CMS Physics Technical Design Report, Volume II: Physics Performance

2007 J. Phys. G: Nucl. Part. Phys. 34 995

(http://iopscience.iop.org/0954-3899/34/6/S01)

J. Phys. G: Nucl. Part. Phys. **34** (2007) 995–1579 doi:10.1088/0954-3899/34/6/S01

CMS Physics Technical Design Report, Volume II: Physics Performance

The CMS Collaboration

Received 3 January 2007
Published 20 April 2007
Online at stacks.iop.org/JPhysG/34/995

Abstract

CMS is a general purpose experiment, designed to study the physics of pp collisions at 14 TeV at the Large Hadron Collider (LHC). It currently involves more than 2000 physicists from more than 150 institutes and 37 countries. The LHC will provide extraordinary opportunities for particle physics based on its unprecedented collision energy and luminosity when it begins operation in 2007.

The principal aim of this report is to present the strategy of CMS to explore the rich physics programme offered by the LHC. This volume demonstrates the physics capability of the CMS experiment. The prime goals of CMS are to explore physics at the TeV scale and to study the mechanism of electroweak symmetry breaking—through the discovery of the Higgs particle or otherwise. To carry out this task, CMS must be prepared to search for new particles, such as the Higgs boson or supersymmetric partners of the Standard Model particles, from the start-up of the LHC since new physics at the TeV scale may manifest itself with modest data samples of the order of a few fb^{-1} or less.

The analysis tools that have been developed are applied to study in great detail and with all the methodology of performing an analysis on CMS data specific benchmark processes upon which to gauge the performance of CMS. These processes cover several Higgs boson decay channels, the production and decay of new particles such as Z' and supersymmetric particles, B_s production and processes in heavy ion collisions. The simulation of these benchmark processes includes subtle effects such as possible detector miscalibration and misalignment. Besides these benchmark processes, the physics reach of CMS is studied for a large number of signatures arising in the Standard Model and also in theories beyond the Standard Model for integrated luminosities ranging from $1\,\mathrm{fb}^{-1}$ to $30\,\mathrm{fb}^{-1}$. The Standard Model processes include QCD, B-physics, diffraction, detailed studies of the top quark properties, and electroweak physics topics such as the W and Z^0 boson properties. The production and decay of the Higgs particle is studied for many observable decays, and the precision with which the Higgs boson properties can be derived is determined. About ten different supersymmetry benchmark points are analysed using full simulation. The CMS discovery reach is evaluated in the SUSY parameter space covering a large variety of decay signatures.

Furthermore, the discovery reach for a plethora of alternative models for new physics is explored, notably extra dimensions, new vector boson high mass states, little Higgs models, technicolour and others. Methods to discriminate between models have been investigated.

This report is organized as follows. Chapter 1, the Introduction, describes the context of this document. Chapters 2–6 describe examples of full analyses, with photons, electrons, muons, jets, missing E_{T}, B-mesons and τ's, and for quarkonia in heavy ion collisions. Chapters 7–15 describe the physics reach for Standard Model processes, Higgs discovery and searches for new physics beyond the Standard Model.

Acknowledgments

This report is the result of several years of work on the preparation for physics analysis at the LHC with CMS. Subprojects in all areas were involved (Detector, PRS, Software, and Computing) in order to produce the large Monte Carlo simulation samples needed, to develop the software to analyse those samples, to perform the studies reported in this Report, and to write and review our findings.

We wish to thank, for the many useful discussions, our theory and phenomenology colleagues, in particular J Campbell, D Dominici, A Djouadi, S Heinemeyer, W Hollik, V Khoze, T Plehn, M Raidal, M Spira and G Weiglein for their contributions to this Report.

For their constructive comments and guidance, we would like to thank the CPT internal reviewers: J Alexander, J Branson, Y Karyotakis, M Kasemann and R Tenchini.

We would like to thank L Malgeri and R Tenchini for their efficient organisation of the CMS Notes.

For their patience in meeting sometimes impossible demands, we wish to thank the CMS Secretariat: K Aspola, M Azeglio, N Bogolioubova, D Denise, D Hudson, G Martin, and M C Pelloux.

We also would like to thank G Alverson and L Taylor for their invaluable technical assistance in the preparation of this manuscript.

Finally, we wish to thank the CMS management for their strong support and encouragement.

The CMS Collaboration

The CMS Collaboration

Yerevan Physics Institute, Yerevan, ARMENIA
G L Bayatian, S Chatrchyan, G Hmayakyan, A M Sirunyan

Institut für Hochenergiephysik der OeAW, Wien, AUSTRIA
W Adam, T Bergauer, M Dragicevic, J Erö, M Friedl, R Fruehwirth, V Ghete, P Glaser, J Hrubec, M Jeitler, M Krammer, I Magrans, I Mikulec, W Mitaroff, T Noebauer, M Pernicka, P Porth, H Rohringer, J Strauss, A Taurok, W Waltenberger, G Walzel, E Widl, C-E Wulz

Research Institute for Nuclear Problems, Minsk, BELARUS
A Fedorov, M Korzhik, O Missevitch, R Zuyeuski

National Centre for Particle and High Energy Physics, Minsk, BELARUS
V Chekhovsky, O Dvornikov, I Emeliantchik, A Litomin, V Mossolov, N Shumeiko, A Solin, R Stefanovitch, J Suarez Gonzalez, A Tikhonov

Byelorussian State University, Minsk, BELARUS
V Petrov

Vrije Universiteit Brussel, Brussel, BELGIUM
J D'Hondt, S De Weirdt, R Goorens, J Heyninck, S Lowette, S Tavernier, W Van Doninck[1], L Van Lancker

Université Libre de Bruxelles, Bruxelles, BELGIUM
O Bouhali, B Clerbaux, G De Lentdecker, J P Dewulf, T Mahmoud, P E Marage, L Neukermans, V Sundararajan, C Vander Velde, P Vanlaer, J Wickens

Université Catholique de Louvain, Louvain-la-Neuve, BELGIUM
S Assouak, J L Bonnet, G Bruno, J Caudron, B De Callatay, J De Favereau De Jeneret, S De Visscher, C Delaere, P Demin, D Favart, E Feltrin, E Forton, G Grégoire, S Kalinin, D Kcira, T Keutgen, G Leibenguth, V Lemaitre, Y Liu, D Michotte, O Militaru, A Ninane, S Ovyn, T Pierzchala, K Piotrzkowski, V Roberfroid, X Rouby, D Teyssier, O Van der Aa, M Vander Donckt

Université de Mons-Hainaut, Mons, BELGIUM
E Daubie, P Herquet, A Mollet, A Romeyer

Universiteit Antwerpen, Wilrijk, BELGIUM
W Beaumont, M Cardaci, E De Langhe, E A De Wolf, L Rurua

Centro Brasileiro de Pesquisas Fisicas, Rio de Janeiro, RJ, BRAZIL
M H G Souza

Universidade do Estado do Rio de Janeiro, Rio de Janeiro, RJ, BRAZIL
V Oguri, A Santoro, A Sznajder

Instituto de Fisica, Universidade Federal do Rio de Janeiro, Rio de Janeiro, RJ, BRAZIL
M Vaz

Instituto de Fisica Teorica, Universidade Estadual Paulista, Sao Paulo, SP, BRAZIL
E M Gregores, S F Novaes

[1] Also at CERN, European Organization for Nuclear Research, Geneva, Switzerland.

Institute for Nuclear Research and Nuclear Energy, Sofia, BULGARIA
T Anguelov, G Antchev, I Atanasov, J Damgov, N Darmenov[1], L Dimitrov, V Genchev[1], P Iaydjiev, B Panev, S Piperov, S Stoykova, G Sultanov, I Vankov

University of Sofia, Sofia, BULGARIA
A Dimitrov, V Kozhuharov, L Litov, M Makariev, A Marinov, E Marinova, S Markov, M Mateev, B Pavlov, P Petkov, C Sabev, S Stoynev, Z Toteva[1], V Verguilov

Institute of High Energy Physics, Beijing, CHINA
G M Chen, H S Chen, K L He, C H Jiang, W G Li, H M Liu, X Meng, X Y Shen, H S Sun, M Yang, W R Zhao, H L Zhuang

Peking University, Beijing, CHINA
Y Ban, J Cai, S Liu, S J Qian, Z C Yang, Y L Ye, J Ying

University for Science and Technology of China, Hefei, Anhui, CHINA
J Wu, Z P Zhang

Technical University of Split, Split, CROATIA
N Godinovic, I Puljak, I Soric

University of Split, Split, CROATIA
Z Antunovic, M Dzelalija, K Marasovic

Institute Rudjer Boskovic, Zagreb, CROATIA
V Brigljevic, D Ferencek, K Kadija, S Morovic, M Planinic[2]

University of Cyprus, Nicosia, CYPRUS
C Nicolaou, A Papadakis, P A Razis, D Tsiakkouri

National Institute of Chemical Physics and Biophysics, Tallinn, ESTONIA
A Hektor, M Kadastik, K Kannike, E Lippmaa, M Müntel, M Raidal

Laboratory of Advanced Energy Systems, Helsinki University of Technology, Espoo, FINLAND
P A Aarnio

Helsinki Institute of Physics, Helsinki, FINLAND
S Czellar, E Haeggstroem, A Heikkinen, J Härkönen, V Karimäki, R Kinnunen, T Lampén, K Lassila-Perini, S Lehti, T Lindén, P R Luukka, S Michal[1], T Mäenpää, J Nysten, M Stettler[1], E Tuominen, J Tuominiemi, L Wendland

Lappeenranta University of Technology, Lappeenranta, FINLAND
T Tuuva

Laboratoire d'Annecy-le-Vieux de Physique des Particules, IN2P3-CNRS, Annecy-le-Vieux, FRANCE
J P Guillaud, P Nedelec, D Sillou

DSM/DAPNIA, CEA/Saclay, Gif-sur-Yvette, FRANCE
M Anfreville, S Beauceron, E Bougamont, P Bredy, R Chipaux, M Dejardin, D Denegri, J Descamps, B Fabbro, J L Faure, S Ganjour, F X Gentit, A Givernaud, P Gras, G Hamel de Monchenault, P Jarry, F Kircher, M C Lemaire[3], B Levesy[1], E Locci, J P Lottin,

[2] Also at University of Zagreb, Zagreb, Croatia.
[3] Also at California Institute of Technology, Pasadena, USA.

I Mandjavidze, M Mur, E Pasquetto, A Payn, J Rander, J M Reymond, F Rondeaux, A Rosowsky, Z H Sun, P Verrecchia

Laboratoire Leprince-Ringuet, Ecole Polytechnique, IN2P3-CNRS, Palaiseau, FRANCE
S Baffioni, F Beaudette, M Bercher, U Berthon, S Bimbot, J Bourotte, P Busson, M Cerutti, D Chamont, C Charlot, C Collard, D Decotigny, E Delmeire, L Dobrzynski, A M Gaillac, Y Geerebaert, J Gilly, M Haguenauer, A Karar, A Mathieu, G Milleret, P Miné, P Paganini, T Romanteau, I Semeniouk, Y Sirois

Institut Pluridisciplinaire Hubert Curien, IN2P3-CNRS, ULP, UHA Mulhouse, Strasbourg, FRANCE
J D Berst, J M Brom, F Didierjean, F Drouhin[1], J C Fontaine[4], U Goerlach[5], P Graehling, L Gross, L Houchu, P Juillot, A Lounis[5], C Maazouzi, D Mangeol, C Olivetto, T Todorov [1], P Van Hove, D Vintache

Institut de Physique Nucléaire, IN2P3-CNRS, Université Claude Bernard Lyon 1, Villeurbanne, FRANCE
M Ageron, J L Agram, G Baulieu, M Bedjidian, J Blaha, A Bonnevaux, G Boudoul[1], E Chabanat, C Combaret, D Contardo[1], R Della Negra, P Depasse, T Dupasquier, H El Mamouni, N Estre, J Fay, S Gascon, N Giraud, C Girerd, R Haroutunian, J C Ianigro, B Ille, M Lethuillier, N Lumb[1], H Mathez, G Maurelli, L Mirabito[1], S Perries, O Ravat

Institute of High Energy Physics and Informatization, Tbilisi State University, Tbilisi, GEORGIA
R Kvatadze

Institute of Physics Academy of Science, Tbilisi, GEORGIA
V Roinishvili

RWTH, I. Physikalisches Institut, Aachen, GERMANY
R Adolphi, R Brauer, W Braunschweig, H Esser, L Feld, A Heister, W Karpinski, K Klein, C Kukulies, J Olzem, A Ostapchuk, D Pandoulas, G Pierschel, F Raupach, S Schael, G Schwering, M Thomas, M Weber, B Wittmer, M Wlochal

RWTH, III. Physikalisches Institut A, Aachen, GERMANY
A Adolf, P Biallass, M Bontenackels, M Erdmann, H Fesefeldt, T Hebbeker, S Hermann, G Hilgers, K Hoepfner[1], C Hof, S Kappler, M Kirsch, D Lanske, B Philipps, H Reithler, T Rommerskirchen, M Sowa, H Szczesny, M Tonutti, O Tsigenov

RWTH, III. Physikalisches Institut B, Aachen, GERMANY
F Beissel, M Davids, M Duda, G Flügge, T Franke, M Giffels, T Hermanns, D Heydhausen, S Kasselmann, G Kaussen, T Kress, A Linn, A Nowack, M Poettgens, O Pooth, A Stahl, D Tornier, M Weber

Deutsches Elektronen-Synchrotron, Hamburg, GERMANY
A Flossdorf, B Hegner, J Mnich, C Rosemann

University of Hamburg, Hamburg, GERMANY
G Flucke, U Holm, R Klanner, U Pein, N Schirm, P Schleper, G Steinbrück, M Stoye, R Van Staa, K Wick

[4] Also at Université de Haute-Alsace, Mulhouse, France.
[5] Also at Université Louis Pasteur, Strasbourg, France.

Institut für Experimentelle Kernphysik, Karlsruhe, GERMANY
P Blüm, V Buege, W De Boer, G Dirkes[1], M Fahrer, M Feindt, U Felzmann, J Fernandez Menendez[6], M Frey, A Furgeri, F Hartmann[1], S Heier, C Jung, B Ledermann, Th. Müller, M Niegel, A Oehler, T Ortega Gomez, C Piasecki, G Quast, K Rabbertz, C Saout, A Scheurer, D Schieferdecker, A Schmidt, H J Simonis, A Theel, A Vest, T Weiler, C Weiser, J Weng [1], V Zhukov[7]

University of Athens, Athens, GREECE
G Karapostoli[1], P Katsas, P Kreuzer, A Panagiotou, C Papadimitropoulos

Institute of Nuclear Physics "Demokritos", Attiki, GREECE
G Anagnostou, M Barone, T Geralis, C Kalfas, A Koimas, A Kyriakis, S Kyriazopoulou, D Loukas, A Markou, C Markou, C Mavrommatis, K Theofilatos, G Vermisoglou, A Zachariadou

University of Ioánnina, Ioánnina, GREECE
X Aslanoglou, I Evangelou, P Kokkas, N Manthos, I Papadopoulos, G Sidiropoulos, F A Triantis

KFKI Research Institute for Particle and Nuclear Physics, Budapest, HUNGARY
G Bencze[1], L Boldizsar, C Hajdu[1], D Horvath[8], A Laszlo, G Odor, F Sikler, N Toth, G Vesztergombi, P Zalan

Institute of Nuclear Research ATOMKI, Debrecen, HUNGARY
J Molnar

University of Debrecen, Debrecen, HUNGARY
N Beni, A Kapusi, G Marian, P Raics, Z Szabo, Z Szillasi, G Zilizi

Panjab University, Chandigarh, INDIA
H S Bawa, S B Beri, V Bhandari, V Bhatnagar, M Kaur, R Kaur, J M Kohli, A Kumar, J B Singh

University of Delhi, Delhi, INDIA
A Bhardwaj, S Bhattacharya[9], S Chatterji, S Chauhan, B C Choudhary, P Gupta, M Jha, K Ranjan, R K Shivpuri, A K Srivastava

Bhabha Atomic Research Centre, Mumbai, INDIA
S Borkar, M Dixit, M Ghodgaonkar, S K Kataria, S K Lalwani, V Mishra, A K Mohanty, A Topkar

Tata Institute of Fundamental Research - EHEP, Mumbai, INDIA
T Aziz, S Banerjee, S Bose, N Cheere, S Chendvankar, P V Deshpande, M Guchait[10], A Gurtu, M Maity[11], G Majumder, K Mazumdar, A Nayak, M R Patil, S Sharma, K Sudhakar, S C Tonwar

[6] Now at Instituto de Física de Cantabria (IFCA), CSIC-Universidad de Cantabria, Santander, Spain.
[7] Also at Moscow State University, Moscow, Russia.
[8] Also at Institute of Nuclear Research ATOMKI, Debrecen, Hungary.
[9] Also at University of California, San Diego, La Jolla, USA.
[10] Also at Tata Institute of Fundamental Research - HECR, Mumbai, India.
[11] Also at University of Visva-Bharati, Santiniketan, India.

Tata Institute of Fundamental Research - HECR, Mumbai, INDIA
B S Acharya, S Banerjee, S Bheesette, S Dugad, S D Kalmani, V R Lakkireddi, N K Mondal, N Panyam, P Verma

Institute for Studies in Theoretical Physics & Mathematics (IPM), Tehran, IRAN
M Arabgol, H Arfaei, M Hashemi, M Mohammadi, M Mohammadi Najafabadi, A Moshaii, S Paktinat Mehdiabadi

University College Dublin, Dublin, IRELAND
M Grunewald

Università di Bari, Politecnico di Bari e Sezione dell' INFN, Bari, ITALY
M Abbrescia, L Barbone, A Colaleo[1], D Creanza, N De Filippis, M De Palma, G Donvito, L Fiore, D Giordano, G Iaselli, F Loddo, G Maggi, M Maggi, N Manna, B Marangelli, M S Mennea, S My, S Natali, S Nuzzo, G Pugliese, V Radicci, A Ranieri, F Romano, G Selvaggi, L Silvestris, P Tempesta, R Trentadue, G Zito

Università di Bologna e Sezione dell' INFN, Bologna, ITALY
G Abbiendi, W Bacchi, A Benvenuti, D Bonacorsi, S Braibant-Giacomelli, P Capiluppi, F R Cavallo, C Ciocca, G Codispoti, I D'Antone, G M Dallavalle, F Fabbri, A Fanfani, P Giacomelli[12], C Grandi, M Guerzoni, L Guiducci, S Marcellini, G Masetti, A Montanari, F Navarria, F Odorici, A Perrotta, A Rossi, T Rovelli, G Siroli, R Travaglini

Università di Catania e Sezione dell' INFN, Catania, ITALY
S Albergo, M Chiorboli, S Costa, M Galanti, G Gatto Rotondo, F Noto, R Potenza, G Russo, A Tricomi, C Tuve

Università di Firenze e Sezione dell' INFN, Firenze, ITALY
A Bocci, G Ciraolo, V Ciulli, C Civinini, R D'Alessandro, E Focardi, C Genta, P Lenzi, A Macchiolo, N Magini, F Manolescu, C Marchettini, L Masetti, S Mersi, M Meschini, S Paoletti, G Parrini, R Ranieri, M Sani

Università di Genova e Sezione dell' INFN, Genova, ITALY
P Fabbricatore, S Farinon, M Greco

Istituto Nazionale di Fisica Nucleare e Universita Degli Studi Milano-Bicocca, Milano, ITALY
G Cattaneo, A De Min, M Dominoni, F M Farina, F Ferri, A Ghezzi, P Govoni, R Leporini, S Magni, M Malberti, S Malvezzi, S Marelli, D Menasce, L Moroni, P Negri, M Paganoni, D Pedrini, A Pullia, S Ragazzi, N Redaelli, C Rovelli, M Rovere, L Sala, S Sala, R Salerno, T Tabarelli de Fatis, S Vigano'

Istituto Nazionale di Fisica Nucleare de Napoli (INFN), Napoli, ITALY
G Comunale, F Fabozzi, D Lomidze, S Mele, P Paolucci, D Piccolo, G Polese, C Sciacca

Università di Padova e Sezione dell' INFN, Padova, ITALY
P Azzi, N Bacchetta[1], M Bellato, M Benettoni, D Bisello, E Borsato, A Candelori, P Checchia, E Conti, M De Mattia, T Dorigo, V Drollinger, F Fanzago, F Gasparini, U Gasparini, M Giarin, P Giubilato, F Gonella, A Kaminskiy, S Karaevskii, V Khomenkov, S Lacaprara, I Lippi, M Loreti, O Lytovchenko, M Mazzucato, A T Meneguzzo, M Michelotto, F Montecassiano[1], M Nigro, M Passaseo, M Pegoraro, G Rampazzo, P Ronchese, E Torassa, S Ventura, M Zanetti, P Zotto, G Zumerle

[12] Also at University of California, Riverside, Riverside, USA.

Università di Pavia e Sezione dell' INFN, Pavia, ITALY
G Belli, U Berzano, C De Vecchi, R Guida, M M Necchi, S P Ratti, C Riccardi, G Sani, P Torre, P Vitulo

Università di Perugia e Sezione dell' INFN, Perugia, ITALY
F Ambroglini, E Babucci, D Benedetti, M Biasini, G M Bilei[1], B Caponeri, B Checcucci, L Fanò, P Lariccia, G Mantovani, D Passeri, M Pioppi, P Placidi, V Postolache, D Ricci[1], A Santocchia, L Servoli, D Spiga

Università di Pisa, Scuola Normale Superiore e Sezione dell' INFN, Pisa, ITALY
P Azzurri, G Bagliesi, A Basti, L Benucci, J Bernardini, T Boccali, L Borrello, F Bosi, F Calzolari, R Castaldi, C Cerri, A S Cucoanes, M D'Alfonso, R Dell'Orso, S Dutta, L Foà, S Gennai[13], A Giammanco, A Giassi, D Kartashov, F Ligabue, S Linari, T Lomtadze, G A Lungu, B Mangano, G Martinelli, M Massa, A Messineo, A Moggi, F Palla, F Palmonari, G Petrucciani, F Raffaelli, A Rizzi, G Sanguinetti, G Segneri, D Sentenac, A T Serban, G Sguazzoni, A Slav, P Spagnolo, R Tenchini, G Tonelli, A Venturi, P G Verdini, M Vos

Università di Roma I e Sezione dell' INFN, Roma, ITALY
S Baccaro[14], L Barone, A Bartoloni, F Cavallari, S Costantini, I Dafinei, D Del Re[9], M Diemoz, C Gargiulo, E Longo, P Meridiani, G Organtini, S Rahatlou

Università di Torino e Sezione dell' INFN, Torino, ITALY
E Accomando, M Arneodo[15], A Ballestrero, R Bellan, C Biino, S Bolognesi, N Cartiglia, G Cerminara, M Cordero, M Costa, G Dellacasa, N Demaria, E Maina, C Mariotti, S Maselli, P Mereu, E Migliore, V Monaco, M Nervo, M M Obertino, N Pastrone, G Petrillo, A Romero, M Ruspa[15], R Sacchi, A Staiano, P P Trapani

Università di Trieste e Sezione dell' INFN, Trieste, ITALY
S Belforte, F Cossutti, G Della Ricca, A Penzo

Kyungpook National University, Daegu, KOREA
K Cho, S W Ham, D Han, D H Kim, G N Kim, J C Kim, W Y Kim, M W Lee, S K Oh, W H Park, S R Ro, D C Son, J S Suh

Chonnam National University, Kwangju, KOREA
J Y Kim

Konkuk University, Seoul, KOREA
S Y Jung, J T Rhee

Korea University, Seoul, KOREA
B S Hong, S J Hong, K S Lee, I Park, S K Park, K S Sim, E Won

Seoul National University, Seoul, KOREA
S B Kim

Universidad Iberoamericana, Mexico City, MEXICO
S Carrillo Moreno

Centro de Investigacion y de Estudios Avanzados del IPN, Mexico City, MEXICO
H Castilla Valdez, A Sanchez Hernandez

[13] Also at Centro Studi Enrico Fermi, Roma, Italy.
[14] Also at ENEA - Casaccia Research Center, S. Maria di Galeria, Italy.
[15] Now at Università del Piemonte Orientale, Novara, Italy.

Benemerita Universidad Autonoma de Puebla, Puebla, MEXICO
H A Salazar Ibarguen

Universidad Autonoma de San Luis Potosi, San Luis Potosi, MEXICO
A Morelos Pineda

University of Auckland, Auckland, NEW ZEALAND
R N C Gray, D Krofcheck

University of Canterbury, Christchurch, NEW ZEALAND
N Bernardino Rodrigues, P H Butler, J C Williams

National Centre for Physics, Quaid-I-Azam University, Islamabad, PAKISTAN
Z Aftab, M Ahmad, U Ahmad, I Ahmed, J Alam Jan, M I Asghar, S Asghar, M Hafeez, H R Hoorani, M Ibrahim, M Iftikhar, M S Khan, N Qaiser, I Rehman, T Solaija, S Toor

Institute of Nuclear Physics, Polish Academy of Sciences, Cracow, POLAND
J Blocki, A Cyz, E Gladysz-Dziadus, S Mikocki, J Turnau, Z Wlodarczyk[16], P Zychowski

Institute of Experimental Physics, Warsaw, POLAND
K Bunkowski, H Czyrkowski, R Dabrowski, W Dominik, K Doroba, A Kalinowski, M Konecki, J Krolikowski, I M Kudla, M Pietrusinski, K Pozniak[17], W Zabolotny[17], P Zych

Soltan Institute for Nuclear Studies, Warsaw, POLAND
M Bluj, R Gokieli, L Goscilo, M Górski, K Nawrocki, P Traczyk, G Wrochna, P Zalewski

Laboratório de Instrumentaçoãe Física Experimental de Partículas, Lisboa, PORTUGAL
R Alemany-Fernandez, C Almeida, N Almeida, A Araujo Trindade, P Bordalo, P Da Silva Rodrigues, M Husejko, A Jain, M Kazana, P Musella, S Ramos, J Rasteiro Da Silva, P Q Ribeiro, M Santos, J Semiao, P Silva, I Teixeira, J P Teixeira, J Varela[1]

Joint Institute for Nuclear Research, Dubna, RUSSIA
S Afanasiev, K Babich, I Belotelov, V Elsha, Y Ershov, I Filozova, A Golunov, I Golutvin, N Gorbounov, I Gramenitski, V Kalagin, A Kamenev, V Karjavin, S Khabarov, V Khabarov, Y Kiryushin, V Konoplyanikov, V Korenkov, G Kozlov, A Kurenkov, A Lanev, V Lysiakov, A Malakhov, I Melnitchenko, V V Mitsyn, K Moisenz, P Moisenz, S Movchan, E Nikonov, D Oleynik, V Palichik, V Perelygin, A Petrosyan, E Rogalev, V Samsonov, M Savina, R Semenov, S Shmatov, S Shulha, V Smirnov, D Smolin, A Tcheremoukhine, O Teryaev, E Tikhonenko, S Vassiliev, A Vishnevskiy, A Volodko, N Zamiatin, A Zarubin, P Zarubin, E Zubarev

Petersburg Nuclear Physics Institute, Gatchina (St Petersburg), RUSSIA
N Bondar, V Golovtsov, A Golyash, Y Ivanov, V Kim, V Kozlov, V Lebedev, G Makarenkov, E Orishchin, A Shevel, V Sknar, I Smirnov, V Sulimov, V Tarakanov, L Uvarov, G Velichko, S Volkov, A Vorobyev

Institute for Nuclear Research, Moscow, RUSSIA
Yu Andreev, A Anisimov, S Gninenko, N Golubev, D Gorbunov, M Kirsanov, A Kovzelev, N Krasnikov, V Matveev, A Pashenkov, V E Postoev, A Sadovski, A Solovey, A Solovey, D Soloviev, L Stepanova, A Toropin

[16] Also at Institute of Physics, Swietokrzyska Academy, Kielce, Poland.
[17] Also at Warsaw University of Technology, Institute of Electronic Systems, Warsaw, Poland.

Institute for Theoretical and Experimental Physics, Moscow, RUSSIA
V Gavrilov, N Ilina, V Kaftanov[1], I Kiselevich, V Kolosov, M Kossov[1], A Krokhotin, S Kuleshov, A Oulianov, G Safronov, S Semenov, V Stolin, E Vlasov[1], V Zaytsev

P N Lebedev Physical Institute, Moscow, RUSSIA
A M Fomenko, N Konovalova, V Kozlov, A I Lebedev, N Lvova, S V Rusakov, A Terkulov

Moscow State University, Moscow, RUSSIA
E Boos, M Dubinin[3], L Dudko, A Ershov, A Gribushin, V Ilyin, V Klyukhin[1], O Kodolova, I Lokhtin, S Petrushanko, L Sarycheva, V Savrin, A Sherstnev, A Snigirev, K Teplov, I Vardanyan

State Research Center of Russian Federation - Institute for High Energy Physics, Protvino, RUSSIA
V Abramov, I Azhguirei, S Bitioukov, K Datsko, A Filine, P Goncharov, V Grishin, A Inyakin, V Kachanov, A Khmelnikov, D Konstantinov, A Korablev, V Krychkine, A Levine, I Lobov, V Petrov, V Pikalov, R Ryutin, S Slabospitsky, A Sourkov[1], A Sytine, L Tourtchanovitch, S Troshin, N Tyurin, A Uzunian, A Volkov, S Zelepoukine[18]

Vinca Institute of Nuclear Sciences, Belgrade, SERBIA
P Adzic, D Krpic[19], D Maletic, P Milenovic, J Puzovic[19], N Smiljkovic[1], M Zupan

Centro de Investigaciones Energeticas Medioambientales y Tecnologicas, Madrid, SPAIN
M Aguilar-Benitez, J Alberdi, J Alcaraz Maestre, M Aldaya Martin, P Arce[1], J M Barcala, C Burgos Lazaro, J Caballero Bejar, E Calvo, M Cardenas Montes, M Cerrada, M Chamizo Llatas, N Colino, M Daniel, B De La Cruz, C Fernandez Bedoya, A Ferrando, M C Fouz, P Garcia-Abia, J M Hernandez, M I Josa, J M Luque, J Marin, G Merino, A Molinero, J J Navarrete, J C Oller, E Perez Calle, L Romero, J Salicio, C Villanueva Munoz, C Willmott, C Yuste

Universidad Autónoma de Madrid, Madrid, SPAIN
C Albajar, J F de Trocóniz, M Fernandez, I Jimenez, R F Teixeira

Universidad de Oviedo, Oviedo, SPAIN
J Cuevas, J M Lopez, H Naves Sordo, J M Vizan Garcia

Instituto de Física de Cantabria (IFCA), CSIC-Universidad de Cantabria, Santander, SPAIN
A Calderon, D Cano Fernandez, I Diaz Merino, L A Garcia Moral, G Gomezo, I Gonzalez Cabellero, J Gonzalez Sanchez, A Lopez Virto, J Marco, R Marco, C Martinez Rivero, P Martinez Ruiz del Arbol, F Matorras, A Patino Revuelta[1], T Rodrigo, D Rodriguez Gonzalez, A Ruiz Jimeno, M Sobron Sanudo, I Vila, R Vilar Cortabitarte

CERN, European Organization for Nuclear Research, Geneva, SWITZERLAND
D Abbaneo, S M Abbas, L Agostino, I Ahmed, S Akhtar, N Amapane, B Araujo Meleiro, S Argiro[20], S Ashby, P Aspell, E Auffray, M Axer, A Ball, N Bangert, D Barney, C Bernet, W Bialas, C Bloch, P Bloch, S Bonacini, M Bosteels, V Boyer, A Branson, A M Brett,

[18] Also at Institute for Particle Physics, ETH Zurich, Zurich, Switzerland.
[19] Also at Faculty of Physics of University of Belgrade, Belgrade, Serbia.
[20] Also at INFN-CNAF, Bologna, Italy.

H Breuker, R Bruneliere, O Buchmuller, D Campi, T Camporesi, E Cano, E Carrone, A Cattai, R Chierici, T Christiansen, S Cittolin, E Corrin, M Corvo, S Cucciarelli, B Curé, A De Roeck, D Delikaris, M Della Negra, D D'Enterria, A Dierlamm, A Elliott-Peisert, M Eppard, H Foeth, R Folch, S Fratianni, W Funk, A Gaddi, M Gastal, J C Gayde, H Gerwig, K Gill, A S Giolo-Nicollerat, F Glege, R Gomez-Reino Garrido, R Goudard, J Gutleber, M Hansen, J Hartert, A Hervé, H F Hoffmann, A Honma, M Huhtinen, G Iles, V Innocente, W Jank, P Janot, K Kloukinas, C Lasseur, M Lebeau, P Lecoq, C Leonidopoulos, M Letheren, C Ljuslin, R Loos, G Magazzu, L Malgeri, M Mannelli, A Marchioro, F Meijers, E Meschi, R Moser, M Mulders, J Nash, R A Ofierzynski, A Oh, P Olbrechts, A Onnela, L Orsini, I Pal, G Papotti, R Paramatti, G Passardi, B Perea Solano, G Perinic, P Petagna, A Petrilli, A Pfeiffer, M Pimiä, R Pintus, H Postema, R Principe, J Puerta Pelayo, A Racz, J Rehn, S Reynaud, M Risoldi, P Rodrigues Simoes Moreira, G Rolandi, P Rosinsky, P Rumerio, H Sakulin, D Samyn, F P Schilling, C Schwick, C Schäfer, I Segoni, A Sharma, P Siegrist, N Sinanis, P Sphicas[21], M Spiropulu, F Szoncsó, O Teller, D Treille, J Troska, E Tsesmelis, D Tsirigkas, A Tsirou, D Ungaro, F Vasey, M Vazquez Acosta, L Veillet, P Vichoudis, P Wertelaers, A Wijnant, M Wilhelmsson, I M Willers

Paul Scherrer Institut, Villigen, SWITZERLAND
W Bertl, K Deiters, W Erdmann, K Gabathuler, S Heising, R Horisberger, Q Ingram, H C Kaestli, D Kotlinski, S König, D Renker, T Rohe, M Spira

Institute for Particle Physics, ETH Zurich, Zurich, SWITZERLAND
B Betev, G Davatz, G Dissertori, M Dittmar, L Djambazov, J Ehlers, R Eichler, G Faber, K Freudenreich, J F Fuchs[1], C Grab, A Holzner, P Ingenito, U Langenegger, P Lecomte, G Leshev, A Lister[22], P D Luckey, W Lustermann, J D Maillefaud[1], F Moortgat, A Nardulli, F Nessi-Tedaldi, L Pape, F Pauss, H Rykaczewski[23], U Röser, D Schinzel, A Starodumov[24], F Stöckli, H Suter, L Tauscher, P Trüb[25], H P von Gunten, M Wensveen[1]

Universität Zürich, Zürich, SWITZERLAND
E Alagoz, C Amsler, V Chiochia, C Hoermann, K Prokofiev, C Regenfus, P Robmann, T Speer, S Steiner, L Wilke

National Central University, Chung-Li, TAIWAN
S Blyth, Y H Chang, E A Chen, A Go, C C Hung, C M Kuo, W Lin

National Taiwan University (NTU), Taipei, TAIWAN
P Chang, Y Chao, K F Chen, Z Gao[1], Y Hsiung, Y J Lei, J Schümann, J G Shiu, K Ueno, Y Velikzhanin, P Yeh

Cukurova University, Adana, TURKEY
S Aydin, M N Bakirci, S Cerci, I Dumanoglu, S Erturk, S Esen, E Eskut, A Kayis Topaksu, P Kurt, H Ozkurt, A Polatöz, K Sogut, H Topakli, M Vergili, T Yetkin, G Önengüt

[21] Also at University of Athens, Athens, Greece.
[22] Now at University of California, Davis, Davis, USA.
[23] Now at ESO, Munich-Garching, Germany.
[24] Also at Institute for Theoretical and Experimental Physics, Moscow, Russia.
[25] Also at Paul Scherrer Institut, Villigen, Switzerland.

Middle East Technical University, Physics Department, Ankara, TURKEY
H Gamsizkan, C Ozkan, S Sekmen, M Serin-Zeyrek, R Sever, E Yazgan, M Zeyrek

Bogaziçi University, Department of Physics, Istanbul, TURKEY
A Cakir[26], K Cankocak[27], M Deliomeroglu, D Demir[26], K Dindar, E Gülmez, E Isiksal[28], M Kaya[29], O Kaya, S Ozkorucuklu[30], N Sonmez[31]

Institute of Single Crystals of National Academy of Science, Kharkov, UKRAINE
B Grinev, V Lyubynskiy, V Senchyshyn

National Scientific Center, Kharkov Institute of Physics and Technology, Kharkov, UKRAINE
L Levchuk, P Sorokin

University of Bristol, Bristol, UNITED KINGDOM
D S Bailey, T Barrass, J J Brooke, R Croft, D Cussans, D Evans, R Frazier, N Grant, M Hansen, G P Heath, H F Heath, B Huckvale, C Lynch, C K Mackay, S Metson, D M Newbold[32], V J Smith, R J Tapper

Rutherford Appleton Laboratory, Didcot, UNITED KINGDOM
S A Baird, K W Bell, R M Brown, D J A Cockerill, J A Coughlan, P S Flower, V B Francis, M French, J Greenhalgh, R Halsall, J Hill, L Jones, B W Kennedy, L Lintern, A B Lodge, J Maddox, Q Morrissey, P Murray, M Pearson, S Quinton, J Salisbury, A Shah, C Shepherd-Themistocleous, B Smith, M Sproston, R Stephenson, S Taghavirad, I R Tomalin, J H Williams

Imperial College, University of London, London, UNITED KINGDOM
F Arteche[1], R Bainbridge, G Barber, P Barrillon, R Beuselinck, F Blekman, D Britton, D Colling, G Daskalakis, G Dewhirst, S Dris[1], C Foudas, J Fulcher, S Greder, G Hall, J Jones, J Leaver, B C MacEvoy, O Maroney, A Nikitenko[24], A Papageorgiou, D M Raymond, M J Ryan, C Seez, P Sharp[1], M Takahashi, C Timlin, T Virdee[1], S Wakefield, M Wingham, A Zabi, Y Zhang, O Zorba

Brunel University, Uxbridge, UNITED KINGDOM
C Da Via, I Goitom, P R Hobson, P Kyberd, C Munro, J Nebrensky, I Reid, O Sharif, R Taylor, L Teodorescu, S J Watts, I Yaselli

Boston University, Boston, Massachusetts, USA
E Hazen, A H Heering, D Lazic, E Machado, D Osborne, J Rohlf, L Sulak, F Varela Rodriguez, S Wu

Brown University, Providence, Rhode Island, USA
D Cutts, R Hooper, G Landsberg, R Partridge, S Vanini[33]

[26] Also at Izmir Institute of Technology (IYTE), Izmir, Turkey.
[27] Also at Mugla University, Mugla, Turkey.
[28] Also at Marmara University, Istanbul, Turkey.
[29] Also at Kafkas University, Kars, Turkey.
[30] Also at Suleyman Demirel University, Isparta, Turkey.
[31] Also at Ege University, Izmir, Turkey.
[32] Also at Rutherford Appleton Laboratory, Didcot, United Kingdom.
[33] Also at Università di Padova e Sezione dell' INFN, Padova, Italy.

University of California, Davis, Davis, California, USA
R Breedon, M Case, M Chertok, J Conway, P T Cox, R Erbacher, J Gunion, B Holbrook, W Ko, R Lander, D Pellett, J Smith, A Soha, M Tripathi, R Vogt

University of California, Los Angeles, Los Angeles, California, USA
V Andreev, K Arisaka, D Cline, R Cousins, S Erhan[1], M Felcini[1], J Hauser, M Ignatenko, B Lisowski, D Matlock, C Matthey, B Mohr, J Mumford, S Otwinowski, G Rakness, P Schlein, Y Shi, J Tucker, V Valuev, R Wallny, H G Wang, X Yang, Y Zheng

University of California, Riverside, Riverside, California, USA
R Clare, D Fortin, D Futyan[1], J W Gary, M Giunta[1], G Hanson, G Y Jeng, S C Kao, H Liu, G Pasztor[34], A Satpathy, B C Shen, R Stringer, V Sytnik, R Wilken, D Zer-Zion

University of California, San Diego, La Jolla, California, USA
J G Branson, E Dusinberre, J Letts, T Martin, M Mojaver, H P Paar, H Pi, M Pieri, A Rana, V Sharma, A White, F Würthwein

University of California, Santa Barbara, Santa Barbara, California, USA
A Affolder, C Campagnari, C Hill, J Incandela, S Kyre, J Lamb, J Richman, D Stuart, D White

California Institute of Technology, Pasadena, California, USA
J Albert, A Bornheim, J Bunn, J Chen, G Denis, P Galvez, M Gataullin, I Legrand, V Litvine, Y Ma, D Nae, H B Newman, S Ravot, S Shevchenko, S Singh, C Steenberg, X Su, M Thomas, V Timciuc, F van Lingen, J Veverka, B R Voicu[1], A Weinstein, R Wilkinson, X Yang, Y Yang, L Y Zhang, K Zhu, R Y Zhu

Carnegie Mellon University, Pittsburgh, Pennsylvania, USA
T Ferguson, M Paulini, J Russ, N Terentyev, H Vogel, I Vorobiev

University of Colorado at Boulder, Boulder, Colorado, USA
J P Cumalat, W T Ford, D Johnson, U Nauenberg, K Stenson, S R Wagner

Cornell University, Ithaca, NY, USA
J Alexander, D Cassel, K Ecklund, B Heltsley, C D Jones, V Kuznetsov, J R Patterson, A Ryd, J Thom, P Wittich

Fairfield University, Fairfield, Connecticut, USA
C P Beetz, G Cirino, V Podrasky, C Sanzeni, D Winn

Fermi National Accelerator Laboratory, Batavia, Illinois, USA
S Abdullin[24], M A Afaq[1], M Albrow, J Amundson, G Apollinari, M Atac, W Badgett, J A Bakken, B Baldin, L A T Bauerdick, A Baumbaugh, U Baur, P C Bhat, F Borcherding, K Burkett, J N Butler, H Cheung, I Churin, S Cihangir, M Demarteau, D P Eartly, J E Elias, V D Elvira, D Evans, I Fisk, J Freeman, P Gartung, F J M Geurts, D A Glenzinski, E Gottschalk, G Graham, D Green, G M Guglielmo, Y Guo, O Gutsche, A Hahn, J Hanlon, S Hansen, R M Harris, T Hesselroth, S L Holm, B Holzman, S Iqbal, E James, M Johnson, U Joshi, B Klima, J Kowalkowski, T Kramer, S Kwan, E La Vallie, M Larwill, S Los, L Lueking, G Lukhanin, S Lusin[1], K Maeshima, P McBride, S J Murray, V O'Dell, M Paterno, J Patrick, D Petravick, R Pordes, O Prokofyev, V Rasmislovich, N Ratnikova, A Ronzhin, V Sekhri, E Sexton-Kennedy, T Shaw, D Skow, R P Smith, W J Spalding, L Spiegel, M Stavrianakou, G Stiehr, I Suzuki, P Tan, W Tanenbaum, S Tkaczyk, S Veseli, R Vidal, H Wenzel, J Whitmore, W J Womersley, W M Wu, Y Wu, A Yagil, J Yarba, J C Yun

[34] Also at KFKI Research Institute for Particle and Nuclear Physics, Budapest, Hungary.

University of Florida, Gainesville, Florida, USA
D Acosta, P Avery, V Barashko, P Bartalini, D Bourilkov, R Cavanaugh, A Drozdetskiy, R D Field, Y Fu, L Gray, D Holmes, B J Kim, S Klimenko, J Konigsberg, A Korytov, K Kotov, P Levchenko, A Madorsky, K Matchev, G Mitselmakher, Y Pakhotin, C Prescott, P Ramond, J L Rodriguez, M Schmitt, B Scurlock, H Stoeck, J Yelton

Florida International University, Miami, Florida, USA
W Boeglin, V Gaultney, L Kramer, S Linn, P Markowitz, G Martinez, B Raue, J Reinhold

Florida State University, Tallahassee, Florida, USA
A Askew, M Bertoldi, W G D Dharmaratna, Y Gershtein, S Hagopian, V Hagopian, M Jenkins, K F Johnson, H Prosper, H Wahl

Florida Institute of Technology, Melbourne, Florida, USA
M Baarmand, L Baksay[35], S Guragain, M Hohlmann, H Mermerkaya, R Ralich, I Vodopiyanov

University of Illinois at Chicago (UIC), Chicago, Illinois, USA
M R Adams, R R Betts, C E Gerber, E Shabalina, C Smith, T Ten

The University of Iowa, Iowa City, Iowa, USA
U Akgun, A S Ayan, A Cooper, P Debbins, F Duru, M Fountain, N George, E McCliment, J P Merlo, A Mestvirishvili, M J Miller, C R Newsom, E Norbeck, Y Onel, I Schmidt, S Wang

Iowa State University, Ames, Iowa, USA
E W Anderson, O Atramentov, J M Hauptman, J Lamsa

Johns Hopkins University, Baltimore, Maryland, USA
B A Barnett, B Blumenfeld, C Y Chien, D W Kim, P Maksimovic, S Spangler, M Swartz

The University of Kansas, Lawrence, Kansas, USA
P Baringer, A Bean, D Coppage, O Grachov, E J Kim, M Murray

Kansas State University, Manhattan, Kansas, USA
D Bandurin, T Bolton, A Khanov[24], Y Maravin, D Onoprienko, F Rizatdinova, R Sidwell, N Stanton, E Von Toerne

University of Maryland, College Park, Maryland, USA
D Baden, R Bard, S C Eno, T Grassi, N J Hadley, R G Kellogg, S Kunori, F Ratnikov, A Skuja

Massachusetts Institute of Technology, Cambridge, Massachusetts, USA
R Arcidiacono, M Ballintijn, G Bauer, P Harris, I Kravchenko, C Loizides, S Nahn, C Paus, S Pavlon, C Roland, G Roland, K Sumorok, S Vaurynovich, G Veres, B Wyslouch

University of Minnesota, Minneapolis, Minnesota, USA
D Bailleux, S Corum, P Cushman, A De Benedetti, A Dolgopolov, R Egeland, G Franzoni, W J Gilbert, J Grahl, J Haupt, Y Kubota, J Mans, N Pearson, R Rusack, A Singovsky

University of Mississippi, University, Mississippi, USA
L M Cremaldi, R Godang, R Kroeger, D A Sanders, D Summers

University of Nebraska-Lincoln, Lincoln, Nebraska, USA
K Bloom, D R Claes, A Dominguez, M Eads, C Lundstedt, S Malik, G R Snow, A Sobol

[35] Also at University of Debrecen, Debrecen, Hungary.

State University of New York at Buffalo, Buffalo, New York, USA
I Iashvili, A Kharchilava

Northeastern University, Boston, Massachusetts, USA
G Alverson, E Barberis, O Boeriu, G Eulisse, Y Musienko[36], S Muzaffar, I Osborne, S Reucroft, J Swain, L Taylor, L Tuura, D Wood

Northwestern University, Evanston, Illinois, USA
B Gobbi, M Kubantsev, H Schellman, M Schmitt, E Spencer, M Velasco

University of Notre Dame, Notre Dame, Indiana, USA
B Baumbaugh, N M Cason, M Hildreth, D J Karmgard, N Marinelli[21], R Ruchti, J Warchol, M Wayne

The Ohio State University, Columbus, Ohio, USA
B Bylsma, L S Durkin, J Gilmore, J Gu, D Herman, P Killewald, K Knobbe, T Y Ling

Princeton University, Princeton, New Jersey, USA
P Elmer, D Marlow, P Piroué, D Stickland, C Tully, T Wildish, S Wynhoff, Z Xie

Purdue University, West Lafayette, Indiana, USA
A Apresyan, K Arndt, K Banicz, V E Barnes, G Bolla, D Bortoletto, A Bujak, A F Garfinkel, O Gonzalez Lopez, L Gutay, N Ippolito, Y Kozhevnikov[1], A T Laasanen, C Liu, V Maroussov, P Merkel, D H Miller, J Miyamoto, N Neumeister, C Rott, A Roy, A Sedov, I Shipsey

Purdue University Calumet, Hammond, Indiana, USA
N Parashar

Rice University, Houston, Texas, USA
G Eppley, S J Lee, J Liu, M Matveev, T Nussbaum, B P Padley, J Roberts, A Tumanov, P Yepes

University of Rochester, Rochester, New York, USA
A Bodek, H Budd, Y S Chung, P De Barbaro[1], R Demina, R Eusebi, G Ginther, Y Gotra, A Hocker, U Husemann, S Korjenevski, W Sakumoto, P Slattery, P Tipton, M Zielinski

Rutgers, the State University of New Jersey, Piscataway, New Jersey, USA
E Bartz, J Doroshenko, E Halkiadakis, P F Jacques, M S Kalelkar, D Khits, A Lath, A Macpherson[1], L Perera, R Plano, K Rose, S Schnetzer, S Somalwar, R Stone, G Thomson, T L Watts

Texas Tech University, Lubbock, Texas, USA
N Akchurin, K W Carrell, K Gumus, C Jeong, H Kim, V Papadimitriou, A Sill, M Spezziga, E Washington, R Wigmans, L Zhang

Vanderbilt University, Nashville, Tennessee, USA
T Bapty, D Engh, W Johns, T Keskinpala, E Luiggi Lopez, S Neema, S Nordstrom, S Pathak, P Sheldon, E W Vaandering, M Webster

[36] Also at Institute for Nuclear Research, Moscow, Russia.

University of Virginia, Charlottesville, Virginia, USA
M W Arenton, S Conetti, B Cox, R Hirosky, R Imlay, A Ledovskoy, D Phillips II, H Powell, M Ronquest, D Smith

University of Wisconsin, Madison, Wisconsin, USA
Y W Baek, J N Bellinger, D Bradley, D Carlsmith, I Crotty[1], S Dasu, F Feyzi, T Gorski, M Grothe[37], W Hogg, M Jaworski, P Klabbers, A Lanaro, R Loveless, M Magrans de Abril, D Reeder, W H Smith, D Wenman

Yale University, New Haven, Connecticut, USA
G S Atoyan[36], S Dhawan, V Issakov, H Neal, A Poblaguev, M E Zeller

Institute of Nuclear Physics of the Uzbekistan Academy of Sciences, Ulugbek, Tashkent, UZBEKISTAN
B S Yuldashev

[37] Also at Università di Torino e Sezione dell' INFN, Torino, Italy.

Contents

Chapter 1. Introduction

The Large Hadron Collider (LHC) [1], at the CERN Laboratory, the European Laboratory for Particle Physics, outside Geneva, Switzerland, will be completed in 2007. The LHC will be a unique tool for fundamental physics research and will be the highest energy accelerator in the world for many years following its completion. The LHC will provide two proton beams, circulating in opposite directions, at an energy of 7 TeV each (centre-of-mass $\sqrt{s} = 14$ TeV). The CMS experiment [2, 3] is a general purpose detector at the LHC to explore physics at an unprecedented physics energy scale, namely that at the TeV scale [4–6]. It is expected that the data produced at the LHC will elucidate the electroweak symmetry breaking mechanism (EWSB) and provide evidence of physics beyond the Standard Model. CMS will also be an instrument to perform precision measurements, e.g., of parameters of the Standard Model, mainly as a result of the very high event rates, as demonstrated for a few processes in Table 1.1 for a luminosity of $\mathcal{L} = 2 \times 10^{33}\,\mathrm{cm}^{-2}\,\mathrm{s}^{-1}$. The LHC will be a Z factory, a W factory, a b quark factory, a top quark factory and even a Higgs or SUSY particle factory if these new particles have TeV scale masses.

The Physics Technical Design Report (PTDR) reports on detailed studies that have been performed with the CMS detector software and analysis tools. The CMS detector and its performance are described in detail in Volume 1 of the PTDR [7], while in the present Volume (Volume 2) the physics reach with the CMS detector is explored.

The CMS detector, shown in Fig. 1.1, measures roughly 22 metres in length, 15 metres in diameter, and 12,500 metric tons in weight. Its central feature is a huge, high field (4 tesla) solenoid, 13 metres in length, and 6 metres in diameter. Its "compact" design is large enough to contain the electromagnetic and hadron calorimetry surrounding a tracking system, and allows a superb muon detection system. All subsystems of CMS are bound by means of the data acquisition and trigger system.

In the CMS coordinate system the origin coincides with the nominal collision point at the geometrical center of the detector. The z direction is given by the beam axis. The rest frame of the hard collision is generally boosted relative to the lab frame along the beam direction, θ is the polar angle with respect to the z axis and ϕ the azimuthal angle with respect to the LHC plane. The detector solid angle segmentation is designed to be invariant under boosts along the z direction. The *pseudorapidity* η, is related to the polar angle θ and defined as $\eta \equiv -\ln(\tan(\theta/2))$. The transverse momentum component z-axis is given by $p_\mathrm{T} = p\sin\theta$ and similarly $E_\mathrm{T} = E\sin\theta$ is the transverse energy of a physics object.

The experiment comprises a tracker, a central calorimeter barrel part for $|\eta| \leqslant 1.5$, and endcaps on both sides, and muon detectors. The tracking system is made of several layers of silicon pixel and silicon strip detectors and covers the region $|\eta| < 2.5$. The electromagnetic calorimeter consists of lead tungstate ($PbWO_4$) crystals covering $|\eta| < 3$ (with trigger coverage $|\eta| < 2.6$). Its resolution at the initial luminosity ($\mathcal{L} = 2 \times 10^{33}\,\mathrm{cm}^{-2}\,\mathrm{s}^{-1}$) is $\Delta E/E = 3\%/\sqrt{E} \oplus 0.5\%$. The surrounding hadronic calorimeter uses brass/scintillator tiles in the barrel and endcaps. Its resolution for jets, when combined with the electromagnetic calorimeter, is $\Delta E/E = 100\%/\sqrt{E} \oplus 5\%$. The region $3 < |\eta| < 5$ is covered by forward calorimeters with a resolution of $\Delta E/E = 180\%/\sqrt{E} \oplus 10\%$. Muons are measured in gas chambers in the iron return yoke. The muon momentum measurement using the muon chambers and the central tracker covers the range $|\eta| < 2.4$ with a resolution of $\Delta p_\mathrm{T}/p_\mathrm{T} = 5\%$ at $p_\mathrm{T} = 1$ TeV and $\Delta p_\mathrm{T}/p_\mathrm{T} = 1\%$ at $p_\mathrm{T} = 100$ GeV. The muon trigger extends over the pseudorapidity range $|\eta| < 2.1$.

In total CMS has $\sim 10^8$ data channels that are checked each bunch crossing. The design data-size per event is about 1 MB. At start-up it is essential to allow for a larger event size,

Table 1.1. Approximate event rates of some physics processes at the LHC for a luminosity of $\mathcal{L} = 2 \times 10^{33}\,\mathrm{cm}^{-2}\,\mathrm{s}^{-1}$. For this table, one year is equivalent to $20\,\mathrm{fb}^{-1}$.

Process	Events/s	Events/year
$W \to e\nu$	40	4×10^8
$Z \to ee$	4	4×10^7
$t\bar{t}$	1.6	1.6×10^7
$b\bar{b}$	10^6	10^{13}
$\tilde{g}\tilde{g}$ ($m = 1\,\mathrm{TeV}$)	0.002	2×10^4
Higgs ($m = 120\,\mathrm{GeV}$)	0.08	8×10^5
Higgs ($m = 120\,\mathrm{GeV}$)	0.08	8×10^5
Higgs ($m = 800\,\mathrm{GeV}$)	0.001	10^4
QCD jets $p_\mathrm{T} > 200\,\mathrm{GeV}$	10^2	10^9

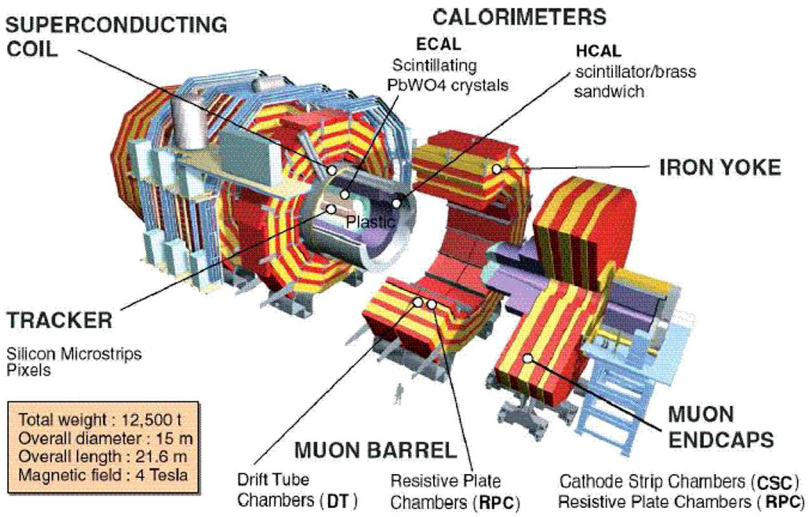

Figure 1.1. Three dimensional view of the CMS detector, and its detector components.

up to 1.5 MB per event, in order to be able to thoroughly study and understand the detector performance.

This Volume is organised in two parts. In the first part a number of physics channels challenging for the detector are studied in detail. Each of these channels is associated with certain physics objects, such as electrons, photons, muons, jets, missing E_T and so on. The analyses are performed in a fully realistic environment as the one expected for real data. Methods on determining the backgrounds from the data as well as on evaluating the experimental systematic effects, e.g., due to miscalibration and misalignment, resolution and signal significance are developed. In short these analyses are performed imitating real data analyses to the maximum possible extent.

In the second part the physics reach is studied for a large number of physics processes, for data samples mostly with luminosities in the range of 1 to $30\,\mathrm{fb}^{-1}$, expected to be collected during the first years of operation at the LHC. Standard model measurements of, e.g., W and top quark mass determinations are studied; many production and decay mechanisms for the SM and MSSM Higgs are studied, and several models beyond the Standard Model are explored.

1.1. The full analyses

In total 11 analyses were studied in full detail. All the studies were performed with detailed Geant4 based simulation of the CMS detector and reconstruction of the data, including event pile-up, and a detailed analysis of the systematics.

The $H \to \gamma\gamma$ analysis covers one of the most promising channels for a low mass Higgs discovery and for precision Higgs mass measurement at the LHC. This channel has been an important motivation for the design of the electromagnetic calorimeter (ECAL) of CMS. It is used here as a benchmark channel for identifying photons with high purity and efficiency, and as a driver for optimising the ECAL energy resolution and calibration of the analyses. Furthermore, new statistical techniques that make use of event kinematics and neural network event selection algorithms have been used to enhance the sensitivity in this channel.

The analysis $H \to ZZ \to 4$ electrons covers electron identification and selection optimisation. In particular, the classification of electron candidates according to quality criteria which depends on their passage through the material of the tracker was studied, and the impact on the Higgs search quantified.

The same process has been studied in the muon decay channel $H \to ZZ \to 4\mu$. This process is an important benchmark for optimising the muon analysis tools. It is one of the cleanest discovery channels for a Standard Model Higgs with a mass up to $600\,\mathrm{GeV/c^2}$. Methods to minimise the systematics errors have been developed.

The channel $H \to WW \to 2\mu 2\nu$ is of particular importance if the mass of the Higgs is around $165\,\mathrm{GeV/c^2}$, and is again an interesting muon benchmark channel. The challenge is to establish with confidence a dimuon excess, since this channel does not allow reconstruction of the Higgs mass on an event by event basis. The event statistics after reconstruction and selection is large enough for an early discovery, even with about $1\,\mathrm{fb}^{-1}$ of integrated luminosity, provided the systematic uncertainty on the background can be kept well under control.

The production of a new gauge boson with a mass in the TeV range is one of the possible early discoveries at the LHC. The clean final state for the decays into two high p_T leptons leads to a clearly detectable signal in CMS. The channel $Z' \to \mu\mu$ was selected as a benchmark to study muons with p_T in the TeV/c range. Dedicated reconstruction techniques were developed for TeV muons and the experimental systematics e.g. due to misalignment effects were studied in detail.

Jets will be omnipresent in the LHC collisions. The analysis of dijets events and the dijet invariant mass has been studied in detail. A pre-scaling strategy of the jet threshold for the trigger, in order to allow a dijet mass measurement starting from approximately $300\,\mathrm{GeV/c^2}$ has been developed. Calibration procedures, and experimental and theoretical systematics on the dijet mass distribution have been evaluated in detail. The results were interpreted as sensitivities to new physics scenarios.

The determination of the missing transverse momentum in collisions at a hadron collider is in general a difficult measurement, since it is very susceptible to detector inefficiencies, mis-measurements, backgrounds such a halo muons or cosmic muons, and instrumental backgrounds. On the other hand, it is probably the most striking signature for new physics with escaping weakly interacting particles, such as the neutralinos in supersymmetry. A low mass mSUGRA SUSY benchmark point was selected to exercise a full analysis, including techniques to suppress spurious backgrounds as well as QCD residual contribution due to mis-measurements. Techniques to calibrate the $E_\mathrm{T}^\mathrm{miss}$ with known Standard Model processes have been also developed. Such a low mass SUSY scenario could already be detected with $0.1\,\mathrm{fb}^{-1}$ of data with a well understood detector and well controlled background.

The decay $B_s \to J/\psi\phi$ is chosen as a benchmark channel since it is representative of exclusive B-physics studies. It allows to study the capability of CMS to identify, select and reconstruct a fully reconstructed decay of the B_s, which presents a significant challenge due to its relatively low momentum and high background. In addition, the measurement is performed of the width difference $\Delta\Gamma$ on a sample of untagged $B_s \to J/\psi\phi \to \mu^+\mu^- K^+K^-$ candidates using a maximum likelihood fit of the time dependent angular distribution.

The detection of the τ particle will be very important at the LHC since, a clear excess of τ production is also a sign of new physics. The τ selection and analysis tools have been used to search for and measure the A/H heavy Higgs bosons in the MSSM. Various decay channels of the τ have been considered, and τ tagging tools have been deployed and refined. A τ-trigger is very challenging but necessary for these physics studies, and has been studied in detail.

The process of associated production of a Higgs particle with top quarks, and with the Higgs decaying into b-quarks, is no doubt one of the most challenging channels studied in this part of the TDR. The physics interest is high since, this channel gives access to a measurement of the $H \to bb$ decay and thus, to the Yukawa coupling of the Higgs to the b quark. The inclusive $H \to bb$ production channel cannot be used due to a too large QCD $b\bar{b}$ background. This analysis uses techniques to tag b quarks and calibration methods to reconstruct top quarks from multi-jet decays. Furthermore, the backgrounds such as $t\bar{t}$ jet-jet have been carefully examined. The results demonstrate that this will be a very challenging measurement even with the highest luminosity in the first phase of the LHC operation.

Finally, a benchmark channel for heavy ions collisions was studied. Quarkonia (J/ψ, Υ) were reconstructed and measured via the two muon decay modes. The particular challenge is an efficient track reconstruction in an environment of 2000 to perhaps even 5000 tracks produced per unit of rapidity. The analysis shows that the detection of the quarkonia is possible with reasonable efficiencies and leads to a good event statistics for detailed studies of the "melting" of these resonances in a hot dense region.

In general, these detailed studies in this first part of the PTDR have demonstrated that the CMS experiment is up and ready to meet the challenge, and can deliver measurements with the quality and precision as anticipated from its detector design.

1.2. The physics reach

The physics reach of the Report contains three main parts: Standard Model processes, Higgs searches and measurements and searches beyond the Standard Model.

The Standard Model sections contain a study of the strong interactions, top quark physics and electroweak physics. Jet production is revisited but this time to measure inclusive single jet p_T spectra, with emphasis placed on the experimental uncertainties related to such a measurement. The underlying event is still enigmatic, and procedures are outlined to get better insight with the first LHC data. B-hadrons will be copiously produced at the LHC and inclusive B production and B_c production have been studied. At the LHC about one top quark pair is produced per second. Such a huge sample of top quarks allows for detailed measurements of the top quark properties such as cross sections and mass, spin properties, single top production, and searches for new physics in top decays. A detailed study on the mass measurement precision, limited by the systematics errors, is reported. In the electroweak part of this chapter, the production of W and Z bosons is discussed, as well as multi-boson production, and a precise measurement of the Drell–Yan process. The precision with which the mass of the W boson can be determined is analysed.

One of the main missions of the LHC is the discovery of the origin of the electroweak symmetry breaking mechanism. Therefore, the search for the Higgs particle is a major task

for the experiments. The Higgs particle search is studied for the SM and MSSM Higgs(es) in the full mass range starting from the LEP exclusion limits. Detailed systematic studies were included in the estimates for the integrated luminosity needed for a 5σ discovery. The methods used to calculate the 5σ discovery limit are detailed in Appendix A. Over a large range of Higgs boson masses, a discovery is possible with a few fb^{-1}, but for the interesting mass region below $130\,\mathrm{GeV/c^2}$, $10\,\mathrm{fb}^{-1}$ will be needed. MSSM Higgs discoveries are studied both for neutral and charged Higgs particles, and discovery regions are presented. Finally, the Higgs chapter also contains studies of other scalar particles such as the radion that emerges in models with warped extra dimensions, and a double charged Higgs that may be produced in Little Higgs scenarios.

The LHC will probe the TeV energy scale and is expected to break new ground. An important part of the CMS program will be to search for new physics. If low mass supersymmetry exists it will be within the reach of the LHC. The studies in this Report are mainly signature based, to test the discovery potential in as many channels as possible, using a number of chosen benchmark points covering a large part of different signatures. The discovery reach for scenarios with extra dimensions, and new vector bosons high mass states are analysed using several different experimental signals. The methods used to calculate the 5σ discovery limit are detailed in Appendix A. Finally alternative signatures for new physics such as technicolour, contact interactions, heavy Majorana neutrinos, heavy top in Little Higgs models, and same sign top quarks have been analysed.

While many signals and processes have been studied, it was not the goal of this PTDR to study and to include all possible channels to give a full physics review. Besides, what is contained here in this Report, there are other ongoing analyses nearing completion on topics such as GMSB SUSY, UED extra dimensions, split SUSY scenarios, invisible Higgs production, TGC sensitivity of dibosons, strongly interacting vector boson scattering, and others. The channels included in this Report have however, been very instrumental to test and deploy the tools and techniques for performing physics studies with CMS at the LHC.

1.3. Tools used in the studies for the PTDR

1.3.1. Detector simulation and reconstruction

For the studies presented in this TDR, the CMS detector response was simulated using the package OSCAR [8]. It is an application of the Geant4 [9] toolkit for detector description and simulation. OSCAR is used to describe the detector geometry and materials. It also includes and uses information about the magnetic field. OSCAR reads the individual generated events and simulates the effects of energy loss, multiple scattering and showering in the detector materials with Geant4. The digitisation (simulation of the electronic response), the emulation of the Level-1 and High-Level Triggers (HLT), and the offline reconstruction of physics objects were performed with the CMS full-reconstruction ORCA package [10].

A number of analyses for the physics reach studies were performed with the fast parameterised simulation FAMOS [11]. FAMOS has been tuned to the detailed simulation and reconstruction and is roughly about a factor 1000 faster. FAMOS allows to perform, e.g., accurate sensitivity scans in a large parameter space of a model for new physics.

1.3.2. Pile-up treatment

The total inelastic cross section at the LHC is assumed to be $\sigma_{\mathrm{T}} \sim 80\,\mathrm{mb}$. The LHC will operate at a bunch crossing rate of 40 MHz. Only 80 % of the bunches will be filled , resulting in an effective bunch crossing rate of 32 MHz. The instantaneous luminosity in the first

two years after start-up is expected to be $\mathcal{L} = 2 \times 10^{33}\,\mathrm{cm}^{-2}\,\mathrm{s}^{-1}$ and subsequently upgraded to $\mathcal{L} = 10^{34}\,\mathrm{cm}^{-2}\,\mathrm{s}^{-1}$ in a second phase. The average number of inelastic non-diffractive interactions per bunch crossing μ is $\mu = 25$ at high and $\mu = 5$ at low luminosity.

Both the detailed simulation and reconstruction chain OSCAR/ORCA and FAMOS allow the overlay of pile-up events, according to a Poisson distribution with average μ, on top of real signal events, exactly as for real data. These events were sampled from a data base of 600K minimum bias events, generated with parameters discussed in Appendix C.

All the studies reported in this TDR include the effects of pile-up on the signal. For all studies with luminosities up to 60 fb^{-1} $\mu = 5$ was used. Several techniques have been developed to minimise the effect of pile-up, and have been used in the studies reported in this TDR. Both in-time and out-of-time pile-up has been included.

1.3.3. Systematic effects on measurements

The results of the PTDR Volume 1 were used to form the baseline for all systematic studies in this Volume. Systematic effects include energy scale uncertainties for the calorimeters, effects of misalignment, uncertainties in the background estimation either from theory or from techniques to estimate these backgrounds from data. Misalignments of the tracker and of the muon system expected at the initial and at the well-advanced stages of the data taking have been taken into account by using two misalignment scenarios developed in the framework of the CMS reconstruction.

A comprehensive review on the experimental and theoretical systematics used in this PTDR is presented in Appendix B.

1.3.4. Event generators

The studies for this physics TDR have been performed with a variety of event generators, suitably chosen for each processes studied. The main work-horse was PYTHIA, the general multi-purpose generator, and in some case checks have been performed with HERWIG. More specialised generators which include a more complete description of the relevant matrix elements, have been used for a number processes, as detailed in the analysis reports. A list of generators used in this TDR is given in Appendix C.

An important aspect for the LHC, is the QCD multi-jet production in various physics channels, and a correct and thorough understanding of Standard Model processes such as W + jets, Z + jets and $t\bar{t}$ + jet production will be paramount before discoveries can be claimed in channels such as jets + $E_{\mathrm{T}}^{\mathrm{miss}}$ and jets + leptons. CMS will measure these Standard Model processes in an early phase of the experiment, to reduce the impact of inherent uncertainties in the Monte Carlo models on searches and discoveries, using methods demonstrated in this TDR. These will allow estimation of the expected backgrounds directly or will allow to tune the generators in order to use these with increased confidence in regions of phase space not directly accessible with measurements from the data.

Generators with multi-parton final states are available at Leading Order (LO) for most Standard Model processes. Recently, Next to Leading Order (NLO) generators have become available as well, be it for a more restricted number of processes. Sophisticated algorithms that match the hard jets generated by the matrix elements, with the softer parton jets, have become available. An example is the ALPGEN generator, which has been used for some studies and comparisons in this Report. For some of the detailed analyses, such as the $E_{\mathrm{T}}^{\mathrm{miss}}$ low mass SUSY search, it was shown that the effect of using ALPGEN instead of PYTHIA did not lead to different result, while for other analyses, such as background to ttH production, the difference was important.

Another difficulty in the estimation of the background to processes is the rate of QCD multi-jet events. Typically, samples of events of more than 10^8 or 10^9 events would be needed to cover possible tails. Detailed simulation of such background samples cannot be easily done, and therefore, other approaches were taken in this TDR. These include pre-selections at the generator level, fast simulation of large samples and factorising the efficiencies of independent selections cuts.

Hence, one has to keep in mind that the exact results presented in this TDR could depend on the generators. They should therefore, be taken as an indication albeit a good indication of what can be expected at the LHC.

1.3.5. Parton distributions and higher order corrections

One of the key differences between a hadron and an e^+e^- collider is that for hadrons the partons collide with a strongly varying incident energy, given by the distribution of the longitudinal momentum fraction x of the parton in the proton. These parton densities are determined from data, in particular from deep inelastic scattering data and other measurements of hard scattering processes. Several groups have fitted parton distribution functions (PDFs) to these data, e.g., the CTEQ [12] and MRST [13] groups.

For the studies in this report, the simulated event samples were generated with CTEQ5L but CTEQ6 was used to normalise cross sections and to study the PDF uncertainties. CTEQ 6.1 has 40 different error PDFs, 20 PDFs at positive error, and 20 PDFs at negative error. We use the CTEQ6.1M eigenvector PDF sets [12] and the "master" equations as detailed in Appendix B to evaluate the uncertainties characterising current knowledge of the parton distributions.

The precise knowledge of the parton distributions will remain an extremely important subject for the physics at the LHC. Currently, a study group in the framework of the HERA-LHC workshop is tackling this topic in order to get as good knowledge as possible of the PDFs [14] and their uncertainties at the time of the startup of the LHC. Once the LHC starts data collection, several QCD process can be used to help to constrain the PDFs, as has been shown, e.g., using W production with studies at the HERA-LHC workshop.

1.4. Outlook

The work detailed in this Volume of the PTDR constitutes the pedestal for the physics studies that the experiment will pursue both at the start-up and the longer term running. In the process of carrying out these studies CMS has gained valuable experience in all aspects, both technical and strategic, in executing a high performance physics program. Of great value is also the identification of shortcomings and challenges that emerged in the context of completing these analyses.

As a follow-up of this work, CMS is planning an elaborate program for the start-up studies and physics commissioning from the combined magnet test effort (MTCC) as well as the experience of the upcoming computing, software and analysis challenge (CSA06) that incorporates the full calibration and alignment framework in combination with the full-trigger path exercise. The whole edifice for data collecting and analysis is expected to be complete and tested by the turn-on of the LHC in 2007.

Part I. Complete Analyses

Chapter 2. Physics Studies with Photons and Electrons

2.1. Benchmark Channel: $H \rightarrow \gamma\gamma$

The $H \rightarrow \gamma\gamma$ channel has been studied since the initial planning of the LHC and SSC as an important channel for the discovery of Higgs particles at masses beyond the upper reach of LEP and below about 150 GeV [3, 15, 16]. The signature sought in the inclusive analysis is two high E_T isolated photons. The challenge for discovery of a Higgs in this mode is the small branching fraction of about 0.002, since in this mass range the dominant decay mode of the Higgs is $b\bar{b}$. The $\gamma\gamma$ decay mode can be well identified experimentally but the signal rate is small compared to the backgrounds coming both from two prompt photons (irreducible), and from those in which one or more of the photons are due to decay products or mis-identified particles in jets (reducible). It has long been understood that $H \rightarrow \gamma\gamma$ can be detected as a narrow mass peak above a large background. The background magnitude can be determined from the region outside the peak. After event selection, for an integrated luminosity of 20 fb^{-1} and for a Higgs boson mass of 120 GeV/c^2, we expect approximately 350 signal events in a mass window of 2 GeV/c^2 over 7000 background events. An example of a $pp \rightarrow H + X$ event with Higgs particle decay $H \rightarrow \gamma\gamma$ is shown in colour plate CP1.

In this study we present two complementary inclusive analyses for the $H \rightarrow \gamma\gamma$ channel: a standard cut based analysis and a high performance, discovery-oriented analysis, based on the method described in [17, 18]. Both are carried out with our present knowledge of the expected background, estimated with full detector simulation. Further details can be found in [19]. The study concentrates on the first years of LHC operation and uses simulated events with pileup corresponding to a luminosity of 2×10^{33} cm^{-2} s^{-1}.

The idea of measuring the rate of background by using the mass regions adjoining the Higgs peak is extended to also measure the characteristics of the background, and using this information to help separate background from signal. The $H \rightarrow \gamma\gamma$ channel is particularly well suited to this technique because the signal is relatively small and can be confined to a narrow mass region thanks to the excellent photon energy and position resolution of the CMS detector [7].

By using photon isolation and photon kinematic information, significant additional discrimination between signal and background can be achieved. The optimised analysis uses this information to discriminate between signal and background by comparing data in mass side-bands with signal Monte Carlo. Use is made of a neural network, but likelihood variables or other techniques may prove to be better in the future. The expected purity in terms of signal/background, corresponding to each event, can be estimated based on this information and each event then can be used optimally to evaluate the likelihood of a signal plus background hypothesis compared to a background-only hypothesis.

In the optimised analysis the expected signal to background ratio is calculated for each event. By dividing the cut-based analysis in various categories with different s/b ratios results improve toward those that are obtained with the optimised analysis. If the maximum s/b ratio in the optimised analysis is limited to the best category used in the cut-based analysis, the performances of the two analyses are nearly identical.

The optimised, discovery-oriented analysis is particularly appropriate to the $H \rightarrow \gamma\gamma$ channel because the Higgs signal appears in a narrow mass peak allowing analysis of the large background in the mass side-bands. The analysis will not be limited by the poor simulation of the background once data will be available.

Table 2.1. NLO cross sections for the different Higgs boson production processes and branching ratios.

M_H	115 GeV/c^2	120 GeV/c^2	130 GeV/c^2	140 GeV/c^2	150 GeV/c^2
σ (gg fusion)	39.2 pb	36.4 pb	31.6 pb	27.7 pb	24.5 pb
σ (WVB fusion)	4.7 pb	4.5 pb	4.1 pb	3.8 pb	3.6 pb
σ (WH, ZH, $t\bar{t}$ H)	3.8 pb	3.3 pb	2.6 pb	2.1 pb	1.7 pb
Total σ	47.6 pb	44.2 pb	38.3 pb	33.6 pb	29.7 pb
$H \to \gamma\gamma$ Branching ratio	0.00208	0.00220	0.00224	0.00195	0.00140
Inclusive $\sigma \times B.R.$	99.3 fb	97.5 fb	86.0 fb	65.5 fb	41.5 fb

The study described requires a comprehensive understanding and simulation of the CMS detector. The electromagnetic calorimeter is used to make the primary measurements of photon energy and position. The tracker is used to measure the position of the interaction vertex. The tracker, ECAL and HCAL are used to determine, if the photon candidate is well isolated. While background characteristics will be measured from data, the signal must be well simulated to perform the analysis described below. This requires a detailed understanding of the detector performance as well as its calibration.

2.1.1. Higgs boson production and decay

For this inclusive study the Higgs boson production mechanisms with the largest cross-sections in the Standard Model have been simulated: gluon fusion, qqH production through Weak Vector Boson Fusion (WBF), associated Higgs production with W or Z bosons, and Higgs production associated with a $t\bar{t}$ pair. The cross sections for the different production processes [20] and the $H \to \gamma\gamma$ branching ratios [21] are summarised in Table 2.1. The analysis described in this chapter has been limited to careful measurement of the inclusive diphoton channel, to address the main detector issues, and no use has been made of tagging leptons or jets. In the future, channel identification, based on additional leptons and jets. will improve the sensitivity. For the moment these 'tagged' channels are investigated individually in other studies [22, 23]. Figure 2.1 shows an event display of a $H \to \gamma\gamma$ event with $M_H = 120\,\text{GeV/c}^2$.

2.1.2. Backgrounds

Backgrounds with two real prompt high E_T photons are called "irreducible", although they can be somewhat reduced due to kinematic differences from signal processes in which high mass particles are produced. Two photons can be produced from two gluons in the initial state through a "box diagram" or from initial quark and anti-quark annihilation.

Backgrounds in which at least one final state jet is interpreted as a photon are called "reducible" and are much harder to simulate since, jets are copiously produced at the LHC and Monte Carlo samples that correspond to $10\,\text{fb}^{-1}$ are much too large to fully simulate. Selections at generator level have been devised in order to be able to select multi-jet and γ plus jets events that contribute to the background of the $H \to \gamma\gamma$ channel and reject events that have negligible chance of producing background to the final analysis.

The γ + jet sample can be viewed, from the selection point of view, as coming from two different sources: one where another photon is radiated during the fragmentation of the jet (two prompt photons), the other where there is only one prompt photon in the final state and the other photon candidate corresponds to a mis-identified jet or isolated π^0 (one prompt plus one fake photon). These two processes have been separated using generator level information, and are listed separately in the tables below. Also, different K-factors are applied.

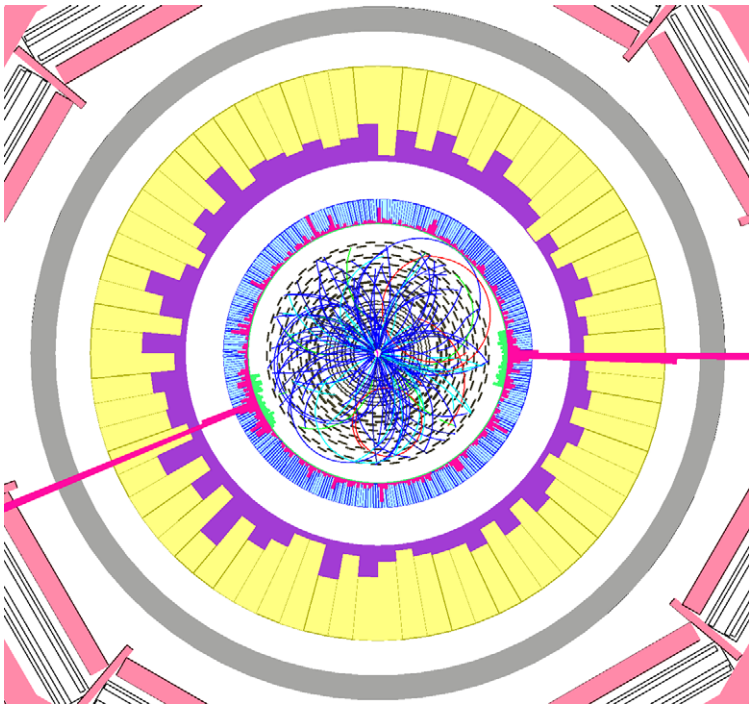

Figure 2.1. $H \to \gamma\gamma$ event produced in gluon fusion with $M_H = 120\,\text{GeV}$ observed in the CMS detector.

The generator level pre-selection of γ + jet events that contribute to the $H \to \gamma\gamma$ background is straightforward. For $pp \to$ jets, a much tighter set of cuts at the particle generator level was carefully developed and studied. Groups of particles, protocandidates, which might form a photon candidate after event simulation are identified. Cuts are applied on the transverse energy of two protocandidates and on their invariant mass, and this involves an estimate on the lower and upper limits to the energy of the photon candidates that might be reconstructed from the protocandidates after the simulation. An estimate is also made on likely level of isolation of the resulting photon candidate.

With such selection a rejection of a factor of about 41000 can be obtained, with an estimated inefficiency of 14% for $pp \to$ jets events generated with PYTHIA with $\hat{p}_\perp > 30\,\text{GeV}$ (transverse momentum of the products of the hard interaction). The inefficiency after the final analysis selection was estimated by using a looser pre-selection similar to that used for the $pp \to \gamma$ + jet simulation. Further details can be found in [19]. Events rejected by the pre-selection have rather low E_T photons and are not very important for the final analysis.

The Monte Carlo samples used are summarised in Table 2.2. All events were generated with PYTHIA [24], simulated with the GEANT-based [9] CMSIM [25] or OSCAR [8], and reconstructed with ORCA version 8.7.3 [10]. Pile-up events from minimum bias interactions were added to the hard interaction, assuming a luminosity of $\mathcal{L} = 2 \times 10^{33}\,\text{cm}^{-2}\,\text{s}^{-1}$.

K-factors are applied to take into account the expected differences between the lowest order cross sections given by PYTHIA and the NLO cross sections of the different background processes [26–30]. The K-factors used for each background are summarised in Table 2.3 and are estimated to have an uncertainty of 20–30%.

Table 2.2. Monte Carlo samples used in the $H \to \gamma\gamma$ analysis with LO cross section from PYTHIA and total corresponding integrated luminosities of the analysed samples.

Process	$\hat{p}_\perp$ (GeV/c)	M_H (GeV/c^2)	σ(pb)	Pre-sel. σ(pb)	Events Analysed	Int Lum. (fb^{-1})
$H \to \gamma\gamma$ (gg fusion)	-	120	-	-	181 K	-
$H \to \gamma\gamma$ (WB fusion)	-	120	-	-	193 K	-
$H \to \gamma\gamma$ (gg fusion)	-	115–150	-	-	20 K	-
$H \to \gamma\gamma$ (WB fusion)	-	115–150	-	-	20 K	-
$H \to \gamma\gamma$ (WH,ZH,ttH)	-	115–150	-	-	20 K	-
$pp \to \gamma\gamma$ (born)	>25	-	82	44	920 K	30
$pp \to \gamma\gamma$ (box)	>25	-	82	31	668 K	20
$pp \to \gamma$ + jet	>30	-	5×10^4	2.5×10^3	5.5 M	2.2
$pp \to$ jets	>50	-	2.8×10^7	4.7×10^3	4.5 M	1.0
Drell–Yan ee	-	-	4×10^3	4×10^3	460 K	0.1

Table 2.3. Background K-factors applied to PYTHIA cross sections.

$pp \to \gamma\gamma$ (Born)	1.5
$pp \to \gamma\gamma$ (Box)	1.2
$pp \to \gamma$ + jet (2 prompt)	1.72
$pp \to \gamma$ + jet (1 prompt + 1 fake)	1
$pp \to$ jets	1

2.1.3. Reconstruction, selection, and signal significance calculation

2.1.3.1. Trigger. $H \to \gamma\gamma$ events are selected with extremely high efficiency both by the Level-1 and High Level triggers that are described in details in Ref. [31]. Since in the analysis selection tighter E_T and isolation cuts are applied, the inefficiency due to the trigger is negligible.

2.1.3.2. Photon reconstruction. Photons are reconstructed with the standard ECAL algorithms [7, 32]. At this level the photon reconstruction efficiency is over 99.5% for photons in the region covered by the ECAL.

The energy resolution of reconstructed photons is excellent for photons that do not convert or that convert late in the tracker. Energy resolution deteriorates somewhat for photons that convert early in the tracker. Nevertheless, the photon energy resolution is substantially less affected by tracker material than is electron energy resolution and the Higgs reconstruction in the calorimeter is quite reliable even for converted photons.

For signal events, where this effect is relevant, the energy response of the individual crystals of the ECAL has been smeared using a miscalibration file randomly generated to correspond to the intercalibration precision expected after calibration with $W \to e\nu$ events obtained with an integrated luminosity of 10 fb^{-1}, as described in [7]. The precision is 0.3% in the central part on the barrel, growing up to 1.0% at the edge of the barrel and in the endcaps.

The tools that have been developed to identify and reconstruct photon conversions in the tracker [33], and π^0 rejection tools developed for the endcap silicon preshower detector and the barrel crystals, have not yet been included in the analysis.

2.1.3.3. Primary vertex identification. The bunch length at LHC has an rms width of 75 mm resulting in a longitudinal spread of interaction vertices of 53 mm. If the mean longitudinal

position is used (nominal vertex), the invariant mass of a two-photon state, such as the $H \to \gamma\gamma$, is smeared by about $1.5\,GeV/c^2$, due to the mis-measurement of the angle between the two photons related to the uncertainty of the photon directions.

The two high E_T photons coming from the Higgs boson decay are produced in association with other tracks that may come from the underlying event and initial state gluon radiation or from the other particles produced with the Higgs boson in the case of WBF fusion, WH or ZH production and $t\bar{t}H$ production.

The charged tracks associated to the Higgs production vertex are typically harder than those coming from minimum bias interactions. Therefore, the vertex can be identified by reconstructing the primary vertices in the event and selecting the one that most likely corresponds to the Higgs boson production, based on charged tracks.

At low luminosity ($2 \times 10^{33} cm^{-2}\,s^{-1}$) we are able to identify the correct vertex, defined as being within 5 mm of the actual vertex, in about 81% of the signal events passing the selection described in Section 2.1.4.1. Clearly, these results will be affected by any significant variation of the characteristics of the pileup events from what is simulated in our pileup samples.

2.1.3.4. Photon isolation. Detailed studies have been made of photon isolation and its optimisation [34, 35]. Fake photon signals due to jets can be rejected by looking for additional energetic particles accompanying the photon candidate. Charged pions and kaons can be detected in the tracker or in the calorimeters. Neutral pions and other particles decaying to photons can be detected in the ECAL. The hadron calorimeter may be important for detecting charged particles not efficiently reconstructed in the tracker, particularly at high η, or other particles like neutrons or K^0_{long}.

2.1.3.5. Separation into categories based on lateral shower shape and pseudorapidity. The shower shape variable R_9, defined as the fraction of the super-cluster energy found inside the 3×3 array of crystals centred around the highest energy crystal, is effective in distinguishing photon conversions in the material of the tracker. Photon candidates with large values of R_9 either did not convert or converted late in the tracker and have good energy resolution. Photons converting early have lower values of R_9 and worse energy resolution.

The variable R_9 has been shown to be very useful also in discriminating between photons and jets. This occurs both because of the conversion discrimination – either of the photons from a π^0 can convert – and because, looking in a small 3×3 crystal area inside the super-cluster, the R_9 variable can provide very local isolation information about narrow jets.

In the multi-category analysis, the events are separated into categories based on R_9 so as to take advantage of better mass resolution where it is expected (the unconverted photons), and yet still use all the events (since the mass resolution varies by at most a factor of 2). This separation also tends to put background events involving jets into categories with lower R_9.

We also find that photons detected in the endcaps have worse energy resolution and higher background than photons detected in the barrel so that it is useful to separate events with one or more photons in the endcaps from those with both photons in the barrel.

2.1.3.6. Calculation of confidence levels. Confidence levels are computed by using the Log Likelihood Ratio frequentist method, as described in [36]. Given the expected signal and background distributions in the final variable (the mass distribution for the cut-based analysis), we simulate many possible outcomes of the experiment by means of Monte Carlo. This is done both in the hypothesis that the signal exists and that it does not exist. To compute a confidence level, we order our trials according to an estimator. This is a single number

that is useful to order random trials from most background-only-like to most signal-plus-background-like. The simplest and probably best estimator is the Log Likelihood Ratio (LLR) which compares the likelihood of the data to come from a background-only distribution to the likelihood to come from a signal-plus-background distribution. Each likelihood is the product of probabilities from all the bins. The median confidence level is computed both for discovery and for exclusion.

2.1.3.7. Effect of systematic errors. To include systematic errors the background and signal expectation are randomised by the systematic error during the generation of the random trials, while keeping their expectations at the nominal value. If necessary, the correlations between the errors on the different analysis bins is included. It is observed that the signal systematic error has no effect on the median LLR of signal-plus-background experiments, nor on that of background-only experiments. Of course, the distribution corresponding to the signal-plus-background experiments is enlarged by the systematic error on the signal and this makes exclusion more difficult. On the other hand the effect of the systematic error on the background is very large, because of the small signal over background ratio. The mean of the distributions is still unchanged but the widths are enlarged both for background-only experiments and for signal-plus-background experiments. This decreases both the discovery and exclusion sensitivities.

2.1.4. Cut-based analysis

2.1.4.1. Selection. Two photon candidates are required with pseudo-rapidity $|\eta| < 2.5$, with transverse energies larger than 40 GeV and 35 GeV respectively, and satisfying the following isolation requirements:

- No tracks with p_T larger than 1.5 GeV/c must be present inside a cone with $\Delta R < 0.3$ around the photon candidate. We only consider tracks with hits in at least two layers of the silicon pixel detector, therefore converted photons are likely to be rejected only if they convert before the second pixel layer.
- The total E_T of all ECAL island basic clusters with $0.06 < \Delta R < 0.35$ around the direction of the photon candidate, regardless of whether they belong to the super-cluster or not must be less than 6 GeV in the barrel and 3 GeV in the endcaps.
- The total transverse energies of HCAL towers within $\Delta R < 0.3$ around the photon candidate must be less than 6 GeV in the barrel and 5 GeV in the endcaps.

In order to further reduce the background that is higher when at least one of the photons is detected in the electromagnetic calorimeter endcaps and to increase the performance of the analysis in the forward region additional isolation requirements are applied for events where one, or more, of the candidates has $|\eta| > 1.4442$. For these events, the candidate in the barrel is required to satisfy the tighter isolation selection that is applied to photons in the endcaps: ECAL isolation less than 3 GeV and HCAL isolation less than 5 GeV.

Figure 2.2 shows the mass distribution after the selection. The efficiency for a 120 GeV/c^2 Higgs boson is 30% and the total expected background is 178 fb/GeV. The number of expected background events for the different types of background is shown in Table 2.4 while the Higgs efficiency in different mass windows is shown in Table 2.5. The efficiency is computed using all generated signal events. The signal contribution to the total number of events is very small, particularly outside the mass region under study. The background can be estimated by a fit to the data mass distribution.

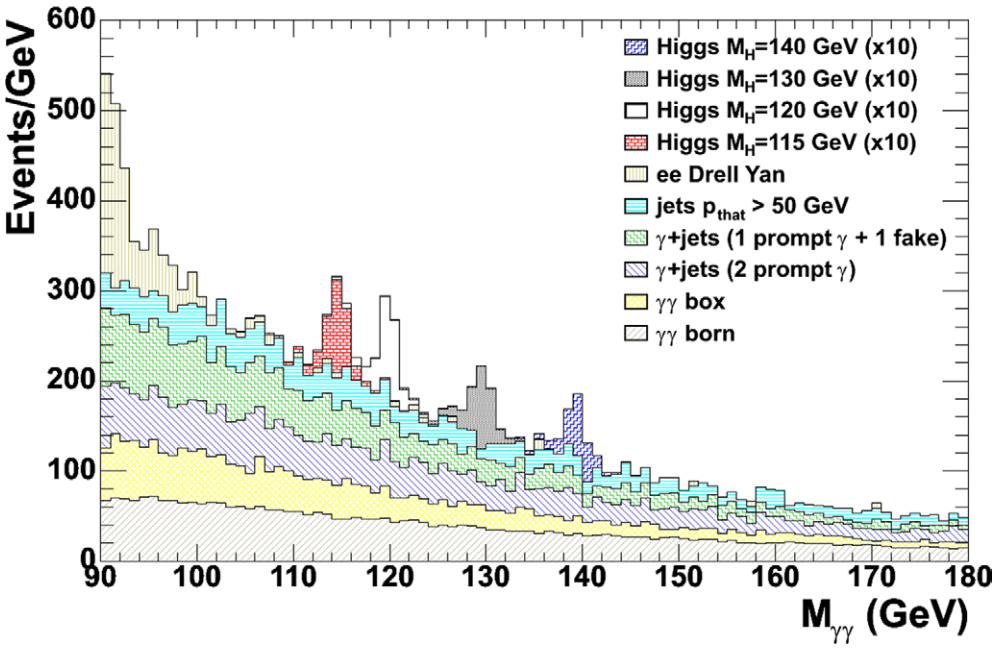

Figure 2.2. Diphoton invariant mass spectrum after the selection for the cut-based analysis. Events are normalised to an integrated luminosity of 1 fb^{-1} and the Higgs signal, shown for different masses, is scaled by a factor 10.

Table 2.4. Expected background after the selection for Higgs boson masses between 115 and 150 GeV/c^2, expressed in fb/GeV.

Process	115 GeV/c^2	120 GeV/c^2	130 GeV/c^2	140 GeV/c^2	150 GeV/c^2
$pp \to \gamma\gamma$ (Born)	48	44	36	29	24
$pp \to \gamma\gamma$ (Box)	36	31	23	16	12
$pp \to \gamma$ + jet (2 prompt)	43	40	32	26	22
$pp \to \gamma$ + jet (prompt + fake)	40	34	22	19	14
$pp \to$ jets	29	27	20	18	14
Drell–Yan ee	2	2	1	1	1
Total background	203	178	134	109	86

Table 2.5. Selection efficiency for the Higgs signal in different mass windows.

M_H (GeV/c^2)	Window ± 1 GeV/c^2	Window ± 1.5 GeV/c^2	Window ± 2.5 GeV/c^2	Window ± 5 GeV/c^2	Window Total
115	17%	21%	25%	28%	29%
120	18%	22%	26%	29%	30%
130	18%	22%	27%	31%	32%
140	18%	23%	28%	32%	34%
150	28%	24%	29%	33%	36%

The error on the background estimation comes from two sources:

- the statistical precision which decreases with the size of the mass range that is used to perform the fit;
- the systematic error related to the shape of the function that is used to fit the distribution.

It is not possible to know the exact functional form of the background shape and the error must be estimated by assuming a function, simulating a distribution and then using a different function to fit the data. Clearly, this error grows with the size of the mass range used. For a reasonable mass range of $\pm 10 - 20\,\mathrm{GeV/c^2}$ excluding +3 and $-5\,\mathrm{GeV/c^2}$ from the Higgs boson mass under study and for an integrated luminosity of $20\,\mathrm{fb}^{-1}$ the statistical and systematic errors are estimated to be 0.4% and 0.5% respectively. The statistical error decreases with the integrated luminosity while the systematic error is constant.

2.1.4.2. Splitting into categories. Changing the cuts or adding new discriminating variables to this analysis does not give large improvements in the sensitivity. This can be seen, for example, from the fact that it is not possible to use the very powerful variable, R_9, to reject events without loosing performance. This is because, the increase in s/b ratio does not compensate the loss in efficiency.

The way to improve the sensitivity of the analysis is to keep all selected events but to split the sample into categories with different s/b ratios.

The following 3 possibilities are considered:

- 1 single category;
- 4 categories from 2 R_9^{min} ranges (R_9^{min} larger or smaller than 0.93) times 2 pseudo-rapidity regions $|\eta|^{\mathrm{max}}$ in barrel or endcaps;
- 12 categories from 3 R_9^{min} ranges ($R_9^{\mathrm{min}} > 0.948$, $0.9 < R_9^{\mathrm{min}} < 0.948$ and $R_9^{\mathrm{min}} < 0.9$) times 4 pseudo-rapidity regions ($|\eta|^{\mathrm{max}} < 0.9$, $0.9 < |\eta|^{\mathrm{max}} < 1.4442$, $1.4442 < |\eta|^{\mathrm{max}} < 2.1$ and $|\eta|^{\mathrm{max}} > 2.1$).

Figure 2.3 shows the mass spectrum after splitting into four categories. The signal over background ratio is much larger in the best category and the composition of the background varies between the different samples: irreducible backgrounds dominate for large R_9 and reducible backgrounds are larger for small R_9.

Table 2.6 shows, for the 12 category analysis, the fraction of events along with the maximum s/b ratio in each category.

2.1.4.3. Systematic errors. The total error on the background is approximately 0.65% and is due to the uncertainty of the function fit to the side-bands of the mass distribution, estimated to be 0.5%, plus the statistical error on the fit that is approximately 0.4% for an integrated luminosity of $20\,\mathrm{fb}^{-1}$.

An error of 0.65% has a very large effect on the discovery CL when only one category is used. The reason is that a large fraction of signal events corresponds to a very low s/b, of the order of a percent. The effect can be reduced by applying a cut on the signal over background s/b. This corresponds to using events in a mass window around the analysed mass, until s/b becomes smaller than the chosen cut. The optimal cut for this analysis is 0.02.

When the events are split into categories the number of background events in each category is reduced on average by $1/N_{\mathrm{cat}}$ and this increases the statistical error on the background estimation by approximately a factor $\sqrt{N_{\mathrm{cat}}}$, but this error is completely uncorrelated between the different categories. The error related to the uncertainty of the fit function remains constant and it is also uncorrelated between the different categories because, due to the different cuts the background shapes are different and described by different

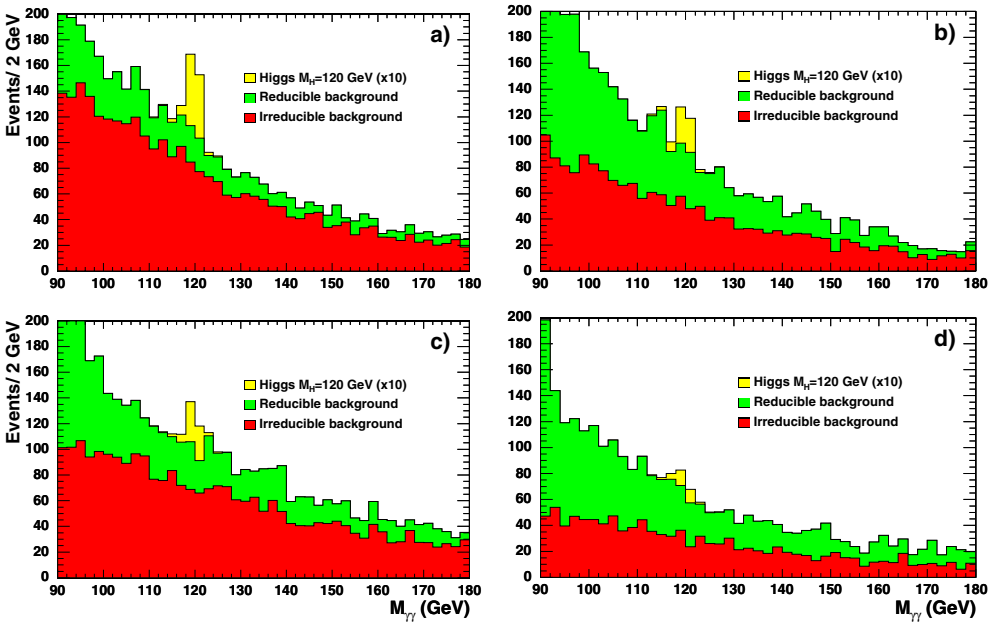

Figure 2.3. Invariant mass spectrum after the selection relative to the cut-based analysis with four categories defined in the text: barrel with large R_9 (a), barrel with small R_9 (b), endcaps with large R_9 (c) and endcaps with small R_9 (d), Events are normalised to an integrated luminosity of 1 fb^{-1} and the Higgs signal, shown for different masses, is scaled by a factor 10.

Table 2.6. Fractions of events in each of the 12 categories and maximum s/b in the mass region of 120 GeV/c^2.

	$\lvert\eta\rvert^{\max} < 0.9$		$0.9 < \lvert\eta\rvert^{\max} < 1.4442$		$1.4442 < \lvert\eta\rvert^{\max} < 2.1$		$\lvert\eta\rvert^{\max} > 2.1$	
	frac.	s/b	frac.	s/b	frac.	s/b	frac.	s/b
$R_9^{\min} > 0.948$	15.5%	14.7%	13.1%	9.0%	10.8%	6.1%	8.5%	4.5%
$0.9 < R_9^{\min} < 0.948$	9.4%	12.2%	6.8%	6.8%	6.7%	4.8%	2.7%	2.8%
$R_9^{\min} < 0.9$	8.3%	7.6%	11.1%	4.3%	5.4%	3.2%	1.7%	2.2%

functions. The total error is then less than the total error reduced by $1/\sqrt{N_{cat}}$. This reduces the effect of the systematic error on the discovery.

The effect of the systematic error on the background estimation is also related to the signal over background of the analysis. A more sensitive analysis, for which a larger part of the signal has a higher s/b ratio, is less affected by the same relative uncertainty on the background.

Clearly the current understanding of the background is affected by larger uncertainties such as: cross section, diphoton kinematic distributions and efficiency of the selection (mainly affected by jet fragmentation, pile-up and by the structure of the underlying events).

The systematic error on the signal, that as has been mentioned has no effect on the discovery CL, has contributions from the theoretical uncertainty of the cross section (+15–12% from the scale variation and +4–5%), from the measurement of the integrated luminosity (∼5%), from the trigger (∼1%), from the analysis selection (that will be measured for example with $Z \to \mu\mu\gamma$) and from the uncertainties on the photon energy resolution.

Table 2.7. Integrated luminosity needed to discover or exclude the Higgs boson with mass 120 GeV/c^2 with or without taking into account the systematic errors (fb^{-1}).

Analysis	5σ discovery no syst	5σ discovery syst	3σ evidence no syst	3σ evidence syst	95% exclusion no syst	95% exclusion syst
counting exp.	27.4	48.7	10.0	13.2	4.5	6.5
1 category	24.5	39.5	8.9	11.5	4.1	5.8
4 categories	21.3	26.0	7.5	9.1	3.5	4.8
12 categories	19.3	22.8	7.0	8.1	3.2	4.4

Other effects that could modify the ability to discover the Higgs boson are: uncertainties on the structure of the underlying events, that could change the efficiency of the primary vertex determination and the amount of material in the tracker before the electromagnetic calorimeter.

The effect on the performances of the analysis of an increase of 20% of the tracker material has been evaluated. The main effects on such change on the analysis would be:

- increase of the inefficiency of the track isolation requirements for early photon conversions, before or inside the second layer of the pixel detector.
- increase of the inefficiency of ECAL isolation cut;
- decrease of the value of R_9 for all photons that would cause a migration of events from more sensitive categories to less sensitive categories.

It was estimated that such change would increase the luminosity needed to achieve a given discovery CL of approximately 6%. Given that the amount of tracker material will be known with a precision of $\sim 2\%$ the related systematic error is less than 1%.

In what follows a conservative 20% systematic error on the signal is assumed. It affects exclusion of a signal, not discovery, since the signal rate is directly measured from data in case of discovery.

2.1.4.4. Results of the cut-based analysis. Table 2.7 shows the integrated luminosity needed to obtain 5σ discovery or 95% CL exclusion for a 120 GeV/c^2 mass Higgs boson with the different splittings. The effect of the systematic errors is also shown. We can observe how the performance increases and the effect of the error on the background estimation decreases with the number of categories. In the three cases (1, 4 and 12 categories) the event selection is the same and that the differences in performance come from the splitting of the total sample in different sub-samples with different sensitivities (s/b). In the split category analyses the computation of the log-likelihood ratio estimator is made separately for each 1 GeV/c^2 bin in mass, whereas in the "counting experiment" only a single (optimum) mass window is evaluated.

The integrated luminosity needed for discovery and exclusion, using the 12-category analysis, for the mass range studied between 115 and 150 GeV/c^2 are shown in the plots at the end of the section (Fig. 2.10). The Higgs boson can be discovered with mass between 115 and 140 GeV/c^2 with less than 30 fb^{-1} and excluded in the same mass range, at 95% CL, with less than 5 fb^{-1}.

As mentioned before, all these results have been obtained assuming an intercalibration of the ECAL, after having collected an integrated luminosity of 10 fb^{-1}. With the whole ECAL intercalibrated to a precision better than 0.5% over all the solid angle, the results improve such that approximately 10% less integrated luminosity is needed for discovery.

2.1.5. Optimised analysis estimating s/b for each event

In the optimised analysis 6 categories are used, 3 in which both photons are in the barrel and 3 in which at least 1 photon is in an endcap. The 3 categories are defined, as for the cut-based analysis, to have the lowest R_9 photon candidate with $R_9 > 0.948$, $0.948 > R_9 > 0.90$ and $R_9 < 0.90$ respectively. The categories are labelled with numbers from 0 to 5: first, the 3 barrel categories with decreasing values of R_9 then the 3 endcap categories again with decreasing values of R_9.

2.1.5.1. Mass distributions in categories. The diphoton mass distributions enable the separation of signal from background. Signal peaks sharply at the Higgs mass while the backgrounds are quite smooth. This allows good estimation of the magnitude of the background under the peak.

The best mass resolution and the best s/b ratio in the peak is found in category 0, with high R_9 in the barrel.

2.1.5.2. Loose selection of events for optimised analysis. Isolation requirements are applied to photon candidates prior to the computation of the neural network isolation variables NN_{isol}:

- the transverse E_T of the photon candidates must be larger than 40 GeV and the absolute value of their pseudo-rapidity less than 2.5;
- no tracks with p_T larger than 1.5 GeV/c must be present inside a cone with $\Delta R < 0.1$ around the photon candidate;
- the total E_T of all ECAL island basic clusters with $\Delta R < 0.3$ around the photon candidate, excluding those belonging to the super-cluster itself must be less than 5 GeV;
- the total transverse energies of HCAL towers within $\Delta R < 0.35$ around the photon candidate must be less than 35 GeV;
- the sum of the transverse momenta of charged tracks within $\Delta R < 0.2$ around the photon candidate must be less than 100 GeV/c.

Before optimising the final analysis, some additional cuts are applied. These both simplify the neural network training and slightly improve the performance. It is required that:

- the events pass the double photon High Level Trigger;
- the isolation neural net output is greater than 0.25 for both photons.

2.1.5.3. Optimised use of kinematic variables to separate signal and background. In addition to the mass, there are kinematic differences between signal and background. In particular the signal has a harder photon E_T distribution than the background – the background can have a high mass by having a large η difference between the photon candidates. Weak Boson Fusion and associated production of a Higgs with other massive particles enhance these differences between signal and background. The large, reducible backgrounds often have photon candidates that are not well isolated.

As with the Higgs searches performed at LEP, higher performance can be achieved if the expected signal over background, s/b, is estimated for each event. This is particularly effective if, the s/b varies significantly from event to event. This is the case here due to wide variations in photon isolation and photon E_T. There is also significant dependence of the s/b on photon conversion and on location in the detector.

One photon isolation variable NN_{isol} for each photon, is combined with kinematic variables to help separate signal and background. A neural net is trained to distinguish background events, taken from the mass side-bands, from signal Monte Carlo events. There is

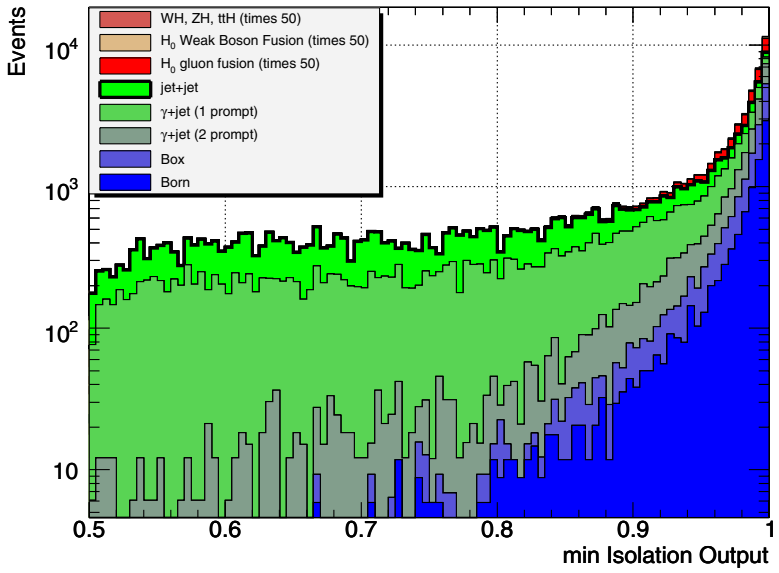

Figure 2.4. Distribution of the minimum value of the NN_{isol} variables of the two photon candidates. Events are normalised to an integrated luminosity of $7.7\,fb^{-1}$ and the signal ($M_H = 120\,GeV/c^2$) is scaled by a factor 50.

no danger of over-training since background events from the signal mass region are not used and independent samples are used for the signal Monte Carlo. The input variables are devised to be insensitive to the diphoton mass so that the background rejection due to the kinematics and isolation is independent of the background rejection from the mass distribution.

Six variables are used as inputs to a neural net. They are the isolation NN outputs NN_{isol} for the 2 photons, the transverse energies of the 2 photons, normalised to the diphoton mass, the absolute value of the rapidity difference between the 2 photons, and the longitudinal momentum of the photon pair.

The distributions of the input variables are shown for signal and background in Figs. 2.4 and 2.5. Kinematic information that are likely to be highly sensitive to higher order corrections to the background simulation has not been used. Such information, like the E_T of the Higgs boson candidate, the E_T transverse to the photon direction, and information about additional jets will ultimately be useful but may not be reliable until better simulations or actual data are available to train on.

The neural net is trained in each of the 6 categories independently. The net has 6 input nodes, 12 intermediate nodes in a single layer, and 1 output node. The error function has been modified from the standard to improve training toward a high signal over background region. A minimum neural net output cut is applied that eliminates 1% of the signal in each category and a function is fit to the distribution above that cut. These functions are used to bin the data and to smooth the background in a limited region.

It is useful to examine the neural net output distribution for events from different sources (Fig. 2.6). Low NN outputs are dominated by photon candidates from jets which are not well isolated. The large peak at 0.85 represents both signal and background where the photon is relatively well isolated and the photon E_T is $M_H/2$, corresponding to events with a large value of NN_{isol}. Higher photon E_T events are found in the peak near 1. There is an enhancement of the signal, particularly for the WBF and associated production processes. The background there is dominated by events with at least one jet interpreted as a photon.

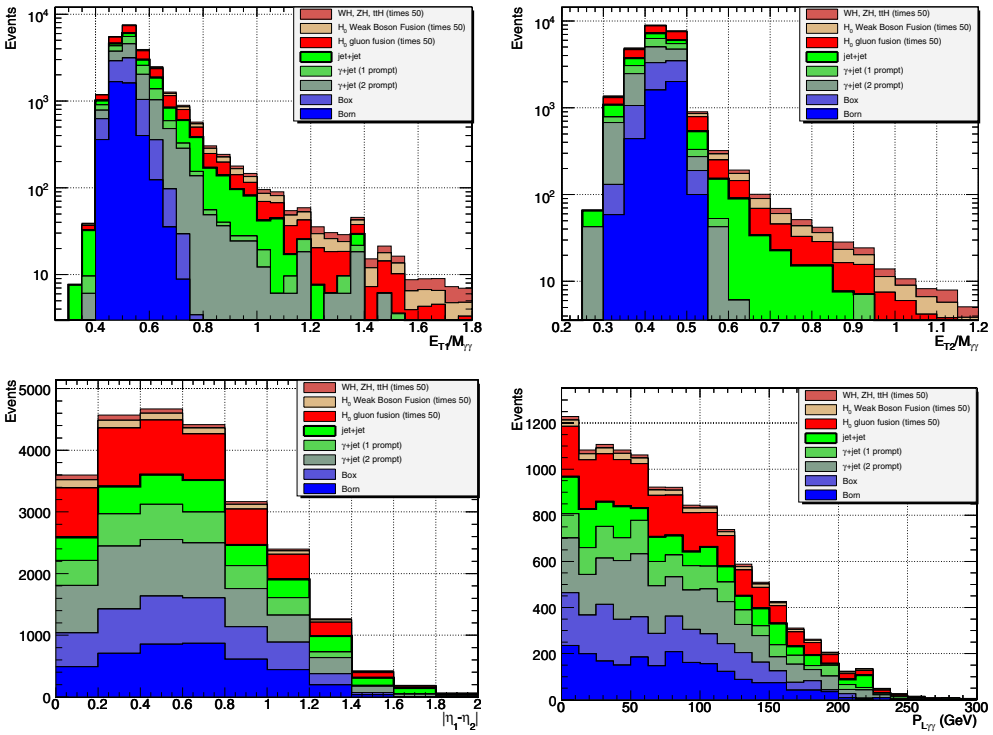

Figure 2.5. Distribution of the kinematic inputs to the neural network for signal and background sources. A value of the neural net output is required to be greater than 0.85. Events are normalised to an integrated luminosity of 7.7 fb^{-1} and the signal ($\mathrm{M_H} = 120\,\mathrm{GeV/c^2}$) is scaled by a factor 50.

2.1.5.4. Estimation of signal to background ratio for each event. In order to get the most information out of each event, the signal over background is estimated for each event. In the simplest analyses, cuts are applied to select only high signal over background events and those are counted. Such a simple analysis looses information because, some of the events that are cut could contribute to the measurement and because, some of the events that are accepted are not used optimally.

Events in the mass peak for the Higgs mass hypothesis under consideration have high signal over background expectation while events outside the peak have lower expected s/b. Similarly, events at high $\mathrm{NN_{kin}}$ output have higher s/b expectation. The kinematics and isolation information in $\mathrm{NN_{kin}}$ has been made independent of mass information so the two s/b ratios can be multiplied to get a good estimate of the s/b expectation for the event:

$$\left(\frac{s}{b}\right)_{\mathrm{est}} = \left(\frac{s}{b}\right)_{\mathrm{mass}} \times \left(\frac{s}{b}\right)_{\mathrm{kin}} .$$

This is an estimate that is to bin signal and background events. If the estimate is bad, the performance of the analysis suffers because good s/b events are not well separated from bad ones. It is not possible for a bad estimate to make the analysis appear to perform too well. The s/b estimate need not be normalised correctly, since it is a relative number used to bin events.

The events are binned according to the s/b estimate. Histograms are made in each of the six categories. The actual signal to background ratio is computed for the binned events and

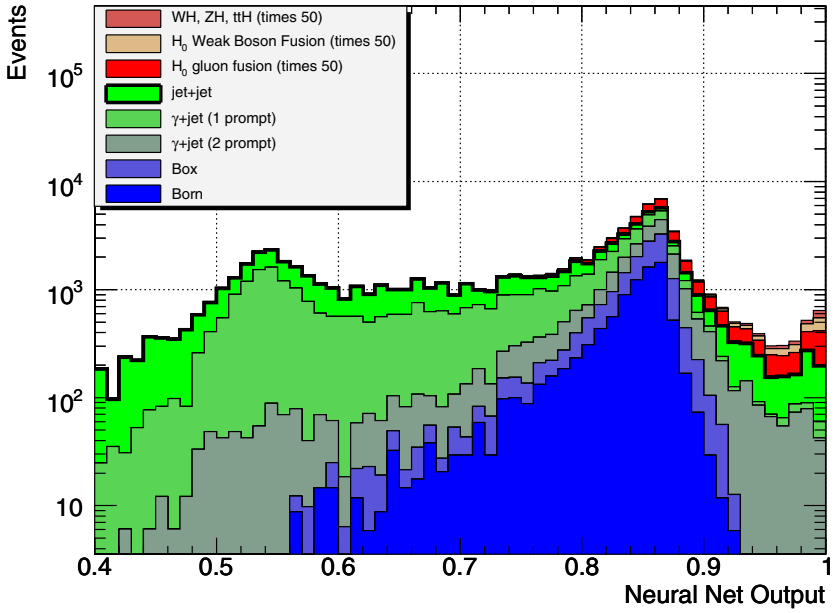

Figure 2.6. The neural net output for events in the barrel for each signal ($M_H = 120\,GeV/c^2$) and background source. Events are normalised to an integrated luminosity of $7.7\,fb^{-1}$ and the Higgs signal is scaled by a factor 50.

used to calculate confidence levels that data are consistent with a background-only hypothesis or with a signal-plus-background hypothesis.

2.1.5.5. Smoothing the background. The $H \to \gamma\gamma$ channel has the good feature that the mass is essentially independent of isolation and suitably chosen kinematic variables. With this factorisation assumption, background can be smoothed well even in regions with low statistics.

The background expectation in a bin must be reliably estimated in order to correctly calculate confidence levels. Downward fluctuations in the background estimation can have a significant impact on the CL. The number of simulated events for the irreducible (jet) backgrounds is about one seventh of the number that will be available in the data at the time it would be expected to discover the Higgs. Therefore, problems with background estimation are even more difficult now than they will be when we have data.

The background distributions are very smooth in the mass variable, so the distribution in mass can be reliably smoothed. This is done by spreading each event over a $\pm 5\,GeV/c^2$ region according to the functions fit to the mass distribution. A wider mass region could be used but this would interfere with the training of the analysis on an independent sample in the mass side-bands.

The background distribution in the neural net output is also smoothed over a region of $\pm\,0.05$ using the fit functions. It is therefore, quite important that the background fit functions accurately represent the neural net distribution. In the smoothing process, the normalisation of the background is carefully maintained to high accuracy.

With this two-dimensional smoothing accurate background expectations are obtained except in the regions with extremely small amounts of background. In such regions, bins must be combined until sufficient background events are available. If a s/b bin has too few MC

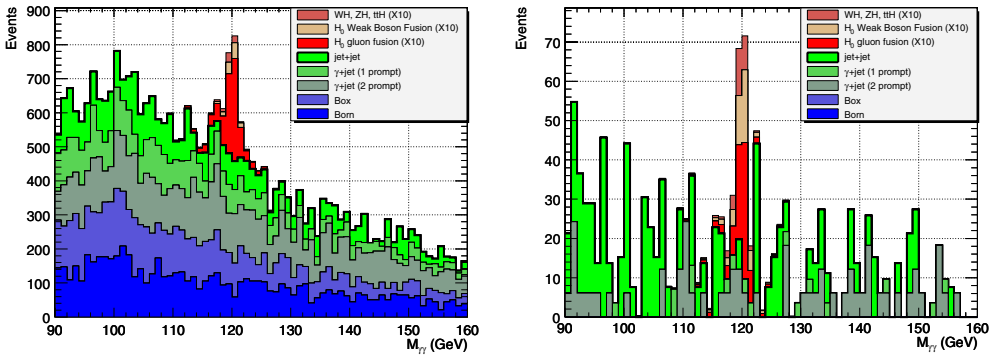

Figure 2.7. The diphoton mass distribution for each source for barrel events with kinematic neural net output greater than 0.85 (left) and 0.97 (right). Events are normalised to an integrated luminosity of 7.7 fb^{-1} and the Higgs signal ($M_H = 120\,GeV/c^2$) is scaled by a factor 10.

background events contributing to it, it is combined with the nearest (lower s/b) bin. This is continued until there are sufficient events. This combination clearly reduces the sensitivity of the analysis but cannot be avoided without a more detailed understanding of the background, which is a goal for the future. At present, at least 20 Monte Carlo background events are required in a bin. Since the current MC samples contain about seven times less events than expected in the data, significant improvements are possible, allowing higher s/b bins to be used, resulting in better performance.

Figure 2.7 shows the mass distributions for barrel events with two different cuts on the neural net output. The looser cut simply excludes most of the obviously non-isolated candidates. It can be seen that all of the backgrounds are important at this level. The tighter cut highly enhances the s/b ratio and emphasises the importance of smoothing, which has not been applied to the background in this distribution.

Figure 2.8 shows the mass distribution for neural net output greater than 0.97 in category 0. Again it is clear that smoothing in two dimensions is needed to get a reasonable estimate of the background. It is useful to note that even in this very high s/b region, the largest contribution to the signal is from gluon fusion, although the relative contributions of the other production processes has increased.

2.1.5.6. Combination of categories into final s/b distribution. At this point the signal and background is binned in s/b in six categories. These could be used to calculate the confidence level, however, it seems most useful, in the light of future plans to analyse separate channels, to combine the categories into one s/b plot in a similar way as may be used to re-combine channels. The six histograms are combined into one which can be used calculate confidence levels. The combination is based on the actual signal to background in each bin. In principle, this is the same as combining results from different channels or even from different experiments in a way that makes optimal use of all channels and does not pollute high quality channels with data of lesser purity.

The final binning of data into s/b bins is shown in Fig. 2.9. The plot extends from very low signal to background to a small number of events with $s/b > 1$.

The relative contribution of barrel and endcap categories can be estimated from the total LLR computed and LLRs computed excluding each category. The six categories have rather widely varying contributions to the Log Likelihood Ratio and hence to the performance of the analysis. Table 2.8 shows the fraction of signal and the fraction of the LLR for each category.

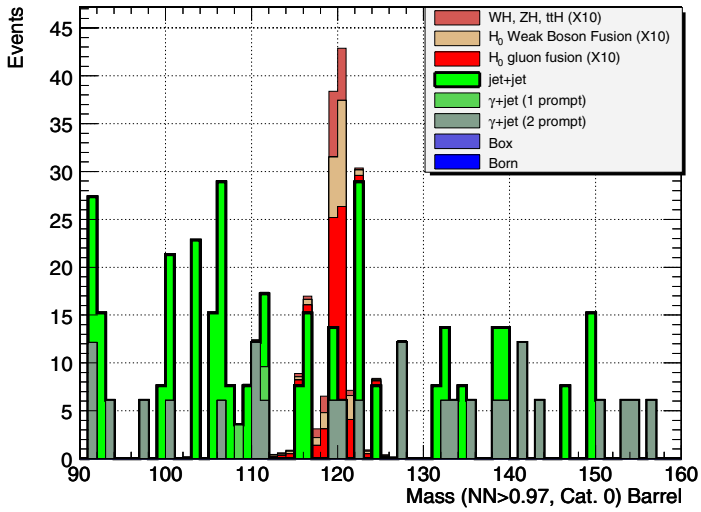

Figure 2.8. The diphoton mass distribution for each source for barrel events with kinematic neural net output greater than 0.97 and $R_9 > 0.948$. Events are normalised to an integrated luminosity of 7.7 fb^{-1} and the Higgs signal ($M_H = 120\,GeV/c^2$) is scaled by a factor 10.

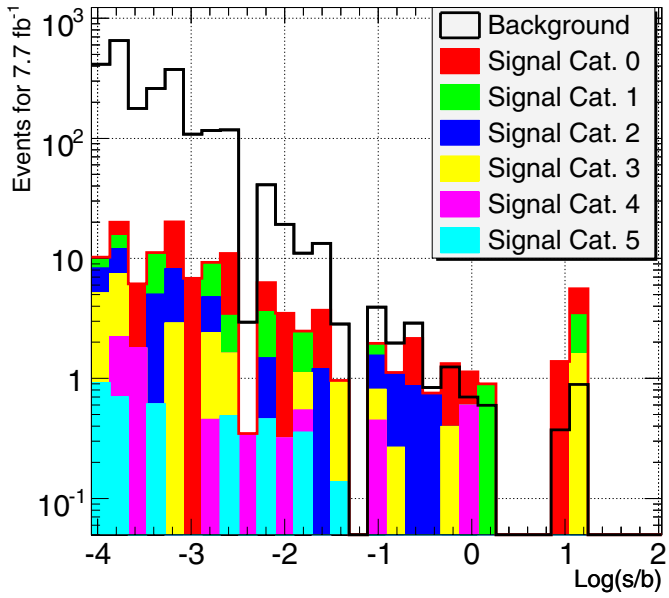

Figure 2.9. The final distribution of binned signal ($M_H = 120\,GeV/c^2$) and background in $\log(s/b)$ for an integrated luminosity of 7.7 fb^{-1}. Here the Higgs signal is normalised to the integrated luminosity and the statistics benefits of the smoothing of the background. Signal and background events are added independently.

Some of the categories have a fairly small effect on the final result. This remains true after the application of systematic normalisation uncertainties described below. It is clear that photon conversions result in a significant deterioration of the performance. It is hoped to mitigate this somewhat by using the conversion track reconstruction in the future, but the poorer mass resolution cannot be recovered and a big effect is not expected.

Table 2.8. Performance in the six categories for $M_H = 120\,GeV/c^2$.

Category	Signal%	LLR %
0	27.8	48.0
1	16.1	24.8
2	21.7	11.9
3	16.6	9.7
4	9.0	4.1
5	8.8	1.5

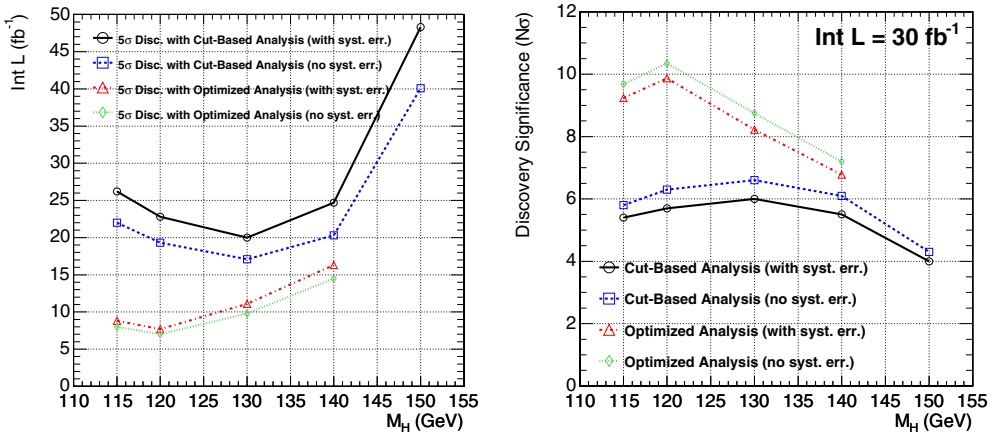

Figure 2.10. Integrated luminosity needed for a 5σ discovery (left) and discovery sensitivity with an integrated luminosity of $30\,fb^{-1}$ (right) with the optimised analysis. The results from the cut-based analysis in 12 categories are also shown for comparison.

2.1.5.7. Results of the optimised analysis. The same estimates of systematic error are used to obtain the results in the optimised analysis as are used in the cut-based analysis. Most of the development and studies have been made for a Higgs mass of $120\,GeV/c^2$. For this mass, a 5σ discovery can be made with about $7\,fb^{-1}$ luminosity. A 1% background normalisation uncertainty corresponds to an increase of the luminosity needed for a 5σ discovery from $7\,fb^{-1}$ to $7.7\,fb^{-1}$.

There is a great deal of uncertainty in this benchmark estimate of luminosity due to our poor understanding of the backgrounds we will contend with when the LHC starts running, however, this is not considered here as a systematic error on a discovery since, it is proposed to measure the background from the data. Figure 2.10 shows the luminosity needed for a 5σ discovery and the discovery sensitivity with an integrated luminosity of $30\,fb^{-1}$ for several Higgs masses, both for the fully optimised analysis and for the cut-based analysis using 12 categories described in Section 2.1.4.4. It seems possible to discover, or at least have strong evidence for a low mass Higgs in the first good year of running.

2.1.6. Measurement of the Higgs boson mass

If the Higgs boson will be discovered in the $H \to \gamma\gamma$ channel then we will be able to measure its mass. We have studied the mass measurements with the cut based analysis with two different methods:

Table 2.9. Expected statistical errors on the Higgs boson mass measurement for 30 fb^{-1}.

M_H	115 GeV/c^2	120 GeV/c^2	130 GeV/c^2	140 GeV/c^2	150 GeV/c^2
All events	184 MeV/c^2	184 MeV/c^2	201 MeV/c^2	222 MeV/c^2	298 MeV/c^2
	0.16%	0.15%	0.15%	0.16%	0.20%
12	127 MeV/c^2	139 MeV/c^2	129 MeV/c^2	156 MeV/c^2	204 MeV/c^2
categories	0.11%	0.12%	0.10%	0.11%	0.14%

- measurement from the Δ Log(likelihood) using all events;
- measurement from the Δ Log(likelihood) using the cut-based analysis split in 12 categories.

The expected statistical errors are shown in Table 2.9 for an integrated luminosity of 30 fb^{-1}. The statistical errors simply scale with $1/\sqrt{\text{Int L}}$. The errors are slightly asymmetric, due to the tail of the reconstructed Higgs mass distribution at lower masses, the positive error being approximately 10% smaller than the negative. The table shows the average between the two.

As we can see the statistical error will be 0.1 to 0.2% already with 30 fb^{-1}, when the significance of the discovery would be 5 to 6 σ with the cut based analysis. Of course, this measurement will be affected by the uncertainty of the absolute scale of the photon energy measurement that will be derived for example by the measurement of the Z mass in the radiative Z decays $Z \to \mu\mu\gamma$.

2.1.7. Summary

A standard cut-based analysis can discover the Higgs boson with 5σ significance between the LEP lower limit and 140 GeV/c^2 with less than 30 fb^{-1} of integrated luminosity. Approximately 5 fb^{-1} are needed to exclude its existence in the same mass range.

It has been shown that the $H \to \gamma\gamma$ channel can be used to discover a low mass Higgs with an integrated luminosity not too different from that needed for higher mass Higgs, 7.7 fb^{-1} at 120 GeV/c^2 with an analysis using an event by event estimation of the s/b ratio. Because of the excellent mass resolution expected in the diphoton channel, the background rate and characteristics from the data can be determined from diphoton events at masses away from the Higgs mass hypothesis.

An inclusive analysis has been presented. In future the various signal channels will be identified by looking for additional jets, leptons, or missing energy. This will clearly improve the sensitivity of the analysis.

2.2. Benchmark Channel: $H \to ZZ^{(*)} \to 4$ electrons

One of the most promising road towards a discovery at the LHC of the Higgs boson postulated in the SM is via single production followed by a cascade decay into charged leptons, $H \to ZZ^{(*)} \to l^+l^-l^+l^-$.

The single Higgs boson production benefits from a high cross-section, with values of about 40×10^3 fb at $m_H = 130$ GeV/c^2 and decreasing monotonically to about 10×10^3 fb around $m_H = 300$ GeV/c^2. The production cross-section is dominated ($\gtrsim 80\%$) over this mass range by gluon-gluon fusion processes via triangular loops involving heavy quark (mostly the top quark) flavours. The branching ratio for the $H \to ZZ^{(*)}$ decay in the SM is sizeable for any m_H value above 130 GeV/c^2. It remains above 2% for $m_H \leqslant 2 \times M_W$ with a peak above 8% around $m_H \simeq 150$ GeV/c^2, and rises to values of 20 to 30% for $m_H \geqslant 2 \times m_Z$. The

Z bosons have a 10% probability to yield a pair of charged leptons. Thus, the decay chain $H \to ZZ^{(*)} \to l^+l^-l^+l^-$ (in short $H \to 4l$) offers a possibly significant and very clean and simple multi-lepton final state signature for the SM Higgs boson at the LHC. An example of an event candidate in the CMS detector for the Higgs boson decay channel $H \to ZZ^* \to 4e$ is shown in colour plate CP2.

Ultimately, the channel can provide a precision determination of the Higgs boson mass and production cross-section. The anti-correlation of the Z spin projections in the $H \to ZZ$ decay and the polarisation of each Z boson can be used to constrain, and eventually determine, the spin and CP quantum numbers of the Higgs resonance. Furthermore, the $ZZ^{(*)}$ and $WW^{(*)}$ decay modes are related via $SU(2)$ and the combination of channels could allow for cancellation of some systematic uncertainties in a determination of the Higgs coupling. But first and foremost is the necessity to be best prepared for a discovery at the LHC.

In this section, the discovery potential of the CMS experiment for the SM Higgs boson is discussed in the mass range of $120 \leqslant m_H \leqslant 300\,GeV/c^2$, focusing on the $4e$ channel. The analysis [37] relies on a detailed simulation of the detector response in the experimental conditions of the first years of low luminosity LHC running. The signal and background Monte Carlo datasets used for this prospective are described in Section 2.2.1. The detailed High Level Trigger (HLT) and reconstruction algorithms used at each step of this analysis have been presented in [7]. Basic, and in part compulsory, triggering and pre-selection steps for data reduction are described in Section 2.2.2. Simple observables from the electron reconstruction are used to characterise the event signature for this pre-selection step. The final event selection relies on more involved requirements for primary electrons coupled with basic event kinematics and is presented in Section 2.2.3. The selection is optimised to preserve a best signal detection efficiency and highest significance for a discovery. Emphasis is put on realistic strategies for the control of experimental errors and the estimation of systematic uncertainties on physics background rates. These are described in Section 2.2.4. Results on the expected discovery reach of the SM Higgs boson in CMS in the $H \to 4e$ channel and for the measurement of its mass, width and cross-section are finally presented in Section 2.2.5.

2.2.1. Datasets for signal and background processes

Monte Carlo data samples for the signal from single SM Higgs boson production as well as for SM background from $ZZ^{(*)}$ pair production, $t\bar{t}$ pair production and $Zb\bar{b}$ associated production are used. The signal and background processes are generated for pp collisions at the LHC at a centre-of-mass energy $\sqrt{pp} = 14\,TeV$, with pile-up conditions from multiple collisions as expected in a collider machine configuration providing an instantaneous luminosity of $2 \times 10^{33}\,cm^{-2}s^{-1}$ (of $\mathcal{O}(10)\,fb^{-1}$/year). All cross-sections are normalised within acceptance to Next to Leading Order (NLO) calculations. The event generators are interfaced with PHOTOS [38, 39] for the simulation of QED final state radiations. The non-perturbative parton density functions (PDFs) in the proton are taken to be the CTEQ6 distributions [12].

The Higgs boson is produced via either gluon fusion and weak boson fusion processes. The $4e$ signal samples are generated at various m_H with PYTHIA [24]. The Higgs boson is forced to decay into a Z boson pair. The Z bosons are subsequently forced to undergo a decay in electron-positron pair. The signal is normalised to the value of total cross-section at NLO calculated including all Higgs boson production processes via HIGLU [40], with branching ratios $BR(H \to ZZ^{(*)})$ calculated via HDECAY [41].

In the $4e$ channel (and similarly for the 4μ channel), an additional enhancement of the signal is considered which is due to the constructive final state interference between like-sign electrons originating from different $Z^{(*)}$ bosons [42]. This enhancement has been

Table 2.10. Total cross-sections at NLO (pb), cross-section in the $4e$ channel within acceptance (fb), and number of accepted events in data samples available for analysis.

m_{H} (GeV/c^2)	σ_{NLO} (pb)	$\sigma_{NLO} \times BR \times Acc.$ (fb)	$N_{simul.}$
115	47.73	0.27	10000
120	44.30	0.48	10000
130	38.44	1.11	10000
140	33.69	1.78	10000
150	29.81	1.94	10000
160	26.56	0.92	10000
170	23.89	0.43	10000
180	21.59	0.98	10000
190	19.67	3.58	10000
200	17.96	3.94	10000
250	12.37	3.07	10000
300	9.58	2.60	10000
$ZZ^{(*)}$	29.0	20.2	150 000
$Zb\bar{b}$	276.3	120.4	87 000
$t\bar{t}$	840	194.0	500 000

re-evaluated with CompHEP [43] and amounts to a factor 1.130 ± 0.006 at $m_{\mathrm{H}} = 115\,\mathrm{GeV/c^2}$, slowly decreasing to a negligible value when approaching $m_{\mathrm{H}} \approx 2m_{\mathrm{Z}}$.

The $ZZ^{(*)}$ SM background continuum is generated using PYTHIA [24]. This includes only the t-channel contribution with $q\bar{q}$ in the initial state. The missing s-channel might contribute up to 10% for low Higgs boson masses and can be neglected for higher masses. The differential cross-section is re-weighted using m_{4e} dependent NLO K-factors obtained with MCFM 4.1, with an average K-factor of $\langle K_{NLO} \rangle = 1.35$. Both Z bosons are constrained within the mass range 5–150 GeV/c^2 and are forced to decay into charged lepton pairs, with the τ leptons subsequently forced to undergo leptonic decays via $\tau \to \mu\nu$ or $\tau \to e\nu$. The missing gg contribution is estimated to be of order 20% at LO [42], with $\pm 8\%$ uncertainties and with unknown NLO K-factors. Recent calculations with TopReX [44] of the gluon fusion production process of two real Z confirm the above assumptions, and this contribution has been shown to remain stable after kinematic cuts for a $\mathrm{H} \to 4l$ analysis. The cross-section here is simply increased by the mean expected contribution.

The $t\bar{t}$ background sample is also generated with PYTHIA [24], with W bosons and τ leptons forced to leptonic decays, but with b quarks left to decay freely. Both gluon fusion and quark annihilation initial states are simulated and the cross-section is normalised to the NLO value of $840 \pm 5\%(\mathrm{scale}) \pm 3\%(\mathrm{PDF})$ pb [45].

The $Zb\bar{b}$ background is generated using all lowest order $gg \to e^+e^-b\bar{b}$ and $qq' \to e^+e^-b\bar{b}$ diagrams (excluding diagrams involving the SM Higgs boson) calculated with CompHEP [43] and interfaced with PYTHIA [24] for showering and hadronisation. All possible combinations of quarks are considered in the initial state. The total LO cross-section for $m_{ee} > 5\,\mathrm{GeV/c^2}$ is 115 pb of which about 89% originates from gg processes, 7.7% involve u-like quarks and 3.2% involve d-like quarks in the initial state. The hadronisation and decay of the b quarks are left free. A NLO K-factor of 2.4 ± 0.3 is applied. Signal and background events are filtered at generator level for further analysis if satisfying the following acceptance requirements: $\geqslant 2e^+$ and $\geqslant 2e^-$ with $p_{\mathrm{T}}^e > 5\,\mathrm{GeV/c}$ in $|\eta| < 2.7$. In addition for the $Zb\bar{b}$ background, at least two e^+e^- pairs with invariant mass in the range 5–400 GeV/c^2 are required. In Table 2.10 cross-sections at NLO and after pre-selection, as well as number of events in data samples available for analysis after pre-selection are given.

Detailed simulation of the CMS detector is performed using the official CMS simulation OSCAR. Reconstruction of physics objects is performed in ORCA.

2.2.2. Data reduction

The events of interest for the Higgs boson search in the $H \to 4e$ channel must satisfy a minimal set of requirements.

A first and compulsory condition for the events is to satisfy the CMS Level 1 (hardware) trigger conditions and the filtering of the (software) HLT. This triggering step is described in Section 2.2.2.1. The basic electron triggers are expected to be saturated by SM processes such as the single Z and W production. Further filtering is obtained with a minimal set of additional electron requirements as described in Section 2.2.2.2.

The pre-selection must preserve the signal acceptance, and especially the electron reconstruction efficiency, until later stages where the analysis can best profit from more involved algorithms applied to reduced event samples.

2.2.2.1. Triggering. The events must have satisfied the *single e*, *double e* or *double relaxed e* requirements at L1/HLT level. The *single e* trigger requires one isolated (charged) "electromagnetic" object with a threshold set at a reconstructed transverse energy in the electromagnetic calorimeter (ECAL) of $E_T = 26\,\text{GeV}$. The *double e* trigger requires two isolated (charged) "electromagnetic" objects, each above a threshold of $E_T = 14.5\,\text{GeV}$. In contrast, the *double relaxed e* trigger does not imposed isolation for the (charged) "electromagnetic" objects and the increased rate is compensated by a higher threshold of $E_T = 21.8\,\text{GeV}$.

The trigger efficiency for the Higgs boson signal, normalised to the cross-section within acceptance as defined in Section 2.2.1, is above 95% for masses $m_H > 130\,\text{GeV/c}^2$.

2.2.2.2. Pre-selection of four electron candidates. Following the Level-1 and HLT filtering steps, the event candidates must further satisfy basic electron pre-selection requirements. These requirements are designed to reduce possible background sources involving "fake" electron contamination from QCD jets.

For Higgs bosons with a mass m_H below $300\,\text{GeV/c}^2$, the $4e$ final state always involves at least one (or few) low p_T^e electron(s). In the range of m_H values below the Z pair production threshold, where the Z and Z^* bosons themselves receive in general only small transverse momentum, the mean p_T^e of the softest electron falls in a range where a full combination of tracking and calorimetry information becomes important. The p_T^e spectra for signal events at $m_H = 150\,\text{GeV/c}^2$ is shown in Fig. 2.11a. The softest electron, which generally couples to the off-shell $Z^{(*)}$, has a most probable p_T^e value below $10\,\text{GeV/c}$ for masses $m_H \lesssim 140\,\text{GeV/c}^2$. Hence, an excellent electron reconstruction is essential down to very low p_T^e values, well below the range of $p_T^e \simeq 40$–$45\,\text{GeV/c}$ for which the reconstruction will be best constrained in CMS via measurements with SM single Z and single W production. The control of systematic uncertainties from experimental data is a major issue for such low p_T^e electrons and this will be discussed in detail in Section 2.2.4.

This analysis makes use of the elaborate reconstruction procedures which have been introduced very recently in CMS and have been described in detail in Ref. [46]. The electron identification and momentum measurements are somewhat distorted by the amount of tracker material which is distributed in front of the ECAL, and by the presence of a strong magnetic field aligned with the collider beam z axis. The procedures introduced in Ref. [46] provide new useful observables that allow to better deal with these detector effects, combining information from the pixel detector, the silicon strip tracker and the ECAL.

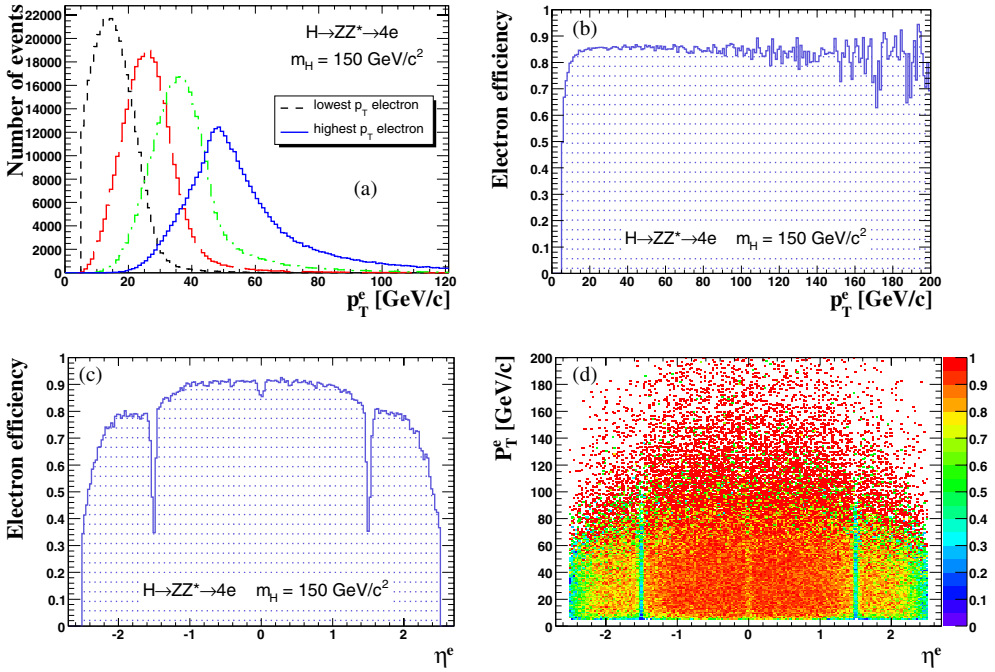

Figure 2.11. Electrons in SM Higgs boson $4e$ decay channel for $m_{\mathrm{H}} = 150\,\mathrm{GeV/c^2}$: (a) transverse momentum of each of the four final state electrons; (b) efficiency at pre-selection as a function of p_{T}^{e}; (c) efficiency at pre-selection as a function of η_e; (d) efficiency in the p_{T}^{e} versus η_e plane.

The pre-selection of the signal event candidates relies on the presence of at least 2 e^+ and 2 e^- candidates within the acceptance $|\eta| < 2.5$ and each with $p_{\mathrm{T}} > 5\,\mathrm{GeV/c}$, verifying the following characteristics:

- $E_{\mathrm{sc}}/p_{\mathrm{in}} < 3$, where E_{sc} is the supercluster energy and p_{in} the track momentum at the interaction vertex;
- $|\Delta\phi_{\mathrm{in}}| = |\phi_{\mathrm{sc}} - \phi_{\mathrm{in}}^{\mathrm{extrap}}| < 0.1$, where ϕ_{sc} is the energy weighted ϕ position of the supercluster and $\phi_{\mathrm{in}}^{\mathrm{extrap}}$ is the ϕ of the track at vertex, extrapolated to the ECAL assuming a perfect helix;
- $|\Delta\eta_{\mathrm{in}}| = |\eta_{\mathrm{sc}} - \eta_{\mathrm{in}}^{\mathrm{extrap}}| < 0.02$, with notations as above;
- $H/E < 0.2$, where H is the energy deposited in the HCAL tower just behind the electromagnetic seed cluster and E the energy of the electromagnetic seed cluster;
- $\sum_{cone} p_{\mathrm{T}}^{\mathrm{tracks}}/p_{\mathrm{T}}^{e} < 0.5$, a loose track isolation requirement, whose calculation will be described in Section 2.2.3.1.

The electron pre-selection efficiency is shown in Fig. 2.11b and Fig. 2.11c as a function of p_{T}^{e} and η^e for the electrons from Higgs boson events at $m_{\mathrm{H}} = 150\,\mathrm{GeV/c^2}$. The efficiency steeply rises and reaches a plateau around 86% for $p_{\mathrm{T}}^{e} \gtrsim 20\,\mathrm{GeV/c}$. The efficiency is above 90% for $|\eta| \lesssim 1.1$ and decreases towards the edge of the tracker acceptance when approaching $|\eta| \simeq 2.5$. The pre-selection efficiency for electrons from the same sample is represented in Fig. 2.11d as a two-dimensional map in the p_{T} versus η plane.

The absolute efficiencies for the Higgs boson signal at different m_{H} values and for the backgrounds are shown in Fig. 2.12a after triggering and the multi-electron pre-selection step. The acceptance for the Higgs boson signal is maintained above 50% in the full relevant mass range.

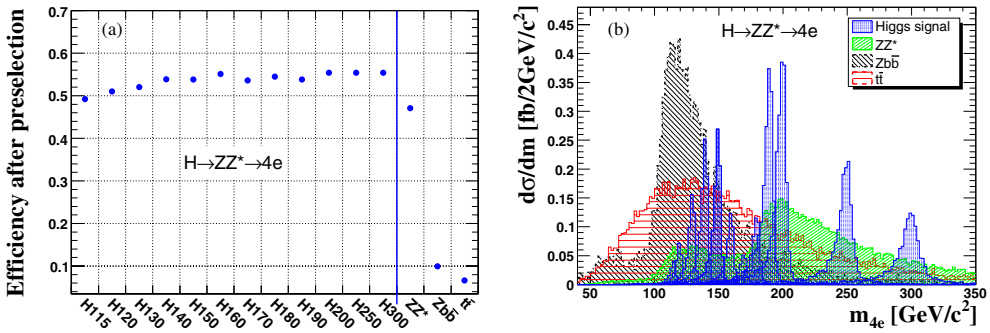

Figure 2.12. Higgs boson signal and dominant background sources after pre-selection step: (a) overall pre-selection efficiency for m_{H} in the range from 115 to 300 GeV/c^2 and the background from ZZ$^{(*)}$ continuum, from Zb$\bar{\mathrm{b}}$ and t$\bar{\mathrm{t}}$; (b) separate signal and background contributions to the spectrum of reconstructed invariant mass m_{4e}.

The signal and background events fulfilling the triggering and pre-selection steps are represented in the reconstructed invariant mass m_{4e} spectrum in Fig. 2.12b. The Higgs boson signal is seen to emerge above the background for masses around 150 GeV/c^2 and above $\simeq 2m_Z$. More background suppression is required elsewhere.

2.2.3. Event selection and kinematic reconstruction

The further steps of the event selection rely on a more detailed characterisation of the electron candidates and simple kinematic expectations. The electrons from the Higgs boson, in contrast to at least one e^+e^- pair from the t$\bar{\mathrm{t}}$ and Zb$\bar{\mathrm{b}}$ backgrounds, are isolated and originate from a common primary vertex. The corresponding analysis requirements are discussed in Section 2.2.3.1. Profiting from the expectation of a narrow resonance in the m_{4e} spectrum, and of the likely presence of a real Z boson in the final state, the kinematics and its simple evolution with m_{H} can be further exploited. The electrons of the e^+e^- pair at lowest m_{ee} have on average a much harder p_{T}^e spectrum for the Higgs boson signal than for the $t\bar{t}$ and $t\bar{t}$ backgrounds. Moreover, the combination of the Z and Z$^{(*)}$ mass spectra distinguishes the Higgs boson signal from the ZZ$^{(*)}$ SM background continuum. These kinematic requirements are discussed in Section 2.2.3.2.

2.2.3.1. Isolated primary electrons. A loose vertex constraint is first imposed on the longitudinal impact parameter for the four electron candidates in each event. All electrons should verify $IP_L/\sigma_L < 13$, where σ_L is the error on the longitudinal impact parameter IP_L. The main vertex constraint is imposed on the transverse impact parameter of the electrons to suppress secondary vertices. Secondary electrons appear for instance in semi-leptonic decays in the hadronisation of the b quark jets in $Zb\bar{b}$ and $t\bar{t}$ background events. The sum of the transverse impact parameter significance ($IP_{\mathrm{T}}/\sigma_{\mathrm{T}}$), i.e. the ratio of the transverse impact parameter IP_{T} over its error σ_{T}, is shown in Fig. 2.13a (Fig. 2.13b) for the e^+e^- pair with invariant mass m_{ee} closest (next-to-closest) to the nominal Z boson mass m_{Z}. For both of these background sources, the displaced vertices are most likely to appear in the softest pair of reconstructed electrons. A best rejection power is obtained by imposing $\sum IP_{\mathrm{T}}/\sigma_{\mathrm{T}} < 30$ for the pair with $m_{ee} \simeq m_{\mathrm{Z}}$ and a more stringent cut of $\sum IP_{\mathrm{T}}/\sigma_{\mathrm{T}} < 15$ for the other pair.

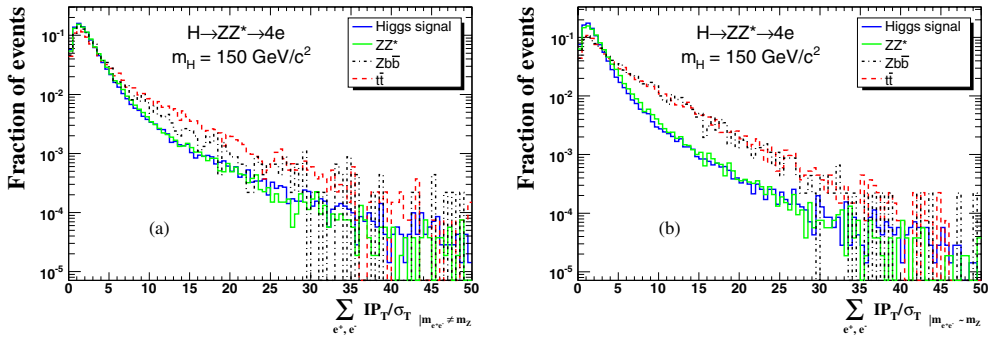

Figure 2.13. Sum of the transverse impact parameter significance ($I P_{\mathrm{T}}/\sigma_{\mathrm{T}}$) of e^+e^- pairs for a Higgs boson at $m_{\mathrm{H}} = 150\,\mathrm{GeV/c^2}$, for the $\mathrm{ZZ}^{(*)}$ continuum, and for $\mathrm{Zb\bar{b}}$ and $\mathrm{t\bar{t}}$: (a) $\sum I P_{\mathrm{T}}/\sigma_{\mathrm{T}}$ from the electrons of the e^+e^- pair with a reconstructed mass m_{ee} best matching the Z boson mass; (b) $\sum I P_{\mathrm{T}}/\sigma_{\mathrm{T}}$ from the second e^+e^- pair.

Another powerful discriminant against secondary electrons in b jets or in general against fake electrons in QCD jets, is provided by isolation requirements. The electrons coupled to the Z or $\mathrm{Z}^{(*)}$ in the $\mathrm{H} \to 4e$ channel are expected to be on average well isolated from hadronic activity. Hadronic activity in single Higgs boson production appears in NLO processes, in the recoil against the Higgs boson. The Higgs boson itself generally receives a significant longitudinal boost in the laboratory reference frame but, as a scalar, decays uniformly in its centre-of-mass reference frame. In contrast, the electrons in the b jets from $\mathrm{t\bar{t}}$ or $\mathrm{Zb\bar{b}}$ are accompanied by significant hadronic activity.

Two partly complementary observables can be best used for the isolation of low p_{T}^e electrons. These rely either on measurements of primary tracks or on the energy flow in the hadronic calorimeter (HCAL). Both observables are insensitive to the eventual electron-induced electromagnetic showering in the tracker material. For the "track isolation", an isolation cone of size $\Delta R = \sqrt{\Delta\eta^2 + \Delta\phi^2} = 0.2$ is defined around the electron direction, and tracks with $p_{\mathrm{T}} > 1.5\,\mathrm{GeV/c}$ originating from the same primary vertex within $|\Delta I P_L| < 0.1$ cm are considered. To avoid suppressing signal events, tracks attached to an electron candidate of opposite charge, and giving $m_{e^+e^-} > 10\,\mathrm{GeV/c^2}$, are discarded. All the 4 electrons from the Higgs boson candidate events must satisfy $\sum_{cone} p_{\mathrm{T}}^{\mathrm{tracks}}/p_{\mathrm{T}}^e < 0.1$. Distributions of this track isolation observable are shown in Fig. 2.14a. For the "hadronic isolation", all HCAL towers in an isolation cone size as above, and contributing with $E_{\mathrm{T}} > 0.5\,\mathrm{GeV}$ are considered in the ratio $\sum_{cone} E_{\mathrm{T}}^{HCAL}/p_{\mathrm{T}}^e$. This ratio is required to be below 0.05 for at least three electrons. The cut is relaxed to 0.2 for the fourth electron. Distributions of this hadronic isolation observable are shown in Fig. 2.14b.

Further electron identification requirements must be imposed to suppress the possible background, involving "fake" electrons, from Drell–Yan processes at NLO where a $\mathrm{Z}^{(*)}$ recoils against jet(s). Different electron identification cuts are used depending on the distinct classes of track-supercluster electron patterns [46] in order to preserve the electron detection efficiency at all η^e. More details can be found in Ref. [37]. This tightening of the electron identification entails an absolute efficiency loss for the Higgs boson signal below 5%.

2.2.3.2. Kinematics. The cascade $\mathrm{H} \to \mathrm{ZZ}^{(*)} \to 4e$ for a Higgs boson, mostly produced at small transverse momentum, leads to very distinctly ordered p_{T}^e spectra for the four final state electrons. Moreover, the p_{T}^e spectra of the softest electrons for the Higgs boson signal is on average harder than the one expected from secondary electrons from the $\mathrm{Zb\bar{b}}$ or $\mathrm{t\bar{t}}$ backgrounds. Thus, it is advantageous to profit from the knowledge of the expected p_{T}^e

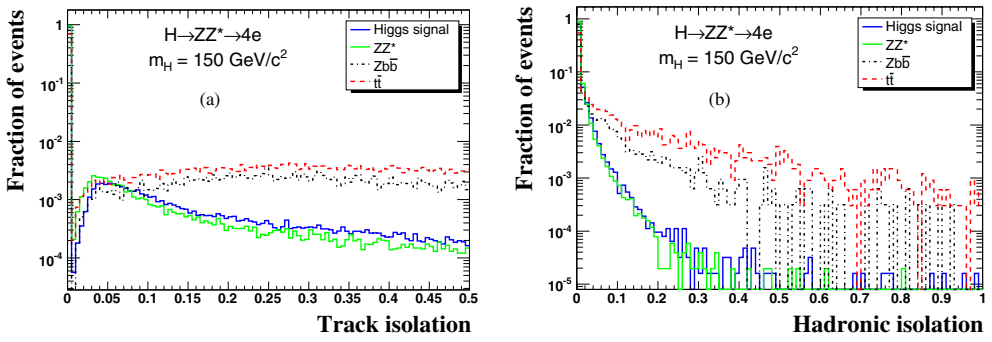

Figure 2.14. Electron isolation observables for the signal at $m_{\mathrm{H}} = 150\,\mathrm{GeV/c^2}$ and the SM backgrounds: (a) track isolation, $\sum_{cone} p_{\mathrm{T}}^{\mathrm{tracks}}/p_{\mathrm{T}}^{e}$; (b) hadronic isolation, $\sum_{cone} E_{\mathrm{T}}^{HCAL}/p_{\mathrm{T}}^{e}$, for the second least isolated electrons.

Table 2.11. Electron p_{T} cuts, from the lowest to the highest p_{T} electron and reconstructed Z_1 and Z_2 invariant mass cuts.

m_{H}	p_{T}^{1}	p_{T}^{2}	p_{T}^{3}	p_{T}^{4}	$m_{\mathrm{Z}_1}^{min}$	$m_{\mathrm{Z}_1}^{max}$	$m_{\mathrm{Z}_2}^{min}$	$m_{\mathrm{Z}_2}^{max}$
($\mathrm{GeV/c^2}$)		($\mathrm{GeV/c}$				($\mathrm{GeV/c^2}$)		
115	7	10	10	15	51	101	10	50
120	7	12	15	15	51	101	10	50
130	7	12	15	15	61	101	10	60
140	7	12	15	15	71	101	10	65
150	7	12	15	15	71	101	15	65
160	7	15	15	15	71	101	15	70
170	7	15	15	20	81	101	20	80
180	7	15	15	20	81	101	30	90
190	7	15	20	30	81	101	40	100
200	7	15	25	30	81	101	40	110
250	7	20	40	50	51	131	20	200
300	7	30	40	60	51	131	15	300

distributions for the Higgs boson signal. A best set of p_{T}^{e} cuts as a function of m_{H} is given in Table 2.11.

The cut on the softest electron is maintained to a lowest value for simplicity and to preserve the signal efficiency at low m_{H}. Otherwise the p_{T}^{e} cuts are seen to slowly evolve for as long as $m_{\mathrm{H}} < 2m_{\mathrm{Z}}$ and then rise faster above the Z pair production threshold. The p_{T}^{e} cuts lead for example [37] to a reduction by a factor of 5 to 10 of the $\mathrm{Zb\bar{b}}$ background, and a factor of 3 to 5 of the $\mathrm{t\bar{t}}$ background for $m_{4e} < 2m_{\mathrm{Z}}$. Both backgrounds are also heavily suppressed above $2m_{\mathrm{Z}}$.

Labelling Z_1 the boson reconstructed with an m_{ee} closest to the nominal Z mass and Z_2 the one reconstructed from the second e^+e^- pair, one expects for $m_{4e} < 2m_{\mathrm{Z}}$ in the case of the Higgs boson signal that $m_{4e} \simeq m_{\mathrm{Z}_1} + m_{\mathrm{Z}_2}$ with most often the presence of a Z boson on its mass shell, $m_{\mathrm{Z}_1} \simeq m_{\mathrm{Z}}$. The Z boson masses saturate the phase space and are dominantly produced with small velocity in the Higgs boson rest frame. The requirement of one real Z boson suppresses further the $\mathrm{t\bar{t}}$ backgrounds for low m_{4e}. The cut on Z_2 is powerful against the $\mathrm{ZZ}^{(*)}$ continuum and further suppresses the $\mathrm{Zb\bar{b}}$ and $\mathrm{t\bar{t}}$ backgrounds. A set of optimal Z_1 and Z_2 cuts is given in Table 2.11 as a function of m_{H}. The cuts lead for example [37]

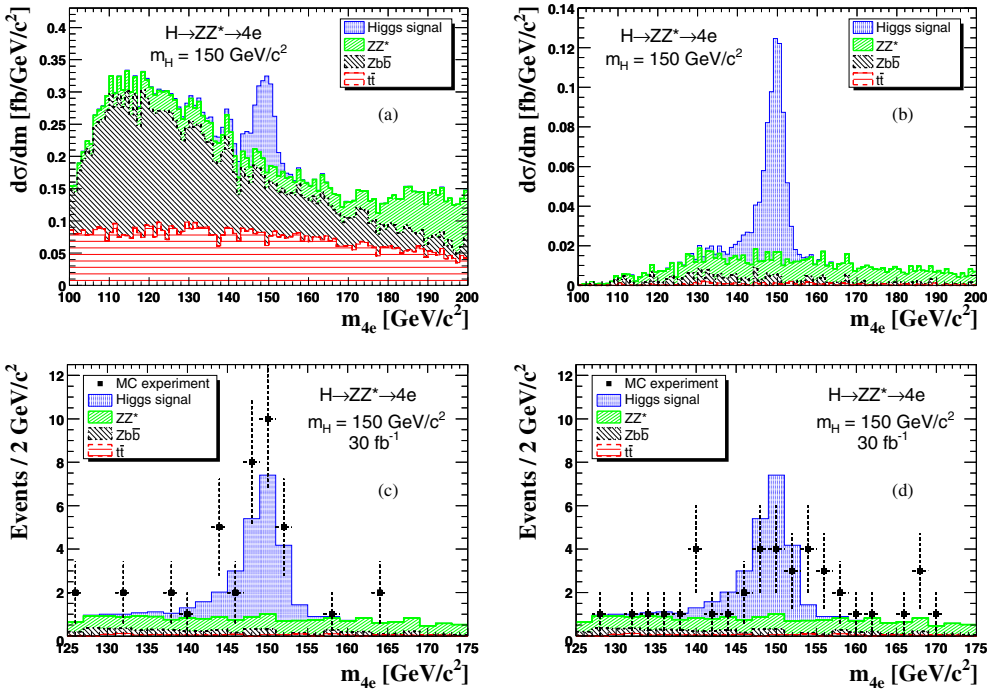

Figure 2.15. Distributions of the reconstructed invariant mass m_{4e} for the SM Higgs bosons signal at $m_{\mathrm{H}} = 150\,\mathrm{GeV/c^2}$ and for the SM backgrounds after (a) pre-selection step and (b) after all cuts. The number of events are normalised in cross-section. Single Monte Carlo experiments corresponding to an integrated luminosity of $30\,\mathrm{fb}^{-1}$ for (c) a favourable case and (d) a less favourable case.

for $m_{4e} \simeq 150\,\mathrm{GeV/c^2}$ to a reduction of the $\mathrm{ZZ}^{(*)}$ continuum by a factor of about 6.5 and a reduction of the $\mathrm{t\bar{t}}$ background by a factor of about 2.5.

Figure 2.15a shows as an illustration the expected m_{4e} invariant mass distributions for the signal at $m_{\mathrm{H}} = 150\,\mathrm{GeV/c^2}$ and for backgrounds after triggering and pre-selection. The further background suppression from the isolated primary electron requirement, the p_{T}^{e} and Z mass cuts is seen by comparison in Fig. 2.15b. The global selection efficiency (normalised to the acceptance defined at the generation level) is given in Table 2.12 for the signal and backgrounds. Figures 2.15c and 2.15d show for illustration the possible outcome of two random Monte Carlo experiments corresponding to favourable and less favourable fluctuations of the Higgs boson signal for an integrated luminosity of $30\,\mathrm{fb}^{-1}$. The Poissonian probability to have equal or more favourable (respectively equal or less favourable) fluctuations is of about 5% for the example cases shown.

2.2.4. Systematics

In this section the systematic errors are discussed in the context of a discovery via a simple event counting method. The "theoretical" and "experimental" sources of errors are distinguished. The theoretical uncertainties concern the estimation of the background rates within the cuts defining the acceptance of the Higgs boson signal and are discussed in Section 2.2.4.1. The experimental uncertainties take into account the limited knowledge of

Table 2.12. Summary of selection efficiencies normalised to the generation pre-selection efficiency.

m_H	115	120	130	140	150	160	170	180	190	200	250	300
						(GeV/c^2)						
Signal	24.3	26.0	31.2	35.2	36.0	37.4	38.0	39.9	40.9	42.5	41.2	38.6
$ZZ^{(*)}$	5.24	4.94	5.68	5.95	5.14	5.23	6.87	17.8	25.1	26.2	22.3	13.9
$Zb\bar{b}$	0.22	0.16	0.17	0.17	0.16	0.10	0.097	0.068	0.037	0.031	0.013	0.001
$t\bar{t}$	0.054	0.044	0.043	0.033	0.032	0.022	0.021	0.011	0.008	0.008	0.013	0.006

the detector responses and efficiencies, and of the corresponding Monte Carlo modelling. These are discussed in Section 2.2.4.2. A comparison of different methods for the control of background systematics is presented in Section 2.2.4.3.

2.2.4.1. Theoretical errors. The theoretical uncertainty on the number of background events in the signal region from PDFs and QCD scales variations has been estimated by the MCFM program [47]. CTEQ6M PDF are used and 20 eigenvector parameters have been varied by $\pm 1\sigma$. Both QCD normalisation and factorisation scales have been varied independently up and down for a factor two from their nominal values of $2m_Z$. The resulting uncertainties from PDF and QCD scale are of the order of 6% for direct estimation of ZZ background, from 2 to 8% for normalisation to single $Z \to 2e$, and from 0.5 to 4% for the normalisation to sidebands (discussed further in Section 2.2.4.3). The gluon fusion cross-section uncertainties in the ZZ background of 8% is also considered as a part of theoretical uncertainties.

The uncertainty on the normalisation of the measurements to the pp luminosity of the LHC collider is estimated to be of the order of 3% for an integrated luminosity above 10 fb^{-1}.

2.2.4.2. Experimental errors. The main remaining sources of experimental systematics expected in the CMS experiment after having collected of $\mathcal{O}(10)$ fb^{-1}, and relevant for the $H \to 4e$ channel, originate from uncertainties on knowledge of the amount of tracker material in front of the ECAL, from the precision of the (pattern dependent) energy calibration of electron objects, and from the control of electron efficiencies. The strategy adopted consists of relying on experimental data, and in particular on single Z and W production, to minimise these systematic errors. The electrons from $W \to e\nu$ and $Z \to ee$ decays are used to control the energy measurements and reconstruction efficiencies.

A change of the integral amount of tracker material traversed by electrons before reaching the ECAL is susceptible of affecting the electron selection and identification efficiencies, as well as energy measurement scales and resolution. The uncertainty on the material budget will limit the precision of the acceptance calculations, when using the Monte Carlo model to extrapolate away from the kinematic domain best constrained via single Z and W measurements.

There are many observables that are directly or indirectly sensitive to the amount of tracker material, and that have been used in collider experiments. Examples are the distribution of converted photon vertices, or the shape of the E/p comparing tracker momentum measurement p to the energy E measured in the calorimeter in finite cluster volume, or a comparison of data and Monte Carlo for the Z mass resolution, etc. A new technique is used which is based on the electron GSF tracking introduced recently in Ref. [46]. The difference between the momentum magnitude at vertex and at the last hit, $p_{in} - p_{out}$, is a measure of the integral amount of bremsstrahlung. The mean fraction f_{brem} of the energy radiated along the complete trajectory is roughly proportional to the integral amount

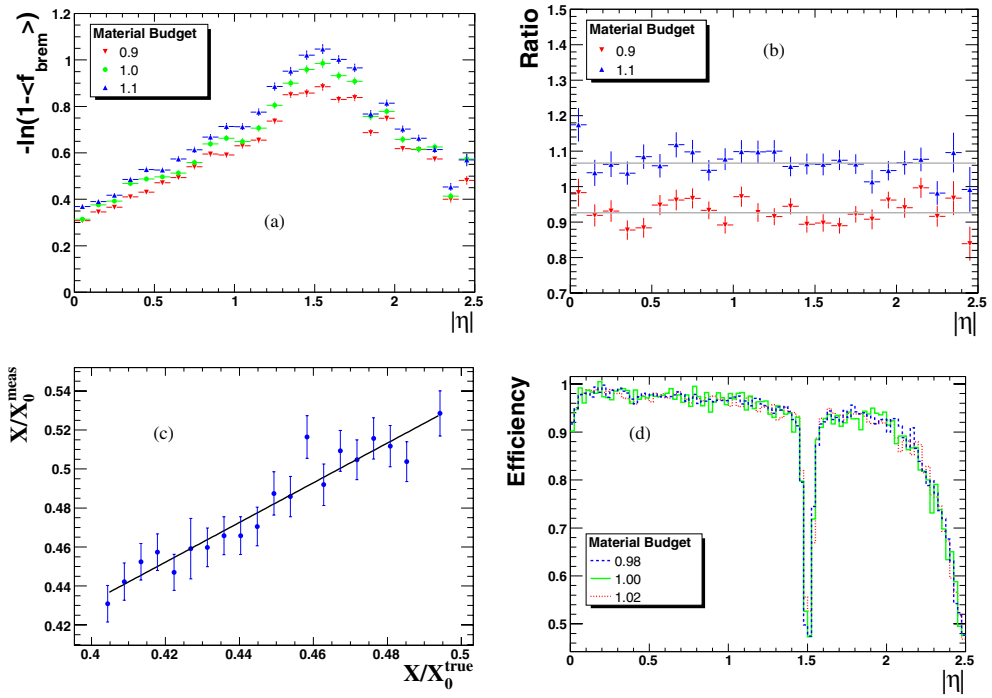

Figure 2.16. Sensitivity to variations of the tracker material budget from electron measurements based on GSF tracks: (a) measured amount of material as a function of $|\eta|$ for the nominal tracker configuration and for an integral material budget changed by $\pm 10\%$; (b) ratio of the measured mount of material as a function of $|\eta|$; (c) measured versus true thickness in X_0 of the tracker material; (d) effect of a change of 2% of the material budget on the electron reconstruction efficiency.

of material traversed. Hence, one can relate $f_{\rm brem}$ to the material thickness X/X_0 where X_0 is the characteristic radiation length via the formula $\langle X\rangle/X_0 \simeq -\ln(1-f_{\rm brem})$, where $f_{\rm brem} = (p_{\rm in} - p_{\rm out})/p_{\rm in}$.

The amount of tracker material measured in this way for single electron data is shown in Fig. 2.16a. The results obtained in the configuration corresponding to the nominal tracker material coincide very well with the known material distribution as given in Ref. [7]. Figure 2.16b shows the ratio of the measured material thickness obtained in configurations where the amount of material was changed by $\pm 10\%$, normalised to the measurement results in the nominal case. The ratio is found to be remarkably stable as a function of η, despite the fact that the integral amount of material has a strong η dependence. Thus, single electrons can be used in CMS to tune the Monte Carlo model of the tracker material per η slice. Figure 2.16c shows that in a given η slice the measured material thickness is linearly correlated to a change (at least within a range of $\pm 10\%$) of the true material thickness. Similar results are obtained when considering various restricted range of $p_{\rm T}^e$ within a sample of uniformly distributed electrons in the $p_{\rm T}^e$ range from 5 to 100 GeV/c. With the electron statistics expected from single Z production for an integrated LHC luminosity of $\mathcal{O}(10)$ fb^{-1}, it should be possible to determine the tracker material thickness to a precision better than 2% over the full acceptance in η. Figure 2.16d shows that such a 2% uncertainty on the material budget will have almost no effect on electron reconstruction efficiency.

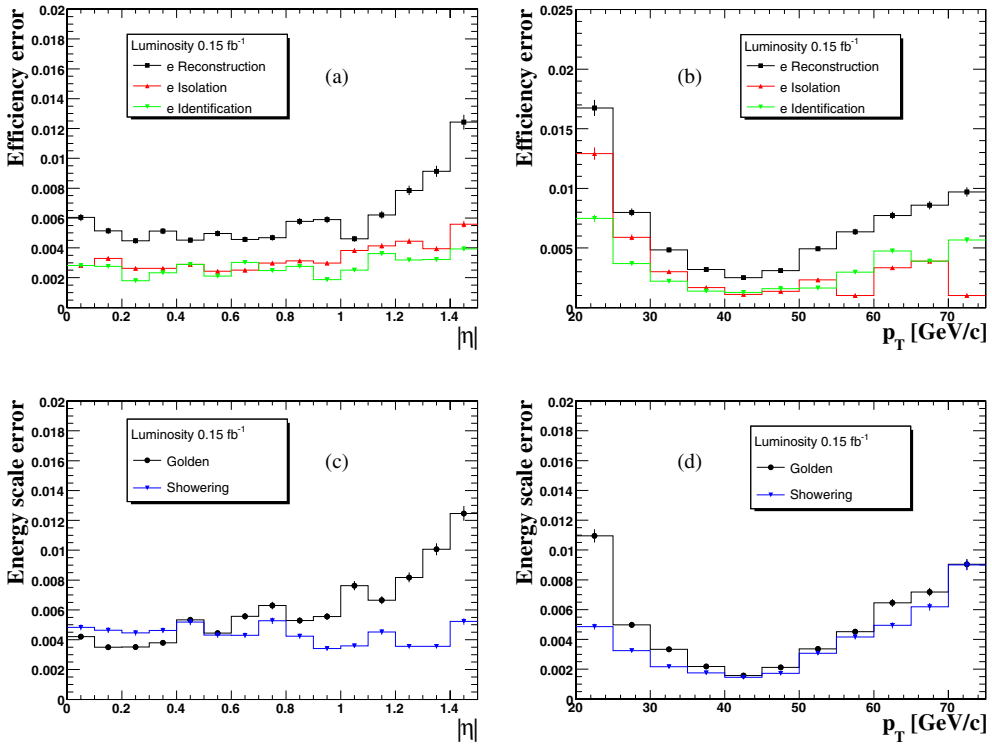

Figure 2.17. Control of experimental uncertainties using SM data; uncertainties on measurements of electron reconstruction, isolation and identification as a function of (a) η and (b) p_{T}; uncertainties on measuring the energy scale for golden and showering electrons as a function of (c) η and (d) p_{T}.

Electron reconstruction efficiencies and energy scales will be controlled by electrons from $\mathrm{W} \to e\nu$ and $\mathrm{Z} \to ee$ decay. Huge cross-sections of these two processes will allow for a significant reduction of reconstruction uncertainties already after few fb^{-1}. Electrons from $\mathrm{Z} \to ee$ are produced centrally with a characteristic Jacobian p_{T} distributions around $45\,\mathrm{GeV/c}$. It is therefore, expected that the best control of experimental systematics is obtained in the central part of the detector and for electrons around the Jacobian peak.

Electron reconstruction uncertainties as a function of η and p_{T} are given in Fig. 2.17a and Fig. 2.17b respectively, for an integrated luminosity of $0.15\,\mathrm{fb}^{-1}$. The expected behaviour of increased uncertainties when moving away from the Jacobian peak or from the central η region can be clearly seen. From the expected reconstruction errors evolution with the luminosity, all reconstruction efficiency uncertainties can be safely absorbed in a single factor of 1% per electron, for integrated luminosities larger than $10\,\mathrm{fb}^{-1}$.

The second important systematic effect is the uncertainty on the energy scale determination. Using single Z production, it has been shown in Ref. [48] that the absolute energy scale for electrons can in principle be controlled with great precision with average uncertainties reaching values below 0.1%. The systematic uncertainty has to be studied as a function of p_{T}^{e} and η^{e} given the different electron spectrum in $\mathrm{H} \to \mathrm{ZZ}^{(*)} \to 4e$ and $\mathrm{Z} \to ee$ decays. The reachable precision depends on the amount of integrated LHC luminosity. In this analysis, the second leg of a Z boson decay, tagged as an electron by imposing stringent

electron identification requirements on the first leg combined with a kinematic constraint to the Z boson mass, is used as a probe to estimate systematics on the energy scale.

Uncertainties versus η and p_T for golden and showering electrons are shown in Fig. 2.17c and Fig. 2.17d, for the integrated luminosity of $0.15\,\text{fb}^{-1}$. With expected evolution of these uncertainties with the luminosity, it is found that an uncertainty in energy scale of 0.5% in the barrel region, and 1% in the endcaps, for integrated luminosities larger than $10\,\text{fb}^{-1}$, can be safely considered.

2.2.4.3. Control of background rates. Following the primary and isolated electron selection and the application of basic kinematic requirements, only the $ZZ^{(*)}$ continuum remains as the dominant or sole background over the full mass range in consideration for the SM Higgs boson search. Thus, the determination of the mean expected number of SM $ZZ^{(*)}$ background events in the signal region, defined e.g. by a simple sliding window in the m_{4e} spectrum, remains as a key issue.

The three main methods for the estimation of $ZZ^{(*)}$ continuum contribution to the background in the signal region are:

- direct simulation of the $ZZ^{(*)} \to 4e$ process,
- normalisation to the $Z \to 2e$ data,
- normalisation to the sidebands.

The first method entirely relies on existing SM constraints and the theoretical knowledge, with uncertainties coming from the PDFs used to describe the colliding protons and from QCD scale variations. It furthermore is reliant on the LHC luminosity uncertainties, and on the Monte Carlo modelling of the acceptance and detector response for the uncertainties arising from electron reconstruction and selection. Otherwise, the method potentially benefits from the fact that the statistical precision on the mean background expectation is only limited by the Monte Carlo statistics, and can therefore be assumed negligible in the context of a prospective for an analysis to be performed in a future CMS experiment.

The second method aims at profiting from the fact that the SM single Z production cross-sections is measured with great precision in an experiment which will have integrated a luminosity of $\mathcal{O}(10)\,\text{fb}^{-1}$ at the LHC. Using the ratio of $ZZ \to 4e$ to $Z \to 2e$ rates allows to profit from a full cancellation of pp luminosity uncertainties, while providing a partial cancellation of PDF and QCD scale variations uncertainties (due to their correlations in a part of the initial state phase space) and a partial cancellation of experimental uncertainties.

In the method of the normalisation from sidebands, the number of background events *inside* the acceptance of the signal region is determined from the number of background events measured *outside* the signal region, by multiplying the latter with the ratio α_{MC} between *inside* and *outside* expectations as determined using Monte Carlo simulation. Using the sidebands one also expects to fully cancel luminosity uncertainties, to reduce PDF and QCD scale variation uncertainties and substantially reduce experimental uncertainties too. Statistical errors with sidebands normalisation come from the statistics of the background rate outside the signal region and can be a limiting factor for the method. By relaxing some of late analysis cuts, such as invariant Z mass, the background events rate outside the signal region increases, reducing therefore statistical errors for this method. The price to pay is an increased background rate in the signal region too and, therefore, some balancing is needed.

Using results from previous sections, both theoretical and experimental uncertainties are evaluated for two methods: normalisation to the $Z \to 2e$ measurements and normalisation to the sidebands. For the normalisation to single $Z \to 2e$ measurements results are shown in Fig. 2.18a. The overall systematic uncertainty with this method is of about 5%. Experimental

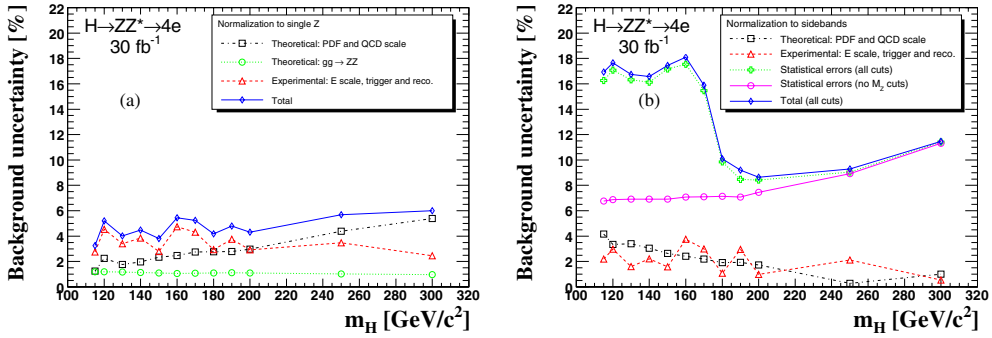

Figure 2.18. Theoretical and experimental uncertainty estimations for both methods for evaluation of background from data: (a) normalisation to the single $Z \to 2e$ measurements and (b) normalisation to the sidebands. Expected statistical errors for sidebands are also shown, for integrated luminosity of 30 fb^{-1}.

Table 2.13. Expected number of Higgs boson signal (N_S) and SM background (N_B) events for an integrated luminosity of 30 fb^{-1}, in the optimised window for the reconstructed invariant mass m_{4e}. The uncertainties (δN_B) are given for systematics from experimental (exp.) and theoretical (theo.) sources, for an analysis where the $ZZ^{(*)}$ continuum has been normalised to the measurement of single Z production.

m_H	115	120	130	140	150	160	170	180	190	200	250	300
							(GeV/c^2)					
N_S	1.52	2.97	8.18	15.80	17.19	8.38	3.76	9.95	34.05	38.20	27.68	21.69
N_B	2.26	1.94	3.71	4.31	3.68	3.10	3.37	6.42	14.62	17.29	13.40	7.63
δN_B												
exp.	0.063	0.089	0.126	0.167	0.105	0.148	0.145	0.187	0.551	0.505	0.466	0.187
theo.	0.039	0.049	0.079	0.098	0.095	0.084	0.100	0.191	0.440	0.549	0.602	0.417

uncertainties are seen to dominate for $m_H \simeq 2m_Z$ while theoretical errors take over above the pair production threshold. Uncertainties for the sidebands normalisation are shown in Fig. 2.18b. Statistical uncertainties scale as the square root of the number of background events outside the signal region and are shown for an integrated luminosity of 30 fb^{-1} and for two analysis scenarios: after all analysis cuts and without cuts on the mass of both Z bosons. A trade-off in the second method is in a somewhat lower nominal significance (for about 8%) while statistical errors decrease by a factor of about 2.5. Full significance calculations with and without systematics and statistical uncertainties are presented in the following section.

2.2.5. $H \to 4e$ Observability, mass and cross-section measurements

2.2.5.1. Discovery reach. A simple counting experiment is used here to quantify the sensitivity of the experiment to the presence of a Higgs boson signal. The expected number of signal (N_S) and background (N_B) events are evaluated in a sliding window whose central position m_{4e} varies between 100 and 320 GeV/c^2. The size of the optimal window increases progressively from 6 GeV/c^2 at $m_{4e} = 115$ GeV/c^2 to 24 GeV/c^2 at $m_{4e} = 300$ GeV/c^2. The Table 2.13 presents for each Higgs boson mass hypothesis the mean expected number of signal and background events, and associated uncertainties.

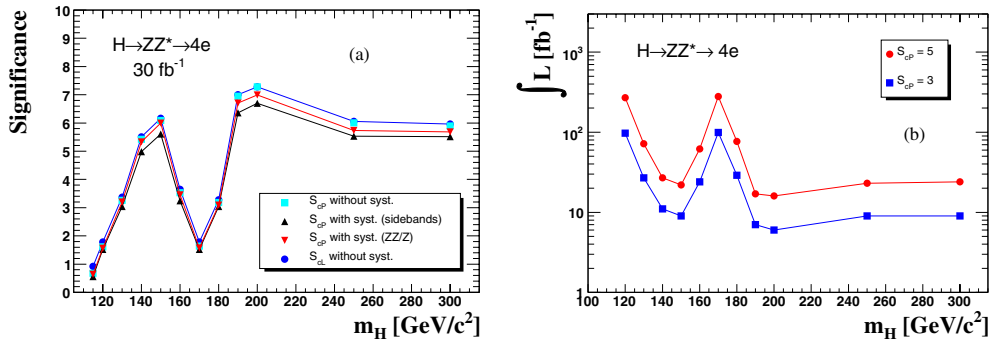

Figure 2.19. (a) Significance S_{cP} for an integrated luminosity of $30\,\mathrm{fb}^{-1}$ as a function of the Higgs boson mass without and with systematics included in both options of $ZZ^{(*)}$ normalisation to the measured sidebands or the measured single Z production cross-section. The significance S_{cL} is also shown. (b) Luminosity needed for a 3σ observation and 5σ discovery with the systematics included using $ZZ^{(*)}$ normalisation to the Z cross-section.

The significance of the $H \to 4e$ signal observation is shown as a function of m_H in Fig. 2.19a as expected for an integrated luminosity of $30\,\mathrm{fb}^{-1}$. The results are given for both the S_{cP} and the S_{cL} significance estimators. The S_{cP} is defined as the probability for a Poisson distribution with mean N_B to observe a number of events equal or greater than $N_S + N_B$, converted in the equivalent number of standard deviations of a Gaussian distribution. The S_{cL} corresponds to the widely used log-likelihood ratio significance [49] and is given for comparison. The effect of including experimental and theoretical systematics, described in section 2.2.4 and listed in Table 2.13, on the significance S_{cP} [50] is also shown, for two different methods of controlling the background uncertainties. A signal observation with a significance above 3 standard deviations is expected in the $H \to 4e$ channel alone for m_H in the range from 130 to $160\,\mathrm{GeV/c^2}$, and above $180\,\mathrm{GeV/c^2}$. The integrated luminosity needed for a 5 standard deviations discovery of the SM Higgs boson in the $H \to 4e$ channel alone is also shown as a function of m_H in Fig. 2.19b. Systematic errors from normalisation to the Z cross-section have been included.

2.2.5.2. Mass, width and cross-section measurements. At an early stage of the Higgs boson search and discovery in the $H \to 4e$ channel, given very low statistics, a robust and simple estimation of m_H can be obtained by a simple mean (or weighted mean) of the m_{4e} values measured for individual events. The events falling in the pre-defined optimal mass window introduced in the above Section 2.2.5.1 and used to establish the signal significance, can be used for such purposes. For higher statistics, a fit of the m_{4e} mass distribution to a signal plus background shape can be used to extract simultaneously the mass and the cross-section $\times$ branching ratio of a Higgs boson signal. Detector effects dominate the Higgs boson mass resolution below the Z pair production threshold and a sensitivity to the Higgs boson intrinsic width is expected only for masses well above $2m_Z$.

The precision on the parameter measurements for the Higgs boson depend on the quality of the reconstructed electrons and can, in general, be improved using event-by-event errors on the electron momentum estimation [46]. Example cases for two different sub-samples of Higgs boson events differing by the pattern of the four reconstructed electrons are presented in Fig. 2.20. Clearly, event candidates built from four *non-showering* electrons in the barrel part of the ECAL, a subset representing only about 1.76% of all signal events, allow for

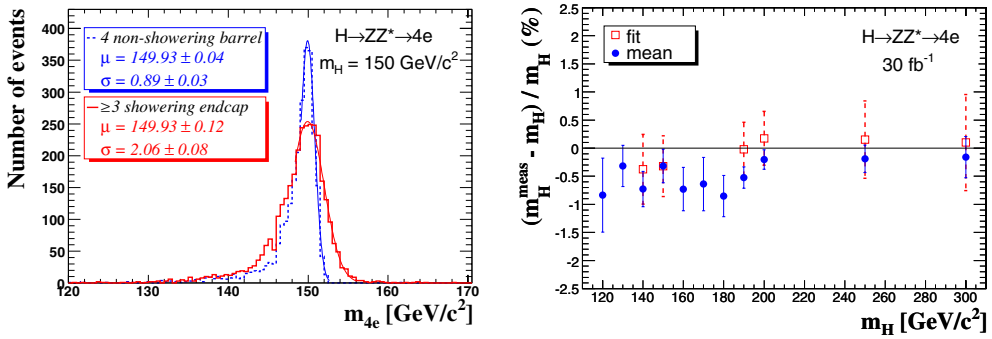

Figure 2.20. Mass measurements: (a) example case for two different event sub-samples differing by the pattern of the four reconstructed electrons; (b) relative errors as a function of the Higgs boson mass using the mean mass and the fitted mass as obtained for an integrated luminosity of 30 fb^{-1}.

a much better m_{H} measurement (smallest errors on average and least dispersion of the mass measurement errors) than candidates built mainly from e.g. *showering* electrons in the endcaps part of the ECAL. About 36.7% of the signal event candidates contain three or more *showering* electrons. A weighted mean of the events of the m_{4e} distribution falling in the signal window has been considered for the estimation of the Higgs boson mass in Ref. [37]. A simple mean can be also used for simplicity.

The reconstructed Higgs boson mass and its error obtained from the mean value for events falling in the expected signal window is presented in Fig. 2.20b. The error is obtained from the dispersion of the mean values obtained from large number of Monte Carlo experiments at an integrated luminosity of 30 fb^{-1}. The results are shown as a function of the Higgs boson mass. The systematic bias on the mass estimate for the low m_{H} cases for this simple mean approach is due to the asymmetric shape of the reconstructed signal and can be modelled. In the mass ranges where the Higgs boson signal significance exceeds 3 standard deviations, the uncertainty on the mass determination is found to be everywhere below 0.4%. It reaches values below 0.2% for $m_{\mathrm{H}} \simeq 200\,\mathrm{GeV/c^2}$. For comparison, results obtained by fitting the m_{4e} distribution are also shown. The fit method requires a significant number of events (typically $\gtrsim \mathcal{O}(10)$) to converge and provide reasonably stable results. The m_{4e} distribution is fitted by a signal plus background shape. The signal contribution is modelled with two Gaussians, describing respectively the core and the low m_{4e} tail of the signal distribution. The tail parameters (fraction, mean and dispersion) are fixed by fitting the "signal only" expectation. The background is modelled using a flat distribution up to about $m_{4e} \approx 2m_{\mathrm{Z}}$ and a linear function (non-zero slope) for higher Higgs boson masses. This has been found to provide a sufficiently good model of the observation in a restricted mass range around the signal region. A likelihood fit is then performed on each Monte Carlo experiments and the reconstructed mass and precision are extracted from the distribution of the fitted values of the peak of the Gaussian core. Where the fit can be performed, Fig. 2.20b shows that an unbiased estimation of m_{H} is obtained within errors.

The fitted number of signal events is used to estimate the production cross-section by correcting for the global acceptance efficiency. The statistical precision on this measurement is here also obtained from the width of the distribution of the fitted parameters in Monte Carlo experiments. An unbiased measurement of the cross-section is obtained over the full mass range considered here, with a precision of the cross-section measurement between

20 and 30%. With such a precision, the influence of the detector systematics (about 5%) and of the uncertainty on the luminosity measurement (less than 3% for 30 fb^{-1}) is marginal. For an integrated luminosity of 60 fb^{-1}, the precision on the cross-section measurement improves to about 15%.

A measurement of the width is possible only for Higgs boson masses above $\gtrsim 2m_{\mathrm{Z}}$ where at the same time the Higgs natural width is becoming large and the detector resolution is improving. A Gaussian width with central values of about 2.3 $\mathrm{GeV/c^2}$ for $m_{\mathrm{H}} = 200\,\mathrm{GeV/c^2}$ and 4.2 $\mathrm{GeV/c^2}$ for $m_{\mathrm{H}} = 300\,\mathrm{GeV/c^2}$ is obtained from the fit, but with a rather large uncertainty of about 50%.

Chapter 3. Physics Studies with Muons

3.1. Benchmark Channel: $H \to ZZ^{(*)} \to 4$ muons

The $H \to Z Z^{(*)} \to 4\,\mu$ process is one of the cleanest channels for discovering the Standard Model Higgs boson at LHC. This section presents the CMS potential for discovering the Higgs boson in this decay mode and measuring its mass, width, and production cross section, in the range of Higgs boson masses from 115 GeV/c^2 to 600 GeV/c^2. Both signal and background event samples are generated at the Leading Order (LO) approximation, and Next to Leading Order (NLO) production cross sections, computed using different methods, are used for their normalisation. To simulate the detector response and reconstruct physics objects, the full CMS detector simulation and reconstruction software was used. A full treatment of the most important theoretical and instrumental systematic uncertainties are presented, together with their effect on the evaluation of the significance of the Higgs boson observation and on the measurement of its parameters. To minimise systematic uncertainties, new methods of reconstructing the most important corrections directly from data were developed.

3.1.1. Physics processes and their simulation

The Higgs boson event samples for 18 Higgs boson mass points and the three main background processes, $t\bar{t}$, $(Z^{(*)}/\gamma^*)b\bar{b}$ and $(Z^{(*)}/\gamma^*)(Z^{(*)}/\gamma^*)$ were simulated using the CMS simulation [8] and reconstruction [10] software. These three backgrounds will be hereafter referred to as $t\bar{t}$, $Zb\bar{b}$ and ZZ, respectively. Details on the generator-level simulation conditions, cross sections and K-factors can be found in [51]. Many other plausible background candidates, $b\bar{b}b\bar{b}$, $b\bar{b}c\bar{c}$, $c\bar{c}c\bar{c}$, single-top, $Zc\bar{c}$, $Wb\bar{b}$, $Wc\bar{c}$, fake and π/K decay muons in QCD, were considered and found to be negligible. An example of an $H \to ZZ \to 4\mu$ event is shown in colour plate CP3.

Only events with at least $2\mu^+$ and $2\mu^-$ in pseudorapidity range $|\eta| < 2.4$ and with $p_T > 3$ GeV/c were retained for further analysis. Muons outside these kinematic limits could not be reconstructed in the CMS detector. Additional cuts were applied on dimuon invariant masses for the Higgs boson samples ($m_Z > 5$ GeV/c^2) and for ZZ and $Zb\bar{b}$ samples ($m\mu^+\mu^- > 5$ GeV/c^2). The first $\mu^+\mu^-$ pair in the ZZ and $Zb\bar{b}$ samples was defined as the one with its invariant mass closest to m_Z, while the second $\mu^+\mu^-$ pair was made out of the two remaining highest p_T muons of opposite charge. These cuts do not bias the Monte Carlo samples since all the analysis cuts, described below, are tighter.

The Higgs boson samples were generated with PYTHIA 6.225 [24] (LO gluon and weak boson fusion, $gg \to H$ and $q\bar{q} \to q\bar{q}H$) interfaced via CMKIN [52]. Events were re-weighted to correspond to the total NLO cross section $\sigma(pp \to H) \cdot BR(H \to ZZ) \cdot BR(Z \to 2\ell)^2$ (Fig. 3.1). The cross section $\sigma(pp \to H)$ and the branching ratio $BR(H \to ZZ)$ were taken from [53]; $BR(Z \to 2\ell) = 0.101$ [54]. Interference of permutations of identical leptons originating from different Z bosons results in an enhancement to the cross section for $H \to ZZ^{(*)} \to 4\ell)$ processes with identical leptons [51], which is about 15% for $m_H = 115$ GeV/c^2 and steadily goes to zero for $m_H = 180$ GeV/c^2. This correction was calculated with COMPHEP.

The $t\bar{t}$ sample was generated with PYTHIA 6.225 (LO $gg \to t\bar{t}$ and $q\bar{q} \to t\bar{t}$). Events were re-weighted to correspond to the total NLO cross section $\sigma(pp \to t\bar{t}) \cdot BR(W \to \ell\nu)^2$. The NLO cross section $\sigma(pp \to t\bar{t}) = 840$ pb was taken from [55] and the branching ratio $BR(W \to \ell\nu) = 0.320$ from [54].

The $Zb\bar{b} \to \mu^+\mu^- b\bar{b}$ sample was generated with the COMPHEP 4.2p1 [43] matrix element generator, interfaced to PYTHIA 6.225 for showering and hadronisation. Included

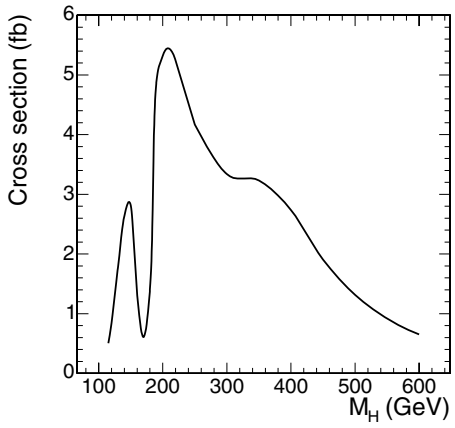

Figure 3.1. Standard Model NLO cross section for the process $(ZZ^{(*)} \to 4\mu$*vs.* Higgs boson mass.

sub-processes were $q\bar{q}/gg \to (Z/\gamma^*)b\bar{b} \to \mu^+\mu^- b\bar{b}$. The corresponding CompHEP LO cross section was found to be 116 pb. To obtain the NLO cross section a NLO K-factor $K_{NLO} = 2.4 \pm 0.3$, computed with MCFM [56], was used.

The $q\bar{q} \to ZZ \to 4\mu$ and $q\bar{q} \to ZZ \to 2\mu 2\tau$ event samples were generated with CompHEP, including both the t- and s-channel diagrams [57]. The CompHEP events were further interfaced to PYTHIA 6.225 for showering and hadronisation. The CompHEP LO cross sections for the two sub-processes were 113 fb and 157 fb. To account for contributions due to all the NLO diagrams and due to the NNLO gluon fusion ($gg \to ZZ$, known to contribute $\sim$ 20% with respect to the LO [42] cross section), events are reweighted with the $m_{4\mu}$-dependent K-factor $K(m_{4\mu}) = K_{NLO}(m_{4\mu}) + 0.2$. The NLO K-factor $K_{NLO}(m_{4\mu})$ was obtained with MCFM. The details on the dynamic differences between NLO and LO are summarised elsewhere [58].

The $m_{4\mu}$ distributions for a Higgs boson signal of $m_H = 140\,\mathrm{GeV/c^2}$ and the main backgrounds are shown in Fig. 3.2 after the pre-selection cuts described above.

3.1.2. Event selection

3.1.2.1. Trigger and offline muon selection. CMS has been designed and optimised to detect and reconstruct muons. These particles provide a very clean signature and thus a very high trigger efficiency, with an average of 98% for the Level-1 Global Muon Trigger [7]. The inclusive muon triggers based on the selection of a single muon with $p_T > 19\,\mathrm{GeV/c}$ or dimuons with $p_T > 7\,\mathrm{GeV/c}$ assures an efficiency of practically 100% for collecting events with four high-p_T muons.

In order to minimise muon reconstruction systematic uncertainties, we select only those reconstructed muons that have transverse momentum $p_T > 7\,\mathrm{GeV/c}$, if they are in the central pseudo-rapidity region ($|\eta| < 1.1$), or with momentum $p > 13/$, GeV/c, if they are in the endcaps ($|\eta| > 1.1$) [59]. These cuts do not affect the number of accepted signal events significantly.

Also, we require that all four possible combinations of the reconstructed dimuon masses be above $12\,\mathrm{GeV/c^2}$, $m_{\mu^+\mu^-} > 12\,\mathrm{GeV/c^2}$. As in the previous case, this cut has a very little effect on the Higgs boson events and is primarily intended to suppress poorly simulated hadron background contributions originating from charmonium and bottomium dimuon decays.

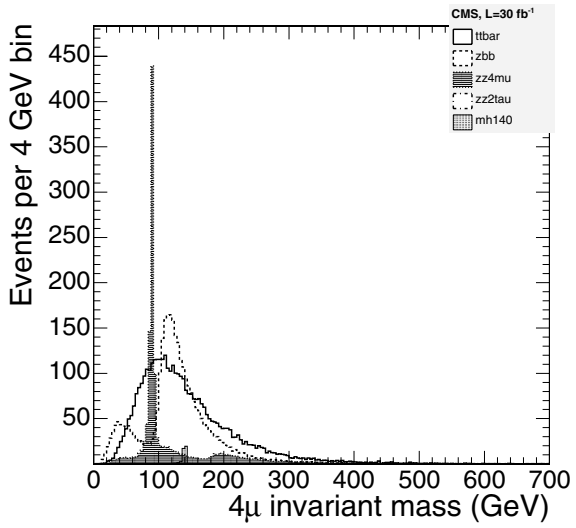

Figure 3.2. Distributions of $m_{4\mu}$ after pre-selection cuts for $t\bar{t}$, Zb$\bar{\text{b}}$, ZZ and a Higgs boson signal of $m_{\text{H}} = 140\,\text{GeV/c}^2$.

3.1.2.2. Discriminating variables. The $\text{H} \to \text{ZZ}^{(*)} \to 4\,\mu$ signal presents a characteristic topology, which consists of two opposite charge muon-pairs in the final state. All four muons are isolated, have a high transverse momentum and point to the same Z-boson mass, depending on the restrictions in the phase space introduced by the Higgs boson mass itself. The four-muon invariant mass peaks at the Higgs boson mass, within the detector resolution. The width of the resonant peak accounts for the natural Higgs boson width and the detector resolution.

In Zb$\bar{\text{b}}$ and $t\bar{t}$ background events, two of the muons come from b-quark decays and are usually found within a jet (i.e., non-isolated), have lower transverse momenta and often exhibit detectable displaced vertices. The isolation is defined as the amount of transverse energy in the calorimeter (calorimeter isolation), or the sum of the transverse momentum of the tracks reconstructed in the tracker (tracker isolation), inside a cone in η-ϕ space with a radius $R \equiv \sqrt{(\Delta\eta)^2 + (\Delta\phi)^2}$ around each muon. Figure 3.3 (left) shows the distribution of the calorimeter isolation variable for the least isolated muon, for two potential Higgs boson signals, $150\,\text{GeV/c}^2$ and $300\,\text{GeV/c}^2$, and for the background. Requiring a maximum isolation in all four muons drastically suppresses $t\bar{t}$ and Zb$\bar{\text{b}}$ contamination.

Further restrictions on the p_{T} spectrum of the 2 lowest p_{T} muons in the event (see Fig. 3.3 (right), for the 2nd lowest p_{T} muon) reduces even more the $t\bar{t}$ and Zb$\bar{\text{b}}$ contamination. In this way, the ZZ background, which presents a topology very similar to that of the signal, becomes the dominant and irreducible background. Only the four-muon mass distribution, the main discriminant, allows the resonant Higgs signal to be identified over the continuum ZZ production.

Distinction on the basis of dimuon invariant mass or displaced vertices does not increase the Higgs boson signal over the ZZ background. However, they may play an important role in eliminating other possible unaccounted for backgrounds, arising from the primary interactions, accelerator beam halo, detector mis-performance, etc.

Additional variables that may help discriminating H from the dominant ZZ background have been studied: $p_{\text{T}}(4\mu)$, number of jets and their E_{T}, etc. However, these variables are driven by the NLO production processes, while our samples were generated at the Leading

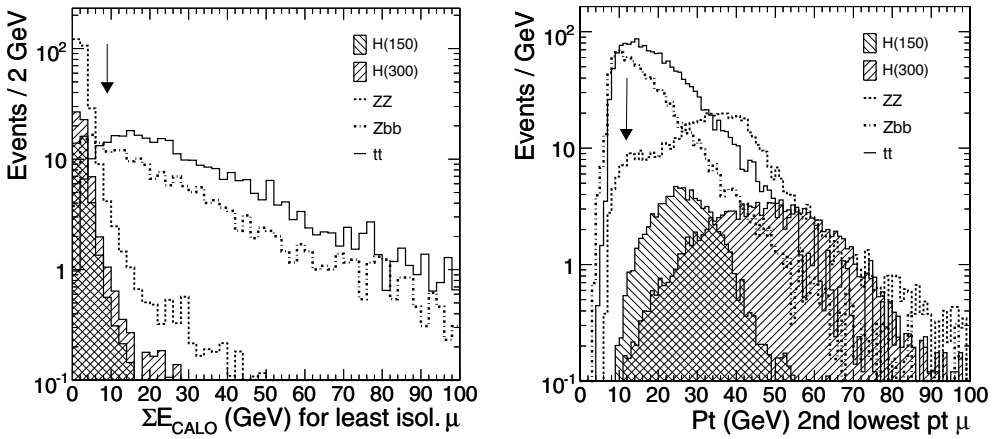

Figure 3.3. Examples of discriminating variables: (left) muon calorimeter-based isolation $\sum E_T$ for the least isolated muon and (right) transverse momentum of the 2nd lowest p_T muon. The hatched histograms represent the Higgs boson signals of masses 150 GeV/c^2 and 300 GeV/c^2, while the solid, dashed and dash-dotted lines indicate the contribution from the $t\bar{t}$, ZZ and Zb$\bar{b}$ backgrounds, respectively. The arrows indicate the positions of the cuts.

Order by PYTHIA and COMPHEP. Therefore, any conclusions that we might derive from these samples would not be reliable. Some muon angular distributions also have some differences originating from the underlying spin structures, but they are not sufficiently discriminating to be used and may be strongly affected by the NLO diagrams.

3.1.3. Higgs boson search analysis

3.1.3.1. Search using $m_{4\mu}$*-independent cuts.* Given the clear signature of the Higgs boson events, the signal extraction has been performed with a unique set of cuts, independent the Higgs boson mass, the details can be found in [60]. A Higgs mass-independent analysis is expected to minimise the dependence on the simulation of the discriminating variables in the Monte Carlo and the sensitivity to systematic errors. It is also readily applicable to real data and robust under variations of the detector conditions (calibrations, resolutions, efficiencies). Moreover, in our case, a mass-dependent selection does not significantly increase the significance of observing a signal.

A unique set of selection cuts has been designed to make the analysis robust when applied to real data. As explained below, some of the cuts (dimuon invariant mass, p_T cuts on the two hardest muons and isolation cuts on the two most isolated muons) slightly decrease the signal significance but make the selection more robust under imperfect conditions in the detector.

A loose requirement on the invariant mass of the pair of unlike-sign muons in the event which is closer to the nominal Z-boson mass, namely, $70\,\text{GeV/c}^2 < m_{\mu^+\mu^-} < 100\,\text{GeV/c}^2$, leaves more than 90% of the signal, while eliminating around 50% of the $t\bar{t}$ contamination. The loss in the signal is due to the internal bremsstrahlung and $Z \to 2\tau \to 2\mu 4\nu$ decays.

Cuts of 12 GeV/c and 8 GeV/c are set on the p_T of the two lowest-p_T muons. The p_T of the two highest-p_T muons must be larger than 15 GeV/c. The latter cut affects neither the signal nor the background, but is considered useful for eliminating unexpected background in real data. The efficiency of the p_T cuts in the signal is close to 90% while it suppresses around 50% of the remaining Zb$\bar{b}$ events, 40% of the $t\bar{t}$ events and about 20% of the ZZ background.

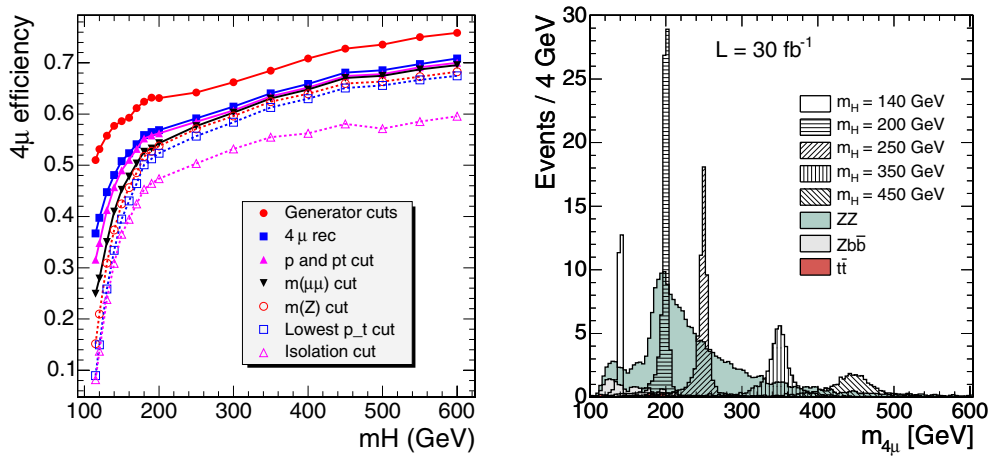

Figure 3.4. (Left) $H \to ZZ^{(*)} \to 4\,\mu$ efficiency *vs.* m_H after different cuts are applied. (Right) Reconstructed four-muon invariant mass distribution, for an integrated luminosity of 30 fb^{-1}, for background (shaded histograms) and several Higgs signals (hatched), after the selection criteria are applied.

For the purposes of the isolation cut optimisation, different cone radii and several energy and transverse momentum thresholds have been studied. Those yielding the maximum signal significance are, for calorimeter isolation, a cone radius of 0.24 and energy thresholds of 5 GeV and 9 GeV, while for tracker isolation a cone radius of 0.20 and p_T thresholds of 2.5 GeV/c and 4 GeV/c. The numbers are given for the two least isolated muons. Although a requirement on the isolation of the two most isolated muons does not increase the signal significance, following the same argument as in the case of the p_T cuts, a cut of 3.5 GeV/c and 5 GeV/c for the calorimeter isolation and 2 GeV/c and 2.5 GeV/c for the tracker isolation is set for the two most isolated muons.

After these cuts, Zbb̄ and $t\bar{t}$ events are suppressed to a negligible level in comparison to the remaining ZZ background. The efficiencies of each selection cut over the signal, for the 18 Higgs mass points studied, are shown in Fig. 3.4 (left). The four-muon mass distributions for signal and background events that survive the selection cuts are displayed in Fig. 3.4 (right).

In order to estimate the statistical significance of the signal, the log-likelihood ratio (LLR) statistical method [61, 62] is used. The distribution to discriminate signal and background is the four-muon invariant mass (Fig. 3.4 (right)). This distribution, for each Higgs boson mass hypothesis and for the background, is used to calculate the log likelihood ratio, $-2\ln Q$, which is then used to evaluate the compatibility of the data with either the *signal plus background* or the *background-only* hypothesis [60]. The $-2\ln Q$ estimator is sensitive both to the normalisation and the shape of the discriminant. Each event in the sum has a weight $\ln(1+s/b)$ which depends on the signal-to-background ratio, s/b, in the bin where it is found, which in turn depends on the m_H hypothesis. The whole spectrum of the discriminant variable enters the LLR calculation. This avoids any ambiguity in the definition of a signal region for determining the signal significance, present in counting methods.

Figure 3.5 (left) shows the statistical significance, $S_L \equiv \sqrt{<2\ln Q>}$, for an integrated luminosity 30 fb^{-1} at different $m_{4\mu}$ invariant masses, should the Higgs boson exist at one of these masses. Based on this distribution, the plot on the right depicts the integrated luminosity required to reach a statistical significance of the signal of 3σ and 5σ, as function of m_H. The expected integrated luminosity required to exclude the signal at the 95% confidence level

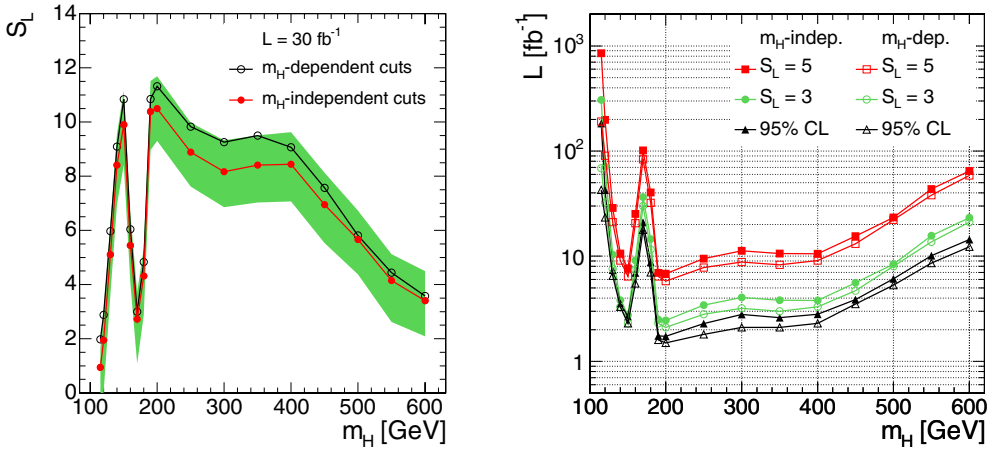

Figure 3.5. (Left) Statistical significance of the signal, S_L, as function of the Higgs boson mass for an integrated luminosity of 30 fb^{-1}, for mass-independent cuts (filled circles) and mass-dependent cuts (empty circles). The shaded band represents the statistical uncertainty on S_L. (Right) Integrated luminosity, for mass-independent (lines with filled squares, circles, and triangles) and mass-dependent cuts (lines with empty pointers), required to achieve a statistical significance of three (middle pair of curves) and five (upper pair of curves) standard deviations, as a function of the Higgs mass. The integrated luminosity required for excluding a Higgs boson signal at the 95% C.L. in a background-only experiment is also displayed (lower pair of curves).

in a background-only experiment is also shown as function of m_{H}. The effect of including systematic uncertainties (subsection 3.1.3.3) in the calculation of S_L is at the level of 15%-20% of the statistical accuracy of the expected significance, supporting that this analysis is not dominated by systematic uncertainties.

In order to more accurately quantify the degree of compatibility of the observed data with any of the two hypotheses, the confidence levels CL_b and CL_s are defined using the $-2\ln Q$ probability density functions, pdf, for both the background-only and the signal-plus-background hypotheses (details can be found in Refs. [60, 61]).

The presence of a signal can be inferred from the behaviour of $1-\mathrm{CL}_b$ for the background-only hypothesis, which is the probability of observing in a sample of simulated background-only experiments a more signal-like value of $-2\ln Q$. The observation of the value $1-\mathrm{CL}_b = 2.85\times10^{-7}$ indicates a 5σ excess in the data with respect to the background expectation. While CL_b quantifies the lack of compatibility of an excess of observed events with the background-only hypothesis, CL_s gives information about how compatible it is with an actual signal (Fig. 3.6).

3.1.3.2. Search using $\mathrm{m}_{4\mu}$*-dependent cuts.* One can take advantage of the fact that the Higgs boson resonance $\mathrm{H}\to\mathrm{ZZ}^{(*)}\to 4\,\mu$ is relatively narrow and use $\mathrm{m}_{4\mu}$-dependent cuts for its search. All details of such search strategy can be found in [51]. The analysis steps in this case would be as follows:

- First, events with 4 muons ($2\mu^+2\mu^-$) satisfying p_{T}, p, and $m_{\mu^+\mu^-}$ quality cuts as described in Section 3.1.2.1 are selected. This ensures that muons are reliably reconstructed and removes a "contamination" originating from heavy quarkonia decays.
- Second, after reconstructing a four-muon invariant mass, the $\mathrm{m}_{4\mu}$-dependent cuts are applied. The cuts, being smooth functions of $\mathrm{m}_{4\mu}$, are optimised in such a way that they maximise the significance of the Higgs signal excess *at all Higgs boson mass points*.

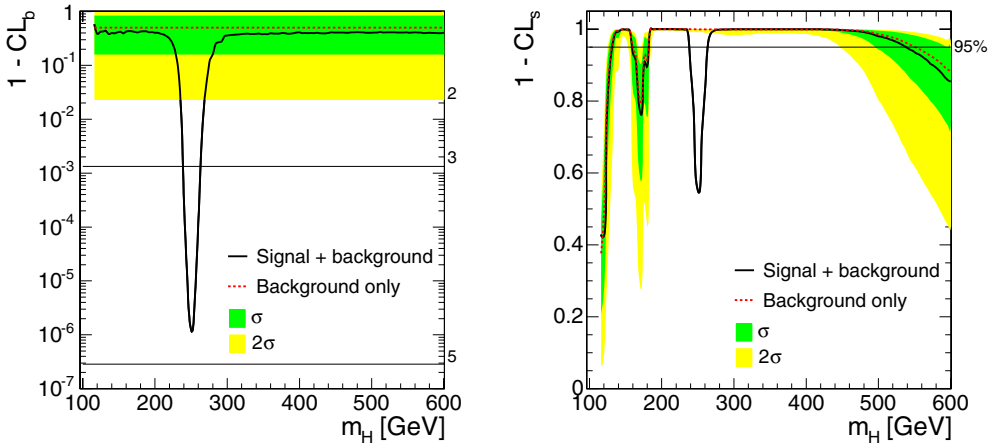

Figure 3.6. Mean values for $1-\mathrm{CL}_b$ (left) and $1-\mathrm{CL}_s$ (right) as a function of the Higgs boson mass hypothesis, assuming existence of Higgs boson at 250 GeV/c^2 mass and for an integrated luminosity of 10 fb^{-1}. The observation of the Higgs is just a little bit shy of the 5σ discovery (left). The mass points for which the curve $1-\mathrm{CL}_s$ is above 0.95 are excluded at 95% CL (right). The 1σ and 2σ bands on $1-\mathrm{CL}_b$ and $1-\mathrm{CL}_s$, originating from the Poisson statistical fluctuations of the number of background events in each bin of the discriminant distribution, are also shown.

- And finally, the resulting $\mathrm{m}_{4\mu}$ distribution is analysed for the presence of a Higgs boson resonance. The search can be done using either the LLR significance S_L estimator built for the whole spectrum or the LLR S_{cL} estimator built for a single-bin, or signal window (counting experiment). The direct comparison of the results can be found in [51].

To perform the desired $\mathrm{m}_{4\mu}$-dependent cut optimisation, we used a recently developed program GARCON [63]. The counting experiment significance estimator S_{cL} is the natural tool for such optimisation. The first half of the available Monte Carlo statistics was used for the cut optimisation. The results for the 18 Higgs mass points were then fit to obtain smooth $\mathrm{m}_{4\mu}$-dependent cuts. It was found that, given the level of the expected dominant backgrounds ($t\bar{t}$, Zb$\bar{\mathrm{b}}$, ZZ), there are only three critical discriminating cuts (details are given in Ref. [51]):

- The muon isolation cut, both tracker- and calorimeter-based, on the worst isolated muon, or equivalently one common cut on all four muons. This cut strongly suppresses $t\bar{t}$ and Zb$\bar{\mathrm{b}}$ backgrounds. The cuts gets tighter and tighter as $\mathrm{m}_{4\mu}$ gets smaller since Zb$\bar{\mathrm{b}}$ and $t\bar{t}$ increase (Fig. 3.2).
- The p_{T} on the second lowest p_{T} muon, or equivalently one common cut on the three highest p_{T} muons. This cut helps to further suppress Zb$\bar{\mathrm{b}}$ background to the level well below ZZ and reduces the ZZ background at high four-muon invariant masses. This cut becomes more stringent with increasing $\mathrm{m}_{4\mu}$.
- The $\mathrm{m}_{4\mu}$ window being used for scanning over the background. It roughly corresponds to the $\pm 2\sigma$ width, where σ is the Higgs boson peak width that includes the detector resolution and the Standard Model Higgs boson width.

The final results are obtained by applying these cuts to the second half of the available Monte Carlo statistics. The observed stability of the results ensures that the cut optimisation did not pick peculiar phase space corners corresponding to statistical flukes. After applying the cuts, the $t\bar{t}$ and Zb$\bar{\mathrm{b}}$ backgrounds are now suppressed well below the irreducible ZZ background.

Figure 3.5 shows, for different Higgs boson masses, the expected significance S_L at $\mathcal{L} = 30\,\mathrm{fb}^{-1}$ (left) and the average integrated luminosities at which a "5σ-discovery", "3σ-evidence", and exclusion at 95%CL are expected (right). The gain in significance with respect to the flat, $\mathrm{m}_{4\mu}$-independent, cuts can be easily translated into probabilistic terms. For example, the Higgs boson with $m_{\mathrm{H}} = 130\,\mathrm{GeV/c^2}$ is right at the "5σ-discovery" threshold for an integrated luminosity $\mathcal{L} = 30\,\mathrm{fb}^{-1}$. The difference in the average expected significance, 5.1 and 6.0, means in this case that the chances of observing significance in excess of 5 for $m_{\mathrm{H}} = 130\,\mathrm{GeV/c^2}$ at $\mathcal{L} = 30\,\mathrm{fb}^{-1}$ are 55% for the flat cuts and 80% for the $\mathrm{m}_{4\mu}$-dependent cuts.

3.1.3.3. Systematic errors. The analysis of the systematic errors can be sub-divided into two distinct stages. First, one needs to understand the level of uncertainties in predicting the level of background in the vicinity of a particular $\mathrm{m}_{4\mu}$ point being investigated for a possible event excess. Second, these uncertainties in the background need to be included in the evaluation of the significance of an excess of events, should it be observed.

Uncertainties in the signal are not very important for establishing an excess of events over the background. It is the uncertainties in the background that are of main concern. After applying the analysis cuts as described earlier, the ZZ production is the dominant irreducible background with all other processes giving much smaller contributions. This reduces the analysis of systematic errors to those of the $\mathrm{ZZ} \to 4\mu$ process.

One can try to evaluate the theoretical and detector performance related uncertainties starting from the first principles. However, especially during the earlier stages of the detector operation when the changes in the system are frequent and hard to monitor and timely incorporate into the detector Monte Carlo simulation, these estimations have limited predictability. Therefore, we developed methods evaluating various corrections, such as muon reconstruction efficiency, muon isolation cut efficiency, directly from data in order to minimise reliance on the Monte Carlo simulation, and, thus, significantly reducing the associated systematic errors. Also, throughout this analysis, we estimate the background around a particular $\mathrm{m}_{4\mu}$ with reference to a *measured* control sample. Note that this completely eliminates uncertainties associated with measuring the luminosity and reduces the sensitivity to PDF and QCD-scales. For the control sample, we use either the inclusive $\mathrm{Z} \to 2\mu$ process or sidebands of the $\mathrm{m}_{4\mu}$ spectrum itself.

The main uncertainties can be grouped as follows:

1. Uncertainties associated with the background production rates, *i.e.* not directly related to CMS Detector performance itself:
   - ZZ: PDF and QCD scale uncertainties described in details in Ref. [47].
   - ZZ: NLO and NNLO contributions vs LO described in details in Ref. [58] plus some related issues are discussed in Ref. [42]. These possible uncertainties are not taken into account in the results shown below, for details see Ref. [51].
   - LHC luminosity: when we estimate the ZZ background events in the signal region via the measured number of events in the control samples, the luminosity uncertainties largely cancel out.
2. Uncertainties associated with the CMS detector performance (hardware/software) and our analysis-specific cuts:
   - ZZ: Trigger efficiency, being very close to 100% due to presence of four muons, does not have substantial systematic errors.

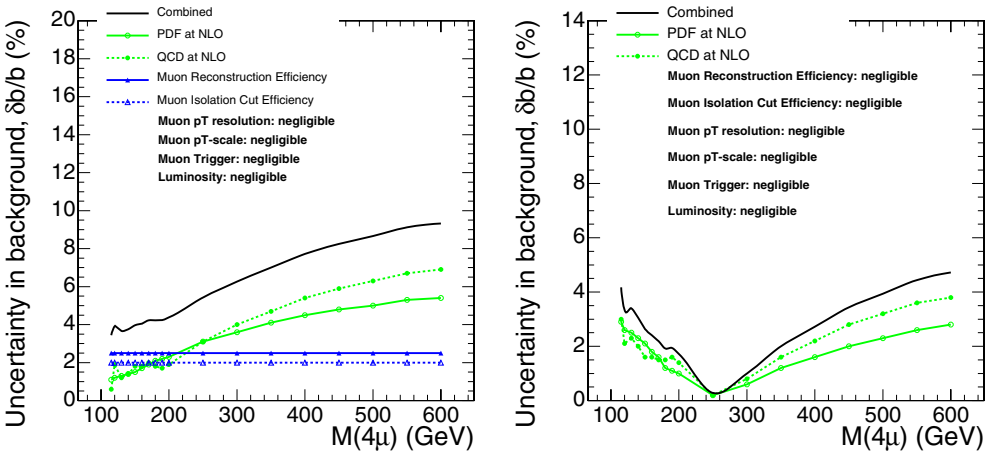

Figure 3.7. Uncertainties in the count of the ZZ $\to 4\mu$ background events in the signal region window at different $m_{4\mu}$. The window size is $\pm 2\sigma$ of the expected experimental Higgs resonance width. (Left) The background event count in the signal region is derived from the measured number of Z $\to 2\mu$ events. (Right) The background event count in the signal region, b, is calculated from the number of ZZ $\to 4\mu$ events B in the range 100 GeV/c^2–700 GeV/c^2 (excluding the signal region window), i.e. $b = \rho \cdot B$.

- ZZ: The muon reconstruction efficiency is determined directly from data [59]. The associated systematic error is less than 1% per muon. Using normalisation to the measured Z $\to 2\mu$ process, this leaves us with 2% uncertainty per event for the ZZ $\to 4\mu$ background production.
- ZZ: The muon isolation cut efficiency is also determined directly from data [64] with about 2% uncertainty per event.
- Higgs: $m_{4\mu}$ resolution is affected by muon p_T resolution. This almost does not affect the background distribution. In [51], we show that even making a mistake in the $m_{4\mu}$ distribution width by as much as 25% has only a tiny effect on evaluating a significance of an excess of events. The muon p_T resolution is fairly easy to measure from data using the measured J/ψ and Z peak widths with the precision much better than needed.
- ZZ: $m_{4\mu}$ scale. The effect of these uncertainties on the number of background events in a signal window appears only on steep slopes of the $m_{4\mu}$ distribution. For the steepest part of the $m_{4\mu}$ distribution in the 180 GeV/c^2–200 GeV/c^2 range, we obtain $\delta b/b \sim 0.1 \delta m_{4\mu}$, where $m_{4\mu}$ is in GeV/c^2 and b is the number of background events. This implies that to be able to neglect this effect, one needs to know the momentum scale with precision of 0.1 GeV at $p_T \sim 50$ GeV/c. This can be easily achieved with just a few hundreds of Z $\to 2\mu$ events.

Fig. 3.7 summaries all systematic errors on the expected number of events in the Z $\to 4\mu$ background for the two methods: via referencing to the total measured Z $\to 2\mu$ cross section and via referencing to the event count in the sidebands of the $m_{4\mu}$ spectrum itself.

Significance with the background uncertainties included

For the Gaussian-like signal over relatively flat background, the S_L and S_{cL} estimators are strongly correlated, with the typical difference of 5%–10% [51]. This stems from the fact that the signal peak is very localised and the background is relatively flat. This allows us to study

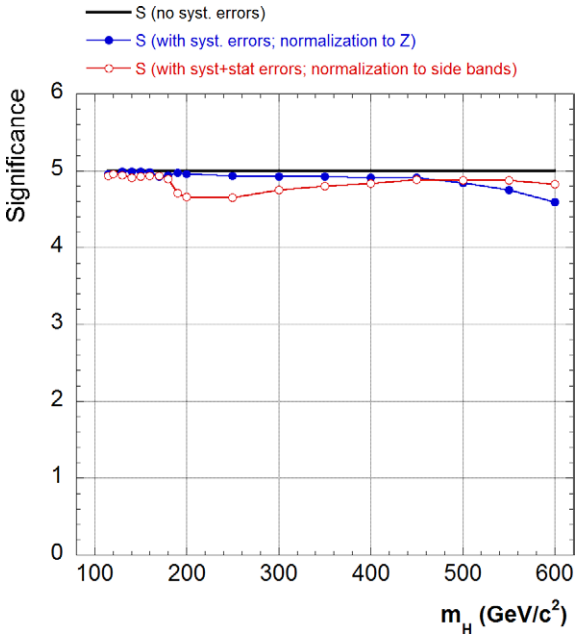

Figure 3.8. Effect of including systematic errors into evaluation of significance at the time of measurements. The reference luminosities, dependent on the Higgs boson mass, are chosen to correspond to an observation of significance $S = 5$ without systematic errors. Solid circles show degrading of significance for the case of systematic errors when the background is evaluated from the measured $Z \to 2\mu$ cross section. Open circles show the effect for the case when the background in signal region is normalised to the sidebands.

the effect of systematic errors on the evaluation of significance at the time of measurements using the counting experiment approach, for which everything can be done analytically. All details on the method we use can be found in Ref. [51]. The method allows to account for the theoretical and instrumental systematic errors as well as for statistical errors when a control sample with a limited event count is used.

The final result of these studies is presented in Fig. 3.8. Starting from an integrated luminosity at which the statistical significance of a Higgs boson observation would be equal to 5 (if the level of background without any errors was known), the figure shows how this significance must be de-rated due to the systematic errors at the time of the measurements as described in the previous sub-section. The effect of systematic errors at low or high luminosities is not as important: at lower luminosity the significance is not sufficient to make serious claims, anyway; while after surpassing the significance of 5, the existence of the Higgs boson can be considered established and the focus must be switched to measuring its parameters.

The two curves with full and open circles show the difference of the two methods for evaluating the background in the signal region: via normalisation to the measured $Z \to 2\mu$ cross section, and via normalisation to the event count in sidebands ($100\,\mathrm{GeV/c^2}$ to $700\,\mathrm{GeV/c^2}$, excluding the signal region). The effect of systematic errors at lower luminosities becomes smaller for the former method and quickly diverges for the latter. As the luminosity increases, the trends obviously reverse. Around the threshold of $S = 5$, the difference between the two methods is not very dramatic; the true benefit of using two approaches to estimating background from data is in their complementarity.

Local significance and overall statistical fluctuation probability

In a search for a relatively narrow 4μ invariant mass peak over a broad background spectrum, one must take into account that the probability of observing a background fluctuation giving an excess of events consistent with a Higgs hypothesis of *some particular mass* might be considerably higher that the local significance calculated for a given mass might imply. This over-estimation of significance strongly depends on how the analysis is set and what constraints/priors on the "phase space" of parameters are used. For example, in a search specifically tailored for the Standard Model Higgs, the only free parameter is the Higgs boson mass; its width, production cross section, and decay branching ratios are dependent on the mass. To make the search even more constrained, one can use a prior on the Higgs mass as it comes out from the precision electroweak measurements. A specific case study showing the potential scope of the effect, which may be comparable or even larger than the effect of the systematic errors discussed above, is given in Appendix A.

3.1.4. Measurement of the Higgs boson properties at $\mathcal{L} = 30\,\mathrm{fb}^{-1}$

The capabilities of the CMS detector to measure the mass, cross section and width of the Higgs boson are determined for an integrated luminosity of $30\,\mathrm{fb}^{-1}$ [65]. These parameters are measured using a binned maximum likelihood fit to the reconstructed four-muon invariant mass, which includes the signal and background contributions after all the selection cuts have been applied (Fig. 3.4 (right)). The 'observed' distribution, f_{sb}, is expressed in terms of the signal, p_s, and background, p_b, probability density functions (pdf) as:

$$f_{sb}(\mathrm{m}_{4\mu}; m_{fit}, \Gamma, N_s, N_b) = N_s \cdot p_s(\mathrm{m}_{4\mu}; m_{fit}, \Gamma) + N_b \cdot p_b(\mathrm{m}_{4\mu})$$

N_s is the number of signal events, N_b the number of background events, m_{fit} the position of the mass peak and Γ the intrinsic width of the Higgs boson. The signal pdf is the sum of two contributions: a convolution of a Breit–Wigner signal shape with a Gaussian distribution that accounts for detector resolution, p_{core}, and a function that reproduces the radiative tail due to internal bremsstrahlung, p_{tail}:

$$p_s = \beta \cdot p_{core}(\mathrm{m}_{4\mu}; m_{fit}, \Gamma, \sigma) + (1-\beta) \cdot p_{tail}(\mathrm{m}_{4\mu}; m_{fit}, \tau)$$

where $1-\beta$ is the fraction of signal events in the radiative tail. The tail shape is parameterised *ad hoc* as

$$p_{tail} = \frac{(\mathrm{m}_{4\mu} - m_{fit})^2}{2\tau^3} \exp\left(\frac{\mathrm{m}_{4\mu} - m_{fit}}{\tau}\right)$$

if $\mathrm{m}_{4\mu} < m_{fit}$ and is zero otherwise [66]. Figure 3.9 (left) illustrates the different contributions to f_{sb}. The p_s function is fitted to the signal-only distributions to obtain the parameters of the radiative tail, which remain fixed in the fit to the signal plus background spectra.

For Higgs boson masses below $190\,\mathrm{GeV/c^2}$, the intrinsic width is negligibly small compared to the mass spread introduced by the experimental resolution and the signal is thus approximated by a Gaussian shape. For masses above $400\,\mathrm{GeV/c^2}$, the natural width of the Higgs is much larger than the experimental resolution, hence the description using a pure Breit–Wigner function yields similar parameters as those obtained from the convolution.

The detector resolution is extracted from the $\mathrm{m}_{4\mu}$ distribution of ZZ events with a four-muon mass above $2m_Z$, for which the kinematics is similar to that of the signal. For masses below $2m_Z$, the intrinsic Higgs boson width is negligible, therefore the resolution is measured directly from the width of the $\mathrm{m}_{4\mu}$ distribution. This width has been found to be consistent with the extrapolation of the resolution determined using ZZ events.

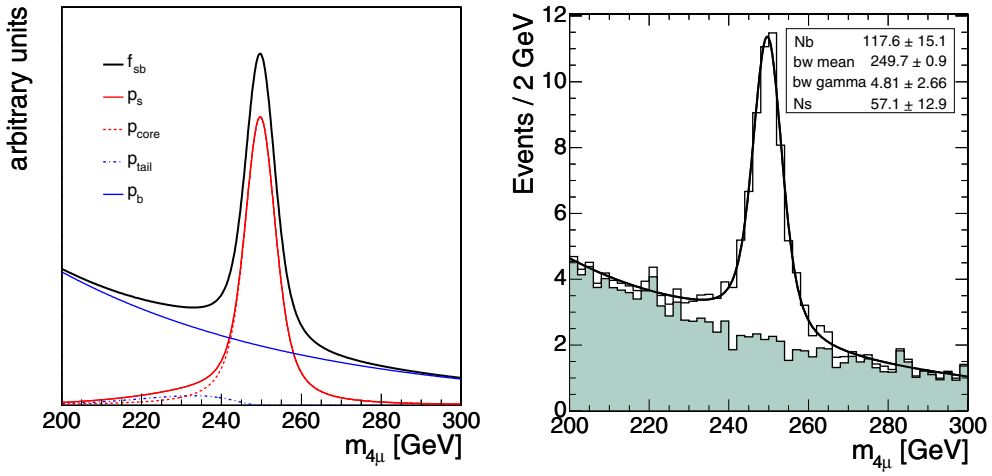

Figure 3.9. (Left) Example of the shapes of the different contributions to f_{sb}. (Right) Data-like distribution expected for a Higgs boson signals of $m_{\mathrm{H}} = 250\,\mathrm{GeV/c^2}$, for an integrated luminosity of $30\,\mathrm{fb}^{-1}$, together with the result of the fit (solid line) and the expected background (shaded area). This pseudo-experiment is selected randomly.

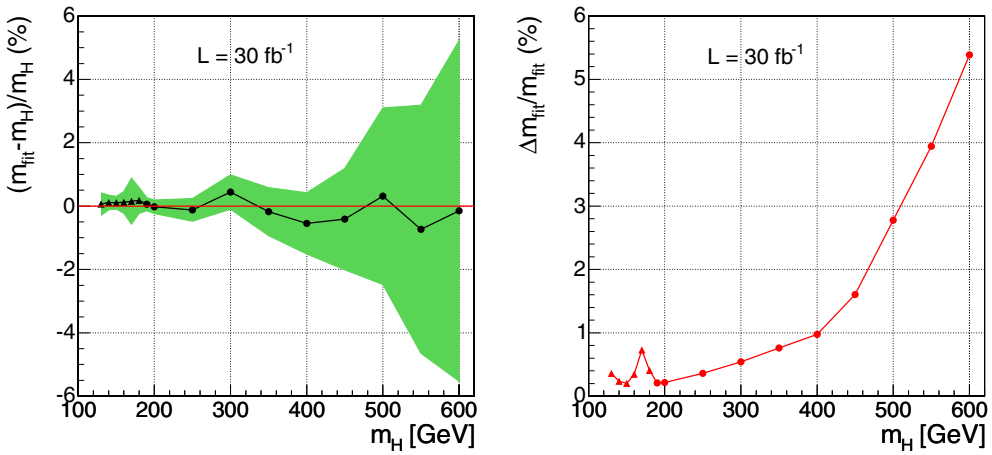

Figure 3.10. (Left) Relative shift of the fitted value of the Higgs boson mass with respect to the input m_{H} value, as function of m_{H}. The shaded area is the error in the determination of the peak value from the fit, also shown as function of the Higgs boson mass (right). The dots correspond to the result of the convolution and the triangles to the Gaussian approximation.

The background pdf, p_b, is approximated by either a polynomial or an exponential function, depending on the mass region under study. The parameters are determined performing a binned maximum likelihood fit to the background sample. The parameters defining the shape of the background are fixed in the global fit to signal plus background, but not its normalisation.

The values of the parameters, together with their errors, are obtained directly from the fit. The result of the fit to the signal plus background distribution is shown in Fig. 3.9 (right) for a Higgs boson signal of $m_{\mathrm{H}} = 250\,\mathrm{GeV/c^2}$. Figure 3.10 (left) depicts the relative shift of the fitted Higgs boson mass with respect to the true mass, together with its statistical error. These values are compatible with zero in the full range of masses, which means that the true mass

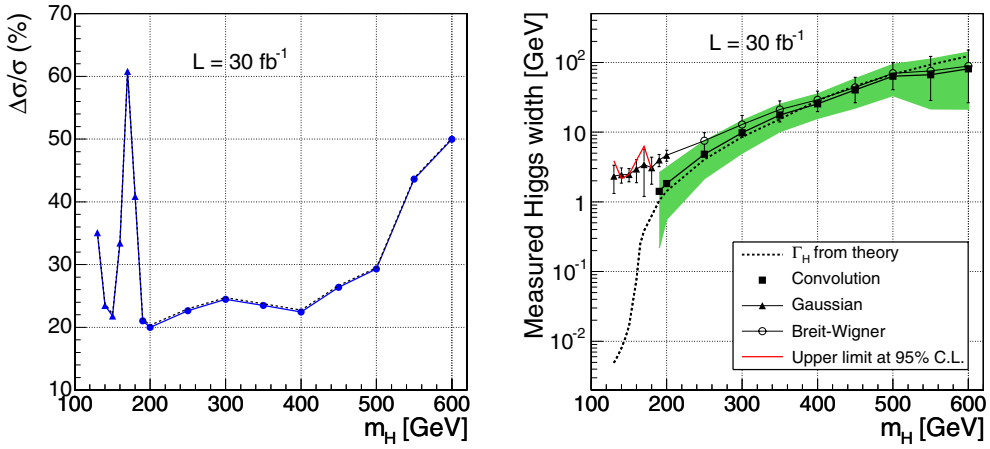

Figure 3.11. (Left) Relative error in the cross-section measurement, $\Delta N_s/N_s$, as a function of the m_H. ΔN_s is the statistical error of N_s obtained from the fit. The dots correspond to the result of the convolution and the triangles to the Gaussian approximation. The dashed line indicates the impact of the systematic uncertainties. (Right) Measured Higgs boson width (squares), its statistical error (green band) and the theoretical calculation of Γ_H (dashed line). Upper limits to the width at 95% C. L. are shown (red line) for $m_H < 190\,\mathrm{GeV/c^2}$. The result of Gaussian (triangles) and Breit–Wigner (dots) fits are also shown for comparison.

is accurately recovered after applying the fitting method to the reconstructed sample. The evolution of the relative error as a function of the true mass is displayed in Fig. 3.10 (right), showing that the mass can be measured with precisions from 0.1% to 5.4%. The increase in this error around $170\,\mathrm{GeV/c^2}$ is due to the smaller signal statistics caused by the suppression of the $H \to ZZ^{(*)}$ decay at this mass. The increasing uncertainty at higher masses is due to the smaller production cross sections, the larger intrinsic width of the Higgs boson and, to a lesser extent, the worse resolution for high p_T muons.

The number of signal and background events is obtained from the fit. The relative error in the cross-section measurement is determined from the number of signal events (N_s) and its statistical uncertainty (ΔN_s) as $\Delta N_s/N_s$, shown in Fig. 3.11 (left) as function of the Higgs boson mass. The contribution of the background is properly taken into account, as its normalisation is a free parameter in the fit. The cross section can be determined with a precision between 20% and 45%, except for masses below $130\,\mathrm{GeV/c^2}$, where the statistics is low.

The measured width, together with its statistical error, is presented in Fig. 3.11 (right) as function of the true mass. The width can be determined with an error between 35% and 45% above $190\,\mathrm{GeV/c^2}$. Below this mass there is no sensitivity to the Higgs boson width and upper limits at 95% confidence level (C.L.) are set. For the sake of comparison, the width obtained by fitting only a Gaussian for masses below $200\,\mathrm{GeV/c^2}$ and only a Breit–Wigner for masses above $200\,\mathrm{GeV/c^2}$ is also shown, together with the statistical uncertainty. The Breit–Wigner-only fits do not take into account the detector resolution, and therefore the intrinsic theoretical values are not recovered.

The measurement of the parameters is affected by systematic uncertainties in the muon momentum resolution (determined from data), in the muon reconstruction efficiency (around 2%) and those associated to the selection cuts (close to 1%) [60]. These systematic uncertainties are mostly uncorrelated. The impact in the measured mass and width is small. The cross-section measurement is also affected by the uncertainty in the luminosity determination, which is around 3% (Fig. 3.11 (left)).

The results obtained for Higgs boson masses around 170 GeV/c^2 and above 500 GeV/c^2, for which the expected number of events is somewhat low for $\mathcal{L} = 30\,\text{fb}^{-1}$, have to be taken as representative results for the typical expected distributions. The higher errors of the parameters for those m_{H} values are consistent with statistics. For extending the measurement of the Higgs boson parameters to smaller masses or to lower luminosities, it should be more appropriate to extract the parameters from a large set of randomly chosen four-muon mass distributions with the correct statistics.

3.1.5. Conclusions

Discovery of the Standard Model Higgs boson and measurement of its mass, production cross section and width in the "golden" decay mode $\text{H} \to \text{ZZ}^{(*)} \to 4\,\mu$ were analysed with the CMS Detector. The explored range of Higgs boson masses was 115 GeV/c^2–600 GeV/c^2. The Monte Carlo samples were normalised to represent the NLO cross sections, including $\text{m}_{4\mu}$-dependent K-factors. To simulate the detector response and reconstruct physics objects, the full CMS Detector simulation and reconstruction software was used. The Higgs boson discovery potential was explored for different analysis variations, including the use of $\text{m}_{4\mu}$-dependent and flat cuts, log-likelihood ratio based on the full $\text{m}_{4\mu}$ spectrum and a straightforward counting experiment approach. A full treatment of the most important theoretical and instrumental systematic errors and their effect on evaluation of significance of the Higgs boson observation as well as measuring its parameters were presented. To minimise systematic errors, a number of methods of reconstructing the necessary corrections directly from data were developed.

It was shown that at $\sim 2\,\text{fb}^{-1}$ of integrated luminosity, CMS would be able to start excluding the Standard Model Higgs boson at 95% CL for m_{H} in vicinity of 200 GeV/c^2. By the time CMS reaches $\sim 30\,\text{fb}^{-1}$, it would exclude the Standard Model Higgs boson in its four-muon decay mode in the mass range $m_{\text{H}} = 120$ GeV/c^2–600 GeV/c^2, if indeed it does not exist.

The discoveries at the level of "5σ" local significance could be already possible at $\sim 10\,\text{fb}^{-1}$ for m_{H} in the range 140 GeV/c^2–150 GeV/c^2 and 190 GeV/c^2–400 GeV/c^2. By the time $\sim 30\,\text{fb}^{-1}$ are collected, the discovery range would open up to 130 GeV/c^2–160 GeV/c^2 and 180 GeV/c^2–500 GeV/c^2. An observation of the Higgs boson with the mass $m_{\text{H}} \sim 170$ GeV/c^2 or ~ 600 GeV/c^2 in the $\text{H} \to \text{ZZ}^{(*)} \to 4\,\mu$ decay channel would require an integrated luminosity of the order of $100\,\text{fb}^{-1}$.

At the integrated luminosity of $\sim 30\,\text{fb}^{-1}$, the Higgs boson mass could be measured with a precision between 0.1 % and 5.4 %, depending on its mass. The intrinsic width could be measured only for the Higgs boson heavier than 190 GeV/c^2, with a precision $\sim 35\%$. For lower masses, the Higgs boson width becomes much smaller than the detector resolution and only upper limits of the order of a few GeV could be set. The production cross section would be determined with a precision $\sim 30\%$.

3.2. Benchmark Channel: $H \to WW^{(*)} \to 2$ muons

3.2.1. Introduction

Previous studies [67, 68] demonstrated the relevance of the $\text{H} \to \text{ZZ}^{(*)} \to 2/2\nu$ channel for the Higgs discovery with an integrated luminosity of less than $5\,\text{fb}^{-1}$. The physics study was performed on the data produced at the end of the full simulation, trigger and off-line detector

reconstruction chain, including realistic assumptions for the sub-detectors misalignments. The goal of this study is to provide the discovery potential as a function of the Higgs mass using detailed simulation reconstruction code, considering all the relevant background contributions and providing an as much as possible complete estimation of the systematic errors. The muon reconstruction has an average efficiency in the detector geometrical acceptance ($\eta < 2.4$) of 95–99% for the transverse momentum ranging from 5 GeV/c up to $P_T = 1$ TeV/c, as extensively discussed in [7], while the fraction of mis-assigned charge for muons with $P_T = 100$ GeV/c is less than 0.1%.

3.2.2. Physics processes

3.2.2.1. Signal processes. The signal was studied in the range between 130 to 180 GeV using 7 samples of datasets (Table 3.1). The generation was done using the PYTHIA program [69], considering the most relevant signal sources:

$$gg \to H \to WW^{(*)} \to 2\mu 2\nu \tag{3.1}$$

$$q\bar{q} \to VVq'\bar{q}' \to Hq'\bar{q}'\,;\; H \to WW^{(*)} \to 2\mu 2\nu \tag{3.2}$$

In the simulation, digitisation and reconstruction the effect of the event pile up expected at the machine luminosity $2 \times 10^{33}\mathrm{cm}^{-1}\mathrm{s}^{-2}$ was included. An example of a pp $\to$ H + X event with H $\to$ WW $\to \mu\nu\mu\nu$ is shown in colour plate CP4.

3.2.2.2. Background processes. The dominant background giving the largest contribution at the end of the complete selection chain, is the irreducible one from the continuum production of W pairs decaying into muons and neutrinos. Other significant or critical sources of backgrounds are the production of top quarks and the Drell–Yan muon pairs. The most important backgrounds are thus the processes:

$$q\bar{q} \to W^+W^- \to 2\mu 2\nu \tag{3.3}$$

$$gg \to t\bar{t} \to 2\mu 2\nu \tag{3.4}$$

$$q\bar{q} \to \gamma^*, Z \to 2\mu \tag{3.5}$$

Further contributions from $b\bar{b}$, $ggWW$, WZ, ZZ, and Wt production processes were also considered. A part from Wt and $gg \to WW$, all the processes have been generated with PYTHIA. For the former process, the TOPREX Monte Carlo [44] has been used which correctly takes into account the top mass and the spin correlations throughout the decay chain. The latter dataset has been simulated starting from a Monte Carlo sample produced by N. Kauer et al. [70]. The full list of dataset samples used for the background study is given in Table 3.2.

3.2.2.3. Cross sections at NLO. All the processes considered in this study have been simulated with LO accuracy. In order to approximate the NLO predictions for the signal and the W-pair background, phase space depended reweighting K-factors has been applied [71]. These factors have been obtained by matching respectively the p_T distribution of the Higgs and of the W^+W^- system provided by PYTHIA to the one predicted by MC@NLO [72][38]. The K(p_T) factors used for each p_T intervals are given in Appendix of [73]. The absolute cross sections for Higgs production through gluon-gluon fusion and vector boson fusion have been calculated [20] and are listed in Table 3.1.

[38] For the signal, only the Higgs production through the gluon–gluon mechanism has been reweighted with K(p_T) factors accordingly to NLO description.

Table 3.1. The cross section at the next-to-leading order for Higgs production through gluon fusion and vector boson fusion (VFB) processes and the number of generated events are reported.

Higgs mass (GeV/c^2)	$\sigma^{NLO} \times BR(2l)$ Gluon Fusion (pb)	$\sigma^{NLO} \times BR(2l)$ VBF (pb)	$\sigma^{NLO} \times BR(2l)$ num. of events
130	0.94	0.12	20000
140	1.39	0.19	20000
150	1.73	0.25	17000
160	2.03	0.31	44000
165	2.04	0.32	49000
170	1.95	0.31	40000
180	1.71	0.28	20000

Table 3.2. The cross section at the next-to-leading order for the background processes. The $gg \to WW$ process is generated using a matrix element program linked to PYTHIA for the showering [70]. This process is only known at LO. (*) For $b\bar{b} \to 2\mu$ the pre-selection $p_T > 20, 10\,GeV/c$ was applied.

Channel	$\sigma^{NLO} \times BR(pb)$	num. of ev.
$qq \to WW \to 2l$	11.7	164000
$t\bar{t}$	840	548000
$gg \to WW \to 2l$	0.54 (LO)	50000
γ^*, Z	145000	2700000
$b\bar{b} \to 2\mu$	710 (LO)(*)	640000
$ZW \to 3l$	1.63	72000
$tWb \to 2l$ (TOPREX)	3.4	191000
$ZZ \to 2l$	1.52	99000

No reweighting has been applied to the other processes, whose total cross sections have been simply rescaled accordingly the NLO calculation performed sing the MCFM Monte Carlo program [55, 74, 75]. These cross sections are reported in Table 3.2.

3.2.3. Event selection

The signal selection requires the identification of two high p_T isolated muons. The background reduction is obtained applying suitable kinematic cuts to the reconstructed muons, a veto on the presence of central jets and a high missing E_T (MET) in the event. As discussed in the following sections, separate optimisations were performed independently on the muon isolation variables, jet and missing energy thresholds and on the muons kinematical variables.

3.2.4. The trigger selection

Events passing the global Level-1 trigger must be reduced with a more restricted trigger requirement to limit the recorded event rate. Two trigger streams were considered in this analysis:

1. the HLT double muon stream;
2. the OR of the HLT single muon and double muon stream.

Before any selection the single or double muon HLT trigger efficiency is 92%, while the double muon HLT trigger efficiency is 80% [76]. After the off-line cuts for the Higgs selection, which will be described in detail in the following section, the overall efficiency of the first stream relative to the second one is found to be $(97 \pm 1)\%$, for $m_H = 165\,\mathrm{GeV/c^2}$. In the following, the trigger selection used was the HLT double muon stream, for which the trigger rate is predicted to be a factor $\sim$7 smaller than the single muon one [76].

3.2.4.1. The muon identification and isolation. A first event selection based on the identification of two prompt muons required:

- Level-1 and HLT dimuon trigger bits found;
- two oppositely charged muons reconstructed by the Global Muon reconstructor algorithm developed in ORCA, as described in [7].

The first requirement assures the events to be found in the CMS dimuon data stream, which currently foresees a symmetric threshold of $7\,\mathrm{GeV/c}$ on the p_T of both muons as reconstructed by the High Level Trigger algorithm, for operations at a machine luminosity of $2 \times 10^{33}\mathrm{cm^{-2}\,s^{-1}}$; in addition, at least one of the muons must fulfill the HLT isolation criteria [76]. As discussed in Ref. [76], the trigger rate for this datastream is predicted to be about 4 Hz.

At the off-line reconstruction and selection stage, two cones were considered for the isolation around each reconstructed muon tracks. The $\sum P_\mathrm{T}$ summed over all the charged track candidates found in the Tracker detector was accounted inside the first cone. The $\sum Et$ over the energy deposits in the ECAL and HCAL towers was accounted in the second cone. The size of a cone around a muon track is defined as $\Delta R = \sqrt{\Delta\eta^2 + \Delta\phi^2}$. A muon is considered to be isolated if the $\sum Pt$ ($\sum Et$) inside the considered cones of size $\Delta R_{Tracker}$ (ΔR_{Calo}) is below the threshold P_T (max) (E_T (max)). An optimisation study was performed to find the four parameters:

$$(1)\ \Delta R_{Tracker} \quad (2)\ P_\mathrm{T}(\mathrm{max}) \quad (3)\ \Delta R_{Calo} \quad (4)\ E_\mathrm{T}(\mathrm{max})$$

searching for the highest signal over background ratio. The optimisation was performed using the signal dataset with $m_H = 165\,\mathrm{GeV/c^2}$ and the $b\bar{b}$ background dataset, which is the most sensitive to the isolation cut. At this first stage of the selection, the background reduction was not requested to be very large, thus keeping the signal reduction relatively small; for each combination of the cones:

$$\Delta R_{Tracker} = 0.25, 0.3, 0.35, 0.4 \quad \Delta R_{Calo} = 0.25, 0.3, 0.35, 0.4 \tag{3.6}$$

the cut efficiency of 85% for the signal was requested. With two free parameters, E_T (max) and P_T (max), several solutions are possible. A reasonable choice is to give the same weight to the Tracker and Calorimeter isolation cuts. The mean and the r.m.s. values of the p_T and energy deposition for the signal dataset within different cones are reported in [77]. For each set of isolation cones ($\Delta R_{Tracker}$,ΔR_{Calo}) the E_T and P_T thresholds were chosen as follows:

$$E_\mathrm{T}^{thresh} = < E_\mathrm{T} > + x \cdot \sigma(E_\mathrm{T}) \tag{3.7}$$

$$P_\mathrm{T}^{thresh} = < P_\mathrm{T} > + x \cdot \sigma(P_\mathrm{T}) \tag{3.8}$$

where the parameter x was set to the value giving the required 85% efficiency for the signal. Figure 3.12 shows the resulting background selection efficiency.

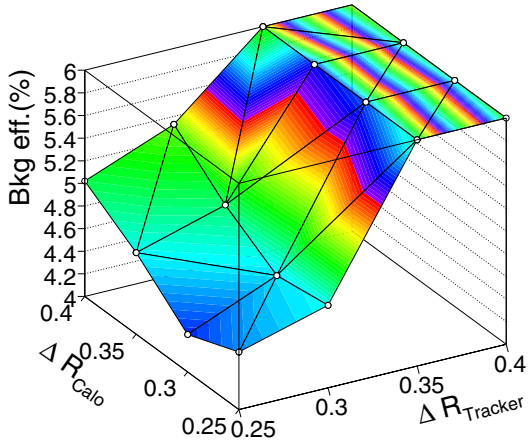

Figure 3.12. $b\bar{b}$ background efficiencies for the 16 combinations of cones considered for the muon isolation selection cut.

The best selection is obtained with:

$$\Delta R_{Tracker} = 0.25 \quad P_{\mathrm{T}} < 2.0\,\mathrm{GeV/c} \quad \Delta R_{Calo} = 0.3 \quad E_{\mathrm{T}} < 4.7\,\mathrm{GeV} \qquad (3.9)$$

corresponding to $x = 1.8$ for the energy deposition and P_{T} cut. The isolation cuts used in the analysis were:

$$\Delta R_{Tracker} = 0.25 \quad P_{\mathrm{T}} < 2.0\,\mathrm{GeV/c} \quad \Delta R_{Calo} = 0.3 \quad E_{\mathrm{T}} < 5.0\,\mathrm{GeV}. \qquad (3.10)$$

3.2.5. Jet reconstruction and the jet veto

The reconstruction of jets is needed to obtain a strong $t\bar{t}$ background reduction by applying a jet veto. The jet reconstruction algorithms can use the raw energy sum of the ECAL and HCAL towers, either with a fixed energy threshold or with η-dependent thresholds. The η-dependent threshold does not improve the $t\bar{t}$ background rejection with respect to a fixed combined E_{T} and E thresholds [73]. The jets reconstructed from raw energies with fixed E_{T} and E thresholds were finally chosen to be used for the JET veto. A strong E_{T} cut helps in the background reduction. However, below $E_{\mathrm{T}} = 25\,\mathrm{GeV}$ the fraction of jets matching with a generated jet starts to decrease, because of ghost jet candidates mainly due to pileup events. The matching was defined within a cone around the reconstructed jet candidate $\Delta R_{rec-genjet} < 0.3$. In order to reduce the number of fake jets, a quality parameter was introduced:

$$\alpha = \sum_{selected\ tracks} P_{\mathrm{T}}/E_{\mathrm{T}}(jet) \qquad (3.11)$$

where the selected tracks are those inside the jet ($\Delta R_{trk-jet} < 0.5$) with more than 5 associated hits, pointing to the primary interaction vertex ($|z_{trk} - z_{vtx}| < 0.4\,\mathrm{cm}$). The mean value of α is 0.66 (two third of the jet energy on average is due to charged particles). A reconstructed jet candidate with E_{T} in the low energy region ($< 20\,\mathrm{GeV}$) was considered only if $\alpha > 0.2$. It has been shown [73] that this selection significantly reduces the number of fake jets (the fraction of matched jets being greater than 90% for $E_{\mathrm{T}} > 15\,\mathrm{GeV}$) with negligible loss of reconstruction efficiency for true jets. Different jet reconstruction algorithms were tested. The best signal ($m_H = 165\,\mathrm{GeV/c^2}$) / background ($t\bar{t}$) ratio was obtained using an iterative

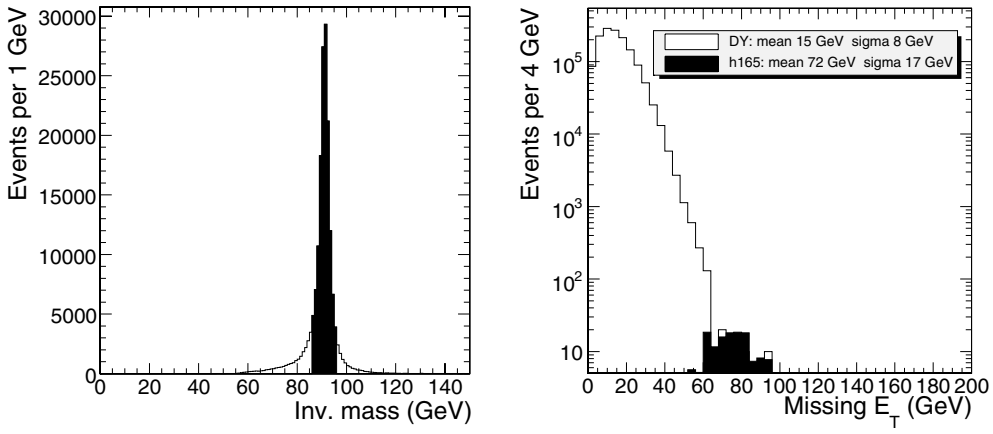

Figure 3.13. Reconstructed dimuon invariant mass for Drell–Yan events selected inside the Z mass region (left, black area); MET distributions for the selected Drell–Yan events and for signal events scaled at the integrated luminosity $\mathcal{L} = 10\,\text{fb}^{-1}$ (right).

cone algorithm [78] with a cone size R = 0.5 and calorimeter towers having raw energies $E_{\text{T}}^{tower} > 0.5\,\text{GeV}$ and $E^{tower} > 0.8$. To summarise, the jet veto is applied if:

$$E_{\text{T}} > 15\,\text{GeV} \quad |\eta_{jet}| < 2.5 \tag{3.12}$$

and the α cut is required in the jet energy range $15\,\text{GeV} < E_{\text{T}} < 20\,\text{GeV}$.

3.2.6. Missing energy reconstruction and the MET cut

The transverse missing energy is reconstructed with the sum of the ECAL and HCAL tower raw energies, corrected for the muons energy contribution. The most sensitive background to the MET cut is the dimuon production from Drell–Yan (DY) process. The right plot in Fig. 3.13 shows the MET distributions for DY events having a reconstructed dimuon invariant mass inside the Z mass region (shown by the black area in the left plot), and for signal events with $m_H = 165\,\text{GeV/c}^2$. The signal and background distribution were normalised to an integrated luminosity $\mathcal{L} = 10\,\text{fb}^{-1}$.

A MET threshold of 47 GeV is 4σ over the mean value for the background and 1.5σ under the mean value for the signal. Drell–Yan events are thus strongly suppressed by applying a MET threshold. The cut used in this analysis was MET > 50 GeV.

3.2.6.1. The kinematic cuts. The kinematic of the two muons is different for signal and background:

- signal events from gluon-gluon scattering are more central than the W^+W^- background from $q\bar{q}$ scattering, thus resulting in a slightly more central rapidity distribution for the decay muons;
- due to the scalar nature of the Higgs boson and of the V-A structure of the weak interaction, for Higgs masses close to $2M_W$, the W^+W^- spin correlation plays in favour of small opening angles between the two muons;
- signal events have a lepton P_{T} spectra peak close to $M_W/2$;
- DY background has a two muons invariant mass peak at M_Z.

In addition, the muons from b quarks (as in the case of the $b\bar{b}$ background and eventually from $t\bar{t}$) have large impact parameters. The following cuts were applied before the optimisation of the kinematical cuts:

1. $|(\mu_1))|, |(\mu_2)| < 2.0$ (pseudorapidity of the two muons);
2. $IP(\mu_1), IP(\mu_2) < 3\sigma$ (impact parameter of the two muons);
3. $P_{\mathrm{T}}(\mu_{max}) < 55\,\mathrm{GeV/c}$ (transverse momentum of the two muons);
4. $m_{\mu_1\mu_2} > 12\,\mathrm{GeV/c_2}$ (invariant mass of the two muons);
5. $\Delta\phi_{\mu_1\mu_2} < 0.8$ (opening angle between the two muons).

Cut 1 is useful for the WW background reduction, as well as cuts 3 and 5. Cut 2 reduces the $b\bar{b}$ events, while cut 4 rejects potential background from b-resonances. After the requirement of the muon isolation described before, the overall signal efficiency for cuts 1 to 4 is about 90%. The distribution of the variable $\Delta\phi\mu 1\mu_2$ will be used to search for the Higgs signal.

The optimisation study was performed by varying the following cuts:

$$P_{\mathrm{T}}(\mu_{max}) > 25, 30, 35, 40\,\mathrm{GeV/c} \quad P_{\mathrm{T}}(\mu_{min}) > 15, 20, 25, 30\,\mathrm{GeV/c^2} \tag{3.13}$$

$$m_{\mu_1\mu_2} < 35, 40, 45, 50, 55, 60\,\mathrm{GeV/c^2} \tag{3.14}$$

to find the set of cuts giving the best significance. The estimator S_{cP} was used, which gives the significance using the Poisson distribution [79]. The input of the estimator are the number of signal and background events, the statistical uncertainties and the theoretical systematics in the background. The optimisation was performed using as before the signal dataset with $M_H = 165\,\mathrm{GeV/c^2}$, and using all the background contributions, properly normalised considering their production cross sections.

The optimisation result could depend on the statistics of the event data samples and on the estimated systematic errors. We searched for the maximum significance in four different conditions:

$$\mathcal{L} = 1\mathrm{fb}^{-1} \quad \mathcal{L} = 2\,\mathrm{fb}^{-1} \quad \text{syst. err.} = 10\% \quad \text{syst. err.} = 15\% \tag{3.15}$$

Figure 3.14 shows, as an example, the significance expected as a function of $p_{\mathrm{T}}(\mu_{max})$ and $p_{\mathrm{T}}(\mu_{min})$ cuts for two different values of the dimuon invariant mass cut, for the case of an integrated luminosity $L = 1\mathrm{fb}^{-1}$ and an overall 10% systematic error.

The following cuts:

$$P_{\mathrm{T}}(\mu_{max}) > 35\,\mathrm{GeV/c} \quad P_{\mathrm{T}}(\mu_{min}) > 25\,\mathrm{GeV/c} \quad m_{\mu_1\mu_2} < 50\,\mathrm{GeV/c^2} \tag{3.16}$$

give the maximum significance (about 3.0 for $\mathcal{L} = 1\,\mathrm{fb}^{-1}$ and an assumed syst. err. = 10%) in all the four conditions.

3.2.7. The selection results

The optimised selection cuts discussed above were applied to the background and signal samples. The list of cuts is described in Table 3.3. The expected number of events for a luminosity of 1 fb^{-1} are given in Table 3.4 for the signals and the backgrounds.

Figure 3.15 shows the distributions of the MET, $P_{\mathrm{T}}(\mu_{max})$, $P_{\mathrm{T}}(\mu_{min})$ and $m_{\mu 1\mu 2}$ variables for the signal and the three most important backgrounds after the jet-veto and the following selection cuts applied in the order reported in the Table 3.3.

Figure 3.16 shows the final distribution obtained for the azimuth angle difference between the muons, expected for an integrated luminosity $\mathcal{L} = 10\,\mathrm{fb}^{-1}$ and for the Higgs signal of mass $m_H = 165\,\mathrm{GeV/c^2}$.

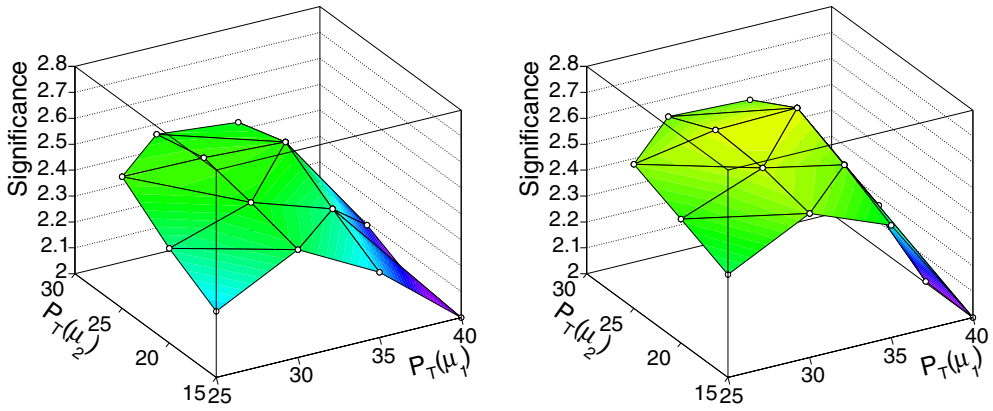

Figure 3.14. Significance as a function of P_T cuts for $m_{\mu_1\mu_2} < 40\,\mathrm{GeV/c^2}$ (left) and for $m_{\mu_1\mu_2} < 50\,\mathrm{GeV/c^2}$ (right) with $\mathcal{L} = 1\,\mathrm{fb}^{-1}$ and syst. err. = 10%

Table 3.3. The list of cuts applied to the signal and background samples.

1	L1+HLT dimuon	6	MET > 50 GeV
2	2 μ opposite charge	7	$35\,\mathrm{GeV/c} < P_T(\mu_{max}) < 55\,\mathrm{GeV/c}$
3	Isolation	8	$25\,\mathrm{GeV/c} < P_T(\mu_{min})$
4	$\eta < 2.0$ $IP < 3\sigma$	9	$m_{\mu_1\mu_2} < 50\,\mathrm{GeV/c^2}$
5	Jet Veto	10	$\Delta\phi_{\mu_1\mu_2} < 0.8$

Table 3.4. The expected number of events for a luminosity of $1\mathrm{fb}^{-1}$ for the signal with Higgs masses between 130 and 180 $\mathrm{GeV/c^2}$ and for the backgrounds.

	L1+HLT dimuon	All cuts	ε_{tot}
$m_H = 130\,\mathrm{GeV/c^2}$	112	0.68 ± 0.19	$(0.07 \pm 0.02)\%$
$m_H = 140\,\mathrm{GeV/c^2}$	162	1.7 ± 0.4	$(0.12 \pm 0.03)\%$
$m_H = 150\,\mathrm{GeV/c^2}$	228	5.3 ± 0.8	$(0.26 \pm 0.04)\%$
$m_H = 160\,\mathrm{GeV/c^2}$	256	12.6 ± 0.7	$(0.58 \pm 0.04)\%$
$m_H = 165\,\mathrm{GeV/c^2}$	264	14.3 ± 0.8	$(0.64 \pm 0.04)\%$
$m_H = 170\,\mathrm{GeV/c^2}$	259	11.0 ± 0.7	$(0.53 \pm 0.03)\%$
$m_H = 180\,\mathrm{GeV/c^2}$	233	5.9 ± 0.8	$(0.30 \pm 0.04)\%$
$qq \to WW$	1040	4.1 ± 0.5	$(0.036 \pm 0.005)\%$
$t\bar{t} \to 2\mu 2\nu$	17007	2.6 ± 0.3	$(0.012 \pm 0.001)\%$
$gg \to WW$	58	1.0 ± 0.1	$(0.18 \pm 0.02)\%$
$\gamma^*, Z \to 2\mu$	720653	0.3 ± 0.3	$(4 \pm 4)10^{-5}\%$
$b\bar{b} \to 2\mu 2\nu$	69374	0	0%
Wt	615	0.57 ± 0.10	$(0.017 \pm 0.003)\%$
ZZ	218	0.18 ± 0.05	$(0.012 \pm 0.003)\%$
ZW	384	0.13 ± 0.05	$(0.008 \pm 0.003)\%$

As stated above, all the numbers at the various selection steps refer to the analysis applied to the HLT dimuon stream. For comparison, the event numbers after all the selection cuts were also studied for the case in which the analysis were performed on the data including the single muon trigger data stream. The inclusion of this datastream, which is foreseen to have a rate about 7 times larger than the dimuon stream [76], would result in a $(3 \pm 1)\%$ increase of

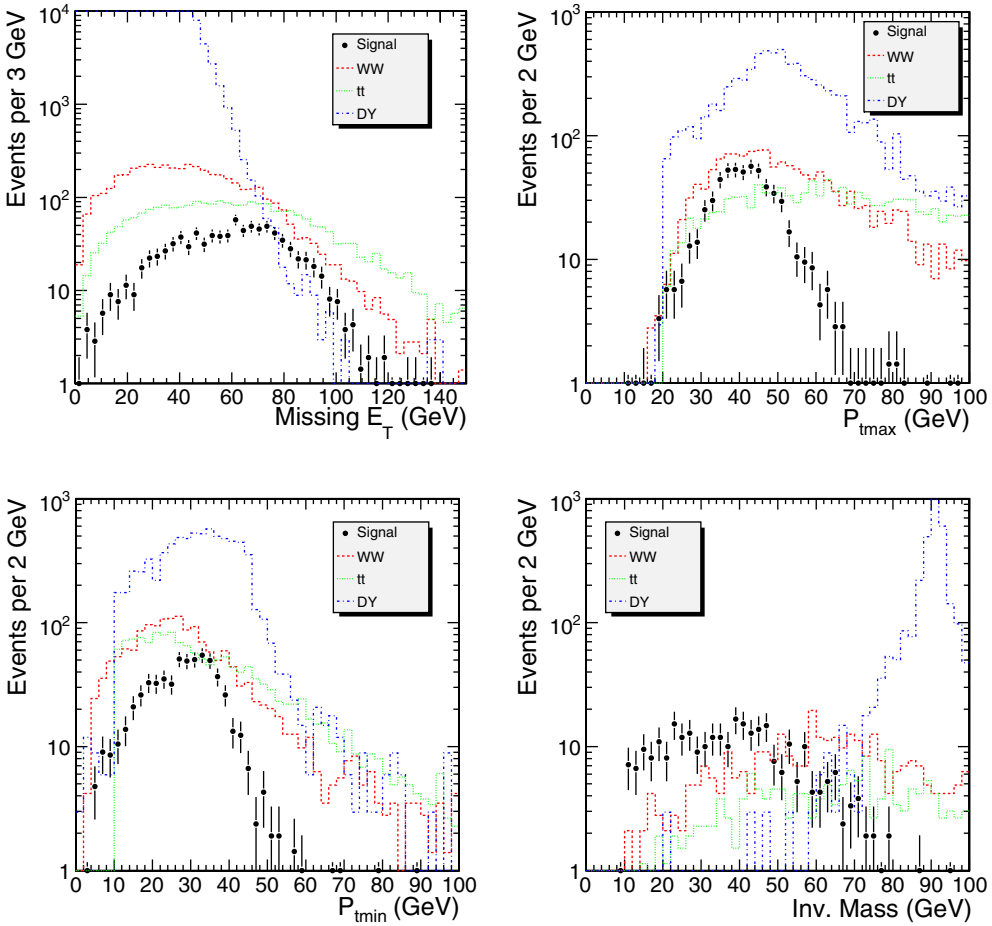

Figure 3.15. Distributions of the missing energy, transverse momentum and invariant mass for a luminosity of 10 fb^{-1} following the cut list order.

the overall signal selection efficiency. The Higgs search with mass appreciably different than 165 $\mathrm{GeV/c^2}$ can take advantage from a dedicated cut optimisation, such as the one reported in [77].

3.2.8. Background estimation and systematics

The precise understanding of the backgrounds is the most critical issue concerning this Higgs discovery channel. The direct use of the Monte Carlo predictions, i.e. $N_{bkg,MC} = \sigma_{bkg,MC} \cdot \varepsilon_{ff}$, leads to high systematic uncertainties due either to theoretical calculation and to experimental systematics. The most reliable approach to address this problem is to measure the different sources of background directly from the data. The commonly used method to extrapolate the background contribution directly from the data consists of selecting a signal-free phase space region (control region) where a given background process is enhanced. The normalisation from data for the two most relevant background, i.e. $t\bar{t}$ and WW has been addressed. For both backgrounds, a dedicated control region was defined. The number of background events in

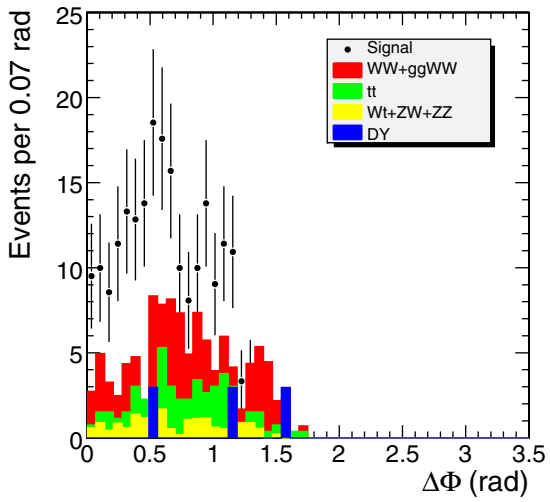

Figure 3.16. Distribution of the angle between the two muons for a luminosity of 10 fb^{-1} at the end of the selection.

the signal region can then be estimated through:

$$N_{signal\_reg} = \frac{N^{MonteCarlo}_{signal\_reg}}{N^{MonteCarlo}_{control\_reg}} N_{control\_reg} \tag{3.17}$$

where $N^{MonteCarlo}_{signal\_reg}$ and $N^{MonteCarlo}_{control\_reg}$ are the numbers of events predicted by the Monte Carlo simulation in the signal and control region. The error on the ratio $N^{MonteCarlo}_{signal\_reg}/N^{MonteCarlo}_{control\_reg}$ accounts for a theoretical contribution (scale variation, PDF uncertainty) and detector systematics effects. The precision with which the number of N_{signal_reg} can be predicted depends also on the statistical error on $N_{control\_reg}$.

3.2.9. $t\bar{t}$ background normalisation

Since the presence of two b-tagged jets is a striking evidence for $t\bar{t}$ events, the most natural control region for this process is then defined by applying the same selection cuts as for the signal region but the jet veto, with the additional request of two b-tagged jets in the detector acceptance[39]. The $t\bar{t}$ evaluation from the data for the $H \to WW^{(*)}$ channel has been studied in Ref. [80] to which we refer for further details. In this study, a jet is tagged as a b-jet if its measured E_{T} is greater then 20 GeV and if there are at least two tracks belonging to the jet (i.e. within a cone of 0.5 around the jet axis) whose σ_{IP} is higher than 2. With such settings the double b-tagging efficiency for $t\bar{t}$ events is $\mathcal{O}(30\%;)$. The mis-tagging rate has been calculated from the ratio between the number of b-tagged jets and the total number of jet with $E_{\mathrm{T}} > 20$ GeV in the fully simulated DY sample and it resulted to be $\mathcal{O}(3\%;)$.

In the following, we consider the background processes in the $t\bar{t}$ control region. For 1fb^{-1} the number of $t\bar{t}$ events in the control region just defined is foreseen to be 17, whereas the contribution from the signal and Wt is completely negligible (in both cases smaller than 0.1 events).

[39] In Ref. [80] an additional control region for $t\bar{t}$ events defined by requiring two high E_{T} jets instead of two b-tagged jets has been proposed. However, it has been shown there, that due to the high contamination from Drell–Yan events, this control region is less indicate for same flavour lepton final states.

Table 3.5. Sources of uncertainty for the $t\bar{t}$ background normalisation procedure. Results are shown for 1, 5 and 10 fb^{-1}.

Luminosity (fb^{-1})	Theoretical error	Detector systematics			Statistical error	Total error
		JES	α criterion	b-tagging		
1	10%	10%	4%	11%	24%	30%
5	10%	6%	4%	9%	11%	19%
10	10%	6%	4%	7%	8%	16%

Not all the processes with $2\mu + 2b + E_t^{\text{miss}}$ as final state have been fully simulated for this analysis, nevertheless general considerations and fast Monte Carlo generator level cross checks lead to exclude other sources of backgrounds, as briefly outlined in the following.

The more natural concurrent process is the non-resonant $W^+W^- \to 2\mu + b\bar{b}$ which is suppressed with respect to $t\bar{t}$. Its cross section is indeed expected to be smaller than $0.3pb$. Assuming the same efficiency for the kinematic selections as for the $W^+W^- \to 2\mu$ ($\sim 0.07\%$) and including the double-b tagging efficiency, less than 0.1 events are expected for 1fb^{-1} in the control region.

In the fully simulated Drell–Yan sample used in this analysis, the eventual additional $b\bar{b}$ pair comes only from a gluon splitting; the main mechanism of $\gamma^*/Z^* + 2b$ is not included. For an estimation of the contamination of the $t\bar{t}$ control region due to this process we thus used a parton level sample generated with a matrix element Monte Carlo (MadGraph [81]). Applying the signal kinematic selections, but the E_{T} cut on the latter sample, ~ 10 events are expected for 1fb^{-1}. The rejection due to E_{T} cut has been calculated from the fully simulated sample where actually two b-quarks were present in the final state and it turned to be smaller than 1%. Considering also the efficiency for the double b-tagging, we can safely exclude this as a dangerous background.

In the following the various contribution of uncertainty in the $t\bar{t}$ normalization procedure are listed and described. The results are summarised in Table 3.5 for 1, 5 and 10 fb^{-1}.

- **Theoretical uncertainty.** The theoretical uncertainty of the $t\bar{t}$ cross section ratio $\sigma_{signal\_reg}/\sigma_{control\_reg}$ has been studied in [82] at parton level with LO precision by varying the reorganisation and factorisation scale. The error has been estimated to range between 3% to 10% mostly due to the choice of PDF. Some studies were done also at NLO: E_{T} spectra and multiplicity of jets are not affected by higher order contributions but the estimate of the theoretical error at NLO is not available. In the following we will, assume the theoretical uncertainty on the $t\bar{t}$ normalisation procedure to be 10%.

- **Jet Energy Scale (JES) uncertainty.** In the background normalisation procedures we proposed, the JES uncertainty is particularly important since it affects in an opposite sense the signal region, defined by vetoing the jets, and the control region where the presence of two jets is required. To take into account this sort of anti-correlation of $\epsilon_{\text{signal\_reg}}$ and $\epsilon_{\text{control\_reg}}$, we estimate the effect of the JES uncertainty directly on their ratio by rescaling the measured jet four momentum by a fractional uncertainty (i.e. $\text{P}^{\mu}_{\text{jet}} = (1+\lambda)P^{\mu}_{\text{jet}}$). The relative variation of $\frac{N^{MonteCarlo}_{signal\_reg}}{N^{MonteCarlo}_{control\_reg}}$ for various values of λ is reported in [77]. The JES uncertainty foreseen at CMS is $\mathcal{O}(5\%)$ for 1fb^{-1} and it is expected to decrease down to $\sim 3\%$ for 5 fb^{-1} (thanks to the calibration on the W mass) [7]. The effect of the JES uncertainty is 10% for 1fb^{-1} and 6% for 5fb^{-1}.

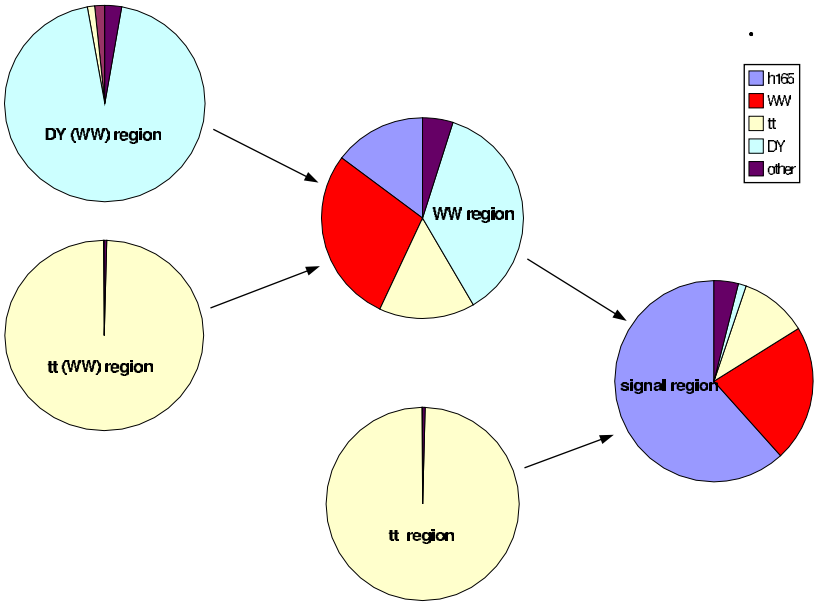

Figure 3.17. Scheme for background normalisation from the data in different phase space regions: the signal region, the $t\bar{t}$ region, the WW region, the DY (WW) region, and the $t\bar{t}$ (WW) region. The arrows indicate the extrapolation of the number of events determined in the corresponding "control region" into the corresponding "target region". Each region is represented by a pie chart that shows the fractions of certain types of events: `h165` is the Higgs signal with $m_h = 165\,\mathrm{GeV/c^2}$, `WW` is the sum of WW backgrounds, $t\bar{t}$ is the $t\bar{t}$ background, `DY` is the Drell–Yan background, and `other` is the sum of the Wt, ZW and ZZ backgrounds. The number of expected events in each region is reported in Table 3.6.

- **α criterion uncertainty.** To estimate the systematic uncertainty due to α criterion, the value of the cut has been varied from 0.15 to 0.25. Moreover, different values of the minimum p_{T} for a track to be included in the sum have been tried, from 2 to 3 GeV/c. The consequent variation of the jet veto efficiency (affecting only $N^{MonteCarlo}_{signal\_reg}$) is relatively small, i.e. of the order of 4%.
- **b-Tagging uncertainty.** The uncertainty on the b-tagging efficiency will be estimated exploiting $t\bar{t}$ events as calibration samples. The precision with which the b-tagging efficiency will be known is expected to be $\pm$ 11% for 1 fb^{-1} integrated luminosity and it is foreseen to improve to $\pm$ 7% with 10 fb^{-1} [83].
- **Uncertainties on the composition of the control region.** As it has been shown in the previous section, $t\bar{t}$ is the dominant process in the chosen control region, other processes contributing less than 1%. It is then safe to simply neglect this source of systematic error.
- **Statistical uncertainty on $N_{control\_reg}$.** Assuming a Poissonian behaviour, the statistical uncertainty scales with the integrated luminosity as the square root of the number of $t\bar{t}$ events in the control region.

3.2.10. WW background normalisation

In contrast to the $t\bar{t}$ background normalisation, which can be performed using an almost completely pure $t\bar{t}$ control sample, it is impossible to isolate the WW background in a

clean way, which means that contributions of other processes have to be subtracted and their systematic uncertainties have to be taken into account during the normalisation procedure of the WW background, including $gg \to W^+W^-$ events. In Fig. 3.17 the overall background normalisation strategy is illustrated. There are four phase space regions involved in the WW background normalisation. Each region is defined with a certain set of cuts:

- signal region: the selection of events in the signal region as described above.
- WW region: same as in the signal region, but $\Delta\phi_{\mu_1\mu_2} = 2 > 0.8$ and $50\,\mathrm{GeV/c^2} < m_{\mu_1\mu_2} < 80\,\mathrm{GeV/c^2}$.
- DY (WW) region: same as in the WW region, but $80\,\mathrm{GeV/c^2} < m_{\mu_1\mu_2} < 100\,\mathrm{GeV/c^2}$.
- $t\bar{t}$ (WW) region: same as in the WW region, but the jet veto is replaced with the requirement of two b-tagged jets ($E_t > 20\,\mathrm{GeV}$ and two tracks with $\sigma_{IP} > 2$).

In all cases, the selection is independent of the Higgs mass hypothesis. The total number of events in each region is given in Table 3.6, and the contributions of individual processes are represented in form of pie charts in Fig. 3.17. The main contamination of the WW region is due to Drell–Yan, $t\bar{t}$ and the Higgs signal. The number of Drell–Yan and $t\bar{t}$ is determined by extrapolating the corresponding numbers from relatively clean control regions and are subtracted from the WW region. Additional small contributions from other backgrounds in the WW region are determined from Monte Carlos and then subtracted. So far, no concrete method has been established to subtract Higgs events from the WW control region. Therefore, we choose the conservative approach to treat these Higgs events as an additional background in the WW region.

- **Theoretical uncertainties.** The theoretical uncertainties of W pair production with subsequent decay to leptons have been studied in detail in Ref. [84], and the main sources of potential uncertainties of the shapes of kinematic variables turn out to be spin correlations, underlying event, and scale dependence. The effect of spin correlations can be taken into account properly with the correct choice of an event generator, and the underlying event is expected to be measured from the data with sufficient precision. The shape dependence on the choice of the reorganisation and factorisation scales is sizable in case of the contribution from the $gg \to W^+W^-$ subprocess, because the higher order corrections are unknown in this case. For the cuts, described below, this uncertainty is about 9% and is taken into account in the following.
- **Statistical error and uncertainties on the composition of the control region.** All background normalisation uncertainties are calculated in the following way:

$$\delta_{\text{extrapolation}} = \sum_i \sqrt{n_{\text{total}} + (n_i \times \delta_i)^2} \times \varepsilon_{\text{control}\to\text{target}} \tag{3.18}$$

  where n_{total} is the total number of events[40] in the corresponding control region, $n_i \times \delta_i$ is the product of the number of events and the systematic uncertainty of an individual process in the control region, and $\varepsilon_{\text{control}\to\text{target}}$ is the extrapolation efficiency from the control region to the target region, e.g. the signal region.

The WW background normalisation requires three extrapolations from control regions to target regions:

- DY (WW) region $\Rightarrow$ WW region: with an extrapolation uncertainty of 5% [85] the extrapolated number of events and the uncertainty from Eq. 3.18 is 15.86 ± 1.23 events (79.29 ± 4.49 events) for $1\,\mathrm{fb^{-1}}$ ($5\,\mathrm{fb^{-1}}$) of integrated luminosity.

[40] This term takes into account the statistical fluctuations of the control sample.

Table 3.6. Number of expected events in all the regions with an integrated luminosity of 1 fb^{-1}. The signal region numbers are referred to $m_H = 165\,GeV/c^2$.

Channel	Signal region	$t\bar{t}$ region	WW region	$t\bar{t}$ (WW) region	DY (WW) region
Signal	**14.3**	0.0	6.0	0.0	0.1
$t\bar{t}$	2.6	**17.0**	6.2	24.7	3.2
WW	5.1	0.0	**11.5**	0.0	4.4
DY	0.3	0.0	15.0	0.0	267
Wt,ZZ,WZ	0.8	0.1	1.9	0.1	7.3
all	23.1	17.1	40.6	24.8	282

- $t\bar{t}$ (WW) region $\Rightarrow$ WW region: with an extrapolation uncertainty of 20% (15%) [80] the extrapolated number of events and the uncertainty from Eq. 3.18 is 6.19 ± 1.75 events (30.93 ± 5.41 events) for 1 fb^{-1} (5 fb^{-1}) of integrated luminosity.
- WW region $\Rightarrow$ signal region: as illustrated in Fig. 3.17, the first two items are inputs to this extrapolation, which means that the obtained numbers of Drell–Yan and $t\bar{t}$ events are subtracted in the WW region and the corresponding uncertainties are propagated. The extrapolation uncertainty of WW events, which is mainly due to the unknown higher order correction of the $gg \rightarrow W^+W^-$ contribution [84], amounts to 9% for the cuts used in this analysis. In addition, the remaining backgrounds are estimated and subtracted with the following uncertainties: δ_{Wt} =40%, δ_{ZW} =20% and δ_{ZZ} =20%. According to Eq. 3.18 we obtain 7.35 ± 3.04 events (36.77 ± 7.85 events) for 1 fb^{-1} (5 fb^{-1}) of integrated luminosity.

The results of the last item are used for the calculation of the Higgs discovery potential with m_h =165 GeV/c^2, and an integrated luminosity of either 1 fb^{-1} or 5 fb^{-1}.

Furthermore, it should be pointed out that the entire background normalisation procedure is performed using only the dimuon data set and therefore no additional data sets are needed. In this way, potential uncertainties due to different trigger efficiencies and different integrated luminosities of other data sets do not play a role.

3.2.11. Other backgrounds normalisation

The Drell–Yan background has been normalised to estimate the contamination in the WW region. The same results can be achieved in the signal region. Figure 3.15 demonstrates that the invariant mass cut 80 GeV/c^2 to 100 GeV/c^2 defines a clean control region. ZW background can be normalised by requiring one additional lepton in the final state and removing the $\Delta\phi$ and the invariant mass cuts. ZZ background can be normalised by requiring two additional leptons in the final state and removing the $\Delta\phi$ and the invariant mass cuts. They are expected to contribute to the total background by only 3% (DY), 1% (ZW) and 1% (ZZ). For the Wt background, it is not easy to define a normalisation region. As this process is expected not to represent a sizable fraction of the total background ($\sim$ 6%), the Monte Carlo prediction will be then directly used, the cross section theoretical uncertainty is estimated to be about 30% at LO and 10% at NLO [75].

3.2.12. Detector misalignment systematics

A study for the misalignment impact on the track reconstruction has been done [86]. In the fist data scenario (100 pb^{-1}–1fb^{-1}) the muon chamber position uncertainty is expected to be 1 mm and the orientation uncertainty about 0.2 mrad. The tracker position uncertainty is expected to be about 5 μm for TPE, 10 μm for TPB, 50 μm for TEC and TOB, 100 μm

Table 3.7. Total background and error for integrated luminosity of 1 and 5 fb^{-1}. The two options for the signal contamination in the WW control region were considered.

Option	Luminosity	Total background	Total error
1.	1 fb^{-1}	8.8	3.2 (36%)
	5 fb^{-1}	44.0	8.3 (19%)
2.	1 fb^{-1}	11.0	3.2 (29%)
	5 fb^{-1}	55.3	8.3 (15%)

for TIB and 400 μm for TID. The results from simulation show the muon reconstruction efficiency will be unaffected, while the momentum resolution (for 100 GeV/c tracks) will be reduced from 1–2 % to 4–5%. Under these circumstances, the systematic contribution to the signal and background selection is expected to be negligible with respect to the background normalisation systematics.

3.2.13. Signal significance

The signal significance can be obtained using counting or Likelihood methods. Here, the counting S_{cP} method (See Appendix A) was used. S_{cP} is the probability, converted in equivalent number of sigmas, to observe at least $N_s + N_b$ events from Poisson distribution with mean N_b. The presence of systematic errors influences the significance calculations. The hypothesis is to find the same number of signal and background events predicted by the Monte Carlo. The systematic errors due to the $t\bar{t}$ and WW background normalisation methods were included. Two options were considered:

1. the signal contamination in the WW control region can be subtracted;
2. the signal contamination in the WW control region must be considered as additional background.

The option 1 was considered to have a comparison with the $H \to WW \to 2l2\nu$ analysis [73]. Table 3.7 summaries the total backgrounds and errors for different integrated luminosities. The systematics and statistical errors due to the limited Monte Carlo statistics are included.

The signal to background ratio as a function of different Higgs masses and the signal significance are shown in Fig. 3.18.

3.2.14. Conclusions

The possibility to discover the Higgs boson particle through its decay channel into $(WW^{(*)} \to 2\mu 2\nu$ was studied in detail. Particular attention was given to the event selection optimisation, in the determination of the number of background events from the data and the evaluation of the experimental and theoretical systematical uncertainties. Taking all these effects into account, it was shown that in the Higgs mass range 155–175 $\mathrm{GeV/c^2}$ a signal significance bigger than 3 standard deviations can be achieved with 5 fb^{-1} integrated luminosity. On the other hand, with 1 fb^{-1} luminosity only a 2 sigma significance can be achieved even in the most favourable case $m_H \sim 2m_W$, when this final state topology alone is used for the Higgs search.

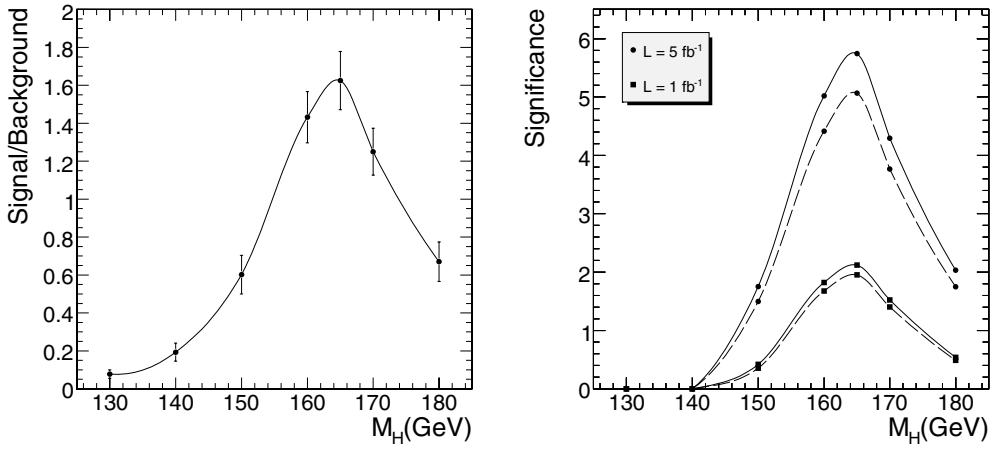

Figure 3.18. Signal to background ratio for the option 1 as a function of different Higgs masses. Error bars are the statistical contribution due to the limited Monte Carlo statistics (left). Significance as a function of different Higgs masses with a luminosity of 1 and 5 fb^{-1}, solid line for the option 1, dashed line for the option 2 (right).

3.3. Benchmark Channel: $Z' \to \mu\mu$

3.3.1. Introduction

Additional heavy neutral gauge bosons (Z′) are predicted in many superstring-inspired [87, 88] and grand unified theories (GUTs) [89], as well as in dynamical symmetry breaking [90] and "little Higgs" [91] models. There are no reliable theoretical predictions, however, of the Z′ mass scale. Current lower limits on the Z′ mass are (depending on the model) of the order of 600–900 GeV/c^2 [54]. The mass region up to about $1TeV/c^2$ is expected to be explored at Run II at the Tevatron [92, 93]. The LHC offers the opportunity to search for Z′ bosons in a mass range significantly larger than $1TeV/c^2$.

Observability of the $Z' \to \mu^+\mu^-$ channel in CMS is discussed in Sections 3.3.2–3.3.4. Since narrow graviton resonances such as those in Randall–Sundrum models [94] can also decay to lepton pairs (Section 14.3.1), much of the discussion in these sections is also applicable to them. If a new resonance is discovered, the characterisation of its spin and couplings will proceed via the traditional methods of measuring production and decay probabilities and distributions. For example, the two-photon decay should be observable for a graviton and not for a Z′, as discussed in Section 14.6. The measurement of forward-backward asymmetries of leptonic decay products, both at the resonance peak and off the peak, yields information on parity-violating couplings and hence can help distinguish among different Z′ models (Section 3.3.5). Angular distributions of the decay products can also be used for spin discrimination (Section 3.3.6). A simulated event of a dimuon decay of $3\,TeV/c^2$ Z′ is shown in colour plate CP5.

3.3.2. Signal and background processes

3.3.2.1. Signal $Z' \to \mu^+\mu^-$. Signal and background samples were generated with PYTHIA [69] version 6.227 (with photon emission off incoming or outgoing quarks and leptons switched on) and the CTEQ6L set of parton distribution functions [12] from LHAPDF [95] version 4.1.1.

Table 3.8. Summary of expected properties of Z′ bosons for six studied models. For each model, the first column shows the ratio of the total Z′ decay width Γ to its mass M, the second column shows the dimuon branching ratio Br. The three middle columns, labelled $\sigma^{\mathrm{LO}} \cdot \mathrm{Br}$, give the product of the pure-Z′ leading-order production cross section and the branching ratio for three studied Z′ masses; the last three columns give $\sigma^{\mathrm{LO}} \cdot \mathrm{Br}$ obtained when the full $\gamma^*/\mathrm{Z}^0/\mathrm{Z}'$ interference structure is included. The numbers quoted are for the mass intervals above 400 GeV/c^2 for $M = 1$ TeV/c^2, above 1.5 TeV/c^2 for $M = 3$ TeV/c^2, and above 3 TeV/c^2 for $M = 5$ TeV/c^2. The values of $\sigma \cdot \mathrm{Br}$ in the three middle columns correspond to Z′-only samples not used in our study; the values in the last three columns refer to the full-interference samples that we did use.

Model	Γ/M%	$\mathrm{Z}' \to \mu^+\mu^-$ BR in %	$\sigma^{\mathrm{LO}} \cdot \mathrm{Br}$, fb (PYTHIA)			$\sigma^{\mathrm{LO}} \cdot \mathrm{Br}$, full interference, fb (PYTHIA)		
			1 TeV/c^2	3 TeV/c^2	5 TeV/c^2	1 TeV/c^2	3 TeV/c^2	5 TeV/c^2
$\mathrm{Z}_{\mathrm{SSM}}$	3.1	3.0	480	1.9	0.034	610	2.8	0.050
Z_{ψ}	0.6	4.0	130	0.5	0.009	340	1.7	0.032
Z_{η}	0.7	3.4	150	0.6	0.011	370	1.8	0.035
Z_{χ}	1.3	5.7	280	1.0	0.014	500	2.2	0.038
$\mathrm{Z}_{\mathrm{LRM}}$	2.2	2.3	310	1.2	0.020	500	2.3	0.040
$\mathrm{Z}_{\mathrm{ALRM}}$	1.6	8.6	580	2.6	0.051	740	3.7	0.077

From a large variety of Z′ bosons described in the literature, we consider six which are frequently discussed, and whose properties are representative of a broad class of extra gauge bosons:

- $\mathrm{Z}_{\mathrm{SSM}}$ within the Sequential Standard Model (SSM), which has the same couplings as the Standard Model Z^0; it is available in PYTHIA [24].
- Z_{ψ}, Z_{η} and Z_{χ}, arising in E_6 and SO(10) GUT groups. Couplings to quarks and leptons were obtained from Refs. [96, 97].
- $\mathrm{Z}_{\mathrm{LRM}}$ and $\mathrm{Z}_{\mathrm{ALRM}}$, arising in the framework of the so-called "left–right" [98] and "alternative left–right" [92, 93] models. Their couplings were obtained from Ref. [92, 93], with the choice of $g_R = g_L$.

The generation of signal events with PYTHIA includes the full $\gamma^*/\mathrm{Z}^0/\mathrm{Z}'$ interference structure. We assume that Z′ bosons decay only to three ordinary families of quarks and leptons and that no exotic decay channels are open. Properties for these models are in Table 3.8. The cross sections are shown at leading order (LO), as predicted by PYTHIA. We scale them by a constant K factor of 1.35, see Appendix C, in order to take into account the next-to-next-to-leading order (NNLO) QCD corrections. Electroweak higher-order corrections are not yet accounted for (see discussion in Section 3.3.4.4.1).

3.3.2.2. Background from Drell–Yan production and other processes. The dominant (and irreducible) background to $\mathrm{pp} \to \mathrm{Z}' \to \mu^+\mu^-$ is the Drell–Yan production of muon pairs, $\mathrm{pp} \to \gamma/Z^0 \to \mu^+\mu^-$. The Drell–Yan cross section in PYTHIA was scaled by the same K factor of 1.35, see Appendix C, to get an agreement with the NNLO QCD calculations.

The overall contribution from ZZ, ZW, WW, and $t\bar{t}$ was found to be at the level of only a few percent of the Drell–Yan background and can be further suppressed by signal-selection criteria with almost no reduction in signal efficiency; we neglect this contribution. A few other potential background sources (like cosmics, jet-jet, W-jet, $b\bar{b}$, hadron punchthroughs, and poorly measured $\mathrm{Z}^0 \to \mu^+\mu^-$ events) have not been studied yet, but their contribution is expected to be small.

3.3.2.3. Simulation and reconstruction. The detector response was simulated with the detailed CMS detector simulation and reconstruction software, including pile-up events. Misalignments of the tracker and of the muon system expected at the initial and at the well-advanced stages of the data taking have been taken into account by using two misalignment scenarios developed in the framework of the CMS reconstruction, referred to as the "first data" and the "long term" scenarios [86]:

- The "first data" scenario gives an estimate of the alignment achieved with an integrated luminosity of about $0.1\,\mathrm{fb}^{-1}$ and corresponds to the situation when the pixel detector is aligned with tracks and the first information from the Laser Alignment System (LAS) is available for the muon detectors.
- The "long term" scenario describes the expected residual alignment uncertainties. Once the performance of the LAS reaches its design level and the alignment with tracks is done in all tracking detectors. The current estimate is that, this can be achieved with an integrated luminosity of about $1\,\mathrm{fb}^{-1}$.

As a result, for each of the Z′ models above, several sets of simulated samples corresponding to different possible combinations of luminosities and misalignment scenarios were produced at each of three mass values of 1, 3, and $5\,\mathrm{TeV/c^2}$. Since the Drell–Yan cross section falls rapidly with the mass of the muon pair, Drell–Yan background was generated in six mass intervals (with lower mass bounds of 0.2, 0.4, 1, 1.5, 2, and $3\,\mathrm{TeV/c^2}$), again for different combinations of luminosities and misalignment scenarios.

3.3.3. Event selection

For $\mu^+\mu^-$ invariant mass between $1\,\mathrm{TeV/c^2}$ and $5\,\mathrm{TeV/c^2}$, the fraction of Drell–Yan events with both muons within the full geometrical acceptance of the muon system ($|\eta| < 2.4$) increases from about 80% at $1\,\mathrm{TeV/c^2}$ to almost 95% at very high masses. The acceptance of $\mathrm{Z}' \to \mu^+\mu^-$ events is very similar.

We require that the event pass the logical OR of single-muon and dimuon triggers, both Level-1 and HLT. We use the default ORCA implementations of low-luminosity and high-luminosity muon trigger algorithms described in Refs. [7, 76], with the exception of the HLT calorimeter isolation criterion requiring that the weighted sum of energy deposits in ECAL and HCAL in a cone around the muon direction be below a pre-defined threshold. Its current implementation leads to significant efficiency losses for *isolated* high-p_T muons (since they are often accompanied by electromagnetic showers); we do not apply HLT calorimeter isolation in this study (tracker isolation is applied). An increase in the trigger rate in the absence of calorimeter isolation should be mitigated by higher p_T thresholds; we have checked that raising the p_T thresholds of the single-muon HLT by 10–20 GeV with respect to their nominal values changes trigger efficiency for our signals by a negligible amount. For the Z′ models that we study (as well as for the Drell–Yan background), the combined Level-1/HLT trigger efficiency is about 98% at $1\,\mathrm{TeV/c^2}$ and decreases with the Z′ mass down to about 95% at $5\,\mathrm{TeV/c^2}$. At high luminosity, the trigger efficiency is 95% at $1\,\mathrm{TeV/c^2}$ and 93% at $5\,\mathrm{TeV/c^2}$. These efficiencies are relative to having at least one muon inside the geometrical acceptance of the muon trigger ($|\eta| < 2.1$) and both muons from the Z′ decay inside the full acceptance of the muon system. No dependence of trigger efficiency on tracker and muon misalignment has been observed, in agreement with the results reported in Ref. [99].

We require that at least two muons of opposite sign charge be reconstructed offline. Detailed description of offline muon reconstruction can be found in Ref. [7]. For each muon candidate, we examine the results of fits to two subsets of hits associated to this

candidate: (1) excluding all muon hits except for those in the innermost muon station, and (2) excluding hits in muon chambers appearing to contain electromagnetic showers. Optimal performance for high-p_T muons is achieved by choosing the best fit on a track-by-track basis using goodness-of-fit variables. The fraction of Z′ events with an opposite-sign dimuon reconstructed offline is about 97% at 1 TeV/c^2 for both the "first data" and the "long term" misalignment scenarios, and decreases slightly with the Z′ mass, to about 95% at 5 TeV/c^2 for the "long term" misalignment scenario. The efficiencies quoted are calculated relative to the number of events accepted by the trigger and with both muons from the Z′ decay within the full geometrical acceptance of the muon system.

The overall efficiency – including acceptance, trigger and offline reconstruction – for $Z' \to \mu^+\mu^-$ events with a mass between 1 and 5 TeV/c^2 lies in the range of 77–85% at low luminosity, and of 75–83% at high luminosity.

3.3.4. Signal observability

The search for a new resonance is performed with an unbinned maximum likelihood fit to the $\mu^+\mu^-$ invariant mass spectrum over a range which includes Drell–Yan continuum as well as a possible peak. The fit takes as input the presumed signal and background shapes, and determines the best-fit background normalisation. More details are given in Refs. [100, 101].

3.3.4.1. Mass spectra and fitting procedure. Prior to the calculation of the invariant mass of an opposite-sign muon pair, $\sqrt{s}$, a search for photon candidates in a cone with a radius of $\Delta R = \sqrt{(\Delta\phi)^2 + (\Delta\eta)^2} < 0.1$ around the trajectory of each muon is performed, and the 4-momentum of the photon candidate with the smallest ΔR in the cone is added to the 4-momentum of the muon. This procedure recovers some of the energy lost by the muon via final state radiation and radiative processes in the detector, thus improving the invariant mass resolution.

The resolution for $\sqrt{s}$ depends strongly on the misalignment scenario, and weakly on the amount of pile-up. If the "long term" misalignment scenario for the tracker and the muon chambers is considered, the sigma of the Gaussian fit to the mass resolution curves varies from 4.2% at 1 TeV/c^2 to 9.0% at 5 TeV/c^2; the RMS truncated at ±30% is ∼ 6% at 1 TeV/c^2 and ∼ 10% at 5 TeV/c^2. The corresponding numbers for the "first data" misalignment scenario at 1 TeV/c^2 are σ=12.5% and RMS ∼ 12%. The bias in the mass resolution does not exceed 1% for the "long term" scenario at all masses considered and for the "first data" scenario at 1 TeV/c^2.

An example of the $\sqrt{s}$ spectra showing 1 TeV/c^2 Z_η signal and Drell–Yan background is in Fig. 3.19. The left-hand plot shows generated mass spectra (100% efficiency with no detector- and reconstruction-related effects); it can be compared to the right-hand plot for fully-recon structed events using the "first data" misalignment scenario. Signal peak is clearly visible in spite of the poor mass resolution.

The mass spectra in Fig. 3.19 are obtained by re-scaling the simulated spectra with large statistics down to a modest number of events characteristic for the regime close to the discovery limit; the statistical fluctuations are thus not to scale. In what follows, we use ensembles of Monte Carlo pseudo-experiments selected from available large-statistics samples. The number of events in each experiment, N_{evt}, fluctuates according to a Poisson distribution with a mean of $\sigma \cdot \mathrm{Br} \cdot \int \mathcal{L}dt \cdot \varepsilon$, where $\int \mathcal{L}dt$ is the integrated luminosity and ε is the combined trigger and reconstruction efficiency.

In order to test for the existence of a resonance and to measure its parameters if it is found to exist, an unbinned maximum likelihood fit of the $\sqrt{s}$ values in each MC experiment

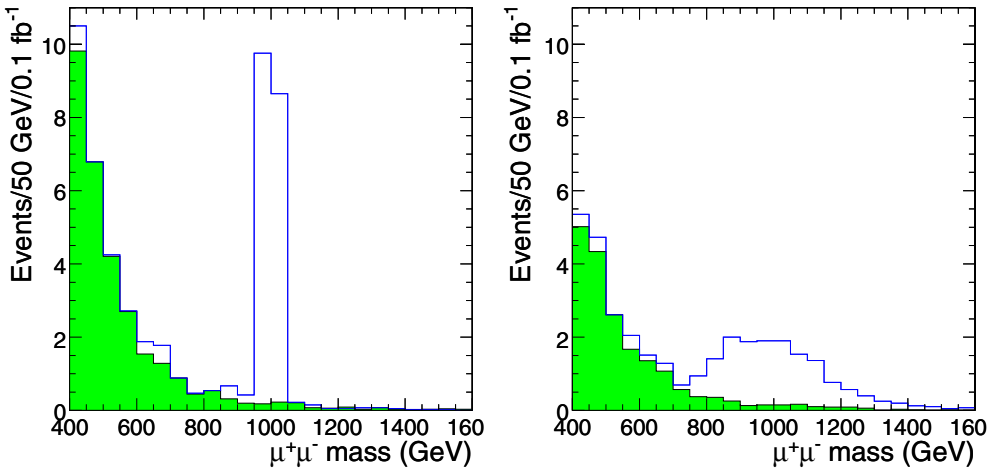

Figure 3.19. Histograms of the $\mu^+\mu^-$ invariant mass for 1 TeV/c^2 Z_η plus background (open histogram) and for background only (shaded histogram), at the event-generator level (left) and for events selected by the Level-1/HLT triggers and reconstructed assuming the "first data" misalignment scenario (right). The number of events per bin is normalised to an integrated luminosity of 0.1 fb^{-1}.

is appropriate. One can imagine that, in the initial data analysis, one is confident about the background shape but not the absolute normalisation. In this case, data can be fit with a sum of signal and background shapes, presumed known, with the signal fraction as a free parameter. In the presence of a signal, one can fix or let vary the mass and the width as well. Thus, as a model of the probability density function (pdf), p, of the parent population of the observed mass spectra, we use

$$p\,(\sqrt{s};\ f_s, m_0, \Gamma) = f_s \cdot p_s\,(\sqrt{s}; m_0, \Gamma) + (1 - f_s) \cdot p_b\,(\sqrt{s}). \tag{3.19}$$

Here:

- p_s, the pdf of the signal, is a convolution of a Breit–Wigner signal shape with a Gaussian accounting for mass resolution smearing. The convolution includes the dependence of the mass resolution on $\sqrt{s}$, but the radiative tail of the signal is not yet accounted for.
- p_b, the pdf of the background, is modelled as an exponential, $\exp(-k\cdot\sqrt{s}^{0.3})$, with the parameter k determined from fits to Drell–Yan events. This pdf, with the value of k of 2.0, gives a good description of the background shape in the whole mass region between 400 and 5000 GeV/c^2.

There are three free parameters in the fit: the signal fraction $f_s = N_s/(N_s + N_b)$, the position of the mass peak m_0, and the full width at half maximum (FWHM), Γ, of the signal. The shape of the background distribution is fixed, while its level is determined by the fit: f_s is a free parameter. Therefore, the fit explores the difference *in shape* between the signal and the background, and is not sensitive to uncertainties in the expected signal and background levels.

The background shape is currently determined from fits to large-statistics background-only simulated distributions in the full mass region of interest, including the region under the signal peak. In the real experiment, the shape will likely have to be extracted from the data in signal-free regions. The accuracy of predicting the background shape is an important contribution to the systematic uncertainty of the analysis and is discussed in Section 3.3.4.4.3.

Table 3.9. Average values of the likelihood-ratio significance estimator $S_{\mathcal{L}}$ for six different Z′ models, at three signal mass points and for a few representative values of an integrated luminosity. The uncertainties shown are statistical only.

Mass	1 TeV/c^2	3 TeV/c^2	5 TeV/c^2
$\int \mathcal{L}dt$	0.1 fb^{-1}	10 fb^{-1}	300 fb^{-1}
Z_{SSM}	12.4 ± 0.2	10.1 ± 0.2	5.8 ± 0.1
Z_{ψ}	5.1 ± 0.2	4.4 ± 0.1	2.4 ± 0.2
Z_{η}	5.5 ± 0.2	5.1 ± 0.1	2.9 ± 0.1
Z_{χ}	9.1 ± 0.2	6.7 ± 0.2	3.2 ± 0.1
Z_{LRM}	9.0 ± 0.2	7.4 ± 0.2	4.1 ± 0.1
Z_{ALRM}	13.3 ± 0.3	11.8 ± 0.2	7.7 ± 0.2

Ref. [100] contains examples of results of fits to Monte Carlo small-event samples. With even the small number of events needed to give evidence of a resonance, the mass is determined fairly well, with a precision of 4–8% depending on the resonance mass and alignment uncertainties. However, for the narrow resonances under study, typically little information can be obtained about the width.

3.3.4.2. Significance estimator. We follow closely the approach of Ref. [102], which is based on the theorem of Wilks [103]. The test statistic is the likelihood-ratio estimator $S_{\mathcal{L}}$:

$$S_{\mathcal{L}} = \sqrt{2 \ln \left(\mathcal{L}_{s+b} / \mathcal{L}_b \right)} \,, \tag{3.20}$$

where $\mathcal{L}_{s+b}$ is the maximum likelihood value obtained in the full signal-plus-background fit, and $\mathcal{L}_b$ is the maximum likelihood from the background-only fit. Studies show [100] that in the small-statistics low-background regime characteristic of a Z′ search, the asymptotic conditions of Wilks's theorem [103] are satisfied well enough and $S_{\mathcal{L}}$ is the number of Gaussian-equivalent standard deviations a measurement lies from the value predicted by a background-only (null) hypothesis. This requires fixing both m_0 and Γ in the fits using the pdf of Eq. (3.19).

We follow a common convention in using the (arbitrary, but useful for comparison) specification that $S > 5$ is necessary to establish a discovery. This S refers to the local excess without accounting for the degree of freedom due to the unknown mass; how one might derate S in a time-dependent way in this context as data comes in will be the subject of a future study.

3.3.4.3. Discovery potential in $Z' \to \mu^+\mu^-$ channel. Table 3.9 gives a summary of the signal significance expected for different Z′ models, masses and integrated luminosities. The numbers shown are for the "first data" misalignment scenario and low luminosity parameters for $\int \mathcal{L}dt = 0.1$ fb^{-1}, the "long term" misalignment scenario and low luminosity parameters for 10 fb^{-1}, and the "long term" misalignment scenario and high luminosity parameters for 300 fb^{-1}. $S_{\mathcal{L}}$ scales as expected with the square root of $\int \mathcal{L}dt$.

We use the same combinations of luminosities and misalignment scenarios to calculate the integrated luminosity needed to reach 5σ significance. The results for various Z′ models are shown in Fig. 3.20 as a function of Z′ mass. One can see that:

- A very low integrated luminosity, less than 0.1 fb^{-1}, and non-optimal alignment of the tracker and the muon detectors should be sufficient to discover Z′ bosons at 1 TeV/c^2, a mass value which will likely be above the Tevatron reach. One would need about 50% less data to reach the same signal significance if, the optimal alignment is achieved.

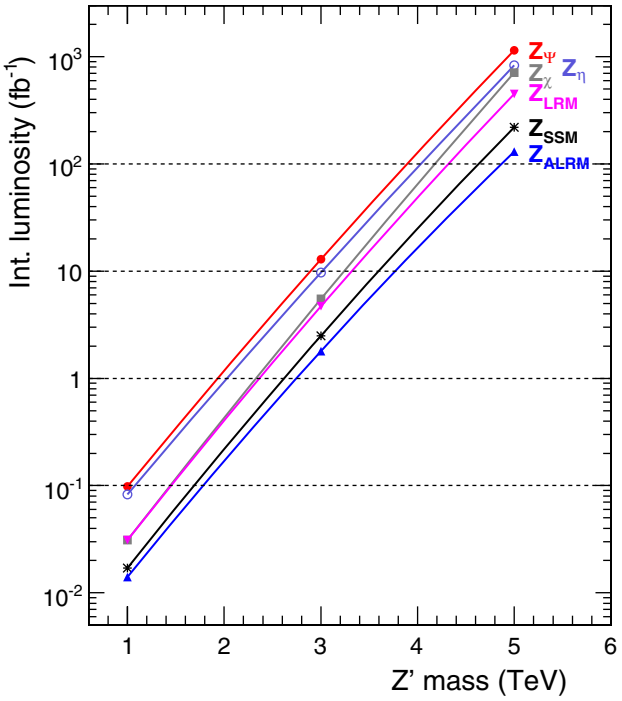

Figure 3.20. Integrated luminosity needed to reach 5σ significanc ($S_{\mathcal{L}}$=5) as a function of Z′ mass for (top to bottom) Z_ψ, Z_η, Z_χ, Z_{LRM}, Z_{SSM} and Z_{ALRM}. Symbols indicate fully-simulated mass-luminosity points, lines are the results of interpolations between the points.

- An integrated luminosity of $10\,\text{fb}^{-1}$ is sufficient to reach 5σ significance at $3\,\text{TeV/c}^2$ for most (but not all) of the Z′ models considered if the optimal alignment is available: depending on the model, the mass reach is in the range between 2.9 and $3.8\,\text{TeV/c}^2$.
- An integrated luminosity of $100\,\text{fb}^{-1}$ does not allow one to obtain 5σ significance at $5\,\text{TeV/c}^2$ with only the $Z' \to \mu^+\mu^-$ channel for any of the models considered: the corresponding mass reach lies in the region between 3.9 and $4.9\,\text{TeV/c}^2$.

These estimates of signal significance do not incorporate systematic uncertainties, which we discuss in the next section.

3.3.4.4. Systematic uncertainties. The main sources of systematic uncertainties are expected to be (a) theoretical uncertainties (parton distributions, higher-order corrections, etc.), (b) uncertainties arising from an imperfect knowledge of the detector (alignment, calibration, magnetic field), and (c) uncertainties in the fitting procedure (background shape, functional forms of pdf's, mass resolution, etc.).

3.3.4.4.1. Theoretical uncertainties. Our current estimates of the Z′ mass reach depend on the accuracy of the modelling of the Standard Model processes and of the Z′ boson production. The following sources of theoretical uncertainties have been studied.

- **Higher-order QCD corrections.** We use a constant $K_{\text{QCD}}^{\text{NNLO}}$ factor of 1.35 to rescale PYTHIA cross sections for Drell–Yan and Z′ bosons to NNLO QCD predictions. This is an approximation, since such a reweight does not take into account variations of the ratio of NNLO and LO cross sections with the invariant mass and other observables, such as rapidity and p_{T}. It is shown in Appendix C that the variations of the $K_{\text{QCD}}^{\text{NNLO}}$ factor with the mass in

the mass interval between 500 GeV/c^2 and 5 TeV/c^2 is in the range of $\Delta K_{\rm QCD} = \pm 0.05$; the dependence on other observables and the ensuing impact on acceptance, efficiency, etc. remains to be studied. Since K is expected to be nearly identical for the signal and dominant background, the effect of changes in K from the nominal value $K_0 = 1.35$ is to scale the expected significance by $\sqrt{K/K_0}$.

- **Higher-order electroweak corrections.** Only preliminary estimates of electroweak next-to-leading order corrections exist for the LHC and $\sqrt{s} > 1$TeV/c^2 [104, 105]. Currently, we use $K_{\rm EW} = 1$ for the central values of signal and background cross-sections, and assign an uncertainty of $\Delta K_{\rm EW} = \pm 0.10$ based on discussions in Refs. [104, 105].
- **Parton distribution functions (PDFs).** We use the CTEQ6.1M eigenvector PDF sets [12] and the "master" equations in Ref. [106] to evaluate the uncertainties characterising current knowledge of the parton distributions. The effect on the total cross section σ was found to be similar for the Drell–Yan background and for the studied Z′ models at any given mass, with uncertainties lying in the range of $\frac{\Delta\sigma}{\sigma} = ^{-7\%}_{+4\%}$ at $\sqrt{s} = 1$ TeV/c^2, rising to $^{-10\%}_{+12\%}$ at $\sqrt{s} = 3$ TeV/c^2, and reaching as much as $^{-20\%}_{+30\%}$ at $\sqrt{s} = 5$ TeV/c^2. The effect on other observables and on the acceptance has not been studied yet, but is expected to be small.
- **Hard process scale.** The dependence of the observables on the choice for renormalisation and factorisation Q^2 scales, μ_R and μ_F, is unphysical and is commonly taken as a rough estimate of the uncertainty due to unaccounted higher orders in QCD calculations. The study of the sensitivity of the Drell–Yan cross section to the choice for the QCD scale is described in Appendix C. Both μ_F and μ_R were varied in the range of $\sqrt{s}\ /2 < \mu < 2\ \sqrt{s}$ around the default choice of $\mu = \sqrt{s}$, and the mass-dependent variations of the cross section obtained. At NNLO, they are smaller than $\pm 1\%$ at 1 TeV/c^2, but as large as -25% (for $\mu = 2\sqrt{s}$) and +5% (for $\mu = 2\sqrt{s}$) at 5 TeV/c^2. We use the NNLO estimates given in Appendix C for both the Drell–Yan and the Z′ bosons.

Since our analysis relies only on the background shape and not on any assumptions about background normalisation, the uncertainties in signal and background cross sections described in this section will not have any direct impact on the calculation of significance once a data set is in hand. They do effect, however, estimates of the Z′ mass reach based on Monte Carlo predictions for the signal and the background. We combine them in quadrature, and use the obtained mass-dependent band as 1σ uncertainty in the expected number of signal and background events. This band is then translated into 1σ uncertainty in the prediction of the mean integrated luminosity needed to reach 5σ significance for any given Z′ model. This uncertainty, and the best estimates of the luminosity, is shown in Fig. 3.21 for the models with the smallest and the largest values of $\sigma \cdot$ Br among the models studied, Z_ψ and $Z_{\rm ALRM}$.

3.3.4.4.2. Uncertainties in the detector performance. The key element in the performance of high-$p_{\rm T}$ muon reconstruction and, therefore, for the Z′ mass reach is the alignment of the tracker and the muon system. Unlike the muons in the region of low and moderate $p_{\rm T}$ values, where the influence of the tracker alignment is predominant, both the tracker alignment and the muon system alignment play an important role for the muons at TeV scale. We take them into account by using the two realistic misalignment scenarios developed in the CMS reconstruction, the "first data" and the "long term". These scenarios, however, are only based on the current best estimates (and sometimes guesses) of expected alignment uncertainties and will be refined as better estimates from alignment studies become available. Therefore, they have intrinsic uncertainties, which at the moment cannot be evaluated. As discussed above and in Ref. [99], neither the trigger efficiency nor the offline reconstruction efficiency for high-$p_{\rm T}$ muons is affected by the misalignment even in the worst-case scenario once the alignment

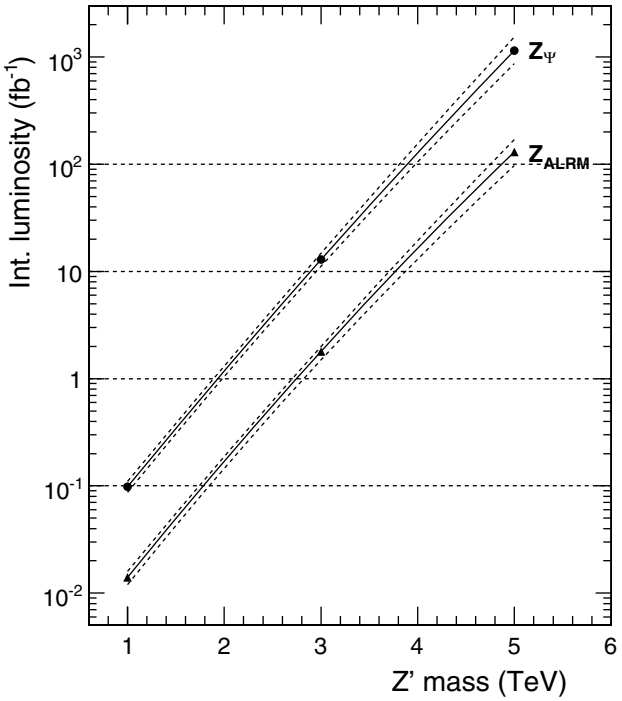

Figure 3.21. Integrated luminosity needed to reach 5σ significance ($S_{\mathcal{L}} = 5$) as a function of Z′ mass for Z_ψ and Z_{ALRM} models. Solid lines show the best estimates, dashed lines indicate boundaries of the band corresponding to the predictions with $\pm 1\sigma$ theoretical uncertainty.

position uncertainties are used in reconstruction algorithms [86]. So uncertainties in alignment translate mainly into uncertainties in the invariant mass resolution. We show below that even sizable variations in the width of the mass resolution have only a small impact on the Z′ mass reach.

Another potentially important source of systematic uncertainties is the uncertainty in the calibration precision of the muon chambers. The impact of uncertainties in the calibration of the Drift Tube chambers on the Z′ mass reach has been studied by (1) changing the t_0 offsets for all chambers by ± 2 ns, and (2) scaling drift velocity (changing time-to-distance relationship) by $\pm 3\%$. These variations represent conservative upper bounds on corresponding effects [107]. The effect of changing t_0 offset was found to be negligible for Z′ samples at all studied mass values and for both misalignment scenarios considered. The scaling of drift velocity has a negligible impact for the "first data" misalignment scenario with its rather poor mass resolution, but results in an increase of 5–10% in the width of the mass resolution for the "long term" scenario (no change in trigger and dimuon reconstruction efficiencies). This translates into a negligible effect in the Z′ mass reach. Uncertainties in the calibration of the Cathode Strip Chambers are less critical and hence are expected to have a negligible impact on the Z′ detection as well.

The effect of uncertainties in the knowledge of the magnetic field remains to be studied.

3.3.4.4.3. Uncertainties in background shape and mass resolution. Many experimental uncertainties have a negligible or small impact on the results of our studies because, the proposed analysis method is not sensitive to uncertainties in the predicted levels of signal and background processes. For example, only the mass dependence of the uncertainty in the

muon reconstruction efficiency needs to be taken into account, not the absolute uncertainty. The same is true for the trigger efficiency and for the uncertainty in the $\sqrt{s}$ scale. Among those uncertainties that do not cancel out, two seem to be particularly important: the uncertainty in the background shape, and the uncertainty in the mass resolution.

As described above, the background shape is currently determined from fits to background distributions predicted by the Monte Carlo simulation. In the analysis of real data, this MC-based shape will be compared with (and perhaps tuned to) the background shape in the region of low masses where one has high statistics of background events. The issue is then the reliability of the extrapolation from the steeply falling spectrum into the candidate signal region. This will have to be studied in detail, once the real data starts to be available. What is interesting to explore at this stage of analysis is how rapidly the significance deteriorates as the ratio of background events in the high-statistics normalisation region to background events in the candidate signal region is wrongly predicted by the MC-motivated background shape. To study this, we multiply our background pdf (p_b in Eq. (3.19)) by a function which is unity in the high-statistics background-only region and smoothly transitions to a tunable value, f, under the candidate mass peak. Values of integrated luminosity were chosen to correspond to 5σ significance for each model at $f = 1$. For $f = 2$ (assuming twice as much background in the signal region as there really is), 5σ becomes 4.2σ for $\mathrm{Z}_{\mathrm{ALRM}}$ and is about 3.7σ for Z_{ψ}. For f around 1.1 or 1.2, the change in S is of the order of a few per cent.

Sensitivity of the Z′ mass reach to uncertainties in the invariant mass resolution has been studied by applying extra Gaussian smearing to the reconstructed values of $\sqrt{s}$ of both the signal and background events and comparing the signal significance obtained with modified $\sqrt{s}$ values to that calculated with the nominal $\sqrt{s}$ values. We found that an increase of 10% in the mass resolution width, σ_M, reduces the signal significance by less than 2% at the values of $S_{\mathcal{L}}$ close to 5; 20% worse resolution gives 5% or less smaller $S_{\mathcal{L}}$. The effect is not very big, indicating that an approximate knowledge of σ_M should suffice. (This exercise does not check, however, the effect of extreme tails of the mass resolution being bigger than expected, which could lead to a background shape (and amount) different from that obtained from the simulation.) The knowledge of σ_M as a function of $\sqrt{s}$ is also used in the pdf of the signal in Eq. (3.19), where it defines the width of a Gaussian accounting for resolution smearing of the signal shape. This does not need to be very precise either: assuming resolution 20% better that it really is reduces $S_{\mathcal{L}}$ by less than 1%.

3.3.5. Distinguishing among Z′ models

The forward–backward asymmetry, A_{FB}, of the leptonic decay products provides information on parity-violating couplings, on and off resonance, as discussed for example in Refs. [96, 108].

The forward–backward asymmetry for $q\bar{q} \to \mu^+\mu^-$ interactions is defined as (e.g., Refs. [109, 110])

$$A_{\mathrm{FB}} = \frac{\sigma_F - \sigma_B}{\sigma_F + \sigma_B}, \tag{3.21}$$

where

$$\sigma_F \equiv \int_0^1 \frac{d\sigma(q\bar{q} \to \mu^+\mu^-)}{d\cos\theta^*} d\cos\theta^*, \quad \sigma_B \equiv \int_{-1}^0 \frac{d\sigma(q\bar{q} \to \mu^+\mu^-)}{d\cos\theta^*} d\cos\theta^*, \tag{3.22}$$

and where θ^* is the angle in the dimuon centre-of-mass (CM) reference frame between the negative muon and the incident quark. For spin-1 $\gamma^*/\mathrm{Z}^0/\mathrm{Z}'$ propagators, the probability density function $P(\cos\theta^*)$ is most generally of the form

$$P(\cos\theta^*;\, A_{\mathrm{FB}}, b) = \frac{3}{2(3+b)}(1 + b\cos^2\theta^*) + A_{\mathrm{FB}}\cos\,\theta^*. \tag{3.23}$$

Although $b = 1$ from general considerations, in the fits described here b is typically left as a free parameter. In Ref. [97], Rosner expresses A_{FB} for $f\overline{f} \to \gamma^*/\mathrm{Z}^0/\mathrm{Z}' \to \mu^+\mu^-$ events in terms of the left- and right-handed couplings of the photon, Z^0, and Z′ to u quarks, d quarks, and charged leptons. More details, including the couplings for the models studied, are given in Ref. [111].

For CM energies well above the Z^0 peak, the Drell–Yan background has a characteristic A_{FB} of about 0.6 [109], and provides a useful starting point.

3.3.5.1. Uncertainty in the sign of $\cos\theta^*$ *in pp collisions.* In proton-proton interactions, the quark direction is ambiguous experimentally since a quark can originate with equal probability from either proton, and the sign of $\cos\theta^*$ is not directly measurable. We follow Ref. [112] and infer the sign of $\cos\theta^*$ by assuming that the longitudinal motion of the dimuon system is in the direction of the proton contributing the annihilating quark, since a quark in a proton typically carries a larger momentum fraction x than does an anti-quark. We refer to the inference of the wrong sign of $\cos\theta^*$ as "mistagging" the sign. If not accounted for, the mistagged events, particularly at low y, reduce ("dilute") the apparent value of A_{FB}. Some authors deal with this problem by removing events below a chosen y threshold [112], or by examining A_{FB} in bins of y [113]; in Ref. [111], an approached is described which assigns the probability of a mistag on an event-by-event basis, thus using all events in a given sample. As knowledge of the mistagging probability depends on the Parton Distribution Functions, the effect of uncertainties in PDFs must be evaluated, and will be the subject of future work.

3.3.5.2. Other uncertainties. The transverse momentum p_{T} of the annihilating quark and/or anti-quark provides another source of uncertainty in the measurement of $\cos\theta^*$, since the observable quantity is the vector sum of these transverse momenta. We use the Collins–Soper reference frame [114], in which angles are measured with respect to the axis that bisects the target and beam axes in the dimuon CM frame, to minimise the effect of p_{T} on the measurement of $\cos\theta^*$, and let θ^*_{CS} denote the polar angle of the μ^- in this frame.

As described in Ref. [111], the effect of detector acceptance, combined with high mistag probability for events near $y = 0$, means that events lying near the edges of acceptance carry the largest information for the A_{FB} measurement. Hence, in addition to trying to obtain maximum acceptance, it is particularly important to understand the effect of any asymmetries in the acceptance which may arise as a result of the real detector efficiencies not being perfectly symmetric or of the beam crossing not being perfectly centred.

3.3.5.3. Likelihood function and fitting procedure. Since a Z′ can be discovered with a small number of events (Section 3.3.4), and since the search for anomalous A_{FB} in the highest mass continuum Drell–Yan events at any given luminosity will use a restricted sample of events, we consider an unbinned likelihood fit. The procedure and results with statistical errors only are described in Ref. [111]. The results of numerous fits can be summarised simply with a nominal statistical uncertainty in A_{FB} of 0.09 in a fit with 400 events for $1\,\mathrm{TeV/c^2}$ Z′ samples, and of 0.08 with 400 events for $3\,\mathrm{TeV/c^2}$ samples. Ref. [111] also reviews an appropriate hypothesis-testing methodology for distinguishing between Z′ models.

Table 3.10. Angular distributions for the decay products of spin-1 and spin-2 resonances, considering only even terms in $\cos\theta^*$.

Channel	d-functions	Normalised density for $\cos\theta^*$
$q\bar{q} \to G^* \to f\bar{f}$	$\lvert d^2_{1,1}\rvert^2 + \lvert d^2_{1,-1}\rvert^2$	$P_q = \frac{5}{8}(1 - 3\cos^2\theta^* + 4\cos^4\theta^*)$
$gg \to G^* \to f\bar{f}$	$\lvert d^2_{2,1}\rvert^2 + \lvert d^2_{2,-1}\rvert^2$	$P_g = \frac{5}{8}(1 - \cos^4\theta^*)$
$q\bar{q} \to \gamma^*/\mathrm{Z}^0/\mathrm{Z}' \to f\bar{f}$	$\lvert d^1_{1,1}\rvert^2 + \lvert d^1_{1,-1}\rvert^2$	$P_1 = \frac{3}{8}(1 + \cos^2\theta^*)$

3.3.6. Discriminating between different spin hypotheses

In order to distinguish the spins of a spin-1 Z′ bosons and a spin-2 gravitons in a dilepton decay mode, Ref. [115] considers an unbinned likelihood ratio statistic incorporating the angles of the decay products. The statistical interpretation of this statistic is discussed in detail in Ref. [116], also considering the possibility of spin 0.

To leading order, the sub-diagram for Z′ formation is quark-anti-quark ($q\bar{q}$) annihilation, while for a graviton there exist both $q\bar{q}$ annihilation and gluon-gluon (gg) fusion. One defines θ^* as the angle in the dilepton centre-of-mass reference frame between the negative lepton ℓ^- and the incident quark or gluon. In this section, we consider only the parity-conserving terms; inference from these terms can be combined with that of the parity-violating terms giving rise to A_{FB}.

For light lepton decay products, the angular probability density functions in the absence of interference are in Table 3.10. These are determined from angular momentum considerations and do not depend on the couplings. For the spin-2 graviton, only the relative fractions of $q\bar{q}$ annihilation, gluon fusion, and background (predominantly from the Drell–Yan continuum) events are needed to arrive at a parameter-free form for the expected distribution. (For spin 1, the resonance and the Drell–Yan background have the same form.)

The fractions of generated events arising from these processes are denoted by ϵ_q, ϵ_g, and ϵ_1, respectively, with $\epsilon_q + \epsilon_g + \epsilon_1 = 1$. Then the form of the probability density $P(\cos\theta^*)$ is

$$P(\cos\theta^*) = \epsilon_q P_q + \epsilon_g P_g + \epsilon_1 P_1. \tag{3.24}$$

As in the A_{FB} measurements, we let θ^*_{CS} denote the polar angle of the ℓ^- in the Collins–Soper frame. Experimentally, one will obtain a set of events with θ^*_{CS} measured along with other quantities such as dilepton transverse momentum $p_{\mathrm{T}}^{\mathrm{dil}}$ and rapidity y^{dil}. From these, one can construct the probability density $P_{\mathrm{acc}}(\cos\theta^*_{\mathrm{CS}})$ for events accepted (observed) in an experiment for each hypothesis H_i, where i labels the model such as Z′ or G*. In this study, we consider only the angular information and integrate over $p_{\mathrm{T}}^{\mathrm{dil}}$, y^{dil}, and any other relevant quantities; if one has confidence that these quantities are well described by the event generators, more variables can be added to P_{acc}. Since we do not add this information, P_{acc} for accepted events approximately factorises:

$$P_{\mathrm{acc}}(\cos\theta^*_{\mathrm{CS}}|H_i) = P(\cos\theta^*_{\mathrm{CS}}|H_i)\,\overline{\Omega}(\cos\theta^*_{\mathrm{CS}}), \tag{3.25}$$

where $P(\cos\theta^*_{\mathrm{CS}}|H_i)$ is from Eq. (3.24) with the ε_j set appropriately for the model considered (e.g. for the spin-1 hypothesis, we set $\epsilon_1 = 1$ and $\epsilon_q = \epsilon_g = 0$), and $\overline{\Omega}$ is the acceptance averaged over p_{T}, y, etc.

Eq. (3.25) has no free parameters, if the fractions ε_q, ε_g, and ε_1 are considered to be fixed. For each observed event, one evaluates $P_{\mathrm{acc}}(\cos\theta^*_{\mathrm{CS}}|H_i)$ at the observed $\cos\theta^*_{\mathrm{CS}}$ to obtain the *likelihood* $\mathcal{L}(H_i)$ of that event under the given hypothesis. The combined likelihood of the data set under a hypothesis is then the product of the events' likelihoods; henceforth in this paper,

Table 3.11. Integrated luminosity and numbers of signal and background events N_s and N_b required to discriminate spin-1 and spin-2 hypotheses with $\alpha = \beta$ corresponding to 2σ (one-tailed). The first column indicates the mass of the resonance; the second column shows the values of the RS ratio $c = k/\bar{M}_{\mathrm{Pl}}$; the third column specifies the integrated luminosity needed for 2σ discrimination; the last two columns show the corresponding numbers of signal and background events.

$\sqrt{s}$, TeV	c	$\int \mathcal{L} dt$, fb^{-1}	N_s	N_b
1.0	0.01	50	200	87
1.0	0.02	10	146	16
1.5	0.02	90	174	41
3.0	0.05	1200	154	22
3.0	0.10	290	148	6

$\mathcal{L}(H_i)$ refers to this product unless otherwise stated. As Ref. [116] discusses, the absence of free parameters means that the Neyman–Pearson hypothesis testing for *simple* hypothesis testing is applicable.

For testing a simple null hypothesis H_A of one spin against another simple alternative spin hypothesis H_B, we use the likelihood ratio $\lambda = \mathcal{L}(H_A)/\mathcal{L}(H_B)$, with critical region again chosen such that $\alpha = \beta$. For investigating and summarising which values of λ^{cut} correspond to which values of α and β, the quantity $-2\ln\lambda = 2\ln\mathcal{L}(H_B) - 2\ln\mathcal{L}(H_A)$ is particularly useful. For simple hypotheses H_A and H_B, the central limit theorem implies that $-2\ln\lambda$ tends to a Gaussian.

3.3.6.1. Testing spin 1 versus spin 2. A detailed discussion of the intermediate steps in applying the above method for discriminating spin 1 from spin 2 is in Ref. [116], using large samples of Z′ and G* events (from the Randall–Sundrum (RS) model [94]) generated with HERWIG. (Generator-level results using PYTHIA are completely compatible.) The ratio λ of the likelihoods of the hypotheses is calculated for each event, assigning spin 1 as the null hypothesis H_A and spin 2 as the alternative hypothesis H_B. In taking the ratio, the average acceptance cancels to good approximation and one essentially recovers the ratios of the angular forms. Histograms of $-2\ln\lambda$ for these events are highly asymmetric and strongly peaked at one side [116]. In view of the asymmetries in the underlying event histograms, the convergence of the sums of $-2\ln\lambda$ values for N selected events toward Gaussians is quite striking. The means and rms deviations of the sums are in excellent agreement with the means and rms deviations of the respective event histograms scaled by N and $\sqrt{N}$, respectively, as expected from the central limit theorem.

The statistical technique of Ref. [116] has been applied to fully-reconstructed Z′ and G* events [117]. Details of simulation, trigger and reconstruction are described in Sections 3.3.2, 3.3.3 and 14.3.1. From ensembles of pseudo-experiments, we determine the number N of events per experiment corresponding to various values of $\alpha = \beta$, expressed in equivalent number of Gaussian standard deviations "σ" for *one*-tailed tests, e.g., for $\alpha = 0.159$, we report $\alpha = 1\sigma$, and so on. The values of α so obtained scale as expected as $\sqrt{N}$.

Table 3.11 contains, for different studied masses and values of the Randall–Sundrum ratio $c = k/\bar{M}_{\mathrm{Pl}}$, the integrated luminosity needed for a 2σ significance, and the corresponding numbers of signal and background events. All numbers are for the "long term" misalignment scenario; the cross section for Z′ production is assumed to be equal to that of G* with the given c value. Of course, because the production cross section falls rather steeply with mass, the integrated luminosity needed for spin discrimination increases with mass. For RS gravitons, the production cross section scales as c^2; therefore, the integrated luminosity required for spin

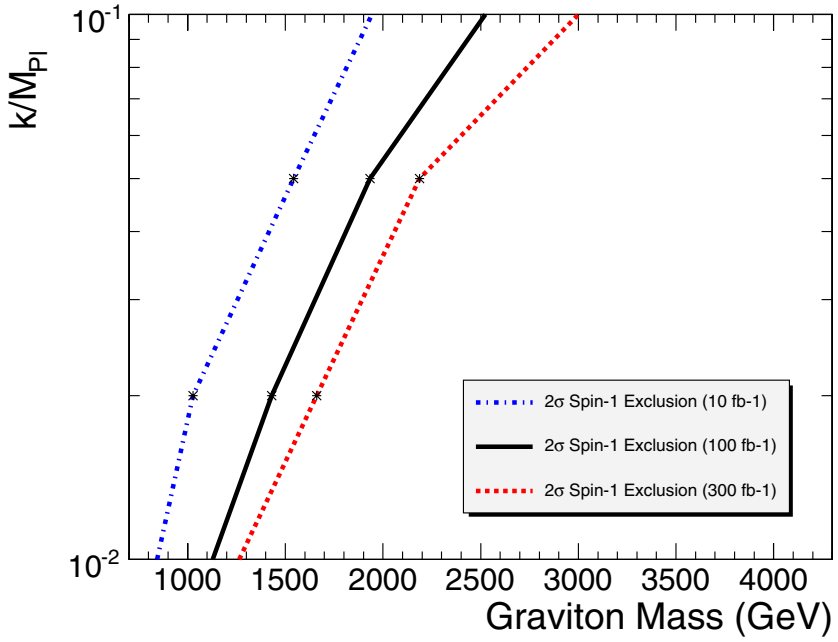

Figure 3.22. Region in the plane of M_{G^*}–c in which Randall–Sundrum G^* can be distinguished from Z' having an equal cross section with 2σ significance if one treats two spin hypotheses symmetrically, for a few representative values of the integrated luminosity. The region which can be probed lies to the left of the lines.

discrimination quickly increases as c gets smaller, and so does the number of signal events, because of a larger background contamination. The region in the plane of M_{G^*}–c in which Randall–Sundrum G^* can be distinguished from Z' with 2σ significance if one treats two spin hypotheses symmetrically is shown in Fig. 3.22 for a few representative values of the integrated luminosity.

Alternatives to the $\alpha = \beta$ criterion, in particular tests in which α is minimised for one hypothesis at the cost of increase in β, are discussed in Ref. [116].

3.3.6.2. Discrimination from spin 0. While the motivation of discriminating Z' from G^* has focused studies on discriminating spin 1 from spin 2, another possibility to be considered is spin 0 resonance (which is uniform in $\cos\theta^*$). For accepted spin-0 events, the probability density for $\cos\theta^*_{CS}$ is somewhat in between the mostly concave-upward function for spin 1 and the predominantly concave-downward function for spin 2.

As discussed in Ref. [116], discriminating either spin 1 or spin 2 from spin 0 requires significantly more events than discriminating spin 2 from spin 1.

Chapter 4. Physics Studies with Jets and $E_{\mathrm{T}}^{\mathrm{miss}}$

4.1. Benchmark Channel: new physics from dijets

Inclusive dijet production ($pp \to 2$ jets $+X$) is the dominant LHC hard scattering process. Simple to observe, and rich in potential signals of new physics, dijets are expected to be one of the earliest CMS measurements. In this section we discuss the measured distributions and their systematic uncertainties [118]. In section 14.5.2 and 15.3 we use these distributions to estimate our sensitivity to specific models of new physics.

4.1.1. Dijet analysis

We use samples generated using PYTHIA dijet processes mixed with pileup of minimum bias interactions for an assumed luminosity of $2 \times 10^{33}\,\mathrm{cm}^{-2}\,\mathrm{s}^{-1}$, simulated with OSCAR and reconstructed with ORCA. Jets are reconstructed as localised energy depositions in the CMS calorimeters arranged in a projective tower geometry. The jet energy E is defined as the scalar sum of the calorimeter tower energies inside a cone of radius $R = \sqrt{(\Delta\eta)^2 + (\Delta\phi)^2} = 0.5$, centred on the jet direction. The jet momentum $\vec{P}$ is the corresponding vector sum of energies, with the vector pointing in the tower direction. Both the jet energy and momentum are corrected back to the particles in the jet cone originating from the hard interaction excluding pileup [119]. We define the dijet system as the two jets with the highest p_{T} in an event (leading jets) and define the dijet mass $m = \sqrt{(E_1 + E_2)^2 - (\vec{P}_1 + \vec{P}_2)^2}$. We select events in which the leading jets each have $|\eta| < 1$. This cut enhances our sensitivity to new physics, produced at low $|\eta|$, compared to the predominantly t-channel processes from the QCD background. In all plots that are a function of dijet mass, we plot in bins of width equal to the Gaussian resolution measured in section 4.1.4.1.

4.1.2. Rates and efficiencies from jet triggers

We use simulated data from the single jet triggers discussed in Appendix E.4.3.2. From the three trigger tables for luminosities of $\mathcal{L} = 10^{32}$, 10^{33}, $10^{34}\,\mathrm{cm}^{-2}\,\mathrm{s}^{-1}$ we expect initial samples of size at least $100\,\mathrm{pb}^{-1}$, $1\,\mathrm{fb}^{-1}$, and $10\,\mathrm{fb}^{-1}$ respectively. This is from 10^6 seconds of collisions, equivalent to one month of continuous operation at 40% efficiency. In Fig. 4.1 we show the rate expected from these triggers as a function of dijet mass. By construction there are comparable events in each trigger, and a high statistics overlap between triggers for a given table. We see that the highest mass dijet is expected to be 5, 6 and 7 TeV for samples of size $100\,\mathrm{pb}^{-1}$, $1\,\mathrm{fb}^{-1}$, and $10\,\mathrm{fb}^{-1}$ respectively. In Fig. 4.2 we show the trigger efficiency vs. dijet mass, measured for each trigger using the neighbouring trigger with a lower p_{T} threshold, and explicitly show the mass cuts that are fully efficient. In Fig. 4.3 we show the data we will use to measure the cross section. We use each trigger where it is fully efficient and stop using the trigger where the next trigger is fully efficient. Fig. 4.3 shows there are adequate numbers of fully efficient events for analysis.

4.1.3. Dijet mass distribution from QCD

In Fig. 4.4 we combine the triggers to produce a cross section across the full mass spectrum. The prescaled triggers allow us to measure mass down to $300\,\mathrm{GeV/c}^2$, or even smaller if we can understand the efficiency of the lowest threshold trigger. The mass measured with the prescaled triggers will allow us to connect to dijet masses measured at the Tevatron.

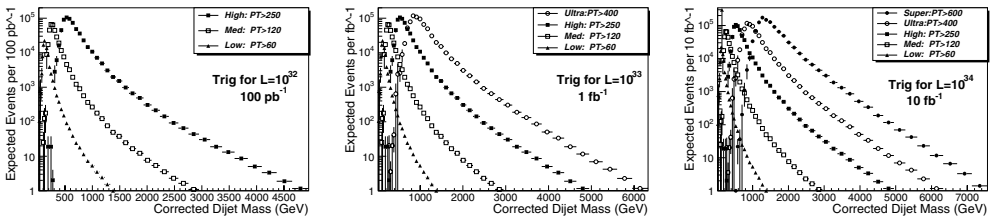

Figure 4.1. Rate of jet trigger as a function of dijet mass. The 3 plots correspond to 3 trigger tables, and each plot shows multiple triggers with various p_T thresholds and prescales.

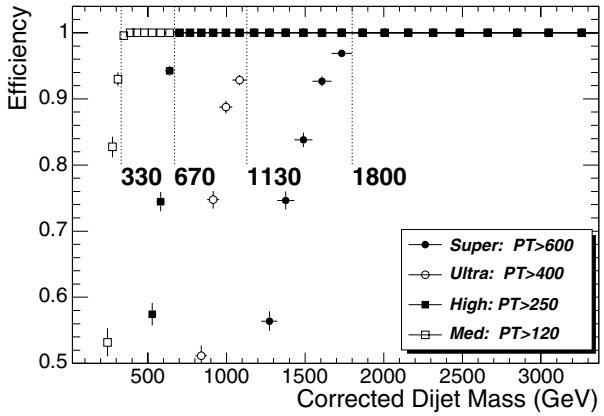

Figure 4.2. Jet trigger efficiency (points) and fully efficient dijet mass cuts (lines).

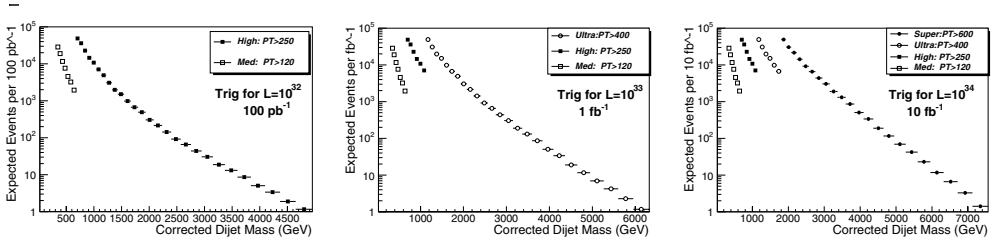

Figure 4.3. Rate of jet trigger for cross section measurement. Same triggers as Fig. 4.1.

In Fig. 4.5 we show the fractional statistical error on the cross section, the simplest measure of our sensitivity to new physics. Figure 4.5 shows that our prescaled triggers will allow a measurement of QCD with 1–3% statistical accuracy. The unprescaled triggers will have 1% error at threshold and the first unprescaled sample begins at a mass of 670 GeV/c^2, giving us full sensitivity to new physics in a region that overlaps with previous dijet mass measurements at the Tevatron.

4.1.4. Searches using dijet mass

Here we will discuss the signal and background distributions that are needed for a dijet resonance search using the mass distribution. In section 14.5.2 we use these techniques to estimate our sensitivity to seven models of narrow dijet resonances.

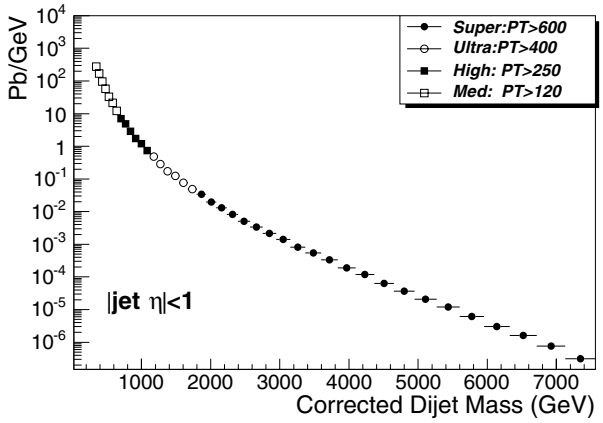

Figure 4.4. Cross section vs. dijet mass and the contributing jet triggers.

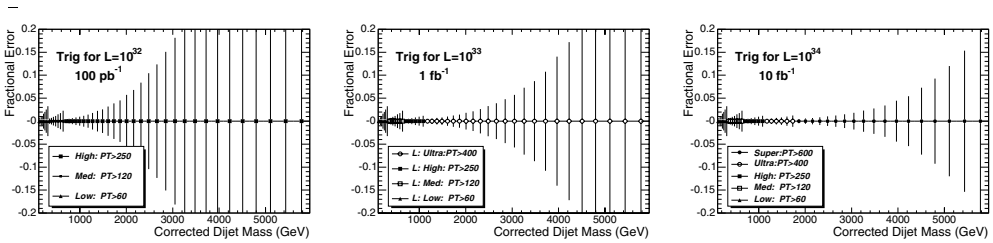

Figure 4.5. Fractional statistical error on the jet cross section for the samples in Fig. 4.5.

4.1.4.1. Narrow dijet resonance shapes. The simulated shape of a narrow dijet resonance in CMS is shown in Figure 4.6. The shape is composed of a Gaussian distribution from jet energy resolution and a long tail to low mass. The measured RMS of the Gaussian component is $\sigma/M = 0.045 + 1.3/\sqrt{M}$. The long tail to low mass comes predominately from final state QCD radiation (extra jets) which reduce the reconstructed mass. All resonances with a natural width significantly less than our resolution should look similar to this in the CMS detector. The model used in Figure 4.6 was a Z' from PYTHIA.

4.1.4.2. QCD background to dijet resonances. Figure 4.6 compares a Z' signal cross section to the QCD background found in section 4.1.3. The differential cross section for the QCD background is well fit by a simple parametrisation of the form

$$\frac{d\sigma}{dm} = \frac{p_0(1-m/\sqrt{s})^{p_1}}{m^{p_2}} \tag{4.1}$$

where m is the dijet mass, $\sqrt{s} = 14000\,\mathrm{GeV/c^2}$ is the collision energy, and p_0, p_1, p_2 are arbitrary parameters. The resonance sensitivity estimates in section 14.5.2 use this parametrisation to smooth away background fluctuations in our simulation sample. In a search with real data, a similar parametrisation could be used to simply model the measured background, as was done by CDF [120], or a full NLO QCD calculation smeared with the jet resolution could be used to model the background, as was done by D0 [121].

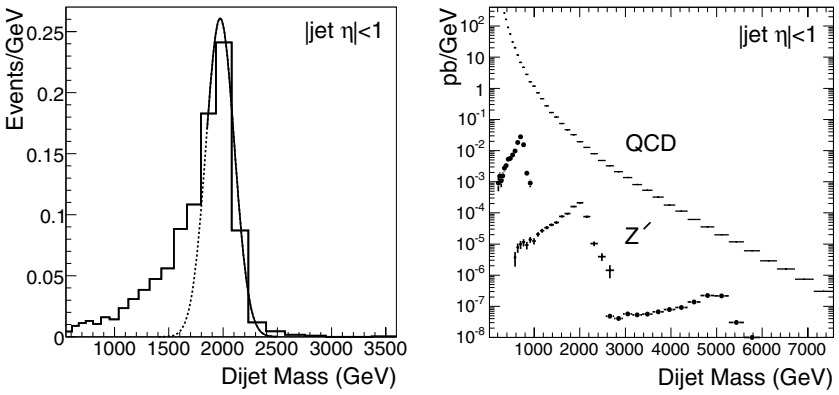

Figure 4.6. (Left) The dijet mass distribution from a 2 TeV/c^2 Z' (histogram) is fit with a Gaussian (solid curve) from the peak region to high mass and the Gaussian is extended to lower mass (dashed curve). (Right) The differential cross section as a function of dijet mass for the QCD background and three Z' signals with a mass of 0.7, 2, and 5 TeV/c^2.

4.1.5. Searches using dijet mass and angle

Here we will discuss the signal and background distributions that are used for searches for new physics in the dijet mass and angular distribution simultaneously. This technique can be used to confirm resonances observed in the dijet mass distribution, and measure their spin, or to discover other new physics that could affect the dijet angular distribution. In section 15.3 we use these techniques to estimate our sensitivity to a model of quark contact interactions.

4.1.5.1. Dijet ratio: $N(|\eta| < 0.5)/N(0.5 < |\eta| < 1.0)$. The ratio of the number of dijets in which both jets have $|\eta| < 0.5$ to the number of dijets in which both jets have $0.5 < |\eta| < 1.0$ was first introduced by D0 to search for contact interactions as a function of dijet mass [122]. It is the simplest measure of the most sensitive part of the angular distribution, providing a single number we can measure as a function of dijet mass. In Figure 4.7 we show our lowest order calculation of the dijet ratio from QCD compared with a left-handed contact interaction among quarks [123, 124] at three different values of the contact interaction scale. For this calculation we used the same code as [125] with modern parton distributions [12]. Lowest order QCD gives a fairly flat dijet ratio around 0.6 while the contact interactions produce an increase in the dijet ratio at high mass. Figure 4.7 also shows that a full CMS detector simulation of the dijet ratio from QCD, using the samples discussed in section 4.1.3, is indistinguishable from a flat ratio of 0.6 within the simulation statistical uncertainty.

4.1.6. Systematic uncertainties

In figure 4.8 we present estimates of systematic uncertainties on both the dijet cross section and the dijet ratio. The systematics discussed below have a large effect on the cross section and little effect on the dijet ratio.

4.1.6.1. Absolute jet energy scale. We have concluded that an overall uncertainty on the jet energy scale in the barrel of ±5% is achievable [126]. We have propagated this energy scale error to the dijet mass cross section by measuring the effect of a ±5% change in mass on a smooth fit to the dijet mass cross section. As shown in figure 4.8, the resulting upper uncertainty on the cross section varies from 30% at a dijet mass of 0.3 TeV/c^2 to 80% at

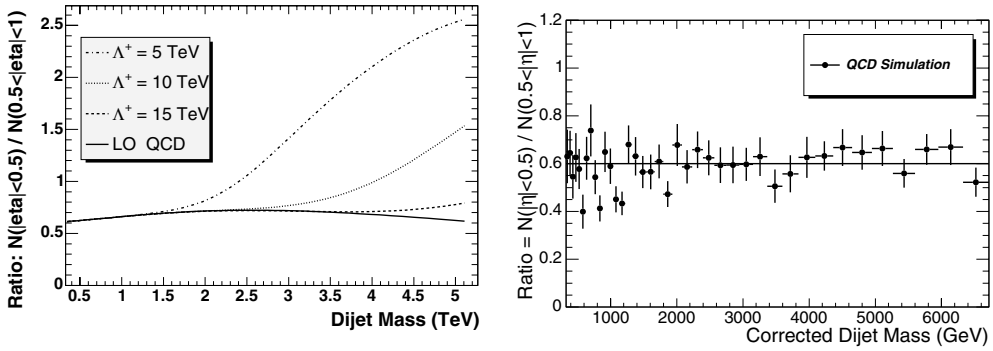

Figure 4.7. (Left) A lowest order calculation of the dijet ratio from QCD (solid curve) is compared with QCD plus a quark contact interaction at a scale Λ^+ of 15 TeV (dashed), 10 TeV (dotted) and 5 TeV (dot-dashed). (Right) The dijet ratio in the CMS simulation from QCD (points) is compared to the value 0.6 (line).

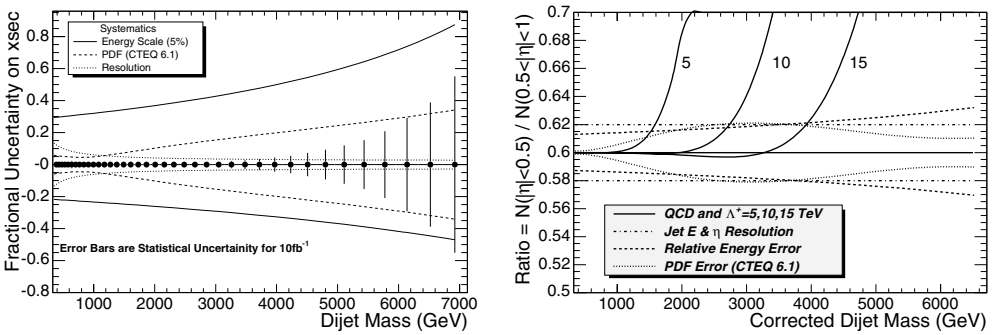

Figure 4.8. (Left) Systematic uncertainty on the dijet cross section due to jet energy scale (solid curve), parton distributions (dashed curve), and calorimeter energy and η resolution (dotted curve) are compared to the statistical uncertainties for 10 fb^{-1} (error bars). (Right) Systematic bounds on the dijet ratio from uncertainties in the relative jet energy scale (dashed curve), parton distributions (dotted curve), and calorimeter energy and η resolution (dot dash curve), are compared to the expectations of QCD and three contact interaction scales (solid line and curves).

a dijet mass of 6.5 TeV/c^2. This large systematic uncertainty, increasing with dijet mass, is the primary reason we do not use the dijet mass distribution to search for quark contact interactions. For the dijet ratio the absolute jet energy scale uncertainty has no effect, because the dijet ratio is flat versus dijet mass. The uncertainty cancels out in the ratio.

4.1.6.2. Relative jet energy scale. We have shown that by using dijet balance an uncertainty of $\pm 0.5\%$ is achievable [127] for the relative jet energy scale as a function of η within the barrel, in 0.1 steps in η. Here we assume that the relative jet energy scale, defined in this analysis as the uniformity in energy scale in the region $0.5 < |\eta| < 1.0$ compared to $|\eta| < 0.5$, can be determined to $\pm 0.5\%$. For the cross section as a function of mass this uncertainty is negligible compare to the $\pm 5\%$ error in the absolute energy scale. We have propagated this error to the dijet ratio by measuring the effect of a $\pm 0.5\%$ change in dijet mass for the measurement of $N(0.5 < |\eta| < 1)$ while keeping $N(|\eta| < 0.5)$ unchanged. As shown in figure 4.8, the resulting upper uncertainty in the ratio varies from 0.013 (2%) at a mass of 0.3 TeV/c^2 to 0.032 (5%) at a mass of 6.5 TeV/c^2.

4.1.6.3. Resolution. The effect of calorimeter resolution is the difference between the measurement with jets constructed from MC particles (Gen Jets) and the measurement with jets constructed from calorimeter depositions and corrected (Rec Jets). This difference, often called the smearing due to calorimeter resolution, is taken as a bound on the size of the systematic uncertainty due to resolution. For the cross section, the difference between Rec Jets and Gen Jets is small. This smearing varies from 15% at 0.3 TeV to 3% at 6.5 TeV, as shown in Figure 4.8. For the ratio, there is no change between Gen Jets and corrected Rec Jets within the Monte Carlo statistics presented in Fig. 4.7, and the statistical error on the simulation gives a bound on the systematic of 0.02 (3%) in the ratio, which is shown in Figure 4.8.

4.1.6.4. Parton distributions. We have used these 40 PDFs of CTEQ6.1 and the recommended procedure [12] to calculate the PDF uncertainties on both the cross section and the dijet ratio using our lowest order QCD calculation. As shown in figure 4.8, the resulting upper uncertainty in the cross section varies from 5% at a dijet mass of 0.3 TeV/c^2 to 32% at a dijet mass of 6.5 TeV/c^2. As shown in figure 4.8, the resulting uncertainty in the dijet ratio peaks at a value of 0.02 (3%) in the ratio at a mass of around 3.5 TeV/c^2, and declines at both lower and higher masses.

4.1.6.5. Luminosity, efficiency and acceptance. The luminosity uncertainty on the cross section is around 10%, small compared to other uncertainties, and has no affect on the dijet ratio. For the masses we consider in this analysis there is full efficiency for finding a dijet in the event with negligible uncertainty. The acceptance for jets is defined by the cut in η, and any measured jet distributions must be compared to calculations using the same η cuts, with negligible uncertainty in the comparison of measured and calculated jet η.

4.2. Benchmark Channel: low mass supersymmetry

4.2.1. Introduction

R-parity conserving SUSY leads to characteristic signatures with missing transverse energy in the final state due to the stable lightest supersymmetric particle (LSP). In the search described below for the bosonic partners of quarks (squarks) and the fermionic partners of gluons (gluinos) it is assumed that the LSP is weakly interacting, as is the case for most of the MSSM parameter space.

This analysis focuses on gluino and squark production within the minimal supergravity model (mSUGRA). In this model the entire SUSY mass spectrum is essentially determined by only five unknown parameters: the common scalar mass at the GUT scale, M_0; the common gaugino mass at the GUT scale, $M_{1/2}$; the common trilinear coupling at the GUT scale, A_0; the sign of the Higgsino mixing parameter, $sign(\mu)$; and the ratio of the Higgs vacuum expectation values, $\tan\beta$.

We investigate whether the production and decay of gluinos and scalar quarks is observable in the rate of $\geqslant$3-jet events with large missing transverse energy. The large missing energy originates from the two LSPs in the final states of the squark and gluino decays. The three or more hadronic jets result from the hadronic decays of the squarks and/or gluinos. We use the ISAJET (7.69) Monte Carlo program interfaced with PYTHIA (6.225) which provides parton shower and an underlying event model to generate squark and gluino production with parameters $M_0 = 60\,\text{GeV/c}^2$, $M_{1/2} = 250\,\text{GeV/c}^2$, $A_0 = 0$, $\mu > 0$ and $\tan\beta = 10$ (LM1 test point). For this set of parameters $m(\tilde{g}) \sim 600\,\text{GeV/c}^2$, $m(\tilde{q}) \sim 550\,\text{GeV/c}^2$, $(m(\tilde{g}) > m(\tilde{q}))$ and production of $\tilde{g}\tilde{q}$ is 53%, $\tilde{q}\tilde{q}$ 28% and $\tilde{g}\tilde{g}$ 12%. The decay $\tilde{g} \to \tilde{q}_{L,R} + q$ is dominant.

Specifically the gluino and squark decays proceed as follows:

$$\tilde{g} \to q\bar{\tilde{q}}_{L,R}, \qquad \text{or} \qquad \tilde{g} \to \bar{q}\tilde{q}_{L,R} \tag{4.2}$$

$$\tilde{q_R} \to q\,\tilde{\chi}_1^0, \ (100\%) \tag{4.3}$$

$$\tilde{q}_L \to q + \tilde{\chi}_2^0, \ (30\%) \tag{4.4}$$

$$\tilde{q}_L \to q + \tilde{\chi}_1^+, \ (70\%) \tag{4.5}$$

while the charginos and neutralinos decay as follows:

$$\tilde{\chi}_2^0 \longrightarrow \tilde{\ell}_R \ell, \ (11.2\%) \tag{4.7}$$

$$\tilde{\chi}_2^0 \longrightarrow \tilde{\tau}_1 \tau, \ (46\%) \tag{4.8}$$

$$\tilde{\chi}_1^+ \longrightarrow \tilde{\nu}_L \ell, \ (36\%). \tag{4.9}$$

The total LO production cross section for squarks and gluinos at this point of the mSUGRA parameter space is 49 pb. An example of a SUSY candidate is shown in colour plate CP6. The major Standard Model background components for a multi-jet plus large missing transverse energy search include production of Z + jets with the Z decaying invisibly, W + jets, top–anti-top pairs, dibosons, single top and QCD jets.

4.2.2. Jets and missing transverse energy at CMS

Jets are defined as localised energy depositions in the calorimeters and are reconstructed using an iterative clustering algorithm with a fixed cone of radius $\Delta R \equiv \sqrt{\Delta\eta^2 + \Delta\phi^2} = 0.5$ in $\eta - \phi$ space [7]. Jets are ordered in transverse energy, $E_{\mathrm{T}} = E\sin\theta$, where E is the scalar sum of energy deposited in the calorimeter towers within the cone, and θ is the angle formed by the beam-line, the event vertex, and the cone centre. Jets with uncorrected $E_{\mathrm{T}} > 30\,\mathrm{GeV}$ and with $|\eta| < 3$ are used throughout this analysis.

The offline missing transverse energy is defined as the negative vector sum of the transverse energy in the electromagnetic and hadronic calorimeter towers, $E_{\mathrm{T}}^{\mathrm{miss}} = -\sum_i (E_i \sin\theta_i)\hat{n}_i$, where E_i is the energy of the i-th tower, $\hat{n}_i$ is a transverse unit vector pointing to the centre of each tower, and θ_i is the polar angle of the tower; the sum extends to $|\eta| < 5$. The data sample is selected with a hardware trigger which requires $E_{\mathrm{T}}^{\mathrm{miss},L1} > 46\,\mathrm{GeV}$ ($|\eta|$ <5 coverage) and a central jet of $E_{\mathrm{T}} > 88\,\mathrm{GeV}$. A parametrisation of the Level-1 trigger efficiency as measured in a dijet sample is applied to all data analysed. For the confirmation of the High Level Trigger (HLT) the $E_{\mathrm{T}}^{\mathrm{miss}}$ is required to be above 200 GeV where the HLT trigger is fully efficient. In the following sections we detail the methodology and analysis strategies towards a search for SUSY using a dataset of events collected according to the missing transverse energy plus jet Level-1 and HLT trigger path.

4.2.3. Clean-up requirements

In anticipation of real data a pre-selection is used to reject accelerator- and detector-related backgrounds (such as beam halo and noise), and cosmic ray events. At least one primary vertex is required in the event and the pre-selection uses the event electromagnetic fraction, F_{em} (defined as the E_{T}-weighted jet electromagnetic fraction sum over the electromagnetic calorimeter acceptance, $|\eta_d| \leqslant 3.0$) and event charged fraction, F_{ch} (defined as the average over the jets ratio of the sum of the P_{T} of the associated to the jet tracks for jets within $|\eta| < 1.7$, over the calorimetric jet transverse energy) to distinguish between real and fake jet events. The pre-selection requirements and their efficiency on the signal are shown in

Table 4.1. Cleanup pre-selection efficiency.

Sample/Requirement	$F_{em} > 0.1$	$F_{ch} > 0.175$	Both (%)
LM1	99.88%	91.32%	91.24%

Table 4.2. The $E_{\mathrm{T}}^{\mathrm{miss}}$ + multi − jet SUSY search analysis path.

Requirement	Remark
Level 1	Level-1 trigger eff. parameter.
HLT, $E_{\mathrm{T}}^{\mathrm{miss}} > 200\,\mathrm{GeV}$	trigger/signal signature
primary vertex $\geqslant 1$	primary cleanup
$F_{em} \geqslant 0.175$, $F_{ch} \geqslant 0.1$	primary cleanup
$N_j \geqslant 3, \lvert\eta_d^{1j}\rvert < 1.7$	signal signature
$\delta\phi_{min}(E_{\mathrm{T}}^{\mathrm{miss}} - jet) \geqslant 0.3$ rad, $R1$, $R2 > 0.5$ rad, $\delta\phi(E_{\mathrm{T}}^{\mathrm{miss}} - j(2)) > 20^{\circ}$	QCD rejection
$Iso^{trk} = 0$	ILV (I) $W/Z/t\bar{t}$ rejection
$f_{em(j(1))}$, $f_{em(j(2))} < 0.9$	ILV (II), $W/Z/t\bar{t}$ rejection
$E_{\mathrm{T},j(1)} > 180\,\mathrm{GeV}$, $E_{\mathrm{T},j(2)} > 110\,\mathrm{GeV}$	signal/background optimisation
$H_{\mathrm{T}} > 500\,\mathrm{GeV}$	signal/background optimisation
SUSY LM1 signal efficiency 13%	

Table 4.1. The values of the requirements are chosen based on the Tevatron data where similar requirements have been used to clean the high p_{T} multi-jet plus large missing transverse energy datasets from a number of spurious and instrumental backgrounds that tend to appear as spikes in the low end of the event electromagnetic and charge fraction distributions.

4.2.4. Analysis path

Events that are accepted by the pre-selection requirements, proceed through the analysis path if they have missing transverse energy $E_{\mathrm{T}}^{\mathrm{miss}} > 200\,\mathrm{GeV}$ and at least three jets with $E_{\mathrm{T}} \geqslant 30\,\mathrm{GeV}$ within $|\eta| < 3$. In addition the leading jet is required to be within the central tracker fiducial volume *i.e.* $|\eta| < 1.7$. These requirements directly define the SUSY signal signature. The rest of the analysis path is designed based on elimination of the major classes of backgrounds: the QCD production, top–anti-top pairs and the W/Z-QCD associated production. In Table 4.2 the path is shown with a remark indicating the reason and aim of each selection step.

In the following sections the motivation and details of the analysis path are discussed.

4.2.5. Missing transverse energy in QCD production

Due the very high QCD production cross section the Standard Model background to a large missing transverse energy plus jets data-sample is dominated by QCD events. The observed missing transverse energy in QCD jet production is largely a result of jet mis-measurements and detector resolution. In Figure 4.9 the missing transverse energy full spectrum is shown for QCD 3-jet events in the $\hat{p_{\mathrm{T}}}$ region between 120 GeV/c and 1.8 TeV/c.

It is to be noted that due to finite computing resources and the large production cross section it is unrealistic to fully simulate and reconstruct samples with adequate Monte Carlo statistics. It is also unrealistic due to the trigger and data acquisition bandwidth constraints and the large QCD production cross section to collect QCD datasets with low E_{T} thresholds during data-taking. However the CMS trigger table includes a large number of prescaled

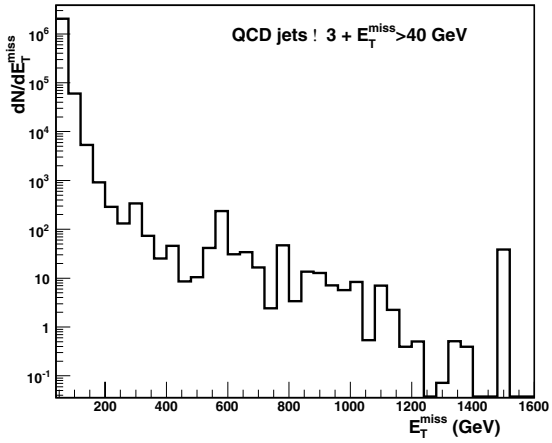

Figure 4.9. $E_{\mathrm{T}}^{\mathrm{miss}}$distribution in QCD 3-jet events.

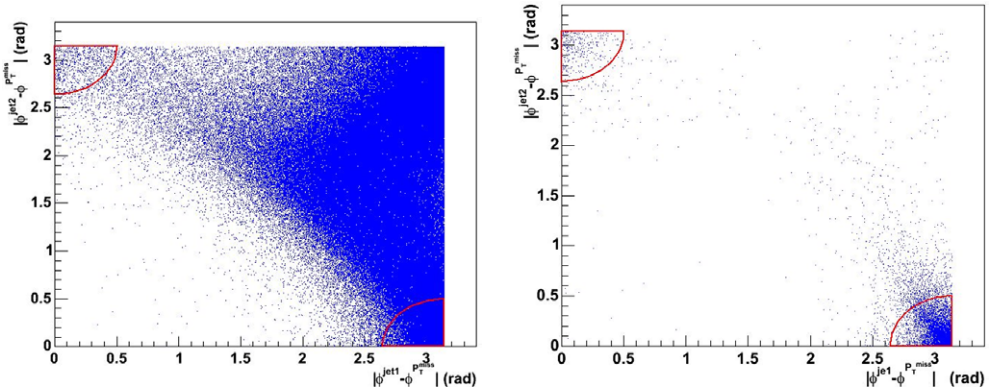

Figure 4.10. $\delta\phi_1$ versus $\delta\phi_2$ for (left) SUSY signal and (right) QCD dijet events.

QCD trigger paths that will be used to extract the shape of the missing transverse energy and the direct normalisation for the QCD background component in all-hadronic events with large missing energy. In addition, topological requirements are designed to eliminate as much as possible the QCD contribution. Well measured QCD dijet events with back-to-back in ϕ jet topology are used for obtaining jet corrections. These are well balanced events with low missing transverse energy. Large missing energy in QCD events originates from jet mis-measurements. In such events the highest E_{T} jet is typically the most accurately measured. When any jet in the event is mis-measured, usually the second or third jet, the $E_{\mathrm{T}}^{\mathrm{miss}}$ direction is pulled close in ϕ to the mis-measured jet direction. We eliminate such residual QCD component by using the correlation in the $\delta\phi_1 = |\phi_{\mathrm{j}(1)} - \phi(E_{\mathrm{T}}^{\mathrm{miss}})|$ versus $\delta\phi_2 = |\phi_{\mathrm{j}(2)} - \phi(E_{\mathrm{T}}^{\mathrm{miss}})|$ plane, as shown is Figure 4.10. Events with $R_1 > 0.5$ rad and $R_2 > 0.5$ rad, where $R_1 = \sqrt{\delta\phi_2^2 + (\pi - \delta\phi_1)^2}$ and $R_2 = \sqrt{\delta\phi_1^2 + (\pi - \delta\phi_2)^2}$, are accepted. In addition we require that no jet in the event be closer than 0.3 rad to the missing energy direction and that the second jet be further than 20° from it (Figure 4.11).

After a baseline selection of $N_j \geqslant 2$ and $E_{\mathrm{T}}^{\mathrm{miss}} > 93$ GeV the cumulative efficiency of the angular requirements is ∼90% for the SUSY signal. They reject ∼85% of all QCD events.

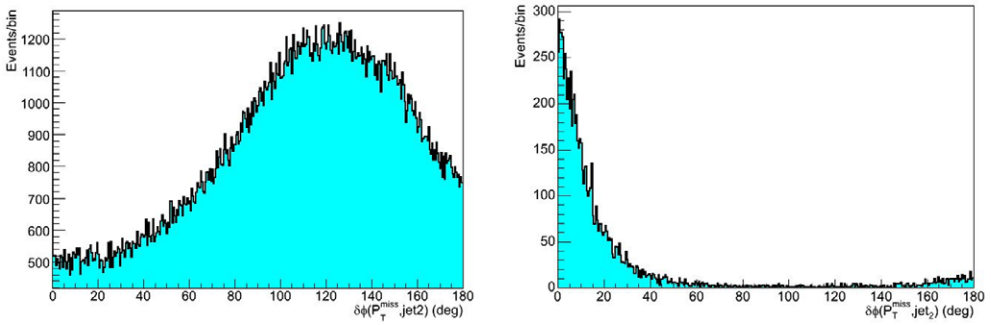

Figure 4.11. $\delta\phi_2 = |\phi_{j(2)} - \phi(E_T^{miss})|$ for (left) SUSY signal and (right) QCD dijet events.

4.2.6. Indirect Lepton Veto

W and Z + jet events with large boson P_T and leptonic decays of the boson are backgrounds to a large missing transverse energy plus multijet search. Similarly semileptonic $t\bar{t}$ events where the W boson decays leptonically constitute a background. In the W leptonic decays there is real missing energy due to the neutrino while in the Z decays the missing energy is mostly due to τ decays or missed leptons. Residual background when the bosons decaying hadronically (with missing energy due to jet mis-measurements) are accounted for using the real multi-jet data triggers.

In this analysis there is no explicit lepton identification. Leptons in the signal SUSY events result from cascade decays of squarks and gluinos through charginos and neutralinos. To reduce the large background contribution mainly from $W(\rightarrow \ell\nu) + jets$ and $t\bar{t}$ production and decays, an *indirect lepton veto* (ILV) scheme is designed. The aim of the indirect lepton veto is twofold: (a) to retain large signal efficiency and (b) to achieve large rejection of the W, Z, $t\bar{t}$ backgrounds (independent of the MC used, namely parton shower only versus complete matrix element in particular for the higher jet multiplicity bins).

Given that electrons are also clustered as jets, the jet electromagnetic fraction, f_{em}, which is close to 1 for electrons, is efficient in rejecting backgrounds events containing electrons while retaining good efficiency in the LM1 SUSY inclusive signal. Events are selected if the two highest E_T jets are not purely electromagnetic, *i.e.* $f_{em,j(1)} < 0.9$ and $f_{em,j(2)} < 0.9$. The leading and second jet electromagnetic fraction distributions for $W \rightarrow e\nu$+$\geqslant 2$ jets are shown in Figure 4.12. The corresponding distributions for the SUSY LM1 signal are shown in Figure 4.13. The signal efficiency is $\sim$87% while 90% of the $W \rightarrow e\nu + \geqslant 2$ jets are rejected. A systematic uncertainty of 5% on the background rejection efficiency is assigned due to a variation between PYTHIA and ALPGEN + PYTHIA samples.

To further reject electrons, muons and taus from W and Z decays while retaining the SUSY signal efficiency a tracking isolation strategy is employed as follows: if the leading track in the event has $p_T \geqslant 15\,\text{GeV/c}$ and the ratio of the sum of the P_T of all tracks around it in a cone of $\Delta R = 0.35$ over the p_T of the track is less than 10% the event is dropped. The requirement of accepting events with a non-isolated leading track is noted in Table 4.2 as $\text{Iso}^{ltrk} = 0$.

The leading isolated track veto has $\sim$92% signal efficiency while it rejects $\sim$50% of the W/Z+jets events (in PYTHIA as well as ALPGEN generated samples). The cumulative W/Z + jets rejection efficiency when both requirements of the indirect lepton veto are applied is between 50% and 90% depending on the lepton flavour, with lower rejection as expected when the boson decay product includes a τ lepton. When applied in the full analyses path it rejects 40% of $t\bar{t}$ inclusive events. The cumulative SUSY signal efficiency is $\sim$80%.

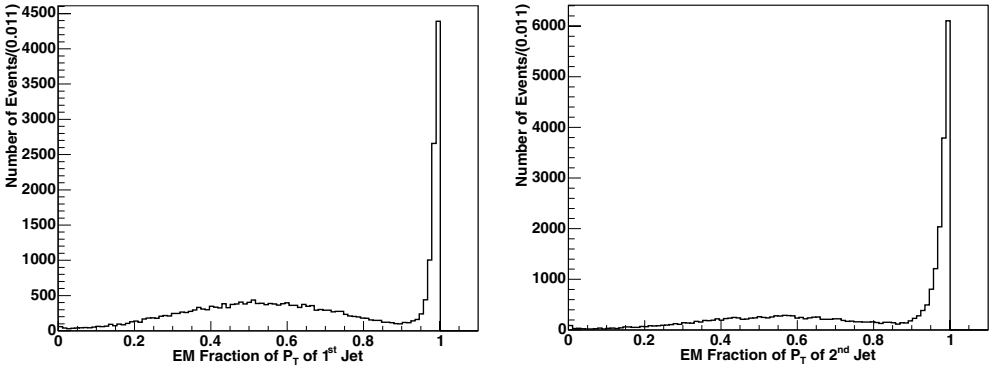

Figure 4.12. Electromagnetic fraction of (left) leading and (right) second jet in $W \to e\nu + \geqslant 2$ jets events.

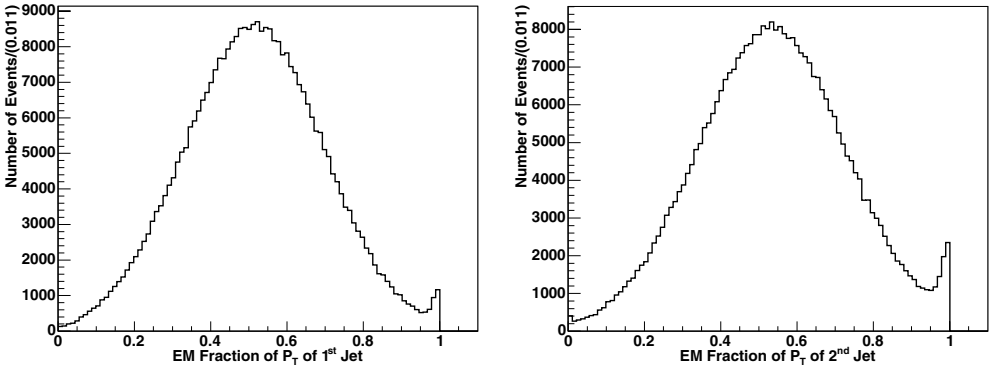

Figure 4.13. Electromagnetic fraction of (left) leading and (right) second jet in SUSY LM1 events.

4.2.7. The standard Z boson "candle" calibration

Events with large missing transverse energy and $\geqslant$3 jets in the final state are expected from $Z(\to \nu\bar{\nu}) + \geqslant 3$ jets and $W(\to \tau\nu) + \geqslant 2$ jets (the third jet originating from the hadronic τ decay) processes. Additional residual contribution is expected also from $W(\to \mu\nu)$, $e\nu + \geqslant 3$ jets. In what follows a comprehensive normalisation program is described that relies on the Z + multi-jet data to accurately estimate the W and Z + multi-jet background contribution in a large $E_{\mathrm{T}}^{\mathrm{miss}}$ plus multi-jet search.

The $Z + N$ jets cross section is proportional to a_s^N: for each additional jet in the Z event the cross section falls by a factor proportional to a_s. The ratio of the number of events in adjacent jet multiplicity bins should remain constant and be proportional to the strong coupling constant. The multiplicity breakdown will be measured in the data and the slope returned by the exponential fit will be $R = \frac{dN_{events}}{dN_{jets}} = \frac{\mathcal{L}d\sigma}{dN_{jets}}$. This ratio measured as the two to three jet ratio in PYTHIA W + jets and Z + jets is ~ 2.3 . An illustration of the result of the measurement that will be performed with the real data is shown in Figure 4.14 using the ALPGEN Monte Carlo cross section after parton shower matching.

The Monte Carlo predictions for events with $\geqslant 3$ jets and Z boson $P_{\mathrm{T}} > 200\,\mathrm{GeV/c}$ will be normalised to the observed $Z(\to \mu\mu) + 2$ jets data sample (where Z boson

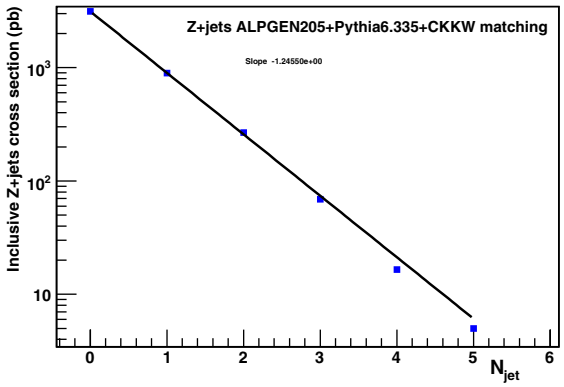

Figure 4.14. Illustration of the measurement of the $R = \frac{dN_{events}}{dN_{jets}}$ ratio in the Z + jets data. Here the ALPGEN Monte Carlo cross section is used after parton shower matching and the theoretical returned ratio is 3.8. No Z boson P_{T} requirement is used for these estimates. Slope $= -1.24550$

$P_{\mathrm{T}} > 200\,\mathrm{GeV/c}$) via the measured $R = \frac{dN_{events}}{dN_{jets}}$ ratio, where dN_{events} is the number of events accumulated with $\sim 1\,\mathrm{fb}^{-1}$ of data.

The ratio $\rho \equiv \frac{\sigma(pp \to W(\to \mu\nu) + jets)}{\sigma(pp \to Z(\to \mu^+\mu^-) + jets)}$ will be used to normalise the W+jets Monte Carlo predictions. Assuming lepton universality, the predictions for the number of events with $\geqslant 2$ jets and $\geqslant 3$ jets from W and Z production and decays to all flavours will be normalised to the $Z(\to \mu^+\mu^-) + \geqslant 2$ jets data. By normalising the MC predictions to data large systematic effects are avoided that are due to the renormalisation scale, the choice of parton density functions, initial- and final-state radiation, and the jet energy scale. The total uncertainty ($\sim$5%) is then dominated by the uncertainty on the luminosity measurement, the uncertainty on the measured ratio $R = \frac{dN_{events}}{dN_{jets}}$ (to be measured with the data), and the uncertainty on the ratio ρ as a function of the jet multiplicity, N_{jet}.

The method will be used to absolutely normalise the Monte Carlo predictions for $Z(\to \nu\bar{\nu}) + \geqslant 3$ jets assuming that after detector simulation they will be tuned to reproduce the kinematic distributions observed in the "candle" data sample and the ratios discussed above. Note that the actual data "candle" sample can be used stand-alone to predict the rate and event kinematics of the $Z(\to \nu\bar{\nu}) + \geqslant 3$ jets process.

In this study the $Z \to \mu\mu + \geqslant 2$ jets with $Z_{pT} > 200\,\mathrm{GeV/c}$ is the "candle" data sample. Both the muon and electron decays of the Z will be used as the standardisable candle, but for the purposes of demonstrating the method, the Z muon decays are chosen. The additional advantage of the muon channel is the efficient CMS muon detection due to the tracking and muon systems. Since the completely raw missing transverse energy is used (as is expected to be the case at the start-up of the experiment), the shape of the $E_{\mathrm{T}}^{\mathrm{miss}}$ distribution of the measured the $Z \to \mu\mu + \geqslant 2$ jet events will be very close to the shape of the invisible $Z \to \nu\nu + \geqslant 2$ jet events as shown in Figure 4.15. The muon decays of the Z are selected from an inclusive sample using the following requirements as baseline selection: (a) at least one primary vertex, (b) at least 2 jets with $E_{\mathrm{T}} \geqslant 30\,\mathrm{GeV}$, and $|\eta_d| \leqslant 3$, (c) $E_{\mathrm{T}}^{\mathrm{miss}} > 200\,\mathrm{GeV}$ and (d) for the Z boson identification two reconstructed muons with invariant mass closest to the measured Z boson mass ($91.2\,\mathrm{GeV/c^2}$) and within $20\,\mathrm{GeV/c^2}$. The "Z-mass" tag requirement is 90% efficient. The selected candle sample dimuon invariant mass is shown in Figure 4.16 overlaid with the one using the Monte Carlo truth. Considering both the electron and muon decays of the Z boson, a statistically adequate (5% precision) "candle" sample to normalise the $Z \to \nu\nu + \geqslant 2$ jet predictions for $E_{\mathrm{T}}^{\mathrm{miss}} > 200\,\mathrm{GeV}$ will be obtained with $\sim 1.5\,\mathrm{fb}^{-1}$.

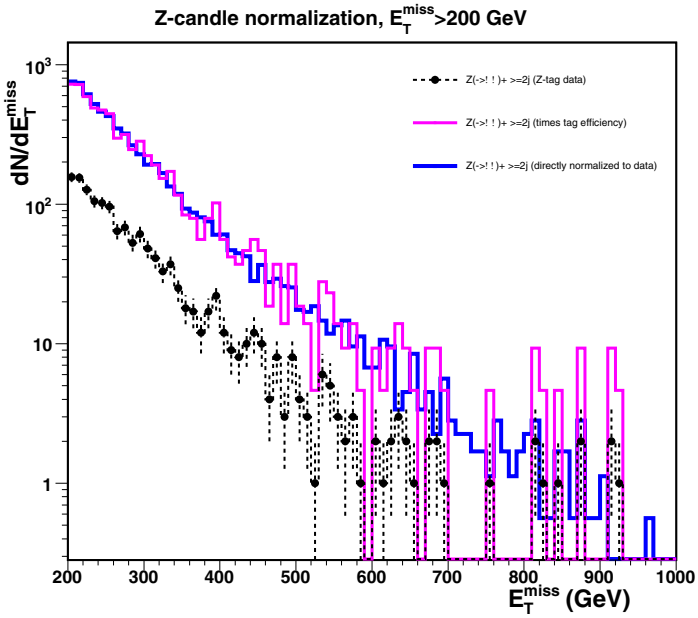

Figure 4.15. $E_{\mathrm{T}}^{\mathrm{miss}}$ in $Z \to \mu\mu + \geqslant 2$ jets candle sample and normalised $E_{\mathrm{T}}^{\mathrm{miss}}$ in $Z \to \nu\bar{\nu} + \geqslant 2$ jets sample.

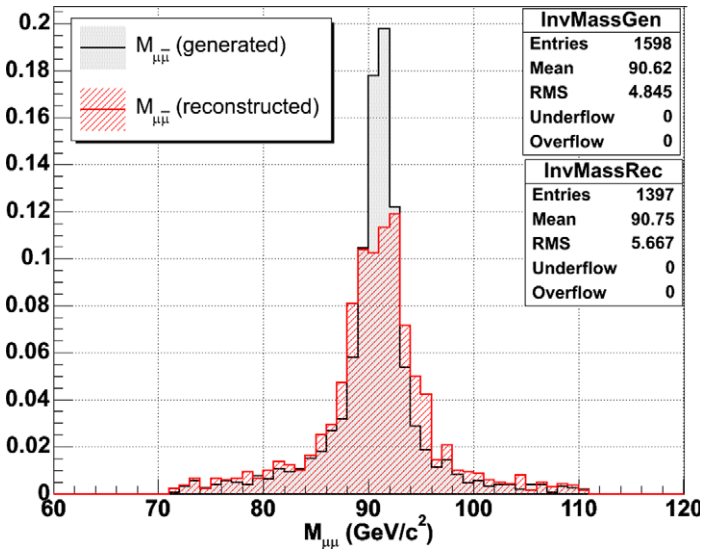

Figure 4.16. Reconstructed and generator level Z dimuon invariant mass for $Z \to \mu\mu + \geqslant 2$ jets and $E_{\mathrm{T}}^{\mathrm{miss}} > 200\,\mathrm{GeV}$.

4.2.8. Analysis results

The signal to background ratio is further enhanced in the final steps of the analysis (shown in Table 4.2) by requiring the two leading jets E_{T} be above 180 and 110 GeV respectively. Furthermore the H_{T} in the event is required to be $H_{\mathrm{T}} \equiv E_{\mathrm{T}(2)} + E_{\mathrm{T}(3)} + E_{\mathrm{T}(4)} + E_{\mathrm{T}}^{\mathrm{miss}} > 500\,\mathrm{GeV}$.

Table 4.3. Selected SUSY and Standard Model background events for 1 fb^{-1}.

Signal	$t\bar{t}$	single t	$Z(\rightarrow \nu\bar{\nu})$ + jets	$(W/Z, WW/ZZ/ZW)$ + jets	QCD
6319	53.9	2.6	48	33	107

The global signal efficiency for the analysis is 13% while the signal to background ratio is ~ 26. The results are shown in Table 4.3.

Due to the QCD Monte Carlo limited statistics to derive the QCD background component the analysis path is followed without the topological QCD clean-up requirements and ILV requirements. The estimate is conservative and is based on factorising the clean-up and ILV efficiency and assuming them uncorrelated with the rest of the analysis requirements. A parametrisation of the QCD topological clean-up requirements efficiency as a function of the $E_{\mathrm{T}}^{\mathrm{miss}}$ is used for $E_{\mathrm{T}}^{\mathrm{miss}} > 700\,\mathrm{GeV}$.

4.2.9. Systematic uncertainties

4.2.9.1. $E_{\mathrm{T}}^{\mathrm{miss}}$ shape systematic uncertainty due to tails in the jet resolution. A bootstrap-like study is performed to estimate the systematic uncertainty of the $E_{\mathrm{T}}^{\mathrm{miss}}$ due to the non Gaussian tails in the jet resolution. The study uses the inclusive $t\bar{t}$ sample. The events are re-weighed according to a grading of the mis-measured jets, and on a jet-by-jet basis. The grading of a jet being considered mis-measured is derived from the jet resolution shape of jets in three E_{T} bins. Jets are considered mis-measured when they fall in the non-Gaussian tails of the jet resolution. The event weight is derived using each jet's weight and for three different scenarios that involve one, two or three jets being simultaneously mis-measured and positively contributing to the enhancement of the $E_{\mathrm{T}}^{\mathrm{miss}}$ tail. As an example when one jet is assumed to be undermeasured, 15% of the events that include the undermeasured jet (as determined by the corresponding resolution curves) are weighted up by up to 15%. A larger weight is assigned to the events with a jet lying on the downward going tail (and depending on the E_{T} of the jet) thus exaggerating the non-Gaussian jet resolution tail. The further the jet in the event is out on the tail the larger is the weight assigned to it.

The ratio of the $E_{\mathrm{T}}^{\mathrm{miss}}$ distribution resulting from the one, two and three under-measured jets scenarios study over the nominal $E_{\mathrm{T}}^{\mathrm{miss}}$ is shown in Figure 4.17 and it shows graphically the positive systematic uncertainty band as a function of the $E_{\mathrm{T}}^{\mathrm{miss}}$ due to jet tails in the resolution.

The positive systematic uncertainty due to one mis-measured jet in the high $E_{\mathrm{T}}^{\mathrm{miss}}$ tails is estimated over the bins where in the nominal distribution we have enough statistics, namely between 180 and 240 GeV (statistical uncertainty $< 5\%$). The result is 8.5%. For the scenario with the two undermeasured jets, and assuming that 50% of the times the simultaneous under-measurement results in the overestimate of the $E_{\mathrm{T}}^{\mathrm{miss}}$ the result is 6% and for the case of the three under-measured jets it is also 6%. We take the weighted average of these three scenarios, namely 7%, as an index of the positive systematic uncertainty due to the tails of the jet resolution in the tails of the $E_{\mathrm{T}}^{\mathrm{miss}}$ above 180 GeV. The result in the method presented is bound to overestimate the increase in the tails, since by design positive interference of all under-measured jets in the event is considered (in reality there is some combinatorial compensation in the $E_{\mathrm{T}}^{\mathrm{miss}}$ vector given the jet topology). The ultimate measurement of the shape of the high $E_{\mathrm{T}}^{\mathrm{miss}}$ tails and its systematic should be done using Standard Model candle physics processes in the real data such as the Z+jets and the $t\bar{t}$ data sample.

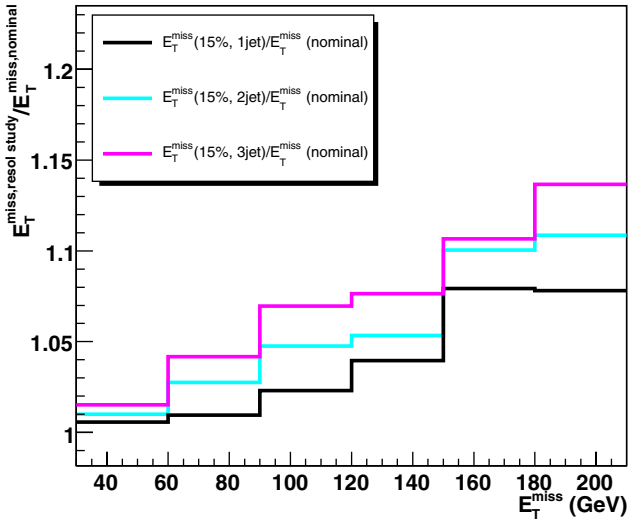

Figure 4.17. Ratio of $E_{\mathrm{T}}^{\mathrm{miss}}$ weighted distribution for one, two and three under-measured jets (described in the text) over the corresponding nominal $E_{\mathrm{T}}^{\mathrm{miss}}$ distribution.

4.2.9.2. Jet energy scale. The jet energy scale (JES) uncertainty in all hadronic analyses is playing an important role since the jet energy spectrum is steeply falling. To determine the effect of the JES uncertainty each jet four-vector is scaled with the uncertainty value α as follow:

$$\begin{aligned} p_{scaled}^{\mu.jet} &= (1 \pm \alpha) \cdot p_{meas}^{\mu.jet} \\ &= (1 \pm \alpha) \cdot (p_x, p_y, p_z, E). \end{aligned} \tag{4.10}$$

The JES uncertainty for the high E_{T} jets that enter this analysis is taken to be about 7% for 1 fb^{-1}. The resulting uncertainty in the overall analysis acceptance times efficiency in $t\bar{t}$ and QCD events is 22%.

4.2.9.3. Luminosity uncertainty. Since the W/Z + jets background is taken to be normalised with real data, the estimate carries the luminosity uncertainty on it. Hence a $\pm$5% uncertainty is taken on the background estimates due to the luminosity measurement.

4.2.9.4. ALPGEN-PYTHIA *ILV.* As discussed in section 4.2.6 a 5% positive systematic on the background estimate is taken due to the variation in efficiency of the ILV requirement between ALPGEN and PYTHIA.

4.2.9.5. Total background systematic. In summary for the major background components the uncertainties are as follows:

- $t\bar{t}$ uncertainties: 7% $E_{\mathrm{T}}^{\mathrm{miss}}$ shape, 22% JES, 13% statistical.
- $Z \to \nu\bar{\nu}$+jets, W/Z+jets: 5% Luminosity (direct candle normalisation to the data).
- QCD: $E_{\mathrm{T}}^{\mathrm{miss}}$ 7% shape, 22% JES, 10% statistical.

The number of backgrounds events per background component and their uncertainties are tabulated in Table 4.4.

Table 4.4. Standard Model background components and uncertainties for 1 fb^{-1}.

$t\bar{t}$, single top	$Z(\rightarrow \nu\bar{\nu})$+ jets	$(W/Z, WW/ZZ/ZW)$ + jets	QCD
56 ± 11(sys) ± 7.5(stat)	48 ± 3.5 (all)	33 ± 2.5 (all)	107 ± 25(sys) ± 10(stat)

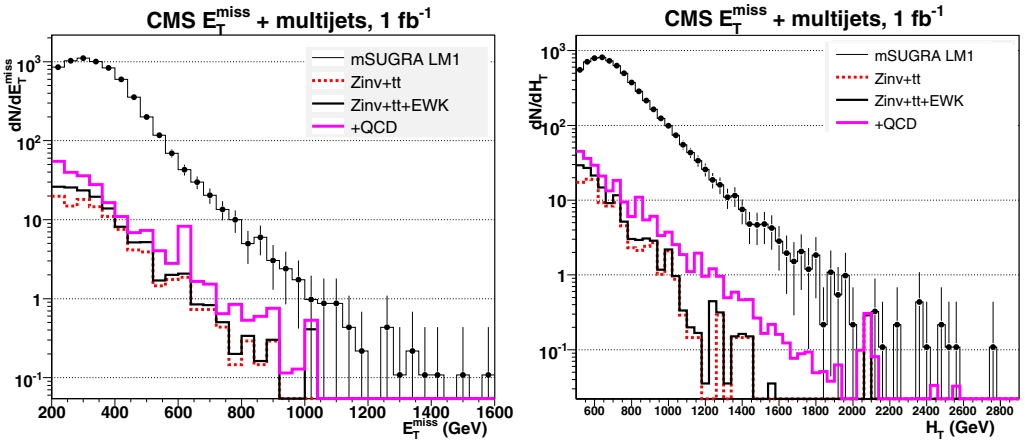

Figure 4.18. LM1 signal and Standard Model background distributions for $E_{\mathrm{T}}^{\mathrm{miss}}$ (left) and H_{T} (right).

4.2.10. Discussion

In conclusion, based on the Standard Model background estimates and their uncertainties, a 5σ observation of low mass SUSY at LM1 (gluino mass 600 GeV/c^2) is in principle achievable with ~ 6/pb in events with large missing energy plus multi-jets. It is found that with ~ 1.5 fb^{-1} the W/Z + jets background including the invisible decays of the Z boson which constitutes a large irreducible background component can be reliably normalised using the $Z \rightarrow \mu\mu$ and $Z \rightarrow ee$ + multi-jet data candle. With adequate data-based strategies of controlling and estimating the Standard Model backgrounds and their uncertainties, low mass SUSY will be discovered with 0.1–1 fb^{-1}. Furthermore the global raw $E_{\mathrm{T}}^{\mathrm{miss}}$ measurement from the calorimeter towers can be calibrated for multi-jet topologies using the tracking and muons systems and the $Z \rightarrow \mu\mu$ + multi-jet candle data sample. This analysis demonstrates that the $E_{\mathrm{T}}^{\mathrm{miss}}$ measurement from the calorimeter towers can be used as such at the startup of the experiment provided that adequate strategies are in place to discard spurious instrumental backgrounds. It is also found that an indirect lepton veto makes possible the $t\bar{t}$ and W/Z+jets background rejection, without compromising the inclusive nature of the search. In anticipation of data, there is no accurate way of accurately predicting the contribution of the QCD background tails; although the full matrix element Monte Carlo predictions (such as ALPGEN) are to date far more complete, the experiment has in place proper prescaled QCD triggers in order to estimate this background component using directly the data.

Finally the comparison of the signal, total background estimated and its components for the $E_{\mathrm{T}}^{\mathrm{miss}}$, H_{T}, N_{jet} and $M_{eff} \equiv E_{\mathrm{T}(1)} + E_{\mathrm{T}(2)} + E_{\mathrm{T}(3)} + E_{\mathrm{T}(4)} + E_{\mathrm{T}}^{\mathrm{miss}}$ are shown in Figure 4.18. It is to be underlined that the slopes of the tails of the missing energy, H_{T}, and M_{eff} distributions are very similar between the Standard Model background and the low mass SUSY signal.

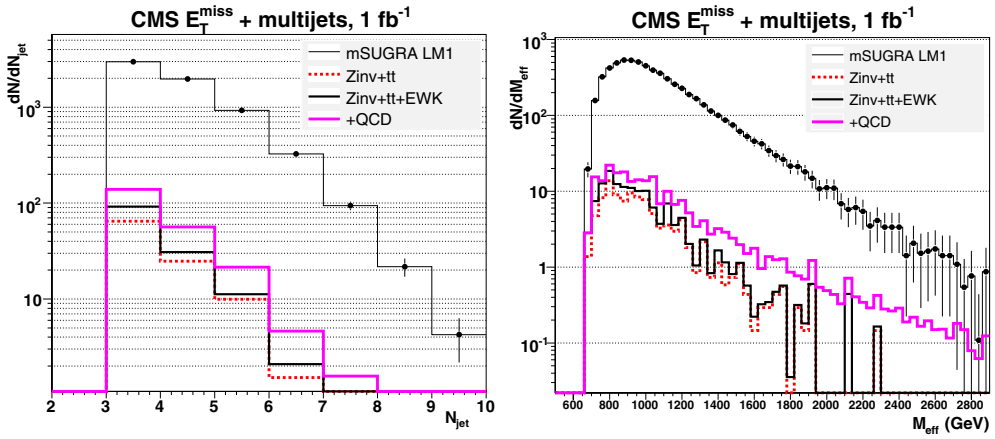

Figure 4.19. LM1 signal and Standard Model background distributions for Jet Multiplicity (left) and M_{eff} (right).

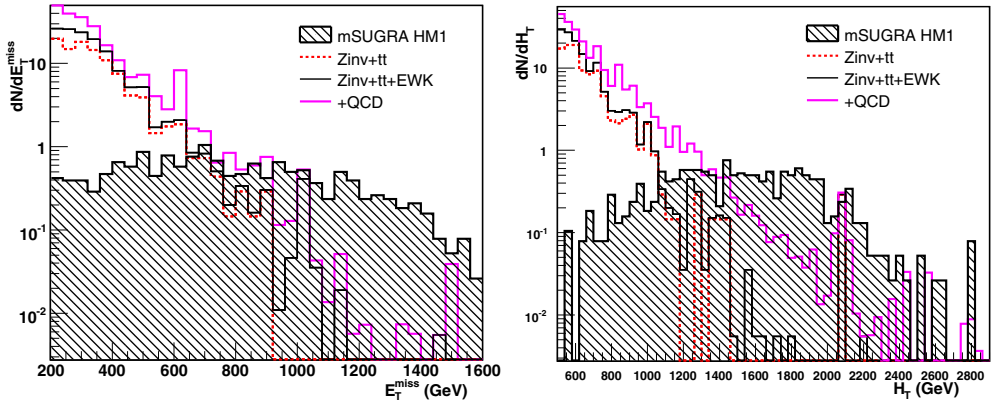

Figure 4.20. HM1 signal and Standard Model background distributions (1 fb^{-1}) for $E_{\mathrm{T}}^{\mathrm{miss}}$ (left) and H_{T} (right).

Applying the analysis in the high mass SUSY test point HM1 (with parameters $M_0 = 180\,\mathrm{GeV/c^2}$, $M_{1/2} = 850\,\mathrm{GeV/c^2}$, $A_0 = 0$, $\mu > 0$ and $\tan\beta = 10$) where $m(\tilde{g}) \sim 1890$ GeV/c^2, $m(\tilde{q}) \sim 1700$ GeV/c^2 the signal efficiency is 28%. The $E_{\mathrm{T}}^{\mathrm{miss}}$ and H_{T} distributions comparison between the HM1 SUSY signal and Standard Model backgrounds are shown in Figure 4.20. To perform a SUSY reach scan over the mSUGRA parameter space the optimised analysis requirements for high mass SUSY are used with $E_{\mathrm{T}}^{\mathrm{miss}} > 600\,\mathrm{GeV}$ and $H_{\mathrm{T}} > 1500\,\mathrm{GeV}$ (cf. section 13.5).

Chapter 5. Physics Studies with Tracks, *B* mesons, and taus

5.1. Benchmark Channels: study of the decay $B_s \to J/\psi\phi$

5.1.1. Introduction

The decay $B_s^0 \to J/\psi\phi \to \mu^+\mu^- K^+K^-$ is of particular interest, since it allows to study many properties of the B_s^0 system, such as the differences between the widths and the masses of the two weak eigenstates, B_s^H and B_s^L. Contrary to the B^0 system, the difference between the widths $\Delta\Gamma_s$ of the two weak eigenstates is expected to be large, with a relative difference $\Delta\Gamma_s/\bar{\Gamma}_s$ predicted to be in the order of 10% in the Standard Model. The first measurement from CDF ($\Delta\Gamma_s/\bar{\Gamma}_s = (65^{+25}_{-33} \pm 1)\%$ [128]) and the new preliminary result from DØ($\Delta\Gamma_s/\bar{\Gamma}_s = (15 \pm 10^{+3}_{-4})\%$ [129]) have discrepancies between the two measured values themselves and with the Standard Model prediction. It is only very recently that a first measurement of the mass difference, Δm_s, has been performed at CDF. Time-integrated measurements are not possible, as the time-integrated mixing probability χ saturates at a value of 0.5 for large mass differences, and in time-dependent measurements, the high mass difference generates very rapid oscillations. As in the B_s^0 system the ratio $\Delta m_s/\Delta\Gamma_s$ depends on the ratio $|V_{cb}V_{cs}|/|V_{tb}V_{ts}|$, which is quite well known, and on QCD corrections, a measurement of $\Delta\Gamma_s$ would therefore yield an independent measurement of Δm_s. With the measurement already performed in the B^0 system, the ratio between the mixing parameters of the B^0 and B_s^0 could provide a measurement of the ratio $|V_{ts}|/|V_{td}|$.

Furthermore, this decay provides one of the best ways to determine the height of the Unitarity Triangle, η in the Wolfenstein parametrisation. At first order of the Wolfenstein parametrisation, the CP-violating weak phase $\phi_{CKM} = [\arg(V_{cs}^* V_{cb}) - \arg(V_{ts}^* V_{tb})]$, measured in the rate asymmetry, cancels, and higher order terms have to be taken, yielding a weak phase $\phi_{CKM} = 2\lambda^2\eta$. The weak phase is therefore expected to be very small, of the order of 0.03. The measurement of a significantly larger phase would indicate contributions from non-Standard Model processes.

Because of the relative orbital angular momentum between the decay products, the $J/\psi\phi$ final state is an admixture of CP-even and CP-odd states, and the total rate asymmetry suffers from a partial cancellation. As the CP-even and CP-odd components have different angular dependences, an analysis of the angular correlation of the decay will allow to separate the two states, thereby permitting to access the different parameters.

With a total B production cross section at $\sqrt{s} = 14\,\text{TeV}$ expected to be as high as $500\,\mu\text{b}$, a substantial number of fully reconstructed B_s^0 candidates can be expected. Nevertheless, a high background has to be dealt with. The main sources of backgrounds identified are those containing a J/ψ decaying to two muons susceptible to satisfy the Level-1 trigger requirements.

The decay $B_s^0 \to J/\psi\phi$ is chosen as a benchmark channel since it is representative of exclusive B physics studies. It allows to study the capability of CMS to identify, select and fully reconstruct the decay of the B_s^0, which presents a significant challenge due to its relatively low momentum and high background. In addition, the measurement of the width difference $\Delta\Gamma_s$ on a sample of untagged $B_s^0 \to J/\psi\phi \to \mu^+\mu^- K^+K^-$ candidates using a maximum likelihood fit of the time dependent angular distribution can be attempted. An example of a pp $\to B_s + X$ event with $B_s \to J\psi\phi$ is shown in colour plate CP7.

5.1.2. Event generation

In addition to the signal itself, the main backgrounds identified have been simulated with low luminosity pile-up ($\mathcal{L} = 2 \times 10^{33}\,\text{cm}^{-2}\,\text{s}^{-1}$). Kinematic requirements were applied in

order to ensure that a significant fraction of the generated events would fulfil the Level-1 trigger requirements and that the final state particles are within the acceptance of the tracker ($|\eta| < 2.5$). The transverse momentum of the muons is thus required to be above 3 GeV/c for muons in the barrel ($|\eta| < 1.2$) and 2 GeV/c elsewhere. For the signal, the momenta of the kaons are required to be above 0.8 GeV/c.

For the samples composed of events with decays of B hadrons, $b\bar{b}$ pairs were generated with PYTHIA 6.215. The MSEL = 1 card was used in order to correctly reproduce the three different contributions to the total cross section (parton fusion, flavour excitation, and gluon splitting). The fragmentation of the b quark is performed by PYTHIA and the subsequent decay of the B hadron is performed using the SIMUB generator [130], a dedicated B physics event generator. The decay $B_s^0 \to J/\psi\phi$ has to be performed with SIMUB, since PYTHIA does not take into account the angular distributions of the final decay products.

One of the b quarks in the event is forced to hadronise to a B_s^0 or $\bar{B}_s^0$ meson and to decay through the complete decay chain. With the kinematic requirements, using the world-average branching ratios for the decays of the B_s^0, J/ψ and ϕ mesons [54], the cross section is predicted to be $\sigma(B_s^0 \to J/\psi\phi \to \mu^+\mu^- K^+K^-) = 74 \pm 27$ pb.

The inclusive decays of B hadrons to final states with a J/ψ resonance are expected to be the most important background for the measurement. These were simulated using PYTHIA, since no detailed simulation of angular distributions of the final decay products is needed. In order to increase the number of events similar to the signal events, a pair of oppositely charged particles with $p_T > 0.5$ GeV/c and $|\eta| < 2.5$ forming a fake ϕ candidate is required in a region ($|\Delta\eta| < 1.5$, $|\Delta\varphi| < 1.5$) around the J/ψ direction and with an invariant mass within 30 MeV/c^2 of the world-average ϕ mass. In addition, this fake ϕ candidate is required to form a fake B_s^0 candidate with an invariant mass within 300 MeV/c^2 of the world-average B_s^0 mass. The cross section, including the kinematic requirements and branching-fractions, is estimated to be $\sigma(b \to J/\psi X) = 3.20 \pm 0.3$ nb.

Furthermore, a sample of $B^0 \to J/\psi K^{*0} \to \mu^+\mu^- K^+\pi^-$ events were simulated, since this final state can be misidentified as a $B_s^0 \to J/\psi\phi$ decay. In addition, this decay has a similar differential decay rate [131,132] to the studied B_s^0 decay. The B^0 decay is simulated with SIMUB, where one of the b quarks in the event is forced to hadronise to a B^0 or $\bar{B}^0$ meson, and to decay through the complete decay chain. With the kinematic requirements, and using the world-average branching ratios, the cross section is predicted to be $\sigma(B^0 \to J/\psi K^{*0} \to \mu^+\mu^- K^+\pi^-) = 366 \pm 22$ pb.

The uncertainties quoted on the estimates above do not include the uncertainties on the total $b\bar{b}$ cross section at LHC energies, the b fragmentation functions, the transverse momentum distribution of b quarks, and the uncertainties introduced by using the model of $b \to J/\psi X$ decays in PYTHIA. However, since both the signal and background are proportional to the same $b\bar{b}$ cross section, the signal-to-background ratio is unaffected by the corresponding uncertainty. The parameters used in the simulation of the $B_s^0 \to J/\psi\phi$ and $B^0 \to J/\psi K^{*0}$ decays are given in Table 5.1.

The direct production of J/ψ mesons is an important background at trigger level. Measurements at the Tevatron [133] have shown that predictions of the colour-singlet model, which is presently the one implemented in the PYTHIA generator, underestimate the measurements by several orders of magnitude. Perturbative QCD is used in this model to generate $c\bar{c}$ pairs, which then hadronise to a charmonium state in a non-perturbative way.

The observed discrepancy has led to a different approach [134], which has been implemented in a modified version of PYTHIA 6.225, tuned on Tevatron data. A $c\bar{c}$ pair is first formed taking into account all perturbative QCD diagrams, regardless of the final colour

Table 5.1. Values used for the mixing parameters, decay amplitudes, strong and weak phases in the simulation of the $B_s^0 \to J/\psi\phi$ and $B^0 \to J/\psi K^{*0}$ Monte Carlo sample.

Parameter	$B_s^0 \to J/\psi\phi$	$B^0 \to J/\psi K^{*0}$
$\tau = 1/\bar{\Gamma}$	1.405×10^{-12} s	1.528×10^{-12} s
$\Delta\Gamma/\bar{\Gamma}$	-0.2	0
Δm	$17.8\,\text{ps}^{-1}$	$0.509\,\text{ps}^{-1}$
$\lvert A_0(0)\rvert^2/\Gamma$	0.570	0.570
$\lvert A_\parallel(0)\rvert^2/\Gamma$	0.217	0.217
$\lvert A_\perp(0)\rvert^2/\Gamma$	0.213	0.213
δ_1	π	π
δ_2	0	0
ϕ	-0.04	0

state. The $c\bar{c}$ state is then transformed into a colour-singlet by non-perturbative processes, such as the emission of a soft gluon.

This version of PYTHIA has been used to simulate a sample of J/ψ decaying to two muons for background studies. The J/ψ production cross section is calculated to be 141μb. Taking the $J/\psi \to \mu^+\mu^-$ branching ratio and the kinematic requirements into account, a cross section of 310 ± 5 nb is expected. Only the statistical uncertainty is quoted and used; the large uncertainties on the total cross section for J/ψ production and on the p_T distribution are not included.

5.1.3. Trigger selection

5.1.3.1. The Level-1 Trigger. The B_s^0 decay chain is selected at Level-1 by the dimuon trigger stream. At low luminosity it is foreseen [76] to use an identical threshold of 3 GeV/c on the transverse momentum of each muon, still keeping a low bandwidth occupancy of 0.9 kHz. Such a low p_T threshold ensures a very high selection efficiency on this channel, with a rate low-enough to allow the use of lower quality muon candidates in the endcap region, recovering full geometrical acceptance of the muon detector up to $|\eta| < 2.4$. For this decay, two of the identified muons are required to have opposite charge.

5.1.3.2. The High-Level Trigger. In the HLT, the signal events are identified by doing a full reconstruction of the B_s^0 decay, imposing invariant mass and vertex constraints. Indeed, at this stage, tracks can be reconstructed in the tracker in restricted (η, ϕ) regions via a partial reconstruction algorithm, where only the first 5 hits are used [7, Section 6.4.3.2]. To define the tracking regions, the primary (interaction) vertex is first identified and reconstructed using only hits in the Pixel detector, with the "Divisive Method" described in reference [135]. Since the primary vertex of $b\bar{b}$ events involves low momentum tracks, the three vertex candidates with the highest sum of the p_T^2 of the tracks, which is the default selection criterion, have to be retained in order to achieve a good efficiency.

For the muons, the tracking regions are chosen around the direction of the muons identified at Level-1. Since no link to the muon detectors can be done at this stage, all track pairs of opposite charge for which the invariant mass is within $150\,\text{MeV/c}^2$ of the world-average J/ψ mass are retained. The resolution on the invariant mass of the J/ψ meson is found to be $51\,\text{MeV/c}^2$. In addition, the p_T of each muon is required to be above 2.5 GeV/c in $|\eta| < 1.2$ or 2 GeV/c in $|\eta| \geqslant 1.2$, and the p_T of the J/ψ candidate above 4 GeV/c. To remove the prompt J/ψ background, the two muon candidates are then fitted to a common

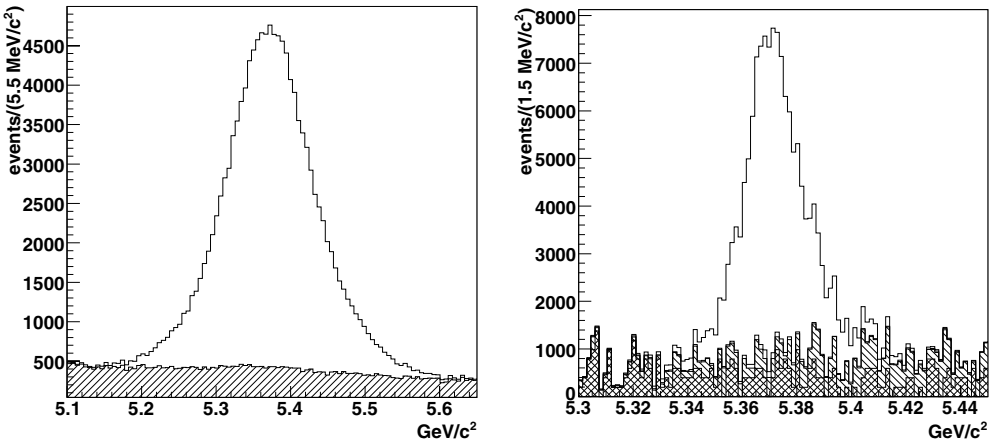

Figure 5.1. Four-track invariant mass distribution after the HLT (left) and offline (right) requirements. The right distribution includes only combinatorial background and the left distribution the expected inclusive $b \to J/\psi X$ and $B^0 \to J/\psi K^{*0}$ background.

decay vertex. The χ^2 of the fit is required to be below 10 and the significance of the transverse decay length is required to be above 3. Furthermore, the transverse momentum of the J/ψ candidate is required to be nearly parallel to its flight path in the transverse plane, since the J/ψ mesons produced in the decays of B_s^0 mesons are collimated around the direction of the B_s^0 meson by the relativistic boost. The cosine of the angle between the reconstructed momentum vector and the vector pointing from the production to the decay vertex is thus required to be larger than 0.9.

To reconstruct the kaons, a tracking region is chosen around the direction of each J/ψ candidate. Assigning the kaon mass to the reconstructed tracks, all oppositely charged track pairs for which the invariant mass is within $20\,\mathrm{MeV/c^2}$ of the world-average mass of the ϕ meson are retained, for a resolution on the invariant mass of the ϕ meson of $4.5\,\mathrm{MeV/c^2}$. The p_T of each of the kaon tracks is required to be above $0.7\,\mathrm{GeV/c}$, the p_T of the ϕ candidate above $1\,\mathrm{GeV/c}$ and the p_T of the B_s^0 candidate above $5\,\mathrm{GeV/c}$. With the two muon candidates, the four-track invariant mass is required to be within $200\,\mathrm{MeV/c^2}$ of the world-average mass of the B_s^0 meson. The resolution on the invariant mass of the B_s^0 meson is found to be $65\,\mathrm{MeV/c^2}$. Here as well, a vertex fit of the four tracks is performed, imposing similar requirements as above.

The distribution of the invariant mass of the candidates after the HLT requirements is shown in Figure 5.1 (left). The efficiencies for the different criteria, which include the respective reconstruction efficiencies, are given in Table 5.2 for the signal and the different background samples, together with the estimated rate. The total rate for this selection is well below 1 Hz, and a yield of approximately 456 000 signal events can be expected within $30\,\mathrm{fb^{-1}}$ of data.

5.1.4. Offline selection and reconstruction

The first step in the offline selection is similar to the HLT selection, with the difference that the complete information from the detector is available. Candidates are reconstructed by combining two muons of opposite charge with two further tracks of opposite charge. As CMS does not possess a particle identification system suitable for this measurement, all

Table 5.2. Trigger selection efficiencies for the signal and background (defined with respect to the number of generated events) after each requirement, and estimated HLT rate.

Requirement	Signal	Background		
	$B_s^0 \to J/\psi\phi$	Inclusive $b \to J/\psi X$	$B^0 \to J/\psi K^{*0}$	Prompt J/ψ
Level-1	45.76(6)%	38.25(13)%	46.91(13)%	36.91(12)%
HLT-J/ψ selection	28.69(7)%	21.91(11)%	30.28(12)%	0.65(2)%
HLT-ϕ selection	20.50(6)%	1.23(3)%	0.961(26)%	0.0007(7)%
HLT rate (Hz)	0.03034(8)	0.0792(18)	0.0077(2)	0.002(2)

measured tracks have to be considered as possible kaon candidates, which adds a substantial combinatorial background. At this stage, only loose requirements are applied, which are tightened after a kinematic fit.

First, all muons in the event are reconstructed using the global muon reconstruction algorithm [7, Section 9.1.3]. This algorithm is not fully efficient for low-p_T muons from J/ψ decays, being more suited to the reconstruction of high-p_T muons. Therefore, all tracks are reconstructed with the standard track reconstruction algorithm [7, Section 6.5]. Track-pairs of opposite charge for which the invariant mass is within $120\,\mathrm{MeV/c^2}$ of the world-average J/ψ mass are retained as a J/ψ candidate. The p_T of each muon is required to be above $3\,\mathrm{GeV/c}$ in $|\eta| < 1.2$ or $2\,\mathrm{GeV/c}$ in $|\eta| \geqslant 1.2$, and the p_T of the J/ψ candidate above $4\,\mathrm{GeV/c}$. The muon identification algorithm which uses information from the muon detector [7, Section 9.2.1.2], is applied to both tracks forming the J/ψ candidate. A J/ψ candidate is confirmed if both tracks share more than half of their hits in the silicon tracker with the muon tracks reconstructed by the global muon reconstructor, or if their compatibility score returned by the muon identification algorithm is greater than 0.1.

To reconstruct the ϕ meson, all tracks reconstructed with the standard track reconstruction algorithm are used. Requiring the p_T of each track to be above $0.8\,\mathrm{GeV/c}$ and assigning a kaon mass to the thus reconstructed tracks, all oppositely charged track pairs for which the invariant mass is within $20\,\mathrm{MeV/c^2}$ of the world-average mass of the ϕ meson are retained. The p_T of the ϕ candidate is required to be above $1\,\mathrm{GeV/c}$, and the p_T of the B_s^0 candidate above $5\,\mathrm{GeV/c}$.

A kinematic fit [136] is then made, where the four tracks are constrained to come from a common vertex and the invariant mass of the two muons is constrained to be equal to the mass of the J/ψ. Since the natural width of the ϕ meson is of the same order as the resolution due to the reconstruction, no mass constraint is applied to the two kaon tracks. With this fit, a resolution on the invariant mass of the B_s^0 meson of $14\,\mathrm{MeV/c^2}$ is found. The confidence level of the fit is required to be greater than 1×10^{-3} (seven degrees of freedom). The invariant mass of the two kaons is required to be within $8\,\mathrm{MeV/c^2}$ of the world-average mass of the ϕ meson. Finally, the cosine of the angle between the reconstructed momentum vector of the B_s^0 candidate and the vector pointing from the production to the decay vertex is required to be larger than 0.95. The distribution of the invariant mass of the candidates after all selection requirements is shown in Figure 5.1 (right).

The primary vertex is not used at this stage, since the efficiency of the standard primary vertex finder [7, Section 6.6.4], which uses all fully reconstructed tracks, is 92%, and drops to 83% if the vertex is required to be within $500\,\mu\mathrm{m}$ from the simulated vertex. In order to prevent this unnecessary loss of efficiency, no use is made of the primary vertex, and all quantities of interest are evaluated in the transverse plane.

Table 5.3. Offline selection efficiencies for the signal and background (defined with respect to the number of generated events) after each requirement.

Requirement	Signal	Background		
	$B_s^0 \to J/\psi\phi$	$b \to J/\psi X$	$B^0 \to J/\psi K^{*0}$	Prompt J/ψ
HLT selection	20.50(6) %	1.23(3) %	0.937(14)%	0.0007(7) %
Reconstruction + Basic p_T req.	18.15(5) %	0.63(2) %	0.675(12) %	0.0007(7) %
Muon Identification	17.89(5) %	0.585(19) %	0.636(11) %	0.0007(7) %
Kinematic fit χ^2 req.	16.58(5) %	0.282(14) %	0.503(10) %	0.0007(7) %
Pointing constraint	16.48(5) %	0.258(13) %	0.497(10) %	–
ϕ mass req.	14.65(5) %	0.113(13) %	0.202(10) %	–

Table 5.4. Expected cross sections for the signal and background, after each requirement, with number of expected events.

	Signal	Background		
	$B_s^0 \to J/\psi\phi$	Inclusive $b \to J/\psi X$	$B^0 \to J/\psi K^{*0}$	Prompt $J\psi$
$\sigma \times$ BR	2.87 ± 1.07 nb	682 ± 64 nb	20.4 ± 1.7 nb	141 μb
Kin. preselection	74 ± 27 pb	3.20 ± 0.3 nb	366 ± 22 pb	176 ± 2 nb
Level-1	34 ± 12 pb	1.22 ± 0.11 nb	172 ± 10 pb	65 ± 1 nb
HLT	15.2 ± 5.5 pb	39.4 ± 3.8 pb	3.52 ± 0.21 pb	1.2 ± 1.2 pb
Offline	10.9 ± 4.0 pb	3.62 ± 0.54 pb	0.74 ± 0.06 pb	–
Events per 30 fb $^{-1}$	327 000	108 500	22 200	–

With this selection, a yield of approximately 327 000 signal events can be expected within 30 fb^{-1} of data, with a background of 108 500 events. The efficiencies for the different criteria, which include the respective reconstruction efficiencies, are given in Table 5.3 for the signal and the different background samples, and the expected cross sections are given in Table 5.4. These do not include a requirement on the four-track invariant mass of the candidates, since the sidebands will be used later in the analysis. However, only a small fraction of these events are directly under the B_s^0 peak, and even a simple cut will reduce the number of background events by a significant factor.

5.1.5. The maximum likelihood analysis

The final state of the decay of a pseudo-scalar B meson into two vector mesons $B \to V_1 V_2$ is an admixture of CP-even and CP-odd states [131,132,137]. The CP-odd states correspond to transitions in which the relative orbital momentum L between the two vector mesons is 1 and the CP-even states to transitions in which L is either 0 or 2. The amplitude of the decay can be decomposed in three independent decay amplitudes which correspond to the linear polarisation states of the two mesons. The first, A_0, describes states in which the linear polarisation vectors are longitudinal and is CP-even. The other two describe states in which the linear polarisation vectors are transverse, either parallel ($A_\parallel$ – CP-even) or perpendicular ($A_\perp$ – CP-odd) to each other.

The differential decay rate can be written as:

$$\frac{\mathrm{d}^4\Gamma(B_s(t))}{\mathrm{d}\Theta\,\mathrm{d}t} = f(\Theta,\alpha,t) = \sum_{i=1}^{6} O_i(\alpha,t)\cdot g_i(\Theta), \tag{5.1}$$

where O_i are the kinematics-independent observables and g_i the angular distributions. The set of physical parameters are represented by α and the angles which define the kinematics are

generically denoted Θ. The time evolution of the different observables is given by bilinear combinations of the polarisation amplitudes, $|A_0(t)|^2$, $|A_\parallel(t)|^2$, $|A_\perp(t)|^2$, $\Im(A_\parallel^*(t)A_\perp(t))$, $R(A_0^*(t)A_\parallel(t))$ and $\Im(A_0^*(t)A_\perp(t))$. These are functions of the widths of the two light and heavy eigenstates, Γ_L and Γ_H, the weak phase ϕ_{CKM}, the magnitudes of the amplitudes at $t=0$ ($A_0(0)$, $A_\parallel(0)$ and $A_\perp(0)$) which describe all hadronisation effects, and, for a flavour-tagged sample, the mass difference $\Delta m_s = m_H - m_L$. Since the overall phase of the polarisation states is not observable, two strong phases are defined as $\delta_1 \equiv \arg|A_\parallel{}^* A_\perp|$ and $\delta_2 \equiv \arg|A_0^* A_\perp|$. These are CP conserving, and are expected to be 0 (mod π) in the absence of final-state interactions. Assuming $SU(3)$ flavour-symmetry, the magnitudes and the two strong phases are equal for the decays $B_s^0 \to J/\psi\phi$ and $B^0 \to J/\psi K^{*0}$ in unmixed samples. The measurement of these parameters is of interest to study and improve the phenomenological models used to calculate all hadronic effects.

In such decays, the kinematics are uniquely defined by a set of three angles. The transversity base is used in this analysis, in which the set of variables is $\Theta = (\cos\theta, \phi, \cos\varphi)$. In this base, (θ, φ) are the polar and azimuthal angles of the momentum of the μ^+ in the J/ψ rest frame. This coordinate system is defined such that the ϕ moves in the positive x direction and the z axis is perpendicular to the decay plane of the decay $\phi \to K^+K^-$. The angle ψ is defined in the rest frame of the ϕ as the negative cosine of the angle between the K^+ direction and the J/ψ direction.

In order to measure the values of the different parameters, an unbinned maximum likelihood fit is performed on the observed time evolution of the angular distribution. In the absence of background and without distortion, the p.d.f. describing the data would be the original differential decay rate $f(\Theta, \alpha, t)$ (Equation (5.1)). The distortion of this distribution by the detector acceptance, trigger efficiency and the different selection criteria is taken into account by an efficiency term $\varepsilon(t, \Theta)$. In addition, a term describing the background has to be added.

It is assumed that the efficiency can be factorised in two functions, the first modelling the effects of the decay length requirements and the second the distortion of the angular distribution,

$$\epsilon(t, \Theta) = \epsilon(t) \cdot \epsilon(\Theta). \tag{5.2}$$

The angular efficiency is described by an expansion of products of spherical harmonics [138]:

$$\epsilon(\Theta) = \sum_{LRM} T^{\epsilon}_{LRM} \cdot \mathcal{Y}_{LRM}(\Theta), \tag{5.3}$$

$$\text{with} \quad \mathcal{Y}_{LRM}(\Theta) = \sqrt{2\pi} \cdot Y_{LM}(\theta, \varphi) \cdot Y_{RM}(\psi, 0), \tag{5.4}$$

where $\mathcal{Y}_{LRM}$ are orthonormal basis functions and Y_{LM}, Y_{RM} are spherical harmonic functions. In principle, L and R run from 0 to infinity and the sum over M from $-\min(L; R)$ to $+\min(L; R)$, but it has been found that the expansion can be limited to $L, R \leqslant 8$. These $\mathcal{Y}_{LRM}$ functions describe the partial waves involved in a scalar $\to$ vector decay [139]. The moments of the efficiency are determined from a Monte Carlo simulation with full detector simulation:

$$T^{\epsilon}_{LRM} = \int \epsilon(\Theta) \cdot \mathcal{Y}^*_{LRM}(\Theta) \mathrm{d}\Theta \tag{5.5}$$

$$\approx \frac{1}{N_{gen}} \sum_{i=1}^{N_{obs}} \frac{1}{f(\Theta_i)} \mathcal{Y}^*_{LRM}(\Theta_i), \tag{5.6}$$

where $f(\Theta_i)$ is the expected time-integrated angular distribution (Equation (5.1)).

The time-dependent efficiency describes mainly the effects of the requirements on the proper decay length distribution. After the initial turn-on and a stable plateau, a deficit of events can be observed. Initial studies attribute this decrease in efficiency to the restrictions imposed on the seeds by the tracking regions in the HLT, which cause an additional track reconstruction inefficiency for displaced tracks such as those originating from B decays. The tolerance on the transverse and the longitudinal direction imposed on the tracking regions in the HLT results in an implicit cut on the impact parameters. Further studies are needed to find solutions to alleviate this inefficiency. Without corrections, the main effect of this inefficiency would be to lower the estimated lifetime of the longer-lived eigenstate B_s^H.

The different features in this distribution cannot easily be described by a simple function. Two sigmoidal functions combined with a quadratic function are used to describe the efficiency:

$$\epsilon(t) = \begin{cases} c \cdot \left(1 + \tanh\left(\frac{t-t_0}{\Delta t_1}\right)\right) & t < t_0 \\ (a \cdot t^2 + b \cdot t + c) \cdot \left(1 + \tanh\left(\frac{t-t_0}{\Delta t_2}\right)\right) & t > t_0. \end{cases} \tag{5.7}$$

The parameters are found by fitting this function to the distribution obtained by the full Monte Carlo simulation.

The best way to gauge our ability to account for all effects and our capacity to correct them through this time-dependent efficiency curve is by comparing the proper time distributions foreseen by the simulation and observed in the data for the different B mesons. The first obvious choice is again the decay $B^0 \to J/\psi K^{*0}$, which is very similar to the studied B_s^0 decay, and for which the lifetime has been measured with a high precision. Any discrepancy between the efficiency determined by Monte Carlo and the data will be reflected in a mismeasurement of the B^0 lifetime. Further studies would be needed to determine the sensitivity of the efficiency on the lifetime of the selected B meson. It is dubious whether the number of B_s^0 events recovered in other trigger streams such as the dimuon stream, which has no decay length requirement, would be enough to estimate the time-dependent efficiency.

The background can be divided in two different types of distributions. The first type arises from misidentified $B^0 \to J/\psi K^{*0} \to \mu^+\mu^- K^+\pi^-$ events, which has a similar differential decay rate [131, 132] to the decay of interest. The width difference of the two eigenstates of the B^0 are assumed to be negligible, and no CP violation is present since the final state is flavour specific. To describe this background in the dataset, it is not possible to use its time dependent angular distribution, which is in principle well known, since all variables are mismeasured because of the misidentification of the π. In addition, the distortion of the distribution due to the various requirements is much more severe than in the case of the B_s^0. Indeed, due to its lower mass, the momentum of the π in the laboratory frame is lower than that of the corresponding K when the π is emitted in the direction opposite to the momentum of the K^{*0}.

The same set of functions $\mathcal{Y}_{LRM}(\Theta)$ (Equation (5.4)) is used to model the angular distribution $f_d(\Theta)$ of this background, with the moments computed in the following way:

$$T^b_{LRM} = \int b(\Theta) \cdot \mathcal{Y}^*_{LRM}(\Theta) \mathrm{d}\Theta \tag{5.8}$$

$$\approx \frac{1}{N_b} \sum_{i=1}^{N_b} \mathcal{Y}^*_{LRM}(\Theta_i)\,. \tag{5.9}$$

Here as well, the expansion is done up to $L, R \leqslant 8$. The functions are obtained by a Monte Carlo simulation and can be cross-checked by a fully reconstructed sample of well-identified $B^0 \to J/\psi K^{*0}$ decays misreconstructed as B_s^0 candidates.

The time dependence of this background is modelled as a single exponential decay, again with a time-dependent efficiency. The lifetime τ_d is left as a free parameter, since the mismeasurement of the proper decay length precludes using the well-measured lifetime of the B^0.

The other sources of background are assumed to have no angular dependence. The distribution of their proper decay time is modelled by two exponential decays, the first describing the short-lived prompt background and the second misidentified long-lived heavy-flavour hadrons.

A better separation of the signal and background is obtained by using the events in a wider invariant mass region between 5.219 and 5.559 $\mathrm{GeV/c^2}$, and including in the fit the distribution of the invariant mass of the candidates. The distribution of the B_s^0 candidates is modelled by a Gaussian $G_s(m; m_s, \sigma_s)$, where m_s is the mass of the B_s^0 meson and σ_s the variance due to the reconstruction. The distribution of the misidentified $B^0 \to J/\psi K^{*0}$ decays can reasonably well be modelled in the chosen region by a Gaussian $G_d(m; m_d, \sigma_d)$. Because of the misidentification of the pion, m_d will not correspond to the true mass of the B^0 meson, and will be left as a free parameter in the fit. The other sources of background are assumed to have a flat mass distribution and will be modelled by a linear function $L(m)$.

The total p.d.f. to be fit is thus given by

$$\begin{aligned}\mathcal{P} = {} & (1 - b_d - b_c) \cdot \epsilon(t, \Theta) \cdot f(\Theta, \alpha, t) \cdot G_s(m; m_s, \sigma_s) \\ & + b_d \cdot f_d(\Theta) \cdot \epsilon(t) \cdot \frac{1}{\tau_d} e^{-t/\tau_d} \cdot G_d(m; m_d, \sigma_d) \\ & + b_c \cdot \epsilon(t) \cdot \left(\frac{1}{\tau_{cl}} e^{-t/\tau_{cs}} + \frac{1}{\tau_{cl}} e^{-t/\tau_{cl}} \right) \cdot L(m), \end{aligned} \tag{5.10}$$

where b_d, respectively b_c, are the fraction of misidentified B^0 background, respectively combinatorial background, in the sample. These parameters are left free in the fit. The resolution of the proper decay length is taken into account by convolving the p.d.f. with a Gaussian resolution function. The standard deviation of the Gaussian is taken as the uncertainty of each candidate's proper decay length measurement multiplied by a scale factor, which is left free in the fit. Since the uncertainties of the measured angles are found to be small, these are not taken into account in the fit. A contribution is added to the systematic uncertainty to reflect this omission.

5.1.6. Result

Due to the high production cross sections of the identified backgrounds, only limited samples could be generated and analysed, which do not permit to have a final dataset with the foreseen signal-to-background ratio. Indeed, the signal sample corresponds to an integrated luminosity of 6.8 $\mathrm{fb^{-1}}$, while the inclusive background corresponds to an integrated luminosity of barely 48 $\mathrm{pb^{-1}}$. The situation is somewhat better for the decay $B^0 \to J/\psi K^{*0}$, for which the sample corresponds to an integrated luminosity of 1.3 $\mathrm{fb^{-1}}$.

First, a fit was performed on the complete set of selected and associated B_s^0 candidates only, using the efficiency functions determined in the previous section. The relative width difference $\Delta\Gamma_s/\bar{\Gamma}_s$ can be determined with an uncertainty of 0.016 (Table 5.5), but no sensitivity on the weak phase and the strong phases is obtained.

Then, a sample corresponding to an integrated luminosity of 1.3 $\mathrm{fb^{-1}}$ is considered, which allows to have a realistic ratio of $B^0 \to J/\psi K^{*0}$ and signal events. With the low number of background events which remain after all selection requirements, an accurate model through the described p.d.f. is not possible. In addition, the low number of $B^0 \to J/\psi K^{*0}$ events

Table 5.5. Results of the maximum likelihood fit for 73813 signal events.

Parameter	Input value	Result	Stat. error	Rel. error
$\|A_0(0)\|^2$	0.57	0.57398	0.00267	0.4%
$\|A_{\|\|}(0)\|^2$	0.217	0.21808	0.00473	2.1%
$\|A_\perp(0)\|^2$	0.213	0.20794	0.00396	1.9%
$\bar{\Gamma}_s$	$0.712\,\mathrm{ps}^{-1}$	$0.712358\,\mathrm{ps}^{-1}$	$0.00350643\,\mathrm{ps}^{-1}$	0.5%
$\Delta\Gamma_s$	$0.142\,\mathrm{ps}^{-1}$	$0.134645\,\mathrm{ps}^{-1}$	$0.0108247\,\mathrm{ps}^{-1}$	8.0%
$\Delta\Gamma_s/\bar{\Gamma}_s$	0.2	0.189013	0.0157993	8.4%
δ_1	π	2.94405	0.632682	
δ_2	0	−0.109493	0.639713	
ϕ_{CKM}	−0.04	−0.0297427	0.0758856	

Table 5.6. Results of the maximum likelihood fit for an integrated luminosity of $1.3\,\mathrm{fb}^{-1}$ (signal only).

Parameter	Input value	Result	Stat. error	Rel. error
$\|A_0(0)\|^2$	0.57	0.5859	0.0062	1.1%
$\|A_{\|\|}(0)\|^2$	0.217	0.2141	0.0078	3.6%
$\|A_\perp(0)\|^2$	0.213	0.2002	0.0064	3.2%
$\bar{\Gamma}_s$	$0.712\,\mathrm{ps}^{-1}$	$0.7018\,\mathrm{ps}^{-1}$	$0.0081\,\mathrm{ps}^{-1}$	1.2%
$\Delta\Gamma_s$	$0.142\,\mathrm{ps}^{-1}$	$0.1470\,\mathrm{ps}^{-1}$	$0.0256\,\mathrm{ps}^{-1}$	17.4%
$\Delta\Gamma_s/\bar{\Gamma}_s$	0.2	0.2095	0.0371	18.1%

Table 5.7. Results of the maximum likelihood fit for an integrated luminosity of $1.3\,\mathrm{fb}^{-1}$ (signal and background).

Parameter	Input value	Result	Stat. error	Rel. error
$\|A_0(0)\|^2$	0.57	0.5823	0.0061	1.1%
$\|A_{\|\|}(0)\|^2$	0.217	0.2130	0.0077	3.6%
$\|A_\perp(0)\|^2$	0.213	0.2047	0.0065	3.2%
$\bar{\Gamma}_s$	$0.712\,\mathrm{ps}^{-1}$	$0.7060\,\mathrm{ps}^{-1}$	$0.0080\,\mathrm{ps}^{-1}$	1.1%
$\Delta\Gamma_s$	$0.142\,\mathrm{ps}^{-1}$	$0.1437\,\mathrm{ps}^{-1}$	$0.0255\,\mathrm{ps}^{-1}$	17.7%
$\Delta\Gamma_s/\bar{\Gamma}_s$	0.2	0.2036	0.0374	18.4%

does not permit an accurate estimate of either the angular distribution or of its time-dependent efficiency. As such, the background events are simply added to the dataset and their expected distribution is not included in the p.d.f. used in the fit. The p.d.f. would thus simply describe the B_s^0 distribution:

$$\mathcal{P} = \epsilon(t, \Theta) \cdot f(\Theta, \alpha, t)\,.$$

With such a fit in which the invariant mass of the candidates is not taken into account, a requirement on the invariant mass of the candidates would obviously be made, choosing a window of $\pm 36\,\mathrm{MeV/c^2}$ around the world-average B_s^0 mass. This reduces the number of B^0 background events by a further 59%, while reducing the number of signal candidates by 2.9%. The results of the fit without background is given in Table 5.6 and with background in Table 5.7. With the lower number of B_s^0 candidates, the statistical uncertainty of the measurement is, as expected, markedly worse. As can be seen, the influence of the background is very small, with only a slight degradation of the width difference. The distribution of the proper decay length of the selected events with the fit projection is shown in Figure 5.2.

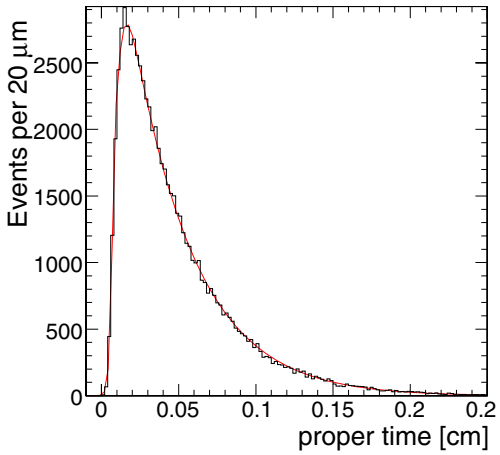

Figure 5.2. Distributions of the proper decay length of the selected signal and background events with fit projection.

Table 5.8. List of systematic uncertainties with effect on the predictions of the rates.

Source	HLT uncert.	Offline uncert.	Common uncert.
Branching ratio B_s^0			36.4 %
Branching ratio B^0			6 %
Branching ratio $b \to J/\psi X$			9 %
Tracking inefficiency	2 %	2%	
Muon reconstruction	-	1.4%	
Misalignment	17%	-	

Table 5.9. List of systematic uncertainties with effect on the measurements.

Source	$\lvert A_0(0)\rvert^2$	$\lvert A_\parallel(0)\rvert^2$	$\lvert A_\perp(0)\rvert^2$	$\bar{\Gamma}_s$	$\Delta\Gamma_s/\bar{\Gamma}_s$
Bckg. distrib.	0.0034	0.0011	0.0045	0.0043	0.0059
S/B ratio	0.0037	0.0001	0.0024	0.0025	0.0055
Resolution	-	-	-	0.00060	0.0045
Ang. distortion	0.0143	0.0061	0.0082	0.00083	0.0010
$c\tau$ distortion	0.0016	0.00073	0.0023	0.0221	0.0146
Alignment	0.00012	0.00042	0.00055	0.00040	0.0014
Total	0.0152	0.0063	0.0099	0.0227	0.0173

5.1.7. Systematics and detector effects

The list of systematic uncertainties which were considered are summarised in two tables. The first, Table 5.8, summarises the uncertainties which affect the HLT rate and the number of foreseen events after all selection requirements. The second, Table 5.9, summarises the uncertainties which affect the measurement of the various parameters.

- **Signal and background statistics.** Among the various uncertainties listed in Section 5.1.2, the largest single source of uncertainty in the estimate of the number of events is obviously

the poor knowledge of the $B_s^0 \to J/\psi\phi$ branching ratio. The uncertainties quoted on the estimates above do not include the uncertainties on the total $b\bar{b}$ cross section at LHC energies, the $b \to B^0$ fragmentation functions, the transverse momentum distribution of b quarks. However, since both the signal and background are proportional to the same $b\bar{b}$ cross section, the signal-to-background ratio is unaffected by the corresponding uncertainty.

- **Track reconstruction efficiency.** A 1% uncertainty per track on the track reconstruction efficiency is assumed for all tracks.
- **Muon reconstruction.** The selection relies heavily on the correct identification of muons. A 1% uncertainty per track on the combined muon identification procedure is assumed.
- **Tracker and muon detector misalignment.** The study has been conducted with a perfectly aligned detector. To gauge the sensitivity of the analysis with respect to the alignment the analysis has been repeated on a detector with the short-term alignment scenario. This scenario is expected to be representative of the relative misalignment of the detector components during the initial data taking period [86]. The effects of misalignment of the tracker on various aspects of track and vertex reconstruction have been extensively studied and reported in [140, 141]. The degradation affect both the selection, mostly through the requirement on the significance of the transverse decay length of the J/ψ in the HLT, and the analysis, through the degradation of the measurement of the proper decay length. The resolution of the latter is degraded from 24 μm for a perfectly aligned detector to 32 μm with the short-term alignment. The HLT efficiency is degraded by some 17% with respect to a perfectly aligned detector.
- **Background distributions.** To gauge the influence of the background on the fit, the variation observed between the fits performed on the reduced 1.3 fb^{-1} dataset with and without these events is added to the systematic uncertainty ("Bckg. distrib." in the table).
  Since the signal-to-background ratio has a significant uncertainty, the fit performed on the reduced 1.3 fb^{-1} sample is repeated varying the number of B_s^0 signal events to match the uncertainty in the signal-to-background ratio. For this estimate, a different uncertainty for the B_s^0 branching fraction has been chosen, since it is believed that it will be measured again in the current run of the Tevatron. Two main uncertainties plagued the measurement done at CDF in Run I, the low number of observed B_s^0 candidates and the uncertainty on the fragmentation. Based on recent publications, it is estimated that approximately 30 times more $B_s^0 \to J/\psi\phi$ decays than in Run 1 should already be collected in the current dataset of 1 fb^{-1}. The uncertainty of the branching fraction is therefore reduced to 20%. For the other uncertainties, the numbers listed in Table 5.8 are used. The variation observed on the fit is listed under the heading "S/B ratio." In a larger dataset, where the full p.d.f. (Eq. 5.11) is used, the influence of the uncertainty on the signal-to-background ratio should be much smaller, since the fractions of background events in the dataset are free parameters in the fit.
- **Distortion of the proper-time distribution ("$c\tau$ distortion").** Other fits were then performed where the parameters of the time dependent efficiency function are varied by one standard deviation. The mean variation of the fitted parameters was added to the systematic uncertainty. As already mentioned, the decay $B^0 \to J/\psi K^{*0}$ can be used to compare the accuracy of this model by comparing the Monte Carlo prediction with the efficiency function observed in the data.
- **Distortion of the angular distributions ("Ang. distortion").** The expansion used to model the distortion of the angular distributions (Equation (5.3)) is limited to $L, R \leqslant 8$. When

Table 5.10. Results of the maximum likelihood fit for an integrated luminosity of $1.3\,\text{fb}^{-1}$ (signal and background).

Parameter	Input value	Result	Stat. error	Sys. error	Total error	Rel. error
$\|A_0(0)\|^2$	0.57	0.5823	0.0061	0.0152	0.0163	2.8%
$\|A_{\|\|}(0)\|^2$	0.217	0.2130	0.0077	0.0063	0.0099	4.6%
$\|A_\perp(0)\|^2$	0.213	0.2047	0.0065	0.0099	0.0118	5.8%
$\bar{\Gamma}_s$	$0.712\,\text{ps}^{-1}$	$0.7060\,\text{ps}^{-1}$	$0.0080\,\text{ps}^{-1}$	$0.0227\,\text{ps}^{-1}$	$0.0240\,\text{ps}^{-1}$	3.4%
$\Delta\Gamma_s$	$0.142\,\text{ps}^{-1}$	$0.1437\,\text{ps}^{-1}$	$0.0255\,\text{ps}^{-1}$	$0.0113\,\text{ps}^{-1}$	$0.0279\text{ps}^{-1}\text{ps}^{-1}$	19%
$\Delta\Gamma_s/\bar{\Gamma}_s$	0.2	0.2036	0.0374	0.0173	0.0412	20%

limiting the expansion to $L, R \leqslant 6$ or $L, R \leqslant 10$, the result of the fit shows negligible differences. In addition, to account for the possibility that the efficiencies do not factorise and that the angular efficiency is grossly miscalculated, the fit is also repeated without the angular efficiency, i.e. without correction of the distortion. While this has little influence on the estimated lifetimes, a large variation is found for the amplitudes. This variation is used as systematic uncertainty.

- **Resolution on the angular variables ("Resolution").** In order to estimate the influence of the uncertainties of the angles and the proper decay length on the fit, a fully controlled toy Monte Carlo was used, in which only the proper time and angles were generated according to the expected p.d.f. and smeared with Gaussian resolution functions. The default standard deviations are taken to be equal to those measured in the Monte Carlo with full detector simulation. The simulation was then repeated without smearing and with a substantial smearing, where the resolution is taken to be two times larger than in the default simulation. The value of parameters found in both cases were very close to the values found with the default smearing, and the observed variation is added to the systematic uncertainty.

5.1.8. Conclusion

The present section describes a study on the selection of the $B_s^0 \to J/\psi\phi$ decay and the measurement of the width difference $\Delta\Gamma_s$ in absence of flavour tagging. An example of a trigger algorithm is presented which would be efficient for this decay and would reject a large fraction of the background. It is based on the identification of J/ψ and B_s^0 candidates with a displaced decay vertex. Nevertheless, this trigger precludes the selection of other decays of the B meson, and should certainly evolve as a true precursor to a B physics trigger. Indeed, the strategy proposed for the Level-2 would select inclusive $b \to J/\psi$ decays with high efficiency and good purity with respect to the prompt J/ψ background. Large uncertainties nevertheless plague the estimates of rates, since large uncertainties remain on the b-quark and prompt J/ψ production cross sections, on their momentum distributions, and on the $b \to B_s^0$ fragmentation function.

A first measurement of one of the main parameters of the B_s^0 system, the relative difference of the widths of the weak eigenstates could be determined with a statistical uncertainty of 0.011 in a sample corresponding to an integrated luminosity of $10\,\text{fb}^{-1}$. A first measurement undertaken on approximately $1.3\,\text{fb}^{-1}$ of data could already yield a measurement with an uncertainty of 20% (Table 5.10). A natural extension of this study should be a tagged analysis, for which flavour tagging algorithms need to be developed.

5.2. Associated production of MSSM heavy neutral Higgs bosons $b\bar{b}H(A)$ with $H(A) \to \tau\tau$

5.2.1. Introduction

The observation of a heavy neutral scalar accompanied by b-jets and decaying into two τ leptons would be an important sign of a MSSM Higgs sector. In the MSSM the associated Higgs boson production $gg \to b\bar{b}H(A)$ is dominant at large values of $\tan\beta$. The cross section of the $gg \to b\bar{b}H(A)$, $H(A) \to \tau\tau$ process is proportional to $\tan^2\beta_{\text{eff}}$ and will be used in a global fit together with other relevant measurements to determine the SUSY parameters simultaneously. An example of a $pp \to H + X$ event with $H \to \tau\nu\tau\nu$ is shown in colour plate CP8.

This channel is an excellent benchmark for the b- and τ-tagging, jet and missing E_T reconstruction. The final state with two τ-jets requires τ tagging both at Level-1 and High Level Trigger. Along with reconstruction and tagging issues, a large number of various Standard Model backgrounds including QCD multi-jet production must be well understood from the real data to be able to establish a discovery.

5.2.2. Event generation

The signal events were generated by PYTHIA using processes the 181 ($gg \to b\bar{b}H$) and 152 ($gg \to H$) for three values of the Higgs boson mass: 200, 500 and 800 GeV/c^2. The backgrounds considered were QCD multi-jet events (for $\tau\tau \to$ jj mode), $t\bar{t}$, $b\bar{b}$, Drell–Yan production of Z/γ^*, W+jet, Wt and $\tau\tau b\bar{b}$. All background processes except $\tau\tau b\bar{b}$ were generated with PYTHIA. The $\tau\tau b\bar{b}$ process was generated by COMPHEP.

In order to reduce CPU time for full detector simulation and event reconstruction loose pre-selections were applied for some of the backgrounds at the generation level. The description of the pre-selections for each final state can be found in the following sections.

The cross sections for the associated Higgs boson production $gg \to b\bar{b}H(A)$ and the branching ratio $H(A) \to \tau\tau$ were calculated using FeynHiggs 2.3.2 [142–144][41] in the $m_h^{\max}$ scenario with $\mu = 200\,\text{GeV}/c^2$ (see Section 11.3.1).

The uncertainty of the measured cross section of the $b(\bar{b})A$, $A \to \tau\tau$ process will include the uncertainty of the Monte Carlo generation. The verification of the Monte Carlo generation for the Higgs boson production with the associated b-jets will be done with the real data using $b\bar{b}Z$ ($Z \to \ell\ell$) events [145].

5.2.3. Level-1 and High Level trigger selections

The $\tau\tau \to$ jj final state is triggered by Level-1 single or double tau triggers with thresholds of 93 GeV for the single and 66 GeV for the double tau trigger. It is followed by the double τ-jet tagging at High Level Trigger. Currently there are two selection strategies at HLT under consideration [146]. In the first strategy the calorimeter isolation using the electromagnetic calorimeter is applied to the first τ-jet in order to reduce the Level-1 output rate by a factor of 3. The tracker isolation is then applied on both jets using the tracks reconstructed with the pixel detector only. The second strategy performs tracker isolation right after the Level-1 trigger decision and uses the full tracker with regional track finding and a restricted number of hits to reconstruct tracks. In this analysis the first method is exploited.

The $\tau\tau \to \mu$j final state uses the single muon trigger at Level-1 with a threshold of 14 GeV. At the High Level the combined muon-plus-τ-jet trigger is used with thresholds of 15 GeV for the muon and of 40 GeV for the τ-jet.

[41] The code can be obtained from http://www.feynhiggs.de

The $\tau\tau \to$ ej final state uses the Level-1 single electron trigger with a threshold of 23 GeV together with the combined electron-plus-τ-jet trigger with thresholds of 14 GeV for the electron and 52 GeV for the τ-jet. At High Level again the single electron trigger with a threshold of 26 GeV and the combined electron-plus-τ-jet trigger with a threshold of 16 GeV for the electron is used. No threshold is applied for the τ-jet candidate.

At High Level Trigger, for both the $\tau\tau \to \mu$j and the $\tau\tau \to$ ej final states, the ECAL and pixel track isolation is applied on the τ-jet candidate similar to what is used in the double τ-jet trigger. For the lepton (e and μ) the same selections are used as for the single electron and muon High Level triggers. The lepton and τ-jet are required to stem from the same vertex found with the pixel detector. Only the tracks from this vertex are used in the tracker isolation.

The search strategy for τ-jet candidates at High Level Trigger for the combined muon-plus-τ-jet and electron-plus-τ-jet triggers is the following: Two calorimeter jets are always reconstructed with the regional jet finder in the regions given by the two highest E_T Level-1 τ-jets. For the muon-plus-τ-jet trigger the first (highest E_T) jet is taken as τ-jet candidate. For the electron-plus-τ-jet trigger the requirement of non collinearity of the jet and the HLT electron candidate, $\Delta R(e - jet) > 0.3$, is checked for each jet, where $\Delta R(e - jet)$ is the distance in η-φ space between the electron and the jet. The first non collinear jet is taken as the τ-jet candidate.

5.2.4. Off-line event selection

The first step in the off-line analysis is the τ-jet identification. The calorimeter jet is reconstructed in the η-φ region of the High Level Trigger τ-jet candidate with the iterative cone algorithm using a cone size of 0.4. A number of requirements for τ-jet identification [146] is applied in addition to the tracker isolation which is tighter off-line than at the HLT and uses the tracks reconstructed with the full tracker. The additional τ-jet identification criteria include requirements to have one or three tracks in the signal cone and opposite charge of the two τ-jets for the $\tau\tau \to$ jj mode or the lepton and the τ-jet for the $\tau\tau \to \ell$j modes and cuts on the transverse impact parameter and on the p_T of the leading track in the signal cone. Finally an electron rejection criterion was applied for the jets. The τ-jet tagging reduces the QCD multi-jet (including $b\bar{b}$) and the W+jet backgrounds.

The associated $b\bar{b}H(A)$ production dominates at high values of $\tan\beta$, thus it is natural to apply b-jet tagging which must suppress Drell–Yan $\tau\tau$ production and eliminate further the QCD multi-jet and the W+jet backgrounds. Since the b-jets in the signal are very soft in E_T and have flat distribution in pseudorapidity only single b tagging is applied. Furthermore, it is possible to veto events with additional jets to reduce $t\bar{t}$ background. The τ-jets found in the first step are not considered for b tagging. Non τ-jet candidates are reconstructed with the iterative cone algorithm using a cone size of 0.5.

The energy of the τ-jet is corrected with a dedicated calibration obtained from Monte-Carlo sample of single τ-jets at low luminosity. The energy of other jets in the event is corrected applying Monte Carlo calibration evaluated from the QCD multi-jet events at low luminosity.

5.2.5. Method of the Higgs boson mass reconstruction

Despite the escaping neutrinos, the Higgs boson mass can be reconstructed in the $H \to \tau\tau$ channels from the visible τ momenta (leptons or τ-jets) and the missing transverse energy (E_T^{miss}) with the collinearity approximation for the neutrinos from highly boosted τ's. The mass resolution depends on the angle $\Delta\varphi$ between the visible τ momenta as $1/\sin(\Delta\varphi)$ and is sensitive to the E_T^{miss} measurement, both in magnitude and particularly in direction. The measurement of E_T^{miss} is affected by the non-linear calorimeter response. A method to improve

the E_T^{miss} scale based on the jet energy corrections was used [147, 148]. The correction of the missing E_T scale improves the reconstruction efficiency by reducing the number of events with negative reconstructed τ lepton and neutrino energies. In particular, for the case of the $\tau\tau \to$ jj final state the efficiency is improved by factor of $\simeq 1.6$. The $\tau\tau$ mass reconstruction method will be verified with the real data using $Z \to \tau\tau \to e(\mu) + \text{jet}$ and $Z \to \tau\tau \to e + \mu$ channels [145, 149].

5.2.6. $H \to \tau\tau \to$ 2jet *analysis*

A detailed description of the analysis can be found in [150].

5.2.6.1. Event generation and pre-selections. The $t\bar{t}$, Drell–Yan production of Z/γ^*, W+jet and Wt backgrounds were generated with PYTHIA, forcing $W \to \tau\nu$ and $Z/\gamma^* \to \tau\tau$ decays. The TAUOLA package was used for τ-lepton decays into all possible decay modes.

The Z/γ^* generation was split into three bins of generated diτ-lepton mass $m_{\tau\tau}$: 80–130 GeV/c^2, 130–300 GeV/c^2 and >300 GeV/c^2. The $\tau\tau b\bar{b}$ generation was divided into two bins of generated diτ-lepton mass $m_{\tau\tau}$: 60–100 GeV/c^2 and >100 GeV/c^2. The $\tau\tau b\bar{b}$ background, generated with COMPHEP, was propagated to PYTHIA for showering, hadronisation and τ lepton decays into all possible modes.

The W + jet background was generated using PYTHIA processes 16 and 31 and with $\hat{p}_T > 65$/GeV/c. The QCD multi-jet background generation was done for four bins in $\hat{p}_T$: 50–80, 80–120, 120–170 and >170 GeV/c.

The loose pre-selections at the level of generation were applied for all backgrounds (except $\tau\tau b\bar{b}$): the event was required to have at least two "τ-like" jets. The jets were reconstructed with the PYTHIA PYCELL routine using a cone size of 0.5. A jet is selected as "τ-like" if it has $E_T^{MC} > 50$ GeV, $|\eta^{MC}| < 2.4$ and a transverse momentum of the leading stable charged particle in the jet, $p_T^{MC} > 30$ GeV/c. These cuts are looser than the ones applied at the trigger and off-line τ-jet selections. For Z/γ^* background no cut was applied on p_T^{MC}.

For the signal events the Higgs boson was forced to decay into two τ leptons and the τ lepton was decayed hadronically using TAUOLA. No pre-selections were applied for the signal events.

5.2.6.2. Event selections. The calorimeter τ-jet jet candidates are reconstructed in the η-φ regions of the High Level Trigger τ-jet candidates, thus no "volunteers" are searched for. This is motivated by the high ($\simeq 100\%$) purity of the HLT τ-jet candidates (fraction of true τ-jets matched with τ-jet candidates).

A cut on the uncalibrated transverse jet energy for each of the two τ-jet candidates was required. It was $E_T > 50$ GeV for $M_A = 200$ GeV/c^2. For higher Higgs boson masses asymmetrical cuts were used: 100, 50 GeV for $M_A = 500$ GeV/c^2 and 150, 50 GeV for $M_A = 800$ GeV/c^2. It allows more effective rejection of the QCD multi-jet background. The following τ-jet identification criteria were then used:

- tracker isolation with parameters: $R_m = 0.1$, $R_S = 0.04$, $R_i = 0.5$, $p_T^i = 1$ GeV/c;
- transverse momentum of the leading track > 35 GeV/c;
- one or three tracks in the signal cone N_{tr}^S for $M_A = 200$ GeV/c^2. For higher Higgs boson masses an effective background rejection is only possible by requiring only one track in the signal cone.

Finally, the two τ-jet candidates were required to have opposite charge. The charge was calculated as the sum of charges of the tracks in the signal cone.

After identification of two τ-jets the other jets in the event were considered. It was required to have only one additional jet with uncalibrated energy $E_T^{raw} > 20$ GeV and $|\eta| < 2.4$. It had to be tagged as b-jet. The b-jet identification was performed using the impact parameter

Table 5.11. The summary table of the selections for signals of $M_A = 200$, 500 and 800 GeV/c^2.

	$m_A = 200$ GeV/c^2 $\tan\beta = 20$	$m_A = 500$ GeV/c^2 $\tan\beta = 30$	$m_A = 800$ GeV/c^2 $\tan\beta = 40$
Cross sections and branching ratios			
$\sigma(gg \to b\bar{b}(A+H))$ (fb)	45795 + 44888	2741 + 2744	677 + 677
BR(H/A $\to \tau\tau$)	0.1	0.082	0.087
BR($\tau \to$ hadrons)^2		0.65×0.65	
$\sigma \times$ BR (fb)	3831	190	49.8
Experimental selection efficiencies			
Level-1 Trigger	0.506	0.854	0.896
HLT	0.289	0.319	0.314
two off-line calo τ jets	0.997	0.999	0.999
cuts on E_T τ jets	0.430	0.755	0.780
two off-line τ candidates	0.674	0.716	0.675
$p_T^{ltr} > 35$ GeV/c	0.326	0.616	0.713
tracker isolation	0.859	0.950	0.954
N_{tracks} in signal cone	0.81	0.67	0.78
$Q_{\tau 1} \times Q_{\tau 2} = -1$	0.98	0.94	0.94
$\geqslant 1$ extra jet, $E_T^{raw} > 20$ GeV, $\lvert\eta\rvert < 2.4$	0.21	0.27	0.31
only 1 extra jet, $E_T^{raw} > 20$ GeV, $\lvert\eta\rvert < 2.4$	0.83	0.82	0.78
$M_{\tau\tau}$ reconstruction efficiency			
$E_{\tau 1,\tau 2} > 0$	0.93	0.93	0.92
$E_{\nu 1,\nu 2} > 0$	0.56	0.67	0.67
total mass reconstruction	0.52	0.62	0.62
b tagging of the extra jet	0.36	0.44	0.41
$M_{\tau\tau}$ mass window	150–300 GeV/c^2	400–700 GeV/c^2	600–1100 GeV/c^2
mass window efficiency	0.81	0.73	0.81
total efficiency	2.5×10^{-4}	2.4×10^{-3}	3.6×10^{-3}
σ after selections (fb)	0.96	0.46	0.19
number of events for 60 fb^{-1}	58.0	27.0	11.0

tagging in 3D space [151]. The jet had to have at least three tracks with an impact parameter significance >2. The purity of the b-tagged jet for the signal is very high ($>95\%$).

The diτ-jet mass reconstruction efficiency is affected by the requirements to have a positive reconstructed energy of both neutrinos, $E_T^{\nu_1,\nu_2} > 0$. In the missing E_T corrections jets with raw energy $E_T^{raw} > 25$ were used.

5.2.6.3. Expected number of selected events. This section summarises the event selections, the corresponding cross sections and expected number of events for the signal and the background processes after the selections. The efficiency of all selections shown in the tables of this section was evaluated relative to the previous selection.

Signal. Table 5.11 summarises the expectations for a signal of $M_A = 200$, 500 and 800 GeV/c^2. The signal cross sections and the branching ratios were obtained for the m_h^{max} scenario with $\mu = 200$ GeV/c^2 (see Section 11.3.1).

QCD multi-jet background. Despite the huge amount of generated events (more than one million) and generation pre-selections, the statistics of the QCD multi-jet background events is not enough to ensure a large number of Monte Carlo events passing all the selections. In order to decrease the statistical uncertainties a factorisation of the selections was applied. All

Table 5.12. The summary table of the selections for the QCD multi-jet background. The selections are factorised as explained in the text. The requirement to have opposite charge τ-jet candidates ($Q_1 \times Q_2 = -1$) is not included.

	QCD dijet background in bins of generated $\hat{p}_T$			
	>170 GeV/c	120–170 GeV/c	80–120 GeV/c	50–80 GeV/c
σ (fb)	1.33×10^8	5.03×10^8	2.94×10^9	2.08×10^{10}
$\varepsilon_{\text{kine pres.}}$	2.12×10^{-1}	4.19×10^{-2}	5.77×10^{-3}	2.44×10^{-4}
Group1 cuts: Level-1 trigger + L2 and offline calo reco + E_T cut				
Level-1 trigger	0.562	0.726	0.715	0.461
Two Level 2 calo jets with $\Delta R_{J\,J} > 1.0$	0.927	0.959	0.982	0.987
two off-line calo τ jets	0.975	0.975	0.982	0.994
cuts on E_T τ jets	0.753	0.804	0.774	0.343
$\varepsilon_{\text{Group1}}$	0.383	0.547	0.534	0.155
Group2 cuts: τ-jet identification at HLT and off-line				
HLT Calo+Pxl τ trigger	7.15×10^{-4}	1.81×10^{-3}	4.44×10^{-3}	1.12×10^{-2}
Two off-line τ candidates	0.86	0.84	0.825	0.84
$p_T^{ltr} > 35$ GeV/c	0.47	0.41	0.42	0.38
Tracker isolation	0.24	0.21	0.25	0.35
	Factorised inside group 2			
1 or 3 prongs in $^{1st}\tau$ *jet*	0.66	0.92	0.63	0.72
1 or 3 prongs in $^{2nd}\tau$ *jet*	0.48	0.54	0.65	0.72
$\varepsilon_{\text{Group2}}/\varepsilon_{\text{Group1}}$	2.30×10^{-5}	6.33×10^{-5}	1.63×10^{-4}	6.54×10^{-4}
Group3 cuts: extra jet reco and b tagging plus $M_{\tau\tau}$ reco and mass window				
$\geqslant 1$ extra jet, $E_T^{raw} > 20$ GeV, $\lvert\eta\rvert < 2.4$	0.463	0.235	0.127	0.090
Only 1 extra jet, $E_T^{raw} > 20$ GeV, $\lvert\eta\rvert < 2.4$	0.661	0.817	0.863	0.855
	Factorised inside group 3: $M_{\tau\tau}$ and b tagging			
$E_{\tau 1,\tau 2} > 0$	0.921	0.898	0.882	0.834
$E_{\nu 1,\nu 2} > 0$	0.701	0.683	0.657	0.625
Total mass reconstruction	0.646	0.613	0.579	0.522
b tagging of the extra jet	0.098	0.050	0.033	0.016
$M_{\tau\tau}$ window: 150–300 GeV/c^2	0.142	0.295	0.433	0.430
$\varepsilon_{\text{Group3}}/\varepsilon_{\text{Group1}}$	2.77×10^{-3}	1.75×10^{-3}	9.15×10^{-4}	2.28×10^{-4}
$\varepsilon_{\text{Group1}} \times \varepsilon_{\text{Group2}} \times \varepsilon_{\text{Group3}}$	2.44×10^{-8}	6.07×10^{-8}	7.98×10^{-8}	2.84×10^{-8}
σ after selections (fb)	0.69	1.28	1.35	0.144
Number of events for 60 fb^{-1}	41.4	76.7	81.2	8.7

selections were combined in three groups as shown in Table 5.12. Group1 includes the Level-1 trigger and the calorimetric reconstruction of the τ-jets (at HLT and offline). It includes also the cut on the transverse energy of the jets. After the event passed the Group1 selections the two other selection groups (Group2 and Group3) were applied independently. Group2 is essentially the τ-jet identification part of the analysis, i.e. the tracker isolation (at HLT and off-line), the cut on the p_T of the leading track and the selection on the number of tracks inside the signal cone. Group3 describes the selections on the one extra jet in the event, the b tagging and the diτ-jet mass reconstruction. The choice of the second and third selection groups was made minimising the correlation among them. A further factorisation was done for some selections inside the groups. Table 5.12 summarises the selections and the QCD multi-jet background estimates for the signal of $M_A = 200\,\text{GeV}/c^2$. The requirement to have opposite charge τ-jet candidates ($Q_1 \times Q_2 = -1$) is not included in Table 5.12. It reduces the QCD multi-jet

Table 5.13. The number of expected events with 60 fb^{-1} and efficiencies of some of the selections for the irreducible backgrounds.

process	$N_{exp.}$ at 60 fb^{-1}	$Q_{\tau 1} \times Q_{\tau 2} = -1$	only one extra jet	b tag. jet	$M_{\tau\tau}$ window
$t\bar{t}$	0.64	0.96	0.36	0.42	0.11
W+j	0.33	0.81	0.15	0.06	0.12
Wt	0.26	0.96	0.49	0.44	0.23
$Z/\gamma^* \to \tau\tau$ in bins of generated $m_{\tau\tau}$					
$130 < m_{\tau\tau} < 300\,GeV/c^2$	3.80	0.96	0.23	0.06	0.61
$m_{\tau\tau} > 300\,GeV/c^2$	0.18	0.95	0.27	0.05	0.04
$\tau\tau b\bar{b}$, $m_{\tau\tau} > 100\,GeV/c^2$	0.86	0.98	0.39	0.44	0.38

background by another factor of two, leading to 104 events of the QCD multi-jet background expected with 60 fb^{-1}. With the selections applied to search for signals of $M_A = 500\,GeV/c^2$ and $M_A = 800\,GeV/c^2$ the expected numbers of the QCD multi-jet background with 60 fb^{-1} are 25.0 and 4.0, respectively.

Irreducible background. The irreducible background which remains after all selections were applied is the small part of the total background dominated by the QCD multi-jet events. Table 5.13 summarises the expected number of events from the irreducible background with 60 fb^{-1} for the selections used to search for a signal of $M_A = 200\,GeV/c^2$. In total, 6.0 events are expected. The efficiencies of some of the selections are also shown in the table. With the selections applied to search for signals of $M_A = 500\,GeV/c^2$ and $M_A = 800\,GeV/c^2$ the expected numbers of the irreducible background with 60 fb^{-1} are 4.0 and 1.0, respectively.

5.2.6.4. Detector effects, experimental systematics and evaluation of the background from data.

E_T^{miss} and jet energy scale uncertainties. The effect of the E_T^{miss} and the jet energy scale uncertainty on the Higgs boson mass reconstruction efficiency was estimated. The E_T^{miss} is reconstructed with the Type 1 corrections in the following form:

$$E^{miss}_{Tx(y)} = -\left(E^{raw}_{Tx(y)} + \sum_{jets} \left(E^{corr.jet}_{Tx(y)} - E^{rawjet}_{Tx(y)} \right) \right) \tag{5.11}$$

where $E^{raw}_{Tx(y)}$ is the sum over the raw calorimeter tower energies from calorimeter towers and the jet sum in the equation is over jets with a reconstructed $E_T^{raw} > 25\,GeV$. The formula can be rewritten in the form:

$$E^{miss}_{Tx(y)} = -\left(\left[E^{raw}_{Tx(y)} - \sum_{jets} E^{rawjet}_{Tx(y)} \right]_{low\,E_T} + \left[\sum_{jets} E^{corr.jet}_{Tx(y)} \right]_{high\,E_T} \right) \tag{5.12}$$

representing of low and high E_T parts. For the low E_T part a scale uncertainty of 10% was applied, while for the high E_T part 3% uncertainty was used. The variation of the scale is applied independently for the two parts to obtain the maximal upper and lower deviations from the case with no uncertainty. It was found that the E_T^{miss} scale uncertainty brings the largest contribution to the uncertainty of the Higgs boson mass reconstruction efficiency. In the worst case the uncertainty reaches 3%. The mean fitted value of the $M_{\tau\tau}$ distribution for a

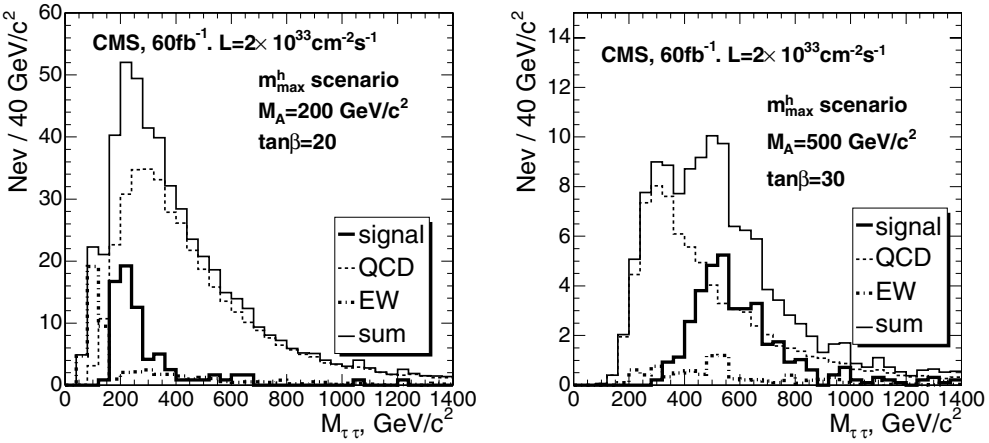

Figure 5.3. The expected $M_{\tau\tau}$ distributions for the signal of $M_A = 200\,\mathrm{GeV/c^2}$, $\tan\beta = 20$ (left plot) and $M_A = 500\,\mathrm{GeV/c^2}$, $\tan\beta = 30$ (right plot) and the background with $60\,\mathrm{fb}^{-1}$. Thick solid histogram – signal in the m_h^{max} scenario; dashed histogram – the QCD multi-jet background; thick dashed-dotted histogram – the irreducible background; normal solid histogram – signal plus background.

signal of $M_A = 500\,\mathrm{GeV/c^2}$ is varied from $-10\,\mathrm{GeV/c^2}$ to $+16\,\mathrm{GeV/c^2}$ relative to the mean value evaluated without the scale uncertainty taken into account.

Tracker misalignment. The effect of the tracker misalignment on the rate of fake τ-jets from the QCD multi-jet background was studied for the first data taking scenario (Scenario 1) and the long term data taking scenario (Scenario 2). The tracker isolation efficiency and the efficiency of the track counting in the signal cone (one or three tracks requirement) was compared with the performance of the perfect tracker alignment (Scenario 0).

It was found that in the Scenario 2 the QCD multi-jet background can be increased by $\simeq$11% due to the change of the tracker isolation efficiency. The efficiency of the requirement to have one track in the signal cone is increased by $\simeq$10% in the Scenario 2 relative to the perfect alignment.

The measurement of the QCD multi-jet background from the data. Figure 5.3 (left plot) shows the expected $M_{\tau\tau}$ distribution for two signal samples and the background. The QCD multi-jet background is the biggest background in this analysis. The following way to evaluate this background from the data is proposed: A control sample must be used where all signal selections are applied except the mass window and the requirement to have an opposite charge of the two τ-jet candidates. It is proposed to select, instead, the sample with the same charge of the two τ-jet candidates (SS sample). The contamination of the signal events and irreducible background is negligible in the SS sample, thus giving the possibility to predict from the data the QCD multi-jet background in a given mass window from the number of event and the measured shape of the diτ-jet mass in SS sample. The expected number of QCD multi-jet SS events after all selections, but the mass window, used for the signal of $M_A = 200\,\mathrm{GeV/c^2}$ is 380 with $60\,\mathrm{fb}^{-1}$. Neglecting the uncertainty of the measured shape of the diτ-jet mass leads to 5% statistical uncertainty of the QCD multi-jet background estimates under the signal mass window. For the $M_A = 500$ (800) $\mathrm{GeV/c^2}$ selections about 80 (28) SS QCD multi-jet events are expected, thus giving $\simeq$10 (20) % statistical uncertainty.

Table 5.14. The lower limit of tan β where a 5σ discovery is possible with $60\,\mathrm{fb}^{-1}$.

Low tanβ limit for 5σ discovery	Higgs boson mass $m_A = 200\,\mathrm{GeV/c^2}$	$m_A = 500\,\mathrm{GeV/c^2}$	$m_A = 800\,\mathrm{GeV/c^2}$
no systematics	20	32	46
with systematics	21	34	49

5.2.6.5. Discovery reach in the $M_A - \tan\beta$ *plane.* Table 5.14 shows the lowest value of $\tan\beta$ for the three Higgs boson masses considered in the analysis, where the 5σ discovery is possible with $60\,\mathrm{fb}^{-1}$. It is shown with and without QCD multi-jet background systematic uncertainty taken into account. The significance of the discovery is calculated with the S_{cP} method.

The extension of the discovery reach to lower values of $\tan\beta$ would be possible with a lower threshold on the energy of the additional jet in the event, provided that the fake jets will be then suppressed with the jet-tracks matching criteria. Another improvement is expected from the increase of the Higgs boson mass reconstruction efficiency using the improved missing E_T measurement from energy-flow like algorithms. Finally, improved b-jet tagging performance is expected to extend the discovery reach to lower values of $\tan\beta$.

5.2.7. $H \to \tau\tau \to \mu + \mathrm{jet}$ *analysis*

A detailed description of the analysis can be found in [152].

5.2.7.1. Event generation and pre-selections. For the irreducible Drell–Yan (DY) $\tau\tau$ background the $\tau_{1(2)} \to \mu\nu\nu$, $\tau_{2(1)} \to$ hadrons $+\,\nu$ decays were forced in PYTHIA. The events containing b quarks were rejected to avoid the double counting with the $\tau\tau b\bar{b}$ background. For the other background processes, $t\bar{t}$, Wt, W+jet and $b\bar{b}$ no specific decay mode was forced.

The DY $\tau\tau$ background was produced in two ranges of the $\tau\tau$ invariant mass: $40 < m_{\tau\tau} < 120\,\mathrm{GeV/c^2}$ and $m_{\tau\tau} > 120\,\mathrm{GeV/c^2}$. For $\tau\tau b\bar{b}$ the following mass bins were used: $60 < m_{\tau\tau} < 100\,\mathrm{GeV/c^2}$ and $m_{\tau\tau} > 100\,\mathrm{GeV/c^2}$. The W+jet background was generated with $\hat{P}_T > 20\,\mathrm{GeV/c^2}$.

The SUSY background has been estimated using the events for the LM2 mSUGRA test point (see Section 13.3.2) with the total NLO SUSY cross section of 9.4 pb. For this point $\tan\beta = 35$, which makes the stau and tau production rate potentially dangerous. The number of events after all selection has been estimated to be less than one, therefore the SUSY background has been considered negligible, and was not studied in detail.

For the signal generation the Higgs boson was forced to decay into a τ pair. The τ leptons were decayed using TAUOLA and events with $\tau_{1(2)} \to \mu\nu\nu$, $\tau_{2(1)} \to$ hadrons $+\,\nu$ decays were selected.

The pre-selections at generation level were chosen in a way that selected events are likely to pass the trigger selection. The requirements were: The isolation of the muon was defined as absence of charged particles with $p_T > 1\,\mathrm{GeV/c}$ within a cone of radius 0.2 in the $\eta - \varphi$ space around the muon momentum direction. Isolation for the τ-like jet allowed for at most one charged particle with $p_T > 1\,\mathrm{GeV/c}$ in the ring with an inner radius of 0.1 and an outer radius of 0.4 around the highest p_T charged particle in the jet. The leading track was required to have $p_T > 3\,\mathrm{GeV/c}$. The $\tau\tau b\bar{b}$ events were generated without the pre-selection requirements.

Details on $b\bar{b}$ generation are explained in [153].

5.2.7.2. Event selection. The off-line τ-jet identification uses the parameters of the pixel HLT τ isolation, but with fully reconstructed tracks instead of pixel tracks. Additionally one or three tracks are required in the signal cone. For the τ-jet direction, the sum of the momenta of the signal tracks was used, improving the direction resolution. The leading τ-jet track is required to have $p_T > 10\,GeV/c$ in case of one track in the signal cone, and $p_T > 20\,GeV/c$ for three tracks, in order to suppress the $b\bar{b}$ and DY $\tau\tau$ backgrounds.

To select events with associated $b\bar{b}H(A)$ production, one b-tagged jet with calibrated $E_T > 20\,GeV$ was required. For the b tagging, the track counting method was used [151]: the jet is b tagged if it has at least two tracks with a 2D transverse impact parameter significance greater than two. The b tagging efficiency, including the jet finding, for the signal is 17% for $M_A = 200\,GeV/c^2$ and 27% for $M_A = 500\,GeV/c^2$. For the backgrounds with a real b-jet it is 67% for $t\bar{t}$ and 46% for Wt processes. For the backgrounds without a real b-jet the mistagging efficiency is 1% for the W+jet and 3% for the DY $\tau\tau$ processes. The b tagging purity for the signal and the $t\bar{t}$ background is 95%; it is 90% for the Wb and the $\tau\tau b\bar{b}$ processes.

Events containing W bosons decaying into $\mu + \nu_\mu$ are suppressed using a cut on the transverse mass of the muon and the missing transverse energy: $m_T = \sqrt{2 \cdot p_T^\mu \cdot \not{E}_T (1 - \cos(\vec{p}_T^{\,\mu}, \vec{\not{E}}_T))}$, where $\vec{\not{E}}_T$ is the missing transverse energy. The distribution of m_T has a Jacobian peak near the W mass. Rejecting events with $m_T > 60\,GeV$ largely reduces the $t\bar{t}$, Wt and W+jet backgrounds while retaining a good fraction of the signal events.

The additional selection against the $t\bar{t}$ background is the central jet veto. All events containing an additional jet (to the τ jet and the b-tagged jet) in the central region, $|\eta| < 2.5$, and with a calibrated $E_T > 20\,GeV$ were rejected.

The electrons from the W boson decays in the $t\bar{t}$ and Wt backgrounds can be misidentified as τ-jets. For the electron rejection a cut on the ratio of the τ-jet energy measured in the HCAL (E^{HCAL}) to the leading track momentum (p^{ltr}), $f = E^{HCAL}/p^{ltr}$, was used for the events with one track in the signal cone. The cut $f > 0.2$ retains 90% of the signal events, while it rejects 95% of the events with the real electrons. The cut on the upper value of the ratio is efficient against jets with a large fraction of neutral hadrons. The requirement $f < 1.1$ rejects 50% of W+j and $b\bar{b}$ events and only 20% of signal events. Figure 5.4 shows the integrated distribution of the parameter f for the signal and the background events selected by the High Level trigger. The labels on the right part of the figure are ordered by decreasing selection efficiency in the acceptance region of $0.2 < f < 1.1$, marked by the arrows.

The Higgs boson mass reconstruction requires the rejection of events with a μ and a τ jet in a back-to-back topology, therefore the cut $\cos(\Delta\varphi(\vec{p}_T, \vec{E}_T^{\,jet})) > -0.9962$ was used. In addition, an upper cut on $\cos(\Delta\varphi(\vec{p}_T, \vec{E}_T^{\,jet})) < -0.5$ was used, retaining most of the signal events, while visibly reducing a fraction of the background events. Finally, the events with a negative reconstructed neutrino energy were rejected.

5.2.7.3. Expected number of selected events. Table 5.15 presents the production cross sections in fb and the individual selection efficiencies for signals of $M_A = 200$ and $500\,GeV/c^2$. The signal cross sections and the branching ratios were obtained for the m_h^{max} scenario with $\mu = 200\,GeV$ (see Section 11.3.1). Tables 5.16–5.18 summarise the cross sections and the individual selection efficiencies for the background processes. The total efficiency of all selections and the cross sections after all selections are also presented at the end of the tables. The events were counted in the $M_{\tau\tau}$ mass windows with the width taken to be $\pm\sigma$, where σ is given by the standard deviation of a Gaussian fit of the signal $M_{\tau\tau}$ distributions. The value of σ is $41\,GeV/c^2$ for $M_A = 200\,GeV/c^2$, whereas it is $83\,GeV/c^2$ for $m_A = 500\,GeV/c^2$. With an integrated luminosity of $20\,fb^{-1}$ the expected number of signal (background) events is

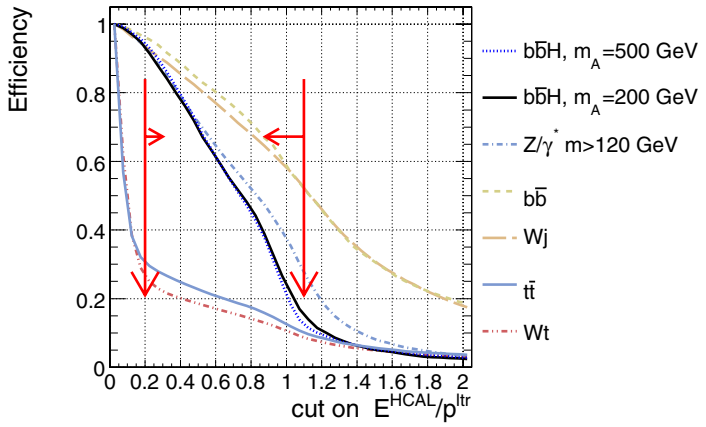

Figure 5.4. The integrated distribution of the parameter $f = E^{HCAL}/p_T^{ltr}$. The acceptance region of $0.2 < f < 1.1$ is marked by the arrows.

Table 5.15. The production cross sections, in fb, and the individual selection efficiencies for the signal.

	$gg \to b\bar{b}(A+H)$, $A, H \to \tau\tau$	
	$M_A = 200\,GeV/c^2$ $\tan(\beta) = 20$	$M_A = 500\,GeV/c^2$ $\tan(\beta) = 30$
$\sigma \times$ BR [fb]	$9.12 \cdot 10^3$	$4.51 \cdot 10^2$
kine pre-selection	$9.47 \cdot 10^{-2}$	$1.65 \cdot 10^{-1}$
Level-1 trigger	$8.99 \cdot 10^{-1}$	$9.09 \cdot 10^{-1}$
HLT	$4.17 \cdot 10^{-1}$	$4.99 \cdot 10^{-1}$
offline τ-jet isolation	$9.54 \cdot 10^{-1}$	$9.60 \cdot 10^{-1}$
1 or 3 tk. in τ-jet signal cone	$9.12 \cdot 10^{-1}$	$9.19 \cdot 10^{-1}$
$p_T^{ltr} > 10\,GeV/c$	$9.05 \cdot 10^{-1}$	$9.55 \cdot 10^{-1}$
$Q_\mu \cdot Q_{jet} = -1$	$9.61 \cdot 10^{-1}$	$9.60 \cdot 10^{-1}$
single b tagging	$1.73 \cdot 10^{-1}$	$2.56 \cdot 10^{-1}$
no jet with $E_T > 20$, $\lvert\eta\rvert < 2.5$	$8.53 \cdot 10^{-1}$	$7.72 \cdot 10^{-1}$
$m_T(l, MET) < 60$ GeV	$8.33 \cdot 10^{-1}$	$7.01 \cdot 10^{-1}$
$-0.996 < \cos(\Delta\varphi) < -0.5$	$8.05 \cdot 10^{-1}$	$7.51 \cdot 10^{-1}$
electron veto: $0.2 < f < 1.1$	$8.22 \cdot 10^{-1}$	$8.54 \cdot 10^{-1}$
$E_{\nu 1} > 0$, $E_{\nu 2} > 0$	$6.84 \cdot 10^{-1}$	$7.68 \cdot 10^{-1}$
total efficiency:	$1.66 \cdot 10^{-3}$	$4.53 \cdot 10^{-3}$
σ after selections [fb]:	$1.52 \cdot 10^1$	2.05

146 (127) for $m_A = 200\,GeV/c^2$, $\tan\beta = 20$, and 21 (61) for $m_A = 500\,GeV/c^2$, $\tan\beta = 30$. Figure 5.5 shows the expected $\tau\tau$ mass distribution for the total background and for the signal plus background for $M_A = 200\,GeV/c^2$, $\tan\beta = 20$ and $M_A = 500\,GeV/c^2$, $\tan\beta = 30$.

5.2.7.4. Background estimates and uncertainty. After all off-line selections the main background is represented by the $\tau\tau b\bar{b}$, DY $\tau\tau$ and the $t\bar{t}$ production processes. The contribution of the non Z/γ^* background, mainly the $t\bar{t}$ events, can be estimated applying the inversion of the electron veto: $f < 0.1$ instead of $0.2 < f < 1.1$. All other cuts must be the same, including the $M_{\tau\tau}$ mass window. A relatively pure sample of $t\bar{t}$ can be selected, since

Table 5.16. The production cross sections, in fb, and the individual selection efficiencies for the reducible background processes.

	$t\bar{t}$	$W + jet$	Wt	$b\bar{b}$
σ [fb]	$8.40 \cdot 10^{5}$	$4.15 \cdot 10^{7}$	$6.20 \cdot 10^{4}$	$2.29 \cdot 10^{10}$
kine preselection	$9.01 \cdot 10^{-2}$	$1.44 \cdot 10^{-2}$	$6.58 \cdot 10^{-2}$	$7.56 \cdot 10^{-4}$
Level-1 trigger	$9.06 \cdot 10^{-1}$	$8.40 \cdot 10^{-1}$	$8.91 \cdot 10^{-1}$	$2.26 \cdot 10^{-2}$
H LT	$9.61 \cdot 10^{-2}$	$4.16 \cdot 10^{-2}$	$1.05 \cdot 10^{-1}$	$2.36 \cdot 10^{-4}$
offline τ-jet isolation	$8.51 \cdot 10^{-1}$	$6.70 \cdot 10^{-1}$	$8.79 \cdot 10^{-1}$	$8.69 \cdot 10^{-1}$
1 or 3 tk. in τ-jet signal cone	$8.92 \cdot 10^{-1}$	$6.30 \cdot 10^{-1}$	$9.07 \cdot 10^{-1}$	$7.19 \cdot 10^{-1}$
$p_T^{ltr} > 10$GeV/c	$9.42 \cdot 10^{-1}$	$8.58 \cdot 10^{-1}$	$9.37 \cdot 10^{-1}$	$7.17 \cdot 10^{-1}$
$Q_\mu \cdot Q_{jet} = -1$	$9.18 \cdot 10^{-1}$	$7.31 \cdot 10^{-1}$	$9.52 \cdot 10^{-1}$	$5.45 \cdot 10^{-1}$
Single b tagging	$6.73 \cdot 10^{-1}$	$1.09 \cdot 10^{-2}$	$4.56 \cdot 10^{-1}$	$9.42 \cdot 10^{-2}$
no jet with $E_T > 20$, $\|\eta\| < 2.5$	$3.43 \cdot 10^{-1}$	$8.17 \cdot 10^{-1}$	$8.60 \cdot 10^{-1}$	$4.30 \cdot 10^{-1}$
$m_T(l, MET) < 60\,\mathrm{GeV/c^2}$	$3.53 \cdot 10^{-1}$	$3.76 \cdot 10^{-1}$	$3.62 \cdot 10^{-1}$	1.00
$-0.996 < \cos(\Delta\varphi) < -0.5$	$4.95 \cdot 10^{-1}$	$6.56 \cdot 10^{-1}$	$4.51 \cdot 10^{-1}$	$4.16 \cdot 10^{-1}$
electron veto: $< 0.2 < f < 1.1$	$1.65 \cdot 10^{-1}$	$4.76 \cdot 10^{-1}$	$1.27 \cdot 10^{-1}$	$2.98 \cdot 10^{-1}$
$E_{\nu 1} > 0$, $E_{\nu 2} > 0$	$4.08 \cdot 10^{-1}$	$2.00 \cdot 10^{-1}$	$4.15 \cdot 10^{-1}$	$3.60 \cdot 10^{-1}$
total efficiency:	$1.54 \cdot 10^{-5}$	$3.31 \cdot 10^{-8}$	$1.66 \cdot 10^{-5}$	$7.86 \cdot 10^{-11}$
σ after selections [fb]:	$1.30 \cdot 10^{1}$	1.37	1.03	1.80

Table 5.17. The production cross sections, in fb, and the individual selection efficiencies for the irreducible background processes.

	$Z/\gamma^* \to \tau\tau \to \mu +$ jet	
	$40 < m_{\tau\tau} < 120\,\mathrm{GeV/c^2}$	$m_{\tau\tau} > 120\,\mathrm{GeV/c^2}$
$\sigma \times$ BR [fb]	$4.63 \cdot 10^{5}$	$4.88 \cdot 10^{3}$
kine preselection	$6.56 \cdot 10^{-2}$	$2.14 \cdot 10^{-1}$
Level-1 trigger	$8.00 \cdot 10^{-1}$	$8.28 \cdot 10^{-1}$
HLT	$1.03 \cdot 10^{-1}$	$2.77 \cdot 10^{-1}$
offline τ-jet isolation	$9.12 \cdot 10^{-1}$	$9.40 \cdot 10^{-1}$
1 or 3 tk. in τ-jet signal cone	$9.03 \cdot 10^{-1}$	$8.93 \cdot 10^{-1}$
$p_T^{ltr} > 10$GeV/c	$8.12 \cdot 10^{-1}$	$9.00 \cdot 10^{-1}$
$Q_\mu \cdot Q_{jet} = -1$	$9.47 \cdot 10^{-1}$	$9.33 \cdot 10^{-1}$
single b tagging	$2.68 \cdot 10^{-2}$	$2.51 \cdot 10^{-2}$
no jet with $E_T > 20$, $\|\eta\| < 2.5$	$7.77 \cdot 10^{-1}$	$6.98 \cdot 10^{-1}$
$m_T(l, MET) < 60\,\mathrm{GeV/c^2}$	$9.41 \cdot 10^{-1}$	$7.74 \cdot 10^{-1}$
$-0.996 < \cos(\Delta\varphi) < -0.5$	$3.75 \cdot 10^{-1}$	$6.57 \cdot 10^{-1}$
electron veto: $0.2 < f < 1.1$	$6.46 \cdot 10^{-1}$	$7.29 \cdot 10^{-1}$
$E_{\nu 1} > 0$, $E_{\nu 2} > 0$	$6.45 \cdot 10^{-1}$	$6.46 \cdot 10^{-1}$
total efficiency:	$1.31 \cdot 10^{-5}$	$1.75 \cdot 10^{-4}$
σ after selections [fb]:	6.08	$8.53 \cdot 10^{-1}$

the requirement $f < 0.1$ rejects more than 95% of all processes except the $t\bar{t}$ and Wt as shown in Figure 5.4. The number of the non Z/γ^* background events in the signal region can be then predicted using the ratio of the $t\bar{t}$ events in the signal region of $0.2 < f < 1.1$ and in the region of $f < 0.1$. This ratio can be obtained from Monte-Carlo simulation or from real $t\bar{t}$ data. The systematic uncertainty on the number of the non Z/γ^* background events predicted using this method has two contributions:

- The uncertainty of the HCAL energy scale, since the variable $f = E^{HCAL}/p^{ltr}$ includes the HCAL part of the τ-jet candidate energy measured by the calorimeter. It is taken as 3%.

Table 5.18. The production cross sections, in fb, and the individual selection efficiencies for the irreducible background processes.

	$bb(Z \to \tau\tau)$	
	$60 < m_{\tau\tau} < 100\,\mathrm{GeV/c^2}$	$m_{\tau\tau} > 100\,\mathrm{GeV/c^2}$
$\sigma \times$ BR [fb]	$2.61 \cdot 10^4$	$1.05 \cdot 10^3$
kine preselection	1.00	1.00
Level-1 trigger	$1.41 \cdot 10^{-1}$	$1.64 \cdot 10^{-1}$
HLT	$4.10 \cdot 10^{-3}$	$1.21 \cdot 10^{-2}$
offline τ-jet isolation	$9.05 \cdot 10^{-1}$	$9.34 \cdot 10^{-1}$
1 or 3 tk. in τ-jet signal cone	$9.12 \cdot 10^{-1}$	$9.17 \cdot 10^{-1}$
$p_T^{ltr} > 10\,\mathrm{GeV/c}$	$8.60 \cdot 10^{-1}$	$8.98 \cdot 10^{-1}$
$Q_\mu \cdot Q_{jet} = -1$	$9.41 \cdot 10^{-1}$	$9.48 \cdot 10^{-1}$
single b tagging	$2.73 \cdot 10^{-1}$	$2.75 \cdot 10^{-1}$
no jet with $E_T > 20$, $\lvert\eta\rvert < 2.5$	$7.20 \cdot 10^{-1}$	$7.72 \cdot 10^{-1}$
$m_T(l, MET) < 60\,\mathrm{GeV}$	$9.68 \cdot 10^{-1}$	$8.80 \cdot 10^{-1}$
$-0.996 < \cos(\Delta\varphi) < -0.5$	$4.23 \cdot 10^{-1}$	$5.84 \cdot 10^{-1}$
electron veto: $0.2 < f < 1.1$	$6.98 \cdot 10^{-1}$	$5.11 \cdot 10^{-1}$
$E_{\nu 1} > 0$, $E_{\nu 2} > 0$	$4.32 \cdot 10^{-1}$	$5.62 \cdot 10^{-1}$
total efficiency:	$6.64 \cdot 10^{-5}$	$2.76 \cdot 10^{-4}$
σ after selections [fb]:	1.74	$2.89 \cdot 10^{-1}$

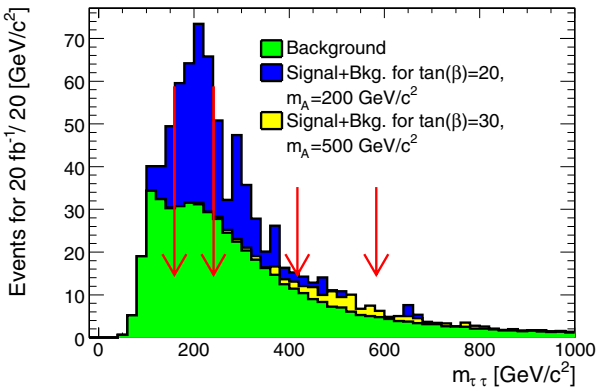

Figure 5.5. The reconstructed $\tau\tau$ mass distribution. The signal and the background contributions are shown with $20\,\mathrm{fb}^{-1}$. The mass windows in which the events are counted for the significance calculations are shown.

- The uncertainty of the shape of the distribution of f. The shape is obtained from $t\bar{t}$ events only, however a small fraction of events from the other processes is present in the "normalisation" region of $f < 0.1$. It leads to an uncertainty of $\simeq$12 %.

The contribution from the other systematic uncertainties, e.g. b tagging is expected to be small, due to the cancellation in the efficiency ratio. The total uncertainty on the number of the non Z/γ^* background events is thus 12.4 %.

The Z/γ^* background consists of two parts: the $\tau\tau b\bar{b}$ process and the DY $\tau\tau$ process without genuine b quarks in the event. The DY $\tau\tau$ background can be predicted using the DY $\ell\ell(\ell =$e, $\mu)$ cross section, to be measured with high precision at LHC, and the selection

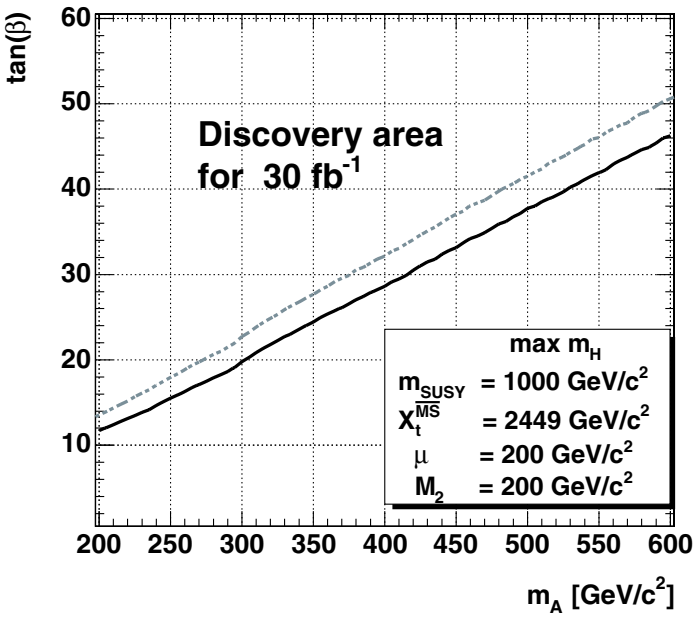

Figure 5.6. The 5σ discovery region in the $M_A - \tan\beta$ plane with $30\,\text{fb}^{-1}$ of the integrated luminosity for the m_h^{max} MSSM scenario. The regions are shown without (lower curve) and with (upper curve) the uncertainty on the background taken into account.

efficiency obtained from the Monte-Carlo. The systematic uncertainty on the number of DY $\tau\tau$ events has two main contributions due to:

- The jet scale uncertainty. The number of the events in the $M_{\tau\tau}$ signal window varies by $\pm 6\%$ for jet scale variations of $\pm 3\%$ and missing transverse energy scale variations of $\pm 5\%$.
- The b-mistagging uncertainty. A conservative estimate of 5% is taken.

The total uncertainty on the number of the DY $\tau\tau$ events with the jet mistagged as a b-jet is therefore 8%.

For the $\tau\tau b\bar{b}$ background estimates the systematic uncertainty has the following main contributions:

- The uncertainty of the $\mu\mu b\bar{b}$ cross section measurement (without the luminosity uncertainty) is 14% [145].
- The jet scale uncertainty. It is assumed to be the same as for the DY $\tau\tau$ events.

The total uncertainty on the number of the $\tau\tau b\bar{b}$ events is 15%.

5.2.7.5. Discovery reach in the $M_A - \tan\beta$ *plane.* The CMS discovery reach in the $M_A - \tan\beta$ plane with $30\,\text{fb}^{-1}$ in the m_h^{max} scenario is shown in Figure 5.6. The 5σ discovery curves are shown without (lower curve) and with (upper curve) the uncertainty on the background taken into account.

5.2.8. $H \to \tau\tau \to e +$ jet *analysis*

A detailed description of the analysis can be found in [154].

5.2.8.1. Event generation. The signal process $gg \to bbH/A$, $H/A \to \tau\tau$, $\tau_1 \to e\nu_e\nu_\tau$, $\tau_2 \to \tau$ jet $+ \nu_\tau$ leads to a final state of one isolated electron, an isolated τ jet and one or two detectable b jets. The background with genuine τ's is due to two types of events, Z/γ^* events decaying into $\tau\tau$, and the $t\bar{t}$ events, where the $e + \tau$ jet final state can come from direct W decays to an electron and a τ or through $W \to \tau\nu_\tau \to e\nu_e\nu_\tau\nu_\tau$ decays:

- $Z/\gamma^* \to \tau\tau \to e + \tau$ jet $+ X$
- $b\bar{b}Z/\gamma^*$, $Z/\gamma^* \to \tau\tau \to e + \tau$jet $+ X$
- $t\bar{t}$ with $W_1 \to \tau\nu_\tau(\tau \to$ jet$)$, $W_2 \to e\nu_e$ or $W_2 \to \tau\nu_\tau \to e\nu_e\nu_\tau\nu_\tau$
- Wt, with $W_1 \to \tau\nu_\tau(\tau \to$ jet$)$, $W_2 \to e\nu_e$ or $W_2 \to \tau\nu_\tau \to e\nu_e\nu_\tau\nu_\tau$.

Background can arise also from the processes where a hadronic jet or an electron leads to a fake τ:

- W+jet, with $W \to e\nu_e$
- $Z/\gamma^* \to e^+e^-$
- $b\bar{b}Z/\gamma^*$, $Z/\gamma^* \to e^+e^-$
- $t\bar{t}$ with $W \to jj$ or $W \to e\nu_e$.

The QCD multi-jet production is a large potential background through hadronic jets faking both the electron and the τ jet.

For the inclusive Z/γ^* production the events containing b quarks in the final state were removed to avoid double counting with the $\tau\tau b\bar{b}$ background. The single top (Wt) events were generated with TopReX [44]. The τ decays in the signal were performed with the TAUOLA package [155].

5.2.8.2. Event selection. In the offline reconstruction an isolated electron from the decay of one of the τ's was first searched for. On the average $\sim$1.3 reconstructed electron candidates were found in the signal events. The reconstructed electrons were first required to be isolated in the tracker demanding that no track with $p_T > 1\,\mathrm{GeV/c}$ was found in a cone of $\Delta R = 0.4$ around the electron candidate direction. The further electron identification was performed following the algorithm of Ref. [156]. The largest contribution to the identification efficiency and purity was obtained from the ratio of hadronic cluster energy to the electromagnetic energy of the cluster ($E^{\mathrm{hadronic}}/E^{\mathrm{elm}} < 0.2$) and from the ratio of the supercluster energy to the track momentum ($E^{\mathrm{super\ cluster}}/p^{\mathrm{track}} > 0.8$). The identification efficiency, including the tracker isolation, was found to be 64.2%. A good purity of 97.5% was obtained for the selected electrons.

The off-line τ-jet identification was applied to the jets with $E_T^{\mathrm{jet}} > 40\,\mathrm{GeV}$ reconstructed in the calorimeter with the cone of 0.4. The leading track with $p_T^{\mathrm{ltr}} > 10\,\mathrm{GeV/c}$ was searched for in a cone of $R_m = 0.1$ around the τ-jet direction. For an efficient isolation against the hadronic jets in the W+jet and QCD multi-jet backgrounds, a small signal cone, $R_S = 0.04$, around the leading track was used. About 83% of the $\tau^\pm \to \mathrm{hadron}^\pm + n\pi^0 + \nu_\tau$ decays were found to be reconstructed as one prong τ's. Due to the small signal cone selected, 50% of the $\tau^\pm \to 3\ \mathrm{hadrons}^\pm + n\pi^0 + \nu_\tau$ decays were reconstructed as one or two prong τ-jets. The cut $p_T^{\mathrm{ltr}} > 20\,\mathrm{GeV/c}$ was found to be optimal for the suppression of the hadronic jets, in the presence of the QCD multi-jet background. The isolation was performed counting tracks with $p_T^i > 1\,\mathrm{GeV/c}$ in the area between the signal cone and the isolation cone, which was taken to be then same as the jet reconstruction cone, $R_i = 0.4$. Following the method described in [146], at least eight hits were required in the full silicon tracker and an upper bound of 0.3 mm on the transverse impact parameter was set on the leading track in order to suppress the background from the fake tracks.

Table 5.19. Production cross sections times branching fraction, efficiencies (%) for the selection cuts and numbers of events for 30 fb^{-1} for the signal with $\tan\beta = 20$ and for $M_A = 130$, 200, 300 and 500 GeV/c^2.

$M_A(GeV/c^2)$	130	200	300	500
$\sigma \times BR$ (pb)	18.2	4.15	0.85	0.071
Level-1 and HLT	1.53 (8.4)	0.64 (15.4)	0.18 (21.6)	2.0×10^{-2} (28.7)
primary vertex	1.44 (94.1)	0.60 (94.2)	0.18 (97.2)	1.9×10^{-2} (93.6)
electron identification	1.11 (77.8)	0.48 (80.8)	0.14 (73.7)	1.4×10^{-2} (73.8)
one identified τ jet	0.127 (11.4)	0.11 (23.4)	4.5×10^{-2} (32.9)	5.9×10^{-3} (41.7)
$Q^{\tau\ jet} \times Q^e = -1$	0.127 (100.0)	0.11 (99.1)	4.5×10^{-2} (99.3)	5.8×10^{-3} (99.0)
$m_T < 40\,GeV/c^2$	9.9×10^{-2} (77.6)	3.8×10^{-2} (73.7)	3.1×10^{-2} (69.3)	3.9×10^{-3} (66.7)
$\geqslant$1 jet, $E_T > 20\,GeV$	4.5×10^{-2} (45.9)	3.8×10^{-2} (46.6)	1.5×10^{-2} (48.6)	2.1×10^{-3} (53.5)
b tagging	1.3×10^{-2} (29.7)	1.2×10^{-2} (32.2)	5.0×10^{-3} (32.9)	7.6×10^{-4} (36.5)
jet veto	8.1×10^{-3} (60.2)	7.2×10^{-2} (62.5)	3.1×10^{-3} (63.2)	4.6×10^{-4} (61.0)
$\Delta\varphi(\tau_1, \tau_2) < 175^\circ$	7.6×10^{-3} (94.8)	6.8×10^{-3} (93.9)	2.7×10^{-3} (85.7)	3.4×10^{-4} (74.5)
$E_{\nu_1,\nu_2} > 0$	4.1×10^{-3} (54.1)	4.2×10^{-3} (61.7)	1.7×10^{-3} (64.3)	2.4×10^{-4} (70.6)
N_{ev} at 30 fb^{-1}	123.9	126.0	51.9	7.3

The $Z/\gamma^* \to e^+e^-$ and $b\bar{b}Z/\gamma^*$, $Z/\gamma^* \to e^+e^-$ backgrounds contain an isolated genuine electron to pass the electron cuts and are not significantly suppressed with the τ-selection cuts. These electronic τ candidates were suppressed requiring a large energy deposition in the hadron calorimeter. A cut in the E_T of the most energetic HCAL cell in the τ jet, $E_T(\text{max HCAL cell}) > 2\,GeV$, was found to suppress the electrons with a factor of ~ 7. A further reduction was obtained comparing the HCAL energy and the leading track momentum of the τ jet. The cut $E^{HCAL}/p^{ltr} > 0.35$, applied on the one-prong τ candidates only, was found to suppress further the electronic τ candidates by a factor of $\sim$1.8. The W + jet events show a tail at large values of E^{HCAL}/p^{ltr} due to the neutral hadron component of the hadronic jets and were suppressed with the cut $E^{HCAL}/p^{ltr} < 1.5$.

Efficiencies of the τ-jet selections are shown in Tables 5.19, 5.20 and 5.21. The purity of $\sim$ 97% is obtained for the signal events. A rejection factor of $\sim$ 400 was obtained for the QCD multi-jet events generated with $50 < \hat{p}_T < 80\,GeV/c$ when the τ-jet selections described above were applied.

Finally, the charges of the electron and τ jet were required to be opposite. The charge of the τ jet was calculated as the sum of charges of the tracks in the signal cone.

The missing transverse energy measurement can be exploited to suppress the $t\bar{t}$ background with an upper bound on the transverse mass $m_T(e, E_T^{miss})$ reconstructed from the electron and the missing transverse energy. Figure 5.7 shows the $m_T(e, E_T^{miss})$ distribution for the signal events with $M_A = 200\,GeV/c^2$ and for the $t\bar{t}$ and $Z/\gamma^* \to e^+e^-$ backgrounds with the electron and τ-jet selections. The selected upper bound $m_T(e, E_T^{miss}) < 40\,GeV/c^2$ reduces the $t\bar{t}$ background with a factor of $\sim$4.

The events were further selected when at least one jet (in addition to the τ jet) with calibrated $E_T^{jet} > 20\,GeV$ and $|\eta| < 2.5$ was found and tagged as the b jet. A probabilistic secondary vertex algorithm with a discriminator cut from Ref. [157] was used for b tagging. The cut in the discriminator was set to 0.8, which suppresses efficiently the Z/γ^*, W+jet and the potential multi-jet background. The efficiency to tag at least one jet, including the jet finding efficiency, was found to be between 13 and 19% for the signal, below 1% for the Z/γ^* backgrounds and 1.3% for the W+jet background. For the signal events the purity of the b-tagged jets is very high (99%).

Table 5.20. Background production cross sections times branching fraction, cross sections and efficiencies (%) for the selection cuts and number of events for 30fb^{-1}.

	$Z/\gamma^* \to \tau\tau$	$b\bar{b}Z/\gamma^* \to \tau\tau$	$Z/\gamma^* \to e^+e^-$	$b\bar{b}Z/\gamma^* e^+e^-$
$\sigma \times$ BR (pb)	331.8	27.0	1890	26.3
pre-selection	173.5 (41.4)		811.2 (42.9)	
Level-1 and HLT	17.3 (10.0)	0.818 (3.1)	617.4 (76.1)	18.2 (67.2)
primary vertex	16.5 (95.4)	0.796 (97.3)	591.9 (95.9)	17.7 (97.3)
no b's in DY Z/γ^*	15.6 (94.6)		561.8 (94.9)	
electron identification	11.6 (74.4)	0.585 (80.2)	278.1 (50.1)	9.31 (52.6)
one identified τ jet	0.13 (1.2)	1.0×10^{-2} (1.8)	3.40 (1.2)	9.0×10^{-2} (1.0)
$Q^{\tau\ jet} \times Q^e = -1$	0.13 (96.3)	1.0×10^{-2} (100)	3.31 (97.4)	8.8×10^{-2} (97.8)
$m_T < 40\,GeV/c^2$	9.8×10^{-2} (76.3)	8.0×10^{-3} (80.0)	2.26 (68.3)	5.5×10^{-2} (62.5)
$\geqslant$1 jet, $E_T > 20\,GeV$	4.0×10^{-2} (40.6)	5.6×10^{-3} (70.0)	0.85 (37.6)	3.0×10^{-2} (54.2)
b tagging	8.0×10^{-4} (2.0)	2.6×10^{-3} (46.4)	1.5×10^{-2} (1.8)	9.6×10^{-3} (32.2)
jet veto	5.2×10^{-4} (65.0)	1.5×10^{-3} (57.7)	6.0×10^{-3} (41.4)	5.9×10^{-3} (67.4)
$\Delta\varphi(\tau_1, \tau_2) < 175^\circ$	4.9×10^{-4} (94.2)	1.4×10^{-3} (90.7)	4.8×10^{-3} (80.0)	5.1×10^{-3} (85.7)
$E_{\nu_1,\nu_2} > 0$	2.0×10^{-4} (40.2)	7.6×10^{-4} (55.9)	1.7×10^{-3} (35.4)	1.9×10^{-3} (50.0)
N_{ev} at 30 fb^{-1}	5.9	22.8	51.3	57.9

Table 5.21. Background production cross sections times branching fraction (pb), cross sections and efficiencies (%) for the selection cuts and number of events for 30fb^{-1}.

	$t\bar{t}$	Wt	W + jet
$\sigma \times$ BR (pb)	840	6.16	673.2
pre-selection			315.0 (46.8)
Level-1 and HLT	94.4 (11.3)	2.00 (32.5)	145.6 (46.2)
primary vertex	93.9 (99.5)	1.97 (98.5)	143.9 (98.8)
electron identification	66.7 (71.0)	1.43 (72.6)	114.2 (79.4)
one id. τ jet	0.66 (0.95)	4.10×10^{-2} (2.87)	0.57 (0.5)
$Q^{\tau\ jet} \times Q^e = -1$	0.57 (89.8)	4.00×10^{-2} (97.6)	0.47 (82.7)
$m_T(e, E_T^{miss}) < 40\,GeV/c^2$	0.14 (24.3)	8.0×10^{-3} (20.0)	0.12 (25.2)
$\geqslant$1 jet, $E_T > 20\,GeV$	0.14 (98.6)	6.9×10^{-3} (86.3)	5.5×10^{-2} (46.2)
b tagging	9.4×10^{-2}(68.6)	4.1×10^{-3} (59.4)	1.6×10^{-3} (2.9)
jet veto	5.1×10^{-3} (5.4)	2.38×10^{-3} (58.1)	6.6×10^{-4} (41.9)
$\Delta\varphi(\tau_1, \tau_2) < 175^\circ$	4.9×10^{-3} (96.4)	2.33×10^{-3} (98.0)	5.6×10^{-4} (83.9)
$E_{\nu_1,\nu} > 0$	2.0×10^{-3} (40.9)	9.60×10^{-4} (41.2)	2.1×10^{-4} (38.5)
N_{ev} at 30 fb^{-1}	60.3	28.8	6.4

The $t\bar{t}$ background, with a genuine electron, τ and b jets, cannot be significantly suppressed with the cuts described above. This background, however, was suppressed applying the jet veto: the event must contain only the b-tagged jet with calibrated $E_T^{jet} > 20$ GeV and $|\eta^{jet}| < 2.5$. The fake jets, which generally do not contain tracks from the signal vertex, were suppressed with a cut in the fraction of the track p_T sum to the jet E_T, $\alpha = \Sigma p_T^{t\ track}/E_T^{jet}$. The cut $\alpha > 0.1$ was found to improve the veto efficiency for the signal by about 10%. The jet veto efficiency is around 60% for the signal and $\sim$5% for the $t\bar{t}$ background.

For the reconstruction of the $\tau\tau$ mass the events with back-to-back configurations between the electron and the τ jet were removed with an upper bound on the angle between the τ jet and the electron in the transverse plane ($\Delta\varphi(e, \tau\ jet)$). The reconstructed neutrino energies were required to be positive ($E_{\nu_1} > 0$ and $E_{\nu_2} > 0$), which leads to a reduction

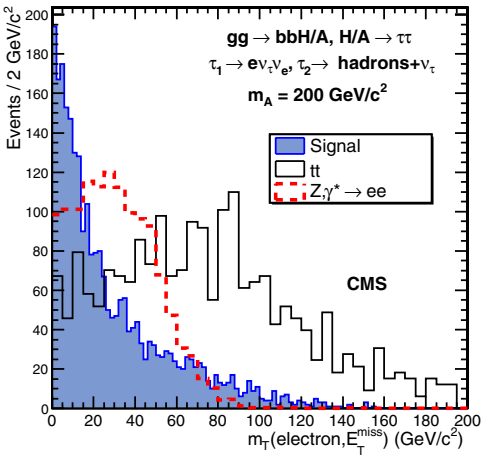

Figure 5.7. Distribution of transverse mass reconstructed from the electron and the missing transverse energy for the signal of $M_A = 200\,GeV/c^2$ and $\tan\beta = 20$ (filled histogram), for the $t\bar{t}$ (solid line) and for the $Z/\gamma^* \to e^+e^-$ (dashed line) background. Histogram normalisation is arbitrary.

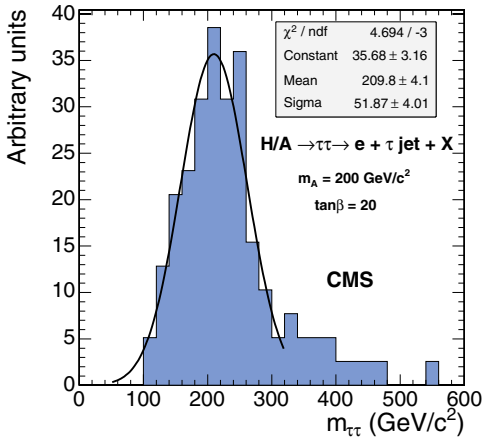

Figure 5.8. Reconstructed Higgs boson mass for $M_A = 200\,GeV/c^2$ and $\tan\beta = 20$.

of ≃40% of the signal events, but rejects ≃ 60% of the $t\bar{t}$, tW and W+jet backgrounds. Figure 5.8 shows the reconstructed Higgs boson mass for the signal events with $M_A = 200\,GeV/c^2$. The Gaussian fit yields a mass resolution of 25%.

Table 5.19 shows the numbers of signal events with M_A = 130–500 GeV/c^2 and $\tan\beta = 20$ for 30 fb^{-1} and the efficiency for all the event selection cuts described above. For $M_A = 130$ and 140 GeV/c^2, the mass of the lighter scalar Higgs boson h is only 4.4 and 11.2 GeV/c^2 smaller than M_A. With the mass resolution, which can be reached in the $H \to \tau\tau$ decay channels, the lighter scalar contributes to the signal and is added in the cross sections for $M_A = 130$ and 140 GeV/c^2. The contribution is 31 and 11% of the total production rate, respectively. Table 5.20 shows the number of events and efficiencies for the backgrounds originating from $Z/\gamma^* \to \tau\tau$ and $Z/\gamma^* \to e^+e^-$ decays in the inclusive and in the associated $b\bar{b}Z/\gamma^*$ production. The efficiency of removing the $b\bar{b}Z/\gamma^*$ component from the inclusive Z/γ^* samples is also shown. Table 5.21 shows the same for the backgrounds involving W's from $t\bar{t}$, Wt and W + jet events. The cross section times branching fraction, trigger efficiency and the efficiency of the primary vertex reconstruction are also shown in the tables. The QCD multi-jet background after all selections was estimated to be 8.4 events for 30 fb^{-1} in the mass window around $M_A = 200\,GeV/c^2$, which is ≃ 10% of all other backgrounds.

Figures 5.9 and 5.10 show the reconstructed Higgs boson mass distributions of the $H/A \to \tau^+\tau^- \to$ electron + jet + X signal and the total background for 30 fb^{-1} for $M_A = 200\,GeV/c^2$, $\tan\beta = 20$ and for $M_A = 300\,GeV/c^2$, $\tan\beta = 25$. The sum of the $Z/\gamma^* \to e^+e^-$ and $b\bar{b}Z/\gamma^* \to e^+e^-$ backgrounds is shown separately in the figures.

5.2.8.3. Systematic uncertainties for the background determination. The background uncertainty was evaluated using the cross-section uncertainties (measured or predicted from the theory) and the experimental uncertainties for the event selections.

The uncertainty of the event selection efficiency is related to the uncertainty of the electron and τ identification, the absolute calorimeter scale and the b-tagging efficiency.

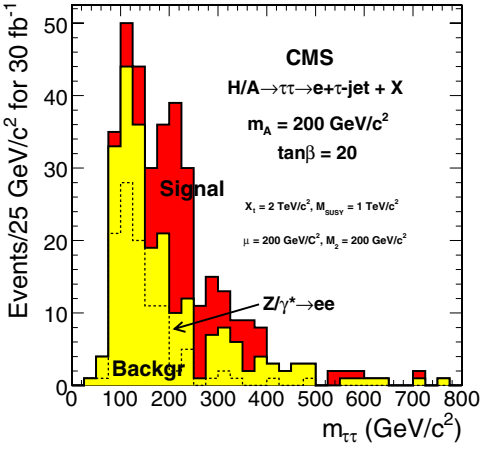

Figure 5.9. Reconstructed Higgs boson mass for the signal of $M_A = 200\,GeV/c^2$, $\tan\beta = 20$ and for the total background for an integrated luminosity of $30\,fb^{-1}$. The dashed line shows the sum of the $Z/\gamma^* \to e^+e^-$ and $b\bar{b}Z/\gamma^* e^+e^-$ backgrounds.

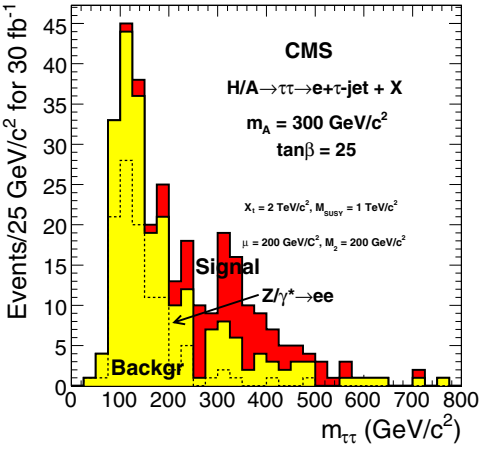

Figure 5.10. Reconstructed Higgs boson mass for the signal with $M_A = 300\,GeV/c^2$, $\tan\beta = 25$ and for the total background for an integrated luminosity of $30\,fb^{-1}$. The dashed line shows the sum of the $Z/\gamma^* \to e^+e^-$ and $b\bar{b}Z/\gamma^* e^+e^-$ backgrounds.

The systematic uncertainty due to the energy scale was estimated varying the jet energy and the E_T^{miss} values with the expected energy scale uncertainties yielding an average 5.1% uncertainty on the number of Z/γ^* events, 3.8% uncertainty on the number of $b\bar{b}Z/\gamma^*$ events, 7.3% uncertainty on the number of $t\bar{t}$ events, 11.3% uncertainty on the number of tW events and 11.8% uncertainty on the number of W+jet events passing the event selection cuts. A 5% uncertainty on the b tagging and mistagging efficiencies and a 2% uncertainty on the electron reconstruction and identification were used.

The uncertainty of the Z/γ^* cross section at the LHC is of the order of 1% [158]. For the $t\bar{t}$ background the theoretical NLO cross section uncertainty derives from the scale uncertainty, taken to be 5% according to Ref. [159], and the PDF uncertainty, about 2.5 %, yielding 5.6% for the total uncertainty. The same uncertainty is used for the cross sections of the Wt and W+jet processes. The uncertainty of the $b\bar{b}Z/\gamma^*$ cross section measurement is estimated to be 14.2% in [145]. With these estimates, the total systematic uncertainty, including the luminosity uncertainty of 3% [7], was found to be 8.1%, 15.9%, 11.1%, 14.0% and 14.5% for the Z/γ^*, $b\bar{b}Z/\gamma^*$, $t\bar{t}$, Wt and W+jet backgrounds, respectively.

5.2.8.4. Discovery reach in the M_A–tan(β) *plane.* Table 5.22 shows the number of signal plus background events and the number of background events for $30\,fb^{-1}$ in the selected mass windows and the signal significance calculated according to Poisson statistics, with and without the background systematics taken into account. The mass windows were selected to optimise the significance. The m_h^{max} scenario was used.

Figure 5.11 shows the 5σ discovery region in the M_A–tan β plane for $30\,fb^{-1}$ in the m_h^{max} scenario, evaluated with and without background systematics.

5.3. Benchmark Channels: $t\bar{t}H$, $H \to b\bar{b}$

5.3.1. Introduction

The Higgs boson decay to $b\bar{b}$ is the dominant mode for the Higgs mass range up to $m_H \sim 135\,GeV/c^2$. Direct Higgs production is almost impossible to detect via this decay

Table 5.22. Number of signal-plus-background events and the number of background events in the selected mass windows for 30 fb^{-1} and the signal significance without ($S_{no\ syst.}$) and with ($S_{syst.}$) the background systematics taken into account.

	$\Delta m_{\tau^+\tau^-}$	N_S+N_B	N_B	$S_{no\ syst.}$	$S_{syst.}$
$M_A = 130\,GeV/c^2$, $\tan\beta = 20$	120–200 GeV/c^2	176	83	8.9	6.4
$M_A = 140\,GeV/c^2$, $\tan\beta = 15$	130–220 GeV/c^2	136	76	9.1	6.7
$M_A = 200\,GeV/c^2$, $\tan\beta = 20$	140–280 GeV/c^2	175	83	8.8	6.3
$M_A = 300\,GeV/c^2$, $\tan\beta = 20$	240–480 GeV/c^2	78	39	5.4	4.3
$M_A = 500\,GeV/c^2$, $\tan\beta = 50$	360–780 GeV/c^2	57	22	6.2	5.3

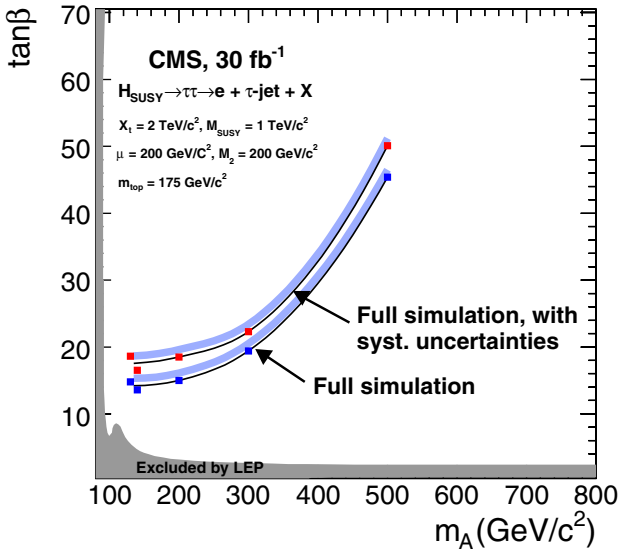

Figure 5.11. The 5σ discovery region in the $M_A - \tan(\beta)$ plane for an integrated luminosity of 30 fb^{-1} in the m_h^{max} scenario. The lower (upper) curve was evaluated without (with) the effect of background systematics taken into account.

as a result of the combination of an overwhelming QCD cross section for $b\bar{b}$ production and the inability to reconstruct the Higgs mass very precisely. While the latter is still true in the case of Higgs production in association with a $t\bar{t}$ or $b\bar{b}$ pair, these channels hold promise because they entail substantially lower backgrounds. The separation of these events into 3 salient topologies follows as a result of the ways in which the two W bosons in the event decay. Thus, in addition to the four b jets, roughly 49% of these events also contain four hadronic jets (the all-hadron channel), while some 28% have two hadronic jets together with an isolated electron or muon and missing E_t (the semi-leptonic channel), with a further 5% of events containing two oppositely-charged leptons (either of which can be an electron or muon) and missing E_t (the dilepton channel). The remaining 14% of events correspond to those cases where one or both of the W bosons decay to a tau lepton and neutrino and are not easily distinguishable as such, as a result of the rich decay repertoire of the tau meson. In fact, these events do make a small contribution to the three other classes of events in the actual analyses. Additional hadronic jets can appear in these events and originate from initial and final state QCD radiation (IFSR).

Table 5.23. NLO signal cross-sections and $H \to b\bar{b}$ branching ratios for different Higgs mass hypotheses

m_H	115 GeV/c^2	120 GeV/c^2	130 GeV/c^2
σ_{NLO} (pb)	0.747	0.664	0.532
$BR(H \to b\bar{b})$	0.731	0.677	0.525

A detailed description of the $t\bar{t}H$ analysis strategies and the results can be found in Reference [160]. All the results presented here are for an integrated luminosity of 60 fb^{-1}.

5.3.2. Event generation and simulation

As the identification of the signal relies upon the presence of top quark decay products, it comes as no surprise that the most significant backgrounds are those associated with $t\bar{t}$ events themselves. The main backgrounds are: $t\bar{t}jj$, $t\bar{t}b\bar{b}$ and $t\bar{t}Z$ with $Z \to b\bar{b}$.

These processes are studied in detail and are presented here. Secondary background sources include pure QCD multi-jet events in the case of the all-hadron channel, and W/Z plus jets or dibosons plus jets events in the case of the semi-leptonic and dilepton channels. With the exception of QCD multi-jets, the latter have substantially lower production cross-sections than $t\bar{t}$ events but very similar topologies. They are therefore not studied in detail.

Details about the primary Monte Carlo data samples used in this analysis are available in Reference [160]. The semi-leptonic and all-hadron $t\bar{t}H$ signal samples were generated using COMPHEP (version 41.10) and PYTHIA (version 6.215), while the dilepton samples used PYTHIA only. Though a leading order Monte Carlo, PYTHIA is known to do a very good job of reproducing IFSR as well as parton shower effects. This is adequate for the signal samples. For the $t\bar{t}$ plus jets backgrounds, greater care must be exercised. In particular, PYTHIA alone cannot be expected to do a realistic job since the relevant processes are not leading order. On the other hand, there is not currently a full next-to-leading order (NLO) MC for $t\bar{t}$ plus jets production. As a result, higher order matrix elements are used including additional radiated partons in conjunction with the parton showering of PYTHIA to produce the appropriate event topologies.

ALPGEN and PYTHIA are used for the matrix elements and parton showering, respectively, for the $t\bar{t}$ plus n jets background samples. The matching of the two generators is done in ALPGEN as discussed in Ref. [161]. In particular, all of the matrix elements for $t\bar{t}$ plus n additional hard partons are included and properly combined at each order taking into account the interference between amplitudes.

QCD events were generated with PYTHIA (version 6.215) in the $\hat{p}_t$ ranges from 120 to 170 GeV/c and greater than 170 GeV/c.

For the simulation of the interaction with the detector, the CMS tools, providing GEANT3 and GEANT4 based simulation of the CMS detector have been used.

The NLO signal cross-sections for different Higgs mass hypotheses are given in Table 5.23 together with the branching ratios for $H \to b\bar{b}$ [162].

The leading order COMPHEP cross-sections for the different background processes together with the effective cross-sections after the application of the generator filters are listed in Table 5.24. The ALPGEN cross sections for the different jet multiplicity processes are listed in Table 5.25. A detailed comparison of ALPGEN versus COMPHEP for the $t\bar{t}jj$ background is available in [160]. All the results that are presented here for the $t\bar{t}Nj$ backgrounds are based on the ALPGEN samples, where available.

Table 5.24. LO COMPHEP cross-sections and effective cross-sections after the generator filters of the considered background processes.

	QCD $\hat{p}_t = 120$–$170\,\mathrm{GeV/c}$	QCD $\hat{p}_t > 170\,\mathrm{GeV/c}$	$t\bar{t}b\bar{b}$	$t\bar{t}Z$
σ_{LO} (pb)	$3.82 \cdot 10^5$	$1.05 \cdot 10^5$	3.28	0.65
$\sigma_{LO} \times \varepsilon$ (pb)	76.4	336.0	2.82	0.565

Table 5.25. LO ALPGEN cross-sections for the different jet multiplicity samples.

	exclusive $t\bar{t}$+1j	exclusive $t\bar{t}$+2j	exclusive $t\bar{t}$+3j	inclusive $t\bar{t}$+4j
σ_{LO} (pb)	170	100	40	61

Table 5.26. Signal and background efficiencies of the Level 1 and High Level Triggers.

	Single μ	Single e	Single e OR μ OR τ	Jets
$H \to b\bar{b}$ (%) with $m_H = 120\,\mathrm{GeV/c^2}$	63.5	52.4	76.7	24.9
$t\bar{t}b\bar{b}$ (%)	19.0	16.1	83.6	18.3
$t\bar{t}$1j (%)	13.9	11.3	53.0	2.9
$t\bar{t}$2j (%)	14.0	11.1	59.8	6.2
$t\bar{t}$3j (%)	14.0	11.1	68.5	11.4
$t\bar{t}$4j (%)	13.4	11.1	78.6	31.4
$t\bar{t}Z$ (%)	20.4	18.8	84.4	25.3
QCD 120–170 GeV/c (%)	0.08	0.8	4.3	1.7
QCD > 170 GeV/c (%)	0.07	2.1	4.4	10.3

5.3.3. Level-1 and high level trigger selections

A dedicated $t\bar{t}H$ trigger was not available and therefore was not implemented in the analysis. As a result, it is assumed in what follows that the signal is recorded by the CMS Level 1 (L1) and High Level Triggers (HLT) as described in [76]. Wherever possible, the cleaner signature of at least one isolated lepton in the final state is exploited. The semi-leptonic channels thus use the single muon (stream #43) or single electron (stream #2) triggers.

A logical "OR" of the single muon, single electron and single tau streams is used for the dilepton channel. The same trigger setups as for streams #43 and #2 were used, except that the p_T threshold was lowered to 15 GeV/c to permit selection of 20 GeV/c leptons later in the analysis. The tau trigger is the official stream (bit #91). Jet triggers are used to select all-hadron events. In particular, the single-jet, 3-jet and 4-jet triggers with low luminosity thresholds [76][163] are combined (stream #120 or #122 or #123).

Efficiencies for the various HLT and Level-1 triggers that were used are presented in Table 5.26. The efficiencies quoted are determined by counting the numbers of accepted events relative to the total numbers of events in each sample. In order to streamline the various studies that were performed, the analyses used different MC samples, produced with different final state constraints. Thus, efficiencies for single muon, single electron and fully hadronic final states were defined with respect to exclusive signal samples and inclusive background samples, as described in the preceding section. The dilepton channel efficiency on the other hand, was defined with respect to samples containing at least one leptonic top decay for the signal and inclusive samples for the backgrounds.

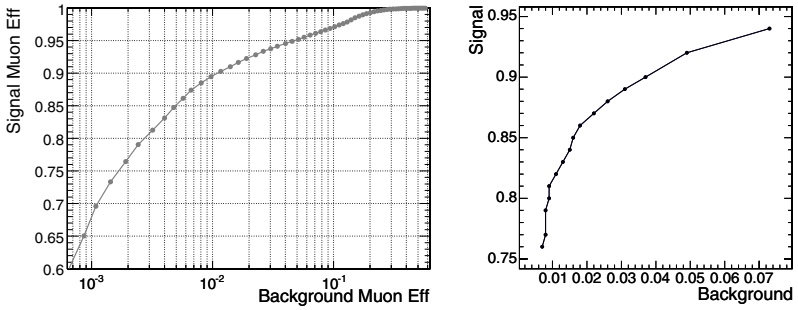

Figure 5.12. (Left) Performance of the muon likelihood discriminator for the semi-leptonic muon $t\bar{t}H$ channel. (Right) *Signal* versus *background* electron efficiencies for likelihood values ranging from 0.006 (the upper point) with a step size of 0.006, (i.e. approximately in the range $1.0 < -\log(L_e) < 2.0$).

5.3.4. Reconstruction

5.3.4.1. Muon reconstruction. The process of muon reconstruction begins in the Muon Chambers and is then extended to the tracking system, as described in Ref. [164]. For the studies presented here it is important to identify muons coming from W decays. To this end, additional selection criteria are applied to distinguish these muons, which will be referred to as *signal* muons, from the muons coming from other sources such as b decays. The latter will be referred to as *background* muons, even though they arise in signal events as well as background events. The desired discrimination between *signal* and *background* muons is achieved by constructing a discriminator that is based upon probability density functions (PDF) for the following observables associated with muon candidates:

- Transverse momentum, p_t.
- Track isolation, *IsoTk*.
- Calorimeter isolation, $IsoCalo$.
- Significance of track impact parameter, $S_{ip} = d/\sigma_d$.

The PDF's associated with these variables for *signal* and *background* muons are obtained by matching to generator-level muons.

The PDF's are combined into the following likelihood ratio:

$$L = \Pi_i \frac{P_i^{sig}(x_i)}{P_i^{sig}(x_i) + P_i^{bkg}(x_i)} \tag{5.13}$$

where P_i^{sig} and P_i^{bkg} are the PDF's of an observable x_i for *signal* and *background* muons, respectively.

The performance for *signal* and *background* muon discrimination are shown in Figure 5.12. For a *signal* muon efficiency of 90%, only 1% of background muons are selected. The PDF's are constructed using a sample of $t\bar{t}H$ events with $m_H = 120\,GeV/c^2$ in which one and only one of the W bosons decays to a muon and neutrino, while the other one decays hadronically.

If the likelihood selection is used after the HLT, a dramatic improvement in QCD ($\hat{p}_t > 170\,GeV/c$) rejection is possible with little or no loss in signal efficiency. For example, a small drop in signal efficiency from 63% to 60% reduces the QCD efficiency by more than a factor of 3 (*i.e.* from 0.07% to 0.02%).

5.3.4.2. Electron reconstruction. A full description of the electron reconstruction in CMS can be found in Ref. [46]. Electrons coming from W boson decays are typically characterised by isolated high transverse energy clusters. These electrons are thus efficiently identified by means of an isolation requirement applied to the electron candidate with respect to other reconstructed tracks in the event.

In analogy to the muon reconstruction and equation 5.13, a likelihood method is used to identify the signal electrons, making use of the following observables:

- the p_t sum of tracks inside an *isolation cone* of radius $\Delta R = 0.3$ around the candidate electron direction.
- the ΔR distance between the electron candidate and the closest track.
- the transverse momentum of the electron candidate, p_t.
- the ratio between the cluster energy and the track momentum, E/p.
- the ratio between the hadronic and electromagnetic energies of the cluster, H/E.

An appropriate choice of likelihood cut value has been studied by comparing *signal* versus *background* electron efficiencies as shown in Figure 5.12.

For a $-\log(L_e)$ cut value of 1.27, *signal* electrons are selected with an efficiency of 84% and *background* electrons with an efficiency of 1.5%. This value was chosen for the analyses described in subsequent sections.

Concerning the efficiency of the likelihood cut with respect to background rejection in $t\bar{t}jj$ events in which there were no isolated electrons coming from W decays, only 6% of these events were accepted for a likelihood cut of 1.27.

As in the case of the muon selection, the likelihood approach can be used to augment the HLT selection efficiency. Maintaining a roughly constant signal efficiency, the likelihood cut in combination with the HLT trigger yields an order of magnitude reduction in the QCD background selection efficiency.

5.3.4.3. Jet and missing E_{T} reconstruction. Jets are reconstructed using the iterative cone algorithm. A cone with $\Delta R = 0.5$ is used when at least one W boson decays into leptons, while a smaller cone size was found to be more suitable for the more dense jet environments associated with the all-hadron channel (see below).

A calorimetric-tower energy threshold of 0.8 GeV and a transverse-energy threshold of 0.5 GeV are used. Calorimeter towers that exceed 1 GeV are considered as jet seeds. For the leptonic channels, the jet energy is calibrated using MC calibrations [165] provided by the JetMET group for the corresponding set of reconstruction parameters.

The single lepton analyses, as described in more detail below, make use of an event likelihood to help select and properly reconstruct events and decay chains. This is facilitated, in part, by making use of the various invariant mass constraints associated with the top quark decays. The corresponding likelihoods thus rely upon the resolutions that are obtained for the invariant masses of the hadronically decaying W boson and the two top quarks. The "best-case" invariant mass distribution for the hadronically decaying top quark is reconstructed by matching to generator-level parton information and shown in Figure 5.13. The distributions for the leptonically decaying top quark and the hadronically decaying W boson (Ref. [160]) have similar shapes but different RMS (25.7 GeV/c^2 and 15.7 GeV/c^2, respectively) since the longitudinal momentum of the leptonically decaying top quark has to be calculated from missing E_t. A reconstructed jet is considered as matched to the corresponding parton if their separation, ΔR_{j-p}, is less than 0.3.

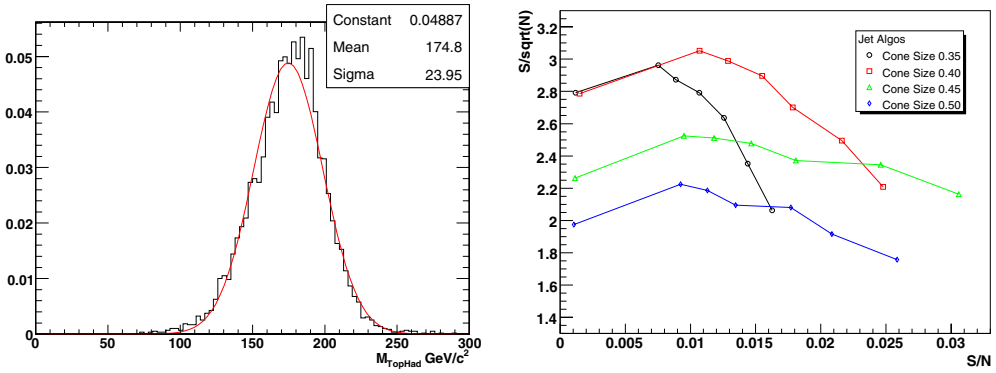

Figure 5.13. (Left) Invariant mass of the hadronically decaying Top quark using jet-parton matching with $\Delta R_{j-p} < 0.3$. (Right) Change in significance and S/N resulting from variations in the b-tagging discriminator for the various cone sizes indicated in the legend.

The missing transverse energy of the event $E_{\mathrm{t}}^{\mathrm{miss}}$ is computed as

$$E_{\mathrm{t}}^{\mathrm{miss}} = \sum_{i} E_{\mathrm{t}}^{\mathrm{tower}} - \left(\sum_{j} E_{\mathrm{t}}^{\mathrm{RawJet}} - \sum_{k} E_{\mathrm{t}}^{\mathrm{CaliJet}} \right) + \sum_{m} E_{\mathrm{t}}^{\mathrm{Muon}} \tag{5.14}$$

where the sum with index i runs over calorimeter towers, that with index j runs over raw jets, k runs over calibrated jets, and m runs over the reconstructed muons of the event. Equation 5.14 thus takes into account the corrections due to jet calibration and the contributions of muons that are not measured in the calorimeter.

The choice of the jet reconstruction algorithm is an important step in the event selection optimisation for the all-hadron $\mathrm{t\bar{t}H}$ channel, where at least 8 jets are expected in the final state. For this reason, an optimisation is obtained by means of a simple "proto" analysis as described in Reference [160].

A dedicated $\mathrm{t\bar{t}}$ H calibration [166] is applied to help recover the original transverse energy of the associated parton. Reconstructed jets with a b-tagging discriminator value higher than 0.4 are calibrated using a separate b-jet calibration procedure.

Figure 5.13 shows the significance with respect to the S/N ratio for a range of b-tag discriminator values for each of the several cone sizes indicated. Lower discriminator values yield higher significance but only at the cost of low S/N while, on the contrary, higher discriminator values give lower significance but higher S/N. A good compromise is in the middle range of each of the curves where neither S/N nor significance are unreasonably low. With this in mind, the best choice for the jet cone is seen to be $\Delta R = 0.40$.

5.3.4.4. b-Tagging. The identification of jets from b-quarks is done with the *Combined Secondary Vertex* algorithm. This algorithm exploits secondary vertex and track properties to calculate a discriminator value which separates b-jets from non b-jets. A detailed description is published in Ref. [157] which also presents results of detailed studies of the performance of the b-tagging algorithm as applied to Monte Carlo $\mathrm{t\bar{t}}$ and QCD samples.

In the $\mathrm{t\bar{t}H}$ analyses, a fixed cut value for the b-tagging discriminator is applied, and four jets are required to pass this cut in the semi-leptonic and all-hadron channels, while only 3 jets are required to be tagged in the dilepton analysis. The misidentification rate of charm and light flavour jets as a function of the b-tagging efficiency is shown in Fig. 5.14 for the $\mathrm{t\bar{t}H}$ and the $\mathrm{t\bar{t}jj}$ samples, respectively. It can be seen that the efficiencies are similar in these samples.

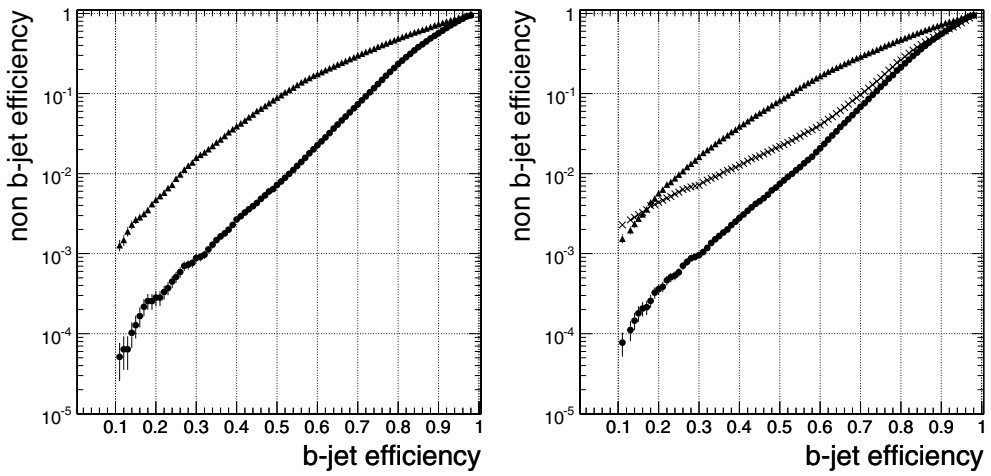

Figure 5.14. On the left: Non-b jet mistagging efficiency versus b-jet tagging efficiency for c-jets (triangles), and uds-jets (stars) for the $t\bar{t}H$ sample with $m_H = 120$ GeV/c^2 and jets with a minimum transverse momentum of 20 GeV/c. For this plot the "physics definition" of the original jet flavour has been used. In this definition there are no original gluon jets in the $t\bar{t}H$ sample. On the right: The corresponding plot for the $t\bar{t}jj$ sample, where gluon jets are represented by crosses.

This fixed-cut b-tagging approach gives reasonable results, but is not necessarily optimal. Some potential improvements are possible such as the combination with a soft lepton tag or a discriminator cut which depends on p_t and η of the jets. Studies have shown that they have the potential to improve the results at the order of some percent. These improvements were not used in the current analyses.

5.3.5. Event selection

In this section the event selection for the different channels under consideration is described. In order to be able to combine the results from all the $t\bar{t}H$ search channels, the different channels use mutually exclusive event samples. This is most easily facilitated by coordinating how high p_t electrons and muons from the W decays (previously referred to as *signal* leptons) are either selected or vetoed by the different analyses.

For the analyses reported here, the different data samples used were separated using selection and/or veto criteria based on the lepton likelihood value, as described in Ref. [160].

5.3.5.1. Semi-leptonic Channel: $t\bar{t}H \to b\bar{b}b\bar{b}qq'\mu\nu_\mu$ *and* $b\bar{b}b\bar{b}qq'e\nu_e$. The strategy for selecting $t\bar{t}H$ events with one isolated muon or electron in the final state can be summarised in the following three steps: pre-selection, choice of jet pairing and finally, selection. The pre-selection requires the HLT stream for a single muon or a single electron, one isolated lepton using the likelihood information as described in section 5.3.4.1 and 5.3.4.2, and 6 or 7 jets in the pseudorapidity region $|\eta| < 3.0$ with a calibrated transverse energy larger than 20 GeV. In order to recover some efficiency, jets with 10 GeV $< E_t <$ 20 GeV are also accepted if they have at least two associated tracks pointing to the signal primary vertex[42] within a distance along the beam (z) axis of ($|z_{PV} - z_{track}| < 1$ mm). The latter condition is required to reject low transverse energy fake jets, (i.e. jets that are not associated with any of the signature

[42] The signal interaction is generally the one which allows the event to be triggered.

partons in the signal event). For the single electron channel, the misidentification of the jet with the isolated electron has been excluded by imposing a veto on the jet if the electron lies inside a jet cone radius of 0.1.

At least 4 jets are required to be tagged as b-jets with a minimal discriminator value corresponding to a b-efficiency of about 70%.

To decrease the contamination from the dilepton channel, a double muon, double electron and muon-electron veto is applied, in which events with the second lowest $-\log(L_\mu) < 1.4$ and events with $-\log(L_e) < 1.2$ are rejected from the analysis. In the case of the semi-leptonic electron channel the previous cuts are applied respectively to the first muon likelihood candidate and to the second electron likelihood candidate. The application of these vetoes results in a lowering of the signal efficiency by about 2%, while the total background rejection is increased by 13%.

In order to perform a complete reconstruction of the event, the longitudinal momentum of the neutrino has to be computed from four-momentum conservation for the W boson: $m_W^2 = (E^\mu + E^\nu)^2 - (\vec{p}^\mu + \vec{p}^\nu)^2$. This equation gives 2 real solutions for p_z^ν in 66% of the cases, while in the remaining 34%, the neutrino is assumed to be collinear with the lepton: $p_z^\nu = p_z^l$. This leads to a small degradation in the longitudinal momentum resolution, but the reconstruction efficiency of the leptonic W boson decay is increased to 100%.

In order to choose the jet combination that does the best job of reconstructing the two top quarks, a likelihood, L_{Event}, is defined using masses, b-tagging and kinematic information from the whole event:

$$L_{Event} = L_{Mass} \times L_{bTag} \times L_{Kine}. \tag{5.15}$$

The mass information considered in the likelihood L_{Mass} is the probability returned by the kinematic fit with invariant mass constraints (top quarks and hadronic W) that is described in Reference [167].

The b-tagging function L_{bTag} is defined as the product of the b-tag discriminators: $L_{bTag} = D_{Top_{Had}} \times D_{Top_{Lep}} \times D_{H_1} \times D_{H_1} \times (1 - D_{W1}) \times (1 - D_{W2})$; where Top_{Had} and Top_{Lep} are expected to be the two b jets from the hadronic and leptonic top, respectively, while H_1 and H_2 are expected to be the two b jets coming from Higgs and W_1 and W_2 are the two jets from the hadronically-decaying W boson.

The kinematic function takes into account the observation that the b-jets coming from top quarks tend to be slightly more energetic than b-jets coming from the Higgs boson (see [160] for a definition).

Among all possible combinations of jet-parton assignments, the one with the highest value of L_{Event} is chosen for use in the final reconstruction of the top quarks and the two remaining jets with highest b-tagging discriminator values are used to reconstruct the Higgs mass.

After the jet assignment is complete, additional criteria are applied to improve background rejection. In particular, a stronger b-tag requirement is applied on the event variable $L_{bSele} = D_{Top_{Had}} \times D_{Top_{Lep}} \times D_{H_1} \times D_{H_1}$.

The signal significance as a function of the selection cut L_{bSele} is shown in Figure 5.15.

The distributions of reconstructed Higgs mass for the final selected events are shown in Figure 5.16 for signal only (left) and for the combination of the different backgrounds (right) for the muon channel only (similar results for the electron channel can be found in [160]). The fraction of signal events where the two b-jets are correctly assigned to the Higgs boson (i.e. the pairing efficiency) is roughly 31% in the muon channel and about 29% for the electron channel.

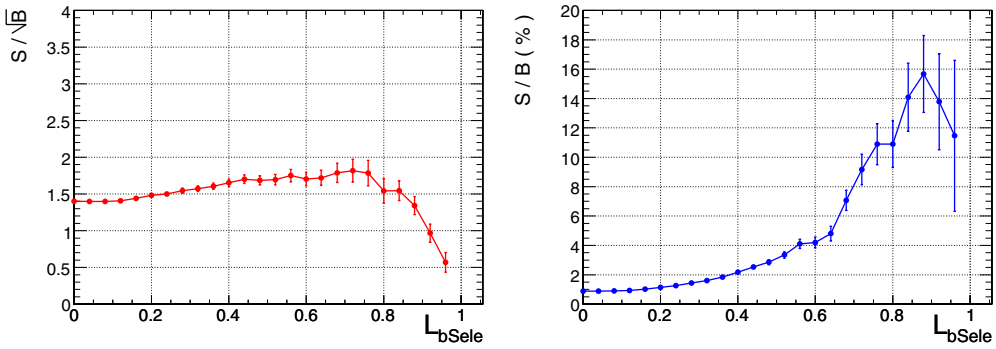

Figure 5.15. $\mathrm{t\bar{t}H}$ ($W \to q\bar{q}'$, $W \to \mu\nu$): Signal Significance (left) and Signal to Background ratio (right) as function of the cut on L_{bSele}.

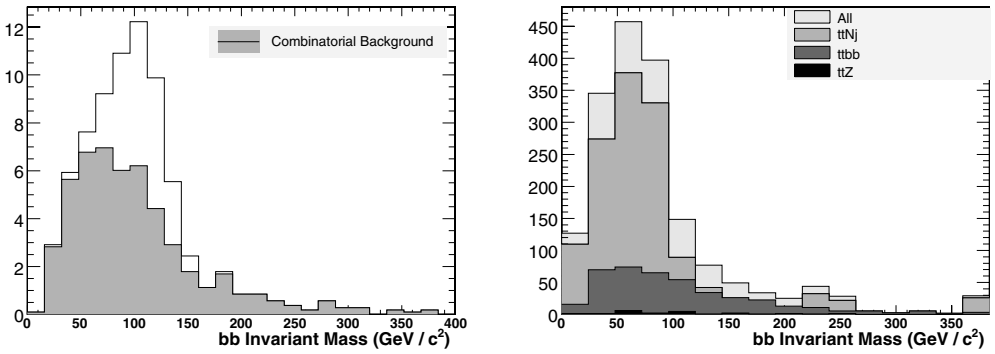

Figure 5.16. $\mathrm{t\bar{t}H}$($W \to q\bar{q}'$, $W \to \mu\nu$). (Left) Invariant $b\bar{b}$ mass for signal only (combinatorial background is shaded grey). (Right) The sum of the reconstructed $m_{b\bar{b}}$ spectra for backgrounds with a value of $L_{bSele} > 0.55$. The distributions are normalised to an integrated luminosity of 60 fb^{-1}.

5.3.5.2. Results. The selection efficiencies with the corresponding numbers of expected events and signal significances are reported in Table 5.27 for the channels with a muon or an electron in the final state. The number of expected events is computed for an integrated luminosity of 60 fb^{-1} in the Standard Model Higgs mass range from 115 to 130 $\mathrm{GeV/c^2}$.

5.3.5.3. Dilepton channel: $\mathrm{t\bar{t}H} \to \mathrm{b\bar{b}b\bar{b}}\ell'\nu'\ell\nu$. Dilepton ttH events are selected by requiring two reconstructed leptons (e, μ) accompanied by significant missing transverse energy and at least four but no more than seven jets, at least three of which have been b-tagged according to the *Combined Secondary Vertex* b-tagging algorithm.

Lepton identification is performed using the electron and muon likelihoods described in Section 5.3.4. In the semi-leptonic analyses, events with more than one identified lepton are vetoed, but in the dilepton analysis those events are retained. The likelihood acceptance cuts used for leptons in the dilepton channel are therefore chosen to be the same as the second-lepton veto cuts for both semi-leptonic channels. In this way, the sample of events for the dilepton $\mathrm{t\bar{t}H}$ analysis is by construction strictly complementary to those used in the semi-leptonic channels.

Table 5.27. Selection efficiency for $L_{bSele} > 0.55$ (ε_{loose}) and for $L_{bSele} > 0.75$ (ε_{tight}), number of expected events and signal significance in 60 fb^{-1} for the muon and electron $t\bar{t}H$ channel. The numbers refer to the complete Higgs mass range.

	Analysed Ev.	$\varepsilon_{\text{loose}}$ (%)	N^{ev}_{loose} 60 fb^{-1}	$\varepsilon_{\text{tight}}$ (%)	N^{ev}_{tight} 60 fb^{-1}
muon channel					
$t\bar{t}H$ (115)	27768	2.00 ± 0.08	96 ± 4	0.80 ± 0.05	38 ± 3
$t\bar{t}H$ (120)	41929	1.90 ± 0.07	75 ± 3	0.74 ± 0.04	29 ± 2
$t\bar{t}H$ (130)	19466	2.23 ± 0.11	55 ± 3	0.84 ± 0.07	21 ± 2
$t\bar{t}b\bar{b}$	372737	0.247 ± 0.008	419 ± 14	0.0877 ± 0.0048	148 ± 8
$t\bar{t}1j$	393000	0.0051 ± 0.0011	520 ± 120	0.00076 ± 0.00044	78 ± 45
$t\bar{t}2j$	568999	0.0105 ± 0.0014	633 ± 82	0.00070 ± 0.00035	42 ± 21
$t\bar{t}3j$	101000	0.0050 ± 0.0022	119 ± 53	0	$<27(68\% C.L)$
$t\bar{t}4j$	86697	0.0035 ± 0.0020	126 ± 73	0	$<48(68\% C.L.)$
$Zt\bar{t}$	50000	0.068 ± 0.012	23 ± 4	0.026 ± 0.007	9 ± 2
Total Background			1840		< 352
$S/\sqrt{B}$ (115)			2.2		2.0
S/B (115)			5.1%		10.8%
$S/\sqrt{B}$ (120)			1.8		1.6
S/B (120)			4.1%		8.2%
$S/\sqrt{B}$ (130)			1.3		1.1
S/B (130)			3.0%		6.0%
electron channel					
$t\bar{t}H$ (115)	27692	1.39 ± 0.07	66 ± 3	0.52 ± 0.04	25 ± 2
$t\bar{t}H$ (120)	42228	1.42 ± 0.06	56 ± 2	0.53 ± 0.04	21 ± 1
$t\bar{t}H$ (130)	19127	1.57 ± 0.09	39 ± 2	0.61 ± 0.06	15 ± 1
$t\bar{t}b\bar{b}$	372737	0.176 ± 0.007	297 ± 12	0.0641 ± 0.0041	109 ± 7
$t\bar{t}1j$	393000	0.0038 ± 0.0010	390 ± 100	0.00025 ± 0.00025	26 ± 26
$t\bar{t}2j$	568999	0.0067 ± 0.0011	401 ± 65	0.00123 ± 0.00046	74 ± 28
$t\bar{t}3j$	101000	0.0040 ± 0.0020	95 ± 48	0	$< 27(68\% C.L)$
$t\bar{t}4j$	86697	0.0023 ± 0.0016	84 ± 60	0	$< 48(68\% C.L.)$
$Zt\bar{t}$	50000	0.064 ± 0.011	22 ± 4	0.022 ± 0.007	7 ± 2
Total Background			1289		< 291
$S/\sqrt{B}$ (115)			1.8		1.5
S/B (115)			5.1%		8.6%
$S/\sqrt{B}$ (120)			1.6		1.2
S/B (120)			4.4%		7.2%
$S/\sqrt{B}$ (130)			1.1		0.9
S/B (130)			3.0%		5.2%

The details of the dilepton $t\bar{t}H$ selection are summarised below:

- 2 oppositely-charged leptons (e, μ) passing identification criteria $-\log(L_\mu) < 1.4$ for muons, $-\log(L_e) < 1.2$ for electrons).
- corrected $E_{\text{T}}^{\text{miss}} > 40\,\text{GeV}$.
- 4 to 7 jets with calibrated $E_{\text{T}} > 20\,\text{GeV}$ and $|\eta| < 2.5$.
- $\geqslant$3 selected jets b-tagged with discriminator $D > 0.7$.

The above is termed the "loose" working point because there is evidence that it is possible to increase the purity (S/B) of the selection, by way of more stringent criteria:

- 4 to 6 jets with calibrated $E_{\text{T}} > 20\,\text{GeV}$ and $|\eta| < 2.5$.
- $\geqslant$4 selected jets b-tagged with discriminator $D > 0.7$.

Table 5.28. Selection efficiency ε_{loose} (including branching fraction where applicable) and resulting number of expected events N_{loose} in 60 fb^{-1}, for the dilepton $\bar{t}tH$ channel. For a glimpse of possible improvements, the same for a tighter set of cuts is provided (ε_{tight}, N_{tight}). Also quoted are binomial errors arising from the finite sizes of processed datasets. The $\bar{t}tH$ datasets are labelled by the generated Higgs mass in GeV/c^2 (parentheses).

	# analysed	ε_{loose}(%)	N^{ev}_{loose}	ε_{tight}(%)	N^{ev}_{tight}
$t\bar{t}H$ (115)	27900	0.511 ± 0.025	168 ± 8	0.088 ± 0.010	29 ± 3
$t\bar{t}H$ (120)	26141	0.490 ± 0.025	132 ± 7	0.070 ± 0.009	19 ± 3
$t\bar{t}H$ (130)	25911	0.490 ± 0.025	82 ± 4	0.072 ± 0.010	12 ± 2
$t\bar{t}b\bar{b}$	313894	0.637 ± 0.014	1080 ± 24	0.094 ± 0.007	159 ± 12
$t\bar{t}1j$	280385	0.0125 ± 0.0021	1270 ± 220	0	< 42 (68% C.L.)
$t\bar{t}2j$	276917	0.0448 ± 0.0040	2690 ± 240	0.00144 ± 0.00072	87 ± 43
$t\bar{t}3j$	90367	0.0553 ± 0.0078	1330 ± 190	0	< 31 (68% C.L.)
$t\bar{t}4j$	12281	0.0716 ± 0.0077	2620 ± 280	0.0025 ± 0.0014	92 ± 53
$t\bar{t}Z$	110156	0.304 ± 0.017	103 ± 6	0.0363 ± 0.0057	12 ± 2
all backgrounds			9090		< 422
$S/\sqrt{B}$ (115)			1.8		1.4
S/B (115)			1.8 (%)		6.9 (%)
$S/\sqrt{B}$ (120)			1.4		0.9
S/B (120)			1.5 (%)		4.5 (%)
$S/\sqrt{B}$ (130)			0.9		0.6
S/B (130)			0.9 (%)		2.9 (%)

The generated W^- was forced to decay leptonically (e, μ, τ), but the W^+ was allowed to decay freely. This "non-exclusive" dataset incurs a branching ratio of 1/3, which has been factored into the selection efficiencies reported in Table 5.28. This choice allows us to obtain a good estimate of the overlap of the contribution to the dilepton sample arising from semi-leptonic top decays which are mis-reconstructed as dilepton events; the same applies to tau decays which are mis-reconstructed as e, μ.

The background events have small efficiency to pass the selection criteria, so very large samples must be analysed. To make these samples more manageable, a loose pre-selection requiring at least 3 b-tags with discriminator $D > 0.7$ is applied before analysis.

5.3.5.4. Results. The selection efficiencies for the two working points, with the corresponding number of expected events and the signal significance, are reported in Table 5.28. The number of expected events is computed for an integrated luminosity of fb^{-1}.

Since the event selection is quite simple for the dilepton channel, it is possible to formulate simple equations predicting the selection efficiencies. This is detailed in Ref. [160], where some back-of-the-envelope calculations to estimate these efficiencies for both signal and backgrounds are presented, including some of the backgrounds that were not taken into account in this analysis.

5.3.5.5. All-hadron channel: $t\bar{t}H \to b\bar{b}b\bar{b}qq'q''q'''$. A number of kinematic variables, together with the b-tagging discriminator, have been studied to optimise the signal selection with respect to background rejection. Moreover, in order to combine the results from the 4 different decay sub-channels, a veto on leptons has been applied using the complementary cut developed within the semi and fully leptonic decays analyses: events are discarded if $-\log(L_\mu) < 1.4$ or $-\log(L_e) < 1.2$.

The final set of variables that are used in this analysis is the following:

- Jet Transverse Energy of the 8 most energetic jets in the tracker acceptance.
- Combined b-Tag discriminator variable for each jet.
- Centrality of the event defined as $\sum_{i=0}^{8} E_{\mathrm{T}}^{i}/E^{i}$.
- Centrality of the Higgs defined similarly, with the sum restricted to the 2 jets paired to the Higgs.

The jet-to-parton matching is performed using a χ^2 method as defined in [160].

Two working points have been chosen: the first uses loose cuts on the b-tagging discriminator to get higher statistical significance (but lower S/B), while the second uses a tighter cut on the b-tagging discriminator to obtain a higher S/B (but lower significance). For the first working point an event is selected if the following conditions are satisfied:

- $E_{\mathrm{T}}^{7th} > 30\,\mathrm{GeV}$ and $E_{\mathrm{T}}^{8th} > 20\,\mathrm{GeV}$ for the E_{T} ordered jets.
- the χ^2 for each of the 2 W bosons and 2 t quarks are within 3 sigma of their expected values.
- the 3 highest combined b-tagging discriminators for the 4 jets associated to the b-partons must satisfy $D_3 > 0.80$.
- Higgs centrality higher than 0.55 and no cut on Event Centrality.

For the tight working point, the b-tagging discriminator for the third highest jet is required to satisfy $D_3 > 0.85$ and the fourth one $D_4 > 0.70$, while the event and Higgs centrality are required to exceed 0.55 and 0.80, respectively.

All the applied cuts have been optimised to obtain the highest significance while keeping the S/B ratio as high as possible. All values chosen for E_{T}^{7th}, E_{T}^{8th}, D_3, D_4, Event and Higgs centrality have been varied simultaneously, thereby mapping out the complete set of combinations within the following limits:

- $20\,\mathrm{GeV} < E_{\mathrm{T}}^{8th} < 40\,\mathrm{GeV}$.
- $E_{\mathrm{T}}^{8th} < E_{\mathrm{T}}^{7th} < E_{\mathrm{T}}^{8th} + 40\,\mathrm{GeV}$.
- $0.5 < D_3$ and $D_4 < 0.95$.
- Event and Higgs Centrality in the range [0.50–0.95].

Variation of more than one cut has also been tested and the final implemented set of cut values is that for which significance and S/B are optimal.

5.3.5.6. Results. The number of analysed events, selection efficiencies with the corresponding number of expected events and the signal significance are reported in Tables 5.29 for the all-hadron decay channel. Both working points are considered.

5.3.6. Discussion of systematic uncertainties

5.3.6.1. Estimation of "standard" CMS systematics. The uncertainties in various quantities, given the knowledge of the CMS experiment at the time of writing this note, are considered first. These differ from what they are expected to be after CMS has collected 60 fb $^{-1}$ of data.

In keeping with other CMS analyses, the following "standard" sources of systematic error are considered:

- Jet energy scale (JES) (3% to 10% depending on p_t).
- Jet resolution (10%).
- b-jet and c-jet tagging efficiencies (4%).
- uds-jet tagging efficiencies (10%).
- Luminosity (3%).

Table 5.29. Analysed events, selection efficiency, number of expected events and signal significance in 60 fb^{-1} for the all-hadron $t\bar{t}H$ channel for 2 different working points: ε_{loose} and ε_{tight}. The numbers refer to the full mass range.

	# analysed	ε_{loose}(%)	N^{ev}_{loose} 60 fb^{-1}	ε_{tight}(%)	N^{ev}_{tight} 60 fb^{-1}
$t\bar{t}H$ (115)	49636	2.32 ± 0.07	347 ± 10	0.294 ± 0.015	44 ± 4
$t\bar{t}H$ (120)	163494	2.55 ± 0.04	314 ± 5	0.366 ± 0.024	45 ± 2
$t\bar{t}H$ (130)	43254	2.80 ± 0.08	214 ± 6	0.358 ± 0.029	27 ± 2
$t\bar{t}b\bar{b}$	203135	0.702 ± 0.019	1190 ± 31	0.0645 ± 0.0056	109 ± 9
$t\bar{t}$1j	1031551	0.0084 ± 0.0009	860 ± 92	0.0005 ± 0.0002	49 ± 22
$t\bar{t}$2j	559111	0.0333 ± 0.0024	2000 ± 150	0.0009 ± 0.0004	54 ± 24
$t\bar{t}$3j	68015	0.079 ± 0.011	1910 ± 260	0.0015 ± 0.0015	35 ± 35
$t\bar{t}$4j	97334	0.182 ± 0.014	6660 ± 500	0.0021 ± 0.0015	75 ± 53
$Zt\bar{t}$	80226	0.358 ± 0.021	121 ± 7	0.0312 ± 0.0062	11 ± 2
qcd170	264310	0.0238 ± 0.0030	4810 ± 610	0.0004 ± 0.0004	76 ± 76
qcd120	55128	0.0018 ± 0.0018	83 ± 83	0 ± 0	$< 95(68\% C.L.)$
Total Backgr.			17600		< 505
$S/\sqrt{B}$ (115)			2.6		2.0
S/B (115)			2.0%		8.7 %
$S/\sqrt{B}$ (120)			2.4		2.0
S/B (120)			1.8%		8.9 %
$S/\sqrt{B}$ (130)			1.6		1.2
S/B (130)			1.2%		5.4 %

It is assumed that the systematics listed above are uncorrelated. Each source is varied independently which produces a change in the selection efficiency $\Delta\varepsilon$ and the corresponding change in expected event yields ΔN_X ($X =$ ttH, tt1j, ...) for the signal and background.

A very detailed breakdown of the various sources of systematic uncertainties and the methods of how they are computed for all the background and signal samples is available in Reference [160]. In Table 5.30, the systematic uncertainties are propagated to the expected signal significance for "tight" and "loose" working points.

5.3.6.2. Background rates from data. There are relatively large theoretical uncertainties in the cross-sections used to normalise the signal yields [162], and even larger theoretical uncertainties in those used for the $t\bar{t}$+jets backgrounds [168]. These have not been included as part of the systematic errors considered above, because when the CMS experiment reaches maturity, estimating the $t\bar{t}$+jets background directly from data ought to be possible. In this way, the uncertainty associated with Monte Carlo derived tagging rates are avoided entirely. For example, the number of mis-tagged $t\bar{t}$+jets which can be factorised as follows:

$$N^{mistag}_{t\bar{t}jj} = N^{no-tag}_{t\bar{t}jj} \times Pr(uds \to b; E_{\mathrm{T}}, \eta, ...)$$

where $N^{no-tag}_{t\bar{t}jj}$ is a high purity (e.g. fully reconstructed with a mass window) top sample that has been obtained without requiring b-tagging and $Pr(uds \to b; E_{\mathrm{T}}, \eta, ...)$ is a parameterised "fake matrix" that is derived from some independent dataset (e.g. dijet data) which yields the probability for a light quark jet to fake a secondary vertex. It may also be possible to derive this fake matrix from the top sample itself. If a high-purity (e.g. double-tagged and fully reconstructed) semi-leptonic top sample were selected, the jets belonging to the hadronic W would provide a source of both light quark and charm jets. From these data, a measurement of the corresponding uds-tag and c-tag rates at the relevant energy could be directly obtained.

Table 5.30. Significance before and after taking into account the uncertainty dB in the total number of background events due to systematics.

muon	S/B	$S/\sqrt{B}$	$S/\sqrt{B+dB^2}$	dilepton	S/B	$S/\sqrt{B}$	$S/\sqrt{B+dB^2}$
	$L_{bSele} > 0.55(\varepsilon_{loose})$				4-7 jets, 3-4 b-tagged (ε_{loose})		
$t\bar{t}H$ (115)	0.052	2.2	0.20	$t\bar{t}H$ (115)	0.018	1.8	0.10
$t\bar{t}H$ (120)	0.041	1.8	0.15	$t\bar{t}H$ (120)	0.015	1.4	0.08
$t\bar{t}H$ (130)	0.030	1.3	0.11	$t\bar{t}H$ (130)	0.009	0.9	0.05
	$L_{bSele} > 0.75(\varepsilon_{tight})$				4-6 jets, 4-6 b-tagged (ε_{tight})		
$t\bar{t}H$ (115)	0.108	2.0	0.44	$t\bar{t}H$ (115)	0.069	1.4	0.42
$t\bar{t}H$ (120)	0.082	1.6	0.34	$t\bar{t}H$ (120)	0.045	0.9	0.27
$t\bar{t}H$ (130)	0.060	1.1	0.24	$t\bar{t}H$ (130)	0.029	0.6	0.18
electron	S/B	$S/\sqrt{B}$	$S/\sqrt{B+dB^2}$	hadron	S/B	$S/\sqrt{B}$	$S/\sqrt{B+dB^2}$
	$L_{bSele} > 0.55(\varepsilon_{loose})$				Working Point ε_{loose}		
$t\bar{t}H$ (115)	0.051	1.8	0.20	$t\bar{t}H$ (115)	0.020	2.6	0.07
$t\bar{t}H$ (120)	0.044	1.6	0.17	$t\bar{t}H$ (120)	0.018	2.4	0.07
$t\bar{t}H$ (130)	0.030	1.1	0.12	$t\bar{t}H$ (130)	0.012	1.6	0.05
	$L_{bSele} > 0.75(\varepsilon_{tight})$				Working Point ε_{tight}		
$t\bar{t}H$ (115)	0.086	1.5	0.37	$t\bar{t}H$ (115)	0.087	2.0	0.22
$t\bar{t}H$ (120)	0.072	1.2	0.31	$t\bar{t}H$ (120)	0.089	2.0	0.22
$t\bar{t}H$ (130)	0.052	0.9	0.22	$t\bar{t}H$ (130)	0.054	1.2	0.13

5.3.7. Combined significance

Since the event samples for the channels studied in this note are strictly disjoint, the results can be combined by simply adding the individual signal yields (background yields) to obtain a summed $S(B)$.

For each of the considered systematics, the resultant error in background yields are added for all four channels, since they are by definition fully correlated. The summed errors are then added by quadratures to get a combined systematic uncertainty dB. One then calculates the significance, inclusive of systematic uncertainties in the background yield, according to the formula $S/\sqrt{B+dB^2}$.

It is of interest to see how much better the results have the potential to be at tighter working points for the various analyses. Since the systematic uncertainties are not well quantified at these "tight" working points, because of a lack in Monte Carlo Statistics, the same uncertainties as for the "loose" working points are used to reduce spurious statistical effects. This procedure can be justified by the observation that the impact of the b-tagging and uds-mistagging uncertainty is smaller at the "tight" working points and the JES uncertainty becomes dominant. Since the "tight" working points are defined by stronger b-tagging cuts, while keeping the E_{T} cuts constant, no major change in the relative systematic uncertainty is expected. A more detailed study of the systematic error at the "tight" working points for samples with enough Monte Carlo Statistics is available in Ref. [160].

It is difficult to predict at this time exactly what will be the level to which the backgrounds can be understood, because the tools required are not yet in existence and because this understanding requires real data. In view of this, it is interesting to consider how the combined significance of the measurements presented in this note would vary as a function of the fractional uncertainty in background cross-sections, i.e. as dB_{xsec}/B.

The solid central line in Figure 5.17 shows how the combined significance $S/\sqrt{B+(dB_{sys}+dB_{xsec})^2}$ degrades as a function of dB_{xsec}/B. The signal and background yields for the tightest working points (N^{ev}_{tight} in Table 5.27, Table 5.28 and Table 5.29)

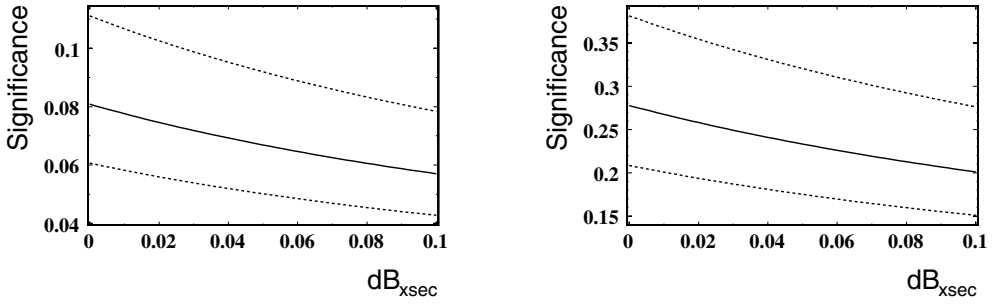

Figure 5.17. Expected range of combined significance (dilepton + semi-leptonic + all-hadron, and includes the systematic uncertainties estimated in Section 5.3.6.1) versus an additional systematic uncertainty on the background cross-section as a fraction of total background. (Left) Results for the "loose" working points. (Right) Results for the "tight" working points.

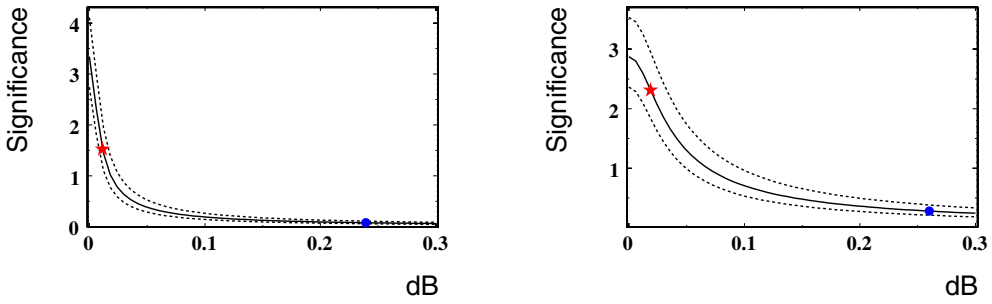

Figure 5.18. Expected range of combined significance (dilepton + semi-leptonic + all-hadron) versus the total systematic uncertainty in background as a fraction of total background. (Left) Results for the "loose" working points. (Right) Results for the "tight" working points.

are used in the right side of Figure 5.17, because these give the best results after inclusion of systematics.

Other than this "fundamental" cross-section uncertainty, there is also the "correctible" errors in the cross-sections used at the time of writing, which can be compensated for once data has been collected. The upper and lower dashed curves in Figure 5.17 show the maximum and minimum allowed excursions, should the signal and background cross-sections be off by 10% and 20% respectively. Thus the upper (lower) dashed line corresponds to the signal cross-section scaled up (down) by 10% while at the same time the background cross-section is scaled down (up) by 20%.

It is also of interest to see how much better the analyses could do if the total systematic uncertainty can be reduced (i.e. the region left of zero in Figure 5.17). Hence, Figure 5.18 shows the full range of obtainable significances, with the dot marking the currently estimated value with no cross-section uncertainty ($dB = dB_{sys}$). The star corresponds to what one would obtain for 1% and 4% uncertainties on the $t\bar{t}$Nj and $t\bar{t}b\bar{b}$ backgrounds, respectively, an arbitrarily chosen reference. It is interesting to note that it does not quite yield a substantial significance, even though background uncertainties of 1% and 4% for $t\bar{t}$Nj and $t\bar{t}b\bar{b}$ are probably substantially better than what will be accessible in reality. This highlights the challenge that is faced in observing $t\bar{t}$H.

Chapter 6. Physics Studies with Heavy Ions

6.1. Benchmark Channel: $PbPb \to Q\overline{Q} + X \to \mu^+\mu^- + X$

The measurement of the charmonium (J/ψ, ψ') and bottomonium (Υ, Υ', Υ'') resonances in PbPb collisions at $\sqrt{s_{NN}} = 5.5$ TeV provides crucial information on the many-body dynamics of high-density QCD matter. First, the step-wise suppression of heavy quarkonia production is generally agreed to be one of the most direct probes of Quark-Gluon-Plasma formation. Lattice QCD calculations of the heavy-quark potential indicate that colour screening dissolves the ground-state charmonium and bottomonium states, J/ψ and Υ, at $T_{\rm diss} \approx 2 \cdot T_{\rm crit}$ and $4 \cdot T_{\rm crit}$, respectively. While the interest of charmonia production studies in heavy-ion collisions is well established from measurements done at the SPS and at RHIC, the clarification of some important remaining questions requires equivalent studies of the Υ family, only possible at the LHC energies. Second, the production of heavy-quarks proceeds mainly via gluon-gluon fusion processes and, as such, is sensitive to saturation of the gluon density at low-x in the nucleus ("Colour Glass Condensate"). Measured departures from the expected "vacuum" (proton-proton) quarkonia cross-sections in PbPb collisions at LHC will thus provide valuable information not only on the thermodynamical state of the produced partonic medium, but also on the initial-state modifications of the nuclear parton (especially, gluon) distribution functions.

This first CMS heavy-ion physics analysis focuses on the measurement of the heavy-quarkonia cross-sections in PbPb collisions at $\sqrt{s_{NN}} = 5.5$ TeV, via their dimuon decay channel. The generation of realistic signals and backgrounds, the dimuon reconstruction algorithm and the trigger, acceptance and efficiency corrections are discussed. The obtained dimuon mass resolutions, the signal over background as well as the expected yields in one-month PbPb running are presented. An example of a $\Upsilon \to \mu^+\mu^-$ event embedded in a PbPb collision is shown in colour plate CP9.

6.1.1. Simulation of physics and background processes

The relatively low Υ production rates ($\sim 10^{-4}$ per PbPb event) and the large number of particles to track in heavy-ion collisions make it very expensive computationally to use a full nucleus-nucleus event generator (such as e.g. HIJING [169]) with detailed detector simulation and reconstruction to obtain a statistically significant sample of signal events. Instead, a combination of fast and slow simulations are used in this analysis. The input signal and backgrounds are obtained from realistic distributions: NLO pQCD for heavy-quark production processes, and HIJING for the soft background, constrained by extrapolations from lower energy heavy-ion data. A full detector and trigger simulation plus reconstruction are carried out for a few 10^7 events with single and pair particles of the different types and the corresponding response functions (acceptances, resolutions, efficiencies, etc) are parameterised in a fast MC, used to obtain the final fully corrected yields. The response functions are cross-checked by comparing the final dimuon spectra obtained with the fast MC against 5×10^5 PbPb HIJING events fully simulated and reconstructed in the detector.

The quarkonium production cross sections in PbPb are obtained from NLO pp calculations at $\sqrt{s} = 5.5$ TeV made in the colour evaporation model (CEM) [170], using MRST PDF modified with the EKS98 prescription for nuclear shadowing [171], with renormalisation and factorisation scales $\mu_R = \mu_F = m_Q$, and scaled by A^2 ($A = 208$ for Pb). The resulting (impact-parameter averaged) inclusive quarkonia production cross sections are: $B_{\mu\mu}\sigma_{Q\overline{Q}}$ = 49 000, 900, 300, 80, 45 μb for J/ψ, ψ', Υ, Υ', and Υ'', respectively. The NLO

double-differential $d^2\sigma/dp_{\mathrm{T}}d\varphi$ distributions of J/ψ and Υ are also used for the other states within each quarkonium family.

The two main sources of background in the dimuon invariant mass spectrum are:

1. Uncorrelated decays of **charged pions and kaons**, which represent about 90% of the produced charged particles. This source was simulated using input pion and kaon $d^2N/dp_{\mathrm{T}}d\eta$ distributions from HIJING, absolutely normalised to give $dN_{ch}/d\eta|_{\eta=0} = 2500\ (low)$ and 5000 $(high)$ multiplicities in central PbPb. Both cases are conservative ("pessimistic"') estimates, since extrapolations from RHIC data indicate that $dN_{ch}/d\eta|_{\eta=0} \approx 2000$ at the LHC.
2. The other source of background muons are **open heavy flavour** (D, B mesons) decaying a few mm away from the interaction vertex. The probability to produce at least one muon at the end of the decay chain of charm (bottom) quarks is ∼18% (38%) according to PYTHIA 6.025. The double differential (p_{T}, η) cross-sections are obtained from pp NLO calculations (with CTEQ5M1 PDF, and $\mu_R = \mu_R = m_Q$), which give $\sigma_{c\bar{c},b\bar{b}}$ = 7.5, 0.2 mb [170], scaled by the nuclear overlap function, $\langle T_{PbPb}(b = 0\,\mathrm{fm})\rangle = 30.4\,\mathrm{mb}^{-1}$, to obtain the expected yields in central PbPb collisions.

A fast MC simulation equivalent to $5 \cdot 10^7$ PbPb events has been carried out superimposing the decay dimuon from the five quarkonium resonances on top of the background from the combinatorial decays of π, K and open heavy flavour. Each muon track (with a given momentum, pseudorapidity, charge and origin) is weighted by a factor that takes into account the corresponding detector acceptance, as well as trigger and reconstruction efficiency for the two event multiplicities considered (see next section).

6.1.2. Reconstruction and analysis

6.1.2.1. Dimuon trigger and acceptance. The response of the CMS detector to muons (as well as long-lived punch through pions and kaons reaching the muon chambers) is parameterised by 2-dimensional p, η acceptance and trigger tables. The particles are fully tracked in CMS using GEANT4 from the vertex to the chambers. Each track is accepted or rejected according to the Level-1,2 heavy-ion dimuon trigger criteria [7] and the corresponding efficiencies, $\varepsilon_{trig}^{LVL1}(p, \eta)$ and $\varepsilon_{trig}^{LVL2}(p, \eta)$, are computed. Trigger efficiencies are of the order of ∼90% for those μ reaching the muon chambers. The J/ψ and Υ acceptances are shown as a function of p_{T} in Fig. 6.1, for two η ranges: full detector and central barrel. Because of its relatively low mass, low energy J/ψ's ($p_{\mathrm{T}} \lesssim 4\,\mathrm{GeV/c}$) cannot be detected since their decay muons don't have enough energy to traverse the calorimeters and they are absorbed due to ionisation losses before reaching the muon chambers. For larger p_{T} values the J/ψ acceptance increases and flattens out at ∼15% for p_{T} 12GeV/c. The Υ acceptance starts at ∼40% at $p_{\mathrm{T}} = 0\,\mathrm{GeV/c}$ and remains constant at 15% (full CMS) or 5% (barrel) for $p_{\mathrm{T}} > 4\,\mathrm{GeV/c}$. The p_{T}-integrated acceptance is about 1.% for the J/ψ and 21% for the Υ as obtained from our input theoretical distribution.

6.1.2.2. Dimuon reconstruction efficiency, purity and mass resolution. The dimuon reconstruction algorithm used in the heavy-ion analysis is a version of the regional track finder based on the muons seeded by the muon stations and on the knowledge of the primary vertex, as described in [172, 173]. It is adapted to deal with the high hit occupancy of the silicon tracker in PbPb collisions. It uses the muon tracks found in the innermost muon stations to identify hits in the outer CMS tracker layer that can form the starting points (seeds) for the matching muon candidate tracks. The propagation in the tracker is performed from the outer

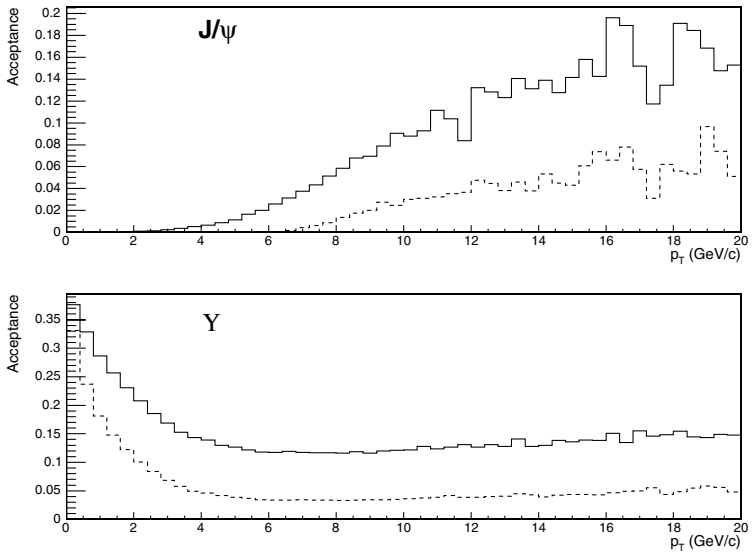

Figure 6.1. J/ψ (top) and Υ (bottom) acceptances as a function of p_{T}, in the full detector (barrel and endcap, $|\eta| < 2.4$, full line) and in the barrel alone ($|\eta| < 0.8$, dashed line).

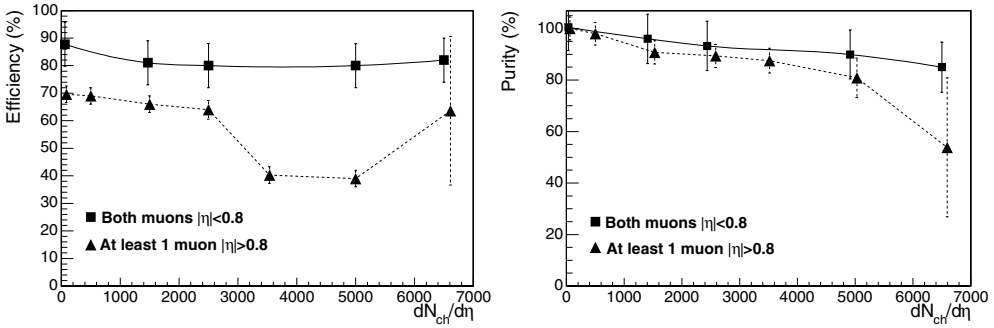

Figure 6.2. Υ reconstruction efficiency (left) and purity (right) as a function of the PbPb charged particle rapidity density, $dN_{ch}/d\eta|_{\eta=0}$.

layer towards the primary vertex, using two-dimensional parametrisation in the transverse and longitudinal planes. The final fit of trajectories is performed with a Kalman-fitter. The efficiency of a given muon pair is: $\varepsilon_{pair}(p,\eta) = \varepsilon_{track_1} \times \varepsilon_{track_2} \times \varepsilon_{vertex}$. The dependence of the Υ reconstruction efficiency on the event multiplicity was obtained from a full GEANT simulation using Υ signal dimuon embedded in HIJING PbPb events. Figure 6.2 shows the Υ efficiency and purity (where purity is defined as the ratio of true Υ reconstructed over all Υ reconstructed) as a function of charged-particle multiplicity. In the central barrel, the dimuon reconstruction efficiency is above $\sim$ 80% for all multiplicities, whereas the purity decreases slightly with $dN_{ch}/d\eta$ but stays also above 80% even at multiplicities as high as $dN_{ch}/d\eta|_{\eta=0}$ = 6500. If (at least) one of the muons is detected in the endcaps, the efficiency and purity drop due to stronger reconstruction cuts. Nonetheless, for the maximum $dN_{ch}/d\eta|_{\eta=0} \approx 2500$ multiplicities expected in central PbPb at LHC, the efficiency (purity) remains above 65% (90%) even including the endcaps.

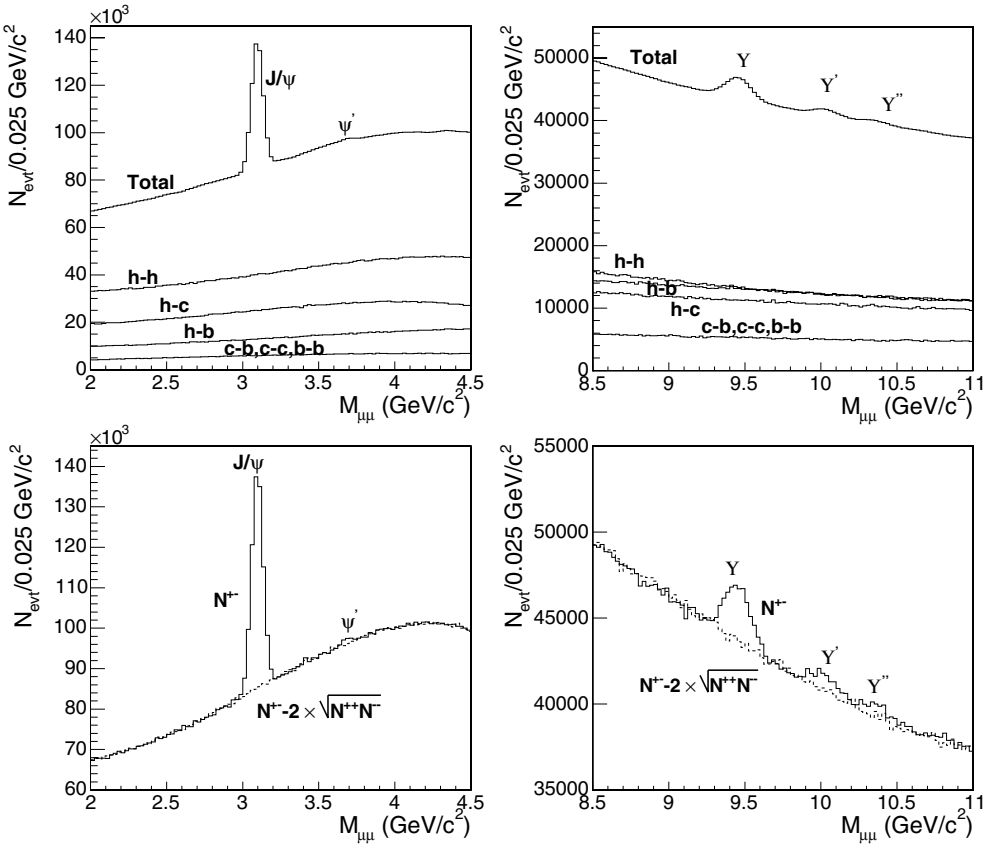

Figure 6.3. Dimuon mass distributions measured within $|\eta| < 2.4$ for PbPb events with $dN_{ch}/d\eta|_{\eta=0} = 5000$ in the J/ψ (left) and Υ (right) mass regions. The main contributions of the background are shown in the top panels (h, c, b stand for $\pi + K$, charm, bottom decay muons resp.), while the bottom panels also show the like-sign pairs (combinatorial background).

If we only consider muon pairs in the central barrel, $|\eta| < 0.8$, the dimuon mass resolution is $\sim$54 MeV/c^2 at the Υ mass, as obtained from a Gaussian fit of the reconstructed $\mu\mu\, m_{\rm inv}$ distribution (using a detailed MC simulation but without background). In the full pseudorapidity range, the dimuon mass resolution amounts to $\sim$1%: 35 MeV/c^2 at the J/ψ mass, and 86 MeV/c^2 at the Υ mass. These dimuon mass resolutions (the best among the LHC experiments) allow for a clean separation of the different quarkonia states. These values are used to smear the dimuon mass distribution in the fast MC studies.

6.1.3. Results

About 5×10^7 PbPb collisions were simulated. Muons passing the acceptance tables are combined to form pairs and each pair is weighted according to the trigger and reconstruction efficiencies (dependent on the momentum, η, purity and event multiplicity). Their invariant mass is calculated and smeared as described in the previous section. The obtained dimuon mass distributions are then scaled to 0.5 nb^{-1}, corresponding to the PbPb luminosity integrated in one month with average luminosity $L = 0.4 \cdot 10^{27}$ cm^{-2} s^{-1} and 50% machine operation efficiency. Figure 6.3 shows the resulting opposite-sign mass distributions, for

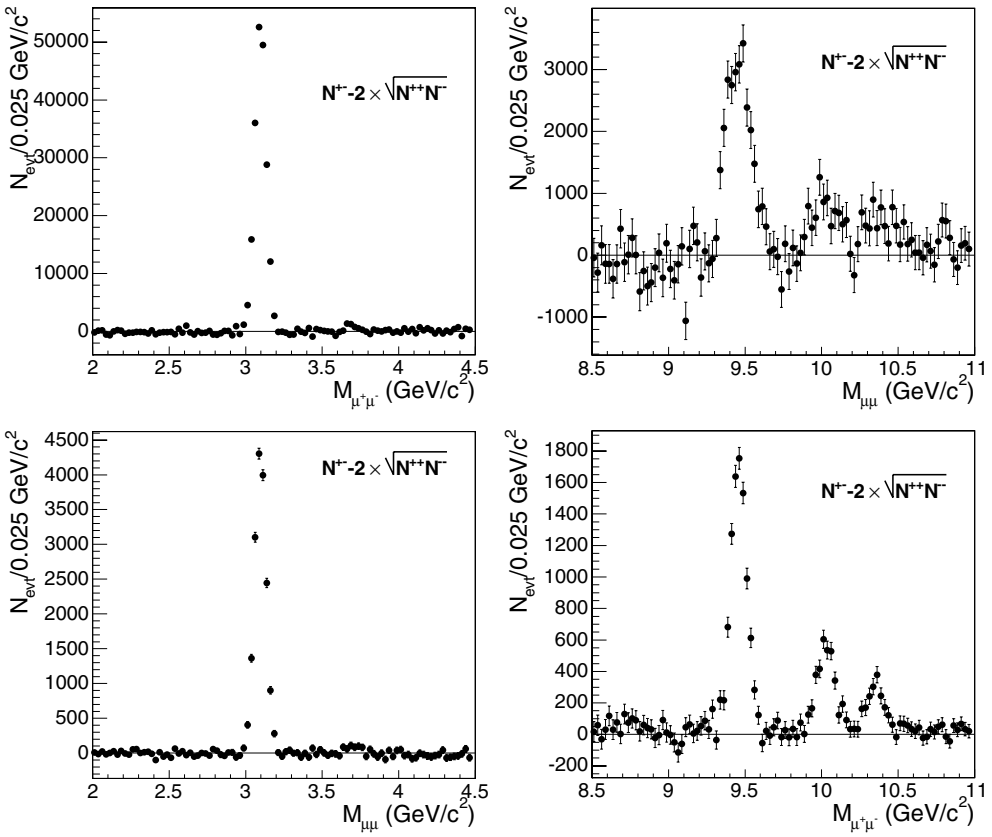

Figure 6.4. Signal dimuon mass distributions after background subtraction in the J/ψ (left) and Υ (right) mass regions expected after one month of PbPb running. Top panels for $dN_{ch}/d\eta|_{\eta=0} = 5000$ and $|\eta| < 2.4$ ("worst" case conditions); bottom panels for $dN_{ch}/d\eta|_{\eta=0} = 2500$ and $|\eta| < 0.8$ ("best" measurement conditions).

the *high* multiplicity case, $dN_{ch}/d\eta|_{\eta=0} = 5000$ and full acceptance ($\eta < 2.4$). The different quarkonia resonances appear on top of a continuum due to several combinatorial background sources, the main ones being identified in the upper plots (h, c and b stand for $\pi + K$, charm and bottom decay muons, respectively). Since the CMS trigger and acceptance conditions treat opposite-sign and like-sign muon pairs in the same way, the uncorrelated background can be subtracted using the like-sign pairs: $N^{\mathrm{Sig}} = N^{+-} - 2\sqrt{N^{++}\,N^{--}}$, shown also in the bottom panels of Fig. 6.3.

Figure 6.4 shows the *signal* dimuon mass distributions, after background subtraction, for two different scenarios: $dN_{ch}/d\eta|_{\eta=0} = 5000$, $|\eta| < 2.4$ ("worst" case conditions); and $dN_{ch}/d\eta|_{\eta=0} = 2500$, $|\eta| < 0.8$ ("best" case). Except for the ψ', all quarkonia states are clearly visible. The corresponding signal-to-background ratios and yields (counted within 1σ of the resonance peaks) are collected in the Table 6.1 for one month of PbPb running.

6.1.4. Conclusions

With its very broad muon acceptance and precise tracking, CMS will provide significant contributions to heavy ion physics at the LHC. Studies of quarkonium production in PbPb

Table 6.1. Signal-to-background ratios and expected quarkonia yields in one month of PbPb running (0.5 nb $^{-1}$ integrated luminosity) for two multiplicity scenarios and two η windows.

$dN_{ch}/d\eta\|_{\eta=0}$, $\Delta\eta$	S/B	N(J/ψ)	S/B	N(Υ)	N(Υ')	N(Υ'')
2500, $\|\eta\| < 2.4$	1.2	180 000	0.12	25 000	7300	4400
2500, $\|\eta\| < 0.8$	4.5	11 600	0.97	6400		
5000, $\|\eta\| < 2.4$	0.6	140 000	0.07	20/000	5900	3500
5000, $\|\eta\| < 0.8$	2.75	12 600	0.52	6000		

collisions at $\sqrt{s_{NN}} = 5.5$ TeV, will provide crucial information on the thermodynamical state of QCD medium formed in these collisions, through the expected step-wise "melting" pattern of the different $Q\overline{Q}$ states due to colour screening. These results will also be sensitive to modifications of the low-x nuclear parton distribution functions, as expected in case of gluon saturation.

CMS can reconstruct the charmonium and bottomonium resonances, via their dimuon decay channel, with high efficiencies (∼80%), good purity (∼90%) and a very good dimuon mass resolution (54 MeV/c^2 at the Υ mass), when both muons are detected in the central barrel ($|\eta| < 0.8$), even in the case of exceptionally high multiplicities ($dN_{ch}/d\eta|_{\eta=0} \approx 5000$). When considering the full pseudorapidity region ($|\eta| < 2.4$), the mass resolution becomes ∼86 MeV/c^2 at the Υ, and 35 MeV/c^2 at the J/ψ, with ∼ 50% dimuon reconstruction efficiencies. The Υ states can be measured all the way down to $p_{\mathrm{T}} = 0$ GeV/c with acceptances as large as 40%, while the lower rest mass of the J/ψ state and the large amount of material in the calorimeters absorbs "low" energy decay muons and prevents from measuring J/ψ's below $p_{\mathrm{T}} \approx 4$ GeV/c. At high p_{T} (above ∼12 GeV/c for the J/ψ and ∼4 GeV/c for the Υ) the dimuon acceptance flattens out at 15%.

The large aperture of the muon detectors and the precise tracking result in a very good separation between the $Q\overline{Q}$ states in the dimuon mass distributions, and in relatively high statistics and good signal to background ratios ($S/B \approx 1(5)$, $S/B \approx 0.1(1)$ for J/ψ and Υ resp. in the full (central) rapidity range). After one month of PbPb running (0.5 nb^{-1}) we should collect ∼180 000 J/ψ and ∼25 000Υ dimuon, enough to compare central and peripheral PbPb collisions, and to carry out some differential studies (dN/dy, dN/dp_{T}) which will surely contribute significantly to clarify the physics mechanisms behind the production (and "destruction") of quarkonia states in nucleus-nucleus collisions at the LHC.

Part II. CMS Physics Reach

Chapter 7. Physics of Strong Interactions

7.1. QCD and jet physics

7.1.1. Introduction

With the start-up of LHC, a new domain of energy will be explored and an extrapolation of our current knowledge in the form of the Standard Model may not be sufficient to describe the new measurements. Even in a first data-taking phase with a rather low luminosity, studies of jet physics in the framework of quantum chromodynamics (QCD) will allow to check our current theory against the new data.

Figure 7.1 presents the decomposition of the total jet cross section into the partonic processes for $p\bar{p}$ collisions at the Tevatron and pp collisions at the LHC in dependence of the scaling variable $x_T = 2p_T/\sqrt{s}$, and illustrates the differences in cross section contributions of the PDFs compared to measurements possible today. In Fig. 7.2 the expected statistical uncertainties on differential cross sections for all rapidities are presented for a pilot run with $0.1\,\text{fb}^{-1}$ and for a first physics run with $10\,\text{fb}^{-1}$. Trigger pre-scales are taken into account. The figure demonstrates that already in the pilot run high statistics will be available up to 1.5 TeV of transverse jet energy.

On the one hand, the measured data have to be corrected for detector effects using fully simulated events. Also, an energy calibration has to be performed on the reconstructed jets which ideally is extracted from data as well, but can also be done employing Monte-Carlo methods. On the other hand, for the theory predictions, which are most precise with respect to the hard parton-parton scattering amplitudes, effects of soft physics modelled in the form of parton showers and hadronisation models with subsequent decays have to be taken into account. Once this is done, parameters of the current theory can be cross-checked or improved in precision by comparing the measured hadronic final state with the corrected theoretical predictions.

7.1.2. Jet algorithms

In order to re-establish a link between the observed particles that appear as collimated streams of hadrons in the detector and the hard process, algorithms are defined to group particles that are supposed to come from the same hard parton into jets. The required ingredients of such a jet algorithm are a distance measure to define the separation between objects, a procedure how to decide when objects are to be combined and a recombination scheme explaining how to combine objects. In addition, it has to be specified how the list of input objects has been determined.

Two principal types of algorithms are in common use: Cone type algorithms [174] that traditionally have been employed in hadron-hadron collisions where objects are clustered together that are close in angle around a high-energetic seed, and clustering algorithms where iteratively objects are combined that have the smallest distance of all pairwise combinations possible. The latter have predominantly been used in e^+e^- and $e^\pm p$ collisions, first in the form of the Jade algorithm [175, 176] and nowadays as k_T algorithm [177].

Both algorithms applied in this study use an angular distance measure based on the azimuthal angle Φ and, instead of the pseudo-rapidity η, the true rapidity $y = 0.5\ \ln((E + p_z)/(E - p_z))$ which has become an established standard in recent publications

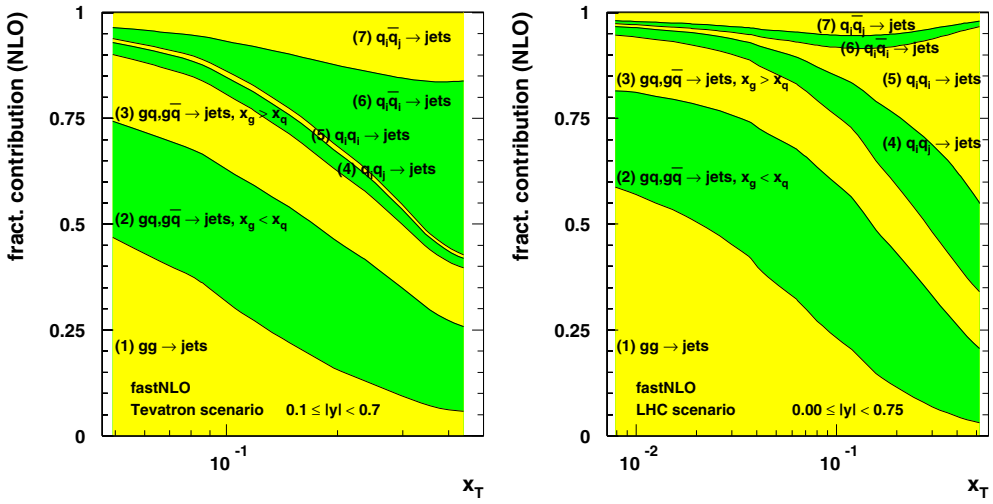

Figure 7.1. Decomposition of the total jet cross section into the partonic processes for $p\bar{p}$ collisions at the Tevatron (left) and pp collisions at the LHC (right). The fractional contributions are shown versus the scaling variable $x_T = 2p_T/\sqrt{s}$.

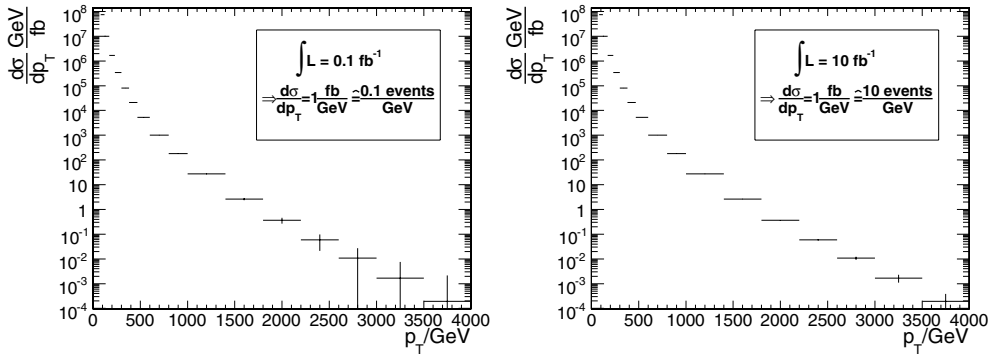

Figure 7.2. Expected statistical uncertainties on differential cross sections for all rapidities; left: for a pilot run with 0.1 fb^{-1}, and right: for a physics run with 10 fb^{-1}. The central cross section values are taken from a leading-order calculation in dependence of the transverse momenta of the hard interaction.

[178, 179]. The distance between two objects i and j hence reads

$$\Delta R_{ij} = \sqrt{(\Delta_{ij}\Phi)^2 + (\Delta_{ij}y)^2}. \tag{7.1}$$

In addition, the most frequently used recombination scheme, the E scheme, implying a simple four-momentum addition, is employed in both cases.

Two types of jet algorithms are used here. The main results have been achieved with the k_T algorithm defined below, some cross checks have been performed with the midpoint

cone algorithm:

1. Iterative clustering-type: Inclusive k_T algorithm [180] with
   - Distances are evaluated according to the ΔR scheme, i.e. $d_{ij} = \min(p_{T,i}^2, p_{T,j}^2)\frac{\Delta R_{ij}^2}{D^2}$ with R_{ij} as in Eq. 7.1
   - Jet resolution parameter $D = 1.0$
2. Cone-type: Midpoint cone algorithm [181, 182] with:
   - Cone radius $R = 0.7$, all objects within a cone have to fulfill $R_{ic} \leqslant R$ with c labelling the four-vector of the current cone.
   - Overlap threshold $f_{\text{merge}} = 0.50$, i.e. overlapping cone jets are merged when they share more than 50% of the energy in the less energetic cone
   - Search-cone radius fraction $f_{\text{search}} = 0.5$, i.e. the first step to find the stable cones (before any splitting/merging is done) is performed with a smaller radius of f_{search}^{*R}

Concerning the k_T algorithm, a jet resolution parameter of $D = 1.0$ is, from a theoretical point of view, best comparable to a cone algorithm with $R = 0.7$. In order to reduce the sensitivity to the underlying event, it is advantageous to reduce the jet resolution parameter D or the cone radius R, respectively.

Note that primarily due to the limited choice of available jet energy calibrations the definition of the midpoint algorithm above has been selected. It does not exactly correspond to the definition given in [181] but to a modified one [182] that is in use by the CDF collaboration [178]. There have been indications that this algorithm leads to an infrared sensitive behaviour [183], so it is recommended to use the original definition of the midpoint algorithm without extra search cone radius.

7.1.3. Trigger scheme, event selection and phase space

The level one (L1) and the high level triggers (HLT) required for this analysis are the single-jet triggers which are described in more detail in Section E.4.3.2. QCD jet production has, by several orders of magnitude, the largest cross section, but in contrast to most other analyses QCD jet events are the signal here. Therefore, the sole other selection requirement for this study demands all jets to have a transverse momentum larger than 50 GeV. The available phase space is then subdivided into 17 ranges in transverse momentum p_T and five ranges in rapidity y, where the focus is mostly on the central region up to 2.5 in rapidity.

7.1.4. Input data

The analysed events were generated with PYTHIA [184] and subsequently subjected to the full GEANT-4 based CMS detector simulation and reconstruction programs. Following the analysis setup presented in the Introduction 7.1.1, four classes of input objects to the jet algorithms have been considered: The initial partons of the hard interaction, partons after parton shower (partonic final state, PFS), all stable particles of the hadronic final state (HFS) other than muons or neutrinos and calorimeter towers. The calorimeter towers fulfilling the requirements $E > 0.8$ GeV and $E_T > 0.5$ GeV were subjected to the same jet algorithms as the generator particles. If necessary, a matching of generator and calorimeter jets was performed by looking for the pairs closest to each other in distance $d = \sqrt{(\Delta\Phi)^2 + (\Delta\eta)^2}$.

7.1.5. Jet energy calibration

The jet energy calibration has been performed with a MC calibration method implying calibration factors that are applied on a jet by jet basis to the calorimeter jets depending on pseudo-rapidity η and transverse momentum p_T. The alternative data based technique of gamma-jet calibration, where jet transverse energies are measured against recoiling high energetic photons could not yet be employed for this study.

7.1.6. NLO calculation

In order to compare to theoretical predictions of perturbative QCD, calculations of at least next-to-leading order (NLO) precision are required. Here, the program CLOSET++ [185] is employed for the NLO calculation. However, since precise computations in NLO are very time consuming, a more efficient set-up in the form of the fastNLO project [186] is used which allows the fast rederivation of the considered cross section for arbitrary input PDFs and α_S values. This is done by separating the PDF dependency from the hard matrix element calculation by interpolating the PDFs between fixed support points in fractional proton momentum x so that the PDF dependency can be evaluated a posteriori from one complete calculation.

Note that neither PYTHIA nor CLOSET++ contain electroweak corrections which may change high p_T cross sections from 1 TeV onwards by up to 30% [187]. Insofar this study is consistent, but before comparing to real data this has to be taken into account.

7.1.7. Experimental and theoretical uncertainties

From the experience at the Tevatron [178, 188, 189], it is known that the jet energy scale with an uncertainty of 3% represents by far the dominant source of uncertainty for high p_T jet cross sections. Similarly, PDF uncertainties lead to the dominant uncertainty of the jet cross sections from the theoretical side.

According to CMS studies the jet energy scale in this analysis has been varied by $\pm 3\%$ in order to estimate the impact on the cross section determination. Figure 7.3 presents on the left hand side the corresponding relative experimental uncertainty on the jet cross section for three regions in rapidity. Starting at about 15% at low p_T it rises up to about 50% at high p_T for central rapidity. In the two non-central rapidity regions the uncertainties are of comparable size below about 1 TeV of transverse momentum, but get considerably larger for higher p_T. In general, a similar behaviour as expected from Tevatron results is observed.

By evaluating the cross section calculation for the error set of the CTEQ6M [12] PDFs the ensuing theoretical uncertainty as shown in fig. 7.3 on the right hand side could be derived. It is of the same order of magnitude as the energy scale uncertainty and rises from about 5% for low transverse momenta with a minimum of 3% at $\approx$ 200 GeV up to $+65\%$ and -30% at the highest transverse momenta for central rapidity.

7.1.8. Summary and outlook

The dominant experimental and theoretical uncertainties on the differential inclusive cross sections of jets with high transverse momentum ranging from 80 GeV up to 4000 GeV have been investigated. A variation of $\pm 3\%$ in the jet energy scale results in an uncertainty of the derived jet cross sections of 15% at low transverse momenta, increasing up to about 50% at the highest p_T for central rapidity. The theoretical uncertainty due to the parton density functions of the proton has been found to be of the same order of magnitude and rises from

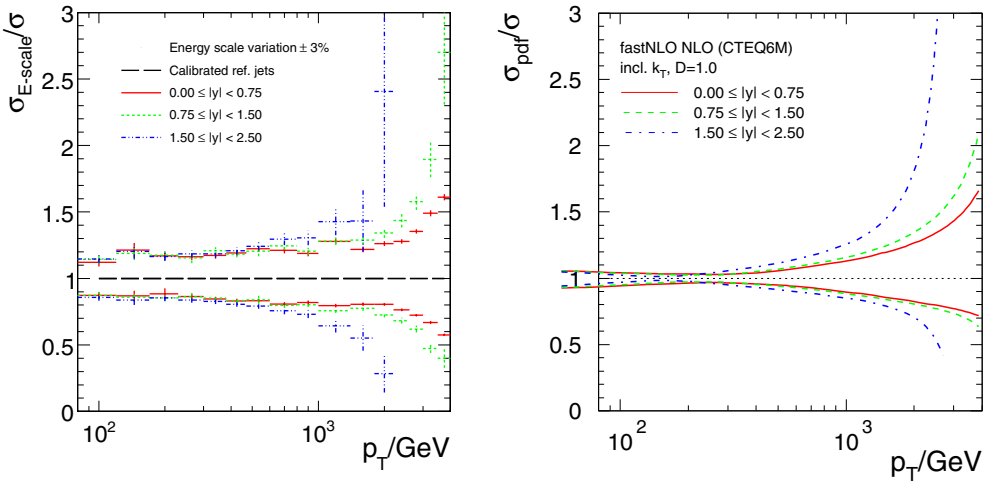

Figure 7.3. Relative systematic uncertainties of the jet cross sections for the k_T algorithm versus p_T due to a change in energy scale of $\pm 3\%$ for three bins in rapidity (left). The error bars represent the statistical uncertainty. On the right hand side, the relative uncertainties due to an evaluation of the error sets of the CTEQ6M [12] PDFs are shown for the same regions in rapidity.

about 5% for low transverse momenta with a minimum of 3% at $\approx 200\,\text{GeV}$ up to $+65\%$ and -30% at the highest transverse momenta. For higher rapidities both uncertainties are considerably larger. The results shown have been derived with the k_T jet algorithm, similar values were obtained with the midpoint cone algorithm.

For transverse momenta below about 500 GeV further sources of uncertainties may give significant contributions to the total uncertainty, e.g. corrections due to pile-up, the underlying event and multiple interactions or hadronisation. Theoretical contributions due to scale variations are of the order of 5% (10% for transverse momenta larger than 3 GeV) for rapidities y below 1.5. Above a rapidity of 1.5 they might be larger especially at the edge of the phase space. In addition, contributions due to α_S and electroweak corrections have to be included before comparing to real data.

In the future, it will be possible to run simultaneous fits of α_S and the parton density functions, especially the gluon density at high x, to the data. To be less sensitive to the jet energy scale other jet related quantities, e.g. jet rates, will be considered. By including other processes into the fit procedure, like W/Z production as a luminosity measure or Drell–Yan reactions to fix the low x gluon density, powerful combined PDF fits to the data of one experiment will become possible.

7.2. Underlying event studies

7.2.1. Definition of the physics process and status of the art

The “Underlying Event” (UE) in a hard scattering process is everything accompanying an event but the hard scattering component of the collision. A CDF analysis [190, 191] showed that the density of particles in the UE of jet events is about a factor of two larger than the density of particles in a typical Minimum Bias (MB) collision. At the LHC the difference might be even larger.

Hard scattering collider events have a distinct topology and one can use the topological structure of the collision to define regions of the $\eta - \phi$ space that are sensitive to the UE components of the interaction. By comparing different processes such as high transverse momentum jets, "back-to-back" dijet production, or Drell–Yan, one can partially isolate the various components contributing to the UE.

Multiple parton interaction (MPI) models [192], extending the QCD perturbative picture to the soft regime, turn out to be particularly adequate to describe the physics of the UE. In the framework of these models one can regard the observed differences between the UE in a hard scattering process and a MB collision as the effect of the increased probability of partonic interactions for small impact parameter hadron-hadron collisions: one hard scattering implies a small impact parameter collision which makes it more likely that an additional parton-parton interaction will occur. Also, a hard scattering promotes initial and final state gluon radiation which inevitably contributes to the UE.

Examples of MPI models are implemented in the general purpose simulation programs PYTHIA [69], JIMMY [193], and SHERPA [194]. Other successful descriptions of UE and MB at hadron colliders are achieved by alternative approaches like PHOJET [195], which rely on both perturbative QCD and the Dual Parton Models (DPM). The purely phenomenological description available in HERWIG [196] provides a very useful reference of a model not implementing multiple interactions.

The QCD models considered in this study are different settings, called tunes, of relevant parameters in HERWIG and PYTHIA 6.2. One of the PYTHIA tunes is the ATLAS tune [197] and the other (PY Tunes DW) is a tune by R. Field which is similar to PYTHIA Tune A [198]. All these tunes use the CTEQ5L parton distribution functions. Details of the settings are given in reference [199].

Both Tune A and Tune DW fit the CDF Run 1 and Run 2 UE data [190, 191]. Tune DW also fits the CDF Run 1 Z-boson transverse momentum distribution [200]. Both Tune A and Tune DW use the same multiple parton interaction energy dependence parameter PARP(90) $= 0.25$, while the ATLAS tune uses the default value of 0.16.

The analyses summarised in this section are described in detail in reference [199].

7.2.2. Underlying event observables discussed for charged jet events

Charged jets are constructed from the charged particles using a simple clustering algorithm and then the direction of the leading charged particle jet is used to isolate regions of $\eta - \phi$ space that are sensitive to the UE. As illustrated in Fig. 7.4, the direction of the leading charged particle jet, chgjet1, is used to define correlations in the azimuthal angle, $\Delta\phi$. The angle $\Delta\phi = \phi - \phi_{\text{chgjet1}}$ is the relative azimuthal angle between a charged particle and the direction of chgjet1. The "transverse" region is almost perpendicular to the plane of the hard 2-to-2 scattering and is therefore very sensitive to the UE. We restrict ourselves to charged particles in the central region $|\eta| < 1$ and consider two p_{T} thresholds, the nominal CMS cut $p_{\mathrm{T}} > 0.9\,\mathrm{GeV/c}$ and a lower threshold with $p_{\mathrm{T}} > 0.5\,\mathrm{GeV/c}$.

Figure 7.5 shows the QCD Monte Carlo models predictions for the average density of charged particles, $dN_{chg}/d\eta d\phi$, and the average charged PT_{sum} density, $dPT_{sum}/d\eta d\phi$, respectively, in the "transverse" region for $|\eta| < 1$ with $p_{\mathrm{T}} > 0.5\,\mathrm{GeV/c}$ and $p_{\mathrm{T}} > 0.9\,\mathrm{GeV/c}$ versus the transverse momentum of the leading charged particle jet. The charged particle density is constructed by dividing the average number of charged particles per event by the area in $\eta - \phi$ space (in this case $4\pi/3$). The charged PT_{sum} density is the average *scalar* p_{T} sum of charged particles per event divided by the area in $\eta - \phi$ space.

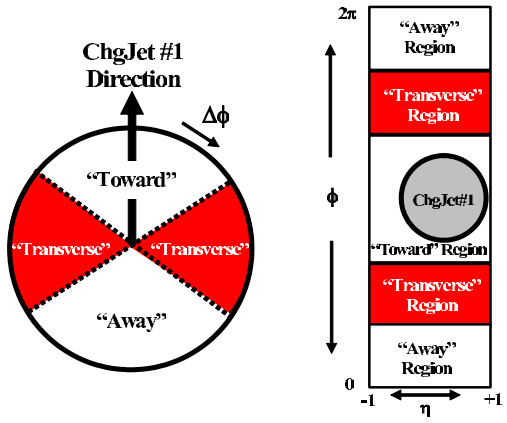

Figure 7.4. Illustration of correlations in azimuthal angle ϕ relative to the direction of the leading charged particle jet ($R = 0.7$) in the event, chgjet1. The angle $\Delta\phi = \phi - \phi_{\text{chgjet1}}$ is the relative azimuthal angle between charged particles and the direction of chgjet1. The "transverse" region is defined by $60^\circ < |\Delta\phi| < 120^\circ$ and $|\eta| < 1$. We examine charged particles in the range $|\eta| < 1$ with $p_{\text{T}} > 0.5\,\text{GeV/c}$ or $p_{\text{T}} > 0.9\,\text{GeV/c}$.

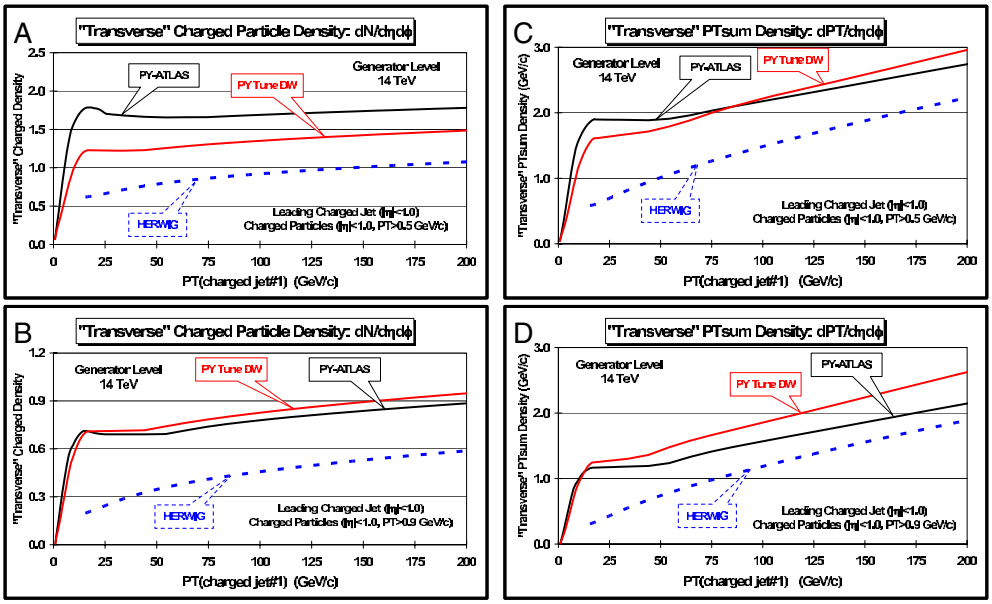

Figure 7.5. QCD Monte Carlo models predictions for charged particle jet production at 14 TeV. Left: Average density of charged particles, $dN_{chg}/d\eta d\phi$, with $|\eta| < 1$ in the "transverse" region versus the transverse momentum of the leading charged particle jet for $p_{\text{T}} > 0.5\,\text{GeV/c}$ (A) and $p_{\text{T}} > 0.9\,\text{GeV/c}$ (B). Right: Average charged PT_{sum} density, $dPT_{sum}/d\eta d\phi$, with $|\eta| < 1$ in the "transverse" region versus the transverse momentum of the leading charged particle jet for $p_{\text{T}} > 0.5\,\text{GeV/c}$ (C) and $p_{\text{T}} > 0.9\,\text{GeV/c}$ (D). The QCD models are HERWIG and two PYTHIA6.2 tunes described in the text.

Due to the multiple parton interactions the PYTHIA tunes rise rapidly and then reach an approximately flat "plateau" region. At very high P_T (chgjet1) they begin to rise again due to initial and final state radiation which increases as the Q^2 scale of the hard scattering increases. HERWIG has considerably fewer particles in the "transverse" region and predicts a steady rise resulting from initial and final state radiation. The ATLAS tune predicts a larger charged particle density than PYTHIA Tune DW for $p_T > 0.5\,\mathrm{GeV/c}$. However, the ATLAS tune and Tune DW have similar charged particle densities for $p_T > 0.9\,\mathrm{GeV/c}$. This is because the ATLAS tune has a "softer" charged particle p_T distribution than Tune DW.

7.2.3. Feasibility studies

Here we concentrate on the UE measurement that will be performed in nominal CMS conditions at low luminosity [199]. All the studies presented in this section have been obtained applying the GEANT-4 based simulation and reconstruction chain of the CMS experiment.

Events corresponding to Drell–Yan dimuon pairs and leading QCD processes with superimposed low luminosity pile-up have been generated with PYTHIA 6.2 in different $\hat{p}_T$ regions. The relevant PYTHIA 6.2 parameters adopted by CMS in simulation production are documented in [201]. The triggers used to collect Jet and Drell–Yan samples are described in reference [76].

Charged track reconstruction uses the Combinatorial Track Finder [202]. The default algorithm allows to reconstruct tracks with p_T above 0.9 GeV/c. However, the same algorithm can be used in special conditions (with reduced thresholds for the seeds) achieving reasonable performances down to 0.5 GeV/c [199]. For $\eta| < 1$, a reconstruction efficiency better than 90% and a fake rate below 1% are quoted for charged tracks with p_T above 0.7 GeV/c.

7.2.3.1. The underlying event as observed in charged jet events. The track-based measurement for the scale of the leading interaction allows to keep an acceptable resolution for jet energies below 20 GeV, where the calorimetric measurement is dominated by large systematic uncertainties.

In principle MB could be studied from any data selection, getting rid of the leading pp interaction and performing the reconstruction of all the primary vertices from all the other piled-up pp interactions. However, this methodology turns out to be challenging as the resolution on the position of the pp vertices degrades when lowering the total p_T of the associated charged tracks. In this study an MB trigger is defined requiring at least a calorimetric jet of $p_T > 20\,\mathrm{GeV/c}$. In order to combine the measurements performed at different leading charged jet scales, on top of the MB trigger, two additional triggers based on the p_T of the leading high level trigger jet are adopted: $p_T > 60\,\mathrm{GeV/c}$ and $p_T > 120\,\mathrm{GeV/c}$, which will be referred to as JET60 and JET120. Jets are reconstructed with an iterative cone algorithm of radius 0.5 in the pseudorapidity-azimuth space.

Tracks arising from the piled-up interactions are suppressed requiring the extrapolated coordinate along the beam axis to be inside 1 mm with respect to the primary vertex associated to the leading charged jet. The selection of the pp interaction with the highest p_T charged jet tends to create a small bias on the MB sample, reducing the statistics available at very low P_T (chgjet1).

The definition of the main UE observables have been introduced in Section 7.2.2. The density of charged particles, $dN_{chg}/d\eta d\phi$, and the charged PT_{sum} density, $dPT_{sum}/d\eta d\phi$, with $p_T > 0.9\,\mathrm{GeV/c}$ and $|\eta| < 1$ in the "transverse" region are reported in Fig. 7.6. Bins of $2\,\mathrm{GeV/c}$ are used up to P_T (chgjet1) $= 20\,\mathrm{GeV/c}$ and bins of $10\,\mathrm{GeV/c}$ above.

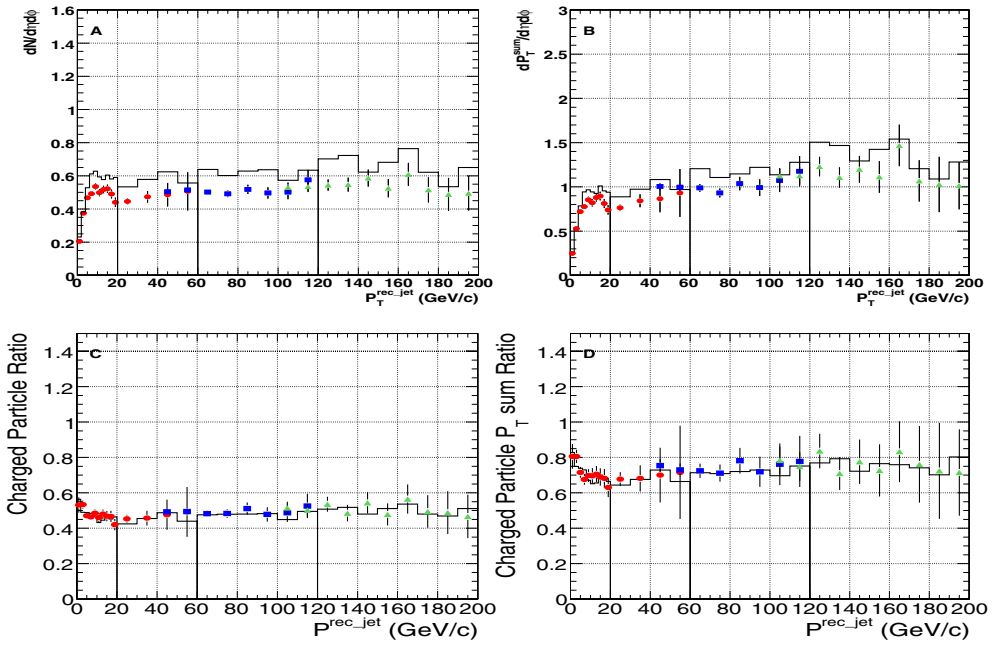

Figure 7.6. Charged jet production at 14 TeV. Charged tracks with $|\eta| < 1$ in the "transverse" region. Density of charged particles, $dN_{chg}/d\eta d\phi(A)$ and PT_{sum} density, $dPT_{sum}/d\eta d\phi(B)$, with $p_{\mathrm{T}} > 0.9\,\mathrm{GeV/c}$ versus the transverse momentum of the leading charged particle jet. Ratio between density of charged particles with $p_{\mathrm{T}} > 0.9\,\mathrm{GeV/c}$ and $p_{\mathrm{T}} > 0.5\,\mathrm{GeV/c}(C)$ and ratio between PT_{sum} density with $p_{\mathrm{T}} > 0.9\,\mathrm{GeV/c}$ and $p_{\mathrm{T}} > 0.5\,\mathrm{GeV/c}(D)$ versus the transverse momentum of the leading charged particle jet. Data from different triggers are superimposed: (circles) = MinimumBias; (squares) = JET60; (triangles) = JET120. The lines show the generator level distributions; the points with error bars correspond to the raw (uncorrected) reconstruction level distributions.

The shapes of uncorrected reconstruction level distributions basically agree with the corresponding generator level ones. The difference in absolute scale (about -20% for both $dN_{chg}/d\eta d\phi$ and $dPT_{sum}/d\eta d\phi$) turns out to be compatible with charged track inefficiencies and fake rates. Further details on these systematic effects, including the calibration and resolution of the leading charged jet have been studied in [199].

Figure 7.6 shows also the ratio between the observables for $p_{\mathrm{T}} > 0.9\,\mathrm{GeV/c}$ and $p_{\mathrm{T}} > 0.5\,\mathrm{GeV/c}$ in the "transverse" region. These ratios, which are sensitive to the differences between the models and/or to the choice of the tuning for a given model, are also nicely free from the systematic effects enumerated above, and basically do not need to be corrected when comparing to the corresponding generator level observables.

7.2.3.2. The underlying event as observed in Drell–Yan muon-pair production. Drell–Yan muon pair production provides an excellent way to study the UE. Here one studies the outgoing charged particles (excluding the $\mu^+\mu^-$ pair) as a function of the muon-pair invariant mass. After removing the muon-pair everything else is the UE. As for the charged jet production, we restrict ourselves to charged particles in the central region $|\eta| < 1$ and consider the two p_{T} thresholds $p_{\mathrm{T}} > 0.5\,\mathrm{GeV/c}$ and $p_{\mathrm{T}} > 0.9\,\mathrm{GeV/c}$.

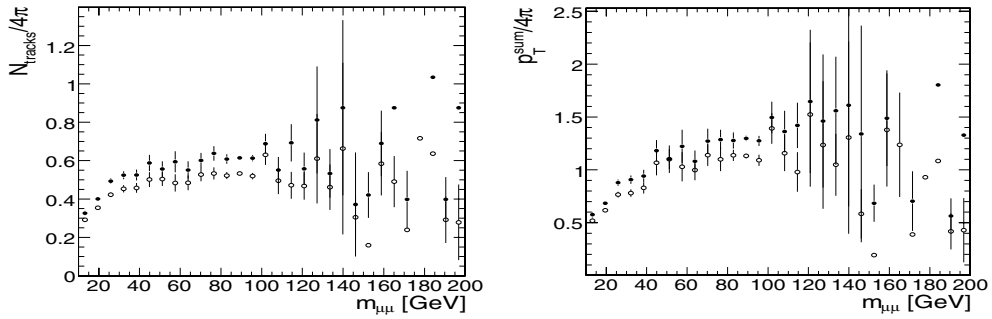

Figure 7.7. Muon-pair production at 14 TeV with two isolated muons. Density of charged particles, $dN_{chg}/d\eta d\phi(left)$, PT_{sum} density, $dPT_{sum}/d\eta d\phi(right)$, with $p_T > 0.9\,\mathrm{GeV/c}$ and $|\eta| < 1$ versus the muon-pair invariant mass. (fullcircles) correspond to the generator level distributions; (empty circles) correspond to the raw (uncorrected) reconstruction level distributions.

Single muon and muon-pair CMS triggers ensure very high efficiencies for the studied process. The relative mass shift and the corresponding resolution of the reconstructed muon-pair are studied in detail in Ref. [199]. Tracks arising from the piled-up interactions are suppressed requiring the extrapolated coordinate along the beam axis to be inside 1 mm with respect to the primary vertex associated to the leading muons.

In our study, we require "isolated muons", not to have charged tracks with $p_T > 0.9\,\mathrm{GeV/c}$ in a cone of radius $R = \sqrt{(\Delta\phi)^2 + (\Delta\eta)^2} = 0.3$ in the azimuth-pseudorapidity space centred along the direction of the muon. Selecting isolated muons turns out to be essential to reduce the QCD background to negligible levels for $p_T > 15\,\mathrm{GeV/c}$, while keeping an efficiency of 76.9% for Drell–Yan muon-pairs in the same p_T region.

The charge particle density, $dN_{chg}/d\eta d\phi$, and the charged PT_{sum} density, $dPT_{sum}/d\eta d\phi$ with $p_T > 0.9\,\mathrm{GeV/c}$ and $|\eta| < 1$ in muon-pair production with isolated muons versus the muon-pair invariant mass are shown in Fig. 7.7. Correlations between isolation and UE activity have been studied in Refs. [64, 199].

7.2.4. Conclusions

Predictions on the amount of activity in UE at the LHC based on extrapolations from the lower energy data differ greatly. In this study we have demonstrated the feasibility of reference UE measurements at CMS under nominal conditions, assessing our capability to distinguish between the predictions of different models. The UE is studied by examining charged particles in the "transverse" region in charged particle jet production and in the central region of Drell–Yan muon-pair production (after removing the muon-pair).

7.3. Physics of b-quarks and hadrons

7.3.1. Inclusive b-quark production

7.3.1.1. Introduction. At the LHC new opportunities to improve our understanding of the physics of *b* quarks will become available because of the high statistics data samples and the high centre-of-mass energy. A study [203] has been performed to investigate methods in CMS of identifying *b* jets (*b* "tagging") in an inclusive sample of events containing jets and at

least one muon. Here we present the capability to measure the inclusive b quark production cross section as a function of the B-hadron transverse momentum and pseudorapidity. An important result of our study is an estimate for the B-hadron p_T range reachable at LHC.

Inclusive b-quark production has been studied at other proton and electron colliders. The observed shapes of distributions and correlations are reasonably well explained by perturbative QCD. However, the observed cross-sections at the Tevatron (Run I) are larger than QCD predictions [204–211] which is confirmed by Run II data. Similar effects are observed in γp collisions at HERA [212–218] and in $\gamma\gamma$ interactions at LEP [219, 220].

The agreement between experiment and theory has improved due to more precise parton density functions and proper estimates of fragmentation effects [221–226]. But the agreement is not complete and the improvement of the phenomenological description is required using also experimental input.

7.3.1.2. Analysis. This study of the CMS capability to measure the inclusive b production is based on full detector simulation. The generated events are passed through the GEANT4 simulation of CMS. Pile-up corresponding to low-luminosity LHC running conditions ($\mathcal{L} = 2 \times 10^{33}\,\mathrm{cm}^{-2}\,\mathrm{s}^{-1}$) is also generated.

7.3.1.2.1 Event selection. About 4 million signal and background events were processed, mainly with high transverse momentum of the partons ($p_T > 50\,\mathrm{GeV/c}$). Samples of QCD jets were used. Jets in those samples cover the full geometrical acceptance in pseudorapidity of the tracking detector, $|\eta| < 2.4$. The measurement of the differential cross sections is studied for B-hadrons of $p_T > 50\,\mathrm{GeV/c}$ and within the fiducial volume of $|\eta| < 2.4$. First, the events are required to pass the Level-1 (L1) trigger selection for the single muon trigger stream which accepts events with muons having $p_T > 14\,\mathrm{GeV/c}$. The most energetic B-hadron inside the phase space defined above is selected. The trigger efficiency is flat as a function of the B-hadron pseudorapidity within the Level-1 trigger acceptance of $|\eta| < 2.1$. It increases with transverse momentum of the B-particle. The average Level-1 trigger efficiency corresponds to the expected value of the branching fractions for the semi-leptonic b quark and c quark decays, about 19% [54]. At Level-1, the single muon trigger is used. At the High Level Trigger (HLT) we require the "muon + b-jet" trigger, fired by non-isolated muons with $p_T > 19\,\mathrm{GeV/c}$ and by jets with $E_T > 50\,\mathrm{GeV/c}$, $|\eta| < 2.4$ and compatible with b tagging.

The event selection requires a b-tagged jet in the fiducial volume to be present in the event. B tagging is based on inclusive secondary vertex reconstruction in jets [157]. The tagging algorithms combine several topological and kinematic secondary vertex related variables into a single tagging variable to discriminate between jets originating from b quarks and those from light quarks and gluons.

To measure differential cross sections for inclusive B-particle production as a function of its transverse momentum p_T and pseudorapidity η, $d\sigma/dp_T$ and $d\sigma/d|\eta|$, we select as the reconstructed B-particle candidate the most energetic b tagged jet. Good correspondence between the generated B-particle and the reconstructed b-tagged jet is observed. The corresponding p_T and pseudorapidity relative resolutions are shown in Fig. 7.8 for B-particles with $p_T > 170\,\mathrm{GeV/c}$. The resolutions are 13% and 6% for p_T and pseudorapidity, respectively.

The efficiency of the b tagging by secondary vertices in jets is shown in Fig. 7.9 as function of the B-particle transverse momentum and pseudorapidity. The b tagging efficiency is defined with respect to events passing the Level-1 trigger and with a single muon of $p_T > 19\,\mathrm{GeV/c}$ selected. The efficiency decreases with increasing transverse momentum, while being rather flat as function of pseudorapidity. The slow degradation for larger

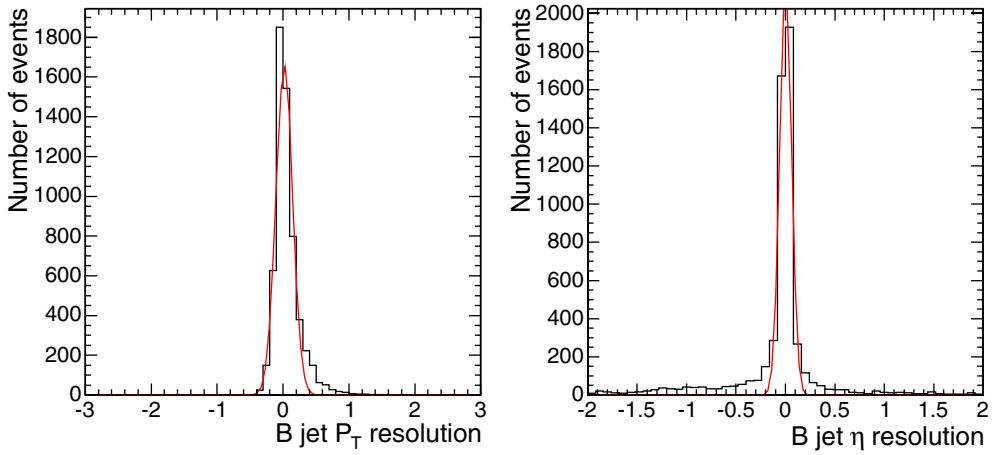

Figure 7.8. Relative resolution, (Reconstructed − True)/True, for p_T and pseudorapidity of b tagged jets in CMS.

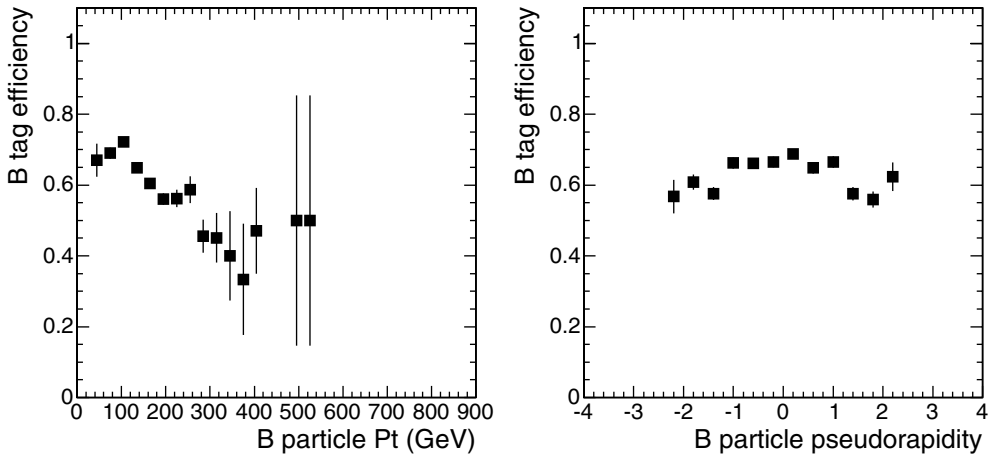

Figure 7.9. The b tagging efficiency versus p_T and pseudorapidity of the generated B-particle.

transverse momenta is caused by the worsening of the tracking resolution with increasing p_T, an increased track multiplicity from fragmentation and more difficult pattern recognition in dense jets. The average b tagging efficiency is 65% in the barrel region, while the efficiency is about 10 % less for the endcap region. The muon plus b-jet cross-channel trigger has a 4.3 Hz rate for the signal and a 6.1 Hz total event rate [203]. This trigger rate corresponds to a low-luminosity LHC run at $\mathcal{L} = 2 \times 10^{33}\,\mathrm{cm}^{-2}\,\mathrm{s}^{-1}$.

To measure the cross section one needs to know the number of selected events, the integrated luminosity, the event sample purity (signal fraction) and the signal efficiency. The signal fraction can be determined from the simulated prediction of the background contribution to the selected event sample. In order to rely less on the absolute prediction for the background one can extract the signal fraction using the prediction of the signal and background shapes for some sensitive variables. A fit to the data distribution using the

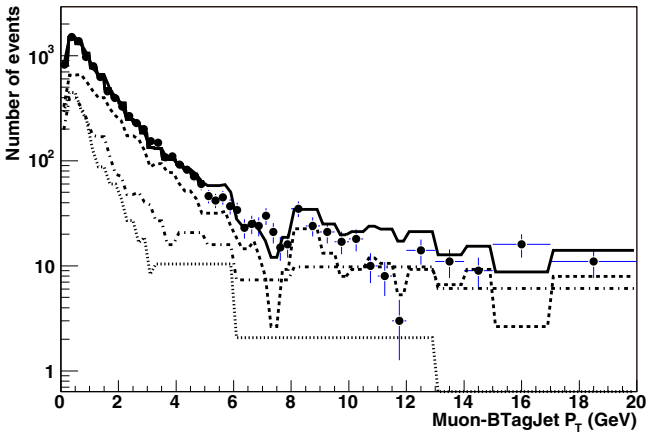

Figure 7.10. Fit of the muon p_{T} spectrum with respect to the closest b tagged jet. The sample of generated QCD events with "p_{T}-hat" parameter in the range $230 < \hat{p_{\mathrm{T}}} < 300\,\mathrm{GeV/c}$ is tested. The contributions of tagged muons from b events (dashed curve), c events (dot-dashed curve) and light quark events (dotted curve) as defined by the fit are shown. The solid curve is the sum of the three contributions.

simulated shapes for the signal and background is performed. To do so we apply a lepton tag by selecting inclusive muons.

7.3.1.2.2 Muon tag. Muons are reconstructed in the muon chambers, matched to the inner tracker information and refitted using both subdetectors information. This provides the most precise muon track measurement. Each reconstructed muon is associated to the most energetic b tagged jet. The muon must be closer to this b tagged jet than to any other jet in the event. Otherwise the event is discarded.

In most cases the tagged muon is inside the b jet. The average efficiency of associating the muon with the b tagged jet is 75%.

7.3.1.2.3 Results. We calculate the transverse momentum of the muon with respect to the b-jet axis which effectively discriminates between b events and background. The slopes of the p_{T} spectra are very different and this is exploited in the fit of the selected events to determine the fractions of the muon sources in the sample.

Figure 7.10 shows an example of the fit of the distribution of the muon p_{T} with respect to the closest jet, using the expected shapes for the muons from b events, charm events and light quark events. The normalisation of the three contributions are free parameters in the fit. The events in this plot are from a sample of QCD events generated with the PYTHIA "p_{T}-" parameter in the range $230 < \hat{p_{\mathrm{T}}} < 300\,\mathrm{GeV/c}$. In the fit, the shapes of the distributions were fixed using an independent QCD sample generated with $170 < \hat{p_{\mathrm{T}}} < 230\,\mathrm{GeV/c}$. The fit results as well as the Monte Carlo input are quoted in Table 7.1. The event fractions are well reproduced within statistical errors. In the actual experiment the shapes will be verified using data at different selection stages. Also the background shape will be derived from the data itself by applying an anti-tag selection (b-suppressed event sample).

In Table 7.2 the b purity, $c\bar{c}$ and light quark event fractions for the different QCD samples are shown. The b purity decreases from about 70% down to 55% from low p_{T} events to the high transverse momentum events. The expected number of $b\bar{b}$ events after event selection is quoted for $10\,\mathrm{fb}^{-1}$ of integrated luminosity. For the phase space of $p_{\mathrm{T}} > 50\,\mathrm{GeV/c}$ and $|\eta| < 2.4$ the event selection will allow for a b event statistics of about 16 million events. We

Table 7.1. Results of the fit to the distribution of the transverse momentum of the muon with respect to the nearest b tagged jet. The number of beauty, charm and light quark events in the Monte Carlo input are compared to the fit result.

	MC input, $230 < \hat{p_T} < 300\,\mathrm{GeV/c}$	Fit result
$N_{b\bar{b}}$	5250	5222 ± 501
$N_{c\bar{c}}$	2388	2050 ± 728
N_{uds}	1740	1778 ± 341

Table 7.2. B purity and expected number of events after final event selection. The expected number of $b\bar{b}$ events is quoted for $10\,\mathrm{fb}^{-1}$ of integrated luminosity.

$\hat{p}_T$ GeVc	$N^{QCD}_{generated}$	$b\bar{b}$ purity, %	$c\bar{c}$ fraction, %	uds fraction, %	$N^{b\bar{b}}_{expected}$
50–80	198993	66	32	2	1.4 M
80–120	294986	66	32	2	6.1 M
120–170	291982	72	26	2	5.1 M
170–230	355978	71	26	3	2.4 M
230–300	389978	73	24	3	0.9 M
300–380	283983	70	25	5	0.3 M
380–470	191989	68	27	5	88 k
470–600	190987	64	29	7	34 k
600–800	94996	60	31	9	10 k
800–1000	89999	60	30	10	2.0 k
1000–1400	89998	55	31	14	0.5 k

conclude that for B-hadrons a p_T range up to 1.5 TeV/c will be accessible with the CMS detector at the LHC.

The background contribution from $t\bar{t}$ events has been estimated from a sample of one million simulated events including all decay modes. The total number of $t\bar{t}$ events passing the selection amounts to 104 thousand events for $10\,\mathrm{fb}^{-1}$ of integrated luminosity, corresponding on average to a less than 1% background contribution. The $t\bar{t}$ background becomes more pronounced for the high p_T part of the inclusive B spectrum. In the region $p_T > 500\,\mathrm{GeV/c}$ it amounts to 2.4%.

The total event selection efficiency is about 5%. By correcting for the semi-leptonic branching ratio of b quarks and c quarks it amounts to about 25% on average. It turns out that the total efficiency is almost independent of transverse momentum and angle of the B-particle. Therefore the measurement of the differential cross section is less affected by systematic uncertainties due to bin-by-bin efficiency corrections.

7.3.1.2.4 Systematics Uncertainties. Several potential sources for systematic uncertainties are considered and their impact on the observed cross section is detailed in Table 7.3. The largest uncertainty arises from the 3% error on the jet energy scale (see Appendix B) which leads to a cross section error of 12% at $E_T > 50\,\mathrm{GeV/c}$. Other important uncertainties arise from the event-selection procedure and the Monte Carlo modelling of the detector response, including the lepton identification and the detector resolution on the energy and angular variables which identify the fiducial volume. The effect of these systematic uncertainties is estimated by varying the corresponding cuts and repeating the fits for the newly selected event samples. It results in an uncertainty of 6%. The expected b-tag systematics for $10\mathrm{fb}^{-1}$ integrated luminosity is 5% [7]. The luminosity uncertainty is also 5% [7].

Table 7.3. Sources of systematic uncertainty in % on the inclusive *b* production cross section measurement. The total systematic uncertainty is calculated by adding all contributions in quadrature.

Source	uncertainty, %
jet energy scale	12
event selection	6
B tagging	5
luminosity	5
trigger	3
muon Br	2.6
misalignment	2
muon efficiency	1
$t\bar{t}$ background	0.7
fragmentation	9
total	18

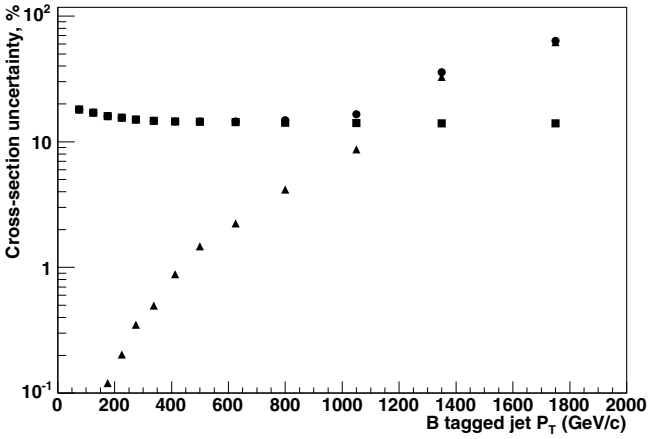

Figure 7.11. The statistical uncertainty for the cross section measurement (triangles), systematic (squares) uncertainty and total (dots) uncertainty as function of the *b* tagged jet transverse momentum with respect to the beam line. Total uncertainty comprises the statistical and systematic uncertainties added in quadrature.

The trigger efficiency will be determined from the data themselves. We estimate its uncertainty from Monte Carlo studies to be 3.0%. The experimental uncertainties on the semi-leptonic branching ratio of b quarks [54] is also propagated to the measurement. The impact of the detector misalignment on the CMS *b* tagging performance has been investigated in [157]. The effect has been found to be small (2%). The muon detection efficiency can be determined with better than 1% precision [7]. The $t\bar{t}$ background subtraction uncertainty is conservatively taken as absolute value of the expected $t\bar{t}$ contribution to the considered phase space.

A large contribution is expected from the fragmentation modelling. We estimate the magnitude of the effect from the DØ b-jet production measurement at Tevatron [211]. This uncertainty propagates to the cross section as a 9% effect independent of jet E_{T}.

The estimated statistical, systematic and total uncertainty as function of the *b* tagged jet transverse momentum with respect to the beam line is shown in Fig. 7.11.

7.3.1.3. Conclusion. The event selection for inclusive b production measurement at CMS will allow to study b production mechanisms on an event sample of 16 million b events for 10 fb^{-1} of integrated luminosity. The b purity of the selected events varies as function of the transverse momentum in a range from 70% to 55%. Our estimate shows that with the CMS detector we can reach 1.5 TeV/c as the highest measured transverse momentum of B hadrons.

7.3.2. Study of B_c hadrons

7.3.2.1. Introduction. The B_c meson is the ground state of the $\bar{b}c$ system, which is doubly heavy flavoured. This unique character provides a window for studying heavy-quark dynamics that is very different from the one of quarkonium. The experimental study of B_c will help us to understand heavy quark dynamics and to test the spin symmetry derived in non-relativistic quantum chromodynamics (NRQCD) [227–236]. B_c mesons have been observed at the Fermilab Tevatron collider by the CDF collaboration through the decay channel $B_c \to J/\psi\ \ell\nu$ [237]. The mass and lifetime are measured to be [238] $\text{M}(B_c) = 6.40 \pm 0.39(stat) \pm 0.13(sys)$ GeV/c^2 and $\tau(B_c) = 0.46^{+0.18}_{-0.16} \pm 0.03(sys)$ps, in agreement with the non-relativistic potential model [239–241] and other approaches [242–244].

Because of the higher colliding energy, the production cross section at the LHC is about a factor of 16 [231] larger than at the Tevatron. As also the LHC luminosity will be higher, CMS has the potential to collect much more B_c mesons than the Tevatron experiments do. We propose to study the B_c meson through $B_c \to J/\psi\ \pi$, $J/\psi \to \mu^+\mu^-$. The goal is to measure the mass and lifetime, and to compare the results with theoretical predictions which do have large uncertainties at the moment. More details on the analysis can be found in reference [245].

7.3.2.2. Monte Carlo data samples. A large amount of Monte Carlo data were produced to study the feasibility for CMS to measure the B_c mass and lifetime with the first fb^{-1}. There are two dedicated B_c generators, one is called BICEPS, developed at ITP, Beijing, by Chang *et al.* [231, 236], and the other is developed at IHEP, Protvino, by Berezhnoy *et al.* [239, 240]. Both packages are based on perturbative QCD, and have been integrated into the SIMUB package [130]. PYTHIA [246] can also generate B_c events, but it takes much more CPU time than the dedicated ones. For comparison, the p_T distribution of B_c mesons, generated by PYTHIA, BICEPS and the Protvino package (named Gouz in the plot), are shown in Fig. 7.12. One can see that the Protvino package produces higher p_T, while PYTHIA agrees with BICEPS. In order to save CPU time, BICEPS is used to generate B_c events. During generation, only events were retained which contain within $|\eta| < 2$ a B_c with $p_T > 10$ GeV/c, together with a muon of $p_T > 4$ GeV/c within $|\eta| < 2.2$. After the kinematic cuts, the cross section multiplied by the branching ratio is 1.78 pb. 52,000 B_c events were produced, corresponding to 29.2 fb^{-1} of integrated luminosity.

Important background sources are J/ψ mesons from decays of other B hadrons and prompt J/ψ mesons. Because of their large cross sections also QCD jets, in particular $b\bar{b} \to \mu^+\mu^- X$, $c\bar{c} \to \mu^+\mu^- X$, as well as W + jets and Z + jets have to be considered.

B hadrons that decay into J/ψ were generated with PYTHIA6.228 with kinematic cuts similar to B_c production, and prompt J/ψ events were generated by PYTHIA6.324, where the colour-octet contribution is included.

The full CMS detector simulation and reconstruction was applied to the generated samples. The fast simulation package FAMOS was also used to produce the B_c events, B hadrons, prompt J/ψ and $c\bar{c} \to \mu^+\mu^- X$ (Table 7.4).

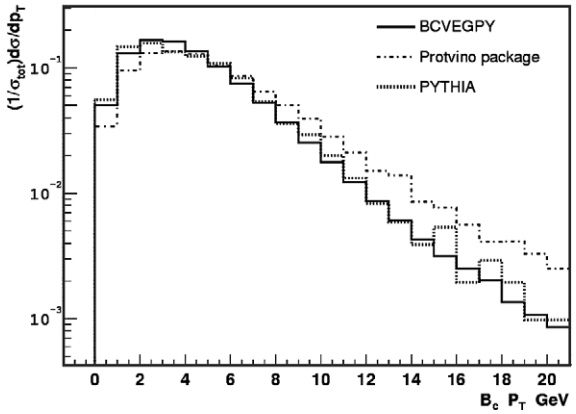

Figure 7.12. Comparison of p_{T} distributions of B_{c} mesons for the generator BICEPS, Gouz and PYTHIA.

Table 7.4. The cross section multiplied by the branching ratio after kinematic cuts and the number of events produced for B hadrons and prompt J/ψ and $c\bar{c} \to \mu^+\mu^- X$.

channel	$\sigma \cdot$ Br.(pb)	N events
B^0	70.3	740,000
B^+	70.7	740,000
B_s	14.8	190,000
Λ_b	19.4	200,000
prompt J/ψ	240.3	500,000
$c\bar{c} \to \mu^+\mu^-$ X	1690	210,000

Samples corresponding to $10\,\mathrm{fb}^{-1}$ of B hadrons, $2\,\mathrm{fb}^{-1}$ of prompt J/ψ and $0.12\,\mathrm{fb}^{-1}$ of $c\bar{c} \to \mu^+\mu^-$ X events were produced for the analysis. Additional background samples of about 950,000 QCD, 880,000 W + jets, 710,000 Z + jets and 100,000 $b\bar{b} \to \mu^+\mu^- X$ events were used.

7.3.2.3. Selection. Signal events should have a b-jet, a c-jet and a B_{c} meson which decays into a J/ψ and a pion, with the subsequent $J/\psi \to \mu^+\mu^-$ decay. The selection starts from 2 muon tracks. The p_{T} of both muons should be larger than 4 GeV/c and the absolute value of η less than 2.2. The two muons should have different charge and share the same vertex. To form a J/ψ candidate the invariant mass of the muons should be in a window between 3.0 and $3.2\,\mathrm{GeV/c}^2$. An additional track must be found at the same vertex of the J/ψ which is inconsistent with a muon or an electron. The p_{T} of it should be larger than 2 GeV/c and the absolute value of η less than 2.4.

The decay length L_{xy}, the proper decay length L_{xy}^{PDL} and the error of the decay length σ_{xy} are calculated from the J/ψ vertex and the primary vertex in the xy-plane. The resolution of the proper decay length is $25\,\mu$m. It is found that the resolution is almost independent of the proper decay length. In order to suppress the prompt backgrounds, the second vertex has to be displaced from the primary one. We require $L_{xy}/\sigma_{xy} > 2.5$ and $L_{xy}^{PDL} > 60\,\mu$m. In addition, the condition $\cos\theta_{sp} > 0.8$ is applied where θ_{sp} is the opening angle between the second vertex (pointing from the primary vertex) and the reconstructed B_{c} momentum. Finally, the reconstructed B_{c} candidate must be in a mass window between 6.25 and $6.55\,\mathrm{GeV/c}^2$.

Table 7.5. Estimated number of signal and background events for 1 fb^{-1}.

B_c	B^+	B_s	B_0	prompt J/ψ	Λ_b	$c\bar{c}$	$b\bar{b}$	QCD
120 ± 11	0.7 ± 0.2	0.1	0.9 ± 0.3	0.1	0.1	0.01	0.01	0.7 ± 0.1

The number of B_c and background events for $1\,\mathrm{fb}^{-1}$ after the selection are listed in Table 7.5. The total number of background events was estimated to be 2.6 ± 0.4, mainly from B hadron decays into J/ψ. So far tagging of the b jet is not used in the analysis.

Because of the high cross section, the number of produced QCD Monte Carlo events is not sufficient to directly determine the QCD background which is therefore estimated in three steps [245]. At first the efficiency to select two muons is obtained directly from the QCD sample, then the efficiency to reconstruct two muons into a J/ψ candidate is calculated from the $c\bar{c} \to \mu^+\mu^- X$ sample, and finally the efficiency for the J/ψ candidate to fake a B_c meson is obtained from the prompt J/ψ sample. The probability of a QCD event to pass the selection cuts is then approximated as the product of the above three efficiencies. In this way, the total number of QCD background for $1\,\mathrm{fb}^{-1}$ is estimated to be 0.7 events.

This study which is aimed at the first fb^{-1} collected with the CMS detector assumes that in this initial phase the dimuon trigger threshold can be set at values such that the applied cut of $p_T > 4\,\mathrm{GeV/c}$ on both muons does not introduce a significant inefficiency at trigger level. In case the available trigger bandwidth will prohibit this, more sophisticated High Level Trigger algorithms like a J/ψ mass window could be invoked to restore the trigger efficiency. A detailed study is underway.

7.3.2.4. Mass and lifetime fitting. A kinematic fit was applied to the selected events imposing a J/ψ mass constraint and forcing the two muon tracks as well as the pion track to share the same vertex. After the kinematic fit the invariant mass of the J/ψ – pion system is shown in Fig. 7.13. A Gaussian fit provides a mean value of 6406 $\mathrm{MeV/c^2}$, close to the input of 6400 $\mathrm{MeV/c^2}$, and a mass resolution of 22 $\mathrm{MeV/c^2}$. The number of signal events in the plot for $1\,\mathrm{fb}^{-1}$ is 120. Backgrounds from B hadrons and prompt J/ψ are included in the plot, while other backgrounds are neglected here.

A binned likelihood fit was done on the proper decay length distribution of the selected B_c events with the likelihood defined as $L = \prod P(n_i, \mu_i)$. $P(n_i, \mu_i)$ denotes the Poisson distribution with n_i events observed and μ_i events predicted in the i-th bin:

$$\mu = N \cdot \epsilon(x) \cdot \exp(-x/c\tau) \otimes G(x, \sigma)$$

Here x represents the proper decay length, N and $c\tau$ are the parameters to be fitted and $G(x, \sigma)$ is a Gaussian smearing function with σ fixed to $25\,\mu\mathrm{m}$ which is the resolution of the proper decay length. The efficiency $\varepsilon(x)$ is obtained from the large B_c sample.

The result of the fit is $c\tau = 148.8 \pm 13.1\,\mu\mathrm{m}$ which is consistent with the used input value of $150\,\mu\mathrm{m}$. The distribution of the proper decay length together with the fit result is shown in Fig. 7.13.

7.3.2.5. Systematic uncertainty. The influence of imperfect detector alignment which is of particular importance at the beginning of the CMS experiment on the track and vertex reconstruction has been studied in [99, 140]. It will affect the study of B_c in three ways: the momentum scale of muons and pions, the mass resolution and finally the vertex precision. Taking the scale uncertainty to be $\Delta(1/p_T) = 0.0005/\,\mathrm{GeV/c}$, the resulting uncertainties on the B_c mass is $11\,\mathrm{MeV/c^2}$ and $0.2\,\mu\mathrm{m}$ on $c\tau$.

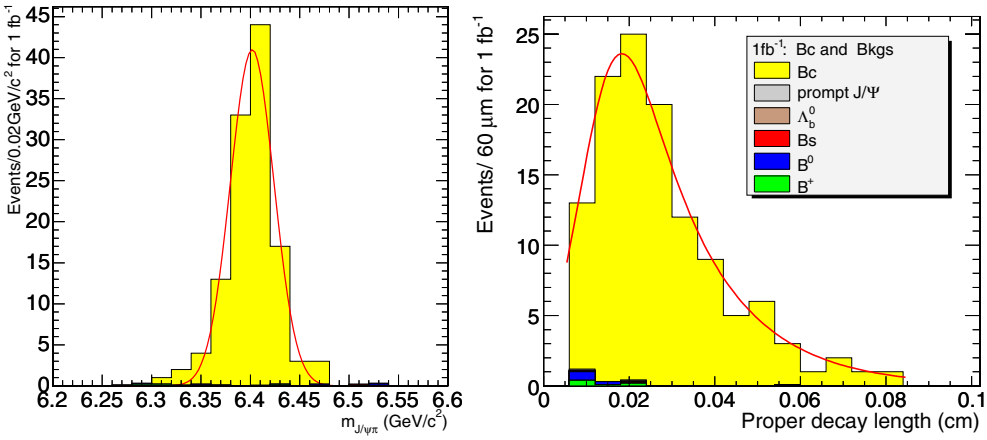

Figure 7.13. Left: The invariant mass of the J/ψ and pion candidate for the selected B_c. Right: The B_c proper decay length distribution. Both plots correspond to 1 fb^{-1}.

The effect of the muon momentum resolution was estimated following [99] and muon p_T-values of 10, 100 and 1000 GeV/c were studied for different η. The Δp_T to be smeared for a muon track from B_c was extrapolated from its p_T and η according to [99]. The resulting B_c mass uncertainty is 10 MeV/c^2, and 0.8 μm on $c\tau$. The error from the vertex uncertainty was determined according to 140 causing an uncertainty on $c\tau$ of 2.4 μm.

The uncertainty on the efficiency as function of the proper decay length origins from the limited Monte Carlo statistics. By subtracting $\sqrt{N}$ events from the sample ($N = 3600$ events), new efficiencies were calculated and the fit was repeated. The observed difference of 0.1 μm on $c\tau$ is taken as systematic uncertainty.

The theoretical uncertainty was estimated from Fig. 7.12 which shows the p_T distributions from different generator packages. The B_c events, generated by BICEPS, were reweighted to agree with the Gouz distribution and the analysis was repeated. The difference on $c\tau$ was found to be 1.5 μm which is taken as the error from this source.

To check the sensitivity on the cuts, the muon and pion p_T cuts were changed by one standard deviation of their resolution, about 1.5% depending on η. Other cuts like on $\cos\theta_{sp}$ and on the proper decay length were changed by 10%. The resulting mass uncertainty is 0.1 MeV/c^2 and 0.2 μm on $c\tau$.

In total the systematic uncertainties on the mass and on $c\tau$ are estimated to be 14.9 MeV/c^2 and 3.0 μm, respectively.

7.3.2.6. Conclusion. With the first fb^{-1} of data CMS is expected to measure the B_c mass with an uncertainty of $22.0(stat.) \pm 14.9(syst.)$ MeV/c^2 and $c\tau$ with $13.1(stat.) \pm 3.0(syst.)$ μm, corresponding to a lifetime uncertainty of $0.044(fit) \pm 0.010(syst.)$ps. About 120 $B_c^+ \to J/\psi\pi^+$, with $J/\psi \to \mu^+\mu^-$, events would be observed. At the moment, the theoretical calculation is at the leading order without the colour-octet contribution. Therefore, the uncertainties on the total cross section and the p_T distribution are large. In the real data analysis, $J/\psi+$ one track with $J/\psi \to \mu^+\mu^-$ will be selected as a control sample, $B^+ \to J/\psi K^+$ will be used to estimate the efficiency, and the side band of the J/ψ peak will be used to estimate the background to B_c.

7.4. Diffraction and forward physics

7.4.1. Introduction

This section outlines the diffractive and forward physics that CMS can do – together with the TOTEM experiment. The CMS and TOTEM detectors involved are presented in Chapter 7 of Volume 1 of the CMS Physics TDR [7].

The combined phase space coverage of the two experiments makes it possible to study many physics subjects in diffractive interactions – from QCD and the investigation of the low-x structure of the proton to the production of SM and MSSM Higgs bosons. Diffractive events are characterised by the fact that the incoming proton(s) emerge from the interaction intact, or excited into a low mass state, with only a small energy loss. Diffractive processes with proton energy losses up to a few per cent are dominated by the exchange of an object with vacuum quantum numbers, the so called Pomeron, now understood in terms of partons from the proton. For larger energy losses, mesonic exchanges – Reggeons and pions – become important. The topology of diffractive events is characterised by a gap in the rapidity distribution of final-state hadrons due to the lack of colour of the exchanged object.

Events with a fast proton in the final state can also originate from the exchange of a photon. In particular, forward tagging one leading proton allows the selection of photon-proton events with known photon energy; likewise, tagging two leading protons gives access to photon-photon interactions of well known centre-of-mass energy.

Triggering of diffractive/forward events is discussed in [247] and in Appendix E.3. More details on the work presented here can be found in [248].

7.4.2. The interest of diffractive interactions

The study of hard diffraction has been pioneered by the UA8 experiment at CERN [249]. There have been major advances in this field recently, largely driven by the study of diffraction at HERA and the Tevatron. The essential results are discussed in [250] and can be summarised as follows:

- Many aspects of hard diffractive processes are well understood in QCD: the presence of a hard scale allows the use of perturbative techniques and thus to formulate the dynamics in terms of quarks and gluons.
- A key to this success are factorisation theorems in electron-proton scattering, which render part of the dynamics accessible to calculation in perturbation theory. The remaining non-perturbative quantities are the so-called diffractive parton distribution functions (dPDFs) and generalised (or "skewed") parton distributions (GPDs). They can be extracted from measurements and contain specific information about small-x partons in the proton that can only be obtained in diffractive processes.
  Diffractive parton densities are determined from inclusive diffractive processes and can be interpreted as conditional probabilities to find a parton in the proton when the final state of the process contains a fast proton of given four-momentum. Generalised parton distributions can be accessed in exclusive diffractive processes; they quantify correlations between parton momenta in the proton. Their t-dependence is sensitive to the distribution of partons in the transverse plane.
- To describe hard diffractive hadron-hadron collisions is more challenging since factorisation is broken by rescattering between spectator partons. These soft re-interactions can produce additional final-state particles which fill the would-be rapidity gap. When such additional particles are produced, a very fast proton can no longer appear in the final state because of

energy conservation. The effect is often quantified in terms of the so called "gap survival probability". These rescattering effects are of interest in their own right because of their intimate relation with multiple scattering effects, which at LHC energies are expected to be crucial for understanding the structure of events in hard collisions.

The dynamics of rescattering and multi-gap events is still not completely understood. The available data can be described in terms of an effective, non-linear Pomeron trajectory [251]; its variation with energy would be a consequence of multi-Pomeron exchange effects [252]. Other models, also testable at the LHC have been proposed (see e.g. [253] and references therein). These topics can be pursued in more detail with the CMS-TOTEM data at the LHC.

- A fascinating link has emerged between diffraction and the physics of heavy-ion collisions through the concept of saturation, which offers a new window on QCD dynamics in the regime of high parton densities.
- Perhaps unexpectedly, the production of a SM or MSSM Higgs boson in diffractive pp collisions is drawing more and more attention as a clean channel to study the properties of a light Higgs boson or even to discover it. The central exclusive reaction, $pp \to pHp$, appears particularly promising.

7.4.3. A survey of the accessible diffractive/forward processes

The accessible physics is a function of the integrated luminosity. We assume standard LHC optics with $\beta^* = 0.5$ m unless stated otherwise. We recall that, in this case, the TOTEM Roman Pots (RP) at 220 m from the CMS interaction point have coverage for $0.02 < \xi < 0.2$, where ξ is the proton fractional momentum loss. Near-beam detectors at 420 m from the interaction point, currently also being considered [254], would cover $0.002 < \xi < 0.02$.

Low-luminosity ($\sim 10^{28}$–$10^{30}\,\mathrm{cm}^{-2}\,\mathrm{s}^{-1}$) studies could profit from running with $\beta^* > 0.5$ m, where the ξ coverage of the 220 m RPs would be wider and the t resolution would improve because of the lower transverse momentum spread of the beam.

7.4.3.1. Inclusive single diffraction and double Pomeron exchange at low luminosity. At modest instantaneous luminosities, up to $10^{32}\,\mathrm{cm}^{-2}\,\mathrm{s}^{-1}$, inclusive single diffractive (SD) events, $pp \to pX$, as well as inclusive double-Pomeron exchange (DPE) events, $pp \to pXp$, can be studied by requiring the presence of one or two rapidity gaps in the event. In the ξ range given above, the scattered proton can be detected and the kinematics of the events fully measured.

The inclusive SD and DPE cross sections, as well as their M_X dependence, even in the absence of a hard scale, are important quantities to measure at the LHC. Here M_X indicates the mass of the system X. These cross sections amount to approximately 15% and 1% of the total proton-proton cross section, respectively; their energy dependence is a fundamental parameter of (non-perturbative) QCD. In addition, since diffractive events constitute a major fraction of the pile-up events, their measurement is mandatory to be able to properly simulate and understand high-luminosity data, where, at instantaneous luminosities of $10^{34}\,\mathrm{cm}^{-2}\mathrm{s}^{-1}$, approximately 35 pile-up events are superimposed, on average, to any event.

7.4.3.2. SD and DPE production of dijets, vector bosons and heavy quarks. The study of SD and DPE events in which the diffractively excited state includes high-E_T jets, heavy quarks or vector bosons opens up the possibility of accessing dPDFs and GPDs. The comparison of the DPE and SD rates for these processes may also give information on the hard diffractive

factorisation breaking at LHC (see Section 7.4.2). A few examples of these processes are given here.

Production of dijets. The measurement of the reaction $pp \to pXjj$ (j indicates a jet) has been used for the first time by CDF to measure the diffractive structure function in antiproton-proton collisions [255]. A similar measurement is possible at LHC with wider kinematic coverage (CDF: $\xi > 0.035$) and larger minimum jet E_{T}. For $E_{\mathrm{T}} > 45\,\mathrm{GeV}$, of the order of 10^8 events per fb^{-1} can be expected.

Production of heavy quarks. Inclusive DPE production of $t\bar{t}$ pairs has been studied in the case in which the final state contains one muon and four jets (i.e. with one top quark decaying to b plus lepton and neutrino, and the other to three jets). The analysis required the detection of both final-state protons. The expected number of events is of order $1-100$ for $10\,\mathrm{fb}^{-1}$, depending on the theoretical model assumed.

SD and DPE production of B-mesons has also been looked at, with $B \to J/\psi X$ and $J/\psi \to \mu^+\mu^-$. Here the number of expected events is much larger, of the order of a few events per $10\,\mathrm{fb}^{-1}$ in the DPE case and thousands in the SD case.

Inclusive DPE production of W bosons. Inclusive DPE production of W bosons, $pp \to pXWp$, is also sensitive to the dPDFs of the proton and is a relatively abundant process that can be studied at instantaneous luminosities where pile-up is small. In these conditions, the requirement that two final state protons be measured in the 220 m RPs suppresses both the QCD background and the inclusive W production. Several thousand events with $W \to e\nu$ or $W \to \mu\nu$ are expected, after cuts, for an integrated luminosity of $1\,\mathrm{fb}^{-1}$. This process, in conjunction with SD production of W bosons, can be used to study hard diffractive factorisation breaking using the LHC data alone, as mentioned above.

7.4.3.3. SM and MSSM central exclusive Higgs production. As the delivered luminosity reaches tens of fb^{-1}, the central exclusive production process (DPE) becomes a tool to search for new physics, delivering signal to background ratios of order 0.1–1 for Standard Model (SM) Higgs production [256] and more than an order of magnitude larger for certain supersymmetric (MSSM) scenarios.

By central exclusive, we refer to the process $pp \to p\phi p$, where there are large rapidity gaps between the outgoing protons and the decay products of ϕ. There are three primary reasons why this process is attractive. Firstly, if the outgoing protons remain intact and scatter through small angles, then, under some general assumptions, the central system ϕ is produced in the $J_Z = 0$, C and P even state. Secondly, the mass of the central system can be determined very accurately from a measurement of the transverse and longitudinal momentum components of the outgoing protons alone. This means an accurate determination of the mass irrespective of the decay mode of the centrally produced particle. Thirdly, the process delivers excellent signal to background ratios, due to the combination of the $J_Z = 0$ selection rules, the mass resolution, and the simplicity of the event in the central detectors. An additional attractive property of central exclusive production is its sensitivity to CP violating effects in the couplings of the object ϕ to gluons.

The left panel of Fig. 7.14 shows the cross section times the branching ratio for central exclusive production of a Standard Model Higgs, with $H \to b\bar{b}$ and $H \to WW$, as a function of the Higgs mass for different theoretical approaches. The $b\bar{b}$ mode is particularly interesting for masses close to the current exclusion limit. The right panel of Fig. 7.14 shows the acceptance assuming various combinations of RPs at 220 m and near-beam detectors at 420 m. Both protons can be detected in the 220 m stations only for Higgs masses larger than $280\,\mathrm{GeV/c^2}$; this reflects the ξ range for which the 220 m RPs have acceptance,

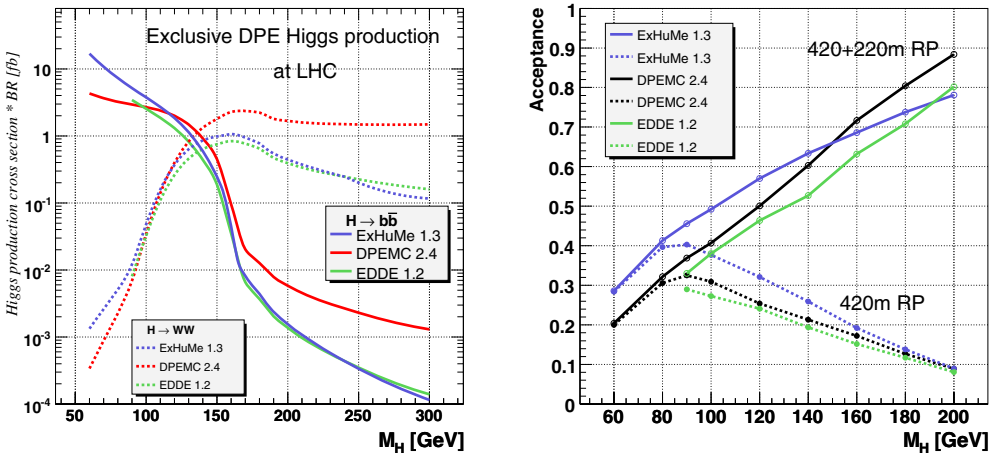

Figure 7.14. Left: The cross section for the exclusive production of the Higgs boson as a function of the Higgs boson mass for $H \to b\bar{b}$ and $H \to WW$. The different curves were obtained with the generators Exhume1.3 [259], DPEMC2.4 [260] and EDDE1.2 [261]. Right: Acceptance for the 420 m detectors alone and for the combination of the 220 m and 420 m detectors as a function of the Higgs boson mass.

$0.02 < \xi < 0.2$ (the mass of the centrally produced Higgs is related to the ξ via $M_H^2 = \xi_1 \xi_2 s$, with ξ_1, ξ_2 the fractional momentum losses of the two protons). However, asymmetric events with one proton at low ξ and another at large ξ can be detected by the combination of the 220 m and 420 m detectors ($0.002 < \xi < 0.02$).

Central exclusive production is generally an attractive way of searching for any new particles that couple strongly to glue. An example studied in [257] is the scenario in which the gluino is the lightest supersymmetric particle. In such models, there should exist a spectrum of gluino-gluino bound states which can be produced in the central exclusive channel. Likewise, central exclusive production of radions, the fields introduced in the Randall–Sundrum model of five-dimensional quantum gravity, has been studied [258].

***H* → *bb̄*.** The analysis is based on the requirement of two back-to-back central b-tagged jets in addition to the detection of both final-state protons yielding a mass of the central system consistent with that calculated from the protons alone. The event yield is very low, about 2–4 events per 30 fb^{-1} after all cuts, depending on the model. The non-resonant continuum b-jet background is largely suppressed by the $J_Z = 0$ rule. The residual background, mostly due to dijet production ($gg \to$ dijets) and diffractive $gg \to b\bar{b}$ production, is a function of the mass resolution, which is about 1.6% for the '420 + 420' combination and 5.6% for the '220 + 420' combination (for $M_H = 120\,\mathrm{GeV/c^2}$). The number of expected background events is of order 10 for 30 fb^{-1}.

***H* → *WW*.** In this case, the suppression of the background does not rely primarily on the mass resolution of the RPs. There are three main categories of WW events. Events in which at least one of the W bosons decays to an electron or a muon are the simplest, and pass the Level-1 trigger thanks to the high-p_T final-state lepton. This holds also if one of the W bosons decays into a tau, which subsequently decays leptonically. The four-jet mode occurs approximately half of the time; here, however, the RP information is necessary already at Level-1. The expected event yields range between 1 and 7 events for 30 fb^{-1}, depending on the mass. Irreducible backgrounds are small and controllable.

MSSM Higgs. Double proton tagging is especially beneficial in the MSSM case. The b-jet channel is very important in the 'intense coupling regime' of MSSM ($M_h \approx M_A \approx M_H \approx 100\,\mathrm{GeV/c^2}$) [262]: couplings of the Higgs to gg, WW^*, ZZ^* are strongly suppressed, making the discovery challenging by conventional means. Rates for central exclusive production of the two scalar (0^+) MSSM Higgs bosons (h, H) are more than a factor 10 larger than for the SM Higgs. The enhancement for $H \to b\bar{b}$ is by orders of magnitude in the M_h-max scenario for $M_H \approx 180$–$250\,\mathrm{GeV/c^2}$; likewise for $h \to b\bar{b}$ and $h \to \tau\tau$ for $M_h \approx 90$–$130\,\mathrm{GeV/c^2}$ [263]. In the small α_{eff} scenario, $h \to b\bar{b}$ and $h \to \tau\tau$ can be heavily suppressed for large $\tan\beta$ and for $M_h \approx 120\,\mathrm{GeV/c^2}$ [263], whereas $h \to WW$ may be enhanced by up to a factor 4 compared to the SM predictions. Also, the pseudo-scalar (0^-) Higgs boson (A) is practically not produced in the central exclusive channel, yielding a clean separation of the scalar and pseudo-scalar Higgs bosons, impossible in conventional channels. The good missing mass resolution allows to resolve h, H and, if enough statistics is available, measure their widths. This makes central exclusive production a possible discovery channel. Central exclusive production is also interesting in the '3-way mixing' scenario of CP-violating MSSM [264]: here the 3 neutral Higgs bosons are nearly degenerate, mix strongly and have masses close to $120\,\mathrm{GeV/c^2}$.

Central exclusive production, with its good mass resolution via the scattered protons, may allow disentangling the Higgs bosons by studying the production lineshape. Explicit CP-violation in the Higgs sector causes an asymmetry in the azimuthal distributions of tagged protons (via the interference of P-even and P-odd amplitudes) – a measurement unique at the LHC [262, 265].

7.4.3.4. High-energy photon interactions. A significant fraction of events at the LHC involves photon interactions at energies above the electroweak scale [266]. The protons radiating the photon often survive the collision intact and are scattered at angles comparable to the beam angular divergence. Detection of such events at the LHC will open up a new field of high-energy photon physics, which is briefly outlined below. By requiring the detection of one or two forward protons like in diffractive interactions, photon-photon and photon-proton interactions can be selected. The photon fluxes, and the effective luminosities of photon-photon and photon-proton collisions are well known [267, 268]. The average proton energy loss is larger and the proton scattering angle smaller in photon exchanges than for the diffractive case. This can be used to establish relative contributions of these two processes.

Two-photon exclusive production of W and Z boson pairs. The cross section for the production of W pairs via photon-photon interactions, $pp \to ppWW$, is slightly above 100 fb; in almost half of these events both forward protons are produced within the acceptance of the TOTEM RPs. About 100 events per $10\,\mathrm{fb^{-1}}$ with leptonic W decays can be detected in CMS. This allows a precise study of the gauge couplings, in particular of the $\gamma\gamma WW$ coupling. The expected sensitivity to anomalous quartic gauge couplings (QGCs) will surpass the LEP and Tevatron limits by orders of magnitude. A deviation from the Standard Model predictions would also allow a clean detection of anomalous WW production as predicted e.g. by A. White's theory of the supercritical Pomeron [269]. Two-photon production of Z pairs, $pp \to ppZZ$, is not allowed at the SM tree level, but yields similar sensitivities to the anomalous QGCs in this channel.

Two-photon exclusive production of pairs of SUSY particles. The cross sections for production of pairs of charginos, sleptons and charged Higgs bosons via photon-photon fusion at the LHC decrease rapidly with the masses of these particles [269]. This limits the

scope of SUSY searches to particle masses below 150–200 GeV/c^2. However, the very clean environment of this reaction makes it attractive compared to other production mechanisms; the final state typically consists of two opposite-sign leptons and of missing p_T. The main background is due to the exclusive production of W pairs discussed above.

Two-photon production of doubly charged Higgs bosons (appearing in GUTs) is strongly enhanced, and leads to exclusive final states with two pairs of same-sign leptons.

Two-photon lepton pair production. Exclusive production of lepton pairs – a purely QED process at low $|t|$ – may serve for calibration of the pp luminosity; it may also be used for calibration of the momentum measurement of the scattered proton. Thousands of exclusive muon pairs are expected to be reconstructed in CMS for an integrated luminosity of 1fb^{-1}. The striking signature of extremely small muon acoplanarity angles of less than about 10 mrad may be exploited already at the trigger level.

Single W and single top photoproduction. The cross section for single W photoproduction, $pp \to pWjX$, reaches almost 100 pb. This process can be therefore studied already at low luminosity. It also provides a means to study rescattering effects [268]. At higher luminosities, studies of high mass Wj states will be possible; for Wj invariant masses above 1 TeV, tens of events are expected to be detected in CMS (and tagged by TOTEM) per 10 fb^{-1}. This will allow to search for, as an example, an anomalous triple gauge coupling γWW. This process is the main background in the search for anomalous photoproduction of single top.

Associated WH and top pair photoproduction. The associated photoproduction of a SM Higgs boson and a W boson has a cross section of about 20 fb for Higgs mass below 180 GeV/c^2. About 50% of the forward protons are tagged by TOTEM, and events with leptonic W decay can be triggered efficiently in CMS. The cross section for photoproduction of top pairs is slightly above 1 pb. Top pair production is the main background for WH production, and in the photoproduction case the signal-to-background ratio for photoproduction of WH pairs is superior to the one in inclusive production.

7.4.3.5. Drell–Yan. The study of forward production of low mass Drell–Yan lepton pairs at the LHC provides a unique opportunity to directly access low-x partons in the proton. In this process, the lepton pair originates from the annihilation of a quark-anti-quark pair whose fractional momenta, x_1 and x_2, are related to the dilepton mass, M, and rapidity, y, through

$$M^2 = sx_1x_2; \qquad x_{1,2} = \frac{M}{\sqrt{s}} \exp^{\pm y}, \tag{7.2}$$

with $\sqrt{s} = 14$ TeV, the centre-of-mass energy of the colliding protons. In order to access low x, a large imbalance in fractional momenta is required, boosting the lepton pair to large rapidities.

The CASTOR calorimeter will cover the pseudorapidity range $5.3 < \eta < 6.6$, corresponding to Bjorken-x values down to 10^{-7}. With CASTOR alone, it may be possible to obtain a crude estimate of the dilepton mass. With the additional information provided by the T2 tracker, one can enhance the signal to background ratio by requiring tracks in association to the electromagnetic energy deposits. As T2 will measure both the azimuthal and polar angles of the tracks, a much more accurate measurement of the opening angle (and therefore of the dilepton mass) and a two-dimensional study in M^2 and x will become possible.

7.4.3.6. Validation of cosmic-ray generators. The correct simulation of the interaction of primary cosmic rays in the PeV energy range with the atmosphere is a key tool in the study of cosmic rays. Unfortunately, the available generators differ significantly in their predictions for the energy flow, multiplicity, hadronic energy fraction etc., in particular at high rapidities. These models can be tested at the LHC: a 100 PeV fixed-target collision in air corresponds to the centre-of-mass energy of a pp collision at the LHC. Several generators were used to simulate inelastic and diffractive collisions at CMS: QGSJET [271], SIBYLL [272], DPMJET [273], NEXUS [271]. There are significant differences in the predictions, notably in the region covered by CASTOR, T1 and T2. A measurement of these features with CASTOR, T1 and T2 may thus be used to validate/tune these generators.

7.5. Physics with heavy ions

7.5.1. High-density QCD: heavy-ion physics

Quantum Chromodynamics (QCD) is the only existing quantum field theory within the Standard Model, whose collective behaviour, phase diagram and phase transitions, are accessible to study in the laboratory. High-energy nucleus-nucleus collisions offer the only experimental means known so far to concentrate a significant amount of energy ($\mathcal{O}(10\,\text{TeV})$ at the LHC) in a "large" volume ($\mathcal{O}(100\,\text{fm}^3)$ at thermalisation times of $\tau_0 \approx 1\text{fm}/c$), allowing the study the many-body dynamics of strongly interacting matter. The programme of high-energy heavy-ion physics addresses several key open questions of the strong interaction:

- **Deconfinement and chiral symmetry restoration.** Lattice QCD calculations predict a new form of matter at energy densities above $\varepsilon \approx 1\,\text{GeV}/\text{fm}^3$ consisting of an extended volume of deconfined and bare-mass quarks and gluons: the Quark Gluon Plasma (QGP) [274]. The scrutiny of this new state of matter (equation-of-state, order of the phase transition, ...) promises to shed light on fundamental questions such as the nature of confinement, the mechanism of mass generation (chiral symmetry breaking, structure of the QCD vacuum) and hadronisation, that still evade a thorough theoretical description due to their highly non-perturbative nature.
- **Non-linear parton evolution at small-x.** At high energies, hadrons consist of a very dense system of gluons with small (Bjorken) parton fractional momenta $x = p_{parton}/p_{hadron}$. At low-$x$, the probability to emit an extra gluon is large $\sim \alpha_S \ln(1/x)$ and non-linear gluon-gluon fusion processes start to dominate the parton evolution in the hadronic wave functions. Whereas at values of $x \gtrsim 10^{-3}$, the parton evolution with Q^2 (or $\ln(1/x)$) is described by the usual DGLAP (or BFKL) equations, at lower values of x and around $Q_s^2 \sim 3\,GeV^2/c^2$, such a saturated configuration is theoretically described in terms of the "Colour Glass Condensate" (CGC) picture [275]. Since the nonlinear growth of the gluon density depends on the transverse size of the system, the effects of gluon saturation are expected to set in earlier (at higher x) for heavy nuclei than for free nucleons.

In addition, the study of heavy-ion collisions has interesting connections to other research areas such as:

- **Early Universe cosmology.** The quark-hadron phase transition took place some 10 μs after the Big-Bang and was the most important event taking place in the Universe between the electro-weak (or SUSY) transition ($\tau \sim 10^{-10}$ s) and Big Bang nucleosynthesis (BBN, at $\tau \sim 200$ s). Depending on the order of the QCD phase transition, several cosmological implications such as the formation of strangelets and cold dark-matter (WIMP) clumps or baryon fluctuations leading to inhomogeneous nucleosynthesis, have been postulated [276].

- **High-energy cosmic-ray physics.** The energy and mass of cosmic particles with energies above 10^{14} eV can only be measured via the ground-based detection of "extended air showers" (EAS) generated in upper-atmosphere interactions of cosmic rays (protons and ions up to Fe) with air (N,O nuclei). The interpretation of the EAS (and the related astro-particle phenomena) relies heavily on the accurate modelling of hadronic multi-particle production in proton-nucleus (p+N, p+O) and nucleus-nucleus (He+N, N+N, Fe+N) collisions in the TeV range. Direct measurements at LHC are needed in order to calibrate and tune the EAS models and correctly extrapolate their predictions to the highest cosmic-ray energies measured ($\sim 10^{20}$ eV).
- **Gauge/String duality.** Theoretical calculations based on the AdS/CFT correspondence permit to obtain results in strongly coupled ($g^2 N_c \gg 1$) gauge theories (QCD-like: SUSY $\mathcal{N} = 4$ Yang-Mills) in terms of a dual gravity theory. Recent applications of this formalism have allowed, for the first time, to compute finite temperature QCD transport coefficients (such as the ratio of the QGP viscosity over entropy density, η/s) experimentally accessible, from black hole thermodynamics calculations [277].

7.5.2. Hard probes of QCD matter at LHC

Nucleus-nucleus collisions at the LHC offer a unique opportunity for studying strongly interacting matter at values of energy and particle densities never reached before. The factor of 30 increase in energy between RHIC and the LHC ($\sqrt{s}_{NN} = 5.5$ TeV for PbPb) leads to copious production of hard QCD probes: high-p_{T} hadrons, jets, quarkonia, direct photons, etc., arising from parton-parton scatterings with large squared momentum transfer, Q^2. Such perturbative processes take place at time scales $\tau \approx 1/p_{\mathrm{T}} \lesssim 0.1\,\mathrm{fm}/c$, and involve primary partons with fractional momenta of order $x \sim 10^{-3}(10^{-5})$ at central (forward) rapidities. The produced hard probes are, thus, sensitive to initial-state modifications of the low-x parton distribution functions, as well as to final-state effects while propagating through the bulk matter formed in the collision.

The contribution of CMS to the heavy-ion physics programme at LHC is extremely competent based on a number of unique experimental capabilities including:

(i) Very large acceptance at midrapidity ($|\eta| < 2.5$, full ϕ) for layered detection of charged hadrons (with the best momentum resolution for charged tracks at LHC) and neutral hadrons as well as muons, electrons, and photons over a wide range of p_{T}.
(ii) The best mass resolution of any LHC detector for quarkonia (J/ψ, Υ) measurements leading to clean separation of the various states, improved signal over background, and large reconstructed yields.
(iii) Complete electromagnetic and hadronic calorimetry since day-1 for full jet triggering and reconstruction over $|\eta| < 3$ and $\Delta\phi = 2\pi$ with a large statistical significance for single jet and jet+X channels ($X =$ jet, γ, Z), and for full b- and c- jet identification, allowing detailed studies of "jet quenching" phenomena.
(iv) Unparalleled forward physics (low-x QCD) capabilities thanks to the forward hadronic calorimeter HF ($3 < |\eta| < 5$), CASTOR-TOTEM ($5.5 < |\eta| < 6.6$), and Zero-Degree-Calorimeter ($|\eta| > 8.1$ for neutrals) detector systems.
(v) A DAQ system capable of delivering almost every PbPb event to the High Level Trigger allowing maximum flexibility to select rare probes at the highest multiplicities expected at the LHC.

Among the various perturbative probes accessible to measurement, we focus on this report on the quarkonia detection via the $\mu^+\mu^-$ decay channel. Other experimental

capabilities, in the hard (notably jet reconstruction in the heavy-ion environment), soft (hadron multiplicities, elliptic flow ...), and low-x (e.g. quarkonia photoproduction in electromagnetic PbPb interactions) sectors will be discussed in detail in CMS Physics TDR addendum for Heavy Ions."

7.5.3. Gluon saturation and QGP colour screening via Quarkonia

The production of heavy-quarks at LHC proceeds mainly via gluon-gluon fusion processes and, as such, is sensitive to nuclear modifications of the gluon density at low-x. At $\sqrt{s}_{NN} = 5.5\,\text{TeV}$, the average fraction of the nucleon momentum carried by the interacting parton producing a J/ψ at mid (forward) rapidity is $\langle x \rangle \approx 3 \cdot 10^{-3} (10^{-5})$. Such a kinematical domain is well in the regime where gluon saturation effects and departures from linear Q^2 (DGLAP) and $\ln(1/x)$ (BFKL) evolutions should be observable. In addition, the final-state formation of $Q\overline{Q}$ bound states is expected to be suppressed in a deconfined medium due to colour screening of the heavy-quark potential. Recent finite-temperature lattice QCD calculations exhibit a substantial reduction of the heavy-quark internal energy $U_{Q\bar{Q}}$, with increasing temperature. The ground-state charmonium state (J/ψ) has been found to dissolve slightly below $2{\cdot}T_{crit} \approx 330\,\text{MeV}$, whereas much higher dissociation temperatures, $T_{diss} \approx 4 \cdot T_{crit}$ reachable at LHC, are needed to dissociate the Υ. Although J/ψ suppression has been indeed observed in central A+A collisions both at CERN-SPS and RHIC energies, competing mechanisms to colour deconfinement (hadronic co-movers interactions and charm quark recombination) have been proposed to explain the observed cross-sections. At variance with charmonia states, the study of the much heavier bottomonia spectroscopy accessible at LHC is free from the distorting hadronic and coalescence contributions, and is directly sensitive to the temperature conditions of the produced partonic medium.

CMS has focused on the quarkonia detection through their decays to muon pairs. The good muon momentum resolution translates in an Υ mass resolution of $\sigma = 54\,\text{MeV/c}^2$ (in the central barrel region $|\eta| < 0.8$), the best of all the LHC detectors. This good resolution provides a clean separation between the members of the Υ family with a consequent improvement in the signal to background ratio, even in head-on PbPb collisions with particle multiplicities as large as $N_{ch}/d\eta|_{\eta=0} = 5000$. The expected signal/background ratios are $S/B \approx 1(5)$, $S/B \approx 0.1(1)$ for J/ψ and Υ respectively in the full ($|\eta| < 0.8$) rapidity range. In the absence of initial- or final-state medium effects, production cross sections of $B_{\mu\mu}\sigma = 50\,\text{mb}$ and $300\,\mu\text{b}$ respectively will be measured in minimum bias PbPb collisions. The expected reconstructed yields for both charmonium and bottomonium resonances after background subtraction, in one-month data taking (with 50% overall efficiency) and nominal PbPb luminosity ($0.5\,\text{nb}^{-1}$), are $\mathcal{O}(1.5 \cdot 10^5)$, $\mathcal{O}(2 \cdot 10^4)$ respectively. These statistics will allow detailed quantitative studies of quarkonia production as a function of p_{T}, rapidity and/or centrality. Any departure from the expected "vacuum" cross-sections will provide valuable information on the initial-state modifications of the nuclear parton (especially, gluon) distribution functions, as well as on the thermodynamical state of the produced medium from the predicted "melting" pattern of different quarkonia states due to colour screening.

Chapter 8. Physics of Top Quarks

8.1. Selection of $t\bar{t}$ events and measurement of the cross sections

8.1.1. Introduction

The goal of top physics at the LHC is to characterise the properties of this heaviest fermion of the Standard Model by measuring observables in its production and decay exploiting all possible decay channels. Important examples are the production cross section and the mass and spin properties of the top quark.

Most of the top quarks at the LHC will be produced as $t\bar{t}$ pairs. The $t\bar{t}$ production cross section is estimated to be 830 pb [278] at NLO and the dominant production mechanisms are gluon-gluon fusion ($\approx 90\%$) and quark-anti-quark annihilation ($\approx$10%). Within the Standard Model the top quark decays almost exclusively to a W boson and a b quark. The decays of the $t\bar{t}$ system are then classified according to the decays of the W^+W^- system as dileptonic, semi-leptonic or fully hadronic. The W can decay into leptons, $e^-\bar{\nu}_e$, $\mu^-\bar{\nu}_\mu$, $\tau^-\bar{\nu}_\tau$, or into quarks, $u\bar{d}'$, $c\bar{s}'$, where the charge conjugate is implicit. Neglecting QCD corrections, branching fractions of 9/81 (11.1%) for the dileptonic, 36/81 (44.4%) for the semi-leptonic and 36/81 (44.4%) for the fully hadronic decay channel are obtained.

For our studies we use PYTHIA for the simulation of signal and background events. As it includes spin correlation in $t\bar{t}$ production also samples generated with TopReX are used for signal events.

8.1.2. Dileptonic channel

8.1.2.1. Event selection for 1 fb^{-1}. The very clean signature of this channel combined with a high signal-to-background ratio makes it possible to select $t\bar{t}$-events with simple kinematic cuts. The selection is therefore suitable for the expected early performance of the CMS detector and will allow to establish the signal as well as to measure the top mass at an early stage of the experiment.

For an integrated luminosity of 1fb^{-1} about 54000 signal events are expected according to the leading-order estimate of PYTHIA. The main backgrounds with a final state mimicking the signal are Z, WW, WZ and ZZ production accompanied by jets. Furthermore, events from semi-leptonic and fully-hadronic top-quark pair production with misidentified leptons and leptons from b-quark jets eventually constitute the dominating background. Here, dilepton events with W bosons decaying into τ-leptons are considered signal events if the τ lepton decays leptonically. Details of the analysis can be found in Reference [279].

Events are required to pass the Level-1 and High Level Trigger, in particular the single and dilepton subtriggers. In addition to trigger criteria, events must contain at least two jets and two oppositely charged leptons. Electrons are identified using an electron likelihood method combining various electromagnetic shower variables and track-to-supercluster-matching criteria. After this pre-selection about 15000 signal events are left in a 1fb^{-1} data set with a signal over background ratio of $S/B = 1/10$. The most important background at this stage consists of Z + jets production with an accepted cross section of about 120 pb and a similar final state.

Isolation criteria reduce the contribution from misidentified leptons and leptons from b-jets. For a lepton candidate no other track or calorimeter hits amounting to 10% or more of the lepton p_{T} are allowed in a cone of $\Delta R < 0.2$. Two charged leptons are then chosen with a discriminant based on the likelihood ratio in case of an electron, the energy deposited in a cone of $\Delta R = 0.2$ around the lepton axis and the p_{T} of the lepton.

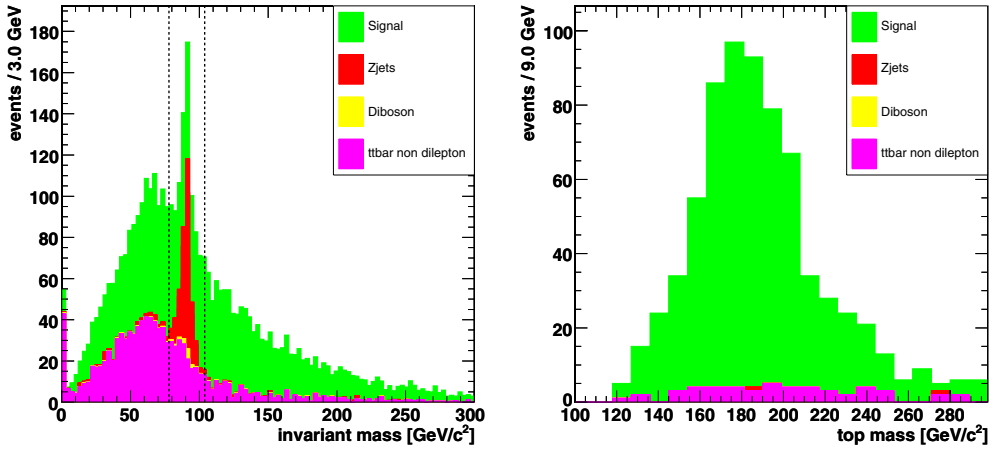

Figure 8.1. Left: Invariant mass of the two lepton candidates indicating the cut window to remove Z + jets events. Right: Most likely top mass after selection for 1fb^{-1}.

Both b-jets are selected with a discriminator based on the jet p_{T}, the invariant mass of tracks inside the jet and the output of the combined b-tagging algorithm [157]. Using this scheme the correct jets and leptons of the signal are selected for more than 90% of the events, if they could be reconstructed. It has been shown in reference [157] that, during the *first data taking phases* of the LHC, the degradation in b-tagging performance is still acceptable. This implies that the b-tagging results presented here remain essentially correct.

Figure 8.1 shows the invariant mass of the two lepton candidates. The Z mass peak of the invariant mass distribution of two same type leptons is used to remove the contamination due to Z + jets events. As a further improvement a cut on the b-tag discriminator is applied to the two selected jets.

The non-dilepton $t\bar{t}$ events usually contain more jets with a p_{T} greater than 30 GeV/c but do not contain two high p_{T} leptons. The second lepton candidate is considerably softer than the corresponding lepton from the signal decay channel. So a cut on the lower transverse momentum lepton is imposed with $p_{\mathrm{T}} > 20\,\mathrm{GeV/c}$. The two neutrinos in the decay of the W bosons lead to significant missing transverse energy $E_{\mathrm{T}}^{\mathrm{miss}}$ whereas the decay of Z bosons into electrons or muons does not generate $E_{\mathrm{T}}^{\mathrm{miss}}$. The cut $E_{\mathrm{T}}^{\mathrm{miss}} > 40\,\mathrm{GeV}$ further improves the signal to background ratio. At this stage about 1800 signal events are left with a signal over background ratio of $S/B = 7.3/1$.

The kinematics of the $t\bar{t}$ dilepton events yield an underconstrained equation system due to the two undetected neutrinos in the final state. However if, all other kinematic quantities have been measured it is possible to make a fit imposing m_W and assuming a top mass parameter in the range of 100 to 300 GeV/c^2. A weight can then be assigned to the different solutions obtained [279]. Figure 8.1 shows the distribution of the most likely top mass for signal and background events in the range $100\,\mathrm{GeV/c^2} < m_t < 300\,\mathrm{GeV/c^2}$.

The event topology of most of the background events passing the previous cuts does not satisfy the dilepton kinematical constraints. Therefore considering only candidates which give a mass estimate in the range of 100 to 300 GeV/c^2 further reduces the background and raises the signal over background ratio to about $S : B = 12 : 1$. The remaining background essentially contains only non-dilepton $t\bar{t}$ events. In a dataset equivalent to 1fb^{-1}, 657 signal events are selected with an overall efficiency of 1.2%.

We conclude that a measurement of the $t\bar{t}$ cross section and the top mass (see Section 8.2.1) in the dileptonic channel will be possible already with a modest amount of luminosity [279].

8.1.2.2. Event selection for higher luminosities. The trigger is based on the presence of one muon or electron which covers with high efficiency all the possible final states in this channel. The selection of events in this channel then requires after trigger selection the presence of just two oppositely charged leptons with $E_T > 20\,\text{GeV}$ within pseudorapidity ranges of ± 2.4 and ± 2.5 for muons and electrons respectively. Details are available in [279].

The reconstruction efficiency is good for both for muons and electrons. More than 97% of the generated muons are correctly reconstructed in the considered range, as well as 90% of the electrons, with p_T above $20\,\text{GeV/c}$ [279]. An electron is considered isolated if the total uncorrected E_T of the jets within a cone $\Delta R \leqslant 0.3$, minus the lepton E_T, is less than 30% of the lepton E_T. In a similar way a muon is considered isolated, if the sum of the p_T of all the tracks present in a cone of $\Delta R \leqslant 0.3$ minus p_T of the muon is less than $2\,\text{GeV/c}$. Candidate events must have $E_T^{\text{miss}} > 40\,\text{GeV}$. The analysis requires at least two jets with uncorrected $E_T > 20\,\text{GeV}$ detected within $|\eta| < 2.5$, where a jet is defined as a fixed-cone cluster with a cone size of $R = 0.5$. Jets produced by electrons are discarded before applying the previous selection by removing those which have an electromagnetic supercluster within $\Delta R = 0.2$ with a ratio between the electromagnetic energy of that supercluster and the uncorrected jet energy above 0.75.

b-tagging techniques based on the explicit reconstruction of a secondary vertex in a jet [157] are used to further suppress backgrounds in which no jets from b-quarks are present. The dominant backgrounds to dilepton $t\bar{t}$ events are those which have real leptons, real E_T^{miss} and jets originating from initial or final state radiation, arising mainly from dibosons (WW, WZ, and ZZ) + jets production, and also from top quark decays, either from the semi-leptonic channel or from tau decays producing leptons. This kind of backgrounds are expected to be determined using MC simulation. Instrumental backgrounds, are characterised in general by their large cross sections but not having real E_T^{miss}, among them are: Z + jets, Drell–Yan ($Z/\gamma^\star \to \ell^+\ell^-$) production, "fake" leptons in $W \to \ell\nu$ + jet events where a jet is falsely reconstructed as a lepton candidate. In principle it is harder to estimate their contribution to the final sample using MC simulation.

After this selection an efficiency close to 5% is obtained, with a very high rejection of all the backgrounds considered at the level of $10^{-3} : 1$ or better, as shown in Table 8.1. A S/B value of 5.5 is obtained, the main background being the one arising from the dilepton channel itself in which at least one of the W decays into $\tau\nu_\tau$ and with a subsequent leptonic tau decay.

Different sources of systematic uncertainties have been identified that affect event selection and background determination and thus the cross section measurement. Detailed studies [279] of these sources have been done based mainly on the results of the studies performed in [7] and [201]. Among the most important experimental sources are uncertainties on the jet energy scale and the b-tag efficiency. The impact of theoretical and phenomenological uncertainties such as those on hadron fragmentation and PDF have been studied using samples generated with different PYTHIA parameters and simulated and reconstructed with the CMS fast simulation and reconstruction program. The uncertainty in the cross section coming from the luminosity estimation was taken as 3% as expected for $10\,\text{fb}^{-1}$ integrated luminosity. As the non-$t\bar{t}$ background is small it does not contribute significantly to the uncertainty. The results are summarised in Table 8.2 and lead to an estimated total error on the $t\bar{t}$ cross section measured in the dileptonic channel using electrons and muons of $\Delta\sigma_{t\bar{t}}/\sigma_{t\bar{t}} = 11\%\,(syst)\ \pm 0.9\%\,(stat)\ \pm 3\%\,(luminosity)$.

Table 8.1. Cumulative effect of the different selection criteria applied to the simulated $t\bar{t}$ dilepton sample (electrons and muons) and simulated backgrounds. The column denoted as τ corresponds to $t\bar{t}$ dilepton sample in which at least one W decays into a τ lepton. The numbers correspond to LO accepted cross sections in pb.

	Signal	τ	WW	WZ	ZZ	Z + jets	other $t\bar{t}$
Before selection	24.3	30.4	7.74	0.89	0.11	3912	438
Level-1 + HLT	19.4	15.1	4.4	0.37	0.07	657	92
2 jets $E_{\mathrm{T}} > 20$ GeV	11.5	9.8	0.6	0.012	0.006	23.9	73.1
$E_{\mathrm{T}}^{\mathrm{miss}} > 40$ GeV	9.6	8.1	0.5	0.01	0.003	5.8	53.6
Two opp. charged leptons	3.2	0.42	0.04	0.001	0.001	1.17	0.12
b-tag of two highest E_{T} jets	1.12	0.15	0.002	$\sim 10^{-4}$	$\sim 10^{-5}$	< 0.01	0.05

Table 8.2. Uncertainties in the $t\bar{t}$ dilepton cross section determination for 10 fb^{-1}.

Effect	$\Delta\sigma_{t\bar{t}\ dil\ e/\mu}/\sigma_{t\bar{t}\ dil\ e/\mu}$
Jet Energy Scale	3.6%
b-tag efficiency	3.8%
Lepton reconstruction	1.6%
$E_{\mathrm{T}}^{\mathrm{miss}}$	1.1%
ISR and FSR	2.5%
Pile-Up	3.6%
Underlying Event	4.1%
Heavy quark fragmentation	5.1%
PDF uncertainties	5.2%
Statistical uncertainty	0.9%
Integrated luminosity	3%

8.1.2.3. Top decays to tau leptons. In this section studies performed to select events with τ leptons in the final state are presented. We consider here dileptonic $t\bar{t}$ decays with one tau lepton decaying into hadrons in the final state $t\bar{t} \to b\bar{b}\tau\nu_\tau\ell\nu_\ell$, $(\ell = \mathrm{e}, \mu)$. The measurement of the ratio $BR(t\bar{t} \to \ell\tau + X)/BR(t\bar{t} \to \ell\ell + X)$ will allow to set new limits on the presence of non-standard physics in top decays. Furthermore, this channel is a source of background for Supersymmetry and Higgs searches, as well as for the other dileptonic top channels.

Tau candidates are selected and identified following the method of the MSSM Higgs and HLT analyses [280], adapting the different selection criteria to the momentum range in which tau candidates are expected to be produced in top decays [279]. The hadronic tau identification efficiency obtained in the dilepton samples is about 30% using this method as can be seen in Fig. 8.2.

Event selection proceeds in a similar way as in Section 8.1.2.2 but only one isolated lepton (electron or muon) is allowed. One isolated tau candidate separated from the isolated lepton has to be present, and the isolated lepton and the tau candidate must have opposite charges. The effect of these selections are described in detail for the $t\bar{t}$ sample in Table 8.3. b-tag for the two accompanying jets is also required. An efficiency close to 2% is obtained, with a very high rejection of all the backgrounds considered. A S/B value close to 1 is obtained, the main background being the one arising from the $t\bar{t}$ semi-leptonic channel. The majority of the systematic uncertainties are described in Section 8.1.2.2. There is another systematic uncertainty intrinsic to this analysis due to the τ reconstruction and identification. Based on preliminary studies, we assigned a 12% uncertainty to the τ reconstruction and identification. Statistical uncertainty in the cross section determination is about 1.3% for an

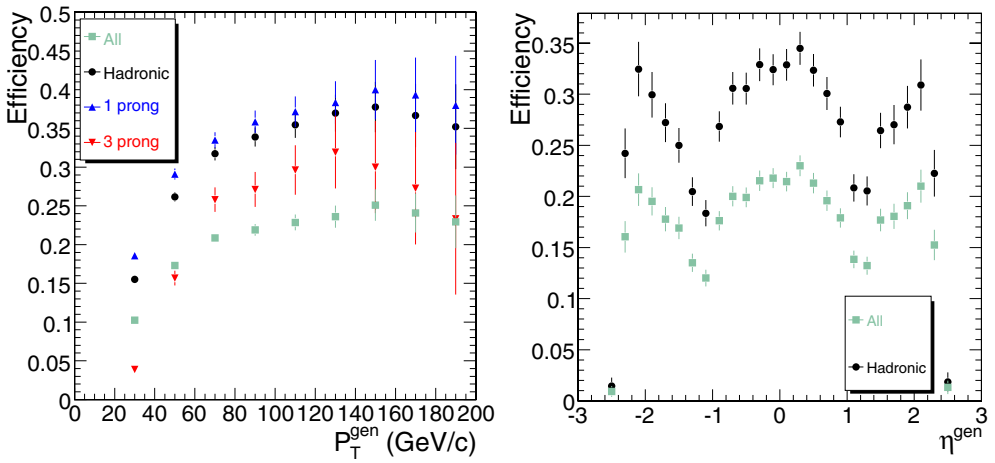

Figure 8.2. Reconstruction efficiency of tau candidates as a function of p_T and η. Errors are statistical only.

Table 8.3. Cumulative effect of the different selection criteria applied to the simulated $t\bar{t}$ sample. Numbers correspond to LO accepted cross sections.

Cut	Efficiency times cross sections (pb)			
	$t\bar{t}$ (signal)	$t\bar{t}$ (other dilepton)	$t\bar{t}$ (semi-leptonic)	$t\bar{t}$ (hadronic)
Before selection	15.62	38.94	218.88	218.88
Trigger	8.61	25.40	85.90	2.08
2 jets	6.97	18.90	80.08	2.04
$\geqslant 1$ Iso lepton	4.27	13.11	34.93	0.11
$E_T^{miss} \geqslant 40$ GeV	3.58	10.89	26.41	0.05
1 lepton	3.48	6.73	25.24	0.04
τ cand. with opp. Q	0.75	0.20	0.75	0.001
b-tagging	0.29	0.07	0.30	0.0005

integrated luminosity of $10\,\text{fb}^{-1}$. Then the relative uncertainty in the estimation of the cross section is given by $\Delta\sigma_{t\bar{t}\,dil\,\tau,e\mu}/\sigma_{t\bar{t}\,dil\,\tau,e\mu} = 16\%\,(syst)\ \pm 1.3\%\,(stat)\ \pm 3\%\,(luminosity)$.

8.1.3. Semi-leptonic channel

The semi-leptonic $t\bar{t}$ decay has a final state topology of four hadronic jets of which two originate from a b-quark, an isolated lepton and missing transverse momentum. In this section, we consider the measurement of the cross section of the semi-leptonic $t\bar{t}$ production where the lepton is a muon [281].

Both the Level-1 and the High-Level Trigger selection criteria are applied on the simulated events, resulting in the efficiencies shown in Table 8.4. The single-muon trigger stream was used. The jets are reconstructed from the combined electromagnetic and hadronic calorimeter energy deposits and clustered with the Iterative Cone algorithm using an opening angle of $\Delta R = 0.5$. A transverse energy threshold of 0.5 GeV is applied on the input objects

Table 8.4. Overview of the selection criteria applied. The expected S/B values take into account the respective Leading-Order cross-sections of the processes.

	Semi-lept. $t\bar{t}$	Other $t\bar{t}$	W + 4j	Wbb + 2j	Wbb + 3j	S/B
Before selection	365k	1962k	82.5k	109.5k	22.5k	5.9
L1 + HLTTrigger	62.2%	5.30%	24.1%	8.35%	8.29%	7.8
Four jets $E_T > 30\,\text{GeV}$	25.4%	1.01%	4.1%	1.48%	3.37%	9.9
$p_T^{lepton} > 20\,\text{GeV/c}$	24.8%	0.97%	3.9%	1.41%	3.14%	10.3
b-tag criteria	6.5%	0.24%	0.064%	0.52%	0.79%	25.4
Kinematic fit	6.3%	0.23%	0.059%	0.48%	0.72%	26.7
Selected cross section (pb)	5.21	1.10	0.10	0.08	0.05	26.7
Scaled $\mathcal{L} = 1\,\text{fb}^{-1}$	5211	1084	104	82	50	26.7

before clustering. Optimisation of the parameter settings of the clustering algorithms are considered in [282]. Only the jets in the vicinity of the primary vertex are considered in the analyses, rejecting in general those jets with a small transverse momentum. The energy scale of the reconstructed jets is calibrated using the methods described in [283]. Among the list of muon candidates identified flavour, the muon originating directly from the W boson decay is selected following the procedure described in [284]. The transverse momentum components of the unobserved neutrino are estimated via the missing transverse momentum which balances the vectorial sum of the energy deposits in the calorimeter above the transverse energy threshold mentioned.

The event selection consists of a series of sequential cuts on kinematic or topological variables. The event is required to have at least four jets after applying the primary vertex constraint with a calibrated transverse energy, E_T, exceeding 30 GeV and within a pseudo-rapidity in the range of the tracker, $|\eta| < 2.4$. If more than four jets match this criterion, the four leading jets are selected as those with the highest E_T. Of these four jets, two have to be b-tagged according to the method applying a combined b-tag variable described in [281, 285, 286]. The selected lepton is required to be within the tracker acceptance and to have a transverse momentum larger than 20 GeV/c.

After classifying two of the four reconstructed jets as b-quark and the other two as light quark jets, only two jet combinations remain to reconstruct the hadronically-decaying top. A kinematic fit [167] was applied on the reconstructed event for both jet combinations forcing the reconstructed W boson mass to its precisely known value. Before applying the kinematic fit the energy scale of the light quark jets is corrected for an overall bias in the reconstructed W boson mass. Following the method described in [287] after the event selection mentioned above, an inclusive jet energy scale correction of -9.7% was obtained and applied to light quark jet candidates. The event is finally selected if the fit converged for at least one of the combinations.

The selection efficiency for the signal events is estimated to be $6.28 \pm 0.04\%$. The fraction of $t\bar{t}$ signal events in the selected sample of inclusive $t\bar{t}$ decays is estimated to be $82.8 \pm 0.2\%$. The signal-to-background ratio after the event selection is 26.7, where all $t\bar{t}$ decay channels are considered as signal. Hence the systematic effect of the background contribution is minor. It is shown in [281] that after the event selection topological observables will not help much in differentiating between signal and background. The cross section is therefore estimated from counting events. The statistical uncertainty on the estimated cross section is 1.2%, 0.6% and 0.4% for integrated luminosities of $1\,\text{fb}^{-1}$, $5\,\text{fb}^{-1}$ and $10\,\text{fb}^{-1}$, respectively.

Table 8.5. Overview of the systematic uncertainties on the cross section.

	$\Delta\hat{\sigma}_{t\bar{t}(\mu)}/\hat{\sigma}_{t\bar{t}(\mu)}$		
	1 fb^{-1}	5 fb^{-1}	10 fb^{-1}
Simulation samples (ε_{sim})		0.6%	
Simulation samples (F_{sim})		0.2%	
Pile-Up (30% On-Off)		3.2%	
Underlying Event		0.8%	
Jet Energy Scale (light quarks) (2%)		1.6%	
Jet Energy Scale (heavy quarks) (2%)		1.6%	
Radiation (Λ_{QCD}, Q_0^2)		2.6%	
Fragmentation (Lund b, σ_q)		1.0%	
b-tagging (5%)		7.0%	
Parton Density Functions		3.4%	
Background level		0.9%	
Integrated luminosity	10%	5%	3%
Statistical Uncertainty	1.2%	0.6%	0.4%
Total Systematic Uncertainty	13.6%	10.5%	9.7%
Total Uncertainty	13.7%	10.5%	9.7%

Systematic effects are introduced only on the signal events, changing the efficiency of the event selection. Similar effects on the background samples should be a second order effect on the inferred cross section. For the theoretical or phenomenological uncertainties the prescription of [201] was used as described in [281]. The list of systematic uncertainties is shown in Table 8.5. The dominant systematic effects are b-tagging, and in the early stage the uncertainty on the integrated luminosity. For an extended discussion on the studied systematic effects we refer to [281]. As a consequence of the kinematic fit, the uncertainty on both the light- and heavy-quark jet energy scale results in a limited systematic uncertainty, of about 1.6%.

The total relative systematic uncertainty on the cross section is 10.5% which can be compared to a relative statistical uncertainty of 0.6% at 5 fb^{-1}. The total uncertainty of 10.5% scales with the integrated luminosity as shown in Fig. 8.3. In this plot it is assumed that the uncertainty on the determination of the integrated luminosity scale as the inverse square root of the integrated luminosity. At an integrated luminosity of about 5 fb^{-1} the total uncertainty is dominated by the uncertainty on the *b*-tagging performance. For the uncertainty on the *b*-tagging efficiency a conservative 5% is taken according to [286] although the Tevatron experience shows that a value of 2% can be reached [288, 289].

8.1.4. Fully hadronic channel

The fully hadronic final state, characterised by a six-jets topology $t\bar{t} \to WWb\bar{b} \to qqqqb\bar{b}$, has the largest branching fraction (46%), and kinematics that can be fully reconstructed. However, this channel is affected by a large background from QCD multi-jet production, which makes the isolation of the signal rather challenging, and internal jet-parton permutation uncertainties. Improvements in the signal-to-background ratio are possible by requiring the presence of *b*-quark jets and by selecting central and very high-energy kinematic configurations which are expected for jets arising from the decay of a massive object like the top quark. A specific multi-jet trigger which uses *b*-tagging information has been devised for this analysis and an optimised selection has been applied. The analysis is described in detail in [279].

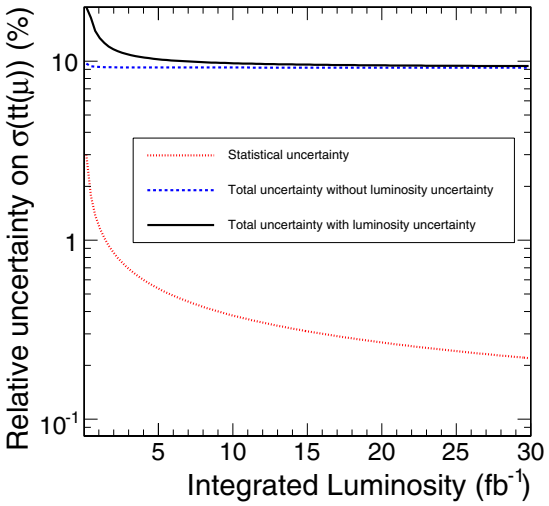

Figure 8.3. Statistical and total uncertainty on the inferred cross section of the process $pp \to t\bar{t} \to bq\bar{q}b\mu\nu_\mu$ as a function of the integrated luminosity.

The signal sample consists of 500000 inclusive $t\bar{t}$ events, from which a sub-sample of 230000 fully hadronic $t\bar{t}$ events is extracted. The background consists of 1.5 million multi-jet events (QCD) generated with $50 < \hat{p_T} < 470\,\mathrm{GeV/c}$, where the $\hat{p_T}$ symbol indicates the transverse momentum of the most energetic parton of the hard scattering before the final-state radiation processes.

8.1.4.1. Trigger pre-selection and event selection. The trigger pre-selection uses the inclusive jet trigger envisaged in [76] and a special inclusive b-jet trigger [290]. The inclusive b-jet trigger combines in the first stage the b-tagging requirement with an inclusive jet trigger which applies tuned E_T thresholds of 350 GeV for single jets, 150 GeV for 3-jet and 55 GeV for 4-jet topologies; then a b-tagging based on pixel and regional track and vertex reconstruction is performed on the two most energetic jets. The trigger requires either multiple jets in the event or a b-tagged jet among the two highest-E_T jets. After the trigger pre-selection the QCD rate is reduced to 23 Hz, the signal efficiency is 16.8% and the signal to background ratio, S/B, amounts to $1/300$.

The selection is designed to optimise the statistical significance $S/\sqrt{S+B}$ for an integrated luminosity of $\mathcal{L} = 1\,\mathrm{fb}^{-1}$. The first step of the selection requires a topology of $6 \leqslant N_{jet} \leqslant 8$. For a jet to be counted, the jet pseudorapidity must satisfy $|\eta| < 2.4$ and its transverse energy must be greater than 30 GeV. Event shape variables, potentially able to separate the signal from the background are then taken into account. The useful ones are centrality, aplanarity and non-leading jet total transverse energy obtained removing the two most energetic jets ($\sum_3 E_T$) of which distributions are shown in Fig. 8.4. After the selection b-tagging is applied to the surviving samples of $t\bar{t}$ fully hadronic and QCD events. Selection criteria of at least one b-jet and two b-jets are considered.

Table 8.6 summarises the selection applied in cascade. The signal-to-background ratio amounts to $1/17$ and $1/9$ for the 1 and 2 b-tag samples,respectively, and resulting in signal efficiencies of 3.8% and 2.7%.

The signal efficiency relative to the total inclusive $t\bar{t}$ sample, to be used in the calculation of the total $t\bar{t}$ production cross section, becomes 2.3% (1.6%), respectively for the 1 (2) b-tag requirement. The estimated statistical uncertainty on the cross section is reported in Table 8.7.

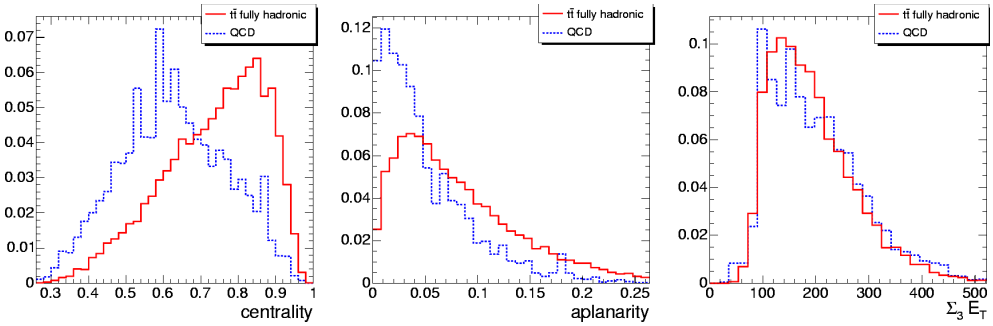

Figure 8.4. Distributions of centrality, aplanarity and $\sum_3 E_T$ for $t\bar{t}$ and QCD events (normalised to the same area).

Table 8.6. $t\bar{t}$ fully hadronic and QCD effective cross sections, signal-to-background ratio, statistical significance for 1 fb^{-1} and signal efficiency at each step of the selection.

Selection	Requirement	$\sigma\varepsilon$ [pb]	$\sigma\varepsilon_{\mathrm{QCD}}$ [pb]	S/B	$S/\sqrt{S+B}$	ε (%)
Before Selection (PYTHIA LO)		225	25M	$1/10^5$	0.04	100
Trigger	HLT multi-jet+b-jet	38	11600	1/300	11.1	16.8
Event	$6 \leqslant N_{jet} \leqslant 8$	35	7900	1/225	12.4	15.5
	$E_T \geqslant 30$ GeV	15	930	1/60	15.4	6.6
	centrality $\geqslant 0.68$	9.9	324	1/33	17.1	4.4
	aplanarity $\geqslant 0.024$	9.0	251	1/28	17.7	4.0
	$\sum_3 E_T \geqslant 148$ GeV	9.0	229	1/25	18.4	4.0
b-tagging	1 b-tag	8.6	148	1/17	21.7	3.8
	2 b-tag	6.0	54	1/9	24.1	2.7

Table 8.7. Number of $t\bar{t}$ and QCD events, $t\bar{t}$ efficiency, absolute and relative statistical uncertainties expected on the cross section measurement for an integrated luminosity of 1fb^{-1}.

Requirement	$\mathcal{L} = 1$ fb^{-1}				
	$t\bar{t}$ events	QCD events	ε (%)	$(\Delta\sigma)_{stat}$ [pb]	$(\Delta\sigma/\sigma)_{stat}$ (%)
1 b-tag	11500	148000	2.3	17	3.5
2 b-tag	8000	54000	1.6	15	3.0

Sources of systematic uncertainty are studied as described in detail in [201] and [7]. From the experience of CDF and DØ experiments at Tevatron [291], one of the dominating systematic uncertainties arises from jet energy scale. The systematic uncertainty related with the trigger selection is calculated considering contributions from b-tagging and jet energy scale. Table 8.8 summarises the contributions to the total uncertainty on the cross section, which combined lead to a relative uncertainty of $\Delta\sigma/\sigma = 3\%(stat) + 20\%(syst) + 5\%(luminosity)$.

8.1.4.2. Event selection based on neural net. A more refined selection is based on a neural net exploiting the same variables considered so far. Such approach is attempted in order to investigate the possibility of improving the S/B ratio and/or the efficiency. The previous

Table 8.8. Contributions to the systematic uncertainty on the $t\bar{t}$ cross section measurement in the fully hadronic channel (cut based approach).

	$\Delta\sigma/\sigma$ (%)
HLT	5.9
Pile Up	10.0
Underlying Event	4.1
Fragmentation	1.9
PDF	4.2
IS/FS Radiation	7.9
Jet Energy Scale	11.2
b-tagging	2.0
Background	5.0
Integrated Luminosity	5.0

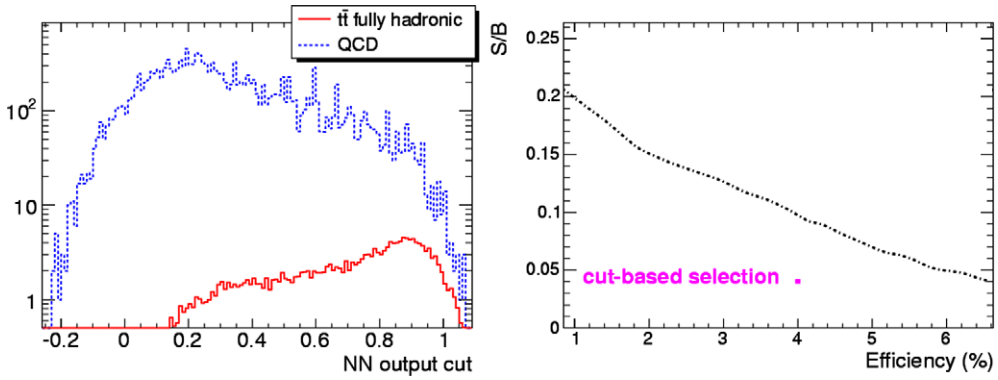

Figure 8.5. Left: distribution of the neural net output for $t\bar{t}$ and QCD. Right: signal-to-background ratio as function of the signal efficiency. For comparison the result of the cut-based selection is also shown.

selection, called “cut-based", could represent a more conservative approach for the first LHC analyses.

The most effective neural network configuration studied is applied to the $t\bar{t}$ and QCD events satisfying the topology request of $6 \leqslant N_{jet} \leqslant 8$ (jet pseudorapidity $|\eta| < 2.4$) after a cut on jet transverse energy of $E_{\mathrm{T}} > 25\,\mathrm{GeV}$ and consists of 6 input nodes: E_{T} of the first and sixth jet with the jets ordered in increasing E_{T}, centrality, aplanarity, $\sum_3 E_{\mathrm{T}}$ and sphericity. The performance of the neural net is shown in Fig. 8.5 which compares the output distributions for signal and QCD background. The S/B ratio as a function of the $t\bar{t}$ efficiency is also shown. With respect to the cut-based selection, the request for a neural net output $\geqslant 0.77$ improves the S/B ratio from $1/25$ to $1/10$ with same efficiency of about 4%.

As done after the cut-based selection, a b-tagging is applied to the surviving samples of $t\bar{t}$ fully hadronic and QCD events, and selection criteria of at least one b-jet and two b-jets are considered. Improved signal-to-background ratio, amounting to $1/7$ ($1/3$) respectively for 1 (2) b-tag samples, can be achieved using the neural net keeping the same signal efficiencies of 3.8% (2.7%). This means an estimated relative statistical uncertainty on the cross section of 2.3% (2.0%), with the same expected number of $t\bar{t}$ events for an integrated luminosity of $\mathcal{L} = 1\,\mathrm{fb}^{-1}$.

8.2. Measurement of the top quark mass

8.2.1. Dileptonic events

The dilepton channel benefits of a clean signature and a large signal-to-background ratio even though the presence of two neutrinos prevents a direct reconstruction of the top-quark mass. However, the event kinematic retains a large sensitivity to the top mass which can be exploited in various ways. The method presented here is discussed in more detail in [279].

The six unmeasured kinematic quantities corresponding to the momentum components of the two neutrinos are reduced by assuming momentum balance in the transverse plane, by imposing the m_W constraint and by requiring both top-quark masses to be equal. The event kinematics can then be written as a fourth order polynomial with the top mass as a parameter. For each candidate event we step through top mass values in the range $100\,\mathrm{GeV/c^2} \leqslant m_t \leqslant 300\,\mathrm{GeV/c^2}$ in $1\,\mathrm{GeV/c^2}$ steps and weight the kinematic solutions, including their fourfold ambiguity, with the Standard Model expectations of the neutrino momentum spectrum. For each event the most likely solution, i.e. the solution with the highest weight, is retained. The mass distribution of these most likely solutions is shown in Fig. 8.1 for $1\mathrm{fb}^{-1}$. The figure shows a clear mass peak at the expected value for the fully-simulated and reconstructed events. A Gaussian fit to the signal in a range corresponding to 40% of the maximum yields $m_t = 178.5 \pm 1.5\,\mathrm{GeV/c^2}$ for an input top mass of $175\,\mathrm{GeV/c^2}$, where the uncertainty is statistical. With $10\,\mathrm{fb}^{-1}$ the statistical uncertainty will be reduced to $0.5\,\mathrm{GeV/c^2}$. The background is small and essentially flat and does not affect the mass determination significantly.

The main systematic effects are due to the assumptions used to reduce the complexity of the kinematic equation system and to detector effects. The dominating systematic effect in the first category is the uncertainty on the initial and final-state radiation which changes the amount of transverse momentum of the $t\bar{t}$-system and the kinematic constraints. This results in an uncertainty on the top mass of $\Delta m_t = 0.3\,\mathrm{GeV/c^2}$ [201]. The zero width approximation for both the W bosons and the top quarks in the equation system gives rise to another shift of about $0.1\,\mathrm{GeV/c^2}$.

The expected uncertainty on the jet energy scale for the early data amounts to 15%, independent of the jet p_T, which corresponds to an uncertainty of $\Delta m_t = 4.2\,\mathrm{GeV/c^2}$ for the first $1\,\mathrm{fb}^{-1}$ of integrated luminosity. This uncertainty is reduced to $2.9\,\mathrm{GeV/c^2}$ with an improved calibration in 1–$10\,\mathrm{fb}^{-1}$ based on photons and jets, especially jets from W-boson decays in semi-leptonic and fully-hadronic $t\bar{t}$ events. Further improvement in the knowledge of the jet energy scale after $10\,\mathrm{fb}^{-1}$ are expected to reduce this uncertainty to about $1\,\mathrm{GeV/c^2}$.

In conclusion, the kinematic reconstruction of the dilepton channel will allow an early measurement of the top-quark mass. Assuming that the goal for a precise jet energy scale determination for b-quarks can be achieved the expected precision on the top mass in this channel with $10\,\mathrm{fb}^{-1}$ is $\Delta m_t = 0.5\,\mathrm{GeV/c^2}(stat) \pm 1.1\,\mathrm{GeV/c^2}(sys)$.

8.2.2. Semi-leptonic events

The semi-leptonic $t\bar{t}$ decay is traditionally called the *golden channel* for measuring the top-quark mass. A measurement based on advanced analysis tools is described in detail in [292]. The event reconstruction and initial event selection follows the one of Section 8.1.3. For the event to be selected, exactly two out of the four leading jets are b-tagged and the other two need to be anti-b-tagged. The four leading jets should not overlap in order to reduce ambiguities in the jet energy scale calibration procedure. The efficiency of each sequential cut is shown in Table 8.9.

Table 8.9. Overview of the selection criteria applied after the lepton cut $p_T^{lepton} > 20\,\mathrm{GeV/c}$ in Table 8.4.

	Signal	Other $t\bar{t}$	W + 4j	Wbb + 2j	Wbb + 3j	S/B
Before selection	365k	1962k	82.5k	109.5k	22.5k	0.032
b-tag criteria	5.5%	0.21%	0.052%	0.47%	0.70%	3.73
No jet overlap	3.0%	0.11%	0.027%	0.25%	0.44%	3.87
P_{χ^2}-cut 20%	1.4%	0.039%	0.0097	0.061	0.07	5.3
P_{sign}-cut 80%	1.2%	0.025%	0.0085	0.052	0.05	6.8
P_{comb}-cut 50%	0.7%	0.013%	0.0036	0.013	0.	8.2
Scaled $\mathcal{L} = 1\,\mathrm{fb}^{-1}$	588	64	6	2	0	8.2

The amount of events produced via a different $t\bar{t}$ decay channel in the selected event sample is reduced by a likelihood-ratio method combining three kinematic observables resulting in a variable L_{sign} which is transformed into a probability P_{sign} for the selected event to be a semi-leptonic muon $t\bar{t}$ event. An extra sequential cut is applied by requiring this probability P_{sign} to exceed 80%.

Among the four reconstructed jets, three have to be chosen to form the hadronic decaying top quark. The efficiency and purity of this selection was significantly enhanced by applying a second likelihood ratio method combining the information from several sensitive variables. The jet combination with the largest L_{comb} value is taken as the best pairing. The L_{comb} value is transformed into a probability P_{comb} for the chosen combination to be the correct one. The event probability P_{comb} is used in the event selection where events are selected if their value for P_{comb} exceeds 60%, increasing the purity of the selected jet pairings to 81.6% in the mass window of $25\,\mathrm{GeV/c^2}$ around the expected m_t of about $175\,\mathrm{GeV/c^2}$.

For each jet combination a kinematic fit was applied as described which imposes the W-boson mass for the hadronically-decaying W boson in the event [167]. Only jet combinations are considered with a probability of the kinematic fit calculated from its χ^2/ndf exceeding 20%. For some events none of the jet combinations fulfill this criterium, therefore reducing the total event selection efficiency. The fraction of fully hadronic $t\bar{t}$ events selected is negligible (less than 0.05 events expected at $1\,\mathrm{fb}^{-1}$). From this we conclude that the also influence of QCD produced jet events is minor.

When estimating m_t from the selected event sample by a simple Gaussian fit in a range of $20\,\mathrm{GeV/c^2}$ in both directions around the modal bin, a value of $176.5 \pm 0.65\,\mathrm{GeV/c^2}$ is obtained before applying the kinematic fit and $172.2 \pm 0.48\,\mathrm{GeV/c^2}$ after applying the kinematic fit, for an input value of $175\,\mathrm{GeV/c^2}$. The errors reflect the statistical precision of the available Monte Carlo signal sample. The top quark mass after the kinematic fit is shown in Fig. 8.6.

Rather than developing m_t estimators on samples of events, an event-by-event likelihood approach is used to estimate m_t from the fitted kinematics of the three jets of the hadronically decaying top quark. The uncertainty on m_t for each event is determined from the covariance matrices of the kinematic fit. This uncertainty can either be assumed Gaussian or the full m_t range can be explicitly scanned with the kinematic fit.

To obtain information about the true value of M_t we convolute the reconstructed resolution function or ideogram with the theoretical expected probability density function $P(m_t|M_t)$ in the reconstruction space

$$\mathcal{L}_i(M_t) = \int P(\{\overline{p}_j\}|m_t) \cdot P(m_t|M_t)\, dm_t \tag{8.1}$$

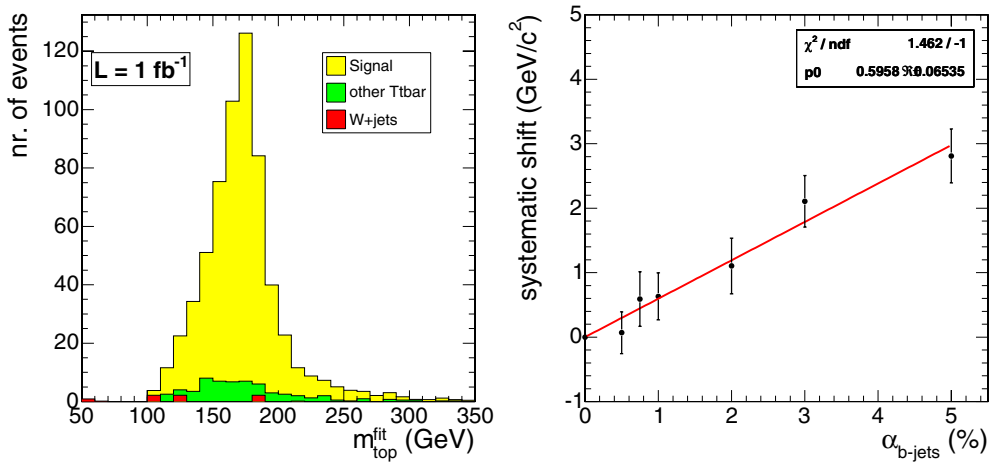

Figure 8.6. Left: Distribution of the mass of the hadronic decaying top quark for the selected events after applying the kinematic fit. Right: Estimated shift in $M_t^{FullIdeo}$ versus a relative shift α applied on the inclusive heavy quark jet energy scale.

where one integrates over the kinematic relevant range of m_t to obtain a likelihood function $\mathcal{L}_i(M_t)$ for each event i. Several contributions are added in the expected density $P(m_t|M_t)$: a Breit–Wigner shape for the correct jet combinations $S(m_t|M_t)$, a parameterised combinatorial background contribution $B_{comb}(m_t)$ and a parameterised background contribution $B_{proc}(m_t)$. This results in a function

$$P(m_t|M_t) = P_{sign} \cdot [P_{comb} \cdot S(m_t|M_t) + (1 - P_{comb}) \cdot B_{comb}(m_t)] + (1 - P_{sign}) \cdot B_{back}(m_t) \quad (8.2)$$

where each contribution is weighted according to the probabilities extracted from the observed event. After combining the likelihoods $\mathcal{L}_i(M_t)$ from all selected events, a maximum likelihood method is applied to obtain the best value for the estimator $\hat{M}_t$.

The linearity of the estimators have been checked and the slopes are found to be compatible with unity. The width of the pull distribution of the top quark mass estimators $\hat{M}_t$ are found to be 0.82 for $\hat{M}_t^{fit}$ (simple fit on reconstructed mass spectrum), 1.04 for $\hat{M}_t^{ParIdeo}$ (convolution with the parameterised ideogram) and 1.02 for $\hat{M}_t^{FullIdeo}$ (convolution with the full scanned ideogram). The resulting top quark mass for the estimator $\hat{M}_t^{fit}$ applied on the simulated events samples with a generated top quark mass of 175 GeV/c^2 is 174.16 ± 0.59 GeV/c^2, hence reflecting a bias of -0.84 GeV/c^2. For the convolution method this is 170.65 ± 0.54 GeV/c^2 and 172.42 ± 0.31 GeV/c^2 for respectively the $\hat{M}_t^{ParIdeo}$ and the $\hat{M}_t^{FullIdeo}$ estimator. Figure 8.7 illustrates the results.

Several systematic effects introduce an uncertainty on the top quark mass estimator. They originate from our understanding of the detector performance, the robustness of the reconstructed objects, for example jets, and the general description of the proton collisions in the simulation. A full description can be found in [292]. The estimation of the systematic uncertainties follows that of the cross section measurement in Section 8.1.3. We conservatively conclude that a total precision on the top quark mass of 1.9 GeV/c^2 can be reached with 10 fb^{-1} of data. The uncertainty is dominated by systematic effects like pile-up collisions and the knowledge of the jet energy scale of b-quark jets (see Fig. 8.6).

After achieving a better understanding of the accelerator settings and the detector performance, however, the total uncertainty will decrease. Our understanding of the

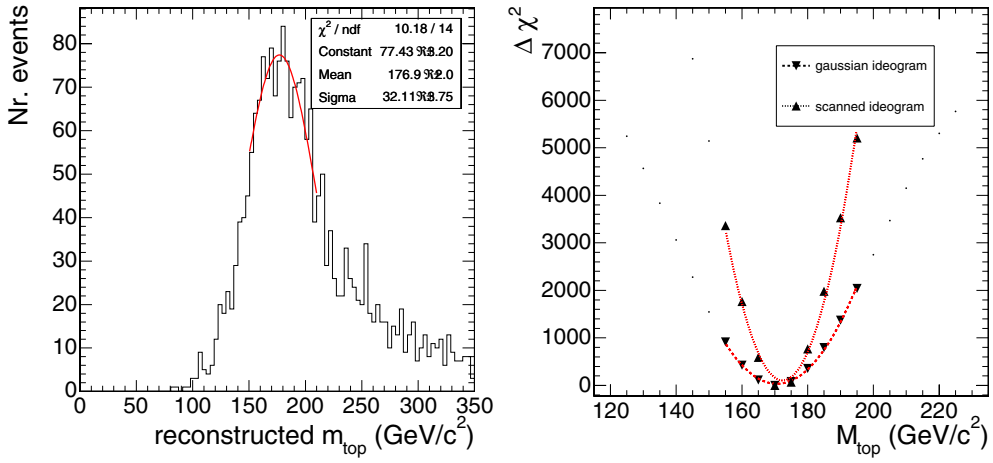

Figure 8.7. Distribution of the mass of the hadronic decaying top quark before the kinematic fit used for the $\hat{M}_t^{fit}$ estimator (left) and the combined $\Delta\chi^2(M_t)$ function over all events for both ideogram based estimators $\hat{M}_t^{ParIdeo}$ and $\hat{M}_t^{FullIdeo}$ (right).

underlying event model will improve in the future significantly when new tuning data become available. The magnitude of pile-up collisions could be monitored to the level of 10%. To take into account the overlap between the pile-up and the jet energy scale uncertainty, the systematic shift due to a 10% variation in the pile-up collisions is divided by two. The uncertainty on the energy scale of b-quark jets can be extrapolated to about 1.5% after a better understanding of the detector performance and with the application of advanced tools like energy flow algorithms or selecting jets only in well understood regions in the detector. The measurement of the b-tag efficiency [286] is dominated by systematic uncertainties of radiation effects. The experience at the Tevatron collider [288, 289] illustrates that an uncertainty of 2% could be reached.

Table 8.10 summarises and combines the extrapolated systematic uncertainties on each of the top quark mass estimators. The uncertainty on the inferred top quark mass of about $1.2\,\mathrm{GeV/c^2}$ is dominated by the uncertainty on the energy scale of the b-quark jets. This relative uncertainty is taken to be 1.5% which defines a goal for the performance of jet calibration methods.

8.2.3. Fully hadronic events

The selection described in Section 8.1.4.1, including the demand for the two b-tags, forms the basis for a selection of fully hadronic $t\bar{t}$ events suitable for a kinematic top-mass reconstruction. An additional cut on the two leading jets, $100\,\mathrm{GeV/c} < p_\mathrm{T} < 300\,\mathrm{GeV/c}$, is effective against background from mis-reconstructed events and combinatorial background.

The six partons in $pp \to t\bar{t} \to bW^+\bar{b}W^- \to bq_1\bar{q}_1'\bar{b}q_2\bar{q}_2'$ are matched to six reconstructed jets by picking the matching which minimises the sum of the angular separation between reconstructed jet and matched parton. Only jets satisfying our initial jet-definition, $p_\mathrm{T} > 30\,\mathrm{GeV/c}$ and $|\eta| < 2.4$, as employed in the selection, are taken into account in the matching process. Based on the amount of the angular separation three disjunctive classes of signal events are defined: good (36%), half-good (45%) and bad jet-parton-matching (19%). The first class being the events where all six partons are matched well by jets, the second class where only the three partons from one top are matched well by jets. The reason for the mismatch

Table 8.10. Overview of all uncertainty components on the top quark mass estimators, extrapolated to a better understanding of both the proton collisions at the LHC and the detector performance.

	Standard Selection		
	Gaussian Fit Δm_t (GeV/c^2)	Gaussian Ideogram Δm_t (GeV/c^2)	Full Scan Ideogram Δm_t (GeV/c^2)
Pile-Up (5%)	0.32	0.23	0.21
Underlying Event	0.50	0.35	0.25
Jet Energy Scale (1.5%)	2.90	1.05	0.96
Radiation (λ_{QCD}, Q_0^2)	0.80	0.27	0.22
Fragmentation (Lund b, σ_q)	0.40	0.40	0.30
b-tagging (2%)	0.80	0.20	0.18
Background	0.30	0.25	0.25
Parton Density Functions	0.12	0.10	0.08
Total Systematical uncertainty	3.21	1.27	1.13
Statistical Uncertainty (10 fb^{-1})	0.32	0.36	0.21
Total Uncertainty	3.23	1.32	1.15

Table 8.11. Distribution of the different signal event classes after jet-pairing and top-choice in the $t\bar{t}$ fully hadronic channel. The label column indicates whether the class is considered signal- or background-like.

reconstruction	pairing	[pb]	top-choice	[pb]	label
good	correct	0.62 (35%)	always correct	0.62(35%)	sig.
	wrong	0.26 (14%)	always wrong	0.26(14%)	bkg.
half-good	correct	0.46 (25%)	correct	0.33(18%)	sig.
			wrong	0.13(7%)	bkg.
	wrong	0.26(15%)	always wrong	0.26(15%)	bkg.
bad	always wrong	0.20 (11%)	always correct	0.20(11%)	bkg.

can be traced to parton-level properties, like high $|\eta|$ and low p_{T}, described in more detail in [279].

In order to perform the correct jet pairing, a likelihood variable is constructed from the following event observables: (a) average of the two W-boson masses, (b) difference of the two W-boson masses, (c) sum of the inter-jet angles of the W-boson candidates $\angle(q_1\bar{q}_1') + \angle(q_2\bar{q}_2')$, (d) difference of the two top-quark masses, (e) sum of the inter-jet angles of the top quark candidates $\angle(bq_1) + \angle(b\bar{q}_1') + \angle(q_1\bar{q}_1') + \angle(\bar{b}q_2) + \angle(\bar{b}\bar{q}_2') + \angle(q_2\bar{q}_2')$, (f) angle between the direction of the two top-quark candidates. Their distributions are shown in [279]. Taking for each event the pairing with the highest likelihood value yields pairing efficiencies of 71% for the good and 64% for the half-good jet-parton-matching.

Only one top per event is chosen for the kinematic mass determination, the choice is once again based on a likelihood variable constructed from the following event observables: (a) p_{T} of the softest of the three jets of each top-quark candidate (b) mass of the W boson as reconstructed in top decay (c) sum of the inter-jet angles of jets from top decay, $\angle(b_i q_i) + \angle(b_i\bar{q}_i') + \angle(q_i\bar{q}_i')$. Taking the top with the larger likelihood value yields a 72% efficiency, far greater than the 50% efficiency of a random choice.

The differentiation of the selected signal events into the now six classes is summarised in Table 8.11, where the six classes are being mapped onto two labels, indicating whether the events are considered signal- or background-like.

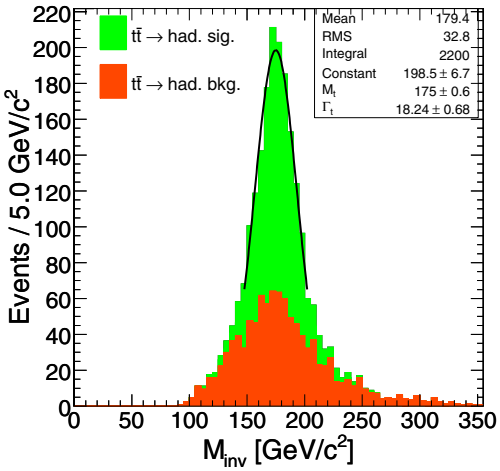

Figure 8.8. Invariant mass distribution of the reconstructed and rescaled, chosen top for both signal classes with a Gaussian fit to the peak.

Table 8.12. Summary of the systematics for the top-mass determination with fully hadronic events.

	Δm_t (GeV/c^2)
Pile Up	0.4
Underlying Event	0.6
PDF	1.4
IS/FS Radiation	2.3
Fragmentation	0.9
Jet Energy Scale	2.3
b-Tagging	0.3
Background	2.0

With all the pieces in place a kinematic reconstruction of the top quarks is straightforward and the resulting invariant mass distribution of the chosen top, with the paired non-b-jets rescaled such that they yield the W-mass, is shown in Figure 8.8.

As expected the signal-like events form a narrow peak, while the wrongly-reconstructed events have a far broader shape. Fitting a Gaussian to the peak of the invariant mass distributions with a fit range corresponding to 0.4 of the peak maximum, as shown in Fig. 8.8 serves as a simple mass estimator. The extracted top-mass is $m_t = 175.0 \pm 0.6(\text{stat.}) \pm 4.2(\text{syst.})\,\text{GeV/c}^2$ for an input top-mass of $175\,\text{GeV/c}^2$ and an integrated luminosity of $\mathcal{L} = 1\,\text{fb}^{-1}$.

Already with this amount of data the statistical error becomes negligible compared to the systematic uncertainties which are summarised in Table 8.12. One of the big systematic uncertainties is the QCD background. The S/B in the displayed mass window of Fig. 8.8 is about $2/3$, although not shown since the currently available number of simulated events does not allow a determination of the QCD background shape and of the uncertainty it introduces into the top-mass determination. Experience from CDF at the Tevatron [293, 294] indicates that this uncertainty can be understood at the $\sim 2\,\text{GeV/c}^2$ level, when using data for background estimation.

8.2.4. Top quark mass from J/ψ final states

8.2.4.1. Introduction. At the LHC the measurement of the top quark mass via direct reconstruction will soon be limited by systematic errors. It is expected that the most severe systematic contributions will be linked to the modelling of the hadronic environment and the knowledge of the jet energies. It would be particularly desirable, therefore, to consider methods for the extraction of m_t from the data which could reduce the contribution from these uncertainties considerably. An alternative method, which is making use of exclusive b decays in semi-leptonic top-pair events with the presence of a J/ψ decaying into an electron or muon pair was proposed in [295, 296].

The top quark mass is determined by its correlation with the invariant mass of the reconstructed J/ψ and the lepton from the W decay coming from the same top decay, $m_{J/\psi l}$. The correlation is present because the reconstruction of the J/ψ gives an accurate measurement of the b quark flight direction and its momentum thanks to the relatively high mass of the meson. Moreover, this measure is expected to have an excellent resolution because of the very clean experimental reconstruction of the lepton three-vectors. Details on the analysis presented here can be found in [297].

8.2.4.2. Event generation and selection. Signal events are generated using the TopReX generator [44] and consist of $t\bar{t}$ events where the presence of at least one J/ψ in the final state from the hadronisation of b-quarks is required. No distinction is made about the origin of the J/ψ; therefore the same samples also contains combinatorial background where the J/ψ is coming from a b quark produced together with a W boson decaying hadronically. Five samples corresponding to five different top masses are generated with a statistics of 200K events each. The event hadronisation and the description of the underlying event and the minimum bias is realised with PYTHIA 6.227 [24].

All the signal samples are passed through full detector simulation (ORCA) [10] with a simulation of the minimum bias corresponding to high luminosity data taking. Indeed, the statistics is expected to be so low that the use of high luminosity data must be considered. The same signal samples, and several millions more for studies on systematics, are passed through the fast simulation of the detector (FAMOS) [11]. The shape of the variables used in the selections are fully compatible in both scenarios.

The studied physics backgrounds are generated with the ALPGEN [161] generator and include W + jets, $Zb\bar{b}$ + jets, $Wb\bar{b}$ + jets. In these cases the samples are not biased by requiring an explicit J/ψ in the final state, therefore the separation from the signal is studied on the basis of cuts not involving the search for a J/ψ and the contribution of the resulting background is then rescaled taking into account the proper branching fractions. The selection, in terms of signal efficiency, is also cross-checked against $t\bar{t}$ + jets signal generated with ALPGEN, and is found to be consistent.

The main difficulty of the analysis comes from the extremely low branching ratio for a $t\bar{t}$ event to give a final state with a leptonic J/ψ. This can be written as:

$$\begin{aligned} BR(t\bar{t} \to (Wb)(Wb) \to (Xb)(\ell\nu J/\psi X)) \; &= \; 2 \cdot BR(W \to \ell\nu) \\ \cdot BR(b(\to X) \to B^{\pm,0}, B_s, B_{baryon} \to J/\psi X) &\cdot BR(J/\psi \to \ell\ell) \end{aligned} \quad (8.3)$$

where charge conjugation is implicit, ℓ indicates either an electron or a muon, and having assumed a $BR(t \to Wb)$ of 1. Replacing the branching ratios with up-to-date numbers [54] one gets for the global branching ratio the value $5.5 \cdot 10^{-4}$ that, in terms of event yield and assuming a cross section for $pp \to t\bar{t}$ of 830 pb, makes approximately 4500 events per $10\,\text{fb}^{-1}$. This number does not include neither the trigger and selection efficiency, nor the efficiency for the correct pairing of the J/ψ to the correct lepton from the W decay.

Table 8.13. Selection performance on signal and expected backgrounds. The first column indicates the channel and its final state, the second the predicted cross section, where the branching ratio for producing at least a J/ψ into leptons from either a b jet or a light jet is accounted for, the third the trigger efficiency, the fourth the selection efficiency, the fifth the expected number of events in 10 fb^{-1}, the sixth the classification of the contribution as signal (S), physics background (B) or combinatorial background (C).

Channel	BR .σ (fb)	ε_{trig} (%)	ε_{sel} (%)	Events in 10 fb^{-1}	Class
$t\bar{t} \to (b \to J/\psi)\ell\nu - b\ell\nu$	107	93.9	15.7 ± 0.4	158	S+C
$t\bar{t} \to (b \to J/\psi)\ell\nu - b\tau\nu$	53	61.1	11.0 ± 0.8	36	S
$t\bar{t} \to (b \to J/\psi)\ell\nu - bqq$	320	55.3	10.9 ± 0.3	193	S
$t\bar{t} \to (b \to J/\psi)\tau\nu - b\ell\nu$	53	61.1	10.6 ± 0.8	34	C
$t\bar{t} \to (b \to J/\psi)\tau\nu - b\tau\nu$	27	14.2	2.8 ± 1.2	1	B
$t\bar{t} \to (b \to J/\psi)\tau\nu - bqq$	160	7.9	1.5 ± 0.5	2	B
$t\bar{t} \to (b \to J/\psi)qq - b\ell\nu$	320	55.3	10.7 ± 0.3	190	C
$t\bar{t} \to (b \to J/\psi)qq - b\tau\nu$	160	7.9	1.5 ± 0.5	2	B
$t\bar{t} \to (b \to J/\psi)qq - bqq$	959	0.1	0.2 ± 0.5	0	B
$W + N$ jets, $N > 1 \to J/\psi X$	394	55.3	2.1 ± 0.1	43	B
$Wb\bar{b}$ + jets $\to J/\psi X$	196	55.3	1.6 ± 0.1	16	B
$Zb\bar{b}$ + jets $\to J/\psi X$	23	93.9	9.4 ± 0.1	20	B
$b\bar{b} \to J/\psi X$	$1.3 \cdot 10^9$	$< 2 \cdot 10^{-8}$	< 1	< 2.6	B

Events are triggered using the inclusive lepton trigger with thresholds described in [76]. The efficiency for triggering signal events is reported in Table 8.13 and is included in all numbers presented here. In events passing the trigger thresholds a J/ψ is searched for by looking for same-flavour, opposite-sign leptons with invariant mass in the range [2.8,3.2] GeV/c^2 and forming an angle greater than 2 and lower than 35 degrees. No isolation requirements must be imposed on these leptons. The efficiency for reconstructing a J/ψ at this stage is (0.386 ± 0.007) and (0.114 ± 0.004) for the muon and electron channels, respectively. It is limited by the low momenta of the leptons and because they are produced inside a jet, making the reconstruction more difficult, particularly for electrons.

If a J/ψ is found in an event, the isolated lepton with the highest p_{T} and higher than 20 GeV/c is considered as the lepton candidate from the W decay. The isolation discriminant is defined as the sum of the energies in the electromagnetic and hadronic calorimeters in a cone of opening angle $\Delta R = 0.3$ around the lepton candidate. The selection requires that the isolation energy is less than 15 GeV for electrons and less than 20 GeV for muons.

We define as background all contributions from processes not resulting in the decay chain $t \to Wb \to \ell\nu J/\psi X$. We call physics background the contribution from processes other than $t\bar{t}$ (semi)leptonic and as combinatorial background the irreducible part of $t\bar{t}$ (semi)leptonic where the J/ψ is wrongly associated to the lepton not coming from the W in the same top decay. Any physics background needs to mimic a final state with the presence of a J/ψ and an isolated and energetic lepton. The obvious candidates are bosons in association with jets. It is important to distinguish between b jets and light jets, which produce J/ψ at very different rates, suppressing the contribution of processes with light jets very much. To remove these contributions the total scalar sum of the transverse jet momenta is required to be greater than 100 GeV/c. This cut is not applied if two isolated leptons are found, in order to preserve dileptonic $t\bar{t}$ events. If the flavour of the two leptons is the same, an explicit cut to remove the presence of leptonic Z is made, vetoing events where the invariant mass of the two leptons is between 85 and 97 GeV/c^2. To further reduce soft background the cut on the transverse momentum of the isolated lepton is brought to 40 GeV/c, making the analysis less sensitive

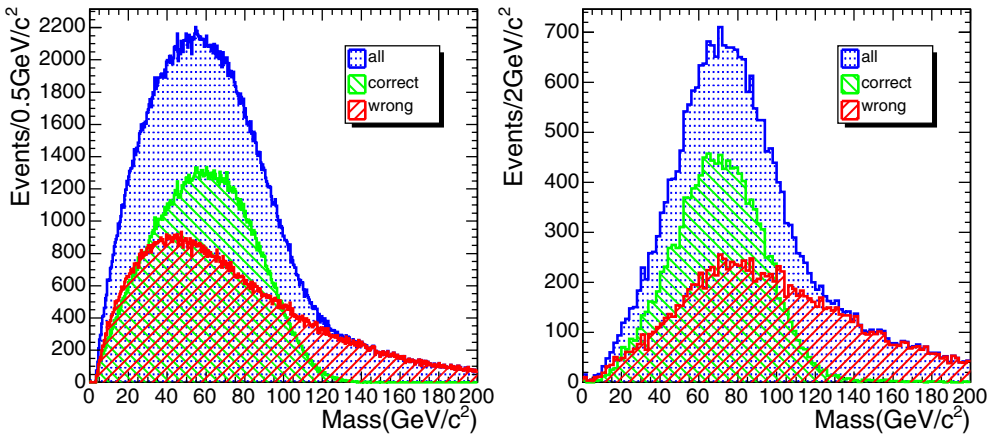

Figure 8.9. Three-lepton mass distribution for $m_t = 175\,\mathrm{GeV/c^2}$ at generator level (left) and after detector simulation and reconstruction (right). In the pictures the components coming from correct and wrong lepton pairing - from both combinatorial and physics backgrounds - are shown.

also to systematic effects involving soft QCD. Table 8.13 presents, in terms of predicted cross sections, efficiencies and events yields per $10\,\mathrm{fb}^{-1}$, the performance of the analysis.

8.2.4.3. Reconstruction of $\mathrm{m}_{J/\psi\ell}$ *and statistical performance.* In order to estimate the correct invariant mass J/ψ-lepton it would be necessary to efficiently discriminate between right pairings, where both particles are coming from the decay of the same top, and from wrong pairings where, in $t\bar{t}$ events, they come from the two different top decays. In the present analysis, in order to increase the available statistics, we propose not to attempt any separation of the combinatorial but, instead, to use the full distribution containing both signal and background.

Figure 8.9 shows the three-lepton invariant mass in $t\bar{t}$ events at generator level without selection and at full reconstruction after the selection described in the previous section. The distribution of the components of signal and background from $t\bar{t}$ are shown, where the Monte Carlo truth is used to judge when the correct pairing is made. No equivalent distribution can be done for non-$t\bar{t}$ backgrounds since no J/ψ is present in those samples. To take this into account the pure background shape is scaled up according to the extra contribution of non $t\bar{t}$ background (Table 8.13), in the hypothesis that the shape of the two samples are the same. Uncertainty in the background description will then be translated into a systematic contribution on the measurement.

The observable most sensitive to the top mass is the position of the maximum of the three-lepton mass distribution. It is determined via a fit of the full shape with a polynomial function of fourth degree. The range chosen for the fit is centred around the maximum and goes from 20 to 120 $\mathrm{GeV/c^2}$. The error on the maximum of the fitted polynomial is determined by propagating the errors on the fitted coefficients and taking into account their correlation. As a cross check, an alternative way of fitting the signal with a Gaussian was tried. In this case the background is first subtracted on a bin-by-bin basis making use of an average background distribution determined by using all the simulated samples. The results obtained are comparable.

The fitted maxima are expected to be correlated to the input value of the top mass. This correlation is proven and fitted by a line (Fig. 8.10). The two results at fast and full simulation are in impressive agreement. The correlation curves can be used to estimate the expected

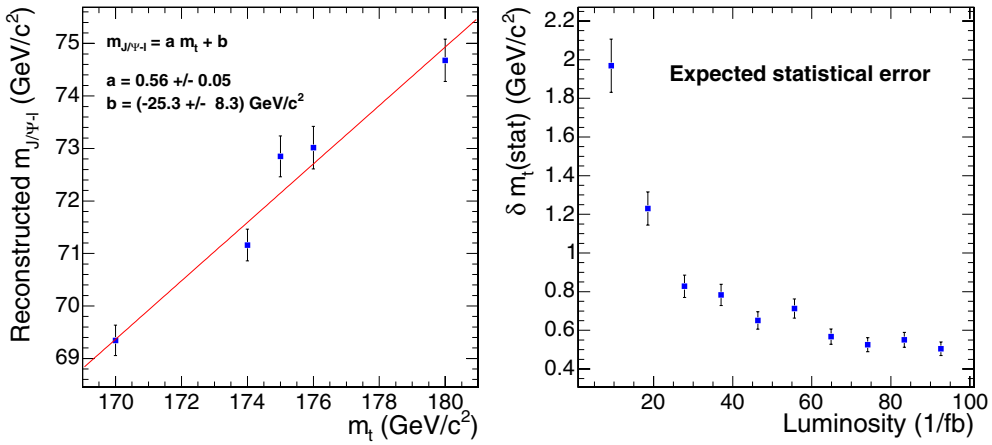

Figure 8.10. Left: correlation between the reconstructed three-lepton invariant mass and the input top mass at full simulation. Right: expected statistical error on the top quark mass as a function of the integrated luminosity.

statistical error on the top mass as a function of the available amount of data. This is done by using the number of events expected according to Table 8.13, and the result is presented in Fig. 8.10. From the figure it can be concluded that the measurement of the top quark mass with this analysis can become, on the statistical footing, competitive already with other analyses' total error after the first years of data taking. Moreover the measurement is expected to be dominated by systematic errors in the long range, as explained in the next section.

8.2.4.4. Systematic errors. The sources of systematic errors can be divided into two main categories: theoretical and experimental. The former include the description of the hard process and the modelling of radiation, fragmentation and the underlying event in the simulation, whereas the latter includes all experimental sources coming from an imperfect detector description. The sources analysed in what follows are considered as uncorrelated and the corresponding resulting errors on the top mass are summed in quadrature to form the total systematic error. To evaluate the effect of various sources the guidelines described in [201] and in Appendix B are followed.

With the exception of the PDF description, for each of the other sources of theoretical uncertainty and for each change in the simulation parameters an independent signal generation with TopRex and PYTHIA has been performed, with statistics of a few 100K events each, and fast simulated. The variations on the resulting top masses are considered as systematics: when the mass difference with respect to the reference sample is smaller than the associated statistical error, this is conservatively quoted as the systematic error.

For all the experimental sources, smearings and shifts on the observed objects (leptons and jets) are applied after reconstruction and before selection in a consistent way. The observed difference on the top mass is taken as an estimation of the associated systematic uncertainty.

Table 8.14 presents the systematic breakdown on the top mass. The systematics error is dominated by theoretical sources, which are the ones affected by the larger statistical uncertainties, quoted here as systematics.

Putting together the systematic and the statistical error one can conclude that, with maybe exception for the first year of data taking, this measurement will be dominated by systematics,

Table 8.14. Systematic error breakdown. For each source either the maximum variation from a reference sample or the resulting statistical error on the difference is quoted as a systematic error.

Source	δm_t (GeV/c^2)
Λ_{QCD}	0.31
Q^2	0.56
Scale definition	0.71
b-quark fragmentation	0.51
Light jet fragmentation	0.46
Minimum bias/Underlying event	0.64
Proton PDF	0.28
Total theoretical	1.37
Electron E scale	0.21
Muon p scale	0.38
Electron E resolution	0.19
Muon p resolution	0.12
Jet E scale	0.05
Jet E resolution	0.05
Background knowledge	0.21
Total experimental	0.54
Total systematic	1.47

in turn dominated by our poor understanding of the theoretical sources. A total error on the top mass below 2 GeV/c^2 can be in reach from the first 20 fb^{-1} already. The present result suggests an uncertainty of 1.5 GeV/c^2 with full statistics, but this number is fully dominated by the theory systematics. A precision much better than this is not out of reach since, by the time this measurement will be made, the analysis will be hopefully repeated at (N)NLO and our understanding of the dominating systematics, for instance the minimum bias and the underlying event, will be drastically improved. More dedicated reconstruction techniques and more sophisticated analyses will considerably improve the statistical treatment of the information.

This analysis reduces to a minimum those systematics which are expected to dominate in more traditional estimations of the top mass, especially the ones from direct reconstruction, like the jet energy scale and the knowledge of the b-tagging.

8.2.5. Summary of top mass determinations

Measuring the mass of the top quark in different channels allows for a combination of the individual results [298]. As the statistical component in the total uncertainty on m_t in each channel is negligible, the correlation between the systematic uncertainties must be determined. The dominant uncertainty arises from the knowledge of the energy scale of *b*-quark jets, a component which is assumed to be fully correlated between decay channels. This uncertainty can however be subdivided in several components: detector understanding, clustering algorithms, related to the modelling of *b*- and light-quark fragmentation and decay and, finally, the statistical precision of the data-based estimates of the *b*-jet energy scale differentiated versus the pseudo-rapidity and the transverse momentum of the observed jet.

The measurement from the J/ψ final states is however limited by other, mainly theoretical, sources of systematic uncertainties. Therefore a reduction of the uncertainty on m_t is expected when combining the direct measurements with the measurement from the J/ψ final states. The knowledge of the top quark mass can be improved by developing alternative

methods which do not rely on the b-jet energy scale [299, 300]. Accounting for these future improvements an uncertainty of $1\,\mathrm{GeV/c^2}$ on the top quark mass is feasible. The combination can be performed by applying techniques described in [301, 302].

8.3. Spin correlation in top-quark pair production

8.3.1. Introduction

Because of its large width of $1.4\,\mathrm{GeV/c^2}$ the top quark decays before either hadronisation, governed by the scale Λ_{QCD}, or depolarisation, governed by the scale Λ^2_{QCD}/m_t, can take place. This unique feature is used to investigate the spin of the top quark; such investigation is not possible in the case of light quarks, where the spin information is diluted by hadronisation. Moreover, the top quark spin-flip time is much larger than its lifetime and the probability of a spin flip due to emission of one or several gluons via chromomagnetic dipole-transition is very small.

The angular distribution of a daughter particle in top quark decays can be written as [303–305]

$$\frac{1}{\Gamma}\frac{d\Gamma}{d\cos\theta_i} = \frac{1}{2}(1+\kappa_i\cos\theta_i), \tag{8.4}$$

where the decay angle θ_i is defined as the angle between the direction of motion of the daughter particle i and the chosen spin quantisation axis. As gluon fusion is the dominant production mechanism at the LHC there is no well defined spin axis in the initial state. This leads to a choice of the helicity basis along the top quark momenta in the partonic centre-of-mass frame. The spin-analyser quality κ of the top quark daughter particle is defined as the degree to which the daughter particle is correlated with the top-quark spin. The analysis presented here is based on the semi-leptonic $t\bar{t}$ decay channel with electrons or muons, which is considered to be the signal. Alternatively, the dileptonic $t\bar{t}$ decay channel can also be considered. The κ values for the daughter particles used in this analysis [306], lepton, b quark and the lower energy quark from W decay, are 1, -0.41 and 0.51, respectively.

The spin correlation in the semi-leptonic $t\bar{t}$ decay channel can be measured in terms of a double differential lepton and quark angular distribution, which, neglecting higher order QCD corrections, is given by

$$\frac{1}{N}\frac{d^2N}{d\cos\theta_l\, d\cos\theta_q} = \frac{1}{4}(1-\mathcal{A}\kappa_l\kappa_q\cos\theta_l\cos\theta_q). \tag{8.5}$$

Here, using the helicity basis the lepton and quark angles θ_l and θ_q are obtained by measuring the angle between the decay particle momentum in its parent top quark rest frame and the parent top quark momentum in the $t\bar{t}$ quark pair rest frame. The correlation coefficient

$$\mathcal{A} = \frac{N_{||}-N_X}{N_{||}+N_X} = \frac{N(t_L\bar{t}_L+t_R\bar{t}_R)-N(t_L\bar{t}_R+t_R\bar{t}_L)}{N(t_L\bar{t}_L+t_R\bar{t}_R)+N(t_L\bar{t}_R+t_R\bar{t}_L)}, \tag{8.6}$$

where $N_{||}$ and N_X give the number of events with parallel and anti-parallel top quark spins, respectively. Two angle combinations are considered: θ_l versus θ_b and θ_l versus $\theta_{q(lower\ energy)}$; in the following description these two combinations are denoted as $b-tl-t$ and $q-tl-t$.

8.3.2. Simulation of $t\bar{t}$ with spin correlation

A $t\bar{t}$ sample of $3.1\cdot10^6$ events containing $9.1\cdot10^5$ semi-leptonic signal events was generated with PYTHIA [24] and reconstructed using ORCA. As PYTHIA does not include spin correlations

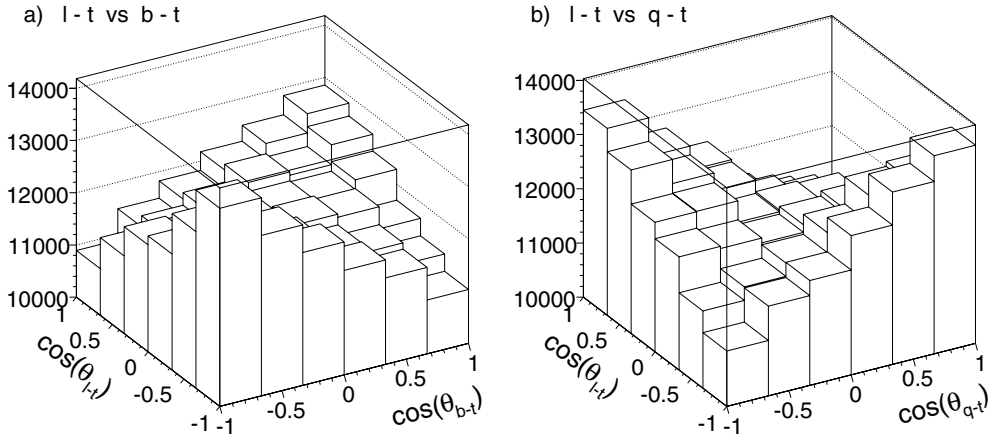

Figure 8.11. Double differential angular distributions obtained from the "analysis" sample, see text.

the events are weighted according to Equation (8.5) with $\mathcal{A} = 0.32$ [44] and appropriate values of κ. Then, this data sample is subdivided into two sub-samples: one is regarded as the "reference" sub-sample (1.61M events), used for determination of the selection efficiency and backgrounds. The other is regarded as the "analysis" sub-sample (1.50M events), used for the measurement of $\mathcal{A}$. This sample provides 436K signal events. The double differential angular distributions obtained from the "analysis" sample are presented in Figure 8.11.

The distributions in Figure 8.11 are fitted according to Equation (8.5). The results are $\mathcal{A}_{b-t\,l-t} = 0.321 \pm 0.011\,(\text{stat.})$ and $\mathcal{A}_{q-t\,l-t} = 0.319 \pm 0.009\,(\text{stat.})$ which are statistically compatible with the input value of $\mathcal{A} = 0.32$.

8.3.3. Online and offline event selection

The Level 1 and High Level Triggers select events with a single isolated electron or muon; the trigger efficiency is 55%.

The following requirements are applied in the offline selection: missing transverse energy $E_{\mathrm{T}}^{\mathrm{miss}} > 20\,\mathrm{GeV}$; at least one isolated lepton with $|\eta| < 2.5$, electron with $p_{\mathrm{T}} > 27\,\mathrm{GeV/c}$ or muon with $p_{\mathrm{T}} > 20\,\mathrm{GeV/c}$; at least four jets with $p_{\mathrm{T}} > 30\,\mathrm{GeV/c}$ and $|\eta| < 2.5$. Jets are reconstructed with a cone algorithm with $\Delta R = 0.5$. At least two jets must be b-jets where the tagging efficiency is 66% for b quarks in $t\bar{t}$ events. This selection results in an overall efficiency of 12%.

The reconstruction of two top quarks includes the following requirements: Two jets that are not b-tagged and have an invariant mass in the range 50–135 $\mathrm{GeV/c^2}$, consistent with the W mass, are found. A b-tag jet which combined with the above reconstructed W gives an invariant mass in the range 130–250 $\mathrm{GeV/c^2}$, consistent with the t mass. In addition to the top quark reconstructed above, another top quark is required based on the other b-tag jet plus lepton and missing energy combination. The neutrino components are determined by fitting the missing energy components, constrained with W and t quark masses. The azimuthal angle between the two top quarks is required to be greater than 2 rad. This selection results in an overall efficiency of 5% (Table 8.15).

A measure of the selection quality can be obtained by comparing the generated and reconstructed momentum directions expressed in terms of the cosine of the angles defined above. Figure 8.12 presents the differences between the generated and reconstructed cosines

Table 8.15. The physics processes considered for signal and background. The number of selected events for the non-$t\bar{t}$ processes are scaled to the same $t\bar{t}$ sample luminosity.

Process	Simulated events	σ(pb)	Efficiency	Selected events
$t\bar{t}$ (signal)	436K	246	$5.0 \cdot 10^{-2}$	21589
$t\bar{t}$ (background)	1.07M	584	$4.0 \cdot 10^{-3}$	4236
WW + jets	310K	188	$4.5 \cdot 10^{-5}$	15
W + jets($\hat{p}_T = 20{-}400$ GeV/c)	2.06M	43K	$3.4 \cdot 10^{-6}$	260
Wbt semi-leptonic decay	328K	63.1	$1.3 \cdot 10^{-3}$	144

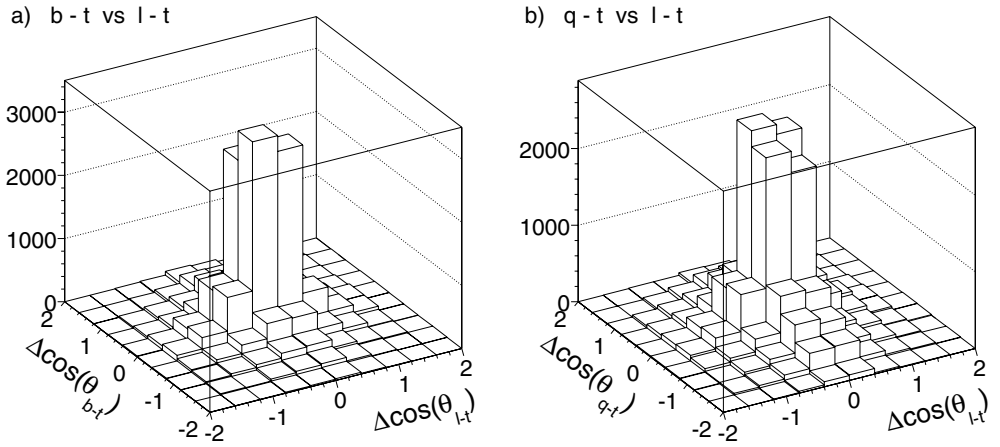

Figure 8.12. Selection quality: Difference between the generated and reconstructed cosine of the analysis angles in the $b-ll-t$ and $q-ll-t$ systems.

of the $b-ll-t$ and $q-ll-t$ systems. Quantifying this selection quality Q as the ratio of the number of events in the four central bins to all bins, one obtains: $Q_{b-tl-t} = 52\%$ and $Q_{q-tl-t} = 45\%$.

The signal-to-background ratio is 4.5. The main background, detailed in Table 8.15, is $t\bar{t}$ production with decays different from those treated as the signal. It amounts to 88% of the total background and is used to model the shape of the total background.

8.3.4. Estimation of correlation coefficient

In order to correct for the selection efficiency, an efficiency (6×6) matrix is determined by taking the ratio of the reconstructed double differential angular distribution to the generated one, using the "reference" sample. The final double differential angular distribution is obtained by subtracting, bin-by-bin, the background obtained from the "reference" sample from the total sample of signal plus background obtained from the "analysis" sample. The resulting distributions are corrected for the selection efficiency, Figure 8.13, and fitted using Equation (8.5).

The correlation coefficients obtained from the fit are:

$$\mathcal{A}_{b-t\,l-t} = 0.375 \pm 0.100(\text{stat}),$$
$$\mathcal{A}_{q-t\,l-t} = 0.346 \pm 0.079(\text{stat}).$$

These results agree, within statistical uncertainties, with those obtained from the generated events of Figure 8.11.

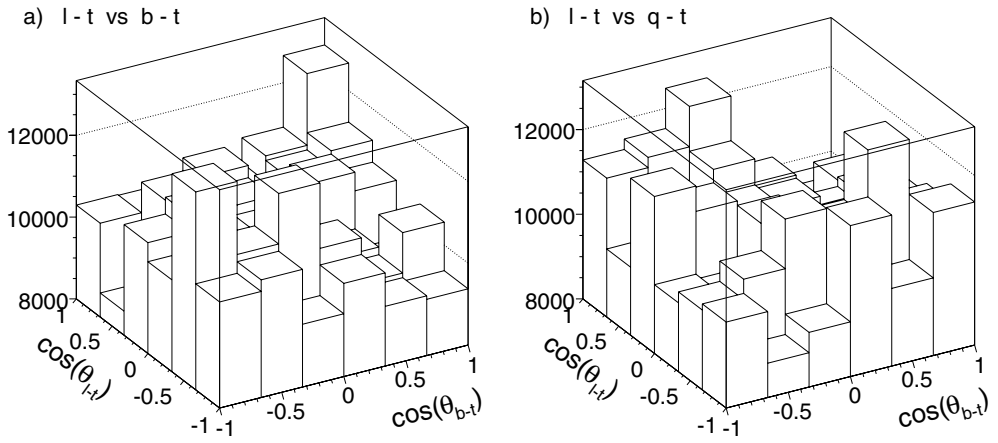

Figure 8.13. Background-subtracted and efficiency-corrected double-differential distribution of the cosine of the analysis angles in the $b-ll-t$ and $q-ll-t$ systems.

The following sources of systematic uncertainties have been evaluated. The choice of the Parton Distribution Function in modelling $t\bar{t}$ production affects the number of $t\bar{t}$ events produced via gluon fusion and that via quark-anti-quark annihilation. The relative variation in $\mathcal{A}$, determined using TopReX with different PDFs (CTEQ6M, MRST2003), is found to be 4%.

The mass of the top quark affects the result of the kinematic fit and the selection. The nominal $m_t = 175\,\mathrm{GeV/c^2}$ is varied by $\pm 5\,\mathrm{GeV/c^2}$ [54] using TopReX. The variation in $\mathcal{A}$ is found to be negligible.

The uncertainty on the $t\bar{t}$ cross section affects the shape of the final angular distribution after background subtraction; varying $\sigma(t\bar{t})$ by 10% results in 1% relative variation in correlation coefficients.

The uncertainty due to b-tagging efficiency is evaluated by varying the b-identification discriminant cut. The corresponding relative variation in $\mathcal{A}_{b-t\,l-t}$ is -20%, and in $\mathcal{A}_{q-t\,l-t}$ it is $+6.5\%/-8.3\%$.

The jet energy scale uncertainty is evaluated by varying the jet P_{T}. The relative variations in $\mathcal{A}_{b-t\,l-t}$ and $\mathcal{A}_{q-t\,l-t}$ are found to be $+7.7\%/-14\%$.

Uncertainties in the initial and final state radiation, quark fragmentation, underlying event and pile up rate could result in an underestimation of the number of non-$t\bar{t}$ jets (not originating from top decays). This possible underestimation of jet multiplicity is estimated to be 8%. To estimate the corresponding uncertainty in $\mathcal{A}$, 10% additional jets per event are generated while processing the data sample. These jets are simulated randomly according to the η and p_{T} distributions of non-$t\bar{t}$ jets, obtained from the $t\bar{t}$ Monte Carlo. The relative variations in $\mathcal{A}_{b-t\,l-t}$ and $\mathcal{A}_{q-t\,l-t}$ are found to be -6.3% and -5.3%, respectively.

Summing up the systematic uncertainties and using the statistical uncertainties estimated for $10\,\mathrm{fb}^{-1}$ of integrated luminosity, the results are:

$$\mathcal{A}_{b-t\,l-t} = 0.375 \pm 0.027(\mathrm{stat.})^{+0.055}_{-0.096}(\mathrm{syst.}),$$
$$\mathcal{A}_{q-t\,l-t} = 0.346 \pm 0.021(\mathrm{stat.})^{+0.026}_{-0.055}(\mathrm{syst.}).$$

In summary, the correlation coefficient of top quark spins in $t\bar{t}$ production is measured with a total relative uncertainty (dominated by systematic uncertainties) of 27% for $\mathcal{A}_{b-t\,l-t}$ and of 17% for $\mathcal{A}_{q-t\,l-t}$.

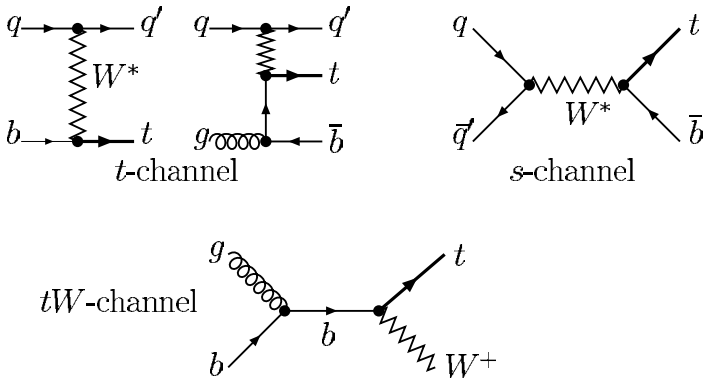

Figure 8.14. Feynman diagrams for the three channels of single top production.

8.4. Single top quark production

8.4.1. Introduction

The single top production cross section at the LHC is known at NLO level for the tree production mechanisms (see Fig. 8.14, which are classified by the virtuality of the W-boson involved as: t-channel ($q_W^2 < 0$), s-channel ($q_W^2 > 0$), and associated tW production ($q_W^2 = M_W^2$) [307–309]. In all cases, the most dangerous background comes from $t\bar{t}$ process. Other dangerous backgrounds are multi-jet QCD and W+jets events, but such background is reduced substantially by considering only leptonic decays of the $W^{\pm}$-bosons from top-quark decays.

All results presented in this Section were done for $10/\text{fb}^{-1}$ of integrated luminosity.

8.4.1.1. Details on the signal and background simulation. Two generators, SINGLETOP [310] (based on the COMPHEP package [43]) and TOPREX [44] were used to generate events for all three single-top production processes. The background processes, namely, $Wb\bar{b}$, $Wb\bar{b}+j$, and $W+2j$ were generated with COMPHEP, TOPREX, MADGRAPH [81], and ALPGEN [161] programs as indicated in the Table 8.16. The hard process events containing all needed information were passed to PYTHIA 6.227 [24] for showering, hadronisation and decays of unstable particles. The $t\bar{t}$ and $W+$jets background events were generated with the same PYTHIA version. All simulations were done with $M_t = 175\,\text{GeV/c}^2$ and $M_b = 4.7\text{–}4.8\,\text{GeV/c}^2$, proper considerations of the spin correlations, and the finite W-boson and t-quark widths. The list of the signal and background process cross sections as well as generators used are given in the Table 8.16. Both the full simulation chain (OSCAR [18] and ORCA [10]) and a fast simulation (FAMOS [11]) were used.

8.4.1.2. Reconstruction algorithms and triggers. Muons are reconstructed by using the standard algorithm combining tracker and muon chamber information as described in [311]; tracker and calorimeter isolation cuts are applied as described in [312]. The electrons are reconstructed by the standard algorithm combining tracker and ECAL information, see [313]. The jets are reconstructed by the Iterative Cone algorithm with the cone size of 0.5, see [314]; for the calibration both the Monte Carlo (in the t-channel analysis) and the $\gamma+$jets (in the tW- and s-channel) methods are used, see [315]. For b-tagging a probability algorithm based on the impact parameter of the tracks is used, as described in [316].

Table 8.16. Cross section values (including branching ratio and kinematic cuts) and generators for the signal and background processes (here $\ell = e, \mu, \tau$). Different generator-level cuts are applied.

Process	$\sigma \times$ BR, pb	generator	Process	$\sigma \times$ BR, pb	generator
t-ch. ($W \to \mu\nu$)	18 (NLO)	SINGLETOP	$Wb\bar{b}$ ($W \to \ell\nu$)	100 (LO)	TOPREX
t-ch. ($W \to \ell\nu$)	81.7 (NLO)	TOPREX	$Wb\bar{b}$ + jets ($W \to \mu$)	32.4 (LO)	MADGRAPH
s-ch. ($W \to \ell\nu$)	3.3 (NLO)	TOPREX	$W + 2j$ ($W \to \mu\nu$)	987 (LO)	COMPHEP
tW (2 $W \to \ell\nu$)	6.7 (NLO)	TOPREX	$W + 2j$ ($W \to \ell\nu$)	2500 (LO)	ALPGEN
tW (1 $W \to \ell\nu$)	33.3 (NLO)	TOPREX	$Z/\gamma^*(\to \mu^+\mu^-)b\bar{b}$	116 (LO)	COMPHEP
$t\bar{t}$ (inclusive)	833 (NLO)	PYTHIA			

The **transverse missing energy** is reconstructed as follows:

$$\vec{E}_{\mathrm{T}}^{\mathrm{miss}} = -\left(\sum \vec{P}_{\mathrm{T}}^{\mu} + \sum \vec{E}_{\mathrm{T}}^{\mathrm{tower}} + \sum (\vec{E}_{\mathrm{T,jet}}^{\mathrm{calib}}) - \sum (\vec{E}_{\mathrm{T,jet}}^{\mathrm{raw}})\right) \tag{8.7}$$

where $E_{\mathrm{T}}^{\mathrm{tower}}$ is the sum of transverse energy of towers, $E_{\mathrm{T,jet}}^{\mathrm{calib}}$ ($E_{\mathrm{T,jet}}^{\mathrm{raw}}$) is the transverse energy of calibrated (uncalibrated) jets. For the final states with one isolated lepton the neutrino ($E_{\mathrm{T}}^{\mathrm{miss}}$) longitudinal component, $P_{z,\nu}$, is extracted from the quadratic equation:

$$M_W^2 = 2\left(E_\mu \sqrt{P_{z,\nu}^2 + (E_{\mathrm{T}}^{\mathrm{miss}})^2} - \vec{P}_{\mathrm{T},\mu} \cdot \vec{E}_{\mathrm{T}}^{\mathrm{miss}} - P_{z,\mu} P_{z,\nu}\right) \tag{8.8}$$

This equation has two solutions:

$$P_{z,\nu}^{(1,2)} = \frac{A P_{z,\mu} \pm \sqrt{\Delta}}{P_{\mathrm{T},\mu}^2}, \quad \text{where } A = \frac{M_W^2}{2} + \vec{P}_{\mathrm{T},\mu} \cdot \vec{E}_{\mathrm{T}}^{\mathrm{miss}},$$
$$\Delta = E_\mu^2 (A^2 - (E_{\mathrm{T}}^{\mathrm{miss}})^2 P_{\mathrm{T},\mu}^2) \tag{8.9}$$

Among the two solutions of Equation (8.8) the minimal value of $|P_{z,\nu}|$ is used for W-boson momentum reconstruction.

About 30% of the events have negative Δ values due to the finite detector resolution and to the presence of extra missing energy. In this case for t-channel analysis the parameter M_W in Equation (8.9) is increased until Δ becomes zero. Using this value of M_W, $P_{z,\nu}$ is calculated from Equation (8.9). For the tW and s-channels analyses, only the real part of $P_{z,\nu}$ is used for further analysis.

The **transverse mass of the W-boson** is defined as

$$M_{\mathrm{T}}^W = \sqrt{2(P_{\mathrm{T},\mu} E_{\mathrm{T}}^{\mathrm{miss}} - \vec{P}_{\mathrm{T},\mu} \cdot \vec{E}_{\mathrm{T}}^{\mathrm{miss}})}. \tag{8.10}$$

The **sum of the transverse momentum vectors** of all reconstructed objects

$$\vec{\Sigma}_{\mathrm{T}} \equiv \vec{P}_{\mathrm{T},\ell} + \vec{E}_{\mathrm{T}}^{\mathrm{miss}} + \sum \vec{E}_{\mathrm{T},jet}, \tag{8.11}$$

is found to be very effective for signal/background separation.

The **"jet charge"** (Q_j) is defined as the sum of the charges of the tracks inside the jet cone, weighted over the projections of the track momenta along the jet axis.

The **lepton isolation** criterion used is to sum the p_{T} of all the tracks in a cone of $\Delta R < 0.2$ around the lepton track, and to reject the event if this sum is greater than 5% of the lepton p_{T}.

The present study is based on leptonic decay channels ($e\nu_e$ or $\mu\nu_\mu$) of the W-boson. The signal is triggered by the trigger on leptons. The HLT p_{T} thresholds from the CMS DAQ-TDR [76] are assumed: 19 GeV/c (29 GeV/c) for the single muon (electron); with $|\eta_\mu| \leqslant 2.1$ and $|\eta_e| \leqslant 2.4$.

8.4.1.3. The contribution from multi-jet backgrounds. A special treatment is required for QCD events with jets, due to the huge cross section. The currently available samples have very small statistics and typically no events remain after the application of pre-selection cuts. Therefore, in order to estimate the impact of the QCD-background the cuts are applied separately, assuming they are uncorrelated.

For t-channel study these cuts are: (a) one isolated muon ($p_{\mathrm{T}} > 19\,\mathrm{GeV/c}$); (b) $E_{\mathrm{T}}^{\mathrm{miss}} > 40\,\mathrm{GeV}$ and only two jets; one B-jet and one light forward jet. It was found a satisfactory suppression of the multi-jet events as compared to other background process ($N_{\mathrm{QCD}}/N_{\mathrm{bckg}} = 6924/(8.9 \times 10^4) = 0.078$ (see [317]) and the QCD-background was not considered in the analysis of the t- and s-channel single top production.

More detailed investigation of this problem was done for tW-channel [318]. The selection cuts are arranged into cut groups whose efficiencies are estimated with the Monte Carlo samples. The product of efficiencies is an indicator of the total efficiency.

Three cut groups are used in the dileptonic channel: lepton, $E_{\mathrm{T}}^{\mathrm{miss}}$, jet. The same procedure is applied on signal sample to find the ratio of total efficiency to the product of efficiencies. The ratio is used to correct the product of efficiencies found in multi-jet sample and the result is 5.6 events. Four cut groups are used in the semi-leptonic channel: jets, leptons, kinematics and finally signal region and b tagging. The b tagging requirement is taken out from jets group to have reasonable statistics for the efficiency measurement. By comparing the product of efficiencies with total efficiency of applying cut groups in series, the cut groups are found to be anti-correlated which would result in an over-estimate of the yield. The result of 508 events is kept to be conservative [318].

8.4.1.4. Systematic uncertainties. The following sources of systematic uncertainty are common for all three channels: (i) the **theoretical errors** to the total rates of the signal is $\Delta_{\mathrm{th}} \approx 4\%$, rising to 10% for tW. The uncertainties in the background events are assumed to be: 5% for $t\bar{t}$ [45], 17% for $Wb\bar{b}j$, 7% for W + jets, 5% for Wjj [319], and 5% for $Wb\bar{b}$. (ii) the **jet energy scale (JES) uncertainty:** using a calibration method based on $t\bar{t}$ events [320], the JES uncertainty after $10\,\mathrm{fb}^{-1}$ integrated luminosity is expected to be $\pm 5\%$ ($\pm 2.5\%$) for jets with $p_{\mathrm{T}} \approx 20\,\mathrm{GeV/c}$ ($p_{\mathrm{T}} > 50\,\mathrm{GeV/c}$). In the region between 20 and 50 GeV/c a linear dependence is assumed. (iii) **b-tagging identification uncertainty:** of $\pm 4\%$ on the overall selection efficiencies is expected on the b-tagging efficiencies [157]. (iv) the **luminosity uncertainty**, expected to be 5% [321].

8.4.2. Selection and cross section: t-channel

The final state in t-channel includes one isolated muon, missing energy (neutrino), one or two jets from b-quarks (B_{jet}), and one "forward" hadronic jet. A specific feature of single top events is production of a light jet in the forward/backward direction (see Figs. 8.15) providing an additional possibility for background suppression. The additional b-quark is produced with small transverse momentum, making the reconstruction of the associated low-p_{T} jet and its b-tagging very difficult. Therefore, in t-channel analysis [317] it is required to have only two hadronic jets in the final state. In this case, the most important background contribution arises from $t\bar{t}$ production and from $W^{\pm}$-boson production in association with heavy quarks ($Wb\bar{b}$ + jet) or light quark jets (W + jets).

8.4.2.1. Analysis of the fully simulated events. The selection requires the presence of only one isolated muon with $p_{\mathrm{T}} > 19\,\mathrm{GeV/c}$ and $|\eta_{\mu}| < 2.1$ (HLT selection). Then, it is required: (i) $E_{\mathrm{T}}^{\mathrm{miss}} > 40\,\mathrm{GeV}$; and (ii) at least two hadronic uncalibrated jets, with $p_{\mathrm{T}} > 20\,\mathrm{GeV/c}$. For

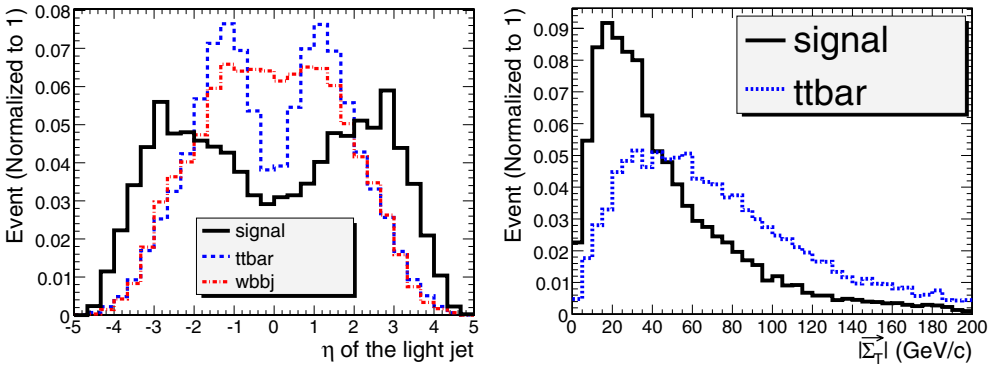

Figure 8.15. The distributions of pseudorapidity (η) of the light jet (left), and of $|\vec{\Sigma}_T|$ (right).

Table 8.17. Number of events (t-channel) and cumulative efficiencies for each cut used in the analysis of t-channel single top production. The symbol "$p_{TB} \times p_{Tj} \times E_T^{miss}$" means: $p_{TB} > 35\,GeV/c$, $p_{Tj} > 40\,GeV/c$, $|\eta_j| > 2.5$, $E_T^{miss} > 40\,GeV$.

	signal	$t\bar{t}$	$Wb\bar{b}j$	Wj	Wjj
N(events) at 10 fb^{-1}	1.8×10^5	8.33×10^6	3.24×10^5	9.7×10^7	9.9×10^5
isolated muon	0.73	0.14	0.52	0.16	0.81
$p_{TB} \times p_{Tj} \times E_T^{miss}$	0.036	6.4×10^{-3}	3.4×10^{-3}	9×10^{-6}	3×10^{-3}
veto on 3^{rd} jet	0.021	5.8×10^{-4}	1.6×10^{-3}	4×10^{-6}	1.1×10^{-3}
$0.0 < \Sigma_T < 43.5\,GeV$	0.018	4.1×10^{-4}	1.2×10^{-3}	4×10^{-6}	6.8×10^{-4}
$50 < M_T^{W*} < 120$	0.015	2.2×10^{-4}	9.6×10^{-4}	1×10^{-6}	5.4×10^{-4}
$110 < M_{rec}(bW)^* < 210$	0.013	1.4×10^{-4}	5.8×10^{-4}	0	4.1×10^{-4}
Number of events	2389	1188	195	0	402

*in GeV/c^2

further analysis the following additional requirements are: at least one of the selected jets should have the b-tag: the second (light) jet should be in the forward region; only two jets (calibrated) with $p_T^{calib} \geqslant 35\,GeV$ and no other hadronic jets with $p_T^{calib} \geqslant 35\,GeV/c$ (jet veto). The GARCON program [63] is used for the final optimisations of the cuts. The signal-over-background ratio times significance is chosen as an optimisation criterion. Finally, the optimal cut values found are:

- muon: $p_T(\mu) > 19.0\,GeV/c$ and $|\eta(\mu)| < 2.1$ and $E_T^{miss} > 40.0\,GeV$;
- b-jet: $p_T > 35.0\,GeV/c$, $|\eta| < 2.5$ and Discriminator > 2.4;
- the light forward: $p_T > 40.0\,GeV/c$ and $|\eta| > 2.5$;
- $|\vec{\Sigma}_T|$ cut window: (0.0, 43.5) GeV; $50 < M_T^W < 120\,GeV/c^2$;
- the reconstructed top mass window: $110\,GeV/c^2 < M_{rec}(bW) < 210\,GeV/c^2$.

The efficiencies of these cuts and the resulting number of events are given in the Table 8.17. The resulting signal-to-background ratio and the significance are: $N_S/N_B = 1.34$ and $S_{stat} = N_S/\sqrt{N_S + N_B} = 37.0$. The final distribution of the reconstructed top mass is shown in Figure 8.16. The cuts provide a satisfactory background suppression.

The systematic uncertainties (see Section 8.4.1.4) evaluated for 10 fb^{-1} are given in Table 8.18. In summary, the statistical error is 2.7%, the total systematic error excluding the 5% luminosity uncertainty is 8%, resulting in a total error of 10%.

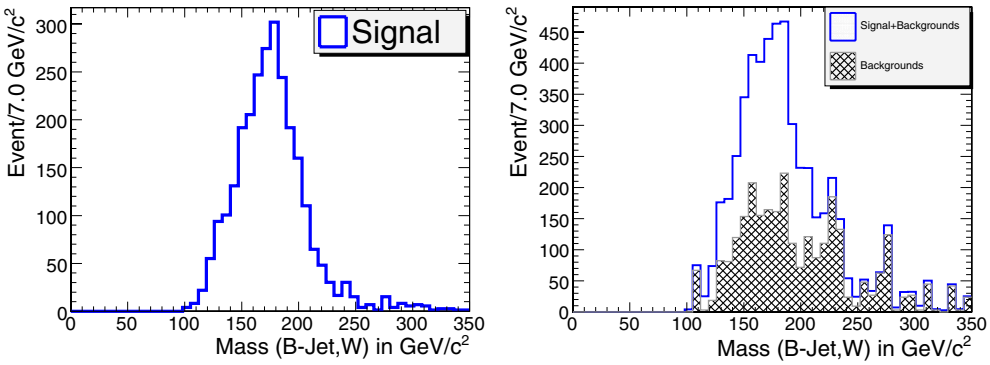

Figure 8.16. The distribution on the reconstructed top mass, for signal only (left) and with background included (right).

Table 8.18. Number of selected events (t-channel) at 10 fb^{-1} with uncertainties due to different sources. ΔN_{syst} represents the theoretical, JES and b-tagging uncertainties. ΔN_{stat} is expected statistical uncertainty.

sample	selected	ΔN_{th}	JES	$\Delta N_{\text{b-tag}}$	ΔN_{syst}	ΔN_{stat}
t-channel	2389	96	71	96	153	49
$t\bar{t}$	1188	59	73	48	105	34
$Wb\bar{b}j$	195	33	6	8	35	14
Wjj	402	20	0	16	26	20

8.4.3. Selection and cross section: tW-channel

The $pp \to tW$ process contains two W-bosons and a b-quark in the final state. In this study only leptonic decays of the W's are considered. The nominal final states are $\ell^+\ell^- E_{\text{T}}^{\text{miss}} b$ and $\ell^{\pm} E_{\text{T}}^{\text{miss}} b\text{jj}$ for the dileptonic and semi-leptonic modes, respectively. The dominant background arises from $t\bar{t}$ production. Other backgrounds are t- and s-channel single top production, $Wb\bar{b}$, W + jets, WW + jets, and to a lesser extent QCD multi-jet background.

8.4.3.1. Jet quality requirements and extra jet reduction. The most significant difference between tW events and $t\bar{t}$ events is the number of jets in the final state. However, most of the time there are also additional jets due to the underlying event, pile-up or calorimeter noise. These "extra jets" were identified and excluded from the counting by consideration of five jet quality variables (see [318]). It was found that the most discriminating variables are E_{T}^{max} (the maximum tower E_{T} in a cone of 0.5) and N_{track} (the number of associated tracks). A Fisher discriminant [322] (F) is constructed from the jet quality variables to separate real jets from extra jets. Each jet is classified value F into one of three categories: good ($F < -0.5$), loose ($|F| < 0.5$) and bad ($F \geqslant 0.5$) jets. This method yields 84.3% efficiency on true jets and rejects 86.9% of extra jets. Only "good" jets and "loose" jets are used in pre-selection and event reconstruction. The jet multiplicity after the extra jet reduction in semi-leptonic channels reveals that the number of good jets peaks at the 2 and 3 jet bins for signal events, and at the 3 and 4 jet bins for $t\bar{t}$ backgrounds.

8.4.3.2. Event selection and reconstruction. The kinematic cuts used for this study are presented in Table 8.19 and Table 8.20. For the semi-leptonic channel, two non-b-like jets with $m_{jj} < 115\,\text{GeV/c}^2$ are used for reconstruction of the W-boson (that decays hadronically). In

Table 8.19. Kinematic cuts used in the dileptonic channel. The final electron and muon should have the opposite charges.

Leptons	**Jets**
$\|\eta(e)\| < 2.4$, $\|\eta(\mu)\| < 2.1$	leading jet: $\|\eta\| < 2.4$, $p_T > 60\,\text{GeV/c}$, disc > 0
$p_T(e, \mu) > 20\,\text{GeV/c}$	at most one extra jet
no other lepton with $p_T > 5\,\text{GeV/c}$	No other jets with $p_T > 20\,\text{GeV/c}$
Missing E_T: $E_T^{miss} > 20\,\text{GeV}$	

Table 8.20. Kinematic cuts used in the semi-leptonic channel. The presence of a good fourth jet would veto the whole event.

Leptons
$p_T(e) > 30\,\text{GeV/c}$, $p_T(\mu) > 20\,\text{GeV/c}$, $\|\eta(e)\| < 2.4$, $\|\eta(\mu)\| < 2.1$
no other lepton $p_T > 10\,\text{GeV/c}$
Jets (after removing all bad quality jets)
b-like jet: good quality, disc >2, $\|\eta\| < 2.5$, $p_T > 35\,\text{GeV/c}$
non-b-like jet: good quality, $\|\eta\| < 3.0$, disc <0 if $\|\eta\| < 2.5$, $p_T > 35\,\text{GeV/c}$
Jet counting: one b-like jet and 2 non-b-like jets
Jet veto: no other "good" or "loose" jets with $p_T > 20\,\text{GeV/c}$ and $\|\eta\| < 3$
Missing E_T : $E_T^{miss} > 40\,\text{GeV}$

events with a 4th jet that survives jet veto cuts, it is required that the invariant mass of the 4th jet with any of the selected non-b-like jets must be outside a window of $M_W \pm 20\,\text{GeV/c}^2$. For the leptonic decays of the W-boson it is required that $M_T^W < 120\,\text{GeV/c}^2$.

To find the correct pairing of b-jet and reconstructed W-boson (coming from top decay) the following variables were used: the p_T of (b, W) systems; the separation of the b-jet with each of the W in (η, ϕ) space; the "charges" of jets (see Section 8.4.1.2) and W-bosons (see Ref. [318] for details). A Fisher discriminant based on these variables is used for discriminating leptonic top events from hadronic top events. A cut of 0.56 is optimal in separating these 2 types of events, and 72% of the events are correctly paired.

To further enhance the signal to background ratio the following "global" cuts are applied:

- p_T of the reconstructed tW system: $|\vec{\Sigma}(t + W)| < 60\,\text{GeV/c}$.
- Scalar sum of transverse energies H_T: $H_T < 850\,\text{GeV}$.
- Reconstructed top quark mass: $110\,\text{GeV/c}^2 < m(t) < 230\,\text{GeV/c}^2$.
- p_T of the reconstructed top quark: $20\,\text{GeV/c} < p_T(t) < 200\,\text{GeV/c}$.

8.4.3.3. Efficiencies and expected yields. The efficiencies estimated with Monte Carlo samples are converted to the effective cross sections by multiplying the production cross sections of each process. The effective cross sections, as well as the expected yields with $10\,\text{fb}^{-1}$ of data for all signal and background samples, are shown in Table 8.21 and 8.22. The signal to background ratio is found to be 0.37 for dileptonic channel and 0.18 for semi-leptonic channel.

8.4.3.4. The ratio method. The *ratio method* is developed to reduce systematic uncertainties related to the dominant $t\bar{t}$ background. We define a $t\bar{t}$-rich control region and use ratio of efficiencies to estimate the yield of $t\bar{t}$ in the signal region. The kinematics of tW and $t\bar{t}$ are similar so tW is present in the control region, therefore the ratio of efficiencies for tW is also

Table 8.21. Summary of cross section times branching ratio times efficiencies at each stage of the analysis for the dileptonic channel. All values are in picobarns The last row is the expected number of events for 10 fb^{-1}. Multi-jet background has been estimated separately (see Section 8.4.1.3). When only a limit on the number of events is stated, this is due to MC statistics.

	tW dil.	$t\bar{t}$ dil.	$t\bar{t}$ oth.	WW dil.	WW oth.	t ch. lept.
Production	6.667	92.222	737.778	11.111	88.889	81.667
HLT	4.865	74.090	346.151	7.674	27.259	41.409
2 ℓ	1.944	25.150	21.012	2.574	0.226	2.309
Lepton p_{T}	0.675	7.919	0.703	0.543	0.012	0.098
$\leqslant 1$ extra jet	0.459	6.574	0.664	0.416	0.010	0.067
Jet p_{T}, η	0.307	5.234	0.556	0.339	0.004	0.033
$\geqslant 1b$-jet	0.184	3.864	0.379	0.017	0.000	0.018
$E_{\mathrm{T}}^{\mathrm{miss}} > 20$	0.170	3.640	0.349	0.017	0.000	0.016
$\leqslant 2$ jet	0.150	2.734	0.221	0.015	0.000	0.012
Final select.	0.057	0.145	0.000	0.006	0.000	0.000
Expected events	567	1450	$\leqslant 55$	61	$\leqslant 10$	$\leqslant 20$

Table 8.22. Summary of cross section times branching ratio times efficiencies at each stage of the analysis for the semi-leptonic channel. All values are in picobarns. The last row is the expected number of events for 10 fb^{-1}.

	tW	$t\bar{t}$	t ch.	s ch.	Wbb	W2j	W3j	W4j	Multi-jet
Total cross section	60	833	245	10	300	7500	2166	522	9.73×10^9
HLT	18.9	263.9	39.5	1.52	34.0	1006	300	73	1.86×10^5
Presel. & isolation	9.05	179.4	12.0	0.54	2.15	52	35	12	1325
jet & lepton p_{T}, jet veto	1.28	18.5	1.31	0.046	0.061	0.60	4.9	1.0	4.23
b-tagging	0.669	6.13	0.476	0.013	0.016	0.10	0.99	0.26	0.85
kinematic cuts	0.223	0.999	0.047	0.002	0.003	0.017	0.101	0.008	0.105
Signal box cuts	0.170	0.771	0.035	0.001	0.001	0.013	0.054	0.008	0.051
Events in 10 fb $^{-1}$	1699	7709	351	14	10	130	539	80	508

used. The signal and background yield is determined by the following equations:

$$S = \frac{R_{t\bar{t}}(N_s - N_s^o) - (N_c - N_c^o)}{R_{t\bar{t}} - R_{tW}}, \tag{8.12}$$

$$B = \frac{(N_c - N_c^o) - R_{tW}(N_s - N_s^o)}{R_{t\bar{t}} - R_{tW}} + N_s^o. \tag{8.13}$$

Here R_x is the ratio of efficiencies $R_x = \varepsilon_x(\text{control region})/\varepsilon_x(\text{signal region})$ for $x = t\bar{t}, tW$; N_s (N_c) is total number of events in the signal (control) region; N_s^o (N_c^o) is the estimated number of non-$t\bar{t}$ background events in the signal (control) region. With S measured with 2 regions and the ratio method, the cross section can be found by $S/\epsilon\mathcal{L}$.

For the ratio method to work it is important to find a control region with similar kinematics except with one more jet. It is expected that systematic uncertainties from PDF, JES and b tagging cancel to a large extent, while the luminosity uncertainty drops out for the $t\bar{t}$ background. The lepton selection and jet quality requirements in the control region are identical to the signal region. The differences are outlined below.

Dileptonic. A second jet is required with $p_{\mathrm{T}} = 20$–$80\,\mathrm{GeV/c}$, $|\eta| < 2.4$ and b-tagged (disc > 0). No other jets with $p_{\mathrm{T}} > 20\,\mathrm{GeV/c}$ are allowed. The background region is found to be filled by 97.9% dileptonic $t\bar{t}$, 0.4% other $t\bar{t}$ decays, 1.6% dileptonic tW, and 0.1% for leptonic t channel single top while WW+jets yield is negligible.

Table 8.23. Summary of uncertainties of cross section measurement.

Source	Uncertainty	$\Delta\sigma/\sigma$(dilept.)	$\Delta\sigma/\sigma$(semi-lept.)
Statistical uncertainty	—	8.8%	7.5%
Integrated luminosity	5%	5.4%	7.8%
$t\bar{t}$ cross-section	9%	*negligible*	*negligible*
t-channel cross-section	5%	*negligible*	0.8%
W+jets cross-section	10%	*not applicable*	3.1%
WW+jets cross-section	10%	1%	*not applicable*
Jet energy scale	5%–2.5%	19.7%	9.4%
b tagging efficiency	4%–5%	8.7%	3.6%
PDF	1σ	+4%/−6.0%	1.6%
Pileup	30%	6.1 %	10.3%
MC statistics	—	9.9%	15.2%
Total uncertainty		±23.9%(syst.) ± 9.9%(MC)	±16.8%(syst.) ±15.2%(MC)

Semi-leptonic. It requires 2 jets with $p_{\mathrm{T}} > 30$, 2 more jets with $p_{\mathrm{T}} > 20$, and no bad jets with $p_{\mathrm{T}} > 20$. It is required that one of the 2 high-p_{T} jets is b-tagged (disc > 2), and that both low-p_{T} jets be not tagged (disc < 0). The $b - W$ pairing is done in the same way, with a 72% correct pairing. It is found that the $t\bar{t}$ purity in the control region is 93.9%. The non-$t\bar{t}$ events are mainly composed of W+jets (2.8%), tW (2.0%) and t-channel single top (1.2%). The ratio of efficiencies are found to be $R_{tW} = 0.319$ and $R_{t\bar{t}} = 3.31$.

8.4.3.5. Systematic uncertainties.

- **Theoretical uncertainties.** The $t\bar{t}$ cross section does not show up in the ratio method. The effect is 0.8% for t-channel single top and 3.1% for W+jets. It is found to be negligible for other background.
- **Pileup amount.** A difference of 30% between normal pileup and no pileup is used as an estimate of the systematic uncertainty, as was done in [201] for the dileptonic $t\bar{t}$ studies.

Dileptonic mode. The analysis is found to be rather sensitive to the pileup, as the relative shift of the "measured" cross section is +20.4% for no pileup, and −16.2% for double pileup, while is the difference between the check sample and the reference sample 4.6% (which has purely statistical origin). The value of 6.1% is used as the systematic uncertainty.

Semi-leptonic mode. The extracted cross section varies by +35% for no pileup and −63% for double pile-up so a systematic uncertainty of 10.3% is obtained. The results for both channels are shown in Table 8.23.

The results from the ratio method were used in the significance calculation. In addition, the uncertainty on the background expectation, evaluated for dileptonic ($\Delta_B/B = \pm 9.6\%$) and semi-leptonic ($\Delta_B/B = +3.6\%/-4.4\%$), was taken into account. The resulting significance is 4.2 for the dileptonic channel and 5.1 for the semi-leptonic channel. Combining the two channels gives a total significance of 6.4.

8.4.4. Selection and cross section: s-channel

The present analysis of the s-channel single top production is based on leptonic channels, i.e. the top is identified and reconstructed by its semi-leptonic decays into $\ell\nu b$ final states, with $\ell = e, \mu$. For this study, a fast simulation of the CMS detector with FAMOS was used, see [317, 318] for details.

Table 8.24. Efficiencies of the pre-selection cuts, with respect to the initial number of events. For all process (except of $t\bar{t}$) the final W decays into charged lepton ($\ell = e, \mu, \tau$) and neutrino. "HLT" includes the 1μ, $1e$ and $e \times j$ triggers. N_{ev} is the number of events surviving these cuts (the uncertainties are only those due to the limited Monte Carlo statistics).

Cut	s-ch.	t-ch.	$t\bar{t}$	$Wb\bar{b}$	Wt ($1\ W \to l\nu$)
"HLT"	$37.5 \pm 0.2\%$	$42.5 \pm 0.1\%$	$30.1 \pm 0.1\%$	$29.4 \pm 0.1\%$	$46.5 \pm 0.1\%$
Isolation	$33.7 \pm 0.2\%$	$39.0 \pm 0.1\%$	$21.7 \pm 0.1\%$	$28.2 \pm 0.1\%$	$42.3 \pm 0.1\%$
$E_{\mathrm{T}}^{\mathrm{miss}}$ cut	$27.3 \pm 0.2\%$	$31.9 \pm 0.1\%$	$17.4 \pm 0.1\%$	$22.6 \pm 0.1\%$	$34.4 \pm 0.1\%$
M_{T}^{W} cut	$23.2 \pm 0.2\%$	$26.3 \pm 0.1\%$	$13.6 \pm 0.1\%$	$18.4 \pm 0.1\%$	$29.2 \pm 0.1\%$
$N_j \geqslant 2j$	$11.9 \pm 0.1\%$	$11.5 \pm 0.1\%$	$11.9 \pm 0.1\%$	$0.88 \pm 0.03\%$	$18.5 \pm 0.1\%$
$N_j = 2j$	$8.9 \pm 0.1\%$	$8.2 \pm 0.1\%$	$1.84 \pm 0.04\%$	$0.76 \pm 0.03\%$	$7.09 \pm 0.05\%$
b-tag	$3.07 \pm 0.07\%$	$0.72 \pm 0.02\%$	$0.28 \pm 0.02\%$	$0.14 \pm 0.01\%$	$0.34 \pm 0.01\%$
N_{ev}	1010 ± 10	5880 ± 70	23300 ± 200	1400 ± 35	1150 ± 40

The signal events are triggered by the single lepton triggers. Since this production mode suffers from low statistics, one could envisage the introduction of a combined trigger $e \times jet$, with threshold 19 GeV/c for the electron (in order to make the electronic sample more coherent with the muonic sample) and 45 GeV/c for the jet. This value has been chosen to be the same as the threshold for the τ-jet in the already existing $e \times \tau - jet$ trigger.

8.4.4.1. Pre-selection. The pre-selection criteria are as follows:

- The event has to fire at least one of the previously described triggers (including the proposed $e \times j$).
- The event must contain one isolated lepton (μ or e) with $p_{\mathrm{T}} \geqslant 19\,\mathrm{GeV/c}$ and $|\eta| \leqslant 2.1$ ($\leqslant 2.4$) for muons (electrons) and no other lepton above 10 GeV/c.
- Exactly two uncalibrated jets must have $p_{\mathrm{T}} \geqslant 30\,\mathrm{GeV/c}$ and $|\eta| \leqslant 2.5$ and no other jet has to be present with $p_{\mathrm{T}} \geqslant 20\,\mathrm{GeV/c}$.
- Both jets should have a positive b-tagging discriminator value.
- The event should have $E_{\mathrm{T}}^{\mathrm{miss}} > 30\,\mathrm{GeV}$.
- The transverse mass of the W-boson M_{T}^{W} should be less than $100\,\mathrm{GeV/c^2}$.

Details on the effect of the pre-selection cuts are given in Table 8.24. Note, that as in Section 8.4.2, the multi-jet QCD contribution is neglected.

8.4.4.2. Genetic algorithm analysis. The following observables have been chosen in order to further discriminate between signal and background after pre-selection: (i) the jet b-tagging discriminants; (ii) the calibrated jet transverse momenta; (iii) the mass of the reconstructed top; (iv) $|\Sigma(t, \bar{b})|$; (v) the scalar sum of the transverse momenta of all the reconstructed objects. The reconstructed top quark is formed by the reconstructed W and one of the two b-jets, chosen according to the value of the "jet charge" (Q_j, see Section 8.4.1.2). Since in top decays the W and the original b quark have opposite sign of the charge, the jet with Q_j "most opposite" to the W is used for top reconstruction, leading to a probability of 67% to identify the correct pairing.

The cuts on these variables are optimised by means of the GARCON program [63]. The surviving events after these cuts are shown in cascade in Table 8.25. With this selection, after an integrated luminosity of $10\,\mathrm{fb^{-1}}$ one gets: $N_S/N_B \approx 0.13$.

Table 8.25. Final cuts and their efficiencies, with respect to the preselected samples, for the signal and the main backgrounds. For s- and t-channel and $Wb\bar{b}$ samples the final W-boson decays into lepton (e, μ, τ) and neutrino. $t\bar{t}$ samples includes all W-boson decay modes.

Cut	s-channel	t-channel	$t\bar{t}$	$Wb\bar{b}$
b-tag(j_1)> 0.4, b-tag(j_2)> 0.1	85%	75%	78%	85%
$p_T(j_1) > 50\,\mathrm{GeV/c}$, $p_T(j_2) > 50\,\mathrm{GeV/c}$	68%	53%	70%	37%
$120 < M(l\nu b) < 220\,\mathrm{GeV/c^2}$	52%	34%	46%	26%
$25 < p_T(l\nu b) < 160\,\mathrm{GeV/c}$	48%	32%	43%	26%
$\Sigma_T < 20\,\mathrm{GeV/c}$	35%	15%	10.6%	12.5%
$H_T < 340\,\mathrm{GeV/c}$	27%	10.7%	5.4%	11.1%
number of surviving events	273 ± 4	630 ± 14	1260 ± 60	155 ± 12

Table 8.26. Number of selected events after 10 fb^{-1} and systematic uncertainties.

sample	selected	$\Delta\sigma$	JES	b-tag	M_{top}	PDF	ISR/FSR
S: s-channel	273	—	±3	±11	±1.5	±2	±1.5
B: t-channel	630	±25	±8	±25	—	—	—
B: $t\bar{t}$	1260	±63	±75	±50	—	—	—
B: $Wb\bar{b}$	155	±8	±7	±6	—	—	—

8.4.4.3. Systematic uncertainties. In addition to systematics described in Section 8.4.1.4 the following sources of systematic uncertainty are considered:

- **Top mass.** The variation of m_t within $\pm2\,\mathrm{GeV/c^2}$ around top mass $m_t = 175\,\mathrm{GeV/c^2}$ leads to the relative systematic error on the selection efficiency $\sigma^{m_t}_{\mathrm{syst}}$ =0.5% for the s-channel single top.
- **Parton Distribution Functions.** To extract the dependence on the PDF uncertainty, two different PDF sets were used: CTEQ61and CTEQ6M [12]. The result is $\sigma^{\mathrm{PDF}}_{\mathrm{syst}}$ =0.7%.
- **Initial/Final State Radiation Modelling.** The model parameters were varied in the ranges Λ_{QCD}=$0.25 \pm 0.1\,\mathrm{GeV}$ and Q^2_{max} from 0.25 to 4 $\hat{s}$ (see [201]). The extreme values of the efficiencies are taken as systematic error: $\sigma^{\mathrm{rad}}_{\mathrm{syst}} = 0.5\%$.

8.4.4.4. Background normalisation. The $t\bar{t}$ events in Table 8.26 are, in 41% of the cases, $t\bar{t} \to l^+\nu b l^-\bar{\nu}\bar{b}$ events with a lepton missed, and in the remain cases $t\bar{t} \to l^+\nu b q\bar{q}'\bar{b}$ events with two jets missed ($t\bar{t} \to q\bar{q}'bq\bar{q}'\bar{b}$ events give a negligible contribution). These two categories of events are very differently affected by the Jet Energy Scale variation. In general, any variation going in the direction of more jets gives a better rejection of the $t\bar{t} \to l^+\nu b q\bar{q}'\bar{b}$ component with respect to the signal, while the $t\bar{t} \to l^+\nu b l^-\bar{\nu}\bar{b}$ events, having two quarks, are affected almost in the same way as the signal.

- $t\bar{t} \to \ell^\pm + X$ *enriched control sample.* In this case the difference with respect to Section 8.4.4.1 is the request of three jets instead of two and only the muon channel is used. The selection efficiency for $t\bar{t} \to \ell^\pm$ events is found to be 1.08%. The ratio R_{c1} between the efficiencies in the main sample and in this control sample is $R_{c1} = 0.0149$, whose variations under JES and b-tagging efficiency systematic shifts are $\Delta R_{c1} = \pm0.0015(\mathrm{JES}) \pm 0.0003$ (b-tag).
- $t\bar{t} \to \ell^{+\ell^-} + X$ *enriched control sample.* This sample is obtained by the same selection as in Section 8.4.4.1, but two leptons with different flavours with the opposite sign are required. The selection efficiency for $t\bar{t} \to 2l$ events is found to be 0.822%. The ratio R_{c2} between the efficiencies in the main sample and in this control sample is $R_{c2} = 0.0681$, whose

variations under JES and b-tagging efficiency systematic shifts are $\Delta R_{c2} = \pm 0.0010$(JES) $\pm\, 0.0004$ (b-tag).

8.4.4.5. Results. The number of the selected signal (N_S) and background (N_B) events and their estimated uncertainties are listed in Table 8.26. The cross section is extracted as

$$\sigma = \frac{N_{tot} - b^0 - R_{c1}(N_{c1} - b^0_{c1}) - R_{c2}(N_{c2} - b^0_{c2})}{\epsilon L}, \tag{8.14}$$

where b^0 is the sum of the non-top backgrounds in the main sample, N_{c1} and N_{c2} are the total events selected in the two control regions, and b^0_{c1} and b^0_{c2} are their contamination by non-top backgrounds, single top and other $t\bar{t}$ decays. The statistical error is evaluated to be 18%. The total systematic uncertainty is 31%, where the largest contribution arises from the effect of the JES uncertainty, on the $t\bar{t}$ single lepton background. The use of "Energy Flow" techniques, including the charged tracks information, is expected to significantly reduce this uncertainty. The total error, including also the 5% luminosity uncertainty, is 36%.

8.4.5. Conclusion

Selection strategies have been proposed for all the three single top production modes, and their effectiveness is shown, taking into account the expected statistics after 10 fb $^{-1}$. All analyses will be systematics dominated. For the s-channel and tW-associated cases, control samples have been proposed in order to constrain the dominant $t\bar{t}$ background.

The resulting signal-to-background ratio and the significance for the t-channel are: $N_S/N_B = 1.34$ and $S_{stat} = N_S/\sqrt{N_S + N_B} = 37.0$, with a statistical error of 2.7%, and a systematic error excluding the 5% luminosity uncertainty of 8%, resulting in a total error of 10%. For tW-channel we expect to reach the significance of 4.2 (5.1) for the dilepton (semi-leptonic) channel, increasing to 6.4 after combining the two channels. The total uncertainty is $\pm$23.9%(syst.) $\pm$9.9%(MC) for dilepton and $\pm$16.8%(syst.) $\pm$15.2%(MC) for semi-leptonic channels. The total systematic uncertainty for the s-channel is 31%. The total error, including also the 5% luminosity uncertainty, is 36%.

8.5. Search for flavour changing neutral currents in top decays

8.5.1. Introduction

The study of Flavour Changing Neutral Current (FCNC) interactions plays an important role in testing the Standard Model (SM) and probing new physics beyond it. The top quark is regarded to be more sensitive to new physics than other fermions, due to its mass close to the electroweak scale. Owing to the GIM mechanism of the SM, top quark FCNC interactions are absent at tree level and extremely small at loop level.

In recent years a lot of work has been done to explore the top quark FCNC couplings. On the theoretical side, various FCNC top quark decays and top-charm associated production at high energy colliders were extensively studied in the SM [323, 324], the Minimal Supersymmetric Standard Model (MSSM) [325–328] and other new physics models [329–333]. In models beyond the SM the top quark FCNC branching fractions may be significantly enhanced. Thus searching for top quark FCNC is a potentially powerful probe of new physics. The CDF and DØ collaborations have reported interesting bounds on the FCNC top quark decays [334–336]. The SM expectations for such top quark FCNC processes are far below the detectable level but the MSSM can enhance them by several orders of magnitude to make them potentially accessible at future collider experiments [337–339]. The theoretical branching ratios and the experimental limits are summarised in Table 8.27. Details of this analysis can be found in [340].

Table 8.27. Theoretical branching ratios of FCNC top quark decays in various models and experimental limits.

Decay	SM	two-Higgs	SUSY with R	Exotic Quarks	Exper. Limits (95% CL)
$t \to gq$	5×10^{-11}	$\sim 10^{-5}$	$\sim 10^{-3}$	$\sim 5 \times 10^{-4}$	< 0.29 (CDF+TH)
$t \to \gamma q$	5×10^{-13}	$\sim 10^{-7}$	$\sim 10^{-5}$	$\sim 10^{-5}$	< 0.0059 (HERA)
$t \to Zq$	$\sim 10^{-13}$	$\sim 10^{-6}$	$\sim 10^{-4}$	$\sim 10^{-2}$	< 0.14 (LEP-2)

8.5.2. Signal and background generation

Both the $t \to \gamma q$ and the $t \to Z^0 q$ decay channels are investigated. The channel $t \to gq$ is not studied because of its very high background. The $t\bar{t}$ signal is generated with TopReX [44], while PYTHIA [184] is used for modelling of quark and gluon hadronisation. The $t\bar{t}$ pair is generated through gluon-gluon and quark-anti-quark annihilation, with subsequent SM decay for one top ($t \to Wb$) and FCNC decay of the other. Only leptonic decay channels of Z and W bosons are studied, where the lepton could be either e or μ. Hadronic Z/W decays as well as decays to tau leptons are not considered because of the large QCD background. On generator level both top quarks are produced on-shell, with a mass of $m_t = 175\,\mathrm{GeV/c^2}$, including the effects of spin-state correlations on final decay products (γq, $Z^0 q$, Wb). Both ISR and FSR are simulated with CTEQ5L PDFs. The generated events are passed through the full detector simulation and digitisation, taking into account low luminosity pile-up.

Several SM processes contributing as background are studied: $t\bar{t}$ production, single top quark production (t-channel), ZW + jets, WW + jets, ZZ + jets, W + jets, Z + jets, $Zb\bar{b}$ and QCD multi-jet production.

8.5.3. Selection strategies

The $t \to \gamma q$ channel is well identified by a high-energy isolated photon accompanying the FCNC top decay. One b-tagged jet and a light jet are also used to distinguish from the standard $t\bar{t}$ decays. For the FCNC $t \to \gamma q$ channel our main selection cuts are: (a) single electron or single muon' trigger criteria at Level-1 and HLT levels; (b) one isolated $e^{\pm}$ (with $p_{\mathrm{T}} > 30\,\mathrm{GeV/c}$) or $\mu^{\pm}$ (with $p_{\mathrm{T}} > 20\,\mathrm{GeV/c}$), and missing transverse energy $E_{\mathrm{T}}^{\mathrm{miss}} > 25\,\mathrm{GeV}$, forming a transverse invariant mass $M_{\mathrm{T}}(bW) < 120\,\mathrm{GeV/c^2}$; (c) only one jet compatible with b-jet with $p_{\mathrm{T}} > 40\,\mathrm{GeV/c}$, that in combination with the W candidate gives an invariant mass in the range between $110\,\mathrm{GeV/c^2}$ and $220\,\mathrm{GeV/c^2}$; (d) one single isolated photon with $p_{\mathrm{T}} > 50\,\mathrm{GeV/c}$; (e) one light-jet (not compatible with b-jet) with $p_{\mathrm{T}} > 50\,\mathrm{GeV/c}$; (f) an invariant mass obtained from the combination of the photon and the light jet that lies in the range between $150\,\mathrm{GeV/c^2}$ and $200\,\mathrm{GeV/c^2}$; (g) the transverse momentum of the photon + light-jet system recoiling against the transverse momentum of the SM-decaying top quark satisfying $\cos\phi(t\bar{t}) < -0.95$.

The total efficiency for the signal is $\varepsilon = 0.021 \pm 0.002$. Only the SM backgrounds $t\bar{t}$ and EW single top (t-channel) contribute to the accepted background, with 54 ± 7 background events accepted for a luminosity of $10\,\mathrm{fb^{-1}}$. The uncertainties are statistical only.

Adopting a factorisation method, QCD background is proven to be not dangerous for the analysis: A set of independent cuts (hard jets, isolated hard lepton, isolated hard photon, b-tagging) is applied to both QCD and $t\bar{t}$ background and the efficiencies for single cuts are assumed to factorise. The b-tagging efficiency and the mistagging are 30% and 0.5%. The number of surviving QCD events for this pre-selection is found to be 42 for a luminosity of $10\,\mathrm{fb^{-1}}$, and the efficiency on the $t\bar{t}$ sample amounts to 2.5%. Assuming that after these

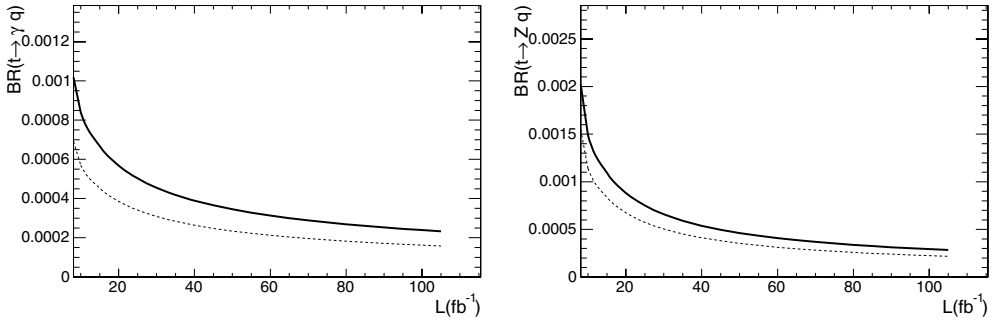

Figure 8.17. Branching Ratios of a FCNC signal detectable at the 5 sigma level as a function of the integrated luminosity, for the $q\gamma$ (left) and qZ (right) channels, shown with (solid line) and without (dashed line) systematic uncertainties.

cuts the further efficiency for the QCD backgrounds and $t\bar{t}$ is the same, leads to expect $\simeq 1$ background events.

For the FCNC $t \to Z^0 q$ channel our main selection cuts are: (a) 'double electron or double muon' trigger criteria at Level-1 and HLT levels; (b) two isolated $e^{\pm}$ (each with $p_{\mathrm{T}} > 20\,\mathrm{GeV/c}$) or $\mu^{\pm}$(each with $p_{\mathrm{T}} > 10\,\mathrm{GeV/c}$), having an invariant mass $\pm 10\,\mathrm{GeV/c^2}$ around the nominal Z^0 mass; (c) third lepton (e with $p_{\mathrm{T}} > 20\,\mathrm{GeV/c}$ or μ with $p_{\mathrm{T}} > 15\,\mathrm{GeV/c}$), which, in combination with the missing transverse energy ($E_{\mathrm{T}}^{\mathrm{miss}} > 20\,\mathrm{GeV}$) have a transverse mass less than $120\,\mathrm{GeV/c^2}$; (d) only one jet compatible with b jet with $p_{\mathrm{T}} > 40\,\mathrm{GeV/c}$; (e) invariant mass of candidate W and b jet in the range [110–220] $\mathrm{GeV/c^2}$; (f) one light-jet (not compatible with b jet) with $p_{\mathrm{T}} > 30\,\mathrm{GeV/c}$ (g) an invariant mass obtained from the combination of the Z and the light jet that lies in the range between $110\,\mathrm{GeV/c^2}$ and $220\,\mathrm{GeV/c^2}$; (h) the transverse momentum of the Z + light-jet system recoiling against the transverse momentum of the SM-decaying top quark satisfying $\cos\phi(t\bar{t}) < 0$.

The total efficiency for the signal is $\varepsilon = 0.041 \pm 0.002$. A total of 1 ± 1 background events are accepted for a luminosity of $10\,\mathrm{fb^{-1}}$. The SM background $t\bar{t} \to (\nu l b)(\nu l b)$ is the only background that gives a significant contribution. The uncertainties are statistical only.

8.5.4. Sensitivity estimation

For the FCNC sensitivity estimation, it is assumed that new physics is observed when the signal significance is 5 at least. When dealing with a small number of background (B) events with respect to signal ones (S), an appropriate definition of significance is [49]:

$$S_{12} = 2\left(\sqrt{B+S} - \sqrt{B}\right). \tag{8.15}$$

S_{12} defines the probability (in number of sigmas) that a background with expected value B fluctuates above observed number of events $S+B$ with Poisson statistics. The number of signal events for the $t \to Zq$ and $t \to \gamma q$ channel can be expressed as:

$$\begin{aligned} S(t \to Zq) &= 2 \times BR(t \to Zq) \times Br\,(W \to l\nu) \times Br\,(Z \to ll) \times \sigma(t\bar{t}) \times L \times \epsilon(t \to Zq) \\ S(t \to \gamma q) &= 2 \times BR(t \to \gamma q) \times Br\,(W \to l\nu) \times \sigma(t\bar{t}) \times L \times \epsilon(t \to \gamma q) \end{aligned} \tag{8.16}$$

where $L = 10\,\mathrm{fb^{-1}}$, $\sigma(t\bar{t}) = 833\,\mathrm{pb}$, $BR(W \to l\nu) = 0.2136$, $BR(Z \to ll) = 0.0673$ ($l = e, \mu$), ε selection efficiency for the signal. From these formulae, the FCNC branching ratios $BR(t \to Zq)$ and $BR(t \to \gamma q)$ can be calculated for a given significance level S_{12}. Without the inclusion of systematic uncertainties, the sensitivity for a significance level

Table 8.28. Effects of systematic uncertainties on the five-sigma observable FCNC branching ratios induced by different sources of systematic uncertainty. The last row indicates the smallest five-sigma observable FCNC branching ratios for 10 fb^{-1} of integrated luminosity including all sources of systematic uncertainty.

	$t \to Zq$ ($\times 10^{-4}$)	$t \to \gamma q$ ($\times 10^{-4}$)
$BR(stat)$	11.4	5.7
jet energy scale	+0.4	+0.6
b jet mistagging	+0.2	+1.8
light jet antitagging	+0.5	+0.9
lepton energy scale	+2.4	+0.5
$\sigma(t\bar{t})$	+0.1	+0.5
MC statistics in B	+2.4	+1.3
MC statistics in S	+0.7	+0.5
Luminosity	+0.1	+0.5
$BR(total)$	14.9	8.4

of $S_{12} = 5$ is $BR(t \to Zq) = 11.4 \times 10^{-4}$ and $BR(t \to \gamma q) = 5.7 \times 10^{-4}$, also shown in Figure 8.17.

The sources of systematic uncertainty are divided into two groups: those related to detector effects and those related to theoretical issues. For both kind of sources, the impact on the selection efficiency and the surviving number of background events is evaluated. Experimental effects considered here include: (a) the lepton energy scale uncertainty, accounted for with relative increase/decrease of the reconstructed photon and electron four-momenta by ± 0.005; (b) the jet energy scale uncertainty, expected to lie in the range from $\pm 5\%$ at $p_T = 20\,GeV/c$ to $\pm 2.5\%$ at $p_T > 50\,GeV/c$, and totally correlated to missing energy uncertainty (assumed to be $\pm 5\%$, [320]); (c) b-tagging uncertainty (4% after 10 fb^{-1} integrated luminosity [285]), that is studied by assuming a non-b-tagged jet is actually a b-tagged jet 4% of the time; (d) uncertainty in anti-tagging b-jet instead of non-*b* ones (4% after 10 fb^{-1} integrated luminosity), simulated by assuming a b-tagged jet is a non-b-tagged jet with the same probability.

The impact of the single sources of systematic uncertainty is detailed in Table 8.28. Experimental sources of systematic uncertainties, such as the control of the lepton energy scale and of the b-tagging procedure are expected to be the most significant. The statistical uncertainty on the prediction of the background level of this analysis has a large contribution to the global systematic uncertainty. Refined techniques for the background estimation will reduce this uncertainty once data will be available.

Including all systematic uncertainties, the smallest detectable FCNC branching ratios, for a five-sigma sensitivity and 10 fb^{-1} of luminosity, are $BR(t \to Zq) = 14.9 \times 10^{-4}$ and $BR(t \to \gamma q) = 8.4 \times 10^{-4}$. Under the assumption that the selection efficiency is unaffected by moderate instantaneous luminosity increases (i.e., pile-up), the decrease in the upper limit on the branching fraction with increasing luminosity can be evaluated in a straightforward way. Figure 8.17 shows the branching ratio for both channels as a function of the integrated luminosity. An improvement in the branching ratio limits by a factor of 2 is expected for a luminosity increase by a factor of 5.

Chapter 9. Electroweak Physics

9.1. Production of W and Z bosons

9.1.1. Introduction

The reactions $pp \to W + X$ and $pp \to Z + X$ with subsequent leptonic decays of the massive electroweak vector bosons, $W \to \ell\nu$ and $Z \to \ell^+\ell^-$, have a large cross section and are theoretically well understood. Cross sections above 10 nb (1 nb) are expected at the LHC for the $W \to \ell\nu$ ($Z \to \ell^+\ell^-$) channel in the fiducial region of the CMS detector. Hence these reactions are useful for many purposes, including a precise luminosity monitor, a high-statistics detector calibration tool and to demonstrate the performance of the CMS experiment. These reactions will be among the first to be measured at the LHC.

Here we discuss prospects for precise measurements of the reactions $pp \to Z + X$ and $pp \to W + X$ at the LHC using the decays of the gauge bosons into electrons and muons. Studies have been performed based on Monte Carlo samples generated with PYTHIA including realistic detector simulation and addressing the most relevant systematic effects. The potentially most dangerous background in these analyses consists of QCD events with leptons from hadron decays or tracks misidentified as leptons. However, these lepton candidates are associated to jets and can be largely suppressed using isolation algorithms.

Robust criteria are developed which allow for a low-background event selection which is rather insensitive to detector inhomogeneities. This robust selection is considered as especially useful for the CMS startup phase. The results show that a determination of the W and Z rates with an experimental precision on the percent level is feasible already in the early phase of the experiment.

9.1.2. W/Z into electrons

The process pp $\to$ ZX and pp $\to$ WX with subsequent decay of Z and W into electrons is studied using the full CMS detector simulation and analysis scheme. The aim is to define some baseline selection which is suppressing background to a very small level and detector inhomogeneities can be controlled. This selection can thus be considered as especially useful for the CMS startup phase. Details can be found in [341].

Electron (positron) candidates are selected with the following criteria [313]:

- The minimal E_{T} of the electromagnetic cluster has to be larger than 20 GeV with $|\eta_{\mathrm{cluster}}| < 1.4$ for barrel electron candidates and $1.6 < |\eta_{\mathrm{cluster}}| < 2.4$ for endcap electron candidates.
- The cluster should be consistent with the shower shape expected for electromagnetic showers. The spread of the electromagnetic shower along the η direction is rather insensitive to bremsstrahlung, thus allowing a good separation of signal and background shower shapes. Therefore it is required that the spread of the electromagnetic shower in η with respect to η of the supercluster, $\sigma_{\eta\eta}$, is smaller than 0.01.
- The energy deposit in the associated hadron calorimeter cluster should be very small. For this selection the ratio $E_{\mathrm{Had}}/E_{\mathrm{EM}}$ has to be smaller than 0.05.
- In order to be identified as an electron, a reconstructed track has to be matched with the cluster such that $\Delta R < 0.15$ (where $\Delta R = \sqrt{\Delta\phi^2 + \Delta\eta^2}$). Furthermore, it is required that the ratio of the cluster energy and the track momentum, E/P, is larger than 0.9 and that $|1/E - 1/P| < 0.02$.
- Finally, it is required that the electron candidate is isolated. The transverse momentum sum of all other tracks found within a cone radius ΔR of 0.35 divided by the electron candidate

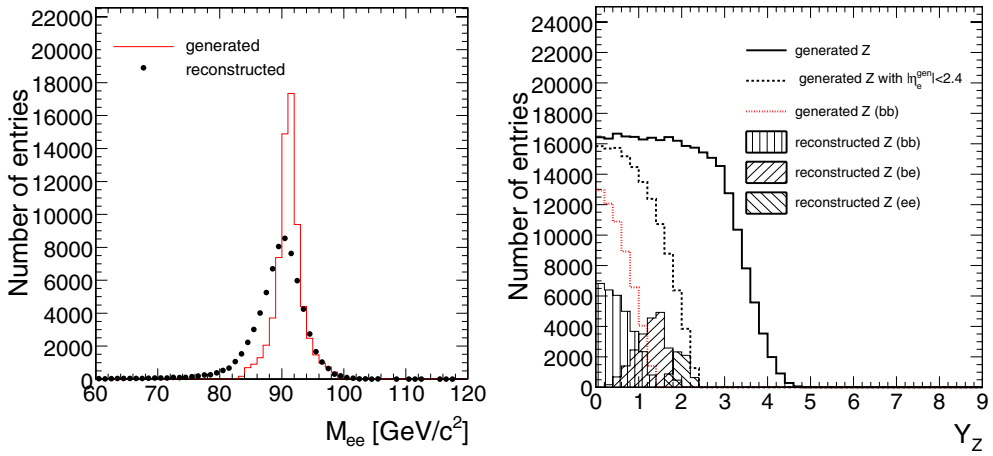

Figure 9.1. Left: Reconstructed and generated Z mass distribution with all cuts. Right: Generated rapidity distribution for all Z candidates and for those where both electrons were generated within the geometrical acceptance of the electromagnetic calorimeter. For comparison, the rapidity distribution of the finally accepted Z events is already shown here.

transverse supercluster energy has to be smaller than 0.2. Only tracks with a transverse momentum above 1.5 GeV/c and with at least four hits in the central tracker which are close to the interaction vertex are considered.

9.1.2.1. $pp \to Z \to eeX$ Selection. We analyse events where one e^+e^- pair consistent with the Z mass is found (if more than two electrons pass the selection criteria, only those two with the highest transverse momenta are considered). The generated and reconstructed mass distribution are shown in Figure 9.1 (left). For now, the "electron" clusters are not corrected for bremsstrahlung within the tracker and the reconstructed Z peak is found to be about 1 GeV lower than the generated one.

Using this selection, the rapidity distribution of the accepted Z events is shown in Fig. 9.1 (right). In addition, the rapidity distribution of the potentially accepted Z bosons, separated for the three cases where both decay electrons are within the acceptance of the barrel calorimeter (BB) $|\eta_{\mathrm{BB}}| < 1.4$, both within the endcaps (EE) $1.6 < |\eta_{\mathrm{EE}}| < 2.4$ or one within the barrel and the other one in the endcaps (EB) are also shown. In the case that both generated electrons are in the barrel, a Z detection efficiency of about 60% is reached.

Here the electron efficiency is defined by the ratio of reconstructed electrons from accepted Z events to the number of electrons from generated Z events, where the generated electrons fulfilled the condition $|\eta^{\mathrm{e}}_{\mathrm{gen}}| < 1.4$. Fig. 9.2 (left) shows the efficiency distribution for all supermodules folded such that the local ϕ angle for all odd supermodules goes from 0–20 degrees and for all even supermodules from 20–40 degrees.

The efficiency drop of about 10% between the supermodules is clearly visible with the available sample of Z events corresponding to roughly 0.2 fb^{-1}. Similar inefficiencies were found in the η direction at supermodule boundaries. From the analysis of the reconstruction efficiency as function of the phi angle, we get an efficiency of $27.1\% \pm 0.4\%$ (if the inter-supermodule regions are excluded) while the average over the whole phi range is $26.5 \pm 0.4\%$.

The average Z efficiency, when both electrons are generated and reconstructed in the barrel calorimeter, is found to be $57.3 \pm 0.2\%$ (where the uncertainties are from the finite number of Monte Carlo events). Half the efficiency loss is caused by the

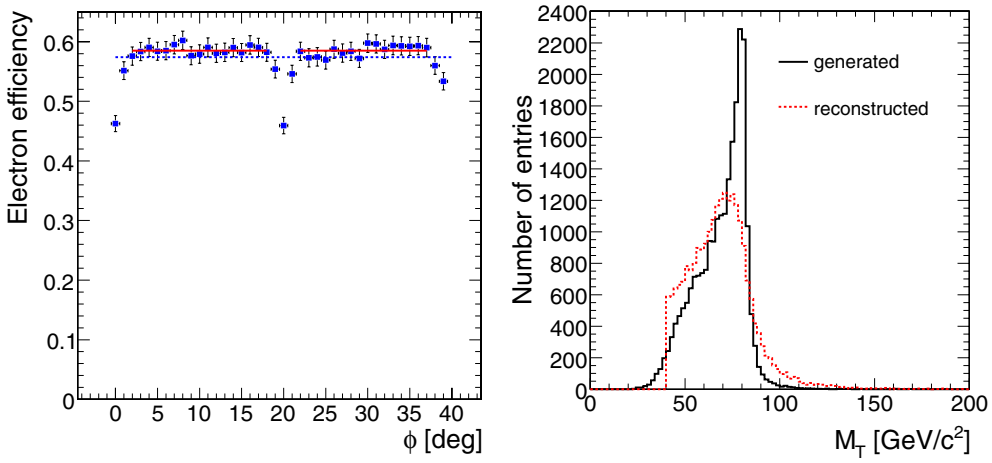

Figure 9.2. Left: The electron reconstruction efficiency in $Z \to e^+e^-$ events as a function of ϕ, all even and odd numbered supermodules are folded such that the odd (even) numbered supermodules always cover local ϕ angles from 0 to 20 degrees and from 20 to 40 degrees respectively. The dotted line corresponds to the average efficiency $57.3 \pm 0.2\%$ over the whole ϕ range and the solid lines correspond to the average efficiency $58.4 \pm 0.2\%$ with the gap regions excluded. Right: Generated (solid line) and reconstructed (dashed line) transverse W mass. The W transverse mass is reconstructed from the electron four-momentum and the missing transverse energy. In this plot, only events with no reconstructed jet above 20 GeV transverse energy are included.

shower-shape requirement, and another quarter by the energy-momentum matching requirement. If events, where at least one electron is reconstructed within the gaps, are removed, the average efficiency is found to be $58.4 \pm 0.2\%$. Assuming that the produced electrons must be homogeneous in ϕ and that the effects from geometrical gaps can be monitored with some reasonable statistics, it should be straightforward to correct for the detector gaps. Already with the available statistics used for this study, the corrections for the efficiency loss in the gaps can certainly be determined with a relative accuracy smaller than about 25%. This number is estimated from comparing the minimal efficiency in the gap and the efficiency in the non-gap regions.

We conclude that already with a few 100 000 reconstructed Z events, collected at the early stage of the experiment, an efficiency determination with a systematic accuracy of better than 1–2% should be possible. Obviously, with the much larger statistics of a few million Z events, these uncertainties can be further reduced. Once data from the CMS detector becomes available, these cuts can be applied on one electron and varied on the other electron to compare the selection efficiency in data and Monte Carlo simulation. This can be used to further improve the detector simulation and to better access systematic uncertainties.

9.1.2.2. $pp \to W \to e\nu X$ Selection. In order to pass the $W \to e\nu$ selection, events must have exactly one electron candidate in the barrel fulfilling the requirements described above, and missing transverse energy associated with the neutrino: a cut on the transverse mass of the $e\nu$ system is applied. The transverse mass m_T is defined as follows:

$$m_T = \sqrt{2 p_T^{(e)} p_T^{(\nu)} (1 - \cos \Delta\phi)} \tag{9.1}$$

where $p_T^{(e,\nu)}$ is the (reconstructed) transverse momentum of the electron and the neutrino respectively and $\Delta\phi$ is the azimuthal angle between the electron and the neutrino.

The missing transverse energy can be determined in several ways, for example:

1. From the vector sum of all clusters in the calorimeter.
2. From the vector sum of hard objects only.

In the electromagnetic calorimeter, the electron transverse energy can be measured accurately. However, the reconstructed transverse missing energy shows a significant bias.

Suspecting that low energy objects (randomly distributed across the detector) are responsible for this bias, we follow the second approach: We select reconstructed jets with a transverse energy above 20 GeV and absolute pseudorapidity less than 2.4 and reconstruct the missing transverse energy only from these jets and the electron. Here we use uncalibrated jets, i.e. whenever we refer to the jet energy we mean raw jet energy.

To study this possibility in more detail, we split our sample into events without jets (as defined in the previous paragraph) and events with one or more jets. Note that in the case of zero accepted jets, only the electron is used to calculate the neutrino transverse energy which is then very close to the electron transverse energy (pointing into opposite directions in ϕ). The transverse mass is equal to twice the electron transverse energy in this case.

No systematic bias is found with this method and the mean value is close to zero. We thus use this method to reconstruct the neutrino transverse energy. The reconstructed W transverse mass is shown in Fig. 9.2 (right). For the purpose of this analysis and the counting of resonant W events, we require the transverse mass to lie in the interval 60 to 100 $\mathrm{GeV}/\mathrm{c}^2$.

We consider two sources of systematic uncertainties here: The uncertainty due to inhomogeneities in the detector geometry and the uncertainty related to the jet veto. We expect that the uncertainty from the reconstruction efficiency as function of the electron azimuthal angle for the efficiency correction will be similar as for the Z selection.

To address the effect of the scale uncertainty of the absolute calibration on the jet definition, we investigated the changes in the selection efficiency when moving the threshold transverse energy for the jet definition. It follows that for a cut on the transverse jet energy at 20 GeV, the efficiency slope is roughly 0.1% (absolute) per GeV, corresponding to a relative uncertainty of about 0.25% per GeV.

Assuming a jet energy scale uncertainty of 15% at the LHC startup we obtain an efficiency uncertainty of 0.75% relative. For 5% uncertainty in the jet energy scale expected after the final detector calibration), this value reduces to 0.25%.

The efficiency change due to the jet veto can also be estimated directly from $\mathrm{Z} \to \mathrm{e}^+\mathrm{e}^-$ events (applying a jet veto to these events). In the future, this can be done directly from the data recorded with the CMS detector. Thus with the expected large data samples of $\mathrm{Z} \to \mathrm{e}^+\mathrm{e}^-$, remaining differences between data and Monte Carlo can be studied and corrected with very small uncertainties.

9.1.3. W/Z into muons

Simple sets of cuts can be used in CMS to select large statistics samples of $Z \to \mu\mu$ and $W \to \mu\nu$ events with high purity. They are described in detail in Ref. [342] and summarised here.

The $Z \to \mu\mu$ selection criteria have been chosen to minimise uncertainties from the muon chamber response and from the matching between the inner tracker and the muon spectrometer. The basic idea is to accept events in which one of the muons is reconstructed as an isolated track in the central tracker detector, even if no associated track in the muon spectrometer is present. This results in a more uniform efficiency as a function of the pseudo-rapidity, as observed in Fig. 9.3 (left). From the kinematics point of view only muons with

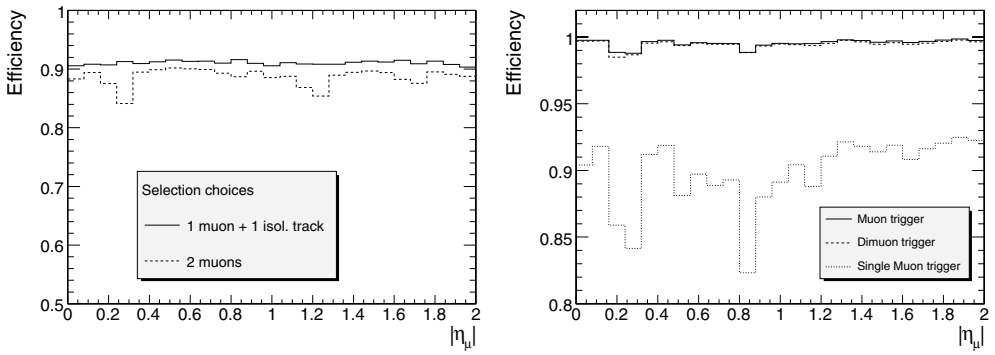

Figure 9.3. Left: Muon efficiency as a function of pseudo-rapidity in the selected $Z \to \mu\mu$ sample. Two cases are considered: a selection using only muons reconstructed in the muon chambers (dashed histogram) and the selection described in the text (solid histogram), which also accepts isolated tracks in the inner tracker. For this test, no HLT trigger criteria have been applied. Right: HLT efficiency on the selected $Z \to \mu\mu$ sample as a function of the pseudorapidity of one of the muons. All but the HLT trigger criteria have been applied. The regions at $|\eta| \approx 0.25$ and $|\eta| \approx 0.8$, with a slightly lower trigger efficiency, are visible. The fraction of events triggered by dimuon and single-muon triggers are also shown.

$p_T > 20\,\text{GeV}$ and pseudorapidity $|\eta_\mu| < 2.0$ are considered in the present analysis. A dimuon mass window of $\pm 3\Gamma_Z = 7.5\,\text{GeV}$ around the reconstructed Z mass is used. Figure 9.3 (right) shows the efficiency of the HLT criteria on the selected sample as a function of the muon pseudo-rapidity. One can clearly observe two regions with smaller efficiency, around $|\eta| \approx 0.25$ and $|\eta| \approx 0.8$, where transitions between two muon wheels take place. The efficiency is dominated by the dimuon component, which represents a unique tool to study the performance of the single-muon subtrigger, which is of relevance for other selections, like $W \to \mu\nu$.

Even if the rate of $W \to \mu\nu$ events is expected to be larger than the $Z \to \mu\mu$ rate by an order of magnitude, the experimental context is more demanding due to a lower trigger efficiency, only moderate transverse missing energy in the event, the absence of a precise mass constraint and a full dependence on tracker and muon spectrometer behaviours. This will lead to larger experimental uncertainties, which can be studied with the $Z \to \mu\mu$ data samples. The selection of $W \to \mu\nu$ events uses the same η cut but a higher p_T threshold, 25 GeV, due to the higher threshold for the single-muon trigger. Figure 9.4 shows the transverse invariant mass distribution of the muon-E_T^{miss} system in $W \to \mu\nu$ events, compared to QCD expectations.

Systematic uncertainties in the determination of $Z \to \mu\mu$ and $W \to \mu\nu$ acceptances are summarised in Tables 9.1 and 9.2. The various sources of uncertainties are discussed in detail in Ref. [342]. Most of them are evaluated for a CMS detector calibrated with $1\,\text{fb}^{-1}$. The experimental components are well under control in the case of the $Z \to \mu\mu$ selection, with the limited knowledge on the track efficiency as the dominant source. In the $W \to \mu\nu$ case, many of them contribute at a similar level, with E_T^{miss} providing the largest uncertainty. Concerning theoretical sources, the boson p_T uncertainties are the dominant contribution. They are estimated from a comparison between LO and NLO CMS simulations using MC@NLO as event generator [343], as shown in Fig. 9.5.

The results of the study can be summarised in terms of cross section measurement accuracies, for $1\,\text{fb}^{-1}$ of integrated luminosity, as follows: $\Delta\sigma/\sigma(pp \to Z + X \to \mu\mu + X) = 0.13\ (stat) \pm 2.3\ (syst.) \pm 10\ (lumi)\%$ and $\Delta\sigma/\sigma(pp \to W + X \to \mu\nu + X) = 0.04\ (stat.) \pm 3.3\ (syst.) \pm 10\ (lumi)\%$, where luminosity represents the dominant uncertainty which will eventually decrease to 5% with more integrated luminosity.

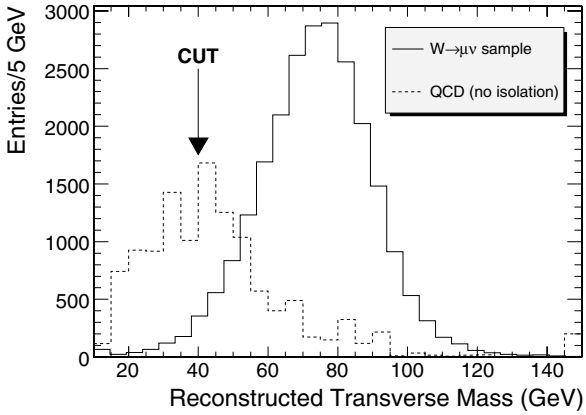

Figure 9.4. Transverse invariant mass reconstructed in $W \to \mu\nu$ events. In order to observe the shape of the QCD background with more statistics, the HLT muon isolation criteria have not been applied to obtain the plot. The position of the lower cut ($M_{\mu\mu} > 40\,\mathrm{GeV/c^2}$) is indicated with an arrow.

Table 9.1. Relative systematic uncertainties on the acceptance for the $Z \to \mu\mu$ sample.

Source	Uncertainty (%)
Tracker efficiency	1
Magnetic field knowledge	0.03
Tracker alignment	0.14
Trigger efficiency	0.2
Jet energy scale uncertainties	0.35
Pile-up effects	0.30
Underlying event	0.21
Total exp.	1.1
PDF choice (CTEQ61 sets)	0.7
ISR treatment	0.18
p_{T} effects (LO to NLO)	1.83
Total PDF/ISR/NLO	2.0
Total	2.3

QCD backgrounds seem to be under control, even if final checks with data will be necessary to determine the level of background with more precision.

Therefore, rates within the fiducial volume of the detector can be determined with high accuracy, even for the first stages of the LHC ($\approx 2.3\%$ for $Z \to \mu\mu$ and $\approx 3.3\%$ for $W \to \mu\nu$). These uncertainties will be significantly reduced with the use of the next generation of NLO Monte Carlos and final detector calibrations, and allow these reactions to be used to determine the luminosity.

9.1.4. Parton distribution functions and parton luminosities

The production of inclusive W and Z events is theoretically well understood and the couplings to quarks and leptons have been measured with accuracies of 1% or better. Thus, it follows from the previous sections that a precise counting of $W \to e\nu$, $\mu\nu$ and $Z \to ee$, $\mu\mu$ events is

Table 9.2. Relative systematic uncertainties on the acceptance for the $W \to \mu\nu$ sample.

Source	Uncertainty (%)
Tracker efficiency	0.5
Muon efficiency	1
Magnetic field knowledge	0.05
Tracker alignment	0.84
Trigger efficiency	1.0
Transverse missing energy	1.33
Pile-up effects	0.32
Underlying event	0.24
Total exp.	2.2
PDF choice (CTEQ61 sets)	0.9
ISR treatment	0.24
p_{T} effects (LO to NLO)	2.29
Total PDF/ISR/NLO	2.5
Total	3.3

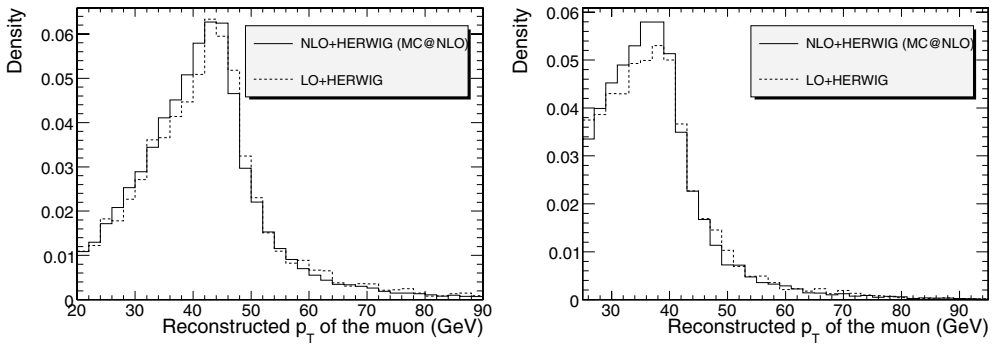

Figure 9.5. Left: Comparison between LO and NLO predictions for the muon p_{T} distribution in $Z \to \mu\mu$ selected events. Both histograms have been normalised to the total number of events generated in the fiducial volume: $|\eta_\mu| < 2.5$, $p_{\mathrm{T}\mu}^{max} > 20\,\mathrm{GeV/c}$, $p_{\mathrm{T}\mu}^{min} > 10\,\mathrm{GeV/c}$ and $M_Z - 6\Gamma_Z < M_{\mu\mu} < M_Z + 6\Gamma_Z$ Right: Comparison between LO and NLO predictions for the muon p_{T} distribution in $W \to \mu\nu$ selected events. Both histograms have been normalised to the total number of events generated in the fiducial volume: $|\eta_\mu| < 2.5$.

equivalent to a precise measurement of the quantity

$$\int_{q,\bar{q}\ partons} \mathrm{d}x_1\,\mathrm{d}x_2\,\sigma_{q\bar{q}\to W,Z} \times L_{pp} \times PDF(x_1, x_2, Q^2), \tag{9.2}$$

where L_{pp} is the LHC integrated luminosity, $\sigma_{q\bar{q}\to W,Z}$ is the cross section for inclusive W or Z production at the partonic level and $PDF(x_1, x_2, Q^2)$ denotes the probability to produce quarks and anti-quarks with proton fractions x_1 and x_2 at a scale Q^2. The prospect studies of Ref. [342], summarised in Table 9.3, show that uncertainties on the parton distribution functions (PDF) have a relatively small influence on the experimental acceptance for the rates, but a large effect on the global rate expectations.

We conclude from Table 9.3 that a comparison between theory and experiment with a 6–7% accuracy is possible. This comparison provides a measurement of the integrated luminosity L_{pp} with a similar level of precision. The small theoretical uncertainties on the experimentally measured rate (from the acceptance uncertainty) allow precise measurements of cross section ratios, such as $\sigma(pp \to ZZ + X)/\sigma(pp \to Z + X)$, in which

Table 9.3. Estimated uncertainties in the rate and in the acceptance for the $pp \to Z + X \to \mu\mu + X$ and $pp \to W + X \to \mu\nu + X$ processes. The global rate is referred to the fiducial volumes used in Ref. [342], which include a pseudorapidity cut of $|\eta_\mu| < 2.5$.

	$Z \to \mu\mu$	$W \to \mu\nu$
Global rate uncertainty (%)	$^{+5.8}_{-7.9}$	$^{+5.6}_{-7.4}$
Acceptance uncertainty (%)	$^{+0.4}_{-0.7}$	$^{+0.6}_{-0.9}$

PDF and luminosity uncertainties cancel. Current studies within theoretical and experimental communities [344] aim to a further reduction of uncertainties associated to PDFs. Finally, PDF validity tests and further reductions in the acceptance uncertainty (below the percent level) will require dedicated studies of the lepton rapidity distributions observed in data, like those suggested in Ref. [345].

9.2. Muon pairs from the Drell–Yan process

9.2.1. Introduction

In the Standard Model, the production of lepton pairs in hadron-hadron collisions, the Drell–Yan (DY) process [346], is described by s-channel exchange of photons or Z bosons. The parton cross section in the lepton-pair centre-of-mass system has the form:

$$\frac{\mathrm{d}\sigma}{\mathrm{d}\Omega} = \frac{\alpha^2}{4s}[A_0(1+\cos^2\theta) + A_1\cos\theta] \tag{9.3}$$

where $\sigma = \frac{4\pi\alpha^2}{3s}A_0$ and $A_{\mathrm{FB}} = \frac{3}{8}\frac{A_1}{A_0}$ are the total cross section and the forward-backward asymmetry, and θ is angle of lepton in the dilepton rest frame with respect to the quark direction. The terms A_0 and A_1 are fully determined by the electroweak couplings of the initial- and final-state fermions. At the Z peak the Z exchange is dominating and the interference term is vanishing. At higher energies both photon and Z exchange contribute and the large value of the forward-backward asymmetry is due to the interference between the neutral currents. Fermion-pair production above the Z pole is a rich search field for new phenomena at present and future high energy colliders. The differential cross section is sensitive to manifestation of new physics from a multi-TeV scale by adding new amplitudes or through their interference with the neutral currents of the SM. At hadron colliders the parton cross sections are folded with the parton density functions (PDF): $pp \to l_1 l_2$

$$\frac{\mathrm{d}^2\sigma}{\mathrm{d}M_{ll}\mathrm{d}y}[pp \to l_1 l_2 + X] \approx \sum_{ij}\left(f_{i/p}(x_1)\, f_{j/p}(x_2) + (i \leftrightarrow j)\right)\hat{\sigma} \tag{9.4}$$

where $\hat{\sigma}$ is the cross section for the partonic subprocess $ij \to l_1 l_2$, $M_{ll} = \sqrt{\tau s} = \sqrt{\hat{s}}$ the mass of the lepton-pair system, y the rapidity of the lepton pair, $x_1 = \sqrt{\tau}e^{y}$ and $x_2 = \sqrt{\tau}e^{-y}$ the parton momentum fractions, and $f_{i/p(\bar{p})}(x_i)$ the probability to find a parton i with momentum fraction x_i in the proton.

The total cross section and the forward-backward asymmetry are function of observables which are well measured experimentally for final states containing e^+e^- or $\mu^+\mu^-$: the invariant mass and the rapidity of the final-state lepton pair. This allows to reconstruct the centre-of-mass energy of the initial partons, even if their flavours are unknown. For a $(x_1 \geqslant x_2)$ pair of partons we have 4 combinations of *up*- or *down*-type quarks initiating the interaction: $u\bar{u}, \bar{u}u, d\bar{d}, \bar{d}d$. In pp collisions the anti-quarks come always from the sea and the quarks can

Table 9.4. x_1 and x_2 for different masses and rapidities.

y	0	2	4	0	2	4	0	2	4
	$M = 91.2\,GeV/c^2$			$M = 200\,GeV/c^2$			$M = 1000\,GeV/c^2$		
x_1	0.0065	0.0481	0.3557	0.0143	0.1056	0.7800	0.0714	0.5278	-
x_2	0.0065	0.0009	0.0001	0.0143	0.0019	0.0003	0.0714	0.0097	-

have valence or sea origin. The x-range probed depends on the mass and rapidity of the lepton pair as shown in Table 9.4.

The results presented here extend the studies for the LHC SM workshop (see [158] and references therein), using more data and the CMS full detector simulation and reconstruction. More details can be found in [347].

9.2.2. Cross section measurements

Simulation of Drell–Yan events in proton-proton collisions at 14 TeV centre-of-mass energy is performed with PYTHIA 6.217 using the CTEQ5L parton distribution functions. The possible contributions from higher-order terms in the dimuon production cross section are taken into account by using a K factor of 1.3 as calculated with the program PHOZPRMS [348]. Eleven samples of 10 000 events each with different cut-off values on the dimuon invariant mass are generated: $M_{inv} \geqslant 0.2, 0.5, 1, 1.5, 2, 2.5, 3, 3.5, 4, 4.5, 5\,TeV/c^2$. Only events with at least two muons in the pseudorapidity range $|\eta| \leqslant 2.5$, with transverse momentum $p_T \geqslant 7\,GeV/c$ are preselected. No cuts on isolation of muons are made at the pre-selection stage. The total efficiency for dimuon pre-selection, ε, is about 87% for a mass of $1\,TeV/c^2$ and 96% for a mass of $5\,TeV/c^2$. To simulate the detector geometry, materials and particle propagation inside the detector, the GEANT 4-based simulation of the CMS detector is used.

The trigger simulation is based on the on-line reconstruction algorithms. Events are selected by the single- and double-muon triggers. This means that at least one muon candidate is within pseudorapidity region $|\eta| \leqslant 2.1$. The total efficiency of triggering including reconstruction and trigger selection efficiency is 98% at 1 TeV. There is significant decrease in trigger efficiency after applying calorimeter isolation cuts (down by 15%). The tracker isolation practically does not affect the trigger efficiency. Thus the additional cuts on calorimeter and tracker isolation of muon tracks are not applied in this analysis.

The off-line muon reconstruction algorithm is applied only to events which have passed trigger selection. At the off-line level two muons inside the CMS acceptance $|\eta| \leqslant 2.4$ are required. The overall efficiency of the full reconstruction procedure taking into account trigger and off-line reconstruction inefficiency is between 97% and 93% for a mass range of 0.2 to $5\,TeV/c^2$, as shown in Fig. 9.6 (left). In the case of an ideal detector the mass resolution smearing for fully-reconstructed events is between 1.8% and 6% for the same mass range, Fig. 9.6 (right). The effect of misalignment on the mass resolution varies from 1.1% up to 2.3% (1.3%) for the *First Data* (*Long Term*) scenarios at the Z and from 5% up to 25% (6%) for $3\,TeV/c^2$.

The cross sections of Drell–Yan production for the simulated CMS runs are shown in Table 9.5. The non-reducible backgrounds considered are vector boson pair production ZZ, WZ, WW, $t\bar{t}$ production etc. The simulation and pre-selection of background events is done with the same cuts as for the signal above. In the SM the expected leading-order cross section of these events is negligible in comparison with the Drell–Yan one, see Table 9.5.

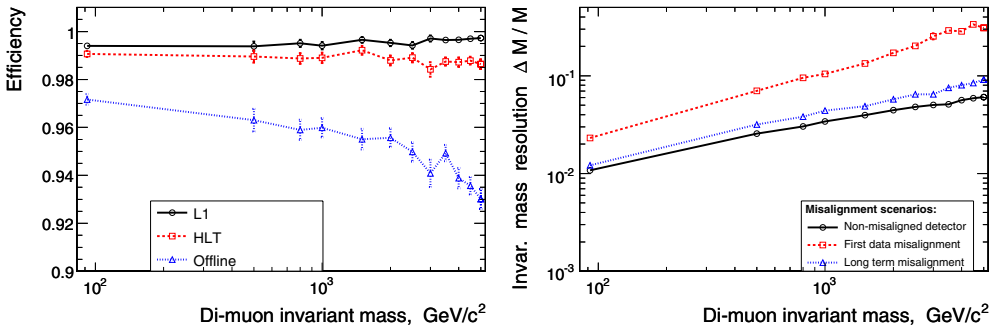

Figure 9.6. Left: dimuon reconstruction efficiency, and right: invariant mass resolution; both as function of the invariant mass cut.

Table 9.5. Leading-order cross sections of Drell–Yan, preselected Drell–Yan, dibosons (ZZ, ZW, WW) and $t\bar{t}$ events in fb. The CTEQ5L parton distributions are used.

$M_{\mu^+\mu^-}$, TeV/c^2	$\geqslant 1.0$	$\geqslant 1.5$	$\geqslant 2.0$	$\geqslant 2.5$	$\geqslant 3.0$	$\geqslant 4.0$
Drell–Yan	6.61	1.04	$2.39 \cdot 10^{-1}$	$6.53 \cdot 10^{-2}$	$1.97 \cdot 10^{-2}$	$2.09 \cdot 10^{-3}$
Pre-sel. D-Y	5.77	$9.53 \cdot 10^{-1}$	$2.24 \cdot 10^{-1}$	$6.14 \cdot 10^{-2}$	$1.87 \cdot 10^{-2}$	$2.00 \cdot 10^{-3}$
Dibosons	$2.59 \cdot 10^{-4}$	$1.51 \cdot 10^{-4}$	$5.6 \cdot 10^{-5}$	$2.26 \cdot 10^{-5}$	$9.06 \cdot 10^{-6}$	$1.66 \cdot 10^{-6}$
$t\bar{t}$	$2.88 \cdot 10^{-4}$	$2.58 \cdot 10^{-4}$	$1.55 \cdot 10^{-4}$	$7.02 \cdot 10^{-5}$	$2.93 \cdot 10^{-5}$	$3.65 \cdot 10^{-6}$

Table 9.6. Relative errors of the Drell–Yan muon pairs cross section measurements in the fiducial volume.

$M_{\mu^+\mu^-}$, TeV/c^2	Detector smearing	Statistical 1 fb^{-1}	Statistical 10 fb^{-1}	Statistical 100 fb^{-1}	Theor. Syst.
$\geqslant 0.2$	$8 \cdot 10^{-4}$	0.025	0.008	0.0026	0.058
$\geqslant 0.5$	0.0014	0.11	0.035	0.011	0.037
$\geqslant 1.0$	0.0049	0.37	0.11	0.037	0.063
$\geqslant 2.0$	0.017		0.56	0.18	0.097
$\geqslant 3.0$	0.029			0.64	0.134

The $\tau\tau$ background (from τ decaying to μ and neutrinos) is 0.8% at the Z pole and 0.7% for masses above 1 TeV/c^2. The background from Drell–Yan production of $q\bar{q}$ pairs (mostly semi-leptonic b or c decays) is 0.3% at the Z pole without applying any isolation cuts and below 0.1% for masses above 1 TeV/c^2. The other background sources are negligible. If the need arises they can be further suppressed by acoplanarity and isolation cuts in the tracker.

The main experimental systematic effects in the cross section measurement arise from the total muon inefficiency and momentum resolution. The latter is very important at high mass as smearing from lower masses from the steeply falling Drell–Yan spectrum can contaminate the high mass measurements, especially if the tails of the momentum resolution are not under control. The main sources of systematic uncertainties on the momentum resolution come from the alignment of the muon chambers and the central tracker, both at start-up and high luminosity.

The statistical errors for 1, 10 and 100 fb^{-1} runs, the systematic uncertainty due to smearing in the detector and from theory side are given in Table 9.6. The modification of the measured cross section due to uncertainty of the mass resolution does not exceed 2.9% which is reached for a mass of 3 TeV/c^2, see Table 9.6. This has been estimated by applying

an additional smearing to the dimuon mass (see [99, 347]). The misalignment does not affect the efficiency of dimuon reconstruction for any masses [99]. Taking into account the trigger efficiency changes from 98.5% to 97% for masses from 0.2 to 5 TeV/c^2, very conservatively we may assign half of this change with mass, i.e., 0.75%, as a systematic uncertainty.

An important ingredient in the cross section measurement is the precise determination of the luminosity. A promising possibility is to go directly to the parton luminosity [345] by using the $W^{\pm}(Z)$ production of single (pair) leptons. New estimates show that in this way the systematic error on $\sigma_{DY}^{high\,Q^2}$ *relative* to σ_Z can be reduced to $\approx$ 5–12% [349].

On the theory side we consider several sources of systematic uncertainties. Higher order QCD corrections are often taken into account with K-factor of 1.3 as calculated with the program PHOZPRMS [348]. It is expected that the total value of additional NNLO contributions does not exceed 8% .

A full-scale analysis of experimental data (comparison data with theory, taking into account acceptance corrections for precise measurement of σ and A_{FB} at large centre-of-mass energies $\hat{s}$) requires good knowledge of the different types of genuine electroweak (EW) radiative corrections to the DY process: vertex, propagator, EW boxes. A complete one-loop parton cross section calculation has been included in [158] and confirmed in [350]. The EW corrections change the cross section by 10–20%. The calculation [105] of the weak radiative corrections to the Drell–Yan processes due to additional heavy bosons contributions shows that these corrections are about 2.9% to 9.7% for mass region between 0.2 TeV/c^2 and 5 TeV/c^2.

The phenomenological origin of PDF gives one additional systematic error. First of all, estimates of cross section obtained by using different sets of structure functions do not give exactly the same values. The results vary within $\pm$7% for $M_{ll} \geqslant 1$ TeV/c^2. The internal PDF uncertainties are estimated using the LHAPDF library [95, 351]. The PDF-dependence of the acceptance efficiency is estimated by using the PDF sets CTEQ5L, CTEQ6L and MRST2001E. The changes in the acceptance efficiency are up to 0.5%. The ambiguity in the acceptance efficiency due to internal PDF uncertainties is larger, but less than 1.4% for any mass region.

The summary of the estimated systematic uncertainties as function of the dilepton mass is given in Fig. 9.7. The CMS experiment has excellent potential to measure the cross section for dimuon pairs up to the highest masses that will be accessible at the LHC, and to test the Standard Model up to very high momentum transfers in a new and unexplored energy range. Current uncertainties from theory are larger than the experimental uncertainties. The statistical errors will dominate for invariant masses larger than 2 TeV/c^2 even for 100 fb^{-1}.

9.2.3. Prospects on the measurement of the forward-backward asymmetry

To measure the forward-backward asymmetry we need the original quark and anti-quark directions of the initiating partons, but these are not known in the case of pp experiments, where the initial state is symmetric. In Ref. [96,112] it is shown that it is possible to approximate the quark direction with the boost direction of the dimuon system with respect to the beam axis. This is due to the fact that the valence quarks have on average larger momentum than the sea anti-quarks, and therefore the dimuon boost direction approximates the quark direction. The most unambiguous tagging occurs for large dimuon rapidity.

The approximation of the original quark direction for pp collisions leads to a flattening out of the original asymmetry ($\approx$ 0.61 for Drell–Yan events) by a factor of almost 2. However, using multi-dimensional fits [111] or reweighting techniques depending on the mistag and acceptance which are under development, we can measure the original asymmetry.

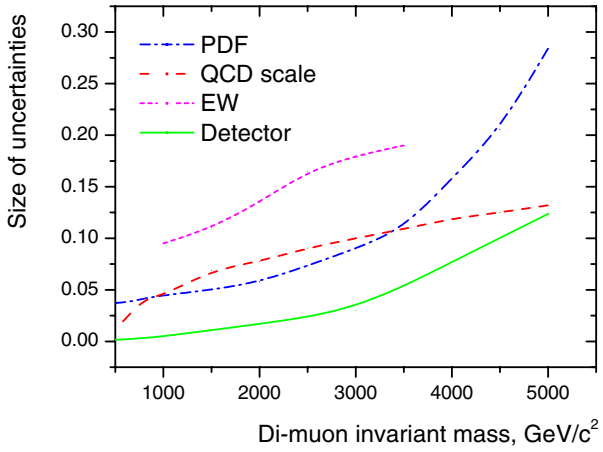

Figure 9.7. Size of the EW corrections and the cross section uncertainties from PDFs, hard process scale and detector understanding as a function of the dimuon invariant mass cut.

The accuracy of asymmetry measurements depends on:

- statistical uncertainty which grows with rising mass cut value, as the number of events for integrated luminosity of e.g. $\int \mathcal{L}\,\mathrm{d}t = 100\,\mathrm{fb}^{-1}$ decreases with mass;
- systematic uncertainty from the variation of the mistag probabilities for various PDF sets, typically below 10%.

We expect the systematic uncertainty to dominate the statistical one for integrated luminosity of $\int \mathcal{L}\,dt = 100\,\mathrm{fb}^{-1}$ and dimuon masses around $500\,\mathrm{GeV/c^2}$, while the statistical one to be more important for dimuon mass cuts above $1000\,\mathrm{GeV/c^2}$.

9.3. Determination of the W mass

9.3.1. Introduction

The precise measurement of the mass of the W boson constitutes an important consistency check of the Standard Model and, together with the top quark mass, is sensitive to supersymmetric corrections. Such a precision measurement of the W mass at the LHC becomes feasible because a huge sample of data available at the LHC will guarantee a nearly negligible statistical uncertainty and a good control of the systematic effects. Extrapolating from traditional approaches based on the reconstruction of the transverse mass $m_{\mathrm{T}} = \sqrt{2p_{\mathrm{T}}^{l}p_{\mathrm{T}}^{\nu}(1-\cos(p_{\mathrm{T}}^{l}, p_{\mathrm{T}}^{\nu}))}$ in leptonic W decays, the most relevant contributions to the systematic uncertainties come from the lepton energy or momentum scale, the lepton energy or momentum resolution, the modelling of the system recoiling against the W boson, the parton distribution functions, the W intrinsic width, from radiative decays and from backgrounds. To accomplish a competitive measurement of the W boson mass, new strategies must be considered [352]. The most promising one consists in predicting the distribution of experimental observables sensitive to the W mass, such as the transverse momentum of the charged lepton (p_{T}^{l}) and the transverse mass of the boson from the corresponding distribution measured in Z boson decays into two charged leptons. The concept of transverse mass measurement can be applied to Z boson events by regarding one of the reconstructed

leptons as missing energy. The theoretical description of both decays is very similar and the resulting distributions in transverse mass are comparable for a wide range in kinematics.

The advantage of this approach, conceptually discussed in [353], is that most of the experimental and theoretical uncertainties, being common between W and Z, cancel in the comparison, leading to a global reduction of the systematic uncertainty. The drawback is a larger statistical uncertainty due to the smaller production rate of Z bosons decaying to charged leptons. Yet a statistical precision of order $10\,\mathrm{MeV/c^2}$ and $30\,\mathrm{MeV/c^2}$ for an integrated luminosity of $10\,\mathrm{fb}^{-1}$ and $1\,\mathrm{fb}^{-1}$ respectively is anticipated. In order not to be limited by statistics, the analyses are performed using large data samples produced with the fast simulation of the CMS experiment [11]. Smaller samples of fully simulated events are used for cross checks.

Two different ways to relate Z to W boson events are considered. One is based on the comparison of the same experimental observables in W- and Z-events scaled to the boson masses. The sensitivity of this method, which can take advantage of the precision calculation of the theoretical ratio of the W and Z boson differential production cross-sections, is fully addressed in the analysis of transverse energy distribution of the electrons from $W \to e\nu$ decays. An alternative approach considered in the analysis of $W \to \mu\nu$ events consists of predicting W boson distributions from Z-events by means of kinematic transformations of measured Z events, parameterised as a function of the boson masses and widths. This more phenomenological approach is exploited in the analysis of the transverse mass distributions, and relies less on the theoretical prediction of the boson p_{T}.

9.3.2. Event selections

In order to obtain a clean signal of $W \to \mathrm{l}\nu$ decays, events that passed the High Level Trigger (HLT) for single leptons are required to satisfy the following selection cuts: one isolated muon with $p_{\mathrm{T}} > 25\,\mathrm{GeV/c}$ within the pseudo-rapidity region $|\eta| < 2.3$ or one isolated electron with $p_{\mathrm{T}} > 25\,\mathrm{GeV/c}$ and within $|\eta| < 2.4$; missing transverse energy $E_{\mathrm{T}}^{\mathrm{miss}} > 25\,\mathrm{GeV}$; no jets in the event with $p_{\mathrm{T}jet} > 30\,\mathrm{GeV/c}$; the transverse momentum of the system recoiling against W has to be lower than $20\,\mathrm{GeV/c}$, measured from the lepton p_{T} and the missing transverse energy.

The difference in minimum p_{T} of the charged lepton is determined by the single lepton trigger threshold. The last two selection cuts are intended to select W bosons produced with a small transverse momentum. The selection efficiency is about 15% for the electron channel and 25% for the muon channel, with a background at the percent level, dominated by leptonic Z decays with one lepton outside the acceptance, as shown in Fig. 9.8.

Z events used to predict the W distribution are also selected from the sample of events passing the HLT for single leptons. Z candidates contain a pair of identified charged leptons consistent with the Z mass hypothesis [352]. One of the two leptons, randomly chosen, is removed from the event to mimic a W decay. The same selections discussed above are then applied, with the cut values on the lepton quantities (minimum lepton p_{T} and event missing transverse energy) scaled by the ratio M_Z/M_W. This choice is intended to minimise kinematic and acceptance differences in Z and W events and thus the theoretical uncertainties implied by the above mentioned approaches.

9.3.3. $W \to e\nu$

The analysis strategy is based on the prediction of the experimental distribution of the electron transverse energy in W events scaled to the boson mass from the corresponding distribution

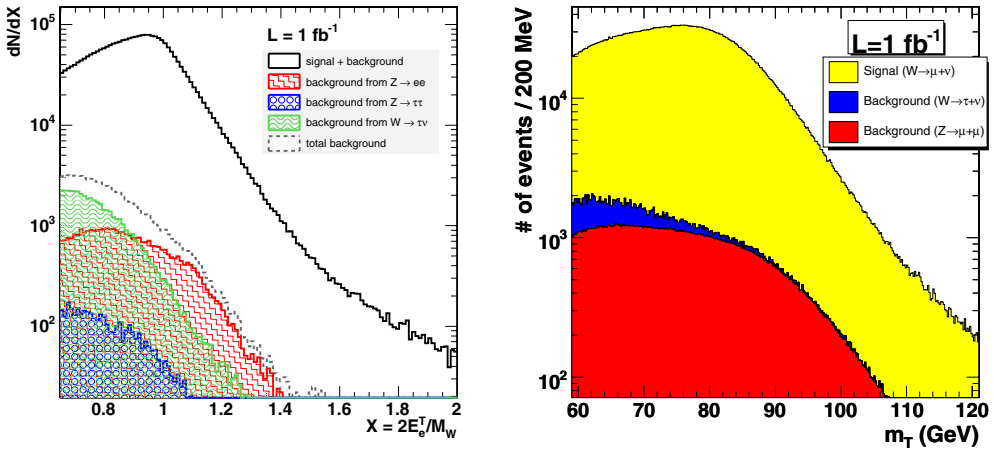

Figure 9.8. W events and main backgrounds for 1 fb^{-1}. Left: Electron scaled transverse energy distribution in $W \to e\nu$ decays and the backgrounds from $Z \to e^+e^-$, from $Z \to \tau^+\tau^-$ and from $W \to \tau\nu$ for 1fb^{-1}. Right: Transverse mass distribution in the muon channel with the fractions of $Z^0/\gamma^* \to \mu^+\mu^-$ (red/grey) $W \to \tau\nu$ (blue/dark), and W $\to \mu\nu$ (yellow/light) events.

measured for Z bosons decaying into e^+e^- pairs, along with the theoretical ratio between the W and Z cross-sections, calculated at a fixed perturbative order. Ideally, the differential cross section for the W boson can be predicted from the one measured for Z boson by scaling the lepton transverse momenta with the boson masses, $p_{\mathrm{T}}^{\mathrm{lept,Z}} = M_Z/M_W\, p_{\mathrm{T}}^{\mathrm{lept,W}}$, as:

$$\left.\frac{\mathrm{d}\sigma^W}{\mathrm{d}p_{\mathrm{T}}^{\mathrm{lept,W}}}\right|_{\mathrm{pred}} = \frac{M_Z}{M_W} R(X) \left.\frac{\mathrm{d}\sigma^Z}{\mathrm{d}p_{\mathrm{T}}^{\mathrm{lept,Z}}}\left(p_{\mathrm{T}}^{\mathrm{lept,Z}} = \frac{M_Z}{M_W} p_{\mathrm{T}}^{\mathrm{lept,W}}\right)\right|_{\mathrm{meas}}, \tag{9.5}$$

where $R(X) = \frac{\mathrm{d}\sigma^W}{\mathrm{d}X^W} / \frac{\mathrm{d}\sigma^Z}{\mathrm{d}X^Z}$ is the ratio, deduced from theoretical calculations, between the differential cross sections in terms of the scaled variable $X^V = \frac{p_{\mathrm{T}}^{\mathrm{lept},V}}{M_V}$, with $V = \mathrm{W}, \mathrm{Z}$. The parameter M_W can be extracted by fitting this prediction to the distribution for W events observed in the experiment. In practice, additional corrections to $R(X)$ are needed to account for the acceptance to Z and W events and for the experimental resolution. This calls for a detailed understanding of the detector response by means of Monte Carlo simulations compared to control samples. Clearly, the definition of $R(X)$ is the most critical aspect and must include both detector effects and theoretical predictions.

The results for 1 fb^{-1} of integrated luminosity using the technique just described are shown in Fig. 9.9. The statistical precision of the method is determined from the resulting χ^2 distribution. The evaluation of the systematic uncertainties affecting the measurement of the W mass is performed by determining the distortions implied by the different systematic effects mentioned above. The effects of instrumental origin have been studied by fixing $R(X)$ to the theoretical prediction exactly describing the samples of generated events (i.e. an exact knowledge of the theory is assumed) and by introducing distortions and biases in the detector response. The resulting shift in M_W is assumed as the systematic uncertainty associated to the effect. The detector response to electrons, the largest source of systematic uncertainty of instrumental origin with this method, can be determined with the required precision from $Z \to ee$ events.

The prediction of the lepton transverse spectrum is plagued by large radiative QCD corrections. Yet, in the method adopted, large cancellations occur and $R(X)$ can be reliably

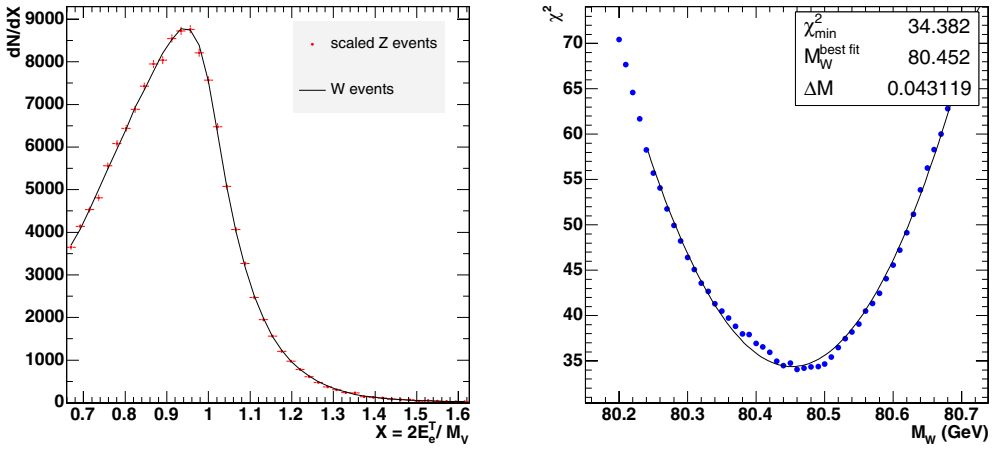

Figure 9.9. Comparison of the scaled electron E_T spectra for Z (dots) and W boson (line) events (left) and χ^2 dependence on M_W (right) for 1 fb^{-1} of integrated luminosity.

predicted. The uncertainty related to the missing orders in the perturbative expansion can be quantified by the dependence of the available NLO prediction on the choice of the renormalisation and factorisation scales. A conservative figure of 30 MeV/c^2 for the mass uncertainty is deduced. This will become the dominant error at 10 fb^{-1}. Yet the reduction of this error by extending the calculation one order higher in α_S is technically feasible [353].

9.3.4. $W \to \mu\nu$

As a complementary method, the transverse mass distribution of W events in the muon channel is modelled from $Z \to \mu^+\mu^-$ events by a kinematic transformation. In the rest frame of the Z boson, the lepton momenta are scaled such that their invariant mass distribution represents that of the W boson [352]. After removing one randomly chosen muon to mimic a neutrino, the whole system is boosted back into the detector frame, thus obtaining a template for the expected distribution of W events, which depends on the W and Z boson masses and widths as parameters. By iterating the procedure for different W boson masses, the best agreement with the observed transverse mass distribution in W events is determined using a χ^2 criterion. In practice, weighting factors take into account unavoidable differences between the W and Z samples, such as the acceptance for the second lepton, photon radiation, and differences in η and p_T of W and Z bosons. Thus perfect agreement of the distributions at the nominal W mass and for the simulated detector is ensured, while systematic effects are studied by introducing distortions of experimental or theoretical origin. The resulting shifts in the extracted W mass are taken as the related systematic uncertainties.

The dominant systematic error arises from scale and resolution uncertainties in the missing energy determined from the calorimeters. These can be controlled by using the Z sample, where the boson p_T can be measured from the two charged leptons, as is shown in Fig. 9.10. The observed differences of 2% on the scale and 5% on the resolution are taken as the systematic uncertainties.

9.3.5. Expected precision and systematic uncertainties

The expected size of various detector effects for the early detector operation, after the analysis of an initial integrated luminosity of 1 fb^{-1}, and for a better detector understanding

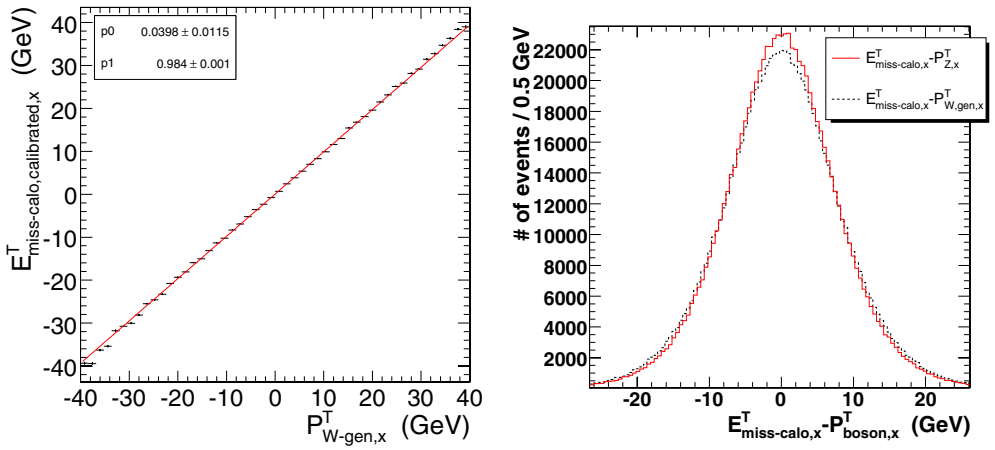

Figure 9.10. Left: x-component of the calibrated missing transverse energy in the calorimeters using the reconstructed muon p_T in Z events, as a function of the transverse W boson momentum at generator level. The slope of a fitted straight line is 0.98. Right: Difference between the reconstructed missing energy in the calorimeters and the measured muon p_T in Z events (red/grey line) or the W boson p_T at generator level (black dashed line). The RMS of the distribution is 8.15 GeV for Z events and 8.65 GeV for W events.

expected after employing an integrated luminosity of 10 fb^{-1}, is shown in Table 9.7 for the scaled p_T-lepton method applied to the electron channel, and for the muon channel using the transformation method.

The measurements of the W mass by means of $W \to e\nu$ and $W \to \mu\nu$ decays are largely independent. Common experimental uncertainties arise from the systematics involving the missing transverse energy in the calorimeters.

Based on the estimated systematic errors, it is clear that the scaled p^T-lepton method suffers less from experimental systematic errors than the transformation method. If systematic uncertainties arising from the theoretical prediction of the transverse momenta of the Z and W bosons can be brought to a level of $\approx 10\,MeV/c^2$, the scaled p^T-lepton method is clearly the first choice. Using the scaled p_T-lepton method in the muon channel leads to a better statistical precision of 30 MeV/c^2 for 1 fb^{-1} due to the higher acceptance for muons compared to electrons. The total instrumental uncertainty of the p_T-lepton method applied to the muon channel is estimated from the findings in the electron channel and amounts to about 25 MeV/c^2 for the initial measurement with an integrated luminosity of 1 fb^{-1}. Uncertainties due to the recoil modelling are fully correlated with the electron channel. The component of the experimental error in common with the electrons amounts to about 20 MeV/c^2. Clearly, all theoretical uncertainties are of similar size and also correlated between the electron and muon channels.

The transformation method has the advantage of providing templates for observables in W events from measured observables in Z events. In particular, the measurement of the transverse momentum of Z bosons and the cross checks on the modelling of the missing energy are of vital importance to quantify systematic uncertainties.

The combination of the electron and muon channels brings the statistical uncertainty to a final precision of better than 10 MeV/c^2 for an integrated luminosity of 10 fb^{-1}, and a systematic uncertainty of instrumental origin below 20 MeV/c^2 should be within reach.

Table 9.7. Expected systematic uncertainties on M_{W} for the scaled E^T-lepton method with electrons (upper part) and for the Z transformation method applied to the muon channel (lower part). The first column lists the systematic effect considered, the second and third columns show the assumed detector uncertainty for an initial integrated luminosity of 1 fb^{-1} and the resulting uncertainty on M_W. The last two columns show the extrapolation to an integrated luminosity of 10 fb^{-1}, when the detector understanding is assumed to have significantly improved.

Source of uncertainty	uncertainty	ΔM_W[MeV/c^2]	uncertainty	ΔM_W [MeV/c^2]
	with 1 fb^{-1}		with 10 fb^{-1}	
	scaled lepton-p_{T} method applied to W $\to$ eν			
statistics		**40**		15
background	10%	10	2%	2
electron energy scale	0.25%	10	0.05%	2
scale linearity	0.00006/ GeV	30	<0.00002/ GeV	<10
energy resolution	8%	5	3%	2
MET scale	2%	15	<1.5%	<10
MET resolution	5%	9	<2.5%	< 5
recoil system	2%	15	<1.5%	<10
total instrumental		**40**		<**20**
PDF uncertainties		20		<10
Γ_W		15		<15
$p_{\mathrm{T}}^{\mathrm{W}}$		30		30 (or NNLO)
	transformation method applied to W $\to \mu\nu$			
statistics		**40**		15
background	10%	4	2%	negligible
momentum scale	0.1%	14	<0.1%	<10
$1/p^T$ resolution	10%	30	<3%	<10
acceptance definition	η-resol.	19	$< \sigma_\eta$	<10
calorimeter $E_{\mathrm{T}}^{\mathrm{miss}}$, scale	2%	38	$\leqslant$1%	<20
calorimeter $E_{\mathrm{T}}^{\mathrm{miss}}$, resolution	5%	30	<3%	<18
detector alignment		12	–	negligible
total instrumental		**64**		<**30**
PDF uncertainties		$\approx$20		<10
Γ_W		10		< 10

9.4. Multi-boson production

9.4.1. Introduction

The study of multiple gauge-boson production at the TeV scale constitutes a unique opportunity to test the Standard Model of Electroweak interactions at the highest possible energies. The production of $W^{\pm}Z^0$ and $W^{\pm}\gamma$ events at the LHC probes the triple gauge-boson couplings and therefore the non-Abelian gauge symmetry of the Standard Model. On the other hand, no neutral gauge-boson couplings exist in the Standard Model, thus anomalies in Z^0Z^0 and $Z^0\gamma$ production, hinting at large s-channel contributions, could be the first indirect manifestation of New Physics. In the following, the selections of $W^{\pm}Z^0$ and Z^0Z^0 events are described, their signal-over-background ratio discussed and the outlook for an early measurement of multiple gauge-boson production is assessed. Further details are given in Ref. [354].

The multi-lepton final states of multiple gauge-boson production are an important background in the search for New Physics, in particular Supersymmetry. A sound

understanding of their production process is therefore needed in the first phase of LHC data-taking before any discovery can be claimed. In particular, Z^0Z^0 production is an irreducible background to the most-coveted discovery at the LHC: the Standard Model Higgs boson. Its early measurement is therefore important.

The cross sections for multiple gauge-boson production at the LHC are of about 50 pb for the $W^{\pm}Z^0$ channel and 20 pb for the Z^0Z^0 channel [158]. These large cross sections and the clean signature of fully-leptonic final states make $W^{\pm}Z^0$ and Z^0Z^0 production observable in the early LHC data. Final states where the gauge bosons decay into electrons and muons are considered: $e^{\pm}e^+e^-$, $\mu^{\pm}e^+e^-$, $e^{\pm}\mu^+\mu^-$ and $\mu^{\pm}\mu^+\mu^-$ for $W^{\pm}Z^0$ production and $e^+e^-e^+e^-$ for the Z^0Z^0 channel. The competing background processes are the Standard Model production of gauge bosons and top quarks, which also yield leptonic final states.

9.4.2. Signal definition and modelling

Both the $W^{\pm}Z^0$ and Z^0Z^0 analyses focus on on-shell gauge bosons. On-shell production of the $W^{\pm}Z^0$ final state proceeds mainly through the s-channel, involving a WWZ triple gauge-boson coupling. Additional contributions from the $W^{\pm}\gamma^*$ final state through a $WW\gamma$ coupling are effectively suppressed by constraining the mass of the observed lepton pair to be compatible with a Z^0 boson. The PYTHIA Monte Carlo generator [24] is used to model $W^{\pm}Z^0$ production and subsequent decay into fully-leptonic final states. Gauge-boson decays into tau leptons are also included. These tau leptons are left free to decay into either leptons or hadrons.

Four-electron final-states can originate from Z^0Z^0 production as well as via either $Z^0\gamma^*$ or $\gamma^*\gamma^*$ production. The requirement of on-shell boson is enforced by considering only electron-positron pairs with a mass between 70 and 110 $\mathrm{GeV/c^2}$. The PYTHIA Monte Carlo is used to generate events of this process, with the additional requirement that the electrons have a rapidity $|\eta| < 2.7$ and a transverse momentum $p_{\mathrm{T}} > 5\,\mathrm{GeV/c}$. Of all generated events, 72% are classified as Z^0Z^0 signal while 26% are ascribed to the $Z^0\gamma^*$ process and 2% to the $\gamma^*\gamma^*$ process.

Taking into account the branching fraction into leptons, $\mathcal{B}$, and the kinematic requirements, ε_{KIN}, the relevant NLO cross sections using the MCFM [56] Monte Carlo are:

$$\sigma_{NLO} \times \mathcal{B} \times \epsilon_{KIN}(pp \to W^+Z^0 \to \ell^+\ell^+\ell^-) = 1034\,\mathrm{fb}$$
$$\sigma_{NLO} \times \mathcal{B} \times \epsilon_{KIN}(pp \to W^-Z^0 \to \ell^-\ell^+\ell^-) = 630\,\mathrm{fb}$$
$$\sigma_{NLO} \times \mathcal{B} \times \epsilon_{KIN}(pp \to Z^0Z^0 \to e^+e^-e^+e^-) = 18.7\,\mathrm{fb}$$

The NLO corrections correspond to k-factors of 1.9 and 1.4 for $W^{\pm}Z^0$ and Z^0Z^0 production, respectively. The NNLO box-diagram contribution to Z^0Z^0 production is not taken into account.

Three-lepton final-states from $W^{\pm}Z^0$ and Z^0Z^0 production are collected with high efficiency by the Level-1 and HLT electron and muon triggers. The Level-1 and HLT efficiencies for events retained by the selections discussed below is 100% [76].

9.4.3. Background processes

The background to the selection of $W^{\pm}Z^0$ and Z^0Z^0 events comprises other processes with multiple leptons in the final states, some of which might be due to fake signals. The most copious sources of multiple leptons at the LHC are $t\bar{t}$ and $Z^0b\bar{b}$ production. The cross section of these processes is large: 830 pb and 1492 pb, respectively, as calculated with MCFM at NLO.

These processes may have two leptons in the final states from leptonic decays of the W bosons arising from $t \to Wb$ decays or of the Z^0 boson, respectively. The other leptons can be produced in the direct or cascade decays of the b quarks. The $Z^0 b\bar{b}$ process is modelled with the COMPHEP Monte Carlo generator [43, 355] and the $t\bar{t}$ process with the TOPREX Monte Carlo program [44]. In addition, the special case in which four electrons are produced in $t\bar{t}$ events is considered in detail and modelled with PYTHIA. Contributions from Wt and $Zc\bar{c}$ to the selected samples are negligible.

Events from Z^0Z^0 production also constitute a background to the $W^{\pm}Z^0$ selection. Events from the $Z^0\gamma^*$ and $\gamma^*\gamma^*$ processes are a background for both the $W^{\pm}Z^0$ and Z^0Z^0 analyses.

9.4.4. $W^{\pm}Z^0$ selection

Events with three charged leptons, either electrons or muons, with $p_{\mathrm{T}} > 10\,\mathrm{GeV/c}$ and $|\eta| < 2.5$, are considered by the $W^{\pm}Z^0$ selection. All possible Z^0-boson candidates from same-flavours opposite-charge lepton pairs are formed. Events are retained if the mass of the Z^0 candidate is within $20\,\mathrm{GeV/c^2}$ of the Z^0-boson mass, m_Z. These criteria effectively suppress Z^0 decays into tau leptons. The background from Z^0Z^0 final states is reduced by rejecting events with a second Z^0 candidate with a mass within $40\,\mathrm{GeV/c^2}$ of m_Z. The remaining lepton is associated to the $W^{\pm}$-boson decay; its transverse momentum must be larger than 20 GeV. This criterion results in lower efficiencies for the $W^{\pm}$ boson decays in tau leptons. The highest-p_{T}lepton associated to the Z^0 boson must satisfy $p_{\mathrm{T}} > 15\,\mathrm{GeV/c}$. If the event contains more than three leptons, the lepton with highest p_{T} is chosen as originating from the $W^{\pm}$. The signal efficiency after these cuts is 9.2% while the $t\bar{t}$, $e^+e^-b\bar{b}$ and $\mu^+\mu^-b\bar{b}$ efficiencies are 0.7%, 0.4% and 0.6%, respectively.

Leptons from the decay of b quarks in the background processes are produced in a higher-multiplicity environment and isolation criteria suppress the background contamination. Electrons associated to the W $^{\pm}$ boson must have no other charged track with $p_{\mathrm{T}} > 2\,\mathrm{GeV/c}$ within a $\Delta R = 0.3$ cone around their direction. All muon candidates must have an energy measured in the calorimeters within a $\Delta R = 0.3$ cone around their direction smaller than 5 GeV and the sum of the p_{T} of tracks within a $\Delta R = 0.25$ cone smaller than 2 GeV/c. The significance of the lepton impact parameter in the plane transverse to the beam, S_{IP}, discriminates against leptons from heavy-quark decays. This variable is defined as the ratio between the measured impact parameter and its uncertainty and is required to satisfy $S_{IP} < 3$. The signal efficiency after these cuts is 7.3% while the $t\bar{t}$, $e^+e^-b\bar{b}$ and $\mu^+\mu^-b\bar{b}$ efficiencies are 0.07%, 0.008% and 0.03%, respectively.

The $t\bar{t}$ and Z^0 $b\bar{b}$ final states are associated with one or more hard jets and their contribution is reduced by removing events containing at least a jet with $E_{\mathrm{T}} > 25\,\mathrm{GeV}$. Only jets outside cones of $\Delta R = 0.3$ around the three leptons are considered. The reconstructed mass of the Z^0 boson is required to be within $10\,\mathrm{GeV/c^2}$ of m_Z, leading to the total efficiencies presented in Table 9.8.

9.4.5. Z^0Z^0 selection

The Z^0Z^0 selection is based on events with four electrons, identified from superclusters in the electromagnetic calorimeter matched with a charged track. The transverse momenta of the electron candidates, ordered from the largest to the smallest, have to be above 30 GeV/c, 20 GeV/c, 15 GeV/c and 10 GeV/c, respectively. This cut suppresses the contribution from the $Z^0\gamma^*$ and $\gamma^*\gamma^*$ final states and reduces by 30% and 60% the $t\bar{t}$ and $Z^0b\bar{b}$ backgrounds,

Table 9.8. Yield of the $W^{\pm}Z^0$ selection for an integrated luminosity of 1fb^{-1}. Signal efficiencies include gauge-boson decays into tau leptons.

	$e^{\pm}e^+e^-$	$\mu^{\pm}e^+e^-$	$e^{\pm}\mu^+\mu^-$	$\mu^{\pm}\mu^+\mu^-$	Total	Efficiency
$W^{\pm}Z^0 \to \ell^{\pm}\ell^+\ell^-$	14.8	26.9	28.1	27.0	96.8	6.1%
Z^0Z^0	0.63	1.54	1.50	1.51	5.18	4.7%
$t\bar{t}$	0.93	1.55	–	0.31	2.79	0.02%
$\mu^+\mu^-b\bar{b}$	–	–	6.54	4.9	11.4	0.005%
$e^+e^-b\bar{b}$	1.21	1.82	–	–	3.03	0.005%

Table 9.9. Yield of the Z^0Z^0 selection for integrated luminosities of $1\,\text{fb}^{-1}$ and $10\,\text{fb}^{-1}$. The last row indicates the signal significance, which include systematic effects.

	Efficiency	$N_{\text{events}}/1\,\text{fb}^{-1}$	$N_{\text{events}}/10\,\text{fb}^{-1}$
Z^0Z^0	38%	7.1	71.1
$Z^0\gamma^*$	4.5%	0.16	1.60
$Z^0b\bar{b}$	0.07%	0.08	0.84
$t\bar{t}$	0.06%	0.12	1.22
S_L		4.8	13.1

respectively. Leptons from b quarks decays in the $t\bar{t}$ and $Z^0b\bar{b}$ background processes are produced in association with hadrons. Their contribution is reduced by requiring the electrons to be isolated: the ratio between the energy deposited in the hadronic and the electromagnetic calorimeters must be below 8%; no more than two other charged track with $p_{\text{T}} > 2\,\text{GeV/c}$ must be within a $\Delta R = 0.3$ cone around the electron; $\Sigma_i (p_{\text{T}}^i - E_{\text{T}})_i / E_{\text{T}} < 0.34$, where E_{T} is the transverse energy of the electron candidate and the sum runs on all tracks with $p_{\text{T}} > 2\,\text{GeV/c}$ within a $\Delta R = 0.3$ cone around the electron.

Electron-positron pairs are combined to form Z^0 candidates. Pairs with reconstructed masses between 50 and 120 GeV/c^2 are retained. Of the two possible Z^0Z^0 pairings, the one where the Z^0 candidate masses are closest to m_Z is chosen. This pairing is correct for almost all events with two on-shell Z^0 bosons. For 2.5% of the events, more than four electrons are present and only the Z^0Z^0 pairing which contains the highest-p_{T} electron is retained. Table 9.9 presents the signal and background selection efficiencies.

9.4.6. Systematic uncertainties

For the first $1\,\text{fb}^{-1}$ of integrated luminosity, the total systematic uncertainties on the $W^{\pm}Z^0$ and Z^0Z^0 cross section measurements are 17.4% and 12.9%, respectively. These figures include a 10% uncertainties on the determination of the integrated luminosity.

The most important sources of systematic uncertainties are lepton identification and isolation, and background subtraction. A 2% uncertainty on the efficiency of each lepton propagates to an uncertainty on the cross section between 2.6% and 7.8%, according to the channel. Background subtraction dominates the $W^{\pm}Z^0$ systematics with an uncertainty of 12%, while it accounts for a 1.3% uncertainty in the Z^0Z^0 channel. An additional uncertainties of 5% on the jet energy scale affects the $W^{\pm}Z^0$ channel, while an uncertainty of 1% on the trigger efficiency affects both channels.

The significance of the observation of the $W^{\pm}Z^0$ and Z^0Z^0 signals in the first $1\,\text{fb}^{-1}$ is not sensitive to the luminosity uncertainty. It is affected by all other sources of systematic uncertainty listed above, with a total effect of 14.8% and 14.2% on the two channels,

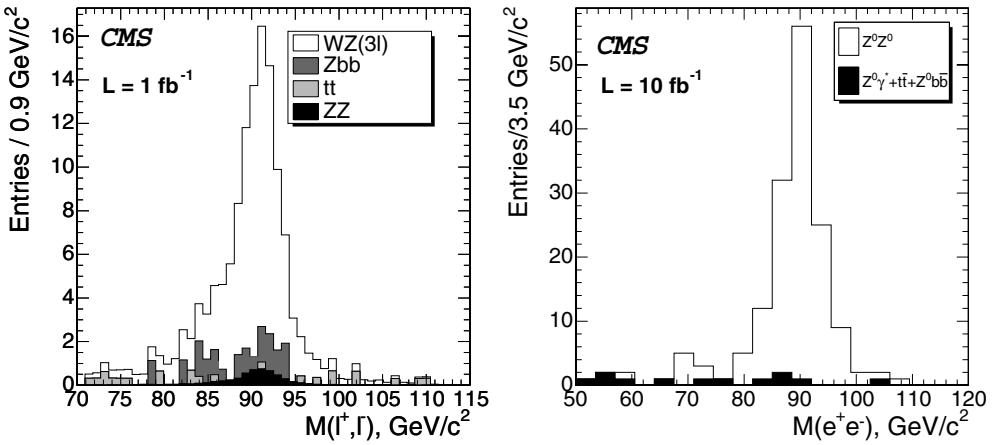

Figure 9.11. Left: Distribution of the mass of the Z^0 candidates for events retained by the $W^{\pm}Z^0$ selection, for an integrated luminosity of 1 fb^{-1}. Right: Distribution of the mass of the Z^0 candidates, two entries per event, retained by the Z^0Z^0 selection, for an integrated luminosity of 10 fb^{-1}.

respectively. These uncertainties include additional PDF and QCD uncertainties in the Monte Carlo modelling, contributing 3.7% and 6.4% for the $W^{\pm}Z^0$ and Z^0Z^0 selections, respectively.

9.4.7. Results

Figure 9.11 left presents the mass distribution of the Z^0 candidates in the $W^{\pm}Z^0$ channel for an integrated luminosity of 1fb^{-1} before the last requirement of a $\pm 10\,\mathrm{GeV/c^2}$ window is applied. A large signal-over-background ratio is observed, as shown in Table 9.8.

Figure 9.11 right shows the mass distribution of the Z^0 candidates, two entries per event, selected by the Z^0Z^0 selection for an integrated luminosity of 10 fb^{-1}. Table 9.9 lists the selection yield for 1 fb^{-1} and 10 fb^{-1}. The selection results into an almost background-free signal sample, which will constitute a valuable input to assess the background in the search for the Higgs boson.

Both the $W^{\pm}Z^0$ and Z^0Z^0 final states can be selected with high purity. A significance of 12.8 and 4.8, respectively, is expected in the first 1 fb^{-1} of integrated luminosity, including systematic uncertainties. The $W^{\pm}Z^0$ channel can be observed with a significance of 5, including systematic effects, in an integrated luminosity of 150 pb^{-1}.

This study of multiple gauge-boson production and couplings at the LHC will be extended to include the $W^{\pm}\gamma$ and $Z^0\gamma$ channels, as well as the other flavours of Z^0Z^0 fully-leptonic decays.

In conclusion, the large signal-over-background ratios achieved by the $W^{\pm}Z^0$ and Z^0Z^0 selections suggest that early observation of these channels will take place at the LHC start up. In addition, precise investigations of triple gauge-boson couplings will be possible with the first 10 fb^{-1} of LHC data.

Chapter 10. Standard Model Higgs Bosons

10.1. Introduction

The Higgs mechanism is a cornerstone of the Standard Model (SM) and its supersymmetric extensions. The introduction of the fundamental Higgs field [356–359] renders the standard electroweak theory weakly interacting up to high energy scales without violating the unitarity bounds of scattering amplitudes [360–363]. Due to spontaneous symmetry breaking in the Higgs sector the electroweak gauge bosons W, Z as well as the fermions acquire masses through the interaction with the Higgs fields. Since the gauge symmetry, though hidden, is still preserved, the theory of electroweak interactions is renormalisable [364–368]. In the Standard Model one weak isospin Higgs doublet is introduced and leads to the existence of one elementary Higgs particle after electroweak symmetry breaking. The Higgs couplings to the electroweak gauge bosons and all fermions grow with their masses. The only unknown parameter of the Higgs boson itself is the value of its mass M_H. Once this is known, all production and decay properties of the SM Higgs boson will be fixed [20, 369, 370]. The search for the Higgs boson is a crucial endeavour for establishing the standard formulation of the electroweak theory.

Although the Higgs mass cannot be predicted in the Standard Model, there are several constraints deduced from consistency conditions on the model [371–381]. Upper bounds can be derived from the requirement that the Standard Model can be extended up to a scale Λ, before perturbation theory breaks down and new non-perturbative phenomena dominate the predictions of the theory. If the SM is required to be weakly interacting up to the scale of grand unified theories (GUTs), which is of $\mathcal{O}(10^{16}\,\mathrm{GeV})$, the Higgs mass has to be less than $\sim 190\,\mathrm{GeV/c^2}$. For a minimal cut-off $\Lambda \sim 1\mathrm{TeV/c^2}$ a universal upper bound of $\sim 700\,\mathrm{GeV/c^2}$ can be obtained from renormalisation group analyses [371–378] and lattice simulations of the SM Higgs sector [379–381]. This issue can be rephrased by stating that the Higgs sector has to be trivial, if the cut-off is extended to arbitrary magnitudes. Triviality means the absence of Higgs self-interactions.

If the top quark mass is large, the Higgs self-coupling can become negative and the Higgs potential deeply negative, thus rendering the SM vacuum unstable. The negative contribution of the top quark, however, can be compensated by a positive contribution due to the Higgs self-interaction, which is proportional to the Higgs mass. For a given top mass $m_t = 175\,\mathrm{GeV/c^2}$ a lower bound of $\sim 60\,\mathrm{GeV/c^2}$ can be obtained for the Higgs mass, if the SM remains weakly interacting up to scales $\Lambda \sim 1\mathrm{TeV/c^2}$. For $\Lambda \sim M_{GUT}$ this lower bound is enhanced to $M_H \gtrsim 130\,\mathrm{GeV/c^2}$. However, the assumption that the vacuum is metastable, with a lifetime larger than the age of the Universe, decreases these lower bounds significantly for $\Lambda \sim 1\mathrm{TeV/c^2}$, but only slightly for $\Lambda \sim M_{GUT}$ [378].

The direct search in the LEP2 experiments via the process $e^+e^- \to ZH$ yields a lower bound of $114.4\,\mathrm{GeV/c^2}$ on the Higgs mass [62]. After LEP2 the search for the SM Higgs particle is continued at the Tevatron for Higgs masses up to $\sim 130\,\mathrm{GeV/c^2}$ [382] and the LHC for Higgs masses up to the theoretical upper limit [383, 384].

The Higgs decay modes can be divided into two different mass ranges. For $M_H \lesssim 135\,\mathrm{GeV/c^2}$ the Higgs boson mainly decays into $b\bar{b}$ and $\tau^+\tau^-$ pairs with branching ratios of about 85% and 8% respectively (see Fig. 10.1, right plot). The decay modes into $c\bar{c}$ and gluon pairs, with the latter mediated by top and bottom quark loops, accumulate a branching ratio of up to about 10%, but do not play a relevant role at the LHC. The QCD corrections to the Higgs decays into quarks are known up to three-loop order [385–391] and the electroweak corrections up to NLO [392–395]. The latter are also valid for leptonic decay modes. One of

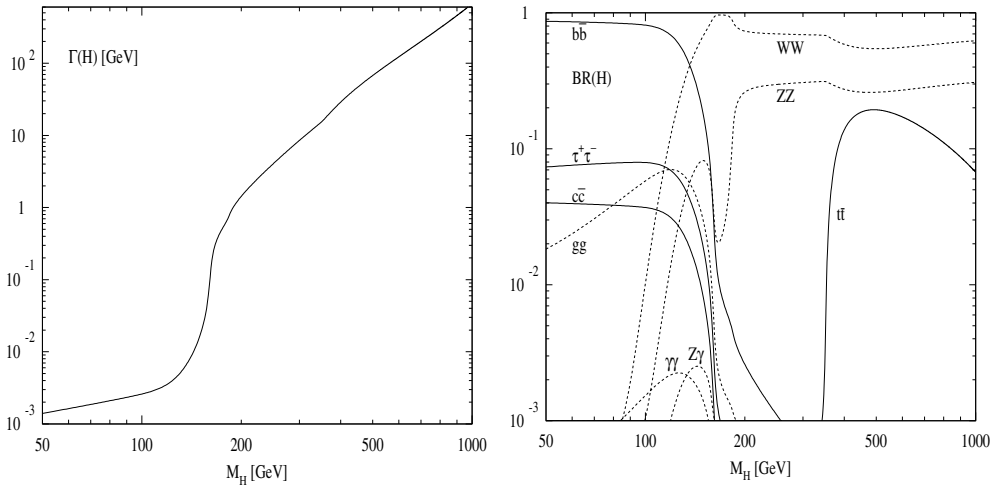

Figure 10.1. Left plot: total decay width (in GeV/c^2) of the SM Higgs boson as a function of its mass. Right plot: Branching ratios of the dominant decay modes of the SM Higgs particle. All relevant higher-order corrections are taken into account.

the most important Higgs decays in this mass range at the LHC is the decay into photon pairs, which is mediated by W, top and bottom quark loops. It reaches a branching fraction of up to 2×10^{-3}. The NLO QCD [396–402] and electroweak [403–405] corrections are known. They are small in the Higgs mass range relevant for the LHC.

For Higgs masses above 135 GeV/c^2 the main decay modes are those into WW and ZZ pairs, where one of the vector bosons is off-shell below the corresponding kinematical threshold. These decay modes dominate over the decay into $t\bar{t}$ pairs, the branching ratio of which does not exceed $\sim 20\%$ as can be inferred from Fig. 10.1 (right plot). The electroweak corrections to the WW, ZZ decays are of moderate size [392, 393, 406, 407]. The total decay width of the Higgs boson, shown in Fig. 10.1 (left plot), does not exceed about 1 GeV/c^2 below the WW threshold. For very large Higgs masses the total decay width grows up to the order of the Higgs mass itself so that the interpretation of the Higgs boson as a resonance becomes questionable. This Higgs mass range coincides with the upper bound of the Higgs mass from triviality.

The dominant Higgs production mechanism at the LHC will be the gluon-fusion process [408]

$$pp \to gg \to H\,,$$

which provides the largest production cross section for the whole Higgs mass range of interest. This process is mediated by top and bottom quark loops (Fig. 10.2a). Due to the large size of the top Yukawa couplings and the gluon densities gluon fusion comprises the dominant Higgs boson production mechanism for the whole Higgs mass range.

The QCD corrections to the top and bottom quark loops have been known a long time including the full Higgs and quark mass dependences [409–411]. They increase the total cross section by 50–100%. The limit of very heavy top quarks provides an approximation within $\sim$10% for all Higgs masses [20, 369, 370, 409–412]. In this limit the NLO QCD corrections have been calculated before [409–411, 413–416] and recently the NNLO QCD corrections [417–420] with the latter increasing the total cross section further by $\sim 20\%$. A full massive NNLO calculation is not available, so that the NNLO results can only be trusted

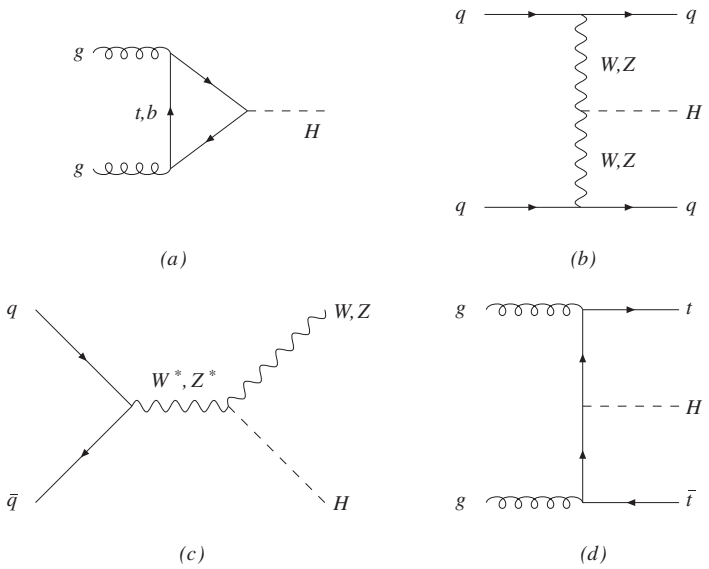

Figure 10.2. Typical diagrams for all relevant Higgs boson production mechanisms at leading order: (a) gluon fusion, (b) vector boson fusion, (c) Higgs-strahlung, (d) Higgs bremsstrahlung off top quarks.

for small and intermediate Higgs masses. The approximate NNLO results have been improved by a soft-gluon resummation at the next-to-next-to-leading log (NNLL) level, which yields another increase of the total cross section by $\sim 10\%$ [421]. Electroweak corrections have been computed, too, and turn out to be small [403, 422–425]. The theoretical uncertainties of the total cross section can be estimated as $\sim 20\%$ at NNLO due to the residual scale dependence, the uncertainties of the parton densities and due to neglected quark mass effects.

At LO the Higgs boson does not acquire any transverse momentum in the gluon fusion process, so that Higgs bosons with non-vanishing transverse momentum can only be produced in the gluon fusion process, if an additional gluon is radiated. This contribution is part of the real NLO corrections to the total gluon fusion cross section. The LO p_{T} distribution of the Higgs boson is known including the full quark mass dependence [426, 427]. The NLO corrections, however, are only known in the heavy quark limit, so that they can only be trusted for small and moderate Higgs masses and p_{T} [428–443]. In this limit a NLL soft gluon resummation has been performed [433–443], which has recently been extended to the NNLL level [444–448] thus yielding a reliable description of the small p_{T} range. It should be noted that these results are only reliable, if the top quark loops provide the dominant contribution and p_{T} is not too large. In the regions where the NLO and resummed results are valid the theoretical uncertainties have been reduced to $\mathcal{O}(20\%)$.

For large Higgs masses the W and Z boson-fusion processes [449–451] (see Fig. 10.2b)

$$pp \to qq \to qq + WW/ZZ \to qqH$$

become competitive. These processes are relevant in the intermediate Higgs mass range, too, since the additional forward jets offer the opportunity to reduce the background processes significantly. Since at NLO there is no colour exchange between the two quark lines, the NLO QCD corrections can be derived from the NLO corrections to deep inelastic lepton-nucleon scattering. They turn out to be $\mathcal{O}(10\%)$ for the total cross section [20, 369, 370, 452].

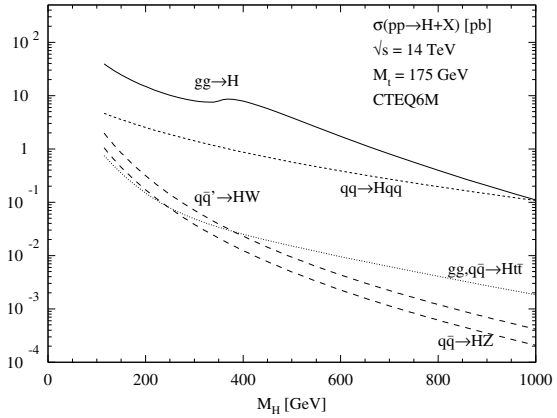

Figure 10.3. Higgs production cross sections at the LHC for the various production mechanisms as a function of the Higgs mass. The full QCD-corrected results for the gluon fusion $gg \to H$, vector-boson fusion $qq \to VVqq \to Hqq$, vector-boson bremsstrahlung $q\bar{q} \to V^* \to HV$ and associated production $gg, q\bar{q} \to Ht\bar{t}$ are shown.

Quite recently the NLO corrections to the differential cross sections have been computed, too, resulting in modifications of the relevant distributions by up to $\sim 30\%$ [453]. The residual uncertainties are of $\mathcal{O}(5\%)$.

In the intermediate mass range $M_H \lesssim 2M_Z$ Higgs-strahlung off W, Z gauge bosons [454, 455] (see Fig. 10.2c)

$$pp \to q\bar{q} \to Z^*/W^* \to H + Z/W$$

provides alternative signatures for the Higgs boson search. Since only the initial state quarks are strongly interacting at LO, the NLO QCD corrections can be inferred from the Drell–Yan process. They increase the total cross section by $\mathcal{O}(30\%)$ [20, 369, 370, 456]. Recently this calculation has been extended up to NNLO [457]. The NNLO corrections are small. Moreover, the full electroweak corrections have been obtained in Ref. [458] resulting in a decrease of the total cross sections by 5–10%. The total theoretical uncertainty is of $\mathcal{O}(5\%)$.

Higgs radiation off top quarks (see Fig. 10.2d)

$$pp \to q\bar{q}/gg \to Ht\bar{t}$$

plays a significant role for smaller Higgs masses below $\sim 150\,\mathrm{GeV/c^2}$. The LO cross section has been computed a long time ago [459–463]. During the last years the full NLO QCD corrections have been calculated resulting in a moderate increase of the total cross section by $\sim 20\%$ at the LHC [162, 464, 465]. These results confirm former estimates based on an effective Higgs approximation [466]. The effects on the relevant parts of final state particle distribution shapes are of moderate size, i.e. $\mathcal{O}(10\%)$, too, so that former experimental analyses are not expected to alter much due to these results. All SM Higgs production cross sections including NLO QCD corrections are shown in Fig. 10.3.

In the following Standard Model Higgs boson analyses the NLO cross sections and branching ratios for the Higgs boson calculated with the programs HDECAY [41], HIGLU [40], VV2H, V2HV and HQQ [20] are used, as well as the NLO cross sections for the background processes, when available.

10.2. Higgs boson channels

10.2.1. Inclusive Higgs boson production with $H \to ZZ^{(*)} \to e + e^- \mu^+ \mu^-$

10.2.1.1. Introduction. The $H \to ZZ^{(*)} \to 4\ell$ channel has a very clean signature with relatively small backgrounds and is therefore an important discovery channel for the Higgs boson for a large range of masses. This channel is also important for the measurement of the mass and width of the Higgs boson.

A detailed description of the analysis can be found in [467].

10.2.1.2. Event generation. All Monte Carlo event samples used in the analysis were generated using the PYTHIA [69] event generator, except for the $Zb\bar{b}$ ($e^+e^-b\bar{b}$ and $\mu^+\mu^-b\bar{b}$) background samples which were generated with COMPHEP [355].

Higgs-boson production was simulated through leading order gluon-gluon scattering and vector-boson fusion. Monte Carlo samples were produced for 18 values of the Higgs boson mass m_H ranging from 115 GeV/c^2 to 200 GeV/c^2 in 10 GeV/c^2 steps, and from 200 GeV/c^2 to 600 GeV/c^2 in 50 GeV/c^2 steps.

Three background processes which yield the same signature of two electrons and two muons in the final state, with significant cross-section times branching ratio, are considered:

1. $q\bar{q}/gg \to t\bar{t} \to W^+W^-b\bar{b} \to e^+e^-\mu^+\mu^-$.
2. $q\bar{q}/gg \to Zb\bar{b} \to e^+e^-\mu^+\mu^-$.
3. $q\bar{q} \to ZZ^\star/\gamma^\star \to e^+e^-\mu^+\mu^-$.

For the $t\bar{t}$ and $Zb\bar{b}$ backgrounds, no restrictions are applied on b decays prior to the pre-selection. Only events with $|\eta_b| < 2.5$ were generated for the $Zb\bar{b}$ background. For the $Zb\bar{b}$ and $ZZ^\star/\gamma^\star$ backgrounds, $m_{\gamma^\star}$ is required to be greater 5 GeV/c^2.

For the $ZZ^\star/\gamma^\star$ background, only the t-channel production through $q\bar{q}$ fusion is simulated. In order to account for contributions from all NLO diagrams and from the NNLO gluon fusion ($gg \to ZZ^\star/\gamma^\star$), all events are re-weighted at analysis level with an $m_{4\ell}$ dependent K-factor, calculated [51][468] using MCFM.

The potential background contribution from $Zc\bar{c} \to e^+e^-\mu^+\mu^-$ was also investigated using fully simulated events and was shown to be negligible.

For all Monte Carlo samples, a pre-selection is applied at generator level with the following requirements:

1. Final state contains $e^+e^-\mu^+\mu^-$.
2. $p_T(e) > 5$ GeV/c and $|\eta(e)| < 2.5$ for both electrons.
3. $p_T(\mu) > 3$ GeV/c and $|\eta(\mu)| < 2.4$ for both muons.

The cross-section times branching ratio and the cross-section times branching ratio times pre-selection efficiency, are shown for the signal as a function of m_H in Fig. 10.4. The NLO cross-section and the cross-section times branching ratio times pre-selection efficiency are shown for each background process in Table 10.1.

10.2.1.3. Online selection. Events selected by the dimuon or the dielectron triggers are considered. This choice follows from the presence of an on-shell Z-boson in most events. The additional use of single-electron and single-muon triggers does not increase the significance of the results.

The efficiencies of the Level-1 and High Level Triggers are shown for the signal as a function of m_H in Fig. 10.5. The corresponding trigger efficiencies for background processes are shown in Table 10.2.

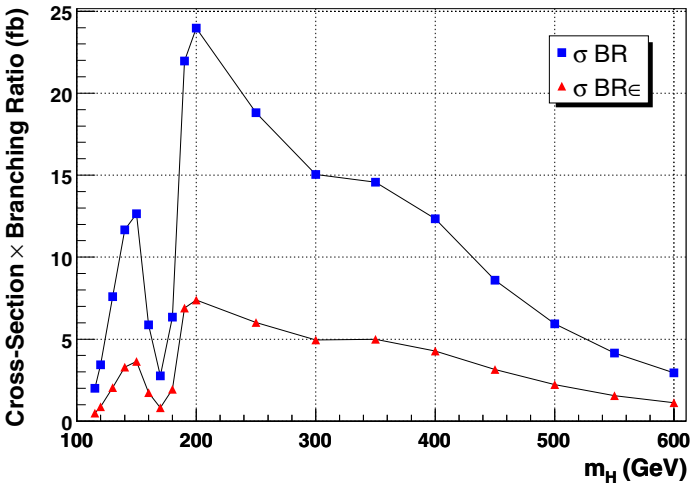

Figure 10.4. Cross-section times branching ratio, and cross-section times branching ratio times pre-selection efficiency for H$\rightarrow$ ZZ $^{(\star)} \rightarrow 2e2\mu$.

Table 10.1. NLO cross-section and the cross-section times branching ratio times pre-selection efficiency for the three background process.

Process	$\sigma_{\rm NLO}$ (pb)	$\sigma_{\rm NLO} \times {\rm BR} \times \varepsilon$ (fb)
$t\bar{t} \rightarrow {\rm W^+W^-b\bar{b}} \rightarrow {\rm e^+e^-}\mu^+\mu^-$	840	744
${\rm e^+e^-b\bar{b}} \rightarrow$ ${\rm e^+e^-}\mu^+\mu^-$	276	262
$\mu^+\mu^-{\rm b\bar{b}} \rightarrow$ ${\rm e^+e^-}\mu^+\mu^-$	279	128
${\rm ZZ}^\star\gamma^\star \rightarrow {\rm e^+e^-}\mu^+\mu^-$	28.9	37.0

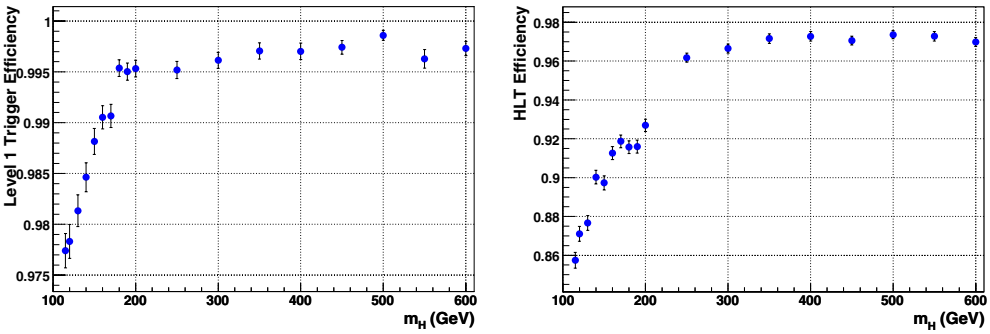

Figure 10.5. Efficiency of the Level-1 and High Level Triggers for the Higgs signal. Monte Carlo Statistical uncertainties are shown.

Table 10.2. Efficiency of the Level-1 and High Level Triggers for each of the three background processes. Monte Carlo Statistical uncertainties are shown.

	$t\bar{t}$	Zbb	ZZ$^*/\gamma^*$
Level-1 Trigger efficiency (%)	95.1 ± 0.1	92.3 ± 0.1	97.9 ± 0.2
HLT efficiency (%)	39.9 ± 0.1	65.8 ± 0.1	89.6 ± 0.4

10.2.1.4. Offline event selection. Offline reconstruction of electrons and muons is performed using standard algorithms. It is required that four leptons of type $e^+e^-\mu^+\mu^-$ are reconstructed.

The two largest backgrounds after the HLT, $t\bar{t}$ and Zbb̄, are reducible, since unlike the Higgs signal, two of the leptons will be associated with b-jets and will therefore be displaced relative to the primary vertex and will not be isolated. These two considerations can be used to powerfully cut against these processes, whereas the $ZZ^\star/\gamma^\star$ background is irreducible by such means. Kinematic cuts are then applied, which further reduce all three backgrounds.

Vertex and Impact Parameter. Three criteria are applied:

1. The transverse distance of the $\mu^+\mu^-$ vertex from the beam line is required to be less than 0.011 cm.
2. The three-dimensional distance between the $\mu^+\mu^-$ vertex and the e^+e^- vertex is required to be less than 0.06 cm.
3. The transverse impact parameter significance of all leptons required to be less than 7.

For events passing this selection, the primary vertex is reconstructed by performing a fit to the tracks of the four reconstructed leptons. The lepton tracks are then refitted using the reconstructed vertex position as an additional point, in order to obtain a more accurate measurement of the momentum at the primary vertex.

Isolation. A cut is applied on the sum of the p_T of reconstructed tracks with $p_T > 0.9$ GeV/c and at least five hits, which satisfy the following conditions:

1. The track lies within the region defined by the sum of cones of size $\Delta R = 0.25$ around each of the four leptons and lies outside veto cones of size $\Delta R = 0.015$ around each lepton.
2. The track is consistent with originating from the reconstructed primary vertex to within $|\Delta z| < 0.2$cm, where Δz is the difference between the z position of the point of closest approach of the track to the reconstructed vertex, and the z position of the reconstructed vertex.

Kinematic Cuts. The following kinematic cuts are applied:

1. Lower thresholds on the transverse momenta of each of the four reconstructed leptons.
2. Upper and lower thresholds on the invariant masses of the reconstructed e^+e^- and $\mu^+\mu^-$ pairs.
3. Upper and lower thresholds on the invariant mass of the four reconstructed leptons.

These kinematic thresholds, together with the threshold on Σp_T for tracker isolation are optimised simultaneously using MINUIT, such that the log-likelihood ratio:

$$S_L = \sqrt{2 \ln Q}, \qquad \text{where} \qquad Q = \left(1 + \frac{N_S}{N_B}\right)^{N_S+N_B} e^{-N_S} \tag{10.1}$$

is maximised. The optimisation is performed separately for each Higgs mass.

10.2.1.5. Results. Tables 10.3 and 10.4 show the production cross-section, cross-section times branching ratio, cross-section times branching ratio times pre-selection efficiency and the cross-section times branching ratio times efficiency after each stage of the online and offline event selection, for Higgs masses of 140 GeV/c^2 and 200 GeV/c^2, respectively. Values are shown for signal and for each of the three background processes. For all values of m_H, the background after all selections is strongly dominated by ZZ^*/γ^*. For low m_H $t\bar{t}$ and Zbb̄ each

Table 10.3. Production cross-section (NLO), cross-section times branching ratio, cross-section times branching ratio times pre-selection efficiency and cross-section times branching ratio times efficiency after each stage of the online and offline event selection, for $m_H = 140\,\mathrm{GeV/c^2}$, for signal and backgrounds. All values in fb, except for expected number of events. Uncertainties are statistical only.

	Signal	$t\bar{t}$	$Zb\bar{b}$	ZZ^*/γ^*
Production cross-section (NLO)	33.6×10^3	840×10^3	555×10^3	28.9×10^3
$\sigma \times$ BR(4 lepton final state)	11.6	-	-	367.5
Pre-selection: $\sigma \times$ BR $\times\varepsilon$	3.29 ± 0.04	743 ± 2	390 ± 1	37.0 ± 0.4
Level-1 trigger	3.24 ± 0.04	707 ± 2	360 ± 1	36.3 ± 0.4
High Level trigger	2.91 ± 0.03	282 ± 1	237 ± 1	32.5 ± 0.4
$e^+e^-\mu^+\mu^-$ reconstructed	2.23 ± 0.03	130 ± 1	141 ± 1	24.1 ± 0.3
Vertex and impact parameter cuts	2.01 ± 0.03	18.9 ± 0.3	18.4 ± 0.2	21.5 ± 0.3
Isolation cuts	1.83 ± 0.03	1.34 ± 0.07	5.8 ± 0.1	20.0 ± 0.3
Lepton p_T cuts	1.61 ± 0.03	0.40 ± 0.04	0.56 ± 0.03	17.6 ± 0.3
Z mass window cuts	1.35 ± 0.02	0.20 ± 0.03	0.23 ± 0.02	13.8 ± 0.3
Higgs mass window cuts	1.17 ± 0.02	0.02 ± 0.01	0.025 ± 0.007	0.15 ± 0.03
Expected events for $\int \mathcal{L} = 10\,\mathrm{fb}^{-1}$	11.7 ± 0.2	0.2 ± 0.1	0.25 ± 0.07	1.5 ± 0.3

Table 10.4. Production cross-section (NLO), cross-section times branching ratio, cross-section times branching ratio times pre-selection efficiency and cross-section times branching ratio times efficiency after each stage of the online and offline event selection, for $m_H = 200\,\mathrm{GeV/c^2}$, for signal and backgrounds. All values in fb, except for expected number of events. Uncertainties are statistical only.

	Signal	$t\bar{t}$	$Zb\bar{b}$	ZZ^*/γ^*
Production cross-section (NLO)	17.9×10^3	840×10^3	555×10^3	28.9×10^3
$\sigma \times$ BR(4 lepton final state)	23.8	-	-	367.5
Pre-selection: $\sigma \times$ BR $\times\varepsilon$	7.39 ± 0.09	743 ± 2	390 ± 1	37.0 ± 0.4
Level-1 trigger	7.36 ± 0.09	707 ± 2	360 ± 1	36.3 ± 0.4
High Level trigger	6.82 ± 0.08	282 ± 1	237 ± 1	32.5 ± 0.4
$e^+e^-\mu^+\mu^-$ reconstructed	5.51 ± 0.07	130 ± 1	141 ± 1	24.1 ± 0.3
Vertex and impact parameter cuts	5.03 ± 0.07	18.9 ± 0.3	18.4 ± 0.2	21.5 ± 0.3
Isolation cuts	4.92 ± 0.07	5.1 ± 0.1	12.3 ± 0.2	21.3 ± 0.3
Lepton p_T cuts	4.78 ± 0.07	1.93 ± 0.09	1.78 ± 0.06	18.7 ± 0.3
Z mass window cuts	4.45 ± 0.07	0.15 ± 0.03	0.12 ± 0.02	14.4 ± 0.3
Higgs mass window cuts	3.64 ± 0.06	0.006 ± 0.005	0.006 ± 0.003	1.61 ± 0.09
Expected events for $\int \mathcal{L} = 10\,\mathrm{fb}^{-1}$	36.4 ± 0.6	0.06 ± 0.05	0.06 ± 0.03	16.1 ± 0.9

contribute around 10-15% to the total residual background, whereas for $m_H > 200\,\mathrm{GeV/c^2}$, ZZ^*/γ^* constitutes more than 99%.

Figure 10.6 shows the invariant mass of the four reconstructed leptons before and after the application of the offline selection, for signal events for $m_H = 140\,\mathrm{GeV/c^2}$ (left) and $m_H = 200\,\mathrm{GeV/c^2}$ (right), and for the three background processes.

Figure 10.7 shows the final cross-section times branching ratio times efficiency for selected events, for signal and background, as a function of the Higgs boson mass. The number of expected events passing all selections for $10\,\mathrm{fb}^{-1}$ of integrated luminosity is shown in Table 10.5 for several values of the Higgs boson mass.

Significance. Figure 10.8 shows the S_{cP} significance after all selection cuts for integrated luminosities of $10\,\mathrm{fb}^{-1}$ and $30\,\mathrm{fb}^{-1}$, with and without the systematic uncertainty on the background estimation taken into account. The background systematic uncertainty will be

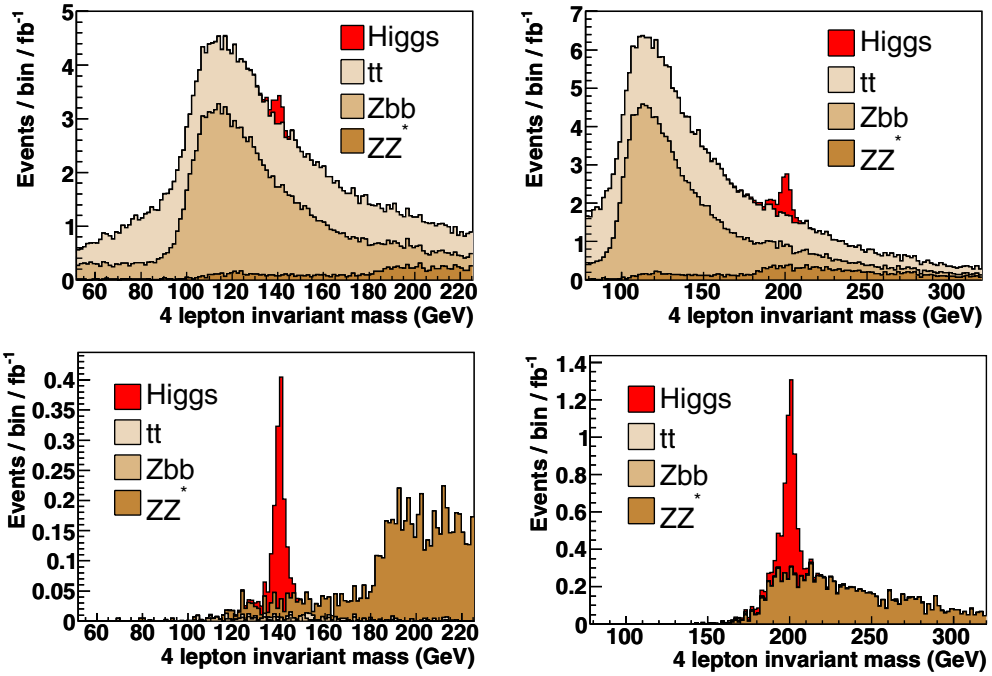

Figure 10.6. Invariant mass of the four reconstructed leptons before (top) and after (bottom) the application of the offline selection, for signal events for $m_H = 140\text{GeV/c}^2$ (left) and $m_H = 200\text{GeV/c}^2$ (right), and for the three background processes.

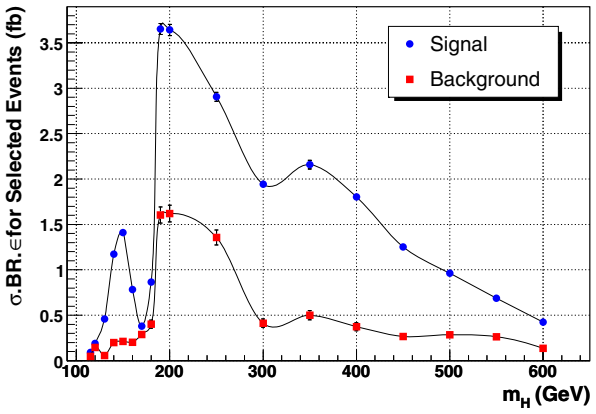

Figure 10.7. Cross-section times branching ratio times efficiency after all selections.

Table 10.5. Expected number of events from signal and background processes after all selections for an integrated luminosity of 10 fb^{-1}.

m_H (GeV/c^2)	120	130	140	150	160	170	180	200	250	300	400	500
N signal for 10 fb^{-1}	1.9	4.6	11.7	14.1	7.8	3.8	8.7	36.4	29.1	19.4	18.0	9.6
N back for 10 fb^{-1}	1.5	0.6	2.0	2.1	2.0	2.9	4.0	16.2	13.6	4.1	3.7	2.6

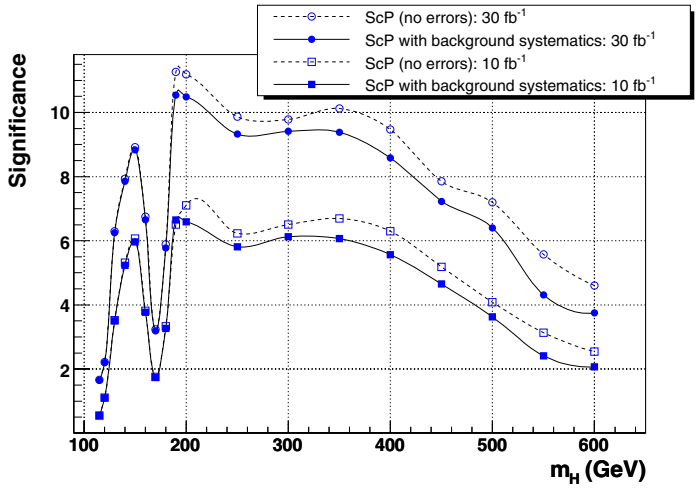

Figure 10.8. The S_{cP} significance after all selection cuts for integrated luminosities of $10\,\mathrm{fb}^{-1}$ and $30\,\mathrm{fb}^{-1}$, with and without the systematic uncertainty on the background estimation taken into account.

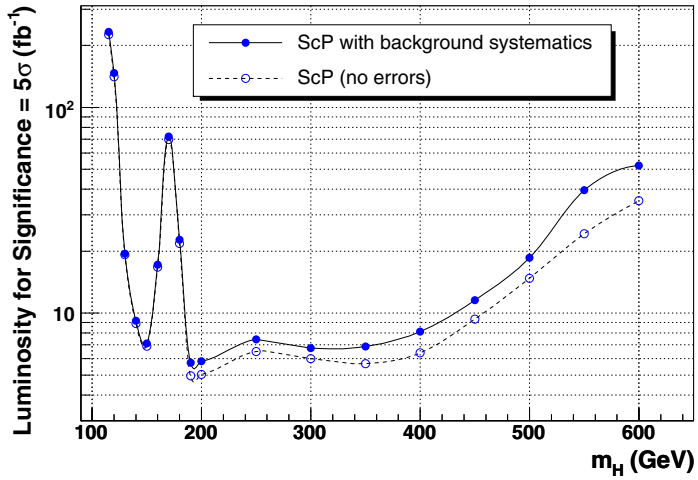

Figure 10.9. Integrated luminosity required to obtain a significance of 5σ using the $\mathrm{H} \to \mathrm{ZZ}^{(*)} \to 2\mathrm{e}2\mu$ channel, with and without the systematic uncertainty on the background estimation taken into account.

discussed in Section 10.2.1.6. Figure 10.9 shows the integrated luminosity required to obtain a significance of 5σ using the $\mathrm{H} \to \mathrm{ZZ}^{(*)} \to 2\mathrm{e}2\mu$ channel alone, with and without the background systematic uncertainty. It can be seen that a significance of 5σ can be achieved with less than $30\,\mathrm{fb}^{-1}$ of integrated luminosity for a Higgs boson with mass in the range $130 \leqslant m_H \leqslant 500\,\mathrm{GeV/c}^2$, excluding a gap of about $15\,\mathrm{GeV/c}^2$ close to $m_H/170\,\mathrm{GeV/c}^2$ for which close to $100\,\mathrm{fb}^{-1}$ is required. If the Higgs boson mass lies in the range $190 \leqslant m_H \leqslant 400\,\mathrm{GeV/c}^2$, 5σ significance can be attained with less than $8\,\mathrm{fb}^{-1}$ of integrated luminosity.

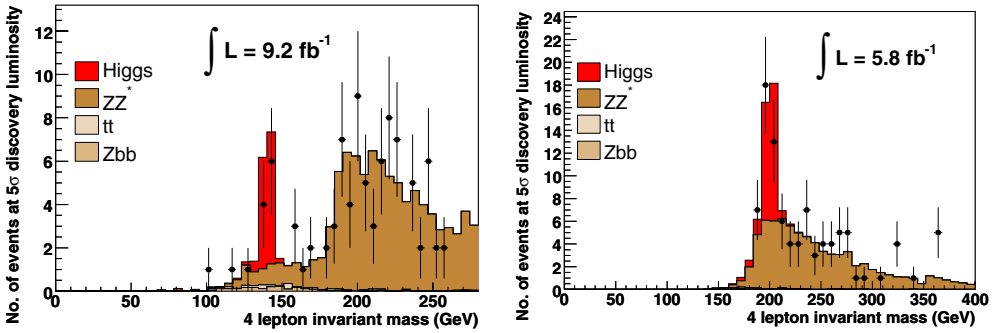

Figure 10.10. Number of expected events for signal and background for an integrated luminosity corresponding to a discovery significance of 5σ, for Higgs boson masses of 140 and 200 GeV/c^2. The results of a simulated experiment are also shown to illustrate the statistical power of the analysis and the determination of the background normalisation from data.

10.2.1.6. Evaluation of background from data. The background normalisation can be estimated from data by using the sidebands in the reconstructed four-lepton invariant mass distribution. Figure 10.10 shows the number of expected events from the signal and background Monte Carlo simulations for an integrated luminosity corresponding to a discovery significance of 5σ, for Higgs boson masses of 140 and 200 GeV/c^2: 9.2 and 5.8 fb^{-1}, respectively. Figure 10.10 also shows the results of a simulated experiments with these luminosities.

The number of background events measured from the data within the signal region, N^{IN}_{Data}, is calculated as:

$$N^{IN}_{Data} = \alpha_{MC} N^{OUT}_{Data}, \qquad \text{where} \qquad \alpha_{MC} = \frac{N^{IN}_{MC}}{N^{OUT}_{MC}}. \tag{10.2}$$

N^{OUT}_{Data} is the number observed events lying outside the signal region and α_{MC} is the ratio of the number of background events inside the signal region (N^{IN}_{MC}) to outside the signal region (N^{OUT}_{MC}), as determined from the background Monte Carlos.

The uncertainty on the number of background events in the signal region measured using this method is given by:

$$\Delta B = \Delta B_{Stat} \oplus \Delta B_{Theory}, \qquad \text{where} \qquad \Delta B_{Stat} = \alpha\sqrt{N^{OUT}_{Data}}.$$

ΔB_{Stat} provides the dominant contribution to the uncertainty. Taking N^{OUT}_{Data} as the expected number of events outside the signal region for an integrated luminosity corresponding to 5σ significance, the value ΔB_{Stat} varies between 2% and 13% for m_H <200 GeV/c^2 and increases to around 30% for high m_H where the statistics in the sidebands are low.

ΔB_{Theory} is the theoretical uncertainty on the shape of the $m_{4\ell}$ distribution for the ZZ$^*/\gamma^*$ background. The value is taken from [51], which takes into account PDF and QCD scale uncertainties in the ZZ$^*/\gamma^*$ production cross-section at NLO, and varies between 0.5 and 4.5% for the range Higgs boson masses considered.

10.2.1.7. Measurement of the properties of the Higgs boson. The H $\rightarrow$ ZZ$^{(*)}$ $\rightarrow 4\ell$ channel can be used to evaluate the mass, width and production cross-section of the Higgs boson.

Mass Measurement. The statistical uncertainty on the Higgs boson mass measurement is given by $\Delta stat = \sigma_{Gauss}/\sqrt{N_S}$, where σ_{Gauss} is the measured Gaussian width of the four

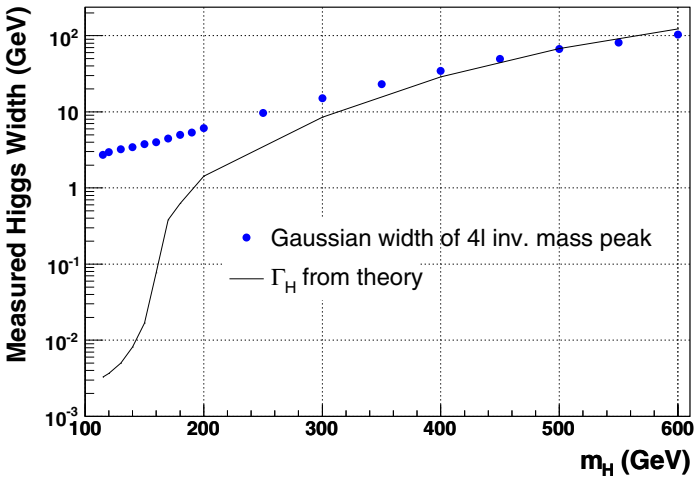

Figure 10.11. Measured width of the Higgs boson mass peak, obtained from a Gaussian fit to the peak, as a function of the true Higgs mass. The true width from theory is also shown.

Table 10.6. Statistical uncertainty on the measurement of the mass, width and production cross-section of the Higgs boson.

m_H (GeV/c^2)	115	120	130	140	150	160	170	180	190
$\Delta_{Stat}(m_H)$(%)	0.722	0.512	0.335	0.206	0.193	0.256	0.388	0.27	0.134
$\Delta_{Stat}(\Gamma_H)$(%)	-	-	-	-	-	-	-	54.8	17.6
$\Delta_{Stat}(\sigma_H)$(%)	75	55.6	28.6	18.2	16.5	23.1	39.2	23.7	11.5
m_H (GeV/c^2)	200	250	300	350	400	450	500	550	600
$\Delta_{Stat}(m_H)$(%)	0.145	0.207	0.328	0.408	0.588	0.896	1.25	1.62	2.43
$\Delta_{Stat}(\Gamma_H)$(%)	14.4	7.38	8.2	5.43	5.8	5.91	6.52	6.61	8.36
$\Delta_{Stat}(\sigma_H)$(%)	11.5	13	14.4	13.8	14.9	18	21.2	25.9	32.3

lepton invariant mass peak from the signal Monte Carlo and N_S is the expected number of signal events passing all selections. The value, as a fraction of the true mass, is shown in Table 10.6, for an integrated luminosity and 30 fb^{-1}, as a function of m_H.

Width Measurement. Figure 10.11 shows the measured width of the Higgs boson mass peak, obtained from the Gaussian fit, as a function of m_H. The true width from theory Γ_H is also shown. The measured width is a convolution of the natural width and the experimental resolution. It can be seen that for m_H less than around 200 GeV/c^2, the measured width is completely dominated by the experimental resolution. The statistical uncertainty on the width measurement is given by $\Delta stat = \sigma_{Gauss}/\sqrt{2N_S}$, where σ_{Gauss} is the measured Gaussian width of the peak and N_S is the expected number of signal events passing all selections. The value, as a fraction of the true width, is shown in Table 10.6, for an integrated luminosity and 30 fb^{-1}, as a function of m_H. The direct measurement the Higgs boson width is possible with $\Delta stat < 30\%$ for $m_H \geqslant 200$ GeV/c^2.

Production Cross-Section Measurement. The Higgs boson production cross-section can be determined from the number of observed events N_{obs} after all selections, given the efficiency ε of the event selection and the integrated luminosity $\mathcal{L}$:

$$\sigma = \frac{N_{obs}}{\mathcal{L}\epsilon}.$$

The total uncertainty on the cross-section measurement is given by:

$$\Delta\sigma^2 = \Delta stat^2 + \Delta syst^2 + \Delta\mathcal{L}^2 + \Delta B^2$$

where $\Delta stat$, $\Delta syst$, $\Delta\mathcal{L}$ and Δ B are the statistical uncertainty, the systematic uncertainty from the event selection, the uncertainty on the luminosity measurement and the background systematic uncertainty, respectively.

The statistical uncertainty $\Delta stat$ is shown in Table 10.6 for an integrated luminosity 30 fb^{-1}, as a function of m_H.

The total systematic uncertainty arising from the offline reconstruction and event selection can be summarised as:

$$\Delta syst^2 = 2\Delta\epsilon_{\text{e}}^2 + 2\Delta\epsilon_{\mu}^2 + \Delta\epsilon_{iso}^2$$

where $\Delta\varepsilon_{\text{e}}$ is the uncertainty in the reconstruction efficiency for electrons, estimated to be around 1% per electron [469], $\Delta\varepsilon_{\mu}$ is the uncertainty in the muon reconstruction efficiency, which has been shown to be measurable to be better than 1% per muon [51], and $\Delta\varepsilon_{iso}$ is the uncertainty in the efficiency of the isolation cut, estimated in the $\text{H} \to \text{ZZ}^{(*)} \to 4\mu$ analysis [51] to be around 2% per event. This gives a total uncertainly $\Delta syst = 3\%$.

The uncertainty on the measurement of the LHC luminosity $\Delta\mathcal{L}$ is expected to be around 3% at the 30 fb^{-1}. The background uncertainty ΔB is discussed in Section 10.2.1.6.

10.2.2. Inclusive Higgs boson production with $\text{H} \to \text{WW}^* \to 2\ell 2\nu$

The Higgs $\text{H} \to \text{WW}^{(*)} \to 2\ell 2\nu$ decay into two Ws and subsequently into two leptons ($\text{H} \to \text{WW} \to \ell\nu\ell\nu$) is the discovery channel for Higgs boson masses between 2m_W and 2m_Z [470]. In this mass range, the Higgs to WW branching ratio is close to one, leading to large number of events. The signature of this decay is characterised by two leptons and missing energy. However, since no narrow mass peak can be reconstructed, good understanding of the background together with a high signal to background ratio is needed. The most important backgrounds, which give similar signature as the signal (i.e. two leptons and missing energy), are the continuum WW production and the $\text{t}\bar{\text{t}}$ production. To reduce these backgrounds, one has to require a small opening angle between the leptons in the transverse plane and apply a jet veto.

A detailed description of the analysis can be found in [471].

10.2.2.1. Signal and background generation. The signal samples were generated using PYTHIA. The two major Higgs production modes for the mass range studied, gluon and vector boson fusion were generated. The $\text{p}_\text{t}(H)$ spectrum predicted by PYTHIA was reweighted to the MC@NLO prediction, defining p_t dependent k-factors, as proposed in [472].

For the backgrounds, continuum vector boson production (WW, ZZ, WZ) was generated using PYTHIA. The p_t(WW) spectrum was reweighted using the same technique than for the signal. A NLO cross section of respectively 16 pb, 50 pb and 114 pb was taken for ZZ, WZ and WW. WW production via gluon box diagram, ggWW, was generated using a parton Monte Carlo provided by N. Kauer and linked to PYTHIA for the parton shower [70]. Top production ($\text{t}\bar{\text{t}}$ and tWb) was generated using TOPREX. NLO cross sections of respectively 840 pb and 33.4 pb were used for $\text{t}\bar{\text{t}}$ and tWb [473].

10.2.2.2. Signal reconstruction. The signal signature is characterised by two leptons in the final state with opposite charge, missing energy and no jet. The leptons, either electrons or muons, are required to have $\text{p}_\text{t} > 20\,\text{GeV/c}$ and $|\eta| < 2$.

Muons candidates are asked to be isolated: The energy left in the calorimeters around the muon candidate within a $\Delta R = 0.3$ cone must be smaller than 5 GeV and the sum of the p_t of the tracks within a $\Delta R = 0.25$ cone around the muon candidate must be smaller than 2 GeV.

Electrons candidates are reconstructed combining tracks and ECAL clusters. They must fulfill in addition the following identification requirements:

- The electron must deposit small energy in the HCAL: $E_{hcal}/E_{ecal} < 0.05$?
- The electron track and cluster must be precisely matched:
  in direction: $|\eta_{track} - \eta_{SC\,corr}| < 0.005$ and $|\phi_{track\,prop} - \phi_{SC}| < 0.02$[43] in magnitude: $E/p > 0.8$ and $|1/E - 1/p| < 0.02$

The electron candidate must be also isolated by requiring, $\sum_{tracks} p_t(track)/E_t(SC) < 0.05$, where the sum runs on all the tracks (excluding electron) which have:

- $\Delta R_{SC-track} < 0.2$ (at vertex);
- $p_t^{track} > 0.9\,GeV/c$;
- $|z_{track} - z_{electron}| < 0.2$ cm.

Finally a cut on the impact parameter significance in the transverse plane is applied in order to reduce the $b\bar{b}$ background. Each lepton is required to have $\sigma_{IP} < 3$ where σ_{IP} is the impact parameter significance. The two leptons are also required to come from the same vertex by asking $|z_{lep1} - z_{lep2}| < 0.2$ cm.

With this lepton selection, the contribution of reducible backgrounds like W+jet where one jet is misidentified as a lepton or $b\bar{b}$ is expected to be less than 5 fb after all cuts applied.

Missing energy is reconstructed by summing the raw energy of all ECAL and HCAL towers, and correcting for muons. Since a jet veto is applied in the signal selection, further correction on the missing energy did not bring a significant improvement.

Jets are reconstructed using a Cone algorithm of size $\Delta R = 0.5$ and requiring its component calorimeter towers to have $E_T^{tow} > 0.5\,GeV$ and $E^{tow} > 0.8\,GeV$. Since jets are reconstructed to be vetoed, no energy calibration was applied. For the events studied, $E_T(jet) \approx (1.5 - 2) \cdot E_T(raw)$. To veto electrons and Bremsstrahlung photons, the jets are also required to be away from the leptons ($\Delta R_{jet-lepton} > 0.5$).

For jets with a raw energy between 15 and 20 GeV an additional cut on their track content was applied in order to reduce the contamination from fake jets coming from the underlying event. For this, the so-called alpha parameter is defined, as the ratio of the sum of p_t of tracks from the signal vertex inside the jet over the transverse jet energy in the calorimeter. For a perfect detector, the alpha parameter of a jet would be around 0.66, as in mean two third of a jet are charged particles. This ratio is smeared and reduced by the detector energy resolution and not 100% efficiency of the charged particle reconstruction in the tracker. In a fake jet, the sum of p_t of tracks from the signal vertex inside the fake jet is small, leading to an alpha parameter around zero.

Alpha is determined using only tracks that are 'inside' the jet, i.e. with $\Delta R_{track-jet} < 0.5$ and coming from the event vertex[44], fulfilling $|z_{trk} - z_{vtx}| < 0.4$ cm. Finally, these tracks should have more than 5 hits and $p_t > 2\,GeV/c$. Alpha is then defined as alpha $= \frac{\sum p_t(tracks)}{E_T(jet)}$. If its raw energy lies between 15 and 20 GeV a jet is then required to have $\alpha > 0.2$ to be kept.

[43] Where $\phi_{track\ prop}$ is the track angle propagated in the magnetic field up to the ECAL cluster position.
[44] The event vertex is defined as the mean z position of the two leptons.

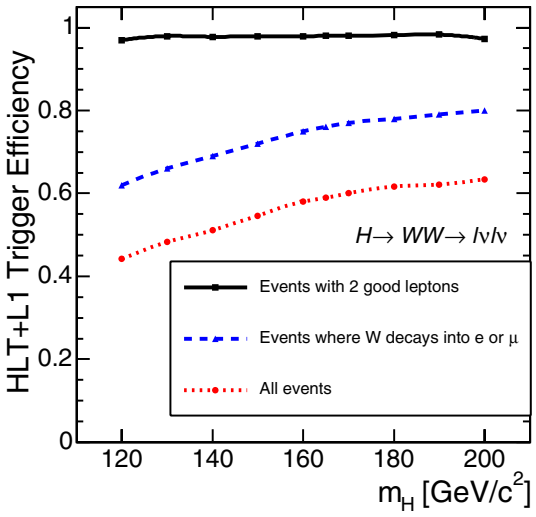

Figure 10.12. Trigger efficiencies (L1+HLT) as a function of the Higgs mass on all events (dotted line), on events where the W decays in electrons and muons (dashed line) and on events with exactly two leptons passing the lepton selection cuts (solid line).

10.2.2.3. Event selection and results. Events are first required to pass globally the Level-1 trigger and at least one of the following HLT triggers: single electron, double electron, single muon or double muon trigger.

Figure 10.12 shows the Level-1 trigger efficiency (blue dashed curve) and the combined L1+HLT trigger efficiencies (red dotted curve) as a function of the Higgs mass. To estimate the numbers of 'useful events' rejected by the trigger it is interesting to look at the trigger efficiency on events having exactly two leptons which fulfill the lepton selection cuts defined before. This is shown by the solid black curve on Fig. 10.12. In this case, the trigger efficiency is higher than 95% on the full mass range and is around 100% for $\mu\mu$ final state, whereas for ee final state it is around 96%.

Then each event has to contain exactly two opposite charge leptons with $p_t > 20\,\mathrm{GeV/c}$ and $|\eta| < 2$ passing the cuts described before. The following kinematic selections were applied:

- $E_t^{miss} > 50\,\mathrm{GeV}$
- $\phi_{\ell\ell} < 45^\circ$ (angle between the leptons in the transverse plane)
- $12\,\mathrm{GeV/c^2} < m_{\ell\ell} < 40\,\mathrm{GeV/c^2}$ (the invariant mass of the two leptons)
- no jet with $E_t^{raw} > 15\,\mathrm{GeV}$ and $|\eta| < 2.5$
- $30\,\mathrm{GeV/c} < p_t^{\ell max} < 55\,\mathrm{GeV/c}$ (lepton with the maximal p_t)
- $p_t^{\ell min} > 25\,\mathrm{GeV/c}$ (lepton with the minimal p_t).

These cuts were optimised for a Higgs mass of $165\,\mathrm{GeV/c^2}$. The expected number of events for the signal for three different Higgs masses and the different backgrounds in fb are given in Table 10.7. The first column shows the signal times branching ratio for the different processes, the second one shows the number of events passing the trigger requirement, the third one the number of events with two opposite charge leptons passing the lepton selection cuts and the last one the number of events after all selection cuts are applied. Figure 10.13, left shows the $\phi_{\ell\ell}$ distribution for the signal plotted on the top of the sum of all background when all selection cuts are applied except the one on $\phi_{\ell\ell}$.

Table 10.7. The expected number of events for the signal for three different Higgs masses and the different backgrounds given in fb. The first column shows the number of expected events after HLT requirement, the second one after having found two opposite charge leptons and the last one the number of events after all selection cuts are applied.

Reaction pp $\to X$	$\sigma_{NLO} \times BR$	L1 + HLT	2 leptons	All cuts
$\ell = e, \mu, \tau$	pb	Expected event rate in fb		
$H \to WW \to \ell\ell$, $m_H = 160\,GeV/c^2$	2.34	1353 (58%)	359 (27%)	42 (12%)
$H \to WW \to \ell\ell$, $m_H = 165\,GeV/c^2$	2.36	1390 (59%)	393 (28%)	46 (12%)
$H \to WW \to \ell\ell$, $m_H = 170\,GeV/c^2$	2.26	1350 (60%)	376 (28%)	33 (8.8%)
$qq \to WW \to \ell\ell$	11.7	6040 (52%)	1400 (23%)	12 (0.9%)
$gg \to WW \to \ell\ell$	0.48	286 (60%)	73 (26%)	3.7 (5.1%)
$tt \to WWbb \to \ell\ell$	86.2	57400 (67%)	15700 (27%)	9.8 (0.06%)
$tWb \to WWb(b) \to \ell\ell$	3.4	2320 (68%)	676 (29%)	1.4 (0.2%)
$ZW \to \ell\ell\ell$	1.6	1062 (66%)	247 (23%)	0.50 (0.2%)
$ZZ \to \ell\ell, \nu\nu$	1.5	485 (32%)	163 (34%)	0.35 (0.2%)
Sum backgrounds	105	67600 (64%)	18300 (27%)	28 (0.2%)

10.2.2.4. Background normalisation and systematics. The following procedure for background normalisation is proposed.

- *Top background normalisation.* Two procedures are proposed. A first possibility is to define a sample with the same lepton and missing energy cuts as for the signal selection but requiring two b-tagged jets with $E_t > 20\,GeV$. A second possibility is to apply the same kinematic cuts on the leptons and require two additional jets with respectively $E_T^{raw} > 50\,GeV$ and $E_T^{raw} > 30\,GeV$. In this case, only $e\mu$ final states are considered in order to avoid a contamination from Drell–Yan. Both methods are expected to give an error of about 16% on $t\bar{t}$ estimate for a luminosity of $5\,fb^{-1}$.
- *WW background normalisation.* A normalisation region can be defined for WW by keeping the same cuts than the signal but requiring $\phi_{\ell\ell} < 140$ and $m_{\ell\ell} > 60\,GeV/c^2$. Moreover only opposite flavour leptons are considered in order to reduce the Drell–Yan and WZ contribution. A systematic error of about 17% is expected with a luminosity of $5\,fb^{-1}$, dominated by statistical uncertainty. Figure 10.13 right shows the $\phi_{\ell\ell}$ distribution for the different process in this normalisation region.
- *WZ background normalisation.* WZ can be normalised by keeping the same signal cut and requiring an additional lepton in the final state. The cuts on $\phi_{\ell\ell}$ and $m_{\ell\ell}$ are removed. An accuracy of about 20% is expected on this background with $5\,fb^{-1}$.
- *ggWW and tWb normalisation.* The contribution of these backgrounds will be estimated using Monte Carlo prediction, since they represent only a small fraction of signal events. The error on ggWW is about 30% whereas the one on tWb is about 22%, both largely dominated by theoretical errors.

Taking into account the sum of the different backgrounds, an overall error of 13% is found on the total background. These results are calculated for a luminosity of $5\,fb^{-1}$. For luminosities of 1,2 and $10\,fb^{-1}$, the total systematic errors scale to 19%, 16% and 11% respectively. Table 10.8 show the signal to background ratio for the different Higgs masses together with the luminosity needed for a 5σ discovery, with and without the inclusion of background uncertainties. For Higgs masses of 120–140 GeV/c^2 and 190–200 GeV/c^2, the background errors are too high to get a significant signal.

Figure 10.14 shows the signal to background ratio (left) and the luminosity needed for a 5σ discovery (right) as a function of the Higgs mass. A signal of more than 5σ significance

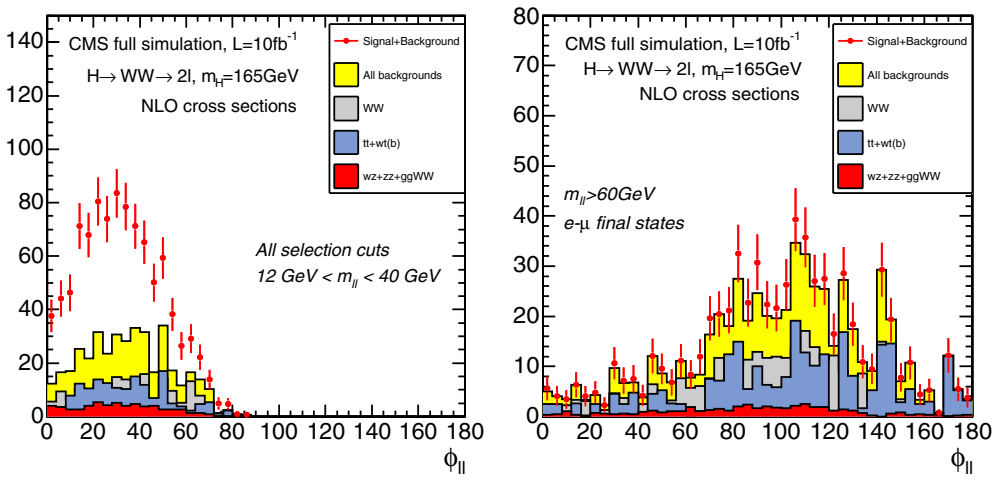

Figure 10.13. The angle between the leptons in the transverse plane for the signal and the different background and a luminosity of $10\,\mathrm{fb}^{-1}$, (Left) For the signal cuts taking out the one on $\varphi_{\ell\ell}$. (Right) For the WW background normalisation region where all signal cuts are applied except the one on the lepton invariant mass, which was set to $\mathrm{m}_{\ell\ell} > 60\,\mathrm{GeV/c}^2$ and only electron-muon final states are kept.

Table 10.8. The signal to background ratio for the different Higgs masses together with the luminosity needed for a 5σ discovery, with and without the inclusion of background uncertainties. Also the statistical errors due to the restricted Monte Carlo statistics are taken into account.

$\mathrm{m_H}$ [GeV]	S/B	Significance for $5\,\mathrm{fb}^{-1}$		$\mathcal{L}_{\mathrm{disc}}$ [fb]	$\mathcal{L}_{\mathrm{disc}}$ [fb]
		no bkg syst	with bkg syst	no bkg syst	with bkg syst
150	0.61	6.6	4.0	3.0	8.2
160	1.51	14	7.7	0.58	1.1
165	1.66	15	8.3	0.50	0.90
170	1.19	11	6.3	0.88	1.7
180	0.65	6.7	3.7	2.7	7.3

could be already observed with a luminosity of $7\,\mathrm{fb}^{-1}$ for a Higgs mass between 150 and $180\,\mathrm{GeV/c}^2$. For a Higgs mass of $165\,\mathrm{GeV/c}^2$ the luminosity needed for a 5σ discovery is expected to be less than $1\,\mathrm{fb}^{-1}$.

10.2.2.5. Selection optimisation for $\mathrm{M_H}$ *in the 130–150* $\mathrm{GeV/c}^2$ *mass range with* $e^+e^-\nu\nu$ *final state.* A dedicated optimisation for the $e^+e^-\nu\nu$ final state in the mass range of $130 \leqslant \mathrm{M_H} \leqslant 150\,\mathrm{GeV/c}^2$ has been performed [474]. The largest significance is searched assuming a known $\mathrm{M_H}$. The latest developments in detailed electron reconstruction are used and allow a good rejection of the W + jets background which is characterised by the misidentification of a jet as an electron. New kinematical variables have been designed to reduce the W+jets background as well as the contribution from Drell–Yan events with recoiling jets (Z+jets). For instance, in the signal, the two electrons tend to be close to each other, and the dielectron system is essentially emitted in the central region. On the contrary, in the Z + jets background, the dielectron pair is emitted uniformly in η, and the electrons candidates in the W + jets backgrounds are well separated. Other selection criteria relying on the absence of a true source of missing transverse energy in the Z + jets events have been introduced: in the events where

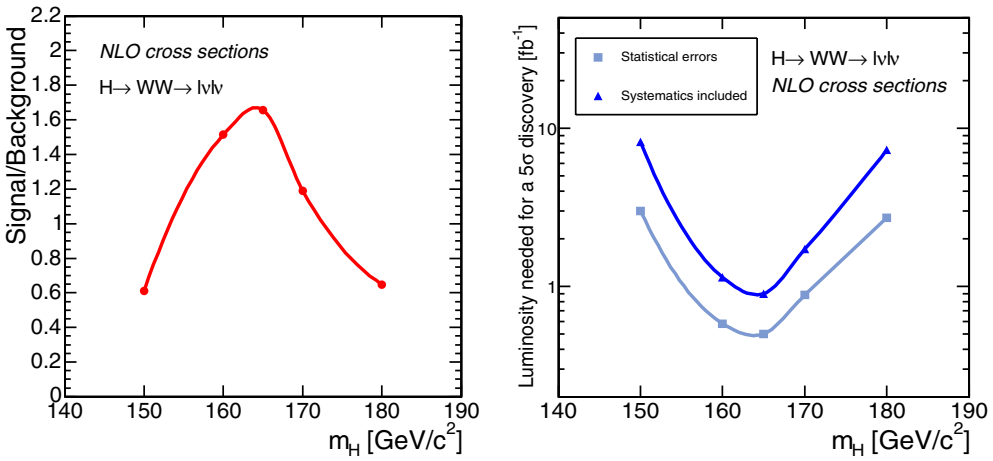

Figure 10.14. Signal to background ratio for a luminosity of $5\,\mathrm{fb}^{-1}$ (left) and the luminosity needed for a 5σ discovery (right) as a function of different Higgs masses for the $\mathrm{H} \rightarrow \mathrm{WW}$ channel.

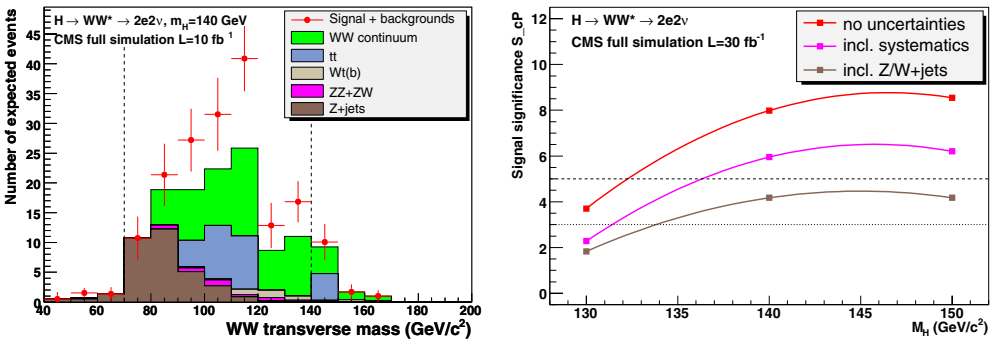

Figure 10.15. Left: the reconstructed WW transverse mass for the 140 GeV Higgs signal selection with $10\,\mathrm{fb}^{-1}$. The dashed lines show the window of events entering in the signal significance calculation. Right: the signal significance as function of the Standard Model Higgs mass for an integrated luminosity of $30\,\mathrm{fb}^{-1}$.

the missing transverse energy is mis-measured, it is usually in the same direction as the leading jet. Similarly, the imbalance of the missing energy and the dilepton system in the transverse plane is exploited.

Both W + jets and Z+jets backgrounds are thus explicitly reduced to a manageable level. Fig. 10.15 (left) shows the reconstructed WW transverse mass for the 140 GeV Higgs signal selection with $10\,\mathrm{fb}^{-1}$. Figure 10.15 (right) shows the signal significance as function of the Standard Model Higgs mass for the integrated luminosity of $30\,\mathrm{fb}^{-1}$ with and without systematics taken into account. A 3σ observation is possible for Higgs masses from 135 GeV. A 5σ discovery is reached with $60\,\mathrm{fb}^{-1}$.

10.2.3. The vector boson fusion production with $\mathrm{H} \rightarrow \tau\tau \rightarrow \ell + \tau$ jet $+ E_{\mathrm{T}}^{\mathrm{miss}}$

In the early parton level simulation studies [475, 476] and fast detector simulation studies of ATLAS and CMS [477] it was shown that the Higgs boson production in the vector boson

fusion qq → qqH (qqH or VBF) and decay into τ lepton pair could be the discovery channel with $\sim 30\,\mathrm{fb}^{-1}$. The cross section measurement of qqH, $H \to \tau\tau$, WW, $\gamma\gamma$ channels will significantly extend the possibility of the Higgs boson coupling measurement [478, 479] and provide the possibility of the indirect measurement of the light Higgs boson width [478]. In the MSSM the qqH(h), H(h)→ $\tau\tau$ channel could be discovered in the largest region of the $M_A - \tan\beta$ parameter plane [475, 480]. The forward jet tagging and the central jet veto are the key selections of the VBF Higgs boson channels. The study of the observability of the VBF Higgs boson production and H→ $\tau\tau \to \ell$ + jet decay with the full detector simulation is presented in the following. A detailed description of the analysis can be found in [481].

10.2.3.1. Signal and background generation and pre-selections. The signal events were generated using PYTHIA for four different values of the Higgs boson mass: 115, 125, 135 and $145\,\mathrm{GeV/c^2}$. The Higgs boson was forced to decay to two τ leptons with one τ decaying to leptons and the other τ to hadrons. The TAUOLA package was used to simulate the τ polarisation.

For background events, following processes are considered:

QCD 2 τ+2/3 j
The QCD production of 2τ+2jet and +3jet events with the invariant mass of two τ leptons, $M_{\tau\tau} > 70\,\mathrm{GeV/c^2}$, was generated using ALPGEN with CTEQ5L PDF. Given the limit of the detector acceptance and requirements in the course of the event reconstruction, all jets were required to satisfy $p_{Tj} > 20\,\mathrm{GeV}$, $|\eta_j| < 5.0$ and $|\Delta R_{jj}| > 0.5$. Further pre-selections were applied on the two highest p_T jets (j1 and j2) reflecting the offline VBF selection cuts: $|\Delta\eta_{j1j2}| > 4.0$, $M_{j1j2} > 600\,\mathrm{GeV/c^2}$. Then the events 2$\tau$+2j and 2$\tau$+3j were added together with the MLM prescription in PYTHIA to avoid double counting of the jets. The TAUOLA package was used in PYTHIA to force one τ lepton to decay leptonically and the other hadronically.

Electro Weak (EW) production of 2 τ+2 j
The EW production of two τ's with $M_{\tau\tau} > 70\,\mathrm{GeV/c^2}$ and two jets in the final state was generated using MADGRAPH with CTEQ5L PDF. Soft pre-selections were applied during generation with MADGRAPH on the kinematics of the jets: $p_{Tj} > 20\,\mathrm{GeV/c}$ and $M_{jj} > 500\,\mathrm{GeV/c^2}$. Further pre-selection cuts were applied on jets and τ's given the limit of the detector acceptance and requirements of the event reconstruction: $|\eta_j| < 5.2$, $|\Delta R_{jj}| > 0.5$, $|\Delta R_{\tau\tau}| > 0.4$. The showering and hadronisation of the MADGRAPH parton level events were carried out using PYTHIA where all decay modes of the τ lepton were open.

W + $jets$
The W + 3j and W + 4j events with $W \to \mu\nu$ decays were generated using ALPGEN with CTEQ5M PDF. In addition to the kinematical cuts on jets used for the QCD Z + jets production described above, further pre-selections were made based on the lepton properties with $|\eta_\ell| < 3$ and $p_{T\ell} > 10\,\mathrm{GeV/c}$. The MLM prescription was applied in PYTHIA.

$t\bar{t} \to WbWb$
The $t\bar{t}$ background was generated using PYTHIA, TOPREX, ALPGEN, COMPHEP and MADGRAPH. All leptonic W decays were included and no kinematical pre-selection was applied.

10.2.3.2. Event reconstruction and selection. Events are triggered at Level 1 by the single isolated e, single μ and combined e-τ triggers. At the High Level the following triggers are used: the single isolated e, single μ, combined e-τ and combined μ-τ triggers.

In the off-line analysis the electron and muon candidates were selected and for the electron candidates three additional requirements are applied: $E/p > 0.9$, tracker isolation, $(\sum_{0.01<\Delta R<0.2}^{trk} p)/E < 0.05$, and E_T of the hottest HCAL tower, $E_T^{Htow} < 2\,GeV$. The highest p_T off-line lepton candidate with $p_T > 15\,GeV/c$ is then selected. The lepton track is used to identify tracks originating from the signal vertex. The tracks are used for the electron isolation, τ tagging and in central jet veto. A track is associated to the signal vertex if its z impact parameter lies within $|\Delta z| < 0.2\,cm$ from that of the lepton track.

The τ-jet identification is seeded from the L1/HLT τ candidates. A jet is formed around each candidate which does not coincide with the identified electron, and the jet is passed through a series of τ-tagging criteria. The τ tagging used in HLT (Ref. [76]) has been adapted to offline use with parameters $R_m = 0.1$, $R_s = 0.07$, $R_i = 0.45$, $p_T^{ltr} = 6\,GeV/c$ and $p_T^i = 1\,GeV/c$. The charge of the τ-jet is required to be opposite of the lepton charge, and $E_T^{Htow} > 2\,GeV$ is required if the jet coincides with any of the electron candidates. A further cut is applied on the transverse energy of the τ-jet, $E_T > 30\,GeV$.

The jets from the VBF process are identified as the two highest E_T calorimeter jets with $E_{Tj} > 40\,GeV$, excluding the electron and the τ-jet. The jets are required to satisfy: $|\eta_j| < 4.5$, $\eta_{j1} \times \eta_{j2} < 0$, $\Delta\eta_{j1j2} > 4.5$, $\Delta_{\phi j1j2} < 2.2$, and the invariant mass, $M_{j1j2} > 1\,TeV$. The jets after these selections will be referred to as tagging jets.

A cut is applied on the transverse mass of the lepton-E_T^{miss} system, $M_T(lep, E_T^{miss}) < 40\,GeV$, in order to reject backgrounds with $W \to \ell\nu$ decays.

The central jet veto was applied. An event is vetoed if there is an additional jet (j3) with $E_{Tj3}^{raw} > 10\,GeV$ in the rapidity gap between the two tagging jets, satisfying the following:

- $(\eta_{min} + 0.5) < \eta_{j3} < (\eta_{max} - 0.5)$
  where η_{min} and η_{max} correspond to the tagging jets which has smaller and larger value of η respectively.
- $\alpha_{j3} = \sum p_{Ttrk}/E_{Tj3}^{raw} > 0.1$
  where p_{Ttrk} is the p_T of the track originating from the signal vertex, which lie within the 0.5 cone around the jet axis, and E_{Tj3}^{raw} is the raw E_T of the jet measured in the calorimeter.

α_{j3} is defined for each additional jet, and the one which satisfies the first criteria and has the highest α_{j3} is considered for the veto.

The invariant mass of the two reconstructed τ's is calculated as described in the MSSM H(A)$\to \tau\tau$ analysis (Section 5.2) using the collinear approximation of the visible part of τ's and neutrinos. The E_T^{miss} is reconstructed by summing the E_T of the calorimeter towers and the muon candidates, and applying the jet energy corrections (Type 1 E_T^{miss}). The events were accepted if $E_{\nu 1,\nu 2} > 0$.

10.2.3.3. Expected number of events. The efficiency of each reconstruction and selection step and the cumulative cross section expected at the LHC are given in Table 10.9. The total selection efficiencies are, 0.32%, 0.34%, 0.42%, 0.39%, for the signal events with the Higgs boson masses, M_H = 115, 125, 135 and 145 GeV/c^2 respectively.

For the W+3/4j background, the efficiencies of some selection cuts have been obtained from factorisation of cuts. The trigger and the lepton identification are carried out as other samples, and the remaining steps are carried out in two uncorrelated parallel streams – A: VBF and $M_T(lep, E_T^{miss})$ cuts, B: central jet veto, τ tagging and mass calculation – after pre-selections of forward jets and τ-jet candidates.

10.2.3.4. Reconstructed mass and fit. The distribution of the invariant mass of two reconstructed τ's for different samples is shown in Fig. 10.16, where the signal sample with

Table 10.9. Cumulative cross sections in fb after successive selection cuts. The efficiency (%) of each cut is listed inside the brackets. The entry, "valid mass", corresponds to the fraction remained after the calculation of the diτ mass when some events are lost due to the negative reconstructed neutrino energies. For the W + 3/4j samples, efficiencies are obtained from factorisation of cuts and the τ-jet ID efficiency includes the p_T cut, and the number of events at 30 fb^{-1} (indicated by*) is calculated for all leptonic decay modes of W.

	cross section, σ [fb] (% from previous cut)				
	signal	background			
Selection	$M_H = 135$	EW2τ+2j	QCD$\tau\tau$+2/3j	W + 3/4j	$t\bar{t} \rightarrow$WbWb
Starting σ	82.38	299.	1615.	14.45×10^3	86×10^3
Level-1	46.50 (56.5)	179.8 (60.1)	543.8 (33.7)	9186. (63.6)	71.39×10^3 (83.0)
L1+HLT	24.60 (52.9)	58.81 (32.7)	201.3 (37.0)	6610. (71.9)	55.42×10^3 (77.6)
lepton ID	23.34 (94.9)	50.67 (86.2)	187.4 (93.1)	6549. (99.1)	54.08×10^3 (97.6)
lepton p_T	23.16 (99.3)	49.13 (97.0)	185.6 (99.0)	6543. (99.9)	53.54×10^3 (99.0)
τ-jet ID	8.276 (35.7)	10.49 (21.3)	39.64 (21.4)	(0.21)	5.056×10^3 (9.4)
τ-jet p_T	6.422 (77.6)	7.360 (70.2)	24.25 (61.2)	-	3.215×10^3 (63.6)
Valid mass	4.461 (69.5)	4.232 (57.5)	14.49 (59.8)	(17.4)	848.6 (26.4)
VBF cuts	0.545 (12.2)	0.391 (9.2)	1.666 (11.5)	(11.0)	2.738 (0.3)
M_T(lep,E_T^{miss})	0.423 (77.6)	0.322 (82.4)	1.382 (83.0)	(30.5)	0.942 (34.4)
Central Jet Veto	0.344 (81.3)	0.230 (71.4)	0.555 (39.7)	(28.9)	0.224 (23.8)
N events at 30 fb^{-1}	10.3	6.9	16.6	1.5*	6.7

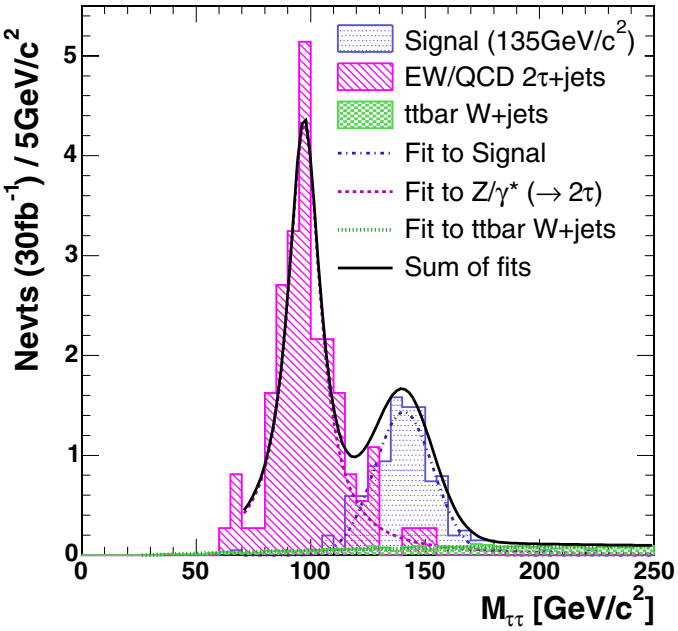

Figure 10.16. The invariant mass of two reconstructed τ's. The number of entries in each histogram is normalised to the expected number of events at an integrated luminosity of 30 fb^{-1}.

the Higgs boson mass, M_H = 135 GeV/c^2 is used. A Gaussian function is used to fit the signal distribution, a Breit–Wigner function for the 2τ+jets background from EW and QCD processes, and a second order polynomial for the reducible background from W+jets and $t\bar{t}$ events. The Higgs boson mass resolution is 9.1%.

Table 10.10. The production cross section and significance of the expected number of signal events within the optimum mass window for each of the four different simulated masses of the Higgs boson.

M_H [GeV]	115	125	135	145
Production σ [fb]	4.65×10^3	4.30×10^3	3.98×10^3	3.70×10^3
$\sigma\times$ BR($H\to\tau\tau\to lj$) [fb]	157.3	112.9	82.38	45.37
N_S at 30 fb^{-1}	10.5	7.8	7.9	3.6
N_B at 30 fb^{-1}	3.7	2.2	1.8	1.4
Significance at 30 fb^{-1} (σ_B = 7.8%)	3.97	3.67	3.94	2.18
Significance at 60 fb^{-1} (σ_B = 5.9%)	5.67	5.26	5.64	3.19

10.2.3.5. Signal significance. The significance is calculated using a window with a fixed width of 40 GeV/c^2, which slides in 5 GeV/c^2 steps. An optimum window position which maximises the significance is chosen for each of the four different masses of Higgs boson. The numbers of signal and background events within the window, N_S and N_B, are estimated from the fits to individual samples. The method S_{cP} (Ref. [79]) is used for calculating the significance, including the systematic uncertainty of 7.8% for 30 fb^{-1} and 5.9% for 60 fb^{-1}. The results are summarised in Table 10.10.

It is envisaged that the shapes of the two background distributions will be extracted experimentally from the LHC data in a region unaffected by the signal contribution, using some relaxation of selection cuts. Since the number of background events in the signal region will be estimated using real data, the fitting procedure is the only contribution to the uncertainty in the significance estimate. The fit uncertainty has been evaluated by performing MC trials, randomly generating a mass distribution from the original fit functions and re-fitting the distribution at each trial. With the data, the Higgs boson mass will be estimated by repeating the fitting procedure for different mass hypotheses and finding the value where the χ^2 of the fit is minimised.

10.2.4. Searching for standard model Higgs via vector boson fusion in $H\to W^+W^-\to \ell^\pm\nu jj$ with m_H from 120 to 250 GeV/c^2

The signal topology of Higgs boson with $H\to W^+W^-\to \ell\nu jj$ via vector boson fusion has been shown as a good potential discovery channel for the medium-high mass range ($m_H > 300$ GeV/c^2). The final state is characterised as two forward jets, two central jets from W hadronic decay, and one high p_T lepton and missing transverse energy (E_T^{miss}) from the W leptonic decay. Extending the use of this channel to the low mass range ($m_H <$ 300 GeV/c^2) makes valuable physics analysis possible and is complementary to the Higgs boson search using $H\to W^+W^-\to \ell\nu\ell\nu$, especially for $160 < m_H < 180$ GeV/c^2, where $H\to ZZ^*$ branching ratio is highly suppressed due to the opening of $H\to W^+W^-$ decay with two on-shell W bosons.

The result of this section shows that in the Higgs boson mass range between 140 and 200 GeV/c^2, a significance of $\sim 5\,\sigma$ can be achieved with integrated luminosity of 30 fb^{-1}. Major backgrounds include $t\bar{t}$ + jets, W + $t\bar{b}(\bar{t}b)$, W + jets, Z+jets, WW/WZ/ZZ + jets, and QCD events. For WW + jets, the QCD and Electroweak (EW) processes are generated separately. A detailed description of the analysis can be found in [482].

10.2.4.1. Event selection strategy. Major difficulties concerning the low mass Higgs analysis using $\ell\nu$jj final state include: many background processes of very large cross section have one

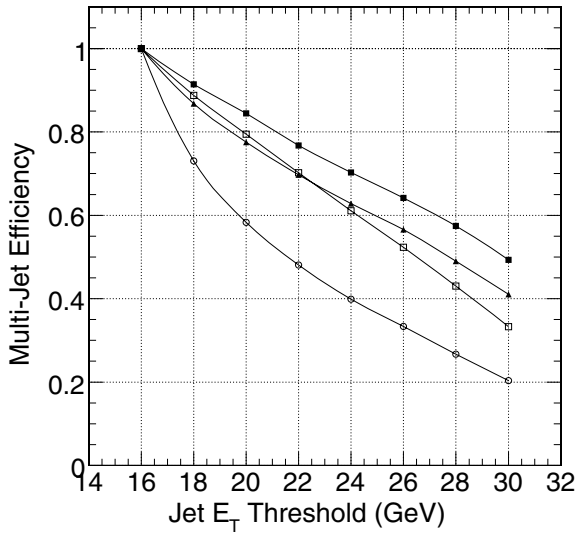

Figure 10.17. Multiple jet selection efficiency (requiring at least 4 jets in an event) as a function of jet E_T threshold. The efficiency is normalised to the rate with jet E_T threshold of 16 GeV for each sample. The physics channels include: $t\bar{t}$ + jets (solid square), W + 3jets (open circle), W + 4jets (solid triangle), and VBF Higgs with $m_H = 170\,GeV/c^2$ (open square).

lepton and multiple jets in the final states; simulating the requisite huge number of background events is both a computing and analysis challenge; hard selection cuts and heavy exploitation of physics signal characteristics are necessary to suppress backgrounds and enhance the statistical significance of the signal, which can lead to large systematic uncertainties; the relatively low Higgs boson mass domain limits the application of high jet E_T thresholds that would normally be used to suppress backgrounds, in contrast to the situation at high mass; low E_T^{miss} and low E_T jets affect the resolution of Higgs mass. To meet these challenges, a robust reconstruction and selection strategy is developed.

Low p_T objects are ignored (e.g. leptons with $p_T < 10\,GeV/c$ and jets with $E_T < 25\,GeV$). The jet E_T threshold is chosen around 25 GeV where there is a stable signal to background ratio (S/B), so that the systematic uncertainty of jet energy scale is minimised (Fig. 10.17). Due to a number of soft jets in the central detector region, the hadronic W reconstruction looks for a dijet mass with the smallest deviation from the true W boson mass. The extra jet veto after forward jet tagging and hadronic W reconstruction is applied. Two schemes are studied: full extra jet veto ($N_{extra} < 1$) and loose extra jet veto ($N_{extra} < 2$). The full extra jet veto is very powerful in reducing the $t\bar{t}$ + jets and W + jets background.

The selection chain is divided into two major steps: basic selection (Table 10.11) and optimised selection. This strategy helps optimise the selection cuts and factorise the selection efficiency to evaluate the systematic uncertainty and QCD background efficiency.

The optimised selection for $m_H \geqslant 160\,GeV/c^2$ ($m_H < 160\,GeV/c^2$) includes 3 steps:

- $E_T^{FH} > 45\,(40)$ GeV, $E_T^{FL} > 35\,(30)$ GeV, $\Delta\eta > 4.2$, and $m_{jj} > 1000\,GeV/c^2$. $E_T^{FH}(E_T^{FL})$ is the high (low) jet E_T threshold for forward jets.
- $E_T^{CH} > 30$ GeV, $E_T^{CL} > 25$ GeV, $\Delta m_W < 20\,GeV/c^2$ ($30 < m_W < 90\,GeV/c^2$), and $N_{extra} < 1$. E_T^{CH} (E_T^{CL}) is the high (low) jet E_T threshold for central jets that are used for hadronic-W reconstruction.

Table 10.11. Summary of basic event selection cuts.

Selection	Configuration
Lepton selection	calorimeter-based e/μ isolation
	$30 < p_T < 120\,GeV/c$
	$\Delta R_{\ell,j} > 0.5$
Jet selection	$N_{jet} \geqslant 4$ jets with $E_T > 25\,GeV$
	$E_T^{miss} > 30\,GeV$
Forward jet tagging	$E_T > 30\,GeV$
	$\eta_1 \cdot \eta_2 < 0$
	$\lvert\eta_1 - \eta_2\rvert > 3.8$
	$m_{jj} > 800\,GeV/c^2$
Hadronic-W	$\Delta m_W < 25\,GeV/c^2$ ($m_H \geqslant 160\,GeV/c^2$)
	$30 < m_W < 90\,GeV/c^2$ ($m_H < 160\,GeV/c^2$)
	select dijet with the least Δm_W
Leptonic-W	using lepton and E_T^{miss}
	select Leptonic-W candidates of
	smaller ΔR(Leptonic − W, Hadronic − W)

Table 10.12. Cross section (fb) of the signal and background in optimised selection with $m_H \geqslant 160\,GeV/c^2$ for full extra jet veto.

Channels	Basic Selection	Step 1	Step 2	Step 3
VBF Higgs ($m_H = 160$)	16.15	9.531	4.580	2.989
VBF Higgs ($m_H = 170$)	15.99	9.814	4.828	3.006
VBF Higgs ($m_H = 180$)	16.28	9.916	4.711	2.738
VBF Higgs ($m_H = 190$)	14.16	9.363	4.294	2.340
VBF Higgs ($m_H = 200$)	13.78	8.626	4.341	1.983
VBF Higgs ($m_H = 210$)	13.43	8.211	4.080	1.571
VBF Higgs ($m_H = 220$)	13.35	8.227	4.128	1.259
VBF Higgs ($m_H = 250$)	10.71	6.900	3.426	0.810
$t\bar{t}$ + jets	1494.2	626.5	16.751	1.232
WW + jets (QCD)	9.27	1.265	0.422	< 0.008
WW + jets (EW)	7.88	9.683	4.454	< 0.0277
ZZ + jets	1.00	0.269	0.0245	< 0.001
ZW + jets	7.23	2.335	0.223	< 0.001
W + $t\bar{b}(\bar{t}b)$	92.8	35.21	4.427	< 0.05787
W + 4j ($W \to e/\mu/\tau + \nu$)	1110.8	583.0	72.066	0.323
Z + 4j ($Z \to ee/\mu\mu$)	82.3	3.713	0.141	0.0104
Z + 3j ($Z \to ee/\mu\mu$)	72.4	2.313	0.233	< 0.0067
Sum of Background	3579.7	1492.5	167.38	1.565

- E_T^{miss}(qqWW) < 40 GeV, ΔR(lepton,Hadronic-W) < 2.0, and ΔR(Leptonic-W, Hadronic-W) < 1.0. E_T^{miss}(qqWW) is the E_T^{miss} of qqWW system that includes reconstructed Higgs boson and two forward jets.

The efficiency of basic selection and three steps of optimised selection is summarised in Table 10.12 and 10.13 for $m_H \geqslant 160\,GeV/c^2$ and $m_H < 160\,GeV/c^2$ respectively. Loose extra jet veto with tightening cuts: $m_{jj} > 1200\,GeV/c^2$ and ΔR(lepton,Hadronic-W) <1.6, gives a conservative result.

The reconstructed Higgs boson mass distributions for signal plus background and background are shown in Fig. 10.18 for $M_H = 160\,GeV/c^2$ (left) and $M_H = 170\,GeV/c^2$ (right) for 60 fb^{-1}.

Table 10.13. Cross section (fb) of signal and background in optimised selection with $m_H < 160\,GeV/c^2$ for full extra jet veto.

Channels	Basic Selection	Step 1	Step 2	Step 3
VBF Higgs ($m_H = 120$)	1.28	0.951	0.363	0.231
VBF Higgs ($m_H = 130$)	4.03	3.004	1.125	0.664
VBF Higgs ($m_H = 140$)	7.12	5.520	2.369	1.656
VBF Higgs ($m_H = 150$)	11.01	8.345	3.505	2.317
$t\bar{t}$ + jets	1483.0	859.5	20.94	0.493
WW + jets (QCD)	9.70	4.215	0.422	< 0.004
WW + jets (EW)	7.94	11.21	5.395	< 0.0277
ZZ + jets	0.96	0.465	0.0979	< 0.001
ZW + jets	7.45	3.781	0.334	< 0.01
$W + t\bar{b}(\bar{t}b)$	101.5	54.37	6.799	< 0.0289
W + 4j ($W \to e/\mu/\tau + \nu$)	1110.7	778.5	118.9	0.667
Z + 4j ($Z \to ee/\mu\mu$)	81.3	4.700	0.152	0.00522
Z + 3j ($Z \to ee/\mu\mu$)	70.0	3.160	0.353	< 0.01333
Sum of Background	3630.6	2066.5	267.2	1.164

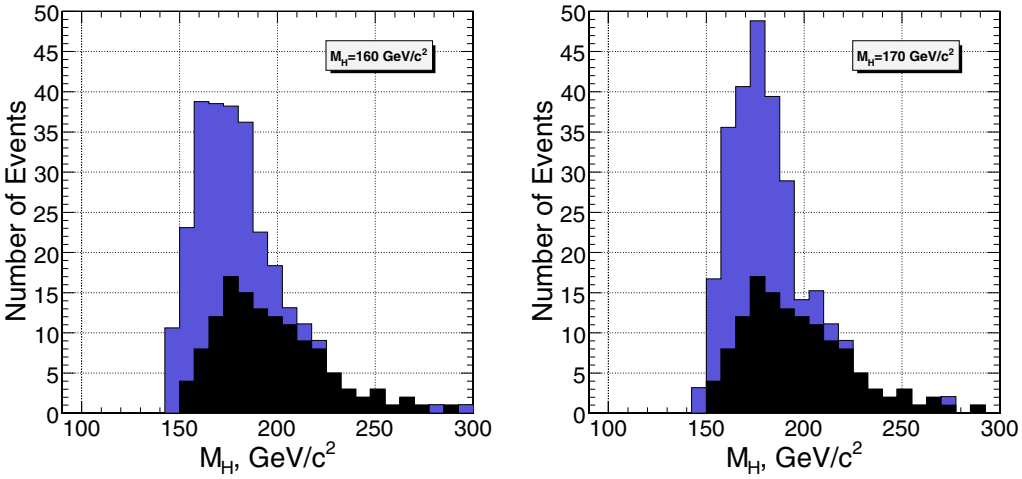

Figure 10.18. The Higgs boson mass reconstruction of signal plus background (blue/grey) and background (black) for $M_H = 160\,GeV/c^2$ (left) and $M_H = 170\,GeV/c^2$ (right).

The overall QCD multi-jet contamination is estimated with the factorisation of the selections as 2-5 events for an upper limit with $60\,fb^{-1}$, which causes possible 2-4% increase of background, which has almost no change in the significance.

10.2.4.2. Detector systematic uncertainties and control. Several calorimeter level systematic uncertainties have significant impact on this channel including: jet energy scale and resolution, E_T^{miss} scale and resolution, and calorimeter-based lepton isolation cut. Their impacts on the rate of signal (S), background (B) and S/B are summarised in Table. 10.14. The total detector level systematic uncertainty is about 16% in the absolute rate of background in the final result.

Table 10.14. Systematic Uncertainties due to Jet and E_T^{miss}.

Source	S	B	S/B
Jet energy scale	10.6%	14.5%	5.2%
Jet energy resolution	0.1%	2.0%	2.0%
E_T^{miss}	2.5%	1.2%	1.7%
Lepton isolation	1.4%	1.3%	0.5%

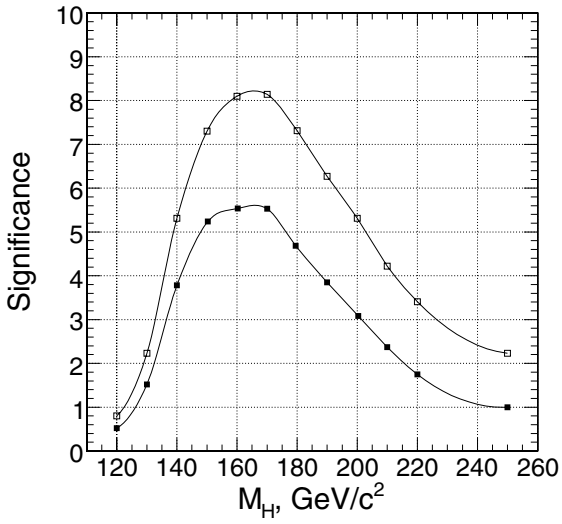

Figure 10.19. The signal significance for 30 fb^{-1}. The high (low) curves correspond to full (loose) extra jet veto.

The data driven technique is able to significantly reduce the detector level systematic uncertainties. For example, the largest uncertainty comes from the selection efficiency with respect to lowest jet E_T threshold. The event rate of the background near this threshold can be measured from data and used to tune the MC prediction, which leaves much less uncertainty due to the systematic bias of jet energy scale. Ignoring the uncertainty in the rate for from lowest jet E_T threshold, the uncertainty of jet energy scale only causes about 5.5% error in the rest of the selection chain which immediately reduces the total detector level systematic uncertainty down to 10% level.

10.2.4.3. Discovery potential. The signal significance for 30 fb^{-1} after optimised selection cuts is shown in Fig. 10.19 for the Higgs boson masses between 120 and 250 GeV/c^2. The background systematic uncertainty of 16% as discussed in the previous section is included.

10.2.5. Vector boson fusion production with $H \to \gamma\gamma$

A detailed description of the analysis can be found in [483].

10.2.5.1. Signal and background generation and simulation. The Higgs boson production from the vector boson fusion $qq \to qqH$ and $H \to \gamma\gamma$ decay was generated by PYTHIA for the Higgs boson masses, $M_H = 115$, 120, 130, 140 and 150 GeV/c^2.

Table 10.15. Cross sections of different types of background.

Background process	Cross section (pb)
QCD hadronic jets	$2.8^{*}10^{7}$
Gluon fusion	83
Drell–Yan	4.1×10^{3}
$\gamma\gamma$ + 2jets, QCD	47.24
$\gamma\gamma$ + 2jets, EW	0.33
γ + 3jets, QCD	5970
γ + 3jets, EW	5.15

The backgrounds considered are:

- QCD multi-jet production, where an electromagnetic energy deposit results from the decay of neutral hadrons (especially isolated π^0s) in a jet. It was generated by PYTHIA with $\hat{p_T} > 50\,\mathrm{GeV/c}$.
- Drell–Yan $e^{-}e^{+}$ production (generated with PYTHIA) which could mimic photons when correspondent electron tracks will not be assigned to the clusters in the ECAL during the reconstruction.
- Diphoton production from the gluon fusion (box diagram) when two additional jets from the initial state radiation are presented in the event. It was generated by PYTHIA with $\hat{p_T} > 20\,\mathrm{GeV/c}$.
- QCD and Electro Weak (EW) pp $\rightarrow \gamma\gamma + 2$ jets process generated with COMPHEP.
- QCD and EW pp $\rightarrow \gamma + 3$ jets generated with COMPHEP.

Table 10.15 shows the cross sections of different types of backgrounds.

Generator level pre-selections for QCD multi-jet background. Selection based on the generated particles was devised, aimed at selecting events which could produce in the detector two electromagnetic showers consistent with isolated photons. In order to apply cuts on the invariant mass of the two candidates an attempt to estimate lower and upper limits to the energy of the candidates that will be reconstructed after the simulation was done.

The idea of this pre-selection, is to pick up events that will give rise to energy depositions in ECAL large enough and isolated enough to be important for this analysis. Pre-selection algorithm is getting all particles which might deposit electromagnetic energy in ECAL, and looking around each particle in a narrow cone, to find another, may be less energetic particles which will make deposits in ECAL as well, and will potentially be reconstructed as one cluster. In addition to that, a very loose tracker isolation was applied: three charged particles were required in a cone $\Delta R = 0.2$ around the "cluster candidate", described above, per one "cluster candidate", and no more than 6 per two first most energetic candidates.

After that some other cuts were applied for the "cluster candidates" as well, $p_T > 37.5\,\mathrm{GeV/c}$ for most energetic one and $p_T > 22.5\,\mathrm{GeV/c}$ for the second most energetic one. The invariant mass of the first most energetic and second most energetic "cluster candidates" should be more than $90\,\mathrm{GeV/c^2}$ for the purpose of this analysis.

Generator level pre-selections for $\gamma + 3jets$ and $\gamma\gamma + 2jets$ backgrounds. At COMPHEP partonic level event generation the following cuts were applied:

- $p_T^{\gamma} > 20\,\mathrm{GeV/c}$
- $p_T^{j} > 20\,\mathrm{GeV/c}$
- $\Delta R_{ij} > 0.4$
- at least one pair of jets must exist with the jets in the opposite hemispheres with the rapidity gap greater than 3.5.

Table 10.16. Number of generated and simulated events for different types of background.

Background process	Number of generated events	Rejection with pre-selections	Number of simulated events	L_{intg} (fb^{-1})
QCD multi-jets	31.2×10^9	6048	4.5M	~ 1
Gluon fusion	2.25×10^6	2	1M	~ 52
Drell–Yan $e^+ e^-$	1.0×10^6	1	1M	0.25
$\gamma\gamma$ + 2jets, QCD	0.5×10^6	2.56	200k	6
$\gamma\gamma$ + 2jets, EW	41×10^3	1	41k	120
γ + 3jets, QCD	0.3×10^6	7.8	40k	0.05

The CTEQ5L PDF set was used; the factorisation and renormalisation scales were set to 50 GeV. Hadronisation was done by PYTHIA and the same pre-selections were applied as it was described above for QCD multi-jet background. Rejection factors of PYTHIA pre-selections are 2.5 for $\gamma\gamma$ + 2jets dataset and 7.8 for γ + 3jets dataset.

The signal and background events passed the full detector simulation and digitisation with pile-up for luminosity $2 \times 10^{33}\,cm^{-2}\,s^{-1}$. The numbers of generated and fully simulated events are shown in Table 10.16 for different types of background. In the last column the corresponding equivalent integrated luminosity is shown.

10.2.5.2. Event reconstruction and selection. The events were triggered by the double-isolated electron trigger at Level 1 and HLT.

Photons are reconstructed with the hybrid algorithm in the ECAL barrel and with the island algorithm in the ECAL endcap. Both photon candidates had to match Level 1 trigger photon candidates, such that, the distance R ($R = \sqrt{\delta\eta^2 + \delta\phi^2}$) between the photon candidate and trigger object be less than 0.5. The transverse energies of the two photon candidates were required to be greater than 40 GeV and 25 GeV respectively. The fiducial volume in rapidity was restricted to $|\eta| < 1.4442$ in the barrel and $1.566 < |\eta| < 2.5$ in the endcap for both photon candidates.

Three different algorithms were studied for the Higgs boson vertex reconstruction:

- **P_T balance.** The P_T balance for charged particle tracks along the reconstructed Higgs boson direction is defined as $P_T^B = -\Sigma P_{Ti} \cos\theta_i$, where θ_i is the angle between the Higgs boson and track i direction in the transverse plane
- **Maximal P_T.** The primary vertex is selected as the vertex with the track of highest P_T
- **Number of charged particle tracks** above P_T cutoff in pixel vertex. The primary vertex is selected as the vertex with a largest number of tracks.

To compare different vertex reconstruction algorithms, the number of events reconstructed in a $5\,GeV/c^2$ mass window are determined. The P_T balance and Maximal P_T algorithms give exactly the same number of events, while track counting algorithm gives a few percent less efficiency. The Higgs boson efficiency in $5\,GeV/c^2$ mass window is improved by 15%.

The photon candidates were required to be isolated in the tracker and calorimeter. The tracker isolation criteria are based on the number of charged particle tracks with p_T greater than a p_T threshold, p_T^{thresh}, calculated in a cone R ($R = \sqrt{\delta\eta^2 + \delta\phi^2}$) around the photon

candidate. The algorithm contains three parameters:

- The size of the cone R around the photon candidate, wherein the number of charged tracks is counted.
- The p_T threshold, p_T^{thresh}. Only charged particle tracks with p_T greater than p_T^{thresh} are considered in isolation calculations.
- The 'number of tracks' threshold N^{thresh}. If the number of charged particle tracks in cone R with p_T greater than the chosen p_T^{thresh} is greater than N^{thresh}, then the photon candidate is considered non-isolated, otherwise isolated.

The jet rejection factor is very sensitive to the 'number of tracks' threshold, N^{thresh}. By increasing N^{thresh} from 0 to 1, the Higgs boson signal efficiency is improved by 6–10%, but the jet rejection factor drops by a factor of ~ 2. Therefore, the parameter N^{thresh} was fixed to zero. The cone size $R = 0.30$ and $p_T^{thresh} = 1.5\,\mathrm{GeV/c}$ were used in this study.

The isolation of the photon candidates in the electromagnetic calorimeter is also required. The isolation criteria is based on the sum of transverse energies deposited in basic clusters in some cone R ($R=\sqrt{\delta\eta^2 + \delta\phi^2}$) around the photon candidate. The basic clusters that belong to the photon candidate's supercluster are not counted as part of the sum. The algorithm contains four parameters:

- The size of the cone R around the photon candidate wherein the transverse energies deposited in the basic clusters are summed.
- The transverse energy sum threshold E_T^{thresh}. If the sum of transverse energies is below this threshold, the photon candidate is considered isolated, otherwise non-isolated.
- The ratio, r, of the transverse energy sum in all surrounded basic clusters to the transverse energy of the most energetic super cluster.
- The ratio (H/E) of the energy deposited in the HCAL behind the super-cluster to the energy of the super-cluster.

There is no strong dependence of the jet rejection factor on the cone size R, though slightly better rejection factors are empirically obtained for a cone size $R = 0.30$–0.35. The cone size $R = 0.30$ is used in this study. The transverse energy sum thresholds, E_T^{thresh}, were chosen to be 1.2 GeV in the barrel and 1.6 GeV in the endcap. Finally, the photon candidate must pass the cuts: $r < 0.01$ and H/E <0.1.

Jet tagging was done based on the jets reconstructed with the iterative cone algorithm using cone size 0.7. The two highest E_T jets were chosen and initial selection cuts were applied:

- $E_T^{jet} > 20\,\mathrm{GeV}$, $|\eta_{jet}| \leqslant 4.5$, $\Delta R_{\gamma jet} \geqslant 0.5$
- $\Delta\eta_{jets} = |\eta_{jet1} - \eta_{jet2}| \geqslant 4.0$, $\eta_{jet1} \times \eta_{jet2} < 0$

Two additional cuts were applied to the already selected two forward jets in order to reduce the background even more than it was done with forward jet tagging procedure:

- $E_T^{jet1} > 50\,\mathrm{GeV}$, where E_T^{jet1} is the transverse momentum of the first most energetic forward jet, selected by forward jet tagging procedure, described above.
- $E_T^{jet2} > 35\,\mathrm{GeV}$, where p_t^{jet2} is the transverse momentum of the second most energetic forward jet, selected by forward jet tagging procedure, described above.
- $m_{j1j2} > 500\,\mathrm{GeV/c^2}$, where m_{j1j2} is the invariant mass of the two most energetic forward jets, selected by forward jet tagging procedure, described above.
- Two photons must in the η region between the two forward jets: $\min(\eta_{jet1}, \eta_{jet2}) + 0.7 < \eta_{\gamma 1,2} < \max(\eta_{jet1}, \eta_{jet2}) - 0.7$.

Table 10.17. The number of signal and background events and signal significance after all selections within the $5\,\mathrm{GeV/c^2}$ mass window around the considered Higgs boson masses for $60\,\mathrm{fb^{-1}}$. The ΔN_b is the background uncertainty estimated from the side bands.

	$m_H = 115$ GeV/c^2	$m_H = 120$ GeV/c^2	$m_H = 130$ GeV/c^2	$m_H = 140$ GeV/c^2	$m_H = 150$ GeV/c^2
N_s	20.2	21.1	19.1	15.7	11.2
γ+3jets (QCD)	2.7	4.7	3.5	2.0	5.8
γ+3jets (EW)	2.5	2.5	2.5	2.5	2.5
$\gamma\gamma$ + 2jets (QCD)	11.2	13.2	9.85	8.9	4.6
$\gamma\gamma$ + 2jets (EW)	10	7.0	7.0	11.0	2.0
Drell–Yan	0	0	0	0	0
N_b	26.0	26.2	21.4	28.2	14.9
ΔN_b	2.8	3.2	2.4	3.0	1.8
S	3.07	3.15	3.21	2.32	2.30

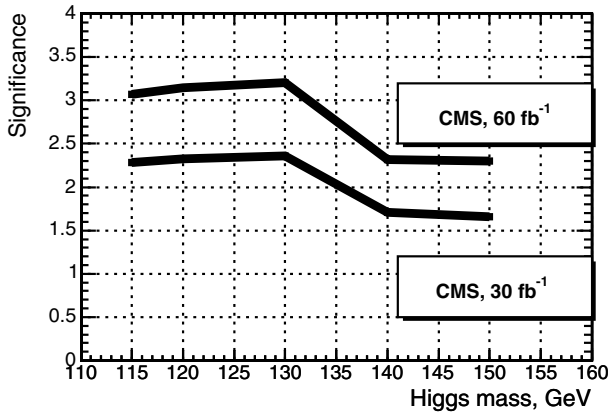

Figure 10.20. Signal significance for 30 and $60\,\mathrm{fb^{-1}}$.

10.2.5.3. Results. After all selections the contribution of the QCD multi-jet events and diphoton events from gluon fusion was found to be negligible. Due to the lack of Monte Carlo statistics only upper limits were estimated conservatively for the contribution from QCD and EW γ+3 jets backgrounds. Table 10.17 shows the number of signal and background events after all selections within $5\,\mathrm{GeV/c^2}$ mass window around the considered Higgs boson masses for $60\,\mathrm{fb^{-1}}$. The ΔN_b shown in the Table is the background uncertainty estimated from the side bands around the Higgs boson mass peak.

The signal significance with the background uncertainty taken into account is shown in Fig. 10.20 for 30 and $60\,\mathrm{fb^{-1}}$.

10.2.6. Associated WH *production with* $\mathrm{H} \to \mathrm{WW}^{(*)} \to 2\ell 2\nu$

The cross-section for this process exhibits a maximum near the Higgs boson mass of 160–180 GeV/c^2 due to the combined behaviour of the production cross-section and the Higgs boson branching ratio. The intermediate mass region between $120\,\mathrm{GeV/c^2}$ and $190\,\mathrm{GeV/c^2}$,

Table 10.18. Background processes considered into the present analysis. The cross-section includes the decay of W and Z bosons into leptons. The generator and the number of events processed are also shown together with the corresponding weight for a luminosity of 1 fb^{-1}.

Background	Cross-section	Generator	MC statistic	weight (1 fb^{-1})
WWW($3l^{\pm}$)	4.95 fb	COMPHEP	10000	5.19×10^{-4}
WZ($3l^{\pm}$)	1.71 pb	PYTHIA	50000	3.46×10^{-2}
ZZ($4l^{\pm}$)	0.17 pb	PYTHIA	50000	3.67×10^{-3}
$t\bar{t}(l^+l^-b\bar{b})$	90.9 pb	TOPREX	100000	0.93
Wt(l^+l^-b)	5.25 pb	TOPREX	50000	0.11

where the cross-section exceeds 300 fb was investigated using the events containing three leptons, electrons and muons (including leptonic tau decays), in the final state.

A detailed description of the analysis can be found in [484].

10.2.6.1. Signal and background generation. The Higgs boson with masses of 115, 125, 130, 140, 150, 160, 170, 180 and 190 GeV/c^2 has been considered. Events were generated with PYTHIA for each of the nine Higgs boson masses, without any kinematical cut. W bosons are forced to decay leptonically (e, μ, τ).

All Standard-Model processes likely to produce three leptons must be considered as background for this analysis. This includes events where three leptons are actually produced in the hard process but also events with a fake or missed lepton. One particular case is the production of leptons in the semi-leptonic decay of a B meson. In the present analysis, we considered the production of WWW, WZ, ZZ, $t\bar{t}$, and Wt. Most of the processes are simulated with PYTHIA, except for WWW, which is generated with COMPHEP, and Wt generated with TOPREX. In all cases, PYTHIA is used for the hadronisation step. Table 10.18 shows the cross-section, the generator used and the number of events produced.

10.2.6.2. Selection streams at Level-1 and HLT. The global (cumulative) trigger efficiency after Level-1 and HLT is found to reach 72% for a 140 GeV/c^2 Higgs boson using the full trigger table. Main contributions come from single and double leptonic (e and μ) triggers (65%). There is a small contribution from the missing transverse energy trigger (E_T^{miss}) and from combined (e and τ) and (μ and τ) triggers, further reduced by the event selection, which favours multi-leptonic patterns. For this analysis, events are selected by the triggers known to have the highest impact on the total efficiency: single- and double-electron and muon triggers. Figure 10.21(a) shows the efficiency for each (exclusive) trigger pattern, given the above choice of interesting bits.

Details about the efficiency for each type of event (defined from the number of muons, electrons and taus in the event) are given in Fig. 10.21(b). Events containing one or more muons are more easily retained (efficiency reaches 85% for events with three muons) while tau events are only marginally selected (efficiency: 12%). Efficiency rises slightly with the Higgs boson mass, from 58% at 115 GeV/c^2 to 74% at 190 GeV/c^2.

Table 10.19 shows the trigger efficiency for each source of background. Efficiency of the single- and double-electron and muon triggers, varies from 64% to 73%, which is the same magnitude as the trigger efficiency for signal events. It is 15% (for $t\bar{t}$) to 5% (for ZZ) less efficient than the inclusive High-Level trigger.

10.2.6.3. Off-line selection. Electrons and muons are reconstructed using default offline reconstruction algorithms. For electrons, additional quality cuts are applied: the energy

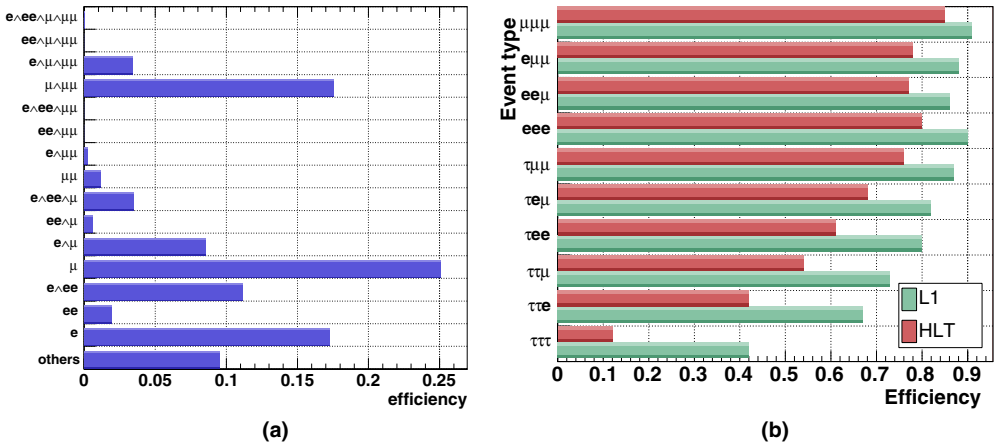

Figure 10.21. (a) Trigger efficiency by trigger pattern, for the signal. Efficiency is calculated as N_x/N_{HLT}, where x is one of the 2^4 exclusive trigger classes. "Others" stands for unconsidered trigger patterns; (b) Trigger efficiency for each class of Monte-Carlo events. Results are given after Level-1 and after HLT. Efficiency is computed as the ratio between the number of triggered events and the total number of generated events.

Table 10.19. Trigger efficiency for each source of background. Efficiency at HLT with the restricted trigger set (e, ee, μ, $\mu\mu$) used in the present analysis is also shown.

Background	Level-1 efficiency	HLT efficiency	e, ee, μ, $\mu\mu$ HLT efficiency
WWW($3l^{\pm}$)	0.87	0.79	0.73
Wt(l^+l^-b)	0.88	0.78	0.67
WZ($3l^{\pm}$)	0.8	0.72	0.65
ZZ($4l^{\pm}$)	0.78	0.69	0.64
$t\bar{t}$($l^+l^-b\bar{b}$)	0.91	0.79	0.65

measured by ECAL and the momentum obtained by the tracker must agree within 50%, and the ratio of energy measured by HCAL and ECAL must be lower than 0.15. Only leptons with $p_T^{\ell} > 14\,\mathrm{GeV/c}$ are retained. A first set of selection criteria is applied to select signal-like topologies, requiring three and only three leptons, for a total charge of either +1 or −1. A cut on the distance in the z direction between the points of closest approach of lepton tracks to the beam is applied to ensure that all of the three leptons are coming from the same interaction. The two closest (in the $\eta - \phi$ plane) opposite-sign leptons are then assigned to the Higgs boson decay. The angle between leptons attributed to the Higgs boson can be used to distinguish signal and background. The acollinearity between two leptons is defined as the angle between the two leptons, in the space, and their acoplanarity is defined as the same angle projected onto the transverse plane. Both the acollinearity ($\theta_{\mathrm{aco}} < 1.75\,\mathrm{rad}$) and the acoplanarity ($0.1\,\mathrm{rad} < \phi_{\mathrm{aco}} < 0.75\,\mathrm{rad}$) between the leptons are used, as they provide complementary information. Leptons required to be isolated in the tracker, i.e. the angle between the lepton's track and the closest track with p_T above $3\,\mathrm{GeV/c}$ must be more than 0.2.

A jet veto is applied rejecting events with a jet, reconstructed with the iterative cone algorithm (using cone size of 0.7) with raw E_T above 25 GeV in the central region, $|\eta| < 2.1$. An additional B veto is applied, imposing that no single B-jet is reconstructed by the default *combined B-tag* algorithm. This removes low-energy b jets passing the jet veto.

Table 10.20. Summary of the optimised selection cuts. The cross-section for the signal and backgrounds, for each step in the selection, is given in fb. An upper limit for the *Wt* and $t\bar{t}$ cross-sections is given when no simulated event remains.

Cut		Signal (fb)	Background (fb)				
Id.	Type	140 GeV/c^2	$t\bar{t}$	Wt	ZW	ZZ	WWW
0	Level-1 and HLT	12.24	72067	4115.8	1238.4	118.438	3.91
1	$N_{lept} = 3$, $\Sigma Q_\ell = \pm 1$	3.81	16432.7	680.0	339.4	34.65	1.05
2	Lepton cuts	2.67	5629.1	245.3	245.9	23.53	0.70
3	Angular cuts	0.87	400.6	15.0	18.3	2.29	0.11
4	B veto	0.43	3.85	0.42	9.77	1.19	0.06
5	Jet veto	0.27	< 1.93	0.31	7.26	0.58	0.04
6	Z veto	0.21	< 1.93	0.21	0.40	0.08	0.03
7–9	Topological	0.13	< 1.93	< 0.11	0.06	0.01	0.02

A cut on the invariant mass of any pair of leptons compatible with the Z hypothesis (via charge flavour and invariant mass constraints, $M_Z \notin$ [65]GeV/c^2) is used to reject ZZ and WZ events. Finally, kinematical cuts are used: $\not{p}_T > 50$ GeV/c, $M_T(W_3) > 40$ GeV/c^2 and $\sum \vec{p}_T^{\,\ell} > 40$ GeV/c, where $\sum \vec{p}_T^{\,\ell}$ is the transverse momentum of the vector sum of momenta of all three leptons, and $M_T(W_3)$ is the reconstructed transverse mass of the associated W boson:

$$M_T(W_3) = \sqrt{2 * p_T^{l_3} \not{p}_T (1 - \cos \Delta\phi_{l_3 \not{p}_T})}, \tag{10.3}$$

with $p_T^{l_3}$ being the transverse momentum of the lepton not associated to the Higgs boson, $\not{p}_T$ the missing transverse momentum, and $\Delta\phi_{l_3 \not{p}_T}$ the polar angle between the lepton and the missing transverse momentum. Optimised cuts are summarised in Table 10.20.

The Higgs boson transverse mass is computed from the two chosen leptons and from the missing transverse momentum:

$$M_T(H) = \sqrt{M_T^{ll\,2} + 2E_T^{ll} \not{p}_T - 2P_T^{ll} \not{p}_T \cos \Delta\phi_{ll \not{p}_T}}, \tag{10.4}$$

Figure 10.22 shows the distribution of M_T(H) for the signal, on top of remaining background, after all cuts for a Higgs boson mass of 140 GeV/c^2 and an integrated luminosity of 100 fb^{-1}. The cumulated efficiency (including trigger and event selection) depends on the Higgs boson mass hypothesis. Starting at 0.5% for a mass hypothesis of 115 GeV/c^2, the efficiency rises to a maximum at the "WW resonance" (1.3%). Beyond the WW production threshold, efficiency drops since W bosons start to be boosted in the Higgs boson frame, which influences the angular distribution of leptons. Efficiency in that region could certainly be improved by optimising the analysis for a Higgs boson mass of 190 GeV/c^2.

10.2.6.4. Systematic uncertainties. Systematic sources considered in this study are related to the normalisation of backgrounds, to the reconstruction, the event selection, the luminosity and the structure functions of protons.

Background will be normalised to signal-free regions of the phase-space. By looking at the acoplanarity distribution when the angular cuts are not applied, data can be fitted to a sum of signal and background shapes. For that purpose, the signal is described by a sigmoid distribution, while the background remains constant. The Monte Carlo distribution for signal and background are first fitted independently, and the shapes obtained that way are used to fit data from pseudo-experiments (Figure 10.23). The uncertainty on the background normalisation is then related to the uncertainty on the background level in that fit. The

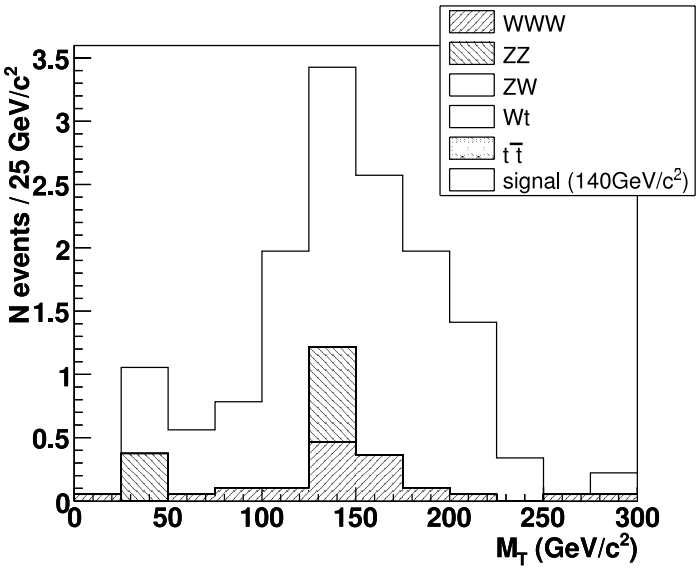

Figure 10.22. Reconstructed transverse mass from Equation (10.4) for a 140 GeV/c^2 Higgs boson and an integrated luminosity of 100 fb^{-1}.

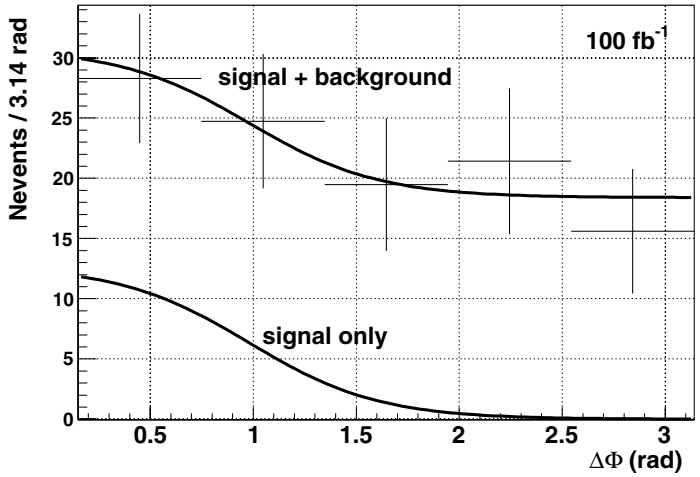

Figure 10.23. Distribution of the acoplanarity for pseudo-experiments, fitted by a signal + background shape, as described in the text.

uncertainty on the background level is found to be 15% for an integrated luminosity of 100 fb^{-1}, and rises up to 20% for 30 fb^{-1}. That value will be used in the following.

Reconstruction and selection uncertainties arise from the jet veto, the b veto and lepton reconstruction. Experience from Tevatron tells that a typical 2% uncertainty on lepton reconstruction efficiency has to be considered, while 5% uncertainty comes from lepton isolation [485] Since three leptons are present in our analysis, a 12% uncertainty from lepton reconstruction and selection has been taken. The additional uncertainties from the jet veto and the b veto will be assumed to be 5% each.

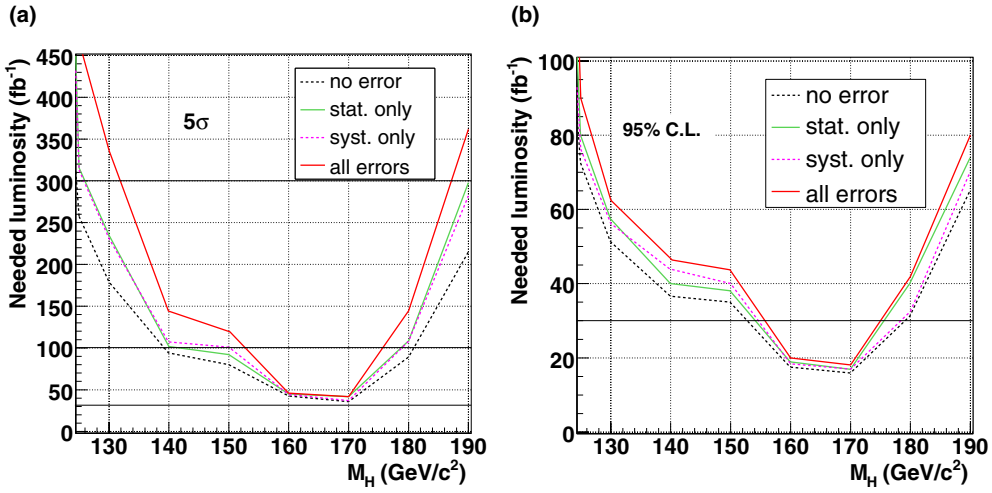

Figure 10.24. (a) Luminosity needed to obtain a 5σ significance using the likelihood-ratio method, with systematics only, Monte-Carlo statistical uncertainties only, or with both effects considered; (b) luminosity needed to exclude a Higgs boson at 95%C.L. if no excess is observed, using the same method.

To take into account other uncertainties related to the event selection, cuts are varied within the resolution of the associated quantity. The signal efficiency and background rejection are found to be stable with respect to such variations. A conservative value of 3% for the associated uncertainty is considered in the following.

The last uncertainty considered comes from the product of the luminosity and the proton structure functions, known as the parton luminosity. Considering these two quantities separately, a 5% uncertainty on the luminosity is assumed, while the uncertainty from the proton parton distribution function (PDF) is taken to be 4% [486]. This latter uncertainty is reduced for the process considered, for which the mid-x region (where uncertainties are small) dominates.

The additional source of systematic uncertainties arising from the limited Monte Carlo statistics is also considered in the following result. With the likelihood ratio method used in the analysis, this is done bin per bin in the distributions of signal and background, so that a single value cannot be quoted. For the time being, this has a large impact on the results, but this effect will easily be reduced in the future, as more events become available.

10.2.6.5. Signal significance. In order to integrate the effect of systematic uncertainties and to exploit the discriminative power from the transverse mass distribution, the likelihood-ratio method (S_{CL}) is used. Figure 10.24(a) shows the luminosity needed to obtain a 5σ significance using this method, with systematics only, with Monte Carlo statistical uncertainties, or with both effects considered. Figure 10.24(b) shows the luminosity needed to exclude a Higgs boson at 95%C.L. if no excess is observed, using the same method. Less than $50\,\mathrm{fb}^{-1}$ are required in most of the mass range, while only $20\,\mathrm{fb}^{-1}$ are needed at $170\,\mathrm{GeV/c}^2$.

One important motivation for studying this channel is also that it is one of the only allowed signatures for a fermiophobic Higgs boson model. If the Higgs boson does not couple to fermions, the usual gluon-fusion diagrams are indeed forbidden, as well as $b\bar{b}$ decays. A fermiophobic Higgs boson will present a large cross-section at low mass, as the branching ratio does not drop down as in the Standard Model. Figure. 10.25(a) shows the luminosity

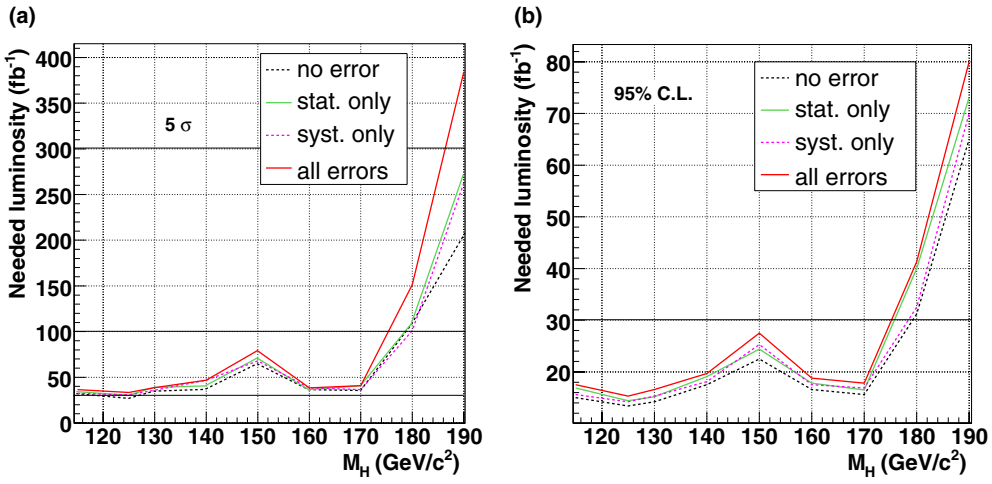

Figure 10.25. Results obtained using the benchmark fermiophobic model; (a) Luminosity needed to obtain a 5σ significance using the likelihood-ratio method, with systematics only, Monte-Carlo statistical uncertainties only, or with both effects considered; (b) luminosity needed to exclude a Higgs boson at 95%C.L. if no excess is observed, using the same method.

needed to obtain a 5σ significance for a fermiophobic Higgs boson. Compared to Fig. 10.24, the needed luminosity is found to be similar in the most favourable mass region for the Standard Model (around 170 GeV/c^2) and above, but far better results are obtained in the low mass region. After 100 fb^{-1}, all masses between the LEP limit and 175 GeV/c^2 will be covered by this analysis alone. Figure 10.25(b) shows the luminosity needed to exclude a fermiophobic Higgs boson at 95%C.L. if no excess is observed. In the absence of signal, less than 30 fb^{-1} are required to reject any fermiophobic Higgs boson up to 175 GeV/c^2.

10.2.7. Associated $\mathrm{t\bar{t}H}$ *production with* $\mathrm{H} \to \gamma\gamma$

10.2.7.1. Introduction. A Higgs boson produced in association with a $\mathrm{t\bar{t}}$ pair, with an $\mathrm{H} \to \gamma\gamma$ decay would share a fully reconstructible mass peak with the inclusive $\mathrm{H} \to \gamma\gamma$ signature. But like the WH and ZH channels [487], the signature could contain an isolated high-transverse- momentum charged lepton which can be used both to discriminate against QCD background and reconstruct the primary vertex; the associated production channels could hence be less dependent on photon energy resolution. In particular, the presence of two top quarks would tend to produce high-multiplicity events, which could offer additional discriminating power against light jet QCD background. In the case of the two-Higgs-doublet MSSM, the gluon fusion Higgs boson production channel could in fact be subject to suppression with respect to the associated production channels in the case of top-stop degeneracy ("maximal mixing") [488]. Prior generator-level studies for the detection of the SM [489] and MSSM [490] Higgs bosons in CMS via this channel have indicated a signal-to-background ratio of approximately 1. A full simulation study in the ATLAS Physics Technical Design Report [491] has predicted a signal significance of $S/\sqrt{B} = 4.3 - 2.8$ for $m_H = 100$–$140\,\mathrm{GeV/c^2}$ with a signal efficiency of ∼30%. A more recent, related ATLAS study involving a 2-photon signature accompanied by missing energy [492] has indicated, for 100 fb^{-1}, a signal-to-background ratio of ~ 2 for $m_H = 120\,\mathrm{GeV/c^2}$.

Table 10.21. Estimated number of signal events for $t\bar{t}H$, $H \to \gamma\gamma$, assuming NLO production cross sections [162], Higgs boson branching ratios to two photons [21], and one electron or muon from top decay (including from tau lepton decays).

Higgs Boson Mass (GeV/c^2)	After 30 fb^{-1}	After 100 fb^{-1}
115	20.80	69.33
120	19.61	65.36
130	15.96	53.20
140	11.20	37.33

10.2.7.2. Signal production cross-sections, event rates and event generation. Production cross-sections for $t\bar{t}H$ have been calculated at next-to-leading order [162, 464, 465]. Taking the branching ratio for $H \to \gamma\gamma$ from HDECAY [21] and assuming in addition that the decay of exactly one of the top quarks yields a lepton (electron or muon) from $W^{\pm} \to l + \nu_l$ (including the possibility of tau lepton decays to muons or electrons), we estimate for several Higgs boson masses the number of signal events for 30 and 100 fb^{-1} (Table 10.21).

Signal events were generated with both the MADGRAPH [81, 493, 494] and ALPGEN [161, 495, 496] LO exact matrix element generators, for each of the Higgs boson masses shown in Table 10.21. Events from both generators were found to yield comparable LO cross-section and kinematical distributions. The LO cross-sections were also found to agree with those from the program HQQ [20] at the percent level. The samples analysed were those generated with ALPGEN. For the current study all signal events have been generated such that exactly one of the two W bosons from the two top quarks decays leptonically.

10.2.7.3. Background processes considered and event generation. Standard Model processes resulting in both irreducible and reducible backgrounds have been identified. A background is called irreducible if it is capable of giving rise to the same signature on the particle level as that searched for in a signal event, that is to say, a lepton and two photons ($l\gamma\gamma$). Special care has been taken to properly treat the irreducible $t\bar{t}\gamma\gamma$ background. Feynman diagrams of three possible types of $t\bar{t}\gamma\gamma$ processes considered are shown in Fig. 10.26. In the first case, called "Type 1", both photons are radiated from either outgoing top quarks or incoming partons. In the third case, called "Type 3", both are radiated from top quark decay products. The second case, "Type 2" combines one photon radiated according to "Type 1" with the second radiated according to "Type 3". (A fourth process arises from both photons being radiated from different decay products of the *same* top quark; for the relevant event selection (see pertinent section below) with $m_{\gamma\gamma} > 70\,GeV/c^2$ we have verified that this contribution is completely negligible). The Types 2 and 3 processes, as well as the process $W\gamma\gamma$+ 4 jets, previously unavailable in any matrix element generator, have been specifically added to ALPGEN for this and future studies. Where applicable in the ALPGEN samples, top quarks and W bosons are decayed within ALPGEN which assures preservation of spin correlation information which could impact kinematical distributions.

Table 10.22 lists the considered irreducible background processes, the generators used to either generate or cross-check event samples, the LO cross-section with statistical errors, the number of events expected for 30 (100)fb^{-1} of integrated luminosity, the number of events generated, simulated, reconstructed and analysed as well as the equivalent integrated luminosity, which ranges from 400 to over 6000 fb^{-1}. The cross-sections reflect pre-selection criteria imposed at generator-level which are described in the next section. In the processes involving real top quarks as well as in the $W\gamma\gamma$+ 4j process, one top quark/the W boson was forced to decay leptonically, and the stated cross-section therefore implicitly includes

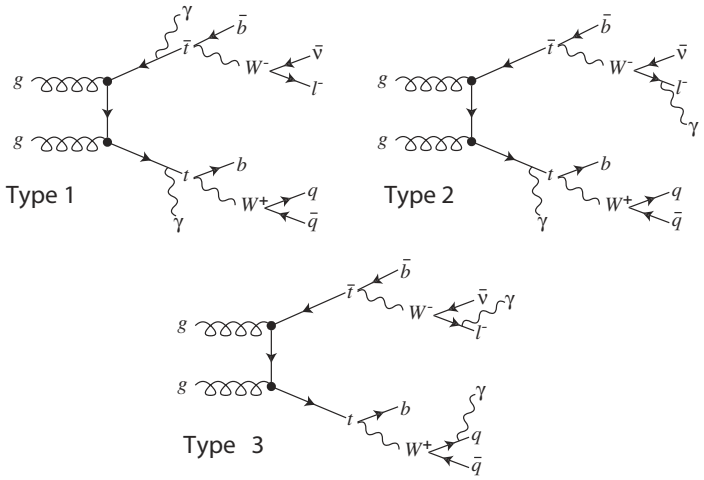

Figure 10.26. A sub-sample of the relative Feynman graphs illustrating the three types of $t\bar{t}\gamma\gamma$ processes.

Table 10.22. Cross-sections at leading order (statistical errors in parentheses), number of events generated, simulated and reconstructed, and equivalent integrated luminosity for the irreducible backgrounds considered.

Process	$\sigma \times$ BR [fb] ($1\,W \to l\nu$)	Ngen	N 30 fb^{-1}	N 100 fb^{-1}	Generator	N simul./ reconstr.	N Anal.	Anal. Eq. Int. Lumi. [fb^{-1}]
tt$\gamma\gamma$ 1	1.6 ($\leqslant$ 1/mil)	52202	48	160	AL,MG	10000	4695	6250
tt$\gamma\gamma$ 2	6.1 ($\leqslant$ 1%)	6238	183	610	AL	6000	5109	1000
tt$\gamma\gamma$ 3	4.9 ($\leqslant$ 1%)	2967	147	490	AL	2500	2250	510
W $\gamma\gamma$ 4j	11.5 (1.2%)	4587	345	1150	AL	4500	3957	400

the relevant branching ratio. The effect of the inclusion of background Types 2 and 3 is to augment the total initial contribution (before selection) from $t\bar{t}\gamma\gamma$ by approximately one order of magnitude.

A background is called reducible if at least one element of the final-state signature is mistakenly identified due to incomplete detector coverage or other instrumental effects. This could arise if one or more electrons or jets are misidentified as photons, or a jet as an electron or a muon. It has been heretofore possible to evaluate only the irreducible backgrounds discussed above with acceptable statistics, so only these will be presented here. Low-statistics tests on most of the reducible background processes have been performed, and strong requirements have been implemented in the following selection in order to veto them.

10.2.7.4. Event simulation and reconstruction. All generated signal and background events were fragmented and hadronised with PYTHIA [69, 246] version 6.227, using the CTEQ5L [12] PDFs. They were then simulated, digitised and reconstructed using the standard CMS tools. All samples were digitised with high-luminosity (10^{34}cm^{-2}s^{-1}) pile-up.

10.2.7.5. Description of generator-level pre-selections. No generator-level pre-selections were made on signal events. For the irreducible background events, the following

pre-selection was made:

- $m_{\gamma\gamma} \geqslant 80\,\mathrm{GeV/c^2}$ for all four processes;
- $p_{T\gamma} \geqslant 20\,\mathrm{GeV/c}$, $|\eta_\gamma| \leqslant 2.5$ (MADGRAPH) or $p_{T\gamma} \geqslant 15\,\mathrm{GeV/c}$, $|\eta_\gamma| \leqslant 2.7$ (ALPGEN) for all four processes;
- $p_{Tl} \geqslant 15\,\mathrm{GeV/c}$ for all processes except $tt\gamma\gamma$ 1;
- $p_{Tj} \geqslant 15\,\mathrm{GeV/c}$, $|\eta_{j,l}| \leqslant 2.7$, Δ R(l, j or j, j or γ,j or γ, γ) $\geqslant 0.3$ for the process $W\gamma\gamma$ 4j, where 'j' refers to one of the four additional light quark jets;

where p_T refers to the transverse momentum of the particle, η its pseudorapidity and $\Delta R = \sqrt{(\Delta\eta^2 + \Delta\phi^2)}$ where ϕ is the azimuthal angle.

The intersection (most restrictive set) of the above generator-level criteria except that pertaining to the additional light quark jets was then imposed on all signal and background event samples at the particle level.

10.2.7.6. Event selections. The events are selected by the single and diphoton triggers at Level-1 and High Level Triggers (HLT) configured for high luminosity ($10^{34}\,\mathrm{cm^{-2}s^{-1}}$).

A prior study of this channel at particle-level [497] found that reliance on p_T alone to identify the two Higgs boson photon candidates results in considerable sidebands (at approximately the 10% level) in the two-photon invariant mass distribution in signal events. It is the choice of the second (lower in p_T) photon which is overwhelmingly contaminated by these combinatorial photons, which originate approximately 80% from π^0s, 10% from ηs, a few percent from ωs, and the remainder from other particles. Fully 80% of these fake Higgs photon 'mother' particles appear to come from parton showers whose origin is one of the two final-state top quarks, and as such are peculiar to the $t\bar{t}H$ process. The other 20% come from showering from the initial-state partons and hence are common to all the associated production channels. For reconstructed signal events, the misidentification percentage grows to $\sim 30\%$ (see the pertinent curve in Fig. 10.28(left)).

To improve the Higgs photon selection procedure, we have evaluated the performance of the photon isolation variables investigated and used by the $H \to \gamma\gamma$ inclusive analysis [7]. We obtain the best results by considering linear combinations of the variables 'ECALIso' (the sum of E_T of ECAL basic clusters within a cone after removing the E_T of those basic clusters constructed with the Island algorithm included in the supercluster matched ($\Delta R < 0.2$) with the offline photon itself) and 'HCALIso' (the sum of E_T of HCAL calorimeter towers within a cone centred on the photon candidate), as illustrated in Fig. 10.27(right).

For this study, the two highest-p_T Offline Photons satisfying the following requirement on the isolation energy Iso = HCALIso + (2.*ECALIso) were retained as Higgs photon candidates:

- For photons in the barrel: Iso $< 25\,\mathrm{GeV}$,
- For photons in the endcap: Iso $< 22\,\mathrm{GeV}$,

with $\Delta R < 0.25$ for ECALIso and $\Delta R < 0.3$ for HCALIso (see comparison of performance with different isolation cone radii in Fig. 10.27 (left). These values yield approximately 95% efficiency for true Higgs photons[45] and less than 40% for combinatorial photons. This strategy successfully restores approximately one-half of the true Higgs photon pairs previously lost to misidentification when selection based on only photon p_T is used, as is demonstrated by Fig. 10.28.

[45] "True Higgs photons" are considered to be those Offline Photons lying within a cone of radius $\Delta R < 0.1$ of one of the two particle-level photons coming from the Higgs boson decay.

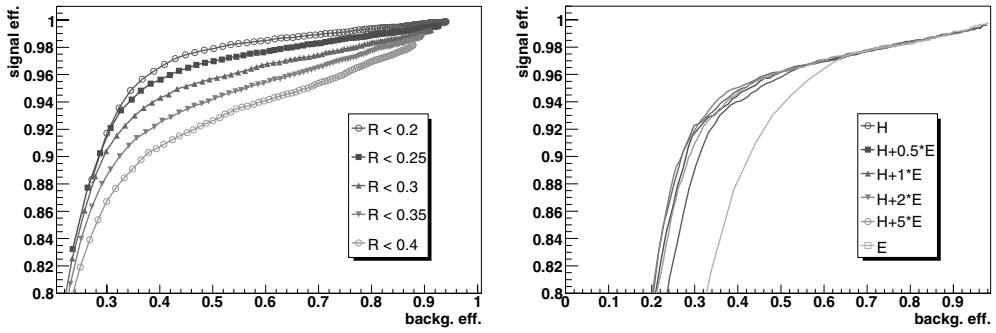

Figure 10.27. Left: Efficiency for true Higgs photons vs. that for combinatorial photons in the ECAL barrel for the ECAL isolation variable, for different isolation cone sizes. Right: Efficiency for true Higgs photons vs. that for combinatorial photons in the ECAL endcap, for several linear combinations of isolation variables.

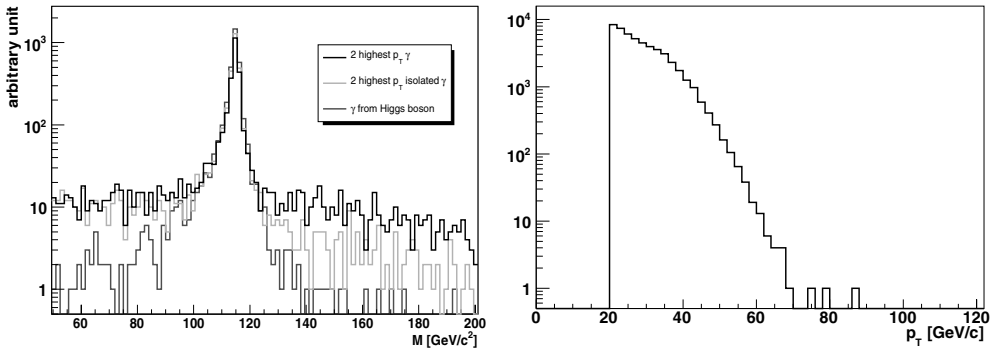

Figure 10.28. Left: Invariant mass of the two Higgs photon candidates selected according to p_T alone (dark grey curve), p_T and isolation (light grey curve), and where both candidates are geometrically matched to particle-level Higgs photons (medium grey curve). Right: Distribution of the p_T of jets from pile-up events. Jets not matched to generated particle jets from the signal are considered to be pile-up jets.

A similar technique is employed for the selection of candidate leptons from top quark decays (via a W boson). We obtain the best performance in selecting 'true' W leptons[46] with the previously-defined ECALIso variable for Offline Electrons and with transverse momentum of tracks in a cone of radius $\Delta R < 0.25$ ('IsoByTkPt025') for GlobalMuons. We retain as the W-decay (top) lepton candidate the highest-E_T OfflineElectron or highest-p_T GlobalMuon satisfying the following requirement:

- For electrons, ECALIso < 5 GeV,
- For muons, IsoByTkPt02 < 9 GeV.

These values yield ∼92% efficiency for 'true' W leptons and approximately 35% for combinatorial leptons. In the selection criteria involving photons described below, as well as those involving leptons described thereafter, the pertinent distributions are constructed using

[46] As for Higgs photons, considered to be those OfflineElectrons or GlobalMuons lying within a cone of radius ΔR <0.1 of a particle-level electron or muon from a W boson which itself is a decay product of one of the final-state top quarks.

the Higgs photon and W lepton candidates selected according to the procedure combining p_T and isolation described above.

After selection of the two Higgs photon and one W lepton candidates, the remainder of the selection aims for a signal efficiency of between 85 and 95% per selection criterion. Five variables involving the Higgs photon candidates have demonstrated effective performance: the p_T of each of the two OfflinePhoton candidates ($p_{T\gamma 1}$, $p_{T\gamma 2}$), the sum of their p_T ($p_{T\gamma 1} + p_{T\gamma 2}$), the angular distance between them ($\Delta R_{\gamma_1,\gamma_2}$), and $\cos\theta^*$, where $\tan\theta^* = \frac{|\vec{p}_i|\sin\theta_i}{\gamma(|\vec{p}_i|\cos\theta_i - \beta E_i)}$, and $\vec{p}_i$ and θ_i refer respectively to the momentum of and the 3-space angle between either of the two Higgs photon candidate directions and the direction of their joint 4-vector, in the laboratory frame (the scalar nature of the Higgs boson should assure a flat distribution of this variable for signal events, and one peaked in the forward and backward directions for background events). We have established the following eventwise selection involving the two Higgs photon candidates:

- $p_{T\gamma 1,\gamma 2} \geqslant 50, 18\,\mathrm{GeV/c}$
- $p_{T\gamma 1} + p_{T\gamma 2} \geqslant 85\,\mathrm{GeV/c}$
- $\Delta R_{\gamma_1,\gamma_2} \leqslant 3.2$
- $\cos\theta^* \leqslant 0.85$.

Three variables involving the W lepton candidates have demonstrated effective performance: the E_T (OfflineElectron) or p_T (OfflineMuon) of the candidate, and the angular distances between the candidate and each of the two Higgs photon candidates ($\Delta R_{\gamma_1,lepton}$, $\Delta R_{\gamma_2,lepton}$). We have established the following eventwise selection involving the W lepton candidate:

- $p_{Tlepton} \geqslant 15\,\mathrm{GeV/c}$
- $\Delta R_{\gamma_1,lepton}$, $\Delta R_{\gamma_2,lepton} \geqslant 0.3, 1.0$.

In order to remove part of the irreducible backgrounds studied here and also eventually to remove backgrounds from QCD processes, we take advantage of the high jet multiplicity of our signal events as well as the presence of two real top quarks yielding b-quark jets as decay products. Jets including those possibly corresponding to b-quarks are constructed with the iterative cone algorithm [7] with a cone radius of $\Delta R = 0.5$. A discriminant (BtagDisc) is then calculated for each candidate b-quark jet with the Combined BTag [7] b-quark-tagging algorithm. We require the presence of a minimum number of jets having a value of p_T greater than $60\,\mathrm{GeV/c}$, which permits the removal of jets from pile-up from consideration (we consider a reconstructed jet to be from pile-up if it is not geometrically matched with a particle-level jet, which has been constructed using the same algorithm and parameters as the reconstruction-level jets). Figure 10.28 (right) shows the p_T distribution of the jets thus attributed to pile-up in a signal sample with $m_H = 115\,\mathrm{GeV/c^2}$. We require $\geqslant 4$ jets with $p_T > 60\,\mathrm{GeV}$.

To specifically target the $W + 2\gamma$ + jets background (and eventually other non-b-quark reducible backgrounds), we make limited use of tagging of b-quark jets. We require that at least one candidate jet having $p_T > 60\,\mathrm{GeV}$ have BtagDisc > 0.8.

10.2.7.7. Performance of off-line selection. Tables 10.23 and 10.24 show the progression of the signal ($m_H = 115\,\mathrm{GeV/c^2}$) and background samples through the selection. Prior to checking for the Level-1 and HLT decision, we apply the pre-selection at particle-level described in Section 10.2.7.5 to all signal and background samples. The number of surviving events is expressed as an effective cross-section in fb. The final results are also expressed as numbers of surviving signal and total background events with statistical errors, for both 30 and $100\,\mathrm{fb}^{-1}$.

Table 10.23. Progression of the signal ($m_H = 115\,GeV/c^2$) and background samples through the trigger portion of the selection, expressed as an effective cross-section in fb. Efficiencies with respect to the previous sequential requirement are expressed as percentages.

Requirement	$M_H = 115\,GeV/c^2$	$tt\gamma\gamma 1$	$tt\gamma\gamma 2$	$tt\gamma\gamma 3$	$W2\gamma 4j$
Before selection	0.693 (100.0)	1.59 (100.0)	6.12 (100.0)	4.95 (100.0)	11.4 (100.0)
Pre-selection	0.533 (76.8)	1.4 (87.9)	5.05 (82.5)	3.94 (79.6)	11.3 (98.9)
L1 + HLTAccept	0.517 (97.0)	1.34 (95.4)	4.71 (93.4)	3.36 (85.7)	10.5 (93.0)
HLT $\gamma\gamma$, γ accept	0.508 (98.3)	1.30 (96.9)	4.57 (96.9)	3.25 (96.6)	10.0 (96.0)

Table 10.24. Progression of the signal ($m_H = 115\,GeV/c^2$) and background samples through the offline portion of the selection, expressed as an effective cross-section in fb. Efficiencies with respect to the previous sequential requirement are expressed as percentages.

Requirement	Criterion	$M_H = 115\,GeV/c^2$	$tt\gamma\gamma 1$	$tt\gamma\gamma 2$	$tt\gamma\gamma 3$	$W2\gamma 4j$
Number of γ's	$\geqslant 2$	0.506 (100.0)	1.29 (100.0)	4.56 (100.0)	3.24 (100.0)	10.0 (100.0)
Number isolated γ's	$\geqslant 2$	0.482 (95.2)	1.22 (94.0)	3.96 (86.8)	2.53 (78.2)	9.58 (95.7)
$pT\gamma_1$(GeV/c)	>50	0.432 (90.0)	1.04 (85.3)	3.14 (79.4)	1.48 (58.5)	7.90 (82.5)
$pT\gamma_2$(GeV/c)	>18	0.386 (89.2)	0.88 (84.7)	2.25 (71.6)	1.03 (69.7)	6.72 (85.0)
$pT\gamma_1 + pT\gamma_2$(GeV/c)	>85	0.379 (98.2)	0.847 (96.3)	2.17 (96.5)	0.926 (89.8)	6.40 (95.3)
$\Delta R(\gamma_1\gamma_2)$(GeV/c)	<3.2	0.364 (96.4)	0.738 (87.2)	1.86 (85.9)	0.719 (77.7)	5.30 (82.8)
$\cos\theta^*$	<0.85	0.332 (91.4)	0.589 (79.8)	1.48 (79.5)	0.583 (81.0)	4.36 (82.3)
pT_{lep} isolated (GeV)	>15	0.238 (72.2)	0.443 (75.2)	0.984 (66.4)	0.387(66.4)	3.15 (72.3)
$\Delta R(\gamma_1 l)$	>0.3	0.236 (99.0)	0.441 (99.5)	0.925 (94.0)	0.321 (83.0)	3.14 (99.6)
$\Delta R(\gamma_2 l)$	>1.0	0.208 (87.4)	0.389 (88.2)	0.607 (65.7)	0.163 (50.7)	2.34 (74.6)
N jets $p_T > 60\,GeV$	$\geqslant 4$	0.179 (86.2)	0.338 (87.0)	0.455 (74.9)	0.110 (67.6)	1.79 (76.6)
Btag Disc for $\geqslant 1$ jet	>0.8	0.110 (61.6)	0.217 (64.0)	0.276 (60.7)	0.051 (46.0)	0.294 (16.4)
$M_H +/- 1.5\,GeV/c^2$		0.074 (67.1)	0.005 (2.51)	0.011 (3.86)	< 0.002 (3.92)	< 0.003 (1.02)
N_{evts} at $30\,fb^{-1}$		$2.22 +/- 0.10$		$0.483 +/- 0.158$		
N_{evts} at $100\,fb^{-1}$		$7.42 +/- 0.334$		$1.61 +/- 0.53$		

10.2.7.8. Uncertainties, systematic errors, and strategy for background measurement from data. To estimate the systematic error on the surviving signal cross-section, the following global source of error is applied directly to the estimated number of signal events:

- Luminosity $<3\%$.

The error due to the inclusion/non-inclusion of initial and final-state photon radiation at the fragmentation/hadronisation level as well as that due to the matrix element generator used (ALPGEN or MADGRAPH) was found to be insignificant.

We have also considered the following sources of uncertainty relevant to the detector:

- Electron/Photon/Muon identification: 1% per identified object.
- Efficiency to tag jets containing b quarks: 5% per identified b-quark jet.
- Uncertainty on the jet energy scale: 3%.

Only the effect of the uncertainty on the jet energy scale is evaluated by propagation through the selection, and yields a net uncertainty of $+1.6/-3.9\%$ for a Higgs boson mass of $115\,GeV/c^2$. All the above contributions are summed in quadrature and a systematic error of $+6.3/-7.2\%$ is obtained for the number of signal events for a Higgs boson mass of $115\,GeV/c^2$. The uncertainty on the number of surviving background events, calculated below and amounting to an average of $\pm 15\%$, is finally added to the above quadratic sum yielding an error of $+16.3/-16.6\%$ on the number of events in a peak containing both signal and background events, corresponding to the case of a signal cross-section measurement.

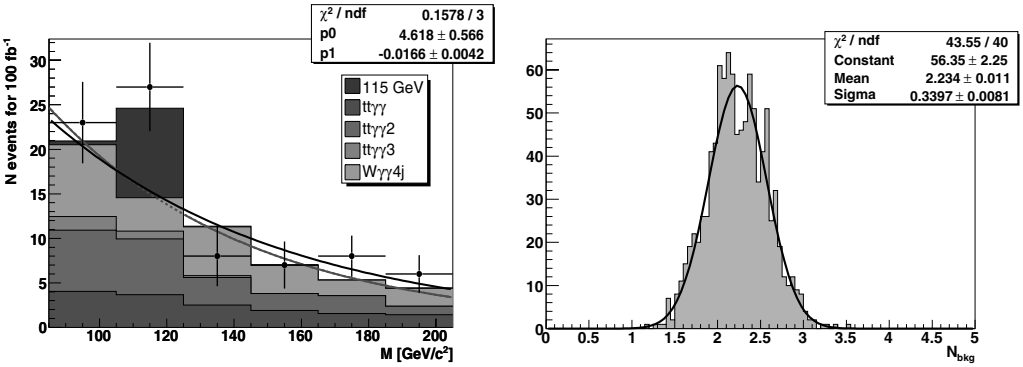

Figure 10.29. Left: Background estimation from the fit of the sidebands: Example of a gedanken experiment giving a possible set of real data points consistent with the Poisson distribution of the simulated number of surviving background events. The fit through these points is superimposed on the original fit. Right: Distribution of the estimated number of background events from the fit of the gedanken experiments.

Table 10.25. The signal selection efficiency, the total number of surviving signal and background events at 100 fb^{-1} with statistical errors (from the number of generated events), the number of background events estimated from the fit with the fit error, and the signal significance calculated using the ScP estimator without and with the background uncertainty evaluated from the fit.

Higgs Boson Mass (GeV)	115	120	130	140
Sig. Selection Eff. (%)	10.7	11.2	11.3	11.3
Number Signal	7.42 ± 0.33	7.33 ± 0.33	5.96 ± 0.27	4.21 ± 0.19
Total Number Bcgkd	1.61 ± 0.53	2.79 ± 0.62	1.98 ± 0.66	1.10 ± 0.51
Total Number Bcgkd from fit w. syst.	2.23 ± 0.34	1.94 ± 0.32	1.60 ± 0.22	1.39 ± 0.22
Signal Significance (ScP)	3.541	3.662	3.257	2.510
Signal Significance (ScP) w. syst.	3.414	3.523	3.184	2.453

The background spectrum can be obtained from the sidebands surrounding the positions of the putative Higgs boson masses and fit to a decreasing exponential function (shown by the grey curve in Fig. 10.29 (left)). The bin width has been chosen to be large enough (20 GeV/c^2) to have a sufficient number of events for an integrated luminosity of 100 fb^{-1} (The bin centred around the generated Higgs boson mass is not used for the fitting procedure). The number of background events and its error are estimated by fitting test distributions obtained with the average of the bin contents according to a Poisson distribution (gedanken experiments corresponding to possible future real data sets). One such fit is shown in the black curve in Fig. 10.29 (left). The mean and width of the gaussian fit of the distribution thus obtained (Fig. 10.29 (right)) yield respectively estimates of the number of background events and its systematic error, which are used to compute the signal significance.

10.2.7.9. Results. Table 10.25 shows, for each of the four Standard Model Higgs boson mass values considered, the signal selection efficiency, the total number of surviving signal and background events at 100 fb^{-1} with statistical errors (from the number of generated events), the number of background events estimated from the fit with the fit error, and the signal significance calculated using the ScP estimator [498] with and without the background uncertainty evaluated from the fit.

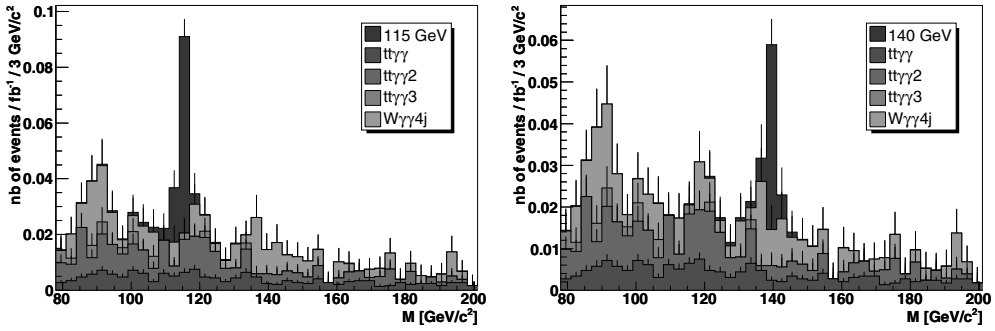

Figure 10.30. The diphoton mass after all selections for signal of $m_H = 115\,\mathrm{GeV/c^2}$ (left) and $140\,\mathrm{GeV/c^2}$ (right) added to the surviving backgrounds.

Figure 10.30 shows the diphoton mass distribution of the signal added to the background after all selections for Higgs boson masses $115\,\mathrm{GeV/c^2}$ (left) and $140\,\mathrm{GeV/c^2}$ (right).

10.2.7.10. Conclusion. A full-reconstruction-level sequential study has been performed for the channel $t\bar{t}H$, with $H \to \gamma\gamma$, taking into account irreducible backgrounds not previously studied. The ratio of signal to background events is approximately 4:1 representing a factor of 2 improvement over prior CMS and ATLAS studies. Signal observability in excess of 3σ is indicated for masses up to $130\,\mathrm{GeV/c^2}$ with full simulation and reconstruction and with estimated systematic errors taken into account for $100\,\mathrm{fb^{-1}}$ of integrated luminosity.

10.2.8. Associated WH, ZH production with $H \to \gamma\gamma$

Compared to the gluon-gluon fusion channel $gg \to H \to \gamma\gamma$, the associated production channels WH/ZH [499, 500] suffer from a much lower production cross section. Several advantages, however, make these channels attractive when the decay of the gauge boson results in a charged lepton: requiring an additional relatively high transverse-momentum lepton greatly reduces the significant QCD background in the $\gamma\gamma$ topology and improves the primary vertex reconstruction [501]. In the context of supersymmetric models, maximal mixing in the stop sector could result in a strong suppression of the $gg \to h$ signal, which the associated production channels would not be subject to [502]. The searched-for final state is therefore comprised of 2 isolated photons and at least one isolated electron or muon. Prior generator-level or fast simulation studies [489, 490, 503, 504] conclude to the possibility of a discovery at the LHC in this channel.

A detailed description of the analysis can be found in [505].

10.2.8.1. Event generation and reconstruction. All the process considered in this study have been simulated at the leading order. Signal events were generated by the matrix element generator COMPHEP [43] for Higgs boson masses ranging from 90 to $150\,\mathrm{GeV/c^2}$, in steps of $5\,\mathrm{GeV/c^2}$. Total cross-sections have been rescaled accordingly to the NLO calculation [20]. K-factors from 1.15 to 1.16 are obtained on the whole mass range. Branching ratios for $H \to \gamma\gamma$ were taken from HDECAY program [21]. The irreducible backgrounds from the processes $W\gamma\gamma$ et $Z\gamma\gamma$ were also generated with COMPHEP, with the same K-factors applied as those pertinent to the signal. Fragmentation and hadronisation was performed by PYTHIA [246].

The reducible background processes $\gamma\gamma$, γ-jet, Wγ, $b\bar{b}$, and $t\bar{t}$, retained due to their capacity to mimic the $l\gamma\gamma$ signal, have been generated with PYTHIA and leading order cross-sections were considered, except for the $t\bar{t}$ production where a NLO cross section of 840 pb is used [278].

To ensure an efficient generation and preserve sufficient statistics of the most signal like events, a pre-selection is applied at generator level. Three electromagnetic candidates or two electromagnetic candidates and one muon candidate with $E_T > 20\,\text{GeV}$ and $|\eta| < 2.7$ are required. An electromagnetic candidate is obtained by clustering electrons and photons in a $\Delta\eta = 0.09$, $\Delta\phi = 0.09$ window. Muon candidates are either μ, τ, π, or K particles.

The generated events were passed through the GEANT3 simulation of CMS [25]. The events were then digitised and reconstructed with the standard CMS software [506] with the addition of pile-up event corresponding to the high luminosity phase ($\mathcal{L} = 10^{34}\,\text{cm}^{-2}\text{s}^{-1}$).

10.2.8.2. Trigger selection. Events are required to pass the global Level 1 trigger [506] and the double photon High Level Trigger (HLT) [76] configured for the high luminosity phase. The trigger efficiencies for the preselected signal events are higher than 95% on the whole Higgs boson mass range (90–150 GeV/c^2) as shown in Table 10.26 and 10.27.

10.2.8.3. Offline event selection. To suppress the reducible backgrounds, four discriminant combined variables are first constructed using a likelihood ratio method to estimate the isolation of the photons, the quality of the lepton reconstruction, the isolation of the lepton and the QCD/multi-jets nature of the event. The reference histograms for the four likelihoods are all produced on independent simulated event samples after a very loose pre-selection requiring two offline photons and one electron or muon reconstructed by the standard algorithms. Photon candidates with a matching seed in the pixel detector are rejected. The two photons with the highest transverse energy are assigned to the Higgs boson decay. Several isolation variables [507] were tested in the likelihood and the best performance is obtained with the sum of the transverse energy of the basic clusters within a cone $\Delta R < 0.3$ around the photon, excluding the basic clusters belonging to the photon supercluster and the sum of the transverse energy of the HCAL towers within a cone $\Delta R < 0.3$ around the photon.

Then the offline lepton with the highest E_T is selected. The reconstruction quality of the electron is carefully checked. The four variables yielding the most significant discriminating power are the ratio E/p between the electron energy as measured in the calorimeter and its momentum measured by the tracker, the hadronic energy fraction E_{had}/E, the distance $\Delta\eta$ between the track and the associated supercluster and the ratio R_9 between the sum of the energies of 9 crystals (3×3 matrix centred on the maximum-energy crystal) and the energy of the corresponding supercluster. In the case of muons the purity obtained by the standard CMS reconstruction algorithms has already proven sufficient; therefore, no additional criteria are applied.

For the lepton isolation, similar calorimeter variables as for photons are used. In addition, the number of pixel lines within a cone $\Delta R < 0.3$ around the lepton improves the discriminative power of the likelihood.

Finally a global discriminant variable against multi-jet background is constructed. The rejection of π^0 faking signal photons, effective against QCD backgrounds, has been accomplished by a neural network procedure exploiting the information on the lateral profile of the electromagnetic shower. Variables involving the multiplicity of reconstructed objects in the electromagnetic calorimeter improve the discriminating power.

The results of the selection applied on the four combined variables are presented in Tables 10.26 and 10.27. The multi-jet backgrounds are entirely suppressed. To obtain a more

Table 10.26. Expected rates (in fb) after each stage of the event selection for signals ($m_H = 120\,GeV/c^2$) and irreducible backgrounds. Errors are statistical only.

	WH	ZH	W$\gamma\gamma$	Z$\gamma\gamma$
σ.BR	0.810	0.137	-	-
Pre-selection: σ.BR.ε	0.460	0.0440	13.58	18.92
Double photons HLT	0.439 ± 0.005	0.0423 ± 0.0004	8.80 ± 0.04	12.13 ± 0.07
2 isolated photons	0.387 ± 0.005	0.0370 ± 0.0004	7.14 ± 0.04	6.51 ± 0.04
1 good quality lepton	0.331 ± 0.004	0.0350 ± 0.0003	5.56 ± 0.04	4.58 ± 0.03
Lepton isolation	0.299 ± 0.004	0.0318 ± 0.0003	4.83 ± 0.04	4.11 ± 0.03
QCD rejection	0.281 ± 0.004	0.0273 ± 0.0003	4.50 ± 0.04	3.53 ± 0.03
$80 < m_{\gamma\gamma} < 160$	0.271 ± 0.004	0.0259 ± 0.0003	2.04 ± 0.02	1.42 ± 0.02

Table 10.27. Expected rates (in fb) after each stage of the event selection for reducible backgrounds. Contributions of the different p_T bins are summed. Errors are statistical only.

	$\gamma\gamma$	Wγ	b$\bar{b}$	t$\bar{t}$	γ-jet (jet)
σ.BR	1.1×10^5	5.79×10^3	1.78×10^9	86.2×10^3	1.21×10^8
Pre-selection: σ.BR.ε	270.1	26.5	2.96×10^5	6.00×10^3	7.16×10^4
Double photons HLT	197.7 ± 1.0	16.8 ± 0.1	77120 ± 764	1948 ± 17	35045 ± 256
2 isolated photons	161.6 ± 0.8	9.97 ± 0.07	682 ± 72	31.2 ± 2.2	7235 ± 115
1 good quality lepton	27.3 ± 0.3	7.98 ± 0.07	311 ± 49	23.5 ± 1.9	2552 ± 68
Lepton isolation	9.8 ± 0.2	6.59 ± 0.06	(0.87)	14.2 ± 1.5	209 ± 20
QCD rejection	7.6 ± 0.2	5.74 ± 0.06	(0.003)	(0.35)	(6.6)
$80 < m_{\gamma\gamma} < 160$	3.2 ± 0.1	2.40 ± 0.04	(0.001)	(0.26)	(3.7)

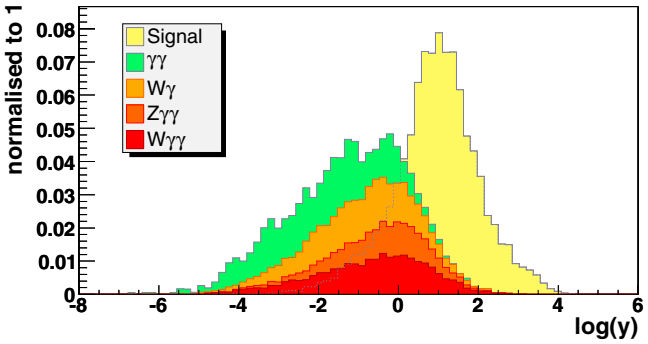

Figure 10.31. Distribution of the final combined variable for the signal ($m_H = 120\,GeV/c^2$) and for the background. The optimal working point is obtained with a cut $\log(y) > 0.35$.

precise estimation of these backgrounds, the cut factorisation method has been applied and the result is given between parentheses in Table 10.27. After rejecting events outside the 80–160 GeV/c^2 diphoton mass window, the expected rate of events is 0.297 ± 0.003 fb for signal and 13.1 ± 2.6 fb for background. Some simple kinematical variables are then used to form a final likelihood. The best discrimination was obtained with the transverse energy of the photons and of the lepton, the ΔR distances between lepton and each photon, the missing transverse energy, and the $\Delta\Phi$ angle between the directions of the missing transverse energy and of the highest E_T photon. The distribution of the resulting combined variable y is shown in Fig. 10.31 for a Higgs boson mass of 120 GeV/c^2.

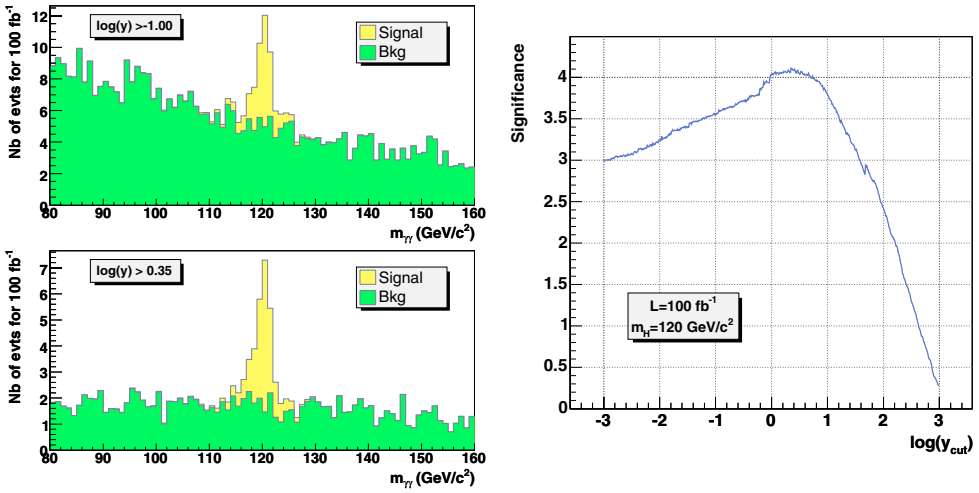

Figure 10.32. Left: Reconstructed $\gamma\gamma$ mass for different selection values on the final combined variable y for an integrated luminosity of 100 fb^{-1}. Right: Statistical significance as a function of the cut on the combined variable $\log(y)$, for $m_{\mathrm{H}} = 120\mathrm{GeV/c^2}$ and an integrated luminosity of 100 fb^{-1}. The highest significance is obtained with a cut $\log(y) > 0.35$.

Table 10.28. Optimal working points for different Higgs boson mass hypotheses. The significance and the expected number of signal and background events are given for an integrated luminosity of 100 fb^{-1}.

m_{H}	working point										
(GeV/c^2)	$\log(y) >$	significance	WH	ZH	W$\gamma\gamma$	Z$\gamma\gamma$	Wγ	$\gamma\gamma$	γ-jet	$\mathrm{t\bar{t}}$	$\mathrm{b\bar{b}}$
115	0.41	4.30 σ	22.1	1.8	49.3	30.9	33.0	10.2	1.7	0.16	10×10^{-5}
120	0.35	4.09 σ	20.7	1.6	51.2	36.2	34.5	12.4	1.9	0.15	10×10^{-5}
130	0.68	3.64 σ	14.6	1.3	30.7	16.9	18.7	6.0	1.4	0.10	4×10^{-5}
140	0.99	3.35 σ	11.4	1.0	18.9	10.3	10.6	3.7	1.0	0.04	1×10^{-5}
150	0.83	2.87 σ	10.4	0.9	20.2	11.7	12.3	5.4	1.1	0.03	3×10^{-5}

10.2.8.4. Statistical method and optimisation. The statistical methods developed by the LEP Higgs working group [508, 509] are used in this analysis to optimise the selection criteria and determine the statistical significance of the final results. To form the test-statistic, the three obvious variables to be used are the counting rates, the $\gamma\gamma$ invariant mass and the kinematic likelihood variable y. The limited statistics of the MC events prohibit however the use of a two-dimensional method for the determination of the Higgs boson discovery potential. So, only the counting rates and shape of the reconstructed $\gamma\gamma$ mass distribution will be used along with a cut on the combined likelihood variable y. The optimal working point is the y cut value which maximises the discovery potential as shown in Fig. 10.32.

The list of the optimal working points obtained for the different Higgs boson mass hypotheses is given in Table 10.28. The significance and the expected number of signal and background events are given for a luminosity of 100 fb^{-1}. For the γ-jet, $\mathrm{t\bar{t}}$ and $\mathrm{b\bar{b}}$ backgrounds, the rates are estimated by the method of cut factorisation.

10.2.8.5. Use of real data in sidebands: systematic uncertainties. The signal is characterised by a strongly peaked diphoton mass and the $m_{\gamma\gamma}$ distribution of the background is quite

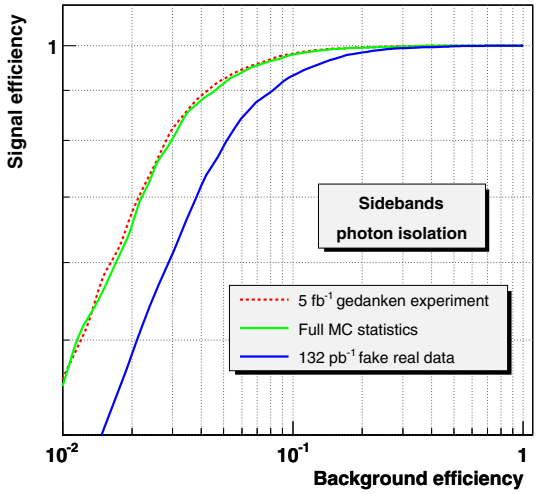

Figure 10.33. Comparison of the performance obtained when optimising the photon isolation likelihood with a sample of 132 fb^{-1} of "fake real data" taken in the $20 < m_{\gamma\gamma} < 80\,\mathrm{GeV/c^2}$ sideband (dash-dotted line) with the performance obtained by the standard analysis using the full MC statistics (solid line). To increase the available statistics in the sideband, gedanken experiments were generated for an equivalent luminosity of 5 fb^{-1}. The results of the optimisation on these sideband events is represented by the dotted line.

smooth at the considered working points. Therefore, when real data will be available, the data taken in $m_{\gamma\gamma}$ sidebands will be used to optimise the likelihood analysis and to estimate the background.

Likelihood optimisation with sideband events. No kinematic observables were used to construct the four primary likelihoods aimed at rejecting multi-jet events to avoid correlations with the diphoton mass. If the shapes of the distributions of the variables used in the likelihoods are sufficiently similar for different diphoton mass regions, then data taken outside the signal region can be used to optimise the likelihoods. To test the feasibility of the method, a sample of "fake real data" (the number of MC events for each background is equal to the expected number of events for a given luminosity) taken in the $20 < m_{\gamma\gamma} < 80\,\mathrm{GeV/c^2}$ sideband is used to produce the reference S/B histograms of the likelihoods. The equivalent luminosity of the sample is limited to 132 pb^{-1} by the available statistics and is composed of 4682 $\mathrm{b\bar{b}}$, 465 γ-jet, 222 $\mathrm{t\bar{t}}$, 2 $\gamma\gamma$, 1 Wγ and 1 Z$\gamma\gamma$ events. The performance obtained with the likelihood on the events in the 80–160 $\mathrm{GeV/c^2}$ band is compared to the results obtained by the standard analysis optimised with the full MC statistics available. For the four global discriminant variables, up to 20% loss of efficiency is observed for the same rejection power. The degradation of the performance is mainly due to the insufficient statistics of γ-jet and $\mathrm{t\bar{t}}$ events in 132 pb^{-1} of data. To increase the size of the "fake data sample", gedanken experiments were generated using the fitted shapes of the variables used in the likelihoods (correlations between the variables are neglected). The results are presented in Fig. 10.33 for the photon isolation likelihood. An integrated luminosity of 5 fb^{-1} will be sufficient to optimise the four primary likelihoods with the real data taken in the $m_{\gamma\gamma}$ sideband and to reproduce the results obtained when using the full MC statistics.

Background measurement from data. The $m_{\gamma\gamma}$ distribution of the background is smooth enough to be easily fit in the sideband to estimate the background in the signal region.

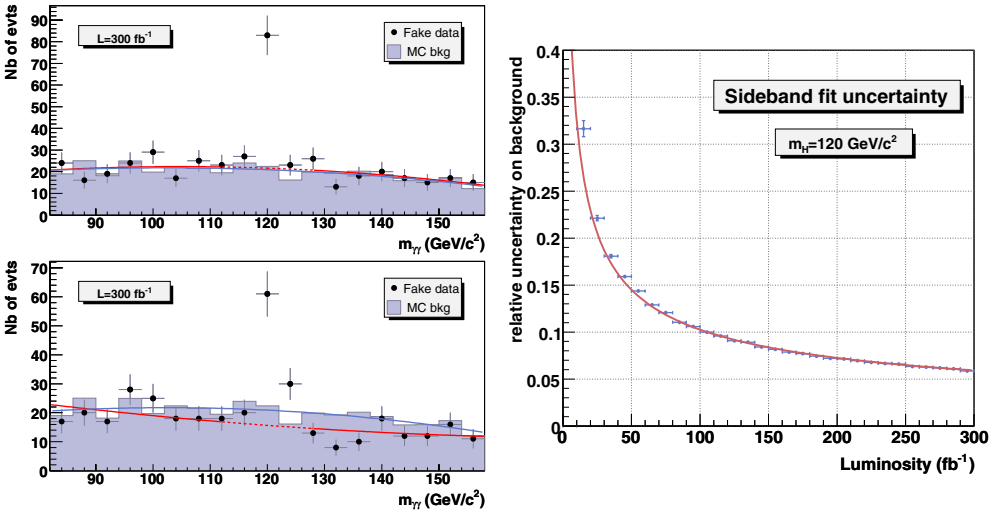

Figure 10.34. Left: Background measurement in the signal region with a fit on the $m_{\gamma\gamma}$ sideband. The fit of the full MC statistics is represented by the solid light gray line. The fit of the fake data (dark grey) is performed on the sidebands (i.e. after the exclusion of the signal window represented by the dotted line). Two gedanken experiments are represented for an integrated luminosity of 300 fb^{-1} and a 120 $\mathrm{GeV/c^2}$ Higgs boson mass hypothesis. Right: Relative uncertainty on the background estimation by the sideband fit method as a function of the integrated luminosity with LHC running at high luminosity for a Higgs boson mass of 120 $\mathrm{GeV/c^2}$.

To optimise the method (size and position of the window, bin width, choice of the fit function) and to estimate the uncertainty on background, 10000 signal + background pseudo-experiments were generated for each Higgs boson mass and luminosity hypothesis, as illustrated in Fig. 10.34. For a luminosity of 100 fb^{-1} and a Higgs boson mass of 120 $\mathrm{GeV/c^2}$, the background is measured with a precision of 11%, and with a precision of 6.6% for 300 fb^{-1}.

Systematic uncertainties for signal and cross-section measurement. The theoretical cross-section error due to the scale variation are estimated to ±3% for WH and ZH production for all considered Higgs boson masses [20]. The uncertainty on the parton density function of the CTEQ collaboration [12] is almost constant for the associated production $\mathrm{q\bar{q}} \rightarrow \mathrm{VH}$ at the LHC and of the order of 4% over a Higgs boson mass range between 100 and 200 $\mathrm{GeV/c^2}$ [510]. The error on the measured luminosity is expected to be 3% for luminosity above 30 fb^{-1}. The error on the lepton or photon reconstruction and identification has been estimated to 1% for each photon and lepton. An error of 5% on the missing transverse energy, see Appendix B, propagated in the final likelihood gives a −1.08% +0.49% variation of the final signal rate for $m_{\mathrm{H}} = 120\,\mathrm{GeV/c^2}$. The quadratic sum of all these errors gives a 6% total error on the expected signal rate.

In the case of a Higgs boson discovery, this channel will be used to measure the cross-section times the branching ratio:

$$\sigma_s \times BR = \frac{N_s}{\epsilon_{sel}\,\mathcal{L}} = \frac{N - N_b^{fit}}{\epsilon_{sel}\,\mathcal{L}}$$

where N_s is the number of signal events given by the difference between the total number N of observed events and the number N_b^{fit} of background events measured by the sideband fit.

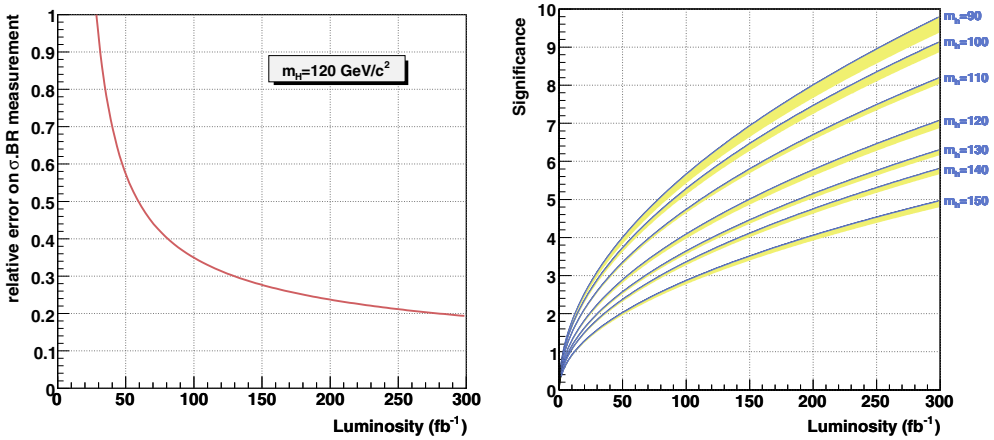

Figure 10.35. Left: Precision on the measurement of the product of cross-section and branching ratio as a function of the integrated luminosity with LHC running at high luminosity for a 120 GeV/c^2 Higgs boson. Right: Statistical significance for different Higgs boson mass hypotheses as a function of the integrated luminosity with LHC running at high luminosity. The 1σ systematic uncertainty is represented by the grey (yellow online) band.

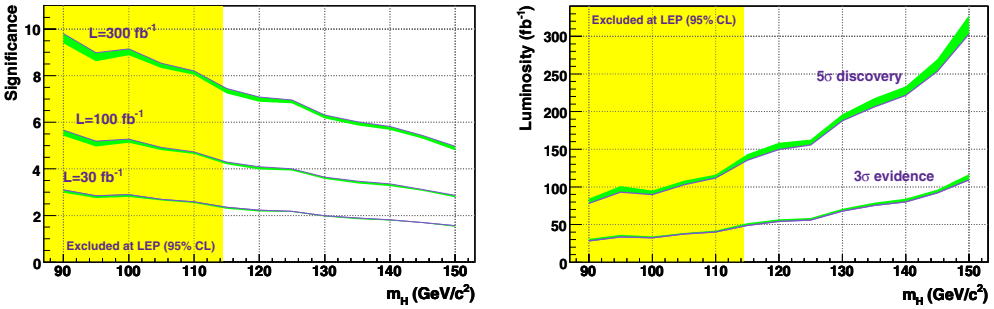

Figure 10.36. Statistical significance (left) and luminosity needed for a 5σ or 3σ observation (right) as a function of m_{H}. The 1σ systematic uncertainty is represented by the grey (yellow online) bands.

The total uncertainty on the measure is given by:

$$\left(\frac{\Delta(\sigma_s \times BR)}{\sigma_s \times BR}\right)^2 = \left(\frac{\Delta N}{N - N_b^{fit}}\right)^2 + \left(\frac{\Delta N_b^{fit}}{N - N_b^{fit}}\right)^2 + \left(\frac{\Delta \mathcal{L}}{\mathcal{L}}\right)^2 + \left(\frac{\Delta \epsilon_{sel}}{\epsilon_{sel}}\right)^2$$

The expected precision on the $\sigma \times BR$ measurement is represented as a function of the integrated luminosity in Fig. 10.35. For a 120 GeV/c^2 Higgs boson, the product of the cross-section and branching ratio will be measured with a precision of 35% after one year of LHC running at high luminosity, and with a precision of 19% after three years of high luminosity running.

10.2.8.6. Results for the Standard Model Higgs boson. The statistical significance is represented as a function of the luminosity in Fig. 10.35 for different m_{H} hypothesis. The statistical significance and the luminosity needed for a 5σ or 3σ observation are represented as a function of m_{H} in Fig. 10.36. One year of high luminosity running allows the observation

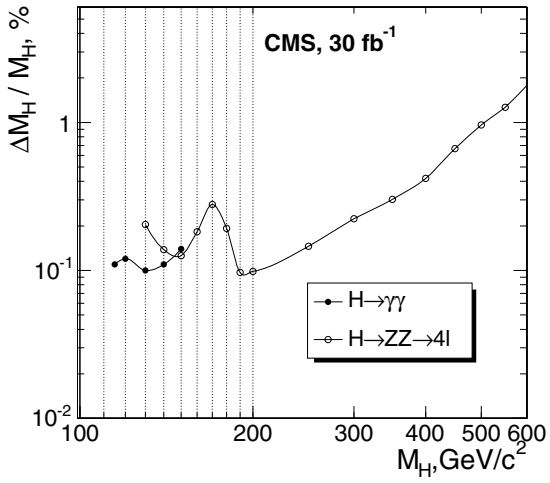

Figure 10.37. The statistical precision of the Higgs boson mass measurement for the $30\,\mathrm{fb}^{-1}$ using inclusive Higgs boson production $\mathrm{pp} \to \mathrm{H} + \mathrm{X}$ and the $\mathrm{H} \to \gamma\gamma$ and $\mathrm{H} \to \mathrm{ZZ} \to 4\ell$ decay modes.

at 3σ of the SM Higgs boson up to $m_{\mathrm{H}} = 150\,\mathrm{GeV/c^2}$, and three years of running at high luminosity are required to reach a 5σ discovery.

10.3. Discovery reach

10.3.1. Accuracy of the Higgs boson mass measurement

Figure 10.37 shows the statistical precision of the Higgs boson mass measurement for the $30\,\mathrm{fb}^{-1}$ using inclusive Higgs boson production $\mathrm{pp} \to \mathrm{H} + \mathrm{X}$ and the $\mathrm{H} \to \gamma\gamma$ and $\mathrm{H} \to \mathrm{ZZ} \to 4\ell$ decay modes.

10.3.2. Discovery reach for the Standard Model Higgs boson

This section summarises the discovery reach for the Standard Model Higgs boson. The NLO cross sections and branching ratios for the Higgs boson calculated with the programs HDECAY [41], HIGLU [40], VV2H, V2HV and HQQ [20] are used, as well as the NLO cross sections for the background processes, when available.

Figure 10.38 shows the integrated luminosity needed for the 5σ discovery of the inclusive Higgs boson production $\mathrm{pp} \to \mathrm{H} + \mathrm{X}$ with the Higgs boson decay modes $\mathrm{H} \to \gamma\gamma$, $\mathrm{H} \to \mathrm{ZZ} \to 4\ell$, and $\mathrm{H} \to \mathrm{WW} \to 2\ell 2\nu$.

Figure 10.39 shows the signal significance as a function of the Higgs boson mass for $30\,\mathrm{fb}^{-1}$ of the integrated luminosity for the different Higgs boson production and decay channels.

10.3.3. Study of CP properties of the Higgs boson using angle correlation in the $\Phi \to ZZ \to \mathrm{e^+e^-}\mu^+\mu^-$ process

The most general ΦVV coupling ($V = W^{\pm}, Z^0$) for spin-0 Higgs boson Φ (Φ means the Higgs particle with unspecified CP-parity, while H (h) and A mean the scalar and

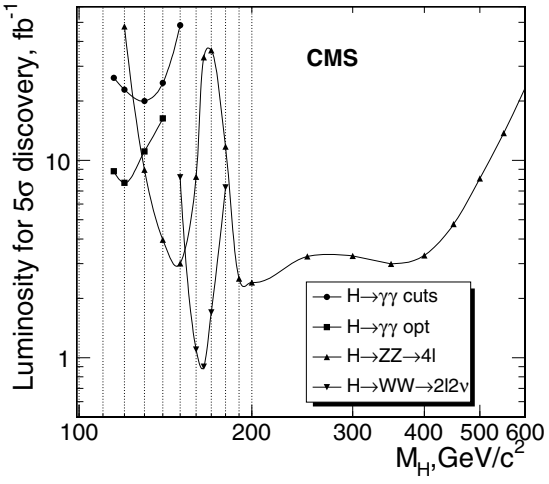

Figure 10.38. The integrated luminosity needed for the 5σ discovery of the inclusive Higgs boson production $pp \to H + X$ with the Higgs boson decay modes $H \to \gamma\gamma$, $H \to ZZ \to 4\ell$, and $H \to WW \to 2\ell 2\nu$.

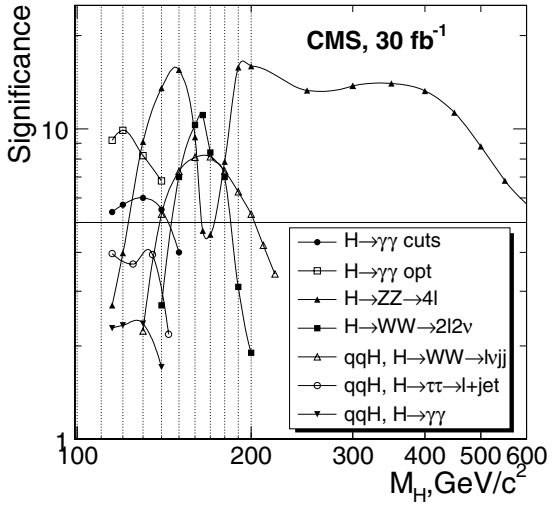

Figure 10.39. The signal significance as a function of the Higgs boson mass for 30 fb $^{-1}$ of the integrated luminosity for the different Higgs boson production and decay channels.

pseudoscalar Higgs particles, respectively) looks as follows [511–514]:

$$C^{J=0}_{\Phi VV} = \kappa \cdot g^{\mu\nu} + \frac{\zeta}{m_V^2} \cdot p^\mu p^\nu + \frac{\eta}{m_V^2} \cdot \epsilon^{\mu\nu\rho\sigma} k_{1\rho} k_{2\sigma}, \tag{10.5}$$

where k_1, k_2 are four-momenta of vector bosons V and $p \equiv k_1 + k_2$ is four-momentum of the Higgs boson. In the present analysis a simplified version of above ΦVV coupling (Eq. 10.5) is studied with a Standard-Model-like scalar and a pseudoscalar contributions (i.e. $\kappa, \eta \neq 0$ and $\zeta = 0$). To study deviations from the Standard Model ΦZZ coupling we take $\kappa = 1$[47].

[47] The ΦVV coupling with $\kappa = 1$ and arbitrary η is implemented in the PYTHIA generator.

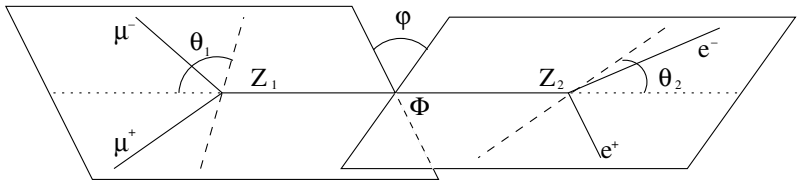

Figure 10.40. Definitions of the angles in the $\Phi \to ZZ \to e^+e^-\mu^+\mu^-$ process.

The decay width for the $\Phi \to ZZ \to (\ell_1\bar{\ell}_1)(\ell_2\bar{\ell}_2)$ process consists now of three terms: a scalar one (denoted by H), a pseudoscalar one $\sim \eta^2$ (denoted by A) and the interference term violating CP $\sim \eta$ (denoted by I):

$$d\Gamma(\eta) \sim H + \eta\, I + \eta^2 A. \tag{10.6}$$

This way the Standard Model scalar ($\eta = 0$) and the pseudoscalar (in the limit $|\eta| \to \infty$) contributions could be recovered. It is convenient to introduce a new parameter ξ, defined by $\tan\xi \equiv \eta$, which is finite and has values between $-\pi/2$ and $\pi/2$. Expressions for H, A and I can be found in article [512].

In study of the CP-parity of the Higgs boson two angular distributions were used. The first one is a distribution of the angle φ (called plane or azimuthal angle) between the planes of two decaying Zs in the Higgs boson rest frame. The negatively charged leptons were used to fix plane orientations. The second one is a distribution of the polar angle θ, in the Z rest frame, between momentum of negatively charged lepton and the direction of motion of Z boson in the Higgs boson rest frame (Figure 10.40).

The analysis was performed for scalar, pseudoscalar and CP-violating Higgs boson states, the latter for $\tan\xi = \pm 0.1, \pm 0.4, \pm 1$ and ± 4.

A detailed description of the analysis can be found in [515].

10.3.3.1. Generation and event selections. The production and decay of the scalar, pseudoscalar and CP-violating Higgs boson states were generated using PYTHIA [69] for three masses of the Higgs boson, $M_\Phi = 200, 300$ and $400\,\mathrm{GeV/c^2}$. Backgrounds and event selections are the same as in the analysis of the Standard Model Higgs boson $H \to ZZ \to e^+e^-\mu^+\mu^-$ described in Section 10.2.1. The reconstructed angular distributions after all selections for the signal with mass $M_\Phi = 300\,\mathrm{GeV/c^2}$ for various values of the parameter ξ, and for the background are shown in Fig. 10.41 at $60\,\mathrm{fb}^{-1}$. The Standard-Model signal cross-section and branching ratio were used for the signal normalisation in Fig. 10.41.

10.3.3.2. Determination of the parameter ξ. The parameter ξ was determined by maximisation of the likelihood function $\mathcal{L}(\xi, R)$, which was constructed from angular distributions and invariant mass distribution of four leptons, for the signal and the background. The function depends on two parameters: ξ describing CP property of the signal, and R describing fraction of the signal in the data sample. The function has the following form:

$$\mathcal{L}(\xi, R) \equiv 2 \sum_{x_i \in data} \log \mathcal{Q}(\xi, R; x_i), \tag{10.7}$$

where $\mathcal{Q}(\xi, R; x_i) \equiv R \cdot \mathcal{PDF}_S(\xi; x_i) + (1 - R) \cdot \mathcal{PDF}_B(x_i)$.

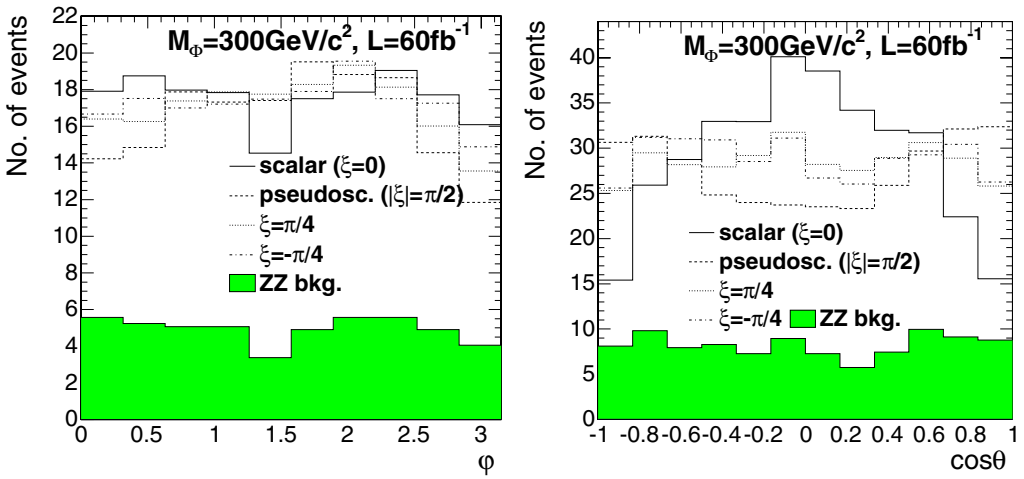

Figure 10.41. The φ-distributions (left) and the θ-distributions (right) for various values of the parameter ξ after final selections at 60 fb^{-1}. Empty histograms - the signal for $M_\Phi = 300\,\mathrm{GeV/c^2}$ and $\xi = 0$ (scalar), $\xi = -\pi/4$, $\xi = +\pi/4$ and $|\xi| = \pi/2$ (pseudoscalar). The filled histogram - the ZZ background. The Standard-Model signal cross-section and branching ratio were used for the signal normalisation.

$\mathcal{PDF}_B(x_i)$ and $\mathcal{PDF}_S(\xi; x_i)$ are probability density functions for background and signal respectively; $\{x_i\}$ are values of the measured quantities (angles and invariant mass) in the event i. $\mathcal{PDF}$s are products of probability densities $\mathcal{P}^M$, $\mathcal{P}^\varphi$, $\mathcal{P}^{\cos\theta_{1,2}}$ of four leptons invariant mass and angles φ and $\cos\theta_{1,2}$: $\mathcal{PDF} \equiv \mathcal{P}^M \cdot \mathcal{P}^\varphi \cdot \mathcal{P}^{\cos\theta_1} \cdot \mathcal{P}^{\cos\theta_2}$. The $\mathcal{P}^M$, $\mathcal{P}^\varphi$, $\mathcal{P}^{\cos\theta_{1,2}}$ are obtained by the Monte Carlo technique, using normalised histograms of given quantities after the final selection.

A part of the function $\mathcal{Q}$ which describes angular distributions of signal depends on the parameter ξ, namely from Eq. (10.6) we obtain:

$$\mathcal{P}(\xi) \equiv \mathcal{P}_S^\varphi(\xi) \cdot \mathcal{P}_S^{\cos\theta_1}(\xi) \cdot \mathcal{P}_S^{\cos\theta_2}(\xi) \equiv$$
$$(\mathcal{H} + \tan\xi \cdot \mathcal{I} + \tan^2\xi \cdot a^2\mathcal{A})/(1 + a^2\tan^2\xi), \tag{10.8}$$

where $\mathcal{H} \equiv \mathcal{P}_H^\varphi \cdot \mathcal{P}_H^{\cos\theta_1} \cdot \mathcal{P}_H^{\cos\theta_2}$ and $\mathcal{A} \equiv \mathcal{P}_A^\varphi \cdot \mathcal{P}_A^{\cos\theta_1} \cdot \mathcal{P}_A^{\cos\theta_2}$ are probability densities obtained by the Monte Carlo technique for the scalar (H) and the pseudoscalar (A) Higgs boson, respectively. The parameter a^2 is a (mass dependent) relative strength of the pseudoscalar and scalar couplings. For example $a^2 = 0.51,\ 1.65,\ 1.79$ for $M_\Phi = 200,\ 300,\ 400\,\mathrm{GeV/c^2}$, respectively. The $\mathcal{I}$ is a normalised product of angular distributions for the CP-violating term. The $\mathcal{I}$ is not always positive, and its integral is equal to zero, so it is not possible to simulate it separately. The $\mathcal{I}$ contribution can be obtained indirectly from the combined probability density for the signal with non-zero value of the parameter ξ. For example by introducing $\mathcal{P}_+ \equiv \mathcal{P}(\pi/4) = (\mathcal{H} + \mathcal{I} + a^2\mathcal{A})/(1 + a^2)$ and $\mathcal{P}_- \equiv \mathcal{P}(-\pi/4) = (\mathcal{H} - \mathcal{I} + a^2\mathcal{A})/(1 + a^2)$ we have $\mathcal{I} = (1 + a^2)/2 \cdot (\mathcal{P}_+ - \mathcal{P}_-)$. Finally we obtain:

$$\mathcal{P}(\xi) \equiv \left[\mathcal{H} + \tan\xi \cdot \frac{1 + a^2}{2} \cdot (\mathcal{P}_+ - \mathcal{P}_-) + \tan^2\xi \cdot a^2\mathcal{A}\right]/(1 + a^2\tan^2\xi). \tag{10.9}$$

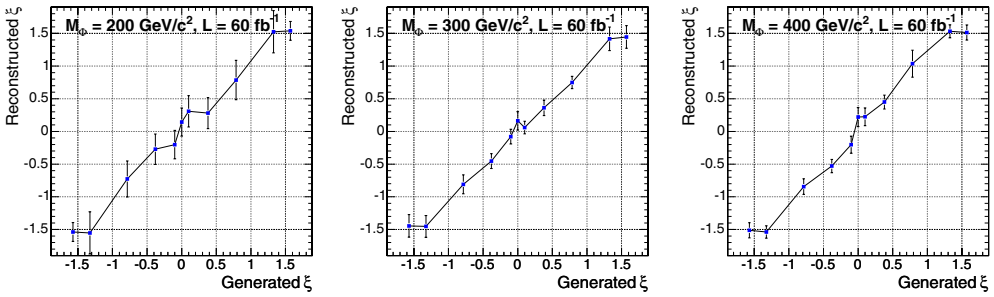

Figure 10.42. Reconstructed value of the parameter ξ as function of the generated value of the parameter ξ for $\mathcal{L}$=60 fb^{-1} and Higgs boson masses $M_\Phi = 200$, 300, 400 GeV/c^2. Uncertainties correspond to one standard deviation. The Standard-Model signal cross-section and branching ratio were used.

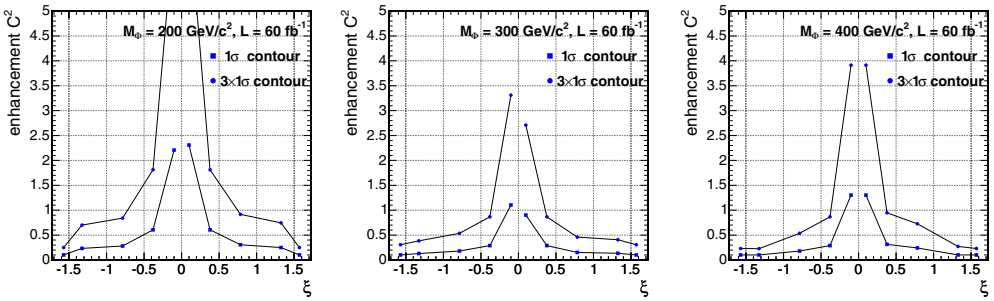

Figure 10.43. The minimal value of the factor C^2 needed to exclude the Standard Model, scalar Higgs boson at Nσ level (N = 1, 3) as a function of the parameter ξ for the Higgs boson masses $M_\Phi = 200$, 300 and 400 GeV/c^2 (from left to right) at 60 fb^{-1}.

10.3.3.3. Results. After selection all background contributions, but ZZ $\rightarrow e^+e^-\mu^+\mu^-$, are negligible, therefore only these events were used to construct probability density function for the background. Signal probability density functions were constructed using samples of scalar Higgs boson (H), pseudoscalar (A) and $\mathcal{P}_+$, $\mathcal{P}_-$ samples ($\xi = \pm\pi/4$).

For each value of the parameter ξ and for each Higgs-boson mass we made 200 pseudo-experiments for the integrated luminosity $\mathcal{L} = 60\,\text{fb}^{-1}$. For each pseudo-experiment we randomly selected events from the signal and background samples to form a test sample. The number of selected events was given by a Poisson probability distribution with mean defined by the process cross-section, selection efficiency and the examined luminosity. Then we performed a maximisation of the likelihood function $\mathcal{L}(\xi, R)$ for the test sample to obtain a value of the parameter ξ. The generated and reconstructed values of the parameter ξ with its uncertainty, obtained for three masses of the Higgs boson are shown in Fig. 10.42. The Standard-Model signal cross-section and branching ratio were used to normalise signal for each value of the parameter ξ.

An influence of enhancement (or suppression) factor C^2 of the Higgs boson production cross section times branching ratio, in respect to the Standard Model

$$C^2 = (\sigma \times Br)/(\sigma_{SM} \times Br_{SM}) \tag{10.10}$$

on the accuracy of the ξ measurement and thus, on possibility to exclude the Standard Model, scalar Higgs boson was studied. It was found that the precision of ξ measurement

is approximately proportional to $1/C$ (i.e. it depends on square-root of number of events, as one can expect):

$$\Delta\xi(\xi, C^2) \equiv \frac{\Delta\xi_{SM}(\xi)}{\sqrt{C^2}}. \tag{10.11}$$

A value of $\Delta\xi_{\mathrm{SM}}(\xi)$ corresponds to the precision of the parameter ξ measurement assuming the Standard Model Higgs boson production cross section times branching ratio. It is shown as the error bars in Fig. 10.42. Figure 10.43 shows the minimal value of the factor C^2 needed to exclude the SM Higgs boson at Nσ level (N = 1, 3), where $\mathrm{N} = \xi/\Delta\xi$, as a function of the parameter ξ.

Chapter 11. MSSM Higgs Bosons

11.1. Introduction

Supersymmetric extensions of the SM [516–520] are strongly motivated by the idea of providing a solution of the hierarchy problem in the Higgs sector. They allow for a light Higgs particle in the context of GUTs [521], in contrast with the SM, where the extrapolation requires an unsatisfactory fine-tuning of the SM parameters. Supersymmetry is a symmetry between fermionic and bosonic degrees of freedom and thus the most general symmetry of the S-matrix. The minimal supersymmetric extension of the SM (MSSM) yields a prediction of the Weinberg angle in agreement with present experimental measurements if embedded in a SUSY–GUT [522, 523]. Moreover, it does not exhibit any quadratic divergences, in contrast with the SM Higgs sector. Owing to the large top quark mass SUSY-GUTs develop electroweak symmetry breaking at the electroweak scale dynamically [524–527]. The lightest supersymmetric particle offers a proper candidate for the Cold Dark Matter content of the universe, if R-parity is conserved. Finally, local supersymmetry enforces gravitational interactions.

In the MSSM two isospin Higgs doublets have to be introduced in order to preserve supersymmetry [525, 528, 529]. After the electroweak symmetry-breaking mechanism, three of the eight degrees of freedom are absorbed by the Z and W gauge bosons, leading to the existence of five elementary Higgs particles. These consist of two CP-even neutral (scalar) particles h, H, one CP-odd neutral (pseudoscalar) particle A, and two charged particles $H^{\pm}$. In order to describe the MSSM Higgs sector one has to introduce four masses M_h, M_H, M_A and $M_{H^{\pm}}$ and two additional parameters, which define the properties of the scalar particles and their interactions with gauge bosons and fermions: the mixing angle β, related to the ratio of the two vacuum expectation values, $\tan\beta = v_2/v_1$, and the mixing angle α in the neutral CP-even sector. Due to supersymmetry there are several relations among these parameters, and only two of them are independent at leading order. In the absence of CP-violation they are usually chosen as M_A and $\tan\beta$. The other Higgs-boson masses and mixing angles are calculable in terms of the other MSSM parameters. Measuring the masses and angles will constitute an important consistency check of the MSSM.

At tree-level the following mass hierarchies hold: $M_h < M_Z$, $M_A < M_H$ and $M_W < M_{H^{\pm}}$. The tree-level bound on M_h receives large corrections from SUSY-breaking effects in the Yukawa sector of the theory. The leading one-loop correction is proportional to m_t^4. The leading logarithmic one-loop term (for vanishing mixing between the scalar top quarks) reads [530–536]

$$\Delta M_h^2 = \frac{3 G_\mu m_t^4}{\sqrt{2}\,\pi^2 \sin^2\beta} \ln\left(\frac{m_{\tilde{t}_1} m_{\tilde{t}_2}}{m_t^2}\right), \tag{11.1}$$

where G_μ is the Fermi constant, and $m_{\tilde{t}_{1,2}}$ are the two stop masses. Corrections of this kind have drastic effects on the predicted value of M_h and many other observables in the MSSM Higgs sector. The higher-order contributions can shift M_h by 50–100% [143, 144, 537–548]. The corrections to the MSSM Higgs boson sector have been evaluated in several approaches. The status of the available calculations can be summarised as follows. For the one-loop part, the complete result within the MSSM is known [530–532, 536, 549–552]. The by far dominant one-loop contribution is the $\mathcal{O}(\alpha_t)$ term due to top and stop loops ($\alpha_t \equiv h_t^2/(4\pi)$, h_t being the top-quark Yukawa coupling). Concerning the two-loop effects, their computation is quite advanced and has now reached a stage such that all the presumably dominant contributions are known [143, 538–543, 545–548, 553–563]. They include (evaluated for vanishing external momenta) the strong corrections, $\mathcal{O}(\alpha_t\alpha_s)$, and Yukawa corrections, $\mathcal{O}(\alpha_t^2)$, to the dominant

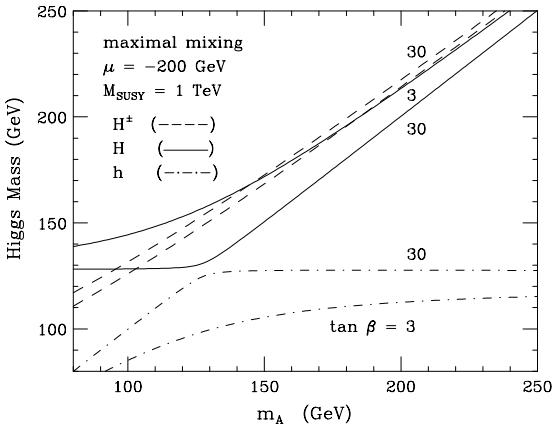

Figure 11.1. The CP-even and charged MSSM Higgs boson masses as a function of M_A for $\tan\beta = 3$ and 30, including radiative corrections [565].

one-loop $\mathcal{O}(\alpha_t)$ term, as well as the strong corrections to the bottom/sbottom one-loop $\mathcal{O}(\alpha_b)$ term ($\alpha_b \equiv h_b^2/(4\pi)$), i.e. the $\mathcal{O}(\alpha_b\alpha_s)$ contribution. The latter can be relevant for large values of $\tan\beta$. For the (s)bottom corrections the all-order resummation of the $\tan\beta$-enhanced terms, $\mathcal{O}(\alpha_b(\alpha_s\tan\beta)^n)$, has also been computed. Finally, the $\mathcal{O}(\alpha_t\alpha_b)$ and $\mathcal{O}(\alpha_b^2)$ corrections have been obtained. The higher-order corrections shift the upper bound of M_h to $M_h \lesssim 135\,\text{GeV}$ [143, 144]. The remaining theoretical uncertainty on M_h has been estimated to be below $\sim 3\,\text{GeV}$[144, 564]. Besides the masses of the Higgs bosons, also their couplings are affected by large higher-order corrections (see below).

An important feature of the MSSM Higgs sector is that for large pseudoscalar masses M_A the light scalar Higgs mass reaches its upper bound and becomes SM-like. Moreover, for large values of $\tan\beta$ the down(up)-type Yukawa couplings are strongly enhanced (suppressed) apart from the region, where the light (heavy) scalar is at its upper (lower) mass bound. The radiatively corrected Higgs masses are depicted in Fig. 11.1.

The LEP experiments have searched for the MSSM Higgs bosons via the Higgs-strahlung process $e^+e^- \to Z + h/H$ and the associated production $e^+e^- \to A + h/H$ for the neutral Higgs particles and $e^+e^- \to H^+H^-$ for the charged Higgs bosons. Neutral Higgs masses $M_A \lesssim 91.9\,\text{GeV/c}^2$ and $M_{h/H} \lesssim 91\,\text{GeV/c}^2$ are excluded [566] as well as charged Higgs masses $M_{H^\pm} \lesssim 78.6\,\text{GeV/c}^2$ [567].

The lightest Higgs boson h will mainly decay into $b\bar{b}$ and $\tau^+\tau^-$ pairs, since its mass is below $\sim 135\,\text{GeV/c}^2$, see Fig. 11.2a. Close to its upper bound in mass all decay modes as for the SM Higgs boson open up rapidly. For large values of $\tan\beta$ the heavy scalar and pseudoscalar Higgs particles H, A will decay predominantly into $b\bar{b}$, $\tau^+\tau^-$ pairs, too, due to the enhanced Yukawa couplings for down-type fermions. The branching ratios for the decays into $b\bar{b}$ and $\tau^+\tau^-$ are about 90% and 10% respectively. Other heavy scalar Higgs decay modes as $H \to t\bar{t}$, W^+W^-, ZZ, hh, AA develop sizeable branching ratios only for small values of $\tan\beta$ (see Fig. 11.2b) and analogously the pseudoscalar Higgs decays $A \to t\bar{t}$, gg, Zh (see Fig. 11.2c). The charged Higgs bosons decay mainly into $\tau\nu_\tau$ pairs for $M_{H^\pm} \lesssim 180\,\text{GeV/c}^2$ and into tb final states above (see Fig. 11.2d). All other decay modes do not acquire branching ratios larger than a few per cent. The (SUSY–)QCD [385–391, 549, 562, 568] and (SUSY–)electroweak corrections [392–395, 568, 569] to the fermionic decay modes are sizeable. In addition to the usual large QCD corrections, significant corrections arise from

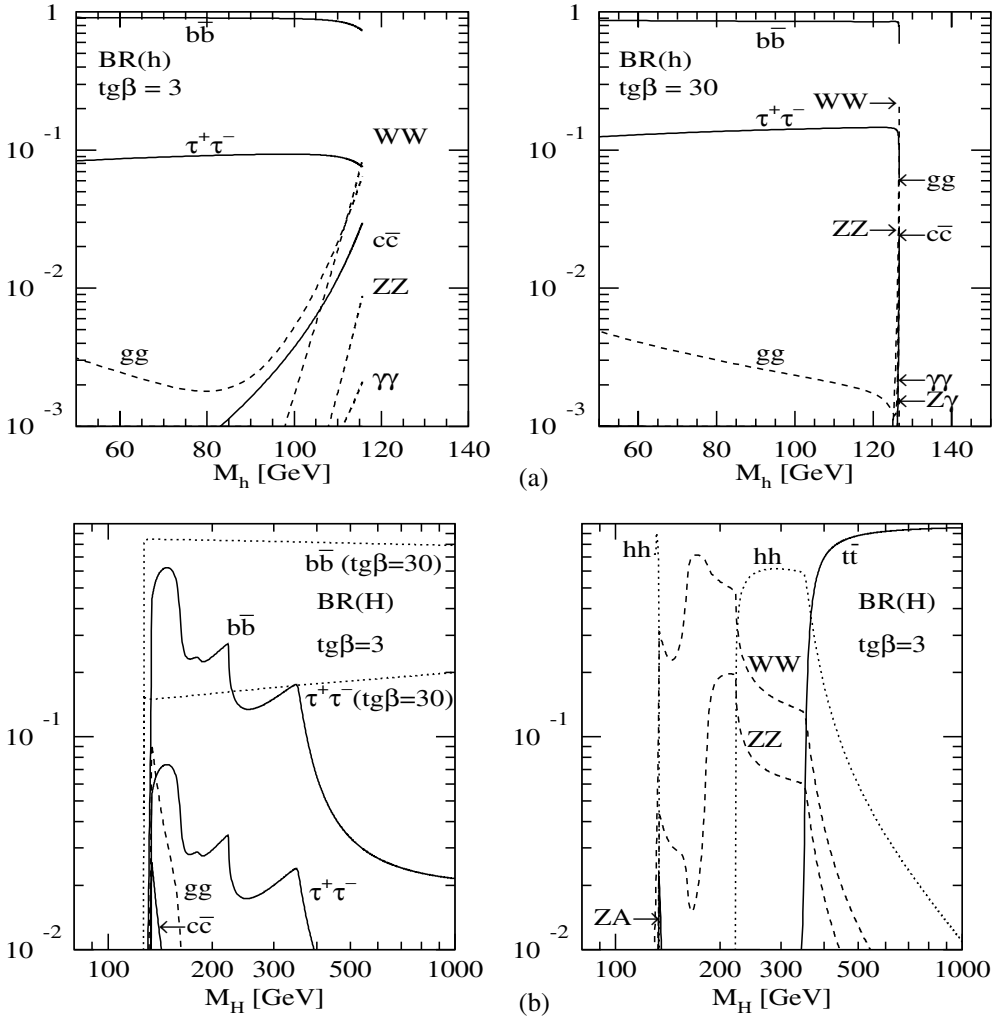

Figure 11.2. Branching ratios of the MSSM Higgs bosons h, H, A, $H^{\pm}$ for non-SUSY decay modes as a function of the masses for two values of $\tan\beta = 3$, 30 and maximal mixing. The common squark mass has been chosen as $M_S = 1\,\mathrm{TeV/c^2}$. The other SUSY–parameters have been chosen as $M_2 = m_{\tilde{g}} = \mu = 1\ \mathrm{TeV/c^2}$ and $A_{t,b} = 2783\,(2483)\,\mathrm{TeV/c^2}$ for $\tan\beta = 3(30)$. (Continued on next page.)

virtual sbottom/stop and gluino/gaugino exchange contributions in the $h, H, A \to b\bar{b}$ and $H^{\pm} \to tb$ decay modes [549, 562, 568, 569]. The dominant part of the latter corrections can be absorbed in improved bottom Yukawa couplings. In this way these contributions can also be resummed up to all orders thus yielding reliable perturbative results [560, 563]. The rare photonic decay modes $h, H, A \to \gamma\gamma$ are mediated by W, t, b loops as in the SM Higgs case and additional contributions from charged Higgs bosons, charginos and sfermions, if these virtual particles are light enough [20, 369, 370]. The QCD corrections to these decay modes can reach a few per cent in the relevant mass regions [396–402]. If decays into supersymmetric particles, i.e. gauginos and sfermions, are possible, they acquire significant branching ratios and can even be the dominant decay modes [20, 369, 370, 570, 571]. In contrast to the SM the

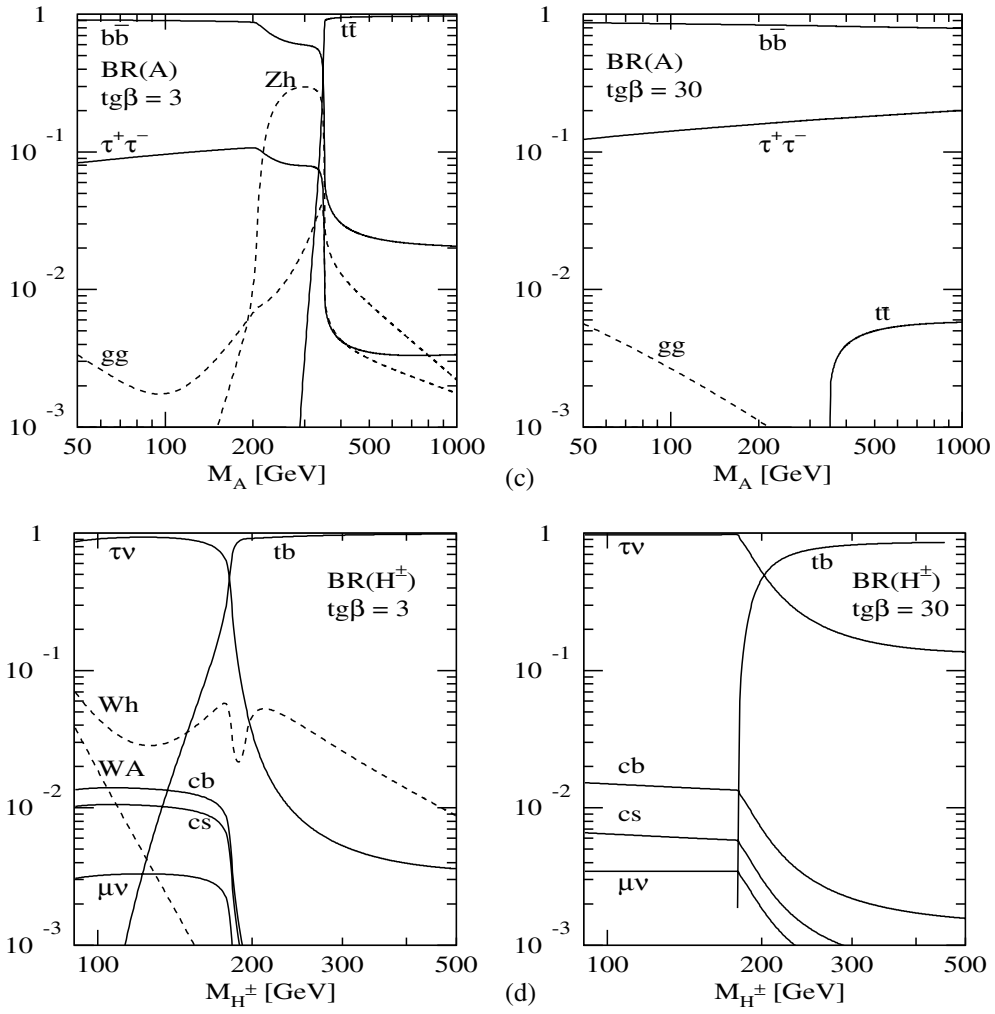

Figure 11.2. Continued.

total widths of the MSSM Higgs bosons do not exceed several tens of GeV, so that the MSSM Higgs particles appear as narrow resonances.

The dominant neutral MSSM Higgs production mechanisms for small and moderate values of $\tan\beta$ are the gluon fusion processes

$$gg \to h, H, A$$

which are mediated by top and bottom loops as in the SM case, but in addition by stop and sbottom loops for the scalar Higgs bosons h, H, if the squark masses are below about $400\,\mathrm{GeV/c^2}$ [572]. The NLO QCD corrections to the quark loops are known in the heavy quark limit as well as including the full quark mass dependence [409–411, 413–416]. They increase the cross sections by up about 100% for smaller $\tan\beta$ and up to about 40% for very large $\tan\beta$, where the bottom loop contributions become dominant due to the strongly enhanced bottom Yukawa couplings. The limit of heavy quarks is only applicable for $\tan\beta \lesssim 5$ within about 20–25%, if full mass dependence of the LO terms is taken into

account [20, 369, 370, 412]. Thus the available NNLO QCD corrections in the heavy quark limit [417–420] can only be used for small and moderate $\tan\beta$, while for large $\tan\beta$ one has to rely on the fully massive NLO results [409–411]. The QCD corrections to the squark loops are only known in the heavy squark limit [572] and the full SUSY–QCD corrections in the limit of heavy squarks and gluinos [573–576]. The pure QCD corrections are of about the same size as those to the quark loops thus rendering the total K factor of similar size as for the quark loops alone with a maximal deviation of about 10% [572]. The pure SUSY–QCD corrections are small [573–576]. The NNLL resummation of the SM Higgs cross section [421] can also be applied to the scalar MSSM Higgs cross sections in the regions, where the heavy quark and squark limits are valid. The same is also true for the NLO QCD corrections to the p_T distributions [428–432] and the NNLL resummation of soft gluon effects [433–443], i.e. for small values of $\tan\beta$, M_H and p_T only. However, for large values of $\tan\beta$ the p_T distributions are only known at LO, since the bottom loops are dominant and the heavy top limit is not valid. An important consequence is that the p_T distributions of the neutral Higgs bosons are softer than for small values of $\tan\beta$ [577].

The vector-boson fusion processes [449, 451]

$$pp \to qq \to qq + WW/ZZ \to qq + h/H$$

play an important role for the light scalar Higgs boson h close to its upper mass bound, where it becomes SM-like, and for the heavy scalar Higgs particle H at its lower mass bound. In the other regions the cross sections are suppressed by the additional SUSY-factors of the Higgs couplings. The NLO QCD corrections to the total cross section and the distributions can be taken from the SM Higgs case and are of the same size [452, 453]. The SUSY–QCD corrections mediated by virtual gluino and squark exchange at the vertices turned out to be small [578].

Higgs-strahlung off W, Z gauge bosons [454, 455]

$$pp \to q\bar{q} \to Z^*/W^* \to H + Z/W$$

does not play a major role for the neutral MSSM Higgs bosons at the LHC. The NLO [456] and NNLO [457] QCD corrections are the same as in the SM case, and the SUSY–QCD corrections are small [578]. The SUSY–electroweak corrections are unknown.

Higgs radiation off top quarks [459–463]

$$pp \to q\bar{q}/gg \to h/H/A + t\bar{t}$$

plays a significant role at the LHC for the light scalar Higgs particle only. The NLO QCD corrections are the same as for the SM Higgs boson with modified top and bottom Yukawa couplings and are thus of moderate size [162, 464, 465]. The SUSY–QCD corrections have been computed recently for the light scalar case [579]. They are of moderate size.

For large values of $\tan\beta$ Higgs radiation off bottom quarks [459–463]

$$pp \to q\bar{q}/gg \to h/H/A + b\bar{b}$$

constitutes the dominant Higgs production process. The NLO QCD corrections can be taken from the analogous calculation involving top quarks. However, they turn out to be very large [580, 581]. The main reason is that the integration over the transverse momenta of the final state bottom quarks generates large logarithmic contributions. The resummation of the latter requires the introduction of bottom quark densities in the proton, since the large logarithms are related to the DGLAP-evolution of these densities. Their DGLAP-evolution

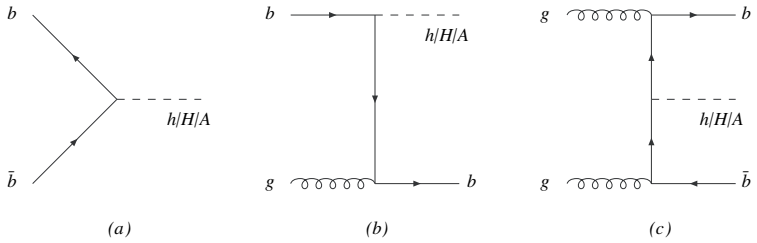

Figure 11.3. Typical diagrams for all Higgs boson production mechanisms related to Higgs radiation off bottom quarks at leading order: (a) $b\bar{b} \to h/H/A$, (b) $gb \to b + h/H/A$, (c) $gg \to b\bar{b} + h/H/A$.

resums them. This leads to an approximate approach starting from the process [582] (see Fig. 11.3a)

$$pp \to b\bar{b} \to h/H/A$$

at LO, where the transverse momenta of the incoming bottom quarks, their masses and their off-shellness are neglected. The NLO [583, 584] and NNLO [585] QCD corrections to this bottom-initiated process are known and of moderate size, if the running bottom Yukawa coupling at the scale of the Higgs mass is introduced. At NNLO the full process $gg \to h/H/A + b\bar{b}$ (see Fig. 11.3c) contributes for the first time. At this order a proper matching to the fully massive result for this process can be performed [586, 587] so that the final expression provides an improved result, which takes into account the resummation of the large logarithms and mass effects. The fully exclusive $gg \to h/H/A + b\bar{b}$ process, calculated with four active parton flavours in a fixed flavour number scheme (FFNS), and this improved resummed result, calculated with 5 active parton flavours in the variable flavour number scheme (VFNS), will converge against the same value at higher perturbative orders. The best agreement between the NLO FFNS and NNLO VFNS is achieved, if the factorisation scale of the bottom quark densities is chosen as about a quarter of the Higgs mass [588, 589]. If only one of the final state bottom jets accompanying the Higgs particle is tagged, the LO bottom-initiated process is $gb \to b + h/H/A$ (see Fig. 11.3b), the NLO QCD corrections of which have been calculated [589, 590]. They turn out to reach $\mathcal{O}(40-50\%)$. The situation concerning the comparison with the FFNS at NLO is analogous to the total cross section. Agreement within the respective theoretical uncertainties is found for a factorisation scale of about a quarter of the Higgs mass [588]. If both bottom jets accompanying the Higgs boson in the final state are tagged, one has to rely on the fully exclusive calculation for $gg \to b\bar{b} + h/H/A$.

All neutral MSSM Higgs production cross sections including the NLO QCD corrections are shown in Fig. 11.4.

The dominant charged Higgs production process is the associated production with heavy quarks [591–593] (see Fig. 11.5a)

$$pp \to q\bar{q}, gg \to H^- + t\bar{b} \qquad \text{and c.c.}$$

The NLO QCD and SUSY–QCD corrections have very recently been computed [594]. They are of significant size due to the large logarithms arising from the transverse-momentum integration of the bottom quark in the final state and the large SUSY–QCD corrections to the bottom Yukawa coupling. The large logarithms can be resummed by the introduction of bottom quark densities in the proton in complete analogy to the neutral Higgs case. In this

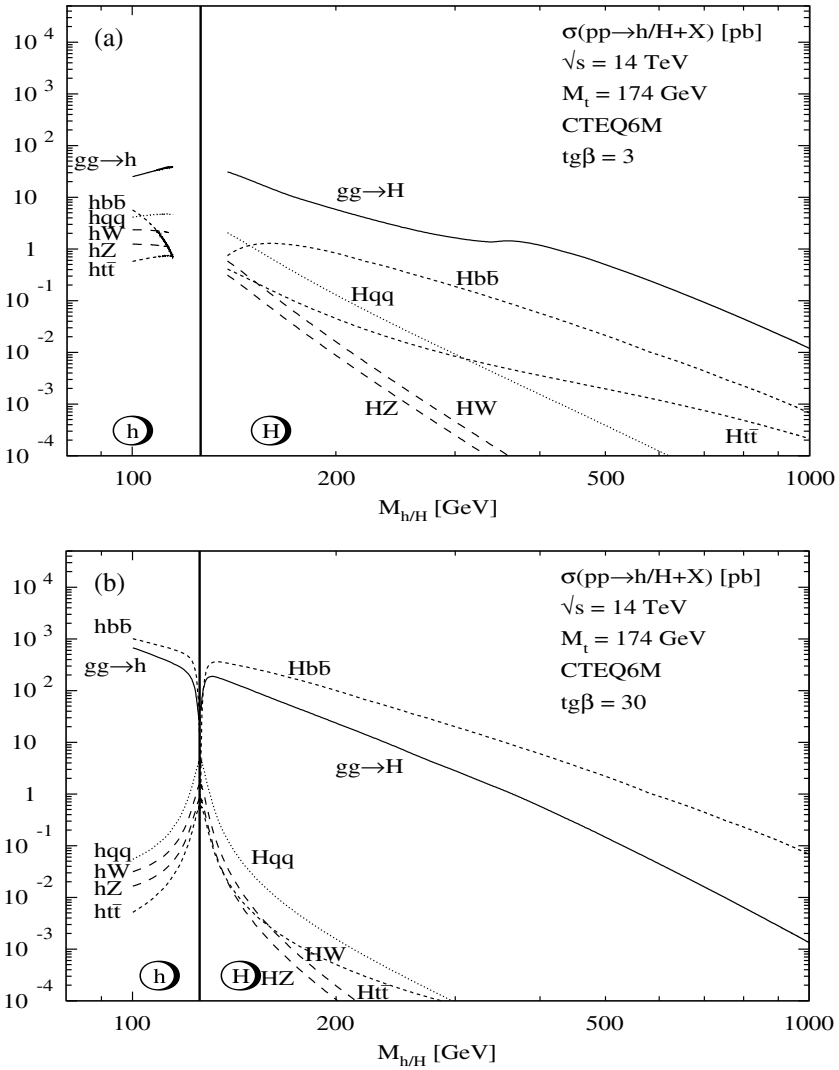

Figure 11.4. Neutral MSSM Higgs production cross sections at the LHC for gluon fusion $gg \to \Phi$, vector-boson fusion $qq \to qqVV \to qqh/qqH$, Higgs-strahlung $q\bar{q} \to V^* \to hV/HV$ and the associated production $gg, q\bar{q} \to b\bar{b}\Phi/t\bar{t}\Phi$, including all known QCD corrections. (a) h, H production for $\tan\beta = 3$, (b) h, H production for $\tan\beta = 30$, (c) A production for $\tan\beta = 3$, (d) A production for $\tan\beta = 30$. The same parameters as in Fig. 11.2 have been adopted. (Continued on next page.)

approach the LO process is $gb \to H^- t$ and the charge conjugate. The NLO SUSY–QCD corrections have been derived in [595–598] and found to be of significant size. This process, however, relies on the same approximations as all bottom-initiated processes. A quantitative comparison of the processes $gb \to H^- t$ and $gg \to H^- + t\bar{b}$ at NLO is missing so far.

The second important charged Higgs production process is charged Higgs pair production in a Drell–Yan type process (see Fig. 11.5b)

$$pp \to q\bar{q} \to H^+ H^-$$

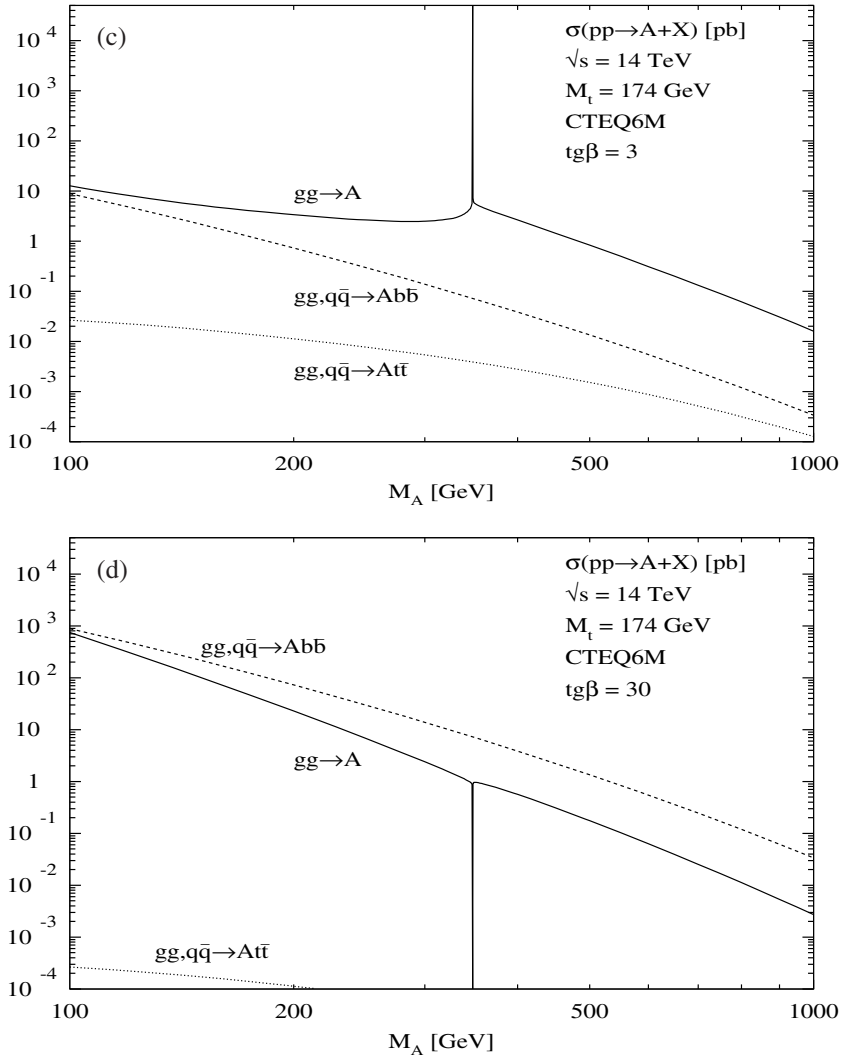

Figure 11.4. Continued.

which is mediated by s-channel photon and Z-boson exchange. The NLO QCD corrections can be taken from the Drell–Yan process and are of moderate size as in the case of the neutral Higgs-strahlung process discussed before. The genuine SUSY–QCD corrections, mediated by virtual gluino and squark exchange in the initial state, are small [578].

Charged Higgs pairs can also be produced from gg initial states by the loop-mediated process [599–603] (see Fig. 11.5c)

$$pp \to gg \to H^+H^-$$

where the dominant contributions emerge from top and bottom quark loops as well as stop and sbottom loops, if the squark masses are light enough. The NLO corrections to this process are unknown. This cross section is of similar size as the bottom-initiated process [603] (see Fig. 11.5e)

$$pp \to b\bar{b} \to H^+H^-$$

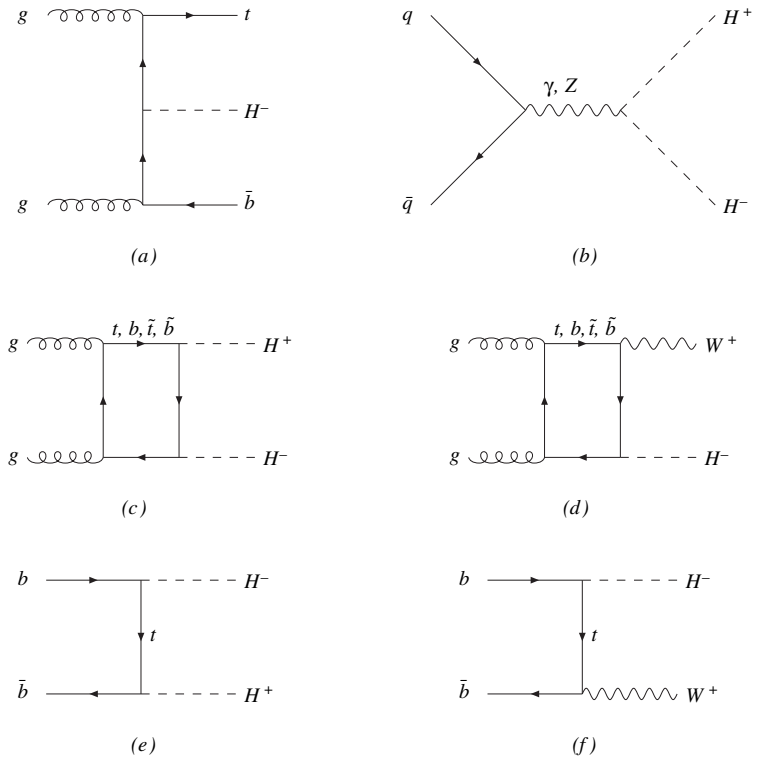

Figure 11.5. Typical diagrams for charged Higgs boson production mechanisms at leading order: (a) $gg \to H^- t\bar{b}$, (b) $q\bar{q} \to H^+H^-$, (c) $gg \to H^+H^-$, (d) $gg \to W^+H^-$, (e) $b\bar{b} \to H^+H^-$, (f) $b\bar{b} \to W^+H^-$.

which relies on the approximations required by the introduction of the bottom densities as discussed before and is known at NLO [604]. The SUSY–QCD corrections are of significant size. The pure QCD corrections and the genuine SUSY–QCD corrections can be of opposite sign.

Finally, charged Higgs bosons can be produced in association with a W boson [605–607] (see Fig. 11.5d)

$$pp \to gg \to H^+W^- \qquad \text{and c.c.}$$

which is generated by top-bottom quark loops and stop-sbottom loops, if the squark masses are small enough. This process is known at LO only. The same final state also arises from the process [605, 606, 608] (see Fig. 11.5f)

$$pp \to b\bar{b} \to H^+W^- \qquad \text{and c.c.}$$

which is based on the approximations of the VFNS. The QCD corrections have been calculated and turn out to be of moderate size [609, 610].

11.2. Higgs boson channels

11.2.1. Associated $b\bar{b}H$ production with $H \to \tau\tau \to e^{\pm}\mu^{\mp} + E_{\mathrm{T}}^{\mathrm{miss}}$

Compared to the hadronic and semi-leptonic final states described in Section 5.2, the fully leptonic final states are suppressed by relatively small branching ratio $\mathrm{BR}(\tau \to \mu\nu\nu) \sim 0.174$ and $\mathrm{BR}(\tau \to e\nu\nu) \sim 0.178$, but the signal is clean and easy to trigger.

The signal consists of events in which the Higgs boson decays into two tau leptons which in turn decay leptonically. Two possibilities exist, either to select any-two-lepton final states, which have larger signal rate, or electron + muon final states for which the background is easier to suppress. Here the electron + muon final state is chosen.

The main backgrounds for $H/A \to \tau\tau$ with $e\mu$ final state are the Drell–Yan $\tau\tau$ production, the $t\bar{t}$ and the Wt production where the W boson coming from top quark decay decays leptonically, the $\tau\tau b\bar{b}$ production, and the $b\bar{b}$ background with b quarks decaying semi-leptonically. Other backgrounds are pairs of vector bosons WW or WZ decaying into leptonic final states, but their contribution is small. The $\tau\tau c\bar{c}$ background is also found negligible. The most biggest background arises from those $t\bar{t}$ and Drell–Yan events which involve genuine τ's and b jets and produce events very similar to the signal. No SUSY particle background is assumed.

A detailed description of the analysis can be found in [611].

11.2.1.1. Event generation. The Higgs boson signal is generated with PYTHIA [246]. The signal cross sections and branching ratios are calculated with FEYNHIGGS [142]. TAUOLA package [155] is used for leptonic τ decays in the signal events.

The Drell–Yan $\tau\tau$ production, $b\bar{b}$, WW, WZ and ZZ backgrounds are generated with PYTHIA. The Drell–Yan $\tau\tau$ next-to-leading order cross section of 1891 pb calculated with the program MCFM [56] for $M_{\tau\tau} > 80\,\mathrm{GeV/c^2}$ is used. The $\tau\tau b\bar{b}$ background is generated with COMPHEP [43] with no p_T and η cuts applied on b quarks and the leading order cross section calculated with COMPHEP are used. The Z/γ^* generation is split into two bins of generated $\tau\tau$ mass $m_{\tau\tau}$: 80–100 $\mathrm{GeV/c^2}$ and $> 100\,\mathrm{GeV/c^2}$, and the $\tau\tau b\bar{b}$ is generated in the $\tau\tau$ mass bins of 60–100 $\mathrm{GeV/c^2}$ and $> 100\,\mathrm{GeV/c^2}$.

The $t\bar{t}$ background is generated with TOPREX [44] and PYTHIA and the single top (Wt) events are generated with TOPREX. A cross section of 840 and 60 pb is used for $t\bar{t}$ and Wt events, respectively.

11.2.1.2. Level-1 and HLT selections. The events are triggered with the single and the double electron and muon triggers. The p_T threshold for single muons is 19 GeV/c, for single electrons 26 GeV/c, for double muons 7 GeV/c and for double electrons 14.5 GeV/c. The Level 1 trigger efficiency for the signal of $M_A = 200\,\mathrm{GeV/c^2}$ is 0.96, and the overall trigger efficiency including the HLT is 0.82. The corresponding trigger efficiencies for the Drell–Yan $\tau\tau$, the $\tau\tau b\bar{b}$, the $t\bar{t}$ and the Wt backgrounds are 0.18, 0.29, 0.68 and 0.68, respectively.

In the future also a combined e+mu trigger with symmetric thresholds of 10 GeV/c for the electron and muon will be included. No large gain is expected since events passing e+mu trigger are most probably already triggered by the single muon trigger.

11.2.1.3. Offline selections. The basic event selection is a requirement of two isolated leptons (one e and one μ) with $p_T > 20\,\mathrm{GeV/c}$ in the central detector acceptance region $|\eta| < 2.5$ coming from a reconstructed primary vertex (PV). The electron candidates are required to pass electron identification cuts described in [156]. The efficiency for the electron identification is about 90% for electrons passing the trigger. The leptons are defined isolated when there are no other tracks from the primary vertex with $p_T > 1\,\mathrm{GeV/c}$ within a cone $\Delta R = \sqrt{\Delta\varphi^2 + \Delta\eta^2} \leqslant 0.4$ around the lepton. The p_T cut and the isolation reduce efficiently the backgrounds with soft leptons ($b\bar{b}$, $c\bar{c}$, ..).

The b jets associated with the Higgs boson provide a powerful tool to separate the $b\bar{b}H/A$ events from the Drell–Yan background. The Drell–Yan background in which Z/γ^* decay into a tau pair has a large cross section compared to the Higgs production. However, these

events are mostly produced with no associated jets, and if they have associated jets they are mostly light quark and gluon jets. Therefore the Drell–Yan background can be suppressed by requiring a reconstructed jets present in the event, and even further by requiring that the associated jets are identified as b jets. The b jets associated with the Higgs bosons are generally very soft, which makes their tagging a challenging task. For low jet E_T values the track multiplicity and momenta tend to be low, and many jets do not have enough significant tracks to be identified as a b jet. As a consequence the b tagging efficiency is not very high. The b tagging efficiency of 43% per jet for the signal events with 2% of the mistagging rate is found.

The $t\bar{t}$ background cannot be suppressed with b tagging due the presence of two energetic genuine b jets in the event. In fact, the jet reconstruction and the b-tagging efficiencies are higher for b jets in $t\bar{t}$ events than for those associated with the signal. This can be exploited using a central jet veto: if more than one jet is found, the event is rejected. The threshold of 20 GeV is set on the calibrated E_T for the jets within the tracker acceptance region, $|\eta| < 2.5$. A suppression factor of 8 is obtained against the $t\bar{t}$ background with an efficiency of 60% for the signal.

A missing energy measurement is needed for estimating the fraction of the energy carried away by neutrinos. This information is used in the Higgs boson mass reconstruction. The amount of missing transverse energy is small and close to the detector resolution.

The τ's from the Higgs boson with $M_A = 200\,\mathrm{GeV/c^2}$ travel on average about 5 mm before they decay. Therefore the leptons coming from τ decays are displaced relative to the primary vertex [612]. The track impact parameter measurements in the transverse plane for the two leptons are combined quadratically into one variable $\sigma_{ip} = \sigma_{ip}(\tau_1) \oplus \sigma_{ip}(\tau_2)$, where $\sigma_{ip}(\tau_1, \tau_2)$ are significances of the lepton impact parameters. The leptons in $t\bar{t}$ background come mostly from W decays. The $t\bar{t}$ events with two intermediate τ's cannot be suppressed by using impact parameter.

The neutrinos-charged lepton collinear approximation method for the mass reconstruction in $H/A \to \tau\tau$ is described in section 5.2.5. The mass reconstruction is possible when the two leptons are not in a back-to-back configuration. The back-to-back events are removed with a cut on the angle between the two leptons in the transverse plane $\Delta\varphi(e, \mu) < 175^\circ$. Uncertainties of the missing transverse energy measurement can lead to negative neutrino energies. For the signal $\sim 40\%$ of events are lost when the positive neutrino energies are required. This requirement, however, yields a further suppression of the $t\bar{t}$ and Wt backgrounds, since for these backgrounds the neutrinos are generally not emitted along the lepton directions. The efficiencies of $E_{\nu 1,\nu 2} > 0$ cut for these backgrounds are about 17% and 15%, respectively. The reconstructed $\tau\tau$ mass with $30\,\mathrm{fb^{-1}}$ after all selections, but the mass window, is shown in Fig. 11.6. In the figure the signal of $M_A = 140$, $\tan\beta = 20$ and $200\,\mathrm{GeV/c^2}$, $\tan\beta = 25$ in the m_h^{max} scenario and the backgrounds are presented.

11.2.1.4. Expected number of events. Table 11.1 shows the cross section times branching ratio for the backgrounds for each step of the selections. The signal cross sections for $M_A = 140$, 200 and $250\,\mathrm{GeV/c^2}$ and $\tan\beta = 20$ in the m_h^{max} scenario are shown in Table 11.2. The expected number of events with $30\,\mathrm{fb^{-1}}$ after all cuts, but mass window, is also shown in Tables 11.1 and 11.2. The expected number of events after all cuts including the mass window is shown for the signal and the total background in Table 11.3.

11.2.1.5. Systematic uncertainties and the discovery reach. The uncertainty of the event selection efficiency is related to the uncertainty of the lepton identification efficiency, the jet

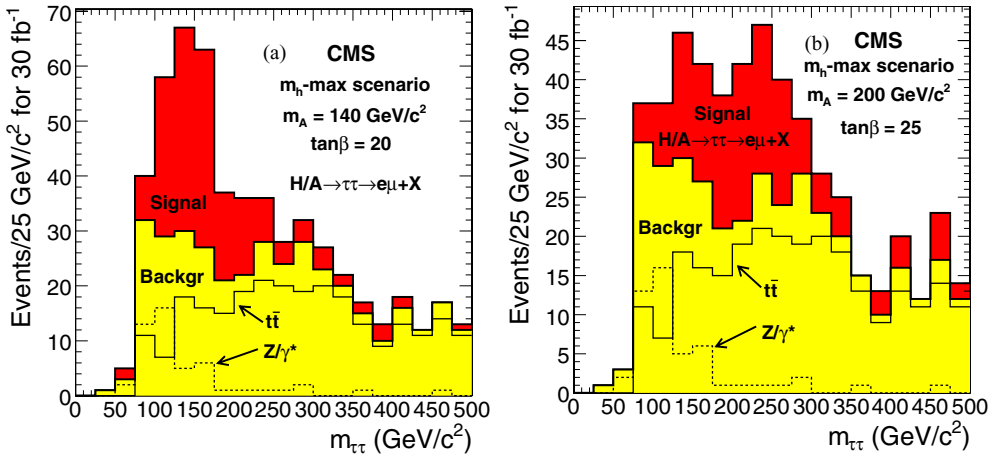

Figure 11.6. The $\tau\tau$ reconstructed mass with 30 fb^{-1} after all selections, but the mass window. The signal in the m_h^{max} scenario and the backgrounds are shown for (a) $M_A = 140\,GeV/c^2$, $\tan\beta = 20$ and (b) $M_A = 200\,GeV/c^2$ and $\tan\beta = 25$.

Table 11.1. The background cross section times branching ratio (in pb) for each step of the selections. The expected number of events at 30 fb^{-1} is also shown.

	Z, γ^*	bbZ, γ^*	tt	tW	bb	VV
$\sigma \times BR$	233.1	3.422	86.2	6.16	36170	7.88
Level 1	83.9	1.85	72.2	5.37	811	5.16
HLT	42.6	0.981	53.7	4.17	78.0	4.10
reconstructed PV	40.8	0.952	53.3	4.11	78.1	3.92
isol e + μ,p_T cut	1.10	0.0270	5.65	0.452	0.0378	0.288
$Q_e + Q_\mu = 0$	1.09	0.0268	5.62	0.451	0.0374	0.248
$\sigma_{ip}(e) \oplus \sigma_{ip}(\mu)$	0.296	0.00745	0.791	0.0550	0.0254	0.0255
N jets > 0	0.0127	0.00527	0.778	0.0509	0.00654	0.0115
b tagging	0.00457	0.00289	0.608	0.0341	0.00312	0.000547
jet veto	0.00344	0.00124	0.0745	0.0166	0.000179	0.000265
$\Delta\varphi(e, \mu)$	0.00295	0.00116	0.0696	0.0159	0.000142	0.000259
$E_{\nu 1,\nu 2} > 0$	0.00124	0.000486	0.0119	0.00246	0.0000661	0.0000546
N_{ev} at 30 fb^{-1}	37.1	14.6	355.8	73.7	2.0	1.6

energy and the missing energy scale and the b tagging efficiency. The jet energy and the missing energy scale uncertainty gives the uncertainty of 7.3% on the $t\bar{t}$ background, which is the dominant background. The uncertainty of the lepton identification efficiency of 2% is used for both electrons and muons. The uncertainty of the b tagging efficiency, 5%, can be estimated from $t\bar{t}$ events as in Ref. [83]. The 5% uncertainty of the mistagging efficiency is assumed [613]. The 5.8% uncertainty of the theoretical prediction of the $t\bar{t}$ cross section is taken. The total systematic uncertainty including the luminosity uncertainty 3% yields a 12% uncertainty for the total background.

The signal significance S with 30 fb^{-1} for the signal of $M_A = 140$, 200 and 250 GeV/c^2 and $\tan\beta = 20$ in the m_h^{max} scenario is shown in Table 11.2 without and with the background systematic uncertainty taken into account. Figure 11.7 shows the discovery reach in the $M_A - \tan(\beta)$ plane in the m_h^{max} scenario with 30 fb^{-1}. The lower (upper) curve corresponds to the case when the background systematic uncertainty is not taken (taken) into account.

Table 11.2. The signal cross section times branching ratio (in pb) for $M_A = 140$, 200 and 250 GeV/c^2 and $\tan\beta = 20$ in the m_h^{max} scenario for each step of the selections. The expected number of events at 30 fb^{-1} is also shown.

m_A	140	200	250
$\sigma \times BR$ (pb)	3.468	1.123	0.493
L1	3.238	1.079	0.479
HLT	2.585	0.923	0.419
reconstructed PV	2.434	0.866	0.395
isol $e^+\mu$, p_T cut	0.258	0.116	0.0613
$Q_e + Q_\mu = 0$	0.256	0.116	0.0612
$\sigma_{ip}(e) \oplus \sigma_{ip}(\mu)$	0.0859	0.044	0.0260
N jets > 0	0.0375	0.0216	0.0130
b tagging	0.0177	0.0104	0.00649
jet veto	0.0115	0.00619	0.00390
$\Delta\varphi(e, \mu)$	0.0106	0.00554	0.00351
$E_{\nu 1,\nu 2} > 0$	0.00601	0.00340	0.00222
N_{ev} at 30 fb^{-1}	180	102	67

Table 11.3. The expected number of the signal plus background and the background events in a given mass windows for 30 fb^{-1} and the signal significance S without and with the background systematic uncertainty taken into account.

	$\Delta m_{\tau\tau}$	N_S+N_B	N_B	$S_{no\,syst.}$	$S_{syst.}$
$m_A = 140$ GeV/c^2, $\tan\beta = 20$	100–200 GeV/c^2	225	107	9.9	7.3
$m_A = 200$ GeV/c^2, $\tan\beta = 20$	140–250 GeV/c^2	163	109	4.8	3.1
$m_A = 250$ GeV/c^2, $\tan\beta = 20$	160–380 GeV/c^2	244	204	2.7	1.4

11.2.2. Associated $b\bar{b}H$ production with $H \to \mu^+\mu^-$

The Higgs boson production in association with b quarks, $pp \to b\bar{b}\phi$ (ϕ = h, H, A) followed by the $\phi \to \mu\mu$ decay can provide the best measurement for the mass and width of the heavy MSSM Higgs bosons H and A. At high $\tan\beta$ the natural width, sensitive to the $\tan\beta$ value, is comparable or dominates the dimuon mass experimental resolution, thus the measured width can be used to constrain the $\tan\beta$.

This analysis uses the dimuon trigger (Level-1 and HLT) stream. Despite of the small $\phi \to \mu\mu$ branching ratio ($\simeq 10^{-4}$) the precise measurement of the dimuon mass in off-line provides an excellent possibility to suppress the $t\bar{t}$ background. The associated Higgs boson production with b quarks is exploited to suppress the huge Drell–Yan $\mu\mu$ background using the b tagging. Irreducible background from $\mu\mu b\bar{b}$ process was also considered and found to be small.

The analysis was performed in the m_h^{max} scenario for three regions of M_A:

- the so-called decoupling regime, $M_A \gg M_h$, where $M_A \sim M_H$. The Higgs bosons A and H with $M_{A(H)} \geqslant 150$ GeV/c^2 and $\tan\beta \geqslant 15$ were generated.
- the "intensive-coupling regime" $M_A \sim M_h$ defined in [614, 615], where the three neutral Higgs bosons have comparable masses, $M_A \simeq M_H \simeq M_h$ The h, A and H bosons were generated for three mass points of $M_A = 125$, 130 and 135 GeV/c^2 at $\tan\beta = 30$.
- the low M_A regime, $M_A < M_h$, where $M_A \sim M_h$. The Higgs bosons h and A were generated at $M_A = 100$ GeV/c^2 and $\tan\beta \geqslant 20$ points.

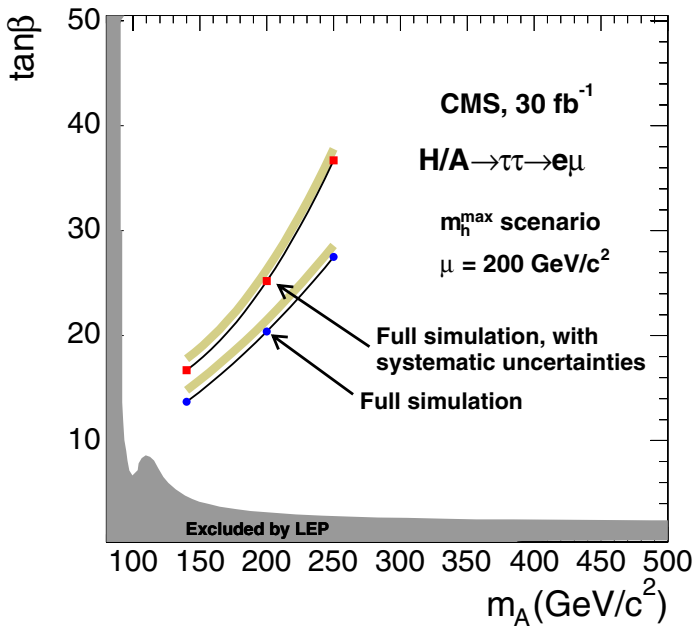

Figure 11.7. The discovery region for $gg \to b\bar{b}H/A$, $H/A \to \tau\tau \to e\mu + X$ channel in M_A-tan β in the m_h^{max} scenario with 30 fb^{-1}.

11.2.2.1. Event generation. The Higgs boson production $pp \to b\bar{b}\phi$ and decay was generated with PYTHIA for the decoupling and low M_A regimes. For the "intensive-coupling regime" events were generated by COMPHEP as described in [615]. The Higgs boson production cross section and branching ratio were evaluated using FeynHiggs 2.3.2 [142–144]. The mass relations between A, H and h bosons and widths were obtained with HDECAY [41] for the "intensive-coupling regime".

The Drell–Yan and $t\bar{t}$ backgrounds were generated with PYTHIA. The Drell–Yan events with b quarks in the final state were excluded to avoid double counting with $\mu\mu b\bar{b}$ background generated with COMPHEP.

11.2.2.2. Offline selection.

Muon identification. The signal is characterised by two well reconstructed, isolated muons. Therefore the event is accepted if there are at least two muons, with opposite charge, both satisfying the following conditions:

- muon transverse momentum $p_T > 20\,GeV/c$;
- a cone of $\Delta R = \sqrt{\Delta\eta^2 + \Delta\phi^2} = 0.35$ is defined around the reconstructed muon track. Then the variable E_{iso} is evaluated as the sum of the energies measured by all the detectors (tracker, ECAL, HCAL) inside this cone with muon momentum excluded. The muon is defined *isolated* if $E_{iso} < 10\,GeV$.

Rejection of $t\bar{t}$ background. The rejection of $t\bar{t}$ events is based on two selection cuts and exploits the presence of the neutrino in the top decay chain and of two well reconstructed energetic jets.

The event is accepted if the following conditions are satisfied:

- the missing transverse energy is less than 40 GeV;
- the jets, reconstructed with the Iterative Cone Algorithm [314], must have transverse energy less than 45 GeV and $|\eta| < 5.0$.

B tagging. The presence of b jets in the Higgs boson production is exploited to suppress Drell–Yan $\mu\mu$ background, which otherwise be dominant, especially for dimuon invariant masses below 200 $\mathrm{GeV/c^2}$.

The b quarks in signal events are mainly produced in the forward region, with lower p_{T} with respect to the b quarks coming from $\mathrm{t\bar{t}}$ background.

Two different strategies, based on two distinct cuts, have been developed for the b tagging:

1. The event must contain at least one jet tagged as b jet with the Combined B-Tagging algorithm [616]. This algorithm has been designed to tag mainly central b jets of high transverse energy, thus it is not optimised for the b jets of the signal. In the following this cut will be refereed to as *hard b-tag*.
2. The tracks in the event are classified as *good tracks* if they satisfy:
   - at least 6 hits in the tracker of which at least two belonging to the pixel detectors;
   - transverse momentum $p_{\mathrm{T}} > 2.4\,\mathrm{GeV/c}$;
   - pseudorapidity $|\eta| < 2.4$;
   - transverse impact parameter IP < 0.5 cm;
   - track fit quality $\chi^2/ndf < 5$.

   The event must contain at least two good tracks with transverse impact parameter (IP) in the range $0.01 < IP < 0.1$ cm (only one track if $0.02 < IP < 0.075$ cm).

The first strategy consists on applying selection 1) only. The second strategy is the logical OR between selection 1) and 2) (this strategy will be refereed to as *soft b-tag*).

Results have been calculated for both selections and the one with the best signal significance has been considered.

11.2.2.3. Fitting procedure. Figure 11.8 shows the distribution of reconstructed dimuon invariant mass after all selections for the backgrounds and, as an example, for the signal of $\mathrm{M_A} = 150\,\mathrm{GeV/c^2}$ and $\tan\beta = 40$. The plot has been obtained assuming an integrated luminosity of $30\,\mathrm{fb^{-1}}$ and the hard b-tag. The signal is visible as a peak over a background that exponentially decreases with increasing $M_{\mu\mu}$.

The background is estimated by fitting the dimuon mass distribution in the off-peak regions, where the signal is not present. To identify this region, the *TSpectrum* class in root is used: this class allows to find a signal peak over a background distribution.

The function used in this analysis to parameterise the background has three free parameters:

$$f_B(M_{\mu\mu};\, P_0,\, P_1,\, P_2) = P_0 \times \frac{\Gamma_Z}{2\pi\left(\left(M_{\mu\mu} - M_Z\right)^2 + \left(\frac{\Gamma_Z}{2}\right)^2\right)} + P_1 + P_2 \times M_{\mu\mu}. \tag{11.2}$$

After the background parametrisation function is determined by fitting the background in the off-peak region, a binned likelihood fit method, with three free parameters, is applied over the whole $\mathrm{M}_{\mu\mu}$ range using the function:

$$f_{tot}(M_{\mu\mu};\, M_A, \sigma_{\mu\mu}, \Gamma_A, N_S) = (N_{TOT} - N_S) \times pdf_B(M_{\mu\mu}) + N_S \times V(M_{\mu\mu};\, M_A, \sigma_{\mu\mu}, \Gamma_A) \tag{11.3}$$

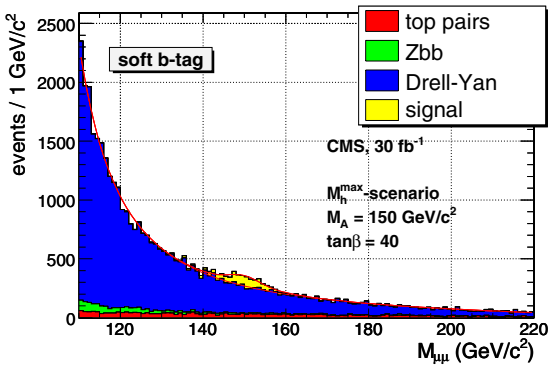

Figure 11.8. Fitting procedure applied to the dimuon reconstruction mass for the main background and for the signal sample with $M_A = 150\,\mathrm{GeV/c^2}$ and $\tan\beta = 40$.

Table 11.4. Effect of the selection cuts on the background and signal cross section (all values in pb). Efficiency w.r.t. previous cut in % is shown in brackets. The *no cut* value for the top pair background refers to the inclusive $t\bar{t}$ production.

	top pairs	Drell–Yan $M_{\mu\mu} > 115\,\mathrm{GeV/c^2}$	Zbb $M_{\mu\mu} > 100\,\mathrm{GeV/c^2}$	signal $\mathrm{M_A} = 130$, $\tan\beta = 30$
No cuts	840	27.8	1.05	0.309
pre-selection cut	20.9 (2.5)	13.0 (46.8)	0.778 (74.1)	0.245 (79.2)
Level-1	19.8 (94.7)	11.9 (91.3)	0.720 (92.5)	0.226 (92.2)
HLT	17.1 (86.1)	11.8 (99.3)	0.712 (98.9)	0.223 (98.7)
Muon Id	5.23 (30.7)	10.4 (87.9)	0.569 (79.9)	0.183 (81.8)
Missing Et	1.20 (23)	9.51 (91.7)	0.503 (88.4)	0.163 (89.2)
Jet Veto	0.317 (26.4)	8.37 (88.1)	0.418 (83.1)	0.138 (84.5)
Soft b-tag	0.238 (75.2)	0.916 (10.9)	0.146 (35.0)	0.0424 (30.9)
$\mathrm{N_{ev}}$ at 30 $\mathrm{fb^{-1}}$	7140	27480	4380	1272
Hard b-tag	0.173 (54.7)	0.0697 (0.83)	0.0616 (14.7)	0.0154 (11.2)
$\mathrm{N_{ev}}$ at 30 $\mathrm{fb^{-1}}$	5190	2091	1848	462

where $pdf_B(M_{\mu\mu})$ is the probability distribution function for the background with fixed parameters, and the second is the Voigt function, i.e. the convolution function between Gaussian and Breit–Wigner functions. The three free parameters are the number of signal events (N_S), the MSSM Higgs boson mass (M_A) and width (Γ_A). The quantity $\sigma_{\mu\mu}$ is the CMS resolution for $M_{\mu\mu}$ and it's value is found from the fit of the Z peak in the Drell–Yan distribution.

To estimate the significance for the potential discovery of the Higgs boson, the likelihood fit is performed in the *signal+background* hypothesis (L_{S+B}) and in the *background* hypothesis (L_B). The significance is defined [102] as:

$$S_L = \sqrt{2\,(\ln L_{S+B} - \ln L_B)}. \tag{11.4}$$

11.2.2.4. Results. Table 11.4 summarises the selection cut efficiency for background and signal. The first set of cuts, down to the Jet Veto cut, is always applied. After that two different b-tags are considered.

Table 11.5. Significance for the decoupling regimes.

Luminosity (fb^{-1})	$\tan\beta = 30$	$\tan\beta = 40$	$\tan\beta = 50$
	$M_A = 150\,GeV/c^2$ - soft b-tag		
10	-	6.5	7.9
20	7.2	10.3	12.1
30	9.7	13.0	15.4
	$M_A = 150\,GeV/c^2$ - hard b-tag		
10	3.8	5.7	6.7
20	6.2	7.3	9.8
30	8.8	9.8	13.1
	$M_A = 200\,GeV/c^2$ - soft b-tag		
20	-	3.1	5.2
30	-	4.7	5.7

Table 11.6. Significance for the intensive coupling regime as a function of the integrated luminosity, for different M_A values.

Luminosity (fb^{-1})	$M_A = 125\,GeV/c^2$	$M_A = 130\,GeV/c^2$	$M_A = 135\,GeV/c^2$
20	7.1	5.4	5.1
30	9.8	7.6	7.1

The systematic effects may be introduced by the experimental technique to fit the background. To estimate such effects, the fitting procedure has been repeated fixing one of the parameters to the measured value increased by its error.

Decoupling regime. Table 11.5 shows the significance as a function of $\tan\beta$, for an Higgs mass of 150 and $200\,GeV/c^2$. In general, where the fitting procedure works properly, the significance is greater then five. Best results are obtained for low values of M_A (as the cross section increases with decreasing Higgs mass) and for high values of $\tan\beta$ (the cross section is proportional to $\tan^2\beta$).

Low M_A regime. In the low M_A regime the background is large due to the presence of the Z^0 peak, thus the signal peak is hidden for the integrated luminosity considered in this study. Better results could be obtained in the LHC high luminosity phase.

Intensive coupling regime. The intensive coupling regime is interesting because all the three neutral Higgs bosons contribute to the signal peak of dimuon mass. Each Higgs boson has rather small intrinsic width (less then $3\,GeV/c^2$ for $\tan\beta = 30$) which is smaller then the mass difference. However, once the mass resolution is taken into account, it becomes impossible to separate the three peaks.

The significance, on the other hand, is quite good despite the vicinity of the Z^0 peak, because the signal cross section is large, thus the discovery can be already done with an integrated luminosity of $20\,fb^{-1}$. Table 11.6 summarises the significance obtained for the three signal samples as a function of the integrated luminosity.

Figure 11.9 shows the discovery contour plot in the plane (M_A, $\tan\beta$) obtained with this analysis. The signal significance inside the grey area is >5 with an integrated luminosity of $30\,fb^{-1}$. The structure of the contour plot near the minimum is due to the features of the signal in the intense coupling regime. The dashed line refers to the analysis without systematic uncertainties. It must be pointed out that the contour of the grey area does not correspond to a significance equal to 5 for $M_A < 180\,GeV/c^2$. The contour for $M_A < 180\,GeV/c^2$ is actually

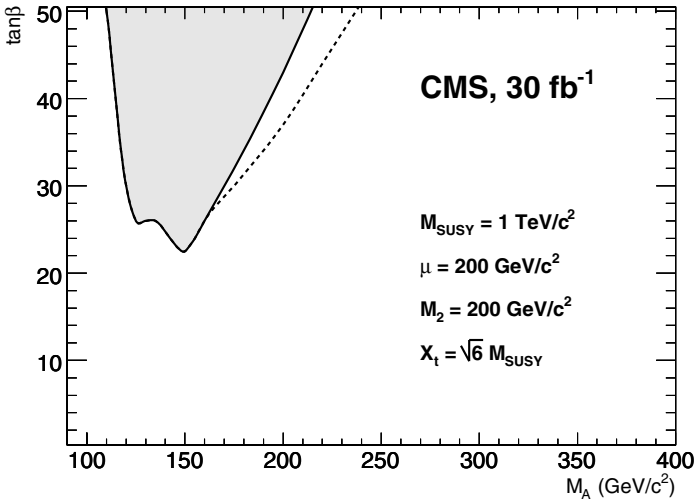

Figure 11.9. Discovery contour plot for the MSSM neutral Higgs in dimuon analysis. The signal significance inside the grey area is > 5 with an integrated luminosity of $30\,\mathrm{fb}^{-1}$.

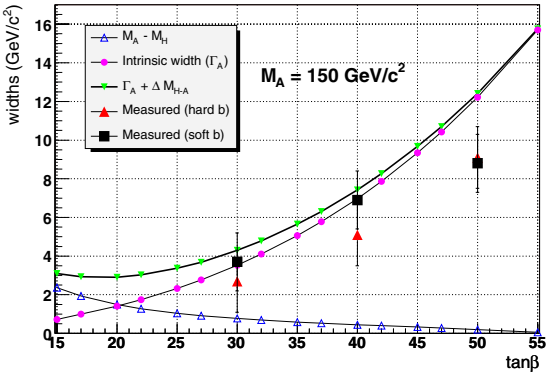

Figure 11.10. The comparison between the expected Higgs boson width and the measured one as a function of $\tan\beta$ for $M_A = 150\,\mathrm{GeV/c^2}$.

determined by the possibility to perform a successful fit to the data, due to the low statistics and the contour plot corresponds to a significance which is actually slightly larger than 5. Only for $M_A > 180\,\mathrm{GeV/c^2}$ the contour corresponds to the signal significance equal to 5. This explains why the effect of the inclusion of the systematic uncertainty is visible only in this mass range. For $M_A < 180\,\mathrm{GeV/c^2}$, the fit fails even if systematic uncertainties are not included in the analysis, and the contour plot does not change.

11.2.2.5. $tan\,\beta$ measurement. The peculiar feature of the dimuon channel at high $\tan\beta$ is the possibility of the direct measurement of the Higgs boson width, $\Gamma_{\mathrm{H/A}}$, which is sensitive to $\tan\beta$ value. Therefore, it is possible to constrain $\tan\beta$ using the measured width. Figures 11.10 compares the intrinsic Higgs boson width (shown as solid circles) with the measured one (solid triangles and solid squares) for $M_A = 150\,\mathrm{GeV/c^2}$. Fitting the mass distribution with a Voigt function, the contribution to the Higgs peak from the muon

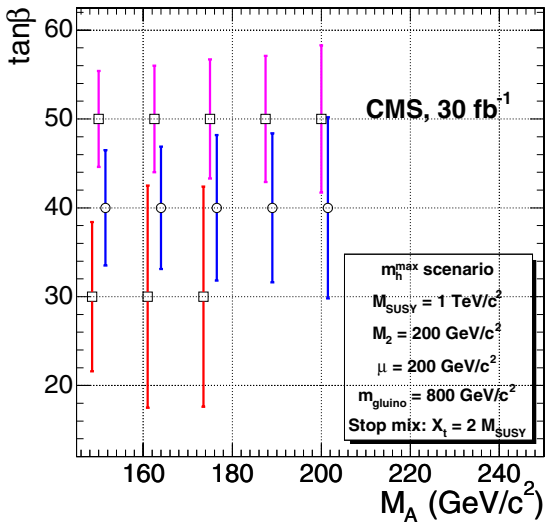

Figure 11.11. Uncertainty on the $\tan\beta$ measurement obtained from the Higgs boson width measurement with an integrated luminosity of 30 fb^{-1}.

invariant mass resolution is subtracted. However, another effect must be taken in account: the degeneracy of the two neutral Higgs bosons, A and H, is not perfect. The value of $M_A - M_H$ is plotted as a function of $\tan\beta$ (open triangles). The effect is particularly evident for $M_A = 150\,\mathrm{GeV/c^2}$ and for low $\tan\beta$, where the mass difference is greater then the intrinsic width. Thus the measured effective width is not the intrinsic one, but it is the sum of the intrinsic width and of Higgs mass difference (inverted triangles): $\Gamma_A + (M_H - M_A)$.

Figure 11.11 shows the uncertainty on the $\tan\beta$ measurement that can be obtained if the MSSM relation between the Higgs boson width and $\tan\beta$ is exploited in the m_h^{max} scenario. A theoretical uncertainty of 15% [560] is included. The $\tan\beta$ can be further constrained using the cross section measurement and exploiting the $\tan\beta$ dependance, $\sigma \times \mathrm{Br} \sim \tan^2\beta_{\mathrm{eff}}$.

11.2.3. Associated $b\bar{b}H$ production with $H \to b\bar{b}$

At high $\tan\beta$ the associated $b\bar{b}H/A$ production followed by the $H/A \to b\bar{b}$ decay has the biggest cross section. Nevertheless, the challenge of observing this channel is driven by the huge QCD multi-jet background expected for the final signature of two soft b-jets from associated Higgs boson production plus two hard b jets from the Higgs boson decay.

In this analysis [617] a study of the observability of this channel is performed using the fast simulation framework of CMS, FAMOS [11]. Signal is also studied with the full GEANT4 [9] CMS detector simulation [8] which allows to validate the fast simulation samples.

This channel can be considered as a cross-check for the discovery once it is known which Higgs boson mass (observed for instance in $b\bar{b}H/A \to b\bar{b}\tau^+\tau^-$ channel) must be looked at. In combination with the $\tau\tau$ mode it can be used to evaluate the ratio of $A(H)b\bar{b}$ and $A(H)\tau\tau$ Yukawa couplings.

11.2.3.1. Event generation. Signal events $b\bar{b}H$, $H \to b\bar{b}$ were produced using PYTHIA for 4 values of M_A: 200, 500, 600 and 800 $\mathrm{GeV/c^2}$. The signal cross sections and branching ratios were calculated with FeynHiggs 2.3.2 [142–144] in the m_h^{max} scenario. The $\tan\beta$ value chosen

Table 11.7. Off-line selection cuts on E_T of the jets (in GeV) for different Higgs boson mass values considered.

M_A	200	500	600	800
E_T^{j1}	90	200	220	260
E_T^{j2}	80	180	200	240
E_T^{j4}		30		

for generation was 50. In the considered M_A-tan β region, A and H Higgs bosons have almost the same mass and can not be distinguished.

Among the Standard Model processes, backgrounds for this channel come mainly from QCD multi-jet production which includes events with four real b jets. Background has been generated with PYTHIA QCD dijet production processes where additional jets are produced from gluon splitting and from the initial and the final state radiation in PYTHIA.

The generation of backgrounds has been weighted in order to get a similar statistics in the whole relevant $\hat{p_T}$ range. Production was split in $\hat{p_T}$ bins of 50 GeV/c from 50 to 1000 GeV/c.

11.2.3.2. Event pre-selection. About 800 million Monte-Carlo events were generated and passed to a pre-selection, requiring a final state containing at least three heavy (b or c) quarks and four jets reconstructed with PYCELL PYTHIA jet finder in the $|\eta| < 4.5$ region, using cone size of 0.5. The thresholds $E_{T_2} > 50$ GeV/c and $E_{T_4} > 10$ GeV/c were applied on the second and fourth highest E_T jet respectively. The QQ + jj background (with Q=b, c and j=light quark or gluon) was estimated to be less than 10% of the total QCD multi-jet background after final selection cuts. After pre-selection, around 30 million events were passed to the detector simulation.

11.2.3.3. Online selection. This channel is triggered at Level 1 by the standard single and multi-jet triggers. At High Level, the inclusive single b-jet trigger [618] stream has been used. The implementation of the High Level double b-jet trigger and relaxing the jet energy thresholds could improve the observability of the signal, especially for low mass Higgs boson ($\sim 200\,\mathrm{GeV/c^2}$).

11.2.3.4. Off-line selection. Analysis has been performed with fast simulated signal and background samples where pile-up was not included, once it was checked with full simulation on signal events that its effect was not significant after requiring jets with reconstructed $E_T > 30$ GeV.

The jets are reconstructed with the iterative cone algorithm [314] using cone size of 0.5. The calorimeter towers with the energy thresholds tuned to minimise the fake jet rate were used as an input for the jet finder. The jet energy corrections were applied using Monte Carlo calibration [619].

The event was required to have at least four jets with the transverse energy of 1st, 2nd and 4th jet greater than thresholds depending upon the M_A point considered, according to Table 11.7. The cut on the 4th jet E_T is motivated by reliability of the analysis simulation without pile-up.

Subsequently, the jets were required to be in the range of the tracker acceptance, $|\eta| < 2.4$. Combined b tagging as described in [616] has been used. At least three b-tagged jets (with discriminant variable > 2), among the 4 highest E_T jets, are requested in the analysis; two of them must be the two highest E_T jets. It would also have been possible to be less restrictive

Table 11.8. Signal selection cumulative efficiencies for $M_A = 600\,GeV/c^2$, $\tan\beta = 50$ and background cumulative efficiencies. The signal to background ratio, S/B, is also shown.

Selection	Signal efficiency	Background efficiency	S/B (full mass range)
None	1	1	1.85×10^{-7}
Pre-selection	5.14E−01	5.94E−03	1.60×10^{-5}
At least 4 jets	5.01E−01	5.85E−03	1.58×10^{-5}
E_T^{j1}	3.10E−01	1.57E−04	3.66×10^{-4}
E_T^{j2}	1.86E−01	4.76E−05	7.21×10^{-4}
E_T^{j4}	1.02E−01	3.24E−05	5.82×10^{-4}
Jets in $\|\eta\| \leqslant 2.4$	8.25E−02	2.26E−05	6.73×10^{-4}
b tagging of 1 jet	3.61E−02	2.44E−06	2.73×10^{-3}
b tagging of 2 jets	1.69E−02	2.81E−07	1.11×10^{-2}
b tagging of 3 jets	8.57E−03	5.62E−08	2.82×10^{-2}
centrality > 0.7	7.05E−03	3.69E−08	3.52×10^{-2}

and accept events where only three of the four jets are in the tracker acceptance, with the other outside the tracker acceptance, but this option is not considered in this analysis.

Finally, the centrality variable, defined as

$$C = \frac{\sum E_T}{\sqrt{(\sum E)^2 + (\sum E_z)^2}} \tag{11.5}$$

using the four highest E_T jets in the event, is used to discriminate between signal and background, given its independence from the signal mass. The analysis uses the discrimination power of this variable to reject background events with C lower than 0.7.

Table 11.8 summarises the selection cut efficiencies for background and signal. The signal to background ratio, S/B, is also shown. The event samples used to calculate numbers given in this table are statistically independent from the ones used to optimise the cuts.

11.2.3.5. Signal significance. The criterion for the presence of signal is based on the distribution of the reconstructed Higgs boson mass, considering as mass estimator the invariant mass distribution of the two leading E_T jets. The signal significance, $S/\sqrt{(B)}$ is calculated in the mass window which maximises this ratio. Figure 11.12 shows the reconstructed Higgs boson mass distribution for signal and background after all selections as expected for $60\,fb^{-1}$.

The signal significances in the optimised mass window after all the cuts applied excluding and including the HLT in the analysis chain, can be found in Table 11.9. The HLT decreases the significance up to a factor 10 for low masses ($M_A = 200\,GeV/c^2$). For higher masses, this factor is reduced to less than 2.

11.2.3.6. Background uncertainty and discovery reach in the $M_A - tan\,\beta$ plane. Given the low S/B ratio and the similarities of the signal and background distributions, a careful evaluation of the background has to be performed. The best source of background events will come from real data samples, when available, as it is being done at the Tevatron experiments [620]. The QCD multi-jet background will be determined from data by normalising distributions outside of the signal region, once the mass of the Higgs is known from other channels for example. Data will be also used to extract the background shape with possibly the help of Monte Carlo.

Figure 11.13 shows the effect of the background uncertainty on the discovery reach (with two sigma signal significance) in the M_A-tan β plane. Different curves correspond to the

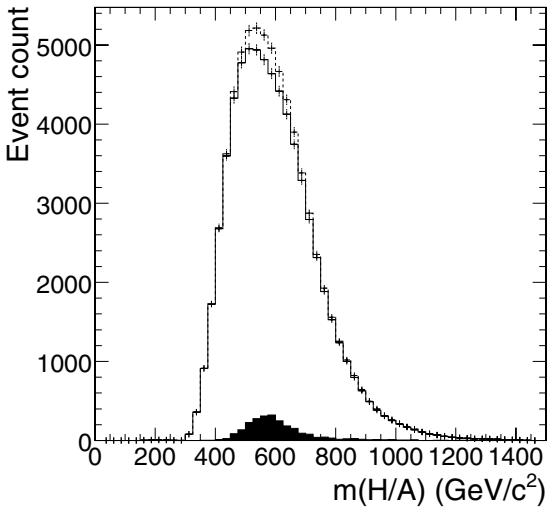

Figure 11.12. The Higgs boson mass distributions after all selections for the signal of $M_A = 600\,GeV/c^2$, $\tan\beta = 50$ in the m_h^{max} scenario (black in foreground), background (solid line) and signal plus background (dashed line) for $60\,fb^{-1}$.

Table 11.9. Signal significance $S/\sqrt{B}$ in optimised mass window after all selections with and without HLT filtering included. The last line shows the low limit of $\tan\beta$ where the 5σ discovery is possible with $60\,fb^{-1}$ in the absence of systematics.

M_A	200	500	600	800
No HLT	30.9	10.4	7.7	2.3
With HLT	2.9	6.4	5.6	3.4
$\tan\beta$ where significance is 5	71	44	47	62

different assumptions on the background uncertainty, from zero uncertainty to 2%. The signal significance is defined as $s = \frac{S}{\sqrt{B+(\varepsilon B)^2}}$, where S is the number of signal events in the mass window, B is the number of background events in the same window and ε is the relative background uncertainty.

The discovery potential of this channel is limited by the low signal-to-background ratio and the similarity of the signal and background distribution shapes. So far, it is not known how well the background can be measured at LHC, thus it is difficult to make predictions about the possibility to observe the MSSM Higgs bosons in the four-b final state.

11.2.4. Charged Higgs boson of $M_H < m_t$ in $t\bar{t} \to H^{\pm}W^{\mp}b\bar{b}$ production with $H^{\pm} \to \tau^{\pm}\nu$, $\tau \to \nu + hadrons$ and $W^{\mp} \to \ell^{\mp}\nu$

A detailed description of the analysis can be found in [621].

11.2.4.1. Event generation and cross sections of signal and background events. The charged Higgs boson in the MSSM can be produced in top quark decays, $t \to H^+b$, if $m_{H^{\pm}} < m_t - m_b$. The branching ratio of top decay to charged Higgs boson depends on both $m_{H^{\pm}}$ and $\tan\beta$ as shown in Fig. 11.14a. The corresponding top decay to $W^{\pm}b$ decreases with increasing $\tan\beta$ so as to keep the sum of branching ratios almost at unity. While the top decay to $H^{\pm}$ or $W^{\pm}$

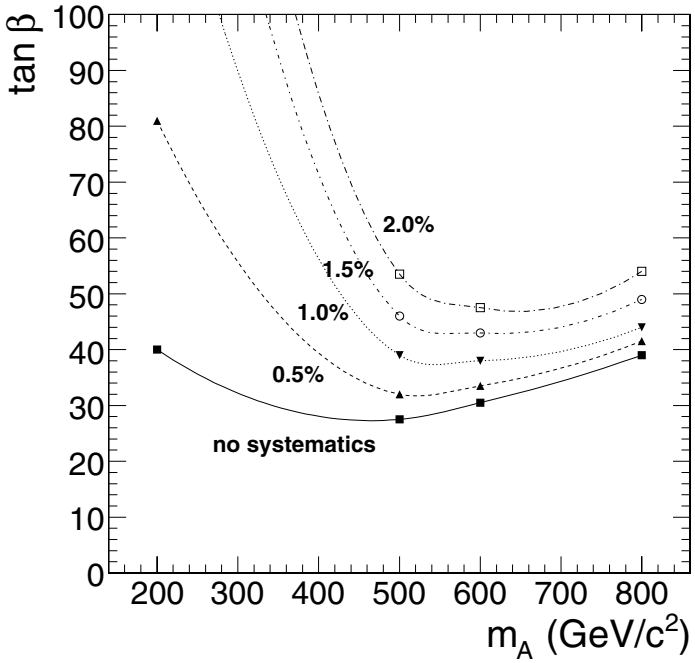

Figure 11.13. Two-sigma significance contours with different assumptions on the background uncertainty at 60 fb^{-1} in the m_h^{max} scenario.

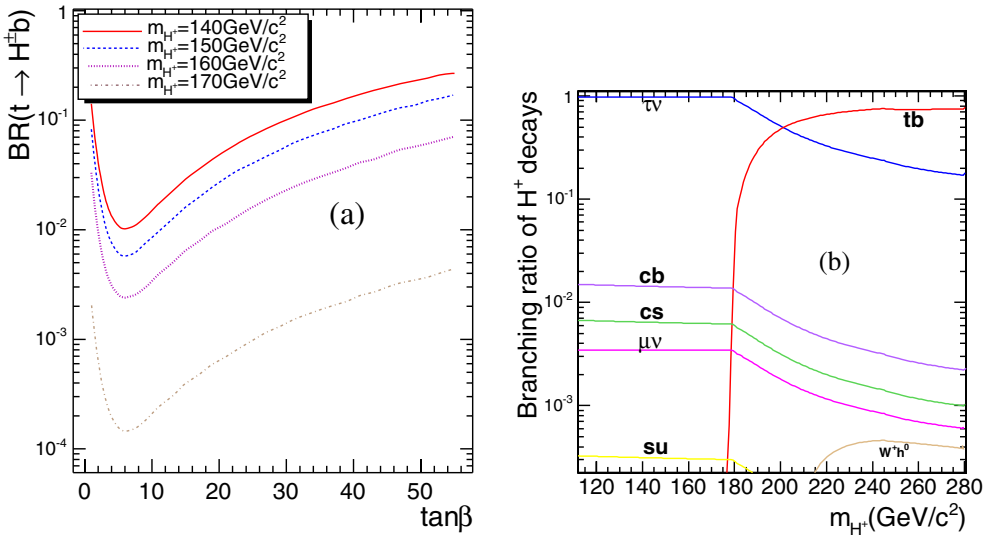

Figure 11.14. (a) Branching ratio of top decay to $H^{\pm}$ vs tan β, and (b) branching ratios for charged Higgs boson decaying to different final states for tan $\beta = 20$.

depends on tan β, the light charged Higgs boson decay to $\tau\nu$ is almost independent of tan β (for tan $\beta > 10$) and is $\sim 98\%$ for all tan $\beta > 10$ and $m_{H^{\pm}} < m_t$ as shown in Fig. 11.14b.

There are two different final states for $t\bar{t} \to H^{\pm}W^{\mp}b\bar{b}$ events depending on $W^{\pm}$ decay to leptons or jets. In this analysis the leptonic decay of $W^{\pm}$ boson is chosen and signal

Table 11.10. Cross section times branching ratio of $t\bar{t} \to H^{\pm}W^{\mp}b\bar{b} \to \tau\nu_{\tau}\ell\nu_{\ell}b\bar{b}$, $\tau \to$ hadrons for $\tan\beta = 20$.

$m_{H^{\pm}}$ (GeV/c^2)	140	150	160	170
Cross section [pb]	10.70	5.06	1.83	0.16

Table 11.11. Cross section times branching ratio of signal events for $m_{H^{\pm}} \simeq m_t$ according to NLO calculations in [597] for $\tan\beta = 20$.

Channel	$gb \to tH^{\pm} \to \ell\nu_{\ell}b\tau\nu_{\tau}$ ($\tau \to$ hadrons) $m_{H^{\pm}} = 170\,\text{GeV/c}^2$	$gg \to tbH^{\pm} \to \ell\nu_{\ell}bb\tau\nu_{\tau}$ ($\tau \to$ hadrons) $m_{H^{\pm}} = 170\,\text{GeV/c}^2$
Cross section [pb]	0.14	0.30

Table 11.12. Cross section times branching ratio of background events.

Channel	$t\bar{t} \to W^+W^-b\bar{b}$ $\to \ell\nu_{\ell}\tau\nu_{\tau}b\bar{b}$ ($\tau \to$ hadrons)	$t\bar{t} \to W^+W^-b\bar{b}$ $\to \ell\nu_{\ell}\ell'\nu_{\ell'}b\bar{b}$ $\ell, \ell' =$ e or μ	$t\bar{t} \to W^+W^-b\bar{b}$ $\to \ell\nu_{\ell}jjb\bar{b}$	$W^{\pm}$ + 3 jets $W^{\pm} \to$ e or μ
Cross section [pb]	25.8	39.7	245.6	840

events are triggered by the single lepton trigger (e or μ). The τ lepton is forced to decay to hadrons. Table 11.10 shows the cross section times branching ratio of $t\bar{t} \to H^{\pm}W^{\mp}b\bar{b}$ events for $\tan\beta = 20$. In this analysis for $m_{H^{\pm}} = 170\,\text{GeV/c}^2$ both $t\bar{t}$ + gb and $gg \to t\bar{b}H^{\pm}$ production processes were used for comparison. The NLO cross section times branching ratio of signal events with $m_{H^{\pm}} \simeq m_t$ is listed in Table 11.11.

The background channels consist of $t\bar{t}$ events with at least a single lepton (e or μ) and τ-jets or jets which could fake τ-jets, $W^{\pm}$ + 3 jet events and also single top (Wt) events which have a small contribution. The cross section of main background channels are shown in Table 11.12.

The $t\bar{t}$, $gb \to tH^{\pm}$ and $gg \to t\bar{b}H^{\pm}$ processes were generated by PYTHIA. The Wt background was generated with TOPREX and the W+3j background was generated by MADGRAPH. The production cross sections for the background processes were normalised to the NLO cross sections (except W + 3 jet).

11.2.4.2. Online event selection and offline reconstruction. Events are triggered by the single lepton triggers (e or μ) at Level 1 and HLT.

In the offline $\geqslant 3$ jets are required to suppress $W^{\pm}$ + njets background with $n < 3$. The jet reconstruction is performed using the iterative cone algorithm and the jet energy corrections, evaluated from γ+jet calibration, were applied. A jet is accepted if it has calibrated $E_T > 40\,\text{GeV}$. Only one b-tagged jet is required in this analysis.

Since events are triggered by lepton from $W \to \ell\nu$ decay, τ jets are identified with an offline τ-tagging algorithm which uses Level 1 τ objects as seeds for τ-jet reconstruction. The first, highest E_T, jet satisfying the conditions of $E_T > 20\,\text{GeV}$ and hottest HCAL tower $E_T > 2\,\text{GeV}$ is used as a τ candidate. A matching cone with $R_m = 0.1$, an isolation cone with $R_i = 0.4$ and a signal cone with $R_S = 0.07$ are defined for checking isolation requirements in the tracker. The ECAL isolation requirement is defined as

$$P_{\text{isol.}} = \sum_{\text{crystals},\,\Delta R_{\text{crystal},\tau-\text{jet}}<0.4} E_{T\text{crystal}} - \sum_{\text{crystals},\,\Delta R_{\text{crystal},\tau-\text{jet}}<0.13} E_{T\text{crystal}} < 5.6\,\text{GeV}. \quad (11.6)$$

Table 11.13. List of selection cuts and their efficiencies for signal events with $m_{H^\pm} < 170\,GeV/c^2$ for $\tan\beta = 20$. Numbers in each row show the remaining cross section after applying the corresponding cut. Numbers in parentheses are relative efficiencies in percent.

	$t\bar{t} \to H^\pm W^\mp b\bar{b}$ $\to \ell\nu_\ell\tau\nu_\tau b\bar{b}$ $m_{H^\pm} = 140\,GeV/c^2$	$t\bar{t} \to H^\pm W^\mp b\bar{b}$ $\to \ell\nu_\ell\tau\nu_\tau b\bar{b}$ $m_{H^\pm} = 150\,GeV/c^2$	$t\bar{t} \to H^\pm W^\mp b\bar{b}$ $\to \ell\nu_\ell\tau\nu_\tau b\bar{b}$ $m_{H^\pm} = 160\,GeV/c^2$
$\sigma \times BR$[fb]	10.7×10^3	5060	1830
L1 + HLT	5170.5(48.3)	2456.3(48.5)	888.9(48.6)
$\geqslant 3$ jets	1889.7(36.5)	795.0(32.4)	264.3(29.7)
$\geqslant 1$ b jet	1103.5(58.4)	427.4(53.8)	131.4(49.7)
< 2 b jets	883.0(80.0)	358.7(83.9)	119.2(90.7)
L1 τ exists	878.4(99.5)	357.4(99.6)	119.0(99.8)
τ-jet reconstruction	875.0(99.6)	356.5(99.7)	118.8(99.8)
Hottest HCAL tower $E_T > 2.GeV$	778.0(88.9)	316.1(88.6)	105.9(89.1)
Tracker isolation	378.2(48.6)	163.5(51.7)	52.7(49.8)
Ecal isolation	292.9(77.4)	134.2(82.1)	43.1(81.8)
τ $E_T > 40\,GeV$	244.3(83.4)	113.0(84.2)	36.5(84.7)
$p_{\text{leading track}}/E_{\tau-\text{jet}} > 0.8$	102.3(41.9)	50.7(44.8)	16.8(45.9)
$Q(\ell) + Q(\tau) = 0$	88.0(86.0)	42.4(83.6)	14.6(87.0)
$E_T^{miss} > 70\,GeV$	51.0(58.0)	25.4(59.9)	9.2(63.3)
Expected Number of events after $10\,fb^{-1}$	510	254	92

When the tracker and ECAL isolation cuts are applied, the τ-jet E_T is required to be more than 40 GeV and the leading track of τ jet is required to carry at least 80% of the visible τ-lepton energy; finally the charges of the τ lepton and the lepton in the event should satisfy the requirement $Q(\ell) + Q(\tau) = 0$.

The missing E_T is reconstructed with the energy corrections applied to jets (Type 1 E_T^{miss} [147, 148]) and a cut on the reconstructed missing E_T ($E_T^{miss} > 70\,GeV$) is applied as a rejection tool against background events, especially $W^\pm + 3$jets.

11.2.4.3. Selection efficiencies and expected number of events. Tables 11.13, 11.14, 11.15 show the selection cuts and their efficiencies for signal and background samples. Other background events such as Wbb, Zbb with $W \to \ell\nu$ ($\ell = e, \mu$) and $Z \to ee$, or $\tau\tau$ turned out to be negligible. Single top background contribution is also small but was considered in the analysis for signal significance calculations.

11.2.4.4. Systematic uncertainties. The systematic uncertainties in the signal significance calculation include the experimental selection uncertainty of the background events and the theoretical cross section calculation uncertainty of the tt and single top background. The $t\bar{t}$ background uncertainty is taken into account as in Eq. 11.7:

$$\Delta^{t\bar{t}}_{\text{sys.}} = \Delta_{\text{lepton reconstruction}} \oplus \Delta_{\geqslant 3\,\text{jet selection}} \oplus \Delta_{1\,\text{b-jet tagging}} \oplus \Delta_{1\,\tau\,\text{tagging}} \oplus \Delta_{\text{lumi.}} \oplus \Delta^{tt}_{\text{theo.}}. \quad (11.7)$$

The $W^\pm + 3$ jets background is assumed to be measured from the real data. The uncertainty of the measurement is estimated by propagating the contribution of events counted in the background area to the signal area and cancelling the common selection cuts

Table 11.14. List of selection cuts and their efficiencies for signal events with $m_{H^\pm} = 170\,\mathrm{GeV/c^2}$ for $\tan\beta = 20$. Numbers in each row show the remaining cross section after applying the corresponding cut. Numbers in parentheses are relative efficiencies in percent.

	$t\bar{t} \to H^\pm W^\mp b\bar{b}$ $\to \ell\nu_\ell \tau\nu_\tau b\bar{b}$ $m_{H^\pm} = 170\,\mathrm{GeV/c^2}$	$gb \to tH^\pm$ $\to \ell\nu_\ell \tau\nu_\tau b$ $m_{H^\pm} = 170\,\mathrm{GeV/c^2}$	$gg \to t\bar{b}H^\pm$ $\to \ell\nu_\ell \tau\nu_\tau b\bar{b}$ $m_{H^\pm} = 170\,\mathrm{GeV/c^2}$
$\sigma \times$ BR[fb]	157	140	297
L1 + HLT	78.0(49.7)	70.5(50.4)	145.4(48.9)
$\geqslant 3$ jets	23.2(29.7)	21.7(30.7)	55.3(38.0)
$\geqslant 1$ bjet	11.5(49.4)	11.7(54.1)	31.9(57.7)
< 2 b jets	10.9(94.8)	10.0(85.5)	25.8(80.9)
L1 τ exists	10.8(99.8)	10.0(99.6)	25.7(99.4)
τ-jet reconstruction	10.8(99.9)	10.0(99.9)	25.5(99.1)
Hottest HCAL tower $E_T > 2.$ GeV	9.6(88.4)	8.9(88.8)	22.6(88.9)
Tracker isolation	4.9(51.3)	5.1(57.2)	11.4(50.5)
Ecal isolation	4.2(84.9)	4.3(84.5)	9.6(84.4)
τ $E_T > 40.$GeV	3.8(90.9)	3.9(90.6)	8.6(89.2)
$p_{\text{leading track}}/E_{\tau-\text{jet}} > 0.8$	1.6(41.7)	1.8(45.9)	3.4(39.6)
$Q(\ell) + Q(\tau) = 0$	1.3(84.4)	1.6(87.2)	2.8(82.6)
$E_T^{\text{miss}} > 70\,\mathrm{GeV}$	0.8(61.7)	1.0(65.2)	1.6(55.3)
Expected Number of events after $10\,\mathrm{fb}^{-1}$	8	10	16

Table 11.15. List of selection cuts and their efficiencies for background events. Numbers in each row show the remaining cross section after applying the corresponding cut. Numbers in parentheses are relative efficiencies in percent.

	$t\bar{t} \to W^+W^-b\bar{b}$ $\to \ell\nu_\ell \tau\nu_\tau b\bar{b}$	$t\bar{t} \to W^+W^-b\bar{b}$ $\to \ell\nu_\ell \ell'\nu_{\ell'} b\bar{b}$	$t\bar{t} \to W^+W^-b\bar{b}$ $\to \ell\nu_\ell jj b\bar{b}$	$W^\pm + 3$ jets $W^\pm \to \ell\nu_\ell$
$\sigma \times$ BR [fb]	25.8×10^3	39.8×10^3	245.6×10^3	$840. \times 10^3$
L1 + HLT	12101.2(46.9)	28429.1(71.4)	99506.6(40.5)	287280(34.2)
$\geqslant 3$ jets	5105.2(42.2)	11306.6(39.8)	66038.6(66.4)	114050(39.7)
$\geqslant 1$ b jet	3428.3(67.1)	7622.0(67.4)	43433.0(65.8)	24292.7(21.3)
< 2 b jets	2325.7(67.8)	5262.7(69.0)	29003.4(66.8)	21207.5(87.3)
L1 τ exists	2310.7(99.3)	5233.7(99.4)	28698.8(98.9)	20613.7(97.2)
τ-jet reconstruction	2303.6(99.7)	5224.4(99.8)	28465.0(99.2)	19438.7(94.3)
Hottest HCAL tower $E_T > 2.$GeV	2034.1(88.3)	3850.6(73.7)	26635.1(93.6)	17125.5(88.1)
Tracker isolation	798.7(39.3)	1120.6(29.1)	6653.3(25.0)	5411.7(31.6)
Ecal isolation	545.6(68.3)	519.5(46.3)	2952.8(44.4)	2554.3(47.2)
τ $E_T > 40.$GeV	405.8(74.4)	341.8(65.8)	1946.8(65.9)	1312.9(51.4)
$p_{\text{leadingtrack}}/E_{\tau-\text{jet}} > 0.8$	123.5(30.4)	131.9(38.6)	377.9(19.4)	224.5(17.1)
$Q(\ell) + Q(\tau) = 0$	95.7(77.5)	56.7(43.0)	78.8(20.9)	27.1(12.1)
$E_T^{\text{miss}} > 70\,\mathrm{GeV}$	51.6(53.9)	29.3(51.8)	36.6(46.4)	10.7(39.3)
Expected Number of events after $10\,\mathrm{fb}^{-1}$	516	293	366	107

uncertainties. Eq. 11.8 describes how systematic uncertainties are taken into account in W+3 jets cross section measurement.

$$\Delta_{\text{sys.}}^{W^\pm+3\,\text{jets}} = \Delta_{\text{stat.}} \oplus \frac{\Delta N_B^{t\bar{t}}}{N_B^{W^\pm+3\,\text{jets}}} \oplus \Delta_{3\,\text{non-b-jet}} \oplus \Delta_{\text{b-jet mistagging}} \oplus \Delta_{\tau\,\text{mistagging}}. \tag{11.8}$$

Table 11.16. The values of different selection uncertainties for $t\bar{t}$ and $W^{\pm}+3$ jets background events at 30 fb^{-1}.

Scale uncertainty of $t\bar{t}$ cross section	5%
PDF uncertainty of $t\bar{t}$ cross section	2.5%
b tagging	5%
τ tagging	4%
Lepton identification	2%
Jet energy scale	3%
Mistagging a non-b jet as a b jet	5%
Mistagging a jet as a τ jet	2%
Non-b-jet identification (anti-b-tagging)	5%
Luminosity uncertainty	5%

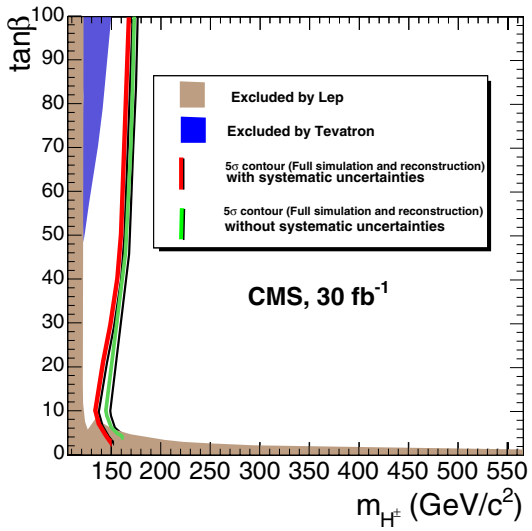

Figure 11.15. The 5σ contour in the $(M_{H^+}, \tan\beta)$ plane for light charged Higgs boson discovery at 30 fb^{-1} including the effect of systematic uncertainties.

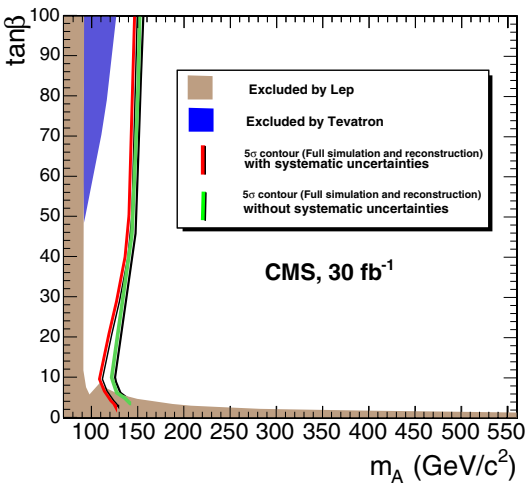

Figure 11.16. The 5σ contour in the $(M_A, \tan\beta)$ plane for light charged Higgs boson discovery at 30 fb^{-1} including the effect of systematic uncertainties.

Table 11.16 lists different sources of systematic uncertainties and their used values corresponding to 30 fb^{-1} in this analysis.

11.2.4.5. Discovery reach in the $M_{A(H^{\pm})} - tan\,\beta$ plane. Figures 11.15 and 11.16 show the 5σ discovery region in the $(M_{H^+}, \tan\beta)$ and $(M_A, \tan\beta)$ planes including the systematic uncertainties. It should be noted that this analysis is systematics dominated and there could be alternative approaches where the systematic uncertainties cancel down to a reasonable level.

11.2.5. Charged Higgs boson of $M_H > m_t$ in $gg \to tbH^{\pm}$ production with $H^{\pm} \to \tau^{\pm}\nu$, $\tau \to hadrons\ \nu$ and $W^{\mp} \to jj$

The $H^{\pm} \to \tau^{\pm}\nu_{\tau}$ decay mode with fully hadronic final state of the charged Higgs boson in the associated production with a top quark has been shown to lead to a clean and almost background-free signature at large $\tan\beta$ in several particle level [622] and fast

simulation [383, 384, 623, 624] studies. The advantages of this decay mode in association with top quark are the large missing transverse energy from $H^{\pm}$, the possibility to disentangle the hadronic τ decay from the hadronic jets, the possibility to reconstruct the top mass to suppress the multi-jet backgrounds, and, in particular, τ helicity correlations favouring the $H^{\pm} \to \tau^{\pm}\nu_{\tau}$ decay over the $W^{\pm} \to \tau^{\pm}\nu_{\tau}$ decay (from the $t\bar{t}$ background). The main backgrounds are due to genuine τ's in multi-jet events from $t\bar{t}$ with $t_1 \to b\tau\nu_{\tau}$, $t_2 \to bqq$, Wt with $W_1 \to \tau\nu_{\tau}$, $W_2 \to qq'$ and W+3 jets with $W \to \tau\nu_{\tau}$. The hadronic QCD multi-jet events can lead to a background through fake τ's and the uncertainty of E_T^{miss} measurement.

A detailed description of the analysis can be found in [625].

11.2.5.1. Helicity correlations. The polarisation states for the τ^+ from $H^+ \to \tau^+\nu_{\tau}$ and from $W^+ \to \tau^+\nu_{\tau}$ are opposite due to the spin-parity properties of the decaying particle. The angular distribution of a pion from the $\tau^{\pm} \to \pi^{\pm}\nu$ decay in the CM frame has the form $(1 + P_{\tau}\cos\theta)$, which leads to more energetic pions in the laboratory frame for the signal ($P_{\tau} = 1$) than for the background ($P_{\tau} = -1$) [622, 626]. The $\tau^{\pm} \to \pi^{\pm}\nu_{\tau}$ decay channel presents 12.5% of the hadronic decay modes. Similarly, the signal pions are more energetic in the τ decays to vector mesons and subsequent decays to one charged pion in the longitudinal polarisation states of the vector meson, $\tau^{\pm} \to \rho_L^{\pm}\nu_{\tau} \to \pi^{\pm}\pi^{\circ}\nu_{\tau}$ (26%) and $\tau^{\pm} \to a_{1L}^{\pm}\nu_{\tau} \to \pi^{\pm}\pi^{\circ}\pi^{\circ}\nu_{\tau}$ (7.5%). For the transverse polarisation states of the vector meson the situation is opposite with more energetic pions from the background. The small contributions from K^* and K in the τ decays lead to similar effects. The helicity correlations can be expressed as a function of the τ-jet momentum fraction carried by the charged pion $R_{\tau} = p_{\pi}/p_{\tau jet}$. As is shown in Refs. [622, 626] the $\tau^{\pm} \to \pi^{\pm}\nu_{\tau}$ decay leads to a δ-function at $R_{\tau} = 1$, the $\rho_L^{\pm}\nu_{\tau} \to \pi^{\pm}\pi^{\circ}\nu_{\tau}$ has contributions at $R_{\tau} \sim 1$ and $R_{\tau} \sim 0$, $\rho_T^{\pm}\nu_{\tau} \to \pi^{\pm}\pi^{\circ}\nu_{\tau}$ and $a_{1T}^{\pm}\nu_{\tau} \to \pi^{\pm}\pi^{\circ}\pi^{\circ}\nu_{\tau}$ have largest contributions around $R_{\tau} \sim 0.5$ while $a_{1L}^{\pm}\nu_{\tau} \to \pi^{\pm}\pi^{\circ}\pi^{\circ}\nu_{\tau}$ peaks at $R_{\tau} \sim 0$.

11.2.5.2. Event generation and simulation. The $gb \to tH^{\pm}$ and $gg \to tbH^{\pm}$ processes contribute to the production of a heavy single charged Higgs boson in association with top quark. In the $gb \to tH^{\pm}$ process the b quark is considered as a massless parton of the incoming proton. Logarithmic factors of the form $\log(p_T^b/m_b)$, due to the collinear b quarks, can be resumed to give a well defined cross section. The $gg \to tbH^{\pm}$ process, where the bottom quarks from the incoming gluons are considered massive, is of the order α_s^2 and is part of the next-to-leading order (LNO) corrections to the leading order (LO) process $gb \to tH^{\pm}$. These processes lead to somewhat different dynamics of the final state objects, visible in particular as a more energetic associated b quark in the $gg \to tbH^{\pm}$ process [627]. Near the top threshold, $m_{H^{\pm}} \sim m_t$, only the exclusive process $gg \to tbH^{\pm}$ can lead to a correct event description. As the correct description of merging these two processes is not possible in the full simulation, signal events were generated with the $gg \to tbH^{\pm}$ process over the full mass range with PYTHIA [69]. The cross sections were normalised to the NLO results of Refs. [597, 628]. The mass of the charged Higgs boson and the $H^{\pm} \to \tau\nu_{\tau}$ branching fraction were calculated with FeynHiggs2.3.2 [142–144] in the m_h^{max} scenario. The $t\bar{t}$ background was generated with PYTHIA, the Wt background with TOPREX [44], the W+3jet background with MADGRAPH [81] and the QCD multi-jet background with PYTHIA. The production cross sections for the background processes were normalised to the NLO cross sections (except W + 3jet). Pre-selections at the particle level, requiring at least one jet with $E_T > 80\,\text{GeV}$, reconstructed with the PYTHIA PYCELL routine with a cone size of 0.5, and containing at least one charged hadron with $p_T > 60\,\text{GeV/c}$, were applied to the $t\bar{t}$ and Wt backgrounds. The τ decays were performed with TAUOLA [155] for the signal and backgrounds. The τ from

Table 11.17. Cross section times branching fraction for $gg \to tbH^{\pm}$, $H^{\pm} \to \tau^{\pm}\nu$, $\tau \to$ hadrons + ν, efficiency for the selection cuts and final number of events for $m_T(\tau\,\text{jet}, E_T^{miss}) > 100\,GeV/c^2$ and for $\Delta\phi(\tau\,\text{jet}, E_T^{miss}) > 60^{\circ}$ with an integrated luminosity of $30\,fb^{-1}$ for the signal events with $m_{H^{\pm}} = 170$, 180, 200 and $400\,GeV/c^2$ and $\tan\beta = 30$.

$m_{H^{\pm}}$ (GeV/c^2)	171.6	180.4	201.0	400.4
σ(NLO) × BR (fb)	1359	1238	776	38
Level-1 trigger	729.9 (53.7%)	688.1 (55.6%)	451.3 (58.2%)	28.5 (75.6%)
HLT trigger	121.0 (16.6%)	128.6 (18.7%)	95.9 (21.2%)	12.1 (42.4%)
Primary vertex	119.9 (99.1%)	127.5 (99.2%)	95.1 (99.2%)	12.0 (99.2%)
Isolated lepton veto	94.4 (78.8%)	104.2 (81.7%)	78.2 (82.2%)	10.1 (85.0%)
$E_T^{miss} > 100\,GeV$	66.7 (70.6%)	70.0 (67.2%)	53.3 (68.2%)	8.2 (80.7%)
$E_T^{\tau jet} > 100\,GeV$	33.7 (50.5%)	36.7 (52.4%)	27.8 (52.1%)	6.7 (81.8%)
$R_\tau > 0.8$	11.2 (33.4%)	11.6 (31.5%)	9.5 (34.2%)	2.3 (34.2%)
1 or 3 signal tracks	10.7 (95.3%)	11.2 (97.1%)	9.1 (95.9%)	2.2 (97.0%)
Tracker isolation	10.0 (93.2%)	10.5 (94.0%)	8.6 (94.9%)	2.1 (93.7%)
ECAL isolation	9.4 (94.4%)	10.0 (95.0%)	8.3 (95.7%)	2.0 (95.8%)
$E_T^{max(HCAL\ cell)} > 2\,GeV$	9.1 (96.5%)	9.4 (93.3%)	7.9 (95.5%)	2.0 (98.7%)
$IP_T^{leading\ track} < 0.3\,mm$	9.0 (97.8%)	9.2 (98.2%)	7.8 (99.0%)	2.0 (99.3%)
$N_{hits}^{leading\ track} \geqslant 10$	8.6 (95.9%)	8.4 (96.5%)	7.4 (94.6%)	2.0 (96.5%)
$\geqslant 3$ jets, $E_T > 20\,GeV$	6.4 (74.4%)	7.2 (80.9%)	5.7 (77.4%)	1.4 (71.9%)
$140 < m_{top} < 210\,GeV/c^2$	4.6 (72.6%)	4.8 (67.2%)	3.6 (63.7%)	0.93 (66.6%)
b discriminator > 1.5	2.0 (43.7%)	2.0 (39.9%)	1.6 (42.7%)	0.37 (40.3%)
$E_T^{bjet} > 30\,GeV$	1.9 (93.2%)	1.8 (95.2%)	1.4 (91.6%)	0.33 (88.2%)
Jet veto, $E_T^{jet} > 25\,GeV$	0.65 (35.2%)	0.63 (34.6%)	0.52 (36.4%)	0.14 (40.9%)
$E_T^{Higgs} > 50\,GeV$	0.61 (91.9%)	0.63 (100%)	0.52 (100%)	0.13 (95.1%)
$m_T > 100\,GeV/c^2$	0.47 (77.3%)	0.49 (78.4%)	0.39 (74.9%)	0.12 (94.8%)
N^{ev}, $m_T > 100\,GeV/c^2$	14.1 ± 3.4	14.7 ± 3.2	11.7 ± 2.3	3.6 ± 0.5
$\Delta\phi(\tau, E_T^{miss}) > 60^0$	0.20 (31.9%)	0.18 (28.5%)	0.28 (53.9%)	0.12 (93.1%)
N^{ev}, $\Delta\phi(\tau, E_T^{miss}) > 60^0$	6.0 ± 2.2	5.4 ± 2.0 (28.5%)	8.3 ± 2.0	3.6 ± 0.5

$H^{\pm}$ was forced to decay to hadrons in the signal samples while all τ decays were generated for the backgrounds.

The analysis was based on event samples from full detector simulation and digitisation at low luminosity $2 \times 10^{33}\,cm^{-2}s^{-1}$.

11.2.5.3. Event selection. Due to an energetic τ jet from $H^{\pm}$ the $gg \to tbH^{\pm}$, $H^{\pm} \to \tau^{\pm}\nu$ ($\tau \to$ hadrons ν, $W^{\mp} \to jj$) events can be most efficiently triggered at the Level-1 with a single τ-jet trigger [76, 280]. At the HLT, a combined E_T^{miss}-τ trigger was used. For this trigger the τ-jet identification was performed in the full tracker (Tracker Tau trigger) [146]. Efficiencies of the Level 1 and HLT triggers are shown in Tables 11.17 and 11.18 for the signal and backgrounds, respectively. Purity of the τ trigger for the signal events is higher than 80%.

In the off-line reconstruction the transverse mass from the τ jet and missing transverse energy requires a fully hadronic event, where E_T^{miss} originates mainly from the $H^{\pm}$. Other sources of E_T^{miss} in the signal events are the leptonic W decays and the semi-leptonic b quark decays. The events with leptonic W decays can be removed with a veto on isolated leptons. The reconstructed electrons and muons were first required to be isolated in the tracker demanding that no track with $p_T > 1\,GeV/c$ was found in a cone of $\Delta R = 0.4$ around the lepton direction. The fraction of events containing at least one muon candidate with $p_T > 15\,GeV/c$ is 24.1%. An isolated muon is found in 8.9% of the signal events.

Table 11.18. Cross section times branching fraction, efficiency for the selection cuts and final number of events for $m_T(\tau\,\text{jet}, E_T^{miss}) > 100\,GeV/c^2$ and for $\Delta\phi(\tau\,\text{jet}, E_T^{miss}) > 60^\circ$ with an integrated luminosity of $30\,fb^{-1}$ for the $t\bar{t}$, Wt, $W^\pm + 3$jets and QCD multi-jet backgrounds background.

	$t\bar{t}$	Wt	$W^\pm$+ 3jets
σ(NLO) × BR (fb)	123820	9140	4.19×10^5
Pre-selection	6440 (5.2%)	237.6 (2.6%)	
Level-1 trigger	4730 (73.4%)	185.6 (78.1%)	1.25×10^5 (29.8%)
HLT trigger	320 (6.9%)	20.5 (11.1%)	4.19×10^3 (3.4%)
Primary vertex	319 (99.8%)	20.4 (99.7%)	4190 (100%)
Isolated lepton veto	314 (89.4%)	18.4 (89.9%)	3456 (82.5%)
$E_T^{miss} > 100\,GeV$	267.4 (85.1%)	15.9 (86.6%)	2674 (77.1%)
$E_T^{\tau\,jet} > 100\,GeV$	167.4 (62.6%)	10.7 (67.2%)	1280 (69.2%)
$R_\tau > 0.8$	35.5 (21.2%)	2.53 (23.7%)	175.4 (13.7%)
1 or 3 signal tracks	31.2 (88.0%)	2.37 (93.7%)	149.3 (85.1%)
Tracker isolation	27.8 (89.1%)	2.18 (91.9%)	132.9 (89.2%)
ECAL isolation	26.1 (93.7%)	2.07 (94.9%)	125.1 (94.1%)
$E_T^{max(HCAL\,cell)} > 2\,GeV$	24.1 (92.4%)	1.95 (94.2%)	105.1 (84.0%)
$IP_T^{leading\,track} < 0.3$	21.4 (88.8%)	1.92 (98.3%)	88.4 (84.1%)
$N_{hits}^{leading\,track} \geqslant 10$	19.9 (92.9%)	1.81 (94.4%)	84.6 (95.7%)
$\geqslant 3$ jets, $E_T > 20\,GeV$	17.3 (87.0%)	1.04 (57.6%)	67.5 (79.8%)
$140 < m_{top} < 210\,GeV/c^2$	12.2 (70.4%)	0.71 (67.7%)	26.6 (39.4%)
b discriminator > 1.5	5.81 (47.7%)	0.34 (48.1%)	1.09 (4.1%)
$E_T^{b\,jet} > 30\,GeV$	5.27 (90.6%)	0.30 (89.2%)	0.82 (75.1%)
Jet veto, $E_T^{jet} > 25\,GeV$	1.48 (28.1%)	0.24 (78.0%)	0.14 (17.2%)
$E_T^{Higgs} > 50\,GeV$	1.44 (97.1%)	0.23 (98.6%)	0.14 (98.3%)
$m_T(\tau\,\text{jet}, E_T^{miss}) > 100\,GeV/c^2$	0.03 (2.0%)	0.003 (1.3%)	0.02 (10.3%)
Events for $m_T > 100\,GeV/c^2$	0.86 ± 0.33	0.09 ± 0.04	0.60 ± 0.60
$\Delta\phi(\tau\text{jet}, E_T^{miss}) > 60^\circ$	0.01 (1.0%)	9.2×10^{-4} (0.4%)	0.013 (6.7%)
Events for $\Delta\phi(\tau\text{jet}, E_T^{miss}) > 60^\circ$	0.30 ± 0.25	0.03 ± 0.02	0.39 ± 0.39

About 84% of these muons were found to originate from $W \to \mu\nu_\mu$. The fraction of events containing at least one electron candidate with $p_T > 15\,GeV/c$ is 72.4% and an isolated electron candidate 41.7%. The final electron identification was done following the methods described in Ref. [156]. The fraction of events removed with a veto on the identified electrons is 7.9%, from which 93.3% are due to genuine electrons from $W \to e\nu_e$.

The missing transverse energy (E_T^{miss}) was reconstructed from the full calorimeter response summing the calorimeter towers and applying the jet energy corrections (Type 1 E_T^{miss} [147, 148]). The hadronic jets with $E_T^{raw} > 20\,GeV$ were calibrated using the corrections from γ+jet calibration. The τ jet was reconstructed in the calorimeter around the Level-1 τ-jet direction in a cone of 0.4 applying energy corrections evaluated for one- and three-prong τ decays. The offline E_T cut on the τ jet was taken to be $E_T^{\tau jet} > 100$ GeV, close to the Level-1 threshold of 93GeV. The tracks were reconstructed inside the jet reconstruction cone. The leading track was searched for in a cone of $R_m = 0.1$ around the τ-jet direction. For an efficient isolation against the hadronic jets a small signal cone of $R_S = 0.04$ was selected. The isolation cone size was taken to be the same as in the HLT Tau trigger, $R_i = 0.4$. The τ-jet isolation in the electromagnetic calorimeter was also applied as described in [280]. The fraction of signal events with $m_{H^\pm} = 200\,GeV/c^2$, where the one-prong (three-prong) τ decays lead to one (three) reconstructed track(s) with $p_T > 1\,GeV/c$ in the signal cone, was found to be in

92.3% (64%). Accidental track reconstruction problems, like shared hits, can lead to fake large-p_T tracks in the hadronic jets [7, 280]. These fake leading tracks are possible in the hadronic multi-jet events but can appear also in the $t\bar{t}$, Wt and W + 3 jet backgrounds if the E_T of the τ jet is below the trigger threshold and the event is triggered with a τ-like hadronic jet. The fake tracks can be suppressed with an upper bound in the transverse impact parameter of the leading track ($IP_T^{\text{leading track}} < 0.3$ mm) and requiring at least 10 hits in the full tracker. The fraction of the $\tau \to e\nu\nu$ events passing the full τ selection was found to be 3% for the $t\bar{t}$ background. This contamination can be efficiently suppressed requiring that the most energetic HCAL tower inside the τ-jet candidate ($E_T^{\text{max(HCAL cell)}}$) has the transverse energy greater than 2 GeV [280].

The τ helicity correlations are best exploited requiring the leading track to carry at least 80% of the τ jet energy. The efficiencies for the $t\bar{t}$ and Wt events, shown in Tables 11.17 and 11.18, are affected by the pre-selection cuts and do not show the expected background suppression for $R_\tau > 0.8$. This cut suppresses the three-prong τ decays leaving 3.1% as the fraction of three-prong τ decays for the signal events with $m_{H^\pm} = 200\,\text{GeV}/c^2$ after all selection cuts.

Due to a limited MC statistics, the trigger simulation was not used in the estimation of the QCD multi-jet background. Events with at least one jet with $E_T > 100$ GeV, containing a track with $p_T > 80$ GeV/c, were used for further analysis. Efficiency for this selection was found to be 5.55×10^{-3} for the QCD multi-jet events generated within the $\hat{p}_T$ interval of $170 < \hat{p}_T < 380\,\text{GeV}/c$. The τ selection cuts, except the E_T^{jet} threshold, are not correlated with the E_T^{miss} cut. Therefore the selection was factorised to E_T^{miss} and τ selections. The efficiency of the τ-selection cuts on the pre-selected events was found to be 1.65%. Combined with the pre-selection, the full τ-selection efficiency for the hadronic multi-jet events in the $\hat{p}_T$ interval considered was found to be 9.2×10^{-5}.

The $gg \to tbH^\pm$ events contain two b jets, one from the decay of the top quark and one associated b jet from the production process. The associated b quark is preferentially emitted in the forward directions and is distributed at smaller p_T values than the b quark from top decay. In about 20% of the signal events, however, this b quark is more energetic than the b quark from the top decay thus contaminating the spectrum of the identified b jet for the top reconstruction. The event reconstruction was performed for events where at least three hadronic jets with $E_T^{\text{jet}} > 20$ GeV were found. A probabilistic secondary vertex algorithm with a discriminator cut was used for b tagging [157]. The fraction of events where the best b-tagged jet is the b jet from $t \to bW$ was found to be 61%. The corresponding fractions for the associated b jets and the quark jets from $W \to qq$ decay were found to be $\sim 26\%$ and $\sim 8\%$, respectively.

The top-quark mass was reconstructed minimising the χ^2 distribution made from the reconstructed and nominal top and W masses, $\chi^2 = ((m_{jj} - m_W)/\sigma_W)^2 + ((m_{jjj} - m_{top})/\sigma_{top})^2$, where m_{jj} and m_{jjj} are the invariant masses of all two- and three-jet combinations in the event and σ_W and σ_{top} are the gaussian widths of the reconstructed true W and top mass distributions. The jet assigned to the top but not to the W presents the b jet from top. For a better reconstruction efficiency, in the presence of a significant contamination from the associated b quark, any of the three jets assigned to the top were tagged requiring the value of the discriminator greater than 1.5 and $E_T > 30$ GeV. A mass resolution of $\sim 11\%$ and a mean reconstructed mass of $\sim 176\ \text{GeV}/c^2$ were obtained, with a fraction of about 40% of correct jet assignments. For a further suppression of the $t\bar{t}$ background, the ordinal jets after top reconstruction were searched for within $|\eta| < 2.5$ and a jet veto was applied. The E_T threshold for the jet veto was set to 25 GeV. The efficiency of this method has decreased compared to

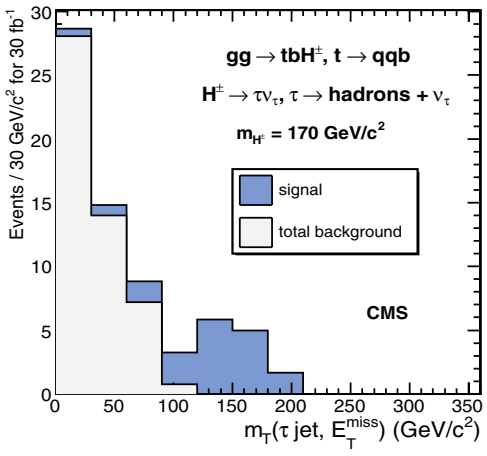

Figure 11.17. Transverse mass reconstructed from the τ jet and missing transverse energy for the $gg \to tbH^{\pm}$, $t \to bW$, $W^{\mp} \to jj$ signal (dark histogram) with $m_{H^{\pm}} = 170\,GeV/c^2$, $\tan\beta = 30$ and for the total background (light histogram) for an integrated luminosity of $30\,fb^{-1}$.

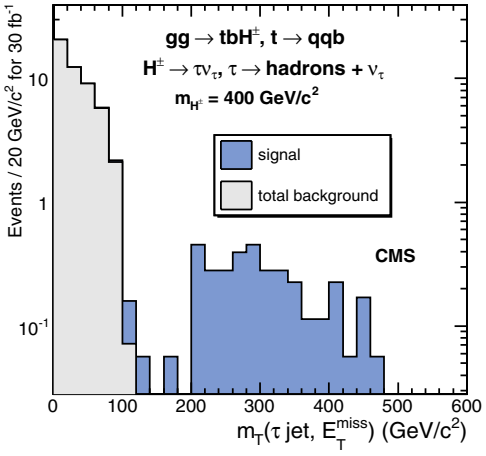

Figure 11.18. Transverse mass reconstructed from the τ jet and missing transverse energy for the $gg \to tbH^{\pm}$, $t \to bW$, $W^{\mp} \to jj$ signal (dark histogram) with $m_{H^{\pm}} = 400\,GeV/c^2$, $\tan\beta = 30$ and for the total background (light histogram) for an integrated luminosity of $30\,fb^{-1}$.

the fast simulation results [623] mainly due to more energetic associated b jets in $gg \to btH^{\pm}$ with respect to the $gb \to tH^{\pm}$ events.

For the $t\bar{t}$, Wt and W + 3jet backgrounds the configuration with large E_T^{miss} and large $E_T^{\tau\,jet}$ can be reached only for strongly boosted W. Therefore to suppress the background from events triggered with a fake τ from a hadronic jet recoiling against the genuine τ jet, a lower bound ($E_T^H > 50\,GeV$) was set on the Higgs boson p_T reconstructed from the τ jet and the missing transverse energy.

The large E_T thresholds lead to an almost two-body (Jacobian peak) situation between the τ jet and missing transverse energy. Therefore an upper edge can be expected in the transverse mass $m_T = \sqrt{2 \times E_T^{\tau jet} \times E_T^{miss} \times (1 - \Delta\phi(\tau jet, E_T^{miss}))}$ at $m_{H^{\pm}}$ for the signal and at m_W for the $t\bar{t}$, Wt and W+3jet backgrounds. The boost required for the $t\bar{t}$, Wt and W+3jet backgrounds to pass the E_T thresholds, leads to small opening angles $\Delta\phi(\tau\,jet, E_T^{miss})$ in the transverse plane. Requiring $\Delta\phi > 60^{\circ}$ removes most of the remaining background for $m_T < 100\,GeV/c^2$. The m_T distributions for the signal and total background are shown in Figs. 11.17 and 11.18 for $m_{H^{\pm}} = 170$ and $400\,GeV/c^2$ and $\tan\beta = 30$, without a cut on $\Delta\phi(\tau\,jet, E_T^{miss})$.

Tables 11.17 and 11.18 show the cross sections and efficiency for the selection cuts for the signal events with $m_{H^{\pm}} = 170$, 180, 200 and $400\,GeV/c^2$ and $\tan\beta = 30$. The trigger efficiency and the efficiency of the primary vertex reconstruction are also shown. Table 11.18 shows the same for the $t\bar{t}$, Wt and W+3jet backgrounds. For the QCD multi-jet background the number of events where at least three jets are found after the E_T^{miss} and τ selections was estimated without the τ selection cuts. At this level of selection the QCD multi-jet events can be assumed to be similar to the W + 3jet events at the same selection level. Therefore the efficiency of the remaining selection cuts was taken from the W+3jet events yielding an estimate of 0.1 ± 0.1 events for $m_T(\tau\,jet, E_T^{miss}) > 100\,GeV/c^2$.

11.2.5.4. Systematic uncertainties on background determination. The background in the signal region $m_T(\tau\,jet, E_T^{miss}) > 100\,GeV/c^2$ may arise from two main sources, the tail due to measurement uncertainties in the backgrounds with $W \to \tau\nu$ decays, and the possibility of

Table 11.19. Value of $\tan\beta$, cross section times branching fraction for $gg \to tbH^{\pm}$, $H^{\pm} \to \tau^{\pm}\nu$, $\tau \to$ hadrons $+\,\nu$, number of selected signal events and the statistical significance (S) for the total background of 1.7 ± 1.0 events with ($S_{syst.}$) and without ($S_{no\,syst.}$) background uncertainty, for the signal with $m_{H^{\pm}} = 170$ to $600\,GeV/c^2$ ($m_A = 150$ to $600\,GeV/c^2$) and for an integrated luminosity of $30\,fb^{-1}$.

$m_{H^{\pm}}$ (GeV/c^2)	171.6	180.4	201.0	300.9	400.7	600.8
$\tan\beta$	30	30	30	30	50	50
σ(NLO) $\times$ BR (fb)	1359.2	1237.6	775.5	118.3	104.9	15.7
Events for $30\,fb^{-1}$	14.1 ± 1.6	14.7 ± 3.2	11.7 ± 2.3	8.3 ± 1.2	10.0 ± 1.4	2.0 ± 0.2
$S_{no\,syst.}$	6.4	6.6	5.5	4.2	4.9	1.2
$S_{syst.}$	5.0	5.2	4.3	3.3	3.8	1.0

fake τ jets, mainly in the QCD multi-jet events. The level of the backgrounds with $W \to \tau\nu$ decays can be measured from data exploiting the precise muon momentum measurement in the W+3jets, $W \to \mu\nu$ events, selecting events in the tail of the transverse mass distribution. The probability of a hadronic jet faking the τ jet can be measured exploiting the γ+jet events, as proposed in Ref. [280]. For this work a Monte-Carlo method was chosen assuming that the probability of the background events to migrate to the signal area depends mainly on the precision of the jet energy and E_T^{miss} measurements. The systematic uncertainty due to the energy scale was estimated varying the jet energy and the E_T^{miss} values with the expected energy scale uncertainties yielding the average values of 3% and 2% for the uncertainties on the efficiency of the E_T^{miss} cut and the efficiency of the selection of three hadronic jets for top reconstruction, respectively. The uncertainty of the τ identification has been estimated to be 8% for the E_T interval of τ jets from $Z \to \tau\tau$ decays [149]. For the b-tagging uncertainty a conservative estimate of 5% was taken. The theoretical uncertainty on the $t\bar{t}$ cross section due to a variation of the scale and PDF has been estimated to be 5.6% [159]. These values yield 11% for the total systematic uncertainty for the $t\bar{t}$ background. For the W+3jet and QCD multi-jet backgrounds the uncertainties due to present MC statistics strongly dominate the measurement uncertainties and therefore the MC statistical uncertainties were used. The total number of background events in the signal region $m_T(\tau\,\text{jet}, E_T^{miss}) > 100GeV$, is 1.7 ± 1.0 events, including the systematic and MC uncertainties.

11.2.5.5. Discovery potential. Table 11.19 shows the number of signal events for $m_{H^{\pm}} = 170$ to $300\,GeV/c^2$ with $\tan\beta = 30$ and for $m_{H^{\pm}} = 400$ to $600\,GeV/c^2$ with $\tan\beta = 50$ and the signal significance (S) calculated according to Poisson statistics [498] with (S_{syst}) and without ($S_{no\,syst.}$) background uncertainty for the total background of 1.7 ± 1.0 events. The cut in the transverse mass $m_T(\tau\,\text{jet}, E_T^{miss}) > 100\,GeV/c^2$ is used to select the signal area. The results are shown for an integrated luminosity of $30\,fb^{-1}$. For the $t\bar{t}$ background the estimated systematic uncertainty of 11% is included. Figure 11.19 shows the 5σ-discovery region in the $m_A - \tan\beta$ plane in the maximal mixing scenario with $\mu = 200\ GeV/c^2$ with and without systematic uncertainties at $30\,fb^{-1}$.

11.2.6. Charged Higgs boson of $M_H > m_t$ *in* $gg \to tbH^{\pm}$ *production with* $H^{\pm} \to tb$

The branching fractions for the decay channels of the charged Higgs boson depend strongly on its mass (see Fig. 11.2). For masses above $m_t + m_b$, the channel $H^{\pm} \to tb$ opens up. Two production channels and corresponding final states were considered in the search for charged Higgs bosons in the $H^{\pm} \to tb$ decay channel [629]:

$$gb \to tH^{\pm} \to ttb \to W^+W^-bbb \to qq'\mu\nu_\mu bbb, \tag{11.9}$$

$$gg \to tH^{\pm}b \to ttbb \to W^+W^-bbbb \to qq'\mu\nu_\mu bbbb. \tag{11.10}$$

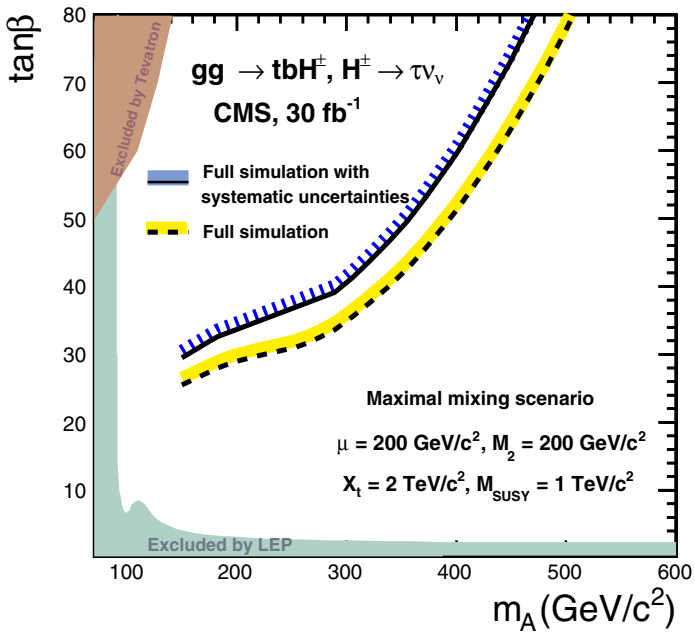

Figure 11.19. The 5σ-discovery region in the m_A-tan β plane for $gg \to tbH^{\pm}$, $H^{\pm} \to \tau\nu_{\tau}$ with an integrated luminosity of 30 fb^{-1} in the maximal mixing scenario with $\mu = 200$ GeV/c^2. The discovery regions with and without systematic uncertainties are shown. The regions excluded by the LEP and Tevatron searches are also shown in the figure.

These final states are the most interesting from the experimental point of view because an isolated muon is present to trigger on and the branching fraction into this decay is high ($\sim 30\%$).

The inclusive final state (11.9) is studied using triple b tagging within the parameterised simulation framework of CMS [11]. The final state (11.10), where a fourth b jet is resolved in the detector, is studied with full GEANT4 [9] CMS detector simulation [8]. Production of the $H^{\pm}$ bosons through heavy sparticle cascades is not taken into account. In addition, supersymmetric particles are supposed to be heavy enough, such that supersymmetric decays of the $H^{\pm}$ can be neglected.

A detailed description of the analysis can be found in [629].

11.2.6.1. Signal and background simulation. Events from the process (11.9) are modelled by considering the initial b quark as a massless parton from the corresponding parton density in the proton. On the other hand, events from the process (11.10) are described with massive spectator b quarks.

The calculation of the total signal cross section was performed at NLO [628], starting from the process (11.9). When calculating the cross section for both processes (11.9) and (11.10) to all orders, however, one expects to obtain the same result, as they both describe the same physics. Therefore, for both processes, the cross section was rescaled to the NLO result for the $pp \to tH^{\pm}X$ channel.

The signal cross section is sensitive to the two parameters $\tan\beta$ and $m_{H^{\pm}}$ (Fig. 11.20). The cross section is enhanced at small and large values of $\tan\beta$, with a minimum at $\tan\beta = \sqrt{m_t/m_b} \approx 6$. Furthermore, the cross section decreases rapidly with rising $m_{H^{\pm}}$. The generation of both processes (11.9) and (11.10) was performed with PYTHIA [69], forcing the

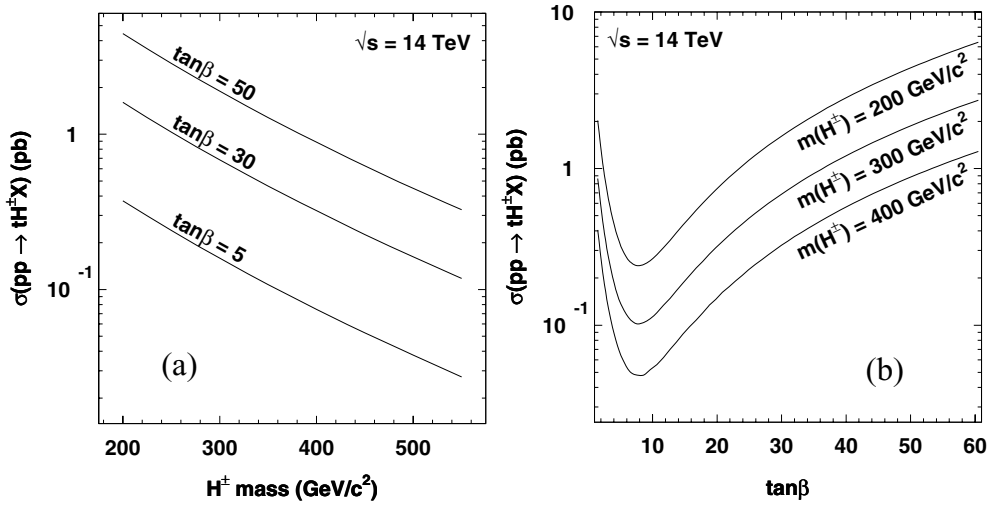

Figure 11.20. NLO cross section for $pp \to tH^{\pm}X$ as a function of (a) $m_{H^{\pm}}$ and (b) $\tan\beta$.

decay $H^{\pm} \to tb$ of the charged Higgs boson. The branching fraction $BR(H^{\pm} \to tb)$ for this decay process was calculated with HDECAY 3.0 [41].

The main background to charged Higgs boson production and decay through $pp \to tH^{\pm}(b) \to ttb(b)$ is the Standard Model top-quark pair production with additional jets. Other potential multi-jet backgrounds are much smaller and neglected.

In the case of process (11.9), the leading order background comes from SM $pp \to t\bar{t}b$ and $pp \to t\bar{t}$ + jet production, where in the latter the extra jet is misidentified as a b jet. The event simulation was performed using the matrix element generator `MadGraph/MadEvent` [81], interfaced to PYTHIA for parton shower, fragmentation and hadronisation, with a cut $p_T > 10\,\text{GeV/c}$ on the transverse momentum and $|\eta| < 2.5$ on the pseudorapidity of the extra jet. This resulted in a cross section of 678 pb.

The background for process (11.10) consists of the irreducible $pp \to t\bar{t}b\bar{b}$ and the reducible $pp \to t\bar{t}jj$ process, where in the latter two jets are misidentified as b jets. Both these backgrounds were simulated using the COMPHEP generator [43]. The generator level cuts $p_T > 15\,\text{GeV}$ and $|\eta| < 3$ were applied on the partons produced in association with the $t\bar{t}$ pair. A separation cut $\Delta R > 0.3$ was also imposed. This resulted in a cross section of 3.285 pb for the $pp \to t\bar{t}b\bar{b}$ process and 507.8 pb for $pp \to t\bar{t}jj$ production. Care was taken to avoid double counting between the $pp \to t\bar{t}b\bar{b}$ and $pp \to t\bar{t}jj$ processes and the cross section for $pp \to t\bar{t}jj$ was scaled to the result from a similar ALPGEN generation, where a jet matching technique was applied to more rigourously handle the transition between the hard interaction and the parton shower.

11.2.6.2. Event selection and reconstruction. On the final states (11.9) and (11.10) a basic event selection is applied on the reconstructed objects (Tables 11.20 and 11.21). Events passing the single muon HLT trigger are required to have at least one muon with $p_T > 20\,\text{GeV}$ and $|\eta| < 2.5$, at least respectively five or six calibrated jets with $E_T > 25\,\text{GeV}$ and $|\eta| < 2.5$ and at least respectively three or four of these jets tagged as b jet with a secondary vertex-based algorithm [157].

In both final states (11.9) and (11.10) the best jet association is selected with a likelihood ratio technique, which combines information from kinematical properties of the extra jets,

Table 11.20. Event selection yield for $\tan\beta = 30$ and an integrated luminosity of 30 fb^{-1}.

30 fb^{-1}	$t\bar{t}b/t\bar{t}j$	$gb \to tH^{\pm}$ ($\tan\beta = 30$)					
$m_{H^{\pm}}$ (GeV/c^2)		263	311	359	408	457	506
cross section × BR (pb)	678	0.850	0.570	0.377	0.251	0.169	0.116
# events before cuts	20.3M	25 489	17 088	11 319	7 529	5 063	3 472
single muon HLT	17%	16%	16%	16%	16%	16%	16%
1 muon	95%	95%	95%	95%	96%	96%	96%
5 jets	18%	35%	42%	44%	46%	49%	51%
3 b-tagged jets	6%	27%	29%	30%	32%	31%	29%
# remaining events	32 880	364	314	230	171	116	80

Table 11.21. Event selection yield for $\tan\beta = 30$ and an integrated luminosity of 30 fb^{-1}.

30 fb^{-1}	$t\bar{t}b\bar{b}$	$t\bar{t}jj$	$gg \to tbH^{\pm}$ ($\tan\beta = 30$)					
$m_{H^{\pm}}$ (GeV/c^2)			263	311	359	408	457	506
cross section × BR (pb)	2.386	235.8	0.850	0.570	0.377	0.251	0.169	0.116
# events before cuts	71 580	7.07M	25 489	17 088	11 319	7 529	5 063	3 472
single muon HLT	19%	19%	13%	13%	13%	13%	13%	13%
1 muon	96%	97%	96%	95%	97%	97%	97%	97%
6 jets	19%	23%	19%	23%	25%	26%	28%	31%
4 b-tagged jets	7%	0.55%	6%	5%	7%	7%	5%	6%
# remaining events	179	1 623	37	24	25	18	9	8

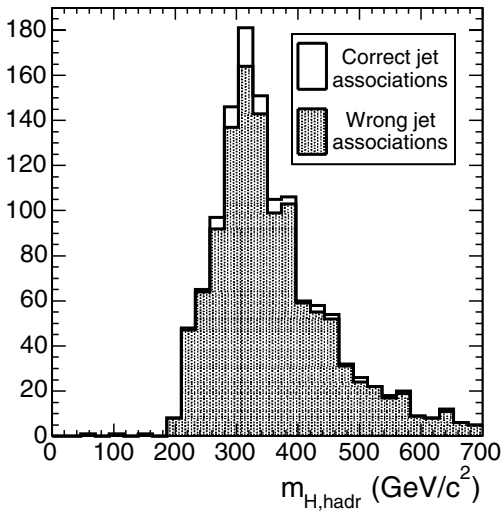

Figure 11.21. Reconstructed $H^{\pm}$ mass with hadronically decaying top for the chosen jet association ($m_{H^{\pm}} = 311\,\text{GeV/c}^2$).

b-tagging of all jets and the result of a kinematic fit on the $t\bar{t}$ system, imposing both $W^{\pm}$ and t mass constraints. Starting from the chosen jet association the Higgs boson mass was reconstructed. An ambiguity remains, as it is not possible to know which top quark candidate the additional b jet should be combined with. In Fig. 11.21 the reconstructed charged Higgs boson mass with hadronically decaying top is shown for correct and wrong jet pairings in the case of three tagged b jets and for $m_{H^{\pm}} = 311\text{GeV}/c^2$. Due to the large combinatorial

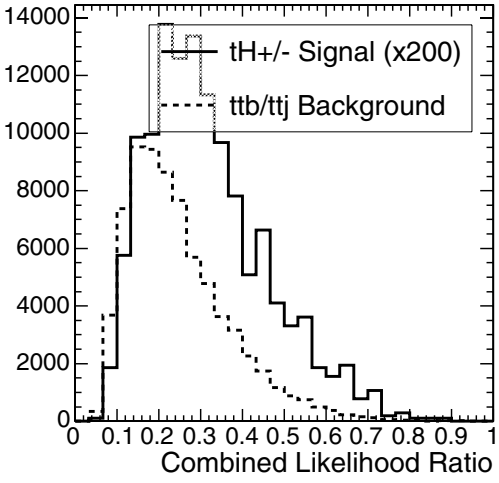

Figure 11.22. Distribution of the discriminator used to distinguish between signal 11.9 and background.

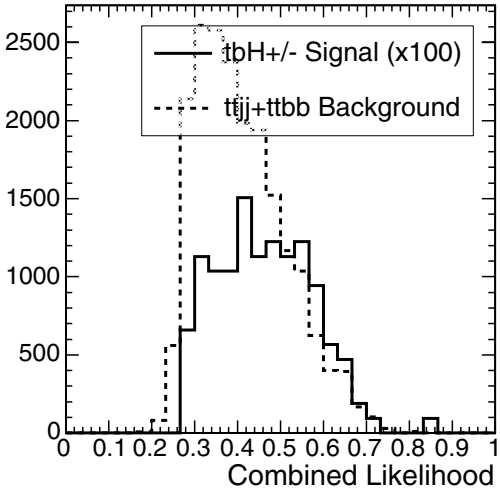

Figure 11.23. Distribution of the discriminator used to distinguish between signal 11.10 and background.

background, the mass information is of limited use for the separation between signal and background, and is therefore not used further on in the analysis.

11.2.6.3. Background suppression. To suppress the large $\mathrm{t\bar{t}}$ + jets background, observables were identified that have different properties for signal and background events. These observables were combined into an overall discriminator. In the case of process (11.9) the b-tagging information for the extra jet was used, together with the p_{T} of the softest jet from the $\mathrm{W}^{\pm}$ decay and the ratio of the E_{T} of the sixth jet and the fifth. For the process (11.10) only the b-tagging information for the two extra jets was used. In Figs. 11.22 and 11.23 the resulting discriminator distributions are shown for the process (11.9) and (11.10) respectively.

11.2.6.4. Discovery reach and systematics. A cut on the discriminating variables of Figs. 11.22 and 11.23 was optimised to obtain the maximal statistical significance for an integrated luminosity of $30\,\mathrm{fb}^{-1}$. The signal cross section required for a significance of 5, corresponding to a discovery, was derived and translated into a minimal value of $\tan\beta$ needed for a discovery for a given value of m_{A}. Performing this analysis and optimisation at different values of m_{A} a discovery contour was obtained in the MSSM $(\tan\beta, m_{\mathrm{A}})$ plane.

The background is large in both final states and therefore the effect of systematic uncertainties on the knowledge of the background is important. A possible way to estimate the background level from data is to require one b-tagged jet less. After such a selection it is possible to calculate the expected number of background events plus its uncertainty, when tagging a third or fourth b jet. Optimistically the uncertainty on the mistag rate can be taken as 5%. Possible large theoretical uncertainties related to this method, like the ratio of events with real extra b jets and events with only light extra jets, should still be accounted for.

Depending on the expected systematic uncertainty on the background level the maximal significance was searched. In Fig. 11.24 the discovery contours are plotted for the final states (11.9) and (11.10) respectively, when supposing perfect knowledge of the background cross section ($\varepsilon = 0$), a 1% uncertainty ($\varepsilon = 0.01$), and a 3% uncertainty ($\varepsilon = 0.03$). From

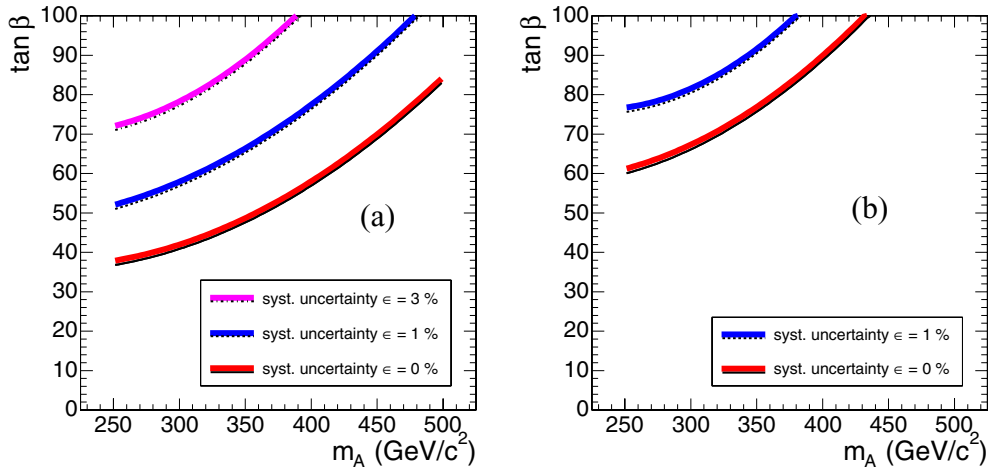

Figure 11.24. Discovery contour for the charged Higgs boson in the $H^{\pm} \to tb$ decay for 30 fb^{-1}, (a) applying 3 b tags, (b) applying 4 b tags; systematic uncertainties on the background of $\varepsilon = 0\%$, $\varepsilon = 1\%$ and $\varepsilon = 3\%$ are taken into account.

the above estimate of the systematic uncertainty on the number of background events, the conclusion is drawn that, neglecting SUSY cascade decays, no visibility for this channel is obtained in the MSSM parameter space during the low luminosity phase of LHC.

11.2.7. Search for the $A \to Zh$ decay with $Z \to \ell^+\ell^-$, $h \to b\bar{b}$

The observation of the CP-odd pseudo-scalar Higgs (A) via its decay into a Z boson and the lighter CP-even scalar Higgs (h) followed by $Z \to e^+e^-$, $\mu^+\mu^-$ and $h \to b\bar{b}$ decays provides an interesting way to detect A and h simultaneously. The largest branching ratio of the $A \to Zh$ appears for low tan β and $m_Z + m_h \leqslant m_A \leqslant 2m_{top}$ mass region. The main production mechanism for A at low tan β is via gg, qq$\to$ A.

The decays of the A into charginos and neutralinos (A$\to \chi\chi$), however, can dominate at certain values of μ and M_2 (Higgs-Higgsino and SU(2) gaugino mass parameters) since the masses of charginos and neutralinos as well as their couplings to the Higgs bosons depend on μ and M_2 (in addition to tan β and M_A). Large values of μ and M_2 are more favourable for the observation of the $A \to Zh$ channel.

In Fig. 11.25 the production cross section multiplied by the appropriate branching ratios (including $Z \to e^+e^-$, $\mu^+\mu^-$ and $h \to b\bar{b}$ decays) is shown as a function of M_A in the m_h^{max} scenario with $\mu = M_2 = 200\,GeV/c^2$ and $\mu = M_2 = 600\,GeV/c^2$ for two values of tan β, 1 and 5. One can see that the difference in the total cross sections for the two choices of the μ and M_2 parameters can be as large as one order of magnitude. The $A \to Zh$ analysis and the discovery reach presented below was evaluated in the m_h^{max} scenario with $\mu = M_2 = 600\,GeV/c^2$.

11.2.7.1. Event generation, simulation and reconstruction. The Higgs boson production processes, gg$\to$ A and pp $\to$ A $b\bar{b}$, were generated using PYTHIA 6.225 [69] for three values of M_A (250, 300, 350 GeV/c^2) and two values of tan β (1.0, 5.0). No pre-selection at generation level was applied. The Standard Model backgrounds considered are: the $Zb\bar{b}$ generated with COMPHEP [355] and ZZ, ZW, Z+jets, W+jets and $t\bar{t}$ generated with PYTHIA 6.215. Events were fully simulated and digitised with pile-up corresponding to a luminosity of $2 \times 10^{33} cm^{-2} s^{-1}$.

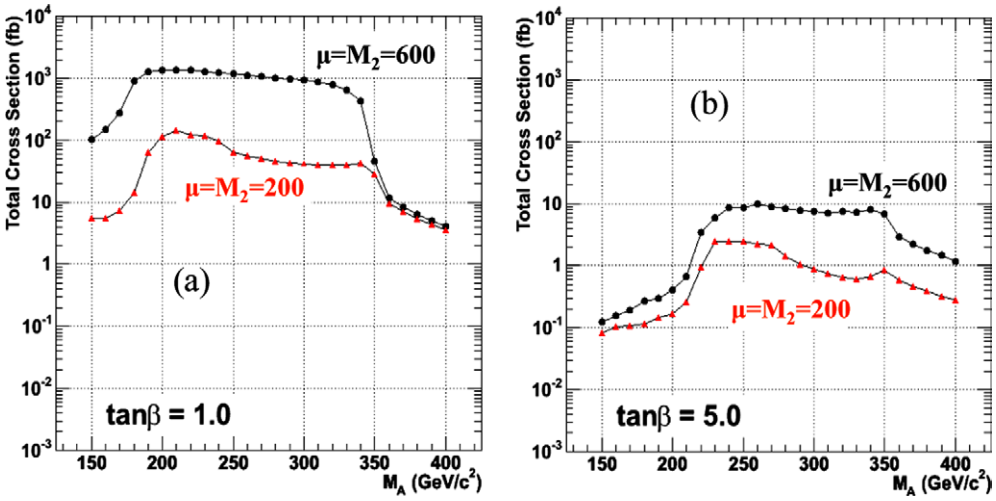

Figure 11.25. The production cross-section multiplied by appropriate branching ratios as a function of M_A in the m_h^{max} scenario with $\mu = M_2 = 600\,GeV/c^2$ (circles) and $\mu = M_2 = 200\,GeV/c^2$ (triangles) for (a) $\tan\beta = 1$ and (b) $\tan\beta = 5$.

Offline reconstruction of electrons, muons, jets and b tagging were performed using standard algorithms.

11.2.7.2. Online selection. The events are required to pass the global Level-1 (L1) and High Level Trigger (HLT) dimuon or dielectron selections since there will always be a real Z in the event decaying into two high p_T electrons or muons. The inclusion of the single muon and electron triggers does not improve the discovery reach in the M_A-tan β plane.

11.2.7.3. Off-line event selection. The baseline selection requires two opposite sign high p_T isolated leptons (e or μ) and two high E_T tagged b-jets separated from the leptons with $\Delta R(\ell, j) > 0.7$. Muons must have $|\eta| < 2.4$ and electrons should be in the ECAL fiducial region ($|\eta| < 2.5$ with $1.444 < |\eta| < 1.566$ region excluded). The event is required to have small missing E_T and reconstructed invariant mass of the leptons close to the Z mass in order to reject a significant fraction of the $t\bar{t}$ background.

Table 11.22 summarises the basic selection variables and thresholds. The variation of the signal significance with the change of the p_T thresholds on the electrons, muons and b-jets, and the thresholds on the b-tagging discriminant for the two tagged jets has been checked. No significant variation was found with small changes of the cut values presented in Table 11.22.

11.2.7.4. Results. The selection efficiencies for the signal vary from 5% to 12% depending on the M_A and tan β values as well as the production mechanism. The details can be found in [630]. The next-to-leading order (NLO) background cross sections before and after selections are shown in Table 11.23.

The signal and the background distributions of $M_{b\bar{b}}$ and $M_{\ell^+\ell^-b\bar{b}}$ after selections are shown in Fig. 11.26 and Fig. 11.27 respectively for 30 fb^{-1} of integrated luminosity.

11.2.7.5. Systematic uncertainties. The method to evaluate the background from the real data measuring the background in the signal free (normalisation) region is proposed.

Table 11.22. Selection variables and thresholds.

Selection Variable	Threshold
most energetic electron/muon p_T	> 30 GeV/c
second-most energetic electron/muon p_T	> 15 GeV/c
most energetic b-jet E_T	> 25 GeV
second-most energetic b-jet E_T	> 20 GeV
missing E_T	< 60 GeV
most energetic b-jet discriminator	> 1.5
second-most energetic b-jet discriminator	> 0.5
Z mass cut	$84\,\mathrm{GeV/c^2} < M_Z < 96\,\mathrm{GeV/c^2}$
Z p_T	> 30.0 GeV/c

Table 11.23. Background cross sections.

	NLO cross sections (fb)	
	before selection	after selection
$Zb\bar{b}$, $Z \to ee, \mu\mu, \tau\tau$	112830	415.26
$t\bar{t}$, $W \to e\nu, \mu\nu, \tau\nu$	88500	70.8
Z+jets, $Z \to ee, \mu\mu, \tau\tau$	5300000	83.05
W+jets, $W \to e\nu, \mu\nu, \tau\nu$	47900000	0.0
ZZ (inclusive)	14985	7.34
ZW (inclusive)	49422	1.98

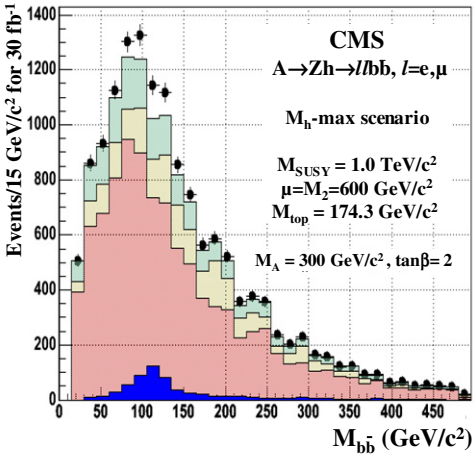

Figure 11.26. Distribution of $M_{b\bar{b}}$ for signal and background after event selection for $30\,\mathrm{fb}^{-1}$ of integrated luminosity. Red (dark gray), yellow (light gray) and green (medium gray) distributions represent the $Zb\bar{b}$, $t\bar{t}$ and Z+jets backgrounds. Blue (black) distribution is the signal ($M_A = 300$, $\tan\beta = 2$) and black dots the data (sum of the signal and the background).

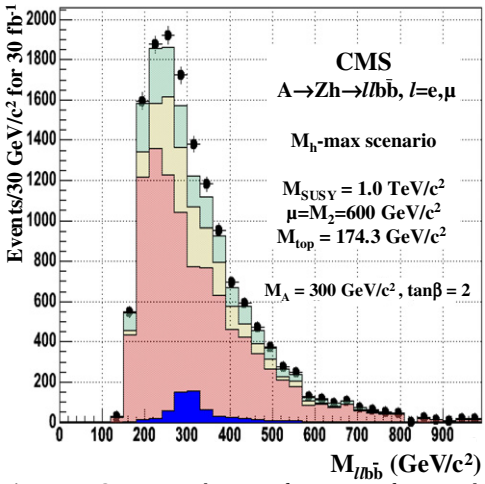

Figure 11.27. Distribution of $M_{\ell^+\ell^-b\bar{b}}$ for signal and background after event selection for $30\,\mathrm{fb}^{-1}$ of integrated luminosity. Red (dark gray), yellow (light gray) and green (medium gray) distributions represent the $Zb\bar{b}$, $t\bar{t}$ and Z+jets backgrounds. Blue (black) distribution is the signal ($M_A = 300$, $\tan\beta = 2$) and black dots the data (sum of the signal and the background).

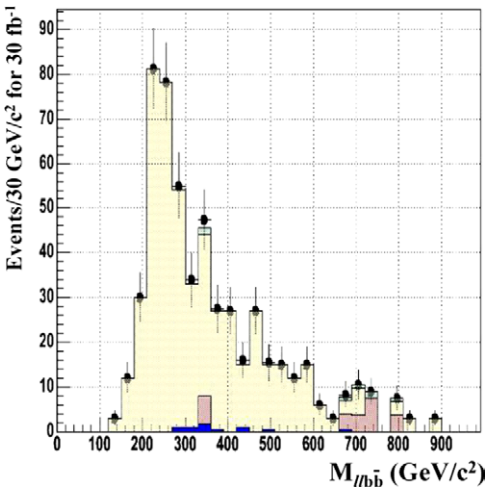

Figure 11.28. Distribution of $M_{\ell^+\ell^-b\bar{b}}$ in the $t\bar{t}$ background normalisation region. Colour code is as in Fig. 11.27.

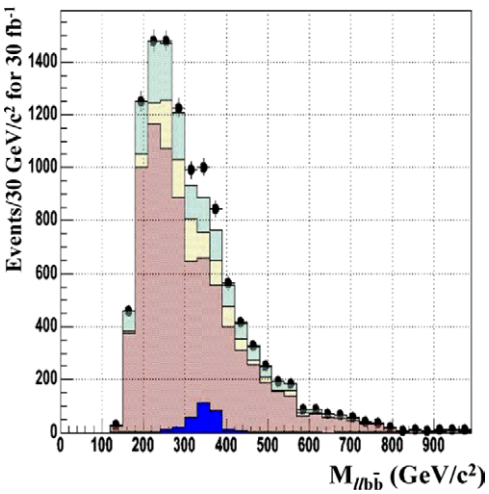

Figure 11.29. Distribution of $M_{\ell^+\ell^-b\bar{b}}$ used in the $Zb\bar{b}$ background estimation. Colour code is as in Fig. 11.27.

The background uncertainty then consists of the statistical uncertainty of the background measurement in the normalisation region and the systematic uncertainty of the ratio of the background in the signal and the normalisation region.

The normalisation region for the $t\bar{t}$ background is defined by the same selection as for the signal search, except the missing E_T which is required to be bigger than 120 GeV. With such a selection 544 events were found for 30 fb^{-1} with high purity (93.4%), thus giving the statistical uncertainty of 4.4%. The distribution of $M_{\ell^+\ell^-b\bar{b}}$ in the $t\bar{t}$ normalisation region can be seen in Figure 11.28. The contamination comes mainly from $Zb\bar{b}$ events (6%). The 5% missing E_T scale uncertainty gives 18.5% uncertainty on the number of the $t\bar{t}$ events in the signal region. Therefore the overall uncertainty in the estimation of the $t\bar{t}$ background is 19.0%.

For the irreducible $Zb\bar{b}$ background a similar idea can be used. In order to suppress the $t\bar{t}$ contribution as much as possible, missing $E_T < 40$ GeV was used. Applying a lower cut in the $M_{\ell^+\ell^-b\bar{b}}$ distribution of 500 GeV/c^2, 920 Zbb events were found with a purity of around 95% for 30 fb^{-1}. Contamination comes mainly from $t\bar{t}$ events. The accuracy of measuring the $Zb\bar{b}$ background is around 3.4% taking into account only statistics. The distribution of $M_{\ell^+\ell^-b\bar{b}}$ for those events can be seen in Figure 11.29 before the application of the $M_{\ell^+\ell^-b\bar{b}}$ 500 GeV/c^2 cut. The uncertainty of 5% on the missing E_T scale and the uncertainty of 3% on the jet energy scale lead to correspondingly 3.6% and 2.5% of the uncertainty of the $Zb\bar{b}$ background estimate in the signal region. Thus the overall uncertainty in the estimation of the $Zb\bar{b}$ background is 5.6%.

11.2.7.6. Discovery reach in the $M_A - tan\,\beta$ plane. Figure 11.30 shows the 5 σ discovery contours in the (M_A, $\tan\beta$) plane for 30 and 60 fb^{-1} of integrated luminosity in the m_h^{max} scenario with $\mu = M_2 = 600$ GeV/c^2. For the calculation of the signal significance the signal and background events were counted in mass windows of $\pm 1.5\sigma$ around the reconstructed masses of M_h and M_A. Since only three different M_A masses and two $\tan\beta$ values were available, the estimations for the rest of M_A, $\tan\beta$ parameter space was done using extra/interpolations of the signal efficiencies from the available parameter points. The

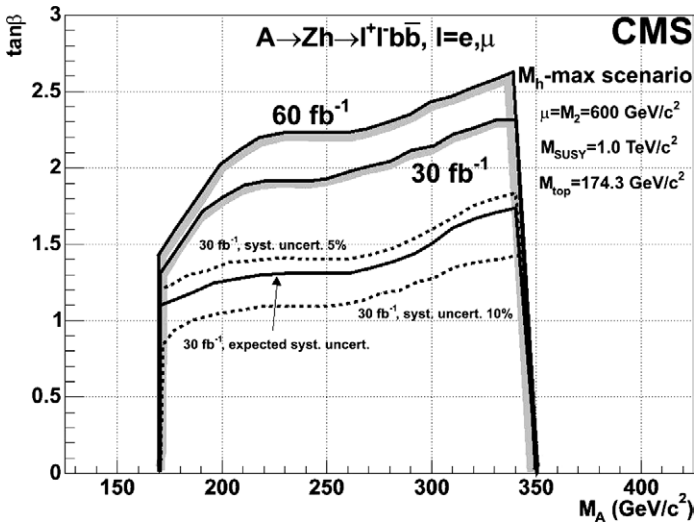

Figure 11.30. The 5σ discovery contours for 30 and 60 fb^{-1} integrated luminosity. The effect of underestimation or overestimation of the background systematic uncertainty can be seen in the curve of 30 fb^{-1}.

statistical significance for 5, 10% (dashed lines) as well as the estimated (full line) uncertainty for the background is also shown for 30 fb^{-1} of integrated luminosity.

11.2.8. Search for $\mathrm{A}^0/\mathrm{H}^0 \to \chi_2^0\chi_2^0 \to 4\ell + E_{\mathrm{T}}^{\mathrm{miss}}$ *channel in mSUGRA*

11.2.8.1. Introduction. In some regions of the SUSY parameter space, heavy neutral Higgs bosons can be searched for using their decay modes to supersymmetric particles. This is the case in particular in the difficult low and intermediate $\tan\beta$ region of the parameter space which is not accessible through the $\mathrm{A}^0/\mathrm{H}^0 \to \tau\tau$ decay channel as the coupling of the Higgs boson to taus is not sufficiently enhanced.

One of the most promising channel is the $\mathrm{A}^0/\mathrm{H}^0$ decay into a pair of next-to-lightest neutralinos, χ_2^0, followed by the decay $\chi_2^0 \to \ell^+\ell^-\chi_1^0$ (with $\ell = e, \mu$). This process results in a clean four leptons plus missing transverse energy final state:

$$\mathrm{A}^0/\mathrm{H}^0 \to \chi_2^0\chi_2^0 \to 4\ell + \mathrm{E}_{\mathrm{T}}^{\mathrm{miss}}.$$

There are two main categories of backgrounds to such process: SUSY and Standard Model backgrounds. In the SUSY category the dominant source of background is the production of leptons from the decays of squarks and gluinos which cascade to charginos and neutralinos. Unlike the neutralinos from the Higgs boson decay, the leptons in this case are produced in association with quarks and gluons. Therefore, the associated large hadronic activity can be used to suppress this type of background. An additional but smaller source of backgrounds come from the direct production of slepton or gaugino pairs via the Drell–Yan processes and the direct production of χ_2^0 pairs. The rejection of these backgrounds is more difficult, as the hadronic activity in these events is very small. In the Standard Model category, three processes which yield the same signature of 4 leptons in the final state contribute as backgrounds: ZZ^*/γ^*, $Zb\bar{b}$ and $t\bar{t}$.

Table 11.24. Chosen benchmark points.

Point	m_0 (GeV/c^2)	$m_{1/2}$ (GeV/c^2)	A_0 (GeV/c^2)	tan β	sign(μ)
A	60	175	0	10	+
B	80	200	0	5	+
C	50	150	0	5	+

11.2.8.2. Analysis. The study is performed in the minimal Super Gravity constrained version of the MSSM (mSUGRA) [631]. To determine the regions where the signal has a sizeable branching ratio times cross section, a scan of the parameters space $(m_0, m_{1/2})$ for tan $\beta = 5, 10$, sign$(\mu) = +$ and $A_0 = 0$ is performed. Three benchmark points are defined for the evaluation of CMS sensitivity. The corresponding mSUGRA parameters are presented in Table 11.24.

The signal and SUSY background datasets are generated using ISASUGRA and PYTHIA. A pre-selection at generator level is applied, asking for $e^+e^-\mu^+\mu^-$ final state with e(μ) $p_T > 7(5)$ GeV/c and $|\eta| < 2.5$. The fast detector simulation is carried out using FAMOS.

The online selection of the events is a logical or of the dielectron and dimuon triggers. The offline reconstruction of electrons and muons is performed using FAMOS standard algorithms. Events are then analysed as follow:

- $e^+e^-\mu^+\mu^-$ final state is selected;
- the four leptons are required to be isolated;
- a jet veto is applied, requiring no jets with $E_T > 25$ GeV and $|\eta| < 5.0$;
- events must have E_T^{miss} and $p_{T(\ell\ell\ell\ell)}$ less than 80 GeV/c;
- a Z veto is imposed, *i.e.* events with a dilepton pair with invariant mass in the range $m_Z \pm 10$ GeV/c^2 are rejected;
- further optimisations are performed by introducing an upper limit to the dilepton invariant masses and by applying a cut on the four lepton invariant mass.

The signal acceptances w.r.t the production cross section times branching ratio are 6.3%, 5.1% and 2.5% respectively for point A, B and C, whereas the acceptances for SUSY backgrounds are 1.5×10^{-4}%, 3.6×10^{-4}% and 2.6×10^{-4}% respectively w.r.t. the total the SUSY production cross section.

11.2.8.3. Results. Figure 11.31 shows the invariant mass distribution of the four leptons for the 3 benchmarks points. Results are given for an integrated luminosity of 30 fb^{-1}.

Figure 11.32 shows the extrapolated 5σ-discovery regions in the $(m_0, m_{1/2})$ plane, for an integrated luminosity of 30 fb^{-1}. The values of the other mSUGRA parameters are $A_0 = 0$, $sign(\mu) = +$ and tan $\beta = 5, 10$. The complex structure of the high significance region is mainly determined by the effective cross section of $A^0/H^0 \to \chi_2^0\chi_2^0 \to 4\ell + E_T^{miss}$. The A^0/H^0 could therefore be discovered through their decays to neutralino pairs in the region $150 < m_{1/2} < 250$ and $m_0 < 120$ for tan $\beta = 10$ and in the region $150 < m_{1/2} < 250$ and $30 < m_0 < 120$ for tan $\beta = 5$.

11.3. Discovery reach and measurement of MSSM parameters

11.3.1. Benchmark scenarios for MSSM Higgs boson searches

11.3.1.1. Why benchmarks — which benchmarks? The tree-level values for the CP-even Higgs bosons of the MSSM, M_h and M_H, are determined by tan β, the CP-odd Higgs-boson

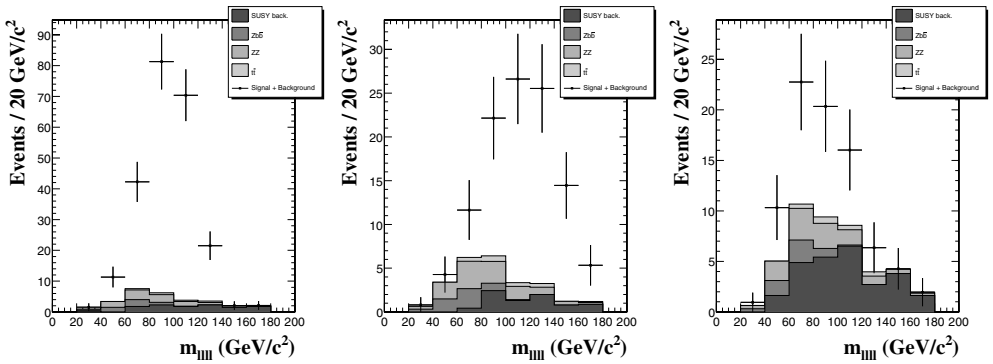

Figure 11.31. Four lepton invariant mass distributions for the 3 benchmark points. Distributions are shown for the signal+backgrounds (points) and for the contribution of each process (histograms).

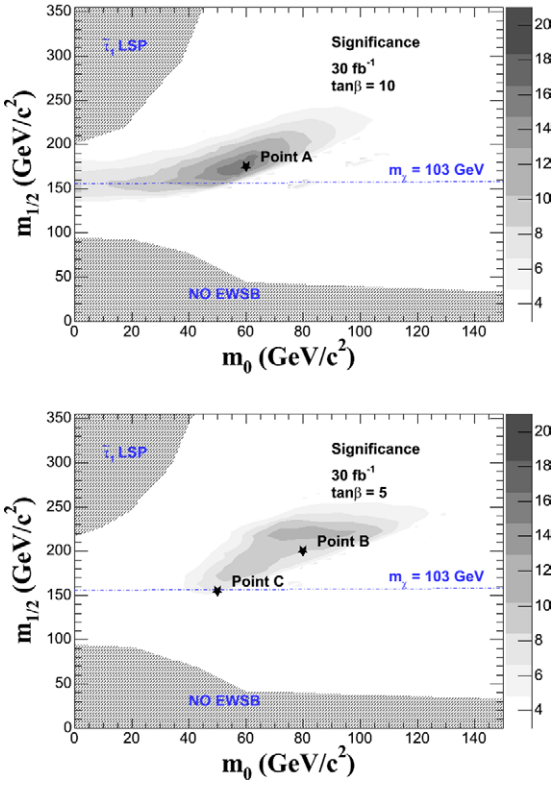

Figure 11.32. For integrated luminosity of $30\,\mathrm{fb}^{-1}$ the 5σ-discovery regions for $\mathrm{A}^0/\mathrm{H}^0 \to \chi_2^0\chi_2^0 \to 4\ell + \mathrm{E}_\mathrm{T}^\mathrm{miss}$ channel in the $(m_0, m_{1/2})$ plane for fixed $A_0 = 0$, $\mathrm{sign}(\mu) = +$ and $\tan\beta = 5, 10$.

mass M_A, and the Z boson mass M_Z. The mass of the charged Higgs boson, $M_{H^\pm}$, is given in terms of M_A and the W boson mass, M_W. Beyond the tree-level, the main correction to the Higgs boson masses stems from the $t/\tilde{t}$ sector, and for large values of $\tan\beta$ also from the $b/\tilde{b}$ sector, see Section 11.1. Sub-leading corrections come from all other sectors of the MSSM.

In this way the Higgs sector phenomenology is connected to the full spectrum of the MSSM via radiative corrections.

In the unconstrained version of the MSSM no particular SUSY breaking mechanism is assumed, but rather a parametrisation of all possible soft SUSY breaking terms is used. This leads to more than a hundred parameters (masses, mixing angles, phases) in this model in addition to the ones of the Standard Model. While a detailed scanning over the more-than-hundred-dimensional parameter space of the MSSM is clearly not practicable, even a sampling of three- or four-dimensional parameter space of certain SUSY-breaking models (such as mSUGRA, GMSB or AMSB) is beyond the present capabilities for phenomenological studies, in particular when it comes to simulating experimental signatures within the detectors. For this reason one often resorts to specific benchmark scenarios, i.e. one studies only specific parameter points [632, 633] or samples of one- or two-dimensional parameter space [263, 634, 635], which exhibit specific characteristics of the MSSM parameter space. Benchmark scenarios of this kind are often used, for instance, for studying the performance of different experiments at the same collider. Similarly, detailed experimental simulations of MSSM particle production with identical parameters in the framework of different colliders can be very helpful for developing strategies for combining pieces of information obtained at different machines [5].

The question of which parameter choices are useful as benchmark scenarios depends on the purpose of the actual investigation. If one is interested, for instance, in setting exclusion limits on the SUSY parameter space from the non-observation of SUSY signals at the experiments performed up to now, it is useful to use a benchmark scenario which gives rise to "conservative" exclusion bounds. An example of a benchmark scenario of this kind is the $m_h^{\max}$-scenario [635] used for the Higgs search at LEP [566]. It gives rise to maximal values of the lightest CP-even Higgs-boson mass (for fixed values of the top-quark mass and the SUSY scale) and thus allows one to set conservative bounds on $\tan\beta$ and M_A [544]. Another application of benchmark scenarios is to study "typical" experimental signatures of SUSY models and to investigate the experimental sensitivities and the achievable experimental precisions for these cases. For this purpose it seems reasonable to choose "typical" (a notion which is of course difficult to define) and theoretically well motivated parameters of certain SUSY-breaking scenarios. Examples of this kind are the benchmark scenarios used so far for investigating SUSY searches at the LHC [632, 633] and at the ILC [636]. As a further possible goal of benchmark scenarios, one can choose them so that they account for a wide variety of SUSY phenomenology. For this purpose, it can also be useful to consider "pathological" regions of parameter space or "worst-case" scenarios. Examples for this are the "small α_{eff} scenario" [635] for the Higgs search at LEP, for which the decay $h \to b\bar{b}$ or $h \to \tau^+\tau^-$ can be significantly suppressed.

A related issue concerning the definition of appropriate benchmarks is whether a benchmark scenario chosen for investigating physics at a certain experiment or for testing a certain sector of the theory should be compatible with additional information from other experiments (or concerning other sectors of the theory). This refers in particular to constraints from cosmology (by demanding that SUSY should give rise to an acceptable dark matter density [637–640]) and low-energy measurements such as the rate for $b \to s\gamma$ [641, 642] and the anomalous magnetic moment of the muon, $(g-2)_\mu$ [643, 644]. On the one hand, applying constraints of this kind gives rise to "more realistic" benchmark scenarios. On the other hand, one relies in this way on further assumptions (and has to take account of experimental and theoretical uncertainties related to these additional constraints), and it could eventually turn out that one has inappropriately narrowed down the range of possibilities by applying these constraints. This applies in particular if slight modifications of the model under

consideration are possible that have a minor impact on collider phenomenology but could significantly alter the bounds from cosmology and low-energy experiments. For instance, the presence of small flavour mixing terms in the SUSY Lagrangian could severely affect the prediction for BR($b \to s\gamma$), while allowing a small amount of R-parity violation in the model would strongly affect the constraints from dark matter relic abundance while leaving collider phenomenology essentially unchanged. The extent to which additional constraints of this kind should be applied to possible benchmark scenarios is related to the actual purpose of the benchmark scenario. For setting exclusion bounds in a particular sector (e.g. the Higgs sector) it seems preferable to apply constraints from this sector only.

11.3.1.2. The relevant MSSM parameters. Beyond the tree-level, the main correction to the Higgs boson masses and couplings comes from the $t/\tilde{t}$ sector, and for large values of $\tan\beta$ also from the $b/\tilde{b}$ sector. In order to fix our notations, we list the conventions for the inputs from the scalar top and scalar bottom sector of the MSSM: the mass matrices in the basis of the current eigenstates $\tilde{t}_L, \tilde{t}_R$ and $\tilde{b}_L, \tilde{b}_R$ are given by

$$\mathcal{M}^2_{\tilde{t}} = \begin{pmatrix} M^2_{\tilde{t}_L} + m_t^2 + \cos 2\beta \left(\frac{1}{2} - \frac{2}{3}s_W^2\right) M_Z^2 & m_t X_t \\ m_t X_t & M^2_{\tilde{t}_R} + m_t^2 + \frac{2}{3}\cos 2\beta s_W^2 M_Z^2 \end{pmatrix}, \tag{11.11}$$

$$\mathcal{M}^2_{\tilde{b}} = \begin{pmatrix} M^2_{\tilde{b}_L} + m_b^2 + \cos 2\beta \left(-\frac{1}{2} + \frac{1}{3}s_W^2\right) M_Z^2 & m_b X_b \\ m_b X_b & M^2_{\tilde{b}_R} + m_b^2 - \frac{1}{3}\cos 2\beta s_W^2 M_Z^2 \end{pmatrix}, \tag{11.12}$$

where

$$m_t X_t = m_t(A_t - \mu\cot\beta), \quad m_b X_b = m_b (A_b - \mu\tan\beta). \tag{11.13}$$

Here A_t denotes the trilinear Higgs-stop coupling, A_b denotes the Higgs-sbottom coupling, and μ is the Higgsino mass parameter.

SU(2) gauge invariance leads to the relation

$$M_{\tilde{t}_L} = M_{\tilde{b}_L}. \tag{11.14}$$

For the numerical evaluation, a convenient choice is

$$M_{\tilde{t}_L} = M_{\tilde{b}_L} = M_{\tilde{t}_R} = M_{\tilde{b}_R} =: M_{\rm SUSY}. \tag{11.15}$$

We furthermore use the short-hand notation

$$M_S^2 := M^2_{\rm SUSY} + m_t^2. \tag{11.16}$$

Accordingly, the most important parameters for the corrections in the Higgs sector are m_t, $M_{\rm SUSY}$, X_t and X_b (or equivalently A_t and A_b), μ and $\tan\beta$. The Higgs sector observables furthermore depend on the SU(2) gaugino mass parameter, M_2. The other gaugino mass parameter, M_1, is usually fixed via the GUT relation

$$M_1 = \frac{5}{3}\frac{s_W^2}{c_W^2} M_2. \tag{11.17}$$

At the loop level also the gluino mass, $m_{\tilde{g}}$, enters the predictions for the Higgs-boson phenomenology.

It should be noted in this context that the results for Higgs boson sector observables have been obtained in different schemes. Most commonly these are the on-shell (OS) renormalisation scheme (in the Feynman-diagrammatic (FD) approach), and $\overline{\rm MS}$ scheme (for the renormalisation group (RG) approach) [645]. Owing to the different schemes used in the FD and the RG approach for the renormalisation in the scalar top sector, the parameters

X_t and M_{SUSY} are also scheme-dependent in the two approaches. This difference between the corresponding parameters has to be taken into account when defining the benchmark scenarios. In a simple approximation the relation between the parameters in the different schemes is at $\mathcal{O}(\alpha_s)$ given by [645]

$$M_S^{2,\overline{\text{MS}}} \approx M_S^{2,\text{OS}} - \frac{8}{3}\frac{\alpha_s}{\pi} M_S^2, \tag{11.18}$$

$$X_t^{\overline{\text{MS}}} \approx X_t^{\text{OS}} + \frac{\alpha_s}{3\pi} M_S \left(8 + 4\frac{X_t}{M_S} - 3\frac{X_t}{M_S}\log\left(\frac{m_t^2}{M_S^2}\right)\right). \tag{11.19}$$

At large $\tan\beta$ and large $|\mu|$ the corrections from the $b/\tilde{b}$ sector can become especially important. The leading effects are included in the effective Lagrangian formalism [563]. Numerically this is by far the dominant part of the contributions from the sbottom sector (see also Refs. [547, 548]). The effective Lagrangian is given by

$$\mathcal{L} = \frac{g}{2M_W}\frac{\overline{m}_b}{1+\Delta_b}\left[\tan\beta\; A\, i\,\bar{b}\gamma_5 b + \sqrt{2}\, V_{tb}\,\tan\beta\; H^+\bar{t}_L b_R + \left(\frac{\sin\alpha}{\cos\beta} - \Delta_b\frac{\cos\alpha}{\sin\beta}\right) h\bar{b}_L b_R \right.$$
$$\left. - \left(\frac{\cos\alpha}{\cos\beta} + \Delta_b\frac{\sin\alpha}{\sin\beta}\right) H\bar{b}_L b_R\right] + \text{h.c.}. \tag{11.20}$$

Here $\overline{m}_b$ denotes the running bottom quark mass including SM QCD corrections. The pre-factor $1/(1+\Delta_b)$ in Eq. 11.20 arises from the resummation of the leading corrections to all orders. The function Δ_b consists of two main contributions, an $\mathcal{O}(\alpha_s)$ correction from a sbottom–gluino loop and an $\mathcal{O}(\alpha_t)$ correction from a stop–Higgsino loop. The explicit form of Δ_b in the limit of $M_S \gg m_t$ and $\tan\beta \gg 1$ reads [563]

$$\Delta_b = \frac{2\alpha_s}{3\pi} m_{\tilde{g}}\,\mu\,\tan\beta\,\times\, I(m_{\tilde{b}_1}, m_{\tilde{b}_2}, m_{\tilde{g}}) + \frac{\alpha_t}{4\pi} A_t\,\mu\,\tan\beta\,\times\, I(m_{\tilde{t}_1}, m_{\tilde{t}_2}, \mu). \tag{11.21}$$

The function I is given by

$$I(a,b,c) = \frac{1}{(a^2-b^2)(b^2-c^2)(a^2-c^2)}\left(a^2b^2\log\frac{a^2}{b^2} + b^2c^2\log\frac{b^2}{c^2} + c^2a^2\log\frac{c^2}{a^2}\right)$$
$$\sim \frac{1}{\max(a^2,b^2,c^2)}. \tag{11.22}$$

It becomes obvious that the size and the sign of μ is especially relevant for this type of corrections.

11.3.1.3. The benchmark scenarios. Since at the tree-level the Higgs sector of the MSSM is governed by two parameters (in addition to M_Z and the SM gauge couplings), it seems reasonable to define benchmarks in which all SUSY parameters are fixed and only the two tree-level parameters, M_A and $\tan\beta$ are varied. For the search of the heavy MSSM Higgs bosons corrections from the $b/\tilde{b}$ sector can be especially relevant. In this case it is also appropriate to vary μ. We review the definition of the benchmark scenarios as defined in Refs. [263, 635]. Another very important parameter is the top-quark mass. For sake of simplicity and to make different analyses readily comparable to each other a fixed value of $m_t = 175$ GeV can be used. Alternatively the current experimental value can be used as input.

The m_h^{max} scenario. This scenario was designed to obtained conservative $\tan\beta$ exclusion bounds [544] at LEP [566]. The parameters are chosen such that the maximum possible

Higgs-boson mass as a function of $\tan\beta$ is obtained (for fixed $M_{\rm SUSY}$, and M_A set to its maximal value, $M_A = 1$ TeV). The parameters are[48]:

$$\begin{aligned} &m_t = 175\,\text{GeV}, \quad M_{\rm SUSY} = 1\,\text{TeV}, \quad \mu = 200\,\text{GeV}, \quad M_2 = 200\,\text{GeV}, \\ &X_t^{\rm OS} = 2\,M_{\rm SUSY}\ \text{(FD calculation)}, \quad X_t^{\overline{\rm MS}} = \sqrt{6}\,M_{\rm SUSY}\ \text{(RG calculation)} \\ &A_b = A_t, \quad m_{\tilde g} = 0.8\,M_{\rm SUSY}. \end{aligned} \tag{11.23}$$

The no-mixing scenario. This benchmark scenario is the same as the $m_h^{\rm max}$ scenario, but with vanishing mixing in the $\tilde t$ sector and with a higher SUSY mass scale to avoid the LEP Higgs bounds [62, 566],

$$\begin{aligned} &m_t = 175\,\text{GeV}, \quad M_{\rm SUSY} = 2\,\text{TeV}, \quad \mu = 200\,\text{GeV}, \quad M_2 = 200\,\text{GeV}, \\ &X_t = 0\ \text{(FD/RG calculation)}, \quad A_b = A_t, \quad m_{\tilde g} = 0.8\,M_{\rm SUSY}. \end{aligned} \tag{11.24}$$

The gluophobic Higgs scenario. In this scenario the main production cross section for the light Higgs boson at the LHC, $gg \to h$, is strongly suppressed. This can happen due to a cancellation between the top quark and the stop quark loops in the production vertex (see Ref. [502]). This cancellation is more effective for small $\tilde t$ masses and hence for relatively large values of the $\tilde t$ mixing parameter, X_t. The partial width of the most relevant decay mode, $\Gamma(h \to \gamma\gamma)$, is affected much less, since it is dominated by the W boson loop. The parameters are:

$$\begin{aligned} &m_t = 175\,\text{GeV}, \quad M_{\rm SUSY} = 350\,\text{GeV}, \quad \mu = 300\,\text{GeV}, \quad M_2 = 300\,\text{GeV}, \\ &X_t^{\rm OS} = -750\,\text{GeV}\ \text{(FD calculation)}, \quad X_t^{\overline{\rm MS}} = -770\,\text{GeV}\ \text{(RG calculation)}, \\ &A_b = A_t, \quad m_{\tilde g} = 500\,\text{GeV}. \end{aligned} \tag{11.25}$$

In the left plot of Fig. 11.33 we show $[\sigma \times \text{BR}]_{\rm MSSM}/[\sigma \times \text{BR}]_{\rm SM}$ for the channel $gg \to h \to \gamma\gamma$ in the $M_A - \tan\beta$-plane. This channel can be strongly suppressed over the whole parameter plane, rendering this detection channel difficult.

The small $\alpha_{\rm eff}$ scenario. Besides the channel $gg \to h \to \gamma\gamma$ at the LHC, other channels for light Higgs searches at the Tevatron and at the LHC rely on the decays $h \to \bar b b$ and $h \to \tau^+\tau^-$. If $\alpha_{\rm eff}$ is small, these two decay channels can be heavily suppressed in the MSSM due to the additional factor $-\sin\alpha_{\rm eff}/\cos\beta$ compared to the SM coupling. Such a suppression occurs for large $\tan\beta$ and not too large M_A for the following parameters:

$$\begin{aligned} &m_t = 175\,\text{GeV}, \quad M_{\rm SUSY} = 800\,\text{GeV}, \quad \mu = 2.5\,M_{\rm SUSY}, \quad M_2 = 500\,\text{GeV}, \\ &X_t^{\rm OS} = -1100\,\text{GeV}\ \text{(FD calculation)}, \quad X_t^{\overline{\rm MS}} = -1200\,\text{GeV}\ \text{(RG calculation)}, \\ &A_b = A_t, \quad m_{\tilde g} = 500\,\text{GeV}. \end{aligned} \tag{11.26}$$

In the right plot of Fig.11.33 we show $[\sigma \times \text{BR}]_{\rm MSSM}/[\sigma \times \text{BR}]_{\rm SM}$ for the channel $WW \to h \to \tau^+\tau^-$ in the $M_A - \tan\beta$-plane. Significant suppression occurs for large $\tan\beta$, $\tan\beta > 20$, and small to moderate M_A, $M_A < 400$ GeV. Thus, Higgs boson search via the WW fusion channel will be difficult in these parts of the parameter space.

11.3.1.4. Variation of μ. The most sensitive channels for detecting heavy MSSM Higgs bosons at the LHC are the channel $pp \to H/A + X$, $H/A \to \tau^+\tau^-$ (making use of different

[48] Better agreement with BR $(b \to s\gamma)$ constraints is obtained for the other sign of X_t (called the "constrained $m_h^{\rm max}$" scenario). However, this lowers the maximum M_h values by ~ 5 GeV.

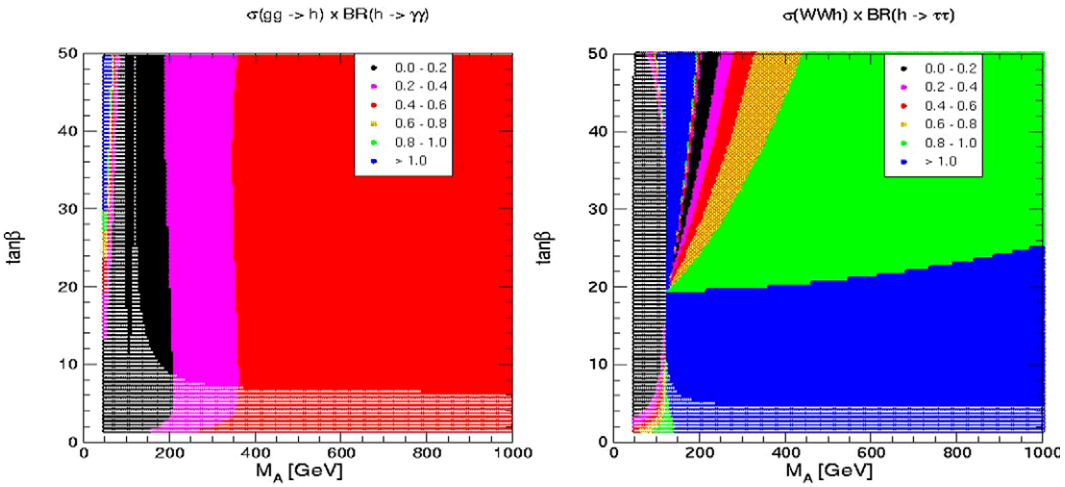

Figure 11.33. $[\sigma \times \mathrm{BR}]_{\mathrm{MSSM}}/[\sigma \times \mathrm{BR}]_{\mathrm{SM}}$ is shown for the channels $gg \to h \to \gamma\gamma$ in the gluophobic Higgs scenario (left plot) and $WW \to h \to \tau^+\tau^-$ in the small α_{eff} scenarios (right plot) in the $M_A - \tan\beta$-plane. The hatched area is excluded by LEP Higgs searches.

decay modes of the two τ leptons) and the channel $tH^{\pm}$, $H^{\pm} \to \tau\nu_{\tau}$ (for $M_{H^{\pm}} > m_t$). These channels show good prospects for $M_A \gg M_Z$ and large $\tan\beta$.

As discussed above, in this part of the parameter space the corrections from the $b/\tilde{b}$ sector can be very important and thus the size and the sign of μ can play a dominant role. This lead to the definition of an extension of the m_h^{max} and the no-mixing scenario by the following values of μ [263]

$$\mu = \pm 200, \pm 500, \pm 1000\,\mathrm{GeV}, \tag{11.27}$$

allowing both an enhancement and a suppression of the bottom Yukawa coupling and taking into account the limits from direct searches for charginos at LEP. It should be noted that the values $\mu = -500, -1000\,\mathrm{GeV}$ can lead to such a large enhancement of the bottom Yukawa coupling that a perturbative treatment is no longer possible in the region of very large values of $\tan\beta$. Some care is therefore necessary to assess up to which values of μ reliable results can be obtained.

A further variation of the discovery reach is caused by the decays of the heavy Higgs bosons into supersymmetric particles. For a given value of μ, the rates of these decay modes are strongly dependent on the particular values of the weak gaugino mass parameters M_2 and M_1. Since the Higgs couplings to neutralinos and charginos depend strongly on the admixture between Higgsino and gaugino states, the rate of these processes is strongly suppressed for large values of $|\mu| > 500$ GeV. In general, the effects of the decays $H/A \to \tilde{\chi}_i^0\tilde{\chi}_j^0$, $\tilde{\chi}_k^{\pm}\tilde{\chi}_l^{\mp}$ only play a role for $M_A > |\mu| + M_1$. Outside this range the dependence of the rates on μ is relatively weak.

11.3.2. Discovery reach in the $\mathrm{M_A} - \tan\beta$ *plane*

This section summarises the discovery reach in the M_{A}-$\tan\beta$ plane for the charged and the neutral MSSM Higgs bosons in the $\mathrm{m_h^{max}}$ scenario. The cross sections and branching ratios for the neutral Higgs bosons and the branching ratios for the charged Higgs boson were calculated with FeynHiggs 2.3.2 [142–144]. The next-to-leading order cross section for the

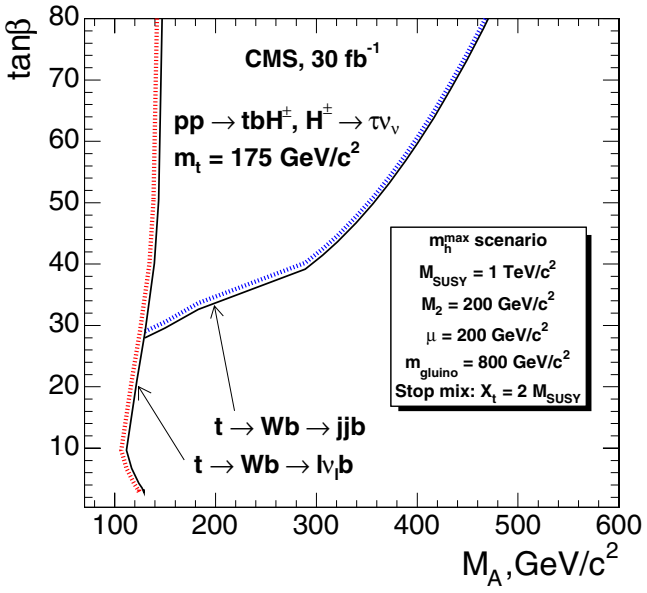

Figure 11.34. The 5σ discovery regions for the charged Higgs boson with the $\tau\nu$ decay mode in the m_h^{max} scenario.

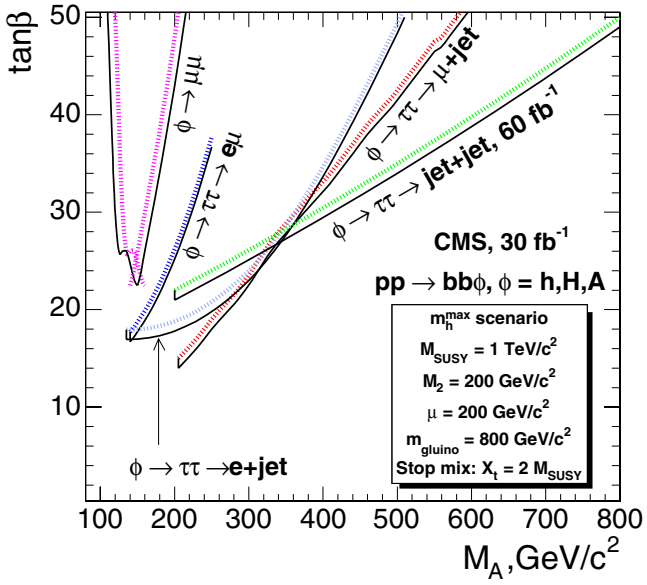

Figure 11.35. The 5σ discovery regions for the neutral Higgs bosons ϕ (ϕ = h, H, A) produced in the association with b quarks $pp \to b\bar{b}\phi$ with the $\phi \to \mu\mu$ and $\phi \to \tau\tau$ decay modes in the m_h^{max} scenario.

charged Higgs production was taken from Refs. [628], [597]. The NLO cross sections for the background processes were used, when available.

Figure 11.34 shows the 5σ discovery regions for the charged Higgs boson produced in the $pp \to tbH^{\pm}$ process with the $H^{\pm} \to \tau^{\pm}\nu_{\tau}$ ($\tau \to$ hadrons) decay mode. Figure 11.35

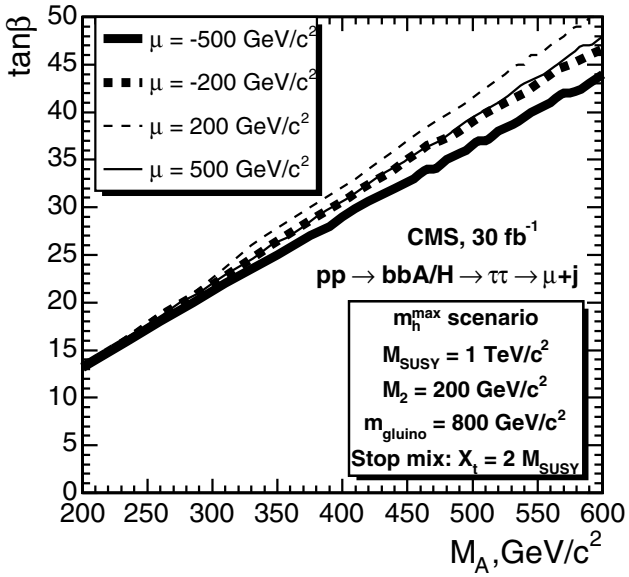

Figure 11.36. Variation of the 5σ discovery potential for the neutral Higgs bosons in the $\tau\tau \to \mu$+jet decay mode with μ in the m_h^{max} scenario.

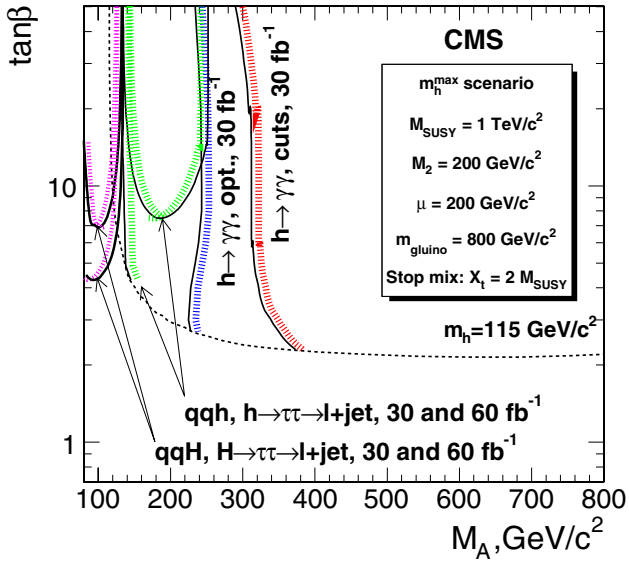

Figure 11.37. The 5σ discovery regions for the light, neutral Higgs boson h from the inclusive pp $\to$ h+X production with the h $\to \gamma\gamma$ decay and for the light and heavy scalar Higgs bosons, h and H, produced in the vector boson fusion qq $\to$ qqh(H) with the h(H) $\to \tau\tau \to \ell$+jet decay in the m_h^{max} scenario.

shows the 5σ discovery regions for the neutral Higgs boson ϕ (ϕ = h, H, A) produced in the association with b quarks pp $\to b\bar{b}\phi$ with the $\phi \to \mu\mu$ and $\phi \to \tau\tau$ decay modes. In both figures the discovery reach was evaluated in the m_h^{max} scenario with $\mu = 200\,\mathrm{GeV/c^2}$ (See Section 11.3.1).

The discovery reach was evaluated also in the extended m_h^{max} scenario (see Section 11.3.1.3 and [263]) with the values of $\mu = -200$ and $\pm 500\,\mathrm{GeV/c^2}$. The Fig. 11.36 presents the variation of the 5σ discovery potential for the neutral Higgs boson produced in the association with b quarks $pp \to b\bar{b}\phi$ with the $\phi \to \tau\tau \to \mu$+jet decay mode. The combination of the effects from supersymmetric radiative corrections and decay modes into supersymmetric particles gives rise to a rather complicated dependence of the discovery contour on μ. This results in a variation of the discovery region, especially for large M_A and large $\tan\beta$. For the positive values of μ the inclusion of the supersymmetric radiative corrections leads to a shift of the discovery region toward higher values of $\tan\beta$.

Figure 11.37 shows the 5σ discovery regions for the light, neutral Higgs boson h from the inclusive $pp \to h+X$ production with the $h \to \gamma\gamma$ decay and for the light and heavy scalar Higgs bosons, h and H, produced in the vector boson fusion $qq \to qqh(H)$ with the $h(H) \to \tau\tau \to \ell$+jet decay.

Chapter 12. Search for Higgs Boson in Non-SUSY Models

12.1. Scalar sector of 5D Randall–Sundrum model

The Randall–Sundrum model (RS) [94, 646] has recently received much attention because it could provide a solution to the hierarchy problem [565], by means of an exponential factor in a five dimensional nonfactorisable metric. In the simplest version the RS model is based on a five dimensional universe with two four-dimensional hypersurfaces (branes), located at the boundary of the fifth coordinate. By placing all the Standard Model fields on the visible brane all the mass terms, which are of the order of the Planck mass, are rescaled by the exponential factor, to a scale of the order of a TeV. The fluctuations in the metric in the fifth dimension are described in terms of a scalar field, the radion, which in general mixes with the Higgs boson. This scalar sector of the RS model is parameterised in terms of a dimensionless Higgs boson radion mixing parameter ξ, of the Higgs boson and radion masses m_h, m_ϕ and the vacuum expectation value of the radion field Λ_ϕ.

The phenomenology of Higgs boson and radion at LHC has been subject to several studies [647–652] concentrating mainly on Higgs and radion processes. The Higgs boson and radion detection is not guaranteed in all the parameter space region. The presence in the Higgs radion sector of trilinear terms opens the possibility of $\phi \to hh$ and $h \to \phi\phi$ decays. For example, for $m_h = 120\,\mathrm{GeV/c^2}$, $\Lambda_\phi = 5\,\mathrm{TeV/c^2}$ and $m_\phi \sim 250$–$350\,\mathrm{GeV/c^2}$ the BR($\phi \to hh$) ranges between 20 and 30%.

The CMS discovery potential is estimated for the decay of the radion in a pair of Higgs bosons, with $\gamma\gamma b\bar{b}$, $\tau\tau b\bar{b}$ and $b\bar{b}b\bar{b}$ final states and for an integrated luminosity of $30\,\mathrm{fb^{-1}}$. The study has been carried out for the radion mass of $300\,\mathrm{GeV/c^2}$ and the Higgs boson mass of $125\,\mathrm{GeV/c^2}$. The sensitivity was evaluated in the (ξ,Λ_ϕ) plane, with systematics uncertainties included.

A detailed description of the analysis can be found in [653]. A brief summary of the analysis and the results is presented below.

12.1.1. The $\phi \to hh$ analysis with the $\gamma\gamma b\bar{b}$ and $\tau\tau b\bar{b}$ final states

Signal events $gg \to \phi \to hh$ were generated with PYTHIA. The cross sections and branching ratios were evaluated using rescaled NLO cross sections for the SM Higgs boson and a modified HDECAY program. For the radion and a Higgs boson mass points considered ($m_h = 125\,\mathrm{GeV/c^2}$, $m_\phi = 300\,\mathrm{GeV/c^2}$) and for $\Lambda_\phi = 1\,\mathrm{TeV/c^2}$ the maximal cross section times branching ratio is 71 fb for $\gamma\gamma b\bar{b}$ final state. For the $\tau\tau b\bar{b}$ final state with the topology considered in the analysis, one τ lepton decaying leptonically and the other τ lepton decaying hadronically (producing a τ jet), the maximal cross section times branching ratio is 960 fb. This maximal cross section is reached for the radion mixing parameter $\xi = -0.35$.

For the $\gamma\gamma b\bar{b}$ final state the irreducible backgrounds $\gamma\gamma$jj (j = u, d, s, g) (generated with CompHEP) and the $\gamma\gamma c\bar{c}$ and $\gamma\gamma b\bar{b}$ (generated with MadGraph) were studied. The reducible background from γ+three jets and four-jet processes was not evaluated directly, but assumed to be the same as in for the inclusive $h \to \gamma\gamma$ analysis [19], namely 40% of the total background after all selection. For the $\tau\tau b\bar{b}$ final state, the $t\bar{t}$, Z+jets, W+jets backgrounds (generated with PYTHIA) and the $b\bar{b}$Z background (generated with CompHEP) were studied.

The $\gamma\gamma b\bar{b}$ events were required to pass the Level-1 and HLT diphoton trigger. In the off-line analysis two photon candidates with $E_T^{\gamma 1,\gamma 2} > 40, 25\,\mathrm{GeV}$ were required to pass tracker cuts and calorimeter isolation cuts. Events with only two calorimeter jets of $E_T > 30\,\mathrm{GeV}$ and within $|\eta| < 2.4$ were selected. At least one of these jets must be tagged as a b-jet. Finally, the

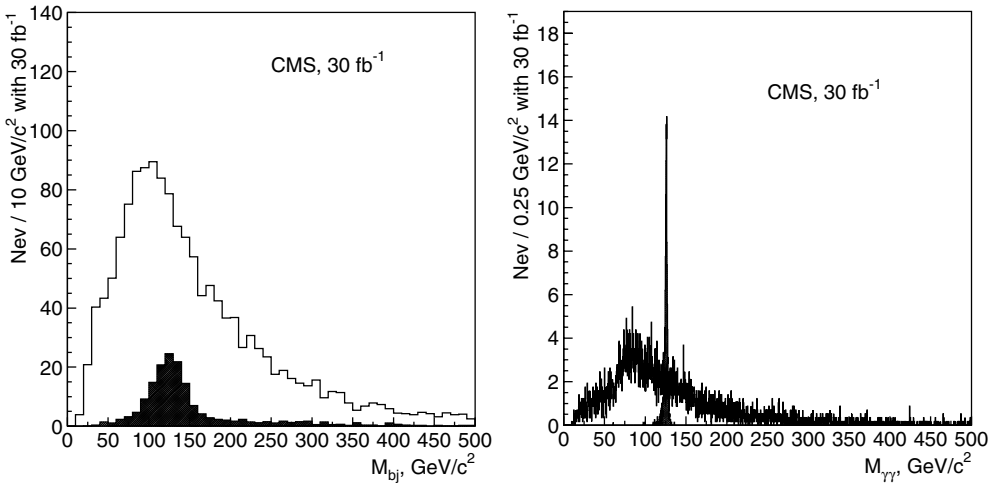

Figure 12.1. The dijet (left plot) and the diphoton (right plot) mass distribution for the background (open histogram) and the signal of $\phi \to hh \to \gamma\gamma b\bar{b}$ (full black histogram) after all selections except the mass window cuts with 30 fb^{-1}. The signal is shown for the maximal cross section times branching ratios point in (ξ $-\Lambda_\phi$) plane.

diphoton mass, $M_{\gamma\gamma}$, was required to be in a window of $\pm 2\,\mathrm{GeV/c^2}$, the dijet mass, $M_{j\bar{b}}$, in a window of $\pm 30\,\mathrm{GeV/c}$ and the diphoton-dijet mass, $M_{\gamma\gamma b\bar{b}}$, in a window $\pm 50\,\mathrm{GeV/c^2}$ around the Higgs and Radion mass. Figure 12.1 shows the dijet (left plot) and the diphoton (right plot) mass distribution for the background (open histogram) and the signal of $\phi \to hh \to \gamma\gamma b\bar{b}$ (full, black histogram) after all selections except the mass window cuts, and for $30\,\mathrm{fb^{-1}}$. The signal is shown for the maximal cross section times branching ratios point in (ξ-Λ_ϕ) plane. Figure 12.2 (left plot) shows the $M_{\gamma\gamma bj}$ distribution for the background (dashed histogram) and for the signal of $\phi \to hh \to \gamma\gamma b\bar{b}$ plus background (solid histogram) after all selections, and for $30\,\mathrm{fb^{-1}}$.

The $\tau\tau b\bar{b}$ events were selected by the single electron and muon triggers and by the combined e-plus-τ-jet and the μ-plus-τ-jet triggers. In the off-line analysis a lepton and τ-jet identification was performed. The requirements on the jets were similar to the ones used in the $\gamma\gamma b\bar{b}$ analysis. In addition a cut of the transverse mass of the lepton and missing transverse momentum, $M_T^{\ell\nu} < 35\,\mathrm{GeV/c^2}$ was applied to suppress the $t\bar{t}$ and W+jets backgrounds. The diτ-lepton mass was reconstructed using the missing transverse energy as described in Section 5.2.5. The significance of the discovery was calculated using expected number of the signal and background events after the mass window selections: $100 < M_{bj} < 150\,\mathrm{GeV/c^2}$, $100 < M_{\tau\tau} < 160\,\mathrm{GeV/c^2}$ and $280 < M_{\tau\tau bj} < 330\,\mathrm{GeV/c^2}$. Figure 12.2 (right plot) shows the $M_{\tau\tau bj}$ distribution for the background (full, grey (yellow) histogram) and for the signal of $\phi \to hh \to \tau\tau b\bar{b}$ plus background (points with error bars) after all selections, for $30\,\mathrm{fb^{-1}}$. Fitted curves for the background and the signal plus background are superimposed.

The four b-jet final state yields the highest rate for the signal. The maximal cross section times branching ratio at $\Lambda_\phi = 1\,\mathrm{TeV/c^2}$ is 10.3 pb, which results in about 3.1×10^5 signal events for $30\,\mathrm{fb^{-1}}$. The effective triggering and selection in the off-line analysis of these events is, however a big challenge due to the huge multi-jet background rate. In fact the remaining background is a few orders of magnitude larger than the signal in the relevant mass range. Techniques can be envisaged to normalise the background directly from a signal-free region and predict the number of background events in the signal region. In order to make a 3σ

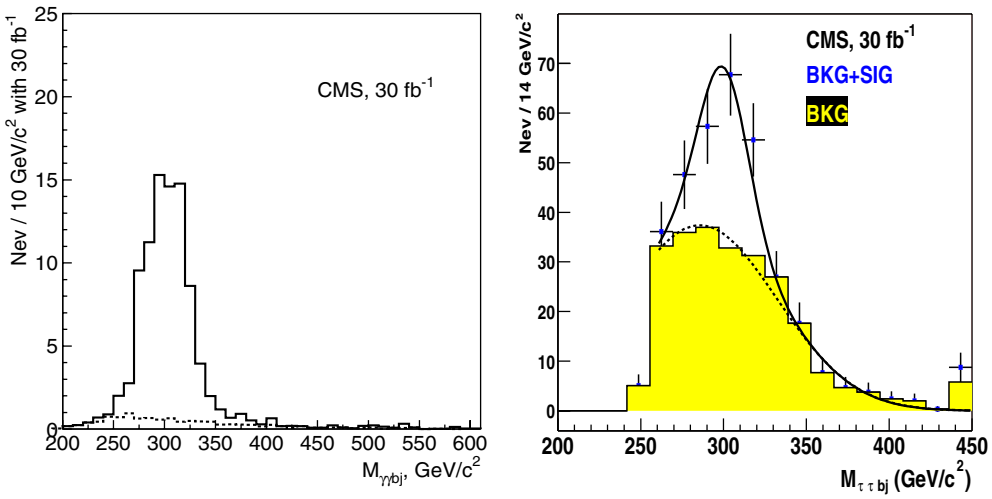

Figure 12.2. Left plot: the $M_{\gamma\gamma bj}$ distribution for the background (dashed histogram) and for the signal of $\phi \to hh \to \gamma\gamma b\bar{b}$ plus background (solid histogram) after all selections for 30 fb^{-1}. Right plot: the $M_{\tau\tau bj}$ distribution for the background (full grey (yellow) histogram) and for the signal of $\phi \to hh \to \tau\tau b\bar{b}$ plus background (black points with the error bars) after all selections for 30 fb^{-1}. The fitted curves for the background and signal plus background are superimposed. On both plots the signal is shown for the maximal cross section times branching ratios point in (ξ-Λ_ϕ).

discovery, such extrapolation needs to be performed with a precision of about 0.1%, making four b-jet channel essentially hopeless.

The background contribution to the $\gamma\gamma b\bar{b}$ final state can be determined directly from the $\gamma\gamma$-plus-two-jets data obtained after all selections, except the final mass window cuts on the $M_{\gamma\gamma}$, $M_{j\bar{b}}$ and $M_{\gamma\gamma b\bar{b}}$. The signal-to-background ratio is always less than 10% before the mass cuts are applied. The final cuts on the $M_{\gamma\gamma}$, $M_{j\bar{b}}$ and $M_{\gamma\gamma b\bar{b}}$ introduce a systematic uncertainty on the number of the background events expected after these cuts. This uncertainty is determined by the following factors: the energy scale uncertainty for the photons and jets, and the theoretical uncertainty of the shape of the mass distributions due to the scale and PDF uncertainties. Figure 12.3 (left plot) shows the 5σ discovery contours for the $\phi \to hh \to \gamma\gamma b\bar{b}$ channel for 30 fb^{-1}. The solid (dashed) contour shows the discovery region without (with) the effects of the systematic uncertainties.

For the $\tau\tau b\bar{b}$ final state the background uncertainty due to the experimental selections was estimated to be between 5% and 10% [653]. Figure 12.3 (right plot) shows the 5σ discovery contours for the $\phi \to hh \to \tau\tau b\bar{b}$ channel for 30 fb^{-1}. The two contours corresponds to the variation of the background NLO cross sections due to the scale uncertainty. The 5% experimental systematics on the background is taken into account.

12.2. Doubly charged Higgs boson pair production in the Littlest Higgs model

The main motivation of the Large Hadron Collider (LHC) experiments is to reveal the secrets of electroweak symmetry breaking. If the standard model (SM) Higgs boson will be discovered, the question arises what stabilises its mass against the Planck scale quadratically divergent radiative corrections. The canonical answer to this question is supersymmetry which implies very rich phenomenology of predicted sparticles in the future collider experiments.

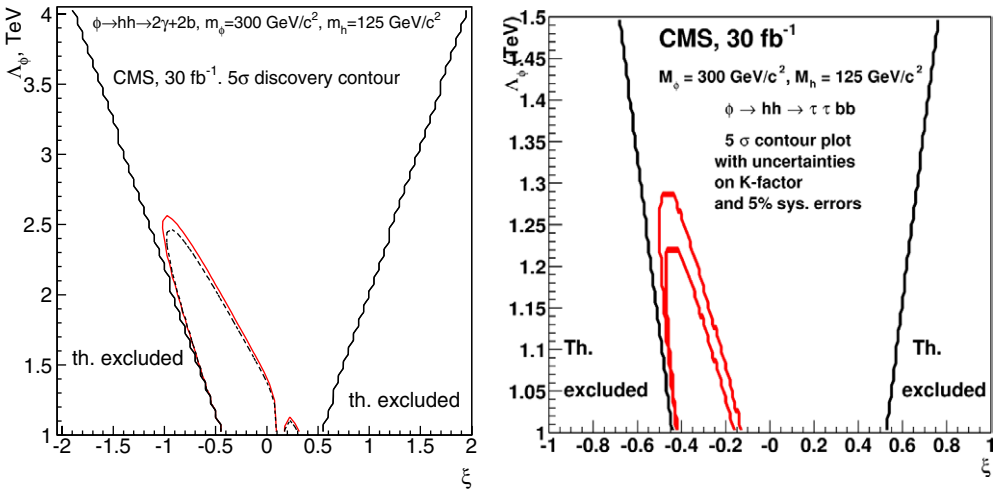

Figure 12.3. Left plot: the 5σ discovery contours for the $\phi \to \mathrm{hh} \to \gamma\gamma\mathrm{b\bar{b}}$ channel for 30 fb^{-1}. The solid (dashed) contour shows the discovery region without (with) the effects of the systematic uncertainties (find more explanations in the text). Right plot: the 5σ discovery contours for the $\phi \to \mathrm{hh} \to \tau\tau\mathrm{b\bar{b}}$ channel for 30 fb^{-1}. The two contours corresponds to the variation of the background NLO cross sections due to the scale uncertainty. The 5% experimental systematics on the background is taken into account (see text).

More recently another possibility of formulating the physics of electroweak symmetry breaking, called the little Higgs, was proposed [654–656]. In those models the SM Higgs boson is a pseudo Goldstone mode of a broken global symmetry and remains light, much lighter than the other new modes of the model which have masses of order the symmetry breaking scale $\mathcal{O}(1)$ TeV. In order to cancel one-loop quadratic divergences to the SM Higgs mass a new set of heavy gauge bosons W', Z' with the SM quantum numbers identical to WZ, and a vector like heavy quark pair T, $\bar{T}$ with charge 2/3 must be introduced. Notice that those fields are put in by hand in order to construct a model with the required properties. However, the minimal model based on the $SU(5)/SO(5)$ global symmetry, the so-called littlest Higgs model [657], has a firm prediction from the symmetry breaking pattern alone: the existence of another $\mathcal{O}(1)$ TeV pseudo Goldstone boson Δ with the $SU(2)_L \times U(1)_Y$ quantum numbers $\Delta \sim (3, 2)$.

Interestingly, the existence of triplet Higgs Δ might also be required to generate Majorana masses to the left-handed neutrinos [658]. Non-zero neutrino masses and mixing is presently the only experimentally verified signal of new physics beyond the SM. In the triplet neutrino mass mechanism [659] the neutrino mass matrix is generated via

$$(m_\nu)_{ij} = (Y_\Delta)_{ij} v_\Delta, \tag{12.1}$$

where $(Y_\Delta)_{ij}$ are the Majorana Yukawa couplings of the triplet to the lepton generations $i, j = e, \mu, \tau$ which are described by the Lagrangian

$$L = i\bar{\ell}^c_{Li}\tau_2 Y^{ij}_\Delta (\tau \cdot \Delta)\ell_{Lj} + \mathrm{h.c.}, \tag{12.2}$$

and v_Δ is the effective vacuum expectation value of the neutral component of the triplet induced via the explicit coupling of Δ to the SM Higgs doublet H as $\mu\Delta^0 H^0 H^0$. Here μ has a dimension of mass. In the concept of seesaw $\mu \sim M_\Delta$, and the smallness of neutrino masses is attributed to the very high scale of triplet mass M_Δ via the smallness of $v_\Delta = \mu v^2/M^2_\Delta$, where $v = 174$ GeV.

However, in the littlest Higgs model the triplet mass scale is $\mathcal{O}(1)$ TeV which alone cannot suppress v_Δ. Therefore in this model $\mu \ll M_\Delta$, which can be achieved, for example, via shining from extra dimensions as shown in ref. [660, 661] or if the triplet is related to the Dark Energy of the Universe [662]. In that case $v_\Delta \sim \mathcal{O}(0.1)$ eV while the Yukawa couplings Y_Δ can be large. For the normally hierarchical light neutrino masses neutrino data implies very small Δ decay branching fractions to electrons and $BR(\Delta^{++} \to \mu^+\mu^+) \approx BR(\Delta^{++} \to \tau^+\tau^+) \approx BR(\Delta^{++} \to \mu^+\tau^+) \approx 1/3$. We remind also that v_Δ contributes to the SM oblique corrections, and the precision data fit $\hat{T} < 2 \cdot 10^{-4}$ [663] sets an upper bound $v_\Delta \leqslant 1.2$ GeV on that parameter.

At LHC Δ^{++} can be produced singly and in pairs. The cross section of the single Δ^{++} production via the WW fusion process [664] $qq \to q'q'\Delta^{++}$ scales as $\sim v_\Delta^2$. In the context of the littlest Higgs model this process, followed by the decays $\Delta^{++} \to W^+W^+$, was studied in ref. [91, 665, 666]. The detailed ATLAS simulation of this channel shows [666] that in order to observe 1 TeV Δ^{++}, one must have $v_\Delta > 29$ GeV. This is in conflict with the precision physics bound $v_\Delta \leqslant 1.2$ GeV as well as with the neutrino data. Therefore the WW fusion channel is not experimentally promising for the discovery of very heavy doubly charged Higgs.

On the other hand, the Drell–Yan pair production process [664, 667] $pp \to \Delta^{++}\Delta^{--}$ is not suppressed by any small coupling and its cross section is known up to next to leading order [668] (possible additional contributions from new physics such as Z' are strongly suppressed for any practical purposes). Followed by the lepton number violating decays $\Delta^{\pm\pm} \to \ell^\pm\ell^\pm$, this process allows to reconstruct $\Delta^{\pm\pm}$ invariant mass from the same charged leptons rendering the SM background to be very small in the signal region. If one also assumes that neutrino masses come from the triplet Higgs interactions, one fixes the $\Delta^{\pm\pm}$ leptonic branching ratios. This allows to test neutrino mass models at LHC.

12.2.1. Search for the final state with four muons

12.2.1.1. Introduction. The doubly charged Higgs bosons $\Delta^{\pm\pm}$ pair-produced via the Drell–Yan process is investigated assuming a branching ratio of 100% into muons. This provides an almost background free channel.

12.2.1.2. Event generation. The signal events are generated using PYTHIA, with doubly charged Higgs bosons pair-produced through the Drell–Yan process. The Higgs bosons are forced to decay into muons. Datasets are produced for several values of the doubly charged Higgs boson mass, ranging from 100 to 800 GeV/c^2.

The leading order (LO) and the next-to-leading order (NLO) cross-sections [668] are shown for the signal as a function of the doubly charged Higgs boson mass in Fig. 12.4.

Important backgrounds for this channel with a four muon final state are:

- $t\bar{t} \to W^+W^-b\bar{b} \to 2\mu + 2\mu$ (generated with PYTHIA);
- $Zb\bar{b} \to 2\mu + 2\mu$ (generated with COMPHEP);
- $ZZ \to 2\mu + 2\mu$ (generated with COMPHEP);
- $ZZ \to 2\tau + 2\mu$ (generated with COMPHEP).

The ZZ production process includes γ^*. The contribution of background from $b\bar{b}$ production has also been investigated. The $b\bar{b}$ background is the QCD multi-jet background which yields the highest probability to fake events with multiple muons. It has been found that the $b\bar{b}$ background can be neglected after the online selection and a cut which requires four well-reconstructed muons with pseudorapidity $|\eta| < 2.1$ and transverse momentum $p_T > 8$ GeV/c. The W bosons in the $t\bar{t}$ data sample are forced to decay into electrons, muons and taus. The tau leptons are forced to decay into electrons and muons. The Z boson in the $Z\bar{b}b$

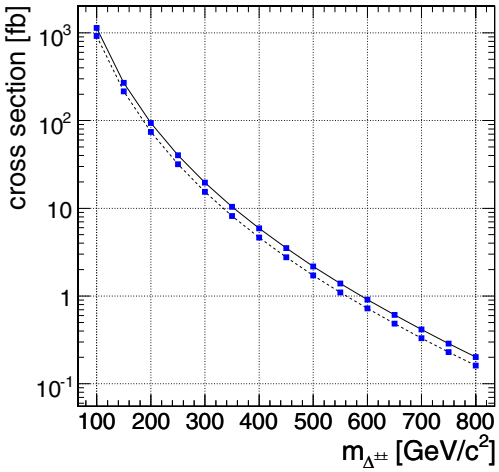

Figure 12.4. The leading order (LO) and the next-to-leading order (NLO) cross-section, for $H^{++} H^{--} \to 4\mu$.

sample is generated with $m_{Z/\gamma^*} > 5\,\mathrm{GeV/c^2}$ and is forced to decay into muons. The Z bosons in the ZZ samples are forced to decay into muons and the taus in the $ZZ \to 2\tau + 2\mu$ sample decay freely.

On all samples pre-selection cuts are applied at the generation level with the following requirements:

- Final state contains two positive and two negative muons.
- Transverse momentum $p_T(\mu) > 3\,\mathrm{GeVc}$ and pseudorapidity $|\eta(\mu)| < 2.4$ for all muons.

12.2.1.3. Event selection and reconstruction. The events are selected by dimuon trigger at Level 1 and the HLT. The p_T threshold for the dimuon HLT is 7 GeV/c. The Level 1 and HLT efficiency for the signal is >99% within uncertainties.

The muons are reconstructed by the Global Muon Reconstructor. At least 4 muons, with a $p_T > 8\,\mathrm{GeV/c}$ and $\eta \leqslant 2.1$, are required. The invariant mass of the doubly charged Higgs is reconstructed, by calculating the invariant mass of the two same charge muons with the highest p_T, after all cuts.

An event, where two or three muons are generated in one collision, and one or two in another, has also to be considered as background to our four muon signal. To suppress this background a vertex cut has been applied. For each muon in an event the impact point is determined. The impact point is the point of closest approach of the extrapolated muon trajectory to the nominal interaction point. The longitudinal distances Δz_{IPS} between the impact point states of all muons in one event are calculated. The biggest calculated Δz_{IPS} is required to be smaller than 0.05 cm. This is much smaller than the longitudinal size of the luminous region of the LHC beam of about 5 cm. So this cut rejects events with muons from different collision vertices with a probability of roughly 99%.

12.2.1.4. Results. Table 12.1 and Table 12.2 show the NLO production cross-section without any forced decay, the cross-section times branching ratio times pre-selection efficiency and the cross-section times branching ratio times efficiency after each stage of the online and offline event selection. Table 12.1 shows these values for each of the background samples.

Table 12.1. The NLO cross sections σ for background events with forced decay modes after each stage of the event selection. Errors are statistical only.

	$t\bar{t}$	$Z\bar{b}b$	$ZZ \to 4\mu$	$ZZ \to 2\mu 2\tau$
Pre-selection [fb]	232	289.8	87.4	1.63
Level-1 Trigger [fb]	232 ± 1	289 ± 1	87.3 ± 0.3	1.63 ± 0.02
High Level Trigger [fb]	149 ± 1	195 ± 1	69.7 ± 0.3	1.10 ± 0.01
4 μ reconstructed ($p_T > 8$ GeV/c, $\|\eta\| < 2.1$) [fb]	45.1 ± 0.4	25.1 ± 0.3	18.5 ± 0.1	0.25 ± 0.01
Impact Point Cut [fb]	22.8 ± 0.3	13.1 ± 0.2	16.9 ± 0.1	0.22 ± 0.01

Table 12.2. Production cross sections (NLO) for signal events with $m_{H^{++}} = 300, 600, 800\,\mathrm{GeV/c^2}$ and forced decay into four muons after each stage of the event selection. Errors are statistical only.

$\Delta^{\pm\pm}$ mass	$300\,\mathrm{GeV/c^2}$	$600\,\mathrm{GeV/c^2}$	$800\,\mathrm{GeV/c^2}$
Production cross section(NLO) [fb]	19.6	0.909	0.201
Pre-selection [fb]	17.4±0.3	0.85 ± 0.02	0.190 ± 0.004
Level-1 Trigger [fb]	17.3 ± 0.3	0.85 ± 0.02	0.190 ± 0.004
High Level Trigger [fb]	17.1 ± 0.3	0.83 ± 0.02	0.188 ± 0.004
4 μ reconstructed ($p_T > 8$ GeV/c, $\|\eta\| < 2.1$) [fd]	13.0 ± 0.2	0.70 ± 0.02	0.158 ± 0.003
Impact Point Cut [fd]	12.5 ± 0.2	0.67 ± 0.02	0.153 ± 0.003

Table 12.2 show these values for signal samples with doubly charged Higgs masses 300, 600 and $800\,\mathrm{GeV/c^2}$.

Figure 12.5 shows the invariant mass spectrum of the reconstructed $\Delta^{\pm\pm}$ before and after the offline cuts, for $m(\Delta^{\pm\pm}) = 300\,\mathrm{GeV/c^2}$ and for $m(\Delta^{\pm\pm}) = 600\,\mathrm{GeV/c^2}$.

12.2.1.5. Statistical interpretation. To interpret the results, the CL_s method [508] is applied, which is based on log-likelihood ratios, calculated for all bins of the invariant mass distribution. CL_s is defined as ratio of the confidence levels for the signal and background hypotheses $CL_s = CL_{s+b}/CL_b$. CL_s can be understood as the probability of excluding an existing signal. The $1 - CL_b$ can be understood as the probability for the background distribution to fake a signal. For high doubly charged Higgs boson masses the amount of simulated background events goes to zero. Nevertheless, zero simulated background events do not necessarily mean zero background events in reality. To estimate the amount of background in this region, empty bins are filled for each background with upper limits to Poisson statistic. Zero background events are compatible with maximal three generated events. Therefore empty bins get filled for each background with three events times the scale factor for an integrated luminosity of $10\,\mathrm{fb^{-1}}$. The left plot in Fig. 12.6 shows the $1 - CL_b$ values for different doubly charged Higgs boson masses. For a doubly charged Higgs Boson mass smaller than $650\,\mathrm{GeV/c^2}$ the signal plus background expectation will exceed the background only expectation by more than 5σ. To claim a discovery, at least three signal events need to be detected. For a mass of $650\,\mathrm{GeV/c^2}$ four detectable events remain after all cuts. The right plot in figure 12.6 shows the CL_s values for different doubly charged Higgs boson masses. If no signal can be detected for an integrated luminosity of $10\,\mathrm{fb^{-1}}$ the existence of a doubly charged Higgs Boson in this decay channel can be excluded with 95% confidence up to a mass of $760\,\mathrm{GeV/c^2}$. The ± 1 and ± 2-sigma bands in figure 12.6 are only for statistical errors.

12.2.1.6. Systematical uncertainties. The uncertainties on the exclusion limit resulting from systematical errors have yet to be studied in detail, once the detector is running.

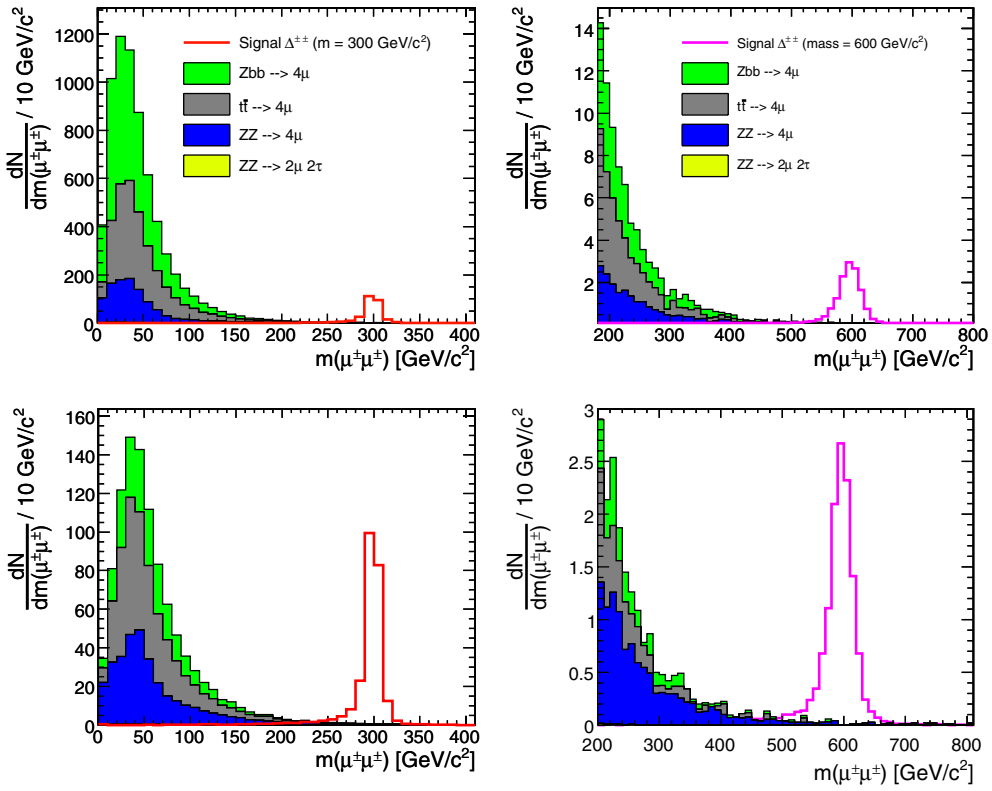

Figure 12.5. The reconstructed $\Delta^{\pm\pm}$ invariant mass after pre-selection and trigger selection (top) and after offline cuts (bottom).

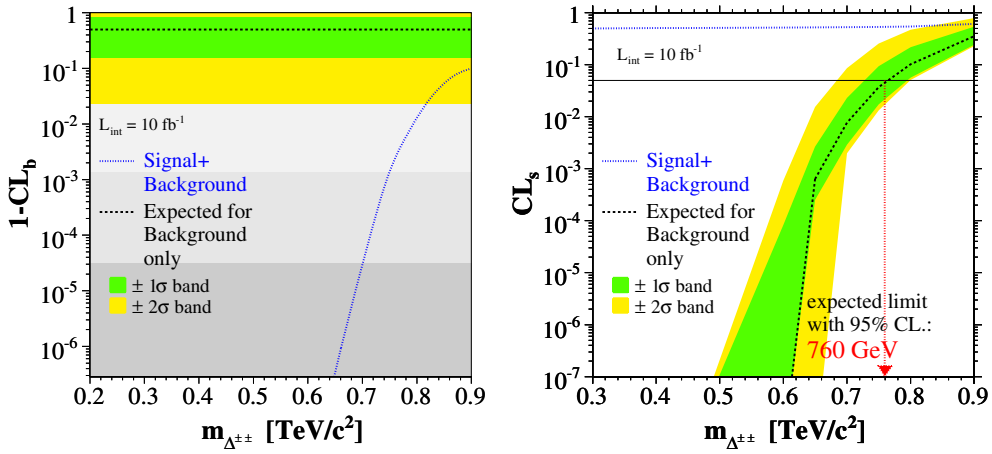

Figure 12.6. $1 - CL_b$ and CL_s as defined in the Log Likelihood Ratio Method after all selection cuts for an integrated luminosity of $10\,\mathrm{fb}^{-1}$.

The considered backgrounds are also backgrounds to the Standard Model $H \to ZZ \to 4\mu$ process. As this process is one of the benchmark processes of the future CMS detector, this backgrounds are studied in detail. The obtained total uncertainty on the background cross

Table 12.3. The NLO background processes cross sections used (in fb).

background	$t\bar{t} \to 4l$	Z $b\bar{b}$	ZZ	$t\bar{t}$ Z
Cross section times BR	$88.4 \cdot 10^3$	$52.4 \cdot 10^3$	229.5	650

section is 1% to 6%. The uncertainty on signal cross section is 10% to 15%. The uncertainty on the luminosity $\mathcal{L}$ is $\sim 5\%$ for an integrated luminosity of $10\,\text{fb}^{-1}$.

Using a background cross section uncertainty of 6%, a signal cross section uncertainty of 10% and a luminosity uncertainty of 5% the approximated uncertainties on the exclusion mass limit and on the discovery mass limit are:

$$\text{Exclusion Limit} = (760\ ^{+0.5}_{-2}(\text{bkg}) \pm 10(\text{signal}) \pm 4(\text{lumi}))\,\text{GeV/c}^2 \tag{12.3}$$

$$\text{Discovery Limit} = (650\ ^{+0.4}_{-0.3}(\text{bkg})\ ^{+3}_{-0.4}(\text{signal}) \pm 0.2(\text{lumi}))\,\text{GeV/c}^2. \tag{12.4}$$

12.2.2. Search for the final states with τ leptons

12.2.2.1. Introduction. In this section, we discuss the doubly charged Higgs boson pair-production via a Drell–Yan process and investigate decays which involve taus and muons. The branching ratios are assumed to be 1/3 for the following three channels: $\Delta^{\pm\pm} \to 2\mu^{\pm}$, $\Delta^{\pm\pm} \to \mu^{\pm}\tau^{\pm}$ and $\Delta^{\pm\pm} \to 2\tau^{\pm}$. The reasoning comes from recent neutrino mixing measurements. As the neutrino mixing matrix and doubly charged Higgs boson decays are directly related then the appropriate branchings can be determined.

12.2.2.2. Event generation. The doubly charged Higgs boson pair-production via Drell–Yan process is generated using PYTHIA. Datasets are produced with Higgs boson mass from $200\,\text{GeV/c}^2$ to $600\,\text{GeV/c}^2$. The taus from Higgs boson decays can decay both leptonically and hadronically while in analysis we only consider hadronic decays.

The backgrounds which were considered for this analysis are as follows:

- $t\bar{t} \to \text{W}^+\text{W}\, b\bar{b}$ generated by PYTHIA, COMPHEP, ALPGEN, TOPREX and MADGRAPH with W boson decay $\text{W} \to \ell\nu$ ($\ell = \text{e}, \mu, \tau$) forced.
- $t\bar{t}\,\text{Z} \to W^+W^-Z\, b\bar{b}$ generated with COMPHEP. The W and Z bosons are allowed to decay arbitrarily.
- Z$b\bar{b}$ where the Z boson decays to muons and τ leptons, generated with COMPHEP.
- ZZ generated with PYTHIA, where the Z bosons are forced to decay leptonically (e, μ, τ). The contribution of γ^* is included with $\text{m}_{\gamma^*} > 12\,\text{GeV/c}^2$.

The next-to-leading order (NLO) cross sections times branching ratios used for the backgrounds can be found in Table 12.3. The Monte Carlo statistics of the generated background exceed $30\,\text{fb}^{-1}$ except Z$b\bar{b}$ background, where it is $8\,\text{fb}^{-1}$. Therefore the results will be presented for an integrated luminosity of $10\,\text{fb}^{-1}$.

12.2.2.3. Event selection and reconstruction. The events are triggered by the single muon trigger at Level 1 and HLT. After HLT the event is only used if it is possible to reconstruct the event primary vertex. If the primary vertex fails to be reconstructed the event is rejected.

The muons are reconstructed using Global Muon Reconstructor. The τ leptons are reconstructed using τ-jet candidates and missing transverse energy after selection cuts. The doubly charged Higgs boson invariant mass is reconstructed from the same charge lepton pairs after all selection cuts.

The selection cuts used on muons are:

- The transverse momentum must be higher than 50 GeV/c. For background events 80% of muons have p_T less than 50 GeV/c while for the signal with Higgs boson mass 200 GeV/c^2 it is 27% and for higher masses it reduces to around 10%.
- The distance to primary vertex in z-direction must not exceed 0.03 cm. It does not cut away any muons from the signal events but limits analysis to leptons coming from the same primary vertex.

The selection cuts used on τ jets are:

- For τ jets we consider τ decays which involve 1 or 3 charged tracks. We use τ-jet candidates which passed the τ-jet filtering algorithms described in [280]. Two isolation criteria are used. Either one or three charged tracks in the signal cone and no charged tracks in the isolation cone or two tracks in signal cone and exactly one charged track in the isolation cone.
- The maximal distance to the primary vertex in the z-direction of any charged track in the τ jet must not exceed 0.2 cm.
- The transverse energy of the hottest HCAL tower of the τ jet must be higher than 2 GeV. This cut eliminates 86% of all electrons taken as τ candidates and only removes 7.5% of real τ jets.
- The transverse energy of the τ jet candidate must exceed 50 GeV. It has been chosen to be the same as the cut used on muons.
- No muon track should be in a cone with $\Delta R = 0.3$ constructed around the τ-jet candidate. If there is, then the candidate is dropped. This eliminates false τ-jet candidates which are generated when a charged muon track passes the same region as photons or hadrons. With this cut only a few real τ jets are discarded however most of the false τ jets coming from this misidentification are rejected.

Missing transverse energy (E_T^{miss}) is reconstructed using calorimeter Type 1 E_T^{miss} (E_T^{miss} with the jet energy corrections) and p_T of muons.

Only events with at least four objects, muons or τ jets, are accepted. The possible final states are:

- $\Delta^{++}\Delta^{--} \to 4\mu$: this channel is investigated in the previous subsection.
- $\Delta^{++}\Delta^{--} \to 3\mu 1\tau$: this channel is easily reconstructible as there is only one neutrino and it goes the direction of the τ jet.
- $\Delta^{++}\Delta^{--} \to 2\mu 2\tau$: this channel can also be reconstructed using the assumption that the neutrinos go in the same directions as the τ jets.
- $\Delta^{++}\Delta^{--} \to 1\mu 3\tau$: this channel can be reconstructed only with very good E_T^{miss} resolution as it requires an additional assumption that the masses of the two reconstructed Higgs bosons are the same. However the reconstruction is very sensitive to E_T^{miss} accuracy and often the event has to be dropped due to negative τ-lepton energies.
- $\Delta^{++}\Delta^{--} \to 4\tau$: this channel can not be reconstructed (and triggered by the single muon trigger).

Once the event leptons are reconstructed, some additional selections are performed:

- Z boson veto: if the odd sign pairing gives an invariant mass of 91 ± 5 GeV/c^2 then these leptons are removed from further use.
- Same charge lepton pairs are reconstructed and only those reconstructed Higgs candidate pairs whose invariant mass difference is within 20% of each other are considered.

The reconstructed mass of doubly charged Higgs boson is shown on Figure 12.7 for the Higgs boson masses 200 and 500 GeV/c^2.

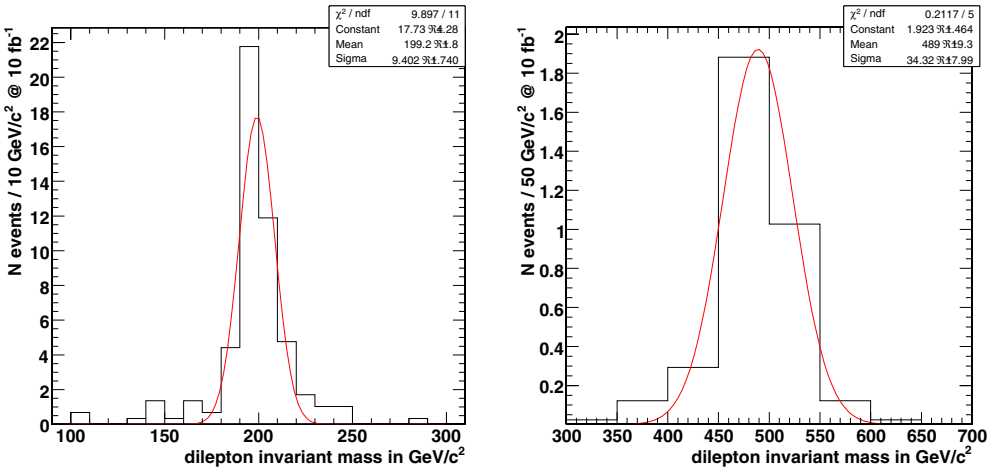

Figure 12.7. The reconstructed invariant mass for $M(\Delta^{\pm\pm}) = 200\,\mathrm{GeV/c^2}$ and $500\,\mathrm{GeV/c^2}$.

Table 12.4. The signal selection efficiencies for different $\Delta^{\pm\pm}$ masses. Total efficiency is the product of the single efficiencies.

$m_{\Delta}^{\pm\pm}$ ($\mathrm{GeV/c^2}$)	200	300	400	500	600
Level 1 and HLT	83.7%	86.0%	86.7%	85.8%	88.3%
Primary vertex	96.9%	98.5%	97.0%	97.5%	98.0%
4 leptons in final state	10.1%	17.2 %	23.6%	24.7%	26.7%
two pairs and at least one τ	44.9%	46.1%	41.7%	53.2%	52.9%
Mass difference	62.5%	77.2%	80.4%	74.3%	63.6%
Total signal efficiency	2.3%	5.1%	6.6%	8.1%	7.7%

12.2.2.4. Selection efficiencies. The upper limit of the signal selection efficiency is given by the fraction of events with $3\mu 1\tau$, $2\mu 2\tau$, $1\mu 3\tau$ ($\tau \to$ hadrons) topology relative to all possible final states with muons and τ leptons from decays of two Higgs bosons. Assuming the above mentioned branching ratios the upper limit is $\simeq 35\%$. The fraction of every selected topology is given below:

- $\Delta^{++}\Delta^{--} \to 3\mu 1\tau = 2/9$ events $\times\, 0.65 = 14.4\%$
- $\Delta^{++}\Delta^{--} \to 2\mu 2\tau = 3/9$ events $\times\, 0.65^2 = 14.1\%$
- $\Delta^{++}\Delta^{--} \to 1\mu 3\tau = 2/9$ events $\times\, 0.65^3 = 6.1\%$.

where 0.65 is the branching ratio of $\tau \to$ hadrons decays. Table 12.4 summarises the efficiencies of each selection (relative to the previous one) for the signal of different $\Delta^{\pm\pm}$ masses. The lepton selection efficiency and purity is shown in Table 12.5. Background efficiencies are shown in Table 12.6.

12.2.2.5. Systematic errors. At the integrated luminosity of $10\,\mathrm{fb^{-1}}$ the cuts implemented above result in an almost background free signal. For datasets with Monte Carlo statistics above $30\,\mathrm{fb^{-1}}$ giving zero Monte Carlo events after all selections ($t\bar{t}$, ZZ^*) we assume the background to be zero. For $t\bar{t}Z$ background where is one Monte Carlo event passing all cuts, which corresponds to 0.05 expected events when scaled with cross section and luminosity.

Table 12.5. Single muon and τ selection efficiencies and purity.

$m_{\Delta}^{\pm\pm}$ (GeV/c^2)	200	300	400	500	600
Single μ selection efficiency	70.7%	82.0%	86.1%	87.2%	89.2%
1 - purity of accepted muons:	0.1%	0.4%	0.8%	0.7%	1.0%
Single τ selection efficiency	36.6%	42.3%	50.6%	53.3%	53.3%
1 - purity of accepted τ jets:	2.2%	2.2%	4.2%	3.6%	3.2%

Table 12.6. Selection efficiencies for background. Total efficiency is the product of the single efficiencies.

Process	$t\bar{t}$	$t\bar{t}$ Z	ZZ	Zbb
Level 1 and HLT trigger	40.7%	20.3%	40.0%	42.1%
Primary vertex	99.3%	99.8%	96.7%	98.2%
4 leptons in final state	0.0015%	0.04 %	3.0%	0.0005%
two pairs and at least one τ	–	0.1%	–	–
Mass difference	–	100%	–	–
Total signal efficiency	–	0.0008%	–	–

For Z $b\bar{b}$ background where the Monte Carlo statistics corresponds to 8 fb^{-1} no events passed all cuts. The analysis was repeated with p_{T} cut on muon (τ jet) of 40 GeV/c, 30 GeV/c and 20 GeV/c, again with no events passing the cuts, which confirms the assumption that leptons coming from Z $b\bar{b}$ are too soft to produce a background. Considering the smallness of all backgrounds we assume no background at 10 fb^{-1} for the following analysis.

The systematic uncertainties used for the signal are the following:

- muon misidentification ($\Delta\mu$): 1% per muon;
- muon isolation ($\Delta\mu_{isol}$): 2% per event;
- τ jets identification ($\Delta\tau$): 9% per τ jet;
- luminosity ($\Delta\mathcal{L}$): 5%;
- PDF and scale ($\Delta\sigma$) 10% (theoretical uncertainty, it is not used for the signal cross section measurement with no background).

As the events are a mixture of different decay modes the total selection efficiency uncertainty ($\Delta\varepsilon_S$) is calculated per decay channel and then added together with the corresponding weights:

$$\Delta 3\mu 1\tau = \sqrt{3\Delta\mu^2 + \Delta\tau^2} = 8.2\%,$$

$$\Delta 2\mu 2\tau = \sqrt{2\Delta\mu^2 + 2\Delta\tau^2} = 11.4\%,$$

$$\Delta 1\mu 3\tau = \sqrt{\Delta\mu^2 + 3\Delta\tau^2} = 13.9\%,$$

giving

$$\Delta\varepsilon_S = \frac{144\Delta 3\mu 1\tau + 141\Delta 2\mu 2\tau + 61\Delta 1\mu 3\tau}{346} = 10.5\%.$$

The total systematic error for cross section measurement is then

$$\frac{\Delta\sigma}{\sigma} = \sqrt{\Delta\mu_{isol}{}^2 + \Delta\mathcal{L}^2 + \Delta\varepsilon_S{}^2} = 13\%.$$

Table12.7. Expected number of events, NLO cross section with expected statistical and systematic uncertainty of the cross section measurement at $10\,\text{fb}^{-1}$, and integrated luminosity needed for exclusion at 95% CL.

$m_{\Delta}^{\pm\pm}$ (GeV)	200	300	400	500
N_{ev} expected at $10\,\text{fb}^{-1}$	26	10	4	2
$\sigma_{NLO} \pm \text{stat} \pm \text{syst}$ (fb)	$93.9^{+19.3}_{-17.5} \pm 12.2$	$19.6^{+6.6}_{-5.6} \pm 2.5$	$5.9^{+3.4}_{-2.5} \pm 0.8$	$2.2^{+1.9}_{-1.3} \pm 0.3$
Luminosity for 95% CL exclusion, fb^{-1}	1.3	3.0	7.7	16.8

The statistical errors were evaluated constructing the shortest Bayesian confidence interval for the confidence level of 67% [669].

12.2.2.6. Results. The expected number of events at $10\,\text{fb}^{-1}$ and the NLO cross section with expected statistical and systematic uncertainty of the cross section measurement are given in Table 12.7. Table 12.7 shows also the integrated luminosity needed for exclusion at 95% CL.

Chapter 13. Supersymmetry

13.1. Introduction

This chapter presents the results of analyses by which evidence for supersymmetry could be obtained in CMS during the "low luminosity" period of the LHC. After a brief reminder of the main phenomenological features of SUSY in Section 13.2, Section 13.3 is devoted to the outline of the scope of present searches. The emphasis was not on a complete study of a specific point in the parameter space, but rather on covering all relevant signatures by which SUSY might be discovered. For this purpose, a set of test points have been defined, for which a full simulation of the CMS detector was performed, to serve as basis for the analyses. An algorithm allowing the separation of the sparticle decay chains, used in several analyses, is presented in Section 13.4. Sections 13.5 to 13.12 summarise the searches for SUSY and the reach as a function of luminosity, demonstrating that low mass supersymmetry can be discovered at the LHC with fairly low integrated luminosity for all these signatures in inclusive searches and show the projected reach at the end of the low luminosity run. They are followed by some exclusive studies, mass reconstruction in ditau final states (Section 13.13), tri-lepton final states from direct chargino/neutralino production (Section 13.14) and slepton pair production (Section 13.15). A possible violation of lepton number in $\tilde{\chi}_2^0$ decay is studied in Section 13.16. Section 13.18 contains some considerations on the robustness of the considered signatures in scenarios beyond mSUGRA, like for non-universal Higgs masses, and shows that the same signatures would still allow the discovery of supersymmetry. The chapter ends with our conclusion on the CMS reach.

13.2. Summary of supersymmetry

13.2.1. The MSSM

The Minimal Supersymmetry Model (MSSM) contains the minimal extension of the Standard Model (SM) particle content. Its gauge sector is fully determined by Supersymmetry. But the unknown mechanism for breaking Supersymmetry introduces a large number of free parameters [670] and makes this general model intractable. Therefore, several more constrained models have appeared in the literature. Below, we will focus on a version derived from Supergravity with minimal superpotential and Kähler potential, called mSUGRA, which guarantees universality of gaugino and scalar masses and of trilinear couplings at a high scale. Other SUSY breaking models, like Gauge Mediated Supersymmetry Breaking (GMSB) or Anomaly Mediated Supersymmetry Breaking (AMSB) have not been included here. R-parity breaking in SUSY is also not considered.

An earlier summary of the potentialities of the CMS experiment at LHC for the discovery of Supersymmetry has been published in 1998 [671]. The potential of the ATLAS experiment for the discovery of supersymmetry was analysed in [491].

13.2.2. mSUGRA parameters and spectrum

The mSUGRA model of supersymmetry is determined by 5 free parameters defined at the Grand Unification (GUT) scale. If it is assumed that the spontaneous gauge symmetry breaking is induced by radiative corrections, the absolute value of μ is determined from the Z^0 mass. The free parameters are then:

$$m_0\,,\ m_{1/2}\,,\ A_0\,,\ \tan\beta, \mathrm{sign}(\mu). \tag{13.1}$$

They are run down to the electroweak scale by Renormalisation Group Equations (RGE) from which the sparticle spectrum, decay branching ratios and production cross sections can be derived.

The gaugino mass parameters M_a at the electroweak scale are approximately:

$$\begin{aligned} M_3 \equiv M_{\tilde{g}} &\simeq 2.7 m_{1/2} \\ M_2(M_Z) &\simeq 0.8 m_{1/2} \\ M_1(M_Z) &\simeq 0.4 m_{1/2} \end{aligned} \tag{13.2}$$

The parameter M_3 determines the gluino mass (after QCD corrections). The masses of neutralinos $\tilde{\chi}_i^0$ ($i = 1$–4) and charginos $\tilde{\chi}_i^{\pm}(i = 1, 2)$ are obtained after diagonalising their mass matrices which are a function of M_1, M_2 and μ. In the mSUGRA framework, the lightest chargino and the two lightest neutralinos are dominantly gaugino-like with masses close to M_1 and M_2.

The sfermions of the first two generations have masses given approximately by:

$$\begin{aligned} m^2_{\tilde{u}_L} &\simeq m_0^2 + 5.0 m_{1/2}^2 + 0.35 cos2\beta M_Z^2 \\ m^2_{\tilde{d}_L} &\simeq m_0^2 + 5.0 m_{1/2}^2 - 0.42 cos2\beta M_Z^2 \\ m^2_{\tilde{u}_R} &\simeq m_0^2 + 4.5 m_{1/2}^2 + 0.15 cos2\beta M_Z^2 \\ m^2_{\tilde{d}_R} &\simeq m_0^2 + 4.4 m_{1/2}^2 - 0.07 cos2\beta M_Z^2 \\ m^2_{\tilde{e}_L} &\simeq m_0^2 + 0.49 m_{1/2}^2 - 0.27 cos2\beta M_Z^2 \\ m^2_{\tilde{\nu}} &\simeq m_0^2 + 0.49 m_{1/2}^2 + 0.50 cos2\beta M_Z^2 \\ m^2_{\tilde{e}_R} &\simeq m_0^2 + 0.15 m_{1/2}^2 - 0.23 cos2\beta M_Z^2 \end{aligned} \tag{13.3}$$

By comparing with the gluino mass, these relations show that the latter cannot be much larger than the squark mass:

$$M_{\tilde{g}} \lesssim 1.2 m_{\tilde{q}} \tag{13.4}$$

This relation (obtained for $m_0 = 0$) is not restricted to the mSUGRA case, as it depends primarily on the α_S contributions to the running down of the mass parameters from the GUT scale.

The masses of the third family scalars are more complicated as the contributions from Yukawa couplings can no longer be neglected and non-negligible off-diagonal elements between left and right states appear (they are proportional to the fermion masses).

13.3. Scope of present searches

13.3.1. Sparticle production and cascade decays

If we assume that Supersymmetry is discovered at the LHC, most likely from fully inclusive studies based on large missing energy and jets, it will be very important to investigate all the typical SUSY signatures to help pin down the underlying model.

If the squarks and/or gluinos are kinematically accessible at the LHC, they are expected to have large production rates. The cross sections for the production of a squark (excluding stop) or a gluino at the LHC are displayed in Fig. 13.1. The nearly diagonal lines delimit three regions:

- Region 1: in this region, the gluinos are heavier than any of the squarks. The decay chains of the produced sparticles are expected to be

$$\tilde{g} \to \tilde{q}\bar{q}, \tilde{q} \to q\chi\,. \tag{13.5}$$

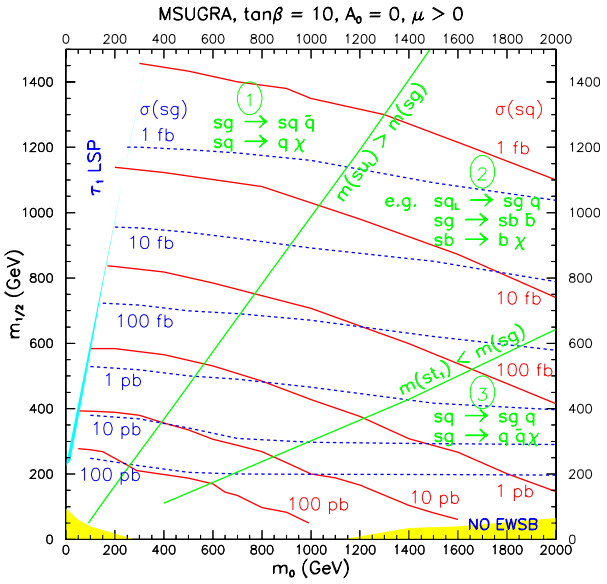

Figure 13.1. Regions of the m_0 versus $m_{1/2}$ plane showing the production cross-sections and with main squark and gluino decays.

- Region 2: in this region some squarks are heavier, other are lighter than the gluino. Hence, rather complicated decay chains are possible, for instance

$$\tilde{q}_L \to \tilde{g}q,\ \tilde{g} \to \tilde{b}\bar{b},\ \tilde{b} \to b\chi \tag{13.6}$$

  as the $\tilde{q}_L$ of the first two generations are expected to be among the heaviest squarks and the $\tilde{b}_1$ (and $\tilde{t}_1$) among the lightest.
- Region 3: in this region, the gluinos are lighter than any of the squarks. A typical decay chain is then

$$\tilde{q} \to \tilde{g}q,\ \tilde{g} \to q\bar{q}\chi \tag{13.7}$$

  where the gluino gives rise to a three-body decay mediated by a virtual squark.

They will cascade down to the LSP, here assumed to be stable. In mSUGRA, the lightest two neutralinos are $\tilde{\chi}_1^0$, which is dominantly bino-like, and $\tilde{\chi}_2^0$, which is dominantly wino-like. The $\tilde{q}_R$ then decays almost exclusively directly into $q\tilde{\chi}_1^0$. But the $\tilde{q}_L$ have usually a non-negligible branching ratio to decay via the $\tilde{\chi}_2^0$ or $\tilde{\chi}_1^\pm$. The decay of the $\tilde{\chi}_2^0$ will then provide an excellent signature for the events which can be observed in inclusive searches.

The main decay modes of the $\tilde{\chi}_2^0$, and hence the signatures, are

$$\tilde{\chi}_2^0 \to \tilde{l}l, \tag{13.8}$$

$$\tilde{\chi}_2^0 \to \tilde{\nu}\nu, \tag{13.9}$$

$$\tilde{\chi}_2^0 \to h^0\tilde{\chi}_1^0, \tag{13.10}$$

$$\tilde{\chi}_2^0 \to Z^0\tilde{\chi}_1^0, \tag{13.11}$$

$$\tilde{\chi}_2^0 \to l^+l^-\tilde{\chi}_1^0 \tag{13.12}$$

where the last decay is mediated by the exchange of an off-shell Z^0 or $\tilde{l}$. The first decay corresponds to a gauge interaction coupling a Wino to a slepton-lepton pair and dominates

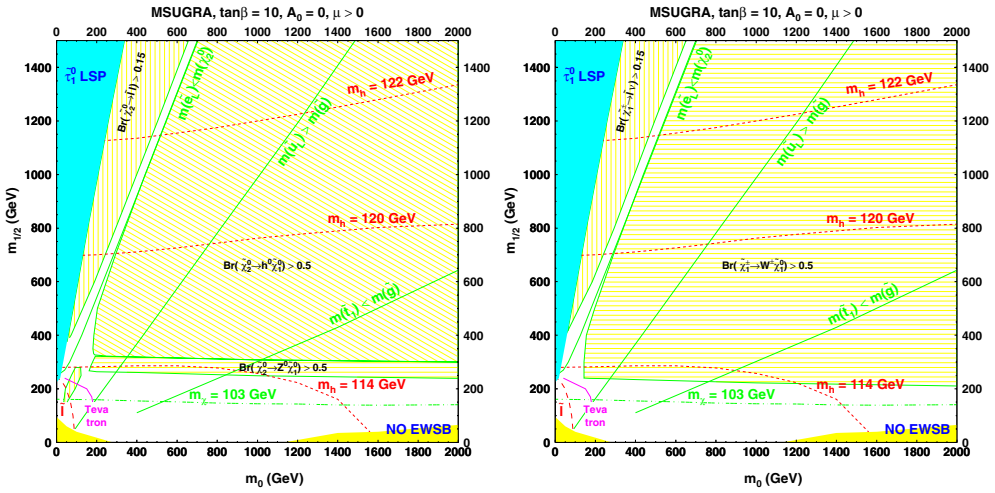

Figure 13.2. Regions of the m_0 versus $m_{1/2}$ plane with main χ_2^0 decays (left) and main decays of $\tilde{\chi}_1^{\pm}$ (right).

if it is kinematically allowed. When this decay is kinematically forbidden and $m_{1/2}$ is large enough, so that $m(\tilde{\chi}_2^0) - m(\tilde{\chi}_1^0) > m(h^0)$, the next preferred decay is to h^0. This corresponds to a gaugino-Higgsino transition and thus requires a non-zero Higgsino component in at least one of the two neutralinos. If also this decay is kinematically forbidden and the neutralino mass difference is sufficient, the $\tilde{\chi}_2^0$ decays to a Z^0 which is suppressed compared to the h^0 decay because it couples to the Higgsino component of both neutralinos. When also this decay is kinematically forbidden, direct three-body decays take place. The corresponding regions in the m_0 versus $m_{1/2}$ plane are illustrated for a mSUGRA case in Fig. 13.2 (left). The exact boundaries of the areas depend on the assumptions (mSUGRA) and on the value of $\tan\beta$ and the parameter A, but their existence is rather generic. It should be emphasised that the existence of these decay modes is a direct consequence of the gauge structure of the theory and is therefore independent of the model details. Their relative importance at a given SUSY point is, however, model dependent.

In addition to the decays via a $\tilde{\chi}_2^0$, a large fraction of squark decays will proceed via a $\tilde{\chi}_1^{\pm}$ decay, which may lead to

$$\tilde{\chi}_1^{\pm} \to \tilde{l}\nu, \tag{13.13}$$

$$\tilde{\chi}_1^{\pm} \to \tilde{\nu}l, \tag{13.14}$$

$$\tilde{\chi}_1^{\pm} \to W^{\pm}\tilde{\chi}_1^0, \tag{13.15}$$

$$\tilde{\chi}_1^{\pm} \to H^{\pm}\tilde{\chi}_1^0, \tag{13.16}$$

$$\tilde{\chi}_1^{\pm} \to l^{\pm}\nu\tilde{\chi}_1^0, \tag{13.17}$$

where the last decay is mediated by the exchange of an off-shell W, $\tilde{\nu}$ or $\tilde{l}$. The localisation of the chargino decay modes in the $(m_0, m_{1/2})$ plane is illustrated for a mSUGRA case in Fig. 13.2 (right).

Further constraints beyond the mSUGRA ones can be imposed, for example the compatibility with the measured relic density. These limit very severely the available parameter space. However, the lack of knowledge of the SUSY breaking mechanism

Table 13.1. mSUGRA parameter values for the test points. Masses are given in units of GeV/c^2.

Point	m_0	$m_{1/2}$	$\tan\beta$	sgn(μ)	A_0
LM1	60	250	10	+	0
LM2	185	350	35	+	0
LM3	330	240	20	+	0
LM4	210	285	10	+	0
LM5	230	360	10	+	0
LM6	85	400	10	+	0
LM7	3000	230	10	+	0
LM8	500	300	10	+	−300
LM9	1450	175	50	+	0
LM10	3000	500	10	+	0
HM1	180	850	10	+	0
HM2	350	800	35	+	0
HM3	700	800	10	+	0
HM4	1350	600	10	+	0

encourages the future experiments to prepare themselves to cope with the broadest possible spectrum of situations. Rather than restricting oneself to a very constrained model, it will be important to understand how to detect departures from the SM in a large variety of topologies and to investigate how to reconstruct the sparticle masses and other SUSY parameters. Of course, there is more information available in the events than just the end points, e.g. momentum asymmetries of the decay leptons, branching ratios and total cross section measurements. This additional information have so far not been used to a large extent.

13.3.2. Test points for mSUGRA

To cover the significantly different experimental signatures, a set of mSUGRA test points have been defined and will be used in the subsequent analyses. First, low mass (LM1 to LM9) test points were chosen to evaluate the sensitivity to SUSY signals in the early period of the LHC but above the Tevatron reach. Then, some high mass test points (HM1 to HM4) near the ultimate reach of the LHC were included.

Their parameters are defined in Table 13.1 and their position in the $(m_0, m_{1/2})$ plane is shown in Fig. 13.3. Points LM1, LM2 and LM6 are compatible with WMAP Cold Dark Matter limits in a strict mSUGRA scenario. The other points are not, but can be made compatible with CDM if universality of the Higgs mass parameters is abandoned (NUHM). Quoted branching ratios are from ISASUGRA7.69 [672] (lepton is e or μ). The post-WMAP benchmark points are found in [633], the NUHM points in [673] and the CMS DAQ TDR points in [76].

- **Point LM1:**
  - Same as post-WMAP benchmark point B′ and near DAQ TDR point 4.
  - $m(\tilde{g}) \geqslant m(\tilde{q})$, hence $\tilde{g} \to \tilde{q}q$ is dominant.
  - $B(\tilde{\chi}_2^0 \to \tilde{l}_R l) = 11.2\%$, $B(\tilde{\chi}_2^0 \to \tilde{\tau}_1 \tau) = 46\%$, $B(\tilde{\chi}_1^\pm \to \tilde{\nu}_l l) = 36\%$.
- **Point LM2:**
  - Almost identical to post-WMAP benchmark point I'.
  - $m(\tilde{g}) \geqslant m(\tilde{q})$, hence $\tilde{g} \to \tilde{q}q$ is dominant ($\tilde{b}_1 b$ is 25%).
  - $B(\tilde{\chi}_2^0 \to \tilde{\tau}_1 \tau) = 96\%$ $B(\tilde{\chi}_1^\pm \to \tilde{\tau}\nu) = 95\%$.

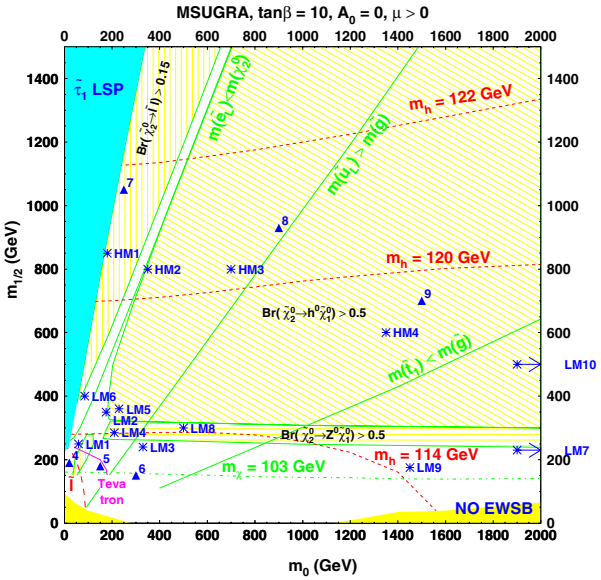

Figure 13.3. Position of the test points in the m_0 versus $m_{1/2}$ plane. The lines in this plane correspond to the assumptions that $\tan\beta = 10$, $A_0 = 0$ and $\mu > 0$. The shaded regions are excluded because either the $\tilde{\tau}_1$ would be the LSP or because there is not radiative electroweak symmetry breaking. The regions excluded by the LEP limit on the h^0 or the $\tilde{\chi}_1^{\pm}$ masses are delineated by dashed lines. The test CMS points are indicated by stars (LM7 and LM10 are outside the boundaries) and the points used in the CMS DAQ TDR by triangles. Also shown are the regions of interest for the decay of the $\tilde{\chi}_2^0$.

- **Point LM3:**
  - Same as NUHM point γ and near DAQ TDR point 6.
  - $m(\tilde{g}) < m(\tilde{q})$, hence $\tilde{g} \to \tilde{q}q$ is forbidden except $B(\tilde{g} \to \tilde{b}_{1,2}b) = 85\%$
  - $B(\tilde{\chi}_2^0 \to ll\tilde{\chi}_1^0) = 3.3\%$, $B(\tilde{\chi}_2^0 \to \tau\tau\tilde{\chi}_1^0) = 2.2\%$, $B(\tilde{\chi}_1^{\pm} \to W^{\pm}\tilde{\chi}_1^0) = 100\%$
- **Point LM4:**
  - Near NUHM point α in the on-shell Z^0 decay region
  - $m(\tilde{g}) \gtrsim m(\tilde{q})$, hence $\tilde{g} \to \tilde{q}q$ is dominant with $\tilde{g} \to \tilde{b}_1 b = 24\%$
  - $B(\tilde{\chi}_2^0 \to Z^0\tilde{\chi}_1^0) = 97\%$, $B(\tilde{\chi}_1^{\pm} \to W^{\pm}\tilde{\chi}_1^0) = 100\%$
- **Point LM5:**
  - In the h^0 decay region, same as NUHM point β.
  - $m(\tilde{g}) \gtrsim m(\tilde{q})$, hence $\tilde{g} \to \tilde{q}q$ is dominant with $B(\tilde{g} \to \tilde{b}_1 b) = 19.7\%$ and $B(\tilde{g} \to \tilde{t}_1 t) = 23.4\%$
  - $B(\tilde{\chi}_2^0 \to h^0\tilde{\chi}_1^0) = 85\%$, $B(\tilde{\chi}_2^0 \to Z^0\tilde{\chi}_1^0) = 11.5\%$, $B(\tilde{\chi}_1^{\pm} \to W^{\pm}\tilde{\chi}_1^0) = 97\%$
- **Point LM6:**
  - Same as post-WMAP benchmark point C′.
  - $m(\tilde{g}) \gtrsim m(\tilde{q})$, hence $\tilde{g} \to \tilde{q}q$ is dominant
  - $B(\tilde{\chi}_2^0 \to \tilde{l}_L l) = 10.8\%$, $B(\tilde{\chi}_2^0 \to \tilde{l}_R l) = 1.9\%$, $B(\tilde{\chi}_2^0 \to \tilde{\tau}_1\tau) = 14\%$, $B(\tilde{\chi}_1^{\pm} \to \tilde{\nu}_l l) = 44\%$
- **Point LM7:**
  - Very heavy squarks, outside reach, but light gluino.
  - $m(\tilde{g}) = 678\,\mathrm{GeV/c^2}$, hence $\tilde{g} \to$ 3-body is dominant

- $B(\tilde{\chi}_2^0 \to ll\tilde{\chi}_1^0) = 10\%$, $B(\tilde{\chi}_1^\pm \to \nu l\tilde{\chi}_1^0) = 33\%$
- EW chargino-neutralino production cross-section is about 73% of total.

- **Point LM8:**
  - Gluino lighter than squarks, except $\tilde{b}_1$ and $\tilde{t}_1$
  - $m(\tilde{g}) = 745$ GeV/c^2, $M(\tilde{t}_1) = 548$ GeV/c^2, $\tilde{g} \to \tilde{t}_1 t$ is dominant
  - $B(\tilde{g} \to \tilde{t}_1 t) = 81\%$, $B(\tilde{g} \to \tilde{b}_1 b) = 14\%$, $B(\tilde{q}_L \to q\tilde{\chi}_2^0) = 26-27\%$,
  - $B(\tilde{\chi}_2^0 \to Z^0\tilde{\chi}_1^0) = 100\%$, $B(\tilde{\chi}_1^\pm \to W^\pm\tilde{\chi}_1^0) = 100\%$
- **Point LM9:**
  - Heavy squarks, light gluino. Consistent with EGRET data on diffuse gamma ray spectrum, WMAP results on CDM and mSUGRA [674]. Similar to LM7.
  - $m(\tilde{g}) = 507$ GeV/c^2, hence $\tilde{g} \to$ 3-body is dominant
  - $B(\tilde{\chi}_2^0 \to ll\tilde{\chi}_1^0) = 6.5\%$, $B(\tilde{\chi}_1^\pm \to \nu l\tilde{\chi}_1^0) = 22\%$
- **Point LM10:**
  - Similar to LM7, but heavier gauginos.
  - Very heavy squarks, outside reach, but light gluino.
  - $m(\tilde{g}) = 1295$ GeV/c^2, hence $\tilde{g} \to$ 3-body is dominant
  - $B(\tilde{g} \to t\bar{t}\tilde{\chi}_4^0) = 11\%$, $B(\tilde{g} \to tb\tilde{\chi}_2^\pm) = 27\%$
- **Point HM1:**
  - $m(\tilde{g}) \geqslant m(\tilde{q})$, hence $\tilde{g} \to \tilde{q}q$ is dominant
  - $B(\tilde{g} \to \tilde{t}_1 t) = 25\%$, $B(\tilde{q}_L \to q\tilde{\chi}_2^0) = 32\%$,
    but $B(\tilde{t}_1 \to t\tilde{\chi}_2^0) = 6\%$, $B(\tilde{t}_1 \to t\tilde{\chi}_3^0) = 18\%$, $B(\tilde{t}_1 \to t\tilde{\chi}_4^0) = 9\%$,
  - $B(\tilde{\chi}_2^0 \to \tilde{l}_L l) = 27\%$, $B(\tilde{\chi}_2^0 \to \tilde{\tau}_1\tau) = 14\%$, $B(\tilde{\chi}_1^\pm \to \tilde{\nu}_l l) = 37\%$
- **Point HM2:**
  - $m(\tilde{g}) \geqslant m(\tilde{q})$, hence $\tilde{g} \to \tilde{q}q$ is dominant
  - $B(\tilde{g} \to \tilde{t}_1 t) = 25\%$, $B(\tilde{q}_L \to q\tilde{\chi}_2^0) = 32\%$,
    but $B(\tilde{t}_1 \to t\tilde{\chi}_2^0) = 6\%$, $B(\tilde{t}_1 \to t\tilde{\chi}_3^0) = 20\%$, $B(\tilde{t}_1 \to t\tilde{\chi}_4^0) = 9\%$,
  - $B(\tilde{\chi}_2^0 \to \tilde{\tau}_1\tau) = 78\%$, $B(\tilde{\chi}_1^\pm \to \tilde{\nu}\tau + \tilde{\tau}_1\nu) = 13 + 76\%$
- **Point HM3:**
  - $m(\tilde{g}) \geqslant m(\tilde{q})$, hence $\tilde{g} \to \tilde{q}q$ is dominant
  - $B(\tilde{g} \to \tilde{t}_1 t) = 52\%$, $B(\tilde{q}_L \to q\tilde{\chi}_2^0) = 32\%$,
    but $B(\tilde{t}_1 \to t\tilde{\chi}_2^0) = 5\%$, $B(\tilde{t}_1 \to t\tilde{\chi}_3^0) = 20\%$, $B(\tilde{t}_1 \to t\tilde{\chi}_4^0) = 11\%$,
  - $B(\tilde{\chi}_2^0 \to h^0\tilde{\chi}_1^0) = 94\%$, $B(\tilde{\chi}_1^\pm \to W^\pm\tilde{\chi}_1^0) = 100\%$
- **Point HM4:**
  - $m(\tilde{g}) < m(\tilde{q})$, hence $\tilde{q} \to \tilde{g}q$ is important
  - $B(\tilde{q}_L \to \tilde{g}q) = 43\%$, $B(\tilde{q}_R \to \tilde{g}q) = 77-93\%$, $B(\tilde{g} \to \tilde{t}_1 t) = 82\%$,
  - $B(\tilde{t}_1 \to t\tilde{\chi}_2^0) = 3\%$, $B(\tilde{t}_1 \to t\tilde{\chi}_3^0) = 22\%$, $B(\tilde{t}_1 \to t\tilde{\chi}_4^0) = 16\%$,
  - $B(\tilde{\chi}_2^0 \to h^0\tilde{\chi}_1^0) = 94\%$, $B(\tilde{\chi}_4^0 \to h^0\tilde{\chi}_2^0) = 30\%$, $B(\tilde{\chi}_1^\pm \to W^\pm\tilde{\chi}_1^0) = 100\%$

The cross sections for the test points are given at NLO and LO from PROSPINO1 in Table 13.2.

Table 13.2. Cross sections for the test points in pb at NLO (LO) from PROSPINO1.

Point	$M(\tilde{q})$	$M(\tilde{g})$	$\tilde{g}\tilde{g}$	$\tilde{g}\tilde{q}$	$\tilde{q}\bar{\tilde{q}}$	$\tilde{q}\tilde{q}$	Total
LM1	558.61	611.32	10.55	28.56	8.851	6.901	54.86
			(6.489)	(24.18)	(6.369)	(6.238)	(43.28)
LM2	778.86	833.87	1.443	4.950	1.405	1.608	9.41
			(0.829)	(3.980)	(1.013)	(1.447)	(7.27)
LM3	625.65	602.15	12.12	23.99	4.811	4.554	45.47
			(7.098)	(19.42)	(3.583)	(4.098)	(34.20)
LM4	660.54	695.05	4.756	13.26	3.631	3.459	25.11
			(2.839)	(10.91)	(2.598)	(3.082)	(19.43)
LM5	809.66	858.37	1.185	4.089	1.123	1.352	7.75
			(0.675)	(3.264)	(0.809)	(1.213)	(5.96)
LM6	859.93	939.79	0.629	2.560	0.768	0.986	4.94
			(0.352)	(2.031)	(0.559)	(0.896)	(3.84)
LM7	3004.3	677.65	6.749	0.042	0.000	0.000	6.79
			(3.796)	(0.028)	(0.000)	(0.000)	(3.82)
LM8	820.46	745.14	3.241	6.530	1.030	1.385	12.19
			(1.780)	(5.021)	(0.778)	(1.230)	(8.81)
LM9	1480.6	506.92	36.97	2.729	0.018	0.074	39.79
			(21.44)	(1.762)	(0.015)	(0.063)	(23.28)
LM10	3132.8	1294.8	0.071	0.005	0.000	0.000	0.076
			(0.037)	(0.004)	(0.000)	(0.000)	(0.041)
HM1	1721.4	1885.9	0.002	0.018	0.005	0.020	0.045
			(0.001)	(0.016)	(0.005)	(0.021)	(0.043)
HM2	1655.8	1785.4	0.003	0.027	0.008	0.027	0.065
			(0.002)	(0.024)	(0.007)	(0.028)	(0.061)
HM3	1762.1	1804.4	0.003	0.021	0.005	0.018	0.047
			(0.002)	(0.018)	(0.004)	(0.019)	(0.043)
HM4	1815.8	1433.9	0.026	0.056	0.003	0.017	0.102
			(0.014)	(0.043)	(0.003)	(0.017)	(0.077)

13.4. Hemisphere algorithm for separation of decay chains

13.4.1. Basic idea and goal

In the MSSM, the primary SUSY particles are heavy and tend to be produced with a large Q^2, whereas the transverse momentum of their decay products with respect to their initial direction is limited by the magnitude of their mass. Moreover, ignoring R_p violation, they are produced in pairs. It may, therefore, be possible to separate the two decay chains by reconstructing the two production directions (in 3D) and collecting the jets and leptons in two clusters according to their "closeness" to these axes. This procedure is inspired by the reconstruction of the thrust or sphericity axis in e^+e^- collisions, except that in hadron collisions two separate axes need to be introduced per event, as the laboratory frame does not coincide with the parton centre of mass frame. Moreover, the back-to-back orientation of the sparticles in the transverse plane cannot be used, as the invisible LSP disturbs significantly the direction of the observable particles.

In hadron colliders like the LHC, the large multiplicity of jets and leptons often lead to a large combinatorial background when trying to reconstruct peaks or to determine end points in effective mass distributions (to reconstruct sparticle masses). Provided the hemisphere algorithm has a large probability to assign correctly the jets to their parents, a reduction of a factor 2 to 4 can be expected in the combinatorial background.

The proposed algorithm consists of a recursive method going through the following steps:

- Starting off by computing two initial axes (called "seeds" below).
- Associating the objects (jets and leptons) to one of these axes according to a certain criterion (hemisphere association method).
- Recalculating the axes as the sum of the momenta of all the connected objects. In order to converge to a stable solution, the axes are only updated after a full iteration is performed.
- Iterating the association until no objects switch from one group to the other.

13.4.2. Seeding methods

Two seeding methods have been tested:

(1) The first axis is chosen as the direction of the highest momentum object and the second axis as the direction of the object with the largest $p \cdot \Delta R$ with respect to the first axis, where ΔR is defined as

$$\Delta R = \sqrt{\Delta\phi^2 + \Delta\eta^2}. \tag{13.18}$$

(2) The axes are chosen as the directions of the pair of objects which have the largest invariant mass.

13.4.3. Association methods

Three association methods are available. An object is assigned to a given axis $\vec{A}$ when:

(1) The scalar product $\vec{p} \cdot \vec{A}$ is maximum, which amounts to choosing the smallest angle
(2) The hemisphere squared masses are minimum, i.e. object k is associated to the hemisphere with mass m_i rather than m_j if $m_{ik}^2 + m_j^2 \leqslant m_i^2 + m_{jk}^2$. This is equivalent to the requirement

$$(E_i - p_i \cos\theta_{ik}) \leqslant (E_j - p_j \cos\theta_{jk}).$$

(3) The Lund distance measure is minimum, i.e.

$$(E_i - p_i \cos\theta_{ik}) \frac{E_i}{(E_i + E_k)^2} \leqslant (E_j - p_j \cos\theta_{jk}) \frac{E_j}{(E_j + E_k)^2}.$$

In order to converge to a stable solution, the axes are only updated after a full iteration is performed.

13.4.4. Results

The performance of the hemisphere assignment was tested on events with production of squarks and/or gluinos. Jets were reconstructed using the Iterative Cone method with $\Delta R = 0.5$ and calibrated with the "GammaJet" procedure. They were selected when $E_T > 30\,\text{GeV}$ and $|\eta| < 3.0$. The momentum vectors used were from the Monte carlo parton level objects which matched with the jets and/or leptons. Some of the CMS test points were used, namely LM1 (dilepton final states via $\tilde{l}_R$), LM5 (with decay of $\tilde{\chi}_2^0$ to $h \to b\bar{b}$) and LM9 (with dileptons from 3-body decays).

The efficiencies quoted below are the ratio between the correctly assigned MC objects and their total number. The correct hemisphere was chosen as the one for which

Table 13.3. Efficiencies for test point LM1.

Type of jet	all jets	quark jets	gluon jets	q from $\tilde{q}$	q from $\tilde{g}$
Seed 1, Assoc 1	79%	80%	74%	85%	69%
Seed 1, Assoc 2	80%	80%	77%	85%	72%
Seed 2, Assoc 2	81%	81%	78%	85%	72%
Seed 2, Assoc 3	81%	81%	79%	86%	73%

Table 13.4. Efficiencies for test points LM1, LM5 and LM9, using the methods Seed 2 and hemisphere association 3.

Point	all jets	quark jets	gluon jets	q from $\tilde{q}$	q from $\tilde{g}$
LM1	81%	81%	79%	86%	73%
LM5	77%	77%	74%	87%	70%
LM9	74%	75%	69%	–	76%

the axis matched most closely the original squark or gluino, after subtracting from it the unobserved $\tilde{\chi}_1^0$.

The efficiencies of various types of jets for the different algorithms at the test point LM1 are summarised in Table 13.3.

It is seen that all the algorithms behave nearly in the same way, with the combination (seed 1, hemisphere association 1) being slightly worse and (seed 2, hemisphere association 3) slightly better.

The efficiencies obtained for the different test points are listed in Table 13.4 for the different types of jets by using the (seed 2, hemisphere association 3) method. Note that at point LM9 the $\tilde{g}$ undergoes a direct 3-body decay, the $\tilde{q}$ being heavier than the $\tilde{g}$.

From these tests it can be concluded that quark jets from $\tilde{q}$ have a rather high efficiency, $\geqslant 85\%$, to be correctly assigned to a hemisphere, whereas the quark jets from a $\tilde{g}$ reach only $\gtrsim 70\%$. This reflects the fact that the latter jets are much softer, on average, than the jets from the $\tilde{q}$ decay.

The same procedure was also applied to leptons (e or μ). However, due to their small mass, the leptons barely "feel" the boost and are sent in any direction. The results were only slightly better than the expectation from random association. Some improvement could be obtained, e.g. for $\tilde{\chi}_2^0 \to e^+e^-\tilde{\chi}_1^0$, by treating the lepton pair as a single (massive) object. But this introduces some model dependence.

The power of the hemisphere separation can be further illustrated by the search for Higgs at point LM5. The reconstructed jets selected as above are identified as b-jets by a combined b-tagging method (see Vol. 1, Section 12.2.2) when the discriminant variable is > 1.5. The invariant mass of all combinations of two b-jets is displayed in Fig. 13.4 (left). The peak from $h^0 \to b\bar{b}$ is visible above a large combinatorial SUSY background, mostly due to the production of $\tilde{b}\tilde{b}$ and $\tilde{t}\tilde{t}$ (directly or from cascade decays). After applying the hemisphere separation method, the 2b invariant mass combinations are separated into the cases where both b-jets are in the same hemisphere (centre), with a clearly visible Higgs peak, and in opposite hemispheres (right), where almost no sign of Higgs remains. Note that these plots were obtained without selection cuts. This method has been used for the Higgs search in Section 13.10 and in other searches.

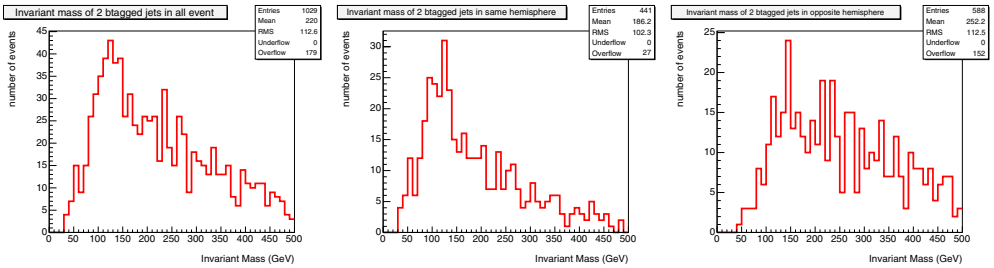

Figure 13.4. $b\bar{b}$ invariant mass distributions in h^0 production with mass $m_h = 116\,\text{GeV}$ for (left) all combinations, (centre) combinations in the same hemisphere, (right) combinations in opposite hemispheres.

13.5. Inclusive analysis with missing transverse energy and jets

The missing transverse energy plus multi-jets final state has been a canonical signature for SUSY searches. This study is a search for the production and decay of gluinos and scalar quarks in $\geqslant$3-jet events with large missing transverse energy. The large missing energy originates from the two LSPs in the final states of the squark and gluino decays. The three or more hadronic jets result from the hadronic decays of the squarks and/or gluinos. The full analysis is presented in section 4.2. The analysis uses the LM1 test-point at which squark and gluino production has a LO cross section of 49 pb. The major Standard Model background components include production of $Z+$ jets with the Z decaying invisibly, W+jets, top-anti-top pairs, dibosons, single top and QCD jets. The trigger path used is the missing energy plus jets both at Level-1 and at HLT.

13.5.1. Analysis path and results

Events that are accepted after clean-up pre-selection requirements, proceed through the analysis path if they have missing transverse energy $E_{\text{T}}^{\text{miss}} > 200\,\text{GeV}$ and at least three jets with $E_{\text{T}} \geqslant 30\,\text{GeV}$ within $|\eta| < 3$. In addition the leading jet is required to be within the central tracker fiducial volume *i.e.* $|\eta| < 1.7$. These requirements directly define the searched for signal signature. The rest of the analysis path is designed based on elimination of the major classes of backgrounds: the QCD production, top–anti-top pairs and the W/Z -QCD associated production. In Table 13.5 the path is shown with a remark indicating the reason and aim of each selection step.

A detailed explanation of the analysis path requirements and variables used is given in section 4.2. The global signal efficiency for the analysis is 13% while the signal to background ratio is ~ 26. The results are shown in Table 13.6 for $1\,\text{fb}^{-1}$.

In summary the major background components and their uncertainties are as follows:

- $t\bar{t}$ uncertainties: 7% $E_{\text{T}}^{\text{miss}}$ shape, 22% JES, 13% statistical;
- $Z \longrightarrow \nu\bar{\nu}+$jets, $W/Z+$jets: 5% Luminosity (direct candle normalisation to the data (*cf.* section 4.2);
- QCD: $E_{\text{T}}^{\text{miss}}$ 7% shape, 22% JES, 10% statistical.

The number of backgrounds events per background component and their uncertainties are tabulated in Table 13.7. Based on the Standard Model background estimates and their uncertainties, a 5σ observation of low mass SUSY at LM1 (gluino mass $600\,\text{GeV}/\text{c}^2$) is achievable with $\sim 6\,\text{pb}^{-1}$ in events with large missing energy plus multi-jets, using a

Table 13.5. The $E_{\mathrm{T}}^{\mathrm{miss}}$ + multi-jet SUSY search analysis path.

Requirement	Remark
Level 1	Level-1 trigger efficiency parametrisation
HLT, $E_{\mathrm{T}}^{\mathrm{miss}} > 200\,\mathrm{GeV}$	trigger/signal signature
primary vertex $\geqslant 1$	primary cleanup
$F_{em} \geqslant 0.175$, $F_{ch} \geqslant 0.1$	primary cleanup
$N_j \geqslant 3$, $\lvert\eta_d^{1j}\rvert < 1.7$	signal signature
$\delta\phi_{min}(E_{\mathrm{T}}^{\mathrm{miss}} - jet) \geqslant 0.3$ rad, $R1$, $R2 > 0.5$ rad,	
$\delta\phi(E_{\mathrm{T}}^{\mathrm{miss}} - j(2)) > 20^{\circ}$	QCD rejection
$Iso^{lead\,trk} = 0$	ILV (I) $W/Z/t\bar{t}$ rejection
$f_{em(j(1))}$, $f_{em(j(2))} < 0.9$	ILV (II), $W/Z/t\bar{t}$ rejection
$E_{\mathrm{T},j(1)} > 180\,\mathrm{GeV}$, $E_{\mathrm{T},j(2)} > 110\,\mathrm{GeV}$	signal/background optimisation
$H_{\mathrm{T}} \equiv E_{\mathrm{T}(2)} + E_{\mathrm{T}(3)} + E_{\mathrm{T}(4)} + E_{\mathrm{T}}^{\mathrm{miss}} > 500\,\mathrm{GeV}$	signal/background optimisation
SUSY LM1 signal efficiency 13%	

Table 13.6. Selected SUSY and Standard Model background events for 1 fb^{-1}.

Signal	$t\bar{t}$	single t	$Z(\rightarrow \nu\bar{\nu})$+ jets	$(W/Z, WW/ZZ/ZW)$ + jets	QCD
6319	53.9	2.6	48	33	107

Table 13.7. Standard Model background components and uncertainties for 1 fb^{-1}.

$t\bar{t}$, single top	$Z(\rightarrow \nu\bar{\nu})$+ jets	$(W/Z, WW/ZZ/ZW)$ + jets	QCD
56 ± 11(sys) $\pm$ 7.5(stat)	48 ± 3.5 (all)	33 ± 2.5 (all)	107 ± 25(sys) $\pm$10(stat)

significance computed with ScPf, defined in Appendix A.1. After $\sim 1.5\,\mathrm{fb}^{-1}$ the W/Z+jets backgrounds, including the invisible decays of the Z boson which constitutes a large irreducible background component, can be reliably normalised using the $Z \rightarrow \mu\mu$ and $Z \rightarrow ee$ + multi-jet data candle. The comparison of the signal, total background estimated and its components for the $M_{eff} \equiv E_{\mathrm{T}(1)} + E_{\mathrm{T}(2)} + E_{\mathrm{T}(3)} + E_{\mathrm{T}(4)} + E_{\mathrm{T}}^{\mathrm{miss}}$ can be found in section 4.2.

To perform the 5 σ reach scan (Fig. 13.5) in the mSUGRA parameter space, the HM1 test point is used as optimisation reference and the $E_{\mathrm{T}}^{\mathrm{miss}}$ and H_{T} requirements are raised to 600 GeV and 1500 GeV correspondingly. The analysis efficiency for HM1 is $\sim$12% while the total Standard Model background for 1 fb^{-1} is 4.36 events with a total uncertainty of 7% . The background composition is 67% Z invisible decays, 19% QCD jets and 14% W/Z+jets.

13.6. Inclusive muons with jets and missing transverse energy

We study the production and decay of new particles in mSUGRA via inclusive final states including muons, high p_{T} jets, and large missing transverse energy. Requiring at least one muon provides a relatively clean experimental signature (complementing searches involving only inclusive jets and missing energy), however requires a well-understood trigger shortly after the LHC start-up. In this work [675], the fully simulated and reconstructed LM1 mSUGRA point is taken as the benchmark for selection optimisation and study of systematic effects. Even though the study was performed within the context of mSUGRA, this method is not specific to the mSUGRA framework and should apply equally well in other contexts.

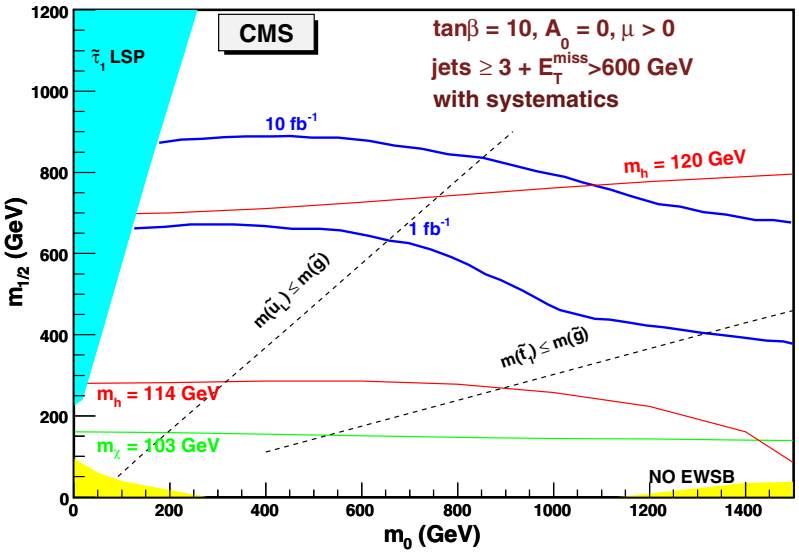

Figure 13.5. 5 σ reach for 1 and 10 fb^{-1} using multi-jets and missing transverse energy final state.

The strategy employed in this analysis is to optimise a set of selection cuts based on an objective function which provides a reasonable estimate of the significance to exclude the Standard Model null-hypothesis while explicitly including systematic uncertainties (thus avoiding regions of phase space which are prone to systematics). This work uses a Genetic Algorithm (GARCON [63]) for the optimisation of cuts.

13.6.1. Signal selection and backgrounds considered

Because this work is an inclusive study of mSUGRA signatures involving at least one muon accompanied by multiple jets and large $E_{\mathrm{T}}^{\mathrm{miss}}$, several Standard Model processes contribute as sources of background and must be taken into account. Accordingly, the main backgrounds studied in this analysis correspond to QCD dijet (2.8 million events with $0 < \hat{p}_{\mathrm{T}} < 4\,\mathrm{TeV/c}$), top ($t\bar{t}$) production (3.3 million events), electroweak single-boson production (4.4 million events with $0 < \hat{p}_{\mathrm{T}} < 4.4\,\mathrm{TeV/c}$) and electroweak dibosons production (1.2 million events). All backgrounds used in this work are fully simulated and reconstructed. This work uses only leading order cross-sections, consistently for both signal and all backgrounds. Considering NLO k-factors for the signal and background processes do not change the final results significantly.

The CMS trigger system is described in [76], and the current working trigger menu is described in Appendix E. This work uses an event sample which is triggered by either of two HLT triggers: the inclusive isolated single-muon trigger or the isolated dimuon trigger.

The following quality criteria are applied to muons and jets. The leading muon is required to have a transverse momentum above $p_{\mathrm{T}} = 30\,\mathrm{GeV/c}$ which ensures that the muon candidate is reconstructed with good efficiency, well above the trigger thresholds. Further, the leading muon is required to be isolated with less than 10 GeV of calorimeter energy within a cone of radius $R = 0.3$, reducing the effects due to fake muons, whilst preserving reasonable efficiency for signal acceptance. Finally, the three leading jets must each have an E_{T} of at least 50 GeV which guarantees that jets are reconstructed with good efficiency.

Table 13.8. Total number of selected events (for $10\,\text{fb}^{-1}$) and significance ("Signif.") with systematic uncertainties (but excluding uncertainties due to finite Monte Carlo simulation statistics and higher order QCD effects). "SM" represents the total of all Standard Model backgrounds considered.

Sample(s)	Events	Signif.	Sample	Events	Signif.	Sample	Events	Signif.
SM	2.54	–	LM4	246	29.2	LM6	277	31.6
LM1	311	34.0	LM5	165	22.9	HM1	13	5.0

The genetic algorithm GARCON [63] used for the optimisation of cuts results in: $E_{\text{T}}^{\text{miss}} > 130\,\text{GeV}$, $E_{\text{T}}^{\text{j1}} > 440\,\text{GeV}$, $E_{\text{T}}^{\text{j2}} > 440\,\text{GeV}$, $|\eta^{\text{j1}}| < 1.9$, $|\eta^{\text{j2}}| < 1.5$, $|\eta^{\text{j3}}| < 3$, $\cos\left[\Delta\phi(\text{j1},\text{j2})\right] < 0.2$, $-0.95 < \cos\left[\Delta\phi(E_{\text{T}}^{\text{miss}},\text{j1})\right] < 0.3$, $\cos\left[\Delta\phi(E_{\text{T}}^{\text{miss}},\text{j2})\right] < 0.85$. Assuming $10\,\text{fb}^{-1}$ of collected data, this set of cuts would expect to select a total of 2.54 background events from the Standard Model and 311 signal events from the mSUGRA LM1 benchmark signal point.

13.6.2. Results for 10 fb^{-1} using full detector simulation and reconstruction

After all selection cuts have been applied, several effects contribute as systematic uncertainties, including: jet energy scale (10%), jet energy resolution (5%), luminosity measurement (5%), and full GEANT simulation versus fast simulation differences (5%), used to determine the analysis reach in mSUGRA parameters in Section 13.6.3). Since this analysis is performed consistently at leading order, the inclusion of higher order effects involving ISR/FSR is not taken into account. A generator-level comparison of the parton shower method for inclusive $t\bar{t}$ used by PYTHIA [69] with the matrix element calculation for $t\bar{t}+1$jet from COMPHEP [355] suggests a $\approx 10\%$ enhancement in the acceptance of $t\bar{t}+1$jet events (generated via the matrix element method) compared with inclusive $t\bar{t}$. When combined with other expected effects – such as underlying event (5%), pile-up (5%), and parton distribution functions (5%) – a total theoretical systematic uncertainty of $\sim 13\%$ is estimated. The dominant uncertainty (32%) arises from an inability to precisely predict the number of background events, due to finite Monte Carlo simulation statistics. We note that by the time $10\,\text{fb}^{-1}$ of data is collected, many of the contributing background processes will be measured from real data, thereby reducing this uncertainty. If one includes the uncertainty due to finite Monte Carlo simulation statistics, the total systematic uncertainty for this work is 37%. Neglecting Monte Carlo simulation statistics, as well as higher order QCD effects, the total systematic uncertainty for this work is 19%.

Table 13.8 shows the main results of this study. For the fully simulated low mass mSUGRA point LM1, and assuming $10\,\text{fb}^{-1}$ of data, this work selects an expected 311 signal events (with an efficiency of 0.074%) compared with 2.54 expected background events, comprised of $t\bar{t}$ (0.73 events), $W+$ jets (1.56 events), and $Z+$ jets (0.24 events). The separation of signal from background for the different low mass mSUGRA points range in values from 23 to 34 in significance, including systematic uncertainties (but excluding uncertainties related to the limited number of simulated events). Such large values of significance merely indicate that the low mass mSUGRA region will either have been discovered or excluded, long before $10\,\text{fb}^{-1}$ of data is collected. We note that shortly after the LHC start-up, the systematic understanding of the CMS detector is expected to be quite different than what is presented in this work, which assumes $\mathcal{L} = 10\,\text{fb}^{-1}$. Nevertheless, if one assumes a similar systematic understanding and extrapolates the results of this work to early running, the expected

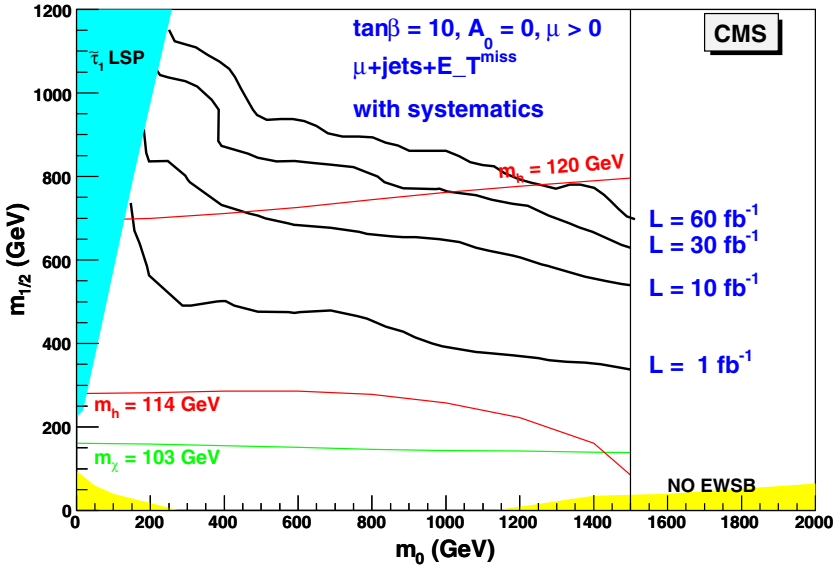

Figure 13.6. CMS discovery reach contours in the m_0–$m_{1/2}$ plane using inclusive muons with jets and missing energy for 10 fb^{-1} (lower contour), 30 fb^{-1} (middle contour), and 60 fb^{-1} (upper contour) including systematics.

luminosity required to discover the LM1 mSUGRA study point would be O(0.1) fb^{-1}. Hence, low mass SUSY is a prime candidate for possible discovery during the very early running of the LHC.

13.6.3. CMS Reach using inclusive muons with jets and missing energy

Since CMS will have either discovered or excluded the lower mass region well in advance of the time required to collect 10 fb^{-1} of data, the selection cuts for 30 fb^{-1} and 60 fb^{-1} are re-optimised using GARCON to select the HM1 mSUGRA point: $E_{\mathrm{T}}^{\mathrm{miss}} > 210\,\mathrm{GeV}$, $E_{\mathrm{T}}^{\mathrm{j1}} > 730\,\mathrm{GeV}$, $E_{\mathrm{T}}^{\mathrm{j2}} > 730\,\mathrm{GeV}$, $\cos\left[\Delta\phi(\mathrm{j1},\mathrm{j2})\right] < 0.95$, $\cos\left[\Delta\phi(\mathrm{E}_{\mathrm{T}}^{\mathrm{miss}},\mathrm{j1})\right] < -0.2$, $\cos\left[\Delta\phi(\mathrm{E}_{\mathrm{T}}^{\mathrm{miss}},\mathrm{j2})\right] < 0.95$. To estimate the reach for 30 fb^{-1} and 60 fb^{-1}, this same cut-set is applied in both cases and results in an estimated Standard Model background yield of $N_{\mathrm{B}} = 0.25$ for 30 fb^{-1}, and $N_{\mathrm{B}} = 0.49$ for 60 fb^{-1}. In both cases the uncertainty on the background levels is $\approx 71\%$, primarily due to a limited number of simulated events; if one neglects that uncertainty, the systematic uncertainty is $\approx 19\%$.

Fast simulation and reconstruction was also performed in order to scan the plane of universal scalar (m_0) and gaugino ($m_{1/2}$) masses for fixed mSUGRA parameters: $\tan\beta = 10$, $\mu > 0$ and $A_0 = 0$. Points were generated on a coarse grid with $\Delta m_0 = 100\,\mathrm{GeV/c^2}$ and $\Delta m_{1/2} = 100\,\mathrm{GeV/c^2}$, starting from the point $m_0 = 100\,\mathrm{GeV}$, $m_{1/2} = 100\,\mathrm{GeV}$. Figure 13.6 shows the discovery reach of this analysis (contours correspond to a significance value of 5), plotted in the mSUGRA m_0–$m_{1/2}$ plane. Assuming 10 fb^{-1} of data, CMS can observe SUSY mass scales of over $\approx 1.5\,\mathrm{TeV/c^2}$; assuming 30 fb^{-1} of integrated luminosity, several of the high mass CMS SUSY benchmark points become interesting for possible discovery; and, assuming 60 fb^{-1} of integrated luminosity, CMS is able to reach in this channel SUSY mass scales of up to $\approx 2\,\mathrm{TeV/c^2}$.

13.7. Inclusive analyses with same sign dimuons

The topology of two same sign isolated muons, high p_T jets, and large missing transverse energy is interesting as it allows for an efficient suppression of the Standard Model backgrounds, and at the same time allows much of the mSUGRA signal to be retained. Like-sign leptons can result from several signal processes because the gluino, being a Majorana particle, has equal probability of yielding either a positively or a negatively charged lepton in its decay chain. Squark production is another important source of like-sign dileptons, since the squark charge tends to be determined by the valence quarks in the proton-proton collision. The same-sign muon topology provides a clean experimental signature and has the extra advantage of an anticipated efficient and well-understood dimuon trigger soon after LHC start-up. Even though this study [676] is performed within the context of mSUGRA, this method is not specific to the mSUGRA framework.

The genetic algorithm GARCON [63] is used to determine the optimal set of cuts for each mSUGRA benchmark point. An interval for each physics cut-parameter is then defined corresponding to its minimal cut value and the maximum cut value, determined over all different optimal mSUGRA benchmark point cut-sets. The interval for each cut-parameter is then coarsely binned and the significance systematically calculated for each possible cut combination within this reduced sub-space.

13.7.1. Signal selection and backgrounds

Because this work is an inclusive study of mSUGRA signatures involving at least two like-sign muons accompanied by multiple jets and large missing transverse energy, several Standard Model processes contribute as sources of background and must be taken into account. Accordingly, the main backgrounds studied in this analysis correspond to QCD dijet (2.8 million fully simulated events with $0 < \hat{p}_T < 4\,\text{TeV/c}$), top ($t\bar{t}$) production (3.3 million fully simulated events), electro-weak single boson production (4.4 million fully simulated events with $0 < \hat{p}_T < 4.4\,\text{TeV/c}$) and electro-weak dibosons production (1.2 million fully simulated events). This work uses only leading order cross-sections, consistently for both signal and all backgrounds.

The dimuon HLT trigger (98% efficient) is required for this analysis. The following selection criteria are applied to muons and jets. The two leading muons are required to be of the same sign and to each have a transverse momentum above $10\,\text{GeV/c}$, ensuring that the muon candidate is reconstructed with good efficiency, above the symmetric thresholds of $7\,\text{GeV/c}$ in the dimuon trigger. Also this analysis requires at least three jets in the event, all of which are required to have $E_T > 50\,\text{GeV}$.

In order to select the particular SUSY diagrams responsible for prompt same-sign dimuons, we apply the following criteria. Each reconstructed muon is required to be separated by at least $\Delta R \geqslant 0.01$ from the other muons. The muon track fit is required to have $\chi^2_\mu \leqslant 3$ and the number of hits associated with the muon must be at least 13. Each muon is required to be isolated, both with respect to the tracker and calorimeter. A combined isolation parameter is used to account for correlations between the tracker (`IsoByTk`) and calorimeter (`IsoByCalo`) isolation variables, $\texttt{Iso} = \texttt{IsoByTk} + 0.75 \times \texttt{IsoByCalo}$, with $\texttt{Iso}_{\mu 1} \leqslant 10\,\text{GeV}$, $\texttt{Iso}_{\mu 2} \leqslant 6\,\text{GeV}$.

In addition to *a priori* requiring three jets in the event, the cut-set maximising the significance (with GARCON) to discover the lowest significant fully simulated mSUGRA test point is then chosen as the final optimal cut-set: $E_T^{j1} > 175\,\text{GeV}$, $E_T^{j2} > 130$ GeV, $E_T^{j3} > 55$ GeV, $E_T^{\text{miss}} > 200\,\text{GeV}$.

Table 13.9. Total number of selected events (for $\mathcal{L} = 10\,\text{fb}^{-1}$) and significance ("Signif.") with systematic uncertainties. "SM" represents the total of all Standard Model backgrounds considered.

Sample(s)	Events	Signif.	Sample	Events	Signif.	Sample	Events	Signif.
SM	1.5	–	LM5	61	14.0	LM10	4	2.2
LM1	341	>37.0	LM6	140	22.3	HM1	4	2.2
LM2	94	17.6	LM7	82	16.3	HM2	2	1.1
LM4	90	17.2	LM8	294	35.9			

13.7.2. Results for full detector simulated mSUGRA samples

After all selection cuts have been applied the main systematic uncertainty is due to the absolute jet energy scale, which is estimated to be 15% after $10\,\text{fb}^{-1}$. In addition, jet energy resolution (10%), muon identification efficiency and fake rate (negligible), luminosity (5%), theory (10%; cross sections, showering, ISR/FSR, etc.) and full simulation versus fast simulation (5%, used to determine the analysis reach in mSUGRA parameters in Section 13.7.3) have been evaluated. Since this analysis is performed consistently at leading order, the inclusion of higher order effects involving ISR/FSR is not taken into account. A generator-level comparison of the parton shower method for inclusive $t\bar{t}$ used by PYTHIA [69] with the matrix element calculation for $t\bar{t}$ + 1jet from COMPHEP [355] suggests a $\approx 10\%$ enhancement in the acceptance of $t\bar{t}$ + 1jet events (generated via the matrix element method) compared with inclusive $t\bar{t}$. The total systematic uncertainty on the number of background events is 24%.

Table 13.9 shows the main results of this study. For the fully simulated low mass mSUGRA point LM1, assuming $10\,\text{fb}^{-1}$ of data, this work selects an expected 341 signal events (with an efficiency of 0.081%) compared with 1.5 expected background events (comprised of $t\bar{t}$). For other fully simulated low mass mSUGRA points (excluding LM10) and an integrated luminosity $10\,\text{fb}^{-1}$ of data, the selection cuts (collectively optimised over all benchmark points) achieve a separation of signal from background with a statistical significance of between 16σ and greater than 37σ, including systematic uncertainties. Such a large significance merely indicates that the low mass mSUGRA region will either have been discovered or excluded, long before $10\,\text{fb}^{-1}$ of data is collected. Hence, low mass SUSY is a prime candidate for possible discovery during the very early running of the LHC. The discovery of high mass SUSY, represented by the fully simulated HM1 and HM2 points, is more difficult and requires more than $10\,\text{fb}^{-1}$ of data.

13.7.3. CMS inclusive reach

Fast simulation and reconstruction was also performed in order to scan the plane of universal scalar (m_0) and gaugino ($m_{1/2}$) masses for fixed mSUGRA parameters: $\tan\beta = 10$, $\mu > 0$ and $A_0 = 0$. Points were generated on a coarse grid with $\Delta m_0 = 100\,\text{GeV/c}^2$ and $\Delta m_{1/2} = 100\,\text{GeV/c}^2$, starting from the point $m_0 = 100\,\text{GeV/c}^2$, $m_{1/2} = 100\,\text{GeV/c}^2$.

The 5σ reach of this analysis, including systematic uncertainties, for different integrated luminosities and assuming no re-optimisation of the selection cuts is shown on Fig. 13.7. By the time CMS collects integrated luminosity $30\,\text{fb}^{-1}$, the high mass point HM1 becomes interesting for possible discovery. For comparison, $\mathcal{L} = 1\,\text{fb}^{-1}$ and $\mathcal{L} = 100\,\text{fb}^{-1}$ are also shown in the figure. Clearly, the systematics for $\mathcal{L} = 1\,\text{fb}^{-1}$ will be higher than that assumed in this work, nevertheless these results strongly suggest (provided systematics can be brought

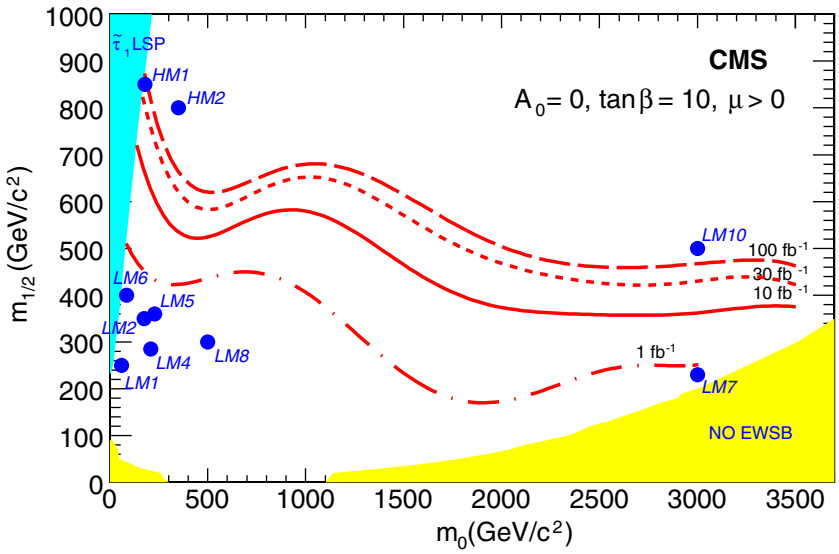

Figure 13.7. CMS reach contours (systematic uncertainties included) in the $(m_0, m_{1/2})$ plane for SUSY processes involving two prompt same-sign muons for $\mathcal{L} = 1\,\text{fb}^{-1}$ (dot-dashed line), $\mathcal{L} = 10\,\text{fb}^{-1}$ (solid line), $\mathcal{L} = 30\,\text{fb}^{-1}$ (short dashed line) $\mathcal{L} = 100\,\text{fb}^{-1}$ (dashed line). The other mSUGRA parameters are fixed to $\tan\beta = 10$, $\mu > 0$ and $A_0 = 0$. Points corresponding to the full detector simulation and reconstruction are also shown (solid circles).

under control) that most of the low mass mSUGRA points are well within reach of CMS during the early running of the LHC.

13.8. Inclusive analyses with opposite sign dileptons

Final states with opposite sign dileptons, originating from the decay $\tilde{\chi}_2^0 \to \tilde{l}_R l \to l^+ l^- \tilde{\chi}_1^0$ in the cascade decays of squarks and gluinos provide a clean signature of SUSY with isolated leptons, high p_T jets and missing transverse energy [677]. In addition, the dilepton invariant mass distribution for this decay is expected to have a triangular shape with a sharp upper edge, which renders this signature striking and useful for further characterisation of SUSY.

13.8.1. Signal selection and backgrounds

The analysis is performed at the LM1 mSUGRA test-point using GEANT-based detailed simulation of the CMS detector [8] and reconstruction [10]. The fast CMS simulation and reconstruction [11] is used to evaluate the discovery reach in the mSUGRA parameter space.

Signal events were generated by ISAJET 7.69 interfaced to PYTHIA 6.225 at the test point LM1, where the NLO cross section at NLO is about 52 pb, dominated by the production of $\tilde{q}\tilde{g}$, $\tilde{g}\tilde{g}$ and $\tilde{q}\bar{\tilde{q}}$. The gluino is the heaviest particle and decays to $\tilde{q}q$. While right squarks decay almost directly to the LSP, due to the bino-like nature of the $\tilde{\chi}_1^0$ at Point LM1, left-handed squarks decay to $\tilde{\chi}_2^0$ with a branching ratio $\sim 30\%$.

The SM backgrounds studied consist of $t\bar{t}$, $W+$ jets, $Z+$ jets, $WW+$ jets, $ZZ+$ jets, Zbb (with leptonic decays of the Z boson), Drell–Yan leptonic events and QCD dijet production processes.

Table 13.10. Cross section at NLO, selection efficiencies and number of events surviving cuts for signal and background processes.

Process	σ (pb)	Ev. analysed	ε	N_{ev} in 1 fb $^{-1}$
SUSY (LM1)	52	478 k	0.016	853
$t\bar{t}$	830	913 k	$1.9 \cdot 10^{-4}$	155
WW+ jets	188	197 k	$1.4 \cdot 10^{-4}$	26
Z+ jets	$5 \cdot 10^3$	606 k	$4.8 \cdot 10^{-6}$	24
DY $\rightarrow 2\mu$	$3.97 \cdot 10^3$	916 k	$< 1.1 \cdot 10^{-6}$	< 4
DY $\rightarrow 2\tau$	$3.97 \cdot 10^3$	514 k	$1.1 \cdot 10^{-6}$	4.5
$Zbb \rightarrow llbb(l = e, \mu, \tau)$ $P^T_{hat} > 60$ GeV/c	57.4	621 k	$8.4 \cdot 10^{-5}$	4.83
$t\bar{t}b\bar{b}$	3.3	50 k	$9.8 \cdot 10^{-4}$	3.2
ZZ+ jets	11	37k	$2.4 \cdot 10^{-4}$	2.7
W+ jets	$1.5 \cdot 10^5$	1765k	$6.7 \cdot 10^{-9}$	1

The SUSY final state studied contains at least two high-p_T isolated leptons, at least two high-p_T jets and large missing transverse energy. The event selection path includes the following requirements:

- the Level-1 and HLT path that requires a single isolated lepton (muon or electron);
- at least two same-flavour opposite-sign (SFOS) isolated leptons (e or μ) with $p_T \geqslant 10$ GeV/c and $\Delta R_{ll} \geqslant 0.2$ and 0.15 for ee and $\mu\mu$, respectively where ΔR_{ll} is the distance of the two leptons in the $\eta - \phi$ space;
- $E_T^{miss} > 200$ GeV;
- at least two jets with $p_T \geqslant 100$ and $\geqslant 60$ GeV/c within $|\eta| < 3$.

The isolation of the leptons is obtained requiring the sum of p_T of the tracks in a cone of $\Delta R = 0.25$ around the lepton track to be less than 5 GeV/c. The E_T^{miss} is computed from the vectorial sum of the jets and leptons.

These selection criteria result in 853 signal events (which correspond to 913 dilepton pairs) for a luminosity of 1 fb^{-1}. The Standard Model background consists of 155 $t\bar{t}$ events, 26 events from WW + jets and 24 events from Z + jets (Table 13.10). All other backgrounds have been found to be negligible and amount in total to at most 20 events.

13.8.2. Results for point LM1

The dilepton invariant mass distribution for 1 fb^{-1} is displayed in Fig. 13.8 showing a clear dilepton edge structure.

The presence of two SFOS leptons can also be due to other processes. Two leptons can result from independent leptonic decays, for example from two charginos or two W's. In that case the final state contains as many SFOS leptons as different-flavour opposite-sign (DFOS) ones and with identical distributions. The background to the SFOS contribution is removed by subtracting the DFOS events, which leads to the dilepton mass distribution of Figure 13.9. The $t\bar{t}$ and WW + jets backgrounds are also strongly reduced by the flavour subtraction. The resulting dilepton invariant mass distribution is fitted using a triangular function smeared (for resolution effects) with a Gaussian to extract the end-point related to the kinematics of the decay $\tilde{\chi}_2^0 \rightarrow \tilde{l}_R l \rightarrow l^+ l^- \tilde{\chi}_1^0$. The value obtained from 1 fb^{-1} of integrated luminosity is:

$$M_{ll}^{max} = 80.42 \pm 0.48 \text{ GeV/c}^2 \tag{13.19}$$

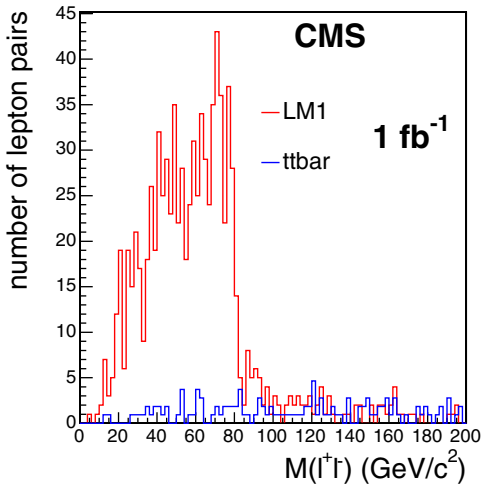

Figure 13.8. Invariant mass distribution of $\mu^+\mu^-$ + e^+e^- and $\mu^\pm e^\mp$ pairs at LM1 for 1 fb^{-1} luminosity. The contribution from the $t\bar{t}$ background is also shown.

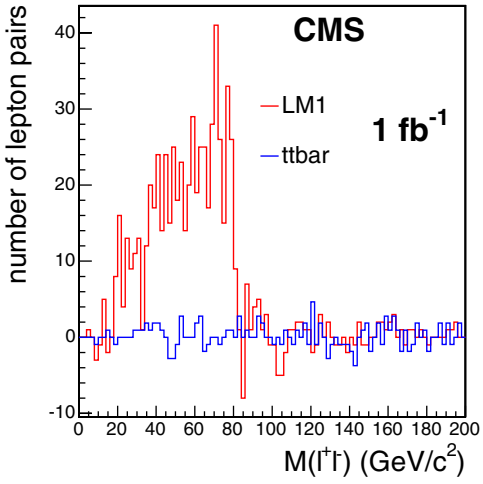

Figure 13.9. Invariant mass distribution of $\mu^+\mu^-$ + e^+e^- and $\mu^\pm e^\mp$ pairs at point LM1 for 1 fb^{-1} luminosity after subtracting $e^+\mu^-$ and μ^+e^- pairs. The contribution from the $t\bar{t}$ background is also shown.

to be compared to the expected value of 81.04 GeV/c^2 for the masses $m(\tilde{\chi}_1^0) = 95$, $m(\tilde{\chi}_2^0) = 180$ and $m(\tilde{l}_R) = 119$ GeV/c^2. The signal-to-background ratio at point LM1 is 4.1, the total signal efficiency is 1.6% and the background composition is 69% of total ttbar, 11.6% of total WW + jets, 10% Z + jets, 3% DY, 2% Zbb, 1% ttbb, 1% ZZ + jets, fractions the others. The total efficiency for the QCD background is too low to be directly calculated, and is then estimated through a factorisation, considering separately the effects due to the single selection cuts. Although the number of surviving QCD events is expected to be negligible, a residual QCD background is still possible, which will be measured using the real data. A statistical significance of 5 sigma, calculated using S_{cP} defined in Appendix A.1, is achieved with 14 pb^{-1} of integrated luminosity. At this luminosity 12.8 signal events are expected with 3.1 Standard Model background events. Therefore this signature is a strong probe for early discovery of low mass supersymmetry.

Systematic uncertainties have been evaluated under the assumption that control data are used for the Standard Model processes. Hence no uncertainties on the theory cross sections, showering, ISR/FSR, are taken into account. The main systematic uncertainty considered is due to the absolute jet energy scale. A $\simeq$ 7% uncertainty on the jet energy scale for 1 fb^{-1} of data is used while this is expected to be $\simeq$ 2% after 10 fb^{-1}. After applying the selection cuts this leads to a $\simeq$ 20% systematic uncertainty on the $t\bar{t}$ background and to a $\simeq$8% systematic uncertainty on the SUSY signal. The electron energy scale uncertainty, expected to be 0.25%, leads to a systematic uncertainty of less than 1% on the background, and less than 0.1% on the signal. The total considered systematic uncertainty on the Standard Model background is 20% at low luminosity, 5% at high luminosity. The effect on the signal of the Tracker and Muon System misalignment in the first months of LHC run has also been evaluated. The number of selected dimuon (dielectron) pairs is lowered by about 30% (10%) while the total signal selection efficiency is decreased by about 20%. The measurement of the distribution end-point is affected by about 1 GeV/c^2. The effect of the electron energy scale uncertainty on the dilepton measurement gives a systematic uncertainty of about 0.15 GeV/c^2.

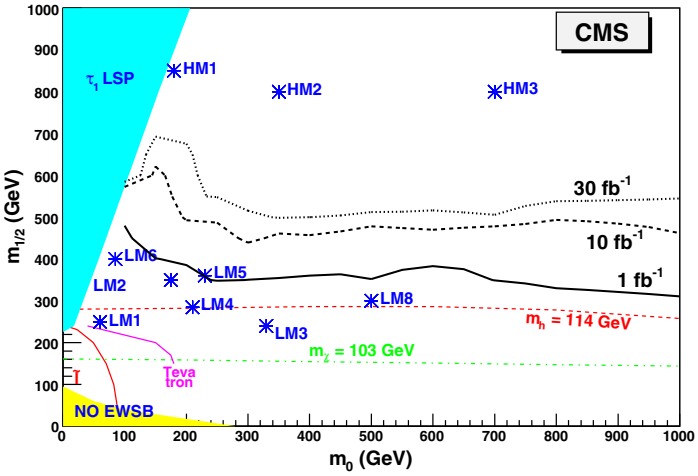

Figure 13.10. 5σ discovery reach for the dilepton final state, assuming $\tan\beta = 10$, $A = 0$, $\mu > 0$ and 1, 10, 30 fb^{-1} integrated luminosity (statistical uncertainties only).

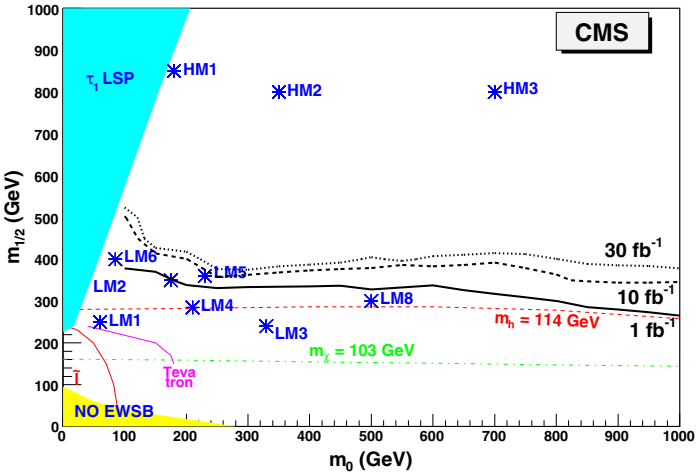

Figure 13.11. 5σ discovery reach for $\tan\beta = 10$ taking into account background systematic uncertainties.

Taking into account the systematic uncertainties on the Standard Model backgrounds expected after the first 1 fb^{-1} of data, the 5 sigma discovery can be achieved with 17 pb^{-1} of integrated luminosity.

13.8.3. CMS inclusive reach

Using the discussed selection path a scan was performed over the mSUGRA parameters in the $(m_0, m_{1/2})$ plane for $\tan\beta = 10$, $A = 0$, $\mu > 0$ to determine the $5\,\sigma$ discovery reach. The observability of the signal over the Standard Model background uses the dilepton estimates before flavour subtraction. The results of the survey are shown for integrated luminosities of 1, 10 and 30 fb^{-1} in Figs. 13.10 and 13.11. It is notable that most of the low mass test-points can be discovered with about 1 fb^{-1}.

13.9. Inclusive analyses with ditaus

In this section, $\tilde{\tau}$ production through the $\tilde{\chi}_2^0$ decays in $\tilde{q}$ or $\tilde{g}$ cascades is investigated. The $\tilde{\tau}$ is produced through $\tilde{\chi}_2^0 \to \tau^{\pm}\tilde{\tau}^{\mp}$, which further decays to $\tau\tilde{\chi}_1^0$ leaving a final state with two taus of opposite sign. The branching fraction of $\tilde{\tau}$ production through $\tilde{\chi}_2^0$ varying with mSUGRA parameters, the analysis is first carried out at large $\tan\beta$, at the LM2 test point, which parameters are given in Section 13.3.2, where the $\tilde{\chi}_2^0$ is predicted to decay 95% of the time into $\tau^{\pm}\tilde{\tau}^{\mp}$. Results are then generalised to any choice of mSUGRA parameters.

This section studies the opportunity of discovering such a model in the first years of data taking of LHC, with integrated luminosities as low as $0.1\,\text{fb}^{-1}$ and up to $10\,\text{fb}^{-1}$. The possibility of measuring the SUSY mass spectra associated to this cascade decay (in particular $\tilde{\chi}_2^0$, $\tilde{\chi}_1^0$ and $\tilde{\tau}$ masses) is investigated in Section 13.13.

13.9.1. Event selection and background studies

For this analysis, 93.5k events (corresponding to an integrated luminosity of $12.6\,\text{fb}^{-1}$) were generated at the LM2 test point using ISASUGRA. Those events were further passed through the full simulation of the CMS detector [8] then digitised and reconstructed [10]. The same procedure was applied to the Monte Carlo samples used as SM background in this analysis. However, in some cases, where large statistics were required, the fast simulation program [11] was used. All Monte Carlo samples used in this analysis are produced with leading order Parton Distribution Functions.

Physics processes responsible for W and Z production and $t\bar{t}$ which final states may contain several taus and jets are considered as potential background sources. In addition, because of its huge cross section ($1.3 \cdot 10^{-4}$ mb) QCD jet production is also considered. The latter can also represent an important source of fake taus as well as fake missing transverse energy ($E_{\text{T}}^{\text{miss}}$) due to imprecision in jet energy measurement.

13.9.1.1. Event selection using all reconstructed taus. In this analysis [678], only events passing the JETMET level1 and HLT triggers are accepted. The event selection is then carried out using only the $E_{\text{T}}^{\text{miss}}$, the reconstructed taus and jets. In order to increase the sensitivity of the selection both tau's decaying hadronically and leptonically are considered in this section.

The mSUGRA events are selected with the following requirement:

- $E_{\text{T}}^{\text{miss}}$ larger than 150 GeV.
  This cut removes a large fraction of Standard Model physics background.
- At least two tau candidates are required.
- At least two jets with $E_{\text{T}} > 150\,\text{GeV}$.
  This requirement is very aggressive on the LM2 events, however it allows to remove most of the Standard Model background.
- ΔR between any pair of tau's should be smaller than two.

This cut makes use of the fact that in $\tilde{\chi}_2^0$ decays, taus belonging to a same cascade decay will be produced relatively close to each other while in Standard Model physics processes taus as well as Supersymmetric physics processes such as chargino production (producing one tau in each cascade) tend to be produced in opposite direction. This cut also reduces the amount of wrong pairing.

Both theoretical and experimental systematic uncertainties are considered in this analysis. The theoretical systematic uncertainty is estimated for the signal according to standard CMS guidelines and involves changing the PDF [351] and varying generator parameters governing

both hard process and fragmentation. Each variation leads to the generation of a new LM2 sample which is then simulated and reconstructed using FAMOS and analysed in the same way as the main signal samples. Variations in the number of selected events are then taken as systematic uncertainty. The relative theoretical systematic uncertainty on the signal was found to be 12%. The experimental systematic uncertainties are coming from the Jet energy scale, the $E_{\mathrm{T}}^{\mathrm{miss}}$ and the tau-jet energy scale. These uncertainties are estimated following standard CMS procedure, see appendix B, by varying the jet and tau energies by an amount corresponding to their respective energy scales and redoing the analysis. The uncertainty on $E_{\mathrm{T}}^{\mathrm{miss}}$ is estimated in a similar way by varying the energy of the jets used to estimate $E_{\mathrm{T}}^{\mathrm{miss}}$ within their energy scale. The experimental systematic uncertainty affect the selection of signal events by 11% for low integrated luminosities (smaller than $1\,\mathrm{fb}^{-1}$) but for large integrated luminosities the systematic effect is less than 3.2%. The experimental systematic uncertainty on the background is 30% for integrated luminosities smaller than $1\,\mathrm{fb}^{-1}$ and 11% for larger integrated luminosities.

At $12.67\,\mathrm{fb}^{-1}$, $N_s = 2735 \pm 273(\mathrm{sys}) \pm 52(\mathrm{stat})$ events from the signal and $N_{bkg} = 938 \pm 103(\mathrm{sys}) \pm 114(\mathrm{stat})$ events from the background survive the selection. 50% of the remaining background is coming from QCD, 39% from $t\bar{t}$ and 11% from W+jets.

To this selection corresponds a ratio signal over background $S/B = 2.9$. The global efficiency of the selection of the signal is around 3% (of which 88% are SUSY events with at least two taus), while only 0.001% of the background remains after selection. Using S_{cL} significance, defined in Appendix A.1, it is possible to estimate that a 5σ discovery can be achieved with only $0.07\,\mathrm{fb}^{-1}$. Using S_{cP} significance [679], which takes into account systematic uncertainties on the background, a 5σ discovery can be expected with a luminosity of $0.125\,\mathrm{fb}^{-1}$.

13.9.1.2. Event selection using only reconstructed taus decaying hadronically. If only taus decaying hadronically are used in the selection described in 13.9.1.1, both signal and backgrounds are affected differently.

At $12.67\,\mathrm{fb}^{-1}$, $N_s = 1447 \pm 144(\mathrm{sys}) \pm 38(\mathrm{stat})$ events from the signal and $N_{bkg} = 543 \pm 60(\mathrm{sys}) \pm 112(\mathrm{stat})$ events from the background survive the selection. 70% of the remaining background is coming from QCD, 20% from $t\bar{t}$ and 10% from W + jets. To this selection corresponds a ratio signal over background $S/B = 2.6$. The global efficiency of the selection of the signal is around 1.5% (of which 88% are SUSY events with at least two taus), while only 0.0006% of the background remains after selection. This time, using S_{cL} a 5σ discovery is achieved with only $0.14\,\mathrm{fb}^{-1}$. Using S_{cP} significance [679], which takes into account systematic uncertainties on the background, a 5σ discovery can be expected with a luminosity of $0.26\,\mathrm{fb}^{-1}$.

13.9.2. Discovery potential of mSUGRA with ditaus final states

A scan of the mSUGRA $(m_0, m_{1/2})$ parameters plane is performed in order to delimit the mSUGRA parameter region where SUSY could be discovered with this analysis. Because the analysis focuses on ditau final states and since the respective branching ratio to ditaus and to other leptons from SUSY may vary by large amounts in the mSUGRA parameter space, allowing large contamination from leptons into ditaus final states the scan is performed using only hadronic tau decays as described in section 13.9.1.2.

This scan is achieved by generating many mSUGRA samples varying m_0 and $m_{1/2}$ values so that the entire region of the plane $(m_0, m_{1/2})$ below $m_0 < 1500\,\mathrm{GeV}$ and $m_{1/2} < 800\,\mathrm{GeV}$ is covered. The samples were generated with ISASUGRA 7.69 then simulated and reconstructed

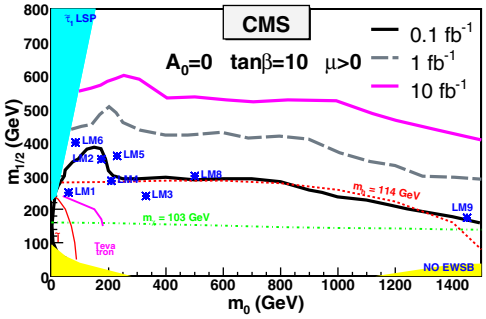

Figure 13.12. Inclusive ditau analysis discovery potential for mSUGRA between 0.1 and 30 fb^{-1} for $\tan\beta = 10$ including only statistical uncertainties.

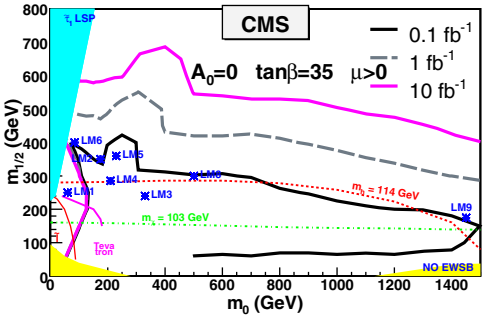

Figure 13.13. Inclusive ditau analysis discovery potential for mSUGRA between 0.1 and 30 fb^{-1} for $\tan\beta = 35$ including only statistical uncertainties.

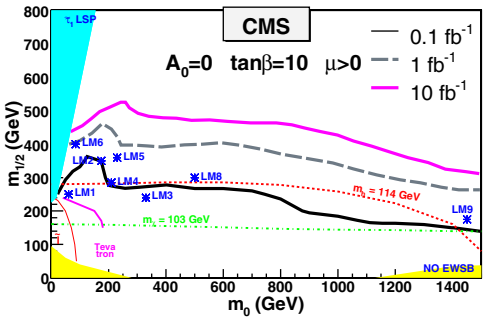

Figure 13.14. Inclusive ditau analysis discovery potential for mSUGRA between 0.1 and 30 fb^{-1} for $\tan\beta = 10$ where both statistical and systematic uncertainties are taken into account.

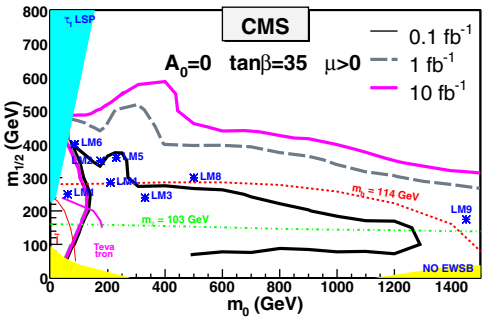

Figure 13.15. Inclusive ditau analysis discovery potential for mSUGRA between 0.1 and 30 fb^{-1} for $\tan\beta = 35$ where both statistical and systematic uncertainties are taken into account.

with FAMOS and analysed in the same way as the LM2 sample. The resulting number of events surviving the selection were used to estimate the significance at each point of the mSUGRA parameter plane. Two types of significance are estimated here, S_{cL} which accounts only for statistical uncertainties and S_{cp} which accounts for both statistical and systematics effects on the background. The resulting 5σ contours over the mSUGRA $(m_0, m_{1/2})$ parameter plane obtained with S_{cl} for several integrated luminosities between 0.1 and 30 fb^{-1} are shown in Figs. 13.12 and 13.13 for $\tan\beta = 10$ and $\tan\beta = 35$, respectively. Results obtained with S_{cp} are shown in Figs. 13.14 and 13.15. The region where a 5σ discovery is possible is somewhat shrunk, especially for the very early measurement at 0.1 fb^{-1} as a precise knowledge of the jet energy scale and of the measurement of the $E_{\mathrm{T}}^{\mathrm{miss}}$ will still be limited. However, a large region is accessible with larger integrated luminosities.

13.10. Inclusive analyses with Higgs

This section describes the potential of the CMS experiment to discover a light supersymmetric Higgs boson (h^0) produced at the end of a cascade of supersymmetric particles starting with the strong production of squarks ($\tilde{q}$) and gluinos ($\tilde{g}$). Because of the cascade production mechanism, the events can be efficiently triggered using inclusive SUSY triggers such as jet $+E_{\mathrm{T}}^{\mathrm{miss}}$, and the dominant $h^0 \to b\bar{b}$ decay mode of the Higgs boson can be exploited.

This analysis focuses on a full CMS detector simulation [8] and event reconstruction [10] at the mSUGRA point LM5, defined in Section 13.3.2. The total SUSY cross section at this parameter point is about 7.75 pb at NLO.

All SUSY channels leading to a light Higgs boson in the final state have been taken into account. The signal events are characterised by at least two b-tagged jets, an important missing transverse energy ($E_{\mathrm{T}}^{\mathrm{miss}}$) and multiple hard jets. This signature allows to suppress the majority of the $b\bar{b}$ background due to SM processes (mainly top pair production $t\bar{t}$, $W^{\pm}$+jets, Z^{0}+jets).

13.10.1. Signal selection and backgrounds

This analysis has been developed based on the CMS reconstruction. The two main algorithms used for the signal reconstruction are the jet reconstruction algorithm (the Iterative cone algorithm with a cone size of 0.5 radians and the GammaJet calibration) and the b-tagging algorithm (Combined b-tagging algorithm, see the PTDR Volume 1, Section 12.2).

A first rejection of the Standard Model backgrounds happens at the online trigger stage. The Level-1 and the High Level Trigger (HLT) efficiencies for the signal and background have been evaluated. The trigger path used for this analysis consists of the Level-1 and HLT Jet + $E_{\mathrm{T}}^{\mathrm{miss}}$ stream. This particular trigger is already an important tool in rejecting Standard Model backgrounds, for example it rejects 96% of the $t\bar{t}$ background while keeping 79% of the signal events.

In order to further remove the SM background events and reduce the SUSY background, a number of offline selection cuts are applied: a minimal number of four jets with a transverse energy above 30 GeV is required, of which at least two are b-tagged with high quality (i.e. a b-tag discriminator greater than 1.5).

The mean b-tagging efficiency is found to be 50% with a mistagging rate of about 1.6%, for u, d, s quarks and gluons, and 12% for c quarks. The mean b jet energy originating from the Higgs decay is approximately 70 GeV, corresponding to a b-tagging efficiency of about 50% at this energy. This means that approximately 25% of the signal events will pass the double b-tag criterion.

Other variables have been identified in order to improve the signal over background ratio, in particular for the most problematic $t\bar{t}$ background: the $E_{\mathrm{T}}^{\mathrm{miss}}$, the first, second and third highest jet P_t. The selection requires a $E_{\mathrm{T}}^{\mathrm{miss}} > 200$ GeV, the highest jet p_t in the event > 200 GeV/c, the second highest jet p_t in event > 150 GeV/c, the third highest jet p_t in event > 50 GeV/c.

Next, in order to select the b-jet pair coming from the Higgs decay, two methods are used. First, the Hemisphere separation technique (see section 13.4) is applied to identify two groups of jets in the detector, each group associated with an initial squark and/or gluino cascade. After that, the b-jet pairing is done only in each of these groups separately, reducing the number of possible combinations by a large factor. In addition, as the Higgs is relatively heavy, its decay products have an important boost leading to a small angle $\Delta R = \sqrt{\Delta\eta^2 + \Delta\phi^2}$ between the two b jets. Therefore, in case of multiple possible combinations inside one hemisphere, the pair with the smallest ΔR value within $\Delta R < 1.5$ is chosen. This procedure gives an efficiency of around 40% and strongly suppresses the combinatorial background.

The full selection chain leads to a signal efficiency of about 8% for all SUSY channels yielding a Higgs. The global rejection factor for $t\bar{t}$ events, including the rejection made by the Jet + $E_{\mathrm{T}}^{\mathrm{miss}}$ trigger, is close to $4.6 \cdot 10^4$. No Z + jets, W + jets nor QCD events from the full simulation samples pass the previously described series of cuts, hence the only remaining background is from $t\bar{t}$. The resulting SUSY signal over SM background ratio is >70. 61%

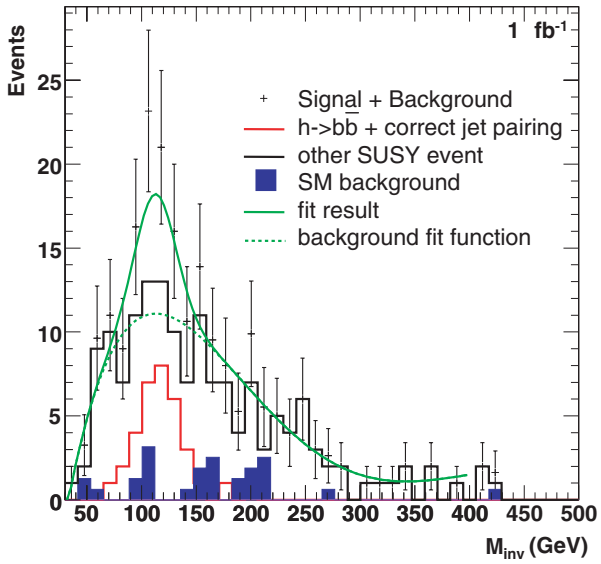

Figure 13.16. Invariant mass distribution of $b\bar{b}$ jets for the search of Higgs final states with 1 fb^{-1}.

of the SUSY signal comes from events with a true h^0, but only part of those have the correct b-jet pairing with both jets from the h^0.

13.10.2. Results at LM5 and systematics

The resulting invariant mass distribution, after the selection cuts described above, is shown in Fig. 13.16. The plot corresponds to the expected statistics equivalent to 1 fb^{-1} of integrated luminosity. A peak around 116 GeV/c^2 is visible. The main background is due to the remaining SUSY background events and some $t\bar{t}$ events.

A fit was performed representing the background by a fifth order polynomial and approximating the Higgs signal by a Gaussian. The r.m.s of the Gaussian has been fixed to 18 GeV, which is the Higgs mass resolution estimated using the Monte Carlo truth. In real data, this number will be determined from studying b-rich samples such as $t\bar{t}$. The results of the fit for the equivalent of 1 fb^{-1} of data are the following: the Higgs mass is found to be (112.9 ± 6.6) GeV/c^2 (for a generated mass of 116 GeV/c^2) and the fraction of signal in the distribution is evaluated to be 0.28 ± 0.08. The significance S_{CL}, directly extracted from the fraction of signal in the histogram, is found to be 4.5. A significance of 5 should be achieved with approximately 1.5 fb^{-1} luminosity.

For 1 fb^{-1}, the jet energy scale and $E_{\mathrm{T}}^{\mathrm{miss}}$ uncertainties have been estimated assuming a linear evolution from $\pm 15\%$ to $\pm 5\%$ for low energy jets (below 50 GeV) and then fixed at $\pm 5\%$ for higher energy jets. As the $E_{\mathrm{T}}^{\mathrm{miss}}$ is computed from the jets, a correction on the jet energy is automatically propagated to its estimation. The effects are about 15% on the SUSY event selection and 17% on the $t\bar{t}$ event rejection respectively. The impact on the Higgs mass measurement have been estimated to be ± 7.5 GeV/c^2; on the signal fraction, the effect is ± 0.04.

Another systematic uncertainty is introduced by the misalignment of the tracker. Both the short and long term misalignment scenarios have been investigated. The short term misalignment corresponds to a displacement of the tracker (strips/pixels) = (100 μm/10 μm), while the long term misalignment takes the following shift of the tracker (strips/pixels) = (20μ m/10 μm) into account. The misalignment of the tracker reduces the

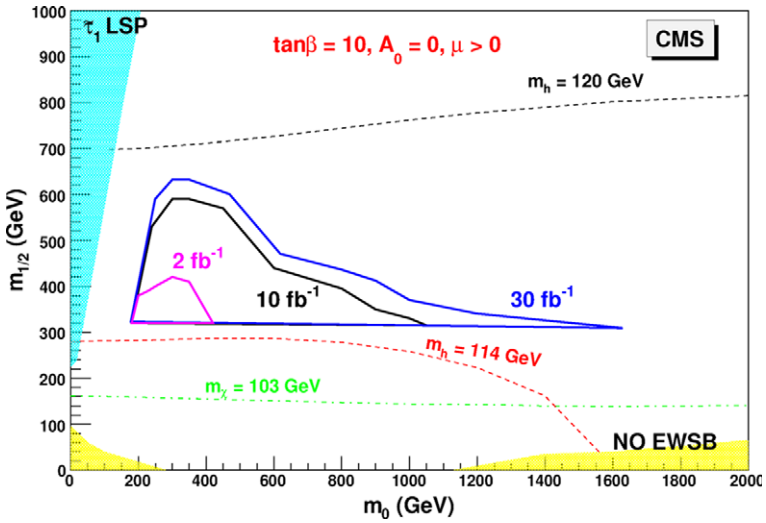

Figure 13.17. Higgs discovery reach in SUSY cascades for 2, 10 and 30 fb^{-1}.

track reconstruction resolution, which results in a reduced b-tagging efficiency and which in its turn causes a reduced signal event selection efficiency. The long term misalignment scenario results in a drop of the signal selection efficiency of (∼10%) compared to the case of an aligned detector; for the short term misalignment case, the reduction is (∼17%). No effect on the position/width of the Higgs mass peak was observed.

Finally, the systematics due to the choice of the background fit function has been estimated to be small (by changing the background function to a third, fourth, sixth or a seventh order polynomial): $\pm 0.3\,\mathrm{GeV/c^2}$ on the Higgs mass and ± 0.01 on the signal fraction.

The final result including all the previously discussed systematics for $1\,\mathrm{fb}^{-1}$ of integrated luminosity is then 112.9 ± 6.6 (stat) ± 7.5 (syst) $\mathrm{GeV/c^2}$ for the Higgs mass and 0.28 ± 0.08 (stat) $\pm$ 0.04 (syst) for the signal fraction.

13.10.3. CMS reach for inclusive Higgs production

After establishing the visibility of the signal for the LM5 point, a scan was performed in the (m_0, $m_{1/2}$) plane in order to determine the region where a 5σ discovery could be made with 2, 10 and 30 fb^{-1}.

First, an effective cross section ($\sigma \times BR(h0)$) was used (calculated with PROSPINO and ISASUGRA) to obtain an estimate of the reach. Using this first estimate, 40 points were chosen for which the full spectrum was calculated and a fast simulation was performed with FAMOS [11]. The same selection criteria as for LM5 point were applied, and the number of Higgs signal and background events was determined. Given that the background is dominated by SUSY events, the signal and background are similarly affected by the systematic uncertainties and the effect on the significance is small. The same significance definition (S_{CL}) was used in order to determine the 5-sigma contours. Comparing the ORCA/FAMOS results at LM5, the significances obtained with both programs were found to agree well.

The result of the scan is displayed in the reach plot in Fig. 13.17. Although for $1\,\mathrm{fb}^{-1}$ the sensitivity remains below 5σ, everywhere a sizeable region of the (m_0, $m_{1/2}$) plane, up to 1100 (1600) GeV in m_0 and 600 (650) GeV in $m_{1/2}$, can be covered with 10 (30) fb^{-1}. With $2\,\mathrm{fb}^{-1}$ of integrated luminosity, a small region of the plane can already be probed. The plot assumes $\tan\beta = 10$, $A_0 = 0$, and a positive sign of μ.

Table 13.11. Number of events for signal ($\tilde{\chi}_2^0 \to Z^0 + \tilde{\chi}_1^0,\ Z^0 \to e^+e^-, \mu^+\mu^-$) and background before and after selection criteria for 10 fb^{-1}. The numbers below Zj specify the range of partonic p_T in GeV/c.

	LM4 with $\tilde{\chi}_2^0$	LM4 no $\tilde{\chi}_2^0$	ZZj	ZWj	WWj	$t\bar{t}$	Zj 85–250
σ NLO (pb)	0.664	17.4	15.5	51.5	270	830	116.7
10 fb^{-1}							
total events	6640	173.8 K	155 K	515 K	2.7 M	8.3 M	1.17 M
L1+HLT	6032	81.7 K	12.6 K	24.4 K	174 K	973 K	462 K
OS leptons	4489	7147	9124	14.7 K	26.3 K	268 K	331 K
M_{ll}	3773	804	6999	11.5 K	2406	23.1 K	249 K
E_T^{miss}	1420	306	32	24	70	149	44
$\Delta\phi_{ll}$	1289	264	31	22	47	61	35

13.11. Inclusive SUSY search with Z^0

13.11.1. Topology of the signal

SUSY processes leading to final states with Z^0 can be detected in CMS using the Z^0 decays into same flavour opposite sign (SFOS) lepton pairs. The detection of SUSY in the mSUGRA framework through the decay $\tilde{\chi}_2^0 \to Z^0 + \tilde{\chi}_1^0$ is the scope of this study. The mSUGRA test-point LM4 with the parameters described in Section 13.3 is chosen. The $\tilde{\chi}_2^0$ is produced mainly through the cascade decays of gluinos ($M_{\tilde{g}} = 695$ GeV) and squarks (mainly the $\tilde{b}_1$ with $M_{\tilde{b}_1} = 601$ GeV). The decays of the second neutralino to Z^0 have a large branching ratio ($\sim$100%). The signal events are characterised by large missing E_T (due to the undetectable LSP) and the SFOS lepton pair from Z^0. The analysis details can be found in [680].

The main Standard Model backgrounds originate from the production of one or more Z^0 bosons in association with jets as well as $t\bar{t}$. In addition SUSY events contain dileptons that do not originate from the above neutralino decay chain and large missing transverse energy. These events are considered as signal for SUSY detection but as background for the $\tilde{\chi}_2^0$ detection. The following backgrounds were considered in this study: dibosons ($ZZ + j$, $ZW + j$, $WW + j$), inclusive top ($t\bar{t}$) and Z+ jets. The signal events were generated interfacing ISAJET 7.69 with PYTHIA. Unless otherwise stated all events are fully simulated and analysed using the CMS full detector simulation [8] and reconstruction [10] packages. The next to leading order (NLO) cross sections of the relevant processes are shown in Table 13.11.

13.11.2. Event selection

The following requirements are imposed in order to efficiently select the signal and reject the background events. All criteria were chosen so that the final SUSY search significance estimator S_{c1} [102, 681] for 10 fb^{-1} integrated luminosity is maximised. Very similar requirements maximise also significance estimator S_{L2} [102] used in the case of 1 fb^{-1} integrated luminosity. The effect of the selection requirements on the signal and on each background sample separately can be seen in Table 13.11 for 10 fb^{-1} integrated luminosity.

- Events are required to pass the HLT dielectron or dimuon triggers.
- An e^+e^- or $\mu^+\mu^-$ pair with lepton $p_T > 17$ GeV for electrons and $p_T > 7$ GeV for muons (as per L1 trigger requirements). Each lepton is required to be within $|\eta| < 2.4$.
- The SFOS lepton pair invariant mass is required to be consistent with the Z^0 mass, i.e. 81 GeV $< M_{ll} <$ 96.5 GeV. The reconstructed masses for the e^+e^- and the $\mu^+\mu^-$ pairs and

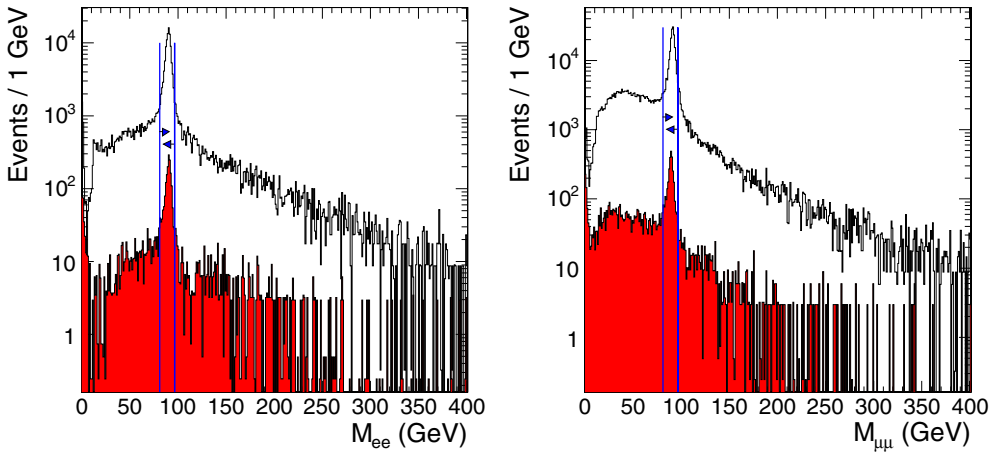

Figure 13.18. Reconstructed masses for (left) e^+e^- and (right) $\mu^+\mu^-$ pairs for the background and for the signal (shaded) events. SUSY events not involving $\tilde{\chi}_2^0$ are considered signal. The vertical lines denote the imposed mass requirement.

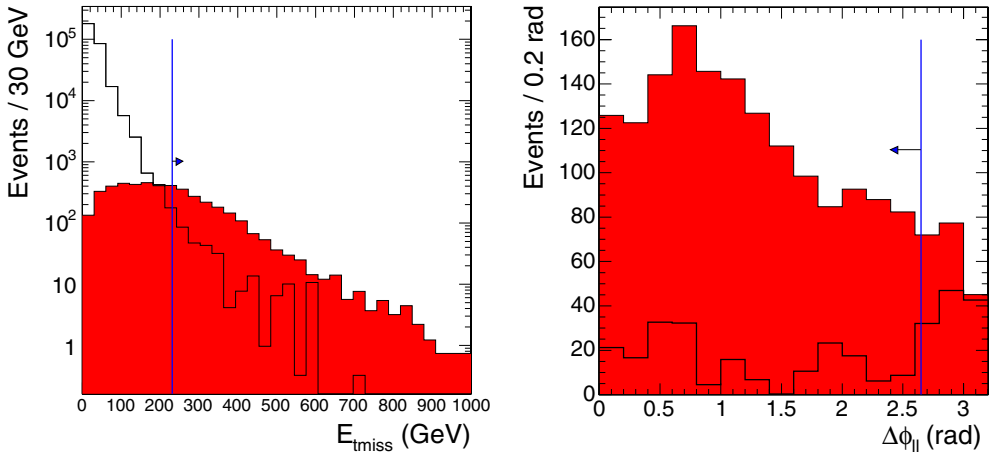

Figure 13.19. $E_{\mathrm{T}}^{\mathrm{miss}}$ (left) and $\Delta\phi$ between the two leptons (right) for background (black line) and signal (shaded) events. SUSY events not involving $\tilde{\chi}_2^0$ are considered signal. The vertical lines denote the $E_{\mathrm{T}}^{\mathrm{miss}}$ and $\Delta\phi$ requirements.

the mass requirements are shown in Figs. 13.18 (left) and (right) respectively. This cut reduces backgrounds not involving a Z^0 ($t\bar{t}$, WW+j) and the sample of SUSY events not involving $\tilde{\chi}_2^0$.

- The missing transverse energy $E_{\mathrm{T}}^{\mathrm{miss}}$ is required to be greater 230 GeV. This requirement reduces all backgrounds as seen in Fig. 13.19 (left). It allows, however, for enough signal and background events in order to maintain good statistics both for 1 fb^{-1} and for 10 fb^{-1} integrated luminosity.
- The angle $\Delta\phi$ between the two leptons of the lepton pair that reconstructs the mass of Z^0 is required to be less than 2.65 rad. The $\Delta\phi$ distribution is shown in Fig. 13.19 (right) for signal and background. This requirement targets the remainder of the $t\bar{t}$ and the WW + j backgrounds that survived the $E_{\mathrm{T}}^{\mathrm{miss}}$ requirement.

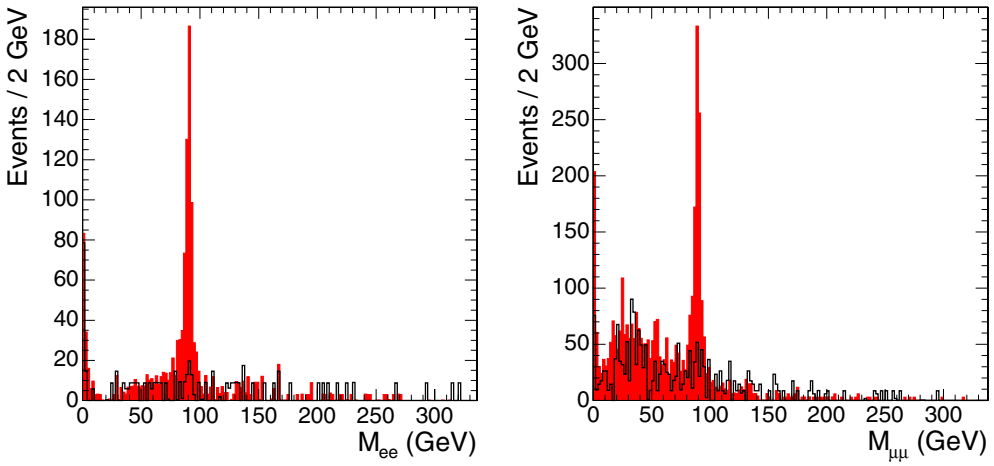

Figure 13.20. Reconstructed masses for (left) e^+e^- and (right) $\mu^+\mu^-$ pairs for the background and for the signal (shaded) events after the cut on $E_{\mathrm{T}}^{\mathrm{miss}}$. SUSY events not involving $\tilde{\chi}_2^0$ are considered signal.

13.11.3. Results and systematic uncertainties

The reconstructed masses for the e^+e^- and the $\mu^+\mu^-$ pairs without the Z^0 mass cut but after the cut on $E_{\mathrm{T}}^{\mathrm{miss}}$ are shown in Fig. 13.20 (left) and (right) respectively. A clear Z^0 peak from the signal is observed.

After the application of the above criteria and for 10 fb^{-1} integrated luminosity we have 1553 SUSY events and 196.5 Standard Model background events in the Z^0 window. This gives a signal over background ratio of 8 and inside the signal events 83% originate from a $\tilde{\chi}_2^0$ decay. The total efficiency for Z^0 events from a $\tilde{\chi}_2^0$ decay is 19.4%. The background is composed of 31% $t\bar{t}$, 24% WW, 18% Zj, 16% ZZ and 11% ZW.

The significance based on statistical uncertainties only has been evaluated by means of S_{cL}, defined in Appendix A.1. A significance of 5σ would be reached after 0.06 fb^{-1} if systematic effects were negligible.

When LHC will start running many uncertainties will be controlled from data. In this analysis relevant uncertainties are the lepton P_t resolution and the $E_{\mathrm{T}}^{\mathrm{miss}}$ uncertainty. The lepton P_t resolution ($\sim$3%) introduces an uncertainty of 2.7% in the number of background events. The dominant systematic, however, is the $E_{\mathrm{T}}^{\mathrm{miss}}$ energy scale uncertainty which is estimated to $\sim$5% and which introduces a 20% uncertainty in the number of background events, nearly independent of the background channel. The significance was recomputed after including the systematic uncertainties using S_{c12s} (see Appendix A.1), which increases the required integrated luminosity for a 5σ discovery to $\sim$0.1 fb^{-1}.

13.11.4. CMS reach for inclusive Z^0 search

A scan was performed over the mSUGRA $m_0, m_{1/2}$ parameter space in order to determine the range over which the above analysis can reveal new physics. The test points were taken at high density in the area where the Z^0 has high production cross section (especially due to the decay $\tilde{\chi}_2^0 \to Z^0 + \tilde{\chi}_1^0$). This is an almost horizontal band in the m_0–$m_{1/2}$ plane between $m_{1/2} \sim 240\,\mathrm{GeV/c^2}$ and $m_{1/2} \sim 340\,\mathrm{GeV/c^2}$. Points were also taken at higher and lower $m_{1/2}$ values, because there is an excess of lepton pairs created due to SUSY processes. These may have invariant mass close to the Z^0 mass and pass analysis cuts assisting in the detection

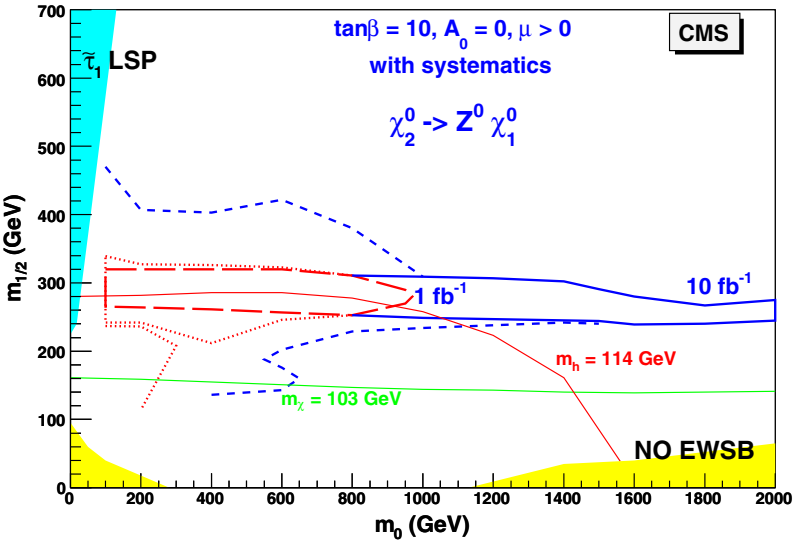

Figure 13.21. The 5σ significance contours of final states with Z^0 for $1\,\text{fb}^{-1}$ (dashed line) and $10\,\text{fb}^{-1}$ (full line) integrated luminosities, taking into account systematic uncertainties, in the region where the $\tilde{\chi}_2^0 \to Z^0\tilde{\chi}_1^0$ decay takes place. Also indicated as dotted and short dashed lines are the extensions at higher and lower $m_{1/2}$ where the Z^0 is off-shell.

of SUSY. For each point 2000 events were produced with an OS lepton pair close to the Z^0 mass. The events were generated interfacing ISAJET 7.69 with PYTHIA 6.227 and they were simulated, reconstructed and analysed using the FAMOS fast simulation package [11]. Systematic uncertainties were taken into account. The 5σ significance contour is shown for integrated luminosities of $1\,\text{fb}^{-1}$ and $10\,\text{fb}^{-1}$ in Fig. 13.21.

13.12. Inclusive analyses with top

The supersymmetric partner of the top quark in most of the supersymmetric scenarios is the lightest squark. Finding evidence of its existence can be a clear signature for supersymmetry. In the main part of the allowed m_0–$m_{1/2}$ plane, the stop can decay to a top plus a neutralino. This neutralino can be either the LSP ($\tilde{\chi}_1^0$) or a heavier neutralino which decays in turn to a LSP which appears as missing transverse energy ($E_{\text{T}}^{\text{miss}}$). Hence in the final state there is at least a top quark plus large $E_{\text{T}}^{\text{miss}}$.

The search for top was tuned on test point LM1, where the stop decays according to

$$\tilde{t}_1 \to t\tilde{\chi}_2^0 \to tl\tilde{l}_R \to tll\tilde{\chi}_1^0 \tag{13.20}$$

giving rise to a final state which also contains two leptons. Although this analysis consists primarily in a search for an excess of top quarks from any SUSY origin with respect to its SM production, it was also optimised for the selection of events where the top results from the production of $\tilde{t}$.

13.12.1. Top quark and lepton reconstruction and identification

Electrons and muons are requested to have $p_{\text{T}} \geqslant 5\,\text{GeV/c}$ and $\eta \leqslant 2.5$.

Electrons are separated from jets by requiring that the ratio of energy deposited in the HCAL to the ECAL $\leqslant 0.1$, the absolute difference in η between the electromagnetic cluster

in the ECAL and the associated track $\Delta\eta \leqslant 0.006$ and the energy weighted spread of the electron shower in η be $\sigma_{\eta\eta} \leqslant 0.015$.

Leptons were required to be isolated, namely that the ratio of p_T of the lepton to the p_T sum of other particles inside a cone of size $\Delta R = 0.1$ around the lepton track be greater than 2. Jets were reconstructed from ECAL and HCAL towers using an Iterative cone algorithm with cone size $\Delta R = 0.5$ and were selected if their uncalibrated transverse energy $E_T \geqslant 30$ GeV in the acceptance of $\eta \leqslant 2.5$. Their energy was calibrated using corrections from photon-jet balancing studies presented in Vol. 1 Section 11.6.3.

In this analysis only hadronic decays of the top quark were considered. A kinematic fit with constraints is utilised to find the best combination of jets to make the top quark. Since the purpose of this analysis is not to measure the top quark mass, its known value was used to constrain the invariant mass of the system of three jets. Among these three jets, one and only one must be tagged as a b-jet and the other two were constrained to be consistent with a hadronically decaying W. The fit then consisted in minimising the χ^2 as a function of the three jet energies and imposing the top and W mass constraints. The solution was obtained by an iterative method based on Lagrange multipliers. As several combinations may lead to a convergent fit for a given event, only the combination with the best χ^2 was kept, with the additional requirement that its χ^2 probability was greater than 0.1.

13.12.2. Signal selection and backgrounds

All events were fully simulated [8], digitised with low luminosity pileup and reconstructed [10].

The signal events consisted of an inclusive SUSY sample at the test point LM1 (see Section 13.3.2), where the total cross section at NLO is about 52 pb. Top quarks are found in the decay of $\tilde{t}$, but other important sources exist, e.g. $\tilde{b} \to t\tilde{\chi}_1^{\pm}$. At an integrated luminosity of 1 fb^{-1}, the total SUSY production amounts to 52000 events, out of which 8375 contain a top quark.

The main backgrounds, generated with PYTHIA 6.225 [69], consist of $t\bar{t}$, $WW + jets$, $WZ + jets$ and QCD. In addition, single top generated with TOPREX 4.11 [44] and $W + jets$ generated with ALPGEN V2.0 [161] were considered.

The selection of SUSY events containing a top quark was based on the following criteria:

- L1T: every event must pass the first level of the Trigger (L1T) cuts corresponding to "Jet/Met" (a jet with $E_T > 88$ and $E_T^{miss} > 46$ GeV/c).
- HLT: events were required to pass High level Trigger (HLT) cuts (a jet with $E_T > 180$ and $E_T^{miss} > 123$ GeV).
- $\geqslant$4 jets with $E_T^{raw} \geqslant 30$ GeV and $\eta \leqslant 2.5$.
- $\geqslant$1 b-jet with $E_T^{raw} \geqslant 30$ GeV and $\eta \leqslant 2.5$.
- $E_T^{miss} \geqslant 150$ GeV to suppress $t\bar{t}$ and other SM backgrounds.
- a convergent fit with $P(\chi^2) \geqslant 0.1$.
- $\Delta\Phi$ between the fitted top and $E_T^{miss} \leqslant 2.6$ rad to suppress semi-leptonic $t\bar{t}$ events.
- $\geqslant$1 isolated lepton (e or μ) with $p_T \geqslant 5$ GeV and $\eta \leqslant 2.5$ to suppress QCD background.

These criteria were simultaneously optimised to reject SM backgrounds and to maximise the ratio of events with a top quark at generator level, called SUSY(with top), to events without top at generator level, called SUSY(no top).

The effect of the cuts is shown in Table 13.12. As a result of the selection, the signal events remaining for a 1 fb^{-1} luminosity consist of 38 events SUSY(with top) and 17 events

Table 13.12. Effect of different cuts on different samples. In every row, the number of the remaining events after that cut is shown. "No.of.used.events" shows the number of events used in this analysis, "NEve(Nor.xsec)1 fb^{-1}" is the same number after normalising to the cross section times 1 fb^{-1} and "wT/noT" means $\frac{SUSY(withTop)}{SUSY(noTop)}$.

cut	SUSY (withTop)	SUSY (noTop)	ttInc	WW	ZW	Single t	wT/noT
x-sec(pb) NLO	52	830	269.91	51.5	250	-	
No.of.used.events	494261	1674500	305000	70000	100000	-	
NEve(Nor.xsec)1 fb^{-1}	8375	43625	830000	269910	51500	250000	0.19
L1T (Jet/Met)	6269	33582	75806	18498	598	10875	0.19
HLT (Jet/Met)	5070	29427	14430	4733	142	1750	0.17
MET $\geqslant$ 150 GeV	4183	25677	4930	2312	99	653	0.16
$n_{bj} \geqslant 1$	3457	14388	3718	792	32	355	0.24
$n_j^{b\ or\ light} \geqslant 4$	1789	4576	769	25	0	33	0.39
A convergent Fit	1335	3062	557	12	0	28	0.44
χ^2 probability >0.1	105	69	56	0	0	5	1.52
$\Delta\phi$ <2.6	79	52	12	0	0	5	1.51
$n_l > 0$	38	17	5	0	0	0	2.19

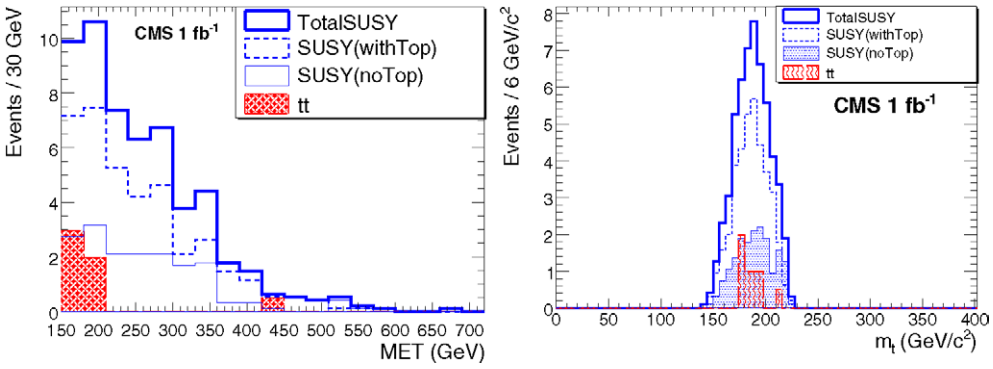

Figure 13.22. (left) Distributions of $E_{\mathrm{T}}^{\mathrm{miss}}$ and (right) fitted top mass after all selection criteria are applied.

SUSY(no top). The remaining backgrounds are 5 events from $t\bar{t}$. The resulting distributions of $E_{\mathrm{T}}^{\mathrm{miss}}$ and of the fitted top mass are displayed in Fig. 13.22.

13.12.3. Results at point LM1

The significance of a discovery was computed from statistical uncertainties only using the formula of S_{c12}, defined in Appendix A.1, where the number of signal events, S, is the sum of SUSY(with top) and SUSY(no top) and B represents the sum of all SM backgrounds. Using this formula, the integrated luminosity required to make a discovery at point LM1 with a significance of 5 amounts to $\sim$210 pb^{-1}.

Many systematic uncertainties (cross section, showering, ISR/FSR, ...) will be rendered very small by using real data. The main uncertainties remaining will be the absolute jet energy scale (estimated to 5% for jets and MET in 1 fb^{-1}), which leads to 5.1% from jets and 18.3% from MET in the $t\bar{t}$ sample and the b-tagging efficiency estimated to 8% for 1 fb^{-1}. Adding them in quadrature yields a total systematic uncertainty of 21%, considered common to all backgrounds. It is seen that this remains negligible compared to the statistical uncertainty.

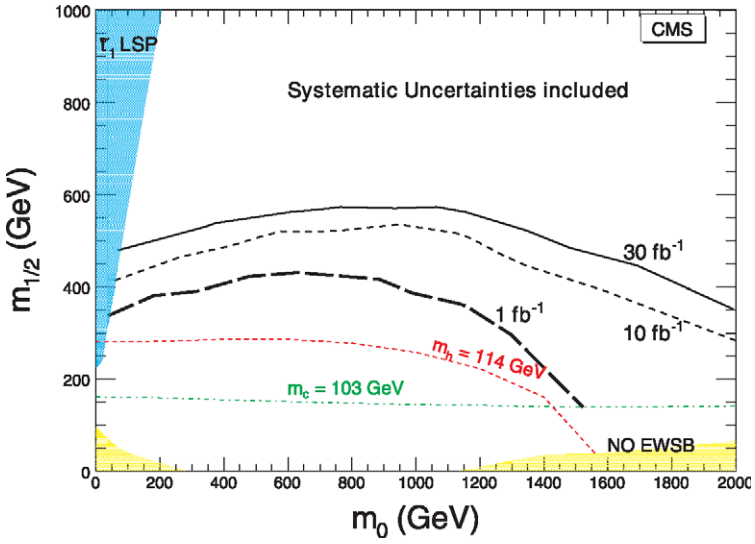

Figure 13.23. The 5σ reach in $m_0, m_{1/2}$ plane with 1, 10 and 30 fb^{-1} obtained for final states with a top quark.

13.12.4. CMS reach for inclusive top search

The CMS fast simulation, FAMOS, was used to find the reach of CMS in this channel in $m_0, m_{1/2}$ plane. In total 36 points have been tried. The ntuples were generated by using the CMS-official ISAPYTHIA. The NLO cross sections were derived by PROSPINO [682].

Figure 13.23 shows the 5σ reach in $m_0, m_{1/2}$ plane with 1, 10 and 30 fb^{-1}.

13.13. Mass determination in final states with ditaus

In this section the determination of the sparticle masses using invariant mass distributions in the ditau final state is investigated. The selection of the events is the same as presented in Section 13.9.

13.13.1. Extraction of mSUGRA mass spectra from the measurement of the end points of invariant mass distributions

Using the kinematics of the successive two body decays in $\tilde{q} \to q\tilde{\chi}_2^0 \to q\tau\tilde{\tau} \to q\tau\tau\tilde{\chi}_1^0$, it is possible to express the mass of the sparticles involved in that cascade as a fully resolved system of equations which depends only on the end-point of the invariant mass distributions obtained by combining the leptons and quark-jets observed in the final state.

However, the tau-lepton always decays, producing at least one undetected neutrino. Therefore, instead of observing a triangle-shaped distribution like for the dilepton invariant mass distribution of chapter 13.8, where the end-point coincides with the maximum of the distribution, the absence of the neutrino smears the resulting mass distribution to lower values. Even though the end-point of the distribution remains unchanged, it now lies at the tail of a gaussian-like distribution.

The $\tilde{\chi}_2^0$ cascade always produces a pair of opposite charge τ's, therefore signal samples are obtained by combining opposite charge tau pairs to the two most energetic jets of the event. In 75% of the cases the quark produced by the decay of the $\tilde{q}$ to $\tilde{\chi}_2^0$ is among these

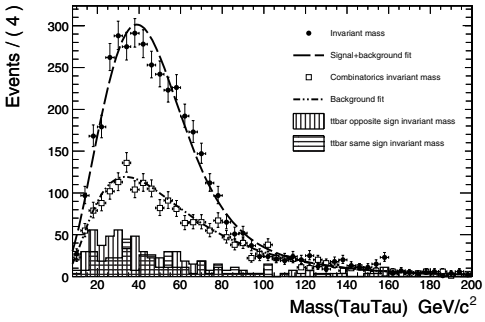

Figure 13.24. Ditau invariant mass distribution.

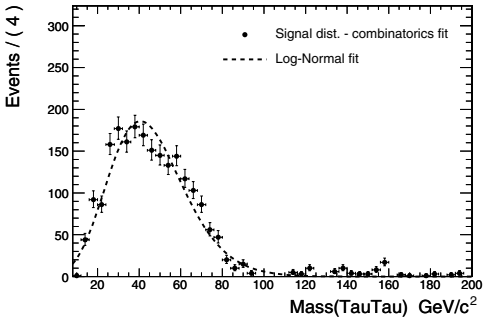

Figure 13.25. Difference between ditau invariant mass distribution and combinatorics fit together with log-normal fit.

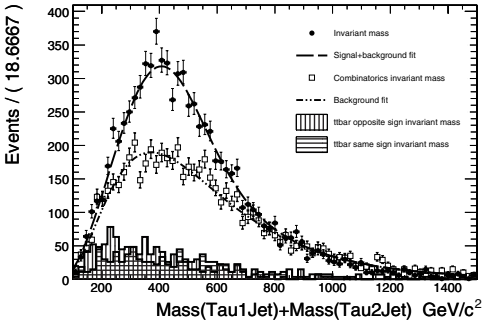

Figure 13.26. τ_1Jet + τ_2Jet invariant mass distribution.

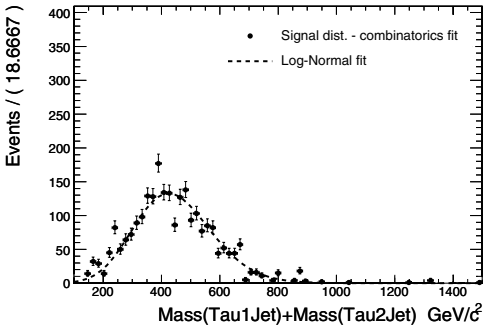

Figure 13.27. Difference between τ_1Jet + τ_2Jet invariant mass distribution and combinatorics fit together with log-normal fit.

two jets, due to the fact that the $\tilde{q}$ is much heavier than the $\tilde{\chi}_2^0$. This large number of tau's and jets is responsible for a high combinatorial background. A good description of this combinatorial background, in particular of its tail, is essential for extracting the true end-points. The combinatorial background in the opposite sign invariant ditau mass is estimated by taking same sign tau pairs. The combinatorial background from the jets is estimated by combining all tau pairs to a jet taken among the 2 most energetic jets of a previous event selected randomly to insure that the jet and tau's are uncorrelated.

Five invariant mass and their associated combinatorial background distributions are then obtained: $M(\tau\tau)$, $M(\tau\tau\text{Jet})$, $M(\tau_1 Jet)$, $M(\tau_2 Jet)$ and $M(\tau_1\text{Jet}) + M(\tau_2\text{Jet})$. ($\tau_1$ is defined as the one which maximises the invariant mass formed by its association with a jet, $M(\tau_1 Jet) > M(\tau_2 Jet)$).

The distributions of combinatorial background are first fitted. Then, the resulting fit parameters are used together with a Log-normal distribution, which gives a good description of the tail of the true distributions, to fit the distributions of the signal. Since it is possible to express the log-normal distribution as a function of the end-point, the end-point can be extracted directly from the fit.

The ditau invariant mass and $M(\tau_1\text{Jet}) + M(\tau_2\text{Jet})$ are fitted first (Figs 13.24–13.27). The three other invariant mass distributions are built using only candidates found to have values for the two previous distributions below the measured end-points. Then, they are fitted using the same procedure. The sparticle masses are evaluated by solving the system of four equations giving the end-points as a function of the sparticle mass [683].

Table 13.13. End-point obtained with the lognormal fit together with sparticle masses measured with the end-point technique for LM2 for integrated luminosities around 40 fb^{-1}.

End-points (GeV)	case 1 (GeV)	case 2 (GeV)
$m(\tau_1\tau_2)^{\max} = 95 \pm 3$	$M(\tilde{\chi}_1^0) = 213 \pm 14$	$M(\tilde{\chi}_1^0) = 147 \pm 23$
$m(\tau_1 Q)^{\max} = 559 \pm 11$	$M(\tilde{\chi}_2^0) = 337 \pm 17$	$M(\tilde{\chi}_2^0) = 265 \pm 10$
$m(\tau_2 Q)^{\max} = 298 \pm 7$	$M(\tilde{\tau}) = 310 \pm 17$	$M(\tilde{\tau}) = 165 \pm 10$
$m(\tau_1\tau_2 Q)^{\max} = 596 \pm 12$	$M(\tilde{q}) = 839 \pm 19$	$M(\tilde{q}) = 763 \pm 33$
$E_5^{meas} = 780 \pm 20$	$E_5^{calc} = 815 \pm 26$	$E_5^{calc} = 765 \pm 30$

Table 13.14. sparticle masses measured with end-point method for LM2 together with theoretical value.

	LM2 benchmark point	
	measured	theory
$M(\tilde{\chi}_1^0)$ (GeV)	$147 \pm 23(\text{stat}) \pm 19(\text{sys})$	138.2
$M(\tilde{\chi}_2^0)$ (GeV)	$265 \pm 10(\text{stat}) \pm 25(\text{sys})$	265.5
$M(\tilde{\tau})$ (GeV)	$165 \pm 10(\text{stat}) \pm 20(\text{sys})$	153.9
$M(\tilde{q})$ (GeV)	$763 \pm 33(\text{stat}) \pm 58(\text{sys})$	753–783 (light $\tilde{q}$)

When several solutions are possible for the SUSY mass spectrum (as it is the case here, where two valid solutions exist), the choice is made by comparing the measured $M(\tau_1\text{Jet}) + M(\tau_2\text{Jet})$ end-point value, E_5, to the one computed from the sparticle masses found by solving the systems of equations.

The most probable mass hypothesis is then chosen as the one for which E_5 computed for each mass spectrum is the closest to the measured one. The measured end-point was found to be 780±20 GeV while the calculations for the mass hierarchy in case 1 and case 2 yield to 815±26 GeV and 765±30 GeV respectively (Table 13.14). The second hypothesis, which corresponds to the correct LM2 mass hierarchy, gives a result compatible with the measured end-point value.

Three main systematic uncertainties are considered, the jet energy scale and tau-jet energy scale as well as systematics uncertainties arising from the extraction procedure.

Results obtained are shown in Table 13.14 for 40 fb^{-1}, together with LM2 generated sparticle masses. They are found to be in good agreement with the theoretical values. Using a 40 fb^{-1} LM2 sample, it is possible to measure the SUSY mass spectra and in particular $\tilde{\tau}$ mass with a precision of 30 GeV.

13.14. Direct $\chi_2^0\chi_1^\pm$ production in tri-leptons

The exclusive tri-lepton final state appears in $pp \to \tilde{\chi}_2^0\tilde{\chi}_1^\pm$ channel with subsequent three body decays of the second neutralino, $\tilde{\chi}_2^0 \to \tilde{\chi}_1^0 ll$, and chargino, $\tilde{\chi}_1^\pm \to \tilde{\chi}_1^0 W^* \to \tilde{\chi}_1^0 l\nu$; or via sleptons in two body decay, $\tilde{\chi}_2^0 \to l\tilde{l} \to l\tilde{\chi}_1^0 l$, and $\tilde{\chi}_1^\pm \to l\tilde{\nu} \to l\tilde{\chi}_1^0\nu$, $\tilde{\chi}_1^\pm \to \nu\tilde{l} \to \nu\tilde{\chi}_1^0 l$. The final signatures are two Opposite-Sign Same-Flavour (SFOS) leptons (e, μ) from the neutralino $\tilde{\chi}_2^0$ decay plus any lepton from the chargino $\tilde{\chi}_1^\pm$. Jets are expected to be only due to gluon state radiation or pile up events. In spite of the escaping $\tilde{\chi}_1^0$, the $E_{\text{T}}^{\text{miss}}$ is relatively small at low $m_{1/2}$ and is comparable with the one of SM backgrounds, especially for three body decays at large m_0. The invariant mass of the SFOS dileptons exhibits a particular shape with a kinematic end point M_{ll}^{max} that depends upon the event topology, see section 13.3.

13.14.1. Datasets

The tri-lepton cross section σ_{3l} was calculated with ISAJET (7.69) and PYTHIA (6.225 CTEQ5L) at LO, the K_{NLO} factor calculated with PROSPINO is in the range of 1.30–1.25 (for $m_{\tilde{\chi}_2^0} = 150-300\,\mathrm{GeV/c^2}$) [684]. The σ_{3l} drops rapidly with the neutralino mass $m_{\tilde{\chi}_2^0} \sim 0.8 m_{1/2}$, $\sigma_{3l} \sim m_{1/2}^{-4}$. This study is restricted to the low $m_{1/2}$ region, where σ_{3l} contributes, for instance, $\sim 0.5\%$ to the total SUSY cross section at $m_0 > 1000\,\mathrm{GeV/c^2}$. The three body decays are dominant in this m_0, $m_{1/2}$ region, except for $m_0 < 150\,\mathrm{GeV/c^2}$ and $\tan\beta \leqslant 20$. The kinematic end point in the invariant mass is approximately $M_{ll}^{max} \sim 0.42^* m_{1/2} - 18.4$ $\mathrm{GeV/c^2}$ (at $m_0 \sim 1000\,\mathrm{GeV/c^2}$), thus moving into the Z-peak region at $m_{1/2} > 250\,\mathrm{GeV/c^2}$ where the SM background is high. Among the CMS benchmark points in this region, LM9 ($m_{1/2} = 175$, $m_0 = 1450$, $\tan\beta = 50$, $A_0 = 0$) has the largest cross section, ~ 3700 events are produced for $30\,\mathrm{fb}^{-1}$, and it was used as a reference.

13.14.2. Backgrounds and trigger path

The main background results from the Drell–Yan, Z + jets, $\mathrm{t\bar{t}} \to WbWb$, ZW, ZZ, Wt+jets, WW+jets, W+jets and inclusive SUSY channels. For all backgrounds, except ZW and ZZ, some leptons originate from jets, mostly $b \to l + j$. The background events were produced with PYTHIA (ALPGEN and TOPREX are also used) and their cross section corrected to NLO. The Z and W bosons are forced to decay leptonically to e, μ, $\tau \to e$, μ. The DY and Z+jets cross section is large ($\sigma_{DY,Zj} \sim 10\,\mathrm{nb}$) and events were preselected by requiring three leptons with $p_\mathrm{T} > 5\,\mathrm{GeV/c}$ and $|\eta| < 2.4$ at the generator level. The full data samples of $30\,\mathrm{fb}^{-1}$ for the LM9 test point and backgrounds are simulated with the CMS fast simulations (FAMOS) validated with smaller statistics samples produced with the full GEANT based simulation (OSCAR, ORCA). Low luminosity pile-up was included.

All events were required to pass Level-1 and HLT triggers. The main trigger paths for LM9 are the dimuons (74%) and dielectrons (25%). The trigger efficiency is 86% at Level-1 and 91% at HLT for LM9 and is increasing for larger $m_{1/2}$ where the leptons become harder. In the off-line selection, at least three isolated leptons in $|\eta| < 2.4$ and $P_\mathrm{T}^{\mu,e} > 10\,\mathrm{GeV/c}$ are required for each event. The leptons are reconstructed using standard reconstruction algorithms. Electrons and muons are required to be isolated, *i.e.* other tracks may only contribute up to $\sum P_\mathrm{T}$ of $1.5\,\mathrm{GeV/c}$ inside a cone of $\Delta R < 0.3$. Moreover, for muons the energy deposit in calorimeters should be $E_\mathrm{T} < 5\,\mathrm{GeV}$ in a cone of $\Delta R < 0.3$. In addition, electron candidates are required to satisfy quality criteria based on a likelihood function, > 0.65. The muons and electrons reconstruction efficiencies in ORCA are found to be 78% ($\mathrm{P}_\mathrm{T}^{\mu} > 5\,\mathrm{GeV/c}$) and 66% ($\mathrm{P}_\mathrm{T}^{e} > 10\,\mathrm{GeV/c}$) respectively. The jets are reconstructed using an iterative cone algorithm with the seed energies $E_\mathrm{T}^{seed} > 0.5\,\mathrm{GeV}$ in a cone $\Delta R < 0.5$.The $E_\mathrm{T}^{\mathrm{miss}}$ was reconstructed from the calorimeter towers. Since the $E_\mathrm{T}^{\mathrm{miss}}$ for the signal events is relatively small and its reconstruction at low energy scale is limited by the $\mathrm{E_T}$ resolution, a $E_\mathrm{T}^{\mathrm{miss}}$ requirement is not as efficient as in other SUSY channels.

13.14.3. Analysis path

The reconstructed events are selected in two steps. First, sequential cuts are applied: 1) No central jets with corrected energy $E_\mathrm{T} > 30\,\mathrm{GeV}$ in $|\eta| < 2.4$, 2) Two SFOS isolated leptons (e, μ) in $|\eta| < 2.4$ with $P_\mathrm{T}^{\mu} > 10\,\mathrm{GeV/c}$, $P_\mathrm{T}^{e} > 17\,\mathrm{GeV/c}$ and the dilepton invariant mass below the Z peak $M_{ll} < 75\,\mathrm{GeV/c^2}$. 3) The third lepton is with $P_\mathrm{T}^{\mu,e} > 10\,\mathrm{GeV/c}$ in $|\eta| < 2.4$. The evolution of statistics and the efficiencies of the selection cuts are presented in Table 13.15.

Table 13.15. Evolution of signal and background statistics with the cuts as expected for 30 fb^{-1}. The last column gives the results of a neural network selection applied after the sequential cuts.

channel	N_{ev} 30 fb^{-1} ($\sigma \times BR$ [pb])	L1+HLT	No Jets	2 SFOS+l SFOS $M_{ll} < 75$ GeV/c^2	NN_{LM9}
LM1	2640 (0.088)	1544 (58%)	864 (56%)	70 (8%)	17 (24%)
LM7	1540 (0.051)	1250 (82%)	738 (59%)	91 (12%)	57 (62%)
LM9	3700 (0.125)	2896 (78%)	1740 (60%)	239 (14%)	158 (68%)
SUSY	$4{\cdot}10^5$ ($13.1^{\,NLO}$)	$2.5{\cdot}10^5$ (63%)	$1.8{\cdot}10^4$ (7%)	34 (0.2%)	22 (65%)
ZW	$5{\cdot}10^4$ ($1.68^{\,NLO}$)	$3.6{\cdot}10^4$ (73%)	$1.9{\cdot}10^4$ (53%)	173 (1%)	44 (25%)
ZZ	$4.8{\cdot}10^3$ ($0.16^{\,NLO}$)	$3.5{\cdot}10^3$ (73%)	$1.7{\cdot}10^3$ (48%)	38 (2.3%)	15 (39%)
$t\bar{t}$	$2.6{\cdot}10^6$ ($88^{\,NLO}$)	$1.8{\cdot}10^6$ (70%)	$1.3{\cdot}10^5$ (7%)	239 (0.2%)	89 (37%)
Z+jets(3l)	$4.6{\cdot}10^5$ ($15.4^{\,LO}$)	$3.7{\cdot}10^5$ (80.5%)	$9.8{\cdot}10^4$ (26.5%)	504 (0.5%)	129 (26%)
DY(3l)	$4.5 \cdot 10^5$ ($15.1^{\,LO}$)	$3.2{\cdot}10^5$ (71%)	$1.4{\cdot}10^5$ (44%)	670 (0.5%)	131 (20%)
$Zb\bar{b}$(3l)	$8.4{\cdot}10^4$ ($2.8^{\,LO}$)	$7.3{\cdot}10^4$ (87%)	$1.5{\cdot}10^4$ (20%)	69 (0.6%)	18 (26%)
Wt+jets	$3{\cdot}10^5$ ($10^{\,NLO}$)	$2.1{\cdot}10^5$ (70%)	$3.9{\cdot}10^4$ (18.5%)	52 (0.1%)	20 (38%)
WW+jets	$6{\cdot}10^5$ ($19.8^{\,LO}$)	$3.8{\cdot}10^5$ (63%)	$1.9{\cdot}10^4$ (50%)	7 (0.04%)	2 (29%)
Tot. bkg	$\sim 4.9 \cdot 10^6$			1786	470 (26%)

In a second step the background suppression is improved with a Neural Network (NN). Five networks for DY, Z+jets, $t\bar{t}$, ZW and ZZ backgrounds are trained on the LM9 signal sample using the following variables: $P_T^{1,2,3}$, $\sum P_T$, M_{ll}, P_T^{2l} (transverse momentum of two SFOS leptons), $A = \frac{P_T^1 - P_T^2}{P_T^1 + P_T^2}$, Θ_{ll} (angle between two SFOS leptons), Φ_{ll} (angle in transverse plane), E_T^{miss}, N_{jets} (number of jets passing the jets veto), E_t^{hj} (of the highest E_T jet), η_{hj} (rapidity of the highest jet). The selection cuts on the NN outputs were optimised for the maximum significance at LM9 with the genetic algorithm GARCON [63]. The efficiency of the NN selection is also shown in Table 13.15.

13.14.4. Results at LM9 and systematics

After the selection based on cuts the S_{cp} significance calculated for all SFOS pair combination is 6.1 at point LM9 for an integrated luminosity of 30 fb^{-1}. The NN improves the S_{cp} for all SFOS combinations to 7.8.

In addition to the real tri-lepton final state, leptons can be produced in the detector volume from $\pi^{\pm}$, $K^{\pm}$ decays, bremsstrahlung, punch-through or faked by jets. The rate per event of such fake leptons was estimated individually for each background by matching the reconstructed lepton with the generated one and is $\sim 10^{-4}$ for electrons and $\sim 10^{-5}$ for muons. The expected fake leptons substantially increase the background, especially for the preselected channels like DY or Z + jets, by $\sim 221 \pm 48$ events and $\sim 31 \pm 16$ events respectively for the tri-muon final state where the fake rate is smaller. The S_{cP} significance defined in Appendix A.1 including fakes but without other systematic uncertainties for all SFOS combinations and for the tri-muon state at LM9 is 6.5 and 5.1 respectively.

The reconstruction uncertainties related to the jet energy scale (5%) and the lepton momentum resolution (2%) contribute 1% to the uncertainties on the background. The average theoretical uncertainty from the PDFs, calculated with the LHPDF subsets using the re-weighting technique for each background channel, amounts to 1.7%. These uncertainties reduce the significances to 5.8 and 4.8 for the all SFOS pairs and for the tri-muon final state, respectively. However the largest uncertainties are coming from the Monte Carlo statistical

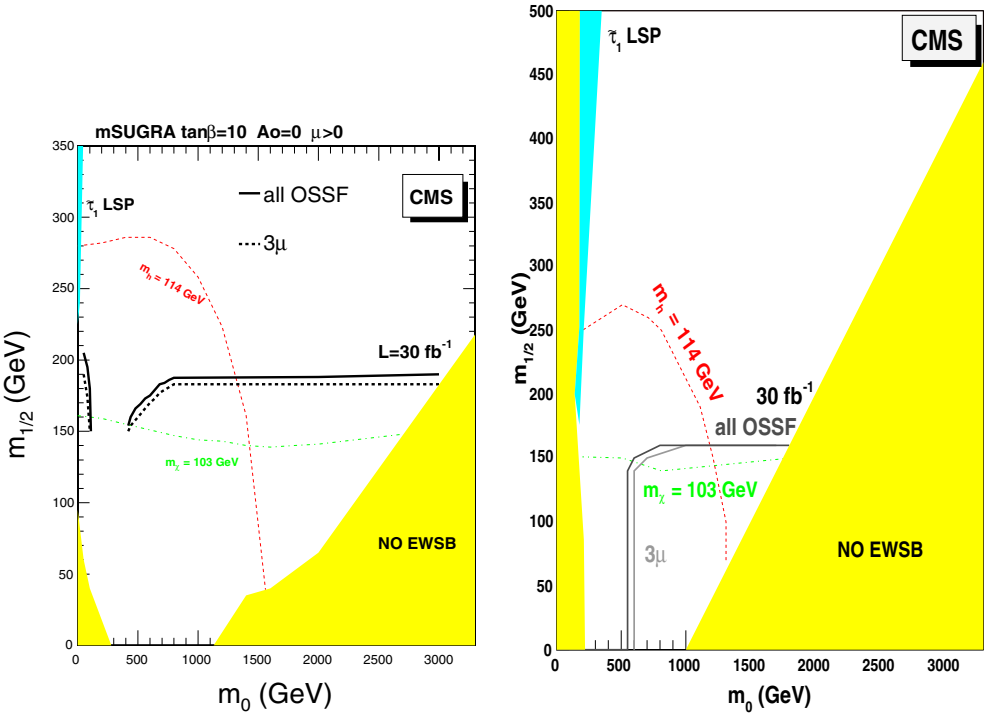

Figure 13.28. Discovery reach of tri-lepton from the $pp \to \tilde{\chi}_2^0 \tilde{\chi}_1^{\pm}$ production at $\mathcal{L}_{int}$=30 fb^{-1} for all SFOS lepton combinations (dashed) and for the tri-muon final state (solid) including systematic uncertainties from reconstruction, for (left) tan $\beta = 10$ and (right) tan $\beta = 50$.

errors in the fake rate estimation which contribute ∼7% to the background uncertainties rendering the signal hardly observable, $S_c p \sim 3.3$. These fake rate uncertainties can be reduced with larger simulation samples.

In summary, for the tri-lepton mSUGRA study presented here, the final signal to background ratio is 0.23, the total signal efficiency is 4.4% and the background composition is 28% Drell–Yan, 27% Z + jets, 19% $t\bar{t}$, 9% WZ, and 17% ZZ, WW, SUSY, W+ jets and QCD. The total considered theoretical and reconstruction systematic uncertainties on the Standard Model background is 2.2%. The Monte Carlo statistics systematic errors in the fake rates increases this to 7.5%.

13.14.5. CMS reach for the tri-lepton final state

Figure 13.28 shows the 5σ discovery reach in m_0 and $m_{1/2}$ plane at $L_{int} = 30\,\text{fb}^{-1}$ for all SFOS combinations and for the tri-muon final state including the systematic uncertainties due to the reconstruction. The signal can be observed at large $m_0 > 1000\,\text{GeV/c}^2$ in a narrow band below $m_{1/2} < 180\,\text{GeV/c}^2$. At low $m_0 < 100\,\text{GeV/c}^2$ the two body decays are visible although a better optimisation is possible in this region, see Sections 13.8 and 13.15. The tri-lepton final state from direct neutralino-chargino production is complementary to the inclusive SFOS dilepton search and provides an additional verification for the leptonic decays of the neutralino at low $m_{1/2}$.

13.15. Production of $\tilde{l}\tilde{l}$

The aim of this section is the study of the possibility of detecting sleptons. Note the previous related papers where the sleptons detection was studied at the level of a toy detector [685–689].

13.15.1. Simulation details

ISASUSY 7.69 [672] was used for the calculation of coupling constants and cross sections in the leading order approximation for SUSY processes. For the calculation of the next-to-leading order corrections to the SUSY cross sections the PROSPINO code [682] was used. Cross sections of the background events were calculated with PYTHIA 6.227 [69] and COMPHEP 4.2pl [355]. For considered backgrounds the NLO corrections are known and they were used. Official datasets (DST) production was used for the study of CMS test point LM1 and backgrounds ($t\bar{t}$, ZZ, WW, Wt, Z $b\bar{b}$, DY2e, DY2τ). For WZ, DY2μ and W + jet backgrounds the events were generated with PYTHIA 6.227. The detector simulation and hits production were made with full CMS simulation [8], digitised and reconstructed [10]. The DY2μ and W + jet backgrounds were simulated with fast simulation [11].

Jets were reconstruction using an iterative cone algorithm with cone size 0.5 and their energy corrected with the GammaJet calibration.

The events are required to pass the Global Level 1 Trigger (L1) and the High Level Trigger (HLT). The events have to pass at least one of the following triggers: single electron, double electron, single muon, double muon.

The CMS fast simulation code was used for the determination of the sleptons discovery plot.

13.15.2. Sleptons production and decays

When sleptons are heavy relative to $\tilde{\chi}_1^{\pm}$, $\tilde{\chi}_2^0$, they are produced significantly at the LHC through the Drell–Yan mechanism (direct sleptons production), via $q\bar{q}$ annihilation with neutral or charged boson exchange in the s-channel, namely, $pp \to \tilde{l}_L\tilde{l}_L, \tilde{l}_R\tilde{l}_R, \tilde{\nu}\tilde{\nu}, \tilde{\nu}\tilde{l}, \tilde{l}_L\tilde{l}_R$. The left sleptons decay to charginos and neutralinos via the following (kinematically accessible) decays:

$$\tilde{l}_L^{\pm} \to l^{\pm} + \tilde{\chi}_{1,2}^0 , \tag{13.21}$$

$$\tilde{l}_L^{\pm} \to \nu_l + \tilde{\chi}_1^{\pm} , \tag{13.22}$$

$$\tilde{\nu} \to \nu_l + \tilde{\chi}_{1,2}^0 , \tag{13.23}$$

$$\tilde{\nu} \to l^{\pm} + \tilde{\chi}_1^{\pm} . \tag{13.24}$$

For right sleptons only decays to neutralino are possible and they decay mainly to LSP:

$$\tilde{l}_R^{\pm} \to l^{\pm} + \tilde{\chi}_1^0 . \tag{13.25}$$

If sleptons are light relative to $\tilde{\chi}_1^{\pm}$, $\tilde{\chi}_2^0$, they can be abundantly produced, besides the Drell–Yan mechanism, also from chargino and neutralino decays $\tilde{\chi}_1^{\pm}$, $\tilde{\chi}_2^0$ (indirect production), equations (13.8), (13.9), (13.13) and (13.14).

13.15.3. Signature and backgrounds

The slepton production and decays described previously lead to the signature with the simplest event topology: *two leptons* $+E_{\mathrm{T}}^{\mathrm{miss}} + jet\ veto$. This signature arises for both direct and indirect slepton pair production. In the case of indirectly produced sleptons not only the event topology with two leptons but with single, three and four leptons is possible. Besides, indirect slepton production from decays of squarks and gluino through charginos, neutralinos can lead to an event topology *two leptons* $+E_{\mathrm{T}}^{\mathrm{miss}} + (n \geqslant 1)\ jets$.

The cut set close to the optimal one is the following:

(a) for leptons:
- p_{T} - cut on leptons ($p_{\mathrm{T}}^{lept} > 20\,\mathrm{GeV/c}$, $|\eta| < 2.4$) and lepton isolation within $\Delta R < 0.3$ cone containing calorimeter cells and tracker;
- effective mass of two opposite-sign and the same-flavour leptons is outside ($M_Z - 15\,\mathrm{GeV}$, $M_Z + 10\,\mathrm{GeV}$) interval;
- $\Phi(l^+l^-) < 140^\circ$ cut on angle between two leptons;

(b) for $E_{\mathrm{T}}^{\mathrm{miss}}$:
- $E_{\mathrm{T}}^{\mathrm{miss}} > 135\,\mathrm{GeV}$ cut on missing E_{T};
- $\Phi(E_{\mathrm{T}}^{\mathrm{miss}}, ll) > 170^\circ$ cut on relative azimuthal angle between dilepton and $E_{\mathrm{T}}^{\mathrm{miss}}$;

(c) for jets:
- jet veto cut: $N_{jet} = 0$ for a $E_{\mathrm{T}}^{jet} > 30\,\mathrm{GeV}$ (corrected jets) threshold in the pseudorapidity interval $|\eta| < 4.5$.

The Standard Model (SM) backgrounds are: $\mathrm{t\bar{t}}$, WW, WZ, ZZ, Wt, $\mathrm{Zb\bar{b}}$, DY, W + jet. The main contributions come from WW and $\mathrm{t\bar{t}}$ backgrounds. There are also internal SUSY backgrounds which arise from $\tilde{q}\tilde{q}$, $\tilde{g}\tilde{g}$ and $\tilde{q}\tilde{g}$ productions and subsequent cascade decays with jets outside the acceptance or below the threshold. Note that when we are interested in new physics discovery we have to compare the calculated number of SM background events N_{SMbg} with new physics signal events $N_{new\ physics} = N_{slept} + N_{SUSYbg}$, so SUSY background events increase the discovery potential of new physics.

13.15.4. Results

For the point LM1 with the used set of cuts for the integral luminosity $\mathcal{L} = 10\,\mathrm{fb}^{-1}$ the number of signal events (direct sleptons plus sleptons from chargino/neutralino decays) is $N_S = 60$, whereas the number of SUSY background events is $N_{SUSYbg} = 4$ and the number of SM background events is $N_{SMbg} = 41$. The total signal efficiency is 1.16×10^{-4} and the background composition is 1.32×10^{-6} of the total ttbar, 1.37×10^{-5} of the total WW, 4×10^{-6} of the total WZ, 4.4×10^{-5} of the total ZZ, 8.1×10^{-6} of the total Wt, 0 of the total Zbb, DY, W + jet.

The SUSY background is rather small compared to the signal, so we can assume $N_S = N_{direct\ sleptons} + N_{chargino/neutralino} + N_{SUSYbg} = 64$. It corresponds to the significances $S_{c12} = 7.7$ and $S_{cL} = 8.3$, defined in Appendix A.1.

Taking into account the systematic uncertainty of 23% related with in exact knowledge of backgrounds leads to the decrease of significance S_{c12} from 7.7 to 4.3.

The ratio of the numbers of background events from two different channels $N(e^+e^- + \mu^+\mu^-)/N(e^\pm\mu^\mp)$=1.37 will be used to keep the backgrounds under control.

The CMS discovery plot for $two\ leptons + E_{\mathrm{T}}^{\mathrm{miss}} + jet\ veto$ signature is presented in Fig. 13.29.

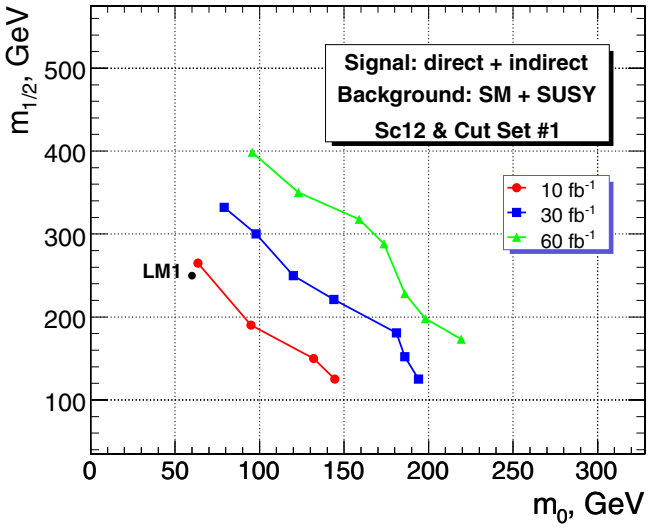

Figure 13.29. Discovery plot ($\tan\beta = 10$, sign(μ) = +, $A = 0$) for final states with l^+l^-, missing transverse energy and a jet veto.

13.16. Lepton flavour violation in neutralino decay

The aim of this section is the study of the possibility to detect SUSY and Lepton Flavour Violation (LFV) using the $e^{\pm}\mu^{\mp} + E_{\mathrm{T}}^{\mathrm{miss}}$ signature.

13.16.1. Signal selection and backgrounds

The simulation details of this study could be found in the Section 13.15.

The SUSY production $pp \to \tilde{q}\tilde{q}^{'}, \tilde{g}\tilde{g}, \tilde{q}\tilde{g}$ with subsequent decays leads to the event topology $e^{\pm}\mu^{\mp} + E_{\mathrm{T}}^{\mathrm{miss}}$. In the MSSM with lepton flavour conserving neutralino decays into leptons $\tilde{\chi}^0_{2,3,4} \to l^+l^-\tilde{\chi}^0_1$ do not contribute to this signature and contribute only to $l^+l^- + E_{\mathrm{T}}^{\mathrm{miss}}$ signature (here $l = e$ or μ). The main backgrounds which contribute to the $e^{\pm}\mu^{\mp}$ events are: $t\bar{t}$, ZZ, WW, WZ, Wt, $Zb\bar{b}$, DY2τ, Z+jet. It has been found that $t\bar{t}$ background is the biggest one and it gives more than 50% contribution to the total background.

Our set of cuts is the following:

- p_{T} - cut on leptons ($p_{\mathrm{T}}^{lept} > 20\,\mathrm{GeV/c}$, $|\eta| < 2.4$) and lepton isolation within $\Delta R < 0.3$ cone.
- $E_{\mathrm{T}}^{\mathrm{miss}} > 300\,\mathrm{GeV}$ cut on missing E_{T}.

13.16.2. Results at CMS test points and reach

For integrated luminosity $\mathcal{L} = 10\,\mathrm{fb}^{-1}$ the number of background events is $N_B = 93$. The results for this luminosity are presented in Table 13.16. At point LM1 the signal over background ratio is 3 and the signal efficiency is 6×10^{-4}. The background composition is 9.5×10^{-6} of the total ttbar, 3.4×10^{-6} of the total WW, 4×10^{-6} of the total WZ, 3.2×10^{-6} of the total Wt, 2.2×10^{-6} of the total Z + jet, 0 of the total ZZ, $Zb\bar{b}$, DY2τ.

The CMS discovery plot for the $e^{\pm}\mu^{\mp} + E_{\mathrm{T}}^{\mathrm{miss}}$ signature is presented in Fig. 13.30.

In the MSSM the off-diagonal components of the slepton mass terms violate lepton flavour conservation. As it was shown in Refs. [690–692] it is possible to look for lepton

Table 13.16. Number of signal events and significances S_{c12} [50] and S_{cL} [100, 102], defined in Appendix A.1, for $\mathcal{L} = 10\,\text{fb}^{-1}$.

Point	N events	S_{c12}	S_{cL}
LM1	329	21.8	24.9
LM2	94	8.1	8.6
LM3	402	25.2	29.2
LM4	301	20.4	23.1
LM5	91	7.8	8.3
LM6	222	16.2	18.0
LM7	14	1.4	1.4
LM8	234	16.9	18.8
LM9	137	11.0	11.9

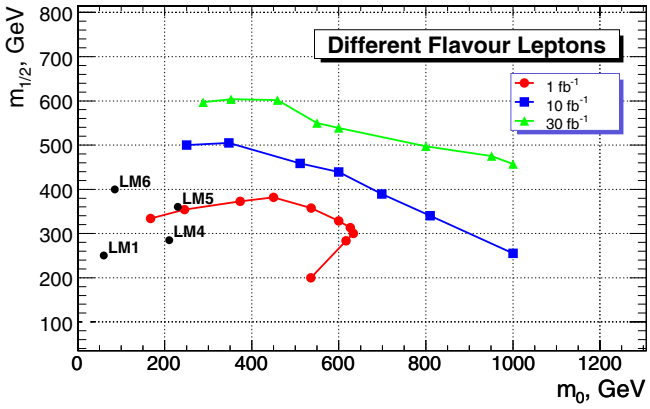

Figure 13.30. Discovery plot ($\tan\beta = 10$, $\text{sign}(\mu) = +$, $A = 0$) for the luminosities $\mathcal{L} = 1$, 10, $30\,\text{fb}^{-1}$ for the $e^{\pm}\mu^{\mp} + E_{\text{T}}^{\text{miss}}$ signature.

flavour violation at supercolliders through the production and decays of the sleptons. For the LFV at the LHC one of the most promising processes is the LFV decay of the second neutralino [693, 694] $\tilde{\chi}_2^0 \to \tilde{l}l \to \tilde{\chi}_1^0\, ll'$, where the non zero off-diagonal component of the slepton mass matrix leads to the different flavours for the leptons in the final state. By using the above mode, LFV in $\tilde{e} - \tilde{\mu}$ mixing has been investigated in Refs. [693, 694] at a parton model level for a toy detector. In this section we study the perspectives of the LFV detection in CMS on the base of full simulation of both signal and background is studied. To be specific, we study the point LM1. We assume that the LFV is due to nonzero mixing of right-handed smuon and selectron. The signal of the LFV $\tilde{\chi}_2^0$ decay is two opposite-sign leptons ($e^+\mu^-$ or $e^-\mu^+$) in the final state with the characteristic edge structure. In the limit of lepton flavour conservation, the process $\tilde{\chi}_2^0 \to \tilde{l}l \to ll\tilde{\chi}_1^0$ has the edge structure for the distribution of the lepton-pair invariant mass m_{ll} and the edge mass m_{ll}^{max} is expressed by the slepton mass $m_{\tilde{l}}$ and the neutralino masses $m_{\tilde{\chi}_{1,2}^0}$ as follows:

$$(m_{ll}^{max})^2 = m_{\tilde{\chi}_2^0}^2 \left(1 - \frac{m_{\tilde{l}}^2}{m_{\tilde{\chi}_2^0}^2}\right)\left(1 - \frac{m_{\tilde{\chi}_1^0}^2}{m_{\tilde{l}}^2}\right). \tag{13.26}$$

The SUSY background for the LFV comes from uncorrelated leptons from different squark or gluino decay chains. The SM background comes mainly from

$$t\bar{t} \to bWbW \to blbl'\nu\nu'. \tag{13.27}$$

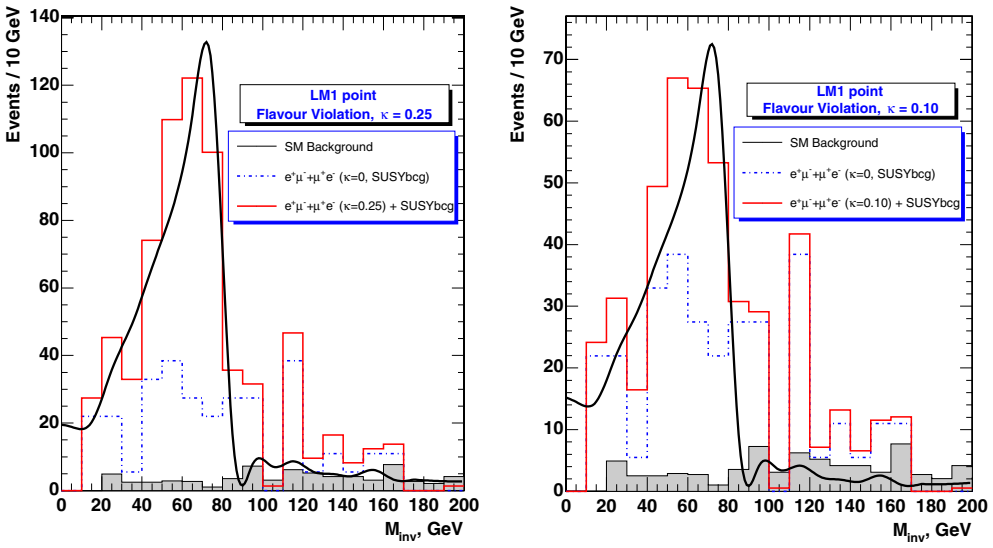

Figure 13.31. The distribution of dilepton invariant mass after selection of two isolated $e^{\pm}\mu^{\mp}$ leptons with $p_{\mathrm{T}}^{lept} > 20\,\mathrm{GeV/c}$ and $E_{\mathrm{T}}^{\mathrm{miss}} > 300\,\mathrm{GeV}$ for flavour violation parameter $k = 0.25$ (left) and $k = 0.1$ (right). The superimposed curves are fits to the invariant mass distribution for the case of 100% LFV.

The Drell–Yan background from $pp \to \tau\tau \to e\mu \ldots$ is negligible. It should be stressed that for the signature with $e^{\pm}\mu^{\mp}$ in the absence of the LFV we do not have the edge structure for the distribution on the invariant mass $m_{inv}(e^{\pm}\mu^{\mp})$. As the result of the LFV the edge structure for $e^{\pm}\mu^{\mp}$ events arises too. Therefore the signature of the LFV is the existence of an edge structure in the $e^{\pm}\mu^{\mp}$ distribution. The rate for a flavour violating decay is

$$Br(\tilde{\chi}_2^0 \to e^{\pm}\mu^{\mp}\tilde{\chi}_1^0) = \kappa\, Br(\tilde{\chi}_2^0 \to e^+e^-\tilde{\chi}_1^0, \mu^+\mu^-\tilde{\chi}_1^0), \tag{13.28}$$

where

$$Br(\tilde{\chi}_2^0 \to e^+e^-\tilde{\chi}_1^0, \mu^+\mu^-\tilde{\chi}_1^0) = Br(\tilde{\chi}_2^0 \to e^+e^-\tilde{\chi}_1^0) + Br(\tilde{\chi}_2^0 \to \mu^+\mu^-\tilde{\chi}_1^0), \tag{13.29}$$

$$\kappa = 2x \sin^2\theta \cos^2\theta, \tag{13.30}$$

$$x = \frac{\Delta m^2_{\tilde{e}\tilde{\mu}}}{\Delta m^2_{\tilde{e}\tilde{\mu}} + \Gamma^2}, \tag{13.31}$$

$$Br(\tilde{\chi}_2^0 \to e^{\pm}\mu^{\mp}) = Br(\tilde{\chi}_2^0 \to e^+\mu^-) + Br(\tilde{\chi}_2^0 \to e^-\mu^+). \tag{13.32}$$

Here θ is the mixing angle between $\tilde{e}_R$ and $\tilde{\mu}_R$ and Γ is the sleptons decay width. The parameter x is the measure of the quantum interference effect. There are some limits on $\tilde{e} - \tilde{\mu}$ mass splitting from lepton flavour violating processes but they are not very strong.

For $\kappa = 0.25$, $\kappa = 0.1$ the distributions of the number of $e^{\pm}\mu^{\mp}$ events on the invariant mass $m_{inv}(e^{\pm}\mu^{\mp})$ (see Figure 13.31) clearly demonstrates the existence of the edge structure [695], i.e. the existence of the lepton flavour violation in neutralino decays. It appears that for the point LM1 the use of an additional cut

$$m_{inv}(e^{\pm}\mu^{\mp}) < 85\,\mathrm{GeV} \tag{13.33}$$

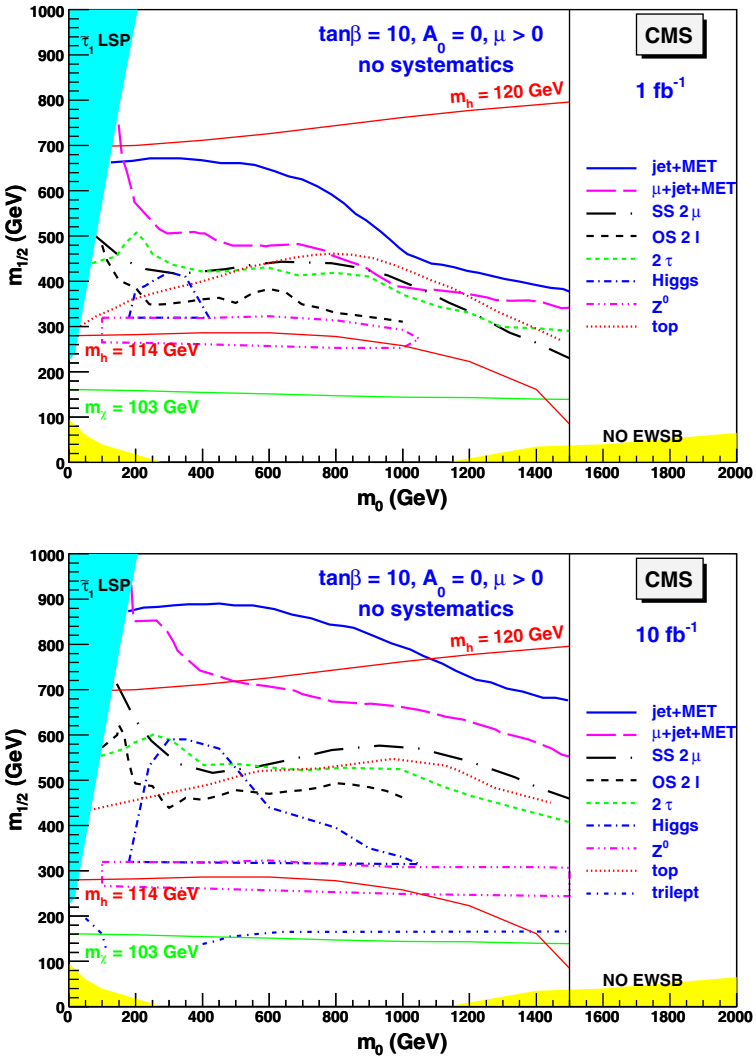

Figure 13.32. Regions of the m_0 versus $m_{1/2}$ plane showing CMS the reach when only statistical uncertainties are taken into account. (Top) for 1 fb^{-1} integrated luminosity, except the Higgs case which assumes 2 fb^{-1}. (Bottom) for 10 fb^{-1}.

reduces both the SM and SUSY backgrounds and increases the discovery potential in the LFV search. For the point LM1 we found that in the assumption of exact knowledge of the background (both the SM and SUSY backgrounds) for the integrated luminosity $\mathcal{L} = 10\,\text{fb}^{-1}$ it would be possible to detect LFV at 5σ level in $\tilde{\chi}_2^0$ decays for $\kappa \geqslant 0.04$.

13.17. Summary of the reach with inclusive analyses

13.17.1. Summary of the mSUGRA studies

In previous sections, several characteristic topologies (or signatures) for MSSM were studied and it was shown that many are already detectable with rather low integrated luminosity

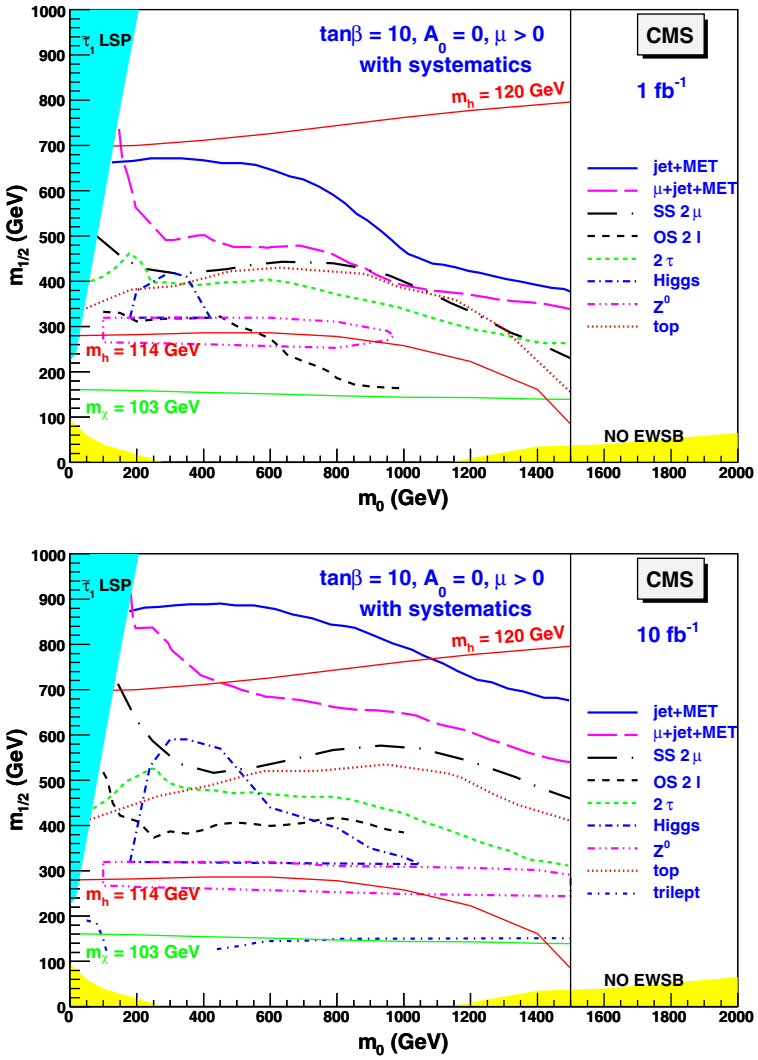

Figure 13.33. Regions of the m_0 versus $m_{1/2}$ plane showing CMS the reach when systematic uncertainties are included. (Top) for 1 fb^{-1} integrated luminosity, except the Higgs case which assumes 2 fb^{-1}. (Bottom) for 10 fb^{-1}.

(few years of LHC running) over a sizeable part of the parameter space, extending well beyond the Tevatron reach.

The curves in Fig. 13.32 summarise the reach estimated for the various topologies of the preceding sections for integrated luminosities of 1 and 10 fb^{-1} when only statistical uncertainties are taken into account. The same results are shown in Fig. 13.33 when systematic uncertainties are included. It is seen that the systematic uncertainties do not degrade the reach very much for integrated luminosities up to 10 fb^{-1}. It should be noted that the analyses have not been reoptimised for the inclusion of systematics nor for higher masses which could be reached with higher luminosity. Moreover, the reach will be further improved by the addition of topologies with electrons, which are presently missing for the muon + jet + MET and same sign dimuon searches.

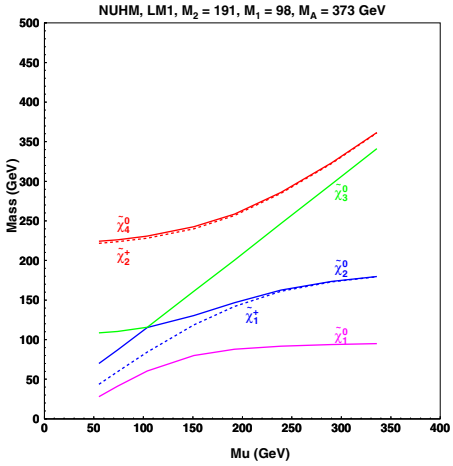

Figure 13.34. Variation of the chargino and neutralino masses as a function of μ for the CMS test point LM1.

The best reach is obtained with the most inclusive channels, the jets + MET and muons + jet + MET. The range of gluino and squark masses up to about 1.5 TeV can be probed with an integrated luminosity of only 1 fb^{-1} and is extended to about 2 TeV with 10 fb^{-1}. Moreover, a large part of the area is covered by several search topologies. The simultaneous observation of a signal in various topologies will help unravel the underlying physics. Examples are the triangular dilepton mass distribution, the observation of the Z^0 or the h^0 in less inclusive channels, which provide a hint that their origin may be the decay of a $\tilde{\chi}_2^0$. If discovered, yet more exclusive analyses should then allow a more quantitative study, e.g. the reconstruction of the sparticle masses and cross section measurements of relevant sub-processes and their ratios.

13.18. Look beyond mSUGRA

13.18.1. Non-universal Higgs masses

It was emphasised in Section 13.3 that the signatures of SUSY with a stable LSP result from the fundamental Supersymmetry gauge couplings, together with the composition of the lightest charginos and neutralinos. As all previous analyses were based on mSUGRA, it is interesting to verify their robustness when relaxing some of the assumptions which might affect the signal observability. As full generality, including giving up all universality assumptions, would lead to an intractable model, a choice needs to be made. Here, a mild extension is considered whereby the two Higgsino mass parameters at the GUT scale are no longer supposed to be degenerate with the other scalar masses, which is sometimes called the Non Universal Higgs Masses (NUHM [696]) scenario. This scenario is conveniently parameterised in terms of two low scale parameters, the mass of the CP-odd Higgs (m_A) and the parameter μ. More specifically, we will analyse the effect of lowering the value of μ compared to its mSUGRA value on the observability of the signatures, as this modifies the composition of the charginos and neutralinos as a function of the gaugino and Higgsino fields. For simplicity, m_A is kept at a fixed value. As exemplified in Fig. 13.34 for the test point LM1, lowering μ also lowers the gaugino masses and in particular their splittings, which affect the

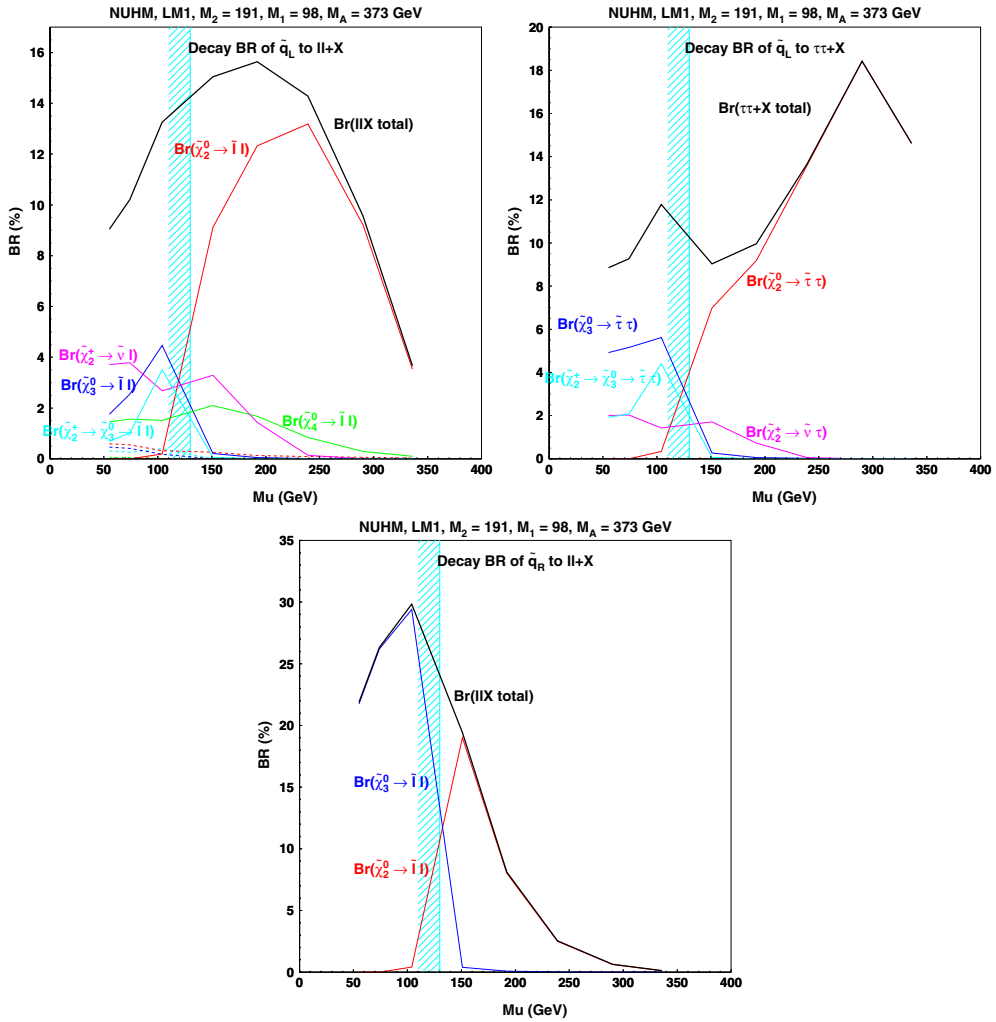

Figure 13.35. Decay branching ratios as a function of μ for $\tilde{q}_L$ into ll and $\tau\tau$ and for $\tilde{q}_R$ into ll at the test point LM1.

branching ratios through phase space effects (a similar behaviour is observed for the other test points). The $\tilde{q}$ and $\tilde{l}$ spectra are almost unaffected. As for low values of μ the lightest chargino becomes lighter than the exclusion from LEP, $m_(\tilde{\chi}_1^{\pm}) \geqslant 103\,\text{GeV}$, this region is excluded and is indicated on Fig. 13.35 by a grey (blue) shaded strip.

13.18.1.1. Signatures at point LM1. The test point LM1 was studied above for its detectability in cascade decays via a $\tilde{\chi}_2^0$ into $\tilde{l}_R l$. Figure 13.35 shows the variation of some branching ratios from the value of μ near the region where radiative electroweak symmetry breaking is not possible up to its value in mSUGRA.

It is seen that by lowering μ, $B(\tilde{q}_L \to q\tilde{\chi}_2^0 \to q\tilde{l}_R l)$ first increases (due to closing the competing decay to $\tilde{\nu}\nu$), then decreases when the $\tilde{\chi}_2^0$ becomes Higgsino-like, but it remains considerably larger than its mSUGRA value for all values of μ down to the LEP limit. In

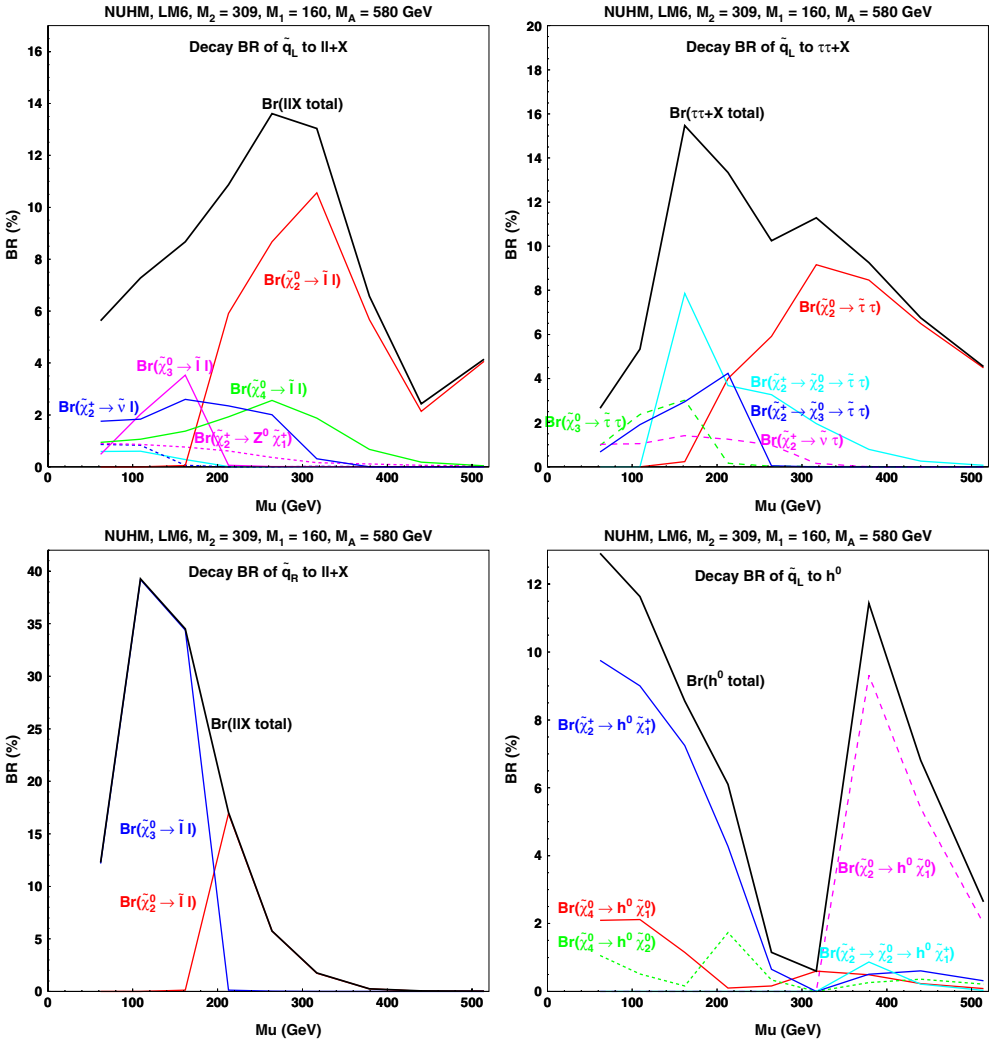

Figure 13.36. Decay branching ratios as a function of μ for $\tilde{q}_L$ into ll, $\tau\tau$ and h^0 and for $\tilde{q}_R$ into ll at the test point LM6.

addition, some new channels open up, like the decay via $\tilde{\chi}_4^0$ into left and right sleptons and the decay via a $\tilde{\chi}_2^\pm \to \tilde{\nu}_l \bar{l}$ followed by $\tilde{\nu}_l \to \tilde{\chi}_1^\pm l$ (the $\tilde{\chi}_4^0$ and $\tilde{\chi}_2^\pm$ become more Wino-like). Other decays via $\tilde{\chi}_3^0$ might also contribute, but only in the region excluded by LEP.

The branching for the decay to $\tilde{\tau}\tau$ shows qualitatively the same behaviour, but is larger than its mSUGRA value in only a small region of μ. Also here a small contribution from the decay $\tilde{\chi}_2^\pm \to \tilde{\nu}\tau$ is present at small μ.

It is interesting to note that, although for mSUGRA the $\tilde{q}_R$ decays exclusively directly to the LSP, it may have for lower μ a non negligible branching ratio to $\tilde{\chi}_2^0$ and also contributes to the dilepton signature.

Finally, there is a non-zero branching ratio for the $\tilde{q}_L$ to the light Higgs via the $\tilde{\chi}_2^\pm$ or $\tilde{\chi}_4^0$ (not shown), but it remains below 1% over the whole range of μ above the LEP limit and will be difficult to detect.

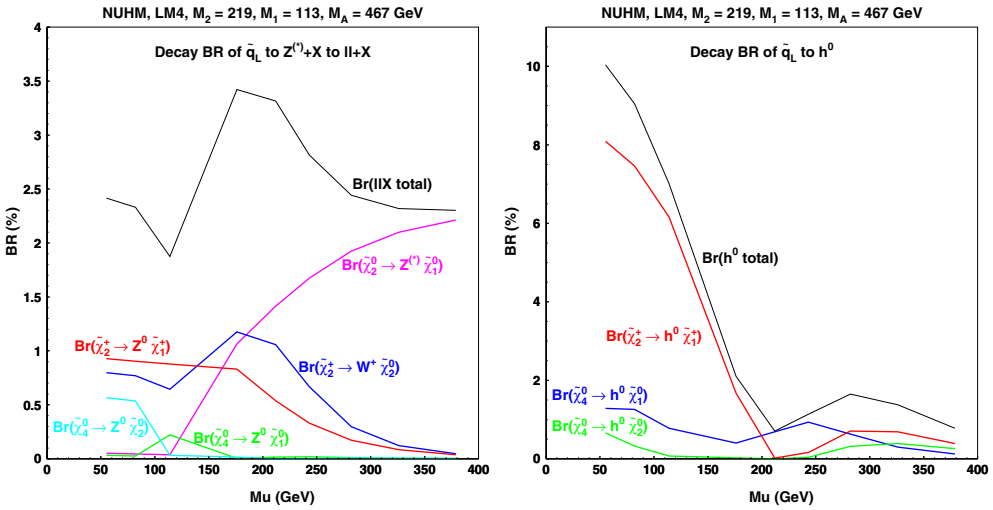

Figure 13.37. Decay branching ratios as a function of μ for $\tilde{q}_L$ into ll and h^0 at the test point LM4.

13.18.1.2. Signatures at point LM6. The test point LM6 has many features in common with LM1, but the $\tilde{\chi}_2^0$ decays mainly to $\tilde{l}_L l$ with a small admixture of $\tilde{l}_R l$. Moreover the decay $\tilde{\chi}_2^0 \to h^0 \tilde{\chi}_1^0$ is kinematically allowed, although suppressed due to the strong gaugino dominance in the $\tilde{\chi}_1^0$ and $\tilde{\chi}_2^0$. The variation of the branching ratios as a function of μ is displayed in Fig. 13.36.

The cascade decays of $\tilde{q}_L$ to $\tilde{l}l$ and $\tilde{\tau}\tau$ via $\tilde{\chi}_2^0$ show grossly the same behaviour as for LM1, with an increase at intermediate values of μ followed by a decrease at low μ. Again, the contributions from other charginos and neutralinos are non negligible near the LEP exclusion limit. Also $\tilde{q}_R$ decays contribute to the dilepton signal via $\tilde{\chi}_2^0$ and $\tilde{\chi}_3^0$ intermediate states.

A distinctive feature of LM6 is its production of final states with h^0. The $\tilde{q}_L$ branching ratio via $\tilde{\chi}_2^0 \to h^0 \tilde{\chi}_1^0$, which is only 2% for mSUGRA increases drastically for lower μ due to the increased Higgsino components in $\tilde{\chi}_1^0$ and $\tilde{\chi}_2^0$, then it drops as the decay becomes kinematically forbidden. After a gap where the branching ratio is below 1%, a strong increase is again visible for lower μ from the cascade dominated by $\tilde{\chi}_1^\pm \to h_0 \tilde{\chi}_1^\pm$ down to the LEP limit. Such an effect is not observed at LM1 due to the smaller spacing of the masses.

13.18.1.3. Signatures at point LM4. Point LM4 was chosen for its characteristic decay of $\tilde{\chi}_2^0$ into $Z^0 \tilde{\chi}_1^0$. Figure 13.37 shows the variation of the branching ratios as a function of μ.

As the decay $\tilde{\chi}_2^0 \to Z^0 \tilde{\chi}_1^0$ requires Higgsino components in both the $\tilde{\chi}_1^0$ and $\tilde{\chi}_2^0$, its branching ratio remains above 90% for all values of μ allowed by the LEP limit. The branching ratio of the $\tilde{q}_L$ into $Z^{(+)}$ via a $\tilde{\chi}_2^0$ decreases mainly due to the decrease of $B(\tilde{q}_L \to q \tilde{\chi}_2^0)$ (the $\tilde{\chi}_2^0$ becomes less gaugino-like). This loss is, however, compensated by the contributions from cascades via $\tilde{\chi}_2^\pm \to W \tilde{\chi}_2^0$ and $\tilde{\chi}_2^\pm \to Z^0 \tilde{\chi}_1^\pm$ and the overall effect is a net increase of the branching ratio of the $\tilde{q}_L$ to final states with a Z^0.

For low values of μ there is also a contribution to h^0 final states via the decay $\tilde{\chi}_2^\pm \to h^0 \tilde{\chi}_1^\pm$, but it remains small above the limit imposed by LEP.

13.18.1.4. Signatures at point LM5. At point LM5, the main signature for mSUGRA is provided by the cascade via $\tilde{\chi}_2^0 \to h^0 \tilde{\chi}_1^0$. The variation of the branching ratios with μ are shown in Fig. 13.38.

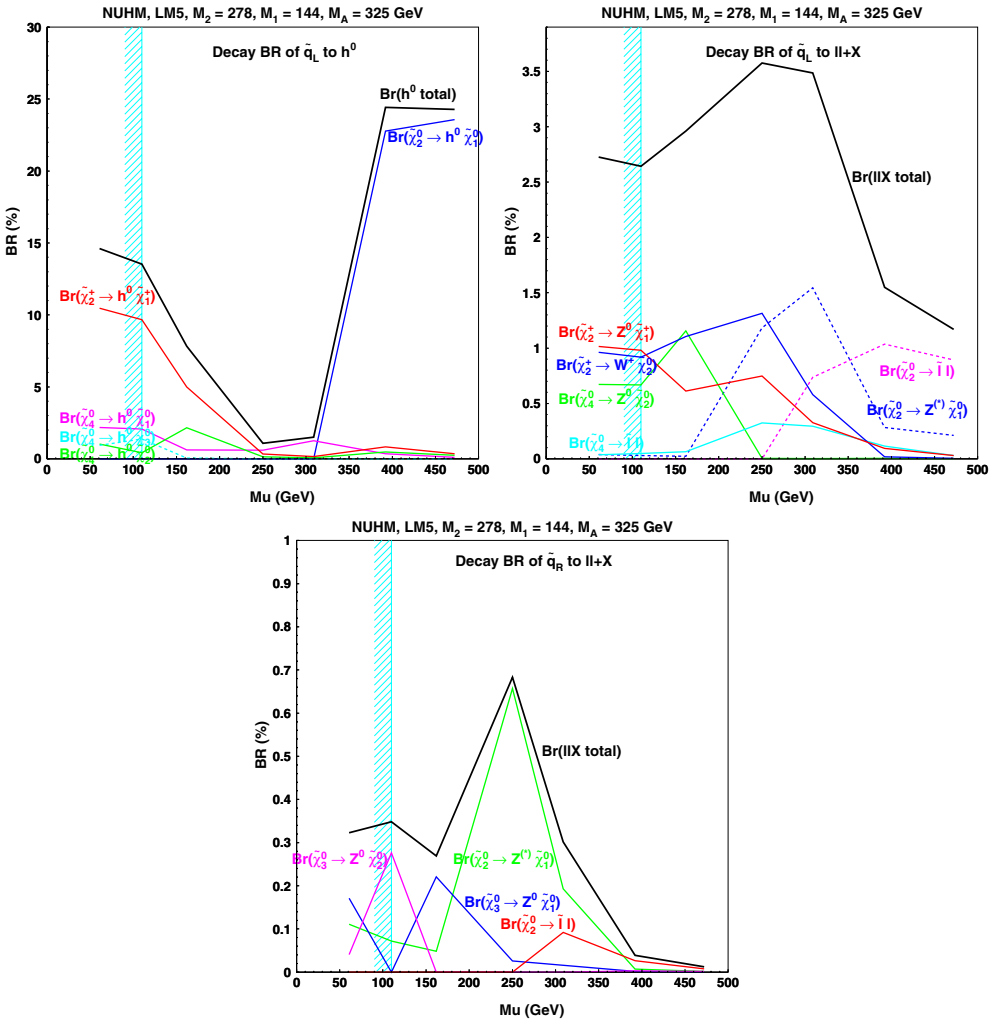

Figure 13.38. Decay branching ratios as a function of μ for $\tilde{q}_L$ into h^0 and ll and for $\tilde{q}_R$ into ll at the test point LM5.

The sharp drop in the branching ratio of $\tilde{\chi}_2^0$ to h^0 below the mSUGRA value of μ results from the decrease in the mass splitting between $\tilde{\chi}_2^0$ and $\tilde{\chi}_1^0$ which suppresses the decay to h^0. For lower values of μ, final states with h^0 are again produced mainly via the $\tilde{\chi}_2^{\pm} \to h^0 \tilde{\chi}_1^{\pm}$. In between these two decay chains, a narrow gap is left where the Higgs branching ratio is less than 2% and hence very difficult to detect.

It is seen that this loss of sensitivity to Higgs final states is to some extent compensated by an increase of the dilepton final states in the region of the gap. The cascade decays of both $\tilde{q}_L$ and $\tilde{q}_R$ contribute in this region, the main contributions being through $\tilde{\chi}_2^0 \to Z^* \tilde{\chi}_1^0$, $\tilde{\chi}_2^{\pm} \to Z^0 \tilde{\chi}_1^{\pm}$ and $\tilde{\chi}_2^{\pm} \to W \tilde{\chi}_2^0$. It gives a branching ratio of up to 3.5% for the dilepton decay of $\tilde{q}_L$ and less than 1% for $\tilde{q}_R$ and hence should be detectable. However, the mixture of intermediate states leading to the dileptons will make the sparticle mass reconstruction very challenging.

13.18.1.5. Conclusion. It can be concluded that the same flavour dilepton signatures originating from the decay of $\tilde{l}l$ or Z^* are quite robust with respect to the chargino and neutralino composition. Lowering μ with respect to its mSUGRA value, a sizeable increase of the branching ratio is even observed for the test points LM1, LM4 and LM6. The h^0 signature at point LM5 is less robust and a region with low branching ratio exists at intermediate values of μ. It is compensated by an increase of dilepton final states. It may be noted that the loss of $\tilde{\chi}_2^0$ decay to h^0 is due to the reduction of the $\tilde{\chi}_2^0$ and $\tilde{\chi}_1^0$ mass splitting. It is therefore a consequence of the low mass spectrum chosen and should disappear at larger values of $m_{1/2}$. Another feature of the NUHM scenario is that for small μ the cascades from $\tilde{q}_R$ also contribute to the signatures, unlike the mSUGRA case. Moreover the signatures at low to intermediate μ tend to be produced by several intermediate neutralino and chargino states. This points to the difficulty of identifying which sparticles are at the origin of the observed end points in the effective mass distributions.

Chapter 14. Extra Dimensions and New Vector Boson High Mass States

14.1. Introduction

The theoretical and phenomenological landscape of beyond the standard model searches extends to a multitude of exotic tendencies today in collider physics. Most are conceived within one kind or another of extra dimensions and supersymmetric scenarios. The strict or loose dualities between different frameworks for physics "beyond the Standard Model" have a direct experimental consequence: the final states and signatures of the models are very similar. This renders the characterisation of an excess or a deviation a fine and probably long challenge. To mention a couple of examples: the question "is it extra dimensions (e.g. UED/ TeV) or is it SUSY?" or "is it a Randall–Sundrum graviton mode or a Z′" is not going to be answered immediately when the excess is observed. The results from all the collider data to date, together with the as yet unobserved Higgs and including the data on the neutrino masses and the composition of the universe, impose a wide program of searches that the LHC experiments are preparing for.

In the present chapter and as well as the "alternatives" chapter that follows, a series of searches is presented with signatures (corresponding to models) as indicated below:

- Dilepton, dijet, diphoton resonances
  - ∗ using ee, $\mu\mu$, $\gamma\gamma$, dijets
  - ∗ searching for Z' (leptons, jets), RS Extra Dimensions (leptons, photons, jets), Z_{KK} in TeV^{-1} (electrons) (can also be interpreted in the context of Little Higgs models)
- Dilepton, dijet continuum modification
  - ∗ using $\mu\mu$, dijets
  - ∗ searching for ADD graviton exchange (dimuons), contact interactions (dimuons, dijets)
- Dilepton + dijets
  - ∗ using ee, $\mu\mu$ + dijets
  - ∗ searching for heavy neutrino from right-handed W (can also be interpreted in the context of leptoquark searches)
- Single photon + missing E_{T}
  - ∗ using γ + missing $\mathrm{E_T}$
  - ∗ searching for ADD direct graviton emission (can also be interpreted in the context of GMSB gravitino-type searches)
- Single lepton + missing E_{T}
  - ∗ using μ + missing $\mathrm{E_T}$
  - ∗ searching for W' (can also be interpreted in the context of little Higgs or W_{KK} excitation in TeV^{-1} models)
- Multilepton + multijet
  - ∗ using top, W and Z reconstruction and constraints
  - ∗ searching for technicolour, littlest Higgs (can also be interpreted in the context of leptoquark searches)
- Same-sign dileptons
  - ∗ using ee, $\mu\mu$, $e\mu$
  - ∗ searching for same-sign top (can be interpreted in the context of technicolour, charged Higgs or SUSY searches)

- High multiplicity/sphericity
  - searching for microscopic black holes in large extra dimensions scenarios

Although not included here, a number of searches are being developed for signatures that involve heavy highly-ionising charged particles and split-SUSY type R-hadrons as well as low P_{T} multi-lepton signatures in UED scenarios. Strategies are being developed to extract the Standard Model backgrounds from data and control its systematic uncertainties. Fake rates are being estimated as possible while machine and cosmic ray induced backgrounds are not included although methods to suppress them are being developed.

14.1.1. Models with heavy vector bosons

Additional heavy neutral gauge bosons (Z') are predicted in many superstring-inspired [87, 88] and grand unified theories (GUTs) [89], as well as in dynamical symmetry breaking [90] and "little Higgs" [91] models. There are no reliable theoretical predictions, however, of the Z' mass scale. Current lower limits on the Z' mass are (depending on the model) of the order of 600–900 $\mathrm{GeV}/\mathrm{c}^2$ [54]. The mass region up to about 1 $\mathrm{TeV}/\mathrm{c}^2$ is expected to be explored at Run II at the Tevatron [92, 93]. The LHC offers the opportunity to search for Z' bosons in a mass range significantly larger than 1 $\mathrm{TeV}/\mathrm{c}^2$. In the Z' studies presented here (Sections 14.3 and 14.2) six models which are frequently discussed and whose properties are representative of a broad class of extra gauge bosons are used:

- $\mathrm{Z}_{\mathrm{SSM}}$ within the Sequential Standard Model (SSM), which has the same couplings as the Standard Model Z^0.
- Z_ψ, $\mathrm{Z}\eta$ and Z_χ, arising in E_6 and SO(10) GUT groups with couplings to quarks and leptons as derived in Refs. [96, 97].
- $\mathrm{Z}_{\mathrm{LRM}}$ and $\mathrm{Z}_{\mathrm{ALRM}}$, arising in the framework of the so-called "left–right" [98] and "alternative left–right" [92, 93] models with couplings as derived in Ref. [92, 93], with the choice of $g_R = g_L$.

The W' search presented in Section 14.4 uses a reference model by Altarelli [697], in which the W' is a heavy copy of the W, with the very same left-handed fermionic couplings (including CKM matrix elements), while there is no interaction with the Standard Model gauge bosons or with other heavy gauge bosons such as a Z'.

14.1.2. Arkani-Hamed–Dimopoulos–Dvali (ADD) models

ADD refers to the class of models which incorporate the large extra dimensions scenario of Arkani-Hamed, Dvali, and Dimopoulos [698]. These were the first extra dimensions models in which the compactified dimensions can be of macroscopic size, consistent with all current measurements, and they are referred to as "large extra dimensions" models. In the most basic version, n extra spatial dimensions are compactified on a torus with common circumference R, and a brane is introduced which extends only in the three infinite spatial directions. Strictly speaking, the brane should have a very small tension (energy per unit volume) in order that it does not significantly warp the extra dimensional space. It is assumed that all standard model fields extend only in the brane. This can be considered as a toy version of what happens in string theory, where chiral gauge theories similar to the standard model are confined to reasonably simple brane configurations in reasonably simple string compactifications [699].

A consequence of these assumptions is that the effective 4d Planck scale is related to the underlying fundamental Planck scale of the $4+n$-dimensional theory and to the volume of

the compactified space. This relation follows from Gauss' law, or by dimensional analysis

$$M_{\text{Planck}}^2 = M_*^{2+n}\, R^n, \tag{14.1}$$

where M_{Planck}^2 is defined by Newton's constant: $M_{\text{Planck}} = 1/\sqrt{G_N} = 1.2 \times 10^{19}\,\text{GeV/c}^2$. M_*^{2+n} is defined as the gravitational coupling which appears in the $4+n$-dimensional version of the Einstein–Hilbert action. It is the quantum gravity scale of the higher dimensional theory.

If M_{Planck}, M^* and $1/R$ are all of the same order, as is usually assumed in string theory, this relation is not very interesting. But it is plausible and experimentally allowed that M^* is equal to some completely different scale. Taking $M^* \sim 1\,\text{TeV/c}^2$ [700] the hierarchy problem of the standard model is translated from an ultraviolet problem to an infrared one. Note that if there is any interface with string theory, ADD-like models must arise from string ground states in which the string scale (and thus the ultraviolet cutoff for gravity) is also in the TeV range. This is difficult to achieve but has been studied in [701].

The ADD scenario renders observations of quantum gravity at the LHC possible. In such models only the graviton, and possibly some non-SM exotics like the right-handed neutrino, probe the full bulk space. There is a Kaluza–Klein (KK) tower of graviton modes, where the massless mode is the standard 4d graviton, and the other KK modes are massive spin 2 particles which also couple to SM matter with gravitational strength.

Whereas bremsstrahlung of ordinary gravitons is a completely negligible effect at colliders, the total cross section to produce *some* massive KK graviton is volume enhanced, and effectively suppressed only by powers of M^* and not M_{Planck}. From Eq. (14.1) it follows:

$$\sigma \sim \frac{1}{M_{\text{Planck}}^2}(E\,R)^n \sim \frac{1}{M_*^2}(E\,M_*)^n, \tag{14.2}$$

where E is the characteristic energy of the subprocess.

For graviton phenomenology it is useful to replace the ADD parameter M^* by other rescaled parameters. The two most useful choices are taken from the work of Giudice, Rattazzi and Wells (GRZ) [702], and Han, Lykken and Zhang (HLZ) [703]:

$$M_*^{n+2} = \frac{S_{n-1}}{(2\pi)^n} M_s^{n+2}\,, \tag{14.3}$$

$$M_*^{n+2} = \frac{8\pi}{(2\pi)^n} M_D^{n+2}\,, \tag{14.4}$$

where M_s is the HLZ scale, M_D is the GRW scale, and S_{n-1} is the surface area of a unit n-sphere:

$$S_{n-1} = \frac{2\pi^{n/2}}{\Gamma(n/2)}\,. \tag{14.5}$$

Both notations are equivalent. To obtain a complete dictionary between ADD, GRZ and HLZ, one also needs to relate the ADD parameter R to those used by the other authors: $R = R_{\text{HLZ}} = 2\pi\, R_{GRW}$, and take note of the different notations for Newton's constant:

$$\kappa^2 = 16\pi\, G_N \text{ (HLZ)}; \quad \overline{\text{M}}_{\text{P}}^2 = \frac{1}{8\pi \text{G}_{\text{N}}} \text{ (GRW)}\,. \tag{14.6}$$

A Kaluza–Klein graviton mode has a mass specified by an n-vector of integers $\vec{k}$:

$$m^2(\vec{k}) = \frac{\vec{k}^2}{R_{\text{GRW}}^2}\,. \tag{14.7}$$

Let $r = |\vec{k}|$. Then for large r (as is often the relevant case for ADD phenomenology) the number of KK graviton states of a given polarisation with $r \leqslant r_{\max}$ is given by the integral

$$S_{n-1}\int_0^{r_{\max}} dr\, r^{n-1} = \frac{1}{n} S_{n-1}\, r_{\max}^n = \int_0^{m_{\max}} \rho(m)\, dm, \tag{14.8}$$

where the KK density of states is

$$\rho(m) = \frac{m^{n-1}}{G_N M_s^{n+2}}. \tag{14.9}$$

M_s is the natural scaling parameter for KK graviton production. The density of states formulation can be applied to a much more general class of models than ADD, and can also include graviton wavefunction factors when the extra dimensions are not flat.

Consider an on-shell production of a KK graviton from a pp or collision. To leading order this is a $2 \to 2$ process with two massless partons in the initial state, plus a massive KK graviton and a massless parton in the final state. Let p_1, p_2 denote the 4-momenta of the initial state partons, p_3 the 4-momentum of the graviton, and p_4 the 4-momentum of the outgoing parton. The total cross section for any particular variety of partonic subprocess has the form

$$\sigma(1+2 \to \mathrm{KK}+4) = \int dx_1 dx_2\; f_1(x_1,\hat{s})\, f_2(x_2,\hat{s}) \int d\hat{t} \int_0^{\sqrt{\hat{s}}} dm\, \rho(m)\, \frac{d\sigma_m}{d\hat{t}}(\hat{s},\hat{t}), \tag{14.10}$$

where $f_1(x_1,\hat{s})$, $f_2(x_2,\hat{s})$ are the parton distribution functions (PDFs) for the initial state partons, $\hat{s} = x_1 x_2 s = (p_1+p_2)^2$ is the square of the total centre of mass (cm) energy of the subprocess, and $\hat{t} = (p_1 - p_3)^2$ is the usual Mandelstam invariant. The formulae for $d\sigma_m/d\hat{t}$, the differential subprocess cross sections for KK gravitons of mass m, are given in [702].

14.1.2.1. Graviton production above the cutoff. At the LHC, proton–proton collisions will probe a distribution of partonic subprocess energies $\sqrt{\hat{s}}$. This creates a problem for the consistent analysis of missing energy signatures in the framework of ADD models. These models are simple low energy effective theories which are only valid for $\sqrt{\hat{s}}$ below some cutoff. This cutoff is at most $2M^*$, and could be a factor of a few smaller if the ultraviolet completion of the model is weakly coupled string theory [704]. The same is true for the Lykken–Randall model [705], which is a low energy description of gravity in a single infinite warped extra dimension, valid up to a cutoff $\sim M^*$. It is inconsistent to use either type of model to describe LHC collisions with subprocess energies greater than the cutoff.

This problem was first noted by the authors of [702], who suggested replacing the ADD graviton density of states $\rho(m)$ by $\rho(m)\theta(\sqrt{\hat{s}} - M_D)$, where θ is a step function. This introduces a systematic theory error into the analysis. The size of this error is very sensitive to the values of M_D and n. For initial LHC data sets, we will be probing the lower range of M_D values, beginning at the current $\simeq 1\,\mathrm{TeV/c^2}$ bounds from Tevatron and LEP. This increases the theory systematic from the cutoff for any fixed n. For fixed M_D, the theory systematic increases rapidly for increasing n. For $n = 2$, the theory uncertainty in the total cross section remains below about 20% even for M_D approaching $1\,\mathrm{TeV/c^2}$.[49] For $n = 6$ and above, the effect of the cutoff is enormous for modest values of M_D, because the rapid rise in the graviton density of states is not compensated by the rapid falloff of the pdfs. The theory error for the total cross section in this case can be as large as an order of magnitude.

[49] To avoid strong astrophysical constraints, $n = 2$ ADD models also require an *ad hoc* infrared cutoff, truncating the massive graviton spectrum for masses below about 20 MeV. This has a negligible effect on LHC analysis.

The resolution of this problem depends upon whether or not there is a signal in the missing energy channels (we will not discuss the related problems which arise in channels affected by virtual graviton exchanges). If there is a signal, the optimal procedure is to measure the observables $d^2\sigma/dp_T d\eta$ as accurately as possible, perhaps at more than one collider energy as suggested in [706, 707]. No theory systematic should be included in these analyses. Instead, one should use the data to find the best fit form for $\rho(m, \sqrt{\hat{s}})$. Simple trial forms can be obtained, for example, from multiplying the ADD density of states by the form factors obtained in models with strings [704, 708, 709] or branes [710]. For the lower range of M_D values, the sensitivity to n suggested in [706, 707] will tend to be washed out. This is not a bad outcome, since it is a result of convolving the n dependence with the effects of strings, branes or other new physics. Thus the theory systematic is replaced by likelihood fits to theories of Planck scale physics.

More problematic is the case where there is no graviton signal in a given data set. Since in this case we are trying to set a limit, we need an estimate of the theory systematic. The simplest possibility is to implement the GRW cutoff defined above, and estimate the theory error by varying the cutoff. For ADD with $n \geqslant 6$, one expects to obtain no lower bound at all on M_D, as noted in [702].

14.1.3. Virtual graviton exchange

The second class of collider signals for large extra dimensions is that of virtual graviton exchange[702, 711] in $2 \to 2$ scattering. This leads to deviations in cross sections and asymmetries in Standard Model processes with difermion final states. It may also give rise to new production processes which are not present at tree-level in the Standard Model, such as $gg \to \ell^+\ell^-$. The signature is similar to that expected in composite theories and provides a good experimental tool for searching for large extra dimensions for the case $\sqrt{s} < M_D$.

Graviton exchange is governed by the effective Lagrangian

$$\mathcal{L} = i\frac{4\lambda}{M_H^4} T_{\mu\nu} T^{\mu\nu} + \text{h.c.} \tag{14.11}$$

The amplitude is proportional to the sum over the propagators for the graviton KK tower which may be converted to an integral over the density of KK states. However, in this case, there is no specific cut-off associated with the process kinematics and the integral is divergent for $n > 1$. This introduces a sensitivity to the unknown ultraviolet physics which appears at the fundamental scale. This integral needs to be regulated and several approaches have been proposed: (i) a naive cut-off scheme [702, 711], (ii) brane fluctuations [710], or (iii) the inclusion of full weakly coupled TeV-scale string theory in the scattering process [704, 708]. The most model independent approach which does not make any assumptions as to the nature of the new physics appearing at the fundamental scale is that of the naive cut-off. Here, the cut-off is set to $M_H \neq M_D$; the exact relationship between M_H and M_D is not calculable without knowledge of the full theory. The parameter $\lambda = \pm 1$ is also usually incorporated in direct analogy with the standard parametrisation for contact interactions [123] and accounts for uncertainties associated with the ultraviolet physics. The substitution

$$\mathcal{M} \sim \frac{i^2\pi}{M_{\text{Pl}}^2} \sum_{\vec{n}=1}^{\infty} \frac{1}{s - m_{\vec{n}}^2} \to \frac{\lambda}{M_H^4} \tag{14.12}$$

is then performed in the matrix element for s-channel KK graviton exchange with corresponding replacements for t- and u-channel scattering. As above, the Planck scale suppression is removed and superseded by powers of $M_H \sim \text{TeV/c}^2$.

The resulting angular distributions for fermion pair production are quartic in $\cos\theta$ and thus provide a unique signal for spin-2 exchange.

The experimental analyses also make use of the cut-off approach. Using virtual Kaluza–Klein graviton exchange in reactions with diphoton, dibosons and dilepton final states, ($G_n \to \gamma\gamma$, VV, $\ell\ell$), the LEP and Tevatron experiments exclude exchange scales up to $\sim 1.1\,\mathrm{TeV/c^2}$.

In the dimuon studies presented here (14.3.2) with $1\,\mathrm{fb}^{-1}$ a 5-sigma effect from the virtual contributions of ADD gravitons to Drell–Yan process is observable for effective fundamental Planck scale of 4.0 TeV and for $n = 6$ extra dimensions.

14.1.4. Inverse TeV sized extra dimensions

The possibility of TeV $^{-1}$-sized extra dimensions naturally arises in braneworld theories [700]. By themselves, they do not allow for a reformulation of the hierarchy problem, but they may be incorporated into a larger structure in which this problem is solved. In these scenarios, the Standard Model fields are phenomenologically allowed to propagate in the bulk. This presents a wide variety of choices for model building: (i) all, or only some, of the Standard Model gauge fields exist in the bulk; (ii) the Higgs field may lie on the brane or in the bulk; (iii) the Standard Model fermions may be confined to the brane or to specific locales in the extra dimension. The phenomenological consequences of this scenario strongly depend on the location of the fermion fields. Unless otherwise noted, our discussion assumes that all of the Standard Model gauge fields propagate in the bulk.

The masses of the excitation states in the gauge boson KK towers depend on where the Higgs boson is located. If the Higgs field propagates in the bulk, the zero-mode state of the Higgs KK tower receives a vacuum expectation value (vev) which is responsible for the spontaneous breaking of the electroweak gauge symmetry. In this case, the resulting mass matrix for the states in the gauge boson KK towers is diagonal and the excitation masses are shifted by the mass of the gauge zero-mode, which corresponds to the Standard Model gauge field, giving

$$m_{\vec{n}} = (m_0^2 + \vec{n}\cdot\vec{n}/R_c^2)^{1/2} \tag{14.13}$$

where $\vec{n} = (n_1, n_2, \ldots)$ labels the KK excitation levels. However, if the Higgs is confined to the brane, its vev induces mixing, amongst the gauge KK states of order $(m_0 R_c)^2$. The KK mass matrix must then be diagonalised in order to determine the excitation masses. For the case of 1 extra TeV $^{-1}$-sized dimension, the coupling strength of the gauge KK states to the Standard Model fermions on the brane is $\sqrt{2}g$, where g is the corresponding Standard Model gauge coupling.

In the case where the Standard Model fermions are rigidly fixed to the brane, they do not feel the effects of the additional dimensions. For models in this class, precision electroweak data place strong constraints on the mass of the first gauge KK excitation. Contributions to electroweak observables arise from the virtual exchange of gauge KK states and a summation over the contributions from the entire KK tower must be performed. For $D > 5$, this sum is divergent. In the full higher dimensional theory, some new, as of yet unknown, physics would regularise this sum and render it finite. An example of this is given by the possibility that the brane is flexible or non-rigid, which has the effect of exponentially damping the sum over KK states. Due to our present lack of knowledge of the full underlying theory, the KK sum is usually terminated by an explicit cut-off, which provides a naive estimate of the magnitude of the effects.

Since the $D = 5$ theory is finite, it is the scenario that is most often discussed and is sometimes referred to as the 5-dimensional Standard Model (5DSM). In this case, a global

fit to the precision electroweak data including the contributions from KK gauge interactions yields $m_1 \sim R_c^{-1} \gtrsim 4\,\mathrm{TeV/c^2}$. In addition, the KK contributions to the precision observables allow for the mass of the Higgs boson to be somewhat heavier than the value obtained in the Standard Model global fit. Given the constraint on R_c from the precision data set, the gauge KK contributions to the anomalous magnetic moment of the muon are small. The first gauge KK state can be produced as a resonance at the LHC in the Drell–Yan channel provided $m_1 \lesssim 6\,\mathrm{TeV/c^2}$. In the studies presented here using the Z_{KK} in the dielectron channel a 5-sigma reach for $m_1 \sim R_c^{-1} \sim 4.97\,\mathrm{TeV/c^2}$ is obtained with $10\,\mathrm{fb}^{-1}$.

In the scenario where the Standard Model fermions are localised at specific points in the extra TeV^{-1}-sized dimensions, the fermions have narrow gaussian-like wave functions in the extra dimensions with width much smaller than R_c^{-1}. The placement of the different fermions at distinct locations in the additional dimensions, along with the narrowness of their wavefunctions, can then naturally suppress operators mediating dangerous processes such as proton decay. The exchange of gauge KK states in $2 \to 2$ scattering processes involving initial and final state fermions is sensitive to the placement of the fermions and can be used to perform a cartography of the localised fermions, i.e., measure the wavefunctions and locations of the fermions. At very large energies, it is possible that the cross section for such scattering will tend rapidly to zero since the fermions' wavefunctions will not overlap and hence they may completely miss each other in the extra dimensions.

14.1.5. Randall–Sundrum (RS) models

Randall–Sundrum refers to a class of scenarios, also known as warped extra dimensions models, originated by Lisa Randall and Raman Sundrum [94, 646]. In these scenarios there is one extra spatial dimension, and the five-dimensional geometry is "warped" by the presence of one or more branes. The branes extend infinitely in the usual three spatial dimensions, but are sufficiently thin in the warped direction that their profiles are well-approximated by delta functions in the energy regime of interest. If we ignore fluctuations of the branes, we can always choose a "Gaussian Normal" coordinate system, such that the fifth dimension is labelled y and the usual 4d spacetime by x^μ. The action for such a theory contains, at a minimum, a 5d bulk gravity piece and 4d brane pieces. The bulk piece has the 5d Einstein–Hilbert action with gravitational coupling M^3, and a 5d cosmological constant Λ. The brane pieces are proportional to the brane tensions V_i, which may be positive or negative. These act as sources for 5d gravity, contributing to the 5d stress-energy terms proportional to

$$\sum_i V_i \delta(y - y_i) \tag{14.14}$$

where the y_i are the positions of the branes. Combined with a negative Λ, this results in a curved geometry, with a 5d metric of the form:

$$\begin{aligned} &g_{\mu\nu}(x^\rho, y) = a^2(y)\, \tilde{g}_{\mu\nu}(x^\rho)\,, \\ &g_{\mu y} = 0\,, \quad g_{yy} = 1\,, \end{aligned} \tag{14.15}$$

where $a(y)$ is called the warp factor, $\tilde{g}$ is a 4d metric, and we have made a useful choice of coordinates. Warping refers to the fact that a 4d distance d_0 measured at $y = y_0$ is related to an analogous 4d distance d_1 measured at $y = y_1$ by $a(y_0)d_0 = a(y_1)d_1$. Thus in Randall–Sundrum scenarios 4d length, time, energy and mass scales vary with y.

Most collider physics phenomenology done with warped extra dimensions so far is based upon one very specific model, the original simple scenario called RSI. In this model the extra dimension is compactified to a circle of circumference $2L$, and then further orbifolded by identifying points related by $y \to -y$. The fifth dimension then consists of two periodically

identified mirror copies of a curved 5d space extending from $y = 0$ to $y = L$. It is assumed that there is a brane at $y = 0$, with positive tension V_0; it is known as the Planck brane – strong gravity resides on that brane. There is another brane at $y = L$, with negative tension V_L, known as the TeV brane–the entire 4d universe is confined to the TeV brane.

Randall and Sundrum showed that, for a tuned choice of input parameters $V_0 = -V_L = -M^2\Lambda$, the 5d Einstein equations have a simple warped solution on $0 < y < L$ with metric:

$$g_{\mu\nu}(x^\rho, y) = \mathrm{e}^{-2ky}\,\eta_{\mu\nu}\,,$$
$$g_{\mu y} = 0\,, \quad g_{yy} = 1\,, \tag{14.16}$$

where $\eta_{\mu\nu}$ is the 4d flat Minkowski metric, and $k = \sqrt{-\Lambda}$. Away from the branes, the 5d curvature is constant and negative; it is thus equivalent locally to AdS_5, with the anti-de Sitter radius of curvature given by $1/k$. At the locations of the branes the curvature is discontinuous, due to the fact that the branes are delta function sources for curvature.

The RSI model is completely described by three parameters: k, M, and L. Restricting the scenario to a low energy effective description implies considering k, $1/L \ll M$. In fact in RSI it is assumed that k is merely parametrically small compared to the 5d Planck scale M, i.e. $k \sim M/10$. The effective 4d Planck scale, which is the same as the coupling of the graviton zero mode, is given by dimensional truncation:

$$M^2_{\mathrm{Planck}} = \frac{M^3}{2k}\left(1 - \mathrm{e}^{-2kL}\right). \tag{14.17}$$

Then, within an order of magnitude, $M \sim k \sim M_{\mathrm{Planck}}$. In RSI the distance L is fixed by requiring that $a(L)M_{\mathrm{Planck}} \simeq 1\,\mathrm{TeV}$, thus $kL \sim 30$. This is *not* a large extra dimension: its inverse size is comparable to the grand unification scale.

Since the standard model fields live on the TeV brane as in ADD models, the phenomenology of RSI is concerned with the effects of the massive KK modes of the graviton. These modes as measured on the TeV brane have their mass splittings of the order of a TeV, and have TeV suppressed couplings to the standard model fields. In RSI, the Standard Model is replaced at the TeV scale by a new effective theory in which gravity is still very weak, but there are exotic heavy spin-two particles.

At the LHC the KK gravitons of RSI would be seen as difermion or dibosons resonances, since (unlike the KK gravitons of ADD) the coupling of each KK mode is only TeV suppressed [712]. The width of these resonances is controlled by the ratio $c = k/M$; the resonances become more narrow as the coupling parameter $c = k/M$ is reduced, as shown in Fig. 14.1.

The studies presented here focus on dilepton and diphoton final states while results using dijets can be found in Section 14.4.1. Note that due to the spin-2 nature of the graviton its branching ratio to diphotons is roughly twice that of a single dilepton channel.

14.2. High mass dielectron final states

This section presents the CMS experiment discovery potential for new heavy resonances, decaying into an electron pair. The $\mathrm{e^+e^-}$ decay channel provides a clean signature in the CMS detector. The presence of a heavy particle would be detected in CMS by the observation of a resonance peak in the dielectron mass spectrum over the Drell–Yan process ($\mathrm{pp} \to \gamma/\mathrm{Z} \to \mathrm{e^+e^-}$) which constitutes the main Standard Model background.

Heavy resonances with mass above $1\,\mathrm{TeV/c^2}$ are predicted by several models beyond the Standard Model. Three models are considered here: Kaluza–Klein (KK) excitations of a Z boson (TeV^{-1} model, see Section 14.1.4) and KK excitation of a graviton (Randall–Sundrum

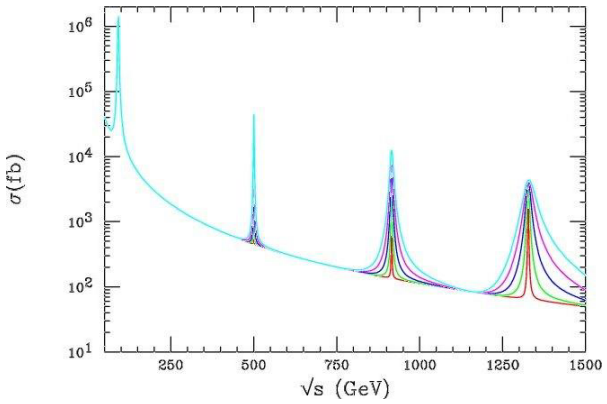

Figure 14.1. The cross section for $e^+e^- \to \mu^+\mu^-$ including the exchange of KK gravitons in the RSI model. The narrowest resonances correspond to $k/M = 0.05$, the widest to $k/M = 0.14$. (Taken from Ref. [713].)

(RS) model, see Section 14.1.5), both predicted in extra dimensions models, and neutral heavy Z' boson predicted by Grand Unified Theories (GUT) (see Section 14.1.1). For the Z' bosons, 6 models are studied, as for the $Z' \to \mu^+\mu^-$ channel [100] that is discussed in Section 14.3.

Details of the analyses presented in this section can be found in [714] and [715].

14.2.1. Event selection and correction

Two electrons are required for this analysis. They are reconstructed as super-clusters (SC) in the ECAL calorimeter in the barrel and the endcap regions [716]. For endcap SC, the energy loss in the preshower detector is taken into account. The two SC with highest energies are selected as the electron candidates.

Reducible backgrounds (like QCD jets and γ-jets) are suppressed by applying the following requirements:

- The ratio of the HCAL to ECAL energy deposits is required to be $H/E < 10$ %.
- The two SC must be isolated: the total additional transverse energy in a cone of radius $0.1 < \Delta R < 0.5$ is required to be below 2% of the SC transverse energy (where $\Delta R = \sqrt{\Delta\eta^2 + \Delta\phi^2}$).
- To identify electrons and reject neutral particles, a track is requested to be associated for each electron candidate. If a track is associated with only one of these SC, the event is however kept if it contains a third SC with $E > 300$ GeV with an associated track and satisfying the H/E and isolation cuts described above.

The selected events are then corrected for the following effects:

- Saturation correction. For very energetic electrons and photons, saturation occurs in the ECAL electronics because of the limited dynamical range of the Multi-Gain-Pre-Amplifier. The saturation threshold has been established to be at 1.7 TeV in crystals of the barrel and 3.0 TeV in the endcaps. A correction method (for barrel only) has been developed using the energy deposit in crystals surrounding the saturated crystal. The correction allows the energy deposits of clusters suffering from saturation to be estimated with a resolution of about 7% [717].

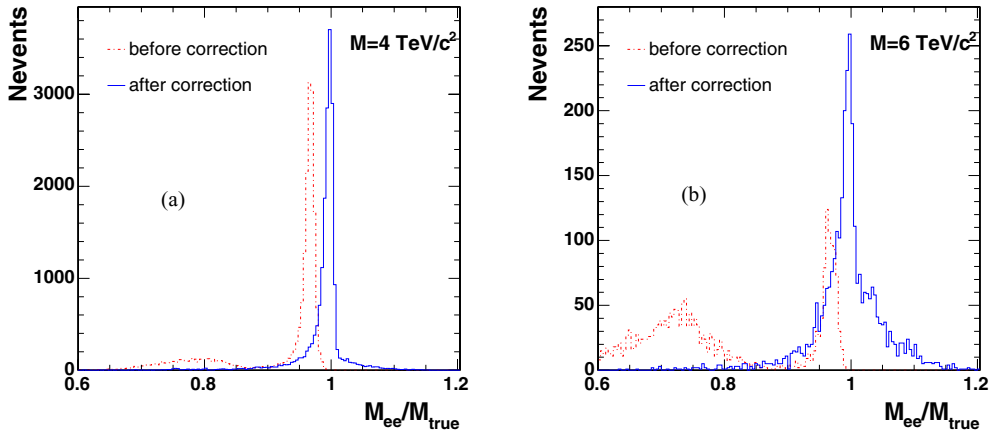

Figure 14.2. Ratio M_{ee}/M_{true} before and after corrections for KK Z boson production, for $M = 4\,\mathrm{TeV/c^2}$ (a) and $M = 6\,\mathrm{TeV/c^2}$ (b).

- Energy correction. The ECAL measured electron energy after preshower, HCAL and saturation corrections, is smaller than the generated energy. Dedicated energy correction factors for very energetic electrons have been determined using calibration files. These factors depend on both energy, η and whether saturation occurs or not. The resolution on the corrected SC energy is 0.6% at $E = 1000\,\mathrm{GeV}$.
- z-vertex distribution. The measurement in η takes into account the knowledge of the z-vertex position.
- FSR recovery. Hard photon emission from Final State Radiation can induce the detection in the event of a third energetic SC If a SC with $E > 300\,\mathrm{GeV}$ satisfying the H/E and isolation cuts is observed very close to the SC of the electron candidates ($\Delta R < 0.1$), this additional SC is associated to the corresponding electron.

14.2.2. Mass peak distributions

The resonance mass is reconstructed from the energies and angles of the 2 electron candidates, after the selection cuts and energy corrections mentioned above. Figures 14.2a and 14.2b show the ratio of the reconstructed and the true masses, M_{ee}/M_{true}, before and after energy corrections for KK Z production with $M = 4$ and $6\,\mathrm{TeV/c^2}$, respectively. The peaks at low values of M_{ee}/M_{true} correspond to events with saturated ECAL electronics. The final resolution on the resonance mass is around 0.6% for events with no saturation, and 7% in case of saturation.

Figure 14.3a presents the signal and the Drell–Yan background for KK Z boson production with $M = 4\,\mathrm{TeV/c^2}$; Fig. 14.3b for Z' boson production with $M = 1.5\,\mathrm{TeV/c^2}$; Fig. 14.3c for graviton production with $M = 1.5\,\mathrm{TeV/c^2}$ and coupling parameter, defined in Section 14.1.5, $c = 0.01$.

14.2.3. Discovery potential of CMS

The discovery potential of a new physics resonance is determined using the likelihood estimator S_{cL} (defined in Appendix A.1) based on event counting, suited for small event samples. The discovery limit is defined by $S_{cL} > 5$.

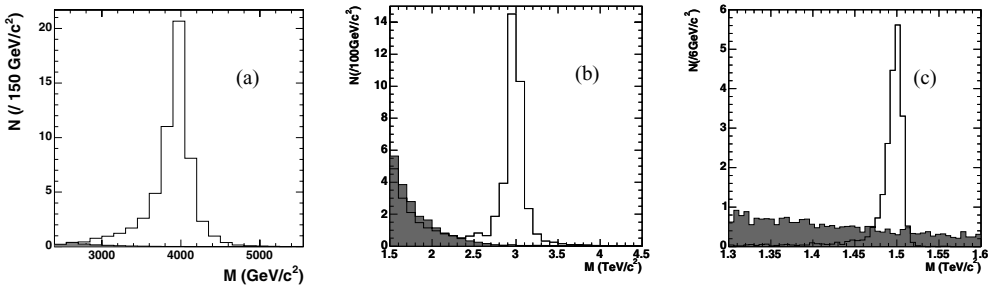

Figure 14.3. Resonance signal (white histograms) and Drell–Yan background (shaded histograms) for KK Z boson production with $M = 4.0\,\mathrm{TeV/c^2}$ (a), SSM Z' boson production with $M = 3.0\,\mathrm{TeV/c^2}$ (b), and graviton production with $M = 1.5\,\mathrm{TeV/c^2}$, coupling parameter $c = 0.01$ (c), for an integrated luminosity of $30\,\mathrm{fb^{-1}}$.

Table 14.1. Number of events for resonant signal, N_s, and for Drell–Yan background, N_b, and corresponding significances S_{cL} for an integrated luminosity of $30\,\mathrm{fb^{-1}}$. The masses M and the mass windows M_w are in $\mathrm{TeV/c^2}$.

	KK Z		G, $c = 0.01$	G, $c = 0.1$	SSM Z'	
M	4.0	6.0	1.5	3.5	1.0	5.0
M_w	3.5–4.5	5.0–6.7	1.47–1.52	3.30–3.65	0.92–1.07	4.18–5.81
N_s	50.6	1.05	18.8	7.30	72020	0.58
N_b	0.13	0.005	4.16	0.121	85.5	0.025
S	22.5	3.0	6.39	6.83	225	1.63

The number of signal and background events, N_s and N_b, computed for a given mass window around the peak, are presented in Table 14.1 for the three models, together with the corresponding significance, for an integrated luminosity of $30\,\mathrm{fb^{-1}}$.

The 5σ discovery limits as a function of mass are given in Fig. 14.4a and Fig. 14.4b, for KK Z boson production and Z' production (for the 6 considered models), respectively. In the graviton case, the 5σ discovery plane as a function of the coupling parameter c and the resonance mass is given in Fig. 14.4c.

For KK Z bosons, a 5σ discovery can be achieved for a resonance mass up to $M = 4.97\,\mathrm{TeV/c^2}$ for an integrated luminosity of $10\,\mathrm{fb^{-1}}$, $M = 5.53\,\mathrm{TeV/c^2}$ for $30\,\mathrm{fb^{-1}}$ and $M = 5.88\,\mathrm{TeV/c^2}$ for $60\,\mathrm{fb^{-1}}$. For gravitons, with an integrated luminosity of $30\,\mathrm{fb^{-1}}$, a 5σ discovery can be extracted for masses up to $1.64\,\mathrm{TeV/c^2}$ for $c = 0.01$ and up to $3.81\,\mathrm{TeV/c^2}$ for $c = 0.1$. For Z' boson production, with an integrated luminosity of $30\,\mathrm{fb^{-1}}$, a 5σ discovery can be extracted for masses up to $3.31\,\mathrm{TeV/c^2}$ for model ψ and up to $4.27\,\mathrm{TeV/c^2}$ for model ARLM. The 5σ discovery limits on the resonance masses for 10, 30 and $60\,\mathrm{fb^{-1}}$ are summarised in Table 14.2.

For KK Z boson production, the luminosities needed for a five σ discovery are 1.5, 4.0, 10.8, 29.4, and $81.4\,\mathrm{fb^{-1}}$ for $M = 4.0$, 4.5, 5.0, 5.5 and $6.0\,\mathrm{TeV/c^2}$, respectively; for SSM Z' boson production, they are 0.015, 3.0 and $260\,\mathrm{fb^{-1}}$ for $M = 1$, 3 and $5\,\mathrm{TeV/c^2}$; for graviton production, most of the interesting region of the (mass, coupling) plane is already covered with $10\,\mathrm{fb^{-1}}$.

For KK Z and Z' production, a K factor of 1 was conservatively taken for both the signal and the Drell–Yan background, since heavy Z production interferes with Z/γ Drell–Yan production. For the graviton analysis, as little interference is present with the Standard Model

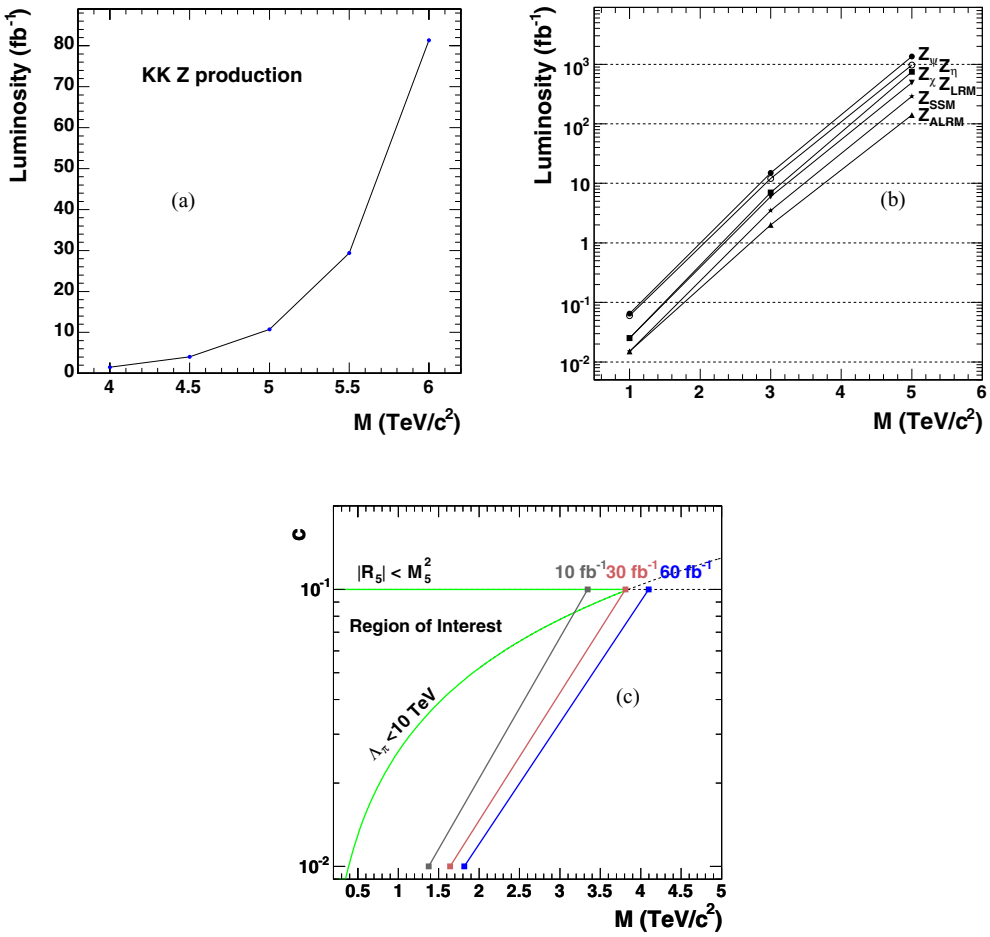

Figure 14.4. Five σ discovery limit as a function of the resonance mass for KK Z boson production (a), for the 6 Z' models (b); five σ discovery plane for graviton production as a function of the coupling parameter c and the graviton mass (c).

Table 14.2. The 5σ discovery limit on the resonance mass (given in TeV/c^2) for the three models, for an integrated luminosity of 10, 30 and 60 fb^{-1}.

Model	Luminosity (fb^{-1})		
	10	30	60
KK Z	4.97	5.53	5.88
G ($c = 0.01$)	1.38	1.64	1.82
G ($c = 0.1$)	3.34	3.81	4.10
Z' (ψ)	2.85	3.31	3.62
Z' (ALRM)	3.76	4.27	4.60

processes, a K factor of 1.0 is used for the signal and of 1.3 for the Drell–Yan background, in order to take into account the higher order terms in the cross section. The latter number comes from the CDF analysis [718] and is compatible with the K factor obtained from theoretical computations [348].

14.2.4. Systematic uncertainties

The uncertainty coming from the choice of the parton distribution function (PDF) was investigated using the set of 20 positive and 20 negative errors, of the CETQ6.1M "best fit" parametrisation [12, 719, 720]. For each event, a weight factor is computed according to the x_1, x_2, and Q^2 variables, for each of the 40 PDF errors, in the case of graviton production with $M = 1.5\,\mathrm{TeV/c^2}$ ($c = 0.01$) and $M = 3.5\,\mathrm{TeV/c^2}$ ($c = 0.1$). The uncertainties on the PDF modify the number of signal events by a factor 1.20 (positive deviations) and 0.86 (negative deviations) for $M = 1.5\,\mathrm{TeV/c^2}$ ($c = 0.01$). The corresponding numbers for $M = 3.5\,\mathrm{TeV/c^2}$ ($c = 0.1$) are 1.47 and 0.78. For the Drell–Yan background, the re-weighting effects on the numbers of events are 1.07 and 0.94 for masses around $1.5\,\mathrm{TeV/c^2}$, and 1.19 and 0.88 for masses around $3.5\,\mathrm{TeV/c^2}$. For an integrated luminosity of $30\,\mathrm{fb^{-1}}$, the significances with the "best fit" and with the positive/negative deviations are equal respectively to 6.40 and 7.25/5.78 for $M = 1.5\,\mathrm{TeV/c^2}$, and to 6.83 and 8.54/5.93 for $M = 3.5\,\mathrm{TeV/c^2}$. The main effect of the variation comes from the gluon-fusion contribution to the graviton production cross section. A lower dependence is observed for the KK Z and Z' channels, which are produced by quark-anti-quark annihilation. For KK Z boson production at $M = 4\,\mathrm{TeV/c^2}$ with an integrated luminosity of $30\,\mathrm{fb^{-1}}$, the significances with the "best fit" and with the positive/negative errors are equal respectively to 22.5 and 23.3/21.9.

Changing to 1 the value of the K factor of the Drell–Yan background for RS graviton production increases the significance from 6.39 to 6.87 ($M = 1.5\,\mathrm{TeV/c^2}$, $c = 0.01$) and from 6.83 to 7.09 ($M = 3.5\,\mathrm{TeV/c^2}$, $c = 0.1$). The discovery limits increase respectively from 1.64 to $1.68\,\mathrm{TeV/c^2}$ and from 3.81 to $3.84\,\mathrm{TeV/c^2}$.

The data themselves will be used to estimate and cross-check the Drell–Yan background at very high energy. For resonance discovery, the number of events in the side-bands of the resonance and their mass dependence will be used to estimate the number of background events under the resonance peak, provided there is enough data in the side-bands. In this approach, the uncertainties on the background cross-sections, the PDF and the luminosity measurement are highly reduced.

14.2.5. Identification of new particles

Once a resonance is found, information will be gained on its characterisation from the study of other decay channels, like $\gamma\gamma$ (see Section 14.6), of angular distributions and of asymmetries, in view of the spin determination (see also Section 14.3).

As an example, RS gravitons with spin 2 can be distinguished from the Standard Model background and Z' bosons with spin 1 using the distribution of the $\cos\theta^*$ variable, computed as the cosine of the polar angle between the electron and the boost direction of the heavy particle in the latter rest frame. In addition to the cuts defined above, the electron and positron candidates are requested to have opposite charges, in order to identify the electron, from which the $\cos\theta^*$ variable is computed.

The $\cos\theta^*$ distributions for graviton production with $M = 1.25\,\mathrm{TeV/c^2}$, $c = 0.01$ and $M = 2.5\,\mathrm{TeV/c^2}$, $c = 0.1$, are presented in Fig. 14.5, for an integrated luminosity of $100\,\mathrm{fb^{-1}}$. The error bars represent the corresponding statistical uncertainties, applied to the signal distribution obtained from a large statistics simulation. The spin-2 hypothesis is compared to the spin-1 hypothesis (dashed red curve in the figures), formed by the Drell–Yan production (Figs. 14.5a and 14.5b) or the ALRM Z' production (Figs. 14.5c and 14.5d). For graviton production, the expected background is included in the $\cos\theta^*$ distributions.

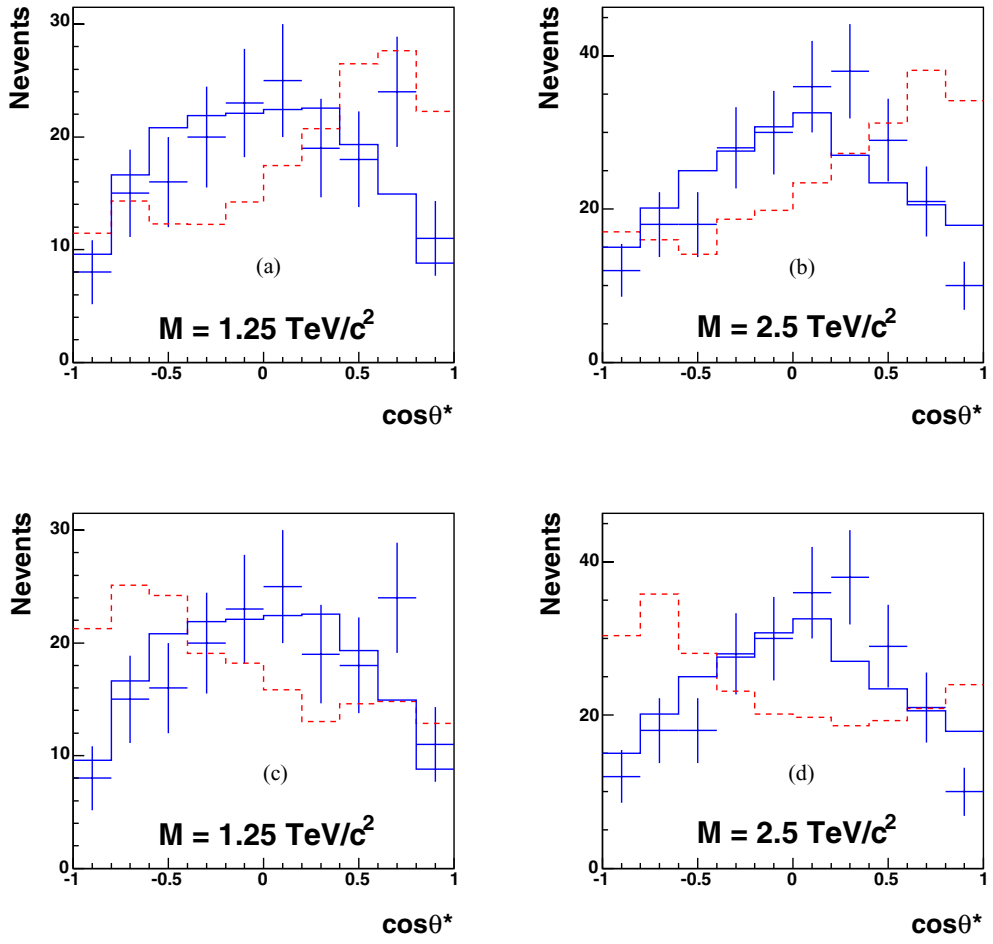

Figure 14.5. Distributions of $\cos\theta^*$ for graviton production (full blue curves) and for Drell–Yan production (dashed red curves) normalised to the signal, for $M = 1.25\,\mathrm{TeV/c^2}$ (a) and $2.5\,\mathrm{TeV/c^2}$ (b), and for Z' boson (ALRM model) (dashed red curves), normalised to the signal, for $M = 1.25\,\mathrm{TeV/c^2}$ (c) and $2.5\,\mathrm{TeV/c^2}$ (d), with an integrated luminosity of $100\,\mathrm{fb}^{-1}$. The error bars represent the "1-experiment" distribution for the graviton production. The expected background is included in the $\cos\theta^*$ distributions.

The spin 2 nature of RS gravitons can be determined in contrast to the Drell–Yan production or the Z' boson production for an integrated luminosity of $100\,\mathrm{fb}^{-1}$ up to $1.25\,\mathrm{TeV/c^2}$ for $c = 0.01$ and $2.5\,\mathrm{TeV/c^2}$ for $c = 0.1$.

14.3. High mass dimuon final states

Many scenarios beyond the Standard Model are expected to manifest themselves through modifications in the mass spectrum of high-mass dimuon pairs. The potential of the CMS experiment to discover dimuon decays of a new heavy neutral gauge boson, Z′, is discussed in Section 3.3.4; the discovery reach for a representative set of Z′ models was found to be in the range between 2.9 and $3.8\,\mathrm{TeV/c^2}$ for an integrated luminosity of $10\,\mathrm{fb}^{-1}$. In this section, we discuss the observability of $\mu^+\mu^-$ final states predicted in two classes of

large extra dimensions models, RS and ADD. While the RS scenario gives rise to relatively narrow resonances, the ADD model is expected to be observed via non-resonant modifications of the dimuon spectrum; therefore, these two searches require somewhat different experimental approaches. The search for compositeness in the dimuon channel is described in Section 15.2.

Once a new physics is discovered, observables other than dimuon invariant mass can be used to determine the theoretical framework to which it belongs. The measurement of the forward-backward asymmetries of leptonic decay products has long been known as a powerful tool to identify Z′; some aspects of such a measurement at the LHC are discussed in Section 3.3.5. Spin discrimination of new heavy resonances based on an unbinned likelihood ratio statistic incorporating the angles of the decay products is described in Section 3.3.6.

14.3.1. The Randall–Sundrum model in the dimuon channel

We consider the range of RS1 graviton masses in the range $1 < m < 4\,\mathrm{TeV/c^2}$ and the dimensionless coupling constant in the expected theoretical range $0.01 \leqslant c \leqslant 0.1$ [721]. A full simulation with PYTHIA [69] version 6.227 and with the GEANT4-based CMS program [8] and reconstruction with the CMS full-reconstruction package [10], including pile-up of minimum-bias collisions is carried out. We derive both the CMS discovery potential for Randall–Sundrum gravitons and the performance of spin determination in this channel (see details in Ref. [117]). The non-reducible backgrounds are the Drell–Yan process, vector boson pair production ZZ, WZ, WW, $t\bar{t}$ production, etc. In the SM the expected leading-order cross section of the Drell–Yan process dominates the other contributions (see the Section 9.2 for details). The trigger simulation is based on the reconstruction package, using the on-line reconstruction algorithm. We require the single or double muon trigger, no requirement for calorimeter isolation of high-p_{T} muons is made. The total trigger + reconstruction efficiency varies between 95% and 90% for dimuons in the mass range $1 < m < 4\,\mathrm{TeV/c^2}$. Only the events which passed both the Level-1 and HLT cuts are selected. Note that the trigger efficiency is significantly decreased after applying of the calorimeter isolation cuts (down to 15%). This drop is caused by electromagnetic showers accompanying high-energy muons. In the following, no cuts on calorimeter isolation of muon tracks are applied at the HLT level.

14.3.1.1. The Randall–Sundrum model discovery potential. The significance estimators used for studying the discovery potential of the RS1 model were S_{cP}, S_{cL} and S_L, defined in Appendix A.1 (see discussion of S_L in Section 3.3.4.1).

Figure 14.6a shows the integrated luminosity required for a 5σ discovery as a function of the dimuon mass. The results for different values of integrated luminosity are summarised in Table 14.3 and Fig. 14.6b. The CMS experiment can observe a RS1 graviton with mass up to $2.3\,\mathrm{TeV/c^2}$ with an integrated luminosity of $\int L\,dt = 1\,\mathrm{fb}^{-1}$ if the coupling c is equal to 0.1. For $c = 0.01$ the mass reach does not exceed $1.9\,\mathrm{TeV/c^2}$, even for the asymptotic regime of LHC operation with $\int \mathcal{L}\,dt = 300\,\mathrm{fb}^{-1}$. The asymptotic reach limit for $c = 0.1$ is $4.5\,\mathrm{TeV/c^2}$.

A combined analysis [721] in the RS1 scenario shows that the value of the coupling constant c is strongly restricted (Fig. 14.6b) due to the theoretical constraints to assure that the model does not introduce a new hierarchy (the scale parameter $\Lambda_\pi = M_{Pl}e^{kL} < 10\,\mathrm{TeV/c^2}$ with the symbols defined in Section 14.1.5). The direct comparison of results on a mass reach region for c with the data of the Fig. 14.6 shows that a luminosity of $100\,\mathrm{fb}^{-1}$ is needed to test the RS1 model everywhere in ($c - M_{\mathrm{grav}}$) space of model parameters. However, these conclusions are not definitive since the initial theoretical constraints are quite arbitrary.

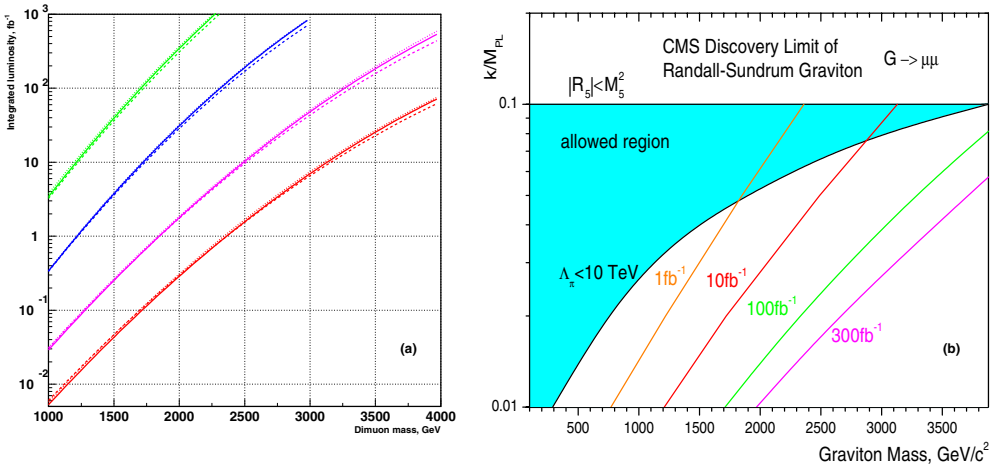

Figure 14.6. (a) Discovery limit for RS1 graviton with $\mu^+\mu^-$ decay mode for different values of RS1 coupling constant $c = 0.01$, 0.02, 0.05 and 0.1 (from top to bottom). Used discovery limit $S > 5$ for the S_{cP} estimator (solid lines), S_L (dashed lines), S_{cL} (dotted lines). (b) Reach of the CMS experiment as a function of the coupling parameter c and the graviton mass for various values of integrated luminosity. The left part of each curve is the region where significance exceeds 5σ.

Table 14.3. CMS discovery potential invariant mass reach (in TeV) to observe the RS1 graviton in $\mu^+\mu^-$ channel.

Coupling constant c	Estimator	1 fb^{-1}	10 fb^{-1}	100 fb^{-1}	300 fb^{-1}
	S_{cP}	0.75	1.20	1.69	1.95
0.01	S_{cL}	0.77	1.21	1.71	1.97
	S_L	0.78	1.23	1.73	1.99
	S_{cP}	1.21	1.72	2.30	2.63
0.02	S_{cL}	1.22	1.72	2.31	2.64
	S_L	1.22	1.74	2.34	2.68
	S_{cP}	1.83	2.48	3.24	3.67
0.05	S_{cL}	1.85	2.49	3.26	3.71
	S_L	1.85	2.51	3.31	3.79
	S_{cP}	2.34	3.11	4.12	4.52
0.1	S_{cL}	2.36	3.13	4.14	4.54
	S_L	2.36	3.16	4.23	4.73

14.3.1.2. Systematic uncertainties. The results taking into account the systematic uncertainties are shown in Fig. 14.7. The expected effects of misalignment are considered in two misalignment scenarios: the First Data and the Long Term scenarios [99], which correspond to different stages of the alignment corrections for the positions of the tracker and muon chambers. The current estimate is that the transition to the Long Term scenario can be achieved at an integrated luminosity of about 1 fb^{-1} [86]. In contrast to Fig. 14.6 which assumed a K-factor equal to unity, a K-factor of $K = 1.30 \pm 0.05$ is used both for the RS1 signal and Drell–Yan background. Additional variations due to EW corrections, hard-scale and PDF uncertainties have been considered, the details being found in Ref. [117].

14.3.1.3. Spin discrimination in angular analysis. A study of muon angular distributions allows a discrimination between the hypotheses of Graviton (spin-2 particle) and Z' (spin-1 particle) – see the discussion and the results in Section 3.3.6.

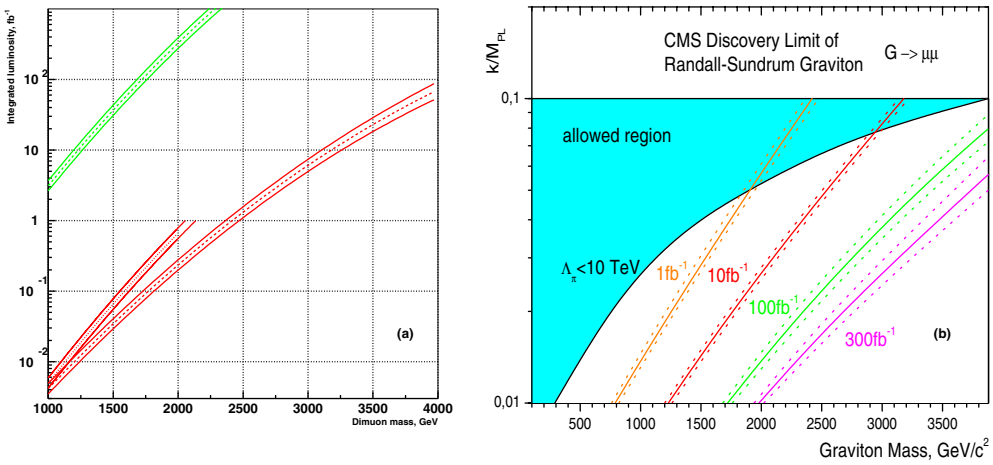

Figure 14.7. (a) Discovery limit for coupling constants $c = 0.01$, 0.1 (upper and lower curves, respectively) after taking into account the systematic uncertainties including misalignment in two scenarios: the curves ending at integrated luminosity of $1\,\text{fb}^{-1}$ correspond the First Data misalignment scenario, the other ones correspond to the Long Term scenario. The ranges show the expected variations due to the systematic uncertainties. (b) The ranges of the expected variations due to the systematic uncertainties for the mass reach of the CMS experiment.

14.3.2. The ADD model in the dimuon channel

We consider the fundamental Planck scale of the ADD model in the range of $3.0 < M_S < 10.0\,\text{TeV/c}^2$ and numbers of extra dimensions in the range of $3 \leqslant n \leqslant 6$ [698]. The contribution of KK-modes of ADD gravitons to the Drell–Yan processes is computed using the leading-order matrix element [722] which was implemented in STAGEN generator collection as external matrix element in PYTHIA [69] version 6.227. A full simulation [8] of the CMS detector and reconstruction [10], without a pile-up of minimum-bias collision is performed to derive the CMS discovery potential for ADD virtual gravitons (see details in Ref. [723]). The non-reducible backgrounds are the Drell–Yan process, vector boson pair production ZZ, WZ, WW, $t\bar{t}$ production, etc. In the SM the expected leading-order cross section of the Drell–Yan process dominates the other contributions (see Section 9.2 for details). The trigger simulation is realised in the reconstruction package, using the on-line reconstruction algorithm. A single or double muon trigger is required, but no requirement for calorimeter isolation of high-p_T muons is made. The total trigger + reconstruction efficiency varies between 70% and 90% for dimuons dependent on the model parameters. Only the events which passed both the Level-1 and HLT cuts are selected.

14.3.2.1. The ADD discovery limit. The CMS discovery potential was estimated using as significance S_{cP} and S_{cL}, defined in Appendix A.1. The computed significance values for the ideal detector as a function of a fundamental theory scale, M_S, are presented in Fig. 41.8 for integrated luminosities of 0.1, 1.0, 10, 100, 300, $1000\,\text{fb}^{-1}$. The main observations are:

- $\int \mathcal{L}\text{d}t = 1\,\text{fb}^{-1}$, even a low luminosity regime allows us to measure the effect from the virtual contributions of ADD gravitons to Drell–Yan process for an effective fundamental Planck scale up to 4.0 TeV for the most unfavourable case with $n = 6$. For a scenario where the number of extra dimensions is $n = 3$ the reach limit is extended to 5.8 TeV.
- $\int \mathcal{L}\text{d}t = 10\,\text{fb}^{-1}$, M_S values of 4.8 and 7.2 TeV can be reached for $n = 3$ and $n = 6$ respectively.

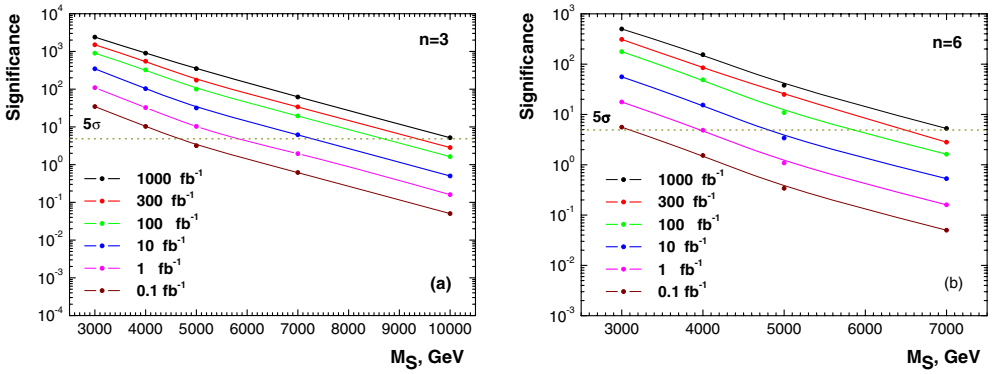

Figure 14.8. Significance as a function of M_S for (a) $n = 3$ and (b) $n = 6$.

- $\int \mathcal{L}dt = 100\,\text{fb}^{-1}$, for LHC operation in a high luminosity regime allow the observation of the ADD signal at $5.8 \div 8.7$ TeV of model scale dependent on a number of extra dimensions.
- $\int \mathcal{L}dt = 300\,\text{fb}^{-1}$, in the asymptotic regime the CMS sensitivity to fundamental Planck scale is increased to values of $6.5 \div 9.3$ TeV.

14.3.2.2. Systematics. The results taking into account the systematical uncertainties with the S_{cP} estimator are shown in Fig. 14.8. To take into account the misalignment effect two scenario of misalignment were considered during reconstruction procedure: *First Data* scenario [99] for 0.1 and $1.0\,\text{fb}^{-1}$ and *Long Term* scenario [99] for 10, 100, 300, $1000\,\text{fb}^{-1}$. The K-factor of $K = 1.30 \pm 0.05$ is used both for ADD signal and Drell–Yan background. Additional variations due to hard-scale and PDF uncertainties as well as trigger and selection uncertainties have been considered, the details being given in Ref. [723].

14.4. High energy single lepton final states

14.4.1. Introduction

Several theoretical models predict, in addition to the well known electroweak vector bosons γ, W, Z, further heavy gauge bosons. These additional particles are postulated for example in Left–Right Symmetric Models [724–727], based on the gauge group $\text{SU(3)}_\text{C} \times \text{SU(2)}_\text{L} \times \text{SU(2)}_\text{R} \times \text{U(1)}_{\text{B}-\text{L}}$ (B, L: baryon-, lepton-number) in theories predicting a substructure of the known "elementary particles", and in Little Higgs Models [91].

Here we investigate the detection capabilities for a hypothetical heavy partner of the W, a charged spin-1 boson W'. We do not assume one of the specific models mentioned above, but derive the W' properties from the Reference Model by Altarelli [697], which has been used in several earlier experiments, so that the resulting limits can be compared easily. In this Reference Model the W' is a carbon copy of the W, with the very same left-handed fermionic couplings (including CKM matrix elements), while there is no interaction with the Standard Model gauge bosons or with other heavy gauge bosons as a Z'. Thus the W' decay modes and corresponding branching fractions are similar to those for the W, with the notable exception of the $\text{t}\bar{\text{b}}$ channel, which opens for W' masses beyond 180 GeV.

In hadron collisions W' bosons can be created through $q\bar{q}$ annihilation, in analogy to W production. Previous searches for the Reference W' at LEP and at the Tevatron give rise to lower bounds approaching 1 TeV [728].

This analysis is based on the decay $W' \to \mu\nu$, with a branching ratio of roughly 10%. The resulting signature of a high energy muon accompanied by missing energy allows an easy separation of signal and background reactions. More details are found in [729].

14.4.2. Data samples

For this study we assume an integrated luminosity of $10\,\text{fb}^{-1}$ and an average instantaneous luminosity of $\mathcal{L} = 2 \times 10^{33}\,\text{cm}^{-2}\,\text{s}^{-1}$ corresponding to an average pile-up of 3.5 pp-collisions per bunch crossing.

Reference Model W' events decaying into muon and neutrino have been generated with PYTHIA v6.227 [69], based on the leading order cross section and the parton density functions CTEQ 5L (leading order) [719]. In total about 300 000 events have been produced for W' masses between 1 TeV and 8 TeV. The product of LO cross section and branching fraction varies between 3.0×10^3 fb (1 TeV) and 3.3×10^{-4} fb (8 TeV), to be compared with 1.7×10^7 fb for Standard Model W production and muonic decay. The detector response was simulated with the full CMS simulation [8] and reconstruction [10] software. Both the signal events and the following background samples were analysed: $\text{W} \to \mu\nu$, $Z \to \mu\mu$, WW inclusive, ZZ inclusive, ZW inclusive, $t\bar{t}$ inclusive. These data sets have been produced in the CMS Data Challenge 2004. On average 3.5 minimum bias reactions have been overlaid to each event.

14.4.3. Event selection and analysis

Events have been preselected requiring at least one globally reconstructed muon which pass the trigger criteria.

The final cuts to select $W' \to \mu\nu$ candidate events are:

- muon quality: at least 13 hits along the global track, $\chi^2/N_{dof} < 50$ for the fit;
- single muon requirement;
- muon isolation: no additional track ($p_\text{T} > 0.8\,\text{GeV}$) within a cone of size $\Delta R = 0.17$.

These cuts have been chosen to maximise the signal/background ratio.

For the selected events the transverse mass

$$M_\text{T} = \sqrt{2 p_{\text{T}_\mu} E_\text{T}^\text{miss} (1 - \cos \Delta\phi_{\mu, E_\text{T}^\text{miss}})}$$

is calculated from the muon transverse momentum p_{T_μ}, the missing energy component in the transverse plane E_T^miss and the angular $\Delta\phi_{\mu, E_\text{T}^\text{miss}}$ between both in this plane. Figure 14.9 shows the resulting distribution for signal (1 and 5 TeV) and background events. The W' boson distributions show a Jacobian peak which is spread out for large M_T due to the detector resolution. It can be seen immediately, that a 1 TeV boson can be discovered or excluded easily, while for higher masses a statistical analysis is needed to quantify the sensitivity.

14.4.4. Discovery and exclusion potential

To interpret the results, the CL_s method [508] is applied, which is based on the likelihood ratios, calculated for all bins of the M_T distribution. CL_s is defined as ratio of the confidence levels for the signal and background hypotheses, $\text{CL}_\text{s} = \text{CL}_{\text{s+b}}/\text{CL}_\text{b}$.

Figure 14.10 shows, that for an integrated luminosity of $10\,\text{fb}^{-1}$, a limit of 4.7 TeV at the 95% CL is reachable, if no signal is present in the CMS data. Both the expected discovery and exclusion limits are displayed in Fig. 14.11 as a function of integrated luminosity and W' mass. To investigate the sensitivity to the signal and background cross sections, they have been varied in a wide range; relative changes by factors of 2 and 10, respectively, lead to a lowering of the accessible mass range by about 0.5 TeV in the worst case.

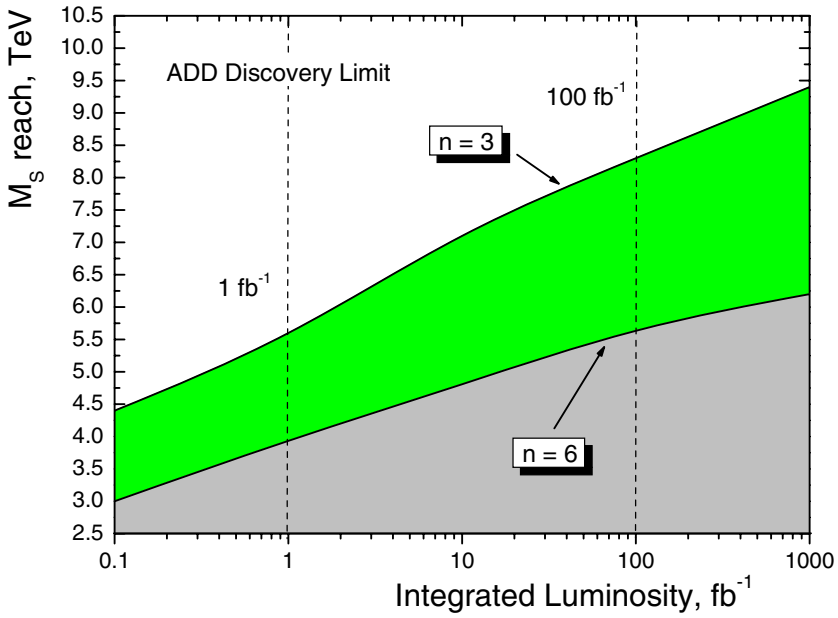

Figure 14.9. 5σ limit on M_S for the number of extra dimensions $n = 3$ and 6.

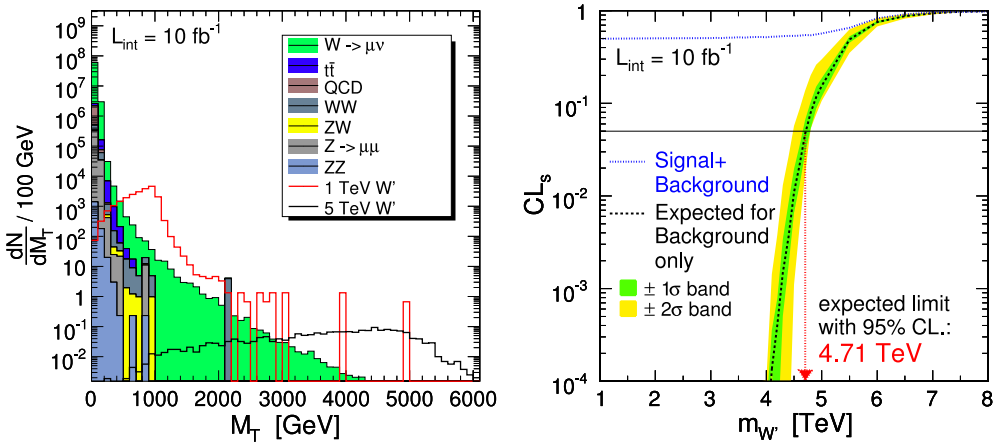

Figure 14.10. (Left) transverse invariant mass spectrum of signal (1 and 5 TeV, non-stacked) and background (stacked) after applying the selection cuts. (Right) result of the CL_s-method: with an integrated luminosity of 10 fb^{-1}. Reference W' bosons can be excluded up to a mass of 4.7 TeV.

14.4.5. Systematic uncertainties

The uncertainties arising from an imperfect knowledge of the PDFs at LHC energies and the error from the hard scale parameters have been investigated by using the Les Houches Accord PDFs [95] and varying the hard scale, respectively. The relative errors on the cross-section of the signal are listed in Table 14.4. The error on the background is comparable to that of the W' at the corresponding invariant mass.

The steep falling invariant mass distribution especially of the W background holds a potential danger for the detection of W' bosons: if only a small fraction of these events is

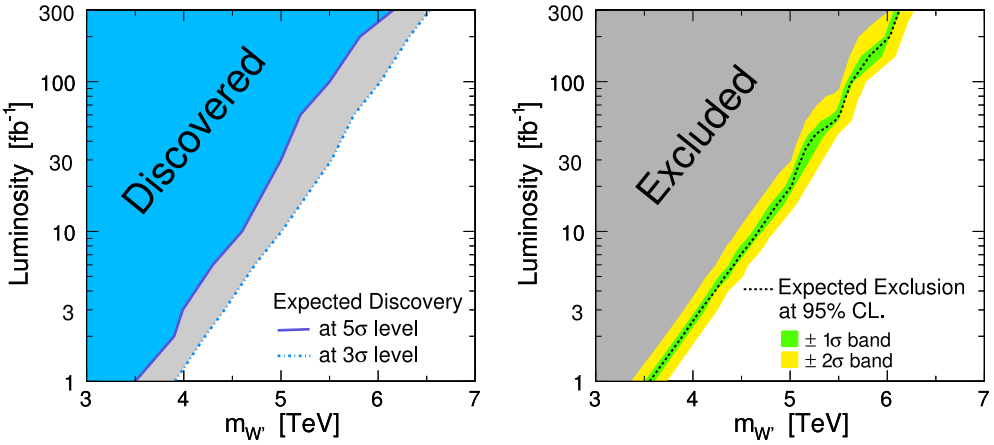

Figure 14.11. The plots show which integrated luminosity is needed to discover (left) or exclude (right) W' bosons of a certain mass.

Table 14.4. Relative systematic uncertainties in percent, arising from an imperfect theoretical knowledge (parton density functions, hard scale) and the expected luminosity error for an integrated luminosity of 10 fb^{-1}.

	Systematic Uncertainties				
Type	1 TeV W'	2 TeV W'	3 TeV W'	4 TeV W'	5 TeV W'
PDF $\Delta\sigma/\sigma$	$^{+3.6}_{-4.3}$	$^{+6.8}_{-5.9}$	$^{+6.2}_{-8.3}$	$^{+17.1}_{-10.6}$	$^{+33.7}_{-18.9}$
Hard Scale $\Delta\sigma/\sigma$	$^{+4.1}_{-4.1}$	$^{+7.5}_{-6.9}$	$^{+10.4}_{-9.2}$	$^{+13.1}_{-10.3}$	$^{+14.8}_{-12.7}$
Luminosity $\Delta\mathcal{L}/\mathcal{L}$	±5%	±5%	±5%	±5%	±5%

reconstructed with a by far too large mass, which might result from a mis-measured muon momentum, the detection of a W' becomes extremely difficult. Such a behaviour would be visible in non-gaussian tails for example in the p_T resolution distribution. Using a large sample of a W events it could be demonstrated, that the alignment precision expected after an integrated luminosity of 10 fb^{-1} has only a small influence on the non-gaussian tails of the muon p_T resolution distribution.

The luminosity uncertainty at the considered integrated luminosity of 10 fb^{-1} is expected to be 5%, while other experimental errors (neutron background, dead detector components, etc.) are expected to be negligible.

14.4.6. Summary

For an integrated luminosity of 10 fb^{-1}, W' bosons of the Reference Model can be discovered or excluded up to a mass of 4.5–5 TeV, from an analysis of the muonic decay mode.

14.5. High mass dijet final states

14.5.1. Dijet resonances and contact interactions

Dijet resonances and contact interactions are the two major signals of new physics with dijets. Dijet resonances are direct and compelling observations of a new physical object at a mass M, requiring an incoming parton-parton collision energy equal to the mass. Contact interactions

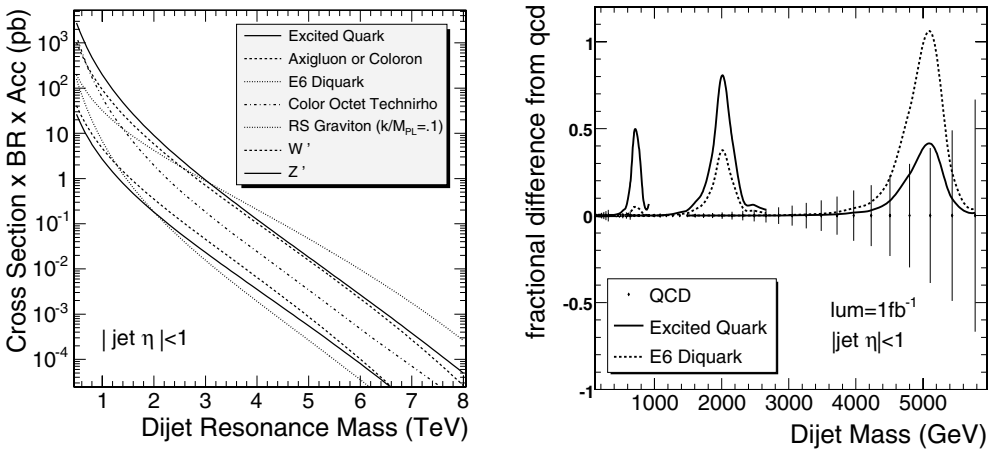

Figure 14.12. (Left) The total cross section times branching ratio times acceptance for dijet resonances from eight different models (see text). (Right) For resonance masses of 0.7, 2.0, and 5.0 TeV/c^2, the fractional difference between an excited quark (solid curve) or an E6 diquark (dashed curve) and the QCD dijet background is compared to the QCD statistical errors (vertical lines).

(discussed in Section 15.3) are indirect observations of an energy scale of new physics, Λ, which can be significantly larger than the available collision energy. Resonances are clear signals but contact interactions are often observed first.

14.5.2. Dijet resonance search

We search for processes producing narrow resonances, X, decaying to dijets: $pp \to X \to$ jet + jet (inclusive) [730]. Our experimental motivation is that LHC is a parton-parton collider, and resonances made from partons must decay to the same partons giving two jets in the final state. The theoretical motivation is broad, since there are many models that predict narrow dijet resonances.

14.5.2.1. Dijet resonance models. In Fig. 14.12 we show the cross section times branching ratio times acceptance calculated to lowest order for eight benchmark models. Here we introduce them in order of descending cross section at low mass. Excited states of composite quarks [731] are strongly produced giving large cross sections ($qg \to q^*$). Axigluons (A) [732] or colorons (C) [733] from an additional colour interaction are also strongly produced, but require an anti-quark in the initial state ($q\bar{q} \to A$ or C) slightly reducing the cross section compared to excited quarks. Diquarks [734] from superstring inspired E_6 grand unified models are produced with electromagnetic coupling from the valence quarks of the proton ($ud \to D$). The cross section for E_6 diquarks at high mass is the largest of all the models considered, because at high parton momentum the probability of finding a quark in the proton is significantly larger than the probability of finding a gluon or anti-quark. Colour octet technirhos [735] from topcolour-assisted technicolour are produced for either gluons or quark-anti-quark pairs in the initial state through a vector-dominance model of mixing between the gluon and the technirho ($q\bar{q}, gg \to g \to \rho_{T8}$). Randall–Sundrum gravitons [94] from a model of large extra dimensions are produced with a significant cross section at masses below 1 TeV/c^2 primarily from gluons in the initial state ($q\bar{q}, gg \to G$). Heavy W bosons [736] inspired by left-right symmetric grand unified models have electroweak couplings and

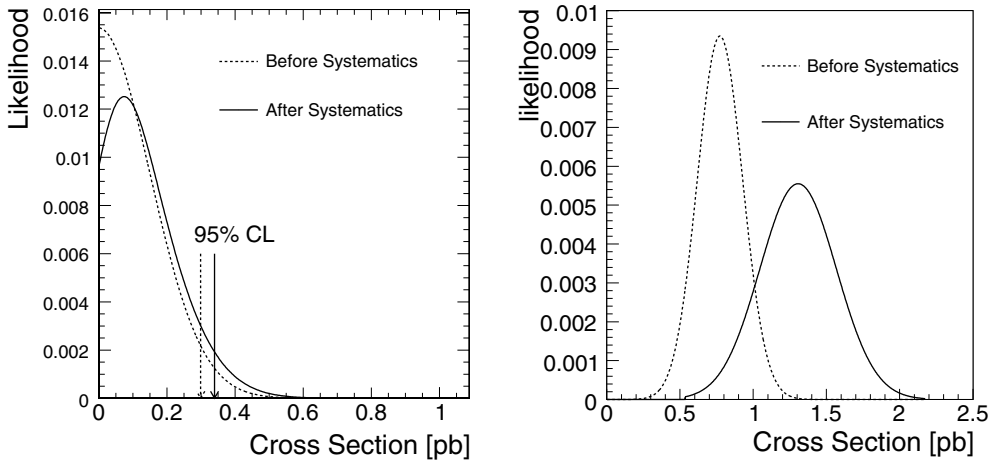

Figure 14.13. Likelihoods for observing a narrow dijet resonance of mass 2 TeV/c^2 in a 1 fb^{-1} data sample that contains only QCD background (left) and a data sample that also contains a resonance with a significance of 5σ (right) are shown with statistical uncertainties only (dashed) and including systematics (solid).

require anti-quarks for their production ($q_1\bar{q}_2 \rightarrow W'$) giving small cross sections. Heavy Z bosons [736] inspired by grand-unified models are widely anticipated by theorists, but they are weakly produced, and require an anti-quark in the initial state ($q\bar{q} \rightarrow Z'$), so their production cross section is around the lowest of the models considered. Lower limits from CDF [120] and D0 [121] on the mass of these models range from 0.4 to 1.0 TeV/c^2.

14.5.2.2. Dijet resonance sensitivity estimates. The signal and background dijet mass distributions for narrow resonances were presented in Section 4.1.4. In Fig. 14.12 we demonstrate the size of the signal for excited quarks and E_6 diquarks compared to the QCD background and it's statistical uncertainty. It is clear that we will be sensitive to such large signals for strongly produced dijet resonances. Here we quantify our sensitivity to any model of narrow dijet resonances. In Fig. 14.13 we show examples of likelihoods for excluding or observing a narrow resonance signal on a QCD background as a function of the signal cross section. In the case where the observed sample is QCD only, the signal likelihood peaks around zero cross section, and the 95% CL excluded signal cross section is shown. In the case where the observed sample is QCD plus a resonance signal, we have varied the signal size until the Gaussian distributed likelihood is 5σ above zero. In Fig. 14.13 we have included estimates of our systematic uncertainties. For a resonance mass of 0.7 (5.0) TeV/c^2 the systematic uncertainty on the observable signal cross section due to the jet energy uncertainty in the background rate is 15% (25%), the uncertainty due to jet resolution in the resonance shape is 10% (10%), the uncertainty due to radiation's affect on the resonance shape is 10% (25%), and the uncertainty due to luminosity is 10% (10%). For resonance masses just above the dijet mass thresholds where the trigger prescale decreases, there is an additional systematic uncertainty from the jet energy uncertainty. Systematic uncertainties have a greater effect on discovery than exclusion, because exclusions occur at a smaller signal cross section and are dominated by statistical uncertainties.

Figure 14.14 demonstrates that the 95% CL exclusion and 5σ discovery signal cross sections, including statistical uncertainties only, have reasonable values when compared to the size of the QCD statistical errors. Also in Fig. 14.13 we present the resonance cross

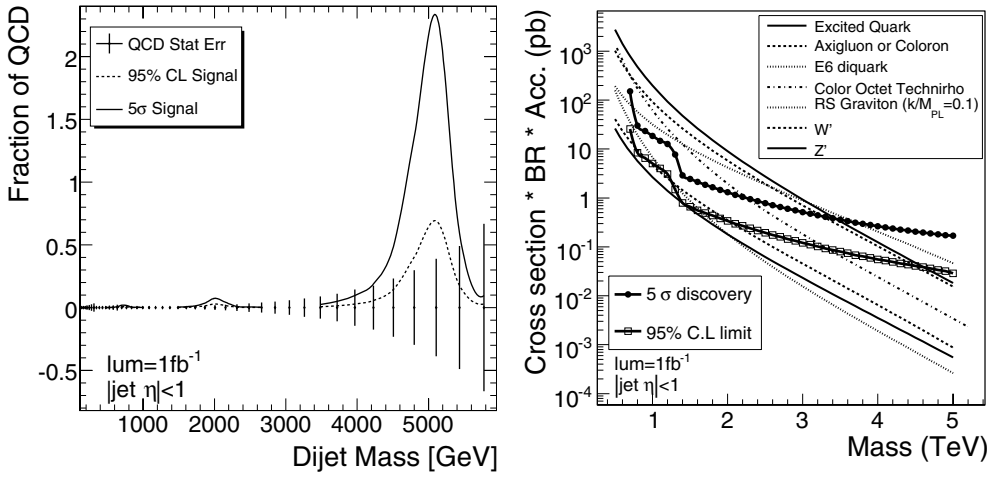

Figure 14.14. (Left) For resonances of mass 0.7, 2.0 and 5.0 TeV/c^2, the rate as a fraction of QCD that CMS expects to exclude (dashed) or discover (solid) including statistical uncertainties only. (Right) The resonance cross section that CMS expects to exclude (boxes) or discover (circles), including systematic uncertainties, is compared to the cross section for eight resonance models.

Table 14.5. Sensitivity to dijet resonances with 100 pb^{-1}, 1 fb^{-1} and 10 fb^{-1}. For each resonance model, we show the range of masses we expect to be able to exclude at a confidence level of 95% or greater, and the range of masses we expect to be able to discover with a significance of 5σ or greater. All estimates are with both statistical and systematic uncertainties.

Resonance Model	95% CL Excluded Mass (TeV/c^2)			5σ Discovered Mass (TeV/c^2)		
	100 pb^{-1}	1 fb^{-1}	10 fb^{-1}	100 pb^{-1}	1 fb^{-1}	10 fb^{-1}
Excited Quark	0.7–3.6	0.7–4.6	0.7–5.4	0.7–2.5	0.7–3.4	0.7–4.4
Axigluon or Colouron	0.7–3.5	0.7–4.5	0.7–5.3	0.7–2.2	0.7–3.3	0.7–4.3
E_6 diquarks	0.7–4.0	0.7–5.4	0.7–6.1	0.8–2.0	0.8–3.7	0.8–5.1
Colour Octet Technirho	0.7–2.4	0.7–3.3	0.7–4.3	0.7–1.5	0.7–2.2	0.7–3.1
Randall–Sundrum	0.7–1.1	0.7–1.1	0.7–1.1			
Graviton		1.3–1.6	1.3–1.6	N/A	N/A	N/A
			2.1–2.3			
W′	0.8–0.9	0.8–0.9	0.8–1.0	N/A	N/A	N/A
		1.3–2.0	1.3–3.2			
Z′	N/A	N/A	2.1–2.5	N/A	N/A	N/A

section values for jet $|\eta| < 1$ that CMS can expect to exclude at 95% CL or discover at 5σ significance for an integrated luminosity of 1 fb^{-1}. These can be compared with the cross section of any model of narrow dijet resonances, and here we compare with our benchmark models. From Fig. 14.14 we can read off the mass limits or discoveries that are possible with 1 fb^{-1} of data, which are listed in Table 14.5 along with the results of repeating the same analysis for 100 pb^{-1} and 10 fb^{-1}. The resonances that are produced via the colour interaction (excited quarks, axigluons, colorons and colour octet technirhos) or from the valence quarks of each proton (E_6 diquarks) have large cross sections and can be discovered up to a mass of a few TeV. A single search for resonances in the dijet mass distribution provides CMS with a sensitive test of many different models of the widely anticipated New Physics at the TeV scale.

14.6. High mass diphoton final states

14.6.1. Introduction

The study of the Randall–Sundrum (RS) graviton decaying into the two photons is particularly interesting as the detection of such few $\mathrm{TeV/c^2}$ mass resonance in such channel together with its observation in the dilepton channel will sign a RS graviton, distinguishing it from a Z′ production. The model is governed by two parameters: the graviton mass M and its coupling to Standard Model particles c, the latter being related to the natural width of the resonance.

14.6.2. Event generation and kinematics pre-selection

The search for the $\mathrm{G} \to \gamma\gamma$ signal at LHC is affected by four types of backgrounds:

- The prompt diphoton production from the quark annihilation and gluon fusion diagrams, which provides an intrinsic or 'irreducible' background.
- The γ + jets production consisting of two parts: i) prompt photon from hard interaction + the second photon coming from the outgoing quark due to final state radiation and ii) prompt photon from hard interaction + the decay of a neutral hadron (mostly isolated π^0) in a jet, which could fake a real photon.
- The background from QCD hadronic jets, where electromagnetic energy deposits result from the decay of neutral hadrons (especially isolated π^0s) in both jets.
- Drell–Yan process with e^+e^- in a final state which could mimic photons when correspondent electron tracks will not be assigned to the superclusters during the reconstruction.

Generator-level pre-selection and parameters used for QCD and bremsstrahlung backgrounds is described in [737].

14.6.3. Offline selection and analysis

The requirements for the analysis were as follows:

1 Two super-clusters (SCs) with $E_\mathrm{T} > 150\,\mathrm{GeV}$ and two HLT trigger bits triggered at the same time: 2p (two photons) and r2p (two photons relaxed).
2 Calorimeter isolation criteria: for each SC the energy in a cone of $\Delta R = 0.5$ (excluding SC itself) should be $< 0.02 E_\mathrm{T}(SC)$
3 $E(HCAL)/E(ECAL) < 0.05$
4 Tracker isolation: the sum of the energy of all tracks in a cone $\Delta R = 0.5$ around the SC should be $< 0.01 E_\mathrm{T}(SC)$
5 Photon energy corrections are done in a simple way so far:
   - For E1 energy $< 1.7\,\mathrm{TeV}$, only a simple energy dependent part of correction is applied (just a shift of the peak).
   - For E1 energy $> 1.7\,\mathrm{TeV}$, the MGPA saturation correction (1d) was applied (see and [738]).

14.6.4. K-factors

To produce the final results and to calculate the expected statistical significance for RS-1 graviton search recently calculated next-to-leading order corrections (K factors) to the cross sections of different types of background are used: $\mathrm{K} = 1.5$ for quark annihilation [26], $\mathrm{K} = 1.2$ for gluon fusion [29], $\mathrm{K} = 1$ for the γ + hadronic jets [29] and $\mathrm{K} = 1$ for QCD jets. For signal, a conservative $\mathrm{K} = 1$ value is taken.

Table 14.6. Number of events passed through the analysis cuts defined above for $M_G = 1.5\,\mathrm{TeV/c^2}$, $c = 0.01$ and $\mathcal{L} = 30\,\mathrm{fb^{-1}}$. Leading column is non-saturated events, all saturated events, passed through the analysis, were added in brackets, where applied.

	signal	Born (K = 1.5)	Box (K = 1.2)	Brem (K = 1)	QCD (K = 1)	DY (K = 1)
trigger + 2SC	28.9	8.6	0.10	29.2	798.7	4.3
+ EM isolation	24.5	5.5	0.08	20.3	361.8	3.5
+ HCAL/ECAL	24.3	5.4	0.08	4.4	12.8	3.5
+ tracker isolation	17.6	4.2(+0.2)	0.05	0.17	0.0	0.0

Table 14.7. Number of events passed through the analysis cuts defined above for $M_G = 3.5\,\mathrm{TeV/c^2}$, $c = 0.1$ and $\mathcal{L} = 30\,\mathrm{fb^{-1}}$. Leading column is non-saturated events, all saturated events, passed through the analysis, were added in brackets, where applied.

	signal	Born (K = 1.5)	Box (K = 1.2)	Brem (K = 1)	QCD (K = 1)	DY (K = 1)
trigger + 2SC	11.6	0.20	$4.4 * 10^{-4}$	0.78	821.9	0.10
+ EM isolation	10.8	0.14	$3.6 * 10^{-4}$	0.32	164.4	0.095
+ HCAL/ECAL	10.6	0.13	$3.4 * 10^{-4}$	0.016	0.0	0.095
+ tracker isolation	8.9(+1.0)	0.10(+0.02)	$2.7(+0.24) * 10^{-4}$	$1.7 * 10^{-3}$	0.0	$7.2 * 10^{-4}$

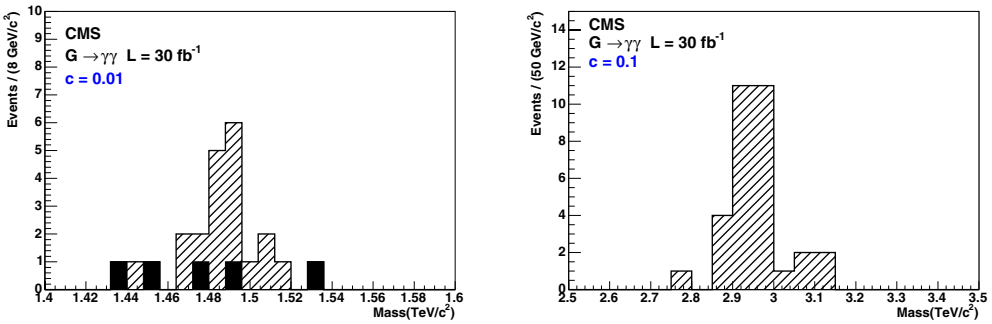

Figure 14.15. Number of events passing all cuts for (1.5 TeV/c^2, 0.01) (left) and (3.0 TeV/c^2,0.1) (right) RSI gravitons for 30 fb^{-1} integrated luminosity.

14.6.5. Results

The numbers of events passing the analysis cuts described above, for the signal and for the backgrounds, are presented in Table 14.6 (1.5 TeV/c^2, 0.01) and in Table 14.7 (3.5 TeV/c^2, 0.1).

Figure 14.15 shows the number of events satisfying all cuts for both signal and backgrounds for the cases (1.5 TeV/c^2, 0.01) and (3.0 TeV/c^2, 0.1) after 30 fb^{-1} luminosity. The results for one year low luminosity of 10 fb^{-1} are presented in Fig. 14.16.

Taking into account the K-factors described above, the number of events for signal and background and the significance S_{cL} (defined in Appendix A.1) for $c = 0.01$ and $c = 0.1$ are shown respectively in Tables 14.8 and 14.9 for an integrated luminosity of 30 fb^{-1}.

The significance as a function of the graviton mass (M_G) for integrated luminosities of 10 fb^{-1}, 30 fb^{-1} and 60 fb^{-1} are displayed in Fig. 14.17.

The discovery region in the plane of the coupling parameter c and the graviton mass is shown in Fig. 14.18.

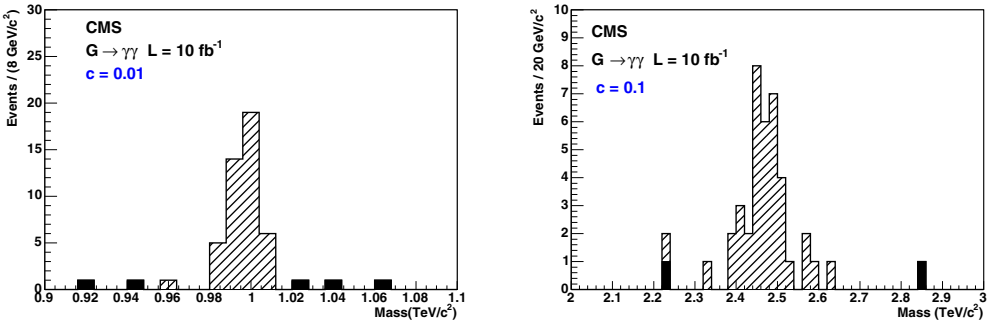

Figure 14.16. Number of events passing all cuts for (1.0 TeV/c^2, 0.01) (left) and (2.5 TeV/c^2,0.1) (right) RS-1 gravitons for 10 fb^{-1} integrated luminosity.

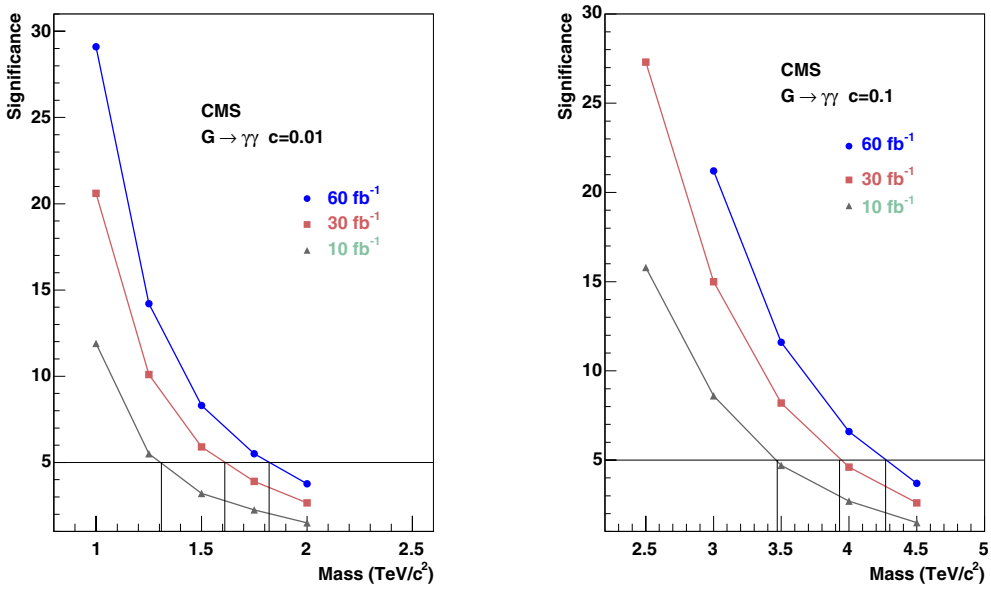

Figure 14.17. Significance as a function of the graviton mass for 10 fb^{-1}, 30 fb^{-1} and 60 fb^{-1} integrated luminosities, with c = 0.01 (left) and c = 0.1 (right).

Table 14.8. Significance for $c = 0.01$ and $\mathcal{L} = 30\,\text{fb}^{-1}$.

	$M_G = 1.0$ TeV/c^2	$M_G = 1.25$ TeV/c^2	$M_G = 1.5$ TeV/c^2	$M_G = 1.75$ TeV/c^2	$M_G = 2.0$ TeV/c^2
N_s	135.8	44.0	17.6	7.3	3.9
N_{bkg}	15.0	8.8	4.6	1.8	1.2
Significance	20.6	10.1	5.9	3.9	2.6

Table 14.9. Significance for $c = 0.1$ and $\mathcal{L} = 30\,\text{fb}^{-1}$.

	$M_G = 2.5$ TeV/c^2	$M_G = 3.0$ TeV/c^2	$M_G = 3.5$ TeV/c^2	$M_G = 4.0$ TeV/c^2	$M_G = 4.5$ TeV/c^2
N_s	103.8	31.6	9.9	3.44	1.11
N_{bkg}	1.11	0.35	0.13	0.06	0.02
Significance	27.3	15.0	8.2	4.6	2.6

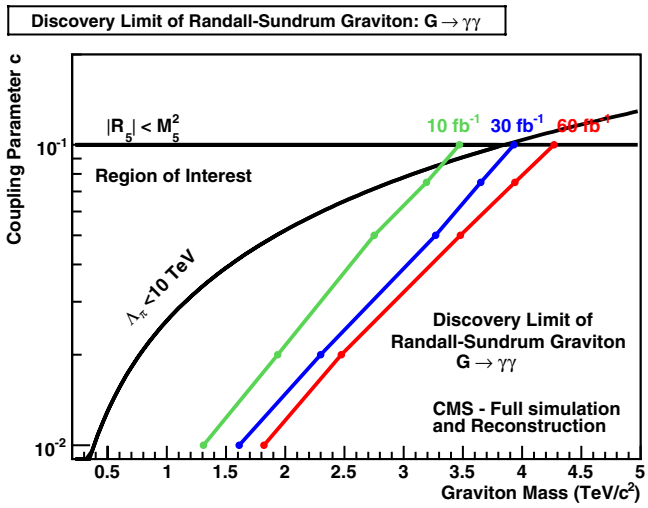

Figure 14.18. Reach of the CMS experiment in the search for the Randall–Sundrum graviton decaying into diphoton channel as a function of the coupling parameter c and the graviton mass for 10 fb^{-1}, 30 fb^{-1} and 60 fb^{-1}. The left part of each curve is the region where the significance exceeds 5σ.

Table 14.10. Hard scale confidence limits uncertainties for 30 fb^{-1}.

	$4\hat{s}$	$0.25\hat{s}$
$c = 0.01$	$-62\,\text{GeV/c}^2$	$+56\,\text{GeV/c}^2$
$c = 0.1$	$-47\,\text{GeV/c}^2$	$+42\,\text{GeV/c}^2$

The discovery region for 60 fb^{-1} extends to $M_G = 1.82\,\text{TeV/c}^2$ if $c = 0.01$ and to $M_G = 4.27\,\text{TeV/c}^2$ if $c = 0.1$. For 30 fb^{-1} it is $M_G = 1.61\,\text{TeV/c}^2$ if $c = 0.01$ and $M_G = 3.95\,\text{TeV/c}^2$ if $c = 0.1$. For 10 fb^{-1} it reaches to $M_G = 1.31\,\text{TeV/c}^2$ if $c = 0.01$ and $M_G = 3.47\,\text{TeV/c}^2$ if $c = 0.1$.

14.6.6. Systematic uncertainties for 30 fb^{-1}

Several systematic uncertainties and their effect on the mass reach have been evaluated for an integrated luminosity of 30 fb^{-1}. The effect of hard scale uncertainties is given in Table 14.10, computed by multiplying and dividing the scale $\hat{s}$ by a factor 2. The uncertainties from the pdfs, computed with LHAPDF, amount for $c = 0.01$ to $-55\,\text{GeV/c}^2$ and for $c = 0.1$ to $-152\,\text{GeV/c}^2$. There is another source of uncertainties due to the fact, that we have used K-factor = 1.5 for the Born process, while the most recent measurements at the Tevatron pointed to a K-factor closer to 2 [739]. The effect of such a change on the mass reach is $-50\,\text{GeV/c}^2$ for $c = 0.01$ and $-30\,\text{GeV/c}^2$ for $c = 0.1$.

14.7. Single γ final state with $E_{\text{T}}^{\text{miss}}$ from extra dimensions

14.7.1. Topology of single-photon final states

An introduction to the signals involving direct graviton emission in ADD type of extra dimensions frameworks is given is Section 14.3.2. The topology of single photon events can

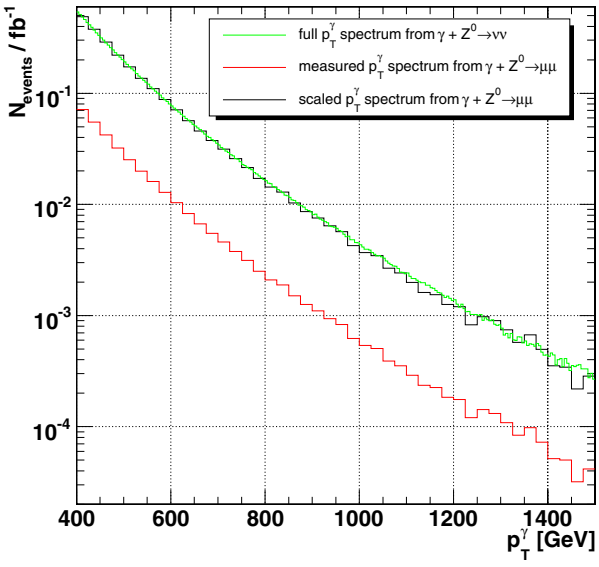

Figure 14.19. Number of expected p_T^γ events per 25 GeV bin at 1 fb^{-1} from measured $\gamma+Z^0 \to \mu^+\mu^-$ events before and after transformation compared with the generator distribution for $\gamma+Z^0 \to \nu_i\bar{\nu}_i$ – the transformed muon distribution models the $\nu_i\bar{\nu}_i$ spectrum well.

be identified by:

- a single high p_T photon in the central η region;
- high missing p_T back-to-back to the photon in the azimuthal plane with a similar p_T distribution.

These characteristics are not strongly dependent on the ADD model parameters. The details of this analysis can be found in [740].

14.7.2. Backgrounds from the Standard Model

All signal and background samples used in the following were simulated using the CMS fast detector simulation [11]. Fully simulated reference samples were generated for the signal and the largest irreducible background, $Z^0\gamma \to \nu\bar{\nu}+\gamma$. A detailed comparison of the resolution, efficiency and purity of all reconstructed objects used in this analysis to the GEANT-based CMS simulation confirmed that the fast simulation provides a very good approximation of the expected detector response. All samples were consistently generated using a generator level cut in PYTHIA $\hat{p_T} > 400$ GeV. The backgrounds considered in the study are, $Z^0\gamma \to \nu\bar{\nu}+\gamma$, $W^\pm \to \ell\nu$ where ℓ is electron, muon or tau, $W^\pm\gamma \to e\nu+\gamma$ γ+Jets, QCD, di γ and Z^0 + jets. For the main background, a normalisation method from measured data is developed employing the reconstructed leptonic decays of the Z^0 into muon and electron pairs.

The detector acceptance for selecting the leptons is parameterised using a two-dimensional function $\alpha(p_T^\gamma, \eta_\gamma)$. Figure 14.19 shows the measured and the p_T^γ spectrum from $\gamma+Z^0 \to \mu^+\mu^-$ after the (acceptance $\times$ efficiency) parameterisation is applied, in comparison with the generator spectrum for $\gamma+Z^0 \to \nu_i\bar{\nu}_i$ events. For $p_T^\gamma > 100$ GeV/c there is 1170 $Z^0 \to \mu^+\mu^-/e^+e^-$ events expected after all selection cuts for 30 fb^{-1}. These can be used as the candle sample that provides a direct normalisation of the $\gamma+Z^0 \to \nu_i\bar{\nu}_i$ with a statistical precision of 3%.

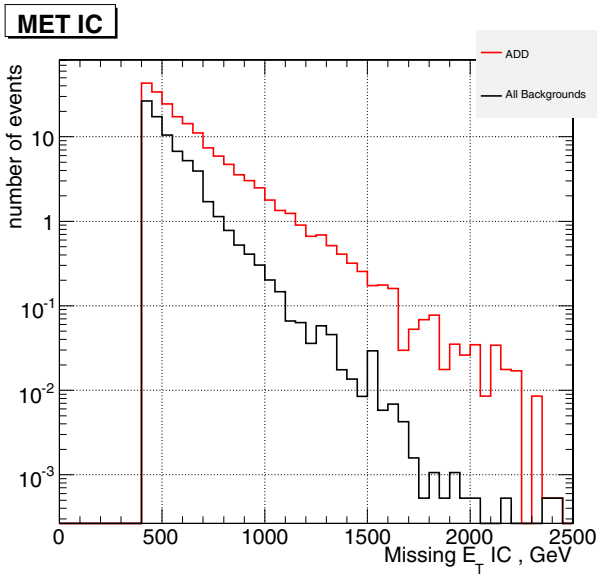

Figure 14.20. Spectrum of the missing E_{T} for all backgrounds (black histogram) and for an example signal sample ($M_{\mathrm{D}} = 2.5$ TeV, $n = 2$). The number of events corresponds to an integrated luminosity of 30 fb^{-1}.

14.7.3. Event selection

The main trigger path for the selection of signal and background events will be the single photon trigger, both at the Level-1 and the HLT. Presently the single photon trigger has a HLT level threshold of 80 GeV, which is far below the selection cut for events with isolated photons above 400 GeV used here. Hence the expected trigger efficiency is close to 100% and its efficiency can be monitored from data with a $E_{\mathrm{T}}^{\mathrm{miss}}$ trigger which will have a threshold in the range of 200–300 GeV, well below the acceptance of the bulk of the signal. Both the topological characteristic and the necessity to reduce the Standard Model background lead to the following selection criteria:

- At least a $E_{\mathrm{T}}^{\mathrm{miss}} > 400$ GeV is required and the photon p_{T} has to be above 400 GeV.
- $|\eta|$ of the photon < 2.4.
- $\Delta\phi(E_{\mathrm{T}}^{\mathrm{miss}}, \gamma) > 2.5$.
- A track veto for high p_{T} tracks > 40 GeV is applied. This is a powerful criterion to reduce all backgrounds containing high-energetic charged particles (such as $e^{\pm}$, $\mu^{\pm}$, jets).
- An Isolated Photon Likelihood criterion is applied to remove residual background from hard photon emission from jets as well as fake photons from jets.

Figure 14.20 shows the missing transverse energy spectra for events surviving the selection path for both the signal and the backgrounds. As expected the $Z^0\gamma$ is by far the most dominant component of the background, followed by $W^{\pm}\gamma$ while the contributions of the other Standard Model backgrounds are small. For all ADD cross section the hard truncation approach is used (see Section 14.1), i.e. events with $M_G < M_D$ are rejected.

14.7.4. Systematic uncertainties and discovery potential

We consider an uncertainty of 2% for the measurement of the photon p_{T}^{γ} in the electromagnetic calorimeter and an uncertainty of 5% for the $E_{\mathrm{T}}^{\mathrm{miss}}$ measurement. The

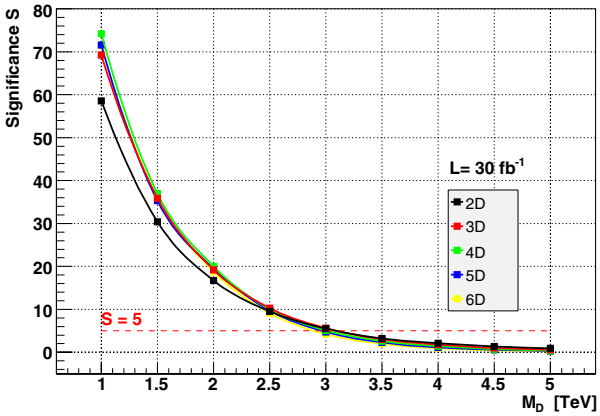

Figure 14.21. Expected significances as function of M_{D} for different number n of extra dimensions.

resulting decrease of the significance is 1.0% and 1.6% respectively. For the main background the systematics can be reduced to the luminosity measurement using the Z^0 candle calibration method. It can thus be measured with a precision of 3% after 30 fb^{-1}. The 5σ discovery reach is achievable for M_D <2.5 TeV/c^2 and all values of extra dimensions while for M_D < 3 TeV/c^{2}5σ reach is achievable for n between 2 and 4. Figure 14.21 shows the expected significances as function of M_{D}.

14.8. Black holes

14.8.1. Introduction to higher-dimensional black holes

One of the consequences of large extra dimensions is the possibility to produce microscopic black hole (BH) at LHC energies. Such a BH formed in a (4+n)-dimensional space-time has a Schwarzschild radius

$$r_{s(4+n)} = \frac{1}{\sqrt{\pi}\,M_{(4+n)}}\left(\frac{M_{BH}}{M_{(4+n)}}\left(\frac{8\Gamma((n+3)/2)}{n+2}\right)\right)^{1/(n+1)} \tag{14.18}$$

where $M_{(4+n)}$ is the reduced Planck scale and n is the number of large extra dimensions [741]. A high energy collision of two partons can result in the formation of a BH when the impact parameter is smaller than $r_{s(4+n)}$. In the semi-classical approach the BH cross section is given by $\sigma(M_{\mathrm{BH}}) = \pi r^2_{s(4+n)}$ at the parton level. If for low masses $M_{(4+n)}$, i.e. around 2 TeV, the BH production cross sections at the LHC is in the pb range.

Once produced, these BHs are expected to decay thermally via Hawking radiation [742]. The Hawking temperature for a BH in 4 + n dimensions is [743]

$$T_{(4+n)} \sim M_{(4+n)}(M_{(4+n)}/M_{\mathrm{BH}})^{1/(n+1)}. \tag{14.19}$$

These BHs have a very short lifetime typically of $\sim 10^{-27}$ seconds.

BH events are expected to evaporate democratically by emission of all particle types that exist in nature, independent of their spin, charge, quantum numbers or interaction properties. Therefore they can be a source of new particles. BH physics at the LHC can provide the possibility of probing quantum gravity in the lab.

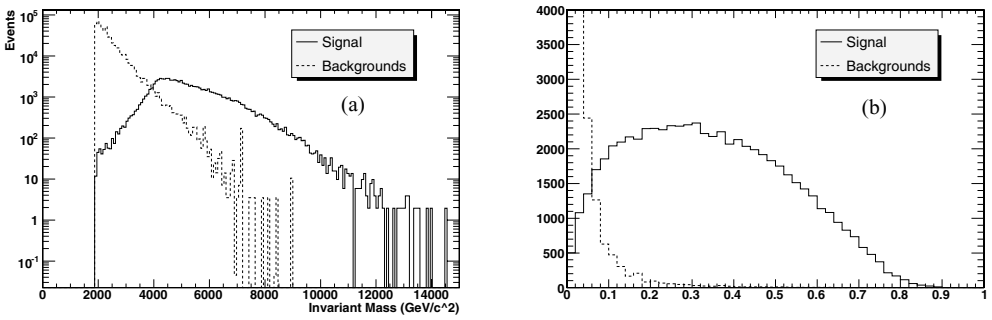

Figure 14.22. (a) Reconstructed invariant mass distribution and (b) event sphericity for black hole and standard model background events.

14.8.2. Analysis selection path and results

Black hole event samples were produced using the CHARYBDIS event generator [744]. As a benchmark the case which is analysed has the following parameters: a) $2\,\mathrm{TeV/c^2}$ effective Planck scale, b) $4\,\mathrm{TeV/c^2}$ minimum and $14\,\mathrm{TeV/c^2}$ maximum black hole mass c) 3 extra dimensions. Time evolution during Hawking radiation and gray body effects are included. The detector response was simulated by us using the CMS fast simulation (FAMOS, version 1.4.0) after validation against the detailed CMS GEANT-based simulation. The Standard Model backgrounds taken into account include QCD jets, top production and boson plus jet production. The invariant mass of all final state objects (electrons, photons, jets and muons) in the event is found to be correlated with the input black hole mass. In addition since the black hole formation can only occur if $M_{\mathrm{BH}} > M_{(4+n)}$, the event invariant mass can indicate the effective Planck scale $M_{(4+n)}$. In the benchmark scenario the invariant mass is required to be greater than $2\,\mathrm{TeV/c^2}$. BH events are characterised by a high multiplicity of the final state particles, which increase as a function of the BH mass (and decreases as a function of Hawking temperature). In particular the ratio of jets to leptons is found to be 5 to 1. In this study with a simple jet and lepton multiplicity counting the jet/lepton ratio is formed. The average value of this ratio is found to be 4.5. The thermal nature of Hawking radiation requires the distribution of BH remnants to be spherical as shown and a sphericity of 0.28 is required which eliminates drastically the Standard Model backgrounds. The invariant mass distribution and sphericity for the signal and background events is shown in Fig. 14.22.

Events are counted when the total sum of the P_{T} of all reconstructed objects plus the missing transverse energy is larger than 2500 GeV. A study of the Level-1 and HLT trigger path shows that the 4 jet trigger has a 93% efficiency for the signal events and is used in the analysis.

The event selection criteria applied to the reconstructed events and the efficiencies of the requirements are listed in Table 14.11.

The minimum integrated luminosity needed for 5σ significance and for the benchmark point is $\sim 2\,\mathrm{pb}^{-1}$. A survey of the parameter space using 25 points shows that for effective Planck scale of 2–3 TeV, minimum black hole mass up to 4 TeV and 2–6 extra dimensions the 5 sigma significance can be obtained with luminosity between fraction of pb^{-1} and 100's of pb^{-1}. For effective Planck scale of 4 TeV a few fb^{-1} is needed for discovery. To account for the systematic uncertainties in the number of signal events, the effect of PDF distribution on cross section is calculated using the CTEQ6 NLO PDF set with the help of LHAPDF interface. PDF uncertainties for the chosen benchmark point is found to be $^{+24.2\%}_{-9.07\%}$. Using these uncertainties, the error in significance calculation was computed to be 12%.

Table 14.11. Event selection and background rejection for signal events and major background processes.

Cut	Signal	tt+nJ	W+nj	Z+nJ	QCD Dijet	WW+nJ
Cross Section (pb)	18.85	371	896	781.84	33076.8	269.91
Events ($10\,\mathrm{fb}^{-1}$)	188500	3.71×10^{6}	8.96×10^{6}	7.82×10^{6}	3.31×10^{8}	2.70×10^{6}
$M\mathrm{Inv} > 2\,\mathrm{TeV/c^2}$	18.71	13.29	6.53	3.85	2634.94	20.53
Tot. Multiplicity > 4	17.72	13.25	6.43	3.84	2613.18	20.42
Sphericity > 0.28	9.27	1.60	0.23	0.10	53.74	0.07
Final No. Events ($10\,\mathrm{fb}^{-1}$)	92740	15990	2328	982	537391	740

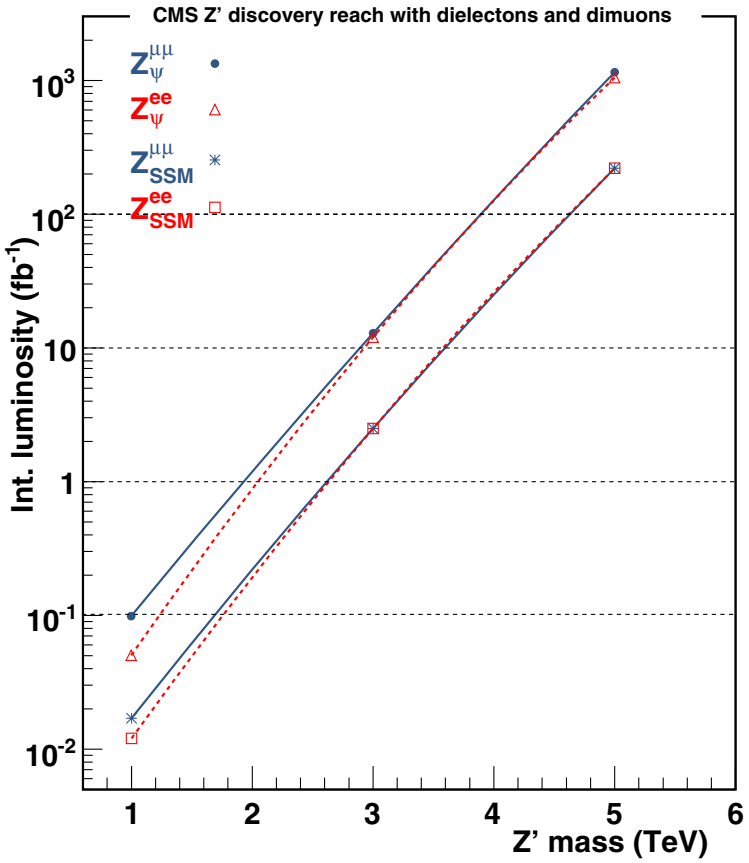

Figure 14.23. Z′ discovery reach for two of the models studied in the dielectron and dimuon channels. The reach for the rest of the models studied is within the band between the two shown here.

14.9. Discussion

The results on Z′s and RS gravitons in the channels studied in this chapter are summarised here.

In Fig. 14.23 the summary of the discovery reach in the dielectron and dimuon channels is shown for two representative Z' models. The reach for the rest of the models studied lies within the band of the two shown in the figure. The results for the dielectron channel are using

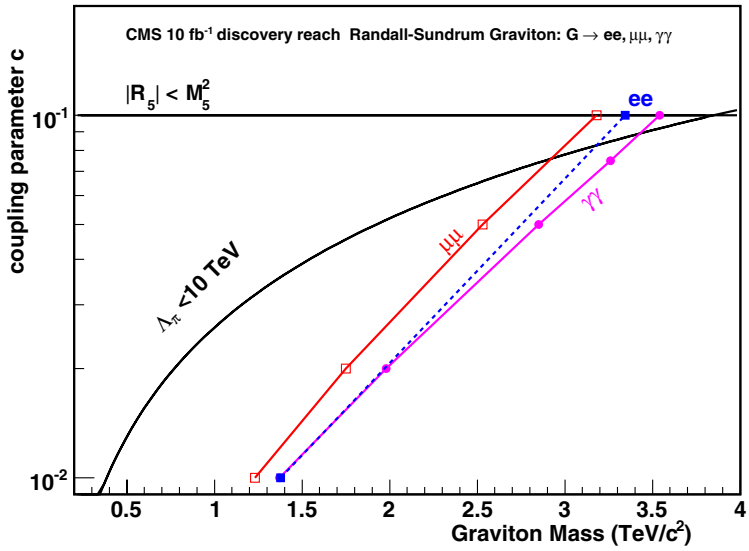

Figure 14.24. RS graviton discovery mass reach as a function of the model coupling parameter in the dielectron, dimuon and diphoton channels for 10 fb^{-1}. The dielectron reach is shown as dashed because only the boundary points (c = 0.01 and c = 0.1) where studied.

here K-factor of 1.3 for the signal and background in order to be directly compared with the dimuon results[50]. Although the analysis strategies and significance computation is different between the two analyses the results are compatible. For low luminosity and mass reach up to 3 TeV/c^2 the muons suffer from misalignment effects which are recovered after 10 fb^{-1}. For high mass reach (above 3 TeV/c^2) the saturation in the ECAL is causing a degradation of the resolution in the dielectron channel. The reach using the dielectron channel is up to 3 TeV better than the dimuons due to less than 1% resolution. Optimising the analysis in the dielectron channel to extract the background from the data and detailed studies of the saturation is expected to further improve the reach in the dielectron channel for high masses. The combined reach of the two channels requires a detailed analysis and is not presented here. Note that a 1 TeV/c^2 Z' is observable with less than 0.1 fb^{-1} for all models and with a single channel while every TeV/c^2 in mass reach corresponds to approximately an order of magnitude increase in integrated luminosity.

In Fig. 14.24 the summary of the RS graviton discovery reach in the dielectron, dimuon and diphoton channels is shown. Here the results for the diphoton channel are using CTEQ6M PDFs to be directly compared with the dielectron and dimuon channels.[51] Although the branching ratio to photons is roughly twice that of electrons or muons the reach for low coupling and graviton mass is comparable between dielectrons and diphotons due to the QCD and prompt photon backgrounds in the photon channel which are harder to efficiently suppress. For higher masses and coupling the diphoton is leading the reach due to the higher branching ratio. The dimuon channel is trailing the reach compared to the dielectrons merely due to resolution.

[50] Recent calculation of K-factors for several of the processes discussed here can be found in reference [745].

[51] In the main analysis the diphoton channel uses CTEQ5L while the dielectron and dimuon analyses use CTEQ6M where the gluon-gluon contribution is enhanced compared to the CTEQ5L; while the Drell–Yan background is largely insensitive to this choice, at low masses the gluon-gluon is the dominant graviton production process while at high masses the qq dominates where CTEQ5L and CTEQ6M are comparable.

Chapter 15. Alternative BSM Signatures

15.1. Technicolour

15.1.1. The $\rho_{TC} \to W + Z$ channel

Technicolour (TC) provides an alternative to the elementary Higgs mechanism of the Standard Model. It introduces a new strong interaction [746] providing a dynamical nature to Electroweak Symmetry Breaking. Technicolour is a QCD-like force, acting on technifermions at an energy scale $\Lambda_{TC} \sim v_{weak} = 246\,\text{GeV}$. A number N_D of technifermion doublet condensates yield the pseudo-Goldstone bosons π_{TC}, together with a wide spectroscopy of excited technimesons. The present simulation is performed using the phenomenology of the lowest-lying technihadrons, commonly referenced as the "Technicolour Straw Man" model (TCSM) [735]. The colour-singlet sector includes the spin-zero π_{TC} and the spin-one technimesons ρ_{TC} and ω_{TC}. The decay cross-section of the ρ_{TC} is expressed as an admixture of π_{TC} and the Standard Model Z and W bosons:

$$\rho_{TC} \to \cos^2\chi\,\langle\pi_{TC}\pi_{TC}\rangle + \cos\chi\,\sin\chi\,\langle\pi_{TC}V_L\rangle + \sin^2\chi\,\langle V_L V_L\rangle \qquad (15.1)$$

where V_L is the longitudinal mode of the $V = Z, W$ and $\sin\chi \simeq 1/\sqrt{N_D} \sim 1/3$. The branching fraction $\text{BR}(\rho_{TC} \to W + Z)$ is competing with the two first terms in Eq. 15.1, hence changing with $\text{M}(\pi_{TC})$.

The decay channel $\rho_{TC} \to W + Z$ is the subject of this analysis [747] as it has the advantage of a very clean final state, namely $3\ell + \nu$. The background contributions arise mainly from Standard Model processes involving weak boson production and decays. Other technicolour decay modes that include jets such as $\rho_{TC} \to \pi_{TC} + W$, have higher branching fractions but are much harder to disentangle from the Standard Model background processes.

15.1.1.1. Event selection. All signal and backgrounds samples used in this analysis are generated with PYTHIA 6.2 [24] with the requirement of at least 3 prompt leptons in the CMS fiducial region. The $Zb\bar{b}$ background is generated using COMPHEP [355] interfaced to PYTHIA. Contributions from processes of type $Z \to 2\ell$ plus an additional fake lepton from a jet have been taken into account in the systematic uncertainties, see Sect. 15.1.1.2. A set of 14 different ρ_{TC} samples are generated within the $[\text{M}(\rho_{TC}), \text{M}(\pi_{TC})]$ phase space.

Nominal CMS Level-1 and High-Level Trigger requirements are applied [76]. The CMS fast simulation [11] is used for detector simulation and event reconstruction. The main reconstructed objects and their efficiencies have been validated against the detailed GEANT-based CMS detector simulation [8, 10].

The analysis is designed to reduce the main Standard Model background contributions WZ, ZZ, $Zb\bar{b}$ and $t\bar{t}$, while retaining high signal efficiency. It is summarised as follows:

(i) Lepton selection: 3 high-p_T and isolated electrons or muons.
(ii) Lepton trigger: single- or two-electron or muon mode (Level-1 and HLT).
(iii) Z : same-flavour and opposite-charge ℓ-pair closest to $\text{M}(Z)$, with $p_T(\ell_{1,2}) > (30, 10)\,\text{GeV/c}$.
(iv) W : solution to 3rd lepton with $p_T > 10\,\text{GeV/c}$ + Missing E_T + $\text{M}(W)$ constraint.
(v) $|\text{M}(\ell^+\ell^-) - \text{M}(Z)| \leqslant 3\sigma_{\text{M}_Z} \cong 7.8\,\text{GeV/c}^2$.
(vi) $p_T(Z)$ and $p_T(W) > 30\,\text{GeV/c}$. For benchmark points with $\text{M}(\rho_{TC}) = 200\,\text{GeV/c}^2$, the minimum $p_T(Z)$ and $p_T(W)$ threshold is $10\,\text{GeV/c}$.
(vii) $|\Delta[\eta(Z) - \eta(W)]| \leqslant 1.2$.

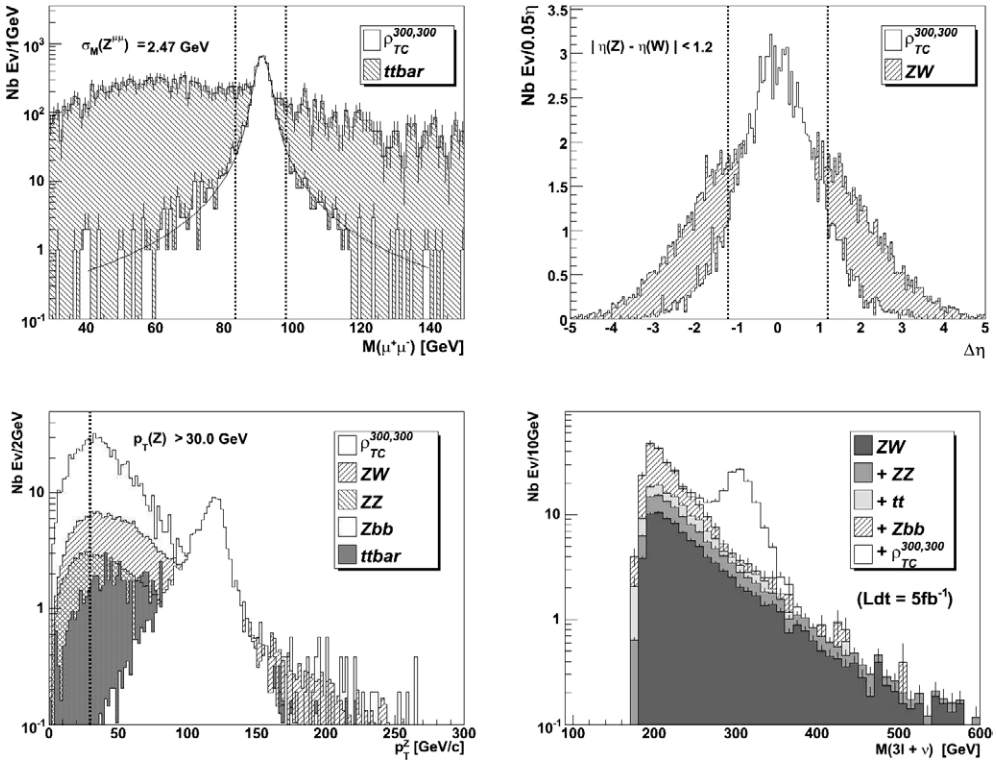

Figure 15.1. (a) $M(\mu^+\mu^-)$ for $\rho_{TC}(300, 300)$ and $t\bar{t}$; (b) $\Delta[\eta(Z) - \eta(W)]$ for $\rho_{TC}(300, 300)$ and WZ; (c) $p_T(Z)$ for $\rho_{TC}(300, 300)$ and all backgrounds ($p_T(W)$ is similar); (d) Reconstructed $M(3\ell + \nu)$ for $\rho_{TC}(300, 300)$ and all backgrounds. The vertical lines indicate the applied requirements.

The Z and W are reconstructed with a purity of $\sim$99%, using the 3 highest-p_T leptons in the event, and the Missing Transverse Energy (MET), obtained as the vector sum of the jets and leptons in the event. The $M(W)$ constraint yields a 2 fold ambiguity in the p_Z component of the reconstructed neutrino: it is found that the most efficient choice for the ρ_{TC} signal is the minimum p_Z solution. The kinematic cuts are illustrated in Fig. 15.1. The main $t\bar{t}$ reduction is obtained via the Z-mass window requirement (v). The irreducible background $WZ \to 3\ell + \nu$ is most efficiently separated from the signal via the $\eta(Z) - \eta(W)$ correlation requirement (vii).

The p_T cut on Z and W further improves the signal to background ratio, however it is kept modest in order to preserve the exponential background hypothesis of the $3\ell + \nu$ invariant mass spectrum, used to compute the signal sensitivity. The $\rho_{TC}(300, 300)$ signal and background yields are shown in Fig. 15.1d and the corresponding reconstruction efficiencies are listed in Table 15.1.

15.1.1.2. Signal sensitivity and systematic uncertainties. The sensitivity of each ρ_{TC} benchmark point is computed by taking into account realistic statistical fluctuations for a given integrated luminosity. The sensitivity estimator is defined as the likelihood-ratio S_L, defined in Appendix A.1. The signal probability density function (p.d.f.) is assumed Gaussian (dominated by detector resolution) and the background p.d.f. is exponential in all ρ_{TC} fit regions. The output of the fitting procedure is shown in the contour plot over the

Table 15.1. $\sigma \times \mathrm{BR}(\ell = e \text{ or } \mu)$, 3-lepton pre-selection efficiency, total efficiency and final yield within 3σ of the signal region (Nev), for $\mathcal{L} = 5\,\mathrm{fb}^{-1}$. $\rho_{TC}(300, 300)$ and the main background contributions are shown. The simulation is repeated for all ρ_{TC} benchmark points.

Sample	$\sigma \times$ BR(pb)	ε(3-lept)	ε(Reco) (%)	Nev($5\,\mathrm{fb}^{-1}$)
$\rho_{TC} \to W + Z \to 3\ell + \nu$	0.13	0.635	25.88 ± 0.40	103
$WZ \to 3\ell + \nu$	0.39	0.471	9.91 ± 0.11	27
$ZZ \to 4\ell$	0.07	0.719	15.80 ± 0.14	10
$Zb\bar{b} \to 2\ell + X$	332	0.046	0.23 ± 0.01	12
$t\bar{t}$	489.72	0.065	0.019 ± 0.001	8

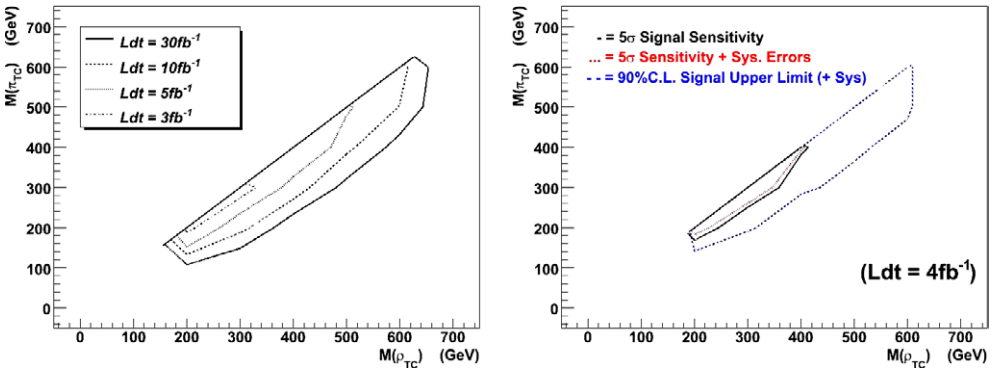

Figure 15.2. Left: Signal 5σ Sensitivity curves for various integrated luminosities. Right: sensitivity for $\mathcal{L} = 4\,\mathrm{fb}^{-1}$: the dotted (resp. dashed) curve shows the sensitivity (resp. the 90% C.L. signal upper limit) after including systematic uncertainties.

$[\mathrm{M}(\rho_{TC}), \mathrm{M}(\pi_{TC})]$ phase space in Fig. 15.2 (left), for various integrated luminosities. A signal sensitivity above 5 is expected for $\mathcal{L} = 3\,\mathrm{fb}^{-1}$ (before including systematic uncertainties).

The ρ_{TC} sensitivity has been simulated for the early CMS data taking phase. Expected detector related systematic uncertainties for $\mathcal{L} = 1\,\mathrm{fb}^{-1}$ are taken into account. While no substantial contribution is found from the tracker and muon system misalignment or the calorimeter miscalibration, the accuracy at which the lepton efficiency will be determined from data affects the result: a 2% uncertainty is considered. Moreover, the lepton fake rate has been simulated on $Zb\bar{b}$ and extrapolated to any $Z + jet(s)$ type background, in order to take into account additional contaminations from pion/kaon decays or from wrongly identified lepton candidates. A production cross-section of 1047 pb per lepton flavour is assumed for $Z + n\text{-}jets$, $n \geqslant 0$. A single lepton fake rate of $\mathrm{O}(10^{-3})$ is obtained using the fast simulation [11], affecting the ρ_{TC} sensitivity as shown below. Finally, a 7.5% uncertainty on the missing transverse energy measurement is considered. The above uncertainties result in the following relative ρ_{TC} sensitivity drop:

$$\Delta_{\mathrm{SYS}}^{\mathrm{tot}} = \sqrt{\left(\Delta_{\mathrm{SYS}}^{\mathrm{Eff}}\right)^2 + \left(\Delta_{\mathrm{SYS}}^{\mathrm{Fake}}\right)^2 + \left(\Delta_{\mathrm{SYS}}^{\mathrm{MET}}\right)^2} = \sqrt{(2.7\%)^2 + (8.5\%)^2 + (6.6\%)^2} = 11\%. \qquad (15.2)$$

Introducing K-factors from next-to-leading-order (NLO) expectations for the signal (a K-factor 1.35 is assumed in similarity with the Drell–Yan process) and background leads to a relative signal sensitivity increase of 6%; however the latter estimate has not been included in the final result.

Table 15.2. Contact interaction models.

Model	LL	RR	LR	RL	VV	AA	LL + RR	LR + RL
	Non-parity conserving				Parity conserving			
η_{LL}	±1	0	0	0	±1	±1	±1	0
η_{RR}	0	±1	0	0	±1	±1	±1	0
η_{LR}	0	0	±1	0	±1	∓1	0	±1
η_{RL}	0	0	0	±1	±1	∓1	0	±1

In summary, the technicolour signature $\rho_{TC} \to W + Z$ in the context of the Straw Man model is studied. The 5 sigma discovery reach is obtained for an integrated luminosity $\mathcal{L} \simeq 4\,\text{fb}^{-1}$.

15.2. Search for contact interactions with dimuons

Contact interactions offer a general framework for describing a new interaction with typical energy scale $\Lambda \gg \sqrt{s}$. The presence of operators with canonical dimension $N > 4$ in the Lagrangian gives rise to effects $\sim 1/\Lambda^{N-4}$. Such interactions can occur for instance, if the SM particles are composite, or when new heavy particles are exchanged.

In the following we will consider lepton-pair production. The lowest order flavour-diagonal and helicity-conserving operators have dimension six [123].

The differential cross section takes the form

$$\frac{d\sigma}{d\Omega} = SM(s,t) + \varepsilon \cdot C_{Int}(s,t) + \varepsilon^2 \cdot C_{NewPh}(s,t) \tag{15.3}$$

where the first term is the Standard Model contribution, the second comes from interference between the SM and the contact interaction, and the third is the pure contact interaction effect. The Mandelstam variables are denoted as s, t and u.

Usually the coupling is fixed, and the structure of the interaction is parameterised by coefficients for the helicity amplitudes:

$$\begin{aligned} &g && \text{coupling (by convention } g^2/4\pi = 1), \\ &|\eta_{ij}| \leqslant 1 && \text{helicity amplitudes } (i,\ j = \text{L, R}), \\ &\varepsilon && \frac{g^2}{4\pi}\frac{\text{sign}(\eta)}{\Lambda^2} \text{ for } f\bar{f}. \end{aligned}$$

Some often investigated models are summarised in Table 15.2. The models in the second half of the table are parity conserving, and hence not constrained by the very precise measurements of atomic parity violation at low energies. The results presented in this contribution cover the LL model, which has the highest sensitivity at LHC energies from the models in the first half of the table. More details can be found in [349].

15.2.1. Analysis

The topology under study is high-mass muon pairs with opposite sign. More details on the analysis are found in [349]. The Global Muon Reconstructor (GMR, described in PTDR, Volume 1, Section 9.1.2) output is used. The dimuon events are triggered by the single and dimuon triggers. We have processed events, generated to cover the whole region of interest

up to dimuon masses of 6 TeV/c^2, through full simulation with OSCAR and reconstruction with ORCA. The dimuon mass resolution is parameterised in two ways:

- as mass dependent one standard deviation (RMS);
- by fitting the mass resolution with a sum of two Gaussians to account for the long tail of less well reconstructed masses.

The results are remarkably stable as a function of the dimuon mass: the second Gaussian contributes around 14% and has a standard deviation 3.3 times bigger than the first Gaussian.

Our strategy is to generate events with PYTHIA and apply parametrisations of the dimuon mass efficiency and resolution obtained from full simulation. We have verified our approach by comparing the resulting mass spectra with the ones obtained with OSCAR/ORCA or FAMOS for Drell–Yan and selected contact interactions samples, observing good agreement in all cases.

Two mass regions: 500–1000 GeV and 1000–6000 GeV are considered. The total cross section and the forward–backward asymmetry as function of the dimuon mass are studied. Our analysis shows that the sensitivity to contact interactions comes almost exclusively from the cross section measurements for the LL model.

In order to reduce the systematic uncertainties both on the experimental and theory sides a "double ratio" method is developed. The number of observed events for a given bin in invariant mass is

$$N_{obs} = L \cdot \sigma \cdot \varepsilon \tag{15.4}$$

where L is the luminosity, σ the differential cross section for the given mass bin, and ε the experimental efficiency. We select a zeroth "normalisation" bin for invariant masses between 250–500 GeV/c^2, both well above the Z pole and in an area well covered by the Tevatron, and define the experimental ratios

$$R_i^{DATA} = \frac{N_i^D}{N_0^D} = \frac{\sigma_i^D \cdot \varepsilon_i^D}{\sigma_0^D \cdot \varepsilon_0^D}. \tag{15.5}$$

Here the cross sections and efficiencies are the ones for the real LHC data. The index i runs for all measured bins with masses above 500 GeV/c^2. The luminosity cancels in the ratio. The choice of this mass bin is not random. If we compare the flavour composition of partons initiating the hard interaction (Table 15.3), at the Z peak 32.1% are heavier flavours (not u or d quarks), with their own parton density functions (PDF) uncertainties. At 250–500 GeV/c^2 the u and d quarks are "initiators" already in 85.6% of the cases, increasing to 96.3% above 1 TeV/c^2, etc. Moreover, at the Z peak d quarks are most abundant, while at higher masses u quarks dominate, asymptotically approaching a ratio 4:1. It is clear that our choice of normalisation bin gives flavour composition much closer to the most interesting high mass events, compared to a normalisation using Z pole events. The PDF uncertainty on cross sections is estimated using LHAPDF [95, 351]. It is interesting to note that this uncertainty reaches a minimum for masses 250–600 GeV/c^2, corresponding to medium values of the parton momentum fractions X, reinforcing our choice of normalisation bin.

We define similar ratios for the Monte Carlo (theory) predictions. The *absolute* values of the cross sections and efficiencies are not important for the ratios, what matters is *the shape* of these quantities as function of invariant mass. For example, the absolute value of K-factors, a way to compensate for missing higher order N(N)LO terms and enable the comparison of leading order Monte Carlo predictions to data (similarly for the electroweak radiative corrections) disappears from the ratios and only the *shape* of the K-function as depending on invariant mass remains – a much smaller effect. And part of the uncertainties introduced due to our limited knowledge of PDFs cancels in the ratio, leaving smaller residual uncertainties due to the change of phase space for changing masses.

Table 15.3. Flavour composition of partons initiating the hard Drell–Yan interaction.The PDF uncertainty on the cross sections (positive and negative asymmetric errors) is estimated using LHAPDF.

Mass [GeV/c^2]	d [%]	u [%]	s [%]	c [%]	b [%]	PDF+ [%]	PDF− [%]
Z peak	35.9	32.1	17.2	9.77	5.10	+4.7	−5.7
250–500	24.3	61.3	6.22	6.64	1.54	+3.4	−4.2
500–600	22.8	68.4	4.03	3.95	0.89	+3.5	−4.1
1000+	21.7	74.6	1.86	1.48	0.33	+5.0	−5.8
2000+	19.9	78.4	0.91	0.63	0.14	+9.0	−7.7

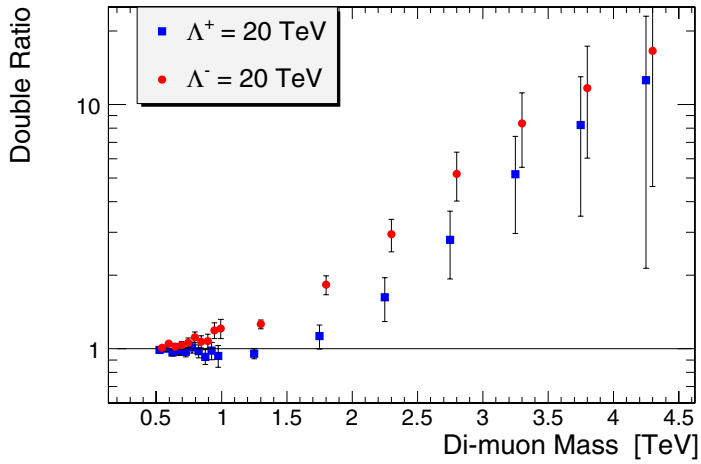

Figure 15.3. Double ratios for contact interactions in the dimuon channel, LL model, scale $\Lambda = 20\,\mathrm{TeV/c^2}$, positive and negative interference, and luminosity $100\,\mathrm{fb^{-1}}$. The errors shown are statistical.

Now let us define the double ratios

$$DR_i = \frac{R_i^{DATA}}{R_i^{MC}}. \tag{15.6}$$

This method is inspired by a study of Drell–Yan events and extraction of proton and pion PDFs at lower masses [748], as well as by the SuperKamiokande double ratio method for measuring atmospheric neutrino oscillations [749]. If our theory understanding and detector modelling are both perfect, we expect $DR_i \equiv 1$. The experimental or Monte Carlo errors introduced in the ratios from the uncertainties in the zeroth bin are negligible, as due to the steeply falling Drell–Yan spectrum this bin has much more data compared to the high mass bins.

An example of double ratios for positive and negative interference is shown in Fig. 15.3. As can be seen, for scale $\Lambda = 20\,\mathrm{TeV/c^2}$ the expected effects are quite sizable (note the log scale), with the sensitivity for negative interference starting around dimuon masses of $750\,\mathrm{GeV/c^2}$, while for positive interference masses above $2\,\mathrm{TeV/c^2}$ are required.

The experimental systematic effects in the cross section measurement are estimated to be 2% from the total muon efficiency and no more than 1.4% from momentum resolution. The former can be controlled quite well with the huge sample of Z events decaying to dimuons, and the effects for TeV muons are taken into account on top of this. The latter is important at high mass as smearing from lower masses from the steeply falling Drell–Yan spectrum can contaminate the high mass measurements, especially if the tails of the momentum resolution

Table 15.4. The PDF uncertainty on the cross section ratios (positive and negative asymmetric errors) as estimated using LHAPDF. Clearly normalising to the 250–500 GeV/c^2 mass bin is superior compared to a normalisation relative to the Z peak (70–120 GeV/c^2).

	$R\left(\frac{M}{250-500}\right)$		$R\left(\frac{M}{Zpeak}\right)$	
Mass [GeV/c^2]	PDF+ [%]	PDF− [%]	PDF+ [%]	PDF− [%]
500–600	+1.5	−1.5	+4.6	−4.2
1000+	+5.2	−4.8	+7.8	−7.1
2000+	+10.7	−7.8	+12.9	−9.4

are not under control. It is estimated by varying the two parametrisations of the mass resolution by ±40%, giving consistent results. The main source of systematic uncertainties on the momentum resolution comes from the alignment of the muon chambers and the central tracker, both at start-up and at high luminosity.

The systematic uncertainties from our limited knowledge of PDFs is estimated using the CTEQ6M PDF set from LHAPDF. From Table 15.4 our estimate of the PDF uncertainty on the cross section ratio is $^{+5.2}_{-4.8}$% above 1 TeV or $^{+10.7}_{-7.8}$% above 2 TeV.

The genuine electro-weak radiative corrections change by ∼10% in the relevant mass range [158, 350]. The K-function changes faster below 250–300 GeV. From our normalisation bin to the highest masses first estimates show a change below 8% on the cross section[52]. Taking conservatively half of these changes with mass as an upper limit on the systematic uncertainty we arrive at 5% and 4% respectively.

Combining all effects in quadrature, we arrive conservatively at systematic uncertainties below 2.5% experimental, 11.5% from theory, 12% total at nominal conditions, 15% shortly after start-up. With the accumulation of data and improved calculations there is hope to improve this number by making progress in our understanding of PDF, electro-weak radiative corrections and K-functions.

The discovery reach for a given model is determined by constructing a negative log-likelihood function combining the deviations between measurements and predictions, including the contact interaction contributions, for all simulated data points. The error on a deviation consists of three parts, which are combined in quadrature: a statistical error, an experimental systematic error and a theoretical uncertainty. The log-likelihood function is integrated in the physically allowed region (all positive Λ for positive interference and all negative Λ for negative interference) to derive the five standard deviations σ discovery reach and one-sided lower limits at 95% confidence level on the scale.

The discovery reach is summarised in Fig. 15.4. The sensitivity is dominated by the cross section measurement, the contribution of the forward-backward asymmetry is minor. The sensitivity for negative interference is substantially better. Even at the highest luminosities the statistical errors at LHC play a major role, as evident from the comparison of the cases with total systematic uncertainties of 3, 15 and 30%. This is not surprising as the Drell–Yan process is probing directly masses up to ∼4–5 TeV/c^2, where due to the steeply falling cross sections the statistical errors remain important for all considered luminosities.

[52] Calculations by M. Schmitt with the program PHOZPRMS [348].

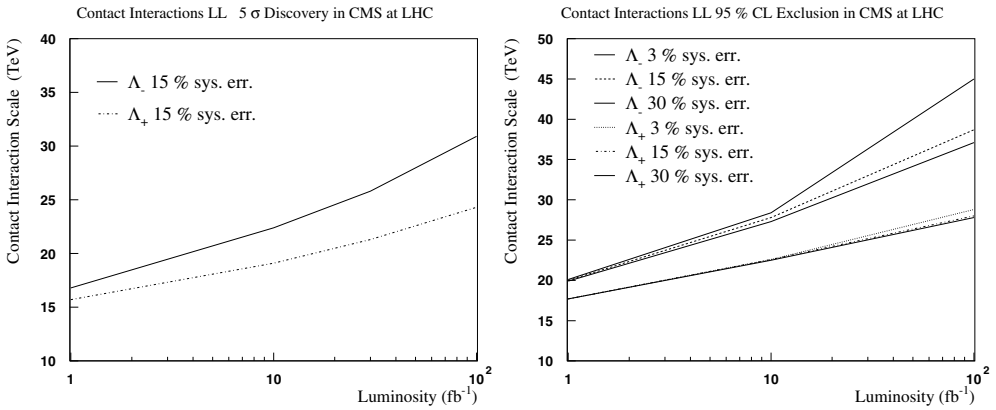

Figure 15.4. Five sigma discovery reach (left) and sensitivity at 95% CL (right) for contact interactions in the dimuon channel for different luminosities and signs of the interference.

15.3. Search for contact interactions with dijets

New physics at a scale Λ above the mass of the final state is effectively modelled as a contact interaction. Here the propagator for a particle of mass $M \sim \Lambda$ exchanged between quarks, or exchanged between constituent particles inside two interacting composite quarks, shrinks to a single point and gives a contact interaction. Quark contact interactions, for example those that arise from a left-handed interaction among composite quarks [123, 124], will always produce a rise in rate relative to QCD at high dijet mass or high inclusive jet E_{T}. However, observation in the mass distribution alone requires precise understanding of the QCD rate as a function of dijet mass, which is complicated by the large systematic uncertainties discussed in Section 4.1.6. Angular distributions benefit from much smaller systematic uncertainties. The contact interaction is often more isotropic than the QCD background, since QCD is dominated by t-channel scattering and produces jets predominantly in the forward direction. Our analysis uses the dijet ratio, discussed in section 4.1.5, to measure the angular distribution as a function of dijet mass, and see any contact interactions which affect the dijet angular distribution [750].

15.3.0.1. Contact interaction sensitivity estimates. The QCD background distribution for the dijet ratio was discussed in section 14.5. In Fig. 15.5 we show a smooth dijet ratio for QCD, estimated at 0.6 from the fit to the full simulation. The error bars shown in Fig. 15.5 are the statistical uncertainties expected with 1 fb^{-1} and the jet trigger prescales discussed in section E.4.3.2. The uncertainties are calculated using Poisson statistics at high dijet mass, where few events are expected and Gaussian statistics is less accurate. In Fig. 4.7 we presented a lowest order calculation of both QCD and a contact interaction among left-handed quarks. The signal in Fig. 15.5 is estimated by scaling the lowest order contact interaction calculation of Fig. 4.7 by the ratio of our full simulation prediction for QCD to the lowest order QCD calculation: signal = contact $\times$ 0.6/QCD. Systematic uncertainties on the dijet ratio are small, as discussed in section 4.1.6 and demonstrated in Fig. 4.8. The calculated chisquared between QCD and the contact interaction signal, including all uncertainties on the dijet ratio, is listed in Table 15.5. In Fig. 15.5 we show the significance in σ, estimated as $\sqrt{\chi^2}$, compared to a smooth fit as a function of $1/\Lambda^+$. The anticipated capability of CMS with 1 fb^{-1} to exclude contact interactions at 95% CL or discover them at 5σ can be read off Fig. 15.5, and they are listed in Table 15.6. This includes the uncertainty on Λ due to the anticipated 5% uncertainty on the observed jet energy. The same analysis is repeated for 100 pb^{-1} and 10 fb^{-1} and the

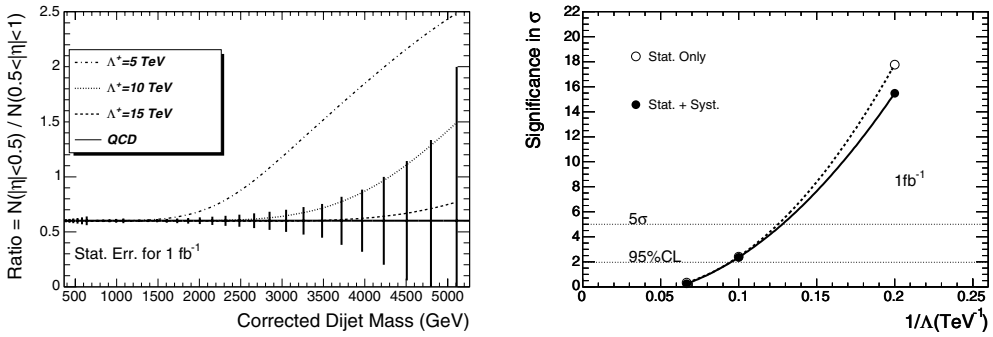

Figure 15.5. Left: The expected value and statistical error of the dijet ratio of QCD in the CMS detector for 1 fb^{-1} (solid) is compared with QCD plus a quark contact interaction at a scale Λ^+ of 15 TeV (dashed), 10 TeV (dotted) and 5 TeV (dot-dashed). Right: The significance with statistical uncertainties only (open circles) and with all uncertainties (solid circles) of the difference between QCD alone and QCD plus a quark contact interaction is plotted vs $1/\Lambda^+$ and fit with a quadratic function. Horizontal lines show the 5σ and 95% CL levels.

Table 15.5. Chisquared between signal and background. For each luminosity and contact interaction scale considered we list the chisquared between QCD alone and QCD plus a contact interaction, for the case where only statistical uncertainties are included (Stat), and for the case where both statistical and systematic uncertainties are included (All).

Luminosity	$100\,\text{pb}^{-1}$			$1\,\text{fb}^{-1}$			$10\,\text{fb}^{-1}$		
Λ^+(TeV)	5	10	15	5	10	15	5	10	15
χ^2 (Stat)	18.3	0.090	0.0037	316	5.82	0.107	3652	133	4.15
χ^2 (All)	16.7	0.082	0.0011	240	5.55	0.061	1340	124	3.56

Table 15.6. Sensitivity to contact interactions with $100\,\text{pb}^{-1}$, $1\,\text{fb}^{-1}$, and $10\,\text{fb}^{-1}$. We list the largest value of the contact interaction scale we expect to be able to exclude at a confidence level of 95% or greater, and the largest value we expect to be able to discover with a significance of 5σ or greater. Estimates include both statistical and systematic uncertainties.

	95% CL Excluded Scale			5σ Discovered Scale		
Luminosity	$100\,\text{pb}^{-1}$	$1\,\text{fb}^{-1}$	$10\,\text{fb}^{-1}$	$100\,\text{pb}^{-1}$	$1\,\text{fb}^{-1}$	$10\,\text{fb}^{-1}$
Λ^+ (TeV)	<6.2	<10.4	<14.8	<4.7	<7.8	<12.0

results are also listed in Table 15.6. The systematic uncertainties on the dijet ratio reduced the CMS sensitivity to a contact interaction between 0.1 and 0.3 TeV/c^2 depending on luminosity and level of significance. To see how quickly CMS jet data will extend the search for new physics, we note that with $100\,\text{pb}^{-1}$ our anticipated 95% CL sensitivity, $\Lambda^+ < 6.3\,\text{TeV}$, is more than twice the sensitivity of the DØ search($\Lambda^+ < 2.7\,\text{TeV}$ at 95% CL) [122]. We note that our contact interaction sensitivity to composite quarks in Table 15.6 is roughly twice our mass resonance sensitivity to excited states of composite quarks in Table 14.5, and is equivalent to observing or excluding a quark radius of order 10^{-18} cm.

15.4. Heavy Majorana neutrinos and right-handed bosons

15.4.1. Introduction

This study is exploring the left–right (LR) symmetric model $SU_C(3) \otimes SU_L(2) \otimes SU_R(2) \otimes U(1)$ [724, 725, 751] at LHC. The model embeds the SM at the scale of the order of 1 TeV

and naturally explains the parity violation in weak interactions as a result of the spontaneously broken parity. It necessarily incorporates three additional gauge bosons W_R and Z' and the heavy right-handed Majorana neutrino states N. The Ns can be the partners (N_l) of the light neutrino states ν_l ($l = e, \mu, \tau$) and can provide their non-zero masses through the see-saw mechanism [726]. Given the results from the atmospheric, solar and reactor neutrino experiments the LR model is very attractive. In the framework of the LR symmetric model, we have studied the production and the experimental signature of heavy Majorana neutrinos and the associated heavy gauge bosons. The detailed analysis is presented in [752].

Existing experimental data constrain the Z' mass to the values $O(1)\,\mathrm{TeV/c^2}$ [753]. The lower bound on the W' mass derived from the $K_L - K_S$ mass difference is quite stringent, $M_{W'} \gtrsim 1.6\,\mathrm{TeV}$ [754], however with some uncertainties from the low energy QCD corrections to the kaon system. The direct searches for W' at the Tevatron yield bounds $M_{W'} \gtrsim 720\,\mathrm{GeV/c^2}$ assuming a light (keV-range) N, and $M_{W'} \gtrsim 650\,\mathrm{GeV/c^2}$ assuming $M_N < M_{W'}/2$ [755]. These bounds are less stringent in more general LR models.

15.4.2. Heavy Majorana neutrino production and decay

The cross sections of $pp \to W_R \to l + N_l + X$ (the process studied here), and $pp \to Z' \to N_l + N_l + X$ (where $N_l \to l + j_1 + j_2$) depend on the value of the coupling constant g_R, the parameters of the CKM mixing matrix for the right-handed sector, the $W_R - W_L$ and $Z' - Z$ mixing strengths, and the masses of the partners N_l of the light neutrino state. In the study presented here the mixing angles are assumed small, the right-handed CKM matrix is identical to the left-handed one and $g_R = g_L$. With these assumptions the Z' is about 1.7 times heavier than W_R and the production cross-section for $pp \to W_R \to eN_e$ is found to be at least one order of magnitude higher than for the $pp \to Z' \to N_eN_e$ process. Finally it is assumed that only the lightest M_{N_e} is reachable at the LHC. In the case of degenerated masses of N_l, the channels with μ's and τ's are open resulting in the increase of the cross section of the process studied here by a factor of $\sim$1.2. The analysis is performed in the M_{W_R}, M_{N_e} parameter space. For the benchmark point considered (referred to as (LRRP)) $M_{N_e} = 500\,\mathrm{GeV/c^2}$ and $M_{W_R} = 2000\,\mathrm{GeV/c^2}$.

For the signal event generation and calculation of cross sections, the PYTHIA Monte Carlo program is used that includes the LR symmetric model with the standard assumptions mentioned above and CTEQ5L parton distribution functions. The fraction of $pp \to W_R^+$ ($pp \to W_R^-$) reactions as a function of M_{W_R} changes from $\simeq$70%($\simeq$ 30%) at $M_{W_R} \simeq 1\,\mathrm{TeV/c^2}$ to $\simeq$ 95%($\simeq$ 5%) at $M_{W_R} \simeq 10\,\mathrm{TeV/c^2}$. For W_R boson masses higher than $M_{W_R} \simeq 2\,\mathrm{TeV/c^2}$ the production of W_R^+ boson dominates. The W_R mass region above $1\,\mathrm{TeV/c^2}$ is studied since smaller masses are excluded by indirect analyses [756].

The signal and background data sample are simulated using the GEANT based CMS full detector simulation [8] and reconstruction package [10].

15.4.3. Analysis

The two major backgrounds considered in this study are the Z+jets and $t\bar{t}$ production. In the event selection two isolated electrons and at least two jets are required. The dielectron invariant mass M_{ee} is required to be above $200\,\mathrm{GeV/c^2}$ to suppress the Z+jets Standard Model background. The invariant mass of each electron with the two leading jets M_{ejj} ($M_{N_e}^{\mathrm{cand}}$ is formed. The M_{eejj} (W_R boson candidate) invariant mass is required to be above $1\,\mathrm{TeV/c^2}$. After this requirement the Standard Model background is suppressed as shown in Fig. 15.6.

The total W_R mass the reconstruction efficiency for $M_{W_R} = 2\,\mathrm{TeV/c^2}$ and for neutrino masses above $500\,\mathrm{GeV/c^2}$ is between 20% and 25% while for neutrino masses much smaller

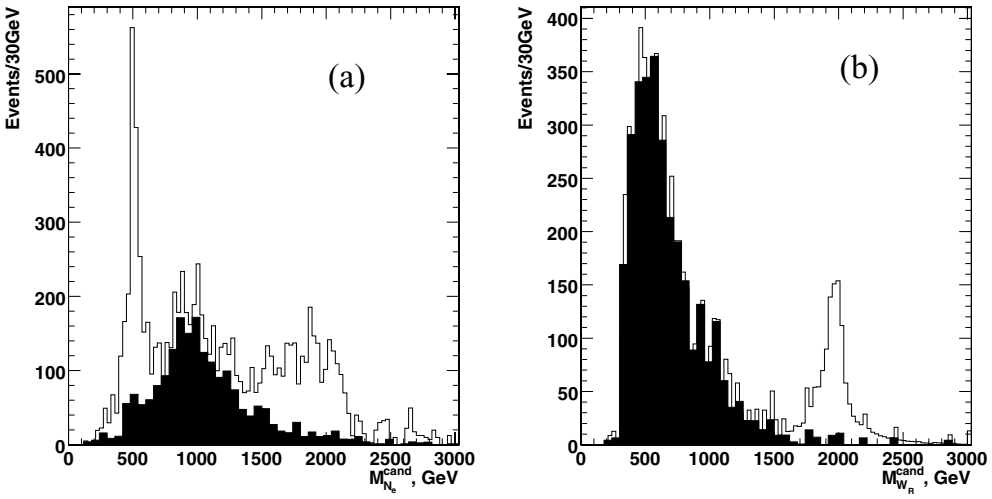

Figure 15.6. M_{ejj} for the signal overlaid with the SM background (shaded histogram) for 30 fb^{-1}: (a) $M_{eejj} > 1$ TeV/c^2, (b) $M_{eejj} < 1$ TeV/c^2.

than the W_R mass the reconstruction efficiency drops due to the significant overlap of the heavy neutrino decay products in $\eta - \phi$.

15.4.4. Results

The 5 sigma discovery contour in the $(M_{W_R}; M_{N_e})$ plane is shown in Fig. 15.7 for 1 and 30 fb^{-1}. With 30 fb^{-1} a 5 sigma observation of W_R and N_e with masses up to 4 TeV/c^2 and 2.4 TeV/c^2 respectively can be achieved. The signal at the LRRP test point (W_R of 2 TeV/c^2 and N_e 500 GeV/c^2) is observable already after one month of running at low luminosity.

15.5. Little Higgs models

15.5.1. Introduction

The Little Higgs model [656] provides an alternative mechanism of electroweak symmetry breaking keeping a light Higgs boson free from one-loop divergences of SM. It breaks a global symmetry spontaneously and invokes a number of new particles of masses in TeV scale. A heavy singlet quark of charge 2/3, marked as T, is the lightest among them and hence we study the viability of its observation with limited integrated luminosity.

The heavy quark T acquires its mass via Yukawa interactions of two gauge groups with couplings λ_1 and λ_2 which are of similar order. T has three dominant decay modes, the corresponding branching ratios following the relation: $BR(T \to th) = BR(T \to tZ) = \frac{1}{2} BR(T \to bW)$.

15.5.2. Analysis

The decay channel T $\to$ tZ, with leptonic decays of Z and W bosons, provides a clean signature at the LHC environment. This channel has not been previously studied in CMS and the work presented here is a feasibility study. Further details can be found in [757].

The signal samples were generated with PYTHIA 6.227 [24] and the T production was mimicked by activating the fourth quark generation through the W-b fusion. The T quark mass

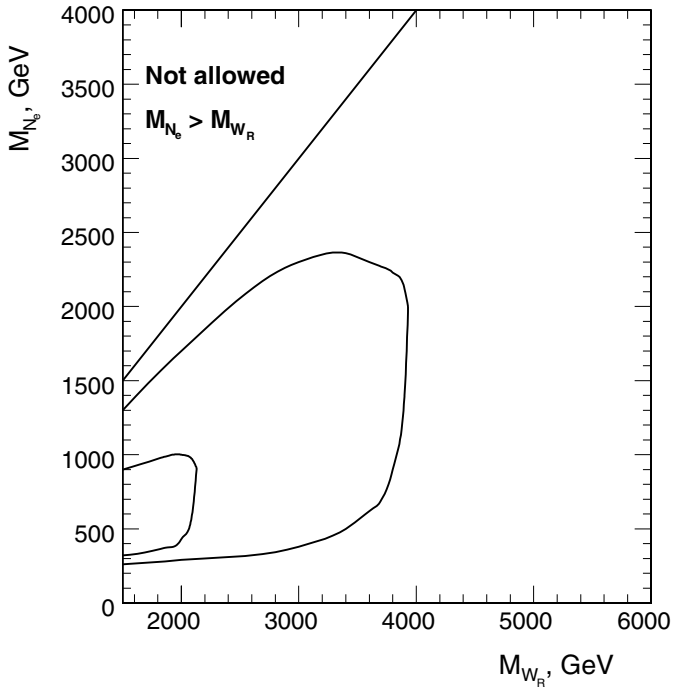

Figure 15.7. CMS discovery potential of the W_R boson and right-handed Majorana neutrinos of the Left–Right Symmetric model for the integrated luminosity $L_t = 30\,\text{fb}^{-1}$ (outer contour) and for $L_t = 1\,\text{fb}^{-1}$ (inner contour).

was set to $1\,\text{TeV/c}^2$ and was treated as a narrow resonance. The CMS full detector simulation was performed with OSCAR [8] and ORCA [10] while pile-up events corresponding to the low luminosity running period of the LHC were taken into account. The major backgrounds considered in this analysis were: $t\bar{t}$, ZW + jets, ZZ + jets, WW + jets, $Zb\bar{b}$, and Z+ jets.

The main selection requirements are summarised below:

- Events are required to pass the "double electron" or "double muon" L1 and HLT trigger criteria.
- Electrons are required to have $p_T > 20\,\text{GeV/c}$ and muons $p_T > 10\,\text{GeV/c}$.
- The combined transverse momentum of the same flavour opposite sign lepton pair is required to be $p_T^{\ell\ell} > 100\,\text{GeV/c}$. The invariant mass of the pair is required to be consistent with the nominal Z mass within $10\,\text{GeV/c}^2$.
- A further third lepton is required in the event ($e^{\pm}$ with $p_T > 20\,\text{GeV/c}$ or $\mu^{\pm}$ with $p_T > 15\,\text{GeV/c}$). The combined transverse momentum of the third lepton with the missing transverse energy is required to be greater than 60 GeV/c. In addition the transverse mass of the third lepton with the missing transverse energy is required to be less than $120\,\text{GeV/c}^2$, to be consistent with the W boson transverse mass.
- Exactly one jet compatible with a b-jet and with calibrated transverse momentum more than $30\,\text{GeV/c}$ is required.
- The combined transverse momentum of the W boson and the b-jet should be more than 150 GeV/c, while their invariant mass is required to be in the range (110–220) GeV/c^2.
- The combined ZWb system invariant mass is required to be in the mass range of the search for heavy quark, namely (850–1150) GeV/c^2.

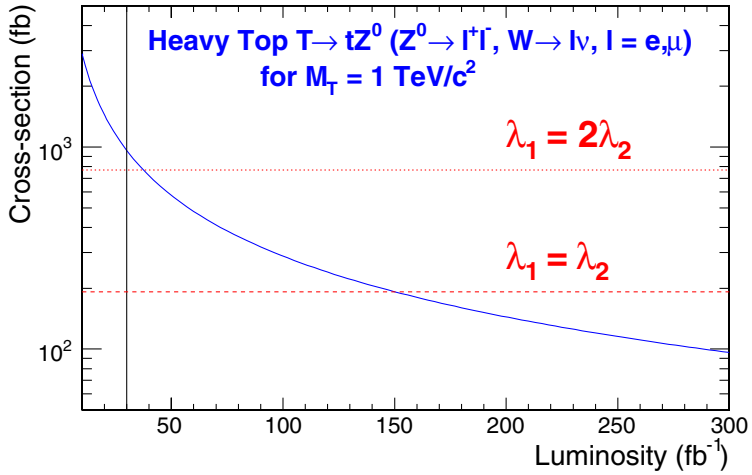

Figure 15.8. Minimum cross section required for a 5σ discovery for a heavy quark of mass $M_{\mathrm{T}} = 1\,\mathrm{TeV/c^2}$ as a function of the luminosity. The horizontal lines correspond to the cross section values for the two cases of λ_1/λ_2. The vertical line indicates the luminosity of $30\,\mathrm{fb}^{-1}$ used for this analysis.

The SM background ZZ $\rightarrow$ leptonic, is the only background that gives non-zero contribution (still less than 1 event at luminosity $30\,\mathrm{fb}^{-1}$). The total efficiency for the signal selection is $(9.7 \pm 0.4)\%$. Assuming the production cross section of T $\rightarrow$ tZ to be 192 fb for $M_{\mathrm{T}} = 1\,\mathrm{TeV/c^2}$ (for the case of $\lambda_1 = \lambda_2$) and folding in the branching ratios involved, a total of $N_S = 2.1 \pm 0.1$ signal events are expected for $30\,\mathrm{fb}^{-1}$. This implies that the discovery potential of the channel is rather limited.

The statistical significance of the channel (S_{c12}, defined in Appendix A.1) is 2.5 with a signal-to-background ratio of 41 for $30\,\mathrm{fb}^{-1}$. Taking into account systematic uncertainties from the electron energy scale, jet and missing energy scale and b-tagging efficiency uncertainty, the significance drops down to 2.0. Figure 15.8 shows the signal cross section as a function of the integrated luminosity at the LHC, for establishing at 5σ level, single production of a heavy quark of mass $= 1\,\mathrm{TeV/c^2}$. The luminosity needed for 5σ evidence is estimated to be around $150\,\mathrm{fb}^{-1}(40\,\mathrm{fb}^{-1})$ for choices of parameters $\lambda_1 = \lambda_2$ ($\lambda_1 = 2\lambda_2$). The vertical line corresponds to the luminosity used for this analysis and demonstrates the inadequacy of statistics for a luminosity of $30\,\mathrm{fb}^{-1}$.

15.6. Same sign top

At the LHC dileptonic $t\bar{t}(+jets)$ events can be selected with a relatively high signal-to-noise ratio and efficiency. Within the clean sample of such events, both leptons (electrons and muons) have an opposite electric charge. In several models beyond the Standard Model however, $tt/\bar{t}\bar{t}(+jets)$ topologies are predicted where both leptons have an equal electric charge. The signal excess is highly enhanced by the application of a combined likelihood variable described in [284]. The likelihood variable is designed to differentiate the lepton from the W boson decay from leptons arising for example in QCD jets or from fake reconstructions. The signal of new physics can be diluted by the mis-identification of the electric charge of the leptons in Standard Model $t\bar{t}(+jets)$ events and the mis-identification of the leptons from the W decay themselves. The observability of an excess of same-sign signals above

Table 15.7. Overview of the selection criteria applied on the events using simulated events with pile-up collisions included. The expected number of events are rescaled to a dataset of 1 fb^{-1} taking into account the respective Leading-Order cross-sections of the processes.

	$\mu\mu$	μe and ee	$t\bar{t} \to \tau + X$	Other $t\bar{t}$	$W^{\pm}W^{\mp}$	$Z + jets$	S/N
Before selection	6915.0	20745.0	34606.2	485973.2	189951.7	578033.3	0.0078
Trigger	6114.7	16314.8	17415.6	100137.2	41288.4	266366.7	0.017
Two jets $E_T > 25$ GeV	4398.2	11982.7	13560.9	93858.2	20593.8	66146.7	0.032
b-tag criteria	989.8	2485.4	2289.6	8784.7	133.5	240.0	0.13
Two leptons identified	888.2	30.1	375.8	801.6	1.7	73.3	1.30
Two leptons selected	481.5	0.07	48.4	3.01	0.4	53.3	4.7
Efficiency (in %)	6.96	0.0003	0.14	0.0006	0.00022	0.0092	
Opposite-sign	481.3	0	48.3	2.19	0	53.3	
Same-sign	0.2	0.07	0.1	0.82	0.4	0	
	ee	μe and $\mu\mu$	$t\bar{t} \to \tau + X$	Other $t\bar{t}$	$W^{\pm}W^{\mp}$	$Z + jets$	S/N
Before selection	6915.0	20745.0	34606.2	485973.2	189951.7	578033.3	0.0078
Trigger	5354.8	17074.7	17415.6	100137.2	41288.4	266366.7	0.015
Two jets $E_T > 25$ GeV	3960.9	12420.0	13560.9	93858.2	20593.8	66146.7	0.029
b-tag criteria	802.7	2672.4	2289.6	8784.7	133.5	240.0	0.11
Two leptons identified	724.5	34.6	453.8	2283.6	73.1	126.7	0.57
Two leptons selected	285.0	0.3	37.5	5.2	0.8	53.3	3.1
Efficiency (in %)	4.12	0.0013	0.11	0.0011	0.00044	0.0092	
Opposite-sign	279.6	0.3	36.8	4.1	0.4	46.7	
Same-sign	5.4	0	0.7	1.1	0.4	6.7	
	$e\mu$	$\mu\mu$ and ee	$t\bar{t} \to \tau + X$	Other $t\bar{t}$	$W^{\pm}W^{\mp}$	$Z + jets$	S/N
Before selection	13830.0	13830.0	34606.2	485973.2	189951.73	578033.3	0.016
Trigger	10960.0	11469.5	17415.6	100137.2	41288.4	266366.7	0.030
Two jets $E_T > 25$ GeV	8021.8	8359.1	13560.9	93858.2	20593.8	66146.7	0.061
b-tag criteria	1682.7	1792.5	2289.6	8784.7	133.5	240.0	0.25
Two leptons identified	1500.6	66.4	822.1	3001.6	30.2	20.0	0.88
Two leptons selected	722.7	0.9	85.2	6.3	0.4	0	8.3
Efficiency (in %)	5.23	0.0065	0.25	0.0013	0.00022	0	
Opposite-sign	715.5	0.9	83.8	4.9	0	0	
Same-sign	7.2	0	1.3	1.4	0.4	0	

the mis-reconstruction of the Standard Model background is determined. The details of the analysis are mentioned in [758].

The jets in the final state are reconstructed with an Iterative Cone jet clustering algorithm using a cone size of $\Delta R = 0.5$. Input objects for the cones are selected from all calorimeter towers above a pseudo-rapidity dependent energy threshold determined from the average underlying event energy deposits [165]. The energy scale of the reconstructed jets is calibrated with corrections from Monte Carlo studies. The primary vertices in the proton bunch crossing are determined, and the vertex with the highest transverse momentum is taken as the one of the hard scattering. Via a track-based algorithm, jets are rejected if they do not match with this hard primary vertex.

The leptons are reconstructed and identified using the methods described in [284]. A likelihood variable is used to suppress leptons from the heavy flavour quark background exploiting several reconstruction aspects of leptons in the CMS detector. This likelihood is determined for each muon or electron in the final state in order to enhance the purity of choosing the correct lepton from the leptonic W decay. The combined likelihood

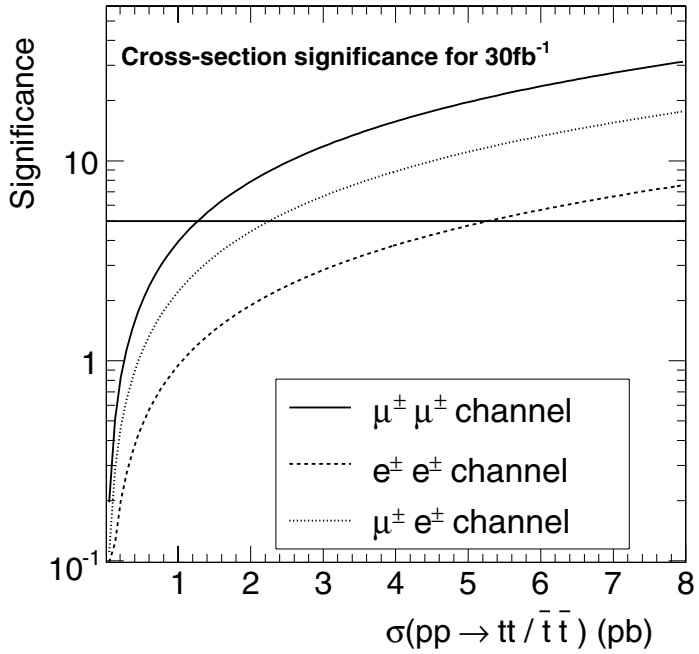

Figure 15.9. For an integrated luminosity of $30\,\mathrm{fb}^{-1}$ the significance of the same-sign tt or $\overline{tt}$ excess above the Standard Model events is indicated as a function of the cross-section of the inclusive process $pp \to tt/\overline{tt}$.

includes observables as tracker isolation, calorimeter isolation, vertex matching significance, transverse momentum of the lepton and angular distance to the closest jet. For the electron likelihood a variable reflecting the reconstruction quality is added. The two muons or electrons having the largest combined likelihood ratio value are taken as the hard leptons of interest.

The inclusive single-muon, single-electron, double muon and double electron triggers are applied as described in [506]. The event should be triggered in at least one of these streams. In total 88.4%, 77.4% and 79.2% of respectively the $\mu\mu$, the ee and the μe signal events remain after applying the trigger criteria. The event is required to have at least 2 jets with a calibrated E_{T} above 25 GeV. These jets need to have a pseudo-rapidity in the range $|\eta| < 2.4$ and a b-tag discriminant larger than 0.5 [157]. The reconstructed hard leptons are required to have transverse momentum p_{T} exceeding $25\,\mathrm{GeV/c}$ in the pseudo-rapidity range of $|\eta| < 2.4$ and a combined likelihood variable larger than 0.05.

In Table 15.7 the efficiencies and signal-to-noise ratios are shown after each selection step. Applying all cuts a signal-to-noise ratio of 4.7, 3.1 and 8.3 is obtained for respectively the $\mu\mu$, the ee and the $e\mu$ final state. Cross-talk between these three considered final states is by construction not possible. As the amount of selected WW and $Z + jets$ events in Table 15.7 is small, their contribution is alternatively estimated by multiplying the efficiencies of the event selection without the b-tagging and the individual b-tagging selection cut efficiency under the assumption that both selection cuts are uncorrelated.

It is illustrated [758] that from the selected topology of dilepton $t\bar{t}$ events, a ratio $R = \frac{N_{++,--}}{N_{+-}}$ can be determined which is sensitive to physics beyond the Standard Model. In the ratio the total amount of events with equally charged leptons is divided by the total amount of events with opposite charged leptons. As the efficiency of reconstructing the leptons electric charge is very high, we can neglect the amount of selected $pp \to tt$ or $pp \to \overline{tt}$

events observed with two opposite-charged leptons. Using the uncertainty on the ratio R, the significance of the observation of new physics channels $pp \to tt$ or $pp \to \overline{tt}$ is determined as a function of the cross section (see Fig. 15.9). The dimuon channel has a larger sensitivity compared to the decay channels with electrons. This is caused by the electron reconstruction where a large fraction of electron energy clusters are matched with a wrong track resulting in a charge ambiguity.

It is assumed that the new physics processes beyond the Standard Model have a similar kinematic topology compared to the $t\bar{t}$ process, therefore the selection efficiency of the new physics channels is taken equal to that of the Standard Model $t\bar{t}$ process. Several models predict an excess of events with same-sign leptons in this topology, via the process $pp \to tt/\overline{tt}$ or $pp \to tt/\overline{tt} + b/c$. These models are motivated by Flavour Changing Neutral Currents (FCNC) [759, 760], topcolour-assisted Technicolour (TC2) [761] or supersymmetry [762]. With a measurement of R these kinematically similar processes $pp \to tt/\overline{tt}$ can be observed with 30 fb^{-1} of integrated luminosity if they have a cross section above 1 pb. Because a ratio of kinematically similar event topologies is measured, most of the experimental and theoretical systematic uncertainties cancel. The uncertainty of the background cross sections on the significances shown in Fig. 15.9 is found to be negligible. A feasibility study is performed to estimate the potential uncertainty on the mis-identification efficiency of the electric charge of electrons and muons from Z boson decays [758]. The effect on the significance of the excess of $tt/\overline{tt}$ events is found to be negligible.

Appendix A. 95% CL limits and 5σ discoveries

A.1. Estimators of significance

Several methods exist to quantify the statistical "significance" of an expected signal at future experiments. Following the conventions in high energy physics, the term significance usually means the "number of standard deviations" an observed signal is above expected background fluctuations. It is understood implicitly that S should follow a Gaussian distribution with a standard deviation of one. In statistics, the determination of the sensitivity is a typical problem of hypothesis testing, aiming at the discrimination between a null-hypothesis H_0 stating that only background and no signal is present, and a alternative hypothesis H_1, which states the presence of a signal on top of the background. The "significance level" is the probability to find a value of a suitably constructed test statistic beyond a certain pre-specified critical value, beyond which the validity of H_1 is assumed. The significance level has to be converted into an equivalent number of Gaussian sigmas to arrive at the common terminology of a high-energy physicist.

Since a signal is usually searched for in many bins of a distribution, and in many channels, a very high value of the significance of a local excess of events must be demanded before an observed "peak" found somewhere in some distribution can be claimed to be an observation of a signal. If the position of the signal peak is not known a-priori and treated as a free parameter in searches for new physics, the probability of background fluctuations is much higher. This is quantified in a case study in Section A.2 below, and this aspect will need careful consideration in the near future before first data taking at the LHC. The general, somewhat arbitrary convention is that the value of S of a local signal excess should exceed five, meaning that the significance level, or the corresponding one-sided Gaussian probability that a local fluctuation of the background mimics a signal, is 2.9×10^{-7}.

Here, the recommendations for the procedures to be used for the studies presented in this document are summarised. The aim of many of these studies is the prediction of the average expected sensitivity to the observation of a new signal in a future experiment. The real experiment might be lucky, i.e. observe a higher significance than the average expectation, or a downward fluctuation of the expected signal could lead to a lower observed significance. The proposed methods have been checked in a large number of pseudo-experiments using Monte Carlo simulation in order to investigate whether the probability of a background fluctuation having produced the claimed significance of the discovery is properly described.

Counting methods use the number of signal events, s, and the number of background events, b, observed in some signal region to define the significance S. These event numbers can be turned into a significance, S_{cP}, by using either the Poisson distribution for small numbers of events, or, in the high-statistics limit, the Gaussian distribution, leading to

$$S_{c1} = \frac{s}{\sqrt{b}}. \tag{A.1}$$

The significance may also be obtained from the ratio of the likelihoods, $\mathcal{L}_1$ and $\mathcal{L}_0$, belonging to the hypothesis H_0 and H_1,

$$S_L = \sqrt{2 \ln Q}, \text{ with } Q = \frac{\mathcal{L}_0}{\mathcal{L}_1}. \tag{A.2}$$

This approach is theoretically well founded and is applicable also to the simple approach of the counting method, leading to

$$S_{cL} = \sqrt{2\left((s+b)\,\ln\left(1+\frac{s}{b}\right)-s\right)}, \tag{A.3}$$

which follows directly from the Poisson distribution. In the Gaussian limit of large numbers s and b, S_{cL} becomes equivalent to S_{c1}. The likelihood approach can be extended to include the full shapes of the signal and background distributions for the hypothesis H_0 and H_1, and the likelihood may be obtained from binned or unbinned likelihood fits of the background-only and the background-plus-signal hypotheses to the observed distributions of events.

Another estimator,

$$S_{c12} = 2\left(\sqrt{s+b}-\sqrt{b}\right), \tag{A.4}$$

has been suggested in the literature [79, 763]. The formula for S_{c12} is strictly only valid in the Gaussian limit, but tabulated values exist for small statistics.

The presence of systematic errors deserves some special care. Two cases must be separated clearly:

(a) If the background and signal contributions can be determined from the data, e.g. by extrapolating the background level into the signal region from sidebands, systematic errors may be irrelevant, and the systematic errors only influence our ability to predict the average expected sensitivity. In this case, simple propagation of the theoretical errors on s and b applied to the above formulae for the various significances is all that is needed.

(b) If systematic errors on the background will affect the determination of the signal in the real experiment, e.g. because an absolute prediction of the background level or a prediction of the background shape are needed, the theoretical uncertainty must be taken into account when estimating the sensitivity. This can be done by numerical convolution of the Poisson distribution, or the Gaussian distribution in the high-statistics limit, with the probability density function of the theoretical uncertainty. Numerical convolutions of the Poisson distribution with a theoretical error of a Gaussian shape, leading to a variant of S_{cP} including systematic errors, were used for this document [679]. Numerical convolutions of the Poisson distribution with a systematic error of a Gaussian shape, leading to a variant of S_{cP} including systematic errors, were used for this document. The program ScPf [679] computes the significance by Monte Carlo integration with the assumption of an additional Gaussian uncertainty Δb on b. The significance can be approximated by an extension of S_{c12}:

$$S_{c12s} = 2\left(\sqrt{s+b}-\sqrt{b}\right)\,\frac{b}{b+\Delta b^2}. \tag{A.5}$$

In the Gaussian limit it leads to

$$S_{c1} = s/\sqrt{b+\Delta b^2}. \tag{A.6}$$

The most crucial point in this context is a realistic description of the probability density function of the systematic theoretical uncertainty, which can be anything ranging from a flat distribution between $b \pm \Delta b$ to a pathological distribution with a significant non-Gaussian tail, but, in practice, is hardly ever known precisely.

The distribution of a significance estimator S in a series of experiments, its probability density function (p.d.f.), is of prime importance for the calculation of discovery probabilities in the presence of a real signal, or of fake probabilities due to fluctuations of the background. In the large-statistics limit, the likelihood-based significance estimators are expected to follow a χ^2-distribution with a number of degrees of freedom given by the difference in the number of free parameters between the alternative hypothesis and the null hypothesis [103]. When

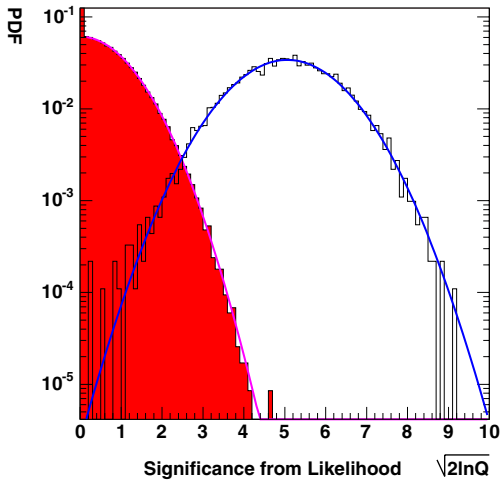

Figure A.1. Probability density functions of the estimator of significance S_L for small statistics (11 signal events over a background of 1.5 events). Filled histogram: pure background sample from 200 000 toy experiments, open histogram: background plus signal from 10 000 toy experiments. Gaussian fits are overlayed; the distribution of S_L for the background-only sample has a mean of -0.004 and a width of $\sigma = 1.0$, the background-plus-signal sample has a width of 1.1.

testing for the presence of a signal on top of background at a fixed peak position, $2 \ln Q = S_L^2$ is expected to follow a χ^2 distribution with one degree of freedom, i.e. a standard Gaussian distribution. All of the above estimators have been tested in a large number of toy experiments, see e.g. [60, 100, 102]. In particular the likelihood based estimators were found to be well-behaved, i.e. the distribution of the values of significance followed the expected behaviour already at moderate statistics, as is shown for one example in Fig. A.1. Good scaling with the square root of the integrated luminosity was also observed in these studies. On the other hand, the estimator S_{c1} cannot be considered a useful measure of significance at low statistics.

A quantitative comparison as a function of the number of background events for fixed values of $s/\sqrt{b}$ of the various estimators discussed above is shown in Fig. A.2. S_{cL} and S_{cP} are found to agree very well, while S_{c12} tends to slightly underestimate the significance, a result which was also verified in the above Monte Carlo studies with large samples of toy experiments. While S_{cL} and S_{cP} remain valid independent of the value of b, the simpler estimator S_{c1} can only be used for background levels larger than 50 events.

A.2. On the true significance of a local excess of events

In searching for new phenomena in a wide range of possible signal hypotheses (e.g. a narrow resonance of unknown mass over a broad range background), a special care must be exercised in evaluating the true significance of observing a local excess of events. In the past, this fact was given substantial scrutiny by statisticians (e.g. [764, 765]) and physicists (e.g., [766–770]) alike. The purpose of this Appendix is to quantify a possible scope of this effect on an example of a search for the Standard Model Higgs boson in the $H \to ZZ^{(*)} \to 4\mu$ decay channel. As the case study, we chose a counting experiment approach widely used in this volume.

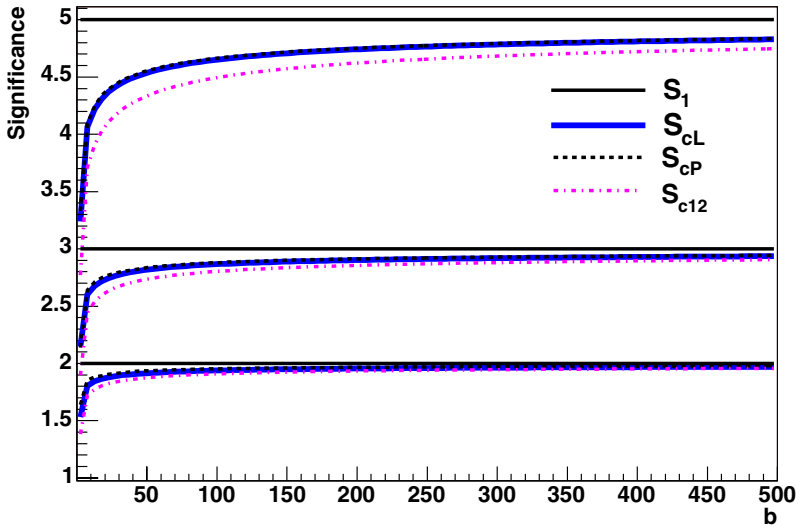

Figure A.2. Comparison of the various significance estimators as a function of the number of background events, b. The number of signal events was taken as $s = S_{c1}\sqrt{b}$, hence the constant black lines represent the value of S_{c1}. As can be seen, S_{cP} and S_{cL} agree perfectly, while S_{12} leads to slightly smaller values of significance. S_1 significantly overestimates the significance at small event numbers.

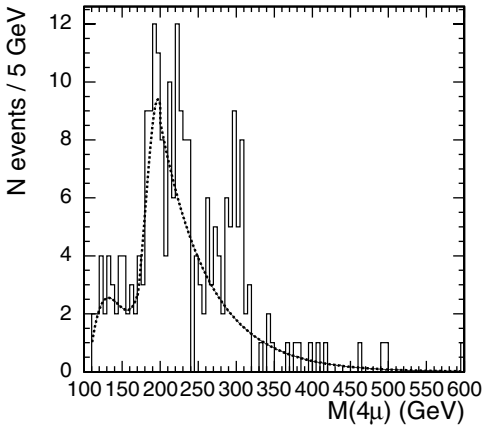

Figure A.3. The background *pdf* and an example of one pseudo-experiment with a statistical fluctuation appearing just like a signal.

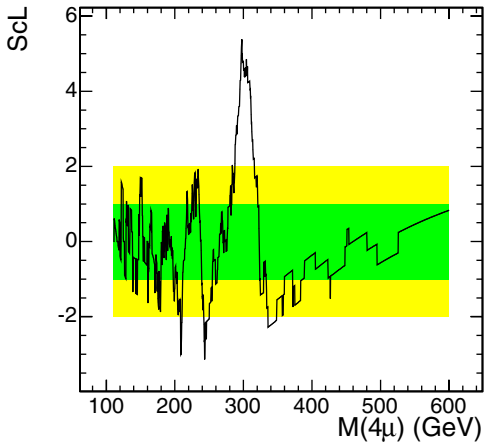

Figure A.4. Profile of the S_{cL} scan corresponding to the pseudo-experiment example shown on the left. Green (inner) and yellow (outer) bands denote $\pm 1\sigma$ and $\pm 2\sigma$ intervals. Spikes that can be seen are due to events coming in or dropping off the trial-window, a feature of low-statistics searches.

The dashed line in Fig. A.3 shows the expected 4μ invariant mass distribution for background at $\mathcal{L} = 30\,\text{fb}^{-1}$ after applying all the $m_{4\mu}$-dependent analysis cuts described in Sec. . Using this distribution, we played out $\sim 10^8$ pseudo-experiments; an example is shown in Fig. A.3. For each pseudo-experiment, we slid a *signal region window* across the spectrum looking for a local event excess over the expectation. The size of the window $\Delta m = w(m_{4\mu})$ was optimised and fixed *a priori* (about $\pm 2\sigma$) to give close to the best significance for a

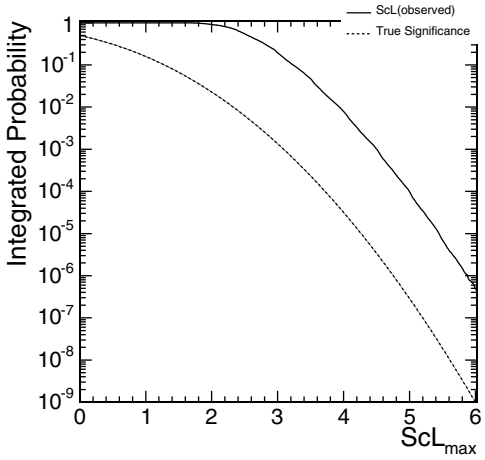

Figure A.5. S_{cL} cumulative probability density function.

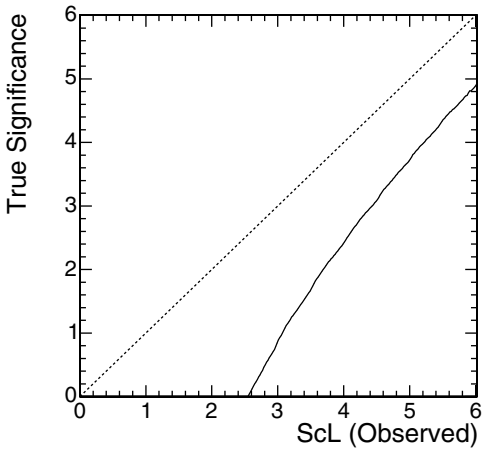

Figure A.6. Local significance "renormalisation" from an observed value to the true significance with a proper probabilistic interpretation.

resonance with a width corresponding to the experimental SM Higgs boson width $\sigma(m_{4\mu})$. The step of probing different values of $m_{4\mu}$ was "infinitesimally" small ($0.05\,\mathrm{GeV/c^2}$) in comparison to the Higgs boson width of more than $1\,\mathrm{GeV/c^2}$. The scanning was performed in *a priori* defined range of 115–600 $\mathrm{GeV/c^2}$.

We used a significance estimator $S_{cL} = \mathrm{sign}(s)\,\sqrt{2\,n_o\,\ln(1+s/b) - 2\,s}$, where b is the expected number of background events, n_o is the number of observed events, and the signal is defined as $s = n_o - b$. This estimator, based on the Log-Likelihood Ratio, is known to follow very closely the true Poisson significance, only slightly over-estimating it in the limit of small statistics [51]. Figure A.4 presents the results of such a scan for the pseudo-experiment shown in Fig. A.3. The maximum value of S_{cL}, S_{max}, and the corresponding mass of a "Higgs boson candidate" obtained in each pseudo-experiment were retained for further statistical studies.

After performing 10^8 pseudo-experiments, the differential probability density function for S_{max} and its corresponding cumulative probability function $P(S_{max} > S)$ (Fig. A.5) were calculated. From Fig. A.5, one can see that the frequency of observing some large values of S_{cL} (solid line) is much higher than its naive interpretation might imply (dashed line). If desired, the actual probability can be converted to the true significance. The result of such "renormalisation" is presented in Fig. A.6. One can clearly see that the required de-rating of significance is not negligible; in fact, it is larger than the effect of including all theoretical and instrumental systematic errors for this channel (see Section 3.1). More details on the various aspects of these studies can be found in [51].

There are ways of reducing the effect. A more detailed analysis of the shape of the $m_{4\mu}$ distribution will help somewhat. Using the predicted number of signal events $s = s_{theory}$ in the significance estimator to begin with and, then, for validating the statistical consistency of an excess $n_o - b$ with the expectation s_{theory} will reduce the effect further. One can also use a non-flat prior on the Higgs mass as it comes out from the precision electroweak measurements. Whether one will be able to bring the effect to a negligible level by using all these additional constraints on the signal hypotheses is yet to be seen. The purpose of this Appendix is not to give the final quantitative answer, but rather to assert that these studies must become an integral part of all future search analyses when multiple signal hypotheses are tried.

Appendix B. Systematic Errors

B.1. Theoretical uncertainties

The simulation of events at the LHC is complex and can be conventionally divided into different parts which either involve the description of the interesting physics process or the description of the initial scattering conditions and the physics environment.

The simulation of the hardest part of the physics process is done via matrix element (ME) calculations at a certain order in the coupling constants and continues with the parton showering (PS) of the resulting partons until a cut-off scale, over which the perturbative evolution stops and the fragmentation of the final partons takes on. This cut-off is often referred to as factorisation scale, because it is the scale at which the two processes (showering and fragmentation) are supposed to factorise.

The interesting event is accompanied by the so-called underlying event (UE), term which identifies all the remnant activity from the same proton-proton (p–p) interaction and whose definition often includes ISR as well, and the pile-up, composed by other minimum bias (MB) p–p interactions in the same bunch crossing (up to 25 at high luminosity at the LHC). Moreover, since the initial state is not defined in p–p collisions, a proper description of the proton parton density functions (PDFs) should be included in the calculations.

Each of these effects needs to be modelled to the best of our knowledge, and the associated uncertainties need to be determined and propagated to the physics measurements. Moreover, many of the sources are correlated: for instance, fragmentation and showering are obviously dependent on each other, and in turn they assume a certain description of the underlying event. The task of assessing systematics due to theory and modelling can therefore be a difficult one and can sometime contain a certain degree of arbitrariness.

In what follows we propose some guidelines for the estimation of errors coming from the above, trying to divide the systematics sources into wider categories as much uncorrelated as possible: QCD radiation, fragmentation description, PDFs, UE and MB.

In attributing systematic errors we believe that one should use motivated recipes, avoiding unrealistic scenarios which will lead to unnecessarily conservative errors or, much worse, totally arbitrary assumptions.

B.1.1. Hard process description and parametric uncertainties

The description of the hard process should be done with Monte Carlo tools which are best suited to the specific analysis. For instance, when precise description of hard gluon emission becomes an issue, then next-to-leading order (NLO) generator tools like MC@NLO [771], or higher leading order (LO) α_s generators like COMPHEP [43], MADGRAPH [81], ALPGEN [161], and SHERPA [194] should be considered. This is in general true for both the signal and the background description.

When adopting a ME tool, one should always keep in mind that its output is often (if not always) supposed to be interfaced to PS Monte Carlo such as HERWIG [196], PYTHIA [24] or ISAJET [672], that treat the soft radiation and the subsequent transition of the partons into observable hadrons. One of the most difficult problems is to eliminate double counting where jets can arise from both higher order ME calculations and from hard emission during the shower evolution. Much theoretical progress has been made recently in this field [772–775]. For what concerns the ME/PS matched description of multi-jet final states, a rich spectrum of processes is currently available in ALPGEN. However, adopting general purpose generators like PYTHIA can still be the best option for topologies that are better described in the Leading

Logarithm Approximation (LLA), for instance in the case of two leading jets and much softer secondary jets. The two different descriptions should be regarded as complementary.

In general, a sensible choice for the selection of the best generation tools can be driven by the HEPCODE data base [776]. However, comparison between different generators is recommended whenever applicable.

Each analysis needs then to make sure that other important effects (e.g. spin correlations in the final state, NLO ME corrections to top decays) are included in the generation mechanism. For example, TopReX [44], as long with some of the Monte Carlo generators already introduced in this section, provides a correct treatment of top quark spin correlations in the final state. Neglecting some of these effects corresponds to introducing an error in the analysis that cannot be considered as coming from a theoretical uncertainty.

For both signal and backgrounds, missing higher orders are a delicate source of uncertainty. Formally, the associated error cannot be evaluated unless the higher order calculation is available. This is often not possible, unless extrapolating by using comparisons with analytical calculations of total or differential cross-sections at the next order, if available. One should keep in mind that simple K-factors are not always enough and that the inclusion of higher orders typically also involves distortions in differential distributions.

Moreover, one should not forget that any Standard Model calculation is performed in certain schemes and that the input parameters are subject to their experimental uncertainties; if the error on most of those and the choice of the renormalisation scheme are expected to give negligible effects in comparison with other uncertainties, this might not be so for the choice of the hard process scale, which we will discuss in the next section, and some of the input parameters.

Among the input parameters, by far the one known with less accuracy will be the top mass. The current uncertainty of about 2% [777] enters in the LO calculations for processes which involve top or Higgs production. For instance, the total $t\bar{t}$ cross-section is known to have a corresponding 10% uncertainty due to this [45]. As far as Higgs production (in association or not with tops) is concerned, gluon–gluon fusion proceeds via a top loop and therefore the total cross-section can have a strong dependence on the top mass when $m_H \approx 2m_t$. Analyses which include Higgs bosons or top are encouraged to estimate the dependence of the significant observables on the top mass itself. Effects of m_t variation on acceptances of these analyses should instead be negligible.

B.1.2. Hard process scale

The hard process under study drives the definition of the Q^2 scale, which directly enters in the parametrisation of PDFs and α_s, hence in the expression of the cross sections.

The dependence of the observables on the choice for the Q^2 hard process scale is unphysical and should be regarded as one important contribution to the total uncertainty in the theoretical predictions. The sensitivity of the predicted observables to such choice is expected to decrease with the increasing order in which the calculation is performed, and can be tested by changing the hard process scale parameters in the generation (where applicable) using a set of sound values according to the characteristics of the hard process.

A sensible choice for the hard process scale in $2 \to 1$ processes is often $\hat{s}$, which is the default in general purpose generators like PYTHIA. Alternative choices to quote theoretical uncertainties can be $0.25\hat{s}$ and $4.0\hat{s}$. In PYTHIA this can be obtained acting on PARP(34).

For $2 \to n$ processes, many reasonable alternatives for the Q^2 scale definition exist. The PYTHIA default (MSTP(32) = 8), corresponds to the average squared transverse mass of the outgoing objects. It is possible to test the sensitivity on the Q^2 scale switching to different options, for example trying $Q^2 = \hat{s}$ (MSTP(32) = 4 in PYTHIA).

B.1.3. PDF description

The parton distribution functions of interacting particles describe the probability density for partons undergoing hard scattering at the hard process scale Q^2 and taking a certain fraction x of the total particle momentum. Since the Q^2 evolution can be calculated perturbatively in the framework of QCD, PDFs measurements can be cross checked using heterogeneous DIS, Drell–Yan and jet data, and achieve predictivity for points where no direct measurements are available yet, for example in a large region of the (x,Q^2) space for p–p interactions at the LHC energy.

Various approaches are currently available to quote the PDFs of the proton, which propose different solutions for what concerns the functional form, the theoretical scheme, the order of the QCD global analysis (including possible QED corrections), and the samples of data retained in the fits: CTEQ [778], MRST [779], Botje [780], Alekhin [781], etc. The CTEQ and MRST PDFs, including Tevatron jet data in the fits, seem to be well suited for use in Monte Carlo simulations for the LHC.

The best way to evaluate theoretical uncertainties due to a certain proton PDFs is to vary the errors on the parameters of the PDF fit itself. With the Les Houches accord [95] PDF (LHAPDF) errors should be easily propagated via re-weighting to the final observables. However, errors are available only for NLO PDF, whereas in most of the cases only LO tools are available for the process calculation. Correctly performing evaluation of theoretical uncertainties in these cases requires some care. The proposed solution is to adopt CTEQxL (LO) for the reference predictions using CTEQxM (NLO) only to determine the errors.

For analyses which are known to be particularly sensitive to PDFs, like cross-section measurements, it would be also desirable to compare two different sets of PDFs (typically CTEQ vs MRST) taking then the maximum variation as an extra error. This is important since, even considering the error boundaries, different set of PDFs may not overlap in some region of the phase space.

The LHAGLUE interface [95] included from the most recent LHAPDF versions simplifies the use of the Les Houches accord PDF in PYTHIA by the switches MSTP(52) = 2, MSTP(51) = LHAPDF$_{id}$.

B.1.4. QCD radiation: the parton shower Monte Carlo

The showering algorithm is basically a numeric Markov-like implementation of the QCD dynamic in the LLA. After the generation of a given configuration at partonic level, the initial state radiation (ISR) and the final state radiation (FSR) are produced following unitary evolutions with probabilities defined by the showering algorithm.

The probability for a parton to radiate, generating a $1\rightarrow 2$ branching, are given by the Altarelli–Parisi equations [782], however various implementations of the showering algorithm exist in parton shower Monte Carlo, which mostly differ for the definition of the Q^2 evolution variable (virtuality scale) in the $1\rightarrow 2$ radiation branching and for the possible prescriptions limiting the phase space accessible to the radiation: PYTHIA, HERWIG, ARIADNE [783], ISAJET etc.

The virtuality scales for both ISR and FSR need to be matched to the hard process scale, the latter setting an upper limit on the former ones; such limit has to be considered in a flexible way, given the level of arbitrariness in the scale definitions. While this matching is somewhat guaranteed if one adopts the same simulation tool for both hard scattering and parton shower, a careful cross check is recommended in all other cases. In general, a critical judgement taking into account the hard process type is needed. Allowing a virtuality scale higher than the hard

process scale may give rise to double counting. This is the case of gg→gg processes with additional hard gluons added in the showering. However other processes are safer from this point of view, for instance the case of the $q\bar{q} \rightarrow Z$ process at LO.

Quantum interference effects in hadronic collisions have been observed by CDF [784] and DØ [785] studying the kinematical correlations between the third jet (regarded as the result of a soft branching in the LLA) and the second one. The implementation of the so called colour coherence in PS Monte Carlo is made in the limit of large number of colours and for soft and collinear emissions, restricting the phase space available to the radiation depending on the developed colour configuration. Different implementations of the colour coherence are available in HERWIG and PYTHIA, while ISAJET doesn't take into account such effects.

The theoretical uncertainty associated to the parton showering descriptions, includes what is normally referred to as ISR or FSR and their interference. In order to achieve practical examples for the recommended parton shower settings, we will consider PYTHIA as the default tool for showering from now on.

Turning OFF ISR and FSR (MSTP(61) = 0, MSTP(71) = 0 respectively) or even the interference part (MSTP(62) = 0, MSTP(67) = 0) is certainly a too crude approach and, to a large extent, a totally arbitrary procedure to assess a systematic error. We believe it is much more realistic to vary, according to sound boundaries, the switches regulating the amount and the strength of the radiation of the showering. These can correspond to Λ_{QCD} and the maximum virtuality scales up to which ISR stops and from which FSR starts. It would be important to switch the parameters consistently going from low to high values in both ISR and FSR.

Notice that the radiation parameters were typically fitted at LEP1 together with the fragmentation parameters, benefiting from a much simplified scenario where no ambiguity on the maximum virtuality scale applies, the only relevant energy scale of the problem being $\hat{s} = s$. One has to take into account that while for instance FSR accompanying heavy boson decays at the LHC can be directly related to the LEP experience, FSR in processes like $gg \rightarrow b\bar{b}$ entails additional uncertainties arising from the maximum allowed virtuality scale and ISR/FSR interference. On top of that, additional complications arise from the fact that ISR at hadron machines contributes to the description of the underlying event. Matching two different tunings of the same parameter (in particular PARP(67)) can be very subtle at the LHC.

These are the suggested settings in PYTHIA, which have been cross-checked with the ones adopted by the CDF experiment and also follow the prescription by the main author:

- Λ_{QCD}: PARP(61), PARP(72), PARJ(81) from 0.15 to 0.35 GeV consistently, symmetric with respect to 0.25. Notice that these settings have been optimised for the CTEQ6L PDFs. In general different ranges apply when changing PDFs. In order to give the user full control on these parameters the option MSTP(3) = 1 has to be set, otherwise Λ_{QCD} is assumed to be derived from the PDFs parametrisation.
- Q^2_{max}: PARP(67) from 0.25 to 4 and PARP(71) from 1 to 16 going from low to high emission in a correlated way. In doing so one should also make sure that the tuning of the underlying event is not changing at the same time. Possible re-tuning of the underlying event in different radiation scenarios may be needed, in particular for what concerns PARP(82).

B.1.5. Fragmentation

Perturbative QCD cannot provide the full description of the transition from primary quarks to observable hadrons, but only the part which involves large momentum transfer. The formation of final hadrons involves a range of interactions which goes above the Fermi scale and where

the strong coupling constant α_s increases above unity, making it necessary to describe this part in a non-perturbative way, normally referred to as fragmentation or hadronisation.

The non-perturbative description of fragmentation is realised via models, which need to be tuned to experimental data. The data correspond, typically, to event shapes and multiplicities at leptonic machines or to the inclusive jet shapes at hadronic machines. A comprehensive overview of the models can be found in [786].

Fragmentation is said to depend only on the factorisation scale if jet universality is assumed, i.e. assuming that jets fragment in the same way at hadron and lepton machines. Jet universality will be ultimately verified at the LHC; one should clarify whether instrumental effects and the LHC environment will have an impact on the final observables. For instance, the much larger fraction of gluon jets or the different description of the underlying event can change the values of the parameters that regulate the fragmentation. Moreover, for events with high multiplicity of jets it will also be crucial to properly describe fragmentation in conditions where large jet overlapping is to be expected and where inclusive tunings might not be ideal.

The consequence of jet universality is that, once the PS cut-off scale is fixed, the fragmentation description for light quarks should be universal, and the LEP/SLD tunings (or the Tevatron ones) could be used as they are for the LHC.

It is important to underline that the description of the non-perturbative part of the radiation also depends on the way the perturbative one is described. This means that one should not use a tuning of fragmentation done with LO(+LL) tools (typically PYTHIA at LEP) attached to perturbative calculation which are done at higher (or different) order.

B.1.5.1. Light quarks fragmentation. In the absence of LHC data, the best choice is therefore to use a model tuned to the LEP and SLD data [787–789]. It is important to choose the tuning in a consistent way from the same experiment, given that a combined LEP/SLD tuning has never been attempted. As a possibility, suggested by the major success in describing the data and by its extensive use in the experimental collaborations, is the use of PYTHIA, which uses the string (or Lund) fragmentation model [790]. The parameters that we consider more relevant in PYTHIA for the description of fragmentation are the following, where the central value is taken by the fit performed by the OPAL Collaboration, as an example:

PARJ(81) = 0.250
PARJ(82) = 1.90
PARJ(41) = 0.11
PARJ(42) = 0.52
PARJ(21) = 0.40

where PARJ(81) (Λ_{QCD}) and PARJ(82) (Q^2_{min}) refer to the radiation part. To properly evaluate a systematic error due to pure fragmentation one should vary only PARJ(42) and PARJ(21) by their respective errors (0.04 and 0.03 for OPAL). The variation should account for the proper parameter correlation if the effect is critical for the analysis. PARJ(41) is totally correlated to PARJ(42).

Alternatively, or additionally, it would also be important to compare PYTHIA with HERWIG with consistent tunings from LEP [787–789]; in doing so it is important to factorise the UE description (see next section) that can induce important differences in the results.

B.1.5.2. Heavy quarks fragmentation. The description of the heavy quarks fragmentation is important for top physics and for those processes with large b production in the final states. Exclusive channels are particularly influenced by the description of the fragmentation of the b quark.

The description of the fragmentation of the heavy quarks has been tuned to Z data at LEP and SLD[778, 791–793] (via a measurement of x_B and x_D) and $b\bar{b}$ data at the Tevatron, using different fragmentation functions like Lund, Bowler [794], Peterson [795], Kartvelishvili [796].

In the spirit of fragmentation universality the LEP/SLD tunings can be adopted for the LHC, but with much care. Significant differences among the fitted values in different experiment can point out that the factorisation scale used for the PS is not the same everywhere. One should make sure that the scale used is set consistently with the chosen fragmentation function parameters. This can be done by using the tuning from only one experiment, making sure to also use the main switches of the parton showering, (PARJ(81) and PARJ(82) in PYTHIA).

The fragmentation function that best describes heavy flavour data at LEP is Bowler. With the same OPAL tuning reported above the best fit of the Bowler parameters, a and $bm_\perp^2$, to data gives:

$bm_\perp^2 = 65^{+17}_{-14}$
$a = 15.0 \pm 2.3.$

The Bowler model would extend the string model to heavy flavours, describing the corrections in terms of the charm and bottom masses. Unfortunately, no tuning exists in the literature which is capable to describe at the same time light and heavy quark fragmentation, i.e. adopting universal parameters $a = \text{PARJ}(41)$ and $b = \text{PARJ}(42)$ for both light and heavy quarks.

Alternatively, the widely used Peterson function can be used, and its parameters are directly switchable in PYTHIA for just b and c fragmentation:

$\text{PARJ}(54) = -0.031 \pm 0.011$
$\text{PARJ}(55) = -0.0041 \pm 0.0004$

where the two parameters correspond, respectively, to ε_c and ε_b fitted in the OPAL tuning. The systematic can then be evaluated by varying the errors on the fitted parameters or by comparing with a different fragmentation function like Kartvelishvili, or Lund.

An important feature of the b fragmentation that should be considered by those analyses in the top sector sensitive to the details of the fragmentation, is the way the b fragments in top decays. At the LHC the b from a t is hadronising with a beam remnant, introducing potentially worrying differences with respect to the fragmentation at LEP. The main effects are presented in [797] and are known as *cluster collapse*, happening when a very low mass strings quark-remnant directly produces hadrons without fragmenting, hence enhancing the original flavour content, and *beam drag*, which is an angular distortion of hadron distribution toward the end of the string in the remnant. If, under reasonable assumptions on the transverse momentum in top events at the LHC, one can exclude to a large extent the importance of the first effect, beam drag could potentially introduce B meson production asymmetries, even though estimations are keeping the effect at the level of 1% at the LHC [797].

B.1.6. Minimum bias and underlying event

Multiple parton interaction models, extending the QCD perturbative picture to the soft regime, turn out to be particularly adequate to describe the physics of minimum bias and underlying event. Examples of these models are implemented in the general purpose simulation programs PYTHIA, HERWIG/JIMMY [193] and SHERPA. Other successful descriptions of underlying event and minimum bias at hadron colliders are achieved by alternative approaches like PHOJET [798], which rely on both perturbative QCD and Double Pomeron Models (DPM).

Huge progress in the phenomenological study of the underlying event in jet events have been achieved by the CDF experiment at Tevatron [799], using the multiplicity and transverse momentum spectra of charged tracks in different regions in the azimuth-pseudorapidity space defined with respect to the direction of the leading jet. Regions that receive contributions only by the underlying event have been identified. The average charged multiplicity per unit of pseudorapidity in these regions turns out to be significantly higher with respect to the one measured in minimum bias events. This effect, referred to as "pedestal effect", is well reproduced only by varying impact parameters models with correlated parton-parton interactions (MSTP(82) $>$ 1 in PYTHIA). Simpler models are definitely ruled out.

The main problem of extrapolating the predictions of the multiple interactions models to the LHC is that some of the parameters are explicitly energy dependent, in particular the colour screening p_T cut-off (PARP(82) at the tuning energy PARP(89) in PYTHIA). The CDF tuning, often referred to as Tune-A, is not concentrating on this particular aspect. Other works [197, 800] have put more emphasis on this issue. However, one of their results is that currently only PYTHIA can be tuned to provide at the same time description of CDF and lower energy minimum bias data from UA5. One of these tunings can be summarised as follows:

- PARP(82) = 2.9
- PARP(83) = 0.5
- PAPR(84) = 0.4
- PARP(85) = 0.33
- PARP(86) = 0.66
- PARP(89) = 14000
- PARP(90) = 0.16
- PARP(91) = 1.0
- MSTP(81) = 1
- MSTP(82) = 4.

Sensible estimation of theoretical uncertainties arising from underlying event and minimum bias modelling can be performed assigning $\pm 3\sigma$ variations to the colour screening p_T cut-off parameter tuned on minimum bias CDF and UA5 data and extrapolated to the LHC energy [800], i.e. varying PARP(82) in the range [2.4–3.4], while keeping the other parameters listed above to their tuned values.

As a new tool for the description of UE and MB we would like to mention PYTHIA 6.3 [801], that allows for new interesting features, including the new p_T-ordered initial- and final-state showers and a new very sophisticated multiple interactions model that achieves description of colliding partons in the proton in terms of correlated multi-parton distribution functions of flavours, colours and longitudinal momenta. However, as stressed by the PYTHIA authors, the new model (PYEVNW) is still not so well explored. Therefore the old model (PYEVNT) is retained as the default choice, with full backward compatibility. Moreover, in the use of PYTHIA 6.3, one should be careful when switching to the new p_T-ordered showers and multiple interaction models, as their parameters are not tuned yet, in particular for what concerns the energy dependence, necessary to get meaningful extrapolations at the LHC energy.

B.1.7. Pile-up and LHC cross sections

The design parameters of the LHC at both low and high luminosity are such that, on top of possible signal events, additional minimum bias interactions are produced in the same beam crossing, the so-called pile-up effect.

Pile-up is a purely statistical effect. The number of minimum bias interactions generated in a single beam crossing is a Poissonian distribution that depends on the instantaneous luminosity, which varies of about a factor 2 during a LHC fill. Although luminosity variation is not arising from theoretical uncertainties, it is recommended to cross check the stability of the results against variation of the nominal luminosity.

An issue which can affect the pile-up is the definition of the minimum bias itself. The latter, indeed, may or may not include the diffractive and elastic contributions, with figures for the total cross section which can vary from 100 mb to 50 mb respectively. If the PYTHIA generator is adopted, these two different options correspond to MSEL 2 and MSEL 1, however, in order to get full control on the different contributions to the cross sections, one can use MSEL 2, setting MSTP(31) = 0, and providing explicit input through SIGT(0, 0, J), where the meaning of the index J is described below:

$J = 0$ Total cross section (reference value = 101.3 mb)
$J = 1$ Elastic cross section (reference value = 22.2 mb)
$J = 2$ Single diffractive cross section XB (reference value = 7.2 mb)
$J = 3$ Single diffractive cross section AX (reference value = 7.2 mb)
$J = 4$ Double diffractive cross section (reference value = 9.5 mb)
$J = 5$ Inelastic, non-diffractive cross section (reference value = 55.2 mb).

Where $J = 0$ has to correspond to the sum of the contributions for $J = 1, \ldots, 5$. With respect to alternative cross section predictions [802], PYTHIA reference values for diffractive cross sections might be slightly shifted on the high side. A possible sound alternative could be to reduce the diffractive cross sections of around 30%, keeping constant the total cross section.

In order to assess the sensitivity of one analysis to the diffractive variations in the pile-up, at least the two options MSEL 1 and MSEL 2 should be tried. Diffractive contribution will in general result in few additional soft charged particles spiralling in the high magnetic fields of the LHC experiments. This effect is most likely to be relevant in the tracker detectors, where multiple hits in the same layer can be generated by the same track.

B.1.8. Decays

In contrast to the simple decay models available in the common PS Monte Carlo, alternative hadron decay models exist, for example EVTGEN [803], which have huge collections of exclusive hadron decays up to branching ratios as low as 10^{-4}.

EVTGEN follows the spin density matrix formalism and has an easily tuneable and upgradeable hadron decay data base which currently constitutes the largest and most refined collection of hadron decay models.

Comparison between the simple default decay models implemented in PS Monte Carlo and those available in EVTGEN should be recommended at least for analyses dealing with B hadrons or relying on b-tagging. However, since switching to a new hadron decay model could have a deep spin-offs on the exclusive description of the final states (multiplicity of kaons, pions, photons and muons, multiplicity of tracks reconstructed in secondary vertices) it might be worth to study also effects on trigger performances.

The LHC version of EVTGEN was initially provided by the LHCb experiment and is currently maintained by LCG Generator [804]. It comprises an interface to PYTHIA simulation that solves the technical problems of switching between the two different scenarios (i.e. hadron decays performed by PYTHIA, hadron decays performed by EVTGEN).

B.1.9. LHAPDF and PDF uncertainties

The detailed investigations of processes at LHC required a well understanding of the systematic theoretical uncertainties [201]. One of the important source of such errors is the parton distribution functions (PDFs).

The Les Houches Accord Parton Density Functions (LHAPDF) package [95] is designed to work with the different PDF sets[53]. In this approach a "fit" to the data is no longer described by a single PDF, but by a PDF set consisting of many individual PDF members. Indeed, PDFs are specified in a parameterised form at a fixed energy scale Q_0, such as

$$f(x, Q_0) = a_0 x^{a_1}(1-x)^{a_2}(1 + a_3 x^{a_4} \ldots). \tag{B.1}$$

The PDFs at all higher Q are determined by NLO perturbative QCD evolution equations. The total number of PDF parameters (d) could be large (for example, for CTEQ parametrisation one has $d = 20$ [12]). Fitting procedure is used for evaluation an effective χ^2 function, which can be used to extract the "best fit" (the global minimum of χ^2) and also to explore the neighbourhood of the global minimum in order to quantify the uncertainties. As a result one has the "best-fit" PDF and $2d$ subsets of PDF [12, 95]:

$$f_0(x, Q), \;\; f_i^{\pm}(x, Q) = f\left(x, Q; \{a_i^{\pm}\}\right), \;\; i = 1, \ldots, d. \tag{B.2}$$

B.1.9.1. Master equations for calculating uncertainties. Let $X(\{a\})$ be any variable that depends on the PDFs. It can be a physical quantity such as the W production cross section, or a differential distribution.

Let $X_0 = X(\{a_0\})$ be the estimate for X calculated with the best-fit PDF and $X_i^{\pm}$ be the observable X calculated with i-th subset $f_i^{\pm}(x, Q)$.

Following to CTEQ6 collaboration one can estimate the variation of X by using a master formula [12]:

$$\Delta X = \sqrt{\sum_{i=1}^{d} \left(X_i^+ - X_i^-\right)^2}. \tag{B.3}$$

However, very often many X_i^+ and X_i^- have different magnitudes and even signs! This failure of the master formula is a result of the simple observation that the PDF set that minimises the uncertainty in a given observable X is not necessarily the same as the one that minimises the fit to the global data set.

The better estimator for the uncertainty of a generic observable X was proposed in [805]. It is defined as the maximum positive and negative errors on an observable X by

$$\begin{aligned} \Delta X_+ &= \sqrt{\textstyle\sum_{i=1}^{d} \left(\max[(X_i^+ - X_0),\ (X_i^- - X_0)\,,\ 0]\right)^2}, \\ \Delta X_- &= \sqrt{\textstyle\sum_{i=1}^{d} \left(\max[(X_0 - X_i^+),\ (X_0 - X_i^-),\ 0]\right)^2}. \end{aligned} \tag{B.4}$$

In Eqs. (B.4) one sums the maximum deviations on the observable in each of the parameter directions, and hence retain both maximal sensitivity to the parameters that vary most and estimate the range of allowed values of the cross section. Note, that the errors in Table C.2 were evaluated with this Eq. (B.4).

[53] Note, at CMS it was recommended to use the CTEQ 5L set for PTDR simulation. Since there is only *one* CTEQ 5L PDF set (without corresponding subsets), it was recommended to use CTEQ 6M for evaluation of uncertainties due to PDFs for PTDR estimates and only in a special case can one use another sets (e.g. MRST).

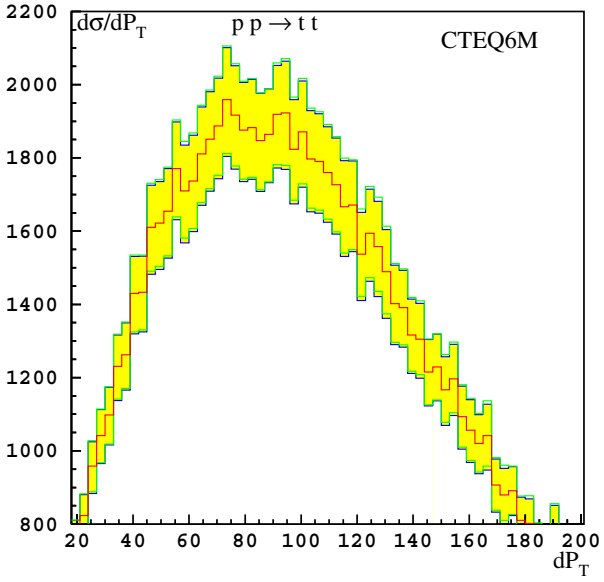

Figure B.1. $d\sigma/dP_{\mathrm{T}}$ distribution for $t\bar{t}$-pair production at LHC. The central histogram corresponds to the 'best-fit' of CTEQ6M PDF, while the shaded area represents the deviation due to PDF uncertainties.

Eq. (B.4 could also be used for calculations of differential distribution. Fig. B.1 presents the differential distribution $d\sigma/dP_{\mathrm{T}}$ for $t\bar{t}$-pair production at LHC.

B.1.9.2. How to calculate $X(\{a_i\})$. The most simple and straightforward method is to simulate a sample with the "best-fit" PDFs and then to repeat a such simulation $2d$ times with different $2d$ PDF subsets. As a results one gets $(1+2d)$ samples of *unweighted* events with *different* kinematics for each samples. Then use these samples to calculate $(1+2d)$ values for observable:

$$X_0 = \sum_{\text{events}} X_n(\{a_0\})), \quad X_i^{\pm} = \sum_{\text{events}} X_n(\{a_i^{\pm}\}), \quad i = 1, \ldots, d. \tag{B.5}$$

In practice, such method requires a large CPU-time and can be recommended only to be used for very few special cases, when a high accuracy is required.

In the second approach (*"re-weighting" method*) one needs to simulate only **one** sample with the 'best-fit' PDF. In doing so the additional weights, corresponding to all other PDF subsets are evaluated. This weight is the ratio of the parton luminosity [PDF($\{a_i\}$) – the product of PDFs] evaluated with PDF subset to the parton luminosity, calculated with the 'best-fit' PDF. As a result, for any n-event one has $2d$ additional weights:

$$w_{(0)} = 1(\text{best fit PDF}), \quad w_{(i)}^{\pm} = \frac{\text{PDF}(\{a_i^{\pm}\})_n}{\text{PDF}(\{a_0\})_n}; \quad w_{(i)}^{\pm} = \mathcal{O}(1). \tag{B.6}$$

The corresponding $(1+2d)$ values for observable X are evaluated as follows:

$$X_0 = \sum_{\text{events}} X_n(\{a_0\})), \quad X_i^{\pm} = \sum_{\text{events}} w_{(i)}^{\pm}\, X_n(\{a_0\}). \tag{B.7}$$

Contrary to the first method (see (B.5)) these $(1+2d)$ samples have the events with *different* weights, but with *identical* kinematics for each samples. Note, that all additional samples have

different "total number of events":

$$N_0 = \sum_{\text{events}} w_{(0)}(=1),\ N_i^{\pm} = \sum_{\text{events}} w_{(i)}^{\pm} \neq N_0,\ \text{and}\ N_i^{\pm} = \mathcal{O}(N_0). \tag{B.8}$$

Starting from CMKIN_6_0_0 version it is possible for each event the evaluation of the additional weights, corresponding to different PDF subsets (i.e. $w_{(i)}^{\pm}$, see (B.6)). This option is available for CMKIN run with PYTHIA-like generators (PYTHIA, MADGRAPH, COMPHEP, ALPGEN, TOPREX, STAGEN, etc) and HERWIG. This information is written in `/mc_param/` user block after all variables filled by CMKIN and a user (by using of `kis_xxx` routines).

B.2. Experimental uncertainties

The systematic uncertainties associated with the detector measurements contributing to an analysis are mostly covered in the corresponding chapters of Volume 1 of this Report [7] and are summarised here.

B.2.1. Luminosity uncertainty

As discussed in Chapter 8 of [7], the design goal for the precision of the luminosity measurement at CMS is 5%, which is assumed to be achieved after 1 fb^{-1} of data has been collected. For integrated luminosities of less than 1 fb^{-1}, it is assumed that the precision is limited to 10%. For studies based on 30 fb^{-1} or more in this Report, it is assumed that further improvement on the uncertainty can be achieved and a 3% uncertainty is assumed, via e.g. W, Z based luminosity measurements.

B.2.2. Track and vertex reconstruction uncertainties

The uncertainty in the silicon track reconstruction efficiency is taken to be 1% for all tracks. The primary vertex precision along the z coordinate is expected to be about 10 μm once 1 fb^{-1} has been collected. The transverse vertex precision is expected to be about 1 μm.

The effects of uncertainties on the alignment of silicon sensors on track and vertex reconstruction are studied using a dedicated software tool (Section 6.6.4 of [7]) that is able to displace tracker elements according to two scenarios: a "First Data Taking Scenario" with placement uncertainties as expected at LHC start-up from measurements using the laser alignment system for the strip tracker and from in-situ track-based alignment of the pixel detector, and a "Long Term Scenario" appropriate after the first few fb^{-1} have been collected and a complete track-based alignment has been carried out for all tracker elements.

The effect of the magnetic field uncertainty in the central region of CMS is expected to contribute a momentum scale uncertainty of 0.0003 GeV/c to $1/p_{\text{T}}$. When combined with the aggregate effect from alignment uncertainties, the overall momentum scale uncertainty is 0.0005 GeV/c at start-up.

B.2.3. Muon reconstruction uncertainties

As with the silicon tracker studies, a dedicated software tool has been developed (Section 3.2.2 of [7]) to study the effects of muon detector placement uncertainties on muon reconstruction. Two scenarios, a "First Data Taking Scenario" with placement uncertainties as expected at LHC start-up and a "Long Term Scenario" appropriate after the first few fb^{-1}, are available and used in analyses sensitive to the alignment precision of the muon detectors. The latter

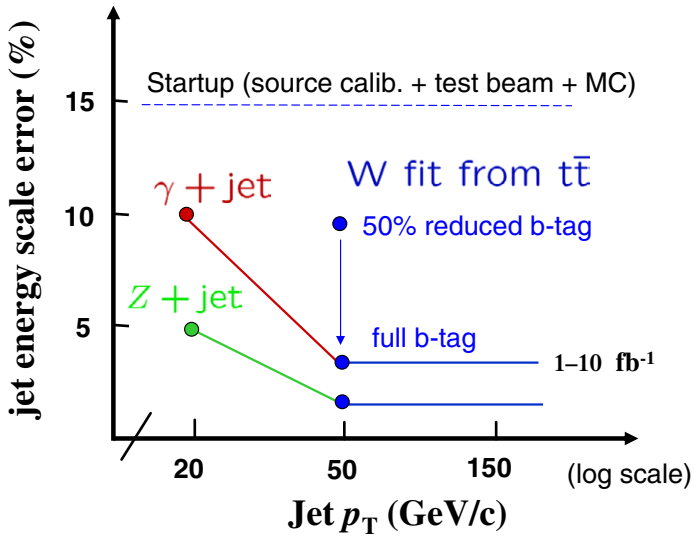

Figure B.2. Jet energy scale uncertainty is applied as a rescaling of the four-momentum of the reconstructed jet $p^{\mu,jet}_{scaled\pm} = (1 \pm \alpha) \cdot p^{\mu,jet}_{meas}$ where α is the percentage uncertainty plotted above.

scenario describes a detector alignment precision of 200 μm in the plane transverse to the beam axis using the laser alignment system and track-based alignment strategies.

The effect of magnetic field uncertainties on the muon momentum will be dominated by the uncertainty in the central region and its impact on the momentum scale determined by fits to the silicon tracker hits for muon momenta well below the TeV/c scale.

B.2.4. Electromagnetic calibration and energy scale uncertainties

The precision to which the ECAL crystals can be intercalibrated from a variety of techniques is discussed in Section 4.4 of [7], and ranges from 0.4–2.0% using about 5 fb^{-1} of *in situ* single isolated electron data. A software tool is used to apply calibration constants to the accuracy expected to be obtained with either 1 fb^{-1} or 10 fb^{-1} of integrated luminosity. The absolute energy scale can be determined using the Z mass constraint in Z $\rightarrow$ ee decays, and is expected to be measured to a precision of about 0.05%.

B.2.5. Jet and missing transverse energy uncertainties

The estimated systematic uncertainty on the jet energy scale is shown in Fig. B.2. At startup the accuracy of the jet energy scale relies on the understanding of single-particle test beam calibration and the level of agreement achieved in the data-to-Monte Carlo simulation comparisons of the detector response. The response of an individual tile or crystals is known to limited accuracy from source calibration in the HCAL and test stand measurements for crystals in the ECAL. Hence, given the limitations of the precalibration of the calorimeters, an overall uncertainty of 15% is expected for the "day-one" absolute energy scale. This applies equally for jet response and the energy scale uncertainty of the missing transverse energy.

In the first 1–10 fb^{-1} of data, the γ+ jet calibration [283] and the hadronic W boson mass calibration in top quark pair production events [287] are currently the best estimates for the accuracy on the absolute jet energy scale. The hadronic W jets in the selected

sample have a mean p_{T} that is approximately 50 GeV/c. A lowering of the jet selection threshold increases the effects of the offset correction from pile-up. The systematic on offset corrections and backgrounds puts the absolute jet energy scale at 3%. The jet reconstruction efficiencies are flat above 50 GeV/c, but drop in the low p_{T} region. The current estimate of the high p_{T} jet energy scale based on the hadronic W calibration is 3%. The calorimeter response curves that are required to extrapolate to high p_{T} are not expected to significantly increase the energy scale uncertainty beyond the 3% from the W calibration. In the low p_{T} region excluded from the hadronic W analysis, the absolute jet energy scale will be set by the γ+jet calibration which will extend down to 20 GeV. Below 20 GeV, only the single-particle calibration methods apply and these will have an accuracy of 10%. The recommended treatment for the jet energy systematic in this report is to apply an uncertainty according to this functional form:

$$\sigma_E^{jet}/E = \begin{cases} 10\% & p_{\mathrm{T}} < 20\,\mathrm{GeV/c} \\ 10\% - 7\% * (p_{\mathrm{T}} - 20\,\mathrm{GeV/c})/(30\,\mathrm{GeV/c}) & 20\,\mathrm{GeV/c} < p_{\mathrm{T}} < 50\,\mathrm{GeV/c} \\ 3\% & p_{\mathrm{T}} > 50\,\mathrm{GeV/c} \end{cases}.$$

It is expected that the Z+jet sample and further analysis of the hadronic W systematics will reduce the overall jet energy scale uncertainty, but these analyses remain under active study.

The low p_{T} region is particularly important for the missing transverse energy (MET) response. As the MET will have significant contributions from low p_{T} jets and unclustered energy, it is expected that the low p_{T} component of the MET will not be understood to better than 10% following the first 1–10 fb^{-1} of data. The recommended treatment of the MET energy scale uncertainty has two approaches (one simple and one more detailed). For a MET which is known to be dominated by low p_{T} jets and unclustered energy, an uncertainty of 10% should be applied to the components of the MET uncorrelated to the jet energy scale uncertainty of the jets. This is the simple approach and gives a conservative error on the MET. For events with reconstructed high p_{T} jets, the contributions to the MET uncertainty are correlated to the jet energy scale uncertainty of the high p_{T} jets. The recommended treatment of the MET uncertainty is to apply separate uncertainties on the low p_{T} and high p_{T} components of the MET. The MET is reconstructed as described in [147] and [148]. This gives a type-1 correction of the following form:

$$E^{\mathrm{miss}}_{\mathrm{Tx(y)}} = -\left[E^{\mathrm{raw}}_{\mathrm{Tx(y)}} + \sum_{\mathrm{jets}} \left(p^{\mathrm{corr.\ jet}}_{\mathrm{Tx(y)}} - p^{\mathrm{raw\ jet}}_{\mathrm{Tx(y)}}\right)\right]$$

where $E^{\mathrm{raw}}_{\mathrm{Tx(y)}}$ is the sum over the raw calorimeter tower energies and the jet sum in the equation is over jets with a reconstructed p_{T} above a given jet $p_{\mathrm{T}}^{\mathrm{cut}}$ selection cut, typically 20–25 GeV/c. The jet p_{T} is used in these formula to account for the angular separation of the towers included in the jet sum, contributing to the jet mass. Rewriting the above equation in this form

$$E^{\mathrm{miss}}_{\mathrm{Tx(y)}} = -\left[\left(E^{\mathrm{raw}}_{\mathrm{Tx(y)}} - \sum_{\mathrm{jets}} p^{\mathrm{raw\ jet}}_{\mathrm{Tx(y)}}\right)_{\mathrm{low}\ p_{\mathrm{T}}} + \left(\sum_{\mathrm{jet}} p^{\mathrm{corr.\ jet}}_{\mathrm{Tx(y)}}\right)_{\mathrm{high}\ p_{\mathrm{T}}}\right]$$

shows explicitly the low p_{T} (in the first set of brackets) and the high p_{T} components (second set of brackets) of the MET. The proposed systematics treatment is to vary the components of the low p_{T} MET by 10% scale uncertainty uncorrelated with the high p_{T} component and to vary the high p_{T} component according the jet energy scale uncertainty for the measured jets.

If a subset of the high p_T jets are identified as electromagnetic objects, isolated electrons or photons, then these EM-jets should be given EM-scale energy corrections which are closer to unity than hadronic jet corrections. The energy scale uncertainty on an EM-object will also be much lower than the jet energy scale systematic. Therefore, if the EM-objects are not removed from the jet list, the quoted energy scale uncertainty will be conservative relative to the lower errors associated with separate treatment of identified EM-objects.

In addition to the jet energy scale uncertainty, there are uncertainties on the jet resolution. At startup the jet resolution is estimated to be accurate to 20% of the quoted resolution based on the test-beam data and simulation studies. The dijet balancing resolution will be determined from data and will further constrain this uncertainty. It is expected that the systematics on the third jet veto and other selection criteria will limit the uncertainty on the jet resolution to 10% in the 1–10 fb^{-1} dataset. The recommended treatment for this systematic is to add an additional smearing to the jet energy which broadens the overall jet resolution by 10%. This can be done by throwing a Gaussian random number and adding an energy term which is 46% of the jet resolution. Therefore, the jet-by-jet event-by-event smearing should be done as follows:

$$E'^{\mathrm{jet}}_{\mathrm{T}} = E^{\mathrm{jet}}_{\mathrm{T}} + \mathrm{Gaus}[0,\ 0.46 * \sigma(E_{\mathrm{T}}, \eta)] \tag{B.9}$$

where $\sigma(E_{\mathrm{T}}, \eta)$ is the reference jet resolution which for the central barrel is given by (using Monte Carlo simulation derived jet calibrations where $E^{\mathrm{MC}}_{\mathrm{T}}$ is equal to $E^{\mathrm{rec}}_{\mathrm{T}}$ on average)

$$\sigma(E^{\mathrm{jet}}_{\mathrm{T}}, |\eta| < 1.4) = (5.8\,\mathrm{GeV}) \oplus \left(1.25 * \sqrt{E^{\mathrm{jet}}_{\mathrm{T}}}\right) \oplus 0.033 * E^{\mathrm{jet}}_{\mathrm{T}} \tag{B.10}$$

(terms added in quadrature) and $\mathrm{Gaus}[0, 0.46 * \sigma(E_{\mathrm{T}}, \eta)]$ is a randomly thrown sampling of a normal distribution per jet with a mean of zero and a width of 46% of the jet resolution and therefore $E'^{\mathrm{jet}}_{\mathrm{T}}$ is the smeared jet energy to be used in the estimation of the jet resolution systematic uncertainty of the measurement. The 46% is chosen so that when added in quadrature to the nominal resolution gives an overall widening of the energy resolution of 10%. The resolutions of the endcap and forward jet regions are found in [165, Table 5]. These are

$$\sigma(E^{\mathrm{jet}}_{\mathrm{T}}, 1.4 < |\eta| < 3.0) = (4.8\mathrm{GeV}) \oplus \left(0.89 * \sqrt{E^{\mathrm{jet}}_{\mathrm{T}}}\right) \oplus 0.043 * E^{\mathrm{jet}}_{\mathrm{T}}$$

$$\sigma(E^{\mathrm{jet}}_{\mathrm{T}}, 3.0 < |\eta| < 5.0) = (3.8\mathrm{GeV}) \oplus 0.085 * E^{\mathrm{jet}}_{\mathrm{T}}$$

where for these jet resolution fits the stochastic term in the forward region is small compared to the noise and constant terms (hence the missing $\sqrt{E^{\mathrm{jet}}_{\mathrm{T}}}$ term for $3.0 < |\eta| < 5.0$). The shift in the +10% direction can be symmetrised to account for the −10% shift. Otherwise, the difference between the reconstructed and generated jet energies must be reduced by 10% in order to estimate the −10% uncertainty from the nominal Monte Carlo jet resolution. The jet resolution uncertainty is particularly important when searching for signals that are on a rapidly falling QCD multi-jet p_T spectrum.

B.2.6. Heavy-flavour tagging uncertainties

A strategy for measuring the b-tag efficiency using an enriched sample of b-jets from $\mathrm{t\bar{t}}$ events, and its estimated precision, is described in Section 12.2.8 of [7]. The relative uncertainty on the b-efficiency measurement is expected to be about 6% (4%) in the barrel and 10% (5%) in

the endcaps for 1 fb^{-1} (10 fb^{-1}) of integrated luminosity. These uncertainties correspond to a b-tag working point efficiency of 50%.

The light-quark (and gluon) mis-tag uncertainty is expected to be larger than the b efficiency uncertainty; however, for this Report a global uncertainty of 5% is assumed for the mis-tag uncertainty. As with the efficiency determination, it is important to identify strategies to measure the mis-tagging probabilities in data as well.

Likewise, a strategy to measure the uncertainty on the efficiency for identifying τ leptons is described in Section 12.1.4 of [7], and involves comparing the ratio of $\mathrm{Z} \to \tau\tau \to \mu +$ jet to $\mathrm{Z} \to \mu\mu$ events. With a 30 fb^{-1} data sample, the relative uncertainty on τ-tagging is estimated to be about 4%. A measurement of the τ misidentification probability can be determined from a sample of $\gamma +$ jet events, and with a 10 fb^{-1} data sample is expected to have an uncertainty at the level of 4–10%.

Appendix C. Monte Carlo Models and Generators

C.1. Introduction

This section presents a short description of the basic event generators used in CMS during preparation of the PTDR (see CMS "Generator Tools group" for details). A comprehensive review of the present Monte Carlo models and generators is given elsewhere [806]. Note that only MC generators used in CMS are described here, and a full description of several popular packages (like ISAJET or AcerMC, see [806]) is omitted.

There are several available Monte Carlo event generators for pp, pA and AA collisions, namely HERWIG [196], HIJING [807], ISAJET [672], PYTHIA [69] and SHERPA [808]. Each of these simulates a hadronic final state corresponding to some particular model of the underlying physics. The details of the implementation of the physics are different in each of these generators, however the underlying philosophy of the generators is the same.

The cross section values and the differential distribution for almost all processes are evalueated as follows:

$$\sigma(pp \to CX) = \sum_{ij} \int f_i^p(x_1, Q^2)\, f_j^p(x_2, Q^2) \hat{\sigma}(ij \to C) \mathrm{d}x_1 \mathrm{d}x_2, \qquad \text{(C.1)}$$

where $f_i^p(x, Q^2)$ are the Parton Distribution Functions (PDF) of ith parton, that carried a fraction x of the initial proton momentum at a scale (Q^2); $\sigma(ij \to C)$ is the cross section for the hard process (i.e. describing two partons, i and j, interaction).

A general scheme of event generation assumes the evaluation of the hard process (the cross section value, the incoming and outgoing particle's momenta and colours), then evolves the event through a parton showering and hadronisation step, and the decay of the unstable particles. The event information (stored in `/HEPEVT/` common block [69]) contains the momenta of the final hadrons, leptons and photons and positions of their decay vertexes. Typically such information contains also the characteristics (momenta, colours, `KF`-codes, mother's and daughter's relations) of all intermediate partons (quarks, gluons, gauge bosons, unstable physical particles, etc) that provide a trace-back the history of particle production inside of an event. By using an acceptance-rejection methods weighted events can be returned.

Parton showering is based on the expansion around the soft and collinear evolution limits and is often ascribed to either the initial or final state. The algorithm used by HERWIG and SHERPA also include some effects due to quantum interference. The events that have more energy in the parton process have more showering, and consequently more jet activity.

The collection of quarks and gluons must then be hadronised into mesons and baryons. This is done differently in each of the event generators, but is described by a set of (fragmentation) parameters that must be adjusted to agree with experimental results. HERWIG looks for colour singlet collections of quarks and gluons with low invariant mass and groups them together; this set then turns into hadrons. PYTHIA splits gluons into quark-anti-quark pairs and turns the resulting set of colour singlet quark-anti-quark pairs into hadrons via a string model. ISAJET simply fragments each quark independently paying no attention to the colour flow.

The dominant cross-section at the LHC consists of events with no hard scattering. There is little detailed theoretical understanding of these minimum-bias events and the event generators must rely on present data. These minimum-bias events are important at LHC, particularly at design luminosity, as they overlap with interesting hard-scattering events. The generators use a different approach in this case. HERWIG uses a parametrisation of data mainly from the CERN $p\bar{p}$ Collider. PYTHIA uses a mini-jet model where the jet cross-section is used at very low

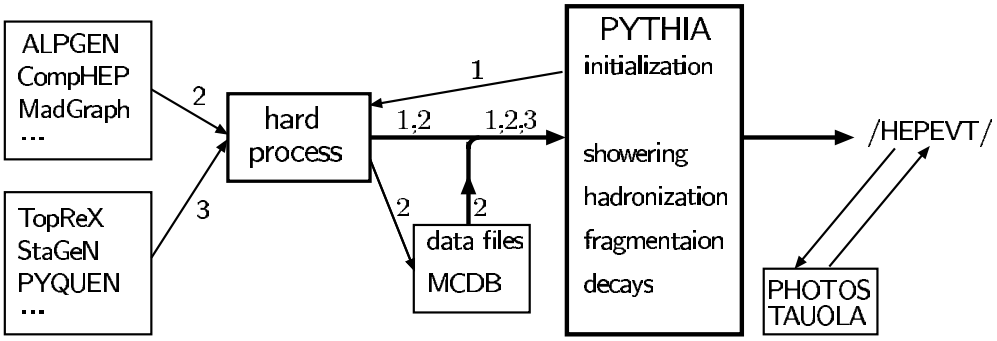

Figure C.1. Purely schematic data flow in PYTHIA and HERWIG.

transverse momenta, i.e the hard scattering process is extrapolated until it saturates the total cross-section. CMS has used the PYTHIA approach with dedicated modifications that agree with present data from Tevatron [69]. The model of the hadronic interactions implemented in the physics generator has a direct impact on physical observables such as jet multiplicity, their average transverse momentum, internal structure of the jets and their heavy flavour content. This led to the choice to use PYTHIA for most processes, allowing for a consistent set of signal and background events to be generated.

Table C.2 presents the predicted cross-section values for the basic SM processes, as used in the simulations for PTDR. The cross-section values (at leading order) were calculated by using PYTHIA 6.327 with `CTEQ5L` (default PDF for PTDR) and with `CTEQ6M` PDFs. α_s at 1st (2nd) order is used with `CTEQ5L` (`CTEQ6M`) PDFs. For `CTEQ6M` the quoted errors are related to the uncertainties due to PDFs (see Subsection B.1.9).

C.2. General scheme of generator usage in CMS

All event generators, included in CMS simulation software, can be separated into two groups.

The first group (HERWIG, HIJING, ISAJET, PYTHIA) provides the *full simulation* of events. The basic package explored in CMS is PYTHIA and only few specific processes were simulated with HERWIG or HIJING.

A purely schematic data flow in PYTHIA and HERWIG is presented in Fig. C.1.

After initialisation the package (HERWIG or PYTHIA) calls "hard process" routines (see "1" arrow lines in Fig. C.1). Then information (the momenta of initial and final partons, the colours and `KF`-codes) is passed to package for parton showering, hadronisation, fragmentation and decays of the unstable particles.

However, all these "full event simulation" generators have very limited number of the hard process matrix elements (typically for $2 \to 2$ reaction at LO). Therefore, several special generators are used for simulation of many other LO processes. In fact, such packages generate the hard processes kinematic quantities, such as masses and momenta, the spin, the colour connection, and the flavour of initial- and final-state partons. The information is stored in the "Les Houches" format [809] (`/HEPEUP/` common block) and is passed to full event simulation package like PYTHIA or HERWIG (see thick "output" line on Fig. C.1).

Three generators, namely ALPGEN [161], COMPHEP [355], and MADGRAPH [81, 493], are widely used for simulation of many processes, especially for the generation of the hard processes with multi-jet final states. For example, ALPGEN allows to generate $Q\bar{Q}$ pair

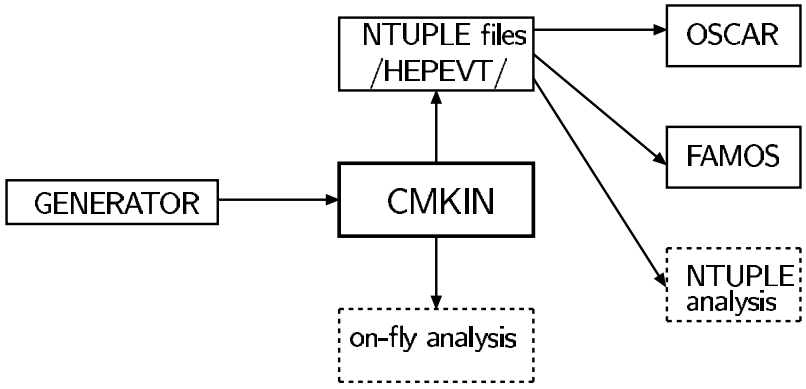

Figure C.2. Illustration of the CMKIN interface.

production with up to 6 jets. Due to the complexity of the matrix elements, describing the multi-jet processes, and a re-weighting procedure the generation of events is very CPU-time consuming. As a result, the information with kinematics is stored in the output files. (see "2" lines on Fig. C.1). Then, like in a generic PYTHIA process, such information is passed to PYTHIA (see thick "output" line on Fig. C.1).

There are several *"dedicated generators"*, TOPREX [44], STAGEN, SINGLETOP, COSMIC, SIMUB, PHASE, PYQUEN [810, 811], HYDJET [812], EDDE. These generators are used for simulation of several specific process (see below for a short description of these codes). The information with hard processes kinematic quantities is stored in `/HEPEUP/` common block [809] and is passed to the "full event simulation" package (see "3" lines on Fig. C.1).

After full simulation of event with PYTHIA or HERWIG the output information is stored in the `/HEPEVT/` common block. In addition two *special functionality* codes provide a better description of photon radiation from a charge final particles (PHOTOS [39]) and $\tau^{\pm}$-lepton decays (TAUOLA [155]). Typically, these codes read information from `/HEPEVT/` common, perform simulation and then add generated information (new particles) into the `/HEPEVT/` common block (see Fig. C.1).

C.3. CMKIN

Almost all generators available in CMS could be used with the CMKIN package. Now the CMKIN is used for OSCAR and FAMOS detector simulation input. This software package provides a common interface between physics event generators and CMS detector simulation (see Fig. C.2). It also provides an environment to make physics plots of generated events. CMKIN provides an interface to a number of physics generators like PYTHIA, ISAJET and HERWIG. It also offers the possibility to use different 'external generators' like ALPGEN [161], COMPHEP [355], MADGRAPH [81, 493] and TOPREX [44]. Cosmic muon simulation is available as well. Simple particle generation is also included, i.e. single and double particles as well as simple multi particle events. The interface is based on a common block `HEPEVT` - a HEP standard to store particle kinematics information for one event [69]. The `/HEPEVT/` common block is converted to HBOOK n-tuples. The event output format follows the `HEPEVT` standard and additional information can be included by the user in the block `/MC_PARAM/`.

There is a unified compilation script which is used as follows:

```
kine_make_ntpl.com <generator> [lhapdf]
```

where the first parameter can have one of the following values: *pythia, herwig, isajet, simple, single, double, simplemulti, cosmic, comphep, alpgen, madgraph, phase, toprex* or *stagen*. The optional second parameter *lhapdf* is given when the user wants to use LHAPDF library [95].

C.4. Full event simulation generators

C.4.1. PYTHIA

The PYTHIA package [69] is a general-purpose generator for hadronic events in pp, e $^{+}$e^{-} and ep colliders. It contains a subprocess library and generation machinery, initial- and final-state parton showers, underlying event, hadronisation and decays, and analysis tools. PYTHIA contains around 240 different $2 \to 2$ (and some $2 \to 1$ or $2 \to 3$) subprocesses, all at leading order. The subsequent decays of unstable resonances (W, Z, top, Higgs, SUSY, ...) brings up the partonic multiplicity, for many processes with full spin correlations in the decays. The external processes can be evolved through the showering and hadronisation (like internal ones).

The final-state shower is based on forward evolution in terms of a decreasing timelike virtuality m^2, with angular ordering imposed by veto. The framework is leading-log, but includes many NLL aspects such as energy–momentum conservation, $\alpha_s(p_\perp^2)$ and coherence. Further features include gluon polarisation effects and photon emission.

The initial-state shower is based on backward evolution, i.e. starting at the hard scattering and moving backwards in time to the shower initiators, in terms of a decreasing spacelike virtuality Q^2. Initial and final showers are matched to each other by maximum emission cones.

The composite nature of hadrons (and resolved photons) allows for several partons from each of the incoming hadrons to undergo scatterings. Such multiple parton–parton interactions are instrumental in building up the activity in the underlying event, in everything from charged multiplicity distributions and long-range correlations to minijets and jet pedestals. The interactions are described by perturbation theory, approximated by a set of more or less separate $2 \to 2$ scatterings; energy conservation and other effects introduce (anti)correlations. The scatterings are colour-connected with each other and with the beam remnants.

The Lund string model, used for hadronisation, is based on a picture with linear confinement, where (anti)quarks or other colour (anti)triplets are located at the ends of the string, and gluons are energy and momentum carrying kinks on the string. The string breaks by the production of new $q\bar{q}$ pairs, and a quark from one break can combine with an anti-quark from an adjacent one to form a colour singlet meson.

Unstable particles are allowed to decay. In cases where better decay models are available elsewhere, e.g. for $\tau^{\pm}$ with spin information or for B hadrons, such decays can be delegated to specialised packages.

At present the parameters from almost all PYTHIA common blocks (see `BLOCK DATA PYDATA`) could be set via data cards. With the CMKIN these parameters could be set in data card file with the following format (note, that only capital letters should be used):

PYTHIA	CMKIN	COMMENT
	parameter	
MSEL = 6	MSEL6	$t\bar{t}$ production
	one- *and* two-dimensional arrays	
CKIN(1) = 100	CKIN1 = 100	min.$\sqrt{\hat{s}}$
i.e. PMAS(6, 1) = 178	PMAS6, 1 = 178	top-quark mass

• *Common cards for* CMKIN

Below we present a list of PYTHIA parameters used for full event simulation for PTDR. Some of these parameters correspond to the old multiple interactions scenario, namely *Tune A* [813].

`MSTP(2)` = 1 : 1(first)/2(second) order running α_s
`MSTP(33)` = 0 : do not include of K-factors in hard cross sections
`MSTP(51)` = 7 : PDF set (here is CTEQ5L)
`MSTP(81)` = 1 : multiple parton interactions is switched ON
`MSTP(82)` = 4 : defines the multiple parton interactions model
`PARP(67)` = 1 : amount of initial-state radiation
`PARP(82)` = 1.9 : P_{T} cut-off for multi-parton interactions
`PARP(83)` = 0.5 : fraction of total hadronic matter in core
`PARP(84)` = 0.4 : radius of core
`PARP(85)` = 0.33 : gluon production mechanism in multiple interactions
`PARP(86)` = 0.66 : gluon prod. mechanism in multiple interactions
`PARP(88)` = 0.5
`PARP(89)` = 1000 : reference energy scale for which `PARP(82)` is set
`PARP(90)` = 0.160 : effective P_{T} cut − off = [PARP(82)/PARP(89)]**PARP(90)
`PARP(91)` = 1.0 : width of Gaussian primordial $k_{\perp}$ distribution inside hadron
`PARJ(71)` = 10 : maximum average $c\tau$ for particles allowed to decay
`MSTJ(11)` = 3 : choice of the fragmentation function
`MSTJ(22)` = 2 : allow to decay those unstable particles
`PMAS(5,1)` = 4.8 : the mass of the b-quark
`PMAS(6,1)` = 175.0 : the mass of the t-quark

C.4.2. HERWIG

HERWIG contains a wide range of Standard Model, Higgs and supersymmetric processes [196]. HERWIG uses the parton-shower approach for initial- and final-state QCD radiation, including colour coherence effects and azimuthal correlations both within and between the jets.

In the treatment of supersymmetric processes, HERWIG itself doesn't calculate the SUSY mass spectrum or decay rates, but reads in an input file containing the low-energy parameters (masses, couplings, decays, ...). This file can be written by hand or more conveniently be generated with the ISAWIG program. This program provides an interface to ISAJET (and therefore to all models in ISASUSY and ISASUGRA), to HDECAY (for NLO Higgs decays), and can also add R-parity violating decays.

Colour coherence effects of (initial and final) partons are taken into account in all hard subprocesses, including the production and decay of heavy quarks and supersymmetric particles. HERWIG uses the angular ordered parton shower algorithm which resumes both soft and collinear singularities. HERWIG includes spin correlation effects in the production and decay of top quarks, tau leptons and supersymmetric particles. For the SUSY decays, there is an option for using either the matrix elements (fast) or the full spin correlations. HERWIG uses a cluster hadronisation model based on non-perturbative gluon splitting, and a similar cluster model for soft and underlying hadronic events. This model gives a good agreement with the LEP data on event shapes, but does not fit the identified particle spectrum well.

C.4.3. ISAJET

ISAJET is a Monte Carlo program which simulates pp, $p\bar{p}$, e^+e^- interactions at high energies [672]. ISAJET is based on perturbative QCD plus phenomenological models for parton and beam jet fragmentation. At CMS ISAJET is used for calculations of SUSY parameters.

C.4.4. HIJING

Hard or semi-hard parton scatterings with transverse momentum of a few GeV/c are expected to dominate high energy heavy ion collisions. The HIJING (Heavy Ion Jet INteraction Generator) Monte Carlo model [807] was developed by M Gyulassy and X-N Wang with special emphasis on the role of minijets in pp, pA and AA reactions at collider energies.

Detailed systematic comparison of HIJING results with a very wide range of data demonstrates that a quantitative understanding of the interplay between soft string dynamics and hard QCD interaction has been achieved. In particular, HIJING reproduces many inclusive spectra two particle correlations, and can explain the observed flavour and multiplicity dependence of the average transverse momentum.

C.5. Tree level matrix element generators

C.5.1. ALPGEN

ALPGEN is designed for the generation of Standard Model processes in hadronic collisions, with emphasis on final states with large jet multiplicities [161]. It is based on the exact leading order evaluation of partonic matrix elements and t and gauge boson decays with helicity correlations. The code generates events in both a weighted and unweighted mode. Weighted generation allows for high-statistics parton-level studies. Unweighted events can be processed in an independent run through shower evolution and hadronisation programs.

The current available processes are:

- $W/Z/H\ Q\bar{Q} + N$ jets ($Q = c, b, t$) with $N \leqslant 4$
- $Q\bar{Q} + N$ jets, with $N \leqslant 6$
- $Q\bar{Q}Q'\bar{Q}' + N$ jets, with $N \leqslant 4$
- W + charm + N jets, with $N \leqslant 5$
- N jets, $W/Z + N$ jets, with $N \leqslant 6$
- $nW + mZ + lH + N$ jets, with $n + m + l + N \leqslant 8$, $N \leqslant 3$
- $N\gamma + M$ jets, with $N \geqslant 1$, $N + M \leqslant 8$ and $M \leqslant 6$
- $H + N$ jets ($N \leqslant 4$), with the Higgs produced via ggH vertex
- single top production.

C.5.2. CompHEP

CompHEP [814] is a package for evaluating Feynman diagrams, integrating over multi-particle phase space and generating events with a high level of automation. CompHEP includes the Feynman rules for SM and several versions of MSSM (SUGRA, GMSB, MSSM with R-parity violation).

CompHEP computes squared Feynman diagrams symbolically and then numerically calculates cross sections and distributions. After numerical computation one can generate the unweighted events with implemented colour flow information. The events are in the form of the Les Houches Accord event record [809] to be used in the PYTHIA program for showering and hadronisation.

CompHEP allows for the computation of scattering processes with up to 6 particles and decay processes with up to 7 particles in the final state.

C.5.3. MadGraph *and* madevent

madevent [81] is a multi-purpose, tree-level event generator which is powered by the matrix element generator MadGraph [493]. Given a user process, MadGraph automatically generates the amplitudes for all the relevant subprocesses and produces the mappings for the integration over the phase space. This process-dependent information is packaged into madevent, and a stand-alone code is produced. It allows the user to calculate cross sections and to obtain unweighted events automatically. Once the events have been generated – event information, (e.g. particle id's, momenta, spin, colour connections) is stored in the "Les Houches" format [809]. Events may be passed directly to a shower Monte Carlo program (interfaces are available for herwig and pythia).

The limitation of the code are related to the maximum number of final state QCD particles. Currently, the package is limited to ten thousand diagrams per subprocess. So, for example, $W+5$ jets is close to its practical limit. At present, only the Standard Model Feynman rules are implemented and the user has to provide his/her own rules for beyond Standard Model physics, such as MSSM.

C.5.4. TopReX

The event generator TopReX [44] provides the simulation of several important processes in pp and $p\bar{p}$ collisions, not implemented in pythia. In the matrix elements used in TopReX the decays of the final t-quarks, $W^{\pm}$, Z and charged Higgs bosons are also included. The final top quark could decay into SM channel ($t \to qW^{+}$, $q = d, s, b$), b-quark and charged Higgs ($t \to bH^{+}$) and the channels with flavour changing neutral current (FCNC): $t \to u(c)V$, $V = g, \gamma, Z$. The implemented matrix elements take into account spin polarisations of the top quark, that provides a correct description of the differential distributions and correlations of the top quarks decay products.

C.6. Supplementary packages

C.6.1. photos

photos is a universal package to simulate QED photon radiative corrections [39]. The precision of the generation may in some cases be limited, in general it is not worse than the complete double bremsstrahlung in LL approximation. The infrared limit of the distributions is also correctly reproduced. The action of the algorithm consists of generating, with internally calculated probability, bremsstrahlung photon(s), which are later added to the `/HEPEVT/` record. Kinematic configurations are appropriately modified. Energy-momentum conservation is assured. When using photos, the QED bremsstrahlung of the principal generator must be switched off. For example in case of pythia one has to use `MSTJ 41=1`.

C.6.2. tauola

tauola is a package for simulation of the $\tau^{\pm}$-lepton decays [155]. It uses the photos package to simulate radiative corrections in the decay. The tauola interface is made with the pythia generator. This interface evaluates also the position of τ-lepton decay (i.e. the information on the production vertex of the decay products of τ-lepton).

C.6.3. PYQUEN

The event generator PYQUEN (PYthia QUENched) [810, 811] provides the simulation of rescattering and energy loss of hard partons in dense QCD-matter (quark-gluon plasma) created in ultrarelativistic heavy ion collisions. The approach relies on an accumulative energy losses, when gluon radiation is associated with each scattering in expanding medium together including the interference effect by the modified radiation spectrum $dE/d\ell$ as a function of decreasing temperature T. The model is implemented as fast Monte Carlo tool, to modify standard PYTHIA jet event.

C.6.4. HYDJET

The event generator HYDJET [812] (HYDrodynamics + JETs) provides the fast simulation of heavy ion events at LHC energy including longitudinal, transverse and elliptic flow effects together with jet production and jet quenching (rescattering and energy loss of hard partons in dense QCD-matter, quark-gluon plasma). The model merges a fast generator of flow effects HYDRO [815] with PYTHIA (for jet production) and PYQUEN [810, 811] (for jet quenching) by simulating full heavy ion event as a superposition of soft, hydro-type state and hard multi-jets.

First of all, HYDJET calculates the number N^{hard} of hard nucleon-nucleon sub-collisions and number N^{part} nucleons-participants (at given impact parameter b of AA collision and minimum P_{T} of hard parton scattering) and generates the initial parton spectra by calling PYTHIA N^{hard} times (fragmentation off). After each jet parton affected by medium-induced rescattering and energy loss according with PYQUEN model. In the end of each PYTHIA sub-event adding new (in-medium emitted) gluons into PYTHIA parton list and rearrangements of partons to update string formation are performed. Then PYQUEN forms final hadrons with `PYEXEC` subroutine (fragmentation on). Finally, HYDJET calculates the multiplicity of soft, hydro-induced part of the event and add new particles in the end of the event record.

C.7. K-factors for dilepton production

Some event generators such as PYTHIA do not employ the most advanced matrix-element calculations. They must be reasonably fast since in most applications, many millions of events must be generated. Experimenters apply an *ad-hoc* correction or "kludge" called the K-factor so that the cross-section value used for, say, the production of muon pairs, is correct. This K-factor amounts to the ratio of a highly accurate cross-section calculation to a less accurate one, typically a leading-order calculation:

$$K_{\text{NLO}} = \frac{\sigma_{\text{NLO}}}{\sigma_{\text{LO}}} \qquad \text{and} \qquad K_{\text{NNLO}} = \frac{\sigma_{\text{NNLO}}}{\sigma_{\text{LO}}}.$$

Clearly the K-factor reflects the accuracy of the better theoretical calculation, and there can be significant differences between K_{NNLO} and K_{NLO}. The most significant contributions to the K-factor come from QCD radiative corrections are expected to be on the order of 10% or more. Usually one does not include electroweak radiative corrections in the K-factor.

We have examined the K-factor for the Drell–Yan production of charged lepton pairs, as well as the signal for new Z' neutral gauge bosons. The program PHOZPRMS is used to compute mass-dependent cross-sections [348], and a generalised version called WUWD is used to study Z' cross-sections [816]. We checked carefully the differential cross-section, $d\sigma/dM$ obtained from PHOZPRMS with the program RESBOS [817, 818] and found very good agreement. We use the MRST parton distribution functions [819] for these calculations. Very similar results are obtained using CTEQ6M [12].

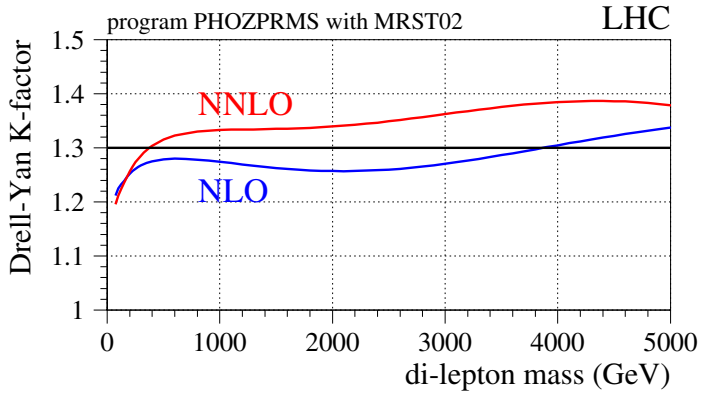

Figure C.3. K-factors as a function of mass for the LHC.

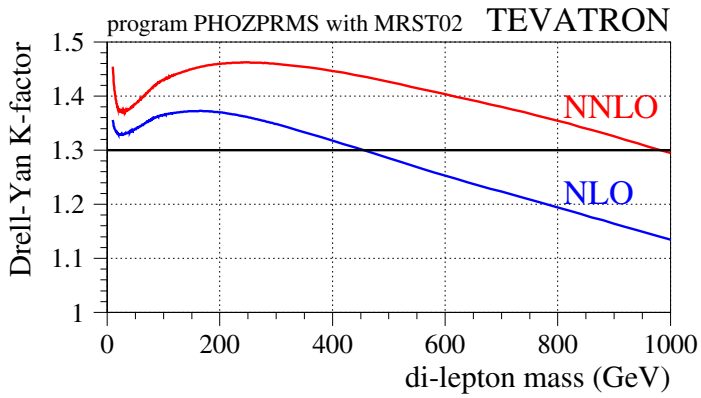

Figure C.4. K-factors as a function of mass for the Tevatron.

Usually experimenters use a constant value for the K-factor, but in fact this is not accurate. The variation of the K-factor with mass is substantial, as shown in Fig. C.3. (There is a similar, though different, variation in the K-factor for Drell–Yan production at the Tevatron – see Fig. C.4.) Notice that $K_{\mathrm{NLO}} \neq K_{\mathrm{NNLO}}$, in general, and the difference can be as large as 7%. A number of values for the K-factor are listed in Table C.1.

It is customary to take the difference $K_{\mathrm{NNLO}} - K_{\mathrm{NLO}}$ as a measure of the theoretical uncertainty due to missing higher orders. According to the results obtained with PHOZPRMS, this uncertainty is on the order of 5%. It is interesting to compare this to the uncertainty coming from the parton distribution functions (PDFs). We used the CTEQ6M set which contains "error" PDFs with which one can estimate this uncertainty [12]. The relative uncertainty of the Drell–Yan cross-section as a function of mass is shown in Fig. C.5. The positive and negative variations of the cross-section were summed separately. The error bands show the full uncertainty obtained from the twenty error-PDFs – no rescaling was done to take into account the fact that these error-PDF's correspond to 2σ variations of the PDF parameters. One sees that the PDF uncertainty varies from about 3% at low masses to 20% toward the upper reach of the LHC. Of course, these uncertainties will be reduces as data from HERA, the Tevatron and fixed-target experiments are used to improve the PDFs.

Table C.1. Values for K_{NNLO}, K_{NLO} and $K_{\mathrm{NNLO}}/K_{\mathrm{NLO}}$ as a function of mass.

mass (GeV/c^2)	K_{NNLO}	K_{NLO}	$K_{\mathrm{NNLO}}/K_{\mathrm{NLO}}$
100	1.212	1.225	0.989
200	1.256	1.252	1.003
300	1.286	1.268	1.014
400	1.303	1.275	1.022
600	1.323	1.280	1.033
800	1.330	1.278	1.040
1000	1.333	1.274	1.046
2000	1.339	1.257	1.065
3000	1.362	1.270	1.073
4000	1.385	1.304	1.061
5000	1.378	1.338	1.031

Table C.2. Leading order cross sections for some typical process at the LHC calculated by using PYTHIA 6.327 with `CTEQ5L` (default PDF for PTDR) and with `CTEQ6M` PDFs. P_0 denotes $\hat{p}_{\mathrm{T}}$-min. for the hard process.

process	cross section	comment	
$\sigma_{\mathrm{tot}}(pp \to X)$	110 ± 10 mb	different models	
$\sigma_{\mathrm{tot}}(pp \to X)$	$111.5 \pm 1.2^{+4.1}_{-2.1}$ mb	COMPETE Coll.	
process	`CTEQ5L`	`CTEQ6M`	comment
Z-boson	48.69 nb	$50.1^{+4.19\%}_{-4.76\%}$ nb	
Z + jet$(g+q)$	13.94 nb	$12.73^{+3.16\%}_{-3.94\%}$ nb	$P_0 = 20$ GeV
$q\bar{q} \to Z\gamma$	44.21 pb	$46.7^{+3.93\%}_{-4.22\%}$ nb	$P_0 = 20$ GeV
$W^{\pm}$-boson	158.5 pb	$161.3^{+4.32\%}_{-4.93\%}$ nb	
$W^{\pm}$ + jet$(g+q)$	41.42 nb	$37.24^{+3.34\%}_{-4.10\%}$ nb	$P_0 = 20$ GeV
$W^{\pm}\gamma$	56.21 pb	$56.42^{+4.11\%}_{-4.38\%}$ nb	$P_0 = 20$ GeV
W^+W^-	69.69 pb	$75.0^{+3.87\%}_{-4.03\%}$ pb	
$W^{\pm}Z$	26.69 pb	$28.76^{+3.93\%}_{-4.08\%}$ pb	
$q\bar{q} \to ZZ$	11.10 pb	$10.78^{+4.02\%}_{-4.21\%}$ pb	
$WQ\bar{Q}$	$m_b = 4.8$ GeV, $m_c = 1.5$ GeV, TopReX		
$W^{\pm}c\bar{c}$	1215 pb	$1086^{+4.12\%}_{-4.53\%}$ pb	$M_{c\bar{c}} \geqslant 3.0$ GeV
$W^{\pm}c\bar{c}$	33.5 pb	$31.3^{+4.00\%}_{-4.18\%}$ pb	$M_{c\bar{c}} \geqslant 50$ GeV
$W^{\pm}b\bar{b}$	328 pb	$297^{+4.04\%}_{-4.37\%}$ pb	$M_{b\bar{b}} \geqslant 9.6$ GeV
$W^{\pm}b\bar{b}$	34.0 pb	$31.3^{+4.00\%}_{-4.18\%}$ pb	$M_{b\bar{b}} \geqslant 50$ GeV
$Zb\bar{b}$, $m_b = 4.62$ GeV	789.6 ± 3.66 pb	MCFM	$M_{b\bar{b}} \geqslant 9.24$ GeV
dijet processes	819 μb	$583^{+4.78\%}_{-6.02\%}$ μb	$P_0 = 20$ GeV
γ + jet	182 nb	$135^{+4.92\%}_{-6.14\%}$ nb	$P_0 = 20$ GeV
$\gamma\gamma$	164 pb	$137^{+4.62\%}_{-5.65\%}$ pb	$P_0 = 20$ GeV
$b\bar{b}$, $m_b = 4.8$ GeV	479 μb	$187^{+9.7\%}_{-13.2\%}$ μb	
$t\bar{t}$, $m_t = 175$ GeV	488 pb	$493^{+3.24\%}_{-3.31\%}$ pb	
$t\bar{t}$, $m_t = 175$ GeV	830 ± 90 pb	NLO+NNLO	
$t\bar{t}\,b\bar{b}$	10 pb		AcerMC 1.2
inclusive Higgs	$m_H = 150$ GeV	23.8 pb	
inclusive Higgs	$m_H = 500$ GeV	3.8 pb	

The variation of the K-factors with mass comes in part because of the Z-resonance. The size of the Z-peak relative to the continuum production of lepton pairs is therefore relevant. This relative size depends on the coupling of the Z-boson to the up and down quarks in

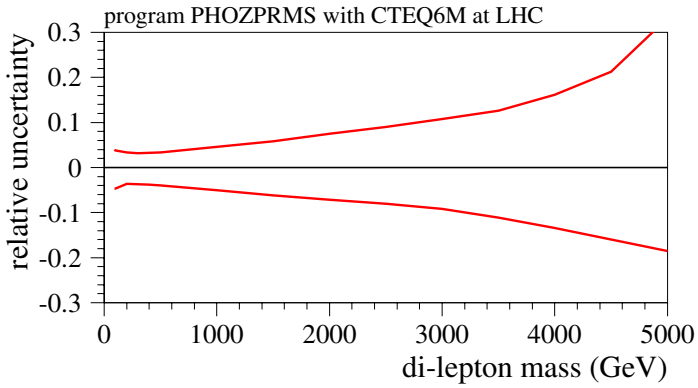

Figure C.5. Uncertainty from the parton distribution functions, evaluated using the CTEQ6M set.

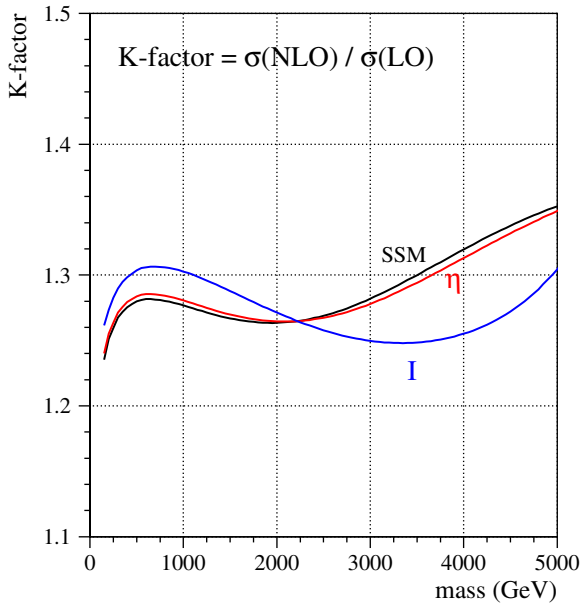

Figure C.6. K-factors as a function of mass of a new Z' resonance, for two cases: η and I (see text). The curve 'SSM' refers to a sequential Standard Model Z'.

the proton. There is practically no uncertainty on those couplings, and they are completely determined in the Standard Model. However, if a new Z' resonances is present, its couplings will not be known *a priori*. Thus it is interesting to consider to what extent the K-factor will depend on those couplings.

We have considered two examples of possible Z' resonances, and computed $K_{\rm NLO}$ as a function of the resonance mass, as shown in Fig. C.6. The first model, labelled "η," illustrates the case of a Z' which couples primarily to up-quarks, and the second one, labelled "I," couples mainly to down-quarks [816]. As is clear from the figure, the radiative corrections as a function of mass are quite different in these two extreme cases. Thus, there will be an ambiguity in the cross-section measurement of a new Z' resonance at the level of about 5% until the relative couplings of that Z' to up and down quarks can be established.

Appendix D. GARCON: Genetic Algorithm for Rectangular Cuts OptimizatioN

Typically HEP analysis has quite a few selection criteria (cuts) to optimise for example a significance of the "signal" over "background" events: transverse energy/momenta cuts, missing transverse energy, angular correlations, isolation and impact parameters, etc. In such cases simple scan over multi-dimensional cuts space (especially when done on top of a scan over theoretical predictions parameters space like for SUSY e.g.) leads to CPU time demand varying from days to many years... One of the alternative methods, which solves the issue is to employ a Genetic Algorithm (GA), see e.g. [820–822].

We wrote a code, GARCON [63], which automatically performs an optimisation and results stability verification effectively trying $\sim 10^{50}$ cut set parameters/values permutations for millions of input events in hours time. Examples of analyses are presented in this Physics TDR; see, for example, Sections 3.1, 8.4.1, 13.6, 13.7, 13.14 and recent papers [51, 317, 675, 676].

The GARCON program among many other features allows user:

- to select an optimisation function among known significance estimators, as well as to define user's own formula, which may be as simple as signal to background ratio, or a complicated one including different systematic uncertainties separately on different signal and background processes, different weights per event and so on;
- to define a precision of the optimisation;
- to restrict the optimisation using different kind of requirements, such us minimum number of signal/background events to survive after final cuts, variables/processes to be used for a particular optimisation run, number of optimisations inside one run to ensure that optimisation converges/finds not just a local maximum(s), but a global one as well (in case of a complicated phase space);
- to automatically verify results stability.

GARCON, like GA-based programs in general, exploits evolution-kind algorithms and uses evolution-like terms:

- Individual is a set of qualities, which are to be optimised in a particular environment or set of requirements. In HEP analysis case Individual is a set of lower and upper rectangular cut values for each of variables under study/optimization.
- Environment or set of requirements of evolutionary process in HEP analysis case is a Quality Function (QF) used for optimisation of individuals. The better QF value the better is an Individual. Quality Function may be as simple as $S/\sqrt{B}$, where S is a number of signal events and B is a total number of background events after cuts, or almost of any degree of complexity, including systematic uncertainties on different backgrounds, etc.
- A given number of individuals constitute a Community, which is involved in evolution process.
- Each individual involved in the evolution: breeding with possibility of mutation of new individuals, death, etc. The higher is the QF of a particular individual, the more chances this individual has to participate in breeding of new individuals and the longer it lives (participates in more breeding cycles, etc.), thus improving community as a whole.
- Breeding in HEP analysis example is a producing of a new individual with qualities (set of min/max cut values) taken in a defined way from two "parent" individuals.
- Death of an individual happens, when it passes over an age limit for it's quality: the bigger it's quality, the more it lives.

- Cataclysmic Updates may happen in evolution after a long period of stagnation in evolution, at this time the whole community gets renewed and gets another chance to evolve to even better quality level. In HEP analysis case it corresponds to a chance to find another local and ultimately a global maximum in terms of quality function. Obviously, the more complicated phase space of cut variables is used the more chances exist that there are several local maximums in quality function optimisation.
- There are some other algorithms involved into GAs. For example mutation of a new individual. In this case newly "born" individual has not just qualities of its "parents", but also some variations, which in terms of HEP analysis example helps evolution to find a global maximum, with less chances to fall into a local one. There are also random creation mechanisms serving the same purpose.

There is nothing special involved in GARCON input preparation. One would need to prepare a set of arrays for each background and a signal process of cut variable values for optimisation. Similar to what is needed to have to perform a classical eye-balling cut optimisation.

In comparison to other automatised optimisation methods GARCON output is transparent to user: it just says what rectangular cut values are optimal and recommended in an analysis. Interpretation of these cut values is absolutely the same as with eye-balling cuts when one selects a set of rectangular cut values for each variable in a "classical" way by eye.

All-in-all it is a simple yet powerful ready-to-use tool with flexible and transparent optimisation and verification parameters setup. It is publicly available along with a paper on it [63] consisting of an example case study and user's manual.

Appendix E. Online Selection

E.1. Introduction

The CMS trigger menu depends upon the luminosity delivered by the LHC and the available bandwidth between and out of the systems. The LHC luminosity is expected to start at $\mathcal{L} = 10^{32}\,\mathrm{cm}^{-2}\,\mathrm{s}^{-1}$ in 2007 and gradually rise to $\mathcal{L} = 10^{34}\,\mathrm{cm}^{-2}\,\mathrm{s}^{-1}$ by 2010. The CMS data acquisition can be operated with one to eight slices of Event Filter Farms that execute High-Level Trigger (HLT) algorithms. It is expected that we start with one slice in 2007, allowing a bandwidth of 12.5 kHz between Level-1 and HLT, and build up to the full eight slices by 2010, when the Level-1 to HLT bandwidth can be raised to 100 kHz. It is assumed that the data logging capability after the HLT selection will remain constant at a rate between 100 Hz to 150 Hz[54]. The Level-1 and HLT algorithms will be configured to operate with the lowest possible thresholds making the best use of the available bandwidth.

Here we focus solely on trigger studies for $\mathcal{L} = 2 \times 10^{33}\,\mathrm{cm}^{-2}\,\mathrm{s}^{-1}$. The scenario of operation assumes that CMS uses four DAQ slices capable of 50 kHz. While the actual choice of trigger thresholds, especially at HLT, depends strongly upon the physics of interest at the time of operation, we propose here an example set of trigger menus within the constraints of the data acquisition system. An effort has been made to optimise the Level-1 and HLT thresholds coherently, taking into account possible bandwidth limitations.

The structure of this note is as follows: first we overview the object-identification algorithms used for these studies. The emphasis is given to the changes that have been introduced since a similar study was performed in the DAQ TDR [76]. We then introduce a series of new trigger paths, aiming at increasing the event yield for various physics analyses. The central idea is to exploit various multi-object (or *cross-channel*) triggers in an attempt to improve the rejection and, at the same time, lower the kinematic thresholds of the corresponding objects. We finally present the performance of the triggers, and we calculate the overlap among them and the total HLT output rate.

E.2. Description of trigger tools

E.2.1. Level-1 reconstruction

There have been no significant changes in the Level-1 algorithms since the DAQ TDR. We have introduced an H_{T} algorithm which sums the corrected jet E_{T} of all the jets found above a programmable threshold, within $|\eta| < 5$. It does not account for E_{T} carried by muons and neutrinos.

The Level-1 strategy is the following: We have made an effort to keep the thresholds at the same levels, or even reduce them in order to be able to study cross-channel triggers (typically appearing with lower kinematic cuts). The notable exception is the tau triggers, where an increase in the HCAL noise and the usage of a new pile-up model in the simulation do affect the Level-1 τ identification tools, and therefore the related trigger rates. We have introduced additional Level-1 conditions for all HLT paths. The determination of thresholds and prescales is a compromise between the desire to distribute reasonably the available L1 bandwidth to the various triggers, and the need to optimise the L1 and HLT thresholds coherently in well-defined trigger paths.

[54] At the time of the writing of this document, several scenarios for the HLT output rate, the disk requirements for the storage manager and the associated cost are under discussion.

E.2.2. HLT reconstruction

Well defined Level-1 terms are used in order to obtain triggers whose behaviour and efficiency can be studied with real data. We have replaced some of the Level-1 conditions with respect to the DAQ TDR with new Level-1 terms when this leads to more reasonable trigger paths or triggers that are more stable and carry less of a bias. The optimisation of the thresholds for the various triggers has been a compromise between the physics needs of the CMS experiment and the total HLT rate available. This study serves only as an intermediate step in a long-term trigger study project. Further improvements in the reconstruction tools, better optimisation of the thresholds, implementation of additional triggers and a CMS-wide discussion of the allocation of the HLT bandwidth to the physics groups according to the priorities of the experiment, are foreseen.

A general and detailed description of the HLT system can be found in Ref. [76]. Here we summarise the recent modifications of the HLT tools, and the expected changes in the rates of the various triggers with respect to the earlier studies.

- **Muons:** The muon algorithm has not changed, with the exception of the drift-tube local reconstruction and segment building. Therefore, no significant changes in the rates of single- and dimuon trigger paths are expected. The option of constructing muon triggers without isolation has been added.
- **Electrons–Photons.** Here the most important change is that all saturated trigger towers at Level-1 are now considered isolated. This increases both the signal efficiency and the background. At HLT, the photon rate can be reduced by increasing the thresholds or by applying some isolation cuts. For the electrons the options include a matching with pixel lines and tracks, as well as isolation requirements in the hadron calorimeter and the tracker. A study of the algorithm optimisation can be found in Ref. [7]. An improvement of the rejection power of the electron–photon algorithms is achieved with a simultaneous decrease of the HLT thresholds. Similar enhancements are expected for cross-channel triggers where one of the objects under consideration is an electron or a photon.
- **Jets and $\boldsymbol{E_{\mathrm{T}}^{\mathrm{miss}}}$.** The main jet-finder algorithm (Iterative Cone with $R = 0.5$) has not been modified. Some optimisations of the tower thresholds have been added, and the jet corrections have been updated ("Scheme C"). Similarly, there are no major algorithm changes for $E_{\mathrm{T}}^{\mathrm{miss}}$, however it has been ensured that all triggers including a $E_{\mathrm{T}}^{\mathrm{miss}}$ object do not have any off-line corrections applied. Another improvement that has been recently introduced is the ability to construct *acoplanar* triggers by combining two jets, or a jet and a $E_{\mathrm{T}}^{\mathrm{miss}}$ object that do not lie "back-to-back" Details of the physics algorithms can be found in Refs. [165] and [148].
- ***b*-jets.** The algorithm now uses muon information for fast rejection. Further improvements have been made for faster decisions and for an increased efficiency in fully hadronic final states. The documentation for the *b*-jet HLT algorithm can be found in Ref. [290].
- **Taus:** The HLT τ algorithm has not changed. However, the increase in the Level-1 rate does propagate into the HLT. The isolation parameters for the electromagnetic calorimeter and the tracker have been tuned after recent studies performed by the Higgs group, described in Ref. [280]. The overall rate for τ-related triggers is expected to be slightly increased.

A new addition to the HLT reconstruction tools is the H_{T} algorithm. It sums the corrected jet E_{T} of all the $E_{\mathrm{T}} > 5\,\mathrm{GeV}$ jets found within $|\eta| < 5$, along with the energy of the $p_{\mathrm{T}} > 5\,\mathrm{GeV/c}$ HLT muons found in the event, and the $E_{\mathrm{T}}^{\mathrm{miss}}$ computed using the calorimeter deposits. It is meant to be driven off the corresponding L1 H_{T} term.

E.3. Triggering with forward detectors

E.3.1. Objective

We discuss[55] the feasibility of a special forward detectors trigger stream, with target output rate of $\mathcal{O}(1)$ kHz at L1 and $\mathcal{O}(1)$ Hz on the HLT, as well as the potential of the already foreseen CMS L1 trigger streams for retaining events with diffractive processes.

The proposed forward detectors trigger stream combines the information of the central CMS detector with that from detectors further downstream of the CMS IP. The forward detectors considered are the TOTEM T1 and T2 tracker telescopes as well as the TOTEM Roman Pot (RP) detectors up to 220 m downstream of CMS [823, 824]. Information from TOTEM will be available to the CMS L1 trigger. We also consider detectors at a distance of 420 m, in the cryogenic region of the LHC ring, currently being studied by the FP420 project [254].

Topologically, diffractive events are characterised by a gap in the rapidity distribution of final-state hadrons. In addition, the fractional momentum loss, ξ, of diffractively scattered protons peaks at $\xi = 0$ ("diffractive peak"). The TOTEM RP detectors will permit to measure protons in the region $0.2 > \xi > 0.02$. Detectors at a distance of 420 m from the IP would provide a coverage of $0.02 > \xi > 0.002$, complementary to that of the TOTEM detectors, but cannot be included in the Level-1 trigger without an increase in the Level-1 latency of 3.2 μs (though a special, long latency running mode might be feasible at lower luminosities).

The studies discussed in the following assume that the RP detectors are 100% efficient in detecting all particles that emerge at a distance of at least $10\,\sigma_{\text{beam}} + 0.5$ mm from the beam axis (1.3 mm at 220 m, 4 mm at 420 m). Their acceptance was calculated for the nominal LHC optics ($\beta^* = 0.55$ m), version V6.5 [825, 826], and by way of a simulation program that tracks particles through the accelerator lattice [827]. LHC bunches with 25 ns spacing were assumed.

The results presented below do not depend on the specific hardware implementation of the TOTEM T1, T2 and RP detectors; they hold for any tracker system with the T1, T2 η coverage in conjunction with RPs at 220 m from the IP.

E.3.2. Level-1 trigger rates for forward detectors trigger stream

E.3.2.1. 2-Jet conditions. A particularly interesting and challenging diffractive channel is the central exclusive production of a Higgs Boson, $pp \to pHp$, with Higgs mass close to the current exclusion limit. The dominant decay of a SM Higgs Boson of mass $\sim$120 GeV/c^2 is into two b-quarks and generates 2 jets with at most 60 GeV/c transverse momentum each. In order to retain as large a signal fraction as possible, as low an E_{T} threshold as possible of the Level-1 2-jet trigger is desirable. In practice, the threshold value cannot be chosen much lower than 40 GeV per jet. The Level-1 trigger applies cuts on the calibrated E_{T} value of the jet. Thus, a threshold of 40 GeV corresponds to 20–25 GeV in reconstructed E_{T}, i.e. to values where noise starts becoming sizable.

For luminosities of $10^{32}\,\text{cm}^{-2}\text{s}^{-1}$ and above, the Level-1 rate from standard QCD processes for events with at least 2 central jets ($|\eta| < 2.5$) with $E_{\text{T}} > 40$ GeV exceeds by far the target output rate of $\mathcal{O}(1)$ kHz. Thus additional conditions need to be employed to reduce the rate from QCD processes. The efficacy of several conditions was investigated [247, 248, 828–830]. In the following, the corresponding rate reduction factors are always quoted with respect to the rate of QCD events that contain at least 2 central jets with $E_{\text{T}} > 40$ GeV per jet.

[55] These studies were carried out in collaboration with TOTEM.

Table E.1. Reduction of the rate from standard QCD processes for events with at least 2 central Level-1 jets with $E_T > 40$ GeV, achievable with requirements on the tracks seen in the RP detectors. Additional rate reductions can be achieved with the H_T condition and with a topological condition. Each of them yields, for all luminosities listed, an additional reduction by about a factor 2.

				Reduction when requiring track in RPs at					
				220 m		420 m	220 & 420 m (asymmetric)		420 & 420 m
Luminosity [$\mathrm{cm^{-2}\,s^{-1}}$]	Pile-up events per BX	Level-1 2-jet rate [kHz] for $E_T > 40$ GeV	Total reduction needed		$\xi < 0.1$			$\xi < 0.1$	
1×10^{32}	0	2.6	2	370					
1×10^{33}	3.5	26	20	7	15	27	160	380	500
2×10^{33}	7	52	40	4	10	14	80	190	150
5×10^{33}	17.5	130	100	3	5	6	32	75	30
1×10^{34}	35	260	200	2	3	4	17	39	10

The QCD background events were generated with the Pythia Monte Carlo generator. In order to assess the effect when the signal is overlaid with pile-up, a sample of 500,000 pile-up events was generated with Pythia. This sample includes inelastic as well as elastic and single diffractive events. Pythia underestimates the number of final state protons in this sample. The correction to the Pythia leading proton spectrum described in [831] was used to obtain the results discussed in the following.

Given a Level-1 target rate for events with 2 central Level-1 jets of $\mathcal{O}(1)$ kHz, a total rate reduction between a factor 20 at $1 \times 10^{33}\,\mathrm{cm^{-2}\,s^{-1}}$ and 200 at $1 \times 10^{34}\,\mathrm{cm^{-2}\,s^{-1}}$ is necessary. Table E.1 summarises the situation for luminosities between $10^{32}\,\mathrm{cm^{-2}\,s^{-1}}$ and $10^{34}\,\mathrm{cm^{-2}\,s^{-1}}$, and for different RP detector conditions: a track at 220 m on one side of the IP (single-arm 220 m), without and with a cut on ξ; a track at 420 m on one side of the IP (single-arm 420 m); a track at 220 m and 420 m (asymmetric); a track at 420 m on both sides of the IP (double-arm 420 m). Because the detectors at 220 m and 420 m have complementary coverage in ξ, the asymmetric condition in effect selects events with two tracks of very different ξ value, in which one track is seen at 220 m on one side of the IP and a second track is seen on the other side at 420 m. If not by the L1 trigger, these asymmetric events can be selected by the HLT and are thus of highest interest. At luminosities where pile-up is present, the rate reduction achievable with the RP detector conditions decreases because of the diffractive component in the pile-up.

A collimator located in front of the LHC magnet Q5, planned to be operative at higher luminosities, will have an effect on the acceptance of the RP detectors resembling that of a ξ cut. This effect has not been taken into account in Table E.1.

Using T1 and T2 as vetoes in events with 2 central Level-1 jets was found to be effective only in the absence of pile-up [832].

In addition to the E_T values of individual Level-1 jets, the CMS Calorimeter Trigger has at its disposal the scalar sum, H_T, of the E_T values of all jets. Requiring that essentially all the E_T be concentrated in the two central Level-1 jets with highest E_T, i.e. $[E_T^1 + E_T^2]/H_T > 0.9$ (H_T condition), corresponds to imposing a rapidity gap of at least 2.5 units with respect to the beam direction. This condition reduces the rate of QCD events by approximately a factor 2, independent of the presence of pile-up and with only a small effect on the signal efficiency.

A further reduction of the QCD rate could be achieved with the help of a topological condition. The 2-jet system has to balance the total momentum component of the two protons along the beam axis. In signal events with asymmetric ξ values, the proton seen on one side

Table E.2. Estimated threshold values that result in a L1 output rate of ~ 1 kHz, for various conditions on central CMS detector quantities and on tracks seen in the RP detectors at 220 m and 420 m.

	L1 E_T or p_T threshold [GeV] at $\mathcal{O}(1)$ KHz L1 output rate for luminosity [cm^{-2} s^{-1}]			
L1 condition	1×10^{33}	2×10^{33}	5×10^{33}	1×10^{34}
1 Jet	115	135	160	190
2 Jet	90	105	130	150
1 Jet+220s	90	115	155	190
2 Jet+220s	65	90	125	150
1 Jet+220d	55	85	130	175
2 Jet+220d	30	60	100	140
1 Jet+220s(c)	70	90	150	185
2 Jet+220s(c)	60	70	115	145
1 Jet+220d(c)	30	65	110	155
2 Jet+220d(c)	20	45	85	125
1 Jet+420s	65	90	125	165
2 Jet+420s	45	70	100	130
1 Jet+420d	20	40	80	115
2 Jet+420d	< 10	30	60	90
1 μ+220s	12	16	23	> 100
1 μ + 220d	4	9	17	80
1 μ+220s(c)	–	11	22	100
1 μ+220d(c)	–	6	13	30
1 μ+420s	7	11	14	37
1 μ+420d	< 2	4	7	14

in the RP detectors at 220 m distance is the one with the larger ξ and thus has lost more of its initial momentum component along the beam axis. Hence the jets tend to be located in the same η-hemisphere as the RP detectors that detect this proton. A trigger condition requiring that $[\eta^{jet1} + \eta^{jet2}] \times \text{sign}(\eta^{220\,mRP}) > 0$ reduces the QCD background by a factor 2, independent of pile-up, and with no loss in signal efficiency.

A reduction of the QCD rate to levels compatible with a Level-1 output target rate of $\mathcal{O}(1)$ kHz by including RP detectors at a distance of 220 m from the CMS IP thus appears feasible for luminosities up to 2×10^{33} cm^{-2} s^{-1}, as long as a ξ cut can be administered in the L1 trigger.

E.3.2.2. Other conditions. The effect of combining already foreseen Level-1 trigger conditions with conditions on the RP detectors is illustrated in Table E.2 [829]. Single- and double-arm RP detector conditions are indicated with 's' and 'd' endings, respectively. Entries marked with a '(c)' indicate thresholds applicable if a cut on $\xi < 0.1$ is implemented for the RP detectors at 220 m. The jet conditions consider all Level-1 jets with $|\eta| < 5$.

A further rate reduction by approximately a factor two can be obtained at luminosities with negligible pile-up by imposing a rough large rapidity gap cut at L1. This was implemented by requiring that there be no forward jets, i.e. jets in the HF, in either hemisphere in the event.

E.3.3. Level-1 signal efficiencies

Of the Level-1 conditions discussed so far, only those based on the RP detectors have a significant impact on the signal efficiency. Of further interest is the question how many signal events are being retained by the already foreseen trigger streams, notably the muon trigger.

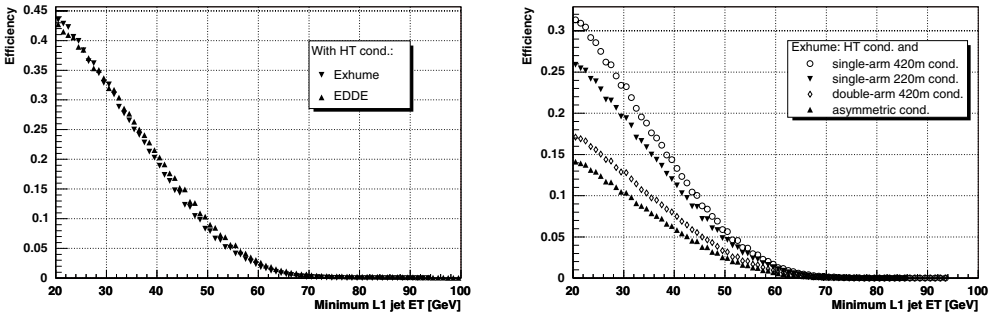

Figure E.1. L1 selection efficiency for $pp \to pHp$ and $H(120, \mathrm{GeV/c^2}) \to b\bar{b}$ as function of the E_T threshold value when at least 2 central Level-1 jets with E_T above threshold are required. All plots are for the non-pile-up case and the H_T condition has been applied. Left: Comparison between the EDDE and Exhume Monte Carlo generators, without applying any additional RP conditions. Right: Comparison of the effect of different RP conditions on the efficiency in the Exhume Monte Carlo sample.

E.3.3.1. Central exclusive Higgs production ($H(120\,\mathrm{GeV/c^2}) \to b\bar{b}$). In order to study the effect of the Level-1 trigger selection on the Higgs signal, signal samples of 100,000 events with central exclusive production of a Higgs Boson were generated with the Monte Carlo programs EDDE [261] (version 1.1) and Exhume [259] (version 1.0).

Figure E.1 shows the Level-1 selection efficiency as a function of the E_T threshold values when at least 2 central Level-1 jets with E_T above threshold are required [829]. For a threshold of 40 GeV per jet, Exhume and EDDE both yield an efficiency of about 20%. The plot on the right-hand side overlays the efficiency curves obtained with Exhume when the 2-jet condition is combines with RP detector conditions. With an E_T threshold of 40 GeV per jet, the single-arm 220 m (420 m) condition results in an efficiency of the order 12% (15%), the double-arm 420 m condition in one of 8% and the asymmetric condition in one of 6%. This also means that, even without the possibility of including the RP detectors at 420 m from the CMS IP in the Level-1 trigger, 6% of the signal events can be triggered on with the single-arm 220 m condition, but will have a track also in the 420 m detectors that can be used in the HLT.

An alternative trigger strategy is to exploit the relatively muon-rich final state from B-decays: about 20% of the events have at least a muon in the final state. Requiring at least one (two) L1 muon(s) with p_T above 14 GeV/c (3 GeV/c) yields an efficiency of 6% (2%). Demanding at least 1 muon and 1 jet, the latter with E_T >40 GeV, is a condition not yet foreseen in the CMS trigger tables. For a muon p_T threshold of 3 GeV/c, the rate at a luminosity of $10^{33}\,\mathrm{cm^{-2}}$ is slightly less than 3 kHz, and about half of the decays with muons in the final state (i.e. 9%) are retained [830].

E.3.3.2. Central exclusive Higgs production ($H(140\,\mathrm{GeV/c^2}) \to WW$). For SM Higgs Boson masses above 120 GeV/c^2, the $H \to WW$ branching ratio becomes sizable; in this case the final state contains high-p_T leptons that can be used for triggering. Efficiencies are in general high [830]. About 23% of the events have at least one muon in the final state. Approximately 70% of these (i.e. 16%) are retained by requiring at least one muon with a p_T threshold of 14 GeV/c. An extra $\approx$ 10% (i.e. 2%) would be retained by implementing the muon/jet slot discussed above with thresholds of 3 GeV/c on the muon p_T and 40 GeV on the jet E_T.

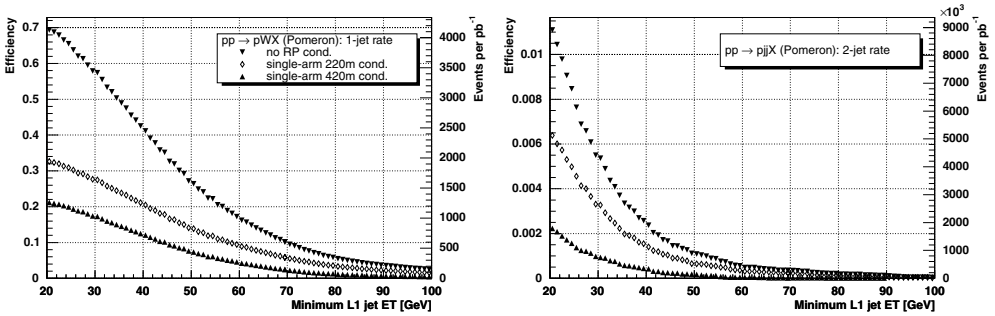

Figure E.2. L1 selection efficiency as function of the E_{T} threshold value for $pp \to pWX$ (left) and $pp \to pjjX$ (right), when at least one (left) or two (right) Level-1 jets ($|\eta| < 5$) above threshold are required. All plots are for the non-pile-up case.

E.3.3.3. Single diffractive hard processes. Double-Pomeron exchange processes constitute only a small part of the diffractive cross section. Hard single-diffraction, $pp \to pX$, where only one proton remains intact and the other is diffractively excited, have much higher cross sections than hard double-Pomeron exchange events. Efficiencies have been studied for $pp \to pX$, with X containing a W or a Z boson that decay to jets and to muons, as well as with X containing a dijet system. Samples of 100,000 signal events each were generated with the POMWIG Monte Carlo generator [833] (version 1.3).

For two example processes, Figure E.2 shows the efficiency as a function of the Level-1 threshold value, normalised to the number of events where for the diffractively scattered proton $0.001 < \xi < 0.2$ holds [829]. Three different trigger conditions are considered: trigger on central detector quantities alone (i), trigger on central detector quantities in conjunction (ii) with the single-arm 220 m condition, and (iii) with the single-arm 420 m condition. Also shown is the number of events expected to pass the L1 selection per pb^{-1} of LHC running. A significant part of events is retained when a proton is required in the 220 m RPs.

E.3.4. Effect of pile-up, beam-halo and beam-gas backgrounds

Pile-up effects are included in all rate and efficiency studies presented. In the 220 m stations, 0.055 protons/pile-up event are expected on average, in the 420 m stations, 0.012 protons/pile-up event. At a luminosity of $10^{34}\,\mathrm{cm}^{-2}\,\mathrm{s}^{-1}$, there are 35 pile-up events on average; this entails, on average, 2 extra tracks in the 220 m stations and less than one in the 420 m stations.

The effect from beam-halo and beam-gas events on the Level-1 rate is not yet included in the studies discussed here. Preliminary estimates suggest that they are chiefly a concern for any trigger condition based solely on the forward detectors. For any trigger condition that includes a requirement on central CMS detector quantities the size of their contribution is such that they do not lead to a significant increase of the Level-1 output rate.

E.3.5. HLT strategies

Jets are reconstructed at the HLT with an iterative cone ($R < 0.5$) algorithm. The Level-1 selection cuts are repeated with HLT quantities. The following conditions are imposed [829]:

(A) The event pass the single-arm 220 m Level-1 condition with $\xi < 0.1$ cut. As demonstrated in Table E.1, this condition reduces the Level-1 output rate to below $\mathcal{O}(1)$ kHz. Additional

Table E.3. Results of HLT selection.

HLT selection condition	A + B + C	A + B + D	A + B + C + E
HLT rate at $1 \times 10^{33}\,\mathrm{cm}^{-2}\,\mathrm{s}^{-1}$	15 Hz	20 Hz	< 1 Hz
line HLT rate at $2 \times 10^{33}\,\mathrm{cm}^{-2}\,\mathrm{s}^{-1}$	60 Hz	80 Hz	1 Hz
e Signal eff. $H(120)\,\mathrm{GeV/c}^2 \to b\bar{b}$	11%	7%	6%

rate reduction factors of ~ 300 (~ 1000) at $1(2) \times 10^{33}$ cm $^{-2}$ s $^{-1}$ are needed to reach the HLT target output rate of $\mathcal{O}(1)$ Hz.

(B) The two jets are back-to-back in the azimuthal angle ϕ ($2.8 < \Delta\phi < 3.48$ rad), and have $(E_{\mathrm{T}}^1 - E_{\mathrm{T}}^2)/(E_{\mathrm{T}}^1 + E_{\mathrm{T}}^2) < 0.4$, and $E_{\mathrm{T}} > 40\,\mathrm{GeV}$ for each jet.

(C) The proton fractional momentum loss ξ is evaluated with the help of calorimeter quantities [834–836]:

$$\xi_{+-} = (1/\sqrt{s})\,\Sigma_i E_{Ti} \exp(\mp\eta_i), \tag{E.1}$$

where the sum runs over the two jets and the $+, -$ signs denote the two hemispheres. The result is compared with the ξ value measured by the RP detectors. At present, no simulation of the RP reconstruction is available. As estimate of the ξ resolution, 15% (10%) is assumed at 220 m (420 m). Events are rejected if the difference between the two values of ξ is larger than $2\,\sigma$.

(D) At least one of the two jets is b-tagged.

(E) A proton is seen at 420 m.

The case without pile-up presents no difficulty: essentially no QCD background events survive the selection. If conditions A+B+C are applied, the signal efficiency for $pp \to pHp$ with $H(120\ \mathrm{GeV/c}^2) \to b\bar{b}$ is at 11% essentially unchanged with respect to the Level-1 selection, but the HLT output rate exceeds the target output rate, see Table E.3. If b-tagging is required but no ξ matching (conditions A +B+D), the efficiency drops to 7%, without any improvement in the rate reduction. The combination of conditions A+B+C+E finally leads to the targeted HLT output rate of $\mathcal{O}(1)$ Hz, without any loss in signal efficiency compared to L1.

E.4. High-Level Trigger paths

We are starting with the DAQ-TDR trigger table as the baseline. This includes single- and double-triggers for the basic objects (e, γ, μ, τ) along with jets and b-jets. Some cross-channel triggers are also present. We are expanding the cross-channel "menu" by introducing additional triggers. We introduce an H_{T} algorithm, which we combine with other objects. We are also adding a series of central single-jets, non-isolated muons, and a diffractive trigger discussed earlier.

E.4.1. Level-1 conditions

Table E.4 summarises the Level-1 conditions used to drive all the trigger paths. A pseudo "L1 bit number" has been assigned for easy reference in the following sections.

E.4.2. Evolution of DAQ-TDR triggers

The trigger paths that have been studied in Ref. [76] have been inherited and constitute the "bulk" of this next iteration of the CMS Trigger Menu for $\mathcal{L} = 2 \times 10^{33}\,\mathrm{cm}^{-2}\,\mathrm{s}^{-1}$.

Table E.4. Level-1 conditions used in High Level Trigger paths.

Level-1 bit #	Trigger	(GeV)	Prescale
0	Single μ	14	1
1	Double μ	3	1
2	Single isolated $e\gamma$	23	1
3	Double isolated $e\gamma$	11	1
4	Double $e\gamma$ (isolated/non-isolated)	19	1
8	Single central jet	177	1
9	Single forward jet	177	1
10	Single τ-jet	100	1
11	2 central jets	130	1
12	2 forward jets	130	1
13	2 τ-jets	66	1
14	3 central jets	86	1
15	3 forward jets	86	1
16	3 τ-jets	40	1
17	4 central jets	70	1
18	4 forward jets	70	1
19	4 τ-jets	30	1
26	(isolated) $e\gamma$ + τ	14, 52	1
31	H_{T}	300	1
32	$E_{\mathrm{T}}^{\mathrm{miss}}$	60	1
33	Single jet (central, forward or τ)	140	10
34	Single jet (central, forward or τ)	60	1 000
35	Single jet (central, forward or τ)	20	100 000
36	Single jet (central, forward or τ)	150	1
37	2 jets (central, forward or τ)	100	1
38	3 jets (central, forward or τ)	70	1
39	4 jets (central, forward or τ)	50	1

Modifications (optimisation of isolation cuts and thresholds) have been made for certain of the triggers, to reflect changes in the physics algorithms, or the improved understanding of the background from Monte Carlo (MC) simulations. The proposed Trigger Tables includes:

- **Muons.** The standard muon triggers include calorimeter-based isolation at L2, and both calorimeter and tracker isolation at L3. The p_{T} thresholds remain at 19 GeV/c for the single-muon and (7, 7) GeV/c for the dimuon trigger. A second set of relaxed single- and double-muons has been added with $p_{\mathrm{T}} > 37$ GeV and $p_{\mathrm{T}} > 10$ GeV, respectively. The main motivation here is Drell–Yan studies. In general, physics analyses that do not need a low p_{T} muon but do suffer from the isolation requirement on the muon. The reduced rejection caused by the removal of the isolation cuts is compensated by the higher-p_{T} thresholds on the muons, without affecting the event yield for the physics signal. The relaxed triggers have the advantage that the muons here are immune to radiative losses for the higher energy spectrum ($p_{\mathrm{T}} > 500$ GeV/c). Both isolated and relaxed triggers run off the corresponding non-isolated single- and double-muon bits at L1.
- **Electrons.** The p_{T} threshold remains at 26 GeV/c for the single electron trigger and has a new value of (12, 12) GeV/c for the dielectron trigger. An additional relaxed dielectron trigger appears with $p_{\mathrm{T}} > 19$ GeV/c. The single-electron and double-electron triggers run off the corresponding Level-1 bits.
- **Photons.** The new p_{T} thresholds are 80 GeV/c for the single-photon trigger and (30, 20) GeV/c for the diphoton trigger (both relaxed and non-relaxed flavours). A few prescaled

single- and double-photon triggers have also been introduced, for the purpose of studying trigger efficiencies. The photon HLT algorithms run off the corresponding Level-1 $e\gamma$ bits (single- and double-triggers).

- **Taus.** The single-τ trigger runs off the corresponding Level-1 bit. The double-τ trigger is driven by the `.OR.`-ing of the single- and double-τ trigger bits at L1. There is no explicit kinematic cut on the tau at HLT. There is, however, a match-to-track requirement in addition to the $p_{\mathrm{T}} > 100(66)\,\mathrm{GeV/c}$ L1 precondition for the inclusive (double) tau trigger. The single-τ has also a $E_{\mathrm{T}}^{\mathrm{miss}} > 65\,\mathrm{GeV}$ requirement at HLT.
- **Tau and electron.** The Level-1 condition is the corresponding τ+$e\gamma$ trigger. The p_{T} threshold remains at $16\,\mathrm{GeV/c}$ for the electron. There is no explicit p_{T} cut for the τ at HLT, but there is the match-to-track requirement for the τ candidate.
- **Jets.** The Level-1 conditions for the single-, double-, triple- and quadruple-jet triggers have been simplified considerably. Single jet triggers run off an `OR.` of a central-, forward- or tau-jet trigger at L1. Double-, triple- and quadruple-jet triggers use an `.OR.` of the all the Level-1 terms requiring the same number of jets or less. For example, the triple-jet trigger is driven by an `OR.` of the single-, double- and triple-jet Level-1 bits. In all cases, jets can be found in either the central or the forward region of the detector, and they include the τ candidates. The additional p_{T} cuts at HLT are: 400 (single), 350 (double), 195 (triple) and 80 (quadruple) GeV. The new double-jet trigger is expected to have a large overlap with the single-jet trigger path. However, it is useful for testing the additional bias introduced by the requirement for a second jet in the event. A series of prescaled triggers have also been introduced, which are discussed later (Sec. E.4.3.2).
- ***b*-jet.** This trigger is also based on the logical `.OR.` of the single-, double-, triple- and quadruple-jet Level-1 terms. At HLT, we have the additional requirement that the event is consistent with *b*-content. The E_{T} cut for the HLT jets is one of the following: 350 GeV if the event has one jet, 150 GeV if the event has three jets, or 55 GeV if the event has four jets.
- **Jet and $\boldsymbol{E}_{\mathbf{T}}^{\mathbf{miss}}$.** The E_{T} thresholds are 180 and 80 GeV, respectively. The Level-1 condition is a single $E_{\mathrm{T}}^{\mathrm{miss}}$ object above 60 GeV.

E.4.3. New triggers

E.4.3.1. Cross-channel triggers. The trigger studies presented in the DAQ TDR [76] have been the most comprehensive CMS effort to date to calculate rates for various trigger paths across many physics channels. For those studies the focus has been the optimisation of the rejection of the individual object-id algorithms (muon, electron, tau, etc.) rather than the combination of them into more powerful trigger tools. However, single (or even double) trigger objects are limited by the rate and, therefore, have their thresholds often higher than desired for many physics analyses. If the signal contains more than one trigger objects, using trigger paths combining different objects may yield a considerable gain by allowing lower trigger thresholds and higher efficiency. Cross-channel triggers can be much more stable and less prone to rate fluctuations from operating conditions. The correlations among trigger objects can help reduce difficult backgrounds and instrumental fakes. The additional advantage is that such cross-channel triggers have noticeably lower rates than the single trigger channels and therefore contribute fairly little to the overall bandwidth.

Some cross-channel triggers have already been considered and their rates estimated [76], such as τ + e and τ + $E_{\mathrm{T}}^{\mathrm{miss}}$, motivated by the Higgs searches with hadronic decays of τ and leptons, and jet + $E_{\mathrm{T}}^{\mathrm{miss}}$, important for searches of super-symmetric particles. The new addition

to the Trigger Menu, expanding the scope of Higgs searches, is a combined $\tau + \mu$ trigger with p_T thresholds at 40 and 15 GeV/c, respectively. It is driven by the single-μ Level-1 bit.

We are presenting here a few additional cross-channel triggers, along with the physics motivation.

- A new category of triggers introduced here is the acoplanar dijet and jet+E_T^{miss} for SUSY signals. The gain is the lower thresholds that become possible because of the topology constraint. Possible biases should be studied, so these triggers are meant to run in parallel with the standard jet and jet + E_T^{miss} triggers without the acoplanarity requirements. We introduce a double-jet trigger with E_T thresholds at (200, 200) GeV and $|\Delta\phi| < 2.1$, and a new jet + E_T^{miss} trigger with E_T thresholds at (100, 80) GeV and $|\Delta\phi| < 2.1$. The former is driven by an .OR. of the single- and double-jet requirements at Level-1 (bits 36, 37). The latter is driven by a simple $E_T^{miss} > 60$ GeV Level-1 requirement.
- "$E_T^{miss} + X$" triggers. A combination of an E_T^{miss} object with an H_T cut, one (or more) jet or lepton may be the only way to access E_T^{miss}-enhanced triggers if there are problems (*e.g.* instrumental fakes) that prevent CMS from running an inclusive E_T^{miss} trigger. At this point we have implemented:
  - Multi-jets and E_T^{miss}. These will be useful for SUSY studies, just like the series of jet triggers. However, the additional E_T^{miss} requirement allows us to lower the thresholds on the jets, and therefore increase the sensitivity of the analyses. We introduce here a dijet + E_T^{miss} trigger with $E_T^{jet} > 155$ GeV, $E_T^{miss} > 80$ GeV, a triple − jet + E_T^{miss} trigger with $E_T^{jet} > 85$ GeV, $E_T^{miss} > 80$ GeV and a quadruple − jet + E_T^{miss} trigger with $E_T^{jet} > 35$ GeV, $E_T^{miss} > 80$ GeV. These all run off the single Level-1 requirement for $E_T^{miss} > 60$ GeV.
  - H_T + E_T^{miss} and H_T + e. It is difficult to contain the rate for an inclusive H_T trigger without any additional cuts. The requirement for a E_T^{miss} cut or an additional electron in the event allows us to access events with lower E_T^{miss} or softer electrons. This can give an increased efficiency for W+jets, top physics, SUSY cascades, and other similar physics channels. Here we propose an H_T + E_T^{miss} trigger with $H_T > 350$ GeV, $E_T^{miss} > 80$ GeV and an H_T + e trigger with $H_T > 350$ GeV and $p_T > 20$GeV/c for the electron. They are both driven by the $E_T^{miss} > 60$ GeV condition at L1.

Some additional cross-channel triggers that have not been included in this Trigger Table iteration but should be considered in future trigger studies are:

- An $e + \mu$ trigger is of interest in many studies, for example:
  - $qqH, H \to \tau\tau \to 2\ell$, with an expected gain thanks to the lower lepton thresholds compared to the single-electron and single-muon trigger paths,
  - many SUSY decays including leptons in the final state,
  - top measurements in the double leptonic channel ($t\bar{t} \to b\bar{b}\ell\nu\ell\nu$), gaining sensitivity at the lower p_T spectrum, and
  - $B_s \to \ell\ell$, to allow for the lepton-number-violating channel to be studied.
- $E_T^{miss} + \ell$. The idea here is to exploit the presence of a W boson or a top decay in many channels. This could be used in many SM channels where lowering the lepton threshold extends the range of the measurement. For example:
  - top measurement in the double leptonic and semi-leptonic channels,
  - single top production, and
  - W measurements.

  Furthermore, this is a typical signature of an event containing super-symmetric particles.

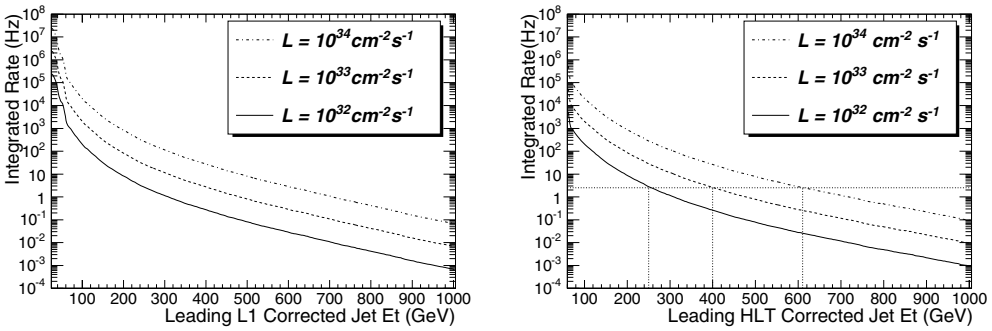

Figure E.3. The integrated trigger rates at Level-1 (left) and HLT (right) above the E_{T} thresholds for the highest E_{T} jet is plotted versus the E_{T} threshold for three luminosity scenarios: $\mathcal{L} = 10^{32}\,\mathrm{cm}^{-2}\,\mathrm{s}^{-1}$ (solid), and $\mathcal{L} = 10^{33}\,\mathrm{cm}^{-2}\,\mathrm{s}^{-1}$ (dashed), and $\mathcal{L} = 10^{34}\,\mathrm{cm}^{-2}\,\mathrm{s}^{-1}$ (dot-dashed). HLT thresholds that give 2.5 Hz are shown by vertical dotted lines.

- Triggers combining a lepton and a jet, or a lepton and a b-jet could be of interest for top measurements. The ℓ + jet signature is also very common in super-symmetric events.
- Finally, a combination of a lepton and a photon ($e+\gamma$ and $\mu+\gamma$) is ideal for Flavour Changing Neutral Current analyses, exploiting the extraordinary capabilities of CMS in detecting photons. These triggers allow to lower the thresholds on the lepton and the photon, increasing the event yield compared to the single-e, μ or γ trigger paths.

E.4.3.2. Single jet triggers. In this section we propose the single jet trigger paths. These have been driven by the needs of the inclusive jet and dijet analysis. The full study can be found in Ref. [118]. Here we summarise conclusions, along with a short description of the strategy for adjusting thresholds and prescales as the luminosity changes. This study looks at the evolution of the single-jet triggers for various luminosities. It serves as an example of how to preserve the long-term continuity of the triggers used for physics analyses. It is, therefore, interesting and instructive beyond the strict scope of the single-jet trigger suite.

To measure jet spectra down to low jet E_{T} and dijet mass requires multiple triggers, of roughly equal total rate, and with appropriately chosen E_{T} thresholds and prescales. In Fig. E.3 we show estimates of the Level-1 and HLT single jet trigger rates vs. corrected jet E_{T}. In Table E.5 we show the single jet trigger paths from Level-1 to HLT including thresholds, prescales and estimates of the rates. We find that the maximum allowed HLT rate is the constraining factor for triggering on jets. For luminosity $\mathcal{L} = 10^{32}\,\mathrm{cm}^{-2}\,\mathrm{s}^{-1}$, $\mathcal{L} = 10^{33}\,\mathrm{cm}^{-2}\,\mathrm{s}^{-1}$ and $\mathcal{L} = 10^{34}\,\mathrm{cm}^{-2}\,\mathrm{s}^{-1}$ the highest E_{T} threshold at HLT was chosen to give a rate of roughly 2.5 Hz, as illustrated in Fig. E.3, so that four triggers would saturate an allowed jet rate of roughly 10 Hz at HLT.

The highest E_{T} threshold in each scenario is not prescaled. Lower thresholds are prescaled and are chosen at roughly half the E_{T} of the next highest threshold. This allows reasonable statistics in the overlap between the two samples, necessary for measuring trigger efficiencies and producing a continuous jet spectrum. Note that the total L1 jet rate required is only around 0.3 KHz, a small fraction of the Level-1 total bandwidth. Since we are limited by HLT, not L1, for each trigger path the Level-1 thresholds are chosen low enough to have a Level-1 trigger efficiency of more than 95% at the corresponding HLT threshold in the path, as shown in Figure E.4. This strategy utilizes ten times more bandwidth at L1 than at HLT to insure that all of the resulting HLT sample has high enough trigger efficiency to be useful for analysis.

Table E.5. Single jet trigger table showing path names, trigger thresholds in corrected E_T, prescales, and estimated rates at Level-1 and HLT for four different luminosity scenarios.

	L1				HLT	
Path	E_T Cut (GeV)	Unpres. Rate (KHz)	Prescale (N)	Presc. Rate (KHz)	E_T Cut GeV)	Rate (Hz)
Single Jet Triggers in Scenario 1: $\mathcal{L} = 10^{32}$ cm^{-2} s^{-1}						
High	140	0.044	1	0.044	250	2.8
Med	60	3.9	40	0.097	120	2.4
Low	25	2.9×10^2	2,000	0.146	60	2.8
Single Jet Triggers in Scenario 2: $\mathcal{L} = 10^{33}$ cm^{-2} s^{-1}						
Ultra	270	0.019	1	0.019	400	2.6
High	140	0.44	10	0.044	250	2.8
Med	60	39	400	0.097	120	2.4
Low	25	2.9×10^3	20,000	0.146	60	2.8
Single Jet Triggers in Scenario 3: $\mathcal{L} = 2 \times 10^{33}$ cm^{-2} s^{-1}						
Ultra	270	0.038	1	0.038	400	5.2
High	140	0.88	20	0.044	250	2.8
Med	60	78	800	0.097	120	2.4
Low	25	5.8×10^3	40,000	0.146	60	2.8
Single Jet Triggers in Scenario 4: $\mathcal{L} = 10^{34}$ cm^{-2} s^{-1}						
Super	450	0.014	1	0.014	600	2.8
Ultra	270	0.19	10	0.019	400	2.6
High	140	4.4	100	0.044	250	2.8
Med	60	3.9×10^2	4,000	0.097	120	2.4
Low	25	2.9×10^4	200,000	0.146	60	2.8

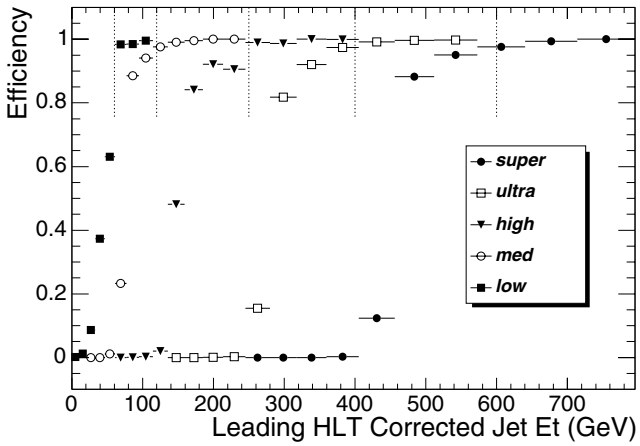

Figure E.4. The efficiency for passing the Level-1 jet trigger is shown as a function of HLT corrected jet E_T for each of the trigger paths shown in table E.5. The Level-1 thresholds were chosen to give an efficiency of greater than 95% at the corresponding HLT threshold.

Table E.5 illustrates a trigger strategy to maintain the continuity of jet analysis as the luminosity increases over a time span of years. The most important feature is that each luminosity scenario maintains the thresholds introduced in the previous scenario, allowing

combination of trigger samples over time. For the prescaled thresholds, we may increase the prescales, either in discrete steps or dynamically, to maintain the allowed HLT rate with increasing luminosity. However, to maintain maximum sensitivity to new physics, the highest E_T threshold must never be prescaled. For example, in table E.5 when the luminosity increases by only a factor of 2 from $\mathcal{L} = 10^{33}\,\mathrm{cm}^{-2}\,\mathrm{s}^{-1}$ to $\mathcal{L} = 2 \times 10^{33}\,\mathrm{cm}^{-2}\,\mathrm{s}^{-1}$, we double the prescales on the prescaled triggers but don't change either the threshold or the prescale of the highest E_T trigger labelled Ultra. This allows us to maintain stability of the single jet trigger thresholds, and analyses that depend on them, with only modest increases in the total rate for single jets. When the HLT rate in the unprescaled trigger becomes intolerably high, a higher E_T threshold unprescaled trigger is introduced, and the old unprescaled trigger can then be prescaled as necessary.

For the particular case of single-jet triggers: To commission the calorimeters, or perform a one-time jet study, it may be desirable to have more jets. If we want to write more than roughly 10 Hz of single jets at HLT, we can still use the same suite of single-jets, but lower the prescales to obtain more jets at low E_T. This is preferable to moving the threshold for the unprescaled trigger, or any of the triggers, and ending up with a special trigger that is only applicable for a given running period and difficult to combine with other samples.

For $\mathcal{L} = 2 \times 10^{33}\,\mathrm{cm}^{-2}\,\mathrm{s}^{-1}$, the suggested jet thresholds have been studied again in the scope of the global High-Level trigger analysis (Sec. E.5) and new Level-1 prescales and rates have been determined. For the trigger table proposed in this study, we have chosen four triggers, with E_T thresholds of 400, 250, 120 and 60 GeV, amd prescales of 1, 10, 1000 and 100 000, respectively.

E.4.3.3. Other triggers. The remaining triggers that have been introduced since the DAQ TDR are:

- Inclusive E_T^{miss} trigger. As discussed earlier, this is a difficult trigger that is subject to the good understanding and control of the detector noise. We suggest here a single E_T^{miss} trigger with $E_T > 91\,\mathrm{GeV}$, driven by the $E_T^{miss} > 60\,\mathrm{GeV}$ L1 condition. This is just an indicative value, rather on the low side, as E_T^{miss} rates appear lower compared to Ref. [76]. It is foreseen that additional E_T^{miss} triggers with different thresholds and prescales will be introduced in the future.
- Diffractive trigger. This trigger is different than all others described earlier in that it uses the TOTEM detector [823, 824]. At Level-1 we ask for two central jets with $E_T > 40\,\mathrm{GeV}$, along with a proton tagged with the 220 m Roman Pot. At HLT, a similar dijet cut and a "back-to-back" azimuthal condition are applied. We also require that we have a consistent measurement of the proton energy loss ξ in the two hemispheres (within $2\,\sigma$, measured at the Roman Pots). A final condition for a tagged proton seen by the 420 m Roman Pot brings the HLT rate down to $\mathcal{O}(1)$ Hz. This trigger is discussed in detail in Sec. E.3.

E.5. Performance

The performance of the trigger system is studied by using simulated data that has been digitised with appropriate pileup[56], taking into account both the inelastic (55.2 mb) and the diffractive (24.1 mb) cross sections. To reduce the amount of simulation time, about 50 million

[56] We have estimated the average number of in-time interactions per bunch crossing to be 5 for $\mathcal{L} = 2 \times 10^{33}\,\mathrm{cm}^{-2}\,\mathrm{s}^{-1}$. Additional, out-of-time interactions have been ignored.

Table E.6. Description and sizes of MC Samples used for the trigger studies. The contribution to the HLT rate does not include pre-scaled triggers.

Sample description	Cuts (Momenta in GeV/c)	Cross section (mb)	# of events	HLT rate (Hz)
Minimum bias with in-time pile-up; $\langle$ # of interactions $\rangle = 5$	—	79.3	50 000 000	—
QCD	$\hat{p_T} \in [15, 20]$	1.46×10^{0}	49 491	
QCD	$\hat{p_T} \in [20, 30]$	6.32×10^{-1}	49 244	
QCD	$\hat{p_T} \in [30, 50]$	1.63×10^{-1}	49 742	
QCD	$\hat{p_T} \in [50, 80]$	2.16×10^{-2}	99 486	
QCD	$\hat{p_T} \in [80, 120]$	3.08×10^{-3}	96 238	
QCD	$\hat{p_T} \in [120, 170]$	4.94×10^{-4}	99 736	
QCD	$\hat{p_T} \in [170, 230]$	1.01×10^{-4}	99 226	
QCD	$\hat{p_T} \in [230, 300]$	2.45×10^{-5}	99 481	
QCD	$\hat{p_T} \in [300, 380]$	6.24×10^{-6}	98 739	
QCD	$\hat{p_T} \in [380, 470]$	1.78×10^{-6}	46 491	
QCD	$\hat{p_T} \in [470, 600]$	6.83×10^{-7}	47 496	
QCD	$\hat{p_T} \in [600, 800]$	2.04×10^{-7}	48 986	
QCD	$\hat{p_T} \in [800, 1000]$	3.51×10^{-8}	45 741	
	Partial total		930 099	55.3 ± 6.9
$W \to e\nu$	1 electron with$\lvert\eta\rvert < 2.7$, $p_T > 25$	7.9×10^{-6}	3 944	9.7 ± 0.2
$Z \to ee$	2 electrons with $\lvert\eta\rvert < 2.7$, $p_T > 5$	8.2×10^{-7}	4 000	1.4 ± 0.0
$pp \to$ jet(s) $+ \gamma$, $\hat{p_T} > 30$ GeV/c	jet: $p_T > 20$,γ: $p_T > 30$	2.5×10^{-6}	4 000	1.0 ± 0.0
$W \to \mu\nu$	1 muon with $\lvert\eta\rvert < 2.5$, $p_T > 14$	9.8×10^{-6}	4 000	14.0 ± 0.3
$Z \to \mu\mu$	2 muons with $\lvert\eta\rvert < 2.5$, $p_T > 20$, 10	7.9×10^{-7}	2 941	1.5 ± 0.0
$pp \to \mu + X$	1 muon with $p_T > 3$	2.4×10^{-2}	839 999	25.5 ± 1.2

minimum bias events were simulated and reused in random combinations. It was ensured that these events do not cause triggers by themselves to avoid over estimating the rates due to this reuse of events.

In the following sections we list trigger rates along with their statistical uncertainties. These take into account the luminosity-dependent weight of the events from the different samples, the corresponding cross sections and the $\hat{p_T}$ of the main interaction and the pile-up contribution. They do *not* take into account the uncertainties of these individual factors, i.e. no systematic effects are studied here.

The Level-1 calorimeter trigger object rate studies are performed using QCD data that has been generated in several bins of $\hat{p_T}$. A special event-weighting procedure has been applied to properly take into account the cross sections of the sub-samples. The Level-1 muon and E_T^{miss} rate studies are performed using a purely minimum bias sample.

The HLT rates are estimated using specially enriched samples. For the triggers invoking muons, electrons and photons we have used a minimum bias sample enriched in muons, as well as $W \to e/\mu\nu$, $Z \to ee/\mu\mu$ and jet(s) + γ MC datasets. For the triggers including jets we have used QCD samples. These samples also contribute to the electron and photon triggers. Events triggered exclusively with muons have been excluded from the QCD samples, to avoid double-counting with the muon-enriched sample. Table E.6 summarises the MC samples used for the trigger studies, and their corresponding contribution to the HLT rate. A more detailed breakdown of the contributions to the electron, photon and muon trigger rates from

Table E.7. Trigger table showing Level-1 rates for DAQ TDR chosen thresholds for $\mathcal{L} = 2 \times 10^{33}\,\mathrm{cm}^{-2}\,\mathrm{s}^{-1}$. Whenever the "95% efficiency point" is reported in DAQ TDR, we also give the actual kinematic threshold that has been applied.

Trigger	95% Eff. point	Threshold (GeV)	Rate (kHz)	Cumulative Rate (kHz)
Single $e\gamma$	29	23.4	3.38 ± 0.23	3.4 ± 0.2
Double $e\gamma$	17	11.5	0.85 ± 0.12	4.0 ± 0.3
Single μ	—	14	2.53 ± 0.20	6.5 ± 0.3
Double μ	—	3	4.05 ± 0.26	10.3 ± 0.4
Single τ	86	93	3.56 ± 0.24	9.7 ± 0.4
Double τ	59	66	1.97 ± 0.18	10.6 ± 0.4
1-, 3-, 4-jets	177, 86, 70	135, 58, 45	2.43 ± 0.20	11.9 ± 0.4
Jet + $E_{\mathrm{T}}^{\mathrm{miss}}$	—	88, 46	1.07 ± 0.13	12.2 ± 0.4
$e\gamma$ + τ	—	21, 45	3.64 ± 0.24	12.9 ± 0.5
	Level-1 Trigger Total			12.9 ± 0.5

the different samples is discussed later (Sec. E.5.3-rates). For our calculations, we have used the standard HLT physics algorithms (`ORCA/_8/_13/_3` [10]) for the implementation of all trigger paths. At the time of this writing, this includes the latest algorithms and jet calibrations. For the global evaluation of the trigger rates we have used the "HLT steering code"

E.5.1. Level-1 rates

The background at Level-1 is entirely dominated by strong interactions. The muon rates at Level-1 are dominated by low p_{T} muons which are reconstructed as high p_{T} muons due to limited resolution at the trigger level. For the electron/photon trigger the rate is dominated by jets that fragment to high E_{T} π^0 s. The jet rates are dominated by true jets in the QCD events. The $E_{\mathrm{T}}^{\mathrm{miss}}$ background is due to the limited energy resolution, and pile-up of minimum bias interactions.

We first produce a trigger table with Level-1 rates for DAQ TDR chosen thresholds for comparison. For the calculations we use a sample of 2 million minimum bias crossings with an average of 5 events per crossing, constructed from the minbias events, without reuse of events. The out-of-time pile-up is neglected. Even though there are small differences for the individual triggers, the integral rate is consistent with the rates reported in Ref. [76]. This comparison serves as a cross-check and is a necessary intermediate step before the introduction of new trigger terms. Table E.7 summarises the Level-1 rate calculations for the DAQ TDR triggers with the new MC samples. Besides the "95% efficiency points" (used throughout the DAQ TDR), the applied L1 thresholds are also given.

For the new trigger table: We select several thresholds for each trigger object type and quote corresponding rates and prescales for $\mathcal{L} = 2 \times 10^{33}\,\mathrm{cm}^{-2}\,\mathrm{s}^{-1}$. For the single objects we have added a series of prescaled triggers to determine the efficiency turn-on. For the multi-object triggers we have picked the lowest common threshold that is allowed for the allocated bandwidth. For the cross-channel triggers we have attempted to keep the lepton thresholds as low as possible, within the allocated bandwidth based on the physics needs of the experiment. The prescales are chosen such that the simulated rate at all times falls below the DAQ bandwidth taking into account a safety factor of 3. The total Level-1 rate for all triggers (including prescaled ones) is 22.6 ± 0.3 kHz.

Table E.8. Comparison of HLT bandwidth given to various trigger paths calculated in this study with the DAQ TDR. See text for details on different kinematic cuts and changes in the HLT algorithms.

Trigger	DAQ TDR Rate (Hz)	New Rate (Hz)
Inclusive e	33.0	23.5 ± 6.7
e-e	1.0	1.0 ± 0.1
Relaxed e-e	1.0	1.3 ± 0.1
Inclusive γ	4.0	3.1 ± 0.2
γ-γ	5.0	1.6 ± 0.7
Relaxed γ-γ	5.0	1.2 ± 0.6
Inclusive μ	25.0	25.8 ± 0.8
μ-μ	4.0	4.8 ± 0.4
τ + $E_{\mathrm{T}}^{\mathrm{miss}}$	1.0	0.5 ± 0.1
τ + e	2.0	< 1.0
Double Pixel τ	1.0	4.1 ± 1.1
Double Tracker τ	1.0	6.0 ± 1.1
Single jet	1.0	4.8 ± 0.0
Triple jet	1.0	1.1 ± 0.0
Quadruple jet	7.0	8.9 ± 0.2
jet + $E_{\mathrm{T}}^{\mathrm{miss}}$	5.0	3.2 ± 0.1
b-jet (leading jet)	5.0	10.3 ± 0.3
b-jet (2^{nd} leading jet)	5.0	8.7 ± 0.3

E.5.2. Level-1 trigger object corrections

The trigger decisions are based on E_{T} of the objects reconstructed by various algorithms. Unfortunately, the energy deposition in the calorimeter and the size of the trigger towers, are not entirely uniform. We have used fits to the reconstructed-to-generated E_{T} ratios to correct for non-uniformity of the response for jets and electron/photon candidates found at all levels of trigger [830]. This correction procedure adjusts the mean response to the generated level.

The energy response of the calorimeters and the limited number of bits used in trigger calculations result in a finite resolution for the reconstructed trigger objects. Similarly, misalignments of the tracking systems and the limited number of patterns in the muon trigger look-up-tables also result in a finite resolution. To avoid systematic problems in understanding the trigger efficiency turn-on with the E_{T} of the trigger objects, it is envisioned that only data where high trigger efficiency is assured is used for analysis.

E.5.3. HLT rates

A rough comparison of the HLT bandwidth given to various triggers, calculated with the latest algorithms and the ones reported in Ref. [76] is shown in Table E.8. It must be noted that not only thresholds but also other cuts are different in the two trigger studies. Furthermore, additional changes in the HLT algorithms (summarised in Sec. E.2.2) must be taken into account. This comparison serves only as a consistency check. It reaffirms that despite the evolution of the CMS reconstruction algorithms over the years, trigger rates remain under control and that no major bandwidth changes are expected.

Table E.10 shows in a similar way the contributions to the single and double standard and relaxed muon rates from the various MC samples.

The contributions to the single and double electron and photon trigger rates at HLT from the various MC samples is given at Table E.9-egamma. The main contributions to the single

Table E.9. Contributions to the HLT rates for the electron and photon triggers from the various MC datasets.

Trigger	Threshold (GeV)	Rates (Hz)			
		QCD	$W \to e\nu$	$Z \to ee$	jet(s) + γ
Inclusive e	26	12.6 ± 6.7	9.7 ± 0.2	1.2 ± 0.0	—
e-e	12, 12	0.1 ± 0.1	—	1.0 ± 0.0	—
Relaxed e-e	19, 19	0.3 ± 0.1	—	1.0 ± 0.0	—
Inclusive γ	80	1.1 ± 0.2	—	—	2.0 ± 0.1
γ-γ	30, 20	1.3 ± 0.8	—	—	0.3 ± 0.0
Relaxed γ-γ	30, 20	0.9 ± 0.6	—	—	0.3 ± 0.0

Table E.10. Contributions to the HLT rates for the muon triggers from the various MC datasets.

Trigger	Threshold	Rates (Hz)		
	(GeV)	Enriched-μ sample	$W \to \mu\nu$	$Z \to \mu\mu$
Inclusive μ	19	10.9 ± 0.8	13.4 ± 0.3	1.5 ± 0.0
Relaxed μ	37	5.1 ± 0.5	5.7 ± 0.1	1.1 ± 0.0
μ-μ	7, 7	3.4 ± 0.4	—	1.3 ± 0.0
Relaxed μ-μ	10, 10	7.1 ± 0.5	—	1.4 ± 0.0

Table E.11. The Level-1 Trigger Menu at $\mathcal{L} = 2 \times 10^{33}\,\mathrm{cm}^{-2}\,\mathrm{s}^{-1}$. Individual and cumulative rates are given for the different trigger paths and selected kinematic thresholds.

Trigger	Level-1 Threshold (GeV)	Level-1 Rate (kHz)	Cumulative Level-1 Rate (kHz)
Inclusive $e\gamma$	22	4.2 ± 0.1	4.2 ± 0.1
Double $e\gamma$	11	1.1 ± 0.1	5.1 ± 0.1
Inclusive μ	14	2.7 ± 0.1	7.8 ± 0.2
Double μ	3	3.8 ± 0.1	11.4 ± 0.2
Inclusive τ	100	1.9 ± 0.1	13.0 ± 0.2
Double τ	66	1.8 ± 0.1	14.1 ± 0.2
1-,2-,3-,4-jets	150, 100, 70, 50	1.8 ± 0.1	14.8 ± 0.3
H_{T}	300	1.2 ± 0.1	15.0 ± 0.3
$E_{\mathrm{T}}^{\mathrm{miss}}$	60	0.3 ± 0.1	15.1 ± 0.3
H_{T} + $E_{\mathrm{T}}^{\mathrm{miss}}$	200, 40	0.7 ± 0.1	15.3 ± 0.3
jet + $E_{\mathrm{T}}^{\mathrm{miss}}$	100, 40	0.8 ± 0.1	15.4 ± 0.3
τ + $E_{\mathrm{T}}^{\mathrm{miss}}$	60, 40	2.7 ± 0.1	17.4 ± 0.3
μ + $E_{\mathrm{T}}^{\mathrm{miss}}$	5, 30	0.3 ± 0.1	17.6 ± 0.3
$e\gamma$ + $E_{\mathrm{T}}^{\mathrm{miss}}$	15, 30	0.7 ± 0.1	17.7 ± 0.3
μ + jet	7, 100	0.1 ± 0.1	17.8 ± 0.3
$e\gamma$ + jet	15, 100	0.6 ± 0.1	17.8 ± 0.3
μ + τ	7, 40	1.2 ± 0.1	18.4 ± 0.3
$e\gamma$ + τ	14, 52	5.4 ± 0.2	20.7 ± 0.3
$e\gamma$ + μ	15, 7	0.2 ± 0.1	20.7 ± 0.3
Prescaled			22.6 ± 0.3
	Total Level-1 Rate		22.6 ± 0.3

Table E.12. The High-Level Trigger Menu at $\mathcal{L} = 2 \times 10^{33}\,\mathrm{cm}^{-2}\,\mathrm{s}^{-1}$ for an output of approximately 120 Hz. The E_T values are the kinematic thresholds for the different trigger paths.

Trigger	Level-1 bits used	Level-1 Prescale	HLT Threshold (GeV)	HLT Rate (Hz)
Inclusive e	2	1	26	23.5 ± 6.7
e-e	3	1	12, 12	1.0 ± 0.1
Relaxed e-e	4	1	19, 19	1.3 ± 0.1
Inclusive γ	2	1	80	3.1 ± 0.2
γ-γ	3	1	30, 20	1.6 ± 0.7
Relaxed γ-γ	4	1	30, 20	1.2 ± 0.6
Inclusive μ	0	1	19	25.8 ± 0.8
Relaxed μ	0	1	37	11.9 ± 0.5
μ-μ	1	1	7, 7	4.8 ± 0.4
Relaxed μ-μ	1	1	10, 10	8.6 ± 0.6
$\tau + E_\mathrm{T}^\mathrm{miss}$	10	1	65 ($E_\mathrm{T}^\mathrm{miss}$)	0.5 ± 0.1
Pixel τ-τ	10, 13	1	—	4.1 ± 1.1
Tracker τ-τ	10, 13	1	—	6.0 ± 1.1
$\tau + e$	26	1	52, 16	< 1.0
$\tau + \mu$	0	1	40, 15	< 1.0
b-jet (leading jet)	36, 37, 38, 39	1	350, 150, 55 (see text)	10.3 ± 0.3
b-jet (2 $^{\mathrm{nd}}$ leading jet)	36, 37, 38, 39	1	350, 150, 55 (see text)	8.7 ± 0.3
Single-jet	36	1	400	4.8 ± 0.0
Double-jet	36, 37	1	350	3.9 ± 0.0
Triple-jet	36, 37, 38	1	195	1.1 ± 0.0
Quadruple-jet	36, 37, 38, 39	1	80	8.9 ± 0.2
$E_\mathrm{T}^\mathrm{miss}$	32	1	91	2.5 ± 0.2
jet + $E_\mathrm{T}^\mathrm{miss}$	32	1	180, 80	3.2 ± 0.1
acoplanar 2 jets	36, 37	1	200, 200	0.2 ± 0.0
acoplanar jet + $E_\mathrm{T}^\mathrm{miss}$	32	1	100, 80	0.1 ± 0.0
2 jets + $E_\mathrm{T}^\mathrm{miss}$	32	1	155, 80	1.6 ± 0.0
3 jets + $E_\mathrm{T}^\mathrm{miss}$	32	1	85, 80	0.9 ± 0.1
4 jets + $E_\mathrm{T}^\mathrm{miss}$	32	1	35, 80	1.7 ± 0.2
Diffractive	Sec. E.3	1	40, 40	< 1.0
$H_\mathrm{T} + E_\mathrm{T}^\mathrm{miss}$	31	1	350, 80	5.6 ± 0.2
$H_\mathrm{T} + e$	31	1	350, 20	0.4 ± 0.1
Inclusive γ	2	400	23	0.3 ± 0.0
γ-γ	3	20	12, 12	2.5 ± 1.4
Relaxed γ-γ	4	20	19, 19	0.1 ± 0.0
Single-jet	33	10	250	5.2 ± 0.0
Single-jet	34	1 000	120	1.6 ± 0.0
Single-jet	35	100 000	60	0.4 ± 0.0
	Total HLT rate			119.3 ± 7.2

electron trigger come from the QCD and $W \to e\nu$ samples, whereas for the single photon trigger the primary source is the jet(s) + γ events.

E.5.4. Trigger tables

Table E.11 summarises the Level-1 triggers used in this study, their kinematic thresholds, the individual and cumulative rates. We have assumed a DAQ capability of 50 kHz, taking into account a safety factor of 3.

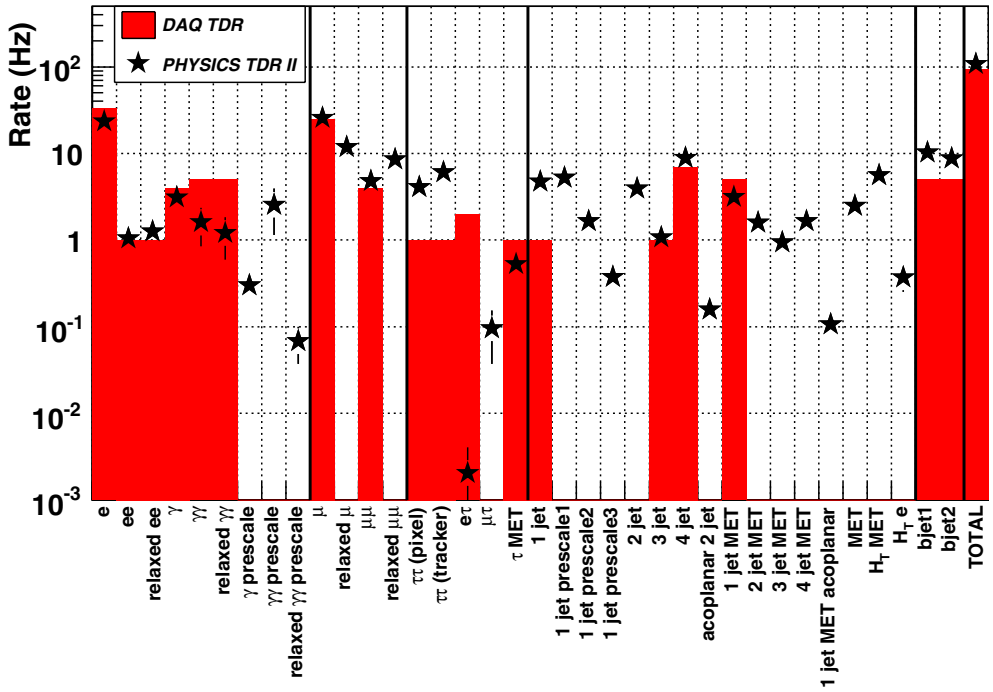

Figure E.5. Heuristic comparison of HLT bandwidth assigned to various trigger paths calculated in this study with the DAQ TDR. For the triggers introduced in this study the DAQ TDR entries appear empty. See text for details on different kinematic cuts and changes in the HLT algorithms.

Table E.12 gives the full list of trigger paths proposed for $\mathcal{L} = 2 \times 10^{33}\,\mathrm{cm}^{-2}\,\mathrm{s}^{-1}$ that have been described earlier for an HLT output rate of approximately 120 Hz.

Fig. E.5 shows a graphic representation of the HLT bandwidth assigned to all trigger paths presented in this study. For the triggers that appeared in the DAQ TDR, the corresponding rates are overlaid, in a heuristic comparison.

Glossary

ADC	Analog to Digital Converter
AdS	Anti de Sitter space
ALEPH	An experiment at LEP
ALICE	A Large Ion Collider Experiment at the LHC
ALPGEN	Monte Carlo event generator for multi-parton processes in hadronic collisions
ATLAS	A Toroidal LHC ApparatuS experiment
BMU	Barrel Muon system
BR	Branching Ratio
BX	Bunch Crossing
BXN	Bunch Crossing Number
CASTOR	Calorimeter in the forward region of CMS
CDF	Collider Detector Facility experiment at the FNAL Tevatron
CL	Confidence Level
CLHEP	Class Library for HEP
CMKIN	CMS Kinematics Package (legacy Fortran)
CMS	Compact Muon Solenoid experiment
CMSIM	CMS Simulation Package (legacy Fortran)
CMSSW	CMS Software framework
CPT	Computing, Physics, TriDAS and software projects of CMS
CPU	Central Processing Unit
CompHEP	Monte Carlo event generator for high-energy physics collisions
CSC	Cathode Strip Chamber muon system
CVS	Concurrent Versions System
DØ	Experiment at the FNAL Tevatron
DAQ	Data Acquisition
DELPHI	An experiment at LEP
DESY	Deutsches Elektronen SYnchrotron laboratory, Hamburg
DST	Data Summary Tape – a compact event format
DT	Drift Tube muon system
DY	Drell–Yan
EB	Electromagnetic Calorimeter (Barrel)
ECAL	Electromagnetic Calorimeter
ED	Extra Dimensions
EE	Electromagnetic Calorimeter (Endcap)
EM	Electromagnetic
EMU	Endcap Muon system
ES	Endcap preShower detector
EW	ElectroWeak
FAMOS	CMS Fast Simulation
FLUKA	Computer program for hadron shower calculations
FNAL	Fermi National Accelerator Laboratory, USA
FSR	Final State Radiation

Gb	Gigabit (10^9 bits)
GB	Gigabyte (10^9 bytes)
GCALOR	Computer program for hadron shower calculations
GEANT	Detector simulation framework and toolkit
GMSB	Gauge Mediated Symmetry Breaking
GUT	Grand Unified Theory
H1	An experiment at the DESY HERA collider
HAD	Hadronic
HCAL	Hadron Calorimeter
HB	Hadron Calorimeter (Barrel)
HE	Hadron Calorimeter (Endcap)
HEP	High Energy Physics
HEPEVT	HEP Event (generated event format)
HERA	Electron-proton collider at DESY
HERWIG	Hadron Emission Reactions With Interfering Gluons, a Monte Carlo event generator for high-energy physics collisions
HF	Hadron Calorimeter (Forward)
HI	Heavy Ion(s)
HIJING	Heavy Ion Jet INteraction Generator, Monte Carlo event generator for heavy-ion collisions
HLT	High-Level Trigger
HO	Hadron Calorimeter (Outer Barrel)
IGUANA	Interactive Graphics for User ANAlysis – used for the CMS Event Display Package
I/O	Input/Output
IP	Impact Parameter, also Impact Point or Internet Protocol
ISR	Initial State Radiation, also Intersecting Storage Ring collider at CERN
JES	Jet Energy Scale
Kalman Filter	Computational method for fitting tracks
kb	kilobit (10^3 bits)
kB	kilobytes (10^3 bytes)
L1	Level-1 hardware-based trigger
L3	An experiment at LEP
LCG	LHC Computing Grid (a common computing project)
LED	Large Extra Dimenstions, also Light Emitting Diode
LEP	Large Electron Positron collider at CERN
LHC	Large Hadron Collider
LHCb	Large Hadron Collider Beauty experiment
LHCC	LHC (review) Committee
LHEP	Physics model of GEANT4
LL	Leading Logarithm, also Log Likelihood
LO	Leading Order calculation
LOI	Letter Of Intent
LPC	LHC Physics Center, Fermilab
LS	Like-Sign
LSP	Lightest Supersymmetric Particle

Mb	Megabit (10^6 bits)
MB	Muon system (Barrel), also Mother Board or Megabyte (10^6 bytes)
MC	Monte Carlo simulation program/technique, also Mini-Crate of DT system
ME	Muon system (Endcap), also Matrix Element or Monitoring Element
MET	Missing Transverse Energy
metadata	Data describing characteristics of other data
MIP	Minimum Ionizing Particle
MSUGRA	Minimal SUper GRAvity model of supersymmetry
MSSM	Minimal SuperSymmetric Model
MTCC	Magnet Test Cosmic Challenge
ndf	number of degrees of freedom
NLO	Next-to-Leading Order calculation
NN	Neural Network
NNLO	Next-to-Next-to-Leading Order calculation
NS	Numbering Scheme
OO	Object Oriented
OPAL	An experiment at LEP
ORCA	Object-oriented Reconstruction for CMS Analysis
OS	Opposite-Sign, also Operating System
OSCAR	Object-oriented Simulation for CMS Analysis and Reconstruction
P5	Point 5 collision area of LHC
PAW	Physics Analysis Workstation (legacy interactive analysis application)
PB	Petabyte (10^5 bytes)
PC	Personal Computer
PD	Pixel Detector
PDF	Parton Density Function, also Probability Distribution Function (p.d.f.)
PRS	Physics Reconstruction and Selection groups
PS	Proton Synchrotron, also Parton Showers
PV	Primary Vertex
PYTHIA	Monte Carlo event generator for high-energy physics collisions
QCD	Quantum Chromodynamics
QED	Quantum Electrodynamics
QGSP	Physics model of GEANT4
RecHit	Reconstructed hit in a detector element
RHIC	Relativistic Heavy Ion Collider (at Brookhaven, USA)
RMS	Root Mean Square
ROOT	An object-oriented data analysis framework
RPC	Resistive Plate Chamber muon system

SLT	Soft Lepton Tag
SM	Standard Model, also SuperModule (ECAL) or Storage Manager (DAQ)
S/N	Signal to Noise ratio
SPS	Super Proton Synchrotron collider at CERN
SS	Same-Sign
SST	Silicon Strip Tracker
SUSY	SUperSYmmetry
SV	Secondary Vertex
T1, T2	Tracking telescopes of TOTEM
TAG	Event index information such as run/event number, trigger bits, etc.
Tb	Terabit (10^{12} bits)
TB	Terabyte (10^{12} bytes)
TDR	Technical Design Report
TEC	Tracker EndCap
TIB	Tracker Inner Barrel
TID	Tracker Inner Disks
TOB	Tracker Outer Barrel
TOTEM	Separate experiment at P5 for forward physics
TPD	Tracker Pixel Detector
TriDAS	Trigger and Data Acquisition project
UA1	An experiment at the CERN SPS collider
UA2	An experiment at the CERN SPS collider
UE	Underlying Event
UED	Universal Extra Dimensions
VBF	Vector Boson Fusion
VPT	Vacuum PhotoTriode
WWW	World Wide Web
ZDC	Zero Degree Calorimeter
ZEUS	An experiment at the DESY HERA collider

References

Blue font in the online PDF indicates links to full-text articles.

DOI numbers are given for some published articles, for which the full text may be accessed by prefixing the number with http://dx.doi.org/

CMS Notes are available at http://cms.cern.ch/iCMS/ unless otherwise noted.

[1] TLS Group 1995 The Large Hadron Collider Conceptual Design *CERN-AC-95-05 Preprint* hep-ph/0601012

[2] CMS Collaboration 1992 The Compact Muon Solenoid Letter of Intent *CERN/LHCC* 1992-3, LHCC/I 1

[3] CMS Collaboration 1994 The Compact Muon Solenoid Technical Proposal *CERN/LHCC* 94-38, LHCC/P1

[4] ATLAS and CMS Collaboration, Branson J G *et al* 2002 High transverse momentum physics at the Large Hadron Collider: The ATLAS and CMS Collaborations *Eur. Phys. J. direct* C **4** N1 (*Preprint* hep-ph/0110021)

[5] LHC/LC Study Group Collaboration, Weiglein G *et al* 2004 Physics interplay of the LHC and the ILC *Preprint* hep-ph/0410364

[6] Krasnikov N and Matveev V 2004 Search for new physics at LHC *Phys. Usp.* **47** 643 (*Preprint* hep-ph/0309200)

[7] CMS Collaboration 2006 The CMS Physics Technical Design Report, Volume 1 *CERN/LHCC* 2006-001, CMS TDR 8.1

[8] OSCAR: CMS Simulation Package Home Page http://cmsdoc.cern.ch/oscar

[9] GEANT4 Collaboration, Agostinelli S *et al* 2003 GEANT4: A simulation toolkit *Nucl. Instrum. Methods* A **506** 250–303

[10] ORCA: CMS reconstruction Package Site located at http://cmsdoc.cern.ch/orca

[11] CMS Collaboration, Acosta D *et al* 2006 CMS Physics Technical Design Report, Volume 1, Section 2.6: Fast simulation p 55 *CERN/LHCC* 2006-001

[12] Pumplin J *et al* 2002 New generation of parton distributions with uncertainties from global QCD analysis *J. High. Energy Phys.* JHEP07(2002)012 (*Preprint* hep-ph/0201195)

[13] Martin A D, Roberts R G, Stirling W J and Thorne R S 2002 MRST2001: Partons and alpha(s) from precise deep inelastic scattering and Tevatron jet data *Eur. Phys. J.* C **23** 73 (*Preprint* hep-ph/0110215)

[14] Alekhin S *et al* 2005 HERA and the LHC - A workshop on the implications of HERA for LHC physics: Proceedings Part A

[15] Seez C *et al* 1990 Photon decay modes of the intermediate mass Higgs *Proceedings of the Large Hadron Collider Workshop* (*Aachen, 4–9 October, 1990), CERN 90-10* volume II ed G Jarlskog and D Rein

[16] CMS Collaboration 1997 The Electromagnetic Calorimeter Technical Design Report *CERN/LHCC*, 97-033 CMS TDR 4, Addendum *CERN/LHCC* 2002-027

[17] Favara A and Pieri M 1997 Confidence Level Estimation and Analysis Optimization *Preprint* DFF 278/4/1997

[18] L3 Collaboration, Acciarri M *et al* 1997 Search for the Standard Model Higgs Boson in e^+e^- Interactions at 161 GeV $< \sqrt{s} <$ 172 GeV *Phys. Lett.* B **411** 373

[19] CMS Collaboration, Pieri M *et al* 2006 Inclusive search for the Higgs boson in the $H \to \gamma\gamma$ channel *CMS Note* AN 2006/112

[20] Spira M 1998 QCD effects in Higgs physics *Fortsch. Phys.* **46** 203–284 (*Preprint* hep-ph/9705337)

[21] Djouadi A, Kalinowski J and Spira M 1998 HDECAY: a program for Higgs boson decays in the Standard Model and its supersymmetric extension *Comput. Phys. Commun.* **108** 56–74 (doi:10.1016/S0010-4655(97)00123-9)

[22] CMS Collaboration, Dubinin M *et al* 2006 The vector boson fusion production with $H \to \gamma\gamma$ *CMS Note* 2006/097

[23] CMS Collaboration, Lethuillier M 2006 Search for SM Higgs boson with W/Z+H, H$\to 2\gamma$ channel *CMS Note* 2006/110

[24] Sjostrand T, Lonnblad L and Mrenna S 2001 PYTHIA 6.2: Physics and manual *Preprint* hep-ph/0108264

[25] CMSIM home page http://cmsdoc.cern.ch/cmsim/cmsim.html

[26] Giele W *et al* 2002 The QCD/SM working group: Summary report *Preprint* hep-ph/0204316

[27] Dobbs M *et al* 2004 The QCD/SM working group: Summary report *Preprint* hep-ph/0403100

[28] Binoth T 2000 Two photon background for Higgs boson searches at the LHC *Preprint* hep-ph/0005194

[29] Bern Z, Dixon L J and Schmidt C 2002 Isolating a light Higgs boson from the di-photon background at the LHC *Phys. Rev.* D **66** 074018 (*Preprint* hep-ph/0206194)

[30] Binoth T, Guillet J P, Pilon E and Werlen M 2002 A next-to-leading order study of photon pion and pion pair hadro-production in the light of the Higgs boson search at the LHC *Eur. Phys. J. Direct* C **4** (doi:10.1007/s1010502c0007)
[31] CMS Collaboration, Agostino L *et al* 2006 HLT Selection of Electrons and Photons *CMS Note* 2006/078
[32] CMS Collaboration, Meschi E *et al* 2001 Electron Reconstruction in the CMS Electromagnetic Calorimeter *CMS Note* 2001/034
[33] CMS Collaboration, Marinelli N 2006 Track Finding and Identification of Converted Photons *CMS Note* 2006/005
[34] CMS Collaboration, Litvin V *et al* 2002 The Rejection of Background to the HGG Process Using Isolation Criteria Based on Information from the Calorimeter and Tracker *CMS Note* 2002-030
[35] CMS Collaboration, Pieri M *et al* 2006 Distinguishing Isolated Photos from Jets *CMS Note* 2006/007
[36] The LEP Collaborations: ALEPH, DELPHI, L3 and OPAL1998 Lower Bound for the Standard Model Higgs Boson Mass from Combining the Results of the Four LEP Experiments *CERN EP* 98-046
[37] CMS Collaboration, Baffioni S *et al* 2006 Discovery potential for the SM Higgs boson in the $H \to ZZ^{(*)} \to e^+e^-e^+e^-$ decay channel *CMS Note* 2006/115
[38] Barberio E, van Eijk B and Was Z 1991 PHOTOS: A Universal Monte Carlo for QED radiative corrections in decays *Comput. Phys. Commun.* **66** 115–128
[39] Barberio E and Was Z 1994 PHOTOS: A Universal Monte Carlo for QED radiative corrections. Version 2.0 *Comput. Phys. Commun.* **79** 291–308 (doi:10.1016/0010-4655(94)90074-4)
[40] Spira M 1995 HIGLU: A Program for the Calculation of the Total Higgs Production Cross Section at Hadron Colliders via Gluon Fusion including QCD Corrections *Preprint* hep-ph/9510347
[41] Djouadi A, Kalinowski J and Spira M 1998 HDECAY: A Program for Higgs Boson Decays in the Standard Model and its Supersymmetric Extension *Comput. Phys. Commun.* **108** 56–74 (*Preprint* hep-ph/9704448)
[42] Zecher C *et al* 1994 Leptonic Signals from off-shell Z Boson Pairs at Hadron Colliders *Preprint* hep-ph/9404295
[43] CompHEP Collaboration, Boos E *et al* 2004 CompHEP 4.4: Automatic computations from Lagrangians to events *Nucl. Instrum. Meth.* A **534** 250–259 (*Preprint* hep-ph/0403113)
[44] Slabospitsky S R and Sonnenschein L 2002 TopReX generator (version 3.25): Short manual *Comput. Phys. Commun.* **148** 87–102 (doi:10.1016/S0010-4655(02)00471-X)
[45] Beneke M *et al* 2000 Top quark physics *Preprint* hep-ph/0003033
[46] CMS Collaboration, Baffioni S, Charlot C, Ferri F, Futyan D, Meridiani P, Puljak I, Rovelli C, Salerno R and Sirois Y 2006 Electron Reconstruction in CMS *CMS Note* 2006/040
[47] Abdullin S *et al* 2006 Study of PDF and QCD scale uncertainties in $H \to ZZ^{(*)} \to 4\mu$ events at the LHC *CMS Note* 2006/068 See also hep-ph/0604120, Les Houches Physics at TeV Colliders 2005, Standard Model and Higgs working group: Summary report. April 2006
[48] Meridiani P and Paramatti R 2006 Use of $Z \to e^+e^-$ events for ECAL calibration *CMS Note* 2006/039
[49] Bartsch V and Quast G 2006 Expected signal observability at future experiments *CMS Note* 2005-004
[50] Bityukov S and Krasnikov N 1998 New physics discovery potential in future experiments *Mod. Phys. Lett.* A **13** 3235–3249
[51] Abdullin S *et al* 2006 Search Strategy for the Standard Model Higgs Boson in the $H \to ZZ^{(*)} \to 4\mu$ Decay Channel using $M(4\mu)$-Dependent Cuts *CMS Note* 2006/122
[52] Karimaki V *et al* 2004 CMKIN v3 User's Guide *CMS IN* 2004-016
[53] Spira M 2005 'SM Higgs boson production cross sections at NLO' and 'SM Higgs boson BRs'Available at http://cmsdoc.cern.ch/∼anikiten/cms-higgs/
[54] Particle Data Group, Eidelman S *et al* 2004 Review of Particle Physics *Phys. Lett.* B **592** 1 (doi:10.1016/j.physletb.2004.06.001)
Particle Data Group, Yao W-M *et al* 2006 Review of Particle Physics *J. Phys. G: Nucl. Part. Phys.* **33** 1 (doi:10.1088/0954-3899/33/1/001)
[55] Maltoni F 2005 Theoretical Issues and Aims at the Tevatron and LHC *Proceedings of the 1st Hadron Collider Physics Symposium (HCP 2005) (Les Diablerets, Switzerland 2005 July)* Available at http://hcp-2005.web.cern.ch/HCP-2005
[56] Campbell J M 2001 W/Z + B anti-B/jets at NLO using the Monte Carlo MCFM Talk given at 36th Rencontres de Moriond on QCD and Hadronic Interactions (*Les Arcs, France, 17–24 March 2001*) *Preprint* hep-ph/0105226
[57] Abdullin S *et al* 2006 Relative Contributions of t- and s-Channels to the $ZZ \to 4\mu$ Process *CMS Note* 2006/057, See also hep-ph/0604120, Les Houches Physics at TeV Colliders 2005, Standard Model and Higgs working group: Summary report. April 2006

[58] Bartalini P *et al* 2006 NLO vs. LO: kinematical differences for signal and background in the H $\rightarrow$ ZZ* $\rightarrow$ 4μ analysis *CMS Note* 2006/130

[59] Acosta D *et al* 2006 Measuring Muon Reconstruction Efficiency from Data *CMS Note* 2006/060

[60] Aldaya M, Arce P, Caballero J, de la Cruz B, Garcia-Abia P, Hernandez J M, Josa M and Ruiz E 2006 Discovery potential and search strategy for the Standard Model Higgs boson in the $H \rightarrow ZZ^{\star} \rightarrow 4\mu$ decay channel using a mass-independent analysis *CMS Note* 2006/106

[61] Read A 2000 Modified Frequentist Analysis of Search Results (The CLs Method) *1st Workshop on Confidence Limits, CERN, Geneva CERN-EP* /2000-005

[62] LEP Working Group for Higgs boson searches Collaboration, Barate R *et al* 2003 Search for the standard model Higgs boson at LEP *Phys. Lett.* B **565** 61–75 (*Preprint* hep-ex/0306033)

[63] Abdullin S and Drozdetskiy A *et al* 2006 GARCON: Genetic Algorithm for Rectangular Cuts Optimization. User's manual for version 2.0 *Preprint* hep-ph/0605143 See also http://drozdets.home.cern.ch/drozdets/home/genetic/

[64] Abdullin S *et al* 2006 Sensitivity of the Muon Isolation Cut Efficiency to the Underlying Event Uncertainties *CMS Note* 2006/033, See also hep-ph/0604120, Les Houches Physics at TeV Colliders 2005, Standard Model and Higgs working group: Summary report. April 2006

[65] Aldaya M *et al* 2006 A method for determining the mass, cross-section and width of the Standard Model Higgs boson using the H $\rightarrow$ ZZ* $\rightarrow$ 4μ decay channel *CMS Note* 2006/107

[66] Bartsch V Simulation of Silicon Sensors and Study of the Higgs Decay

[67] Dittmar M and Dreiner H 1997 How to find a Higgs boson with a mass between 155GeV to to 180GeV at the CERN LHC *Phys. Rev.* D **55** 167–172 (*Preprint* hep-ph/9608317) (doi:10.1103/PhysRevD.55.167)

[68] Dittmar M and Dreiner H 1997 LHC Higgs Search with $l^{+}\nu l^{-}\overline{\nu}$ final states *CMS Note* 1997/083

[69] Sjostrand T *et al* 2001 High-energy-physics event generation with PYTHIA 6.1 *Comput. Phys. Commun.* **135** 238–259 (doi:10.1016/S0010-4655(00)00236-8)

[70] Binoth T, Ciccolini M, Kauer N and Kramer M 2005 Gluon-induced W W background to Higgs boson searches at the LHC *J. High. Energy Phys.* JHEP03(2005)065 (*Preprint* hep-ph/0503094)

[71] Davatz G *et al* 2004 Effective k-factors for $H \rightarrow WW^{(*)} \rightarrow 2\mu 2\nu$ at the LHC *J. High. Energy Phys.* JHEP0405(2004)009 (*Preprint* hep-ph/0402218) (doi:10.1088/1126-6708/2004/05/009)

[72] Frixione S and Webber B R 2002 Matching NLO QCD computations and parton shower simulations *J. High. Energy Phys.* JHEP0206(2002)029 (*Preprint* hep-ph/0204244)

[73] Davatz G, Dittmar M and Giolo-Nicollerat A S 2006 Standard Model Higgs Discovery Potential of CMS in the $H \rightarrow WW^{(*)} \rightarrow l\nu l\nu$ Channel *CMS Note* 2006/047

[74] Campbell J M and Ellis R K 1999 An update on vector boson pair production at hadron colliders *Phys. Rev.* D **60** 113006 (doi:10.1103/PhysRevD.60.113006)

[75] Campbell J and Tramontano F 2005 Next-to-leading order corrections to Wt production and decay *Nucl. Phys.* B **726** 109–130 (doi:10.1016/j.nuclphysb.2005.08.015)

[76] CMS Collaboration 2002 The TriDAS Project Technical Design Report, Volume 2: Data Acquisition and High-Level Trigger *CERN/LHCC* 2002-26, CMS TDR 6.2

[77] Drollinger V, Gasparini U, Torassa E and Zanetti M 2006 Physics study of the Higgs decay chanel $H \rightarrow WW^{(*)} \rightarrow 2\mu 2\nu$ *CMS Note* 2006/055

[78] Chekanov S V 2002 Jet algorithms: a mini review *Proceedings of the 14th Topical Conference on Hadron Collider Physics (HCP 2002)* September-October (Karlsruhe, Germany)

[79] Bityukov S I and Krasnikov N V 2002 Uncertainties and discovery potential in planned experiments *CMS CR* 2002/05

[80] Davatz G, Giolo-Nicollerat A and Zanetti M 2006 Systematics uncertainties of the top background in the $H \rightarrow WW$ channel *CMS Note* 2006/048

[81] Maltoni F and Stelzer T 2003 MadEvent: Automatic event generation with MadGraph *J. High. Energy Phys.* JHEP02(2003)027 (doi:10.1088/1126-6708/2003/02/027)

[82] Kauer N 2004 Top background extrapolation for $H \rightarrow WW$ searches at the LHC *Preprint* hep-ph/0404045

[83] Lowette S, D'Hondt J, Heyninck J and Vanlaer P 2006 Offline Calibration of b-Jet Identification Efficiencies *CMS Note* 2006/013

[84] Drollinger V *et al* 2005 Modeling the production of W pairs at the LHC *CMS Note* 2005/024

[85] Anastasiou C *et al* 2004 High precision QCD at hadron colliders: Electroweak gauge boson rapidity distribution at NNLO *Phys. Rev.* D **69**

[86] Belotelov I *et al* 2006 Simulation of misalignment scenarios for CMS tracking devices *CMS Note* 2006-008

[87] Cvetic M and Langacker P 1996 Implications of abelian extended gauge structures from string models *Phys. Rev.* D **54** 3570–3579 (*Preprint* hep-ph/9511378)

[88] Cvetic M and Langacker P 1996 New gauge bosons from string models *Mod. Phys. Lett.* A **11** 1247–1262 (*Preprint* hep-ph/9602424)
[89] Leike A 1999 The phenomenology of extra neutral gauge bosons *Phys. Rept.* **317** 143–250 (*Preprint* hep-ph/9805494)
[90] Hill C T and Simmons E H 2003 Strong dynamics and electroweak symmetry breaking *Phys. Rept.* **381** 235–402 (*Preprint* hep-ph/0203079)
[91] Han T, Logan H, McElrath B and Wang L-T 2003 Phenomenology of the little Higgs model *Phys. Rev.* D **67** 095004 (doi:10.1103/PhysRevD.67.095004)
[92] Cvetic M and Godfrey S 1996 Discovery and identification of extra gauge bosons *Electroweak symmetry breaking and new physics at the TeV scale* ed T L Barlow and S Dawson (World Scientific) 383–415 *Preprint* hep-ph/9504216
[93] Godfrey S 2001 Update of discovery limits for extra neutral gauge bosons at hadron colliders *Proceedings of Snowmass 2001* (Snowmass, Colorado: June–July) p P344 *Preprint* hep-ph/0201093
[94] Randall L and Sundrum R 1999 A large mass hierarchy from a small extra dimension *Phys. Rev. Lett.* **83** 3370–3373 (doi:10.1103/PhysRevLett.83.3370)
[95] Whalley M R, Bourilkov D and Group R C 2005 The Les Houches accord PDFs (LHAPDF) and LHAGLUE *Preprint* hep-ph/0508110
[96] Rosner J L 1987 Off peak lepton asymmetries from new Zs *Phys. Rev.* D **35** 2244
[97] Rosner J L 1996 Forward-Backward asymmetries in hadronically produced lepton pairs *Phys. Rev.* D **54** 1078–1082 (*Preprint* hep-ph/9512299)
[98] Mohapatra R N, Goldstein S A and Money D (eds) 2002 *Unification and supersymmetry: The Frontiers of quark - lepton physics* 3rd ed. (Springer-Verlag)
[99] Belotelov I *et al* 2006 Influence of misalignment scenarios on muon reconstruction *CMS Note* 2006-017
[100] Cousins R, Mumford J and Valuev S 2005 Detection of Z' gauge bosons in the dimuon decay mode in CMS *CMS Note* 2005-002
[101] Cousins R, Mumford J and Valuev V 2006 Detection of Z′ gauge bosons in the dimuon decay mode in CMS *CMS CR* 2004/050
[102] Bartsch V and Quast G 2005 Expected signal observability at future experiments *CMS Note* 2005-004
[103] Wilks S S 1938 The large-sample distribution of the likelihood ratio for testing composite hypotheses *Annals of Math. Stat.* **9** 60
[104] Baur U, Brein O, Hollik W, Schappacher C and Wackeroth D 2002 Electroweak radiative corrections to neutral-current Drell–Yan processes at hadron colliders *Phys. Rev.* D **65** 033007 (*Preprint* hep-ph/0108274)
[105] Zykunov V 2005 Weak radiative corrections to Drell–Yan process for large invariant mass of di-lepton pair *Preprint* hep-ph/0509315
[106] De Roeck A and Slabospitsky S Evaluation of the PDF Uncertainties (in CMS) available at http://cmsdoc.cern.ch/cms/PRS/gentools/www/pdfuncert/uncert.html
[107] Cerminara G private communication
[108] Langacker P, Robinett R W and Rosner J L 1984 New heavy gauge bosons in pp and $p\bar{p}$ collisions *Phys. Rev.* D **30** 1470
[109] Rosner J L 1989 Observability of charge asymmetries for lepton pairs produced in present collider experiments *Phys. Lett.* B **221** 85
[110] Cheng T P and Li L F 1988 *Gauge theory of elementary particle physics* (Oxford University Press)
[111] Cousins R, Mumford J and Valuev V 2005 Measurement of Forward-Backward Asymmetry of Simulated and Reconstructed $Z' \to \mu^+\mu^-$ Events in CMS *CMS Note* 2005-022
[112] Dittmar M 1997 Neutral current interference in the TeV region: The experimental sensitivity at the LHC *Phys. Rev.* D **55** 161–166 (*Preprint* hep-ex/9606002)
[113] Wulz C-E 1996 Z' at LHC *Proceedings of the 1996 DPF/DPB Summer Study on New Directions in High-Energy Physics* available at http://www.slac.stanford.edu/pubs/snowmass96
[114] Collins J C and Soper D E 1977 Angular distribution of dileptons in high-energy hadron collisions *Phys. Rev.* D **16** 2219
[115] Allanach B C, Odagiri K, Parker M A and Webber B R 2000 Searching for narrow graviton resonances with the ATLAS detector at the Large Hadron Collider *J. High. Energy Phys.* JHEP09(2000)019 (*Preprint* hep-ph/0006114)
[116] Cousins R, Mumford J, Tucker J and Valuev V 2005 Spin discrimination of new heavy resonances at the LHC *J. High. Energy Phys.* JHEP11(2005)046 (doi:10.1088/1126-6708/2005/11/046)
[117] Belotelov I *et al* 2006 Search for Randall-Sandrum Graviton Decay into Muon Pairs *CMS Note* 2006/104
[118] Esen S and Harris R M 2006 Jet Triggers and Dijet Mass *CMS Note* 2006/069

[119] CMS Collaboration, Acosta D *et al* 2006 CMS Physics Technical Design Report, Volume 1, Section 11.3: Monte Carlo Corrections *CERN/LHCC*, 2006-001 p 409

[120] CDF Collaboration, Abe F *et al* 1997 Search for new particles decaying to dijets at CDF *Phys. Rev.* D **55** 5263–5268 (doi:10.1103/PhysRevD.55.R5263)

[121] DØ Collaboration, Abazov V M *et al* 2004 search for new particles in the two-jet decay channel with the DØdetector *Phys. Rev.* D **69** 111101 (*Preprint* hep-ex/0308033)

[122] DØ Collaboration, Abbott B *et al* 1999 The dijet mass spectrum and a search for quark compositeness in $\bar{p}p$ collisions at $\sqrt{s} = 1.8$-TeV *Phys. Rev. Lett.* **82** 2457–2462 (doi:10.1103/PhysRevLett.82.2457)

[123] Eichten E, Lane K D and Peskin M E 1983 New tests for quark and lepton substructure *Phys. Rev. Lett.* **50** 811–814 (doi:10.1103/PhysRevLett.50.811)

[124] Lane K D 1996 Electroweak and flavor dynamics at hadron colliders *Preprint* hep-ph/9605257

[125] CDF Collaboration, Abe F *et al* 1996 Measurement of dijet angular distributions at CDF *Phys. Rev. Lett.* **77** 5336–5341 (doi:10.1103/PhysRevLett.77.5336)

[126] CMS Collaboration, Acosta D *et al* 2006 CMS Physics Technical Design Report, Volume 1, Section 11.6.1: Data-driven calibration strategy *CERN/LHCC*, 2006-001 p 421

[127] CMS Collaboration, Acosta D *et al* 2006 CMS Physics Technical Design Report, Volume 1, Section 11.6.2: Dijet Balancing *CERN/LHCC*, 2006-001 p 422

[128] CDF Collaboration, Acosta D *et al* 2005 Measurement of the lifetime difference between B_s mass eigenstates *Phys. Rev. Lett.* **94** 101803 (*Preprint* hep-ex/0412057) (doi:10.1103/PhysRevLett.94.101803)

[129] DØ Collaboration 2006 Measurement of the lifetime difference in the B_s system *DØ Conference note 5052*

[130] Belkov A and Shulga S 2004 Studies of angular correlations in the decays $B_s^0 \to J/\psi\phi$ by using the SIMUB generator *Comput. Phys. Commun.* **156** 221–240 (*Preprint* hep-ph/0310096) (doi:10.1016/S0010-4655(03)00465-X)

[131] Dighe A S, Dunietz I and Fleischer R 1999 Extracting CKM phases and $B_s - \bar{B}_s$ mixing parameters from angular distributions of non-leptonic B decays *Eur. Phys. J.* C **6** 647–662 (doi:10.1007/s100529800954)

[132] Dighe A S, Dunietz I, Lipkin H J and Rosner J L 1996 Angular distributions and lifetime differences in $B_s \to J/\psi\phi$ decays *Phys. Lett.* B **369** 144–150 (doi:10.1016/0370-2693(95)01523-X)

[133] CDF Collaboration, Abe F *et al* 1997 Production of J/ψ mesons from χ_c meson decays in $p\bar{p}$ collisions at $\sqrt{s} = 1.8$ TeV *Phys. Rev. Lett.* **79** 578–583 (doi:10.1103/PhysRevLett.79.578)

[134] Cano-Coloma B and Sanchis-Lozano M A 1997 Charmonia production in hadron colliders and the extraction of colour-octet matrix elements *Nucl. Phys.* B **508** 753–767 (*Preprint* hep-ph/9706270) (doi:10.1016/S0550-3213(97)00660-3)

[135] Cucciarelli S, Konecki M, Kotlinski D and Todorov T 2006 Track reconstruction, primary vertex finding and seed generation with the Pixel Detector *CMS Note* 2006/026

[136] Prokofiev K and Speer T 2005 A kinematic fit and a decay chain reconstruction library *CERN Yellow Report* http://doc.cern.ch/yellowrep/2005/2005-002/p411.pdf, 2005-002 Proc. of the 2004 Conference for Computing in High-Energy and Nuclear Physics (CHEP 04) (Interlaken, Switzerland, 2004) available at http://indico.cern.ch

[137] Dunietz I, Fleischer R and Nierste U 2001 In pursuit of new physics with B_s decays *Phys. Rev.* D **63** 114015 (doi:10.1103/PhysRevD.63.114015)

[138] BABAR Collaboration, Aubert B *et al* 2005 Ambiguity-free measurement of $\cos(2\beta)$: Time-integrated and time-dependent angular analyses of $B \to J/\psi K\pi$ *Phys. Rev.* D **71** 032005 (doi:10.1103/PhysRevD.71.032005)

[139] Dunietz I, Quinn H, Snyder A, Toki W and Lipkin H J 1991 How to extract CP-violating asymmetries from angular correlations *Phys. Rev.* D **43** 2193–2208 (doi:10.1103/PhysRevD.43.2193)

[140] Vanlaer P *et al* 2006 Impact of CMS Silicon Tracker Misalignment on Track and Vertex Reconstruction *CMS Note* 2006/029

[141] Speer T *et al* 2006 Vertex Fitting in the CMS Tracker *CMS Note* 2006/032

[142] Heinemeyer S, Hollik W and Weiglein G 2000 FeynHiggs: A program for the calculation of the masses of the neutral CP-even Higgs bosons in the MSSM *Comput. Phys. Commun.* **124** 76–89 (*Preprint* hep-ph/9812320)

[143] Heinemeyer S, Hollik W and Weiglein G 1999 The masses of the neutral CP-even Higgs bosons in the MSSM: accurate analysis at the two-loop level *Eur. Phys. J.* C **9** 343–366 (*Preprint* hep-ph/9812472)

[144] Degrassi G, Heinemeyer S, Hollik W, Slavich P and Weiglein G 2003 Towards high-precision predictions for the MSSM Higgs sector *Eur. Phys. J.* C **28** 133–143 (*Preprint* hep-ph/0212020)

[145] Lehti S 2006 Study of bbZ as a benchmark for MSSM bbH *CMS Note* 2006/099

[146] Bagliesi G, Dutta S, Gennai S, Kalinowski A, Konecki M, Kotlinski D, Moortgat F, Nikitenko A, Wendland L and Wakefield S 2006 Tau jet reconstruction and tagging at high level trigger and off-line *CMS Note* 2006/028
[147] Kunori S, Kinnunen R and Nikitenko A 2001 Missing transverse energy measurement with jet energy correctioins *CMS Note* 2001/040
[148] Pi H *et al* 2006 Measurement of missing transverse energy with the CMS detector at the LHC *CMS Note* 2006/035
[149] Kalinowski A and Nikitenko A 2006 Measurement of the τ-tagging efficiency using the Z$\rightarrow \tau\tau \rightarrow \mu$ + hadrons + X events *CMS Note* 2006/074
[150] Gennai S, Nikitenko A and Wendland L 2006 Search for MSSM Heavy Neutral Higgs Boson in $\tau\tau \rightarrow$ two Jet Decay Mode *CMS Note* 2006/126
[151] Rizzi A, Palla F and Segneri G 2006 Track impact parameter based b-tagging with CMS *CMS Note* 2006/019
[152] Kalinowski A, Konecki M and Kotlinski D 2006 Search for MSSM Heavy Neutral Higgs Boson in $\tau\tau \rightarrow \mu$ + jet Decay Mode *CMS Note* 2006/105
[153] Kalinowski A, Konecki M and Kotliński D 2006 Search for MSSM heavy neutral Higgs boson in $\tau + \tau \rightarrow \mu +$ jet decay mode *CMS Note* 2006/105
[154] Kinnunen R and Lehti S 2006 Search for the Heavy Neutral MSSM Higgs Bosons with the H/A$\rightarrow \tau\tau \rightarrow$ Electron plus Jet Decay Mode *CMS Note* 2006/075
[155] Jadach S, Was Z, Decker R and Kuhn J H 1993 The tau decay library TAUOLA: Version 2.4 *Comput. Phys. Commun.* **76** 361–380 (doi:10.1016/0010-4655(93)90061-G)
[156] Giolo-Nicollerat A-S 2006 *CMS Note*
[157] Weiser C 2006 A Combined Secondary Vertex Based B-Tagging Algorithm in CMS *CMS Note* 2006/014
[158] Haywood S *et al* 1999 Electroweak physics *Preprint* hep-ph/0003275 In 'Standard Model Physics (and more) at the LHC', Geneva, 1999
[159] Chakraborty D, Konigsberg J and Rainwater D L 2003 Review of top quark physics *Ann. Rev. Nucl. Part. Sci.* **53** 301–351 (*Preprint* hep-ph/0303092)
[160] Benedetti D, Cucciarelli S, Hill C, Incandela J, Koay S, Riccardi C, Santocchia A, Schmidt A, Torre P and Weiser C 2006 Search for $H \rightarrow bb$ in association with a tt pair at CMS *CMS Note* 2006/119
[161] Mangano M L, Moretti M, Piccinini F, Pittau R and Polosa A D 2003 ALPGEN, a generator for hard multiparton processes in hadronic collisions *J. High. Energy Phys.* JHEP07(2003)001 (*Preprint* hep-ph/0206293) (doi:10.1088/1126-6708/2003/07/001)
[162] Beenakker W, Dittmaier S, Kraemer M, Pluemper B, Spira M and Zerwas P 2003 NLO QCD corrections to $t\bar{t}H$ production in hadron collisions *Nucl. Phys.* B **653** 151–203 (*Preprint* hep-ph/0211352)
[163] Roberfroid V *et al* 2006 Validation and status of the HLT Steering Code and default menu *CMS IN* 2006/001
[164] James E, Maravin Y, Mulders M and Neumeister N 2006 Muon Identification in CMS *CMS Note* 2006/010
[165] Heister A, Kodolova O, Konoplianikov V, Petrushanko S, Rohlf J, Tully C and Ulyanov A 2006 Measurement of Jets with the CMS Detector at the LHC *CMS Note* 2006/036
[166] Santocchia A 2006 Optimization of Jet Reconstruction Settings and Parton-Level Correction for the ttH Channel *CMS Note* 2006/059
[167] D'Hondt J, Lowette S, Buchmuller O, Cucciarelli S, Schilling F P, Spiropulu M, Mehdiabadi S, Benedetti D and Pape L 2006 Fitting of Event Topologies with External Kinematic Constraints in CMS *CMS Note* 2006/023
[168] Mangano M private communication
[169] Wang X-N and Gyulassy M 1991 HIJING: A Monte Carlo model for multiple jet production in p p, p A and A A collisions *Phys. Rev.* D **44** 3501–3516
[170] Bedjidian M *et al* 2004 Hard probes in heavy ion collisions at the LHC: heavy flavour physics *Preprint* hep-ph/0311048
[171] Eskola K J, Kolhinen V J and Salgado C A 1999 The scale dependent nuclear effects in parton distributions for practical applications *Eur. Phys. J.* C **9** 61–68 (*Preprint* hep-ph/9807297)
[172] Kodolova O, Bedjidian M and Petrouchanko S 1999 Dimuon reconstruction in heavy ion collisions using a detailed description of CMS geometry *CMS Note* 1999-004
[173] Bedjidian M and Kodolova O 2006 Quarkonia measurements in heavy-ion collisions in CMS *CMS Note* 2006/089
[174] Sterman G and Weinberg S 1977 Jets from Quantum Chromodynamics *Phys. Rev. Lett.* **39** 1436
[175] JADE Collaboration, Bartel W *et al* 1986 Experimental studies on multi-jet production in e^+e^+ annihilation at petra energies *Z. Phys.* C **33** 23
[176] JADE Bethke S *et al* 1988 Experimental investigation of the energy dependence of the strong coupling strength *Phys. Lett.* B **213** 235

[177] Catani S, Dokshitzer Y L, Olsson M, Turnock G and Webber B R 1991 New clustering algorithm for multi-jet cross-sections in e^+e^+ annihilation *Phys. Lett.* B **269** 432–438

[178] CDF Run II Collaboration, Abulencia A *et al* 2005 Measurement of the inclusive jet cross section in $p\bar{p}$ interactions at $\sqrt{s} = 1.96$ TeV using a cone-based jet algorithm *Preprint* hep-ex/0512020

[179] DØ, Collaboration, Strohmer R 2006 Inclusive jet cross-sections and dijet azimuthal decorrelations with DØ*PoS* HEP **2005** 051 (*Preprint* hep-ex/0601016)

[180] Butterworth J, Couchman J, Cox B and Waugh B 2003 KtJet: A C^{++} implementation of the K(T) clustering algorithm *Comput. Phys. Commun.* **153** 85–96 (*Preprint* hep-ph/0210022)

[181] ed U Baur, R K Ellis and D Zeppenfeld 2000 *QCD and Weak Boson Physics in Run II* (Batavia, IL, USA: FERMILAB) Prepared for Physics at Run II: QCD and Weak Boson Physics Workshop: Final General Meeting, Batavia, Illinois, 4–6 November, 1999

[182] Ellis S D, Huston J and Tonnesmann M 2001 On building better cone jet algorithms *eConf* C 010630 P513 (*Preprint* hep-ph/0111434)

[183] Wobisch M private communication

[184] Sjostrand T 1994 High-energy physics event generation with PYTHIA 5.7 and JETSET 7.4 *Comput. Phys. Commun.* **82** 74–90

[185] Nagy Z 2002 Three-jet cross sections in hadron hadron collisions at next-to-leading order *Phys. Rev. Lett.* **88** 122003 (*Preprint* hep-ph/0110315)

[186] Kluge T, Rabbertz K and Wobisch M fast NLO—fast pQCD calculations for hadron-induced processes To be published, available at http://hepforge.cedar.ac.uk/fastnlo

[187] Moretti S, Nolten M R and Ross D A 2005 Weak corrections and high E(T) jets at Tevatron *Preprint* hep-ph/0503152

[188] DØ Collaboration, Abazov V M *et al* 2002 The inclusive jet cross-section in p anti-p collisions at s**(1/2)=1.8-TeV using the k(T) algorithm *Phys. Lett.* B **525** 211–218 (*Preprint* hep-ex/0109041)

[189] DØ Collaboration, Abbott B *et al* 2001 High-p_{T} jets in $\bar{p}p$ collisions at $\sqrt{s} = 630$ GeV and 1800 GeV *Phys. Rev.* D **64** 032003 (doi:10.1103/PhysRevD.64.032003)

[190] CDF Collaboration, Affolder A A *et al* 2002 Charged jet evolution and the underlying event in proton anti-proton collisions at 1.8-TeV *Phys. Rev.* D **65** 092002

[191] CDF Collaboration, Acosta D *et al* 2004 The underlying event in hard interactions at the Tevatron anti-p p collider *Phys. Rev.* D **70** 072002 (*Preprint* hep-ex/0404004)

[192] Sjostrand T and van Zijl M 1987 A multiple interaction model for the event structure in hadron collisions *Phys. Rev.* D **36** 2019

[193] Butterworth J, Forshaw J R and Seymour M 1996 Multiparton interactions in photoproduction at HERA *Z. Phys.* C **72** 637–646 (*Preprint* hep-ph/9601371)

[194] Gleisberg T *et al* 2004 SHERPA 1.alpha, a proof-of-concept version *J. High. Energy Phys.* JHEP02(2004)056 (*Preprint* hep-ph/0311263)

[195] Bopp F W, Engel R and Ranft J 1998 Rapidity gaps and the PHOJET Monte Carlo *Preprint* hep-ph/9803437

[196] Corcella G *et al* 2001 HERWIG 6: An event generator for hadron emission reactions with interfering gluons (including supersymmetric processes) *J. High. Energy Phys.* JHEP01(2001)010 (*Preprint* hep-ph/0011363) (doi:10.1088/1126-6708/2001/01/010)

[197] Buttar C M, Clements D, Dawson I and Moraes A 2004 Simulations of minimum bias events and the underlying event, MC tuning and predictions for the LHC *Acta Phys. Polon.* B **35** 433–441

[198] CDF Collaboration, Field R 2005 Min-bias and the underlying event in Run 2 at CDF *Acta Phys. Polon.* B **36** 167–178

[199] Acosta D *et al* 2006 The underlying event at the LHC *CMS Note* 2006/067

[200] CDF Collaboration, Abe F *et al* 1991 Measurement of the Z-boson p_{T} distribution in $\bar{p}p$ collisions at $\sqrt{s} = 1.8$ TeV *Phys. Rev. Lett.* **67** 2937–2941 (doi:10.1103/PhysRevLett.67.2937)

[201] Bartalini P, Chierici R and De Roeck A 2005 Guidelines for the estimation of theoretical uncertainties at the LHC *CMS Note* 2005/013

[202] Adam W, Mangano B, Speer T and Todorov T 2006 Track reconstruction in the CMS tracker *CMS Note* 2006/041

[203] Andreev V P, Cline D.B and Otwinowski S 2006 Inclusive b quark production *CMS Note* 2006/120

[204] CDF Collaboration, Abe F *et al* 1993 Measurement of the bottom quark production cross section using semileptonic decay electrons in $p\bar{p}$ collisions at $\sqrt{s} = 1.8$ TeV *Phys. Rev. Lett.* **71** 500 (doi:10.1103/PhysRevLett.71.500)

[205] CDF Collaboration, Abe F *et al* 1994 Measurement of the B meson and b quark cross sections at $\sqrt{s} = 1.8$ TeV using the exclusive decay $B^0 \to J/\psi K^*(892)^0$ *Phys. Rev.* D **50** 4252 (doi:10.1103/PhysRevD.50.4252)

[206] CDF Collaboration, Abe F *et al* 1995 Measurement of the B Meson Differential Cross Section $d\sigma/dp_{\mathrm{T}}$ in $p\bar{p}$ Collisions at $\sqrt{s} = 1.8$ TeV *Phys. Rev. Lett.* **75** 1451 (doi:10.1103/PhysRevLett.75.1451)

[207] CDF Collaboration Abe F *et al* 2002 Measurement of the B^+ total cross section and B^+ differential cross section $d\sigma/dp_{\mathrm{T}}$ in $p\bar{p}$ collisions at $\sqrt{s} = 1.8$ TeV *Phys. Rev.* D **65** 052005 (doi:10.1103/PhysRevD.65.052005)

[208] CDF Collaboration, Abe F *et al* 2002 Measurement of the ratio of b quark production cross sections in $\bar{p}p$ collisions at $\sqrt{s} = 630$ GeV and $\sqrt{s} = 1800$ GeV *Phys. Rev.* D **66** 032002 (doi:10.1103/PhysRevD.66.032002)

[209] DØ Collaboration, Abachi S *et al* 1995 Inclusive μ and b-quark production cross-sections in $p\bar{p}$ collisions at $\sqrt{s} = 1.8$ TeV *Phys. Rev. Lett.* **74** 3548 (doi:10.1103/PhysRevLett.74.3548)

[210] DØ Collaboration, Abbott B *et al* 2000 The $b\bar{b}$ production cross section and angular correlations in $p\bar{p}$ collisions at $\sqrt{s} = 1.8$ TeV *Phys. Lett.* B **487** 264 (doi:10.1016/S0370-2693(00)00844-3)

[211] DØ Collaboration, Abbott B *et al* 2000 Cross section for b-Jet production in $\bar{p}p$ collisions at $\sqrt{s} = 1.8$ TeV *Phys. Rev. Lett.* **85** 5068 (doi:10.1103/PhysRevLett.85.5068)

[212] H1 Collaboration, Adloff C *et al* 1999 Measurement of open beauty production at HERA *Phys. Lett.* B **467** 156 (doi:10.1016/S0370-2693(99)01099-0)

[213] H1 Collaboration, Adloff C *et al* 2001 Erratum *Phys. Lett.* B **518** 331

[214] ZEUS Collaboration, Breitweg J *et al* 2001 Measurement of open beauty production in photoproduction at HERA *Eur. Phys. J.* C **18** 625–637 (doi:10.1007/s100520100571)

[215] H1 Collaboration, Aktas A *et al* 2005 Measurement of F2(c anti-c) and F2(b anti-b) at high Q**2 using the H1 vertex detector at HERA *Eur. Phys. J.* C **40** 349–359 (*Preprint* hep-ex/0411046)

[216] ZEUS Collaboration, Chekanov S *et al* 2004 Bottom photoproduction measured using decays into muons in dijet events in e p collisions at s**(1/2)=318 GeV *Phys. Rev.* D **70** 012008

[217] ZEUS Collaboration, Chekanov S *et al* 2004 Measurement of beauty production in deep inelastic scattering at HERA *Phys. Lett.* B **599** 173–189 (*Preprint* hep-ex/0405069)

[218] H1 Collaboration, Aktas A *et al* 2005 Measurement of beauty production at HERA using events with muons and jets *Eur. Phys. J.* C **41** 453–467 (*Preprint* hep-ex/0502010)

[219] L3 Collaboration, Acciarri M *et al* 2001 Measurements of the cross sections for open charm and beauty production in $\gamma\gamma$ collisions at $\sqrt{s} = 189$ GeV–202 GeV *Phys. Lett.* B **503** 10 (doi:10.1016/S0370-2693(01)00134-4)

[220] L3 Collaboration, Achard P *et al* 2005 Measurement of the cross section for open-beauty production in photon photon collisions at LEP *Phys. Lett.* B **619** 71

[221] Nason P, Dawson S and Ellis R K 1988 The total cross-section for the production of heavy quarks in hadronic collisions *Nucl. Phys.* B **303** 607

[222] Nason P, Dawson S and Ellis R K 1989 The one particle inclusive differential cross-section for heavy quark production in hadronic collisions *Nucl. Phys.* B **327** 49–92

[223] Beenakker W, Van Neerven W L, Meng R, Schuler G A and Smith J 1991 QCD corrections to heavy quark production in hadron-hadron collisions *Nucl. Phys.* B **351** 507–560 (doi:10.1016/S0550-3213(05)80032-X)

[224] Cacciari M, Frixione S, Mangano M L, Nason P and Ridolfi G 2004 QCD analysis of first b cross section data at 1.96-TeV *J. High. Energy Phys.* JHEP07(2004)033 (doi:10.1088/1126-6708/2004/07/033)

[225] Mangano M L 2005 The saga of bottom production in proton antiproton collisions *AIP Conf. Proc.* **753** 247–260 (*Preprint* hep-ph/0411020)

[226] Frixione S 2004 Bottom production *Preprint* hep-ph/0408317

[227] Weinberg S 1990 Unitarity vonstraints on CP nonconservation in Higgs exchange *Phys. Rev.* D **42** 860–866

[228] Lavoura L 1993 Maximal CP violation via Higgs boson exchange *Int. J. Mod. Phys.* A **8** 375–390

[229] Jenkins E, Luke M E, Manohar A V and Savage M J 1993 Semileptonic B_c decay and heavy quark spin symmetry *Nucl. Phys.* B **390** 463–473 (*Preprint* hep-ph/9204238)

[230] Kiselev V V, Kovalsky A E and Likhoded A K 2000 B_c decays and lifetime in QCD sum rules *Nucl. Phys.* B **585** 353–382 (doi:10.1016/S0550-3213(00)00386-2)

[231] Wu X-G, Chang C-H, Chen Y-Q and Fang Z-Y 2003 The meson B_c annihilation to leptons and inclusive light hadrons *Phys. Rev.* D **67** 094001 (doi:10.1103/PhysRevD.67.094001)

[232] Chang C-H and Chen Y-Q 1992 The Production of B_c or $\bar{B}_c$ meson associated with two heavy quark jets in Z^0 boson decay *Phys. Rev.* D **46** 3845–3855 (doi:10.1103/PhysRevD.46.3845)

[233] Chang C-H and Chen Y-Q 1993 Hadronic production of the B_c meson at TeV energies *Phys. Rev.* D **48** 4086 (doi:10.1103/PhysRevD.48.4086)

[234] Chang C-H, Chen Y-Q, Han G-P and Jiang H-T 1995 On hadronic production of the B_c meson *Phys. Lett.* B **364** 78 (doi:10.1016/0370-2693(95)01235-4)

[235] Chang C-H, Chen Y-Q and Oakes R J 1996 Comparative study of the hadronic production of B_c mesons *Phys. Rev.* D **54** 4344 (doi:10.1103/PhysRevD.54.4344)

[236] Chang C-H and Wu X-G 2004 Uncertainties in estimating hadronic production of the meson B/c and comparisons between TEVATRON and LHC *Eur. Phys. J.* C **38** 267–276 (doi:10.1140/epjc/s2004-02015-0)

[237] CDF Collaboration, Abe F *et al* 1998 Observation of the B_c meson in $p\bar{p}$ collisions at $\sqrt{s} = 1.8$ TeV *Phys. Rev. Lett.* **81** 2432–2437 (doi:10.1103/PhysRevLett.81.2432)

[238] CDF Collaboration, Acosta D *et al* 2006 Evidence for the exclusive decay $B_c^{\pm} \to J/\psi\pi^{\pm}$ and measurement of the mass of the B_c meson *Phys. Rev. Lett.* **96** 082002 (doi:10.1103/PhysRevLett.96.082002)

[239] Berezhnoi A V, Kiselev V V, Likhoded A K and Onishchenko A I 1997 B_c meson at LHC *Phys. Atom. Nucl.* **60** 1729–1740 (*Preprint* hep-ph/9703341)

[240] Gouz I P, Kiselev V V, Likhoded A K, Romanovsky V I and Yushchenko O P 2004 Prospects for the B_c studies at LHCb *Phys. Atom. Nucl.* **67** 1559–1570 (doi:10.1134/1.1788046)

[241] Chang C-H and Chen Y-Q 1994 Decays of the B_c meson *Phys. Rev.* D **49** 3399–3411 (doi:10.1103/PhysRevD.49.3399)

[242] Kwong W-K and Rosner J L 1991 Masses of new particles containing b quarks *Phys. Rev.* D **44** 212–219 (doi:10.1103/PhysRevD.44.212)

[243] Eichten E J and Quigg C 1994 Mesons with beauty and charm: Spectroscopy *Phys. Rev.* D **49** 5845–5856 (*Preprint* hep-ph/9402210)

[244] Chen Y-Q and Kuang Y-P 1992 Improved QCD motivated heavy quark potentials with explicit $\Lambda_{\overline{MS}}$ dependence *Phys. Rev.* D **46** 1165–1171 (doi:10.1103/PhysRevD.46.1165)

[245] Chen G, Meng X and Tao J 2006 Feasibility to study the B_c meson at CMS *CMS Note* 2006/118

[246] Sjostrand T, Lonnblad L, Mrenna S and Skands P 2003 PYTHIA 6.3: Physics and manual *Preprint* hep-ph/0308153

[247] Grothe M *et al* 2006 Triggering on Forward Physics *CMS Note* 2006/054. Also available as TOTEM NOTE 2006-01

[248] CMS/TOTEM Collaboration, CMS/TOTEM document on diffractive and forward physics, in preparation 2006

[249] UA8 Collaboration, Bonino R *et al* 1988 Evidence for transverse jets in high mass diffraction *Phys. Lett.* B **211** 239

[250] Arneodo M and Diehl M 2005 Diffraction for non-believers *Preprint* hep-ph/0511047

[251] UA8 Collaboration, Brandt A *et al* 1998 Measurements of single diffraction at $\sqrt{s} = 630$ GeV: Evidence for a non-linear $\alpha(t)$ of the pomeron *Nucl. Phys.* B **514** 3–44 (doi:10.1016/S0550-3213(97)00813-4)

[252] Erhan S and Schlein P E 2000 Inelastic diffraction data and the Pomeron trajectory *Phys. Lett.* B **481** 177–186 (doi:10.1016/S0370-2693(00)00467-6)

[253] Goulianos K 2005 Twenty years of diffraction at the TevatronPresented at 11th international conference on elastic and diffractive scattering: towards high energy frontiers: the 20th anniversary of the blois workshops *Preprint* hep-ph/0510035

[254] FP420 Collaboration, Albrow M G *et al* 2005 FP420: A proposal to investigate the feasibility of installing proton tagging detectors in the 420 m region of the LHC *CERN/LHCC*, 2005-025

[255] CDF Collaboration, Affolder A A *et al* 2000 Diffractive dijets with a leading antiproton in anti-p p collisions at $\sqrt{s}$ = 1800 GeV *Phys. Rev. Lett.* **84** 5043–5048

[256] De Roeck A, Khoze V A, Martin A D, Orava R and Ryskin M G 2002 Ways to detect a light Higgs boson at the LHC *Eur. Phys. J.* C **25** 391–403 (*Preprint* hep-ph/0207042)

[257] Khoze V, Martin A and Ryskin M 2002 Prospects for new physics observations in diffractive processes at the LHC and Tevatron *Eur. Phys. J.* C **23** 311–327 (*Preprint* hep-ph/0111078)

[258] Kisselev A, Petrov V and Ryutin R 2005 5-dimensional quantum gravity effects in exclusive double diffractive events *Phys. Lett.* B **630** 100–107 (doi:10.1016/j.physletb.2005.09.059)

[259] Monk J and Pilkington A 2005 ExHuME: a Monte Carlo event generator for exclusive diffraction *Preprint* hep-ph/0502077

[260] Boonekamp M *et al* 2005 Monte-Carlo generators for central exclusive diffraction *Proceedings of the HERA-LHC Workshop (CERN/DESY, January, 2005)* available at http://www.desy.de/ heralhc/proceedings/wg4montecarlo.pdf

[261] Ryutin R 2004 EDDE Monte Carlo event generator *Preprint* hep-ph/0409180

[262] Kaidalov A, Khoze V A, Martin A D and Ryskin M G 2003 Central exclusive diffractive production as a spin parity analyser: From hadrons to Higgs *Eur. Phys. J.* C **31** 387–396 (*Preprint* hep-ph/0307064)

[263] Carena M, Heinemeyer S, Wagner C E M and Weiglein G 2006 MSSM Higgs boson searches at the Tevatron and the LHC: Impact of different benchmark scenarios *Eur. Phys. J.* C **45** 797–814 (*Preprint* hep-ph/0511023)

[264] Ellis J R, Lee J S and Pilaftsis A 2005 Diffraction as a CP and lineshape analyzer for MSSM Higgs bosons at the LHC *Phys. Rev.* D **71** 075007 (*Preprint* hep-ph/0502251)
[265] Petrov A, Ryutin R, Sobol A and Guillaud J-P 2005 Azimuthal angular distributions in EDDE as spin-parity analyser and glueball filter for LHC *J. High. Energy Phys.* JHEP06(2005)007 (*Preprint* hep-ph/0409118)
[266] Piotrzkowski K 2001 Tagging two-photon production at the LHC *Phys. Rev.* D **63** 071502 (*Preprint* hep-ex/0009065)
[267] Budnev V, Ginzburg I, Meledin G and Serbo V 1974 The Two photon particle production mechanism. physical problems. applications. equivalent photon approximation *Phys. Rept.* **15** 181–281 (doi:10.1016/0370-1573(75)90009-5)
[268] Khoze V, Martin A and Ryskin M 2002 Photon-exchange processes at hadron colliders as a probe of the dynamics of diffraction *Eur. Phys. J.* C **24** 459–468 (*Preprint* hep-ph/0201301) (doi:10.1007/s10052-002-0964-4)
[269] White A R 2005 The physics of a sextet quark sector *Phys. Rev.* D **72** 036007 (*Preprint* hep-ph/0412062)
[270] Piotrzkowski K 2002 High energy two-photon interactions at the LHC *Preprint* hep-ex/0201027
[271] Kalmykov N N, Ostapchenko S S and Pavlov A I 1997 Quark-gluon string model and EAS simulation problems at ultra-high energies *Nucl. Phys. Proc. Suppl.* B **52** 17–28
[272] Engel R, Gaisser T K, Stanev T and Lipari P 1999 Air shower calculations with the new version of SIBYLL *Prepared for 26th International Cosmic Ray Conference* (ICRC 99) (Salt Lake City, Utah, 17–25 August 1999)
[273] Roesler S, Engel R and Ranft J The Event generator DPMJET-III at cosmic ray energies Prepared for 27th International Cosmic Ray Conference (ICRC 2001) (Hamburg, Germany, 7-15 Aug 2001)
[274] Karsch Frithjof 2002 Lattice QCD at high temperature and density *Lect. Notes Phys.* **583** 209–249 (*Preprint* hep-lat/0106019)
[275] Iancu Edmond and Venugopalan Raju 2003 The color glass condensate and high energy scattering in QCD *Preprint* hep-ph/0303204
[276] Schwarz Dominik J 2003 The first second of the universe *Annalen Phys.* **12** 220–270 (*Preprint* astro-ph/0303574)
[277] Starinets Andrei O 2005 Transport coefficients of strongly coupled gauge theories: Insights from string theory *Preprint* nucl-th/0511073
[278] Bonciani Roberto, Catani Stefano, Mangano Michelangelo L and Nason Paolo 1998 NLL resummation of the heavy-quark hadroproduction cross-section *Nucl. Phys.* B **529** 424–450 (*Preprint* hep-ph/9801375)
[279] Davids M *et al* 2006 Measurement of top-pair cross section and top-quark mass in the di-lepton and full-hadronic channels with CMS *CMS Note* http://cms.cern.ch/iCMS/jsp/openfile.jsp?tp=draft&files=2907_ttbar.pdf2006/077
[280] Gennai S *et al* 2006 Tau jet reconstruction and tagging at High Level Trigger and off-line *CMS Note* http://cms.cern.ch/iCMS/jsp/openfile.jsp?type=NOTE&year=2006&files=NOTE2006_028.pdf2006/028
[281] D'Hondt J, Heyninck J and Lowette S 2006 Measurement of the cross section of single leptonic $t\bar{t}$ events *CMS Note* http://cms.cern.ch/iCMS/jsp/openfile.jsp?type=NOTE&year=2006&files=NOTE2006_064.pdf2006/064
[282] Buttar C *et al* 2006 Les Houches Physics at TeV Colliders 2005, Standard Model and Higgs working group: Summary report *Preprint* hep-ph/0604120
[283] Konoplianikov V, Kodolova O and Ulyanov A 2006 Jet calibration using γ+jet events in the CMS Detector *CMS Note* http://cms.cern.ch/iCMS/jsp/openfile.jsp?type=NOTE&year=2006&files=NOTE2006_042.pdf2006/042
[284] D'Hondt J *et al* 2006 Electron and muon reconstruction in single leptonic $t\bar{t}$ events *CMS Note* http://cms.cern.ch/iCMS/jsp/openfile.jsp?type=NOTE&year=2006&files=NOTE2006_024.pdf2006/024
[285] CMS Collaboration, Acosta D *et al* 2006 CMS Coll. Physics TDR Vol. I, Section 12.2.8 *CERN/LHCC* 2006-001
[286] Lowette S, D'Hondt J, Heyninck J and Vanlaer P 2006 Offline calibration of b-jet identification efficiency, *CERN-CMS-NOTE* -2006-013
[287] D'Hondt J, Lowette S, Heyninck J and Kasselmann S 2006 Light quark jet energy scale calibration using the W mass constraint in single-leptonic $t\bar{t}$ events *CERN-CMS-NOTE* -2006-025
[288] The CDF Collaboration, Acosta D *et al* 2005 Measurement of the $t\bar{t}$ cross section in $p\bar{p}$ collisions at $\sqrt{s}$=1.96 TeV using kinematic characteristics of lepton plus jets events *Phys. Rev.* D **71** 072005 (doi:10.1103/PhysRevD.71.072005)
[289] DØ Collaboration, Abazov V M *et al* 2005 Measurement of the $t\bar{t}$ cross section in $p\bar{p}$ collisions at $\sqrt{s}$=1.96 TeV using kinematic characteristics of lepton plus jets events *Phys. Lett.* B **626** 55 (doi:10.1016/j.physletb.2005.08.105)

[290] Vos M and Palla F 2006 B-tagging in the High Level Trigger *CMS Note* http://cmsdoc.cern.ch/documents/06/note06_030.pdf2006-030
[291] CDF and DØ, Wicke D 2005 Top pair production cross-section measurement in the all-hadronic channel at CDF and DØCollaboration *Int. J. Mod. Phys. A* **20** 3183–3186 (*Preprint* hep-ex/0411009) (doi:10.1142/S0217751X05026091)
[292] D'Hondt J, Heyninck J and Lowette S 2006 Top Quark mass measurement in single-leptonic $t\bar{t}$ events *CMS Note* http://cms.cern.ch/iCMS/jsp/openfile.jsp?type=NOTE&year=2006&files=NOTE2006_066.pdf2006/066
[293] CDF Collaboration, Abe F *et al* 1997 First Observation of the All-Hadronic Decay of $t\bar{t}$ pairs *Phys. Rev. Lett.* **79** 1992–1997 (doi:10.1103/PhysRevLett.79.1992)
[294] Tevatron Electroweak Working Group Collaboration 2006 Combination of CDF and DØresults on the mass of the top quark *Preprint* hep-ex/0603039
[295] Kharchilava Avto 2000 Top mass determination in leptonic final states with J/psi *Phys. Lett.* **B476** 73–78 (*Preprint* hep-ph/9912320)
[296] Grenier P 2001 *ATLAS Physics Note* 2001-023
[297] Chierici R and Dierlamm A 2006 Determination of the top mass in exclusive JPsi decays *CMS Note* http://cmsdoc.cern.ch/documents/06/note06_058.pdf2006-058
[298] Tevatron Electroweak Working Group Collaboration 2006 Combination of CDF and DØ results on the mass of the top quark *Preprint* hep-ex/0603039
[299] Hill C S, Incandela J R and Lamb J M 2005 A method for measurement of the top quark mass using the mean decay length of *b* hadrons in *t* anti-*t* events *Phys. Rev.* D **71** 054029 (*Preprint* hep-ex/0501043)
[300] Borjanovic I *et al* 2005 Investigation of top mass measurements with the ATLAS detector at LHC *Eur. Phys. J.* **C39S2** 63–90 (*Preprint* hep-ex/0403021)
[301] Lyons Louis, Gibaut Duncan and Clifford Peter 1988 How to combine correlated estimates of a single physical quantity *Nucl. Instrum. Methods* A **270** 110
[302] Valassi A 2003 Combining correlated measurements of several different physical quantities *Nucl. Instrum. Methods* A **500** 391–405
[303] Mahlon G and Parke S 1996 Angular correlation in top quark pair production and decay at hadron collider *Phys. Rev.* D **53** 4886–4896 (*Preprint* hep-ph/9512264)
[304] Stelzer T and Willenbrock S 1996 Spin correlation in top-quark production at hadron collider *Phys. Lett.* B **374** 169–172 (*Preprint* hep-ph/9512292)
[305] Brandenburg A 1996 Spin-spin correlations of top quark pairs at Hadron colliders *Phys. Lett.* B **387** 626–632 (*Preprint* hep-ph/9606379)
[306] Baarmand M, Mermerkaya H and Vodopiyanov I 2006 Measurement of spin correlation in top quark pair production in semi-leptonic final state *CMS Note* 2006/111
[307] Tait T 2000 The tW^- mode of single top production *Phys. Rev.* D **61** 034001 (*Preprint* hep-ph/9909352) (doi:10.1103/PhysRevD.61.034001)
[308] Belyaev A and Boos E 2001 Single top quark t W + X production at the LHC: A closer look *Phys. Rev.* D **63** 034012 (*Preprint* hep-ph/0003260)
[309] Zhu S 2002 Next-to-leading order QCD corrections to b g $\rightarrow$ t W- at the CERN Large Hadron Collider *Phys. Lett.* B **524** 283–288
[310] Boos E, Bunichev V, Dudko L, Savrin V and Sherstnev A 2005 A simulation method of the electroweak top quark production events in the NLO approximation: a Monte-Carlo generator 'singletop'abstract available at http://www.npi.msu.su/eng/science.php3?sec=preprint&ref_pp=1262
[311] CMS Collaboration, Acosta D *et al* 2006 CMS Physics Technical Design Report, Volume 1, Section 9.1.2: Global muon reconstruction *CERN/LHCC*, 2006-001 p 333
[312] CMS Collaboration, Acosta D *et al* 2006 CMS Physics Technical Design Report, Volume 1, Section 9.3: Muon identification *CERN/LHCC*, 2006-001 p 351
[313] CMS Collaboration, Acosta D *et al* 2006 CMS Physics Technical Design Report, Volume 1, Section 10.4: Electron reconstruction and selection *CERN/LHCC*, 2006-001 p 390
[314] CMS Collaboration, Acosta D *et al* 2006 CMS Physics Technical Design Report, Volume 1, Section 11.2.1: Iterative cone *CERN/LHCC*, 2006-001 p 408
[315] CMS Collaboration, Acosta D *et al* 2006 CMS Physics Technical Design Report, Volume 1, Section 11.6.3: γ+jet events *CERN/LHCC*, 2006-001 423
[316] CMS Collaboration, Acosta D *et al* 2006 CMS Physics Technical Design Report, Volume 1, Section 12.2: b-tagging tools *CERN/LHCC*, 2006-001 p 461
[317] Abramov V *et al* 2006 Selection of single top events with the CMS detector at LHC *CMS Note* 2006/084
[318] Yeh P *et al* 2006 Search for W-associated Production of Single Top Quarks in CMS *CMS Note* 2006/086

[319] Campbell J, Ellis R K and Rainwater D L 2003 Next-to-leading order QCD predictions for W + 2jet and Z + 2jet production at the CERN LHC *Phys. Rev.* D **68** 094021 (doi:10.1103/PhysRevD.68.094021)
[320] CMS Collaboration, Acosta D *et al* 2006 CMS Coll. Physics Technical Design Physics, Volume I, Section 11.6.5 *CERN/LHCC*, 2006-001
[321] CMS Collaboration, Acosta D *et al* 2006 CMS Physics Technical Design Physics, Volume I, Section 8.5: Sources of systematic effects *CERN/LHCC*, 2006-001 p 229
[322] Fisher R A 1936 The use of multiple measurements in taxonomic problems *Annuals of Eugenics* **7** 179–188
[323] Mele B, Petrarca S and Soddu A 1998 A new evaluation of the $t \to cH$ decay width in the standard model *Phys. Lett.* B **435** 401–406 (*Preprint* hep-ph/9805498)
[324] Huang C-S, Wu X-H and Zhu S-H 1999 Top-charm associated production at high energy $e^+ e^-$ colliders in standard model *Phys. Lett.* B **452** 143–149 (*Preprint* hep-ph/9901369)
[325] de Divitiis G M, Petronzio R and Silvestrini L 1997 Flavour changing top decays in supersymmetric extensions of the standard model *Nucl. Phys.* B **504** 45–60 (*Preprint* hep-ph/9704244)
[326] Guasch J and Sola J 1999 FCNC top quark decays: A door to SUSY physics in high luminosity colliders? *Nucl. Phys.* B **562** 3–28 (*Preprint* hep-ph/9906268)
[327] Eilam G, Gemintern A, Han T, Yang J M and Zhang X 2001 Top quark rare decay $t \to ch$ in R-parity-violating SUSY *Phys. Lett.* B **510** 227–235 (*Preprint* hep-ph/0102037) (doi:10.1016/S0370-2693(01)00598-6)
[328] Li C S, Zhang X-M and Zhu S H 1999 SUSY-QCD effect on top charm associated production at linear collider *Phys. Rev.* D **60** 077702 (*Preprint* hep-ph/9904273)
[329] Bejar S, Guasch J and Sola J 2001 FCNC top quark decays beyond the standard model *Preprint* hep-ph/0101294
[330] Diaz R A, Martinez R and Alexis Rodriguez J 2001 The rare decay $t \to c\gamma$ in the general 2HDM type III *Preprint* hep-ph/0103307
[331] Han T and Hewett J L 1999 Top charm associated production in high energy $e^+ e^-$ collisions *Phys. Rev.* D **60** 074015 (*Preprint* hep-ph/9811237)
[332] del Aguila F, Aguilar-Saavedra J A and Miquel R 1999 Constraints on top couplings in models with exotic quarks *Phys. Rev. Lett.* **82** 1628–1631 (*Preprint* hep-ph/9808400)
[333] Aguilar-Saavedra J A and Nobre B M 2003 Rare top decays $t \to c\gamma$, $t \to cg$ and CKM unitarity *Phys. Lett.* B **553** 251–260 (*Preprint* hep-ph/0210360)
[334] CDF and DØ Collaboration, Paulini M 1996 Heavy flavor physics from top to bottom *Preprint* hep-ex/9701019
[335] CDF Collaboration, Abe F *et al* 1998 Search for flavor-changing neutral current decays of the top quark in $p\bar{p}$ collisions at $\sqrt{s} = 1.8$ TeV *Phys. Rev. Lett.* **80** 2525–2530 (doi:10.1103/PhysRevLett.80.2525)
[336] Heinson A 1996 Future top physics at the Tevatron and LHC *Preprint* hep-ex/9605010
[337] Aguilar-Saavedra J A and Branco G C 2000 Probing top flavour-changing neutral scalar couplings at the CERN LHC *Phys. Lett.* B **495** 347–356 (*Preprint* hep-ph/0004190)
[338] Aguilar-Saavedra J A 2001 Top flavour-changing neutral coupling signals at a linear collider *Phys. Lett.* B **502** 115–124 (*Preprint* hep-ph/0012305)
[339] Aguilar-Saavedra J A and Riemann T 2001 Probing top flavor-changing neutral couplings at TESLA *Preprint* hep-ph/0102197
[340] Karafasoulis K *et al* 2006 Study of flavour changing neutral currents in top quark decays with the CMS detector *CMS Note* 2006/093
[341] Dissertori G *et al* 2006 How accurately can we count the number of $pp \to ZX$ and $pp \to WX$ events using decays to electrons *CMS Note* 2006/124
[342] Alcaraz J 2006 Measurement of Z $\to \mu^+\mu^-$ and W $\to \mu\nu$ rates in CMS *CMS Note* 2006/082
[343] Frixione S and Webber B R 2006 The MC@NLO 3.2 event generator *Preprint* hep-ph/0601192
[344] For further details see Proceedings of the 2004/2005 HERA-LHC workshop
[345] Dittmar M, Pauss F and Zurcher D 1997 Towards a precise parton luminosity determination at the CERN LHC *Phys. Rev.* D **56** 7284–7290 (*Preprint* hep-ex/9705004)
[346] Drell S D and Yan T-M 1970 Massive lepton pair production in hadron-hadron collisions at high-energies *Phys. Rev. Lett.* **25** 316–320 (doi:10.1103/PhysRevLett.25.316)
[347] Belotelov I *et al* 2006 Study of Drell–Yan di-muon production with the CMS detector *CMS Note* 2006/123
[348] Hamberg R, van Neerven W L and Matsuura T 1991 A Complete calculation of the order α_s^2 correction to the Drell–Yan K-factor *Nucl. Phys.* B **359** 343–405 (doi:10.1016/0550-3213(91)90064-5)
[349] Bourilkov D 2006 Compositeness search with di-muons in CMS *CMS Note* 2006/085
[350] Baur U and Wackeroth D 2003 Electroweak radiative corrections to weak boson production at hadron colliders *Nucl. Phys. Proc. Suppl.* **116** 159–163 (*Preprint* hep-ph/0211089)

[351] Bourilkov D 2003 Study of parton density function uncertainties with LHAPDF and PYTHIA at LHC*Prepared for the LHC/LC Study Group Meeting (Geneva, Switzerland, 9 May 2003) Preprint* hep-ph/0305126
[352] Buege V *et al* 2006 Prospects for the precision measurement of the W mass with the CMS detector *CMS Note* 2006-061
[353] Giele W T and Keller S 1998 Determination of W boson properties at hadron colliders *Phys. Rev.* D **57** 4433–4440 (*Preprint* hep-ph/9704419)
[354] Brigljević V *et al* 2006 Study of di-boson production with the CMS detector at the LHC *CMS Note* 2006/108
[355] Pukhov A *et al* 1999 CompHEP: A package for evaluation of Feynman diagrams and integration over multi-particle phase space. User's manual for version 33 *Preprint* hep-ph/9908288
[356] Higgs P W 1964 Broken symmetries, massless particles and gauge fields *Phys. Lett.* **12** 132–133
[357] Higgs P W 1966 Spontaneous symmetry breakdown without massless bosons *Phys. Rev.* **145** 1156–1163
[358] Englert F and Brout R 1964 Broken symmetry and the mass of gauge vector mesons *Phys. Rev. Lett.* **13** 321–322
[359] Guralnik G S, Hagen C R and Kibble T W B 1964 Global conservation laws and massless particles *Phys. Rev. Lett.* **13** 585–587
[360] Cornwall J M, Levin D N and Tiktopoulos G 1973 Uniqueness of spontaneously broken gauge theories *Phys. Rev. Lett.* **30** 1268–1270 (doi:10.1103/PhysRevLett.30.1268)
[361] Cornwall J M, Levin D N and Tiktopoulos G 1974 Derivation of gauge invariance from high-energy unitarity bounds on the S-Matrix *Phys. Rev.* D **10** 1145
[362] Llewellyn Smith C H 1973 High-energy behavior and gauge symmetry *Phys. Lett.* B **46** 233–236
[363] Joglekar S D 1974 S-matrix derivation of the Weinberg model *Ann. Phys.* **83** 427
[364] Veltman M 1968 Perturbation theory of massive Yang-Mills fields *Nucl. Phys.* B **7** 637–650
[365] 't Hooft G 1971 Renormalization of massless Yang-Mills fields *Nucl. Phys.* B **33** 173–199
[366] 't Hooft G 1971 Renormalizable lagrangians for massive Yang-Mills fields *Nucl. Phys.* B **35** 167–188
[367] 't Hooft G and Veltman M J G 1972 Regularization and renormalization of gauge fields *Nucl. Phys.* B **44** 189–213
[368] 't Hooft G and Veltman M J G 1972 Combinatorics of gauge fields *Nucl. Phys.* B **50** 318–353
[369] Djouadi A 2005 The anatomy of electro-weak symmetry breaking I: The Higgs boson in the standard model *Preprint* hep-ph/0503172
[370] Djouadi A 2005 The anatomy of electro-weak symmetry breaking II: The Higgs bosons in the minimal supersymmetric model *Preprint* hep-ph/0503173
[371] Cabibbo N, Maiani L, Parisi G and Petronzio R 1979 Bounds on the fermions and higgs boson masses in grand unified theories *Nucl. Phys.* B **158** 295
[372] Chanowitz M S, Furman M A and Hinchliffe I 1978 Weak interactions of ultraheavy fermions *Phys. Lett.* B **78** 285
[373] Flores R A and Sher M 1983 Upper limits to fermion masses in the Glashow-Weinberg-Salam model *Phys. Rev.* D **27** 1679
[374] Lindner M 1986 Implications of triviality for the standard model *Zeit. Phys.* C **31** 295
[375] Sher M 1989 Electroweak Higgs potentials and vacuum stability *Phys. Rept.* **179** 273–418
[376] Sher M 1993 Precise vacuum stability bound in the standard model *Phys. Lett.* B **317** 159–163 (*Preprint* hep-ph/9307342)
[377] Altarelli G and Isidori G 1994 Lower limit on the Higgs mass in the standard model: an update *Phys. Lett.* B **337** 141–144
[378] Espinosa J and Quiros M 1995 Improved metastability bounds on the standard model Higgs mass *Phys. Lett.* B **353** 257–266 (*Preprint* hep-ph/9504241)
[379] Hasenfratz A, Jansen K, Lang C B, Neuhaus T and Yoneyama H 1987 The triviality bound of the four component phi**4 model *Phys. Lett.* B **199** 531
[380] Kuti J, Lin L and Shen Y 1988 Upper bound on the Higgs mass in the standard model *Phys. Rev. Lett.* **61** 678
[381] Luscher M and Weisz P 1989 Scaling laws and triviality bounds in the lattice φ^4 theory (III) n-component model *Nucl. Phys.* B **318** 705 (doi:10.1016/0550-3213(89)90637-8)
[382] Higgs Working Group Collaboration, Carena M *et al* 2000 Report of the Tevatron Higgs working group *Preprint* hep-ph/0010338
[383] ATLAS Collaboration, 1994 Technical Design Report *CERN/LHCC*, 94-14, ATLAS TDR 14
[384] Abdullin S *et al* 2005 Summary of the CMS potential for the Higgs boson discovery *Eur. Phys. J.* C **39S2** 41–61 (doi:10.1140/epjcd/s2004-02-003-9)
[385] Braaten E and Leveille J P 1980 Higgs boson decay and the running mass *Phys. Rev.* D **22** 715

[386] Sakai N 1980 Perturbative QCD Corrections to the hadronic decay width of the Higgs boson *Phys. Rev.* D **22** 2220
[387] Inami T and Kubota T 1981 Renormalization group estimate of the Hadronic decay width of the Higgs boson *Nucl. Phys.* B **179** 171
[388] Gorishnii S G, Kataev A L and Larin S A 1984 The width of Higgs Boson decay into Hadrons: three loop corrections of strong interactions *Sov. J. Nucl. Phys.* **40** 329–334
[389] Drees M and Hikasa K-i 1990 Heavy quark thresholds in Higgs physics *Phys. Rev.* D **41** 1547
[390] Drees M and Hikasa K 1990 Note on QCD corrections to Hadronic Higgs decay *Phys. Lett.* B **240** 455
[391] Chetyrkin K G 1997 Correlator of the quark scalar currents and Gamma(tot)(H → hadrons) at O(alpha(s)**3) in pQCD *Phys. Lett.* B **390** 309–317 (*Preprint* hep-ph/9608318)
[392] Fleischer J and Jegerlehner F 1981 Radiative Corrections to Higgs Decays in the Extended Weinberg-Salam Model *Phys. Rev.* D **23** 2001–2026
[393] Bardin D Y, Vilensky B M and Khristova P K 1991 Calculation of the Higgs boson decay width into fermion pairs *Sov. J. Nucl. Phys.* **53** 152–158
[394] Dabelstein A and Hollik W 1992 Electroweak corrections to the fermionic decay width of the standard Higgs boson *Z. Phys.* C **53** 507–516
[395] Kniehl B A 1992 Radiative corrections for $H \to f\bar{f}(\gamma)$ in the standard model *Nucl. Phys.* B **376** 3–28 (doi:10.1016/0550-3213(92)90065)-J
[396] Zheng H-Q and Wu D-D 1990 First order QCD corrections to the decay of the Higgs boson into two photons *Phys. Rev.* D **42** 3760–3763
[397] Djouadi A, Spira M, van der Bij J and Zerwas P 1991 QCD corrections to gamma gamma decays of Higgs particles in the intermediate mass range *Phys. Lett.* B **257** 187–190
[398] Dawson S and Kauffman R P 1993 QCD corrections to H → gamma gamma *Phys. Rev.* D **47** 1264–1267
[399] Djouadi A, Spira M and Zerwas P 1993 Two photon decay widths of Higgs particles *Phys. Lett.* B **311** 255–260 (*Preprint* hep-ph/9305335)
[400] Melnikov K and Yakovlev O I 1993 Higgs → two photon decay: QCD radiative correction *Phys. Lett.* B **312** 179–183 (*Preprint* hep-ph/9302281)
[401] Inoue M, Najima R, Oka T and Saito J 1994 QCD corrections to two photon decay of the Higgs boson and its reverse process *Mod. Phys. Lett.* A **9** 1189–1194
[402] Steinhauser M 1996 Corrections of O(alpha(s)**2) to the decay of an intermediate-mass Higgs boson into two photons *Preprint* hep-ph/9612395
[403] Djouadi A, Gambino P and Kniehl B A 1998 Two-loop electroweak heavy-fermion corrections to Higgs-boson production and decay *Nucl. Phys.* B **523** 17–39 (*Preprint* hep-ph/9712330)
[404] Aglietti U, Bonciani R, Degrassi G and Vicini A 2004 Two-loop light fermion contribution to Higgs production and decays *Phys. Lett.* B **595** 432–441 (*Preprint* hep-ph/0404071)
[405] Degrassi G and Maltoni F 2005 Two-loop electroweak corrections to the Higgs-boson decay H→ gamma gamma *Preprint* hep-ph/0504137
[406] Kniehl B A 1991 Radiative corrections for $H \to ZZ$ in the standard model *Nucl. Phys.* B **352** 1–26 (doi:10.1016/0550-3213(91)90126-I)
[407] Kniehl B A 1991 Radiative corrections for $H \to W^+W^-(\gamma)$ in the standard model *Nucl. Phys.* B **357** 439–466 (doi:10.1016/0550-3213(91)90476-E)
[408] Georgi H, Glashow S, Machacek M and Nanopoulos D 1978 Higgs bosons from two gluon annihilation in proton proton collisions *Phys. Rev. Lett.* **40** 692 (doi:10.1103/PhysRevLett.40.692)
[409] Graudenz D, Spira M and Zerwas P M 1993 QCD corrections to Higgs boson production at proton proton colliders *Phys. Rev. Lett.* **70** 1372–1375 (doi:10.1103/PhysRevLett.70.1372)
[410] Spira M, Djouadi A, Graudenz D and Zerwas P 1993 SUSY Higgs production at proton colliders *Phys. Lett.* B **318** 347–353 (doi:10.1016/0370-2693(93)90138-8)
[411] Spira M, Djouadi A, Graudenz D and Zerwas P 1995 Higgs boson production at the LHC *Nucl. Phys.* B **453** 17–82 (*Preprint* hep-ph/9504378) (doi:10.1016/0550-3213(95)00379-7)
[412] Kramer M, Laenen E and Spira M 1998 Soft gluon radiation in Higgs boson production at the LHC *Nucl. Phys.* B **511** 523–549 (*Preprint* hep-ph/9611272) (doi:10.1016/S0550-3213(97)00679-2)
[413] Djouadi A, Spira M and Zerwas P 1991 Production of Higgs bosons in proton colliders: QCD corrections *Phys. Lett.* B **264** 440–446
[414] Dawson S 1991 Radiative corrections to Higgs boson production *Nucl. Phys.* B **359** 283–300
[415] Kauffman R P and Schaffer W 1994 QCD corrections to production of Higgs pseudoscalars *Phys. Rev.* D **49** 551–554 (*Preprint* hep-ph/9305279)
[416] Dawson S and Kauffman R 1994 QCD corrections to Higgs boson production: nonleading terms in the heavy quark limit *Phys. Rev.* D **49** 2298–2309 (*Preprint* hep-ph/9310281)

[417] Harlander R V and Kilgore W B 2002 Next-to-next-to-leading order Higgs production at hadron colliders *Phys. Rev. Lett.* **88** 201801 (*Preprint* hep-ph/0201206)

[418] Harlander R V and Kilgore W B 2002 Production of a pseudo-scalar Higgs boson at hadron colliders at next-to-next-to leading order *J. High. Energy Phys.* JHEP10(2002)017 (*Preprint* hep-ph/0208096)

[419] Anastasiou C and Melnikov K 2002 Higgs boson production at hadron colliders in NNLO QCD *Nucl. Phys.* B **646** 220–256 (*Preprint* hep-ph/0207004)

[420] Ravindran V, Smith J and van Neerven W L 2003 NNLO corrections to the total cross section for Higgs boson production in hadron hadron collisions *Nucl. Phys.* B **665** 325–366 (*Preprint* hep-ph/0302135)

[421] Catani S, de Florian D, Grazzini M and Nason P 2003 Soft-gluon resummation for Higgs boson production at hadron colliders *J. High. Energy Phys.* JHEP07(2003)028 (*Preprint* hep-ph/0306211)

[422] Djouadi A and Gambino P 1994 Leading electroweak correction to Higgs boson production at proton colliders *Phys. Rev. Lett.* **73** 2528–2531 (*Preprint* hep-ph/9406432)

[423] Chetyrkin K G, Kniehl B A and Steinhauser M 1997 Virtual top-quark effects on the H → b anti-b decay at next-to-leading order in QCD *Phys. Rev. Lett.* **78** 594–597 (*Preprint* hep-ph/9610456)

[424] Chetyrkin K G, Kniehl B A and Steinhauser M 1997 Three-loop O(alpha(s)**2 G(F) M(t)**2) corrections to hadronic Higgs decays *Nucl. Phys.* B **490** 19–39 (*Preprint* hep-ph/9701277)

[425] Ghinculov A and van der Bij J J 1996 The Higgs resonance shape in gluon fusion: Heavy Higgs effects *Nucl. Phys.* B **482** 59–72 (*Preprint* hep-ph/9511414)

[426] Ellis R K, Hinchliffe I, Soldate M and van der Bij J J 1988 Higgs Decay to tau + tau-: A Possible Signature of Intermediate Mass Higgs Bosons at the SSC *Nucl. Phys.* B **297** 221

[427] Baur U and Glover E W N 1990 Higgs Boson Production at Large Transverse Momentum in Hadronic Collisions *Nucl. Phys.* B **339** 38–66

[428] Schmidt C R 1997 $H \to ggg(gq\bar{q})$ at two loops in the large-M_t limit *Phys. Lett.* B **413** 391–395 (doi:10.1016/S0370-2693(97)01102-7)

[429] de Florian D, Grazzini M and Kunszt Z 1999 Higgs production with large transverse momentum in hadronic collisions at next-to-leading order *Phys. Rev. Lett.* **82** 5209–5212 (*Preprint* hep-ph/9902483)

[430] Ravindran V, Smith J and Van Neerven W L 2002 Next-to-leading order QCD corrections to differential distributions of Higgs boson production in hadron hadron collisions *Nucl. Phys.* B **634** 247–290 (*Preprint* hep-ph/0201114)

[431] Glosser C J and Schmidt C R 2002 Next-to-leading corrections to the Higgs boson transverse momentum spectrum in gluon fusion *J. High. Energy Phys.* JHEP12(2002)016 (*Preprint* hep-ph/0209248)

[432] Anastasiou C, Melnikov K and Petriello F 2005 Fully differential Higgs boson production and the di-photon signal through next-to-next-to-leading order *Nucl. Phys.* B **724** 197–246 (*Preprint* hep-ph/0501130)

[433] Catani S, D'Emilio E and Trentadue L 1988 The Gluon Form-Factor to Higher Orders: Gluon Gluon Annihilation at Small Q-Transverse *Phys. Lett.* B **211** 335–342

[434] Hinchliffe I and Novaes S F 1988 On the Mean Transverse Momentum of Higgs Bosons at the SSC *Phys. Rev.* D **38** 3475–3480

[435] Kauffman R P 1991 Higgs boson p(T) in gluon fusion *Phys. Rev.* D **44** 1415–1425

[436] Kauffman R 1992 Higher order corrections to Higgs boson p(T) *Phys. Rev.* D **45** 1512–1517

[437] Balazs C and Yuan C P 2000 Higgs boson production at the LHC with soft gluon effects *Phys. Lett.* B **478** 192–198 (*Preprint* hep-ph/0001103)

[438] Berger E L and Qiu J-w 2003 Differential cross section for Higgs boson production including all-orders soft gluon resummation *Phys. Rev.* D **67** 034026 (*Preprint* hep-ph/0210135)

[439] Kulesza A and Stirling W J 2003 Non-perturbative effects and the resummed Higgs transverse momentum distribution at the LHC *J. High. Energy Phys.* JHEP12(2003)056 (*Preprint* hep-ph/0307208)

[440] Kulesza A, Sterman G and Vogelsang W 2004 Joint resummation for Higgs production *Phys. Rev.* D **69** 014012 (*Preprint* hep-ph/0309264)

[441] Gawron A and Kwiecinski J 2004 Resummation effects in Higgs boson transverse momentum distribution within the framework of unintegrated parton distributions *Phys. Rev.* D **70** 014003 (*Preprint* hep-ph/0309303)

[442] Watt G, Martin A and Ryskin M 2004 Unintegrated parton distributions and electroweak boson production at hadron colliders *Phys. Rev.* D **70** 014012 (*Preprint* hep-ph/0309096)

[443] Lipatov A and Zotov N 2005 Higgs boson production at hadron colliders in the k(T)-factorization approach *Eur. Phys. J.* C **44** 559–566 (*Preprint* hep-ph/0501172)

[444] de Florian D and Grazzini M 2000 Next-to-next-to-leading logarithmic corrections at small transverse momentum in hadronic collisions *Phys. Rev. Lett.* **85** 4678–4681 (*Preprint* hep-ph/0008152)

[445] Catani S, De Florian D and Grazzini M 2001 Higgs production at hadron colliders in (almost) NNLO QCD *Bologna 2001, Deep Inelastic Scattering (Bologna, Italy, April, 2001)* pp 518–521 *Preprint* hep-ph/0106049
[446] Catani S, de Florian D and Grazzini M 2001 Universality of non-leading logarithmic contributions in transverse momentum distributions *Nucl. Phys.* B **596** 299–312 (*Preprint* hep-ph/0008184)
[447] Bozzi G, Catani S, de Florian D and Grazzini M 2003 The q(T) spectrum of the Higgs boson at the LHC in QCD perturbation theory *Phys. Lett.* B **564** 65–72 (*Preprint* hep-ph/0302104)
[448] Bozzi G, Catani S, de Florian D and Grazzini M 2006 Transverse-momentum resummation and the spectrum of the Higgs boson at the LHC *Nucl. Phys.* B **737** 73–120 (*Preprint* hep-ph/0508068)
[449] Cahn R N and Dawson S 1984 Production of Very Massive Higgs Bosons *Phys. Lett.* B **136** 196
[450] Hikasa K-i 1985 Heavy Higgs Production in e+ e- and e- e- Collisions *Phys. Lett.* B **164** 385
[451] Altarelli G, Mele B and Pitolli F 1987 Heavy Higgs production at future colliders *Nucl. Phys.* B **287** 205–224
[452] Han T, Valencia G and Willenbrock S 1992 Structure function approach to vector boson scattering in p p collisions *Phys. Rev. Lett.* **69** 3274–3277 (*Preprint* hep-ph/9206246)
[453] Figy T, Oleari C and Zeppenfeld D 2003 Next-to-leading order jet distributions for Higgs boson production via weak-boson fusion *Phys. Rev.* D **68** 073005 (*Preprint* hep-ph/0306109)
[454] Glashow S, Nanopoulos D and Yildiz A 1978 Associated production of Higgs bosons and Z particles *Phys. Rev.* D **18** 1724–1727
[455] Kunszt Z, Trocsanyi Z and Stirling W J 1991 Clear signal of intermediate mass Higgs boson production at LHC and SSC *Phys. Lett.* B **271** 247–255
[456] Han T and Willenbrock S 1991 QCD correction to the p p → W H and Z H total cross- sections *Phys. Lett.* B **273** 167–172
[457] Brein O, Djouadi A and Harlander R 2004 NNLO QCD corrections to the Higgs-strahlung processes at hadron colliders *Phys. Lett.* B **579** 149–156 (*Preprint* hep-ph/0307206)
[458] Ciccolini M L, Dittmaier S and Kramer M 2003 Electroweak radiative corrections to associated W H and Z H production at hadron colliders *Phys. Rev.* D **68** 073003 (*Preprint* hep-ph/0306234)
[459] Raitio R and Wada W W 1979 Higgs Boson production at large transverse momentum in QCD *Phys. Rev.* D **19** 941
[460] Ng J N and Zakarauskas P 1984 A QCD Parton calculation of conjoined production of Higgs Bosons and heavy flavors in p anti-p collision *Phys. Rev.* D **29** 876
[461] Kunszt Z 1984 Associated production of heavy Higgs boson with top quarks *Nucl. Phys.* B **247** 339
[462] Gunion J F 1991 Associated top anti-top Higgs production as a large source of W H events: Implications for Higgs detection in the lepton neutrino gamma gamma final state *Phys. Lett.* B **261** 510–517
[463] Marciano W J and Paige F E 1991 Associated production of Higgs bosons with t anti-t pairs *Phys. Rev. Lett.* **66** 2433–2435
[464] Beenakker W, Dittmaier S, Kraemer M, Pluemper B, Spira M and Zerwas P 2001 Higgs radiation off top quarks at the Tevatron and the LHC *Phys. Rev. Lett.* **87** 201805 (*Preprint* hep-ph/0107081)
[465] Dawson S, Orr L H, Reina L and Wackeroth D 2003 Associated top quark Higgs boson production at the LHC *Phys. Rev.* D **67** 071503 (*Preprint* hep-ph/0211438)
[466] Dawson S and Reina L 1998 QCD corrections to associated Higgs boson production *Phys. Rev.* D **57** 5851–5859 (*Preprint* hep-ph/9712400)
[467] Futyan D, Fortin D and Giordano D 2006 Search for the Standard Model Higgs Boson in the Two-Electron and Two-Muon Final State with CMS *CMS Note* 2006/136
[468] Bartalini P *et al* 2006 NLO vs. LO: kinematical differences for signal and background in the $H \to ZZ^{(*)} \to 4\mu$ analysis *CMS Note* 2006/130
[469] Baffioni S *et al* 2006 Discovery potential for the SM Higgs boson in the $H \to ZZ^{(*)} \to e^+e^-e^+e^-$ decay channel *CMS Note* 2006/115
[470] Dittmar M and Dreiner H K 1997 How to find a Higgs boson with a mass between 155-GeV to 180-GeV at the LHC *Phys. Rev.* D **55** 167–172 (*Preprint* hep-ph/9608317)
[471] Davatz G, Dittmar M and Giolo-Nicollerat A-S 2006 Standard Model Higgs Discovery Potential of CMS in H→WW→ $\ell\nu\ell\nu$ Channel *CMS Note* 2006/047
[472] Davatz G, Dissertori G, Dittmar M, Grazzini M and Pauss F 2004 Effective K-factors for $gg \to H \to WW \to \ell\nu\ell\nu$ at the LHC *J. High. Energy Phys.* JHEP05(2004)009 (*Preprint* hep-ph/0402218)
[473] Campbell J and Tramontano F 2005 Next-to-leading order corrections to W t production and decay *Nucl. Phys.* B **726** 109–130 (*Preprint* hep-ph/0506289)
[474] CMS Collaboration, Beaudette F *et al* 2006 Search for a Light Standard Model Higgs Boson in the $H \to WW^{(*)} \to e^+\nu e^-\bar{\nu}$ Channel *CMS Note* 2006/114

[475] Plehn T, Rainwater D L and Zeppenfeld D 2000 A method for identifying $H \to \tau\tau \to e^{\pm}\mu^{\mp}_{P_T}$ at the CERN LHC *Phys. Rev.* D **61** 093005 (doi:10.1103/PhysRevD.61.093005)

[476] Rainwater D L, Zeppenfeld D and Hagiwara K 1999 Searching for $H \to \tau\tau$ in weak boson fusion at the LHC *Phys. Rev.* D **59** 014037 (doi:10.1103/PhysRevD.59.014037)

[477] Cavalli D *et al* 2002 The Higgs working group: Summary report *Preprint* hep-ph/0203056

[478] Zeppenfeld D, Kinnunen R, Nikitenko A and Richter-Was E 2000 Measuring Higgs boson couplings at the LHC *Phys. Rev.* D **62** 013009 (*Preprint* hep-ph/0002036)

[479] Duhrssen M *et al* 2004 Extracting Higgs boson couplings from LHC data *Phys. Rev.* D **70** 113009 (*Preprint* hep-ph/0406323)

[480] Plehn T, Rainwater D L and Zeppenfeld D 1999 Probing the MSSM Higgs sector via weak boson fusion at the LHC *Phys. Lett.* B **454** 297–303 (*Preprint* hep-ph/9902434)

[481] Foudas C, Nikitenko A and Takahashi M 2006 Observation of the Standard Model Higgs boson via H$\to \tau\tau \to$ lepton+jet Channel *CMS Note* 2006/088

[482] Pi H, Avery P, Rohlf J, Tully C and Kunori S 2006 Search for Standard Model Higgs Boson via Vector Boson Fusion in the H$\to$W$^+$W$^-$ to $\ell^{\pm}\nu$jj with $120 < m_H < 250$ GeV/c^2 *CMS Note* 2006/092

[483] Dubinin M, Litvin V, Ma Y, Newman H and Pieri M 2006 Vector Boson Fusion Production with H$\to \gamma\gamma$ *CMS Note* 2006/097

[484] Delaere C 2006 Study of associated WH production with H$\to$WW* in the 3 leptons final state *CMS Note* 2006/053

[485] CDF Collaboration, Acosta D *et al* 2005 Measurement of the ttbar Production Cross Section in ppbar Collisions at sqrt(s) = 1.96 TeV using Lepton + Jets Events with Secondary Vertex b-tagging *Phys. Rev.* D **71** 052003

[486] Djouadi A and Ferrag S 2003 PDF Uncertainties In Higgs Production At Hadron Colliders *Preprint* hep-ph/0310209

[487] Higgs Working Group Collaboration, Assamagan K *et al* 2004 The Higgs working group: Summary report 2003 *Preprint* hep-ph/0406152

[488] Belanger G, Boudjema F and Sridhar K 2000 SUSY Higgs at the LHC: Large stop mixing effects and associated production *Nucl. Phys.* B **568** 3–39 (*Preprint* hep-ph/9904348)

[489] Dubinin M, Ilyin V and Savrin V 1997 Light Higgs Boson Signal at LHC in the reaction pp $\to \gamma\gamma$+jet and pp $\to \gamma\gamma$+lepton *CMS Note* 1997/101

[490] Kinnunen R and Denegri D 1997 Expected SM/SUSY Higgs Observability in CMS *CMS Note* 1997/057

[491] ATLAS Collaboration, 1999 ATLAS Detector and Physics Performance. Technical Design Report. Vol. 2 *CERN/LHCC, CERN-LHCC* -99-15

[492] Beauchemin P, Azuelos G and Burgess C 2004 Dimensionless coupling of bulk scalars at the LHC *J. Phys.* **G30** N17 (doi:10.1088/0954-3899/30/10/N01)

[493] Stelzer T and Long W F 1994 Automatic generation of tree level helicity amplitudes *Comput. Phys. Commun.* **81** 357–371 (doi:10.1016/0010-4655(94)90084-1)

[494] Murayama H, Watanabe I and Hagiwara K HELAS: HELicity amplitude subroutines for Feynman diagram evaluations KEK-91-11

[495] Mangano M, Moretti M and Pittau R 2002 Multijet matrix elements and shower evolution in hadronic collisions: $Wb\bar{b}+n$-jets as a case study *Nucl. Phys.* B **632** 343–362 (*Preprint* hep-ph/0108069) (doi:10.1016/S0550-3213(02)00249-3)

[496] Caravaglios F, Mangano M, Moretti M and Pittau R 1999 A new approach to multi-jet calculations in hadron collisions *Nucl. Phys.* B **539** 215–232 (*Preprint* hep-ph/9807570)

[497] Buttar C *et al* Les Houches physics at TeV colliders 2005, standard model, QCD, EW, and Higgs working group: Summary report 2006 *Preprint* hep-ph/0604120

[498] Bityukov S, Erofeeva S, Krasnikov N and Nikitenko A 2005 Program for evaluation of significance, confidence intervals and limits by direct calculation of probabilities *Proceedings of PhyStat 2005*

[499] Lethuillier M *et al* 2006 Search for a neutral Higgs boson with WH / ZH, H$\to \gamma\gamma$ channel *CMS Note* 2006/110

[500] Ravat O 2004 Etude du Calorimètre électromagnétique de l'expérience CMS et recherche de bosons de Higgs neutres dans le canal de production associée PhD Thesis, IPN, Lyon, 2004. LYCEN-T2004-29

[501] Graham D J 1995 An algorithm using tracks to locate the two photon vertex at high luminosity *CMS TN* 1995/115

[502] Djouadi A 1998 Squark effects on Higgs boson production and decay at the LHC *Phys. Lett.* B **435** 101–108 (*Preprint* hep-ph/9806315)

[503] Eynard G 1998 Study of associated Higgs boson production HW, Ht$\bar{t}$, HZ $\to \gamma\gamma + e^{\pm}/\mu^{\pm} +$ X with the ATLAS detector at LHC. (In French) PhD Thesis, Annecy, *CERN-THESIS* -2000-036

[504] Beauchemin P-H and Azuelos G 2004 Search for the Standard Model Higgs Boson in the $\gamma\gamma + E_{\mathrm{T}}^{miss}$ channel *ATL-PHYS-2004-028*
[505] Lethuillier M, Agram J-L, Baty C, Gascon-Shotkin S, Perries S and Ravat O 2006 Search for a Neutral Higgs Boson with WH/ZH, H$\rightarrow \gamma\gamma$ Channel *CMS Note* 2006/110
[506] CMS Collaboration 2000 The TriDAS Project Technical Design Report, Volume 1: The Trigger Systems *CERN/LHCC*, 2000-38, CMS TDR 6.1
[507] CMS Collaboration, Acosta D *et al* 2006 CMS Physics Technical Design Report, Volume 1, Section 10.3.2: Photon isolation *CERN/LHCC*, 2006-001 p 376
[508] Read A L 2002 Presentation of search results: The CL(s) technique *J. Phys.* G **28** 2693–2704
[509] Junk T 1999 Confidence level computation for combining searches with small statistics *Nucl. Instrum. Meth.* A **434** 435–443 (*Preprint* hep-ex/9902006)
[510] Djouadi A and Ferrag S 2004 PDF uncertainties in Higgs production at hadron colliders *Phys. Lett.* B **586** 345–352 (*Preprint* hep-ph/0310209)
[511] Dell'Aquila J R and Nelson C A 1986 Simple tests for CP or P violation by sequential decays: V_1V_2 modes with decays into $\bar{\ell}_A\ell_B$ and/or $\bar{q}_Aq_B$ *Phys. Rev.* D **33** 101 (doi:10.1103/PhysRevD.33.101)
[512] Skjold A and Osland P 1994 Signals of CP violation in Higgs decay *Phys. Lett.* B **329** 305–311 (*Preprint* hep-ph/9402358)
[513] Choi S Y, Miller D J, Muhlleitner M M and Zerwas P M 2003 Identifying the Higgs spin and parity in decays to Z pairs *Phys. Lett.* B **553** 61–71 (*Preprint* hep-ph/0210077)
[514] Buszello C P, Fleck I, Marquard P and van der Bij J J 2004 Prospective analysis of spin- and CP-sensitive variables in H $\rightarrow$ ZZ $\rightarrow$ l(1)+ l(1)- l(2)+ l(2)- at the LHC *Eur. Phys. J.* C **32** 209–219 (*Preprint* hep-ph/0212396)
[515] Bluj M 2006 A Study of Angular Correlations in H$\rightarrow$ZZ$\rightarrow$2e2μ *CMS Note* 2006/094
[516] Wess J and Zumino B 1974 Supergauge transformations in four-dimensions *Nucl. Phys.* B **70** 39–50
[517] Fayet P and Ferrara S 1977 Supersymmetry *Phys. Rept.* **32** 249–334
[518] Nilles H P 1984 Supersymmetry, supergravity and particle physics *Phys. Rept.* **110** 1
[519] Barbieri R 1988 Looking beyond the standard model: the supersymmetric option *Riv. Nuovo Cim.* **11N4** 1–45
[520] Haber H E and Kane G L 1985 The search for supersymmetry: probing physics beyond the standard model *Phys. Rept.* **117** 75
[521] Witten E 1981 Mass hierarchies in supersymmetric theories *Phys. Lett.* B **105** 267
[522] Dimopoulos S, Raby S and Wilczek F 1981 Supersymmetry and the scale of unification *Phys. Rev.* D **24** 1681–1683
[523] Ibanez L E and Ross G G 1981 Low-energy predictions in supersymmetric grand unified theories *Phys. Lett.* B **105** 439
[524] Ibanez L E and Ross G G 1982 $SU(2)_L \times U(1)$ Symmetry breaking as a radiative effect of supersymmetry breaking in GUTs *Phys. Lett.* B **110** 215–220 (doi:10.1016/0370-2693(82)91239-4)
[525] Inoue K, Kakuto A, Komatsu H and Takeshita S 1982 Aspects of grand unified models with softly broken supersymmetry *Prog. Theor. Phys.* **68** 927
[526] Alvarez-Gaume L, Claudson M and Wise M B 1982 Low-energy supersymmetry *Nucl. Phys.* B **207** 96
[527] Ellis J R, Nanopoulos D V and Tamvakis K 1983 Grand unification in simple supergravity *Phys. Lett.* B **121** 123
[528] Dimopoulos S and Georgi H 1981 Softly broken supersymmetry and SU(5) *Nucl. Phys.* B **193** 150
[529] Sakai N 1981 Naturalness in supersymmetric 'GUTS' *Zeit. Phys.* C **11** 153
[530] Okada Y, Yamaguchi M and Yanagida T 1991 Upper bound of the lightest Higgs boson mass in the minimal supersymmetric standard model *Prog. Theor. Phys.* **85** 1–6
[531] Haber H E and Hempfling R 1991 Can the mass of the lightest Higgs boson of the minimal supersymmetric model be larger than m(Z)? *Phys. Rev. Lett.* **66** 1815–1818
[532] Ellis J R, Ridolfi G and Zwirner F 1991 Radiative corrections to the masses of supersymmetric Higgs bosons *Phys. Lett.* B **257** 83–91
[533] Barbieri R, Frigeni M and Caravaglios F 1991 The supersymmetric Higgs for heavy superpartners *Phys. Lett.* B **258** 167–170
[534] Yamada A 1991 Radiative corrections to the Higgs masses in the minimal supersymmetric standard model *Phys. Lett.* B **263** 233–238
[535] Brignole A, Ellis J R, Ridolfi G and Zwirner F 1991 The supersymmetric charged Higgs boson mass and LEP phenomenology *Phys. Lett.* B **271** 123–132
[536] Chankowski P H, Pokorski S and Rosiek J 1992 Charged and neutral supersymmetric Higgs boson masses: Complete one loop analysis *Phys. Lett.* B **274** 191–198

[537] Espinosa J R and Quiros M 1991 Two loop radiative corrections to the mass of the lightest Higgs boson in supersymmetric standard models *Phys. Lett.* B **266** 389–396
[538] Hempfling R and Hoang A H 1994 Two loop radiative corrections to the upper limit of the lightest Higgs boson mass in the minimal supersymmetric model *Phys. Lett.* B **331** 99–106 (*Preprint* hep-ph/9401219)
[539] Casas J A, Espinosa J R, Quiros M and Riotto A 1995 The lightest Higgs boson mass in the minimal supersymmetric standard model *Nucl. Phys.* B **436** 3–29 (*Preprint* hep-ph/9407389)
[540] Carena M, Espinosa J R, Quiros M and Wagner C 1995 Analytical expressions for radiatively corrected Higgs masses and couplings in the MSSM *Phys. Lett.* B **355** 209–221 (*Preprint* hep-ph/9504316)
[541] Carena M, Quiros M and Wagner C E M 1996 Effective potential methods and the Higgs mass spectrum in the MSSM *Nucl. Phys.* B **461** 407–36 (*Preprint* hep-ph/9508343)
[542] Heinemeyer S, Hollik W and Weiglein G 1998 QCD corrections to the masses of the neutral CP-even Higgs bosons in the MSSM *Phys. Rev.* D **58** 091701 (*Preprint* hep-ph/9803277)
[543] Heinemeyer S, Hollik W and Weiglein G 1998 Precise prediction for the mass of the lightest Higgs boson in the MSSM *Phys. Lett.* B **440** 296–304 (*Preprint* hep-ph/9807423)
[544] Heinemeyer S, Hollik W and Weiglein G 2000 Constraints on tan(beta) in the MSSM from the upper bound on the mass of the lightest Higgs boson *J. High. Energy Phys.* JHEP06(2000)009 (*Preprint* hep-ph/9909540)
[545] Espinosa J R and Zhang R-J 2000 Complete two-loop dominant corrections to the mass of the lightest CP-even Higgs boson in the minimal supersymmetric standard model *Nucl. Phys.* B **586** 3–38 (*Preprint* hep-ph/0003246)
[546] Brignole A, Degrassi G, Slavich P and Zwirner F 2002 On the $\mathcal{O}(\alpha_t^2)$ two-loop corrections to the neutral Higgs boson masses in the MSSM *Nucl. Phys.* B **631** 195–218 (doi:10.1016/S0550-3213(02)00184-0)
[547] Brignole A, Degrassi G, Slavich P and Zwirner F 2002 On the two-loop sbottom corrections to the neutral Higgs boson masses in the MSSM *Nucl. Phys.* B **643** 79–92 (*Preprint* hep-ph/0206101)
[548] Heinemeyer S, Hollik W, Rzehak H and Weiglein G 2005 High-precision predictions for the MSSM Higgs sector at $\mathcal{O}(\alpha_b\alpha_s)$ *Eur. Phys. J.* C **39** 465–481 (doi:10.1140/epjc/s2005-02112-6)
[549] Coarasa J A, Jimenez R A and Sola J 1996 Strong effects on the hadronic widths of the neutral Higgs Bosons in the MSSM *Phys. Lett.* B **389** 312–320 (*Preprint* hep-ph/9511402)
[550] Chankowski P H, Pokorski S and Rosiek J 1994 Complete on-shell renormalization scheme for the minimal supersymmetric Higgs sector *Nucl. Phys.* B **423** 437–496 (*Preprint* hep-ph/9303309)
[551] Dabelstein A 1995 The One loop renormalization of the MSSM Higgs sector and its application to the neutral scalar Higgs masses *Z. Phys.* C **67** 495–512 (*Preprint* hep-ph/9409375)
[552] Brignole A 1992 Radiative corrections to the supersymmetric neutral Higgs boson masses *Phys. Lett.* B **281** 284–294
[553] Haber H E, Hempfling R and Hoang A H 1997 Approximating the radiatively corrected Higgs mass in the minimal supersymmetric model *Z. Phys.* C **75** 539–554 (*Preprint* hep-ph/9609331)
[554] Zhang R-J 1999 Two-loop effective potential calculation of the lightest CP-even Higgs-boson mass in the MSSM *Phys. Lett.* B **447** 89–97 (*Preprint* hep-ph/9808299)
[555] Espinosa J R and Zhang R-J 2000 MSSM lightest CP-even Higgs boson mass to O(alpha(s) alpha(t)): The effective potential approach *J. High. Energy Phys.* JHEP03(2000)026 (*Preprint* hep-ph/9912236)
[556] Degrassi G, Slavich P and Zwirner F 2001 On the neutral Higgs boson masses in the MSSM for arbitrary stop mixing *Nucl. Phys.* B **611** 403–422 (*Preprint* hep-ph/0105096)
[557] Hempfling R 1994 Yukawa coupling unification with supersymmetric threshold corrections *Phys. Rev.* D **49** 6168–6172
[558] Hall L J, Rattazzi R and Sarid U 1994 The Top quark mass in supersymmetric SO(10) unification *Phys. Rev.* D **50** 7048–7065 (*Preprint* hep-ph/9306309)
[559] Carena M, Olechowski M, Pokorski S and Wagner C 1994 Electroweak symmetry breaking and bottom-top Yukawa unification *Nucl. Phys.* B **426** 269–300 (*Preprint* hep-ph/9402253)
[560] Guasch J, Hafliger P and Spira M 2003 MSSM Higgs decays to bottom quark pairs revisited *Phys. Rev.* D **68** 115001 (*Preprint* hep-ph/0305101)
[561] Dedes A, Degrassi G and Slavich P 2003 On the two-loop Yukawa corrections to the MSSM Higgs boson masses at large tan(beta) *Nucl. Phys.* B **672** 144–162 (*Preprint* hep-ph/0305127)
[562] Eberl H, Hidaka K, Kraml S, Majerotto W and Yamada Y 2000 Improved SUSY QCD corrections to Higgs boson decays into quarks and squarks *Phys. Rev.* D **62** 055006 (*Preprint* hep-ph/9912463)
[563] Carena M, Garcia D, Nierste U and Wagner C 2000 Effective Lagrangian for the $\bar{t}bH^+$ interaction in the MSSM and charged Higgs phenomenology *Nucl. Phys.* B **577** 88–120 (doi:0.1016/S0550-3213(00)00146-2)

[564] Heinemeyer S, Hollik W and Weiglein G 2006 Electroweak precision observables in the minimal supersymmetric standard model *Phys. Rept.* **425** 265–368 (*Preprint* hep-ph/0412214)
[565] Carena M and Haber H E 2003 Higgs boson theory and phenomenology. ((V)) *Prog. Part. Nucl. Phys.* **50** 63–152 (*Preprint* hep-ph/0208209)
[566] ALEPH, DELPHI, L3, OPAL Collaboration 2006 LEP Working Group for Higgs Boson Searches, Search for neutral MSSM Higgs bosons at LEP *Preprint* hep-ex/0602042
[567] LEP Higgs Working Group for Higgs boson searches Collaboration 2001 Search for charged Higgs bosons: Preliminary combined results using LEP data collected at energies up to 209 GeV *Preprint* hep-ex/0107031
[568] Dabelstein A 1995 Fermionic decays of neutral MSSM Higgs bosons at the one loop level *Nucl. Phys.* B **456** 25–56 (*Preprint* hep-ph/9503443)
[569] Heinemeyer S, Hollik W and Weiglein G 2000 Decay widths of the neutral CP-even MSSM Higgs bosons in the Feynman-diagrammatic approach *Eur. Phys. J.* C **16** 139–153 (*Preprint* hep-ph/0003022)
[570] Djouadi A, Janot P, Kalinowski J and Zerwas P M 1996 SUSY Decays of Higgs Particles *Phys. Lett.* B **376** 220–226 (*Preprint* hep-ph/9603368)
[571] Djouadi A, Kalinowski J, Ohmann P and Zerwas P M 1997 Heavy SUSY Higgs bosons at e+ e- linear colliders *Z. Phys.* C **74** 93–111 (*Preprint* hep-ph/9605339)
[572] Dawson S, Djouadi A and Spira M 1996 QCD Corrections to SUSY Higgs Production: The Role of Squark Loops *Phys. Rev. Lett.* **77** 16–19 (*Preprint* hep-ph/9603423)
[573] Harlander R V and Steinhauser M 2003 Hadronic Higgs production and decay in supersymmetry at next-to-leading order *Phys. Lett.* B **574** 258–268 (*Preprint* hep-ph/0307346)
[574] Harlander R and Steinhauser M 2003 Effects of SUSY-QCD in hadronic Higgs production at next-to-next-to-leading order *Phys. Rev.* D **68** 111701 (*Preprint* hep-ph/0308210)
[575] Harlander R V and Steinhauser M 2004 Supersymmetric Higgs production in gluon fusion at next-to-leading order *J. High. Energy Phys.* JHEP09(2004)066 (*Preprint* hep-ph/0409010)
[576] Harlander R V and Hofmann F 2005 Pseudo-scalar Higgs production at next-to-leading order SUSY-QCD *Preprint* hep-ph/0507041
[577] Langenegger U, Spira M, Starodumov A and Trueb P 2006 SM and MSSM Higgs boson production: spectra at large transverse momentum *Preprint* hep-ph/0604156
[578] Djouadi A and Spira M 2000 SUSY-QCD corrections to Higgs boson production at hadron colliders *Phys. Rev.* D **62** 014004 (*Preprint* hep-ph/9912476)
[579] Wu P *et al* 2005 NLO supersymmetric QCD corrections to t anti-t h0 associated production at hadron colliders *Preprint* hep-ph/0505086
[580] Dittmaier S, Kramer M and Spira M 2004 Higgs radiation off bottom quarks at the Tevatron and the LHC *Phys. Rev.* D **70** 074010 (*Preprint* hep-ph/0309204)
[581] Dawson S, Jackson C B, Reina L and Wackeroth D 2004 Exclusive Higgs boson production with bottom quarks at hadron colliders *Phys. Rev.* D **69** 074027 (*Preprint* hep-ph/0311067)
[582] Dicus D A and Willenbrock S 1989 Higgs boson production from heavy quark fusion *Phys. Rev.* D **39** 751
[583] Dicus D, Stelzer T, Sullivan Z and Willenbrock S 1999 Higgs boson production in association with bottom quarks at next-to-leading order *Phys. Rev.* D **59** 094016 (*Preprint* hep-ph/9811492)
[584] Balazs C, He H-J and Yuan C P 1999 QCD corrections to scalar production via heavy quark fusion at hadron colliders *Phys. Rev.* D **60** 114001 (*Preprint* hep-ph/9812263)
[585] Harlander R V and Kilgore W B 2003 Higgs boson production in bottom quark fusion at next-to-next-to-leading order *Phys. Rev.* D **68** 013001 (*Preprint* hep-ph/0304035)
[586] Aivazis M A G, Olness F I and Tung W-K 1994 Leptoproduction of heavy quarks. 1. General formalism and kinematics of charged current and neutral current production processes *Phys. Rev.* D **50** 3085–3101 (*Preprint* hep-ph/9312318)
[587] Aivazis M A G, Collins J C, Olness F I and Tung W-K 1994 Leptoproduction of heavy quarks. 2. A unified QCD formulation of charged and neutral current processes from fixed target to collider energies *Phys. Rev.* D **50** 3102–3118 (*Preprint* hep-ph/9312319)
[588] Campbell J *et al* 2004 Higgs boson production in association with bottom quarks *Preprint* hep-ph/0405302 Contributed to 3rd Les Houches Workshop: Physics at TeV Colliders, Les Houches, France, 26 May–6 June 2003
[589] Campbell J, Ellis R K, Maltoni F and Willenbrock S 2003 Higgs boson production in association with a single bottom quark *Phys. Rev.* D **67** 095002 (*Preprint* hep-ph/0204093)
[590] Dawson S, Jackson C B, Reina L and Wackeroth D 2005 Higgs boson production with one bottom quark jet at hadron colliders *Phys. Rev. Lett.* **94** 031802 (doi:10.1103/PhysRevLett.94.031802)
[591] Bawa A C, Kim C S and Martin A D 1990 Charged Higgs production at hadron colliders *Z. Phys.* C **47** 75–82

[592] Borzumati F, Kneur J-L and Polonsky N 1999 Higgs-strahlung and R-parity violating slepton-strahlung at hadron colliders *Phys. Rev.* D **60** 115011 (*Preprint* hep-ph/9905443)

[593] Belyaev A, Garcia D, Guasch J and Sola J 2002 Prospects for heavy supersymmetric charged Higgs boson searches at hadron colliders *J. High. Energy Phys.* JHEP06(2002)059 (*Preprint* hep-ph/0203031)

[594] Wu P *et al* 2006 NLO supersymmetric QCD corrections to the t anti-b H-associated production at hadron colliders *Phys. Rev.* D **73** 015012 (*Preprint* hep-ph/0601069) (doi:10.1103/PhysRevD.73.015012)

[595] Zhu S-H 2003 Complete next-to-leading order QCD corrections to charged Higgs boson associated production with top quark at the CERN large hadron collider *Phys. Rev.* D **67** 075006 (doi:10.1103/PhysRevD.67.075006)

[596] Plehn T Charged Higgs boson production in bottom-gluon fusion Prepared for 10th International Conference on Supersymmetry and Unification of Fundamental Interactions (SUSY02), Hamburg, Germany, 17–23 June 2002

[597] Berger E L, Han T, Jiang J and Plehn T 2005 Associated production of a top quark and a charged Higgs boson *Phys. Rev.* D **71** 115012 (*Preprint* hep-ph/0312286)

[598] Gao G, Lu G, Xiong Z and Yang J M 2002 Loop effects and non-decoupling property of SUSY QCD in $gb \to tH^-$ *Phys. Rev.* D **66** 015007 (doi:10.1103/PhysRevD.66.015007)

[599] Willenbrock S S D 1987 Pair production of supersymmetric charged Higgs bosons *Phys. Rev.* D **35** 173

[600] Krause A, Plehn T, Spira M and Zerwas P M 1998 Production of charged Higgs boson pairs in gluon–gluon collisions *Nucl. Phys.* B **519** 85–100 (*Preprint* hep-ph/9707430)

[601] Jiang Y, Han L, Ma W-G, Yu Z-H and Han M 1997 Pair production of charged Higgs bosons in gluon–gluon collisions *J. Phys.* **G23** 385–400 (*Preprint* hep-ph/9703275)

[602] Brein O and Hollik W 2000 Pair production of charged MSSM Higgs bosons by gluon fusion *Eur. Phys. J.* C **13** 175–184 (*Preprint* hep-ph/9908529)

[603] Barrientos Bendezu A A and Kniehl B A 2000 H^+H^- pair production at the large hadron collider *Nucl. Phys.* B **568** 305–318 (doi:10.1016/S0550-3213(99)00732-4)

[604] Hou H-S *et al* 2005 Pair production of charged Higgs bosons from bottom-quark fusion *Phys. Rev.* D **71** 075014 (doi:10.1103/PhysRevD.71.075014)

[605] Barrientos Bendezu A A and Kniehl B A 1999 $W^\pm H^\mp$ associated production at the large hadron collider *Phys. Rev.* D **59** 015009 (*Preprint* hep-ph/9807480) (doi:10.1103/PhysRevD.59.015009)

[606] Brein O, Hollik W and Kanemura S 2001 The MSSM prediction for $W^\pm H^\mp$ production by gluon fusion *Phys. Rev.* D **63** 095001 (*Preprint* hep-ph/0008308)

[607] Barrientos Bendezu A A and Kniehl B A 2001 Squark loop correction to $W^\pm H^\mp$ associated hadroproduction *Phys. Rev.* D **63** 015009 (*Preprint* hep-ph/0007336)

[608] Dicus D, Hewett J, Kao C and Rizzo T G 1989 $W^\pm H^\mp$ production at hadron colliders *Phys. Rev.* D **40** 787

[609] Hollik W and Zhu S-h 2002 $\mathcal{O}(\alpha_s)$ corrections to $b\bar{b} \to W^\pm H^\mp$ at the CERN large hadron collider *Phys. Rev.* D **65** 075015 (*Preprint* hep-ph/0109103) (doi:10.1103/PhysRevD.65.075015)

[610] Zhao J, Li C S and Li Q 2005 SUSY-QCD corrections to $W^\pm H^\mp$ associated production at the CERN large hadron collider *Phys. Rev.* D **72** 114008 (*Preprint* hep-ph/0509369)

[611] Lehti S 2006 Study of H/A$\to \tau\tau \to$ eμ+X in CMS *CMS Note* 2006/101

[612] Lehti S 2002 Study of $gg \to b\bar{b}H_{SUSY}$, $H_{SUSY} \to \tau\tau \to \ell\ell + X$ *CMS Note* 2002/035

[613] Bloch D private communication

[614] Boos E, Djouadi A, Muhlleitner M and Vologdin A 2002 The MSSM Higgs bosons in the intense-coupling regime *Phys. Rev.* D **66** 055004 (*Preprint* hep-ph/0205160)

[615] Boos E, Djouadi A and Nikitenko A 2004 Detection of the neutral MSSM Higgs bosons in the intense-coupling regime at the LHC *Phys. Lett.* B **578** 384–393 (*Preprint* hep-ph/0307079)

[616] CMS Collaboration, Acosta D *et al* 2006 CMS Physics Technical Design Report, Volume 1, Section 12.2.3: Combined secondary vertex tag *CERN/LHCC*, 2006-001 p 466

[617] Fernandez J 2006 Search for MSSM heavy neutral Higgs bosons in the four-b final state *CMS Note* 2006/080

[618] CMS Collaboration, Acosta D *et al* 2006 CMS Physics Technical Design Report, Volume 1, Section 12.2.6: HLT b tag *CERN/LHCC*, 2006-001 p 474

[619] CMS Collaboration, Acosta D *et al* 2006 CMS Physics Technical Design Report, Volume 1, Section 11.6.4: Parton-level corrections *CERN/LHCC*, 2006-001 p 428

[620] DØ Collaboration, Abazov V M *et al* 2005 Search for neutral supersymmetric Higgs bosons in multijet events at $\sqrt{s}$ =1.96 TeV *Phys. Rev. Lett.* **95** 151801 (doi:10.1103/PhysRevLett.95.151801)

[621] Baarmand M, Hashemi M and Nikitenko A 2006 Light Charged Higgs Discovery Potential of CMS in the $H^+ \to \tau\nu$ with single lepton trigger *CMS Note* 2006/056

[622] Roy D 1999 The hadronic tau decay signature of a heavy charged Higgs boson at LHC *Phys. Lett.* B **459** 607–614 (*Preprint* hep-ph/9905542)

[623] Kinnunen R 2004 Study of $A/H \to \tau\tau$ and $H^{\pm} \to \tau\nu$ in CMS *Czech. J. Phys.* **54** A93–A101
[624] Assamagan K A and Coadou Y 2002 The hadronic tau decay of a heavy $H^{\pm}$ in ATLAS *Acta Phys. Polon.* B **33** 707–720
[625] Baarmand M, Hashemi M and Nikitenko A 2006 Search for the heavy charged MSSM Higgs bosons with the $H^{+} \to \tau\nu$ decay mode in fully hadronic final state *CMS Note* 2006/100
[626] Roy D P 2004 Looking for the charged Higgs boson *Mod. Phys. Lett.* A **19** 1813–1828 (*Preprint* hep-ph/0406102)
[627] Alwall J and Rathsman J 2004 Improved description of charged Higgs boson production at hadron colliders *J. High Energy Phys.* JHEP12(2004)050 (*Preprint* hep-ph/0409094)
[628] Plehn T 2003 Charged Higgs boson production in bottom gluon fusion *Phys. Rev.* D **67** 014018 (*Preprint* hep-ph/0206121)
[629] Lowette S, D'Hondt J and Vanlaer P 2006 Charged MSSM Higgs boson observability in the $H^{\pm} \to tb$ Decay *CMS Note* 2006/109
[630] CMS Collaboration, Anagnostou G and Daskalakis G 2006 Search for the MSSM A → Zh decay with Z → $\ell^{+}\ell^{-}$, h → bb *CMS Note* 2006/063
[631] CMS Collaboration, Charlot C, Salerno R and Sirois Y 2006 Observability of the heavy neutral SUSY Higgs Bosons decaying into neutralinos *CMS Note* 2006/125
[632] Allanach B C *et al* 2002 The snowmass points and slopes: benchmarks for SUSY searches *Eur. Phys. J.* C **25** 113–123 (*Preprint* hep-ph/0202233)
[633] Battaglia M *et al* 2004 Updated post-WMAP benchmarks for supersymmetry *Eur. Phys. J.* C **33** 273–296 (*Preprint* hep-ph/0306219)
[634] Carena M, Heinemeyer S, Wagner C and Weiglein G 1999 Suggestions for improved benchmark scenarios for Higgs-boson searches at LEP2 *Preprint* hep-ph/9912223
[635] Carena M, Heinemeyer S, Wagner C and Weiglein G 2003 Suggestions for benchmark scenarios for MSSM Higgs boson searches at hadron colliders *Eur. Phys. J.* C **26** 601–607 (*Preprint* hep-ph/0202167)
[636] ECFA/DESY LC Physics Working Group Collaboration, Aguilar-Saavedra J A *et al* 2001 TESLA Technical Design Report Part III: Physics at an e+e- Linear Collider *Preprint* hep-ph/0106315
[637] Bennett C L *et al* 2003 First year Wilkinson Microwave Anisotropy Probe (WMAP) observations: preliminary maps and basic results *Astrophys. J. Suppl.* **148** 1 (*Preprint* astro-ph/0302207)
[638] WMAP Collaboration, Spergel D N *et al* 2003 First year Wilkinson Microwave Anisotropy Probe (WMAP) observations: determination of cosmological parameters *Astrophys. J. Suppl.* **148** 175 (*Preprint* astro-ph/0302209)
[639] Goldberg H 1983 Constraint on the photino mass from cosmology *Phys. Rev. Lett.* **50** 1419
[640] Ellis J R, Hagelin J, Nanopoulos D, Olive K A and Srednicki M 1984 Supersymmetric relics from the big bang *Nucl. Phys.* B **238** 453–476
[641] Heavy Flavor Averaging Group Collaboration, Barberio E *et al* 2006 Averages of b-hadron properties at the end of 2005 *Preprint* hep-ex/0603003
[642] Asatrian H M, Hovhannisyan A, Poghosyan V, Greub C and Hurth T 2005 Towards the NNLL precision in anti-B→X/s gamma *Preprint* hep-ph/0512097
[643] Muon Collaboration, Bennett G W 2006 Final report of the muon E821 anomalous magnetic moment measurement at BNL *Preprint* hep-ex/0602035
[644] Czarnecki A and Marciano W J 2001 The muon anomalous magnetic moment: A harbinger for 'new physics' *Phys. Rev.* D **64** 013014 (*Preprint* hep-ph/0102122)
[645] Carena M *et al* 2000 Reconciling the two-loop diagrammatic and effective field theory computations of the mass of the lightest CP-even Higgs boson in the MSSM *Nucl. Phys.* B **580** 29–57 (*Preprint* hep-ph/0001002)
[646] Randall L and Sundrum R 1999 An alternative to compactification *Phys. Rev. Lett.* **83** 4690–4693 (doi:10.1103/PhysRevLett.83.4690)
[647] Giudice G F, Rattazzi R and Wells J D 2001 Graviscalars from higher-dimensional metrics and curvature- Higgs mixing *Nucl. Phys.* B **595** 250–276 (*Preprint* hep-ph/0002178)
[648] Chaichian M, Datta A, Huitu K and Yu Z-h 2002 Radion and Higgs mixing at the LHC *Phys. Lett.* B **524** 161–169 (*Preprint* hep-ph/0110035)
[649] Hewett J L and Rizzo T G 2003 Shifts in the properties of the Higgs boson from radion mixing *J. High. Energy Phys.* JHEP08(2003)028 (*Preprint* hep-ph/0202155)
[650] Dominici D, Grzadkowski B, Gunion J F and Toharia M 2003 The scalar sector of the Randall-Sundrum model *Nucl. Phys.* B **671** 243–292 (*Preprint* hep-ph/0206192)
[651] Battaglia M, De Curtis S, De Roeck A, Dominici D and Gunion J F 2003 On the complementarity of Higgs and radion searches at LHC *Phys. Lett.* B **568** 92–102 (*Preprint* hep-ph/0304245)

[652] Azuelos G, Cavalli D, Przysiezniak H and Vacavant L 2002 Search for the radion using the ATLAS detector *Eur. Phys. J. direct* C **4** 16
[653] Dominici D, Dewhirst G, Nikitenko A, Gennai S and Fanò L 2005 Search for radion decays into Higgs boson pairs in the $\gamma\gamma b\bar{b}$, $\tau\tau b\bar{b}$ and $b\bar{b}b\bar{b}$ final states *CMS Note* 2005/007
[654] Arkani-Hamed N, Cohen A G and Georgi H 2001 (De)constructing dimensions *Phys. Rev. Lett.* **86** 4757–4761 (*Preprint* hep-th/0104005)
[655] Cheng H-C, Hill C T, Pokorski S and Wang J 2001 The standard model in the latticized bulk *Phys. Rev.* D **64** 065007 (*Preprint* hep-th/0104179)
[656] Arkani-Hamed N, Cohen A G and Georgi H 2001 Electroweak symmetry breaking from dimensional deconstruction *Phys. Lett.* B **513** 232–240 (*Preprint* hep-ph/0105239)
[657] Arkani-Hamed N, Cohen A G, Katz E and Nelson A E 2002 The littlest Higgs *J. High Energy Phys.* JHEP07(2002)034 (*Preprint* hep-ph/0206021)
[658] Schechter J and Valle J 1980 Neutrino masses in $SU(2) \times U(1)$ Theories *Phys. Rev.* D **22** 2227 (doi:10.1103/PhysRevD.22.2227)
[659] Ma E and Sarkar U 1998 Neutrino masses and leptogenesis with heavy Higgs triplets *Phys. Rev. Lett.* **80** 5716–5719 (*Preprint* hep-ph/9802445)
[660] Ma E, Raidal M and Sarkar U 2000 Verifiable model of neutrino masses from large extra dimensions *Phys. Rev. Lett.* **85** 3769–3772 (*Preprint* hep-ph/0006046)
[661] Ma E, Raidal M and Sarkar U 2001 Phenomenology of the neutrino-mass-giving Higgs triplet and the low-energy seesaw violation of lepton number *Nucl. Phys.* B **615** 313–330 (*Preprint* hep-ph/0012101)
[662] Ma E and Sarkar U 2006 Connecting dark energy to neutrinos with an observable Higgs triplet *Preprint* hep-ph/0602116
[663] Marandella G, Schappacher C and Strumia A 2005 Little-Higgs corrections to precision data after LEP2 *Phys. Rev.* D **72** 035014 (*Preprint* hep-ph/0502096)
[664] Huitu K, Maalampi J, Pietila A and Raidal M 1997 Doubly charged Higgs at LHC *Nucl. Phys.* B **487** 27–42 (*Preprint* hep-ph/9606311)
[665] Han T, Logan H E and Wang L-T 2005 Smoking-gun signatures of little Higgs models *Preprint* hep-ph/0506313
[666] Azuelos G *et al* 2005 Exploring little Higgs models with ATLAS at the LHC *Eur. Phys. J.* C **39S2** 13–24 (*Preprint* hep-ph/0402037)
[667] Gunion J F, Grifols J, Mendez A, Kayser B and Olness F I 1989 Higgs bosons in left-right symmetric models *Phys. Rev.* D **40** 1546 (doi:10.1103/PhysRevD.40.1546)
[668] Muhlleitner M and Spira M 2003 A note on doubly-charged Higgs pair production at hadron colliders *Phys. Rev.* D **68** 117701 (*Preprint* hep-ph/0305288)
[669] Bityukov S, Krasnikov N and Taperechkina V 2001 Confidence intervals for Poisson distribution parameter *Preprint* hep-ex/0108020
[670] Martin S P 1997 A supersymmetry primer *Perspectives in Supersymmetry* ed G. Kane (World Scientific) *Preprint* hep-ph/9709356
[671] CMS Collaboration Abdullin S *et al* 2002 Discovery potential for supersymmetry in CMS *J. Phys.* G **28** 469 (doi:10.1088/0954-3899/28/3/401)
[672] Paige F E, Protopopescu S D, Baer H and Tata X 2003 ISAJET 7.69: A Monte Carlo Event Generator for pp, $\bar{p}p$, and e^+e^- Reactions (*Preprint* hep-ph/0312045)
[673] De Roeck A *et al* 2005 Supersymmetric benchmarks with non-universal scalar masses or gravitino dark matter *Preprint* hep-ph/0508198
[674] de Boer W *et al* 2004 Excess of EGRET galactic gamma ray data interpreted as dark matter annihilation *Preprint* astro-ph/0408272
[675] Acosta D *et al* 2006 Potential to Discover SUSY in Events with Muons Jets and Large Missing Transverse Energy in pp Collisions at $\sqrt{s} = 14$ TeV *CMS Note* 2006/134
[676] Acosta D *et al* 2006 CMS Discovery Potential for mSUGRA in Same Sign Di-muon Events with Jets and Large Missing Transverse Energy in pp collisions at $\sqrt{s} = 14$ TeV*CMS Note*
[677] Chiorboli M, Galanti M and Tricomi A 2006 Leptons + Jets + Missing Energy analysis at LM1 *CMS Note* 2006/133
[678] Mangeol D and Goerlach U 2006 Search for $\tilde{\tau}$ production in di-tau final states and measurements of SUSY masses in mSUGRA cascade decays *CMS Note* 2006/096
[679] Bityukov S I 2005 Uncertainty, Systematics, Limits Available at http://cmsdoc.cern.ch/bityukov
[680] Kyriazopoulou S and Markou C 2006 Search for SUSY in Final States with Z Bosons *CMS Note* 2006/116
[681] Nikitenko A, Quast G and Ciulli V Minimal requirements for significance estimates of the physics resultInfo located at http://cmsdoc.cern.ch/ anikiten/cms-higgs/stat.txt

[682] Beenakker W, Hopker R and Spira M 1996 PROSPINO: A program for the PROduction of Supersymmetric Particles In Next-to-leading Order QCD *Preprint* hep-ph/9611232
[683] Allanach B C, Lester C G, Parker M A and Webber B R 2000 Measuring sparticle masses in non-universal string inspired models at the LHC *J. High. Energy Phys.* JHEP09(2000)004 (*Preprint* hep-ph/0007009)
[684] Beenakker W *et al* 1999 The production of charginos/neutralinos and sleptons at hadron colliders *Phys. Rev. Lett.* **83** 3780–3783 (doi:10.1103/PhysRevLett.83.3780)
[685] del Aguila F and Ametller L 1991 On the detectability of sleptons at large hadron colliders *Phys. Lett.* B **261** 326–333 (doi:10.1016/0370-2693(91)90336-O)
[686] Baer H, Chen C-h, Paige F and Tata X 1994 Detecting sleptons at hadron colliders and supercolliders *Phys. Rev.* D **49** 3283–3290 (*Preprint* hep-ph/9311248)
[687] Denegri D, Rurua L and Stepanov N 1996 Detection of Sleptons in CMS, Mass Reach *CMS TN* 96-059
[688] Andreev Y M, Bityukov S I and Krasnikov N V 2005 Sleptons at post-WMAP benchmark points at LHC(CMS) *Phys. Atom. Nucl.* **68** 340–347 (*Preprint* hep-ph/0402229)
[689] Bityukov S I and Krasnikov N V 1999 The search for sleptons and lepton-flavor-number violation at LHC (CMS) *Phys. Atom. Nucl.* **62** 1213–1225 (*Preprint* hep-ph/9712358)
[690] Krasnikov N 1994 Flavor lepton number violation at LEP-2 *Mod. Phys. Lett.* A **9** 791–794
[691] Arkani-Hamed N, Cheng H-C, Feng J L and Hall L J 1996 Probing lepton flavor violation at future colliders *Phys. Rev. Lett.* **77** 1937–1940 (*Preprint* hep-ph/9603431) (doi:10.1103/PhysRevLett.77.1937)
[692] Krasnikov N V 1997 Search for flavor lepton number violation in slepton decays at LHC *JETP Lett.* **65** 148 (doi:10.1134/1.567315)
[693] Agashe K and Graesser M 2000 Signals of supersymmetric lepton flavor violation at the LHC *Phys. Rev.* D **61** 075008 (*Preprint* hep-ph/9904422)
[694] Hisano J, Kitano R and Nojiri M M 2002 Flavor mixing in slepton production at the large hadron collider *Phys. Rev.* D **65** 116002
[695] Baer H, Chen C-h, Paige F and Tata X 1994 Trileptons from chargino - neutralino production at the CERN Large Hadron Collider *Phys. Rev.* D **50** 4508–4516 (*Preprint* hep-ph/9404212) (doi:10.1103/PhysRevD.50.4508)
[696] Ellis J R, Olive K A and Santoso Y 2002 The MSSM parameter space with non-universal Higgs masses *Phys. Lett.* B **539** 107–118 (*Preprint* hep-ph/0204192)
[697] Altarelli G, Mele B and Ruiz-Altaba M 1989 Searching for new heavy vector bosons in $p\bar{p}$ colliders *Z. Phys.* C **45** 109 (doi:10.1007/BF01556677)
[698] Arkani-Hamed N, Dimopoulos S and Dvali G R 1998 The hierarchy problem and new dimensions at a millimeter *Phys. Lett.* B **429** 263–272 (*Preprint* hep-ph/9803315)
[699] Lykken J D, Poppitz E and Trivedi S P 1999 Branes with GUTs and supersymmetry breaking *Nucl. Phys.* B **543** 105–121 (*Preprint* hep-th/9806080)
[700] Antoniadis I 1990 A possible new dimension at a few TeV *Phys. Lett.* B **246** 377–384 (doi:10.1016/0370-2693(90)90617-F)
[701] Lykken J D 1996 Weak scale superstrings *Phys. Rev.* D **54** 3693–3697 (*Preprint* hep-th/9603133) (doi:10.1103/PhysRevD.54.R3693)
[702] Giudice G F, Rattazzi R and Wells J D 1999 Quantum gravity and extra dimensions at high-energy colliders *Nucl. Phys.* B **544** 3–38 (*Preprint* hep-ph/9811291)
[703] Han T, Lykken J D and Zhang R-J 1999 On Kaluza-Klein states from large extra dimensions *Phys. Rev.* D **59** 105006 (*Preprint* hep-ph/9811350) (doi:10.1103/PhysRevD.59.105006)
[704] Cullen S, Perelstein M and Peskin M E 2000 TeV strings and collider probes of large extra dimensions *Phys. Rev.* D **62** 055012 (*Preprint* hep-ph/0001166)
[705] Lykken J D and Randall L 2000 The shape of gravity *J. High. Energy Phys.* JHEP06(2000)014 (*Preprint* hep-th/9908076)
[706] Vacavant L and Hinchliffe I 2001 Signals of models with large extra dimensions in ATLAS *J. Phys.* G **27** 1839–1850
[707] Ruppert J, Rahmede C and Bleicher M 2005 Determination of the fundamental scale of gravity and the number of space-time dimensions from high energetic particle interactions *Phys. Lett.* B **608** 240–243 (*Preprint* hep-ph/0501028)
[708] Dudas E and Mourad J 2000 String theory predictions for future accelerators *Nucl. Phys.* B **575** 3–34 (doi:10.1016/S0550-3213(00)00082-1)
[709] Chialva D, Iengo R and Russo J G 2005 Cross sections for production of closed superstrings at high energy colliders in brane world models *Phys. Rev.* D **71** 106009 (*Preprint* hep-ph/0503125)
[710] Bando M, Kugo T, Noguchi T and Yoshioka K 1999 Brane fluctuation and suppression of Kaluza-Klein mode couplings *Phys. Rev. Lett.* **83** 3601–3604 (doi:10.1103/PhysRevLett.83.3601)

[711] Hewett J L 1999 Indirect collider signals for extra dimensions *Phys. Rev. Lett.* **82** 4765–4768 (doi:10.1103/PhysRevLett.82.4765)
[712] Davoudiasl H, Hewett J L and Rizzo T G 2000 Phenomenology of the Randall-Sundrum gauge hierarchy model *Phys. Rev. Lett.* **84** 2080 (doi:10.1103/PhysRevLett.84.2080)
[713] Hewett J and Spiropulu M 2002 Particle physics probes of extra spacetime dimensions *Ann. Rev. Nucl. Part. Sci.* **52** 397–424 (doi:10.1146/annurev.nucl.52.050102.090706)
[714] Clerbaux B, Mahmoud T, Collard C and Miné P 2006 Search with the CMS detector for heavy resonances decaying into an electron pair *CMS Note* 2006/083
[715] Collard C and Lemaire M-C 2004 Search with the CMS Detector for Randall-Sundrum Excitations of Gravitons Decaying Into Electron Pairs *CMS Note* 2004/024
[716] CMS Collaboration, Acosta D *et al* 2006 CMS Physics Technical Design Report Volume 1, Section 10 *CERN/LHCC*, 2006-001
[717] Clerbaux B, Mahmoud T, Collard C, Lemaire M-C and Litvin V 2006 TeV electron and photon saturation studies *CMS Note* 2006/004
[718] CDF Collaboration, Affolder T *et al* 2001 Measurement of ds/dM and Forward-Backward charge asymmetry for high-mass Drell–Yan e $^{+}$e $^{-}$ pairs from collisions at $\sqrt{s} = 1.8$ TeV *Phys. Rev. Lett.* **87** 131802
[719] CTEQ Collaboration, Lai H L *et al* 2000 Global QCD analysis of parton structure of the nucleon: CTEQ5 parton distributions *Eur. Phys. J.* C **12** 375–392 (doi:10.1007/s100529900196)
[720] CTEQ Collaboration, Stump D *et al* 2003 Inclusive jet production, parton distributions, and the search for new physics *J. High. Energy Phys.* JHEP0310(2003)046 (*Preprint* hep-ph/0303013)
[721] Davoudiasl H, Hewett J L and Rizzo T G 2001 Experimental probes of localized gravity: on and off the wall *Phys. Rev.* D **63** 075004 (*Preprint* hep-ph/0006041)
[722] Cheung K-m and Landsberg G 2000 Drell–Yan and diphoton production at hadron colliders and low scale gravity model *Phys. Rev.* D **62** 076003 (*Preprint* hep-ph/9909218)
[723] Belotelov I, Golutvin I, Bourilkov D, Lanyov A, Rogalev E, Savina M and Shmatov S 2006 Search for ADD extra dimensional gravity in di-muon channel with the CMS Detector *CMS Note* 2006/076
[724] Mohapatra R and Pati J 1975 Left-right gauge symmetry and an 'isoconjugate' model of CP violation *Phys. Rev.* D **11** 566–571 (doi:10.1103/PhysRevD.11.566)
[725] Senjanovic G and Mohapatra R 1975 Exact left-right symmetry and spontaneous violation of parity *Phys. Rev.* D **12** 1502 (doi:10.1103/PhysRevD.12.1502)
[726] Mohapatra R and Senjanovic G 1980 Neutrino mass and spontaneous parity nonconservation *Phys. Rev. Lett.* **44** 912 (doi:10.1103/PhysRevLett.44.912)
[727] Pati J and Salam A 1974 Lepton number as the fourth color *Phys. Rev.* D **10** 275–289
[728] CDF Collaboration, Affolder T *et al* 2001 Search for quark lepton compositeness and a heavy W' boson using the e nu channel in p anti-p collisions at s $^{**}(1/2) = 1.8$-TeV *Phys. Rev. Lett.* **87** 231803 (*Preprint* hep-ex/0107008)
[729] Hof C, Hebbeker T and Hoepfner K 2006 Detection of New Heavy Charged Gauge Bosons in the Muon Plus Neutrino Channel *CMS Note* 2006/117
[730] Gumus K, Akchurin N, Esen S and Harris R M 2006 CMS sensitivity to dijet resonances *CMS Note* 2006/070
[731] Baur U, Hinchliffe I and Zeppenfeld D 1987 Excited quark production at Hadron colliders *Int. J. Mod. Phys.* A **2** 1285
[732] Bagger J, Schmidt C and King S 1988 Axigluon production in hadronic collisions *Phys. Rev.* D **37** 1188
[733] Chivukula R S, Cohen A G and Simmons E H 1996 New strong interactions at the Tevatron? *Phys. Lett.* B **380** 92–98 (*Preprint* hep-ph/9603311)
[734] Hewett J L and Rizzo T G 1989 Low-energy phenomenology of superstring inspired E(6) models *Phys. Rept.* **183** 193
[735] Lane K and Mrenna S 2003 The collider phenomenology of technihadrons in the technicolor Straw man model *Phys. Rev.* D **67** 115011 (doi:10.1103/PhysRevD.67.115011)
[736] Eichten E, Hinchliffe I, Lane K D and Quigg C 1984 Super collider physics *Rev. Mod. Phys.* **56** 579–707
[737] CMS Collaboration, Lemaire M-C, Newman H and Litvin V 2006 Search for Randall-Sundrum excitations of gravitons decaying into two photons for CMS at LHC *CMS Note* 2006/051
[738] CMS Collaboration, Clerbaux B, Mahmoud T, Collard C, Lemaire M-C and Litvin V 2006 TeV electron and photon saturation studies *CMS Note* 2006/004
[739] Acosta D *et al* 2005 Measurement of the Cross Section for Prompt Diphoton Production in $p\bar{p}$ Collisions at $\sqrt{s} = 1.96$ TeV *Phys. Rev. Lett.* **95** 022003 (doi:10.1103/PhysRevLett.95.022003)
[740] Weng J *et al* 2006 Search for ADD Direct Graviton Emission in Photon plus Missing Transverse Energy Final States at CMS *CMS Note* 2006/129
[741] Myers R C and Perry M J 1986 Black holes in higher dimensional space-times *Ann. Phys.* **172** 304

[742] Hawking S W 1975 Particle creation by black holes *Commun. Math. Phys.* **43** 199–220
[743] Argyres P C, Dimopoulos S and March-Russell J 1998 Black holes and sub-millimeter dimensions *Phys. Lett.* B **441** 96–104 (*Preprint* hep-th/9808138)
[744] Harris C M, Richardson P and Webber B R 2003 CHARYBDIS: A black hole event generator *J. High. Energy Phys.* JHEP08(2003)033 (*Preprint* hep-ph/0307305)
[745] Mathews P, Ravindran V and Sridhar K 2005 NLO-QCD corrections to dilepton production in the Randall-Sundrum model *J. High. Energy Phys.* JHEP10(2005)031 (*Preprint* hep-ph/0506158)
[746] Lane K D 2000 Technicolor 2000 *Preprint* hep-ph/0007304
[747] Kreuzer P 2006 Search for Technicolour at CMS in the $\rho_{TC} \to WZ$ channel *CMS Note* 2006/135
[748] Betev B, Bourilkov D and Mavrodiev S. Shch Structure functions of pion and nucleon determined from high mass muon pair production JINR-E2-85-312
[749] Super-Kamiokande Collaboration, Fukuda Y *et al* 1998 Evidence for oscillation of atmospheric neutrinos *Phys. Rev. Lett.* **81** 1562–1567 (*Preprint* hep-ex/9807003)
[750] Esen S and Harris R 2006 CMS sensitivity to quark contact interactions using dijets *CMS Note* 2006/071
[751] Pati J C and Salam A 1975 Anomalous lepton-hadron interactions and gauge models *Phys. Rev.* D **11** 1137–1154 (doi:10.1103/PhysRevD.11.1137)
[752] CMS Collaboration, Gninenko N, Kirsanov M, Krasnikov N and Matveev N 2006 Detection of Heavy Majorana Neutrinos and Right-Handed Bosons *CMS Note* 2006/098
[753] Particle Data Group, Hagiwara K *et al* 2002 Review of Particle Physics *Phys. Rev.* D **66** 010001
[754] Barenboim G, Bernabeu J, Prades J and Raidal M 1997 Constraints on the W(R) mass and CP-violation in left-right models *Phys. Rev.* D **55** 4213–4221 (*Preprint* hep-ph/9611347)
[755] DØ Collaboration, Abachi S *et al* 1996 Search for right-handed W bosons and heavy W' in $p\bar{p}$ collisions at $\sqrt{s}$ =1.8 TeV *Phys. Rev. Lett.* **76** 3271–3276 (*Preprint* hep-ex/9512007)
[756] Datta A, Guchait M and Roy D P 1993 Prospect of heavy right-handed neutrino search at SSC/LHC energies *Phys. Rev.* D **47** 961–966 (*Preprint* hep-ph/9208228)
[757] CMS Collaboration, Karafasoulis K, Kyriakis A, Petrakou H and Mazumdar K 2006 Little Higgs model and top-like heavy quark at CMS *CMS Note* 2006/079
[758] D'Hondt J, Lowette S, Hammad G, Heyninck J and Van Mulders P 2006 Observability of same-charge lepton topology in di-leptonic ttbar events *CMS Note* 2006/065
[759] Larios F and Penunuri F 2004 FCNC production of same sign top quark pairs at the LHC *J. Phys.* G **30** 895–904 (*Preprint* hep-ph/0311056)
[760] Gouz Y P and Slabospitsky S R 1999 Double top production at hadronic colliders *Phys. Lett.* B **457** 177–185 (doi:10.1016/S0370-2693(99)00516-X)
[761] Yue C-X, Zong Z-J, Xu L-L and Chen J-X 2006 Associated production of the top-pions and single top at hadron colliders *Phys. Rev.* D **73** 015006 (*Preprint* hep-ph/0601058)
[762] Kraml S and Raklev A R 2006 Same-sign top quarks as signature of light stops at the LHC *Phys. Rev.* D **73** 075002 (*Preprint* hep-ph/0512284)
[763] Bityukov S I and Krasnikov N V 2000 On the observability of a signal above background *Nucl. Instrum. and Methods* A **452** 518–524 (doi:10.1016/S0168-9002(00)00454-X)
[764] Lehmann E L 1957 A theory of some multiple decision problems *The Annals of Mathematical Statistics* **28 1**
[765] O'Neill R and Wetherill G B 1971 The present state of multiple comparison methods *Journal of the Royal Statistical Society, Series B (Methodological)* **33 2**
[766] Hauser J 2006 Search for new physics in tails of distributionsPrivate communications, paper in preparation
[767] DØ Collaboration, Abazov V M *et al* 2005 Measurement of the $t\bar{t}$ production cross section in $p\bar{p}$ collisions at $\sqrt{s} = 1.96$ TeV using kinematic characteristics of lepton + jets events *Phys. Lett.* B **626** 45–54 (*Preprint* hep-ex/0504043) (doi:10.1016/j.physletb.2005.08.104)
[768] Abbott B *et al* 2000 Search for New physics in $e\mu X$ data at DØ Using Sleuth: a quasi-model-independent search strategy for new physics *Phys. Rev.* D **62** (doi:10.1103/PhysRevD.62.092004)
[769] Abbott B *et al* 2001 A Quasi-Model-Independent search for new physics at large transverse momentum *Phys. Rev.* D **64** (*Preprint* hep-ex/0011067)
[770] Finley C *et al* 2004 On the evidence for clustering in the arrival directions of AGASA's ultrahigh energy cosmic rays *Astroparticle Physics* **21**
[771] Frixione S, Nason P and Webber B R 2003 Matching NLO QCD and parton showers in heavy flavour production *J. High. Energy Phys.* JHEP08(2003)007 (*Preprint* hep-ph/0305252)
[772] Lonnblad L 2002 Correcting the colour-dipole cascade model with fixed order matrix elements *J. High. Energy Phys.* JHEP05(2002)046 (*Preprint* hep-ph/0112284)
[773] Frixione S and Webber B R 2002 Matching NLO QCD computations and parton shower simulations *J. High. Energy Phys.* JHEP06(2002)029 (*Preprint* hep-ph/0204244)

[774] Krauss F 2002 Matrix elements and parton showers in hadronic interactions *J. High. Energy Phys.* JHEP08(2002)015 (*Preprint* hep-ph/0205283)

[775] Mrenna S and Richardson P 2004 Matching matrix elements and parton showers with HERWIG and PYTHIA *J. High. Energy Phys.* JHEP05(2004)040 (*Preprint* hep-ph/0312274)

[776] Butterworth J, Butterworth S, Waugh B, Stirling W and Whalley M 2004 The CEDAR project *Preprint* hep-ph/0412139

[777] LEP Collaboration, 2004 A combination of preliminary electroweak measurements and constraints on the standard model *Preprint* hep-ex/0412015

[778] Stump D R 2002 A new generation of CTEQ parton distribution functions with uncertainty analysis Prepared for 31st International Conference on High Energy Physics (ICHEP 2002), (*Amsterdam, The Netherlands, 24–31 July 2002*)

[779] Stirling W J, Martin A D, Roberts R G and Thorne R S 2005 MRST parton distributions *AIP Conf. Proc.* **747** 16–21

[780] Botje M 2000 A QCD analysis of HERA and fixed target structure function data *Eur. Phys. J.* C **14** 285–297 (*Preprint* hep-ph/9912439)

[781] Alekhin S I 2001 Global fit to the charged leptons DIS data: alpha(s), parton distributions, and high twists *Phys. Rev.* D **63** 094022 (*Preprint* hep-ph/0011002)

[782] Altarelli G and Parisi G 1977 Asymptotic freedom in parton language *Nucl. Phys.* B **126** 298

[783] Lonnblad L 1992 ARIADNE version 4: A program for simulation of QCD cascades implementing the color dipole model *Comput. Phys. Commun.* **71** 15–31

[784] CDF Collaboration, Abe F *et al* 1994 Evidence for color coherence in $p\bar{p}$ collisions at $\sqrt{s} = 1.8$ TeV *Phys. Rev.* D **50** 5562–5579 (doi:10.1103/PhysRevD.50.5562)

[785] DØ Collaboration, Abbott B *et al* 1997 Color coherent radiation in multijet events from $p\bar{p}$ collisions at $\sqrt{s} = 1.8$ TeV *Phys. Lett.* B **414** 419–427 (doi:10.1016/S0370-2693(97)01190-8)

[786] Knowles I G *et al* 1995 QCD event generators *Preprint* hep-ph/9601212

[787] ALEPH Collaboration, Buskulic D *et al* 1992 Properties of hadronic Z decays and test of QCD generators *Z. Phys.* C **55** 209–234

[788] DELPHI Collaboration, Abreu P *et al* 1996 Tuning and test of fragmentation models based on identified particles and precision event shape data *Z. Phys.* C **73** 11–60 (doi:10.1007/s002880050295)

[789] OPAL Collaboration, Alexander G *et al* 1996 A Comparison of b and (u d s) quark jets to gluon jets *Z. Phys.* C **69** 543–560

[790] Andersson B, Gustafson G and Soderberg B 1983 A general model for jet fragmentation *Z. Phys.* C **20** 317

[791] ALEPH Collaboration, Heister A *et al* 2001 Study of the fragmentation of b quarks into B mesons at the Z peak *Phys. Lett.* B **512** 30–48 (*Preprint* hep-ex/0106051)

[792] OPAL Collaboration, Abbiendi G *et al* 2003 Inclusive analysis of the b quark fragmentation function in Z decays at LEP ((B)) *Eur. Phys. J.* C **29** 463–478 (*Preprint* hep-ex/0210031)

[793] SLD Collaboration, Abe K *et al* 2002 Measurement of the b-quark fragmentation function in Z^0 decays *Phys. Rev.* D **65** 092006 (doi:10.1103/PhysRevD.65.092006)

[794] Bowler M G 1981 e+ e- Production of heavy quarks in the String Model *Zeit. Phys.* C **11** 169

[795] Peterson C, Schlatter D, Schmitt I and Zerwas P M 1983 Scaling violations in inclusive e^+e^- annihilation spectra *Phys. Rev.* D **27** 105

[796] Kartvelishvili V, Likhoded A and Petrov V 1978 On the fragmentation functions of heavy quarks into hadrons *Phys. Lett.* B **78** 615

[797] Norrbin E and Sjostrand T 2000 Production and hadronization of heavy quarks *Eur. Phys. J.* C **17** 137–161 (*Preprint* hep-ph/0005110)

[798] Engel R and Ranft J 1999 Color singlet exchange between jets and the PHOJET Monte Carlo *Nucl. Phys. Proc. Suppl.* A **75** 272–274 (doi:10.1016/S0920-5632(99)00263-7)

[799] CDF Collaboration, Affolder T *et al* 2002 Charged jet evolution and the underlying event in proton anti-proton collisions at 1.8 TeV *Phys. Rev.* D **65** 092009 (doi:10.1103/PhysRevD.65.092009)

[800] Nason P *et al* 1999 Bottom production *Preprint* hep-ph/0003142

[801] Sjostrand T and Skands P Z 2005 Transverse-momentum-ordered showers and interleaved multiple interactions *Eur. Phys. J.* C **39** 129–154 (*Preprint* hep-ph/0408302) (doi:10.1140/epjc/s2004-02084-y)

[802] Sapeta S and Golec-Biernat K 2005 Total, elastic and diffractive cross sections at LHC in the Miettinen-Pumplin model *Phys. Lett.* B **613** 154–161 (*Preprint* hep-ph/0502229)

[803] Lange D J 2001 The EvtGen particle decay simulation package *Nucl. Instrum. Methods* A **462** 152–155

[804] Bartalini P 2005 Supporting Monte Carlo Generators at the LHC *Proceedings of the 10th International Conference on B-Physics at Hadron Machines* (Assisi Perugia, Italy June, 2005) ed M Biasini and S Erhan volume 156, *Published in Nucl. Phys B - Proceedings Supplements 1* (doi:10.1016/j.nuclphysbps.2006.02.123)
[805] Sullivan Z 2002 Fully differential W production and decay at next-to- leading order in QCD *Phys. Rev.* D **66** 075011 (*Preprint* hep-ph/0207290)
[806] Dobbs M A *et al* 2004 Les Houches guidebook to Monte Carlo generators for hadron collider physics *Preprint* hep-ph/0403045
[807] HIJING Web Site Located at http://www-nsdth.lbl.gov/ xnwang/hijing/index.html
[808] Gleisberg T *et al* 2005 Event generator for the LHC *Preprint* hep-ph/0508315
[809] Boos E *et al* 2001 Generic user process interface for event generators *Preprint* hep-ph/0109068
[810] Lokhtin I P and Snigirev A M 2000 Nuclear geometry of jet quenching *Eur. Phys. J.* C **16** 527–536 (*Preprint* hep-ph/0004176) (doi:10.1007/s100520000437)
[811] Lokhtin I P and Snigirev A M 2004 Fast simulation of jet quenching in ultrarelativistic heavy ion collisions SINP MSU-13/752 *Preprint* hep-ph/0406038
[812] Lokhtin I P and Snigirev A M 2003 Fast simulation of flow effects in central and semi-central heavy ion collisions at LHC *Preprint* hep-ph/0312204
[813] CDF Collaboration, Field R D 2001 The underlying event in hard scattering processes *eConf* C **010630** P501 (*Preprint* hep-ph/0201192)
[814] CompHEP Collaboration, Boos E, Bunichev V, Dubinin M, Dudko L, Edneral V, Ilyin V, Kryukov A, Savrin V, Semenov A and Sherstnev A 2004 Web site at http://theory.sinp.msu.ru/comphep. See also [355]
[815] Lokhtin I P, Sarycheva L I and Snigirev A M 2002 The method for analysing jet azimuthal anisotropy in ultrarelativistic heavy ion collisions *Phys. Lett.* B **537** 261–267 (*Preprint* hep-ph/0203144) (doi:10.1016/S0370-2693(02)01913-5)
[816] Carena M, Daleo A, Dobrescu B A and Tait T M P 2004 Z' gauge bosons at the Tevatron *Phys. Rev.* D **70** 093009 (doi:10.1103/PhysRevD.70.093009)
[817] Balazs C, Qiu J-w and Yuan C P 1995 Effects of QCD resummation on distributions of leptons from the decay of electroweak vector bosons *Phys. Lett.* B **355** 548–554 (doi:10.1016/0370-2693(95)00726-2)
[818] Balazs C and Yuan C P 1997 Soft gluon effects on lepton pairs at hadron colliders *Phys. Rev.* D **56** 5558–5583 (doi:10.1103/PhysRevD.56.5558)
[819] Martin A D, Roberts R G, Stirling W J and Thorne R S 2003 Uncertainties of predictions from parton distributions I: Experimental errors *Eur. Phys. J.* C **28** 455–473 (*Preprint* hep-ph/0211080)
[820] Holland J H 1975 Adaptation in natural and artificial systems (The University of Michigan Press, Ann Arbor)
[821] Goldberg D E 1989 Genetic algorithms in search, optimization and machine learning (Addison: Wesley)
[822] Abdullin S 2003 Genetic algorithm for SUSY trigger optimization in CMS detector at LHC *NIM A* **502** 693–695 (doi:10.1016/S0168-9002(03)00546-1)
[823] TOTEM Collaboration, 2004 TOTEM Technical Design Report *CERN/LHCC*, 2004-002
[824] TOTEM Collaboration, 2004 Addendum to the TOTEM-TDR *CERN/LHCC*, 2004-020
[825] Avati V and Österberg K 2005 TOTEM forward measurements: leading proton acceptance *Proceedings of the HERA-LHC Workshop* (CERN/DESY: January, 2005) Available at http://www.desy.de/ heralhc/proceedings/wg4avati.pdf
[826] Kalliopuska J *et al* 2005 TOTEM forward measurements: exclusive central diffraction *Proceedings of the HERA-LHC Workshop* (CERN/DESY: January, 2005) Available at http://www.desy.de/ heralhc/proceedings/wg4pXp_heralhc.pdf
[827] The MAD-X Program, Methodical Accelerator Design Information available at http://www.cern.ch/mad
[828] Arneodo M *et al* 2005 Diffractive Higgs: CMS/TOTEM Level-1 Trigger Studies *Proceedings of the HERA-LHC Workshop* (CERN/DESY: January, 2005) Available at http://www.desy.de/ heralhc/proceedings/wg4arneodo.pdf
[829] Croft R 2006 (In preparation) PhD Thesis, University of Bristol
[830] Oljemark F 2006 First level triggering of diffractively produced low-mass Higgs at The Large Hadron Collider, University of Helsinki
[831] Bruni G *et al* 2005 Leading proton production in ep and pp, experiments: how well do high-energy physics Monte Carlos reproduce the data? *Proceedings of the HERA-LHC Workshop* (CERN/DESY: January, 2005) Available at http://www.desy.de/ heralhc/proceedings/wg5lps.pdf
[832] Ferro F 2005 Diffractive Higgs in CMS/TOTEM: study of L1 trigger conditions from T1 and T2 *TOTEM Note* **04-2005**
[833] Cox B and Forshaw J 2002 Herwig for diffractive interactions *Comput. Phys. Commun.* **144** 104–110 (doi:10.1016/S0010-4655(01)00467-2)

[834] Collins J C 1997 Light-cone variables, rapidity and all that *Preprint* hep-ph/9705393
[835] Albrow M G and Rostovtsev A 2000 Searching for the Higgs at hadron colliders using the missing mass method *Preprint* hep-ph/0009336
[836] Albrow M G 2005 Double pomeron physics at the LHC *AIP Conf. Proc.* **792** 509–514 (*Preprint* hep-ex/0507095)

Colour plates CP1–CP9

Various figures are in colour throughout the online edition but only plates CP1–CP9 are in colour in both the print and online editions.

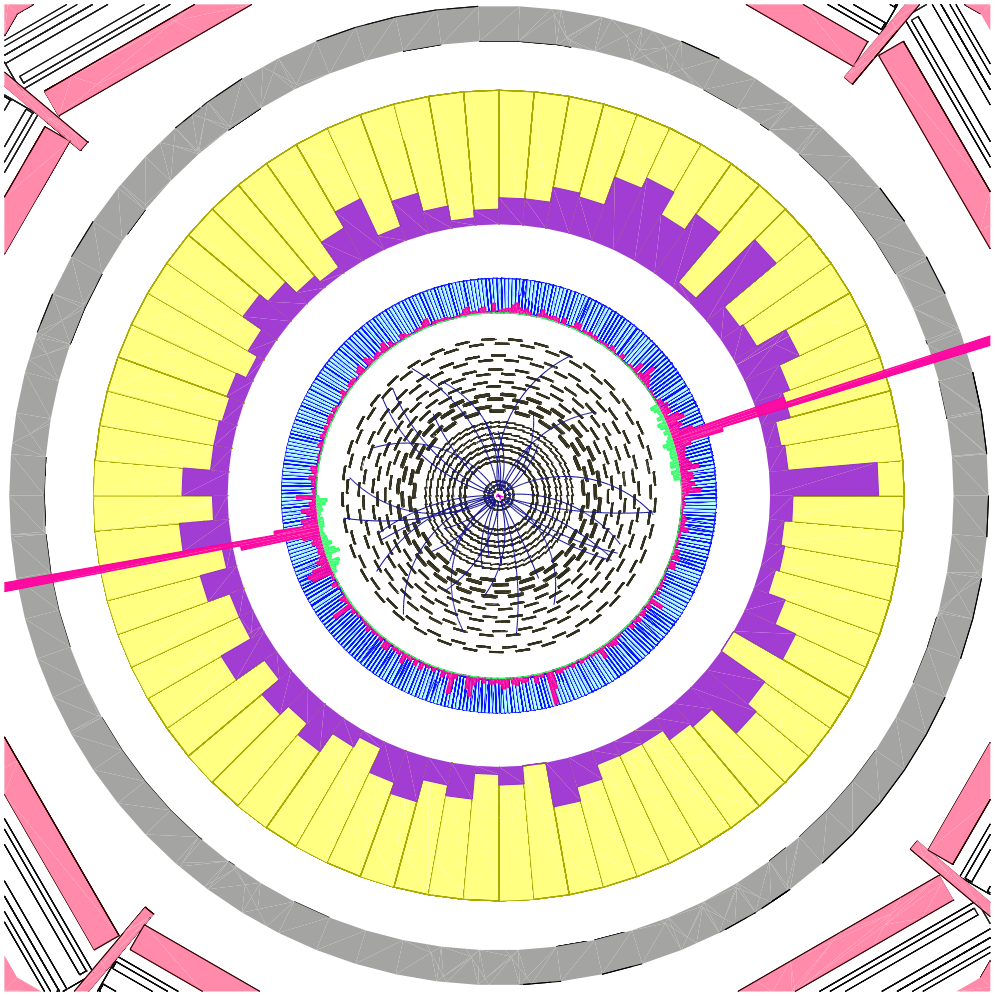

Figure CP1. Example of a $pp \to H + X$ event with Higgs particle decay $H \to \gamma\gamma$. (See section 2.1.)

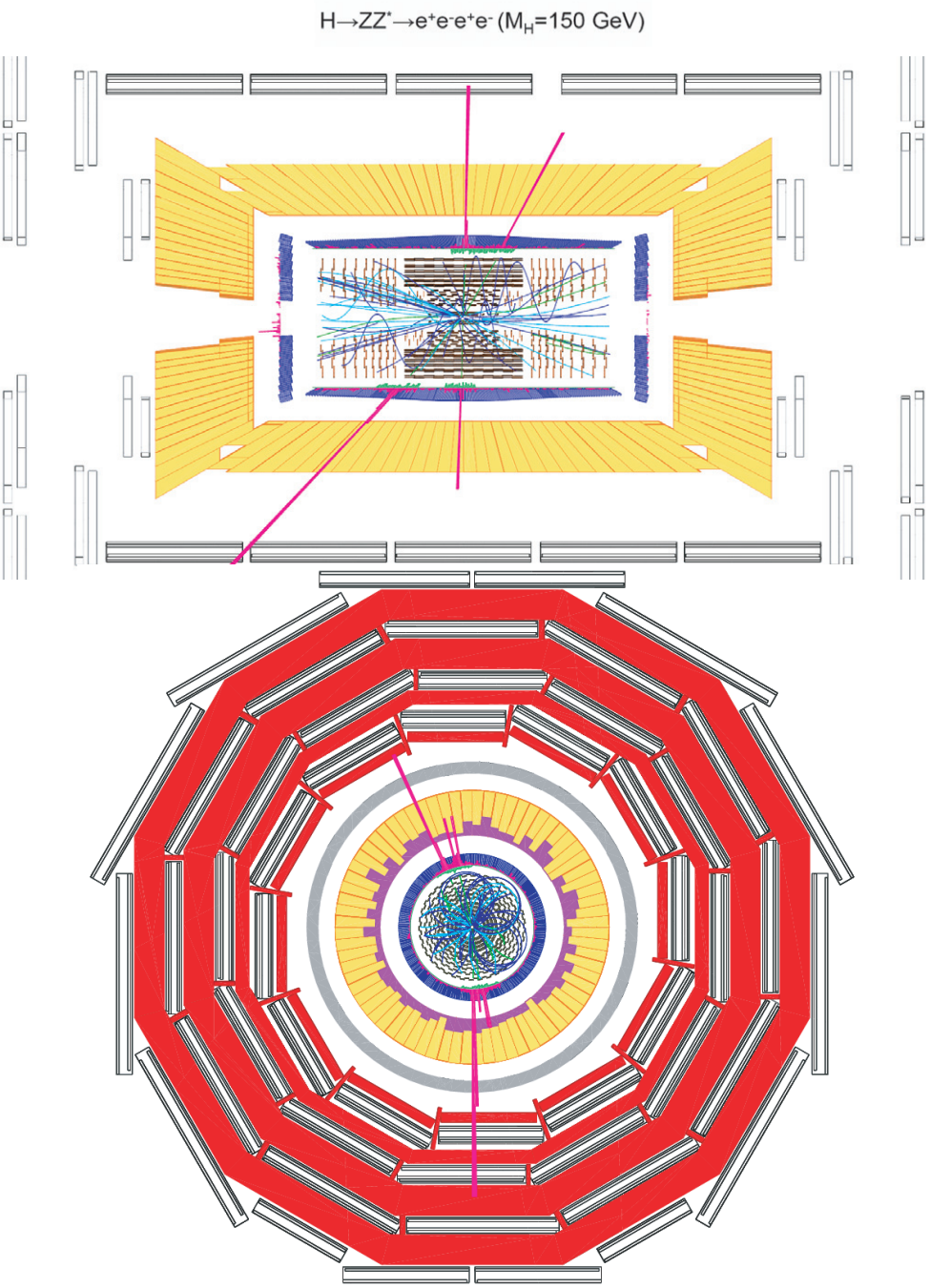

Figure CP2. Display of an event candidate in the CMS detector at the LHC for the Standard Model Higgs boson decay channel $H \rightarrow ZZ^* \rightarrow 4e$. The event is shown in a longitudinal (top) and transversal (bottom) projection of the detector. A mass of $150\,GeV/c^2$ is measured from the reconstructed electrons. (See section 2.2.)

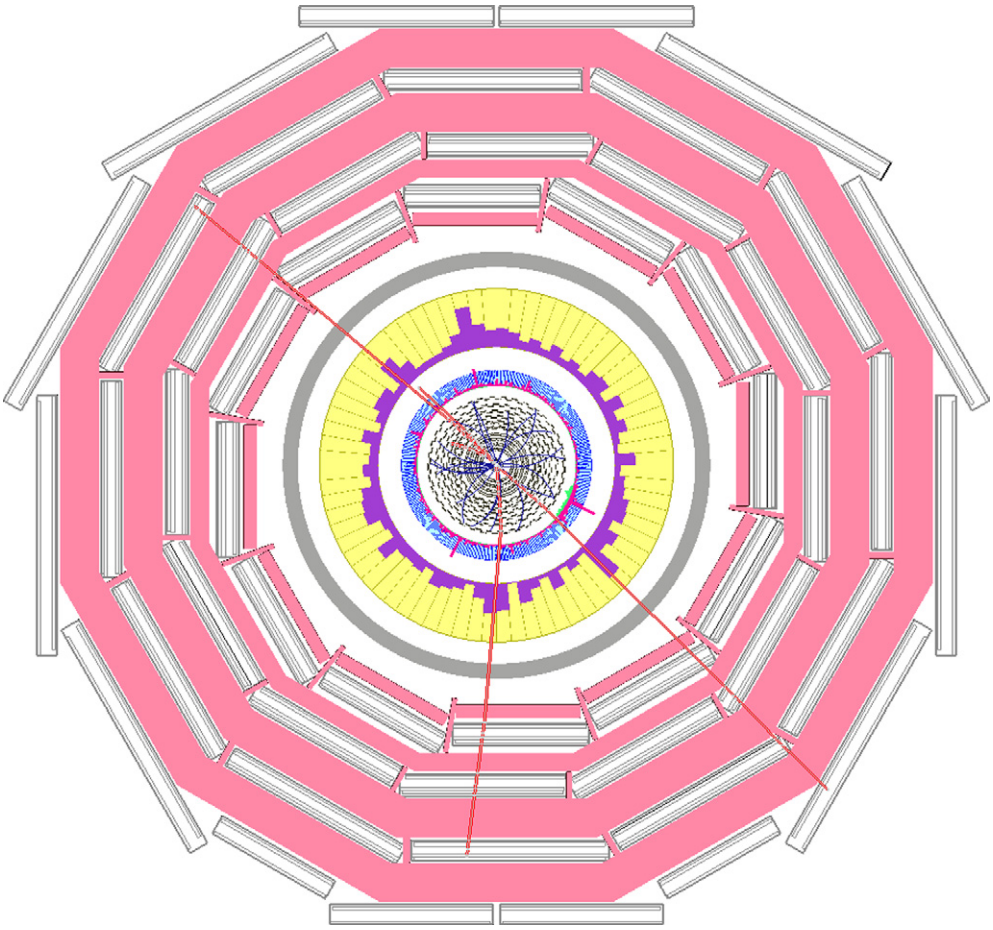

Figure CP3. Example of a $H \rightarrow ZZ \rightarrow 4\mu$ event showing only the reconstructed tracks. One muon goes in the endcap detectors. (See section 3.1.1.)

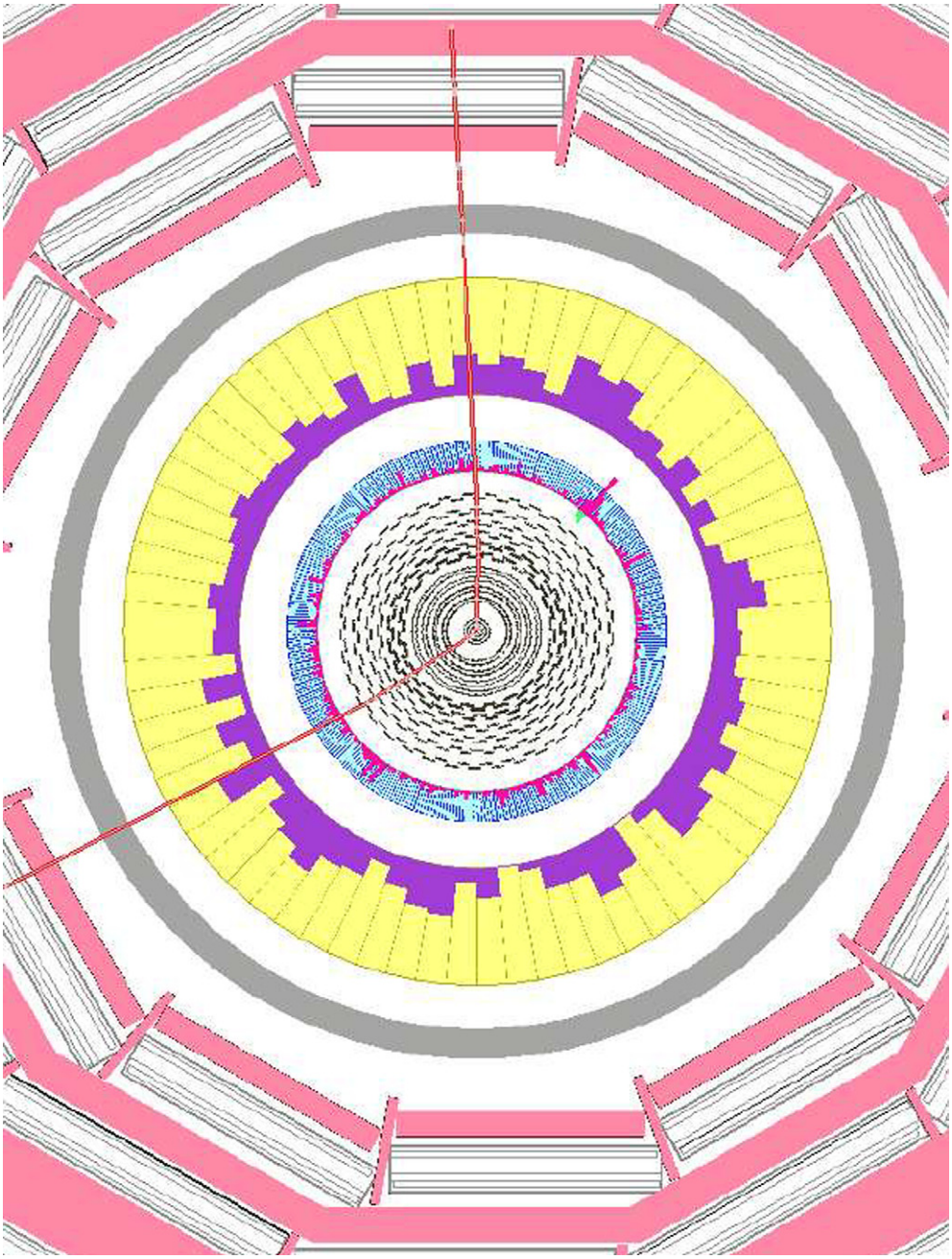

Figure CP4. Example of a pp $\rightarrow$ H + X event with H $\rightarrow$ WW $\rightarrow \mu\nu\mu\nu$. (See section 3.2.2.1.)

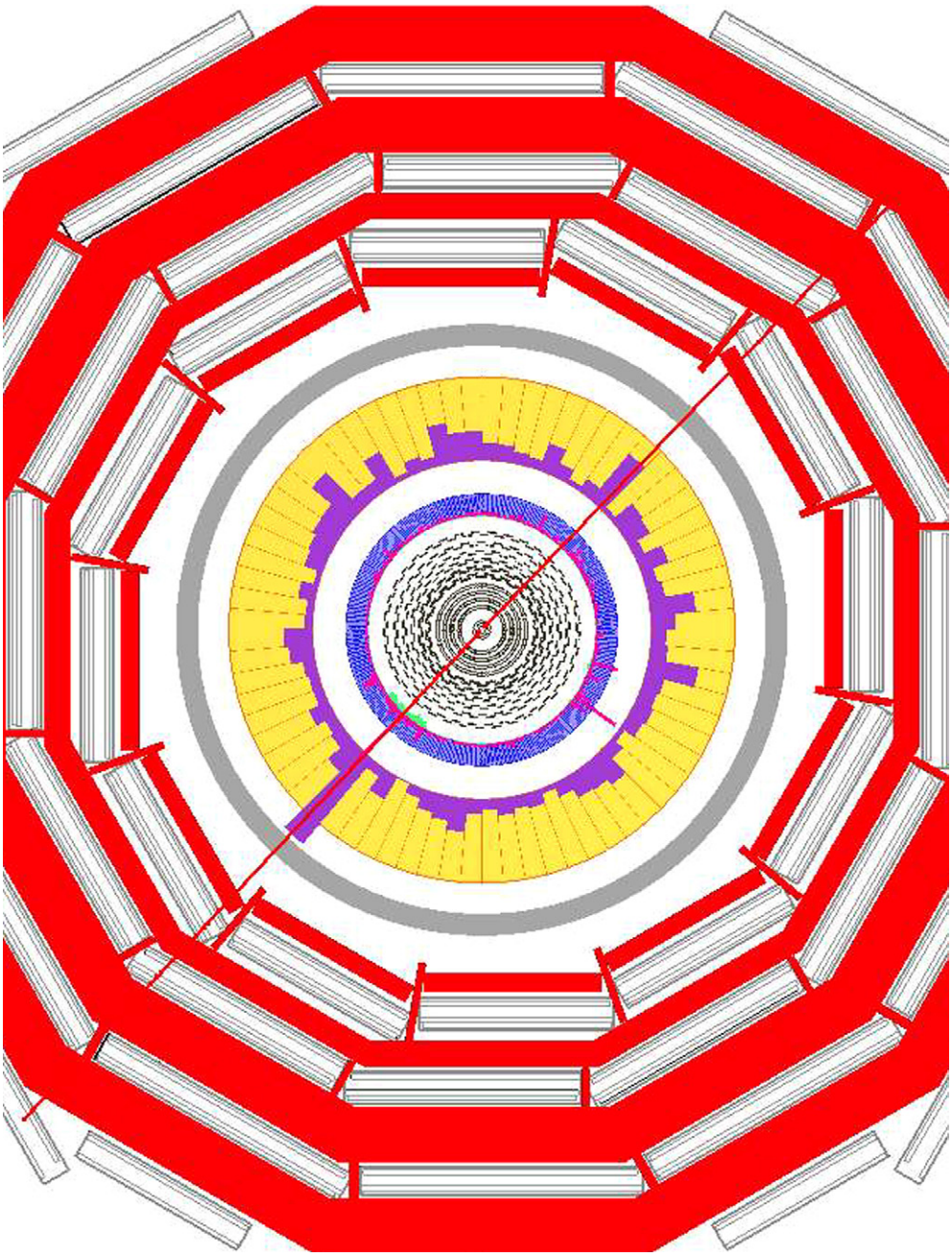

Figure CP5. Typical simulated event of a dimuon decay of $3\,\mathrm{TeV}/c^2$ Z' produced at $\mathcal{L} = 2 \times 10^{33}\,\mathrm{cm}^{-2}\,\mathrm{s}^{-1}$, showing the muon tracks only. (See section 3.3.1.)

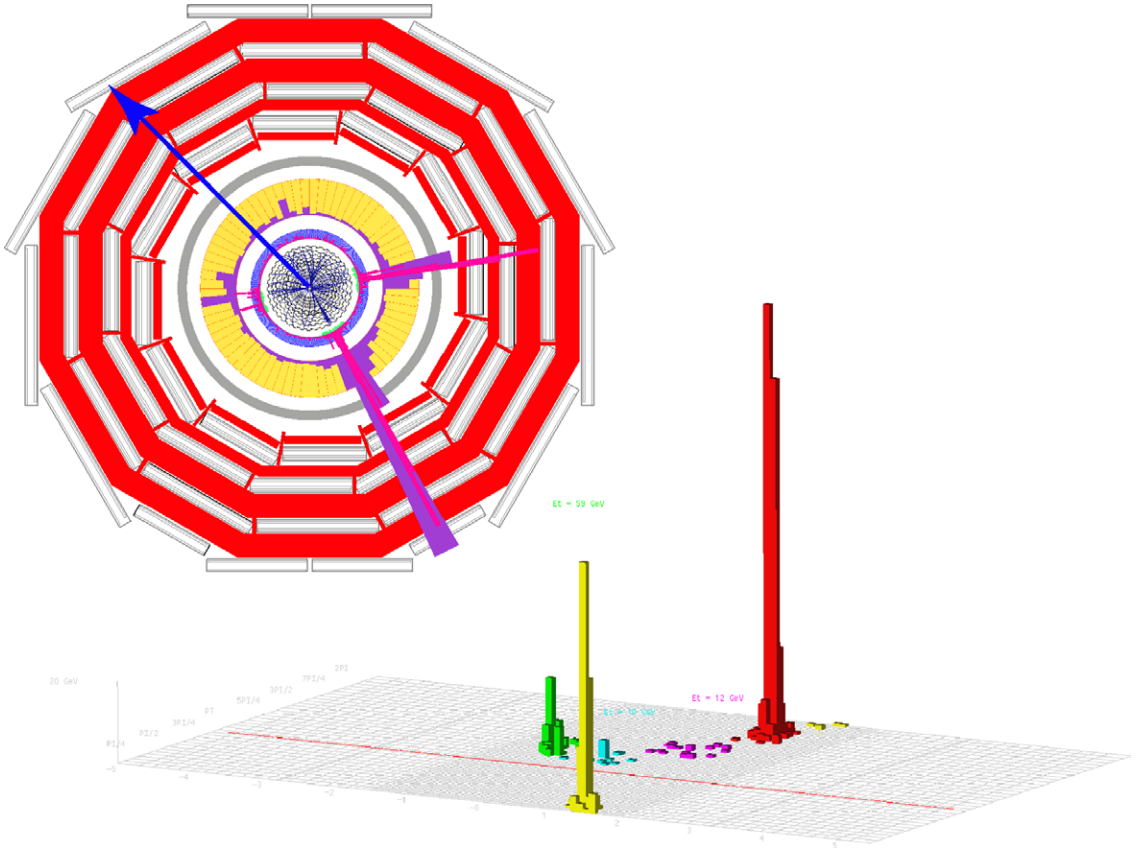

Figure CP6. Event display of SUSY candidate event that survives the requirements of the multijet + missing energy analysis of section 13.5. The three highest E_{T} jets are 330, 140 and 60 GeV while the missing transverse energy is 360 GeV. The Lego $\eta - \phi$ calorimeter display shows the three leading jets, colour coded red-yellow-green, while the missing energy ϕ is indicated with the red line. The transverse $x - y$ view shows relative depositions of the jets in the calorimeter systems as well as the reconstructed tracks and the missing energy vector direction (in blue).

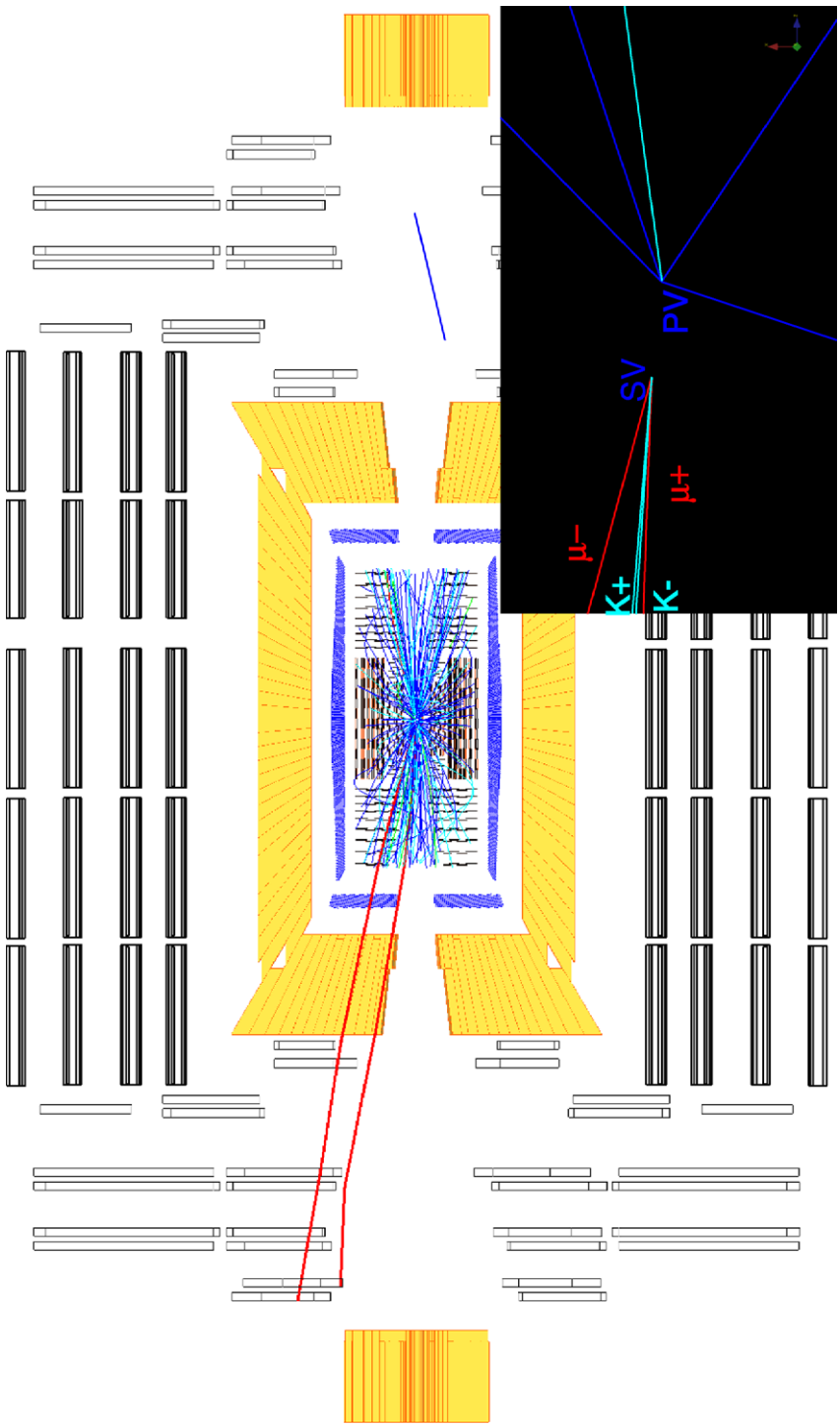

Figure CP7. Example of a pp $\rightarrow B_s + X$ event with $B_s \rightarrow J/\psi\phi$. (See section 5.1.1.)

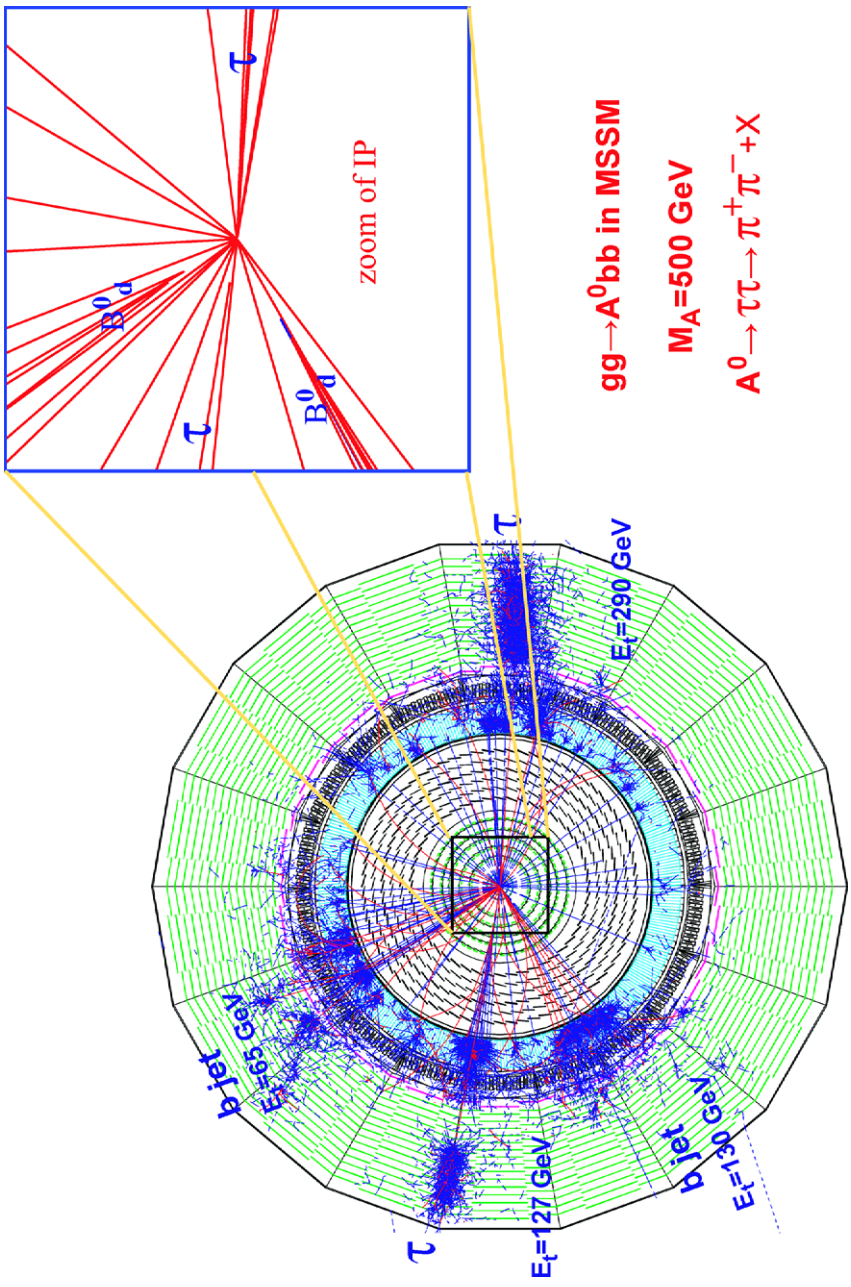

Figure CP8. Example of a pp → H + X event with H → $\tau\nu\tau\nu$. (See section 5.2.1.)

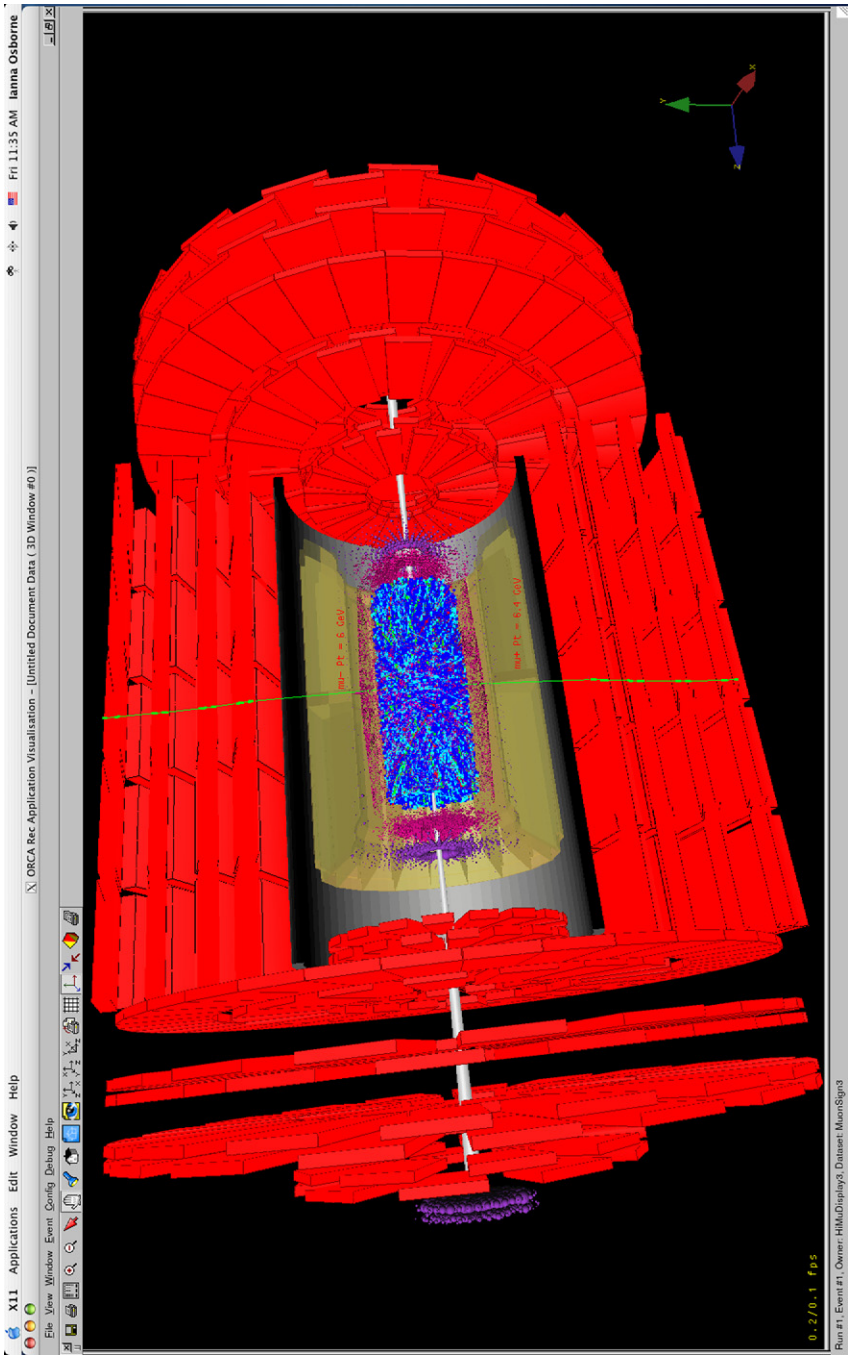

Figure CP9. $\Upsilon \to \mu^+\mu^-$ event embedded in a PbPb collision at $\sqrt{s_{NN}} = 5.5$ TeV with charged multiplicities at mid-rapidity $dN_{ch}/d\eta|_{\eta=0} = 3500$. (See section 6.1.)

The CMS experiment at the CERN LHC

2008 JINST 3 S08004

(http://iopscience.iop.org/1748-0221/3/08/S08004)

PUBLISHED BY INSTITUTE OF PHYSICS PUBLISHING AND SISSA

RECEIVED: *January 9, 2008*
ACCEPTED: *May 18, 2008*
PUBLISHED: *August 14, 2008*

THE CERN LARGE HADRON COLLIDER: ACCELERATOR AND EXPERIMENTS

The CMS experiment at the CERN LHC

CMS Collaboration

ABSTRACT: The Compact Muon Solenoid (CMS) detector is described. The detector operates at the Large Hadron Collider (LHC) at CERN. It was conceived to study proton-proton (and lead-lead) collisions at a centre-of-mass energy of 14 TeV (5.5 TeV nucleon-nucleon) and at luminosities up to $10^{34}\,\mathrm{cm}^{-2}\mathrm{s}^{-1}$ ($10^{27}\,\mathrm{cm}^{-2}\mathrm{s}^{-1}$). At the core of the CMS detector sits a high-magnetic-field and large-bore superconducting solenoid surrounding an all-silicon pixel and strip tracker, a lead-tungstate scintillating-crystals electromagnetic calorimeter, and a brass-scintillator sampling hadron calorimeter. The iron yoke of the flux-return is instrumented with four stations of muon detectors covering most of the 4π solid angle. Forward sampling calorimeters extend the pseudo-rapidity coverage to high values ($|\eta| \leq 5$) assuring very good hermeticity. The overall dimensions of the CMS detector are a length of 21.6 m, a diameter of 14.6 m and a total weight of 12500 t.

KEYWORDS: Instrumentation for particle accelerators and storage rings - high energy; Gaseous detectors; Scintillators, scintillation and light emission processes; Solid state detectors; Calorimeters; Gamma detectors; Large detector systems for particle and astroparticle physics; Particle identification methods; Particle tracking detectors; Spectrometers; Analogue electronic circuits; Control and monitor systems online; Data acquisition circuits; Data acquisition concepts; Detector control systems; Digital electronic circuits; Digital signal processing; Electronic detector readout concepts; Front-end electronics for detector readout; Modular electronics; Online farms and online filtering; Optical detector readout concepts; Trigger concepts and systems; VLSI circuits; Analysis and statistical methods; Computing; Data processing methods; Data reduction methods; Pattern recognition, cluster finding, calibration and fitting methods; Software architectures; Detector alignment and calibration methods; Detector cooling and thermo-stabilization; Detector design and construction technologies and materials; Detector grounding; Manufacturing; Overall mechanics design; Special cables; Voltage distributions.

2008 JINST 3 S08004

CMS Collaboration

Yerevan Physics Institute, Yerevan, Armenia
S. Chatrchyan, G. Hmayakyan, V. Khachatryan, A.M. Sirunyan

Institut für Hochenergiephysik der OeAW, Wien, Austria
W. Adam, T. Bauer, T. Bergauer, H. Bergauer, M. Dragicevic, J. Erö, M. Friedl, R. Frühwirth, V.M. Ghete, P. Glaser, C. Hartl, N. Hoermann, J. Hrubec, S. Hänsel, M. Jeitler, K. Kastner, M. Krammer, I. Magrans de Abril, M. Markytan, I. Mikulec, B. Neuherz, T. Nöbauer, M. Oberegger, M. Padrta, M. Pernicka, P. Porth, H. Rohringer, S. Schmid, T. Schreiner, R. Stark, H. Steininger, J. Strauss, A. Taurok, D. Uhl, W. Waltenberger, G. Walzel, E. Widl, C.-E. Wulz

Byelorussian State University, Minsk, Belarus
V. Petrov, V. Prosolovich

National Centre for Particle and High Energy Physics, Minsk, Belarus
V. Chekhovsky, O. Dvornikov, I. Emeliantchik, A. Litomin, V. Makarenko, I. Marfin, V. Mossolov, N. Shumeiko, A. Solin, R. Stefanovitch, J. Suarez Gonzalez, A. Tikhonov

Research Institute for Nuclear Problems, Minsk, Belarus
A. Fedorov, M. Korzhik, O. Missevitch, R. Zuyeuski

Universiteit Antwerpen, Antwerpen, Belgium
W. Beaumont, M. Cardaci, E. De Langhe, E.A. De Wolf, E. Delmeire, S. Ochesanu, M. Tasevsky, P. Van Mechelen

Vrije Universiteit Brussel, Brussel, Belgium
J. D'Hondt, S. De Weirdt, O. Devroede, R. Goorens, S. Hannaert, J. Heyninck, J. Maes, M.U. Mozer, S. Tavernier, W. Van Doninck,[1] L. Van Lancker, P. Van Mulders, I. Villella, C. Wastiels, C. Yu

Université Libre de Bruxelles, Bruxelles, Belgium
O. Bouhali, O. Charaf, B. Clerbaux, P. De Harenne, G. De Lentdecker, J.P. Dewulf, S. Elgammal, R. Gindroz, G.H. Hammad, T. Mahmoud, L. Neukermans, M. Pins, R. Pins, S. Rugovac, J. Stefanescu, V. Sundararajan, C. Vander Velde, P. Vanlaer, J. Wickens

2008 JINST 3 S08004

Ghent University, Ghent, Belgium
M. Tytgat

Université Catholique de Louvain, Louvain-la-Neuve, Belgium
S. Assouak, J.L. Bonnet, G. Bruno, J. Caudron, B. De Callatay, J. De Favereau De Jeneret, S. De Visscher, P. Demin, D. Favart, C. Felix, B. Florins, E. Forton, A. Giammanco, G. Grégoire, M. Jonckman, D. Kcira, T. Keutgen, V. Lemaitre, D. Michotte, O. Militaru, S. Ovyn, T. Pierzchala, K. Piotrzkowski, V. Roberfroid, X. Rouby, N. Schul, O. Van der Aa

Université de Mons-Hainaut, Mons, Belgium
N. Beliy, E. Daubie, P. Herquet

Centro Brasileiro de Pesquisas Fisicas, Rio de Janeiro, Brazil
G. Alves, M.E. Pol, M.H.G. Souza

Instituto de Fisica - Universidade Federal do Rio de Janeiro,
Rio de Janeiro, Brazil
M. Vaz

Universidade do Estado do Rio de Janeiro, Rio de Janeiro, Brazil
D. De Jesus Damiao, V. Oguri, A. Santoro, A. Sznajder

Instituto de Fisica Teorica-Universidade Estadual Paulista,
Sao Paulo, Brazil
E. De Moraes Gregores,[2] R.L. Iope, S.F. Novaes, T. Tomei

Institute for Nuclear Research and Nuclear Energy, Sofia, Bulgaria
T. Anguelov, G. Antchev, I. Atanasov, J. Damgov, N. Darmenov,[1] L. Dimitrov, V. Genchev,[1] P. Iaydjiev, A. Marinov, S. Piperov, S. Stoykova, G. Sultanov, R. Trayanov, I. Vankov

University of Sofia, Sofia, Bulgaria
C. Cheshkov, A. Dimitrov, M. Dyulendarova, I. Glushkov, V. Kozhuharov, L. Litov, M. Makariev, E. Marinova, S. Markov, M. Mateev, I. Nasteva, B. Pavlov, P. Petev, P. Petkov, V. Spassov, Z. Toteva,[1] V. Velev, V. Verguilov

Institute of High Energy Physics, Beijing, China
J.G. Bian, G.M. Chen, H.S. Chen, M. Chen, C.H. Jiang, B. Liu, X.Y. Shen, H.S. Sun, J. Tao, J. Wang, M. Yang, Z. Zhang, W.R. Zhao, H.L. Zhuang

Peking University, Beijing, China
Y. Ban, J. Cai, Y.C. Ge, S. Liu, H.T. Liu, L. Liu, S.J. Qian, Q. Wang, Z.H. Xue, Z.C. Yang, Y.L. Ye, J. Ying

2008 JINST 3 S08004

Shanghai Institute of Ceramics, Shanghai, China (Associated Institute)
P.J. Li, J. Liao, Z.L. Xue, D.S. Yan, H. Yuan

Universidad de Los Andes, Bogota, Colombia
C.A. Carrillo Montoya, J.C. Sanabria

Technical University of Split, Split, Croatia
N. Godinovic, I. Puljak, I. Soric

University of Split, Split, Croatia
Z. Antunovic, M. Dzelalija, K. Marasovic

Institute Rudjer Boskovic, Zagreb, Croatia
V. Brigljevic, K. Kadija, S. Morovic

University of Cyprus, Nicosia, Cyprus
R. Fereos, C. Nicolaou, A. Papadakis, F. Ptochos, P.A. Razis, D. Tsiakkouri, Z. Zinonos

National Institute of Chemical Physics and Biophysics, Tallinn, Estonia
A. Hektor, M. Kadastik, K. Kannike, E. Lippmaa, M. Müntel, M. Raidal, L. Rebane

Laboratory of Advanced Energy Systems,
Helsinki University of Technology, Espoo, Finland
P.A. Aarnio

Helsinki Institute of Physics, Helsinki, Finland
E. Anttila, K. Banzuzi, P. Bulteau, S. Czellar, N. Eiden, C. Eklund, P. Engstrom,[1] A. Heikkinen, A. Honkanen, J. Härkönen, V. Karimäki, H.M. Katajisto, R. Kinnunen, J. Klem, J. Kortesmaa,[1] M. Kotamäki, A. Kuronen,[1] T. Lampén, K. Lassila-Perini, V. Lefébure, S. Lehti, T. Lindén, P.R. Luukka, S. Michal,[1] F. Moura Brigido, T. Mäenpää, T. Nyman, J. Nystén, E. Pietarinen, K. Skog, K. Tammi, E. Tuominen, J. Tuominiemi, D. Ungaro, T.P. Vanhala, L. Wendland, C. Williams

Lappeenranta University of Technology, Lappeenranta, Finland
M. Iskanius, A. Korpela, G. Polese,[1] T. Tuuva

Laboratoire d'Annecy-le-Vieux de Physique des Particules,
IN2P3-CNRS, Annecy-le-Vieux, France
G. Bassompierre, A. Bazan, P.Y. David, J. Ditta, G. Drobychev, N. Fouque, J.P. Guillaud, V. Hermel, A. Karneyeu, T. Le Flour, S. Lieunard, M. Maire, P. Mendiburu, P. Nedelec, J.P. Peigneux, M. Schneegans, D. Sillou, J.P. Vialle

2008 JINST 3 S08004

DSM/DAPNIA, CEA/Saclay, Gif-sur-Yvette, France
M. Anfreville, J.P. Bard, P. Besson,* E. Bougamont, M. Boyer, P. Bredy, R. Chipaux, M. Dejardin, D. Denegri, J. Descamps, B. Fabbro, J.L. Faure, S. Ganjour, F.X. Gentit, A. Givernaud, P. Gras, G. Hamel de Monchenault, P. Jarry, C. Jeanney, F. Kircher, M.C. Lemaire, Y. Lemoigne, B. Levesy,[1] E. Locci, J.P. Lottin, I. Mandjavidze, M. Mur, J.P. Pansart, A. Payn, J. Rander, J.M. Reymond, J. Rolquin, F. Rondeaux, A. Rosowsky, J.Y.A. Rousse, Z.H. Sun, J. Tartas, A. Van Lysebetten, P. Venault, P. Verrecchia

Laboratoire Leprince-Ringuet, Ecole Polytechnique,
IN2P3-CNRS, Palaiseau, France
M. Anduze, J. Badier, S. Baffioni, M. Bercher, C. Bernet, U. Berthon, J. Bourotte, A. Busata, P. Busson, M. Cerutti, D. Chamont, C. Charlot, C. Collard,[3] A. Debraine, D. Decotigny, L. Dobrzynski, O. Ferreira, Y. Geerebaert, J. Gilly, C. Gregory,* L. Guevara Riveros, M. Haguenauer, A. Karar, B. Koblitz, D. Lecouturier, A. Mathieu, G. Milleret, P. Miné, P. Paganini, P. Poilleux, N. Pukhaeva, N. Regnault, T. Romanteau, I. Semeniouk, Y. Sirois, C. Thiebaux, J.C. Vanel, A. Zabi[4]

Institut Pluridisciplinaire Hubert Curien,
IN2P3-CNRS, Université Louis Pasteur Strasbourg, France, and
Université de Haute Alsace Mulhouse, Strasbourg, France
J.L. Agram,[5] A. Albert,[5] L. Anckenmann, J. Andrea, F. Anstotz,[6] A.M. Bergdolt, J.D. Berst, R. Blaes,[5] D. Bloch, J.M. Brom, J. Cailleret, F. Charles,* E. Christophel, G. Claus, J. Coffin, C. Colledani, J. Croix, E. Dangelser, N. Dick, F. Didierjean, F. Drouhin[1,5], W. Dulinski, J.P. Ernenwein,[5] R. Fang, J.C. Fontaine,[5] G. Gaudiot, W. Geist, D. Gelé, T. Goeltzenlichter, U. Goerlach,[6] P. Graehling, L. Gross, C. Guo Hu, J.M. Helleboid, T. Henkes, M. Hoffer, C. Hoffmann, J. Hosselet, L. Houchu, Y. Hu,[6] D. Huss,[6] C. Illinger, F. Jeanneau, P. Juillot, T. Kachelhoffer, M.R. Kapp, H. Kettunen, L. Lakehal Ayat, A.C. Le Bihan, A. Lounis,[6] C. Maazouzi, V. Mack, P. Majewski, D. Mangeol, J. Michel,[6] S. Moreau, C. Olivetto, A. Pallarès,[5] Y. Patois, P. Pralavorio, C. Racca, Y. Riahi, I. Ripp-Baudot, P. Schmitt, J.P. Schunck, G. Schuster, B. Schwaller, M.H. Sigward, J.L. Sohler, J. Speck, R. Strub, T. Todorov, R. Turchetta, P. Van Hove, D. Vintache, A. Zghiche

Institut de Physique Nucléaire,
IN2P3-CNRS, Université Claude Bernard Lyon 1, Villeurbanne, France
M. Ageron, J.E. Augustin, C. Baty, G. Baulieu, M. Bedjidian, J. Blaha, A. Bonnevaux, G. Boudoul, P. Brunet, E. Chabanat, E.C. Chabert, R. Chierici, V. Chorowicz, C. Combaret, D. Contardo,[1] R. Della Negra, P. Depasse, O. Drapier, M. Dupanloup, T. Dupasquier, H. El Mamouni, N. Estre, J. Fay, S. Gascon, N. Giraud, C. Girerd, G. Guillot, R. Haroutunian, B. Ille, M. Lethuillier, N. Lumb, C. Martin, H. Mathez, G. Maurelli, S. Muanza, P. Pangaud, S. Perries, O. Ravat, E. Schibler, F. Schirra, G. Smadja, S. Tissot, B. Trocme, S. Vanzetto, J.P. Walder

Institute of High Energy Physics and Informatization,
Tbilisi State University, Tbilisi, Georgia
Y. Bagaturia, D. Mjavia, A. Mzhavia, Z. Tsamalaidze

2008 JINST 3 S08004

Institute of Physics Academy of Science, Tbilisi, Georgia
V. Roinishvili

RWTH Aachen University, I. Physikalisches Institut, Aachen, Germany
R. Adolphi, G. Anagnostou, R. Brauer, W. Braunschweig, H. Esser, L. Feld, W. Karpinski, A. Khomich, K. Klein, C. Kukulies, K. Lübelsmeyer, J. Olzem, A. Ostaptchouk, D. Pandoulas, G. Pierschel, F. Raupach, S. Schael, A. Schultz von Dratzig, G. Schwering, R. Siedling, M. Thomas, M. Weber, B. Wittmer, M. Wlochal

RWTH Aachen University, III. Physikalisches Institut A, Aachen, Germany
F. Adamczyk, A. Adolf, G. Altenhöfer, S. Bechstein, S. Bethke, P. Biallass, O. Biebel, M. Bontenackels, K. Bosseler, A. Böhm, M. Erdmann, H. Faissner,* B. Fehr, H. Fesefeldt, G. Fetchenhauer,[1] J. Frangenheim, J.H. Frohn, J. Grooten, T. Hebbeker, S. Hermann, E. Hermens, G. Hilgers, K. Hoepfner, C. Hof, E. Jacobi, S. Kappler, M. Kirsch, P. Kreuzer, R. Kupper, H.R. Lampe, D. Lanske,* R. Mameghani, A. Meyer, S. Meyer, T. Moers, E. Müller, R. Pahlke, B. Philipps, D. Rein, H. Reithler, W. Reuter, P. Rütten, S. Schulz, H. Schwarthoff, W. Sobek, M. Sowa, T. Stapelberg, H. Szczesny, H. Teykal, D. Teyssier, H. Tomme, W. Tomme, M. Tonutti, O. Tsigenov, J. Tutas,* J. Vandenhirtz, H. Wagner, M. Wegner, C. Zeidler

RWTH Aachen University, III. Physikalisches Institut B, Aachen, Germany
F. Beissel, M. Davids, M. Duda, G. Flügge, M. Giffels, T. Hermanns, D. Heydhausen, S. Kalinin, S. Kasselmann, G. Kaussen, T. Kress, A. Linn, A. Nowack, L. Perchalla, M. Poettgens, O. Pooth, P. Sauerland, A. Stahl, D. Tornier, M.H. Zoeller

Deutsches Elektronen-Synchrotron, Hamburg, Germany
U. Behrens, K. Borras, A. Flossdorf, D. Hatton, B. Hegner, M. Kasemann, R. Mankel, A. Meyer, J. Mnich, C. Rosemann, C. Youngman, W.D. Zeuner[1]

University of Hamburg, Institute for Experimental Physics, Hamburg, Germany
F. Bechtel, P. Buhmann, E. Butz, G. Flucke, R.H. Hamdorf, U. Holm, R. Klanner, U. Pein, N. Schirm, P. Schleper, G. Steinbrück, R. Van Staa, R. Wolf

Institut für Experimentelle Kernphysik, Karlsruhe, Germany
B. Atz, T. Barvich, P. Blüm, F. Boegelspacher, H. Bol, Z.Y. Chen, S. Chowdhury, W. De Boer, P. Dehm, G. Dirkes, M. Fahrer, U. Felzmann, M. Frey, A. Furgeri, E. Gregoriev, F. Hartmann,[1] F. Hauler, S. Heier, K. Kärcher, B. Ledermann, S. Mueller, Th. Müller, D. Neuberger, C. Piasecki, G. Quast, K. Rabbertz, A. Sabellek, A. Scheurer, F.P. Schilling, H.J. Simonis, A. Skiba, P. Steck, A. Theel, W.H. Thümmel, A. Trunov, A. Vest, T. Weiler, C. Weiser, S. Weseler,* V. Zhukov[7]

Institute of Nuclear Physics "Demokritos", Aghia Paraskevi, Greece
M. Barone, G. Daskalakis, N. Dimitriou, G. Fanourakis, C. Filippidis, T. Geralis, C. Kalfas, K. Karafasoulis, A. Koimas, A. Kyriakis, S. Kyriazopoulou, D. Loukas, A. Markou, C. Markou,

2008 JINST 3 S08004

N. Mastroyiannopoulos, C. Mavrommatis, J. Mousa, I. Papadakis, E. Petrakou, I. Siotis, K. Theofilatos, S. Tzamarias, A. Vayaki, G. Vermisoglou, A. Zachariadou

University of Athens, Athens, Greece
L. Gouskos, G. Karapostoli, P. Katsas, A. Panagiotou, C. Papadimitropoulos

University of Ioánnina, Ioánnina, Greece
X. Aslanoglou, I. Evangelou, P. Kokkas, N. Manthos, I. Papadopoulos, F.A. Triantis

KFKI Research Institute for Particle and Nuclear Physics, Budapest, Hungary
G. Bencze,[1] L. Boldizsar, G. Debreczeni, C. Hajdu,[1] P. Hidas, D. Horvath,[8] P. Kovesarki, A. Laszlo, G. Odor, G. Patay, F. Sikler, G. Veres, G. Vesztergombi, P. Zalan

Institute of Nuclear Research ATOMKI, Debrecen, Hungary
A. Fenyvesi, J. Imrek, J. Molnar, D. Novak, J. Palinkas, G. Szekely

University of Debrecen, Debrecen, Hungary
N. Beni, A. Kapusi, G. Marian, B. Radics, P. Raics, Z. Szabo, Z. Szillasi,[1] Z.L. Trocsanyi, G. Zilizi

Panjab University, Chandigarh, India
H.S. Bawa, S.B. Beri, V. Bhandari, V. Bhatnagar, M. Kaur, J.M. Kohli, A. Kumar, B. Singh, J.B. Singh

University of Delhi, Delhi, India
S. Arora, S. Bhattacharya,[9] S. Chatterji, S. Chauhan, B.C. Choudhary, P. Gupta, M. Jha, K. Ranjan, R.K. Shivpuri, A.K. Srivastava

Bhabha Atomic Research Centre, Mumbai, India
R.K. Choudhury, D. Dutta, M. Ghodgaonkar, S. Kailas, S.K. Kataria, A.K. Mohanty, L.M. Pant, P. Shukla, A. Topkar

Tata Institute of Fundamental Research — EHEP, Mumbai, India
T. Aziz, Sunanda Banerjee, S. Bose, S. Chendvankar, P.V. Deshpande, M. Guchait,[10] A. Gurtu, M. Maity,[11] G. Majumder, K. Mazumdar, A. Nayak, M.R. Patil, S. Sharma, K. Sudhakar

Tata Institute of Fundamental Research — HECR, Mumbai, India
B.S. Acharya, Sudeshna Banerjee, S. Bheesette, S. Dugad, S.D. Kalmani, V.R. Lakkireddi, N.K. Mondal, N. Panyam, P. Verma

Institute for Studies in Theoretical Physics & Mathematics (IPM), Tehran, Iran
H. Arfaei, M. Hashemi, M. Mohammadi Najafabadi, A. Moshaii, S. Paktinat Mehdiabadi

2008 JINST 3 S08004

University College Dublin, Dublin, Ireland
M. Felcini, M. Grunewald

Università di Bari, Politecnico di Bari e Sezione dell' INFN, Bari, Italy
K. Abadjiev, M. Abbrescia, L. Barbone, P. Cariola, F. Chiumarulo, A. Clemente, A. Colaleo,[1] D. Creanza, N. De Filippis,[25] M. De Palma, G. De Robertis, G. Donvito, R. Ferorelli, L. Fiore, M. Franco, D. Giordano, R. Guida, G. Iaselli, N. Lacalamita, F. Loddo, G. Maggi, M. Maggi, N. Manna, B. Marangelli, M.S. Mennea, S. My, S. Natali, S. Nuzzo, G. Papagni, C. Pinto, A. Pompili, G. Pugliese, A. Ranieri, F. Romano, G. Roselli, G. Sala, G. Selvaggi, L. Silvestris,[1] P. Tempesta, R. Trentadue, S. Tupputi, G. Zito

Università di Bologna e Sezione dell' INFN, Bologna, Italy
G. Abbiendi, W. Bacchi, C. Battilana, A.C. Benvenuti, M. Boldini, D. Bonacorsi, S. Braibant-Giacomelli, V.D. Cafaro, P. Capiluppi, A. Castro, F.R. Cavallo, C. Ciocca, G. Codispoti, M. Cuffiani, I. D'Antone, G.M. Dallavalle, F. Fabbri, A. Fanfani, S. Finelli, P. Giacomelli,[12] V. Giordano, M. Giunta, C. Grandi, M. Guerzoni, L. Guiducci, S. Marcellini, G. Masetti, A. Montanari, F.L. Navarria, F. Odorici, A. Paolucci, G. Pellegrini, A. Perrotta, A.M. Rossi, T. Rovelli, G.P. Siroli, G. Torromeo, R. Travaglini, G.P. Veronese

Università di Catania e Sezione dell' INFN, Catania, Italy
S. Albergo, M. Chiorboli, S. Costa, M. Galanti, G. Gatto Rotondo, N. Giudice, N. Guardone, F. Noto, R. Potenza, M.A. Saizu,[48] G. Salemi, C. Sutera, A. Tricomi, C. Tuve

Università di Firenze e Sezione dell' INFN, Firenze, Italy
L. Bellucci, M. Brianzi, G. Broccolo, E. Catacchini, V. Ciulli, C. Civinini, R. D'Alessandro, E. Focardi, S. Frosali, C. Genta, G. Landi, P. Lenzi, A. Macchiolo, F. Maletta, F. Manolescu, C. Marchettini, L. Masetti,[1] S. Mersi, M. Meschini, C. Minelli, S. Paoletti, G. Parrini, E. Scarlini, G. Sguazzoni

Laboratori Nazionali di Frascati dell' INFN, Frascati, Italy
L. Benussi, M. Bertani, S. Bianco, M. Caponero, D. Colonna,[1] L. Daniello, F. Fabbri, F. Felli, M. Giardoni, A. La Monaca, B. Ortenzi, M. Pallotta, A. Paolozzi, C. Paris, L. Passamonti, D. Pierluigi, B. Ponzio, C. Pucci, A. Russo, G. Saviano

Università di Genova e Sezione dell' INFN, Genova, Italy
P. Fabbricatore, S. Farinon, M. Greco, R. Musenich

Laboratori Nazionali di Legnaro dell' INFN,
Legnaro, Italy (Associated Institute)
S. Badoer, L. Berti, M. Biasotto, S. Fantinel, E. Frizziero, U. Gastaldi, M. Gulmini,[1] F. Lelli, G. Maron, S. Squizzato, N. Toniolo, S. Traldi

2008 JINST 3 S08004

INFN e Universita Degli Studi Milano-Bicocca, Milano, Italy
S. Banfi, R. Bertoni, M. Bonesini, L. Carbone, G.B. Cerati, F. Chignoli, P. D'Angelo, A. De Min, P. Dini, F.M. Farina,[1] F. Ferri, P. Govoni, S. Magni, M. Malberti, S. Malvezzi, R. Mazza, D. Menasce, V. Miccio, L. Moroni, P. Negri, M. Paganoni, D. Pedrini, A. Pullia, S. Ragazzi, N. Redaelli, M. Rovere, L. Sala, S. Sala, R. Salerno, T. Tabarelli de Fatis, V. Tancini, S. Taroni

Istituto Nazionale di Fisica Nucleare de Napoli (INFN), Napoli, Italy
A. Boiano, F. Cassese, C. Cassese, A. Cimmino, B. D'Aquino, L. Lista, D. Lomidze, P. Noli, P. Paolucci, G. Passeggio, D. Piccolo, L. Roscilli, C. Sciacca, A. Vanzanella

Università di Padova e Sezione dell' INFN, Padova, Italy
P. Azzi, N. Bacchetta,[1] L. Barcellan, M. Bellato, M. Benettoni, D. Bisello, E. Borsato, A. Candelori, R. Carlin, L. Castellani, P. Checchia, L. Ciano, A. Colombo, E. Conti, M. Da Rold, F. Dal Corso, M. De Giorgi, M. De Mattia, T. Dorigo, U. Dosselli, C. Fanin, G. Galet, F. Gasparini, U. Gasparini, A. Giraldo, P. Giubilato, F. Gonella, A. Gresele, A. Griggio, P. Guaita, A. Kaminskiy, S. Karaevskii, V. Khomenkov, D. Kostylev, S. Lacaprara, I. Lazzizzera, I. Lippi, M. Loreti, M. Margoni, R. Martinelli, S. Mattiazzo, M. Mazzucato, A.T. Meneguzzo, L. Modenese, F. Montecassiano,[1] A. Neviani, M. Nigro, A. Paccagnella, D. Pantano, A. Parenti, M. Passaseo,[1] R. Pedrotta, M. Pegoraro, G. Rampazzo, S. Reznikov, P. Ronchese, A. Sancho Daponte, P. Sartori, I. Stavitskiy, M. Tessaro, E. Torassa, A. Triossi, S. Vanini, S. Ventura, L. Ventura, M. Verlato, M. Zago, F. Zatti, P. Zotto, G. Zumerle

Università di Pavia e Sezione dell' INFN, Pavia, Italy
P. Baesso, G. Belli, U. Berzano, S. Bricola, A. Grelli, G. Musitelli, R. Nardò, M.M. Necchi, D. Pagano, S.P. Ratti, C. Riccardi, P. Torre, A. Vicini, P. Vitulo, C. Viviani

Università di Perugia e Sezione dell' INFN, Perugia, Italy
D. Aisa, S. Aisa, F. Ambroglini, M.M. Angarano, E. Babucci, D. Benedetti, M. Biasini, G.M. Bilei,[1] S. Bizzaglia, M.T. Brunetti, B. Caponeri, B. Checcucci, R. Covarelli, N. Dinu, L. Fanò, L. Farnesini, M. Giorgi, P. Lariccia, G. Mantovani, F. Moscatelli, D. Passeri, A. Piluso, P. Placidi, V. Postolache, R. Santinelli, A. Santocchia, L. Servoli, D. Spiga[1]

Università di Pisa, Scuola Normale Superiore e Sezione dell' INFN, Pisa, Italy
P. Azzurri, G. Bagliesi,[1] G. Balestri, A. Basti, R. Bellazzini, L. Benucci, J. Bernardini, L. Berretta, S. Bianucci, T. Boccali, A. Bocci, L. Borrello, F. Bosi, F. Bracci, A. Brez, F. Calzolari, R. Castaldi, U. Cazzola, M. Ceccanti, R. Cecchi, C. Cerri, A.S. Cucoanes, R. Dell'Orso, D. Dobur, S. Dutta, F. Fiori, L. Foà, A. Gaggelli, S. Gennai,[13] A. Giassi, S. Giusti, D. Kartashov, A. Kraan, L. Latronico, F. Ligabue, S. Linari, T. Lomtadze, G.A. Lungu,[48] G. Magazzu, P. Mammini, F. Mariani, G. Martinelli, M. Massa, A. Messineo, A. Moggi, F. Palla, F. Palmonari, G. Petragnani, G. Petrucciani, A. Profeti, F. Raffaelli, D. Rizzi, G. Sanguinetti, S. Sarkar, G. Segneri, D. Sentenac, A.T. Serban, A. Slav, P. Spagnolo, G. Spandre, R. Tenchini, S. Tolaini, G. Tonelli,[1] A. Venturi, P.G. Verdini, M. Vos, L. Zaccarelli

2008 JINST 3 S08004

Università di Roma I e Sezione dell' INFN, Roma, Italy
S. Baccaro,[14] L. Barone, A. Bartoloni, B. Borgia, G. Capradossi, F. Cavallari, A. Cecilia,[14] D. D'Angelo, I. Dafinei, D. Del Re, E. Di Marco, M. Diemoz, G. Ferrara,[14] C. Gargiulo, S. Guerra, M. Iannone, E. Longo, M. Montecchi,[14] M. Nuccetelli, G. Organtini, A. Palma, R. Paramatti, F. Pellegrino, S. Rahatlou, C. Rovelli, F. Safai Tehrani, A. Zullo

Università di Torino e Sezione dell' INFN, Torino, Italy
G. Alampi, N. Amapane, R. Arcidiacono, S. Argiro, M. Arneodo,[15] R. Bellan, F. Benotto, C. Biino, S. Bolognesi, M.A. Borgia, C. Botta, A. Brasolin, N. Cartiglia, R. Castello, G. Cerminara, R. Cirio, M. Cordero, M. Costa, D. Dattola, F. Daudo, G. Dellacasa, N. Demaria, G. Dughera, F. Dumitrache, R. Farano, G. Ferrero, E. Filoni, G. Kostyleva, H.E. Larsen, C. Mariotti, M. Marone, S. Maselli, E. Menichetti, P. Mereu, E. Migliore, G. Mila, V. Monaco, M. Musich, M. Nervo, M.M. Obertino,[15] R. Panero, A. Parussa, N. Pastrone, C. Peroni, G. Petrillo, A. Romero, M. Ruspa,[15] R. Sacchi, M. Scalise, A. Solano, A. Staiano, P.P. Trapani,[1] D. Trocino, V. Vaniev, A. Vilela Pereira, A. Zampieri

Università di Trieste e Sezione dell' INFN, Trieste, Italy
S. Belforte, F. Cossutti, G. Della Ricca, B. Gobbo, C. Kavka, A. Penzo

Chungbuk National University, Chongju, Korea
Y.E. Kim

Kangwon National University, Chunchon, Korea
S.K. Nam

Kyungpook National University, Daegu, Korea
D.H. Kim, G.N. Kim, J.C. Kim, D.J. Kong, S.R. Ro, D.C. Son

Wonkwang University, Iksan, Korea
S.Y. Park

Cheju National University, Jeju, Korea
Y.J. Kim

Chonnam National University, Kwangju, Korea
J.Y. Kim, I.T. Lim

Dongshin University, Naju, Korea
M.Y. Pac

Seonam University, Namwon, Korea
S.J. Lee

2008 JINST 3 S08004

Konkuk University, Seoul, Korea
S.Y. Jung, J.T. Rhee

Korea University, Seoul, Korea
S.H. Ahn, B.S. Hong, Y.K. Jeng, M.H. Kang, H.C. Kim, J.H. Kim, T.J. Kim, K.S. Lee, J.K. Lim, D.H. Moon, I.C. Park, S.K. Park, M.S. Ryu, K.-S. Sim, K.J. Son

Seoul National University, Seoul, Korea
S.J. Hong

Sungkyunkwan University, Suwon, Korea
Y.I. Choi

Centro de Investigacion y de Estudios Avanzados del IPN, Mexico City, Mexico
H. Castilla Valdez, A. Sanchez Hernandez

Universidad Iberoamericana, Mexico City, Mexico
S. Carrillo Moreno

Universidad Autonoma de San Luis Potosi, San Luis Potosi, Mexico
A. Morelos Pineda

Technische Universiteit Eindhoven, Eindhoven, Netherlands (Associated Institute)
A. Aerts, P. Van der Stok, H. Weffers

University of Auckland, Auckland, New Zealand
P. Allfrey, R.N.C. Gray, M. Hashimoto, D. Krofcheck

University of Canterbury, Christchurch, New Zealand
A.J. Bell, N. Bernardino Rodrigues, P.H. Butler, S. Churchwell, R. Knegjens, S. Whitehead, J.C. Williams

National Centre for Physics, Quaid-I-Azam University, Islamabad, Pakistan
Z. Aftab, U. Ahmad, I. Ahmed, W. Ahmed, M.I. Asghar, S. Asghar, G. Dad, M. Hafeez, H.R. Hoorani, I. Hussain, N. Hussain, M. Iftikhar, M.S. Khan, K. Mehmood, A. Osman, H. Shahzad, A.R. Zafar

National University of Sciences And Technology,
Rawalpindi Cantt, Pakistan (Associated Institute)
A. Ali, A. Bashir, A.M. Jan, A. Kamal, F. Khan, M. Saeed, S. Tanwir, M.A. Zafar

Institute of Nuclear Physics, Polish Academy of Sciences, Cracow, Poland
J. Blocki, A. Cyz, E. Gladysz-Dziadus, S. Mikocki, M. Rybczynski, J. Turnau, Z. Wlodarczyk, P. Zychowski

2008 JINST 3 S08004

Institute of Experimental Physics, Warsaw, Poland
K. Bunkowski, M. Cwiok, H. Czyrkowski, R. Dabrowski, W. Dominik, K. Doroba, A. Kalinowski, K. Kierzkowski, M. Konecki, J. Krolikowski, I.M. Kudla, M. Pietrusinski, K. Pozniak,[16] W. Zabolotny,[16] P. Zych

Soltan Institute for Nuclear Studies, Warsaw, Poland
R. Gokieli, L. Goscilo, M. Górski, K. Nawrocki, P. Traczyk, G. Wrochna, P. Zalewski

Warsaw University of Technology, Institute of Electronic Systems,
Warsaw, Poland (Associated Institute)
K.T. Pozniak, R. Romaniuk, W.M. Zabolotny

Laboratório de Instrumentação e Física Experimental de Partículas,
Lisboa, Portugal
R. Alemany-Fernandez, C. Almeida, N. Almeida, A.S. Araujo Vila Verde, T. Barata Monteiro, M. Bluj, S. Da Mota Silva, A. David Tinoco Mendes, M. Freitas Ferreira, M. Gallinaro, M. Husejko, A. Jain, M. Kazana, P. Musella, R. Nobrega, J. Rasteiro Da Silva, P.Q. Ribeiro, M. Santos, P. Silva, S. Silva, I. Teixeira, J.P. Teixeira, J. Varela,[1] G. Varner, N. Vaz Cardoso

Joint Institute for Nuclear Research, Dubna, Russia
I. Altsybeev, K. Babich, A. Belkov,* I. Belotelov, P. Bunin, S. Chesnevskaya, V. Elsha, Y. Ershov, I. Filozova, M. Finger, M. Finger Jr., A. Golunov, I. Golutvin, N. Gorbounov, I. Gramenitski, V. Kalagin, A. Kamenev, V. Karjavin, S. Khabarov, V. Khabarov, Y. Kiryushin, V. Konoplyanikov, V. Korenkov, G. Kozlov, A. Kurenkov, A. Lanev, V. Lysiakov, A. Malakhov, I. Melnitchenko, V.V. Mitsyn, K. Moisenz, P. Moisenz, S. Movchan, E. Nikonov, D. Oleynik, V. Palichik, V. Perelygin, A. Petrosyan, E. Rogalev, V. Samsonov, M. Savina, R. Semenov, S. Sergeev,[17] S. Shmatov, S. Shulha, V. Smirnov, D. Smolin, A. Tcheremoukhine, O. Teryaev, E. Tikhonenko, A. Urkinbaev, S. Vasil'ev, A. Vishnevskiy, A. Volodko, N. Zamiatin, A. Zarubin, P. Zarubin, E. Zubarev

Petersburg Nuclear Physics Institute, Gatchina (St Petersburg), Russia
N. Bondar, Y. Gavrikov, V. Golovtsov, Y. Ivanov, V. Kim, V. Kozlov, V. Lebedev, G. Makarenkov, F. Moroz, P. Neustroev, G. Obrant, E. Orishchin, A. Petrunin, Y. Shcheglov, A. Shchetkovskiy, V. Sknar, V. Skorobogatov, I. Smirnov, V. Sulimov, V. Tarakanov, L. Uvarov, S. Vavilov, G. Velichko, S. Volkov, A. Vorobyev

High Temperature Technology Center of Research & Development Institute of Power Engineering, (HTTC RDIPE),
Moscow, Russia (Associated Institute)
D. Chmelev, D. Druzhkin,[1] A. Ivanov, V. Kudinov, O. Logatchev, S. Onishchenko, A. Orlov, V. Sakharov, V. Smetannikov, A. Tikhomirov, S. Zavodthikov

2008 JINST 3 S08004

Institute for Nuclear Research, Moscow, Russia
Yu. Andreev, A. Anisimov, V. Duk, S. Gninenko, N. Golubev, D. Gorbunov, M. Kirsanov, N. Krasnikov, V. Matveev, A. Pashenkov, A. Pastsyak, V.E. Postoev, A. Sadovski, A. Skassyrskaia, Alexander Solovey, Anatoly Solovey, D. Soloviev, A. Toropin, S. Troitsky

Institute for Theoretical and Experimental Physics, Moscow, Russia
A. Alekhin, A. Baldov, V. Epshteyn, V. Gavrilov, N. Ilina, V. Kaftanov,* V. Karpishin, I. Kiselevich, V. Kolosov, M. Kossov,[1] A. Krokhotin, S. Kuleshov, A. Oulianov, A. Pozdnyakov, G. Safronov, S. Semenov, N. Stepanov, V. Stolin, E. Vlasov,[1] V. Zaytsev

Moscow State University, Moscow, Russia
E. Boos, M. Dubinin,[18] L. Dudko, A. Ershov, G. Eyyubova, A. Gribushin, V. Ilyin, V. Klyukhin, O. Kodolova, N.A. Kruglov, A. Kryukov, I. Lokhtin, L. Malinina, V. Mikhaylin, S. Petrushanko, L. Sarycheva, V. Savrin, L. Shamardin, A. Sherstnev, A. Snigirev, K. Teplov, I. Vardanyan

P.N. Lebedev Physical Institute, Moscow, Russia
A.M. Fomenko, N. Konovalova, V. Kozlov, A.I. Lebedev, N. Lvova, S.V. Rusakov, A. Terkulov

State Research Center of Russian Federation - Institute for High Energy Physics, Protvino, Russia
V. Abramov, S. Akimenko, A. Artamonov, A. Ashimova, I. Azhgirey, S. Bitioukov, O. Chikilev, K. Datsko, A. Filine, A. Godizov, P. Goncharov, V. Grishin,[1] A. Inyakin,[19] V. Kachanov, A. Kalinin, A. Khmelnikov, D. Konstantinov, A. Korablev, V. Krychkine, A. Krinitsyn, A. Levine, I. Lobov, V. Lukanin, Y. Mel'nik, V. Molchanov, V. Petrov, V. Petukhov, V. Pikalov, A. Ryazanov, R. Ryutin, V. Shelikhov, V. Skvortsov, S. Slabospitsky, A. Sobol, A. Sytine, V. Talov, L. Tourtchanovitch, S. Troshin, N. Tyurin, A. Uzunian, A. Volkov, S. Zelepoukine[20]

Electron National Research Institute, St Petersburg, Russia (Associated Institute)
V. Lukyanov, G. Mamaeva, Z. Prilutskaya, I. Rumyantsev, S. Sokha, S. Tataurschikov, I. Vasilyev

Vinca Institute of Nuclear Sciences, Belgrade, Serbia
P. Adzic, I. Anicin,[21] M. Djordjevic, D. Jovanovic,[21] D. Maletic, J. Puzovic,[21] N. Smiljkovic[1]

Centro de Investigaciones Energeticas Medioambientales y Tecnologicas (CIEMAT), Madrid, Spain
E. Aguayo Navarrete, M. Aguilar-Benitez, J. Ahijado Munoz, J.M. Alarcon Vega, J. Alberdi, J. Alcaraz Maestre, M. Aldaya Martin, P. Arce,[1] J.M. Barcala, J. Berdugo, C.L. Blanco Ramos, C. Burgos Lazaro, J. Caballero Bejar, E. Calvo, M. Cerrada, M. Chamizo Llatas, J.J. Chercoles Catalán, N. Colino, M. Daniel, B. De La Cruz, A. Delgado Peris, C. Fernandez Bedoya, A. Ferrando, M.C. Fouz, D. Francia Ferrero, J. Garcia Romero, P. Garcia-Abia, O. Gonzalez Lopez, J.M. Hernandez, M.I. Josa, J. Marin, G. Merino, A. Molinero, J.J. Navarrete, J.C. Oller, J. Puerta Pelayo, J.C. Puras Sanchez, J. Ramirez, L. Romero, C. Villanueva Munoz, C. Willmott, C. Yuste

2008 JINST 3 S08004

Universidad Autónoma de Madrid, Madrid, Spain
C. Albajar, J.F. de Trocóniz, I. Jimenez, R. Macias, R.F. Teixeira

Universidad de Oviedo, Oviedo, Spain
J. Cuevas, J. Fernández Menéndez, I. Gonzalez Caballero,[22] J. Lopez-Garcia, H. Naves Sordo, J.M. Vizan Garcia

Instituto de Física de Cantabria (IFCA), CSIC-Universidad de Cantabria, Santander, Spain
I.J. Cabrillo, A. Calderon, D. Cano Fernandez, I. Diaz Merino, J. Duarte Campderros, M. Fernandez, J. Fernandez Menendez,[23] C. Figueroa, L.A. Garcia Moral, G. Gomez, F. Gomez Casademunt, J. Gonzalez Sanchez, R. Gonzalez Suarez, C. Jorda, P. Lobelle Pardo, A. Lopez Garcia, A. Lopez Virto, J. Marco, R. Marco, C. Martinez Rivero, P. Martinez Ruiz del Arbol, F. Matorras, P. Orviz Fernandez, A. Patino Revuelta,[1] T. Rodrigo, D. Rodriguez Gonzalez, A. Ruiz Jimeno, L. Scodellaro, M. Sobron Sanudo, I. Vila, R. Vilar Cortabitarte

Universität Basel, Basel, Switzerland
M. Barbero, D. Goldin, B. Henrich, L. Tauscher, S. Vlachos, M. Wadhwa

CERN, European Organization for Nuclear Research, Geneva, Switzerland
D. Abbaneo, S.M. Abbas,[24] I. Ahmed,[24] S. Akhtar, M.I. Akhtar,[24] E. Albert, M. Alidra, S. Ashby, P. Aspell, E. Auffray, P. Baillon, A. Ball, S.L. Bally, N. Bangert, R. Barillère, D. Barney, S. Beauceron, F. Beaudette,[25] G. Benelli, R. Benetta, J.L. Benichou, W. Bialas, A. Bjorkebo, D. Blechschmidt, C. Bloch, P. Bloch, S. Bonacini, J. Bos, M. Bosteels, V. Boyer, A. Branson, H. Breuker, R. Bruneliere, O. Buchmuller, D. Campi, T. Camporesi, A. Caner, E. Cano, E. Carrone, A. Cattai, J.P. Chatelain, M. Chauvey, T. Christiansen, M. Ciganek, S. Cittolin, J. Cogan, A. Conde Garcia, H. Cornet, E. Corrin, M. Corvo, S. Cucciarelli, B. Curé, D. D'Enterria, A. De Roeck, T. de Visser, C. Delaere, M. Delattre, C. Deldicque, D. Delikaris, D. Deyrail, S. Di Vincenzo,[26] A. Domeniconi, S. Dos Santos, G. Duthion, L.M. Edera, A. Elliott-Peisert, M. Eppard, F. Fanzago, M. Favre, H. Foeth, R. Folch, N. Frank, S. Fratianni, M.A. Freire, A. Frey, A. Fucci, W. Funk, A. Gaddi, F. Gagliardi, M. Gastal, M. Gateau, J.C. Gayde, H. Gerwig, A. Ghezzi, D. Gigi, K. Gill, A.S. Giolo-Nicollerat, J.P. Girod, F. Glege, W. Glessing, R. Gomez-Reino Garrido, R. Goudard, R. Grabit, J.P. Grillet, P. Gutierrez Llamas, E. Gutierrez Mlot, J. Gutleber, R. Hall-wilton, R. Hammarstrom, M. Hansen, J. Harvey, A. Hervé, J. Hill, H.F. Hoffmann, A. Holzner, A. Honma, D. Hufnagel, M. Huhtinen, S.D. Ilie, V. Innocente, W. Jank, P. Janot, P. Jarron, M. Jeanrenaud, P. Jouvel, R. Kerkach, K. Kloukinas, L.J. Kottelat, J.C. Labbé, D. Lacroix, X. Lagrue,* C. Lasseur, E. Laure, J.F. Laurens, P. Lazeyras, J.M. Le Goff, M. Lebeau,[28] P. Lecoq, F. Lemeilleur, M. Lenzi, N. Leonardo, C. Leonidopoulos, M. Letheren, M. Liendl, F. Limia-Conde, L. Linssen, C. Ljuslin, B. Lofstedt, R. Loos, J.A. Lopez Perez, C. Lourenco, A. Lyonnet, A. Machard, R. Mackenzie, N. Magini, G. Maire, L. Malgeri, R. Malina, M. Mannelli, A. Marchioro, J. Martin, F. Meijers, P. Meridiani, E. Meschi, T. Meyer, A. Meynet Cordonnier, J.F. Michaud, L. Mirabito, R. Moser, F. Mossiere, J. Muffat-Joly, M. Mulders, J. Mulon, E. Murer, P. Mättig, A. Oh, A. Onnela, M. Oriunno, L. Orsini, J.A. Osborne,

2008 JINST 3 S08004

C. Paillard, I. Pal, G. Papotti, G. Passardi, A. Patino-Revuelta, V. Patras, B. Perea Solano, E. Perez, G. Perinic, J.F. Pernot, P. Petagna, P. Petiot, P. Petit, A. Petrilli, A. Pfeiffer, C. Piccut, M. Pimiä, R. Pintus, M. Pioppi, A. Placci, L. Pollet, H. Postema, M.J. Price, R. Principe, A. Racz, E. Radermacher, R. Ranieri, G. Raymond, P. Rebecchi, J. Rehn, S. Reynaud, H. Rezvani Naraghi, D. Ricci, M. Ridel, M. Risoldi, P. Rodrigues Simoes Moreira, A. Rohlev, G. Roiron, G. Rolandi,[27] P. Rumerio, O. Runolfsson, V. Ryjov, H. Sakulin, D. Samyn, L.C. Santos Amaral, H. Sauce, E. Sbrissa, P. Scharff-Hansen, P. Schieferdecker, W.D. Schlatter, B. Schmitt, H.G. Schmuecker, M. Schröder, C. Schwick, C. Schäfer, I. Segoni, P. Sempere Roldán, S. Sgobba, A. Sharma, P. Siegrist, C. Sigaud, N. Sinanis, T. Sobrier, P. Sphicas,[28] M. Spiropulu, G. Stefanini, A. Strandlie, F. Szoncsó, B.G. Taylor, O. Teller, A. Thea, E. Tournefier, D. Treille, P. Tropea, J. Troska, E. Tsesmelis, A. Tsirou, J. Valls, I. Van Vulpen, M. Vander Donckt, F. Vasey, M. Vazquez Acosta, L. Veillet, P. Vichoudis, G. Waurick, J.P. Wellisch, P. Wertelaers, M. Wilhelmsson, I.M. Willers, M. Winkler, M. Zanetti

Paul Scherrer Institut, Villigen, Switzerland
W. Bertl, K. Deiters, P. Dick, W. Erdmann, D. Feichtinger, K. Gabathuler, Z. Hochman, R. Horisberger, Q. Ingram, H.C. Kaestli, D. Kotlinski, S. König, P. Poerschke, D. Renker, T. Rohe, T. Sakhelashvili,[29] A. Starodumov[30]

Institute for Particle Physics, ETH Zurich, Zurich, Switzerland
V. Aleksandrov,[31] F. Behner, I. Beniozef,[31] B. Betev, B. Blau, A.M. Brett, L. Caminada,[32] Z. Chen, N. Chivarov,[31] D. Da Silva Di Calafiori, S. Dambach,[32] G. Davatz, V. Delachenal,[1] R. Della Marina, H. Dimov,[31] G. Dissertori, M. Dittmar, L. Djambazov, M. Dröge, C. Eggel,[32] J. Ehlers, R. Eichler, M. Elmiger, G. Faber, K. Freudenreich, J.F. Fuchs,[1] G.M. Georgiev,[31] C. Grab, C. Haller, J. Herrmann, M. Hilgers, W. Hintz, Hans Hofer, Heinz Hofer, U. Horisberger, I. Horvath, A. Hristov,[31] C. Humbertclaude, B. Iliev,[31] W. Kastli, A. Kruse, J. Kuipers,* U. Langenegger, P. Lecomte, E. Lejeune, G. Leshev, C. Lesmond, B. List, P.D. Luckey, W. Lustermann, J.D. Maillefaud, C. Marchica,[32] A. Maurisset,[1] B. Meier, P. Milenovic,[33] M. Milesi, F. Moortgat, I. Nanov,[31] A. Nardulli, F. Nessi-Tedaldi, B. Panev,[34] L. Pape, F. Pauss, E. Petrov,[31] G. Petrov,[31] M.M. Peynekov,[31] D. Pitzl, T. Punz, P. Riboni, J. Riedlberger, A. Rizzi, F.J. Ronga, P.A. Roykov,[31] U. Röser, D. Schinzel, A. Schöning, A. Sourkov,[35] K. Stanishev,[31] S. Stoenchev,[31] F. Stöckli, H. Suter, P. Trüb,[32] S. Udriot, D.G. Uzunova,[31] I. Veltchev,[31] G. Viertel, H.P. von Gunten, S. Waldmeier-Wicki, R. Weber, M. Weber, J. Weng, M. Wensveen,[1] F. Wittgenstein, K. Zagoursky[31]

Universität Zürich, Zürich, Switzerland
E. Alagoz, C. Amsler, V. Chiochia, C. Hoermann, C. Regenfus, P. Robmann, T. Rommerskirchen, A. Schmidt, S. Steiner, D. Tsirigkas, L. Wilke

National Central University, Chung-Li, Taiwan
S. Blyth, Y.H. Chang, E.A. Chen, A. Go, C.C. Hung, C.M. Kuo, S.W. Li, W. Lin

2008 JINST 3 S08004

National Taiwan University (NTU), Taipei, Taiwan
P. Chang, Y. Chao, K.F. Chen, Z. Gao,[1] G.W.S. Hou, Y.B. Hsiung, Y.J. Lei, S.W. Lin, R.S. Lu, J.G. Shiu, Y.M. Tzeng, K. Ueno, Y. Velikzhanin, C.C. Wang, M.-Z. Wang

Cukurova University, Adana, Turkey
S. Aydin, A. Azman, M.N. Bakirci, S. Basegmez, S. Cerci, I. Dumanoglu, S. Erturk,[36] E. Eskut, A. Kayis Topaksu, H. Kisoglu, P. Kurt, K. Ozdemir, N. Ozdes Koca, H. Ozkurt, S. Ozturk, A. Polatöz, K. Sogut,[37] H. Topakli, M. Vergili, G. Önengüt

Middle East Technical University, Physics Department, Ankara, Turkey
H. Gamsizkan, S. Sekmen, M. Serin-Zeyrek, R. Sever, M. Zeyrek

Bogaziçi University, Department of Physics, Istanbul, Turkey
M. Deliomeroglu, E. Gülmez, E. Isiksal,[38] M. Kaya,[39] O. Kaya,[39] S. Ozkorucuklu,[40] N. Sonmez[41]

Institute of Single Crystals of National Academy of Science, Kharkov, Ukraine
B. Grinev, V. Lyubynskiy, V. Senchyshyn

National Scientific Center, Kharkov Institute of Physics and Technology, Kharkov, UKRAINE
L. Levchuk, S. Lukyanenko, D. Soroka, P. Sorokin, S. Zub

Centre for Complex Cooperative Systems, University of the West of England, Bristol, United Kingdom (Associated Institute)
A. Anjum, N. Baker, T. Hauer, R. McClatchey, M. Odeh, D. Rogulin, A. Solomonides

University of Bristol, Bristol, United Kingdom
J.J. Brooke, R. Croft, D. Cussans, D. Evans, R. Frazier, N. Grant, M. Hansen, R.D. Head, G.P. Heath, H.F. Heath, C. Hill, B. Huckvale, J. Jackson,[42] C. Lynch, C.K. Mackay, S. Metson, S.J. Nash, D.M. Newbold,[42] A.D. Presland, M.G. Probert, E.C. Reid, V.J. Smith, R.J. Tapper, R. Walton

Rutherford Appleton Laboratory, Didcot, United Kingdom
E. Bateman, K.W. Bell, R.M. Brown, B. Camanzi, I.T. Church, D.J.A. Cockerill, J.E. Cole, J.F. Connolly,* J.A. Coughlan, P.S. Flower, P. Ford, V.B. Francis, M.J. French, S.B. Galagedera, W. Gannon, A.P.R. Gay, N.I. Geddes, R.J.S. Greenhalgh, R.N.J. Halsall, W.J. Haynes, J.A. Hill, F.R. Jacob, P.W. Jeffreys, L.L. Jones, B.W. Kennedy, A.L. Lintern, A.B. Lodge, A.J. Maddox, Q.R. Morrissey, P. Murray, G.N. Patrick, C.A.X. Pattison, M.R. Pearson, S.P.H. Quinton, G.J. Rogers, J.G. Salisbury, A.A. Shah, C.H. Shepherd-Themistocleous, B.J. Smith, M. Sproston, R. Stephenson, S. Taghavi, I.R. Tomalin, M.J. Torbet, J.H. Williams, W.J. Womersley, S.D. Worm, F. Xing

2008 JINST 3 S08004

Imperial College, University of London, London, United Kingdom
M. Apollonio, F. Arteche, R. Bainbridge, G. Barber, P. Barrillon, J. Batten, R. Beuselinck, P.M. Brambilla Hall, D. Britton, W. Cameron, D.E. Clark, I.W. Clark, D. Colling, N. Cripps, G. Davies, M. Della Negra, G. Dewhirst, S. Dris, C. Foudas, J. Fulcher, D. Futyan, D.J. Graham, S. Greder, S. Greenwood, G. Hall, J.F. Hassard, J. Hays, G. Iles, V. Kasey, M. Khaleeq, J. Leaver, P. Lewis, B.C. MacEvoy, O. Maroney, E.M. McLeod, D.G. Miller, J. Nash, A. Nikitenko,[30] E. Noah Messomo, M. Noy, A. Papageorgiou, M. Pesaresi, K. Petridis, D.R. Price, X. Qu, D.M. Raymond, A. Rose, S. Rutherford, M.J. Ryan, F. Sciacca, C. Seez, P. Sharp,[1] G. Sidiropoulos,[1] M. Stettler,[1] M. Stoye, J. Striebig, M. Takahashi, H. Tallini, A. Tapper, C. Timlin, L. Toudup, T. Virdee,[1] S. Wakefield, P. Walsham, D. Wardrope, M. Wingham, Y. Zhang, O. Zorba

Brunel University, Uxbridge, United Kingdom
C. Da Via, I. Goitom, P.R. Hobson, D.C. Imrie, I. Reid, C. Selby, O. Sharif, L. Teodorescu, S.J. Watts, I. Yaselli

Boston University, Boston, Massachusetts, U.S.A.
E. Hazen, A. Heering, A. Heister, C. Lawlor, D. Lazic, E. Machado, J. Rohlf, L. Sulak, F. Varela Rodriguez, S. X. Wu

Brown University, Providence, Rhode Island, U.S.A.
A. Avetisyan, T. Bose, L. Christofek, D. Cutts, S. Esen, R. Hooper, G. Landsberg, M. Narain, D. Nguyen, T. Speer, K.V. Tsang

University of California, Davis, Davis, California, U.S.A.
R. Breedon, M. Case, M. Chertok, J. Conway, P.T. Cox, J. Dolen, R. Erbacher, Y. Fisyak, E. Friis, G. Grim, B. Holbrook, W. Ko, A. Kopecky, R. Lander, F.C. Lin, A. Lister, S. Maruyama, D. Pellett, J. Rowe, M. Searle, J. Smith, A. Soha, M. Squires, M. Tripathi, R. Vasquez Sierra, C. Veelken

University of California, Los Angeles, Los Angeles, California, U.S.A.
V. Andreev, K. Arisaka, Y. Bonushkin, S. Chandramouly, D. Cline, R. Cousins, S. Erhan,[1] J. Hauser, M. Ignatenko, C. Jarvis, B. Lisowski,* C. Matthey, B. Mohr, J. Mumford, S. Otwinowski, Y. Pischalnikov, G. Rakness, P. Schlein,* Y. Shi, B. Tannenbaum, J. Tucker, V. Valuev, R. Wallny, H.G. Wang, X. Yang, Y. Zheng

University of California, Riverside, Riverside, California, U.S.A.
J. Andreeva, J. Babb, S. Campana, D. Chrisman, R. Clare, J. Ellison, D. Fortin, J.W. Gary, W. Gorn, G. Hanson, G.Y. Jeng, S.C. Kao, J.G. Layter, F. Liu, H. Liu, A. Luthra, G. Pasztor,[43] H. Rick, A. Satpathy, B.C. Shen,* R. Stringer, V. Sytnik, P. Tran, S. Villa, R. Wilken, S. Wimpenny, D. Zer-Zion

University of California, San Diego, La Jolla, California, U.S.A.
J.G. Branson, J.A. Coarasa Perez, E. Dusinberre, R. Kelley, M. Lebourgeois, J. Letts, E. Lipeles,

2008 JINST 3 S08004

B. Mangano, T. Martin, M. Mojaver, J. Muelmenstaedt, M. Norman, H.P. Paar, A. Petrucci, H. Pi, M. Pieri, A. Rana, M. Sani, V. Sharma, S. Simon, A. White, F. Würthwein, A. Yagil

University of California, Santa Barbara, Santa Barbara, California, U.S.A.
A. Affolder, A. Allen, C. Campagnari, M. D'Alfonso, A. Dierlamm,[23] J. Garberson, D. Hale, J. Incandela, P. Kalavase, S.A. Koay, D. Kovalskyi, V. Krutelyov, S. Kyre, J. Lamb, S. Lowette, M. Nikolic, V. Pavlunin, F. Rebassoo, J. Ribnik, J. Richman, R. Rossin, Y.S. Shah, D. Stuart, S. Swain, J.R. Vlimant, D. White, M. Witherell

California Institute of Technology, Pasadena, California, U.S.A.
A. Bornheim, J. Bunn, J. Chen, G. Denis, P. Galvez, M. Gataullin, I. Legrand, V. Litvine, Y. Ma, R. Mao, D. Nae, I. Narsky, H.B. Newman, T. Orimoto, C. Rogan, S. Shevchenko, C. Steenberg, X. Su, M. Thomas, V. Timciuc, F. van Lingen, J. Veverka, B.R. Voicu,[1] A. Weinstein, R. Wilkinson, Y. Xia, Y. Yang, L.Y. Zhang, K. Zhu, R.Y. Zhu

Carnegie Mellon University, Pittsburgh, Pennsylvania, U.S.A.
T. Ferguson, D.W. Jang, S.Y. Jun, M. Paulini, J. Russ, N. Terentyev, H. Vogel, I. Vorobiev

University of Colorado at Boulder, Boulder, Colorado, U.S.A.
M. Bunce, J.P. Cumalat, M.E. Dinardo, B.R. Drell, W.T. Ford, K. Givens, B. Heyburn, D. Johnson, U. Nauenberg, K. Stenson, S.R. Wagner

Cornell University, Ithaca, New York, U.S.A.
L. Agostino, J. Alexander, F. Blekman, D. Cassel, S. Das, J.E. Duboscq, L.K. Gibbons, B. Heltsley, C.D. Jones, V. Kuznetsov, J.R. Patterson, D. Riley, A. Ryd, S. Stroiney, W. Sun, J. Thom, J. Vaughan, P. Wittich

Fairfield University, Fairfield, Connecticut, U.S.A.
C.P. Beetz, G. Cirino, V. Podrasky, C. Sanzeni, D. Winn

Fermi National Accelerator Laboratory, Batavia, Illinois, U.S.A.
S. Abdullin,[1] M.A. Afaq,[1] M. Albrow, J. Amundson, G. Apollinari, M. Atac, W. Badgett, J.A. Bakken, B. Baldin, K. Banicz, L.A.T. Bauerdick, A. Baumbaugh, J. Berryhill, P.C. Bhat, M. Binkley, I. Bloch, F. Borcherding, A. Boubekeur, M. Bowden, K. Burkett, J.N. Butler, H.W.K. Cheung, G. Chevenier,[1] F. Chlebana, I. Churin, S. Cihangir, W. Dagenhart, M. Demarteau, D. Dykstra, D.P. Eartly, J.E. Elias, V.D. Elvira, D. Evans, I. Fisk, J. Freeman, I. Gaines, P. Gartung, F.J.M. Geurts, L. Giacchetti, D.A. Glenzinski, E. Gottschalk, T. Grassi, D. Green, C. Grimm, Y. Guo, O. Gutsche, A. Hahn, J. Hanlon, R.M. Harris, T. Hesselroth, S. Holm, B. Holzman, E. James, H. Jensen, M. Johnson, U. Joshi, B. Klima, S. Kossiakov, K. Kousouris, J. Kowalkowski, T. Kramer, S. Kwan, C.M. Lei, M. Leininger, S. Los, L. Lueking, G. Lukhanin, S. Lusin,[1] K. Maeshima, J.M. Marraffino, D. Mason, P. McBride, T. Miao, S. Moccia, N. Mokhov, S. Mrenna, S.J. Murray, C. Newman-Holmes, C. Noeding, V. O'Dell, M. Paterno, D. Petravick, R. Pordes, O. Prokofyev, N. Ratnikova, A. Ronzhin, V. Sekhri, E. Sexton-Kennedy, I. Sfiligoi,

2008 JINST 3 S08004

T.M. Shaw, E. Skup, R.P. Smith,* W.J. Spalding, L. Spiegel, M. Stavrianakou, G. Stiehr, A.L. Stone, I. Suzuki, P. Tan, W. Tanenbaum, L.E. Temple, S. Tkaczyk,[1] L. Uplegger, E.W. Vaandering, R. Vidal, R. Wands, H. Wenzel, J. Whitmore, E. Wicklund, W.M. Wu, Y. Wu, J. Yarba, V. Yarba, F. Yumiceva, J.C. Yun, T. Zimmerman

University of Florida, Gainesville, Florida, U.S.A.
D. Acosta, P. Avery, V. Barashko, P. Bartalini, D. Bourilkov, R. Cavanaugh, S. Dolinsky, A. Drozdetskiy, R.D. Field, Y. Fu, I.K. Furic, L. Gorn, D. Holmes, B.J. Kim, S. Klimenko, J. Konigsberg, A. Korytov, K. Kotov, P. Levchenko, A. Madorsky, K. Matchev, G. Mitselmakher, Y. Pakhotin, C. Prescott, L. Ramond, P. Ramond, M. Schmitt, B. Scurlock, J. Stasko, H. Stoeck, D. Wang, J. Yelton

Florida International University, Miami, Florida, U.S.A.
V. Gaultney, L. Kramer, L.M. Lebolo, S. Linn, P. Markowitz, G. Martinez, J.L. Rodriguez

Florida State University, Tallahassee, Florida, U.S.A.
T. Adams, A. Askew, O. Atramentov, M. Bertoldi, W.G.D. Dharmaratna,[49] Y. Gershtein, S.V. Gleyzer, S. Hagopian, V. Hagopian, C.J. Jenkins, K.F. Johnson, H. Prosper, D. Simek, J. Thomaston

Florida Institute of Technology, Melbourne, Florida, U.S.A.
M. Baarmand, L. Baksay,[44] S. Guragain, M. Hohlmann, H. Mermerkaya, R. Ralich, I. Vodopiyanov

University of Illinois at Chicago (UIC), Chicago, Illinois, U.S.A.
M.R. Adams, I. M. Anghel, L. Apanasevich, O. Barannikova, V.E. Bazterra, R.R. Betts, C. Dragoiu, E.J. Garcia-Solis, C.E. Gerber, D.J. Hofman, R. Hollis, A. Iordanova, S. Khalatian, C. Mironov, E. Shabalina, A. Smoron, N. Varelas

The University of Iowa, Iowa City, Iowa, U.S.A.
U. Akgun, E.A. Albayrak, A.S. Ayan, R. Briggs, K. Cankocak,[45] W. Clarida, A. Cooper, P. Debbins, F. Duru, M. Fountain, E. McCliment, J.P. Merlo, A. Mestvirishvili, M.J. Miller, A. Moeller, C.R. Newsom, E. Norbeck, J. Olson, Y. Onel, L. Perera, I. Schmidt, S. Wang, T. Yetkin

Iowa State University, Ames, Iowa, U.S.A.
E.W. Anderson, H. Chakir, J.M. Hauptman, J. Lamsa

Johns Hopkins University, Baltimore, Maryland, U.S.A.
B.A. Barnett, B. Blumenfeld, C.Y. Chien, G. Giurgiu, A. Gritsan, D.W. Kim, C.K. Lae, P. Maksimovic, M. Swartz, N. Tran

The University of Kansas, Lawrence, Kansas, U.S.A.
P. Baringer, A. Bean, J. Chen, D. Coppage, O. Grachov, M. Murray, V. Radicci, J.S. Wood, V. Zhukova

2008 JINST 3 S08004

Kansas State University, Manhattan, Kansas, U.S.A.
D. Bandurin, T. Bolton, K. Kaadze, W.E. Kahl, Y. Maravin, D. Onoprienko, R. Sidwell, Z. Wan

Lawrence Livermore National Laboratory, Livermore, California, U.S.A.
B. Dahmes, J. Gronberg, J. Hollar, D. Lange, D. Wright, C.R. Wuest

University of Maryland, College Park, Maryland, U.S.A.
D. Baden, R. Bard, S.C. Eno, D. Ferencek, N.J. Hadley, R.G. Kellogg, M. Kirn, S. Kunori, E. Lockner, F. Ratnikov, F. Santanastasio, A. Skuja, T. Toole, L. Wang, M. Wetstein

Massachusetts Institute of Technology, Cambridge, Massachusetts, U.S.A.
B. Alver, M. Ballintijn, G. Bauer, W. Busza, G. Gomez Ceballos, K.A. Hahn, P. Harris, M. Klute, I. Kravchenko, W. Li, C. Loizides, T. Ma, S. Nahn, C. Paus, S. Pavlon, J. Piedra Gomez, C. Roland, G. Roland, M. Rudolph, G. Stephans, K. Sumorok, S. Vaurynovich, E.A. Wenger, B. Wyslouch

University of Minnesota, Minneapolis, Minnesota, U.S.A.
D. Bailleux, S. Cooper, P. Cushman, A. De Benedetti, A. Dolgopolov, P.R. Dudero, R. Egeland, G. Franzoni, W.J. Gilbert, D. Gong, J. Grahl, J. Haupt, K. Klapoetke, I. Kronkvist, Y. Kubota, J. Mans, R. Rusack, S. Sengupta, B. Sherwood, A. Singovsky, P. Vikas, J. Zhang

University of Mississippi, University, Mississippi, U.S.A.
M. Booke, L.M. Cremaldi, R. Godang, R. Kroeger, M. Reep, J. Reidy, D.A. Sanders, P. Sonnek, D. Summers, S. Watkins

University of Nebraska-Lincoln, Lincoln, Nebraska, U.S.A.
K. Bloom, B. Bockelman, D.R. Claes, A. Dominguez, M. Eads, M. Furukawa, J. Keller, T. Kelly, C. Lundstedt, S. Malik, G.R. Snow, D. Swanson

State University of New York at Buffalo, Buffalo, New York, U.S.A.
K.M. Ecklund, I. Iashvili, A. Kharchilava, A. Kumar, M. Strang

Northeastern University, Boston, Massachusetts, U.S.A.
G. Alverson, E. Barberis, O. Boeriu, G. Eulisse, T. McCauley, Y. Musienko,[46] S. Muzaffar, I. Osborne, S. Reucroft, J. Swain, L. Taylor, L. Tuura

Northwestern University, Evanston, Illinois, U.S.A.
B. Gobbi, M. Kubantsev, A. Kubik, R.A. Ofierzynski, M. Schmitt, E. Spencer, S. Stoynev, M. Szleper, M. Velasco, S. Won

University of Notre Dame, Notre Dame, Indiana, U.S.A.
K. Andert, B. Baumbaugh, B.A. Beiersdorf, L. Castle, J. Chorny, A. Goussiou, M. Hildreth, C. Jessop, D.J. Karmgard, T. Kolberg, J. Marchant, N. Marinelli, M. McKenna, R. Ruchti, M. Vigneault, M. Wayne, D. Wiand

2008 JINST 3 S08004

The Ohio State University, Columbus, Ohio, U.S.A.
B. Bylsma, L.S. Durkin, J. Gilmore, J. Gu, P. Killewald, T.Y. Ling, C.J. Rush, V. Sehgal, G. Williams

Princeton University, Princeton, New Jersey, U.S.A.
N. Adam, S. Chidzik, P. Denes,[47] P. Elmer, A. Garmash, D. Gerbaudo, V. Halyo, J. Jones, D. Marlow, J. Olsen, P. Piroué, D. Stickland, C. Tully, J.S. Werner, T. Wildish, S. Wynhoff,* Z. Xie

University of Puerto Rico, Mayaguez, Puerto Rico, U.S.A.
X.T. Huang, A. Lopez, H. Mendez, J.E. Ramirez Vargas, A. Zatserklyaniy

Purdue University, West Lafayette, Indiana, U.S.A.
A. Apresyan, K. Arndt, V.E. Barnes, G. Bolla, D. Bortoletto, A. Bujak, A. Everett, M. Fahling, A.F. Garfinkel, L. Gutay, N. Ippolito, Y. Kozhevnikov,[1] A.T. Laasanen, C. Liu, V. Maroussov, S. Medved, P. Merkel, D.H. Miller, J. Miyamoto, N. Neumeister, A. Pompos, A. Roy, A. Sedov, I. Shipsey

Purdue University Calumet, Hammond, Indiana, U.S.A.
V. Cuplov, N. Parashar

Rice University, Houston, Texas, U.S.A.
P. Bargassa, S.J. Lee, J.H. Liu, D. Maronde, M. Matveev, T. Nussbaum, B.P. Padley, J. Roberts, A. Tumanov

University of Rochester, Rochester, New York, U.S.A.
A. Bodek, H. Budd, J. Cammin, Y.S. Chung, P. De Barbaro,[1] R. Demina, G. Ginther, Y. Gotra, S. Korjenevski, D.C. Miner, W. Sakumoto, P. Slattery, M. Zielinski

The Rockefeller University, New York, New York, U.S.A.
A. Bhatti, L. Demortier, K. Goulianos, K. Hatakeyama, C. Mesropian

Rutgers, the State University of New Jersey, Piscataway, New Jersey, U.S.A.
E. Bartz, S.H. Chuang, J. Doroshenko, E. Halkiadakis, P.F. Jacques, D. Khits, A. Lath, A. Macpherson,[1] R. Plano, K. Rose, S. Schnetzer, S. Somalwar, R. Stone, T.L. Watts

University of Tennessee, Knoxville, Tennessee, U.S.A.
G. Cerizza, M. Hollingsworth, J. Lazoflores, G. Ragghianti, S. Spanier, A. York

Texas A&M University, College Station, Texas, U.S.A.
A. Aurisano, A. Golyash, T. Kamon, C.N. Nguyen, J. Pivarski, A. Safonov, D. Toback, M. Weinberger

2008 JINST 3 S08004

Texas Tech University, Lubbock, Texas, U.S.A.
N. Akchurin, L. Berntzon, K.W. Carrell, K. Gumus, C. Jeong, H. Kim, S.W. Lee, B.G. Mc Gonagill, Y. Roh, A. Sill, M. Spezziga, R. Thomas, I. Volobouev, E. Washington, R. Wigmans, E. Yazgan

Vanderbilt University, Nashville, Tennessee, U.S.A.
T. Bapty, D. Engh, C. Florez, W. Johns, T. Keskinpala, E. Luiggi Lopez, S. Neema, S. Nordstrom, S. Pathak, P. Sheldon

University of Virginia, Charlottesville, Virginia, U.S.A.
D. Andelin, M.W. Arenton, M. Balazs, M. Buehler, S. Conetti, B. Cox, R. Hirosky, M. Humphrey, R. Imlay, A. Ledovskoy, D. Phillips II, H. Powell, M. Ronquest, R. Yohay

University of Wisconsin, Madison, Wisconsin, U.S.A.
M. Anderson, Y.W. Baek, J.N. Bellinger, D. Bradley, P. Cannarsa, D. Carlsmith, I. Crotty,[1] S. Dasu, F. Feyzi, T. Gorski, L. Gray, K.S. Grogg, M. Grothe, M. Jaworski, P. Klabbers, J. Klukas, A. Lanaro, C. Lazaridis, J. Leonard, R. Loveless, M. Magrans de Abril, A. Mohapatra, G. Ott, W.H. Smith, M. Weinberg, D. Wenman

Yale University, New Haven, Connecticut, U.S.A.
G.S. Atoian, S. Dhawan, V. Issakov, H. Neal, A. Poblaguev, M.E. Zeller

Institute of Nuclear Physics of the Uzbekistan Academy of Sciences, Ulugbek, Tashkent, Uzbekistan
G. Abdullaeva, A. Avezov, M.I. Fazylov, E.M. Gasanov, A. Khugaev, Y.N. Koblik, M. Nishonov, K. Olimov, A. Umaraliev, B.S. Yuldashev

[1]Also at CERN, European Organization for Nuclear Research, Geneva, Switzerland
[2]Now at Universidade Federal do ABC, Santo Andre, Brazil
[3]Now at Laboratoire de l'Accélérateur Linéaire, Orsay, France
[4]Now at CERN, European Organization for Nuclear Research, Geneva, Switzerland
[5]Also at Université de Haute-Alsace, Mulhouse, France
[6]Also at Université Louis Pasteur, Strasbourg, France
[7]Also at Moscow State University, Moscow, Russia
[8]Also at Institute of Nuclear Research ATOMKI, Debrecen, Hungary
[9]Also at University of California, San Diego, La Jolla, U.S.A.
[10]Also at Tata Institute of Fundamental Research - HECR, Mumbai, India
[11]Also at University of Visva-Bharati, Santiniketan, India
[12]Also at University of California, Riverside, Riverside, U.S.A.
[13]Also at Centro Studi Enrico Fermi, Roma, Italy
[14]Also at ENEA - Casaccia Research Center, S. Maria di Galeria, Italy
[15]Now at Università del Piemonte Orientale, Novara, Italy

2008 JINST 3 S08004

[16]Also at Warsaw University of Technology, Institute of Electronic Systems, Warsaw, Poland
[17]Also at Fermi National Accelerator Laboratory, Batavia, U.S.A.
[18]Also at California Institute of Technology, Pasadena, U.S.A.
[19]Also at University of Minnesota, Minneapolis, U.S.A.
[20]Also at Institute for Particle Physics, ETH Zurich, Zurich, Switzerland
[21]Also at Faculty of Physics of University of Belgrade, Belgrade, Serbia
[22]Now at Instituto de Física de Cantabria (IFCA), CSIC-Universidad de Cantabria, Santander, Spain
[23]Also at Institut für Experimentelle Kernphysik, Karlsruhe, Germany
[24]Also at National Centre for Physics, Quaid-I-Azam University, Islamabad, Pakistan
[25]Also at Laboratoire Leprince-Ringuet, Ecole Polytechnique, IN2P3-CNRS, Palaiseau, France
[26]Also at Alstom Contracting, Geneve, Switzerland
[27]Also at Scuola Normale Superiore and Sezione INFN, Pisa, Italy
[28]Also at University of Athens, Athens, Greece
[29]Also at Institute of High Energy Physics and Informatization, Tbilisi State University, Tbilisi, Georgia
[30]Also at Institute for Theoretical and Experimental Physics, Moscow, Russia
[31]Also at Central Laboratory of Mechatronics and Instrumentation, Sofia, Bulgaria
[32]Also at Paul Scherrer Institut, Villigen, Switzerland
[33]Also at Vinca Institute of Nuclear Sciences, Belgrade, Serbia
[34]Also at Institute for Nuclear Research and Nuclear Energy, Sofia, Bulgaria
[35]Also at State Research Center of Russian Federation - Institute for High Energy Physics, Protvino, Russia
[36]Also at Nigde University, Nigde, Turkey
[37]Also at Mersin University, Mersin, Turkey
[38]Also at Marmara University, Istanbul, Turkey
[39]Also at Kafkas University, Kars, Turkey
[40]Also at Suleyman Demirel University, Isparta, Turkey
[41]Also at Ege University, Izmir, Turkey
[42]Also at Rutherford Appleton Laboratory, Didcot, United Kingdom
[43]Also at KFKI Research Institute for Particle and Nuclear Physics, Budapest, Hungary
[44]Also at University of Debrecen, Debrecen, Hungary
[45]Also at Mugla University, Mugla, Turkey
[46]Also at Institute for Nuclear Research, Moscow, Russia
[47]Now at Lawrence Berkeley National Laboratory, Berkeley, U.S.A.
[48]Now at National Institute of Physics and Nuclear Engineering, Bucharest, Romania
[49]Also at University of Ruhuna, Matara, Sri Lanka
[*]Deceased

Corresponding author: Roberto Tenchini (Roberto.Tenchini@cern.ch)

2008 JINST 3 S08004

Contents

2008 JINST 3 S08004

2008 JINST 3 S08004

2008 JINST 3 S08004

2008 JINST 3 S08004

Chapter 1

Introduction

The Compact Muon Solenoid (CMS) detector is a multi-purpose apparatus due to operate at the Large Hadron Collider (LHC) at CERN. The LHC is presently being constructed in the already existing 27-km LEP tunnel in the Geneva region. It will yield head-on collisions of two proton (ion) beams of 7 TeV (2.75 TeV per nucleon) each, with a design luminosity of $10^{34}\,\mathrm{cm}^{-2}\mathrm{s}^{-1}$ ($10^{27}\,\mathrm{cm}^{-2}\mathrm{s}^{-1}$). This paper provides a description of the design and construction of the CMS detector. CMS is installed about 100 metres underground close to the French village of Cessy, between Lake Geneva and the Jura mountains.

The prime motivation of the LHC is to elucidate the nature of electroweak symmetry breaking for which the Higgs mechanism is presumed to be responsible. The experimental study of the Higgs mechanism can also shed light on the mathematical consistency of the Standard Model at energy scales above about 1 TeV. Various alternatives to the Standard Model invoke new symmetries, new forces or constituents. Furthermore, there are high hopes for discoveries that could pave the way toward a unified theory. These discoveries could take the form of supersymmetry or extra dimensions, the latter often requiring modification of gravity at the TeV scale. Hence there are many compelling reasons to investigate the TeV energy scale.

The LHC will also provide high-energy heavy-ion beams at energies over 30 times higher than at the previous accelerators, allowing us to further extend the study of QCD matter under extreme conditions of temperature, density, and parton momentum fraction (low-x).

Hadron colliders are well suited to the task of exploring new energy domains, and the region of 1 TeV constituent centre-of-mass energy can be explored if the proton energy and the luminosity are high enough. The beam energy and the design luminosity of the LHC have been chosen in order to study physics at the TeV energy scale. A wide range of physics is potentially possible with the seven-fold increase in energy and a hundred-fold increase in integrated luminosity over the previous hadron collider experiments. These conditions also require a very careful design of the detectors.

The total proton-proton cross-section at $\sqrt{s} = 14\,\mathrm{TeV}$ is expected to be roughly 100 mb. At design luminosity the general-purpose detectors will therefore observe an event rate of approximately 10^9 inelastic events/s. This leads to a number of formidable experimental challenges. The online event selection process (*trigger*) must reduce the huge rate to about 100 events/s for storage and subsequent analysis. The short time between bunch crossings, 25 ns, has major implications for the design of the read-out and trigger systems.

At the design luminosity, a mean of about 20 inelastic collisions will be superimposed on the event of interest. This implies that around 1000 charged particles will emerge from the interaction region every 25 ns. The products of an interaction under study may be confused with those from other interactions in the same bunch crossing. This problem clearly becomes more severe when the response time of a detector element and its electronic signal is longer than 25 ns. The effect of this pile-up can be reduced by using high-granularity detectors with good time resolution, resulting in low occupancy. This requires a large number of detector channels. The resulting millions of detector electronic channels require very good synchronization.

The large flux of particles coming from the interaction region leads to high radiation levels, requiring radiation-hard detectors and front-end electronics.

The detector requirements for CMS to meet the goals of the LHC physics programme can be summarised as follows:

- Good muon identification and momentum resolution over a wide range of momenta and angles, good dimuon mass resolution ($\approx 1\%$ at 100 GeV), and the ability to determine unambiguously the charge of muons with $p < 1$ TeV;
- Good charged-particle momentum resolution and reconstruction efficiency in the inner tracker. Efficient triggering and offline tagging of τ's and b-jets, requiring pixel detectors close to the interaction region;
- Good electromagnetic energy resolution, good diphoton and dielectron mass resolution ($\approx 1\%$ at 100 GeV), wide geometric coverage, π^0 rejection, and efficient photon and lepton isolation at high luminosities;
- Good missing-transverse-energy and dijet-mass resolution, requiring hadron calorimeters with a large hermetic geometric coverage and with fine lateral segmentation.

The design of CMS, detailed in the next section, meets these requirements. The main distinguishing features of CMS are a high-field solenoid, a full-silicon-based inner tracking system, and a homogeneous scintillating-crystals-based electromagnetic calorimeter.

The coordinate system adopted by CMS has the origin centered at the nominal collision point inside the experiment, the y-axis pointing vertically upward, and the x-axis pointing radially inward toward the center of the LHC. Thus, the z-axis points along the beam direction toward the Jura mountains from LHC Point 5. The azimuthal angle ϕ is measured from the x-axis in the x-y plane and the radial coordinate in this plane is denoted by r. The polar angle θ is measured from the z-axis. Pseudorapidity is defined as $\eta = -\ln\tan(\theta/2)$. Thus, the momentum and energy transverse to the beam direction, denoted by p_T and E_T, respectively, are computed from the x and y components. The imbalance of energy measured in the transverse plane is denoted by E_T^{miss}.

1.1 General concept

An important aspect driving the detector design and layout is the choice of the magnetic field configuration for the measurement of the momentum of muons. Large bending power is needed

2008 JINST 3 S08004

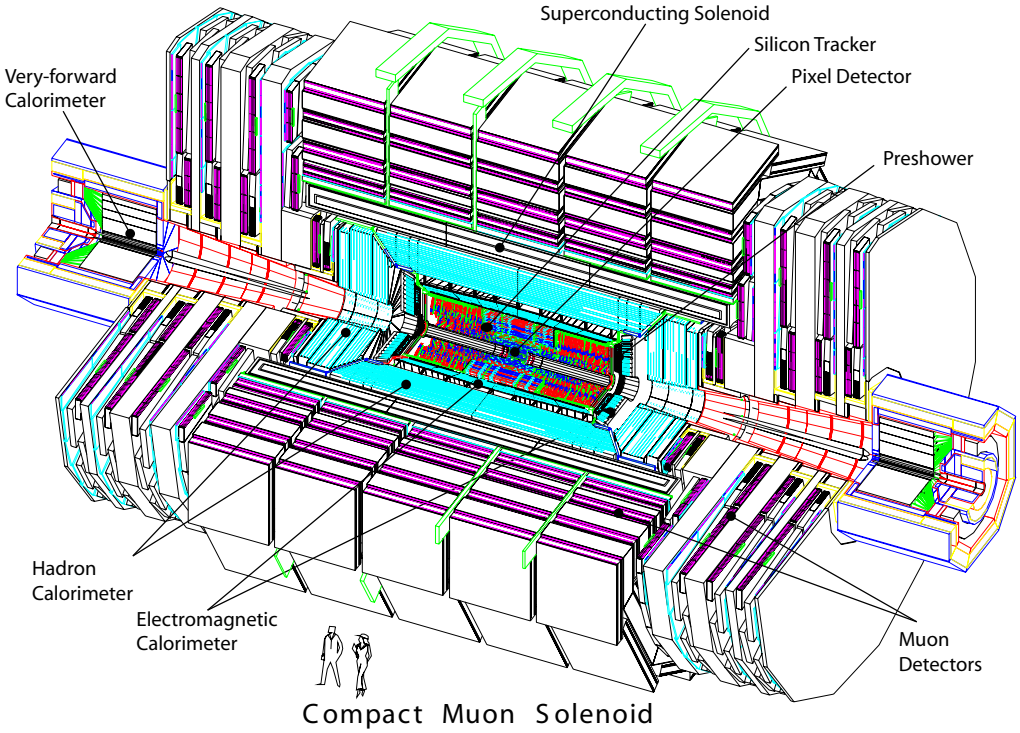

Figure 1.1: A perspective view of the CMS detector.

to measure precisely the momentum of high-energy charged particles. This forces a choice of superconducting technology for the magnets.

The overall layout of CMS [1] is shown in figure 1.1. At the heart of CMS sits a 13-m-long, 6-m-inner-diameter, 4-T superconducting solenoid providing a large bending power (12 Tm) before the muon bending angle is measured by the muon system. The return field is large enough to saturate 1.5 m of iron, allowing 4 muon *stations* to be integrated to ensure robustness and full geometric coverage. Each muon station consists of several layers of aluminium drift tubes (DT) in the barrel region and cathode strip chambers (CSC) in the endcap region, complemented by resistive plate chambers (RPC).

The bore of the magnet coil is large enough to accommodate the inner tracker and the calorimetry inside. The tracking volume is given by a cylinder of 5.8-m length and 2.6-m diameter. In order to deal with high track multiplicities, CMS employs 10 layers of silicon microstrip detectors, which provide the required granularity and precision. In addition, 3 layers of silicon pixel detectors are placed close to the interaction region to improve the measurement of the impact parameter of charged-particle tracks, as well as the position of secondary vertices. The expected muon momentum resolution using only the muon system, using only the inner tracker, and using both sub-detectors is shown in figure 1.2.

The electromagnetic calorimeter (ECAL) uses lead tungstate ($PbWO_4$) crystals with coverage in pseudorapidity up to $|\eta| < 3.0$. The scintillation light is detected by silicon avalanche photodiodes (APDs) in the barrel region and vacuum phototriodes (VPTs) in the endcap region. A preshower system is installed in front of the endcap ECAL for π^0 rejection. The energy resolution

2008 JINST 3 S08004

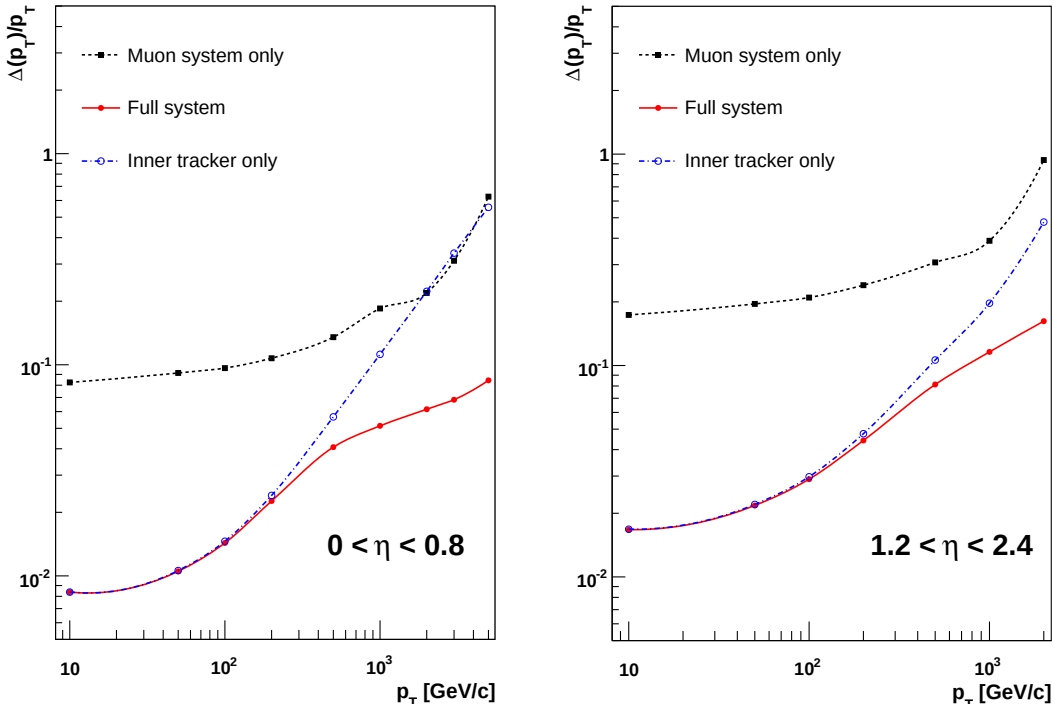

Figure 1.2: The muon transverse-momentum resolution as a function of the transverse-momentum (p_T) using the muon system only, the inner tracking only, and both. Left panel: $|\eta| < 0.8$, right panel: $1.2 < |\eta| < 2.4$.

of the ECAL, for incident electrons as measured in a beam test, is shown in figure 1.3; the stochastic (S), noise (N), and constant (C) terms given in the figure are determined by fitting the measured points to the function

$$\left(\frac{\sigma}{E}\right)^2 = \left(\frac{S}{\sqrt{E}}\right)^2 + \left(\frac{N}{E}\right)^2 + C^2 . \tag{1.1}$$

The ECAL is surrounded by a brass/scintillator sampling hadron calorimeter (HCAL) with coverage up to $|\eta| < 3.0$. The scintillation light is converted by wavelength-shifting (WLS) fibres embedded in the scintillator tiles and channeled to photodetectors via clear fibres. This light is detected by photodetectors (hybrid photodiodes, or HPDs) that can provide gain and operate in high axial magnetic fields. This central calorimetry is complemented by a *tail-catcher* in the barrel region (HO) ensuring that hadronic showers are sampled with nearly 11 hadronic interaction lengths. Coverage up to a pseudorapidity of 5.0 is provided by an iron/quartz-fibre calorimeter. The Cerenkov light emitted in the quartz fibres is detected by photomultipliers. The forward calorimeters ensure full geometric coverage for the measurement of the transverse energy in the event. An even higher forward coverage is obtained with additional dedicated calorimeters (CASTOR, ZDC, not shown in figure 1.1) and with the TOTEM [2] tracking detectors. The expected jet transverse-energy resolution in various pseudorapidity regions is shown in figure 1.4.

The CMS detector is 21.6-m long and has a diameter of 14.6 m. It has a total weight of 12 500 t. The ECAL thickness, in radiation lengths, is larger than 25 X_0, while the HCAL thickness, in interaction lengths, varies in the range 7–11 λ_I (10–15 λ_I with the HO included), depending on η.

2008 JINST 3 S08004

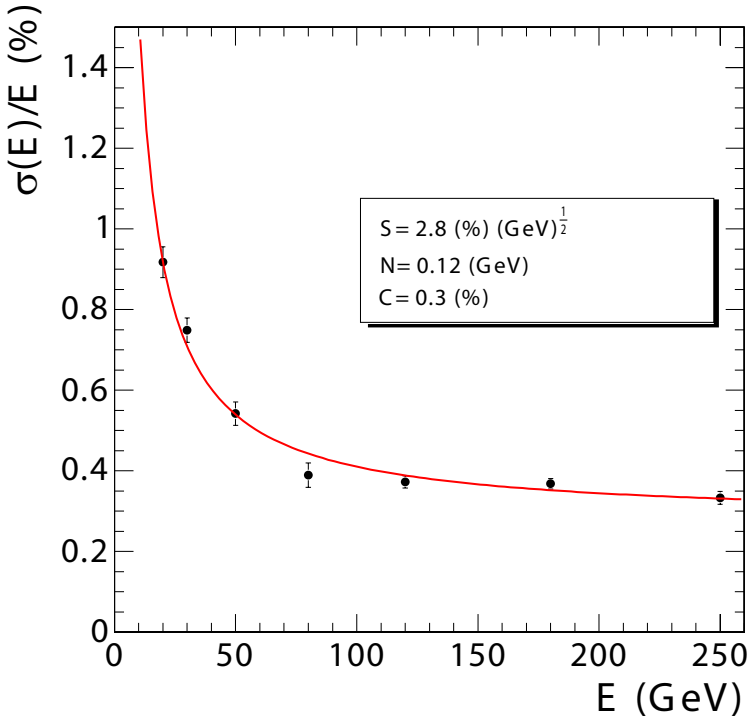

Figure 1.3: ECAL energy resolution, $\sigma(\mathrm{E})/\mathrm{E}$, as a function of electron energy as measured from a beam test. The energy was measured in an array of 3×3 crystals with an electron impacting the central crystal. The points correspond to events taken restricting the incident beam to a narrow (4×4 mm^2) region. The stochastic (S), noise (N), and constant (C) terms are given.

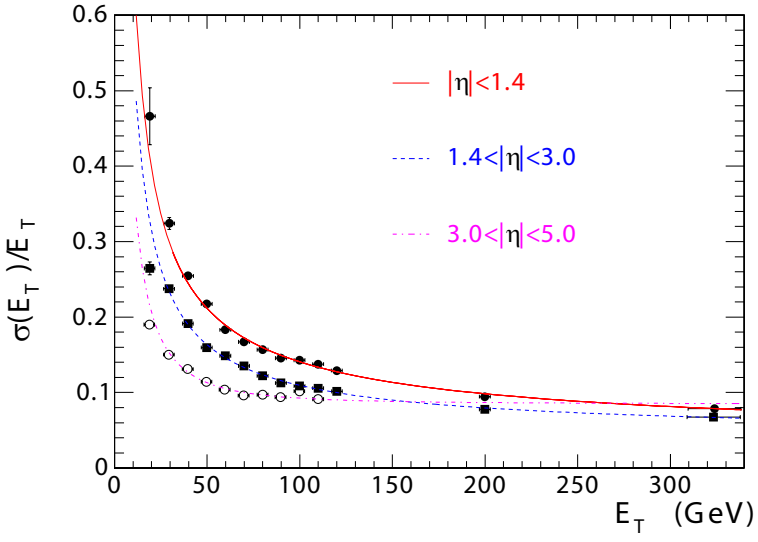

Figure 1.4: The jet transverse-energy resolution as a function of the jet transverse energy for barrel jets ($|\eta| < 1.4$), endcap jets ($1.4 < |\eta| < 3.0$), and very forward jets ($3.0 < |\eta| < 5.0$). The jets are reconstructed with an iterative cone algorithm (cone radius = 0.5).

2008 JINST 3 S08004

Chapter 2

Superconducting magnet

2.1 Overview

The superconducting magnet for CMS [3–6] has been designed to reach a 4-T field in a free bore of 6-m diameter and 12.5-m length with a stored energy of 2.6 GJ at full current. The flux is returned through a 10 000-t yoke comprising 5 wheels and 2 endcaps, composed of three disks each (figure 1.1). The distinctive feature of the 220-t cold mass is the 4-layer winding made from a stabilised reinforced NbTi conductor. The ratio between stored energy and cold mass is high (11.6 KJ/kg), causing a large mechanical deformation (0.15%) during energising, well beyond the values of previous solenoidal detector magnets. The parameters of the CMS magnet are summarised in table 2.1. The magnet was designed to be assembled and tested in a surface hall (SX5), prior to being lowered 90 m below ground to its final position in the experimental cavern. After provisional connection to its ancillaries, the CMS Magnet has been fully and successfully tested and commissioned in SX5 during autumn 2006.

2.2 Main features of the magnet components

2.2.1 Superconducting solenoid

The superconducting solenoid (see an artistic view in figure 2.1 and a picture taken during assembly in the vertical position in SX5 in figure 2.2) presents three new features with respect to previous detector magnets:

- Due to the number of ampere-turns required for generating a field of 4 T (41.7 MA-turn), the winding is composed of 4 layers, instead of the usual 1 (as in the Aleph [7] and Delphi [8] coils) or maximum 2 layers (as in the ZEUS [9] and BaBar [10] coils);
- The conductor, made from a Rutherford-type cable co-extruded with pure aluminium (the so-called insert), is mechanically reinforced with an aluminium alloy;
- The dimensions of the solenoid are very large (6.3-m cold bore, 12.5-m length, 220-t mass).

For physics reasons, the radial extent of the coil (ΔR) had to be kept small, and thus the CMS coil is in effect a "thin coil" ($\Delta R/R \sim 0.1$). The hoop strain (ε) is then determined by the

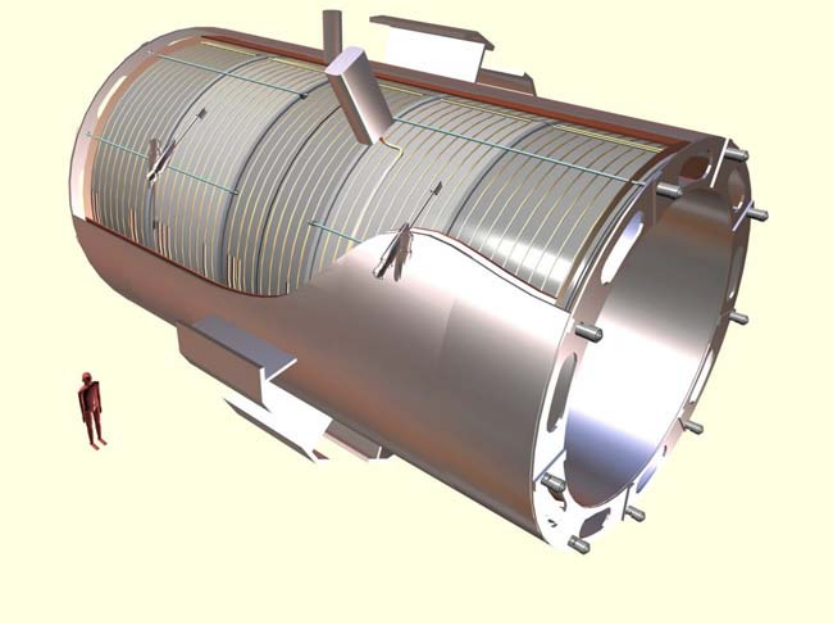

Figure 2.1: General artistic view of the 5 modules composing the cold mass inside the cryostat, with details of the supporting system (vertical, radial and longitudinal tie rods).

magnetic pressure ($P = \frac{B_0^2}{2\mu_0} = 6.4$ MPa), the elastic modulus of the material (mainly aluminium with Y= 80 GPa) and the structural thickness (ΔR_s = 170 mm i.e., about half of the total cold mass thickness), according to $\frac{PR}{\Delta R_s} = Y\varepsilon$, giving $\varepsilon = 1.5 \times 10^{-3}$. This value is high compared to the strain of previous existing detector magnets. This can be better viewed looking at a more significant figure of merit, i.e. the E/M ratio directly proportional to the mechanical hoop strain according to $\frac{E}{M} = \frac{PR}{2\Delta R_s \delta}\frac{\Delta R_s}{\Delta R} = \frac{\Delta R_s}{\Delta R}\frac{Y\varepsilon}{2\delta}$, where δ is the mass density. Figure 2.3 shows the values of E/M as function of stored energy for several detector magnets. The CMS coil is distinguishably far from other detector magnets when combining stored energy and E/M ratio (i.e. mechanical deformation). In order to provide the necessary hoop strength, a large fraction of the CMS coil must have a structural function. To limit the shear stress level inside the winding and prevent cracking the insulation, especially at the border defined by the winding and the external mandrel, the structural material cannot be too far from the current-carrying elements (the turns). On the basis of these considerations, the innovative design of the CMS magnet uses a self-supporting conductor, by including in it the structural material. The magnetic hoop stress (130 MPa) is shared between the layers (70%) and the support cylindrical mandrel (30%) rather than being taken by the outer mandrel only, as was the case in the previous generation of thin detector solenoids. A cross section of the cold mass is shown in figure 2.4.

The construction of a winding using a reinforced conductor required technological developments for both the conductor [11] and the winding. In particular, for the winding many problems had to be faced mainly related to the mandrel construction [12], the winding method [13], and the module-to-module mechanical coupling. The modular concept of the cold mass had to face the problem of the module-to-module mechanical connection. These interfaces (figure 2.5) are critical

2008 JINST 3 S08004

Table 2.1: Main parameters of the CMS magnet.

General parameters	
Magnetic length	12.5 m
Cold bore diameter	6.3 m
Central magnetic induction	4 T
Total Ampere-turns	41.7 MA-turns
Nominal current	19.14 kA
Inductance	14.2 H
Stored energy	2.6 GJ
Cold mass	
Layout	Five modules mechanically and electrically coupled
Radial thickness of cold mass	312 mm
Radiation thickness of cold mass	3.9 X_0
Weight of cold mass	220 t
Maximum induction on conductor	4.6 T
Temperature margin wrt operating temperature	1.8 K
Stored energy/unit cold mass	11.6 kJ/kg
Iron yoke	
Outer diameter of the iron flats	14 m
Length of barrel	13 m
Thickness of the iron layers in barrel	300, 630 and 630 mm
Mass of iron in barrel	6000 t
Thickness of iron disks in endcaps	250, 600 and 600 mm
Mass of iron in each endcap	2000 t
Total mass of iron in return yoke	10 000 t

because they have to transmit the large magnetic axial force corresponding to 14 700 t, without allowing local displacements due to possible gaps. These displacements can be partially converted into heat, causing a premature quench. A construction method which involved the machining of the upper surface of the modules and a local resin impregnation during the mechanical mounting allowed us to get an excellent mechanical coupling between the modules.

Figure 2.2: The cold mass mounted vertically before integration with thermal shields and insertion in the vacuum chamber.

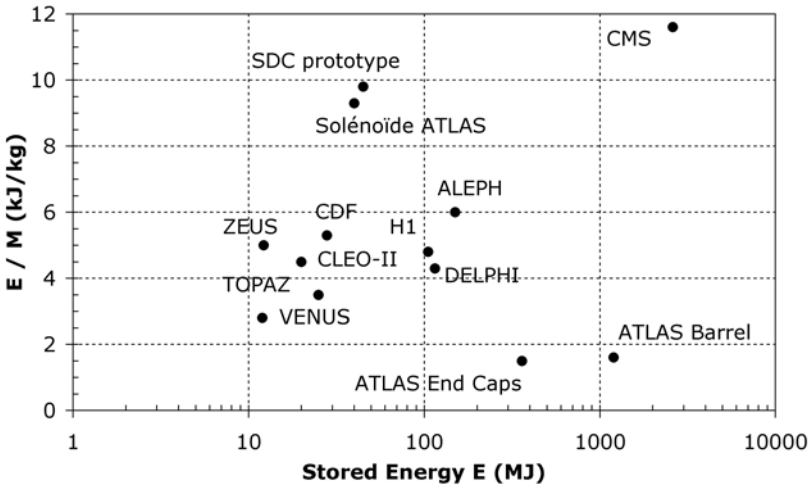

Figure 2.3: The energy-over-mass ratio E/M, for several detector magnets.

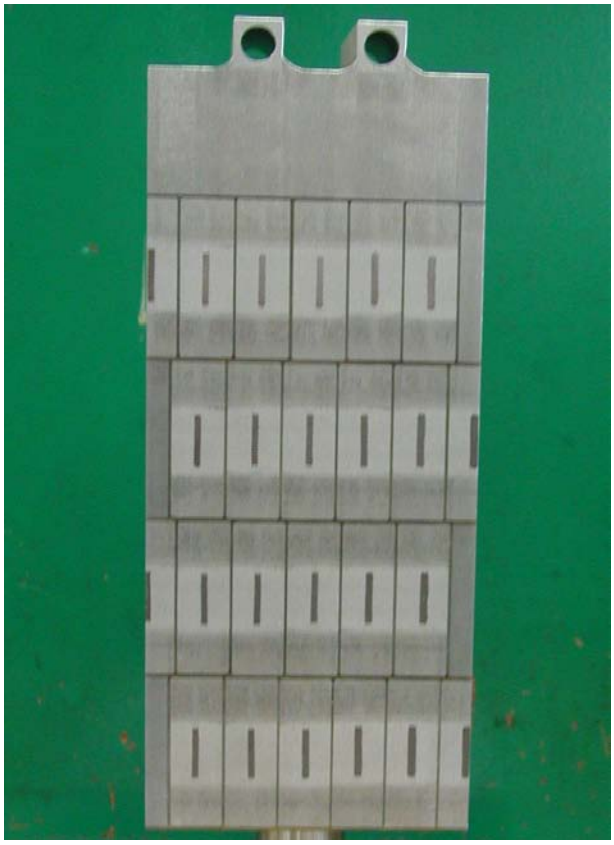

Figure 2.4: Cross section of the cold mass with the details of the 4-layer winding with reinforced conductor.

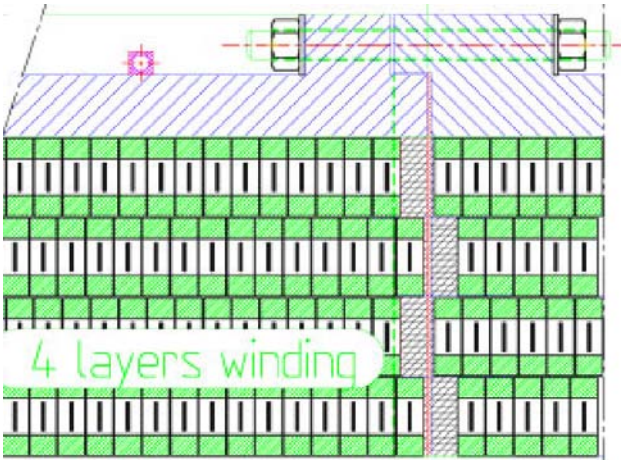

Figure 2.5: Detail of the interface region between 2 modules. In order to guarantee mechanical continuity, false turns are involved. The modules are connected through bolts and pins fixed through the outer mandrels.

Figure 2.6: A view of the yoke at an early stage of magnet assembly at SX5. The central barrel supports the vacuum chamber of the superconducting coil. At the rear, one of the closing end cap disks is visible.

2.2.2 Yoke

The yoke (figure 2.6) is composed of 11 large elements, 6 endcap disks, and 5 barrel wheels, whose weight goes from 400 t for the lightest up to 1920 t for the central wheel, which includes the coil and its cryostat. The easy relative movement of these elements facilitates the assembly of the sub-detectors. To displace each element a combination of heavy-duty air pads plus grease pads has been chosen. This choice makes the system insensitive to metallic dust on the floor and allows transverse displacements. Two kinds of heavy-duty high-pressure air pads with a capacity of either 250 t (40 bars) or 385 t (60 bars) are used. This is not favourable for the final approach when closing the detector, especially for the YE1 endcap that is protruding into the vacuum tank. A special solution has been adopted: for the last 100 mm of approach, flat grease-pads (working pressure 100 bar) have been developed in order to facilitate the final closing of the detector. Once they touch the axially-installed z-stops, each element is pre-stressed with 100 t to the adjacent element. This assures good contact before switching on the magnet. In the cavern the elements will be moved on the 1.23% inclined floor by a strand jacking hydraulic system that ensures safe operation for uphill pulling as well as for downhill pushing by keeping a retaining force. The maximum movements possible in the cavern are of the order of 11 meters; this will take one hour.

To easily align the yoke elements, a precise reference system of about 70 points was installed in the surface assembly hall. The origin of the reference system is the geometrical center of the coil. The points were made after loading the coil cryostat with the inner detectors, the hadronic barrel in particular which weights 1000 t. A mark on the floor was made showing the position of each foot in order to pre-position each element within a $\pm$ 5 mm tolerance. Finally, all the elements were aligned with an accuracy of 2 mm with respect to the ideal axis of the coil.

2008 JINST 3 S08004

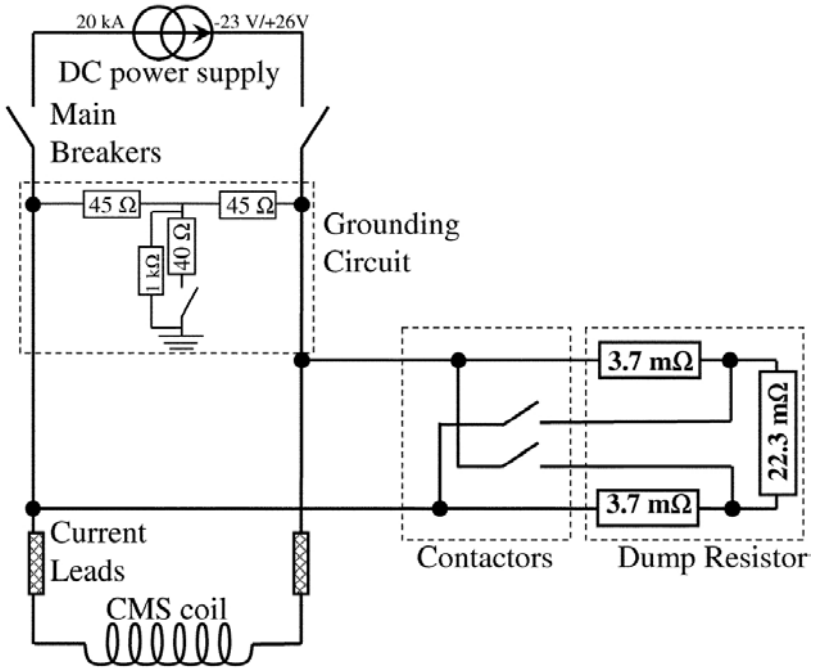

Figure 2.7: The electrical scheme of the magnet with the protection circuit. One of the main components of the protection is the dump resistor, made of three elements.

2.2.3 Electrical scheme

The CMS solenoid can be represented as a 14 H inductance mutually coupled with its external mandrel. This inductive coupling allows for the so-called *quench back* effect, as the eddy currents, induced in the external mandrel at the trigger of a current fast discharge, heat up the whole coil above the superconducting critical temperature. This is the fundamental basis of the protection system, which, in case of a superconducting to resistive transition of the coil, aims at keeping the lowest possible thermal gradients and temperature increase in the superconducting windings, and prevents the occurrence of local overheating, hence reducing the thermal stresses inside the winding. A diagram of the powering circuit with protection is shown in figure 2.7.

A bipolar thyristor power converter rated at 520 kW with passive L-C filters is used to power the CMS solenoid. It covers a range of voltages from +26 V to -23 V, with a nominal DC current of 19.1 kA. In case of a sudden switch off of the power converter, the current decays naturally in the bus-bar resistance and through the free-wheel thyristors until the opening of the main breakers. Inside the power converter, an assembly of free-wheel thyristors, mounted on naturally air-cooled heat sinks, is installed. In case of non-opening of the main switch breakers, the thyristors are rated to support 20 kA DC for 4 minutes. The current discharge is achieved by disconnecting the electrical power source by the use of two redundant 20 kA DC normally-open switch breakers, leaving the solenoid in series with a resistor, in a L-R circuit configuration. The stored magnetic energy is therefore extracted by thermal dissipation in the so-called dump resistor. This resistor is external to the solenoid cryostat and is designed to work without any active device. It is positioned

outdoors taking advantage of natural air convection cooling. The fast discharge (FD) is automatically triggered by hardwired electronics only in case of a superconductive-to-resistive transition, a so-called quench, and for unrecoverable faults which require fast current dumping. The FD time constant is about 200 s. An emergency FD button is also available to the operator in case of need. As the coil becomes resistive during the FD, energy is dissipated inside the coil, which heats up. As a consequence, this necessitates a post-FD cool-down of the coil. The FD is performed on a 30 mΩ dump resistor, as a compromise to keep the dump voltage lower than 600 V, and to limit the coil warm-up and subsequent cool-down time. For faults involving the 20 kA power source, a slow discharge (SD) is triggered through hardwired electronics on a 2 mΩ dump resistor. The SD current evolution is typically exponential, and its time constant is 7025 s, but the coil stays in the superconducting state as the heat load, about 525 W, is fully absorbed by the cooling refrigerator. For current lower than 4 kA, a FD is performed in any case, as the heat load is small enough for the refrigerator. The same resistor is used in both cases for the FD and the SD, using normally open contactors, leaving the dump resistor modules either in series (FD) or in parallel (SD). For other cases, and depending on the alarms, the coil current can be adjusted by the operator, or ramped down to zero, taking advantage of the two-quadrant converter.

2.2.4 Vacuum system

The vacuum system has been designed to provide a good insulation inside the 40 m^3 vacuum volume of the coil cryostat. It consists of 2 double-primary pumping stations, equipped with 2 rotary pumps and 2 Root's pumps, that provide the fore vacuum to the two oil diffusion pumps located at the top of CMS and connected to the coil cryostat via the current leads chimney and the helium phase separator. The rotary pumps have a capacity of 280 m^3/h while the two Root's pumps have a flow of 1000 m^3/h. The biggest oil diffusion pump, installed via a DN 400 flange on the current leads chimney, has a nominal flow of 8000 l/s at 10^{-4} mbar of fore vacuum. The smallest one delivers 3000 l/s at the phase separator.

2.2.5 Cryogenic plant

The helium refrigeration plant for CMS is specified for a cooling capacity of 800 W at 4.45 K, 4500 W between 60 and 80 K, and simultaneously 4 g/s liquefaction capacity. The primary compressors of the plant have been installed, in their final position, while the cold box, as well as the intermediate cryostat which interfaces the phase separator and the thermo-syphon, were moved underground after the completion of the magnet test. These components were commissioned with the help of a temporary heat load of 6.5 kW that simulated the coil cryostat which was not yet available. The performance of the cold box has been measured in cool-down mode and in nominal and operation mode.

2.2.6 Other ancillaries

- *Current leads*. The two 20-kA current leads are made of a high purity copper braid, having a cross section of 1800 mm^2 and RRR (Residual Resistivity Ratio) of 130, placed inside a conduit and cooled by circulating helium gas. Without cooling, the current leads are able

2008 JINST 3 S08004

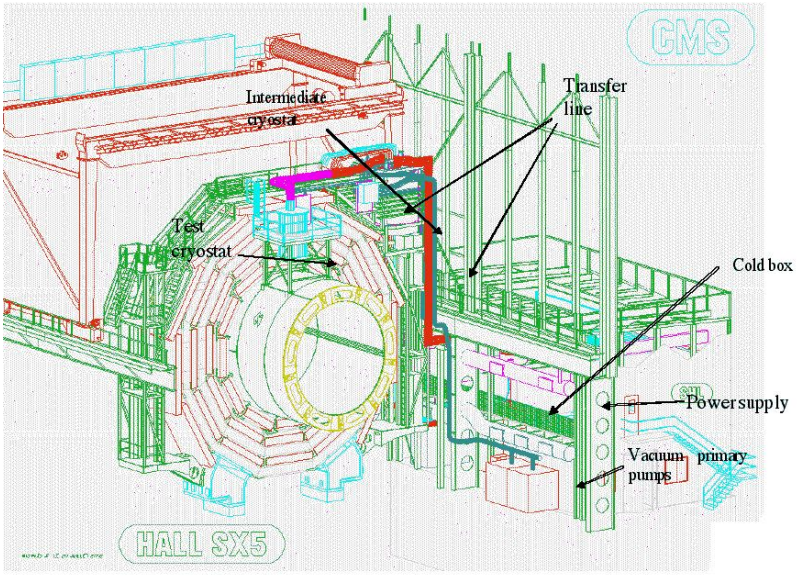

Figure 2.8: The layout for the surface test at SX5, showing only the central barrel. The magnet is connected to the cryoplant (through the proximity cryogenics), the vacuum and the power systems.

to hold a current of 20 kA for 5 minutes, followed by a FD without any damage, as the temperature at the hot spot stays below 400 K [14].

- *Grounding circuit*. The grounding circuit is connected across the solenoid terminals. It fixes the coil circuit potential, through a 1 kΩ resistor, dividing by two the potential to ground. The winding insulation quality is monitored by continuously measuring the leakage current through a 10 Ω grounding resistor.

- *Quench detection system*. The quench detection system is a key element of the Magnet Safety System (MSS). The role of the quench detection system is to detect a resistive voltage between two points of the coil, whose value and duration are compared to adjustable thresholds. The voltage taps are protected by 4.7 kΩ, 6 W resistors. There are 2 redundant systems, with resistor bridge detectors and differential detectors. For each system, there are 5 detectors. Each resistor bridge detector spans two modules and one detector spans the whole solenoid. Each coil module is compared with two other modules through two differential detectors.

2.3 Operating test

The magnet and all its ancillaries were assembled for testing in SX5 and ready for cool-down in January 2006. Figure 2.8 shows the test layout.

2008 JINST 3 S08004

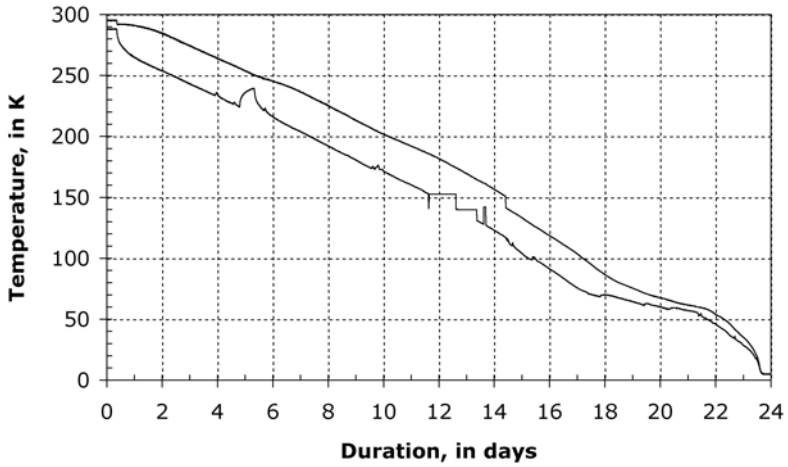

Figure 2.9: Graph of the coil minimum and maximum temperatures during the cool-down from room temperature to 4.5 K.

2.3.1 Cool-down

The cool-down of the solenoid started on February, the 2nd, 2006 and in a smooth way brought the cold mass to 4.6 K in 24 days. Figure 2.9 shows the cool-down curve. The only glitch was due to an overpressure on a safety release valve that stopped cooling for one night before the system was restarted.

One important aspect monitored during the cool-down was the amount of coil shrinkage. In order to explain this point, we refer to the coil suspension system inside the cryostat (figure 2.1), made of longitudinal, vertical, and axial tie-rods in Ti alloy. The magnet is supported by 2×9 longitudinal tie rods, 4 vertical tie rods, and 8 radial tie rods. The tie rods are equipped with compensated strain gauges to measure the forces on 2×3 longitudinal, plus the vertical and radial tie rods. The tie rods are loaded in tension and flexion. To measure the tension and flexion strain, 3 strain gauges are placed on the tie rods at 0°, 90°, and 180°.

The measured stresses in the tie bars due to the cool-down, causing a shrinkage of the cold mass and putting the tie-bars in tension, are shown in table 2.2. A comparison with the expected values is provided as well. The measured axial and radial shrinkage of the cold mass is shown in figure 2.10.

2.3.2 Charge and discharge cycles

The magnetic tests took place during August 2006, with additional tests during the magnet field mapping campaign in October 2006. The current ramps for the field mapping are detailed in figure 2.11. The tests were carried out through magnet charges to progressively higher currents, setting increasing $\mathrm{d}I/\mathrm{d}t$, followed by slow or fast discharges. During these current cycles all the relevant parameters related to electrical, magnetic, thermal, and mechanical behaviours have been

Table 2.2: Calculated and measured cold mass displacements and related stresses on tie-rods due to the cool-down to 4.5 K.

	Expected value	Measured value
Cold Mass Shrinkage		
Longitudinal	26 mm	27 mm
Radial	14 mm	15 mm
Tie rod stress due to cool-down		
Vertical	315 MPa	310±45 MPa
Radial	167 MPa	153±20 MPa
Longitudinal	277 MPa	260±20 MPa

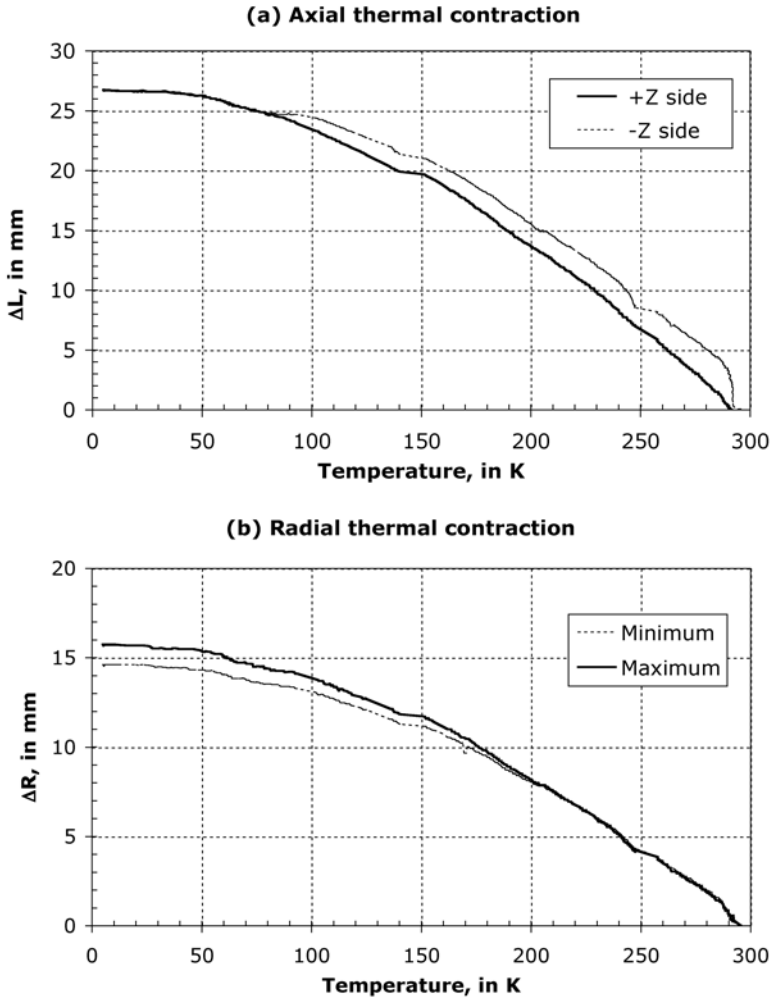

Figure 2.10: Axial (a) and radial (b) shrinkage of the cold mass from 300 K to 4.5 K.

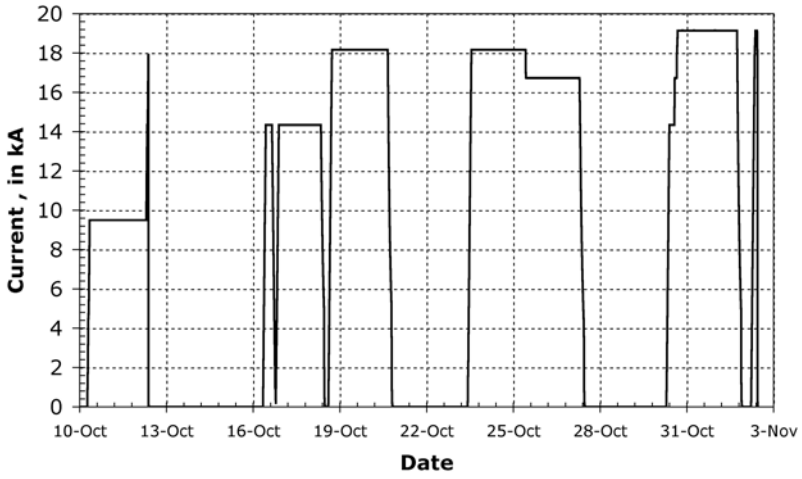

Figure 2.11: Magnet cycles during the CMS magnet tests in October 2006.

recorded. Depending on the level of the current at the trigger of a fast discharge, the time needed for re-cooling the coil can be up to 3 days.

2.3.3 Cold mass misalignment

The support system is designed to withstand the forces created by a 10 mm magnetic misalignment, in any direction of the cold mass with respect to the iron yoke. Geometrical surveys were performed at each step of the magnet assembly to ensure a good positioning. Nevertheless, the monitoring of the coil magnetic misalignment is of prime importance during magnet power test. The misalignment can be calculated either by analysing the displacement of the cold mass or the stresses of the tie rods when the coil is energised. The displacement is measured at several locations and directions at both ends of the coil with respect to the external vacuum tank wall, by the use of rectilinear potentiometers. Results are displayed in figures 2.12 and 2.13. The displacement of the coil's geometric centre is found to be 0.4 mm in z, in the $+z$ direction. According to the computations, such a displacement indicates that the coil centre should be less than 2 mm off the magnetic centre in $+z$. As the coil supporting system is hyper-static, the tie rods are not all initially identically loaded. But the force increase during energising is well distributed, as shown in figure 2.14 and figure 2.15, giving the force measurements on several tie rods. These figures also indicate the forces computed in the case of a 10-mm magnetic misalignment, together with forces calculated for the ideally-centred model, showing there is no noticeable effect of misalignment on the forces.

Using the strain gauges glued on the cold mass (outer mandrel of the central module, CB0), one can determine the Von Mises stress. The cold mass Von Mises stress versus the coil current is given in figure 2.16. The measured value of Von Mises stress at 4.5 K and zero current is 23 MPa. The value at 19.1 kA is 138 MPa. These values are in agreement with computations done during design [3, 6].

2008 JINST 3 S08004

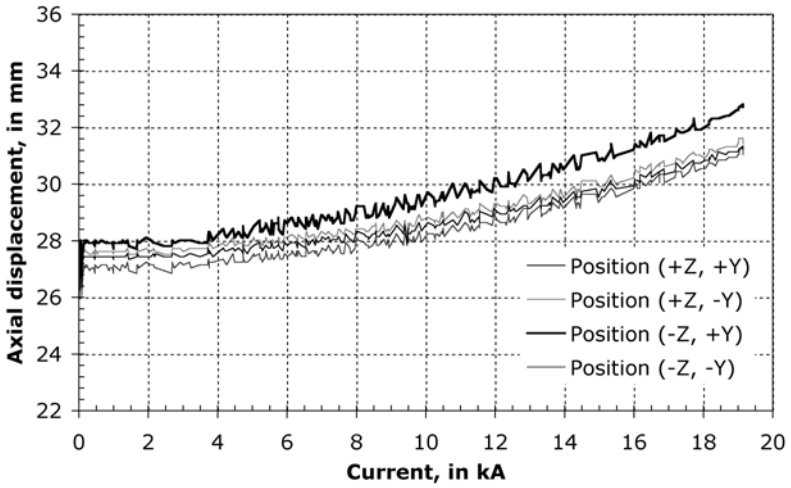

Figure 2.12: Axial displacement in Z at both ends of the coil in different positions during energising.

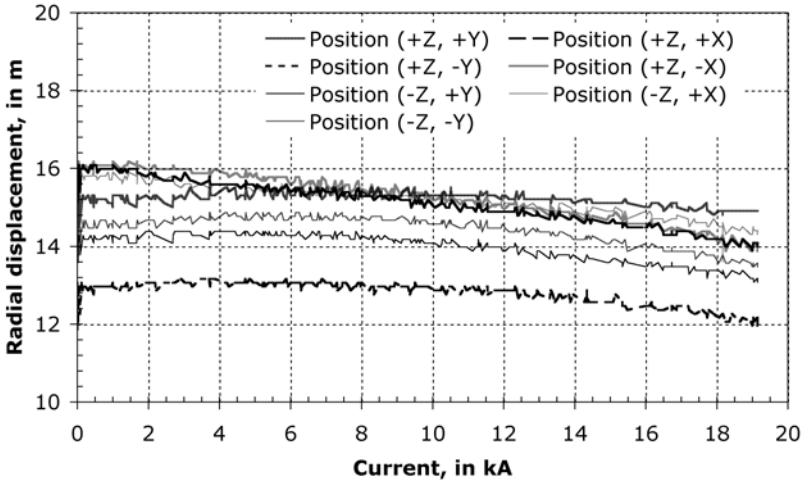

Figure 2.13: Radial displacement at both ends of the coil in different positions during energising.

2.3.4 Electrical measurements

The apparent coil inductance measured through the inductive voltage $V = L\mathrm{d}I/\mathrm{d}t$ is decreasing while increasing the current, as the iron yoke reaches the saturation region. From voltage measurements at the coil ends in the cryostat, while ramping up the coil current at a regulated $\mathrm{d}I/\mathrm{d}t$, the inductance is calculated and results are given in figure 2.17. Initially the apparent inductance of the coil is 14.7 H at zero current, and then it decreases to 13.3 H at 18 kA. The 21 resistive electrical joints, which connect the 5 modules together and, for each module, the 4 layers, are positioned externally to the coil, on the outer radius of the external mandrel, in low magnetic field regions. The

2008 JINST 3 S08004

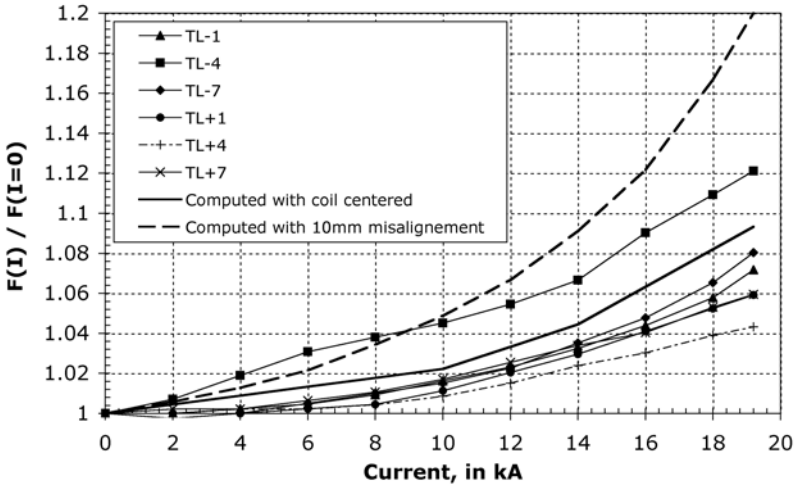

Figure 2.14: Force increase on several axial tie rods; the average force at zero current is 45 t.

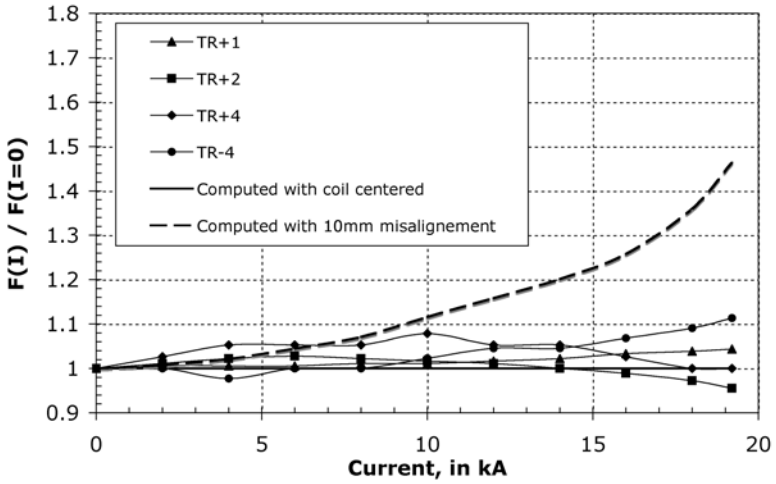

Figure 2.15: Force increase on several radial tie rods; the average force at zero current is 15 tons.

resistance measurements of the joints indicate values ranging from 0.7 nΩ to 1.6 nΩ at 19.1 kA, corresponding to a maximum dissipation in the joint of 0.6 W. The specific joint cooling system is fully efficient to remove this local heat deposit in order to avoid that the resistive joints generate a local quench of the conductor. As mentioned above, the fast discharge causes a quench of the coil, through the quench-back process. The typical current decay at the nominal current of 19.14 kA is given in figure 2.18.

The effect of the mutual coupling of the coil with the external mandrel is clearly visible at the beginning of the current fast discharge as shown in the zoomed detail of figure 2.18. It appears clearly that a high $\mathrm{d}I/\mathrm{d}t$ of about 500 A/s occurs at the very beginning of the discharge. The

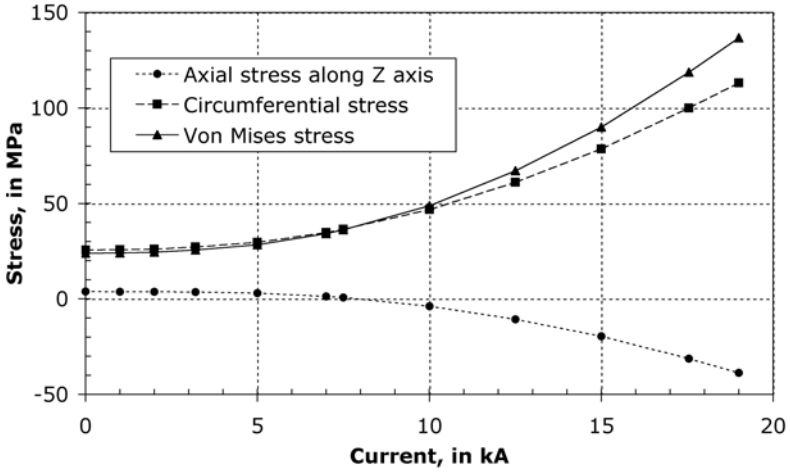

Figure 2.16: Stresses measured on the CB0 module as a function of the current.

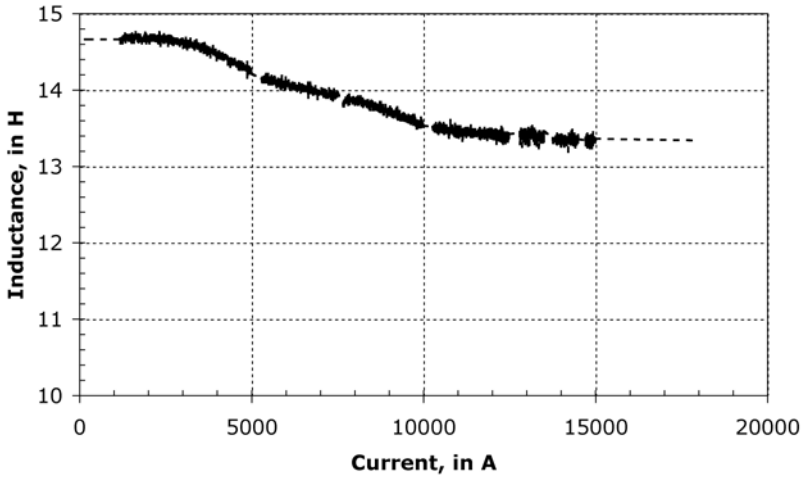

Figure 2.17: Coil inductance as a function of the magnet current.

minimum and maximum temperatures of the coil are displayed in figure 2.19 for a fast discharge at 19.14 kA. A maximum temperature difference of 32 K is measured on the coil between the warmest part, located on the coil central module internal radius, and the coldest part, located on the external radius of the mandrel. It should be noted that the thermal gradient is mainly radial. The temperature tends to equilibrate over the whole coil 2 hours after the trigger of the fast discharge. The average cold mass temperature after a fast discharge at 19 kA is 70 K.

During a magnet discharge, the dump resistor warms up, with a maximum measured temperature increase of 240°C, resulting in an increase of the total dump resistance value by up to 19%. Also the coil internal electrical resistance is increased by up to 0.1 Ω at the end of a FD at 19.14 kA.

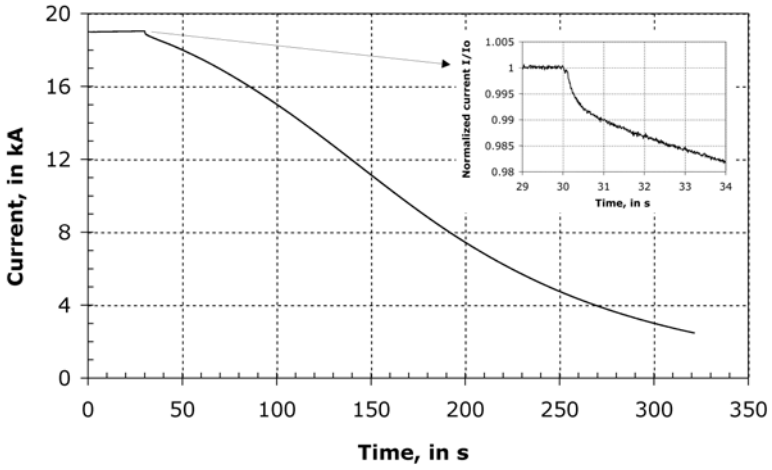

Figure 2.18: Magnet current during fast discharge at the nominal field of 4 T. The insert shows the details at the beginning of the discharge.

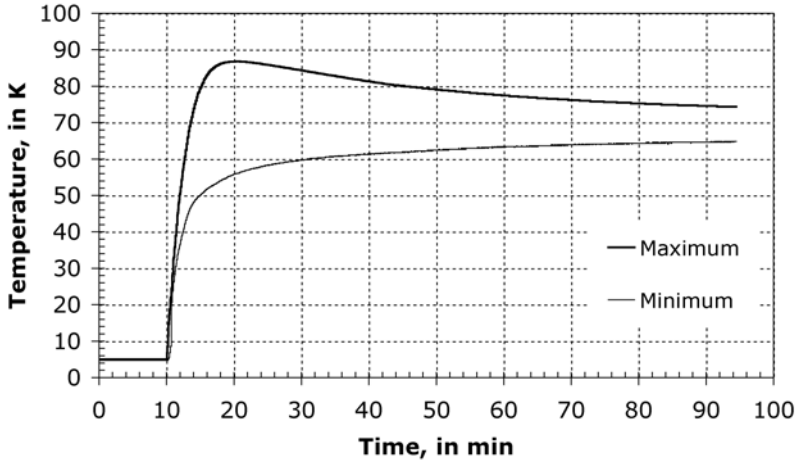

Figure 2.19: Minimum and maximum temperatures detected on the cold mass during the fast discharge from 19.1 kA.

The effect of both the dump resistor and the magnet electrical resistance increasing was revealed through the measurement of the discharge time constant, which was equal to 177 s, 203 s, 263 s, 348 s and 498 s for fast discharges respectively at 19 kA, 17.5 kA, 15 kA, 12.5 kA and 7.5 kA. This is visible in figure 2.20. The temperature recovery of the dump resistor is achieved in less than 2 hours after the trigger of a fast dump. It is 5 hours after the trigger of a slow dump.

In the case of a fast dump at 19.14 kA, typically half of the total energy (1250 MJ) is dissipated as heat in the external dump resistor. The energy dissipated in the dump resistor as a function of the

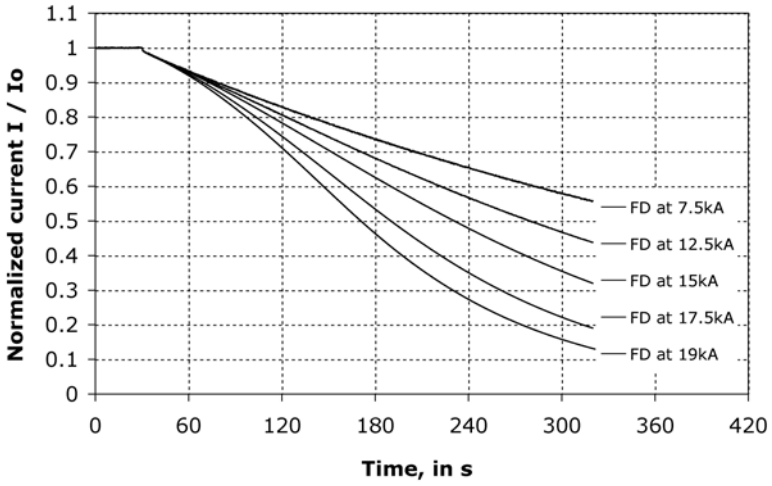

Figure 2.20: The normalised discharge current as a function of time for different initial currents, showing the effect of the increase in magnet and external dump resistance with current.

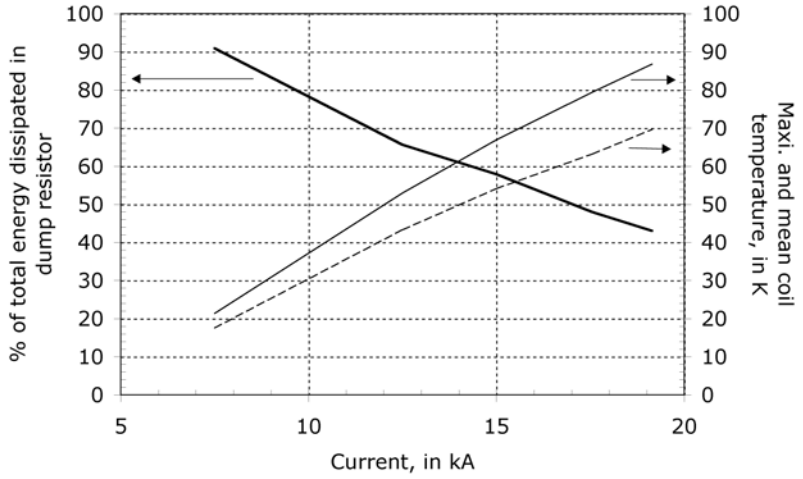

Figure 2.21: Energy dissipated in the external dump resistor and the mean and maximum temperatures of the coil during FD.

magnet current at the trigger of a FD was measured for each FD performed during the magnet tests and is given in figure 2.21. The magnet current is precisely measured by the use of two redundant DCCTs (DC current transformer). The peak-to-peak stability of the current is 7 ppm with a voltage ripple of 2.5% (0.65 V). In order to gain on the operation time, an acceleration of the slow dump has been tested and validated by switching to the fast dump configuration at 4 kA. It has been checked that the cryogenic refrigerator can take the full heat load, and the magnet stays in the superconducting state. This Slow Dump Accelerated (SDA) mode was tested in semi-automatic mode through the cryogenics supervisory system and the magnet control system, and it will be fully automatic for the final installation in the cavern.

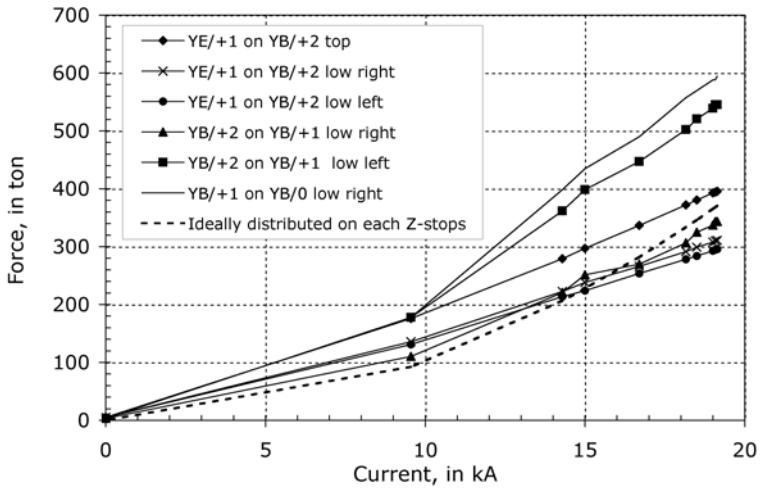

Figure 2.22: Axial forces acting on the yoke Z-stops during the coil energising.

2.3.5 Yoke mechanical measurements

The elements of the return yoke, barrels and endcaps, are attached with several hydraulic locking jacks, which are fixed on each barrel and endcap. They are pre-stressed in order to bring the barrels and endcaps into contact at specific areas using the aluminium-alloy Z-stop blocks. There are 24 Z-stops between each barrel and endcap. A computation of the total axial compressive force gives 8900 tons. The stresses are measured on some Z-stops; the forces on these Z-stops are given in figure 2.22 and compared to the case of a uniformly distributed load on all the Z-stops. To allow for uniform load distribution and distortion during magnet energising, the yoke elements are positioned on grease pads. During magnet energising, the displacement of the barrel yoke elements under the compressive axial force is very limited, while the displacement of the yoke end cap disk YE+1 is clearly noticeable on the outer radius of the disk, due to the axial attraction of the first yoke endcaps towards the interaction point. The measurement of the distance between the barrel elements parallel to the axial axis of the detector is given in figure 2.23. The endcap YE+1 disk is equipped with rosette strain gauges on its inner face, under the muon chambers and near the bolts at the interface between two adjacent segments. The main stresses measured in these regions do not exceed 88 MPa.

2.3.6 Coil stability characteristics

The NbTi superconductor critical temperature is T_c = 9.25 K at zero field. At B = 4.6 T (peak field on the conductor), T_c = 7.30 K. The current-sharing temperature T_g is defined as the maximum temperature for which the current can flow, with no dissipation, in the superconducting part. For CMS the operating current is 19 143 A, while the critical current, according to the measurements done on a short sample extracted from the length used in the inner layer of the central module (the one exposed to the higher field), is I_c (T= 4.5 K, B= 4.6 T) = 62 kA leading to T_g = 6.44 K, i.e., the temperature margin is 1.94 K. This margin is a little higher than the designed one (1.83

2008 JINST 3 S08004

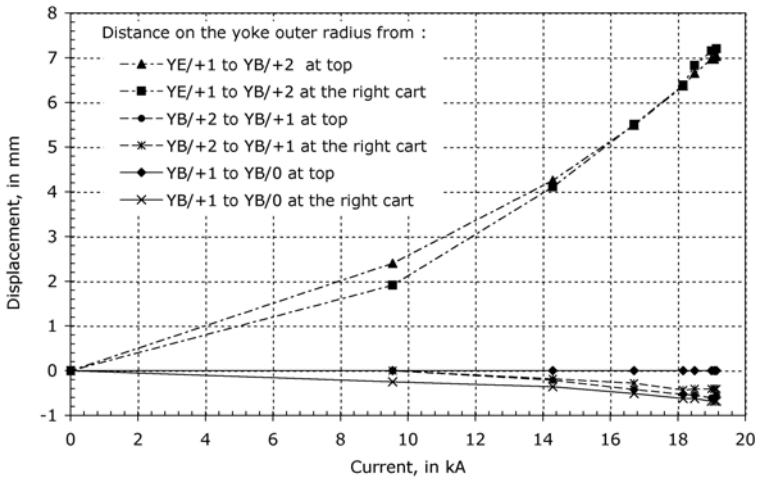

Figure 2.23: Measured displacement of the yoke during the coil energising.

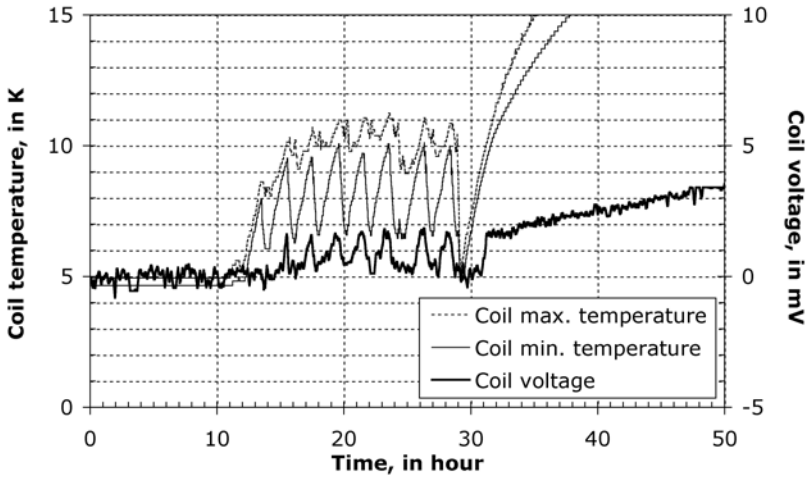

Figure 2.24: The minimum and maximum temperatures and voltage of the coil as a function of time, with only a few amperes of current, showing the superconducting-to-resistive-state transition at around 9.3 K.

K) because the nominal current is less than the one used in this kind of computation (19.5 kA) and the expected conductor critical current was from 7% to 10% lower than the real one obtained through advanced and qualified processes. The T_c value was confirmed at 9.3 K during cryogenic recovery tests (figure 2.24) at zero field. The conductor pure-aluminium stabilizer RRR, deduced from electrical measurements during cool-down, is found to be above 1800.

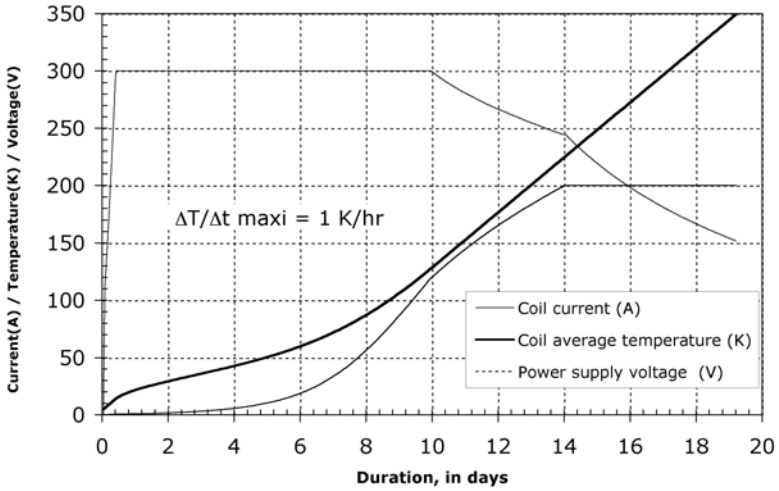

Figure 2.25: Measurements of the coil warm-up behaviour as a function of time; the Y-axis scale is common for all the three curves.

2.3.7 Coil warm-up

Following the test of the magnet on the surface, the cold mass had to be warmed up to room temperature before lowering. The coil, inside its cryostat, was attached to the central barrel YB0 to avoid any risk due to vacuum degradation during the transport operations. The warm-up was performed using a dedicated power supply (200 V-300 A DC) to maintain integrity of the coil/mandrel interface. Knowing the temperature dependence of both the electrical resistivity and the specific heat of the coil materials, the temperature increase for a given electrical power is calculated. Taking into account the capacity of the warm-up supply, and limiting the temperature increase to 1 K/hour, the warm-up was performed as shown in figure 2.25. As the warm-up was done after a fast discharge, the coil temperature was already at 70 K. Nevertheless, the warm-up took place only at night as the yoke was opened to continue integration activities inside the detector. Ultimately, the warm-up lasted only 3 weeks. The maximum temperature gradient across the coil during the warm-up exercise was less than 9 K.

Chapter 3

Inner tracking system

3.1 Introduction

The inner tracking system of CMS is designed to provide a precise and efficient measurement of the trajectories of charged particles emerging from the LHC collisions, as well as a precise reconstruction of secondary vertices. It surrounds the interaction point and has a length of 5.8 m and a diameter of 2.5 m. The CMS solenoid provides a homogeneous magnetic field of 4 T over the full volume of the tracker. At the LHC design luminosity of $10^{34}\,\mathrm{cm}^{-2}\,\mathrm{s}^{-1}$ there will be on average about 1000 particles from more than 20 overlapping proton-proton interactions traversing the tracker for each bunch crossing, i.e. every 25 ns. Therefore a detector technology featuring high granularity and fast response is required, such that the trajectories can be identified reliably and attributed to the correct bunch crossing. However, these features imply a high power density of the on-detector electronics which in turn requires efficient cooling. This is in direct conflict with the aim of keeping to the minimum the amount of material in order to limit multiple scattering, bremsstrahlung, photon conversion and nuclear interactions. A compromise had to be found in this respect. The intense particle flux will also cause severe radiation damage to the tracking system. The main challenge in the design of the tracking system was to develop detector components able to operate in this harsh environment for an expected lifetime of 10 years. These requirements on granularity, speed and radiation hardness lead to a tracker design entirely based on silicon detector technology. The CMS tracker is composed of a pixel detector with three barrel layers at radii between 4.4 cm and 10.2 cm and a silicon strip tracker with 10 barrel detection layers extending outwards to a radius of 1.1 m. Each system is completed by endcaps which consist of 2 disks in the pixel detector and 3 plus 9 disks in the strip tracker on each side of the barrel, extending the acceptance of the tracker up to a pseudorapidity of $|\eta| < 2.5$. With about $200\,\mathrm{m}^2$ of active silicon area the CMS tracker is the largest silicon tracker ever built [15, 16].

The construction of the CMS tracker, composed of 1440 pixel and 15 148 strip detector modules, required the development of production methods and quality control procedures that are new to the field of particle physics detectors. A strong collaboration of 51 institutes with almost 500 physicists and engineers succeeded over a period of 12 to 15 years to design, develop and build this unique device.

3.1.1 Requirements and operating conditions

The expected LHC physics program [17] requires a robust, efficient and precise reconstruction of the trajectories of charged particles with transverse momentum above 1 GeV in the pseudorapidity range $|\eta| < 2.5$. A precise measurement of secondary vertices and impact parameters is necessary for the efficient identification of heavy flavours which are produced in many of the interesting physics channels. Together with the electromagnetic calorimeter and the muon system the tracker has to identify electrons and muons, respectively. Tau leptons are a signature in several discovery channels and need to be reconstructed in one-prong and three-prong decay topologies. In order to reduce the event rate from the LHC bunch crossing rate of 40 MHz to about 100 Hz which can be permanently stored, tracking information is heavily used in the high level trigger of CMS.

The operating conditions for a tracking system at the LHC are very challenging. As already mentioned, each LHC bunch crossing at design luminosity creates on average about 1000 particles hitting the tracker. This leads to a hit rate density of $1\,\mathrm{MHz}/\,\mathrm{mm}^2$ at a radius of 4 cm, falling to 60 kHz/mm^2 at a radius of 22 cm and 3 kHz/mm^2 at a radius of 115 cm. In order to keep the occupancy at or below 1% pixelated detectors have to be used at radii below 10 cm. For a pixel size of $100 \times 150\,\mu\mathrm{m}^2$ in r-ϕ and z, respectively, which is driven by the desired impact parameter resolution, the occupancy is of the order 10^{-4} per pixel and LHC bunch crossing. At intermediate radii ($20\,\mathrm{cm} < r < 55\,\mathrm{cm}$) the reduced particle flux allows the use of silicon micro-strip detectors with a typical cell size of $10\,\mathrm{cm} \times 80\,\mu\mathrm{m}$, leading to an occupancy of up to 2–3% per strip and LHC bunch crossing. In the outer region ($55\,\mathrm{cm} < r < 110\,\mathrm{cm}$) the strip pitch can be further increased. Given the large areas that have to be instrumented in this region, also the strip length has to be increased in order to limit the number of read-out channels. However, the strip capacitance scales with its length and therefore the electronics noise is a linear function of the strip length as well. In order to maintain a good signal to noise ratio of well above 10, CMS uses thicker silicon sensors for the outer tracker region (500 μm thickness as opposed to the 320 μm in the inner tracker) with correspondingly higher signal. These thicker sensors would in principle have a higher depletion voltage. But since the radiation levels in the outer tracker are smaller, a higher initial resistivity can be chosen such that the initial depletion voltages of thick and thin sensors are in the same range of 100 V to 300 V. In this way cell sizes up to about $25\,\mathrm{cm} \times 180\,\mu\mathrm{m}$ can be used in the outer region of the tracker, with an occupancy of about 1%. These occupancy-driven design choices for the strip tracker also satisfy the requirements on position resolution.

CMS is the first experiment using silicon detectors in this outer tracker region. This novel approach was made possible by three key developments:

- sensor fabrication on 6 inch instead of 4 inch wafers reduced the sensor cost to 5–10 CHF/cm^2 and allowed the coverage of the large required surfaces with silicon sensors,
- implementation of the front-end read-out chip in industry-standard deep sub-micron technology led to large cost savings and to an improved signal-to-noise performance,
- automation of module assembly and use of high throughput wire bonding machines.

The radiation damage introduced by the high particle fluxes at the LHC interaction regions is a severe design constraint. Table 3.1 shows the expected fast hadron fluence and radiation dose

2008 JINST 3 S08004

Table 3.1: Expected hadron fluence and radiation dose in different radial layers of the CMS tracker (barrel part) for an integrated luminosity of 500 fb^{-1} ($\approx$ 10 years). The fast hadron fluence is a good approximation to the 1 MeV neutron equivalent fluence [17].

Radius (cm)	Fluence of fast hadrons (10^{14} cm^{-2})	Dose (kGy)	Charged particle flux (cm^{-2}s^{-1})
4	32	840	10^8
11	4.6	190	
22	1.6	70	6×10^6
75	0.3	7	
115	0.2	1.8	3×10^5

in the CMS barrel tracker for an integrated luminosity of 500 fb^{-1} corresponding to about 10 years of LHC operation [15, 17]. Neutrons generated by hadronic interactions in the ECAL crystals make up a substantial contribution to the fast hadron fluence, which actually dominates in the outer tracker close to the ECAL surface. The uncertainties on these estimates due to the extrapolation error of the inelastic proton proton cross-section, momentum distributions and multiplicities to $\sqrt{s} = 14$ TeV and in the Monte Carlo description of the cascade development lead to a safety factor of 1.5 (2 in regions where the neutron contribution dominates) which was applied to these estimates in order to define the design requirements for the tracker.

Three different effects had to be considered in the design of a radiation tolerant silicon tracker. Surface damage is created when the positively charged holes, generated by the passage of an ionizing particle, get trapped in a silicon oxide layer. This is mostly a concern for the front-end chips where this additional space charge changes for instance the characteristics of MOS structures. Surface damage simply scales with the absorbed dose. The silicon sensors are mainly affected by bulk damage, i.e. modifications to the silicon crystal lattice which are caused by non-ionizing energy loss (NIEL) and lead to additional energy levels in the band gap. NIEL is a complicated process, depending on particle type and energy, but is found to scale approximately with the fast hadron fluence. The consequences are an increase of the leakage current (linear in fluence), a change in the doping from n- to p-type with a corresponding change in depletion voltage by a few hundred volts over the lifetime of the tracker, and the creation of additional trapping centers which will reduce the signal by roughly 10% after 10 years of LHC running [18]. The design of the silicon sensors and the read-out electronics has to take this into account and assure a signal-to-noise ratio of 10:1 or better over the full lifetime of the detector, in order to guarantee a robust hit recognition at an acceptable fake hit rate. Finally, transient phenomena due to the generation of charge by ionizing particles in the electronic circuitry can change for instance the state of memory cells and therefore disturb or even stop the correct functioning of the read-out (single event upset, SEU).

The increased detector leakage current can lead to a dangerous positive feedback of the self heating of the silicon sensor and the exponential dependence of the leakage current on temperature, called thermal runaway. This has to be avoided by efficient coupling of the silicon sensors to the cooling system and by a low operating temperature. For this reason it is foreseen that the whole tracker volume will be operated at or slightly below -10°C. After 10 years of operation it is

2008 JINST 3 S08004

expected that this will require a cooling fluid temperature of about $-27°C$ which in turn means that all structures in the tracker have to survive temperature cycles between room temperature and about $-30°C$. A second effect, called reverse annealing, requires to keep the silicon sensors permanently well below 0°C except for short maintenance periods. This effect is caused by the interaction of radiation induced defects in the silicon sensors which can lead to more serious damage and to an even stronger change in depletion voltage with fluence. Experimentally it is found that reverse annealing becomes insignificant for temperatures roughly below 0°C [18].

The read-out chips employed in the CMS tracker are fabricated in standard 0.25 μm CMOS technology which is inherently radiation hard due to the thin gate oxide (and special design rules). The lifetime of the silicon strip tracker is therefore limited by the radiation damage to the silicon sensors. For efficient charge collection they always need to be over-depleted, requiring bias voltages up to 500 V after 10 years of LHC operation. This reaches the limit of the typical high voltage stability of current sensor layouts. Furthermore, the increased leakage currents of the sensors will at some point lead to thermal runaway. All tests have shown that the silicon strip tracker will remain fully operational for 10 years of LHC running. For the pixel detector on the other hand, which has to survive even higher radiation doses, under-depleted operation is possible due to a different sensor layout. Its lifetime reaches from at least 2 years at full LHC luminosity for the innermost layer to more than 10 years for the third layer.

The ultimate position resolution of the pixel and strip sensors is degraded by multiple scattering in the material that is necessary to precisely hold the sensors, to supply the electrical power (in total about 60 kW for the CMS tracker) and to cool the electronics and the silicon sensors. Nuclear interactions of pions and other hadrons in this material reduce significantly the tracking efficiency for these particles. In addition, this material leads to photon conversion and bremsstrahlung which adversely affect the measurement accuracy of the electromagnetic calorimeter. It was therefore a requirement to keep the amount of this material to a minimum.

3.1.2 Overview of the tracker layout

A schematic drawing of the CMS tracker is shown in figure 3.1. At radii of 4.4, 7.3 and 10.2 cm, three cylindrical layers of hybrid pixel detector modules surround the interaction point. They are complemented by two disks of pixel modules on each side. The pixel detector delivers three high precision space points on each charged particle trajectory. It is described in detail in section 3.2. In total the pixel detector covers an area of about $1\,m^2$ and has 66 million pixels.

The radial region between 20 cm and 116 cm is occupied by the silicon strip tracker, which is described in detail in section 3.3. It is composed of three different subsystems. The Tracker Inner Barrel and Disks (TIB/TID) extend in radius towards 55 cm and are composed of 4 barrel layers, supplemented by 3 disks at each end. TIB/TID delivers up to 4 r-ϕ measurements on a trajectory using 320 μm thick silicon micro-strip sensors with their strips parallel to the beam axis in the barrel and radial on the disks. The strip pitch is 80 μm on layers 1 and 2 and 120 μm on layers 3 and 4 in the TIB, leading to a single point resolution of 23 μm and 35 μm, respectively. In the TID the mean pitch varies between 100 μm and 141 μm. The TIB/TID is surrounded by the Tracker Outer Barrel (TOB). It has an outer radius of 116 cm and consists of 6 barrel layers of 500 μm thick micro-strip sensors with strip pitches of 183 μm on the first 4 layers and 122 μm on

2008 JINST 3 S08004

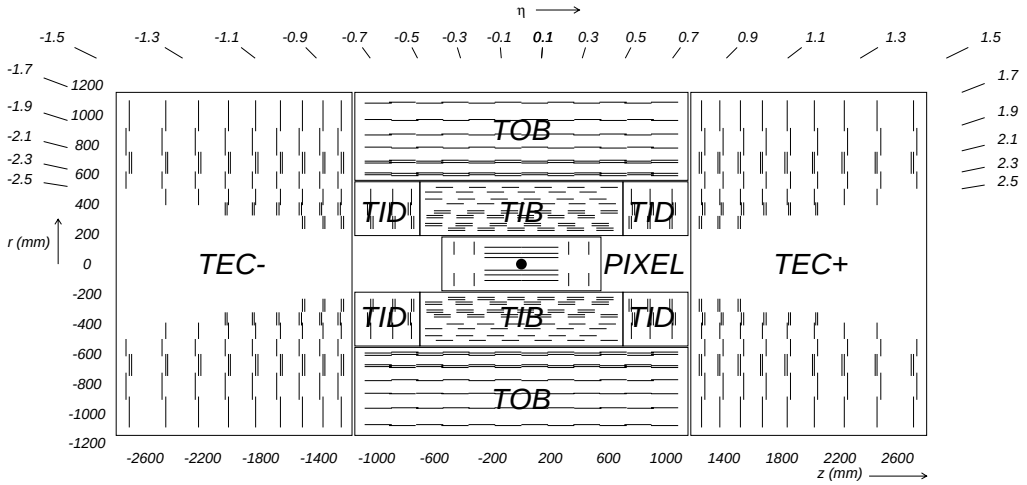

Figure 3.1: Schematic cross section through the CMS tracker. Each line represents a detector module. Double lines indicate back-to-back modules which deliver stereo hits.

layers 5 and 6. It provides another 6 r-ϕ measurements with single point resolution of 53 μm and 35 μm, respectively. The TOB extends in z between $\pm$118 cm. Beyond this z range the Tracker EndCaps (TEC+ and TEC- where the sign indicates the location along the z axis) cover the region 124 cm $< |z| <$ 282 cm and 22.5 cm $< |r| <$ 113.5 cm. Each TEC is composed of 9 disks, carrying up to 7 rings of silicon micro-strip detectors (320 μm thick on the inner 4 rings, 500 μm thick on rings 5-7) with radial strips of 97 μm to 184 μm average pitch. Thus, they provide up to 9 ϕ measurements per trajectory.

In addition, the modules in the first two layers and rings, respectively, of TIB, TID, and TOB as well as rings 1, 2, and 5 of the TECs carry a second micro-strip detector module which is mounted back-to-back with a stereo angle of 100 mrad in order to provide a measurement of the second co-ordinate (z in the barrel and r on the disks). The achieved single point resolution of this measurement is 230 μm and 530 μm in TIB and TOB, respectively, and varies with pitch in TID and TEC. This tracker layout ensures at least ≈ 9 hits in the silicon strip tracker in the full range of $|\eta| < 2.4$ with at least ≈ 4 of them being two-dimensional measurements (figure 3.2). The ultimate acceptance of the tracker ends at $|\eta| \approx 2.5$. The CMS silicon strip tracker has a total of 9.3 million strips and 198 m^2 of active silicon area.

Figure 3.3 shows the material budget of the CMS tracker in units of radiation length. It increases from 0.4 X_0 at $\eta \approx 0$ to about 1.8 X_0 at $|\eta| \approx 1.4$, beyond which it falls to about 1 X_0 at $|\eta| \approx 2.5$.

3.1.3 Expected performance of the CMS tracker

For single muons of transverse momenta of 1, 10 and 100 GeV figure 3.4 shows the expected resolution of transverse momentum, transverse impact parameter and longitudinal impact parameter, as a function of pseudorapidity [17]. For high momentum tracks (100 GeV) the transverse momentum resolution is around $1-2\%$ up to $|\eta| \approx 1.6$, beyond which it degrades due to the reduced lever arm. At a transverse momentum of 100 GeV multiple scattering in the tracker material accounts for 20 to

2008 JINST 3 S08004

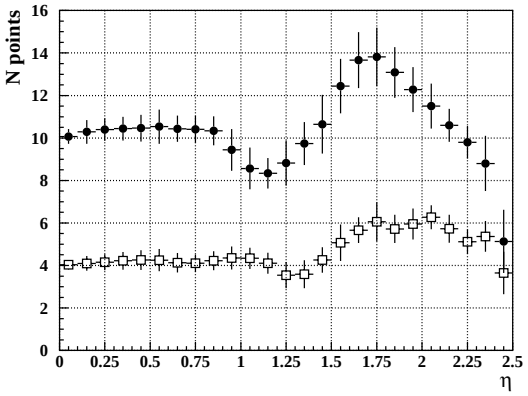

Figure 3.2: Number of measurement points in the strip tracker as a function of pseudorapidity η. Filled circles show the total number (back-to-back modules count as one) while open squares show the number of stereo layers.

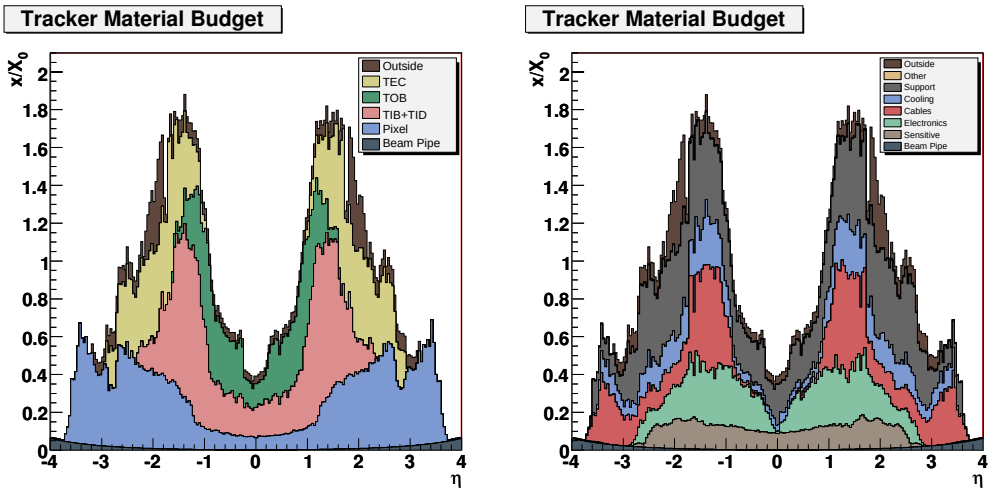

Figure 3.3: Material budget in units of radiation length as a function of pseudorapidity η for the different sub-detectors (left panel) and broken down into the functional contributions (right panel).

30% of the transverse momentum resolution while at lower momentum it is dominated by multiple scattering. The transverse impact parameter resolution reaches $10\,\mu$m for high p_T tracks, dominated by the resolution of the first pixel hit, while at lower momentum it is degraded by multiple scattering (similarly for the longitudinal impact parameter). Figure 3.5 shows the expected track reconstruction efficiency of the CMS tracker for single muons and pions as a function of pseudorapidity. For muons, the efficiency is about 99% over most of the acceptance. For $|\eta| \approx 0$ the efficiency decreases slightly due to gaps between the ladders of the pixel detector at $z \approx 0$. At high η the efficiency drop is mainly due to the reduced coverage by the pixel forward disks. For pions and hadrons in general the efficiency is lower because of interactions with the material in the tracker.

2008 JINST 3 S08004

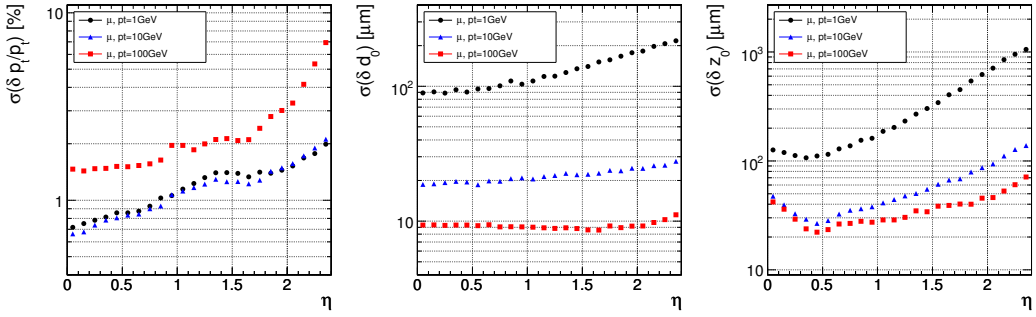

Figure 3.4: Resolution of several track parameters for single muons with transverse momenta of 1, 10 and 100 GeV: transverse momentum (left panel), transverse impact parameter (middle panel), and longitudinal impact parameter (right panel).

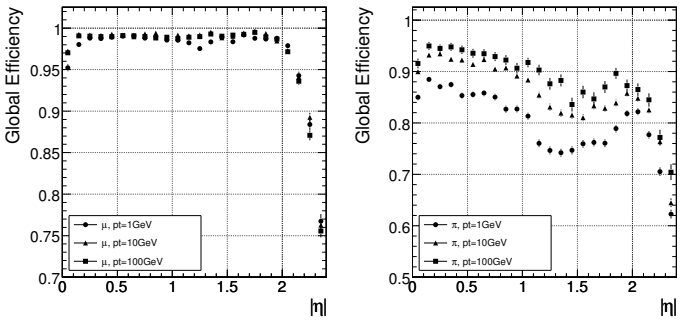

Figure 3.5: Global track reconstruction efficiency for muons (left panel) and pions (right panel) of transverse momenta of 1, 10 and 100 GeV.

3.1.4 Tracker system aspects

All elements of the CMS tracker are housed in the tracker support tube, which is suspended on the HCAL barrel. The tracker support tube is a large cylinder 5.30 m long with an inner diameter of 2.38 m. The 30-mm-thick wall of the cylinder is made by two 950-1/T300 carbon fiber composite skins, 2 mm in thickness, sandwiching a 26-mm-high Nomex core. Over the entire length of the tube's inner surface, two carbon fiber rails are attached on the horizontal plane. The tracker outer barrel (TOB) and both endcaps (TEC+ and TEC-) rest on these rails by means of adjustable sliding pads. The tracker inner barrel and disks (TIB/TID) are in turn supported by the TOB. The angle between the guiding elements of these rails is controlled to better than 0.183 mrad, corresponding to a parallelism between the guides better than ± 0.5 mm in all directions over the full length.

An independent support and insertion system for the pixel detectors, the central section of the beam pipe and the inner elements of the radiation monitor system spans the full length of the tracker at its inner radius. This is composed of three long carbon fiber structures, joined together during tracker assembly to form two continuous parallel planes, on which precision tracks for the installation, support and positioning of each element are machined. The central element is a 2266.5-mm-long and 436-mm-wide cylinder which is connected with flanges to the TIB/TID detector. This element provides support and accurate positioning to the pixel detectors. Two 2420-

2008 JINST 3 S08004

mm-long side elements are coupled to it only by very precise pinned connections, bridging the gap between the faces of the TIB/TID and the closing flanges of the tracker without direct contact to the TEC detectors. These side elements are therefore structurally decoupled from the silicon strip detectors and can be installed and removed at any time with no impact on the strip detectors. They serve several purposes: they provide support and alignment features for the central section of the beam pipe, they allow the installation of the inner elements of the radiation monitor system, and they are used for installation and removal of all the components permanently or temporarily housed in the inner region of the tracker: beam pipe, bake-out equipment, pixel barrel, pixel disks and radiation monitor. This system of permanent tracks, light but very stiff and stable, installed in the core of the tracker will allow for the quickest possible intervention in this region during maintenance, inducing no disturbance to the volume occupied by the silicon strip detectors. This feature will be extremely valuable after some years of operation, when activation of components and radiation damage on sensors will start becoming an issue.

The outer surface of the tracker tube faces the electromagnetic calorimeter, which is operated at room temperature and requires good temperature stability. The surface of the electromagnetic calorimeter must be kept at (18 ± 4)°C while the tracker volume needs to be cooled to below -10°C. In order to achieve this thermal gradient over a very limited radial thickness, the inside surface of the tracker support tube is lined with an active thermal screen. It ensures a temperature below -10°C inside the tracker volume even when the sub-detectors and their cooling are switched off, while maintaining a temperature above $+12$°C on the outer surface of the support tube in order to avoid condensation. It also reduces the thermal stress across the support tube structure. The thermal screen consists of 32 panels. On the inside, cold fluid is circulated in a thin aluminium plate whilst, separated by 8 mm of Rohacell foam, several polyimide-insulated resistive circuits are powered to heat up the outer surface to the required temperature. The system is feed-back controlled, based on 64 temperature sensors.

The total power dissipation inside the tracker volume is expected to be close to 60 kW. Mainly for robustness in operation, the CMS tracker is equipped with a mono-phase liquid cooling system. The liquid used for refrigeration of the silicon strip and pixel detector as well as the thermal screen is C_6F_{14}. It has a sufficiently low viscosity even at the lowest required temperature, excellent behaviour under irradiation and is extremely volatile (with practically no residues) thus minimizing eventual damages from accidental leaks. The cooling system provides up to 77 m^3/hour of C_6F_{14} liquid to the tracker, at a temperature of down to -35°C and with a pressure drop of up to 8 bar. This corresponds to a cooling capacity of up to 128 kW.

The full tracker volume (about 25 m^3) is flushed with pre-chilled dry nitrogen gas at a rate of up to one volume exchange per hour.

3.2 Pixel detector

3.2.1 Pixel system general

The pixel system is the part of the tracking system that is closest to the interaction region. It contributes precise tracking points in r-ϕ and z and therefore is responsible for a small impact parameter resolution that is important for good secondary vertex reconstruction. With a pixel cell

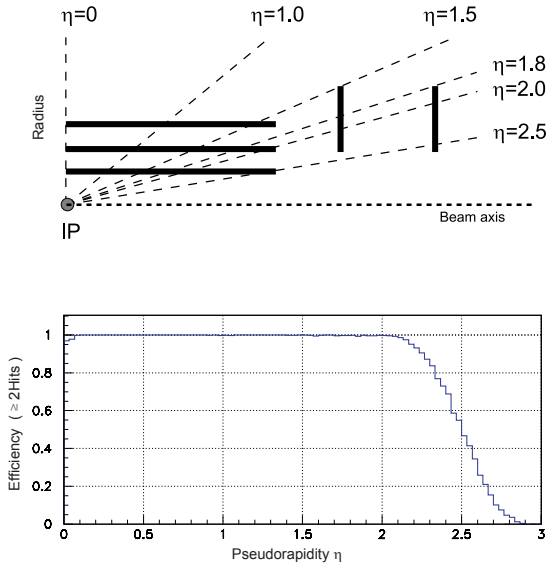

Figure 3.6: Geometrical layout of the pixel detector and hit coverage as a function of pseudorapidity.

size of $100 \times 150\ \mu\text{m}^2$ emphasis has been put on achieving similar track resolution in both r-ϕ and z directions. Through this a 3D vertex reconstruction in space is possible, which will be important for secondary vertices with low track multiplicity. The pixel system has a zero-suppressed read out scheme with analog pulse height read-out. This improves the position resolution due to charge sharing and helps to separate signal and noise hits as well as to identify large hit clusters from overlapping tracks.

The pixel detector covers a pseudorapidity range $-2.5 < \eta < 2.5$, matching the acceptance of the central tracker. The pixel detector is essential for the reconstruction of secondary vertices from b and tau decays, and forming seed tracks for the outer track reconstruction and high level triggering. It consists of three barrel layers (BPix) with two endcap disks (FPix). The 53-cm-long BPix layers will be located at mean radii of 4.4, 7.3 and 10.2 cm. The FPix disks extending from $\approx$6 to 15 cm in radius, will be placed on each side at z=$\pm$34.5 and z=$\pm$46.5 cm. BPix (FPix) contain 48 million (18 million) pixels covering a total area of 0.78 (0.28) m^2. The arrangement of the 3 barrel layers and the forward pixel disks on each side gives 3 tracking points over almost the full η-range. Figure 3.6 shows the geometric arrangement and the hit coverage as a function of pseudorapidity η. In the high η region the 2 disk points are combined with the lowest possible radius point from the 4.4 cm barrel layer.

The vicinity to the interaction region also implies a very high track rate and particle fluences that require a radiation tolerant design. For the sensor this led to an n+ pixel on n-substrate detector design that allows partial depleted operation even at very high particle fluences. For the barrel layers the drift of the electrons to the collecting pixel implant is perpendicular to the 4 T magnetic field of CMS. The resulting Lorentz drift leads to charge spreading of the collected signal charge over more than one pixel. With the analog pulse height being read out a charge interpolation allows

to achieve a spatial resolution in the range of 15–20 μm. The forward detectors are tilted at 20° in a turbine-like geometry to induce charge-sharing. The charge-sharing is mainly due to the geometric effect of particles entering the detector at an average angle of 20° away from normal incidence [19]; charge-sharing is also enhanced by the $\vec{E} \times \vec{B}$ drift. A position resolution of approximately 15 μm in both directions can be achieved with charge-sharing between neighbouring pixels. The reduction in the depletion depth or the increase in bias voltage will lead to a reduction of charge-sharing and therefore a degradation of the spatial resolution with radiation damage.

In order to allow a replacement of the innermost layers the mechanics and the cabling of the pixel system has been designed to allow a yearly access if needed. At full LHC luminosity we expect the innermost layer to stay operational for at least 2 years. The 3 layer barrel mechanics as well as the forward disks are divided into a left and a right half. This is required to allow installation along the beam pipe and to pass beyond the beam pipe support wires at z=± 1632 mm. The 6 individual mechanical pieces are referenced to each other through precisely machined rails inside the TIB cylinder. Power, cooling, the optical controls as well as the optical read-out lines are brought to the detector through supply tube shells. In case of the barrel pixel system the supply tubes have a flexible connection that needs to bend by a few degrees during insertion following the slightly curved rails around the beam pipe support ring.

The pixel system is inserted as the last sub-detector of CMS after the silicon strip tracker has been installed and after the central section of the beam pipe has been installed and baked out.

3.2.2 Sensor description

Technological choices

The sensors for the CMS-pixel detector adopt the so called n-on-n concept. The pixels consist of high dose n-implants introduced into a high resistance n-substrate. The rectifying pn-junction is placed on the back side of the sensor surrounded by a multi guard ring structure. Despite the higher costs due to the double sided processing this concept was chosen as the collection of electrons ensures a high signal charge at moderate bias voltages (< 600 V) after high hadron fluences. Furthermore the double sided processing allows a guard ring scheme keeping all sensor edges at ground potential.

The isolation technique applied for the regions between the pixel electrodes was developed in close collaboration with the sensor vendors. Open p-stops [20] were chosen for the disks and moderated p-spray [21] for the barrel. Both types of sensors showed sufficient radiation hardness during an extensive qualification procedure including several test beams [22, 23].

Disk sensors

The disk sensors use the p-stop technique for interpixel isolation. To maximize the charge collection efficiency and minimize the pixel capacitance within the design rules of the vendor a width of 8 μm for the p-stop rings and a distance of 12 μm between implants was chosen. Figure 3.7 shows a photograph of 4 pixel cells. The open ring p-stops, the bump-bonding pad and the contact between the aluminium and the implanted collecting electrode are highlighted.

2008 JINST 3 S08004

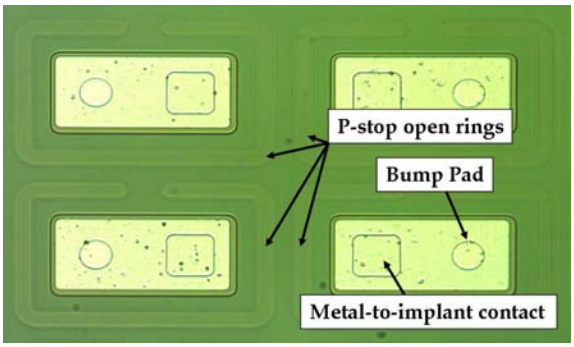

Figure 3.7: Picture of four pixels in the same double column for a pixel disk sensor.

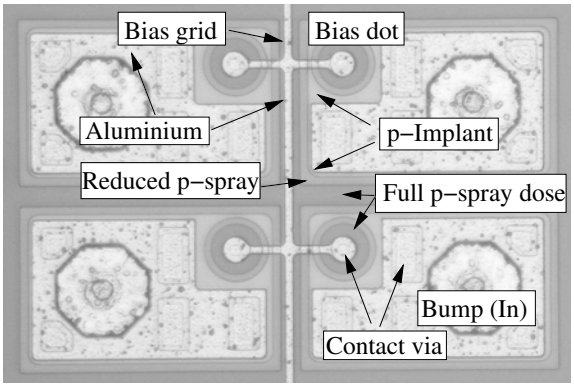

Figure 3.8: Photograph of four pixel cells. The Indium bumps are already deposited but not yet reflown.

The opening on the p-stop rings provides a low resistance path until full depletion is reached to allow IV (current-voltage) characterization of the sensor on wafer and a high resistance path when the sensor is over-depleted (10–20 V over-depletion) to assure interpixel isolation.

The process is completely symmetric with five photolithographic steps on each side to minimize the mechanical stress on the silicon substrate and the potential bowing of the diced sensors.

The sensors were all fabricated in 2005 on 4 inch wafers. The depletion voltage is 45–50 V and the leakage current is less than 10 nA per cm^2. The 7 different sensor tiles needed to populate a disk blade, ranging from 1×2 read-out chips (ROCs) to 2×5 ROCs, are implemented on a single wafer.

A production yield higher than 90% has been achieved and 150 good sensors for each of the seven flavours are available to the project for module assembly.

Barrel sensors

The sensors for the pixel barrel use the moderated p-spray technique for interpixel isolation. A photograph of four pixels in a barrel sensor is shown in figure 3.8. Most area of a pixel is covered with the collecting electrode formed by the n-implant. The gap between the n-implants is kept small ($20\,\mu$m) to provide a homogeneous drift field which leads to a relatively high capacitance of the order of 80-100 fF per pixel.

2008 JINST 3 S08004

In one corner of each pixel the so called *bias dot* is visible. They provide a high resistance punch-through connection to all pixels which allows on-wafer IV measurements which are important to exclude faulty sensors from the module production.

The dark *frame* around the pixel implants visible in figure 3.8 indicates the opening in the nitride covering the thermal oxide. In this region the p-spray dose reaches the full level. Close to the lateral pn-junction between the pixel implant and the p-sprayed inter-pixel region the boron dose is reduced.

The sensor shown in figure 3.8 has undergone the bump deposition process. The Indium bumps are visible as roughly 50 μm wide octagons.

The sensors are processed on n-doped DOFZ-silicon [24] with $\langle 111 \rangle$ orientation and a resistivity of about 3.7 kΩcm (after processing). This leads to a full depletion voltage of 50-60 V of the 285 μm thick sensors. All wafers for the production of the barrel sensors come from the same silicon ingot to provide the best possible homogeneity of all material parameters.

The pixel barrel requires two different sensor geometries, 708 full (2×8 ROCs) and 96 half modules (1×8 ROCs). They were processed in 2005 and 2006 using two different mask sets.

3.2.3 Pixel detector read-out

System overview

The pixel read-out and control system [25] consists of three parts: a read-out data link from the modules/blades to the pixel front end driver (pxFED), a fast control link from the pixel front end controller (pFEC) to the modules/blades and a slow control link from a standard FEC to the supply tube/service cylinder. The latter is used to configure the ASICs on the supply tube/service cylinder through a I^2C protocol. Figure 3.9 shows a sketch of the system.

The front end consists of a Token Bit Manager (TBM) chip which controls several read-out chips (ROCs). The pFEC sends the 40MHz clock and fast control signals (e.g. trigger, reset) to the front end and programs all front end devices. The pxFED receives data from the front end, digitizes it, formats it and sends it to the CMS-DAQ event builder. The pFEC, FEC and pxFED are VME modules located in the electronics room and are connected to the front end through 40 MHz optical links. The various components are described in the following sections.

Read-out chip

Sensor signals are read out by ROCs bump bonded to the sensors. A ROC is a full custom ASIC fabricated in a commercial 0.25-μm 5-metal-layer CMOS process and contains 52×80 pixels [26]. Its main purposes are:

- Amplification and buffering of the charge signal from the sensor.
- Zero suppression in the pixel unit cell. Only signals above a certain threshold will be read out. This threshold can be adjusted individually for each pixel by means of four trim bits. The trim bits have a capacitive protection against single event upset (SEU), which has shown to reduce SEUs by 2 orders of magnitude [26]. The mean threshold dispersion after trimming at T$= -10$°C is 90 electrons equivalent with a noise of 170 electrons.

2008 JINST 3 S08004

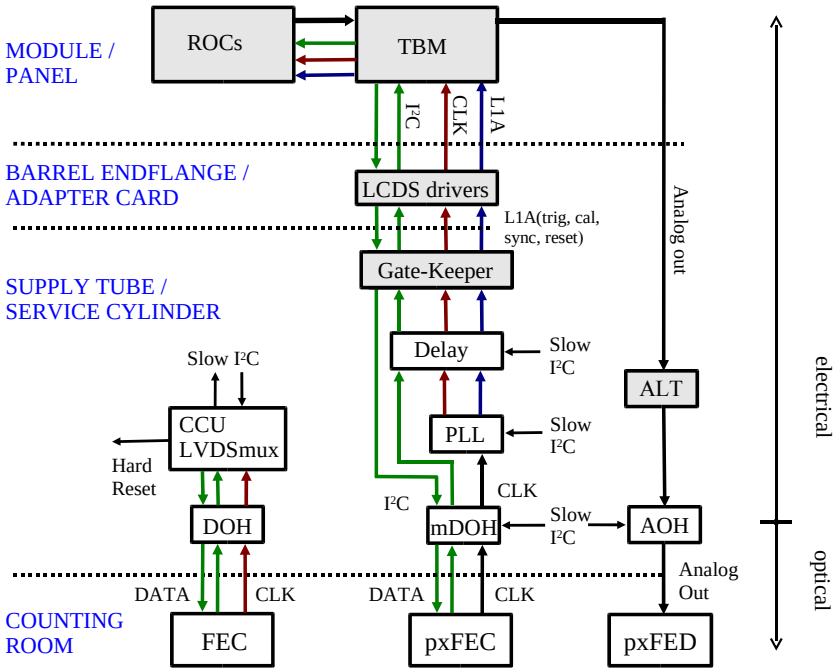

Figure 3.9: Block diagram of the pixel control and read-out system.

- Level 1 trigger verification. Hit information without a corresponding L1 trigger is abandoned.
- Sending hit information and some limited configuration data (analog value of last addressed DAC) to the TBM chip. Pixel addresses are transferred as 6 level analog encoded digital values within 5 clock cycles (125ns) while the pulse height information is truly analog.
- Adjusting various voltage levels, currents and offsets in order to compensate for chip-to-chip variations in the CMOS device parameters. There are a total of 29 DACs on the chip.

The ROC needs two supply voltages of 1.5 V and 2.5 V. There are 6 on chip voltage regulators. They compensate for differences in supply voltage due to voltage drops in module cables of different lengths, improve AC power noise rejection and strongly reduce intermodule cross-talk. An on-chip temperature sensor allows the monitoring of the module temperature online. The ROC is controlled through a modified I^2C interface running at 40 MHz. The configuration data can be downloaded without stopping data acquisition.

There are a few architecture inherent data loss mechanisms. The particle detection inefficiency has been measured in a high-rate pion beam. It is in fairly good agreement with expectations and reaches 0.8%, 1.2% and 3.8% respectively for the three layers at a luminosity of 10^{34} $s^{-1}cm^{-2}$ and 100 kHz L1 trigger rate.

The power consumption depends on the pixel hit rate. At the LHC design luminosity, the ROC contributes with 34 μW per pixel about 88% (62%) to the total pixel detector front end power budget before (after) the detector has received a total fluence of $6\times10^{14}/cm^2$.

Token Bit Manager chip

The TBM [27] controls the read-out of a group of pixel ROCs. The TBM is designed to be located on the detector near to the pixel ROCs. In the case of the barrel, they will be mounted on the detector modules and will control the read-out of 8 or 16 ROCs depending upon the layer radius. In the case of the forward disks, they will be mounted on the disk blades and will control the read-out of 21 or 24 ROCs depending on blade side. A TBM and the group of ROCs that it controls will be connected to a single analog optical link over which the data will be sent to the front end driver, a flash ADC module located in the electronics house. The principal functions of the TBM include the following:

- It will control the read-out of the ROCs by initiating a token pass for each incoming Level-1 trigger.
- On each token pass, it will write a header and a trailer word to the data stream.
- The header will contain an 8 bit event number and the trailer will contain 8 bits of error status. These will be transferred as 2 bit analog encoded digital.
- It will distribute the Level-1 triggers, and clock to the ROCs.

Each arriving Level-1 trigger will be placed on a 32-deep stack awaiting its associated token pass. Normally the stack will be empty but is needed to accommodate high burst rates due to noise, high track density events, or trigger bursts. Since there will be two analog data links per module for the inner two layers of the barrel, the TBMs will be configured as pairs in a Dual TBM Chip. In addition to two TBMs, this chip also contains a Control Network. The Hub serves as a port addressing switch for control commands that are sent from the DAQ to the front end TBMs and ROCs. These control commands will be sent over a digital optical link from a front end controller in the electronics house to the front end Hubs. The commands will be sent using a serial protocol, running at a speed of 40 MHz. This high speed is mandated by the need to rapidly cycle through a refreshing of the pixel threshold trim bits that can become corrupted due to single event upsets. There are four external, write only ports on each Hub for communicating with the ROCs and there is one internal read/write port for communicating with the TBMs within the chip. The first byte of each command will contain a 5-bit Hub address and a 3-bit port address. When a Hub is addressed, it selects the addressed port, strips off the byte containing the Hub/port address and passes the remainder of the command stream unmodified onto the addressed port. The outputs of the external ports consist of two low voltage differential lines for sending clock and data.

Analog chain

The hit information is read out serially through analog links in data packets containing all hits belonging to a single trigger. Within such packets a new analog value is transmitted every 25 ns and digitized in the Front End Driver (pxFED) at the same rate. Each pixel hit uses 6 values, or 150 ns. Five values are used to encode the address of a pixel inside a ROC and the sixth value represents the signal charge. Only the charge signals are truly analog while headers and addresses are discrete levels generated by DACs. No ROC IDs are sent but every ROC adds a header, whether

2008 JINST 3 S08004

it has hits or not in order to make the association of hits to ROCs possible. The sequential read-out is controlled by a token bit which is emitted by the TBM, passed from ROC to ROC and back to the TBM. The differential electrical outputs of the ROCs are multiplexed by the TBM onto either one or two output lines. On the same lines the TBM transmits a header before starting the ROC read-out. After receiving the token back from the last ROC in the chain the TBM sends a trailer containing status information. From the TBM to the end ring of the pixel barrel the read-out uses the module Kapton cable. The Kapton cable has a ground mesh on the back side and the differential analog lines are separated by quiet lines from the fast digital signals. Nevertheless, cross-talk from LVDS signals was found to be unacceptable and a low swing digital protocol is being used instead. On the end ring the analog signals are separated from the digital and all analog signals of the sector are sent on a separate Kapton cable to a printed circuit board that houses the Analog Optical Hybrids (AOH). The signal path between TBM and AOH is designed with a constant impedance of 40 Ω and terminated on the AOH. The optical links of the pixel system are identical to those used in the silicon strip tracker. An ASIC that adapts the output levels of the pixel modules to those expected by the laser driver has been added to the AOH of the pixel system. A clean identification of the six levels used for encoding pixel addresses is crucial for the reconstruction of hits. The ratio of RMS width to separation of the digitized levels after the full read-out chain is 1:30. The rise-time at the digitizer input is 3 ns which makes corrections from previously transmitted levels negligible. The full read-out chain adds a noise equivalent to 300 electrons to the analog pulse height, dominated by baseline variations of the laser drivers.

Front End Driver

Optical signals from the pixel front end electronics (ROCs and TBMs) are digitized using the pixel Front End Digitizer (pxFED). A pxFED is a 9U VME module. It has 36 optical inputs each equipped with an optical receiver and an ADC. The ADC converts at LHC frequency supplied by the TTC system which can be adjusted by an individually programmed phase shift (16 steps within 25 ns) for precise timing. A programmable offset voltage to compensate bias shifts can also be set. The output of the 10 bit-ADC is processed by a state machine to deliver pixel event fragments consisting of header, trailer, input channel number, ROC numbers, double column numbers and addresses and amplitudes of hit pixels all at a subject-dependent resolution of 5 to 8 bits. Event fragments are strobed into FIFO-1 (1k deep $\times$ 36 bit wide) which can be held on demand to enable read-out via VME. In normal processing mode FIFO-1 is open and data of 4 (5) combined input channels are transmitted to 8 FIFO-2 memories (8k $\times$ 72 bits). In order to determine thresholds and levels required for the state machine, FIFO-1 can alternatively be operated in a transparent mode making unprocessed ADC output data available. The output from FIFO-2 is clocked into two FIFO-3 memories (8k $\times$ 72 bits) whose outputs are combined to provide the data now at a frequency of 80 MHz (twice the common operating pxFED-frequency) to the S-Link interface acting as a point-to-point link with the CMS-DAQ system. Parallel to the data flow spy FIFOs are implemented (restricted in size) to hold selected event fragments and make them available for checking data integrity. Error detection takes place in the data stream from FIFO-1 to FIFO-2 and corresponding flags are embedded in the event trailer and also accessible from VME. A selected DAC output from each ROC (on default representing the ROC's temperature) is available as well.

2008 JINST 3 S08004

In addition, errors are directly transmitted to the CMS-TTS system using a dedicated connector on the S-Link supplementary card. A histogramming feature has been implemented to monitor the rate of double column hits. This histogram is intended to be read out via VME periodically to check for dead or overloaded columns. The pxFED houses an internal test system which, when enabled, replaces the normal ADC input by a pattern of 256 clocked analog levels simulating a normal pixel event. There are three test DACs (10-bit) available to generate such a pattern meaning that every third input channel receives the same simulated event. This test system allows to test most of the features of the pxFED without the need of external optical input signals. All FIFOs, the state machine with its adjustable parameters, the VME protocol, error detection and histogramming features are integrated into several FPGAs mounted on daughter cards making the pxFED flexible to changes and improvements. The corresponding firmware can be downloaded via VME or using a JTAG bus connector mounted on the mother board. The whole pixel read-out system will consist of 40 pxFED modules (32 for the barrel and 8 for the forward) set up in three 9U VME crates located in the electronics room. Individual modules can be accessed by VME geographical addressing.

Front End Controller

The Pixel Front End Controller (pFEC) supplies clock and trigger information to the front end, and provides a data path to the front end for configuration settings over a fiber optic connection. The pFEC uses the same hardware as the standard CMS FEC-CCS [28]. The firmware which defines the behaviour of the mezzanine FEC (mFEC) module has been replaced by a pixel specific version, converting the FEC into a pFEC. Each mFEC board becomes two command links to the front end. The Trigger Encoder performs all trigger transmission functions, encoding TTC triggers to match the pixel standard, block triggers to a given channel, generate internal triggers, either singly, or continuously, for testing purposes. Within each command link are a one kilobyte output buffer for data transmission, and a two kilobyte input buffer for data receiving. All data, whether write or read operations, are retransmitted back from the front end for possible verification. To minimize the VME data transfer time, the pFEC uses several data transfer modes. When transferring pixel trim values to the front end, the pFEC calculates the row number information for a given column of pixels on the fly. This results in nearly a 50% reduction in the time required to transfer trim values over VME to a given command link buffer. In this way, the entire pixel front end trims can be reloaded in 12 s. Another 2 s are used to load the other configuration registers, for a total of 14 s to reload the front end completely. This column mode is also the reason that the return buffer is twice as big as the transmit buffer. The return buffer receives the row number as well as the trim value for each pixel. Once data is loaded into an output buffer, the transfer may be initiated either by computer control, or by a signal from the TTC system. Since single event upsets are expected to occur in the front end registers, it is anticipated that periodic updates will be necessary. Since updating the front end may disrupt data taking, it is preferable to perform small updates synchronized to orbit gaps or private orbits. This is done through the TTC initiated downloads. For transmission verification purposes, the number of bytes transmitted is compared to the number of bytes returned from the front end. Also, the returning Hub/port address is compared to the transmitted address. Status bits are set with the results of this comparison, and these values are stored, for possible review, should an error condition occur.

2008 JINST 3 S08004

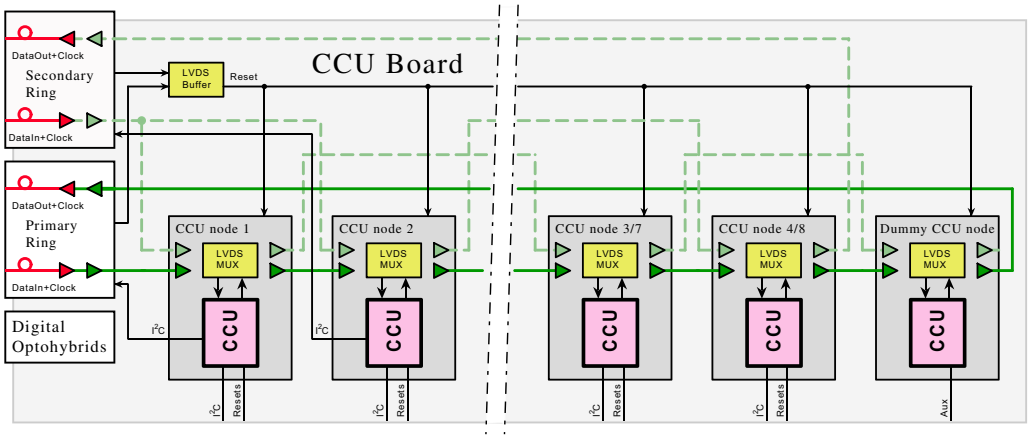

Figure 3.10: Block diagram of the Pixel front end control system. Note that the total number of CCU nodes is 9 for the BPix and 5 for the FPix.

The detector front end control system

The CMS Pixel detector front end control system for both the barrel (BPix) and the forward (FPix) detectors consists of four communication and control unit boards (CCU Boards). Each CCU board controls a quarter of the detector with eight Barrel read-out sectors or twelve Forward port cards. Figure 3.10 shows the block diagram of a CCU Board. The same ring topology configured as a local area network as in the silicon strip tracker is used. The front end controller (FEC) module is the master of the network and uses two optical fibers to send the timing and data signals to a number of slave CCU nodes, and another two fibers to receive return communication traffic. The two receiver channels on the digital optohybrid (DOH) transmit the 40 MHz clock and control data at 40 Mbit/s in the direction from the FEC to the ring of communication and control units (CCUs). The two transmitter channels send clock and data back to the FEC from the ring of CCUs. The CCU is the core component developed for the slow control, monitoring and timing distribution in the tracking system [29]. To improve system reliability against a single component failure a redundant interconnection scheme based on doubling signal paths and bypassing of faulty CCUs is implemented. An additional "dummy" CCU node allows to mitigate a single DOH failure preserving complete functionality. A CCU node failure leads to a loss of communication to all electronics attached to that CCU. The first two CCU nodes in the ring provide also the I^2C data channels necessary to control the digital optohybrids on the CCU boards.

In the BPix each read-out sector is controlled by a separate CCU node. Eight active and one dummy CCU node build a single control ring. One I^2C data channel is used to access and control the front end read-out electronics and three output channels generate the necessary signals to reset the digital and the analog optohybrids as well as the read-out chips (ROCs) in one read-out sector. The FPix control ring consists of four active and one dummy CCU node. Each of the active CCU nodes control 3 port cards, which constitute a 45° sector in the detector coverage at one end. A connection between a CCU and a port card includes a bi-directional 100 KHz I^2C communication channel and two reset signals. One reset signal is for the port card electronics, and the other one goes to the read-out chips on the detector panels.

2008 JINST 3 S08004

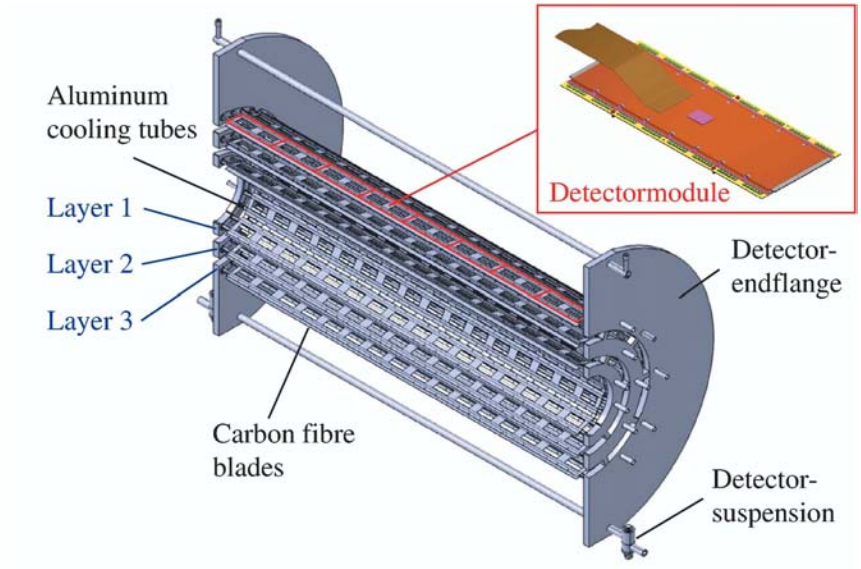

Figure 3.11: Complete support structure half shell with the three detector layers.

3.2.4 The pixel barrel system

The pixel barrel system as installed inside CMS comprises the barrel itself, i.e. detector modules mounted on their cylindrical support structure, as well as supply tubes on both sides. The barrel with its length of 570 mm is much shorter than the Silicon Strip Tracker inside which it is installed. Supply tubes carry services along the beam pipe from patch panels located outside of the tracker volume to the barrel. The supply tubes also house electronics for read-out and control. The length of the full system is 5.60 m. Support structure and supply tubes are split vertically to allow installation in the presence of the beam-pipe and its supports. Electrically the $+z$ and $-z$ sides of the barrel are separated. Each side is divided in 16 sectors which operate almost independently, sharing only the slow control system.

Pixel barrel support structure

The detector support structure for the three layers at the radii of four, seven and eleven centimeters equipped with silicon pixel modules has a length of 570 mm ranging from -285 mm to $+285$ mm closest to the CMS interaction region. Figure 3.11 shows a sketch of a complete support structure half shell.

Aluminium cooling tubes with a wall thickness of 0.3 mm are the backbones of the support structure. Carbon fiber blades with a thickness of 0.24 mm are glued onto the top or bottom of two adjacent cooling tubes in such a way that their normal directions alternate pointing either to the beam or away from it. The tubes have trapezoidal cross sections defined by the azimuthal angles of the ladders they hold.

Four to five of these tubes are laser welded to an aluminium container which distributes the cooling fluid. The resulting manifold provides the necessary cooling of the detector modules to

2008 JINST 3 S08004

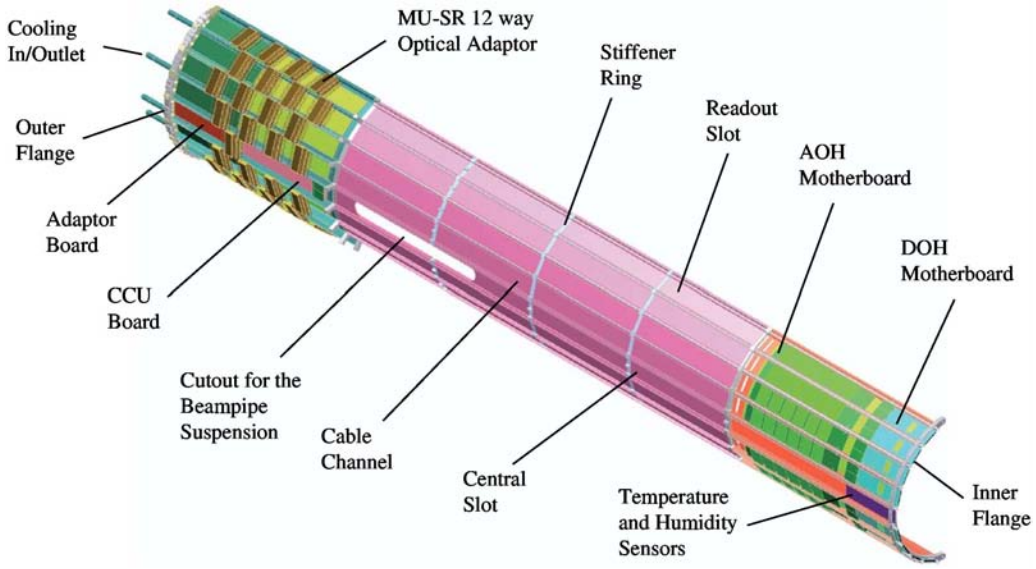

Figure 3.12: Overview of a supply tube half shell.

about $-10\,^{\circ}\mathrm{C}$ with C_6F_{14}. Support frames on both ends, which connect the single segments, build a complete detector layer half shell. These flanges consist of thin fibreglass frames (FR4) that are filled with foam and covered by carbon fibre blades.

Printed circuit boards mounted on the the flanges hold the connectors for the module cables and provide control signal fan-out and power distribution to the individual modules of a sector.

Pixel detector supply tube. The electrical power lines, the electrical control signal and the optical signals as well as the cooling fluid are transferred across the supply tubes to the pixel barrel. The two supply tube parts of a half shell in $+z$ and $-z$ direction have a length of 2204 mm (figure 3.12).

The supporting elements of the basic structure are the stainless steel tubes with a wall thickness of 0.1 mm running along the z-direction connected to the stiffener rings (FR4) and the inner and outer flanges made out of aluminium. The tubes supply the detector with the cooling fluid. The gaps in between are filled with foamed material with the corresponding shape to guarantee the necessary rigidity. All power and slow control leads are embedded in the supply tube body. This allows a clear layout of the wiring and also makes the system more reliable.
The motherboards, which hold the optical hybrids for the analog and digital control links, are installed in the eight read-out slots near the detector on the integrated supply boards. The corresponding boards at the outer ends carry the power adapter boards, which provide the detector power and the bias voltage for this sector. In the central slot the digital communication and control board (CCU Board) is installed. From here the digital control signals are distributed to the individual read-out boards in each of the eight read-out sectors. Here also all slow control signals like temperatures, pressures and the humidity are brought together and connected by the dedicated slow control adapter board to the cables. The optical fibres are installed in the cable channels. The 36 single fibres for the analog read-out and the eight fibres for the digital control of the detector

2008 JINST 3 S08004

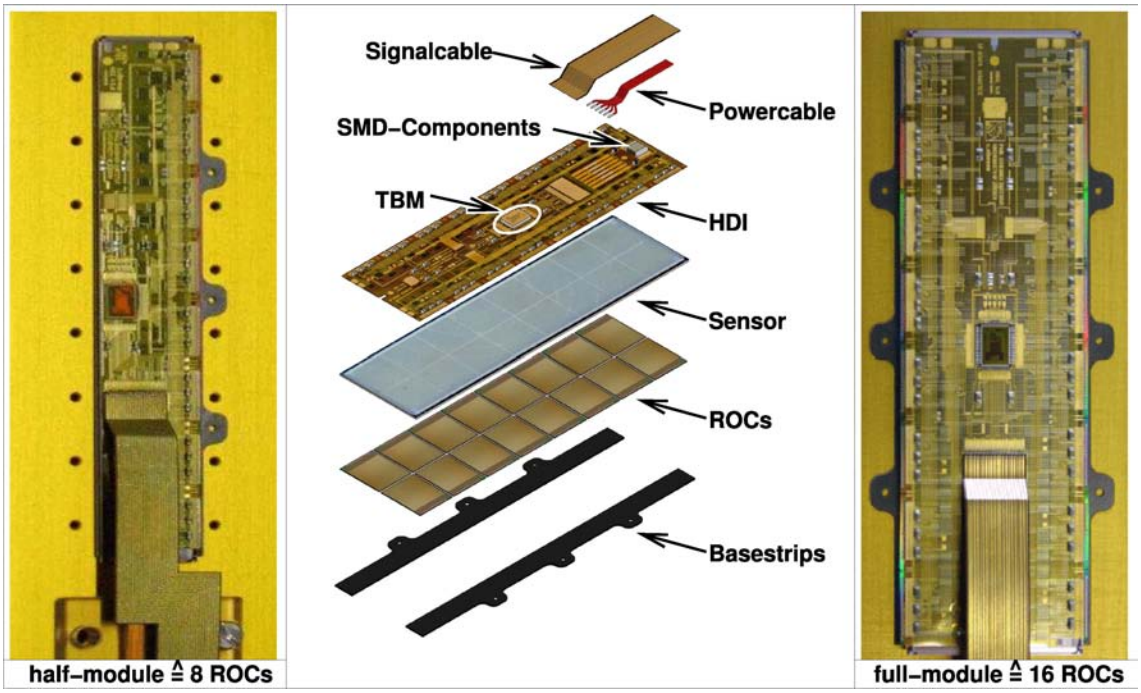

Figure 3.13: Exploded view (middle panel) of a barrel pixel detector full module (right panel) and picture of an assembled half module (left panel).

modules will then be connected through the MUSR connector to the optical ribbon cable. These adapters are mounted at the circumference in the first part of the supply tube. The length of each supply tube is 2204 mm. Only a flexible mechanical connection is made between the barrel and the supply tube.

Pixel barrel detector modules

The barrel part of the CMS pixel detector consists of about 800 detector modules. While the majority of the modules (672) are full modules as seen in figure 3.13 on the right, the edges of the six half-shells are equipped with 16 half-modules each (96 in total, see figure 3.13 on the left).

Geometry and components. A module is composed of the following components (figure 3.13). One or two basestrips made from 250 μm thick silicon nitride provide the support of the module. The front end electronics consists of 8 to 16 read-out chips with 52×80 pixels of size 100×150 μm^2 each, which are bumpbonded to the sensor. The chips are thinned down to 180 μm . The High Density Interconnect, a flexible low mass 3 layer PCB with a trace thickness of 6 μm equipped with a Token Bit Manager chip that controls the read-out of the ROCs, forms the upper layer of a module and distributes signals and power to the chips. The signals are transferred over an impedance matched 2 layer Kapton/copper compound cable with 21 traces and 300 μm pitch. The module is powered via 6 copper coated aluminium wires of 250 μm diameter.

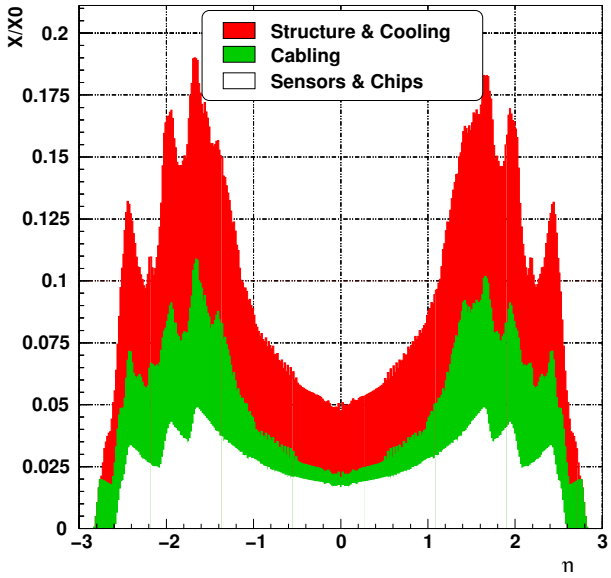

Figure 3.14: Material budget of the pixel barrel in units of radiation length versus rapidity. The plot does not contain contributions from the pixel support cylinder, the supply tube and cabling from the detector end flange to the supply tube.

A completed full-module has the dimensions 66.6×26.0 mm^2, weights 2.2 g plus up to 1.3 g for cables, and consumes 2 W of power. The material of the pixel barrel amounts to 5 percent of a radiation length in the central region. Sensors and read-out chips contribute one third of the material while support structure and cooling fluid contribute about 50 percent. The distribution of material as a function of pseudorapidity is shown in figure 3.14.

3.2.5 The forward pixel detector

The FPix detector consists of two completely separate sections, one on each side of the interaction region. They are located inside the BPix supply tube but are mounted on separate insertion rails. Each section is split vertically down the middle so the detector can be installed around the beam-pipe and its vertical support wire and so it can also be removed for servicing during major maintenance periods without disturbing the beam-pipe. Each of these four sections is called a *half-cylinder*.

Mechanics of a half-cylinder

Each half-cylinder consists of a carbon fiber shell with two half-disks located at its front end, one at 34.5 cm from the IP and the other at 46.5 cm. The half-disks support the actual pixel detectors that extend from 6 cm to 15 cm in radius from the beam.

The half-disk has 12 cooling channels (each in the shape of a “U”) assembled between a half ring shown in figure 3.15. The assembly requires three slightly different types of cooling channels. Each channel is made by Al-brazing two blocks of Al with the channel for the cooling fluid already

Figure 3.15: The FPix half-disk cooling channels mounted in the outer half-ring structure. The turbine-like geometry is apparent. Panels are mounted on both sides of the cooling channels.

machined in the two parts. The brazed parts are then machined to their final shape. The walls of the channels are 0.5 mm thick. The average weight of the channels is 8.21 g.

All channels passed a Helium leak test at 1.33×10^{-8} mbar-litre/s. The pressure drop of the individual cooling channels for a flow of 2600 sccm of dry N_2 is 0.49 $\pm$ 0.02 mbar. Six daisy-chained cooling channels form a *cooling loop*. The pressure drop over a loop (for a flow rate of 1230 sccm) of dry N_2 is 0.96 ± 0.13 mbar. For C_6F_{14} at -20°C with a rate of 12cc-s the pressure drop is 294 mbar.

Each of the twelve cooling channels of a half-disk has trapezoidal beryllium *panels* attached to each side. The panels support the sensors and read-out chips that constitute the actual particle detectors. As explained above, the cooling channels are rotated to form a turbine-like geometry to enhance charge-sharing. The panels are made of 0.5mm beryllium. The beryllium provides a strong, stable and relatively low-mass support for the actual pixel detectors. The cooling channels are supplied with C_6F_{14} at about -15°C. A single cooling channel with panels mounted on both sides forms a subassembly called a *blade*. There are 24 panels, forming 12 blades, in each half-disk.

Powering up the electronics on one blade increases the temperature by $\approx$2°C. The temperature of each ROC is part of the information available for each event. Each panel also has a resistance temperature detection sensor. The pixel sensors have fiducial marks visible with a coordinate measuring machine (CMM). Their position is then related to reference marks mounted on the half-disk units.

After installing the half-disks in the half-cylinder, the disk position is measured relative to the half-cylinder using a CMM and also by photogrammetry. This permits relating the position of the sensors to the CMS detector. The detector is surveyed at room temperature but operated at

2008 JINST 3 S08004

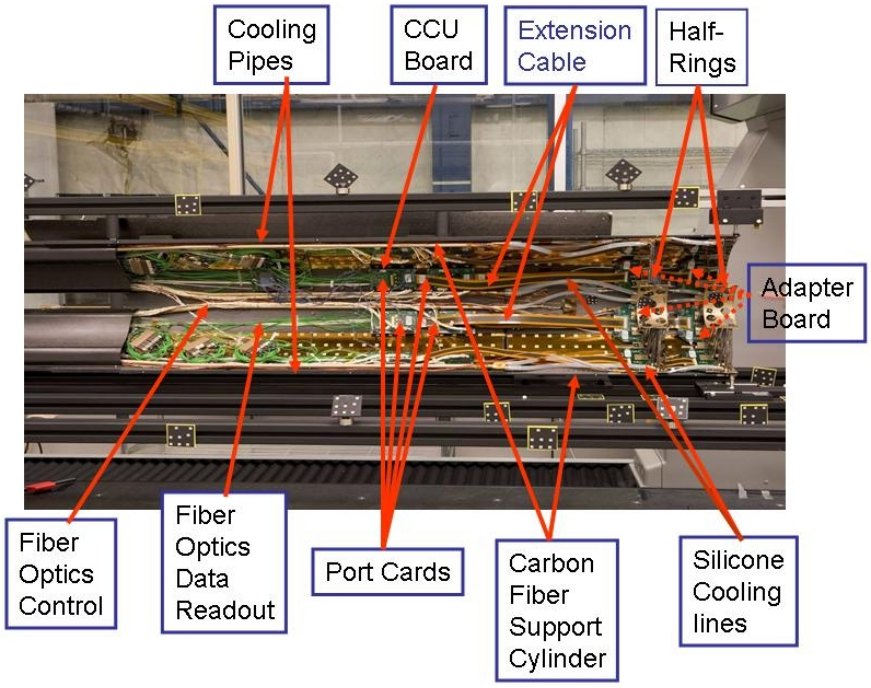

Figure 3.16: Overview of the Forward Pixel half-cylinder. A photograph of the portion of the first production half-cylinder facing the interaction region (IR). The aluminium flange, the filter boards (see below), and the CCU board are not shown. The half-cylinder is mounted in a survey fixture. The carbon fiber cover at the end away from the IR protects the downstream components during insertion of the beam pipe suspension wires that run through a slot in the half-cylinder towards the left end of the picture.

about $-10°$C. The deformation (magnitude and direction) of the panels on a half-disk, when its temperature changes from 20°C to $-20°$C has been measured to be 150 μm. This result has been reproduced by a finite element analysis of the half-disk and it will be used in the final alignment of the pixels. We anticipate knowing the pixel geometry to a few tens of microns before the final alignment with tracks.

The service half-cylinder also contains all the mechanical and electrical infrastructure needed to support, position, cool, power, control and read out the detector. In particular, it contains electronics for providing bias voltage to the sensors, power to the read-out chips, signals for controlling the read-out chip via optical fibers linking it to the control room, and laser drivers for sending the signals (address and energy deposition) off the detector to the data acquisition system. The service half-cylinder also provides the path for cooling fluid necessary to remove the heat generated by the sensors and read-out chips.

At the end of each service half-cylinder there is an annular aluminium flange that contains holes to pass the power cables, cooling tubes, control and monitoring cables, and fiber optic read-out from intermediate patch panels to the FPix detector. The electronics cards needed for the operation of the detector are mounted on the inner surface of the half-cylinder. A picture of a half-cylinder is shown in figure 3.16.

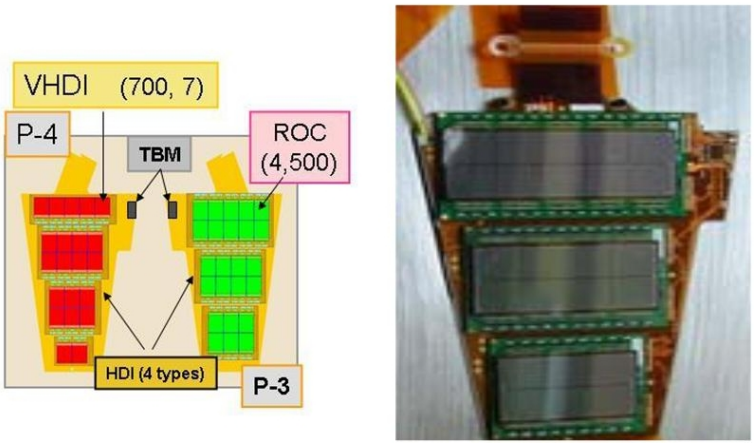

Figure 3.17: Sketches of the two types of FPix panels showing the different sizes and numbers of the plaquettes on each (left side). A photograph of an actual 3-plaquette panel (right side).

Forward pixel detection elements - the plaquettes

The basic unit of construction for the forward pixel detector is the *plaquette*. A plaquette consists of a single pixel sensor bump-bonded to an appropriate number of Read-Out Chips (ROCs) and wire-bonded to a very-high-density-interconnect (VHDI) that provides power, control, and data connections.

In order to cover the trapezoidal or *pie-shaped* panels without leaving cracks, five different sizes of plaquettes are needed. These are respectively 1×2, 2×3, 2×4, 1×5, 2×5, where the first digit refers to the number of rows and the second to the number of columns of read-out chips that are attached to a given sensor. The largest plaquette, the 2×5, has dimensions of 16 mm × 35 mm. The panels on the side of the cooling channel closest to the IP contain 1×2, 2×3, 2×4, and 1×5 plaquettes or a total of 21 ROCs. The panels on the side of the cooling channels farthest from the IP contain 2×3, 2×4 and 2×5 type plaquettes with a total of 24 ROCs. The sensors are offset on the upstream and downstream panels so that there are no cracks in the coverage due to the ROC read-out periphery. The two types of panels are shown in figure 3.17. A total of 672 plaquettes are needed.

The joining, or *hybridization*, of the pixel sensors and the pixel unit cells of the ROC is achieved by fine-pitch bumping using Pb/Sn solder and then flip-chip mating. The bumping is done on the 8" ROC wafers and the 4" sensor wafers. After bumping, the ROC wafers are thinned by backside grinding to 150 μm and then diced. Finally, each of the 5 different types of sensors are mated to the appropriate number of ROCs. The sensor with its ROCs bump-bonded to it is called a module. For FPix, the hybridization was done in industry. The fraction of broken, bridged, or missing bumps is at the level of a few 10^{-3}.

After delivery from the vendor, the bump-bonded pixel detector module is then installed on a Very High Density Interconnect (VHDI). The VHDI is a two-layer flexible printed circuit, laminated to a 300 μm thick silicon substrate, whose trace geometry and characteristics (impedance, low intrinsic capacitance, and low cross-talk) have been optimized for the intended use of conveying digital control and analog output signals to and from the sensors and ROCs.

The VHDI is made as follows. A bulk 6" silicon wafer is laminated to a flexible sheet containing several VHDI circuits. Passive components are also attached using surface-mount solder techniques. The wafer of populated circuits is then diced into individual circuits using a diamond saw. The circuits are then electrically tested.

The hybridized pixel module is attached and wire bonded to a populated VHDI to become a *plaquette*. The joining is made using parallel plate fixtures aligned on linear rails. The alignment of components is inspected using a coordinate measuring machine. A flexible plate is used for fine adjustments on the fixtures resulting in alignments between joined components within 100 μm. The adhesive bond between plaquette components is made in a vacuum at 60°C, to soften the adhesive and prevent air entrapment. An air cylinder applies and controls the mating pressure, which is limited by the compression allowed on the bump-bonds.

The effects of thermal cycling and radiation on the assembled plaquettes have been extensively tested. The tests demonstrate that the adhesive and the application method mitigate warping due to temperature changes, and provide reliable strength and thermal conductivity.

Once plaquettes are mechanically joined, they are clamped in cassettes that accommodate all processing steps such as wirebonding which provides electrical connections between the ROCs and the VHDI. After wirebonding we encapsulate the feet of wirebonds. This encapsulation is necessary due to periodic $I\vec{d}l \times \vec{B}$ forces expected to occur during actual CMS operation. The encapsulant acts as a damping force on the wire, preventing large resonant oscillations to work harden the wire and cause eventual breakage [30]. Finally the plaquettes undergo quick testing at room temperature. During this test the quality of the plaquettes is evaluated in terms of the characteristics of the sensor, the read-out chip, the number of bad pixels and missing bonds. The assembly and testing rate is optimized for a rate of six plaquettes per day.

The completed plaquettes are subjected to a quick plug-in test. Then they are loaded into a *Burn-In Box* where they undergo 10 temperature cycles between 20°C and −15°C. These cycles can take up to 2 days to complete, depending upon the thermal load. During these cycles, the plaquettes are monitored for electrical operation. We have seen no failures during the cycling. After the burn-in process is completed, the plaquettes are subjected to a series of electrical tests to ensure their suitability for their eventual mounting on a panel. These tests, at the operating temperature of −15°C, include the functionality of the ROC, the integrity of the bump-bond, and the I-V characteristics of the sensor. Other tests measure the thresholds and noise characteristics of each pixel on the entire plaquette assembly, and the individual pixel thresholds are trimmed via the ROC capability. We have found that the pixel trim values from the plaquette test on each pixel remain valid even after subsequent steps of the assembly process. After testing the plaquette data is loaded into the Pixel Construction Database and the plaquettes are graded. We have three main categories of grades:

- A - the plaquette is available for immediate mounting on a panel;
- B - potential issues have been found during testing and need further analysis;
- C - the plaquettes are unsuitable for mounting.

The data on each B-grade plaquette are examined carefully. In many cases, the plaquettes are found to have missed being classified as A-grade due to very minor deficiencies (e.g. slightly

2008 JINST 3 S08004

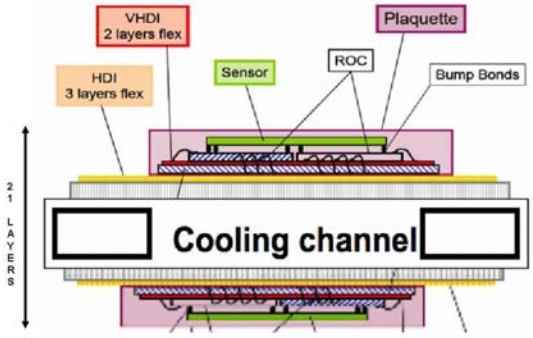

Figure 3.18: Sketch of a plaquette mounted on a panel showing its several layers.

too many noisy pixels) which will not be significant when an entire panel's quality is assessed. These are "promoted" to A-grade and declared usable on panels. Current plaquette yields, based on an original grade of A or a promotion to A-grade from B, are in the 80% range, varying slightly according to plaquette size.

Panel assembly

A panel is formed from three or four plaquettes attached to an assembly of a High Density Interconnect (HDI) laminated to a beryllium plate. The HDI is a three-layer flexible printed circuit whose trace geometry and characteristics (impedance, low cross-talk) have been optimized for the intended use of transferring digital control and analog output signals.

The process by which a panel is assembled is as follows. A single HDI circuit is laminated to a trapezoidal-shaped 0.5 mm thick beryllium plate. Passive components are attached using surface-mount solder techniques. The Token Bit Manager (TBM) is attached to the corner tab of the HDI using a die attach method and wire-bonding. After functional and burn-in tests with only the TBM, the individual plaquettes are attached to the HDI using adhesive for mechanical attachment and wire-bonds for electrical connection.

There are four types of panels, a right and left 3-plaquette version, and a right and left 4-plaquette version. The right and left handed versions have their TBMs on opposite sides of the panel centerline. Both types are required so that no panel part projects past a line in the vertical plane. The reason for the "3" and "4" type panels is that they are eventually mounted on opposite side of a blade, and the gaps between plaquettes on one type are covered by the active area of the other.

A panel is built up out of several layers of components. These are shown in figure 3.18. The total number of panels in all eight half-disks is 192.

Final detector assembly validation

The panels are attached onto the front and back of the half-disk cooling channels. The 4-plaquette panels are mounted on the side closest to the interaction region (IR), and the 3-plaquette versions on the opposite side. The half-disk assembly is mounted onto the half-service cylinder and is again tested.

Electronics chain

Each HDI is connected to another flexible printed circuit board, the *adapter board*. Each adapter board serves three blades (or 6 panels). One important purpose of the adapter board is to send and receive signals from the panels, which are mounted perpendicular to the axis of the service cylinder to and from the electronics mounted on the inner surface of the service cylinder. This is done by a *pigtail* at the end of each panel that plugs into connectors on the fingers of the adapter board.

The adapter board has three types of ASICs mounted on it. These are used to pass the clock, trigger and control data signals to each panel and return the received control signals back to the pFEC.

The adapter board is connected to another printed circuit board, the *port card*, by a light-weight extension cable. These cables are of two types, a power cable which distributes the power to the ROCs and TBMs, and the HV bias to the sensors. The other cable is to transmit the pixel data and control signals to the panel from the port card. The port card is a low-mass printed circuit board. It houses the electronics needed to interface the front-end chips with the VME electronics (the pFEC and pxFED) and power supplies located in the counting room. The port card transmits the clock signal, L1 trigger and slow control signals to the front end electronics. It distributes the power and bias voltages to the chips and sensors. It also monitors the currents and voltages as well as the temperature on some panels. These functions are done by various ASICs that are common to the CMS tracker. These ASICs include the DCU for monitoring, the TPLL for regenerating the trigger and timing signal, the gatekeeper for keeping the optical up and down links open as needed.

To control and monitor the various ancillary chips and optohybrids, there is a CCU board for each half service cylinder, as described above.

The port card contains the Analog Optohybrid (AOH). Each of the 6 laser diodes of the AOH chip receives data from one panel via its TBM and sends it over its own optical fiber to the Front end Driver (FED).

The control of the ROCs is achieved through the Pixel Front End Controller. Optical signals are sent from it to the Digital Optohybrids on the port card, through the extension cables to the adapter board, then to the TBM on the panel, through the HDI and the VHDI to the ROCs.

Power and monitoring

Power connections are made from CAEN power supplies via cables that run through the flange at the end of the half-cylinder away from the IR into a set of power/filter boards. From these boards, it is sent along wires to the port card, in the case of low voltages, and directly to the adapter board in the case of the sensor bias voltage.

Monitoring points for temperature are distributed throughout the service cylinder. There are also humidity sensors. Additional temperature sensors are mounted on the panels. High and low voltage and detector monitoring are connected to the DCS system described below.

Testing

Testing is a key element of quality assurance in the assembly process. While rework is possible, it is difficult and error prone. At every step, we confirm that we are using only “known good parts”.

2008 JINST 3 S08004

Testing must keep up with the driving assembly step, plaquette production. Full characterization of a plaquette requires hundreds of thousands of measurements. To accomplish this, we have developed special read-out hardware and software that can carry out these measurements quickly and efficiently. A software using a USB-based data acquisition scheme is employed when flexibility is needed to develop measurement programs of modest complexity and duration, such as the burn-in procedure. For the most extensive measurements, including plaquette testing and characterization, we use a PCI-based system and a software program called Renaissance [31].

Final testing is performed using the real data-acquisition and control hardware and prototype data-acquisition software and constitutes an end-to-end system test. Detailed testing also establishes an initial set of parameters for the many DACs and thresholds in the system.

3.2.6 Power supply

All needed high and low DC voltages are generated by means of a commercial modular system of the type CAEN-EASY4000 . This system is also employed by the CMS silicon strip tracker for which the main regulating cards (A4601H) were custom designed [32]. Only small changes in hard- and firmware were necessary for adaptation to the pixel project.

The core of this system, accessed through LAN, is located in the detector control room (USC55) and consists of one main controller (SY1527) containing 3 branch controllers (A1676A). The actual power supply cards are placed in two racks of 5 crates in close proximity to the detector thanks to their radiation tolerance and magnetic field resistance. This has been chosen in order to reduce power loss in the cables. The power supply crates are connected by flat cables (≈ 100 m) to the branch controllers. They are fed by local 3-phase 230 V_{AC} to 48 V_{DC} master converters of each 2 kW (A3486H) also suited for operation at hostile environments.

The crates house two types of electronic cards, one of 4 channels of 2.5 V/7 A (A4602) feeding the service electronics on the supply tubes (auxiliary power), while the other (A4603H) deliver 2 complex channels of each 2 low (1.75 V/7 A and 2.5 V/15 A) and 2 high voltage lines (-600 V/20 mA) for ROC and sensor biasing respectively. Each of these channels contains floating pulse-width-modulated DC/DC switching transformers with a common ground return for the 1.75 and 2.5 V lines. The isolation resistance (ground return versus earth on the racks) is typically 100 Ω at 5 MHz. Every card is controlled by an optically decoupled microprocessor for setting and measuring voltages, currents, ramp times, trip parameters, interlocks and others.

The DC levels are regulated over sense lines. The reaction time of the sensing circuit (typically 200 μs) is subject to fine tuning to comply with capacitive load, cable impedance and length (typically 50 m). The line drop in the cables amounts to roughly 2 V, while the regulators would allow for a maximum of 6 V. Fourteen A4602 cards, yielding 40 independent channels of auxiliary power, feed the 32 slots of the barrel service tubes with each 2 DOHs and 6 AOHs as well as 4 groups of each 12 port cards of the forward half disks. The main supplies of 112 complex LV and HV channels (56 A4603H cards) feed the 64 barrel groups (192 ROCs, this contains groups with half size modules) of each 12 detector modules, and 48 forward groups (135 ROCs) of each 3 disk blades. Each of these groups draws a typical current of 4.6 A on the analogue (1.75 V) and 9 A on the digital (2.5 V) line respectively. The large current reserve of the supplies is needed to comply with conditions during bootstrapping where the ROCs remain briefly in an undefined state. It was

verified that the regulators undergo a smooth transition from the constant-voltage to the constant-current regime if the programmed current limits are approached. Beside microprocessor controlled actions (1 s) fast over-current security is guaranteed by various solid state fuses (10 ms) as well as crowbars (100 μs) for over-voltage.

Noise levels are typically 5 mV_{pp} on the LV and 50 mV_{pp} on the HV outputs which can easily be accepted thanks to the LV regulators in the ROCs and the intrinsically small sensor capacitances respectively. Of major concern in the overall design were fast drops in the digital current consumption (2.5 V line) in case of low ROC activity like in orbit gaps. Due to the cable inductance a typical current drop of 2 A per group generates over-voltage spikes at the module level in the order of some Volts depending on local buffer capacitors. The integrity of the cable-module-ROC circuit was therefore checked by a full simulation in SPICE together with measurements on pulsed current loads. This served for the designs of the cables and the electronic layout, e.g. grounding or HV distribution. (In one sector layer-1 modules are fed by one line while layer-2,3 modules are commonly fed by the other.) Finally a $6\times4\,mm^2$ shielded copper cable was chosen for the 40 m from the power supply cards to the patch panel (PP1) located in the HCAL with alternating current directions between adjacent lines. Two twisted pair lines for the senses and a bunch of 10 commonly shielded lines for HV are contained in the same cable complex ($0.1\,mm^2$).

Inductance, capacitance and characteristic impedance between two of the main lines were measured to be 6 μH/m, 0.13 nF/m and 24 Ω respectively. The 4 m connection between PP1 and PP0 (tracker bulkhead) uses Al conductors in the cable. The auxiliary power cable is also shielded and contains $26\times0.75\,mm^2$ and 4 twisted pair copper lines with $0.1\,mm^2$ for the sense wires.

3.2.7 Cooling

The power consumption per pixel amounts to around 55 μW, including about 13 μW from the sensor leakage current at final fluences of $6\times10^{14}/cm^2$. For the total of $\approx$ 66 million pixels this adds up to 3.6 kW. The power load on the aluminium cooling tubes is therefore expected to be about 50 W/m. The sensor temperature will be maintained at around -10°C. As for the strip detectors, liquid phase cooling with C_6F_{14} is used. To keep the temperature increase of the coolant below 2°C, a total flow rate of 1 litre/s is required.

The pixel system is cooled by a total of 18 cooling loops: 10 for the barrel and 4 for each of the two end disk systems. For the barrel, the coolant enters at $+z$ and exits at $-z$, or vice versa. The coolant for the two disk sets on each side of the interaction region is supplied and reclaimed from the same z side. One barrel loop feeds in parallel 9 thin-walled aluminium pipes, each cooling 8 modules in series. One disk loop cools in parallel one quarter of each of the 2 disks; inside the quarter disks the 6 blade loops are connected serially. The coolant flow at the pixel modules is turbulent. The total lengths of the cooling loops starting from and returning to the pixel cooling rack amount to about 80 m, resulting in pressure drops of below 2 bar.

3.2.8 Slow controls

The safe operation of the barrel and forward pixel detectors is guaranteed by the CMS Pixel slow controls system (DCS). Its tasks are to monitor temperatures and humidities at different locations

of the detector and to monitor and control the high and low voltages necessary for operation of the on-detector electronics.

The monitoring of temperatures and humidities is based on a commercial Siemens S7–300 modular mini Programmable Logic Controller (PLC) system. The Siemens S7–300 system monitors a total of 192 temperature and 8 humidity sensors installed in the Pixel barrel and forward endcap disks. For the temperature sensors, platinum resistance temperature detection sensors with a nominal resistance of 1 kΩ (Pt1000 RTD) have been chosen. The measurement of humidity is based on detecting the water vapor induced shear stress in a small polymer element that is connected to a Wheatstone Bridge piezoresistor circuit [33]. This circuit provides a small (mV) output signal that is linearly proportional to relative humidity (RH) between the full range of 0% to 100% RH and is amplified by the same kind of conditioning electronics that is used by the silicon strip tracker. The PLC of the Siemens S7–300 system is programmed in the Statement List (STL) language [34] to convert the currents and voltages of the temperature and humidity sensors into calibrated physical units (i.e. degrees Celsius for temperatures and percentages for humidities). For the purpose of avoiding damage to the detector in case the cooling system (dry air supply) fails, routines are programmed within the PLC to interlock the CAEN power supplies (shut-off the cooling) in that case.

An additional 96 Pt1000 temperature sensors are read out via the data-acquisition (DAQ) system, together with the temperature dependent voltage sources integrated into each one of the pixel read-out chips. The temperatures recorded by the DAQ system are passed to the slow controls system by means of a dedicated software interface [35].

The Barrel and Forward Pixel slow controls system is integrated into the PVSS graphical user interface (chapter 9) of the main CMS DCS.

3.3 Silicon strip tracker

3.3.1 Silicon sensors

The sensor elements in the strip tracker are single sided p-on-n type silicon micro-strip sensors [36, 37]. They have been manufactured on 6 inch wafers in a standard planar process, leading to significant cost reduction per unit area when compared to the more traditional 4 inch wafers. The base material is n doped float zone silicon with $\langle 100 \rangle$ crystal orientation. This crystal orientation was preferred over the more common $\langle 111 \rangle$ orientation because measurements [38] have shown that the built-up of surface charge on $\langle 100 \rangle$ wafers due to irradiation is much smaller and consequently irradiation causes less inter-strip capacitance increase on this material.

In TIB/TID and on the inner 4 rings of the TECs (figure 3.1), thin sensors of $(320 \pm 20)\,\mu$m wafer thickness are used, with substrate resistivity of $\rho = 1.55 - 3.25\,$kΩcm. TOB and the outer 3 rings of the TECs are equipped with thicker sensors of $(500 \pm 20)\,\mu$m thickness, with substrate resistivity of $\rho = 4 - 8\,$kΩcm. Due to the single sided processing, these sensors show a significant bow, which is required to be less than $100\,\mu$m.

A uniform n^+ implantation on the back side of the wafers, covered by aluminium, forms an ohmic contact which is connected to positive voltage up to about 500 V. Those sensors which are penetrated by the beams of the laser alignment system (section 3.3.7) feature a 10 mm hole in the

2008 JINST 3 S08004

back side metalization, as well as anti-reflective coating in order to achieve transmission through up to four sensors with a sufficient signal on a fifth sensor.

On the front side, strip shaped diodes are formed by p^+ implantation into the n type bulk. Due to the radiation damage to the crystal lattice, the bulk material will undergo type inversion and change to p type. At this point, the pn junction moves from the strip side of the wafer to the rear side contact. Each implanted strip is covered by an aluminium strip from which it is electrically insulated by means of a silicon oxide and nitride multilayer. This integrated capacitor allows for AC coupling of the signals from the strips to the read-out electronics, which is thus protected from the high leakage currents after irradiation. Each metal strip has two bond pads on each end, which are used to make a wire bond connection to the read-out chip and in case of the daisy chained sensors to make a wire bond connection between the two sensors in one detector module. For testing purposes there is also a DC pad connected to the p^+ implant. Each strip implant is connected via a (1.5 ± 0.5) MΩ polysilicon bias resistor to a p^+ bias ring which encloses the strip region and also defines the active area of the sensor.

For all sensors in the CMS strip tracker the ratio of p^+ implant width over strip pitch is $w/p = 0.25$, leading to a uniform total strip capacitance per unit length of about 1.2 pF/cm across all sensor geometries [38]. The actual w/p value was chosen in order to minimize the strip capacitance while still maintaining a good high voltage behaviour of the sensor. The aluminium strips feature a metal overhang of 4 to 8 μm on each side of the strip which pushes the high field region into the silicon oxide where the breakdown voltage is much higher, leading to stable high voltage operation. For the same reason, the bias ring is surrounded by a floating guard ring p^+ implant. It gradually degrades the electric field between the n^+ implant at the cut edge of the sensor and the bias ring, which are at backplane potential (high voltage) and ground, respectively. Figure 3.19 shows the layout of a corner of the active region of a sensor.

In order to equip all regions in the CMS tracker, 15 different sensor geometries are needed [36] (figure 3.19): two rectangular sensor types each for TIB and TOB, and 11 wedge-shaped sensor types for TEC and TID. They have either 512 or 768 strips, reflecting the read-out modularity of 256 channels (two 128-channel front-end chips multiplexed to one read-out channel). Since the sensors are fabricated on 6 inch wafers, they can be made rather large. Typical dimensions are for instance about $6 \times 12\,\mathrm{cm}^2$ and $10 \times 9\,\mathrm{cm}^2$ in the inner and outer barrel, respectively. The total number of silicon sensors in the strip tracker is 24 244, making up a total active area of $198\,\mathrm{m}^2$, with about 9.3 million of strips [36].

3.3.2 Read-out system

The signals from the silicon sensors are amplified, shaped, and stored by a custom integrated circuit, the APV25 [39]. Upon a positive first level trigger decision the analogue signals of all channels are multiplexed and transmitted via optical fibers to Front End Driver (FED) boards in the service cavern where the analogue to digital conversion takes place. This read-out scheme brings the full analogue information to a place where it can be used for accurate pedestal and common mode subtraction as well as data sparsification. Clock, trigger, and control signals are transmitted by optical links as well. A schematic view of the silicon strip tracker read-out scheme is given in figure 3.20. This analogue read-out scheme was chosen for several reasons: optimal spatial reso-

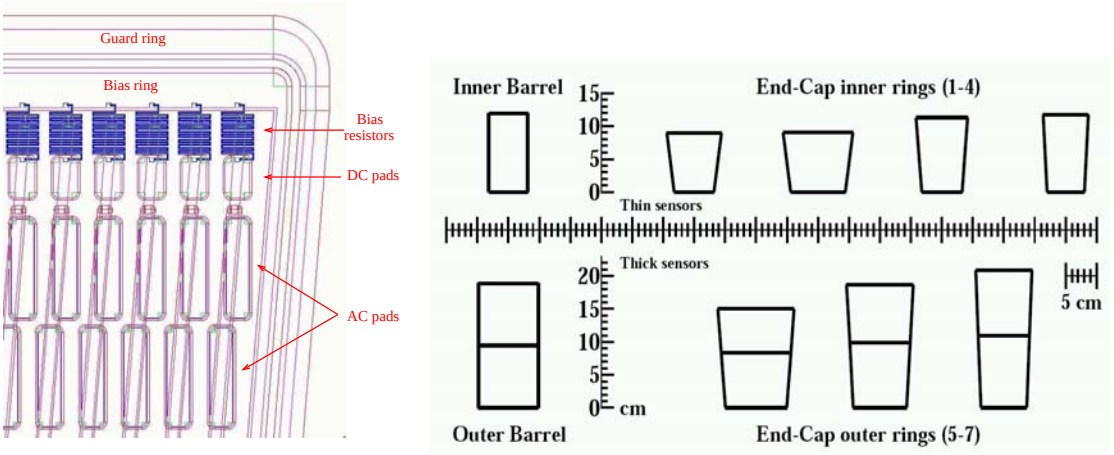

Figure 3.19: Left panel: drawing of one corner of the active region of a wedge-shaped silicon strip sensor for the tracker endcaps. Right panel: silicon sensor geometries utilized in the CMS tracker. In the outer layers the sensors are paired to form a single module, as shown in the figure. The Inner Barrel and Outer Barrel sensors exist in two types, of same area and different pitch. The sensors utilized for the first inner ring exist in two different versions, one for TID and one for TEC, respectively. (Only the TEC version is shown.)

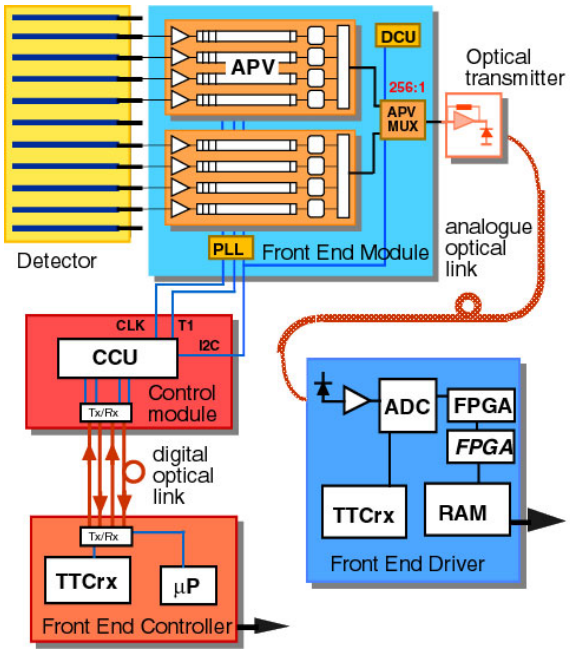

Figure 3.20: Read-out scheme of the CMS tracker.

lution from charge sharing, operational robustness and ease of monitoring due to the availability of the full analogue signal, robustness against possible common mode noise, less custom radiation hard electronics and reduced material budget as the analogue to digital conversion and its power needs are shifted out of the tracker volume.

2008 JINST 3 S08004

Front-end ASICs

The APV25 has been designed in an IBM 0.25 μm bulk CMOS process. Compared to processes with bigger feature sizes, the thin gate oxide inherent to this deep sub-micron process is much less affected by radiation induced charge-up and thereby, in conjunction with special design techniques, ensures radiation tolerance [40]. The APV25 has 128 read-out channels, each consisting of a low noise and power charge sensitive pre-amplifier, a 50 ns CR-RC type shaper and a 192 element deep analogue pipeline which samples the shaped signals at the LHC frequency of 40 MHz. This pipeline is used to store the data for a trigger latency of up to 4 μs and to buffer it. A subsequent stage can either pass the signal as sampled at the maximum of the 50 ns pulse (peak mode) or form a weighted sum of three consecutive samples which effectively reduces the shaping time to 25 ns (deconvolution mode). The latter is needed at high luminosity in order to confine the signals to the correct LHC bunch crossing. The pulse shape depends linearly (linearity better than 5%) on the signal up to a charge corresponding to 5 minimum ionizing particles (MIPs, one MIP is equivalent to 25 000 electrons in this case), with a gradual fall off beyond. When a trigger is received, the analogue data from all 128 channels of the appropriate time slice in the pipeline are multiplexed and output at a rate of 20 MS/s (mega-samples per second) as a differential bi-directional current signal, together with a digital header. Due to the tree structure of the analogue multiplexer the order in which the channels are output is non-consecutive and therefore re-ordering is necessary prior to the actual data processing. An internal calibration circuit allows to inject charge with programmable amplitude and delay into the amplifier inputs in order to be able to monitor the pulse shape.

The APV25 needs supply voltages of 1.25 V and 2.5 V with a typical current consumption of about 65 mA and 90 mA respectively, leading to a total power consumption of typically around 300 mW for one APV25 or 2.3 mW per channel. The noise of the analogue read-out chain is dominated by the front end MOSFET transistor in the APV25. Measurements have shown that the total noise for an APV25 channel depends linearly on the connected detector capacitance C_{det}. The equivalent noise charge is found to be $ENC_{\mathrm{peak}} = 270e + 38e/\mathrm{pF} \cdot C_{\mathrm{det}}$ in peak mode and $ENC_{\mathrm{deconv}} = 430e + 61e/\mathrm{pF} \cdot C_{\mathrm{det}}$ in deconvolution mode, both measured at room temperature [39]. Mainly due to the MOSFET characteristics, the noise reduces with temperature approximately as $ENC \sim \sqrt{T}$. Therefore, the noise at operating temperature is about 10% lower.

More than 100 APV25 chips from all production lots have been irradiated with X-rays to 10 Mrad ionizing dose, in excess of the expectation for 10 years of LHC operation. No significant degradation in pulse shape or noise level has been observed.

The APV25 is fabricated on 8 inch wafers with 360 chips per wafer. More than 600 wafers corresponding to 216 000 chips have been manufactured and probe-tested. After initial yield problems were solved, an average yield of 88% was achieved.

Another custom ASIC, the APVMUX, is used to multiplex the data streams from two APV25 chips onto one optical channel by interleaving the two 20 MS/s streams into one 40 MS/s stream, which is then sent to a laser driver of the optical links. One APVMUX chip contains 4 such multiplexers.

2008 JINST 3 S08004

Optical links

Analogue optical links are used to transmit the data streams from the tracker to the service cavern over a distance of about 100 m at 40 MS/s. Likewise, the digital timing and control signals (see below) are transmitted by digital optical links running at 40 Mb/s [41]. Optical links are superior to an electrical distribution scheme mainly since they have minimal impact on the material budget and are immune to electrical interference. The transmitters are commercially available multi-quantum-well InGaAsP edge-emitting devices, selected for their good linearity, low threshold current and proven reliability. Epitaxially grown planar InGaAs photo-diodes are used as receivers. The optical fiber itself is a standard, single-mode, non dispersion shifted telecommunication fiber. The fibers are grouped in ribbons of 12 fibers which in turn are packaged in a stack of 8 inside a 96-way ribbon cable, which features a small diameter (< 10 mm) and a low bending radius (8 cm). For the analogue data link up to three transmitters are connected to a laser driver ASIC on an Analogue Opto-Hybrid (AOH), one of which sits close to each detector module. The electrical signals from the APVMUX are transmitted differentially over a distance of a few centimeters to the laser driver, which modulates the laser diode current accordingly and provides a programmable bias current to the diode. For the bi-directional digital optical link a set of two receivers and two transmitters is mounted on a Digital Opto-Hybrid (DOH), converting the optical signals to electrical LVDS [42] and vice versa.

Front End Drivers

The strip tracker Front End Driver (FED) is a 9U VME module which receives data from 96 optical fibres, each corresponding to 2 APV25 or 256 detector channels [45]. All 96 fibres are processed in parallel. The optical signals are converted to electrical levels by opto-receivers [43] and then digitized by a 40 MHz, 10 bit ADC. The ADC sampling point for each fibre can be programmed independently in 1 ns steps. After auto-synchronization to the APV data stream, pedestal corrections are applied and the common mode subtracted. The common mode correction is calculated for each trigger and each APV separately. The samples are then re-ordered to restore the physical sequence of detector channels which is essential for the following step of cluster finding. Pedestal values for each detector channel and thresholds for cluster finding are stored in look up tables. The digital functionality of the FED is implemented in FPGAs and can therefore be adjusted with considerable flexibility. In zero suppression mode, which is the standard for normal data taking, the output of the FED is a list of clusters with address information and signal height (8-bit resolution) for each strip in the cluster, thus passing to the central DAQ only those objects which are relevant for track reconstruction and physics analysis. In this way an input data rate per FED of about 3.4 GB/s, at LHC design luminosity, is reduced to roughly 50 MB/s per percent strip occupancy. Other modes are, however, available which suppress one or more steps in the processing chain and therefore transmit additional data to the central DAQ to be used mainly for debugging and system analysis. There are a total of 450 FEDs in the final system.

2008 JINST 3 S08004

Control and monitoring

Clock, trigger and control data are transmitted to the tracker by Front End Controller (FEC) cards [44]. These are VME modules, located in the service cavern, as close as possible to the tracker in order to reduce trigger latency. They receive clock and trigger signals from the global Timing Trigger and Command (TTC) system and distribute those as well as control signals via digital optical links and the digital opto-hybrids to LVDS token ring networks (control rings) inside the tracker volume. Several Communication and Control Units (CCU) [46] participate in one token ring. These are custom ASICs which interface the ring network to the front-end chips. One CCU is mounted on a Communication and Control Unit Module (CCUM) and is dedicated to a set of detector modules. A combined clock and trigger signal is distributed to Phase Locked Loop (PLL) chips [47] on each detector module while the industry standard I^2C protocol [48] is used to send control signals to the APV chips as well as to the other ancillary chips. One CCU can control up to 16 units so that one FEC ring typically controls a set of several tens of detector modules. The PLL chips decode the trigger signals and provide a very low jitter, phase adjustable clock signal to the local electronics.

Detector Control Unit (DCU) ASICs [49] on the detector modules are used to monitor the low voltages on the hybrid, the silicon sensor leakage current, and the temperatures of the silicon sensors, the hybrid and the DCU itself. For this purpose, each DCU contains eight 12 bit ADCs. The DCUs are read out through the control rings and digital links so that these readings are only available when the control rings and the detector modules are powered.

Hybrids

The front-end read-out electronics for a detector module is mounted onto a multi chip module called hybrid [50]. Due to the different detector module geometries 12 different types of hybrids are needed in the CMS silicon strip tracker. Each hybrid carries 4 or 6 APV25 read-out chips which are mounted as bare dies, and one APVMUX chip, one PLL chip and one DCU chip which are packaged components. The main features of the hybrid are to distribute and filter the supply voltages to the chips, to route clock, control and data lines between the chips and to remove the heat from the chips into the cooling system. No high voltage is present on the CMS tracker hybrids. The hybrid substrate is fabricated as a four layer polyimide copper multilayer flex circuit (figure 3.21). It is laminated onto a ceramic (Al_2O_3) carrier plate using double sided acrylic adhesive. A polyimide cable is integrated into the layout of the hybrid. The minimal feature sizes are 120 μm for via diameter and line width. Large metalized through holes under the chips transfer the heat to the underlying ceramic plate, from where it is removed through the frame of the module into the cooling system. Three different flex circuit types (one each for TIB/TID, TOB and TEC) combined with different geometries of the ceramic plates, different connector orientations and different number of APV25 chips (4 or 6) make up the total of 12 different hybrid flavours.

Power supplies

Silicon strip modules are grouped into 1944 detector power groups in order to share the power services. Each group is supplied by a power supply unit (PSU) [32], featuring two low-voltage

2008 JINST 3 S08004

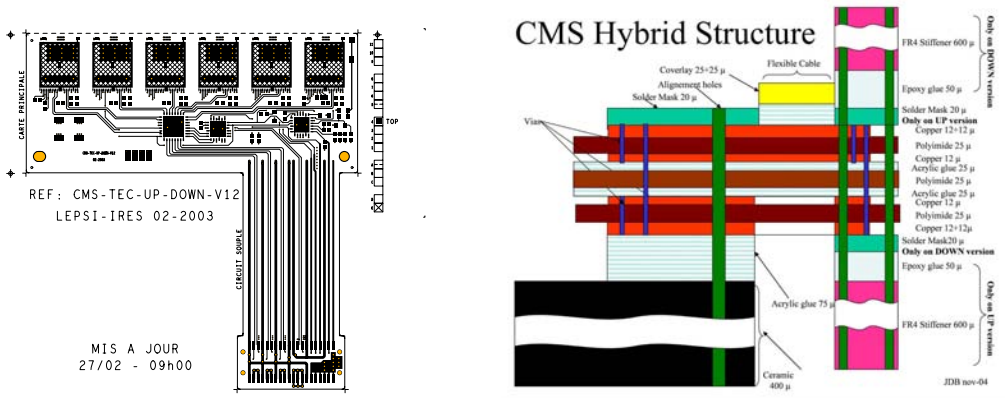

Figure 3.21: Front-end hybrid layout (example for TEC shown on the left) and arrangement of layers.

regulators, respectively 1.25 V (up to 6 A) and 2.5 V (up to 13 A), and two high-voltage regulators (0-600 V, up to 12 mA). All regulators are "floating" (return line isolated from the local earth). The two low-voltage channels share the same return line and use the sensing wire technique to compensate, up to 4 V, the voltage drop along the cables. The two high-voltage regulators are fanned out at the PSU exit into 8 lines; each silicon strip sensor is connected to one of these lines. Two PSU are combined into one power supply module (PSM, A4601H model). In total 984 A4601H boards are needed to power the detector groups; they are located on 129 EASY 4000 crates, disposed on 29 racks, around 10 m away from the beam crossing region, and operate in a "hostile" radiation and magnetic field environment, powering the detector through $\approx$ 50-m-long low impedance cables [32]. The 356 control rings require a separate power at 2.5 V. This is provided by a different set of 110 control power supply modules (A4602, four 2.5 V channels per module), fully integrated in the same system of the A4601H units and located on the same crates. Both A4601H and A4602 units require two distinct 48V power sources, one source (48Vp) for the regulators, the other (48Vs) for the service electronics. They are both provided by AC-DC converters, CAENs A3486 ("MAO"), disposed on the same racks. Each EASY 4000 crate hosts up to 9 boards (A4601H mixed to A4602) and provides 48Vp and 48Vs rails, interlock and general reset bus lines. The first slot in the crate (*slot 0*) hosts one interlock-card, which interfaces the interlock and reset lines to the control and safety systems (section 3.3.8). The average power consumption of each silicon strip module with 6 (4) APV25 chips is about 2662 mW (1845 mW). The total power supplied by A4601H and A4602 boards is approximately 68 kW, of which nearly 50% is dissipated on power cables. The power consumption is foreseen to increase with the aging of the detector; the power supply system is dimensioned to cope with up to 60% increase of the low-voltage currents, corresponding to a total consumption of nearly 150 kW.

2008 JINST 3 S08004

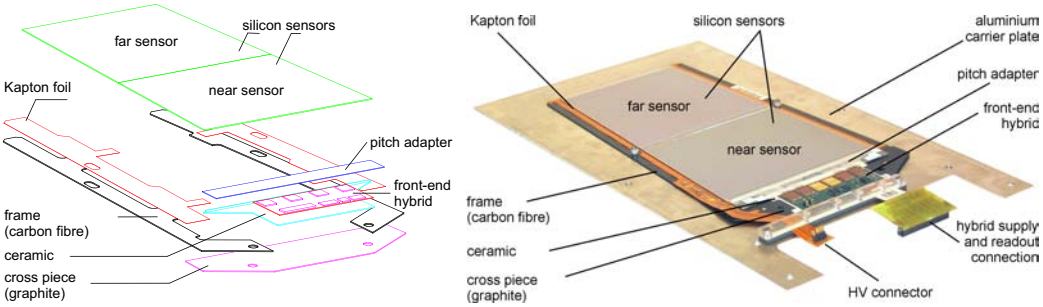

Figure 3.22: Left panel: exploded view of a module housing two sensors. Right panel: photograph of a TEC ring 6 module, mounted on a carrier plate.

3.3.3 Silicon modules

Module design

The silicon strip tracker is composed of 15 148 detector modules distributed among the four different subsystems (TIB, TID, TOB, TEC). Each module carries either one thin (320 μm) or two thick (500 μm) silicon sensors from a total of 24 244 sensors. All modules are supported by a frame made of carbon fiber or graphite, depending on the position in the tracker. A Kapton circuit layer is used to insulate the silicon from the module frame and to provide the electrical connection to the sensor back plane, i.e. bias voltage supply and temperature probe read-out. In addition the module frame carries the front-end hybrid and the pitch adapter. Figure 3.22 shows an exploded view and a photograph of a TEC module.

Modules for the inner barrel, the inner disks and rings 1 to 4 in the endcaps are equipped with one sensor, modules in the outer barrel and rings 5 to 7 in the endcaps have two sensors. In the case of two sensors, their corresponding strips are connected electrically via wire bonds. Depending on the geometry and number of sensors the active area of a module varies between 6243.1 mm^2 (TEC, ring 1) and 17202.4 mm^2 (TOB module). In total 29 different module designs, 15 different sensor designs and twelve different hybrid designs are used in TIB, TOB, TID and TEC. For alignment purposes special modules are prepared with etched holes in the aluminium back plane to allow a laser ray to traverse up to five modules.

The module frame provides the stability, safety and heat removal capability needed in the sensor support and carries the read-out electronics. In addition it has to remove the heat generated in the electronics and the silicon sensor(s) into the cooling points. In the endcaps the frame for the one-sensor modules is U-shaped and made of (780$\pm$5) μm thick graphite (FE779 carbon). For the two-sensor modules a similar U-shaped support structure is obtained by gluing two (640$\pm$40) μm thick carbon fiber legs (K13D2U CFC, 5 $\times$ 125 μm fabric, cyanate ester resin (CE3)) on a 800 μm thick graphite cross-piece (FE779 carbon) which holds the front end electronics. In the inner barrel a 550 μm thick carbon fiber frame that surrounds the silicon sensor on all sides is used . For the TOB, U-shaped module frames are obtained by gluing two carbon fiber legs (K13D2U CFC, 5 $\times$ 125 μm fabric, cyanate ester resin (CE3)) on a carbon fiber cross piece made of the same material.

Both graphite and carbon fiber fulfil the requirements of high stiffness, low mass, efficient heat removal from the sensors, and radiation hardness. Differences in the expansion coefficients need to be compensated by the glue joint between the frames and the silicon. Several types of glues are used in module construction which all comply with the requirements of radiation hardness, good thermal conductivity and thermal stability. Among them are e. g. Epoxy AW 106 (Araldit, Novartis), silicone glue RTV 3140 (Dow Corning) to compensate for different thermal expansion coefficients and the conductive glue EE 129-4 (Polytec) between the silicon sensor back plane and the HV lines on the Kapton bias strips (see below).

Different types of aluminium inserts and precision bushings in the module frames are used to position and attach the modules to the larger support structures with high precision. TIB/TID and TEC modules are mounted using four points, two being high precision bushings that allow for a mounting precision of better than 20 μm while all four provide thermal contact between the module and the cooling pipes. For TOB modules two Cu-Be springs give the precision positioning and four screws ensure thermal contact.

The high voltage supply to the silicon back plane is provided by Kapton bias circuits running along the legs of the modules between the silicon sensor and the carbon fiber support frame. The connection of the bias voltage to the back plane is done via wire bonds. Thermal probes are placed on the Kapton foil to measure the temperature of the silicon. The glue joint between the temperature sensor and the back plane is done with the silicone glue RTV 3140.

The pitch adapter between the front end hybrid and the silicon sensor adjusts the strip pitch of the sensor (80 μm–205 μm depending on sensor type) to the APV pitch of 44 μm. It also allows placing the heat producing front end electronics farther away from the silicon sensors. A pitch adapter for TOB and TEC consists of a 550 μm thick glass substrate (Schott D263 glass), cut to the correct dimensions, with a pattern of low resistivity aluminium strips. For TIB 300 μm thick glass (Corning 1737F or G glass) is used. The 10 μm narrow lines are etched on a (1.0–1.5) μm thick aluminium layer deposited on a chromium base, resulting in less than 25 m$\Omega/\square$.

Module assembly and testing

Sensors and front end hybrids are glued to the frames by high precision gantry robots. The components are aligned by cameras surveying special fiducial marks with a pattern recognition algorithm. In total seven institutes shared the responsibility for the assembly of all modules. The assembly rate was about 20 modules per day per gantry robot. A positioning precision of approximately 10 μm (RMS) has been achieved and one example from the quality control can be seen in figure 3.23.

Thin wire wedge bonding is used in several places on the modules to make electrical connections: APV chip to front-end hybrid, APV chip to pitch adapter, pitch adapter to sensor, sensor to sensor (in case of two-sensor-modules), bias voltage connection to the sensor back plane. In total 15 institutes *(bonding centers)* shared the responsibility for wire bonding all modules. The bonding rate was approximately 1 Hz. Bonding wire (99% aluminium, 1% silicon) with a diameter of 25 μm was used for all connections.

For the TEC and TOB modules the line of bonding wires connecting the hybrid pitch adapter to the silicon strips, and in the case of two sensor modules the strips of the two sensors, can be damaged by vibration during transport. As a protection for the TEC modules the silicon is glued

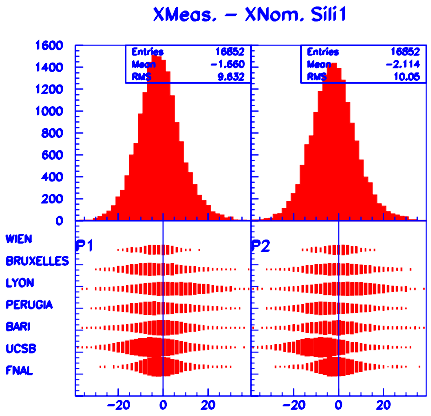

Figure 3.23: A typical residual distribution (in μm) for a reference point on the modules is shown for the different module assembly centers, indicating a precision of 10 μm (RMS) in the module production.

to a supporting strip (400 μm thin ceramic Al_2O_3) which in the case of the pitch adapter-sensor connection is also glued to the graphite cross piece. The reinforcement for the TOB modules was done by dispensing Sylgard 186 glue on the backside of the modules, between the two sensors and between the near sensor and the edge of the hybrid. For the TOB modules the sensor-sensor bonds and the backside APV bondings are encapsulated by Sylgard 186 glue across the bonding wires. For TIB modules no reinforcement was done.

After wire bonding each module was tested and graded, using the ARC system [51]. A detailed description of all tests performed and the acceptance criteria for good channels is given in the reference. Modules were graded A if fewer than 1% of the channels were failing the quality acceptance criteria (due to high noise, open bondings, oxide defects) and B if the failure rate was less than 2%. The remaining modules were graded C and were not used in the experiment. Other reasons to reject modules were imperfect mechanical precision or poor high voltage behaviour. All relevant test results are stored in the central CMS tracker data base. The yield of module production was greater than 97%.

3.3.4 Tracker Inner Barrel and Disks (TIB/TID)

Introduction and mechanics

The Tracker Inner Barrel (TIB) consists of four concentric cylinders placed at radii of 255.0 mm, 339.0 mm, 418.5 mm, and 498.0 mm respectively from the beam axis that extend from -700 mm to $+700$ mm along the z axis. The two innermost layers host double sided modules with a strip pitch of 80 μm, while the outer two layers host single sided modules with a strip pitch of 120 μm. Each cylinder is subdivided into four sub-assemblies ($\pm z$, up/down) for ease of handling and integration. Each of these sub-assemblies (half-shells) hosts an independent array of services from cooling to electronics and thus can be fully equipped and tested before being mechanically coupled to each other during final assembly.

2008 JINST 3 S08004

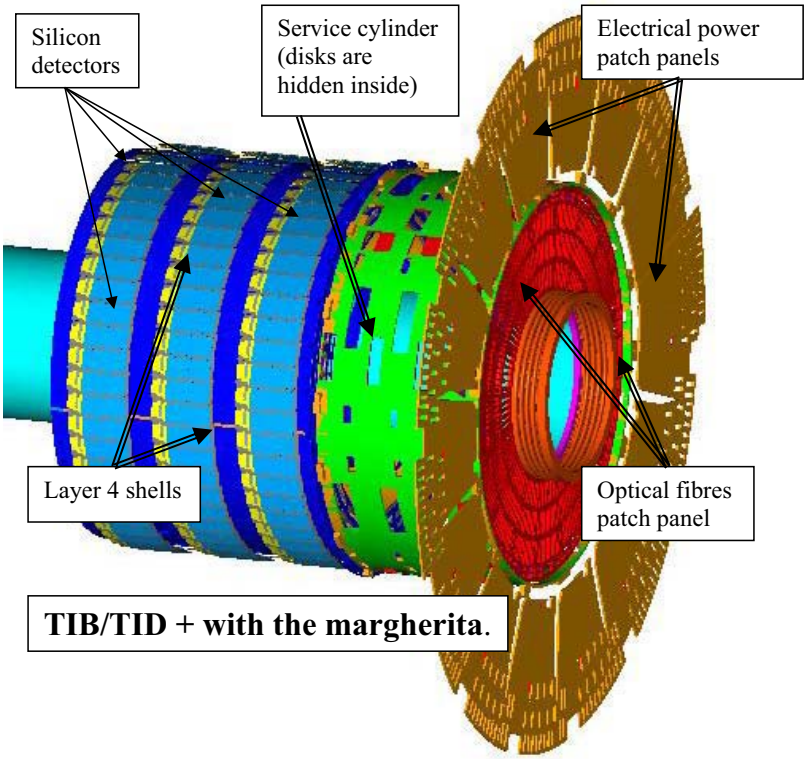

Figure 3.24: Schematic drawing of the TIB/TID+ subassembly. This structure and its twin (TIB/TID-) nest inside the Tracker Outer Barrel (TOB), one for each end. Services routed out from the margherita consist of copper cables for powering and slow controls, optical fibers for signals and controls and also cooling fluid supply lines made of aluminium tubing.

Two service cylinders are coupled to the ends of TIB$\pm$ (referring to $+z$ or $-z$) which end in a service distribution disk called the *margherita* (see below). These service cylinders play a dual role: one is to route out services from the shells to the margherita, the other is to support the Tracker Inner Disks (TID) which sit inside them. Figure 3.24 shows a schematic drawing of one half TIB/TID structure together with its corresponding margherita.

The TID$\pm$ are assemblies of three disks placed in z between $\pm$800 mm and $\pm$900 mm. The disks are identical and each one consists of three rings which span the radius from roughly 200 mm to 500 mm. The two innermost rings host back-to-back modules while the outer one hosts single sided ones. Just like the TIB shells each individual ring can be fully equipped and tested independently of the others before final assembly. Together the full TIB/TID guarantee hermetical coverage up to pseudorapidity $\eta = 2.5$.

All mechanical parts like shells, disks and service cylinders are made of high strength low deformation carbon fiber chosen both for its lightness and its low material budget. The margherita is instead made of conventional G-10 fiber epoxy with 30 μm copper on both sides.

The silicon detector modules are mounted directly on the structure's shells and rings. Thus, while a large number of modules has to be integrated and tested at any one time, the approach chosen allows for far greater precision of assembly. The individual components of a TIB shell,

some of which not only service the silicon detector needs but also define its geometric position in space, will be described in some detail in next paragraphs.

Cooling

The cooling circuits must be able to efficiently cool the detectors with a cooling liquid temperature down to about $-25°C$, while keeping the material budget as low as possible. For the TIB/TID the decision was made to use aluminium piping of 6 mm cross section and 0.3 mm wall thickness. These pipes are bent into loops and soldered to inlet/outlet manifolds which connect several loops in parallel. The thermal connection between pipes and silicon modules is made with aluminium ledges which are glued to the pipes. On each ledge there are two threaded M1 holes onto which the modules are tightened. For the TIB each loop hosts three modules placed in straight row (figure 3.25), while in the TID arrangements are more varied even though the number of modules per cooling loop is similar.

Since the position of the ledges defines the position in space of the modules, after the glue has hardened the whole half cylinder is surveyed with a precision measuring machine. Before gluing, the circuits are tested individually for leaks both at cold temperatures ($-30°C$) and at high pressure (20 bars). It is only after the survey that the TIB cylinders (or TID disks) are available for the integration of the electrical parts including the detector modules. The dimensions of the cooling circuit vary from layer to layer and depend on the amount of power dissipated by the modules used for that specific layer. The cooling circuits vary from a minimum of four loops (12 modules equivalent) for the double sided layers to a maximum of 15 loops for the outer single sided ones where individual module heat dissipation is much lower. The TIB/TID uses a total of 70 independent cooling circuits so that in case of an accidental break in one of the circuits only a small part of the tracker is affected. The TIB thus is organized in three module ladders (the cooling loop) which cover the outer and inner surface of the four layers. The same concept applies to the TID with the only difference that the number of modules per cooling loop varies with the ring radius. The electrical grouping which we now describe takes this mechanical distribution into account.

Electrical grouping

The modules have been grouped together electrically. The basic group consists of three modules which sit on any given cooling loop (figure 3.25). The three modules are interconnected through a Kapton circuit (mother cable) through which powering, detector biasing and controls are distributed. At the top of a mother cable sits a CCUM which takes care of clock, trigger and I^2C distribution. These mother cables are then electrically joined in a more complex group called the control ring which distributes trigger, clock and slow control signals to the CCUMs. Control ring groups never straddle two different cooling loops and are dimensioned so that a reasonable compromise between granularity and complexity is achieved. Control rings in the TIB/TID make use of a unit called the DOHM (Digital opto-hybrid module) which receives all the signals from the optical fibers coming from the front end controllers (FEC) and converts them to electrical LVDS signals that are then distributed to up to 45 detector modules (15 mother cables) via CCUs. Given the high number of modules belonging to a Control Ring, TIB/TID has implemented redundancy in its DOHM hardware.

2008 JINST 3 S08004

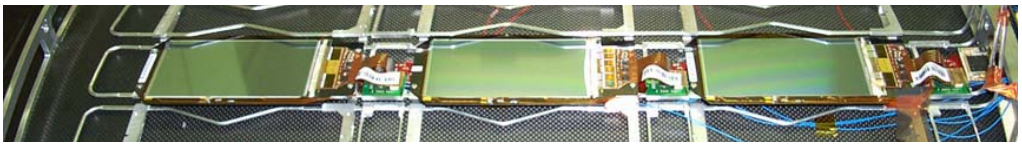

Figure 3.25: Three TIB modules mounted on a layer 3 shell. The Kapton mother cable runs underneath. A CCUM module at the end of the string interfaces the modules to the control ring. Also visible are the three analog opto-hybrids (see text) and fibers.

Modules have been grouped together to keep the number of power supplies down to a manageable level. The smallest power group consists of three modules (one mother cable) while the largest comprises up to 12 modules (four mother cables). Power groups are contained within a control ring (i.e. there is no straddling across control ring boundaries) and are fed by a specific power supply unit (PSU) developed for the tracker which also supplies HV biasing for the detectors.

Analog signals from the detector front end are converted to optical by analog opto-hybrids which sit next to the silicon modules and are connected directly to the front end hybrids. Thus the system is completely optically decoupled from the DAQ which helps preserve signal integrity while avoiding ground loops.

Grounding of the TIB/TID relies on the cooling circuits which are made of aluminium. The return current wires are connected to the cooling manifolds for all mother cables and DOHMs. The cooling inlet and outlet pipes run along the service cylinder across the margherita, making electrical contact with it. Outside the tracker volume these pipes are then connected to the CMS detector ground. Power cable shields are connected to the margherita which hosts all of the connectors. All detector modules have their own carbon fiber frame directly connected to the front end hybrid local ground. The shells are grounded through the cooling manifolds.

3.3.5 Tracker Outer Barrel (TOB)

Mechanical structure and layout

The Tracker Outer Barrel consists of a single mechanical structure (*wheel*) supporting 688 self-contained sub-assemblies, called *rods*.

The wheel is composed by four identical disks joined by three outer and three inner cylinders (figure 3.26). Disks and cylinders are made of carbon fiber epoxy laminate. The cylinders have a core of aramid-fiber honeycomb. The joints between disks and cylinders are realized with aluminium elements glued to the carbon fiber parts on precision fixtures, and then bolted together. Each of the disks contains 344 openings, in which the rods are inserted. Each rod is supported by two disks, and two rods cover the whole length of the TOB along the z axis. The wheel has a length of 2180 mm, and inner and outer radii of 555 mm and 1160 mm, respectively. With cabling at its two ends the TOB has a total length of 2360 mm. The openings in the disks form six detection layers with average radii of 608, 692, 780, 868, 965, 1080 mm. Within each layer, the centers of gravity of the rods are displaced by ± 16 mm with respect to the average radius of the layer, thus allowing for overlap in ϕ and therefore full coverage within each layer. The rod mechanics are designed in such a way to implement overlap of the silicon sensors at $z = 0$. In each layer, the

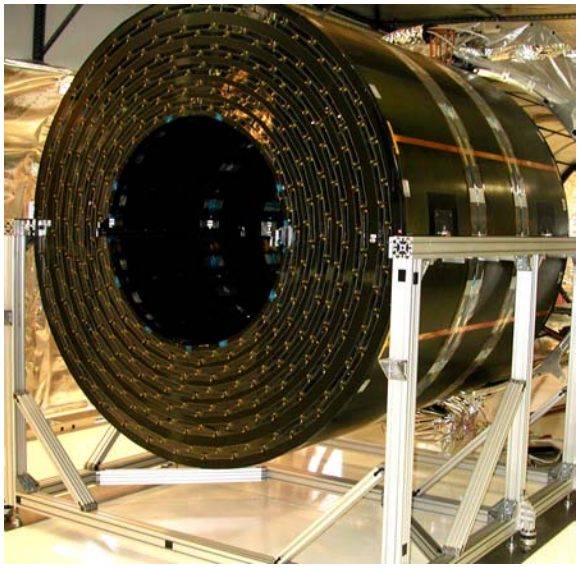

Figure 3.26: Picture of the TOB wheel.

overlap in the r-ϕ view between neighboring rods is always larger than 1.5 mm or 12 strips, while the overlap around $z = 0$ is precisely 1.5 mm. Inside the disk openings, the rod support spheres are held by precision elements made of polyetherimide plastic that are glued to the carbon fiber structure. The four disks have all been assembled in a temperature-controlled room on one single precision table, ensuring a precision on the relative positions of the rod holding elements and the aluminium elements joining disks and cylinder of 100 μm, and a reproducibility between different disks at the 10 μm level.

The wheel is equipped with *targets* for measurements of the geometrical precision of the assembled structure. Photogrammetry, theodolites, and 3D coordinate measurement systems have been used for survey and alignment of the wheel structure. Some of these targets remain visible after insertion of the TOB in the *tracker support tube*, for a precise measurement of the TOB positioning in the tracker reference frame, and even after integration of TIB, to monitor possible movements due to deformations of the loaded structure. The wheel mechanics has been thoroughly measured before starting rod integration, and the relative positioning of the precision elements has been found to be typically within 100 μm of nominal values over the whole TOB dimensions, with maximum deviations observed around 200 μm.

The rod mechanics

The rods are self-contained assemblies providing support and cooling for 6 or 12 silicon detector modules, together with their interconnection and read-out electronics.

The mechanical structure consists of two 1130 mm long carbon fiber C-shaped profiles, joined by several transverse carbon fiber ribs and plates. All rod components are contained in an envelope of $159 \times 1130 \times 22$ mm^3, except the four supporting spheres that stick out laterally in correspondence of the two disks of the wheel, and the *z-stops* that block the rod against the outer disk surface after insertion in the wheel.

2008 JINST 3 S08004

A U-shaped cooling pipe runs around the rod, inside the C-profiles; 24 aluminium inserts are glued through openings along the profiles to the carbon fiber and around the cooling pipe; these inserts provide support and cooling to the detector modules, that are mounted in six positions along the rod, three per side. Each detector is supported by four inserts, two close to the read-out hybrid, and two close to the sensor-to-sensor bonds. The two inserts close to the hybrid implement pins on which the Cu-Be springs on the module frame are clamped, determining the precision of the module positioning; all four inserts have a threaded hole for the fixation of the module to the rod: cup-shaped washers together with a calibrated torque used in tightening the screw ensure efficient cooling contact between the aluminium heat spreader on the module frame and the rod support inserts. On the cooling pipe side, the shape and the size of the inserts is optimized to minimize the thermal impedance of the contact, which in turn allows to minimize the cross section of the cooling pipe.

In single-sided rods, which populate layers 3–6, one detector module is mounted in each of the six positions, with the strips facing the central plane of the rod. In double-sided rods, which populate layers 1 and 2, two detectors are mounted in each position, the inner one as in single-sided rods and the outer one with the backplane facing the backplane of the first module. The distance between the sensor and the middle plane of the rod is $\pm$3.3 mm in single-sided rods, $\pm$3.3 mm and $\pm$7.6 mm in double-sided rods.

The rod cooling pipes, and the manifolds housed on the outer disks of the wheel, are realized in CuNi 70/30 alloy. This material is chosen for its corrosion resistance, and as it allows reliable solder joints to be made relatively easily, avoiding the use of o-rings or ferrules in the pipe connections; the reliability of the cooling circuits is a crucial issue for the tracker, and particularly so for the TOB, which is the most inaccessible subsystem once the detector is fully integrated. The rather high density of the material (its radiation length of about 1.4 cm is 6 times shorter than that of aluminium) is compensated by the reduced thickness of the walls that this technology allows: rod pipes and manifolds have 100 μm and 200 μm wall thickness, respectively. In addition the design of the cooling circuit has been optimized (as already mentioned above), to minimize the cross section of the pipes (the cooling fluid also gives a non-negligible contribution to the material budget), and to maximize the number of rod pipes served by a single manifold (within the constraints of the desired cooling performance). An outer diameter of 2.2 mm is chosen for single-sided rod pipes (providing cooling to 6 detectors), 2.5 mm for double-sided rod pipes (providing cooling to 12 detectors), and 6 mm for the manifolds; one manifold serves on average more than 15 rod pipes, the actual number varying between 8 and 22 depending on the region of the TOB. Overall, the whole TOB is served by 44 cooling lines, giving an average of 118 detectors, or 550 read-out chips, per line.

Rod electrical design

The 6 or 12 modules housed in a rod form a power group, i.e. they are supplied by a single power supply unit. The low voltage lines supplying the front-end hybrids and the Analogue Opto-Hybrids (AOHs) run in the Inter-Connect-Bus (ICB), a 700 mm long printed circuit board sitting in the middle plane of the rod (figure 3.27). The Communication and Control Unit Module (CCUM) is plugged to one end of the ICB. The clock and the control signals issued by the CCUM are also routed to the final destinations through the ICB. The distribution of power, clock and signals to front-end hybrids and AOHs proceeds through four other PCBs, the Inter-Connect-Cards

2008 JINST 3 S08004

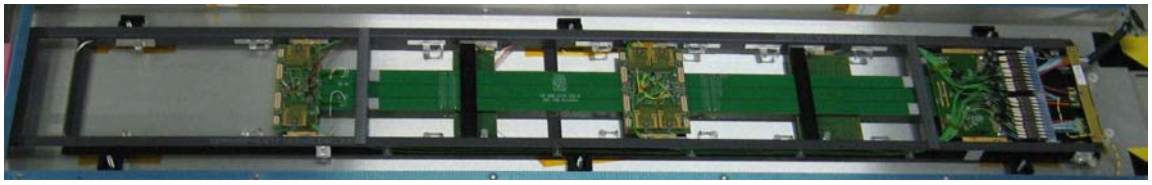

Figure 3.27: Photo of a rod frame equipped with electronics components, ready to receive silicon detector modules.

(ICCs). Two ICCs serve one module position and two other ICCs serve two module positions. ICCs have different design in single-sided rods and double-sided rods, which have one and two modules mounted in each module position, respectively; therefore there are in total four different ICC flavours in the TOB.

The ICB is held in place by small transverse carbon fiber plates; the ICCs and the CCUM are plugged to the ICB and screwed to the aluminium module support inserts (on the opposite side of the module), which also provide a good cooling contact to those boards. The AOHs are supported and cooled only by the connector that plugs to the ICCs. In addition to distributing LV power and CTRL signals, the ICCs receive the data lines from the read-out hybrid and route them to the AOHs (a few cm away) where they are converted to optical signals. The ICCs also receive lines carrying temperature information from the module frame Kapton circuit and route them to the ICB. The optical fibers leaving the AOHs travel inside the carbon fiber profiles, guided by dedicated plastic holders. The only electrical lines not integrated in the ICB/ICCs distribution system are the bias lines for the sensors. These run in dedicated wires (size AWG 26) housed in the carbon fiber profiles, while the line with the return current is integrated in the ICB. There are six lines in single-sided rods (one per module), and 8 lines in double-sided rods (four serving one module each, and four serving two modules each). The LV lines and the HV lines go in separate connectors in the rod end-panel, each of which also hosts some temperature lines, and then run all together to the back-end in one multi-service cable plus low-impedance cable. At the power supply backplane the six or eight bias lines are connected to the two independent high-voltage supply lines in such a way that each line powers one side of the rod. The clock and control lines as well as the LV lines powering the CCUM leave the rod through a short cable which plugs into the next rod of the control ring. The first and the last rod of a control ring are connected to the Digital Opto-Hybrid Module (DOHM). This board houses the digital opto-hybrids optically connected to the remote control system and distributes the clock and the control signals through a token-ring 40 MHz LVDS-based protocol to the connected rods (up to 10). The length of the optical fibers coming from the AOHs is chosen so that all fibers end at the same location near the CCUM, where the connectors of the 12-fiber ribbons are integrated (figure 3.28). The choice of including the optical patch panel inside the rod volume was made to reduce the thickness of the TOB services on the TOB end-flanges, so minimizing the inactive volume between TOB and TEC.

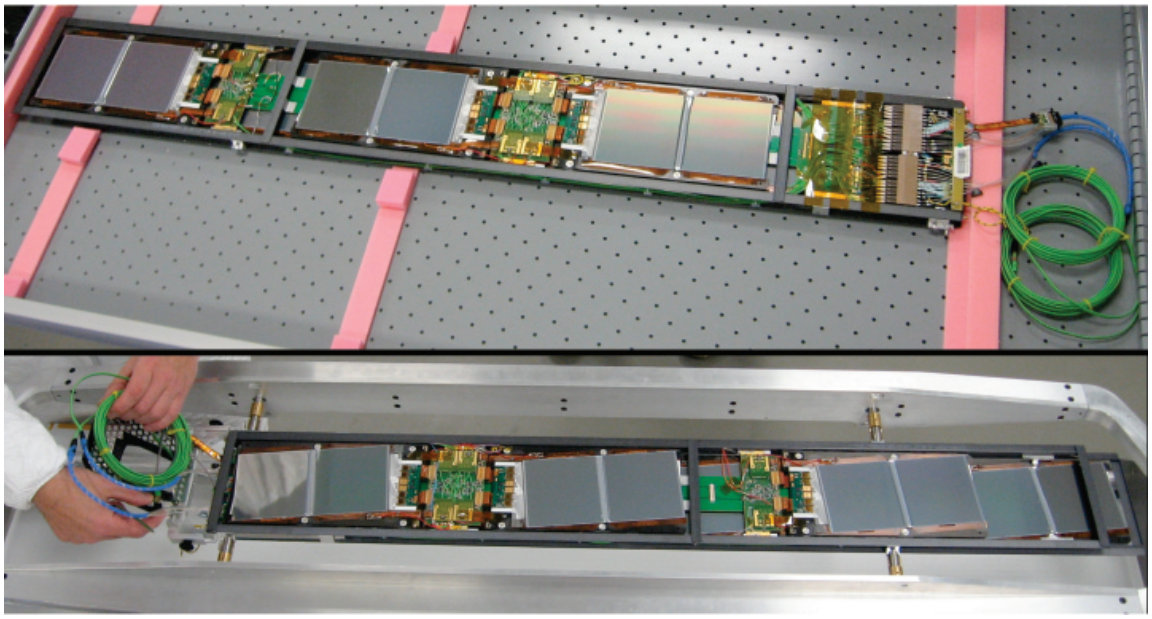

Figure 3.28: Top panel: photo of an assembled double-sided rod, showing the CCUM side, with the 12-way optical ribbons connected to the AOH fibers. Bottom panel: double-sided rod being prepared for insertion in the TOB mechanics; the side opposite to the CCUM is shown.

Electrical and read-out grouping

The grouping of the rods into control rings is designed primarily to avoid having control rings spanning across two different cooling segments, while maximizing the size of a control ring (to reduce cost and material budget) within the recommended limit of 10 CCUMs per ring. This logic results in two or three control rings per cooling segment, with a single exception of a cooling segment containing one control ring only. The average number of CCUMs (i.e. of rods) per ring in the TOB is 7.5. Within a control ring, rods are clustered in groups that are read out by the same FED. Again, a read-out group never spans over two control rings, and the grouping is optimized to minimize the number of unused channels in the FEDs (to reduce cost). The average FED occupancy in the TOB is 94%. In summary, the TOB is made of 688 rods read out by 134 FEDs, controlled by 92 DOHMs, and cooled by 44 independent lines.

Grounding

In each rod the return line of LV and bias is connected inside the CCUM to the return line of the LV power of DOHM and CCUMs, and connected through a short multi-wire cable to the cooling manifold serving the rod: this is the main ground connection of the rod. The grounding is improved by additional ground connections in each ICC, implemented through metalization around the mounting holes.

The DOHMs, mounted on the TOB end-flange (figure 3.29), are protected by alodyned aluminium plates of 0.5 mm thickness, which are locally connected to the power return line.

2008 JINST 3 S08004

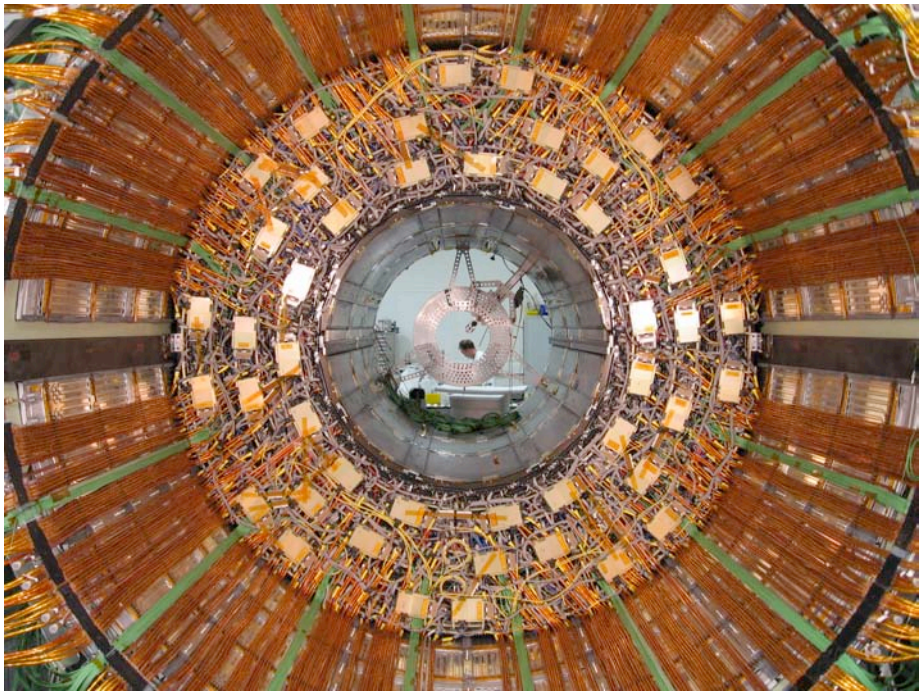

Figure 3.29: Photo of the completed z+ side of the TOB. The DOHMs form the outer layer of the services on the TOB end flange. Optical ribbons (green) run out, grouped in 16 channels. Power cables and feeding pipes run parallel to each other on the thermal screen panels.

The cooling circuits of the different segments are then connected electrically through short multi-wire cables soldered to the radial pipes feeding the manifolds (or to the manifolds themselves, for the outer layer) and screwed to the *ground rings*: an alodyned aluminium bar of 10×10 mm^2 square section bent to round shape and equipped all along with threaded holes, which is installed at the outer radius of the TOB, on both sides. Gold-coated copper strips of 30 mm width and 0.2 mm thickness connect the ground ring to the carbon fiber structure of the outer cylinder, in eight locations in ϕ. The connection to the carbon fiber is realized with conductive araldite. The same strip material is used to realize the electrical connections between outer cylinders and disks, and inner cylinders and disks, again in eight locations in ϕ. In addition, copper strips as long as the whole TOB are added on the outer surface of the outer cylinder (visible in figure 3.26); for the inner cylinder instead, which is inside the tracking volume, it was decided to rely on the conductivity of the carbon fiber.

Such design of the grounding scheme ensures good electrical connection of mechanical structures and power return lines making efficient use of the existing conductive materials (cooling pipes and carbon fiber parts), with minimal amount of added metallic elements.

2008 JINST 3 S08004

3.3.6 Tracker EndCaps (TEC)

Mechanical structure

The endcaps extend radially from 220 mm to 1135 mm and from $\pm$1240 mm to $\pm$2800 mm along the z-direction. The two endcaps are called TEC+ and TEC- (according to their location in z in the CMS coordinate system). Each endcap consists of nine disks that carry substructures on which the individual detector modules are mounted plus an additional two disks serving as front/back termination. A sketch of one endcap and a photograph of the completed TEC+ is shown in figures 3.30 and 3.31. Eight U-profiles, referred to as service channels because all services are grouped in their vicinity, join the disks together along their outer periphery, while at its inner diameter each disk is attached at four points to an inner support tube. To preserve the envelope necessary for the insertion of the pixel detector, the last six disks have a larger inner radius (309 mm) as compared to the first three (229 mm).

The disks are Carbon Fiber Composite (CFC) / honeycomb structures. The honeycomb core is 16 mm thick NOMEX, 3.2-92 with a border of epoxy potting. On either side of the core there is a symmetric layup of CFC skins (0.4 mm thickness). The skin material is CF-fabric THENAX HTA 5131,3K (T300) impregnated with EP121 epoxy resin. The same material is used for the service channels and the inner support tube. The latter has a thickness of 3 mm and is azimuthally segmented into four 90° segments. Each of these segments is attached to the disks and the gaps at the joints between segments are filled with epoxy glue so that they are gas tight. A thin cylindrical skin made of 0.5 mm thick CFC panels surrounds the endcaps on the outside and serves as a gas envelope for the atmosphere of dry nitrogen. The front plate has the same function and consists of a 5 mm NOMEX core with 0.2 mm CFC skins on each side. The back plate provides an additional thermal shielding for the cold silicon volume and is considerably thicker. The NOMEX core is 45 mm with each CFC skin 1.5 mm thick. The back plate also serves to make the overall structure rigid in the z-direction. The back plate is covered by another carbon fibre disk, the bulkhead, which is, however, mechanically detached from the TEC and supported by the tracker support tube. The bulkhead carries the outer connectors of all TEC cables, thereby forming a patch panel for the electrical connection of the TEC to the external power cables. It is covered by panels with heating foils which close the thermal screen at the end face of the tracker support tube.

Ten different module types are arranged in rings around the beam pipe. For reasons of modularity they are mounted on substructures called *petals*, which in turn are mounted on the disks. Disks 1 to 3 carry seven rings of modules, ring 1 is missing on disks 4 to 6, rings 1 and 2 are missing on disks 7 and 8, and disk 9 carries rings 4 to 7 only. Rings 1, 2 and 5 are built up of so-called double sided modules: two modules are mounted back-to-back with a stereo angle of 100 mrad. This provides space information perpendicular and parallel to the strip orientation.

Petals

To allow easy access to the detector modules they are mounted on modular elements, the petals (figures 3.32 and 3.33). Petals can be individually removed from the endcaps without uncabling and/or disassembling the entire structure. A total of 16 petals are mounted on each of the nine disks of one endcap, eight on the front face of the disk — as seen from the interaction point —

2008 JINST 3 S08004

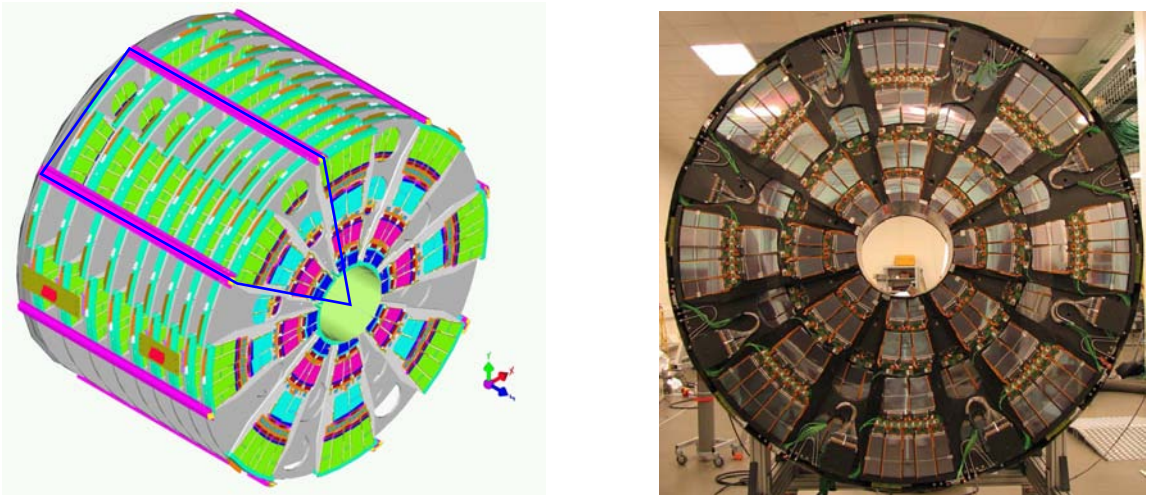

Figure 3.30: Left panel: Sketch of one tracker endcap. Modules are arranged in rings around the beam axis. They are mounted on trapezoidal sub-structures called *petals*. One sector, indicated with a line, consists of nine front petals mounted on the disk sides facing the interaction point (3 FD13, 3 FD46, 2 FD78, 1 FD9) and nine back petals mounted in the opposite side of a disk (3 BD13, 3 BD46, 2 BD78, 1 BD9). Right panel: Photograph of a TEC as seen from the interaction point. The diameter of the TECs is 2.3 m.

Figure 3.31: Side view of a TEC.

(front petals) and eight on the back face (back petals). Mechanically there are two types each of front and back petals, long petals for disks 1–3 and short ones for disks 4–9. As described above, the front and back petals on disks 1–3 carry all seven rings of modules and are labelled FD13 and BD13, respectively. Petals on disks 4–6 carry rings 2 to 7 (FD46/BD46), those on disks 7 and 8 carry rings 3 to 7 (FD78/BD78), and on disk 9 the petals carry rings 4 to 7 (FD9/BD9). The petals have a structure similar to the disks, consisting of a 10 mm NOMEX core sandwiched between

0.4 mm CFC skins. As viewed from the interaction point the modules belonging to rings 1, 3, 5, 7 are mounted on the petal front side (A-side and C-side for the front and back petals, respectively), while modules in rings 2, 4, 6 are mounted on the back side of each petal (B-side and D-side for the front and back petals, respectively). On a given disk the front petals overlap azimuthally with the back petals, as do, for a given petal, detector modules belonging to the same ring. Detectors in adjacent rings are arranged to overlap radially, thus providing full coverage. Each petal is mounted on inserts in the main disks using a three point fixation: one point fixed in x, y and z, one fixed only in phi, and one fixed only in z.

Cooling

The heat generated by all electronic components on a petal must be removed efficiently. In addition the silicon sensors must be operated at a temperature of about -10°C to reduce the effects of radiation damage. The silicon sensors and front end hybrids are cooled via the CFC frames of the detector modules, for which carbon fiber of high thermal conductivity is used (800 W/(m K)). The aluminium inserts for positioning the modules serve at the same time for the coupling to the cooling pipe. The two inserts along the legs of the module frame provide primarily for the cooling of the sensors, while the inserts on the frame base are heat sinks for the front end hybrid. Each petal contains two cooling circuits traversing the petal longitudinally and meandering from one cooling point to the next. The cooling pipes are made of titanium with an outer diameter of 3.9 mm and a wall thickness of 0.25 mm. They are embedded in the petal and serve to cool the components on both back and front side. The tubing is pre-bent into the proper shape. The input/output manifolds are laser welded onto the cooling pipes. After having milled the corresponding grooves and holes into the petals, the tubing is inserted. Gluing jigs are used to position the cooling inserts and to glue them to the pipes and to the petal. To close the grooves and re-establish the integrity of the petal a CFC skin with holes at the location of the inserts is glued onto the petal face. The inserts are then machined to the precision required for module positioning. The maximum heat load from the electronics on a petal is about 87 W, including the heating of the sensors after ten years of LHC operation. In these conditions a mass flow of 2.3 kg/min of the C_6F_{14} coolant gives a temperature difference of 2°C between petal inlet and outlet. The connection of the petal circuits to the piping running along z is done at the outer periphery of the petal. These connections can be undone easily in case the petal needs to be removed. A pair of longitudinal pipes serves either 4 or 5 petals, which are connected in parallel. A total of 64 longitudinal stainless steel pipes with 11 mm inner diameter are used per endcap.

Electrical system design

The silicon modules, AOHs and CCUMs on the petals are connected to motherboards, called InterConnect Boards or ICBs, which are mounted on both sides of the petal. In figure 3.32 photos of a bare front petal equipped with ICBs only are shown. There are five individual boards: the main board ICB_46 on side B/D, which carries all the connectors for the cables and two CCUM boards and transmits power and signals to the modules of rings 4 and 6, and four smaller boards, which provide the power and signals for the other rings (ICB_2 on side B/D and ICB_1, ICB_3 and ICB_57 on side A/C, where the numbers correspond to the number of the ring to which the

2008 JINST 3 S08004

Figure 3.32: The different ICBs on the two sides of a front petal: ICB_2 and ICB_46 on side B, and ICB_1, ICB_3 and ICB_57 on side A (from left to right). On ICB_46, the two CCUMs are plugged.

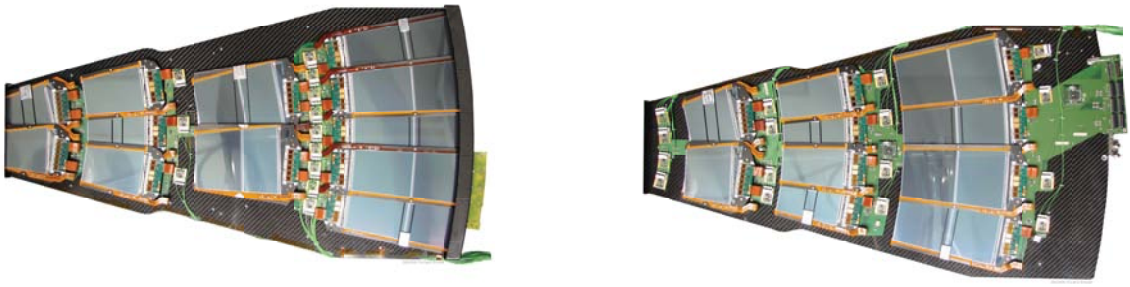

Figure 3.33: Left photograph: front side of a TEC Petal. Right photograph: back side.

connected modules belong). These four boards are connected to the main board. The ICB brings the ground, the various supply voltages and the bias voltage to the electrical devices on the petal, and transmits LVDS and I^2C signals. In addition analogue data from the FE hybrids are transmitted differentially to the AOHs over distances of a few centimetres.

To keep the number of low voltage power supplies and connections relatively small while limiting the current that must be provided by one power supply, the modules are organized in three low voltage (LV) groups, which are served by individual power supplies. The LV group 1 consists of rings 1 and 2, group 2 contains rings 3, 4 and 6 and finally rings 5 and 7 belong to group 3. This corresponds to 8/11/9 (4/8/11) modules or 48/44/44 (24/32/56) APVs on front (back) petals in LV group 1/2/3. In total there are eleven power rails on ICB_46, which must carry a current of up to 12 A. Sensing is implemented for the low voltage connections. The sense resistors are located in the electrical centre of each power group. Capacitances are implemented on the ICB near the power input connectors as well as near the front-end connectors to suppress ripples and minimize a possible voltage overshoot caused by switching off the FE-hybrids.

For each low voltage group, two high voltage channels are provided. For each HV channel there are up to four single HV lines, which bias one or two silicon modules.

The ICB_46 and ICB_57 have six copper layers, while the smaller boards have only four layers. To limit the contribution to the material budget, the copper layers are rather narrow and thin.

2008 JINST 3 S08004

The layer thickness amounts to 17 and 25 μm for the inner four and outer two layers, respectively, except for the innermost layer of boards ICB_1, ICB_3 and ICB_57 on front petals and ICB_1, ICB_2 and ICB_3 on back petals, which has a thickness of 35 μm. Digital and data traces are shielded by power and ground layers.

Two petals, one back and one front petal, are connected in a control ring. The front petal is the first in the control loop. Both on back and front petals, rings 1–4 and 5–7 are connected to one CCU, respectively. The Digital Opto-Hybrid (DOH) converts the optical signals to electrical LVDS signals and vice versa. Two DOHs are located on a separate PCB, the Digital Opto-Hybrid Module (DOHM), which is mounted on the back petal. From the DOHM, which also distributes the power for the DOHs, electrical signals are transmitted to the CCUMs on the petal. For the control ring, a redundancy scheme is implemented on the ICB. Each CCU can be bypassed electrically in case of a problem, so that the functionality of the control ring is maintained. The second DOH is needed for redundancy purposes only. To allow also the last CCU on the ring to be bypassed, a fifth CCU is located on the DOHM. It is used only in this special case. However, if two consecutive CCUs are faulty, the complete control ring is lost.

Low-pass filters are implemented for the traces of the temperature signals that are brought out via power cables, to ensure that noise is not coupled in via these lines. In addition to the thermistors located on the Kapton of the silicon modules, several temperature and humidity probes are located on or connected to the ICB. Two 10 kΩ NTC thermistors are located on ICB_46 on front petals and read out via the power cable of low voltage group 2. Both on front and back petals, four 10 kΩ NTC thermistors are glued to the cooling inserts of the ring 6 modules. They are read out via the DCU that is present on each CCUM. On both petal types, a humidity sensor can be connected to ICB_46. For back petals, this sensor is read out via the power cable of LV group 2. On each z-side in total 12 hardwired humidity sensors are distributed over the TEC volume. For front petals, the humidity sensor is read out via the DCU on the CCUM. Front petals of all disks of the top and bottom sectors carry these additional humidity sensors, providing detailed information on the relative humidity along the z-direction.

Kapton cables of about 15 cm length are used to link the petals inside one control ring with each other and with the DOHM, providing the electrical digital signals and the power for the CCUMs. These cables consist of two copper layers with a thickness of 35 μm each, separated by a 100 μm thick polyimide layer.

Each TEC LV group is supplied by one so-called multiservice cable, which transmits the analogue power and the bias voltage and brings out signals from temperature or humidity sensors. Inside the tracker support tube, power cables are arranged around the main TEC cooling pipes that run along the z direction, and end at the bulkhead. These cables implement silver-plated aluminium conductors to minimize the impact on the material budget. Typical currents per cable range from about 5 A to 11 A, depending on the number of APVs connected. Therefore three cable types exist, with wire cross-sections tailored to the differing needs.

The connection from the bulkhead to the so-called patch panel 1, located outside of the tracker volume, is provided by power cables implementing tinned copper conductors. The control power is transmitted via separate cables, which also break at the bulkhead. In this case tinned copper conductors are used both inside and outside the tracker volume.

2008 JINST 3 S08004

The grounding scheme

The so-called TEC common ground is located at the back end of each TEC. It is realized by means of a 5 cm wide and 150 μm thick copper ring, which is glued to the outer radius of each back disk and tied to the brackets that connect the tracker support tube to the hadron calorimeter. The material of the hadron calorimeter represents a very solid ground. The shields of all cables, the reference points of all power groups, the cooling manifolds that are used to connect the cooling pipes of the petals to the main tubes that are mounted on the TEC, the CF skins of the disks and petals and the outer aluminium shields of the TEC are connected to this TEC common ground. On the petal side, one common analogue ground is implemented per petal. This so-called local petal ground is distributed via a 2 cm wide and 20 μm thick copper path along the ICBs as a reference rail. The LV and HV supplies of all power groups are referenced to this local petal ground at the geometrical/electrical centre of each group. The digital ground of a control group is referenced once to the local petal ground. The local petal ground of each petal is connected to the TEC common ground. Copper strips glued to the outer radii of the disks and along the service channels that connect all disks with the back disk provide the electrical connection to the TEC common ground. These copper strips are connected via short copper braids to the ICBs on the petals. The carbon frames of the silicon detectors are connected via a conductive glue spot to the bias Kapton and finally via the ICB to the FE hybrid ground. To avoid ground loops, the frames are electrically insulated from the cooling pipes by an anodized layer between the cooling inserts and the pipe.

3.3.7 Geometry and alignment

The deviation of true position and orientation of tracker modules from their nominal values as specified in the engineering drawings depends on many factors with different origin, some of them time-dependent: the achieved assembly precision, deformation due to tracker cooling, stress from access and magnetic field, out-gassing of components in dry nitrogen. This leads to a degradation of the track parameter resolution (figure 3.4), which needs to be recovered by determining true module position and orientation, called *alignment*.

Alignment of the tracker relies on three key components: the various data about assembly gathered during the integration process, the Laser Alignment System and the alignment with tracks, ordered by increasing precision and availability with time.

For alignment purposes, modules with two sensors are treated as they would have one large sensor with identical active area coverage. This is justified by sensor mask design [36] and achieved sensor placement accuracy (figure 3.23).

The CMS tracker alignment task thus consists of the determination of three translational and three rotational parameters for each of the 15 148 tracker modules. To achieve ultimate precision, it might be necessary to consider additional parameters, e.g. the sensor bow due to single-sided processing.

Geometry

Two methods are mainly used for measuring tracker component assembly precision: survey with coordinate measurement machines with a typical accuracy of a few μm to a few tens of μm, and

2008 JINST 3 S08004

Table 3.2: Estimated assembly precision (RMS, in μm) of tracker components. Values are given with respect to the next level in the hierarchy, e.g. the position accuracy of sensors in modules is 10 μm.

TIB		TID		TOB		TEC	
Sensor	10	Sensor	10	Sensor	10	Sensor	10
Module	180	Module	54	Module	30	Module	20
Shell	450	Ring	185	Rod	100	Petal	70
Cylinder	750	Disc	350	Wheel	140 ($r\phi$), 500 (z)	Disc	150
Tube		Cylinder	450	Tube	1000	TEC	600
		Tube		CMS		Tube	

photogrammetry with an accuracy of 150 μm (80 μm) under good (optimal) conditions for relative measurements. The measured and expected mounting precision from those data are summarized in table 3.2. It should be noted that structure deformations due to loading as well as temperature and humidity variations have not been taken into account.

The software description of the position and orientation of the active detector volumes has been validated with survey data and reconstructed tracks from test beams and cosmic muons recorded in various test and integration setups.

Laser Alignment System

The Laser Alignment System (LAS, figure 3.34) uses infrared laser beams with a wavelength $\lambda = 1075$ nm to monitor the position of selected tracker modules. It operates globally on tracker substructures (TIB, TOB and TEC discs) and cannot determine the position of individual modules. The goal of the system is to generate alignment information on a continuous basis, providing geometry reconstruction of the tracker substructures at the level of 100 μm, which is mandatory for track pattern recognition and for the High Level Trigger. In addition, possible tracker structure movements can be monitored at the level of 10 μm, providing additional input for the track based alignment.

In each TEC, laser beams cross all nine TEC discs in ring 6 (ray 2) and ring 4 (ray 3) on back petals, equally distributed in ϕ. Here special silicon sensors with a 10 mm hole in the backside metalization and an anti-reflective coating are mounted. The beams are used for the internal alignment of the TEC discs. The other eight beams (ray 4), distributed in ϕ, are foreseen to align TIB, TOB, and both TECs with respect to each other. Finally, there is a link to the Muon system (ray 1), which is established by 12 laser beams (six on each side) with precise position and orientation in the tracker coordinate system.

The signal induced by the laser beams in the silicon sensors decreases in height as the beams penetrate through subsequent silicon layers in the TECs and through beam splitters in the align-

2008 JINST 3 S08004

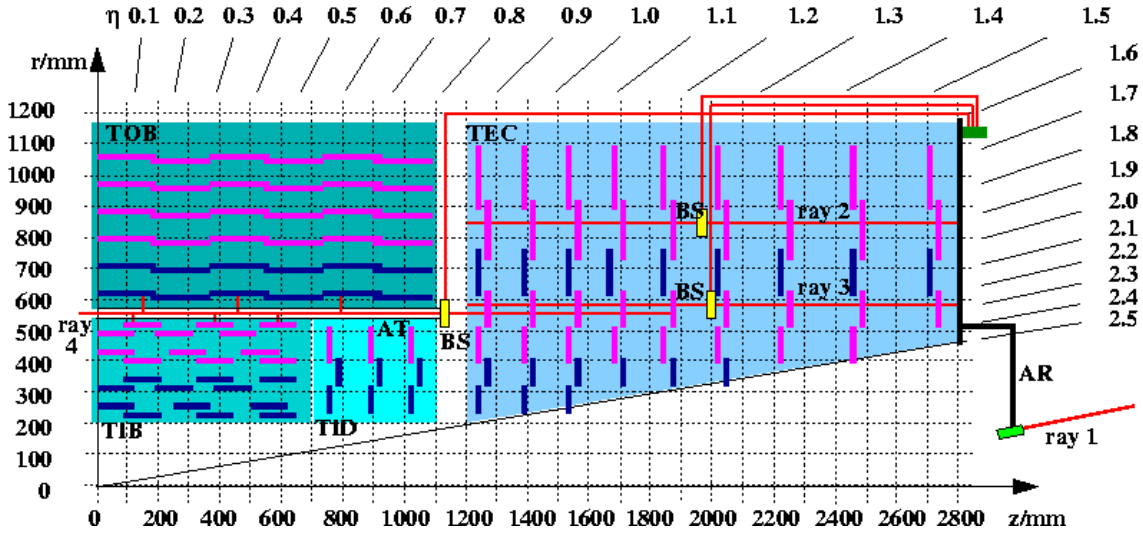

Figure 3.34: Overview of the CMS Laser Alignment System.

ment tubes that partly deflect the beams on TIB and TOB sensors. To obtain optimal signals on all sensors, a sequence of laser pulses with increasing intensities, optimized for each position, is generated. Several triggers per intensity are taken and the signals are averaged. In total, a few hundred triggers are needed to get a full picture of the alignment of the tracker structure. Since the trigger rate for the alignment system is around 100 Hz, this will take only a few seconds. These data will be taken at regular intervals, both in dedicated runs and during physics data taking.

Alignment with tracks

CMS pursues the development of two novel track-based alignment algorithms that allow to quickly solve the system of linear equations of order $\mathcal{O}(100\,000)$. The first is an extension to the well-known global Millepede algorithm [52], that takes all correlations into account and has been shown to successfully align the most sensitive 50 000 parameters. The second is a novel approach using a Kalman Filter [53], which bridges the gap between global and local algorithms by taking into account the most important correlations. In addition the HIP [54] algorithm, which is local in the sense that it takes into account only correlations of parameters within a module, is developed in parallel. In this algorithm, correlations between modules are dealt with implicitly by iterating the alignment many times. All three methods are expected to be able to provide alignment constants for the full silicon pixel and strip tracker.

Experience from other experiments has shown that collision data are not sufficient to constrain certain correlated module movements well enough to obtain a unique set of alignment constants. Therefore complementary data and constraints need to be exploited. Examples are tracks from cosmic muons (with and without magnetic field) that constrain the tracker barrel modules, or beam halo muons for the endcap. Beam gas and minimum bias events are also under consideration. Typical examples of constraints are a vertex constraint for decay particles e.g. from $Z \rightarrow \mu^+\mu^-$ or jets, mass constraints, measurements from the Laser Alignment System, and survey constraints. First studies indicate that those data will provide a unique alignment parameter set.

2008 JINST 3 S08004

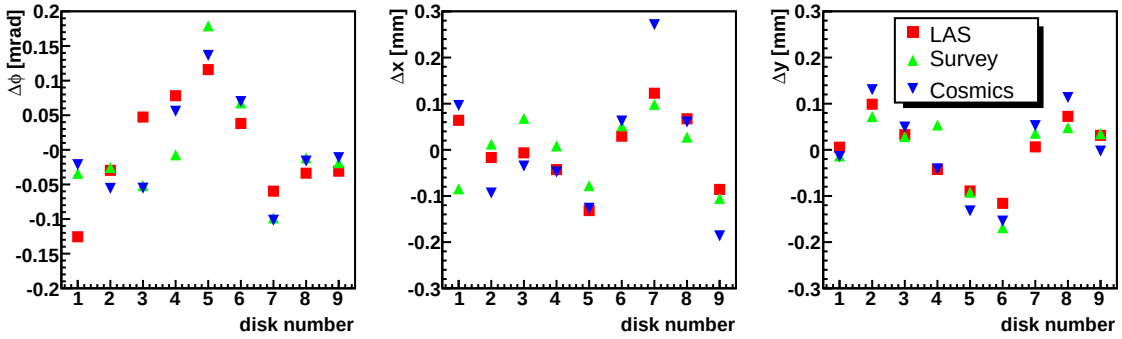

Figure 3.35: TEC+ disk rotation $\Delta\phi$ (around the beam axis) and displacements $\Delta x, \Delta y$ (in the disk plane) as determined from survey, LAS and cosmic muon tracks.

During integration of the TEC+, deviation of disk positions and rotations from nominal values have been determined from survey with photogrammetry, the LAS, and tracks from cosmic muons. Figure 3.35 shows the results from the three complementary methods. The global degrees of freedom (absolute position and orientation, torsion and shear around the symmetry axis) have been fixed by requiring the average displacement and rotation as well as torsion and shear to be zero. The values agree within 60 μm and 80 μrad with each other, which can be taken as an upper value on the precision of each method.

3.3.8 Detector control and safety system

The Tracker Detector Safety System (TDSS) and tracker Detector Control System (tracker DCS) is a two pillar system. The TDSS ensures independently the safety, with a large PLC (Programmable Logical Controller) system, occupying 6 LHC racks. A limited set of around 1000 hardwired temperature and humidity sensors are evaluated and out of limit states interlock power supplies. The tracker DCS, as a complementary partner, controls, monitors and archives all important parameters. The heart of the DCS is composed out of an industrial SCADA program (Supervisory Control And Data Acquisition) PVSS (Prozessvisualisierungs- und Steuerungssystem from ETM Austria, chapter 9) together with a Finite State Machine written in SMI++, a derivative of the former DELPHI control software; thus using the standard control software framework for all LHC experiments. The main task of the DCS is to control about 2000 power supplies for silicon module low and high voltage power and about 100 low voltage control power supplies via the OPC (OLE for Process Automation) protocol. Detector interdependencies of control, low and high voltages are handled, as well as fast ramp downs in case of higher than allowed temperatures or currents in the detector, experimental cavern problems, etc. All this is ensured by evaluating 10^4 power supply parameters, 10^3 data points from DSS via a Siemens S7 driver and 10^5 readings from the DCUs situated on all front end hybrids and control units CCUs. Several passive alarms and warning levels are defined for temperature, relative humidity, voltages, currents, etc. and are reported in a global warning panel as well as limits that, if surpassed, would result in automatic shutdown. Information from the tracker cooling plant, the thermal screen, beam conditions and the dry gas system are crucial for safe running and are accessible from the tracker DCS and TDSS.

2008 JINST 3 S08004

All parameters are archived to ORACLE. The TDSS (tracker DCS) system is fully implemented in the global CMS DSS (DCS) and Run Control system.

3.3.9 Operating experience and test results

Performance in test beam experiments

The system performance of integrated structures of the silicon strip tracker and its data acquisition chain as well as the performance of the silicon strip modules themselves has been studied in various test beam experiments at CERN and the Paul Scherrer Institut (PSI), Villigen (CH). In test beam campaigns, performed in May and October 2004 at the X5 test beam complex in the CERN west area, large substructures of TIB, TOB and TEC were exposed to a secondary pion beam with an energy of 120 GeV and a tertiary muon beam with muon energies ranging from 70 to 120 GeV. The TIB setup comprised a prototype half-shell structure of layer 3, equipped with eight single-sided strings, plus four double-sided strings, mounted on a custom support structure. For the TOB, the so-called cosmic rack, a precise mechanical telescope-like structure equipped with four single-sided and two double-sided rods, was used in the beam tests. The TEC setup consisted of one back and one front petal [55]. These setups corresponded to about 1% of the complete TIB, TOB and TEC detectors, respectively. The TOB and TEC setups were operated at a temperature below -10°C, while the TIB setup was operated at room temperature. Typical primary trigger rates for the pion beam were 600 000 pions per spill (a 2.2 s long period within a 12 s long SPS cycle during which particles are delivered) corresponding to a mean occupancy of 15 Hz/cm^2.

In the strip-cluster finding the cuts for the signal-to-noise ratio, S/N, of the cluster seed / neighbour strips / total cluster are 4/3/5 for TIB, 5/2/5 for TOB and 3/2/5 for TEC, respectively. The cluster noise is calculated by adding the single strip noise values in quadrature (TIB, TEC) or by taking the seed noise as the cluster noise (TOB). To determine the most probable value for the S/N of a module, a Landau distribution convoluted with a Gaussian is fitted to the signal-to-noise distribution, and the most probable value of the fitted function is quoted as the S/N.

The mean most probable S/N values for all module types, together with their strip length, pitch and abbreviations used in the following, are summarized in table 3.3. For thin (thick) TEC sensors, most probable S/N values of 29–33 (36–42) in peak mode and 19–22 (20–24) in deconvolution mode have been observed [55]. For the thick TOB OB1 (OB2) modules a S/N of typically 36 (38) and 25 (27) was found in peak and deconvolution mode, respectively [17], while the thin TIB IB1 (IB2) modules exhibited a S/N of 26 (30) in peak mode and 18 (20) in deconvolution mode.

Assuming that a MIP creates 24 000 electrons in a 300 μm thick layer of silicon [16], and assuming that the beam particles can be treated as MIPs, the S/N can be used to calculate the equivalent noise charge, ENC. The common mode subtracted noise depends on the capacitance of the sensor, which depends linearly on the strip length and the ratio between strip width and pitch, w/p [16]. Since $w/p = 0.25$ for all sensor types, the ENC varies between different module types according to the strip length. Results for all module types except W1TID are summarized in table 3.3. Measurements performed at low temperature (for the TEC, typically hybrid temperatures of $+10$°C and 0°C were reached for hybrids with six and four APVs, respectively) are plotted versus the strip length in figure 3.36. A linear fit to these data yields the following dependence of

2008 JINST 3 S08004

the ENC on the strip length L:

$$\begin{aligned} \mathrm{ENC_{peak}} &= (36.6 \pm 1.9)\, e^-/\mathrm{cm} \cdot L + (405 \pm 27)\, e^-, \\ \mathrm{ENC_{dec}} &= (49.9 \pm 3.2)\, e^-/\mathrm{cm} \cdot L + (590 \pm 47)\, e^-. \end{aligned}$$

The common mode noise is the standard deviation of the common mode, calculated per APV from a certain number of events. The mean common mode noise has been evaluated and amounts to (173 ± 38) and (299 ± 76) electrons for TEC (mean from all APVs in the setup) and (265 ± 36) and (300 ± 19) electrons for TIB (mean from all APVs of TIB2 modules) in peak and deconvolution mode, respectively.

Although no dedicated beam telescope was available, efficiency studies have been performed both with the TOB and TEC setups, exploiting the fact that in both cases the beam penetrated several layers of modules. Efficiencies of above 99% have been observed in all such studies.

The uniformity of the module performance along and perpendicular to the strip direction has been studied in 2003 with several TIB modules in a test beam experiment at the X5 complex. Two single-sided strings equipped with IB2 modules were mounted on a structure corresponding to a portion of a layer 3 half-shell, and operated at room temperature. To study the uniformity across the strips, the strips read out by three APVs (on two different modules) were exposed to a pion beam, and between 1000 and 8000 events were collected per strip. A cluster was associated to a strip if the centre of gravity x of the cluster was reconstructed within $(n-0.5) \cdot p < x < (n+0.5) \cdot p$ for strip n and pitch p. The uniformity, defined as the ratio between the RMS and the mean of the respective distribution, was 1.3% for the cluster noise, with an increase close to the APV chip edges. The cluster charge uniformity was of the order of 1.4%, but dropped to 0.5% if calculated separately for groups of 32 adjacent strips. A uniformity of the S/N of 1.6% on average and of 1.0% for groups of 32 strips was measured. To investigate the uniformity along the strips, a muon beam was used for its uniform particle density. The cluster position along the strip could be obtained from the TOB setup that was operated in the same test beam, since the strip direction of the TOB modules was perpendicular to that of the TIB modules. The clusters were binned in 24 intervals according to their centre of gravity, corresponding to length intervals of 5 mm, and about 1500 events were accumulated per bin. Both the uniformity of cluster charge and S/N were found to be 1.4%.

Performance during integration

Testing during integration consisted typically of checks of the control ring functionality, tests of the I^2C communication of all chips, tests of the gain of the optical connections, commissioning (i.e. tuning of chip operation parameters), pedestal runs in peak and deconvolution mode, bias voltage ramping up to 450 V, read-out of currents and module and hybrid temperatures through the DCUs, and a functionality check of the temperature and humidity sensors.

In the following sections the performance of TEC, TIB/TID and TOB during integration is described. Two comments apply to all three sub-detectors:

- Numbers of dead and noisy strips are given below. While dead strips can be identified reliably, the noisiness of strips depends on external conditions such as grounding and the APV read-out mode and the figures given should be regarded as estimates only. APV edge strips

2008 JINST 3 S08004

Table 3.3: Pitch, strip length, signal-to-noise ratio and equivalent noise charge after common mode subtraction for different module types. The TEC and TOB measurements are for hybrid temperatures of below 0 °C, the TIB measurements were performed at room temperature. Sensors of type IB1 and IB2 are used in TIB, layers 1 and 2 and layers 3 and 4, respectively. In the TOB, layers 1–4 are equipped with OB2 sensors, layers 5 and 6 with OB1 sensors. The sensor geometries abbreviated with W are wedge-shaped sensors used in TEC and TID, with the number corresponding to the ring. W1 sensors have a slightly different geometry in TID and TEC.

Module type	Pitch [μm]	Strip length [mm]	S/N Peak mode	S/N Dec. mode	ENC [e^-] Peak mode	ENC [e^-] Dec. mode
IB1	80	116.9	25.8 ± 1.3	18.3 ± 0.5	931 ± 48	1315 ± 37
IB2	120	116.9	29.5 ± 1.4	20.3 ± 0.6	815 ± 37	1182 ± 31
OB1	122	183.2	36	25	1110 ± 47	1581 ± 75
OB2	183	183.2	38	27	1057 ± 17	1488 ± 22
W1TEC	81–112	85.2	33.1 ± 0.7	21.9 ± 0.6	714 ± 23	1019 ± 37
W2	113–143	88.2	31.7 ± 0.5	20.7 ± 0.4	741 ± 25	1068 ± 51
W3	123–158	110.7	29.2 ± 0.6	20.0 ± 0.4	802 ± 16	1153 ± 48
W4	113–139	115.2	28.6 ± 0.5	19.2 ± 0.3	819 ± 21	1140 ± 26
W5	126–156	144.4	42.2 ± 1.1	24.1 ± 1.1	971 ± 29	1354 ± 57
W6	163–205	181.0	37.8 ± 0.6	23.0 ± 0.4	1081 ± 26	1517 ± 47
W7	140–172	201.8	35.5 ± 1.0	20.3 ± 1.1	1155 ± 40	1681 ± 107

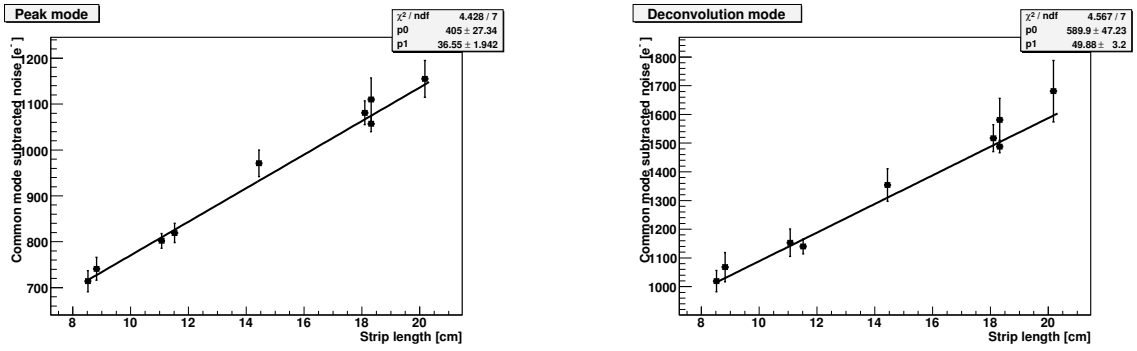

Figure 3.36: Equivalent noise charge after common mode subtraction versus strip length for all TOB and TEC module types, in peak (left panel) and deconvolution mode (right panel).

show typically an increased noise and are frequently flagged as noisy, especially when a fixed noise cut is used for all strips. These edge strips are included in the numbers of flagged strips, although they are usually fully efficient.

- Although all components (petals, rods, single modules in case of the TIB/TID) were tested before insertion and components not fulfilling strict quality criteria were rejected, several defects have been observed during integration. Typical defects are broken optical fibers, bad APVs (i.e. with many noisy or dead strips), and missing or unreliable I^2C communication

of complete modules or single chips. Most of the problems are assumed to be caused by mishandling during insertion or cabling. Since the exchange of components bears a considerable risk, not all defective components have been exchanged. Additional defects could be introduced by any following handling step, such as cabling of the tracker. The numbers given below should thus be regarded as a snapshot reflecting the situation right after integration of the single sub-detectors.

TEC Performance during integration

The TEC petals were integrated sector-wise, where one sector corresponds to one eighth of a TEC in ϕ, and comprises 18 petals that share nine control rings and four cooling circuits. After integration of one sector, a read-out test of the full sector was performed at room temperature, with the coolant at $+15$°C and mean silicon and hybrid temperatures of about $+23$°C and $+33$°C, respectively.

During integration a flaw in the crimping of the connectors of the multiservice power cables was found. After all such connectors had been replaced on both TECs, the system performance observed during integration was very robust. In figure 3.37, left side, the common mode subtracted noise of all strips of both TECs is shown for deconvolution mode. Since the measured noise depends on the gain of the optical chain, the noise was normalized to the digital output of the APV (scale on upper x-axis in figure 3.37). In addition, the number of ADC counts in the FED was converted to ENC according to the following method: with a nominal digital APV output of $\pm\,4$ mA and a nominal APV gain of 1 MIP/mA for thin sensors, the height of the digital output corresponds to 8 MIPs or 200 000 electrons. This method allows a direct comparison of the measurements from different optical channels and delivers an approximate absolute calibration of the equivalent noise charge. Cross-checks with cosmic muon data performed during TIB/TID integration indicate that this scaling agrees with the real ENC within 10–20%. Furthermore, the noise depends on the strip capacitance and thus on the strip length, i.e. on the module type. For this reason the noise of all strips was normalized to the strip length of modules of ring 1 (8.52 cm). In addition a correction was applied to TEC- data to account for the fact that they were taken with other chip parameter settings than TEC+ data. The common mode subtraction was performed assuming a constant common mode per APV. To extract the mean noise, a gaussian was fitted to the distribution. The resulting mean common mode subtracted noise amounts to 1693 ± 75 electrons in this normalization.

The mean common mode noise, calculated per APV, amounts to $(22 \pm 4)\%$ and $(21 \pm 3)\%$ of the mean intrinsic noise in peak and deconvolution mode, respectively (figure 3.38, left, for all non-defective APVs of TEC+).

The flatness of the noise across the APV is a good indicator for the quality of the grounding. The relative spread of the total noise (before common mode subtraction), i.e. the RMS of the noise divided by the mean noise, both calculated per APV, can be used to quantify the flatness. The relative spread is $(2.5 \pm 0.2)\%$ in both read-out modes, as shown in figure 3.38, right, indicating that the grounding scheme implemented by the TEC works well.

Strips are counted as noisy or dead if their noise is more than five times the RMS of the noise above or below the mean noise of the respective APV. Edge strips are counted as noisy, if

2008 JINST 3 S08004

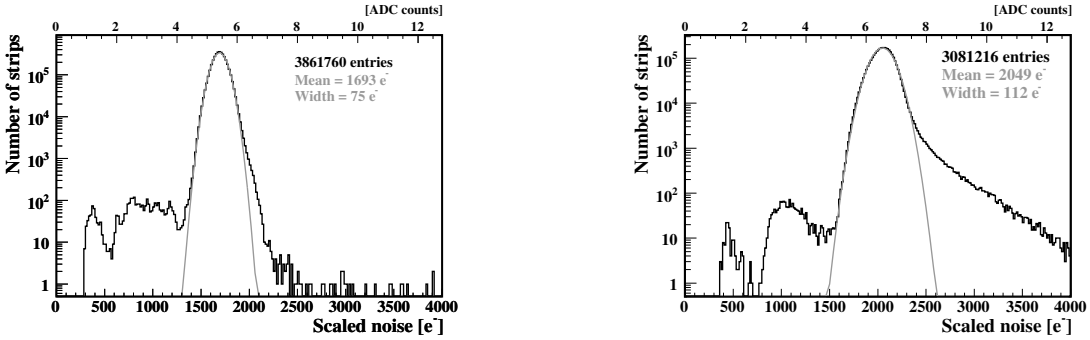

Figure 3.37: Normalized common mode subtracted noise of all strips (scaled to the strip length of ring 1 sensors) of both TECs (left panel) and the TOB (right panel), in deconvolution mode. Details are described in the text.

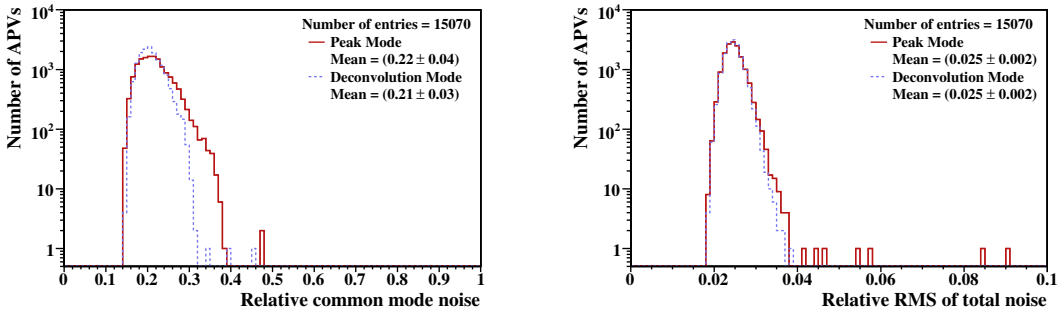

Figure 3.38: Ratio between common mode noise and mean intrinsic noise (left panel) and ratio between the RMS of the total noise and the mean total noise (right panel), calculated per APV, in peak and deconvolution mode for all non-defective APVs of TEC+.

their noise is more than seven sigma above the mean noise. In total, there are 3.0 per mille of bad channels in TEC+, while TEC- has 2.7 per mille of bad channels.

TIB and TID performance during integration

During TIB/TID integration [56], modules and AOHs were assembled onto half layers and disks and tested extensively for functionality, including pedestals, once a mother cable was completed (corresponding to a string in the TIB and three single-sided or five double-sided modules in the TID). Completed disks and half layers were then subjected to a burn-in in a climatic chamber, during which the structures were operated at a silicon sensor temperature of about $-15°$C. The complete half layers and disks were read out during these tests. Typically, the structures underwent 2–3 cooling cycles during a five day measurement period. After-wards disks and half layers were assembled into the complete TIB/TID+ and TIB/TID- structures and shipped to CERN, where the last integration operations were performed, such as connection of fibers to the final ribbons and cabling of the margherita.

After optimization of the grounding scheme, the noise performance observed in the TIB and TID structures was very good. For the TIB and TID structures the scaled common mode subtracted noise of all strips, except for two TIB half-shells for which data were taken under non-final running conditions and three half-shells for which the proper grounding scheme was not yet implemented, is shown in figure 3.39 for deconvolution mode. Scaling and common mode subtraction have been implemented as previously described in this section. These data have been taken under nominal CMS conditions, with a mean silicon sensor temperature of about -15°C, hybrid temperatures ranging from -4°C (TID double-sided modules) to -14°C (TIB single-sided modules) and APV parameters set as intended for this temperature range. The mean noise, taken from a gaussian fit, amounts to (1233 ± 87) electrons in the TIB and (1246 ± 76) electrons in the TID. Measurements with a silicon sensor temperature of about $+10$°C and hybrid temperatures of $+10$°C to $+30$°C show a mean noise about 20% larger. In contrast to the TEC, a strip is flagged as dead if its noise is below 75% of the average noise of the APV, and APV edge strips are not treated differently. The total number of bad channels is 4.4 per mille in TIB/TID+ and 3.4 per mille in TIB/TID-.

TOB performance during integration

Fully equipped and tested rods were integrated cooling segment-wise. After a first functional test, the cooling connection was soldered and a leak test was performed. Then the cooling segment was cabled, and a full read-out test, including pedestals, was performed at room temperature. During these measurements, the silicon sensor temperature was about $+24$°C and the hybrid temperature about $+30$°C.

During integration, a sensitivity to pick-up noise has been observed, which leads to non-flat, wing-like common mode subtracted noise distributions. This sensitivity is especially pronounced for layers 3 and 4, which are equipped with single-sided 4 APV modules, and within these layers the effect is worst for modules mounted closest to the CCUM. Defining as a figure of merit the ratio of the highest noise amplitude (taken from a parabola fit to the noise distribution) to the flat noise baseline, and counting all APVs with a ratio above 1.25 as "in the wings", the fraction of APVs in the wings is about 30% in layers 3 and 4 and about 7% and 1% in layers 1/2 and 5/6, respectively. In total, 11.4% of all APVs are found to be in the wings according to this criterion. It has been verified that either with adjusted cluster cuts or with a linear online common mode subtraction the increase in the cluster width and occupancy is negligible.

The normalized noise of all TOB strips is shown in figure 3.37, right. The tail to high noise values comes from the non-flat noise distributions. The mean noise from a gaussian fit amounts to (2049 ± 112) electrons.

Due to this wing-like noise structure, a special algorithm has been adopted to evaluate the number of dead and noisy strips. A parabola is fitted to the noise distribution of each APV in an iterative procedure, and strips are flagged as bad if their noise deviates more than ten times the RMS of the distribution of fit residuals from the fitted function.

Only very few permanent defects, corresponding to 0.6 per mille of lost channels, have been introduced during TOB integration. Including the number of noisy and dead strips, the number of bad channels amounts to 0.6 per mille in TOB+ and 1.9 per mille in TOB-.

2008 JINST 3 S08004

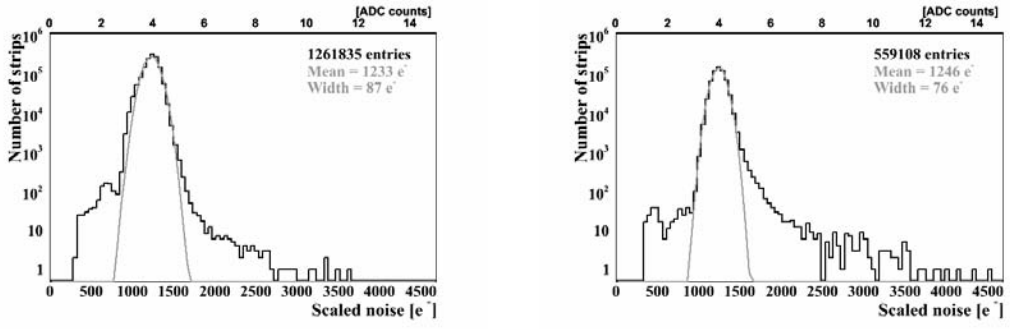

Figure 3.39: Normalized common mode subtracted single strip noise for TIB (left panel) and TID (right panel), in deconvolution mode. Details are described in the text.

Irradiation studies

As already discussed in detail in section 3.1.1, the silicon strip tracker will suffer from a severe level of radiation during its 10 year long lifetime: up to $1.8 \times 10^{14}\,\mathrm{n_{eq}cm^{-2}}$ for TIB/TID and TEC and up to $0.5 \times 10^{14}\,\mathrm{n_{eq}cm^{-2}}$ for TOB, assuming an integrated luminosity of $500\,\mathrm{fb^{-1}}$. The radial and z dependence of the fluence both for fast hadrons and neutrons is described in detail in [15, 16]. Hadrons are expected to dominate in the inner part of the tracker, up to a radius of about 0.5 m, while neutrons backscattered off the electromagnetic calorimeter dominate further outside. Safety factors of 1.5 and 2.0 on the fluence are typically applied for TIB/TID and TOB/TEC, respectively.

To ensure that both the FE electronics and the silicon sensors can be operated safely and with satisfactory performance after such an irradiation, several irradiation tests with neutrons and protons have been carried out. Neutron irradiation was usually performed at the isochronous cyclotron of the Centre de Recherches du Cyclotron, Louvain-la-Neuve, which delivers neutrons with a mean energy of 20 MeV (hardness factor 1.95 relative to 1 MeV neutrons [58]). Proton irradiation has been carried out e.g. at the compact cyclotron of the Forschungszentrum Karlsruhe, where a 26 MeV proton beam (hardness factor 1.85 relative to 1 MeV neutrons) with a current of $100\,\mu\mathrm{A}$ and a beam spot diameter of 1 cm is available.

To study the performance of complete irradiated modules, several OB1 and OB2 modules (table 3.3 for explanation) were irradiated with a proton fluence ranging from $0.1 \times 10^{14}\,\mathrm{n_{eq}cm^{-2}}$ to $0.7 \times 10^{14}\,\mathrm{n_{eq}cm^{-2}}$, and one OB2 module was subjected to a neutron fluence of about $1.2 \times 10^{14}\,\mathrm{n_{eq}cm^{-2}}$ [57]. Two TEC W5 modules were irradiated with a proton fluence of about $1.1 \times 10^{14}\,\mathrm{n_{eq}cm^{-2}}$, and three TIB IB1 modules were subjected to a proton fluence of $0.5 \times 10^{14}\,\mathrm{n_{eq}cm^{-2}}$ to $2.1 \times 10^{14}\,\mathrm{n_{eq}cm^{-2}}$. The effect of annealing was simulated by heating the modules for 80 minutes at 60°C and afterwards storing them at room temperature for at least two hours. To prevent uncontrolled annealing, the modules were stored at −20°C between the irradiation or annealing steps. Measurements were performed at −15°C.

As expected from inversion from n- to p-type doping, the full depletion voltage increased with the fluence, as shown in figure 3.40 (left). However, the required depletion voltage stays below 500 V, which is the maximum depletion voltage for which the sensors are specified. The dependence of the depletion voltage on annealing time was studied as well and found to be in

2008 JINST 3 S08004

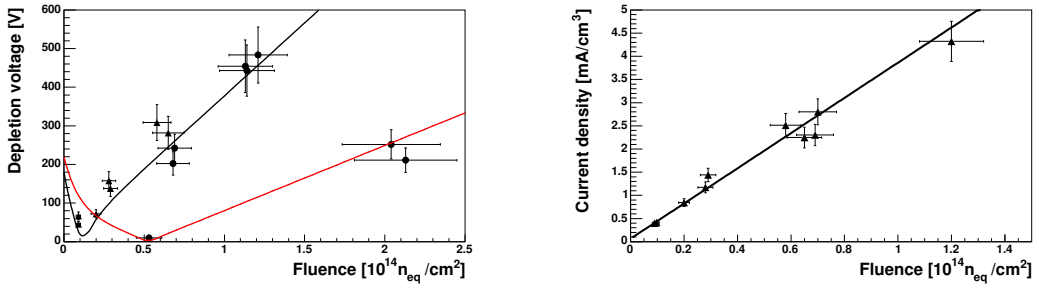

Figure 3.40: Left panel: Variation of depletion voltage with fluence for OB1 (triangles), OB2 and W5 (dots on upper curve) and IB2 (dots on lower curve) modules, after an annealing time of 80 minutes after each irradiation step. The curves correspond to calculations for 500 μm (upper curve) and 320 μm (lower curve) sensors for an annealing time of 80 minutes at 60°C. Right panel: Current density, scaled to 20°C, versus fluence after annealing for 80 minutes at 60°C.

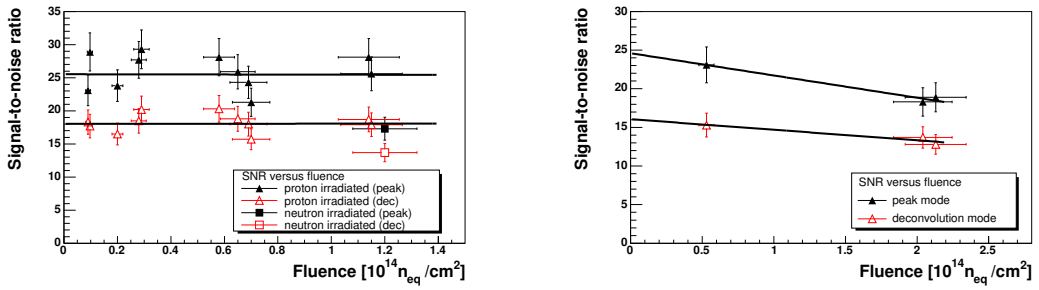

Figure 3.41: Signal-to-noise ratio versus fluence for modules with 500 μm (left panel) and 320 μm thick sensors (right panel) in peak (filled symbols) and deconvolution mode (open symbols).

excellent agreement with the Hamburg model [59], with a minimum at 80 minutes annealing time, corresponding to a 10 day shut down period at room temperature.

The leakage current is expected to increase with fluence, leading to a larger heat dissipation and increased noise. In figure 3.40 (right) the dependence of the current density on the fluence is shown. The current related damage rate, defined as the current increase, scaled to 20°C, per sensor volume and equivalent neutron fluence, amounts to $(3.79 \pm 0.27) \times 10^{-17}$ A/cm, which is in good agreement with literature and measurements from test structures.

Measurements of the signal-to-noise ratio, S/N, of irradiated modules have been performed with a ^{90}Sr source. Due to an increase of the noise and a decrease of the charge collection efficiency, the S/N is expected to decrease with fluence. The dependence of the S/N on the accumulated fluence for thick and thin sensors in both read-out modes is shown in figure 3.41. For thick sensors, the S/N decreased from 23 (35) to 15 (21) in deconvolution (peak) mode, while for thin sensors a decrease from 18 (24) to 13 (18) was observed. These figures ensure a hit finding efficiency of above 95% even after 10 years of operation at the LHC [60, 61].

2008 JINST 3 S08004

Chapter 4

Electromagnetic calorimeter

The electromagnetic calorimeter of CMS (ECAL) is a hermetic homogeneous calorimeter made of 61 200 lead tungstate ($PbWO_4$) crystals mounted in the central barrel part, closed by 7 324 crystals in each of the two endcaps. A preshower detector is placed in front of the endcap crystals. Avalanche photodiodes (APDs) are used as photodetectors in the barrel and vacuum phototriodes (VPTs) in the endcaps. The use of high density crystals has allowed the design of a calorimeter which is fast, has fine granularity and is radiation resistant, all important characteristics in the LHC environment. One of the driving criteria in the design was the capability to detect the decay to two photons of the postulated Higgs boson. This capability is enhanced by the good energy resolution provided by a homogeneous crystal calorimeter.

4.1 Lead tungstate crystals

The characteristics [62] of the $PbWO_4$ crystals make them an appropriate choice for operation at LHC. The high density (8.28 g/cm^3), short radiation length (0.89 cm) and small Molière radius (2.2 cm) result in a fine granularity and a compact calorimeter. In recent years, $PbWO_4$ scintillation properties and other qualities have been progressively improved, leading to the mass production of optically clear, fast and radiation-hard crystals [63, 64]. The scintillation decay time of these production crystals is of the same order of magnitude as the LHC bunch crossing time: about 80% of the light is emitted in 25 ns. The light output is relatively low and varies with temperature ($-2.1\%^{\circ}C^{-1}$ at 18°C [65]): at 18°C about 4.5 photoelectrons per MeV are collected in both APDs and VPTs. The crystals emit blue-green scintillation light with a broad maximum at 420–430 nm [64, 66]. Longitudinal optical transmission and radioluminescence spectra are shown in figure 4.1.

To exploit the total internal reflection for optimum light collection on the photodetector, the crystals are polished after machining. For fully polished crystals, the truncated pyramidal shape makes the light collection non-uniform along the crystal length. The effect is large because of the high refractive index ($n = 2.29$ around the peak wavelength [67]) and the needed uniformity [68] is achieved by depolishing one lateral face. In the endcaps, the light collection is naturally more uniform because the crystal faces are nearly parallel. Pictures of barrel and endcap crystals with the photodetectors attached are shown in figure 4.2.

2008 JINST 3 S08004

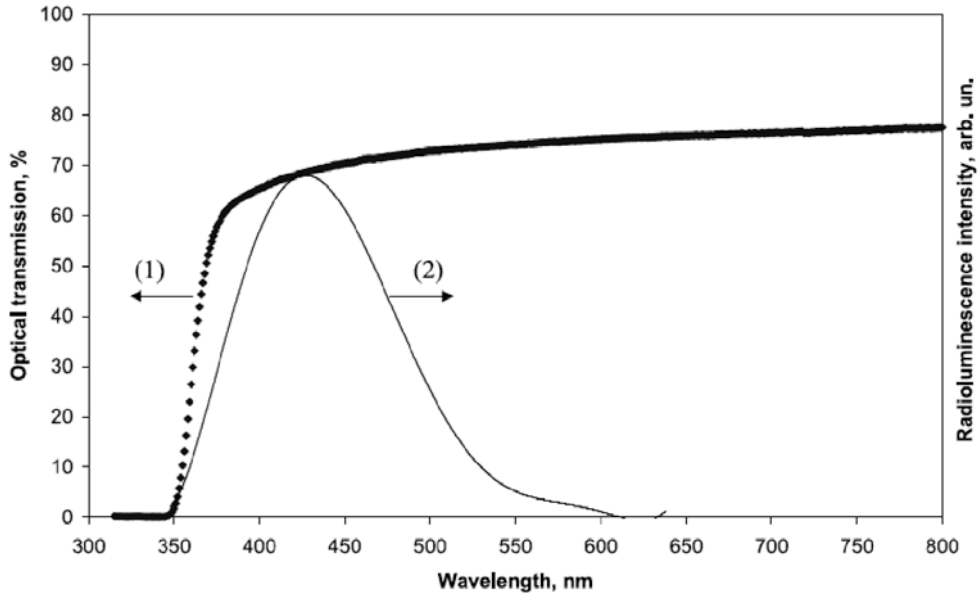

Figure 4.1: Longitudinal optical transmission (1, left scale) and radioluminescence intensity (2, right scale) for production $PbWO_4$ crystals.

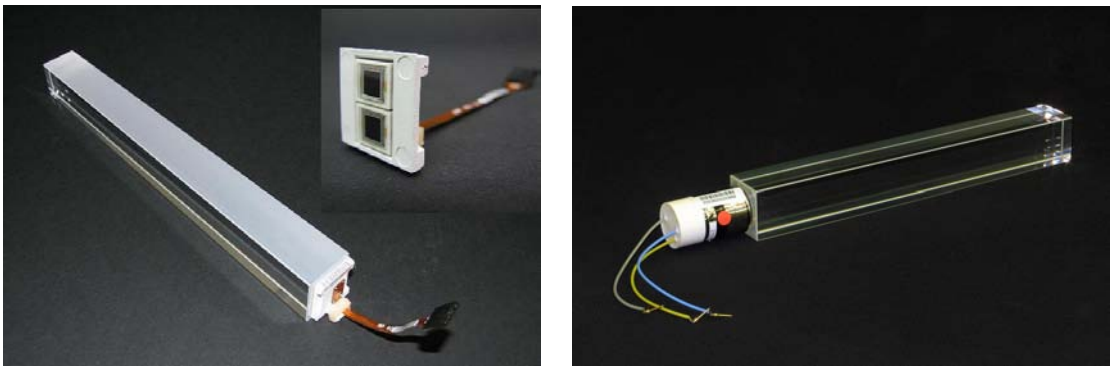

Figure 4.2: $PbWO_4$ crystals with photodetectors attached. Left panel: A barrel crystal with the upper face depolished and the APD capsule. In the insert, a capsule with the two APDs. Right panel: An endcap crystal and VPT.

The crystals have to withstand the radiation levels and particle fluxes [69] anticipated throughout the duration of the experiment. Ionizing radiation produces absorption bands through the formation of colour centres due to oxygen vacancies and impurities in the lattice. The practical consequence is a wavelength-dependent loss of light transmission without changes to the scintillation mechanism, a damage which can be tracked and corrected for by monitoring the optical transparency with injected laser light (section 4.9). The damage reaches a dose-rate dependent equilibrium level which results from a balance between damage and recovery at 18°C [64, 70].

To ensure an adequate performance throughout LHC operation, the crystals are required to exhibit radiation hardness properties quantified as an induced light attenuation length (at high dose rate) greater than approximately 3 times the crystal length even when the damage is saturated. Hadrons have been measured to induce a specific, cumulative reduction of light transmission, but the extrapolation to LHC conditions indicates that the damage will remain within the limits required for good ECAL performance [71, 72].

4.2 The ECAL layout and mechanics

The barrel part of the ECAL (EB) covers the pseudorapidity range $|\eta| < 1.479$. The barrel granularity is 360-fold in ϕ and (2×85)-fold in η, resulting in a total of 61 200 crystals. The crystals have a tapered shape, slightly varying with position in η. They are mounted in a quasi-projective geometry to avoid cracks aligned with particle trajectories, so that their axes make a small angle (3^{o}) with respect to the vector from the nominal interaction vertex, in both the ϕ and η projections. The crystal cross-section corresponds to approximately 0.0174×0.0174 in η-ϕ or 22×22 mm^2 at the front face of crystal, and 26×26 mm^2 at the rear face. The crystal length is 230 mm corresponding to 25.8 X_0. The barrel crystal volume is 8.14 m^3 and the weight is 67.4 t.

The centres of the front faces of the crystals are at a radius 1.29 m. The crystals are contained in a thin-walled alveolar structure (submodule). The alveolar wall is 0.1 mm thick and is made of an aluminium layer, facing the crystal, and two layers of glass fibre-epoxy resin. To avoid oxidation, a special coating is applied to the aluminium surface. The nominal crystal to crystal distance is 0.35 mm inside a submodule, and 0.5 mm between submodules. To reduce the number of different types of crystals, each submodule contains only a pair of shapes, left and right reflections of a single shape. In total, there are 17 such pairs of shapes. The submodules are assembled into modules of different types, according to the position in η, each containing 400 or 500 crystals. Four modules, separated by aluminium conical webs 4-mm thick, are assembled in a supermodule, which contains 1700 crystals (figures 4.3 and 4.4).

In each module, the submodules are held in partial cantilever by an aluminium grid, which supports their weight from the rear. At the front the submodule free ends are connected together by pincers that cancel the relative tangential displacements. The submodule cantilever is reduced by the action of a 4-mm thick cylindrical plate where the front of the submodules are supported by setpins. Not all the submodules are connected to the cylindrical plate but only four rows in ϕ from a total of ten. The portion of the submodule load taken at the front by the cylindrical plate is transmitted to the aluminium grids of the different modules via the conical webs interspaced between the modules [73]. Each module is supported and positioned in the supermodule at the rear end through the grid by a spine beam. The spine is provided with pads which slide into rails housed on the front face of the HCAL barrel, allowing the installation and support of each single supermodule. The cylindrical plate in front of the supermodule also provides the fixation of the monitoring system (see below) and the holes for its optical fibres.

All services, cooling manifolds and cables converge to a patch panel at the external end of the supermodule. Eighteen supermodules, each covering 20° in ϕ, form a half barrel.

The endcaps (EE) cover the rapidity range $1.479 < |\eta| < 3.0$. The longitudinal distance between the interaction point and the endcap envelope is 315.4 cm, taking account of the estimated

2008 JINST 3 S08004

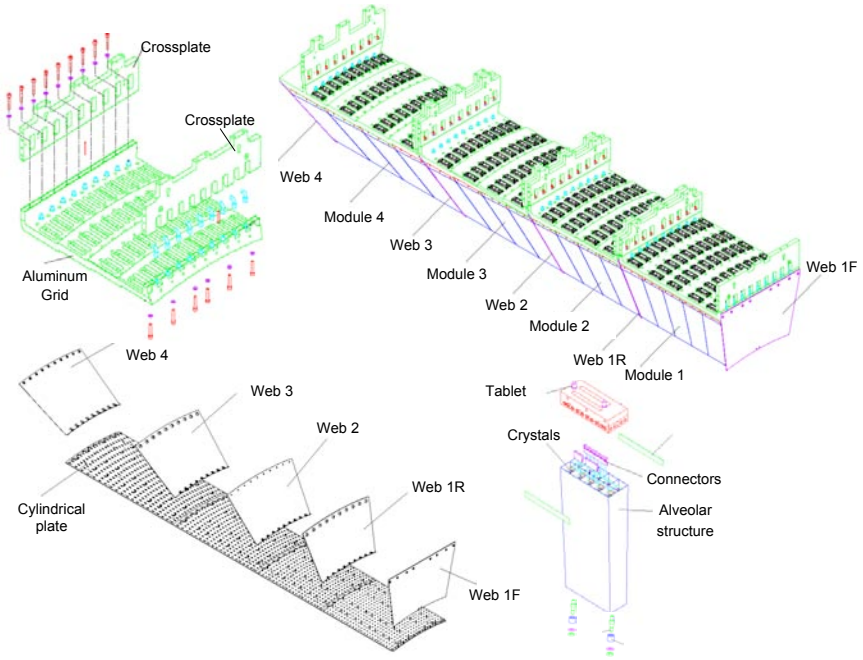

Figure 4.3: Layout of the ECAL barrel mechanics.

shift toward the interaction point by 1.6 cm when the 4-T magnetic field is switched on. The endcap consists of identically shaped crystals grouped in mechanical units of 5×5 crystals (supercrystals, or SCs) consisting of a carbon-fibre alveola structure. Each endcap is divided into 2 halves, or *Dees*. Each Dee holds 3 662 crystals. These are contained in 138 standard SCs and 18 special partial supercrystals on the inner and outer circumference. The crystals and SCs are arranged in a rectangular *x*-*y* grid, with the crystals pointing at a focus 1 300 mm beyond the interaction point, giving off-pointing angles ranging from 2 to 8 degrees. The crystals have a rear face cross section $30\times30\,\mathrm{mm}^2$, a front face cross section $28.62\times28.62\,\mathrm{mm}^2$ and a length of 220 mm (24.7 X_0). The endcaps crystal volume is 2.90 m^3 and the weight is 24.0 t. The layout of the calorimeter is shown in figure 4.5. Figure 4.6 shows the barrel already mounted inside the hadron calorimeter, while figure 4.7 shows a picture of a Dee.

The number of scintillation photons emitted by the crystals and the amplification of the APD are both temperature dependent. Both variations are negative with increasing temperature. The overall variation of the response to incident electrons with temperature has been measured in test beam [74] to be $(-3.8\pm0.4)\%^{\circ}\mathrm{C}^{-1}$. The temperature of the system has therefore to be maintained constant to high precision, requiring a cooling system capable of extracting the heat dissipated by the read-out electronics and of keeping the temperature of crystals and photodetectors stable within $\pm0.05^{\circ}$C to preserve energy resolution. The nominal operating temperature of the CMS ECAL is 18°C. The cooling system has to comply with this severe thermal requirement. The system employs water flow to stabilise the detector. In the barrel, each supermodule is independently supplied

2008 JINST 3 S08004

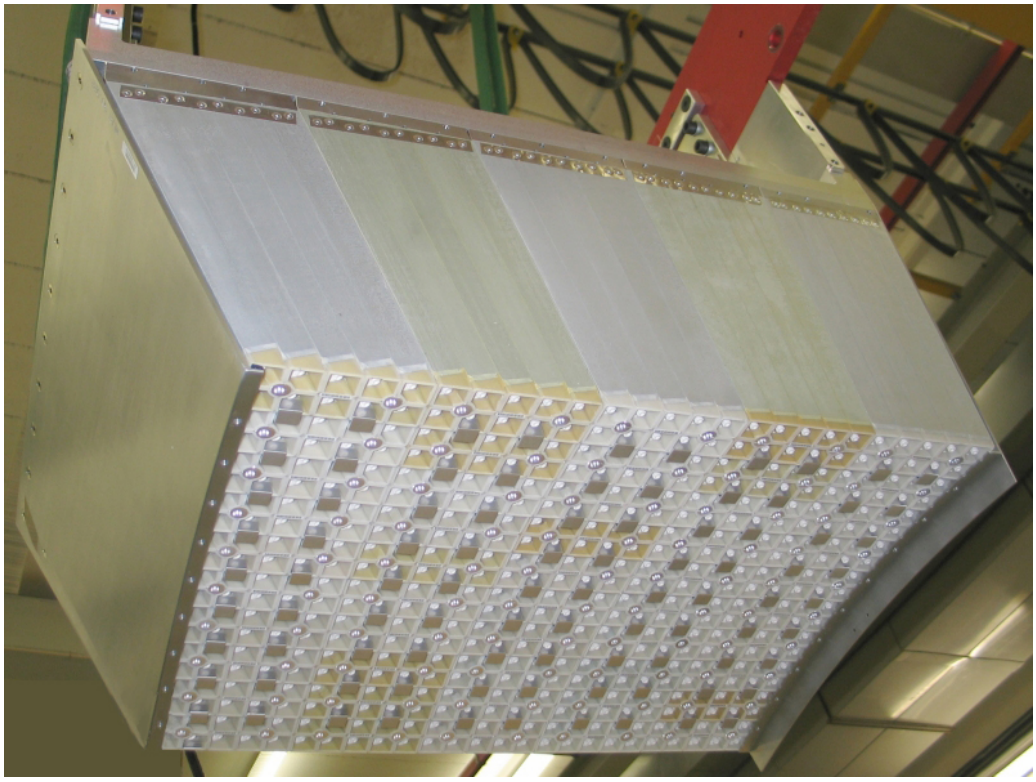

Figure 4.4: Front view of a module equipped with the crystals.

with water at 18°C. The water runs through a thermal screen placed in front of the crystals which thermally decouples them from the silicon tracker, and through pipes embedded in the aluminium grid, connected in parallel. Beyond the grid, a 9 mm thick layer of insulating foam (Armaflex) is placed to minimise the heat flowing from the read-out electronics towards the crystals. Return pipes distribute the water through a manifold to a set of aluminium cooling bars. These bars are in close contact with the very front end electronics (VFE) cards and absorb the heat dissipated by the components mounted on these cards. A thermally conductive paste (gap filler 2000, produced by Bergquist) is used to provide a good contact between the electronic components and a metal plate facing each board. This plate is coupled to the cooling bar by a conductive pad (ultrasoft gap pad, also produced by Bergquist). Both the gap pad and the gap filler have been irradiated with twice the dose expected in the ECAL endcaps after 10 years at the LHC and have shown no change in character or loss of performance.

Extended tests of the cooling system have been performed with good results [74]. Residual effects caused by a possible variation of the power dissipated by the electronics were measured in the extreme case of electronics switched on and off. The conclusion is that contributions to the constant term of the energy resolution due to thermal fluctuations will be negligible, even without temperature corrections.

2008 JINST 3 S08004

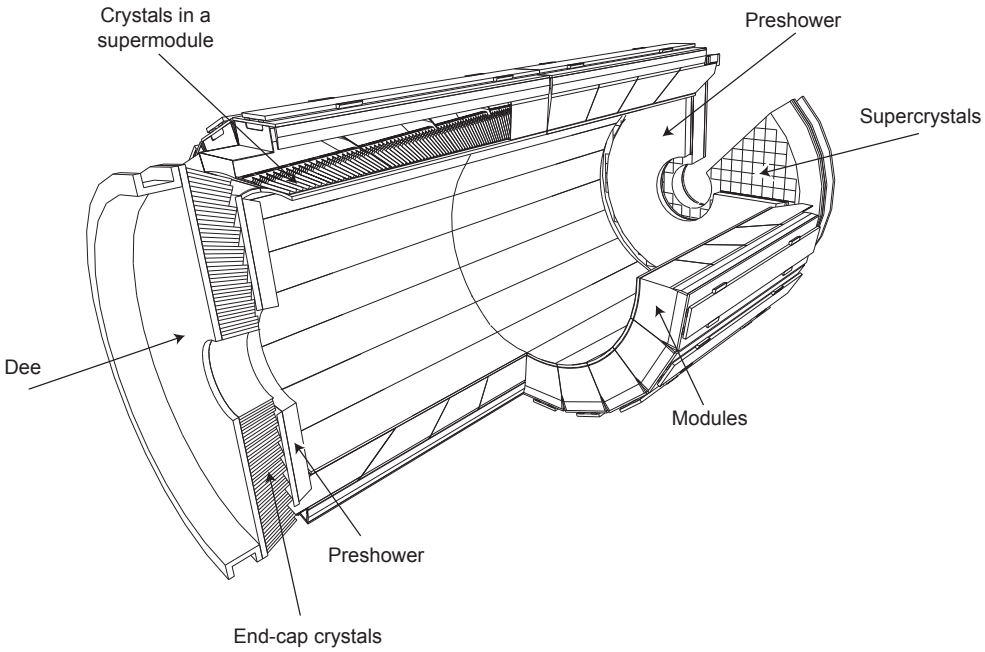

Figure 4.5: Layout of the CMS electromagnetic calorimeter showing the arrangement of crystal modules, supermodules and endcaps, with the preshower in front.

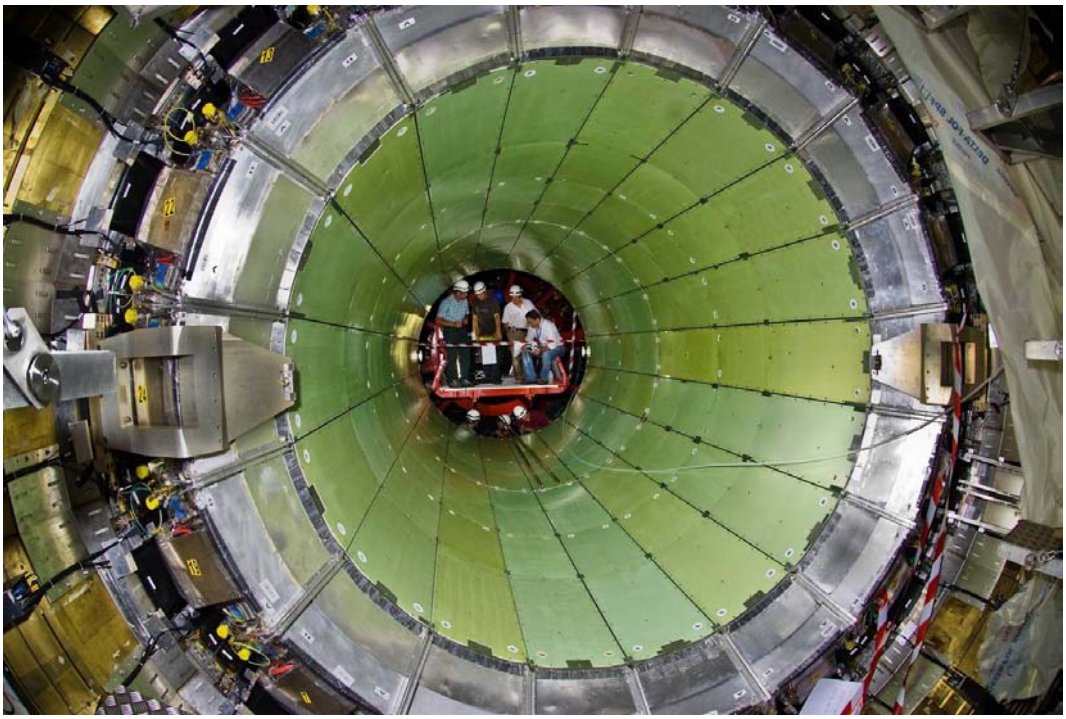

Figure 4.6: The barrel positioned inside the hadron calorimeter.

Figure 4.7: An endcap Dee, fully equipped with supercrystals.

4.3 Photodetectors

The photodetectors need to be fast, radiation tolerant and be able to operate in the longitudinal 4-T magnetic field. In addition, because of the small light yield of the crystals, they should amplify and be insensitive to particles traversing them (*nuclear counter effect*). The configuration of the magnetic field and the expected level of radiation led to different choices: avalanche photodiodes in the barrel and vacuum phototriodes in the endcaps. The lower quantum efficiency and internal gain of the vacuum phototriodes, compared to the avalanche photodiodes, is offset by their larger surface coverage on the back face of the crystals.

4.3.1 Barrel: avalanche photodiodes

In the barrel, the photodetectors are Hamamatsu type S8148 reverse structure (i.e., with the bulk n-type silicon behind the p-n junction) avalanche photodiodes (APDs) specially developed for the CMS ECAL. Each APD has an active area of $5\times5\,\mathrm{mm}^2$ and a pair is mounted on each crystal. They are operated at gain 50 and read out in parallel. The main properties of the APDs at gain 50 and 18°C are listed in table 4.1.

The sensitivity to the nuclear counter effect is given by the effective thickness of 6 μm, which translates into a signal from a minimum ionizing particle traversing an APD equivalent to about 100 MeV deposited in the $PbWO_4$.

Table 4.1: Properties of the APDs at gain 50 and 18°C.

Sensitive area	$5\times5\,\mathrm{mm}^2$
Operating voltage	340–430 V
Breakdown voltage - operating voltage	45 ± 5 V
Quantum efficiency (430 nm)	$75 \pm 2\%$
Capacitance	80 ± 2 pF
Excess noise factor	2.1 ± 0.2
Effective thickness	$6 \pm 0.5\ \mu$m
Series resistance	$< 10\ \Omega$
Voltage sensitivity of the gain $(1/M \cdot \mathrm{d}M/\mathrm{d}V)$	$3.1 \pm 0.1\%$/V
Temperature sensitivity of the gain $(1/M \cdot \mathrm{d}M/\mathrm{d}T)$	$-2.4 \pm 0.2\%/^\circ$C
Rise time	< 2 ns
Dark current	< 50 nA
Typical dark current	3 nA
Dark current after 2×10^{13} n/cm^2	$5\ \mu$A

For ECAL acceptance each APD was required to be fully depleted and to pass through a screening procedure involving 5 kGy of ^{60}Co irradiation and 1 month of operation at 80°C. Each APD was tested to breakdown and required to show no significant noise increase up to a gain of 300. The screening and testing aimed to ensure reliable operation for 10 years under high luminosity LHC conditions for over 99% of the APDs installed in the ECAL [75]. Based on tests with hadron irradiations [76] it is expected that the dark current after such operation will have risen to about 5 μA, but that no other properties will have changed. Small samples of APDs were irradiated with a ^{251}Cf source to monitor the effectiveness of the screening procedure in selecting radiation resistant APDs.

The gain stability directly affects the ECAL energy resolution. Since the APD gain has a high dependence on the bias voltage ($\alpha_V = 1/M\mathrm{d}M/\mathrm{d}V \simeq 3.1\%/\mathrm{V}$ at gain 50), to keep this contribution to the resolution at the level of per mille, the APDs require a very stable power supply system: the stability of the voltage has to be of the order of few tens of mV. This requirement applies to all the electrical system characteristics: noise, ripple, voltage regulation and absolute precision, for short and long term periods. A custom high voltage (HV) power supply system has been designed for the CMS ECAL in collaboration with the CAEN Company [77]. To remain far from high doses of radiation, the HV system is located in the CMS service cavern, some 120 m away from the detector. The HV channels are floating and use sense wires to correct for variations in the voltage drop on the leads. The system is based on a standard control crate (SY1527) hosting 8 boards expressly designed for this application (A1520E). The SY1527 integrate a PC capable of communicating with the board controller via an internal bus and different interfaces are available to integrate the SY1527 on the ECAL detector control system (DCS). The board design is based on a modular concept so that each HV channel is implemented on a separate module and up to 9 channels can be hosted on a single A1520E board. Each channel can give a bias voltage to 50 APD pairs from 0 to 500 V with maximum current of 15 mA. In total, there are 18 crates and 144 boards. Temperature

2008 JINST 3 S08004

drift compensation is possible due to the presence on the crate of temperature probes that can be used to monitor the environment temperature for adjustments of the voltage setting.

The operating gain of 50 requires a voltage between 340 and 430 V. The APDs are sorted according to their operating voltage into bins 5 V wide, and then paired such that each pair has a mean gain of 50. Each pair is mounted in parallel in a *capsule*, a moulded receptacle with foam, which is then glued on the back of each crystal. The capsules are connected to the read-out electronics by Kapton flexible printed circuit boards of variable length, dictated by the capsule's position within the submodule. Each capsule receives the bias voltage through an RC filter network and a protection resistor.

One 100 kΩ negative temperature coefficient thermistor from Betatherm, used as temperature sensor, is embedded in every tenth APD capsule. There are twenty-two different types of capsules, differing by the Kapton length and by the presence of the thermistor.

4.3.2 Endcap: vacuum phototriodes

In the endcaps, the photodetectors are vacuum phototriodes (VPTs) (type PMT188 from National Research Institute Electron in St. Petersburg). Vacuum phototriodes are photomultipliers having a single gain stage. These particular devices were developed specially for CMS [78] and have an anode of very fine copper mesh (10 μm pitch) allowing them to operate in the 4-T magnetic field. Each VPT is 25 mm in diameter, with an active area of approximately 280 mm^2; one VPT is glued to the back of each crystal. One Betatherm thermistor is embedded into each supercrystal. The VPTs have a mean quantum efficiency of the bialkali photocathode (SbKCs) of 22% at 430 nm, and a mean gain of 10.2 at zero field. When placed in a strong axial magnetic field, the response is slightly reduced and there is a modest variation of response with the angle of the VPT axis with respect to the field over the range of angles relevant to the CMS endcaps (6° to 26°). The mean response in a magnetic field of 4 T, with the VPT axis at 15° to the field direction, is typically $> 90\%$ of that in zero field [79].

All VPTs are tested by the manufacturer before delivery, without an applied magnetic field. All VPTs are also tested on receipt by CMS to determine their response as a function of magnetic field up to 1.8 T. Each device is measured at a set of angles with respect to the applied field, spanning the range of angles covered by the endcaps. In addition, at least 10% of the tubes, selected at random, are also tested in a 4-T superconducting magnet, at a fixed angle of 15°, to verify satisfactory operation at the full field of CMS.

The estimated doses and particle fluences for 10 years of LHC operation are 0.5 kGy and 5×10^{13} n/cm^2 at the outer circumference of the endcaps and 20 kGy and 7×10^{14} n/cm^2 at $|\eta| = 2.6$. Sample faceplates from every glass production batch were irradiated with a ^{60}Co source to 20 kGy. The faceplates were required to show a transmission loss, integrated over the wavelength range corresponding to $PbWO_4$ emission, of less than 10%. Irradiation of VPTs in a nuclear reactor to 7×10^{14} n/cm^2 showed a loss in anode sensitivity entirely consistent with discolouration of the faceplate caused by the accompanying gamma dose (100 kGy) [80]. Irradiations of tubes biased to the working voltage, with both gammas and neutrons showed no adverse effects, apart from an increase in anode current, attributable to the production of Cerenkov light in the faceplates.

2008 JINST 3 S08004

The VPTs are operated with the photocathode at ground potential and the dynode and anode biased at +600 V and +800 V respectively. The high voltage system is based (like the APD system) on CAEN SY1527 standard control crates, although for the VPTs, the crates are equipped with standard 12-channel A1735P boards, each channel rated at 1.5 kV and 7 mA. At the operating bias, the VPT gain is close to saturation thus the voltages do not have to be controlled very precisely. However, care must be taken to minimise ripple and noise, since these would feed directly into the input of the sensitive preamplifier that is connected to the anode. Filtering is achieved with RC networks mounted inside the supercrystals (SC), close to the VPTs. An entire endcap is biased using one SY1527 crate equipped with just two A1735P boards. On each board, only eight of the twelve output channels will initially be used, leaving four spare channels. The spare outputs may be used at a later stage, if noisy channels develop which can be recovered by operating at a lower bias voltage. The HV from the CAEN power supplies is transmitted to the SCs via a custom designed HV distribution system which provides hard-wired protection against over-voltage and over-current, and sensitive current monitoring. For each endcap, this system is housed in five crates. Each crate hosts up to five input cards, receiving the HV from the power supplies, and up to six output cards, with each output card serving up to twelve SCs. The HV supplies and distribution system are mounted in two racks (one for each endcap) located in the Service Cavern. Each SC is served by two coaxial cables (one for the anode, one for the dynode) running from the Service Cavern to the detector, via intermediate patch panels. The total cable length is approximately 120 m and the cable capacitance forms part of the filter network. Inside an SC the HV is distributed to the VPTs via five filter cards, each serving five VPTs. The spread in anode sensitivity among the VPTs is 25% (RMS). They are therefore sorted into six groups which are distributed on the endcaps with the highest sensitivities at the outer circumference grading to the lowest sensitivities at the inner circumference. This arrangement provides a roughly constant sensitivity to the transverse energy across the endcaps.

The anode sensitivity of a VPT may show a dependence on count rate (anode current) under certain conditions. For example, in the absence of a magnetic field, if the count rate falls to a few Hz, following a period of high rate operation, the anode sensitivity may rise suddenly and take several hours to return to the nominal value. The magnitude of the effect may vary from a few percent to a few tens of percent. In the presence of a strong magnetic field (as in normal CMS operation), the effect is strongly suppressed or absent. Nevertheless, it has been judged prudent to incorporate a light pulser system on the ECAL endcaps. This delivers a constant background rate of at least 100 Hz of pulses of approximately 50 GeV equivalent energy to all VPTs, thus ensuring that they are kept “active”, even in the absence of LHC interactions.

The system consists of a control and trigger unit located in the Service Cavern, and sets of pulsed light sources mounted on the circumference of each Dee. The light is produced by Luxeon III light emitting diodes (type LXHL-PR09), whose peak emission wavelength is 455 nm. The LEDs are driven by high output current op-amps (LT6300 from Linear Technology). The drive pulses have amplitudes of 1.2 A and a widths of 80 ns. A single light source consists of a cluster of seven LEDs and associated drive-circuits. These are configured singly or in pairs, with the drive-circuits and LEDs mounted on double-sided printed circuit boards housed within metal enclosures. There are four such enclosures distributed around the circumference of each Dee, housing 19 light sources. A schematic representation of the system for distributing the light pulses is shown in figure 4.8.

2008 JINST 3 S08004

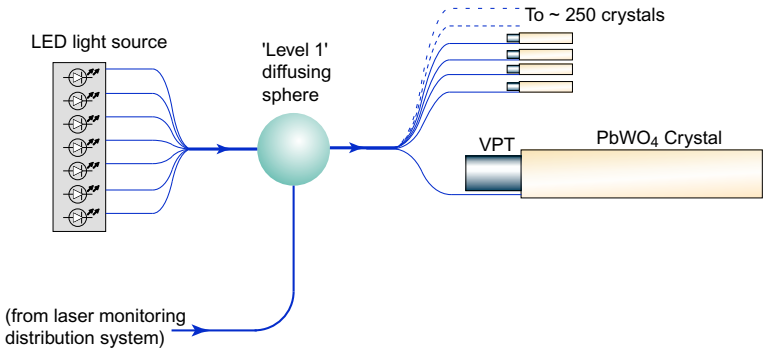

Figure 4.8: Distribution system for VPT stabilisation light pulses.

An all-silica optical fibre (CF01493-43 from OFS (Furukawa)) is inserted into a hole drilled into the lens of each LED and collects light by *proximity focusing*. The seven fibres from a given light source are combined into a single bundle that transports light to a diffusing sphere which has a dual role, acting also as part of the distribution network of the laser monitoring system. Light from each diffusing sphere is distributed to up to 220 individual detector channels through the set of optical fibres that also carry the laser monitoring pulses. Light is injected via the rear face of a crystal, which carries the VPT, and reaches the VPT via reflection from the front of the crystal. The system is synchronized to pulse during a fraction of the 3 μs abort gaps that occur during every 89 μs cycle of the LHC circulating beams.

4.4 On-detector electronics

The ECAL read-out has to acquire the small signals of the photo-detectors with high speed and precision. Every bunch crossing digital sums representing the energy deposit in a trigger tower are generated and sent to the trigger system. The digitized data are stored during the Level-1 trigger latency of $\approx 3\,\mu$s.

The on-detector electronics has been designed to read a complete trigger tower (5×5 crystals in $\eta \times \phi$) or a super-crystal for EB and EE respectively. It consists of five Very Front End (VFE) boards, one Front End (FE) board, two (EB) or six (EE) Gigabit Optical Hybrids (GOH), one Low Voltage Regulator card (LVR) and a motherboard.

The motherboard is located in front of the cooling bars. It connects to 25 photo-detectors and to the temperature sensors using Kapton flexible printed circuit boards and coaxial cables for EB and EE respectively. In the case of the EB the motherboard distributes and filters the APD bias voltage. Two motherboards are connected to one CAEN HV supply located at a distance of about 120 m with remote sensing. In the case of the EE the operating voltages for the VPTs are distributed and filtered by a separate HV filter card, hosting as well the decoupling capacitor for the anode signals. Five of these cards serving five VPTs each are installed into each super-crystal. One LVR and five VFE cards plug into the motherboard.

Each LVR card [81] uses 11 radiation-hard low voltage regulators (LHC4913) developed by ST-microelectronics and the RD49 project at CERN. The regulators have built in over-temperature

2008 JINST 3 S08004

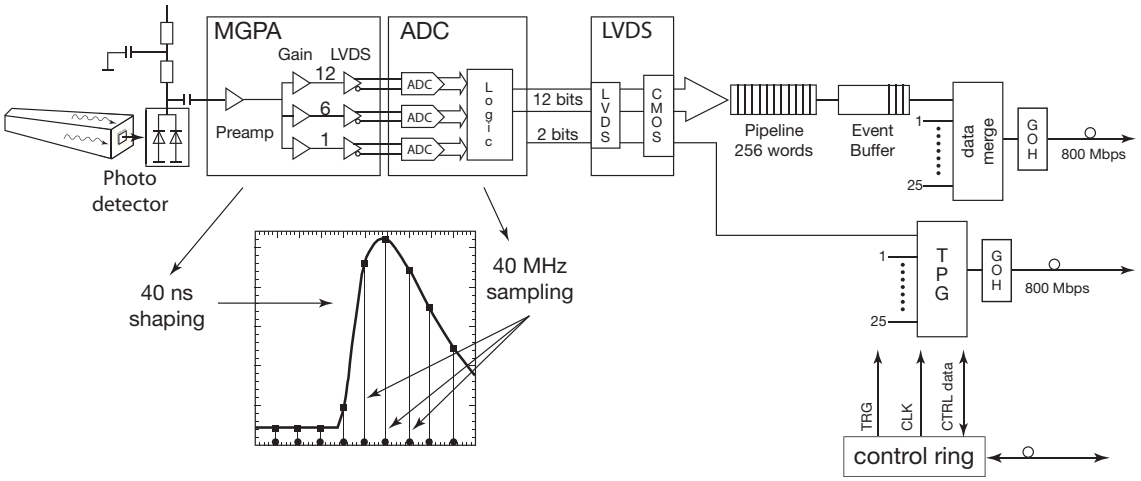

Figure 4.9: Schematic view of the on-detector electronics: the scintillation light is collected by photodetectors (in the figure the case of APD is presented), the signal is shaped by a Multi-Gain Pre-Amplifier and digitized by 40-MHz ADC; a radiation-hard buffer (LVDS) adapts the ADC output to the FE card, where data pipeline and Trigger Primitives Generation (TPG) are performed; trigger words are sent at 25 ns rate, while data are transmitted on receipt of a Level-1 trigger; GOHs provide in both cases the data serializer and the laser diode, sending the signals on a fibre to the off-detector electronics over a distance of about 100 m. A control token ring connects groups of FE cards, providing Level-1 trigger (TRG) and clock (CLK) signals, together with control data in and out (CTRL data).

protection, output current limitation and an inhibit input. The output voltages of 2.5 V are distributed to the FE card and via the motherboard to the VFE cards. Three Detector Control Unit (DCU) ASICs on each LVR card, interfaced to the FE card, monitor all input and output voltages. All regulators, excluding the one providing power to the control interface of the FE card, can be powered down remotely by an external inhibit. Four LVR cards are connected by a passive low voltage distribution (LVD) block to one radiation and magnetic field tolerant Wiener low voltage power supply located about 30 m away in racks attached to the magnet yoke.

The signals are pre-amplified and shaped and then amplified by three amplifiers with nominal gains of 1, 6 and 12. This functionality is built into the Multi Gain Pre-Amplifier (MGPA) [82], an ASIC developed in 0.25 μm technology. The full scale signals of the APDs and VPTs are 60 pC and 12.8 pC corresponding to $\approx$ 1.5 TeV and 1.6–3.1 TeV for EB and EE respectively. The shaping is done by a CR-RC network with a shaping time of $\approx$ 40 ns. The MGPA has a power consumption of 580 mW at 2.5 V. The output pulse non-linearity is less than 1%. The noise for gain 12 is about 8000 e^- for the APD configuration and about 4000 e^- for the VPT configuration. The MGPA contains three programmable 8-bit DACs to adjust the baseline to the ADC inputs. An integrated test-pulse generator with an amplitude adjustable by means of an 8-bit DAC allows a test of the read-out electronics over the full dynamic range.

A schematic view of the signal read-out is given in figure 4.9. The 3 analog output signals of the MGPA are digitized in parallel by a multi-channel, 40-MHz, 12-bit ADC, the AD41240 [83], developed in 0.25 μm technology. It has an effective number of bits of 10.9. An integrated logic

selects the highest non-saturated signal as output and reports the 12 bits of the corresponding ADC together with two bits coding the ADC number.

If the read-out switches to a lower gain as the pulse grows, it is prevented from immediately reverting to the higher gain when the pulse falls: once the pulse has declined to the point where it could be read out at the higher gain again, the read-out is then forced to continue reading out at the lower gain for the next five samples.

A radiation-hard buffer (LVDS_RX) developed in 0.25 μm technology, adapts the low voltage differential output signals of the AD41240 to the single ended CMOS inputs on the FE card. Five identical read-out channels are integrated into a VFE card, together with a Detector Control Unit (DCU) for the measurement of the APD leakage currents and the read-out of the thermistors. The noise obtained with the VFE cards installed into supermodules is typically 1.1, 0.75 and 0.6 ADC counts for gains 12, 6 and 1 respectively. This corresponds to ≈ 40 MeV for gain 12.

The FE card [84] stores the digitized data during the Level-1 trigger latency in 256-word-deep dual-ported memories, so called pipelines. Five such pipelines and the logic to calculate the energy sum of the 5 channels once every bunch crossing are integrated into an ASIC developed in 0.25 μm technology called FENIX. Each VFE card is serviced by a FENIX chip. Thus the energy is summed in strips of 5 crystals along ϕ. In the case of the EE the five strip sums are transmitted by five GOHs (see below) to the off-detector electronics Trigger Concentrator Card (TCC), while in the case of the EB a sixth FENIX sums the five strip sums and calculates the "fine-grain" electromagnetic bit, set to identify electromagnetic shower candidates on the basis of the energy profile of the trigger tower. The trigger tower energy sum together with the fine-grain bit is transmitted using one GOH to the TCC. On receipt of a Level-1 trigger the corresponding data, ten 40-MHz samples per channel, are transmitted in $\approx 7.5\,\mu$s to the off-detector electronics Data Concentrator Card (DCC) using an identical GOH. The Clock and Control Unit (CCU) ASIC together with the LVDS_MUX ASIC provide the interface to the token rings.

The ECAL serial digital data links are based on the technology developed for the CMS Tracker analog links (section 3.3). The GOH consists of a data serializer and laser driver chip, the GOL, and a laser diode with an attached fibre pigtail. Fibres, fibre interconnections and a 12-channel NGK receiver module complete the optical link system. It uses single mode fibres operating at 1310 nm wavelength over a distance of about 100 m. The fibre attenuation of ≈ 0.04 dB is negligible. The optical links are operated at 800 Mbit/s.

The VFE and FE electronics are controlled using a 40-MHz digital optical link system, controlled by the off-detector Clock and Control System (CCS) boards. A 12-fibre ribbon is connected to the token ring link board, generating an electrical control ring, the token ring. Each supermodule has 8 token rings which connect to groups of eight to ten FE cards including the two FE cards of the laser monitoring electronics module (MEM). The system has redundancy, as long as there are no two consecutive FE cards malfunctioning, by means of two independent bi-directional optical links, using 4 fibres each. It provides fast and slow control functions. While the fast control transmits the level one trigger information and the 40-MHz clock, the slow control comprises the configuration of the FE and VFE electronics as well as the read-out of status information, temperatures, voltages and APD leakage currents.

2008 JINST 3 S08004

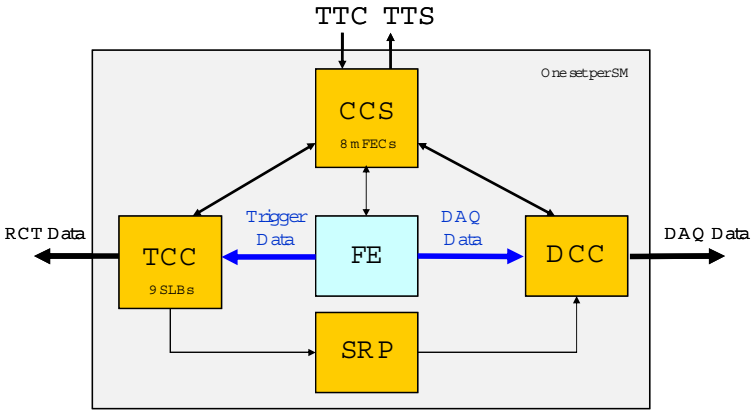

Figure 4.10: Schematic view of ECAL off-detector electronics.

4.5 Off-detector electronics

4.5.1 Global architecture

The ECAL off-detector read-out and trigger architecture [85, 86] is illustrated schematically in figure 4.10. The system is composed of different electronic boards sitting in 18 VME-9U crates (the CCS, TCC and DCC modules) and in 1 VME-6U crate (the selective read-out processor, SRP, system). The system serves both the DAQ and the trigger paths. In the DAQ path, the DCC performs data read-out and data reduction based on the selective read-out flags computed by the SRP system. In the trigger path, at each bunch crossing, trigger primitive generation started in the FE boards is finalized and synchronized in the TCC before transmission to the regional calorimeter trigger.

The clock and control system (CCS) board distributes the system clock, trigger and broadcast commands, configures the FE electronics and provides an interface to the trigger throttling system. The TTC signals are translated and encoded by suppression of clock edges and sent to the *mezzanine* Front End Controller cards (mFEC). The mFEC interfaces optically with a FE token ring. The 8 mFECs of the CCS board control a supermodule.

The trigger concentration card (TCC) [87] main functionalities include the completion of the trigger primitive generation and their transmission to the synchronization and link board (SLB) mezzanines [88] at each bunch crossing, the classification of each trigger tower and its transmission to the Selective Read-out Processor at each Level-1 trigger accept signal, and the storage of the trigger primitives during the Level-1 latency for subsequent reading by the DCC.

Each TCC collects trigger data from 68 FE boards in the barrel, corresponding to a supermodule, and from 48 FE boards in the endcaps corresponding to the inner or outer part of a 20° ϕ sector. In the endcaps, trigger primitive computation is completed in the TCCs, which must perform a mapping between the collected pseudo-strips trigger data from the different supercrystals and the associated trigger towers. The encoded trigger primitives (8 bits for the nonlinear representation of the trigger tower E_T plus the fine-grain bit) are time aligned and sent to the regional trigger processors by the SLB. The trigger primitives are stored in the TCC during the Level-1 latency for subsequent reading by the DCC. In the barrel region a single TCC is interfaced with 1 DCC. In the endcap region, a DCC serves 4 TCCs covering a 40° sector.

2008 JINST 3 S08004

The data concentration card (DCC) [89, 90] is responsible for collecting crystal data from up to 68 FE boards. Two extra FE links are dedicated to the read-out of laser monitoring data (PN diodes). The DCC also collects trigger data transmitted from the TCC modules and the selective read-out flags transmitted from the SRP system. A data suppression factor near 20 is attained using a programmable selective read-out algorithm. When operating in the selective read-out mode the SRP flags indicate the level of suppression that must be applied to the crystal data of a given FE read-out. For the application of zero suppression, time samples pass through a finite impulse response filter with 6 consecutive positions and the result is compared to a threshold. If any time sample of the 6 has been digitized at a gain other than the maximum, then zero suppression is not applied to the channel.

Data integrity is checked, including verification of the event-fragment header, in particular the data synchronization check, verification of the event-fragment word count and verification of the event-fragment parity bits. Identified error conditions, triggered by input event-fragment checks, link errors, data timeouts or buffer memory overflows are flagged in the DCC error registers and incremented in associated error counters. Error conditions are flagged in the DCC event header.

Input and output memory occupancy is monitored to prevent buffer overflows. If a first occupancy level is reached, the Trigger Throttling System (TTS) signal *Warning Overflow* is issued, requesting a reduction of the trigger rate. In a second level a TTS signal *Busy* inhibits new triggers and empty events (events with just the header words and trailer) are stored. DCC events are transmitted to the central CMS DAQ using a S-LINK64 data link interface at a maximum data rate of 528 MB/s, while an average transmission data flow of 200 MB/s is expected after ECAL data reduction. Laser triggers (for crystal transparency monitoring) will occur with a programmable frequency and synchronously with the LHC gap. No data reduction is applied for these events, which are read-out following a TTC test enable command. A VME memory is used for local DAQ, allowing VME access to physics events and laser events in spy mode.

The selective read-out processor (SRP) [91] is responsible for the implementation of the selective read-out algorithm. The system is composed by a single 6U-VME crate with twelve identical algorithm boards (AB). The AB computes the selective read-out flags in different calorimeter partitions. The flags are composed of 3 bits, indicating the suppression level that must be applied to the associated read-out units.

4.5.2 The trigger and read-out paths

The ECAL data, in the form of trigger primitives, are sent to the Level-1 calorimeter trigger processor, for each bunch crossing. The trigger primitives each refer to a single trigger tower and consist of the summed transverse energy deposited in the tower, and the fine-grain bit, which characterizes the lateral profile of the electromagnetic shower. The accept signal, for accepted events, is returned from the global trigger in about $3\mu s$. The selected events are read out through the data acquisition system to the Filter Farm where further rate reduction is performed using the full detector data.

The read-out system is structured in sets of 5×5 crystals. The FE card stores the data, in 256-clock cycles deep memory banks, awaiting a Level-1 trigger decision during at most 128 bunch crossings after the collision occurred. It implements most of the Trigger Primitives Generation (TPG) pipeline (section 4.5.3).

2008 JINST 3 S08004

In the barrel, these 5×5 crystal sets correspond to the trigger towers. Each trigger tower is divided into 5 ϕ-oriented strips, whose energy deposits are summed by the FE board trigger pipeline to give the total transverse energy of the tower, called the main trigger primitive. Each FE is served by two optical links for sending the data and trigger primitives respectively and a third electrical serial link which transmits the clock, control and Level-1 trigger signals.

In the endcaps, the read-out modularity maps onto the 5×5 mechanical units (supercrystals). However the sizes of the trigger towers vary in order to approximately follow the η, ϕ geometry of the HCAL and Level-1 trigger processor. The supercrystals are divided into groups of 5 contiguous crystals. These groups are of variable shape and referred to as pseudo-strips. The trigger towers are composed of several pseudo-strips and may extend over more than one supercrystal. Since the read-out structure does not match the trigger structure, only the pseudo-strip summations are performed on the detector. The total transverse energy of the trigger tower is computed by the off-detector electronics. Hence, each endcap FE board is served by 6 optical links, 5 of them being used to transmit the trigger primitives. As in the barrel an electrical serial link transmits the clock, control and Level-1 trigger signals.

After time alignment the ECAL trigger primitives are sent at 1.2 Gb/s to the regional calorimeter trigger, via 10-m-long electrical cables, where together with HCAL trigger primitives, the electron/photon and jets candidates are computed as well as the total transverse energy.

4.5.3 Algorithms performed by the trigger primitive generation

The TPG logic implemented on the FE boards combines the digitized samples delivered by the VFE boards to determine the trigger primitives and the bunch crossing to which they should be assigned. The logic must reconstruct the signal amplitude to be assigned to each bunchcrossing from the continuous stream of successive digitizations.

The TPG logic is implemented as a pipeline, operated at the LHC bunch crossing frequency. The trigger primitives are delivered to the regional calorimeter trigger after a constant latency of 52 clock cycles, of which 22 are used for transmission over the optical fibres and cables. The signal processing performed in the VFE and FE barrel electronics has a total duration of only 17 clock cycles. The remaining part of the latency is mainly due to formatting and time alignment of the digital signals. Ideally, the output of this processing should be a stream of zeroes, unless there is a signal in the tower resulting from a bunch crossing exactly 17 clock cycles before. In this case the output is a word encoding the summed transverse energy in the tower together with the fine-grain bit. The endcap pipeline is split between the on-detector and off-detector electronics and implements very similar algorithms. The trigger primitives are expected to be delivered to the regional calorimeter trigger in 50 clock cycles in the endcap case.

4.5.4 Classification performed by the selective read-out

About 100 kB per event has been allocated for ECAL data. The full ECAL data for an event, if all channels are read out, exceeds this target by a factor of nearly 20. Reduction of the data volume, *selective read-out*, can be performed by the Selective Read-out Processor [86, 91] so that the suppression applied to a channel takes account of energy deposits in the vicinity. For the measure of the energy in a region, the trigger tower sums are used. In the barrel the read-out

2008 JINST 3 S08004

modularity corresponds exactly to the 5×5-crystal trigger towers. In the endcap, the situation is more complex. The simplified and illustrative description below is given for the barrel case.

The selective read-out algorithm classifies the trigger towers of the ECAL into 3 classes using the Level-1 trigger primitives. The energy deposited in each trigger tower is compared to 2 thresholds. Trigger towers with an energy above the higher threshold are classified as high interest trigger towers, those with an energy between the 2 thresholds as medium interest, and those with an energy below the lower threshold as low interest trigger towers.

These classifications can be used flexibly to implement a range of algorithms by using different thresholds to define the classes, and different suppression levels for the read-out of the channels within each class. The algorithm currently used in the simulation provides adequate data reduction even at high luminosity. The algorithm functions as follows: if a trigger tower belongs to the high interest class ($E_{\mathrm{T}} > 5\,\mathrm{GeV}$) then the crystals of this trigger tower and of its neighbour trigger towers (225 crystals in total in the barrel case) are read with no zero suppression. If a trigger tower belongs to the medium interest class ($E_{\mathrm{T}} > 2.5\,\mathrm{GeV}$), then the crystals of this trigger tower (25 crystals in the barrel case) are read with no suppression. If a trigger tower belongs to the low interest class and it is not the neighbour of a high interest trigger tower, then the crystals in it are read with zero suppression at about $3\sigma_{\mathrm{noise}}$.

For debugging purposes, the selective read-out can be deactivated and either a global zero suppression (same threshold for every channel) or no zero suppression applied. Even when the selective read-out is not applied the selective read-out flags are inserted into the data stream and can be used offline for debugging purposes.

4.6 Preshower detector

The principal aim of the CMS Preshower detector is to identify neutral pions in the endcaps within a fiducial region $1.653 < |\eta| < 2.6$. It also helps the identification of electrons against minimum ionizing particles, and improves the position determination of electrons and photons with high granularity.

4.6.1 Geometry

The Preshower is a sampling calorimeter with two layers: lead radiators initiate electromagnetic showers from incoming photons/electrons whilst silicon strip sensors placed after each radiator measure the deposited energy and the transverse shower profiles. The total thickness of the Preshower is 20 cm.

The material thickness of the Preshower traversed at $\eta = 1.653$ before reaching the first sensor plane is $2\,X_0$, followed by a further $1\,X_0$ before reaching the second plane. Thus about 95% of single incident photons start showering before the second sensor plane. The orientation of the strips in the two planes is orthogonal. A major design consideration is that all lead is covered by silicon sensors, including the effects of shower spread, primary vertex spread etc. For optimum Level-1 trigger performance the profile of the outer edge of the lead should follow the shape of the ECAL crystals behind it. For the inner radius the effect of the exact profiling of the lead is far less

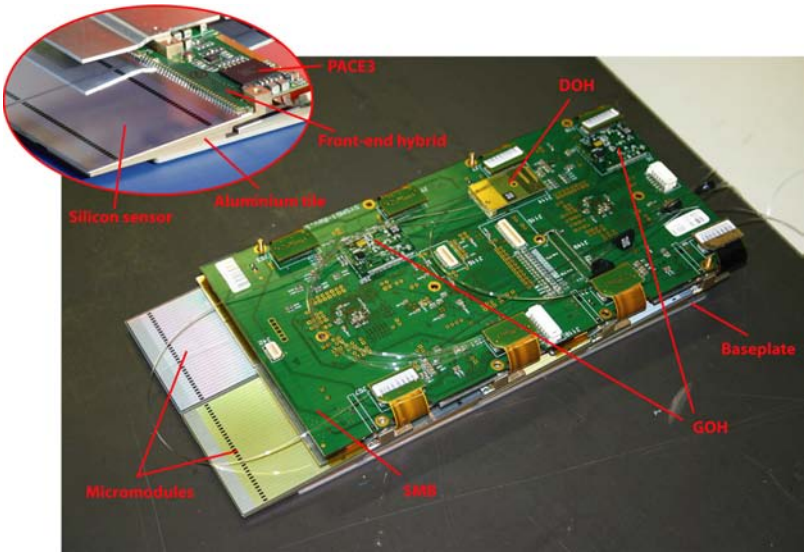

Figure 4.11: Photograph of a complete type-1 ladder, with an inset showing details of a micromodule.

critical, and thus a circular shape has been chosen. The lead planes are arranged in two Dees, one on each side of the beam pipe, with the same orientation as the crystal Dees.

Each silicon sensor measures $63\times63\,\mathrm{mm}^2$, with an active area of $61\times61\,\mathrm{mm}^2$ divided into 32 strips (1.9 mm pitch). The nominal thickness of the silicon is $320\,\mu$m; a minimum ionizing particle (MIP) will deposit 3.6 fC of charge in this thickness (at normal incidence). The sensors are precisely glued to ceramic supports, which also support the front-end electronics assembly (see below), and this is in turn glued to an aluminium tile that allows a 2 mm overlap of the active part of the sensors in the direction parallel to the strips. In order to improve noise performance the tile is constructed in two parts, with a glass fibre insulation in between. The combination of sensor + front-end electronics + supports is known as a micromodule.

The micromodules are placed on baseplates in groups of 7, 8 or 10 that, when coupled to an electronics system motherboard (SMB) placed above the micromodules, form a ladder. The spacing between silicon strips (at the edges) in adjacent micromodules within a ladder is 2.4 mm, whilst the spacing between strips in adjacent ladders is normally 2.5 mm. For the region where the two Dees join this spacing is increased to 3.0 mm.

Figure 4.11 shows a complete ladder (*Type-1* for 8 micromodules) and an inset shows the micromodule.

The ladders are attached to the radiators in an *x*-*y* configuration. Around 500 ladders are required, corresponding to a total of around 4 300 micromodules and 137 000 individual read-out channels. Further details of the layout can be found in [92].

4.6.2 Preshower electronics

Each silicon sensor is DC-coupled to a front-end ASIC (PACE3 [93]) that performs preamplification, signal shaping and voltage sampling. Data is clocked into an on-chip high dynamic range 192-cell deep analogue memory at 40 MHz.

For each Level-1 trigger received, 3 consecutive cells of the memory, corresponding to time samples on the baseline, near the peak and after the peak, are read out for all 32 channels through a 20 MHz multiplexer. The PACE3 has a switchable gain:

- Low gain: For normal physics running with a large dynamic range (0-1600 fC) with a S/N of around 3 for a single MIP;
- High gain: For MIP calibration purposes [94], with a reduced dynamic range (0-200 fC) but with a S/N approaching 10 for a single MIP.

The PACE3 are soldered to front-end hybrids that contain embedded polyimide cables to connect to the SMBs. The SMBs contain AD41240 12-bit ADCs that digitize the data from 1 or 2 PACE3. The digital data are then formatted and packaged by a second Preshower ASIC known as the K-chip [95]. The K-chip also performs synchronization checks on the data, adds bunch/event counter information to the data packets and transmits the data to the Preshower-DCC (see below) via gigabit optical hybrids (GOH). The SMB also contains an implementation of the CMS tracker control system.

Groups of up to 12 ladders are connected via polyimide cables to form control rings. Off-detector CCS cards (identical to those of the ECAL except not all FEC mezzanines are mounted for the Preshower) communicate via digital optical hybrids (DOH) mounted on 2 of the SMBs in each control ring. The full Preshower comprises 4 planes of 12 control rings each.

The Preshower-DCC [96] is based on the DCC of the ECAL except it is a modular design incorporating a VME host board mounted with optoRx12 [97] mezzanines. The modular design has allowed a development collaboration with the TOTEM experiment which uses the same components but in a different manner. The optoRx12 incorporates an NGK 12-way optical receiver and an Altera Stratix GX FPGA that performs data deserialization, pedestal subtraction, common-mode noise reduction, bunch crossing assignment, charge reconstruction and zero suppression [98]. The sparsified data from up to 3 optoRx12 are merged by another FPGA on the host board that then transmits data packets to the event builder via an Slink64 interface. The host board also provides data spying as well as TTC and VME interfaces. A provision has been made on the host board to allow the plug-in of an additional mezzanine board mounted with FPGAs/processors that could provide more data reduction power if necessary in the future.

4.7 ECAL detector control system

The ECAL Detector Control System (DCS) comprises the monitoring of the detector status, in particular various kinds of environmental parameters, as well as the ECAL safety system (ESS), which will generate alarms and hardwired interlocks in case of situations which could lead to damaging the detector hardware. It consists of the following sub-systems: ECAL Safety System (ESS), Precision Temperature Monitoring (PTM), Humidity Monitoring (HM), High Voltage (HV), Low Voltage (LV) and monitoring of the laser operation, the cooling system and of the parameters (temperatures in capsules, temperatures on the printed circuit boards, APD leakage currents) read out by the DCUs on the VFE and LVR boards. Further details on the ECAL DCS are available [99].

2008 JINST 3 S08004

The whole DCS software is based on the commercial SCADA package PVSS II (chapter 9). A distributed system is built out of several applications dedicated to the DCS sub-systems. Every application is implemented as a Finite State Machine (FSM) and linked to a supervisory level, which summarizes the overall ECAL DCS status and itself incorporates a FSM. Finally, this ECAL DCS supervisor is linked to the general CMS DCS supervisory node, in order to communicate the status and alarms and to receive commands which are propagated down to the relevant sub-systems.

4.7.1 Safety system

The purpose of the ESS [100] is to monitor the air temperature of the VFE and FE environment (expected to be around 25–30°C) and the water leakage detection cable, which is routed inside the electronics compartment, to control the proper functioning of the cooling system and to automatically perform pre-defined safety actions and generate interlocks in case of any alarm situation. One pair of temperature sensors is placed at the centre of each module. The read-out system, with full built-in redundancy, is independent of the DAQ and control links and based on a Programmable Logic Controller (PLC) situated in the Service Cavern. In case of any critical reading hardwired interlock signals will be routed to the relevant crates in order to switch off the HV and LV and/or the cooling PLC in order to stop the water flow on a certain cooling line. The proper functioning of the ESS PLC itself is monitored by the general CMS detector safety system.

4.7.2 Temperature

The number of scintillation photons emitted by the crystals and the amplification of the APD are both temperature dependent, as described in section 4.2. Therefore a major task for the ECAL DCS is the monitoring of the system's temperature and the verification that the required temperature stability of (18 ± 0.05)°C of the crystal volume and the APDs is achieved. The PTM is designed to read out thermistors, placed on both sides of the crystal volume, with a relative precision better than 0.01°C. In total there are ten sensors per supermodule. Two immersion probes measure the temperature of the incoming and outgoing cooling water, whereas two sensors per module, one on the grid and one on the thermal screen side of the crystal volume, monitor the crystal temperature. The read-out is based on the Embedded Local Monitoring Board (ELMB) developed by ATLAS which functions completely independently of the DAQ and control links. In addition, sensors fixed to the back surface of every tenth crystal in the barrel, and one in 25 crystals in the endcap, are read out by the DCUs placed on the VFE boards. With this temperature monitoring it has been shown that the water cooling system can indeed ensure the required temperature stability [74].

4.7.3 Dark current

The APD dark current will increase during CMS operation due to bulk damage of the silicon structure by neutrons. Part of this damage anneals, but the overall effect will be an increase in electronics noise, due to an increasing dark current, over the lifetime of the detector. The dark current of all APD channels will be continuously monitored.

2008 JINST 3 S08004

4.7.4 HV and LV

The DCS system operates the CAEN HV system via an OPC server. The functionalities include the independent configuration of the HV channels with various set of voltages, the monitor of the voltage and the current delivered by each channel and the database recording of the settings. The ECAL Safety System can switch off the HV via the individual board interlocks.

The ECAL amplification and digitization electronics located on the VFE electronics cards require a very stable low voltage to maintain constant signal amplification. The system uses Low Voltage Regulators that guarantee the required stability of the signal amplification. The Low Voltage Regulator Boards are equipped with DCUs that measure the voltages and these measurements are read via the Token Ring. Overall the power is supplied by MARATON crates (WIENER), which are operated and monitored by the DCS.

4.8 Detector calibration

Calibration is a severe technical challenge for the operation of the CMS ECAL. Many small effects which are negligible at low precision need to be treated with care as the level of precision of a few per mille is approached. ECAL calibration is naturally seen as composed of a global component, giving the absolute energy scale, and a channel-to-channel relative component, which is referred to as intercalibration. The essential issues are uniformity over the whole ECAL and stability, so that showers in different locations in the ECAL in data recorded at different times are accurately related to each other.

The main source of channel-to-channel response variation in the barrel is the crystal-to-crystal variation of scintillation light yield which has an RMS of $\approx 8\%$ within most supermodules, although the total variation among all barrel crystals is $\approx 15\%$. In the endcap the VPT signal yield, the product of the gain, quantum efficiency and photocathode area, has an RMS variation of almost 25%. Preliminary estimates of the intercalibration coefficients are obtained from laboratory measurements of crystal light yield and photodetector/electronics response [101]. Applying this information reduces the channel-to-channel variation to less than 5% in the barrel and less than 10% in the endcaps.

All 36 supermodules were commissioned in turn by operating them on a cosmic ray stand for a period of about one week. A muon traversing the full length of a crystal deposits an energy of approximately 250 MeV, permitting intercalibration information to be obtained for the barrel ECAL [102]. In 2006, nine supermodules were intercalibrated with high energy electrons (90 and 120 GeV), in a geometrical configuration that reproduced the incidence of particles during CMS operation. One of the supermodules was exposed to the beam on two occasions, separated by an interval of one month. The resulting sets of inter-calibration coefficients are in close agreement, the distribution of differences having an RMS spread of 0.27%, indicating a reproducibility within the statistical precision of the individual measurements (figure 4.12).

A comparison of the cosmic ray and high energy electron data demonstrates that the precision of the cosmic ray inter-calibration is better than 1.5% over most of the volume of a supermodule, rising to just above 2% at the outer end (corresponding to $\eta \approx 1.5$). The mean value of the precision

2008 JINST 3 S08004

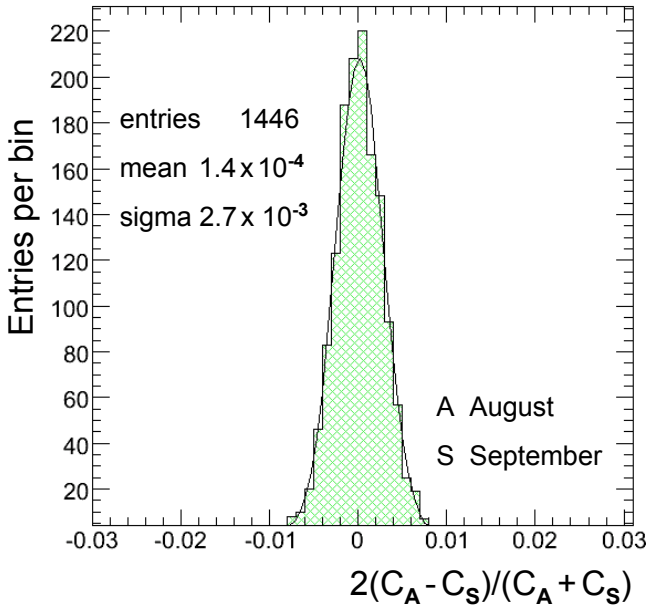

Figure 4.12: Distribution of differences of inter-calibration coefficients from a supermodule exposed to a high energy electron beam on two occasions, separated by a period of one month. The reproducibility of the intercalibration coefficients (RMS/$\sqrt{2}$) is measured to be 0.2%.

of the cosmic intercalibration, averaged over all the channels in the nine supermodules for which a comparison with electrons can be made, is 1.5% (figure 4.13).

The ultimate intercalibration precision will be achieved *in situ* with physics events. As a first step, imposing the ϕ-independence of the energy deposited in the calorimeter can be used to rapidly confirm, and possibly improve on, the start-up intercalibration within fixed η regions. The intercalibration method that has been investigated in the most detail uses the momentum of isolated electrons measured in the tracker. These electrons, mainly from $W \rightarrow e\nu$, are abundant ($\sigma \approx 20$ nb) and have a similar p_T to the photons of the benchmark channel $H \rightarrow \gamma\gamma$. A complementary method, not relying on the tracker momentum measurement, is based on $\pi^0 \rightarrow \gamma\gamma$ and $\eta \rightarrow \gamma\gamma$ mass reconstruction. Most methods of intercalibration will be local to a region of the ECAL, and a further step intercalibrating these regions to one another will be needed. This is a consequence of the significant systematic variations that occur as a function of pseudorapidity such as (or including): the large variation of the thickness of the tracker material, the variation of the structure of the ECAL (both the major differences between the barrel and endcap, and the small continuous variation of the geometry along the length of the barrel), and the variation of background characteristics for $\pi^0 \rightarrow \gamma\gamma$.

Over the period of time in which the physics events used to provide an intercalibration are taken the response must remain stable to high precision. Where there is a source of significant variation, as in the case of the changes in crystal transparency caused by irradiation and subsequent annealing, the variation must be precisely tracked by an independent measurement. The changes in crystal transparency are tracked and corrected using the laser monitoring system.

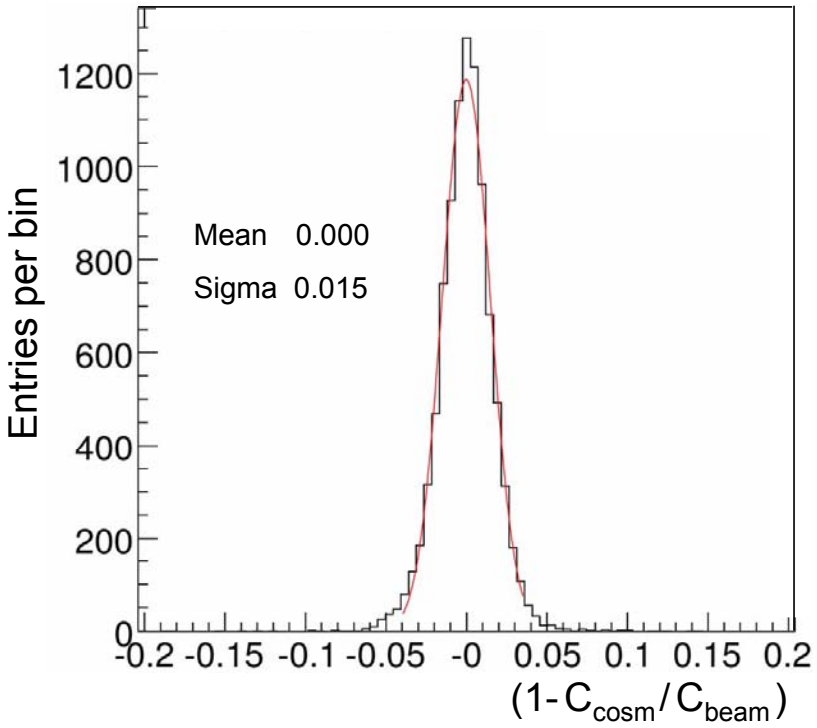

Figure 4.13: Distribution of the relative differences between the inter-calibration coefficients measured with high energy electrons and those obtained from cosmic ray muons.

The final goal of calibration is to achieve the most accurate energy measurements for electrons and photons. Different reconstruction algorithms are used to estimate the energy of different electromagnetic objects, i.e., unconverted photons, electrons and converted photons, each of them having their own correction functions. At present these "algorithmic" corrections are obtained from the simulated data by accessing the generated parameters of the Monte Carlo simulation. For some of the corrections, for example the containment corrections, this is an acceptable procedure provided that test beam data is used to verify the simulation, so that, in effect, the simulation is being used only as a means of interpolating and extrapolating from data taken in the test beam. In other cases, where the test beam provides no useful information, for example in issues related to conversions and bremsstrahlung radiation in the tracker material, it will be important to find ways of using information that can be obtained from data taken in situ with the running detector. Two particularly useful channels which can be used to obtain such information, and also assist in the step of intercalibrating regions of the ECAL to one another, are under investigation: $Z \rightarrow e^+e^-$, and $Z \rightarrow \mu^+\mu^-\gamma$ (the photon coming from inner bremsstrahlung).

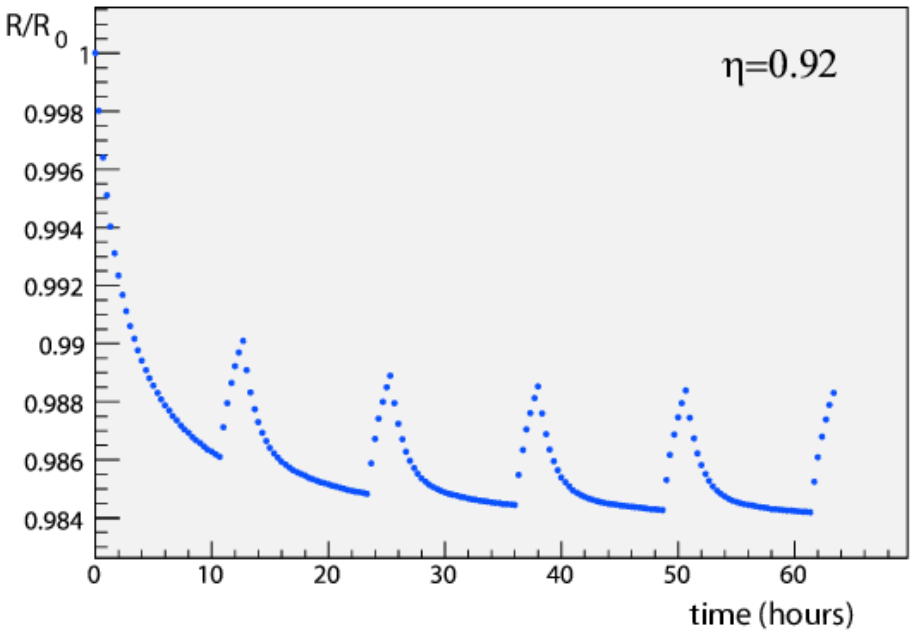

Figure 4.14: Simulation of crystal transparency evolution at LHC based on test-beam results. For this illustrative example a luminosity of $\mathscr{L} = 2 \times 10^{33}$ cm^{-2}s^{-1} was assumed, together with a machine cycle consisting of a 10 hour coast followed by 2 hours filling time. The crystal behaviour under irradiation was modeled on data taken during a crystal irradiation in the test beam.

4.9 Laser monitor system

Although radiation resistant, ECAL $PbWO_4$ crystals show a limited but rapid loss of optical transmission under irradiation due to the production of colour centres which absorb a fraction of the transmitted light. At the ECAL working temperature (18°C) the damage anneals and the balance between damage and annealing results in a dose-rate dependent equilibrium of the optical transmission, if the dose rate is constant. In the varying conditions of LHC running the result is a cyclic transparency behaviour between LHC collision runs and machine refills (figure 4.14). The magnitude of the changes is dose-rate dependent, and is expected to range from 1 or 2 per cent at low luminosity in the barrel, to tens of per cent in the high η regions of the endcap at high luminosity. The performance of the calorimeter would be unacceptably degraded by these radiation induced transparency changes were they not measured and corrected for.

The evolution of the crystal transparency is measured using laser pulses injected into the crystals via optical fibres. The response is normalized by the laser pulse magnitude measured using silicon PN photodiodes. PN type photodiodes were chosen because of their very narrow depletion zone (≈ 7 μm with +4 V reverse bias), making them much less sensitive to type inversion than the faster PIN photodiodes. Thus $R(t) = APD(t)/PN(t)$ is used as the measure of the crystal transparency. The laser monitoring system [69] performing this task is briefly outlined in the next section. Because of the different optical paths and spectra of the injected laser pulses and the scintillation light, the changes in crystal transparency cause a change in response to the laser light which is not necessarily equal to the change in response to scintillation light. For attenuations $< 10\%$ the

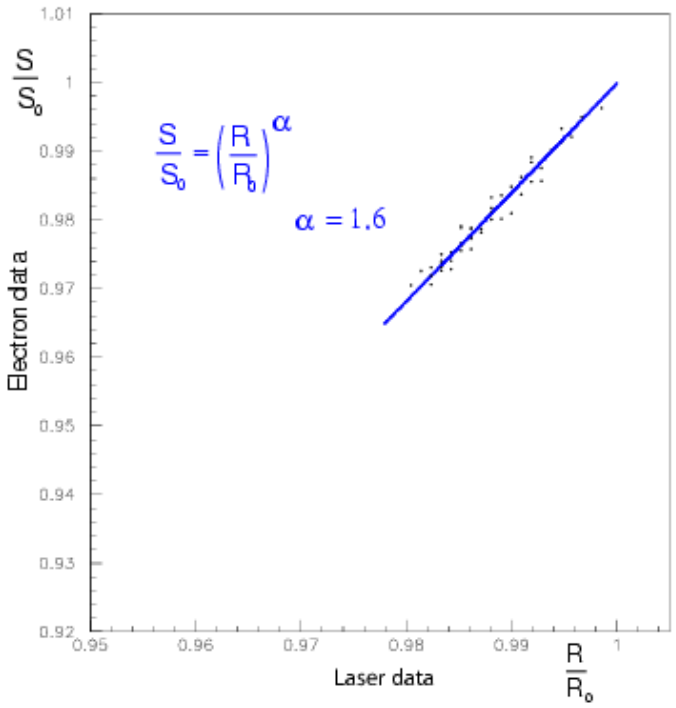

Figure 4.15: Relation between the transmission losses for scintillation light and for laser light for a given crystal. The signals are followed during the irradiation and the recovery.

relationship between the changes can be expressed by a power law,

$$\frac{S(t)}{S(t_0)} = \left[\frac{R(t)}{R(t_0)}\right]^{\alpha}, \tag{4.1}$$

where $S(t)$ represents the response to scintillation light and α is characteristic of the crystal which depends on the production method ($\alpha \approx 1.53$ for BCTP crystals, and $\alpha \approx 1.0$ for SIC crystals). An example of this relationship is given in figure 4.15. This power law describes well the behaviour of all the crystals that have been evaluated in the test beam, and this formula is expected to be valid in the barrel for both low and high luminosity at LHC.

4.9.1 Laser-monitoring system overview

Figure 4.16 shows the basic components of the laser-monitoring system: two laser wavelengths are used for the basic source. One, blue, at λ=440 nm, is very close to the scintillation emission peak, which is used to follow the changes in transparency due to radiation, and the other, near infra-red, at λ=796 nm, is far from the emission peak, and very little affected by changes in transparency, which can be used to verify the stability of other elements in the system. The spectral contamination is less than 10^{-3}. The lasers are operated such that the full width at half maximum of the pulses is $\approx$ 30 ns. The lasers can be pulsed at a rate of $\approx$ 80 Hz, and the pulse timing jitter is less than 3 ns which allows adequate trigger synchronization with the LHC bunch train and ECAL ADC clock.

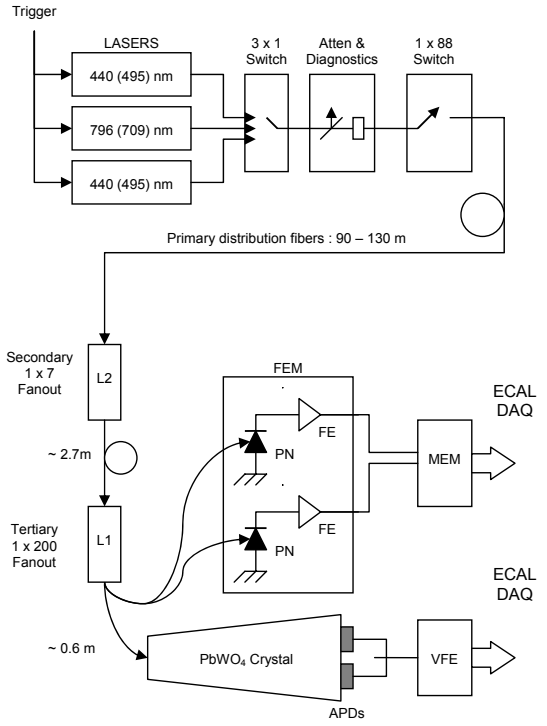

Figure 4.16: The components of the laser monitoring system.

The pulse energy of 1 mJ/pulse at the principal monitoring wavelength corresponds to $\approx$ 1.3 TeV, and a linear attenuator allows 1% steps down to 13 GeV. The pulse intensity instability is less than 10% which guarantees a monitoring precision of 0.1% by using the PN silicon photodiode normalization.

There are 3 light sources, 2 blue and 1 near infrared. The duplication of the blue source provides fault tolerance and allows maintenance of one while the other is in use, ensuring that a source at the wavelength used to track changes in transparency is always available. Each source consists of an Nd:YLF pump laser, its power supply and cooler unit and corresponding transformer, a Ti:Sapphire laser and its controller, and a NESLAB cooler for an LBO crystal in the Ti:S laser. Each pair of the YLF and Ti:S lasers and their corresponding optics are mounted on an optical table. Each source has its own diagnostics, 2 fibre-optic switches, internal monitors and corresponding PC based controllers. Further details can be found in [103].

The monitoring light pulses are distributed via a system of optical fibres. A fibre optic switch at the laser directs the laser pulses to 1 of 88 calorimeter regions (72 half supermodules in the barrel and 8 regions in each endcap). A two-stage distribution system mounted on each calorimeter region delivers the light to each crystal.

To provide continuous monitoring, about 1% of the 3.17 μs beam gap in every 88.924 μs LHC beam cycle will be used to inject monitoring light pulses into crystals. The time needed to scan the entire ECAL is expected to be about 30 minutes.

The first laser system was installed in the CERN H4 test beam site in August 2001. The other two laser systems were installed at H4 in August, 2003. All three laser systems have been used in

2008 JINST 3 S08004

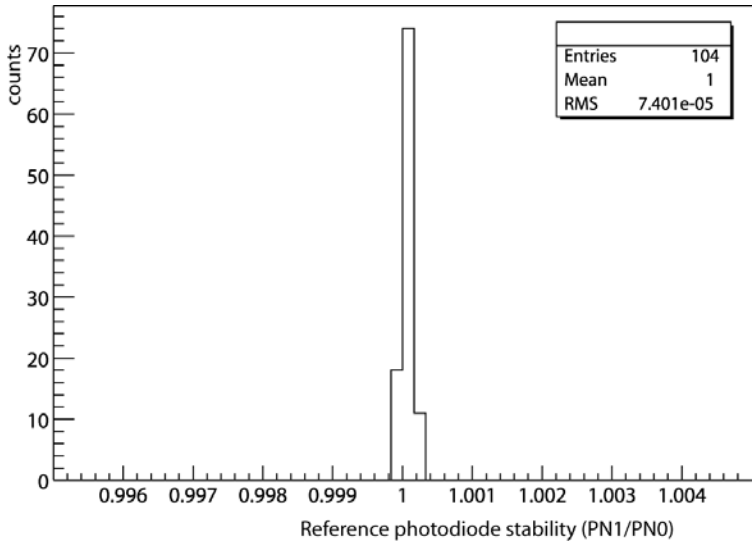

Figure 4.17: Relative stability between a pair of reference PN photodiodes monitoring 200 crystals measured in autumn 2004 at the CERN test beam facility.

the ECAL test beam program since their installation, and more than 10 000 laser hours have been cumulated.

The relative stability between a pair of reference PN photodiodes monitoring the same group of 200 crystals is shown in figure 4.17. The system achieves 0.0074% RMS over 7.5 days operation.

The response to injected laser light (normalized by the reference PN photodiodes) is presented in figure 4.18 for a group of 200 crystals measured for 11.5 days at the wavelength of 440 nm, showing that a stability of 0.068% is achieved at the scintillation wavelength.

The effect of the monitor correction procedure is presented in figure 4.19, showing that electron signals taken during an irradiation test at H4 are effectively corrected using laser monitor runs taken during the same data-taking period, providing an equalisation of the corrected response at the level of few per mille [104] .

4.10 Energy resolution

For energies below about 500 GeV, where shower leakage from the rear of the calorimeter starts to become significant, the energy resolution can be parametrized as in equation (1.1) (chapter 1.1), that is repeated for convenience here:

$$\left(\frac{\sigma}{E}\right)^2 = \left(\frac{S}{\sqrt{E}}\right)^2 + \left(\frac{N}{E}\right)^2 + C^2, \tag{4.2}$$

where S is the stochastic term, N the noise term, and C the constant term. The individual contributions are discussed below.

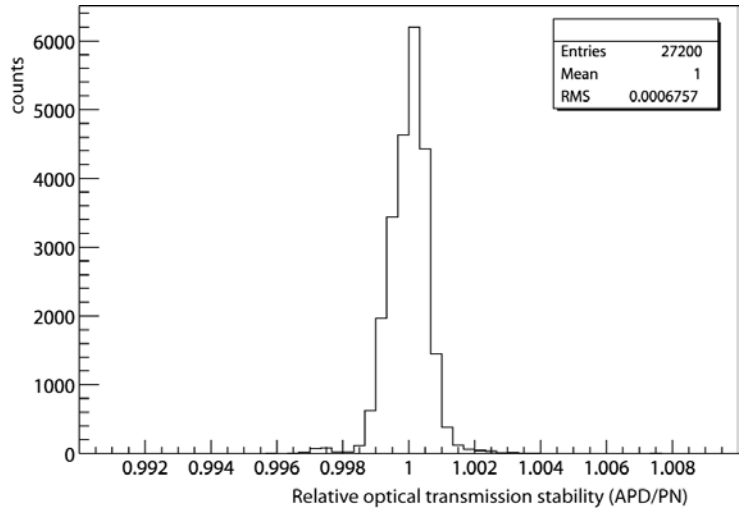

Figure 4.18: Stability of crystal transmission measurements at 440 nm (blue laser) over 11.5 days operation for a module of 200 crystals.

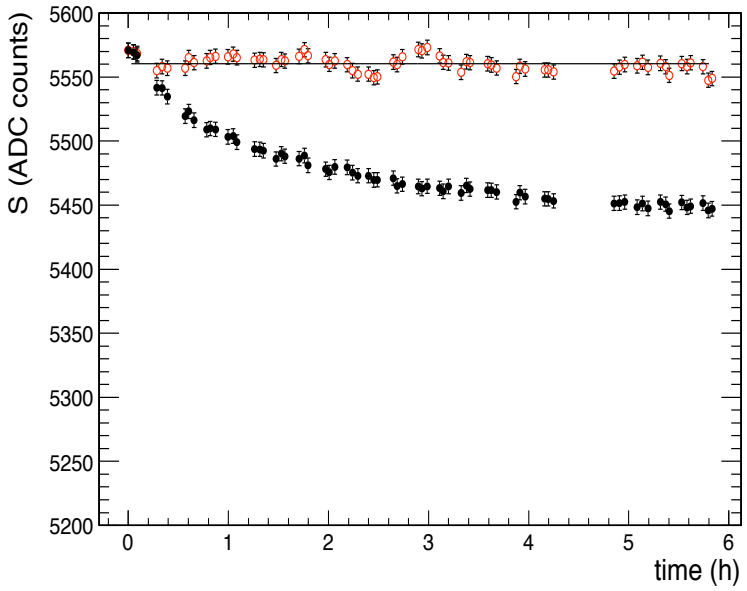

Figure 4.19: Effect of the monitor correction procedure on test beam data: full black points refer to signals measured during test beam irradiation, open red points are the same after the monitor corrections.

The stochastic term

There are three basic contributions to the stochastic term:

1. event-to-event fluctuations in the lateral shower containment,

2. a photostatistics contribution of 2.1%,

3. fluctuations in the energy deposited in the preshower absorber (where present) with respect to what is measured in the preshower silicon detector.

The contribution to the stochastic term coming from fluctuations in the lateral containment is expected to be about 1.5% when energy is reconstructed by summing an array of 5×5 crystals, and about 2% when using 3×3 crystals.

The photostatistics contribution is given by:

$$a_{\mathrm{pe}} = \sqrt{\frac{F}{N_{\mathrm{pe}}}} \tag{4.3}$$

where N_{pe} is the number of primary photoelectrons released in the photodetector per GeV, and F is the excess noise factor which parametrizes fluctuations in the gain process. This factor has a value close to 2 for the APDs, and is about 2.5 for the VPTs. A value of $N_{\mathrm{pe}} \approx 4500$ pe/GeV is found for the barrel, giving $\approx 2.1\%$ for the photostatistics contribution to the stochastic term. In the endcap the photostatistics contribution is similar, since the larger collection area of the VPT largely compensates for the reduced quantum efficiency of the photocathode.

The contribution to the energy resolution from the preshower device can be approximately parametrized as a stochastic term with a value of $5\%/\sqrt{E}$, where E is in GeV. But, because it samples only the beginning of the shower, the resolution is, in fact, predicted to vary like $\sigma/E \propto 1/E^{0.75}$. A beam test in 1999 [105] verified this prediction.

The constant term

The most important contributions to the constant term may be listed as follows:

1. non-uniformity of the longitudinal light collection,

2. intercalibration errors,

3. leakage of energy from the back of the crystal.

The effects of the longitudinal light collection curve have been studied in detail. Quite stringent requirements are made on the crystal longitudinal uniformity. Requiring the constant term contribution due to non-uniformity be less than 0.3%, sets a limit on the slope of the longitudinal light collection curve in the region of the shower maximum of $\approx 0.35\%$ per radiation length. A small increase in response towards the rear of the crystal helps to compensate the rear leakage from late developing showers, which would otherwise cause a low energy tail. The required response is achieved in the barrel by depolishing one long face of the crystals to a designated roughness. This surface treatment is incorporated into the crystal production process.

The effect of rear leakage is very small. Charged particles leaking from the back of the crystals can also give a direct signal in the APDs (nuclear counter effect), but test beam data show that this effect is negligible for isolated electromagnetic showers: no tails on the high side of the energy distribution are observed even at the highest electron energy tested (280 GeV).

2008 JINST 3 S08004

The noise term

There are three contributions to the noise term:

1. electronics noise,
2. digitization noise,
3. pileup noise.

The signal amplitude in the test beam is reconstructed using a simple digital filter. The noise measured, after this amplitude reconstruction, for channels in barrel supermodules is $\approx$ 40 MeV/channel in the highest gain range. This noise includes both electronics and digitization noise. The amplitude reconstruction makes use of an event-by-event baseline subtraction using 3 digitization samples taken directly before the signal pulse. This procedure removes the small channel-to-channel correlated noise. Its success is evidenced by the fact that, after this procedure, the noise in the sum of 25 channels is almost exactly 5 times the noise in a single channel [106].

In the endcap it is intended to sort the VPTs in bins of overall signal yield, which includes the photocathode area, the quantum efficiency and the VPT gain. The VPTs with higher overall signal yield are used for the larger radius regions of the endcap. This has the result that the transverse energy equivalent of the noise will be more or less constant, with a value of $\sigma_{\mathrm{ET}} \approx 50$ MeV.

Neutron irradiation of the APDs in the barrel induces a leakage current which contributes to the electronics noise. The evolution of the leakage current and induced noise over the lifetime of the experiment has been extensively studied. The expected contribution is equivalent to 8 MeV/channel after one year of operation at $\mathscr{L} = 10^{33}$ cm^{-2}s^{-1}, and 30 MeV/channel at the end of the first year of operation at $\mathscr{L} = 10^{34}$ cm^{-2}s^{-1} [69].

The shaped signals from the preamplifier output will extend over several LHC bunch crossings. When using a multi-weights method to reconstruct the signal amplitude [106], up to 8 time samples are used. Pileup noise will occur if additional particles reaching the calorimeter cause signals which overlap these samples.

The magnitude of pileup noise expected at low luminosity ($\mathscr{L} = 2 \times 10^{33}$ cm^{-2}s^{-1}) has been studied using detailed simulation of minimum bias events generated between -5 and $+3$ bunch crossings before and after the signal. The average number of minimum bias events per bunch crossing was 3.5. Figure 4.20 shows the reconstructed amplitude observed with and without pileup in the absence of any signal. The fraction of events with a signal beyond the Gaussian distribution of the electronics noise is small, showing that at low luminosity the pileup contribution to noise is small.

Energy resolution in the test beam

In 2004 a fully equipped barrel supermodule was tested in the CERN H4 beam. The energy resolution measured with electron beams having momenta between 20 and 250 GeV/c confirmed the expectations described above [107]. Since the electron shower energy contained in a finite crystal matrix depends on the particle impact position with respect to the matrix boundaries, the intrinsic performance of the calorimeter was studied by using events where the electron was limited to a 4×4 mm^2 region around the point of maximum containment (*central impact*). Figure 1.3 shows

2008 JINST 3 S08004

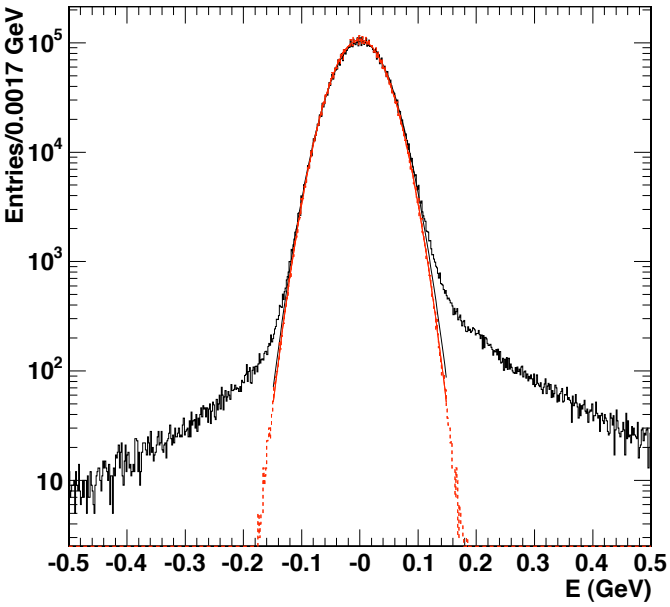

Figure 4.20: Reconstructed amplitude in ECAL barrel channels in the absence of a signal, without pileup (dashed histogram) and with pileup (solid histogram). A Gaussian of width 40 MeV is superimposed on the dashed histogram.

the resolution as a function of energy when the incident electrons were restricted in this way. The energy is reconstructed by summing 3×3 crystals. A typical energy resolution was found to be:

$$\left(\frac{\sigma}{E}\right)^2 = \left(\frac{2.8\%}{\sqrt{E}}\right)^2 + \left(\frac{0.12}{E}\right)^2 + (0.30\%)^2 ,$$

where E is in GeV. This result is in agreement with the expected contributions detailed in the earlier part of this section. (Results from beam-test runs taken in 2006, using the final VFE card, show a 10% improvement of the noise performance.)

The energy resolution was also measured with no restriction on the lateral position of the incident electrons except that provided by the 20×20 mm^2 trigger. The trigger was roughly centred (± 3 mm) on the point of maximum response of a crystals. In this case a shower containment correction was made as a function of incident position, as measured from the distribution of energies in the crystal, to account for the variation of the amount of energy contained in the matrix. For energy reconstruction in either a 3×3 or a 5×5 matrix an energy resolution of better than 0.45% is found for 120 GeV electrons after correction for containment. Figure 4.21 shows an example of the energy distributions before and after correction for the case of reconstruction in a 5×5 matrix, where the correction is smaller than for the 3×3 case.

The energy resolution has also been measured for a series of 25 runs where the beam was directed at locations uniformly covering a 3×3 array of crystals. In this case a resolution of 0.5% was measured for 120 GeV electrons.

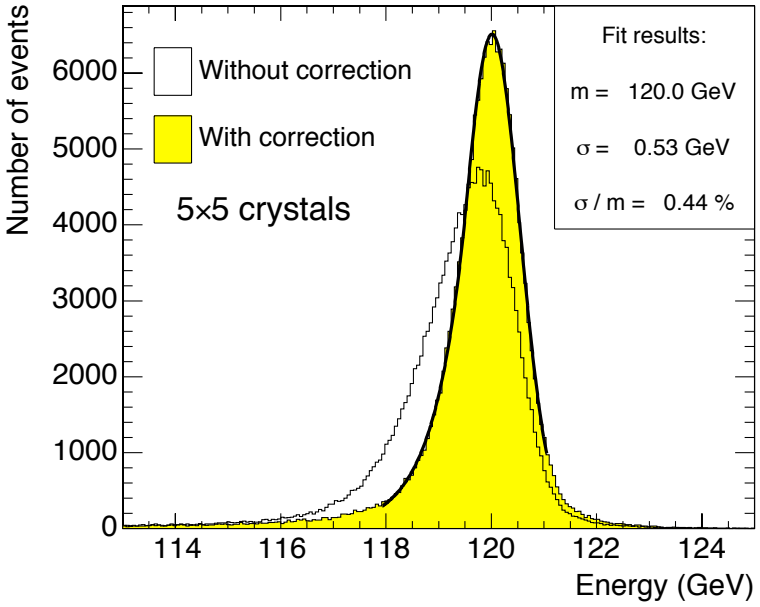

Figure 4.21: Distribution of energy reconstructed in a 5×5 matrix, before and after correction for containment, when 120 GeV electrons are incident over a $20 \times 20\text{mm}^2$ area.

Chapter 5

Hadron calorimeter

The CMS detector is designed to study a wide range of high-energy processes involving diverse signatures of final states. The hadron calorimeters are particularly important for the measurement of hadron jets and neutrinos or exotic particles resulting in apparent missing transverse energy [1].

Figure 5.1 shows the longitudinal view of the CMS detector. The dashed lines are at fixed η values. The hadron calorimeter barrel and endcaps sit behind the tracker and the electromagnetic calorimeter as seen from the interaction point. The hadron calorimeter barrel is radially restricted between the outer extent of the electromagnetic calorimeter (R = 1.77 m) and the inner extent of the magnet coil (R = 2.95 m). This constrains the total amount of material which can be put in to absorb the hadronic shower. Therefore, an outer hadron calorimeter or *tail catcher* is placed outside the solenoid complementing the barrel calorimeter. Beyond $|\eta| = 3$, the forward hadron calorimeters placed at 11.2 m from the interaction point extend the pseudorapidity coverage down to $|\eta| = 5.2$ using a Cherenkov-based, radiation-hard technology. The following sections describe these subdetectors in detail.

5.1 Barrel design (HB)

The HB is a sampling calorimeter covering the pseudorapidity range $|\eta| < 1.3$. The HB is divided into two half-barrel sections (figure 5.2), each half-section being inserted from either end of the barrel cryostat of the superconducting solenoid and subsequently hung from rails in the median plane. Since the HB is very rigid compared to the cryostat, great care has been taken to ensure that the barrel load is distributed evenly along the rails [108].

Absorber geometry

The HB consists of 36 identical azimuthal wedges which form the two half-barrels (HB+ and HB–). The wedges are constructed out of flat brass absorber plates (table 5.1) aligned parallel to the beam axis. The numbering scheme of the wedges is shown in figure 5.3. Each wedge is segmented into four azimuthal angle (ϕ) sectors. The plates are bolted together in a staggered geometry resulting in a configuration that contains no projective dead material for the full radial extent of a wedge (figure 5.4). The innermost and outermost plates are made of stainless steel for structural strength. The plastic scintillator is divided into 16 η sectors, resulting in a segmentation

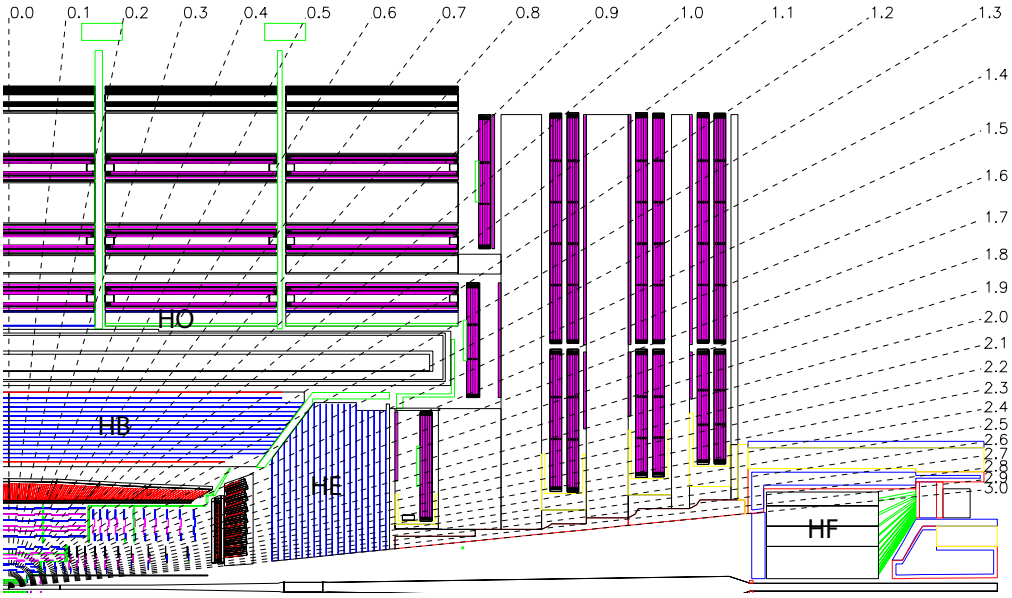

Figure 5.1: Longitudinal view of the CMS detector showing the locations of the hadron barrel (HB), endcap (HE), outer (HO) and forward (HF) calorimeters.

Table 5.1: Physical properties of the HB brass absorber, known as C26000/cartridge brass.

chemical composition	70% Cu, 30% Zn
density	8.53 g/cm^3
radiation length	1.49 cm
interaction length	16.42 cm

$(\Delta\eta, \Delta\phi) = (0.087, 0.087)$. The wedges are themselves bolted together, in such a fashion as to minimize the crack between the wedges to less than 2 mm.

The absorber (table 5.2) consists of a 40-mm-thick front steel plate, followed by eight 50.5-mm-thick brass plates, six 56.5-mm-thick brass plates, and a 75-mm-thick steel back plate. The total absorber thickness at 90° is 5.82 interaction lengths (λ_I). The HB effective thickness increases with polar angle (θ) as $1/\sin\theta$, resulting in 10.6 λ_I at $|\eta| = 1.3$. The electromagnetic crystal calorimeter [69] in front of HB adds about 1.1 λ_I of material.

Scintillator

The active medium uses the well known tile and wavelength shifting fibre concept to bring out the light. The CMS hadron calorimeter consists of about 70 000 tiles. In order to limit the number of individual elements to be handled, the tiles of a given ϕ layer are grouped into a single mechanical scintillator tray unit. Figure 5.5 shows a typical tray. The tray geometry has allowed for construction and testing of the scintillators remote from the experimental installation area. Furthermore,

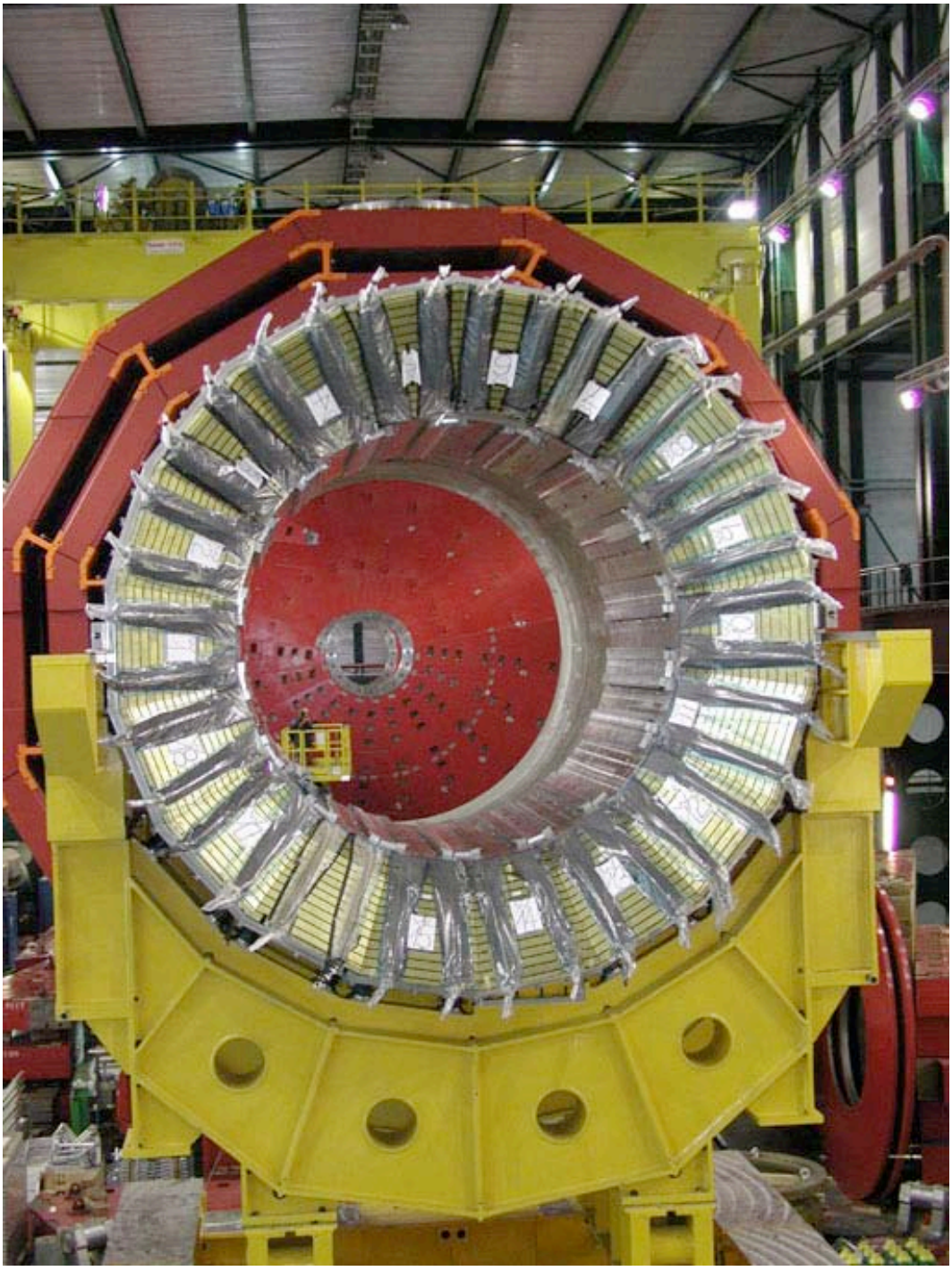

Figure 5.2: Assembled HCAL half-barrel in SX5, the above ground assembly hall.

individual scintillator trays may be replaced without disassembly of the absorber in the event of catastrophic damage. Each HB wedge has four ϕ divisions (ϕ-index = 1–4). Trays with segmentation of ϕ-index 2 and 3 go into the center of a wedge while trays with segmentation of ϕ-index 1 and 4 go into the edge slots in a wedge (figure 5.4). Each layer has 108 trays. Figure 5.6 shows a cross section of the tray.

2008 JINST 3 S08004

Table 5.2: Absorber thickness in the HB wedges.

layer	*material*	*thickness*
front plate	steel	40 mm
1-8	brass	50.5 mm
9-14	brass	56.5 mm
back plate	steel	75 mm

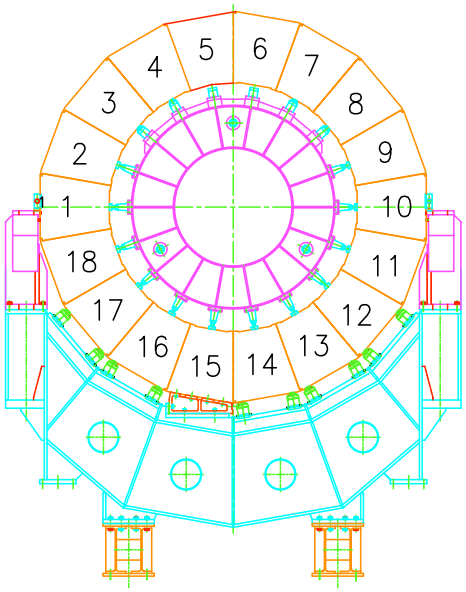

Figure 5.3: Numbering scheme for the HB wedges. Wedge 1 is on the inside ($+x$ direction) of the LHC ring.

The HB baseline active material is 3.7-mm-thick Kuraray SCSN81 plastic scintillator, chosen for its long-term stability and moderate radiation hardness. The first layer of scintillator (layer 0) is located in front of the steel support plate. It was originally foreseen to have a separate read-out [108] and is made of 9-mm-thick Bicron BC408. The scintillators are summarized in table 5.3. The purpose of layer zero is to sample hadronic showers developing in the inert material between the EB and HB. The larger thickness of layer 16 serves to correct for late developing showers leaking out the back of HB.

A tray is made of individual scintillators with edges painted white and wrapped in Tyvek 1073D which are attached to a 0.5-mm-thick plastic substrate with plastic rivets. Light from each tile is collected with a 0.94-mm-diameter green double-cladded wavelength-shifting fibre (Kuraray Y-11) placed in a machined groove in the scintillator. For calibration purposes, each tray has 1-mm-diameter stainless steel tubes, called *source tubes*, that carry Cs^{137} (or optionally Co^{60}) radioactive sources through the center of each tile. An additional quartz fibre is used to inject ultraviolet (337 nm) laser light into the layer 9 tiles. The top of the tray is covered with 2-mm-thick white polystyrene. The cover is grooved to provide routing paths for fibres to the outside of the tray and

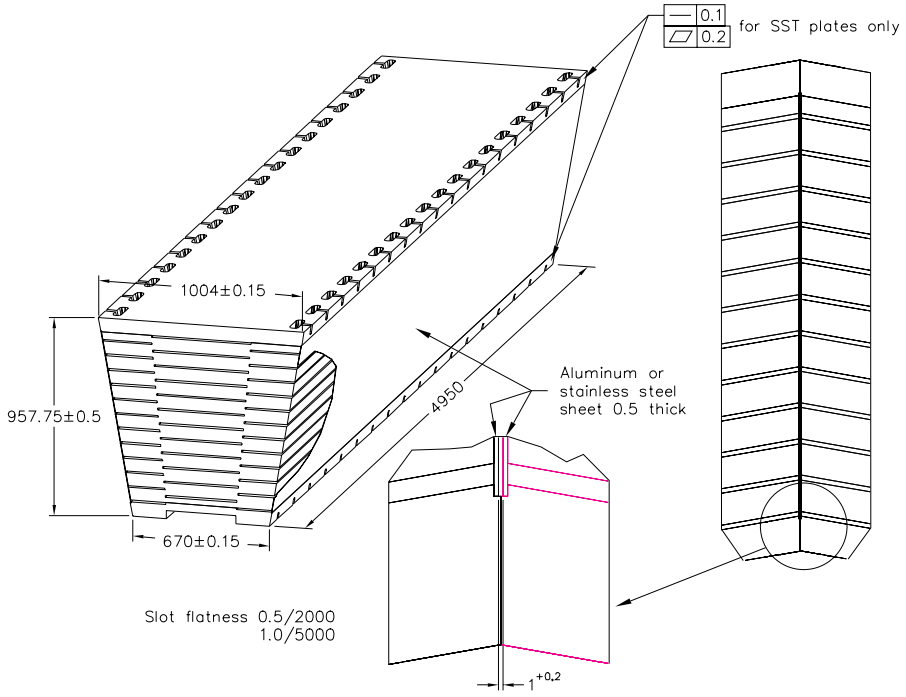

Figure 5.4: Isometric view of the HB wedges, showing the hermetic design of the scintillator sampling.

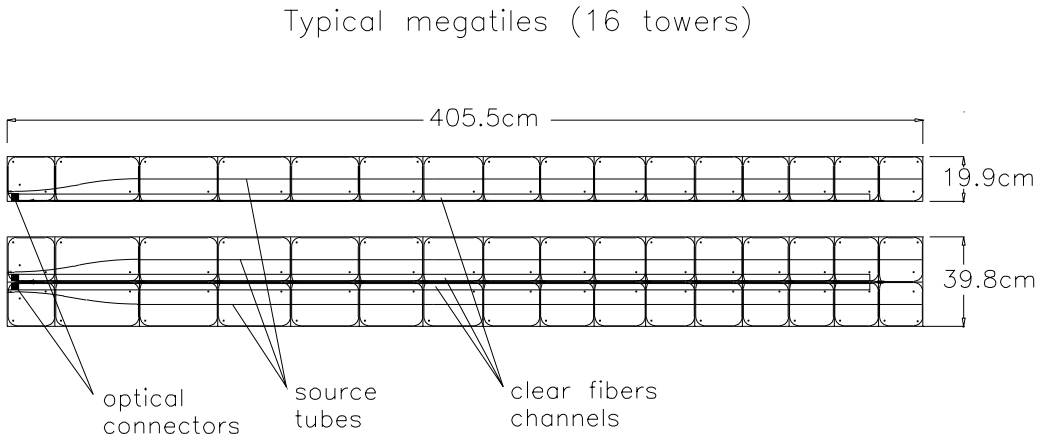

Figure 5.5: Scintillator trays.

also to accommodate the tubes for moving radioactive sources.

After exiting the scintillator, the wavelength shifting fibres (WLS) are spliced to clear fibres (Kuraray double-clad). The clear fibre goes to an optical connector at the end of the tray. An optical cable takes the light to an optical decoding unit (ODU). The ODU arranges the fibres into read-out towers and brings the light to a hybrid photodiode (HPD) [109]. An additional fibre enters each

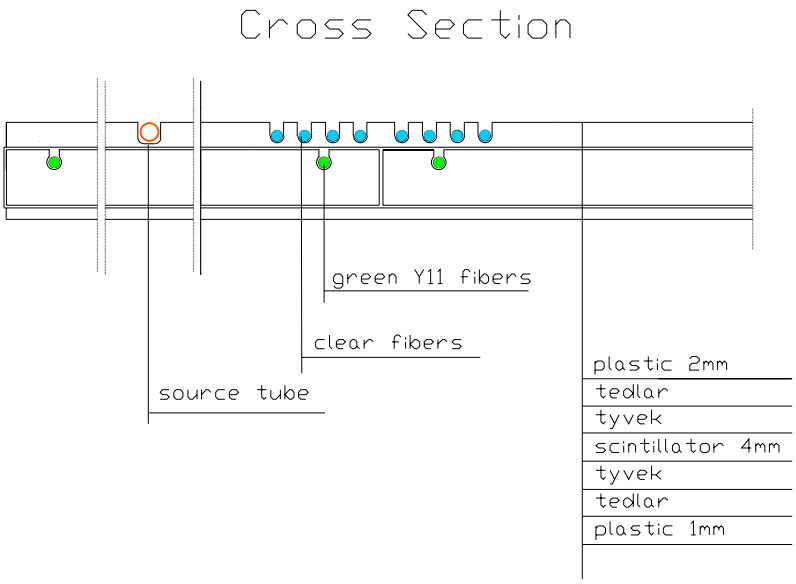

Figure 5.6: Cross-sectional view of a scintillator tray.

Table 5.3: Scintillator in the HB wedges.

layer	*material*	*thickness*
0	Bicron BC408	9 mm
1-15	Kuraray SCSN81	3.7 mm
16	Kuraray SCSN81	9 mm

HPD for direct injection of light using either the laser or a light emitting diode (LED). A schematic of the fibre optics is shown in figure 5.7 and the actual cabling is shown in figure 5.8.

The HPD consists of a photocathode held at a HV of -8 kV at a distance of approximately 3.3 mm from a pixelated silicon photodiode. The ionization produced by the accelerated photo-electron in the diode results in a gain of the HPD of approximately 2000. There are 19 hexagonal 20-mm^2 pixels in a single HPD, the centermost of which is not read-out. A cross sectional view of an HPD is shown in figure 5.9.

During the production and assembly process, the WLS fibres are cut, polished, and mirrored. The reflectivity of the mirror is checked by measuring test fibres which are mirrored along with the fibres used in the calorimeter. Measuring the reflectivity of the mirror is done with a computer controlled UV scanner with the fibres read out by photodiodes. Clear fibres are spliced onto WLS fibres with a fusion splicer. The transmission across the splice is checked by splicing a sample of WLS fibres onto WLS fibres. The splice region is measured with the UV scanner. The transmission across the splice is 92.6% with an RMS of 1.8%. Next, the optical fibres are glued into a 10 fibre connector. This configuration is called a pigtail. In order to get the fibre lengths correct, the pigtail is assembled in a template. The connector is diamond polished. The fibres are measured with the

2008 JINST 3 S08004

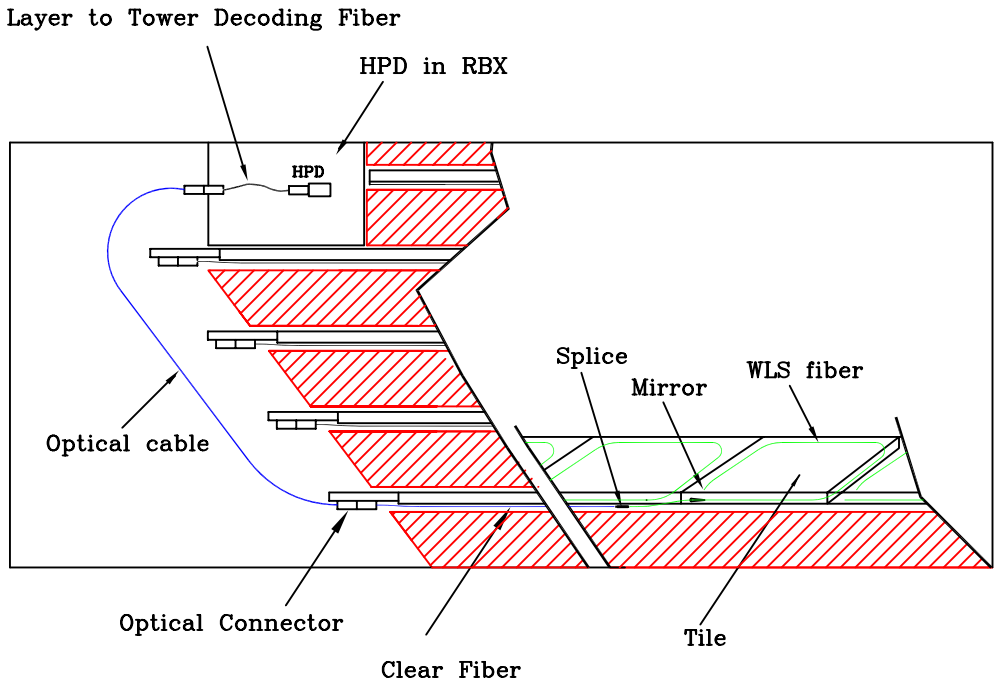

Figure 5.7: Schematic of the HB optics.

UV scanner. The scanner checks the green fibre, clear fibre, splice, and mirror. The RMS of the light from the fibres is 1.9%. After the pigtail is inserted into the tray, the completed tray is checked with an automated source scanner using a Cs^{137} source inside a lead collimator. This yields a 4 cm diameter source spot on the tray. The collimator is moved with a computer controlled x-y motor. From the scanner we determine the relative light yield of each tile and the uniformity of each tray. The light yield of the individual tiles has an RMS of 4.6%, while the transverse uniformity of the tile is 4.5%. A Cs^{137} wire source is run through the 4 source tubes and the light yield is measured. The RMS of the ratio of collimated source to wire source is 1.3%. This means the line sources, which can be used when the calorimeter is completely assembled, can calibrate individual tiles to better than 2%. In addition to the moving wire source, there are laser and LED light injection systems.

Longitudinal segmentation

The η towers 1–14 have a single longitudinal read-out. The η towers closest to the endcap transition region (15 and 16) are segmented in depth. The front segment of tower 15 contains either 12 or 13 scintillators, due to the placement of the read-out box and the staggering of the layers (layers 0–11 for the middle two ϕ sectors and 0–12 layers for the outer two ϕ sectors). The rear segment of tower 15 has three scintillators. Tower 16, which is in front of the endcap (HE) has one scintillators in the front segment and seven in the rear. The front segment of tower 16 does not have a layer-0 scintillator. The tower segmentation is summarized in figure 5.10 and table 5.4.

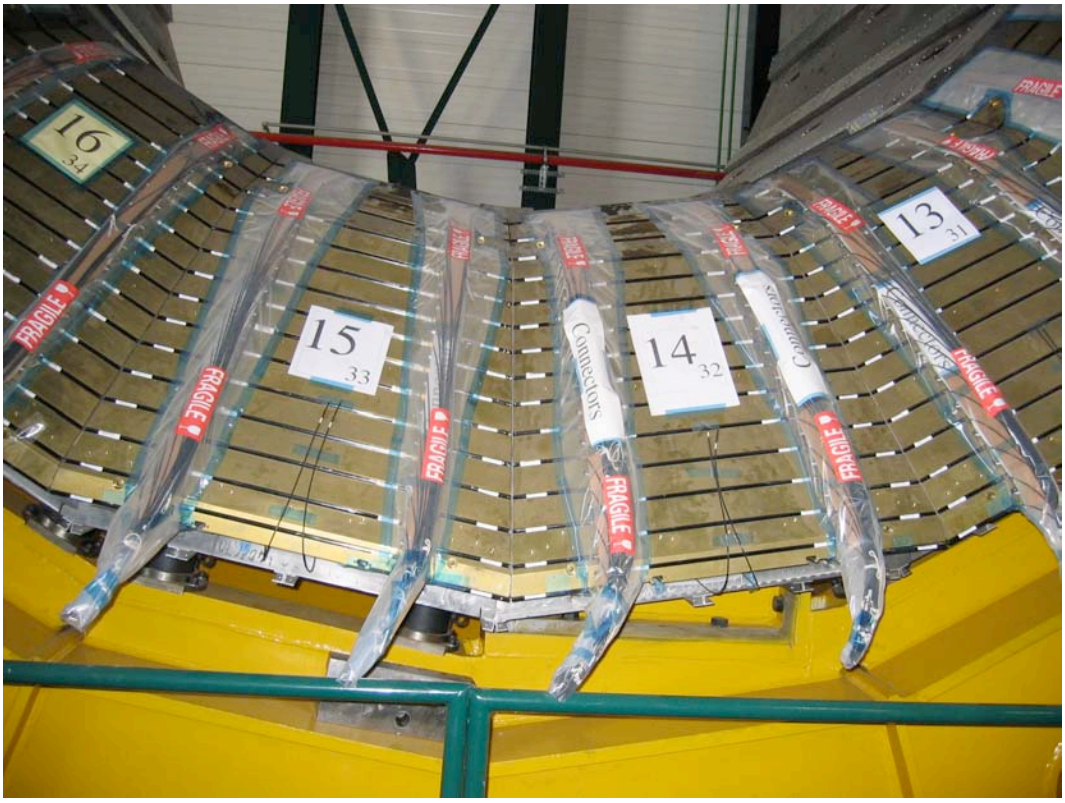

Figure 5.8: Close up view of the assembled HB wedges, showing the optical cabling.

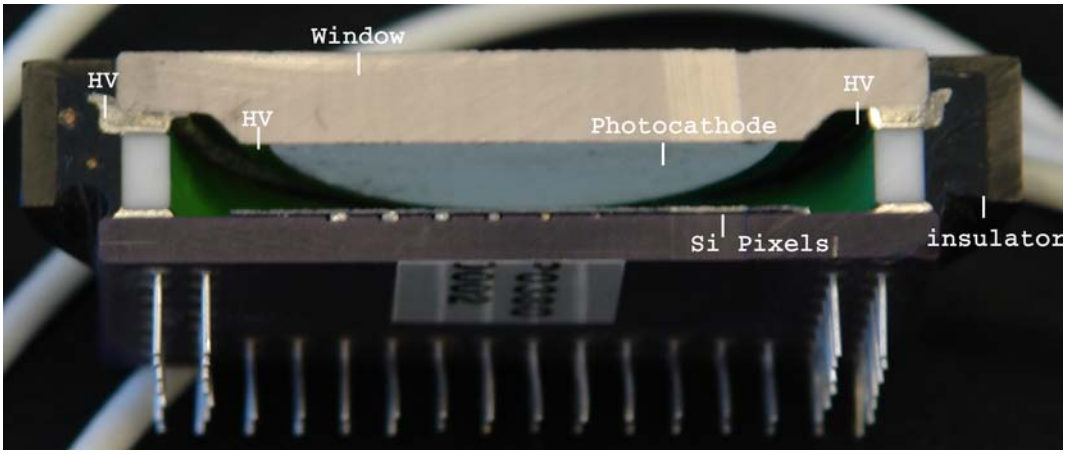

Figure 5.9: Cross sectional view of an HPD.

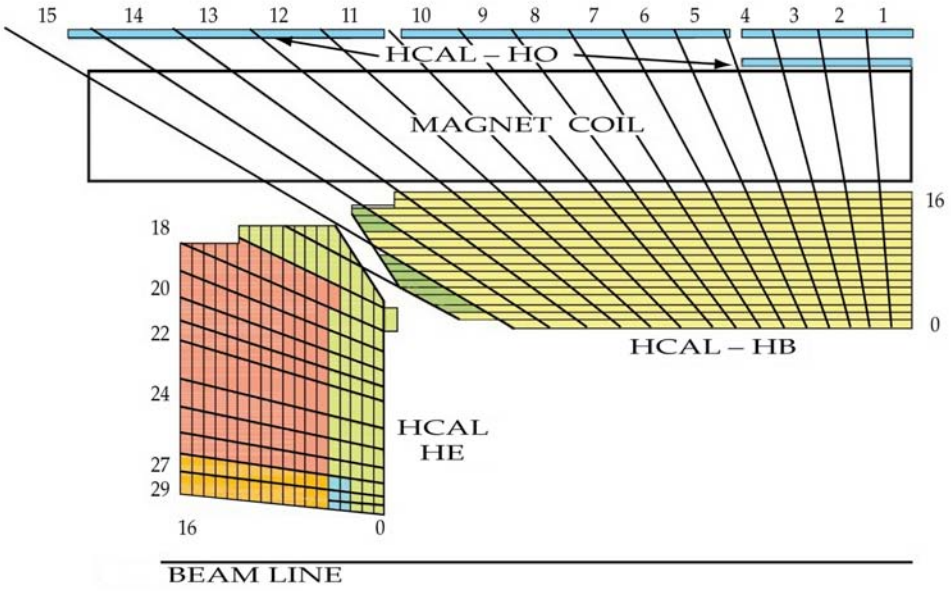

Figure 5.10: The HCAL tower segmentation in the r,z plane for one-fourth of the HB, HO, and HE detectors. The shading represents the optical grouping of scintillator layers into different longitudinal readouts.

Table 5.4: Tower data for HB. The given thicknesses correspond to the center of the tower. Note that tower 16 overlaps with HE.

tower	η *range*	*thickness* (λ_I)
1	0.000 – 0.087	5.39
2	0.087 – 0.174	5.43
3	0.174 – 0.261	5.51
4	0.261 – 0.348	5.63
5	0.348 – 0.435	5.80
6	0.435 – 0.522	6.01
7	0.522 – 0.609	6.26
8	0.609 – 0.696	6.57
9	0.696 – 0.783	6.92
10	0.783 – 0.870	7.32
11	0.870 – 0.957	7.79
12	0.957 – 1.044	8.30
13	1.044 – 1.131	8.89
14	1.131 – 1.218	9.54
15	1.218 – 1.305	10.3
16	1.305 – 1.392	overlaps with HE

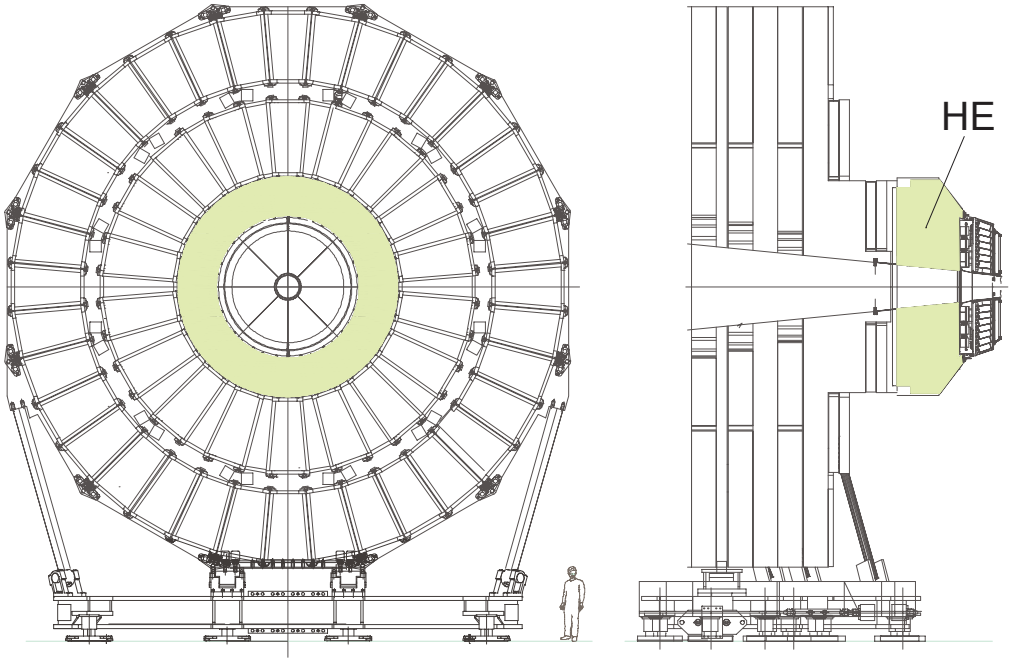

Figure 5.11: Hadron endcap (HE) calorimeter mounted on the endcap iron yoke.

5.2 Endcap design (HE)

The hadron calorimeter endcaps (HE) [108] cover a substantial portion of the rapidity range, $1.3 < |\eta| < 3$ (13.2% of the solid angle), a region containing about 34% of the particles produced in the final state. The high luminosity of the LHC (10^{34} cm^{-2} s^{-1}) requires HE to handle high (MHz) counting rates and have high radiation tolerance (10 MRad after 10 years of operation at design luminosity) at $|\eta| \simeq 3$. Since the calorimeter is inserted into the ends of a 4-T solenoidal magnet, the absorber must be made from a non-magnetic material. It must also have a maximum number of interaction lengths to contain hadronic showers, good mechanical properties and reasonable cost, leading to the choice of C26000 cartridge brass. The endcaps are attached to the muon endcap yoke as shown in figures 5.11 and 5.12. Only a small part of the calorimeter structure can be used for the fixation to the magnet iron, because the majority of the space between HE and muon absorber is occupied with muon cathode strip chambers. A 10-t electromagnetic calorimeter (EE) with a 2-t preshower detector (ES) is attached at the front face of HE. The large weight involved (about 300 t) and a strict requirement to minimize non-instrumented materials along particle trajectories, has made the design of HE a challenge to engineers. An interface kinematic scheme was developed in order to provide precise positioning of the endcap detectors with respect to the adjacent muon station, and to minimize the influence of deformation under magnetic forces. The interface kinematic contains a sliding joint between the interface tube, and HE back-flange and the hinge connection between brackets and the iron disk (YE1). Structural materials used in the interface system are non-magnetic in order not to distort the axial magnetic field of up to 4 T.

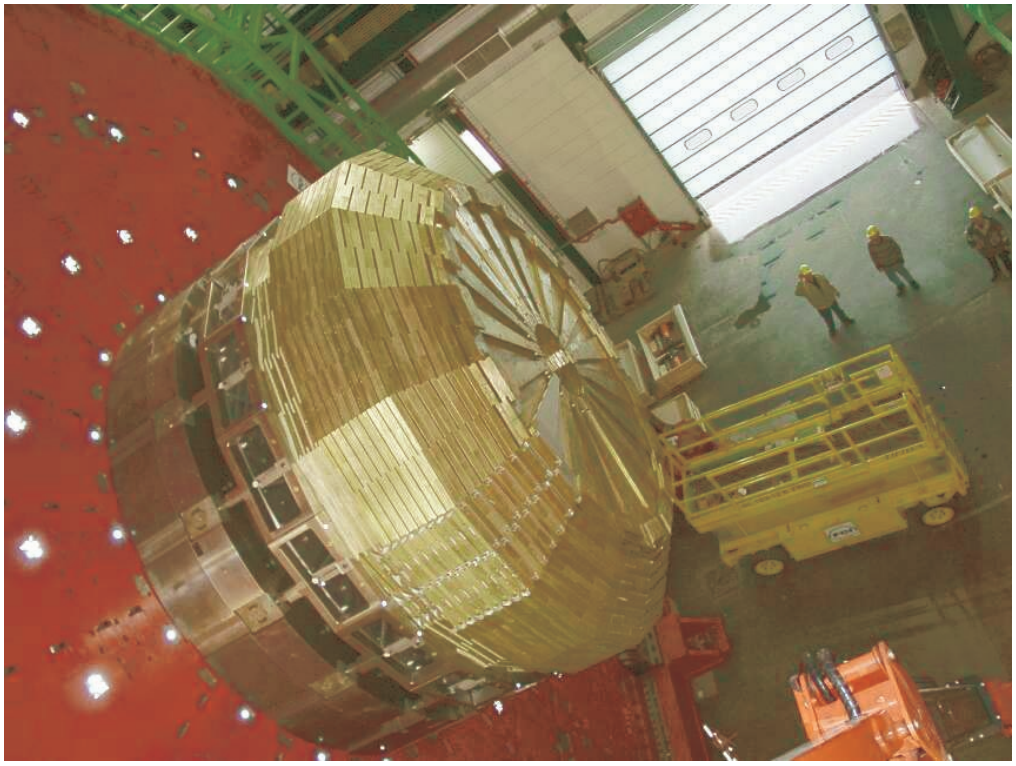

Figure 5.12: Partially assembled HE-minus absorber in the CMS surface hall (SX5). Scintillator trays can be seen to be inserted in some of the outer sectors.

Absorber geometry

The design of the absorber is driven by the need to minimize the cracks between HB and HE, rather than single-particle energy resolution, since the resolution of jets in HE will be limited by pileup, magnetic field effects, and parton fragmentation [110, 111]. The plates are bolted together in a staggered geometry resulting in a configuration that contains no projective "dead" material (figure 5.13). The design provides a self-supporting hermetic construction. The brass plates are 79-mm-thick with 9-mm gaps to accommodate the scintillators. The total length of the calorimeter, including electromagnetic crystals, is about 10 interaction lengths (λ_I).

The outer layers of HE have a cutout region for installation of the photodetectors and front-end electronics. To compensate for the resulting reduction of material, an extra layer (-1) is added to tower 18 [112]. The outer layers are fixed to a 10-cm-thick stainless steel support plate. The optical elements are inserted into the gaps after the absorber is completely assembled; therefore, the optical elements must have a rigid structure to allow insertion from any position.

Scintillator trays

The scintillation light is collected by wavelength shifting (WLS) fibres [113, 114]. The design minimizes dead zones because the absorber can be made as a solid piece without supporting structures while at the same time the light can be easily routed to the photodetectors. Trapezoidal-

2008 JINST 3 S08004

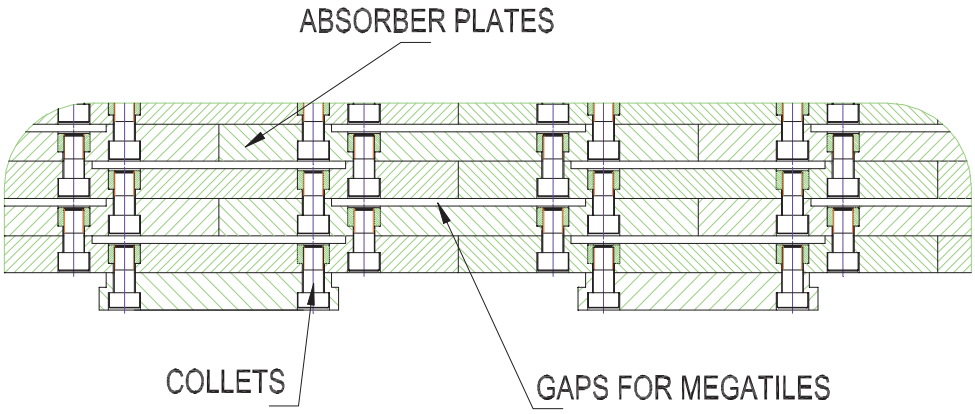

Figure 5.13: Mechanical structure of the HE absorber. Particles enter the calorimeter from the bottom.

shaped scintillators (figure 5.14), 3.7-mm-thick SCSN81 for layers 1–17 and 9-mm-thick Bicron BC408 for layer 0, have grooves in which the WLS fibres are inserted. The ends of the fibres are machined with a diamond fly cutter and one end is covered with aluminium to increase the light collection. The other end is spliced to a clear fibre, which is terminated in an optical connector. The connector with the glued fibres is also machined by a diamond fly cutter. The scintillator is painted along the narrow edges and put into a frame to form a tray. The total number of tiles for both HE calorimeters is 20 916 and the number of trays is 1368. The design of a tray is presented in figure 5.15. The numbering scheme in η is shown in figure 5.16, and the CMS convention for ϕ as applied to HE is shown in figure 5.17. The scintillators are wrapped with Tyvek and sandwiched between sheets of duraluminum. The stack contains holes for fibres which are terminated with optical connectors. The gap between the duraluminum plates is fixed by brass spacers screwed together. The granularity of the calorimeters is $\Delta\eta \times \Delta\phi = 0.087 \times 0.087$ for $|\eta| < 1.6$ and $\Delta\eta \times \Delta\phi \approx 0.17 \times 0.17$ for $|\eta| \geq 1.6$.

The tray design is very robust and reliable. The trays are relatively stiff which is very important for insertion into the absorber. To control the scintillator tray quality, a UV nitrogen laser was used to excite the scintillators. The light is fed by quartz fibres to the connector and is fanned out as shown in figure 5.15. These fibres are terminated with aluminium reflectors and distribute the light to all tiles. The light signal produced by a UV flash in the scintillator is similar to the signal induced by a charged particle. This allows a performance check of the entire optical route from scintillator to electronics, providing an important technique to track possible degradation of transparency due to radiation damage. For further calibration and monitoring, a radioactive source moving in a stainless steel tube is used to study the time-dependence of calibration coefficients.

The trays are inserted into the gaps in the absorber and fixed by screws. At the back of the calorimeter, boxes with photodetectors and electronics are located in the notch shown in figure 5.18. Optical cables transfer signals from the scintillator trays to the photodetectors. The partially assembled HE is shown in figure 5.12. Multipixel hybrid photodiodes (HPDs) are used as photodetectors due to their low sensitivity to magnetic fields and their large dynamical range.

2008 JINST 3 S08004

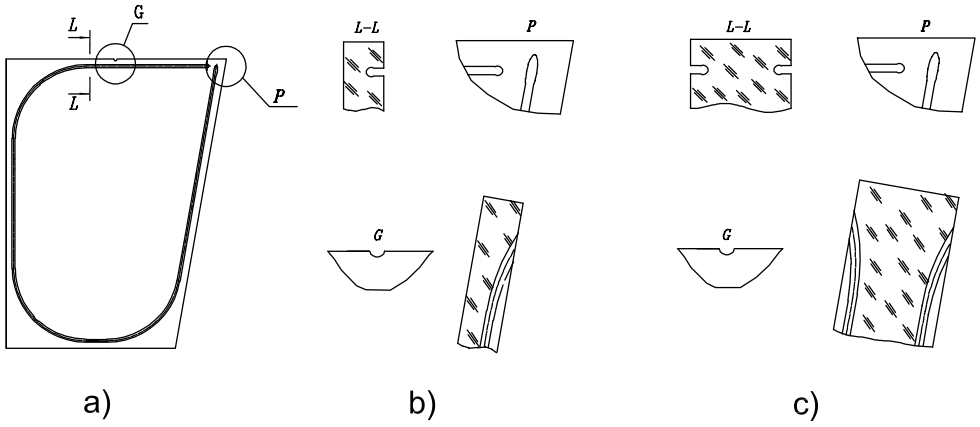

Figure 5.14: a) Basic structure of a scintillator tile with a groove to fix wavelength shifting fibre, b) cross section of the 3.7-mm-thick scintillator for layers 1–17, and c) cross section of the 9-mm-thick scintillator for layer zero. Two layers of reflecting paint cover the side surfaces of the tile.

Longitudinal segmentation

The longitudinal segmentation of HE (figure 5.10) is, in part, motivated by the radiation environment. Correction of the calibration coefficients after scintillator degradation can be applied, in order to restore the energy resolution. The towers nearest the beam line (27 and 28 plus guard ring "29") have 3 divisions in depth which are read-out separately. The other towers (except 16 and 17 which overlap with the electromagnetic barrel calorimeter) have two longitudinal readouts for potential use during the time period when the electromagnetic endcap calorimeter (EE) may not yet be available. A special scintillator layer of 9 mm BC408 (layer 0) is installed in front of the absorber to partially correct for the different response of EE to electrons and hadrons and for particle absorption in the mechanical structure supporting EE.

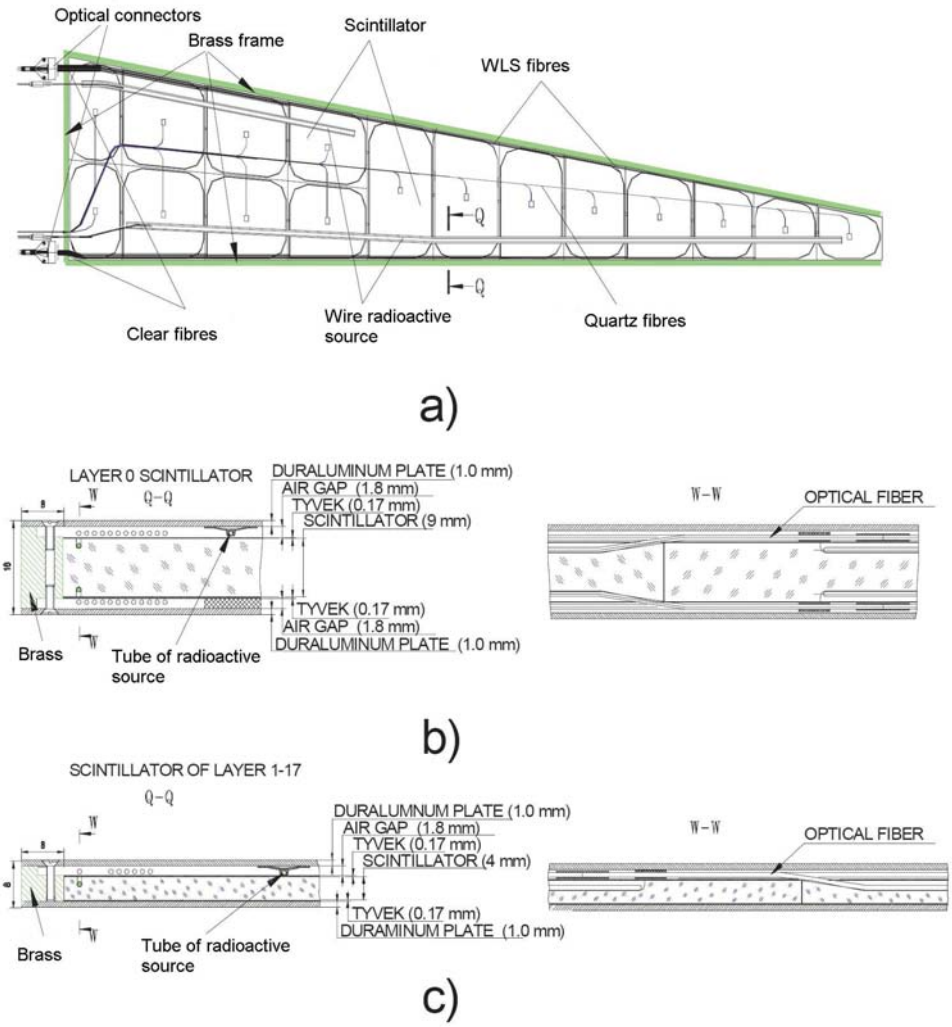

Figure 5.15: The design of the calorimeter scintillator trays: a) front view of a tray without upper aluminium cover, b) cut out view of the layer-0 tray with two fibres from a tile, c) cut out view of a tray for layers 1–17.

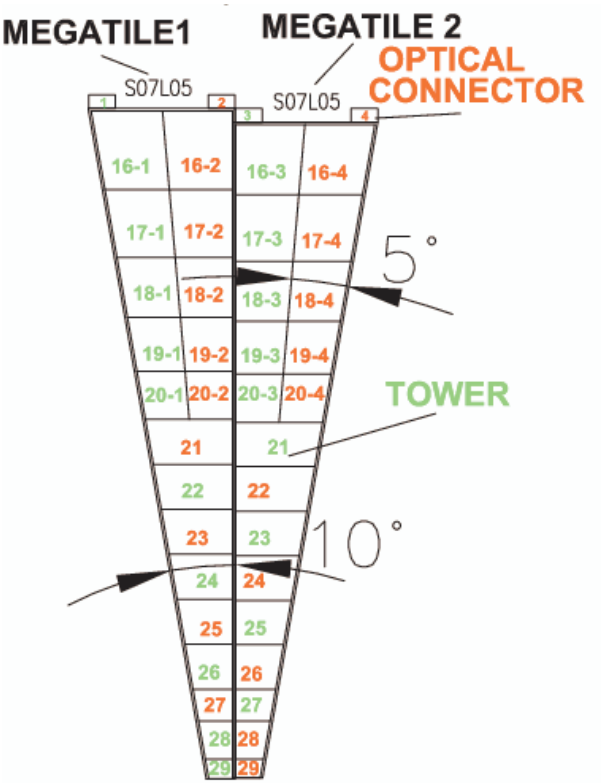

Figure 5.16: Numbering scheme for the tiles in adjacent scintillator trays.

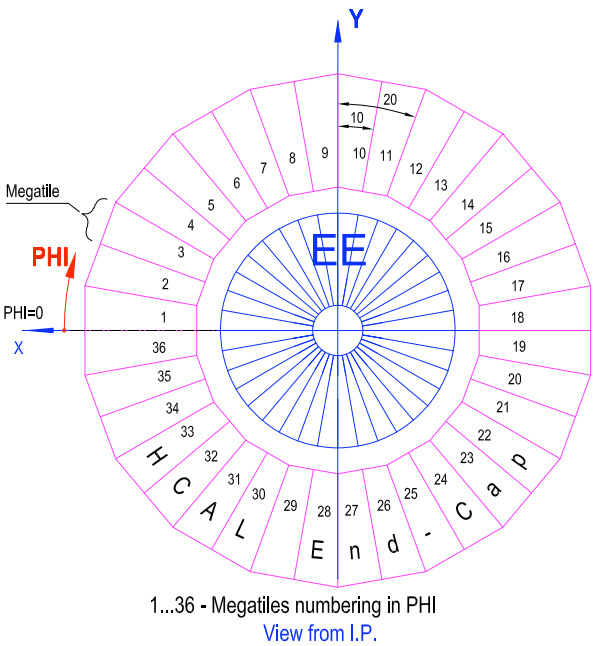

Figure 5.17: Numbering scheme for the HE wedges as viewed from the interaction point. The $+x$ direction points to the center of the LHC ring.

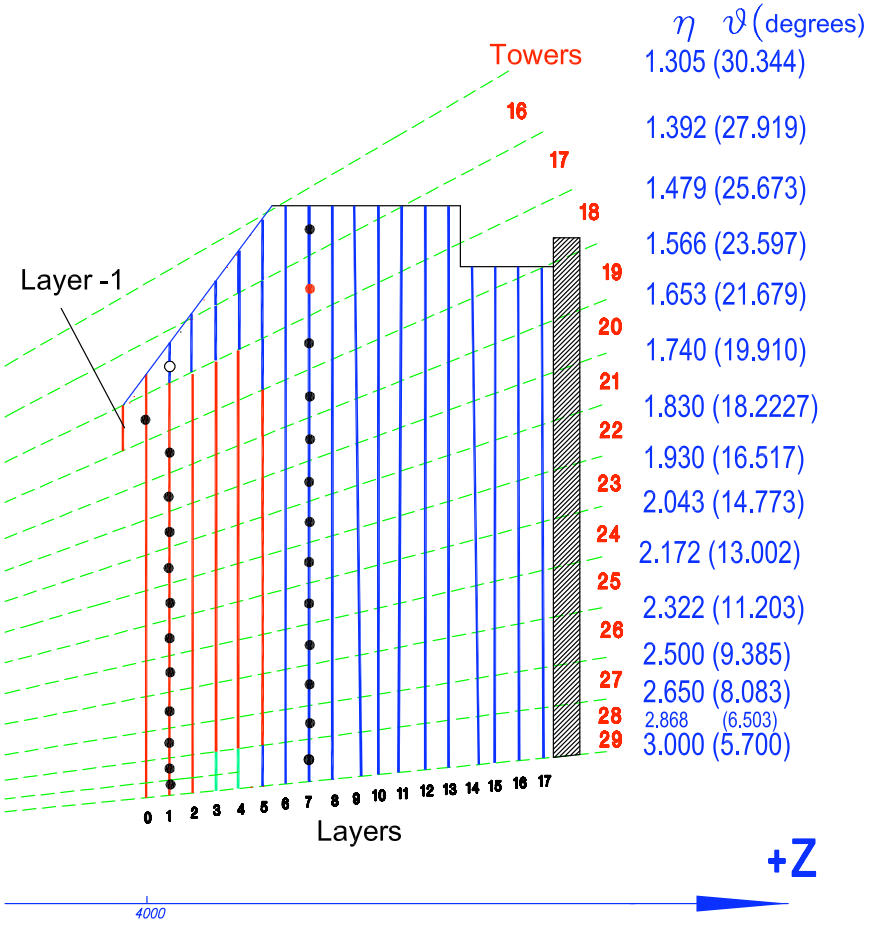

Figure 5.18: Longitudinal and angular segmentation of the HE calorimeter. The dashed lines point to the interaction point.

2008 JINST 3 S08004

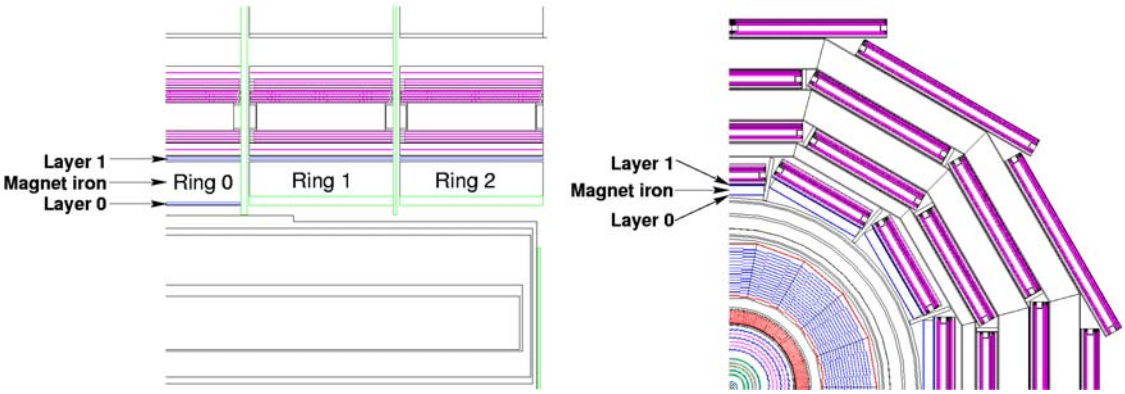

Figure 5.19: Longitudinal and transverse views of the CMS detector showing the position of HO layers.

5.3 Outer calorimeter design (HO)

In the central pseudorapidity region, the combined stopping power of EB plus HB does not provide sufficient containment for hadron showers. To ensure adequate sampling depth for $|\eta| < 1.3$, the hadron calorimeter is extended outside the solenoid with a tail catcher called the HO or outer calorimeter. The HO utilises the solenoid coil as an additional absorber equal to $1.4/\sin\theta$ interaction lengths and is used to identify late starting showers and to measure the shower energy deposited after HB.

Outside the vacuum tank of the solenoid, the magnetic field is returned through an iron yoke designed in the form of five 2.536 m wide (along z-axis) rings. The HO is placed as the first sensitive layer in each of these five rings. The rings are identified by the numbers -2, -1, 0, $+1$, $+2$. The numbering increases with z and the nominal central z positions of the five rings are respectively -5.342 m, -2.686 m, 0, $+2.686$ m and $+5.342$ m. At $\eta = 0$, HB has the minimal absorber depth. Therefore, the central ring (ring 0) has two layers of HO scintillators on either side of a 19.5 cm thick piece of iron (the tail catcher iron) at radial distances of 3.82 m and 4.07 m, respectively. All other rings have a single HO layer at a radial distance of 4.07 m. The total depth of the calorimeter system is thus extended to a minimum of 11.8 λ_I except at the barrel-endcap boundary region.

The HO is constrained by the geometry of the muon system. Figure 5.19 shows the position of HO layers in the rings of the muon stations in the overall CMS setup. The segmentation of these detectors closely follows that of the barrel muon system. Each ring has 12 identical ϕ-sectors. The 12 sectors are separated by 75-mm-thick stainless steel beams which hold successive layers of iron of the return yoke as well as the muon system. The space between successive muon rings in the η direction and also the space occupied by the stainless steel beams in the ϕ direction are not available for HO. In addition, the space occupied by the cryogenic "chimneys" in sector 3 of ring -1, and sector 4 of ring $+1$ are also not available for HO. The chimneys are used for the cryogenic transfer lines and power cables of the magnet system. Finally, the mechanical structures needed to position the scintillator trays further constrain HO along ϕ.

2008 JINST 3 S08004

In the radial direction each HO layer has been allocated a total of 40 mm, of which only 16 mm is available for the detector layer, the rest being used for the aluminium honeycomb support structures. In addition, the HO modules are independently supported from the steel beams located on either side of each ϕ sector. The thickness and position of the iron ribs in the yoke structure further constrain the shape and segmentation of the HO.

The sizes and positions of the tiles in HO are supposed to roughly map the layers of HB to make towers of granularity 0.087$\times$ 0.087 in η and ϕ. The HO consists of one (rings $\pm$1 and $\pm$2) or two (ring 0) layers of scintillator tiles located in front of the first layer of the barrel muon detector. Scintillation light from the tiles is collected using multi-clad Y11 Kuraray wavelength shifting (WLS) fibres of diameter 0.94 mm, and transported to the photo detectors located on the structure of the return yoke by splicing a multi-clad Kuraray clear fibre (also of 0.94 mm diameter) with the WLS fibre. In order to simplify installation of HO, the scintillator tiles are packed into a single unit called a tray. Each tray corresponds to one ϕ slice (5° wide in ϕ). However, along the z (η) direction, a tray covers the entire span of a muon ring. Figure 5.20 shows a schematic view of a HO tray where one tile is mapped to a tower of HB and the optical cable from the tray is connected to the read-out box.

The physics impact of HO has been studied [115] using a simulation of the CMS detector. Single pions of fixed energies are shot at specific η values and the resulting energy deposits in the electromagnetic calorimeter and in the layers of the hadron calorimeter are combined to measure the energy. Figure 5.21 shows distributions of the measured energy scaled to the incident energy for 200 GeV pions at η = 0 and 225 GeV at η = 0.5 (pointing towards the middle of ring 1). The solid and dashed lines in the figure indicate measurements without and with HO, respectively. As can be seen in figure 5.21, there is an excess in Energy/$\mathrm{E_{incident}} < 1$ for measurements without HO, because of leakage. The measurements with HO are more Gaussian in nature indicating that the addition of HO recovers the effect of leakage. The effect of leakage is visible at η = 0 (ring 0) from 70 GeV, increasing with energy. The mean fraction of energy in HO increases from 0.38% for 10 GeV pions to 4.3% for 300 GeV pions. There is some evidence of leakage without HO in ring 1 but it is reduced due to the greater HB thickness at larger $|\eta|$. The amount of leakage in ring 2 is found to be negligible at energies below 300 GeV.

The effect of shower leakage has a direct consequence on the measurement of missing transverse energy (E_T^{miss}). Study of QCD events shows that the cross section for those events, where at least one particle has E_T above 500 GeV, is several pb. For these events the HO is useful to decrease the leakage and improve the E_T^{miss} measurement. Figure 5.22 shows the dijet integrated cross section for E_T^{miss} above a certain value. It is clear from the figure that the inclusion of HO reduces the dijet rate by a factor of 1.5 or more for moderate E_T^{miss} values, a region important for searches of supersymmetric particles.

Module specification

HO is physically divided into 5 rings in η conforming to the muon ring structure. The rings are numbered $-2, -1, 0, +1$ and $+2$ with increasing η. Each ring of the HO is divided into 12 identical ϕ sectors and each sector has 6 slices (numbered 1 to 6 counting clockwise) in ϕ. The ϕ slices of a layer are identical in all sectors. The widths of the slices along ϕ are given in table 5.5. In each ϕ

2008 JINST 3 S08004

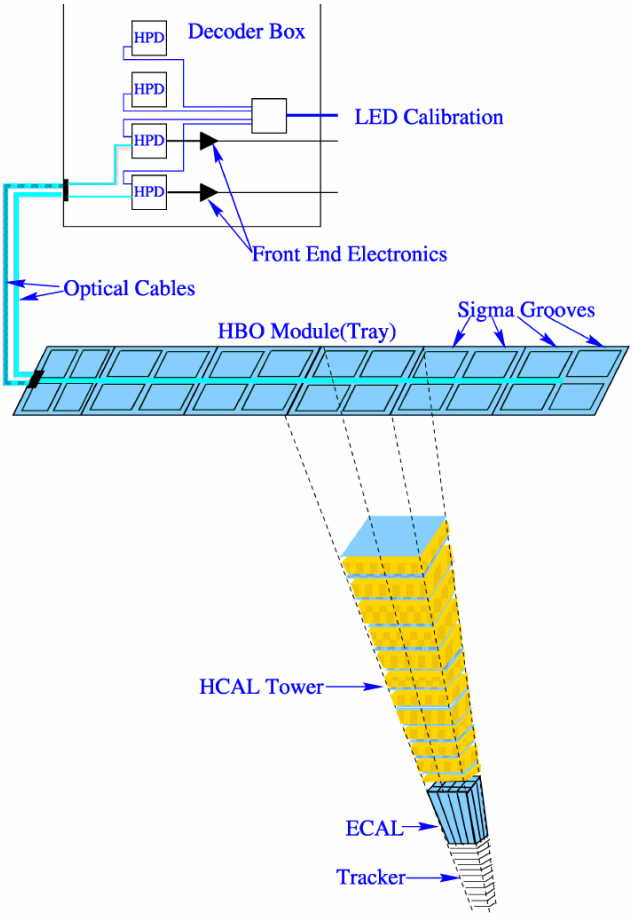

Figure 5.20: Schematic view of a HO tray shown with individual tiles and the corresponding grooves for WLS fibres. Each optically independent (4 WLS fibres) tile is mapped to a tower of HB. Optical fibres from the tray are routed to the decoder box which contains the photodetector and read-out electronics.

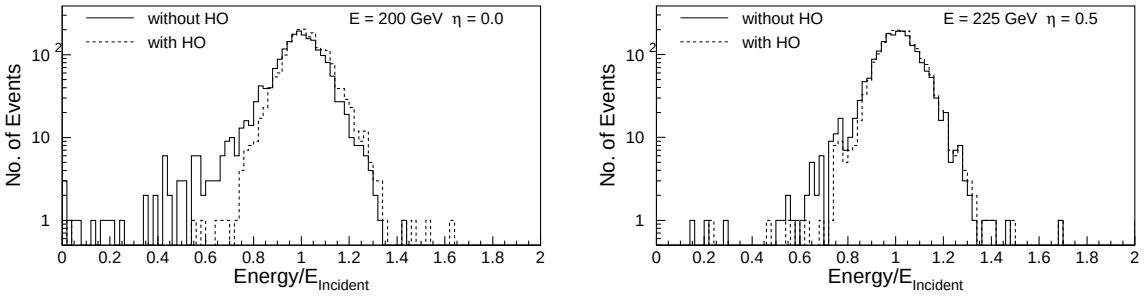

Figure 5.21: A simulation of the distribution of the measured energy scaled to the incident energy for pions with incident energies of (left panel) 200 GeV at $\eta = 0$ and (right panel) 225 GeV at $|\eta| = 0.5$. The solid and dashed histograms are measurements without and with HO, respectively.

2008 JINST 3 S08004

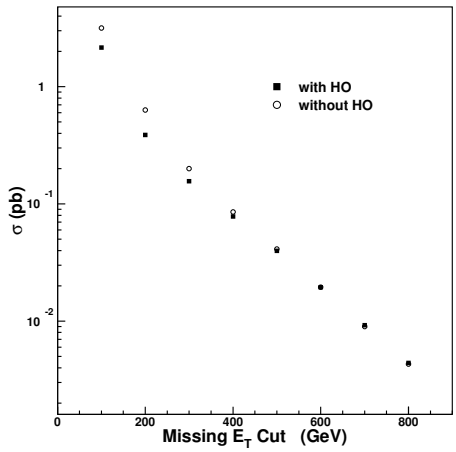

Figure 5.22: Integrated cross section above threshold for intrinsically balanced QCD dijet events as a function of missing E_{T} with or without HO.

Table 5.5: Dimension of tiles along ϕ for different trays. Each tray corresponds to one ϕ-slice in a ϕ sector.

Ring	Layer	Width along ϕ in mm					
		Tray 1	Tray 2	Tray 3	Tray 4	Tray 5	Tray 6
0	0	274	343	332	327	327	268
0	1	300	364	352	347	347	292
±1, ±2	1	317	366	354	349	349	406

slice, there is a further division along η. The smallest scintillator unit in HO thus obtained is called a tile. The scintillator tiles in each ϕ sector belong to a plane. The perpendicular distance of this plane from the z-axis is 3.82 m for layer 0 and 4.07 m for layer 1. The tiles in each ϕ slice of a ring are mechanically held together in the form of a tray.

Both layers of ring 0 have 8 η-divisions (i.e. 8 tiles in a tray): -4, -3, -2, -1, $+1$, $+2$, $+3$, $+4$. Ring 1 has 6 divisions: $5\cdots10$ and ring 2 has 5 divisions: $11\cdots15$. Ring -1 and ring -2 have the same number of divisions as rings 1 and 2 but with $-$ve indices. The η-dimension of any tile with $-$ve tower number is the same as the one with $+$ve number. The tile dimensions along η are shown in table 5.6.

Figure 5.23 shows the final layout of all the HO trays in the CMS detector. The length of a full tray is 2510 mm whereas the shorter trays, the sizes of which are constrained because of the chimney (trays 4 and 5 in sector 4 of ring $+1$ and trays 3, 4, 5 and 6 in sector 3 of ring -1), are 2119-mm long. The shorter trays are constructed without the tile corresponding to tower number ±5. Because of the constraints imposed by the gap between ring 0 and rings ±1, the η boundaries of HO tower 4 do not match the barrel η boundaries; therefore, part of HO tower 5 overlaps with tower 4 in the barrel.

2008 JINST 3 S08004

Table 5.6: HO tile dimensions along η for different rings and layers. The tile sizes, which are constrained by muon ring boundaries, are also given.

Tower #	η_{max}	Length (mm)	Tower #	η_{max}	Length (mm)
Ring 0 Layer 0			Ring 0 Layer 1		
1	0.087	331.5	1	0.087	351.2
2	0.174	334.0	2	0.174	353.8
3	0.262	339.0	3	0.262	359.2
4	0.326	248.8	4	0.307	189.1
Ring 1 Layer 1			Ring 2 Layer 1		
5	0.436	391.5	11	0.960	420.1
6	0.524	394.2	12	1.047	545.1
7	0.611	411.0	13	1.135	583.3
8	0.698	430.9	14	1.222	626.0
9	0.785	454.0	15	1.262	333.5
10	0.861	426.0			

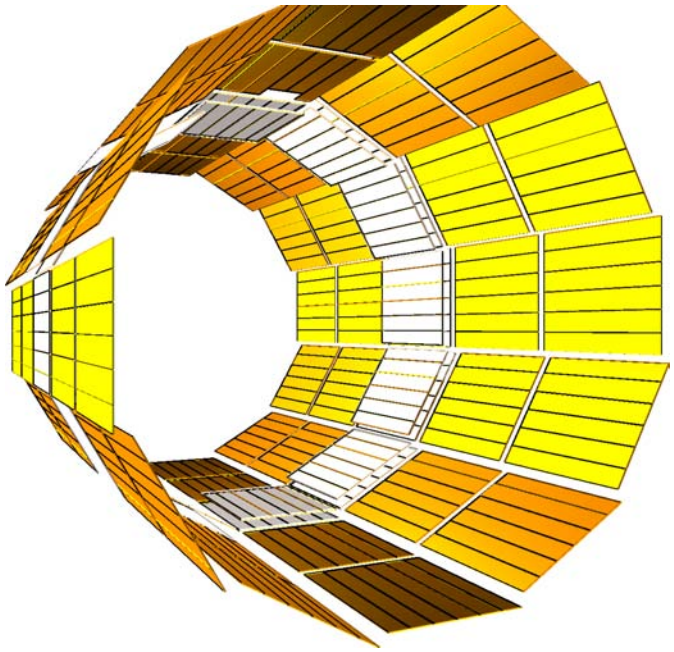

Figure 5.23: Layout of all the HO trays in the CMS detector.

Figure 5.24: View of a typical tile of HO with WLS fibres inserted in the 4 grooves of the tile.

Tiles

Scintillator tiles are made from Bicron BC408 scintillator plates of thickness 10^{+0}_{-1} mm. Figure 5.24 shows a typical HO scintillator tile. The WLS fibres are held inside the tile in grooves with a key hole cross section. Each groove has a circular part (of diameter 1.35 mm) inside the scintillator and a neck of 0.86 mm width. The grooves are 2.05-mm deep. Each tile has 4 identical grooves, one groove in each quadrant of the tile. The grooves closely follow the quadrant boundary. The corners of the grooves are rounded to prevent damage to the fibre at the bend and to ease fibre insertion. The groove design is slightly different for the tile where the optical connector is placed at the end of the tray. Since the tiles are large, 4 grooves ensure good light collection and less attenuation of light.

The HO has 95 different tile dimensions, 75 for layer 1 and 20 for layer 0. The total number of tiles is 2730 (2154 for layer 1 and 576 for layer 0).

Trays

All tiles in each ϕ slice of a sector are grouped together in the form of a tray. Each tray contains 5 tiles in rings ± 2; 6 tiles in rings ± 1 and 8 tiles in ring 0. The edges of the tiles are painted with Bicron reflecting white paint for better light collection as well as isolating the individual tiles of a tray. Further isolation of tiles is achieved by inserting a piece of black tedler in between the adjacent tiles. The tiles in a tray are covered with a single big piece of white, reflective tyvek paper. Then they are covered with black tedlar paper to prevent light leakage. This package is placed between two black plastic plates for mechanical stability and ease of handling. The top plastic cover is 2-mm-thick and the bottom one is 1-mm-thick. Figure 5.25 shows a cross section of a tray to illustrate the different components. The plastic covers (top and bottom) have holes matching with the holes in the tiles. Specially designed countersunk screws passing through these holes fix the plastic covers firmly on the tiles.

The 2 mm plastic sheet on the top has 1.6 mm deep channels grooved on it (on the outer side) to route the fibres from individual tiles to an optical connector placed in a groove at the edge of the tray. A 1.5-mm-wide straight groove runs along the edge of the top cover to accommodate a stainless steel tube. This is used for the passage of a radioactive source which is employed in calibrating the modules. Each connector has two holes and they are fixed to the scintillator-plastic assembly through matching holes. Each ϕ sector in each ring has 6 trays. There are 360 trays for layer 1 and 72 trays for layer 0.

2008 JINST 3 S08004

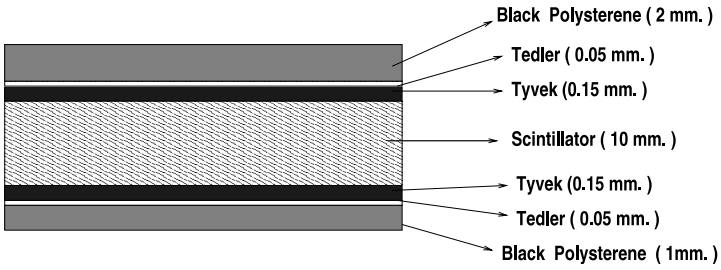

Figure 5.25: Cross section of a HO tray showing the different components.

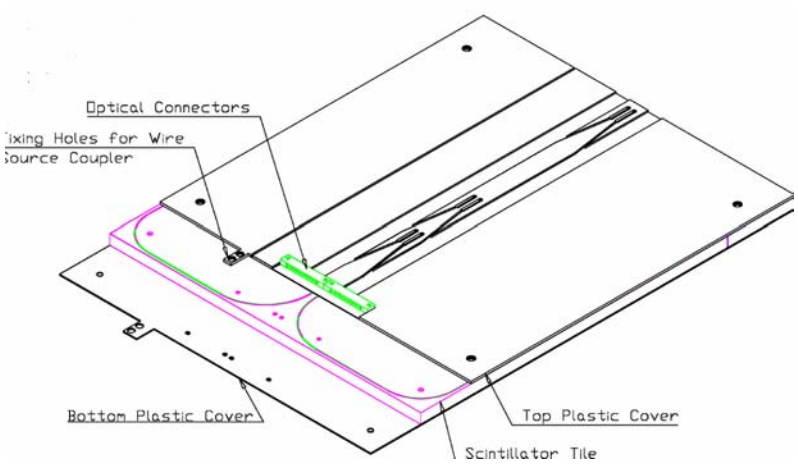

Figure 5.26: The arrangement of scintillation tiles, plastic covers and connectors in a tray. The components are slightly displaced from their true positions to show their matching designs.

Pigtails

The light collected by the WLS fibres inserted in the tiles needs to be transported to photodetectors located far away on the muon rings. The captive ends of the WLS fibres, which reside inside the groove, are polished, aluminized and protected using a thin polymer coating. The other end of the WLS fibre comes out of the tile through a slot made on the 2-mm-thick black plastic cover sheet. To minimise the loss of light in transportation, the WLS fibre (attenuation length of $\approx$ 1.8 m) is spliced to a clear fibre (attenuation length of $\approx$ 8.0 m). A fibre is spliced only if the potential WLS light loss is larger than the light loss at a spliced joint. Thus depending on tile length (along η) 2–3 fibres in each pigtail are made only of WLS fibres. The clear fibres from each tile follow the guiding grooves on the top plastic to the optical connector at the end. Each tray has two optical connectors mounted on one end of the tray. In a tray, the grooves of the tiles form two rows along η. The fibres from all grooves on one row terminate on one connector (figure 5.26). The number of fibres from trays in different rings are given in table 5.7.

The bunch of fibres fixed to the optical connector is called a pigtail (figure 5.27). Each tray has 2 pigtails and there are 864 pigtails in total: 720 for layer 1 and 144 for layer 0. Each fibre in a pigtail is cut to the proper length to match the groove length in the scintillator plus the distance from the scintillator to the optical connector at the end of the tray.

Table 5.7: Tray specifications for different rings of HO.

Ring #	Tiles/tray	Fibres/tray	Fibres/connector
0	8	32	16
±1	6	24	12
±2	5	20	10

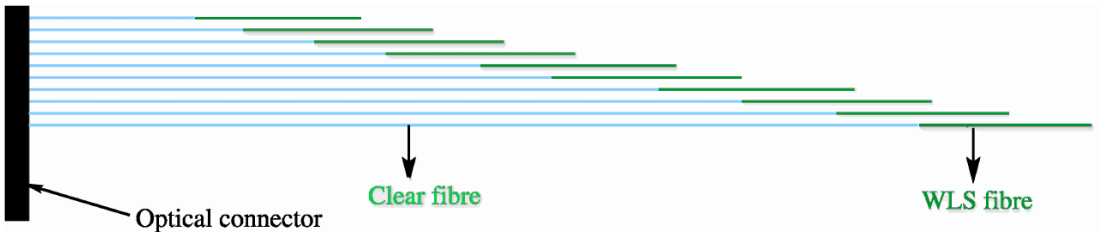

Figure 5.27: Illustration of an assembled pigtail (not drawn to scale).

5.4 Forward calorimeter design (HF)

The forward calorimeter will experience unprecedented particle fluxes. On average, 760 GeV per proton-proton interaction is deposited into the two forward calorimeters, compared to only 100 GeV for the rest of the detector. Moreover, this energy is not uniformly distributed but has a pronounced maximum at the highest rapidities. At $|\eta| = 5$ after an integrated luminosity of $5 \times 10^5\,\mathrm{pb}^{-1}$ (≈ 10 years of LHC operation), the HF will experience ≈ 10 MGy. The charged hadron rates will also be extremely high. For the same integrated luminosity, inside the HF absorber at 125 cm from the beam-line, the rate will exceed 10^{11} per cm^2 [108]. This hostile environment presents a considerable challenge to calorimetry, and the design of the HF calorimeter was first and foremost guided by the necessity to survive in these harsh conditions, preferably for at least a decade. Successful operation critically depends on the radiation hardness of the active material. This was the principal reason why quartz fibres (fused-silica core and polymer hard-cladding) were chosen as the active medium.

The signal is generated when charged shower particles above the Cherenkov threshold ($E \geq 190$ keV for electrons) generate Cherenkov light, thereby rendering the calorimeter mostly sensitive to the electromagnetic component of showers [116]. A small fraction of the generated light is captured, $f_{\mathrm{trap}} = \mathrm{NA}/2n_{\mathrm{core}}^2$, where NA is the numerical aperture ($\mathrm{NA} = 0.33 \pm 0.02$) and n_{core} is the refractive index of the quartz core. Only light that hits the core-cladding interface at an angle larger than the critical angle (71°) contributes to the calorimeter signal. The half-angle $\theta = 19°$ is determined by the refractive indices of the core (n_{core}) and the cladding (n_{clad}), $\sin\theta = \sqrt{n_{\mathrm{core}}^2 - n_{\mathrm{clad}}^2}$. The fibres measure 600 ± 10 μm in diameter for the fused-silica core, 630^{+5}_{-10} μm with the polymer hard-cladding, and 800 ± 30 μm with the protective acrylate buffer. Over 1000 km of fibres are used in the HF calorimeters. The fibres are cleaved at both ends by a diamond cutter. The attenuation length of these fibres is measured to be ≈15 m using high energy electrons at 90° to the fibres.

The optical attenuation at a wavelength λ in these types of fibres scales as $a(\lambda)(D/D_0)^{b(\lambda)}$ where D is the accumulated dose, which is normalized to a reference dose ($D_0 = 1$ MGy) for convenience. For example, at a wavelength $\lambda = 450$ nm at the accumulated dose of $D = 1$ MGy, the induced attenuation is ≈ 1.5 dB/m, thus defining a. The a and b parameters characterize the radiation hardness of a given fibre. For high OH^- (300–500 ppm) HF fibres at 450 nm, the measured values are $a \approx 1.5$ and $b \approx 0.3$ [117–119]. An accumulated dose of 10 MGy will result in a loss of optical transmission by a half, which is the worst case for HF after a decade.

The calorimeter consists of a steel absorber structure that is composed of 5 mm thick grooved plates. Fibres are inserted in these grooves. The detector is functionally subdivided into two longitudinal segments. Half of the fibres run over the full depth of the absorber (165 cm $\approx 10\lambda_I$) while the other half starts at a depth of 22 cm from the front of the detector. These two sets of fibres are read out separately. This arrangement makes it possible to distinguish showers generated by electrons and photons, which deposit a large fraction of their energy in the first 22 cm, from those generated by hadrons, which produce nearly equal signals in both calorimeter segments on average. The long fibre section is referred as L (measuring the total signal), and the short fibre section as S (measuring the energy deposition after 22 cm of steel). The absorber has grooves ($0.90^{+0.12}_{-0}$ mm wide and $1.06^{+0.6}_{-0}$ mm in depth) which make a square grid separated by 5.0 ± 0.1 mm center-to-center. Long and short fibres alternate in these grooves. The packing fraction by volume (fibre/total) in the first 22 cm is 0.57% and is twice as large beyond that depth.

The forward calorimeter is essentially a cylindrical steel structure with an outer radius of 130.0 cm. The front face of the calorimeter is located at 11.2 m from the interaction point. The hole for the beam pipe is cylindrical, with radius 12.5 cm from the center of the beam line. This structure is azimuthally subdivided into 20° modular wedges. Thirty-six such wedges (18 on either side of the interaction point) make up the HF calorimeters. A cross sectional view of the HF is shown in figure 5.28. The fibres run parallel to the beam line, and are bundled to form 0.175×0.175 ($\Delta\eta \times \Delta\phi$) towers (figure 5.29 and table 5.8). The detector is housed in a hermetic radiation shielding which consists of layers of 40 cm thick steel, 40 cm of concrete, and 5 cm of polyethylene. A large plug structure in the back of the detector provides additional shielding.

Bundled fibres are held in ferrules which illuminate one end of the air-core light guides that penetrate through 42.5 cm of the shielding matrix (steel, lead, and polyethylene). This shielding is necessary to protect the photomultipliers and the front-end electronics housed in the read-out boxes. The air-core light guide consists of a hollow tube lined on the inside with highly reflective custom-made sheets. These metal-coated reflectors are designed to be very efficient ($> 90\%$) in the visible spectrum at the relevant angles (≈ 70 degrees from normal). Light typically makes five bounces before reaching the photocathode and nearly half the light is lost in this transport. Each light guide is coupled to a standard bialkaline, 8-stage photomultiplier tube with a borosilicate glass window. A read-out box (RBX) houses 24 PMTs and services half of a wedge (10° in ϕ).

The entire calorimeter system, with its shielding components, is mounted on a rigid table which supports more than 240 t with less than 1 mm deflection. The absorber alone weighs 108 t. The table is also designed for horizontal separation of the detector into two sections to clear the beam pipe at installation and removal. It is possible to align the forward calorimeters within ± 1 mm with respect to the rest of the CMS experiment.

2008 JINST 3 S08004

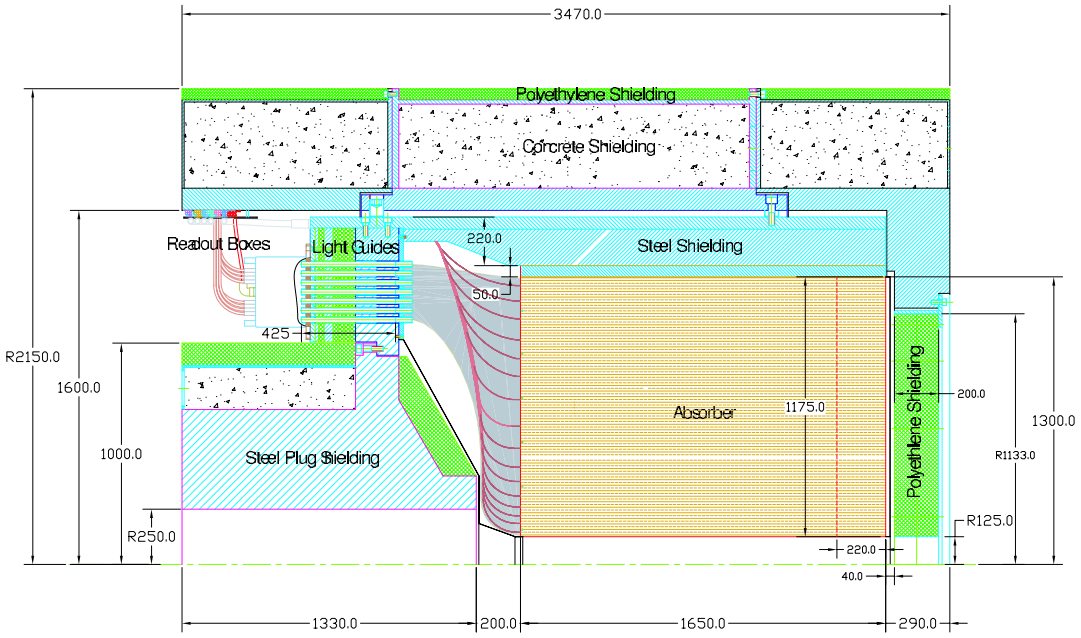

Figure 5.28: The cross sectional view of the HF calorimeter shows that the sensitive area extends from 125 to 1300 mm in the radial direction. The absorber in the beam direction measures 1650 mm. Bundled fibres (shaded area) are routed from the back of the calorimeter to air-core light guides which penetrate through a steel-lead-polyethlene shielding matrix. Light is detected by PMTs housed in the read-out boxes. Stainless steel radioactive source tubes (red lines) are installed for each tower and are accessible from outside the detector for source calibration. The interaction point is at 11.2 meters from the front of the calorimeter to the right. All dimensions are in mm.

The inner part of HF ($4.5 < |\eta| < 5$) will experience radiation doses close to 100 Mrad/year, and large neutron fluxes leading to activation of the absorber material, reaching several mSv/h in the region closest to the beam line after 60 days of running at $10^{34}\,\mathrm{cm}^{-2}\mathrm{s}^{-1}$ luminosity and one day of cooling down. The active elements of HF (quartz fibres) are sufficiently radiation-hard to survive these levels of radiation with limited deterioration. The PMTs are shielded behind 40 cm of steel and borated polyethylene slabs. HF, using Cherenkov light from quartz fibres, is practically insensitive to neutrons and to low energy particles from the decay of activated radionucleids. Further shielding around HF achieves activation levels below 10 μSv/h on the periphery of the detector. A 10-cm-thick lead plate, located in front of HF during operations around the detector, reduces personal exposure to radiation from the absorber. Maintenance of read-out boxes will be performed with the help of semi-automatic extractor tools. HF is equipped with radiation monitors located at the periphery of the detector, and with a system (Raddam) to measure the transmission properties of a few reference quartz fibres embedded in the absorber, as a function of integrated luminosity.

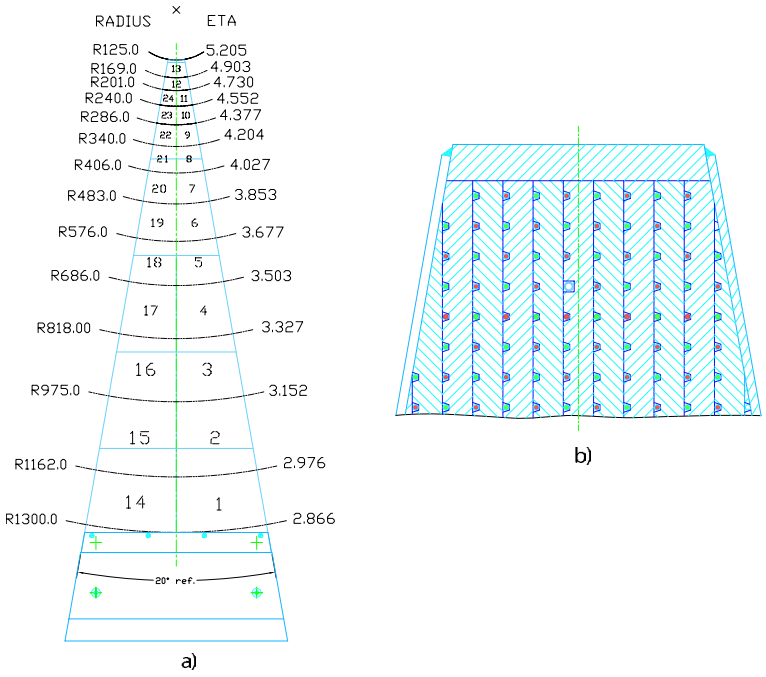

Figure 5.29: a) Transverse segmentation of the HF towers. b) An expanded view of the wedge shows the squared out groove holding the radioactive source tube.

Table 5.8: The tower sizes, number of fibres, bundle sizes and the percentage of photocathode area utilized are listed below for each tower. The air-core light guides are tapered to better match the photocathode area for towers 1, 2 and 3.

Ring No	$(r_{\text{in}}, r_{\text{out}})$ [mm]	$\Delta\eta$	$\Delta\phi$ [degree]	N_{fib}	A_{bundle} [mm^2]	$\frac{A_{\text{bundle}}}{A_{\text{photocathode}}}$
1	(1162–1300)	0.111	10	594	551	1.14
2	(975–1162)	0.175	10	696	652	1.33
3	(818–975)	0.175	10	491	469	0.96
4	(686–818)	0.175	10	346	324	0.66
5	(576–686)	0.175	10	242	231	0.47
6	(483–576)	0.175	10	171	167	0.34
7	(406–483)	0.175	10	120	120	0.25
8	(340–406)	0.175	10	85	88	0.18
9	(286–340)	0.175	10	59	63	0.13
10	(240–286)	0.175	10	41	46	0.94
11	(201–240)	0.175	10	30	35	0.71
12	(169–201)	0.175	20	42	52	0.11
13	(125–169)	0.300	20	45	50	0.10

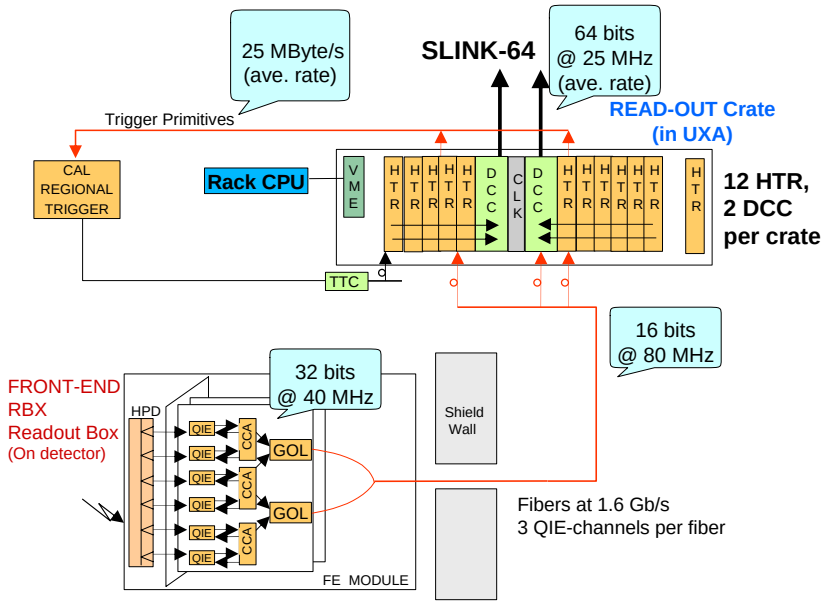

Figure 5.30: Overview of HCAL read-out electronics.

5.5 Read-out electronics and slow control

The overview of the full HCAL read-out chain is shown in figure 5.30. The read-out consists of an optical to electrical transducer followed by a fast charge-integrating ADC. The digital output of the ADC is transmitted for every bunch over a gigabit digital optical fibre to the service cavern, housing the off-detector electronics. In the service cavern, the signal is deserialized and used to construct trigger primitives which are sent to the calorimeter trigger. The data and trigger primitives are also pipelined for transmission to the DAQ upon a Level-1 Accept (L1A) decision.

The optical signals from the scintillator-based detectors (HB/HE/HO) are converted to electrical signals using multichannel hybrid photodiodes (HPDs) which provide a gain of ≈ 2000. A detailed view of the scintillator-based front-end read-out chain is given in figure 5.31. The optical signals from individual sampling layers are brought out on clear fibres. The fibres corresponding to a projective calorimeter tower are mapping via an optical decoding unit (ODU) to a cookie that interfaces to individual pixels on the HPD. In the forward calorimeter, where the magnetic fields are much smaller than in the central detector, conventional photomultiplier tubes (Hamamatsu R7525HA) are used and quartz-fibre bundles are routed directly to the phototube windows.

An overview of the HCAL controls is given in figure 5.32. Several PCs in the CMS control room operated through PVSS are used to control high and low voltages. The control system also downloads pedestal DAC and timing parameters to front-ends and controls many of the calibration and monitoring systems including the source calibration drivers, the LED pulsers, and the laser system. These systems record temperature, humidity and other constants useful for correlation studies of detector/calibration stability.

The configuration database contains the relationships or mapping for all HCAL detector components: wedges, layers, read-out boxes (RBX), cables, HCAL Trigger (HTR) cards, and calibra-

2008 JINST 3 S08004

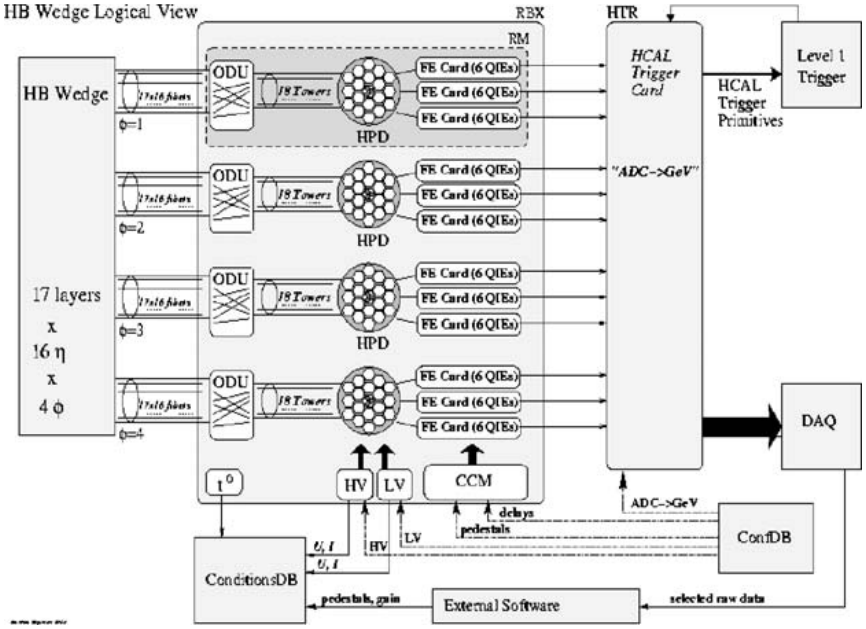

Figure 5.31: Overview of HCAL read-out/trigger chain and connections to database.

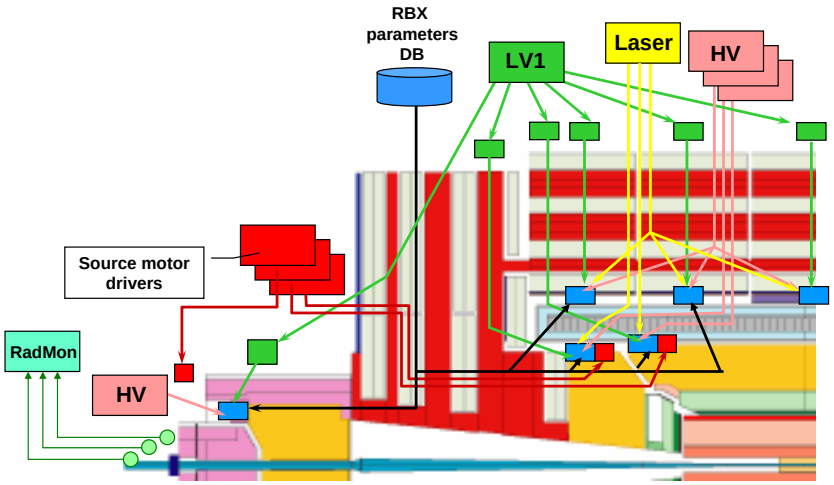

Figure 5.32: Overview of HCAL detector controls.

tion parameters for various components e.g. RBX, QIE, source types and strength. The conditions database has the slow-controls logging, the calibration constants (pedestals, gains, timing information, etc.) and the configuration database downloaded to the read-out system during the initialization.

The analogue signal from the HPD or photomultiplier is converted to a digital signal by a charge-integrating ADC ASIC called the QIE (Charge-Integrator and Encoder). The QIE internally contains four capacitors which are connected in turn to the input, one during each 25 ns period. The integrated charge from the capacitors is converted to a seven-bit non-linear scale to cover the

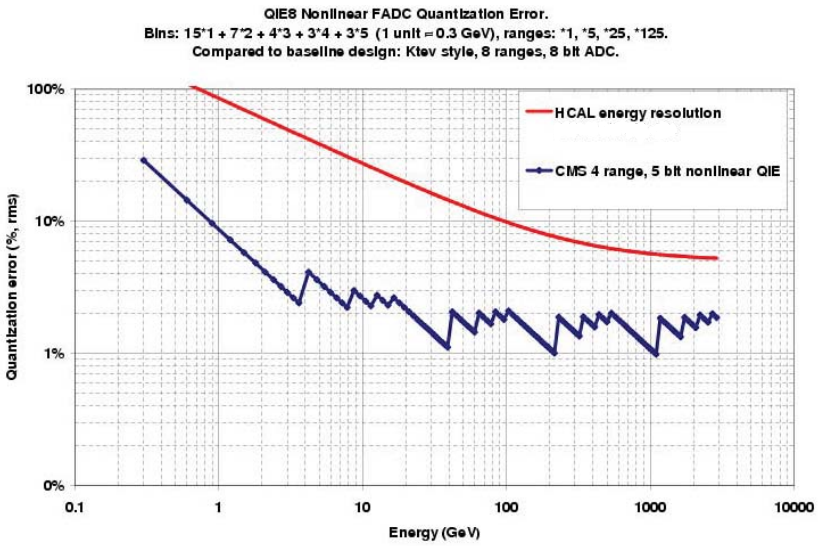

Figure 5.33: Contribution of the FADC quantization error to the resolution, compared with a representative HCAL resolution curve.

large dynamic range of the detector. The ADC is designed so its contribution to the detector energy resolution over its multi-range operation is negligible, as shown in figure 5.33. The QIE input characteristics were chosen from test beam data to optimize speed and noise performance. This resulted in a per channel RMS noise of 4600 electrons (0.7 fC) corresponding to about 180 MeV.

The digital outputs of three QIE channels are combined with some monitoring information to create a 32-bit data word. The 32-bit data, at a rate of 40 MHz, is fed into the Gigabit Optical Link (GOL) chip and transmitted using 8b/10b encoding off the detector to the service cavern. In the service cavern, the data is received by the HCAL Trigger/Read-out (HTR) board. The HTR board contains the Level-1 pipeline and also constructs the trigger primitives for HCAL. These trigger primitives are sent to the Regional Calorimeter trigger via Serial Link Board mezzanine cards. The HTR board receives data for 48 channels (16 data fibres) and may host up to six SLBs.

When a L1A is received by the HTR through the TTC system, it prepares a packet of data for the DAQ including a programmable number of precision read-out values and trigger primitives around the triggered bunch crossing. For normal operations, the HTR will transmit 7 time samples for each non-zero channel and a single trigger primitive for every trigger tower. These packets of data, each covering 24 channels, are transmitted by LVDS to the HCAL Data Concentrator Card (DCC). The DCC is the HCAL Front-End Driver (FED) and concentrates the data from up to 360 channels for transmission into the DAQ.

The Level-1 trigger primitives (TPG) are calculated in the HTR modules. The QIE data are linearized and converted to transverse energy with a single look up table. Two or more consecutive time samples are summed. A sum over depth is made for those towers having longitudinal segmentation. A final look up table is used to compress the data before sending the data across the trigger link to the regional calorimeter trigger. Table 5.9 summarizes the geometry of the trigger towers. The HF towers are summed in η and ϕ before being sent to the trigger.

2008 JINST 3 S08004

Table 5.9: Sizes of the HCAL trigger towers in η and ϕ.

Tower index	$\lvert\eta_{\text{max}}\rvert$	Detector	Size	
			η	ϕ
1–15	$0.087\times\eta$	HB	0.087	5°
16	1.392	HB, HE	0.087	5°
17–20	$0.087\times\eta$	HE	0.087	5°
21	1.830	HE	0.090	5°
22	1.930	HE	0.100	5°
23	2.043	HE	0.113	5°
24	2.172	HE	0.129	5°
25	2.322	HE	0.150	5°
26	2.500	HE	0.178	5°
27	2.650	HE	0.150	5°
28	3.000	HE	0.350	5°
29	3.314	HF	0.461	20°
30	3.839	HF	0.525	20°
31	4.363	HF	0.524	20°
32	5.191	HF	0.828	20°

Timing and synchronization

The QIE integration clock is controlled by the Channel Control ASIC (CCA) which allows for fine-skewing of the integration phase of each tower relative to the machine clock. This allows each channel's integration phase to correct for differences in the time-of-flight from the interaction region as well as differences in the optical pathlength within the detector.

Figure 5.34 shows that scintillator tile signals produce relatively fast pulses such that 68% of the pulse is contained within a 25 ns window. Figure 5.35 shows the pulse shape for the forward calorimeter. The Cerenkov process and the phototubes used in the forward calorimeter are extremely fast, so the pulse in HF is only 10 ns wide. The HF is thus subject only to in-time pile-up which is important in the highly active forward region of CMS.

An additional important effect on the HCAL pulse timing in HB/HE/HO comes from the input stage of the QIE. The QIE has an amplitude-dependent impedance which implies a faster pulse shape for large signals than for small ones, as seen in figure 5.36. The amount of time slewing is dependent on the noise characteristics of the QIE, so the final QIE ASICs for the barrel and endcap were chosen to limit the timeslew to the "medium" case in exchange for somewhat increased noise. In the outer calorimeter, the noise level is a critical factor for muon identification and pile-up is much less important so the quieter "slow" characteristics were chosen for the HO QIEs.

The in-situ synchronization of HCAL is performed using the HCAL laser system. The laser system consists of a single UV laser which can illuminate an entire half-barrel of HB or a single endcap at once through a series of optical splitters. The quartz fibres which lead from the laser to the detector have been carefully controlled to equalize the optical path length to each wedge. The laser can be directed either straight onto a scintillator block connected to the HPD or into the

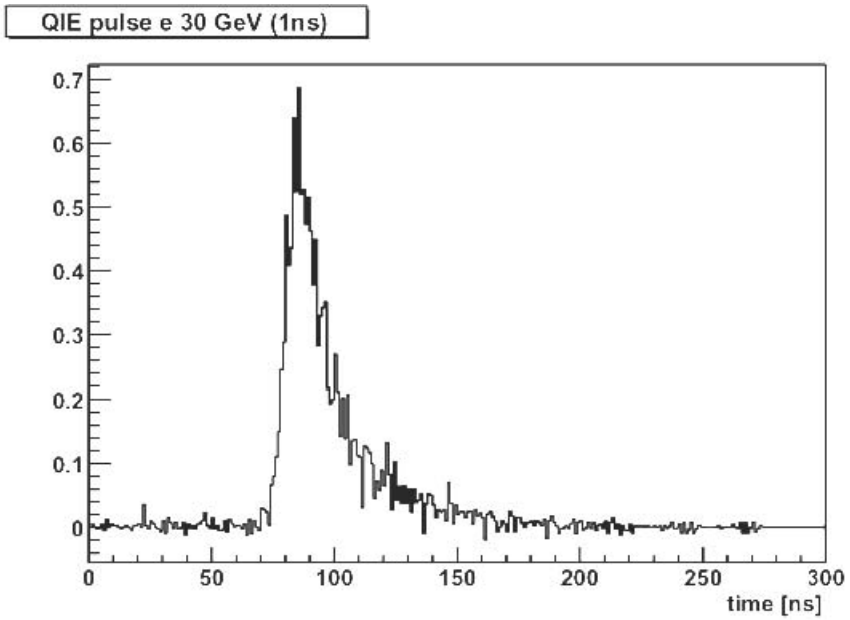

Figure 5.34: Measured single event pulse shape from the scintillator tiles, representative of HB/HE/HO pulse shapes.

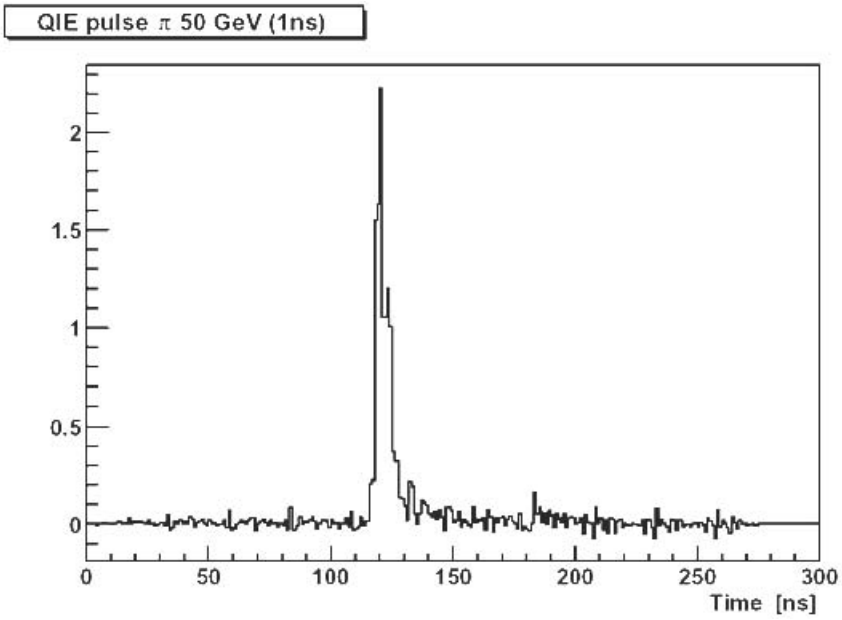

Figure 5.35: Measured pulse shape, energy collected vs. time, for HF.

wedge. Within layer 9 of each wedge is an arrangement of optical fibres which mimic the time-of-flight from the interaction region. This arrangement allows the timing of HCAL to be flattened and monitored, as has been demonstrated in test beam data taking, which verified the timing determined by the laser using the synchronized beam. In the HO and HF detectors, only the photodetector can be illuminated so the alignment will be based on construction and test beam data.

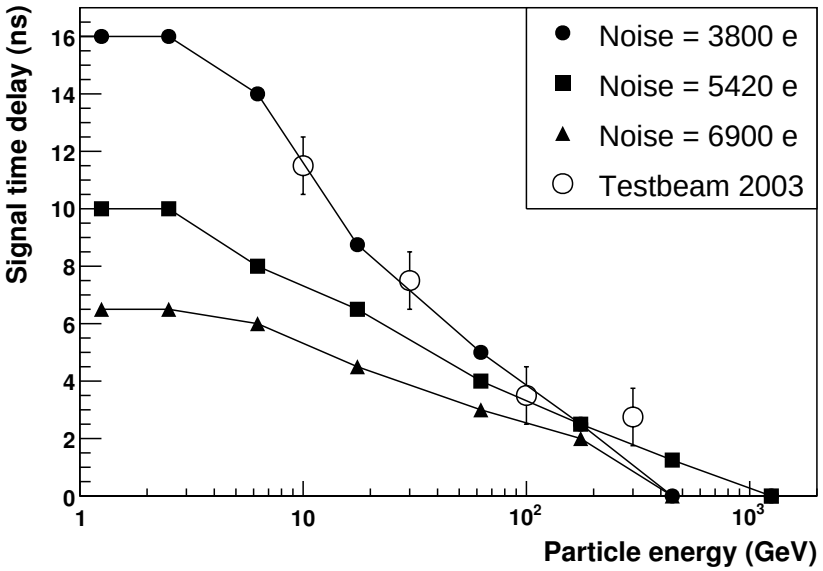

Figure 5.36: Pulse time variation as a function of signal amplitude as measured on the bench (solid points) for several input amplifier configurations compared with test beam measurements from 2003.

The channel-by-channel bunch synchronization of HCAL will be determined using a histogramming procedure in the serial link boards (SLBs) which determine the bunch synchronization using the beam structure of the LHC. The event and bunch synchronization is monitored using fast control signals originating from the TTC system which are transmitted in the data stream between the front-ends and the HTR. On a global scale, the bunch and event synchronization between the HCAL and other detector subsystems is determined using muons and other correlated physics signals.

5.6 HF luminosity monitor

The CMS luminosity measurement will be used to monitor the LHC's performance on a bunch-by-bunch basis in real time and to provide an overall normalization for physics analyses. The design goal for the real-time measurement is to determine the average luminosity with a 1% statistical accuracy with an update rate of 1 Hz. For offline analyses, the design goal is a systematic accuracy of 5%, although every reasonable effort will be made to produce a more accurate result. Both of these requirements must be met over a very large range of luminosities, extending from roughly 10^{28} cm^{-2}s^{-1} to 10^{34} cm^{-2}s^{-1}, and possibly beyond.

A number of techniques capable of providing suitable luminosity information in real time have been identified [17]. One technique employs signals from the forward hadron calorimeter (HF) while another, called the Pixel Luminosity Telescope (PLT), uses a set of purpose-built particle tracking telescopes based on single-crystal diamond pixel detectors. At the time of writing, the PLT has not been formally approved, but is under study. The methods based on signals from the HF are the ones being most vigorously pursued.

2008 JINST 3 S08004

Two methods for extracting a real-time relative instantaneous luminosity with the HF have been studied. The first method is based on *zero counting* in which the average fraction of empty towers is used to infer the mean number of interactions per bunch crossing. The second method exploits the linear relationship between the average transverse energy per tower and the luminosity.

Outputs of the QIE chips used to digitize the signals from the HF PMTs on a bunch-by-bunch basis are routed to a set of 36 HCAL Trigger and Read-out (HTR) boards, each of which services 24 HF physical towers. In order to derive a luminosity signal from the HTR, an additional mezzanine board called the HF luminosity transmitter (HLX) is mounted on each of the HTR boards. The HLX taps into the raw HF data stream and collects channel occupancy and E_T-sum data and transmits them to a central collector node over standard 100-Mbps Ethernet. The HLX boards have the same form factor as the Synchronization and Link Boards (SLBs) used to interface the ECAL and HCAL readouts to the Regional Calorimeter Trigger (RCT) system.

Although all HF channels can be read by the HLX, MC studies indicate that the best linearity for occupancy histograms is obtained using just two η rings. Hence two sets of two rings are used for the occupancy histograms. Four rings are combined to form the E_T-sum histogram. The algorithm has been optimized to minimize sensitivity to pedestal drifts, gain changes and other related effects. Each of the two sets of rings sends 12 bits of data to the HLX. There are three occupancy histograms dedicated to each of the following possible states for each tower: enabled-below-threshold, over-threshold-1, over-threshold-2. In addition, a 15-bit E_T sum value is sent to the HLX and a further histogram based on all 13 HF η rings is filled for use by the LHC. As a result, the input to the HLX is used to create eight histograms: two sets of three occupancy histograms, one E_T-sum histogram, and one additional occupancy histogram.

Each histogram has 3564 bins, one for each bunch in the LHC orbit. Each occupancy-histogram bin uses two bytes, and there are four bytes per bin in the E_T sum histogram. The baseline design is to add the results from all desirable channels into a single set of histograms.

The histograms are transmitted as UDP (User Datagram Protocol) packets from the HLX cards once roughly every 0.37 s, which is safely within the 1.45 s (worst case) histogram overflow time. The Ethernet core in the HLX automatically packages the data to make optimal use of network bandwidth. Each histogram spans several Ethernet packets, the precise number depending on the type of histogram. The eight sets of histograms comprise about 70 kB of data, which is transmitted at a rate of approximately 1.6 Mbps to an Ethernet switch that aggregates the data from multiple HLX boards. The switch multi-casts the data to a pair of luminosity server nodes. One of the servers is responsible for publishing the luminosity information to various clients, such as the CMS and LHC control rooms and the Fermilab Remote Operations Center (ROC). The second server archives the data for each luminosity section (one luminosity section corresponds to 2^{20} orbits, or about 93 s). An XDAQ layer on this server makes it possible to communicate with other CMS DAQ systems.

2008 JINST 3 S08004

Chapter 6

Forward detectors

6.1 CASTOR

The CASTOR (Centauro And Strange Object Research) detector is a quartz-tungsten sampling calorimeter [120], designed for the very forward rapidity region in heavy ion and proton-proton collisions at the LHC. Its physics motivation is to complement the nucleus-nucleus physics programme [122], developed essentially in the baryon-free mid-rapidity region, and also the diffractive and low-x physics in pp collisions [123]. CASTOR will be installed at 14.38 m from the interaction point, covering the pseudorapidity range $5.2 < |\eta| < 6.6$. Figure 6.1 shows the location of CASTOR in the CMS forward region. The calorimeter will be constructed in two halves surrounding the beam pipe when closed, as shown in figure 6.2. The calorimeter and its readout are designed in such a way as to permit the observation of the cascade development of the impinging particles as they traverse the calorimeter. The typical total and electromagnetic energies in the CASTOR acceptance range (about 180 TeV and 50 TeV, respectively, according to HIJING [121] Pb-Pb simulations at 5.5 TeV) can be measured with a resolution better than $\approx$1%.

The main advantages of quartz calorimeters are radiation hardness, fast response and compact detector dimensions [124], making them suitable for the experimental conditions encountered in the very forward region at the LHC. The typical visible transverse sizes of hadronic and electromagnetic showers in quartz calorimeters are 5–10 cm and about 10 mm respectively (for 95% signal containement), i.e. are a factor 3 to 4 times narrower than those in "standard" (scintillation) calorimeters [124]. A detailed description of the operation principle (including optimal geometrical specifications of the quartz and tungsten plates, and performances of light-guides, reflectors and photodetectors) can be found in references [125, 126].

Tungsten-Quartz plates

The CASTOR detector is a Cerenkov-based calorimeter, similar in concept to the HF. It is constructed from layers of tungsten (W) plates (alloy density $\approx$ 18.5 g/cm^3) as absorber and fused silica quartz (Q) plates as active medium. For the electromagnetic (EM) section, the W plates have a thickness of 5.0 mm and the Q plates 2.0 mm. For the hadronic (HAD) section, the W and Q plates have thicknesses of 10.0 mm and 4.0 mm, respectively. The W/Q plates are inclined 45° with respect to the direction of the impinging particles, in order to maximize the Cerenkov light

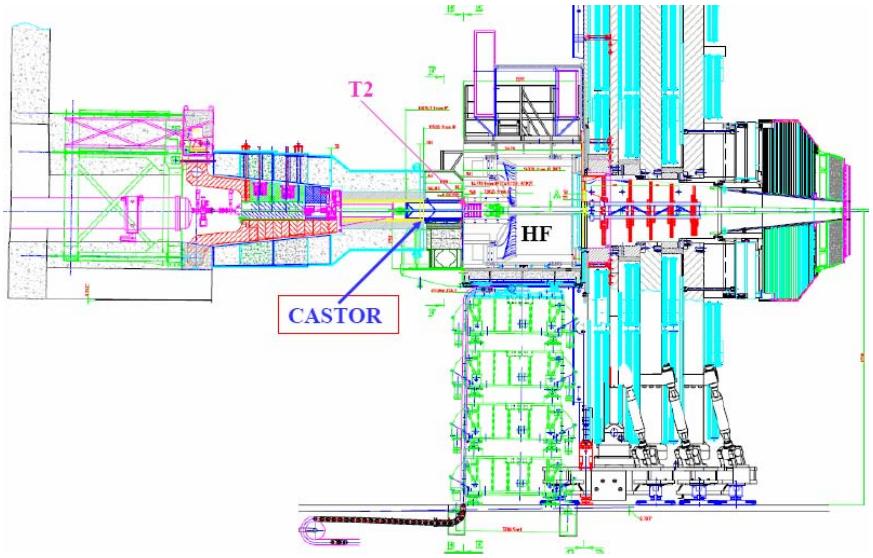

Figure 6.1: Location of CASTOR in the CMS forward region.

output in the quartz. The combination of one W and one Q plate is called a sampling unit (SU). Figure 6.3 shows the complicated geometry of the W/Q plates, due to their 45° inclination.

In the EM section, each sampling unit corresponds to 2.01 X_0 (0.077 λ_I). Each readout unit (RU) consists of 5 SUs and is 10.05 X_0 (0.385 λ_I) deep. The EM section is divided in two successive RUs and has a total of 20.1 X_0 (0.77 λ_I). In the hadronic section, a sampling unit corresponds to 0.154 λ_I. Each readout unit consists of 5 SUs and is 0.77 λ_I deep. The HAD section has 12 RUs, corresponding to 9.24 λ_I. In total, the calorimeter has 10 λ_I. The total number of channels is 224.

Light-guides and photodetectors

The Cerenkov light, produced by the passage of relativistic charged particles through the quartz medium, is collected in sections (RUs) along the length of the calorimeters and focused by air-core light guides onto the photomultiplier (PMT), as shown in figure 6.3. The inside surfaces of the light guides are covered with Dupont [AlO+ SiO_2+TiO_2] reflective foil. The light guide is made out of a 0.8 mm stainless steel sheet. Each light guide subtends 5 SUs in both the EM and HAD sections. The PMT is located in the aluminium housing on the top. Two types of PMTs are currently under consideration: (i) a Hamamatsu R7899 PMT, and (ii) a radiation-hard multi-mesh, small-size PMT FEU-187 produced by Research Institute Electron (RIE, St. Petersburg), with cathode area ≈2 cm^2. Both PMTs allow the muon MIP peak to be separated from the pedestal, an important feature for calibration purposes.

Beam tests results

The energy linearity and resolution as well as the spatial resolution of two CASTOR prototypes have been studied at CERN/SPS tests in 2003 [125] and 2004 [126] (as well as in tests end-of-summer 2007, for the final prototype). The response of the calorimeter to electromagnetic and

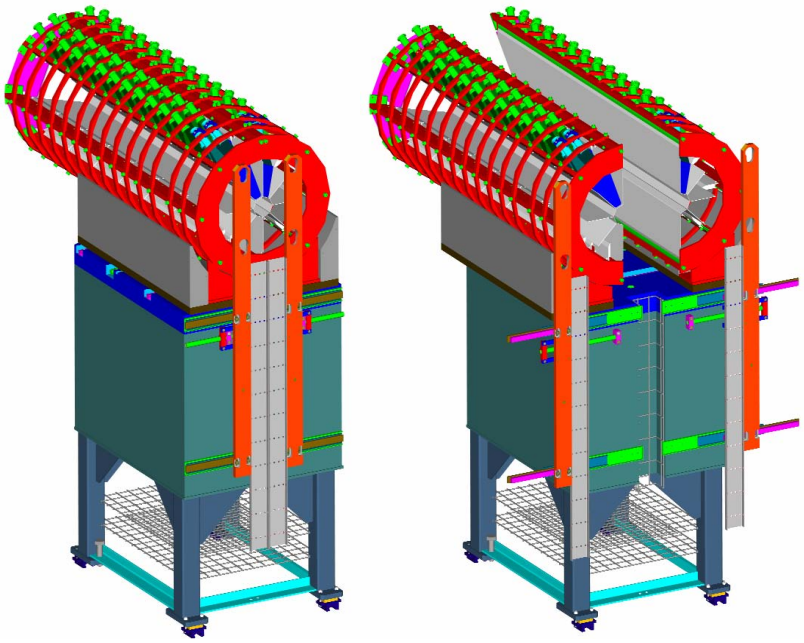

Figure 6.2: CASTOR calorimeter and support.

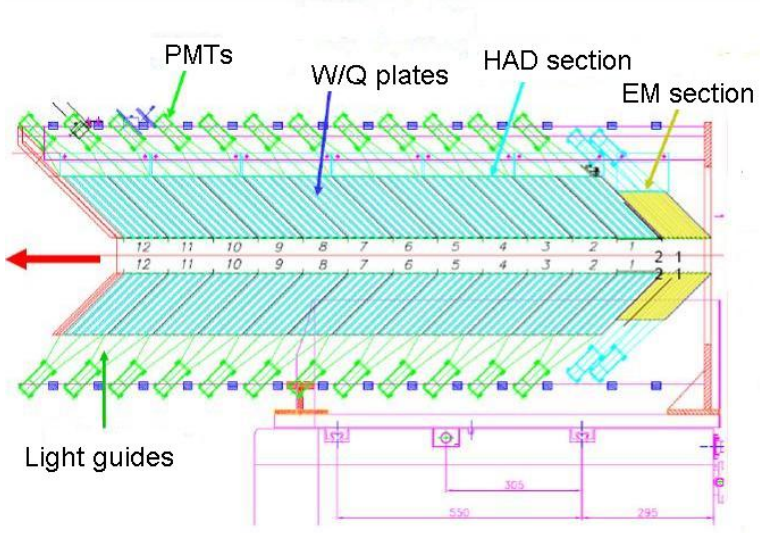

Figure 6.3: Details of the components and geometry of the CASTOR calorimeter.

hadronic showers has been analysed with $E = 20$–200 GeV electrons, $E = 20$–350 GeV pions, and $E = 50$, 150 GeV muons. Good energy linearity for electrons and pions in the full range tested is observed. For the EM section, the constant term of the energy resolution, that limits performance at high energies, is less than 1%, whereas the stochastic term is $\approx 50\%$. The measured spatial resolution of the electron (pion) showers is $\sigma_{\mathrm{EM(HAD)}} = 1.7$ (6.4) mm.

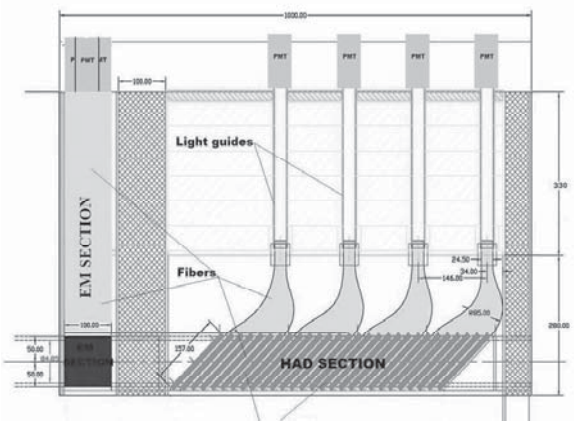

Figure 6.4: The side view of the ZDC showing the EM and HAD sections.

Figure 6.5: Photograph of the ZDC HAD section.

6.2 Zero degree calorimeter (ZDC)

A set of two zero degree calorimeters [127, 128], with pseudorapidity coverage of $|\eta| \geq 8.3$ for neutral particles, are designed to complement the CMS very forward region, especially for heavy ion and pp diffractive studies. Each ZDC has two independent parts: the electromagnetic (EM) and hadronic (HAD) sections. Two identical ZDCs will be located between the two LHC beam pipes at ≈140 m on each side of the CMS interaction region at the detector slot of 1 m length, 96 mm width and 607 mm height inside the neutral particle absorber TAN [129]. The TAN is located in front of the D2 separation dipole. It was designed to protect magnets and detectors against debris generated in the pp collisions, and against beam halo and beam losses. During heavy ion running the combined (EM + HAD) calorimeter should allow the reconstruction of the energy of 2.75 TeV spectator neutrons with a resolution of 10–15%. Sampling calorimeters using tungsten and quartz fibers have been chosen for the detection of the energy in the ZDCs with a design similar to HF and CASTOR. The quartz-quartz fibers [127] can withstand up to 30 GRad with only a few percent loss in transparency in the wavelength range 300–425 nm. During the low-luminosity pp (10^{33} cm^{-2}s^{-1}) and design-luminosity Pb-Pb (10^{27} cm^{-2}s^{-1}) runs, the expected average absorbed radiation doses is about 180 MGy and 300 kGy, respectively, per data-taking year.

Figure 6.4 shows a side view of the ZDC with the EM section in front and the HAD section behind. A photo of the HAD section is shown in figure 6.5. The total depth of the combined system is ≈7.5 hadronic interaction lengths (λ_I). The configuration includes 9 mm Cu plates in the front and back of each section. For the TAN's final detector configuration an LHC real-time luminosity monitor (BRAN, Beam RAte of Neutrals [130]) will be mounted in the 120 mm space between the ZDC's calorimetric sections. The HAD section consists of 24 layers of 15.5 mm thick tungsten plates and 24 layers of 0.7 mm diameter quartz fibers (6.5 λ_I). The tungsten plates are tilted by 45° to optimize Cerenkov-light output. The EM section is made of 33 layers of 2-mm-thick tungsten plates and 33 layers of 0.7-mm-diameter quartz fibers (19 X_0). The tungsten plates are oriented vertically. The fibers are laid in ribbons. The hadronic section of each ZDC requires 24 fiber ribbons. After exiting the tungsten plates the fibers from 6 individual ribbons are grouped together to form a readout bundle. This bundle is compressed and glued with epoxy into a tube. From there,

2008 JINST 3 S08004

an optical air-core light guide will carry the light through radiation shielding to the photomultiplier tube. The full hadronic section will consist of four identical towers divided in the longitudinal direction. For the electromagnetic section, fibers from all 33 fiber ribbons will be divided in the horizontal direction into five identical fiber bundles. These 5 bundles will form five horizontal towers and each fiber bundle will be mounted with a 0.5 mm air gap from the photocathode of a phototube. The EM and HAD sections will be instrumented with the same type of phototube as the HF: Hamamatsu R7525 phototubes with a bi-alkali photocathode, resulting in an average quantum efficiency for Cerenkov light of about 10%.

There are a total of 18 readout channels for the two ZDCs. The signals from the ZDCs are transmitted through a long (210 m) coaxial cable to the front-end HCAL VME crates in the underground counting room (USC55). The signal from each channel will be split, with 90% going to the QIE (Charge Integrator and Encoder) while 10% will be used for making trigger signals. An analog sum, proportional to the total energy deposition in each detector, will provide the basic Level 1 trigger in the heavy-ion running mode: the coincidence of (neutron) signals from both sides of the interaction point is sensitive to most of the nuclear and electromagnetic cross section. A left-right timing coincidence will also be used as a fast vertex trigger, to suppress beam-gas events in the heavy ion runs. Information from scalers will be used for tuning the interaction of beams and for defining the real-time luminosity. Finally it may be possible to improve the overall energy resolution of the system by looking at the correlation between the ZDC and the BRAN detector, which sits between the electromagnetic and hadronic sections, near the shower maximum.

The response of the ZDC EM and HAD sections has been studied in beam tests at the CERN/SPS in 2006 [131] and 2007. The calorimeter is found to be linear within 2% in the range from 20 GeV to 100 GeV. The energy resolution obtained for the different positron energies can be parametrized as

$$\left(\frac{\sigma}{E}\right)^2 = \left(\frac{70\%}{\sqrt{E}}\right)^2 + (8\%)^2 \tag{6.1}$$

where E is in GeV. Positive pions with energies of 150 GeV and 300 GeV were used to measure the response of the combined EM+HAD system. The pion energy resolution, obtained by a Landau fit, can be parametrized as

$$\frac{\sigma}{E} = \frac{138\%}{\sqrt{E}} + 13\% \tag{6.2}$$

where E, again, is in GeV. The width of EM showers is ≈5 mm. Such a good position resolution will allow measurement of the beam crossing angle with a resolution of ≈10 mrad.

The performance of both the left and right ZDCs has been studied with electron, pion and muon beams in 2007. Figure 6.6 shows online plots for positrons entering the electromagnetic section of one calorimeter.

2008 JINST 3 S08004

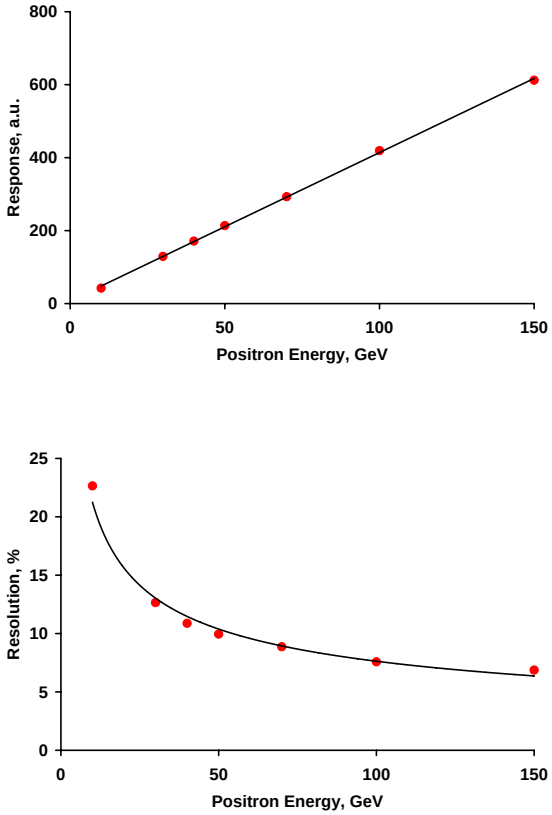

Figure 6.6: Online results for positrons from the 2007 test beam. The top panel shows the response linearity, while the bottom panel gives the energy resolution as a function of the incoming positron beam energy.

Chapter 7

The muon system

Muon detection is a powerful tool for recognizing signatures of interesting processes over the very high background rate expected at the LHC with full luminosity. For example, the predicted decay of the Standard Model Higgs boson into ZZ or ZZ*, which in turn decay into 4 leptons, has been called "gold plated" for the case in which all the leptons are muons. Besides the relative ease in detecting muons, the best 4-particle mass resolution can be achieved if all the leptons are muons because they are less affected than electrons by radiative losses in the tracker material. This example, and others from SUSY models, emphasize the discovery potential of muon final states and the necessity for wide angular coverage for muon detection.

Therefore, as is implied by the experiment's middle name, the detection of muons is of central importance to CMS: precise and robust muon measurement was a central theme from its earliest design stages. The muon system has 3 functions: muon identification, momentum measurement, and triggering. Good muon momentum resolution and trigger capability are enabled by the high-field solenoidal magnet and its flux-return yoke. The latter also serves as a hadron absorber for the identification of muons. The material thickness crossed by muons, as a function of pseudorapidity, is shown in figure 7.1.

The CMS muon system is designed to have the capability of reconstructing the momentum and charge of muons over the the entire kinematic range of the LHC. CMS uses 3 types of gaseous particle detectors for muon identification [132]. Due to the shape of the solenoid magnet, the muon system was naturally driven to have a cylindrical, barrel section and 2 planar endcap regions. Because the muon system consists of about 25 000 m^2 of detection planes, the muon chambers had to be inexpensive, reliable, and robust.

In the barrel region, where the neutron-induced background is small, the muon rate is low, and the 4-T magnetic field is uniform and mostly contained in the steel yoke, drift chambers with standard rectangular drift cells are used. The barrel drift tube (DT) chambers cover the pseudorapidity region $|\eta| < 1.2$ and are organized into 4 stations interspersed among the layers of the flux return plates. The first 3 stations each contain 8 chambers, in 2 groups of 4, which measure the muon coordinate in the r-ϕ bending plane, and 4 chambers which provide a measurement in the z direction, along the beam line. The fourth station does not contain the z-measuring planes. The 2 sets of 4 chambers in each station are separated as much as possible to achieve the best angular resolution. The drift cells of each chamber are offset by a half-cell width with respect to their

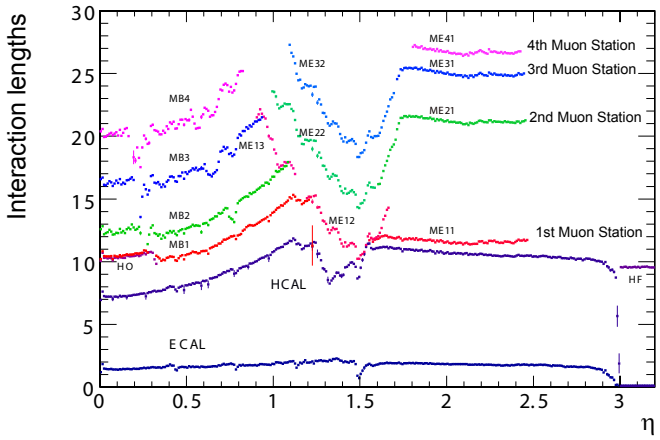

Figure 7.1: Material thickness in interaction lengths at various depths, as a function of pseudorapidity.

neighbor to eliminate dead spots in the efficiency. This arrangement also provides a convenient way to measure the muon time with excellent time resolution, using simple meantimer circuits, for efficient, standalone bunch crossing identification. The number of chambers in each station and their orientation were chosen to provide good efficiency for linking together muon hits from different stations into a single muon track and for rejecting background hits.

In the 2 endcap regions of CMS, where the muon rates and background levels are high and the magnetic field is large and non-uniform, the muon system uses cathode strip chambers (CSC). With their fast response time, fine segmentation, and radiation resistance, the CSCs identify muons between $|\eta|$ values of 0.9 and 2.4. There are 4 stations of CSCs in each endcap, with chambers positioned perpendicular to the beam line and interspersed between the flux return plates. The cathode strips of each chamber run radially outward and provide a precision measurement in the r-ϕ bending plane. The anode wires run approximately perpendicular to the strips and are also read out in order to provide measurements of η and the beam-crossing time of a muon. Each 6-layer CSC provides robust pattern recognition for rejection of non-muon backgrounds and efficient matching of hits to those in other stations and to the CMS inner tracker.

Because the muon detector elements cover the full pseudorapidity interval $|\eta| < 2.4$ with no acceptance gaps, muon identification is ensured over the range corresponding to $10^\circ < \theta < 170^\circ$. Offline reconstruction efficiency of simulated single-muon samples (figure 7.2) is typically 95–99% except in the regions around $|\eta| = 0.25$ and 0.8 (the regions between 2 DT wheels) and $|\eta| = 1.2$ (the transition region between the DT and CSC systems), where the efficiency drops. Negligible punchthrough reaches the system due to the amount of material in front of the muon system, which exceeds 16 interaction lengths [132].

Due to multiple-scattering in the detector material before the first muon station, the offline muon momentum resolution of the standalone muon system is about 9% for small values of η and p for transverse momenta up to 200 GeV [17]. At 1 TeV the standalone momentum resolution varies between 15% and 40%, depending on $|\eta|$. A global momentum fit using also the inner tracker

2008 JINST 3 S08004

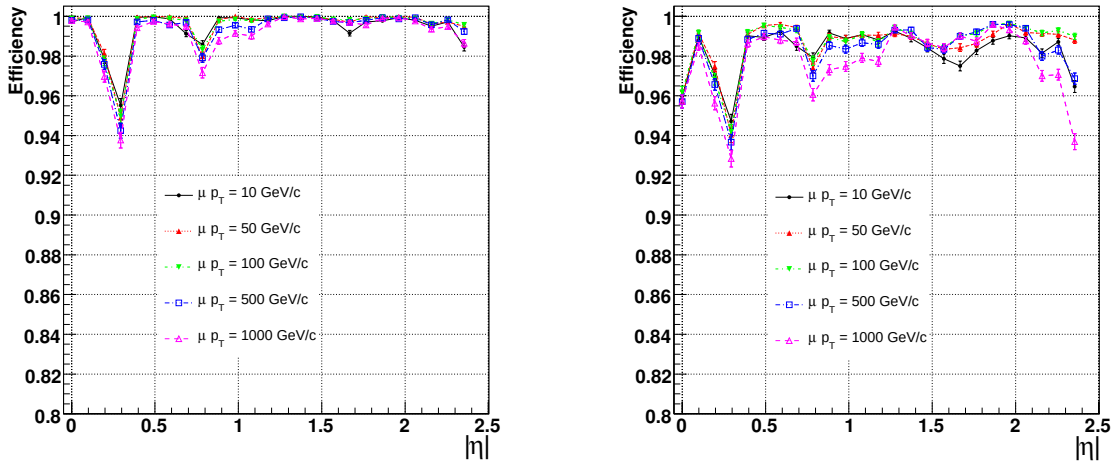

Figure 7.2: Muon reconstruction efficiency as a function of pseudorapidity for selected values of p_T. Left panel: standalone reconstruction (using only hits from the muon system with a vertex constraint). Right panel: global reconstruction (using hits from both the muon system and the tracker).

improves the momentum resolution by an order of magnitude at low momenta. At high momenta (1 TeV) both detector parts together yield a momentum resolution of about 5% (figure 1.2). Note that the muon system and the inner tracker provide independent muon momentum measurements; this redundancy enhances fault finding and permits cross-checking between the systems.

A crucial characteristic of the DT and CSC subsystems is that they can each trigger on the p_T of muons with good efficiency and high background rejection, independent of the rest of the detector. The Level-1 trigger p_T resolution is about 15% in the barrel and 25% in the endcap.

Because of the uncertainty in the eventual background rates and in the ability of the muon system to measure the correct beam-crossing time when the LHC reaches full luminosity, a complementary, dedicated trigger system consisting of resistive plate chambers (RPC) was added in both the barrel and endcap regions. The RPCs provide a fast, independent, and highly-segmented trigger with a sharp p_T threshold over a large portion of the rapidity range ($|\eta| < 1.6$) of the muon system. The RPCs are double-gap chambers, operated in avalanche mode to ensure good operation at high rates. They produce a fast response, with good time resolution but coarser position resolution than the DTs or CSCs. They also help to resolve ambiguities in attempting to make tracks from multiple hits in a chamber.

A total of 6 layers of RPCs are embedded in the barrel muon system, 2 in each of the first 2 stations, and 1 in each of the last 2 stations. The redundancy in the first 2 stations allows the trigger algorithm to work even for low-p_T tracks that may stop before reaching the outer 2 stations. In the endcap region, there is a plane of RPCs in each of the first 3 stations in order for the trigger to use the coincidences between stations to reduce background, to improve the time resolution for bunch crossing identification, and to achieve a good p_T resolution.

Finally, a sophisticated alignment system measures the positions of the muon detectors with respect to each other and to the inner tracker, in order to optimize the muon momentum resolution.

2008 JINST 3 S08004

7.1 Drift tube system

7.1.1 General description

The CMS barrel muon detector consists of 4 stations forming concentric cylinders around the beam line: the 3 inner cylinders have 60 drift chambers each and the outer cylinder has 70. There are about 172 000 sensitive wires. It is possible to use drift chambers as the tracking detectors for the barrel muon system because of the low expected rate and the relatively low strength of the local magnetic field.

The wire length, around 2.4 m in the chambers measured in an r-ϕ projection, is constrained by the longitudinal segmentation of the iron barrel yoke. The transverse dimension of the drift cell, i.e., the maximum path and time of drift, was chosen to be 21 mm (corresponding to a drift time of 380 ns in a gas mixture of 85% Ar + 15% CO_2). This value is small enough to produce a negligible occupancy and to avoid the need for multi-hit electronics, yet the cell is large enough to limit the number of active channels to an affordable value. A tube was chosen as the basic drift unit to obtain protection against damage from a broken wire and to partially decouple contiguous cells from the electromagnetic debris accompanying the muon itself.

The amount of iron in the return yoke was dictated by the decision to have a large and intense solenoidal magnetic field at the core of CMS. Two detector layers, one inside the yoke and the other outside, would be insufficient for reliable identification and measurement of a muon in CMS. Therefore, 2 additional layers are embedded within the yoke iron (figure 7.3). In each of the 12 sectors of the yoke there are 4 muon chambers per wheel, labeled MB1, MB2, MB3, and MB4. The yoke-iron supports that are between the chambers of a station generate 12 unavoidable dead zones in the ϕ coverage, although the supports are placed so as not to overlap in ϕ.

A drift-tube (DT) chamber is made of 3 (or 2) superlayers (SL, see figure 7.4), each made of 4 layers of rectangular drift cells staggered by half a cell. The SL is the smallest independent unit of the design.

The wires in the 2 outer SLs are parallel to the beam line and provide a track measurement in the magnetic bending plane (r-ϕ). In the inner SL, the wires are orthogonal to the beam line and measure the z position along the beam. This third, z-measuring, SL is not present in the fourth station, which therefore measures only the ϕ coordinate. A muon coming from the interaction point first encounters a ϕ-measuring SL, passes through the honeycomb plate, then crosses the z-measuring SL and the second ϕ-measuring SL. In this scenario, there still exist limited regions of η in which the combined effect of the ϕ and z discontinuities limits to only 2 (out of 4), the number of stations crossed by a muon.

At high momenta ($\geq$40 GeV), the probability of electromagnetic cascades accompanying the parent muon becomes relevant. A reliable way to cope with this effect in the regions where only 2 stations are available is to have a good tracking efficiency in each station even in the presence of electromagnetic debris. Redundancy is also needed to cope with the uncorrelated background hits generated by neutrons and photons whose rate is much larger than that from prompt muons. Redundancy is obtained by having several layers of separated drift cells per station. The separation, i.e., the thickness of the tube walls, should be large enough to decouple the basic units against low-energy electrons. The relatively thick wall of the DTs, 1.5 mm, gives an effective decoupling among

2008 JINST 3 S08004

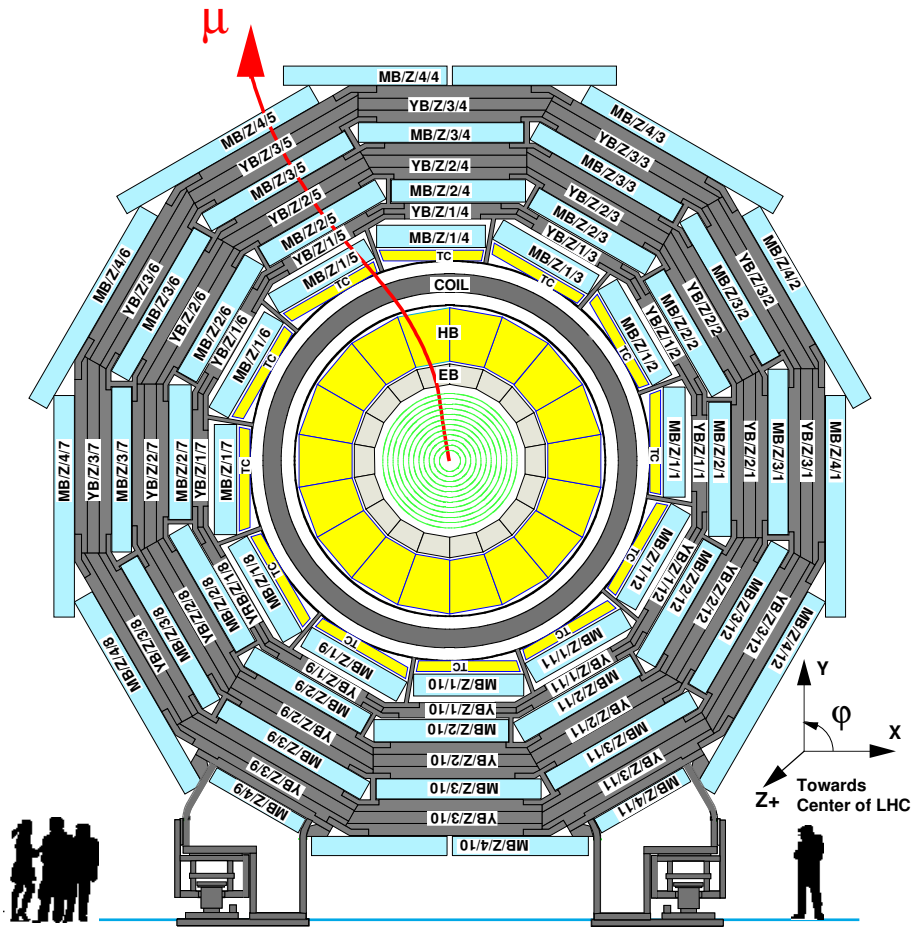

Figure 7.3: Layout of the CMS barrel muon DT chambers in one of the 5 wheels. The chambers in each wheel are identical with the exception of wheels –1 and +1 where the presence of cryogenic chimneys for the magnet shortens the chambers in 2 sectors. Note that in sectors 4 (top) and 10 (bottom) the MB4 chambers are cut in half to simplify the mechanical assembly and the global chamber layout.

the several layers of tubes inside the same station. With this design, the efficiency to reconstruct a high p_T muon track with a momentum measurement delivered by the barrel muon system alone is better than 95% in the pseudorapidity range covered by 4 stations, i.e., $\eta < 0.8$. The constraints of mechanical stability, limited space, and the requirement of redundancy led to the choice of a tube cross section of 13×42 mm^2.

The many layers of heavy tubes require a robust and light mechanical structure to avoid significant deformations due to gravity in the chambers, especially in those that lie nearly horizontal. The chosen structure is basically frameless and for lightness and rigidity uses an aluminium honeycomb plate that separates the outer superlayer(s) from the inner one (figure 7.4). The SLs are glued to the outer faces of the honeycomb. In this design, the honeycomb serves as a very light spacer,

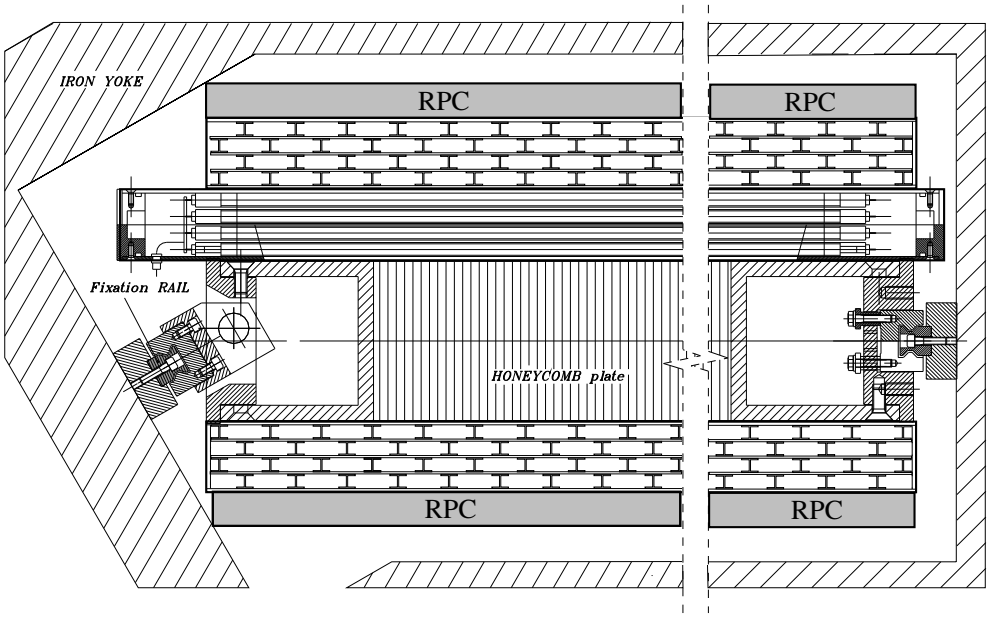

Figure 7.4: A DT chamber in position inside the iron yoke; the view is in the (r-ϕ) plane. One can see the 2 SLs with wires along the beam direction and the other perpendicular to it. In between is a honeycomb plate with supports attached to the iron yoke. Not shown are the RPCs, which are attached to the DT chambers via support plates glued to the bottom and/or top faces, depending on chamber type.

with rigidity provided by the outer planes of tubes. A thick spacer also helps to improve angular resolution within a station. Table 7.1 provides a summary of the general DT chamber parameters.

One SL, that is, a group of 4 consecutive layers of thin tubes staggered by half a tube, gives excellent time-tagging capability, with a time resolution of a few nanoseconds. This capability provides local, stand-alone, and efficient bunch crossing identification. The time tagging is delayed by a constant amount of time equal to the maximum possible drift-time, which is determined by the size of the tube, the electrical field, and the gas mixture. Within the angular range of interest, the time resolution was shown to be largely independent of the track angle, but this requires the cell optics to maintain a linear relationship between the distance from the wire of the crossing track and the drift-time of the electrons along the entire drift path. bunch crossing tagging is performed independently in each of the 3 SLs by fast pattern-recognition circuitry. Together with the bunch crossing assignment, this circuit delivers the position of the centre of gravity of the track segment and its angle in the SL reference system with precisions of 1.5 mm and 20 mrad, respectively. This information is used by the first-level muon trigger for the time and transverse momentum assignment.

The goal of the mechanical precision of the construction of a chamber was to achieve a global resolution in r-ϕ of 100 μm. This figure makes the precision of the MB1 chamber (the innermost layer) comparable to the multiple scattering contribution up to $p_T = 200$ GeV. The 100-μm target chamber resolution is achieved by the 8 track points measured in the two ϕ SLs, since

Table 7.1: Chambers of the CMS DT system. Notation: MB/wheel/station/sector. W stands for all 5 wheels (numbered –2, –1, 0, 1, and 2) and S means any sector (1 to 12, see figure 7.3). The SLs of type Φ(Θ) measure the $\phi(z)$ coordinate in the CMS coordinate system.

chamber type	No. of chambers	No. of SL Φ	No. of SL Θ	No. of ch. SL Φ	No. of ch. SL Θ	Wire length Φ (mm)	Wire length Θ (mm)	Sum of ch.
MB/W/1/S	58	2	1	196	228	2379	2038	35960
MB/1/1/4	1	2	1	196	190	1989	2038	582
MB/-1/1/3	1	2	1	196	190	1989	2038	582
MB/W/2/S	58	2	1	238	228	2379	2501	40832
MB/1/2/4	1	2	1	238	190	1989	2501	666
MB/-1/2/3	1	2	1	238	190	1989	2501	666
MB/W/3/S	58	2	1	286	228	2379	3021	46400
MB/1/3/4	1	2	1	286	190	1989	3021	762
MB/-1/3/3	1	2	1	286	190	1989	3021	762
MB/W/4/S	29	2	0	382	0	2379	0	22156
MB/-1/4/3	1	2	0	382	0	1989	0	764
MB/W/4/4	8	2	0	286	0	2379	0	4576
MB/1/4/4	2	2	0	286	0	1989	0	1144
MB/W/4/8,12	10	2	0	372	0	2379	0	7440
MB/W/4/9,11	10	2	0	190	0	2379	0	3800
MB/W/4/10	10	2	0	238	0	2379	0	4760
total	250							171852

the single wire resolution is better than 250 μm. To avoid corrections to the primary TDC data (section 7.1.3), the deviation from linearity of the space-time relation in each drift cell must be less than 100–150 μm. This figure matches well with the requirements of linearity for the bunch crossing (section 7.1.3) identifier. The cell design includes 5 electrodes, 1 anode wire, 2 field shaping strips, and 2 cathode strips (figure 7.5 and section 7.1.2). The requirements of 250-μm resolution and 150-μm nonlinearity can be obtained by operating the tubes at atmospheric pressure with an Ar/CO_2 gas mixture and by keeping the CO_2 concentration in the 10–20% range. The multi-electrode design also ensures this performance in the presence of the stray magnetic field present in some regions of the chambers. It is worth noting that to reach this local performance in a single tube, the precision requirement on the position of the field-shaping electrodes, including the wires, is about 300 μm, which is considerably less demanding than the 100 μm required for the mechanical construction.

7.1.2 Technical design

Drift cell

Figure 7.5 shows the drift lines in a cell. The anode is a 50-μm-diameter gold-plated stainless-steel wire. The field electrode is made of a 16-mm-wide, 50-μm thick aluminium tape, glued on a 100-μm thick, 23-mm-wide mylar tape that insulates the electrode with respect to the aluminium plate set to ground. Both the conductive and insulating ribbons are self-adhesive with a pressure-activated glue. Field electrodes are positioned at the top and bottom of the drift cell. Cathodes

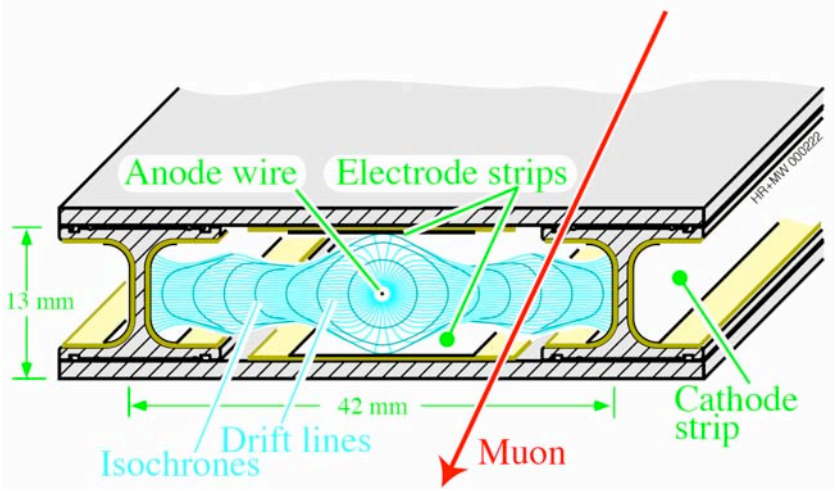

Figure 7.5: Sketch of a cell showing drift lines and isochrones. The plates at the top and bottom of the cell are at ground potential. The voltages applied to the electrodes are +3600V for wires, +1800V for strips, and −1200V for cathodes.

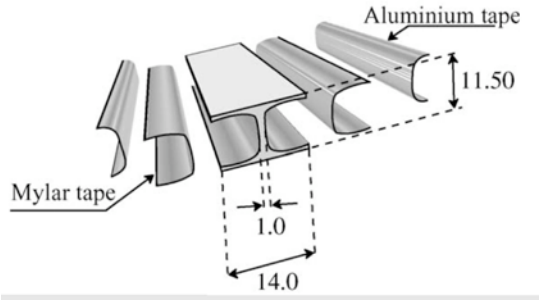

Figure 7.6: Exploded view of the cathode electrodes, glued on the I-beams.

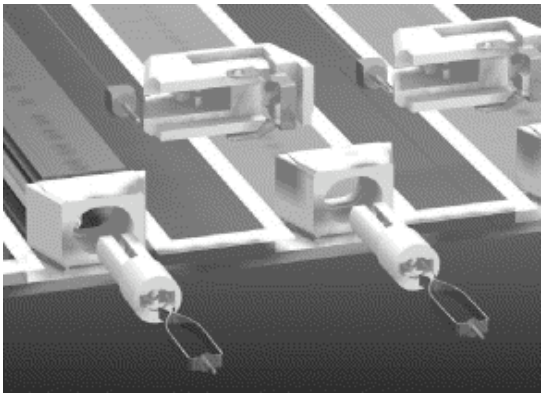

Figure 7.7: Exploded view of the end part of the drift cells showing the different end-plugs and spring contacts for high voltage connections.

are placed on both sides of the I-beams (figure 7.6) following a technique similar to that used for the strip electrodes on the aluminium plates. A cathode consists of a 50-μm-thick, 11.5-mm-wide aluminium tape insulated from the I-beam by 19-mm-wide, 100-μm-thick mylar tape. This design allows for at least 3.5 mm separation of the electrode from the sides of the grounded I-beam. At the extremities the mylar tape is cut flush with respect to the I-beam ends while the aluminium tape is recessed by 5 mm. Special tools were designed and built to glue the electrode strips to both the plates and the I-beams. The only difference between the tapes used for the electrode strips and the

2008 JINST 3 S08004

ones just described is the width: the mylar tape used for the electrode strips is 23-mm wide and the aluminium tape is 16-mm wide. These strips are set to a positive voltage and help to improve the shaping of the electric field and the linearity of the space-time relation, most noticeably in the presence of magnetic fields.

The cathode and wire end-plugs were designed to protect against discharges from the border at the end of the cathode strips and to house the wire holder, which is crucial for the wire position precision. The wire holders protrude inside the cell providing 12 mm of additional protection around the wire. The I-beam and wire end-plug pieces, as well as the springs connecting the electrodes to the high voltage, are shown in figure 7.7. The Ar-CO_2 mixture and the drift-cell optics described above provide a linear relationship between time and drift path. This is an essential requirement for the use of the chamber as a first-level trigger device [133]. A calculation of the drift velocity using GARFIELD [134] showed that drift velocity saturation occurs between 1 and 2 kV/cm (figure 7.8). This may be compared to the the drift velocity as measured with the Drift Velocity Chamber (VdC) (figure 7.9).

The drift cells will operate at a gas gain of 10^5, allowing them to work within an efficiency plateau with a wide threshold range, which is convenient for the operation of large chambers in the environment expected at CMS. A computation of equipotential lines [136] (figure 7.10) is useful for better understanding of the role of each electrode. The position of the 0 V equipotential in the region between the central strips and the cathodes is mainly determined by the size of the electrodes and not by their voltage values. The gas gain is mainly determined by the voltage drop from the wire to the nearest electrode, the strips. The wire/strip voltage difference must be kept between 1.75 and 1.85 kV to achieve a gain not far from the expected value of 10^5. Under the rough assumption of a uniform drift field of 1.5 kV/cm, the distances between the various electrodes imply that the strips should be set to a voltage larger than or equal to 1.7 kV and the cathodes to around -1 kV. As described below, during the chamber commissioning in laboratories and at CERN (with B=0), satisfactory performance was obtained with the voltages of cathodes, strips, and wires set to -1.2, $+1.8$, and $+3.6$ kV, respectively.

Chamber mechanics and services

A chamber is assembled by gluing 3 (or 2) SLs to an aluminium honeycomb plate to ensure the required stiffness. Each SL is made of 5 aluminium sheets, 1.5-mm thick, separated by 11.5-mm-high, 1-mm-thick aluminium I-beams, as described in section 7.1.2. The cell pitch is 42 mm, while the layer pitch is 13 mm. For the construction of the SLs, a full layer of cells is built at the same time by gluing together 2 aluminium plates separated by an array of parallel aluminium I-beams. The pitch and height of an I-beam determine the larger and smaller dimensions of a cell, respectively. An SL has an independent gas and electronics enclosure. Each SL is assembled and tested individually before being glued to the honeycomb plate and/or to the other SL to form a chamber.

HV connections to the cells and the front-end electronics are located at opposite ends of the wires. The HV is fed into each SL via two 52-pin custom connectors and distributed to the drift cells via printed-circuit HV boards (HVB). Each HVB is mounted along the edge of the aluminium plate separating 2 layers of drift cells and serves the 8 cells above and the 8 cells below it. One

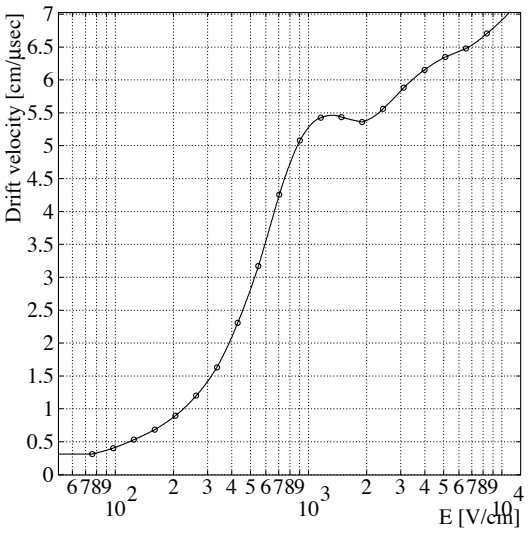

Figure 7.8: Calculated drift velocity (in cm/μs) as a function of the electric field (in V/cm) for a gas mixture Ar/CO_2 (85%/15%). The values obtained are very similar for the 2 different environment pressures, 973 and 1027 hPa.

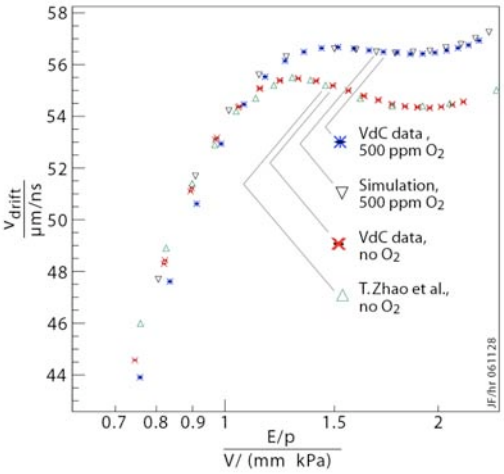

Figure 7.9: Measured and calculated drift velocities (in μm/ns) as functions of electric field and gas pressure for a pure gas mixture Ar/CO_2 (85%/15%) and for a gas mixture with air impurities corresponding to 500-ppm O_2. The measurements were obtained with the VdC, a dedicated reference drift chamber that will be used for drift-velocity monitoring during CMS running. For comparison, results of measurements from [135] for a pure gas mixture, and a simulation with Magboltz [134] for a mixture with impurities are also shown.

HV channel is dedicated to each group of 8 anode wires, while for the other 2 voltages there is 1 HV channel for 16 cells in the same layer. The strip and the cathode voltages can be daisy chained from an HVB to the next one. On the HVB there is 1 capacitor for filtering for each group. As a current limiter, a 50-MΩ ceramic resistor is used in series. There is 1 resistor for each anode and 1 for each group of 4 strips or cathodes. Due to the restricted space as required to minimise dead space, the size of the HVB is only about 307 $\times$ 37 mm^2 and special care had to be taken to maximise the distance between the printed HV lines and to avoid any embedded gas pocket within the HVB volume.

The gas enclosures are different: on the HV side they contain the HV distribution system and gas connector, whereas on the front-end sides there are the HV decoupling capacitors, the front-end circuitry, the pulse distribution system, the gas distribution, and the necessary cooling for the electronics. Inside the SL, gas is distributed as a "shower", with each cell being fed through a small-diameter (1 mm^2) outlet hole to guarantee that the same amount of gas is circulated to each

2008 JINST 3 S08004

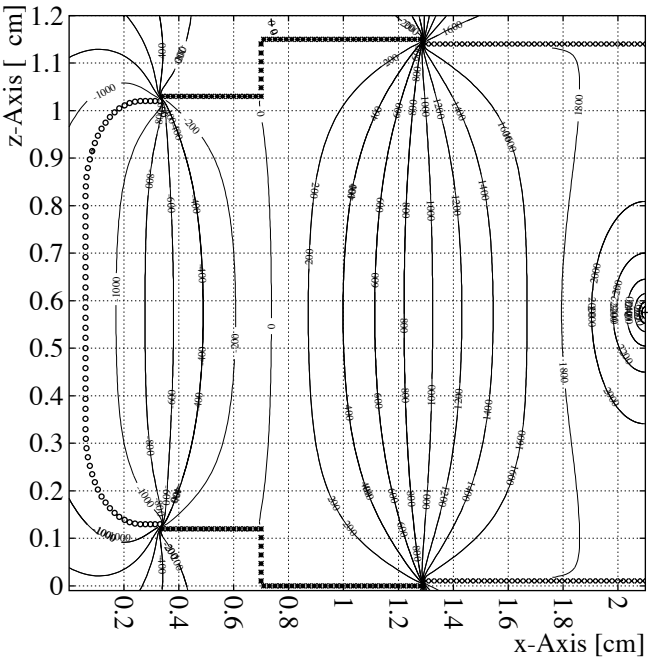

Figure 7.10: Equipotential lines in half of a drift cell. The anode wire is on the right side. The lines are labeled with the potentials in volts (the x-axis is perpendicular to the wires on the wire plane, while the z-axis is orthogonal to the wire plane).

channel. The distance between the position where the wire enters the end plug and the outer face of the gas enclosure, which determines the SL dead area, corresponds to 60 mm on both the HV and the front-end side (corresponding to ≈10% dead space).

It is very important that the individual SLs of the DT chambers are gas tight because contamination by nitrogen (from air) changes the drift velocity by a sizeable amount, while oxygen reduces the signal efficiency, when its contamination exceeds 2000 ppm. Contamination by air including 1000 ppm of O_2 changes the maximum drift time by about 2% with respect to no contamination, with a sizeable effect on the trigger performance of the detector. In the DT chambers, the gas tightness of the SLs is obtained by gluing profiles to the outer aluminium skins. Along 2 sides of the SL, C-shaped profiles are used and the ends of these profiles are glued to reference blocks (figure 7.11), forming the corners of the SL box. The front and back of the box have L-shaped profiles glued along the plate border to form an open frame, which is then closed with removable long cover plates that contain all necessary gas connectors, HV connectors, and signal outputs, equipped with O-rings that seal the structure. A 3-dimensional computer model of the gas enclosure for one SL, where the outer aluminium plates have been removed to expose all details of the gas enclosure, is shown in figure 7.12. With this type of gas enclosure we can obtain a level of oxygen contamination of 10–20 ppm, downstream of the 3 SLs flushed in parallel with about 1 volume change per day.

During SL assembly, before the fifth aluminium plate is glued closing the structure, reference blocks are glued such that their positions with respect to the wires can be measured precisely. Thus, when the chamber is completed, the wire positions may be determined by measuring the reference

2008 JINST 3 S08004

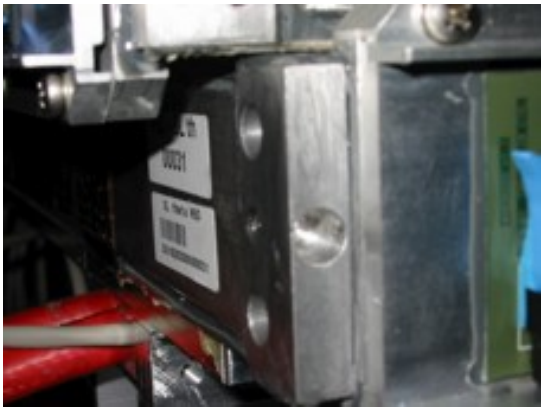

Figure 7.11: Corner blocks of an SL. These pieces also carry the reference marks with respect to which the wire positions are measured.

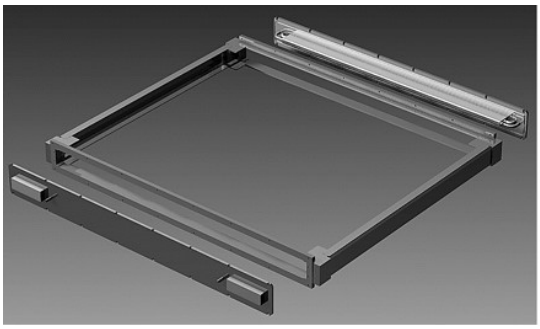

Figure 7.12: A 3-dimensional computer model of the gas enclosure of the SLs.

marks on the blocks. Pressure and temperature monitoring probes, ground straps that connect all the aluminium planes to form a unique ground reference, and a Faraday cage for the signals, front-end electronics, and HV distribution complete the equipment that is in the gas enclosures of each SL.

Each SL is fully independent with respect to gas tightness, HV, and front-end electronics; hence an SL can be fully tested before it is glued to form a DT chamber. SLs are glued to a honeycomb panel (figure 7.4) that sustains and gives rigidity to the chamber and provides the fixation points from which it is suspended in the CMS barrel steel yoke (two Φ-type SLs and one Θ-type SL in the case of layers 1, 2, and 3; and two Φ-type SLs for layer 4). The panel thickness varies from 125 mm for the first three stations, to 178 mm for the fourth station. It is delivered with the correct dimensions and equipped with the C-shaped profiles at the periphery that are used for the supports and for part of the electronics.

The space for the chamber supports and attachments, the passages for alignment, and the local read-out and trigger electronics is provided by a channel running around the border of the honeycomb plate. The channel is approximately as wide and deep as the honeycomb plate thickness. The 2 channels parallel to the beam line and to the yoke steel supports house the kinematic fixations to the yoke supports themselves, and the longitudinal alignment passages. One of the 2 remaining sides houses the read-out and trigger electronics that collect the full chamber information (*minicrates*). To ease chamber handling, all services are connected on the same side of the chamber. All the general services for the chambers are located around each barrel wheel on the 4 balconies along the walls of the CMS cavern where there is space for the racks and crates. Each wheel is thus an independent, large subsystem.

2008 JINST 3 S08004

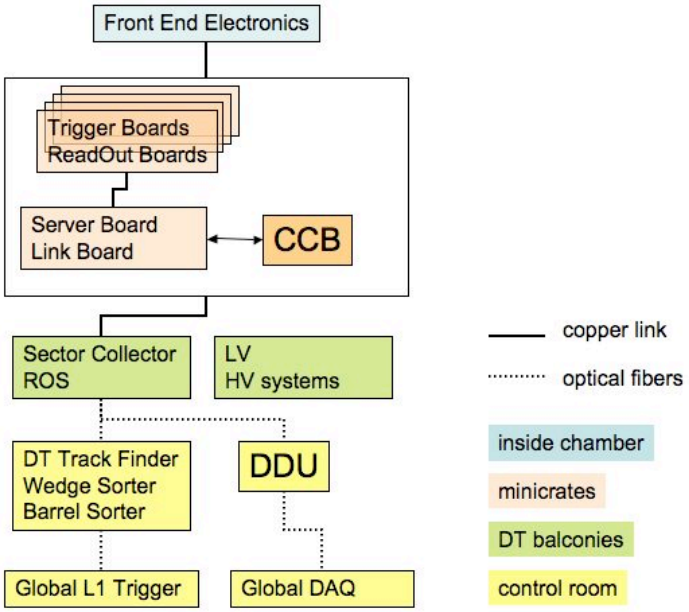

Figure 7.13: Block diagram of the DT electronic system.

7.1.3 Electronics

The DT electronics is a complex, heavily integrated system, which includes L1 trigger logic, read-out data handling, and service electronics, such as the LV and HV systems. A description of the electronic system layout together with the functions associated to each sub-task is shown in figure 7.13 and briefly summarized, whereas detailed information will be described in the following sections.

Front-end electronics and HV distribution are physically embedded in the chamber gas volume. Amplified and shaped signals are directly fed to the *minicrates*. A minicrate, as described previously, is an aluminium structure attached to the honeycomb of the drift tube chambers that houses both the first level of the read-out and of the trigger electronics. The trigger boards located in the minicrates are the Trigger Boards (TRB) and the Server Boards (SB), as described in detail in section 8.2. In each TRB are located the Bunch Crossing and Track Identifier (BTI), which provides independent segments from each chamber SL, and the Track Correlator (TRACO), which correlates ϕ segments in the same chamber by requiring a spatial matching between segments occurring at the same bunch crossing (BX). TRB output signals are fed to the Server Board (SB) which selects the best two tracks from all TRACO candidates and sends the data out of the minicrate. In parallel to the trigger signals, chamber data are fed to the read-out system through the Read Out Boards (ROB), which are in charge of the time digitization of chamber signals related to the Level-1 Accept (L1A) trigger decision and the data merging to the next stages of the data acquisition chain. The Chamber Control Board (CCB) located at the centre of the minicrate, allows ROB and TRB configuration and monitoring. It works together with the CCB link board, on one of the minicrate ends, that receives data from the Slow Control and global experiment Timing and Trigger Control (TTC) system. Among other tasks, the CCB distributes the LHC 40.08 MHz clock and other TTC signals to every board in the minicrate.

2008 JINST 3 S08004

Trigger and data signals coming out of the minicrates are collected by VME electronics installed in the iron balconies attached to the DT wheels, respectively to the Sector Collector (SC, section 8.2) and to the Read Out Server (ROS, section 7.1.3) where data merging is performed. From the wheel balconies, data are sent via optical links, both to the CMS central acquisition system through the Detector Dependent Unit (DDU) (section 7.1.3) and to the CMS L1 system through the Sector Collector (SC) and the Drift Tube Track Finder (DTTF, section 8.2).

Front-end electronics

The front-end electronics for the barrel muon detector must satisfy many stringent requirements. Its functions are to amplify the signals produced by the detector, compare them with a threshold, and send the results to the trigger and read-out chains located on the chamber. Analog signal processing must use a short shaping time to achieve a high spatial resolution while introducing minimal noise; this allows low-gain operation of the drift tubes, thus improving reliability and chamber lifetime. The downstream comparator has to be very fast and precise to allow the use of low threshold values, which reduce the influence of the signal amplitude on the time response. The output driver also must be very fast, and it must deliver differential levels that minimise mutual interferences and can be transmitted through low-cost cables. Besides the above functions, several features that simplify the control and monitoring of the data acquisition have been implemented. The large number of channels and the resulting need for both high reliability and low cost, limited space, and concerns about power consumption led to the necessity to integrate the front-end electronics as much as possible.

The resulting custom front-end application specific integrated circuit chip (ASIC), named MAD, was developed using 0.8 μm BiCMOS technology [138]. This chip integrates signal processing for 4 channels (4 drift tubes) plus some ancillary functions in a 2.5 $\times$ 2.5 mm^2 die and 80 000 pieces were produced with a fabrication yield better than 95%. Figure 7.14 shows the ASIC block diagram and the pinout of the TQFP44 package used for it. Each of the 4 identical analog chains begins with a charge preamplifier that uses a single gain stage, folded/unfolded cascode, having a GBW product in excess of 1 GHz (result from simulation). The feedback time constant is 33 ns while input impedance is $\approx$100 Ω in the range 5–200 MHz.

The shaper that follows is a low-gain integrator with a small time constant. Its output is directly connected to 1 input of a latched discriminator made of 2 differential gain stages, the other input being connected to the external threshold pin V_{th}, common to all channels. Auxiliary circuits allow the masking of individual channels at the shaper input (pins A_ENn in high state) thus stopping the propagation of excessive noise background to the trigger and DAQ electronics. A similar but faster enable/disable function was implemented on the cable-driver stage to select channels that output signals in response to a test input. A temperature probe was also included for monitoring the operating conditions of the detector.

The ASIC operates with 2 distinct supply voltages, 5 V for the analog section and 2.5 V for the output stage, with a total power consumption of 100 mW (25 mW/ch) equally split between the 2 voltages and almost independent of the temperature and signal rate. Several tests have been carried out on the MAD ASIC both on the bench and in the field in various configurations. For the analog section an average gain of about 3.7 mV/fC was found for bare chips with (1370$\pm$48)/pF

2008 JINST 3 S08004

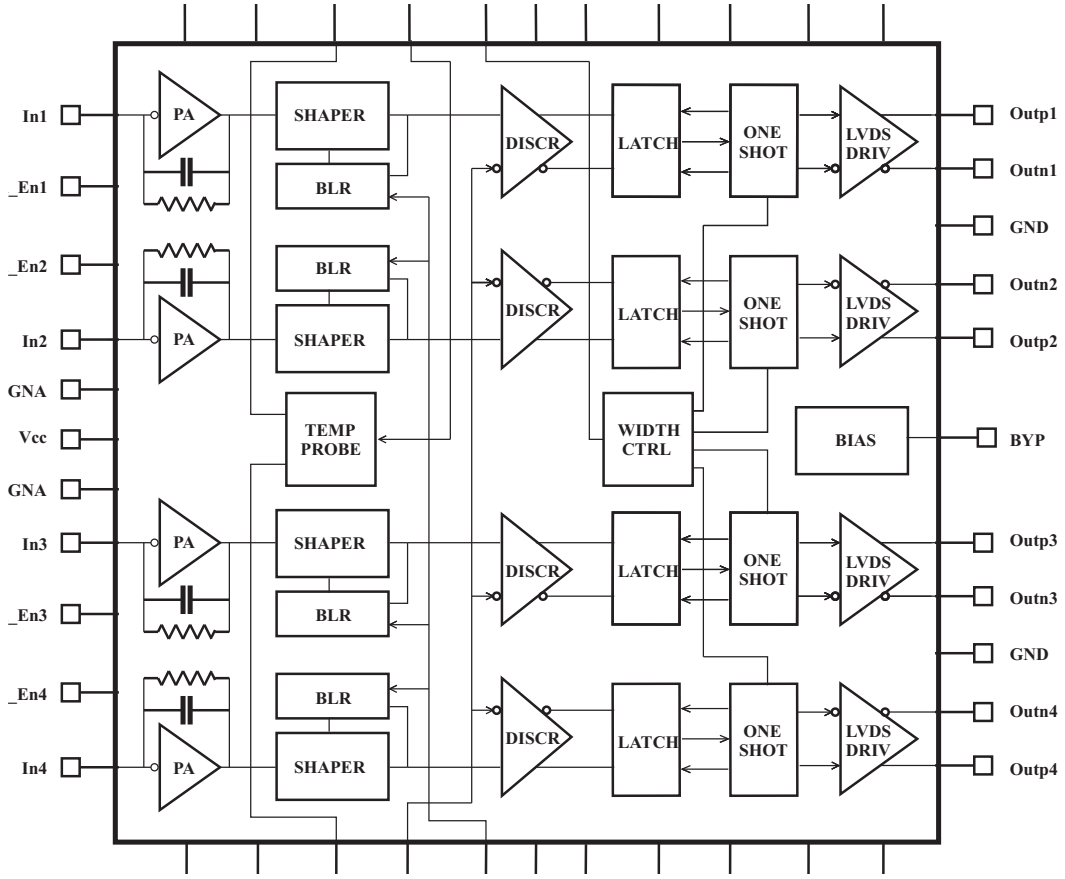

Figure 7.14: Block diagram of the MAD ASIC.

electrons ENC. Another key characteristic for operation with low signals is the crosstalk, which is less than 0.1%; moreover, the baseline restorer and the comparator offsets sum up to less than ± 2 mV total error.

The chip performance is somewhat degraded when it is mounted on a front-end board (figure 7.15): the gain reduces to 3.4 mV/fC and noise and crosstalk increase to (1850$\pm$60)/pF electrons and 0.2%, respectively. These effects are caused by the input protection network, which is made of an external resistor and diodes that together with 100 μm gaps included in the PCB are capable of dissipating the energy stored in the 470 pF capacitors that connect the detector wires (biased at 3.6 kV) to the ASIC inputs. This protection is effective even in the case of repeated sparks (ASICs survive $>$105 sparks at 3.6 kV amplitude with 1 spark/s on all channels).

The above figures enable front-end operation at a threshold well below 10 fC (the value used during test beams was 5 fC) when connected to the detector, which has a maximum capacitance of 40 pF. The propagation delay of the chip is less than 5 ns with little dependence on signal amplitude (time walk is less than 7 ns). The rate capability of the MAD ASIC largely exceeds demand: 800 fC charge pulses (just below saturation) at 2 MHz rate do not affect the efficiency in detecting 5 fC interleaved signals, so there is a wide safety margin with respect to the total rate (about 10 kHz) foreseen per drift tube during CMS operation.

Figure 7.15: Front-end board (FEB).

Finally, the radiation tolerance and overall reliability of the front-end board and associated electronics were investigated [139]. Radiation testing involved a series of tests with thermal and high-energy neutrons, protons, and γ-rays to simulate the behaviour in a CMS-like environment. The results can be summarized in latch-up immunity (undetected SELs even with heavy ions on naked dies), very little sensitivity to SEUs (only a few thousand spurious counts/channel calculated for the whole detector lifetime), and tolerance to total integrated dose orders of magnitude higher than foreseen in 10 years of CMS operation. In addition, accelerated ageing in a climatic chamber at 125°C was carried out for >3000 hours on 20 FEBs and related circuits without revealing any fault.

Read-out electronics

The electronics of the read-out system of the CMS DTs is responsible for the time digitization of the signals generated in the drift chambers and for the data transmission to higher levels of the DAQ system. The time digitization of the signals is performed at the Read-Out Boards (ROB [140]), located in minicrates, as described in section 7.1.3, together with the DT muon trigger electronics. Two FTP cables are used to send digitized data from each minicrate to the rack 30 m away in the towers beside the CMS wheels where the Read-Out Server (ROS) boards are located. Each ROS merges data coming from chambers of one wheel sector through a 70-m optical link to the Detector Dependent Units (DDU) in the USC55 control room, performing the multiplexing of 1500 copper links into 60 optical links. The Read-Out Systems have been developed according to the requirements both of the expected trigger rates (100 kHz) at the high luminosity of LHC, with an average occupancy of 0.76% in the whole detector, a L1 trigger latency of 3.2 μs, and of the need of operating in an environment where the integrated neutron fluence will reach 10^{10}cm^{-2} in 10 years of activity.

Read-Out Boards are built around a 32-channel high performance TDC, the HPTDC, which is the third generation of TDC's developed by the CERN Microelectronics group [141], and it has been implemented in IBM 0.25 μm CMOS technology. This highly programmable TDC is based on the Delay Locked Loop (DLL) principle, providing a time bin of 25/32 ns = 0.78 ns, which corresponds to 265-ps resolution, when it is clocked at the LHC 40.08-MHz frequency. This time resolution is enough to obtain a single wire position resolution of 250 μm.

The number of HPTDCs per ROB has been decided following a compromise between the number of unused channels when the granularity is too small and the multiplication of common components when it is too big. Finally, each ROB has 4 HPTDCs connected in a clock synchronous token ring passing scheme, where one of them is configured as a master to control the token of the

2008 JINST 3 S08004

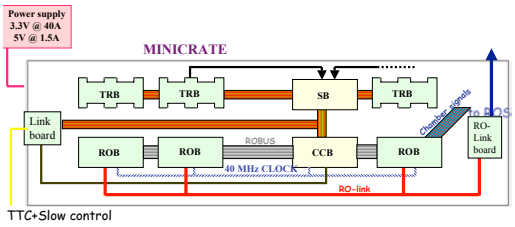

Figure 7.16: Sketch of the read-out and trigger electronics located inside a minicrate.

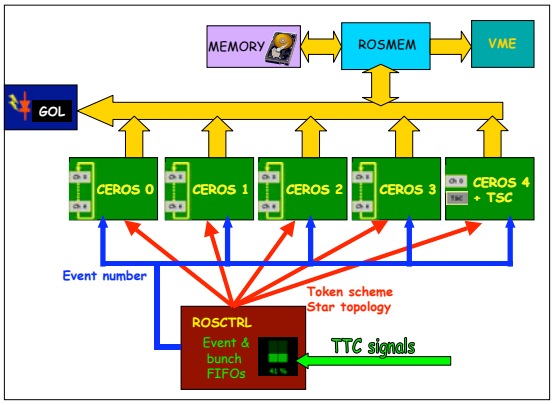

Figure 7.17: Sketch of the splitting of the 25 channels in four groups.

read-out data chain. The token ring scheme is designed following a failsafe mechanism, which avoids that the failure in one of the TDCs interrupts the whole ROB operation. Both hardware and software bypassing systems have been implemented.

Depending on the chamber type, the number of channels is different and accordingly, the number of ROBs per minicrate. The smallest minicrate has 3 ROBs and the biggest has 7. They are all connected to the Control Board (CCB) that manages, among others, the Timing and Trigger Control (TTC) signals. As can be seen in figure 7.16, Trigger Boards (TRB), located inside the minicrate are connected to the ROBs to receive TTL translated hit signals. As described at the beginning of this section, FTP cables connect the output of the ROBs to the ROS boards [142]. Located in the barrel tower racks there are 60 ROS boards, 12 per wheel, 1 per sector (four to five minicrates), so each ROS receives 25 channels of the LVDS copper ROB-ROS link. These 9U boards have to multiplex data coming from the ROBs, adding necessary information of ROB number, link status and other information, and send them to the DDU through a fast link. Another feature of the ROS board is that it also includes a power supply protection circuitry, current and temperature monitoring, and a 512 kB memory to test and perform data flow snapshots for traceability in case of transmission errors. In Figure 7.17 it can be seen how the 25 channels are split in four groups of six channels each, so-called CEROS, controlled by an FPGA that manages the FIFO read-out performing a pooling search for the next event to be read. These FPGAs also filter the events, discarding headers and trailers of those channels without timing or error information, reducing accordingly the data overhead.

A test performed on 10 prototypes, keeping them in an oven at 125°C for 2000 hours, in order to simulate 10 years of CMS activity, gave no faults. The DT Front-End-Driver (FED, also called DDU [143]) is the last component of the DT read-out electronics. The DT FED system consists of 5 VME64X 9U boards housed in the CMS service cavern; each board collects data through serial optical connections from 12 ROS, corresponding to an entire DT wheel, and transmits a formatted event fragment to the CMS common DAQ through a S-Link transmitter module. The synchronization with the trigger system is guaranteed by the TTC network, providing the LHC timing signal, the L1 trigger accept and fast commands, that are distributed to the different parts of the FED board. The layout of the board is depicted in figure 7.18.

2008 JINST 3 S08004

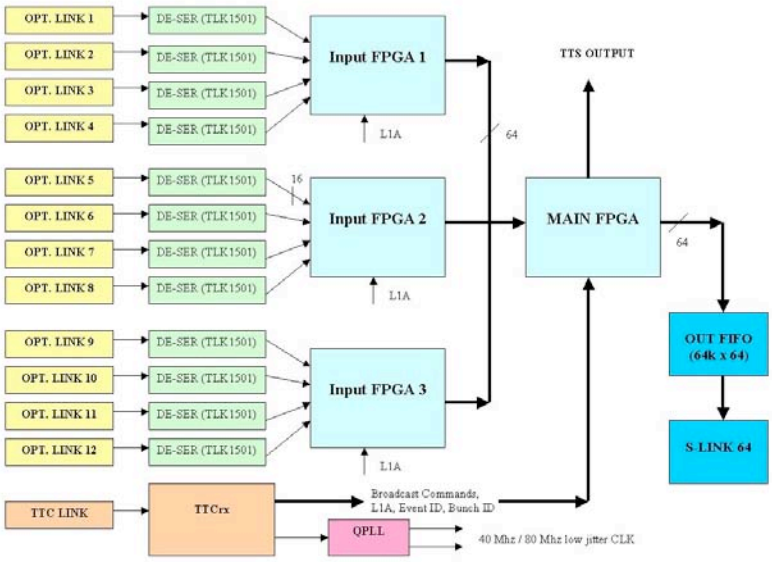

Figure 7.18: Scheme of the DDU architecture.

The data rate in each DT FED board is limited by the maximum rate the CMS DAQ can accept from an S-Link connection (about 200 Mbytes/s). The number of boards has been chosen to deal with the expected DT event size (7 kbytes/event) at 100 kHz trigger rate.

High Voltage and Low Voltage systems

The CAEN SY1527 universal multichannel power supply systems are used to supply high and low voltages (HV and LV) to the muon DT chambers. The basic modules of the DT HV system consist of A876 master boards and A877 remote boards. A maximum of 8 A876 master boards can be housed in the SY1527 mainframe. Each of them supplies high voltages and low voltages, controls and monitoring, to a maximum of 4 independent A877 remote boards, each one powering one DT chamber (two in the case of MB4 of Sectors 4 or 10). The A877 remote boards are located in a separate non-powered mechanical crate sitting in racks on the towers next to the wheels. The A876 delivers to each A877 HV board: a positive HV in the range from 0 to +4.2 kV (2.5 mA maximum output current), a negative HV in the range from 0 to −2.2 kV (1 mA maximum output current), a dual LV of ±15V (1.5 A maximum output current). The A877 HV outputs are subdivided into 12 groups (8 for the special A877 boards powering the MB4 chambers) conventionally called macro-channels. Each macro-channel supplies 4 HV channels per layer: 2 anodes (the wires of each layer are divided into 2 groups), 1 strip and 1 cathode. For all HV channels, the maximum output current is hardware limited to 100 μA.

The DT LV system uses three different types of CAEN Easy3000 modules: the A3009 to provide V_{CC} and V_{DD} voltages to the chamber front-end electronics and the V_{CC} voltage to the mini-crates, the A3050 for the mini-crate V_{DD} and the A3100 to power the Sector Collector Crates. The control of the Easy3000 power supply system is done remotely using a branch controller (Mod. A1676A) plugged in a SY1527 mainframe located in the control room. Each A1676A

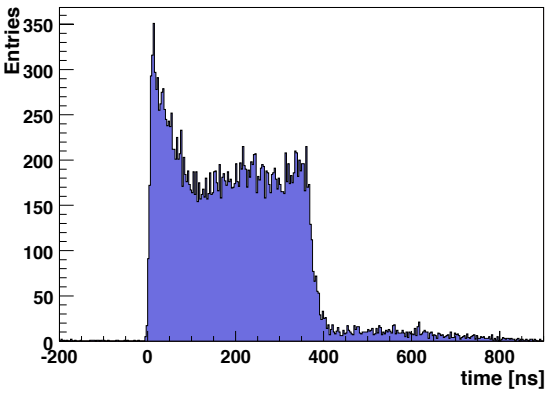

Figure 7.19: Drift Time distribution of a good cell. Wire position corresponds to time 0.

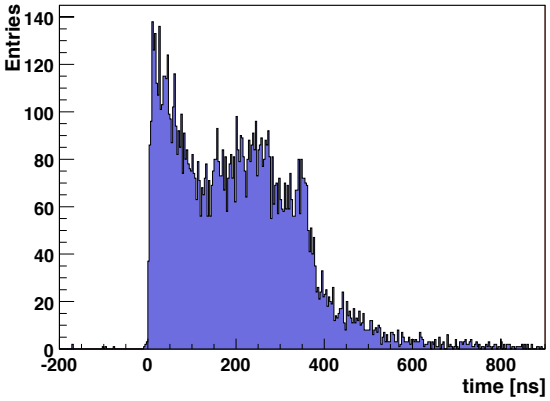

Figure 7.20: Drift Time distribution of a cell with a disconnected cathode.

branch controller can handle up to 6 Easy3000 crates. The Easy3000 crate is powered by external 48 V DC that is provided by the CAEN AC/DC converter A3486S module. The following voltages are delivered:

- VCCMC = 5.8 V, software current limit i_0 = 3 A;
- VDDMC = 4 V, software current limit i_0 = 30 A;
- VCCFE = 5.2 V, software current limit i_0 = 3 A;
- VDDFE = 2.6 V, software current limit i_0 = 4 A;
- VSC = 2.6 V, the current limit depends on the number of SC and ROS boards plugged in the crate.

7.1.4 Chamber assembly, dressing, and installation

Chamber assembly

Mass chamber assembly was started in January 2002 and was fully completed (spares included) in June 2006, with a constant production rate for all the four production sites involved. The collection of a good sample of cosmic muons allowed full testing of a constructed chamber, before sending it to CERN. In each laboratory cosmic-ray events were triggered by an external scintillator system which covered the full acceptance of the chamber. Since final minicrate electronics was not available during chamber assembly, drift times were measured with external TDCs and a custom DAQ. Typical trigger rates were 50–100 Hz, resulting in $\approx 10^6$ events in a few hours. With such a large data sample it was possible to spot and cure problems which could not be detected in previous tests, like disconnected cathodes (figures 7.19 and 7.20) and disconnected strips (figure 7.21).

Beside efficiencies, other relevant working parameters are measured from cosmic-ray data, as calibration stability (drift velocity measured to be stable within $\pm 5\%$), deviation from linear drift parametrization, measured to be well within 100 μm (figure 7.22), wire positions and comparison with CCD measurements during assembly, relative alignment of layers, and noise (typically below 100 Hz per cell, see figure 7.23).

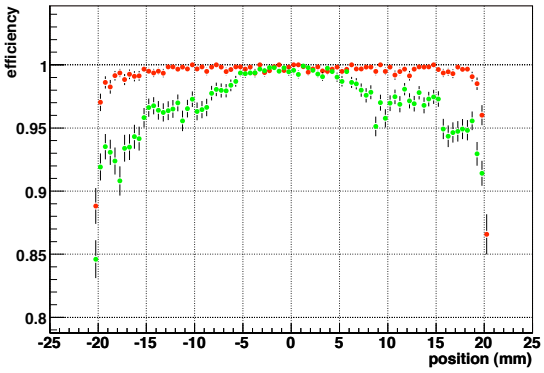

Figure 7.21: Single cell efficiency for a good cell (red dots) and for a cell with a disconnected strip (green dots).

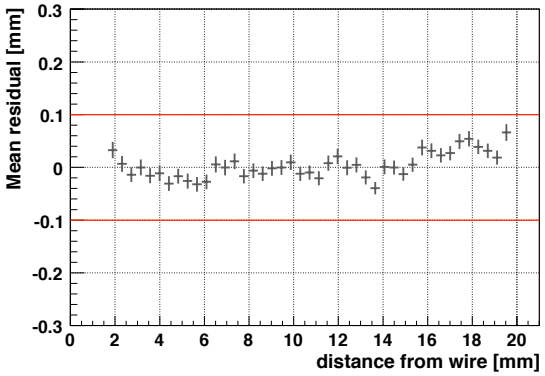

Figure 7.22: Residuals as a function of the distance from the wire, indicating a linear dependence well within ± 100 μm in the full cell range.

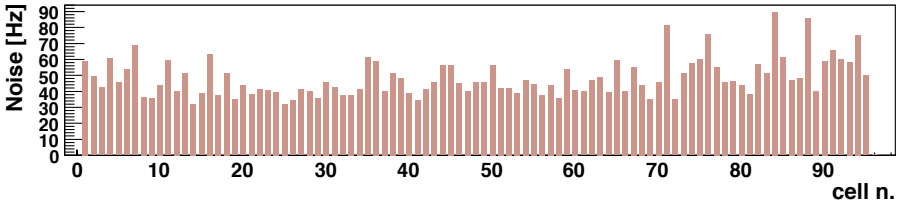

Figure 7.23: Typical hit rate distribution in one layer, as measured during the test of a SuperLayer with cosmic rays. This rate is dominated by noise and is typically below 100 Hz per cell.

Chamber dressing

All chambers, built and fully tested at the production sites, were sent to CERN for final testing and commissioning prior to installation in the experiment. Since the arrival of the first chamber at CERN (an MB2 type chamber arrived in summer 2000, prepared for a test beam [144]), a total of 272 more chambers (including spares) have been received from all four production sites, leading to a continuous workflow of dressing and testing.

At a first stage chambers are assigned to a particular position in CMS, depending on their orientation. Before any test, each chamber undergoes the optical alignment procedure described in section 7.1.4. After going through the alignment procedure, chambers are equipped with gas components (cooling pipes, gas manifolds, PADC pressure meters), HV cables and additional items like stickers, protectors, grounding straps, etc. Basically all components except for the minicrates (section 7.1.3), minicrates-related items and external protections are installed at this stage.

After dressing the chamber the following tests were performed:

- High voltage long term tests;
- Gas tightness tests;

- Cosmic-muon tests.

The high voltage long term test consists of a continuous monitoring of the high voltage performance (electric current) under the nominal values for all components (3600 V for wires, 1800 V for strips, and −1200 V for cathodes) for a minimum of 6 weeks. The time constant of the chamber with the final gas connections is also computed as a measurement of gas tightness. No significant degradation has been observed with respect to the values measured at the sites.

Finally a cosmic test stand has been set up with trigger scintillators, independent cabling, LV and HV supplies and several HPTDCs, capable of measuring one chamber at a time, and registering several millions of triggers in a few hours. The later analysis of these data allows the recognition of almost all kind of problems related to the chamber itself and its internal electronics.

Once this first certification step is passed, the chamber dressing is completed and the chamber is declared ready for minicrate installation (section 7.1.3). All signal cables from the chamber to the minicrate are installed and tested, and then the minicrate itself is inserted. The performance of the minicrate is tested at this stage for the first time together with a real chamber. All internal connections are checked, as well as configurability and data processing performance of the full local electronics chain.

At this point the chamber has passed all tests and can be considered *ready to install*. Last dressing steps are performed (installation of carters and additional protections) and then DT chambers are coupled together to RPCs, forming an installable barrel muon package.

Chamber survey

To determine the chamber positions in the CMS coordinate system and to follow their movements a position monitoring Alignment System was built (section 7.4). All the 250 DT-chambers positions are recorded by this system via optical connections using LED light sources mounted on the chambers and specially designed video-cameras fixed to the return yoke of the barrel. Four LED-holders called forks are mounted on the side-profile of the honeycomb structure (two per side), using the rectangular 50×65 mm^2 tube as the light-passage. Each fork has 10 LEDs, 6 and 4 respectively, on each side of the fork. The control of the LEDs (on-off, current) is performed via I^2C bus system integrated in the minicrate.

The primary aim of the alignment is to give the positions of the anode wires but this is not directly possible. On the other hand all the wire positions are measured with respect to the SL corner during the chamber construction. To establish the connection between the LEDs and the corner blocks a calibration bench was built at the CERN ISR site (figure 7.24). This bench had two functions. The first one was to measure the corner block positions with respect to each other, allowing the full-chamber geometry, including the relative positions of the superlayers in 3D and their planarity, to be measured. The second function was to measure the LED positions in the chamber coordinate system stretched on the corner blocks. The bench contained video-cameras that could observe the LEDs and photogrammetry targets to measure the corner blocks with respect to the LEDs by photogrammetric methods. The bench allowed us to measure all the types of chambers from MB1 to MB4. The full bench was calibrated and recalibrated before each chamber calibration campaign by the CERN survey group. Also, additional LEDs were mounted on the bench to detect any significant deformation of the bench itself. The precision of the bench measurements for the locations of the corner blocks was σ <40 μm and the position of the forks relative to the chamber

2008 JINST 3 S08004

Figure 7.24: The chamber calibration bench in the CERN ISR Lab.

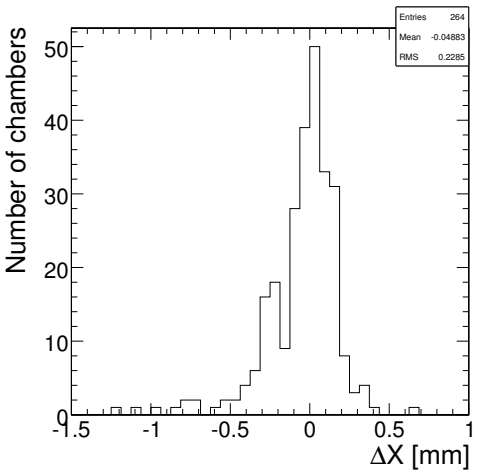

Figure 7.25: Distribution of the ϕ-deviation from the nominal design value for the two Φ-type superlayers.

was σ <70 μm. Both values are within the acceptable range defined by physics requirements. Figure 7.25 shows the result of the residual distributions of Φ-type SL corner block positions for all measured chambers.

Gas system

For the DT chambers a safe and inexpensive gas mixture is used, namely Ar/CO_2 in the ratio 85/15 volume. The gas is distributed in parallel to all drift cells in four steps: (1) the main line is split into 5 lines to feed each of the 5 barrel wheels; (2) on the wheel it is split into 50 lines to feed the 50 chambers on the wheel; (3) on the chambers it is split into 3 lines to feed the 3 SuperLayers; (4) within the SL a long tube with small holes distributes the gas over the drift cells. The nominal flow is 50 l/h for each chamber. Due to the large total number of 250 chambers, a closed loop circuit with a cleaning station is used. It is foreseen to add about 10% fresh gas daily. The gas system is run at constant absolute pressure inside the chambers, to avoid any variation of the drift velocity inside the chamber. The pressure is regulated for each wheel. There are flowmeters at the inlet and outlet of each line at the gas distribution rack on the wheel. The gas pressure is also measured with two sensors at the inlet and outlet gas manifolds on the chambers, amounting to 1000 sensors in total. They should ensure a safe and redundant measurement of the pressure at every chamber, as needed for unaccessible chambers. To be able to analyze the gas actually present in every chamber, a return line brings a sample to the gas room. There is one such line per wheel and a remotely controlled multiway valve permits the selection of the desired chamber or the gas arriving at the wheel, for analysis.

The gas is also analysed independently for each of the 5 wheels and consists of a measurement of the oxygen and of the humidity content of the gas, as well as a direct measurement of the main parameter of the DT chambers, the drift velocity. The drift velocity is measured with a small drift chamber (VdC), which features a very homogeneous, constant, known and adjustable electric field in a region where two thin beams of electrons from a beta-source cross the chamber volume and

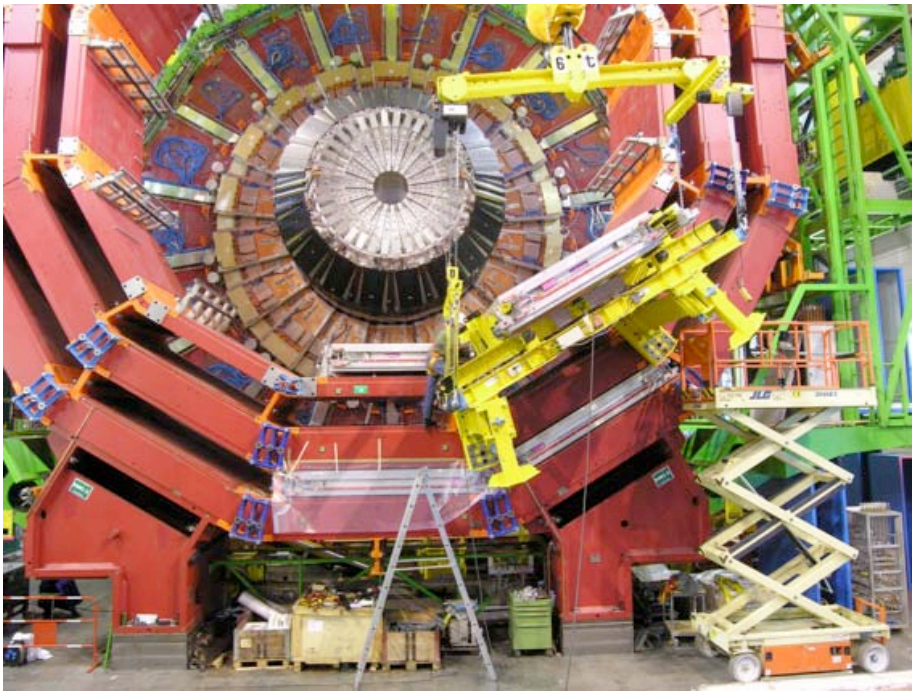

Figure 7.26: Installation of MB1 station on Wheel -2. The yellow frame is the *cradle* used to insert the chamber in its location inside the iron slot.

trigger a counter outside the chamber. The distribution of times between the trigger signal and the signal from the anode wire of the chamber is recorded. The distance between the two beams being well known by construction, by measuring the distance in time between the peaks from the two sources, one reads directly the drift velocity. Variations of the drift velocity can be monitored accurately by accumulating data for about 5 min. The data shown in figure 7.8 demonstrate that the absolute values measured with the VdC agree with the expectation. The special merit of a direct monitoring of the drift velocity is that one does not need to know which impurities are affecting the drift velocity to monitor it.

Chamber installation in CMS

The main installation tool is a platform (*cradle*) with the same support rail as in the iron pockets that can be anchored to interface pads mounted on the wheel (figure 7.26). Pneumatic movements allow the precise alignment of the chamber with respect to the iron pockets. Once the rails on the cradle and those in the iron pockets are aligned, the chamber is pushed into position with an electric motor. The installation of the chamber in the MB1 station of Wheel -2 sector 11 is shown in figure 7.26.

The first chambers were installed in the bottom sectors of Wheel +2 in July 2004 and the surface installation was completed in Wheel -2 in December 2006. Installation completion, for sectors 1 and 7, which could not be filled on the surface since these parts of the wheel were reserved for handling during the heavy lowering operation, was made underground.

2008 JINST 3 S08004

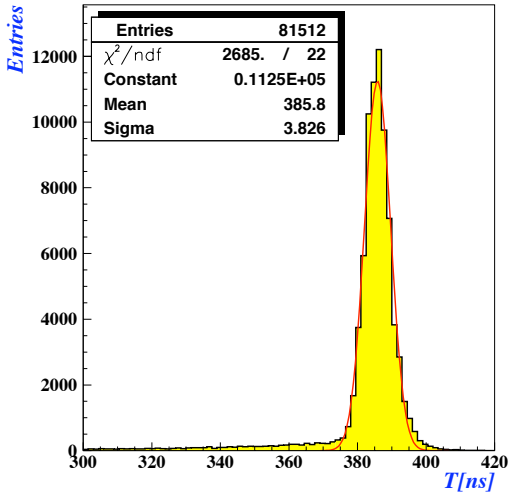

Figure 7.27: Gaussian fitted MT distribution with $\sigma_t = 170$ μm. The position of the MT peak allows the determination of an average drift velocity of 54.4 μm/ns.

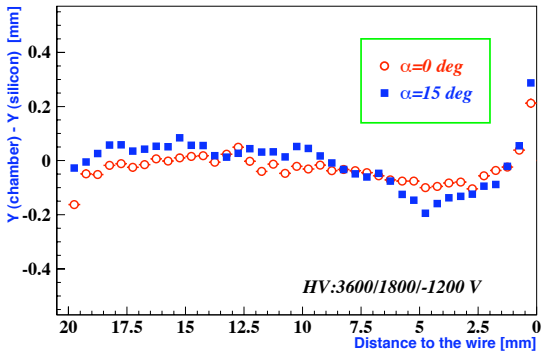

Figure 7.28: Deviation from linearity as a function of the distance to the wire for tracks with angles of incidence α=0° and 15°. The cathode is centred at 21 mm.

7.1.5 Chamber performance

Chamber and trigger performances have been thoroughly analyzed at various stages, on prototypes before mass production (with and without external magnetic field [145]), on final chambers with test beams and with the CERN Gamma Irradiation Facility [144, 146, 147], with cosmic-rays both at production sites and at the commissioning of the installed chambers, and finally with the so-called *Magnet Test and Cosmic Challenge* (MTCC) in 2006, where part of the DT system, completely installed and equipped with final hardware, was tested together with the final CMS DAQ system.

Test beam data: chamber performance

Several dedicated muon test beam runs were set up in order to test chamber performance under different conditions. Single cell spatial resolution could be determined [144] simply by the dispersion of the $MT = (t_1 + t_3)/2 + t_2$ distribution, MT being the meantime obtained from the time of the signals (t_1, t_2, t_3) generated by the incoming muon in 3 consecutive, staggered layers. The smoothness of the drift time box and the fast drop of the trailing edge (figure 7.19) are both signs of the saturation of the drift velocity. Under the assumption that the time resolution is the same in all layers $\sigma_t = \sqrt{\frac{2}{3}} \cdot \sigma_{\mathrm{MT}}$, one can easily observe an average spatial resolution of 170 μm (figure 7.27). Using a Silicon Beam Telescope, it was possible to measure the deviation from the extrapolated hit on the SL and the reconstructed position. As can be seen in figure 7.28 deviations from linearity are within $\pm$ 100 μm, which corresponds to a trigger jitter smaller than 5 ns.

Silicon Beam Telescope data can also be used to measure precisely the chamber efficiency (figure 7.29). The geometrical acceptance associated with the presence of the I-beam is clearly seen by the drop of efficiency in that region. In the rest of the cell the efficiency is always higher than

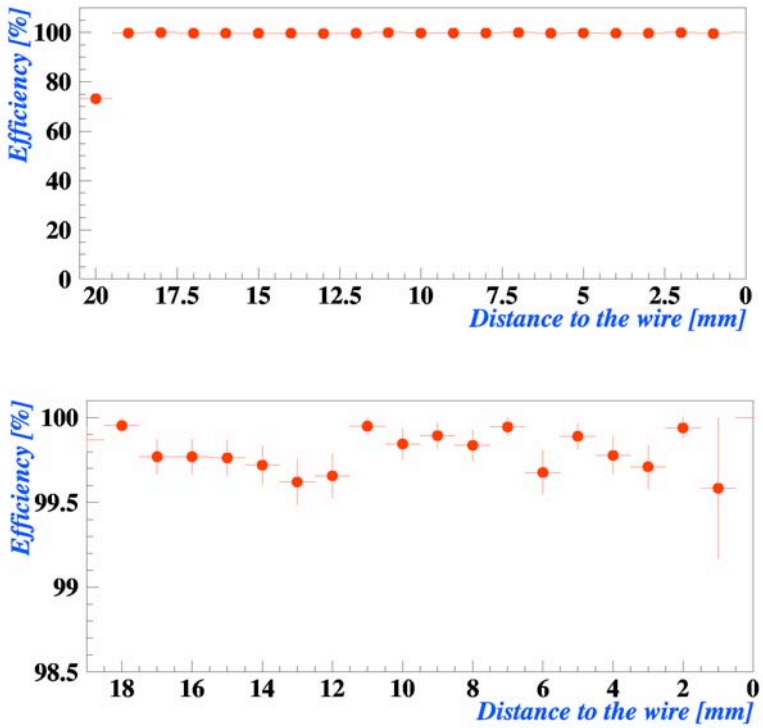

Figure 7.29: Efficiency as a function of the distance to the wire (top), for tracks orthogonal to chamber surface; (bottom) with an expanded scale excluding the I-beam region.

99.5%. The typical intrinsic average noise, as measured during chamber construction or during a test beam in dedicated random trigger runs [146], is shown in figure 7.30. It is reasonably stable, at values of ≈50 Hz, and does not vary much with channel number. Also the effect of higher noise levels, generated at the CERN Irradiation Facility, by photo-conversion in the chamber aluminum walls at chosen rates, both on reconstruction and trigger efficiency, was studied. The SL segment reconstruction efficiency is shown in figure 7.31 for various filter values of the gamma source, showing no significant dependence of the reconstruction algorithm on the gamma irradiation level, even at noise rates higher than the maximum levels expected in any DT chamber during normal LHC operations. Since the chambers are operated in the iron yoke of CMS, where important stray magnetic fields are present, the impact of the radial and longitudinal components of the field were carefully simulated (finite element analysis program ANSYS, figure 7.32), and tested both at dedicated muon test beams where the chambers were operated inside a magnetic field [145, 146], and during the CMS Magnet Test and Cosmic Challenge, with comsic rays. The distortion of the electron drift lines caused by a field of 0.5 T parallel to the wires can be seen in figure 7.33. This distortion can be roughly approximated by a rotation of the drift lines around the wire, simulating a rotation of the drift cell with respect to the direction of the incident particles. A change in the maximum drift path and time is generated, together with a drop of efficiency for inclined tracks which go through the I-beam region where the drift lines do not reach the wire. The staggering of the four layers minimizes the impact on track measurement of this last effect. In the case of

2008 JINST 3 S08004

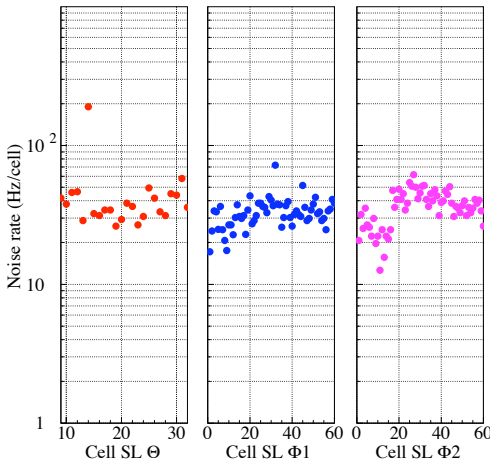

Figure 7.30: The noise cell occupancy as a function of the cell number, for the three SLs.

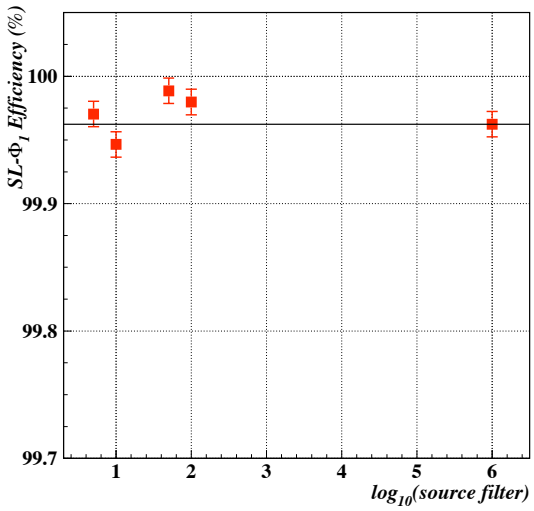

Figure 7.31: The cell efficiency in superlayer Φ_1 as a function of the irradiation filter value. The smallest filter value provides a background a factor 2 larger than the maximum one to be expected during LHC operation in any of the DT chambers in CMS.

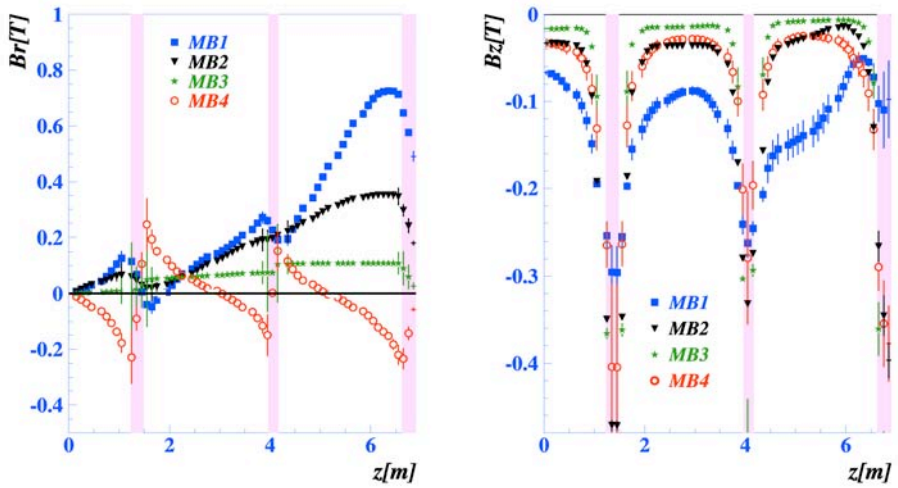

Figure 7.32: Radial (B_r) and longitudinal (B_z) components of the CMS magnetic field in the regions where the barrel chambers are placed as a function of the position along the beam direction (the centre of the detector is at z=0). Vertical bands indicate the separation between chamber wheels (in these particular regions B_z becomes significant). The biggest B_r values (0.7–0.8 T) occur in the MB1 region near the endcaps.

2008 JINST 3 S08004

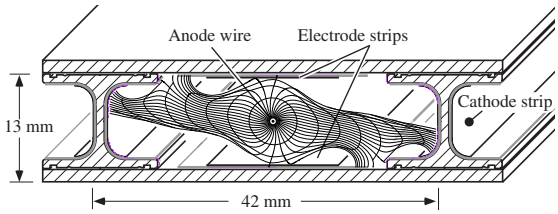

Figure 7.33: Simulation of the distortion produced in the drift lines by a 0.5 T magnetic field parallel to the wires.

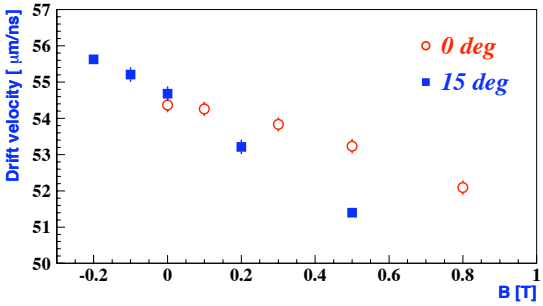

Figure 7.34: Drift velocity for several magnetic fields for perpendicular (0°) and inclined (15°) tracks.

a homogeneous magnetic field along the wire, the main consequence would be an effective lower drift velocity, but in CMS the magnetic field is not homogeneous. Figure 7.34 shows the drift velocity values obtained for several magnetic field values in the case of perpendicular tracks. A variation in the drift velocity of around 3% is observed from B=0 to 0.5 T. This corresponds to a change in the maximum drift time of less than 12 ns, which is acceptable both for reconstruction and trigger efficiency. The effects of the magnetic field on linearity are not very important below 0.3 T but increase dramatically for higher fields, mainly near the I-beams. The resolution is also slightly deteriorated by low magnetic fields, but it is still better than 300 μm below 0.3 T. In CMS the magnetic field component parallel to the wires measuring the coordinate in the bending plane is expected to be below 0.1 T, with only very limited regions reaching 0.3 T. In such conditions, the results obtained confirm that the performance of the drift tube chambers fulfil the requirements.

Test beam data: trigger performance

Like the chamber performance, the DT local trigger has also been tested extensively using test beam facilities at CERN [147, 148]. In particular, to fully test the performance of the trigger electronics, bunched beams having the same time structure as the LHC were used at the CERN SPS, producing high momentum muon tracks separated by multiples of 25 ns.

The bunch crossing (BX) identification efficiency is defined as the fraction of selected single muon events for which the local trigger delivered at least one trigger segment at the correct BX. This quantity was measured as a function of the muon momentum, and results are shown in figure 7.35. The measurement was also performed after inserting iron slabs, for a total depth of 15 cm, in front of the muon chamber. The effect of the iron absorber is the enhancement of the probability for a high momentum muon to produce electromagnetic showers. Such a probability also increases as a function of the muon momentum. This has the effect to decrease the BX identification efficiency. Results are also shown in figure 7.35, superimposed on results without iron absorber. Ghosts are copies of the trigger segment at the correct BX, as well as fake triggers at the wrong BX. They may originate from wrong alignment of hits in a DT muon station, due to the presence of extra hits produced by electromagnetic cascades and δ-rays, or from redundancies in the trigger electronics. In the case of single muon events, if two trigger segments are delivered at the same

2008 JINST 3 S08004

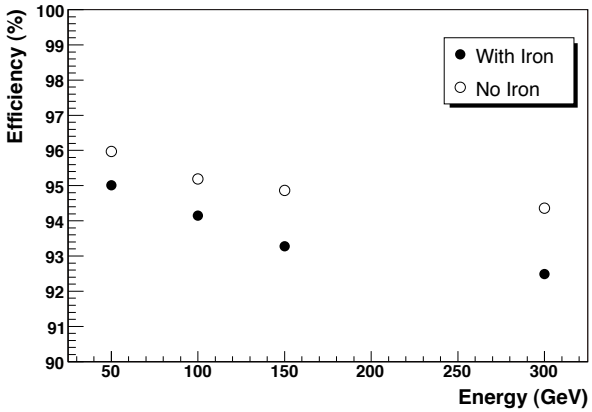

Figure 7.35: BX identification efficiency in a muon station in single muon events, as a function of the incident muon momentum, for events with and without the iron absorber placed in front of the muon station.

BX by the local trigger system in a muon station, the second trigger is considered a ghost copy of the first one. Although generally with a poorer quality, ghosts at the correct BX reproduce the characteristics of the main trigger segment in terms of position and angle. The production of segments associated to a wrong BX, arising from wrong hit alignment, is intrinsic to the BTI algorithm (section 8.2). In addition there are also cases in which the hit alignment is spoiled by δ-ray production or electromagnetic showering. Such fake triggers, which are called out-of-time ghosts, are almost entirely uncorrelated low quality segments, and are distributed over a wide range of BXs. The fraction of ghost triggers at the correct BX as a function of incident muon momentum, and the fraction of out-of-time triggers, as defined above, are shown respectively in figures 7.36 and 7.37 as a function of the incident muon momentum, for events with and without the iron absorber. The performance of the Φ Track Finder (PHTF, section 8.2) was also tested within the same muon test beam at CERN [148]. The PHTF was used to reconstruct muon trigger candidates using both muon stations, using ϕ-view local trigger primitives. Figure 7.38 shows the distribution of the BX assigned to the tracks found by the PHTF. The BX is correctly identified when its value is 24. Superimposed are the distributions of the same quantity determined independently by the local trigger in MB1 and MB3, as well as the distribution of the determined BX when a trigger segment with the same BX was delivered in coincidence in MB1 and MB3. It can be seen that the PHTF is fully efficient to deliver track candidates at the correct BX, whereas for out-of-time triggers the corresponding PHTF trigger rate is suppressed at the level of 1% or less.

A large fraction of the out-of-time triggers is due to real muons crossing the experimental apparatus at a BX different from 24, and which are correctly reconstructed by the PHTF. This is confirmed by the fact that the trigger segments that are matched together to form such tracks, are mainly of the type HH (four hits in both Φ-type SL), thus indicating a real muon track. Figure 7.39 shows the PHTF efficiency to reconstruct a trigger track in events with a MB1 and MB3 coincidence as a function of the BX. Superimposed are the efficiency to reconstruct a trigger track when the two trigger segments are both of HH type, and both of L (three out of four hits in a SL) quality

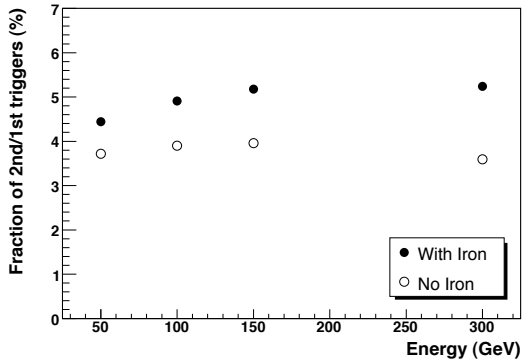

Figure 7.36: Fraction of ghost triggers observed in a muon station in single muon events, defined as the ratio of the number of second tracks over the number of first tracks, delivered by the local trigger at the correct BX, as a function of the muon momentum, for events with and without the iron absorber.

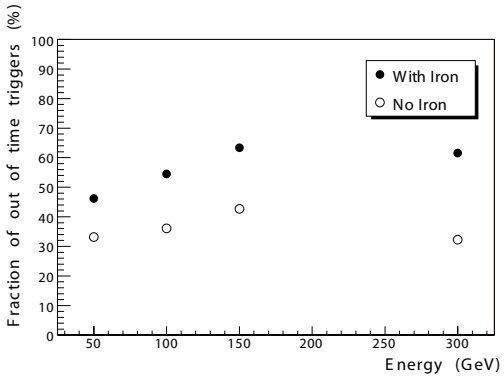

Figure 7.37: The fraction of out-of-time triggers in a muon station in single muon events, defined as the number of out-of-time trigger segments divided by the number of selected single muon events, as a function of the muon momentum, for events with and without the iron absorber.

respectively. The correct BX is 24. The PHTF efficiency for HH coincidences is 99.7±0.1% and is practically constant for any BX. This fits with the expectations, as such tracks are real muons crossing the apparatus. On the other hand, when the trigger segments have a low quality, which is typical for fake triggers, the PHTF ghost suppression is very effective. The rejection power for ghosts (L coincidences at BX $\neq$ 24) is 9.5±0.4. Therefore, although the out-of-time local trigger rate in a single station is rather high (as shown for example in figure 7.37), the PHTF is very effective in ghost rejection.

Commissioning of installed chambers

After installation in their final positions in the five CMS barrel wheels in the CMS surface hall, the chambers, including read-out and trigger electronics, were tested again with the goal of identifying potential problems before final cabling. Given the previous testing stages, it was mainly a test of the electronics and connections. Possible damage or loose connections as a consequence of installation (where chambers undergo some mechanical movement) could also be detected at this stage. This commissioning step was performed before final cabling (since the cables cover the minicrates and would prevent access for potential repairs) and involved all chambers in the ten sectors (84% of the full system). The commissioning consisted in the following steps:

1. connection to the power supplies and to the test-stand, which handled the trigger and read-out, in order to verify the functionality of the connectors and cabling of the chamber;

2. check of the minicrate performance by testing the internal connections and by monitoring the electronics boards inside the minicrate;

2008 JINST 3 S08004

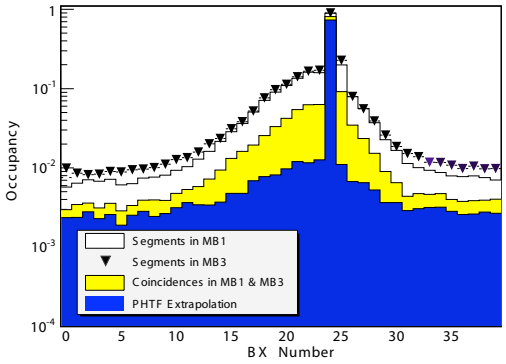

Figure 7.38: Distribution of the BX assigned to the tracks found by the PHTF. The BX is correctly identified when its value is 24. Superimposed are the distributions of the same quantity determined independently by the local trigger in MB1 and MB3, as well as the distribution of the determined BX when a trigger segment at the same BX was delivered in coincidence in MB1 and MB3.

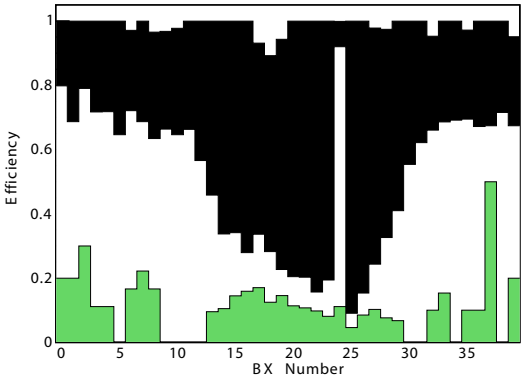

Figure 7.39: Efficiency to reconstruct a trigger track by the PHTF, as a function of the BX (white), in events with a two stations (MB1-MB3) coincidence. The correct BX is 24. Superimposed are the efficiency to reconstruct a trigger track when there is a coincidence of two trigger segments both of HH quality (black), and a coincidence of two trigger segments both of L quality (light green).

3. T0 determination (the starting point) of the drift time spectrum with test pulses. The T0 is specific for every cell, its cell-to-cell variation within a chamber is of the order of ≈1–2 ns;

4. cosmics data taking in different trigger configurations;

5. analysis of the cosmics data and verification of the chamber and electronics performance.

Depending on the amount of repairs, between two and five chambers per week were commissioned. Cosmic muon tracks were recorded in auto-trigger mode in different trigger configurations. Trigger rates varied from 80 Hz to 600 Hz per chamber depending on the sector inclination, the trigger configuration, and the chamber type. Higher level trigger components (tower electronics) as well as RPC connections were not tested at this stage since they required full cabling to the tower electronics.

The chamber orientation with respect to incoming cosmic-rays is purely horizontal only in sectors 4 and 10. This yields a reduction in the occupancy near the edges of the Φ-type superlayer for sectors near the vertical. An example comparing the bottom sectors 8, 9, 11 and 12 is shown in figure 7.40, where the occupancy per wire is summed over the four layers of superlayer Φ2. The reduced geometrical acceptance at the chamber edges is caused by the combination of two effects: i) the direction of cosmic rays, which is mainly vertical, and ii) the shielding of the iron yoke on soft muons.

Data recorded with highly selective trigger condition, 4 hits in both Φ-type superlayers or 3 hits in one and 4 in the other, are used to calculate the efficiency. The cell efficiency is calculated

2008 JINST 3 S08004

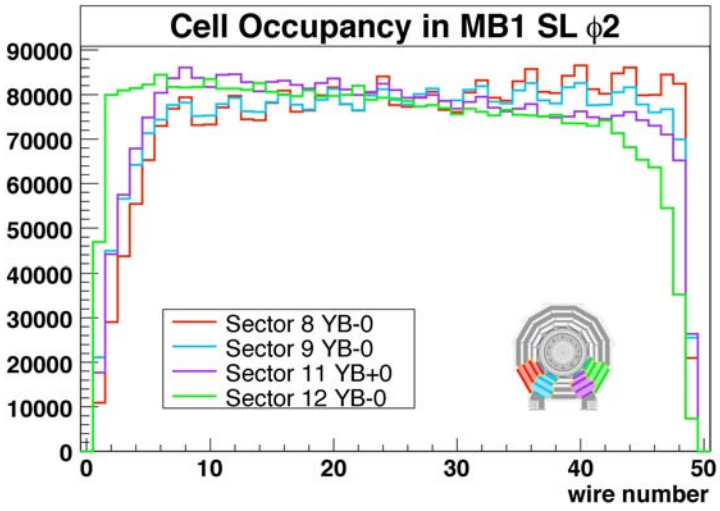

Figure 7.40: Sum of the occupancy of the four layers in MB1 Φ2 superlayer for sectors 8, 9, 11 and 12. The sectors have different inclinations as shown on the right. Material inside the yoke along with the iron yoke itself shield partly the soft cosmic ray muons.

from reconstructed tracks with hits found in the traversed cell or its 2 neighbours (N_{h}), normalized to the total reconstructed tracks traversing the considered layer (N_{track}):

$$\varepsilon_{\mathrm{Layer}} = N_{\mathrm{h}}/N_{\mathrm{track}} \tag{7.1}$$

requiring $\geq$5 hits in ϕ and $\geq$3 hits in z. Figure 7.41 (left panel) illustrates the combined track fit in the case of the ϕ projection. Because of the normalization to the number of tracks, the reduced occupancy near the chamber edges does not play a role. The cell efficiency is almost constant across the chamber, usually $\geq$98%, as seen, for example, in figure 7.41 (right panel).

Similarly the reconstruction efficiency is determined as the fraction of reconstructed tracks when requiring $\geq$7 hits per track, an example of which can be seen in figure 7.42. Here we should remark that the overall number of dead cells, as measured during chamber commissioning at CERN, amounts to $\approx$0.2% of the total number of channels (298 out of 171 852).

Results from Magnet Test and Cosmic Challenge

A further important test of the muon system with emphasis on integration into the overall CMS DAQ and Trigger system, is the aforementioned Magnet Test and Cosmic Challenge (MTCC), performed at CERN during summer 2006. For the first time, the three muon subsystems were operated together. The DT system made use of the complete read-out and trigger chain with final hardware, and the recorded data allowed the study of cosmic muon tracks in magnetic field. Another important task was the generation of a cosmic-muon trigger for the read-out of all CMS subsystems participating in the MTCC. Several goals were accomplished by the DT system during the MTCC:

1. Check of chamber performance and read-out

2008 JINST 3 S08004

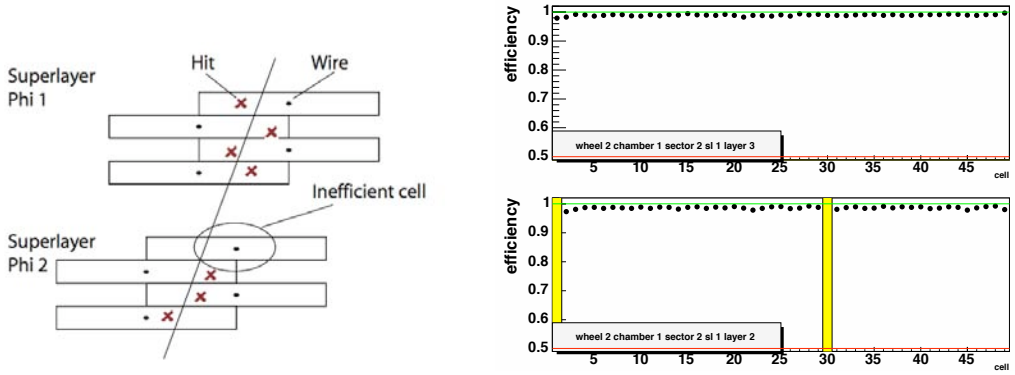

Figure 7.41: Cell efficiencies for two of the four layers of Φ1, MB1 sector 2.

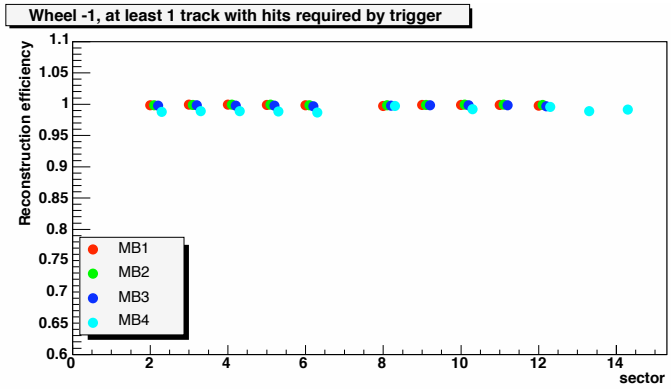

Figure 7.42: Reconstruction efficiency with 7 points in both Φ-type superlayers, according to the trigger condition, requiring either two 4-hit segments in both of the two Φ-type superlayers or one 4-hit and one 3-hit segment.

- check the effect of the fringe field on chamber performance in terms of HV behaviour, drift velocity, position resolution, and efficiency;
- exercise the complete read-out chain from the chamber through the ROS-25 up to the DDU;
- test of HV and LV in the final set-up. Integrate HV and LV control into central CMS services.

2. Trigger

   - operate the complete trigger chain with final hardware;
   - provide a cosmic-ray trigger to CMS;
   - check the effect of magnetic field on trigger timing (i.e. bunch crossing identification), requiring the RPC trigger to set a reference T0.

3. Software

   - integration of DAQ and Data Quality Monitoring;

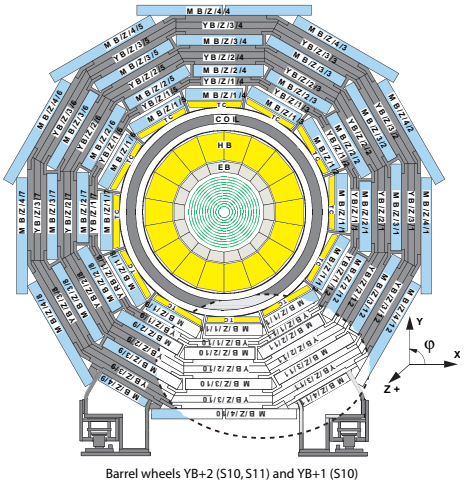

Figure 7.43: The MTCC exploited in the barrel region three sectors in wheels YB+1 (sector 10) and YB+2 (sectors 10, 11) instrumented with DTs and RPCs.

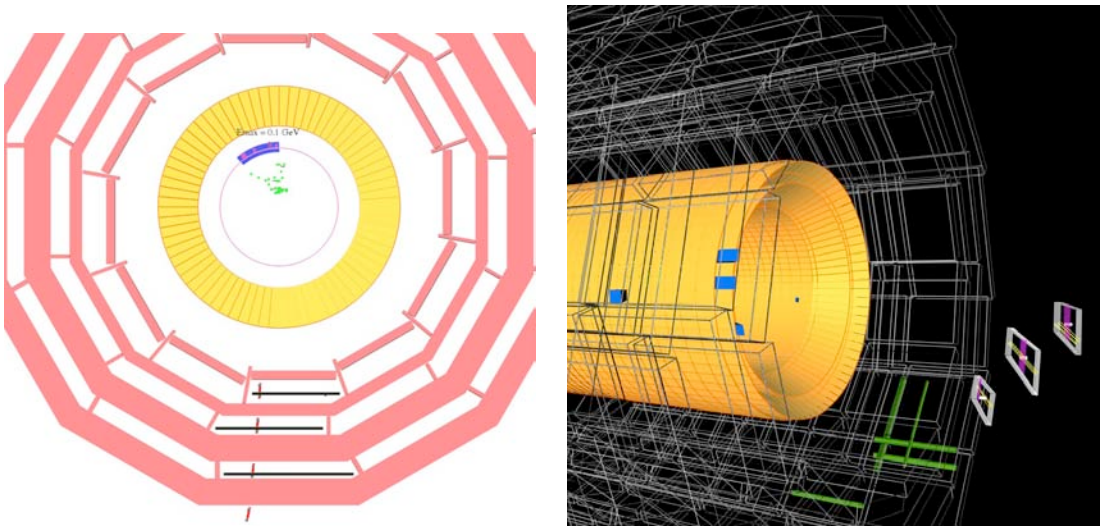

Figure 7.44: Event displays from the MTCC. Left panel: muon reconstructed in a DT sector in conjunction with Tracker activity. Right panel: muon track passing through both DT and CSC chambers.

- exercise the reconstruction software under realistic conditions.

4. Take data with other CMS subsystems.

For the DTs (as well as for the barrel RPCs) three instrumented sectors were read-out, the bottom sector 10 and the adjacent sector 11, both in YB+2, along with sector 10 in YB+1 (figure 7.43). This accounted for 14 DT chambers, corresponding to about 10 000 channels. Beside the cross-check of chamber performance previously carried out in test beams, MTCC data provided a unique opportunity to test the reconstruction algorithms for different magnetic field strengths (figure 7.44(left)) and to observe for the first time tracks combined in different detectors (figure 7.44(right)). As de-

2008 JINST 3 S08004

scribed in section 7.1.5, because of the radial component of the magnetic field between the solenoid and endcap disks, the electron drift direction in the r-ϕ view changes, acquiring a Lorentz angle. The angle is increasingly larger as the B radial component increases along z. Thus signals generated by muon hits in a r-ϕ drift tube at a given distance from the wire but at different z positions will appear at different times. The effect has implications both for the trigger synchronization and for the muon track reconstruction and it should be calibrated out before LHC start-up. During the MTCC a total of 159 million cosmic-muon events (48 million DT triggered) were collected at several values of the B field. Data were collected at 0 T (as a reference), then at 2, 3, 3.5, 3.8, and 4 T (93 million events at 3.8 and 4 T), which allowed a detailed mapping of the Lorentz angle effect in an MB1 and an MB2 chamber. Some 15 million events at 0 T and 3.8 T (1.6 million DT triggered) have been taken with the MB1 local trigger configured to select only muon segments pointing to the centre of the CMS barrel (LHC beam interaction point): this sample is specific for trigger timing studies in the DT-CSC overlap, in particular also the muon time-of-flight is the same as in a LHC run.

While procedures for the synchronization of the DT system in stand-alone were studied in Phase I of the MTCC, in Phase II (during the magnetic field mapping operations) effort was put in tools for fine inter-synchronization of the muon detectors (DT, CSC and RPC). In particular the analysis of the DT trigger data at the chamber output as function of RPC-originated L1A has proven to be sensitive to desynchronization by a few nanoseconds.

To study the efficiency of the DT Local Trigger (DTLT), events were selected by requiring the presence of the RPC triggers RBC1 (for wheel YB+1) or RBC2 (for RPCs in wheel YB+2) triggers. In such events, track segments were reconstructed in each muon station independently, whenever possible, using TDC hits. If more than one track segment was reconstructed in a given station, the one with the largest number of associated hits was taken. The efficiency of the DTLT was computed for each muon station separately, by counting events with a reconstructed muon segment, and comparing them with events which also had a trigger segment at any BX in the same muon station. Accepting a trigger regardless of its BX position was dictated by the fact that cosmic rays are likely to generate triggers in nearby BXs, as with non-bunched particles the system is intrinsically not synchronized. Only correlated trigger segments, namely of quality High-High (HH), High-Low (HL) or Low-Low (LL), as defined in section 7.1.5, were released by the trigger sector collector and thus used to compute the DTLT efficiency.

This efficiency was found to be about 65–70% in all stations, independent of the magnetic field. The measurements obtained using 40 MHz bunched muon beams [148] provided a much higher efficiency, of the order of 85% or more, and for which only triggers at the correct BX were considered.

The observed lower efficiency of the DTLT can be explained by the fact that, while the trigger system is clocked every 25 ns, cosmic rays occur at any time. In bunched beams the BTIs can be properly synchronized by choosing the best phase which maximizes the number of HH triggers with respect to higher level triggers. In the case of cosmic rays, this is not possible, due to the random arrival time of the muons thus making the BTI synchronization itself meaningless. In such conditions the rate of Low-quality trigger segments released by the BTIs increases, and also the associated BX can easily fluctuate. As only correlated trigger segments were released by the trigger Sector Collector in each station, we also expect an increase in TRACOs (section 8.2) failing

2008 JINST 3 S08004

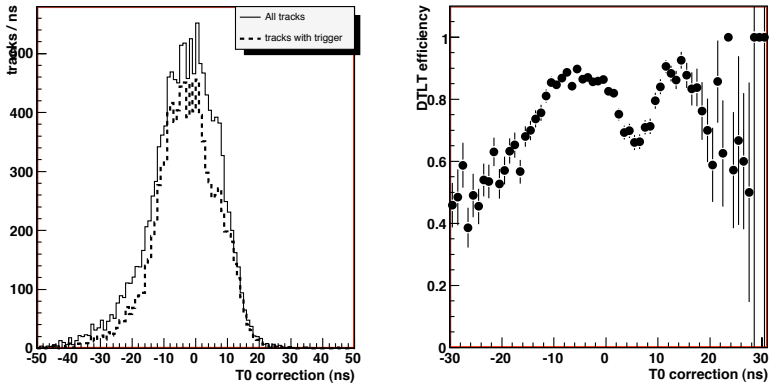

Figure 7.45: Left panel: distribution of t_0 for all track segments in a station, for events triggered by RPC (solid line). The distribution of the same quantity for events also triggered by the DT is superimposed (dashed line). Right panel: DT local trigger efficiency as a function of the quantity t_0, obtained by the ratio of the two histograms shown on the left.

to correlate segments among the two superlayers of a given station, with respect to a perfectly synchronized system, which will turn into a DTLT efficiency loss.

Consequently, one expects that muons crossing the detector at the "correct time" (for which the BTIs behave as perfectly synchronized to the clock) will be detected with the highest efficiency, as such a condition is the same as in the bunched beam tests. On the other hand, muons crossing the detector out of such a "correct time" will be detected with lower efficiency, as for them the synchronization of the system is not optimised.

The quantity t_0 is the time correction to be added to the t_{Trig} of the event to obtain the effective time at which the given muon crossed the detector. It can be computed event-by-event by minimizing the space resolution of the reconstructed track segment in a station. Figure 7.45 (left) shows the distribution of the t_0 correction of the reconstructed track segments in events triggered by the barrel RPC, superimposed to the one for events which also had a DT local trigger. The best trigger efficiency is obtained only at some preferred t_0 values. This can be seen in figure 7.45 (right) which shows the DTLT efficiency as a function of the t_0-correction time, obtained as the ratio of the two distributions previously described. Two peaks at efficiency around 90% are visible. They correspond to the case in which the muon crosses the detector at the "correct time" for which BTIs are synchronized. The two peaks correspond to two adjacent BXs. For other t_0 values, the efficiency can be very low, as in this case the system is not synchronized. The observed DTLT efficiency is therefore explained by the fact that cosmic rays occur at random time with respect to the "correct time" at which the BTIs have maximum efficiency.

The magnetic field modifies the shape of the field lines in the drift cell, thus affecting the effective drift velocity, as discussed in section 7.1.5. The largest effect in the barrel is expected to occur in station MB1 in Wheels +2 and -2. From the point of view of the DTLT, a change of the effective drift velocity, if large enough, could make the BX determination less precise, and shift its value by one unit.

Figure 7.46 shows this effect for the two MB1 stations in Wheel 2, displaying the BX value determined by the DTLT as a function of the z-position of the track in the chamber, with and

2008 JINST 3 S08004

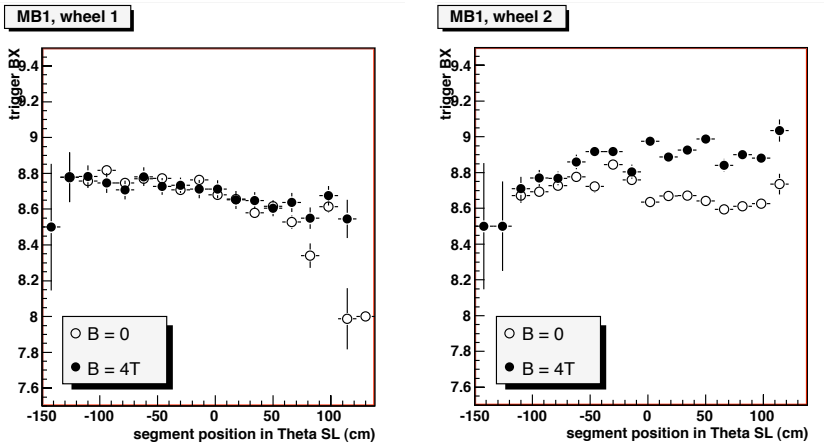

Figure 7.46: BX determined by the DTLT as a function of the track position in the z-direction of the muon station, with and without magnetic field, for MB1 in Wheel 1 on the left, where no effect of the B-field is expected. On the right, the same quantities are shown for MB1 in Wheel 2, where an influence of the magnetic field on the drift velocity is expected.

without magnetic field. While no clear effect is visible in MB1-Wheel 1, in MB1-Wheel 2 there is a slight delay of the average BX value which tends to increase as the track approaches the edge of the wheel, corresponding to larger values of z, where the stray field components are larger. This delay is at most of the order of 0.3 units of BX.

7.2 Cathode strip chambers

At the time of the LHC start-up, the CMS Endcap Muon system will consist of 468 cathode strip chambers (CSC) arranged in groups as follows: 72 ME1/1, 72 ME1/2, 72 ME1/3, 36 ME2/1, 72 ME2/2, 36 ME3/1, 72 ME3/2, and 36 ME4/1 (figures 7.47 and 7.48). The de-scoped 72 ME4/2 chambers will not be available during early years of CMS operation. The chambers are trapezoidal and cover either 10° or 20° in ϕ; all chambers, except for the ME1/3 ring, overlap and provide contiguous ϕ-coverage. A muon in the pseudorapidity range $1.2 < |\eta| < 2.4$ crosses 3 or 4 CSCs. In the endcap-barrel overlap range, $0.9 < |\eta| < 1.2$, muons are detected by both the barrel drift tubes (DT) and endcap CSCs. In the baseline design, muons with $|\eta| < 2.1$ are also detected by resistive plate chambers (RPC); however, in the initial detector this coverage is reduced to $|\eta| < 1.6$.

The CSCs are multiwire proportional chambers comprised of 6 anode wire planes interleaved among 7 cathode panels (figure 7.49). Wires run azimuthally and define a track's radial coordinate. Strips are milled on cathode panels and run lengthwise at constant $\Delta\phi$ width. Following the original CSC idea [149], the muon coordinate along the wires (ϕ in the CMS coordinate system) is obtained by interpolating charges induced on strips (figure 7.50). The largest chambers, ME2/2 and ME3/2, are about 3.4×1.5 m^2 in size. The overall area covered by the sensitive planes of all chambers is about 5000 m^2, the gas volume is >50 m^3, and the number of wires is about 2 million. There are about 9000 high-voltage channels in the system, about 220 000 cathode strip read-out channels with 12-bit signal digitisation, and about 180 000 anode wire read-out channels.

2008 JINST 3 S08004

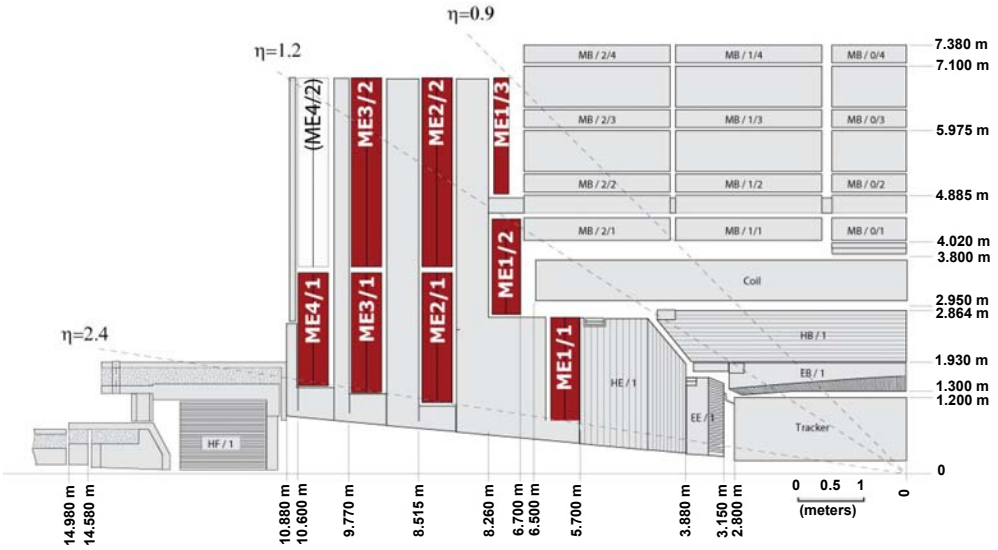

Figure 7.47: Quarter-view of the CMS detector. Cathode strip chambers of the Endcap Muon system are highlighted.

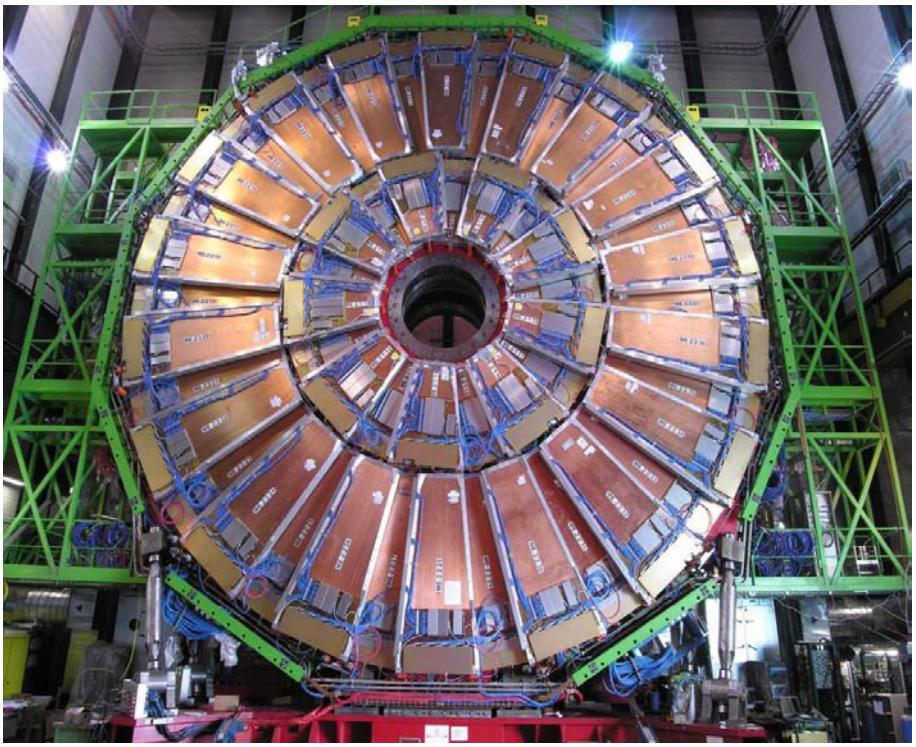

Figure 7.48: The ME2 station of CSCs. The outer ring consists of 36 ME2/2 chambers, each spanning 10° in ϕ, and the inner ring of eighteen 20° ME2/1 chambers. The chambers overlap to provide contiguous coverage in ϕ.

2008 JINST 3 S08004

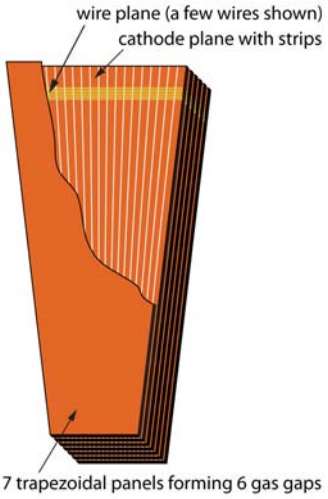

Figure 7.49: Layout of a CSC made of 7 trapezoidal panels. The panels form 6 gas gaps with-planes of sensitive anode wires. The cut-out in the top panel reveals anode wires and cathode strips. Only a few wires are shown to indicate their azimuthal direction. Strips of constant $\Delta\phi$ run lengthwise (radially). The 144 largest CSCs are 3.4 m long along the strip direction and up to 1.5 m wide along the wire direction.

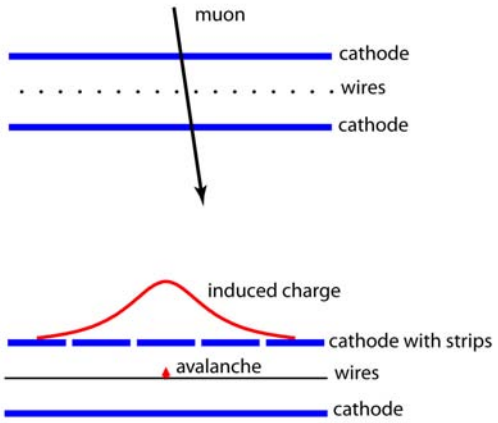

Figure 7.50: A schematic view of a single gap illustrating the principle of CSC operation. By interpolating charges induced on cathode strips by avalanche positive ions near a wire, one can obtain a precise localisation of an avalanche along the wire direction.

The CSCs provide the functions of precision muon measurement and muon trigger in one device. They can operate at high rates and in large and non-uniform magnetic fields. They do not require precise gas, temperature, or pressure control. Moreover, a radial fan-shaped strip pattern, natural for measurements in the endcap region, can be easily arranged on the cathode planes.

The performance requirements for the CMS cathode strip chamber system include the following:

- Reliable and low-maintenance operation for at least 10 years at the full LHC luminosity, i.e., at estimated random hit rates up to 1 kHz/cm^2;
- At least 99% efficiency per chamber for finding track stubs by the first-level trigger;
- At least 92% probability per chamber of identifying correct bunch crossings by the first-level trigger. With such an efficiency per chamber and 3–4 CSCs on a muon track path, a simple majority rule ensures that the reconstructed muons will be assigned the correct bunch crossing number in more than 99% of cases;
- About 2 mm resolution in r-ϕ at the first-level trigger.
- About 75 μm off-line spatial resolution in r-ϕ for ME1/1 and ME1/2 chambers and about 150 μm for all others.

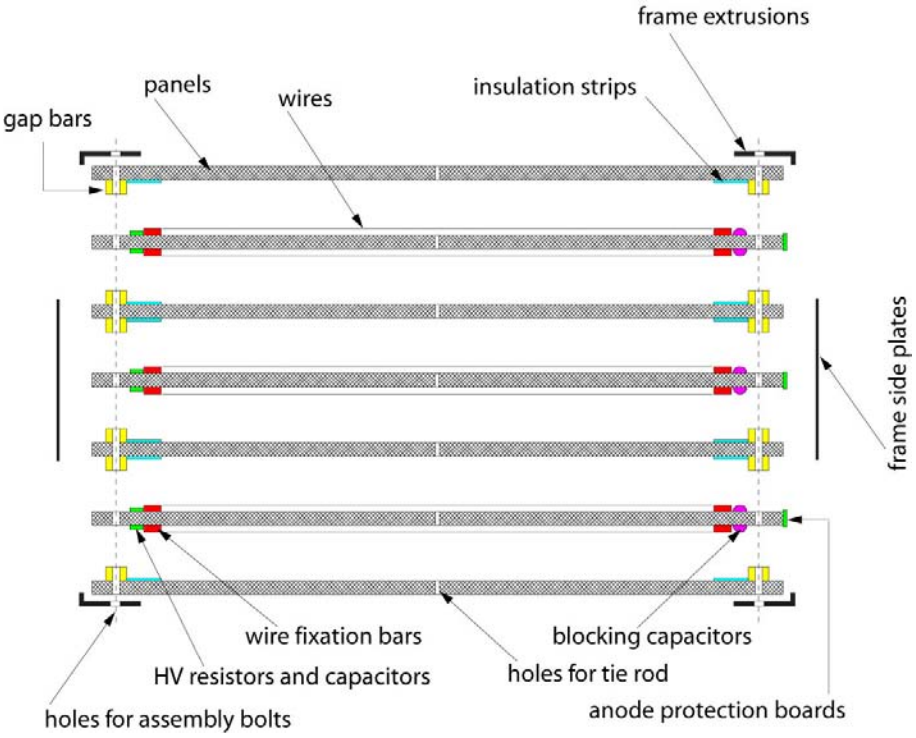

Figure 7.51: Mechanical design of the CMS cathode strip chambers (exploded view).

7.2.1 Chamber mechanical design

The 72 ME1/1 chambers and the larger 396 chambers have somewhat different mechanical designs. Below, we describe the design of the larger chambers using ME2/2 as an example and, then, at the end of this section, summarise the ME1/1-specific features that distinguish them from the other chambers.

The mechanical structure is based on seven 16.2-mm-thick trapezoidal panels (figure 7.51). The panels are made of a 12.7-mm-thick polycarbonate honeycomb core with two 1.6-mm FR4 skins commercially glued on each side. FR4 is a fire-retardant fibreglass/epoxy material widely used for printed circuit boards. The FR4 skins are clad with 36-μm-thick copper on their outer surfaces, forming the cathode planes.

FR4 cathode gap bars are glued to both sides of every other panel (panels 1, 3, 5, 7 in figure 7.51) so that when the panels are stacked together, these cathode bars define 6 gas gaps of 9.5 mm. To provide additional support, there are 4 spacers placed between panels along the chamber centreline. When all 7 panels are put together, the entire stack is tightened down with bolts along the chamber perimeter (through holes in the cathode gap bars) and at 4 points along the chamber centreline (through holes in the spacers). Such an arrangement ensures that no panel has more than 60 cm of unsupported length. Measurements show that most of the panels are flat within the required $\pm$300 μm on such spans. This specification arises from the desire to keep gas-gain variations within a factor of 2.

Six of the panels have a pattern of 80 strips milled on one side. Strips, being radial, have a pitch that varies from 8.4 mm at the narrow chamber end to 16 mm at the wide end. The gap

between strips is about 0.5 mm. The precision of milling was better than 50 μm (rms). Milling was done with a cutter tilted at 45° to make the groove edges smoother (otherwise, sharp edges and burrs might provoke sparking and discharges).

Three of the panels are so-called *anode* panels (panels 2, 4, 6 in figure 7.51) around which anode wires were wound (these panels do not have gap bars). A specially designed winding machine wound wires directly on a panel by rotating it around its long axis at a speed of about 5 turns per minute; one panel could be completed (about 1000 wires on each side) in less than 4 hours. The wire spacing of about 3.2 mm was defined by combs: threaded rods running the full panel length and attached to the panel edges during winding. Gold-plated tungsten wires, 50 μm in diameter, were stretched at 250-g tension (about 70% of the elastic limit) and run their full length up to 1.2 m without any intermediate supports. The electrostatic stability limit for the longest wires is above 6 kV (the nominal operational point is 3.6 kV). Based on measurements during production, the wire tension non-uniformity does not exceed $\pm$10%, while wire spacing variations are less than $\pm$150 μm. Wires found to fall outside of these specifications were replaced.

After winding, the wires were first glued and then soldered to anode bars 4.75 mm in height (half of the gas gap). The anode bars are made of copper-clad FR4 and carry the electric artwork. An automated soldering machine allowed for soldering at a speed of 3.5 s per joint. Groups of 16 wires make 1 anode read-out channel with a width of about 5 cm. High voltage (HV) is distributed to the wire groups on one end and signals are read out on the other end via 1 nF blocking capacitors.

Each wire plane is sub-divided by spacer bars into 5 independent HV segments, which allows us to independently regulate or turn off HV on any of the 5 sections. In places where the spacer bars were inserted (and prior to their installation), 8 wires were removed. Two gold-plated 200-μm guard wires were inserted in place of the first and eighth thin wires that were removed to eliminate edge effects. The very first and last wires in each plane are also thicker. If the edge thin wires were to be left unguarded, the electric field on them would be much larger than for the rest of the wires, which would provoke discharges. Such plane segmentation, because of the intermediate panel supports and the individual HV control over smaller wire-plane sections, makes the overall chamber performance very robust.

After stacking the panels and tightening the bolts (with O-rings), continuous beads of RTV sealant were applied along the outer seams between the panels and gap bars. The O-rings around the bolts and the RTV seal make the chambers hermetic. Should it be necessary, a chamber can be opened, serviced, and resealed. Gas enters into one of the outer gas gaps via an inlet in a cathode gap bar, flows from one plane to another in a zigzag manner via special holes in the panels, then exits from the last gas gap via an outlet in a gap bar. The leak rate, measured during production and after installation of the chambers, was required to be $<$1% of the chamber volume per day at an over-pressure of 7.5 mbar (e.g., $<$2 cm^3/min for the largest chambers whose gas volume is about 200 litres).

Side plates made of 3.2-mm-thick Al extrusions were attached around the chamber perimeter. They stiffen the chamber and connect the top and bottom copper skins to form a Faraday cage.

The nominal gas mixture is $40\%\mathrm{Ar} + 50\%\mathrm{CO_2} + 10\%\mathrm{CF_4}$. The CO_2 component is a non-flammable quencher needed to achieve large gas gains, while the main function of the CF_4 is to prevent polymerisation on wires. A detailed discussion of the gas optimisation can be found elsewhere [150].

2008 JINST 3 S08004

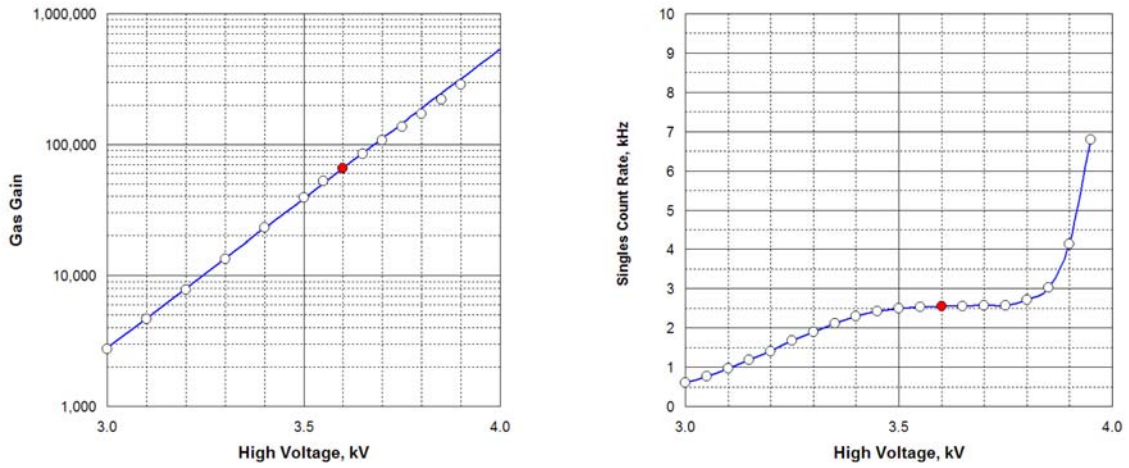

Figure 7.52: Left panel: CSC gas gain vs. high voltage. Right panel: ME2/1 chamber singles rate vs. high voltage (the overall sensitive area of all 6 planes in this chamber is ≈9.5 m^2).

Figure 7.52 (left) shows the chamber gas gain vs. high voltage. The nominal operating HV was chosen to be 3.6 kV, which corresponds to a gas gain on the order of 7×10^4. A minimum ionising particle (MIP) produces about 100 electrons in a gas gap, thus the charge per MIP in an avalanche is about 1 pC. As is shown below, at this operational point, the cathode and anode electronics have a very high efficiency and an adequate signal-to-noise ratio. The operational range of the chambers extends to 3.9 kV. Typically, we start seeing a sharp rise in the rate of spurious pulses at about 3.9–4.0 kV (figure 7.52 (right)).

The 72 ME1/1 chambers have differences in their mechanical design with respect to the other CSCs. The gas gap is 7 mm, wire diameter is 30 μm, and wire spacing is 2.5 mm, so the nominal HV for these chambers is somewhat lower: 2.9 kV. Most notably, the ME1/1 anode wires are not azimuthal, but are tilted by an angle $\alpha_L = 29^\circ$ (figure 7.53). Unlike the other CSCs, the ME1/1 chambers are inside the CMS solenoid and see its strong and uniform 4 T axial field. The wire tilt compensates for the Lorentz angle so that electrons drift parallel to the strips, enabling a precise measurement of the r-ϕ-coordinate.

7.2.2 Electronics design

Figure 7.54 shows a schematic layout of the custom-made trigger and read-out electronic boards developed for the CSC system.

An anode front-end board (AFEB) has one 16-channel amplifier-discriminator application-specific integrated circuit (ASIC). The amplifier has a 30-ns shaper (semi-Gaussian with 2-exponent tail cancellation designed to suppress the slow signal component associated with a drift of positive ions away from the anode wires), about 7 mV/fC sensitivity, and 1.4 fC noise at a typical wire group capacitance of 180 pF for the largest chambers. With the 30-ns shaping time, an AFEB sees about 12% of the total avalanche charge, i.e., an average of about 130 fC. A typical chamber signal as seen at the output of this amplifier is shown in figure 7.55 (left). The constant-fraction discriminator has a threshold nominally set at 20 fC (input equivalent charge) and its slewing time is less than 3 ns for the 60–600 fC signal range. Depending on chamber size, there are 12 to 42 AFEBs per chamber. Further details on the AFEB design and performance can be found elsewhere [151].

2008 JINST 3 S08004

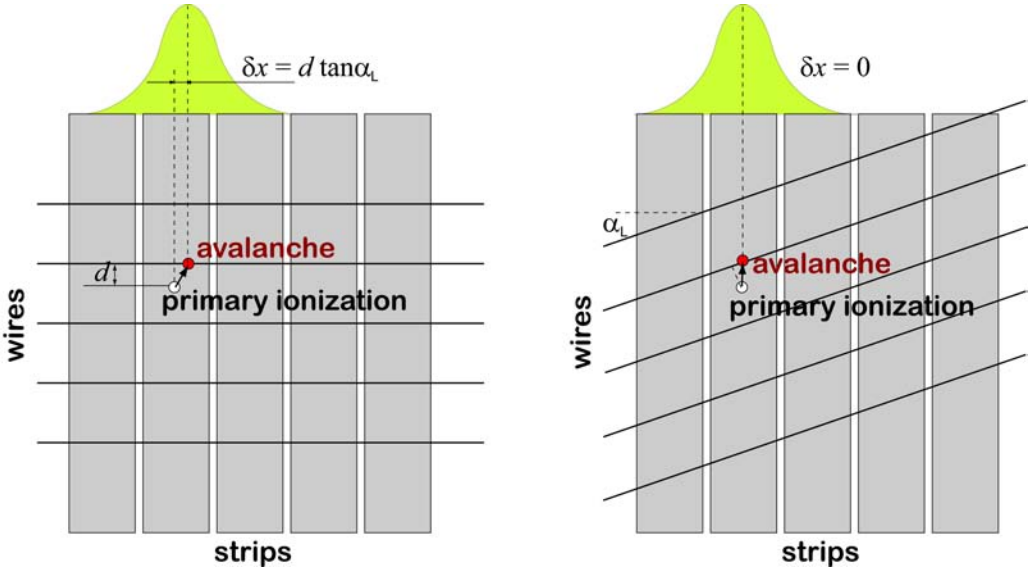

Figure 7.53: Left panel: if the ME1/1 wires were not tilted, ionisation electrons, as they drift toward the anode wires in the strong magnetic field normal to the plane of the drawing, would be carried sideways by the Lorentz force. The direction and size of the shift would depend on whether the electrons drift upwards or downwards and on how far away they were from the wires to begin with. These sideways displacements would spread the charge over the anode wires. Right panel: by tilting the wires at the Lorentz angle α_L, all ionisation electrons arrive near the same point.

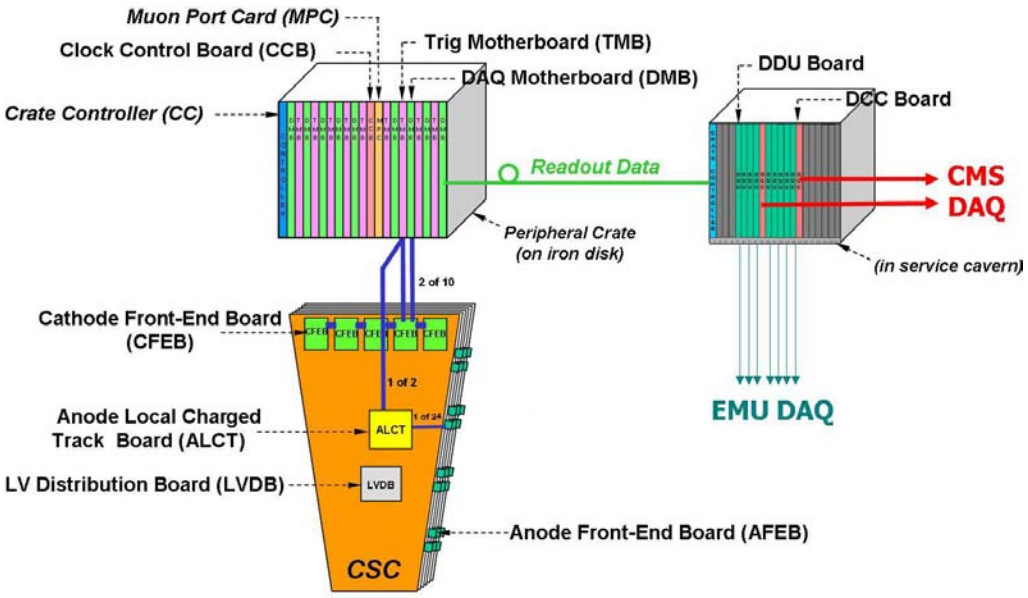

Figure 7.54: Schematic layout of the CSC trigger and read-out electronics.

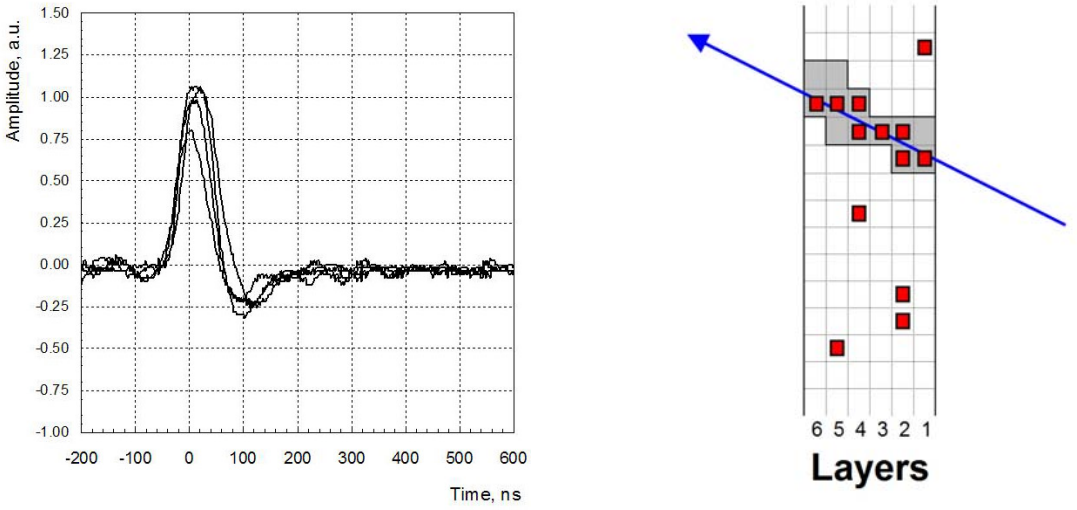

Figure 7.55: Left panel: muon signals as seen at the AFEB amplifier output. Right panel: a schematic event display showing anode signals in the 6 planes of a CSC (small dark squares). The ALCT board FPGA logic is programmed to scan the chamber and search for hits falling inside predefined patterns (grey cells) consistent with muons originating from the interaction point. Hits must be present in at least 4 planes for an ALCT pattern to be found.

Every 25 ns, in synchronization with the LHC collisions, all AFEB outputs, 40-ns-long step pulses, are sampled by an FPGA-based anode local charged track (ALCT) board, 1 board per chamber. The recorded *yes/no* information is stored in a FIFO. Upon receiving a CMS-wide Level-1 Accept (L1A) trigger command, the recorded information within the proper time window is extracted and reported to the DAQ. The latency of the L1A command with respect to the time of a collision is 3.2 μs. The temporal length of the raw-hit record transmitted to the DAQ can be as large as 800 ns.

The ALCT board has another important function. Based on the information from all anode channels, the FPGA code constantly (every 25 ns) searches for patterns of hits among the 6 planes that would be consistent with muon tracks originating from the interaction point. For a pattern to be valid, we require that hits from at least 4 planes be present in the pattern. Figure 7.55 (right) illustrates how patterns are identified in the presence of spurious single-plane hits. Due to a large neutron-induced photon background, a substantial rate of such single-plane hits is expected. However, these hits, being completely uncorrelated, would not typically line up to form track-like patterns. Found patterns, called ALCTs, are trigger primitives. They are transmitted further downstream to the muon Level-1 trigger electronics that builds muon track candidates from these primitives. The time it takes to form an anode track trigger primitive is 225 ns (including drift time). Each ALCT board can find up to 2 such patterns per bunch crossing, which is adequate for the expected chamber track occupancy at the nominal LHC luminosity.

For the cathode strips, 1 cathode front-end board (CFEB) serves (6 planes)$\times$(16 strips) = 96 channels and has 6 parallel chains of the following chips (figure 7.56 (left)): 16-channel amplifier-shaper ASIC, 16-channel switched capacitor array (SCA) ASIC, 12-bit 1-channel ADC, and 16-channel comparator ASIC. There are 4 to 5 CFEBs per chamber.

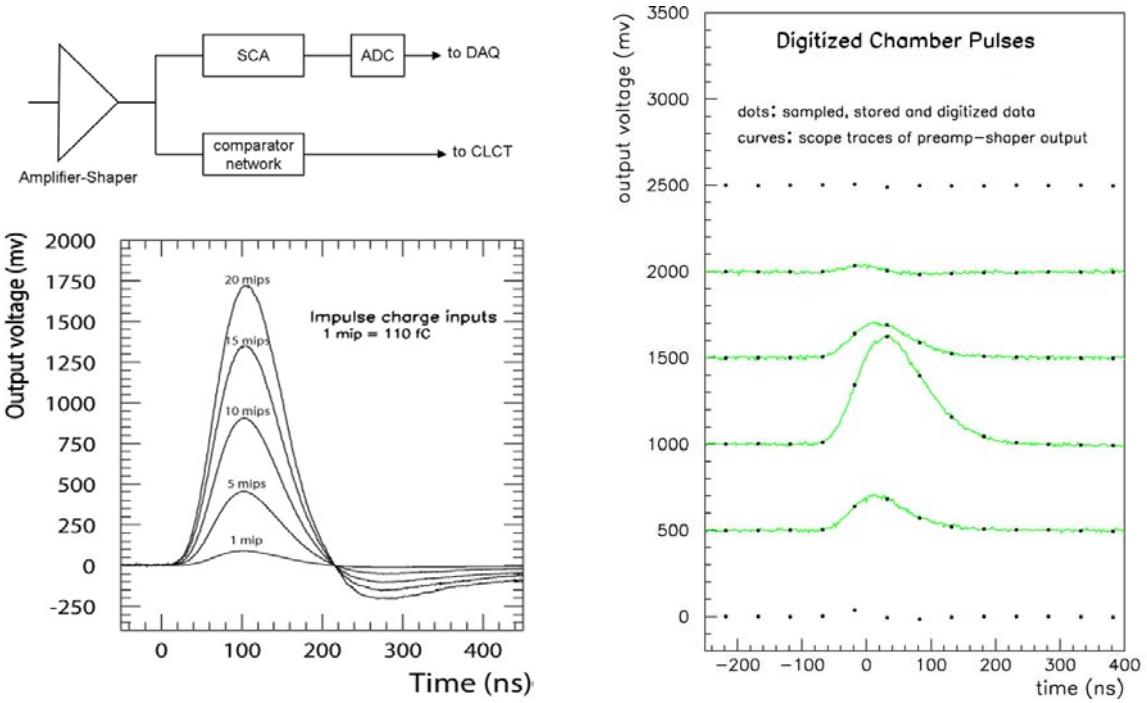

Figure 7.56: Left panel: basic functional diagram of a CFEB and the CFEB amplifier-shaper response to a δ-function input pulse. The undershoot is intended to compensate for the long tail present in muon hit signals resulting from the slow drift of positive ions away from the anode wires. Right panel: signals from a muon track on 6 contiguous strips in a layer. The 4 curves are oscilloscope traces and the 6 lines of dots are digitised outputs. The signals have an arbitrary vertical offset for ease of viewing.

The amplifier-shaper ASIC has 100-ns shaping time and a sensitivity of 0.85 mV/fC over a linear range up to 1 V. The equivalent noise level at ≈300-pF strip capacitance is typically 1.5 fC. The shaping is based on a semi-Gaussian transfer function with an undershoot designed to compensate for the $1/t$ signal tail due to the slow drift of positive ions. After convolution with the current pulse produced in a chamber by a muon, the amplifier-shaper signal peaks around 150 ns and has no tail (figure 7.56 (right)). The CFEB sees about 8% of the total avalanche charge, i.e., about 100 fC on average.

The output from this chip is split into 2 pathways. One leads to the SCA chip [152], which samples the waveform of each strip signal every 50 ns in sync with the LHC clock and stores this analog information on its capacitors. The depth of this analog memory is 96 capacitor cells per channel, or 96 × 50 ns = 4.8 μs. Upon receiving the L1A command 3.2 μs following a collision, 8 or 16 consecutive samples from the proper time range among the SCA capacitors are retrieved and digitised individually by the 12-bit flash ADCs. The digital information is passed to the DAQ via an intermediate digital data buffer. For the digitisation and subsequent read-out by the DAQ to happen, the L1A signal must be in coincidence with the *cathode local charged track* (CLCT) primitive decision described below.

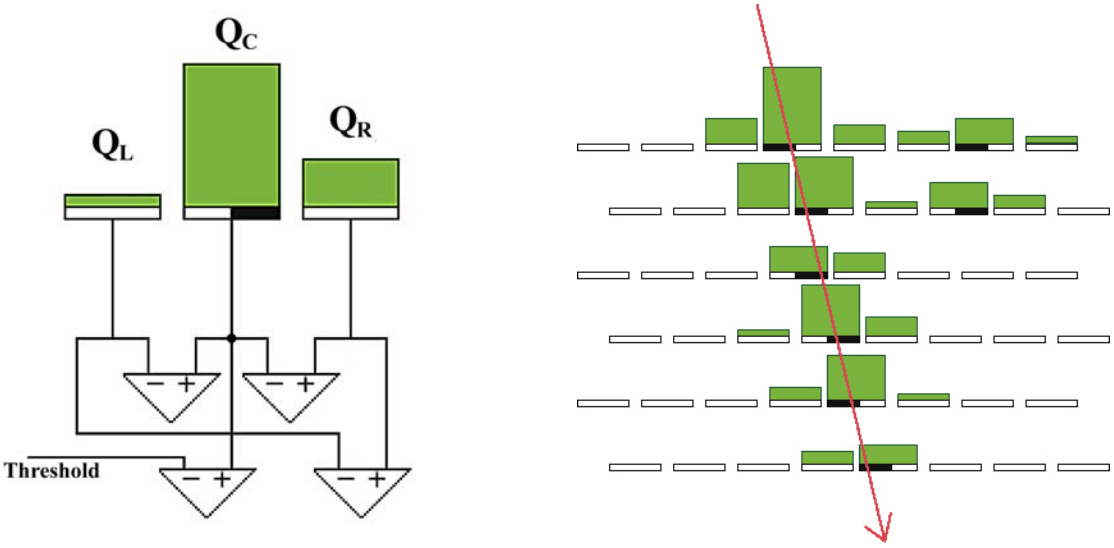

Figure 7.57: Left panel: a simplified schematic of the idea behind the comparator network. For each group of 3 adjacent strips, comparators compare the central strip signal Q_c with a threshold and with the central-to-left $Q_c - Q_l$, central-to-right $Q_c - Q_r$, and right-to-left $Q_r - Q_l$ strip signal differences. If $Q_c >$ threshold, $Q_c - Q_l > 0$, $Q_c - Q_r > 0$, and $Q_r - Q_l > 0$ (as shown here), the hit position is somewhere within the right half of the central strip. Right panel: a *cathode local charged track* is a pattern of half-strip hits consistent with a muon track.

The second amplifier-shaper output goes to the comparator network. This chip compares signals on triplets of adjacent strips at the time when signals reach their maximum amplitude. By means of such comparisons, the comparator network can identify a muon hit location to within one half of a strip width, independent of the signal amplitude, the induced charge shape (as long as it is "bell"-like), and the strip width itself [153] (figure 7.57 (left)).

Comparator half-strip hits are sent to the trigger motherboard (TMB). Like the ALCT board, the TMB searches for patterns of half-strip comparator hits that would be consistent with muon tracks of interest (figure 7.57 (right)). There is 1 TMB per chamber and up to 2 CLCTs per bunch crossing can be found per TMB. As in the ALCT pattern search, for a CLCT pattern to be found, half-strip hits must be present from at least 4 planes. Unlike the ALCT boards, the TMBs are not mounted on the chambers, but are in peripheral VME crates mounted along the outer rim of the endcap steel disks.

The TMB also matches ALCT and CLCT patterns found within a chamber to make correlated 2-dimensional LCTs (2D-LCT = ALCT×CLCT), up to 2 per bunch crossing. These 2D-LCTs are sent to muon port cards (MPC), each of which serves 9 chambers covering either 60°- or 30°-sectors in ϕ. For each bunch crossing, an MPC performs a preliminary sorting of all received correlated 2D-LCTs and finds the 3 best-quality candidates — these are then sent further upstream to the muon L1-trigger electronics.

Raw data are collected by the DAQ motherboards (DMB) located in the peripheral crates. There is one DMB for each chamber. The data consist of anode and comparator hits within a time window up to 32 bunch crossings long, ALCT and CLCT decisions in the same window, and

digitised strip signal waveforms (eight or sixteen 50-ns time samples). The status of the various electronic boards is also a part of the event record. The data collected by the DMB are passed to a detector-dependent unit (DDU) board, then to a data concentration card (DCC), and finally to the CMS filter farm to be processed by the CMS high-level trigger (HLT) software. The expected event size per chamber is about 5 kBytes.

It is important to note that the CSC read-out is intrinsically zero-suppressed. The anode raw data in a particular chamber are passed downstream only if there is an ALCT pattern in coincidence with the L1A signal. Likewise, the cathode information, comparator hits and digitised strip signal waveforms, are passed downstream to the DAQ only if there was a similar CLCT$\times$L1A coincidence. The coincidence window is programmable, but is nominally set at 75 ns, i.e., $\pm$1 bunch crossing.

At the design LHC luminosity, we expect on average to find track stubs in 2 chambers for each L1A signal. With the maximum CMS L1A rate of 100 kHz, the data flow rate from CSCs to HLT is estimated to be around 1 GB/s.

Operation of the peripheral VME crates is supported by clock-control boards (CCB) and custom crate controllers. As its name implies, the CCB distributes the LHC clock and all CMS control commands (like L1A signals).

The HV system is custom made and provides channel-by-channel regulated voltage up to 4.0 kV with about 10 V precision. Currents of less than 10 μA can be measured with a precision of 100 nA, while the precision for larger currents is about 1%. The system can provide more than 100 μA current for individual channels as long as the average consumption does not exceed 40 μA per channel. The maximum expected current at the design LHC luminosity for the most-loaded HV segment is $<$10 μA.

7.2.3 Performance

The results presented in this section come from tests conducted with final-design CSCs in high-energy muon beams at CERN, with cosmic-ray muons in a lab or in situ after installation, and at the Gamma Irradiation Facility (GIF).

A high-energy muon beam provides a test environment with maximum control, but it can expose only a small portion of a chamber. We typically used 100–300 GeV beams, which also allowed us to study chamber performance in the presence of bremsstrahlung radiation. To study performance over the entire chamber area, for many years we have tested individual large chambers with cosmic-ray muons at various research laboratories.

During the CMS Magnet Test and Cosmic Challenge (MTCC) in 2006, a substantial part of CMS was operated as a unified system. The CSC subsystem was represented by a 60° sector, or 36 chambers. This allowed us to obtain in situ performance results for a large number of CSCs operating simultaneously with other CMS subsystems. Figure 7.58 shows a muon event as detected by CSCs at the MTCC.

At the design LHC luminosity, we expect a large neutron flux in the underground cavern, which upon thermalization and capture is predicted to result in a substantial flux of $\approx$1 MeV photons. Of the photons that enter a chamber, about 1% will convert to electrons. These electrons will give rise to large rates of random hits up to 1 kHz/cm^2 in the CSCs. The GIF at CERN has a

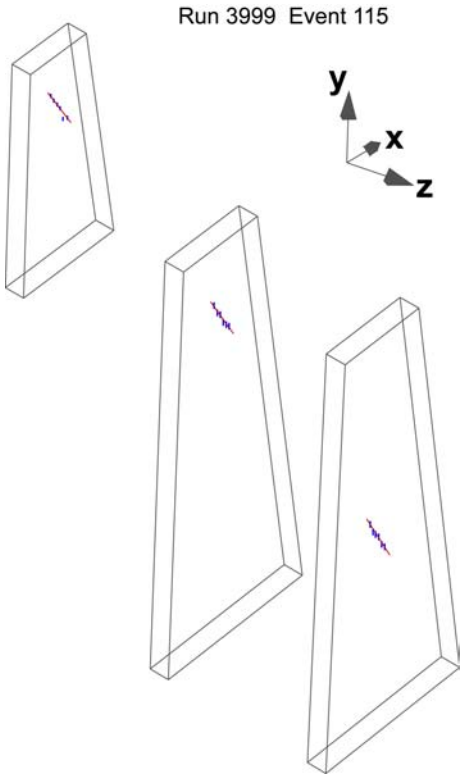

Figure 7.58: Part of a CMS event display showing a muon event detected by CSCs during the MTCC. Only those chambers containing muon hits are displayed.

Cs-137 source of 0.7 MeV photons with an intensity of $\approx 0.7 \times 10^{12}$ Bq. Tests at the GIF allowed us to study the chamber performance in an environment of high random-hit rates. We also used these facilities for chamber-ageing studies.

Trigger primitives

It is important to note that the efficiency of finding trigger primitives (LCTs) directly affects not only the muon trigger, but also the DAQ path. As was described earlier, the CSC read-out is driven by an LCT×L1A coincidence. If an LCT is not found, there will not be a coincidence, and no raw hits will be recorded and available for the offline reconstruction.

The anode signal efficiency of a single plane is shown in figure 7.59 (left). The same figure also shows the efficiency for finding ALCTs, patterns of hits in 6 planes consistent with a muon track. The desired ALCT-finding efficiency of 99% is reached above 3.4 kV. At 3.6 kV, the ALCT-finding efficiency is about 99.9%. These results were obtained for test-beam muons going through a small area of a chamber free of dead zones. For CLCT patterns, similar results are achieved at about 50 V higher. This is because the cathode signal is somewhat smaller than the anode signal.

The overall efficiency of finding 2D-LCT patterns (ALCT×CLCT) averaged over the entire area of many chambers was studied with cosmic-ray muons at the MTCC. At the nominal HV of 3.6 kV, the average 2D-LCT efficiency in 6 ME2/2 chambers was found to be (99.93±0.03)%. For the 0.07% of events with missing 2D-LCTs in ME2/2 chambers, the majority of tracks (reconstructed

2008 JINST 3 S08004

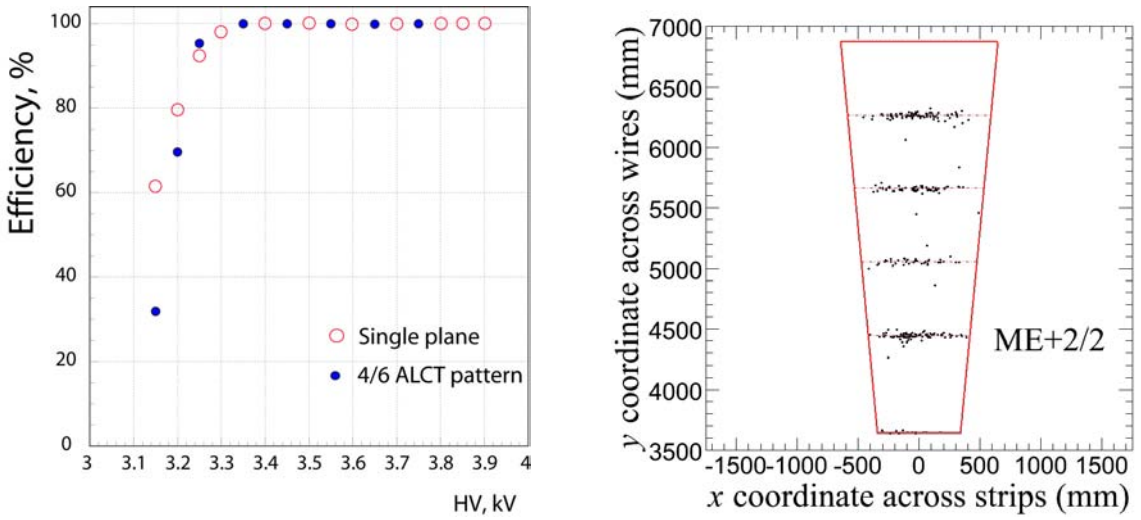

Figure 7.59: Left panel: single-plane anode signal efficiency (open circles) and ALCT pattern finding efficiency (filled circles) vs. high voltage. Right panel: predicted position of muon tracks in ME2/2 chambers for events when no LCT was found in these chambers (superimposed results for 6 chambers). The dashed lines indicate where wire planes of the ME2/2 chambers have inefficient bands separating independent HV segments.

using the ME1 and ME3 LCT stubs) were found to cross ME2/2 chambers in inefficient bands separating the chamber high-voltage segments (figure 7.59 (right)).

To test whether the found LCTs are indeed associated with the muons going through the chambers, we looked at the relative distance between the (x,y) coordinates of 2D-LCTs found in ME2/2 chambers and the muon track (x,y) coordinates in the ME2 station as predicted from the 2D-LCTs in the ME1 and ME3 stations. (Here x and y are the local chamber coordinates across the cathode strips and anode wires, respectively.) The 2D-residuals between the measured and predicted (x,y) coordinates are shown in figure 7.60 (left). The observed spread of $\approx$0.5 cm along the x axis is consistent with the expected multiple scattering of cosmic-ray muons penetrating the endcap steel disks. As is shown below, the intrinsic precision of CLCT localisation is better than that. The distribution along the y axis is noticeably broader due to a much coarser wire group segmentation of 5 cm, which defines the precision of ALCT localisation in these chambers.

For studying the intrinsic CLCT-localisation precision, we used a test chamber in a muon beam and a telescope of Si micro-strip detectors to precisely determine the position of a muon going through the test chamber. To achieve the best results, a given CLCT pattern is assigned an x coordinate corresponding to the average of all muons that can generate such a pattern. Figure 7.60 (right) shows the residuals between the Si-based track coordinate and the CLCT-based coordinate. The distribution is Gaussian and has $\sigma \approx 0.11$ in strip width units, which is better than the desired 2 mm for even the widest 16-mm strips. In the more conservative approach currently implemented in the muon trigger firmware, CLCT patterns are localised within a half-strip. Therefore, in this approach the CLCT spatial resolution is approximately $(w/2)/\sqrt{12} \approx 0.14w$, where w is the strip width.

The time distribution of anode signals from a single chamber plane (figure 7.61 (left, top)) has an RMS of about 11 ns. Clearly this is too wide for a chamber hit to be assigned unambiguously to

2008 JINST 3 S08004

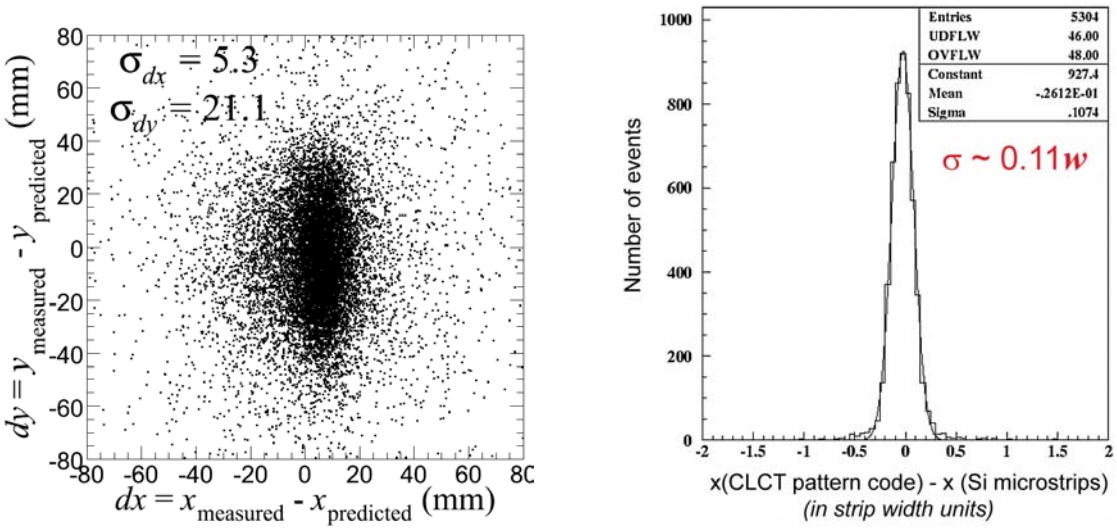

Figure 7.60: Left panel: 2D-coordinate residuals between LCTs found in ME2/2 chambers and muon-track positions. The *x* axis runs along the wires and the *y* axis along the strips. The observed spread is consistent with multiple scattering of cosmic-ray muons in the steel disks and the expected CLCT and ALCT spatial resolutions. Right panel: residuals between the CLCT pattern-defined muon coordinate and the coordinate predicted by the Si beam telescope in a 300-GeV muon beam. The residuals are shown in units of strip width.

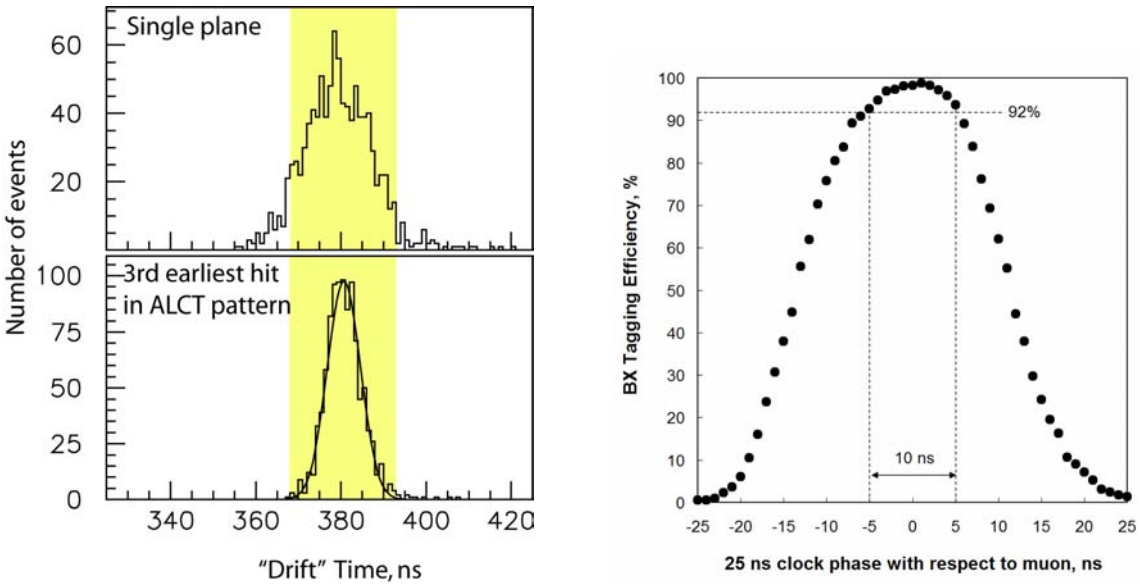

Figure 7.61: Left panel: time distributions of the response of a single plane to a passing muon (top) and for the 3rd earliest hit in an ALCT pattern (bottom). The horizontal scale has an arbitrary offset. The shaded band indicates the 25-ns window, the time between bunch crossings at the LHC. Right panel: probability for correct bunch crossing tagging vs. relative phase shift between the 25-ns clock on an ALCT board and the LHC 25-ns clock.

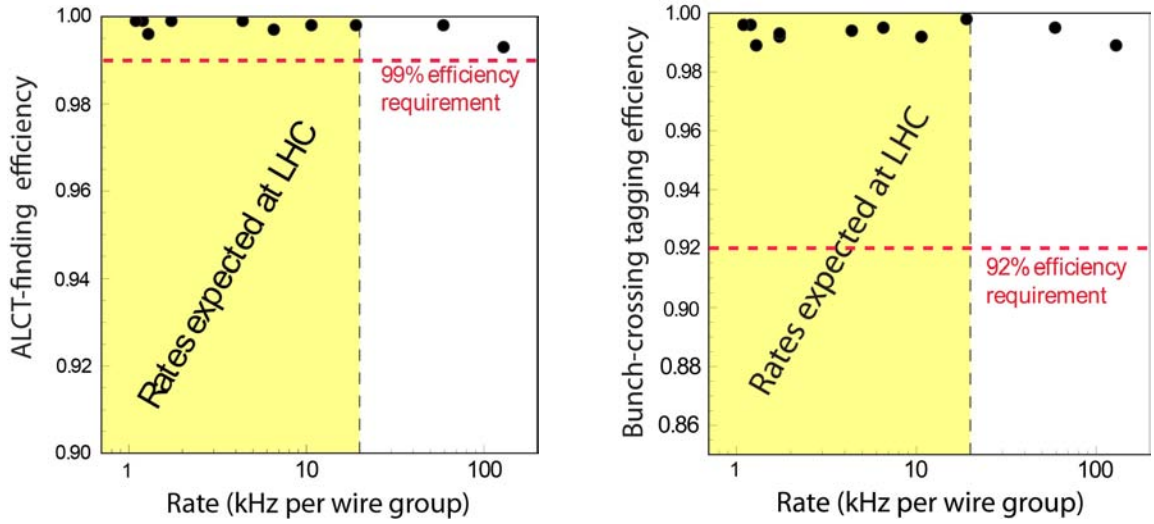

Figure 7.62: Left panel: ALCT-finding efficiency vs. rate of random hits per wire group. Right panel: efficiency of correct bunch tagging vs. rate of random hits per wire group. The shaded areas show the range of rates expected in different chambers at full LHC luminosity.

the correct bunch crossing. We overcome this problem by making use of all 6 planes in a chamber. The time distribution for the 3rd earliest hit in an ALCT pattern (figure 7.61 (left, bottom)) is a much narrower Gaussian with $\sigma < 5$ ns, the use of which results in a bunch-tagging efficiency of 98–99%, well above the desired 92% level. Figure 7.61 (right) shows the accuracy required for aligning the phase of the 25-ns clock on an ALCT board with the LHC clock. The acceptable range of phase misalignment is ± 5 ns. CLCTs tend to have slightly worse timing properties due to the slower CFEB shaping time and smaller amplitude of strip signals, so we assign the time tagged by the ALCT pattern to the matched 2D-LCT.

Results obtained from a CSC irradiated with 0.7 MeV photons in a muon beam at the GIF (figure 7.62) show that the ALCT-finding and bunch-tagging efficiencies remain very robust even at random-hit rates far exceeding those expected at full LHC luminosity.

During 300-GeV muon-beam tests, a 30-cm-thick steel slab was moved in front of the test chamber to study the effect of bremsstrahlung radiation on the reconstruction of muon stubs at the trigger level. In offline analysis of strip data, we classified each muon as either "clean" (multiple charge clusters observed in only 1 plane) or otherwise "contaminated." Without the steel slab, the fraction of "clean" muons was 94% and CLCT patterns were formed from half-strips with a 99.5% efficiency. With the steel slab, the fraction of "clean" muons dropped to 80%, while the CLCT-finding efficiency remained very high (98.9%). Figure 7.63 shows an example of a badly "contaminated" muon where the muon track is nevertheless successfully identified.

2008 JINST 3 S08004

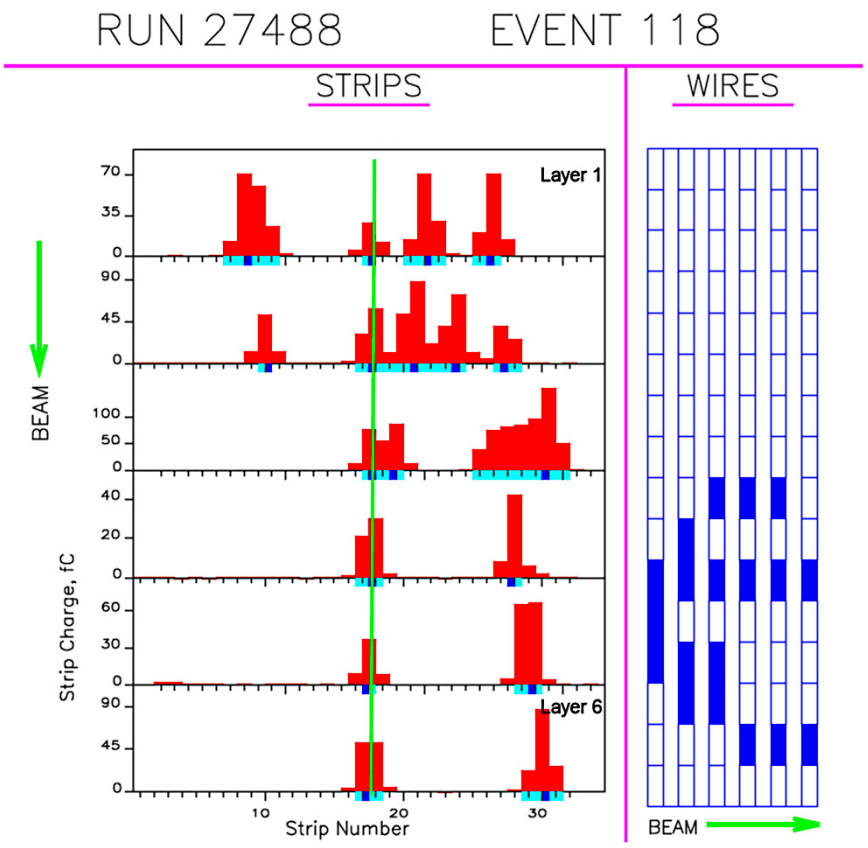

Figure 7.63: A sample CSC event of a muon accompanied by substantial bremsstrahlung radiation. The left side of the plot shows the charge (blocks just above the axes) on each of the 32 strips in each of the 6 chamber layers, while the right side shows the information from the anode wire groups. Strips with charge above the trigger threshold are marked with light shading below the axes, while the half-strip "peaks" are marked with dark squares. The vertical line at $\lambda = 17.56$ shows the track position extrapolated from the Si beam telescope. This event was assigned a 6-layer CLCT code that corresponds to an average track position $\lambda = 17.59$.

Spatial resolution based on digitised strip signals

An avalanche on a wire induces charge on a cathode plane. In a first approximation, the shape of the induced charge can be parameterized by the so-called Gatti function [155]:

$$\frac{1}{Q}\frac{dQ}{d\lambda} = K_1 \left[\frac{1-\tanh^2(K_2\lambda)}{1+K_3\tanh^2(K_2\lambda)} \right], \tag{7.2}$$

where $\lambda = x/h$, in which x is the coordinate across a strip and h is the cathode-anode spacing, and the coefficients K_1, K_2, and K_3 are defined by the chamber geometry.

Given the geometry of the CSCs, most of the induced charge is shared among 3–4 strips. As described earlier, a strip signal waveform is sampled and digitised every 50 ns. The signal peaks in about 150 ns and comes back very close to the baseline within the next 150 ns so that the

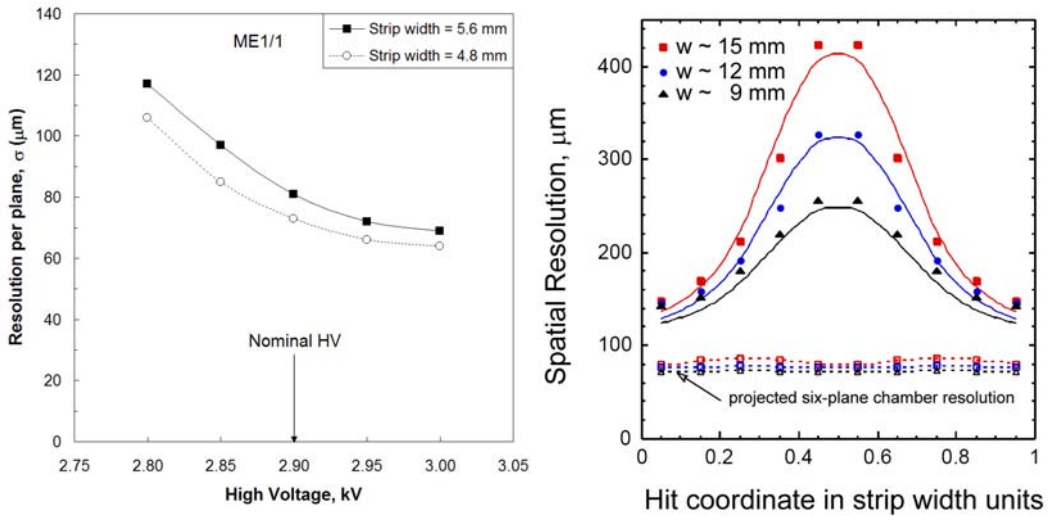

Figure 7.64: Left panel: ME1/1 chamber single-plane resolution vs. HV. Right panel: ultimate large CSC offline resolutions per plane for different muon passage points across a strip for areas with different strip widths for data (closed symbols) and simulation (solid lines). The expected overall 6-plane CSC resolutions are shown by open symbols and dashed lines.

overall pulse duration is roughly 300 ns. Such a 2-dimensional charge cluster can be fit to obtain the spatial coordinate, time, and cluster charge. To achieve the best possible resolution, we take into account empirical corrections for the induced charge shape, the time structure of the signal waveform, strip-to-strip cross-talk, electronic-noise correlations between nearby time samples, and electronic pedestal and gain calibrations.

By design, ME1/1 and ME1/2 chambers have narrower strips and thus deliver better resolution. The ME1/1 single-plane resolution (figure 7.64 (left)) is about 80 μm at nominal HV. The 6-plane chamber resolution is estimated to be $\approx 80/\sqrt{6} = 33$ μm, plus alignment errors. Clearly, the desired resolution of 75 μm per 6-plane chamber is within reach.

The single-plane spatial resolution of the larger CSCs (with very wide strips up to 16 mm) depends very strongly on the muon coordinate across a strip. Muons that pass through a strip centre will be measured poorly (and the wider the strip, the worse the measurement). On the other hand, muons hitting between strips will be measured nearly equally well for any strip width. We took advantage of this feature in our design. In the larger chambers, strips in adjacent planes are staggered by one half of the strip pitch. High-energy muons, for which we need the best chamber resolution, appear as nearly straight-through tracks. If such a muon goes through areas with poor resolution in odd planes, it will have very good measurements in even planes, and vice versa. Therefore, by combining measurements from 6 planes with proper weighting, a muon track segment is accurately localised. Figure 7.64 (right) shows single-plane resolutions, σ_i, for chamber regions with different strip widths and the resulting combined 6-plane resolution, $\sigma_{\rm CSC}$, which is estimated by

$$\frac{1}{\sigma^2_{\rm CSC}(x/w)} = \sum \frac{1}{\sigma^2_i(x/w)} \,. \tag{7.3}$$

2008 JINST 3 S08004

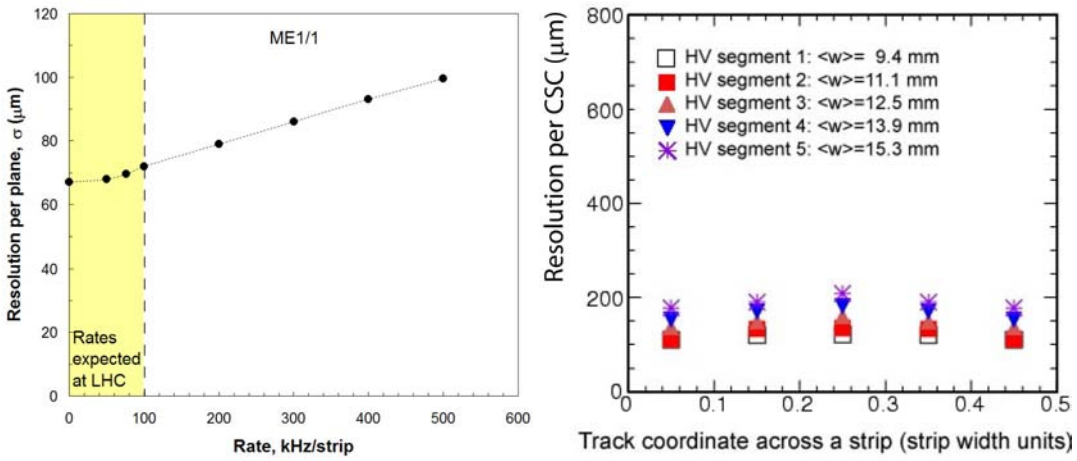

Figure 7.65: Left panel: deterioration of spatial resolution (ME1/1 chambers) with increasing rate of signals. The resolution remains well within the design specs even at rates far exceeding those expected at the LHC. Right panel: expected 6-plane chamber resolution for nearly perpendicular tracks vs. muon coordinate across a strip as evaluated from the single-plane resolution obtained with a simplified and fast reconstruction specifically targeted for the HLT.

The expected combined resolution for a 6-plane chamber is ≈80 μm almost independent of the hit position in a chamber, better than the 150-μm goal.

Even at the highest rates expected at the LHC, the CSC resolution will stay well within the design specifications (figure 7.65 (left)). A simplified algorithm for hit-position reconstruction that does not use any fitting, iterative procedures, or chamber- or electronics-specific corrections/calibrations was tested on the 12 largest chambers in the MTCC cosmic-ray runs. Being simple and fast, this algorithm is specifically targeted for the HLT. First, 2D-track segments in the chambers are identified by directly accessing the ALCT- and CLCT-pattern records available in the DAQ. Then, the coordinate is calculated by using a simple analytical function $f_w(r)$ of the ratio r built from the charges Q on 3 adjacent strips (centre, right, and left strips):

$$(x/w)_{\text{measured}} = f_w(r), \quad \text{where } r = \frac{1}{2}\left[\frac{Q_{\text{right}} - Q_{\text{left}}}{Q_{\text{centre}} - min(Q_{\text{right}}, Q_{\text{left}})}\right]. \tag{7.4}$$

This algorithm localises muon stubs in a chamber with a precision of <200 μm (figure 7.65 (right)), which is more than adequate for the HLT. The highest muon p_T threshold used by the HLT is 40 GeV. Due to the muon multiple scattering in the calorimeters and in the steel disks, for muons with transverse momenta $p_T < 40$ GeV, one need not measure muon coordinates with a precision much better than ≈0.5 mm. This holds true for a muon momentum measurement in the stand-alone muon system, for associating stand-alone muons with tracks in the central tracker, and for the ultimate muon momentum measurement, which is achieved by means of combining information from the central tracker and the muon system.

2008 JINST 3 S08004

Radiation tolerance

The high radiation rates at the LHC could result in devastating problems; thus, the detectors and electronics were designed to be robust. To validate the design, we carried out a series of detailed tests of chamber ageing and electronic board radiation damage.

Ageing studies were conducted [156] by irradiating CSCs at the GIF for several months. The prototype gas system operated in recycling mode as envisioned for full-system operation (2 gas volume exchanges per day with about 5% fresh gas added in each 1-volume cycle). The chambers showed little change in gas gain, dark current, and spurious pulse rate. The total accumulated charge on the wires was about 0.4 C/cm, corresponding to about 50 years of operation at full LHC luminosity in the worst areas closest to the beam line. Upon opening the chambers, we observed a layer of deposits on the cathode surfaces, but not on the anode wires. The deposits on the cathodes, being slightly conductive (established by a small reduction of resistance between strips), did not affect performance (e.g., by the Malter effect [157]).

To test the stability of electronic board performance, we dealt separately with 2 distinct radiation components: total ionisation dose and neutron fluence. The total ionising dose for 10 LHC years is ≈20 Gy for on-chamber boards and 2 Gy for peripheral crate electronics. The integrated neutron flux over 10 years ranges from about 10^{10} to 10^{12} cm^{-2}. Analog components of the electronics may suffer a steady and permanent deterioration in performance, while the main danger for digital electronics are Single Event Effects (SEE), including Single Event Upsets (SEU) and Single Event Latching (SEL). Upon an SEE occurrence, the electronics can typically be reset by reloading the FPGAs or cycling the power: SEEs can thus be characterised by the meantime between occurrences.

All electronic chips and components were tested with radiation doses far exceeding the 10 LHC-year equivalent [158]. For final-design boards, no significant deterioration in analog performance was observed (noise, gain, threshold, etc.). All digital-electronic FPGAs were tested for SEEs using typical fluences of $\approx 3\times10^{11}$ cm^{-2}. No SEL was observed on any FPGA during testing. SEU rates were dominated by the control logic on the CFEB boards. The SEU rate was lowered significantly by introducing a design with triple-voting logic. The mean time between SEEs on a single CFEB was measured and extrapolated to be 700 h at the LHC neutron fluence. With ≈2400 CFEBs in our system, a single CFEB will fail due to an SEU about every 30 min during LHC running, which is an acceptable rate, and will need to be reset.

Reliability

Extensive testing of prototypes has shown that the CMS Endcap Muon System based on CSC technology would meet all performance requirements and could be built within the constraints of the construction budget. There are 468 six-plane CSCs in the system, with CSC planes comprising ≈5000 m^2 of sensitive area. The total number of read-out channels is about 400 000. During the years of construction and commissioning, the CMS CSCs have proven to be very reliable in operation (e.g., not a single wire out of about 2 000 000 in the system has ever snapped) and have confirmed the expected performance. As an example, analyses of the first data taken in situ with 36 chambers and cosmic-ray muons showed that chambers had a 99.9% efficiency to detect muon-

2008 JINST 3 S08004

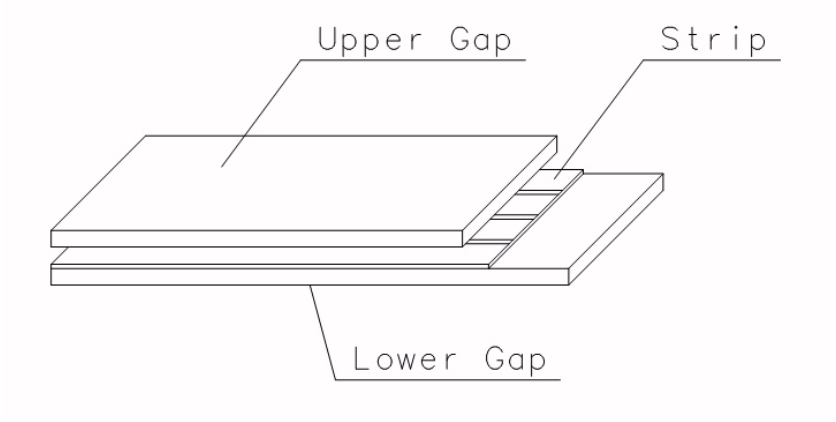

Figure 7.66: Layout of a double-gap RPC.

Table 7.2: Basic construction parameters.

Bakelite thickness	2 mm
Bakelite bulk resistivity	1–2 $\times 10^{10}$ Ω·cm
Gap width	2 mm

track segments (input to the Level-1 trigger) and the spatial resolution attainable at the high-level trigger and offline was ≈150 μm.

7.3 Resistive Plate Chamber system

Resistive Plate Chambers (RPC) are gaseous parallel-plate detectors that combine adequate spatial resolution with a time resolution comparable to that of scintillators [159, 160]. An RPC is capable of tagging the time of an ionising event in a much shorter time than the 25 ns between 2 consecutive LHC bunch crossings (BX). Therefore, a fast dedicated muon trigger device based on RPCs can identify unambiguously the relevant BX to which a muon track is associated even in the presence of the high rate and background expected at the LHC. Signals from such devices directly provide the time and position of a muon hit with the required accuracy. A trigger based on RPCs has to provide the BX assignment to candidate tracks and estimate the transverse momenta with high efficiency in an environment where rates may reach 10^3 Hz/cm^2.

The CMS RPC basic double-gap module consists of 2 gaps, hereafter referred as *up* and *down* gaps, operated in avalanche mode with common pick-up read-out strips in between (figure 7.66) [161, 162]. The total induced signal is the sum of the 2 single-gap signals. This allows the single-gaps to operate at lower gas gain (lower high voltage) with an effective detector efficiency higher than for a single-gap. Table 7.2 lists the basic construction and operating parameters of the CMS double-gap RPCs.

Extensive ageing tests have been performed over the past years with both neutron and gamma sources to verify long term detector performance in the LHC background environment [163, 164]. Results confirm that over a period equivalent to 10 CMS-operation years, no efficiency degradation is expected while all other characteristic parameters stay well within the project specifications. Six layers of RPC chambers are embedded in the barrel iron yoke, 2 located in each of the first and second muon stations and 1 in each of the 2 last stations. The redundancy in the first 2 stations allows the trigger algorithm to perform the reconstruction always on the basis of 4 layers, even for low p_T particles, which may stop inside the iron yoke. In the endcap region, the baseline design foresees the instrumentation of the iron disks with 4 layers of RPCs to cover the region up to η = 2.1. However, in the first phase, due to budget limitations, only 3 layers up to η = 1.6 are built. In addition, the background rate in the high η region is significantly higher, well beyond the limit reached during the ageing test. Additional R&D to certify the detector performance under such conditions is ongoing.

7.3.1 Detector layout

Barrel system

In the barrel iron yoke, the RPC chambers form 6 coaxial sensitive cylinders (all around the beam axis) that are approximated with concentric dodecagon arrays arranged into 4 stations (figure 7.67).

In the first and second muon stations there are 2 arrays of RPC chambers located internally and externally with respect to the Drift Tube (DT) chambers: RB1in and RB2in at smaller radius and RB1out and RB2out at larger radius. In the third and fourth stations there are again 2 RPC chambers, both located on the inner side of the DT layer (named RB3+ and RB3–, RB4+ and RB4–). A special case is RB4 in sector 4, which consists of 4 chambers: RB4++, RB4+, RB4–, and RB4– –. Finally, in sectors 9 and 11 there is only 1 RB4 chamber.

In total there are 480 rectangular chambers (table 7.3), each one 2455 mm long in the beam direction. Exceptions are the chambers in sector 3 of wheel –1 and sector 4 of wheel +1, which are 2055 mm long to allow passage of the magnet cooling chimney. Chambers RB1, RB2, and RB3 have widths 2080, 2500, and 1500 mm, respectively. The widths of the RB4 chambers (which depend on location) are given in table 7.4.

Physics requirements demand that the strips always run along the beam direction and are divided into 2 parts for chambers RB1, RB3, and RB4. The RB2 chambers, a special case for the trigger algorithm, have strips divided into 2 parts (RB2in in wheels +2 and –2 and RB2out in wheels +1, 0, and –1) and into 3 parts (RB2out in wheels +2 and –2 and RB2in in wheels +1, 0, and –1). Each chamber therefore consists of either 2 or 3 double-gap modules mounted sequentially in the beam direction to cover the active area. For each double-gap module (up to 96 strips/double-gap), the front-end electronics boards are located at the strip end, which minimises the signal arrival time with respect to the interaction point. The strip widths increase accordingly from the inner stations to the outer ones to preserve projectivity (each strip covers 5/16° in ϕ). Figures 7.68 and 7.69 show schematic views of chamber modules with 2 and 3 double-gaps, respectively. Table 7.5 lists some global information regarding the barrel detector.

2008 JINST 3 S08004

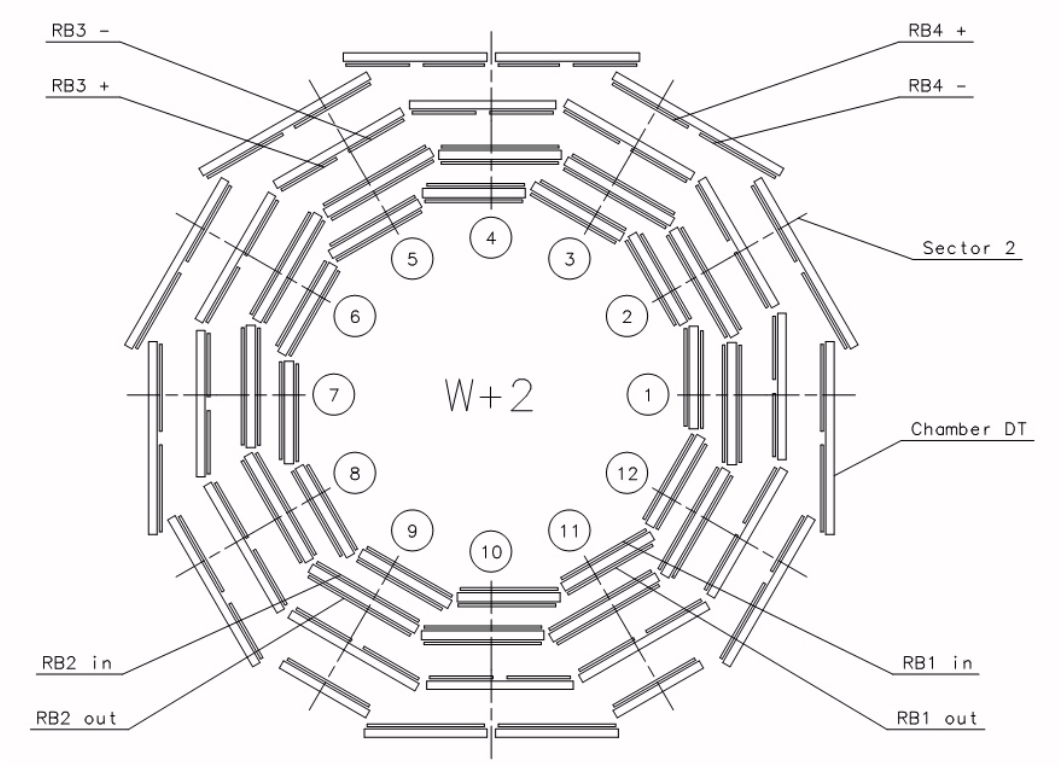

Figure 7.67: Schematic layout of one of the 5 barrel wheels, which are labeled –2, –1, 0, +1, and +2, respectively. Each wheel is divided into 12 sectors that are numbered as shown.

Table 7.3: Number of RPCs for different wheels.

RPC	W+2	W+1	W0	W–1	W–2	Total
RB1in	12	12	12	12	12	60
RB1out	12	12	12	12	12	60
RB2/2in	12	-	-	-	12	24
RB2/2out	-	12	12	12	-	36
RB2/3in	-	12	12	12	-	36
RB2/3out	12	-	-	-	12	24
RB3	24	24	24	24	24	120
RB4	24	24	24	24	24	120
Total	96	96	96	96	96	480

Endcap system

In the forward and backward regions of the CMS detector, 3 iron disks constitute the endcap yokes. Like in the barrel, 2 complementary muon detector systems are deployed for robust muon identifi-

Table 7.4: Widths of the RB4 chambers.

Sector	RB4+	RB4++	RB4–	RB4– –	RB4
S1–S3					
S5–S7	2000 mm		2000 mm		
S8	1500 mm		2000 mm		
S12	2000 mm		1500 mm		
S9, S11					2000 mm
S10	2500 mm		2500 mm		
S4	1500 mm	1500 mm	1500 mm	1500 mm	

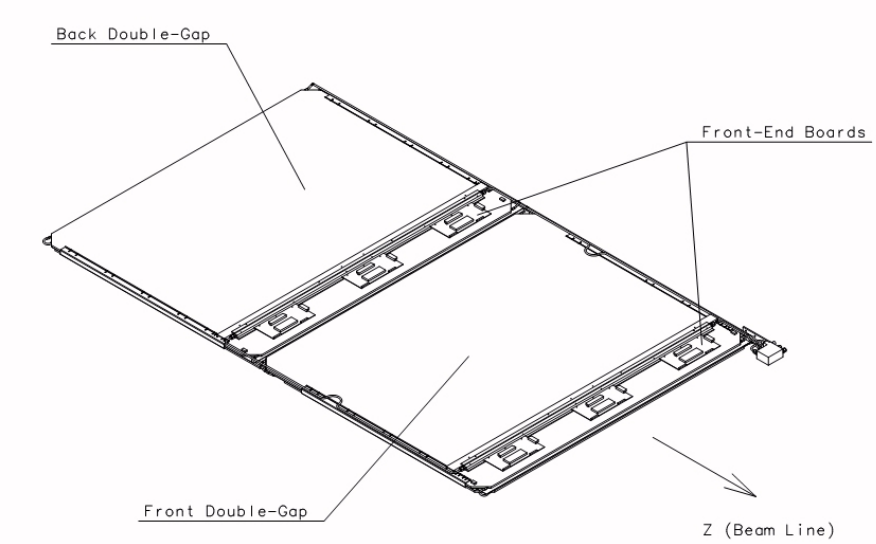

Figure 7.68: Schematic layout of chamber module with 2 double-gaps.

Table 7.5: Barrel RPC system global parameters.

Number of stations	480
Total surface area	2400 m^2
Number of double-gaps	1020
Number of strips	80 640

cation: cathode strip chambers (CSC) and RPCs. They are mounted on both faces of the disks to yield 4 CSC stations (ME1–4) and, for the initial detector, 3 RPC stations (RE1–3). The double-gaps in every station have a trapezoidal shape and are arranged in 3 concentric rings as shown in the r-ϕ view of figure 7.70. They overlap in ϕ as to avoid dead space at chamber edges. Except

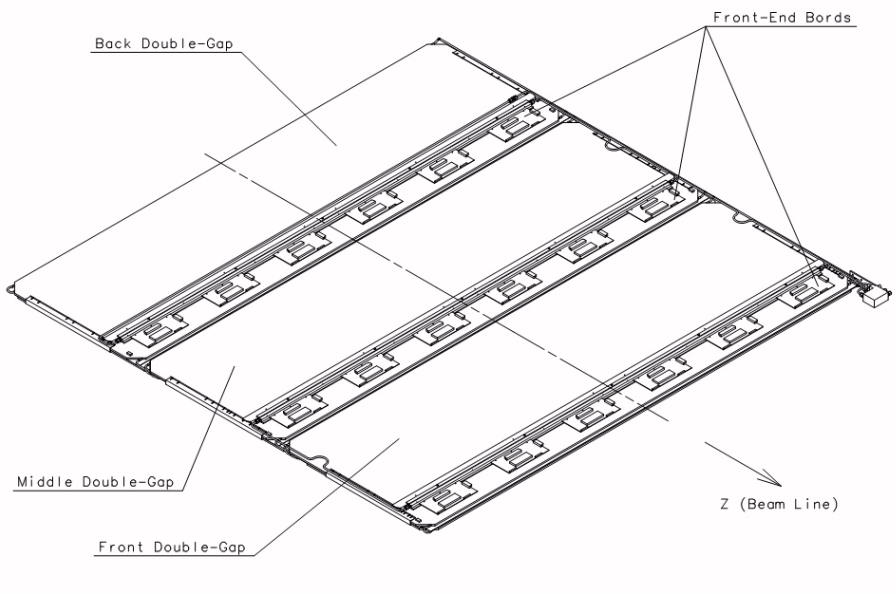

Figure 7.69: Schematic layout of chamber module with 3 double-gaps.

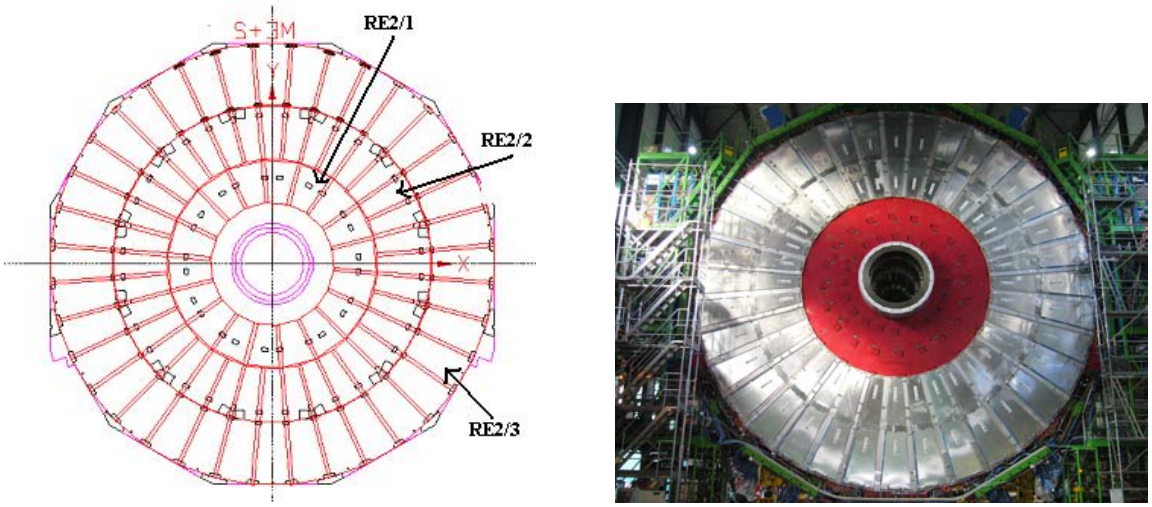

Figure 7.70: Left panel: schematic r-ϕ layout of RPC station RE2 on the back side of the first endcap yoke. Right panel: RPC station RE2 on the back side of the YE-1 yoke. The inner ring has been staged and is absent here.

for station 1, the chambers of the innermost ring span 20° in ϕ, all others span 10°. As mentioned before, the high η part of the RPC system (beyond $\eta \approx 1.6$) has been staged until the LHC is scheduled to deliver its design luminosity of 10^{34} cm^{-2}s^{-1}.

Station RE1 is mounted on the interaction point (IP) side of the first endcap disk (YE1), underneath the CSC chambers of ME1. Stations RE2 and 3 are mounted on the back side of YE1 and on the IP side of YE3, respectively. They remain uncovered since the corresponding CSC stations 2 and 3 are mounted on both faces of YE2. Figure 7.71 shows a schematic layout

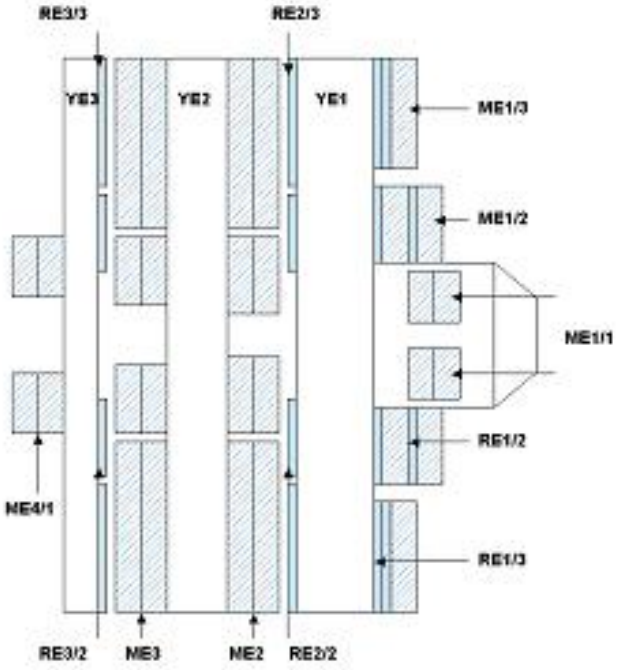

Figure 7.71: Schematic layout of the CMS endcap for the initial muon system.

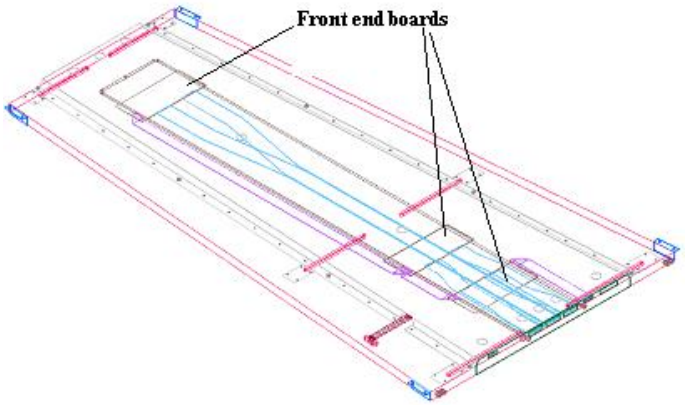

Figure 7.72: A view of an endcap RPC chamber.

of the CMS endcap defining the nomenclature of the muon stations. Each endcap RPC chamber consists of a double-gap structure enclosed in a flat trapezoidal shaped box made of 2 aluminium honeycomb panels of 6 mm thickness each and a 16×16 mm^2 section spacer frame (figure 7.72). The strip panel, sandwiched in between the gas gaps, has copper strip sections on a G10 support. Strips run radially and are radially segmented into 3 trigger sections for the REn/2 and REn/3 chambers (n = 1–3). The 32 strips of the 10° RPC chambers are projective to the beam line, following a homothetic pattern. Besides the different mechanical shape and assembly, the front-end electronics, services, trigger, and read-out schemes of the endcap RPC system are identical to the barrel system. To an operator, the CMS barrel and endcap RPC systems look identical.

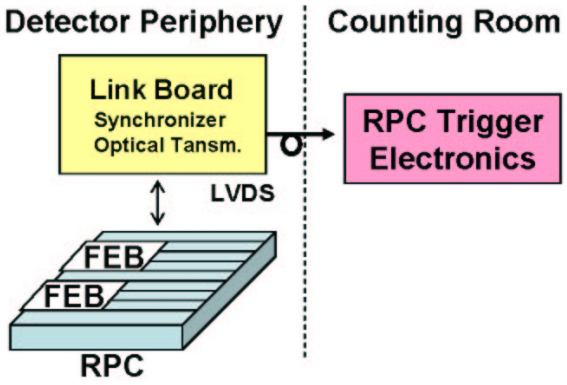

Figure 7.73: Block diagram of RPC read-out electronics.

7.3.2 Readout electronics

Front-end electronics

The read-out strips are connected to Front-End Boards (FEB). After having been amplified and discriminated, signals are sent unsynchronized to Link Boards (LB) placed around the detector. The LBs synchronize the signals with the 40-MHz LHC clock and transmit them to the trigger electronics located in the CMS counting room over a 90-m optical link at 1.6 GHz, as shown in the block diagram of figure 7.73.

The FEBs house two (barrel version) or four (endcap version) front-end chips, which are custom ASICs designed in AMS 0.8 μm CMOS technology [165]. Each chip is made of 8 identical channels, each consisting of an amplifier, zero-crossing discriminator, one-shot, and LVDS driver. The preamplifier is a trans-resistance stage with 15-Ω input impedance to match the characteristic impedance of the strips. It is followed by a gain stage to provide an overall charge sensitivity of 2 mV/fC.

Since accurate RPC timing information is crucial for providing an unambiguous bunch crossing assignment of the event, the zero-crossing discrimination technique was adopted to make the timing response amplitude-independent. In fact, considering that the RPC signals have a wide dynamic range (from few tens of fC to 10 pC), the implemented architecture provides a time walk below 1 ns, while the simpler leading-edge discrimination technique would have provided a time walk of $\approx$10 ns. The discriminator is followed by a one-shot circuit. This produces a pulse shaped at 100 ns to mask possible after-pulses that may follow the avalanche pulse. Finally, an LVDS driver is used to send the signals to the LB in differential mode.

Gamma-irradiation tests showed no performance degradation of either the front-end chip or the control electronics on the FEB [166]. Moreover, tests with thermal and fast reactor neutrons (0.4 eV–10 MeV) and with more energetic neutrons (65 MeV), have certified that the circuit can sustain the expected CMS operational conditions [167].

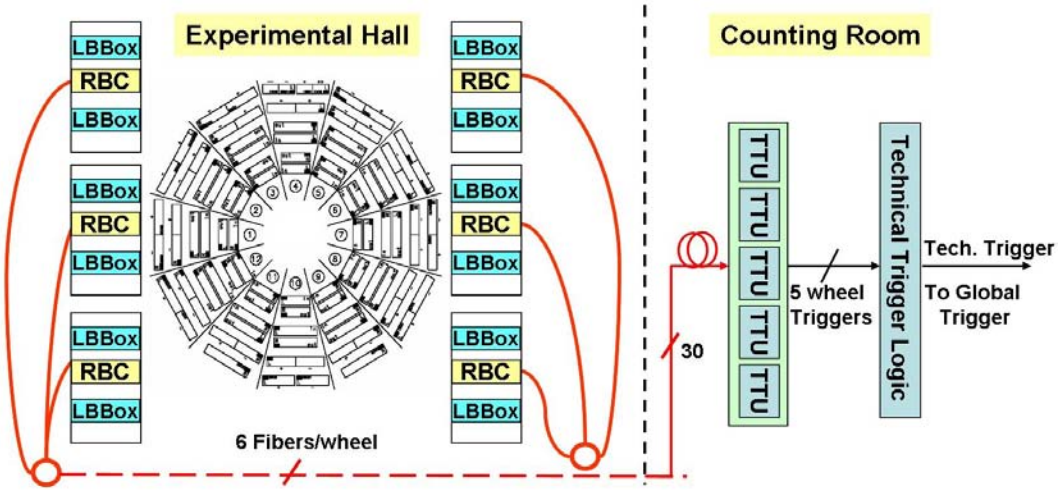

Figure 7.74: Technical Trigger schematic layout.

RPC technical trigger electronics

Study of the detector performance is a crucial aspect during the detector-commissioning phase. The RPC trigger system was designed to identify muon tracks starting from the interaction point. Therefore, all interconnections among the LBs and trigger electronics were optimised to fulfil a projective vertex geometry, not adequate for triggering on cosmic rays. Therefore, an RPC-based trigger (Technical Trigger in the following) has been implemented by means of 2 types of electronic boards: the RPC Balcony Collector (RBC) housed in the cavern and the Technical Trigger Unit (TTU) located in the counting room (figure 7.74) [168].

The RBC collects 96-strip OR signals from the barrel LBs and produces a "local" sector-based cosmic trigger to be used during commissioning or calibration of the detector. The RBC transmits the ORs optically to the TTU boards in the Counting Room (30 fibres in total), where a wheel-level cosmic trigger is produced and sent as a Technical Trigger to the CMS Global Trigger. A proper algorithm for searching for cosmic-muon tracks is implemented in the TTU.

7.3.3 Low voltage and high voltage systems

General requirements

The RPC power systems operate in a hostile environment due to the high magnetic field and high radiation flux. Large portions of the power systems are near the detectors on the balcony racks placed around the barrel wheels and the endcap disks. In these areas the magnetic field can reach 1 T with radiation around $5{\cdot}10^{10}$ protons/cm^2 and $5{\cdot}10^{11}$ neutrons/cm^2. In cooperation with the ATLAS, ALICE, and LHCb groups, the CMS collaboration developed a new design for an RPC power system able to operate in such conditions. The main requirements for the RPC HV and LV power supplies are collected in table 7.6.

The HV and LV systems are both based on a master/slave architecture. The master, called the mainframe, is devoted to controlling and monitoring one or more slaves and is placed in a

Table 7.6: HV and LV power supply requirements.

	HV	LV
Maximum Voltage	12 kV	7 V
Maximum Current	1 mA	3 A
Ripple	<100 mV pp at load (freq <20 MHz)	<10 mV pp at load (freq <20 MHz)
Programmable Voltage	from 0 to 12 kV	from 0 to 7 V
Current monit. precision	0.1 μA	100 mA
Voltage monit. precision	<10 V	100 mV

safe and accessible area like the control room. The slaves can be located near the detector and are designed to be modular and multi-functional to accept both HV and LV boards. These have to work in a hostile and inaccessible area and are based on radiation-tolerant and magnetic-field-tolerant electronics.

Past experience with RPC detector systems, however, suggested that it is important to have the HV power supplies in an accessible area. In case of unsustainable high current on a detector, the possibility of removing a channel during operation should be available. Therefore, the CMS RPC collaboration decided to keep the master/slave architecture for both the HV and LV systems but to move all HV system components into the control room.

HV and LV system description

The system is based on the EASY (Embedded Assembly SYstem) project. It is made of a master SY1527 (mainframe) which houses up to 16 branch controller boards (A1676A) and of EASY3000 crates (slaves). The EASY3000 crate can house different boards (high and low voltage, ADC, and DAC). Each EASY3000 board operates as a channel of the A1676A and can be accessed through the mainframe. The EASY architecture foresees 2 independent 48-V power supplies to power independently the channel regulators and the control logic. The EASY system is connected to the external world through a serial port and an ETHERNET3 interface that allows the user to monitor and control the whole system with various software from a very easy TELNET interface to a more sophisticated OPC protocol.

HV hardware. The A3512 double-width board is equipped with 6 floating 12 kV/1 mA channels of either positive or negative polarity. The 6 channels have an independent return to avoid ground loops. The board is designed with an output voltage that can be programmed and monitored in the 0–12 kV range with 1 V resolution and with a monitored current resolution of 0.1 μA. This current resolution allows the Detector Control System (DCS) to study the current behaviour of every chamber with an accuracy of at least 1/10 of the measured current (between 10 and 20 μA per chamber). In the barrel there is 1 HV channel per chamber, while in the endcap region 1 channel supplies 2 chambers. In this last case, an upgrade of the system will depend on future budget availability. A summary of the HV systems is given in table 7.7.

Table 7.7: Summary of HV systems.

	Barrel	Endcap
HV channels	480	216
HV boards	80	36
Easy3000 Crates	14	6

Table 7.8: Summary of LV systems.

	Barrel	Endcap
LV channels	720	432
LV boards	60	36
Easy3000 Crates	20	14

LV hardware. The CAEN A3009 board is a 12-channel 8V/9A power-supply board for the EASY Crate. It was developed for operation in magnetic fields and radioactive environments. The output-voltage range is 1.5–8 V with 5-mV monitor resolution; channel control includes various alarms and protections. The output current is monitored with 10-mA resolution.

Each chamber is supplied by 2 LV lines for the front-end analog (LV_a) and digital (LV_d) parts. To avoid ground loops on the detector, it is important to preserve, when possible, a 1-to-1 correspondence between LV channel and chamber. This is achieved in the barrel system, where there is 1 LV_a and 1 LV_d channel per chamber. However, for the endcap detector, at the start-up 1 LV_a and 1 LV_d are distributed between 2 chambers. A summary of the LV systems is given in table 7.8.

7.3.4 Temperature control system

RPC operation is sensitive to both temperature and atmospheric pressure. Therefore, the chambers are constantly monitored to compensate in real time for the detector operating point (HV value). A network of 420 sensors located inside the barrel chambers is available to monitor the temperature. The AD592BN sensor (Analog Devices) can work in a hostile environment with a resolution of about 0.5°C, better than the CMS requirement (1°C). Sensors are read out by a 128-channel ADC equipped with a 12-V input stage.

Additional sensors are available on each front-end board; they are read out through the LB electronics to monitor the temperature.

7.3.5 Gas system

Test results [169] showed that RPCs are suitably operated with a 3-component non-flammable mixture of 96.2% R134a ($C_2H_2F_4$), 3.5% iC_4H_{10} and 0.3% SF_6. Water vapour is added to the gas mixture to maintain a relative humidity of about 45% and to avoid changes of the bakelite

Table 7.9: Main gas parameters of the CMS RPC system.

Gas volume	14 m^3
Gas mixture composition	96.2% R134a, 3.5% iC_4H_{10}, and 0.3% SF_6
Internal chamber pressure above atmosphere	3 mbar
Nominal flow rate	10 m^3/h
Fresh gas replenishing rate	0.2 m^3/h
Number of gas channels	250 (barrel) + 144 (endcaps)

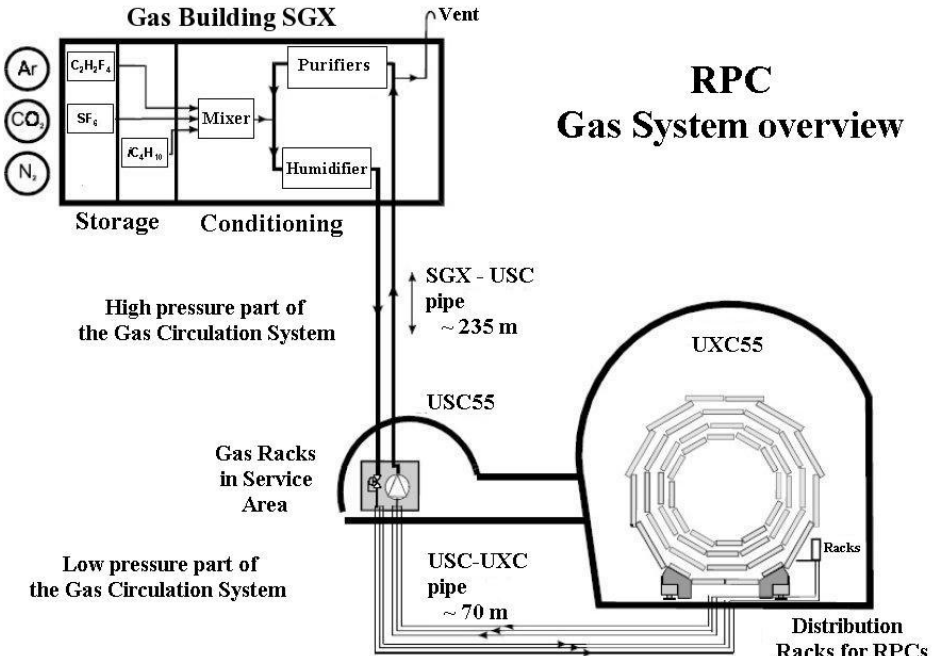

Figure 7.75: Closed-loop circulation system.

resistivity. The basic function of the gas system is to mix the different gas components in the appropriate proportions and to distribute the mixture to the individual chambers. The large detector volume and the use of a relatively expensive gas mixture make a closed-loop circulation system mandatory. The main gas-system parameters are given in table 7.9.

The system consists of several modules: the primary gas supply, mixer and closed-loop circulation system, gas distributors to the chambers, purifier, pump, and gas-analysis station [132]. The full closed-loop circulation system (figure 7.75) extends from the surface gas building SGX to the USC55 service cavern and UXC55 experimental cavern.

Mixer

The primary gas supplies and the mixer are situated in the SGX building. The flow of component gases is controlled by mass-flow meters. Flows are monitored by a computer-controlled process,

Table 7.10: Chamber volumes and gas flow for a single wheel of the barrel detector.

Station	RPCs in that station	Volume per RPC (l)	number of gas channels	Volume per gas channel (l)	Operating channel flow (l/h)	total flow per station type (l/h)
RB1	24	20.6	12	41.2	27.5	330
RB2	24	25.4	12	50.8	33.9	406
RB3	12	31.4	12	31.4	20.9	251
RB4	12	43.4	14	43.4	28.9	347
Total	72		50			1334

which constantly calculates and adjusts the mixture percentages supplied to the system. The gas mixture is maintained non-flammable by permanent monitoring. The gas flow is stopped automatically if the $i C_4H_{10}$ fraction increases beyond the flammability limit. For fast detector filling, parallel rotameters are used, instead of the mass-flow controllers, yielding a complete volume renewal in about 8 hours.

Closed-loop circulation

The mixed gas is circulated in a common closed loop for the barrel and both endcaps. The circulation loop is distributed among 3 locations:

- the purifier, gas input, and exhaust gas connections are located in the SGX building;
- the pressure controllers, separation of barrel and endcaps systems, compressor, and analysis instrumentation are located in the USC (accessible at any time);
- the manifolds for the chamber-gas supplies and channel flow meters are mounted in the distribution racks near the detector.

The high density of the used mixture generates a hydrostatic pressure of about 0.3 mbar/m above atmospheric pressure. Since the total RPC detector height is about 15 m, the barrel detector is split into 2 zones (top and bottom) that have independent pressure regulation systems (figure 7.76). Each barrel muon station has an independent gas line. The 2 RPC chambers located in a station are supplied in parallel from the same patch panel sitting nearby. This configuration leads to 250 gas channels (50 per wheel) for the full barrel detector (table 7.10).

Each endcap detector consists of 3 disks, RE1, RE2, and RE3, with a total of 216 double-gap chambers. Each disk is composed of 2 concentric rings (i.e., for REn: REn/2 and REn/3) of 36 chambers each. In the RE1 rings the chambers are divided in 6 ϕ sections of 60°. A section contains 6 chambers and is supplied with 2 gas lines for the up and down gaps (figure 7.77a). The gas flow in the up gap is in the opposite sense to that in the down gap to improve the average gas quality. In the RE2 and RE3 stations, the chambers are divided into 12 ϕ sections of 30°. Each section contains 3 chambers of the external ring and the corresponding 3 chambers of the internal ring, i.e., an RE2 section includes 3 RE2/2 and 3 RE2/3 chambers (figure 7.77b). In RE2 and RE3

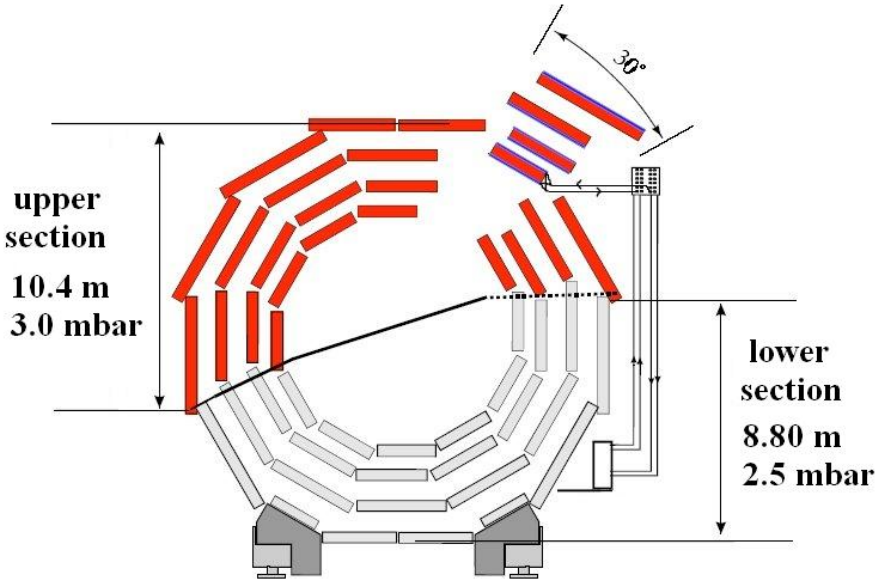

Figure 7.76: The 2 zones into which a wheel is sub-divided. Each station (2 chambers) is supplied by a gas line.

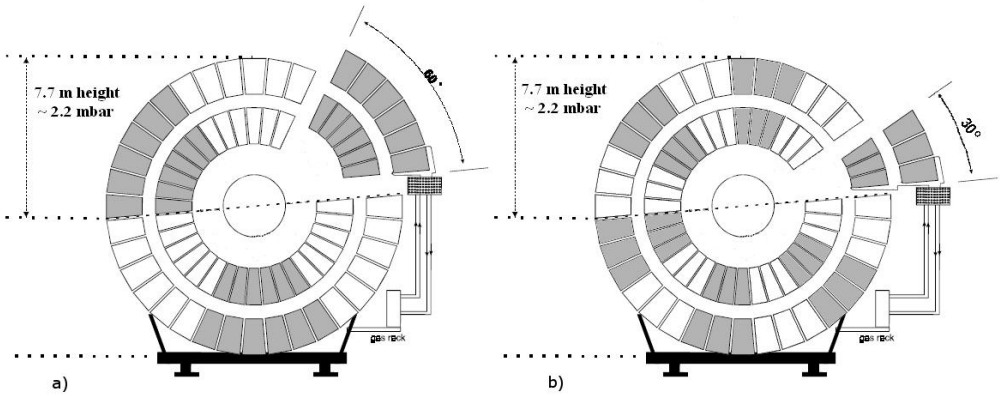

Figure 7.77: In each endcap disk the RPC detectors are divided in 2 rings. RE1 (a) is divided into 60° sectors, while in RE2 and in RE3 (b) sectors are composed of 3 chambers of the internal ring and the corresponding 3 of the external ring. Every sector is supplied by 2 independent gas lines.

as well there are 2 gas lines per section (for the up and down gaps) and the flows are in the opposite sense between the two. The total number of channels and the relative gas flows are summarised in table 7.11.

2008 JINST 3 S08004

Table 7.11: Chamber volumes and gas flows for a single endcap of the CMS RPC system.

Module	RPCs in that module	Volume per RPC (l)	Number of gas channels	Volume per gas channel (l)	Operating channel flow (l/h)	Total flow per module type (l/h)
RE/1/2	36	5.1	12	30.6	20.4	122
RE/1/3	36	7.4	12	44.4	29.6	178
RE/2/2	36	5.1	24	20.3	13.5	324
RE/2/3	36	8.4				
RE/3/2	36	5.1	24	20.3	13.5	324
RE/3/3	36	8.4				
Total	216		72			948

Pressure regulation system and gas distribution in UXC

Pressure regulation is achieved in the USC area for each of the 2 zones. Each height section has its own pressure control and protection system consisting of bubblers located in the distribution racks at the bottom of the wheels/disks. The oil level is adjusted to account for the hydrostatic pressure differences in the 2 zones. The distribution racks are installed at the bottom of each wheel/disk. The supply and return lines for each station are equipped with a mass-flow meter and a needle valve (only at the inlet). The flow measurements allow the detection of possible leaks, while the needle valves are used for the flow adjustment between different stations.

Purifier

Results from long term tests performed by CMS showed that the impurity concentrations produced in the RPC chambers are high enough to influence the detector performance if they are not properly removed from the mixture. Therefore, to achieve a high recycling rate the closed-loop circulation system is equipped with a purifier module containing 3 cleaning agents. In the first running phase the 3 cleaning agents are contained in 2 purifiers. Both the purifiers are 24-l cartridges. The first is filled with a 0.5-nm molecular sieve, while the second is filled with the following combination: 25% Cu-Zn filter (type R12, BASF), 25% Cu filter (type R3-11G, BASF), and 50% Ni-Al2O3 filter (type 6525, Leuna). During the high luminosity running period the second purifier will be split into 2 separate 24-l cartridges, the first containing the R12 and R3-11G cleaning agents and the second containing the 6525 Leuna filter. Each purifier is equipped with an automatic regeneration system: 2 identical cartridges are present allowing the regeneration of a cartridge while the other is in use.

Gas-quality monitoring

Two independent systems are in preparation to continuously monitor the gas quality. The gas-gain monitoring system [170] is based on several small (50×50 cm^2) single-gap RPCs whose working points (gain and efficiency) are continuously monitored online. The system is designed to provide a fast and accurate determination of any shift in the working points. The small single-gap

RPCs are divided into several sub-groups supplied with gas coming from different parts of the full system (i.e., fresh gas mixture, input to the chambers in closed-loop circulation, and return from the closed-loop circulation). The second gas monitoring system [171] performs both qualitative and quantitative gas chemical analyses with a set-up that includes a gas chromatograph, pH sensors, and specific fluoride electrodes. In the underground service cavern (USC), many sampling points equipped with manual valves allow the analysis of the gas mixtures that return from every half wheel. In the surface gas building (SGX), sampling points are available to monitor the effectiveness as well as the status of each cartridge in the purifier module.

7.3.6 Chamber construction and testing

In view of the extremely large-scale production (a factor of 10 greater than in past experiments), impressive quality control and certification protocols were set along the production chain at many different levels:

- selection of electrodes and resistivity certification;
- certification of single-gaps and double-gaps;
- chamber testing.

Details regarding the quality certification procedures have been reported elsewhere [172]. Only a short summary of the chamber testing results is given below.

Chamber performance at the test sites

Several RPC test stands were in operation. Each telescope consisted of a tower in which several detectors could be placed horizontally and read out in coincidence with the passage of the crossing of cosmic muons. Two sets of scintillators, at the top and the bottom of the telescope, were used for triggering purposes. Atmospheric and environmental conditions were continuously monitored during the tests. These values were used to scale the applied HV for temperature and pressure variations to evaluate the effective high voltage (HV_{eff}) [173] at given reference values ($T_0 = 293$ K and $P_0 = 1010$ mbar).

The final gas mixture (96.2% $C_2H_2F_4$, 3.5% iC_4H_{10}, and 0.3% SF_6) was used and water vapour was added to keep the gas relative humidity at a value of about 45%.

The tracking capabilities of the test telescope provided a full characterisation of the detectors in terms of efficiency, cluster size, and noise rate. Also the chambers' local efficiency and the spatial resolution were studied. Rigourous and automatic protocols were developed and systematically applied at all test sites in order to accept chambers that satisfied the CMS requirements.

First, the chamber efficiency was studied with the "coincidence" method by evaluating the ratio between the number of events in which an RPC module had at least 1 fired strip in the trigger window (100 ns) and the total number of recorded events. In figure 7.78 the distribution of the maximum efficiency for all the barrel RPCs is shown. The mean value of the distribution is 97.2%. In figure 7.79 the efficiency distribution at HV = 9.3 kV for the first 27 endcap chambers is shown.

The chamber response uniformity was also studied by performing track recognition through the telescope. Muon trajectories were reconstructed in 2-dimensional views, where the x coordinate

2008 JINST 3 S08004

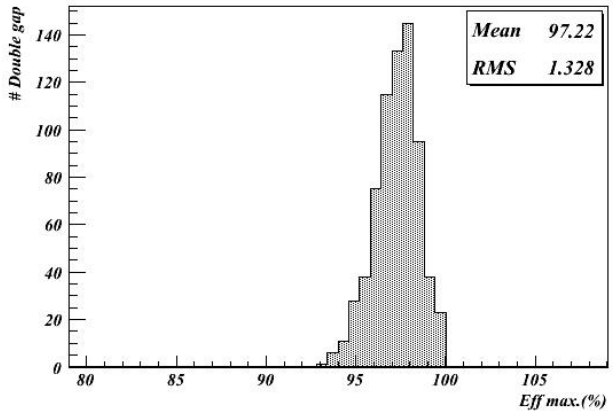

Figure 7.78: Distribution of plateau efficiency for all the barrel chambers.

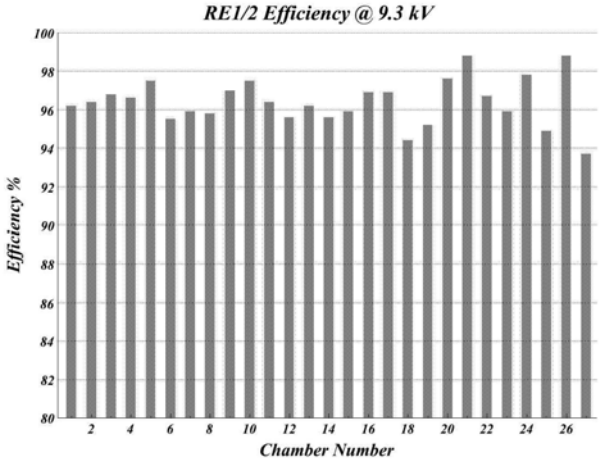

Figure 7.79: Efficiency at HV = 9.3 kV for the first 27 endcap chambers.

is defined by the strip position along the chamber and the y coordinate by the chamber position in the tower. Details about the pattern recognition algorithm have been presented elsewhere [174]. The track-impact point on the chamber under test was also determined and the distance to the nearest cluster centre was evaluated. A chamber was considered efficient if the reconstructed muon trajectory matched the fired strip. A typical strip-by-strip efficiency plot is shown in figure 7.80.

The chamber cluster size is defined as the average value of the cluster-size distribution. In Figure 7.81 the profile histogram of the cluster-size distribution as a function of the HV_{eff} is shown for all the barrel chambers. A chamber was accepted if the cluster size was below 3 strips at the knee of the efficiency plateau.

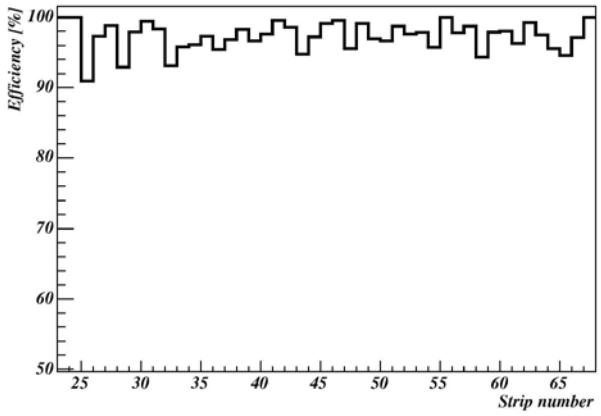

Figure 7.80: Local efficiency at HV_{eff} = 9.6 kV for a barrel chamber.

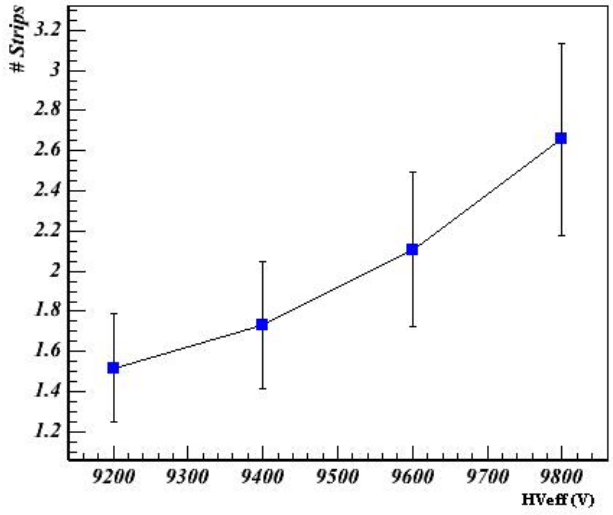

Figure 7.81: Profile histogram of the chambers' cluster-size distribution as a function of HV_{eff}. The dots and bars are the average and the root-mean-square of the cluster-size distributions, respectively.

Magnet Test and Cosmic Challenge (MTCC)

During the summer and fall of 2006 a first integrated test of an entire CMS "slice" was performed in the SX5 experimental surface hall. For the RPC system, 3 barrel sectors and a 60° portion of the first positive endcap disk were involved in the test. The chambers were operated with their final power system configuration, and CMS DAQ software, data quality monitor (DQM), and detector control system (DCS) were implemented for the detector read-out and control.

The RPC Balcony Collector (RBC) board provided a cosmic trigger with a selectable majority level of signals from the 6 RPC barrel chambers. A trigger rate of about 30 Hz/sector for a majority level of 5/6, and 13 Hz/sector for a 6/6 majority was found while operating the detector on the surface. The RBC trigger was well synchronized with the other muon detector (DT and CSC) triggers.

2008 JINST 3 S08004

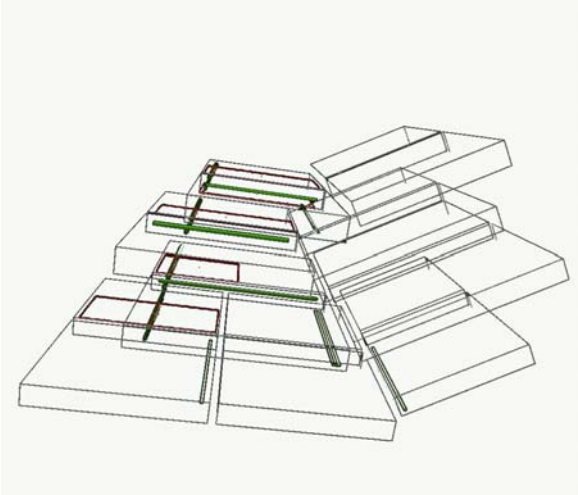

Figure 7.82: Iguana muon reconstruction: RPC-fired strips are in red and DT hits in green.

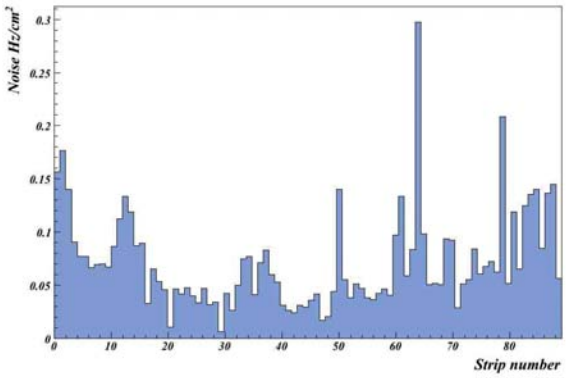

Figure 7.83: Barrel chamber noise profile at HV_{eff} = 9.6 kV.

Several millions of events were collected with different trigger configurations. The DQM was used successfully during the MTCC. It allowed the online checking of the quality of the data and the chamber behaviour in terms of cluster size, number of clusters, etc. Figure 7.82 shows the event display of a typical cosmic muon triggered by the RBC and crossing both RPCs and DTs.

Specific runs were taken before and during the test to evaluate the noise rate. Preliminarily, all the threshold values on the front-end electronic discriminators were set to achieve the best noise configuration with higher efficiency. The chamber noise rate profile for a barrel station is shown in figure 7.83 at HV_{eff} = 9.6 kV, while figure 7.84 shows the overall noise distribution for all the barrel strips involved in the test.

The RPC efficiency can be studied by extrapolating DT segments to the corresponding RPC layer and by requiring matching hits within an appropriate width. In figure 7.85 the chamber efficiency as a function of the HV_{eff} is shown for some RPC stations.

Results are in agreement with those obtained during testing at construction sites and fully meet the design specifications.

2008 JINST 3 S08004

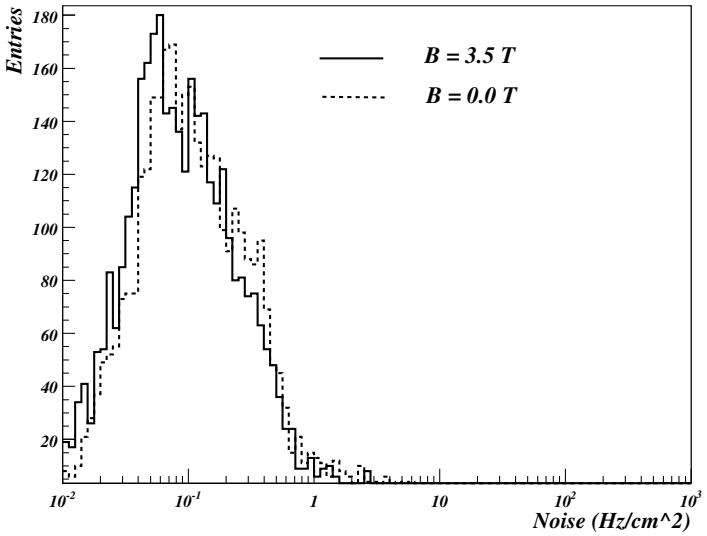

Figure 7.84: Noise distributions in 2 different magnetic fields. All strips of the barrel stations are included in the distribution.

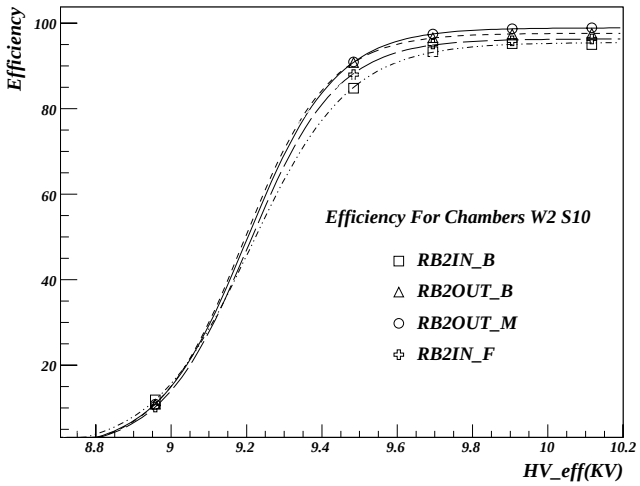

Figure 7.85: Global efficiency vs. HV_{eff}, estimated by means of DT segment extrapolation.

7.4 Optical alignment system

For optimal performance of the muon spectrometer [132] over the entire momentum range up to 1 TeV, the different muon chambers must be aligned with respect to each other and to the central tracking system to within a few hundred μm in $r\phi$. The required alignment precision for the endcap chambers is 75–200 μm, while for the barrel the precision varies from 150 μm for the inner chambers of Station 1 to 350 μm for the outer chambers of Station 4. To this end, after following strict chamber construction specifications, CMS combines precise survey and photogrammetry measurements, measurements from an opto-mechanical system, and the results of alignment algorithms based on muon tracks (both from cosmic rays and from pp collisions) crossing the spectrometer.

There are several potential sources of misalignment in the muon spectrometer, from chamber production to final detector operating conditions, including:

- Chamber construction tolerances. These are unavoidable geometrical tolerances in the production of the chamber parts, such as mis-positioning of wires or strips within a layer and relative shifts in the layer-superlayer assembly. The relative positioning of the different internal components of a chamber was measured during construction to be within the required tolerances (section 7.1 and 7.2). After assembly, all chambers were tested with cosmic muon data and showed good correlation between those measurements and the results of muon track fits. Furthermore, the geometry of the DT chambers was measured at the CERN ISR assembly hall using optical and survey techniques. These data are compared with construction drawings and cosmic data to provide corrections to the nominal chamber geometry when necessary.

- Detector assembly, closing tolerances. Gravitational distortions of the return yoke lead to static deformations of the steel support. This effect, together with the installation tolerances, results in displacements of the chambers in the different barrel wheels and endcap disks of up to several millimetres with respect to their nominal detector positions. After chamber installation, survey and photogrammetry measurements were performed for each wheel and disk. These measurements provide an initial geometry — position and orientation of each muon chamber in the different yoke structures — which absorbs installation tolerances and static steel deformations [175].

- Solenoid effects. Magnetic field distortions lead to almost perfect elastic deformations of the return yoke, at the level of a few centimetres. They result in further displacement of the chambers. The new detector geometry resulting from the magnetic forces is accessed with measurements of the optical system and track-based alignment techniques.

- Time-dependent effects. During operation, thermal instabilities and other time-dependent factors can cause dynamic misalignments at the sub-millimetre level.

The Muon Alignment (MA) system was designed to provide continuous and accurate monitoring of the barrel and endcap muon detectors among themselves as well as alignment between them and the inner tracker detector. To fulfil these tasks the system is organized in separate blocks:

2008 JINST 3 S08004

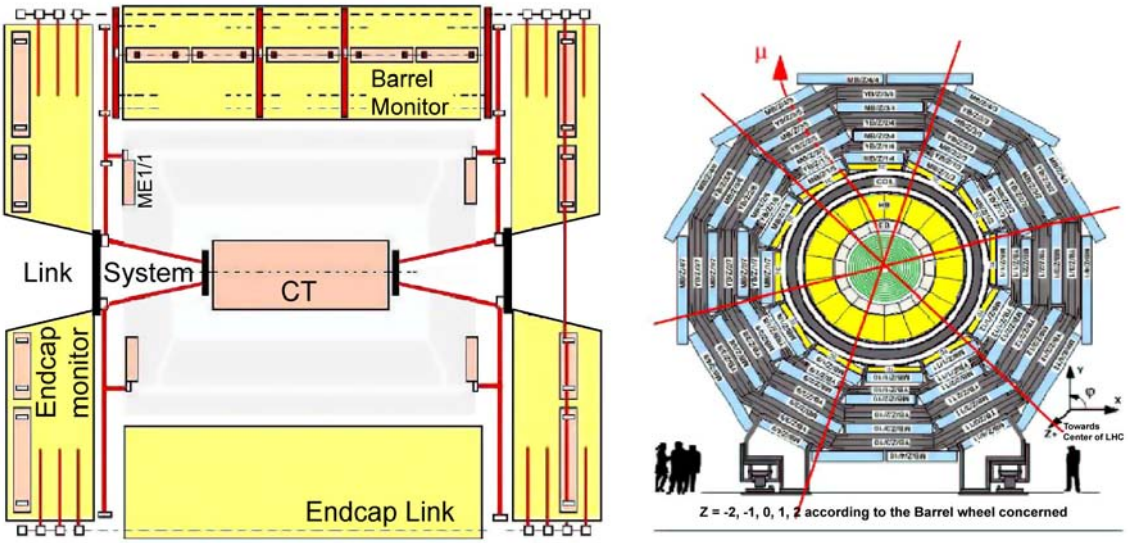

Figure 7.86: Schematic view of the alignment system. Left panel: longitudinal view of CMS. The continuous and dotted lines show different optical light paths. Right panel: transverse view of the barrel muon detector. The crossing lines indicate the r-z alignment planes with 60° staggering in ϕ.

local systems for barrel and endcap muon detectors to monitor the relative positions of the chambers, and a link system that relates the muon and central tracker systems and allows simultaneous monitoring of the detectors.

The system must generate alignment information for the detector geometry with or without collisions in the accelerator. The dynamic range of the system allows it to work in the solenoidal magnetic field between 0 and 4 T. Its goal is to provide independent monitoring of the CMS tracking detector geometry with respect to an internal light-based reference system. This will help to disentangle geometrical errors from sources of uncertainty present in the track-based alignment approach, e.g., knowledge of the magnetic field, material description, and drift velocity.

The basic geometrical segmentation consists of 3 r-z alignment planes with 60° staggering in ϕ. This segmentation is based on the 12-fold geometry of the barrel muon detector. Within each plane, the 3 tracking sub-detectors of CMS (central tracker, barrel and endcap muon detectors) are linked together. Figure 7.86 shows schematic longitudinal and transverse views of CMS, with the light paths indicated. Furthermore, the barrel and endcap monitoring systems can work in stand-alone mode, in which they provide reconstruction of the full geometry of each independent sub-detector. The layout of the optical paths allows the monitoring of each of the 250 DT chambers, while only one sixth of selected CSCs in the 4 endcap stations are directly monitored. Alignment sensors located in the region between the muon barrel wheels and endcap disks allow the tracker and muon detectors to be aligned with respect to each other.

7.4.1 System layout and calibration procedures

The optical network uses two types of light sources: LEDs and laser beams. It is composed of 10 000 LEDs and 150 laser beams together with precise measuring devices: ≈ 900 photo-detectors

and $\approx$ 600 analog sensors (distance sensors and inclinometers), complemented by temperature, humidity and Hall probes. The system is structured into three basic blocks whose main features are described below.

Muon barrel alignment

The monitoring of the barrel muon detector (figure 7.87) is based on the measurement of all the 250 DT chamber positions with respect to a floating network of 36 rigid reference structures, called MABs (Module for the Alignment of Barrel). The MAB design was optimised to achieve adequate mechanical rigidity of the structures under load and in thermal and humidity gradients. Long term measurements showed deviations below 100 μm and 50 μrad [176]. The MABs are fixed to the barrel yoke forming 12 r-z planes parallel to the beam line and distributed in ϕ every 60°. Each structure contains 8 specially designed video cameras that observe LED sources mounted on the DT chambers. Extra light sources and video-cameras in specific MABs serve to connect MABs in different planes forming a closed optical network (called diagonal connections). The MAB positions in the z coordinate are measured with respect to 6 calibrated carbon-fibre bars (z-bars) sitting on the outer surface of the vacuum tank of the solenoid. The MABs in the external wheels, YB$\pm$2, are equipped with extra alignment sensors and light sources that connect the barrel monitoring system with the endcap and tracker detectors.

The 4 corners of the DTs are equipped with LED light sources. Four LED-holders, or forks, are rigidly mounted on the side-profile of the honeycomb structure (2 per side) and use the rectangular 50 $\times$ 65 mm^2 tube as a light passage. Each fork contains 10 LEDs, 6 and 4, respectively, on each side. There are 10 000 light sources mounted on the DT chambers. The position of the forks with respect to the chamber geometry was measured on a dedicated bench with a precision of < 70 μm. As an important by-product, the calibration also provides the full geometry, including the planarity, trapezoidity, and the relative positions of superlayers for each DT chamber with < 40 μm precision, as described in section 7.1.4. Each LED-holder and video-sensor was individually calibrated before its assembly on the DT chambers or MABs and z-bars. LED-holders were measured and the position of the light centroid was determined with respect to the holder mechanics with an accuracy of 10 μm. Long term measurements showed good stability of the centroids and light intensity distributions. CMOS miniature video sensors, containing 384 $\times$ 288 pixels with 12 $\times$ 12 μm^2 pixel size, were calibrated to absorb residual response non-uniformities and the intensity nonlinearities. The video cameras, consisting of a video sensor and a single-element lens assembled in an aluminium box, were also calibrated to determine their inner geometrical parameters. Fully instrumented MABs containing the necessary number of survey fiducials were calibrated on a special bench, where the whole geometry of the structure, positions, and orientations of elements were determined with overall accuracies of 70 μm and 50 μrad.

Once MABs were installed (figure 7.88), the initial MAB positions on the barrel wheels were determined by photogrammetry measurements.

The control, read-out, and data preprocessing [177] are performed by a network of local minicomputers (1 per MAB, 36 in total) that makes it possible to run the full system in parallel. The minicomputers are connected to the main control PC via an Ethernet network capable of working in magnetic fields. The main control PC synchronizes the operation of the light sources mounted on

2008 JINST 3 S08004

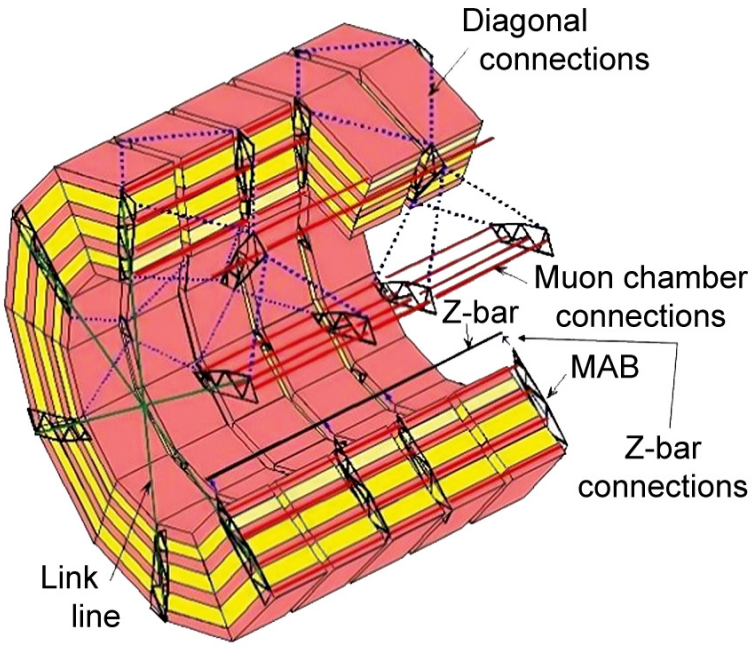

Figure 7.87: Schematic view of the barrel monitoring system showing the optical network among the MAB structures.

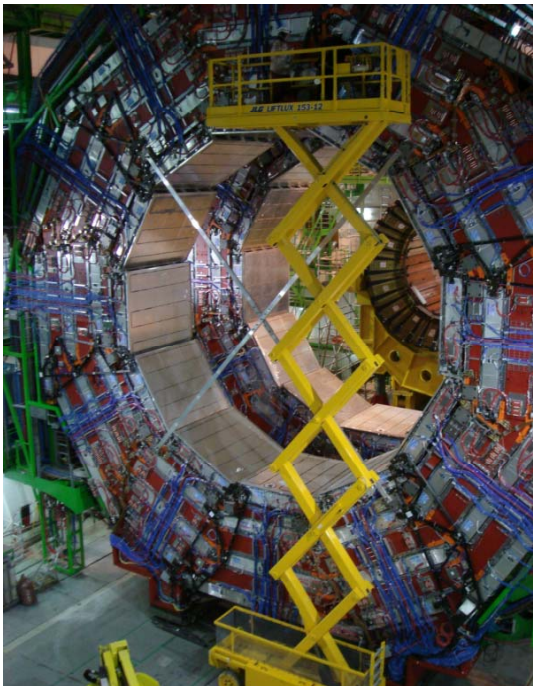

Figure 7.88: Installation of the MABs on wheel YB+2.

the DT chambers and the read-out of the images taken by the cameras. The minicomputers control the light sources mounted on the MABs and the z-bars, read out the temperature and humidity sensors, perform the image read-out and digitisation, and calculate the image centroids of the light sources. The results are transferred to the main control PC, which is connected to the corresponding central CMS units.

Based on simulation, the barrel monitoring system should provide a stand-alone measurement of the barrel chambers with an average r-ϕ position accuracy of 100 μm for chambers in the same sector and about 250 μm between barrel sectors. The current understanding of its performance is discussed in section 7.4.3.

Muon endcap alignment

The muon endcap alignment system [178] is designed to continuously and accurately monitor the actual positions of the 486 CSCs relative to each other, relative to the tracking system, and ultimately within the absolute coordinates of CMS. Due to the large magnetic field, the chambers mounted on the endcap yoke undergo substantial motion and deformation, on the order of a few centimetres, when the field is switched on and off. The alignment system must measure the disk deformation and monitor the absolute positions of the CSCs in the r-ϕ plane and in z. From simulations, the required absolute alignment accuracies were found to run from 75 to 200 μm in r-ϕ. Because the r and r-ϕ accuracies are directly coupled, the required accuracy in the r-position is $\approx$400 μm. The z displacement due to the deformation of the iron yoke disks caused by the strong and non-uniform magnetic field in the endcaps requires the alignment sensors to be able to accommodate a dynamic range of $\approx$2 cm with an accuracy of $\approx$1 mm.

The system uses a complex arrangement of 5 types of sensors for the transferring and monitoring of ϕ, r, and z coordinates (figure 7.89). The system measures one sixth of all endcap chambers. The main monitoring tools within the r-ϕ plane are the Straight Line Monitors (SLM). Each SLM consist of 2 cross-hair lasers, which emit a nearly radial laser beam across 4 chambers from each end, and provide straight reference lines that are picked up by 2 optical sensors (Digital CCD Optical Position Sensors, DCOPS [179]). This arrangement provides references for the chamber positions relative to the laser lines. Figure 7.90 shows a photograph of a complete SLM on station ME+2. The figure also indicates r-sensors for monitoring radial chamber positions, z-sensors for axial distance measurements between stations, and a clinometer for monitoring the tilt of the mechanical support assembly (transfer plate) onto which lasers, reference DCOPS, and z-sensors are mounted. The inset in figure 7.90 shows the location of proximity sensors on the outer ring of the ME+1 station, which monitor the azimuthal distance between neighbouring chambers. These are necessary because the outer ring of ME1 chambers is the only ring for which the CSCs do not overlap in ϕ. Furthermore, every CSC and alignment device is equipped with photogrammetry targets to allow absolute magnet-off measurements.

The ϕ coordinate alignment is handled by optical SLMs and transfer lines. Transfer laser lines run parallel to the CMS z-axis along the outer cylindrical envelope of CMS at 6 points separated by 60° in ϕ. The SLMs run across the surface of one sixth of all the CSCs, along radial directions, and link transfer lines on opposite sides of a disk. Both laser lines have a similar basic configuration: a laser beam defines a direction in space that is picked up by several DCOPS precisely mounted

2008 JINST 3 S08004

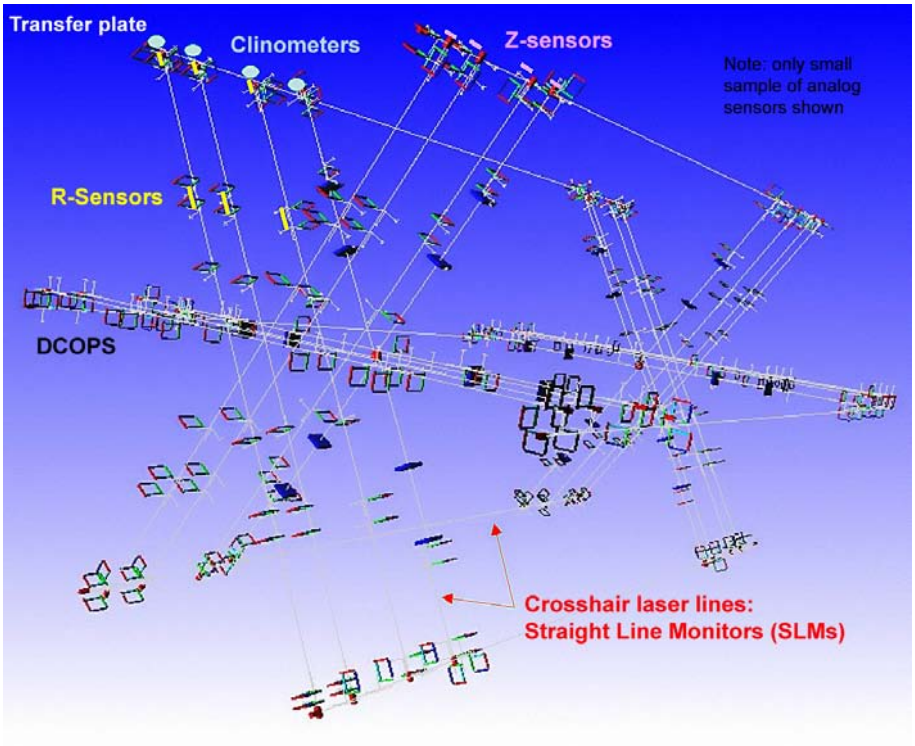

Figure 7.89: Visualisation of the geometry and components of the muon endcap alignment system. The square objects represent optical sensors (DCOPS) for monitoring 3 straight laser lines across each endcap station.

on CSCs or transfer plates to reference their own positions. Mounting accuracies due to tolerances of dowel pins and dowel holes are ≈50 μm. Every DCOPS comprises 4 linear CCDs, each with 2048 pixels and 14 μm pixel pitch. The CCDs are basically arranged in the shape of a square and can be illuminated by cross-hair lasers from either side. The r and z coordinate measurements are performed by analog linear potentiometers and optical distance devices in contact with aluminium tubes of calibrated length.

All analog sensors were calibrated with a 1D precision linear mover with 6.4 μm step size. The uncertainty in the absolute distance calibration is 100 μm for r sensors and 53 μm for z sensors [180]. Calibration for optical DCOPS consisted in determining the distance from the surface of the mount hole for a reference dowel pin to the first active CCD pixel and measuring the projected pixel pitch of each of the 4 CCDs. This was done on a calibration bench where a fibre-bundle variable light source at the focus of a parabolic mirror illuminated a mask with 8 optical slits. A simple geometry reconstruction, based on coordinate-measuring-machine data for the calibration mask and sensor mounts, determined the physical pixel positions. Calibration errors were typically 30 to 50 μm.

2008 JINST 3 S08004

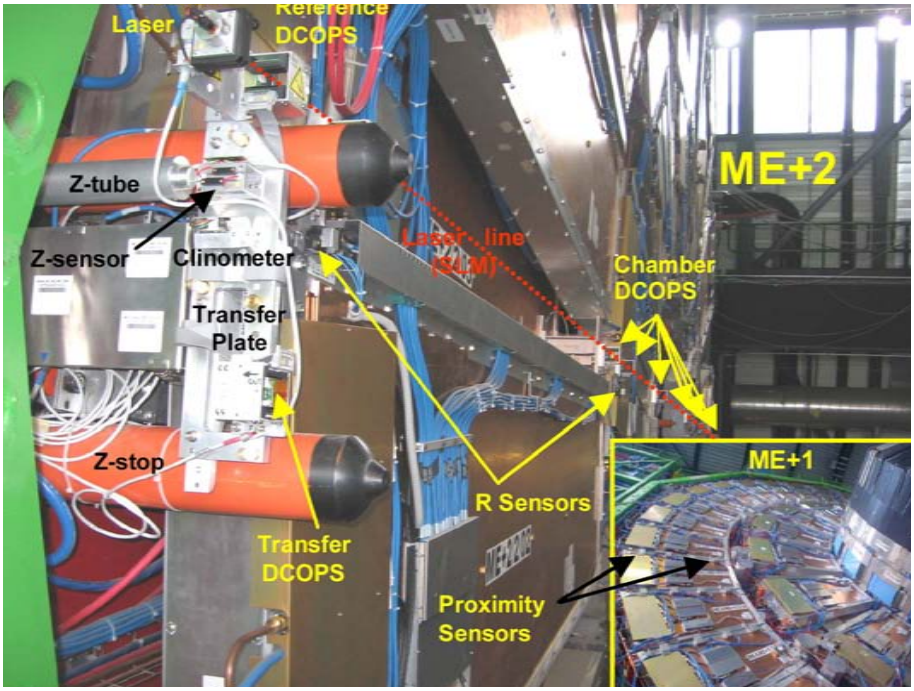

Figure 7.90: Close-up of one of the 3 Straight Line Monitors (SLM) on the ME+2 station with cross-hair laser, DCOPS, and analog sensors (r, z, and Tiltmeter). The insert indicates the location of proximity sensors on ME+1.

Link system

The purpose of the link alignment system is to measure the relative position of the muon spectrometer and the tracker in a common CMS coordinate system. It is designed to work in a challenging environment of very high radiation and magnetic field, meet tight space constraints, and provide high precision measurements over long distances. A distributed network of opto-electronic position sensors, ASPDs (amorphous-silicon position detectors) [181], placed around the muon spectrometer and tracker volumes are connected by laser lines. The entire system is divided into 3 ϕ-planes 60° apart; this segmentation allows a direct reference of each muon barrel sector with the tracker detector and provides a direct reference also to the endcap alignment lines in the first endcap station, ME1. Each plane consists of 4 quadrants (figure 7.86) resulting in 12 laser paths: 6 on each z-side of the CMS detector, and generated by 36 laser sources. The system uses 3 types of reference structures: rigid carbon-fibre annular structures placed at both ends of the tracker (alignment rings, AR) and at the YE$\pm$1 wheels of the endcap muon spectrometer (link disks, LD); and the MAB structures attached at the external barrel wheels, YB$\pm$2. Figure 7.91 (left) shows the LD and AR carbon fibre structures installed in the inner $\eta = 3$ cone. The link measurement network is complemented by electrolytic tiltmeters, proximity sensors in contact with aluminium tubes of calibrated length, magnetic probes, and temperature sensors.

The ARs are rigidly attached to the endcap tracker detectors, TECs, through a purely mechanical connection with the instrumented silicon volume (section 3.3.7). Three pillars, acting as support fixations, connect the last instrumented disk of each TEC with the corresponding AR, at

2008 JINST 3 S08004

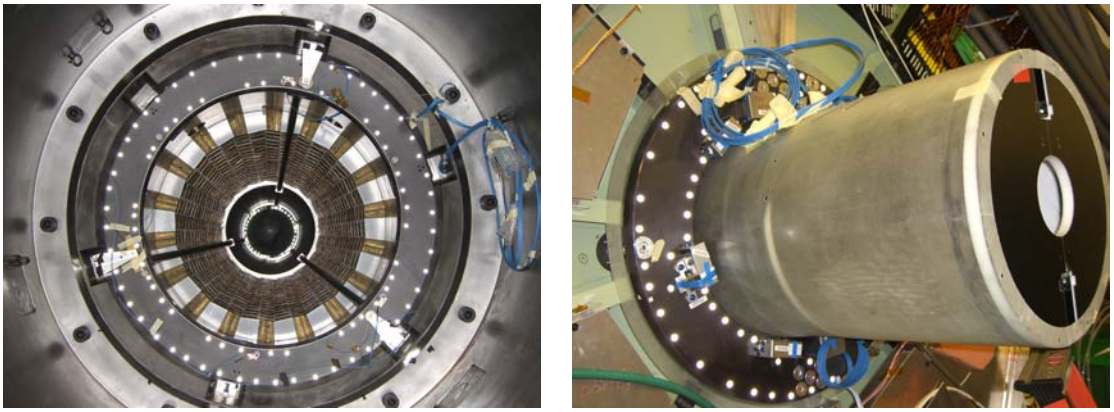

Figure 7.91: Left panel: Link Disk and Alignment Ring installed in the inner $\eta = 3$ cone during the first closing of the detector in summer 2006, MTCC period. Right panel: Alignment Ring mounted in the TEC end flange.

both ends of the tracker volume, see figure 7.91 (right). The position and orientation of the ARs with respect to the TEC disks 9 and 10 were measured with a coordinate-measurement machine using the external survey fiducials prior to the TEC assembly and instrumentation. Changes in angular orientations are monitored by high precision tiltmeters placed at the AR and TEC disk 10. Laser sources originating at the AR and running along the inner detector boundary reach ASPD sensors on the first endcap disk, ME1, and on the external barrel wheel.

The ASPDs are 2D semitransparent photo-sensors, which consist of 2 groups of 64 silicon micro-strips with a pitch of 430 μm oriented perpendicularly. With $\geq$80% transmittance for the 685 nm wavelength used in the system, they allow multi-point measurements along the light path without significant distortions in the beam direction. The intrinsic position resolution is about 2 μm. The location, centre position, and orientation of the ASPD with respect to reference pins in their mechanical mount are measured with a non-contact CMM (Coordinate Measuring Machine) with an overall accuracy of 15 μm. Distance measurement devices (optical distance sensors and linear potentiometers) already mounted in their final mechanics were calibrated using 2 μm resolution linear movers and pre-measured calibration fixtures. The uncertainties in absolute and relative calibration [182] are below 50 μm and 20 μm, respectively, for the different sensor types. The intrinsic accuracy of the tiltmeters sensors, after calibration, is about 2 μrad; mechanical offsets inherent to the mechanical mounts and assembly tolerances are determined by survey and photogrammetry techniques.

The light sources (collimators) and specific optical devices housed on the alignment reference structures (AR, LD, and MABs) create the laser beam paths with the layout described above. Each collimator is focused to its working distance to ensure Gaussian beam profiles along the propagation path to avoid beam-shape-induced bias in the position reconstruction. The adjustment and calibration [183] of the laser rays for the AR and LD structures were done on a dedicated bench instrumented with a precise survey network that mimics the nominal detector geometry. Beams were adjusted to their nominal geometry with a precision better than 100 μrad. Long term measurements were performed after beam adjustments. Beam pointing stability, including temperature

2008 JINST 3 S08004

effects, was found to be better than 30 μrad. The adjustment and calibration accuracy was limited to 30–100 μrad due to the finite dimension of the structures combined with the intrinsic accuracy of the survey and photogrammetry measurement techniques of 70 μm.

Survey and photogrammetry measurements are also performed during the installation of the alignment structures in the detector. An installation accuracy of the order of a few millimetres and milliradians is needed to ensure correct functionality of the system, taking into account the standard CMS assembly tolerances of the big endcap disks and barrel wheels.

The control, read-out, and data preprocessing are performed by two types of electronic boards. Analog sensors read-out and laser control use standard ELMB (embedded local monitor board) cards [184]. For the read-out of ASPD sensors, custom made LEB (local electronic board) cards were developed. LEBs are intelligent imaging acquisition boards made to read and control up to 4 ASPD sensors. They are based on Hitachi micro-controllers. ELMB and LEB boards use the CAN communication protocol to connect the front-end electronics and the main control PC unit.

7.4.2 Geometry reconstruction

The DAQ, monitoring, and control software are integrated into the DCS (detector control system) environment. Data are recorded in an online Oracle database and subsequently converted into ntuples by specialised programs that perform database queries and apply calibrations to convert raw values into meaningful physical quantities. This provides the necessary information for global geometry reconstruction, which is handled by COCOA (CMS Object-Oriented Code for Optical Alignment) [185], an offline program to simulate and reconstruct the complex optical alignment system. Due to the unknown movements of different CMS structures, the sensors of the optical alignment systems will not measure the expected nominal values. The aim of COCOA is to analyse the observed changes in these measurements to determine which are the displacements and/or rotations that caused them. The approach adopted by COCOA to tackle this problem is to solve the system of equations that relate the measurement values to all the positions, rotations, and internal parameters of all the objects that make up the system. In fact, to solve the system of equations, one does not need to know the explicit form of the equations, but only the derivatives of each measurement value with respect to each object parameter. COCOA uses a geometrical approximation of the propagation of light to calculate numerically these derivatives and then solves the system of equations through a nonlinear least squares method. Due to the large number of parameters in CMS (about 30 000), big matrices are needed. COCOA matrix manipulations are based on the Meschach Library [186].

COCOA has proved its robustness through its extensive use in CMS for several design studies, as well as for the analysis of several test benches and magnet test results. Its output, the aligned geometry, will be used as input geometry for track reconstruction as well as for further alignment studies based on muon tracks from cosmic rays and from pp collisions.

7.4.3 System commissioning and operating performance

A first test of the large superconducting solenoid magnet in the CMS detector was successfully performed between June and November 2006, during which stable operation at full field (4 T) was achieved (section 3.3). The alignment sensors, read-out, and DAQ software were commissioned

2008 JINST 3 S08004

during this test period for about one third of the system, instrumented at the $+z$ side of the detector. This allowed the first full-scale dynamic test of the system. The performance of the system as well as the main features of the yoke displacement and deformation were studied. The relevant results are summarised below:

- Measurement of relative movements due to thermal changes.
  The effects of thermal changes (day-night variations) for DT and CSC chambers were recorded for the conditions present during the test, with the detector in the surface assembly hall and power on only ≈5% of the muon spectrometer. The measured relative movement did not exceed 50 μm over the entire test period, with changes in position showing a good correlation with temperature. Although a movement of this magnitude is not relevant from the physics analysis point of view, its measurement illustrates the good resolution of the alignment system.

- Measurement of the displacements and deformations of the yoke structures.

  Two effects were observed. The first is the change in the original positions of the structures (the positions before any magnet operation). The displacements of the structures along the z direction towards the solenoid seem to stabilise after the first 2.5–3 T are reached. This compression is permanent, meaning it is not reversed/recovered in subsequent magnet off states, and it is interpreted as the final closing of the structures due to the magnetic forces acting on the iron. These measured displacements are specific to the first CMS closing experience and cannot be extrapolated to other scenarios.

  The second effect is the almost perfectly elastic deformations between magnet-on and magnet-off states, as illustrated in figure 7.92. At 4 T, the elastic deformation of the barrel yoke, measured at the end of the $+z$ side with respect of the plane of the interaction point, is about 2.5 mm. Figure 7.92 shows the elastic compression of the barrel wheels versus the magnet current as recorded in the second phase of the Magnet Test period. Despite the large overall compression of the barrel spectrometer, an important measurement was the stability of the barrel chambers during the whole data-taking period. The relative movements in the r-ϕ direction did not exceed 60 μm.

  The behaviour of the endcap disk is more complicated. Due to the strong gradient in the magnetic field near the end of the solenoid, strong magnetic forces pull the central portions of the endcap disks towards the center of the detector. As shown in figure 7.92, the nose is pulled towards the interaction point, the magnitude of the compression is perfectly correlated with the magnet current, reaching up to ≈16 mm at 4 T. The various z-stops, which prevent the disks from getting pushed into each other and onto the barrel wheels, cause the endcap disks to bend into a cone shape. The z-stops between endcap and barrel, positioned at nearly half the disk radius, cause the side of the YE1 disk facing the barrel to compress radially around them by ≈600 μm, while expanding azimuthally by ≈800 μm. This explains the radial compression of the face of ME+1 and the larger bending angles at mid-radius than at the outer edge (figure 7.93). Endcap disk deformations are predicted by finite element analysis (FEA) using the ANSYS program [3]. The measurements are in reasonable quantitative agreement for all displacements and deformations, as shown in figure 7.93. Note that the

2008 JINST 3 S08004

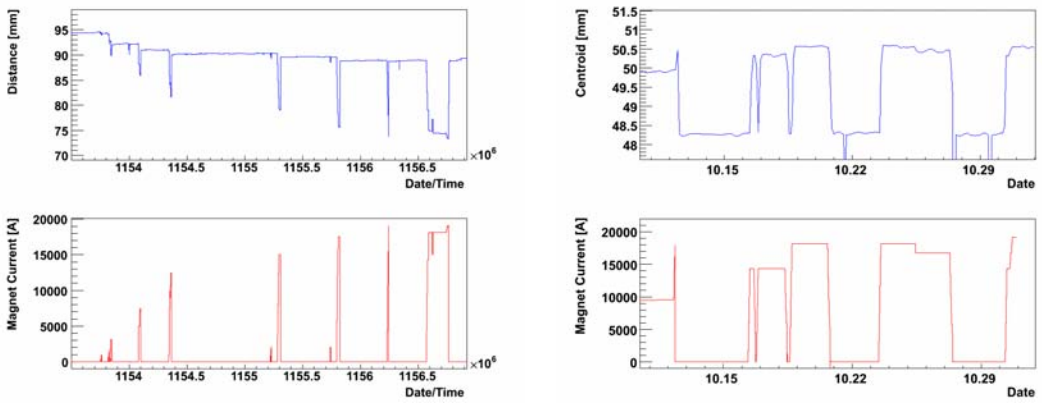

Figure 7.92: Deformations of endcap disks and barrel wheels vs magnet current cycling. Left panel: The bottom plot shows the magnet powering cycle exercised during the first phase of the Magnet Test period. The top plot shows the measured YE+1 nose compression towards the interaction point. Right panel: The bottom plot shows the magnet powering cycle exercised during the second phase of the Magnet Test period. The top plot shows the calculated approximate YB+2 compression towards the interaction point.

front z-stops, between the ME1 and barrel wheels, were not included in the FEA, which explains the difference. The difference between top and bottom is also explained by the presence of the carts that support the disks.

The rest of the endcap stations on YE+2 and YE+3 experience a maximum bending angle of ≈2.5 mrad relative to the vertical, as sketched in figure 7.94. As in the case of the barrel chambers, with stable 4 T field, the observed relative movements were very small.

- Detector closing tolerances and reproducibility.
  The test of the magnet was divided into 2 phases, separated by a short period during which the yoke was open to extract the inner detectors, tracker, and ECAL modules. This allowed a test of the reproducibility in the closing procedure and tolerances, as well as the study of the compatibility of measurements between the two phases. Reproducibility in the closing was at the level of a few millimetres for the barrel wheels and about an order of magnitude higher for the endcap disks. The particular conditions of the test did not allow the establishment of a solid understanding of reproducibility for the process of closing the different structures. Instead, the system was able to reproduce the same magnetic-force-induced effects as measured in the first period.

From this test we conclude that the system operates adequately under magnetic fields both in terms of dynamic range and measurement performance. The system precision achieved is ≤ 300 μm and the measurement accuracy has been validated against results from photogrammetry and cosmic ray tracks.

2008 JINST 3 S08004

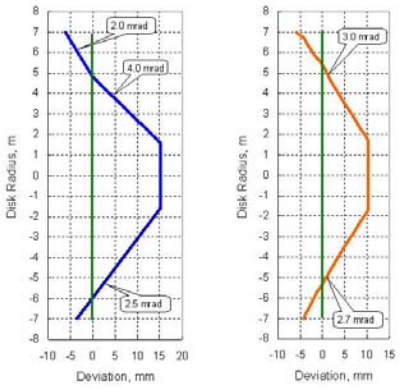

Figure 7.93: Comparison of the YE+1 disk deformations in the *r*-*z* plane at full magnetic field (4 T) measured by the alignment system (left panel) and predictions from finite element analysis (right panel). The vertical lines correspond to 0 magnetic field.

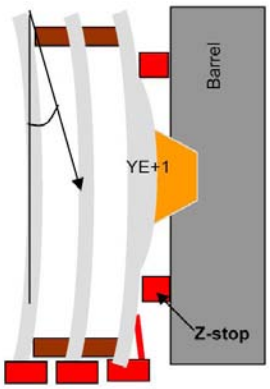

Figure 7.94: Current understanding of disk deformation due to magnetic forces based on alignment system measurements. The *z*-stops (red) prevent the disks from getting pushed into each other. Note that the indicated bending angle is exaggerated for illustrative purposes. Its measured magnitude is 2.5 mrad.

2008 JINST 3 S08004

Chapter 8

Trigger

The LHC provides proton-proton and heavy-ion collisions at high interaction rates. For protons the beam crossing interval is 25 ns, corresponding to a crossing frequency of 40 MHz. Depending on luminosity, several collisions occur at each crossing of the proton bunches (approximately 20 simultaneous pp collisions at the nominal design luminosity of 10^{34} $cm^{-2}s^{-1}$). Since it is impossible to store and process the large amount of data associated with the resulting high number of events, a drastic rate reduction has to be achieved. This task is performed by the trigger system, which is the start of the physics event selection process. The rate is reduced in two steps called Level-1 (L1) Trigger [187] and High-Level Trigger (HLT) [188], respectively. The Level-1 Trigger consists of custom-designed, largely programmable electronics, whereas the HLT is a software system implemented in a filter farm of about one thousand commercial processors. The rate reduction capability is designed to be at least a factor of 10^6 for the combined L1 Trigger and HLT. The design output rate limit of the L1 Trigger is 100 kHz, which translates in practice to a calculated maximal output rate of 30 kHz, assuming an approximate safety factor of three. The L1 Trigger uses coarsely segmented data from the calorimeters and the muon system, while holding the high-resolution data in pipelined memories in the front-end electronics. The HLT has access to the complete read-out data and can therefore perform complex calculations similar to those made in the the analysis off-line software if required for specially interesting events. Since HLT algorithms will evolve with time and experience they are not described here. More information may be found in [189]. For reasons of flexibility the L1 Trigger hardware is implemented in FPGA technology where possible, but ASICs and programmable memory lookup tables (LUT) are also widely used where speed, density and radiation resistance requirements are important. A software system, the Trigger Supervisor [190], controls the configuration and operation of the trigger components.

The L1 Trigger has local, regional and global components. At the bottom end, the Local Triggers, also called Trigger Primitive Generators (TPG), are based on energy deposits in calorimeter trigger towers and track segments or hit patterns in muon chambers, respectively. Regional Triggers combine their information and use pattern logic to determine ranked and sorted trigger objects such as electron or muon candidates in limited spatial regions. The rank is determined as a function of energy or momentum and quality, which reflects the level of confidence attributed to the L1 parameter measurements, based on detailed knowledge of the detectors and trigger electronics and on the amount of information available. The Global Calorimeter and Global Muon Triggers

2008 JINST 3 S08004

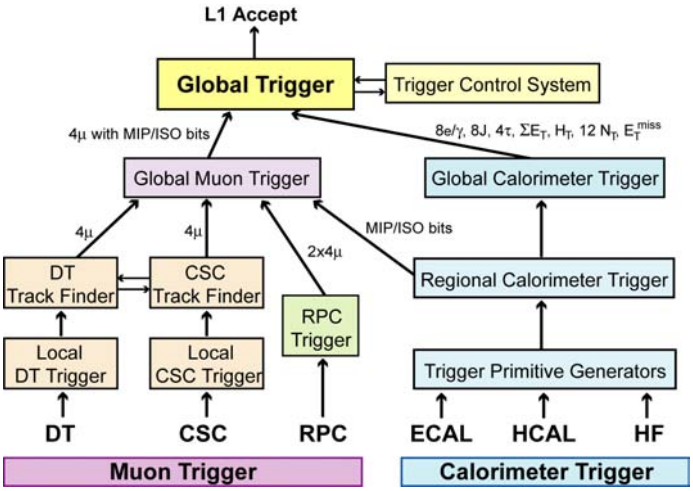

Figure 8.1: Architecture of the Level-1 Trigger.

determine the highest-rank calorimeter and muon objects across the entire experiment and transfer them to the Global Trigger, the top entity of the Level-1 hierarchy. The latter takes the decision to reject an event or to accept it for further evaluation by the HLT. The decision is based on algorithm calculations and on the readiness of the sub-detectors and the DAQ, which is determined by the Trigger Control System (TCS). The Level-1 Accept (L1A) decision is communicated to the sub-detectors through the Timing, Trigger and Control (TTC) system. The architecture of the L1 Trigger is depicted in figure 8.1. The L1 Trigger has to analyze every bunch crossing. The allowed L1 Trigger latency, between a given bunch crossing and the distribution of the trigger decision to the detector front-end electronics, is 3.2 μs. The processing must therefore be pipelined in order to enable a quasi-deadtime-free operation. The L1 Trigger electronics is housed partly on the detectors, partly in the underground control room located at a distance of approximately 90 m from the experimental cavern.

8.1 Calorimeter trigger

The Trigger Primitive Generators (TPG) make up the first or local step of the Calorimeter Trigger pipeline. For triggering purposes the calorimeters are subdivided in trigger towers. The TPGs sum the transverse energies measured in ECAL crystals or HCAL read-out towers to obtain the trigger tower E_T and attach the correct bunch crossing number. In the region up to $|\eta| = 1.74$ each trigger tower has an (η, ϕ)-coverage of 0.087×0.087. Beyond that boundary the towers are larger. The TPG electronics is integrated with the calorimeter read-out. The TPGs are transmitted through high-speed serial links to the Regional Calorimeter Trigger, which determines regional candidate electrons/photons, transverse energy sums, τ-veto bits and information relevant for muons in the form of minimum-ionizing particle (MIP) and isolation (ISO) bits. The Global Calorimeter Trigger determines the highest-rank calorimeter trigger objects across the entire detector.

2008 JINST 3 S08004

Calorimeter trigger primitive generators

The ECAL on-detector front-end electronics boards, each serving 25 crystals, receive the ADC signals from the very front-end electronics located at the rear of the detector modules. They contain most of the TPG pipeline in six radiation-hard 0.25 μm CMOS ASIC chips named FENIX. An off-detector Trigger Concentrator Card (TCC) collects the primitives from 68 front-end boards in the barrel and 48 boards in the endcaps through optical links. The TCCs finalize the TPG generation and encoding, store the trigger primitives during the L1 latency time and transmit them to the RCT by dedicated daughter boards, the Synchronization and Link Boards (SLB), upon reception of a L1A signal. The SLBs synchronize the trigger data through circuits that histogram the LHC bunch crossing structure. Each trigger tower is aligned with the bunch crossing zero signal. A Data Concentrator Card (DCC) performs the opto-electronic conversion and deserialization of the serial input data streams and sends the read-out data collected from the front-end boards to the DAQ. Clock and Control System (CCS) boards distribute the clock, the L1A and control signals to the TCC, the DCC and the on-detector electronics. The ECAL TPG hardware is contained in twelve 9U VME crates for the barrel and six for the endcaps.

The front-end modules of the hadron calorimeter contain Charge Integrator and Encoder (QIE) ADC chips to digitize the signals from the photo detectors. Optical links transmit the data to the HCAL Trigger and Readout (HTR) boards. Each HTR board processes 48 channels. It linearizes, filters and converts the input data to generate the HCAL trigger primitives. The energy values of front and back towers are added and the bunch crossing number is assigned by a peak filtering algorithm. As for the ECAL, the primitives are sent to the RCT by SLBs, and read-out data are collected by a DCC. The HCAL trigger electronics is contained in 26 9U VME crates. Each crate houses 18 HTR boards and one DCC.

Regional Calorimeter Trigger

The Regional Calorimeter Trigger [191] determines electron/photon candidates and transverse energy sums per calorimeter region. Information relevant for muons about isolation and compatibility with minimally ionizing particles is also calculated. A region consists of 4×4 trigger towers except in HF where a region is one trigger tower. Electromagnetic and hadronic transverse energies are summed in each tower.

The e/γ trigger algorithm (figure 8.2) starts by determining the tower with the largest energy deposit and is applied across the entire ECAL region. The energy of the tower with the next-highest deposit in one of the four broad side neighbours is then added. Isolated and non-isolated e/γ within $|\eta| \leq 2.5$ are determined by the trigger. A non-isolated e/γ requires passing of two shower profile vetoes. The first one is based on a fine-grain crystal energy profile reflecting the lateral extension of a shower. The fine-grain bit is set by the TPG if the shower is contained in a matrix of 2×5 crystals. The matrix is dimensioned such that it also allows for the detection of bremsstrahlung due to the magnetic field. The second one is based on the ratio of the deposited energies in the hadronic and in the electromagnetic sections. A typical maximal value of 5% is allowed for that ratio. An isolated electron/photon candidate has to pass the previous vetoes for all eight neighbouring towers. In addition, at least one quiet corner made of four groups of five electromagnetic towers surrounding the hit tower is required. Four isolated and four non-isolated e/γ per region are forwarded to the GCT.

2008 JINST 3 S08004

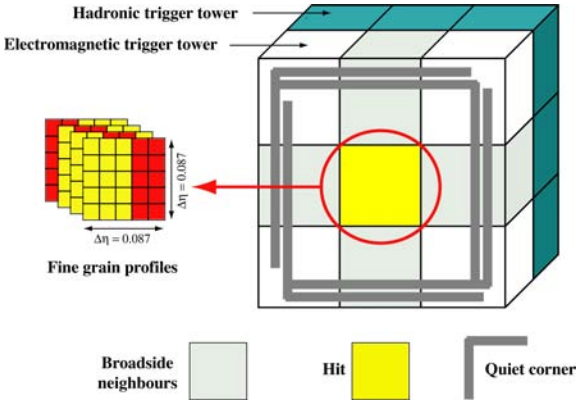

Figure 8.2: Electron/photon algorithm.

Figure 8.3: Electron Isolation Card.

The RCT also sums the transverse energy in a given region of the central calorimeter (HF is not included) and determines τ-veto bits for the identification of jets from one- and three-prong τ-decays, which are narrower than ordinary quark/gluon jets. A τ-veto bit is set unless the pattern of active towers corresponds to at most 2×2 contiguous trigger towers within a 4×4 tower region. Jets can be classified as τ-jet only at $|\eta| < 3.0$ (not in HF).

The RCT hardware consists of 18 regional 9U VME crates and one 6U clock distribution crate located in the underground control room. Each crate covers a region of $\Delta\eta \times \Delta\phi = 5.0 \times 0.7$. Receiver cards are plugged into the rear of the regional crates. Seven cards per crate receive the ECAL and HCAL primitives. The HF primitives are directly received on a Jet/Summary card. The serial input data are converted to 120 MHz parallel data, deskewed, linearized and summed before transmission on a 160 MHz custom monolithic backplane to seven Electron Isolation Cards (EIC) and one Jet/Summary Card (JSC) mounted at the front side of the crate. Different ASICs perform the algorithm calculations. An EIC is shown in figure 8.3.

Global Calorimeter Trigger

The Global Calorimeter Trigger determines jets, the total transverse energy, the missing transverse energy, jet counts, and H_T (the scalar transverse energy sum of all jets above a programmable threshold). It also provides the highest-rank isolated and non-isolated e/γ candidates.

Jets are found by a four-stage clustering technique based on jet finders operating in 2×12 cells in ϕ and η, spanning 40° and half the detector, respectively, in these directions. The cell at η=0 is duplicated. In the first stage mini-clusters are created by summing energies within 2×3 cells if a central cell has more energy than neighbouring cells. In the second stage the three largest mini-clusters in each of the two ϕ-strips are transferred in opposite ϕ-directions. These are compared against the existing mini-clusters on the receiving ϕ-strip. Mini-clusters adjacent or diagonally adjacent to a larger mini-cluster are removed. In the third and fourth stages the received mini-clusters that survive have their three adjacent cells in the receiving ϕ-strip combined to make a 3×3 cell. A jet is classified as a τ jet if none of the corresponding RCT regions had a τ-veto bit set. After sorting, up to four jets and four τ jets from the central HCAL and four jets from HF are forwarded to the GT. The magnitude and direction of the missing energy and the total transverse energy are

2008 JINST 3 S08004

computed from the regional transverse energy sums in the two coordinates transverse to the beam within $|\eta| < 5$. Twelve jet counts for different programmable E_T-thresholds and optionally also different (η, ϕ)-regions are computed. Muon MIP/ISO bits are received from the RCT along with the e/γ data and are forwarded to the GMT through a dedicated muon processing system. Apart from triggering, the GCT also acts as the read-out system for the RCT. The GCT has in addition the capability to monitor rates for certain trigger algorithms and from those deduce information about the LHC luminosity as seen by the CMS trigger system.

All GCT electronics is located in the underground control room. The large amount of data from the RCT crates are transmitted electronically to 63 Source Cards, which reorder the data onto 252 optical fibres. The core of the GCT processing is performed by Leaf Cards, which can be configured as electron or jet cards. Several Leaf Cards can be connected with each other in order to perform complex tasks such as the jet finding. There are two Leaf Cards for electrons and six for jets. Each electron leaf card receives the e/γ data from one half of the RCT crates on 27 fibres and sorts them. Each jet card receives 30 regional sum fibres from three RCT crates via the source cards. They perform the jet clustering and transmit the jet candidates to two Wheel Cards for sorting and data compression. They also calculate partial energy sums and jet counts and forward them to the Wheel Cards. A Concentrator Card finally collects the data from all Electron Leaf and Wheel Cards and performs the final sorting for electrons/photons, completes the jet finding in the boundaries between groups of three Leaf Cards, sorts all jets, calculates the global energy and jet count quantities and sends the final results to the GT and the DAQ. In addition to the tasks involving e/γ's, jets and energy sums, the GCT also handles MIP/ISO bits for muons. They are processed by three muon processing cards, which receive 6 muon fibres each from Source Cards. The processor design is built on an evolution of the leaf concept and uses a modular, low-latency architecture based on the μTCA industry standard [193]. An active custom backplane based on the principle of a crosspoint switch allows a programmable routing of the 504 MIP/ISO bits, which are then transmitted to the GMT on 24 links.

8.2 Muon trigger

All three muon systems – the DT, the CSC and the RPC – take part in the trigger. The barrel DT chambers provide local trigger information in the form of track segments in the ϕ-projection and hit patterns in the η-projection. The endcap CSCs deliver 3-dimensional track segments. All chamber types also identify the bunch crossing from which an event originated. The Regional Muon Trigger consists of the DT and CSC Track Finders, which join segments to complete tracks and assign physical parameters to them. In addition, the RPC trigger chambers, which have excellent timing resolution, deliver their own track candidates based on regional hit patterns. The Global Muon Trigger then combines the information from the three sub-detectors, achieving an improved momentum resolution and efficiency compared to the stand-alone systems. The initial rapidity coverage of the muon trigger is $|\eta| \leq 2.1$ at the startup of LHC. The design coverage is $|\eta| \leq 2.4$.

2008 JINST 3 S08004

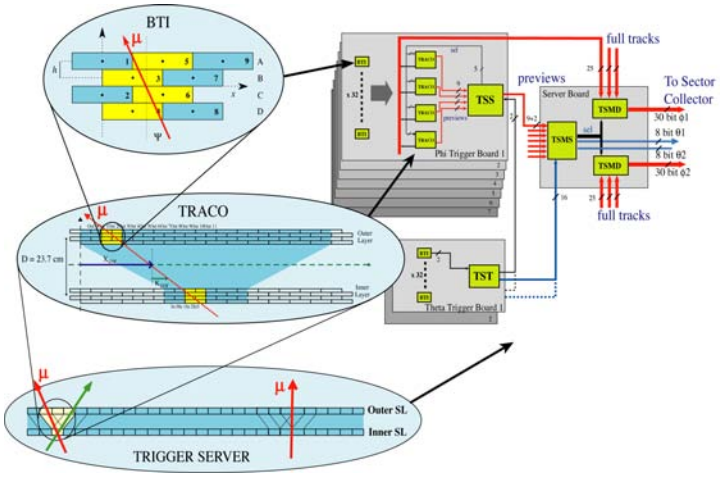

Figure 8.4: Drift Tube Local Trigger.

Drift Tube local trigger

The electronics of the DT local trigger consists of four basic components (figure 8.4): Bunch and Track Identifiers (BTI), Track Correlators (TRACO), Trigger Servers (TS) and Sector Collectors (SC). While the SCs are placed on the sides of the experimental cavern, all other trigger and read-out electronics is housed in minicrates on the front side of each chamber. All devices are implemented in custom-built integrated circuits. The BTIs are interfaced to the front-end electronics of the chambers. Using the signals from the wires they generate a trigger at a fixed time after the passage of the muon. Each BTI searches for coincident, aligned hits in the four equidistant planes of staggered drift tubes in each chamber superlayer. The association of hits is based on a mean-timer technique [194], which uses the fact that there is a fixed relation between the drift times of any three adjacent planes. From the associated hits, track segments defined by position and angular direction are determined. The spatial resolution of one BTI is better than 1.4 mm, the angular resolution better than 60 mrad. The BTI algorithm is implemented in a 64-pin ASIC with CMOS 0.5 μm Standard Cell technology. There are a few hundred BTIs per chamber.

The DT chambers have two Φ-type superlayers, measuring ϕ coordinates. The TRACO attempts to correlate the track segments measured in each of them. If a correlation can be found, the TRACO defines a new segment, enhancing the angular resolution and producing a quality hierarchy. Four BTIs in the inner Φ-type superlayer and 12 BTIs in the outer Φ-type superlayer are connected to one TRACO. The number of TRACOs is 25 for the largest muon chamber type. The TRACO is implemented in a 240-pin ASIC with CMOS 0.35 μm Gate Array technology. The trigger data of at most two track segments per bunch crossing reconstructed by each TRACO are transmitted to the TS, whose purpose is to perform a track selection in a multitrack environment.

The TS has two components, one for the transverse projection (TSϕ) and the other for the longitudinal projection (TSθ). The first one processes the output from the TRACO, whilst the second uses directly the output of the BTIs of the θ view delivered by the Θ-type superlayers present in the three innermost muon stations. The TSϕ consists itself of two components, the

2008 JINST 3 S08004

Track Sorter Slave (TSS) and the Track Sorter Master (TSM). The TSS preselects the tracks with the best quality and the smallest bending angle based on a reduced preview data set coming from the TRACOs in order to save processing time. A select line in the TRACO with the best track is then activated and the TRACO is allowed to send the full data to the TSM. The corresponding preview data are also sent to the TSM for a second stage processing. The TSM analyzes up to seven preview words from the TSSs. The output consists of the two tracks with the highest transverse momentum. There is one TSM per muon station. In the longitudinal view the TSθ groups the information from the 64 BTIs per chamber. From each BTI two bits are received, a trigger bit and a quality bit. A logic OR of groups of eight bits is applied. The output data consist of 8 bits indicating the position of the muon and 8 quality bits.

The requirement of robustness implies redundancy, which introduces, however, a certain amount of noise or duplicate tracks giving rise to false triggers. Therefore the BTIs, the TRACOs and the different parts of the TS contain complex noise and ghost reduction mechanisms. The trigger and also the read-out data from each of the sixty 30°-sectors of CMS are sent to Sector Collector (SC) units, where the trigger information — the position, transverse momentum and track quality — is coded and transmitted to the DT regional trigger, called the Drift Tube Trigger Track Finder (DTTF), through high-speed optical links.

Cathode Strip Chamber local trigger

The endcap regions are challenging for the trigger since many particles are present and muons at a given p_T have a higher momentum than in the barrel, which gives rise to more bremsstrahlung photons. In addition, photon conversions in a high-radiation (neutron-induced) environment occur frequently. Therefore the CSCs consist of six layers equipped with anode wires and cathode strips, which can be correlated. Muon track segments, also called Local Charged Tracks (LCT), consisting of positions, angles and bunch crossing information are first determined separately in the nearly orthogonal anode and cathode views. They are then correlated in time and in the number of layers hit. The cathode electronics is optimized to measure the ϕ-coordinate, the anode electronics to identify the bunch crossing with high efficiency.

An electric charge collected by the anode wires induces a charge of opposite sign in the cathode strips nearby. The trigger electronics determines the centre of gravity of the charge with a resolution of half a strip width, between 1.5 and 8 mm, depending on the radius. By demanding that at least four layers are hit, the position of a muon can be determined with a resolution of 0.15 strip widths. Due to the finite drift time the anode signals in the six chamber layers are spread out over an interval of more than two bunch crossings. As for the cathodes, at least four coincident hits are required, since in contrast to neutron-induced background a real muon leaves coincident signals in at least four layers with a probability that exceeds 99%. Actually a coincidence of two signals (pre-trigger) is used to identify the crossing, in order to allow for long drift time hits to arrive. A validation of the track occurs if in the following two bunch crossings at least four coincident signals are found. In order to reduce the number of trigger channels 10 to 15 anode wires are ORed. Figure 8.5 shows the principles of the cathode and anode trigger electronics and the bunch crossing assignment.

2008 JINST 3 S08004

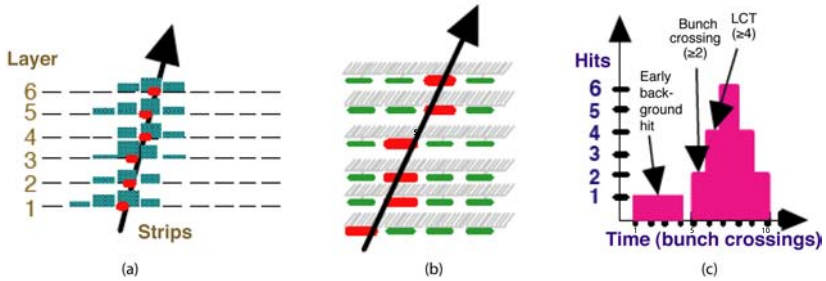

Figure 8.5: Cathode Strip Chamber Local Trigger: (a) Cathode LCT formation from strips, (b) Anode LCT formation from wire group hits, (c) Bunch crossing assignment.

The track segments from the cathode and anode electronics are finally combined into three-dimensional LCTs. They are characterized by the high-precision ϕ-coordinate in the bending plane, the bending angle ϕ_b, a rough η-value and the bunch crossing number. The best two LCTs of each chamber are transmitted to the regional CSC trigger, called the CSC Track Finder (CSCTF), which joins segments to complete tracks.

The hardware of the CSC local trigger consists of seven types of electronics boards. Cathode and anode front-end boards (CFEB and AFEB) amplify and digitize the signals. Anode LCT-finding boards (ALCT) latch the anode hits at 40 MHz, find hit patterns in the six chamber layers that are consistent with having originated at the vertex, and determine the bunch crossing. They send the anode information to the Cathode LCT-finding plus Trigger Motherboard (CLTC/TMB) cards. The CLCT circuits look for strip hit patterns consistent with high-momentum tracks. The TMB circuits perform a time coincidence of cathode and anode LCT information. If a coincidence is found, they send the information to the Muon Port Cards (MPC). The TMB selects up to two LCTs based on quality cuts. In order to cancel out ghosts a coincidence with RPC hits is established if two or more LCTs are found. A MPC receives the LCTs from the CLTC/TMBs of one endcap muon station sector, selects the best two or three LCTs depending on the station number and sends them over optical links to the CSC Track Finder. The anode and cathode LCTs and the raw hits are recorded by DAQ motherboards (DAQMB) and transmitted to the CSC detector-dependent units (DDU) belonging to the DAQ system upon reception of a L1A signal. The LHC timing reference, the L1A decision, the bunch crossing number and bunch counter reset signals are distributed by the Clock and Control Boards (CCB). The front-end boards and the ALCTs are mounted directly on the chambers. The rest of the local trigger electronics is housed in 48 peripheral crates on the endcap disks. The optical fibres to the control room depart from there. Except for the comparator-network ASIC implemented in the CLCT module, the CSC trigger electronics is built in FPGA technology.

Resistive Plate Chamber trigger

The RPCs are dedicated trigger detectors. Several layers of double-gap RPCs are mounted on the DT and CSC tracking chambers, six in the central region (two layers on the inside and outside of the two innermost muon stations, one on the inside of the two outermost stations) and four in the forward parts (one layer on the inside of each station). Their main advantage is their excellent

2008 JINST 3 S08004

timing resolution of about 1 ns, which ensures an unambiguous bunch crossing identification. For triggering purposes the measurement of the momentum of a particle is also important. In the magnetic field, muons are bent in the plane transverse to the LHC beams. It is sufficient to measure the azimuthal coordinate ϕ at several points along the track to determine the bending and thus the p_T. Therefore the RPC strips run parallel to the beam pipe in the barrel, and radially in the endcaps. There are about 165 000 strips in total, which are connected to front-end boards (FEB) handling 16 channels each.

The RPC trigger is based on the spatial and temporal coincidence of hits in several layers. It is segmented in 33 trigger towers in η, which are each subdivided in 144 segments in ϕ. As opposed to the DT/CSC, there is no local processing on a chamber apart from synchronization and cluster reduction. The Pattern Comparator Trigger (PACT) logic [195] compares strip signals of all four muon stations to predefined patterns in order to assign p_T and electric charge, after having established at least three coincident hits in time in four planes. Spatially the PACT algorithm requires a minimum number of hit planes, which varies depending on the trigger tower and on the p_T of the muon. Either 4/6 (four out of six), 4/5, 3/4 or 3/3 hit layers are minimally required. A quality parameter reflects the numbers of hit layers. For six planes there are typically 14 000 possible patterns. The outer section of the hadron calorimeter (HO) consists of scintillators placed after the magnet coil up to $|\eta| < 1.24$. Their signals can also be taken into account by the RPC trigger in order to reduce rates and suppress background [196]. The algorithm requires HO confirmation for low-quality RPC triggers. The optical links from the four HO HTR boards are received by the RPC trigger boards, and the signals are treated and incorporated in the PACT logic like an additional RPC plane, with the required number of planes hit increased by one.

The RPC signals are transmitted from the FEBs, which contain ASICs manufactured in 0.8 μm BiCMOS technology, to the Link Boards (LB), where they are synchronized, multiplexed, serialized and then sent via 1732 optical links to 108 Trigger Boards in 12 trigger crates in the control room. The 1640 LBs are housed in 136 Link Board Boxes. The Trigger Boards contain the complex PACT logic which fits into a large FPGA. There are 396 PACT chips in the system. Since duplicate tracks may be found due to the algorithm concept and the geometry, a *ghost busting* logic is also necessary. The RPC muon candidates are sorted separately in the barrel and forward regions. The best four barrel and the best four forward muons are sent to the Global Muon Trigger. The RPC data record is generated on the Data Concentrator Card, which receives data from the individual trigger boards.

Drift Tube and Cathode Strip Chamber track finders

The regional muon trigger based on the precision tracking chambers consists of the Drift Tube Track Finder (DTTF) in the barrel [197] and the CSC Track Finder (CSCTF) in the endcaps [198]. They identify muon candidates, determine their transverse momenta, locations and quality. The candidates are sorted by rank, which is a function of p_T and quality. The DTTF and the CSCTF each deliver up to four muons to the Global Muon Trigger.

The track finding principle relies on extrapolation from a source track segment in one muon station to a possible target segment in another station according to a pre-calculated trajectory originating at the vertex. If a compatible target segment with respect to location and bending angle is

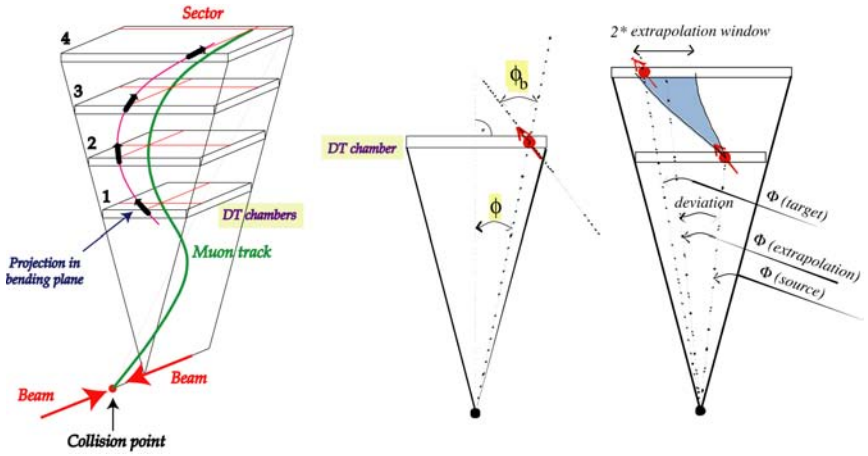

Figure 8.6: Track Finder extrapolation scheme.

found, it is linked to the source segment. A maximum number of compatible track segments in up to four muon stations is joined to form a complete track, to which parameters are then assigned. The extrapolation principle is shown in figure 8.6. While the CSCTF incorporates 3-dimensional spatial information from the CSC chambers in the track finding procedure, the DTTF operates 2-dimensionally in the ϕ-projection. A coarse assignment of η is nevertheless possible by determining which chambers were crossed by the track. In most cases an even more refined η-value can be assigned using the information from the θ-superlayers. Both for the DTTF and the CSCTF, the track finder logic fits into high-density FPGAs. For the regional trigger the DT chambers are organized in sectors and wedges. There are twelve horizontal wedges parallel to the beams. Each wedge has six 30°-sectors in ϕ. The central wheel has 2×12 half-width sectors, whereas the four outer wheels are subdivided in 12 full-width sectors each. In the two endcaps the track finding is partitioned in 2×6 60°-sectors. In the overlap region between the DT and CSC chambers, around $|\eta| \approx 1$, information from both devices is used.

In the DTTF the track finding in ϕ is performed by 72 sector processors, also called Phi Track Finders (PHTF). Per chamber they receive at most two track segments from the DT local trigger through optical links. The segment information is composed of the relative position of the segments inside a sector, its bending angle and a quality code. If there are two segments present in a chamber, the second one is sent not at the bunch crossing from which it originated but at the subsequent one, provided that in that crossing no other segment occured. A tag bit to indicate this *second track segment* status is therefore necessary. The sector processors attempt to join track segments to form complete tracks. The parameters of all compatible segments are pre-calculated. Extrapolation windows, which are adjustable, are stored in look-up tables. Muon tracks can cross sector boundaries, therefore data are exchanged between sector processors and a cancellation scheme to avoid duplicated tracks has to be incorporated.

The track finding in η, with the goal to refine η-values, is performed by 12 η assignment units, also called Eta Track Finders (ETTF). A pattern matching rather than an extrapolation method is used, since for muon stations 1, 2 and 3 the η-information coming from the DT lo-

2008 JINST 3 S08004

cal trigger is contained in a bit pattern representing adjacent chamber areas. The tracks in η are matched with those of the ϕ-projection, if possible. For each wedge, the combined output of the PHTFs and the ETTFs, which consists of the transverse momentum including the electric charge, the ϕ- and η-values and quality for at most 12 muon candidates corresponding to a maximum of two track candidates per 30°-sector, is delivered to a first sorting stage, the Wedge Sorter (WS). There are twelve of these sorters, which have to sort at most 144 candidates in total by p_T and quality. Suppression of remaining duplicate candidates found by adjacent sector processors and track quality filtering is also performed by these units. The two highest-rank muons found in each WS, at most 24 in total, are then transmitted to the final Barrel Sorter (BS). The latter selects the best four candidates in the entire central region, which are then delivered to the Global Muon Trigger for matching with the RPC and CSC candidates.

The DTTF data are recorded by the data acquisition system. A special read-out unit, the DAQ Concentrator Card (DCC) has been developed. It gathers the data from each wedge, through six Data Link Interface Boards (DLI). Each DLI serves two wedges. The DTTF electronics is contained in three racks in the control room. Two racks contain six track finder crates, which each house the electronics for two wedges as well as a crate controller. There is also one Timing Module (TIM) in each of these crates to distribute the clock and other timing signals. The third rack houses the central crate containing the BS, the DCC, a TIM module and boards for interfacing with the LHC machine clock and the Trigger Control System.

As for the DTTF, the core components of the CSCTF are the sector processors. They receive, through optical links, the LCT data from the Muon Port Cards in the peripheral crates. Each sector processor receives up to six LCTs from ME1 and three LCTs each from stations ME2, ME3 and ME4. Up to four track segments are also transmitted from DT station MB2. First the data are latched and synchronized, and the original LCT information is converted to reflect global (η, ϕ)-coordinates. Then nearly all possible pairwise combinations of track segments are tested for consistency with a single track in the processors' extrapolation units. In contrast to the DTTF, no data exchange between neighbour processors is performed. Complete tracks are assembled from the extrapolation results and redundant tracks canceled as in the DTTF. The best three muons per processor are selected and assigned kinematic and quality parameters. The p_T assignment, through SRAM look-up tables, is based on the ϕ-information from up to three muon stations. The data are collected in a detector-dependent unit (DDU) for the read-out. The twelve sector processors are housed in a single crate in the counting room. This crate also contains a Clock and Control Board (CCB) similar to the ones in the local CSC trigger electronics, which distributes the clock, bunch crossing reset, bunch crossing zero and other timing signals. Over the custom-developed GTL+ backplane a maximum of 36 candidate tracks is transmitted to the forward Muon Sorter board, which determines the best four muons in the two endcaps and sends them to the GMT.

Global Muon Trigger

The purpose of the Global Muon Trigger [199] is to improve trigger efficiency, reduce trigger rates and suppress background by making use of the complementarity and redundancy of the three muon systems. It receives for every bunch crossing up to four muon candidates each from the DTs and barrel RPCs, and up to four each from the CSCs and endcap RPCs. The candidate information

2008 JINST 3 S08004

consists of p_T and charge, η, ϕ and a quality code. From the GCT it also receives isolation and minimally ionizing particle bits for each calorimeter region sized $\Delta\eta \times \Delta\phi = 0.35 \times 0.35$. A muon is considered isolated if its energy deposit in the calorimeter region from which it emerged is below a defined threshold. DT and CSC candidates are first matched with barrel and forward RPC candidates based on their spatial coordinates. If a match is possible, the kinematic parameters are merged. Several merging options are possible and can be selected individually for all of these parameters, taking into account the strengths of the individual muon systems. Unmatched candidates are optionally suppressed based on η and quality. Cancel-out units reduce duplication of muons in the overlap region between the barrel and the endcaps, where the same muon may be reported by both the DT and CSC triggers. Muons are back-extrapolated through the calorimeter regions to the vertex, in order to retrieve the corresponding MIP and ISO bits, which are then added to the GMT output and can be taken into account by the Global Trigger. Finally, the muons are sorted by transverse momentum and quality, first separately in the barrel and forward regions, and then together to deliver four final candidates to the GT. A read-out processor collects the input muon data and the output record. The GMT electronics is housed in the same crate as the GT (figure 8.7). The 16 muon cables are directly connected to the GMT logic board, which has a special four VME slot wide front panel. The logic itself, which is contained in FPGA chips, only occupies one slot. The MIP/ISO bits from the GCT are received and synchronized by three Pipeline Synchronizing Buffer (PSB) input modules, which are also used in the GT. The PSB boards receive the bits via 1.4 Gbit/s serial links and are mounted at the back of the crate, behind the wide logic front panel. The MIP/ISO bits are transmitted from the PSBs to the logic board by GTL+ point-to-point links on the GT backplane.

8.3 Global Trigger

The Global Trigger [200] takes the decision to accept or reject an event at L1 based on trigger objects delivered by the GCT and GMT. These objects consist in candidate-particle, such as e/γ (isolated and non-isolated), muons, central and forward hadronic jets, τ jets, as well as global quantities: total and missing transverse energies, the scalar sum (H_T) of the transverse energies of jets above a programmable threshold, and twelve threshold-dependent jet multiplicities. Objects representing particles and jets are ranked and sorted. Up to four objects are available. They are characterized by their p_T or E_T, (η, ϕ)-coordinates, and quality. For muons, charge, MIP and ISO bits are also available.

The GT has five basic stages: input, logic, decision, distribution and read-out. The corresponding electronics boards use FPGA technology [201]. All of them, as well as the boards of the GMT, are housed in one central 9U high crate, which is shown in figure 8.7. Three Pipeline Synchronizing Buffer (PSB) input boards receive the calorimeter trigger objects from the GCT and align them in time. The muons are received from the GMT through the backplane. An additional PSB board can receive direct trigger signals from sub-detectors or the TOTEM experiment for special purposes such as calibration. These signals are called *technical triggers*. The core of the GT is the Global Trigger Logic (GTL) stage, in which algorithm calculations are performed. The most basic algorithms consist of applying p_T or E_T thresholds to single objects, or of requiring the jet multiplicities to exceed defined values. Since location and quality information is available, more

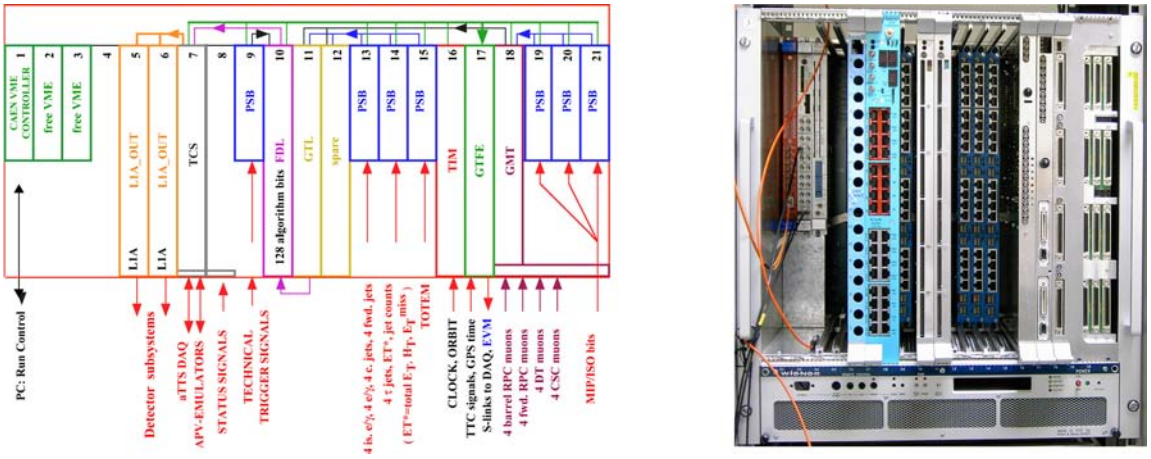

Figure 8.7: Global Trigger central crate.

complex algorithms based on topological conditions can also be programmed into the logic. A graphical interface [202] is used to set up the trigger algorithm menu. The results of the algorithm calculations are sent to the Final Decision Logic (FDL) in the form of one bit per algorithm. The number of algorithms that can be executed in parallel is 128. Up to 64 technical trigger bits may in addition be received directly from the dedicated PSB board. For normal physics data taking a single trigger mask is applied, and the L1A decision is taken accordingly. For commissioning, calibration and tests of individual subsystems up to eight final ORs can be applied and correspondingly eight L1A signals can be issued. The distribution of the L1A decision to the subsystems is performed by two L1A_OUT output boards, provided that it is authorized by the Trigger Control System described in section 8.4. A Timing Module (TIM) is also necessary to receive the LHC machine clock and to distribute it to the boards. Finally, the Global Trigger Frontend (GTFE) board collects the GT data records, appends the GPS event time received from the machine, and sends them to the data acquisition for read-out.

8.4 Trigger Control System

The Trigger Control System (TCS) [203] controls the delivery of the L1A signals, depending on the status of the sub-detector read-out systems and the data acquisition. The status is derived from signals provided by the Trigger Throttle System (TTS). The TCS also issues synchronization and reset commands, and controls the delivery of test and calibration triggers. It uses the Timing, Trigger and Control distribution network [204], which is interfaced to the LHC machine.

The TCS architecture is represented in figure 8.8. Different subsystems may be operated independently if required. For this purpose the experiment is divided into 32 partitions, each representing a subsystem or a major component of it. Each partition is assigned to a partition group, also called a TCS partition. Within such a TCS partition all connected partitions operate concurrently. For commissioning and testing up to eight TCS partitions are available, with their own L1A signals distributed in different time slots allocated by a priority scheme or in round robin mode.

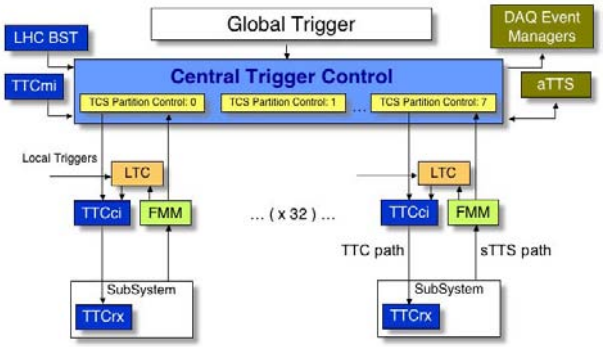

Figure 8.8: Trigger Control System architecture.

During normal physics data taking there is only one single TCS partition. Subsystems may either be operated centrally as members of a partition or privately through a Local Trigger Controller (LTC). Switching between central and local mode is performed by the TTCci (TTC CMS interface) module, which provides the interface between the respective trigger control module and the destinations for the transmission of the L1A signal and other fast commands for synchronization and control. The TTC Encoder and Transmitter (TTCex) module encodes the signals received from the TTCci and drives optical splitters with a laser transmitter. The LHC clock is received from the TTC machine interface (TTCmi). At the destinations the TTC signals are received by TTC receivers (TTCrx) containing low-jitter quartz PLLs. The Beam Synchronous Timing (BST) system of the LHC sends the GPS time.

The central TCS module, which resides in the Global Trigger crate, is connected to the LHC machine through the TIM module, to the FDL through the GT backplane, and to 32 TTCci modules through the LA1_OUT boards. The TTS, to which it is also connected, has a synchronous (sTTS) and an asynchronous (aTTS) branch. The sTTS collects status information from the front-end electronics of 24 sub-detector partitions and up to eight tracker and preshower front-end buffer emulators. The status signals, coded in four bits, denote the conditions *disconnected*, *overflow warning*, *synchronization loss*, *busy*, *ready* and *error*. The signals are generated by the Fast Merging Modules (FMM) through logical operations on up to 32 groups of four sTTS binary signals and are received by four conversion boards located in a 6U crate next to the GT central crate. The aTTS runs under control of the DAQ software and monitors the behaviour of the read-out and trigger electronics. It receives and sends status information concerning the 8 DAQ partitions, which match the TCS partitions. It is coded in a similar way as the sTTS. Depending on the meaning of the status signals different protocols are executed. For example, in case of warning on the use of resources due to excessive trigger rates, prescale factors may be applied in the FDL to algorithms causing them. A loss of synchronization would initiate a reset procedure. General trigger rules for minimal spacing of L1As are also implemented in the TCS. The total deadtime estimated at the maximum L1 output rate of 100 kHz is estimated to be below 1%. Deadtime and monitoring counters are provided in the TCS. The central board sends to the DAQ Event Manager (EVM) located in the surface control room the total L1A count, the bunch crossing number in the range from 1 to 3564, the orbit number, the event number for each TCS/DAQ partition, all FDL algorithm bits and other information.

2008 JINST 3 S08004

Chapter 9

Data Acquisition

The architecture of the CMS Data Acquisition (DAQ) system is shown schematically in figure 9.1. The CMS Trigger and DAQ system is designed to collect and analyse the detector information at the LHC bunch crossing frequency of 40 MHz. The rate of events to be recorded for offline processing and analysis is on the order of a few 10^2 Hz. At the design luminosity of $10^{34}\,\mathrm{cm}^{-2}\mathrm{s}^{-1}$, the LHC rate of proton collisions will be around 20 per bunch crossing, producing approximately 1 MByte of zero-suppressed data in the CMS read-out systems. The first level trigger is designed to reduce the incoming average data rate to a maximum of 100 kHz, by processing fast trigger information coming from the calorimeters and the muon chambers, and selecting events with interesting signatures. Therefore, the DAQ system must sustain a maximum input rate of 100 kHz, for a data flow of $\approx$ 100 GByte/s coming from approximately 650 data sources, and must provide enough computing power for a software filter system, the High Level Trigger (HLT), to reduce the rate of stored events by a factor of 1000. In CMS all events that pass the Level-1 (L1) trigger are sent to a computer farm (Event Filter) that performs physics selections, using faster versions of the offline reconstruction software, to filter events and achieve the required output rate. The design of the CMS Data Acquisition System and of the High Level Trigger is described in detail in the respective Technical Design Report [188].

The read-out parameters of all sub-detectors are summarized in table 9.1. Each data source to the DAQ system is expected to deliver an average event fragment size of $\approx$2 kByte (for pp

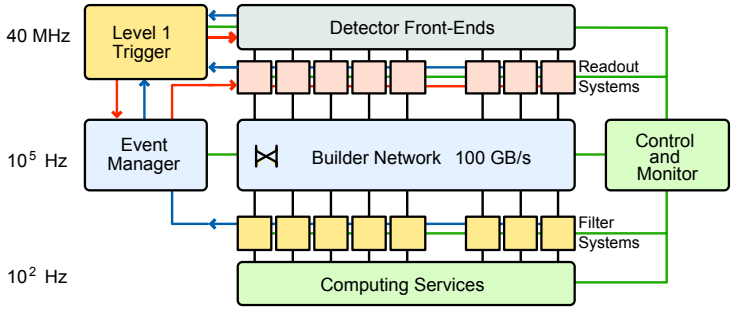

Figure 9.1: Architecture of the CMS DAQ system.

Table 9.1: Sub-detector read-out parameters.

sub-detector	number of channels	number of FE chips	number of detector data links	number of data sources (FEDs)	number of DAQ links (FRLs)
Tracker pixel	≈ 66 M	15840	≈ 1500	40	40
Tracker strips	≈ 9.3 M	≈ 72 k	≈ 36 k	440	250 (merged)
Preshower	144384	4512	1128	56	56
ECAL	75848	≈ 21 k	≈ 9 k	54	54
HCAL	9072	9072	3072	32	32
Muons CSC	≈ 500 k	≈ 76 k	540	8	8
Muons RPC	192 k	≈ 8.6 k	732	3	3
Muons DT	195 k	48820	60	10	10
Global Trigger	n/a	n/a	n/a	3	3
CSC, DT Track Finder	n/a	n/a	n/a	2	2
Total	≈ 55 M			626	458

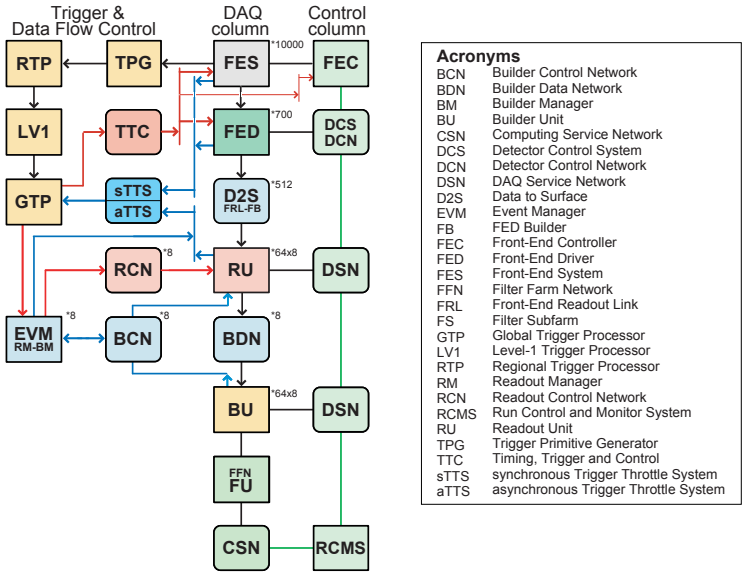

Figure 9.2: Schematic of the functional decomposition of the DAQ. The multiplicity of each entity is not shown for clarity.

collisions at design luminosity). In some case two data sources are merged in order to reach this nominal size.

A schematic view of the components of the CMS DAQ system is shown in figure 9.2. The various sub-detector front-end systems (FES) store data continuously in 40-MHz pipelined buffers. Upon arrival of a synchronous L1 trigger (3.2 μs latency) via the Timing, Trigger and Control (TTC) system [204, 207], the corresponding data are extracted from the front-end buffers and pushed into the DAQ system by the Front-End Drivers (FEDs). The data from the FEDs are read

2008 JINST 3 S08004

into the Front-end Read-out Links (FRLs) that are able to merge data from two FEDs. The number of FRLs corresponding to the CMS read-out parameters of table 9.1 is 458. In the "baseline" configuration, there are 512 FRLs. These additional inputs are used for combined operation with the TOTEM experiment [2], and for inputs from local trigger units, among others. The sub-detector read-out and FRL electronics are located in the underground electronics room (USC).

The event builder assembles the event fragments belonging to the same L1 from all FEDs into a complete event and transmits it to one Filter Unit (FU) in the Event Filter for further processing. The event builder is implemented in two stages (referred to as FED-builder and RU-builder) and comprises a number of components, which are described below (section 9.4). The DAQ system can be deployed in up to 8 *slices*, each of which is a nearly autonomous system, capable of handling a 12.5 kHz event rate. The event builder is also in charge of transporting the data from the underground to the surface building (SCX), where the filter farm is located.

The DAQ system includes back-pressure all the way from the filter farm through the event builder to the FEDs. Back-pressure from the down-stream event-processing, or variations in the size and rate of events, may give rise to buffer overflows in the sub-detector's front-end electronics, which would result in data corruption and loss of synchronization. The Trigger-Throttling System (TTS) protects against these buffer overflows. It provides fast feedback from any of the sub-detector front-ends to the Global Trigger Processor (GTP) so that the trigger can be throttled before buffers overflow. During operation, trigger thresholds and pre-scales will be optimized in order to fully utilize the available DAQ and HLT throughput capacity. However, instantaneous fluctuations might lead to L1 trigger throttling and introduce dead-time. CMS has defined a *luminosity section* as a fixed period of time (set to 2^{20} LHC orbits, corresponding to 93 s), during which trigger thresholds and pre-scales are not changed. The GTP counts the live-time (in numbers of bunch crossings) for each luminosity section and records them in the Conditions Database for later analysis.

The required computing power of the filter farm to allow the HLT algorithms to achieve the design rejection factor of 1000 is substantial and corresponds to O(1000) processing nodes. At the LHC luminosity of $2 \times 10^{33}\,\mathrm{cm}^{-2}\mathrm{s}^{-1}$ it is foreseen to operate at a maximum L1 rate of 50 kHz, corresponding to 4 installed DAQ slices. It has been estimated [189] that under these conditions the HLT algorithms will demand a mean processing time of around 50 ms on a 3-GHz Xeon CPU-core. This implies for the 50-kHz DAQ system that an equivalent of about 2500 CPU-cores must be deployed for the HLT. After optimising the trigger selection for the LHC design luminosity, the estimated required computing power is expected to be roughly twice as much for 8 DAQ slices operating at a 100 kHz L1 rate.

For the first LHC run, the Event Filter is foreseen to comprise 720 PC-nodes (with two quad-core processors) for 50 kHz operation. Based on initial experience and evaluation of candidate hardware, the additional filter farm nodes for 100 kHz operation at design luminosity will be procured. The design of the DAQ system allows for this gradual expansion in event building rate and processing.

9.1 Sub-detector read-out interface

The design of the FED is sub-detector specific, however, a common interface from the FED to the central DAQ system has been implemented. The hardware of this interface is based on S-

2008 JINST 3 S08004

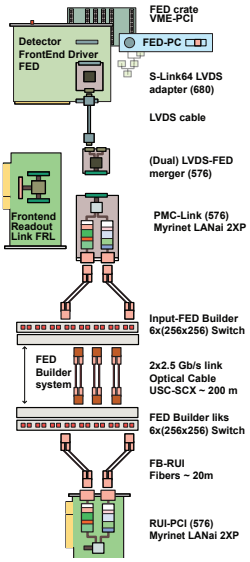

Figure 9.3: Diagram of a generic sub-detector read-out into the FED builder.

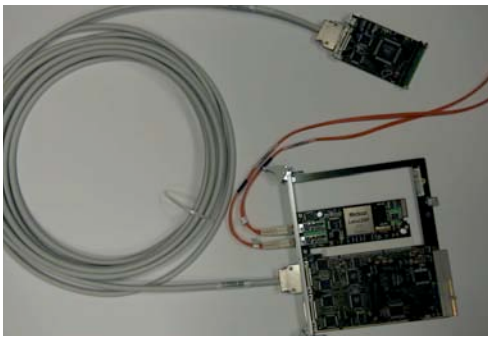

Figure 9.4: Photograph of S-link64 sender card, LVDS cable and compact-PCI FRL card with embedded LANai2XP NIC. Connected to the NIC are fibres that go to the FED Builder input switch.

Link64 [208]. The FED encapsulates the data received from the front-end electronics in a common data structure by adding a header and a trailer that mark the beginning and the end of an event fragment. The header and trailer partially consists of event information used in the event building process, such as the event number derived from the TTC L1A signals. The trailer includes a CRC (Cyclic Redundancy Check) of the data record. The payload of the event fragments is only inspected in the Event Filter.

The physical implementation of one element of the sub-detector read-out interface and its FED builder port is shown in figures 9.3 and 9.4.

The S-Link64 Sender card

The S-Link64 Sender card is a custom developed Common Mezzanine Card (CMC), directly plugged into the sub-detector FED. It receives data from the FED via an S-Link64 port and checks the CRC in order to check transmission errors over the S-Link. The card is able to buffer up to 1.6 kByte of data before generating back-pressure to the FED. The CMC has an LVDS converter to interface with a copper cable which can have a maximum length of 11 m. This cable (Multi-conductor round cable v98 manufactured by 3M) comprises 14 twisted pairs, which are individually shielded. The link provides feedback lines in order to signal back-pressure and to initiate an automatic self test. The nominal data transfer rate over the LVDS cable is 400 MByte/s (50 MHz clock, 64 bits), which is twice the maximum sustained design throughput of the DAQ system.

2008 JINST 3 S08004

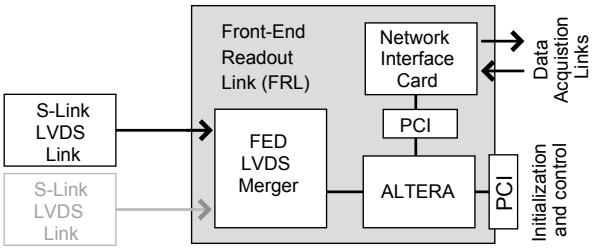

Figure 9.5: FRL layout.

The Front-end Read-out Link

The FRL is a custom 6U Compact-PCI card (figure 9.5). It has three interfaces: an input interface which handles up to two LVDS cables; an output interface to the FED Builder implemented as a 64-bit/66-MHz PCI connector for a Network Interface Card (NIC); and a configuration and control interface which is a PCI bus interface connected to the Compact-PCI backplane. The function of the FRL board is performed by two FPGAs (Altera EP20K100EFC324-1 for the PCI bridge and EP1S10F672C6 for the main logic).

The FRL receives event fragments and checks the CRC in order to check transmission errors over the LVDS cable. In the case where the FRL receives data from two FEDs, the two data records are merged. Data are buffered in memories of 64 kByte size and pushed into the NIC in fixed size blocks via the onboard PCI bus.

The FRL card also provides monitoring features, such as the ability to spy on a fraction of events via the Compact-PCI bus, and to accumulate histograms of quantities such as fragment size.

Up to 16 FRL cards are placed in a crate with a Compact-PCI backplane. Each crate is connected to a PC via a compact PCI bridge (StarFabric CPCI/PCI system expansion board from Hartmann Elektronik), which is used for configuration, control and monitoring. There are 50 FRL crates in total.

9.2 The Trigger Throttling System and sub-detector fast-control interface

The TTS provides the feedback from all FEDs and their associated front-end systems to the GTP. It is a hardwired system, acting on the dataflow with a reaction time of less than 1 μs. Each FED provides fast signals indicating the state of the read-out. The states *Ready, Warning, Busy, Out-Of-Sync* and *Error* are defined (listed in order of increasing priority). Ready, Warning and Busy are generated according to the amount of internal data buffering available and are used to indicate if more triggers can be accepted. Given the trigger rules (section 8.4) and a TTS latency of 1 μs, a FED has to be able to accept 2 more triggers after asserting Busy state. Out-Of-Sync and Error indicate that synchronization was lost or an error occurred in the front-end electronics. The GTP attempts to recover automatically from these states by issuing a L1-Resync or L1-Reset command

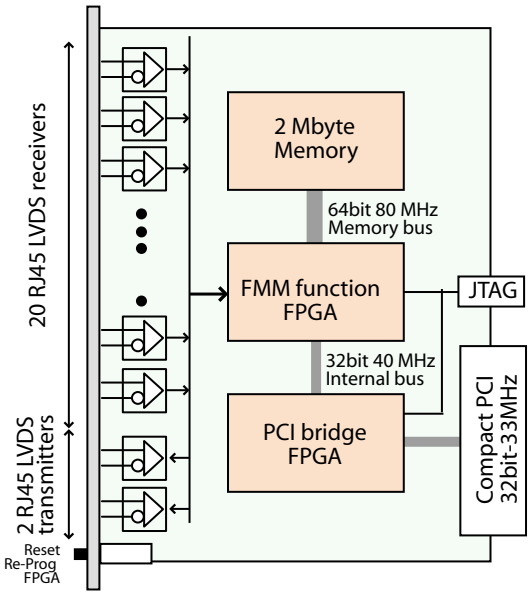

Figure 9.6: Block diagram of the FMM.

Figure 9.7: Photograph of a FMM module.

via the TTC system. These fast TTS signals are transmitted over shielded RJ-45 cables with four twisted pairs using the LVDS signaling standard.

The Fast Merging Module

For flexibility, FEDs are grouped into 32 TTC partitions which may be operated independently of each other. The Level-1 Trigger Control System separately distributes triggers to these 32 TTC partitions and separately receives trigger throttling signals for each TTC partition. TTS signals from all FEDs in a TTC partition thus need to be merged with low latency. Dedicated Fast Merging Modules (FMMs), have been designed for this task. These modules can merge and monitor up to 20 inputs and have quad outputs. Optionally, FMMs can be configured to merge two independent groups of 10 inputs with two independent twin outputs. For partitions with more than 20 FEDs, FMMs are cascaded in two layers.

The FMM is a custom-built 6U compact-PCI card (figures 9.6 and 9.7). It has three main components: a PCI Interface FPGA, a main logic FPGA and an on-board memory block. The 80 MHz internal clock of the FMM is not synchronized to the LHC clock. Input signals are synchronized to the internal clock by requiring two successive samples in the same state. The input signals are then merged by selecting the highest priority input signal from the enabled inputs according to the signal priorities listed above. Optionally, Out-of-Sync input signals are only taken into account if the number of inputs in Out-of-Sync state exceeds a programmable threshold.

The FMM also provides extensive monitoring capabilities in order to diagnose the causes for dead-times. Each state transition at the inputs is detected and stored with a time-stamp (25 ns resolution) in a circular buffer memory that can hold up to 128 k transitions. The times spent in the states Warning and Busy are counted with 25 ns resolution for each input channel and for the output(s).

2008 JINST 3 S08004

FMM cards are configured, controlled and monitored by a PC via a compact-PCI interface (StarFabric CPCI/PCI system expansion board from Hartmann Elektronik). The total system comprises 8 FMM crates with up to 9 FMMs in each crate. A total of 60 FMM modules are needed in order to merge the TTS signals of all TTC partitions of CMS.

9.3 Testing

In order to test and commission the central DAQ system independently of the GTP and of the subdetector DAQ systems, a number of additional components have been developed. These are not used in standard data taking.

The Global Trigger Processor emulator (GTPe) [205] emulates the functionality of the GTP (see figure 9.2). It reproduces the LHC beam structure, generates random or clocked triggers up to 4 MHz, respects the trigger rules, applies partitioning, transmits the GTPe data fragment over S-Link64 and receives and handles sTTS and aTTS backpressure signals. The hardware implementation is based on the Generic-III PCI card [206] and an interface module GTPe-IO.

In normal data taking mode, triggers from the global trigger are distributed to the FEDs via the TTC. When using the GTPe, special test triggers are sent directly to the FRL crates via a lemo cable to a trigger distributer card which distributes the trigger over the backplane to all the FRLs in the crate. Because the FEDs are not being used in this mode, busy signals from the FRLs are collected by the trigger distributer card and sent to a dedicated set of FMM modules for fast merging of this subset of sTTS signals. A dedicated mode of the FRL firmware handles the GTPe test triggers and instead of reading out the FEDs, the FRL generates data fragments with sizes according to a predefined table. In this way, the full central DAQ system can be tested.

9.4 The Event Builder

A schematic view of the Event Builder system is shown in figure 9.8. The event builder is composed of two stages: the FED-builder and the RU-builder. Each of the ≈512 FRLs generate event fragments with an average size of ≈2 kByte and the FED-builder is in charge of transporting these fragments to the surface building (SCX) and assembling them into 72 super-fragments with an average size of ≈16 kByte. The super-fragments are then stored in large buffers in Read-out Units (RU), waiting for the second stage of event building (RU-builder), which is implemented with multiple 72×72 networks. There can be up to 8 RU-builders, or DAQ slices, connected to the FED-builder layer. Each FED-builder is in charge of distributing the super-fragments, on an event by event basis, to the RU-builders and ensures that all super-fragments corresponding to one event go to one and only one DAQ slice, and are read by one Builder Unit (BU) of the RU-builder network. The complete event is then transferred to a single unit of the Event Filter. By utilising an architecture with two-stage event building, the full size system can be progressively deployed slice by slice while the traffic load to the second stage is optimized. The event builder is implemented with commodity equipment, including processing nodes, network switches and network interfaces. The processing nodes are server PC's with PCI busses to host the NICs. They run the Linux operating system.

2008 JINST 3 S08004

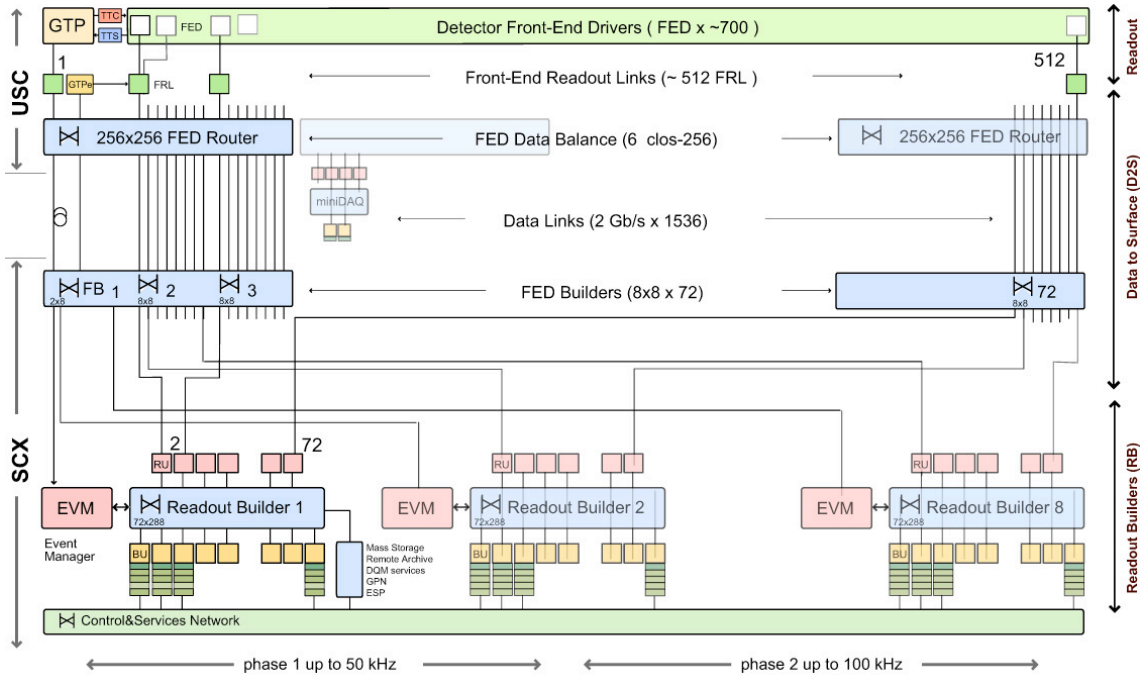

Figure 9.8: Schematic view of the Event Builder.

The event builder is lossless and when necessary back-pressure is propagated up to the FRL and subsequently to the FED, which can throttle the trigger via the TTS.

The FED-Builder stage

The FED Builder is based on Myrinet [209], an interconnect technology for clusters, composed of crossbar switches and NICs, connected by point to point bi-directional links. It employs wormhole routing and flow control at the link level. The LANai ASIC on the NIC contains an embedded RISC processor.

The FED-builder stage is implemented using multiple $N \times M$ FED-builders. In the baseline configuration, $N \leq 8$ and M equals the number of DAQ slices, which is 8 for the full system. In general, one $N \times M$ FED-builder comprises N input NICs hosted by the FRL, M output NICs hosted by the RU PCs, and two independent $N \times M$ switches to form 2 rails (figure 9.9). The NIC (M3F2-PCIXE-2 based on the LANai2XP) has two bi-directional fibre optic ports, with 2 Gbit/s data rate each. Each rail of one NIC is connected to an independent switch. In practice, instead of a large amount of small physical switches, a single large switching fabric is used per rail (see below). This 2-rail configuration doubles the bandwidth to 4 Gbit/s per FRL and provides redundancy.

The software running on the NICs has been custom developed in the C language. The FED-builder input NICs are programmed to read fragments from the FRL and to send them to the switch fabric, with a destination assigned on the basis of the fragment event number and a predefined look-up table. The FED-builder output NICs are hosted by the RU-builder PCs. They are programmed to concatenate fragments with the same event number from all the connected input cards,

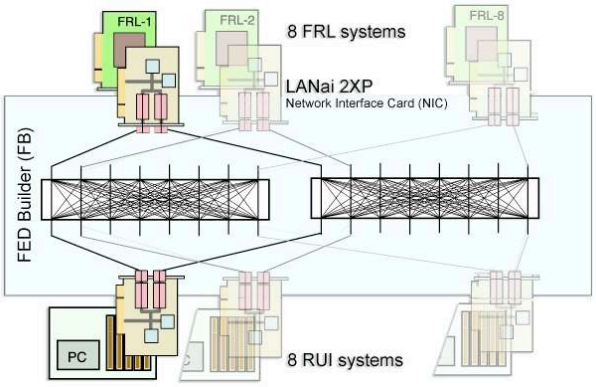

Figure 9.9: 8×8 FED builder with a two-rail network.

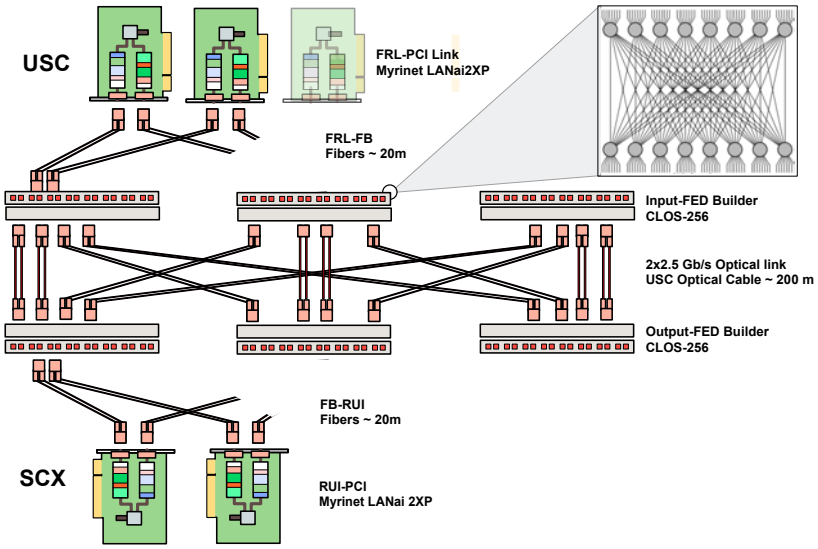

Figure 9.10: The FED builder stage switching fabric (only 1 rail is shown).

in order to build the super-fragments. The FED-builder is lossless due to a basic flow control and retransmission protocol, implemented on the RISC processor on the NIC.

The physical switching fabric is composed of six Clos-256 enclosures per rail (figure 9.10). A Clos-256 enclosure is internally composed of two layers of 16×16 (Xbar32) cross-bars. Three Clos-256 enclosures are located in the underground electronics room (USC), while the other three are in the surface DAQ building (SCX). They are connected by 768 200 m optical fiber pairs per rail, bundled in 12 cables. The Clos-256 enclosures are partly populated with linecards. Currently, the system has ports to accommodate a total of 576 FRLs and 576 RU PCs. In the baseline it is configured as 72 times 8×8 FED-builders. The use of a large switching fabric allows for a high

2008 JINST 3 S08004

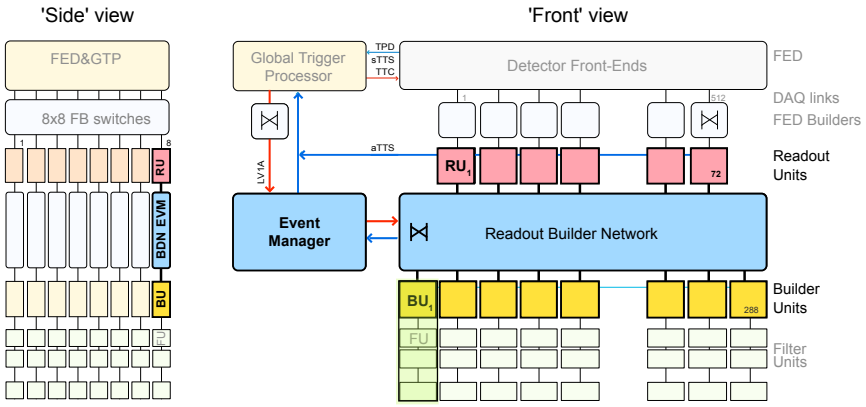

Figure 9.11: A Read-out Builder slice.

re-configurability of the FED-builders in software, which enables traffic balancing by redefining the super-fragment composition and traffic rerouting in case of a hardware failure.

The Myrinet NIC can transfer 4.0 Gbit/s data rate over the two optical rails. For random traffic the network efficiency is approximately 60%, due to head-of-line blocking. An event building throughput of about 300 MBbyte/s per node is achieved for variable sized fragments with a nominal average of 2 kBytes by using two rails [210]. Hence, the sustained aggregate throughput through the FED-builder stage is ≈1.4 Tbit/s, satisfying the CMS DAQ requirements. A maximum peak throughput of ≈2 Tbit/s is possible, if fully exploiting the FRL and Myrinet bandwidth, and using traffic shaping in the FED-builders.

The RU-builder stage

The RU-builder stage assembles super-fragments into complete events. Each RU-builder must collect event superfragments of average size ≈16 kByte from 72 data sources and build them into complete events at a rate of 12.5 kHz. A diagram of one slice of the RU-builder, indicating its various components is shown in figure 9.11. A RU-builder is made up of a number of Read-out Units (RU), Builder Units (BU) and a single Event Manager (EVM) connected together by a switching network. The EVM supervises the data flow in the RU-builder and receives a data record from the GTP via a dedicated FED-builder. The EVM allocates events on request to a BU, which subsequently collects the super-fragments from all RUs. From the BUs the complete events are sent to the Filter Units (FU).

In the baseline configuration the number of RUs per RU-builder is 72 and there is a factor of 4 more FU nodes. The RU, BU and EVM software components can be distributed in various ways on the PC nodes. In the baseline, there are two layers of PCs: RUs and BU-FUs. Here, the events are built by the BU software component in the same PC that runs the filter unit (FU) software, referred to as BU-FU. The RU nodes are server PCs with two 2 GHz dual-core Xeon processors (e5120) and 4 GByte of main memory (Dell PowerEdge 2950). They host a Myrinet NIC (M3F2-PCIXE-2) for the input from the FED-builder and a 4-port GbE NIC (PEG4I-ROHS Quad port copper Gigabit

Ethernet PCI Express Server Adapter from Silicom Ltd.). In the baseline, two links of the 4-port NIC are cabled to the network switch, which is sufficient to satisfy the throughput requirement of at least 200 MByte/s per RU node. A single ethernet link for each BU-FU node is sufficient, as the required throughput is 50 MByte/s. The EVB switching network is implemented with eight E-1200 switches (Terascale E-1200 router from Force10), one per DAQ-slice.

The RU-builder is based on TCP/IP over Gigabit Ethernet. The design choice of TCP/IP over Gigabit Ethernet has the advantage of using standard hardware and software. When operating an event builder over Ethernet close to wire speed, typically packet loss occurs because hardware flow control is not propagated from end-point to end-point through the switches. TCP/IP provides a reliable transport service that removes the need for the event building application to detect and deal with lost packets. It also provides flow control and congestion control. TCP/IP uses a substantial amount of host resources. Roughly 20% of a 2 GHz Xeon CPU core is required to transmit 1 Gbit/s, when using jumbo-frames (MTU=9000 Bytes).

For the event builder with 2 Ethernet links per RU node, a throughput of ≈240 MByte/s per RU node has been achieved at the nominal super-fragment size of 16 kBytes [211]. This can be increased, if needed for higher trigger rate or larger event sizes, to ≈360 MByte/s per RU node by installing a third Ethernet link per RU node. At a nominal throughput of 60 MByte/s, corresponding to 1/4 of the RU throughput, the event building tasks consume roughly 10% of the CPU resources on the BU-FU event filter nodes.

9.5 The Event Filter

The primary goal of the Event Filter complex is to reduce the nominal Level-1 Trigger accept rate of 100 kHz to a manageable level for the mass storage and offline processing systems while preserving interesting physics events and not introducing additional experiment dead-time.

The Event Filter complex:

- collects events accepted by the Level-1 Trigger system from the Event Builder and distributes them to worker nodes for further processing;
- performs basic consistency checks on the event data;
- runs offline-quality reconstruction modules and filters to process and select events for storage (High Level Trigger, “HLT”);
- generates, collects, and distributes Data Quality Monitoring (DQM) information resulting from online event processing in the HLT;
- serves a subset of the events to local and remote online consumers (EventServer, ES) for calibration and DQM;
- routes selected events to local storage in several online streams according to their trigger configuration;
- transfers data from local storage at the CMS site to mass storage in the CERN data centre at the Meyrin site.

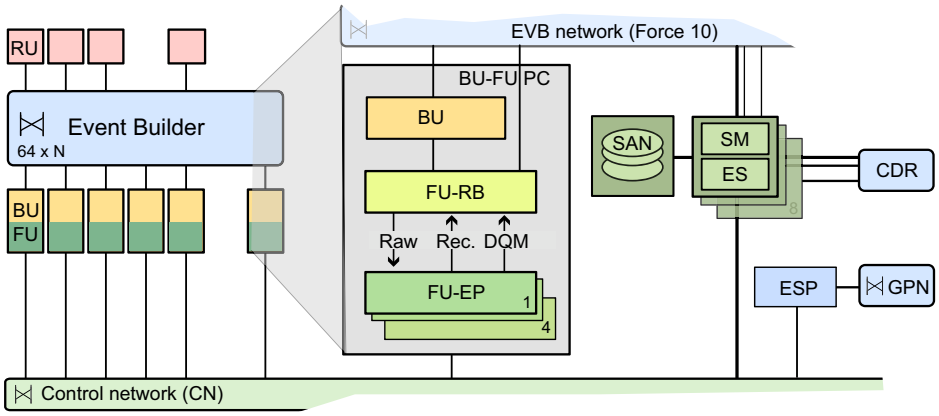

Figure 9.12: Architecture and data flow of the Filter Farm.

Architecture and data flow

The architecture of the CMS Event Filter is schematically illustrated in figure 9.12. The Event Filter hardware consists of a large farm of processors (on the order of 1000), running the HLT selection (Filter Farm), and a data logging system connected to a Storage Area Network (SAN). The Builder Unit (BU), belonging to the event builder, delivers complete events to one of multiple copies of the Filter Unit Event Processors (FU-EP) via the Filter Unit Resource Broker (FU-RB). A logically separate switch fabric provides the connectivity from the Filter Units to the data logging nodes. These data logging nodes are connected to a Fibre-Channel SAN, that is capable of a peak bandwidth of 1 GByte/s and has a capacity of several hundred TBytes.

The filter farm is logically subdivided into groups of processing nodes (Builder/Filter Unit, BU-FU). Each BU-FU hosts an identical set of software modules in a distributed environment based on the XDAQ online framework (section 9.7). As mentioned above, there are three separate applications, the Builder Unit (BU), the Filter Unit "Resource Broker" (RB) and the Event Processor (EP). The RB is responsible for managing memory resources for input and output to/from the HLT processes, and the communication with the Event Builder and the data logger. A complete event is handed by the RB, upon request, to the Event Processor (EP). The EP process uses the CMS reconstruction framework (CMSSW) [212] to steer the execution of reconstruction and selection code forming the HLT selection. Multiple EP processes can coexist in a single processor to provide concurrent execution and thus saturate the processing CPU resources.

Event processing

The EP reconstruction and selection algorithms are configured at the start of each data-taking run, by a configuration management system based on Oracle and working under run control supervision. The reconstruction, selection, and analysis modules specified in the configuration are instructed to obtain calibration constants and other time-dependent information from an Oracle database using standard access methods supported by the reconstruction framework.

2008 JINST 3 S08004

Each reconstruction or selection algorithm runs in a predefined sequence, starting from raw data unpacking modules, which deal with sub-detector specific raw-data formats. The binary raw-data is formatted into C++ objects associated with sub-detector channels through a channel map using the FED block identifiers. Reconstruction modules can attach reconstructed objects to the event data structure. A full history of the execution of the HLT is attached to each accepted event. In addition, bookkeeping information is maintained by each EP process, and periodically collected by a supervising system to provide full accounting of events accepted and rejected by each HLT path. When a decision is reached, accepted events, comprising raw data and event reconstruction information produced by the HLT, are handed back to the RB for transfer to the data logging process.

Monitoring

The operation of unpacking and reconstruction modules running in the Event Processors is monitored using the Physics and Data Quality Monitoring infrastructure (DQM). Additional analysis modules may be executed in the process, outside the normal selection sequences, to provide fast feedback about the quality of the data using the same infrastructure. Information collected by the DQM on the individual FU nodes is periodically forwarded to the data logging system via the RB, providing a DQM Collector functionality (DQMC).

Data logging and Event Server

Events accepted for storage by one of the EP processes are transmitted to the RB, which forwards them to the Storage Manager (SM) process running in the data logger nodes via the data logging network. The SM is responsible of managing the various online streams to provide an appropriate granularity of event data for transfer, processing and bookkeeping. The data logger supports both disk streams for physics or calibration data, and network streams for the usage of consumer processes carrying out calibration or monitoring tasks. The network streams are created "on demand" by a consumer process connecting to the EventServer (ES) function of each SM. In normal operation with multiple SMs, the ES is multiplexed across the various sub-farm SMs by a caching Event Server Proxy (ESP). File and network streams can deal transparently with event data or DQM data.

Each data logger node hosting a SM is responsible for direct management of its disk pool in the storage area network. This includes correct interleaving of write transactions of the SM and data transfer, via the Central Data Recording (CDR) network to the offline systems for analysis and distribution to remote sites.

9.6 Networking and Computing Infrastructure

Networking Infrastructure

The general networking infrastructure of the experiment is based on Ethernet and is separated into:

- CMS Technical Network (CMS-TN);
- CERN general purpose network (CERN-GPN);

- Connection to the Central Data Recording (CDR);
- LHC technical network (LHC-TN).

These four networks are interconnected. In addition there are the dedicated DAQ event building networks (Myrinet and Ethernet) and dedicated networks for equipment control which have no connection to any of those four.

The CMS-TN is a general purpose network connecting all machines directly related to the operation of the experiment. It is used for system administration of all computers and for configuration, control and monitoring of all online applications. This network is not accessible directly from outside, but can be reached through dual-homed Application Gateway (AG) machines, which have one connection to CMS-TN and one to CERN-GPN switches. The CMS-TN is implemented as a distributed backbone with two routers located in SCX, and two in USC. Typically all computers in a rack are served by a switch in that rack. Each switch has two Gigabit Ethernet uplinks to the backbone routers. The desktop computers in the control room are also connected to the CMS-TN.

The CERN-GPN is the CERN-site network. The GPN will be used at all places to connect visitors (wired or wireless), who will use the application gateways to connect to the CMS-TN. This network will typically provide 1 Gbit/s connections to the GPN backbone.

The CDR connects to the Tier0 (chapter 11) system at the CERN Meyrin site using a minimum of 10 Gbit/s. A set of 8 triple-homed servers (one connection on the DAQ, one to CERN-TN, one on the CDR switches) are dedicated to this task. These are the Storage Manager nodes.

The LHC-TN allows data exchange between some of the CMS equipment and the LHC controls. The CMS-TN interconnects with the CERN-GPN and the LHC-TN using a filter implemented in the backbone routers.

Computing infrastructure

As previously discussed, the DAQ system comprises thousands of computing nodes. These are all rack mounted PCs. All PCs are Intel x86 based, running the CERN distribution of the Redhat Linux OS. The PC cluster includes a global file server and other services to be able to operate independently from the CERN-GPN. System installation is done with the Quattor toolkit [213]. In addition around a hundred PCs are used for DCS, running Microsoft Windows.

Database services are provided by a 6-node Oracle Real Application Cluster.

9.7 DAQ software, control and monitor

As stated previously, the CMS DAQ is designed in a way such that its hardware implementation can be staged as the LHC accelerator luminosity increases as well as the experiment's need for higher throughput. Thus the CMS DAQ online software must be highly scalable and must also support a diverse hardware base. The online software encompasses a distributed processing environment, data acquisition components, the run control and the detector control system. All subsystems of the DAQ have adopted the central online software frameworks with the philosophy of using common and standardized software technologies in order to reduce the effort associated with the maintenance and evolution of the detector read-out system over the long lifetime of the experiment.

2008 JINST 3 S08004

XDAQ Framework

The XDAQ (Cross-Platform DAQ Framework) framework [214] is designed for the development of distributed data acquisition systems. XDAQ includes a distributed processing environment called the "executive" that provides applications with the necessary functions for communication, configuration control and monitoring. Written entirely in C++, it provides applications with efficient, asynchronous communication in a platform independent way, including the use of memory pools for fast and predictable buffer allocation, support for zero-copy operation and a dispatching mechanism for an event-driven processing scheme. A copy of the executive process runs on every processing node in the data acquisition network.

XDAQ Applications are modeled according to a software component model [216] and follow a prescribed interface. They are compiled and the object code is loaded and configured dynamically at run-time into a running executive using the XML schema [221]. Multiple application components, even of the same application class, may coexist in a single executive process.

All configuration, control and monitoring can be performed through the SOAP/http [217] protocol, widely used in Web enabled applications. A rich set of data structures, including lists, vectors and histograms are exportable and can be inspected by clients through the executive SOAP services. Additional utility components provide support for hardware and database access.

XDAQ Applications and Libraries

XDAQ components [219] developed for CMS include applications such as the distributed Event Builder (EVB), sub-detector electronics configuration and monitoring components (FEC and FED), and central DAQ applications.

The generic event builder application consists of the main XDAQ components: a read-out unit (RU), a builder unit (BU) and an event manager (EVM). Data that are recorded by custom read-out devices are forwarded to the read-out unit application. A RU buffers data from subsequent single events until it receives a control message to forward a specific event fragment to a BU. A BU collects the event fragments belonging to a single event from all the RUs and combines them into a complete event. The BU provides an interface to the event data processors that apply event-filtering algorithms and provide data persistency (section 9.5). The EVM interfaces to the trigger read-out electronics and so controls the event building process by mediating control messages between RUs and BUs. For efficient transmission of binary (i.e. event) data the I2O specification [218] is followed. The event builder is a generic application that can run on a wide range of underlying hardware and is also used in local data acquisition systems, such as sub-detector test beams [215].

Data transmission in the XDAQ programming environment is carried out by special application components named peer transports. Peer transports register themselves with the XDAQ executive as being capable of resolving addresses as well as transmitting and receiving data. Communication between XDAQ applications is then accomplished by using an executive function that, when invoked, redirects the outgoing message to the proper peer-transport that in turn delivers the data over the associated medium. In this way the framework is independent of any transport protocol or network and can be extended at any time to accommodate newly appearing communication technologies. Baseline peer transports have been implemented for efficient binary data transmission using an asynchronous TCP/IP protocol and for simple message handling using the

2008 JINST 3 S08004

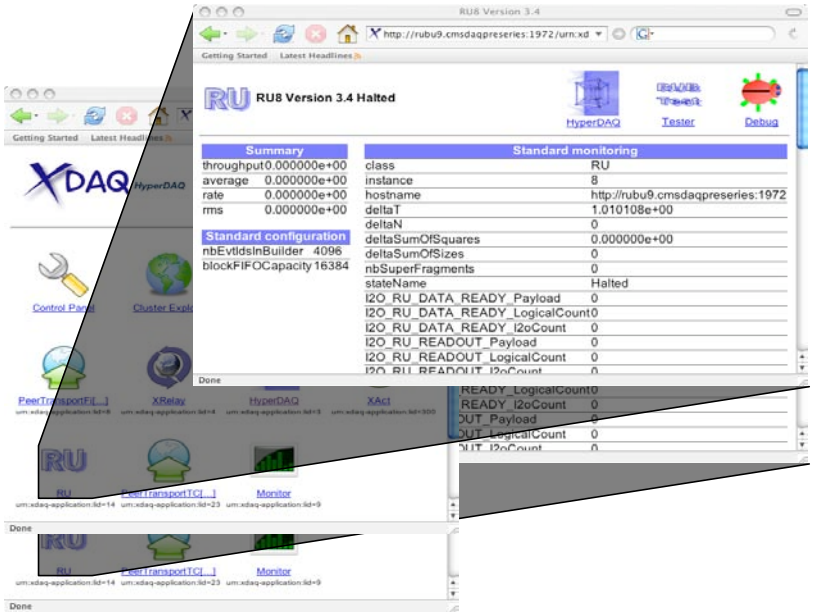

Figure 9.13: Example HyperDAQ page. Clicking on the RU application in the HyperDAQ page brings up monitoring information for the Read-out Unit application.

SOAP XML message format, however the framework is independent of the peer transport used, so optimisation of this layer is transparent to the rest of the XDAQ applications.

Libraries and device drivers have been developed that provide generic user access to VME and PCI modules and support Myrinet. Additional XDAQ components include support for the CMS custom front end devices, persistent monitoring message support and a gateway application to interface the XDAQ SOAP environment to the Detector Control System (section 9.8).

HyperDAQ

An extension to the XDAQ framework, HyperDAQ [220], exploits the http protocol which creates an entry point into XDAQ executives. A combination of HyperDAQ and Peer-to-Peer technology, used to discover new XDAQ applications providing data content, presents to the user links to the data content providers as they become available (figure 9.13). In this way, any node in the distributed online cluster can become an access point from which the entire distributed system can be explored by navigating from one application to another as the links become available. The HyperDAQ system has proved to be invaluable in debugging and monitoring the DAQ during full system integration tests.

Run Control System

The Run Control System configures and controls the online applications of the DAQ components and interfaces to the Detector Control Systems. It is an interactive system furnishing diagnostic

2008 JINST 3 S08004

and status information and providing the entry point for control. There are O(10000) applications to manage, running on O(1000) PCs.

The Run Control structure is organized into eleven different sub-systems, with each sub-system corresponding to a sub-detector or self-contained component, e.g. the Hadron Calorimeter, central DAQ or global trigger. The Run Control and Monitoring System (RCMS) framework, provides a uniform API to common tasks like storage and retrieval of process configuration data, state-machine models for process control and access to the online monitoring system.

Run Control applications and services are implemented in Java as components of a common web application "RCMS" provided by the framework. The Run Control is designed as a scalable and distributed system to run on multiple machines, thus the system can be easily expanded by adding additional hardware.

In RCMS the basic unit is the Function Manager (section 9.7). The interfaces are specified with the Web Service Description Language (WSDL) using the Axis [222] implementation of Web Services (WS). Various Web Service clients including Java, LabView and Perl have been implemented to provide access to the Run Control services. The publicly available official reference implementation of the Java Servlet technology Tomcat [223], by the Apache Software Foundation, has been chosen as the platform to run the Run Control web-applications. For persistency both Oracle and MySQL are supported by the RCMS framework.

For the baseline DAQ system, ten PCs running Linux are sufficient to control the experiment. A special copy of the XDAQ executive, the job control, is always running on each online node to accept SOAP commands from the run control to start and configure additional XDAQ executives. One common database (Oracle) is shared by all online processes and RCMS installations. Configuration management across sub-systems is achieved using global configuration keys (section 9.7).

The services and tools provided by RCMS comprise:

- Function Manager Framework;
- Resource and Account Management Services;
- Configurator;
- Log Message Collector.

In the following a few key components of Run Control are discussed.

Function Manager

A hierarchical control tree, with a central controller on the top and one or more controllers for each sub-system, structures the flow of commands and state information. The controllers are written using a common design paradigm, the so-called "Function Manager" (FM).

The FM has available a finite state machine, an interface for remote invocation, and a set of services to start, configure and control remote processes and to access configuration information from a DBMS. The FM is the basic element in the control tree. A standardized state machine model has been adopted by the sub-system for the first level of FMs which are directly steered by the central controller in the control tree (figure 9.14).

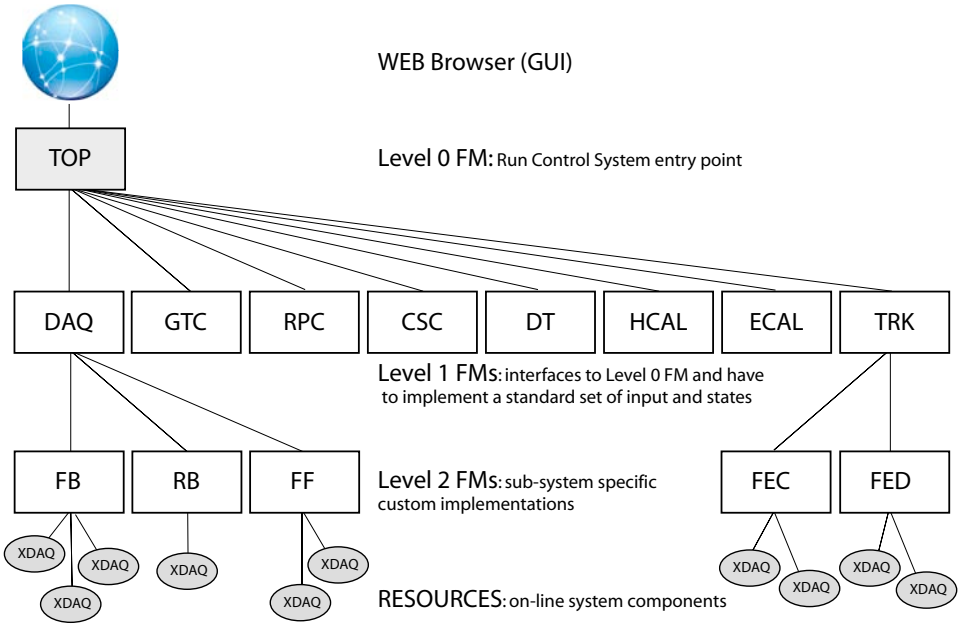

Figure 9.14: The RC hierarchy showing the full DAQ system. The Top Function Manager controls the next layer (Level 1) of Function Managers who in turn control the Level 2 (sub-detector level) Function Managers. The sub-detector Function Managers are responsible for managing the online system component resources.

Resource and Account Management Services

The Resource Service (RS) stores all information necessary to start and configure the online processes of the DAQ and sub-detectors. The data is represented as Java objects which are made persistent in the DBMS both as blobs and optionally as relational tables. RCS views the experiment as a collection of configurations, where a configuration is one or more groups of resources and one or more function manager implementations for control. The configuration is specific to each sub-system. Each sub-system has its own schema instance of the RS in the DBMS. The resource definition of a run is then the set of configurations of all participating sub-systems. The configuration of a given sub-system is resolved via a key mechanism. The sub-systems register a "configuration key" to a given global key identifying the configuration of the global run. All changes to configurations and global keys are versioned and trackable.

Users have to be authenticated to get access to the RCS resources. The resource service manages the configurations based on RCMS user accounts. Multiple configurations by multiple users can be run simultaneously in the same instance of the RCMS web-application.

Configurator

In order to create central DAQ configurations for different data taking scenarios, the CMS DAQ configurator application has been developed. The configurations can be tailored for reading out

2008 JINST 3 S08004

specific sub-sets of FEDs with specific throughput requirements, using different FED-Builder configurations and different sub-sets of the available event builder hardware. The configurations can be adapted to different versions and parameter settings of the online software components. The process of parametrising tens of thousands applications on thousands of hosts is largely simplified by factorizing the structure of the DAQ system and of the software settings. The structural representations of the DAQ configurations are stored in the CMS DAQ hardware and configuration database which also holds a representation of the available hardware components and their connectivity. Templates of software parameters for all software components are stored in a separate software template database. The CMS DAQ configurator application reads from both databases. It automatically calculates application parameters such as those depending on the connectivity information of the underlying hardware and creates the Java objects of the Resource Service. XML configuration files for the XDAQ executive processes are generated from these Java objects and stored in the Resource Service database. The CMS DAQ configurator application can also be used to generate configurations for test-bed hardware.

Log Message Collector

The Log Message Collector (LMC) is a web application to collect logging information from log4j and log4c compliant applications. The LMC has receiver modules for log4c messages used with C++ applications and log4j messages used with Java applications in XML and in binary format. Appender modules are implemented for TCP socket, TCP socket hub and JMS connections. Log messages can be stored on files with a File Appender, or in a DBMS with a DB Appender. Appenders can be active concurrently. Log messages are filtered by severity in the appender modules.

Each subsystem has its own instance of a LMC. A central LMC concentrates the messages of the subsystems and forms the entry point for the visualization client of messages, e.g. the Apache Chainsaw log message viewer.

9.8 Detector Control System

Function

The main purpose of the Detector Control System (DCS) is to ensure the correct operation of the CMS experiment, so that high quality data is taken with the apparatus. The scope of DCS includes all subsystems involved in the control and monitor of the detector, its active elements, the electronics on and off the detector and the overall environment.

The Detector Control Systems of individual sub-detectors are connected to the central DCS Supervisor (figure 9.15) for combined operation. These sub-detector DCS subsystems handle all the individual detector electronics such as the CAEN high-voltage power supplies and other electronics both commercial and custom made. The low-voltage system and the gas system are common for all sub-detectors whereas the cooling systems are built individually by each sub-detector. Additional components such as front-end detector read-out links are also monitored by the DCS.

The DCS provides both bookkeeping of detector parameters (table 9.2) and safety-related functions, including alarm handling and limiting the control of critical components via a software

2008 JINST 3 S08004

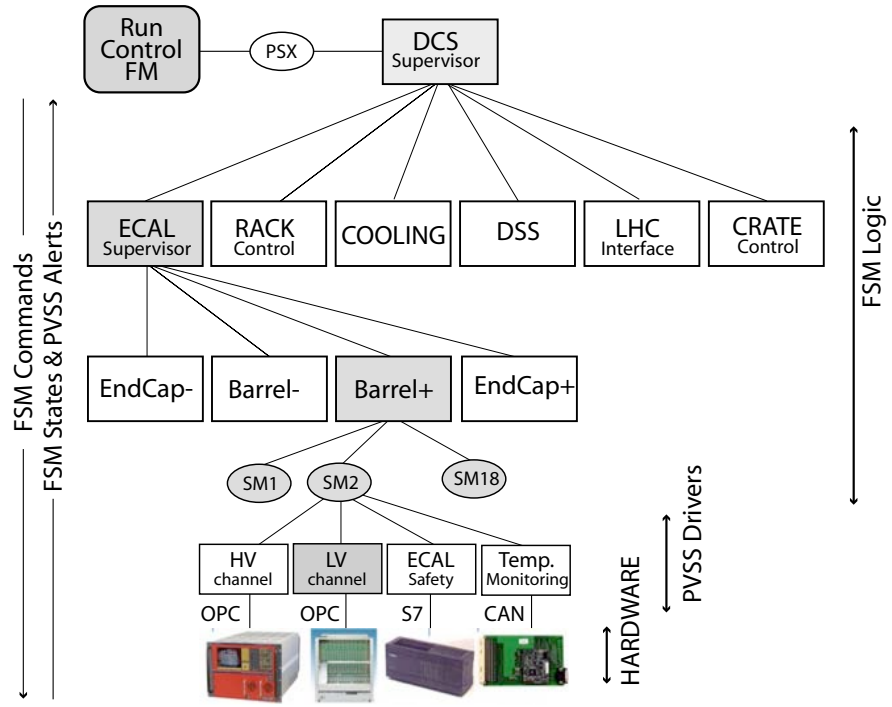

Figure 9.15: Outline of the Detector Control System hierarchy. Shown are all global services and ECAL as an example of a sub-detector control.

access control. The alarm handling and automated actions are designed in a way to anticipate major problems that would otherwise initiate Detector Safety System (DSS) actions, and warn the operator in advance that some action is needed. The alarm handling includes an SMS (mobile "text messaging") system that warns DCS users (for example a sub-detector expert) about abnormal system parameters. These SMS messages may require an acknowledgment by replying to the received alert SMS, and the status of both the alerts and acknowledgment's is displayed in the control room so that the operators in the control room are aware that experts are investigating the alarms. The DCS also collects relevant information from DSS. Monitoring of DCS parameters is possible via the Oracle Portal web pages that allow users to analyse both real time and archived data.

The DCS has to communicate with external entities as well, in particular the DAQ run control, and serves as the interface between the CMS experiment and the LHC accelerator. Many of the features provided by the DCS are needed at all times, and as a result selected parts of the DCS must function continually on a 24-hour basis during the entire year. To ensure this continuity UPS and redundant software and hardware systems are implemented in critical areas, however even non-critical nodes can be recovered in the order of minutes thanks to a CMS specific automated software recovery system.

2008 JINST 3 S08004

Table 9.2: Summary of detector parameters that are specific to each sub-detector.

Sub-detector	Monitored Parameters	Drivers	PCs / PLCs
muon CSCs	HV: 11 k channels, 218 k params LV: 8 k params Peripheral crate controller: 24 k params	Wiener and CAEN OPC custom: HV controller, Peripheral crate ctr CANopen-ELMB OPC	16
muon DTs	HV: 15 k channels - 110 k params LV: 1100 channels - 10 k parameters trigger: ≈12 k params	CAEN OPC CAEN OPC custom	7 5
muon RPCs	HV: 1200 channels LV: 1400 channels sensors: 500 channels Front end: 50 k params	CAEN OPC CAEN OPC same as LV custom	2 2
HCAL	HV: 450 channels, 3500 params LV: 270 channels, ≈1600 params HSS: 220 params Front end: 21 k params	custom CAEN OPC custom	
ECAL	LV: ≈4500 params HV: ≈2600 params Cooling: ≈200 params FE monitoring: ≈80 k params ESS: ≈600 params PTM/HM: ≈1 k params	CAN (Wiener) CAEN OPC Simatic S7, PSX custom: PSX Simatic S7 CANopen-ELMB OPC	3 4 2 / 1 1 1 / 2 2
Strip tracker	HV: 4 k channels LV: 4 k channels + 365 ctrl ch, 160 k params Temperature: 1100 sensors DCUs: 18 k channels, ≈ 100 k params	CAEN OPC, Siemens S7 custom: PSX	10 / 9
Pixel tracker	HV: 192 channels, 384 params LV: 192 channels, 384 params Temperature: 200 sensors	CAEN OPC, Siemens S7 custom: PSX	2 / 1
Alignment	LV: 200 channels 10 k LEDs, 150 lasers ≈2 k sensors	CAEN OPC ELMB, custom	5
Central DCS Services	rack control: 10 k params LHC interface: 1 k params cooling and ventilation DSS	Wiener OPC, CAN, SNMP custom: PSX	15

2008 JINST 3 S08004

Implementation

The DCS software is based on the Siemens commercial SCADA package PVSS-II and the CERN Joint Controls Project (JCOP) framework [224]. Industrial controls hardware is interfaced by PVSS-II via various supported drivers OPC (OLE for Process Automation) [225] protocol, Siemens S7, SNMP, or Modbus. The JCOP framework provides common solutions to similar problems across all LHC experiments. This framework includes PVSS-II components to control and monitor the most commonly used commercial hardware (CAEN and Wiener) as well as control for additional hardware devices designed at CERN like the widely used ELMB (Embedded Local

Monitoring Board). It also provides a Data Interchange Protocol (DIP). For hardware not covered by JCOP, PVSS-II offers the possibility of implementing new drivers and components, and CMS has developed sub-detector specific software.

The control application behaviour of all sub-detectors and support services are modeled as Finite State Machine (FSM) nodes, using the FSM toolkit provided by the JCOP framework. The detector controls are organized in a tree-like FSM node hierarchy representing the logical structure of the detector, where commands flow down and states and alarms are propagated up (figure 9.15). The different control systems of the experiment have been integrated into a single control tree, whose top node is referred to as the CMS DCS Supervisor. CMS has put policies into place to ensure a homogeneous and coherent use of the DCS [226].

The DCS is a distributed system and comprises all control applications dedicated to sub-systems, communicating via the PVSS proprietary network protocol. In total there will be around 100 PCs with the majority of them running Microsoft Windows, although Linux is also supported.

PVSS-II includes a proprietary database that is used to store in real time the values of all the parameters defining the current state of the system (e.g. high-voltage settings, alarms, etc.). The configuration of PVSS-II itself is also stored in this database. For static and large amounts of data, an external Oracle database is used to store configuration data, and to archive measured values of parameters from PVSS to Oracle tables. Selected data from DCS is exported to the CMS conditions database, which contains all the data describing the detector environment needed for the offline reconstruction. The DCS access control system uses the LDAP and Oracle identity management tools which has web support for account management.

During normal physics data taking the DCS will act as a slave to run control and will therefore have to receive commands and send back status information. A communication mechanism between DCS and external entities is provided by the CMS specific PVSS SOAP interface (PSX). The PSX is a SOAP server implemented with XDAQ (section 9.7) using the PVSS native interface and JCOP framework, and allows access to the entire PVSS-II system via SOAP.

2008 JINST 3 S08004

Chapter 10

Detector infrastructures and safety systems

The common term *infrastructures* includes very different systems, ranging from basic site facilities to more detector-specific and safety-related services. In this section, the main general systems are described.

10.1 Detector powering

CMS, like any other modern particle physics detector, needs considerable electrical power for its front-end electronics (FEE), for electronics racks in counting rooms and in site control centres, and finally for auxiliary services (cranes, ventilation and cooling stations, lifts and access facilities, etc.). Different power sources are available on site. Uninterruptible Power Systems (UPS), for valuable equipment that must stay on in case of power disruption, secure power for specific users for a short period, before being backed-up by a diesel engine. Common users are connected to standard network power. Table 10.1 gives an overview of the power requirements for CMS.

With the exception of the cooling stations, the racks system is the most important client in

Table 10.1: Power requirements for CMS.

System	Power (kW)
General site services	2200
Electronics racks	2300
Low voltage to front-end electronics	1000
Magnet and cryogenics	1250
Ventilation stations	1250
Surface cooling stations	4000
Underground cooling stations	1500
Total steady-state consumption	9000

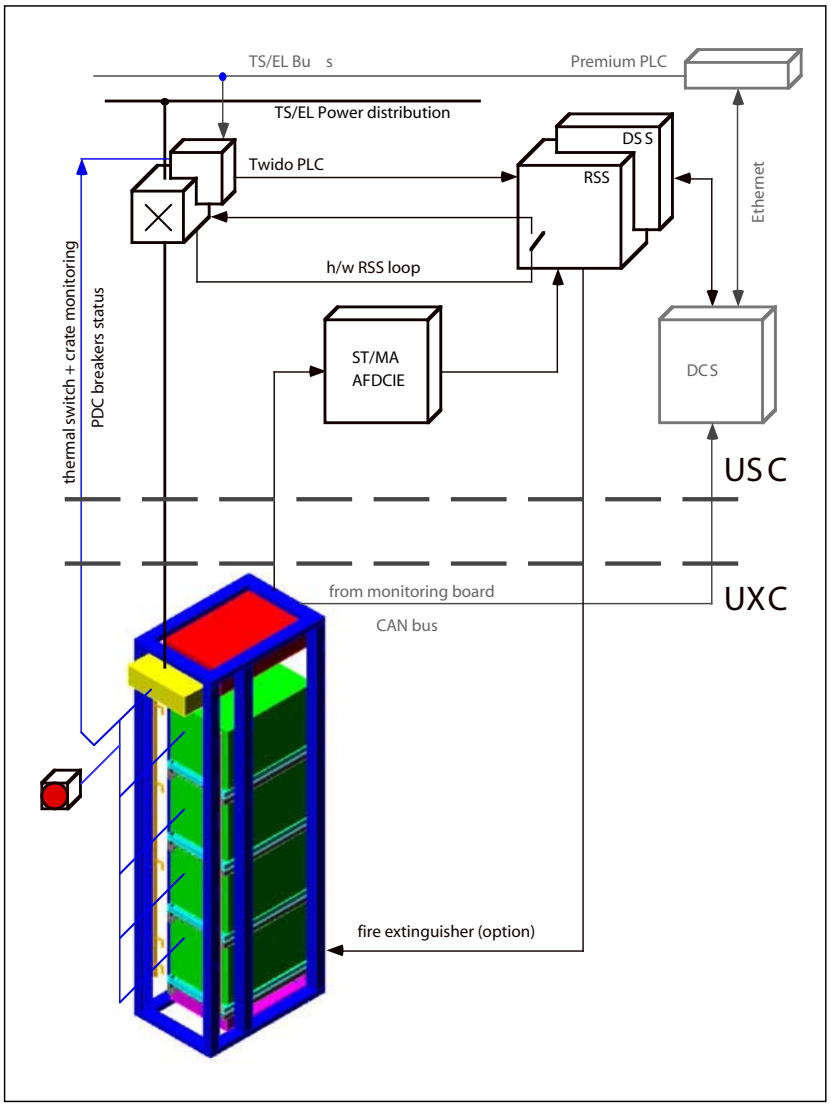

Figure 10.1: Control loops for rack powering.

terms of power. Rows of racks are fed by power bus-bars. Each single rack has a main breaker piloted by a dedicated PLC, the whole system being located in a box attached to the bus-bar. A power and a control cable run from this box to the power distributor cabinet inside each rack. Cabinets provide single-phase, three-phase or three-phase + neutral current distribution. The breaker PLC is controlled by the Detector Control System (DCS) via a network connection. Single racks can be switched on-off upon DCS request and the status of each breaker is known by DCS as well. Moreover, a hardwired connection to the Detector Safety System (DSS) secures the system in case of smoke or a high temperature is detected inside a rack. Figure 10.1 describes the logic behind the power controls.

Table 10.2: Cooling power for different sub-systems.

System	Power (kW)
Muon Endcaps	100
Muon Barrel	50
HCAL and Yoke Barrel	60
ECAL	300
Rack system	1600
Tracker, Pixel, Preshower	150

10.2 Detector cooling

10.2.1 Front-end electronics cooling

The CMS front-end electronics dissipates some 800 kW in the experimental cavern. This huge amount of heat is intercepted by cooling water at 18°C for the ECAL, HCAL and Muon systems, and by C_6F_{14} fluid at temperature ranging from -15°C to -25°C for the Preshower, Pixel and Tracker systems. In addition, some 1600 kW are dissipated by the rack system. Table 10.2 shows the power dissipated by each system.

Chilled water at 14°C is produced at the surface in the SU5 building and then transferred to the USC55 cooling plant, where five independent water circuits, each one with its own heat-exchangers, pumps and controls, produce and distribute water at 18°C to the experiment cavern. The Tracker, Pixel, and Preshower systems have on their primary side chilled water at 6°C, and they have their own cooling cabinets in UXC55 to shorten the transfer lines. Cooling status is monitored by the central DCS via ethernet connection to TS/CV control units. The DSS monitors crucial parameters such as flow rate, temperature, and dew point, in order to take actions in case of need. Loss of coolant is detected by measuring the fluid level in the expansion tanks of every cooling loop.

10.2.2 Cryogenics

The cryogenic plant at the CMS site has the function to cool down and keep at 4.7 K the 230 t of the CMS superconducting coil. The refrigerator system can deliver a cooling power of 800 W at 4.7 K, plus 4500 W at 60 K to cool the coil's thermal screens, in addition to the 4 g/s of liquid helium used to cool the 20 kA coil current leads. Cooling the coil down from room temperature takes 3 weeks, with a maximum thermal gradient inside the cold mass of 30 K. In case of a quench, the temperature rises to 70 K and 3 days are necessary to bring the cold mass down to 4.7 K. A 6000 l liquid helium storage tank sits close to the coil cryostat to allow a slow discharge from full current without warming up the coil.

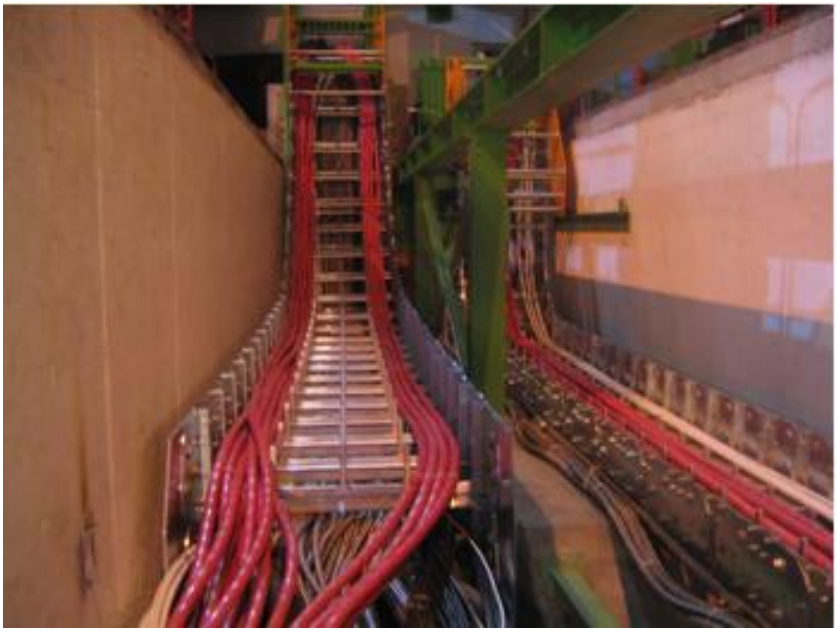

Figure 10.2: YB+2 and YE+1 cable-chains in UXC55 basement trenches.

10.3 Detector cabling

Due to the specific CMS design, with one central element (YB0) that is fixed and 6 mobile elements for each side moving on the cavern floor during shut-down periods, power cables, coolant, gas and optical fibres have to run through huge cable-chains in order to open and close the detector without disconnecting everything (figure 10.2).

Cables are labeled and stored in a database with web interface, that allows identification of each cable by sub-system, type, length, starting point, endpoint and routing. The main cable types can be summarised as follows:

- HV cables;
- LV cables for DC power to FEE;
- FEE read-out cables;
- optical fibres read-out;
- monitoring and control (DCS) cables;
- general pourpose power cables (230-400 V AC);
- safety system cables (DSS) for hard-wired signals and interlocks.

The cable-trays include also the gas-sniffer soft-pipes. Some 30 000 cables are referenced in the data-base.

2008 JINST 3 S08004

10.4 Detector moving system

The CMS moving system has been designed according to the following criteria: affordability, robustness, preciseness, easyness in handling and compactness. The boundary conditions have been determined on the one hand by the weight and dimensions of the assemblies and on the other hand by the friction, the slope and the size of the cavern.

10.4.1 Sliding system

In order to limit friction and thus the power of the pulling system, CMS has chosen a heavy duty air pad system for the long movements (10 cm to 10 m) and a flat grease pad system for the final approach (up to 10 cm). In addition, these systems allow, without any additional structure, movement perpendicular to the beam. The air pads (figure 10.3) have rubber sealing rings that prevent air losses. The system can be used with compressed air bottles only. At the same time, this sealing increases somewhat the friction factor, which lies around 0.8% before moving and goes down to around 0.4% once moving has begun. The grease pad system produces a final approach with practically no friction.

10.4.2 Pulling system

The pulling system consists of a hydraulic strand jack system and includes 6 jacks with strands (of which the two in the center are pivotable) and a strand storage mandrel. Taking into account the slope of the cavern (1.234%) and the friction of the airpads and cable chain, the system must be capable of safely pulling uphill 2.5% of the maximum load, which is 2600 t (3 endcaps together). Whereas going uphill is a pure pulling, going downhill needs a retaining force in order to produce a smooth, constant movement of the load. This was integrated into the design of the hydraulic control unit.

10.5 The Detector Safety System

The Detector Safety System (DSS) is a common development carried out by the 4 large LHC experiments together with the CERN IT department. The purpose of the DSS is to protect the detector and the experimental equipment from hazards. The DSS works complementary to the Detector Control System (DCS) and the CERN Safety System (CSS) (figure 10.4).

Normal operation of the experiments proceeds with the DCS which monitors and controls any deviation from normal operation or the occurrence of anomalies. In this respect, the DCS is ensuring a safe operation of the experiment. The DCS is designed such as to monitor and react up to a very detailed level and in a highly granular way, a necessary feature which on the other hand makes the system quite complex and thus vulnerable.

For emergency situations though, the LHC experiments are equipped with the CERN Safety System. The CSS is designed to reliably detect the main hazards, like smoke, flammable gas, oxygen deficiency, etc. that could endanger the human life, and will transmit a corresponding alarm to the CERN fire brigade. The CSS, however, does not foresee immediate actions for the protection of the equipment.

Figure 10.3: A transport beam for barrel rings with 4 air pads fixed on it.

Equipment protection is the purpose of the DSS which triggers automatic actions in order to avoid or to reduce eventual damage to the experimental equipment when it detects abnormal and potentially dangerous situations. The DSS is designed to be simple and reliable and consequently the DSS actions have to be fast and quite coarse, e.g., cutting the power to the entire cavern in the case that smoke is detected. In order to do so, the DSS partially recuperates signals from the CSS (e.g., smoke detection) and triggers actions on the main infrastructure, as cutting the 18 kV supply. DSS actions thus will in general disrupt the data taking, but in the long run, by avoiding damage to experimental equipment, will increase the overall data taking efficiency of the experiment.

10.5.1 DSS Requirements

In order to fulfill its purpose, the DSS has the following characteristics:

- high reliability and availability to make the system simple and robust;

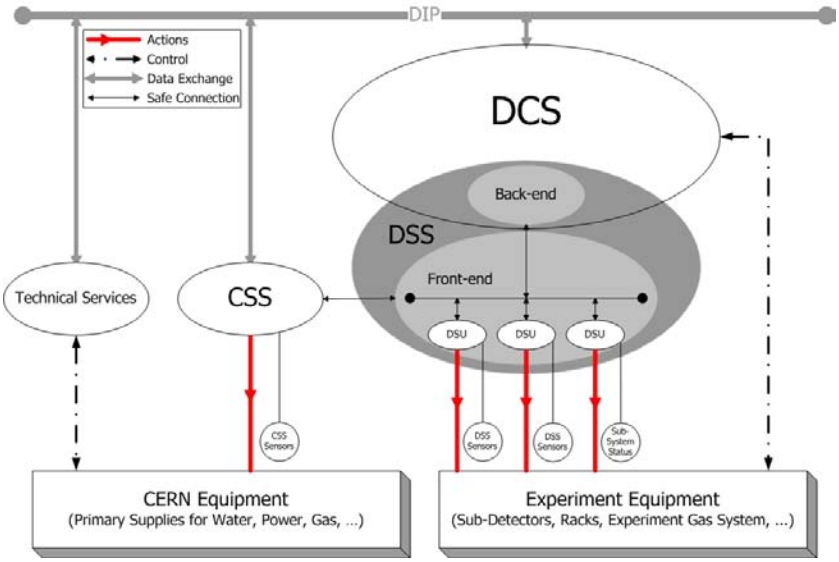

Figure 10.4: Context diagram of the DSS system, showing its rôle with respect to the CERN Safety System (CSS), the Detector Control System (DCS) and other technical services. The interconnection network is provided by the Data Interchange Protocol (DIP).

- operational independence of all other systems, running in stand alone system mode;
- autonomy from outside services, especially power supply and computer network;
- input from its own sensors and actuators (nevertheless some are owned by the CSS);
- capability of immediate and automatic actions;
- flexibility to be adopted and configured in order to adapt to the evolving needs of the experiments;
- full integration into the DCS.

10.5.2 DSS Architecture

The DSS consists of two main pillars: the front-end and the back-end.

The front-end is a redundant array of two Siemens S7-400 H PLCs. These PLCs interpret the signals coming from the connected sensors according to a programmable alarm-action matrix. Actuators, attached to the output of the PLCs trigger actions. The PLCs are scanning all input channels, processing the alarm-action matrix and modifying the state of the outputs accordingly. Such a cycle will take about 500 ms, allowing the DSS to react to any hazardous situation with a response time below one second. Different type of sensors can be connected to the DSS that are digital inputs, analogue inputs (4–20 mA) and PT100 temperature probes. The front-end can operate completely independent from the back-end and is thus the safety relevant part of the DSS. It is also connected to an uninterruptible power supply which gives the DSS autonomy of several hours.

The back-end of the DSS consists of a standard PC running the PVSS software. It serves as interface between the front end and the operator. The back-end provides tools for post mortem and data analysis, e.g. the possibility to retrieve and display data based on user-defined selection criteria, trending tools and the possibility to filter alarms according to criteria such as time, origin, alarm priority. However, it is not necessary for the user to initiate any DSS actions, as these are all performed as automated actions in the DSS front-end.

10.5.3 CMS Implementation of DSS

Due to the rather large number of input channels for the CMS experiment, the DSS is split into two completely separate entities. One entity collects input channels from the equipment housed in the USC cavern and the surface buildings and one entity for the UXC cavern. Both systems, each equipped with a set of redundant PLCs, are stand alone and communicate only via hard wired input and output. The USC/surface system consists of 6 Detector Safety Units (DSU) each housed in a rack, where the UXC system consists of 10 DSU's. A typical DSU is made of 224 digital input channels, 64 analogue or PT100 input channels and a few digital output channels. The bulk amount of signals originates form the 230 V rack power distribution system and from the low voltage system. The about 200 racks in the USC cavern produce each an individual smoke detection alarm and an alarm from the power distribution box (TWIDO). The about 200 racks in the UXC cavern will give as additional signals the status of the electrical breaker inside the TWIDO box and a signal in case of an electrical fault since the racks in the UXC cavern are not accessible during the LHC operation. Concerning the low voltage supply for the UXC racks, the DSS receives about 180 status- and electrical-fault bits, and it is able to cut the low voltage power supply to each rack individually.

In addition to the protection of the racks, the DSS also directly safeguards the sub-detectors via a number of sensors. These are temperature sensors placed directly on the sub-detector or in the vicinity of them, flow meters measuring their cooling circuit, water leak detectors inside the vacuum tank of the solenoid, etc. Since the functioning of the DCS is mandatory for the operation of the DSS, every sub-detector shall send a status bit to DSS, such that DSS can take appropriate actions in case the DCS of a sub-detector or the central DCS is not functioning. The typical DSS action is to cut the power to part of the detector equipment, but other actions can be taken as, for example, triggering the CO_2 rack extinguishing system, as well as the water mist system.

10.6 Beam and Radiation Monitoring systems

10.6.1 Introduction

The Beam and Radiation Monitoring systems (BRM) [227] perform both a monitoring and a protection function for CMS. To this end, multiple and redundant systems have been installed, some of which can be used to initiate LHC beam aborts and/or CMS equipment control, others of which can be used for fast beam/detector optimisations. All systems will provide long term monitoring of the received radiation dose in various regions of the CMS detector.

2008 JINST 3 S08004

The CMS experiment sits in an unprecedentedly high radiation field for a HEP experiment and much effort has gone into the design and construction of systems with very high radiation tolerance. Nevertheless, the LHC is designed to run with 362 MJ of stored energy in one beam and with proton intensities in excess of 10^{14} per beam. Even very small fractional losses of this beam risk causing serious damage to detector elements. Whilst the LHC itself has extensive instrumentation designed for machine protection, CMS requirements dictate that CMS must be able to detect beam-related problems as they develop and to assert beam aborts if required. In addition, CMS must be able to log data and perform post-mortem analyses in the case of accidents and understand the accumulated dosage and potential longer term damage to the detector elements. To this end CMS has implemented the BRM systems.

While radiation damage can lead to long term effects, the most likely damage scenarios involve very fast bursts of radiation/energy-dissipation in detector elements. Thus the protection systems must be sensitive to very fast changes in beam conditions; the BRM systems can detect changes at the 25 ns level, though the initially deployed protection systems will react in times of order 3–40 μs. Additionally, the BRM systems provide monitoring and tuning data to permit operator intervention to diagnose and improve beam conditions. In addition, all BRM systems can be used to monitor integrated dose and detector component aging over the years of LHC operation.

In designing the BRM, CMS imposed several design constraints; namely to implement systems which can stay alive at any time when beam may be in the LHC independently of the state of CMS operations; that have readout and post-mortem capabilities extremely close to those of the LHC machine protection systems; and that offer a high degree of redundancy and a wide dynamic range for protection and monitoring scenarios. Given these constraints, the BRM protection system, summarised in table 10.3, has been implemented. The BRM system, its nomenclature and sub-system locations in CMS are also represented in figure 10.5.

10.6.2 Protection systems

The protection systems are based on chemical vapour deposition diamond detectors [228] similar to those that have been widely used in recent collider experiments [229, 230] where they have proven to be radiation hard [231], fast enough to match beam abort scenarios, and small enough to be inserted into areas close to key detector components without adding substantial material or services.

In CMS there are two protection systems foreseen for initial LHC operation. The first is the BCM1L made of four polycrystalline diamonds, each $10 \times 10 \times 0.4$ mm^3, positioned on either side of the IP at z values of $\pm$ 1.8 m, close to the beam pipe and the inner-tracker pixel detectors (chapter 3) at a radius of 4.5 cm. The second protection system is the BCM2L. This is a set of twelve polycrystalline diamonds, each $10 \times 10 \times 0.4$ mm^3, on either side of the IP behind the TOTEM T2 detector at a z position of $\pm$ 14.4 m. On each side of the IP, a set of eight sensors are deployed at an outer radius of 29 cm and an additional four at an inner radius of 5 cm. Here BCM refers to Beam Conditions Monitor, the index 1 or 2 refers to the two locations in z and L indicates that these detectors are used in a leakage current measurement mode as relative flux monitors, typically integrating the leakage current over μs time scales. The BCM1L diamonds are arranged on the x and y axes. The BCM2L comprise eight diamonds at 45° intervals at large radius

2008 JINST 3 S08004

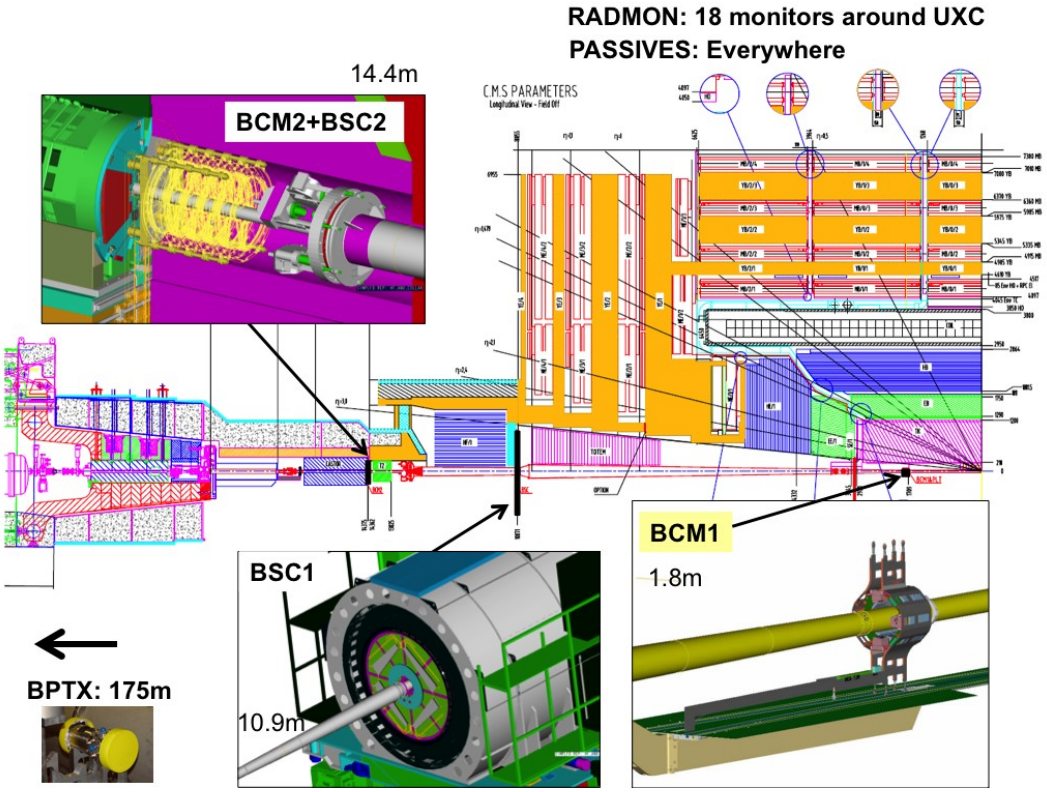

Figure 10.5: Layout of CMS BRM sub-systems.

and four on the x, y axes at small radius. The BCM1L and inner BCM2L diamonds measure a rate which is dominated by pp interactions at the IP. The outer BCM2L diamonds are hidden from the beam-spot and are expected to be largely sensitive to beam-halo rates.

The diamonds used for BCM1L and BCM2L are essentially identical, but the two systems differ in the readout methods adopted. The BCM2L uses a standard LHC Beam Loss Monitor (BLM) electronics and data processing [232, 233] that is read out asynchronously with respect to the LHC machine with 40 μs sampling. The BCM1L readout uses the same LHC BLM back-end electronics, but uses an additional mezzanine card to provide sub-orbit sampling. The readout is synchronized with the 89-μs LHC orbit, allowing user-configurable sampling, so that the sampling can be matched to the LHC bunch trains. In addition the BCM1L allows sampling of the LHC abort gap, which must be kept empty to avoid a spray of particles being directed at CMS during a beam dump.

Using a set of thresholds in the readout systems and a combinatorial logic to reduce sensitivity to individual noise events, a hardware beam abort signal can be generated and transmitted to the LHC machine via the Beam Interlock System [234], leading to the dumping of the beams within 3 orbits. A lower threshold value can be used to send hardware signals to CMS sub-detector clients to initiate high and/or low voltage ramp-downs.

In the event of a beam abort initiated by CMS, or by any of the other LHC (or experiment) protection systems, a full history of the BCM1L and BCM2L signals is produced and transmitted to the LHC control room.

2008 JINST 3 S08004

Table 10.3: The sub-systems to be deployed as part of the initial BRM. The table is ordered from top to bottom in increasing time resolution.

sub-system (Sensor type)	Location Distance from IP (m)	Sampling Time	Function	Readout + Interface LHC or CMS type	Number of Sensors
Passives (TLD+Alanine)	CMS and UXC	$\sim$ months	Monitoring	N/A	Many
RADMON (RadFets+SRAM)	CMS and UXC	1 s	Monitoring	Standard LHC	18
BCM2L (Polycrystalline Diamond)	Behind TOTEM T2 z=$\pm$14.4 m	40 μs	Protection	Standard LHC	24
BCM1L (Polycrystalline Diamond)	Pixel Volume z=$\pm$1.8 m	5 μs	Protection	Standard LHC	8
BCM2F (Polycrystalline Diamond)	Behind TOTEM T2 z=$\pm$14.4 m	$\sim$ns	Monitoring	CMS Standalone	8
BSC (Scintillator Tiles)	Front of HF z=$\pm$10.9 m	$\sim$ns	Monitoring	CMS Standalone	32
BCM1F (Single Crystal Diamond)	Pixel Volume z=$\pm$1.8 m	$\sim$ns	Monitoring	CMS Standalone	8
BPTX (Button Beam Pickup)	Upstream of IP5 z=$\pm$175 m	200 ps	Monitoring	CMS Standalone	2

10.6.3 Monitoring systems

Several monitoring systems are listed in table 10.3: the BCM1F and BCM2F are also based upon diamond sensors, but with readouts able to resolve the sub-bunch structure, the Beam Scintillator Counters (BSC) are a series of scintillator tiles designed to provide hit and coincidence rates, the Button Beam Pickup (BPTX) is designed to provide precise information on the bunch structure and timing of the beam, and the RADMON and Passives systems give calibrated information on the radiation field within the CMS cavern.

The BCM1F, BSC and BPTX are sensitive to time structure below the 25-ns level; as such they also provide technical trigger inputs into the global CMS trigger. In particular, the inputs from the BPTX and BSC provide zero- and minimum-bias triggers, respectively. Additionally, all three of these systems are sensitive to all foreseen beam intensities including the LHC pilot beam, where a single low intensity bunch is injected for studies or to confirm parameter settings prior to full intensity injection.

The BCM1F consists of four single crystal diamonds, each $5\times5\times0.5$ mm^3, positioned on either side of the IP at z values of $\pm$ 1.8 m at a radius of 4.5 cm, in close proximity to the BCM1L detectors. The BCM1F is used as a diagnostic tool to flag problematic beam conditions resulting in "bursts" of beam loss over very short periods of time. Such beam losses are expected to be one of the principle damage scenarios for the CMS detector systems. The location of the BCM1F is close to the optimal position in terms of timing separation between ingoing and outgoing particles from the IP (i.e. 6.25 ns from the IP). The gated rate information from the BCM1F should therefore give a very good handle on the comparative rate of background from beam halo to that from lumonisity products. The sensor is connected to the JK16 radiation hard amplifier [235], after which the

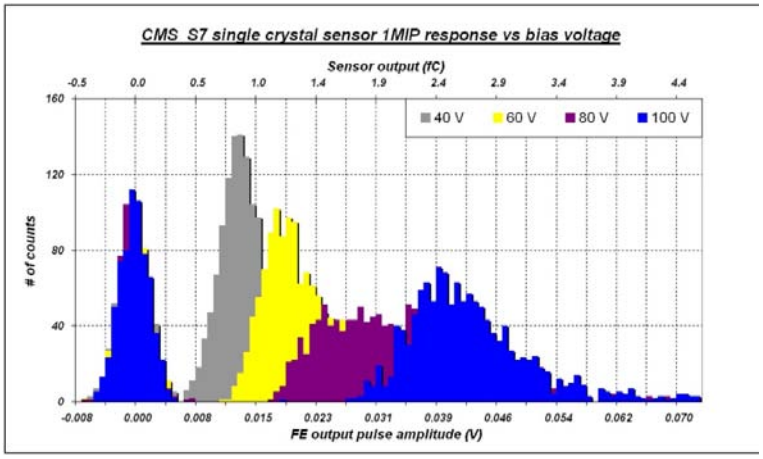

Figure 10.6: MIP response of BCM1F single-crystal diamond with front-end electronics, as a function of bias voltage of the sensor. The superposition of histograms around 0-V output amplitude indicates the noise.

signal is transmitted to the counting room over an analog optical link built from the tracker optical components [236].

The detector is sensitive to one MIP and has a timing resolution for single hits of a few ns. The performance of the front end electronics is shown in figure 10.6. Good separation can be seen between the signal and the noise. The pulse height was found to saturate at 100 V bias voltage across the sensor. The back-end readout produces rate, multiplicity, timing and coincidence information independently of the CMS DAQ. However, there is the possibility to feed information into the event stream via a standard CMS SLINK.

In a similar vein to the BCM1F, the BCM2F is composed of four diamonds at the BCM2L location, read out by a fast digitiser. The aim of this system is to provide additional diagnostic information at this location, as the digitiser can sample at 1 GHz, giving information on the sub-bunch level [237]. Whilst this will not be MIP-sensitive, it will help resolve the timing structure of periods of enhanced background.

The Beam Scintillator Counters (BSC) are a series of scintillator tiles designed to provide hit and coincidence rates, with a design similar to those used at previous experiments [238]. The scintillators and PMTs used for the BSC are recycled from OPAL [239]. The layout and geometry of the scintillator tiles are shown in figure 10.7. The BSC1 is located on the front of the HF, at $\pm$10.9 m from the IP, and consists of two types of tiles. Next to the beampipe are the disks, segmented into 8 independent slices in ϕ, with an inner radius of 22 cm and an outer radius of 45 cm. The primary function of the disks is to provide the rate information corresponding to the beam conditions. In addition, there are four large area "paddles" further out, at a radial distance of between $\approx$ 55 cm and $\approx$ 80 cm, which in addition to providing rate information, will also provide coincidence information which can be used to tag halo muons passing through the detector, for calibration purposes. The area covered by the BSC is about 25% of the tracker; therefore these tiles can be indicative of activity within this bunch crossing, and can be used to provide a minimum-

2008 JINST 3 S08004

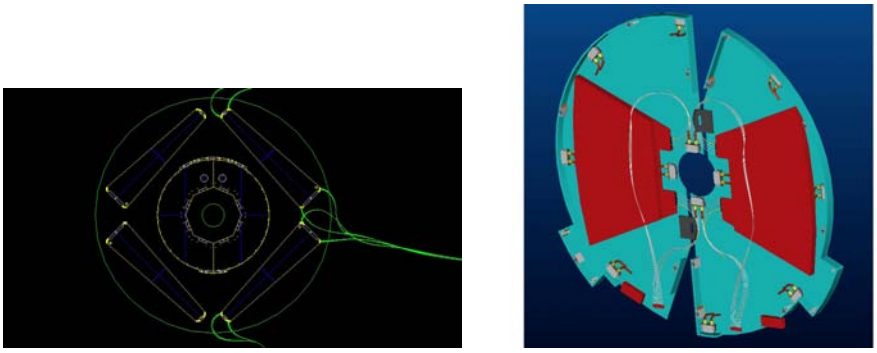

Figure 10.7: Layout of the Beam Scintillator Counters tiles. The left-hand panel shows the layout for BSC1, the right-hand panel for BSC2. The locations of the BCM2 sensors can also be seen in the right-hand panel.

bias trigger for commissioning and systematic studies. The BSC2 is located behind TOTEM T2 at $\pm$14.4 m from the IP. The BSC2 consists of two tiles on each side of the IP, with a minimum inner radius of 5 cm and a maximum outer radius of 29 cm. The primary function of the BSC2 is to distinguish between ingoing and outgoing particles along the beamline, as there is a 4-ns timing difference between them. The rates at this location can therefore be tagged as to whether they are incoming (beam halo only) or outgoing (collision products and beam halo).

The Beam Timing for the experiments (BPTX) is a beam pickup device specifically installed to provide the experiments with the timing structure of the LHC beam. This beam pickup is a standard button monitor used everywhere around the LHC ring for the beam position monitors. Two are installed for CMS: 175 m left and right upstream of the IP. At this location there are two beampipes, and therefore the timing measurement is only of the incoming beam. To optimise the timing measurement, the four buttons (left, right, up, down) of the pickup have been electrically connected together. This is done to maximise the signal strength and hence the resolution on the timing, at the price of loosing the position information.

An oscilloscope-based read-out was chosen for the BPTX and developed in common with ATLAS [240]. The BPTX will provide accurate information on the timing and phase of each bunch and its intensity. The phases of all the experimental clocks can be compared to the measured phase of each bunch with a precision better than 200 ps. This will also allow the interaction-point z position to be calculated from the relative phases of the BPTX measurements on opposite sides of the IP. The BPTX can also detect problems with the bunch structure, and measure the proportion of beam which has drifted into the neighbouring RF bucket.

In parallel to the oscilloscope based read-out, the signals from the BPTX will also be discriminated and sent as three technical trigger inputs to the CMS global trigger. This will provide three flags on each bunch crossing as to whether: a) bunch in beam 1 is occupied; b) bunch in beam 2 is occupied; c) both beams are occupied. The flag where both beams are occupied is indicative of whether collisions can occur in this bunch crossing, and therefore provides a zero-bias trigger for commissioning of the trigger system.

At 18 locations around the CMS cavern, RADMON [241] detectors are installed. The RADMON detectors each provide well calibrated measurements of: a) the dose and dose rate using

2008 JINST 3 S08004

RadFETs; b) the hadron flux with energies above 20 MeV and the single event upset rate using SRAM; c) the 1-MeV-equivalent neutron fluence using pin diodes. RADMON detectors are installed all around the LHC ring, and in the experimental insertions. The RADMON detectors at CMS will be integrated into and read out via the accelerator-wide RADMON system.

The integrated radiation dose throughout the CMS cavern will be measured during each run period with passive dosimetry. This allows to map the radiation field throughout the cavern and will be used to validate the simulations of the anticipated doses. This gives an absolute scale to the other measurements. The dosimeters chosen are TLDs and Alanine.

2008 JINST 3 S08004

Chapter 11

Computing

11.1 Overview

The CMS offline computing system must support the storage, transfer and manipulation of the recorded data for the lifetime of the experiment. The system accepts real-time detector information from the data acquisition system at the experimental site; ensures safe curation of the raw data; performs pattern recognition, event filtering, and data reduction; supports the physics analysis activities of the collaboration. The system also supports production and distribution of simulated data, and access to conditions and calibration information and other non-event data.

The users of the system, and the physical computer centres it comprises, are distributed worldwide, interconnected by high-speed international networks. Unlike previous generations of experiments, the majority of data storage and processing resources available to CMS lie outside the host laboratory. A fully distributed computing model has therefore been designed from the outset. The system is based upon Grid middleware, with the common Grid services at centres defined and managed through the Worldwide LHC Computing Grid (WLCG) project [242], a collaboration between LHC experiments, computing centres, and middleware providers.

The nature of the CMS experimental programme poses several challenges for the offline computing system:

- The requirement to analyse very large statistics datasets in pursuit of rare signals, coupled with the fine granularity of the CMS detector, implies a volume of data unprecedented in scientific computing. This requires a system of *large scale*, supporting efficient approaches to data reduction and pattern recognition.

- The system is required to be *highly flexible*, allowing any user access to any data item recorded or calculated during the lifetime of the experiment. A software framework is required which supports a wide variety of data processing tasks in a consistent way, and which must evolve along with the goals of the experiment. Since the CMS programme centres on discovery of new phenomena, under new experimental conditions, analysis requirements cannot be wholly defined in advance.

- A complex distributed system of such large scale must be designed from the outset for *manageability*, both in the operation of computing resources for physics, and in terms of software

construction and maintenance. The *longevity* of the system, of 15 years or more, implies several generations of underlying hardware and software, and many changes of personnel, during the lifetime of the system.

Key components of the computing system include:

- An event data model and corresponding application framework;
- Distributed database systems allowing access to non-event data;
- A set of computing services, providing tools to transfer, locate, and process large collections of events;
- Underlying generic Grid services giving access to distributed computing resources;
- Computer centres, managing and providing access to storage and CPU at a local level.

At each level, the design challenges have been addressed through construction of a modular system of loosely coupled components with well-defined interfaces, and with emphasis on scalability to very large event samples [243].

11.2 Application framework

The CMS application software must perform a variety of event processing, selection and analysis tasks, and is used in both offline and online contexts. The software must be sufficiently modular that it can be developed and maintained by a large group of geographically dispersed collaborators. The chosen architecture consists of a common framework which is adaptable for each type of computing environment, physics modules which plug into the framework via a well-defined interface, and a service and utility toolkit which decouples the physics modules from details of event I/O, user interface, and other environmental constraints [212].

The central concept of the CMS data model is the *Event*. The Event provides access to the recorded data from a single triggered bunch crossing, and to new data derived from it. This may include raw digitised data, reconstructed products, or high-level analysis objects, for real or simulated crossings. The Event also contains information describing the origin of the raw data, and the provenance of all derived data products. The inclusion of provenance information allows users to unambiguously identify how each event contributing to a final analysis was produced; it includes a record of the software configuration and conditions / calibration setup used to produce each new data product. Events are physically stored as persistent ROOT files [244].

The Event is used by a variety of *physics modules*, which may read data from it, or add new data, with provenance information automatically included. Each module performs a well-defined function relating to the selection, reconstruction or analysis of the Event. Several module types exist, each with a specialised interface. These include: *event data producers*, which add new data products into the event; *filters* used in online triggering and selection; *analysers*, producing summary information from an event collection; and *input and output modules* for both disk storage and DAQ.

2008 JINST 3 S08004

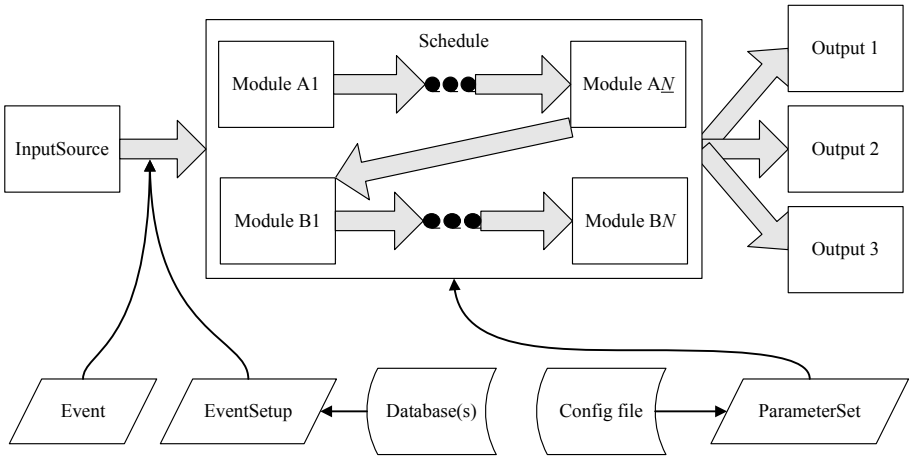

Figure 11.1: Modules within the CMS Application Framework.

Modules are insulated from the computing environment, execute independently from one another, and communicate only though the Event; this allows modules to be developed and verified independently. A complete CMS application is constructed by specifying to the Framework one or more ordered sequences of modules through which each Event must flow, along with the configuration for each. The Framework configures the modules, schedules their execution, and provides access to global services and utilities (figure 11.1).

11.3 Data formats and processing

In order to achieve the required level of data reduction, whilst maintaining flexibility, CMS makes use of several event formats with differing levels of detail and precision. Other specialised event formats are used for heavy-ion data. The process of data reduction and analysis takes place in several steps, typically carried out at different computer centres.

RAW format

RAW events contain the full recorded information from the detector, plus a record of the trigger decision and other metadata. RAW data is accepted into the offline system at the HLT output rate (nominally 300 Hz for pp collisions). An extension of the RAW data format is used to store the output of CMS Monte Carlo simulation tools. The RAW data is permanently archived in safe storage, and is designed to occupy around 1.5 MB/event (2 MB/event for simulated data, due to additional Monte Carlo truth information).

The RAW data will be classified by the online system into several distinct *primary datasets*, based upon the trigger signature. Event classification at the earliest possible stage has several advantages, including the possibility of assigning priorities for data reconstruction and transfer in the case of backlog, and balancing of data placement at centres outside CERN. CMS will also define one or more flexible "express streams" used for prompt calibration and rapid access to interesting or anomalous events.

2008 JINST 3 S08004

RECO format

Reconstructed (RECO) data is produced by applying several levels of pattern recognition and compression algorithms to the RAW data. These algorithms include: detector-specific filtering and correction of the the digitised data; cluster- and track-finding; primary and secondary vertex reconstruction; and particle ID, using a variety of algorithms operating on cross-detector information.

Reconstruction is the most CPU-intensive activity in the CMS data processing chain. The resulting RECO events contain high-level *physics objects*, plus a full record of the reconstructed hits and clusters used to produce them. Sufficient information is retained to allow subsequent application of new calibrations or algorithms without recourse to RAW data, though basic improvements in pattern recognition or event formats will probably require re-production of the RECO data at least once per year. RECO events are foreseen to occupy around 0.5 MB/event.

AOD format

AOD (Analysis Object Data) is the compact analysis format, designed to allow a wide range of physics analyses whilst occupying sufficiently small storage so that very large event samples may be held at many centres. AOD events contain the parameters of high-level physics objects, plus sufficient additional information to allow kinematic refitting. This format will require around 100 kB/event, small enough to allow a complete copy of the experimental data in AOD format to be held at computing centres outside CERN. AOD data is produced by filtering of RECO data, either in bulk production, or in a skimming process which may also filter a primary dataset into several analysis datasets.

Non-Event data

In addition to event data recorded from the detector, a variety of *non-event data* is required in order to interpret and reconstruct events. CMS makes use of four types of non-event data: construction data, generated during the construction of the detector; equipment management data; configuration data, comprising programmable parameters related to detector operation; and conditions data, including calibrations, alignments and detector status information. We concentrate here on the lattermost category.

Conditions data are produced and required by both online and offline applications, and have a well-defined interval of validity (IOV). For instance, calibration constants for a given run may be derived from prompt reconstruction of a subset of recorded events, and then used both by the HLT system and for subsequent reconstruction and analysis at computing centres around the world. Non-event data are held in a number of central Oracle databases, for access by online and offline applications. New conditions data, including calibration and alignment constants produced offline, may be replicated between the databases as required. Conditions data access at remote sites takes place via the FroNTier system [245] which uses a distributed network of caching http proxy servers.

2008 JINST 3 S08004

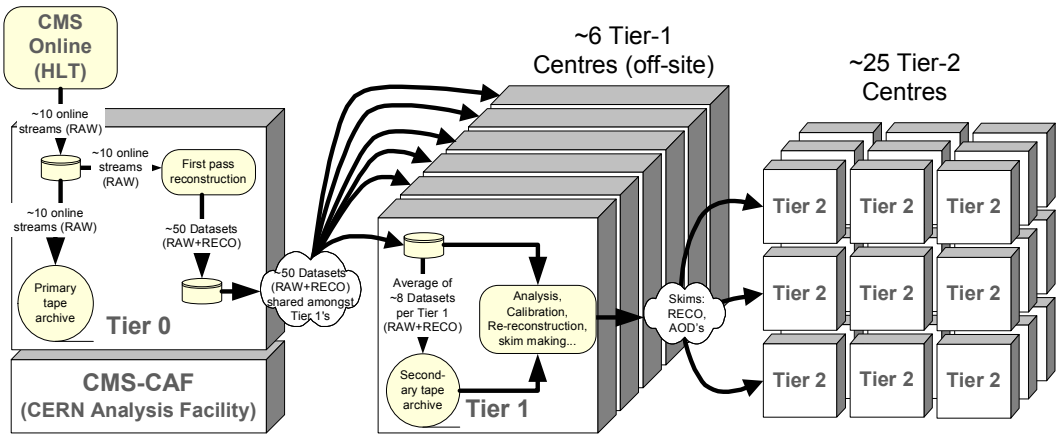

Figure 11.2: Dataflow between CMS Computing Centres.

11.4 Computing centres

The scale of the computing system is such that it could not, even in principle, be hosted entirely at one site. The system is built using computing resources at a range of scales, provided by collaborating institutes around the world. CMS proposes to use a hierarchical architecture of Tiered centres, similar to that originally devised in the MONARC working group [246], with a single Tier-0 centre at CERN, a few Tier-1 centres at national computing facilities, and several Tier-2 centres at institutes. A representation of the dataflow between centres is shown in figure 11.2.

The CMS computing model depends upon reliable and performant network links between sites. In the case of transfers between Tier-0 and Tier-1 centres, these network links are implemented as an optical private network (LHC-OPN) [247]. Data transfers between Tier-1 and Tier-2 centres typically takes place over general-purpose national and international research networks.

Tier-0 centre

A single Tier-0 centre is hosted at CERN. Its primary functions are to:

- Accept data from the online system with guaranteed integrity and latency, and copy it to permanent mass storage;
- Carry out prompt reconstruction of the RAW data to produce first-pass RECO datasets. The centre must keep pace with the average rate of data recording, and must provide sufficient input buffering to absorb fluctuations in data rate;
- Reliably export a copy of RAW and RECO data to Tier-1 centres. Data is not considered "safe" for deletion from Tier-0 buffers until it is held at at least two independent sites. (One of these is CERN computing centre, playing the role of a Tier-1.)

During the LHC low-luminosity phase, the Tier-0 is intended to be available outside data-taking periods for second-pass reconstruction and other scheduled processing activities. High-luminosity running will require the use of the Tier-0 for most of the year. The Tier-0 is a common CMS facility used only for well-controlled batch work; it is not accessible for analysis use.

2008 JINST 3 S08004

Tier-1 centres

A few large Tier-1 centres are hosted at collaborating national labs and computing centres around the world. These centres are operated by a professional staff on a 24/365 basis, with the emphasis on extremely reliable delivery of data-intensive processing services. Each site provides large batch CPU facilities, a mass storage system including a robotic tape archive, and very high speed international network links including a dedicated link to the LHC-OPN. The primary functions of a Tier-1 are to:

- Provide long-term safe storage of RAW data from CMS, providing a second complete copy outside CERN distributed across the centres. Each Tier-1 takes long-term custodial responsibility for a fraction of the CMS dataset;
- Store and serve to Tier-2 centres simulated and derived data. Each Tier-1 holds a fraction of the CMS simulated and RECO data, and a complete copy of the AOD data. It can rapidly transfers these data to any Tier-2 centre which requires them for analysis;
- Carry out second-pass reconstruction: a Tier-1 provides access to its archive of RAW data to allow reproduction of RECO datasets using improved algorithms or calibrations;
- Provide rapid access to very large data samples for skimming and data-intensive analysis: a Tier-1 can support high-statistics analysis projects which would be infeasible at a Tier-2 centre.

Since each Tier-1 centre holds unique RAW and RECO datasets, it must be capable of serving data to any CMS Tier-2. However, for the purposes of Monte Carlo data receipt and AOD data serving, the Tier-1 serves a defined set of a few "associated" Tier-2 centres, usually defined by geographical proximity.

Tier-2 centres

Several Tier-2 centres of varying sizes are hosted at CMS institutes. A Tier-2 centre typically divides its resources between the local user community and CMS as a whole. Tier-2 centres are subject to less stringent requirements on availability and data security than a Tier-1 centre, making them feasible to manage with the resources available to a typical University group. The functions of a Tier-2 centre may include:

- Support of analysis activities, including local storage of data samples transferred from Tier-1 centres, and access to a flexible CPU farm; in particular, the Tier-2 centres are designed to support final-stage analysis requiring repeated passes over a reduced dataset;
- Support of specialised activities such as offline calibration and alignment tasks, and detector studies;
- Production of Monte Carlo data, and its transfer to an associated Tier-1 centre for long term storage.

2008 JINST 3 S08004

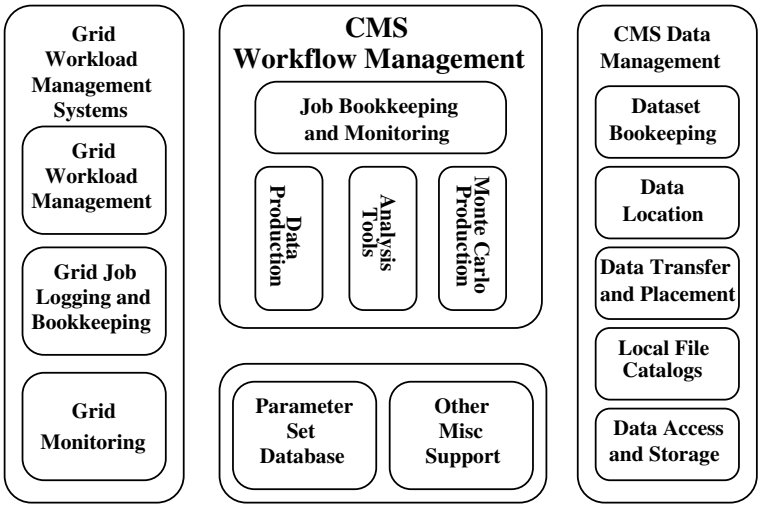

Figure 11.3: Overview of the CMS Computing Services.

CERN Analysis Facility

In addition to the Tier-0 centre, CERN also hosts an Analysis Facility which combines flexible CPU resources with rapid access to the entire CMS dataset. This centre supports fast turn-around analysis when required, and a variety of other specialised functions (calibration, performance monitoring) related to the operation of the CMS detector. The centre effectively combines the rapid data access capabilities of a Tier-1 with the flexibility of a very large Tier-2.

11.5 Computing services

Grid computing

The integration of the resources at CMS computing centres into a single coherent system relies upon Grid middleware which presents a standardised interface to storage and CPU facilities at each WLCG (Worldwide LHC Computing Grid) site. The Grid allows remote job submission and data access with robust security and accounting. The detailed architecture of the Grid is described in the WLCG Technical Design Report [242].

A number of CMS-specific distributed computing services operate above the generic Grid layer, facilitating higher-level data and workload management functions. These services require CMS-specific software agents to run at some sites, in addition to generic Grid services. CMS also provides specialised user-intelligible interfaces to the Grid for analysis job submission and monitoring, and tools for automated steering and monitoring of large-scale data production and processing. An overview of the CMS Computing Services components is shown in figure 11.3.

2008 JINST 3 S08004

Data management

CMS requires tools to catalogue the data which exist, to track the location of the corresponding physical data files on site storage systems, and to manage and monitor the flow of data between sites. In order to simplify the data management problem, the data management system therefore defines higher-level concepts including: *dataset*, a logical collection of data grouped by physical-meaningful criteria; *event collection*, roughly corresponding to an experiment "run" for a given dataset definition; and *file block*, an aggregation of a few TB of data files, representing the smallest unit of operation of the data transfer system.

To provide the connection between abstract datasets and physical files, a multi-tiered catalogue system is used. The *Dataset Bookkeeping System* provides a standardised and queryable means of cataloguing and describing event data [249]. It is the principle means of data discovery for the end user, answering the question "which data of this type exists in the system?" A second catalogue system, the *Data Location Service* provides the mapping between file blocks to the particular sites at which they are located, taking into account the possibility of replicas at multiple sites. *Local File Catalogues* at each site map logical files onto physical files in local storage.

The *data transfer and placement system* is responsible for the physical movement of file-blocks between sites on demand; it is currently implemented by the PhEDEx system [248]. This system must schedule, monitor and verify the movement of data in conjunction with the storage interfaces at CMS sites, ensuring optimal use of the available bandwidth. The baseline mode of operation for the data management system is that the collaboration will explicitly place datasets at defined sites, where they will remain for access by CMS applications until removed.

Workload management

Processing and analysis of data at sites is typically performed by submission of batch jobs to a remote site via the Grid workload management system. A standard job wrapper performs the necessary setup, executes a CMSSW application upon data present on local storage at the site, arranges for any produced data to be made accessible via Grid data management tools, and provides logging information. This process is supported by several CMS-specific services.

A *parameter set management system*, implemented with either global or local scope according to the application, allows the storage and tracking of the configuration of CMSSW applications submitted to the Grid. A lightweight *job bookkeeping and monitoring system* allows users to track, monitor, and retrieve output from jobs currently submitted to and executing at remote sites [250]. The system also provides a uniform interface to a variety of Grid-based and local batch-system based submission tools. In addition, a suite of software distribution tools provide facilities for automated installation of standard CMS applications and libraries at remote sites.

Bulk workflow management

For very large-scale data processing (including Monte Carlo production, skimming and event reconstruction), a specialised bulk workflow management tool has been developed. The ProdAgent system comprises a collaborative distributed network of automated job managers, operating at Tier-0, Tier-1 and Tier-2 sites [250]. The system provides facilities for large-scale Grid job submission,

2008 JINST 3 S08004

interface to the CMS data catalogues and data management system, and handling of large flows of logging and status information. A highly automated system such as ProdAgent is essential in order to allow the CMS data processing system to be controlled and monitored by a moderately-sized data operations team.

User workflow management

For a generic CMS physicist, a dedicated tool (CRAB) for workflow management is available [250]. It allows to submit user-specific jobs to a remote computing element which can access data previously transferred to a close storage element. CRAB takes care of interfacing with the user environment, it provides data-discovery and data-location services, and Grid infrastructure. It also manages status reporting, monitoring, and user job output which can be put on a user-selected storage element. Via a simple configuration file, a physicist can thus access data available on remote sites as easily as he can access local data: all infrastructure complexities are hidden to him as much as possible. There is also a client-server architecture available, so the job is not directly submitted to the Grid but to a dedicated CRAB server, which, in turn, handles the job on behalf of the user, interacting with the Grid services.

11.6 System commissioning and tests

It has been recognised since the very start of preparations for LHC that the construction and organisation of the experiment computing systems would be a key challenge. Each component of the system must be designed with attention to both scalability and flexibility, and rigorously tested at realistic scale. The reliance on distributed computing, using the relatively new Grid approach, has many advantages, but adds further complexity in controlled deployment and testing compared to a system located primarily at a single site.

The relatively large cost of the computing system dictates that centres must build up their resources in a carefully controlled way; the rapidly falling price of hardware dictates that full-scale resources will only become available shortly before they are required, and that efficient use of resources is a strong requirement. The emphasis in CMS has been on a series of increasing scale full-system tests ("data challenges") over the last three years, exercising all available components in a realistic way.

In 2006 and 2007, CMS carried out large-scale Computing, Software and Analysis challenges (CSA06, CSA07). The scale of the two tests was set at 25% and 50% of the nominal 2008 performance, respectively, with the computing system operated continuously at this level for more than four weeks. The challenges were carried out using realistic application software and computing tools. Typical targets for the tests were:

- Preparation of large Monte Carlo datasets ($\approx$ 100 million events) at around twenty CMS Tier-1 and Tier-2 centres in the weeks preceding the challenge, and upload to CERN;
- Playback of the MC dataset for prompt Tier-0 reconstruction at around 100 Hz, including the application of calibration constants from the offline database, and splitting the event sample into around ten datasets;

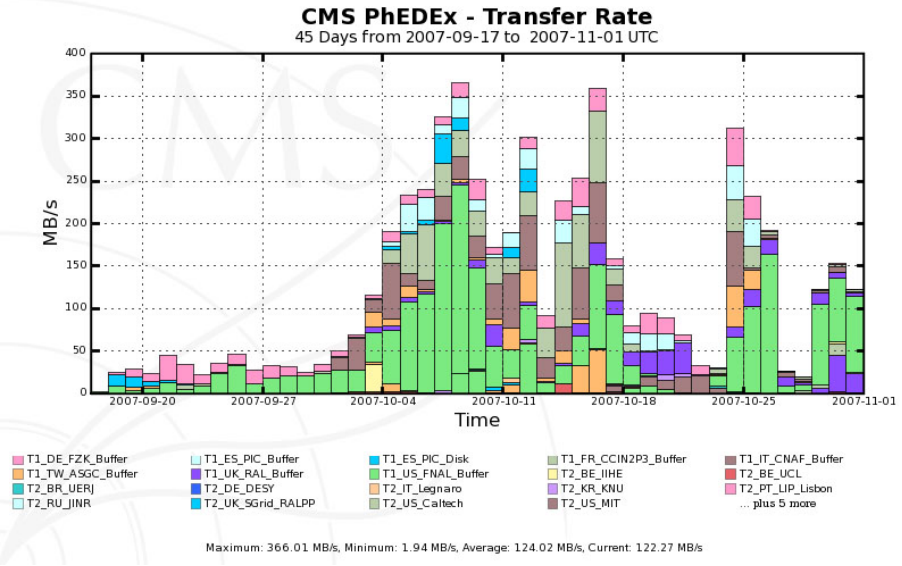

Figure 11.4: Dataflow from CERN during the CSA07 Data Challenge.

- Distribution of AOD and RAW to all Tier-1 centres, and subsequent alignment / calibration, reconstruction and skimming operations at several sites;
- Transfer of skimmed data to Tier-2 centres and running of physics analysis jobs.

Overall, many of the key metrics for success in the challenges were met: the reconstruction rate at the Tier-0 exceeded 100 Hz for periods of time; an export rate of over 350 MB/s was achieved from CERN (figure 11.4). CMS will finalise its data challenge programme with additional scale tests during 2008, which are in the final stages of preparation at the time of writing. In parallel with data challenges, continuous programmes are under way to deploy, commission and test the increasing hardware resources at the computing centres, and to debug and demonstrate reliable and high-speed data network links between them. The CMS computing model itself is also under ongoing review, with many new lessons expected to be learnt as detector data begins to flow.

2008 JINST 3 S08004

Chapter 12

Conclusions

The Compact Muon Solenoid detector has been described in detail. The expected physics performance of the apparatus has been described elsewhere [17].

At the time of this paper, the apparatus is essentially completed and installed.

After more than 10 years of design and construction, the CMS magnet has been constructed and successfully tested. Most of the magnetic, electrical, mechanical, and cryogenics parameters measured during the tests are in good agreement with calculated values. The CMS magnet is the largest superconducting solenoid ever built for a physics experiment in terms of bending power for physics, total stored energy, and stored energy per unit of cold mass.

The silicon-strip inner tracker, with about 200 m^2 of active silicon, has been integrated into its support tube, commissioned, and thoroughly tested with cosmic rays. Its performance is excellent, fulfilling the design specifications. The silicon tracker was installed into CMS in december 2007. All the pixel modules are completed; it is planned to install the Pixel detector into CMS in mid-2008.

The ECAL, comprising over 75 000 lead tungstate crystals, is the largest crystal calorimeter ever built. The crystals in the barrel part, comprising over 60 000 crystals, have been intercalibrated using cosmic rays and about a third in particle beams, demonstrating the ability to measure the energies ranging from those deposited by minimum ionising particles to high-energy electrons. An energy resolution of 0.5% for 120 GeV electrons has been attained. The ECAL barrel has been installed in the experiment and is being commissioned. The endcaps are foreseen to be inserted into the experiment in 2008.

The entire HCAL has been completed and commissioned on the surface. The HCAL modules are currently being commissioned in the experiment proper.

The various components of the Muon System (drift tubes, cathode strip chambers, resistive plate chambers) have been completed. A significant fraction of the Muon System has been commissioned and tested on surface with cosmic rays, and it is now being integrated into the experiment and being commissioned in-situ.

In the very forward region, the Zero Degree Calorimeter has been completed and CASTOR is expected to be completed in 2008.

The off-detector electronics are currently being installed and operations for trigger commissioning are taking place.

Common data-acquisition runs with various sub-detectors, sometimes using cosmic rays, are regularly taking place at the experiment and will continue into spring 2008 in anticipation of collisions at LHC in mid-2008.

2008 JINST 3 S08004

Acknowledgements

The design, construction, installation and commissioning of CMS would have been impossible without the devoted efforts of our numerous technical colleagues from the CERN departments and from all the CMS Institutes. The cost of the detectors, computing infrastructure, data acquisition and all other systems without which CMS would not be able to operate, was generously supported by the financing agencies involved in the experiment. We are particularly indebted to: Austrian Federal Ministry of Science and Research; FNRS and FWO (Belgium); CNPq and FAPERJ (Brazil); Bulgarian Ministry of Education and Science; CERN; CAS and NSFC (China); Croatian Ministry of Science and Technology; University of Cyprus; Estonian Academy of Sciences and NICPB; Academy of Finland, Finish Ministry of Education and Helsinki Institute of Physics; CEA and CNRS/IN2P3 (France); BMBF and DESY (Germany); General Secretariat for Research and Technology (Greece); NKTH (Hungary); DAE and DST (India); IPM (Iran); UCD (Ireland); INFN (Italy); KICOS (Korea); CINVESTAV (Mexico); PAEC (Pakistan); State Commission for Scientific Research (Poland); FCT (Portugal); JINR (Armenia, Belarus, Georgia, Ukraine, Uzbekistan), Ministry of Education and Science of the Russian Federation, Russian Federal Agency of Atomic Energy; Ministry of Science and Environmental Protection of the Republic of Serbia; Oficina de Ciencia y Tecnologia (Spain); ETHZ, PSI, University of Zurich (Switzerland); National Science Council (Taipei); TUBITAK and TAEK (Turkey); STFC (United Kingdom); DOE and NSF (USA).

We also acknowledge the important contributions provided by the following institutes: Research Institute of Applied Physical Problems, Minsk, Belarus; University for Science and Technology of China, Hefei, Anhui, China; Digital and Computer Systems Laboratory, Tampere University of Technology, Tampere, Finland; Seoul National University of Education, Seoul, Korea; Benemerita Universidad Autonoma de Puebla, Puebla, Mexico; Myasishchev Design Bureau, Zhukovsky, Russia; Russian Federal Nuclear Centre, Scientific Research Institute for Technical Physics, Snezhinsk, Russia; Kharkov State University, Kharkov, Ukraine; University of Strathclyde, Glasgow, United Kingdom; Virginia Polytechnic Institute and State University, Blacksburg, Virginia, USA.

2008 JINST 3 S08004

CMS acronym list

AB	Algorithm Board
AC	Alternating Current
ADC	Analog to Digital Converter
AFEB	Anode Front-End Board, CSC system
AG	Application Gateway
ALCT	Anode Local Charged Track trigger primitive, CSC system
AOD	Analysis Object Data - a compact event format for physics analysis
AOH	Analog Opto-Hybrid
APD	Avalanche Photo-Diode
API	Application Programming Interface
APV	Analogue Pipeline (Voltage mode), front-end read-out chip of Tracker
ASIC	Application Specific Integrated Circuit
ATLAS	A Toroidal LHC ApparatuS experiment
aTTS	Asynchronous Trigger Throttle System
AWG	American Wire Gauge
BMU	Barrel Muon system
BD	Back Disk
BP	Back Petal
BPix	Barrel Pixel
BR	Branching Ratio
BRAN	Beam RAte of Neutrals
BST	Beam Synchronous Timing
BTI	Bunch and Track Identifier trigger primitive, DT system
BU	Builder Unit
BX	Bunch Crossing
BXN	Bunch Crossing Number
CASTOR	Centauro And Strange Object Research
CC	Cosmic Challenge
CCS	Clock and Control System
CCU	Communication and Control Unit
CCUM	Communication and Control Unit Module
CDR	Central Data Recording
CFC	Carbon Fiber Composite

2008 JINST 3 S08004

CFEB	Cathode Front-End Board of the CSC system
CLCT	Cathode Local Charged Track trigger primitive, CSC system
CMM	Coordinate Measuring Machine
CMN	Common Mode Noise
CMOS	Complementary Metal Oxide Semiconductor
CMS	Compact Muon Solenoid experiment
CMSSW	CMS SoftWare framework
COSINE	Consistent Online Software INtegration Environment, project integrating online with offline software
CPU	Central Processing Unit
COCOA	CMS Object-oriented Code for optical Alignment
CRAB	CMS Remote Analysis Builder
CRack	Cosmic Rack, a set of TOB rods
CRC	Cyclic Redundancy Check error detection
CSC	Cathode Strip Chamber muon system
CSCTF	Cathode Strip Chamber Trigger Track Finder
D2S	Data to Surface
DAC	Digital to Analog Converter
DAQ	Data Acquisition
DAQMB	Data Acquisition Motherboard, CSC L1 trigger
DBMS	Database Management System
DC	Direct Current
DCC	Data Concentrator Card
DCCT	DC Current Transformer
DCS	Detector Control System
DCU	Detector Control Unit
DDD	Detector Description Database
DDL	Data Description Language
DDU	Detector Dependent Unit in DAQ system
DIP	Data Interchange Protocol (CERN)
DMB	DAQ MotherBoard of CSC system
DOFZ	Diffusion Oxygenated Float Zone
DOH	Digital Opto-Hybrid
DOHM	Digital Opto-Hybrid Module
DQM	Data Quality Monitoring
DQMC	Data Quality Monitoring Collector
DSS	Detector Safety System
DT	Drift Tube muon system
DTTF	Drift Tube Trigger Track Finder, DT L1 trigger
EB	Electromagnetic Calorimeter (Barrel)
ECAL	Electromagnetic Calorimeter
EDM	Event Data Model
EDMS	Engineering Database Management System

EE	Electromagnetic Calorimeter (Endcap)
EIC	Electromagnetic Isolation Card, regional calorimeter trigger
ELMB	Embedded Local Monitoring Board (ECAL)
EMDB	Equipment Management DataBase
EMU	Endcap Muon system
ENC	Equivalent Noise Charge
EP	Event Processor
ES	Endcap preShower detector, also Event Server
ESP	Event Server Proxy
ESS	ECAL Safety System
ETTF	Eta Track Finder, DT regional muon trigger
EVB	EVent Builder
EVF	Event Filter Farm
EVM	Event Manager
FB	FED builder
FD	Front Disk
FDL	Final Decision Logic, L1 Global Trigger
FE	Front-End
FEB	Front-End Board
FEC	Front-End Card, Front End Controller
FED	Front-End Driver
FEE	Front-End Electronics
FES	Front-End System
FENIX	ECAL front-end read-out ASIC
FEVT	Event format comprising the union of RAW and RECO data
FF	Filter Farm
FMM	Fast Merging Module
FIFO	First In First Out buffer
FP	Front Petal
FPGA	Field Programmable Gate Array
FPix	Forward Pixel
FRL	Front-End Read-out Link
FSM	Finite State Machine
FTP	Foil screened Twisted Pair cables
FU	Filter Unit
Gb	Gigabit (10^9 bits)
GB	Gigabyte (10^9 bytes)
GBW	Gain BandWidth product
GCALOR	Computer program for hadron shower calculations
GCT	Global Calorimeter Trigger (L1)
GIF	Gamma Irradiation Facility
GMR	Global Muon Reconstructor
GMT	Global Muon Trigger (L1)

GOH	Giga Optical Hybrid
GOL	Gigabit Optical Link
GPN	General Purpose Network (CERN campus)
GT	Global Trigger (L1)
GTFE	Global Trigger Front-end board (L1)
GTL	Global Trigger Logic board (L1)
GTL+	Gunning Transceiver Logic, upgraded version, developed by Fairchild Semiconductor
GTP	Global Trigger Processor
GTPe	Global Trigger Processor emulator
GUI	Graphical User Interface
H2	Beamline at CERN
HCAL	Hadron Calorimeter
HB	Hadron Calorimeter (Barrel)
HDI	High Density Interconnect
HE	Hadron Calorimeter (Endcap)
HF	Hadron Calorimeter (Forward)
HG	High Gain
HI	Heavy Ion(s)
HIJING	Heavy Ion Jet INteraction Generator, Monte Carlo event generator for heavy-ion collisions
HIP	Hits and Impact Point alignment method, also Highly Ionizing Particle
HLT	High-Level Trigger
HM	Humidity Monitoring
HO	Hadron Calorimeter (Outer Barrel)
HPD	Hybrid Photo-Diode
HTML	HyperText Mark-up Language
HTR	HCAL Trigger and Read-out
HV	High Voltage
IGUANA	Interactive Graphics for User ANAlysis
I^2C	Inter-Integrated Circuit
ICB	InterConnect Board (TEC), InterConnect Bus (TOB)
ICC	InterConnect Card
I/O	Input/Output
IOV	Interval Of Validity
IP	Interaction Point or Internet Protocol
ISO	Isolation bit in muon trigger
ISR	Intersecting Storage Ring collider at CERN
JCOP	Joint controls Project at CERN
JSC	Jet Summary Card, in Regional Calorimeter Trigger
JTAG	Joint Test Action Group
kb	kilobit (10^3 bits)
kB	kilobytes (10^3 bytes)

L1	Level-1 hardware-based trigger
L1A	Level-1 Accept
LAN	Local Area Network
LAS	Laser Alignment System
LCG	LHC Computing Grid (a common computing project)
LCT	Local Charged Track trigger primitive of CSC system
LDAP	Lightweight Directory Access Protocol
LED	Light Emitting Diode
LEP	Large Electron Positron collider at CERN
LG	Low Gain
LHC	Large Hadron Collider
LSB	Least Significant Bit
LUT	Lookup table
LTC	Local Trigger Controller
LV	Low Voltage
LVD	Low Voltage Distribution
LVDS	Low Voltage Differential Signaling
LVR	Low Voltage Regulator
MA	Module Alignment
MAB	Module Alignment of Barrel
Mb	Megabit (10^6 bits)
MB	Muon system (Barrel), also Mother Board or Megabyte (10^6 bytes)
MC	Monte Carlo simulation program/technique, also Mini-Crate of DT system
ME	Muon system (Endcap) or Monitoring Element
MEM	Monitoring Electronics Module
mFEC	mezzanine Front End Controller
MGPA	Multiple Gain Pre-Amplifier chip, ECAL
MILLEPEDE	Algorithm for tracker alignment
MIP	Minimum Ionizing Particle
MOS	Metal Oxide Semiconductor
MOSFET	Metal Oxide Semiconductor Field Effect Transistor
MPC	Muon Port Card, CSC L1 trigger
MSS	Magnet Safety System
MT	Mean Time
MTCC	Magnet Test Cosmic Challenge
MTU	Maximum Transfer Unit
NIC	Network Interface Card
NIEL	Non-Ionizing Energy Loss
O2O	Online to Offline
ODBMS	Object Database Management System
OMDS	Online Master Data Storage
OPC	OLE for Process Automation
ORCOF	Offline ReConstruction OFfline subset, conditions database

ORCON	Offline ReConstruction ONline subset, conditions database
OS	Operating System
P5	Point 5 collision area of LHC
PACE	Preshower front end ASIC
PACT	PAttern Comparator Trigger, RPC system
PB	Petabyte (10^{15} bytes)
PC	Personal Computer
PCB	Printed Circuit Board
PCI	Peripheral Component Interconnect
PD	Pixel Detector
PDF	Parton Density Function, also Probability Distribution Function
PHTF	Phi Track Finder, DT regional muon trigger
PLC	Programmable Logic Controller
PLD	Programmable Logic Device
PLL	Phase-Locked Loop
PP	Patch Panel
PLT	Pixel Luminosity Telescope
PS	Proton Synchrotron
PSB	Pipeline Synchronizing Buffer, L1 Global Trigger and Global Muon Trigger
PSX	PVSS SOAP Interface
PTM	Precision Temperature Monitoring, ECAL
PV	Primary Vertex
PVSS	Prozessvisualisierungs- und Steuerungs-System
QIE	Charge Integrator and Decoder, ECAL frontend electronics
QPLL	Quartz Phase-Locked Loop
RAW	Event format from the online containing full detector and trigger data
RB	Read-out Unit Builder, also Resource Broker
RCT	Regional Calorimeter Trigger (L1)
RCS	Run Control System
RECO	Event format for reconstructed objects such as tracks, vertices, jets, etc.
RH	Relative Humidity
RISC	Reduced Instruction Set Computer
RMS	Root Mean Square
ROB	ReadOut Board, DT system
ROC	ReadOut Chip, pixels
ROS	ReadOut Server board, DT system
RPC	Resistive Plate Chamber muon system
RS	Resource Service
RU	Read-out Unit
SAN	Storage Area Network
SC	Sector Collector, DT muon L1 trigger or Super Crystal, ECAL
SCA	Switched Capacitor Array buffer, CSC system
SCADA	Supervisory Control And Data Acquisition

SCX	Surface Control eXperimental building at P5
SDA	Slow Dump Accelerated
SEL	Single Event Lathcup
SEU	Single Event Upset
SFM	SubFarm Manager
Skim	Subset of events selected from a larger set
SLB	Sychronization and Link Board
SM	SuperModule (ECAL) or Storage Manager (DAQ)
SMB	System Mother Board
SMD	Surface Mounted Device
SMS	Short Message Service (mobile phones)
S/N	Signal to Noise ratio
SNMP	Simple Network Management Protocol
SOAP	Simple Object Access Protocol
SPS	Super Proton Synchrotron
SRP	Selective Read-out Processor
SST	Silicon Strip Tracker
STL	Standard Template Library
sTTS	Synchronous Trigger Throttle System
SV	Secondary Vertex
SX5	Surface hall at Point 5 for CMS
T1, T2	Tracking telescopes of TOTEM
TAG	Event index information such as run/event number, trigger bits, etc.
Tb	Terabit (10^{12} bits)
TB	Terabyte (10^{12} bytes)
TBM	Token Bit Manager
TCA	Telecom Computing Architecture
TCC	Trigger Concentrator Card
TCP	Transmission Control Protocol
TCS	Trigger Control System
TDC	Time to Digital Converter
TDR	Technical Design Report
TDSS	Tracker Detector Safety System
TEC	Tracker EndCap
TF	Track-Finder, muon L1 trigger
TIB	Tracker Inner Barrel
TID	Tracker Inner Disks
TIM	Timing Module, Global Trigger and Drift Tube Trigger Track Finder
TMB	Trigger MotherBoard, CSC L1 trigger
TN	Technical Network
TOB	Tracker Outer Barrel
TOTEM	TOTal Elastic and diffractive cross section Measurement
TPD	Tracker Pixel Detector

TPG	Trigger Primitive Generator
TRACO	Track Correlator, DT L1 trigger
TriDAS	Trigger and Data Acquisition project
TRLB	Token Ring Link Board
TS	Trigger Server, DT L1 trigger
TSM	Track Sorter Master, DT L1 trigger
TSS	Track Sorter Slave, DT L1 trigger
TTC	Trigger Timing and Control
TTCex	TTC Encoder and Transmitter
TTCmi	TTC Machine Interface
TTCrx	TTC Receiver
TTS	Trigger Throttling System
UDP	User Datagram Protocol
USC55	Underground Service Cavern at Point 5 for CMS
UXC55	Underground eXperimental Cavern at Point 5 for CMS
VFE	Very Front End
VHDI	Very High Density Interconnect
VME	Versa Module Eurocard
VPT	Vacuum PhotoTriode
WAN	Wide Area Network
WLCG	Worldwide LHC Computing Grid
WLS	WaveLength Shifting
XDAQ	Software framework for CMS Data Acquisition
XML	eXtensible Markup Language
YB	Yoke (Barrel)
YE	Yoke (Endcap)
ZDC	Zero Degree Calorimeter

Bibliography

[1] CMS collaboration, *The Compact Muon Solenoid technical proposal*, CERN-LHCC-94-38, http://cdsweb.cern.ch/record/290969.

[2] TOTEM collaboration, *The TOTEM Experiment at the LHC*, 2008 *JINST* **3** S08007.

[3] CMS collaboration, *The CMS magnet project: technical design report*, CERN-LHCC-97-010, http://cdsweb.cern.ch/record/331056.

[4] A. Hervé et al., *Status of the construction of the CMS magnet*, *IEEE Trans. Appl. Supercond.* **14** (2004) 524.

[5] A. Hervé, *The CMS detector magnet*, *IEEE Trans. Appl. Supercond.* **10** (2000) 389.

[6] F. Kircher et al., *Final design of the CMS solenoid cold mass*, *IEEE Trans. Appl. Supercond.*. **10** (2000) 407.

[7] ALEPH collaboration, *ALEPH: a detector for electron-positron annihilation at LEP*, *Nucl. Instrum. Meth.* **A 294** (1990) 121.

[8] DELPHI collaboration, *The DELPHI detector at LEP*, *Nucl. Instrum. Meth.* **A 303** (1991) 233.

[9] ZEUS collaboration, *The ZEUS detector*, unpublished, available at http://www-zeus.desy.de/bluebook/bluebook.html.

[10] BABAR collaboration, *The BABAR detector*, *Nucl. Instrum. Meth.* **A 479** (2000) 1.

[11] I. Horvath et al., *The CMS conductor*, *IEEE Trans. Appl. Supercond.* **12** (2002) 345.

[12] S. Sgobba et al., *Mechanical performance at cryogenic temperature of the modules of the external cylinder of CMS and quality controls applied during their fabrication*, *IEEE Trans. Appl. Supercond.* **14** (2004) 556.

[13] P. Fabbricatore et al., *The construction of the modules composing the CMS superconducting coil*, *IEEE Trans. Appl. Supercond.* **14** (2004) 552.

[14] P. Fazilleau et al., *Design, construction and tests of the* 20*kA current leads for the CMS solenoid*, *IEEE Trans. Appl. Supercond.* **14** (2004) 1766.

2008 JINST 3 S08004

[15] CMS collaboration, *The CMS tracker system project: technical design report*, CERN-LHCC-98-006, http://cdsweb.cern.ch/record/368412.

[16] CMS collaboration, *The CMS tracker: addendum to the technical design report*, CERN-LHCC-2000-016, http://cdsweb.cern.ch/record/490194.

[17] CMS collaboration, *CMS Physics Technical Design Report Volume 1: Detector Performance and Software*, CERN-LHCC-2006-001, http://cdsweb.cern.ch/record/922757; CMS collaboration, *CMS Physics Technical Design Report Volume 2: Physics Performance*, *J. Phys.* **G 34** (2006) 995, CERN-LHCC-2006-021, http://cdsweb.cern.ch/record/942733.

[18] ROSE collaboration, 2nd *RD*48 *status report: R & D on silicon for future experiments*, CERN-LHCC-98-039, http://cdsweb.cern.ch/record/376432.

[19] M. Atac et al., *Beam test results of the US-CMS forward pixel detector*, *Nucl. Instrum. Meth.* **A 488** (2002) 271.

[20] G. Bolla et al., *Design and test of pixel sensors for the CMS experiment*, *Nucl. Instrum. Meth.* **A 461** (2001) 182.

[21] J. Kemmer et al., *Streifendetektor*, Patentoffenlegungsschrift DE 19620081 A1, Munich, Germany, 21 October 1997.

[22] K. Arndt et al., *Silicon sensors development for the CMS pixel system*, *Nucl. Instrum. Meth.* **A 511** (2003) 106.

[23] Y. Allkofer et al., *Design and performance of the silicon sensors for the CMS barrel pixel detector*, *Nucl. Instrum. Meth.* **584** (2008) 25.

[24] G. Lindström et al., *Radiation hard silicon detectors — Developments by the RD*48 *(ROSE) collaboration*, *Nucl. Instrum. Meth.* **A 466** (2001) 308.

[25] D. Kotlinski, *The control and readout system of the CMS pixel barrel detector*, *Nucl. Instrum. Meth.* **A 565** (2006) 73.

[26] H.C. Kästli, *Design and performance of the CMS pixel detector readout chip*, *Nucl. Instrum. Meth.* **A 565** (2006) 188.

[27] E. Bartz, *The* 0.25μ*m token bit manager chip for the CMS pixel readout*, in *Proceedings of the* 11th *Workshop on Electronics for LHC and Future Experiments*, Heidelberg Germany (2005).

[28] K. Kloukinas et al., *FEC-CCS: a common front-end controller card for the CMS detector electronics*, in *Proceedings of the* 12th *Workshop on Electronics for LHC and Future Experiments*, Valencia Spain (2006), http://cdsweb.cern.ch/record/1027434.

[29] CERN ASICs manuals, online at http://cmstrackercontrol.web.cern.ch/cmstrackercontrol/manuals.htm.

2008 JINST 3 S08004

[30] G. Bolla et al., *Wire-bond failures induced by resonant vibrations in the CDF silicon detector*, *IEEE Nucl. Sci. Symp. Conf. Rec.* **3** (2003) 1641.

[31] D. Menasce, M. Turqueti and L. Uplegger, *The renaissance: a test-stand for the forward CMS pixel tracker assembly*, *Nucl. Instrum. Meth.* **A 579** (2007) 1141.

[32] S. Paoletti et al., *The powering scheme of the CMS silicon strip tracker*, in 10th *Workshop on Electronics for LHC and future experiments*, CERN-2004-010, CERN-LHCC-2004-030, http://cdsweb.cern.ch/record/814088.

[33] R. Fenner and E. Zdankiewicz, *Micromachined water vapor sensors: a review of sensing technologies*, *IEEE Sens. J.* **1** (2001) 309.

[34] SIEMENS, SIMATIC, *Statement List (STL) for S7-300 and S7-400 programming*, reference manual, Siemens ag automation and drives, http://www.fer.hr/_download/repository/S7_300_STL_programming_manual.pdf.

[35] *Interface for accessing the PVSS system through SOAP XML protocol*, online at http://xdaqwiki.cern.ch/index.php/PSX.

[36] L. Borrello et al., *Sensor design for the CMS silicon strip tracker*, CMS-NOTE-2003-020, http://cdsweb.cern.ch/record/687861.

[37] J.L. Agram et al., *The silicon sensors for the Compact Muon Solenoid tracker: design and qualification procedure*, *Nucl. Instrum. Meth.* **A 517** (2004) 77.

[38] S. Braibant et al., *Investigation of design parameters for radiation hard silicon microstrip detectors*, *Nucl. Instrum. Meth.* **A 485** (2002) 343.

[39] M. Raymond et al., *The CMS Tracker APV*25 0.25 μ*mCMOS readout chip*, in *Proceedings of the* 6th *Workshop on Electronics for LHC Experiments*, Cracow Poland (2000).

[40] A. Marchioro, *Deep submicron technologies for HEP*, in *Proceedings of the* 4th *Workshop on Electronics for LHC Experiments*, Rome Italy, CERN-LHCC-98-36, CERN-LHCC-40-46, http://cdsweb.cern.ch/record/405093.

[41] J. Troska et al., *Optical readout and control systems for the CMS tracker*, *IEEE Trans. Nucl. Sci.* **50** (2003) 1067.

[42] Telecommunications Industry Association, *Electrical characteristics of Low Voltage Differential Signaling (LVDS) interface circuits*, ANSI/TIA/EIA-644-A-2001.

[43] F. Vasey, C. Biber, M. Sugiyama and J. Troska, *A* 12*-channel analog optical-receiver module*, *J. Lightwave Technol.* **23** (2005) 4270.

[44] K. Gill et al., *Progress on the CMS tracker control system*, in *Proceedings of the* 11th *Workshop on Electronics for LHC and Future Experiments*, Heidelberg Germany (2005), http://cdsweb.cern.ch/record/921198.

2008 JINST 3 S08004

[45] J. Coughlan et al., *The CMS tracker front-end driver*, in *Proceedings of the* 9th *Workshop on Electronics for LHC Experiments*, Amsterdam, The Netherlands (2003), http://cdsweb.cern.ch/record/722058.

[46] C. Ljuslin, A. Marchioro and C. Paillard, *The CCU25: a network oriented communication and control unit integrated circuit in a* 0.25 *µmCMOS technology*, in *Proceedings of the* 8th *Workshop on Electronics for LHC Experiments*, Colmar France (2002), http://cdsweb.cern.ch/record/593914.

[47] K. Kloukinas, A. Marchioro, P. Moreira and P. Placidi, *A* 40 *MHz clock and trigger recovery circuit for the CMS tracker fabricated in a* 0.25 *µmCMOS technology and using a self calibration technique*, in *Proceedings of the* 5th *Workshop on Electronics for LHC Experiments*, Snowmass U.S.A. (1999).

[48] Philips Semiconductors, *The I^2C-bus specification, version* 2.1, document order number 9398 393 40011, January (2001), http://www.semiconductors.philips.com/i2c.

[49] G. Magazzu, A. Marchioro and P. Moreira, *The detector control unit: an ASIC for the monitoring of the CMS silicon tracker*, *IEEE Trans. Nucl. Sci.* **51** (2004) 1333.

[50] U. Goerlach, *Industrial production of front-end hybrids for the CMS silicon tracker*, in *Proceedings of the* 9th *Workshop on Electronics for LHC Experiments*, Amsterdam, The Netherlands (2003), http://cdsweb.cern.ch/record/720615.

[51] M. Axer et al., *The qualification of silicon microstrip detector modules for the CMS inner tracking detector*, CMS-NOTE-2006-141, http://cdsweb.cern.ch/record/1000390.

[52] P. Schleper, G. Steinbrück and M. Stoye, *Software alignment of the CMS tracker using MILLEPEDE II*, CMS-NOTE-2006-011, http://cdsweb.cern.ch/record/926543.

[53] E. Widl, R. Frühwirth and W. Adam, *A Kalman filter for track-based alignment*, CMS-NOTE-2006-022, http://cdsweb.cern.ch/record/927376.

[54] V. Karimäki, A. Heikkinen, T. Lampén and T. Lindén, *Sensor alignment by tracks*, in *Proceedings of the CHEP2003 - International Conference on Computing in High Energy and Nuclear Physics*, La Jolla U.S.A. (2003), CMS-CR-2003-022, http://cdsweb.cern.ch/record/619975.

[55] R. Brauer et al., *Design and test beam performance of substructures of the CMS tracker end caps*, CMS-NOTE-2005-025, http://cdsweb.cern.ch/record/927381.

[56] CMS TIB collaboration, *Validation tests of CMS TIB/TID structures*, in preparation.

[57] W. deBoer et al., *The performance of irradiated CMS silicon micro-strip detector modules*, CMS-NOTE-2006-049, http://cdsweb.cern.ch/record/951391.

[58] A. Chilingarov et al., *Radiation studies and operational projections for silicon in the ATLAS inner detector*, *Nucl. Instrum. Meth.* **A 360** (1995) 432.

2008 JINST 3 S08004

[59] CERN DETECTOR R&D collaboration RD2, E. Fretwurst et al., *Reverse annealing of the effective impurity concentration and long term operational scenario for silicon detectors in future collider experiments*, *Nucl. Instrum. Meth.* **A 342** (1994) 119.

[60] M.M. Angarano et al., *Study of radiation damage and substrate resistivity effects from beam test of silicon microstrip detectors using LHC readout electronics*, CMS-NOTE-2000-053, http://cdsweb.cern.ch/record/593000.

[61] H.W. Gu et al., *High voltage operation of heavily irradiated silicon microstrip detectors*, CMS-CR-1999-010, http://cdsweb.cern.ch/record/687105.

[62] PARTICLE DATA GROUP collaboration, S. Eidelman et al., *Review of particle physics*, *Phys. Lett.* **B 592** (2004) 1.

[63] P. Lecoq et al, *Lead tungstate ($PbWO_4$) scintillators for LHC EM calorimetry*, *Nucl. Instrum. Meth.* **A 365** (1995) 291;
S. Baccaro et al., *Influence of La^{3+}-doping on radiation hardness and thermoluminescence characteristics of $PbWO_4$*, *Phys. Status Solidi* **A 160** (1997) R5;
E. Auffray et al., *Improvement of several properties of lead tungstate crystals with different doping ions*, *Nucl. Instrum. Meth.* **A 402** (1998) 75;
M. Kobayashi et al., *Improvement of radiation hardness of $PbWO_4$ scintillating crystals by La-doping*, *Nucl. Instrum. Meth.* **A 404** (1998) 149;
H.F. Chen et al., *Radiation damage measurements of undoped lead tungstate crystals for the CMS electromagnetic calorimeter at LHC*, *Nucl. Instrum. Meth.* **A 414** (1998) 149;
H. Hofer et al., *Afterglow measurements of lead tungstate crystals*, *Nucl. Instrum. Meth.* **A 433** (1999) 630;
M. Kobayashi et al., *Significant improvement of $PbWO_4$ scintillating crystals by doping with trivalent ions*, *Nucl. Instrum. Meth.* **A 434** (1999) 412.

[64] A.A. Annenkov, M.V. Korzhik and P. Lecoq, *Lead tungstate scintillation material*, *Nucl. Instrum. Meth.* **A 490** (2002) 30.

[65] I. Dafinei, E. Auffray, P. Lecoq M. Schneegans, *Lead tungstate for high energy calorimetry*, *Mat. Res. Soc. Symp. Proc.* **348** (1994) 99, also in *Proceedings of Scintillator and Phosphor Materials Symposium*, San Francisco U.S.A. (1994).

[66] X.D. Qu, L.Y. Zhang and R.Y. Zhu, *Radiation induced color centers and light monitoring for lead tungstate crystals*, *IEEE Trans. Nucl. Sci.* **47** (2000) 1741.

[67] S. Baccaro et al., *Ordinary and extraordinary complex refractive index of the lead tungstate ($PbWO_4$) crystals*, *Nucl. Instrum. Meth.* **A 385** (1997) 209.

[68] D. Graham and C. Seez, *Simulation of Longitudinal Light Collection Uniformity in PbWO4 crystals*, CMS-NOTE-1996-002, http://cdsweb.cern.ch/record/687541.

[69] CMS collaboration, *The electromagnetic calorimeter project: technical design report*, CERN-LHCC-97-033, http://cdsweb.cern.ch/record/349375; *Changes to CMS ECAL*

2008 JINST 3 S08004

electronics: addendum to the technical design report, CERN-LHCC-2002-027, http://cdsweb.cern.ch/record/581342.

[70] R.Y. Zhu, *Radiation damage in scintillating crystals*, *Nucl. Instrum. Meth.* **A 413** (1998) 297.

[71] M. Huhtinen et al., *High-energy proton induced damage in $PbWO_4$ calorimeter crystals*, *Nucl. Instrum. Meth.* **A 545** (2005) 63.

[72] P. Lecomte et al., *High-energy proton induced damage study of scintillation light output from $PbWO_4$ calorimeter crystals*, *Nucl. Instrum. Meth.* **A 564** (2006) 164.

[73] M. Lebeau, F. Mossire and H. Rezvani Naraghi, *The super-basket: incorporation of conical reinforcements in the CMS ECAL EB support structure*, CMS-NOTE-2003-010, http://cdsweb.cern.ch/record/687869.

[74] THE CMS ELECTROMAGNETIC CALORIMETER group, P. Adzic et al., *Results of the first performance tests of the CMS electromagnetic calorimeter*, *Eur. Phys. J.* **C44** (2006) S1.1

[75] K. Deiters et al., *Double screening tests of the CMS ECAL avalanche photodiodes*, *Nucl. Instrum. Meth.* **A 543** (2005) 549.

[76] S. Baccaro et al., *Radiation damage effect on avalanche photo diodes*, *Nucl. Instrum. Meth.* **A 426** (1999) 206.

[77] A. Bartoloni, *The power supply system for CMS-ECAL APDs*, in *Proceedings of the* 7th *Workshop on Electronics for LHC Experiments*, Stockholm Sweden (2001), http://cdsweb.cern.ch/record/530694;
A. Bartoloni et al., *High voltage system for the CMS electromagnetic calorimeter*, *Nucl. Instrum. Meth.* **A 582** (2007) 462.

[78] K.W. Bell et al., *Vacuum phototriodes for the CMS electromagnetic calorimeter endcap*, *IEEE Trans. Nucl. Sci.* **51** (2004) 2284;
N.A. Bajanov et al., *Fine-mesh photodetectors for CMS endcap electromagnetic calorimeter*, *Nucl. Instrum. Meth.* **A 442** (2000) 146;
Yu. Blinnikov et al., *Radiation hardness, excess noise factor and short-term gain instability of vacuum phototriodes for the operation in pseudorapidity range* $1.5 \leq \eta \leq 3.0$ *at CMS ECAL*, *Nucl. Instrum. Meth.* **A 504** (2003) 228.

[79] K.W. Bell et al., *The response to high magnetic fields of the vacuum photriodes for the Compact Muon Solenoid endcap electromagnetic calorimeter*, *Nucl. Instrum. Meth.* **A 504** (2003) 255.

[80] Yu. I. Gusev et al., *Super radiation hard vacuum phototriodes for the CMS endcap ECAL*, *Nucl. Instrum. Meth.* **A 535** (2004) 511.

[81] B. Betev et al., *Low voltage supply system for the very front end readout electronics of the CMS electromagnetic calorimeter*, in 9th *Workshop on Electronics for LHC Experiments*,

2008 JINST 3 S08004

Amsterdam The Netherlands (2003), CERN-LHCC-2003-055 page 353, http://cdsweb.cern.ch/record/744282.

[82] M. Raymond et al., *The MGPA electromagnetic calorimeter readout chip for CMS*, in 9th *Workshop on Electronics for LHC Experiments*, Amsterdam The Netherlands (2003), CERN-LHCC-2003-055 page 83, http://cdsweb.cern.ch/record/712053.

[83] G. Minderico et al., *A CMOS low power, quad channel,* 12 *bit,* 40 *MS/s pipelined ADC for applications in particle physics calorimetry*, in 9th *Workshop on Electronics for LHC Experiments*, Amsterdam The Netherlands (2003), CERN-LHCC-2003-055 page 88, http://cdsweb.cern.ch/record/712054.

[84] M. Hansen, *The new readout architecture for the CMS ECAL*, in 9th *Workshop on Electronics for LHC Experiments*, Amsterdam The Netherlands (2003), CERN-LHCC-2003-055 page 78, http://cdsweb.cern.ch/record/712052.

[85] R. Alemany et al., *CMS ECAL off-detector electronics*, in *Proceedings of the* 11th *International Conference on Calorimetry in High Energy Physics (CALOR2004)*, Perugia Italy (2004), CMS-CR-2004-022, http://cdsweb.cern.ch/record/787474.

[86] R. Alemany et al., *Overview of the ECAL off-detector electronics of the CMS experiment*, *IEEE Nucl. Sci. Symp. Conf. Rec.* **2** (2004) 1053.

[87] P. Paganini et al., *Tests of the boards generating the CMS ECAL trigger primitives: from the on-detector electronics to the off-detector electronics system*, in *Proceedings of the* 10th *Workshop on Electronics for LHC Experiments*, Boston U.S.A. (2004), CMS-CR-2004-066, http://cdsweb.cern.ch/record/814461.

[88] N. Almeida et al., *Calorimeter trigger synchronization in CMS, implementation and test system*, in *Proceedings of the* 10th *Workshop on Electronics for LHC Experiments*, Boston U.S.A. (2004), CMS-CR-2004-068, http://cdsweb.cern.ch/record/823745.

[89] N. Almeida et al., *Data concentrator card and test system for the CMS ECAL readout*, in *Proceedings of the* 9th *Workshop on Electronics for the LHC Experiments*, Amsterdam The Netherlands (2003), CMS-CR-2003-056, http://cdsweb.cern.ch/record/692739.

[90] R. Alemany et al., *Test results of the data concentrator card of the CMS electromagnetic calorimeter readout system*, in *Proceedings of the* 10th *Workshop on Electronics for LHC Experiments*, Boston U.S.A. (2004), http://cdsweb.cern.ch/record/814237.

[91] N. Almeida et al., *The selective read-out processor for the CMS electromagnetic calorimeter*, *IEEE Nucl. Sci. Symp. Conf. Rec.* **3** (2004) 1721.

[92] R. Loos et al., *CMS ECAL Preshower and Endcap Engineering Design Review. v.2 - Preshower*, CMS-2000-054-MEETING, CERN-ECAL-EDR-4, http://cdsweb.cern.ch/record/539819.

2008 JINST 3 S08004

[93] P. Aspell et al., *PACE3: A large dynamic range analogue memory ASIC assembly designed for the readout of silicon sensors in the LHC CMS preshower*, in *Proceedings of the* 10th *Workshop on Electronics for LHC Experiments*, Boston U.S.A. (2004), http://cdsweb.cern.ch/record/814076.

[94] I. Evangelou, *CMS Preshower in-situ absolute calibration*, in *Proceedings of the* 9th *ICATPP conference*, Villa-Olmo, Como Italy (2005), http://cdsweb.cern.ch/record/981557.

[95] K. Kloukinas et al., *Kchip: a radiation tolerent digital data concentrator chip for the CMS Preshower detector*, in *Proceedings of the* 9th *Workshop on Electronics for LHC Experiments*, Amsterdam The Netherlands (2003), CERN-LHCC-2003-055 page 66, http://cdsweb.cern.ch/record/712049.

[96] G. Antchev et al., *A VME-based readout system for the CMS preshower sub-detector*, *IEEE Trans. Nucl. Sci.* **54** (2007) 623.

[97] S. Reynaud and P. Vichoudis, *A multi-channel optical plug-in module for gigabit data reception*, in *Proceedings of the* 12th *Workshop on Electronics for LHC and Future Experiments*, Valencia Spain (2006), CERN-LHCC-2007-006, http://cdsweb.cern.ch/record/1027469.

[98] D. Barney et al., *Implementation of on-line data reduction algorithms in the CMS endcap preshower data concentrator card*, 2007 *JINST* **2** P03001.

[99] P. Adzic et al., *The detector control system for the electromagnetic calorimeter of the CMS experiment at the LHC*, in *Proceedings of the* 10th *International Conference on Accelerator and Large Experimental Physics Control Systems (ICALEPS2005)*, Geneva Switzerland, CMS-CR-2005-028, http://cdsweb.cern.ch/record/904796.

[100] P. Milenovic et al., *Performance of the CMS ECAL safety system for Super Modules SM*0 *and SM*1, *Nucl. Instrum. Meth.* **A 554** (2005) 427.

[101] F. Cavallari et al., *CMS ECAL intercalibration of ECAL crystals using laboratory measurements*, CMS-NOTE-2006-073, http://cdsweb.cern.ch/record/962038.

[102] W. Bertl et al., *Feasibility of intercalibration of CMS ECAL supermodules with cosmic rays*, *Eur. Phys. J.* **C 41** (2005) S2.11;
F. Ferri and P. Govoni, *The CMS electromagnetic calorimeter pre-calibration with cosmic rays and test beam electrons*, in *Proceedings of VCI2007*, Vienna Austria, CMS-CR-2007-012, http://cdsweb.cern.ch/record/1027034.

[103] L. Zhang et al., *Performance of the monitoring light source for the CMS lead tungstate crystal calorimeter*, *IEEE Trans. Nucl. Sci.* **52** (2005) 1123;
M. Anfreville et al., *Laser monitoring system for the CMS lead tungstate crystal calorimeter*, CMS-NOTE-2007-028, http://cdsweb.cern.ch/record/1073694.

2008 JINST 3 S08004

[104] A. Ghezzi et al., *Analysis of the response evolution of the CMS electromagnetic calorimeter under electron and pion irradiation*, CMS-NOTE-2006-038, http://cdsweb.cern.ch/record/934066.

[105] P. Aspell et al., *Results from the* 1999 *beam test of a preshower prototype*, CMS-NOTE-2000-001, http://cdsweb.cern.ch/record/687210.

[106] P. Adzic et al., *Reconstruction of the signal amplitude of the CMS electromagnetic calorimeter*, *Eur. Phys. J.* **C 46** (2006) S1.23.

[107] P. Adzic et al., *Energy resolution of the barrel of the CMS electromagnetic calorimeter*, 2007 *JINST* **2** P04004.

[108] CMS collaboration, *The hadron calorimeter project: technical design report*, CERN-LHCC-97-031, http://cdsweb.cern.ch/record/357153.

[109] P. Cushman, A. Heering and A. Ronzhin, *Custom HPD readout for the CMS HCAL*, *Nucl. Instrum. Meth.* **A 442** (2000) 289.

[110] A. Heister et al., *Measurement of jets with the CMS detector at the LHC*, CMS-NOTE-2006-036, http://cdsweb.cern.ch/record/933705.

[111] H. Pi et al., *Measurement of missing transverse energy with the CMS detector at the LHC*, *Eur. Phys. J.* **C 46** (2006) 45, CMS-NOTE-2006-035, http://cdsweb.cern.ch/record/933706.

[112] S. Abdullin et al., *Design, performance, and calibration of CMS hadron-barrel calorimeter wedges*, *Eur. Phys. J.* **55** (2008) 159, CMS-NOTE-2006-138, http://cdsweb.cern.ch/record/1049915.

[113] V.I. Kryshkin and A.I. Ronzhin, *An optical fiber readout for scintillator calorimeters* *Nucl. Instrum. Meth.* **A 247** (1986) 583.

[114] M.G. Albrow et al., *A uranium scintillator calorimeter with plastic-fibre readout*, *Nucl. Instrum. Meth.* **A 256** (1987) 23.

[115] S. Banerjee and S. Banerjee, *Performance of hadron calorimeter with and without HO*, CMS-NOTE-1999-063, http://cdsweb.cern.ch/record/687178.

[116] N. Akchurin and R. Wigmans, *Quartz fibers as active elements in detectors for particle physics*, *Rev. Sci. Instrum.* **74** (2002) 2955.

[117] I. Dumanoglu et al., *Radiation-hardness studies of high OH^- content quartz fibers irradiated with* 500 *MeV electrons*, *Nucl. Instrum. Meth.* **A 490** (2002) 444.

[118] N. Akchurin et al., *Effects of radiation damage and their consequences for the performance of the forward calorimeters in the CMS experiment*, *Nucl. Instrum. Meth.* **B 187** (2002) 66.

[119] R. Thomas, *Study of radiation hardness of optical fibers*, M.Sc. Thesis, Texas Tech University, U.S.A. (2004).

2008 JINST 3 S08004

[120] A. Panagiotou et al., *CASTOR engineering design report*, CMS Note in preparation (2008).

[121] X.N. Wang and M. Gyulassy, *HIJING: a Monte Carlo model for multiple jet production in pp, pA and AA collisions*, *Phys. Rev.* **D 44** (1991) 3501;
X.N. Wang, *A pQCD-based approach to parton production and equilibration in high-energy nuclear collisions*, *Phys. Rept.* **280** (1997) 287.

[122] D. D'Enterria et al., *CMS physics technical design report: addendum on high density QCD with heavy ions*, *J. Phys.* **G 34** (2007) 2307, CERN-LHCC-2007-009, http://cdsweb.cern.ch/record/1019832.

[123] M. Albrow et al., *Prospects for diffractive and forward physics at the LHC*, CMS-NOTE-2007-002, CERN-LHCC-2006-039, http://cdsweb.cern.ch/record/1005180.

[124] G. Mavromanolakis, *Quartz fiber calorimetry and calorimeters*, physics/0412123v1.

[125] X. Aslanoglou et al., *First performance studies of a prototype for the CASTOR forward calorimeter at the CMS experiment*, arXiv:0706.2576v3.

[126] X. Aslanoglou et al., *Performance studies of prototype II for the CASTOR forward calorimeter at the CMS experiment*, *Eur. Phys. J.* **C 52** (2007) 495 [arXiv:0706.2641v2].

[127] A.S. Ayan et al., *CMS Zero-Degree-Calorimeter (ZDC). Technical design report*, in preparation.

[128] O.A. Grachov et al., *Status of zero degree calorimeter for CMS experiment*, *AIP Conf. Proc.* **867** (2006) 258 [nucl-ex/0608052].

[129] E.H. Hoyer, W.C. Turner and N.V. Mokhov, *Absorbers for the high luminosity insertions of the LHC*, in *Proceedings of the* 6th *European Particle Accelerator Conference*, Stockholm Sweden (1998), http://accelconf.web.cern.ch/AccelConf/e98/PAPERS/MOP13C.PDF.

[130] J.-F. Beche et al., *An ionization chamber shower detector for the LHC luminosity monitor*, *IEEE Nucl. Sci. Symp. Conf. Rec.* **1** (2000) 5.

[131] O.A. Grachov et al., *Measuring photons and neutrons at zero degrees in CMS*, nucl-ex/0703001.

[132] CMS collaboration, *The CMS muon project, technical design report*, CERN-LHCC-97-032, http://cdsweb.cern.ch/record/343814.

[133] M. De Giorgi et al., *Design and simulations of the trigger electronics for the CMS muon barrel chambers*, *Proceedings of the first Workshop on Electronics for LHC Experiments*, Lisbon Portugal (1995), CERN-LHCC-95-56, http://cdsweb.cern.ch/record/1062706.

[134] R. Veenhof, *Garfield. A drift chamber simulation program user's guide*, CERN Program Library W5050 (1994).

2008 JINST 3 S08004

[135] T. Zhao et al., *A study of electron drift velocity in Ar-CO_2 and Ar-CO_2-CF_4 gas mixtures*, *Nucl. Instrum. Meth.* **A 340** (1994) 485.

[136] A. Benvenuti et al., *Simulations in the development of the barrel muon chambers for the CMS detector at LHC*, *Nucl. Instrum. Meth.* **A 405** (1998) 20.

[137] CMS MUON group, G. Alampi et al., *Electrode strip deposition for the CMS barrel drift tube system*, CMS-NOTE-2006-144, http://cdsweb.cern.ch/record/1000408.

[138] F. Gonella and M. Pegoraro, *A prototype frontend ASIC for the readout of the drift tubes of CMS barrel muon chambers*, in 4th *Workshop on Electronics for LHC Experiments*, CERN-LHCC-98-036 page 257, http://cdsweb.cern.ch/record/1062709.

[139] L. Barcellan et al., *Single events effects induced by heavy ions on the frontend ASIC developed for the muon DT chambers*, LNL Annual Report (2000) page 247, http://cdsweb.cern.ch/record/1062712.

[140] C. Fernandez Bedoya et al., *Electronics for the CMS muon drift tube chambers: the read-out minicrate*, *IEEE Trans. Nucl. Sci.* **52** (2005) 944.

[141] J. Christiansen et al., *A data driven high performance time to digital converter*, *Proceedings of the* 6th *Workshop on Electronics for LHC Experiments*, Cracow Poland (2000), CERN-2000-010 page 169, http://cdsweb.cern.ch/record/478865.

[142] P. Moreira et al., *A radiation tolerant gigabit serializer for LHC data transmission*, *Proceedings of the* 7th *workshop on electronics for LHC experiments*, Stockholm Sweden (2001), CERN-2001-005 page 145, http://cdsweb.cern.ch/record/588665.

[143] G. Dellacasa, V. Monaco and A. Staiano, *DDU: the front end driver system (FED) of the CMS drifttube detector*, *Nucl. Phys.* **B 177-178** *(Proc. Suppl.)* (2008) 281, also in *Proceedings of hadron collider physics*, La Biodola, Isola d'Elba Italy (2007).

[144] C. Albajar et al., *Test beam analysis of the first CMS drift tube muon chamber*, *Nucl. Instrum. Meth.* **A 525** (2004) 465.

[145] M. Aguilar-Benitez et al., *Study of magnetic field effects in drift tubes for the barrel muon chambers of the CMS detector at the LHC*, *Nucl. Instrum. Meth.* **A 416** (1998) 243.

[146] M. Aguilar-Benitez et al., *Construction and test of the final CMS barrel drift tube muon chamber prototype*, *Nucl. Instrum. Meth.* **A 480** (2002) 658.

[147] P. Arce et al., *Bunched beam test of the CMS drift tubes local muon trigger*, *Nucl. Instrum. Meth.* **A 534** (2004) 441.

[148] M. Aldaya et al., *Results of the first integration test of the CMS drift tubes muon trigger*, *Nucl. Instrum. Meth.* **A 579** (2007) 951.

[149] G. Charpak and F. Sauli, *High-accuracy, two-dimensional read-out in multiwire proportional chambers*, *Nucl. Instrum. Meth.* **113** (1973) 381.

2008 JINST 3 S08004

[150] C. Anderson et al., *Effect of gas composition on the performance of cathode strip chambers for the CMS endcap muon system*, CMS-NOTE-2004-033, http://cdsweb.cern.ch/record/837542.

[151] T. Ferguson et al., *Anode front-end electronics for the cathode strip chambers of the CMS endcap muon detector*, *Nucl. Instrum. Meth.* **A 539** (2005) 386.

[152] R. Breedon et al., *Performance and radiation testing of a low-noise switched capacitor array for the CMS endcap muon system*, in *Proceedings of the* 6th *Workshop on Electronics for LHC Experiments*, CMS-CR-2000-013, http://cdsweb.cern.ch/record/478866.

[153] M.M. Baarmand et al., *Spatial resolution attainable with cathode strip chambers at the trigger level*, *Nucl. Instrum. Meth.* **A 425** (1999) 92.

[154] V. Barashko, *Performance validation tests of the cathode strip chambers for CMS muon system*, *IEEE Nucl. Sci. Symp. Conf. Rec.* **2** (2005) 827.

[155] E. Gatti et al., *Optimum geometry for strip cathodes on grids in MWPC for avalanche localization along the anode wires*, *Nucl. Instrum. Meth.* **163** (1979) 83.

[156] D. Acosta et al., *Aging tests of full scale CMS muon cathode strip chambers*, *Nucl. Instrum. Meth.* **A 515** (2003) 226.

[157] L. Malter, *Thin film field emission*, *Phys. Rev.* **50** (1936) 48.

[158] R. Breedon et al., *Results of radiation test of the cathode front-end board for CMS endcap muon chambers*, *Nucl. Instrum. Meth.* **A 471** (2001) 340.

[159] R. Santonico and R. Cardarelli, *Development of resistive plate counters*, *Nucl. Instrum. Meth.* **187** (1981) 377.

[160] R. Cardarelli, A. Di Ciaccioa and R. Santonico, *Performance of a resistive plate chamber operating with pure CF_3Br*, *Nucl. Instrum. Meth.* **A 333** (1993) 399.

[161] M. Abbrescia et al., *The simulation of resistive plate chambers in avalanche mode: charge spectra and efficiency*, *Nucl. Instrum. Meth.* **A 431** (1999) 413.

[162] M. Abbrescia et al., *Local and global performance of double-gap resistive plate chambers operated in avalanche mode*, *Nucl. Instrum. Meth.* **A 434** (1999) 244.

[163] M. Abbrescia et al., *Study of long term performance of CMS RPC under irradiation at the CERN GIF*, *Nucl. Instrum. Meth.* **A 533** (2004) 102.

[164] M. Abbrescia et al., *Neutron irradiation of the RPCs for the CMS experiment*, *Nucl. Instrum. Meth.* **A 508** (2003) 120.

[165] M. Abbrescia et al., *New developments on front-end electronics for the CMS resistive plate chambers*, *Nucl. Instrum. Meth.* **A 456** (2000) 143.

2008 JINST 3 S08004

[166] M. Abbrescia et al., *Long term perfomance of double gap resistive plate chamber under gamma irradiation*, *Nucl. Instrum. Meth.* **A 477** (2002) 293.

[167] M. Abbrescia et al., *Neutron induced single event upset on the RPC front-end chips for the CMS experiment*, *Nucl. Instrum. Meth.* **A 484** (2002) 494.

[168] M. Abbrescia et al., *An RPC-based technical trigger for the CMS experiment*, in *Proceedings of the* 12th *Workshop on Electronics for LHC and Future Experiments*, Valencia Spain (2006), http://cdsweb.cern.ch/record/1000404.

[169] G. Iaselli et al., *Properties of $C_2H_2F_4$-based gas mixture for avalanche mode operation of Resistive Plate Chambers*, *Nucl. Instrum. Meth.* **A 398** (1997) 173.

[170] M. Abbrescia et al., *Gas analysis and monitoring systems for the RPC detector of CMS at LHC*, *IEEE Nucl. Sci. Symp. Conf. Rec.* **2** (2006) 891 [Frascati preprint LNF-06-34(P)].

[171] M. Abbrescia et al., *HF production in CMS-resistive plate chambers*, *Nucl. Phys.* **B 158** *(Proc. Suppl.)* (2006) 30.

[172] M. Abbrescia et al., *The bakelite for the RPCs of the experiment CMS*, *Nucl. Instrum. Meth.* **A 456** (2000) 132;
M. Abbrescia et al., *Production and quality control of the Barrel RPC chambers of the CMS experiment*, *Nucl. Phys.* **B 150** *(Proc. Suppl.)* (2006) 290;
M. Abbrescia et al., *Quality control tests for the CMS barrel RPCs*, *Nucl. Phys.* **B 158** *(Proc. Suppl.)* (2006) 73;
A. Ball et al., *Cosmic ray certification of the first* 100 *CMS endcap RPCs and the corresponding construction database*, *Nucl. Phys.* **B 158** *(Proc. Suppl.)* (2006) 99;
Z. Aftab et al., *Production and quality control for the CMS endcap RPCs*, *Nucl. Phys.* **B 158** *(Proc. Suppl.)* (2006) 16;
Z. Aftab et al., *Assembly and quality certification for the first station of the endcap RPCs (RE1)*, *Nucl. Phys.* **B 158** *(Proc. Suppl.)* (2006) 103.

[173] M. Abbrescia et al., *Resistive plate chambers performances at cosmic rays fluxes*, *Nucl. Instrum. Meth.* **A 359** (1995) 603.

[174] M. Abbrescia et al., *Cosmic ray tests of double-gap resistive plate chambers for the CMS experiment*, *Nucl. Instrum. Meth.* **A 550** (2005) 116.

[175] CMS, *CMS muon detector survey documents*, EDMS document CMS-00000083880, https://edms.cern.ch/cedar/plsql/cms.

[176] C. Carneiro, R. Goudard and C. Humbertclaude, *CMS MAB prototype-deformation test under load and humidity-measurements from July to October* 2002, EDMS Doc. CMS-MA-UR-0001, http://cdsweb.cern.ch/record/1062715, also https://edms.cern.ch/cedar/plsql/cms.

2008 JINST 3 S08004

[177] G. Szekely et al., *Muon barrel alignment system based on a net of PC/*104 *board computers*, in *Proceedings of the* 9th *workshop on electronics for LHC experiments*, Amsterdam The Netherlands (2003), CERN-2003-006, http://cdsweb.cern.ch/record/722098.

[178] M. Hohlmann et al., *Design and performance of the alignment system for the CMS muon endcaps*, *IEEE Nucl. Sci. Symp. Conf. Rec.* **1** (2006) 489;
R.H. Lee, *Simulation and study of the CMS Endcap Muon alignment scheme*, Ph.D. Thesis, Purdue University, U.S.A (2002).

[179] J. Moromisato et al., *The development of totally transparent position sensors*, *Nucl. Instrum. Meth.* **A 538** (2005) 234.

[180] M. Ripert, *Calibration of analog sensors for the alignment of muon chambers in the CMS experiment*, M.Sc. thesis, Florida Institute of Technology, U.S.A. (2005).

[181] A. Calderón et al., *Large size high performance transparent amorphous silicon sensors for laser beam position detection*, *Nucl. Instrum. Meth.* **A 565** (2006) 603.

[182] A. Lopez Virto, *Caracterizacion y pruebas de validacion del sistema link de alineamiento de CMS*, Ph.D. Thesis, Universidad de Cantabria, Spain (2003).

[183] A. Calderón, *Construccion, calibracion y evaluacion del sistema link de alineamiento del espectrometro de muones del experimento CMS*, PhD Thesis, Universidad de Cantabria, Spain (2006).

[184] *ELMB Boards*, http://elmb.web.cern.ch/ELMB/elmb128.html.

[185] P. Arce, *Object oriented software for simulation and reconstruction of big alignment systems*, *Nucl. Instrum. Meth.* **A 502** (2003) 696.

[186] D.E. Stewart and Z. Leyk, *Meschach library*, http://www.netlib.org/c/meschach/readme.

[187] CMS collaboration, *The TriDAS project, technical design report. Volume 1: The level-1 trigger*, CERN-LHCC-2000-038, http://cdsweb.cern.ch/record/706847.

[188] CMS collaboration, *The TriDAS project, technical design report. Volume 2: Data acquisition and high-level trigger technical design report*, CERN-LHCC-2002-026, http://cdsweb.cern.ch/record/578006.

[189] CMS COLLABORATION group, W. Adam et al., *The CMS high level trigger*, *Eur. Phys. J.* **C 46** (2005) 605 [hep-ex/0512077].

[190] I. Magrans de Arbril, C.-E. Wulz and J. Varela, *Conceptual design of the CMS trigger supervisor*, *IEEE Trans. Nucl. Sci.* **53** (2006) 474.

[191] P. Chumney et al., *Level-*1 *regional calorimeter trigger system for CMS*, in *Proceedings of Computing in High Energy Physics and Nuclear Physics*, La Jolla (2003), hep-ex/0305047.

2008 JINST 3 S08004

[192] See http://www.hep.ph.ic.ac.uk/cms/gct.

[193] See http://www.picmg.org/v2internal/microTCA.htm.

[194] RD5 collaboration, F. Gasparini et al., *Bunch crossing identification at LHC using a mean-timer technique*, *Nucl. Instrum. Meth.* **A 336** (1993) 91.

[195] M. Andlinger et al., *Pattern Comparator Trigger (PACT) for the muon system of the CMS experiment*, *Nucl. Instrum. Meth.* **A 370** (1996) 389.

[196] C. Albajar et al., *Conceptual design of an improved CMS RPC muon trigger using the hadron outer scintillators*, *Nucl. Instrum. Meth.* **A 545** (2005) 97.

[197] J. Erö et al., *The CMS drift tube trigger track finder*, CMS-NOTE-2008-009, http://cdsweb.cern.ch/record/1103001.

[198] D. Acosta et al., *Performance of a pre-production track-finding processor for the level-1 trigger of the CMS endcap muon system*, in *Proceedings of the* 10th *Workshop on Electronics for LHC and Future Experiments*, Boston U.S.A. (2004), http://cdsweb.cern.ch/record/814321.

[199] H. Sakulin et al., *Implementation and test of the first-level global muon trigger of the CMS experiment*, in *Proceedings of the* 11th *Workshop on Electronics for LHC and Future Experiments*, Heidelberg Germany (2005), http://cdsweb.cern.ch/record/921035.

[200] C.-E. Wulz, *Concept of the first level global trigger for the CMS experiment at LHC*, *Nucl. Instrum. Meth.* **A 473** (2001) 231.

[201] A. Taurok, H. Bergauer and M. Padrta, *Implementation and synchronisation of the first level global trigger for the CMS experiment at LHC*, *Nucl. Instrum. Meth.* **A 473** (2001) 243.

[202] P. Glaser et al., *Design and development of a graphical setup software for the CMS global trigger*, *IEEE Trans. Nucl. Sci.* **53** (2006) 1282.

[203] CMS TRIGGER and DATA ACQUISITION GROUP, *CMS L1 trigger control system*, CMS-NOTE-2002-033, http://cdsweb.cern.ch/record/687458.

[204] B.G. Taylor, *Timing distribution at the LHC*, in *Proceedings of the* 8th *Workshop on Electronics for LHC and Future Experiments*, Colmar France (2002), http://cdsweb.cern.ch/record/592719.

[205] T. Geralis et al., *The global trigger processor emulator system for the CMS experiment*, *IEEE Trans. Nucl. Sci.* **52** (2005) 1679.

[206] E. Cano et al., *FED-kit design for CMS DAQ system*, *Proceedings of the* 8th *Workshop on Electronics for LHC Experiments*, Colmar France (2002), http://cdsweb.cern.ch/record/594312.

[207] B.G. Taylor, *TTC distribution for LHC detectors*, *IEEE Trans. Nucl. Sci.* **45** (1998) 82, see, http://www.cern.ch/TTC/intro.html.

2008 JINST 3 S08004

[208] A. Racz, R. McLaren and E. van der Bij, *The S-Link64 bit extension specification: S-Link64*, http://hsi.web.cern.ch/HSI/s-link.

[209] N.J. Boden et al., *Myrinet — A gigabit per second local area network*, *IEEE Micro* **15** (1995) 29.

[210] G. Bauer et al., *The Tera-bit/s super-fragment builder and trigger throttling system for the Compact Muon Solenoid experiment at CERN*, *IEEE Trans. Nucl. Sci.* **55** (2008) 190, also in 15th *IEEE Real Time Conference* 2007, Batavia U.S.A., CMS-CR-2007-020, http://cdsweb.cern.ch/record/1046342.

[211] G. Bauer et al., *CMS DAQ event builder based on gigabit ethernet*, *IEEE Trans. Nucl. Sci.* **55** (2008) 198, also in 15th *IEEE real time conference* 2007, Batavia U.S.A., CMS-CR-2007-016, http://cdsweb.cern.ch/record/1046338.

[212] C.-D. Jones et al., *The new CMS data model and framework*, in *Proocedings of the Conference on Computing in High Energy Physics*, Mumbai India (2006).

[213] QUATTOR is a system administration toolkit, http://www.quattor.org or http://quattor.web.cern.ch.

[214] J. Gutleber and L. Orsini, *Software architecture for processing clusters based on I2O*, *Cluster Comput.* **5** (2002) 55.

[215] V. Briglijevic et al., *Using XDAQ in application scenarios of the CMS experiment*, in *Proocedings of Computing in High Energy Physics*, La Jolla U.S.A. (2003), CMS-CR-2003-007, http://cdsweb.cern.ch/record/687845.

[216] O. Nierstrasz, S. Gibbs and D. Tsichritzis, *Component-oriented software development*, *Comm. ACM* **35** (1992) 160.

[217] D. Box et al., *Simple Object Access Protocol (SOAP)* 1.1, W3C Note 08, http://www.w3.org/TR/SOAP.

[218] For the I2O standard, http://developer.osdl.org/dev/opendoc/Online/Local/I20/index.html.

[219] See http://xdaqwiki.cern.ch, and references therein.

[220] R. Arcidiacono et al., *HyperDAQ — Where data acquisition meets the web*, in 10th *ICALEPCS International Conference on Accelerator and Large Experimental Physics Control Systems*, Geneva Switzerland (2005), http://accelconf.web.cern.ch/AccelConf/ica05/proceedings/pdf/O5_004.pdf.

[221] J. Boyer, *Canonical XML version* 1.0, W3C Recommendation, 16 August 2006, http://www.w3c.org/XML.

[222] Apache Axis is an XML based Web service framework, http://ws.apache.org/axis/.

[223] The Apache Tomcat servlet container, http://tomcat.apache.org.

2008 JINST 3 S08004

[224] *JCOP framework*, http://itcobe.web.cern.ch/itcobe/Projects/Framework/welcome.html.

[225] OLE for Process Control (OPC), http://www.opcfoundation.org/.

[226] R. Arcidiacono et al., *CMS DCS design concepts*, in *Proceedings of the* 10th *International Conference on Accelerator and Large Experimental Physics Control Systems (ICALEPCS2005)*, Geneva Switzerland (2005).

[227] L. Fernandez-Hernando et al., *Development of a CVD diamond beam condition monitor for CMS at the Large Hadron Collider*, *Nucl. Instrum. Meth.* **A 552** (2005) 183;
A. Macpherson, *Beam condition monitoring and radiation damage concerns of the experiment*, in *Proceedings of the XV LHC Project Chamonix Workshop*, Divonne Switzerland (2006);
D. Chong et al., *Validation of synthetic diamond for a beam condition monitor for the Compact Muon solenoid experiment*, *IEEE Trans. Nucl. Sci.* **54** (2007) 182.

[228] R.J. Tapper, *Diamond detectors in particle physics*, *Rept. Prog. Phys.* **63** (2000) 1273.

[229] R. Eusebi et al., *A diamond-based beam condition monitor for the CDF experiment*, *IEEE Trans. Nucl. Sci.* **2** (2006) 709.

[230] M. Brunisma et al., *CVD diamonds in the BaBar radiation monitoring system*, *Nucl. Phys.* **B 150** *(Proc. Suppl.)* (2006) 164.

[231] W. de Boer et al., *Radiation hardness of diamond and silicon sensors compared*, *Phys. Status Solidi* **A 204** (2007) 3004.

[232] B. Dehning et al., *The beam loss monitoring system*, in *Proceedings of the XIII LHC Project Chamonix Workshop*, Chamonix France (2004), http://cdsweb.cern.ch/record/726322;
E. Effinger et al., *The LHC beam loss monitoring system's data acquisition card*, in *Proceedings of LECC*, Valencia Spain (2006), http://cdsweb.cern.ch/record/1027422;
C. Zamantzas et al., *The LHC beam loss monitoring system's surface building installation*, in *Proceedings of LECC*, Valencia Spain (2006), http://cdsweb.cern.ch/record/1020105.

[233] C. Zamantzas, *The real-time data analysis and decision system for particle flux detection in the LHC accelerator at CERN*, Ph.D. Thesis, Brunel University, U.K., CERN-THESIS-2006-037, http://cdsweb.cern.ch/record/976628.

[234] R. Schmidt et al., *Beam interlocks for LHC and SPS*, in *Proceedings of the International Conference on Accelerator and Large Experimental Physics Control Systems (ICALEPCS)*, Gyeongju South Korea (2003), CERN-AB-2003-106-CO, http://cdsweb.cern.ch/record/693161;
B. Todd, *A beam interlock system for CERN high energy accelerators*, Ph.D. Thesis, Brunel University, U.K., CERN-THESIS-2007-019, http://cdsweb.cern.ch/record/1019495.

[235] J. Kaplon and W. Dabrowski, *Fast CMOS binary front end for silicon strip detectors at LHC experiments*, *IEEE Trans. Nucl. Sci.* **52** (2005) 2713.

2008 JINST 3 S08004

[236] J. Troska et al., *Optical readout and control systems for the CMS tracker*, *IEEE Trans. Nucl. Sci.* **50** (2003) 1067.

[237] J. Bol, *Strahlmonitore aus Diamant für primäre Teilchenstrahlen hoher Intensität*, Ph.D. Thesis, Karlsruhe University, Germany (2006), IEKP-KA-2006-8.

[238] J. Furletova, *Search for exotic processes in events with large missing transverse momentum in ZEUS at HERA*, Ph.D. thesis, Hamburg University, Germany, DESY-THESIS-2004-046, http://cdsweb.cern.ch/record/824243.

[239] G. Aguillion et al., *Thin scintillating tiles with high light yield for the OPAL endcaps*, *Nucl. Instrum. Meth.* **A 417** (1998) 266.

[240] C. Ohm, *Phase and intensity monitoring of the particle beams at the ATLAS experiment*, M.Sc. thesis, Linköping University, Sweden, http://www.ep.liu.se/abstract.xsql?dbid=9614.

[241] T. Wijnands, *Radiation monitoring for equipment in the LHC tunnel, functional specification*, 2005 EDMS Document 565013, https://edms.cern.ch/file/565013/0.2/LHC-PM-ES-0006-00-10.pdf;
C. Pignard and T. Wijnands, *Radiation tolerant commercial of the shelf components for the remote readout of PIN diodes and Radfets*, in *Proceedings of the RADECS Conference*, Cap d'Agde France (2005).

[242] J. Knobloch et al., *LHC computing grid: technical design report*, CERN-LHCC-2005-024, http://cdsweb.cern.ch/record/840543.

[243] CMS collaboration, *CMS computing: technical design report*, CERN-LHCC-2005-023, http://cdsweb.cern.ch/record/838359.

[244] R. Brun and F. Rademakers, *ROOT — An object oriented data analysis framework*, *Nucl. Instrum. Meth.* **A 389** (1997) 81, see also http://root.cern.ch.

[245] S. Kosyakov et al., *FroNtier: high performance database access using standard web components in a scalable multi-tier architecture*, in *Proceedings of the Conference on Computing in High Energy Physics*, Interlaken Switzerland (2004), http://cdsweb.cern.ch/record/865676.

[246] M. Aderholz et al., *Models of networked analysis at regional centres for LHC experiments (MONARC) — Phase* 2 *report,* 24$^{\text{th}}$ *March* 2000, CERN-LCB-2000-001, http://cdsweb.cern.ch/record/510694.

[247] http://lhcopn.cern.ch.

[248] J. Rehn et al., *PhEDEx high-throughput data transfer management system*, in *Proocedings of the conference on computing in high energy physics*, Mumbai India (2006).

[249] A. Fanfani et al., *Distributed Data Management in CMS*, in *Proocedings of the conference on computing in high energy physics*, Mumbai India (2006), CMS-CR-2006-013, http://cdsweb.cern.ch/record/933704.

[250] D. Spiga et al., *CMS workload management*, *Nucl. Phys.* **B 172** *(Proc. Suppl.)* (2007) 141.

2008 JINST 3 S08004

Physics Letters B 695 (2011) 424–443

Contents lists available at ScienceDirect

Physics Letters B

www.elsevier.com/locate/physletb

First measurement of the cross section for top-quark pair production in proton–proton collisions at $\sqrt{s} = 7$ TeV ☆

CMS Collaboration

CERN, Switzerland

ARTICLE INFO

Article history:
Received 30 October 2010
Received in revised form 18 November 2010
Accepted 26 November 2010
Available online 1 December 2010
Editor: M. Doser

Keywords:
CMS
LHC
Physics
Top quark
Cross section

ABSTRACT

The first measurement of the cross section for top-quark pair production in pp collisions at the Large Hadron Collider at center-of-mass energy $\sqrt{s} = 7$ TeV has been performed using a data sample corresponding to an integrated luminosity of 3.1 ± 0.3 pb^{-1} recorded by the CMS detector. This result utilizes the final state with two isolated, highly energetic charged leptons, large missing transverse energy, and two or more jets. Backgrounds from Drell–Yan and non-W/Z boson production are estimated from data. Eleven events are observed in the data with 2.1 ± 1.0 events expected from background. The measured cross section is $194 \pm 72(\text{stat.}) \pm 24(\text{syst.}) \pm 21(\text{lumi.})$ pb, consistent with next-to-leading order predictions.

Since its discovery [1,2], the properties of the top quark have been subject to numerous detailed studies [3], which until recently have only been possible at the Tevatron proton–antiproton collider. With the advent of the Large Hadron Collider (LHC) era [4], top-quark processes can be studied for the first time in multi-TeV proton–proton collisions. In both $p\bar{p}$ and pp collisions, top quarks are expected to be produced primarily via the strong interaction in top–antitop ($t\bar{t}$) pairs. At the LHC, the $t\bar{t}$ production mechanism is expected to be dominated by a gluon fusion process, whereas at the Tevatron, top-quark pairs are predominantly produced through quark–antiquark annihilation. Measurements of top-quark production at the LHC are therefore important new tests of our understanding of the $t\bar{t}$ production mechanism. This is a crucial component of the early LHC physics program, since many signatures of new physics models accessible at the LHC either suffer from top-quark production as a significant background or contain top quarks themselves.

In this Letter we present the first measurement of the cross section for $t\bar{t}$ production in proton–proton collisions at the LHC at center-of-mass energy $\sqrt{s} = 7$ TeV. The results are based on a data sample corresponding to an integrated luminosity of 3.1 ± 0.3 pb^{-1} [5] recorded by the CMS experiment [6] between March and August 2010. This measurement is an important milestone for CMS, demonstrating the experiment's capabilities in extracting an intricate signature.

Within the standard model, the top quark decays via the weak process $t \to Wb$ almost exclusively. Experimentally, top-quark pair events are categorized according to the decay of the two W bosons: the all-hadronic channel, in which both W bosons decay into quarks; the lepton + jets channel, in which one W boson decays leptonically, the other into quarks; and the dilepton channel, in which both W bosons decay into leptons. The measurement described herein is performed using the e^+e^-, $\mu^+\mu^-$, and $e^\pm\mu^\mp$ dilepton $t\bar{t}$ modes. These modes comprise $(6.45 \pm 0.11)\%$ [7] of the total branching fraction for $t\bar{t}$ when including contributions from tau leptons that subsequently decay to electrons and muons, as is done here. Therefore, the final state studied in this analysis contains two oppositely charged leptons (electrons or muons), two neutrinos from the W boson decays, and at least two jets of particles resulting from the hadronization of the b quarks. Similar measurements have been performed recently at the Tevatron [8,9].

The central feature of the CMS apparatus is a superconducting solenoid, 13 m in length and 6 m in diameter, which provides an axial magnetic field of 3.8 T. The bore of the solenoid is outfitted with various particle detection systems. Charged particle trajectories are measured by the silicon pixel and strip tracker, covering $0 < \phi < 2\pi$ in azimuth and $|\eta| < 2.5$, where the pseudorapidity η is defined as $\eta = -\ln[\tan\theta/2]$, with θ being the polar angle of the trajectory of the particle with respect to the beam direction. A crystal electromagnetic calorimeter (ECAL)

☆ © CERN, for the benefit of the CMS Collaboration.

E-mail address: cms-publication-committee-chair@cern.ch.

0370-2693/$ – see front matter
doi:10.1016/j.physletb.2010.11.058

and a brass/scintillator hadronic calorimeter (HCAL) surround the tracking volume; in this analysis the calorimetry provides high-resolution energy and direction measurements of electrons and hadronic jets. Muons are measured in gas detectors embedded in the steel return yoke outside the solenoid. The detector is nearly hermetic, allowing for energy balance measurements in the plane transverse to the beam directions. A two-tier trigger system selects the most interesting pp collision events for use in physics analysis. A more detailed description of the CMS detector can be found elsewhere [6].

The trigger providing the data sample used in this analysis is based on the presence of at least one charged lepton, either an electron or a muon, with a minimum transverse momentum p_T of 9 (15) GeV/c for the muon (electron). This data sample is used both for the selection of the signal and for signal-depleted control regions used for studies related to background processes. Simulated signal events that pass the event selection, as described below, satisfy the trigger requirements with an efficiency above 97% in the $\mu^+\mu^-$ decay mode and above 99% in the other two modes, in agreement with estimates from Z boson events in the data.

Before further consideration, events are required to have at least one good reconstructed pp interaction vertex [10]. Among these events, selection criteria are applied to reconstructed objects to identify candidates consistent with dilepton $t\bar{t}$ processes.

Muon candidates are reconstructed [11] using two algorithms that require consistent hits in the tracker and muon systems: one is an algorithm based on the matching of extrapolated trajectories from the silicon tracker to hits in the muon system (tracker-based muons); the second is an algorithm based on performing a global fit of consistent hits in the tracker and the muon system (globally-fitted muons). Candidates are required to have $p_T > 20$ GeV/c and $|\eta| < 2.5$. Additionally, the track associated with the muon candidate is required to have a minimum number of hits in the silicon tracker, to be consistent with originating from the beam spot, and to have a high-quality global fit including a minimum number of hits in the muon detector.

Electron candidates are reconstructed [12] starting from a cluster of energy deposits in the crystals of the ECAL, which is then matched to hits in the silicon tracker, used to initiate a special track reconstruction algorithm. The electron reconstruction algorithm takes into account the possibility of significant energy loss of the electron through bremsstrahlung as it traverses the material of the tracker. Electron candidates are required to have $p_T >$ 20 GeV/c and pseudorapidity $|\eta| < 2.5$. The electron candidate track is required to be consistent with originating from the beam spot. Requirements on the values of electron identification variables based on shower shape and track-cluster matching are applied to the reconstructed candidates; the criteria are optimized for inclusive $W \to e\nu$ selection and are designed to maximize the rejection of electron candidates from QCD multijet production while maintaining 90% efficiency for electrons from the decay of W/Z bosons. Electron candidates within $\Delta R = \sqrt{\Delta\phi^2 + \Delta\eta^2} < 0.1$ of a tracker-based or globally-fitted muon are rejected to remove fake electron candidates due to muon bremsstrahlung. In addition, electrons consistent with anomalous depositions in the ECAL or with photon conversions are rejected.

Charged leptons from the decay of W bosons are expected to be isolated from other activity in the event. For selected muon and electron candidates, a cone of $\Delta R < 0.3$ is constructed around the track direction at the origin and the scalar sum of the track transverse momenta and calorimeter energy deposits, projected onto a plane transverse to the beam, is calculated. The contribution from the candidate itself is excluded. If the value of this scalar sum is more than 15% of the candidate's transverse momentum, the candidate is considered to be non-isolated and is rejected.

Lepton trigger, identification, and isolation efficiencies are measured using inclusive Z events from data and are compared with simulation. All comparisons show good agreement, generally within 2%. The residual differences between the efficiencies estimated in data and simulation are treated as systematic uncertainties.

Events are required to have at least one pair of oppositely charged leptons. Both charged leptons are required to originate from within 1 cm along the beam line of the reconstructed pp interaction location. To veto contributions from Z production, the invariant mass of the dilepton system, $M_{\ell\ell}$, is required to be outside a ± 15 GeV/c^2 window centered at the mass of the Z boson for the e^+e^- and $\mu^+\mu^-$ modes. Additionally, dilepton candidate events with $M_{\ell\ell} < 10$ GeV/c^2 are removed, at essentially no penalty for the collected signal.

The neutrinos from the W boson decays do not interact with the detector and escape without depositing any of their energy. The presence of a neutrino manifests itself as an imbalance in the measured energy depositions; the imbalance in the projection perpendicular to the beam line (missing transverse energy, $\not\!\!E_T$) is an important distinguishing feature of $t\bar{t}$ events in this channel. At CMS there are several techniques for calculating $\not\!\!E_T$ [13]; here, the raw $\not\!\!E_T$, calculated from calorimeter signals, is made more accurate through a series of corrections taking into account the contribution from the minimally interacting muons and, most importantly, a per-track correction for the expected imperfect response of the calorimeter, derived from simulation. This track correction results in an improved energy resolution, especially for low-energy charged particles. Neither the dominant background processes, Drell–Yan $Z/\gamma^\star \to e^+e^-$ and $\mu^+\mu^-$, nor the difficult-to-model background from isolated lepton candidates produced in QCD multijet events, contain a natural source of large $\not\!\!E_T$. Hence, in the e^+e^- and $\mu^+\mu^-$ modes, $\not\!\!E_T > 30$ GeV is required; in the $e^\pm\mu^\mp$ mode a looser requirement of $\not\!\!E_T > 20$ GeV is used due to the significantly smaller contribution of Drell–Yan background.

Dilepton $t\bar{t}$ events will have at least two hadronic jets from the hadronization of the two b quarks. The anti-k_T clustering algorithm [14] with $R = 0.5$ is used for jet clustering. Jets are reconstructed using calorimeter information and corrected using reconstructed tracks [15]. Further corrections are applied to the raw jet momenta to establish a relative uniform response of the calorimeter in jet η and an absolute uniform response in jet p_T. The jet energy scale uncertainty for these track-corrected jets is 5%. Jet candidates are required to have $p_T > 30$ GeV/c, $|\eta| < 2.5$, and must not overlap with any electron or muon candidate within $\Delta R < 0.4$. Events with fewer than two jets are not used in the measurement.

The selection efficiency of signal events is evaluated in a simulated $t\bar{t}$ event sample modeled with the MadGraph event generator version 4.4.12 [16] with up to three additional hadronic jets. The events are subsequently processed with pythia (v. 6.420) [17] to provide showering of generated particles, and then processed with a full CMS detector simulation based on geant4 (v. 9.2 Rev01) [18]. The total next-to-leading order (NLO) cross section for top-quark pair production used here to scale simulated signal distributions is $\sigma_{t\bar{t}} = 158^{+23}_{-24}$ pb, as obtained with MCFM [19–22] for a top-quark mass of 172.5 GeV/c^2. Approximate next-to-next-to-leading order (NNLO) calculations for the $t\bar{t}$ cross section have been completed (see for example [23–29]) but are not used here. The theoretical uncertainty on the cross section includes the scale uncertainties, determined by varying the factorization and renormalization scales by factors of 2 and 0.5 around the central scale, corresponding to the assumed top-quark mass, and the uncertainties from the parton distribution functions (PDFs) and the value of α_S,

Table 1
The expected number of dilepton $t\bar{t}$ signal and background events passing the full selection criteria, compared to the number of observed events. The procedures for estimating the expected numbers of events and their uncertainties are described in the text. For the backgrounds estimated from data, the statistical and systematic uncertainties are quoted separately. The expected signal yield assumes a $t\bar{t}$ cross section of $\sigma_{t\bar{t}} = 158^{+23}_{-24}$ pb.

Source	Number of events
Expected $t\bar{t}$	7.7 ± 1.5
Dibosons (VV)	0.13 ± 0.07
Single top (tW)	0.25 ± 0.13
Drell–Yan $Z/\gamma^\star \to \tau^+\tau^-$	0.18 ± 0.09
Drell–Yan $Z/\gamma^\star \to e^+e^-$, $\mu^+\mu^-$	$1.4 \pm 0.5 \pm 0.5$
Events with non-W/Z leptons	$0.1 \pm 0.5 \pm 0.3$
Total backgrounds	2.1 ± 1.0
Expected total, including $t\bar{t}$	9.8 ± 1.8
Data	11

following the procedures from the MSTW2008 [30], CTEQ6.6 [31], and NNPDF2.0 [32] sets. From the simulated $t\bar{t}$ sample, the total signal acceptance, including geometric acceptance and event reconstruction and selection efficiencies, is found to be $(23.0 \pm 1.4)\%$ for events contributing to the e^+e^-, $\mu^+\mu^-$, and $e^\pm\mu^\mp$ modes combined, where the systematic uncertainty on the acceptance is described later in the text. The expected yield of events passing the selection criteria, assuming the NLO production cross section, is 1.5 ± 0.3, 1.7 ± 0.3, and 4.5 ± 0.9 for the e^+e^-, $\mu^+\mu^-$, and $e^\pm\mu^\mp$ decay modes, respectively. The uncertainties on these predicted event yields combine the systematic uncertainties on the event selection, the theoretical production cross section, and the integrated luminosity of the sample, where the contribution from the last two sources dominates the total. Note that the simulated $t\bar{t}$ signal sample used for the estimate of the expected signal events was generated with the $W \to \ell\nu$ branching fraction set to 1/9, which is different from the standard value (0.1080 ± 0.0009) [7] used in the cross section measurement.

The selected sample is not 100% pure in dilepton $t\bar{t}$ events. There are two types of background estimation techniques used in this analysis. One strategy utilizes simulated pp collision events to model background processes. There are, however, some pathological backgrounds that are harder to model accurately. In such cases, it is preferred to estimate the yields of these events from the data.

Contributions from diboson production (VV, where V = W or $Z/\gamma^\star$), based on a leading-order production cross section of $\sigma_{VV} = 4.8$ pb [16], and electroweak single-top production in the tW channel ($\sigma_{tW} = 10.6$ pb [33]) are modeled with the MadGraph event generator and are processed in an equivalent fashion as the simulated $t\bar{t}$ sample used to assess the signal yield. The Drell–Yan $Z/\gamma^\star \to \tau\tau$ process ($\sigma_{Z/\gamma^\star \to \tau\tau} = 1666$ pb [34]) is modeled with pythia and MadGraph. The uncertainties on these production cross sections are well within the total systematic uncertainty of 50% used for each of these backgrounds. Table 1 gives the simulation-based predictions for the event yields from these processes.

The contributions from two important background sources are estimated from the data: exceptional Drell–Yan events that evade the Z veto and are accompanied by significant missing transverse energy; and dilepton candidate events from multijet and W + jets production. Difficult-to-simulate instrumental effects influence both topologies and hence it is preferable to use calibration samples from the data in these estimations.

The events rejected by the Z veto are used to estimate the residual contributions from Drell–Yan $Z/\gamma^\star \to e^+e^-$ and $\mu^+\mu^-$ in the surviving selected sample. In the $\mu^+\mu^-$ final state the rate of events surviving the Z veto is equal to an estimate of the Drell–Yan contribution near the $M_{\ell\ell}$ peak, scaled by the expected ratio of off-peak to near-peak events derived from simulation. The near-peak Drell–Yan $Z/\gamma^\star$ contribution is estimated from the number of all events failing the Z veto, after subtraction of the non-Drell–Yan contribution estimated from $e^\pm\mu^\mp$ events passing the same selection and corrected for the differences between the electron and muon identification efficiencies. The estimate in the e^+e^- mode is done in a similar fashion; the summed contribution is shown in Table 1. The systematic uncertainty of this method, evaluated in each mode separately, is estimated to be 50%. This is dominated by detector calibration effects and changes of the fraction of Z-vetoed Drell–Yan $Z/\gamma^\star$ events with increasingly stringent requirements (additional jets and missing transverse energy) as estimated from simulation.

Dilepton candidate events from multijet and W + jets production mostly arise from jets that are able to satisfy the tight lepton identification criteria. These contributions to the selected sample from isolated lepton candidates from non-W/Z decays are also derived from data. A superset of dilepton candidate events is chosen by loosening the lepton identification criteria in the data samples used for the measurement. The number of these candidates passing the loosened selection criteria from non-W/Z leptons can be weighted by the ratio of yields of tight-to-loose lepton candidates (R_{TL}) to produce an estimate of non-W/Z leptons passing the tight selections. The ratio R_{TL} is measured as a function of candidate transverse momentum and pseudorapidity in a multijet-dominated data sample containing events with one lepton candidate passing loose selection criteria. Additional selection criteria, based on the missing transverse energy and on the transverse mass of the system defined by the $\not\!\!E_T$ and charged lepton candidate p_T, are applied to suppress the residual contribution to the loose lepton sample from electroweak processes. We assume this R_{TL} is appropriate for use in the dilepton signal sample, and we also consider R_{TL} to be independent from the other lepton in events with two leptons. In this measurement, the value of R_{TL} changes slightly as a function of candidate p_T and $|\eta|$; for both muon and electron candidates, R_{TL} is in the interval between 0.2 and 0.4.

Estimates for the contributions from lepton candidates in pure multijet QCD, with two such non-W/Z candidates, and in W + jets, with one such candidate beyond that from the decay of the W, are derived separately. A sample of loose dilepton events both failing the tight selections is used to estimate the multijet QCD contribution. Loose dilepton events with only one lepton failing the tight requirements include contributions from W + jets events, but are contaminated by multijets and leptons from W/Z decays. The multijet QCD contamination is subtracted using the previous estimate, while the contamination from W/Z leptons is measured from a sample of Z events fulfilling loose selection requirements.

The prediction for these non-W/Z leptons is shown in Table 1. The systematic uncertainty on the non-W/Z lepton estimate is primarily from differences in the jet momentum spectrum and flavor composition between the QCD-dominated sample in which R_{TL} is measured and the sample where it is applied. Other subdominant contributions to the systematic uncertainties include the R_{TL} measurement biases due to electroweak signal contribution, the dissimilarity in the trigger between the R_{TL} calibration sample and the signal sample to which it is applied, and from the statistical limitations on the R_{TL} calibration sample. The systematic uncertainty on the electron R_{TL} is 50%, which corresponds to a 50% (100%) uncertainty on a raw estimate of the W + jets (QCD multijets) non-W/Z isolated lepton contribution, prior to accounting for the signal contribution to the estimate. Similarly, the systematic uncertainty on the muon R_{TL} is $^{+50}_{-100}\%$, which corresponds to a $^{+50}_{-100}\%$ ($^{+100}_{-100}\%$) uncertainty on the estimate of the W + jets (QCD multijets) non-W/Z isolated lepton contribution.

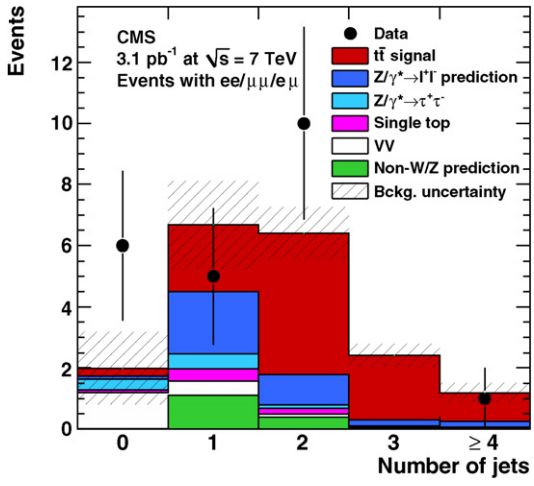

Fig. 1. Number of jets in events passing all dilepton selection criteria before the $\geqslant$2-jet requirement for all three dilepton modes combined, compared to signal and background predictions. The hatched bands reflect the uncertainties on the background predictions.

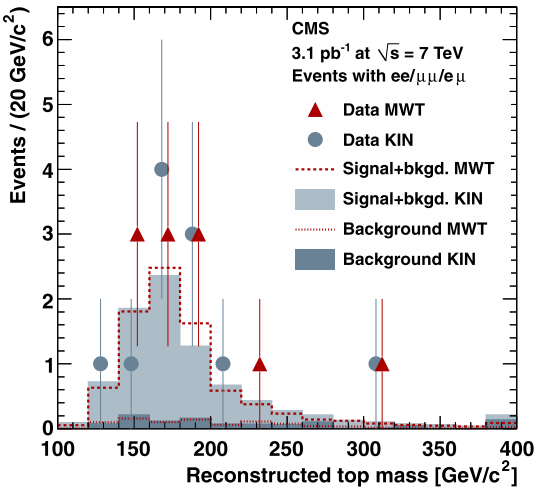

Fig. 2. Distribution of the top-quark mass using two different reconstruction methods [35,36], compared with the expected yields from simulated signal-plus-background and background-only hypotheses. The points in each bin for the two methods are slightly offset in reconstructed mass to allow coincident points to be visible. The last bin contains the overflow.

Expected yields from simulated signal and background processes, normalized to estimates from data where appropriate, are shown in Fig. 1 as a function of jet multiplicity for events satisfying the complete dilepton event selection criteria except the $\geqslant$2-jet requirement; the $t\bar{t}$ signal dominates the bins with at least two jets.

Eleven dilepton events (3 e^+e^-, 3 $\mu^+\mu^-$, 5 $e^\pm\mu^\mp$) are observed in the data after applying the event selection criteria, with a total of 2.1 ± 1.0 background events expected. We attribute the excess of events above the background expectation to top-quark pair production.

The top-quark mass reconstruction methods of [35] (KIN, i.e., KINematic, method) and [36] (MWT, i.e., Matrix Weighting Technique) are applied to the selected events. In both methods, numerical solutions to the kinematic equations appropriate for a $t\bar{t}$ decay with two charged leptons in the final state are found for each event. The solutions are based on an ensemble of values of jet momenta and missing energy, generated corresponding to their expected resolution around the measured values. In the KIN method the underconstrained system is solved by introducing an additional constraint on the longitudinal momentum of the $t\bar{t}$ system, whose probability distribution is expected to have a negligible dependence on the top-quark mass and is therefore assumed from simulation. The top-quark mass value corresponding to the largest number of solutions is the reconstructed mass for each event. In the MWT method the system is solved for a range of top-quark mass values, and weights, dependent on the momentum of the initial partons and the lepton energies in the top-quark rest frame, are assigned based on the likelihood of each solution. The mass for which the sum of the weights of all solutions is maximized is used as the mass estimator. Fig. 2 shows that the kinematics of the selected events are statistically compatible with predictions based on a top-quark mass of 172.5 GeV/c^2, demonstrating the consistency of the selected sample with top-quark pair production.

Further, beyond the complete event selection described above, the property that the two jets expected in dilepton $t\bar{t}$ events both originate from b quarks is exploited to further confirm the top-quark signal. A b-quark jet identification algorithm that relies on the presence of charged particle tracks displaced from the primary pp interaction location, as expected from the decay products of long-lived b hadrons [37], is used. A jet is identified to be from a b quark if there are at least two tracks satisfying a minimum impact parameter significance requirement. The efficiency of this algorithm for a b-quark jet in dilepton $t\bar{t}$ signal events is about 80% with a 10% false positive rate, as estimated in simulated QCD multijet events with no b quarks. This algorithm is applied to events passing all the selection criteria. The multiplicity of jets satisfying these b-tagging criteria in events passing the full dilepton event selection is shown in Fig. 3. Although not used directly in the cross section extraction, the b-tag multiplicity provides additional support for the hypothesis that the selected data are consistent with dilepton $t\bar{t}$ production.

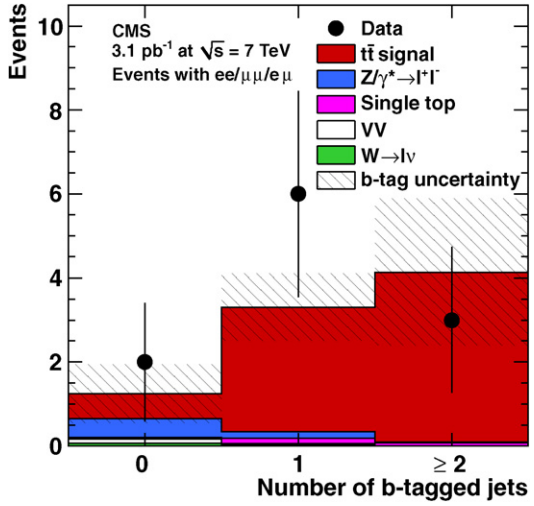

Fig. 3. Number of b-tagged jets in events passing all dilepton selection criteria for all three dilepton modes combined, compared to signal and background directly from simulations. The hatched bands reflect the expected uncertainties on the b-tag efficiency for signal events.

The top-quark pair production cross section is determined from the ratio of the number of observed events in the data after background subtraction with the product of the total signal acceptance, the branching fractions, and the integrated luminosity. The impact of systematic uncertainty is included on each piece, as described below.

Various sources of systematic uncertainty related to the event selection have been evaluated. The systematic uncertainty assigned to the dilepton selection efficiency is 4.4%, obtained from a comparison of Z events in data and simulation, together with half of the difference between the efficiencies obtained in simulated Z and $t\bar{t}$ events. The effect of multiple pp interactions in a single beam crossing — an effect that is present in the data but not in these simulated samples — is included in this uncertainty. The systematic uncertainty due to the reconstruction of jets and missing transverse energy is estimated by varying the jet energy scale by ±5%, simultaneously with a ±5% variation in the hadronic part of the missing transverse energy, resulting in a value of 3.7%. Uncertainties on the simulation of the signal selection efficiency include the amount of QCD radiation, hadron and tau decay modeling, and the W leptonic branching fraction; these sources combined give a systematic uncertainty of 2.8%. Other sources of systematic uncertainty pertaining to the signal, including uncertainties in the parton distribution functions inside the colliding protons, the effect of uncertainty on the world-average top-quark mass measurement [38], and the effect of additional minimum bias interactions in the signal selection, are neglected because they were found to have a relatively small impact. The overall systematic uncertainty on the total $t\bar{t}$ cross section from the above sources is 6.4%.

The background contributions from single-top, diboson, and Drell–Yan $Z/\gamma^\star \to \tau^+\tau^-$ processes shown in Table 1 are obtained from simulation and found to be small compared to the total event yield. Each of these backgrounds is assigned a 50% systematic uncertainty. The contributions from Drell–Yan e^+e^- and $\mu^+\mu^-$ processes and events with non-W/Z isolated leptons are estimated from data with absolute systematic uncertainties of 0.5 and 0.3 events, respectively. The contribution to the systematic uncertainty on the cross section from the uncertainties on the background estimates is 11%.

The total systematic uncertainty on the measured cross section, dominated by the uncertainty on the estimated background yield, is 24 pb. An additional systematic effect of 21 pb, due to a 11% relative uncertainty on the integrated luminosity measurement [5], is quoted separately.

Taking into account the data yield, the background estimation, the branching fraction, the signal acceptance, the integrated luminosity, and all associated statistical and systematic uncertainties, the top-quark pair production cross section is measured to be

$$\sigma(\mathrm{pp} \to t\bar{t} + \mathrm{X}) = 194 \pm 72(\mathrm{stat.}) \pm 24(\mathrm{syst.}) \pm 21(\mathrm{lumi.})\ \mathrm{pb}.$$

An alternative analysis, exploiting jets constructed only from silicon tracker information [39] and without missing transverse energy requirements in the event selection, yields a similar cross section. The quoted measurement can be compared with the calculated NLO theoretical cross section of 158^{+23}_{-24} pb for a top-quark mass of 172.5 GeV/c^2 [19,20].

In conclusion, the first measurement at the LHC of the cross section for $t\bar{t}$ production has been completed. This measurement, made with an integrated luminosity of $3.1 \pm 0.3\ \mathrm{pb}^{-1}$, is only the beginning of a rich top-quark physics program to be conducted at the CMS experiment.

Acknowledgements

We wish to congratulate our colleagues in the CERN accelerator departments for the excellent performance of the LHC machine. We thank the technical and administrative staff at CERN and other CMS institutes, and acknowledge support from: FMSR (Austria); FNRS and FWO (Belgium); CNPq, CAPES, FAPERJ, and FAPESP (Brazil); MES (Bulgaria); CERN; CAS, MoST, and NSFC (China); COLCIENCIAS (Colombia); MSES (Croatia); RPF (Cyprus); Academy of Sciences and NICPB (Estonia); Academy of Finland, ME, and HIP (Finland); CEA and CNRS/IN2P3 (France); BMBF, DFG, and HGF (Germany); GSRT (Greece); OTKA and NKTH (Hungary); DAE and DST (India); IPM (Iran); SFI (Ireland); INFN (Italy); NRF and WCU (Korea); LAS (Lithuania); CINVESTAV, CONACYT, SEP, and UASLP-FAI (Mexico); PAEC (Pakistan); SCSR (Poland); FCT (Portugal); JINR (Armenia, Belarus, Georgia, Ukraine, Uzbekistan); MST and MAE (Russia); MSTD (Serbia); MICINN and CPAN (Spain); Swiss Funding Agencies (Switzerland); NSC (Taipei); TUBITAK and TAEK (Turkey); STFC (United Kingdom); DOE and NSF (USA).

Open access

References

[1] F. Abe, et al., Phys. Rev. Lett. 74 (1995) 2626, doi:10.1103/PhysRevLett.74.2626, arXiv:hep-ex/9503002.
[2] S. Abachi, et al., Phys. Rev. Lett. 74 (1995) 2632, doi:10.1103/PhysRevLett.74.2632, arXiv:hep-ex/9503003.
[3] J.R. Incandela, A. Quadt, W. Wagner, D. Wicke, Prog. Part. Nucl. Phys. 63 (2009) 239, doi:10.1016/j.ppnp.2009.08.001, arXiv:0904.2499.
[4] L. Evans, P. Bryant (Eds.), LHC Machine, JINST 3 (2008) S08001, doi:10.1088/1748-0221/3/08/S08001.
[5] CMS Collaboration, Measurement of CMS luminosity, CMS Physics Analysis Summary CMS-PAS-EWK-10-004, http://cdsweb.cern.ch/record/1279145.
[6] R. Adolphi, et al., JINST 0803 (2008) S08004, doi:10.1088/1748-0221/3/08/S08004.
[7] K. Nakamura, J. Phys. G 37 (2010) 075021, doi:10.1088/0954-3899/37/7A/075021.
[8] T. Aaltonen, et al., Phys. Rev. D 82 (2010) 052002, doi:10.1103/PhysRevD.82.052002, arXiv:1002.2919.
[9] V.M. Abazov, et al., Phys. Lett. B 679 (2009) 177, doi:10.1016/j.physletb.2009.07.032, arXiv:0901.2137.
[10] CMS Collaboration, CMS tracking performance results from early LHC operation, CMS Physics Analysis Summary CMS-PAS-TRK-10-001, arXiv:1007.1988, http://cdsweb.cern.ch/record/1277738.
[11] CMS Collaboration, Performance of muon identification in pp collisions at $\sqrt{s} = 7$ TeV, CMS Physics Analysis Summary CMS-PAS-MUO-10-002, http://cdsweb.cern.ch/record/1279140.
[12] CMS Collaboration, Electron reconstruction and identification at $\sqrt{s} = 7$ TeV, CMS Physics Analysis Summary CMS-PAS-EGM-10-004, http://cdsweb.cern.ch/record/1299116.
[13] CMS Collaboration, CMS MET performance in events containing electroweak bosons from pp collisions at $\sqrt{s} = 7$ TeV, CMS Physics Analysis Summary CMS-PAS-JME-10-005, http://cdsweb.cern.ch/record/1294501.
[14] M. Cacciari, G.P. Salam, G. Soyez, JHEP 0804 (2008) 063, doi:10.1088/1126-6708/2008/04/063, arXiv:0802.1189.
[15] CMS Collaboration, Jet performance in pp collisions at $\sqrt{s} = 7$ TeV, CMS Physics Analysis Summary CMS-PAS-JME-10-003, http://cdsweb.cern.ch/record/1279362.
[16] F. Maltoni, T. Stelzer, JHEP 0302 (2003) 027, arXiv:hep-ph/0208156.
[17] T. Sjöstrand, S. Mrenna, P. Skands, JHEP 0605 (2006) 026, arXiv:hep-ph/0603175.
[18] J. Allison, et al., IEEE Trans. Nucl. Sci. 53 (2006) 270, doi:10.1109/TNS.2006.869826.
[19] J.M. Campbell, R.K. Ellis, MCFM for the Tevatron and the LHC, arXiv:1007.3492, 2010.
[20] R. Kleiss, W.J. Stirling, Z. Phys. C 40 (1988) 419, doi:10.1007/BF01548856.
[21] P. Nason, S. Dawson, R.K. Ellis, Nucl. Phys. B 303 (1988) 607, doi:10.1016/0550-3213(88)90422-1.
[22] W. Beenakker, H. Kuijf, W.L. van Neerven, J. Smith, Phys. Rev. D 40 (1989) 54, doi:10.1103/PhysRevD.40.54.
[23] N. Kidonakis, Next-to-next-to-leading soft-gluon corrections for the top quark cross section and transverse momentum distribution, arXiv:1009.4935, 2010.
[24] N. Kidonakis, R. Vogt, Phys. Rev. D 78 (2008) 074005, doi:10.1103/PhysRevD.78.074005, arXiv:0805.3844.

[25] M. Cacciari, S. Frixione, M.L. Mangano, P. Nason, G. Ridolfi, JHEP 0809 (2008) 127, doi:10.1088/1126-6708/2008/09/127, arXiv:0804.2800.
[26] S. Moch, P. Uwer, Phys. Rev. D 78 (2008) 034003, doi:10.1103/PhysRevD.78.034003, arXiv:0804.1476.
[27] U. Langenfeld, S. Moch, P. Uwer, New results for $t\bar{t}$ production at hadron colliders, arXiv:0907.2527, 2009.
[28] U. Langenfeld, S. Moch, P. Uwer, Phys. Rev. D 80 (2009) 054009, doi:10.1103/PhysRevD.80.054009, arXiv:0906.5273.
[29] V. Ahrens, A. Ferroglia, M. Neubert, B.D. Pecjak, L.L. Yang, JHEP 1009 (2010) 097, doi:10.1007/JHEP09(2010)097, arXiv:1003.5827.
[30] A.D. Martin, W.J. Stirling, R.S. Thorne, G. Watt, Eur. Phys. J. C 64 (2009) 653, doi:10.1140/epjc/s10052-009-1164-2, arXiv:0905.3531.
[31] H.-L. Lai, et al., Uncertainty induced by QCD coupling in the CTEQ-TEA global analysis of parton distributions, arXiv:1004.4624, 2010.
[32] F. Demartin, S. Forte, E. Mariani, J. Rojo, A. Vicini, Phys. Rev. D 82 (2010) 014002, doi:10.1103/PhysRevD.82.014002, arXiv:1004.0962.
[33] J.M. Campbell, F. Tramontano, Nucl. Phys. B 726 (2005) 109, doi:10.1016/j.nuclphysb.2005.08.015, arXiv:hep-ph/0506289.
[34] K. Melnikov, F. Petriello, Phys. Rev. D 74 (2006) 114017, doi:10.1103/PhysRevD.74.114017, arXiv:hep-ph/0609070.
[35] A. Abulencia, et al., Phys. Rev. D 73 (2006) 112006, doi:10.1103/PhysRevD.73.112006, arXiv:hep-ex/0602008.
[36] V.M. Abazov, et al., Phys. Rev. D 80 (2009) 092006, doi:10.1103/PhysRevD.80.092006, arXiv:0904.3195.
[37] CMS Collaboration, Commissioning of b-jet identification with pp collisions at $\sqrt{s} = 7$ TeV, CMS Physics Analysis Summary CMS-PAS-BTV-10-001, http://cdsweb.cern.ch/record/1279144.
[38] Tevatron Electroweak Working Group, Combination of CDF and D0 results on the mass of the top quark, arXiv:1007.3178, 2010.
[39] CMS Collaboration, Commissioning of TrackJets in pp collisions at $\sqrt{s} = 7$ TeV, CMS Physics Analysis Summary CMS-PAS-JME-10-006, http://cdsweb.cern.ch/record/1275133.

CMS Collaboration

V. Khachatryan, A.M. Sirunyan, A. Tumasyan

Yerevan Physics Institute, Yerevan, Armenia

W. Adam, T. Bergauer, M. Dragicevic, J. Erö, C. Fabjan, M. Friedl, R. Frühwirth, V.M. Ghete, J. Hammer [1], S. Hänsel, C. Hartl, M. Hoch, N. Hörmann, J. Hrubec, M. Jeitler, G. Kasieczka, W. Kiesenhofer, M. Krammer, D. Liko, I. Mikulec, M. Pernicka, H. Rohringer, R. Schöfbeck, J. Strauss, A. Taurok, F. Teischinger, W. Waltenberger, G. Walzel, E. Widl, C.-E. Wulz

Institut für Hochenergiephysik der OeAW, Wien, Austria

V. Mossolov, N. Shumeiko, J. Suarez Gonzalez

National Centre for Particle and High Energy Physics, Minsk, Belarus

L. Benucci, L. Ceard, E.A. De Wolf, X. Janssen, T. Maes, L. Mucibello, S. Ochesanu, B. Roland, R. Rougny, M. Selvaggi, H. Van Haevermaet, P. Van Mechelen, N. Van Remortel

Universiteit Antwerpen, Antwerpen, Belgium

V. Adler, S. Beauceron, S. Blyweert, J. D'Hondt, O. Devroede, A. Kalogeropoulos, J. Maes, M. Maes, S. Tavernier, W. Van Doninck, P. Van Mulders, G.P. Van Onsem, I. Villella

Vrije Universiteit Brussel, Brussel, Belgium

O. Charaf, B. Clerbaux, G. De Lentdecker, V. Dero, A.P.R. Gay, G.H. Hammad, T. Hreus, P.E. Marage, L. Thomas, C. Vander Velde, P. Vanlaer, J. Wickens

Université Libre de Bruxelles, Bruxelles, Belgium

S. Costantini, M. Grunewald, B. Klein, A. Marinov, D. Ryckbosch, F. Thyssen, M. Tytgat, L. Vanelderen, P. Verwilligen, S. Walsh, N. Zaganidis

Ghent University, Ghent, Belgium

S. Basegmez, G. Bruno, J. Caudron, J. De Favereau De Jeneret, C. Delaere, P. Demin, D. Favart, A. Giammanco, G. Grégoire, J. Hollar, V. Lemaitre, J. Liao, O. Militaru, S. Ovyn, D. Pagano, A. Pin, K. Piotrzkowski, L. Quertenmont, N. Schul

Université Catholique de Louvain, Louvain-la-Neuve, Belgium

N. Beliy, T. Caebergs, E. Daubie

Université de Mons, Mons, Belgium

G.A. Alves, D. De Jesus Damiao, M.E. Pol, M.H.G. Souza

Centro Brasileiro de Pesquisas Fisicas, Rio de Janeiro, Brazil

W. Carvalho, E.M. Da Costa, C. De Oliveira Martins, S. Fonseca De Souza, L. Mundim, H. Nogima, V. Oguri, J.M. Otalora Goicochea, W.L. Prado Da Silva, A. Santoro, S.M. Silva Do Amaral, A. Sznajder, F. Torres Da Silva De Araujo

Universidade do Estado do Rio de Janeiro, Rio de Janeiro, Brazil

F.A. Dias, M.A.F. Dias, T.R. Fernandez Perez Tomei, E.M. Gregores [2], F. Marinho, S.F. Novaes, Sandra S. Padula

Instituto de Fisica Teorica, Universidade Estadual Paulista, Sao Paulo, Brazil

N. Darmenov [1], L. Dimitrov, V. Genchev [1], P. Iaydjiev [1], S. Piperov, M. Rodozov, S. Stoykova, G. Sultanov, V. Tcholakov, R. Trayanov, I. Vankov

Institute for Nuclear Research and Nuclear Energy, Sofia, Bulgaria

M. Dyulendarova, R. Hadjiiska, V. Kozhuharov, L. Litov, E. Marinova, M. Mateev, B. Pavlov, P. Petkov

University of Sofia, Sofia, Bulgaria

J.G. Bian, G.M. Chen, H.S. Chen, C.H. Jiang, D. Liang, S. Liang, J. Wang, J. Wang, X. Wang, Z. Wang, M. Yang, J. Zang, Z. Zhang

Institute of High Energy Physics, Beijing, China

Y. Ban, S. Guo, Z. Hu, W. Li, Y. Mao, S.J. Qian, H. Teng, B. Zhu

State Key Lab. of Nucl. Phys. and Tech., Peking University, Beijing, China

A. Cabrera, B. Gomez Moreno, A.A. Ocampo Rios, A.F. Osorio Oliveros, J.C. Sanabria

Universidad de Los Andes, Bogota, Colombia

N. Godinovic, D. Lelas, K. Lelas, R. Plestina [3], D. Polic, I. Puljak

Technical University of Split, Split, Croatia

Z. Antunovic, M. Dzelalija

University of Split, Split, Croatia

V. Brigljevic, S. Duric, K. Kadija, S. Morovic

Institute Rudjer Boskovic, Zagreb, Croatia

A. Attikis, R. Fereos, M. Galanti, J. Mousa, C. Nicolaou, F. Ptochos, P.A. Razis, H. Rykaczewski

University of Cyprus, Nicosia, Cyprus

A. Abdel-basit [4], Y. Assran [5], M.A. Mahmoud [6]

Academy of Scientific Research and Technology of the Arab Republic of Egypt, Egyptian Network of High Energy Physics, Cairo, Egypt

A. Hektor, M. Kadastik, K. Kannike, M. Müntel, M. Raidal, L. Rebane

National Institute of Chemical Physics and Biophysics, Tallinn, Estonia

V. Azzolini, P. Eerola

Department of Physics, University of Helsinki, Helsinki, Finland

S. Czellar, J. Härkönen, A. Heikkinen, V. Karimäki, R. Kinnunen, J. Klem, M.J. Kortelainen, T. Lampén, K. Lassila-Perini, S. Lehti, T. Lindén, P. Luukka, T. Mäenpää, E. Tuominen, J. Tuominiemi, E. Tuovinen, D. Ungaro, L. Wendland

Helsinki Institute of Physics, Helsinki, Finland

K. Banzuzi, A. Korpela, T. Tuuva

Lappeenranta University of Technology, Lappeenranta, Finland

D. Sillou

Laboratoire d'Annecy-le-Vieux de Physique des Particules, IN2P3–CNRS, Annecy-le-Vieux, France

M. Besancon, M. Dejardin, D. Denegri, B. Fabbro, J.L. Faure, F. Ferri, S. Ganjour, F.X. Gentit, A. Givernaud, P. Gras, G. Hamel de Monchenault, P. Jarry, E. Locci, J. Malcles, M. Marionneau, L. Millischer, J. Rander, A. Rosowsky, M. Titov, P. Verrecchia

DSM/IRFU, CEA/Saclay, Gif-sur-Yvette, France

S. Baffioni, L. Bianchini, M. Bluj [7], C. Broutin, P. Busson, C. Charlot, L. Dobrzynski, R. Granier de Cassagnac, M. Haguenauer, P. Miné, C. Mironov, C. Ochando, P. Paganini, D. Sabes, R. Salerno, Y. Sirois, C. Thiebaux, B. Wyslouch [8], A. Zabi

Laboratoire Leprince-Ringuet, Ecole Polytechnique, IN2P3–CNRS, Palaiseau, France

J.-L. Agram [9], J. Andrea, A. Besson, D. Bloch, D. Bodin, J.-M. Brom, M. Cardaci, E.C. Chabert, C. Collard, E. Conte [9], F. Drouhin [9], C. Ferro, J.-C. Fontaine [9], D. Gelé, U. Goerlach, S. Greder, P. Juillot, M. Karim [9], A.-C. Le Bihan, Y. Mikami, P. Van Hove

Institut Pluridisciplinaire Hubert Curien, Université de Strasbourg, Université de Haute Alsace Mulhouse, CNRS/IN2P3, Strasbourg, France

F. Fassi, D. Mercier

Centre de Calcul de l'Institut National de Physique Nucleaire et de Physique des Particules (IN2P3), Villeurbanne, France

C. Baty, N. Beaupere, M. Bedjidian, O. Bondu, G. Boudoul, D. Boumediene, H. Brun, N. Chanon, R. Chierici, D. Contardo, P. Depasse, H. El Mamouni, A. Falkiewicz, J. Fay, S. Gascon, B. Ille, T. Kurca, T. Le Grand, M. Lethuillier, L. Mirabito, S. Perries, V. Sordini, S. Tosi, Y. Tschudi, P. Verdier, H. Xiao

Université de Lyon, Université Claude Bernard Lyon 1, CNRS–IN2P3, Institut de Physique Nucléaire de Lyon, Villeurbanne, France

V. Roinishvili

E. Andronikashvili Institute of Physics, Academy of Science, Tbilisi, Georgia

G. Anagnostou, M. Edelhoff, L. Feld, N. Heracleous, O. Hindrichs, R. Jussen, K. Klein, J. Merz, N. Mohr, A. Ostapchuk, A. Perieanu, F. Raupach, J. Sammet, S. Schael, D. Sprenger, H. Weber, M. Weber, B. Wittmer

RWTH Aachen University, I. Physikalisches Institut, Aachen, Germany

M. Ata, W. Bender, M. Erdmann, J. Frangenheim, T. Hebbeker, A. Hinzmann, K. Hoepfner, C. Hof, T. Klimkovich, D. Klingebiel, P. Kreuzer [1], D. Lanske [†], C. Magass, G. Masetti, M. Merschmeyer, A. Meyer, P. Papacz, H. Pieta, H. Reithler, S.A. Schmitz, L. Sonnenschein, J. Steggemann, D. Teyssier

RWTH Aachen University, III. Physikalisches Institut A, Aachen, Germany

M. Bontenackels, M. Davids, M. Duda, G. Flügge, H. Geenen, M. Giffels, W. Haj Ahmad, D. Heydhausen, T. Kress, Y. Kuessel, A. Linn, A. Nowack, L. Perchalla, O. Pooth, J. Rennefeld, P. Sauerland, A. Stahl, M. Thomas, D. Tornier, M.H. Zoeller

RWTH Aachen University, III. Physikalisches Institut B, Aachen, Germany

M. Aldaya Martin, W. Behrenhoff, U. Behrens, M. Bergholz [10], K. Borras, A. Cakir, A. Campbell, E. Castro, D. Dammann, G. Eckerlin, D. Eckstein, A. Flossdorf, G. Flucke, A. Geiser, I. Glushkov, J. Hauk, H. Jung, M. Kasemann, I. Katkov, P. Katsas, C. Kleinwort, H. Kluge, A. Knutsson, D. Krücker, E. Kuznetsova, W. Lange, W. Lohmann [10], R. Mankel, M. Marienfeld, I.-A. Melzer-Pellmann, A.B. Meyer, J. Mnich, A. Mussgiller, J. Olzem, A. Parenti, A. Raspereza, A. Raval, R. Schmidt [10], T. Schoerner-Sadenius, N. Sen, M. Stein, J. Tomaszewska, D. Volyanskyy, R. Walsh, C. Wissing

Deutsches Elektronen-Synchrotron, Hamburg, Germany

C. Autermann, S. Bobrovskyi, J. Draeger, H. Enderle, U. Gebbert, K. Kaschube, G. Kaussen, R. Klanner, B. Mura, S. Naumann-Emme, F. Nowak, N. Pietsch, C. Sander, H. Schettler, P. Schleper, M. Schröder, T. Schum, J. Schwandt, A.K. Srivastava, H. Stadie, G. Steinbrück, J. Thomsen, R. Wolf

University of Hamburg, Hamburg, Germany

J. Bauer, V. Buege, T. Chwalek, D. Daeuwel, W. De Boer, A. Dierlamm, G. Dirkes, M. Feindt, J. Gruschke, C. Hackstein, F. Hartmann, S.M. Heindl, M. Heinrich, H. Held, K.H. Hoffmann, S. Honc, T. Kuhr, D. Martschei, S. Mueller, Th. Müller, M.B. Neuland, M. Niegel, O. Oberst, A. Oehler, J. Ott, T. Peiffer, D. Piparo, G. Quast, K. Rabbertz, F. Ratnikov, M. Renz, A. Sabellek, C. Saout, A. Scheurer, P. Schieferdecker, F.-P. Schilling, G. Schott, H.J. Simonis, F.M. Stober, D. Troendle, J. Wagner-Kuhr, M. Zeise, V. Zhukov [11], E.B. Ziebarth

Institut für Experimentelle Kernphysik, Karlsruhe, Germany

G. Daskalakis, T. Geralis, S. Kesisoglou, A. Kyriakis, D. Loukas, I. Manolakos, A. Markou, C. Markou, C. Mavrommatis, E. Petrakou

Institute of Nuclear Physics "Demokritos", Aghia Paraskevi, Greece

L. Gouskos, T. Mertzimekis, A. Panagiotou [1]

University of Athens, Athens, Greece

I. Evangelou, C. Foudas, P. Kokkas, N. Manthos, I. Papadopoulos, V. Patras, F.A. Triantis

University of Ioánnina, Ioánnina, Greece

A. Aranyi, G. Bencze, L. Boldizsar, G. Debreczeni, C. Hajdu [1], D. Horvath [12], A. Kapusi, K. Krajczar [13], A. Laszlo, F. Sikler, G. Vesztergombi [13]

KFKI Research Institute for Particle and Nuclear Physics, Budapest, Hungary

N. Beni, J. Molnar, J. Palinkas, Z. Szillasi, V. Veszpremi

Institute of Nuclear Research ATOMKI, Debrecen, Hungary

P. Raics, Z.L. Trocsanyi, B. Ujvari

University of Debrecen, Debrecen, Hungary

S. Bansal, S.B. Beri, V. Bhatnagar, M. Jindal, M. Kaur, J.M. Kohli, M.Z. Mehta, N. Nishu, L.K. Saini, A. Sharma, R. Sharma, A.P. Singh, J.B. Singh, S.P. Singh

Panjab University, Chandigarh, India

S. Ahuja, S. Bhattacharya, S. Chauhan, B.C. Choudhary, P. Gupta, S. Jain, S. Jain, A. Kumar, R.K. Shivpuri

University of Delhi, Delhi, India

R.K. Choudhury, D. Dutta, S. Kailas, S.K. Kataria, A.K. Mohanty [1], L.M. Pant, P. Shukla, P. Suggisetti

Bhabha Atomic Research Centre, Mumbai, India

T. Aziz, M. Guchait [14], A. Gurtu, M. Maity [15], D. Majumder, G. Majumder, K. Mazumdar, G.B. Mohanty, A. Saha, K. Sudhakar, N. Wickramage

Tata Institute of Fundamental Research – EHEP, Mumbai, India

S. Banerjee, S. Dugad, N.K. Mondal

Tata Institute of Fundamental Research – HECR, Mumbai, India

H. Arfaei, H. Bakhshiansohi, S.M. Etesami, A. Fahim, M. Hashemi, A. Jafari, M. Khakzad, A. Mohammadi, M. Mohammadi Najafabadi, S. Paktinat Mehdiabadi, B. Safarzadeh, M. Zeinali

Institute for Studies in Theoretical Physics & Mathematics (IPM), Tehran, Iran

M. Abbrescia [a,b], L. Barbone [a,b], C. Calabria [a,b], A. Colaleo [a], D. Creanza [a,c], N. De Filippis [a,c], M. De Palma [a,b], A. Dimitrov [a], F. Fedele [a], L. Fiore [a], G. Iaselli [a,c], L. Lusito [a,b,1], G. Maggi [a,c], M. Maggi [a], N. Manna [a,b], B. Marangelli [a,b], S. My [a,c], S. Nuzzo [a,b], N. Pacifico [a,b], G.A. Pierro [a], A. Pompili [a,b], G. Pugliese [a,c], F. Romano [a,c], G. Roselli [a,b], G. Selvaggi [a,b], L. Silvestris [a], R. Trentadue [a], S. Tupputi [a,b], G. Zito [a]

[a] *INFN Sezione di Bari, Bari, Italy*
[b] *Università di Bari, Bari, Italy*
[c] *Politecnico di Bari, Bari, Italy*

G. Abbiendi [a], A.C. Benvenuti [a], D. Bonacorsi [a], S. Braibant-Giacomelli [a,b], P. Capiluppi [a,b], A. Castro [a,b], F.R. Cavallo [a], M. Cuffiani [a,b], G.M. Dallavalle [a], F. Fabbri [a], A. Fanfani [a,b], D. Fasanella [a], P. Giacomelli [a], M. Giunta [a], C. Grandi [a], S. Marcellini [a], M. Meneghelli [a,b], A. Montanari [a], F.L. Navarria [a,b], F. Odorici [a], A. Perrotta [a], A.M. Rossi [a,b], T. Rovelli [a,b], G. Siroli [a,b], R. Travaglini [a,b]

[a] *INFN Sezione di Bologna, Bologna, Italy*
[b] *Università di Bologna, Bologna, Italy*

S. Albergo [a,b], G. Cappello [a,b], M. Chiorboli [a,b,1], S. Costa [a,b], A. Tricomi [a,b], C. Tuve [a]

[a] *INFN Sezione di Catania, Catania, Italy*
[b] *Università di Catania, Catania, Italy*

G. Barbagli [a], V. Ciulli [a,b], C. Civinini [a], R. D'Alessandro [a,b], E. Focardi [a,b], S. Frosali [a,b], E. Gallo [a], C. Genta [a], P. Lenzi [a,b], M. Meschini [a], S. Paoletti [a], G. Sguazzoni [a], A. Tropiano [a,1]

[a] *INFN Sezione di Firenze, Firenze, Italy*
[b] *Università di Firenze, Firenze, Italy*

L. Benussi, S. Bianco, S. Colafranceschi [16], F. Fabbri, D. Piccolo

INFN Laboratori Nazionali di Frascati, Frascati, Italy

P. Fabbricatore, R. Musenich

INFN Sezione di Genova, Genova, Italy

A. Benaglia [a,b], G.B. Cerati [a,b], F. De Guio [a,b,1], L. Di Matteo [a,b], A. Ghezzi [a,b,1], P. Govoni [a,b], M. Malberti [a,b], S. Malvezzi [a], A. Martelli [a,b], A. Massironi [a,b], D. Menasce [a], L. Moroni [a], M. Paganoni [a,b], D. Pedrini [a], S. Ragazzi [a,b], N. Redaelli [a], S. Sala [a], T. Tabarelli de Fatis [a,b], V. Tancini [a,b]

[a] *INFN Sezione di Milano-Biccoca, Milano, Italy*
[b] *Università di Milano-Bicocca, Milano, Italy*

S. Buontempo [a], C.A. Carrillo Montoya [a], A. Cimmino [a,b], A. De Cosa [a,b,1], M. De Gruttola [a,b], F. Fabozzi [a,17], A.O.M. Iorio [a], L. Lista [a], M. Merola [a,b], P. Noli [a,b], P. Paolucci [a]

[a] *INFN Sezione di Napoli, Napoli, Italy*
[b] *Università di Napoli "Federico II", Napoli, Italy*

P. Azzi [a], N. Bacchetta [a], P. Bellan [a,b], D. Bisello [a,b], A. Branca [a], R. Carlin [a,b], P. Checchia [a], M. De Mattia [a,b], T. Dorigo [a], U. Dosselli [a], F. Gasparini [a,b], U. Gasparini [a,b], P. Giubilato [a,b], A. Gresele [a,c], S. Lacaprara [a,18], I. Lazzizzera [a,c], M. Margoni [a,b], M. Mazzucato [a], A.T. Meneguzzo [a,b], M. Nespolo [a], L. Perrozzi [a,1], N. Pozzobon [a,b], P. Ronchese [a,b], F. Simonetto [a,b], E. Torassa [a], M. Tosi [a,b], A. Triossi [a], S. Vanini [a,b], P. Zotto [a,b], G. Zumerle [a,b]

[a] *INFN Sezione di Padova, Padova, Italy*
[b] *Università di Padova, Padova, Italy*
[c] *Università di Trento (Trento), Padova, Italy*

P. Baesso [a,b], U. Berzano [a], C. Riccardi [a,b], P. Torre [a,b], P. Vitulo [a,b], C. Viviani [a,b]

[a] *INFN Sezione di Pavia, Pavia, Italy*
[b] *Università di Pavia, Pavia, Italy*

M. Biasini [a,b], G.M. Bilei [a], B. Caponeri [a,b], L. Fanò [a,b], P. Lariccia [a,b], A. Lucaroni [a,b,1], G. Mantovani [a,b], M. Menichelli [a], A. Nappi [a,b], A. Santocchia [a,b], L. Servoli [a], S. Taroni [a,b], M. Valdata [a,b], R. Volpe [a,b,1]

[a] *INFN Sezione di Perugia, Perugia, Italy*
[b] *Università di Perugia, Perugia, Italy*

P. Azzurri [a,c], G. Bagliesi [a], J. Bernardini [a,b], T. Boccali [a,1], G. Broccolo [a,c], R. Castaldi [a], R.T. D'Agnolo [a,c], R. Dell'Orso [a], F. Fiori [a,b], L. Foà [a,c], A. Giassi [a], A. Kraan [a], F. Ligabue [a,c], T. Lomtadze [a], L. Martini [a], A. Messineo [a,b], F. Palla [a], F. Palmonari [a], S. Sarkar [a,c], G. Segneri [a], A.T. Serban [a], P. Spagnolo [a], R. Tenchini [a,*], G. Tonelli [a,b,1], A. Venturi [a,1], P.G. Verdini [a]

[a] *INFN Sezione di Pisa, Pisa, Italy*
[b] *Università di Pisa, Pisa, Italy*
[c] *Scuola Normale Superiore di Pisa, Pisa, Italy*

L. Barone [a,b], F. Cavallari [a], D. Del Re [a,b], E. Di Marco [a,b], M. Diemoz [a], D. Franci [a,b], M. Grassi [a], E. Longo [a,b], G. Organtini [a,b], A. Palma [a,b], F. Pandolfi [a,b,1], R. Paramatti [a], S. Rahatlou [a,b,1]

[a] *INFN Sezione di Roma, Roma, Italy*
[b] *Università di Roma "La Sapienza", Roma, Italy*

N. Amapane [a,b], R. Arcidiacono [a,c], S. Argiro [a,b], M. Arneodo [a,c], C. Biino [a], C. Botta [a,b,1], N. Cartiglia [a], R. Castello [a,b], M. Costa [a,b], N. Demaria [a], A. Graziano [a,b,1], C. Mariotti [a], M. Marone [a,b], S. Maselli [a], E. Migliore [a,b], G. Mila [a,b], V. Monaco [a,b], M. Musich [a,b], M.M. Obertino [a,c], N. Pastrone [a], M. Pelliccioni [a,b,1], A. Romero [a,b], M. Ruspa [a,c], R. Sacchi [a,b], V. Sola [a,b], A. Solano [a,b], A. Staiano [a], D. Trocino [a,b], A. Vilela Pereira [a,b,1]

[a] *INFN Sezione di Torino, Torino, Italy*
[b] *Università di Torino, Torino, Italy*
[c] *Università del Piemonte Orientale (Novara), Torino, Italy*

F. Ambroglini [a,b], S. Belforte [a], F. Cossutti [a], G. Della Ricca [a,b], B. Gobbo [a], D. Montanino [a,b], A. Penzo [a]

[a] *INFN Sezione di Trieste, Trieste, Italy*
[b] *Università di Trieste, Trieste, Italy*

S.G. Heo

Kangwon National University, Chunchon, Republic of Korea

S. Chang, J. Chung, D.H. Kim, G.N. Kim, J.E. Kim, D.J. Kong, H. Park, D. Son, D.C. Son

Kyungpook National University, Daegu, Republic of Korea

Zero Kim, J.Y. Kim, S. Song

Chonnam National University, Institute for Universe and Elementary Particles, Kwangju, Republic of Korea

S. Choi, B. Hong, M. Jo, H. Kim, J.H. Kim, T.J. Kim, K.S. Lee, D.H. Moon, S.K. Park, H.B. Rhee, E. Seo, S. Shin, K.S. Sim

Korea University, Seoul, Republic of Korea

M. Choi, S. Kang, H. Kim, C. Park, I.C. Park, S. Park, G. Ryu

University of Seoul, Seoul, Republic of Korea

Y. Choi, Y.K. Choi, J. Goh, J. Lee, S. Lee, H. Seo, I. Yu

Sungkyunkwan University, Suwon, Republic of Korea

M.J. Bilinskas, I. Grigelionis, M. Janulis, D. Martisiute, P. Petrov, T. Sabonis

Vilnius University, Vilnius, Lithuania

H. Castilla Valdez, E. De La Cruz Burelo, R. Lopez-Fernandez, A. Sánchez Hernández, L.M. Villasenor-Cendejas

Centro de Investigacion y de Estudios Avanzados del IPN, Mexico City, Mexico

S. Carrillo Moreno, F. Vazquez Valencia

Universidad Iberoamericana, Mexico City, Mexico

H.A. Salazar Ibarguen

Benemerita Universidad Autonoma de Puebla, Puebla, Mexico

E. Casimiro Linares, A. Morelos Pineda, M.A. Reyes-Santos

Universidad Autónoma de San Luis Potosí, San Luis Potosí, Mexico

P. Allfrey, D. Krofcheck, J. Tam

University of Auckland, Auckland, New Zealand

P.H. Butler, R. Doesburg, H. Silverwood

University of Canterbury, Christchurch, New Zealand

M. Ahmad, I. Ahmed, M.I. Asghar, H.R. Hoorani, W.A. Khan, T. Khurshid, S. Qazi

National Centre for Physics, Quaid-I-Azam University, Islamabad, Pakistan

M. Cwiok, W. Dominik, K. Doroba, A. Kalinowski, M. Konecki, J. Krolikowski

Institute of Experimental Physics, Warsaw, Poland

T. Frueboes, R. Gokieli, M. Górski, M. Kazana, K. Nawrocki, M. Szleper, G. Wrochna, P. Zalewski

Soltan Institute for Nuclear Studies, Warsaw, Poland

N. Almeida, A. David, P. Faccioli, P.G. Ferreira Parracho, M. Gallinaro, P. Martins, G. Mini, P. Musella, A. Nayak, L. Raposo, P.Q. Ribeiro, J. Seixas, P. Silva, D. Soares, J. Varela [1], H.K. Wöhri

Laboratório de Instrumentação e Física Experimental de Partículas, Lisboa, Portugal

I. Belotelov, P. Bunin, M. Finger, M. Finger Jr., I. Golutvin, A. Kamenev, V. Karjavin, G. Kozlov, A. Lanev, P. Moisenz, V. Palichik, V. Perelygin, S. Shmatov, V. Smirnov, A. Volodko, A. Zarubin

Joint Institute for Nuclear Research, Dubna, Russia

N. Bondar, V. Golovtsov, Y. Ivanov, V. Kim, P. Levchenko, V. Murzin, V. Oreshkin, I. Smirnov, V. Sulimov, L. Uvarov, S. Vavilov, A. Vorobyev

Petersburg Nuclear Physics Institute, Gatchina (St Petersburg), Russia

Yu. Andreev, S. Gninenko, N. Golubev, M. Kirsanov, N. Krasnikov, V. Matveev, A. Pashenkov, A. Toropin, S. Troitsky

Institute for Nuclear Research, Moscow, Russia

V. Epshteyn, V. Gavrilov, V. Kaftanov †, M. Kossov [1], A. Krokhotin, N. Lychkovskaya, G. Safronov, S. Semenov, I. Shreyber, V. Stolin, E. Vlasov, A. Zhokin

Institute for Theoretical and Experimental Physics, Moscow, Russia

E. Boos, M. Dubinin [19], L. Dudko, A. Ershov, A. Gribushin, O. Kodolova, I. Lokhtin, S. Obraztsov, S. Petrushanko, L. Sarycheva, V. Savrin, A. Snigirev

Moscow State University, Moscow, Russia

V. Andreev, M. Azarkin, I. Dremin, M. Kirakosyan, S.V. Rusakov, A. Vinogradov

P.N. Lebedev Physical Institute, Moscow, Russia

I. Azhgirey, S. Bitioukov, V. Grishin [1], V. Kachanov, D. Konstantinov, A. Korablev, V. Krychkine, V. Petrov, R. Ryutin, S. Slabospitsky, A. Sobol, L. Tourtchanovitch, S. Troshin, N. Tyurin, A. Uzunian, A. Volkov

State Research Center of Russian Federation, Institute for High Energy Physics, Protvino, Russia

P. Adzic [20], M. Djordjevic, D. Krpic [20], J. Milosevic

University of Belgrade, Faculty of Physics and Vinca Institute of Nuclear Sciences, Belgrade, Serbia

M. Aguilar-Benitez, J. Alcaraz Maestre, P. Arce, C. Battilana, E. Calvo, M. Cepeda, M. Cerrada, N. Colino, B. De La Cruz, C. Diez Pardos, C. Fernandez Bedoya, J.P. Fernández Ramos, A. Ferrando, J. Flix, M.C. Fouz, P. Garcia-Abia, O. Gonzalez Lopez, S. Goy Lopez, J.M. Hernandez, M.I. Josa, G. Merino, J. Puerta Pelayo, I. Redondo, L. Romero, J. Santaolalla, C. Willmott

Centro de Investigaciones Energéticas Medioambientales y Tecnológicas (CIEMAT), Madrid, Spain

C. Albajar, G. Codispoti, J.F. de Trocóniz

Universidad Autónoma de Madrid, Madrid, Spain

J. Cuevas, J. Fernandez Menendez, S. Folgueras, I. Gonzalez Caballero, L. Lloret Iglesias, J.M. Vizan Garcia

Universidad de Oviedo, Oviedo, Spain

I.J. Cabrillo, A. Calderon, M. Chamizo Llatas, S.H. Chuang, J. Duarte Campderros, M. Felcini [21], M. Fernandez, G. Gomez, J. Gonzalez Sanchez, R. Gonzalez Suarez, C. Jorda, P. Lobelle Pardo, A. Lopez Virto, J. Marco, R. Marco, C. Martinez Rivero, F. Matorras, J. Piedra Gomez [22], T. Rodrigo, A. Ruiz Jimeno, L. Scodellaro, M. Sobron Sanudo, I. Vila, R. Vilar Cortabitarte

Instituto de Física de Cantabria (IFCA), CSIC – Universidad de Cantabria, Santander, Spain

D. Abbaneo, E. Auffray, P. Baillon, A.H. Ball, D. Barney, F. Beaudette [3], A.J. Bell [23], D. Benedetti, C. Bernet [3], W. Bialas, P. Bloch, A. Bocci, S. Bolognesi, H. Breuker, G. Brona, K. Bunkowski, T. Camporesi, E. Cano, G. Cerminara, T. Christiansen, J.A. Coarasa Perez, R. Covarelli, B. Curé, D. D'Enterria, T. Dahms, A. De Roeck, A. Elliott-Peisert, W. Funk, A. Gaddi, S. Gennai, G. Georgiou, H. Gerwig, D. Gigi, K. Gill, D. Giordano, F. Glege, R. Gomez-Reino Garrido, M. Gouzevitch, S. Gowdy, L. Guiducci, M. Hansen, J. Harvey, J. Hegeman, B. Hegner, C. Henderson, H.F. Hoffmann, A. Honma, V. Innocente, P. Janot,

E. Karavakis, P. Lecoq, C. Leonidopoulos, C. Lourenço, A. Macpherson, T. Mäki, L. Malgeri, M. Mannelli, L. Masetti, F. Meijers, S. Mersi, E. Meschi, R. Moser, M.U. Mozer, M. Mulders, E. Nesvold [1], T. Orimoto, L. Orsini, E. Perez, A. Petrilli, A. Pfeiffer, M. Pierini, M. Pimiä, G. Polese, A. Racz, G. Rolandi [24], T. Rommerskirchen, C. Rovelli [25], M. Rovere, H. Sakulin, C. Schäfer, C. Schwick, I. Segoni, A. Sharma, P. Siegrist, M. Simon, P. Sphicas [26], D. Spiga, M. Spiropulu [19], F. Stöckli, M. Stoye, P. Tropea, A. Tsirou, A. Tsyganov, G.I. Veres [13], P. Vichoudis, M. Voutilainen, W.D. Zeuner

CERN, European Organization for Nuclear Research, Geneva, Switzerland

W. Bertl, K. Deiters, W. Erdmann, K. Gabathuler, R. Horisberger, Q. Ingram, H.C. Kaestli, S. König, D. Kotlinski, U. Langenegger, F. Meier, D. Renker, T. Rohe, J. Sibille [27], A. Starodumov [28]

Paul Scherrer Institut, Villigen, Switzerland

P. Bortignon, L. Caminada [29], Z. Chen, S. Cittolin, G. Dissertori, M. Dittmar, J. Eugster, K. Freudenreich, C. Grab, A. Hervé, W. Hintz, P. Lecomte, W. Lustermann, C. Marchica [29], P. Martinez Ruiz del Arbol, P. Meridiani, P. Milenovic [30], F. Moortgat, A. Nardulli, P. Nef, F. Nessi-Tedaldi, L. Pape, F. Pauss, T. Punz, A. Rizzi, F.J. Ronga, L. Sala, A.K. Sanchez, M.-C. Sawley, B. Stieger, L. Tauscher [†], A. Thea, K. Theofilatos, D. Treille, C. Urscheler, R. Wallny [21], M. Weber, L. Wehrli, J. Weng

Institute for Particle Physics, ETH Zurich, Zurich, Switzerland

E. Aguiló, C. Amsler, V. Chiochia, S. De Visscher, C. Favaro, M. Ivova Rikova, A. Jaeger, B. Millan Mejias, C. Regenfus, P. Robmann, A. Schmidt, H. Snoek, L. Wilke

Universität Zürich, Zurich, Switzerland

Y.H. Chang, K.H. Chen, W.T. Chen, S. Dutta, A. Go, C.M. Kuo, S.W. Li, W. Lin, M.H. Liu, Z.k. Liu, Y.J. Lu, J.H. Wu, S.S. Yu

National Central University, Chung-Li, Taiwan

P. Bartalini, P. Chang, Y.H. Chang, Y.W. Chang, Y. Chao, K.F. Chen, W.-S. Hou, Y. Hsiung, K.Y. Kao, Y.J. Lei, R.-S. Lu, J.G. Shiu, Y.M. Tzeng, M. Wang, J.T. Wei

National Taiwan University (NTU), Taipei, Taiwan

A. Adiguzel, M.N. Bakirci, S. Cerci [31], Z. Demir, C. Dozen, I. Dumanoglu, E. Eskut, S. Girgis, G. Gökbulut, Y. Güler, E. Gurpinar, I. Hos, E.E. Kangal, T. Karaman, A. Kayis Topaksu, A. Nart, G. Önengüt, K. Ozdemir, S. Ozturk, A. Polatöz, K. Sogut [32], B. Tali, H. Topakli, D. Uzun, L.N. Vergili, M. Vergili, C. Zorbilmez

Cukurova University, Adana, Turkey

I.V. Akin, T. Aliev, S. Bilmis, M. Deniz, H. Gamsizkan, A.M. Guler, K. Ocalan, A. Ozpineci, M. Serin, R. Sever, U.E. Surat, E. Yildirim, M. Zeyrek

Middle East Technical University, Physics Department, Ankara, Turkey

M. Deliomeroglu, D. Demir [33], E. Gülmez, A. Halu, B. Isildak, M. Kaya [34], O. Kaya [34], M. Özbek, S. Ozkorucuklu [35], N. Sonmez [36]

Bogazici University, Istanbul, Turkey

L. Levchuk

National Scientific Center, Kharkov Institute of Physics and Technology, Kharkov, Ukraine

P. Bell, F. Bostock, J.J. Brooke, T.L. Cheng, D. Cussans, R. Frazier, J. Goldstein, M. Grimes, M. Hansen, G.P. Heath, H.F. Heath, B. Huckvale, J. Jackson, L. Kreczko, S. Metson, D.M. Newbold [37], K. Nirunpong, A. Poll, V.J. Smith, S. Ward

University of Bristol, Bristol, United Kingdom

L. Basso, K.W. Bell, A. Belyaev, C. Brew, R.M. Brown, B. Camanzi, D.J.A. Cockerill, J.A. Coughlan, K. Harder, S. Harper, B.W. Kennedy, E. Olaiya, D. Petyt, B.C. Radburn-Smith, C.H. Shepherd-Themistocleous, I.R. Tomalin, W.J. Womersley, S.D. Worm

Rutherford Appleton Laboratory, Didcot, United Kingdom

R. Bainbridge, G. Ball, J. Ballin, R. Beuselinck, O. Buchmuller, D. Colling, N. Cripps, M. Cutajar, G. Davies, M. Della Negra, J. Fulcher, D. Futyan, A. Guneratne Bryer, G. Hall, Z. Hatherell, J. Hays, G. Iles, G. Karapostoli, L. Lyons, A.-M. Magnan, J. Marrouche, R. Nandi, J. Nash, A. Nikitenko [28], A. Papageorgiou, M. Pesaresi, K. Petridis, M. Pioppi [38], D.M. Raymond, N. Rompotis, A. Rose, M.J. Ryan, C. Seez, P. Sharp, A. Sparrow, A. Tapper, S. Tourneur, M. Vazquez Acosta, T. Virdee [1], S. Wakefield, D. Wardrope, T. Whyntie

Imperial College, London, United Kingdom

M. Barrett, M. Chadwick, J.E. Cole, P.R. Hobson, A. Khan, P. Kyberd, D. Leslie, W. Martin, I.D. Reid, L. Teodorescu

Brunel University, Uxbridge, United Kingdom

K. Hatakeyama

Baylor University, Waco, USA

T. Bose, E. Carrera Jarrin, A. Clough, C. Fantasia, A. Heister, J.St. John, P. Lawson, D. Lazic, J. Rohlf, D. Sperka, L. Sulak

Boston University, Boston, USA

A. Avetisyan, S. Bhattacharya, J.P. Chou, D. Cutts, S. Esen, A. Ferapontov, U. Heintz, S. Jabeen, G. Kukartsev, G. Landsberg, M. Narain, D. Nguyen, M. Segala, T. Speer, K.V. Tsang

Brown University, Providence, USA

M.A. Borgia, R. Breedon, M. Calderon De La Barca Sanchez, D. Cebra, M. Chertok, J. Conway, P.T. Cox, J. Dolen, R. Erbacher, E. Friis, W. Ko, A. Kopecky, R. Lander, H. Liu, S. Maruyama, T. Miceli, M. Nikolic, D. Pellett, J. Robles, T. Schwarz, M. Searle, J. Smith, M. Squires, M. Tripathi, R. Vasquez Sierra, C. Veelken

University of California, Davis, USA

V. Andreev, K. Arisaka, D. Cline, R. Cousins, A. Deisher, J. Duris, S. Erhan, C. Farrell, J. Hauser, M. Ignatenko, C. Jarvis, C. Plager, G. Rakness, P. Schlein [†], J. Tucker, V. Valuev

University of California, Los Angeles, USA

J. Babb, R. Clare, J. Ellison, J.W. Gary, F. Giordano, G. Hanson, G.Y. Jeng, S.C. Kao, F. Liu, H. Liu, A. Luthra, H. Nguyen, G. Pasztor [39], A. Satpathy, B.C. Shen [†], R. Stringer, J. Sturdy, S. Sumowidagdo, R. Wilken, S. Wimpenny

University of California, Riverside, USA

W. Andrews, J.G. Branson, E. Dusinberre, D. Evans, F. Golf, A. Holzner, R. Kelley, M. Lebourgeois, J. Letts, B. Mangano, J. Muelmenstaedt, S. Padhi, C. Palmer, G. Petrucciani, H. Pi, M. Pieri, R. Ranieri, M. Sani, V. Sharma [1], S. Simon, Y. Tu, A. Vartak, F. Würthwein, A. Yagil

University of California, San Diego, La Jolla, USA

D. Barge, R. Bellan, C. Campagnari, M. D'Alfonso, T. Danielson, P. Geffert, J. Incandela, C. Justus, P. Kalavase, S.A. Koay, D. Kovalskyi, V. Krutelyov, S. Lowette, N. Mccoll, V. Pavlunin, F. Rebassoo, J. Ribnik, J. Richman, R. Rossin, D. Stuart, W. To, J.R. Vlimant, M. Witherell

University of California, Santa Barbara, USA

A. Bornheim, J. Bunn, Y. Chen, M. Gataullin, D. Kcira, V. Litvine, Y. Ma, A. Mott, H.B. Newman, C. Rogan, K. Shin, V. Timciuc, P. Traczyk, J. Veverka, R. Wilkinson, Y. Yang, R.Y. Zhu

California Institute of Technology, Pasadena, USA

B. Akgun, A. Calamba, R. Carroll, T. Ferguson, Y. Iiyama, D.W. Jang, S.Y. Jun, Y.F. Liu, M. Paulini, J. Russ, N. Terentyev, H. Vogel, I. Vorobiev

Carnegie Mellon University, Pittsburgh, USA

J.P. Cumalat, M.E. Dinardo, B.R. Drell, C.J. Edelmaier, W.T. Ford, B. Heyburn, E. Luiggi Lopez, U. Nauenberg, J.G. Smith, K. Stenson, K.A. Ulmer, S.R. Wagner, S.L. Zang

University of Colorado at Boulder, Boulder, USA

L. Agostino, J. Alexander, F. Blekman, A. Chatterjee, S. Das, N. Eggert, L.J. Fields, L.K. Gibbons, B. Heltsley, K. Henriksson, W. Hopkins, A. Khukhunaishvili, B. Kreis, V. Kuznetsov, Y. Liu, G. Nicolas Kaufman, J.R. Patterson, D. Puigh, D. Riley, A. Ryd, M. Saelim, X. Shi, W. Sun, W.D. Teo, J. Thom, J. Thompson, J. Vaughan, Y. Weng, L. Winstrom, P. Wittich

Cornell University, Ithaca, USA

A. Biselli, G. Cirino, D. Winn

Fairfield University, Fairfield, USA

S. Abdullin, M. Albrow, J. Anderson, G. Apollinari, M. Atac, J.A. Bakken, S. Banerjee, L.A.T. Bauerdick, A. Beretvas, J. Berryhill, P.C. Bhat, I. Bloch, F. Borcherding, K. Burkett, J.N. Butler, V. Chetluru, H.W.K. Cheung, F. Chlebana, S. Cihangir, M. Demarteau, D.P. Eartly, V.D. Elvira, I. Fisk, J. Freeman, Y. Gao, E. Gottschalk, D. Green, K. Gunthoti, O. Gutsche, A. Hahn, J. Hanlon, R.M. Harris, J. Hirschauer, B. Hooberman, E. James, H. Jensen, M. Johnson, U. Joshi, R. Khatiwada, B. Kilminster, B. Klima, K. Kousouris, S. Kunori, S. Kwan, P. Limon, R. Lipton, J. Lykken, K. Maeshima, J.M. Marraffino, D. Mason, P. McBride, T. McCauley, T. Miao, K. Mishra, S. Mrenna, Y. Musienko [40], C. Newman-Holmes, V. O'Dell, S. Popescu, R. Pordes, O. Prokofyev, N. Saoulidou, E. Sexton-Kennedy, S. Sharma, A. Soha, W.J. Spalding, L. Spiegel, P. Tan, L. Taylor, S. Tkaczyk, L. Uplegger, E.W. Vaandering, R. Vidal, J. Whitmore, W. Wu, F. Yang, F. Yumiceva, J.C. Yun

Fermi National Accelerator Laboratory, Batavia, USA

D. Acosta, P. Avery, D. Bourilkov, M. Chen, G.P. Di Giovanni, D. Dobur, A. Drozdetskiy, R.D. Field, M. Fisher, Y. Fu, I.K. Furic, J. Gartner, S. Goldberg, B. Kim, S. Klimenko, J. Konigsberg, A. Korytov, K. Kotov, A. Kropivnitskaya, T. Kypreos, K. Matchev, G. Mitselmakher, L. Muniz, Y. Pakhotin, M. Petterson, C. Prescott, R. Remington, M. Schmitt, B. Scurlock, P. Sellers, N. Skhirtladze, M. Snowball, D. Wang, J. Yelton, M. Zakaria

University of Florida, Gainesville, USA

C. Ceron, V. Gaultney, L. Kramer, L.M. Lebolo, S. Linn, P. Markowitz, G. Martinez, D. Mesa, J.L. Rodriguez

Florida International University, Miami, USA

T. Adams, A. Askew, J. Bochenek, J. Chen, B. Diamond, S.V. Gleyzer, J. Haas, S. Hagopian, V. Hagopian, M. Jenkins, K.F. Johnson, H. Prosper, S. Sekmen, V. Veeraraghavan

Florida State University, Tallahassee, USA

M.M. Baarmand, B. Dorney, S. Guragain, M. Hohlmann, H. Kalakhety, R. Ralich, I. Vodopiyanov

Florida Institute of Technology, Melbourne, USA

M.R. Adams, I.M. Anghel, L. Apanasevich, Y. Bai, V.E. Bazterra, R.R. Betts, J. Callner, R. Cavanaugh, C. Dragoiu, E.J. Garcia-Solis, C.E. Gerber, D.J. Hofman, S. Khalatyan, F. Lacroix, C. O'Brien, C. Silvestre, A. Smoron, D. Strom, N. Varelas

University of Illinois at Chicago (UIC), Chicago, USA

U. Akgun, E.A. Albayrak, B. Bilki, K. Cankocak[41], W. Clarida, F. Duru, C.K. Lae, E. McCliment, J.-P. Merlo, H. Mermerkaya, A. Mestvirishvili, A. Moeller, J. Nachtman, C.R. Newsom, E. Norbeck, J. Olson, Y. Onel, F. Ozok, S. Sen, J. Wetzel, T. Yetkin, K. Yi

The University of Iowa, Iowa City, USA

B.A. Barnett, B. Blumenfeld, A. Bonato, C. Eskew, D. Fehling, G. Giurgiu, A.V. Gritsan, Z.J. Guo, G. Hu, P. Maksimovic, S. Rappoccio, M. Swartz, N.V. Tran, A. Whitbeck

Johns Hopkins University, Baltimore, USA

P. Baringer, A. Bean, G. Benelli, O. Grachov, M. Murray, D. Noonan, V. Radicci, S. Sanders, J.S. Wood, V. Zhukova

The University of Kansas, Lawrence, USA

D. Bandurin, T. Bolton, I. Chakaberia, A. Ivanov, M. Makouski, Y. Maravin, S. Shrestha, I. Svintradze, Z. Wan

Kansas State University, Manhattan, USA

J. Gronberg, D. Lange, D. Wright

Lawrence Livermore National Laboratory, Livermore, USA

A. Baden, M. Boutemeur, S.C. Eno, D. Ferencek, J.A. Gomez, N.J. Hadley, R.G. Kellogg, M. Kirn, Y. Lu, A.C. Mignerey, K. Rossato, P. Rumerio, F. Santanastasio, A. Skuja, J. Temple, M.B. Tonjes, S.C. Tonwar, E. Twedt

University of Maryland, College Park, USA

B. Alver, G. Bauer, J. Bendavid, W. Busza, E. Butz, I.A. Cali, M. Chan, V. Dutta, P. Everaerts, G. Gomez Ceballos, M. Goncharov, K.A. Hahn, P. Harris, Y. Kim, M. Klute, Y.-J. Lee, W. Li, C. Loizides, J. Lopez, P.D. Luckey, T. Ma, S. Nahn, C. Paus, C. Roland, G. Roland, M. Rudolph, G.S.F. Stephans, K. Sumorok, K. Sung, E.A. Wenger, S. Xie, M. Yang, Y. Yilmaz, A.S. Yoon, M. Zanetti

Massachusetts Institute of Technology, Cambridge, USA

P. Cole, S.I. Cooper, P. Cushman, B. Dahmes, A. De Benedetti, P.R. Dudero, G. Franzoni, J. Haupt, K. Klapoetke, Y. Kubota, J. Mans, V. Rekovic, R. Rusack, M. Sasseville, A. Singovsky

University of Minnesota, Minneapolis, USA

L.M. Cremaldi, R. Godang, R. Kroeger, L. Perera, R. Rahmat, D.A. Sanders, D. Summers

University of Mississippi, University, USA

K. Bloom, S. Bose, J. Butt, D.R. Claes, A. Dominguez, M. Eads, J. Keller, T. Kelly, I. Kravchenko, J. Lazo-Flores, C. Lundstedt, H. Malbouisson, S. Malik, G.R. Snow

University of Nebraska-Lincoln, Lincoln, USA

U. Baur, A. Godshalk, I. Iashvili, A. Kharchilava, A. Kumar, K. Smith, J. Zennamo

State University of New York at Buffalo, Buffalo, USA

G. Alverson, E. Barberis, D. Baumgartel, O. Boeriu, M. Chasco, K. Kaadze, S. Reucroft, J. Swain, D. Wood, J. Zhang

Northeastern University, Boston, USA

A. Anastassov, A. Kubik, N. Odell, R.A. Ofierzynski, B. Pollack, A. Pozdnyakov, M. Schmitt, S. Stoynev, M. Velasco, S. Won

Northwestern University, Evanston, USA

L. Antonelli, D. Berry, M. Hildreth, C. Jessop, D.J. Karmgard, J. Kolb, T. Kolberg, K. Lannon, W. Luo, S. Lynch, N. Marinelli, D.M. Morse, T. Pearson, R. Ruchti, J. Slaunwhite, N. Valls, J. Warchol, M. Wayne, J. Ziegler

University of Notre Dame, Notre Dame, USA

B. Bylsma, L.S. Durkin, J. Gu, C. Hill, P. Killewald, T.Y. Ling, M. Rodenburg, G. Williams

The Ohio State University, Columbus, USA

N. Adam, E. Berry, P. Elmer, D. Gerbaudo, V. Halyo, P. Hebda, A. Hunt, J. Jones, E. Laird, D. Lopes Pegna, D. Marlow, T. Medvedeva, M. Mooney, J. Olsen, P. Piroué, X. Quan, H. Saka, D. Stickland, C. Tully, J.S. Werner, A. Zuranski

Princeton University, Princeton, USA

J.G. Acosta, X.T. Huang, A. Lopez, H. Mendez, S. Oliveros, J.E. Ramirez Vargas, A. Zatserklyaniy

University of Puerto Rico, Mayaguez, USA

E. Alagoz, V.E. Barnes, G. Bolla, L. Borrello, D. Bortoletto, A. Everett, A.F. Garfinkel, Z. Gecse, L. Gutay, M. Jones, O. Koybasi, A.T. Laasanen, N. Leonardo, C. Liu, V. Maroussov, M. Meier, P. Merkel, D.H. Miller, N. Neumeister, K. Potamianos, I. Shipsey, D. Silvers, H. Sun, A. Svyatkovskiy, H.D. Yoo, J. Zablocki, Y. Zheng

Purdue University, West Lafayette, USA

P. Jindal, N. Parashar

Purdue University Calumet, Hammond, USA

C. Boulahouache, V. Cuplov, K.M. Ecklund, F.J.M. Geurts, J.H. Liu, J. Morales, B.P. Padley, R. Redjimi, J. Roberts, J. Zabel

Rice University, Houston, USA

B. Betchart, A. Bodek, Y.S. Chung, P. de Barbaro, R. Demina, Y. Eshaq, H. Flacher, A. Garcia-Bellido, P. Goldenzweig, Y. Gotra, J. Han, A. Harel, D.C. Miner, D. Orbaker, G. Petrillo, D. Vishnevskiy, M. Zielinski

University of Rochester, Rochester, USA

A. Bhatti, L. Demortier, K. Goulianos, G. Lungu, C. Mesropian, M. Yan

The Rockefeller University, New York, USA

O. Atramentov, A. Barker, D. Duggan, Y. Gershtein, R. Gray, E. Halkiadakis, D. Hidas, D. Hits, A. Lath, S. Panwalkar, R. Patel, A. Richards, K. Rose, S. Schnetzer, S. Somalwar, R. Stone, S. Thomas

Rutgers, the State University of New Jersey, Piscataway, USA

G. Cerizza, M. Hollingsworth, S. Spanier, Z.C. Yang, A. York

University of Tennessee, Knoxville, USA

J. Asaadi, R. Eusebi, J. Gilmore, A. Gurrola, T. Kamon, V. Khotilovich, R. Montalvo, C.N. Nguyen, J. Pivarski, A. Safonov, S. Sengupta, A. Tatarinov, D. Toback, M. Weinberger

Texas A&M University, College Station, USA

N. Akchurin, C. Bardak, J. Damgov, C. Jeong, K. Kovitanggoon, S.W. Lee, P. Mane, Y. Roh, A. Sill, I. Volobouev, R. Wigmans, E. Yazgan

Texas Tech University, Lubbock, USA

E. Appelt, E. Brownson, D. Engh, C. Florez, W. Gabella, W. Johns, P. Kurt, C. Maguire, A. Melo, P. Sheldon, J. Velkovska

Vanderbilt University, Nashville, USA

M.W. Arenton, M. Balazs, S. Boutle, M. Buehler, S. Conetti, B. Cox, B. Francis, R. Hirosky, A. Ledovskoy, C. Lin, C. Neu, T. Patel, R. Yohay

University of Virginia, Charlottesville, USA

S. Gollapinni, R. Harr, P.E. Karchin, V. Loggins, M. Mattson, C. Milstène, A. Sakharov

Wayne State University, Detroit, USA

M. Anderson, M. Bachtis, J.N. Bellinger, D. Carlsmith, S. Dasu, J. Efron, L. Gray, A. Gregerson, K.S. Grogg, M. Grothe, R. Hall-Wilton [1], M. Herndon, P. Klabbers, J. Klukas, A. Lanaro, C. Lazaridis, J. Leonard, J. Liu, D. Lomidze, R. Loveless, A. Mohapatra, W. Parker, D. Reeder, I. Ross, A. Savin, W.H. Smith, J. Swanson, M. Weinberg

University of Wisconsin, Madison, USA

* Corresponding author.
E-mail address: Roberto.Tenchini@cern.ch (R. Tenchini).
† Deceased.
[1] Also at CERN, European Organization for Nuclear Research, Geneva, Switzerland.
[2] Also at Universidade Federal do ABC, Santo Andre, Brazil.
[3] Also at Laboratoire Leprince-Ringuet, Ecole Polytechnique, IN2P3–CNRS, Palaiseau, France.
[4] Also at Cairo University, Cairo, Egypt.
[5] Also at Suez Canal University, Suez, Egypt.
[6] Also at Fayoum University, El-Fayoum, Egypt.
[7] Also at Soltan Institute for Nuclear Studies, Warsaw, Poland.
[8] Also at Massachusetts Institute of Technology, Cambridge, USA.
[9] Also at Université de Haute-Alsace, Mulhouse, France.
[10] Also at Brandenburg University of Technology, Cottbus, Germany.
[11] Also at Moscow State University, Moscow, Russia.
[12] Also at Institute of Nuclear Research ATOMKI, Debrecen, Hungary.
[13] Also at Eötvös Loránd University, Budapest, Hungary.
[14] Also at Tata Institute of Fundamental Research – HECR, Mumbai, India.
[15] Also at University of Visva-Bharati, Santiniketan, India.
[16] Also at Facoltà Ingegneria, Università di Roma “La Sapienza”, Roma, Italy.
[17] Also at Università della Basilicata, Potenza, Italy.
[18] Also at Laboratori Nazionali di Legnaro dell’INFN, Legnaro, Italy.
[19] Also at California Institute of Technology, Pasadena, USA.
[20] Also at Faculty of Physics of University of Belgrade, Belgrade, Serbia.
[21] Also at University of California, Los Angeles, Los Angeles, USA.
[22] Also at University of Florida, Gainesville, USA.
[23] Also at Université de Genève, Geneva, Switzerland.
[24] Also at Scuola Normale e Sezione dell’INFN, Pisa, Italy.
[25] Also at INFN Sezione di Roma; Università di Roma “La Sapienza”, Roma, Italy.
[26] Also at University of Athens, Athens, Greece.
[27] Also at The University of Kansas, Lawrence, USA.
[28] Also at Institute for Theoretical and Experimental Physics, Moscow, Russia.
[29] Also at Paul Scherrer Institut, Villigen, Switzerland.
[30] Also at University of Belgrade, Faculty of Physics and Vinca Institute of Nuclear Sciences, Belgrade, Serbia.
[31] Also at Adiyaman University, Adiyaman, Turkey.
[32] Also at Mersin University, Mersin, Turkey.

[33] Also at Izmir Institute of Technology, Izmir, Turkey.
[34] Also at Kafkas University, Kars, Turkey.
[35] Also at Suleyman Demirel University, Isparta, Turkey.
[36] Also at Ege University, Izmir, Turkey.
[37] Also at Rutherford Appleton Laboratory, Didcot, United Kingdom.
[38] Also at INFN Sezione di Perugia; Università di Perugia, Perugia, Italy.
[39] Also at KFKI Research Institute for Particle and Nuclear Physics, Budapest, Hungary.
[40] Also at Institute for Nuclear Research, Moscow, Russia.
[41] Also at Istanbul Technical University, Istanbul, Turkey.

Eur. Phys. J. C 47, 547–587 (2006)
Digital Object Identifier (DOI) 10.1140/epjc/s2006-02569-7

THE EUROPEAN PHYSICAL JOURNAL C

Search for neutral MSSM Higgs bosons at LEP

The LEP Collaborations ALEPH, DELPHI, L3 and OPAL
The LEP Working Group for Higgs Boson Searches[a]

The ALEPH Collaboration

S. Schael[1], R. Barate[2], R. Brunelière[2], I. De Bonis[2], D. Decamp[2], C. Goy[2], S. Jézéquel[2], J.-P. Lees[2], F. Martin[2], E. Merle[2], M.-N. Minard[2], B. Pietrzyk[2], B. Trocmé[2], S. Bravo[3], M.P. Casado[3], M. Chmeissani[3], J.M. Crespo[3], E. Fernandez[3], M. Fernandez-Bosman[3], L. Garrido[3,44], M. Martinez[3], A. Pacheco[3], H. Ruiz[3], A. Colaleo[4], D. Creanza[4], N. De Filippis[4], M. de Palma[4], G. Iaselli[4], G. Maggi[4], M. Maggi[4], S. Nuzzo[4], A. Ranieri[4], G. Raso[4,49], F. Ruggieri[4], G. Selvaggi[4], L. Silvestris[4], P. Tempesta[4], A. Tricomi[4,38], G. Zito[4], X. Huang[5], J. Lin[5], Q. Ouyang[5], T. Wang[5], Y. Xie[5], R. Xu[5], S. Xue[5], J. Zhang[5], L. Zhang[5], W. Zhao[5], D. Abbaneo[6], T. Barklow[6,50], O. Buchmüller[6,50], M. Cattaneo[6], B. Clerbaux[6,48], H. Drevermann[6], R.W. Forty[6], M. Frank[6], F. Gianotti[6], J.B. Hansen[6], J. Harvey[6], D.E. Hutchcroft[6,52], P. Janot[6], B. Jost[6], M. Kado[6,37], P. Mato[6], A. Moutoussi[6], F. Ranjard[6], L. Rolandi[6], D. Schlatter[6], F. Teubert[6], A. Valassi[6], I. Videau[6], F. Badaud[7], S. Dessagne[7], A. Falvard[7,46], D. Fayolle[7], P. Gay[7], J. Jousset[7], B. Michel[7], S. Monteil[7], D. Pallin[7], J.M. Pascolo[7], P. Perret[7], J.D. Hansen[8], J.R. Hansen[8], P.H. Hansen[8], A.C. Kraan[8], B.S. Nilsson[8], A. Kyriakis[9], C. Markou[9], E. Simopoulou[9], A. Vayaki[9], K. Zachariadou[9], A. Blondel[10,42], J.-C. Brient[10], F. Machefert[10], A. Rougé[10], H. Videau[10], V. Ciulli[11], E. Focardi[11], G. Parrini[11], A. Antonelli[12], M. Antonelli[12], G. Bencivenni[12], F. Bossi[12], G. Capon[12], F. Cerutti[12], V. Chiarella[12], G. Mannocchi[12], P. Laurelli[12], G. Mannocchi[12,40], G.P. Murtas[12], L. Passalacqua[12], J. Kennedy[13], J.G. Lynch[13], P. Negus[13], V. O'Shea[13], A.S. Thompson[13], S. Wasserbaech[14], R. Cavanaugh[15,39], S. Dhamotharan[15,47], C. Geweniger[15], P. Hanke[15], V. Hepp[15], E.E. Kluge[15], A. Putzer[15], H. Stenzel[15], K. Tittel[15], M. Wunsch[15,45], R. Beuselinck[16], W. Cameron[16], G. Davies[16], P.J. Dornan[16], M. Girone[16,36], N. Marinelli[16], J. Nowell[16], S.A. Rutherford[16], J.K. Sedgbeer[16], J.C. Thompson[16b], R. White[16], V.M. Ghete[17], P. Girtler[17], E. Kneringer[17], D. Kuhn[17], G. Rudolph[17], E. Bouhova-Thacker[18], C.K. Bowdery[18], D.P. Clarke[18], G. Ellis[18], A.J. Finch[18], F. Foster[18], G. Hughes[18], R.W.L. Jones[18], M.R. Pearson[18], N.A. Robertson[18], M. Smizanska[18], O. van der Aa[19], C. Delaere[19c], G. Leibenguth[19d], V. Lemaitre[19e], U. Blumenschein[20], F. Hölldorfer[20], K. Jakobs[20], F. Kayser[20], A.-S. Müller[20], B. Renk[20], H.-G. Sander[20], S. Schmeling[20], H. Wachsmuth[20], C. Zeitnitz[20], T. Ziegler[20], A. Bonissent[21], P. Coyle[21], C. Curtil[21], A. Ealet[21], D. Fouchez[21], P. Payre[21], A. Tilquin[21], F. Ragusa[22], A. David[23], H. Dietl[23,53], G. Ganis[23,51], K. Hüttmann[23], G. Lütjens[23], W. Männer[23,53], H.-G. Moser[23], R. Settles[23], M. Villegas[23], G. Wolf[23], J. Boucrot[24], O. Callot[24], M. Davier[24], L. Duflot[24], J.-F. Grivaz[24], P. Heusse[24], A. Jacholkowska[24,41], L. Serin[24], J.-J. Veillet[24], P. Azzurri[25], G. Bagliesi[25], T. Boccali[25], L. Foà[25], A. Giammanco[25], A. Giassi[25], F. Ligabue[25], A. Messineo[25], F. Palla[25], G. Sanguinetti[25], A. Sciabà[25], G. Sguazzoni[25], P. Spagnolo[25], R. Tenchini[25], A. Venturi[25], P.G. Verdini[25], O. Awunor[26], G.A. Blair[26], G. Cowan[26], A. Garcia-Bellido[26], M.G. Green[26], T. Medcalf[26,†], A. Misiejuk[26], J.A. Strong[26], P. Teixeira-Dias[26], R.W. Clifft[27], T.R. Edgecock[27], P.R. Norton[27], I.R. Tomalin[27], J.J. Ward[27], B. Bloch-Devaux[28], D. Boumediene[28], P. Colas[28], B. Fabbro[28], E. Lançon[28], M.-C. Lemaire[28], E. Locci[28], P. Perez[28], J. Rander[28], B. Tuchming[28], B. Vallage[28], A.M. Litke[29], G. Taylor[29], C.N. Booth[30], S. Cartwright[30], F. Combley[30,†], P.N. Hodgson[30], M. Lehto[30], L.F. Thompson[30], A. Böhrer[31], S. Brandt[31], C. Grupen[31], J. Hess[31], A. Ngac[31], G. Prange[31], C. Borean[32], G. Giannini[32], H. He[33], J. Putz[33], J. Rothberg[33], S.R. Armstrong[34], K. Berkelman[34], K. Cranmer[34], D.P.S. Ferguson[34], Y. Gao[34,43], S. González[34], O.J. Hayes[34], H. Hu[34], S. Jin[34], J. Kile[34], P.A. McNamara III[34], J. Nielsen[34], Y.B. Pan[34], J.H. von Wimmersperg-Toeller[34], W. Wiedenmann[34], J. Wu[34], S.L. Wu[34], X. Wu[34], G. Zobernig[34], G. Dissertori[35]

The DELPHI Collaboration

J. Abdallah[82], P. Abreu[79], W. Adam[111], P. Adzic[68], T. Albrecht[74], T. Alderweireld[55,56,57], R. Alemany-Fernandez[65], T. Allmendinger[74], P.P. Allport[80], U. Amaldi[86], N. Amapane[104], S. Amato[108], E. Anashkin[93], A. Andreazza[85], S. Andringa[79], N. Anjos[79], P. Antilogus[82], W.-D. Apel[74], Y. Arnoud[71], S. Ask[83], B. Asman[103], J.E. Augustin[82], A. Augustinus[65], P. Baillon[65], A. Ballestrero[105], P. Bambade[77], R. Barbier[84], D. Bardin[73], G.J. Barker[74], A. Baroncelli[96], M. Battaglia[65], M. Baubillier[82], K.-H. Becks[113], M. Begalli[61,62,63], A. Behrmann[113], E. Ben-Haim[77], N. Benekos[89], A. Benvenuti[60], C. Berat[71], M. Berggren[82], L. Berntzon[103], D. Bertrand[55,56,57], M. Besancon[97], N. Besson[97], D. Bloch[66], M. Blom[88], M. Bluj[112], M. Bonesini[86], M. Boonekamp[97], P.S.L. Booth[80,†], G. Borisov[78], O. Botner[109], B. Bouquet[77], T.J.V. Bowcock[80], I. Boyko[73], M. Bracko[100,101,102],

R. Brenner[109], E. Brodet[92], P. Bruckman[75], J.M. Brunet[64], B. Buschbeck[111], P. Buschmann[113], M. Calvi[86], T. Camporesi[65], V. Canale[95], F. Carena[65], N. Castro[79], F. Cavallo[60], M. Chapkin[99], P. Charpentier[65], P. Checchia[93], R. Chierici[65], P. Chliapnikov[99], J. Chudoba[65], S.U. Chung[65], K. Cieslik[75], P. Collins[65], R. Contri[70], G. Cosme[77], F. Cossutti[106,107], M.J. Costa[110], D. Crennell[94], J. Cuevas[91], J. D'Hondt[55,56,57], J. Dalmau[103], T. da Silva[108], W. Da Silva[82], G. Della Ricca[106,107], A. De Angelis[106,107], W. De Boer[74], C. De Clercq[55,56,57], B. De Lotto[106,107], N. De Maria[104], A. De Min[93], L. de Paula[108], L. Di Ciaccio[95], A. Di Simone[96], K. Doroba[112], J. Drees[113,65], G. Eigen[59], T. Ekelof[109], M. Ellert[109], M. Elsing[65], M.C. Espirito Santo[79], G. Fanourakis[68], D. Fassouliotis[68,58], M. Feindt[74], J. Fernandez[98], A. Ferrer[110], F. Ferro[70], U. Flagmeyer[113], H. Foeth[65], E. Fokitis[89], F. Fulda-Quenzer[77], J. Fuster[110], M. Gandelman[108], C. Garcia[110], P. Gavillet[65], E. Gazis[89], R. Gokieli[65,112], B. Golob[100,101,102], G. Gomez-Ceballos[98], P. Goncalves[79], E. Graziani[96], G. Grosdidier[77], K. Grzelak[112], J. Guy[94], C. Haag[74], A. Hallgren[109], K. Hamacher[113], K. Hamilton[92], S. Haug[90], F. Hauler[74], V. Hedberg[83], M. Hennecke[74], H. Herr[65,†], J. Hoffman[112], S.-O. Holmgren[103], P.J. Holt[65], M.A. Houlden[80], K. Hultqvist[103], J.N. Jackson[80], G. Jarlskog[83], P. Jarry[97], D. Jeans[92], E.K. Johansson[103], P.D. Johansson[103], P. Jonsson[84], C. Joram[65], L. Jungermann[74], F. Kapusta[82], S. Katsanevas[84], E. Katsoufis[89], G. Kernel[100,101,102], B.P. Kersevan[65,100,101,102], U. Kerzel[74], B.T. King[80], N.J. Kjaer[65], P. Kluit[88], P. Kokkinias[68], C. Kourkoumelis[58], O. Kouznetsov[73], Z. Krumstein[73], M. Kucharczyk[75], J. Lamsa[54], G. Leder[111], F. Ledroit[71], L. Leinonen[103], R. Leitner[87], J. Lemonne[55,56,57], V. Lepeltier[77], T. Lesiak[75], W. Liebig[113], D. Liko[111], A. Lipniacka[103], J.H. Lopes[108], J.M. Lopez[91], D. Loukas[68], P. Lutz[97], L. Lyons[92], J. MacNaughton[111], A. Malek[113], S. Maltezos[89], F. Mandl[111], J. Marco[98], R. Marco[98], B. Marechal[108], M. Margoni[93], J.-C. Marin[65], C. Mariotti[65], A. Markou[68], C. Martinez-Rivero[98], J. Masik[69], N. Mastroyiannopoulos[68], F. Matorras[98], C. Matteuzzi[86], F. Mazzucato[93], M. Mazzucato[93], R. Mc Nulty[80], C. Meroni[85], E. Migliore[104], W. Mitaroff[111], U. Mjoernmark[83], T. Moa[103], M. Moch[74], K. Moenig[65,67], R. Monge[70], J. Montenegro[88], D. Moraes[108], S. Moreno[79], P. Morettini[70], U. Mueller[113], K. Muenich[113], M. Mulders[88], L. Mundim[61,62,63], W. Murray[94], B. Muryn[76], G. Myatt[92], T. Myklebust[90], M. Nassiakou[68], F. Navarria[60], K. Nawrocki[112], R. Nicolaidou[97], M. Nikolenko[73,66], A. Oblakowska-Mucha[76], V. Obraztsov[99], A. Olshevski[73], A. Onofre[79], R. Orava[72], K. Osterberg[72], A. Ouraou[97], A. Oyanguren[110], M. Paganoni[86], S. Paiano[60], J.P. Palacios[80], H. Palka[75], T.D. Papadopoulou[89], L. Pape[65], C. Parkes[81], F. Parodi[70], U. Parzefall[65], A. Passeri[96], O. Passon[113], L. Peralta[79], V. Perepelitsa[110], A. Perrotta[60], A. Petrolini[70], J. Piedra[98], L. Pieri[96], F. Pierre[97], M. Pimenta[79], E. Piotto[65], T. Podobnik[100,101,102], V. Poireau[65], M.E. Pol[61,62,63], G. Polok[75], V. Pozdniakov[73], N. Pukhaeva[55,56,57,73], A. Pullia[86], J. Rames[69], A. Read[90], P. Rebecchi[65], J. Rehn[74], D. Reid[88], R. Reinhardt[113], P. Renton[92], F. Richard[77], J. Ridky[69], M. Rivero[98], D. Rodriguez[98], A. Romero[104], P. Ronchese[93], P. Roudeau[77], T. Rovelli[60], V. Ruhlmann-Kleider[97], D. Ryabtchikov[99], A. Sadovsky[73], L. Salmi[72], J. Salt[110], C. Sander[74], A. Savoy-Navarro[82], U. Schwickerath[65], A. Segar[92,†], R. Sekulin[94], M. Siebel[113], A. Sisakian[73], G. Smadja[84], O. Smirnova[83], A. Sokolov[99], A. Sopczak[78], R. Sosnowski[112], T. Spassov[65], M. Stanitzki[74], A. Stocchi[77], J. Strauss[111], B. Stugu[59], M. Szczekowski[112], M. Szeptycka[112], T. Szumlak[76], T. Tabarelli[86], A.C. Taffard[80], F. Tegenfeldt[109], J. Timmermans[88], L. Tkatchev[73], M. Tobin[80], S. Todorovova[69], B. Tome[79], A. Tonazzo[86], P. Tortosa[110], P. Travnicek[69], D. Treille[65], G. Tristram[64], M. Trochimczuk[112], C. Troncon[85], M.-L. Turluer[97], I.A. Tyapkin[73], P. Tyapkin[73], S. Tzamarias[68], V. Uvarov[99], G. Valenti[60], P. Van Dam[88], J. Van Eldik[65], N. van Remortel[72], I. Van Vulpen[65], G. Vegni[85], F. Veloso[79], W. Venus[94], P. Verdier[84], V. Verzi[95], D. Vilanova[97], L. Vitale[106,107], V. Vrba[69], H. Wahlen[113], A.J. Washbrook[80], C. Weiser[74], D. Wicke[65], J. Wickens[55,56,57], G. Wilkinson[92], M. Winter[66], M. Witek[75], O. Yushchenko[99], A. Zalewska[75], P. Zalewski[112], D. Zavrtanik[100,101,102], V. Zhuravlov[73], N.I. Zimin[73], A. Zintchenko[73], M. Zupan[68]

The L3 Collaboration

P. Achard[133], O. Adriani[130], M. Aguilar-Benitez[138], J. Alcaraz[138], G. Alemanni[136], J. Allaby[131], A. Aloisio[142], M.G. Alviggi[142], H. Anderhub[162], V.P. Andreev[119,147], F. Anselmo[121], A. Arefiev[141], T. Azemoon[116], T. Aziz[122], P. Bagnaia[152], A. Bajo[138], G. Baksay[139], L. Baksay[139], S.V. Baldew[115], S. Banerjee[122], Sw. Banerjee[117], A. Barczyk[162,160], R. Barillère[131], P. Bartalini[136], M. Basile[121], N. Batalova[159], R. Battiston[146], A. Bay[136], F. Becattini[130], U. Becker[126], F. Behner[162], L. Bellucci[130], R. Berbeco[116], J. Berdugo[138], P. Berges[126], B. Bertucci[146], B.L. Betev[162], M. Biasini[146], M. Biglietti[142], A. Biland[162], J.J. Blaising[117], S.C. Blyth[148], G.J. Bobbink[115], A. Böhm[114], L. Boldizsar[125], B. Borgia[152], S. Bottai[130], D. Bourilkov[162], M. Bourquin[133], S. Braccini[133], J.G. Branson[154], F. Brochu[117], J.D. Burger[126], W.J. Burger[146], X.D. Cai[126], M. Capell[126], G. Cara Romeo[121], G. Carlino[142], A. Cartacci[130], J. Casaus[138], F. Cavallari[152], N. Cavallo[149], C. Cecchi[146], M. Cerrada[138], M. Chamizo[133], Y.H. Chang[157], M. Chemarin[137], A. Chen[157], G. Chen[120], G.M. Chen[120], H.F. Chen[135], H.S. Chen[120], G. Chiefari[142], L. Cifarelli[153], F. Cindolo[121], I. Clare[126], R. Clare[151], G. Coignet[117], N. Colino[138], S. Costantini[152], B. de la Cruz[138], S. Cucciarelli[146], R. de Asmundis[142], P. Déglon[133], J. Debreczeni[125], A. Degré[117], K. Dehmelt[139], K. Deiters[160], D. della Volpe[142], E. Delmeire[133], P. Denes[150], F. DeNotaristefani[152], A. De Salvo[162], M. Diemoz[152], M. Dierckxsens[115], C. Dionisi[152], M. Dittmar[162], A. Doria[142], M.T. Dova[123,f], D. Duchesneau[117], M. Duda[114], B. Echenard[133], A. Eline[131], A. El Hage[114], H. El Mamouni[137], A. Engler[148], F.J. Eppling[126], P. Extermann[133], M.A. Falagan[138], S. Falciano[152], A. Favara[145], J. Fay[137], O. Fedin[147], M. Felcini[162], T. Ferguson[148], H. Fesefeldt[114], E. Fiandrini[146], J.H. Field[133], F. Filthaut[144],

P.H. Fisher[126], W. Fisher[150], G. Forconi[126], K. Freudenreich[162], C. Furetta[140], Yu. Galaktionov[141,126], S.N. Ganguli[122], P. Garcia-Abia[138], M. Gataullin[145], S. Gentile[152], S. Giagu[152], Z.F. Gong[135], G. Grenier[137], O. Grimm[162], M.W. Gruenewald[129], M. Guida[153], V.K. Gupta[150], A. Gurtu[122], L.J. Gutay[159], D. Haas[118], D. Hatzifotiadou[121], T. Hebbeker[114], A. Hervé[131], J. Hirschfelder[148], H. Hofer[162], M. Hohlmann[139], G. Holzner[162], S.R. Hou[157], J. Hu[144], B.N. Jin[120], P. Jindal[127], L.W. Jones[116], P. de Jong[115], I. Josa-Mutuberría[138], M. Kaur[127], M.N. Kienzle-Focacci[133], J.K. Kim[156], J. Kirkby[131], W. Kittel[144], A. Klimentov[126,141], A.C. König[144], M. Kopal[159], V. Koutsenko[126,141], M. Kräber[162], R.W. Kraemer[148], A. Krüger[161], A. Kunin[126], P. Ladron de Guevara[138], I. Laktineh[137], G. Landi[130], M. Lebeau[131], A. Lebedev[126], P. Lebrun[137], P. Lecomte[162], P. Lecoq[131], P. Le Coultre[162], J.M. Le Goff[131], R. Leiste[161], M. Levtchenko[140], P. Levtchenko[147], C. Li[135], S. Likhoded[161], C.H. Lin[157], W.T. Lin[157], F.L. Linde[115], L. Lista[142], Z.A. Liu[120], W. Lohmann[161], E. Longo[152], Y.S. Lu[120], C. Luci[152], L. Luminari[152], W. Lustermann[162], W.G. Ma[135], L. Malgeri[131], A. Malinin[141], C. Ma na[138], J. Mans[150], J.P. Martin[137], F. Marzano[152], K. Mazumdar[122], R.R. McNeil[119], S. Mele[131,142], L. Merola[142], M. Meschini[130], W.J. Metzger[144], A. Mihul[124], H. Milcent[131], G. Mirabelli[152], J. Mnich[114], G.B. Mohanty[122], G.S. Muanza[137], A.J.M. Muijs[115], B. Musicar[154], M. Musy[152], S. Nagy[128], S. Natale[133], M. Napolitano[142], F. Nessi-Tedaldi[162], H. Newman[145], A. Nisati[152], T. Novak[144], H. Nowak[161], R. Ofierzynski[162], G. Organtini[152], I. Pal[159], C. Palomares[138], P. Paolucci[142], R. Paramatti[152], G. Passaleva[130], S. Patricelli[142], T. Paul[123], M. Pauluzzi[146], C. Paus[126], F. Pauss[162], M. Pedace[152], S. Pensotti[140], D. Perret-Gallix[117], D. Piccolo[142], F. Pierella[121], M. Pieri[154], M. Pioppi[146], P.A. Piroué[150], E. Pistolesi[140], V. Plyaskin[141], M. Pohl[133], V. Pojidaev[130], J. Pothier[131], D. Prokofiev[147], G. Rahal-Callot[162], M.A. Rahaman[122], P. Raics[128], N. Raja[122], R. Ramelli[162], P.G. Rancoita[140], R. Ranieri[130], A. Raspereza[161], P. Razis[143], S. Rembeczki[139], D. Ren[162], M. Rescigno[152], S. Reucroft[123], S. Riemann[161], K. Riles[116], B.P. Roe[116], L. Romero[138], A. Rosca[161], C. Rosemann[114], C. Rosenbleck[114], S. Rosier-Lees[117], S. Roth[114], J.A. Rubio[131], G. Ruggiero[130], H. Rykaczewski[162], A. Sakharov[162], S. Saremi[119], S. Sarkar[152], J. Salicio[131], E. Sanchez[138], C. Schäfer[131], V. Schegelsky[147], H. Schopper[134], D.J. Schotanus[144], C. Sciacca[142], L. Servoli[146], S. Shevchenko[145], N. Shivarov[155], V. Shoutko[126], E. Shumilov[141], A. Shvorob[145], D. Son[156], C. Souga[137], P. Spillantini[130], M. Steuer[126], D.P. Stickland[150], B. Stoyanov[155], A. Straessner[133], K. Sudhakar[122], G. Sultanov[155], L.Z. Sun[135], S. Sushkov[114], H. Suter[162], J.D. Swain[123], Z. Szillasi[139,g], X.W. Tang[120], P. Tarjan[128], L. Tauscher[118], L. Taylor[123], B. Tellili[137], D. Teyssier[137], C. Timmermans[144], S.C.C. Ting[126], S.M. Ting[126], S.C. Tonwar[122], J. Tóth[125], C. Tully[150], K.L. Tung[120], J. Ulbricht[162], E. Valente[152], R.T. Van de Walle[144], R. Vasquez[159], G. Vesztergombi[125], I. Vetlitsky[141], G. Viertel[162], M. Vivargent[117], S. Vlachos[118], I. Vodopianov[139], H. Vogel[148], H. Vogt[161], I. Vorobiev[148,141], A.A. Vorobyov[147], M. Wadhwa[118], Q. Wang[144], X.L. Wang[135], Z.M. Wang[135], M. Weber[131], S. Wynhoff[150], L. Xia[145], Z.Z. Xu[135], J. Yamamoto[116], B.Z. Yang[135], C.G. Yang[120], H.J. Yang[116], M. Yang[120], S.C. Yeh[158], An. Zalite[147], Yu. Zalite[147], Z.P. Zhang[135], J. Zhao[135], G.Y. Zhu[120], R.Y. Zhu[145], H.L. Zhuang[120], A. Zichichi[121,131,132], B. Zimmermann[162], M. Zöller[114]

The OPAL Collaboration

G. Abbiendi[164], C. Ainsley[167], P.F. Åkesson[165,219], G. Alexander[183], J. Allison[177], P. Amaral[170], G. Anagnostou[163], K.J. Anderson[170], S. Asai[184,185], D. Axen[189], G. Azuelos[179,196], I. Bailey[188], E. Barberio[169,210], T. Barillari[194], R.J. Barlow[177], R.J. Batley[167], P. Bechtle[187,197], T. Behnke[187], K.W. Bell[181], P.J. Bell[163], G. Bella[183], A. Bellerive[168], G. Benelli[166], S. Bethke[194], O. Biebel[193], O. Boeriu[171], P. Bock[172], M. Boutemeur[193], S. Braibant[169], L. Brigliadori[164], R.M. Brown[181], K. Buesser[187], H.J. Burckhart[169], S. Campana[166], R.K. Carnegie[168], A.A. Carter[174], J.R. Carter[167], C.Y. Chang[178], D.G. Charlton[163], C. Ciocca[164], A. Csilling[191], M. Cuffiani[164], S. Dado[182], S. de Jong[173,214], A. De Roeck[169], E.A. De Wolf[169,213h], K. Desch[187], B. Dienes[192], M. Donkers[168], J. Dubbert[193], E. Duchovni[186], G. Duckeck[193], I.P. Duerdoth[177], E. Etzion[183], F. Fabbri[164], L. Feld[171], P. Ferrari[169], F. Fiedler[193], I. Fleck[171], M. Ford[167], A. Frey[169], P. Gagnon[173], J.W. Gary[166], S.M. Gascon-Shotkin[178], G. Gaycken[187], C. Geich-Gimbel[165], G. Giacomelli[164], P. Giacomelli[164], M. Giunta[166], J. Goldberg[182], E. Gross[186], J. Grunhaus[183], M. Gruwé[169], P.O. Günther[165], A. Gupta[170], C. Hajdu[191], M. Hamann[187], G.G. Hanson[166], A. Harel[182], M. Hauschild[169], C.M. Hawkes[163], R. Hawkings[169], R.J. Hemingway[168], G. Herten[171], R.D. Heuer[187], J.C. Hill[167], K. Hoffman[170], D. Horváth[191,198], P. Igo-Kemenes[172], K. Ishii[184,185], H. Jeremie[179], U. Jost[172], P. Jovanovic[163], T.R. Junk[168,203], N. Kanaya[188], J. Kanzaki[184,185,215], D. Karlen[188], K. Kawagoe[184,185], T. Kawamoto[184,185], R.K. Keeler[188], R.G. Kellogg[178], B.W. Kennedy[181], S. Kluth[194], T. Kobayashi[184,185], M. Kobel[165], S. Komamiya[184,185], T. Krämer[187], P. Krieger[168,206], J. von Krogh[172], K. Kruger[169], T. Kuhl[187], M. Kupper[186], G.D. Lafferty[177], H. Landsman[182], D. Lanske[175], J.G. Layter[166], D. Lellouch[186], J. Letts[209], L. Levinson[186], J. Lillich[171], S.L. Lloyd[174], F.K. Loebinger[177], J. Lu[189,217], A. Ludwig[165], J. Ludwig[171], W. Mader[165], S. Marcellini[164], A.J. Martin[174], G. Masetti[164], T. Mashimo[184,185], P. Mättig[207], J. McKenna[189], R.A. McPherson[188], F. Meijers[169], W. Menges[187], F.S. Merritt[170], H. Mes[168,196], N. Meyer[187], A. Michelini[164], S. Mihara[184,185], G. Mikenberg[186], D.J. Miller[176], S. Moed[182], W. Mohr[171], T. Mori[184,185], A. Mutter[171], K. Nagai[174], I. Nakamura[184,185,216], H. Nanjo[184,185], H.A. Neal[195], R. Nisius[194], S.W. O'Neale[163,†], A. Oh[169], M.J. Oreglia[170], S. Orito[184,185,†], C. Pahl[194], G. Pásztor[166,201], J.R. Pater[177], J.E. Pilcher[170], J. Pinfold[190], D.E. Plane[169], B. Poli[164], O. Pooth[175], M. Przybycień[169,208], A. Quadt[165], K. Rabbertz[169,212], C. Rembser[169], P. Renkel[186], J.M. Roney[188], Y. Rozen[182], K. Runge[171], K. Sachs[168], T. Saeki[184,185], E.K.G. Sarkisyan[169,204],

A.D. Schaile[193], O. Schaile[193], P. Scharff-Hansen[169], J. Schieck[194], T. Schörner-Sadenius[169,220], M. Schröder[169], M. Schumacher[165], W.G. Scott[181], R. Seuster[175,200], T.G. Shears[169,202], B.C. Shen[166], P. Sherwood[176], A. Skuja[178], A.M. Smith[169], R. Sobie[188], S. Söldner-Rembold[176], F. Spano[170], A. Stahl[165,218], D. Strom[180], R. Ströhmer[193], S. Tarem[182], M. Tasevsky[169,213,g], R. Teuscher[170], M.A. Thomson[167], E. Torrence[180], D. Toya[184,185], P. Tran[166], I. Trigger[169], Z. Trócsányi[192,199], E. Tsur[183], M.F. Turner-Watson[163], I. Ueda[184,185], B. Ujvári[192,199], C.F. Vollmer[193], P. Vannerem[171], R. Vértesi[192,199], M. Verzocchi[178], H. Voss[169,211], J. Vossebeld[169,202], C.P. Ward[167], D.R. Ward[167], P.M. Watkins[163], A.T. Watson[163], N.K. Watson[163], P.S. Wells[169], T. Wengler[169], N. Wermes[165], G.W. Wilson[177,205], J.A. Wilson[163], G. Wolf[186], T.R. Wyatt[177], S. Yamashita[184,185], D. Zer-Zion[166], L. Zivkovic[186],

S. Heinemeyer[221,222], A. Pilaftsis[223], G. Weiglein[224]

The ALEPH Collaboration

[1] Physikalisches Institut das RWTH-Aachen, 52056 Aachen, Germany
[2] Laboratoire de Physique des Particules (LAPP), IN^2P^3-CNRS, 74019 Annecy-le-Vieux Cedex, France
[3] Institut de Física d'Altes Energies, Universitat Autònoma de Barcelona, 08193 Bellaterra (Barcelona), Spain[i]
[4] Dipartimento di Fisica, INFN Sezione di Bari, 70126 Bari, Italy
[5] Institute of High Energy Physics, Academia Sinica, Beijing, P.R. China[j]
[6] European Laboratory for Particle Physics (CERN), 1211 Geneva 23, Switzerland
[7] Laboratoire de Physique Corpusculaire, Université Blaise Pascal, IN^2P^3-CNRS, Clermont-Ferrand, 63177 Aubière, France
[8] Niels Bohr Institute, 2100 Copenhagen, Denmark[k]
[9] Nuclear Research Center Demokritos (NRCD), 15310 Attiki, Greece
[10] Laoratoire Leprince-Ringuet, Ecole Polytechnique, IN^2P^3-CNRS, 91128 Palaiseau Cedex, France
[11] Dipartimento di Fisica, Università di Firenze, INFN Sezione di Firenze, 50125 Firenze, Italy
[12] Laboratori Nazionali dell'INFN (LNF-INFN), 00044 Frascati, Italy
[13] Department of Physics and Astronomy, University of Glasgow, Glasgow G128QQ, UK[l]
[14] Utah Valley State College, Orem, UT 84058, U.S.A.
[15] Kirchhoff-Institut für Physik, Universität Heidelberg, 69120 Heidelberg, Germany[m]
[16] Department of Physics, Imperial College, London SW7 2BZ, UK[k]
[17] Institut für Experimentalphysik, Universität Innsbruck, 6020 Innsbruck, Austria[n]
[18] Department of Physics, University of Lancaster, Lancaster LA1 4YB, UK[k]
[19] Institut de Physique Nucléaire, Département de Physique, Université Catholique de Louvain, 1348 Louvain-la-Neuve, Belgium
[20] Institut für Physik, Universität Mainz, 55099 Mainz, Germany[o]
[21] Centre de Physique des Particules de Marseille, Univ Méditerranée, IN^2P^3-CNRS, 13288 Marseille, France
[22] Dipartimento di Fisica, Università di Milano e INFN Sezione di Milano, 20133 Milano, Italy
[23] Max-Planck-Institut für Physik, Werner-Heisenberg-Institut, 80805 München, Germany[n]
[24] Laboratoire de l'Accélérateur Linéaire, Université de Paris-Sud, IN^2P^3-CNRS, 91898 Orsay Cedex, France
[25] Dipartimento di Fisica dell'Università, INFN Sezione di Pisa, e Scuola Normale Superiore, 56010 Pisa, Italy
[26] Department of Physics, Royal Holloway & Bedford New College, University of London, Egham, Surrey TW20 OEX, UK[k]
[27] Particle Physics Dept., Rutherford Appleton Laboratory, Chilton, Didcot, Oxon OX11 OQX, UK[k]
[28] CEA, DAPNIA/Service de Physique des Particules, CE-Saclay, 91191 Gif-sur-Yvette Cedex, France[p]
[29] Institute for Particle Physics, University of California at Santa Cruz, Santa Cruz, CA 95064, USA[q]
[30] Department of Physics, University of Sheffield, Sheffield S3 7RH, UK[k]
[31] Fachbereich Physik, Universität Siegen, 57068 Siegen, Germany[n]
[32] Dipartimento di Fisica, Università di Trieste e INFN Sezione di Trieste, 34127 Trieste, Italy
[33] Experimental Elementary Particle Physics, University of Washington, Seattle, WA 98195, U.S.A.
[34] Department of Physics, University of Wisconsin, Madison, WI 53706, USA[l]
[35] Institute for Particle Physics, ETH Hönggerberg, 8093 Zürich, Switzerland
[36] Also at CERN, 1211 Geneva 23, Switzerland
[37] Now at Fermilab, PO Box 500, MS 352, Batavia, IL 60510, USA
[38] Also at Dipartimento di Fisica di Catania and INFN Sezione di Catania, 95129 Catania, Italy
[39] Now at University of Florida, Department of Physics, Gainesville, Florida 32611-8440, USA
[40] Also IFSI sezione di Torino, INAF, Italy
[41] Also at Groupe d'Astroparticules de Montpellier, Université de Montpellier II, 34095 Montpellier, France
[42] Now at Departement de Physique Corpusculaire, Université de Genève, 1211 Genève 4, Switzerland
[43] Also at Department of Physics, Tsinghua University, Beijing, P.R. China
[44] Permanent address: Universitat de Barcelona, 08208 Barcelona, Spain
[45] Now at SAP AG, 69185 Walldorf, Germany

[46] Now at Groupe d' Astroparticules de Montpellier, Université de Montpellier II, 34095 Montpellier, France
[47] Now at BNP Paribas, 60325 Frankfurt am Mainz, Germany
[48] Now at Institut Inter-universitaire des hautes Energies (IIHE), CP 230, Université Libre de Bruxelles, 1050 Bruxelles, Belgique
[49] Now at Dipartimento di Fisica e Tecnologie Relative, Università di Palermo, Palermo, Italy
[50] Now at SLAC, Stanford, CA 94309, USA
[51] Now at CERN, 1211 Geneva 23, Switzerland
[52] Now at Liverpool University, Liverpool L69 7ZE, UK
[53] Now at Henryk Niewodnicznski Institute of Nuclear Physics, Polish Academy of Sciences, Cracow, Poland

The DELPHI Collaboration

[54] Department of Physics and Astronomy, Iowa State University, Ames IA 50011-3160, USA
[55] Physics Department, Universiteit Antwerpen, Universiteitsplein 1, 2610 Antwerpen, Belgium
[56] IIHE, ULB-VUB, Pleinlaan 2, 1050 Brussels, Belgium
[57] Faculté des Sciences, Univ. de l'Etat Mons, Av. Maistriau 19, 7000 Mons, Belgium
[58] Physics Laboratory, University of Athens, Solonos Str. 104, 10680 Athens, Greece
[59] Department of Physics, University of Bergen, Allégaten 55, 5007 Bergen, Norway
[60] Dipartimento di Fisica, Università di Bologna and INFN, Via Irnerio 46, 40126 Bologna, Italy
[61] Centro Brasileiro de Pesquisas Físicas, rua Xavier Sigaud 150, 22290 Rio de Janeiro, Brazil
[62] Depto. de Física, Pont. Univ. Católica, C.P. 38071, 22453 Rio de Janeiro, Brazil
[63] Inst. de Física, Univ. Estadual do Rio de Janeiro, rua São Francisco Xavier 524, Rio de Janeiro, Brazil
[64] Collège de France, Lab. de Physique Corpusculaire, IN2P3-CNRS, 75231 Paris Cedex 05, France
[65] CERN, 1211 Geneva 23, Switzerland
[66] Institut de Recherches Subatomiques, IN2P3 - CNRS/ULP - BP20, 67037 Strasbourg Cedex, France
[67] Now at DESY-Zeuthen, Platanenallee 6, 15735 Zeuthen, Germany
[68] Institute of Nuclear Physics, N.C.S.R. Demokritos, P.O. Box 60228, 15310 Athens, Greece
[69] FZU, Inst. of Phys. of the C.A.S. High Energy Physics Division, Na Slovance 2, 180 40 Praha 8, Czech Republic
[70] Dipartimento di Fisica, Università di Genova and INFN, Via Dodecaneso 33, 16146 Genova, Italy
[71] Institut des Sciences Nucléaires, IN2P3-CNRS, Université de Grenoble 1, 38026 Grenoble Cedex, France
[72] Helsinki Institute of Physics and Department of Physical Sciences, P.O. Box 64, 00014 University of Helsinki, Finland
[73] Joint Institute for Nuclear Research, Dubna, Head Post Office, P.O. Box 79, 101 000 Moscow, Russian Federation
[74] Institut für Experimentelle Kernphysik, Universität Karlsruhe, Postfach 6980, 76128 Karlsruhe, Germany
[75] Institute of Nuclear Physics PAN,Ul. Radzikowskiego 152, 31142 Krakow, Poland
[76] Faculty of Physics and Nuclear Techniques, University of Mining and Metallurgy, 30055 Krakow, Poland
[77] Université de Paris-Sud, Lab. de l'Accélérateur Linéaire, IN2P3-CNRS, Bât. 200, 91405 Orsay Cedex, France
[78] School of Physics and Chemistry, University of Lancaster, Lancaster LA1 4YB, UK
[79] LIP, IST, FCUL - Av. Elias Garcia, 14-1^{o}, 1000 Lisboa Codex, Portugal
[80] Department of Physics, University of Liverpool, P.O. Box 147, Liverpool L69 3BX, UK
[81] Dept. of Physics and Astronomy, Kelvin Building, University of Glasgow, Glasgow G12 8QQ, UK
[82] LPNHE, IN2P3-CNRS, Univ. Paris VI et VII, Tour 33 (RdC), 4 place Jussieu, 75252 Paris Cedex 05, France
[83] Department of Physics, University of Lund, Sölvegatan 14, 223 63 Lund, Sweden
[84] Université Claude Bernard de Lyon, IPNL, IN2P3-CNRS, 69622 Villeurbanne Cedex, France
[85] Dipartimento di Fisica, Università di Milano and INFN-MILANO, Via Celoria 16, 20133 Milan, Italy
[86] Dipartimento di Fisica, Univ. di Milano-Bicocca and INFN-MILANO, Piazza della Scienza 2, 20126 Milan, Italy
[87] IPNP of MFF, Charles Univ., Areal MFF, V Holesovickach 2, 180 00, Praha 8, Czech Republic
[88] NIKHEF, Postbus 41882, 1009 DB Amsterdam, The Netherlands
[89] National Technical University, Physics Department, Zografou Campus, 15773 Athens, Greece
[90] Physics Department, University of Oslo, Blindern, 0316 Oslo, Norway
[91] Dpto. Fisica, Univ. Oviedo, Avda. Calvo Sotelo s/n, 33007 Oviedo, Spain
[92] Department of Physics, University of Oxford, Keble Road, Oxford OX1 3RH, UK
[93] Dipartimento di Fisica, Università di Padova and INFN, Via Marzolo 8, 35131 Padua, Italy
[94] Rutherford Appleton Laboratory, Chilton, Didcot OX11 OQX, UK
[95] Dipartimento di Fisica, Università di Roma II and INFN, Tor Vergata, 00173 Rome, Italy
[96] Dipartimento di Fisica, Università di Roma III and INFN, Via della Vasca Navale 84, 00146 Rome, Italy
[97] DAPNIA/Service de Physique des Particules, CEA-Saclay, 91191 Gif-sur-Yvette Cedex, France
[98] Instituto de Fisica de Cantabria (CSIC-UC), Avda. los Castros s/n, 39006 Santander, Spain
[99] Inst. for High Energy Physics, Serpukov P.O. Box 35, Protvino, (Moscow Region), Russian Federation
[100] J. Stefan Institute, Jamova 39, 1000 Ljubljana, Slovenia
[101] Laboratory for Astroparticle Physics, Nova Gorica Polytechnic, Kostanjeviska 16a, 5000 Nova Gorica, Slovenia
[102] Department of Physics, University of Ljubljana, 1000 Ljubljana, Slovenia
[103] Fysikum, Stockholm University, Box 6730, 113 85 Stockholm, Sweden
[104] Dipartimento di Fisica Sperimentale, Università di Torino and INFN, Via P. Giuria 1, 10125 Turin, Italy

[105] INFN,Sezione di Torino and Dipartimento di Fisica Teorica, Università di Torino, Via Giuria 1, 10125 Turin, Italy
[106] Dipartimento di Fisica, Università di Trieste and INFN, Via A. Valerio 2, 34127 Trieste, Italy
[107] Istituto di Fisica, Università di Udine, 33100 Udine, Italy
[108] Univ. Federal do Rio de Janeiro, C.P. 68528 Cidade Univ., Ilha do Fundão 21945-970 Rio de Janeiro, Brazil
[109] Department of Radiation Sciences, University of Uppsala, P.O. Box 535, 751 21 Uppsala, Sweden
[110] IFIC, Valencia-CSIC, and D.F.A.M.N., U. de Valencia, Avda. Dr. Moliner 50, 46100 Burjassot (Valencia), Spain
[111] Institut für Hochenergiephysik, Österr. Akad. d. Wissensch., Nikolsdorfergasse 18, 1050 Vienna, Austria
[112] Inst. Nuclear Studies and University of Warsaw, Ul. Hoza 69, 00681 Warsaw, Poland
[113] Fachbereich Physik, University of Wuppertal, Postfach 100 127, 42097 Wuppertal, Germany

The L3 Collaboration

[114] III. Physikalisches Institut, RWTH, 52056 Aachen, Germany[r]
[115] National Institute for High Energy Physics, NIKHEF, and University of Amsterdam, 1009 DB Amsterdam, The Netherlands
[116] University of Michigan, Ann Arbor, MI 48109, USA
[117] Laboratoire d'Annecy-le-Vieux de Physique des Particules, LAPP, IN2P3-CNRS, BP 110, 74941 Annecy-le-Vieux CEDEX, France
[118] Institute of Physics, University of Basel, 4056 Basel, Switzerland
[119] Louisiana State University, Baton Rouge, LA 70803, USA
[120] Institute of High Energy Physics, IHEP, 100039 Beijing, China[s]
[121] University of Bologna and INFN-Sezione di Bologna, 40126 Bologna, Italy
[122] Tata Institute of Fundamental Research, Mumbai (Bombay) 400 005, India
[123] Northeastern University, Boston, MA 02115, USA
[124] Institute of Atomic Physics and University of Bucharest, 76900 Bucharest, Romania
[125] Central Research Institute for Physics of the Hungarian Academy of Sciences, 1525 Budapest 114, Hungary[t]
[126] Massachusetts Institute of Technology, Cambridge, MA 02139, USA
[127] Panjab University, Chandigarh 160 014, India
[128] KLTE-ATOMKI, 4010 Debrecen, Hungary[f]
[129] UCD School of Physics, University College Dublin, Belfield, Dublin 4, Ireland
[130] INFN Sezione di Firenze and University of Florence, 50125 Florence, Italy
[131] European Laboratory for Particle Physics, CERN, 1211 Geneva 23, Switzerland
[132] World Laboratory, FBLJA Project, 1211 Geneva 23, Switzerland
[133] University of Geneva, 1211 Geneva 4, Switzerland
[134] University of Hamburg, 22761 Hamburg, Germany
[135] Chinese University of Science and Technology, USTC, Hefei, Anhui 230 029, China[r]
[136] University of Lausanne, 1015 Lausanne, Switzerland
[137] Institut de Physique Nucléaire de Lyon, IN2P3-CNRS, Université Claude Bernard, 69622 Villeurbanne, France
[138] Centro de Investigaciones Energéticas, Medioambientales y Tecnológicas, CIEMAT, 28040 Madrid, Spain[u]
[139] Florida Institute of Technology, Melbourne, FL 32901, USA
[140] INFN-Sezione di Milano, 20133 Milan, Italy
[141] Institute of Theoretical and Experimental Physics, ITEP, Moscow, Russia
[142] INFN-Sezione di Napoli and University of Naples, 80125 Naples, Italy
[143] Department of Physics, University of Cyprus, Nicosia, Cyprus
[144] Radboud University and NIKHEF, 6525 ED Nijmegen, The Netherlands
[145] California Institute of Technology, Pasadena, CA 91125, USA
[146] INFN-Sezione di Perugia and Università Degli Studi di Perugia, 06100 Perugia, Italy
[147] Nuclear Physics Institute, St. Petersburg, Russia
[148] Carnegie Mellon University, Pittsburgh, PA 15213, USA
[149] INFN-Sezione di Napoli and University of Potenza, 85100 Potenza, Italy
[150] Princeton University, Princeton, NJ 08544, USA
[151] University of Californa, Riverside, CA 92521, USA
[152] INFN-Sezione di Roma and University of Rome, "La Sapienza", 00185 Rome, Italy
[153] University and INFN, Salerno, 84100 Salerno, Italy
[154] University of California, San Diego, CA 92093, USA
[155] Bulgarian Academy of Sciences, Central Lab. of Mechatronics and Instrumentation, 1113 Sofia, Bulgaria
[156] The Center for High Energy Physics, Kyungpook National University, 702-701 Taegu, Republic of Korea
[157] National Central University, Chung-Li, Taiwan, China
[158] Department of Physics, National Tsing Hua University, Taiwan, China
[159] Purdue University, West Lafayette, IN 47907, USA
[160] Paul Scherrer Institut, PSI, 5232 Villigen, Switzerland
[161] DESY, 15738 Zeuthen, Germany
[162] Eidgenössische Technische Hochschule, ETH Zürich, 8093 Zürich, Switzerland

The OPAL Collaboration

[163] School of Physics and Astronomy, University of Birmingham, Birmingham B15 2TT, UK
[164] Dipartimento di Fisica dell' Università di Bologna and INFN, 40126 Bologna, Italy
[165] Physikalisches Institut, Universität Bonn, 53115 Bonn, Germany
[166] Department of Physics, University of California, Riverside CA 92521, USA
[167] Cavendish Laboratory, Cambridge CB3 0HE, UK
[168] Ottawa-Carleton Institute for Physics, Department of Physics, Carleton University, Ottawa, Ontario K1S 5B6, Canada
[169] CERN, European Organisation for Nuclear Research, 1211 Geneva 23, Switzerland
[170] Enrico Fermi Institute and Department of Physics, University of Chicago, Chicago IL 60637, USA
[171] Fakultät für Physik, Albert-Ludwigs-Universität Freiburg, 79104 Freiburg, Germany
[172] Physikalisches Institut, Universität Heidelberg, 69120 Heidelberg, Germany
[173] Indiana University, Department of Physics, Bloomington IN 47405, USA
[174] Queen Mary and Westfield College, University of London, London E1 4NS, UK
[175] Technische Hochschule Aachen, III Physikalisches Institut, Sommerfeldstrasse 26–28, 52056 Aachen, Germany
[176] University College London, London WC1E 6BT, UK
[177] Department of Physics, Schuster Laboratory, The University, Manchester M13 9PL, UK
[178] Department of Physics, University of Maryland, College Park, MD 20742, USA
[179] Laboratoire de Physique Nucléaire, Université de Montréal, Montréal, Québec H3C 3J7, Canada
[180] University of Oregon, Department of Physics, Eugene OR 97403, USA
[181] CCLRC Rutherford Appleton Laboratory, Chilton, Didcot, Oxfordshire OX11 0QX, UK
[182] Department of Physics, Technion-Israel Institute of Technology, Haifa 32000, Israel
[183] Department of Physics and Astronomy, Tel Aviv University, Tel Aviv 69978, Israel
[184] International Centre for Elementary Particle Physics and Department of Physics, University of Tokyo, Tokyo 113-0033, Japan
[185] Kobe University, Kobe 657-8501, Japan
[186] Particle Physics Department, Weizmann Institute of Science, Rehovot 76100, Israel
[187] Universität Hamburg/DESY, Institut für Experimentalphysik, Notkestrasse 85, 22607 Hamburg, Germany
[188] University of Victoria, Department of Physics, P O Box 3055, Victoria BC V8W 3P6, Canada
[189] University of British Columbia, Department of Physics, Vancouver BC V6T 1Z1, Canada
[190] University of Alberta, Department of Physics, Edmonton AB T6G 2J1, Canada
[191] Research Institute for Particle and Nuclear Physics, 1525 Budapest, P O Box 49, Hungary
[192] Institute of Nuclear Research, 4001 Debrecen, P O Box 51, Hungary
[193] Ludwig-Maximilians-Universität München, Sektion Physik, Am Coulombwall 1, 85748 Garching, Germany
[194] Max-Planck-Institute für Physik, Föhringer Ring 6, 80805 München, Germany
[195] Yale University, Department of Physics, New Haven, CT 06520, USA
[196] Now at TRIUMF, Vancouver V6T 2A3, Canada
[197] Now at SLAC, Stanford, CA 94309, USA
[198] And Institute of Nuclear Research, Debrecen, Hungary
[199] And Department of Experimental Physics, University of Debrecen, Hungary
[200] And MPI München, München, Germany
[201] And Research Institute for Particle and Nuclear Physics, Budapest, Hungary
[202] Now at University of Liverpool, Dept. of Physics, Liverpool L69 3BX, UK
[203] Now at Dept. Physics, University of Illinois at Urbana-Champaign, USA
[204] And Manchester University, Manchester, UK
[205] Now at University of Kansas, Dept. of Physics and Astronomy, Lawrence, KS 66045, USA
[206] Now at University of Toronto, Dept. of Physics, Toronto, Canada
[207] Current address Bergische Universität, Wuppertal, Germany
[208] Now at University of Mining and Metallurgy, Cracow, Poland
[209] Now at University of California, San Diego, USA
[210] Now at The University of Melbourne, Victoria, Australia
[211] Now at IPHE Université de Lausanne, 1015 Lausanne, Switzerland
[212] Now at IEKP Universität Karlsruhe, Germany
[213] Now at University of Antwerpen, Physics Department, 2610 Antwerpen, Belgium
[214] Now at University of Nijmegen, Nijmegen, The Netherlands
[215] And High Energy Accelerator Research Organisation (KEK), Tsukuba, Ibaraki, Japan
[216] Now at University of Pennsylvania, Philadelphia, Pennsylvania, USA
[217] Now at TRIUMF, Vancouver, Canada
[218] Now at DESY-Zeuthen, Zeuthen, Germany
[219] Now at CERN, 1211 Geneva 23, Switzerland
[220] Now at DESY, Hamburg, Germany

[221] Departamento de Fisica Teorica, Facultad de Ciencias, Universidad de Zaragoza, 50009 Zaragoza, Spain
[222] CERN TH division, Dept. of Physics, 1211 Geneva 23, Switzerland
[223] Department of Physics and Astronomy, University of Manchester, Manchester M13 9PL, UK
[224] Institute for Particle Physics Phenomenology, University of Durham, Durham DH1 3LE, UK

† Deceased

Received: 17 January 2006 / Revised version: 12 April 2006 /
Published online: 18 July 2006 –

Abstract. The four LEP collaborations, ALEPH, DELPHI, L3 and OPAL, have searched for the neutral Higgs bosons which are predicted by the Minimal Supersymmetric standard model (MSSM). The data of the four collaborations are statistically combined and examined for their consistency with the background hypothesis and with a possible Higgs boson signal. The combined LEP data show no significant excess of events which would indicate the production of Higgs bosons. The search results are used to set upper bounds on the cross-sections of various Higgs-like event topologies. The results are interpreted within the MSSM in a number of "benchmark" models, including CP-conserving and CP-violating scenarios. These interpretations lead in all cases to large exclusions in the MSSM parameter space. Absolute limits are set on the parameter $\tan\beta$ and, in some scenarios, on the masses of neutral Higgs bosons.

1 Introduction

One of the outstanding questions in particle physics is that of electroweak symmetry breaking and the origin of mass. The leading candidate for an answer is the Higgs mechanism [1] whereby fundamental scalar Higgs fields acquire nonzero vacuum expectation values and spontaneously break the electroweak symmetry. Gauge bosons and fermions obtain their masses by interacting with the resulting vacuum Higgs fields. Associated with this description is the existence of massive scalar particles, the Higgs bosons.

The standard model [2] requires one complex Higgs field doublet and predicts a single neutral Higgs boson of unknown mass. After extensive searches at LEP, a lower bound of $114.4\,\mathrm{GeV/c^2}$ has been established for the mass of the standard model Higgs boson, at the 95% confidence level (CL) [3].

Supersymmetric (SUSY) [4] extensions of the standard model are of interest since they provide a consistent framework for the unification of the gauge interactions at a high energy scale and for the stability of the electroweak scale. SUSY is also a basic ingredient of models such as Supergravity and Superstring which aim at a unified description of all fundamental forces, including the gravitational force. It is remarkable that the predictions of SUSY extensions of the standard model are found to be compatible with existing high-precision data [5].

In SUSY, each of the standard model fermions has a bosonic superpartner "sfermion", and each boson has a fermionic superpartner "gaugino" or "Higgsino". These additional particles, if they exist, have several virtues. Their presence modifies the renormalisation group evolution of the gauge couplings, improving the convergence of the couplings at a unique (GUT) energy. The new particles lead to a naturally light Higgs boson (close to the electroweak energy scale) since the divergent loop contributions of the standard model particles are almost completely compensated by corresponding contributions from

[a] The LEP Working Group for Higgs Boson Searches consists of members of the four LEP Collaborations and of theorists among whom S. Heinemeyer, A. Pilaftsis and G. Weiglein are authors of this paper.

[b] Supported by the Leverhulme Trust.
[c] Research Fellow of the Belgium FNRS.
[d] Supported by the Federal Office for Scientific, Technical and Cultural Affairs through the Interuniversity Attraction Pole P5/27.
[e] Research Associate of the Belgium FNRS.
[f] Also supported by CONICET and Universidad Nacional de La Plata, CC 67, 1900 La Plata, Argentina.
[g] Also supported by the Hungarian OTKA fund under contract number T026178.
[h] Supported by Interuniversity Attraction Poles Programme – Belgian Science Policy.
[i] Supported by CICYT, Spain.
[j] Supported by the National Science Foundation of China.
[k] Supported by the Danish Natural Science Research Council.
[l] Supported by the UK Particle Physics and Astronomy Research Council.
[m] Supported by the US Department of Energy, grant DE-FG0295-ER40896.
[n] Supported by the Austrian Ministry for Science and Transport.
[o] Supported by Bundesministerium für Bildung und Forschung, Germany.
[p] Supported by the Direction des Sciences de la Matière, C.E.A.
[q] Supported by the US Department of Energy, grant DE-FG03-92ER40689.
[r] Supported by the German Bundesministerium für Bildung, Wissenschaft, Forschung und Technologie.
[s] Supported by the National Natural Science Foundation of China.
[t] Supported by the Hungarian OTKA fund under contract numbers T019181, F023259 and T037350.
[u] Supported also by the Comisión Interministerial de Ciencia y Tecnología.

the superpartners (the compensation would be perfect if SUSY were an exact symmetry). SUSY models also provide a perfect cold dark matter candidate, the neutralino, which arises from the mixing of the neutral gaugino and Higgsino fields.

The Minimal Supersymmetric standard model (MSSM) (reviewed, e.g., in [6]) is the SUSY extension with minimal new particle content. It requires two Higgs field doublets and predicts the existence of three neutral and two charged Higgs bosons. The lightest of the neutral Higgs bosons is predicted to have a mass less than about $140\,\mathrm{GeV/c^2}$ including radiative corrections [7]. This prediction provided a strong motivation for the searches at LEP energies.

Most of the experimental investigations carried out in the past at LEP and elsewhere were interpreted in MSSM scenarios where CP conservation in the Higgs sector was assumed. In such scenarios the neutral Higgs bosons are CP eigenstates. However, CP violation in the Higgs sector cannot be a priori excluded [8]. Scenarios with CP violation are theoretically appealing since they provide one of the ingredients needed to explain the observed cosmic matter-antimatter asymmetry. The observed size of CP violation in B and K meson systems is not sufficient to drive this asymmetry. In the MSSM, however, substantial CP violation can be induced by complex phases in the soft SUSY-breaking sector, through radiative corrections, especially from third-generation scalar quarks [9]. In such scenarios the three neutral Higgs mass eigenstates are mixtures of CP-even and CP-odd fields, with production and decay properties different from those in the CP-conserving scenarios. Hence, the experimental exclusions published so far for the CP-conserving MSSM scenarios may be weakened by CP-violating effects. There is currently one publication on searches interpreted in CP-violating scenarios [10].

In this paper we describe the results of a statistical combination based on the searches of the four LEP collaborations [10–13], which was carried out by the LEP Working Group for Higgs Boson Searches. These searches include all LEP2 data up to the highest energy, 209 GeV; in the case of [10, 12] they also include the LEP1 data collected at energies in the vicinity of 91 GeV (the Z boson resonance). The combined LEP data show no significant signal for Higgs boson production. The search results are used to set upper bounds on topological cross-sections for a number of Higgs-like final states. Furthermore, they are interpreted in a set of representative MSSM "benchmark" models, with and without CP-violating effects in the Higgs sector.

2 The MSSM framework

The LEP searches and their statistical combination presented in this paper are interpreted in a constrained MSSM model. At tree level, two parameters are sufficient (besides the known parameters of the standard model fermion and gauge sectors) to fully describe the Higgs sector. A convenient choice is one Higgs boson mass (m_{A} is chosen in CP-conserving scenarios and $m_{\mathrm{H}^\pm}$ in CP-violating scenarios), and the ratio $\tan\beta = v_2/v_1$ of the vacuum expectation values of the two Higgs fields (v_2 and v_1 refer to the fields which couple to the up- and down-type fermions). Additional parameters, M_{SUSY}, M_2, μ, A and $m_{\tilde{\mathrm{g}}}$, enter at the level of radiative corrections. M_{SUSY} is a soft SUSY-breaking mass parameter and represents a common mass for all scalar fermions (sfermions) at the electroweak scale. Similarly, M_2 represents a common SU(2) gaugino mass at the electroweak scale. The "Higgs mass parameter" μ is the strength of the supersymmetric Higgs mixing; $A = A_{\mathrm{t}} = A_{\mathrm{b}}$ is a common trilinear Higgs-squark coupling at the electroweak scale and $m_{\tilde{\mathrm{g}}}$ is the mass of the gluino (the superpartner of the gluons). Three of these parameters define the stop and sbottom mixing parameters $X_{\mathrm{t}} = A - \mu\cot\beta$ and $X_{\mathrm{b}} = A - \mu\tan\beta$. In CP-violating scenarios, the complex phases related to A and $m_{\tilde{\mathrm{g}}}$, $\arg(A)$ and $\arg(m_{\tilde{\mathrm{g}}})$, are supplementary parameters. In addition to all these MSSM parameters, the top quark mass also has a strong impact on the predictions through radiative corrections. In this paper, three fixed values are used in the calculations: $m_{\mathrm{t}} = 169.3$, 174.3 and $179.3\,\mathrm{GeV/c^2}$. For the purposes of illustration, $m_{\mathrm{t}} = 174.3\,\mathrm{GeV/c^2}$ is used in producing the figures (unless explicitly specified otherwise), which is a previous world-average value [14] and which is within the current experimental range of $172.7 \pm 2.9\,\mathrm{GeV/c^2}$ [15]. The influence of the top quark mass on the exclusion limits is discussed in Sects. 5 and 6 along with the other results.

The combined LEP data are compared to the predictions of a number of MSSM "benchmark" models [16]. Within each of these models, the two tree-level parameters, $\tan\beta$ and m_{A} (in the CP-conserving scenarios) or $m_{\mathrm{H}^\pm}$ (in the CP-violating scenarios) are scanned while the other parameters are set to fixed values. Each scan point thus represents a specific MSSM model. The ranges of the scanned parameters and the values of the fixed parameters are listed in Table 1 for the main scenarios studied. The first five models represent the main benchmarks for CP-conserving scenarios while the last model, labelled *CPX*, is a benchmark model for CP-violating scenarios. Some variants of these benchmark scenarios, which are also investigated, are presented in the text below.

The scan range of $\tan\beta$ is limited by the following considerations. For values of $\tan\beta$ below the indicated lower bounds, the calculations of the observables in the Higgs sector (masses, cross-sections and decay branching ratios) become uncertain; for values above the upper bounds, the decay width of the Higgs bosons may become larger than the experimental mass resolution (typically a few $\mathrm{GeV/c^2}$) and the modelling of the kinematic distributions of the signal becomes inaccurate[1]. The scan range of m_{A} is limited in most cases to less than $1000\,\mathrm{GeV/c^2}$; at higher values the Higgs phenomenology is insensitive to the choice of m_{A}.

[1] The DELPHI Collaboration included the variation of the Higgs boson decay width with $\tan\beta$ in their simulation for $\tan\beta$ between 30 and 50. With increasing $\tan\beta$, DELPHI observed an increase of the mass resolutions and hence a loss in the signal detection efficiencies; but this was compensated by the increase of the cross-sections, such that DELPHI found no significant drop in the overall sensitivity.

Table 1. Parameters of the main benchmark scenarios investigated in this paper. The values of $\tan\beta$ and the mass parameters m_{A} (in the CP-conserving scenarios) or $m_{\mathrm{H}^\pm}$ (in the CP-violating scenarios) are scanned within the indicated ranges. For the definitions of A and X_{t}, the Feynman-diagrammatic on-shell renormalisation scheme is used in the CP-conserving scenarios and the $\overline{\mathrm{MS}}$ renormalisation scheme in the CP-violating scenarios

	Benchmark parameters					
	(1) m_{h}-*max*	(2) *no-mixing*	(3) *large-*μ	(4) *gluophobic*	(5) *small-*α_{eff}	(6) *CPX*
	Parameters varied in the scan					
$\tan\beta$	0.4–40	0.4–40	0.7–50	0.4–40	0.4–40	0.6–40
m_{A} (GeV/c^2)	0.1–1000	0.1–1000	0.1–400	0.1–1000	0.1–1000	–
$m_{\mathrm{H}^\pm}$ (GeV/c^2)	–	–	–	–	–	4–1000
	Fixed parameters					
M_{SUSY} (GeV)	1000	1000	400	350	800	500
M_2 (GeV)	200	200	400	300	500	200
μ (GeV)	-200	-200	1000	300	2000	2000
$m_{\tilde{\mathrm{g}}}$ (GeV/c^2)	800	800	200	500	500	1000
X_{t} (GeV)	$2M_{\mathrm{SUSY}}$	0	-300	-750	-1100	$A-\mu\cot\beta$
A (GeV)	$X_{\mathrm{t}}+\mu\cot\beta$	$X_{\mathrm{t}}+\mu\cot\beta$	$X_{\mathrm{t}}+\mu\cot\beta$	$X_{\mathrm{t}}+\mu\cot\beta$	$X_{\mathrm{t}}+\mu\cot\beta$	1000
$\arg(A)=\arg(m_{\tilde{\mathrm{g}}})$	–	–	–	–	–	90°

For a given scan point, the observables in the Higgs sector are calculated using two theoretical approaches, both including one- and two-loop corrections. The `FeynHiggs2.0` code [17] is based on a Feynman-diagrammatic approach and uses the on-shell renormalization scheme. The `SUBHPOLE` calculation and its CP-violating variant `CPH` [18] are based on a renormalization-group improved effective potential calculation [19] and use the $\overline{\mathrm{MS}}$ scheme[2].

In the CP-conserving case, the `FeynHiggs` calculation is retained for the presentation of the results since it yields slightly more conservative results (the theoretically allowed parameter space is wider) than `SUBHPOLE` does. Also, `FeynHiggs` is preferred on theoretical grounds since its radiative corrections are more detailed than those of `SUBHPOLE`.

In the CP-violating case, neither of the two calculations is preferred on theoretical grounds. While `FeynHiggs` contains more advanced one-loop corrections, the `CPH` code has a more precise phase dependence at the two-loop level. We opted therefore for a solution where, in each scan point, the `CPH` and `FeynHiggs` calculations are compared and the calculation yielding the weaker exclusion (more conservative) is retained. However, we also discuss in Sect. 6 the effect of using separately either one or the other of the two calculations. Rather large discrepancies between the two codes are found in calculating the partial width for the Higgs boson cascade decay $\Gamma(\mathcal{H}_2\to\mathcal{H}_1\mathcal{H}_1)$ ($\mathcal{H}_1$ and $\mathcal{H}_2$ are the lightest and the second-lightest neutral MSSM Higgs bosons). Aiming at conservative exclusion limits, therefore, the `CPH` formula for this decay was also used within the `FeynHiggs` code.

All codes are implemented in a modified version of the `HZHA` program package [21], which takes into account initial-state radiation and the interference between identical final states from Higgsstrahlung and boson fusion processes.

[2] New developments in this approach are implemented in the code `CPsuperH` [20].

2.1 CP-conserving scenarios

Assuming CP conservation, the spectrum of MSSM Higgs bosons consists of two CP-even neutral scalars, h and H (h is defined to be the lighter of the two), one CP-odd neutral scalar, A, and one pair of charged Higgs bosons, $\mathrm{H}^\pm$. The following ordering of masses is valid at tree level: $m_h<(m_{\mathrm{Z}},m_{\mathrm{A}})<m_{\mathrm{H}}$ and $m_{\mathrm{W}^\pm}<m_{\mathrm{H}^\pm}$. This ordering may be substantially modified by radiative corrections [7] where the largest contribution arises from the incomplete cancellation between top and scalar top (stop) loops. The corrections affect mainly the neutral Higgs boson masses and decay branching ratios.

In $\mathrm{e^+e^-}$ collisions at LEP energies, the main production processes of h, H and A are the Higgsstrahlung processes $\mathrm{e^+e^-}\to hZ$ and HZ and the pair production processes $\mathrm{e^+e^-}\to hA$ and HA (in most of the MSSM parameter space only the hZ and hA processes are possible by kinematics). The fusion processes $\mathrm{e^+e^-}\to(WW\to h)\nu_{\mathrm{e}}\bar{\nu_{\mathrm{e}}}$ and $\mathrm{e^+e^-}\to(ZZ\to h)\mathrm{e^+e^-}$ play a marginal role at LEP energies but they are also taken into account in the derivation of the results.

The cross-sections for Higgsstrahlung and pair production can be expressed in terms of the standard model Higgs boson production cross-section $\sigma^{\mathrm{SM}}_{HZ}$. The following expressions hold for the processes involving the lightest scalar boson h:

$$\sigma_{hZ}=\sin^2(\beta-\alpha)\sigma^{\mathrm{SM}}_{HZ} \quad (1)$$

$$\sigma_{hA}=\cos^2(\beta-\alpha)\bar{\lambda}\sigma^{\mathrm{SM}}_{HZ}\,. \quad (2)$$

Here α is the mixing angle which diagonalises the CP-even Higgs mass matrix (at lowest order it can be expressed in terms of m_A, M_Z and $\tan\beta$) and $\bar{\lambda}$ is a kinematic factor:

$$\bar{\lambda}=\lambda_{Ah}^{3/2}/\left[\lambda_{Zh}^{1/2}\left(12M_Z^2/s+\lambda_{Zh}\right)\right] \quad (3)$$

with

$$\lambda_{ij} = [1-(m_i+m_j)^2/s][1-(m_i-m_j)^2/s]\,, \qquad (4)$$

where s is the square of the centre-of-mass energy. The cross-sections for the processes involving the heavy scalar boson H are obtained by interchanging the MSSM suppression factors $\sin^2(\beta-\alpha)$ and $\cos^2(\beta-\alpha)$ in (1) and (2) and replacing the index h by H in (1)–(3). The Higgsstrahlung and pair production cross-sections are complementary, as seen from (1) and (2). At LEP energies, the process $e^+e^- \to hZ$ is typically more abundant at small $\tan\beta$ and $e^+e^- \to hA$ at large $\tan\beta$, but the latter process can be suppressed also by the kinematic factor $\bar{\lambda}$.

The following decay features are relevant to the neutral MSSM Higgs bosons. The h boson decays mainly to fermion pairs, with only a small fraction of WW^* and ZZ^* decays, since its mass is below the threshold of the on-shell processes $h \to WW$ and $h \to ZZ$. However, for particular choices of the parameters, the fermionic final states may be strongly suppressed. The A boson also decays predominantly to fermion pairs, independently of its mass, since its coupling to vector bosons is zero at leading order. For $\tan\beta > 1$, decays of h and A to $b\bar{b}$ and $\tau^+\tau^-$ pairs are preferred while the decays to $c\bar{c}$ and gluon pairs are suppressed. Decays to $c\bar{c}$ may become important for $\tan\beta < 1$. The decay $h \to AA$ may be dominant if allowed by kinematics [22]. Higgs boson decays into SUSY particles, such as sfermions, charginos or invisible neutralinos, are suppressed due to the high values of the SUSY-breaking scale $M_{\rm SUSY}$ which have been chosen.

In the following we describe the CP-conserving benchmark scenarios [16] which are examined in this paper. The corresponding parameters are listed in Table 1.

2.1.1 The $m_{\rm h}$-*max* scenario

In the $m_{\rm h}$-*max* scenario the stop mixing parameter is set to a large value, $X_{\rm t} = 2M_{\rm SUSY}$. This model is designed to maximise the theoretical upper bound on m_h for a given $\tan\beta$ and fixed $m_{\rm t}$ and $M_{\rm SUSY}$ (uncertainties due to unknown higher-order corrections are ignored). This model thus provides the largest parameter space in the $m_{\rm h}$ direction and conservative exclusion limits for $\tan\beta$.

We also examine a variant of this scenario where the sign of μ is changed to positive, since, in the context of SUSY extensions of the standard model, a positive sign of μ is favoured by presently available results on $(g-2)_\mu$ [23, 24]. This variant is labelled $m_{\rm h}$-*max* (a) below. Furthermore, we examine the case where, besides changing the sign of μ to positive, the sign of the mixing parameter $X_{\rm t}$ is changed to negative. This choice of parameters gives better agreement with measurements of the branching ratios and of the CP- and isospin-asymmetries for the process $b \to s\gamma$ [16, 25]. This variant is labelled $m_{\rm h}$-*max* (b) below.

2.1.2 The *no-mixing* scenario

In the *no-mixing* scenario the stop mixing parameter $X_{\rm t}$ is set to zero, giving rise to a relatively restricted MSSM parameter space. Like in the $m_{\rm h}$-*max* scenario, we also examine a variant of the *no-mixing* scenario where the sign of μ is changed to positive. At the same time, we raise $M_{\rm SUSY}$ to 2 TeV in order to enlarge the allowed parameter space [16]. In the case of this variant, which is labelled *no-mixing* (a) below, the scan in $\tan\beta$ is done only from 0.7 upward, due to numerical instabilities, at lower values, in the diagonalisation of the mass matrix.

2.1.3 Special scenarios

Some scenarios were designed to illustrate choices of the MSSM parameters for which the detection of Higgs bosons at LEP, at the Tevatron and at the LHC is expected to be difficult a priori due to the suppression of some main discovery channels [16].

- The *large-*μ scenario is constructed in such a way that, while the h boson is accessible by kinematics at LEP for all scan points, the decay $h \to b\bar{b}$, on which most of the searches at LEP and at the Tevatron are based, is typically strongly suppressed. For many of the scan points the decay $h \to \tau^+\tau^-$ is also suppressed, such that the dominant decay modes are $h \to c\bar{c}$, gg and WW^*. The detection of Higgs bosons thus relies mainly on flavour- and decay-mode-independent searches. Moreover, for some of the scan points, the $e^+e^- \to hZ$ process is suppressed altogether by a small value of $\sin^2(\beta-\alpha)$. In such cases, however, the heavy neutral scalar H is within reach ($m_{\rm H} < 111\,{\rm GeV/c^2}$) and the cross-section for $e^+e^- \to HZ$, proportional to $\cos^2(\beta-\alpha)$, is large; the search may thus proceed via the heavy Higgs boson H.
- The *gluophobic* scenario is constructed in such a way that the Higgs boson coupling to gluons is suppressed due to a cancellation between the top and the stop loops at the hgg vertex. Since at the LHC the searches will rely heavily on producing the Higgs boson in gluon-gluon fusion, and since the mass determination will rely in part on the decays into gluon pairs, such a scenario may present experimental difficulties.
- In the *small-*$\alpha_{\rm eff}$ scenario the couplings governing the decays $h \to b\bar{b}$ and $h \to \tau^+\tau^-$ are suppressed with respect to their standard model values by a factor $-\sin\alpha_{\rm eff}/\cos\beta$ ($\alpha_{\rm eff}$ is the effective mixing angle of the neutral CP-even Higgs sector including radiative corrections). This suppression is most prominent for $\tan\beta > 15$ and $170 < m_{\rm A} < 350\,{\rm GeV/c^2}$. (One should note that in most models which fall in this domain, all three neutral Higgs bosons are beyond the kinematic reach of LEP.)

2.2 CP-violating scenarios

In CP-violating MSSM scenarios the three neutral Higgs mass eigenstates $\mathcal{H}_i$ ($i = 1, 2, 3$) do not have well defined CP quantum numbers. Each of them can thus be produced by Higgsstrahlung ($e^+e^- \to \mathcal{H}_i Z$) via the CP-even field component and in pairs ($e^+e^- \to \mathcal{H}_i\mathcal{H}_j$ ($i \neq j$)). The relative rates depend on the choice of the parameters describing the CP-even/odd mixing.

Table 2. A typical parameter set which is difficult to address by the present searches. The results of the two calculations, `FeynHiggs` and `CPH`, are given for a centre-of-mass energy of 206 GeV. The main input parameters are listed in the first two lines; all other input parameters correspond to the *CPX* benchmark scenario and are listed in the last column of Table 1. The output masses $m_{\mathcal{H}_1}$, $m_{\mathcal{H}_2}$ and the relevant topological cross-sections are listed in the *lower part*

Parameters	`FeynHiggs`	`CPH`
H^+ ($\mathrm{GeV/c^2}$)	129.0	129.0
$\tan\beta$	5.0	5.0
$m_{\mathcal{H}_1}$ ($\mathrm{GeV/c^2}$)	38.1	33.4
$m_{\mathcal{H}_2}$ ($\mathrm{GeV/c^2}$)	105.4	102.4
$\sigma(\mathcal{H}_1 Z \to b\bar{b}Z)$ (pb)	0.0051	0.0019
$\sigma(\mathcal{H}_2 Z \to b\bar{b}Z)$ (pb)	0.0156	0.0197
$\sigma(\mathcal{H}_2 Z \to \mathcal{H}_1\mathcal{H}_1 Z \to b\bar{b}b\bar{b}Z)$ (pb)	0.0866	0.0978
$\sigma(\mathcal{H}_1\mathcal{H}_2 \to b\bar{b}b\bar{b})$ (pb)	0.0066	0.0094

Experimentally, the CP-violating scenarios are more challenging than the CP-conserving scenarios. For a wide range of model parameters, the coupling of the lightest Higgs boson $\mathcal{H}_1$ to the Z boson may be suppressed. Furthermore, the second- and third-lightest $\mathcal{H}_2$ and $\mathcal{H}_3$ bosons may both have masses close to or beyond the kinematic reach of LEP. Also, in CP-violating scenarios, the decays to the main "discovery channels", $\mathcal{H}_1 \to b\bar{b}$, $\mathcal{H}_2 \to b\bar{b}$ and $\mathcal{H}_2 \to \mathcal{H}_1\mathcal{H}_1 \to b\bar{b}b\bar{b}$[3], may have lower branching ratios. One therefore anticipates less search sensitivity in the CP-violating scenarios than in the CP-conserving scenarios. An example illustrating this situation is given in Table 2.

The cross-sections for Higgsstrahlung and pair production are given by [9]

$$\sigma_{\mathcal{H}_i Z} = g^2_{\mathcal{H}_i ZZ}\sigma^{\mathrm{SM}}_{HZ} \tag{5}$$

$$\sigma_{\mathcal{H}_i\mathcal{H}_j} = g^2_{\mathcal{H}_i\mathcal{H}_j Z}\bar{\lambda}\sigma^{\mathrm{SM}}_{HZ} \tag{6}$$

(in the expression for $\bar{\lambda}$, (3), the indices h and A have to be replaced by $\mathcal{H}_i$ and $\mathcal{H}_j$). The couplings

$$g_{\mathcal{H}_i ZZ} = \cos\beta\mathcal{O}_{1i} + \sin\beta\mathcal{O}_{2i} \tag{7}$$

$$g_{\mathcal{H}_i\mathcal{H}_j Z} = \mathcal{O}_{3i}(\cos\beta\mathcal{O}_{2j} - \sin\beta\mathcal{O}_{1j}) - \mathcal{O}_{3j}(\cos\beta\mathcal{O}_{2i} - \sin\beta\mathcal{O}_{1i}) \tag{8}$$

obey the complementarity relation

$$\sum_{i=1}^{3} g^2_{\mathcal{H}_i ZZ} = 1 \tag{9}$$

$$g_{\mathcal{H}_k ZZ} = \varepsilon_{ijk} g_{\mathcal{H}_i\mathcal{H}_j Z} \tag{10}$$

where ε_{ijk} is the usual Levi–Civita symbol.

[3] Regarding the decay properties, the CP-violating scenarios maintain a certain similarity to the CP-conserving scenarios although the branching ratios are, in general, different. The lightest mass eigenstate $\mathcal{H}_1$ predominantly decays to $b\bar{b}$ if allowed by kinematics, with a small fraction decaying to $\tau^+\tau^-$ and $c\bar{c}$. The second-lightest Higgs boson $\mathcal{H}_2$ may decay to $\mathcal{H}_1\mathcal{H}_1$ when allowed by kinematics; otherwise it decays preferentially to $b\bar{b}$.

In CP-violating scenarios, the orthogonal matrix $\mathcal{O}_{ij}$ $(i,j = 1,2,3)$ relating the weak CP eigenstates to the mass eigenstates has non-vanishing off-diagonal elements. These elements, giving rise to CP-even/odd mixing, are proportional to

$$\frac{m_t^4 \mathrm{Im}(\mu A)}{v^2 M^2_{\mathrm{SUSY}}} \tag{11}$$

with $v = \sqrt{v_1^2 + v_2^2}$. Substantial deviations from the CP-conserving scenarios are thus expected for small M_{SUSY} and large $\mathrm{Im}(\mu A)$, which are obtained if the CP-violating phase $\arg(A)$ takes values close to 90°. Furthermore, the effects from CP violation strongly depend on the precise value of the top quark mass [15].

The parameters of the benchmark model *CPX* have been chosen [18] to maximise the phenomenological differences with respect to the CP-conserving scenarios. Constraints from measurements of the electron and neutron electric dipole moments [26] were also taken into account. The basic set of parameters is listed in the last column of Table 1. Note that the scan of $m_{\mathrm{H}^\pm}$ started at $4\,\mathrm{GeV/c^2}$ but values less than about $100\,\mathrm{GeV/c^2}$ give unphysical results and are thus considered as theoretically inaccessible.

The parameters which follow have been varied one-by-one while all the other parameters were kept at their standard *CPX* value.

- Top quark mass: $m_{\mathrm{t}} = 169.3$, 174.3, and $179.3\,\mathrm{GeV/c^2}$, embracing the current experimental value, $m_{\mathrm{t}} = 172.7 \pm 2.9\,\mathrm{GeV/c^2}$ [15].
- The CP-violating phases: $\arg(A) = \arg(m_{\tilde{\mathrm{g}}}) = 0°$, 30°, 60°, 90° (*CPX* value), 135° and 180° (the values 0° and 180° correspond to CP-conserving limits).
- The Higgs mass parameter: $\mu = 0.5$, 1.0, 2.0 (*CPX* value) and 4.0 TeV.
- The SUSY-breaking scale: $M_{\mathrm{SUSY}} = 0.5\,\mathrm{TeV}$ (*CPX* value) and 1.0 TeV. The proposal of the *CPX* scenario [18] predicts a weak dependence on M_{SUSY} if the relations $|A| = |m_{\tilde{\mathrm{g}}}| = \mu/2 = 2M_{\mathrm{SUSY}}$ are preserved. This behaviour is examined by studying a model where M_{SUSY} is increased from 0.5 TeV to 1 TeV and the values of A, $m_{\tilde{\mathrm{g}}}$ and μ are scaled to 2000 GeV, 2000 GeV and 4000 GeV, respectively.

3 Experimental searches

The searches carried out by the four LEP collaborations are based on $\mathrm{e^+e^-}$ collision data which span a large range of centre-of-mass energies, from 91 GeV to 209 GeV. The searches include the Higgsstrahlung and pair production processes, ensuring, by their complementarity, a high sensitivity over the accessible MSSM parameter space. It is important to note that the kinematic properties of the signal processes are to a large extent independent of the CP composition of the Higgs bosons. This implies that the same topological searches can be applied to study the CP-conserving and CP-violating scenarios. For Higgsstrahlung this is natural since only the CP-even components of the

Higgs fields couple to the Z boson. In pair production involving CP-even and CP-odd field components, the similarity of the kinematic properties (e.g., angular distributions) arises from the scalar nature of the Higgs bosons. Small differences may occur from spin-spin correlations between final-state particles but these were found to have no noticeable effect on the signal detection efficiencies. We therefore adopt in the following a common notation for the CP-conserving and CP-violating processes in which $\mathcal{H}_i$ ($i = 1, 2, 3$) designate three generic neutral Higgs bosons of increasing mass, with undefined CP properties; in the CP-conserving limit ($\arg(A) = \arg(m_{\tilde{g}}) = 0°$), these become the CP eigenstates h, A, H (the correspondence depends on the mass hierarchy).

In each of the four LEP experiments, the data analysis is done in several steps. A preselection is applied to reduce some of the largest backgrounds, in particular, from two-photon processes. The remaining background, mainly from production of fermion pairs and WW or ZZ (possibly accompanied by photon or gluon radiation), is further reduced by more selective cuts or by applying multivariate techniques such as likelihood analyses and neural networks. The identification of b-quarks in the decay of the Higgs bosons plays an important role in the discrimination between signal and background, as does the kinematic reconstruction of the Higgs boson masses. The detailed implementation of these analyses, as well as the data samples used by the four collaborations, are described in the individual publications. A full catalog of the searches provided by the four LEP collaborations for this combination, with corresponding references to the detailed descriptions, is given in Appendix A.

3.1 Search topologies

Searches have been carried out for the two main signal processes, the Higgsstrahlung process $e^+e^- \to \mathcal{H}_1 Z$ (which also apply in some cases to $e^+e^- \to \mathcal{H}_2 Z$) and the pair production process $e^+e^- \to \mathcal{H}_2\mathcal{H}_1$.

(a) Considering first the Higgsstrahlung process $e^+e^- \to \mathcal{H}_1 Z$, the principal signal topologies are those used in the search for the standard model Higgs boson at LEP [3], namely:

- the four-jet topology, $(\mathcal{H}_1 \to b\bar{b})(Z \to q\bar{q})$, in which the invariant mass of two jets is close to the Z boson mass m_Z while the other two jets contain b-flavour;
- the missing energy topology, $(\mathcal{H}_1 \to b\bar{b}, \tau^+\tau^-)(Z \to \nu\bar{\nu})$, in which the event consists of two b-jets or identified tau decays and substantial missing momentum and missing mass, compatible with m_Z;
- the leptonic final states, $(\mathcal{H}_1 \to b\bar{b})(Z \to e^+e^-, \mu^+\mu^-)$, in which the invariant mass of the two leptons is close to m_Z;
- the final states with tau-leptons, $(\mathcal{H}_1 \to \tau^+\tau^-)(Z \to q\bar{q})$ and $(\mathcal{H}_1 \to b\bar{b}, \tau^+\tau^-)(Z \to \tau^+\tau^-)$, in which either the $\tau^+\tau^-$ or the $q\bar{q}$ pair has an invariant mass close to m_Z.

Most of these signatures are relevant for Higgs boson masses above the $b\bar{b}$ threshold and rely on the identification of b-quarks in the final state. Searches for lighter Higgs bosons, listed in Appendix A, use signatures which are described in the specific publications. In some regions of the MSSM parameter space, the $\mathcal{H}_1 \to b\bar{b}$ decay may be suppressed while decays into other quark flavours or gluon pairs are favoured. The above searches are therefore complemented or replaced[4] by flavour-independent searches for $(\mathcal{H}_1 \to q\bar{q})Z$ in which there is no requirement on the quark-flavour of the jets. Finally, the searches for Higgsstrahlung also include the Higgs cascade decay $e^+e^- \to \mathcal{H}_2 Z \to (\mathcal{H}_1\mathcal{H}_1)Z$, giving rise to a new class of event topologies. These processes may play an important role in those regions of the parameter space where they are allowed by kinematics.

(b) In the case of the pair production process, $e^+e^- \to \mathcal{H}_2\mathcal{H}_1$, the principal signal topologies at LEP are:

- the four-b final state $(\mathcal{H}_2 \to b\bar{b})(\mathcal{H}_1 \to b\bar{b})$;
- the mixed final states $(\mathcal{H}_2 \to \tau^+\tau^-)(\mathcal{H}_1 \to b\bar{b})$ and $(\mathcal{H}_2 \to b\bar{b})(\mathcal{H}_1 \to \tau^+\tau^-)$;
- the four-tau final state $(\mathcal{H}_2 \to \tau^+\tau^-)(\mathcal{H}_1 \to \tau^+\tau^-)$.

The Higgs cascade decay, $e^+e^- \to \mathcal{H}_2\mathcal{H}_1 \to (\mathcal{H}_1\mathcal{H}_1)\mathcal{H}_1$, gives rise to event topologies ranging from six b-jets to six tau-leptons. Most of these searches are relevant for Higgs boson masses above the $\tau^+\tau^-$ threshold. Similarly to the Higgsstrahlung case, the above searches for pair production are complemented or replaced, whenever more efficient, by flavour-independent searches.

3.2 Additional experimental constraints

If the combination of the above searches is not sufficiently sensitive for excluding a given model point, additional constraints are applied; these are listed below.

- Constraint from the measured decay width of the Z boson, Γ_Z, and its possible deviation, $\Delta\Gamma_Z$, from the standard model prediction. The model point is regarded as excluded if the following relation between the relevant cross-sections is found to be true:

$$\sum_i \sigma_{\mathcal{H}_i Z}(m_Z) + \sum_{i,j} \sigma_{\mathcal{H}_i\mathcal{H}_j}(m_Z) > \frac{\Delta\Gamma_Z}{\Gamma_Z} \cdot \sigma_Z^{\mathrm{tot}}(m_Z)\,, \tag{12}$$

  where $\Delta\Gamma_Z = 2.0\,\mathrm{MeV}$ [27] stands for the 95% CL upper bound on the possible additional decay width of the Z boson, beyond the standard model prediction, and σ_Z^{tot} is the Z pole cross-section.
- Constraint from a decay mode independent search for $e^+e^- \to \mathcal{H}_1 Z$ [28]. The model point is regarded as excluded if the condition

$$\sigma_{\mathcal{H}_i Z} > k(m_{\mathcal{H}_i}) \cdot \sigma_{HZ}^{\mathrm{SM}} \tag{13}$$

  is fulfilled, where $k(m_{\mathcal{H}_i})$ is a mass-dependent factor which scales the standard model Higgs production cross-section to the value that is excluded at the 95% CL.

[4] The replacement is necessary whenever the overlap in terms of selected events is important, in order to avoid double-counting.

– Constraint from a search for light Higgs bosons produced by the Yukawa process[5]. The model point is regarded as excluded if the predicted Yukawa enhancement factor $\xi(m_{\mathcal{H}_1})$, defined in [29], is excluded by this search. To be conservative, the weaker of the two enhancement factors, for CP-even and CP-odd couplings, is used.

These additional constraints are particularly useful at small $m_{\mathcal{H}_1}$ and $m_{\mathcal{H}_2}$, below the $b\bar{b}$ threshold.

3.3 Statistical combination of search channels

The statistical method by which the topological searches are combined is described in [3, 30].

After selection, the combined data configuration (distribution of all selected events in several discriminating variables) is compared in a frequentist approach to a large number of simulated configurations generated separately for two hypotheses: the background (b) hypothesis and the signal-plus-background ($s+b$) hypothesis. The ratio

$$Q = \mathcal{L}_{s+b}/\mathcal{L}_b\,, \tag{14}$$

of the corresponding likelihoods is used as the test statistic. The predicted, normalised, distributions of Q (probability density functions) are integrated to obtain the p-values [31] $1-CL_b = 1-\mathcal{P}_b(Q \le Q_{\rm observed})$ and $CL_{s+b} = \mathcal{P}_{s+b}(Q \le Q_{\rm observed})$; these measure the compatibility of the observed data configuration with the two hypotheses. Here $\mathcal{P}_b$ and $\mathcal{P}_{s+b}$ are the probabilities for a single experiment to obtain a value of Q smaller than or equal to the observed value, given the background or the signal-plus-background hypothesis. More details can be found in [3].

Systematic errors are incorporated in the calculation of the likelihoods by randomly varying the signal and background estimates in each channel[6] according to Gaussian error distributions and widths corresponding to the systematic errors. For a given source of uncertainty, correlations are addressed by applying these random variations simultaneously to all those channels for which the source of uncertainty is relevant. Errors which are correlated among the experiments arise mainly from using the same Monte Carlo generators and cross-section calculations for the signal and background processes. The uncorrelated errors arise mainly from the limited statistics of the simulated background event samples.

In a purely frequentist approach, the exclusion limit is computed from the confidence CL_{s+b} for the signal-plus-background hypothesis: a signal is regarded as excluded at the 95% CL, for example, if an observation is made such that CL_{s+b} is lower than 0.05. However, this procedure may lead to the undesired situation in which a large downward fluctuation of the background would exclude a signal hypothesis for which the experiment has no sensitivity since the expected signal rate is too small. This problem is avoided by using the ratio

$$CL_s = CL_{s+b}/CL_b \tag{15}$$

instead of CL_{s+b}. We adopt this quantity for setting exclusion limits and consider a given model to be excluded at the 95% CL if the corresponding value of CL_s is less than 0.05. Since CL_b is a positive number less than one, CL_s is always larger than CL_{s+b} and the limits obtained in this way are therefore conservative.

3.4 Comparisons of the data with the expected background

The distribution of the p-value $1-CL_b$ over the parameter space covered by the searches provides a convenient way of studying the agreement between the data and the expected background and of discussing the statistical significance of any local excess in the data. While a purely background-like behaviour[7] would yield p-values close to 0.5, much smaller values are expected in the case of a signal-like excess. For example, a local excess of three or five standard deviations would give rise to a p-value $1-CL_b$ of 2.7×10^{-3} or 5.7×10^{-7}, respectively.

One has to be careful, however, when interpreting these numbers as probabilities for local excesses occurring over the extended domains covered by the searches. For example, the probability for a fluctuation of three standard deviations to occur anywhere in the parameter space is much larger than the number 2.7×10^{-3} just quoted. A multiplication factor has to be applied to the probability $1-CL_b$ which reflects the number of independent "bins" of the parameter space; this factor can be estimated from the total size of the parameter space and the experimental resolutions. For example, the searches for the Higgsstrahlung process $\mathrm{e^+e^-}\to\mathcal{H}_1Z$, covering the range $0 < m_{\mathcal{H}_1} < 120\ \mathrm{GeV/c^2}$ with a mass resolution $\Delta m_{\mathcal{H}_1}$ of about $3\ \mathrm{GeV/c^2}$, would yield about twenty fairly independent mass-bins of width $2\Delta m_{\mathcal{H}_1}$; hence, a multiplication factor of about twenty. Much bigger multiplication factors are expected in the searches for the pair production process $\mathrm{e^+e^-}\to\mathcal{H}_2\mathcal{H}_1$ with two independent search parameters (masses).

These simple considerations do not take into account, for example, possible correlations from resolution tails extending over several adjacent bins or correlations between different searches sharing candidate events. A more elaborate evaluation of the multiplication factor has therefore been performed. A large number of background experiments was simulated, covering the whole parameter space, using realistic resolution functions and taking correlations into account. From these random experiments, the probability to obtain $1-CL_b$ smaller than a given value, anywhere in the parameter space of a given scenario, has

[5] Note that, in the case of DELPHI, the Yukawa channels are not used as external constraints but are combined with the other search channels.

[6] The word "channel" designates any subset of the data in which a search has been carried out. These subsets may correspond to specific final-state topologies, to data sets collected at different centre-of-mass energies or to the subsets of data collected by different experiments.

[7] Single, background-like, experiments have values of $1-CL_b$ uniformly distributed between zero and one.

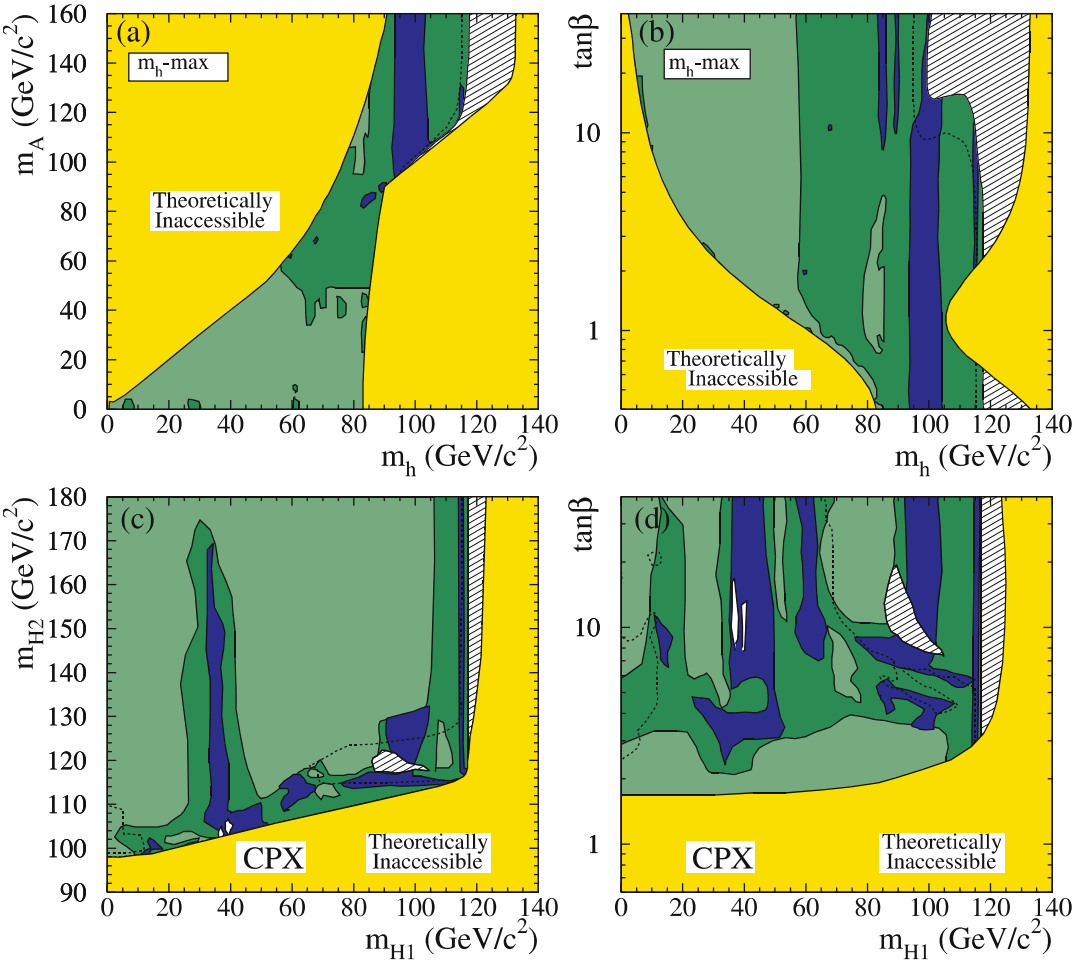

Fig. 1. Contours of the observed p-values, $1-CL_b$, indicating the statistical significances of local excesses in the data. Plots **a** and **b** refer to the CP-conserving MSSM benchmark scenario m_{h}-*max* and plots **c** and **d** to the CP-violating scenario *CPX*. For each scenario, the parameter space is shown in two projections. Regions which are not part of the parameter space (labelled "Theoretically Inaccessible") are shown in *light-grey* or *yellow*. In the *medium-grey* or *light-green* regions the data show an excess of less than one standard deviation above the expected background. Similarly, in the *dark-grey* or *dark-green* regions the excess is between one and two standard deviations while in the *darkest-grey* or *blue* regions it is between two and three standard deviations. In plots **c** and **d**, two small regions with excesses larger than three standard deviations are shown in *white*. The *dashed lines* show the expected exclusion limit at 95% CL. The *hatched areas* represent regions where the median expected value of CL_s in the background hypothesis is larger than 0.4; apparent excesses in these regions would not be significant

been determined (the m_{h}-*max* scenario was taken for this study). A scale factor of at least 60 was obtained in this manner. According to this estimate, the probability of observing a background fluctuation of three standard deviations anywhere in the parameter space of a given scenario (e.g., m_{h}-*max*) can be 16% or more. Also, to observe two fluctuations with two standard deviations turns out to be more likely than to observe only one.

Figure 1 shows the distribution of the p-value $1-CL_b$, determined from the present combined searches, for the CP-conserving benchmark scenario m_{h}-*max* and the CP-violating scenario *CPX*. Over the largest part of the parameter space, the local excesses are smaller than two standard deviations. In the m_{h}-*max* scenario, the lowest value, $1-CL_b = 1.3\times10^{-2}$, lies within the vertical band at m_h around $100\,\mathrm{GeV/c^2}$ and corresponds to 2.5 standard deviations. This excess, and a less significant excess at about $115\,\mathrm{GeV/c^2}$, come from the Higgsstrahlung search; both are discussed in [3] in the context of the search for the standard model Higgs boson. In the *CPX* scenario, one observes two small regions at $m_{\mathcal{H}_1} \approx 35$–$40\,\mathrm{GeV/c^2}$, $m_{\mathcal{H}_2} \approx 105\,\mathrm{GeV/c^2}$ and $\tan\beta \approx 10$, where the significance exceeds three standard deviations; they arise from the search for the pair production process.

The exact position and size of these fluctuations may vary from one scenario to the other. In Tables 3 and 4 we list the parameters of the most significant excesses for all CP-conserving and CP-violating benchmark scenarios considered in this paper. The largest fluctuation of all has a significance of 3.5 standard deviations; its probability is estimated as 3.6% at least, when the scale factor of 60 or more is applied.

From these studies one can conclude that there is a reasonable agreement between the data and the simulated

Table 3. The most significant excesses with respect to the predicted background, for each of the CP-conserving benchmark scenarios. Columns 2 to 6 show the mass parameters (in GeV/c^2) and $\tan\beta$ at which the excess occurs. Column 7 gives the corresponding p-values $1-CL_b$. In the last column, the significances of the excesses, in standard deviations, are listed

Benchmark	m_{h}	m_{H}	m_{A}	$m_{\mathrm{H}^\pm}$	$\tan\beta$	$1-CL_b$	σ (st.dev.)
m_{h}-*max*	99	253	169	184	0.7	1.3×10^{-2}	2.5
m_{h}-*max (a)*	99	277	156	171	0.6	1.4×10^{-2}	2.5
m_{h}-*max (b)*	99	345	310	319	0.9	1.6×10^{-2}	2.4
no-mixing	99	165	152	171	3.7	1.4×10^{-2}	2.5
no-mixing (a)	99	134	114	138	5.4	1.1×10^{-2}	2.5
large-μ	59	108	67	104	3.1	1.0×10^{-2}	2.6
gluophobic	56	124	69	105	4.1	5.5×10^{-3}	2.8
small-α_{eff}	60	121	75	109	5.5	2.4×10^{-3}	3.0

Table 4. The most significant excesses with respect to the predicted background in the CP-violating benchmark scenario *CPX* and its variants. The first column indicates either the *CPX* scenario or the parameter value which differs from the standard *CPX* set listed in the last column of Table 1. Columns 2 to 6 show the mass parameters (in GeV/c^2) and $\tan\beta$ at which the excesses occur (the more conservative of the `CPH` and `FeynHiggs` calculations is used). Columns 7 and 8 give the corresponding p-values, $1-CL_b$, using in turn the `CPH` and `FeynHiggs` codes (note the overall agreement of the two calculations in this respect). In the last column, the significances of the excesses, in standard deviations, are listed

	$m_{\mathcal{H}_1}$	$m_{\mathcal{H}_2}$	$m_{\mathcal{H}_3}$	$m_{\mathrm{H}^\pm}$	$\tan\beta$	$1-CL_b$ (`CPH`)	$1-CL_b$ (`FeynH.`)	σ (st.dev.)
CPX scenario	35–40	105	120	120	10	1×10^{-3}	2×10^{-3}	3.1
[1ex] m_{t}= 169 GeV/c^2	40	100	125	120	10–15	8×10^{-4}	9×10^{-4}	3.3
m_{t}= 179 GeV/c^2	95	125	145	155	3	4×10^{-3}	4×10^{-3}	2.9
m_{t}= 183 GeV/c^2	95	130	150	155	3	4×10^{-3}	4×10^{-3}	2.9
$\arg(A)$=$\arg(m_{\tilde{\mathrm{g}}})=0^\circ$	40	95	125	115	12	8×10^{-4}	1×10^{-3}	3.1
$\arg(A)=\arg(m_{\tilde{\mathrm{g}}})=30^\circ$	45	100	125	110	10-20	1×10^{-3}	1×10^{-3}	3.1
$\arg(A)=\arg(m_{\tilde{\mathrm{g}}})=60^\circ$	45	95	130	115	5-20	5×10^{-4}	6×10^{-4}	3.5
$\arg(A)=\arg(m_{\tilde{\mathrm{g}}})=135^\circ$	40	105	120	110	>20	2×10^{-3}	3×10^{-3}	3.0
$\arg(A)=\arg(m_{\tilde{\mathrm{g}}})=180^\circ$	95	130	170	170	6	4×10^{-3}	4×10^{-3}	2.9
$\mu=500$ GeV	95	100	125	130	1	4×10^{-3}	4×10^{-3}	2.9
$\mu=1000$ GeV	95	110	125	135	2	5×10^{-3}	5×10^{-3}	2.8
$\mu=4000$ GeV	95	180	330	300	4	5×10^{-3}	5×10^{-3}	2.8
M_{SUSY}=1 TeV	95	105	145	130	2	4×10^{-3}	4×10^{-3}	2.9
M_{SUSY}=1 TeV, scaled	40	105	120	130	10	2×10^{-3}	2×10^{-3}	3.1

background, with no compelling evidence for a Higgs boson signal, and that the excesses observed are compatible with random fluctuations of the background.

4 Limits on topological cross-sections

In this section we present upper bounds on the cross-sections for the most important final-state topologies expected from the Higgsstrahlung process $\mathrm{e^+e^-}\to\mathcal{H}_1Z$ and the pair production process $\mathrm{e^+e^-}\to\mathcal{H}_2\mathcal{H}_1$. These can be used to test a wide range of specific models.

We define the scaling factor

$$S_{95}=\sigma_{\max}/\sigma_{\mathrm{ref}}\,, \tag{16}$$

where $\sigma_{\max}$ is the largest cross-section compatible with the data, at the 95% CL, and σ_{ref} is a reference cross-section. For the topologies motivated by Higgsstrahlung, σ_{ref} is taken to be the standard model Higgs production cross-section; for final states motivated by the pair production process, σ_{ref} is taken to be the MSSM Higgs production cross-section of (2) with the MSSM suppression factor set to 1. Numerical values for the cross-section limits are listed in Appendix B.

Figure 2 shows the upper bound S_{95} for final states motivated by the Higgsstrahlung process $\mathrm{e^+e^-}\to\mathcal{H}_1Z$ (the figure is reproduced from [3]). In part (a), the Higgs boson is assumed to decay into fermions and bosons with branching ratios as given by the standard model. Contributions from the fusion processes $WW\to\mathcal{H}_1$ and $ZZ\to\mathcal{H}_1$, according to the standard model, corrected for initial-state radiation, are assumed to scale with energy like the Hig-

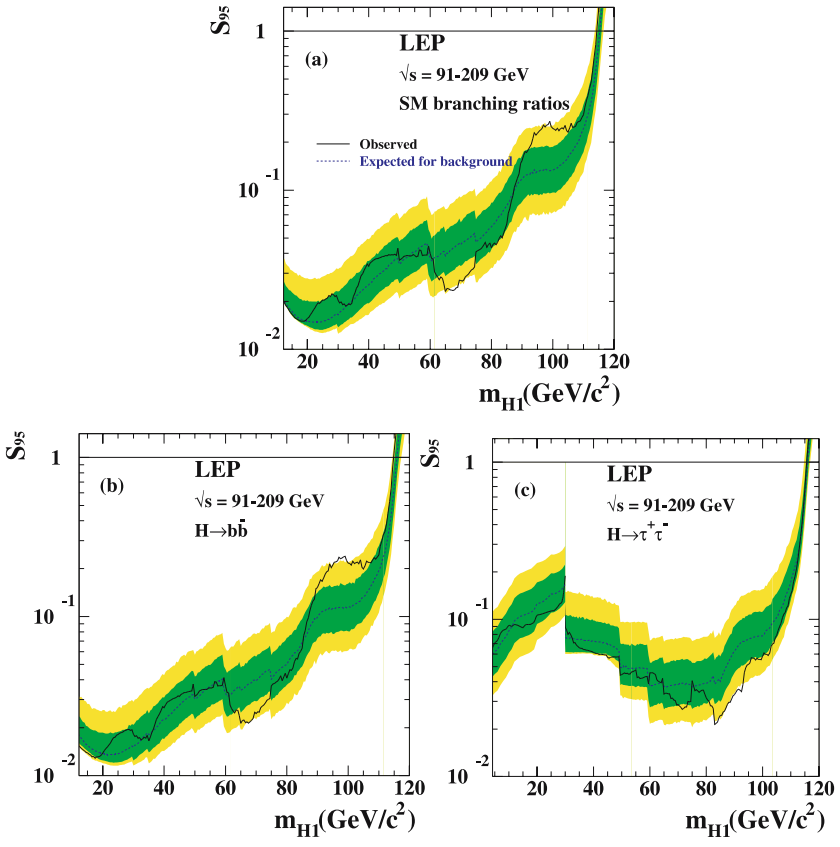

Fig. 2. The 95% CL upper bounds, S_{95} (see text), for various topological cross-sections motivated by the Higgsstrahlung process $e^+e^- \to \mathcal{H}_1 Z$, as a function of the Higgs boson mass (the figure is reproduced from [3]). The *full lines* represent the observed limits. The *dark* (*green*) and *light* (*yellow*) *shaded bands* around the median expectations (*dashed lines*) correspond to the 68% and 95% probability bands. The *horizontal lines* correspond to the standard model cross-sections. In part **a** the Higgs boson decay branching ratios are assumed to be those predicted by the standard model; in part **b** the Higgs boson is assumed to decay exclusively to $b\bar{b}$ and in part **c** exclusively to $\tau^+\tau^-$. In part **c**, the discontinuity at about 30 GeV/c^2 arises because at lower masses only one of the LEP experiments is contributing to the cross-section limit

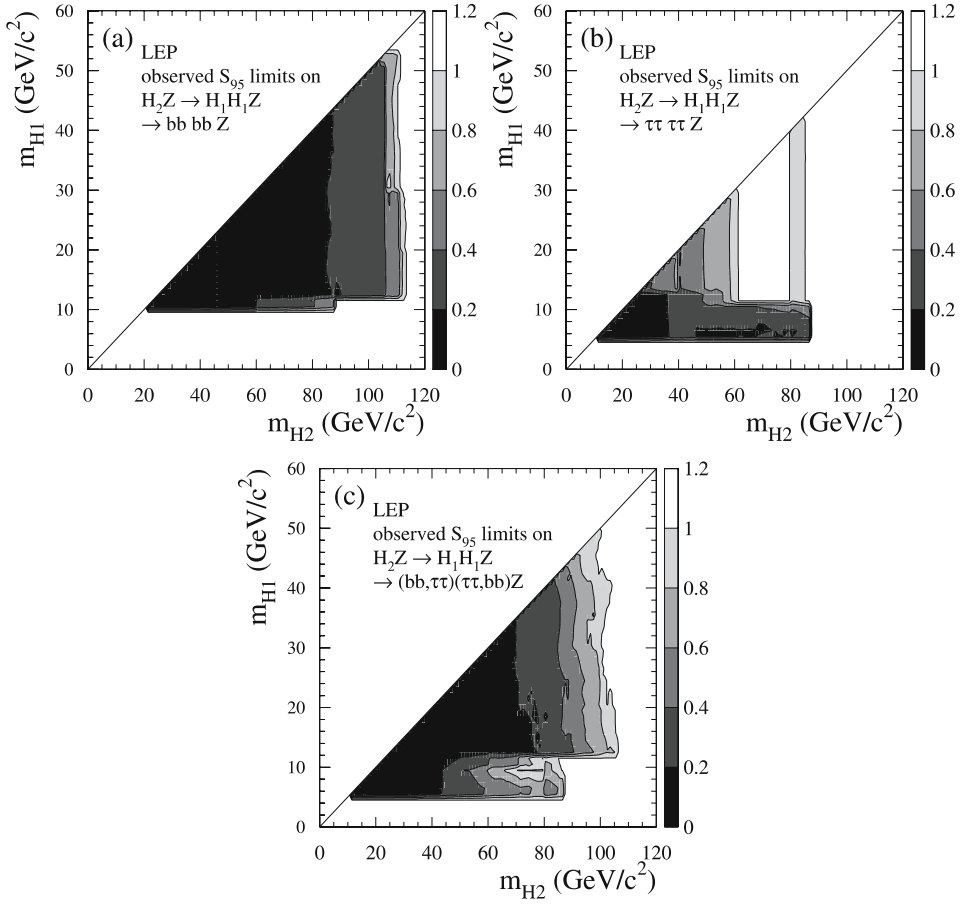

Fig. 3. Contours of the 95% CL upper bound, S_{95} (see text), for various topological cross-sections motivated by the Higgsstrahlung cascade process $e^+e^- \to (\mathcal{H}_2 \to \mathcal{H}_1\mathcal{H}_1)Z$, projected onto the $(m_{\mathcal{H}_2}, m_{\mathcal{H}_1})$ plane. The scales for the shadings are given on the right-hand side of each plot. In plot **a** the $\mathcal{H}_1$ boson is assumed to decay exclusively to $b\bar{b}$ and in plot **b** exclusively to $\tau^+\tau^-$; in plot **c** it is assumed to decay with equal probabilities to $b\bar{b}$ and to $\tau^+\tau^-$

gsstrahlung process. In part (b) it is assumed that the Higgs boson decays exclusively to $b\bar{b}$ and in part (c) exclusively to $\tau^+\tau^-$. Besides representing bounds on topological cross-sections, this figure also illustrates the overall agreement between the data and the expected background from standard model processes. The largest deviations observed barely exceed two standard deviations.

Figure 3 shows contours of S_{95} for the cascade process $e^+e^- \to \mathcal{H}_2 Z \to (\mathcal{H}_1\mathcal{H}_1)Z$, projected onto the ($m_{\mathcal{H}_2}$, $m_{\mathcal{H}_1}$) plane, assuming that the $\mathcal{H}_2$ boson decays exclusively to $\mathcal{H}_1\mathcal{H}_1$. In part (a) it is assumed that the $\mathcal{H}_1$ boson decays exclusively to $b\bar{b}$ and in part (b) exclusively to $\tau^+\tau^-$. In part (c), as an example, an equal mixture of $\mathcal{H}_1 \to b\bar{b}$ and $\mathcal{H}_1 \to \tau^+\tau^-$ is assumed, which implies 25% $b\bar{b}b\bar{b}Z$, 25% $\tau^+\tau^-\tau^+\tau^-Z$ and 50% $b\bar{b}\tau^+\tau^-Z$ final states. The sensitivity of the $b\bar{b}b\bar{b}Z$ channel starts at the $b\bar{b}$ threshold and extends almost to the kinematic limit. In the $\tau^+\tau^-\tau^+\tau^-Z$ channel the sensitivity is altogether weaker (the discontinuities reveal the limited and inhomogeneous mass coverage of the four experiments in this channel).

Figure 4 shows S_{95} for final states motivated by the pair-production process $e^+e^- \to \mathcal{H}_2\mathcal{H}_1$, for the particular case where the masses $m_{\mathcal{H}_2}$ and $m_{\mathcal{H}_1}$ are approximately equal. Such is the case, for example, in the CP-conserving MSSM scenario m_h-*max* for $\tan\beta$ larger than about 10 and small $m_{\mathcal{H}_2}$ ($\equiv m_A$). In part (a), the $\mathcal{H}_2$ and $\mathcal{H}_1$ decay branching ratios correspond to the m_h-*max* benchmark scenario with $\tan\beta = 10$ (see the caption for the exact values); in part (b), both $\mathcal{H}_2$ and $\mathcal{H}_1$ are assumed to decay exclusively to $b\bar{b}$; in part (c), one Higgs boson is assumed to decay exclusively to $b\bar{b}$ while the other exclusively to $\tau^+\tau^-$; in part (d), $\mathcal{H}_2$ and $\mathcal{H}_1$ are both assumed to decay exclusively to $\tau^+\tau^-$. At low masses, the exclusion limits are completed using the constraint from the measured decay width of the Z boson (see Sect. 3.2). This figure also illustrates the overall agreement between the data and the expected background from standard model processes since the largest deviations are within two standard deviations.

Figure 5 shows contours of S_{95} for final states motivated by the process $e^+e^- \to \mathcal{H}_2\mathcal{H}_1$, projected onto the ($m_{\mathcal{H}_2}$, $m_{\mathcal{H}_1}$) plane. In part (a), both Higgs bosons are assumed to

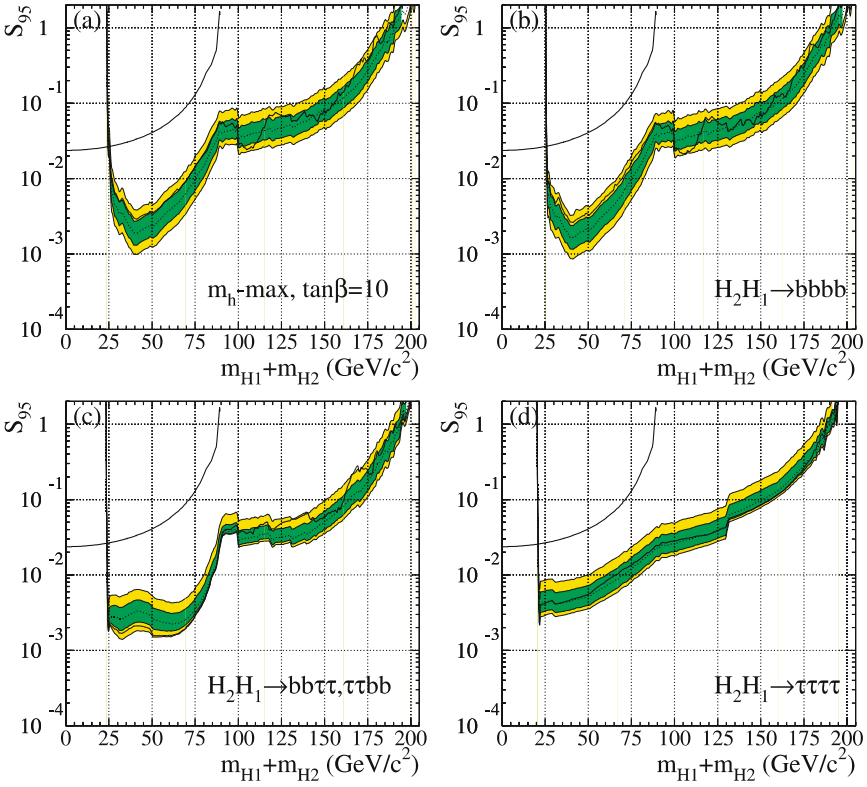

Fig. 4. The 95% CL upper bounds, S_{95} (see text), for various topological cross-sections motivated by the pair production process $e^+e^- \to \mathcal{H}_2\mathcal{H}_1$. The bounds are obtained for the particular case where $m_{\mathcal{H}_2}$ and $m_{\mathcal{H}_1}$ are approximately equal. Such is the case, for example, in the CP-conserving MSSM scenario m_h-*max* for $\tan\beta$ greater than 10 and small $m_{\mathcal{H}_2}$($\equiv m_A$). The abscissa is the sum of the two Higgs boson masses. The *full lines* represent the observed limits. The *dark* (*green*) and *light* (*yellow*) *shaded bands* around the median expectations (*dashed lines*) correspond to the 68% and 95% probability bands. The *curves* which complete the exclusions at low masses are obtained using the constraint from the measured decay width of the Z boson, see Sect. 3.2. Plot **a**: the Higgs boson decay branching ratios correspond to the m_h-*max* benchmark scenario with $\tan\beta = 10$, namely 94% $\mathcal{H}_1 \to b\bar{b}$, 6% $\mathcal{H}_1 \to \tau^+\tau^-$, 92% $\mathcal{H}_2 \to b\bar{b}$ and 8% $\mathcal{H}_2 \to \tau^+\tau^-$; plot **b**: both Higgs bosons are assumed to decay exclusively to $b\bar{b}$; plot **c**: one of the Higgs bosons is assumed to decay exclusively to $b\bar{b}$ and the other exclusively to $\tau^+\tau^-$; plot **d**: both Higgs bosons are assumed to decay exclusively to $\tau^+\tau^-$

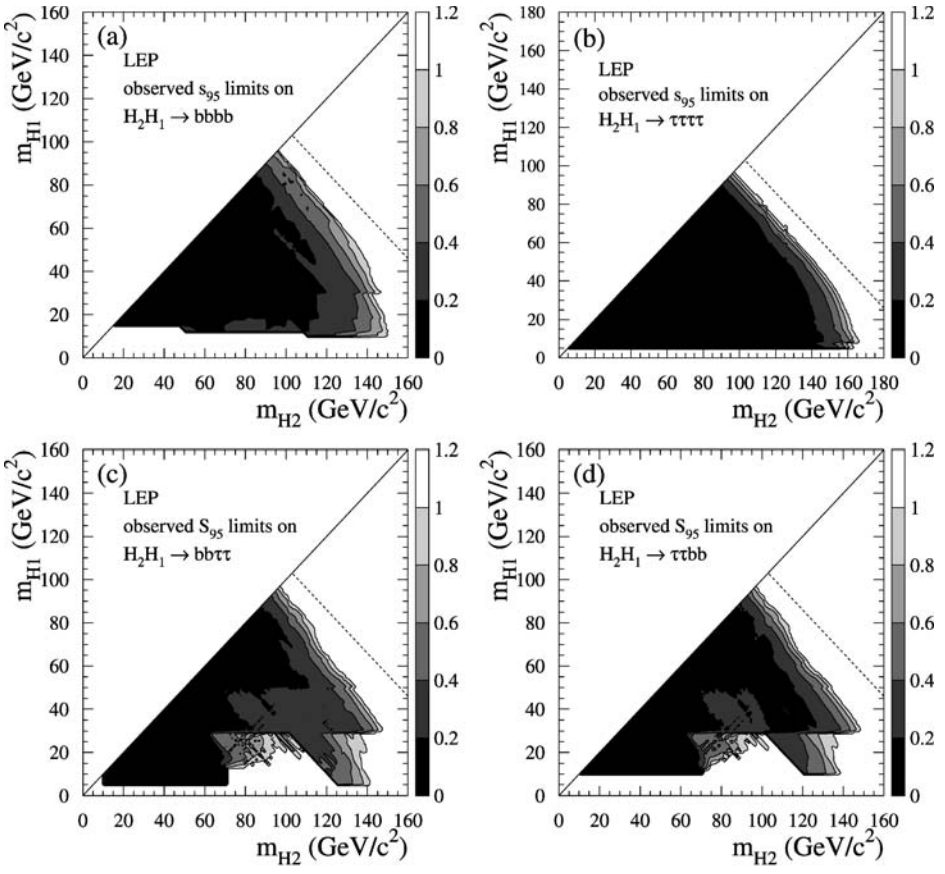

Fig. 5. Contours of the 95% CL upper bound, S_{95} (see text), for various topological cross-sections motivated by the pair production process $e^+e^- \to \mathcal{H}_2\mathcal{H}_1$, projected onto the $(m_{\mathcal{H}_2}, m_{\mathcal{H}_1})$ plane. The scales in terms of the shadings are given on the right-hand side of each plot. In plot **a** both Higgs bosons are assumed to decay exclusively to $b\bar{b}$ and in plot **b** exclusively to $\tau^+\tau^-$. In plot **c** the $\mathcal{H}_2$ boson is assumed to decay exclusively to $b\bar{b}$ and the $\mathcal{H}_1$ boson exclusively to $\tau^+\tau^-$ and in plot **d** the $\mathcal{H}_1$ boson is assumed to decay exclusively to $b\bar{b}$ and the $\mathcal{H}_2$ boson exclusively to $\tau^+\tau^-$. The *dashed lines* represent the approximate kinematic limits of the processes

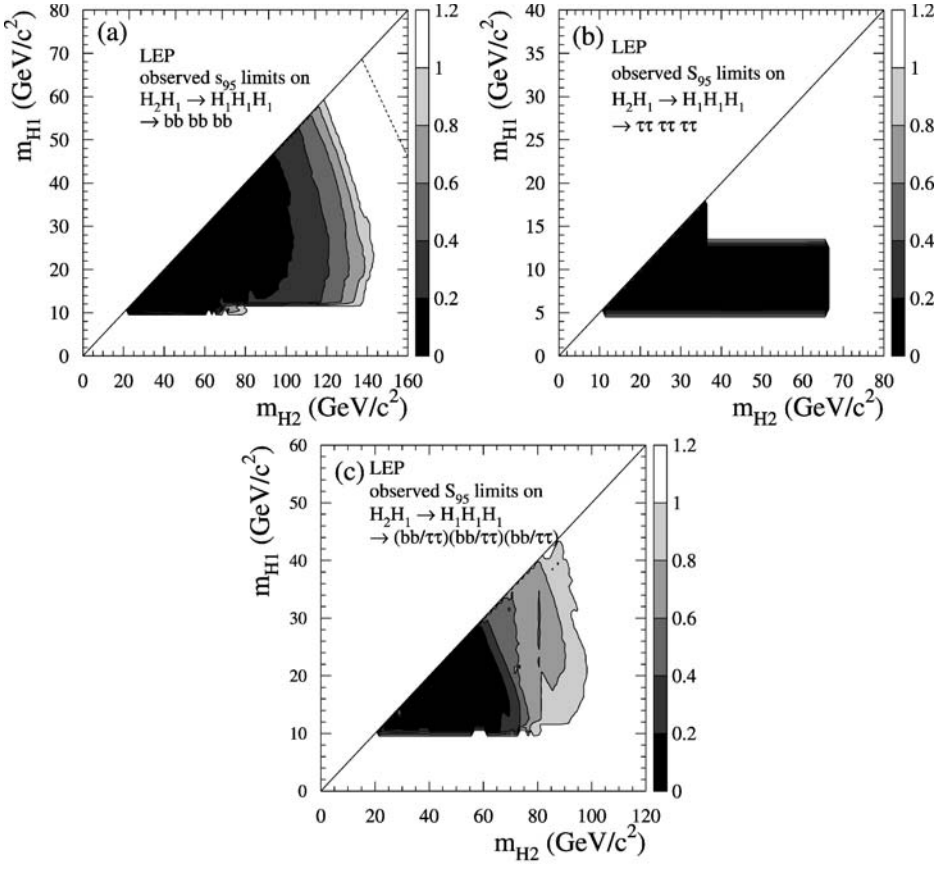

Fig. 6. Contours of the 95% CL upper bound, S_{95} (see text), for various topological cross-sections motivated by the pair production cascade process $e^+e^- \to (\mathcal{H}_2 \to \mathcal{H}_1\mathcal{H}_1)\mathcal{H}_1$, projected onto the $(m_{\mathcal{H}_2}, m_{\mathcal{H}_1})$ plane. The scales in terms of the shadings are given on the right-hand side of each plot. In plot **a** the $\mathcal{H}_1$ boson is assumed to decay exclusively to $b\bar{b}$ and in plot **b** exclusively to $\tau^+\tau^-$. In plot **c** the $\mathcal{H}_1$ boson is assumed to decay with equal probability to $b\bar{b}$ and to $\tau^+\tau^-$. The *dashed line* in part **a** represents the approximate kinematic limit of the process

decay exclusively to $b\bar{b}$ and in part (b) exclusively to $\tau^+\tau^-$. In parts (c)/(d), the $\mathcal{H}_2/\mathcal{H}_1$ boson is assumed to decay exclusively to $b\bar{b}$ while the other boson is assumed to decay exclusively to $\tau^+\tau^-$.

Figure 6 shows contours of S_{95} for the cascade process $e^+e^- \to \mathcal{H}_2\mathcal{H}_1 \to (\mathcal{H}_1\mathcal{H}_1)\mathcal{H}_1$, projected onto the ($m_{\mathcal{H}_2}$, $m_{\mathcal{H}_1}$) plane, assuming that the $\mathcal{H}_2$ boson decays exclusively to $\mathcal{H}_1\mathcal{H}_1$. In part (a), the $\mathcal{H}_1$ boson is assumed to decay exclusively to $b\bar{b}$ and in part (b) exclusively to $\tau^+\tau^-$. In part (c), as an example, an equal mixture of $\mathcal{H}_1 \to b\bar{b}$ and $\mathcal{H}_1 \to \tau^+\tau^-$ is assumed, which implies 12.5% $b\bar{b}b\bar{b}b\bar{b}$, 37.5% $b\bar{b}b\bar{b}\tau^+\tau^-$, 37.5% $bb\tau^+\tau^-\tau^+\tau^-$ and 12.5% $\tau^+\tau^-\tau^+\tau^-\tau^+\tau^-$ final states.

A word of caution is in place concerning the correlations which exist between some of the above cross-section limits which arise from overlapping candidates in the corresponding selections. Such correlations are present, for example, between b-tagged and flavour-independent searches of a given experiment or between searches addressing direct decays (e.g. $\mathcal{H}_1 Z \to b\bar{b}b\bar{b}$) and cascade decays (e.g. $(\mathcal{H}_2 \to \mathcal{H}_1\mathcal{H}_1)Z \to b\bar{b}b\bar{b}b\bar{b}$); they may be a source of problems if several of the cross-section limits are used in conjunction to test a given model. Note, however, that these correlations are properly taken into account in the model interpretations which follow.

5 Results interpreted in CP-conserving MSSM scenarios

In this section, the search results are interpreted in the CP-conserving benchmark scenarios presented in Sect. 2.1. The exclusion limits, which are shown in the figures below at the 95% CL and the 99.7% CL, are obtained from the values of CL_s (see (15)), for an assumed top quark mass of $m_t = 174.3\,\mathrm{GeV/c^2}$. The exclusion limits are presented in four projections of the MSSM parameter space. The limits expected on the basis of Monte Carlo simulations with no signal, at the 95% CL, are also indicated. The exact mass bounds and exclusions for $\tan\beta$ are listed in Table 5, for three values of m_t.

The exclusions for the m_h-*max* benchmark scenario are shown in Fig. 7. In the region with $\tan\beta$ less than about five, the exclusion is provided mainly by the Higgsstrahlung process, giving a lower bound of about $114\,\mathrm{GeV/c^2}$ for m_h. At high $\tan\beta$, the pair production

Table 5. Lower mass bounds and exclusions in $\tan\beta$, at 95% CL, obtained in the case of the CP-conserving MSSM benchmark scenarios, for three values of the top quark mass. In each case, the observed limit is followed, between parentheses, by the value expected on the basis of Monte Carlo simulations with no signal. $\tan\beta$ for $m_t = 183.0\,\mathrm{GeV/c^2}$ or larger. The *no-mixing* scenario is entirely excluded for $m_t = 169.3\,\mathrm{GeV/c^2}$ or smaller. In the *no-mixing* scenario and for m_t larger than $169.3\,\mathrm{GeV/c^2}$, the quoted mass limits are only valid for $\tan\beta \geq 0.7$ and the exclusion in $\tan\beta$ is only valid for m_A larger than about $3\,\mathrm{GeV/c^2}$. The *large-μ* scenario is entirely excluded for $m_t = 174.3\,\mathrm{GeV/c^2}$ or smaller

Benchmark scenario	m_t(GeV/c^2)	m_h (GeV/c^2)	m_A (GeV/c^2)	Exclusions of $\tan\beta$
m_h-*max*	169.3	92.9 (94.8)	93.4 (95.1)	0.6–2.6 (0.6–2.7)
	174.3	92.8 (94.9)	93.4 (95.2)	0.7–2.0 (0.7–2.1)
	179.3	92.9 (94.8)	93.4 (95.2)	0.9–1.5 (0.9–1.6)
m_h-*max*	169.3	92.7 (94.9)	93.1 (95.1)	0.7–2.1 (0.7–2.2)
(a)	174.3	92.7 (94.8)	93.1 (95.1)	0.7–2.1 (0.7–2.2)
	179.3	92.6 (94.8)	93.1 (95.1)	0.9–1.6 (0.8–1.7)
m_h-*max*	169.3	92.8 (94.8)	93.2 (95.2)	0.5–3.3 (0.5-3.5)
(b)	174.3	92.6 (94.9)	93.4 (95.1)	0.6–2.5 (0.6–2.7)
	179.3	92.6 (94.8)	93.4 (95.1)	0.7–2.0 (0.7–2.1)
no-mixing	169.3	excl. (excl.)	excl. (excl.)	excl. (excl.)
	174.3	93.6 (96.0)	93.6 (96.4)	0.4–10.2 (0.4–19.4)
	179.3	93.3 (95.0)	93.4 (95.0)	0.4–5.5 (0.4–6.5)
no-mixing	169.3	93.2 (95.2)	93.4 (95.4)	0.7–7.1 (0.7–9.3)
(a)	174.3	92.8 (94.9)	93.1 (95.1)	0.7–4.6 (0.7–5.1)
	179.3	92.8 (94.9)	93.1 (95.0)	0.7–3.5 (0.7–3.8)
large-μ	169.3	excl. (excl.)	excl. (excl.)	excl. (excl.)
	174.3	excl. (excl.)	excl. (excl.)	excl. (excl.)
	179.3	109.2 (109.2)	225.0 (225.0)	0.7–43 (0.7–43)
gluophobic	169.3	90.6 (93.2)	95.7 (98.2)	0.4–10.3 (0.4–21.5)
	174.3	90.5 (92.3)	96.3 (98.0)	0.4–5.4 (0.4–6.4)
	179.3	90.0 (91.8)	96.5 (98.2)	0.4–3.9 (0.4–4.2)
small-α_{eff}	169.3	88.2 (90.0)	98.2 (99.6)	0.4–6.1 (0.4–7.4)
	174.3	87.3 (89.0)	98.8 (100.0)	0.4–4.2 (0.4–4.5)
	179.3	86.6 (88.0)	99.8 (100.7)	0.5–3.2 (0.5–3.4)

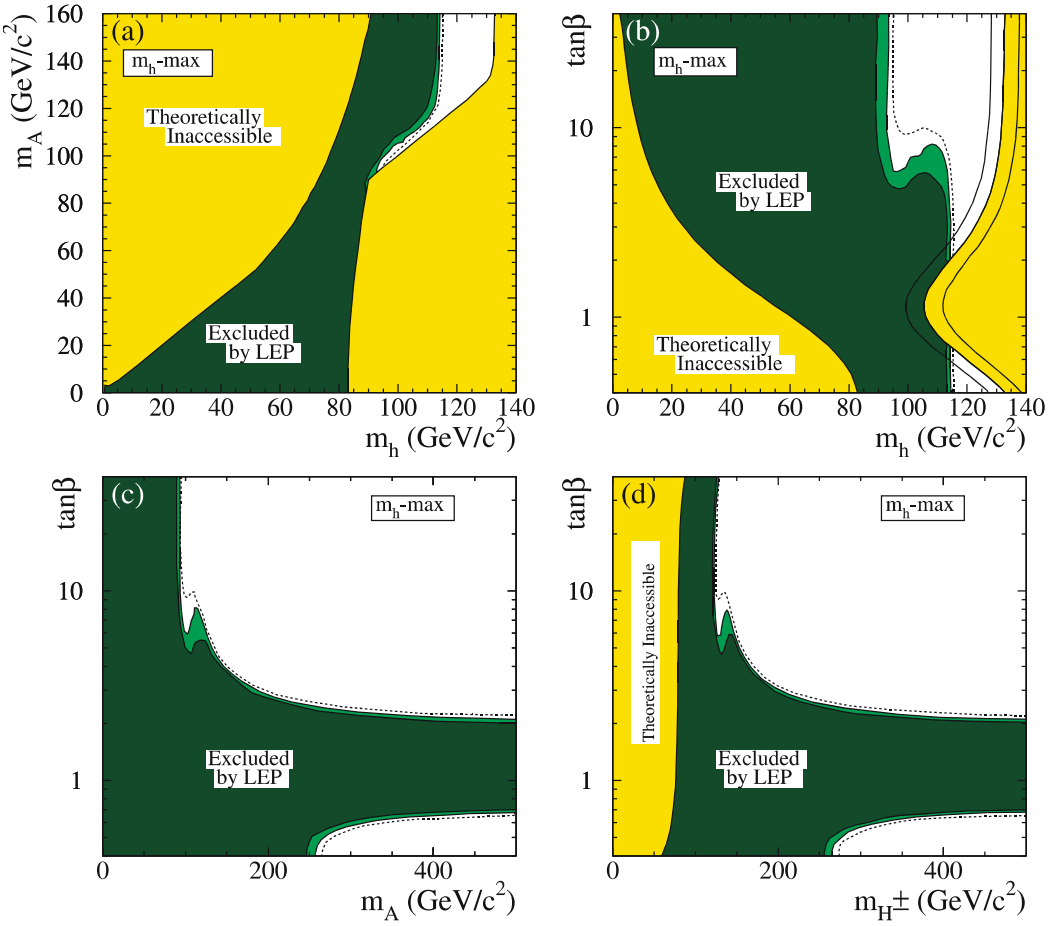

Fig. 7. Exclusions, at 95% CL (*medium-grey* or *light-green*) and the 99.7% CL (*dark-grey* or *dark-green*), in the case of the CP-conserving m_{h}-*max* benchmark scenario, for $m_{\mathrm{t}} = 174.3\,\mathrm{GeV/c^2}$. The figure shows the theoretically inaccessible domains (*light-grey* or *yellow*) and the regions excluded by this search, in four projections of the MSSM parameters: **a**: $(m_{\mathrm{h}}, m_{\mathrm{A}})$; **b**: $(m_{\mathrm{h}}, \tan\beta)$; **c**: $(m_{\mathrm{A}}, \tan\beta)$; **d**: $(m_{\mathrm{H}^\pm}, \tan\beta)$. The *dashed lines* indicate the boundaries of the regions which are expected to be excluded, at 95% CL, on the basis of Monte Carlo simulations with no signal. In the $(m_{\mathrm{h}}, \tan\beta)$ projection (plot **b**), the upper boundary of the parameter space is indicated for three values of the top quark mass; from left to right: $m_{\mathrm{t}} = 169.3, 174.3$ and $179.3\,\mathrm{GeV/c^2}$

process is most useful, providing limits in the vicinity of $93\,\mathrm{GeV/c^2}$ for both m_{h} and m_{A}. For m_{h} in the vicinity of $100\,\mathrm{GeV/c^2}$, one observes a deviation between the expected and the experimental exclusions. This deviation, which is also present in other CP-conserving scenarios, is due to the excess in the Higgsstrahlung channel which was discussed in [3] and gives rise to the vertical bands in Fig. 1a and b. Note that the mass bounds obtained are largely insensitive to the top quark mass.

The data also exclude certain domains of $\tan\beta$. This is best illustrated in the $(m_h, \tan\beta)$ projection (plot b) where the upper boundary of the parameter space along m_{h} is indicated for three values of m_{t}; the intersections of these boundaries with the experimental exclusions define the regions of $\tan\beta$ which are excluded. The exclusion in $\tan\beta$, as a function of the assumed top quark mass, is summarised in Fig. 8.

One should be aware that the upper boundary of the parameter space along m_{h} also depends moderately on the choice of M_{SUSY}. For example, changing M_{SUSY} from 1 TeV to 2 TeV would broaden the parameter space by about $2\,\mathrm{GeV/c^2}$ along m_{h}, with corresponding effects on the exclusions in $\tan\beta$. This observation holds for all CP-conserving scenarios which follow.

Figures 9 and 10 show the same set of plots for the two variants, a and b, of the m_{h}-*max* scenario introduced in Sect. 2.1.1. The change of the sign of the Higgs mass

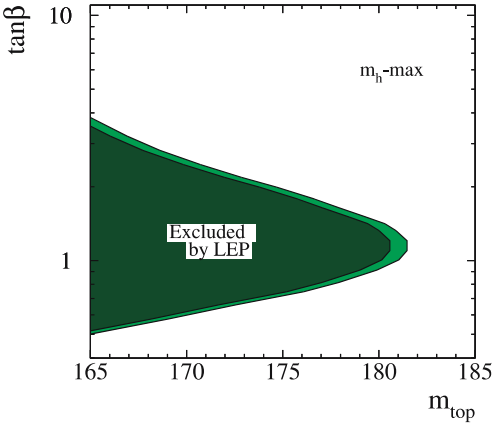

Fig. 8. Domains of $\tan\beta$ which are excluded at the 95% CL (*light-grey* or *light-green*) and the 99.7% CL (*dark-grey* or *dark-green*), in the case of the CP-conserving m_{h}-*max* benchmark scenario, as a function of the assumed top quark mass

parameter μ or of the mixing parameter X_{t} barely affect the mass limits; differences occur, however, in the exclusions of $\tan\beta$ (see Table 5). Note, in Fig. 9, the small domains at m_{h} between 60 and $75\,\mathrm{GeV/c^2}$, small m_{A} and $\tan\beta < 0.9$ which are excluded at the 95% CL but not at the 99.7% CL.

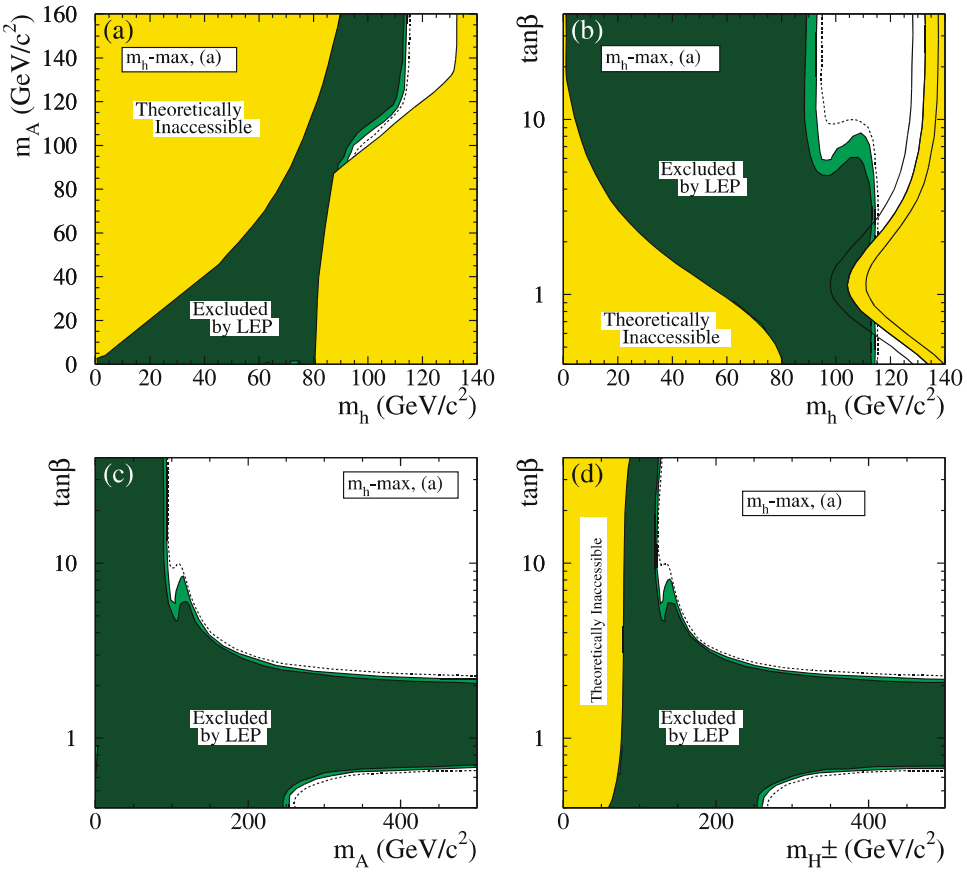

Fig. 9. Exclusions in the case of the CP-conserving m_{h}-*max* benchmark scenario, variant **a** (see Sect. 2.1.1). See the caption of Fig. 7 for the legend. Note the small domains at m_{h} between 60 and 75 GeV/c^2, small m_{A} and $\tan\beta < 0.9$ which, although excluded at the 95% CL, are not excluded at the 99.7% CL

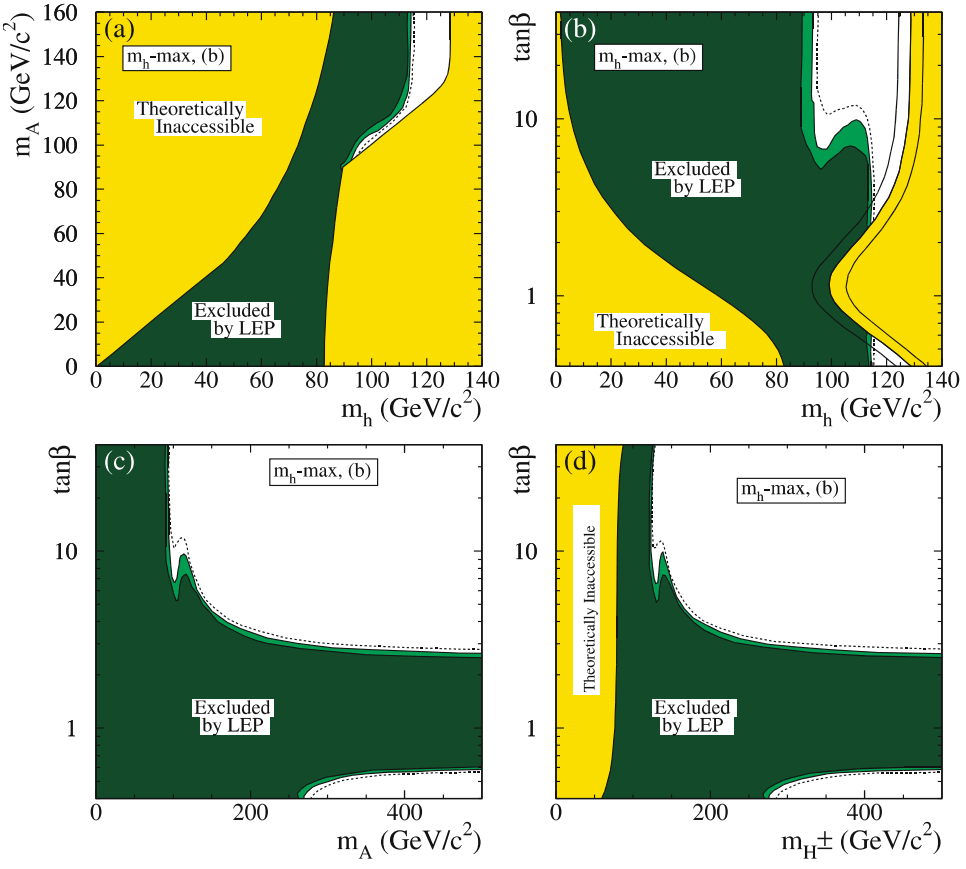

Fig. 10. Exclusions in the case of the CP-conserving m_{h}-*max* benchmark scenario, variant **b** (see Sect. 2.1.1). See the caption of Fig. 7 for the legend

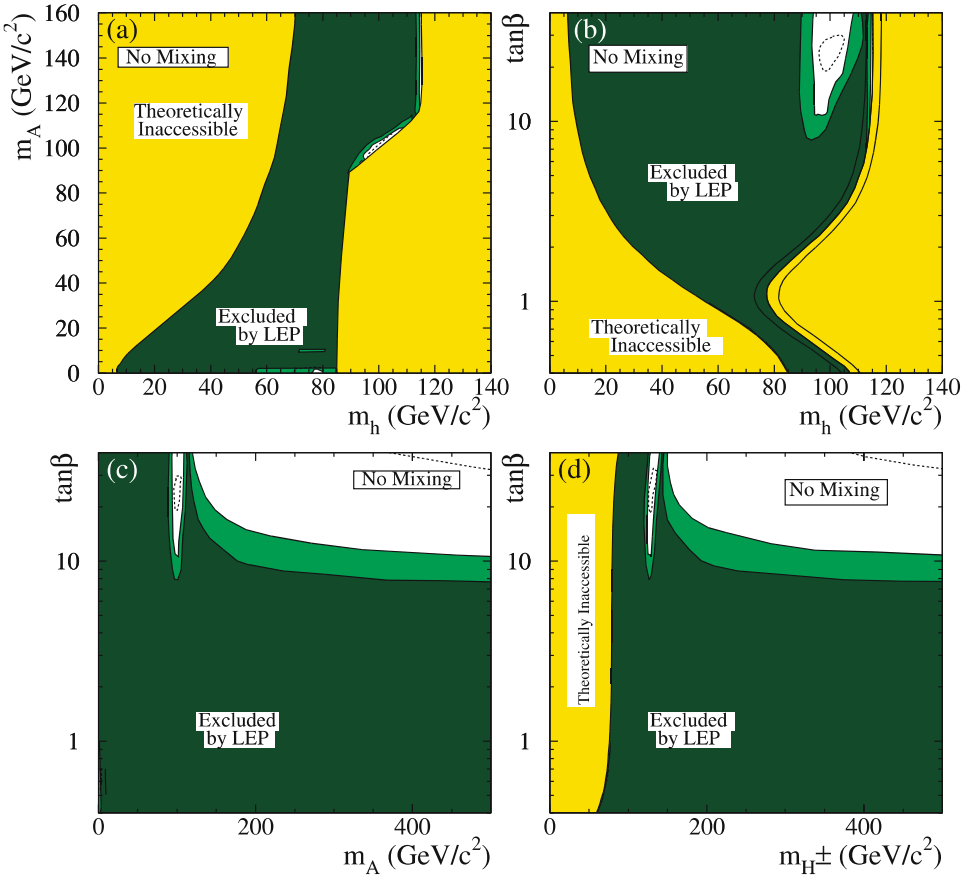

Fig. 11. Exclusions in the case of the CP-conserving *no-mixing* benchmark scenario. See the caption of Fig. 7 for the legend. Note the small domain at m_{h} between 75 and 80 $\mathrm{GeV/c^2}$, small m_{A} and $\tan\beta < 0.7$ which is not excluded at the 95% CL

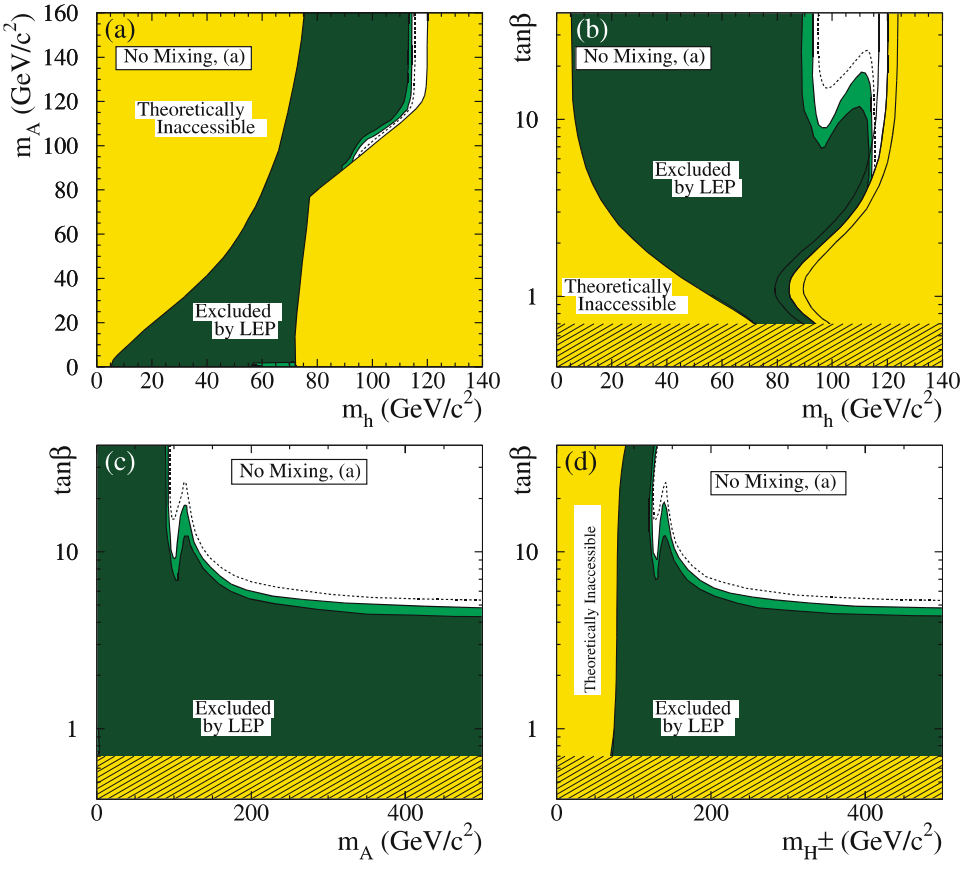

Fig. 12. Exclusions in the case of the CP-conserving *no-mixing* benchmark scenario, variant **a** (see Sect. 2.1.2). See the caption of Fig. 7 for the legend. In the hatched domain ($\tan\beta < 0.7$), the contributions from top and stop quark loops to the radiative corrections are large and uncertain. Note the small domain at m_{h} between 56 and 72 $\mathrm{GeV/c^2}$, small m_{A} and $\tan\beta < 1$ which, although excluded at the 95% CL, is not excluded at the 99.7% CL

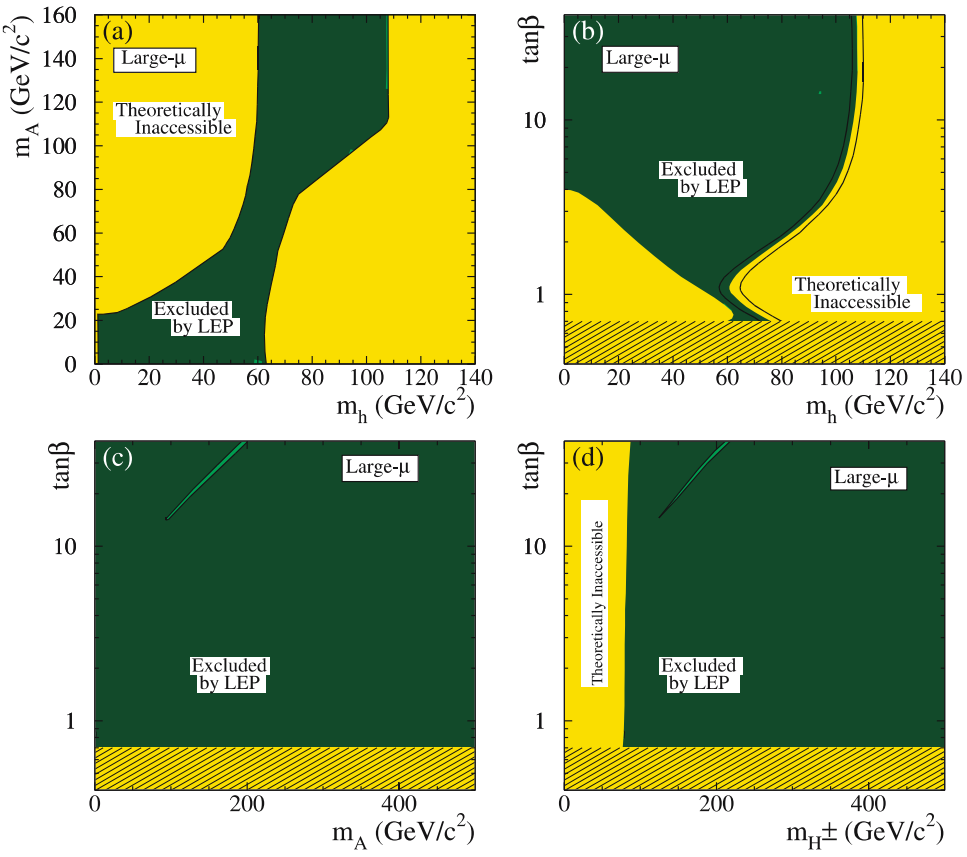

Fig. 13. Exclusions in the case of the CP-conserving *large-μ* benchmark scenario (see Sect. 2.1.3). See the caption of Fig. 7 for the legend. In the hatched domain ($\tan\beta < 0.7$), the contributions from top and stop quark loops to the radiative corrections become large and uncertain; hence, no exclusions can be claimed there

The exclusions for the CP-conserving *no-mixing* benchmark scenario are shown in Fig. 11. In this scenario, the theoretical boundaries of the parameter space are more restricted than in the m_h-*max* scenario. As a consequence, large domains of $\tan\beta$ are excluded for all the top quark masses considered. Note the relatively strong variation of the exclusion limits with m_t in this scenario (see Table 5), which is caused by the proximity of the experimental lower bound of m_h from the Higgsstrahlung searches and the theoretical upper bound of m_h.

An interesting feature of this scenario is that, for m_h larger than about $100\,\mathrm{GeV/c^2}$ and large $\tan\beta$, the heavy scalar boson H is within kinematic reach. Moreover, the cross-section for the process $e^+e^- \to HZ$ is increasing with $\tan\beta$, resulting in an improved search sensitivity; this explains the nearly circular shape of the expected limit in Fig. 11b.

Note the small domain at m_h between 75 and $80\,\mathrm{GeV/c^2}$, small m_A and $\tan\beta < 0.7$, barely perceptible in the plots, which is not excluded in this scenario at 95% CL (this domain is excluded for $m_t = 169.3\,\mathrm{GeV/c^2}$). The branching ratio for $h \to b\bar{b}$ is small and the decay $h \to AA$ is dominant in this region. The A boson, with mass below the $\tau^+\tau^-$ threshold, may decay to final states which are not sufficiently covered by the present searches. For this reason, the mass limits given in Table 5 for this scenario and for m_t larger than $169.3\,\mathrm{GeV/c^2}$ are valid only for $\tan\beta \geq 0.7$. Conversely, for m_t larger than $169.3\,\mathrm{GeV/c^2}$, the quoted exclusion of $\tan\beta$ is valid only for m_A larger than about $3\,\mathrm{GeV/c^2}$.

Figure 12 shows the exclusion plots for the a variant of the *no-mixing* scenario introduced in Section 2.1.2. The change of sign of the Higgs mass parameter μ and the increase of the weak SUSY-breaking scale from 1 TeV to 2 TeV affect only the theoretical bounds of the parameter space but barely change the mass limits, except for $m_t = 169.3\,\mathrm{GeV/c^2}$. There are moderate changes though in the exclusions of $\tan\beta$. In the hatched domain ($\tan\beta < 0.7$), the contributions from top and stop quark loops to the radiative corrections are large and uncertain; hence, no exclusions can be claimed there.

The exclusions for the *large-μ* benchmark scenario are shown in Fig. 13. As mentioned in Sect. 2.1, this scenario was constructed to test the sensitivity of LEP to MSSM scenarios which may be a priori difficult to handle experimentally since the Higgs boson decays to $b\bar{b}$ are largely suppressed. It turns out that the flavour-independent and decay-mode-independent searches are sufficiently powerful to exclude all such situations at 95% CL, for top quark masses up to $174.3\,\mathrm{GeV/c^2}$. There remains a thin strip at $\tan\beta$ larger than about 10 and running from m_A of about 100 to about $200\,\mathrm{GeV/c^2}$, which is excluded at the 95% CL but not at 99.7% CL because the suppression of the $b\bar{b}$ channel is particularly strong in that region. This strip is found to grow with increasing m_t and becomes gradually non-excluded at the 95% CL. Other small, weakly excluded, regions are located at $m_h \approx 60\,\mathrm{GeV/c^2}$ and small m_A, and along the $m_h \approx m_A$ "diagonal" of plot a.

Similar plots are shown in Figs. 14 and 15 for the *gluophobic* and *small-*α_{eff} scenarios defined in Sect. 2.1.3.

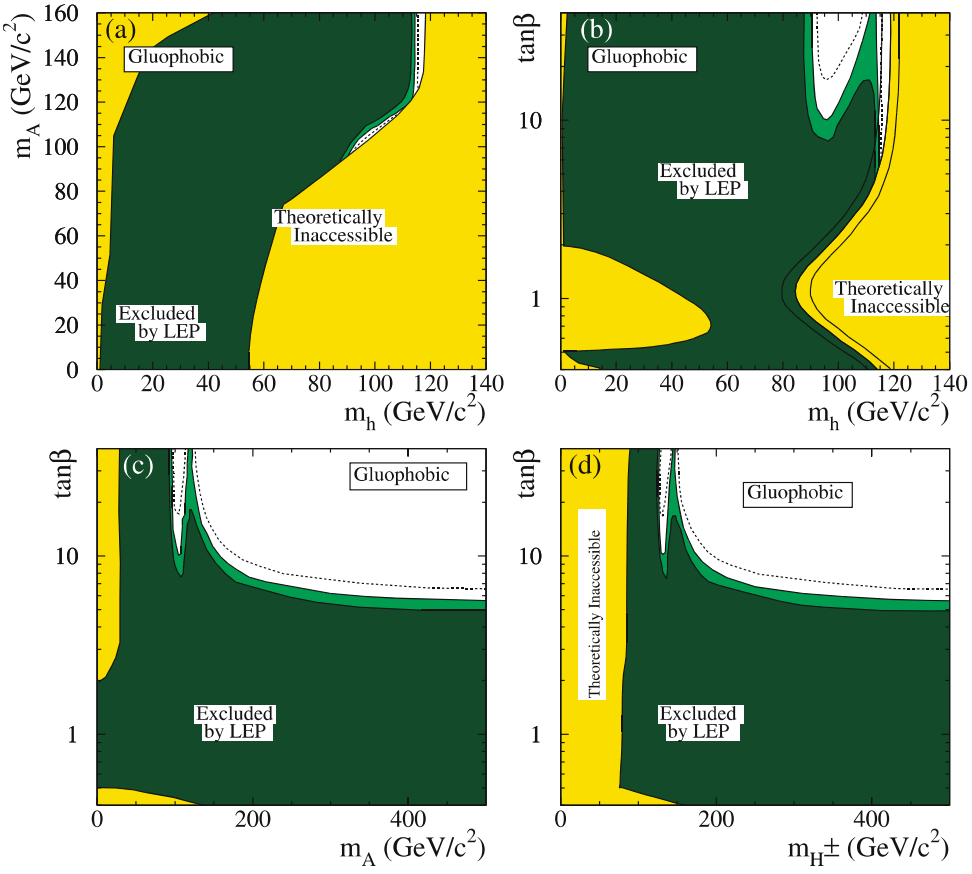

Fig. 14. Exclusions in the case of the *gluophobic* benchmark scenario (see Sect. 2.1.3). See the caption of Fig. 7 for the legend

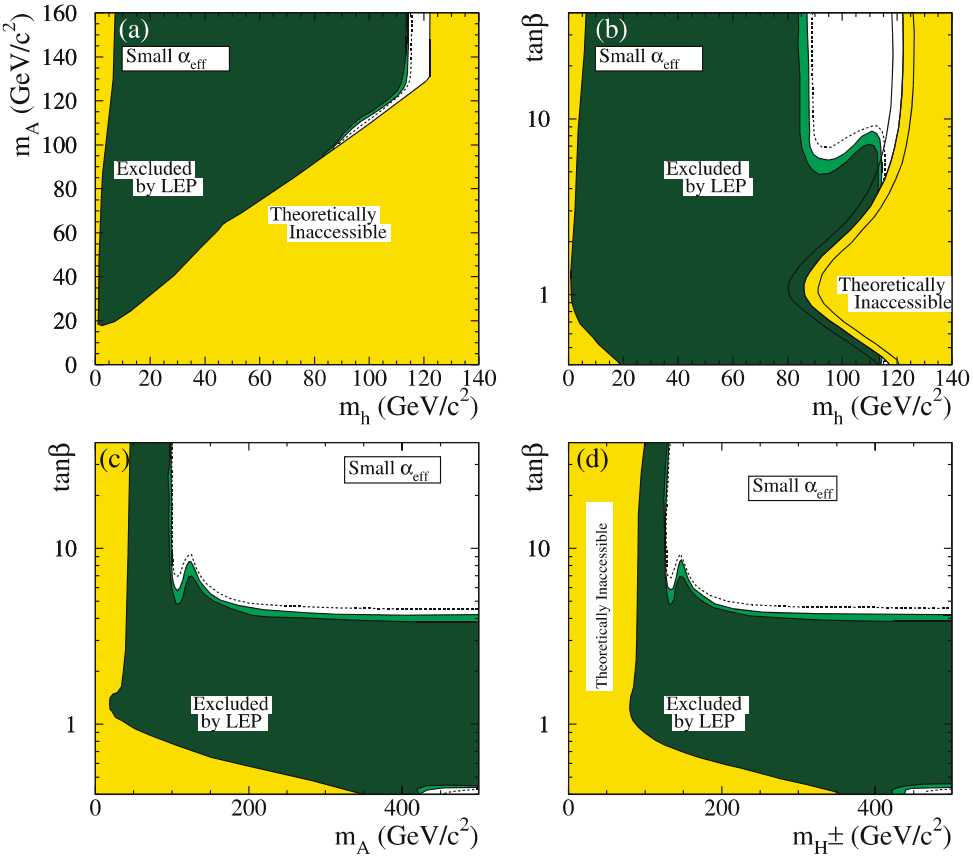

Fig. 15. Exclusions in the case of the CP-conserving *small-*$\alpha_{\rm eff}$ benchmark scenario (see Sect. 2.1.3). See the caption of Fig. 7 for the legend

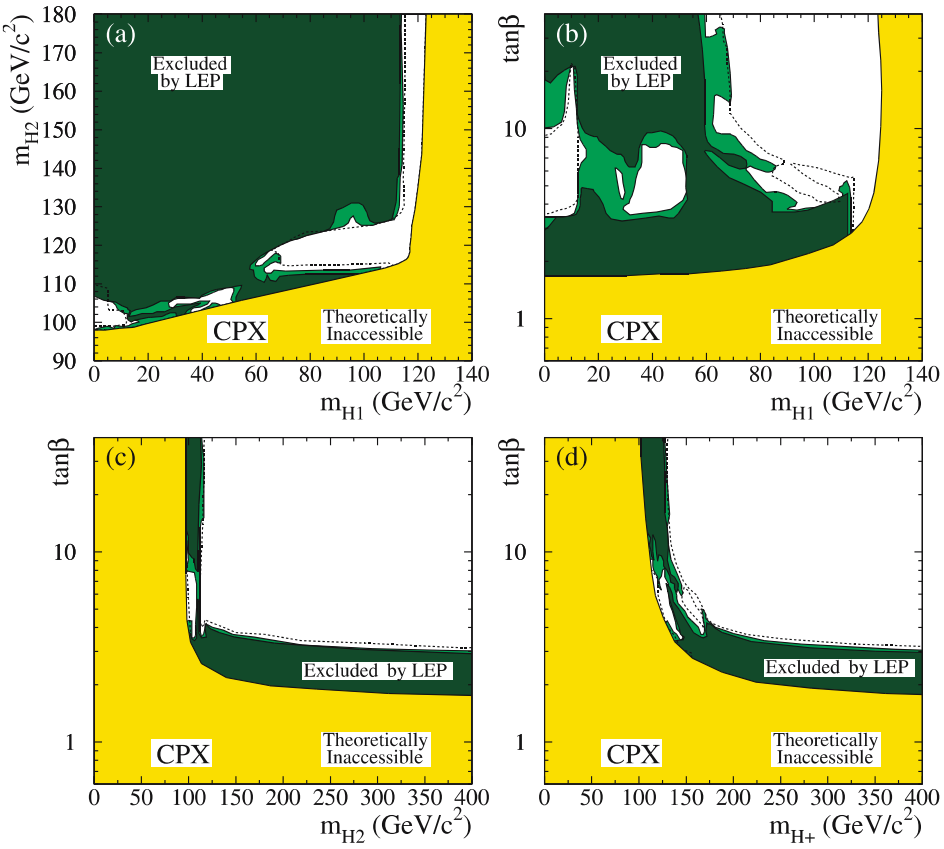

Fig. 16. Exclusions, at 95% CL (*medium-grey* or *light-green*) and the 99.7% CL (*dark-grey* or *dark-green*), for the CP-violating *CPX* scenario with $m_t = 174.3\,\mathrm{GeV/c^2}$. The figure shows the theoretically inaccessible domains (*light-grey* or *yellow*) and the regions excluded by the present search, in four projections of the MSSM parameter space: ($m_{\mathcal{H}_1}$, $m_{\mathcal{H}_2}$), ($m_{\mathcal{H}_1}$, $\tan\beta$), ($m_{\mathcal{H}_2}$, $\tan\beta$) and (m_{H^+}, $\tan\beta$). The *dashed lines* indicate the boundaries of the regions expected to be excluded, at the 95% CL, on the basis of Monte Carlo simulations with no signal. In each scan point, the more conservative of the two theoretical calculations, `FeynHiggs` or `CPH`, is used

These scenarios were designed to test situations which can be problematic at the Tevatron and LHC colliders. In both cases, large domains of the parameter space are excluded by the LEP searches.

6 Results interpreted in CP-violating MSSM scenarios

In this section, the search results are interpreted in the CP-violating benchmark scenario *CPX* presented in Sect. 2.2, and in some variants of *CPX* where the basic model parameters are varied one-by-one. Note that in these scenarios $m_{\mathcal{H}_3}$ is always larger than $120\,\mathrm{GeV/c^2}$, except where the CP-violating phases $\arg(A) = \arg(m_{\tilde{g}})$ are put to 0° or 180°.

The experimental exclusions for the *CPX* benchmark scenario are shown in Fig. 16, in four projections. For large $m_{\mathcal{H}_2}$, the $\mathcal{H}_1$ is almost completely CP-even; in this case the limit on $m_{\mathcal{H}_1}$ is close to $114\,\mathrm{GeV/c^2}$, the limit obtained for the standard model Higgs boson [3]. For example, for $m_{\mathcal{H}_2}$ larger than $133\,\mathrm{GeV/c^2}$, one can quote a lower bound of $113\,\mathrm{GeV/c^2}$ for $m_{\mathcal{H}_1}$. Large CP-odd admixtures to $\mathcal{H}_1$ occur, however, for smaller $m_{\mathcal{H}_2}$, giving rise to domains at lower $m_{\mathcal{H}_1}$ which are not excluded.

The exclusion is particularly weak for $\tan\beta$ between about 3.5 and 10. Here, the signal is spread over several channels arising from the Higgsstrahlung and pair-production processes, including the $\mathcal{H}_2 \to \mathcal{H}_1\mathcal{H}_1$ cascade decays, which give rise to complex final states with six jets. The parameter set of Table 2 is a typical example of this situation. This is illustrated in Fig. 17 where the main final-state cross-sections are plotted as a function of $\tan\beta$ (the `FeynHiggs` calculation is used). In general, these signal contributions cannot be added up statistically because of a large overlap in the selected events; hence, a relatively low overall detection efficiency is expected. Moreover, one of the experiments presents a local excess of about two standard deviations in this domain of $\tan\beta$ and for $m_{\mathcal{H}_1}$ of about $45\,\mathrm{GeV/c^2}$ [10], which lowers the exclusion power

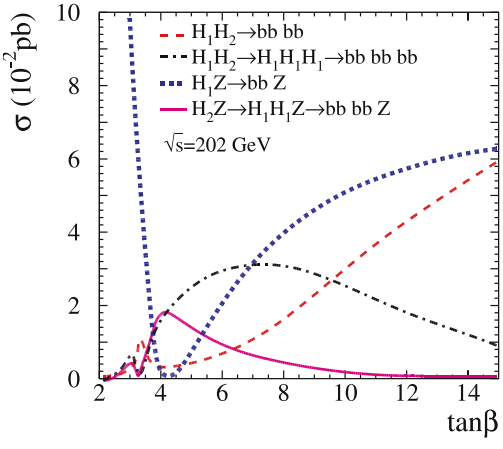

Fig. 17. Cross-sections, as a function of $\tan\beta$, for some of the dominant signal processes, in the CP-violating scenario *CPX*, using the `FeynHiggs` calculation, with a centre-of-mass energy of 202 GeV, $m_t = 175\,\mathrm{GeV/c^2}$, and $m_{\mathcal{H}_1}$ between 35 and $45\,\mathrm{GeV/c^2}$

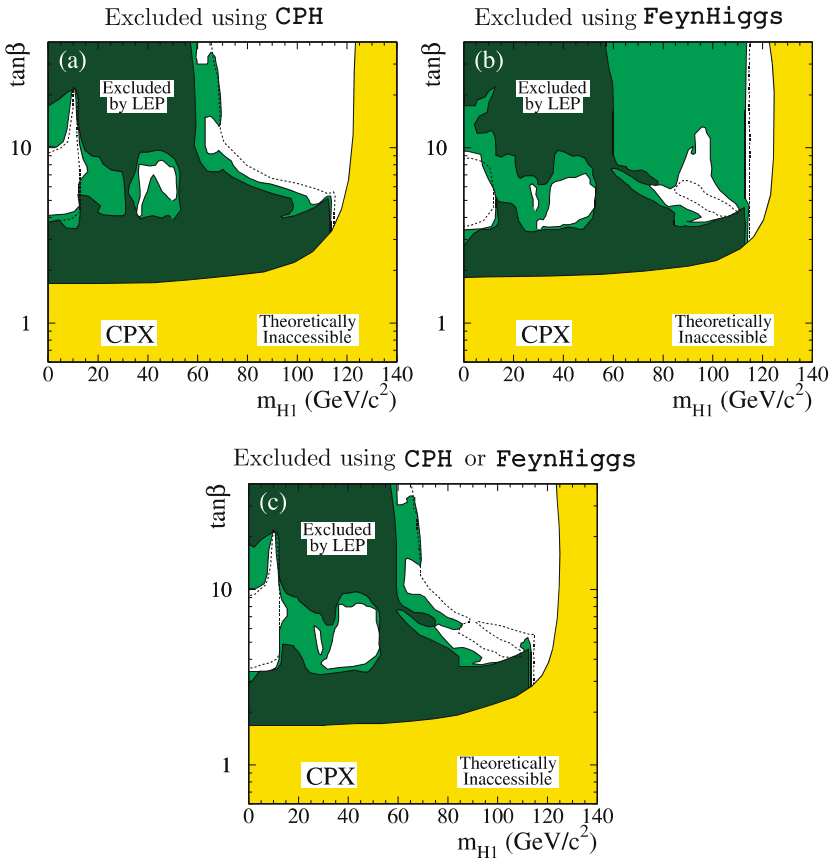

Fig. 18. Exclusions, in the case of the CP-violating *CPX* scenario, for the two theoretical approaches, `CPH` and `FeynHiggs`. See the caption of Fig. 16 for the legend. In part **a** the `CPH` calculation is used and in part **b** the `FeynHiggs` calculation. In part **c** the procedure is adopted where, in each scan point of the parameter space, the more conservative of the two calculations is used

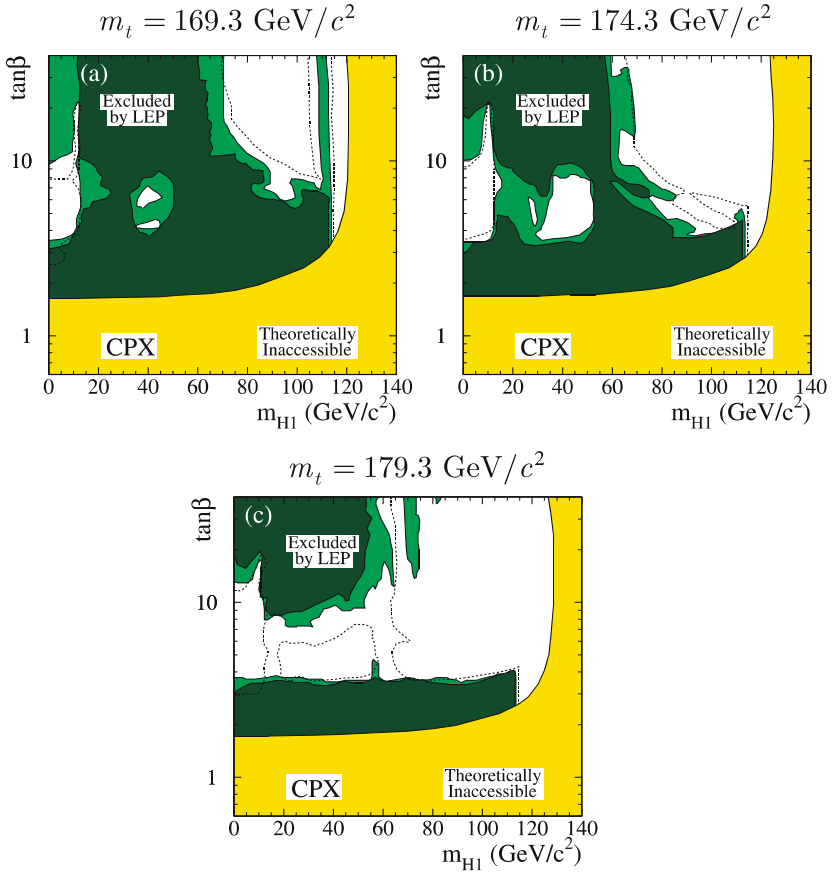

Fig. 19. Exclusions, in the case of the CP-violating *CPX* scenario, for three top quark masses: $m_{\mathrm{t}} = 169.3, 174.3$ and $179.3\,\mathrm{GeV/c^2}$. See the caption of Fig. 16 for the legend

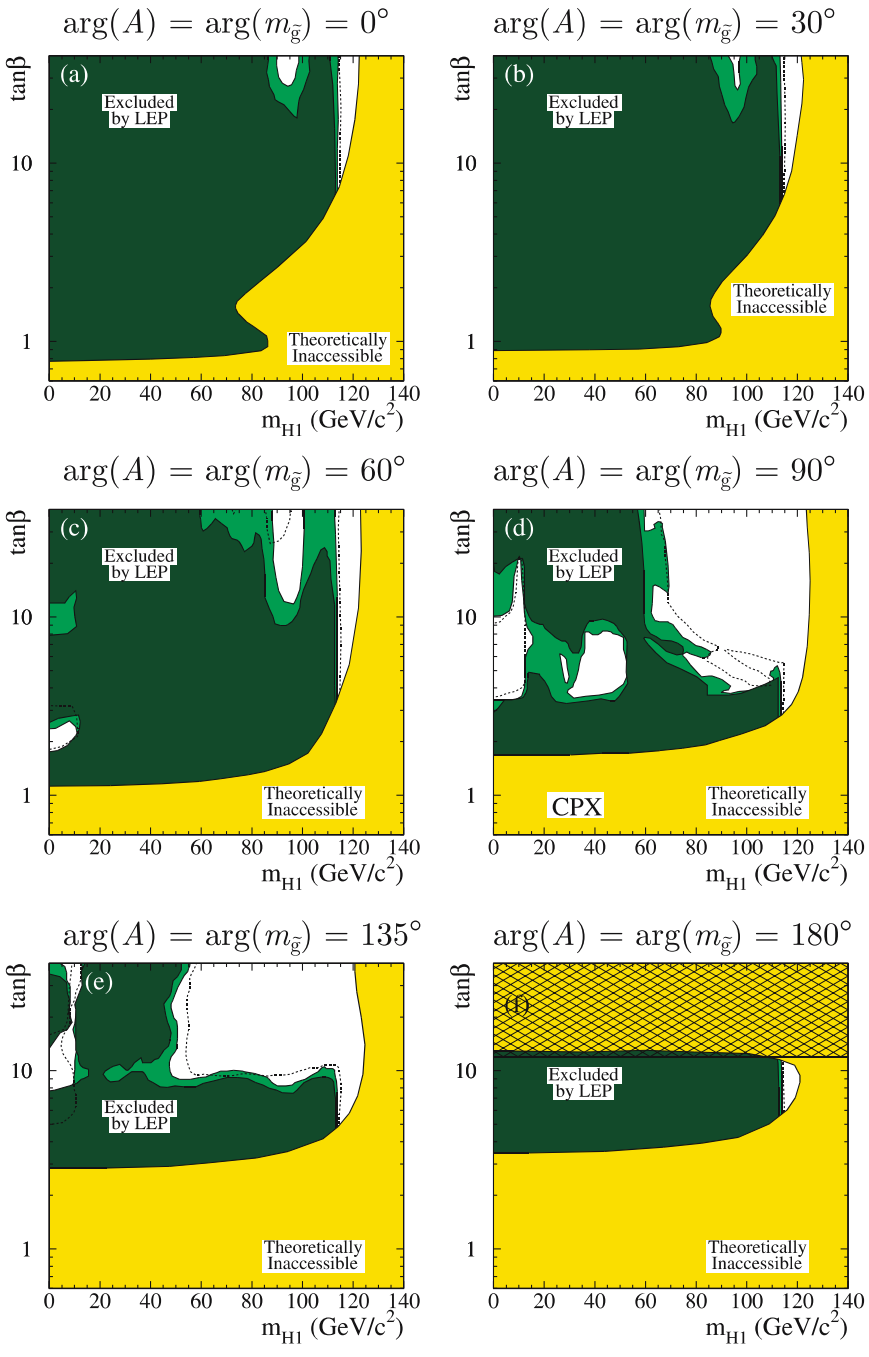

Fig. 20. Exclusions, in the case of the *CPX* scenario with various CP-violating phases, $\arg(A) = \arg(m_{\tilde{g}})$: $0°, 30°, 60°, 90°$ (the *CPX* value), $135°$ and $180°$. See the caption of Fig. 16 for the legend. In the hatched region in part **f** the calculations are uncertain (see text)

below the expectation. Nonetheless, the region defined by $m_{\mathcal{H}_1} < 114\,\mathrm{GeV/c^2}$ and $\tan\beta < 3.0$ is excluded by the data (see Fig. 16b) and a 95% CL lower bound of 2.9 can be set on $\tan\beta$ in this scenario. The two distinct domains in Fig. 16b, at moderate $\tan\beta$, with $m_{\mathcal{H}_1} < 15\,\mathrm{GeV/c^2}$ and $30\,\mathrm{GeV/c^2} < m_{\mathcal{H}_1} < 55\,\mathrm{GeV/c^2}$, which are not excluded at the 95% CL, are found to be excluded, respectively, at the 50% CL and 66% CL.

Figure 18 illustrates the exclusions in the $(m_{\mathcal{H}_1}, \tan\beta)$ projection, using the `CPH` calculation (part a) and the `FeynHiggs` calculation (part b). Differences occur mainly at large $\tan\beta$ where the `FeynHiggs` calculation predicts a larger Higgsstrahlung cross-section and hence a better search sensitivity than the `CPH` calculation. The two distinct domains at moderate $\tan\beta$, with $m_{\mathcal{H}_1} < 15\,\mathrm{GeV/c^2}$ and $30\,\mathrm{GeV/c^2} < m_{\mathcal{H}_1} < 55\,\mathrm{GeV/c^2}$, which are not excluded at the 95% CL, are found to be excluded, respectively, at the 55% CL and 77% CL using the `CPH` calculation, and at the 50% CL and 66% CL, respectively, using the `FeynHiggs` calculation. A third domain appears in part b at higher $m_{\mathcal{H}_1}$ (where the `CPH` calculation indicates no exclusion power at all); this domain is excluded at the 42% CL using `FeynHiggs`.

As explained in Sect. 2, neither of the two approaches, `CPH` or `FeynHiggs`, are preferred on theoretical grounds. For this reason, part (c) of this figure was obtained by choosing in each scan point of the parameter space the more conservative of the two approaches, i.e., the one for

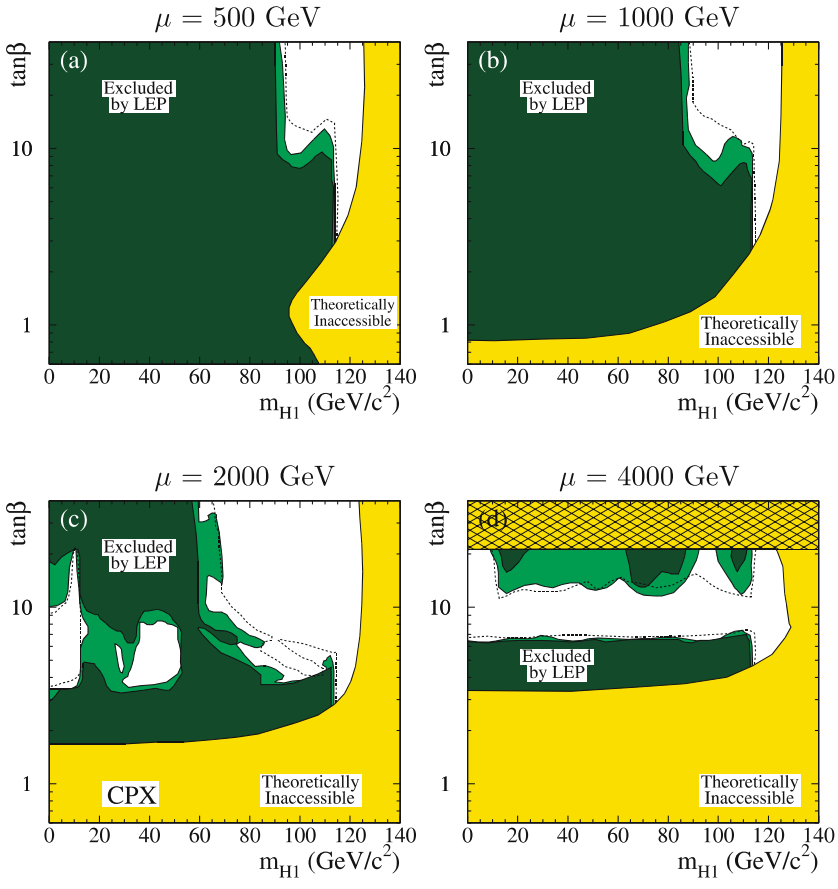

Fig. 21. Exclusions, for the CP-violating *CPX* scenario with various values of the Higgs mass parameter μ: 500 GeV, 1000 GeV, 2000 GeV (the standard *CPX* value) and 4000 GeV. See the caption of Fig. 16 for the legend. In the hatched region in part **d** the calculations are uncertain (see text)

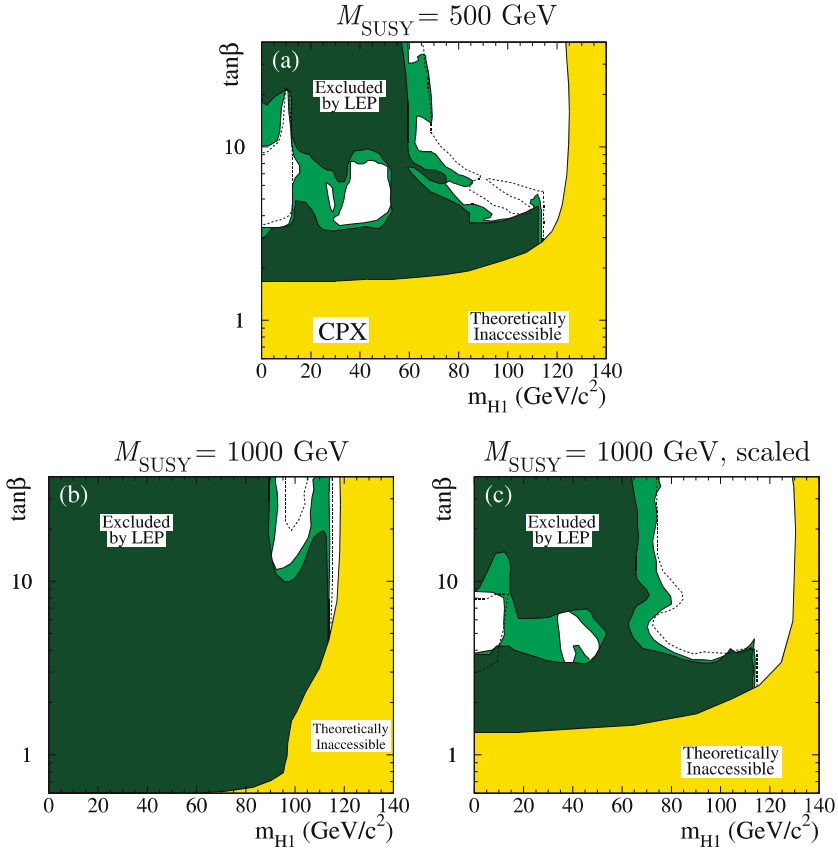

Fig. 22. Exclusions, for the CP-violating *CPX* scenario with various values of the soft SUSY-breaking scale $M_{\rm SUSY}$. **a**: $M_{\rm SUSY} = 500$ GeV (the standard *CPX* value); **b**: $M_{\rm SUSY} = 1000$ GeV while all other parameters are kept at their standard *CPX* values; **c**: $M_{\rm SUSY} = 1000$ GeV while $A, m_{\tilde{\rm g}}$ and μ are "scaled" to 2000 GeV, 2000 GeV and 4000 GeV, respectively. See the caption of Fig. 16 for the legend

which the less significant exclusion is observed. The same procedure was adopted in Fig. 16 and in all the figures which follow.

The significant impact of the top mass on the CP-violating effects, indicated by (11), is illustrated in Fig. 19 where the $(m_{\mathcal{H}_1}, \tan\beta)$ projection is shown for three values of m_{t}. With increasing m_{t}, one observes a reduction of the exclusion power, especially in the region of $\tan\beta$ between 3.5 and 10. No lower bound on $m_{\mathcal{H}_1}$ can be quoted in this domain. In plot (a) (for $m_{\mathrm{t}} = 169.3\,\mathrm{GeV/c^2}$), the two domains with $m_{\mathcal{H}_1} < 15\,\mathrm{GeV/c^2}$ and $30\,\mathrm{GeV/c^2} < m_{\mathcal{H}_1} < 55\,\mathrm{GeV/c^2}$ are excluded at the 60% CL and 88% CL, respectively. (The levels of exclusion for the two domains which appear in plot (b) (for $m_{\mathrm{t}} = 174.3\,\mathrm{GeV/c^2}$), have been quoted above, in the discussion of Fig. 16.)

Figure 20 illustrates the exclusion in the $(m_{\mathcal{H}_1}, \tan\beta)$ plane as a function of the CP-violating phases, $\arg(A) = \arg(m_{\tilde{\mathrm{g}}})$, which are varied together. For phase angles close to 0°, the experimental exclusions are similar to those in the CP-conserving scenarios (see, for example, Fig. 7 but note the differences in the allowed parameter space). Sizable differences are observed for larger phase angles, especially for $\arg(A) = \arg(m_{\tilde{\mathrm{g}}}) = 90°$ (the *CPX* value). At $\arg(A) = \arg(m_{\tilde{\mathrm{g}}}) = 180°$ (another CP-conserving scenario), the allowed parameter space is excluded almost completely. Note however that in the hatched region, with $\tan\beta$ greater than about 12, the calculation of the bottom-Yukawa coupling has large theoretical uncertainties; hence no exclusion can be claimed in this domain.

In Figure 21, the value of the Higgs mass parameter μ is varied from 500 GeV through 1000 GeV and 2000 GeV (the *CPX* value) to 4000 GeV. At small values, the CP-violating effects are small (see (11)) and the exclusion power is strong (as in the CP-conserving case). For μ larger than 2000 GeV and large $\tan\beta$, the `FeynHiggs` and `CPH` calculations both provide bottom-Yukawa coupling in the non-perturbative regime, giving rise to negative values for the square of $m_{\mathcal{H}_1}$ and to other unphysical results. For $\mu \leq 2000\,\mathrm{GeV}$ this regime sets in only at $\tan\beta$ larger than 40 whereas for $\mu = 4000\,\mathrm{GeV}$ this situation already occurs at $\tan\beta$ abowe 20. Hence, in Fig. 21d, the hatched domain should not be considered as being integrally part of the allowed parameter space.

Figure 22 illustrates the dependence on the soft SUSY-breaking scale parameter, M_{SUSY}, which is increased from the *CPX* value of 500 GeV in part (a) to 1000 GeV in part (b). This decreases the CP-violating effects (see (11)) and leads to a larger exclusion. The "scaling" behaviour mentioned in Sect. 2.2, namely the relative insensitivity of the exclusions to changes in M_{SUSY} as long as the relations $|A_{\mathrm{t},b}| = |m_{\tilde{\mathrm{g}}}| = \mu/2 = 2M_{\mathrm{SUSY}}$ are preserved, is qualitatively confirmed by comparing parts (a) and (c) of the figure.

7 Summary

The searches for neutral MSSM Higgs bosons described in this paper are based on the data collected by the four LEP collaborations, ALEPH, DELPHI, L3 and OPAL, which were statistically combined by the LEP Working Group for Higgs Boson Searches. The data samples include those collected during the LEP 2 phase at $\mathrm{e^+e^-}$ centre-of-mass energies up to 209 GeV; two experiments also provided LEP 1 data, at energies in the vicinity of the Z boson resonance. The searches address a large number of final-state topologies arising from the Higgsstrahlung process $\mathrm{e^+e^-} \to \mathcal{H}_1 Z$ and from the pair production process $\mathrm{e^+e^-} \to \mathcal{H}_2\mathcal{H}_1$. The combined LEP data do not reveal any excess of events which would indicate the production of Higgs bosons. The differences with respect to the background predictions are compatible with statistical fluctuations of the background.

From these results, upper bounds are derived for the cross-sections of a number of Higgs-like event topologies. These upper bounds cover a wide range of Higgs boson masses and are typically well below the cross-sections predicted within the MSSM framework; these limits can be used to constrain a large number of theoretical models.

The combined search results are used to test several MSSM scenarios which include CP-conserving and CP-violating benchmark models. These models are motivated mainly by physics arguments but some of them are constructed to test specific situations where the detection of Higgs bosons at the Tevatron and LHC colliders might present experimental difficulties. It is found that in all these scenarios the searches conducted at LEP exclude sizeable domains of the theoretically allowed parameter space.

In the CP-conserving case, lower bounds can be set on the masses of neutral Higgs bosons and the value of $\tan\beta$ can be restricted. Taking, for example, the CP-conserving scenario m_{h}-*max* and a top quark mass of $174.3\,\mathrm{GeV/c^2}$, values of m_{h} and m_{A} less than $92.8\,\mathrm{GeV/c^2}$ and $93.4\,\mathrm{GeV/c^2}$, respectively, are excluded at the 95% CL. In the same scenario, values of $\tan\beta$ between 0.7 and 2.0 are excluded, but this range depends considerably on the assumed top quark mass and may also depend on M_{SUSY}.

In the CP-violating benchmark scenario *CPX* and the variants which have been studied, the combined LEP data show large domains which are not excluded, down to the lowest mass values; hence, no absolute limits can be set for the Higgs boson masses. The excluded domains vary considerably with the precise value of the top quark mass and the MSSM model parameters. For example, in the *CPX* scenario with standard parameters and $m_{\mathrm{t}} = 174.3\,\mathrm{GeV/c^2}$, $\tan\beta$ can be restricted to values larger than 2.9 at the 95% CL.

Acknowledgements. We congratulate the LEP Accelerator Division for the successful running of LEP over twelve years, up to the highest energies. We also would like to express our thanks to the engineers and technicians in all our institutions for their contributions to the excellent performance of the four LEP experiments.

Appendix A: Catalog of searches

The searches of the four LEP collaborations which contribute to this combined analysis are listed in Tables 6

to 13. The list is structured into two tables per experiment, one for the Higgsstrahlung process $e^+e^- \to \mathcal{H}_1 Z$ and one for the pair production process $e^+e^- \to \mathcal{H}_2\mathcal{H}_1$. In each of these tables, the upper part contains the final states of the direct process and the lower part contains, where it applies, those of the cascade process $\mathcal{H}_2 \to \mathcal{H}_1\mathcal{H}_1$.

The final-state topologies are listed in the first column. In the notation adopted, $\mathcal{H}_1$ represents the lightest and $\mathcal{H}_2$ the second-lightest neutral Higgs boson. In the CP-conserving case, $\mathcal{H}_1$ is identified with the CP-even eigenstate h and $\mathcal{H}_2$ is identified with the CP-odd eigenstate A, except in the case of the cascade process $\mathcal{H}_2 \to \mathcal{H}_1\mathcal{H}_1$ which is identified with $h \to AA$. The symbol q indicates an arbitrary quark flavour, u, d, s, c or b. "Hadrons" include quarks and gluons. In the missing energy channel, in addition to the $\mathcal{H}_1 Z \to \mathcal{H}_1 \nu\bar{\nu}$ process, the W fusion process $\mathcal{H}_1 \nu_e \bar{\nu}_e$ (including interference) is also considered; similarly, in the leptonic channel, in addition to the $\mathcal{H}_1 Z \to \mathcal{H}_1 \ell^+\ell^-$ process, the Z fusion process $\mathcal{H}_1 e^+e^-$ (including interference) is also considered.

The contributions based on LEP1 data (from two experiments only) can be identified by their value "91" in the second column which indicates the e^+e^- collision energy, $\sqrt{s}$(GeV); the LEP1 data used in this combination represent an integrated luminosity $\mathcal{L}$ of about 125 pb^{-1}. The LEP2 data span an energy range between 133 GeV and 209 GeV; they represent an integrated luminosity of about 2400 pb^{-1}. The integrated luminosities for the individual searches are listed in the third column.

Table 6. Summary of the ALEPH searches for the Higgsstrahlung process $e^+e^- \to \mathcal{H}_1 Z$. The top part of the table lists the searches originally developed for the standard model Higgs boson. The bottom part lists flavour-independent searches where the decays of the Higgs boson into a quark pair of any flavour, a gluon pair or a tau pair were considered; the signal efficiencies were evaluated for all indicated hadronic decays of the Higgs boson. In the cases of the $(\tau^+\tau^-)(q\bar{q})$ and leptonic channels listed in the flavour-independent part, the event selections of the standard model Higgs boson searches were used

	$\sqrt{s}$(GeV)	$\mathcal{L}$ (pb^{-1})	Mass range (GeV/c^2)	Ref.
$\mathcal{H}_1 Z \to (\dots)(\dots)$			$m_{\mathcal{H}1}$	
$(b\bar{b})(q\bar{q})$, $(b\bar{b}, c\bar{c}, \tau\tau, gg)(\nu\bar{\nu})$	189	176.2	75–110	[32]
(any)$(e^+e^-, \mu^+\mu^-)$	189	176.2	75–110	[32]
$(b\bar{b})(\tau^+\tau^-), (\tau^+\tau^-)(q\bar{q})$	189	176.2	65–110	[32]
$(b\bar{b})(q\bar{q}, \nu\bar{\nu})$	192–202	236.7	60–120	[33]
$(b\bar{b}, \tau^+\tau^-, c\bar{c}, gg)(e^+e^-, \mu^+\mu^-)$	192–202	236.7	60–120	[33]
$(b\bar{b}, \tau^+\tau^-, c\bar{c}, gg)(\tau^+\tau^-), (\tau^+\tau^-)(q\bar{q})$	192–202	236.7	60–120	[33]
$(b\bar{b})(q\bar{q})$	199–209	217.2	75–120	[11, 34]
$(b\bar{b}, \tau^+\tau^-, c\bar{c}, gg, WW)(\tau^+\tau^-, \nu\bar{\nu})$	199–209	217.2	75–120	[11, 34]
$(b\bar{b}, \tau^+\tau^-, c\bar{c}, gg)(e^+e^-, \mu^+\mu^-)$	199–209	217.2	70–120	[11, 34]
$(b\bar{b}, c\bar{c}, s\bar{s}, gg)(q\bar{q})$	189	176.2	40–100	[35]
$(b\bar{b}, c\bar{c}, s\bar{s}, gg)(\nu\bar{\nu})$	189	176.2	60–100	[35]
$(b\bar{b}, c\bar{c}, s\bar{s}, gg)(e^+e^-, \mu^+\mu^-)$	189	176.2	60–115	[32, 35]
$(\tau^+\tau^-)(q\bar{q})$	189	176.2	65–110	[32]
$(b\bar{b}, c\bar{c}, s\bar{s}, gg)(q\bar{q})$	192–202	236.7	40–110	[35]
$(b\bar{b}, c\bar{c}, s\bar{s}, gg)(\nu\bar{\nu})$	192–202	236.7	60–116	[35]
$(b\bar{b}, c\bar{c}, s\bar{s}, gg)(e^+e^-, \mu^+\mu^-)$	192–202	236.7	60–115	[33, 35]
$(\tau^+\tau^-)(q\bar{q})$	192–202	236.7	60–120	[33]
$(b\bar{b}, c\bar{c}, s\bar{s}, gg)(q\bar{q})$	199–209	217.2	40–115	[35]
$(b\bar{b}, c\bar{c}, s\bar{s}, gg)(\nu\bar{\nu})$	199–209	217.2	75–120	[35]
$(b\bar{b}, c\bar{c}, s\bar{s}, gg)(e^+e^-, \mu^+\mu^-)$	199–209	217.2	70–120	[11, 34, 35]
$(\tau^+\tau^-)(q\bar{q})$	199–209	217.2	60–120	[11, 34]

Table 7. Summary of the ALEPH searches for the pair production process $e^+e^- \to \mathcal{H}_2\mathcal{H}_1$. The searches are restricted to $|m_{\mathcal{H}_2} - m_{\mathcal{H}_1}|$ less than about 20 GeV/c^2

	$\sqrt{s}$ (GeV)	$\mathcal{L}$ (pb^{-1})	Mass range (GeV/c^2)	Ref.
$\mathcal{H}_2\mathcal{H}_1 \to (\dots)(\dots)$			$(m_{\mathcal{H}_2} + m_{\mathcal{H}_1})/2$	
$(b\bar{b})(b\bar{b})$, $(\tau^+\tau^-)(b\bar{b})$, $(b\bar{b})(\tau^+\tau^-)$	189	176.2	65–95	[32]
$(b\bar{b})(b\bar{b})$, $(b\bar{b}, \tau^+\tau^-, c\bar{c}, \mathrm{gg})(\tau^+\tau^-)$, $(\tau^+\tau^-)(b\bar{b}, \tau^+\tau^-, c\bar{c}, \mathrm{gg})$	192–202	236.7	60–$\sqrt{s}/2$	[33]
$(b\bar{b})(b\bar{b})$, $(b\bar{b}, \tau^+\tau^-, c\bar{c}, \mathrm{gg})(\tau^+\tau^-)$, $(\tau^+\tau^-)(b\bar{b}, \tau^+\tau^-, c\bar{c}, \mathrm{gg})$	199–209	217.2	75–$\sqrt{s}/2$	[11, 34]

Table 8. List of the DELPHI searches for the Higgsstrahlung processes $e^+e^- \to \mathcal{H}_1 Z$ and $\mathcal{H}_2 Z$

	$\sqrt{s}$ (GeV)	$\mathcal{L}$ (pb^{-1})	Mass ranges (GeV/c^2)		Ref.
$e^+e^- \to \mathcal{H}_1 Z \to (\dots)(\dots)$			$m_{\mathcal{H}_1}$		
(any)(e^+e^-, $\mu^+\mu^-$), (V^0)(any)	91	2.5	< 0.21		[36]
(2 prongs)($q\bar{q}$)	91	0.5	0.21–2		[37]
(jet)(e^+e^-, $\mu^+\mu^-$)	91	0.5	1–20		[37]
(jet jet)($\ell^+\ell^-$, $\nu\bar{\nu}$)	91	3.6	12–50		[38]
(jet jet)(e^+e^-, $\mu^+\mu^-$, $\nu\bar{\nu}$)	91	33.4	35–70		[39]
($b\bar{b}$)(any), ($\tau^+\tau^-$)($q\bar{q}$)	161,172	19.9	40–80		[40]
($b\bar{b}$)(any), ($\tau^+\tau^-$)($q\bar{q}$)	183	52.0	45–95		[41]
($b\bar{b}$)(any), ($\tau^+\tau^-$)(qq)	189	158.0	65–100		[42]
($b\bar{b}$)(any)	192-209	452.4	12–120		[43, 44]
($\tau^+\tau^-$)(qq)	192-209	452.4	45–120		[43, 44]
($q\bar{q}$, gg)($q\bar{q}$, $\nu\bar{\nu}$, e^+e^-, $\mu^+\mu^-$)	189-209	610.4	4–116		[45]
$e^+e^- \to \mathcal{H}_2 Z \to (\mathcal{H}_1\mathcal{H}_1)Z \to (\dots)(\dots)$			$m_{\mathcal{H}_2}$	$m_{\mathcal{H}_1}$	
(any)($q\bar{q}$)	91	16.2	12–70	< 0.21	[46]
(V^0V^0)(any but $\tau^+\tau^-$)	91	9.7	0.5–55	< 0.21	[46]
($\gamma\gamma$)(any)	91	12.5	0.5–60	< 0.21	[46]
(4 prongs)(any)	91	12.9	0.5–60	0.21–10	[46]
(hadrons)($\nu\bar{\nu}$)	91	15.1	1–60	0.21–30	[46]
($\tau^+\tau^-\tau^+\tau^-$)($\nu\bar{\nu}$)	91	15.1	9–73	3.5–12	[46]
(any)($q\bar{q}$, $\nu\bar{\nu}$)	161,172	20.0	40–70	20–35	[40]
($b\bar{b}b\bar{b}$)($q\bar{q}$)	183	54.0	45–85	12–40	[41]
($b\bar{b}b\bar{b}$, $b\bar{b}c\bar{c}$, $c\bar{c}c\bar{c}$)($q\bar{q}$)	192-208	452.4	30–105	12–50	[43, 44]
($c\bar{c}c\bar{c}$)($q\bar{q}$)	192-208	452.4	10–105	4–12	[47]

Table 9. List of the DELPHI searches for the pair production process $e^+e^- \to \mathcal{H}_2\mathcal{H}_1$

	$\sqrt{s}$ (GeV)	$\mathcal{L}$ (pb^{-1})	Mass ranges (GeV/c^2)		Ref.
$e^+e^- \to \mathcal{H}_2\mathcal{H}_1 \to (\dots)(\dots)$			$m_{\mathcal{H}_2}$	$m_{\mathcal{H}_1}$	
4 prongs	91	5.3	0.2–10	0.2–10	[39]
($\tau^+\tau^-$)(hadrons)	91	0.5	4–35	4–35	[48]
($\tau^+\tau^-$)(jet jet)	91	3.6	25–42	25–42	[49]
($b\bar{b}$)($b\bar{b}$), ($b\bar{b}$)($c\bar{c}$)	91	33.4	15–46	15–46	[38]
$\tau^+\tau^- b\bar{b}$	91	79.4	4–70	4–70	[47]
$b\bar{b}b\bar{b}$	91	79.4	12–40	20–70	[50]
$b\bar{b}b\bar{b}$	133	6.0	40–68	35–73	[51]
$b\bar{b}b\bar{b}$, $\tau^+\tau^- b\bar{b}$	161,172	20.0	40–70	35–75	[40]
$b\bar{b}b\bar{b}$, $\tau^+\tau^- b\bar{b}$	183	54.0	50–80	25–105	[41]
$b\bar{b}b\bar{b}$, $\tau^+\tau^- b\bar{b}$	189	158.0	65–90	40–115	[42]
$\tau^+\tau^- b\bar{b}$	192-208	452.4	50–100	60–150	[43, 44]
$b\bar{b}b\bar{b}$	192-208	452.4	12–100	40–190	[43, 44]
$\tau^+\tau^-\tau^+\tau^-$	189-208	570.9	4–90	4–170	[50]
$b\bar{b}b\bar{b}$	189-208	610.2	12–70	30–170	[50]
quarks or gluons	189-208	610.4	4–170	4–170	[45]
$e^+e^- \to \mathcal{H}_2\mathcal{H}_1 \to (\mathcal{H}_1\mathcal{H}_1)\mathcal{H}_1 \to (\dots)(\dots)$			$m_{\mathcal{H}_2}$	$m_{\mathcal{H}_1}$	
($\gamma\gamma$)($\gamma\gamma$)	91	12.5	0.5–60	< 0.21	[46]
(4 prongs)(2 prongs)	91	12.9	0.5–60	0.21–10	[46]
(hadrons)(hadrons)	91	15.1	1–60	0.21–30	[46]
($\tau^+\tau^-\tau^+\tau^-$)($\tau^+\tau^-$)	91	15.1	9–60	3.5–12	[46]
(any)(any)	161,172	20.0	40–70	20–35	[40]

Table 10. List of the L3 searches for the Higgsstrahlung processes $e^+e^- \to \mathcal{H}_1 Z$ and $\mathcal{H}_2 Z$

	$\sqrt{s}$ (GeV)	$\mathcal{L}$ (pb^{-1})	Mass ranges (GeV/c^2)		Ref.
$e^+e^- \to \mathcal{H}_1 Z \to (\dots)(\dots)$			$m_{\mathcal{H}_1}$		
$(b\bar{b})$(any),$(\tau^+\tau^-)(q\bar{q})$	189	176.4	60–100		[52]
$(b\bar{b})$(any),$(\tau^+\tau^-)(q\bar{q})$	192–202	233.2	60–110		[53]
$(b\bar{b})$(any),$(\tau^+\tau^-)(q\bar{q})$	203–209	217.3	60–120		[54]
$(b\bar{b}, c\bar{c}, gg)$(any)	189	176.4	60–100		[55]
$(b\bar{b}, c\bar{c}, gg)$(any)	192–202	233.2	60–110		[55]
$(b\bar{b}, c\bar{c}, gg)$(any)	204–209	214.5	60–120		[55]
$e^+e^- \to \mathcal{H}_2 Z \to (\mathcal{H}_1\mathcal{H}_1)Z \to (\dots)(\dots)$			$m_{\mathcal{H}_2}$	$m_{\mathcal{H}_1}$	
$(\mathcal{H}_1 \to b\bar{b}, cc, gg)(q\bar{q})$	189 – 209	626.9	30 – 85	10 – 42	[56]

Table 11. List of the OPAL searches for the Higgsstrahlung processes $e^+e^- \to \mathcal{H}_1 Z$ and $\mathcal{H}_2 Z$

	$\sqrt{s}$ (GeV)	$\mathcal{L}$ (pb^{-1})	Mass ranges (GeV/c^2)		Ref.
$\mathcal{H}_1 Z \to (\dots)(\dots)$			$m_{\mathcal{H}_1}$		
$(b\bar{b})(q\bar{q})$	161–172	20.4	40–80		[59, 60]
$(b\bar{b})(q\bar{q})$	183	54.1	40–95		[61]
$(b\bar{b})(q\bar{q})$	189	172.1	40–100		[62]
$(b\bar{b})(q\bar{q})$	192–209	421.2	80–120		[63]
$(b\bar{b})(\nu\bar{\nu})$	161–172	20.4	50–70		[59, 60]
$(b\bar{b})(\nu\bar{\nu})$	183	53.9	50–95		[61]
$(b\bar{b})(\nu\bar{\nu})$	189	171.4	50–100		[62]
$(b\bar{b})(\nu\bar{\nu})$	192–209	419.9	30–120		[63]
$(b\bar{b})(\tau^+\tau^-)$, $(\tau^+\tau^-)(q\bar{q})$	161–172	20.4	30–95		[59, 60]
$(b\bar{b})(\tau^+\tau^-)$, $(\tau^+\tau^-)(q\bar{q})$	183	53.7	30–100		[61]
$(b\bar{b})(\tau^+\tau^-)$, $(\tau^+\tau^-)(q\bar{q})$	189	168.7	30–100		[62]
$(b\bar{b})(\tau^+\tau^-)$, $(\tau^+\tau^-)(q\bar{q})$	192–209	417.4	80–120		[63]
$(b\bar{b})(e^+e^-)$, $(b\bar{b})(\mu^+\mu^-)$	183	55.9	60–100		[61]
$(b\bar{b})(e^+e^-)$, $(b\bar{b})(\mu^+\mu^-)$	189	170.0	70–100		[62]
$(b\bar{b})(e^+e^-)$, $(b\bar{b})(\mu^+\mu^-)$	192–209	418.3	40–120		[63]
$(q\bar{q}, gg)(\tau^+\tau^-, \nu\bar{\nu})$, $(\tau^+\tau^-)(q\bar{q})$	91	46.3	0–70		[64, 65]
$(q\bar{q}, gg)(e^+e^-, \mu^+\mu^-)$	91	46.3	20–70		[64, 65]
(any)$(e^+e^-, \mu^+\mu^-)$	161–172	20.4	35–80		[59, 60]
$(q\bar{q}, gg)(q\bar{q})$	189	174.1	60–100		[66]
$(q\bar{q}, gg)(q\bar{q})$	192–209	424.2	60–120		[67]
$(q\bar{q}, gg)(\nu\bar{\nu})$	189	171.8	30–100		[66]
$(q\bar{q}, gg)(\nu\bar{\nu})$	192–209	414.5	30–110		[67]
$(q\bar{q}, gg)(\tau^+\tau^-)$, $(\tau^+\tau^-)(q\bar{q})$	189	168.7	30–100		[66]
$(q\bar{q}, gg)(\tau^+\tau^-)$, $(\tau^+\tau^-)(q\bar{q})$	192–209	418.9	60–115		[67]
$(q\bar{q}, gg)(e^+e^-, \mu^+\mu^-)$	189	170.0	70–100		[66]
$(q\bar{q}, gg)(e^+e^-, \mu^+\mu^-)$	192–209	422.0	60–120		[67]
$e^+e^- \to \mathcal{H}_2 Z \to (\mathcal{H}_1\mathcal{H}_1)Z \to (\dots)(\dots)$			$m_{\mathcal{H}_2}$	$m_{\mathcal{H}_1}$	
$(q\bar{q}q\bar{q})(\nu\bar{\nu})$	91	46.3	10–75	0–35	[64, 65]
$(b\bar{b}b\bar{b})(q\bar{q})$	183	54.1	40–80	10.5–38	[61]
$(b\bar{b}b\bar{b})(q\bar{q})$	189	172.1	40–100	10.5–48	[62]
$(b\bar{b}b\bar{b})(q\bar{q})$	192–209	421.2	80–120	12–$m_{\mathcal{H}_2}/2$	[10]
$(b\bar{b}b\bar{b})(\nu\bar{\nu})$	183	53.9	50–95	10.5–$m_{\mathcal{H}_2}/2$	[61]
$(q\bar{q}q\bar{q})(\nu\bar{\nu})$	189	171.4	50–100	10.5–$m_{\mathcal{H}_2}/2$	[62]
$(b\bar{b}b\bar{b})(\nu\bar{\nu})$	199–209	207.2	100–110	12–$m_{\mathcal{H}_2}/2$	[10]
$(b\bar{b}b\bar{b})(\tau^+\tau^-)$	183	53.7	30–100	10.5–$m_{\mathcal{H}_2}/2$	[61]
$(b\bar{b}b\bar{b})(\tau^+\tau^-)$	189	168.7	30–100	10.5–$m_{\mathcal{H}_2}/2$	[62]
$(c\bar{c}c\bar{c}, gggg, c\bar{c}gg, c\bar{c}\tau^+\tau^-, gg\tau^+\tau^-,$ $\tau^+\tau^-\tau^+\tau^-)(\nu\bar{\nu}, e^+e^-, \mu^+\mu^-)$	189–209	598.5	45–86	2–11	[68]

Table 12. List of the L3 searches for the pair production process $e^+e^- \to \mathcal{H}_2\mathcal{H}_1$

	$\sqrt{s}$ (GeV)	$\mathcal{L}$ (pb^{-1})	Mass ranges (GeV/c^2)		Ref.
$e^+e^- \to \mathcal{H}_2\mathcal{H}_1 \to (\dots)(\dots)$			$m_{\mathcal{H}_2}$	$m_{\mathcal{H}_1}$	
$(b\bar{b})(b\bar{b})$, $(b\bar{b})(\tau^+\tau^-)$, $(\tau^+\tau^-)(b\bar{b})$	189	176.4	50–95	50–95	[57]
$(b\bar{b})(b\bar{b})$, $(b\bar{b})(\tau^+\tau^-)$, $(\tau^+\tau^-)(b\bar{b})$	192–202	233.2	50–105	50–105	[58]
$(b\bar{b})(b\bar{b})$, $(b\bar{b})(\tau^+\tau^-)$, $(\tau^+\tau^-)(b\bar{b})$	204–209	216.6	50–110	50–110	[56]

Table 13. List of the OPAL searches for the pair production process $e^+e^- \to \mathcal{H}_2\mathcal{H}_1$. The symbols Σ and Δ stand for the mass sum $m_{\mathcal{H}_2} + m_{\mathcal{H}_1}$ and mass difference $|m_{\mathcal{H}_2} - m_{\mathcal{H}_1}|$

	$\sqrt{s}$ (GeV)	$\mathcal{L}$ (pb^{-1})	Mass ranges (GeV/c^2)		Ref.
$\mathcal{H}_2\mathcal{H}_1 \to (\dots)(\dots)$			$m_{\mathcal{H}_2}$	$m_{\mathcal{H}_1}$	Ref.
$(b\bar{b})(b\bar{b})$	130–136	5.2	Σ : 80–130	Δ : 0–50	[60]
$(b\bar{b})(b\bar{b})$	161	10.0	Σ : 80–130	Δ : 0–60	[59, 60]
$(b\bar{b})(b\bar{b})$	172	10.4	Σ : 80–130	Δ : 0–60	[59, 60]
$(b\bar{b})(b\bar{b})$	183	54.1	Σ : 80–150	Δ : 0–60	[61]
$(b\bar{b})(b\bar{b})$	189	172.1	Σ : 80–180	Δ : 0–70	[62]
$(b\bar{b})(b\bar{b})$	192	28.9	Σ : 83–183	Δ : 0–70	[10]
$(b\bar{b})(b\bar{b})$	196	74.8	Σ : 80–187	Δ : 0–70	[10]
$(b\bar{b})(b\bar{b})$	200	77.2	Σ : 80–191	Δ : 0–70	[10]
$(b\bar{b})(b\bar{b})$	202	36.1	Σ : 80–193	Δ : 0–70	[10]
$(b\bar{b})(b\bar{b})$	199–209	207.3	Σ : 120–190	Δ : 0–70	[10]
$(b\bar{b})(b\bar{b})$	199–209	207.3	Σ : 100–140	Δ : 60–100	[10]
$(b\bar{b})(\tau^+\tau^-)$, $(\tau^+\tau^-)(b\bar{b})$	161	10.0	40–160	52–160	[59, 60]
$(b\bar{b})(\tau^+\tau^-)$, $(\tau^+\tau^-)(b\bar{b})$	172	10.4	37–160	28–160	[59, 60]
$(b\bar{b})(\tau^+\tau^-)$, $(\tau^+\tau^-)(b\bar{b})$	183	53.7	Σ : 70–170	Δ : 0–70	[61]
$(b\bar{b})(\tau^+\tau^-)$, $(\tau^+\tau^-)(b\bar{b})$	189	168.7	Σ : 70–190	Δ : 0–90	[62]
$(b\bar{b})(\tau^+\tau^-)$, $(\tau^+\tau^-)(b\bar{b})$	192	28.7	Σ : 10–174	Δ : 0–182	[10]
$(b\bar{b})(\tau^+\tau^-)$, $(\tau^+\tau^-)(b\bar{b})$	196	74.7	Σ : 10–182	Δ : 0–191	[10]
$(b\bar{b})(\tau^+\tau^-)$, $(\tau^+\tau^-)(b\bar{b})$	200	74.8	Σ : 10–182	Δ : 0–191	[10]
$(b\bar{b})(\tau^+\tau^-)$, $(\tau^+\tau^-)(b\bar{b})$	202	35.4	Σ : 10–174	Δ : 0–182	[10]
$(b\bar{b})(\tau^+\tau^-)$, $(\tau^+\tau^-)(b\bar{b})$	199–209	203.6	Σ : 70–190	Δ : 0–90	[10]
$(q\bar{q})(\tau^+\tau^-)$, $(\tau^+\tau^-)(q\bar{q})$	91	46.3	12–75	10–78	[64, 65]
$(q\bar{q})(q\bar{q})$, $(q\bar{q})(gg)$, $(gg)(q\bar{q})$, $(gg)(gg)$	192–209	424.0	Σ : 60–175	Δ : 0–113	[69]
$e^+e^- \to \mathcal{H}_2\mathcal{H}_1 \to (\mathcal{H}_1\mathcal{H}_1)\mathcal{H}_1 \to (\dots)(\dots)$			$m_{\mathcal{H}_2}$	$m_{\mathcal{H}_1}$	
$(b\bar{b}b\bar{b})(b\bar{b})$	91	27.6	40–70	5–35	[64, 65]
$(b\bar{b}b\bar{b})(b\bar{b})$	130–136	5.2	55–65	> 27.5	[60]
$(b\bar{b}b\bar{b})(b\bar{b})$	161	10.0	55–65	> 20.0	[59, 60]
$(b\bar{b}b\bar{b})(b\bar{b})$	172	10.4	55–65	25–35	[59, 60]
$(b\bar{b}b\bar{b})(b\bar{b})$	183	54.1	30–80	12–40	[61]
$(b\bar{b}b\bar{b})(b\bar{b})$	189	172.1	24–80	12–40	[62]
$(b\bar{b}b\bar{b})(b\bar{b})$	199–209	207.3	Σ : 90–200	Δ : 40–160	[10]
6τ, $4\tau 2q$, $2\tau 4q$	91	46.3	30–75	4–30	[64, 65]

Responding to the increasing data samples and e^+e^- energies, the searches were gradually upgraded or replaced so as to become more efficient in detecting Higgs bosons of higher masses. The mass ranges where the searches are relevant are listed in the next column(s). In the last column, references are given to the publications where the details of the searches can be found.

Appendix B: Limits on topological cross-sections

The tables presented below summarise the 95% CL upper bounds, as a function of the Higgs boson masses, of the scaling factor S_{95} defined in the text (see (16)). Tables 14, 15 and 16 refer to final-state topologies aris-

Table 14. The 95% CL upper bound, S_{95}, obtained for the normalised ross-section (see text) of the Higgsstrahlung process $e^+e^- \to \mathcal{H}_1 Z$, as a function of the Higgs boson mass. The numbers listed in this table correspond to the observed limit (*full line*) in Fig. 2, which is reproduced from [3]. In the columns labelled (a) the Higgs boson is assumed to decay as in the standard model; in columns (b) it is assumed to decay exclusively to $b\bar{b}$ and in columns (c) exclusively to $\tau^+\tau^-$

$m_{\mathcal{H}_1}$ (GeV/c^2)	(a)	(b)	(c)	$m_{\mathcal{H}_1}$ (GeV/c^2)	(a)	(b)	(c)
12	0.0204	0.0154	0.0925	66	0.0236	0.0218	0.0287
14	0.0176	0.0143	0.0899	68	0.0236	0.0218	0.0287
16	0.0158	0.0134	0.0923	70	0.0271	0.0246	0.0287
18	0.0150	0.0131	0.0933	72	0.0291	0.0274	0.0271
20	0.0156	0.0139	0.1060	74	0.0320	0.0301	0.0297
22	0.0177	0.0156	0.1080	76	0.0421	0.0380	0.0351
24	0.0194	0.0174	0.1110	78	0.0469	0.0424	0.0350
26	0.0207	0.0186	0.1140	80	0.0435	0.0410	0.0316
28	0.0223	0.0195	0.1110	82	0.0467	0.0475	0.0281
30	0.0203	0.0181	0.0893	84	0.0539	0.0585	0.0222
32	0.0193	0.0173	0.0796	86	0.0762	0.0816	0.0257
34	0.0191	0.0172	0.0682	88	0.112	0.118	0.0296
36	0.0241	0.0187	0.0653	90	0.153	0.152	0.0331
38	0.0299	0.0235	0.0634	92	0.179	0.175	0.0354
40	0.0333	0.0267	0.0615	94	0.229	0.214	0.0491
42	0.0367	0.0297	0.0599	96	0.239	0.220	0.0570
44	0.0378	0.0310	0.0594	98	0.256	0.233	0.0565
46	0.0387	0.0328	0.0572	100	0.244	0.216	0.0582
48	0.0391	0.0337	0.0575	102	0.237	0.216	0.0588
50	0.0363	0.0316	0.0445	104	0.255	0.227	0.0704
52	0.0386	0.0344	0.0454	106	0.263	0.223	0.0896
54	0.0387	0.0349	0.0464	108	0.266	0.227	0.110
56	0.0384	0.0360	0.0403	110	0.297	0.244	0.144
58	0.0390	0.0367	0.0427	112	0.435	0.343	0.212
60	0.0398	0.0365	0.0456	114	0.824	0.640	0.410
62	0.0293	0.0264	0.0444	116	1.41	1.79	1.79
64	0.0278	0.0258	0.0394				

Table 15. The 95% CL upper bound, S_{95}, obtained for the normalised cross-section (see text) of the Higgsstrahlung cascade process $e^+e^- \to (\mathcal{H}_2 \to \mathcal{H}_1\mathcal{H}_1)Z \to (b\bar{b}b\bar{b})Z$, as a function of the Higgs boson masses $m_{\mathcal{H}_1}$ and $m_{\mathcal{H}_2}$. The numbers correspond to the contours shown in Fig. 3a

$m_{\mathcal{H}_2}$(GeV/c^2)	$m_{\mathcal{H}_1}$(GeV/c^2)									
	10	15	20	25	30	35	40	45	50	55
20	0.020									
25	0.026									
30	0.037	0.046								
35	0.048	0.042								
40	0.053	0.056	0.051							
45	0.066	0.059	0.046							
50	0.087	0.058	0.048	0.049						
55	0.11	0.055	0.050	0.050						
60	0.29	0.103	0.094	0.094	0.053					
65	0.30	0.099	0.091	0.088	0.084					
70	0.25	0.098	0.097	0.095	0.083	0.059				
75	0.34	0.11	0.10	0.11	0.10	0.096				
80	0.39	0.13	0.14	0.14	0.13	0.12	0.13			
85	0.52	0.20	0.20	0.20	0.21	0.19	0.18			
90	≥ 1	0.23	0.23	0.23	0.27	0.26	0.24	0.28		
95	≥ 1	0.29	0.27	0.29	0.31	0.29	0.28	0.30		
100	≥ 1	0.30	0.29	0.31	0.30	0.27	0.28	0.29	0.29	
105	≥ 1	0.27	0.32	0.36	0.40	0.36	0.31	0.35	0.35	
110	≥ 1	0.44	0.54	0.55	0.96	0.97	≥ 1	≥ 1	0.89	≥ 1

Table 16. The 95% CL upper bound, S_{95}, obtained for the normalised cross-section (see text) of the Higgsstrahlung cascade process $e^+e^- \to (\mathcal{H}_2 \to \mathcal{H}_1\mathcal{H}_1)Z \to (\tau^+\tau^-\tau^+\tau^-)Z$, as a function of the Higgs boson masses $m_{\mathcal{H}_1}$ and $m_{\mathcal{H}_2}$. The numbers correspond to the contours shown in Fig. 3b

	5	10	15	20	25	30	35	40	45
10	0.26								
15	0.033								
20	0.048	0.32							
25	0.070	0.076							
30	0.10	0.11	0.38						
35	0.18	0.19	0.51						
40	0.22	0.22	0.40	0.39					
45	0.30	0.31	0.49	0.49					
50	0.18	0.38	0.66	0.66	0.63				
55	0.18	0.37	0.68	0.69	0.68				
60	0.20	0.38	0.95	0.96	0.96	0.94			
65	0.20	0.38	≥ 1	≥ 1	≥ 1	≥ 1			
70	0.21	0.43	≥ 1	≥ 1	≥ 1	≥ 1	≥ 1		
75	0.19	0.46	≥ 1	≥ 1	≥ 1	≥ 1	≥ 1		
80	0.20	0.44	0.83	0.83	0.83	0.83	0.84	0.84	
85	0.25	0.56	≥ 1	≥ 1	≥ 1	≥ 1	≥ 1	≥ 1	

Table 17. The 95% CL upper bound, S_{95}, obtained for the normalised cross-section (see text) of the pair production process $e^+e^- \to \mathcal{H}_2\mathcal{H}_1$, as a function of the Higgs boson mass sum $m_{\mathcal{H}_1} + m_{\mathcal{H}_2}$. The bounds are given for the particular case where $m_{\mathcal{H}_2}$ and $m_{\mathcal{H}_1}$ are approximately equal. This occurs, for example, in the CP-conserving MSSM scenario m_h-*max* for $\tan\beta$ greater than 10 and small $m_{\mathcal{H}_2}$ ($\equiv m_A$). The numbers listed in this table correspond to the four plots in Fig. 4 (see the corresponding labels). For $m_{\mathcal{H}_1} + m_{\mathcal{H}_2}$ less than 30 GeV/c^2, the bounds are derived from the measured decay width of the Z boson, see Sect. 3.2. Columns labelled (a): the Higgs boson decay branching ratios correspond to the m_h-*max* benchmark scenario with $\tan\beta = 10$, giving 94% for $\mathcal{H}_1 \to b\bar{b}$, 6% for $\mathcal{H}_1 \to \tau^+\tau^-$, 92% for $\mathcal{H}_2 \to b\bar{b}$ and 8% for $\mathcal{H}_2 \to \tau^+\tau^-$; columns (b): both Higgs bosons are assumed to decay exclusively to $b\bar{b}$; columns (c): one Higgs boson is assumed to decay exclusively to $b\bar{b}$only and the other exclusively to $\tau^+\tau^-$; columns (d): both Higgs bosons are assumed to decay exclusively to $\tau^+\tau^-$

$m_{\mathcal{H}_1}+m_{\mathcal{H}_2}$ (GeV/c^2)	(a)	(b)	(c)	(d)	$m_{\mathcal{H}_1}+m_{\mathcal{H}_2}$ (GeV/c^2)	(a)	(b)	(c)	(d)
0	0.0237	0.0237	0.0237	0.0237	105	0.0243	0.0213	0.0354	0.0300
5	0.0238	0.0238	0.0238	0.0238	110	0.0297	0.0250	0.0418	0.0313
10	0.0242	0.0242	0.0242	0.0242	115	0.0472	0.0387	0.0484	0.0332
15	0.0248	0.0248	0.0248	0.0248	120	0.0682	0.0599	0.0409	0.0348
20	0.0255	0.0255	0.0255	0.0255	125	0.0676	0.0542	0.0493	0.0387
25	0.0266	0.0266	0.0266	0.0042	130	0.0688	0.0541	0.0524	0.0429
30	0.0054	0.0054	0.0018	0.0043	135	0.0618	0.0478	0.0571	0.0604
35	0.0044	0.0041	0.0018	0.0043	140	0.0669	0.0524	0.0660	0.0665
40	0.0029	0.0026	0.0021	0.0048	145	0.0600	0.0540	0.0506	0.0739
45	0.0033	0.0030	0.0021	0.0051	150	0.0798	0.0726	0.0591	0.0847
50	0.0036	0.0034	0.0017	0.0055	155	0.0967	0.0895	0.0696	0.0995
55	0.0043	0.0042	0.0016	0.0067	160	0.136	0.125	0.0847	0.118
60	0.0055	0.0057	0.0016	0.0083	165	0.179	0.122	0.175	0.144
65	0.0073	0.0070	0.0010	0.0097	170	0.323	0.237	0.234	0.188
70	0.0097	0.0106	0.0021	0.0117	175	0.352	0.294	0.245	0.269
75	0.0142	0.0163	0.0029	0.0134	180	0.765	0.596	0.408	0.391
80	0.0203	0.0227	0.0043	0.0165	185	0.838	0.702	0.582	0.700
85	0.0357	0.0383	0.0101	0.0198	190	1.04	0.855	0.764	1.07
90	0.0527	0.0522	0.0292	0.0247	195	1.93	1.81	1.10	2.88
95	0.0520	0.0493	0.0400	0.0266	200	6.97	6.47	3.49	5.29
100	0.0298	0.0257	0.0370	0.0283					

Table 18. The 95% CL upper bound, S_{95}, obtained for the normalised cross-section (see text) of the pair production process $e^+e^- \to \mathcal{H}_2\mathcal{H}_1 \to b\bar{b}b\bar{b}$, as a function of the Higgs boson masses $m_{\mathcal{H}_1}$ and $m_{\mathcal{H}_2}$. The numbers correspond to the contours shown in Fig. 5a

$m_{\mathcal{H}_2}$(GeV/c^2)	$m_{\mathcal{H}_1}$(GeV/c^2)								
	10	15	20	25	30	35	40	45	50
15	≥ 1	0.012							
20	≥ 1	0.013	0.010						
25	≥ 1	0.017	0.013	0.011					
30	≥ 1	0.015	0.013	0.012	0.020	0.023			
40	≥ 1	0.016	0.018	0.022	0.028	0.039	0.043		
45	≥ 1	0.029	0.029	0.026	0.037	0.048	0.067	0.041	
50	≥ 1	0.035	0.026	0.042	0.044	0.069	0.043	0.035	0.028
55	≥ 1	0.063	0.056	0.076	0.071	0.058	0.050	0.038	0.030
60	≥ 1	0.075	0.084	0.098	0.051	0.051	0.050	0.044	0.039
65	≥ 1	0.14	0.13	0.10	0.065	0.064	0.070	0.068	0.069
70	≥ 1	0.20	0.16	0.11	0.072	0.074	0.066	0.072	0.071
75	≥ 1	0.23	0.13	0.14	0.076	0.075	0.083	0.066	0.093
80	≥ 1	0.26	0.19	0.12	0.078	0.089	0.072	0.064	0.093
85	≥ 1	0.26	0.17	0.13	0.095	0.080	0.070	0.071	0.10
90	≥ 1	0.18	0.13	0.11	0.073	0.070	0.076	0.081	0.13
95	≥ 1	0.20	0.13	0.095	0.073	0.078	0.081	0.11	0.15
100	≥ 1	0.21	0.12	0.092	0.085	0.091	0.12	0.16	0.18
105	≥ 1	0.16	0.13	0.12	0.11	0.13	0.18	0.20	0.20
110	0.297	0.16	0.14	0.15	0.14	0.17	0.20	0.20	0.19
115	0.338	0.22	0.20	0.20	0.18	0.20	0.21	0.21	0.23
120	0.355	0.28	0.25	0.23	0.22	0.22	0.23	0.27	0.36
125	0.409	0.29	0.26	0.25	0.22	0.25	0.29	0.40	0.51
130	0.494	0.35	0.32	0.32	0.24	0.32	0.46	0.57	0.72
135	0.617	0.44	0.42	0.42	0.36	0.51	0.67	0.84	0.98
140	0.696	0.57	0.53	0.66	0.62	0.83	0.97	≥ 1	≥ 1
145	0.811	0.73	0.80	≥ 1	0.94	≥ 1	≥ 1	≥ 1	≥ 1
	65	70	75	80	85	90	95	100	105
65	0.067								
70	0.082	0.078							
75	0.10	0.10	0.098						
80	0.11	0.11	0.14	0.14					
85	0.12	0.14	0.16	0.15	0.21				
90	0.17	0.16	0.17	0.25	0.24	0.41			
95	0.19	0.21	0.30	0.35	0.44	0.51	0.64		
100	0.21	0.31	0.39	0.42	0.43	0.74	≥ 1	≥ 1	
105	0.32	0.42	0.55	0.53	0.90	≥ 1	≥ 1	≥ 1	≥ 1
110	0.47	0.55	0.63	≥ 1	≥ 1	≥ 1	≥ 1	≥ 1	≥ 1
115	0.56	0.65	≥ 1	≥ 1	≥ 1	≥ 1	≥ 1	≥ 1	≥ 1
120	0.64	≥ 1	≥ 1	≥ 1	≥ 1	≥ 1	≥ 1	≥ 1	≥ 1
125	≥ 1	≥ 1	≥ 1	≥ 1	≥ 1	≥ 1	≥ 1	≥ 1	≥ 1

Table 19. The 95% CL upper bound, S_{95}, obtained for the normalised cross-section (see text) of the pair production process $e^+e^- \to \mathcal{H}_2\mathcal{H}_1 \to \tau^+\tau^-\tau^+\tau^-$, as a function of the Higgs boson masses $m_{\mathcal{H}_1}$ and $m_{\mathcal{H}_2}$. The numbers correspond to the contours shown in Fig. 5b

$m_{\mathcal{H}_2}$(GeV/c^2)	$m_{\mathcal{H}_1}$(GeV/c^2)									
	5	10	15	20	25	30	35	40	45	50
5	0.00041									
10	0.00047	0.00035								
15	0.0036	0.0032	0.0032							
20	0.0033	0.0035	0.0037	0.0040						
25	0.0037	0.0039	0.0043	0.0043	0.0046					
30	0.0052	0.0058	0.0045	0.0047	0.0055	0.0060				
35	0.0060	0.0058	0.0056	0.0065	0.0070	0.0081	0.0084			
40	0.0063	0.0064	0.0071	0.0070	0.0078	0.0092	0.011	0.0099		
45	0.0079	0.0068	0.0066	0.0083	0.0088	0.011	0.011	0.012	0.016	
50	0.0096	0.011	0.0086	0.0089	0.011	0.011	0.015	0.018	0.017	0.018
60	0.013	0.012	0.011	0.014	0.017	0.019	0.022	0.022	0.024	0.024
65	0.015	0.015	0.015	0.016	0.019	0.022	0.023	0.023	0.024	0.026
70	0.019	0.017	0.017	0.021	0.021	0.022	0.023	0.024	0.025	0.033
75	0.023	0.023	0.021	0.023	0.024	0.024	0.025	0.028	0.031	0.035
80	0.028	0.026	0.024	0.025	0.025	0.026	0.030	0.032	0.036	0.041
85	0.032	0.029	0.028	0.027	0.030	0.031	0.032	0.035	0.040	0.043
90	0.033	0.031	0.028	0.030	0.031	0.032	0.035	0.041	0.045	0.049
95	0.037	0.034	0.031	0.034	0.036	0.037	0.041	0.047	0.050	0.054
100	0.040	0.036	0.036	0.037	0.038	0.044	0.048	0.053	0.059	0.062
105	0.045	0.040	0.042	0.043	0.047	0.052	0.055	0.065	0.068	0.072
110	0.051	0.044	0.050	0.053	0.054	0.057	0.062	0.076	0.081	0.085
115	0.055	0.050	0.060	0.065	0.064	0.069	0.074	0.083	0.089	0.105
120	0.067	0.060	0.071	0.075	0.077	0.083	0.085	0.093	0.12	0.145
125	0.075	0.071	0.086	0.084	0.089	0.097	0.109	0.12	0.17	0.198
130	0.085	0.088	0.10	0.10	0.11	0.13	0.14	0.16	0.20	0.317
135	0.11	0.11	0.13	0.15	0.16	0.16	0.19	0.23	0.31	0.436
140	0.14	0.13	0.18	0.19	0.21	0.23	0.26	0.30	0.50	≥ 1
145	0.18	0.18	0.25	0.26	0.28	0.33	0.42	0.59	≥ 1	≥ 1
150	0.25	0.26	0.35	0.37	0.42	0.51	0.69	≥ 1	≥ 1	≥ 1
	55	60	65	70	75	80	85	90	95	100
55	0.021									
60	0.025	0.028								
65	0.030	0.033	0.036							
70	0.033	0.039	0.039	0.042						
75	0.038	0.040	0.044	0.048	0.049					
80	0.043	0.049	0.047	0.051	0.057	0.064				
85	0.048	0.050	0.055	0.061	0.071	0.075	0.097			
90	0.053	0.059	0.065	0.077	0.080	0.10	0.14	0.21		
95	0.059	0.067	0.076	0.080	0.10	0.14	0.21	0.38	0.70	
100	0.069	0.077	0.086	0.11	0.15	0.21	0.39	0.71	≥ 1	≥ 1
105	0.083	0.096	0.11	0.15	0.22	0.39	0.73	≥ 1	≥ 1	≥ 1
110	0.11	0.13	0.16	0.21	0.39	0.76	≥ 1	≥ 1	≥ 1	≥ 1
115	0.14	0.20	0.27	0.36	0.79	≥ 1	≥ 1	≥ 1	≥ 1	≥ 1
120	0.19	0.28	0.49	0.83	≥ 1	≥ 1	≥ 1	≥ 1	≥ 1	≥ 1
125	0.26	0.53	0.65	≥ 1	≥ 1	≥ 1	≥ 1	≥ 1	≥ 1	≥ 1
130	0.46	0.85	≥ 1	≥ 1	≥ 1	≥ 1	≥ 1	≥ 1	≥ 1	≥ 1
135	0.89	≥ 1	≥ 1	≥ 1	≥ 1	≥ 1	≥ 1	≥ 1	≥ 1	≥ 1

Table 20. The 95% CL upper bound, S_{95}, obtained for the normalised cross-section (see text) of the pair production cascade process $e^+e^- \to (\mathcal{H}_2 \to \mathcal{H}_1\mathcal{H}_1)\mathcal{H}_1 \to (b\bar{b}b\bar{b})b\bar{b}$, as a function of the Higgs boson masses $m_{\mathcal{H}_1}$ and $m_{\mathcal{H}_2}$. The numbers correspond to the contours shown in Fig. 6a

$m_{\mathcal{H}_2}$(GeV/c^2)	$m_{\mathcal{H}_1}$(GeV/c^2)										
	10	15	20	25	30	35	40	45	50	55	60
20	≥ 1										
25	0.096										
30	0.11	0.17									
35	0.13	0.075									
40	0.028	0.034	0.19								
45	0.15	0.047	0.034								
50	0.063	0.063	0.029	0.039							
55	0.074	0.087	0.042	0.055							
60	0.11	0.12	0.099	0.086	0.12						
65	0.25	0.17	0.13	0.14	0.13						
70	≥ 1	0.15	0.14	0.13	0.12	0.13					
75	0.72	0.17	0.16	0.14	0.13	0.13					
80	0.99	0.18	0.14	0.11	0.11	0.12	0.13				
85	≥ 1	0.19	0.15	0.13	0.14	0.14	0.16				
90	≥ 1	0.19	0.15	0.15	0.15	0.16	0.15	0.17			
95	≥ 1	0.20	0.17	0.17	0.16	0.15	0.17	0.20			
100	≥ 1	0.22	0.20	0.19	0.18	0.18	0.20	0.23	0.30		
105	≥ 1	0.26	0.22	0.21	0.23	0.24	0.27	0.32	0.38		
110	≥ 1	0.30	0.26	0.27	0.28	0.31	0.36	0.40	0.43	0.55	
115	≥ 1	0.35	0.32	0.33	0.33	0.38	0.43	0.47	0.54	0.70	
120	≥ 1	0.43	0.39	0.39	0.42	0.46	0.50	0.58	0.71	0.93	≥ 1
125	≥ 1	0.53	0.49	0.48	0.51	0.56	0.63	0.77	0.99	≥ 1	≥ 1
130	≥ 1	0.66	0.59	0.62	0.64	0.72	0.86	≥ 1	≥ 1	≥ 1	≥ 1
135	≥ 1	0.82	0.66	0.75	0.84	0.98	≥ 1	≥ 1	≥ 1	≥ 1	≥ 1
140	≥ 1	≥ 1	0.90	0.96	0.98	≥ 1	≥ 1	≥ 1	≥ 1	≥ 1	≥ 1

Table 21. The 95% CL upper bound, S_{95}, obtained for the normalised cross-section (see text) of the pair production cascade process $e^+e^- \to (\mathcal{H}_2 \to \mathcal{H}_1\mathcal{H}_1)\mathcal{H}_1 \to (\tau^+\tau^-\tau^+\tau^-)\tau^+\tau^-$, as a function of the Higgs boson masses $m_{\mathcal{H}_1}$ and $m_{\mathcal{H}_2}$. The numbers correspond to the contours shown in Fig. 6b

$m_{\mathcal{H}_2}$(GeV/c^2)	$m_{\mathcal{H}_1}$(GeV/c^2)			
	5	10	15	20
10	0.0006			
15	0.0016			
20	0.0017	0.011		
25	0.0018	0.0019		
30	0.0021	0.0021	0.013	
35	0.0024	0.0025	0.017	
40	0.0009	0.0016	≥ 1	≥ 1
45	0.0010	0.0019	≥ 1	≥ 1
50	0.0013	0.0023	≥ 1	≥ 1
55	0.0017	0.0029	≥ 1	≥ 1
60	0.0024	0.0043	≥ 1	≥ 1
65	0.0058	0.014	≥ 1	≥ 1

ing from the Higgsstrahlung processes $e^+e^- \to \mathcal{H}_1 Z$ and $e^+e^- \to (\mathcal{H}_2 \to \mathcal{H}_1\mathcal{H}_1)Z$; Tables 18 to 21 refer to those arising from the pair production processes $e^+e^- \to \mathcal{H}_2\mathcal{H}_1$ and $e^+e^- \to (\mathcal{H}_2 \to \mathcal{H}_1\mathcal{H}_1)\mathcal{H}_1$. The corresponding figures, showing the same results, are mentioned in the table captions.

References

1. P.W. Higgs, Phys. Lett. **12**, 132 (1964); Phys. Rev. Lett. **13**, 508 (1964); Phys. Rev. **145**, 1156 (1966); F. Englert, R. Brout, Phys. Rev. Lett. **13**, 321 (1964); G.S. Guralnik, C.R. Hagen, T.W.B. Kibble, Phys. Rev. Lett. **13**, 585 (1964).
2. S. Weinberg, Phys. Rev. Lett. **19**, 1264 (1967); A. Salam, Elementary Particle Theory, ed. by N. Svartholm (Almquist and Wiksells, Stockholm, 1968), 367
3. ALEPH, DELPHI, L3 and OPAL Collaborations, The LEP Working Group for Higgs Boson Searches, Phys. Lett. B **565**, 61 (2003)
4. J. Wess, B. Zumino, Nucl. Phys. B **70**, 39 (1974); Phys. Lett. B **49**, 52 (1974); P. Fayet, Phys. Lett. B **69**, 489 (1977); Phys. Lett. B **84**, 421 (1979); Phys. Lett. B **86**, 272 (1979)
5. W. de Boer, C. Sander, Phys. Lett. B **585**, 276 (2004); J.R. Ellis, S. Heinemeyer, K. Olive, G. Weiglein, JHEP **0502**, 13 (2005); S. Heinemeyer, W. Hollik, G. Weiglein, hep-ph/0412214
6. H.E. Haber, G.L. Kane, Phys. Rep. C **117**, 75 (1985); J.F. Gunion, H.E. Haber, G.L. Kane, S. Dawson, The Higgs Hunter's Guide (Addison-Wesley, 1990); H.E. Haber, Supersymmetry, Phys. Rev. D **66**, 010 001-895 (2002); A. Djouadi, The Anatomy of Electro-Weak Symmetry Breaking, Tome II: The Higgs boson in the Minimal Supersymmetric Model, hep-ph/0503173
7. Y. Okada, M. Yamaguchi, T. Yanagida, Theor. Phys. **85**, 1 (1991); H. Haber, R. Hempfling, Phys. Rev. Lett. **66**, 1815

(1991); J. Ellis, G. Ridolfi, F. Zwirner, Phys. Lett. B **257**, 83 (1991); R. Barbieri, M. Frigeni, Phys. Lett. B **258**, 395 (1991); M. Carena, M. Quiros, C.E.M. Wagner, Nucl. Phys. B **461**, 407 (1996); H. Haber, R. Hempfling, A. Hoang, Z. Phys. C **75**, 539 (1997); S. Heinemeyer, W. Hollik, G. Weiglein, Eur. Phys. J. C **9**, 343 (1999); Phys. Rev. D **58**, 091 701 (1998); Phys. Lett. B **440**, 296 (1998); JHEP **0006**, 009 (2000); J.R. Espinosa, R.-J. Zhang, Nucl. Phys. B **586**, 3 (2000); A. Brignole, G. Degrassi, P. Slavich, F. Zwirner, Nucl. Phys. B **631**, 195 (2002); G. Degrassi, S. Heinemeyer, W. Hollik, P. Slavich, G. Weiglein, Eur. Phys. J. C **28**, 133 (2003)

8. A.D. Sakharov, JETP Lett. **5**, 24 (1967); A. Pilaftsis, Phys. Rev. D **58**, 096 010 (1998); Phys. Lett. B **435**, 88 (1998)
9. D. Demir, Phys. Rev. D **60**, 055 006 (1999); A. Pilaftsis, C. Wagner, Nucl. Phys. B **553**, 3 (1999); S. Choi, M. Drees, J. Lee, Phys. Lett. B **481**, 57 (2000); M. Carena, J. Ellis, A. Pilaftsis, C. Wagner, Nucl. Phys. B **586**, 92 (2000); M. Carena et al., Nucl. Phys. B **599**, 158 (2001); S. Heinemeyer, Eur. Phys. J. C **22**, 521 (2001); T. Ibrahim, P. Nath, Phys. Rev. D **63**, 035 009 (2001); Phys. Rev. D **66**, 015 005 (2002); M. Frank, S. Heinemeyer, W. Hollik, G. Weiglein, hep-ph/0212037, Proceedings, SUSY02, DESY, Hamburg (Germany), July 2002, Vol. 2, p. 637
10. OPAL Collaboration, G. Abbiendi et al., Eur. Phys. J. C **37**, 49 (2004)
11. ALEPH Collaboration, Phys. Lett. B **526**, 191 (2002)
12. DELPHI Collaboration, J. Abdallah et al., Eur. Phys. J. C **32**, 145 (2004); DELPHI 2005-020-CONF-740, paper in preparation
13. L3 Collaboration, P. Achard et al., Phys. Lett. B **545**, 30 (2002)
14. D.E. Groom et al., Eur. Phys. J. C **15**, 1 (2000)
15. The CDF and D0 Collaborations, and the Tevatron Electroweak Working Group, hep-ex/0507091 (July 2005)
16. M. Carena, S. Heinemeyer, C.E.M. Wagner, G. Weiglein, hep-ph/9912223; Eur. Phys. J. C **26**, 601 (2003)
17. S. Heinemeyer, W. Hollik, G. Weiglein, Comput. Phys. Commun. **124**, 76 (2000); S. Heinemeyer, hep-ph/0407244; M. Frank, T. Hahn, S. Heinemeyer, W. Hollik, H. Rzehak, G. Weiglein, in preparation. The code is accessible via http://www.feynhiggs.de
18. M. Carena, J.R. Ellis, A. Pilaftsis, C.E. Wagner, Phys. Lett. B **495**, 155 (2000); Nucl. Phys. B **586**, 92 (2000)
19. M. Carena, M. Quirós, C.E.M. Wagner, Nucl. Phys. B **461**, 407 (1996); M. Carena, S. Mrenna, C. Wagner, Phys. Rev. D **60**, 075 010 (1999); M. Carena, H.E. Haber, S. Heinemeyer, W. Hollik, C.E.M. Wagner, G. Weiglein, Nucl. Phys. B **580**, 29 (2000); J.R. Espinosa, R.-J. Zhang, JHEP **0003**, 026 (2000)
20. J.S. Lee, A. Pilaftsis, M. Carena, S.Y. Choi, M. Drees, J.R. Ellis, C.E.M. Wagner, Comput. Phys. Commun. **156**, 283 (2004)
21. P. Janot, Physics at LEP2, ed. by G. Altarelli, T. Sjöstrand, F. Zwirner, CERN 96-01 Vol. 2, p. 309.
22. S. Heinemeyer, W. Hollik, Nucl. Phys. B **474**, 32 (1996)
23. G.W. Bennett et al., Phys. Rev. Lett. **92**, 161 802 (2004); M. Davier, W. Marciano, Ann. Rev. Nucl. Part. Sci. **54**, 115 (2004)
24. T. Moroi, Phys. Rev. D **53**, 6565 (1996); [Erratum: Phys. Rev. D **56**, 4424 (1997)]
25. ALEPH Collaboration, R. Barate et al., , Phys. Lett. B **429**, 169 (1998); CLEO Collaboration, T.E. Coan et al., Phys. Rev. Lett. **84**, 5283 (2000); CLEO Collaboration, S. Chen et al., Phys. Rev. Lett. **87**, 251 807 (2001); BELLE Collaboration, K. Abe et al., Phys. Lett. B **511**, 151 (2001); BABAR Collaboration, B. Aubert et al., Phys. Rev. Lett. **88**, 101 815 (2002); BABAR Collaboration, B. Aubert et al., hep-ex/0407003, submitted to Phys. Rev. Lett. (2004); BELLE Collaboration, M. Nakao et al., Phys. Rev. D **69**, 112 001 (2004); A.L. Kagan, M. Neubert, Phys. Rev. D **58**, 094 012 (1998); Phys. Lett. B **539**, 227 (2002)
26. E.D. Commins, S.B. Ross, D. DeMille, B.C. Regan, Phys. Rev. A **50**, 2960 (1994); P.G. Harris et al., Phys. Rev. Lett. **82**, 904 (1999)
27. ALEPH, DELPHI, L3, OPAL and SLD Collaborations, LEP Electroweak Working Group, SLD Electroweak and Heavy Flavour Groups, CERN-PH-EP/2005-041, Phys. Rep. **427**, 257–454 (2006) [hep-ex/0509008]
28. OPAL Collaboration, G. Abbiendi et al., Eur. Phys. J. C **27**, 311 (2003)
29. OPAL Collaboration, G. Abbiendi et al., Eur. Phys. J. C **23**, 397 (2002)
30. T. Junk, Nucl. Instrum. Methods Phys. Res. A **434**, 435 (1999); A. Read, In: 1st Workshop on Confidence Limits, CERN-2000-005; P. Bock, hep-ex/0405072 (2004)
31. K. Hagiwara et al., Phys. Rev. D **66**, 010001-1 (2002), Review No. 31 on Statistics, p. 229
32. ALEPH Collaboration, Eur. Phys. J. C **17**, 223 (2000)
33. ALEPH Collaboration, Phys. Lett. B **499**, 53 (2001)
34. ALEPH Collaboration, Phys. Lett. B **495**, 1 (2000)
35. ALEPH Collaboration, Phys. Lett. B **544**, 25 (2002)
36. DELPHI Collaboration, P. Abreu et al., Z. Phys. C **51**, 25 (1991)
37. DELPHI Collaboration, P. Abreu et al., Nucl. Phys. B **342**, 1 (1990)
38. DELPHI Collaboration, P. Abreu et al., Nucl. Phys. B **373**, 3 (1992)
39. DELPHI Collaboration, P. Abreu et al., Nucl. Phys. B **421**, 3 (1994)
40. DELPHI Collaboration, P. Abreu et al., Eur. Phys. J. C **2**, 1 (1998)
41. DELPHI Collaboration, P. Abreu et al., Eur. Phys. J. C **10**, 563 (1999)
42. DELPHI Collaboration, P. Abreu et al., Eur. Phys. J. C **17**, 187 (2000); [Addendum: Eur. Phys. J. C **17**, 529 (2000)]
43. DELPHI Collaboration, J. Abdallah et al., Eur. Phys. J. C **32**, 145 (2004)
44. DELPHI Collaboration, J. Abdallah et al., Eur. Phys. J. C **23**, 409 (2002)
45. DELPHI Collaboration, J. Abdallah et al., Eur. Phys. J. C **44**, 147 (2005)
46. DELPHI 92-80 Dallas PHYS 191, Neutral Higgs Bosons in a Two Doublet Model, contribution to the 1992 ICHEP conference; quoted by G. Wormser, In: Proc. of the XXVI ICHEP conference (Dallas, August 1992), Vol. 2, pages 1309–14, ref. 4
47. DELPHI 2003-045-CONF-665, DELPHI results on neutral Higgs bosons in MSSM benchmark scenarios, contribution to the 2003 summer conferences
48. S. Dagoret, PhD Thesis, Université de Paris-Sud, Centre d'Orsay, LAL-preprint 91-12 (May 1991)
49. DELPHI Collaboration, P. Abreu et al., Phys. Lett B **245**, 276 (1990)

50. DELPHI Collaboration, J. Abdallah et al., Eur. Phys. J. C **38**, 1 (2004)
51. DELPHI Collaboration, P. Abreu et al., Z. Phys. C **67**, 69 (1995)
52. L3 Collaboration, M. Acciarri et al., Phys. Lett. B **461**, 376 (1999)
53. L3 Collaboration, M. Acciarri et al., Phys. Lett. B **508**, 225 (2001)
54. L3 Collaboration, P. Achard et al., Phys. Lett. B **517**, 319 (2001)
55. L3 Collaboration, P. Achard et al., Phys. Lett. B **583**, 14 (2004)
56. L3 Collaboration, P. Achard et al., Phys. Lett. B **545**, 30 (2002)
57. L3 Collaboration, M. Acciarri et al., Phys. Lett. B **471**, 321 (1999)
58. L3 Collaboration, M. Acciarri et al., Phys. Lett. B **503**, 21 (2001)
59. OPAL Collaboration, K. Ackerstaff et al., Eur. Phys. J. C **1**, 425 (1998)
60. OPAL Collaboration, K. Ackerstaff et al., Eur. Phys. J. C **5**, 19 (1998)
61. OPAL Collaboration, G. Abbiendi et al., Eur. Phys. J. C **7**, 407 (1999)
62. OPAL Collaboration, G. Abbiendi et al., Eur. Phys. J. C **12**, 567 (2000)
63. OPAL Collaboration, G. Abbiendi et al., Eur. Phys. J. C **26**, 479 (2003)
64. OPAL Collaboration, G. Alexander et al., Z. Phys. C **73**, 189 (1997)
65. OPAL Collaboration, R. Akers et al., Z. Phys. C **64**, 1 (1994)
66. OPAL Collaboration, G. Abbiendi et al., Eur. Phys. J. C **18**, 425 (2001)
67. OPAL Collaboration, G. Abbiendi et al., Phys. Lett. B **594**, 11 (2004)
68. OPAL Collaboration, G. Abbiendi et al., Eur. Phys. J. C **27**, 483 (2003)
69. OPAL Collaboration, G. Abbiendi et al., Eur. Phys. J. C **40**, 317 (2005)

Eur. Phys. J. C 55, 1–38 (2008)
DOI 10.1140/epjc/s10052-008-0585-7

THE EUROPEAN PHYSICAL JOURNAL C

Regular Article – Experimental Physics

Measurement of the mass and width of the W boson in e^+e^- collisions at $\sqrt{s} = 161$–$209\,\mathrm{GeV}$

This paper is dedicated to the memory of Carlo Caso.

The DELPHI Collaboration

J. Abdallah[26], P. Abreu[23], W. Adam[55], P. Adzic[12], T. Albrecht[18], R. Alemany-Fernandez[9], T. Allmendinger[18], P.P. Allport[24], U. Amaldi[30], N. Amapane[48], S. Amato[52], E. Anashkin[37], A. Andreazza[29], S. Andringa[23], N. Anjos[23], P. Antilogus[26], W-D. Apel[18], Y. Arnoud[15], S. Ask[9], B. Asman[47], J.E. Augustin[26], A. Augustinus[9], P. Baillon[9], A. Ballestrero[49], P. Bambade[21], R. Barbier[28], D. Bardin[17], G.J. Barker[57], A. Baroncelli[40], M. Battaglia[9], M. Baubillier[26], K-H. Becks[58], M. Begalli[7], A. Behrmann[58], E. Ben-Haim[21], N. Benekos[33], A. Benvenuti[5], C. Berat[15], M. Berggren[26], D. Bertrand[2], M. Besancon[41], N. Besson[41], D. Bloch[10], M. Blom[32], M. Bluj[56], M. Bonesini[30], M. Boonekamp[41], P.S.L. Booth[24,†], G. Borisov[22], O. Botner[53], B. Bouquet[21], T.J.V. Bowcock[24], I. Boyko[17], M. Bracko[44], R. Brenner[53], E. Brodet[36], P. Bruckman[19], J.M. Brunet[8], B. Buschbeck[55], P. Buschmann[58], M. Calvi[30], T. Camporesi[9], V. Canale[39], F. Carena[9], N. Castro[23], F. Cavallo[5], M. Chapkin[43], Ph. Charpentier[9], P. Checchia[37], R. Chierici[9], P. Chliapnikov[43], J. Chudoba[9], S.U. Chung[9], K. Cieslik[19], P. Collins[9], R. Contri[14], G. Cosme[21], F. Cossutti[50], M.J. Costa[54], D. Crennell[38], J. Cuevas[35], J. D'Hondt[2], T. da Silva[52], W. Da Silva[26], G. Della Ricca[50], A. De Angelis[51], W. De Boer[18], C. De Clercq[2], B. De Lotto[51], N. De Maria[48], A. De Min[37], L. de Paula[52], L. Di Ciaccio[39], A. Di Simone[40], K. Doroba[56], J. Drees[58,9], A. Duperrin[28], G. Eigen[4], T. Ekelof[53], M. Ellert[53], M. Elsing[9], M.C. Espirito Santo[23], G. Fanourakis[12], D. Fassouliotis[12,3], M. Feindt[18], J. Fernandez[42], A. Ferrer[54], F. Ferro[14], U. Flagmeyer[58], H. Foeth[9], E. Fokitis[33], F. Fulda-Quenzer[21], J. Fuster[54], M. Gandelman[52], C. Garcia[54], Ph. Gavillet[9], E. Gazis[33], R. Gokieli[9,56], B. Golob[44,46], G. Gomez-Ceballos[42], P. Goncalves[23], E. Graziani[40], G. Grosdidier[21], K. Grzelak[56], J. Guy[38], C. Haag[18], A. Hallgren[53], K. Hamacher[58], K. Hamilton[36], S. Haug[34], F. Hauler[18], V. Hedberg[27], M. Hennecke[18], J. Hoffman[56], S-O. Holmgren[47], P.J. Holt[9], M.A. Houlden[24], J.N. Jackson[24], G. Jarlskog[27], P. Jarry[41], D. Jeans[36], E.K. Johansson[47], P. Jonsson[28], C. Joram[9], L. Jungermann[18], F. Kapusta[26], S. Katsanevas[28], E. Katsoufis[33], G. Kernel[44], B.P. Kersevan[44,46], U. Kerzel[18], B.T. King[24], N.J. Kjaer[9], P. Kluit[32], P. Kokkinias[12], C. Kourkoumelis[3], O. Kouznetsov[17], Z. Krumstein[17], M. Kucharczyk[19], J. Lamsa[1], G. Leder[55], F. Ledroit[15], L. Leinonen[47], R. Leitner[31], J. Lemonne[2], V. Lepeltier[21], T. Lesiak[19], W. Liebig[58], D. Liko[55], A. Lipniacka[47], J.H. Lopes[52], J.M. Lopez[35], D. Loukas[12], P. Lutz[41], L. Lyons[36], J. MacNaughton[55], A. Malek[58], S. Maltezos[33], F. Mandl[55], J. Marco[42], R. Marco[42], B. Marechal[52], M. Margoni[37], J-C. Marin[9], C. Mariotti[9], A. Markou[12], C. Martinez-Rivero[42], J. Masik[13], N. Mastroyiannopoulos[12], F. Matorras[42], C. Matteuzzi[30], F. Mazzucato[37], M. Mazzucato[37], R. Mc Nulty[24], C. Meroni[29], E. Migliore[48], W. Mitaroff[55], U. Mjoernmark[27], T. Moa[47], M. Moch[18], K. Moenig[9,11], R. Monge[14], J. Montenegro[32], D. Moraes[52], S. Moreno[23], P. Morettini[14], U. Mueller[58], K. Muenich[58], M. Mulders[32], L. Mundim[7], W. Murray[38], B. Muryn[20], G. Myatt[36], T. Myklebust[34], M. Nassiakou[12], F. Navarria[5], K. Nawrocki[56], R. Nicolaidou[41], M. Nikolenko[17,10], A. Oblakowska-Mucha[20], V. Obraztsov[43], A. Olshevski[17], A. Onofre[23], R. Orava[16], K. Osterberg[16], A. Ouraou[41], A. Oyanguren[54], M. Paganoni[30], S. Paiano[5], J.P. Palacios[24], H. Palka[19], Th.D. Papadopoulou[33], L. Pape[9], C. Parkes[25], F. Parodi[14], U. Parzefall[9], A. Passeri[40], O. Passon[58], L. Peralta[23], V. Perepelitsa[54], A. Perrotta[5], A. Petrolini[14], J. Piedra[42], L. Pieri[40], F. Pierre[41], M. Pimenta[23], E. Piotto[9], T. Podobnik[44,46], V. Poireau[9], M.E. Pol[6], G. Polok[19], V. Pozdniakov[17], N. Pukhaeva[17], A. Pullia[30], D. Radojicic[36], J. Rames[13], A. Read[34], P. Rebecchi[9], J. Rehn[18], D. Reid[32], R. Reinhardt[58], P. Renton[36], F. Richard[21], J. Ridky[13], M. Rivero[42], D. Rodriguez[42], A. Romero[48], P. Ronchese[37], P. Roudeau[21], T. Rovelli[5], V. Ruhlmann-Kleider[41], D. Ryabtchikov[43], A. Sadovsky[17], L. Salmi[16], J. Salt[54], C. Sander[18], A. Savoy-Navarro[26], U. Schwickerath[9], R. Sekulin[38], M. Siebel[58], L. Simard[41], A. Sisakian[17], G. Smadja[28], O. Smirnova[27], A. Sokolov[43], A. Sopczak[22], R. Sosnowski[56], T. Spassov[9], M. Stanitzki[18], A. Stocchi[21], J. Strauss[55], B. Stugu[4], M. Szczekowski[56], M. Szeptycka[56], T. Szumlak[20], T. Tabarelli[30], F. Tegenfeldt[53], J. Thomas[36], J. Timmermans[32,a], L. Tkatchev[17], M. Tobin[24], S. Todorovova[13], B. Tome[23], A. Tonazzo[30], P. Tortosa[54], P. Travnicek[13], D. Treille[9], G. Tristram[8], M. Trochimczuk[56], C. Troncon[29], M-L. Turluer[41], I.A. Tyapkin[17], P. Tyapkin[17], S. Tzamarias[12], V. Uvarov[43], G. Valenti[5], P. Van Dam[32], J. Van Eldik[9], N. van Remortel[16], I. Van Vulpen[9], G. Vegni[29], F. Veloso[23], W. Venus[38], P. Verdier[28], V. Verzi[39], D. Vilanova[41], L. Vitale[50], V. Vrba[13], H. Wahlen[58], A.J. Washbrook[24], C. Weiser[18], D. Wicke[9], J. Wickens[2], G. Wilkinson[36], M. Winter[10], M. Witek[19], O. Yushchenko[43], A. Zalewska[19], P. Zalewski[56], D. Zavrtanik[45], V. Zhuravlov[17], N.I. Zimin[17], A. Zintchenko[17], M. Zupan[12]

† deceased

[1] Department of Physics and Astronomy, Iowa State University, Ames IA 50011-3160, USA
[2] IIHE, ULB-VUB, Pleinlaan 2, 1050 Brussels, Belgium
[3] Physics Laboratory, University of Athens, Solonos Str. 104, 10680 Athens, Greece
[4] Department of Physics, University of Bergen, Allégaten 55, 5007 Bergen, Norway
[5] Dipartimento di Fisica, Università di Bologna and INFN, Via Irnerio 46, 40126 Bologna, Italy
[6] Centro Brasileiro de Pesquisas Físicas, rua Xavier Sigaud 150, 22290 Rio de Janeiro, Brazil
[7] Inst. de Física, Univ. Estadual do Rio de Janeiro, rua São Francisco Xavier 524, Rio de Janeiro, Brazil
[8] Collège de France, Lab. de Physique Corpusculaire, IN2P3 – CNRS, 75231 Paris Cedex 05, France
[9] CERN, 1211 Geneva 23, Switzerland
[10] Institut de Recherches Subatomiques, IN2P3 – CNRS/ULP – BP20, 67037 Strasbourg Cedex, France
[11] Now at DESY-Zeuthen, Platanenallee 6, 15735 Zeuthen, Germany
[12] Institute of Nuclear Physics, N.C.S.R. Demokritos, P.O. Box 60228, 15310 Athens, Greece
[13] FZU, Inst. of Phys. of the C.A.S. High Energy Physics Division, Na Slovance 2, 182 21 Praha 8, Czech Republic
[14] Dipartimento di Fisica, Università di Genova and INFN, Via Dodecaneso 33, 16146 Genova, Italy
[15] Institut des Sciences Nucléaires, IN2P3 – CNRS, Université de Grenoble 1, 38026 Grenoble Cedex, France
[16] Helsinki Institute of Physics and Department of Physical Sciences, P.O. Box 64, 00014 University of Helsinki, Finland
[17] Joint Institute for Nuclear Research, Dubna, Head Post Office, P.O. Box 79, 101 000 Moscow, Russian Federation
[18] Institut für Experimentelle Kernphysik, Universität Karlsruhe, Postfach 6980, 76128 Karlsruhe, Germany
[19] Institute of Nuclear Physics PAN, Ul. Radzikowskiego 152, 31142 Krakow, Poland
[20] Faculty of Physics and Nuclear Techniques, University of Mining and Metallurgy, 30055 Krakow, Poland
[21] Université de Paris-Sud, Lab. de l'Accélérateur Linéaire, IN2P3 – CNRS, Bât. 200, 91405 Orsay Cedex, France
[22] School of Physics and Chemistry, University of Lancaster, Lancaster LA1 4YB, UK
[23] LIP, IST, FCUL – Av. Elias Garcia, 14-1^{o}, 1000 Lisboa Codex, Portugal
[24] Department of Physics, University of Liverpool, P.O. Box 147, Liverpool L69 3BX, UK
[25] Dept. of Physics and Astronomy, Kelvin Building, University of Glasgow, Glasgow G12 8QQ, UK
[26] LPNHE, IN2P3 – CNRS, Univ. Paris VI et VII, Tour 33 (RdC), 4 place Jussieu, 75252 Paris Cedex 05, France
[27] Department of Physics, University of Lund, Sölvegatan 14, 223 63 Lund, Sweden
[28] Université Claude Bernard de Lyon, IPNL, IN2P3 – CNRS, 69622 Villeurbanne Cedex, France
[29] Dipartimento di Fisica, Università di Milano and INFN-MILANO, Via Celoria 16, 20133 Milan, Italy
[30] Dipartimento di Fisica, Univ. di Milano-Bicocca and INFN-MILANO, Piazza della Scienza 3, 20126 Milan, Italy
[31] IPNP of MFF, Charles Univ., Areal MFF, V Holesovickach 2, 180 00 Praha 8, Czech Republic
[32] NIKHEF, Postbus 41882, 1009 DB Amsterdam, The Netherlands
[33] National Technical University, Physics Department, Zografou Campus, 15773 Athens, Greece
[34] Physics Department, University of Oslo, Blindern, 0316 Oslo, Norway
[35] Dpto. Fisica, Univ. Oviedo, Avda. Calvo Sotelo s/n, 33007 Oviedo, Spain
[36] Department of Physics, University of Oxford, Keble Road, Oxford OX1 3RH, UK
[37] Dipartimento di Fisica, Università di Padova and INFN, Via Marzolo 8, 35131 Padua, Italy
[38] Rutherford Appleton Laboratory, Chilton, Didcot OX11 OQX, UK
[39] Dipartimento di Fisica, Università di Roma II and INFN, Tor Vergata, 00173 Rome, Italy
[40] Dipartimento di Fisica, Università di Roma III and INFN, Via della Vasca Navale 84, 00146 Rome, Italy
[41] DAPNIA/Service de Physique des Particules, CEA-Saclay, 91191 Gif-sur-Yvette Cedex, France
[42] Instituto de Fisica de Cantabria (CSIC-UC), Avda. los Castros s/n, 39006 Santander, Spain
[43] Inst. for High Energy Physics, Serpukov P.O. Box 35, Protvino, (Moscow Region), Russian Federation
[44] J. Stefan Institute, Jamova 39, 1000 Ljubljana, Slovenia
[45] Laboratory for Astroparticle Physics, University of Nova Gorica, Kostanjeviska 16a, 5000 Nova Gorica, Slovenia
[46] Department of Physics, University of Ljubljana, 1000 Ljubljana, Slovenia
[47] Fysikum, Stockholm University, Box 6730, 113 85 Stockholm, Sweden
[48] Dipartimento di Fisica Sperimentale, Università di Torino and INFN, Via P. Giuria 1, 10125 Turin, Italy
[49] INFN, Sezione di Torino and Dipartimento di Fisica Teorica, Università di Torino, Via Giuria 1, 10125 Turin, Italy
[50] Dipartimento di Fisica, Università di Trieste and INFN, Via A. Valerio 2, 34127 Trieste, Italy
[51] Istituto di Fisica, Università di Udine and INFN, 33100 Udine, Italy
[52] Univ. Federal do Rio de Janeiro, C.P. 68528 Cidade Univ., Ilha do Fundão 21945-970 Rio de Janeiro, Brazil
[53] Department of Radiation Sciences, University of Uppsala, P.O. Box 535, 751 21 Uppsala, Sweden
[54] IFIC, Valencia-CSIC, and D.F.A.M.N., U. de Valencia, Avda. Dr. Moliner 50, 46100 Burjassot (Valencia), Spain
[55] Institut für Hochenergiephysik, Österr. Akad. d. Wissensch., Nikolsdorfergasse 18, 1050 Vienna, Austria
[56] Inst. Nuclear Studies and University of Warsaw, Ul. Hoza 69, 00681 Warsaw, Poland
[57] Now at University of Warwick, Coventry CV4 7AL, UK
[58] Fachbereich Physik, University of Wuppertal, Postfach 100 127, 42097 Wuppertal, Germany

Received: 12 July 2007 / Revised version: 12 March 2008 /
Published online: 22 April 2008 –

Abstract. A measurement of the W boson mass and width has been performed by the DELPHI collaboration using the data collected during the full LEP2 programme (1996–2000). The data sample has an integrated luminosity of 660 pb^{-1} and was collected over a range of centre-of-mass energies from 161 to 209 GeV.
Results are obtained by applying the method of direct reconstruction of the mass of the W from its decay products in both the $W^+W^- \to \ell\overline{\nu}_\ell q\bar{q}'$ and $W^+W^- \to q\bar{q}'\bar{q}q'$ channels. The W mass result for the combined data set is

$$M_W = 80.336 \pm 0.055(\mathrm{Stat.}) \pm 0.028(\mathrm{Syst.}) \pm 0.025(\mathrm{FSI}) \pm 0.009(\mathrm{LEP})\ \mathrm{GeV}/c^2\,,$$

where FSI represents the uncertainty due to final state interaction effects in the $q\bar{q}'\bar{q}q'$ channel, and LEP represents that arising from the knowledge of the collision energy of the accelerator. The combined value for the W width is

$$\Gamma_W = 2.404 \pm 0.140(\mathrm{Stat.}) \pm 0.077(\mathrm{Syst.}) \pm 0.065(\mathrm{FSI})\ \mathrm{GeV}/c^2\,.$$

These results supersede all values previously published by the DELPHI collaboration.

1 Introduction

The measurement of the W boson mass can be used, in combination with other electroweak data, to test the validity of the Standard Model and obtain estimates of its fundamental parameters. In particular the measurement is sensitive, through loop corrections, to the masses of the top quark and the Higgs boson.

The W boson mass and width results presented in this paper are obtained from data recorded by the DELPHI experiment during the 1996–2000 operation of the LEP collider, known as the LEP2 period. This corresponds to a total of 660 pb^{-1} collected over a range of centre-of-mass energies: $\sqrt{s} = 161$–209 GeV.

Initially, data were recorded close to the W^+W^- pair production threshold. At this energy the W^+W^- cross-section is sensitive to the W boson mass, M_W. Subsequently, LEP operated at higher centre-of-mass energies, where the $e^+e^- \to W^+W^-$ cross-section has little sensitivity to M_W. For these data, which constitute the bulk of the DELPHI data sample, M_W and the W boson width, Γ_W, are measured through the direct reconstruction of the W boson's invariant mass from the observed jets and leptons. The analysis is performed on the final states in which both W bosons in the event decay hadronically ($W^+W^- \to q\bar{q}'\bar{q}q'$ or fully-hadronic) and in which one W boson decays hadronically while the other decays leptonically ($W^+W^- \to \ell\overline{\nu}_\ell q\bar{q}'$ or semi-leptonic).

The M_W analyses of the relatively small quantity of data ($\sim 20\,\mathrm{pb}^{-1}$) collected during 1996 at centre-of-mass energies of 161 and 172 GeV were published in [1, 2]. These data are not reanalysed in this paper but are discussed in Sects. 7.1.1 and 7.1.2 and included in the final M_W combination.

The data recorded during 1997 and 1998 at $\sqrt{s} = 183$ and 189 GeV have also been the subject of previous DELPHI publications [3, 4]. These data have been reprocessed and are reanalysed in this paper; the results given here supersede those in the previous publications. Results on the data collected during the final two years of LEP operation are published here for the first time. The data quality, simulation samples and analysis techniques have all been improved with respect to those used in previous DELPHI publications. The W mass and width have also been determined by the other LEP collaborations [5–7] and at hadron colliders [8].

The results on the W mass, M_W, and width, Γ_W, presented below correspond to a definition based on a Breit–Wigner denominator with an s-dependent width, $|(s - {M_W}^2) + \mathrm{i}s\Gamma_W/M_W|$.

After these introductory remarks, the paper starts in Sect. 2 by describing the LEP accelerator and the determination of its collison energy. A brief description of the DELPHI detector is provided as Sect. 3. This is followed by Sect. 4, which presents the properties of the data sample and of the Monte Carlo simulation samples used in the analysis.

The analysis method is presented in Sect. 5, first for $W^+W^- \to \ell\overline{\nu}_\ell q\bar{q}'$ events, then for $W^+W^- \to q\bar{q}'\bar{q}q'$ events. The text describes how the events are selected and the mass and width estimated from M_W- and Γ_W-dependent likelihood functions. The potential sources of systematic uncertainty are considered in Sect. 6. These include: inaccuracies in the modelling of the detector; uncertainties on the background; uncertainties on the effects of radiative corrections; understanding of the hadronisation of the W boson jets; possible cross-talk between two hadronically decaying W bosons, the effects of which the $q\bar{q}'\bar{q}q'$ M_W analysis has been specifically designed to minimise; and uncertainty on the LEP centre-of-mass energy determination. The paper concludes in Sect. 7 with a presentation of the results and their combination.

2 LEP characteristics

2.1 Accelerator operation

The LEP2 programme began in 1996 when the collision energy of the beams was first ramped to the W^+W^- pro-

[a] e-mail: jan.timmermans@cern.ch

duction threshold of 161 GeV and approximately 10 pb^{-1} of integrated luminosity was collected by each experiment. Later in that year LEP was run at 172 GeV and a dataset of similar size was accumulated. In each of the four subsequent years of operation the collision energy was raised to successively higher values, and the accelerator performance improved such that almost half the integrated luminosity was delivered at nominal collision energies of 200 GeV and above. The main motivation for this programme was to improve the sensitivity of the search for the Higgs boson and other new particles. The step-by-step nature of the energy increase was dictated by the evolving capabilities of the radio frequency (rf) accelerating system.

During normal operation the machine would be filled with four electron and four positron bunches at $E_{\mathrm{beam}} \approx 22$ GeV, and the beams then ramped to physics energy, at which point they would be steered into collision and experimental data taking begun. The *fill* would last until the beam currents fell below a useful level, or an rf cavity trip precipitated loss of beam. The mean fill lengths ranged from 5 h in 1996 to 2 h in 1999. After de-Gaussing the magnets the cycle would be repeated.

In 2000, the operation was modified in order to optimise still further the high energy reach of LEP. Fills were started at a beam energy safely within the capabilities of the rf system. When the beam currents had decayed significantly, typically after an hour, the dipoles were ramped and luminosity delivered at a higher energy. This procedure was repeated until the energy was at the limit of the rf, and data taken until the beam was lost through a klystron trip. These *mini-ramps* lasted less than a minute, and varied in step size with a mean value of 600 MeV. The luminosity in 2000 therefore was delivered through a near-continuum of collision energies between 201 and 209 GeV.

In addition to the high energy running, a number of fills each year were performed at the Z resonance. This was to provide calibration data for the experiments. Finally, several fills were devoted to energy calibration activities, most notably resonant depolarisation (RDP), spectrometer and Q_{s} measurements (see below for further details).

The machine optics that was used for physics operation and for RDP measurements evolved throughout the programme in order to optimise the luminosity at each energy point. Certain optics enhanced the build-up of polarisation, and thus were favoured for RDP measurements. The optics influence E_{beam} in several ways, and are accounted for in the energy model, full details of which are available in [9].

2.2 The LEP energy model

A precise measurement of the LEP beam energy, and thus the centre-of-mass energy, is a crucial ingredient in the determination of the W mass as it sets the overall energy scale. The absolute energy scale of LEP is set by the technique of RDP, which is accurate to better than 1 MeV. This technique allowed very precise measurements of the mass and width of the Z boson to be made at LEP1. However, this technique is only possible for beam energies between about 41 and 61 GeV. The LEP2 energy scale is set mainly by the nuclear magnetic resonance (NMR) model. This makes use of 16 NMR probes, positioned in selected dipoles, which were used to obtain local measurements of the bending field. These probes thus sample the total bending field, which is the primary component in determining the beam energy. Onto this must be added time-dependent corrections coming from other sources. These include effects from earth tides, beam orbit corrections, changes in the rf frequency, and other smaller effects. Details of all these can be found in [9]. Using this LEP energy model, the LEP energy group provided DELPHI with an estimate of the centre-of-mass energy at the start of each fill and thereafter in intervals of 15 mins. For the year 2000 the values before and after the mini-ramps were also supplied. No data are used that are taken during the mini-ramps, as the energy is not accurately known during these periods.

The main assumption that is made in the LEP energy model is that the beam energy scales linearly with the readings of the NMR probes. This assumption of linearity has been tested by three different methods:

1) *Flux loop*. Each dipole magnet of LEP is equipped with a single-turn flux loop. Measurements are made for a series of dipole magnet currents, which correspond roughly to the operating beam energies of LEP2. This allows the change in flux over almost the entire LEP dipole field to be measured as the machine is ramped in dedicated experiments. This change in flux can be compared with the local bending field measurements of the NMR probes. The flux loop is calibrated against the LEP energy model in the range 41–61 GeV, using the NMR coefficients determined from RDP. The measurements from the flux loop in the high energy regime (up to 106 GeV beam energy) are then compared to those from the LEP energy model. The flux loop measurements were made in all years of LEP2 running.
2) *Spectrometer magnet*. In 1999 a special steel spectrometer magnet, equipped with three beam position monitors to measure the beam position both on entry and exit from the magnet, was installed in the LEP ring. The magnetic field of this magnet was carefully mapped before and after installation in the LEP ring. All these measurements were very compatible. The beam energy is determined by measuring the bending angle of the beam in passing through the dipole magnet. The device was calibrated against RDP in the 41–61 GeV region and the spectrometer results were compared to the LEP energy model at beam energies of 70 and 92 GeV.
3) Q_s *versus* V_{rf}. The synchrotron tune Q_{s} can be expressed as a function of the beam energy and the total rf voltage, V_{rf}, plus some additional small corrections. By measuring Q_{s} as a function of the total rf voltage the beam energy can be determined. These measurements were performed in 1998–2000, at beam energies from 80 to 91 GeV. Again the measurements were normalised against RDP in the region 41–61 GeV, and compared to the LEP energy model at LEP2 energies.

The three methods are in good agreement, both with each other and the LEP energy model. Based on these comparisons a small energy offset compared to the LEP energy

model was supplied for each of the 10 beam energies used in LEP2. This offset is always smaller than 2 MeV. The estimated centre-of-mass energy uncertainties range between 20 and 40 MeV and are discussed further in Sect. 6.8.

The LEP centre-of-mass energy has also been determined by the LEP collaborations using LEP2 events containing on-shell Z bosons and photons (radiative return to the Z events) [10–13]. The DELPHI analysis measured the average difference between the centre-of-mass energy from radiative return events in the $e^+e^- \to \mu^+\mu^-(\gamma)$ and $e^+e^- \to q\bar{q}(\gamma)$ channels and the energy reported by the LEP energy working group,

$$\Delta E_{\rm cm} = +0.073 \pm 0.094(\text{Stat.}) \pm 0.065(\text{Syst.})\ \text{GeV}\,.$$

Thus the DELPHI result, relying on similar reconstruction procedures to those described in this paper, is in agreement with the values reported by the LEP energy working group.

3 Detector description

The DELPHI detector [14, 15] was upgraded for LEP2. Changes were made to the subdetectors, the trigger system, the run control and the algorithms used in the offline reconstruction of tracks, which improved the performance compared to the earlier LEP1 period.

The major change was the inclusion of the Very Forward Tracker (VFT) [16], which extended the coverage of the innermost silicon tracker out to $11^\circ < \theta < 169^\circ$[1]. Together with improved tracking algorithms and alignment and calibration procedures optimised for LEP2, these changes led to an improved track reconstruction efficiency in the forward regions of DELPHI.

Changes were made to the electronics of the trigger and timing system, which improved the stability of the running during data taking. The trigger conditions were optimised for LEP2 running, to give a high efficiency for Standard Model two- and four-fermion processes and also to give sensitivity for events that may be signatures of new physics. In addition, improvements were made to the operation of the detector during the LEP cycle, to prepare the detector for data taking at the very start of stable collisions of the e^+e^- beams, and to respond to adverse background from LEP were they to arise. These changes led to an overall improvement of $\sim 10\%$ in the efficiency for collecting the delivered luminosity from $\sim 85\%$ in 1995, before the start of LEP2, to $\sim 95\%$ at the end in 2000.

During the operation of the DELPHI detector in 2000 one of the 12 sectors of the central tracking chamber, the TPC, failed. After the 1st September 2000 it was not possible to detect the tracks left by charged particles inside the broken sector. The data affected correspond to $\sim 1/4$ of the total dataset of the year 2000. Nevertheless, the redundancy of the tracking system of DELPHI meant that tracks passing through the sector could still be reconstructed from signals in any of the other tracking detectors. A modified track reconstruction algorithm was used in this sector, which included space points reconstructed in the Barrel RICH detector. As a result, the track reconstruction efficiency was only slightly reduced in the region covered by the broken sector, but the track parameter resolutions were degraded compared with the data taken prior to the failure of this sector.

[1] The DELPHI coordinate system is right-handed with the z-axis collinear with the incoming electron beam, and the x-axis pointing to the centre of the LEP accelerator. The radius in the xy plane is denoted R and θ is used to represent the polar angle to the z-axis.

4 Data and simulation samples

4.1 Data

The W mass and width are measured in this paper with the data samples collected during the 1996–2000 operation of the LEP collider. A summary of the available data samples is reported in Table 1, where the luminosity-weighted centre-of-mass energies and the amount of data collected at each energy are shown. The luminosity is determined from Bhabha scattering measurements making use of the very forward electromagnetic calorimetry [17]. The total integrated luminosity for the LEP2 period corresponds to approximately 660 pb^{-1}. The integrated luminosities used for the different selections correspond to those data for which all elements of the detector essential to each specific analysis were fully functional. The additional requirements on, for example, the status of the calorimetry and the muon chambers mean that the integrated luminosity of the semi-leptonic analysis is slightly less than that of the hadronic dataset.

All the data taken from the year 1997 onwards have been reprocessed with an improved reconstruction code, and the analyses on these data are updated with respect to the previously published ones and supersede them. The data taken in 1996 have not been reanalysed; the results from this year are taken from the previous publications with minor revisions as reported in Sect. 7.

In addition to these data taken above the W^+W^- pair production threshold, data were also recorded during this period at the Z peak. These samples, containing a total of over 0.5 million collected Z decays, were taken each year typically at the start and end of the data taking periods. These Z peak samples were used extensively in the alignment and calibration of the detector and are used in many of the systematic uncertainty studies reported in Sect. 6.

4.2 Simulation

The response of the detector to various physical processes was described using the simulation program DELSIM [14, 15], which includes modelling of the resolution, granularity and efficiency of the detector components. In addition, detector correction factors, described in Sect. 6, were included to improve the description of jets, electrons and muons. To allow use of the data taken

Table 1. Luminosity-weighted centre-of-mass energies and integrated luminosities in the LEP2 data taking period. The hadronic integrated luminosity is used for the fully-hadronic channel, the leptonic one is used for the semi-leptonic channels

Year	$\mathcal{L}$-weighted $\sqrt{s}$ (GeV)	Hadronic int. $\mathcal{L}$ (pb^{-1})	Leptonic int. $\mathcal{L}$ (pb^{-1})
1996	161.31	10.1	10.1
	172.14	10.1	10.1
1997	182.65	52.5	51.8
1998	188.63	154.4	152.5
1999	191.58	25.2	24.4
	195.51	76.1	74.6
	199.51	82.8	81.6
	201.64	40.3	40.2
2000	205.86	218.4	215.9

after the 1st September in 2000, samples of events were simulated dropping information from the broken sector of the TPC. A variety of event generators were used to describe all the physics processes relevant for the analysis. W^+W^- events and all other four-fermion processes were simulated with the program described in [18], based on the WPHACT 2.0 generator [19, 20] interfaced with PYTHIA 6.156 [21] to describe quark hadronisation and TAUOLA 2.6 [22] to model τ leptons decays. The most recent $\mathcal{O}(\alpha)$ electroweak radiative corrections in the so-called double pole approximation (DPA) were included in the generation of the signal via weights computed by YFSWW 3.1.16 [23, 24], and the treatment of initial state radiation (ISR) of this calculation was adopted. The photon radiation from final state leptons was computed with PHOTOS 2.5 [25]. For systematic studies the alternative hadronisation descriptions implemented in ARIADNE 4.08 [26] and HERWIG 6.2 [27] were also used. All the hadronisation models were tuned on the DELPHI Z peak data [28].

The background process $e^+e^- \to q\bar{q}(\gamma)$ was simulated with KK 4.14 [29] interfaced with PYTHIA 6.156 for the hadronisation description. The two-photon events giving rise to those $e^+e^-q\bar{q}$ final states not described in the four-fermion generation above were produced with PYTHIA 6.143 as discussed in [18]. The contribution from all other background processes was negligible.

The simulated integrated luminosity used for the analysis was about a factor 350 higher than for the real data collected for four-fermion processes, about a factor 60 higher for two-fermion final states and about 3.5 times greater for $e^+e^-q\bar{q}$ two-photon final states (those not already included in the four-fermion simulation).

5 Analysis method

The measurement of M_W and of Γ_W are performed on samples of $W^+W^- \to \ell\overline{\nu}_\ell q\bar{q}'$ and $W^+W^- \to q\bar{q}'\bar{q}q'$ events; these two channels are discussed in turn below. The reconstruction of events where both Ws decay leptonically has very limited sensitivity to the W mass and width, as they contain at least two undetected neutrinos, and hence are not used in this analysis.

The first stage in the analysis is to select events from these decay channels, using either a neural network or a sequential cut-based approach. In some channels, after preliminary cuts, the probability is assessed for each event of how W^+W^--like it is and a corresponding weight is applied in the analysis.

The resolution of the kinematic information extracted from the observed particles in the event can be improved by applying energy and momentum conservation constraints to the event; this is discussed in Sect. 5.1. In the fully-hadronic channel, the jet directions used as the input to the kinematic fit are also assessed excluding particles from the inter-jet regions. This alternative approach reduces the sensitivity of the W mass analysis to final state interaction systematics and is discussed in Sect. 5.3.2.

The next stage in the analysis is to produce a likelihood function expressing the relative probability of observing an event as a function of M_W and Γ_W. The likelihood functions used below depend not only on the reconstructed W mass of the event but make use of other event characteristics to assess the relative weight and resolution of each event. These likelihood functions are then calibrated against simulated events.

The W mass and width are then extracted by maximising the combined likelihood function of the full observed dataset.

5.1 Application of kinematic constraints to event reconstruction

The event-by-event uncertainty on the centre-of-mass energy, i.e. the energy spread, at LEP is typically 0.1%, while the overall momentum and energy resolution of the observed final state is about 10%. Hence, the precise knowledge of the kinematics in the initial state can be used to significantly improve the reconstructed kinematic information obtained from the clustered jets and observed leptons in the final state. This is accomplished by means of a χ^2 fit based on the four constraints from the conservation laws of energy and momentum.

The reconstructed jets and leptons of the event may be associated with one of the two hypothesised W bosons in the event. A fifth constraint may then be applied to the event by assigning equal masses to these W boson candidates. As the decay width of the $W^{\pm}$ bosons is finite, this constraint is non-physical. However, as the event mass resolution and $2\,\mathrm{GeV}/c^2$ W width are of comparable magnitude in practice this constraint provides a useful approximation. It is of particular use in the semi-leptonic decay channels where, after applying the four constraints, the event mass resolution is still larger than the W width and, due to the unseen neutrino, the two fitted masses are strongly anticorrelated. However, in the fully-hadronic decay channel the mass resolution after the four-constraint fit is better and the correlation is less; hence more information is available in the two four-constraint masses than the combined five-constraint event mass.

Parameterisation of jets and leptons. Each fitted object, jet or lepton, is described by three parameters. Muons are described by their measured momenta and their polar and azimuthal angles. The uncertainties on these parameters are obtained directly from the track fit. Electrons are characterized by their measured energies and their detected angular position in the electromagnetic calorimeters. The energy uncertainties are obtained from parameterisations of the responses of the electromagnetic calorimeters, which were tuned to the responses found in Bhabha and Compton scattering events. The angular uncertainties were determined from the detector granularity and were significant only for the forward electromagnetic calorimeter. In semi-leptonic events, the neutrino momentum vector is considered as unknown, which leads to a reduction by three in the number of effective constraints in the kinematic fit.

Each fitted jet momentum $\vec{p}_j^{\,f}$ is projected onto a set of axes with one component parallel to the measured jet momentum $\vec{p}_j^{\,m}$ and two transverse components, $\vec{p}_j^{\,b}$ and $\vec{p}_j^{\,c}$, each normalized in magnitude to $1\,\mathrm{GeV}/c$. In this coordinate system $\vec{p}_j^{\,f}$ can be described by three parameters, a_j, b_j and c_j:

$$\vec{p}_j^{\,f} = \mathrm{e}^{a_j}\vec{p}_j^{\,m} + b_j\vec{p}_j^{\,b} + c_j\vec{p}_j^{\,c}\,, \qquad (1)$$

where each component is shown in Fig. 1. The measured jet energy $E_j^{\,m}$ is rescaled with the same factor e^{a_j} as the jet momentum. The exponential parameterisation e^{a_j} of the factor in front of $\vec{p}_j^{\,m}$ makes the fit more stable and results in uncertainties that have a more Gaussian distribution. The values of the parameters are determined by performing a constrained fit, while the transverse directions are given by the eigenvectors of the momentum tensor described below.

Form of χ^2. The algorithm minimizes a χ^2, defined for fully-hadronic events as

$$\chi^2 = \sum_{j=1}^{\text{jets}} \frac{(a_j - a_0)^2}{\sigma_{a_j}^2} + \frac{b_j^{\,2}}{\sigma_{b_j}^2} + \frac{c_j^{\,2}}{\sigma_{c_j}^2}\,, \qquad (2)$$

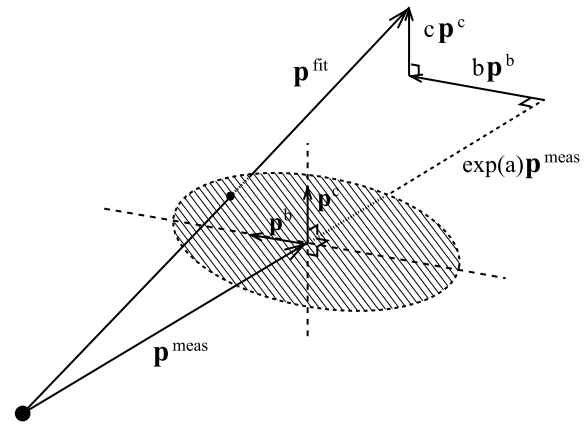

Fig. 1. Parameterisation used for jets in the constrained fit, as explained in the text and in (1)

while forcing the fitted event to obey the constraints. The appropriate terms are included in the χ^2 for events with a leptonic W decay. The expected energy loss parameter a_0 and the energy spread parameter σ_{a_j}, together with the parameters σ_{b_j} and σ_{c_j}, are parameterised as functions of the jet polar angles.

Jet error parameterisation. The jet error parameters, a_0, σ_{a_j}, σ_{b_j} and σ_{c_j} were obtained from a study of hadronic Z events. Hadronic Z events with a two-jet topology were selected from the Z calibration run data or from the corresponding Monte Carlo simulation. The reconstructed jet energies were compared with the beam energy. In general an energy loss of around 10% was observed for jets in the barrel region of the detector while this increased to 15% in the forward regions. A good agreement between the data and simulation was found. The energy loss increases if the event jet topology becomes less two-jet like, resulting in energy losses of around 15% for the barrel region and up to 35% in the forwards regions.

The uncertainties on the jet parameters for the first stage of the fit were determined from this study as a function of the polar angle of the jet. However, a dependence of these parameters on the properties of the individual jets has also been observed.

Jet breadth. The dependence of the uncertainties on the individual jet properties is included in a second stage of the fit, where the parameterisation of the transverse momentum uncertainties depends upon the breadth of the jet. This breadth is calculated by projecting the momenta of all particles in the jet on to the plane transverse to the jet axis. From these projections a two-dimensional momentum tensor $\mathcal{T}_{\beta\gamma}$ is created:

$$\mathcal{T}_{\beta\gamma} = \sum_k p_\beta^k p_\gamma^k\,, \qquad (3)$$

where p_β^k and p_γ^k are the two components of the projection of the momentum of particle k in the transverse plane. The normalized eigenvectors of the tensor, $\vec{p}_j^{\,b}$ and $\vec{p}_j^{\,c}$, reflect the

directions where the jet is broadest and slimmest. The corresponding eigenvalues are B_b and B_c. By comparing the resulting jet energies from the first stage of the fit with the measured ones, an estimate is made of how much energy remained undetected in the jet, referred to as $E_{j,\mathrm{miss}}$. The uncertainties on the jet breadths were then parametrised as a function of the eigenvalues, the measured jet energy and the missing energy $E_{j,\mathrm{miss}}$.

Use of χ^2. The χ^2 of the resulting fit is a function of the collection of jet parameters (a_j, b_j, c_j) and lepton parameters. The jets and leptons are paired appropriately to each W boson decay and constraints applied. The total χ^2 is then minimized by an iterative procedure using Lagrange multipliers for the constraints.

Events for which the χ^2 of the fit is larger than the number of degrees of freedom for the fit, NDF, had their errors scaled by a factor of $\sqrt{\chi^2/\mathrm{NDF}}$ in order to take non-Gaussian resolution effects into account.

In the semi-leptonic analysis described in Sect. 5.2.3 the value of the best fit mass from the χ^2 minimum and the error on this mass is used for each event. In the fully-hadronic analysis described in Sect. 5.3.3 each event uses the χ^2 distribution as a function of the masses of the two W bosons in the event.

5.2 Semi-leptonic decay channel

The $W^+W^- \to \ell\overline{\nu}_\ell q\bar{q}'$ events constitute 44% of all W^+W^- decays. The W^+W^- event candidates are classified according to their leptons and their selection is performed using a neural network. An event W mass is reconstructed in a kinematic fit, by imposing momentum conservation, the measured centre-of-mass energy and equality of the leptonic and hadronic decay W masses. An estimate of the mass resolution in each individual event is also obtained from the kinematic fit and an estimate of the event purity is obtained from the neural network output; these quantities are both used in producing the likelihood function from which M_W and Γ_W are determined.

5.2.1 Event selection

Events are selected from the recorded data sample requiring that all detectors essential for this measurement were fully efficient: these comprise the central tracking detectors and the electromagnetic calorimeters. The data recorded during the period with a damaged sector of the TPC are also used with matching simulation samples produced. The corresponding integrated luminosities, at each centre-of-mass energy, are given in Table 1.

Events containing at least three charged particle tracks and with a visible mass greater than $20\,\mathrm{GeV}/c^2$ are considered for analysis. Events containing lepton candidates are then identified in this sample, either by direct lepton identification (electrons and muons), or by clustering the events into a three-jet configuration and selecting the jet with the lowest charged multiplicity as the tau candidate. At this stage, events can be considered as candidates in multiple channels.

Electron and muon identification. Charged particles are identified as muons if they are associated with a hit in the muon chambers, or have an energy deposit in the hadron calorimeter that is consistent with a minimum ionising particle. Muon identification is performed in the polar angle range between 10° and 170°. Muons with an unambiguous association [14, 15] with the hits in the muon chambers, or with a loose association in addition to a good pattern in the hadron calorimeter are classified as good candidates, with the remainder being classified as possible candidates.

Electron identification is performed in the polar angle range between 15° and 165° by selecting charged particles with a characteristic energy deposition in the electromagnetic calorimeters. In the central region of the detector, covered by the HPC electromagnetic calorimeter, the electron selection followed the criteria described in [14, 15] for candidates below 30 GeV. This selection is based on a neural network using the electron energy to momentum ratio (E/p), the spatial matching between the extrapolated track and the shower, the shower shape and the track energy loss per unit path length in the TPC ($\mathrm{d}E/\mathrm{d}x$) as the discriminating variables. Above 30 GeV, a simplified selection is adopted, the main deposit associated with a charged particle track is identified and the surrounding electromagnetic showers are clustered into this electron candidate. Only candidates with E/p greater than 0.5 are used. In the polar angle region corresponding to the forward electromagnetic calorimeter acceptance, below 36° and above 144°, electron candidates are selected from among the calorimetric shower clusters. Only clusters with an energy above 8 GeV and which could be geometrically associated to extrapolated charged particle tracks are used. The electron candidates are separated into categories of good and possible candidates based on the quality of the track associated with the electron. The association of vertex detector hits to the track is a primary criterion used in assessing the track quality.

Tau reconstruction. As mentioned above, tau candidate events are clustered into a three-jet configuration using the LUCLUS [30] algorithm. Tracks at large angle (more than 40° from the nearest jet axis) or ones that contribute a large mass to the jet they belong to (ΔM bigger than $3.5\,\mathrm{GeV}/c^2$) are removed from the tau candidate. As the tau lepton predominantly decays into a final state with one or three charged particles, with few neutrals, a pseudo-multiplicity defined as the sum of the charged multiplicity and one quarter of the neutral multiplicity is used and the jet with the lowest pseudo-multiplicity is chosen as the tau candidate. Then a further cleaning is applied on this tau candidate: tracks at more than 20° from the tau axis, or which contribute a large mass (ΔM bigger than $2.5\,\mathrm{GeV}/c^2$) are removed from the tau candidate. Only tau candidates containing between one and four charged particle tracks after this cleaning, and with a polar angle between 15° and 165° are kept. Two classes of events are then defined, those with only one charged particle track, and all others.

Event reconstruction and pre-selection. After the lepton identification is performed, the events are reconstructed

as the lepton and a two- or three-jet system. Pre-selection cuts are then applied.

All tracks not associated to the lepton are clustered using the LUCLUS algorithm. These jet tracks in semi-leptonic electron and muon decay channel events are clustered with $d_{\rm join} = 7.5\,\mathrm{GeV}/c$,where $d_{\rm join}$ is a measure of the clusterisation scale used inside LUCLUS. If more than three jets are obtained the tracks are forced into a three-jet configuration. This procedure correctly treats events with hard gluon radiation (the proportion of three-jet events is about 20%). In semi-leptonic tau decay events the tracks not associated to the tau candidate are forced into a two-jet configuration.

A set of pre-selection cuts is then applied. First, a common set of criteria is applied to the system of jets:

- Visible mass greater than $30\,\mathrm{GeV}/c^2$;
- At least five charged particle tracks, with at least two with momentum transverse to the beam greater than $1.5\,\mathrm{GeV}/c$ and compatible with the primary vertex (impact parameter in $R < 0.15$ cm and in $z < 0.4$ cm);
- No electromagnetic cluster with an energy bigger than 50 GeV.

Then, for electron and muon semi-leptonic decay channel events, the following additional cuts are used:

- Energy of the lepton bigger than 20 GeV;
- If there is another isolated lepton of the same flavour and opposite charge, the event acollinearity should be bigger than 25°. The acollinearity used here is that between the two 'jets' when forcing the event into a two-jet (including the lepton) configuration.

Further cuts are made for electron decay channel events:

- Missing transverse momentum should be greater than $8\,\mathrm{GeV}/c$;
- The cut on missing transverse momentum is increased to $12\,\mathrm{GeV}/c$ for electron candidates in the 'possible' class;
- The angle between the lepton and the nearest jet greater than 15°.

The cuts specific to the muon decay channel events are as follows.

- The angle between the lepton and the nearest jet is greater than 15° in the case of 'possible' class muons;
- The angle between the missing momentum and the beam axis greater than 10° for muon candidates in the 'possible' class.

While for tau decay channel events, the cuts applied are as follows:

- The visible hadronic mass is smaller than $130\,\mathrm{GeV}/c^2$;
- The energy of the tau is greater than 5 GeV;
- The fraction of energy of the tau associated to charged tracks is greater than 5%;
- At least one of the charged particle tracks from the tau must have a vertex detector hit;
- The angle between the tau and the nearest jet is greater than 15°;
- The angle between the tau and the nearest charged particle is greater than 10°;
- The missing transverse momentum is greater than $8\,\mathrm{GeV}/c$;
- The cut on the missing transverse momentum is increased to $12\,\mathrm{GeV}/c$ in the case of tau candidates with several charged particles.

The semi-leptonic electron and muon events are then reconstructed using a constrained fit imposing conservation of four-momentum and equality of the two W masses in the event. As the energy of the tau lepton is unknown, due to the emission of at least one neutrino in its decay, the mass in the $\tau\overline{\nu}_\tau q\bar{q}'$ channel is entirely determined by the jet system and no improvement can be made from applying a constrained fit.

Selection. The event selection is based upon a multi-layer perceptron neural network[2]. The network has been optimised separately for the six classes of events (good and possible $e\overline{\nu}_e q\bar{q}'$, good and possible $\mu\overline{\nu}_\mu q\bar{q}'$, and $\tau\overline{\nu}_\tau q\bar{q}'$ candidates containing either only one or several charged particles).

The choice of the variables used in the neural networks is a compromise between their independence from the W mass and their discriminant power. The number of input–hidden–output nodes were 12–8–1, 11–7–1 and 17–12–1 for the e, μ and τ channels respectively. The detailed list of variables is given below. The network has been tuned on samples of signal and background simulation events, and examples of the distribution of the neural network output value are shown in Fig. 2. The applied selection cut is at 0.40, 0.50 and 0.35 for the e, μ and τ channels respectively, independent of the centre-of-mass energy. Any discrepancy in the background rate between data and simulation is accounted for in the systematic uncertainty applied.

The event selection procedure ensures that the events are only selected in one of the channels: events that pass the chosen cut in the muon channel are selected, the remaining events are considered as electron channel candidates and, if they are again rejected, are then analysed under the tau channel hypothesis. This ordering follows the hierarchy of purities in these channels (and is not dependent on the good or possible lepton classes). After applying the cut on the network output the selection performance is as shown in Table 2. As an example, the global efficiencies for CC03 events are 79.8, 89.8 and 59.3% respectively for the $e\overline{\nu}_e q\bar{q}'$, $\mu\overline{\nu}_\mu q\bar{q}'$ and $\tau\overline{\nu}_\tau q\bar{q}'$ events in the data taken at $\sqrt{s} = 189$ GeV. These numbers are integrated over all event selections as there is a non-negligible cross-contamination of events in the event selections (e.g. $e\overline{\nu}_e q\bar{q}'$ event selected by the $\tau\overline{\nu}_\tau q\bar{q}'$ selection), which still add useful information in the W mass and width fits. Here CC03 refers to the three charged current processes producing the W^+W^- state for which this analysis is intended: s-channel photon or Z production and t-channel ν_e exchange.

For each of the six classes of events, the fraction of semi-leptonic W^+W^- events in the sample has been extracted from simulation as a function of the neural net-

[2] Code kindly provided by J. Schwindling and B. Mansoulie.

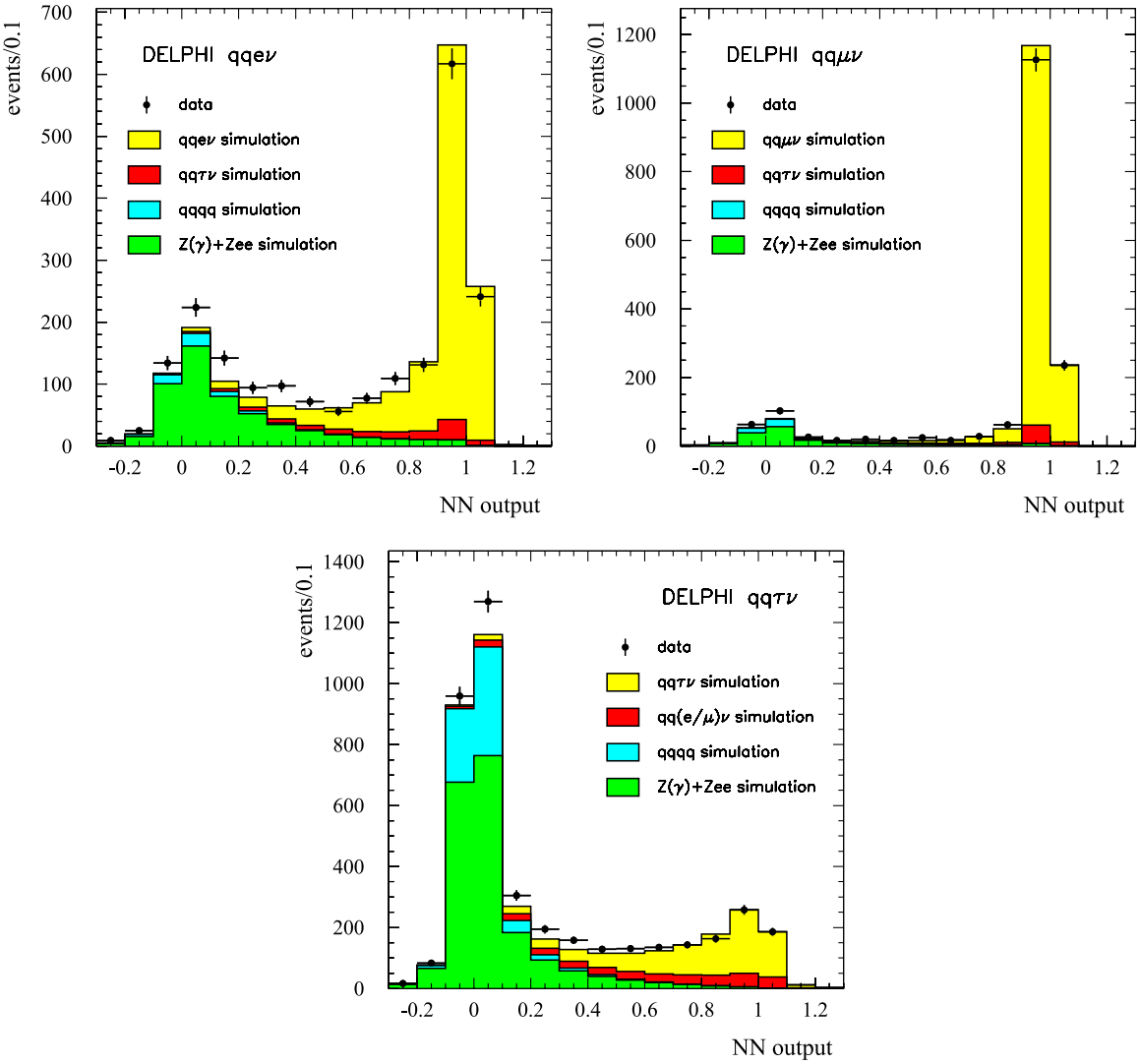

Fig. 2. The output of the neural network used for the selection of the semi-leptonic channels for the data sample recorded at $\sqrt{s} = 183$–209 GeV. The data are indicated by the data points with *error bars*. The *histograms* show the signal and background simulation contributions normalised to the integrated luminosity of the data sample

work output: this is referred to below as the event purity P_e. This feature is particularly useful for the tau selection, where the proportion of background events is highest.

5.2.2 Variables used in the selection neural networks

Common variables for all leptonic channels.

- Polar angle of the leptonic W (after applying the constrained fit);
- Angle of the charged lepton with respect to the direction of the leptonic W (in the W rest frame, and after the constrained fit);
- Polar angle of the lepton;
- Polar angle of the missing momentum vector;
- Angle between the lepton and the nearest jet;
- Angle between the lepton and the nearest charged hadron track (of energy greater than 1 GeV);
- Missing transverse momentum;
- The invariant mass of the measured system of particles $\sqrt{s'}$ [31] – this is measured using planar kinematics, by forcing the event into two jets (using all particles in the event including the lepton) and assuming a photon is emitted down the beam pipe;
- Aplanarity (cosine of the angle between the lepton and the normal to the plane formed by the jets[3]);
- Acollinearity (complement of the angle between the two "jets" when forcing the event into a two-jet configuration);
- The minimum d_{join} distance in the LUCLUS jet clusterisation algorithm between two jets in the final configuration, where the whole event (hadronic and leptonic system) is forced into three jets. This is known as d_{j3all}.

[3] For three-jets events in the electron and muon channels, the jets-plane is the plane formed by the most energetic jet and the sum of the two others.

Additional variable for the electron channel only.

– Angle between the missing momentum and the nearest jet.

Additional variables for the tau channel only.

– Angle between the missing momentum and the nearest jet;
– Fraction of the tau energy coming from charged particle tracks;
– Missing energy;
– Reconstructed tau energy;
– Reconstructed tau mass;
– d_{j4all}, as d_{j3all} (see above) but with the final event configuration forced into four jets.

5.2.3 Likelihood function

A likelihood function, $\mathcal{L}_{\mathrm{e}}(M_W, \Gamma_W)$, is evaluated for each selected event with a reconstructed mass in a defined range. The range was 67–91 GeV/c^2 for the data collected in 1997, 67–93 GeV/c^2 for 1998, 67–95 GeV/c^2 for 1999, and 67–97 GeV/c^2 for 2000. The increase in range with rising centre-of-mass energy is to account for the increasing ISR tail. The likelihood function is defined as follows:

$$\mathcal{L}_{\mathrm{e}}(M_W, \Gamma_W) = P_{\mathrm{e}} S''(m^{\mathrm{fit}}, \sigma^{\mathrm{fit}}, M_W, \Gamma_W) + (1 - P_{\mathrm{e}}) B(m^{fit}) ,$$

where P_{e} is the event purity, discussed above, S'' is the signal function that describes the reconstructed mass distribution of the semi-leptonic W decays, and B is used to describe background processes. The reconstructed event mass m^{fit} and its estimated error σ^{fit} are both obtained from the constrained fit. The distribution of background events is extracted from simulation as a function of m^{fit}.

The signal function S'' is defined in terms of S and S' as discussed below. The function S relies on the convolution of three components, using x and m as the dummy integration variables:

$$\begin{aligned} &S(m^{\mathrm{fit}}, \sigma^{\mathrm{fit}} | M_W, \Gamma_W) \\ &= \int_0^{E_{\mathrm{BEAM}}} \mathrm{d}m G[m^{\mathrm{fit}} - m, \sigma^{\mathrm{fit}}] \\ &\quad \times \int_0^1 \mathrm{d}x \mathrm{PS}(m(1-x)) \mathrm{BW}[m(1-x) | M_W, \Gamma_W] R_{\mathrm{ISR}}(x) . \end{aligned} \tag{4}$$

BW is a relativistic Breit–Wigner distribution representing the W mass distribution,

$$\mathrm{BW}(m | M_W, \Gamma_W) = \frac{1}{\pi} \frac{\Gamma_W}{M_W} \frac{m^2}{\left(m^2 - {M_W}^2\right)^2 + \left(m^2 \frac{\Gamma_W}{M_W}\right)^2} , \tag{5}$$

and PS is a phase-space correction factor

$$\mathrm{PS}(m) = \sqrt{1 - \frac{4m^2}{s}} .$$

The convolution with the Gaussian function G describes the detector resolution. The width of the Gaussian depends upon the reconstructed mass error obtained in the constrained fit for that event.

Table 2. Number of selected events in the decay channel event selections from the 1998 and 2000 data samples and the combined 1997–2000 data sample, and the corresponding number of expected events from the simulation. The table is split into rows giving the results of each of the event selection routines. The primary-l and other-l $\overline{\nu}_\ell q\bar{q}'$ columns relate to the nature of the semi-leptonic event selections e.g. for the $e\overline{\nu}_e q\bar{q}'$ selection the results are for the $e\overline{\nu}_e q\bar{q}'$ and $(\mu\overline{\nu}_\mu q\bar{q}' + \tau\overline{\nu}_\tau q\bar{q}')$ channels respectively

			Simulation				
1998, 189 GeV	(Primary-l) $\overline{\nu}_\ell q\bar{q}'$	(Other-l) $\overline{\nu}_\ell q\bar{q}'$	$q\bar{q}'\bar{q}q'$	$q\bar{q}(\gamma)$	Other $4f$	Total	Data
$e\overline{\nu}_e q\bar{q}'$	257.5	10.5	0.7	9.3	6.5	284.5	256
$\mu\overline{\nu}_\mu q\bar{q}'$	321.2	10.2	0.4	1.1	2.2	335.1	320
$\tau\overline{\nu}_\tau q\bar{q}'$	198.2	56.6	3.5	18.6	10.9	287.9	294
$q\bar{q}'\bar{q}q'$	–	34.0	1029.9	341.6	50.8	1456.3	1506
2000, 206 GeV							
$e\overline{\nu}_e q\bar{q}'$	373.9	16.9	1.0	13.6	11.4	416.8	395
$\mu\overline{\nu}_\mu q\bar{q}'$	457.0	14.8	0.6	1.7	4.1	478.2	467
$\tau\overline{\nu}_\tau q\bar{q}'$	290.2	87.6	5.7	22.3	21.4	427.2	426
$q\bar{q}'\bar{q}q'$	–	40.6	1514.5	460.9	107.8	2123.8	2134
1997–2000 183–206 GeV							
$e\overline{\nu}_e q\bar{q}'$	1091.5	47.7	2.9	39.9	30.7	1212.7	1182
$\mu\overline{\nu}_\mu q\bar{q}'$	1356.7	43.3	1.7	15.2	11.0	1417.8	1402
$\tau\overline{\nu}_\tau q\bar{q}'$	849.3	248.6	16.0	72.2	55.6	1241.6	1270
$q\bar{q}'\bar{q}q'$	–	131.6	4421.0	1399.5	269.8	6222.0	6446

The ISR spectrum is parameterised as

$$R_{\mathrm{ISR}}(x_\gamma) = \beta x_\gamma^{(\beta-1)} ,$$

where x_γ is the ratio of the photon energy to the centre-of-mass energy and β is calculated from the electromagnetic coupling constant (α), the centre-of-mass energy squared (s) and the electron mass (m_e):

$$\beta = \frac{2\alpha}{\pi}\left[\ln\left(s/m_e^2\right) - 1\right] .$$

Due to the constrained fit, a W produced at mass m will be reconstructed to a good approximation as $m/(1-x_\gamma)$ in the presence of an undetected ISR photon, giving a tail at high mass in the measured spectrum. This tail is well described by the integration on the photon spectrum in (4).

The event selection contains a significant fraction of $\tau\overline{\nu}_\tau q\bar{q}'$ events in the electron and muon channel samples, and of $e\overline{\nu}_e q\bar{q}'$ events in the tau sample (see Table 2). In the tau channel the mass of the event is determined from the jet system. The behaviour of true $\tau\overline{\nu}_\tau q\bar{q}'$ and $e\overline{\nu}_e q\bar{q}'$ events in this fit are found to be similar, and $S'' = S$ in this channel. However, in the electron and muon channel samples the behaviour of the $\tau\overline{\nu}_\tau q\bar{q}'$ events is somewhat different to that of the $e\overline{\nu}_e q\bar{q}'$, $\mu\overline{\nu}_\mu q\bar{q}'$ events. The $\tau\overline{\nu}_\tau q\bar{q}'$ events have a worse mass resolution and introduce a small negative offset on the mass. The fraction of tau events that have been wrongly classified and are contained in the electron and muon channel samples has been parameterised in bins of the lepton energy and the measured missing mass. This fraction $P\tau_{\mathrm{e}}$ is then taken into account in the likelihood function for the electron and muon samples, by defining the signal function S'' as

$$S'' = (1 - P\tau_{\mathrm{e}})S + P\tau_{\mathrm{e}}S' ,$$

where S' is analogous to S, but with the width of the Gaussian resolution function increased according to a factor determined from simulation studies. All remaining biases in the analysis due to using this approximate likelihood description are corrected for in the calibration procedure as described in Sect. 5.4.

5.3 Fully-hadronic decay channel

The $W^+W^- \to q\bar{q}'\bar{q}q'$ events constitute 46% of all W^+W^- decays. The event masses can be reconstructed from the observed set of jets. The kinematics of the jets can be significantly over-constrained in a kinematic fit, improving the event mass resolution, by imposing momentum conservation and the measured centre-of-mass energy. The influence of the many ambiguities in the event reconstruction, which dilute the statistical information, is minimised by optimally weighting the different hypotheses in the likelihood fit of M_W or Γ_W.

The dominant systematic error is due to the possible influence of final state interference effects between particles from the two decaying Ws. Reconstructing the jet directions using only the particles from the core of the jet reduces the possible effects of these final state interference effects. This technique and the mass estimator based on all observed particles are both discussed in Sect. 5.3.2.

5.3.1 Event selection

As in the semi-leptonic analysis, appropriate criteria were imposed on the functionality of the detector when selecting the data sample for analysis. The corresponding integrated luminosities, at each centre-of-mass energy, are given in Table 1.

The event selection can be separated into three stages. First a pre-selection is performed to reduce the data sample to events with a high multiplicity and high visible energy. In the second stage events with a four or five jet topology are retained. The observables on which the selection is made are chosen to be, to a good approximation, independent of the centre-of-mass energy $\sqrt{s}$: the same selection criteria are used for all energies for the pre-selection and jet topology selection. The final stage of the event selection is to use the inter-jet angles and jet momenta to estimate the probability that this was a $W^+W^- \to q\bar{q}'\bar{q}q'$ event.

The pre-selection cuts applied are as follows:

- The charged particle multiplicity should be larger than 13;
- The total visible energy of the event must exceed $1.15\,\frac{\sqrt{s}}{2}$;
- The scaled effective centre-of-mass energy $\frac{\sqrt{s'}}{\sqrt{s}}$ [31] is required to be equal to or larger than 0.8;
- Rejection of events tagged as likely to be containing b quarks [32, 33].

The last criterion removes 7% of the remaining $Z \to q\bar{q}(\gamma)$ and 18% of the remaining ZZ events, while changing the signal selection efficiency by less than 1%. The distributions of data and simulation events for the scaled effective centre-of-mass energy and combined b-tag variable are shown in Fig. 3; the cut on the combined b-tag variable retains all events below 2.

The remaining events are then clustered using the DURHAM [34, 35] jet clustering algorithm with a fixed y_{cut} of 0.002. The jets obtained are required to have an invariant mass of greater than 1 GeV/c^2 and contain at least three particles. If the jets do not meet these criteria or more than five jets are obtained, the clustering is continued to higher values of y_{cut}. Events that cannot be clustered into either four or five jets that fulfill these criteria are rejected. The initial y_{cut} value of this procedure was optimised for maximal sensitivity to M_W and results in a sample of approximately 50% four- and 50% five-jet events.

The jets obtained from this procedure are then used in a constrained fit, described in Sect. 5.1, where momentum conservation and the measured centre-of-mass energy are enforced. From the fitted jets a topological observable, D_{pur}, was formed to discriminate between signal events and $Z \to q\bar{q}$ events with hard gluon radiation:

$$D_{\mathrm{pur}} = \theta^{\mathrm{fit}} E^{\mathrm{fit}} \sqrt{\tilde{\theta}^{\mathrm{fit}} \tilde{E}^{\mathrm{fit}}} ,$$

where E_j^{fit} and $\tilde{E}_j^{\mathrm{fit}}$ are the smallest and second smallest fitted jet energies and $\theta_{ij}^{\mathrm{fit}}$ and $\tilde{\theta}_{ij}^{\mathrm{fit}}$ are the smallest and sec-

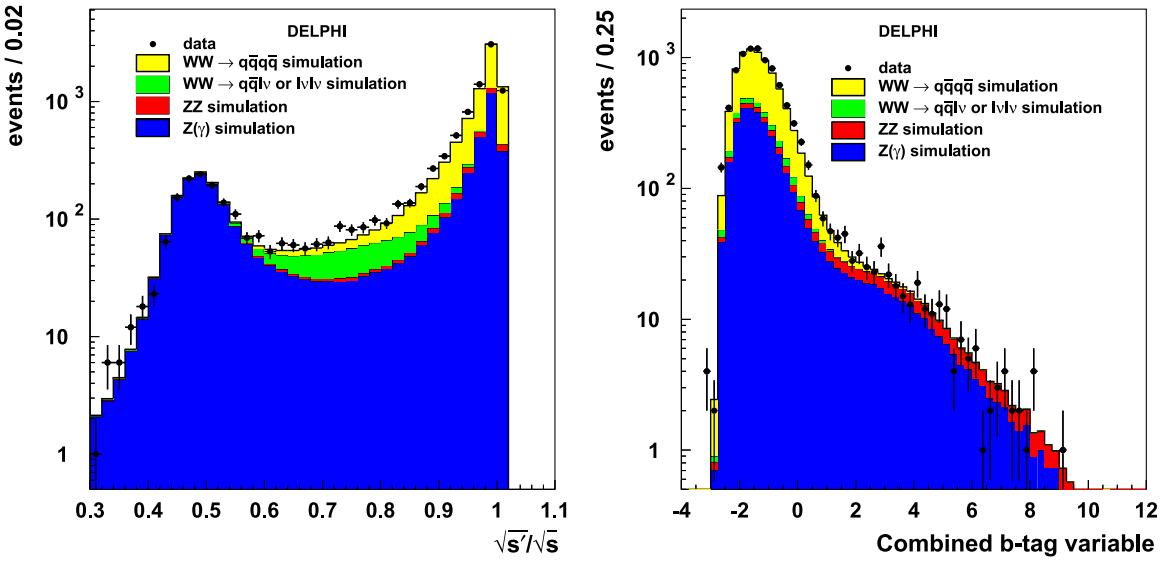

Fig. 3. The distribution of two event selection variables for candidate $q\bar{q}'\bar{q}q'$ events from the full LEP2 data sample and the corresponding simulation samples. The *left hand plot* shows the scaled effective centre-of-mass energy, the *right hand plot* the combined b-tag variable. The distributions are shown after the cuts on all other pre-selection variables have been applied

ond smallest fitted inter-jet angles. The expected fraction of $q\bar{q}'\bar{q}q'$ events (W^+W^- or ZZ) in the selected sample, the event purity P^{4f}, is parameterised as a function of this variable. This fraction of $q\bar{q}'\bar{q}q'$ events, i.e. doubly resonant events rather than just W^+W^- events, is used in the theoretical distribution function described below. Events with an estimated purity below 25% are rejected. The distribution of the $D_{\rm pur}$ observable is shown in Fig. 4 for both the four- and five-jet topology events, and the numbers of selected events are given in Table 2. An excess of data events over the expected number of simulation events was observed.

5.3.2 Cone jet reconstruction

The largest contribution to the systematic uncertainty in the fully-hadronic decay channel arises from the hypothesis, used throughout the likelihood construction, that the fragmentation of the partons from both W bosons happens independently. However, Bose–Einstein correlations (Sect. 6.11) and colour reconnection (Sect. 6.12) effects may result in cross-talk between the two W systems. A jet reconstruction technique is presented here that has been designed to have reduced sensitivity to colour reconnection effects.

Conventionally, as used for the jets in the semi-leptonic analysis, the particles in the event are clustered into jets using a jet clustering algorithm and the energy, magnitude of the momentum and direction of the jet are reconstructed from the clustered particles. The jet momentum and energy are then used as the input to the kinematic fit. This technique is referred to in this paper as the standard reconstruction method and provides the optimal statistical sensitivity.

In the alternative reconstruction algorithm discussed here the effect of particles in the inter-jet regions on the reconstructed jet direction is reduced. This is achieved by using a cone algorithm. The initial jet direction $\vec{p}^{\,\rm jet}$ is defined by the standard clustering algorithms (DURHAM [34, 35], CAMBRIDGE [36] or DICLUS [37]) and a cone of opening angle $R_{\rm cone}$ defined around this as in Fig. 5. The jet direction is recalculated (direction (1) on the figure) using those particles that lie inside the cone. This process is iterated by constructing a cone (of the same opening angle $R_{\rm cone}$) around this new jet direction and the jet direction is recalculated again. The iteration is continued until a stable jet direction $\vec{p}^{\,\rm jet}_{\rm cone}$ is found. Only the jet direction is changed in this procedure, the magnitude of the momentum and the jet energy are rescaled to compensate for the lost energy of particles outside the stable cone. The value of the cone opening angle $R_{\rm cone}$ is set to 0.5 rad, a value optimised for the measurement of the colour reconnection effect as reported in [38].

This cone jet reconstruction technique reduces the sensitivity to the colour reconnection effect (see Sect. 6.12) at the expense of some statistical sensitivity. The expected statistical uncertainty increases by approximately 14%. This technique has been applied only to the W mass and not to the W width analysis.

This technique of jet reconstruction should not be confused with the alternative jet clustering algorithms (DURHAM, CAMBRIDGE or DICLUS) used in the analysis (see below). The alternative jet clustering algorithms are used as the starting point for the cone jet reconstruction in order to improve the statistical sensitivity of the analysis rather than to reduce the sensitivity to colour reconnection effects.

5.3.3 Likelihood function

Event ideograms. Each of the selected events is analysed through the use of a likelihood ratio function, which we will

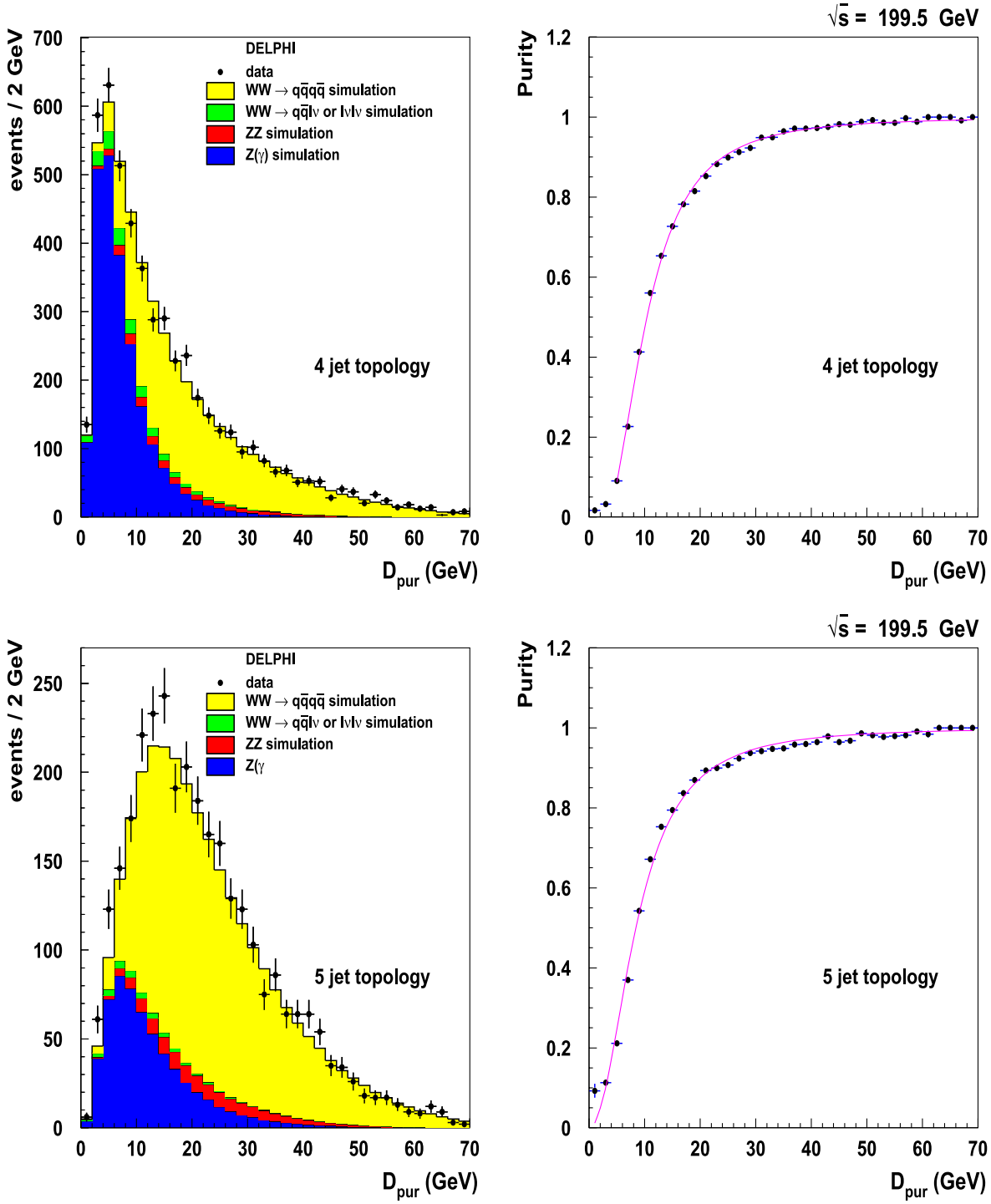

Fig. 4. The *left hand plots* show the distribution of the $D_{\rm pur}$ variable for four-jet (*top*) and five-jet (*bottom*) events from the full LEP2 data sample and the corresponding simulation samples. The *right hand plots* show the distribution of the four-fermion event purity with this variable at a centre-of-mass energy of 199.5 GeV extracted from simulation events. The fitted parameterisation of this distribution is given by the *line*

label here as the event ideogram. The final ideogram for each event consists of the weighted sum of the ideograms produced using a range of event reconstruction hypotheses h_i. These reconstruction hypotheses, including for example the possible different associations of the jets to their parent W bosons, are discussed below. The details of how these hypotheses are combined is then described below under the heading of 'Ideogram sum'.

The ideogram reflects the relative compatibility of the kinematics of the event with the premise that two heavy objects, with masses m_x and m_y, were produced. The ideogram is based on the least square, χ^2_{4C}, of the

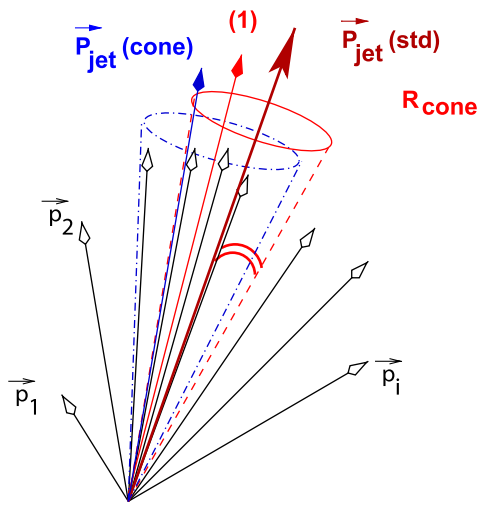

Fig. 5. Illustration of the iterative cone jet reconstruction algorithm used for the fully-hadronic W mass analysis as discussed in the text

energy and momentum constrained fit of the observed set of jet kinematics, $\{\bar{p}_j\}$, of the reconstructed final state.

Thus, for each pair of test masses $\vec{m} = (m_x, m_y)$, we can obtain the $\chi^2_{4C}(\{\bar{p}_j\}|\vec{m}, h_i)$. As the calculation of the χ^2 over the full mass $\vec{m}$-plane is computationally intensive we apply the following approximation in the analysis. The χ^2 is only calculated once per hypothesis h_i at the minimum of the $\chi^2_{4C}(\vec{m})$ in the full $\vec{m}$-space. The probability in all other points $\vec{m} = (m_x, m_y)$ is calculated using a Gaussian approximation for the $\chi^2(\vec{m})$ given by

$$\chi^2_i(m_x, m_y) \simeq \chi^2_{4C} + (\mathbf{m} - \mathbf{m}^{\mathrm{fit}})^{\mathrm{T}} \mathbf{V}^{-1} (\mathbf{m} - \mathbf{m}^{\mathrm{fit}}) \,,$$

with

$$\mathbf{m} = \begin{pmatrix} m_x \\ m_y \end{pmatrix},$$

$$\mathbf{m}^{\mathrm{fit}} = \begin{pmatrix} m_x^{\mathrm{fit}} \\ m_y^{\mathrm{fit}} \end{pmatrix}.$$

The masses m_x^{fit}, m_y^{fit}, and the covariance matrix $\mathbf{V}$ are taken from the $4C$ kinematic fit. When the χ^2_{4C} is larger than the number of degrees of freedom (NDF = 4), the $\chi^2_i(m_x, m_y)$ is rescaled with a factor NDF/χ^2_{4C} in order to compensate for non-Gaussian resolution effects.

This procedure decreases the computing time taken by an order of magnitude compared with the full six constraint fit [3], while resulting in only a minimal reduction in the W mass precision obtained ($2 \pm 1\%$).

We denote the ideogram of the event under hypothesis h_i as $P(\{\bar{p}_j\}|\vec{m}, h_i)$. Assuming a Gaussian form, this is calculated from the χ^2 as follows:

$$P(\{\bar{p}_j\}|\vec{m}, h_i)\,\mathrm{d}\vec{m} = \exp\left(-\frac{1}{2}\chi^2_{4C}(\{\bar{p}_j\}|\vec{m}, h_i)\right)\,\mathrm{d}\vec{m}\,.$$

Example ideograms are shown in Fig. 6. These ideograms show the weighted sum of the reconstruction hypothesis ideogram terms for an individual event. The reconstruction hypotheses, which we will discuss in the following sections, include a range of options for the jet clustering algorithms that assign particles to jets, the possible associations of jets to W bosons, and a treatment for events that may have significant initial state radiation.

Jet pairings. As discussed in Sect. 5.3.1, the reconstructed particles in the event were clustered into four or five jets. These jets can then be associated to their parent W

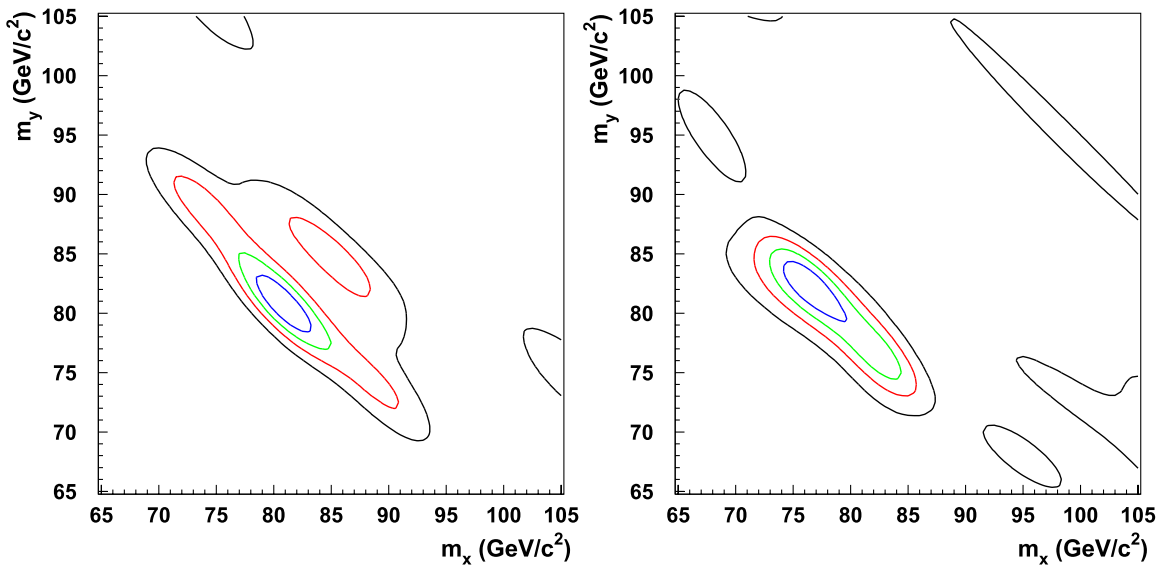

Fig. 6. Examples of a reconstruction hypothesis weighted sum of two-dimensional probability ideograms (see text) for a four-jet (*left*) and five-jet (*right*) hadronic event. The ideograms include terms from each potential jet pairing, three jet clustering algorithms and possible ISR emission. The 1, 2, 3 and 4 sigma contours are shown

bosons. For events clustered into four (five) jets there are three (ten) combinatorial possibilities for the jet pairing into W bosons. The relative probability of each of these jet pairings to be the correct jet association is estimated.

This jet to W boson association weight, w_k, is estimated as a function of the reconstructed polar angle of the W boson and the estimated charge difference between the two reconstructed W bosons in the event. For the five-jet events the transverse momentum of the gluon jet is also used.

The production angle θ_W of the W^+ (W^-) boson is correlated with the flight direction of the incoming e^+ (e^-) beam. For each jet pairing the W boson polar angle was calculated and its probability $P_\theta(\theta_W)$ assessed from a centre-of-mass-dependent parameterisation of correctly paired simulation events.

The jet charge Q^i_{jet} for jet i in the clustered event can be measured as

$$Q^i_{\rm jet} = \frac{\sum_{n=1}^{n_{\rm jet}} |\vec{p}_n|^{0.5} q_n}{\sum_{n=1}^{n_{\rm jet}} |\vec{p}_n|^{0.5}} ,$$

where $n_{\rm jet}$ are all charged particles in jet i, while q_n and $\vec{p}_n$ are their charge and momentum. For each association k of the jets to their parent W bosons the charge difference $\Delta Q_k = Q_k^{W_1} - Q_k^{W_2}$ is obtained. Again, the probability of this being the correct jet assignment is assessed using a Monte Carlo simulation-derived parameterisation. The relative weight for each jet pairing k can be expressed as

$$\begin{aligned} w_k^W = {} & P_{W^+}(\Delta Q_k) P_\theta \left(\theta^k_{W_1}\right) \\ & + (1 - P_{W^+}(\Delta Q_k)) P_\theta \left(\pi - \theta^k_{W_1}\right) . \end{aligned}$$

In five-jet events, a two-jet and a three-jet system are considered. The three-jet system is considered as comprising a $q\bar{q}$ pair and a gluon jet. The probability of emission of a gluon from a $q\bar{q}$ pair is approximately inversely proportional to the transverse momentum of the gluon with respect to the original quarks. Hence, the most probable gluon jet in the three-jet system is the jet with the smallest transverse momentum ($k_{\rm T}$) with respect to the two other jets in the candidate W boson rest frame. Each of the ten possible jet associations, in this five-jet event, is then given a relative weight from its most probable gluon jet of $w_k^{\rm gluon} = 1/k_{\rm T}$.

The combined relative jet pairing weight of each combination is given by multiplying the jet pairing weights w_k^W and, for five-jet events, also multiplying by the $w_k^{\rm gluon}$ weight. The relative weights are then normalised so that the sum of the weights for all the jet pairing combinations of the event is 1, giving combination weights w_k. The use of all the jet pairings, rather than simply picking the best one, improves the statistical precision of this analysis by 4%.

Jet clustering algorithms. Several standard jet clustering algorithms are used in this analysis. Whilst the overall performances of the algorithms are similar, the reconstruction of an individual event can differ significantly. In this analysis, the event ideograms were reconstructed with three clustering algorithms DURHAM, CAMBRIDGE and DICLUS. The ideograms resulting from each clustering algorithm are summed with fixed optimised relative weights, w_c, determined from simulation events. The sum of the three-jet clustering weights for one event is normalised to 1.

The use of a range of jet clustering algorithms, rather than taking only one, improves the statistical precision of this analysis by 5%.

Initial state radiation hypotheses. A kinematic fit (see Sect. 5.1) is performed with modified constraints and an extra free parameter $p_z^{\rm fit}$ to account for the possible emission of an ISR photon of momentum p_z inside the beam pipe. The modified constraints are

$$\sum_{i=1}^{n_{\rm objects}} (E, p_x, p_y, p_z)_i = \left(\sqrt{s} - \left|p_z^{\rm fit}\right|, 0, 0, p_z^{\rm fit}\right) .$$

The probability that the missing momentum in the z direction is indeed due to an unseen ISR photon was extracted from the simulation as a function of $|p_z^{\rm fit}|/\sigma_{p_z}$, where σ_{p_z} is the estimated error on the fitted z momentum component; only events with this ratio greater than 1.5 are treated with the mechanism described below.

Additional ideograms are then calculated for these events, with a relative weight factor derived from the ISR hypothesis probability. The ideogram obtained without the ISR hypothesis is given a relative weight 1, while the other ideograms obtained from this procedure are given relative weight factors according to the distribution shown in Fig. 7. The weights are then normalised such that the sum of the ISR and no ISR hypotheses for an event sum to 1, giving ISR weights $w_{\rm isr}$.

This treatment is applied to 15% of the events and results in an improvement of the expected W mass error for these events of 15%.

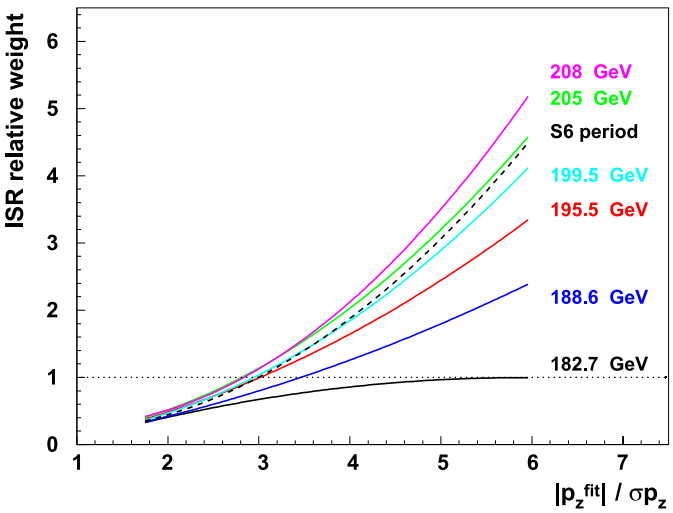

Fig. 7. Parameterised weight given to the ISR solution of the kinematic fit, relative to the unity weight of the no ISR solution, as a function of the $|p_z^{\rm fit}|/\sigma_{p_z}$ value of the event for different centre-of-mass energies. The period with a damaged TPC sector (S6) is indicated with a *dashed line*

Ideogram sum. An ideogram is produced for each event under each of the possible reconstruction hypotheses. For four-jet events there are three jet association hypotheses to be performed with three clustering algorithms and maximally two ISR hypotheses, giving a total of eighteen ideograms. For five-jet events there are sixty possible ideograms. The final ideogram for each event is produced as a weighted sum of these:

$$P(\{\bar{p}_j\}|\vec{m},\{h_i\}) = \sum_{k=1}^{3\text{ or }10}\sum_{\mathrm{isr}=1}^{2}\sum_{c=1}^{3} w_k w_{\mathrm{isr}} w_c P(\{\bar{p}_j\}|\vec{m},h_{k,\mathrm{isr},c})\,,$$

where the sum over k takes into account the three or ten possible jet pairings in the event, the sum over isr the two different initial state radiation hypotheses used in the kinematic fit and the sum over c the three jet clustering algorithms. The sum of all weights for each event is fixed to unity, so that while possible reconstruction hypotheses within an individual event have different weights the overall weight for each event is the same.

Likelihood. To obtain information about M_W and Γ_W a theoretical probability distribution function, $P(\vec{m}|M_W,\Gamma_W)$, is required predicting the population density in the $\vec{m}$-plane of the event ideogram. The ideogram in $\vec{m}$-space can then be transformed into a likelihood, $\mathcal{L}_{\mathrm{e}}(M_W,\Gamma_W)$, in the (M_W,Γ_W)-space by convoluting it with this expected distribution $P(\vec{m}|M_W,\Gamma_W)$:

$$\mathcal{L}_{\mathrm{e}}(M_W,\Gamma_W) = \int_{m_{\min}}^{m_{\max}}\int_{m_{\min}}^{m_{\max}} P(\{\bar{p}_j\}|\vec{m},\{h_i\})\cdot P(\vec{m}|M_W,\Gamma_W)\,\mathrm{d}\vec{m}\,, \tag{6}$$

where the two-dimensional integral is over the relevant kinematic region in the $\vec{m}$-space. This region is taken to be $m_{\min} = 60\,\mathrm{GeV}/c^2$ and $m_{\max} = 110\,\mathrm{GeV}/c^2$, and the combined ideogram is normalized to unity in the same region:

$$\int_{m_{\min}}^{m_{\max}}\int_{m_{\min}}^{m_{\max}} P(\{\bar{p}_j\}|\vec{m},\{h_i\})\,\mathrm{d}\vec{m} = 1\,.$$

Theoretical distribution function. The theoretical probability distribution function, $P(\vec{m}|M_W,\Gamma_W)$, predicts the population density in the $\vec{m}$-plane of the event ideogram for a given M_W and Γ_W. To provide an accurate description of the data the form assumed for $P(\vec{m}|M_W,\Gamma_W)$ must take into account not only the expected distribution for the $W^+W^- \to q\bar{q}'\bar{q}q'$ signal events but also that of the background events in the selected sample. The two principal components of the background, $Z \to q\bar{q}(\gamma)$ and $ZZ \to q\bar{q}'\bar{q}q'$, are considered.

The background process $Z \to q\bar{q}(\gamma)$ does not have a doubly resonant structure and a uniform population of these events is expected in the $\vec{m}$-space independent of the values of the parameters (M_W, Γ_W). Therefore, the probability density function from this background source is assumed to be a constant denoted B. The probability (P^{4f}) that a given event is a $q\bar{q}'\bar{q}q'$ event was calculated from the event topology as described in Sect. 5.3.1.

The $W^+W^- \to q\bar{q}'\bar{q}q'$ and $ZZ \to q\bar{q}'\bar{q}q'$ events both have a doubly resonant Breit–Wigner structure in the $\vec{m}$-plane, modulated by a phase-space correction factor $\mathrm{PS}(\vec{m}|\sqrt{s})$ due to the nearby kinematic limit $m_{W^+} + m_{W^-} \leq \sqrt{s}$. The probability density function component used to model four-fermion events is given by

$$S(\vec{m}|M_W,\Gamma_W) = \mathrm{PS}(\vec{m}|\sqrt{s}) \times \left[\frac{\tilde{\sigma}_{\mathrm{s}}^{WW}}{\tilde{\sigma}_{\mathrm{s}}^{WW}+\tilde{\sigma}_{\mathrm{s}}^{ZZ}}\mathrm{BW}_{WW}(\vec{m}|M_W,\Gamma_W) + \frac{\tilde{\sigma}_{\mathrm{s}}^{ZZ}}{\tilde{\sigma}_{\mathrm{s}}^{WW}+\tilde{\sigma}_{\mathrm{s}}^{ZZ}}\cdot\mathrm{BW}_{ZZ}(\vec{m}|M_Z,\Gamma_Z)\right],$$

where $\tilde{\sigma}_{\mathrm{s}}^{WW}$ and $\tilde{\sigma}_{\mathrm{s}}^{ZZ}$ reflect the accepted cross-sections, calculated from simulation, of respectively the W^+W^- and the ZZ final states. These cross-sections are centre-of-mass energy dependent but are independent of the reconstructed event topology.

The two-dimensional Breit–Wigner distribution is approximated as the product of two one-dimensional Breit–Wigner expressions:

$$\mathrm{BW}_{WW}(\vec{m}|M_W,\Gamma_W) = \mathrm{BW}_W(m_{W^+}|M_W,\Gamma_W)\times\mathrm{BW}_W(m_{W^-}|M_W,\Gamma_W)\,,$$

with BW_W given by the expression in (5) of Sect. 5.2.3. An expression of the same form is assumed for the ZZ component.

A dependence on the centre-of-mass energy is also introduced into $S(\vec{m}|M_W,\Gamma_W)$ through the phase-space correction factor $\mathrm{PS}(\vec{m}|\sqrt{s})$:

$$\mathrm{PS}(\vec{m}|\sqrt{s}) = \frac{1}{s}\sqrt{(s-m_{W^+}^2-m_{W^-}^2)^2 - 4m_{W^+}^2 m_{W^-}^2}\,.$$

The combined density function is then constructed from the signal and background terms:

$$P(\vec{m}|M_W,\Gamma_W,\sqrt{s}) = P^{4f}S(\vec{m}|M_W,\Gamma_W,\sqrt{s}) + (1-P^{4f})B\,.$$

Utilising this probability density function, and the event ideogram, (6) may be used to calculate the event likelihood function. The extraction of the parameters of interest, M_W and Γ_W, from the event likelihood functions are discussed below.

5.4 Mass and width extraction

The mass and width of the W boson are extracted from maximum likelihood fits to data samples. This section describes this procedure, the calibration applied and the cross-checks of this method that have been performed.

The distribution of the reconstructed invariant masses of the selected events after applying a kinematic fit, imposing four-momentum conservation and the equality of the

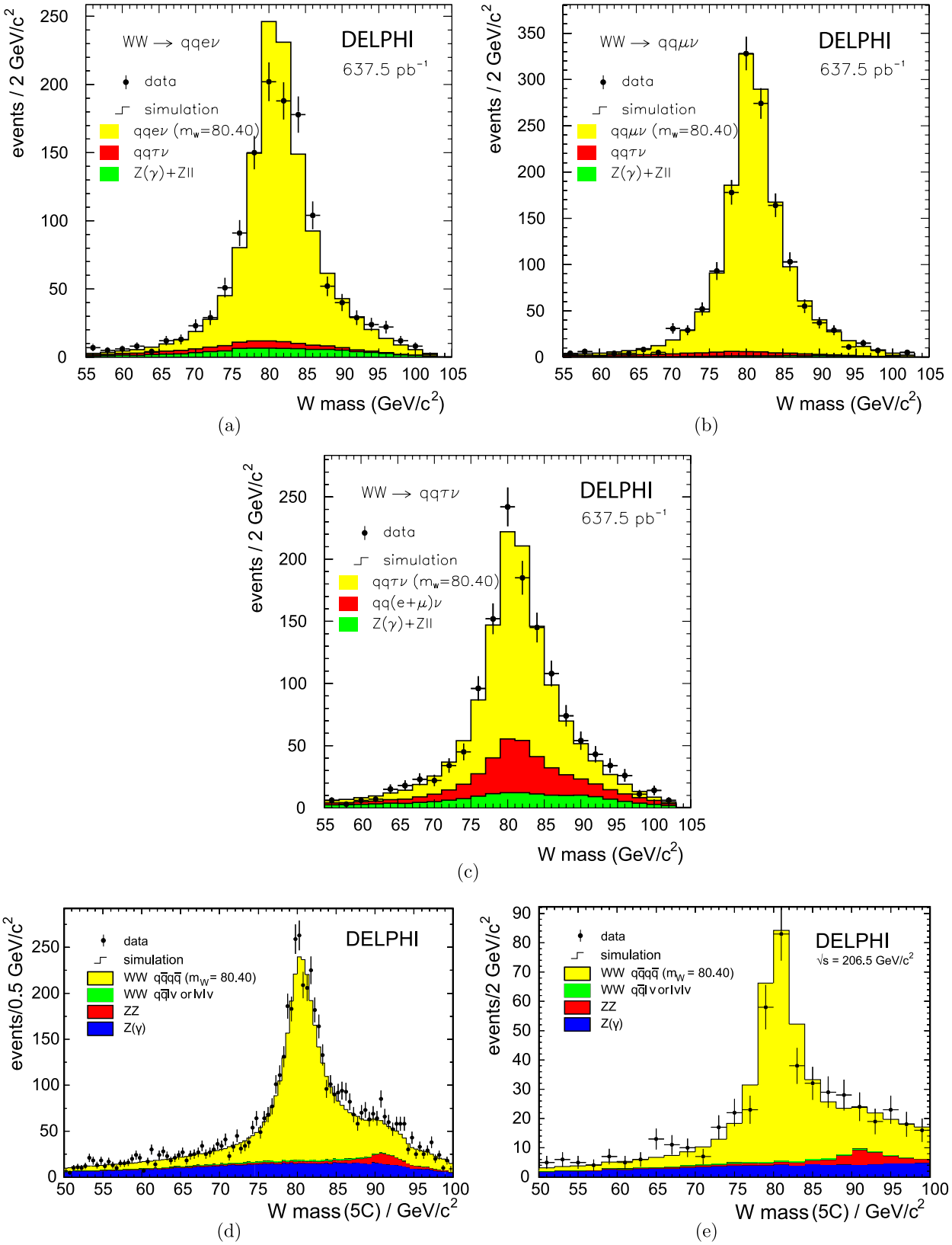

Fig. 8. The distribution of the reconstructed W masses from a kinematic fit with five constraints imposed in the **a** $e\overline{\nu}_e q\bar{q}'$, **b** $\mu\overline{\nu}_\mu q\bar{q}'$, **c** $\tau\overline{\nu}_\tau q\bar{q}'$ and **d** and **e** $q\bar{q}'\bar{q}q'$ analysis channels at all energies. **d** shows the data sample taken at all energies until September 2000, the data taken after that with a damaged TPC sector are shown in **e**. In **d** and **e** only the jet pairing with the highest probability is included in the figures. The simulation samples have been normalised to the same integrated luminosity as the data

two di-jet masses, are shown in Fig. 8. This figure is provided for illustrative purposes only, the mass and width fitting procedure is described below.

The combined likelihood of the data can be obtained from the product of the event likelihoods described above. In practice this is achieved by performing the sum of the logarithms of the individual event likelihoods. The fitted data samples are divided by data taking year and applied event selection. For the mass fit the data from the fully-hadronic event selection and the electron, muon and tau semi-leptonic selections are all fitted separately. In the determination of the W width, where the relative precision is much worse, the data are divided only into fully-hadronic and semi-leptonic selection samples. The procedure for combining the results from each of these fits is discussed in Sect. 7.

The W mass and width are extracted from maximum likelihood fits. The W mass fit is performed assuming the Standard Model value for the W width ($2.11\,\mathrm{GeV}/c^2$). The W width was obtained assuming a mass of $80.4\,\mathrm{GeV}/c^2$. The correlation between M_W and Γ_W was found to have a negligible impact on the extracted mass and width value: the current uncertainty of $44\,\mathrm{MeV}/c^2$ on Γ_W [42] gives rise to a $0.6\,\mathrm{MeV}/c^2$ uncertainty in the extracted M_W.

The terms used in the likelihood and described above are functions that approximate a description of the underlying physics and detector response. Hence, this approach necessitates a calibration of the analysis procedure. The calibration is performed using signal and background simulation events for which the true mass and width values are known. Rather than regenerating the events at a range of mass and width values, the calibration of the analysis uses reweighted events. The reweighting was performed using the extracted matrix element of the WPHACT and YFSWW generators. The reweighting procedure is cross-checked using independent simulation events generated at three W mass and width values. In the fully-hadronic channel where both the standard method and the cone jet reconstruction technique are applied to the W mass measurement, both analyses are calibrated separately: the illustrative values reported in this section are for the standard analysis.

A high statistics simulation sample is used to calibrate the analysis, comprised of an appropriate mixture of signal and background events. The result of the likelihood fit as a function of the simulated W mass is shown in Fig. 9 for the $\mu\overline{\nu}_\mu q\bar{q}'$ channel analysis at $\sqrt{s} = 189\,\mathrm{GeV}$. The analysis has a linear behaviour in the mass window of interest, and the calibration curves are defined by two parameters:

- The slope of the generated mass against fitted mass line;
- The offset defined at a fixed reference point. This point is chosen to be the value used in our simulation; $80.4\,\mathrm{GeV}/c^2$ for the mass and $2.11\,\mathrm{GeV}/c^2$ for the width.

The slopes at different energies are found to be compatible, and their mean values are respectively 0.984 ± 0.013, 0.993 ± 0.006 and 0.963 ± 0.013 in the $e\overline{\nu}_e q\bar{q}'$, $\mu\overline{\nu}_\mu q\bar{q}'$ and $\tau\overline{\nu}_\tau q\bar{q}'$ analyses. In the $q\bar{q}'\bar{q}q'$ analysis the slope was compatible with unity to within 2% at all centre-of-mass energies and no slope calibration was applied.

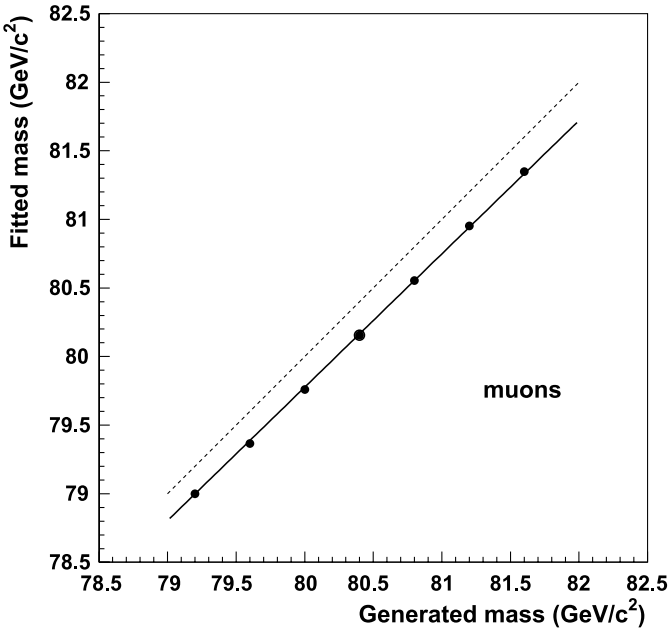

Fig. 9. W mass calibration curve in the $\mu\overline{\nu}_\mu q\bar{q}'$ channel at $\sqrt{s} = 189\,\mathrm{GeV}$. The *dashed line* indicates the result that would be obtained without any analysis bias

The highly linear behavior, with a value of the slope close to unity is an a posteriori justification of the fitting functions used in the likelihood fit and described in Sect. 5.3.3. The remaining effects not taken into account by these fitting functions give rise to the offset. As an example, the calibration offsets at $\sqrt{s} = 189\,\mathrm{GeV}$ are respectively -0.108 ± 0.012, -0.215 ± 0.010, -0.252 ± 0.015 and $-0.222 \pm 0.006\,\mathrm{GeV}/c^2$ in the $e\overline{\nu}_e q\bar{q}'$, $\mu\overline{\nu}_\mu q\bar{q}'$, $\tau\overline{\nu}_\tau q\bar{q}'$ and $q\bar{q}'\bar{q}q'$ analyses for the mass. The offsets vary slightly with the centre-of-mass energy.

The same procedure is also applied for the W width analyses. In the $\ell\overline{\nu}_\ell q\bar{q}'$ channel a slope of 0.894 ± 0.008 is obtained independent of the centre-of-mass energy and the offset at $\sqrt{s} = 189\,\mathrm{GeV}$ was $+0.065 \pm 0.015\,\mathrm{GeV}/c^2$. However, in the $q\bar{q}'\bar{q}q'$ analysis the slope is found to be dependent on the centre-of-mass energy, the slopes at $\sqrt{s} = 189$ and 205 GeV are approximately 1.1 and 1.2 respectively and furthermore the relation between the reconstructed and generated Γ_W is not perfectly linear. Hence the offset is parameterised as a function of the generated W width and the centre-of-mass energy. The calibration offset at $\sqrt{s} = 189\,\mathrm{GeV}$ is $183 \pm 13\,\mathrm{MeV}/c^2$ at the reference width.

The analyses are corrected with these calibration results, and the statistical error on the offset is included in the systematic error (see below).

After applying the calibration procedure, the consistency of the analyses is checked. Sets of simulation events, with a sample size the same as the data, containing the expected mixture of signal and background events were used to test the analyses. Figure 10 shows error and pull plots from analysing 20 000 or more such samples, where the pull

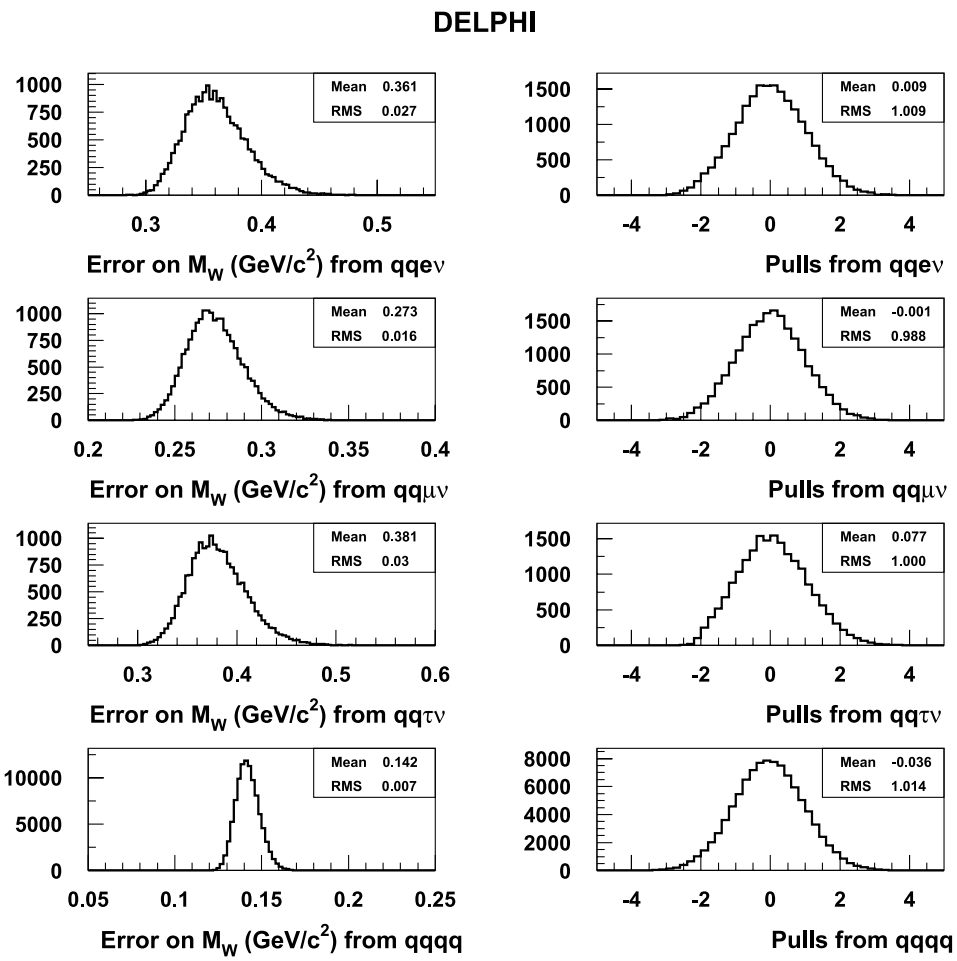

Fig. 10. The errors (*left*) and pulls (*right*) of the W mass fits for each semi-leptonic analysis channel and the fully-hadronic channel. These plots were obtained using simulated event samples with the same statistics as the data sample collected at 200 GeV. The errors obtained on the fits to the data samples were 365 MeV/c^2 for the $e\overline{\nu}_e q\bar{q}'$ analysis, 282 MeV/c^2 for $\mu\overline{\nu}_\mu q\bar{q}'$, 438 MeV/$c^2$ for $\tau\overline{\nu}_\tau q\bar{q}'$ and 149 MeV/c^2 for the standard $q\bar{q}'\bar{q}q'$ analysis

is defined as

$$\text{pull} = \frac{(M_{W\,\text{fit}} - M_{W\,\text{gen}})}{\sigma_{\text{fit}}},$$

here the subscript 'fit' and 'gen' distinguish the result from the calibrated analysis fit and the generated parameter in the simulation respectively. The σ_{fit} is the error estimated by the analysis. This error has been scaled in the analysis to obtain a Gaussian width of one for the pull distributions, as shown in the plots. These plots were produced at all centre-of-mass energies for both parameters. The error distributions in Fig. 10 also demonstrate that this quantity is in good agreement with the value obtained from the data.

6 Systematic uncertainties

The sources of systematic error that have been considered for the W mass and width determinations are described in the subsections below. The results of these studies at example centre-of-mass energies are summarised in Tables 14–16. In the fully-hadronic channel, the standard method and the cone jet reconstruction technique have been applied as described in Sect. 5.3.2. The systematic uncertainties are in agreement between these two techniques except for the error sources from final state interactions (FSI), where separate values for the two techniques are given.

6.1 Calibration

The analysis calibration procedure is described above in Sect. 5.4. The accuracy with which the offset of the analyses can be determined is limited by the size of the generated simulation samples. Sufficient events were generated to limit this error to 5% or less of the statistical error on the mass or width determination in any given channel.

6.2 Detector effects – muons

Contributions to the systematic error on the W mass and width due to the reconstruction of muons are considered in this section. These were evaluated using the $Z \to \mu^+\mu^-$ events collected at the Z peak during the LEP2 period. The systematic uncertainties determined by these studies for the W mass analysis are presented in Table 3.

Inverse momentum scale. The primary sources of systematic error on the muon momentum scale are the detector

Table 3. Contributions to the systematic error on the W mass measurement at 189 and 205 GeV related to the lepton reconstruction. The uncertainties on each of these numbers are typically 3 MeV/c^2

M_W lepton correction systematic errors (MeV/c^2)		
Sources of systematic error	$e\overline{\nu}_e q\bar{q}'$ 189 GeV	$e\overline{\nu}_e q\bar{q}'$ 205 GeV
Electron energy scale	18	22
Electron energy resolution	–	–
Electron energy linearity	16	11
	$\mu\overline{\nu}_\mu q\bar{q}'$ 189 GeV	$\mu\overline{\nu}_\mu q\bar{q}'$ 205 GeV
Muon $1/p$ scale	16	21
μ^+ μ^- $1/p$ difference	1	4
Muon $1/p$ resolution	–	–

alignment or possible reconstruction distortions (particularly in the TPC). As a result of these effects, we may also anticipate an opposite bias on the measured track curvature for positive and negative muons.

Corrections to the inverse momentum scale, $1/p$, are calculated from the selected $\mu^+\mu^-$ samples. The mean inverse momentum, $\langle 1/p\rangle$, is calculated separately for positive and negative muons in different bins of the polar angle, and a correction for the positive muons is defined as

$$\frac{1}{2}\left(\left\langle\frac{1}{p-}\right\rangle-\left\langle\frac{1}{p+}\right\rangle\right), \tag{7}$$

with the opposite sign correction applied to negative muons. These corrections are typically of the order 1 to $2\times10^{-4}\,\mathrm{GeV}^{-1}\,c$, except in the polar angle regions at the junction between the barrel and endcaps where the correction can reach $10^{-3}\,\mathrm{GeV}^{-1}\,c$ in the worst case. In the simulation this correction is, as expected, compatible with zero. After applying the corrections $\langle 1/p\rangle_{\mathrm{data}}$ and $\langle 1/p\rangle_{\mathrm{simulation}}$ are found to be in agreement within 0.2%, and this value is used to calculate the systematic on the muon inverse momentum scale. The systematic uncertainty on the positive and negative muon inverse momentum scale difference is estimated by varying the correction by ±50% of its value.

Inverse momentum resolution. The momentum resolution (typically $0.001\,\mathrm{GeV}^{-1}\,c$ in $1/p$) was found to be commonly around 10% better in simulation events than in the data. This discrepancy, determined for all years of LEP2 and polar angle regions, is corrected by smearing the simulation with a Gaussian. An additional smearing of $\pm0.0003\,\mathrm{GeV}^{-1}\,c$ in $1/p$ is used to estimate the systematic error resulting from this correction. This systematic does not affect the M_W determination but is a small component of the Γ_W measurement uncertainty for events containing muons.

6.3 Detector effects – electrons

Contributions to the systematic error on the W mass and width due to the reconstruction of electrons are considered in this section. These were evaluated using the Bhabha and Compton events collected at the Z peak and high energies during the LEP2 period. The systematic uncertainties determined by these studies for the W mass analysis are presented in Table 3.

Energy scale. The reconstructed energy of electrons was compared between data collected at the Z peak and fully simulated samples of Bhabha events. In the barrel region of the detector the data and simulation are in good agreement. However, in the forward directions a slight difference is observed between the data and simulation (see Fig. 11) and attributed to an underestimation of the quantity of material in the simulation before the electromagnetic calorimeter in the DELPHI endcaps. A correction is applied to the simulation by introducing the effect of extra bremsstrahlung emission corresponding to an additional 3% of a radiation length. Following [43], the probability w that an electron of initial energy E_0 has an observed energy between E and $E+\mathrm{d}E$ after traversing a thickness of t radiation lengths is

$$w(E_0,E,t)\,\mathrm{d}E=\frac{\mathrm{d}E}{E_0}\frac{[\ln(E_0/E)]^{(t/\ln 2)-1}}{\Gamma(t/\ln 2)}\,. \tag{8}$$

For each event, the corrected energy E is chosen randomly according to the distribution w. The optimal value of the parameter t was adjusted from the data and simulation comparison.

After the endcap correction was applied, good agreement between data and simulation was obtained throughout the detector. The residual systematic error on this absolute energy scale is estimated to be ±0.3% of the measured energy and is estimated from the selection cut stability and statistical precision of the data and simulation comparison.

Energy resolution. The resolution on the reconstructed electron energies was also compared between the data and simulation Bhabha samples. The agreement is improved by applying a Gaussian smearing to the simulation with a width varying between 1 and 2% of the measured electron energy in the barrel, and 2 to 4% in the endcaps, depending on the year of data taking. The systematic error on this smearing Gaussian width is estimated to be ±1% of the measured energy. This systematic does not affect the M_W determination but is a small component of the Γ_W measurement uncertainty for events containing electrons.

Energy linearity. The reconstructed electron energy was also studied as a function of the true energy. The Z peak and high energy running provided high statistic Bhabha samples with which to study electrons of 45 GeV and above 100 GeV energy. For these samples the "true" electron energy is taken from the beam energy. The reconstructed electron energy was also checked using low energy electrons from Compton events at the Z peak, and high energy electrons from radiative Bhabha scattering at high centre-of-mass energy. In these cases the true energy of the lepton is deduced from 3-body kinematics using only the angular in-

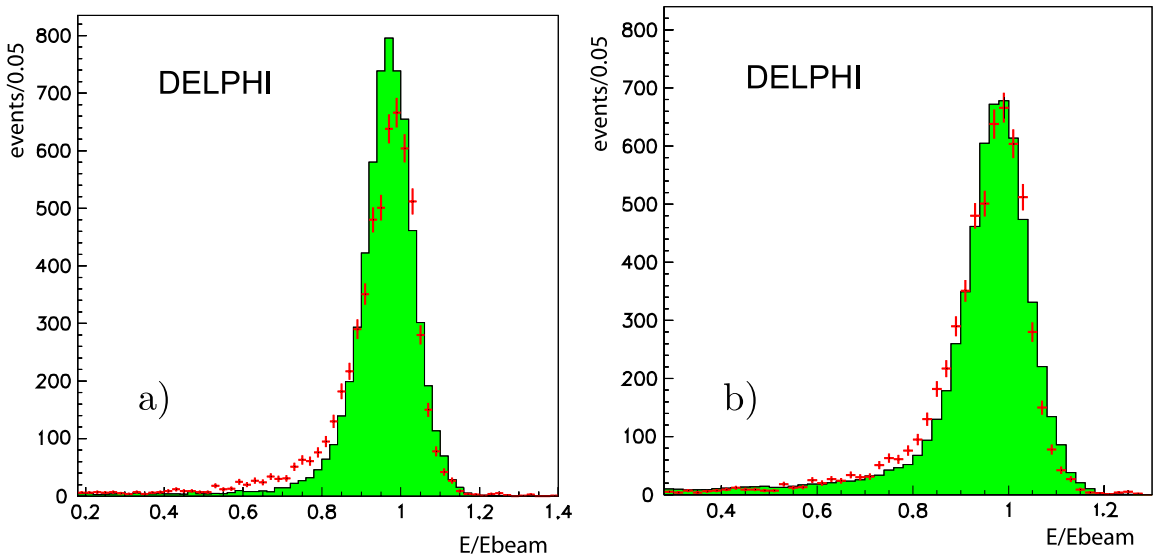

Fig. 11. The ratio $E/E_{\rm beam}$ for electrons in the endcaps from Bhabha events recorded at the Z peak in 1998. The *shaded histogram* is the simulation and the points are the data. Plot (**a**) shows the raw distribution, while plot (**b**) gives this after the bremsstrahlung correction discussed in the text. The resolution correction (see text) has also been applied

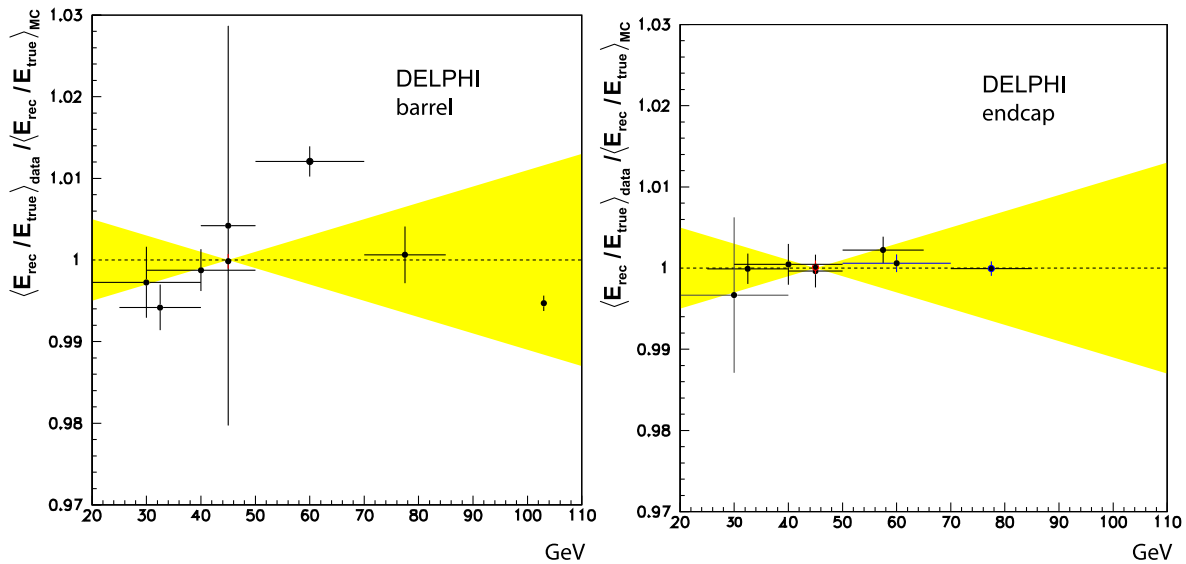

Fig. 12. The double ratio of reconstructed and true average energy values in data and simulation, $\langle E_{\rm rec}/E_{\rm true}\rangle_{\rm data}/\langle E_{\rm rec}/E_{\rm true}\rangle_{\rm MC}$, for data taken in 2000. The *shaded area* represents the quoted systematics due to a possible dependence of the energy calibration with the electron energy. The *left hand plot* is for electrons observed in the barrel electromagnetic calorimeter and the *right hand plot* for electrons in the endcap. Note that, by construction, the Bhabha point at 45 GeV is at one

formation and assuming that the unseen particle was along the beam axis. Figure 12 shows the compatibility of the reconstructed electron energy in data and simulation, only statistical errors are shown. One of the three points measured for radiative Bhabhas in the Barrel shows a discrepancy but this effect is not confirmed by the better measured high energy (non-radiative) Bhabha point, whereas physical calibration problems such as threshold effects or leakage in the calorimeter would be expected to increase in size with energy. Hence, no additional corrections are applied. A systematic error is estimated assuming a deviation of the energy calibration slope $E_{\rm data}/E_{\rm simulation}$ versus $E_{\rm simulation}$ of 1% over the range 25 to 70 GeV. These values approximately correspond to the relevant energy range for the observed electrons in the analysis.

6.4 Detector effects – taus

The $\tau\overline{\nu}_\tau q\bar{q}'$ channel differs from the other W^+W^- semi-leptonic decay channels as these events contain two (or three for leptonic tau decays) neutrinos in the final state.

Thus, the mass of the event can be determined only from the decay products of the other W. As a result the lepton systematics described in the preceding sections are not relevant to the $\tau\overline{\nu}_\tau q\bar{q}'$ channel. The only relevant systematic involving the tau decay products arises from uncertainties in the assignment of the reconstructed tracks between the tau product and the hadronically decaying W. This effect is small compared with the overall uncertainty on the jet energy and direction, the systematic on which is considered in the sections below.

6.5 Jet description

Jets are composite objects, and the detector and analysis response to them can be dependent on their internal structure. Therefore it is not straightforward to separate in a clean way uncertainties arising from the modelling of the detector in the simulation from those due to the theoretical description of the jet structure.

Moreover this description is not based on exact calculations, whose uncertainty can be in principle reasonably well estimated, but on phenomenological models tuned to best reproduce the data at the Z peak: the Lund model as implemented in PYTHIA is the standard choice for this analysis. In this situation the comparison of different models may be a useful tool to understand which parts of the fragmentation description the measurement is sensitive to, but only a direct comparison of the chosen model with well understood data samples, in particular Z hadronic decays, can give the ultimate estimate of the uncertainty from the observed data-simulation disagreements.

The jet studies performed are described in the text below and the corresponding jet correction systematic errors are provided in Table 4. The most relevant jet characteristics were calibrated on real data control samples, and uncertainties on these calibrations are propagated through the analysis.

Table 4. Contributions to the systematic error on the W mass measurement at 189 and 205 GeV related to jet reconstruction. The uncertainties on each of these numbers are typically 6 MeV/c^2

M_W Jet correction systematic errors (MeV/c^2)				
Sources of systematic error	189 GeV			
	$e\overline{\nu}_e q\bar{q}'$	$\mu\overline{\nu}_\mu q\bar{q}'$	$\tau\overline{\nu}_\tau q\bar{q}'$	$q\bar{q}'\bar{q}q'$
Energy scale	8	6	11	8
Energy resolution	3	3	5	9
Energy linearity	12	9	12	16
Angular bias	3	5	5	2
Angular resolution	–	–	–	8
Jet mass	9	8	8	10
	205 GeV			
	$e\overline{\nu}_e q\bar{q}'$	$\mu\overline{\nu}_\mu q\bar{q}'$	$\tau\overline{\nu}_\tau q\bar{q}'$	$q\bar{q}'\bar{q}q'$
Energy scale	11	9	16	8
Energy resolution	8	5	8	10
Energy linearity	15	11	20	8
Angular bias	9	8	7	19
Angular resolution	–	–	–	1
Jet mass	13	12	17	13

Energy scale. The absolute jet energy scale was studied in on-peak $Z \to q\bar{q}$ decays, by comparing the reconstructed energies, $E_{\rm rec}$, in data and simulation in selected two jets events. The b-tagging technique is used to remove b quark jets, which are essentially not present in W^+W^- decays. The true jet energy in these events is assumed to be the beam energy $E_{\rm beam}$, under the assumption that the bias introduced by QED ISR is described with negligible error in the simulation (the KK2f generator was used for these events). The double ratio of average values $\langle E_{\rm rec}/E_{\rm beam}\rangle_{\rm data}/\langle E_{\rm rec}/E_{\rm beam}\rangle_{\rm MC}$ was evaluated as a function of the jet polar angle and applied as a scale factor correction to the four-momentum components of the jet in simulated events. The correction value depends on the year as well as the angular region, with the deviation from unity ranging typically from a few per mille up to 3%–4% in the most forward region.

The systematic uncertainty on this correction is determined by the limited on-peak Z statistics, and it is estimated to be $\pm 0.3\%$.

Energy resolution. The same event sample used to study the jet absolute energy scale was also used to calibrate the jet energy resolution in the simulation. A Gaussian smearing was determined from the data and is applied to the simulated jet energy with a magnitude dependent on the ratio of the reconstructed and true jet energies. This procedure takes into account the asymmetric shape of the jet energy observable. When applying the correction to the simulated W^+W^- events an estimate of the true jet energy is required. When the event is reconstructed with two jets from each hadronically decaying W, the generated quark energies are used. However, when gluon radiation has given rise to an additional jet the true jet energy estimate is determined by applying the same clustering algorithm as used in the analysis to the simulated partons prior to the detector simulation. In both cases the association of the true and reconstructed jets is performed according to geometric criteria.

The average resolution correction ranges from 4.5% of the jet energy in the barrel to 6.6% in the endcaps. The correction is also dependent on the year. The systematic uncertainty on the correction is estimated to be $\pm 2\%$ of the jet energy.

Energy linearity. The dependence of the energy calibration as a function of the jet energy was checked using low energy jets from $q\bar{q}+$gluon events at the Z peak and high energy jets from $e^+e^- \to q\bar{q}$ decays at high energy.

In the first case, the true jet energy is determined using three-body massless kinematics. The jet energy range used in this study is restricted to the region where the data and simulation true energy distributions do not show sizeable discrepancies. This energy selection avoids introducing an

unnecessary sensitivity in this analysis to the modelling of hard gluon radiation in the simulation.

In the second high energy jet case the effective hadronic mass $\sqrt{s'}$ is required to be such that $\sqrt{s'/s} > 0.95$. The true jet energy is then again determined using three-body massless kinematics but now the third object is an hypothetical ISR photon emitted along the beam pipe. The difference between the estimated jet energy and the nominal beam energy is constrained to be smaller than 10 GeV.

A jet energy linearity slope in $E_{\rm data}/E_{\rm simulation}$ versus $E_{\rm simulation}$ is then determined. The study was performed separately in the barrel and endcap regions of the detector and for each data taking year. The results from the different data taking years are compatible within statistical errors. The study showed agreement in the slope at typically the 0.5% level over the range 25 to 75 GeV, and this deviation value is used to determine the systematic uncertainty.

Angular bias. As reported in [13], the reprocessing of data and simulation used for this analysis has a noticeable excess of tracks at low polar angles (forward tracks) in data as compared to the simulation. The most likely cause of this effect is an underestimation in the simulation of the track reconstruction efficiency for low-momentum particles at low polar angle.

This effect introduces a small bias in the distribution of the jets' reconstructed polar angle in the simulation compared with data. In order to evaluate the effect of such a bias, a systematic shift of the jets' polar angle is applied to the simulation. The shift as a function of the polar angle itself has been determined using on-resonance Z hadronic decays, and is found to have the form $0.008 \cos\theta_j^{5.3}$, where $0 < \theta_j < \pi/2$ is the polar angle of the jet. The corresponding W mass and width shifts have been evaluated and symmetric systematic errors of these values applied. The W mass uncertainty is reported in Table 4.

Angular resolution. A study of the acollinearity of jets in on-peak $Z \to q\bar{q}$ events was performed and appropriate smearings to the simulation of the jet angular direction, dependent on the polar angle of the jet, were estimated. The smearings on the polar angle are typically 5 mrads. A systematic error is estimated by applying an extra 5 mrad angular smearing.

Jet mass. The jet mass is known not to be exactly described in the simulation; both inaccuracies in the fragmentation description (related to the jet breadth due to soft and hard gluon radiation) and imperfections in the modelling of the detector response (reconstruction efficiencies and noise) are responsible for these discrepancies. However, only those data-simulation differences in the jet mass that are not compensated by differences in the inter-jet angle are relevant for the systematic uncertainty, since these cause systematic biases in the reconstructed W mass.

For this reason the fragmentation-induced differences are only marginally relevant for the mass measurement. Furthermore, the calibration procedure adopted, in particular for the energy and angular smearing, corrects for most of the effects given by the differences in jet breadth. The jet breadth is relevant as broader jets are worse reconstructed: they are detected with larger uncertainties on the jet direction; are likely to lose more energy due to the imperfect hermeticity of the detector; and cause more confusion in the jet clustering.

The jet correction procedure described above, as well as the constrained kinematic fit, modifies all the four-momentum components of the jet but leaves unchanged the jet boost, i.e. the E/m ratio. It is therefore useful to study this observable, instead of the simple jet mass.

Detector noise is a source of data-simulation discrepancy, which clearly biases the reconstructed boson mass, since it changes the mass and boost of the jets while leaving, on average, the inter-jet angle unchanged. Significant data-simulation differences in low energy neutral clusters, both in the electromagnetic and hadronic calorimeters, are attributed primarily to an imperfect noise description, while the discrepancies in the charged particles of jets are considered to be almost entirely due to the modelling of the fragmentation.

The average effect of removing low energy neutrals below 2 GeV on the jet m/E was evaluated as a function of the polar angle and of the m/E of the jet itself, since the impact of the noise depends on the breadth of the jet. The expected effect on the neutrals from fragmentation was subtracted. The fragmentation effect was obtained from charged particles, suitably scaled for the relative neutral and charged particle multiplicity.

This m/E effect was then propagated in the full analysis chain to extract the relative systematic uncertainty on the full mass and width measurements.

Fragmentation model. The effect of using different hadronisation models on the analysis was studied by replacing the standard choice, PYTHIA, with both the ARIADNE and HERWIG models, each tuned by DELPHI to best match experimental data. The mass and width shifts were evaluated at 189 GeV and 207 GeV centre-of-mass energies and are reported in Tables 5 and 6. Detailed studies performed

Table 5. Effect of different fragmentation models on the W mass determination

	ΔM_W MeV/c^2			
	$e\overline{\nu}_e q\bar{q}'$	$\mu\overline{\nu}_\mu q\bar{q}'$	$\tau\overline{\nu}_\tau q\bar{q}'$	$q\bar{q}'\bar{q}q'$
HERWIG – PYTHIA	-7 ± 10	-16 ± 9	-17 ± 13	-9 ± 5
ARIADNE – PYTHIA	-11 ± 9	-12 ± 9	-10 ± 12	-15 ± 5

Table 6. Effect of different fragmentation models on the W width determination

	$\Delta\Gamma_W$ MeV/c^2	
	$\ell\overline{\nu}_\ell q\bar{q}'$	$q\bar{q}'\bar{q}q'$
HERWIG – PYTHIA	$+46 \pm 13$	-2 ± 11
ARIADNE – PYTHIA	-9 ± 15	$+1 \pm 11$

Table 7. Effect of different fragmentation models on the W mass determination, after reweighting the heavy particle species rates in the Monte Carlo simulations to the measured rates

	ΔM_W MeV/c^2			
	$e\overline{\nu}_e q\bar{q}'$	$\mu\overline{\nu}_\mu q\bar{q}'$	$\tau\overline{\nu}_\tau q\bar{q}'$	$q\bar{q}'\bar{q}q'$
HERWIG Rew. – PYTHIA	-2 ± 10	-8 ± 9	-5 ± 13	-11 ± 6
ARIADNE Rew. – PYTHIA	-10 ± 9	-10 ± 9	-10 ± 12	-1 ± 4

Table 8. Effect of different fragmentation models on the W width determination, after reweighting the heavy particle species rates in the Monte Carlo simulations to the measured rates

	$\Delta\Gamma_W$ MeV/c^2	
	$\ell\overline{\nu}_\ell q\bar{q}'$	$q\bar{q}'\bar{q}q'$
HERWIG Rew. – PYTHIA Rew.	$+29\pm13$	$+3\pm8$
ARIADNE Rew. – PYTHIA Rew.	-11 ± 15	-1 ± 8

at the Z peak showed that for several observables all the models showed disagreements with the data and that these disagreements were all in the same direction: the jet mass variable, discussed in the previous paragraph, is a clear example. Hence the results of the hadronisation model comparison were used only to investigate the sensitivity of the analysis to specific features of the models, and not used directly as an evaluation of the systematic uncertainty due to the choice of model.

The biggest difference was found to be between PYTHIA and HERWIG and was shown to be largely due to the different production rates of heavy particles, mainly kaons, protons and neutrons. At parton level these differences modify not only the jet masses but also change the jet–jet angles accordingly, leaving the bosons invariant masses unchanged. However, the reconstruction and analysis procedure breaks this compensation since in the fully-hadronic event reconstruction all charged particle tracks are assigned the pion mass, and all neutrals are assumed to be massless (photon-like). In the semi-leptonic analysis, the nominal masses are used in the jet reconstruction for those particles with a positive identification, i.e. for charged kaons and protons identified by the RICH and for $K^0_{\rm S}$ and lambdas reconstructed as secondary vertexes from their decay products [14, 15].

The HERWIG version used, although tuned to best reproduce the Z peak DELPHI data, is known to describe the particle production rates poorly. This is especially the case for baryons, therefore using HERWIG accentuates this particle mass assignment effect. Generally the measured particle rates are closer to those in PYTHIA and ARIADNE. Reweighting in the models the production rates of the most abundant heavy particles species, kaons and protons, reduces the disagreement among the different models, bringing it to the level of the statistical uncertainty of the fit. Tables 7 and 8 show the residual discrepancies obtained between the models after they have been reweighted to the PYTHIA values. The component

Table 9. Effect on the W mass of reweighting the heavy particle species rates in the Monte Carlo simulations. The mass shifts were evaluated between the DELPHI tune of PYTHIA and versions reweighted to 1 sigma above and below the measured particle rates. The shift value reported is the average of the modulus of these two shifts. The measured charged multiplicity in a Z peak event for kaons is 2.242 ± 0.063 [42], whereas for protons the measured multiplicity is 1.048 ± 0.045 [42]

	ΔM_W MeV/c^2			
Particle type	$e\overline{\nu}_e q\bar{q}'$	$\mu\overline{\nu}_\mu q\bar{q}'$	$\tau\overline{\nu}_\tau q\bar{q}'$	$q\bar{q}'\bar{q}q'$
$K^\pm$	0.1 ± 0.3	0.9 ± 0.3	1.5 ± 0.4	0.2 ± 0.5
Proton	2.0 ± 0.4	1.5 ± 0.3	3.2 ± 0.5	3.5 ± 0.5

of the fragmentation systematic error that is not due to the heavy particle multiplicity effect is obtained from these numbers. The largest value – either the central value or its uncertainty – from either model is taken as the systematic error estimate.

The component of the fragmentation error that is due to the heavy particle rate was also evaluated for the W mass analysis; this small component of the error is neglected for the W width analysis. The W mass shift was evaluated between the DELPHI tune of PYTHIA and the same events reweighting to the measured particle rates $\pm1\sigma$ of their uncertainty. The average of the modulus of the two shifts is reported in Table 9 and is taken as the estimate of the fragmentation error due to the heavy particle multiplicity.

The combined fragmentation error was evaluated for the W mass by adding the particle reweighting effects and the model variation uncertainty in quadrature. This fragmentation error is listed separately from the other jet description uncertainties in the systematic uncertainty summary tables (Tables 14–16).

6.6 Mixed Lorentz boosted Zs

An alternative method of evaluating the jet description systematic is to use the technique of mixed Lorentz boosted Zs (MLBZ). This method attempts to emulate W^+W^- events using two on-peak Z events. The emulated W^+W^- events are constructed both from simulated events and the large statistics sample of Z peak data events. Standard W mass and W width analyses can then be performed on these event samples. Hence, the MLBZ method provides a direct comparison between data and the simulation

model of choice. The difference between the measurements made from the data and simulation MLBZs can be interpreted as primarily providing a statistically sensitive cross-check of the fragmentation systematic assigned to the W mass and width measurements. This method would also identify some sources of detector modelling error.

A $W^+W^- \to f\bar{f}'\bar{f}f'$ event is emulated by selecting two Z events and rotating and Lorentz boosting them so that their superposition reflects a true W^+W^- event. The mixture of quark species will not be the same as in true W^+W^- events, it will however be the same between the data and simulated Z samples that are used in the comparison. To emulate a $q\bar{q}'\bar{q}q'$ event two hadronically decaying Z events were used. To emulate a $\ell\overline{\nu}_\ell q\bar{q}'$ event one Z decaying into hadrons and one Z decaying into charged leptons was used. One hemisphere of the $Z \to l^+l^-$ decay is removed to represent the $W \to \ell\overline{\nu}_\ell$ decay. The emulation process is performed by manipulating the reconstructed tracks and calorimeter energy clusters.

A realistic distribution of W^+W^- events is obtained by using event templates. The four momenta of the four primary fermions in a WPHACT W^+W^- event are used as the event template. The Z events are chosen such that they have a thrust axis direction close to the polar angle of one of the W fermions. This ensures that the distribution in the detector of the tracks and energy clusters selected in the Z event follows that expected in W^+W^- events. Each of the template Ws is then boosted to its rest frame. The particles in a final state of a selected Z event are rotated to match the rest-frame direction of the fermions from the template W. The energy and momentum of the Z events are then rescaled to match the kinematic properties of the W boson decay. The two Z events are then each boosted into the lab frame of the template W^+W^- event and mixed together. The same W^+W^- event templates are used for the construction of both the data and Monte Carlo simulation MLBZ events, thus increasing the correlation between both emulated samples.

Tests were performed to confirm the reliability of the MLBZ method in assessing systematic errors. MLBZs were produced using Zs with the PYTHIA, HERWIG and ARIADNE models and the observed mass shifts were compared and found to agree with the statistically limited mass shifts observed in W^+W^- simulation events. A significant mass shift ($300\,\mathrm{MeV}/c^2$) was introduced by using the cone rejection algorithm (discussed in Sect. 5.3.2) for the W mass measurement in the $q\bar{q}'\bar{q}q'$ channel. The real and simulated MLBZs and W^+W^- events agreed on the estimated size of the mass shift between the standard and cone estimators at the 15% level.

The MLBZ method was used to create emulated W^+W^- event samples. The Z events were selected from data recorded during the LEP2 calibration runs of the same year or from the corresponding Monte Carlo simulation samples. Values for the M_W and Γ_W estimators were determined separately for the data and simulation samples. This method has been applied on a cross-check analysis in the semi-leptonic channels and to the standard fully-hadronic analysis. The results from the fully-hadronic analysis are shown in Table 10. The semi-leptonic cross-check analysis applied the MLBZ procedure to the W mass determination separately in the electron, muon, and tau channels with uncertainties of around $8\,\mathrm{MeV}/c^2$ being obtained and the results being compatible with the systematic uncertainties quoted in this paper. The MLBZ method provides a useful cross-check of the size of the systematic uncertainty arising from fragmentation and other jet description errors reported in the previous section. From the values obtained from the MLBZ method we conclude that the systematic uncertainties have not been significantly underestimated.

Table 10. Results obtained with the MLBZ method (see text)

	$\sqrt{s}$ GeV MLBZ	ΔM_W MeV/c^2	$\Delta\Gamma_W$ MeV/c^2
$q\bar{q}'\bar{q}q'$ Data – PYTHIA	206.5	-7.9 ± 4.9	20.1 ± 10.5

6.7 Electroweak radiative corrections

The measurements of the W mass and width described in this paper rely upon the accuracy of the event description provided by the simulation. Hence, the modelling accuracy of the electroweak radiative corrections implemented in the event generator is a source of systematic uncertainty.

The radiative corrections for four-fermion events are described in [18] and in Sect. 4.2. For W^+W^- (CC03) events, the signal used in this analysis, the corrections are based on YFSWW [23, 24] and the effect of the theoretical uncertainties in it on the W mass measurement were initially studied in [44] at pure event generator level.

In [45] this study has been performed in the context of the full DELPHI simulation and analysis procedure; furthermore the main uncertainties due to non-CC03 four-fermion background events have been studied. Radiative corrections uncertainties on non-four-fermion background events are included in the uncertainty estimated on the background.

Several categories of uncertainty sources have been studied, which are considered here in turn.

W^+W^- Production: initial state radiation (ISR). ISR plays a key role in the W mass analysis as it is one of the main sources of the bias on the fitted result with respect to the true value. This bias, which is removed by calibrating the fits with the simulation, is due to the energy-momentum conservation constraint used in the kinematical constrained fits. The ISR is computed in the YFS exponentiation approach, using a leading logarithm (LL) $\mathcal{O}(\alpha^3)$ matrix element.

The difference between the best result, obtained from implementing the $\mathcal{O}(\alpha^3)$ ISR matrix element, and the $\mathcal{O}(\alpha^2)$ one provides an estimate of the effect of missing the matrix element for higher orders. The missing higher orders lead to the use of a wrong description for events with

more than three hard photons or more than one photon with high p_{t}.

The difference between the best result and the $\mathcal{O}(\alpha)$ result includes the previous study, and can be used as an estimate of the upper limit of the effect of missing the non-leading logarithm (NLL) terms at $\mathcal{O}(\alpha^2)$; this effect of missing NLL terms is expected to be smaller than the effect from the LL terms given by this $\mathcal{O}(\alpha^3)$ to $\mathcal{O}(\alpha)$ difference.

Also taking into account the study performed in [44], the ISR related uncertainty can be conservatively estimated at $1\,\mathrm{MeV}/c^2$ for the mass and $2\,\mathrm{MeV}/c^2$ on the width.

W decay: final state radiation (FSR). The FSR description and uncertainty is tightly linked to the final state considered. QED FSR from quarks is embedded in the parton shower describing the first phase of the hadronisation process. It is therefore essentially impossible to separate it from the rest of the hadronisation process, and the related uncertainty is considered as included in the jet and fragmentation related systematics.

FSR from leptons is described by PHOTOS. The difference between the best result, based on the NLL treatment, and the LL one can give an estimate of the effect of the missing part of the $\mathcal{O}(\alpha)$ FSR correction. While the result depends on the semi-leptonic channel, the difference is always less than $1\,\mathrm{MeV}/c^2$.

In [44] the effect of the missing higher orders beyond $\mathcal{O}(\alpha^2)$ has been found to be negligible at generator level. Simple perturbative QED considerations suggest that the size of the effect should not exceed the size of the effect from the missing part of the $\mathcal{O}(\alpha)$ FSR correction; therefore conservatively the $1\,\mathrm{MeV}/c^2$ can be doubled to take into account both of these components of the uncertainty.

Non-factorizable QED interference: NF $\mathcal{O}(\alpha)$ corrections. Non-factorizable $\mathcal{O}(\alpha)$ QED interference between Ws is effectively implemented through the so-called Khoze–Chapovsky [46] (KC) ansatz.

The effect of using the KC ansatz with respect to the Born calculation, where this interference is not described, can be considered as an upper limit of the missing part of the full $\mathcal{O}(\alpha)$ calculation and of the higher order terms. A dedicated study shows that the effect is less than $2\,\mathrm{MeV}/c^2$ for all the measurements.

Ambiguities in leading pole approximation (LPA) definition: non-leading (NL) $\mathcal{O}(\alpha)$ corrections. Two sources of uncertainties are considered, following the study in [44]. The effect of missing higher orders can be, at least partly, evaluated by changing the electroweak scheme used in the $\mathcal{O}(\alpha)$ calculation. This essentially means changing the definition of the QED fine structure constant used in the $\mathcal{O}(\alpha)$ matrix element. The effect is very small, at the limit of the fit sensitivity, both for the mass and the width.

The second, more relevant, source of uncertainty connected to the LPA is in its possible definitions, i.e. the ambiguity present in the way of expanding the amplitude around the doubly resonant W pole. The standard YFSWW uses the so-called LPA_A definition; a comparison with the LPA_B one can give an estimate of the effect from the intrinsic ambiguity in the LPA definition. A dedicated study has been performed evaluating the difference

$$\begin{aligned}\Delta\mathcal{O}(\alpha)(\mathrm{LPA}_A - \mathrm{LPA}_B) = {} & \Delta(\text{Best LPA}_A - \text{no NL LPA}_A) \\ & - \Delta(\text{Best LPA}_B - \text{no NL LPA}_B)\end{aligned}$$

in order to evaluate only the effect of the different scheme on the radiative corrections (and not at Born level). The size of the effect is less than $1\,\mathrm{MeV}/c^2$ for the mass and less than $4\,\mathrm{MeV}/c^2$ for the width.

Radiative corrections on 4-f background diagrams: single W. The double pole approximation (DPA) is known to be valid within a few W widths of the double resonant pole. The DPA correction is applied only to the CC03 part of the matrix element (and partly to the interference, see [18]); non-CC03 diagrams contributions are not directly affected by the DPA uncertainty (except for possible effects in the interference term that is relevant for the electron channel).

It is clear that this procedure still leaves the problem of the approximated radiative corrections treatment for the non-CC03 part of the matrix element (and the interference). The ISR studies previously discussed can reasonably cover the most relevant part of the electroweak radiative corrections uncertainties present also for the W^+W^--like 4-f background diagrams, e.g. the non-CC03 part. There is, however, a notable exception: the so-called single W diagrams for the $q\bar{q}'e\nu$ final state.

The bulk of single W events are rejected in the W mass and width analysis, since the electron in these events is lost in the beam pipe. But the CC03-single W interference is sizeable, and it has a strong impact on the W mass result in the electron channel. The situation is different in the W width analysis, where in $e\overline{\nu}_e q\bar{q}'$ events reconstructed by the electron analysis the effects of non-CC03 diagrams and the CC03–non-CC03 interference are opposite in sign and almost completely cancel.

The situation is made even more complex by the cross-talk between channels, e.g. events belonging in reality to one channel but reconstructed as belonging to another one. This cross-talk is particularly relevant between semi-leptonic electron and tau decays, and this explains why the τ channel analysis is also sensitive to this uncertainty source.

The effect of this uncertainty has been studied in two ways. Firstly, since the uncertainty on the single W rate associated to radiative corrections is known in literature to be about 4%, the non-CC03 part of the matrix element, assumed to be dominated by the single W contribution, has been varied by 4% for $q\bar{q}'e\nu$ final states. Another possible source of uncertainty related to 4-f background is estimated by partly applying the DPA correction to the interference term (see the discussion in [18]). The effect of this way of computing the corrections can be considered as another estimate of the uncertainty related to the 4-f background presence.

The maximal size of these effects is about $6\,\mathrm{MeV}/c^2$ (for the mass in $qqe\nu$ and the width in $qq\tau\nu$).

Total uncertainty. The results of all the studies presented are combined in a single uncertainty for each channel. Ta-

Table 11. Summary of the systematic uncertainties on the W mass due to electroweak corrections. The total is computed adding linearly the absolute values of all the contributions

M_W electroweak correction systematic errors (MeV/c^2)				
Uncertainty source	$e\overline{\nu}_e q\bar{q}'$	$\mu\overline{\nu}_\mu q\bar{q}'$	$\tau\overline{\nu}_\tau q\bar{q}'$	$q\bar{q}'\bar{q}q'$
ISR	1.0	1.0	1.0	1.0
FSR	0.5	0.5	1.0	–
NF $\mathcal{O}(\alpha)$	1.0	1.0	1.0	2.0
NL $\mathcal{O}(\alpha)$	1.0	1.0	1.0	1.0
4-f background	5.5	0.5	1.0	0.5
Total	9	4	5	4.5

Table 12. Summary of the systematic uncertainties on the W width due to electroweak corrections. The total is computed adding linearly the values of all the contributions

Γ_W electroweak correction systematic errors (MeV/c^2)				
Uncertainty source	$e\overline{\nu}_e q\bar{q}'$	$\mu\overline{\nu}_\mu q\bar{q}'$	$\tau\overline{\nu}_\tau q\bar{q}'$	$q\bar{q}'\bar{q}q'$
ISR	2.0	2.0	2.0	2.0
FSR	1.0	1.0	2.0	–
NF $\mathcal{O}(\alpha)$	2.0	2.0	2.0	2.0
NL $\mathcal{O}(\alpha)$	4.0	4.0	4.0	4.0
4-f background	2.0	1.0	6.0	1.0
Total	11	10	16	9

bles 11 and 12 present the estimates for the mass and width from the different sources of uncertainties discussed above.

The total uncertainty per channel is conservatively computed summing linearly the values of the contributions. All the numbers have been rounded to 0.5 MeV/c^2.

Reference [18] also reports a comparison of YFSWW with the other completely independent Monte Carlo generator RacoonWW [47, 48], which implements radiative corrections in the DPA. This study has not been directly used in the error estimation presented here due to the limitations in the treatment of non-collinear radiation in RacoonWW. However, this study does provide additional confidence in the validity of the YFSWW calculation.

As can be seen, the uncertainty on the W mass associated with the electroweak radiative corrections is found to be less than 10 MeV/c^2.

6.8 LEP collision energy

The average LEP collision energy is evaluated at 15 min intervals of running or after significant changes in the beam energy. The measured centre-of-mass energy is imposed as a constraint in the kinematic fit, and hence the relative error on the collision energy translates to approximately the same fractional error on the W mass determination. The effect of the uncertainty on the W width determination is negligible.

The beam energy is estimated using the LEP energy model, discussed in Sect. 2 based on 16 NMR probes in dipole magnets around the LEP ring calibrated with the RDP technique. The compatibility of three cross-check methods with this determination was used to determine a set of small energy offsets. The relative size of this offset was energy dependent, rising to a maximum of 1.6×10^{-5} at 207 GeV centre-of-mass energy.

The LEP energy working group also assessed the uncertainties in the collision energies and supplied these in the form of a 10×10 correlation matrix. The uncertainties increase as the collision energy increases, due to the fact that higher energies are further from the RDP normalisation region. The errors are given in Table 13. At 183 GeV centre-of-mass energy the uncertainty on the collision energy is 20.3 MeV. This rises to 23.7 MeV at 202 GeV. For the energy points at values of 205 and 207 GeV, taken in the year 2000, there is an additional uncertainty due to the 'bending field spreading' strategy, in which the corrector magnets were powered in a coherent manner to increase the overall dipole field and thus the LEP energy [9]. This leads to a larger error for the year 2000. For the energy points at 161 and 172 GeV, taken in the year 1996, there is also a small increase in the error, compared to 183 GeV, due to increased uncertainties in the NMR calibration for this year.

The mean energy difference between the electron and positron beams is less than 4 MeV at all energies and hence the effect on the W mass or width determination is negligible. The momentum spread of the electrons or positrons in a bunch gives rise to a variation in the centre-of-mass energy of the collisions and boost of the centre-of-mass frame with respect to the laboratory frame. The spreads in centre-of-mass collision energies have been evaluated by the LEP energy working group [9] and range from 144 to 265 MeV. The corresponding effects for the W mass and width analyses are negligible.

6.9 Aspect ratio

The aspect ratio is defined as the ratio of the length to the width of the detector. As all the subdetectors of DELPHI are aligned with respect to the vertex detector, the knowledge of the aspect ratio is limited by the precision to which the position and dimensions of the Vertex Detector can

Table 13. Uncertainties on the LEP energies for the different centre-of-mass energy points

	$\sqrt{s}$ nominal [GeV]									
	161	172	183	189	192	196	200	202	205	207
E_{cm} error [MeV]	25.4	27.4	20.3	21.6	21.6	23.2	23.7	23.7	36.9	41.7

be measured. The effect of a mismeasurement of the aspect ratio is to introduce a bias on the measurement of the polar angle, θ. As the W boson production polar angle is not isotropic but forward peaked, a mismeasurement of the aspect ratio would result in a small bias on the average opening angle of the W decay products, and hence induce a small bias on the reconstructed W mass.

The correspondence of hits in the overlapping silicon modules is sensitive to a misalignment of the Vertex Detector. In fact the study of these overlaps constitutes an essential part of the procedure for the alignment of the Vertex Detector. From this study, discussed further in [13], it is concluded that a reasonable estimate of the aspect ratio uncertainty is 3×10^{-4}. Such a bias would result in a shift in W mass below $1\,\mathrm{MeV}/c^2$ for the semi-leptonic channel, and of $2\,\mathrm{MeV}/c^2$ for the fully-hadronic one. The effect on the W width is negligible.

6.10 Background description

The background events for the W pair selection are from four-fermion or hadronic two-fermion processes.

The four-fermion background uncertainty is studied and described in the electroweak corrections uncertainties (Sect. 6.7) and in the jet description studies (Sect. 6.5) parts of this paper.

The dominant source of background to W pair production, both in the semi-leptonic and in the fully-hadronic channel, is from $Z \to q\bar{q}(\gamma)$ events.

In the semi-leptonic channel, the two-fermion background is relatively small with the main uncertainty in its rate arising from the discrepancy between data and simulation in the rate of misidentification of energetic photons (from radiative return to the Z peak events) as electrons. This misidentification is mainly due to the electron–positron conversion of photons and the spurious associations of forward vertex detectors hits to an electromagnetic cluster in the calorimeter. A data-simulation comparison shows that a 10% fluctuation of the background is possible without significantly degrading the agreement between the data and simulation. The theory uncertainty on the two-fermion cross-section is generally small, in the worst case at the 2% level [49].

In the fully-hadronic channel, the two-fermion background is more important, and the major contribution to the uncertainty is from the four-jet final state production mechanism. The study performed in [50] has shown that the maximal difference in the estimated two-fermion background rate is 10% coming from changing from PYTHIA to HERWIG as the hadronisation model, with the ARIADNE model giving intermediate results. The effect on the W mass is $13\,\mathrm{MeV}/c^2$ at $\sqrt{s} = 189\,\mathrm{GeV}$, and $4\,\mathrm{MeV}/c^2$ at $\sqrt{s} = 206.5\,\mathrm{GeV}$, while the effect on the W width is $40\,\mathrm{MeV}/c^2$ over the whole range of centre-of-mass energies.

In summary, applying a variation of $\pm 10\%$ on the $Z \to q\bar{q}(\gamma)$ event rate is used to provide an estimate of the systematic uncertainty on the background level for both the semi-leptonic and fully-hadronic channel mass and width measurements. This variation also covers any discrepancies seen in the data and simulation comparison plots shown in this paper.

The importance of the background event mass distribution has also been investigated. In the semi-leptonic analyses the mass distribution taken from the simulation has been replaced with a constant level and half of the variation in the result has been taken as a systematic. In the fully-hadronic channel this systematic was assessed by changing the generator used for the background between PYTHIA, HERWIG and ARIADNE.

The background level and background shape uncertainties were added in quadrature and the resulting errors are reported in Tables 14–16 below.

6.11 Bose–Einstein correlations

Correlations between final state hadronic particles are dominated by Bose–Einstein correlations (BEC), a quan-

Table 14. Contributions to the systematic error on the W mass measurement for data taken at a nominal centre-of-mass energy of 189 GeV. Where two uncertainties are reported in the $q\bar{q}'\bar{q}q'$ analysis column the first corresponds to the standard analysis and the second to the cone jet reconstruction analysis

	M_W systematic errors (MeV/c^2) at 189 GeV			
Sources of systematic error	$e\overline{\nu}_e q\bar{q}'$	$\mu\overline{\nu}_\mu q\bar{q}'$	$\tau\overline{\nu}_\tau q\bar{q}'$	$q\bar{q}'\bar{q}q'$
Statistical error on calibration	12	10	15	4
Lepton corrections	24	16	–	–
Jet corrections	18	15	19	24
Fragmentation	10	10	13	12
Electroweak corrections	9	4	5	5
Background	5	1	12	17
LEP energy	9	9	9	9
Bose–Einstein correlations	–	–	–	31/26
Colour reconnection	–	–	–	212/116

Table 15. Contributions to the systematic error on the W mass measurement for data taken at a nominal centre-of-mass energy of 205 GeV. Where two uncertainties are reported in the $q\bar{q}'\bar{q}q'$ analysis column the first corresponds to the standard analysis and the second to the cone jet reconstruction analysis

M_W systematic errors (MeV/c^2) at 205 GeV				
Sources of systematic error	$e\overline{\nu}_e q\bar{q}'$	$\mu\overline{\nu}_\mu q\bar{q}'$	$\tau\overline{\nu}_\tau q\bar{q}'$	$q\bar{q}'\bar{q}q'$
Statistical error on calibration	15	10	17	4
Lepton corrections	25	21	–	–
Jet corrections	26	21	33	28
Fragmentation	10	10	13	12
Electroweak corrections	9	4	5	5
Background	4	6	19	5
LEP energy	15	15	15	15
Bose–Einstein correlations	–	–	–	31/26
Colour reconnection	–	–	–	212/116

tum mechanical effect that enhances the production of identical bosons close in phase space. The net effect is that multiplets of identical bosons are produced with smaller energy-momentum differences than non-identical ones.

BEC for particles produced from the same W boson affect the normal fragmentation and are therefore treated implicitly in the fragmentation uncertainties, which are constrained by the large amount of Z-data. BEC for pairs of particles coming from different Ws cannot be constrained or safely predicted by the information from single hadronically decaying vector bosons.

A dedicated and model-independent measurement of the BEC effect was performed by the DELPHI collaboration in [51] while other LEP experiments have made similar measurements [52–54]. Comparing these results with Monte Carlo models constitutes the only way to estimate potential systematic uncertainties from BEC. The LUBOEI model BE_{32} [55] was found to give the largest shift in the measured value of M_W for a given amount of BEC. Other models give smaller shifts and some models predict no appreciable BEC shifts at all. It was decided not to apply any corrections due to BEC and evaluate the systematic error as the largest predicted shift consistent with the DELPHI data. The predicted shift plus one standard deviation of its error is used as the estimator of the systematic error.

The DELPHI result for BEC is a 2.4 standard deviation evidence for BEC between different Ws and a correlation strength, Λ, which can be compared to the BE_{32} prediction at the same effective correlation length scale:

$$\Lambda_{\mathrm{data}}/\Lambda_{\mathrm{BE}_{32}} = 0.55 \pm 0.20(\mathrm{Stat.}) \pm 0.11(\mathrm{Syst.})\,. \qquad (9)$$

The predicted mass shift, BEC inside Ws only – BEC inside and between Ws, using BE_{32} (with model parameters $\mathrm{PARJ}(92) = 1.35$ and $\mathrm{PARJ}(93) = 0.34$) is $40 \pm 10\,\mathrm{MeV}/c^2$ for the standard mass analysis, $33 \pm 11\,\mathrm{MeV}/c^2$ for the cone jet mass reconstruction analysis and $-17 \pm 20\,\mathrm{MeV}/c^2$ for the W width analysis. The observed mass shift in BE_{32} is linear in the observed correlation, $\Lambda_{\mathrm{BE}_{32}}$. Applying the one standard deviation upper bound of the correlation parameter this translates into a systematic error of $31\,\mathrm{MeV}/c^2$ from BEC for the standard analysis and $26\,\mathrm{MeV}/c^2$ for the cone analysis. A systematic error of $20\,\mathrm{MeV}/c^2$ is applied for the W width. The mass and width shifts were evaluated with the simulation model over the full range of centre-of-mass energies and no energy dependence was observed. The shifts reported are the average values. Conservatively, these errors are applied as symmetric uncertainties.

The combined DELPHI BEC measurements of the correlation strength and effective correlation length scale suggest that the between-W BEC occur with an effective correlation length scale that is larger than the one predicted by BE_{32}. If this is the case, the number of pairs effectively affected by the BEC is reduced and also the effect per pair is diminished. Furthermore, the other LEP experiments have reported smaller values of $\Lambda_{\mathrm{data}}/\Lambda_{\mathrm{BE}_{32}}$ than that observed by DELPHI. Hence the systematic uncertainties applied in this analysis are considered conservative.

Table 16. Contributions to the systematic error on the W width measurement for data taken at a nominal centre-of-mass energy of 205 GeV

Γ_W systematic errors (MeV/c^2) at 205 GeV		
Sources of systematic error	$\ell\overline{\nu}_\ell q\bar{q}'$	$q\bar{q}'\bar{q}q'$
Statistical error on calibration	15	9
Lepton corrections	48	–
Jet corrections	38	169
Fragmentation	29	8
Electroweak corrections	11	9
Background	43	51
Bose–Einstein correlations	–	20
Colour reconnection	–	247

6.12 Colour reconnection

In the reaction $e^+e^- \to W^+W^- \to (q_1\bar{q}_2)(q_3\bar{q}_4)$ the hadronisation models used for this analysis treat the colour

singlets $q_1\bar{q}_2$ and $q_3\bar{q}_4$ coming from each W boson independently. However, interconnection effects between the products of the two W bosons may be expected since the lifetime of the W bosons ($\tau_W \simeq \hbar/\Gamma_W \simeq 0.1\,\mathrm{fm}/c$) is an order of magnitude smaller than the typical hadronisation times.

The exchange of coloured gluons between partons from hadronic systems from different W bosons can induce the so-called colour reconnection (CR) effect in the development of the parton shower. This effect can in principle distort the properties of the final hadronic system and therefore affect the W mass measurement, if not properly accounted for in the simulation.

At perturbative level the effects are expected to be small [56], and the impact on the reconstructed W mass has been evaluated to be at most $5\,\mathrm{MeV}/c^2$. However, CR effects can be large at hadronisation level, due to the large numbers of soft gluons sharing the space-time region. These effects have been studied by introducing CR effects into hadronisation models and comparing with DELPHI data and are reported in [38].

The most studied model, and the one used for the evaluation of the systematic uncertainty on the W mass and width measurement, is the Sjöstrand–Khoze "Type 1" model (SK-I) [57, 58]. This model of CR is based on the Lund string fragmentation phenomenology: the strings are considered as colour flux tubes with some volume, and reconnection occurs when these tubes overlap. The probability of reconnection in an event, P_{reco}, is parameterised by the value κ, according to the volume of overlap between the two strings V_{overlap}:

$$P_{\mathrm{reco}} = 1 - \mathrm{e}^{-\kappa V_{\mathrm{overlap}}} \,. \tag{10}$$

The parameter κ determines the reconnection probability. By comparing the data with the model predictions evaluated at several κ values it is possible to determine the value most consistent with the data and extract the corresponding reconnection probability.

Another model has been developed by the same authors (SK-II') and also implemented in PYTHIA but is found to predict a smaller shift on the reconstructed W mass than SK-I for the same reconnection probability.

Further CR models are available in the HERWIG and ARIADNE Monte Carlo programs. In ARIADNE, which implements an adapted version of the Gustafson–Häkkinen model [59], the model used [60] allows for reconnections between partons originating in the same W boson, or from different W bosons if they have an energy smaller than the width of the W boson. The mass shift from CR is evaluated from the difference between the shift when the reconnections are made only in the same W boson and when the full reconnections are made. In the standard DELPHI analysis, the shift was found to be $11 \pm 11\,\mathrm{MeV}/c^2$.

In HERWIG the partons are reconnected, with a reconnection probability of 1/9, if the reconnection results in a smaller total cluster mass. The shift in the reconstructed W mass at 189 GeV centre-of-mass energy was found to be $29 \pm 7\,\mathrm{MeV}/c^2$, the same shift as obtained from a κ value of 0.29 in the SK-I model.

DELPHI has performed two analyses to compare these simulation models with data that are described in detail in [38].

The first one is based on the measurement of the particle flow between the jets in a four-jet W^+W^- event. On a subsample of strictly four-jet events two regions can be defined, the region between jets from the same W (called inside-W regions) and the region between jets from different W bosons (called between-W regions). The ratio R of the particle fluxes in the inside-W and between-W regions (limiting the analysis to the central part of these regions) is an observable sensitive to CR effects. The comparison of the flux measured in real data with the prediction of the SK-I model as a function of κ allows the value to be determined that is most consistent with data and the uncertainty on the value.

The second method used exploits the observation that in the direct reconstruction analysis of the W mass, different W mass estimators have different sensitivities to CR effects. As discussed in Sect. 5.3.2 removing particles

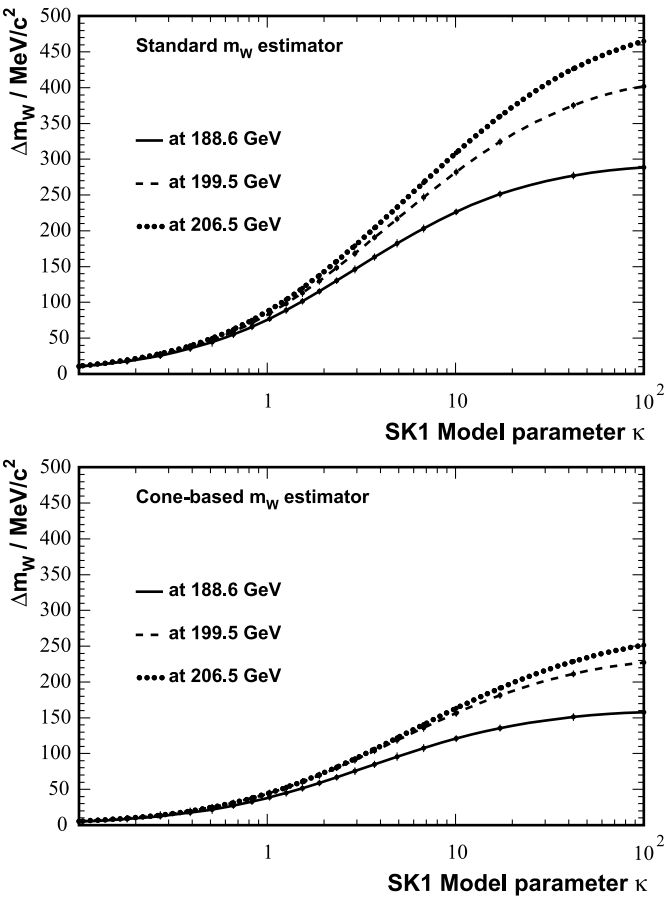

Fig. 13. W mass shift caused by the colour reconnection effect as described in the SK-I model plotted as a function of the model parameter κ, which controls the fraction of reconnected events. The *upper plot* is for the standard W mass analysis and the *lower plot* for when the cone jet reconstruction technique is applied

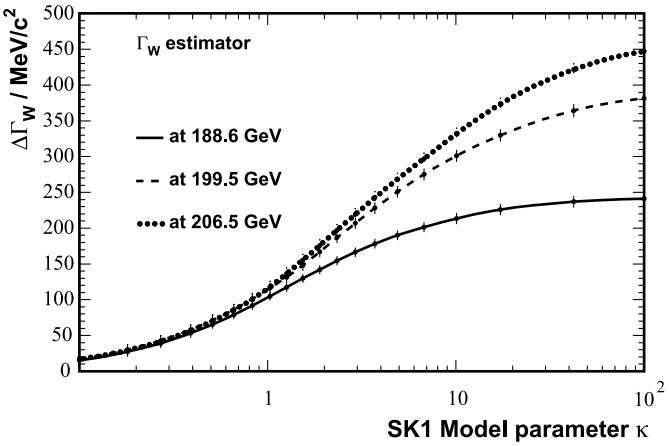

Fig. 14. W width shift caused by the colour reconnection effect as described in the SK-I model plotted as a function of the model parameter κ, which controls the fraction of reconnected events

from the inter-jet regions reduces the sensitivity to CR effects and hence can be used to measure the CR effect. The correlation between the measurement of the mass shift (using the standard or cone jet reconstruction techniques) and the measurement of the mass from these techniques is only 11%.

From the combination of these two analyses and in the framework of the SK-I model, the value of the κ parameter most compatible with the data is found to be [38]

$$\kappa = 2.2 \pm^{2.5}_{1.3} .$$

The CR shift in the reconstructed W mass as a function of the SK-I κ parameter is provided as Fig. 13, the results of the standard and cone jet reconstruction techniques are indicated. Figure 14 shows the CR shift for the W width reconstruction analysis.

The systematic uncertainty on the W mass and width is calculated using the one standard deviation upper bound of κ of 4.7. As reported above, this systematic error is considerably larger than that which would be evaluated from the ARIADNE or HERWIG CR models. Furthermore, this value of κ is larger than that reported by the other LEP experiments [39–41]. The CR W mass shift is dependent on the centre-of-mass energy in the SK-I model as shown in Figs. 13 and 14. However, we prefer not to rely on the centre-of-mass energy evolution of the SK-I CR shift (leading to a change in relative weights when averaging the results from different centre-of-mass energies) and instead choose to quote the systematic errors at 200 GeV (close to the average centre-of-mass energy of the data). In light of the significant range of CR effect estimates no correction is made to the W mass or width results and for simplicity a symmetric systematic uncertainty is applied. The corresponding systematics uncertainties on the W mass are 212 MeV/c^2 (standard), 116 MeV/c^2 (cone jet reconstruction) and 247 MeV/c^2 for the W width analysis.

7 Results

The results of the analyses and the final combinations of these results are presented in this section. The results are obtained at a range of nominal centre-of-mass energies and in the four event selection channels. Combined results are obtained from an average of these results and also an average with the previously published DELPHI data [1, 2] that have not been reanalysed in this paper.

Subdividing the results by data taking years and nominal centre-of-mass energies enables a proper treatment of the correlated systematic uncertainty from the LEP collision energy and other dependences on the centre-of-mass energy or data taking period. A detailed breakdown of the sources of systematic uncertainty, as shown in Tables 14–16, is provided for each result and the correlations specified.

The combination is performed and the evaluation of the components of the total error assessed using the best linear unbiased estimate (BLUE) technique [61].

7.1 W mass

The W mass is extracted separately in the analyses designed to select the $e\overline{\nu}_e q\bar{q}'$, $\mu\overline{\nu}_\mu q\bar{q}'$ and $\tau\overline{\nu}_\tau q\bar{q}'$ decay channels. The values obtained are given in Table 17 for the analysed centre-of-mass collision energies. The semi-leptonic channel analysis results are combined into a single $\ell\overline{\nu}_\ell q\bar{q}'$ value for each year of data taking. When performing these combinations the following sources of systematic uncertainty are taken as fully correlated between lepton channels and between years: electroweak corrections, fragmentation, jet corrections, lepton corrections, background. The LEP energy measurement correlations are taken from the matrix supplied in [9]. The simulation calibration statistics are taken as uncorrelated.

The W mass is also obtained from the $q\bar{q}'\bar{q}q'$ channel using both the standard and cone jet reconstruction technique. The results obtained from these analyses are given in Table 18.

In addition to the analyses presented in this paper, measurements of the W mass have also been made using the data collected in 1996.

7.1.1 W mass from the W^+W^- cross-section

The DELPHI collaboration has measured the total CC03 W^+W^- cross-section, as a function of centre-of-mass energy, using the full data sample collected by the collaboration during LEP2 operations [50]. Assuming the validity of the cross-section dependence predicted by the Standard Model these measurements can be translated into a measurement of the W mass. Only the cross-section measurements close to the W^+W^- threshold have significant sensitivity to the W mass.

The Standard Model cross-section dependence on the W mass is obtained from the WPHACT and YFSWW generator setup, as discussed in Sect. 4.2, and cross-checked

Table 17. Measured W mass (in GeV/c^2) from the semi-leptonic decay channel analyses with the nominal centre-of-mass energies (in GeV) of each data sample indicated. The values marked $\ell\overline{\nu}_\ell q\bar{q}'$ are the combined values of the three semi-leptonic channel analyses. The values obtained from the data recorded in 1996 and analysed in [2] are also included

Year	Energy	Channel	M_W GeV/c^2
1996	172	$e\overline{\nu}_e q\bar{q}'$	$80.450 \pm 0.870(\text{Stat.}) \pm 0.085(\text{Syst.}) \pm 0.013(\text{LEP})$
	172	$\mu\overline{\nu}_\mu q\bar{q}'$	$80.560 \pm 0.760(\text{Stat.}) \pm 0.062(\text{Syst.}) \pm 0.013(\text{LEP})$
	172	$\ell\overline{\nu}_\ell q\bar{q}'$	$80.510 \pm 0.570(\text{Stat.}) \pm 0.051(\text{Syst.}) \pm 0.013(\text{LEP})$
1997	183	$e\overline{\nu}_e q\bar{q}'$	$80.852 \pm 0.411(\text{Stat.}) \pm 0.034(\text{Syst.}) \pm 0.009(\text{LEP})$
		$\mu\overline{\nu}_\mu q\bar{q}'$	$80.573 \pm 0.331(\text{Stat.}) \pm 0.024(\text{Syst.}) \pm 0.009(\text{LEP})$
		$\tau\overline{\nu}_\tau q\bar{q}'$	$80.233 \pm 0.396(\text{Stat.}) \pm 0.025(\text{Syst.}) \pm 0.009(\text{LEP})$
		$\ell\overline{\nu}_\ell q\bar{q}'$	$80.548 \pm 0.216(\text{Stat.}) \pm 0.024(\text{Syst.}) \pm 0.009(\text{LEP})$
1998	189	$e\overline{\nu}_e q\bar{q}'$	$79.848 \pm 0.275(\text{Stat.}) \pm 0.035(\text{Syst.}) \pm 0.009(\text{LEP})$
		$\mu\overline{\nu}_\mu q\bar{q}'$	$80.238 \pm 0.195(\text{Stat.}) \pm 0.026(\text{Syst.}) \pm 0.009(\text{LEP})$
		$\tau\overline{\nu}_\tau q\bar{q}'$	$80.055 \pm 0.288(\text{Stat.}) \pm 0.030(\text{Syst.}) \pm 0.009(\text{LEP})$
		$\ell\overline{\nu}_\ell q\bar{q}'$	$80.096 \pm 0.139(\text{Stat.}) \pm 0.026(\text{Syst.}) \pm 0.009(\text{LEP})$
1999	192	$e\overline{\nu}_e q\bar{q}'$	$80.025 \pm 0.789(\text{Stat.}) \pm 0.036(\text{Syst.}) \pm 0.009(\text{LEP})$
		$\mu\overline{\nu}_\mu q\bar{q}'$	$80.604 \pm 0.467(\text{Stat.}) \pm 0.028(\text{Syst.}) \pm 0.009(\text{LEP})$
		$\tau\overline{\nu}_\tau q\bar{q}'$	$80.161 \pm 0.664(\text{Stat.}) \pm 0.033(\text{Syst.}) \pm 0.009(\text{LEP})$
	196	$e\overline{\nu}_e q\bar{q}'$	$80.391 \pm 0.349(\text{Stat.}) \pm 0.037(\text{Syst.}) \pm 0.010(\text{LEP})$
		$\mu\overline{\nu}_\mu q\bar{q}'$	$80.024 \pm 0.270(\text{Stat.}) \pm 0.031(\text{Syst.}) \pm 0.010(\text{LEP})$
		$\tau\overline{\nu}_\tau q\bar{q}'$	$80.269 \pm 0.417(\text{Stat.}) \pm 0.036(\text{Syst.}) \pm 0.010(\text{LEP})$
	200	$e\overline{\nu}_e q\bar{q}'$	$80.383 \pm 0.365(\text{Stat.}) \pm 0.037(\text{Syst.}) \pm 0.010(\text{LEP})$
		$\mu\overline{\nu}_\mu q\bar{q}'$	$80.374 \pm 0.282(\text{Stat.}) \pm 0.032(\text{Syst.}) \pm 0.010(\text{LEP})$
		$\tau\overline{\nu}_\tau q\bar{q}'$	$80.197 \pm 0.438(\text{Stat.}) \pm 0.040(\text{Syst.}) \pm 0.010(\text{LEP})$
	202	$e\overline{\nu}_e q\bar{q}'$	$80.193 \pm 0.453(\text{Stat.}) \pm 0.039(\text{Syst.}) \pm 0.010(\text{LEP})$
		$\mu\overline{\nu}_\mu q\bar{q}'$	$80.120 \pm 0.341(\text{Stat.}) \pm 0.033(\text{Syst.}) \pm 0.010(\text{LEP})$
		$\tau\overline{\nu}_\tau q\bar{q}'$	$81.399 \pm 0.574(\text{Stat.}) \pm 0.042(\text{Syst.}) \pm 0.010(\text{LEP})$
	192–202	$\ell\overline{\nu}_\ell q\bar{q}'$	$80.296 \pm 0.113(\text{Stat.}) \pm 0.030(\text{Syst.}) \pm 0.009(\text{LEP})$
2000	206	$e\overline{\nu}_e q\bar{q}'$	$80.814 \pm 0.267(\text{Stat.}) \pm 0.040(\text{Syst.}) \pm 0.016(\text{LEP})$
		$\mu\overline{\nu}_\mu q\bar{q}'$	$80.340 \pm 0.193(\text{Stat.}) \pm 0.032(\text{Syst.}) \pm 0.016(\text{LEP})$
		$\tau\overline{\nu}_\tau q\bar{q}'$	$80.701 \pm 0.272(\text{Stat.}) \pm 0.042(\text{Syst.}) \pm 0.016(\text{LEP})$
		$\ell\overline{\nu}_\ell q\bar{q}'$	$80.551 \pm 0.136(\text{Stat.}) \pm 0.034(\text{Syst.}) \pm 0.016(\text{LEP})$

with the improved Born approximation calculation. The theoretical error on the total W^+W^- cross-section near threshold was estimated as 2% decreasing with increasing collision energy to 0.5% in the DPA-valid region [62], the corresponding error on the W mass is marked below as Theor. The sources of experimental systematic error have not been reevaluated and are as reported in [1], apart from use of the revised collision energy uncertainty.

From a χ^2 fit of the measured cross-sections at centre-of-mass energies of 161.31, 172.14 and 182.65 GeV the mass has been determined to be

$$M_W = 80.448 \pm 0.434(\text{Stat.}) \pm 0.090(\text{Syst.}) \pm 0.043(\text{Theor.}) \pm 0.013(\text{LEP})\,\text{GeV}/c^2\,.$$

7.1.2 W mass from direct reconstruction at $\sqrt{s} = 172\,\text{GeV}$

For completeness, we also report here on the relatively small data sample ($10\,\text{pb}^{-1}$) recorded in 1996 at $\sqrt{s} = 172\,\text{GeV}$. This sample was analysed and W mass results published using the $e\overline{\nu}_e q\bar{q}'$, $\mu\overline{\nu}_\mu q\bar{q}'$ and $q\bar{q}'\bar{q}q'$ decay channels in [2]. The $q\bar{q}'\bar{q}q'$ analysis was performed using a standard analysis rather than a cone jet reconstruction-based analysis.

This data sample has not been reprocessed, nor have W width results been produced with this sample. The estimates of systematic uncertainties are retained from the original paper except for the uncertainties arising from colour reconnection and Bose–Einstein correlations in the $q\bar{q}'\bar{q}q'$ channel, where the errors reported above for the standard analysis are used, and the use of the final LEP collision energy uncertainty. The revised values are

$$M_W = 80.51 \pm 0.57(\text{Stat.}) \pm 0.05(\text{Syst.}) \pm 0.01(\text{LEP})\,\text{GeV}/c^2\,,$$

for the combined semi-leptonic channels, and

$$M_W = 79.90 \pm 0.59(\text{Stat.}) \pm 0.05(\text{Syst.}) \pm 0.21(\text{FSI.}) \pm 0.01(\text{LEP})\,\text{GeV}/c^2\,,$$

for the fully-hadronic decay channel. These values have been included in Tables 17 and 18.

Table 18. Measured W mass (in GeV/c^2) from the fully-hadronic decay channel analysis with the nominal centre-of-mass energies (in GeV) of each data sample indicated. Results are provided for both the standard (std) and cone jet reconstruction techniques applied. The value obtained from the data recorded in 1996 and analysed in [2] is also included

Year	Energy	Analysis	M_W GeV/c^2
1996	172	std	$79.900 \pm 0.590(\text{Stat.}) \pm 0.050(\text{Syst.}) \pm 0.214(\text{FSI}) \pm 0.013(\text{LEP})$
1997	183	std	$80.137 \pm 0.185(\text{Stat.}) \pm 0.046(\text{Syst.}) \pm 0.214(\text{FSI}) \pm 0.009(\text{LEP})$
		cone	$80.100 \pm 0.191(\text{Stat.}) \pm 0.046(\text{Syst.}) \pm 0.119(\text{FSI}) \pm 0.009(\text{LEP})$
1998	189	std	$80.519 \pm 0.107(\text{Stat.}) \pm 0.032(\text{Syst.}) \pm 0.214(\text{FSI}) \pm 0.009(\text{LEP})$
		cone	$80.533 \pm 0.119(\text{Stat.}) \pm 0.032(\text{Syst.}) \pm 0.119(\text{FSI}) \pm 0.009(\text{LEP})$
1999	192	std	$80.711 \pm 0.281(\text{Stat.}) \pm 0.032(\text{Syst.}) \pm 0.214(\text{FSI}) \pm 0.009(\text{LEP})$
		cone	$81.076 \pm 0.294(\text{Stat.}) \pm 0.032(\text{Syst.}) \pm 0.119(\text{FSI}) \pm 0.009(\text{LEP})$
	196	std	$80.248 \pm 0.159(\text{Stat.}) \pm 0.032(\text{Syst.}) \pm 0.214(\text{FSI}) \pm 0.010(\text{LEP})$
		cone	$80.240 \pm 0.192(\text{Stat.}) \pm 0.032(\text{Syst.}) \pm 0.119(\text{FSI}) \pm 0.010(\text{LEP})$
	200	std	$80.274 \pm 0.149(\text{Stat.}) \pm 0.032(\text{Syst.}) \pm 0.214(\text{FSI}) \pm 0.010(\text{LEP})$
		cone	$80.227 \pm 0.164(\text{Stat.}) \pm 0.032(\text{Syst.}) \pm 0.119(\text{FSI}) \pm 0.010(\text{LEP})$
	202	std	$80.537 \pm 0.199(\text{Stat.}) \pm 0.031(\text{Syst.}) \pm 0.214(\text{FSI}) \pm 0.010(\text{LEP})$
		cone	$80.248 \pm 0.231(\text{Stat.}) \pm 0.031(\text{Syst.}) \pm 0.119(\text{FSI}) \pm 0.010(\text{LEP})$
	192–202	std	$80.365 \pm 0.090(\text{Stat.}) \pm 0.032(\text{Syst.}) \pm 0.214(\text{FSI}) \pm 0.010(\text{LEP})$
		cone	$80.339 \pm 0.103(\text{Stat.}) \pm 0.032(\text{Syst.}) \pm 0.119(\text{FSI}) \pm 0.010(\text{LEP})$
2000	206	std	$80.318 \pm 0.092(\text{Stat.}) \pm 0.032(\text{Syst.}) \pm 0.214(\text{FSI}) \pm 0.015(\text{LEP})$
		cone	$80.171 \pm 0.104(\text{Stat.}) \pm 0.032(\text{Syst.}) \pm 0.119(\text{FSI}) \pm 0.015(\text{LEP})$

7.1.3 Combined results

The combinations of the results are performed, assuming that the following components of the error are fully correlated between years (and energy points) and between the fully-hadronic and semi-leptonic channels: electroweak corrections, fragmentation and jet correction. The lepton-related detector systematic in the semi-leptonic channel is also assumed to be fully correlated between years. The colour reconnection and Bose–Einstein effect in the fully-hadronic channel is assumed to be fully correlated between years. The error arising from calibration statistics is uncorrelated between years in the semi-leptonic analysis, as it was determined from independent Monte Carlo simulation samples, but this error is correlated in the fully-hadronic channel as the values were obtained from an overall fit to the samples at all centre-of-mass energies. This error source is uncorrelated in the combination of the semi-leptonic and fully-hadronic channel. The background-related systematic is assumed to be fully correlated between years in both the fully-hadronic and semi-leptonic analyses but uncorrelated between the two channels. The LEP centre-of-mass energy uncertainty is, of course, fully correlated between the semi-leptonic and fully-hadronic decay channels but is only partially correlated between years. The inter-year correlations were assessed by the LEP energy working group [9] and this correlation matrix was applied when performing the combinations reported here.

The results from the semi-leptonic W mass analyses in each year of data taking (1996–2000) have been combined. The result for the analysis aimed at selecting events in the $e\overline{\nu}_e q\bar{q}'$ decay channel is

$$M_W = 80.388 \pm 0.133(\text{Stat.}) \pm 0.036(\text{Syst.}) \pm 0.010(\text{LEP})\ \text{GeV}/c^2\,,$$

the combination has a χ^2 probability of 25%.

The result for the analysis aimed at selecting events in the $\mu\overline{\nu}_\mu q\bar{q}'$ decay channel is

$$M_W = 80.294 \pm 0.098(\text{Stat.}) \pm 0.028(\text{Syst.}) \pm 0.010(\text{LEP})\ \text{GeV}/c^2\,,$$

the combination has a χ^2 probability of 96%.

The $\tau\overline{\nu}_\tau q\bar{q}'$ selection includes significant cross-talk from events in other decay channels (see Table 2) and a result from the 1996 data is not available. The result for the analysis aimed at selecting events in the $\tau\overline{\nu}_\tau q\bar{q}'$ decay channel (in the years 1997–2000) is

$$M_W = 80.387 \pm 0.144(\text{Stat.}) \pm 0.033(\text{Syst.}) \pm 0.010(\text{LEP})\ \text{GeV}/c^2\,,$$

the combination has a χ^2 probability of 56%.

The result for the combined semi-leptonic W mass analyses is

$$M_W = 80.339 \pm 0.069(\text{Stat.}) \pm 0.029(\text{Syst.}) \pm 0.009(\text{LEP})\ \text{GeV}/c^2\,,$$

the combination has a χ^2 probability of 16%.

Similarly, the results on the W mass extracted from the fully-hadronic event analysis have also been combined.

The value from 1996 uses the standard reconstruction technique; the results of the cone jet reconstruction technique are used for the other data taking years (1997–2000). The combined result is

$$M_W = 80.311 \pm 0.059(\text{Stat.}) \pm 0.032(\text{Syst.}) \pm 0.119(\text{FSI}) \pm 0.010(\text{LEP})\,\text{GeV}/c^2\,,$$

the combination also has a χ^2 probability of 16%.

The mass difference between the W boson mass measurements obtained from the fully-hadronic and semi-leptonic channels $\Delta M_W(q\bar{q}'\bar{q}q' - \ell\overline{\nu}_\ell q\bar{q}')$, has been determined. A significant non-zero value for ΔM_W could indicate that Bose–Einstein or colour reconnection effects are biasing the value of M_W determined from $q\bar{q}'\bar{q}q'$ events. Since ΔM_W is primarily of interest as a cross-check of the possible effects of final state interactions, the errors from CR and BEC are set to zero in its determination and the results of the standard reconstruction technique, rather than the FSI effect-reducing cone jet reconstruction technique, are used for the $q\bar{q}'\bar{q}q'$ analysis. The result provides no evidence for FSI effects:

$$\Delta M_W(q\bar{q}'\bar{q}q' - \ell\overline{\nu}_\ell q\bar{q}') = 0.024 \pm 0.090\,\text{GeV}/c^2\,,$$

the combination has a χ^2 probability of 20%.

The final DELPHI result for the W mass for the full LEP2 data sample is obtained by combining the values obtained from the direct reconstruction method in the $\ell\overline{\nu}_\ell q\bar{q}'$ analysis and cone jet reconstruction technique $q\bar{q}'\bar{q}q'$ analysis in each data taking year. The value obtained from the threshold cross-section is also included in this average. The combined result is

$$M_W = 80.336 \pm 0.055(\text{Stat.}) \pm 0.028(\text{Syst.}) \pm 0.025(\text{FSI}) \pm 0.009(\text{LEP})\,\text{GeV}/c^2\,,$$

the combination has a χ^2 probability of 15%.

Although the statistical error in the $\ell\overline{\nu}_\ell q\bar{q}'$ and $q\bar{q}'\bar{q}q'$ channels is similar, owing to the large systematic error attributed to final state cross-talk effects the weight of the fully-hadronic channel results in this average is 21%. The weight of the threshold cross-section measurement of the W mass is only 2% due to the small data sample collected at 161 GeV centre-of-mass energy. The full error breakdown of the averages is provided in Table 19.

Table 19. The final results (in GeV/c^2) of the W mass analyses and the breakdown of the uncertainty into its component categories. The $\ell\overline{\nu}_\ell q\bar{q}'$ and $q\bar{q}'\bar{q}q'$ results use the values obtained in these analysis channels from the direct reconstruction method. The column marked 'All' uses the full direct reconstruction analyses and the threshold cross-section measurement. The $q\bar{q}'\bar{q}q'$ results are taken from the cone jet reconstruction analysis, for all data except 1996 where the standard analysis was used

	$\ell\overline{\nu}_\ell q\bar{q}'$	$q\bar{q}'\bar{q}q'$	All
Value	80.339	80.311	80.336
Statistical error	0.069	0.059	0.055
Statistical error on calibration	0.003	0.004	0.002
Lepton corrections	0.015	–	0.012
Jet corrections	0.020	0.026	0.021
Fragmentation	0.011	0.012	0.011
Background	0.007	0.013	0.006
Threshold systematics	–	–	0.002
Electroweak corrections	0.006	0.005	0.006
LEP energy	0.009	0.010	0.009
Bose–Einstein correlations	–	0.026	0.005
Colour reconnection	–	0.116	0.024

The DELPHI measurement of the colour reconnection effect is reported in [38]. This measurement places relatively loose constraints on the size of the W mass uncertainty from CR effects, and thus leads to the small impact of the fully-hadronic mass in the DELPHI average. For comparison the value of the combined DELPHI W mass as a function of the CR uncertainty is shown in Table 20. All other errors, including that arising from Bose–Einstein correlations, have been kept constant in these results.

7.2 W width

The W width has been measured from the semi-leptonic and the fully-hadronic decay channel events. As the analysis is less sensitive to the W width than the W mass, the width is extracted by performing a combined fit of the three semi-leptonic channels rather than from each channel individually. The results are given in Table 21. The correlations assumed for the combinations are identical to those reported above for the W mass.

Table 20. The combined DELPHI W mass value as a function of the uncertainty ascribed to colour reconnection effects in the fully-hadronic decay channel. The values of the $\kappa_{\text{SK-I}}$ parameter that give rise to this shift in the $q\bar{q}'\bar{q}q'$ W mass at a centre-of-mass energy of 200 GeV are also given

CR MeV/c^2	$\kappa_{\text{SK-I}}$	M_W GeV/c^2
0	0.00	$80.326 \pm 0.045(\text{Stat.}) \pm 0.028(\text{Syst.}) \pm 0.013(\text{FSI}) \pm 0.010(\text{LEP})$
20	0.40	$80.326 \pm 0.045(\text{Stat.}) \pm 0.028(\text{Syst.}) \pm 0.016(\text{FSI}) \pm 0.010(\text{LEP})$
40	0.89	$80.328 \pm 0.046(\text{Stat.}) \pm 0.028(\text{Syst.}) \pm 0.021(\text{FSI}) \pm 0.010(\text{LEP})$
60	1.51	$80.330 \pm 0.048(\text{Stat.}) \pm 0.028(\text{Syst.}) \pm 0.024(\text{FSI}) \pm 0.010(\text{LEP})$
80	2.30	$80.333 \pm 0.051(\text{Stat.}) \pm 0.028(\text{Syst.}) \pm 0.026(\text{FSI}) \pm 0.010(\text{LEP})$
100	3.36	$80.335 \pm 0.054(\text{Stat.}) \pm 0.028(\text{Syst.}) \pm 0.026(\text{FSI}) \pm 0.009(\text{LEP})$

Table 21. Measured W widths (in GeV/c^2) from the semi-leptonic decay and fully-hadronic decay channel analyses with the nominal centre-of-mass energies (in GeV) of each data sample indicated

Year	Energy	Channel	Γ_W GeV/c^2
1997	183	$\ell\overline{\nu}_\ell q\bar{q}'$	$2.495 \pm 0.590(\text{Stat.}) \pm 0.069(\text{Syst.})$
		$q\bar{q}'\bar{q}q'$	$2.572 \pm 0.460(\text{Stat.}) \pm 0.092(\text{Syst.}) \pm 0.248(\text{FSI})$
1998	189	$\ell\overline{\nu}_\ell q\bar{q}'$	$3.056 \pm 0.401(\text{Stat.}) \pm 0.071(\text{Syst.})$
		$q\bar{q}'\bar{q}q'$	$2.337 \pm 0.260(\text{Stat.}) \pm 0.114(\text{Syst.}) \pm 0.248(\text{FSI})$
1999	192	$\ell\overline{\nu}_\ell q\bar{q}'$	$2.342 \pm 0.953(\text{Stat.}) \pm 0.071(\text{Syst.})$
		$q\bar{q}'\bar{q}q'$	$2.390 \pm 0.756(\text{Stat.}) \pm 0.126(\text{Syst.}) \pm 0.248(\text{FSI})$
	196	$\ell\overline{\nu}_\ell q\bar{q}'$	$1.805 \pm 0.440(\text{Stat.}) \pm 0.072(\text{Syst.})$
		$q\bar{q}'\bar{q}q'$	$2.545 \pm 0.508(\text{Stat.}) \pm 0.142(\text{Syst.}) \pm 0.248(\text{FSI})$
	200	$\ell\overline{\nu}_\ell q\bar{q}'$	$2.153 \pm 0.477(\text{Stat.}) \pm 0.073(\text{Syst.})$
		$q\bar{q}'\bar{q}q'$	$2.210 \pm 0.376(\text{Stat.}) \pm 0.157(\text{Syst.}) \pm 0.248(\text{FSI})$
	202	$\ell\overline{\nu}_\ell q\bar{q}'$	$1.707 \pm 0.649(\text{Stat.}) \pm 0.076(\text{Syst.})$
		$q\bar{q}'\bar{q}q'$	$1.797 \pm 0.488(\text{Stat.}) \pm 0.165(\text{Syst.}) \pm 0.248(\text{FSI})$
	192-202	$\ell\overline{\nu}_\ell q\bar{q}'$	$1.950 \pm 0.277(\text{Stat.}) \pm 0.072(\text{Syst.})$
		$q\bar{q}'\bar{q}q'$	$2.210 \pm 0.243(\text{Stat.}) \pm 0.152(\text{Syst.}) \pm 0.248(\text{FSI})$
2000	206	$\ell\overline{\nu}_\ell q\bar{q}'$	$2.814 \pm 0.364(\text{Stat.}) \pm 0.083(\text{Syst.})$
		$q\bar{q}'\bar{q}q'$	$1.979 \pm 0.225(\text{Stat.}) \pm 0.183(\text{Syst.}) \pm 0.248(\text{FSI})$

The results from the semi-leptonic W width analyses in each year of data taking (1997–2000) have been combined, and the result obtained is

$$\Gamma_W = 2.452 \pm 0.184(\text{Stat.}) \pm 0.073(\text{Syst.})\,\text{GeV}/c^2\,,$$

the combination has a χ^2 probability of 9%.

Similarly, the results on the W width extracted from the fully-hadronic event analysis have also been combined, and the result obtained is

$$\Gamma_W = 2.237 \pm 0.137(\text{Stat.}) \pm 0.139(\text{Syst.}) \pm 0.248(\text{FSI})\,\text{GeV}/c^2\,,$$

the combination has a χ^2 probability of 62%.

Table 22. The final results (in GeV/c^2) of the W width analyses and the breakdown of the uncertainty into its component categories. The $\ell\overline{\nu}_\ell q\bar{q}'$ and $q\bar{q}'\bar{q}q'$ results use the values obtained in these analysis channels from the direct reconstruction method. The column marked 'All' provides the result from combining the measurements made in both channels

	$\ell\overline{\nu}_\ell q\bar{q}'$	$q\bar{q}'\bar{q}q'$	All
Value	2.452	2.237	2.404
Statistical error	0.184	0.137	0.140
Statistical error on calibration	0.006	0.009	0.005
Lepton corrections	0.041	–	0.030
Jet corrections	0.036	0.129	0.059
Fragmentation	0.029	0.008	0.024
Electroweak corrections	0.011	0.009	0.010
Background	0.037	0.051	0.031
Bose–Einstein correlations	–	0.020	0.005
Colour reconnection	–	0.247	0.065

The final DELPHI result for the W width for the full LEP2 data sample is obtained by combining the values obtained from the direct reconstruction method in the $\ell\overline{\nu}_\ell q\bar{q}'$ analysis and $q\bar{q}'\bar{q}q'$ analysis in each data taking year. The combined result is

$$\Gamma_W = 2.404 \pm 0.140(\text{Stat.}) \pm 0.077(\text{Syst.}) \pm 0.065(\text{FSI})\,\text{GeV}/c^2\,,$$

the combination has a χ^2 probability of 27%.

Although the statistical error in the $\ell\overline{\nu}_\ell q\bar{q}'$ and $q\bar{q}'\bar{q}q'$ channels is similar, owing to the large systematic error attributed to final state cross-talk effects the weight of the fully-hadronic channel results in this average is 26%. The full error breakdown of the averages is provided in Table 22.

8 Conclusions

The mass and width of the W boson have been measured using the reconstructed masses in $e^+e^- \to W^+W^-$ events decaying to $q\bar{q}'\bar{q}q'$ and $\ell\overline{\nu}_\ell q\bar{q}'$ states. The W mass was also extracted from the dependence of the W^+W^- cross-section close to the production threshold. The full LEP2 data sample of 660 pb^{-1} collected by the DELPHI experiment at centre-of-mass energies from 161 to 209 GeV has been used. The final results are

$$\begin{aligned} M_W &= 80.336 \pm 0.055(\text{Stat.}) \pm 0.028(\text{Syst.}) \pm 0.025(\text{FSI}) \\ &\quad \pm 0.009(\text{LEP})\,\text{GeV}/c^2\,, \\ \Gamma_W &= 2.404 \pm 0.140(\text{Stat.}) \pm 0.077(\text{Syst.}) \\ &\quad \pm 0.065(\text{FSI})\,\text{GeV}/c^2\,. \end{aligned}$$

These results supersede the previously published DELPHI results [1–4].

Acknowledgements. We are greatly indebted to our technical collaborators, to the members of the CERN-SL Division for the excellent performance of the LEP collider, and to the funding agencies for their support in building and operating the DELPHI detector. We also wish to offer our thanks to the LEP energy working group for their measurement of the LEP collision energy, which plays an important role in the analysis presented in this paper.

We acknowledge in particular the support of Austrian Federal Ministry of Education, Science and Culture, GZ 616.364/2-III/2a/98, FNRS–FWO, Flanders Institute to encourage scientific and technological research in the industry (IWT) and Belgian Federal Office for Scientific, Technical and Cultural affairs (OSTC), Belgium, FINEP, CNPq, CAPES, FUJB and FAPERJ, Brazil, Ministry of Education of the Czech Republic, project LC527, Academy of Sciences of the Czech Republic, project AV0Z10100502, Commission of the European Communities (DG XII), Direction des Sciences de la Matière, CEA, France, Bundesministerium für Bildung, Wissenschaft, Forschung und Technologie, Germany, General Secretariat for Research and Technology, Greece, National Science Foundation (NWO) and Foundation for Research on Matter (FOM), The Netherlands, Norwegian Research Council, State Committee for Scientific Research, Poland, SPUB-M/CERN/PO3/DZ296/2000, SPUB-M/CERN/PO3/DZ297/2000, 2P03B 104 19 and 2P03B 69 23 (2002–2004), FCT – Fundação para a Ciência e Tecnologia, Portugal, Vedecka grantova agentura MS SR, Slovakia, Nr. 95/5195/134, Ministry of Science and Technology of the Republic of Slovenia, CICYT, Spain, AEN99-0950 and AEN99-0761, The Swedish Research Council, Particle Physics and Astronomy Research Council, UK, Department of Energy, USA, DE-FG02-01ER41155, EEC RTN contract HPRN-CT-00292-2002.

References

1. DELPHI Collaboration, P. Abreu et al., Phys. Lett. B **397**, 158 (1997)
2. DELPHI Collaboration, P. Abreu et al., Eur. Phys. J. C **2**, 581 (1998)
3. DELPHI Collaboration, P. Abreu et al., Phys. Lett. B **462**, 410 (1999)
4. DELPHI Collaboration, P. Abreu et al., Phys. Lett. B **511**, 159 (2001)
5. ALEPH Collaboration, S. Schael et al., Eur. Phys. J. C **47**, 309 (2006)
6. L3 Collaboration, P. Achard et al., Eur. Phys. J. C **45**, 569 (2006)
7. OPAL Collaboration, G. Abbiendi et al., Eur. Phys. J. C **45**, 307 (2006)
8. CDF Collaboration, D0 Collaboration, Tevatron Electroweak Working Group, V.M. Abazov et al., Phys. Rev. D **70**, 092 008 (2004)
9. LEP Energy Working Group, R. Assmann et al., Eur. Phys. J. C **39**, 253 (2005)
10. ALEPH Collaboration, R. Barate et al., Phys. Lett. B **464**, 339 (1999)
11. L3 Collaboration, P. Achard et al., Phys. Lett. B **585**, 42 (2004)
12. OPAL Collaboration, G. Abbiendi et al., Phys. Lett. B **604**, 31 (2004)
13. DELPHI Collaboration, J. Abdallah et al., Eur. Phys. J. C **46**, 295 (2006)
14. DELPHI Collaboration, P. Aarnio et al., Nucl. Instrum. Methods A **303**, 233 (1991)
15. DELPHI Collaboration, P. Abreu et al., Nucl. Instrum. Methods A **378**, 57 (1996)
16. DELPHI Silicon Tracker Group, P. Chochula et al., Nucl. Instrum. Methods A **412**, 304 (1998)
17. S.J. Alvsvaag et al., Nucl. Instrum. Methods A **425**, 106 (1999)
18. A. Ballestrero, R. Chierici, F. Cossutti, E. Migliore, Comput. Phys. Commun. **152**, 175 (2003)
19. E. Accomando, A. Ballestrero, Comput. Phys. Commun. **99**, 270 (1997)
20. E. Accomando, A. Ballestrero, E. Maina, Comput. Phys. Commun. **150**, 166 (2003)
21. T. Sjöstrand et al., Comput. Phys. Commun. **135**, 238 (2001)
22. S. Jadach, Z. Was, R. Decker, J.H. Kuehn, Comput. Phys. Commun. **76**, 361 (1993)
23. S. Jadach, W. Placzek, M. Skrzypek, B.F.L. Ward, Z. Was, Phys. Lett. B **417**, 326 (1998)
24. S. Jadach, W. Placzek, M. Skrzypek, B.F.L. Ward, Z. Was, Comput. Phys. Commun. **140**, 432 (2001)
25. E. Barberio, Z. Was, Comput. Phys. Commun. **79**, 291 (1994)
26. L. Lönnblad, Comput. Phys. Commun. **71**, 15 (1992)
27. G. Corcella et al., JHEP **0101**, 010 (2001)
28. DELPHI Collaboration, P. Abreu et al., Z. Phys. C **73**, 11 (1996)
29. S. Jadach, B.F.L. Ward, Z. Was, Comput. Phys. Commun. **130**, 260 (2000)
30. T. Sjöstrand, PYTHIA 5.7 and JETSET 7.4: Physics and manual, CERN-TH-7112-93-REV (1995)
31. P. Abreu et al., Nucl. Instrum. Methods A **427**, 487 (1999)
32. G. Borisov, Nucl. Instrum. Methods A **417**, 384 (1998)
33. DELPHI Collaboration, P. Abreu et al., Eur. Phys. J. C **10**, 415 (1999)
34. S. Catani, Yu.L. Dokshitzer, M. Olsson, G. Turnock, B.R. Webber, Phys. Lett. B **269**, 432 (1991)
35. N. Brown, W. Stirling, Z. Phys. C **53**, 629 (1992)
36. Y.L. Dokshitzer, G.D. Leder, S. Moretti, B.R. Webber, JHEP **9708**, 001 (1997)
37. L. Lönnblad, Z. Phys. C **58**, 471 (1993)
38. DELPHI Collaboration, J. Abdallah et al., Eur. Phys. J. C **51**, 249 (2007)
39. L3 Collaboration, P. Achard et al., Phys. Lett. B **561**, 202 (2003)
40. OPAL Collaboration, G. Abbiendi et al., Eur. Phys. J. C **45**, 291 (2006)
41. ALEPH Collaboration, S. Schael et al., Eur. Phys. J. C **47**, 309 (2006)
42. Particle Data Group, S. Eidelman et al., Phys. Lett. B **592**, 1 (2004)
43. H.A. Bethe, W. Heitler, Proc. R. Soc. London A **146**, 83 (1934)
44. S. Jadach, W. Placzek, M. Skrzypek, B.F.L. Ward, Z. Was, Phys. Lett. B **523**, 117 (2001)
45. F. Cossutti, Eur. Phys. J. C **44**, 383 (2005)
46. A.P. Chapovsky, V.A. Khoze, Eur. Phys. J. C **9**, 449 (1999)
47. A. Denner, S. Dittmaier, M. Roth, D. Wackeroth, Nucl. Phys. B **560**, 33 (1999)
48. A. Denner, S. Dittmaier, M. Roth, D. Wackeroth, Nucl. Phys. B **587**, 67 (2000)

49. F. Boudjema, B. Mele et al., Standard Model Process, Physics at LEP2, ed. by G. Altarelli, T. Sjöstrand, F. Zwirner, CERN 96-01 (1996) vol. 1, p. 207
50. DELPHI Collaboration, J. Abdallah et al., Eur. Phys. J. C **34**, 127 (2004)
51. DELPHI Collaboration, J. Abdallah et al., Eur. Phys. J. C **44**, 161 (2005)
52. ALEPH Collaboration, S. Schael et al., Phys. Lett. B **606**, 265 (2005)
53. OPAL Collaboration, G. Abbiendi et al., Eur. Phys. J. C **36**, 297 (2004)
54. L3 Collaboration, P. Achard et al., Phys. Lett. B **547**, 139 (2002)
55. L. Lönnblad, T. Sjöstrand, Eur. Phys. J. C **2**, 165 (1998)
56. V. Khoze et al., Colour Reconnection, Physics at LEP2, ed. by G. Altarelli, T. Sjöstrand, F. Zwirner, CERN 96-01 (1996), vol. 1, p. 191
57. T. Sjöstrand, V. Khoze, Z. Phys. C **62**, 281 (1994)
58. T. Sjöstrand, V. Khoze, Phys. Rev. Lett. **72**, 28 (1994)
59. G. Gustafson, J. Häkkinen, Z. Phys. C **64**, 659 (1994)
60. L. Lönnblad, Z. Phys. C **70**, 107 (1996)
61. L. Lyons, D. Gibaut, P. Clifford, Nucl. Instrum. Methods A **270**, 110 (1988)
62. LEP2 Monte Carlo Workshop: Report of the Working Groups on Precision Calculations for LEP2 Physics, ed. by G. Passarino, R. Pittau, S. Jadach, CERN-2000-009 (2000)